NAT'L INST. OF STAND & TECH
A11107 245627

NBS SPECIAL PUBLICATION 594

U.S. DEPARTMENT OF COMMERCE/National Bureau of Standards

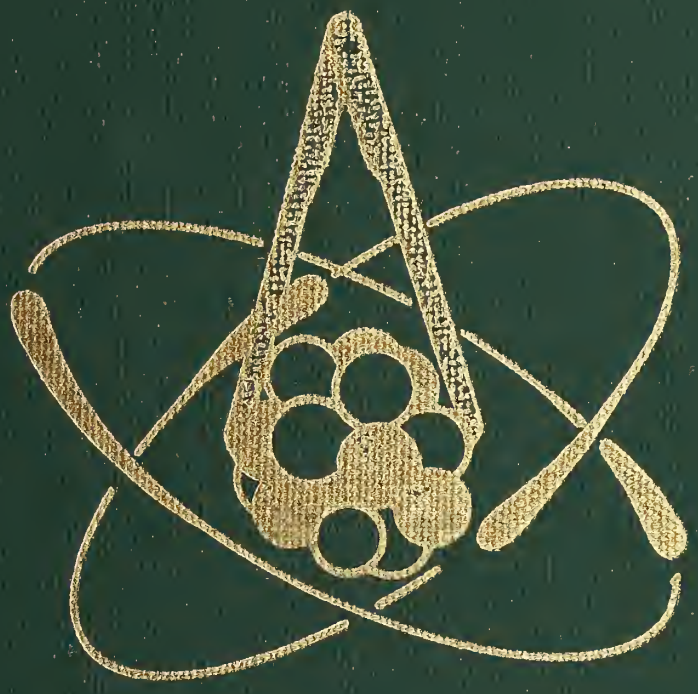

NUCLEAR CROSS SECTIONS FOR TECHNOLOGY

PROCEEDINGS OF THE INTERNATIONAL CONFERENCE

NATIONAL BUREAU
OF STANDARDS
LIBRARY
NOV 24 1980
191356

Nuclear Cross Sections for Technology

Proceedings of the International Conference
on Nuclear Cross Sections for Technology,
Held at the University of Tennessee
Knoxville, TN, October 22-26, 1979

Edited by:

J. L. Fowler and C. H. Johnson

Oak Ridge National Laboratory
Oak Ridge, TN 37830

C. D. Bowman

Center for Radiation Research
National Measurement Laboratory
National Burea of Standards
Washington, DC 20234

Sponsored by:

U.S. Department of Energy
National Bureau of Standards
U.S. Department of Commerce
International Union of Pure and Applied Physics
American Physical Society
American Nuclear Society
Oak Ridge National Laboratory
University of Tennessee
with the Cooperation of the
International Atomic Energy Agency

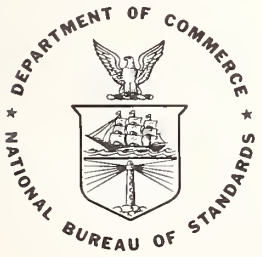

U.S. DEPARTMENT OF COMMERCE, Philip M. Klutznick, Secretary
Luther H. Hodges, Jr., Deputy Secretary
Jordan J. Baruch, Assistant Secretary for Productivity, Technology and Innovation
NATIONAL BUREAU OF STANDARDS, Ernest Ambler, Director

Issued September 1980

Library of Congress Catalog Card Number: 80-600128

National Bureau of Standards Special Publication 594
Nat. Bur. Stand. (U.S.), Spec. Publ. 594, 1056 pages (Sept. 1980)
CODEN: XNBSAV

U.S. GOVERNMENT PRINTING OFFICE
WASHINGTON: 1980

For sale by the Superintendent of Documents, U.S. Government Printing Office
Washington, D.C. 20402 Price $21.00

(Add 25 percent for other than U.S. mailing)

PREFACE

These are the proceedings of the International Conference on Nuclear Cross Sections for Technology held at the University of Tennessee, Knoxville, October 22-26, 1979. This was the fifth such conference held in the United States. The first three, however, were entitled "Neutron Cross Sections and Technology" and were not intended to be international, although there was sizable international attendance, particularly for the later conferences. The 1975 conference on "Nuclear Cross Sections and Technology" became international and was co-sponsored by the International Union of Pure and Applied Physics (I.U.P.A.P.). This 1975 conference brought out a number of serious discrepancies in nuclear data and made experimental nuclear physicists aware of some of the critical needs for cross sections for the fission and fusion programs as well as the cross section needs for radiotherapy.

Basil Rose from AERE, Harwell, who took an active role in the 1975 conference, suggested that these conferences be held annually but with the location interchanged between U.S.S.R., Western Europe, and America on a 3-year cycle. In April 1977 the Soviets held their "Fourth National Soviet Conference on Neutron Physics" in Kiev, U.S.S.R. In 1978 the O.E.C.D. Nuclear Energy Agency, Paris, France and the United Kingdom Atomic Energy Authority, Harwell, England held the conference at Harwell September 25-29, 1978. This "International Conference on Neutron Physics and Nuclear Data for Reactor and Other Applied Purposes" was with the cooperation of the International Atomic Energy Agency.

The October 22-26, 1979 conference on Nuclear Cross Sections for Technology was organized by Oak Ridge National Laboratory and the University of Tennessee and was sponsored by the U.S. Department of Energy, the U.S. National Bureau of Standards, the International Union of Pure and Applied Physics, the American Physical Society, the American Nuclear Society, the Oak Ridge National Laboratory, and the University of Tennessee, Knoxville. The International Atomic Energy Agency extended its cooperation to the conference.

An international program committee arranged for invited speakers on such subjects as: nuclear data needs for fission and fusion reactors; for waste management-actinide production and burnup; and for safeguards. Other subjects discussed included: biomedical applications of nuclear data; application of nuclear physics in industry and in space; nuclear cross sections and flux standards; nuclear instruments and techniques; and nuclear theory in applications. In an evening session October 25, 1979, two invited papers of general interest were presented. Etienne Roth gave a review of the natural fission reactor at Gabon, and A. R. Buhl discussed the "Lessons of Three Mile Island".

The papers are printed in the proceedings in the order in which they were presented in the sessions, and in the Bulletin of the American Physical Society, Vol. 24, number 7, pp. 860-891, September 1979. We have preserved the conference notation for the sessions. The following papers for which abstracts appeared in the Bulletin were not submitted: AB9, DA1, DC1, DC5, DC8, EB10 and EB11. Several papers have been added which arrived after the deadline for the Bulletin.

In order to speed the publication of the proceedings, we requested the authors to submit their papers in camera-ready form. The editors, who have made minor corrections in some of the papers, hope they have not altered the meaning intended by the authors.

J. L. Fowler
C. H. Johnson
C. D. Bowman

In the interests of accuracy and clarity in describing various items of equipment or apparatus, occasional mention has been made of commercial sources or brand names. This in no way implies endorsement of such products by the U.S. Government.

Abstract

These proceedings are the compilation of 203 papers presented at the International Conference on Nuclear Cross Sections for Technology held at the University of Tennessee, Knoxville, October 22-26, 1979. Invited papers reviewed nuclear data needs for standard fission reactors, alternate fuel cycles, fusion reactors, biomedical applications, and applications in industry, as well as integral experiments, cross section measurements, cross section standards, and cross section evaluations. There were 165 contributed papers on these subjects with some emphasis on cross section measurement techniques and evaluation of cross section data.

Key words: Biomedical; conference; fission; fusion; nuclear cross sections; reactors; standards; technology.

CONFERENCE PERSONNEL

CONFERENCE OFFICERS

J. L. Fowler, Charman -- University of Tennessee and
Oak Ridge National Laboratory
F. C. Maienschein, Deputy Chairman -- Oak Ridge National Laboratory
C. H. Johnson, Secretary -- Oak Ridge National Laboratory
M. E. Ross, Conference Coordinator -- Oak Ridge National Laboratory
University of Tennessee

ORGANIZING COMMITTEE

W. M. Bugg, University of Tennessee
R. E. Chrien, Brookhaven National Laboratory
J. L. Fowler, University of Tennessee and Oak Ridge National Laboratory
D. G. Gardner, Lawrence Livermore Laboratory
P. B. Hemmig, Department of Energy
H. T. Motz, Los Alamos Scientific Laboratory
S. F. Pasqua, University of Tennessee
S. Pearlstein, Brookhaven National Laboratory
W. P. Poenitz, Argonne National Laboratory
G. L. Rogosa, Department of Energy

PROGRAM COMMITTEE

From U.S.A.

H. H. Barschall, University of Wisconsin
C. D. Bowman, National Bureau of Standards
J. C. Browne, Lawrence Livermore Laboratory
R. E. Chrien, Brookhaven National Laboratory
C. L. Cowan, General Electric F.B.R.D.
A. J. Elwyn, Argonne National Laboratory
W. W. Havens, Columbia University
G. A. Keyworth, Los Alamos Scientific Laboratory
H. J. Kouts, Brookhaven National Laboratory
F. C. Maienschein, Oak Ridge National Laboratory
Odelli Ozer, Electric Power Research Institute

From Abroad

S. W. Cierjacks, Karlsruhe, Germany
W. G. Cross, Chalk River, Canada
U. Farinelli, C.N.E.N., Italy
T. Fuketa, J.A.E.R.I., Japan
J. E. Lynn, Harwell, England
A. F. Michaudon, C.E.N. Bruyeres-le-Chatel, France
B. Rose, GEEL, Belgium
J. L. Rowlands, Winfrith, England
L. N. Usachev, Obninsk, U.S.S.R.

CINDA INDEX

Gail Waite, Brookhaven National Laboratory

SESSION CHAIRMEN

SESSION AA: STANDARD FISSION REACTORS
H. J. Kouts

SESSION AB: NUETRON INTERACTIONS WITH LIGHT AND MEDIUM WEIGHT NUCLEI
D. G. Gardner

SESSION AC: CHEMICAL BINDING EFFECTS
P. F. Pasqua

SESSION BA: ALTERNATE FUEL CYCLES
C. L. Cowan

SESSION BB: NEUTRON INTERACTIONS WITH MEDIUM WEIGHT NUCLEI
J. A. Harvey

SESSION BC: INTEGRAL EXPERIMENTAL AND CROSS ACTION PROCESSING
R. E. Schenter

SESSION CA: FUSION
F. C. Maienshein

SESSION CB: INTEGRAL EXPERIMENTS
T. Fuketa

SESSION CC: NUCLEON CROSS SECTIONS, $75 < A < 200$
R. C. Block

SESSION DA: FISSILE FUEL BREEDING AND DISPOSAL
R. E. Chrien

SESSION DB: CROSS SECTION MEASUREMENTS
L. N. Usachev

SESSION DC: HIGH ENERGY BIOMEDICAL INSTRUMENTATION
R. O. Lane

SESSION EA: BIOMEDICAL APPLICATIONS
H. H. Barschall

SESSION EB: FISSION CROSS SECTIONS
G. A. Keyworth

SESSION EC: DETECTOR AND ACCELERATOR TECHNIQUES
A. B. Smith

SESSION ED: INTEGRAL EXPERIMENTS
P. B. Hemmig

SESSION FA: APPLICATION IN SPACE AND INDUSTRY
W. W. Havens, Jr.

SESSION FB: EVALUATION OF CROSS SECTIONS
A. Elwyn

SESSION FC: NEUTRON INTERACTIONS FOR $A > 200$
R. W. Peelle

SESSION GA: NUCLEON CROSS SECTIONS AND FLUX STANDARDS
S. W. Cierjacks

SESSION GB: MODEL CALCULATIONS
P. A. Moldauer

SESSION GC: FUSION
D. Steiner

SESSION GD: POST DEADLINE PAPERS
A. T. G. Ferguson

SESSION HA: GENERAL INTEREST
G. Rogosa

SESSION IA: NUCLEAR INSTRUMENTS AND TECHNIQUES
C. D. Bowman

SESSION IB: STANDARDS
S. L. Whetstone

SESSION JA: CONCLUDING
M. Motz

TABLE OF CONTENTS

NUCLEAR DATA NEEDS FOR LWR APPLICATIONS

Odelli Ozer
Electric Power Research Institute
Palo Alto, California 94303, USA

ABSTRACT

LWR's have been successfully built and operated with the use of methods and data libraries adjusted on the basis of realistic benchmark experiments. As part of an effort to develop an accurate standard data base that could be used to upgrade design methods, EPRI has participated in the development of the ENDF/B library. Sensitivity studies and banchmark analyses were carried out to determine data types that are important for the calculation of various LWR parameters and to determine problem areas associated with the use of ENDF/B data in LWR calculations. Discrepancies between calculations and measurements involving captures in ^{238}U and plutonium critical systems are identified as source for concern.

[LWR data needs, Benchmark Analysis, Fuel Cycle Sensitivities, ENDF/B-V]

Introduction

The Light Water Reactor (LWR) industry can be considered to have reached a high level of maturity. LWR's have been designed, built and operated successfully for a number of years using available data bases and methods of analysis. This has been accomplished by conducting integral experiments of increasingly realistic complexity and benchmarking the calculational capability against this integral information. In producing a three dimensional, one or two group nodal parametrization of a nuclear reactor, the basic nuclear data must be averaged over neutron fluxes and spectra that are characteristic of a reactor under various operating conditions. This averaging process must adequately account for flux perturbations due to various geometric effects such as the presence of control rods, burnable absorbers, instrumentation channels, wide and narrow water gaps, etc., as well as for variations in the thermal-hydraulic state of the moderator.[1,2] The uncertainties introduced by this procedure could be large compared to those due to nuclear data. However, because of the difficulty of modifying the calculational procedures, often data adjustments were found to be the easiest solution for resolving discrepancies between measured and calculated parameters. Such an approach has resulted in the production of methods of analysis and associated libraries that can be used reliably for predicting the behavior of parameters not too different from those used in benchmarking. However, predictions involving different systems or non-benchmarked parameters may be inadequate. Thus, for example, a multigroup library that has been adjusted to predict the correct criticality, reaction rates and isotopic variation as a function of burnup, may produce large uncertainties or biases in calculations involving temperature coefficients of reactivity. Because of the coupling between data and methods in such a system, improvements in the accuracy of the data library may actually result in worse results for the benchmark parameters unless accompanied by corresponding method improvements.

EPRI Objectives

EPRI has supported the development of a LWR core analysis capability primarily for the use of of the U.S. utility industry. This capability known as the ARMP system[3] is based on state-of-the-art design methods and it utilizes a multigroup data library derived from early versions of the ENDF/B files. The system has been benchmarked against a a wide range of experiments including water moderated UO_2 critical lattice experiments, mixed oxide (UO_2 with PuO_2) critical lattices and experiments involving the production of tans-uranic isotopes in reactor fuel as a function of exposure.

Data adjustments found to be necessary to obtain agreement with benchmark parameters involved primarily a reduction in the ^{238}U resonance capture cross sections and an increase in the ^{240}Pu 1 eV resonance capture width. Since its release, the ARMP system has been adapted by some forty utility groups, national labs and DOE contractors and found to give adequate results in LWR analysis.

In parallel with the development of ARMP, EPRI has also supported the development of the ENDF/B data library, particularly in areas of importance to LWR applications. The reason for this support has been the need for an accurate and up-to-date nuclear data base that can be used as a standard for comparing LWR design codes with more accurate calculational methods such as Monte Carlo. To this end, modules linking ENDF/B files with the ARMP lattice physics codes EPRI-CELL and CPM have been written and implemented within the Los Alamos data processing code NJOY,[4] and the capabilities of the (MAGI) Monte Carlo code SAM-CE[5,6] have been extended to include a rigorous representation of ENDF/B data down to thermal energies together with the capability of representing the geometric complexities of a reactor core. This Monte Carlo capability is needed in order to provide an accurate test of the adequacy of ENDF/B files in LWR applications as well as to test the limitations of the design codes.

Finally, in order to better focus its support of ENDF/B on cross sections of greatest importance to thermal reactors, EPRI undertook an extensive data testing and sensitivity analysis program. Sensitivity analyses were used to determine what data types are important in general, whereas data testing and benchmark calculations were used to determine specific problem areas relating to the use of ENDF/B version IV library in LWR analysis.

Data Type of Importance to LWR Fuel Cycle Calculations

Materials of importance to LWR analysis initially consist of ^{235}U, ^{238}U, cladding and structual materials, burnable poisons and water. As a reactor is operated fission product and heavy actinide nuclides are produced and become increasingly important. In order to determine the relative importance of different types of cross sections in the calculation of various LWR parameters, an interactive sensitivity analysis system was implemented at RPI under the guidance of M. Becker and D. Harris.[7] In a typical study of fuel cycle cost sensitivities, cross sections were divided into three energy ranges labeled thermal, epi-thermal and fast (with boundaries at 0.625eV, 5.53Kev and 10Mev) and it was assumed that uncertainties must be made up by increasing the fissile content of the fuel in an amount necessary to maintain criticality at end-of-life. Both BWR's, PWR's and heavy water reactors were considered under various operating conditions. The sensitivities (defined as percent change in cost divided by percent change in quantity) were found to be dependent on reactor type and assumptions about the back end of the fuel cycle (i.e., whether recycling of plutonium is permitted or not).

The sensitivities for a throwaway cycle, summarized in tables 1 though 4 were fond to be considerably larger than for cases with plutonium recycle. In general, as expected, the sensitivities to the thermal capture and fission cross sections of the fissile materials were found to be the largest. This high sensitivity was not confined to the 0.0253eV point, focused upon by many studies, but was found to extend into higher energies corresponding to the hardened Maxwellian flux distribution within the fuel. In all situations considered involving UO_2 fuel the thermal fission and capture cross sections of ^{239}Pu emerged as the most important parameters, particularly in the area of the .3 eV resonance. In contrast resonance capture cross sections of fertile materials such as ^{238}U and ^{240}Pu which are extremely important for criticality calculations were found to have a lesser impact on fuel cycle cost studies. This is because the negative effects of neutron capture in fertile materials are to a great extent compensated by the positive effects of the bred fuel.

Cross Section Type		Sensitivities BWR	PWR
$^{239}Pu(n,f)$	Thermal	-.688	-.753
$^{239}Pu(n,\gamma)$	Thermal	.549	.619
^{235}U (n,f)	Thermal	-.578	-.568
^{235}U (n,γ)	Thermal	.232	.232
H (n,γ)	Thermal	.169	.135
^{238}U (n,γ)	Epi-thermal	.216	.344
^{238}U (n,f)	Fast	-.127	-.141
^{241}Pu(n,f)	Thermal	-.123	-.130
^{235}U (n,γ)	Epi-thermal	.094	.129
^{235}U (n,f)	Epi-thermal	-.091	-.134
^{241}Pu(n,γ)	Thermal	.080	.089
^{238}U (n,γ)	Thermal	.151	.147
^{239}Pu(n,f)	Epi-thermal	-.053	-.078
^{239}Pu(n,γ)	Epi-thermal	.045	.062
Zr(n,γ)	Epi-thermal	.033	.027
^{238}U (n,γ)	Fast	.026	.040
O (n,γ)	Fast	.024	.030
^{135}Xe(n,γ)	Thermal	.024	.029
^{241}Pu(n,f)	Epi-thermal	-.018	-.030
^{236}U (n,γ)	Epi-thermal	.020	.029

TABLE 1 -- Fuel cycle cost sensitivities to fiew group data (Assuming no recycle)

In addition to cross section data, parameters such as $\bar{\nu}$, number of neutrons produced per fission (Table 2) and κ, energy released in fission (Table 3), were seen to result in very high sensitivities. The fuel cycle cost sensitivities to fission product data (Table 4) were relatively smaller

Nuclide	BWR	PWR
^{252}Cf	-3.952	-4.326
^{235}U	-1.764	-1.889
^{239}Pu	-1.696	-1.895
^{241}Pu	-0.342	-0.386
^{238}U	-0.181	-0.205

TABLE 2 -- Fuel Cycle Cost Sensitivity to Fission Neutron Yield ($\bar{\nu}$).

Nuclide	BWR	PWR
^{235}U	-0.503	-0.492
^{239}Pu	-0.214	-0.220
^{241}Pu	-0.028	-0.032
^{238}U	-0.028	-0.034

TABLE 3 -- Fuel Cycle Cost Sensitivity to Energy Per Fission (κ).

	BWR	PWR
^{135}Xe Pu Fission Yield	.042	.051
^{135}Xe U Fission Yield	.038	.042
^{143}Nd U Fission Yield	.026	.028
^{143}Nd Thermal Capture σ	.025	.027
^{135}Xe Thermal Capture σ	.023	.029
^{135}Xe Decay Constant	-.023	-.025
^{103}Rh Pu Fission Yield	.018	.022
^{147}Pm U Fission Yield	.016	.020
^{149}Sm Pu Fission Yield	.016	.019
^{103}Rh U Fission Yield	.015	.017

TABLE 4 -- Fuel Cycle Cost Sensitivity to Important Fission Product Data

A similar study carried out for thorium cycles of interest for resource utilization and proliferation resistance indicated the thermal cross sections of ^{233}U to be the most important parameter. ^{239}Pu was again found to be very important in a denatured thorium-uranium cycle. Because of the reduced resonance self-shielding in the lower concentrations of ^{238}U, plutonium productions was found to be larger than might have been anticipated.

In addition to the RPI fuel cycle cost sensitivity study the detailed energy dependent sensitivity profiles for two H_2O moderated critical uranium metal and mixed oxide fueled lattice experiments were determined at Oak Ridge National Laboratory. These studies indicated the importance of an accurate representation of the wings of the resonances of fertile materials such as ^{238}U.

The relative importance of various fission product nuclides has been determined by W. B. Wilson and T. R. England[8] by calculating the contributions of various fission product nuclides to the total fission product capture in a PWR fuel pin at various exposure points. This study has shown that the importance of isotopes such as ^{135}Xe and ^{149}Sm which dominate the fission product absorbtion rate at early exposure points (73% of total absorbtions in ^{135}Xe, 17% in ^{149}Sm at an exposure of 1GWd/MT) is reduced at higher exposures (15% for ^{135}Xe, 6% for ^{149}Sm at 33 GWd/MT) with a corresponding increase in the importance of isotopes such as ^{143}Nd, ^{103}Rh, ^{133}Cs, ^{131}Xe and a spread of the absorbtion rate among a larger number of isotopes.

Problem Areas Relating to the Utilization of ENDF/B Data Libraries in LWR Calculations

The ENDF/B library constitutes a very comprehensive source of data for a wide range of LWR applications. However, in the past it has not been possible to utilize these files in thermal reactor analysis without making a number of key modifications. These modifications were necessitated primarily because of discrepancies between parameters measured in water moderated, slightly enriched uranium lattice experiments and calculations using ENDF/B data. ENDF/B-IV calculations underpredicted the eigenvalues of uranium-metal fueled systems by 0.8 to 1.2% and those of the UO_2 fueled lattices more typical of power reactors by ~0.5 - 0.7%. This underprediction was found to be closely correlated to an overprediction of resonance capture rates in ^{238}U.

In Table 5, ENDF/B-IV calculations using a combination of Monte Carlo and transport theory are compared with measurements and design calculations for three UO_2 benchmark lattices.

A new (fifth) version of ENDF/B containing a number of modifications expected to have a significant impact on the analysis of thermal systems has recently been released. Unfortunately, at the present time only a very limited number of preliminary benchmark calculations have been carried out. A set of these is shown on the last column of Table 5. On the basis of these preliminary calculations as well as earlier analyses and a review of modifications incorporated into ENDF/B-V, it is possible to point out a number of areas where problems may exist.

If the file is to be adapted for use in LWR's these potential problem areas should be investigated with the use of the newly developed Monte Carlo Capabilities and data uncertainties should be reduced.

Lattice ID	Vmod/Vfuel	Parameter	Measured Values	Calculated Values		
				Design Lib.	ENDF/B-IV	ENDF/B-V*
BAPL UO_2-1	1.43	keff	1.00	1.0007	.9929	1.0028
		ρ_{28}	1.39±.01	1.37	1.418	1.414
		δ_{25}	.084±.002	.085	.0828	.0840
		δ_{28}	.078±.004		.0731	.0762
BAPL UO_2-2	1.78	keff	1.00	1.0004	.9936	1.0031
		ρ_{28}	1.12±.01	1.14	1.18	1.17
		δ_{25}	.068±.001	.068	.0671	.068
		δ_{28}	.070±.004		.0628	.065
BAPL UO_2-3	2.40	keff	1.00	.9999	.995	1.0055
		ρ_{28}	.906±.01	.90	.928	.914
		δ_{25}	.052±.001	.054	.0521	.0525
		δ_{28}	.057±.003		.0514	.0533

TABLE 5 -- Summary of H_2O moderated UO_2 lattice calculations

***Preliminary results.**

^{238}U Capture Cross Sections

A 15% reduction in the capture widths of the lowest three S-wave resonances on the basis of recent experimental evidence has resulted in a 50% reduction of the discrepancy between measured and calculated resonance capture rates. However, this reductions was to a great extend counteracted by increases in the higher energy cross sections. It would be very desirable to have the uncertainties in the KeV region reduced. Reactor temperature coefficient calculations using design methods and libraries result in this coefficient being overpredicted for both PWR's and BWR's. Such calculations, although methods dependent, are sensitive to the shape of the ^{238}U capture cross section in the thermal energy range. If the overpredictions are found to persist with ENDF/B-V data, a more accurate determination of the cross section shape below 1 eV may be needed.

Number of Neutrons Produced in Fission ($\bar{\nu}$)

The sensitivity of reactor criticality calculations to $\bar{\nu}$ is almost equal to unity (i.e., a 1% change in $\bar{\nu}$ results is a 1% change in the eigenvalue). Even though the increased $\bar{\nu}$ values in ENDF/B-V give better agreement with uranium fueled critical experiments, the implications of a 0.7% change in $\bar{\nu}$ between versions 4 and 5 are not acceptable.

The uncertainty associated with the $\bar{\nu}$ value of ^{252}Cf is to a great extent due to disagreements between two types of experiments (Manganese Bath and Liquid Scintillator). It has recently been pointed out that up to 50% of this discrepancy may be due to inadequate knowledge of the cross sections of sulfur which appears in the Manganese Bath experiment as an impurity. Measurements of this cross section in the thermal energy range have not been carried out since the late forties.

Fission Spectra

Small integral experiments and leaky systems are highly sensitive to the correct representation of the fission spectra. The harder spectra included in ENDF/B-V are expected to make calculations of small homogenous criticals more consistent.

^{239}Pu Cross Sections

END/B-IV calculations of homogeneous critical experiments containing solutions of plutonium nitrate, consistently overpredict the eigenvalues of such systems[10] by up to 2% (Figure 1). Although the calculated results could be improved by increased leakage due to a harder fission spectrum, the increased ENDF/B-V $\bar{\nu}$ values can be expected to result in an even larger disagreement. A BNWL evaluation of the thermal energy range cross sections using a non-linear least squares method capable of accounting for an energy dependence in $\bar{\nu}$ has been delayed because of discrepancies between the most recent experimental data. However, the magnitude of the uncertainty associated with the cross sections is not large enough to explain the observed high eigenvalues.

Calculations involving mixed UO_2-PuO_2 fueled lattices result in eigenvalues very close to unity. However, this agreement may be fortuitous since captures in ^{238}U are overpredicted (Table 6). In view of the high sensitivities of fuel cycle calculations to the cross sections of this isotope an apparent disagreement in such benchmark calculations is highly disturbing.

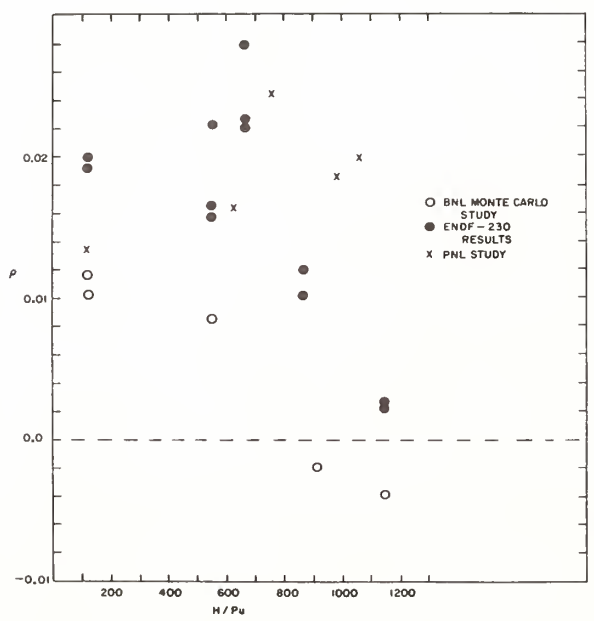

Figure 1 -- Calculated Reactivity of Homogeneous Plutonium Systems.

Lattice ID	Vmod/Vfuel	Boron(ppm)	keff
BNWL UL-266	1.20	--	.9818
UL-250	1.20	681	.9917
BNWL UL-189	2.53	--	1.0006
UL-212	2.53	1090	1.0012
BNWL UL-282	3.64	--	1.0058
UL-232	3.64	767	1.0011

TABLE 6 -- Summary of Eigenvalue Calculations for H_2O moderated mixed oxide (UO_2 + 2% PuO_2) critical lattices. (ENDF/B-IV data)

^{240}Pu Cross Sections

The importance of the ^{240}Pu cross sections to LWR analysis is completely dominated by the 1 eV resonance. The parameters of this resonance are not known accurately enough (uncertainty in $\Gamma\gamma$ is 6% and $\Gamma\eta$ is 15%).[11] Design code calculations of the buildup of trans-uranic isotopes in an operating PWR fuel pin[12] were able to match the experimentally determined ^{241}Pu production rates only after the ^{240}Pu 1 eV resonance capture width was arbitrarily increased by ~10%.

	Exposure (GWd/MTU)	^{239}Pu / ^{240}Pu	^{240}Pu / ^{241}Pu	^{241}Pu / ^{242}Pu
Measurement	24.57	2.55± .07	1.83± .07	3.03± .27
CPM($\Gamma\gamma$=29.9mV)	24.57	2.43	1.93	3.41
CPM($\Gamma\gamma$=33.0mV)	24.57	2.58	1.82	3.41
Measurement	30.92	2.15± .05	1.79± .05	2.33± .19
CPM($\Gamma\gamma$=29.9)	30.92	2.05	1.91	2.53
CPM($\Gamma\gamma$=33.0)	30.92	2.19	1.79	2.53

TABLE 7 -- Plutonium Isotopic Ratios (Robinson-2 Reactor)

^{235}U Cross Sections

A recent evaluation by B. A. Leonard et al has indicated a number of problems which include the possibility of systematic errors in the interpretation of the energy scale in a set of Belgian measurements involving the fission cross sections of this isotope as well as those of ^{233}U, ^{237}Pu and ^{241}Pu. A need for an upward re-normalization of the capture cross sections of ^{235}U above 0.4 eV has also been found to be necessary.[13]

Gadolinium Cross Sections

Gadolinium is included in BWR's as a burnable absorber in order to establish a more uniform flux distribution. Because of its high absorption cross section the calculation of the burnup of

gadolinium loaded pins presents a difficult methods problem. Although discrepancies observed between different design calculations can be ascribed to differences in methods, a set of integral experiments carried out of Battelle Northwest Laboratories has indicated the possibility of data problems as well. These experiments involved homogeneous plutonium nitrate solutions that have been poisoned by varying amounts of gadolinium. BNWL calculations indicated that in spite of an overprediction of the eigenvalues of unpoisoned plutonium nitrate systems by up to 2% the eigenvalues of gadolinium loaded systems are too low by about the same amount.

Thermal Scattering Law Data

A number of investigators[13,9] have suggested the possibility of problems relating to the use of the ENDF/B thermal scattering law data. This data has not been revised since it was produced in 1968 (ENDF/B Version I).

The Haywood Kernel on which the ENDF/B data is based has been observed[9] to result in harder neutron spectra than the Nelkin model incorporated in various design codes. The effect of such differences was considered to be small in uranium systems but may be significant for systems containing significant amounts of plutonium.

Discussion

There exists a considerable incentive for the utilization of the ENDF/B Version V library in LWR analysis. The small decrease in the ^{238}U resonance capture cross section, the higher $\bar{\nu}$ values and the harder fission spectra included in this version result in closer agreement between preliminary calculations and uranium fueled benchmark experiments. Discrepancies in plutonium systems however must be resolved in order for the library to be adequate for fuel cycle calculations.

References

1. A. Jonson, J.R. Rec, U.N. Singh, Symposium Proceedings, EPRI NP-1098 (1979)

2. W.J. Eich, Symposium Proceedings, EPRI NP-1098 (1979)

3. W.J. Eich, "Advanced Recycle Methodology Programs System Documentation", EPRI RP 118-1 (1977)

4. R.E. MacFarlane, R.J. Barrett, D.W. Muir and R.M. Boicourt, The NJOY Nuclear Data Processing System: User's Manual LA-7584-MS to be published

5. H. Lichtenstein, M.O. Cohen, H.A. Steinberg, E.S. Troubetzkoy, M. Beer, EPRI CCM-8 (1979)

6. H. Lichtenstein, E. Troubetzkoy, H. Steinberg, M.O. Cohen, EPRI NP-1042 (1979)

7. M. Becker, D.R. Harris, EPRI NP-985 (1979)

8. W.B. Wilson and T.R. England, Symposium Proceedings EPRI NP-1098 (1979)

9. M. Edenius, Symposium Proceedings, EPRI NP-985 (1979)

10. National Nuclear Data Center, EPRI RP 975-1 Interim report for 1978 to be published

11. L.W. Eston, Symposium Proceedings, EPRI NP-1098 1979

12. R.D. Mosteller, W.M. Andrews, O. Ozer, W.J. Eich, Nuclear Technology 44 192 (1979)

13. B.R. Leonard, Jr., D.A. Kottwitz and J.K. Thompson, EPRI NP-167 (1976)

14. U.P. Jenquin, "The Effect of Substitutions for ENDF/B-IV Data on Plutonium Benchmarks" CSEWG Thermal Data Testing Memo 78-2 (1978)

NUCLEAR DATA NEEDS FOR PLUTONIUM BREEDERS

Ph. Hammer
DRNR/SEDC/SPNR/LPR
CEN/CADARACHE - B.P. N°1
13115 - SAINT-PAUL-LEZ-DURANCE -
(France)

This paper aims at summarizing the present major nuclear data needs for fast breeders. The corresponding requirements are deduced from the target accuracies which are associated to the design, operation and safety related parameters. Due to the fact that these target accuracies may somewhat change from one country to another the requirements quoted here must be considered more as the present order of magnitudes than as precise figures.

The maximum admissible uncertainties which are asked presently for the nuclear data are due in particular to :

- the necessity of reducing the supplementary investment costs which result from the security margins taken by the designers to take into account the present neutronic uncertainties ;
- the necessity of improving the optimization studies devoted to the future commercial fast breeders : these studies involve the comparison of neutronics performances of new concepts, such as the heterogeneous core concept, to the classical one.

[Nuclear data - Fast breeders]

Introduction

It may appear rather surprising that there are still nuclear data needs to be expressed for the fast breeders, since several evaluated data files have been completed and several specific data sets have been adjusted these last years, which should provide all the necessary information for the neutronic calculations.

In spite of this situation, several reasons remain for asking to the nuclear and reactor physicists to improve and enlarge the nuclear data for fast breeders :

1) a benchmark exercice has been recently performed [1] on a typical power reactor : some major design parameters, such as critical mass, radial power distribution, control rod antireactivity, were calculated with various cross section sets.

The dispersion between the calculated results was in most cases significantly higher than the target accuracies for the design parameters.

Taking into account that the calculational method was the same with all the nuclear data sets, this means that these data have still to be analyzed and improved.

2) For the commercial size power plants (1200 to 1500 MWe) which are presently designed in several countries, it is necessary to reduce the investment costs with respect to the prototype situation in order to reach the industrial level. In this context, it is clear that the reduction of the uncertainties applied to the neutronic parameters can contribute directly and significantly to the cost reductions.

3) For the first fast breeders which have been built, either experimental reactors or power plans, the first requests for an improvement of the nuclear data concerned mainly the fuel investment through the core critical mass.

For the power plants which are now in operation , such as PHENIX or PFR, and for the designed commercial reactors, the requests include now :

- the operation related problems (burn-up, corrosion, contamination, handling, storage) ;
- the fuel cycle related problems (Plutonium production, reprocessing and refabrication).

4) For the future, new concepts are studied in order to improve the fast breeder characteristics with respect to the classical two core zone concept.

To be significant such optimization studies imply that the calculated parameters are affected with low uncertainties.

Most of the requests concerning the nuclear data expressed by different laboratories are included in the world request list for Nuclear Data (WRENDA).

The requirements which are deduced from the target accuracies on design operation or safety related parameters depend upon the target accuracies choosen : therefore they may change according to each laboratory.

Nevertheless, from WRENDA and from the specialist meetings devoted to structural materials [2], fission products [3], or transactinium isotopes [4], one can deduce the present status of the main requests for nuclear data related to the fast breeder neutronic problems. Such an attempt is done is this paper which does not aim at presenting a new request list but rather to underline and to analyze the present major requests for fast breeders.

In the following sections, the main design neutronic problems which originate the nuclear data requirements are recalled, the procedure generally used to deduce the maximum admittable uncertainties on the nuclear data from the target accuracies on the design parameters is briefly described and the main nuclear data needs for fast breeders are summarized.

Nuclear data need motivations

Target accuracies for the prediction of fast breeder characteristics

In the design of a power reactor, the uncertainties which are applied to the calculated neutronic parameters are due in particular to :

- the uncertainties on the basic nuclear data ;
- the approximations included in the calculational methods.

These uncertainties are taken into account in the reactor design by the use of security margins leading to supplementary costs. A typical example of such a situation is given by the SUPER-PHENIX 1 power plant, where the global uncertainty on the start-up core critical mass : ± 1% ΔK/K leads to increase the corresponding fuel enrichments by 4% to guarantee the fulfilment of all the operation conditions [5].

The following table provides a comparison between the present uncertainties on the main neutronic parameters and the target accuracies which are expected for the next commercial fast power plants (all the uncertainties quoted correspond to 2 S.D.) :

DESIGN PARAMETERS	PRESENT ACCURACY	TARGET ACCURACY
Reactivity for a fresh core	± 0.5 % $\frac{\Delta K}{K}$	± 0.3 % $\frac{\Delta K}{K}$
Critical mass	± 1.2 % $\frac{\Delta K}{K}$	± 1 % $\frac{\Delta K}{K}$
Reactivity loss per cycle	± 0.7 % $\frac{\Delta K}{K}$	± 0.5 % $\frac{\Delta K}{K}$
Global breeding gain	± 0.04	± 0.03
Doppler effect	≃ 20 %	±15 %
Sodium void effect	±40 %	±20 %
Control rod antireactivity	±20 %	±10 %
$q_{max}/\bar{q}$	± 4 %	± 3 %
βeff	±10 %	± 6 %
TCF	± 5 %	± 3 %
Displacements per atom (D.P.A.)	±10 %	± 5 %
Decay heat	±10 %	± 5 %

On these figures, the following comments can be made :

. The global uncertainty on the critical mass can be taken into account by defining enrichments which will be higher for the start-up core than for the nominal one.

Such a strategy has been choosen for SUPER-PHENIX 1 with the following consequences on the neutronic characteristics [5] :

	NOMINAL CORE	START-UP CORE
Volumic enrichments (%)	13.79 17.60	14.43 18.17
Total Pu mass (Kg)	5560	5780
Cycle length (days)	320	320
Rectivity loss per cycle (%) ΔK/K	1.68	2.07
Breeding gain	0.25	0.21
Linear power (Max.) W/cm	455	457

One sees thaht higher enrichments lead to a supplementary fuel investment (220 Kg of Plutonium) and to a higher reactivity loss per cycle which must be taken into account for the first cycle operation.

. The uncertainty on the reactivity of the fresh core is mainly due to the uncertainties on the nuclear data of the main fissile isotopes and of the structural materials, and to a less extent to the design calculational method.

This uncertainty can be reduced by improving the basic nuclear data, and such an improvement can be achieved with integral experiments [6].

. The reactivity loss per cycle uncertainty is related to the uncertainties on the Fission Product capture cross-sections and to the heavy atom balance associated to the burn-up. It must be noted that the reactivity loss per cycle determines the operational control requirements, so that the core is critical at the end of cycle.

In a SUPER-PHENIX type reactor, the reactivity loss due to the Fission Product amounts to 75% of the total reactivity loss per cycle. The present uncertainty on the fission product bulk reactivity is ≃ ± 15% and the target accuracy is ≃ ± 10%.(2S.D.,[32].

. The uncertainty on the global breeding gain is not independant of the uncertainty on the critical mass [7] : ± 1% ΔK/K correspond to ± 0.03 for the breeding gain. This uncertainty contributes directly to the uncertainty on the doubling time of a fast breeder.

A typical figure for given operating conditions of a fast breeder is : ± 0.04 on the breeding gain absolute value leads to ± 10 years on the doubling time (≃ 40 years).

. The Doppler effect is one of the safety related parameters which has to be known mainly to predict the reactor kinetic behaviour and the energy yield corresponding to an accidental configuration. The uncertainty on this parameter is due to :

- the uncertainties on the shapes of the fission and capture cross-sections ;
- the uncertainties associated to calculational methods.

The present accuracy given is around ≃ ± 15% to ± 30% (see for example [8], [9]) and appears to be sufficient [9].

. The uncertainty applied to the Sodium void effect -which is another safety parameter) is mainly due to the present design calculational methods [10, 11]. The target accuracy ± 20% should be reached mainly by improving these methods, and to a less extent by improving the Sodium scattering cross-sections [12].

There is no need for a better accuracy than ± 20% since the other problems related to a hypothetical accident description are very roughly described by the calculations (e.g. dynamic behaviour of the core, accident sequences).

. The uncertainty on the control rod efficiency quoted here, takes into account :

- the uncertainties on the antireactivity on each absorber rod. These are related to the usual design calculational methods [13, 14], but also to a large extent to the basic nuclear data as it appears from the discrepancies observed for the benchmark problem [1] ;
- the uncertainties on the prediction of the interaction effects between the rods, which are very important for the commercial size breeders. Recent studies [15] confirm that these interactions effects are in fact rather will predicted by the usual design calculations.

. The uncertainty on the power form factor $q_{max}/\overline{q}$ has a direct influence on the total power output as far as this total power is limitable by the temperature of the hottest subassembly. In order to respect the limits on this highest temperature, one can be led to increase the core size. In the axial direction, the power form factor is used to predict the bowing of the core subassemblies.

. The βeff value has to be known in order to get significant reactivity measurements by using the calibrated control rods : such accurate measurements are necessary to get information on the temperature and power coefficients of a power reactor and on the internal breeding gain [16].

. Both the TCF or D.P.A. values can be used as criterion for limiting the residence time of the subassemblies.

The reduction of uncertainty margins on the DPA value involves an improvement of the damage cross-sections of the structural materials.

. The determination of decay heat of the whole core and of each core subassembly is needed to define the emergency cooling conditions and to design the appropriate systems for fuel transfer out of the core and for fuel transportration.

The problems related to decay heat will be analyzed at this conference [34].

Remarks on the procedures used to improve the nuclear data

As said before the uncertainties on the design neutronic parameters are mainly due to the basic nuclear data and to the design calculational methods.

While the design calculational methods are checked and improved with integral experiments of various types (clean experiments or mock-up ones), the basic nuclear data can be improved by two approachs :

- differential measurements and evaluation ;
- specific integral measurements on critical facilities or power reactors.

In some cases, the differential measurements and evaluations represent the only mean to determine the cross-sections :

. for all the isotopes which are not easily available in a sufficient quantity for experimental studies. Such cases occur for :

- many isotopes of each structural materials (for corrosion and contamination studies) ;
- most of the separate Fission Products: of ≃600 identified isotopes only 40 play an important part in the core physics and can be available as samples [17] ;
- most of the actinides, at least presently (for reprocessing, refabrication, storage and studies) [18].

In such cases, the nuclear data can be improved only by improving the microscopic measurements, when they are possible, or by the evaluation technics.

For the major isotopes present in fast breeder cores, the nuclear data requirements can be met by using specific integral measurements [19 to 26]. The role of such experiments has been extensively discussed in many papers, summarized in [27], and will not be discussed in detail here. Only some points will be underlined in the present paper :

1. In order to get significant informations on the nuclear data, simple integral experiments must be performed, where the integral parameters are studied parametrically VS the fuel enrichment or the diluant volumetric percentage.

The media to be studied are determined by sensitivity studies so that the informations obtained cover the complete energy range of interest for fast breeders.

Moreover, one has to check that the integral parameters measured provide significant informations on the nuclear data under study. Such a verification is necessary in particular for the structural material studies where several measured parameters (k_∞, reaction rate ratios) are not simply related to the structural material nuclear data.

The configurations built in critical facilities must be simple from the geometrical point of view in order to minimize the influence of the calculational methods on the result analysis and to avoid any ambiguity when determining the sources of the Calculation to Experiment deviations.

Typical examples of such speicific programmes are those performed at CEA :

- . R-Z programme : for the clean core neutron balance [19, 20] ;
- . PLUTO programme : for the higher Plutonium isotope study [28] ;
- . F.P. programm : for the F.P. capture cross-section determination [17].

2. The parameters which are measured correspond in many cases to the fundamental mode situation and provide direct informations on the neutron balance. Typical integral parameters are :

- . reaction rate ratios (± 1 to 2%) ;
- . material buckling (± 1%) ;
- . reactivity worth measurements (± 5 to 10%) ;
- . spectrum measurements (± 5 to 10%) ;
- . critical mass (± 0.2 % ΔK/K).

Determination of the nuclear data requirements

In order to reduce the maximum admittable uncertainties on the nuclear data from the target accuracies wanted for the design parameters, sensitivity studies are widely performed, using the USACHEV generalized perturbation theory.

Such sensitivity studies aim at providing :

- . the global accuracies which are desirable for each cross-sections in order to reach the design parameter accuracies ;
- . the sensitivity profile of a given integral parameter P to a cross-section variations : $dP/P \Big/ d\sigma/\sigma = f(E)$, which determines the cross-section variation VS energy and contribute directly to the definition of integral experiment study to the improvement of the cross-section under study [29].

The following figures provide as examples the sensitivity profiles of the internal breeding ratio and Keff to the Iron section for the two core zones of a 1200 MWe power plant [7].

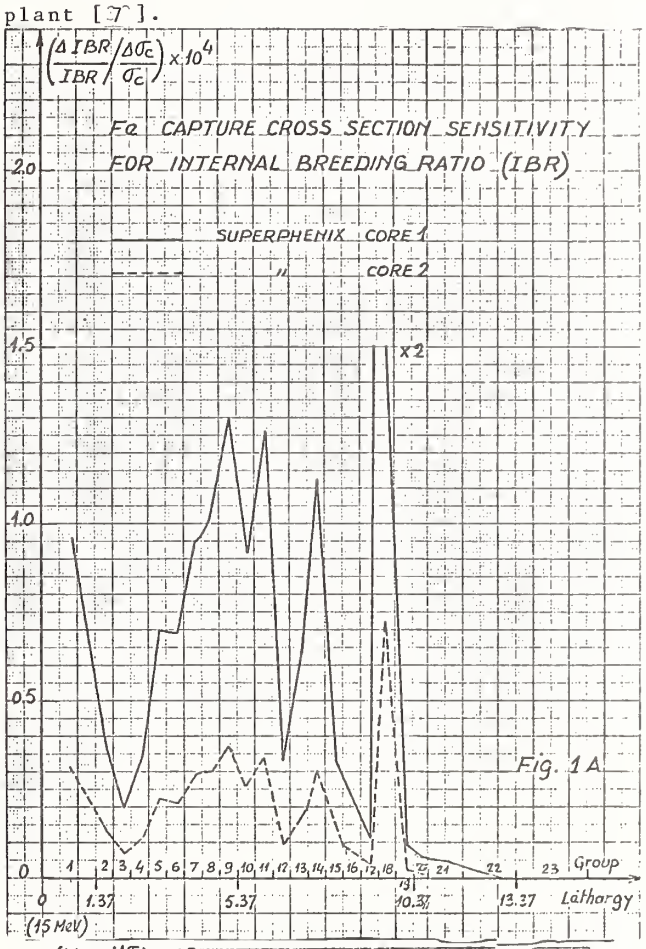

Fig. 1A

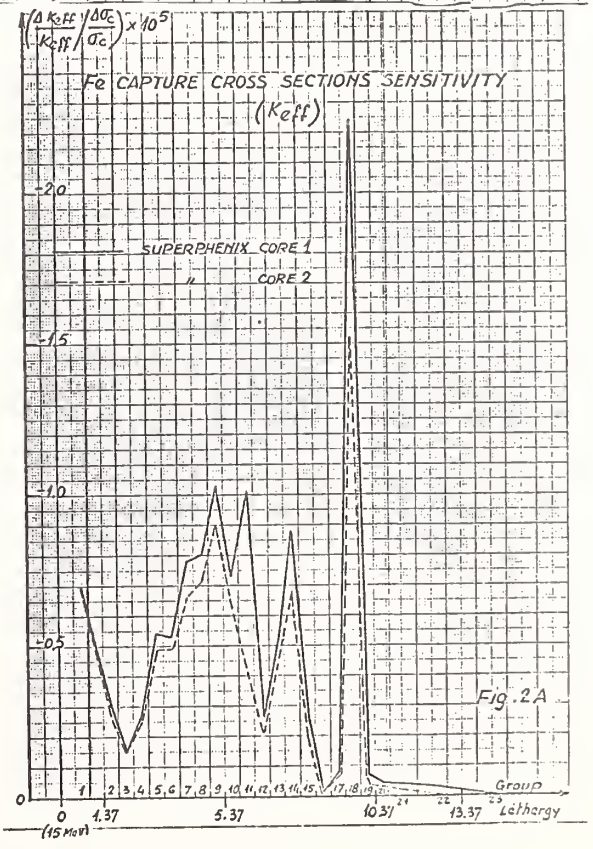

Fig. 2A

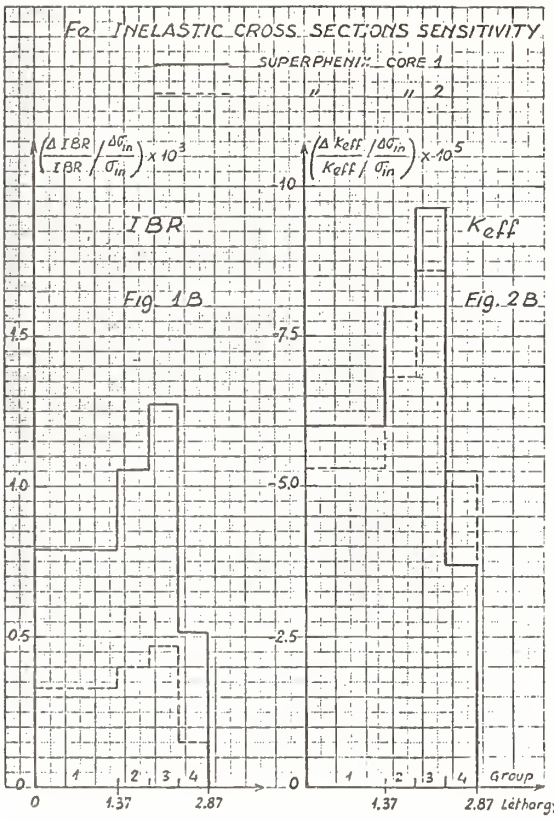

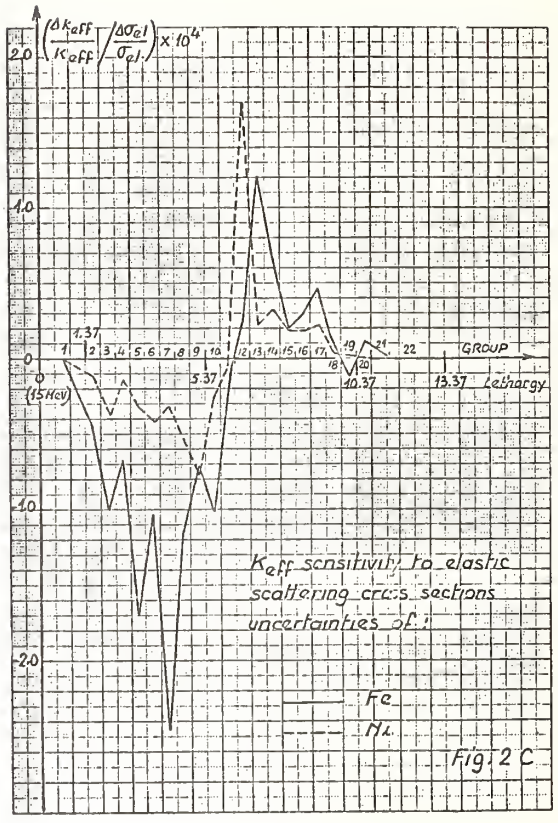

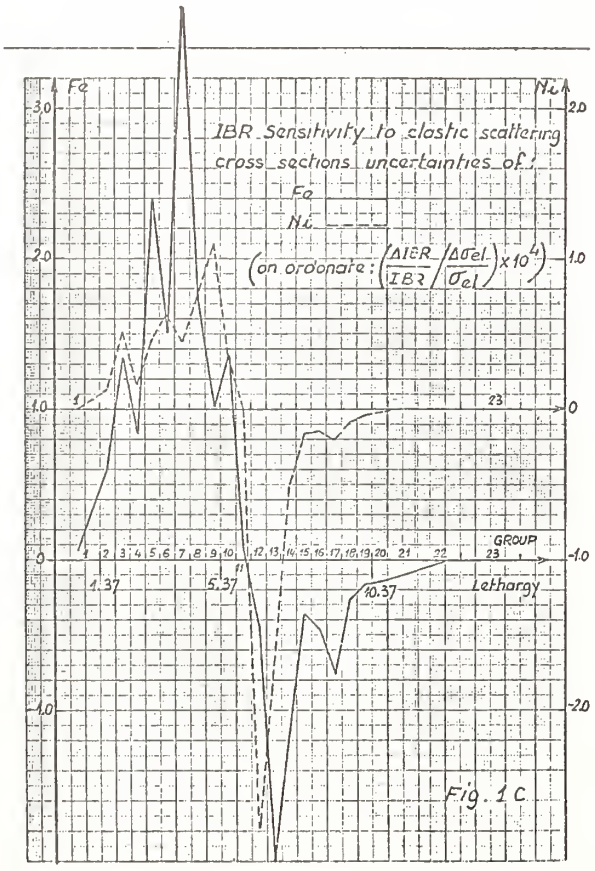

One notes that the sensitivity profiles as those given on the precedent figures provides the necessary complementary informations :

- on the energy range of interest for each core parameter (e.g. for Keff or internal breeding ratio with respect to capture and inelastic iron cross-sections) ;
- on the possible compensation effects between different energy ranges (e.g. for elastic cross-section of iron and Ni).

In order to identify the cross-sections which play a major part in the uncertainties applied to the design parameters, the following table presents, for several isotopes, the cross-section variations which lead to a given change of two integral parameters :

- ± 0.05 % ΔK/K on the critical mass ;
- ± 0.02 % on the absolute value of the internal breeding gain.

The calculations have been performed successively for two media rather close to the inner and outer core zones of SUPERPHENIX : the global variations indicated in the following table correspond to an uniform variation of the cross-section over the whole energy range.

Cross-Section Variation (%)	±0.5% ΔK/K		±0.02 on the IBG	
	$\frac{Pu}{Pu+U}$ ≃14%	$\frac{Pu}{Pu+U}$ ≃18%	$\frac{Pu}{Pu+U}$ ≃14%	$\frac{Pu}{Pu+U}$ ≃18%
ν (239Pu)	0.65	0.64	2.0	1.2
σ_f (239Pu)	0.91	0.91	20	7.6
σ_c (238 U)	2.2	2.9	4.3	5.1
ν (238 U)	4.1	4.4	9.1	12
σ_f (238 U)	6.5	7.0	13	14
σ_c (239Pu)	8.3	8.7	6.6	8.1
σ_{eR} (O_2)	10	15	21	33
σ_{inel} (238U)	10	13	22	34
σ_{tr} (238 U)	12	7.8	26	21
σ_{tr} (O_2)	13	8.2	29	23
σ_f (240Pu)	15	14	23	23
σ_f (241Pu)	15	16	110	119
σ_{tr} (Fe)	16	10	35	28
σ_{inel} (Fe)	21	25	45	66
σ_{tr} (Na)	24	15	53	42
σ_c (240Pu)	29	30	46	50
σ_c (F.P.)	31	52	69	143
ν (235 U)	32	38	70	104
σ_c (Fe)	33	42	77	118
σ_{eR} (Na)	37	54	82	142

. One observes that the sensitivities of the integral parameters such as Keff or the Internal breeding gain to the cross-section variations may depend to some extent upon the spectrum of the medium under study.

On the other hand, the influence of a given cross-section can be much more important for one parameter than for another : a typical example is the 239 Pu fission cross-section for which a 0.9% variation leads to 0.5% ΔK/K variation whereas a 7.6% variation is necessary to change the breeding gain by 0.02.

. It must kept in mind than in such studies the cross-section variations which lead to ± 0.5% ΔK/K or ± 0.02 on the I.B.G. are considered separately.

With . ± 0.5% ΔK/K target accuracy associated to the uncertainties on all the cross-sections lead to more stringent requests on the maximum admittable uncertainties of each cross-section.

Finally, the requests on the nuclear data have to take into account : the complete spectrum range of interest for fast breeders and the request issued from the most severe parameters.

Classification of the nucear data request for core calculations

From the precedent table, it appears clearly that three main kinds of requests can be distinguisted according to their contribution to the core parameter uncertainties :

1. requests on the main fissile isotopes (235U - 238U - 239Pu) ;
2. requests on the structural material isotopes ;
3. requests on the fission products and higher Plutonium isotopes.

These successive priorities are typically reflected by the successive versions of the CARNAVAL adjusted cross-section set where the efforts to meet the design requirements have concerned successively the three items indicated here above.

The following table presents the progression between the successive versions II, III et IV of the CARNAVAL, where the adjusments are done in order to meet the target accuracies on design parameters.

CARN. / ISOT.	II		III		IV	
	Data before 68	After Adjust.	Before Adjust.	After Adjust.	Before Adjust.	After Adjust.
235 U 238 U 239 Pu	EV	A	CII	A	CIII	A
240 Pu 241 Pu	EV	EV	New EV	A	CIII	A
242 Pu	EV	EV	CII	A	CIII	A
241 Am 238 Pu	EV	EV	New EV	EV	New EV	A
Fe	EV	A	CII	A	New EV	A
Cr Ni	EV	EV	CII	EV (CII)	New EV	A
O	EV	EV	CII	EV (CII)	New EV	EV
Na	EV	EV	CII	EV (CII)	New EV	EV
PF	EV	EV	CII	EV (CII)	New EV	A

A refers to adjusted data ;
EV refers to evaluated data.

Influence of the reactor concept on the nuclear data requests :

Most of the nuclear data requests which are related to neutronic core parameters such as critical mass or internal breeding gain correspond to the fast breeders presently in operation or in construction (typically 250 MWe to 1200 MWe).

For the future, new concepts such as the heterogeneous core concept are under study. The following tables provide a comparison of the cross-section variations leading to ± 0.5% ΔK/K change to a ± 0.02 charge of the Internal Breeding gain for some typical cross-sections in three cases :

- . core with low enrichment zones (9%/12%) ;
- . a classical 1200 MWe core (14%/18%);
- . a heterogeneous core (fissile ≃ 20%).

The calculations are performed in a 1D cylindreical geometry and concern only the core zones :

Fissile zone enrichment %	± 0.5 % $\frac{\Delta K}{K}$			± 0.02 on the Internal Breeding Gain		
Cross-sec. variation %	10/12	14/18	20	9/12	14/18	20
σ_f 239 Pu	2.2	1.6	1.6	3.1	2.9	3.1
σ_c 238 U	2.5	2.1	2.9	2.2	2.9	3.1
σ_f 238 U	8.8	7.6	8.5		68	96
σ_c 239Pu	12	7.6	8.5	11.5	10	10.6
σ_{inel} 238U)	12	11	13.2	43	50	88
$\sigma_{el}(O_2)$	13	12	15	/	/	/
σ_f 240 Pu	19	17	17	/	/	/
σ_{fe}(Fe)	/	21	23	/	/	/
σ_c 240 Pu	/	/	/	40	35	27

One observes that the sensitivity coefficients of the critical mass and the internal breeding gain do not depend very tightly of the core enrichment. This indicates that the present requests should not be modified by the introduction of new core concepts at least for the main isotopes.

Nuclear data requests

The main nuclear data requests have been recently reviewed by J. ROWLANDS [27] at the International Conference on Neutron Physics and Nuclear Data, held in HARWELL (September 1978). In most of the cases, the values quoted here under are close to the values given by J. ROWLANDS since no major reason has appeared since last year to modify the requests. To be consistent with the values given by J. ROWLANDS, all the figures quoted correspond to 1 S.D., in the following tables.

Fissile isotopes

Typical target accuracies for the fissile isotopes : 235U - 239Pu - 238U, given in the following table are taken from [27] :

PARAMETER	FISSILE ISOTOPES	FERTILE ISOTOPES
ν_f	0.3 %	1 %
σ_f	2 %	2 %
σ_c or α	4 %	3 %
σ_t, σ_s	20 %	5 %
σ_{inel}	10 %	5 %
$\sigma_{l,2n}$	10 %	10 %
Resonance Parameters	10 %	3 %
ν for delayed neutrons	3 %	5 %

The safety requirements may lead to more specific requests :

- . the target accuracy on the Doppler effect requires an improvement of the data on resonance parameters especially for 238 U [27] ;
- . the target accuracy on the Sodium void effect can lead to an improvement of the 238 U capture cross-sections [12].

Structural and coolant materials

. The structural materials -mainly Fe, Cr, Ni- play an important part on the neutron balance (3 to 5% ΔK/K), on the internal breeding gain of the core, and their characteristics influence directly upon the residence time of the core subassemblies through the damage effects on the claddings or on the wrappers.

As an example, the following table gives the sensitivity percentage per energy range to the structural material capture cross-sections for the Keff value [7].

One observes that the energy range of interest for the capture effects lies between ≃ 0.5 KeV and ≃3 MeV :

ENERGY RANGE	Fe	Cr	Ni	Mo	Mn
3.23MeV→14.5MeV	9	2	41	1	4
3.36KeV→3.23MeV	69	76	55	70	38
0.45KeV→3.36MeV	21	21	3	25	34
23 eV→450 eV	1	1	1	4	24

Moreover the structural material neutronic characteristics play also a major part in the propagation studies (e.g. blanket, shielding) : the corresponding requests have been reviewed by J. BUTLER at the HARWELL Conference [30].

. The requests which concern all the cross-sections of each isotope (Fe, Cr, Ni) may change very significantly according to the data concerned : microscopic data, or final adjusted data. As an example the following table provides a comparison between typical requests for microscopic data (measured or evaluated) and target accuracies which are aimed at for adjusted data [7]. Such accuracies involve the use of integral experiments whenever it is possible. Improved data on the resonance structure of the cross-sections are also required for the treatment of the resonance shielding and Doppler effects.

ISOTOPE		TYPICAL REQUEST FOR MICROSCOPIC DATA	TARGET ACCURACY FOR ADJUSTED DATA
Fe	σ_c	± 10 %	± 3 %
	σ_{inel}	± 5 %	± 3 %
	$\sigma_{(n,p)}$	± 30 %	± 15 %
	$\sigma_{(n,\alpha)}$	± 30 %	± 15 %
	σ_{tot}	/	± 2 %
Cr	σ_c	± 20 %	± 6 %
	σ_{inel}	/	± 8 %
	$\sigma_{(n,p)}$	± 30 %	± 15 %
	$\sigma_{(n,\alpha)}$	± 30 %	± 15 %
	σ_{tot}	/	± 3 %
Ni	σ_c	± 15 %	± 5 %
	σ_{inel}	± 5 %	± 8 %
	$\sigma_{(n,p)}$	± 30 %	± 15 %
	$\sigma_{(n,\alpha)}$	± 30 %	± 15 %
	σ_{tot}	/	± 3 %

For the future power plants, new steel compositions are being investigated, which lead to complementary requirements for Mn, Mo, Ti isotopes. The capture cross-sections of these isotopes should be known with a target accuracy of ± 5% (1 S.D. fpr final adjusted data) [7].

Sodium

The Sodium used as a coolant in fast breeders does not have a significant contribution to the core neutronic parameters such as the critical mass on the breeding gain, but from the safety point of view, the Sodium nuclear data play a major part in the determination of the Sodium voiding reactivity effect, which is related to an hypothetic accidental boiling of the coolant.

The Sodium voiding reactivity effect is the sum of two main component contributions :

- a "central component" which depends upon the neutronic properties of the core ;
- a leakage component which depends mainly on the geometry of the voided zone.

The uncertainty applied to the central component may reach ≃ 20% [12], and is mainly due to the Sodium scattering cross-sections (elastic and inelastic).

The Sodium total cross-section being well known (≃ ± 3%), the problem would be to get a better discrimination between the elastic and inelastic scattering so that each type of cross-section is known with a 10 - 15% accuracy for E > 1 MeV.

To a less extent an improvement of the Sodium capture cross-section seems desirable [12] in order to reduce the uncertainty applied to the central component.

Activations Nuclear Data

These data needs are related to the design calculations performed in order to determine :

- the contamination of various components of the reactor such as the primary circuit, the pumps and the heat exchangers ;
- the activation of subassemblies which will be handled, transported, and stored.

It must be noted that in some cases significant informations can be obtained either from integral measurements performed on critical facilities [31] or eventually from power reactors.

The required accuracies are not very high due to the fact that in many cases the calculational methods lead by themselves to rather high uncertainties.

The following table presents the major reactions involved in the activation calculations :

TYPICAL ACTIVATION REACTIONS	REQUIRED ACCURACY
54 Fe (n,p) 54 Mn	± 10 - 15 %
58 Ni (n,p) 58 Co	± 10 - 15 %
59 Co (n,γ) 60 Co	± 10 - 15 %
58 Fe (n,γ) 59 Fe	± 10 - 15 %
50 Cr (n,γ) 51 Cr	± 10 - 15 %
54 Fe (n,α) 51 Cr	± 10 - 15 %
58 Co (n,γ) 59 Co	± 10 - 15 %
62 Ni (n,γ) 63 Ni	± 10 - 15 %
58 Ni (n,γ) 59 Ni	± 10 - 15 %
54 Fe (n,γ) 55 Fe	± 10 - 15 %
22 Na (n,γ) 23 Na	± 15 %
40 Ar (n,γ) 41 Ar	± 15 %

Absorber Materials

The absorber materials used for fast breeders in operation or in design, are mainly natural and Enriched B4C (typical B.10 enrichments are for example 47% for the first PHENIX rods, 90% for the designed SUPER-PHENIX rods). To a less extent Tantalum and Europium oxide are also considered.

The typical requirements on the nuclear data for the absorber materials have been given by J. ROWLANDS [27] :

- $\leq \pm$ 5% for the capture cross-sections
- $\leq$ 10 % for the scattering cross-sections.

. The recent results obtained on the benchmark exercice[1] seem to indicate that the complementary improvements are needed to reach these target accuracies.

Resonance shielding effect are important for Tantalum and Europium, and require an improvement of the resonance structure, as previously indicated [27]. Data are also required in order to predict the Helium production in the B4C absorber rod and the gamma-heating effects which have to be taken into account in the rod design.

Fission Product Nuclear Data Needs

The fission product build-up resulting from the fuel irradiation contributes directly to the reactivity loss per cycle (75% for a 1200 MWe power plant), influes on the Plutonium build-up during the cycle and contributes highly to the residual power after a stop of the power plant operation.

The fission product nuclear data needs have been reviewed at the HARWELL Conference [27, 32] and only the main conclusions will be summarized here.

The target accuracy on the bulk reactivity effects is : ± 5% to ± 10%.

This leads to the following typical requirements on the Fission Products, which contribute mostly to the global capture effect (a partial list of these isotopes is given in the table hereunder :

- capture cross-sections : ±5% to ±10% (± 25% is sufficient for the isotopes which do not contribute significantly to the total capture) ;
- scattering cross-sections : ±15% to ±30% ;
- fission yields : ±3% to ±5% ;
- decay periods : ±2% ;

The fulfiment of the two last items do not seem to give rise to major problems [17, 33].

For achieving the target accuracy on the capture cross-sections of the main Fission Products, the integral measurements on critical facilities or in power reactors -when they are possible- play a major role.

This appears clearly in the following table, where one compares the target accuracies and the values obtained for data adjusted with integral experiments performed either on critical facilities or in power reactors (PHENIX) :

ISOTOPE	TARGET ACCURACY %	PRESENT ACHIEVED ACCURACY %
105 Pd	± 5	± 4.6
101 Ru	± 5	± 4.5
103 Rh	± 5	/
99 Tc	± 5	± 5
107 Pd	± 5	± 7
149 Sm	± 5	± 4.5
151 Sm	± 5	± 10
147 Pm	± 5	± 6
97 Mo	± 5	± 5
145 Na	± 5	± 5.5
133 Cs	± 5	± 5
135 Cs	± 5	/
109 Ag	± 5	/
103 Ru	± 5	/
143 Nd	± 5	± 6
104 Ru	± 5	± 6

The fission product nuclear data required for decay heat problems will be examined in another paper at this conference [34].

Higher Plutonium Isotopes and Major Actinides (241 Am - 238 Pu)

There are important amounts of higher Plutonium isotopes and of major actinides (241 Am, 238 Pu) in the fast breeder fuels. The following table gives typical compositions for gaz-graphite and PWR Plutonium [5]:

ISOTOPE	GAZ-GRAPHITE	P.W.R.
238 Pu	0	1.7
239 Pu	76.7	56.6
240 Pu	20.1	23.6
241 Pu	2.4	10.9
242 Pu	0.4	5.6
241 Am	0.4	1.6

The higher Plutonium isotopes and 241 Am have significant effects on the core neutronic characteristics : fresh core reactivity, reactivity loss per cycle and internal breeding gain.

Moreover the 241 Am build up during the fuel storage has a quite important effect on the reactivity of this fuel :

STORAGE TIME YEARS	REACTIVITY LOSS OF A P.W.R. Pu ΔK/K
1	0.62 %
3	- 1.8 %

The target accuracies which are given hereunder are typically determined by the following criteria :

. the uncertainty on the core critical mass due to these isotopes must no exceed ± 0.2% ΔK/K ;

. the maximum uncertainty on the internal breeding gain due to these isotopes should not exceed ± 0.01 (absolute value) :

	240Pu	241Pu	242Pu	241Am	238Pu
σ_f	±3%	±2%	±5 to 10%	±3%	±4
σ_c	±3%	±5%	/	±5%	±

For these isotopes as for the Fission Products the internal measurement performed either on critical facilities or in power reactor permit to meet these requirements [28].

Conclusion

1. In spite of the various data libraries, evaluated or adjusted which are available for the fast breeder designs, there are still strong motivations for nuclear data requirements.

These requiremetns are related to :

. the necessity of understanding and reducing the discrepancies between the various data files. In this respect, the discrepancies which can be observed between evaluated and adjusted data files require a better understanding of the discrepancies between the microscopic and integral measurements ;

. the need of reaching the target accuracies for the design parameters by limitating the contribution of the uncertainties on the nuclear data. This particular aspect, related to the fact that fast breeders reach the industrial level, is a strong incentive for improving the nuclear data ;

. the introduction of new concepts for commercial size breeders which aim at improving the characteristics of the future commercial power plants. The associated optimization neutronic studies require reduced uncertainties on the design parameters and consequently reduced uncertainties on nuclear data.

2. Since the design and the start-up of the prototype fast power reactor such as P.F.R. (U.K.), PHENIX (FRANCE), or BN 350 (U.S.S.R.), the need for carefully improved nuclear data has extended from the main fissile isotopes to other isotopes, mainly :

. structural materials ;
. fission products ;
. transactinium isotopes.

The corresponding requests are associated to the necessity of predicting with acceptable accuracy the design parameters related to the power plant operation, the fuel handling, storage, transportation, reprocessing and refabrication.

3. The nuclear data need have been recently precised by sensitivity studies performed in various countries, which can provide a more refined description of the needs VS energy.

A better definition of the required accuracies implies to take into account the correlations which exist either between different cross-sections or for a given cross-section between the various energy ranges. Up to now, in most cases quite qimple assumptions have been made to take into account these correlations. If this problem was not a first priority one for the main fissile isotopes due to the number of available experimental data, it becomes quite important for the isotopes such as structural materials or Fission Products for which only few experimental data exist.

4. The differential measurements and evaluations are necessary for providing the basic nuclear data for all isotopes and for providing detailed informations on particular energy ranges (such for threshold reactions or for resonance regions) : as far as they are the only mean to get the nuclear data of particular isotopes (e.g. Fission Products or Actinides) an improvement of these data requires an improvement of the microscopic data or of the evaluation techniques.

Specific integral experiments are essential to achieve the requested accuracies on some major nuclear data in order to get the target accuracies on the design parameters. Moreover the integral measurements can provide mean values V.S. energy which in some case may be sufficient (e.g. activation cross-sections). In this respect, the results which have been obtained from the power reactors such as PHENIX represent clearly a particularly valuable information.

Acknowledgments

The author wants to express his gratitude to MM. BOUGET and THERDON for performing the sensitivity studies which have been presented and used in this communication.

-o0o-

References

[1] Lesage et al., "Assessement of Evaluated Nuclear Data files via Benchmark calculations", A preliminary report on the NEACRP/IAEA International comparison calculation of a large LMFBR ; ANS Topical Meeting on Advanced in Reactor Physics, GATLINBURG (April 1978).

[2] Böckhoff, "Neutron data of structural materials for fast reactors", Proceedings of a Specialists' Meeting held at GEEL (Belgium), (5-8 December 1977), Jointly sponsored by NEANDC and NEACRP.

[3] IAEA 213, "Fission Product Nuclear Data 1977", Proceedings of the second advisory group meeting on Fission Product Nuclear Data organized by IAEA and held at PETTEN (5-9 Septembre 1977).

[4] IAEA (to be published), "Transactinium Isotope Nuclear Data", Proceeding of the Second advisory group meeting on Transactinium Isotope Nuclear Data, organised by IAEA and held at CADARACHE (France), (2-5 May 1979).

[5] Giacometti et al., "Caractéristiques neutroniques du Réacteur SUPER-PHENIX 1 de CREYS-MALVILLE", Colloque International sur la Physique des Réacteurs à Neutrons Rapides, IAEA-SM-244/24, AIX-EN-PROVENCE (24-28 Septembre 1978).

[6] Chaudat et al., "Data Requirements for fast reactor design", ANS Winter Meeting SAN-FRANCISCO, (November 27, December 2, 1977).

[7] Filip et al., "Needs of Nuclear Data of structural materials for fast reactors" NEANDC, NEACRP Specialist Meeting on Neutron Data of Structural Materials for Fast Reactor, GEEL (5-8 December 1977)

[8] Bennet et al., "Status of Safety Related FFTF Neutronic Parameters", International Meeting on Fast Reactor Safety and Related Physics, (October 5-8, 1976), CHICAGO.

[9] Butland et al., "An assessement of methods of calculations Doppler effects in Plutonium fuelled Sodium cooled Fast Reactors, IAEA-SM-244/32, International Symposium on Fast Reactor Physics, AIX-EN-PROVENCE (France),(24-28 September 1979).

[10] Butland et al., "An assessement of Calculating Sodium Voiding Reactivity in Plutonium fuelled Sodium cooled Fast Reactors, IAEA-SM-244/39, International Symposium on Fast Reactor Physics, AIX-EN-PROVENCE, (24-28 September 1979).

[11] Lyon et al., "Etude de l'effet de Vidange Sodium dans les milieux représentatifs des centrales à neutrons rapides de type classique ou hétérogène : expériences faites au cours du programme PRE-RACINE sur MASURCA, IAEA-SM-244/23, Colloque International sur la Physique des Réacteurs à Neutrons Rapides, AIX-EN-PROVENCE, (24-28 Septembre 1979).

[12] Rimpault, Thèse présentée pour obtenir le titre d'Ingénieur-Docteur, Université de Provence (à paraître).

[13] Bouget et al., "Etude expérimentale des barres de commande pour les réacteurs de puissance à neutrons rapides dans MASURCA", IAEA-SM-244/27, Colloque International sur la Physique des Réacteurs à Neutrons Rapides, AIX-EN-PROVENCE (24-28 Septembre 1979).

[14] Rowlands et al., "The development and validation of control-rod calculation methods", IAEA-SM-244/36, International Symposium on Fast Reactor Physics, AIX-EN-PROVENCE, (24-28 Septembre 1979).

[15] Collins et al., "Experimental studies of 350 MWe heterogeneous LMFBR cores at ZPPR, IAEA-SM-244/70, International Symposium on Fast Reactors Physics, AIX-EN-PROVENCE, (24-28 Septembre 1979).

[16] Hammer, "Requirements of delayed neutron data for the design, operation, dynamics and safety of fast breeder and thermal power reactors", Consultent Meeting on Delayed Neutron Properties, VIENNE, (26-30 March 1979).

[17] Coppé, "Etude de la représentation des produits de fission dans les réacteurs de la filière à neutrons rapides", Thèse présentée à l'Université de PARIS-SUD, Faculté d'ORSAY, le 28 Juin 1978.

[18] Bouchard, "Revue des besoins en données nucléaires des isotopes de Transactinium pour les réacteurs thermiques et rapides à combustible U et U-Pu, ainsi que pour les cycles associés", Second Advisory Group Meeting on Transactinium isotope Nuclear Data", AIEA, CADARACHE (2-5 May 1979).

[19] Barré et al., "Fast reactor physics at CEA : studies of the characteristics of the "clean core" cell neutron balance, control rods, power distributions", International Symposium on Physics of Fast Reactors, TOKYO, (16-19 October 1973).

[20] Barré et., "Complementary rods of Integral experiments and differntial measurements for a fast reactor project. The case of Plutonium isotopes", Conference on Nuclear Data for Reactors, HELSINKI, (June 1970).

21 Campbell et al., "The Relations ship of microscopic and integral data", Conference on Nuclear Data for Reactors, HELSINKI, (June 1970).

22 Weisbin et al., "Application of sensitivity and uncertainty methodology to Fast Reactor Integral Experiment Analysis", NSE, 66 307, (1978).

23 Kuroĭ et al., "Adjusted cross-section library AGL1 and the reliability analysis of integral data", International Symposium on Physics of Fast Reactors, TOKYO, (October 1973).

24 Salvatores, "Recent developments in cross-section adjustment procedures", ANS Topycal Meeting on Advanced in Reactor Physics, GATLINBURG, (April 1978).

25 Barré et al., "After PHENIX, what is the importance of nuclear data programmes for fast breeder reactor development", Conference on Nuclear Cross-Sections and Technology, WASHINGTON, (March 1975).

26 Usachev et al., "Determining the Necessary Accuracy of Nuclear Data with allowance for integral experiments", INDC Neutron Physics Conference, KIEV (1975).

27 Rowlands, "Nuclear data for reactor design, operation and safety", International Confernece on Neutron Physics and Nuclear Data, HARWELL (Sept. 1979).

28 Chaudat at al., "Integral experiments performed at CEA to improve the Pu higher isotopes nuclear data", Specialist Meeting on the Nuclear Data of Higher Plutonium and Americium Isotopes for Reactor Operations", BROOKHAVEN, (November 1978).

29 Bobkov et al., "Planning of neutron data experiments and evaluations for Reactors", OBNINSK (1974). INDC.

30 Butler, "Nuclear Data for shielding", International Conference on Neutron Physics and Nuclear Data, HARWELL, (September 1978).

31 Murphy et al., "Tests of some FD5 Activation cross-sections by ZEBRA irradiations", NEANDC/NEACRP Sepcialist Meeting on Neutron Data of Structural Material for Fast Reactors, GEEL, (December 1977).

32 Hammer, "Besoins en données nucléaires des produits de fission et actinides pour les calculs des réacteurs de puissance à neutrons rapides", International Conference on Neutron Physics and Nuclear Data, HARWELL, (September 1978).

33 Meek et al., "Fission product yields", Second Advisory Group Meeting on Fission Product Nuclear Data, organized by IAEA, PETTEN (5-9 September 1977).

34 , "Decay-heat", paper presented at this Conference.

NUCLEAR DATA NEEDS FOR THE ANALYSIS OF GENERATION AND BURN-UP OF ACTINIDE ISOTOPES IN NUCLEAR REACTORS

H. Küsters

Nuclear Research Center Karlsruhe, Institute of Neutron Physics and Reactor Technology
Postfach 3640, D-7500 Karlsruhe 1, Federal Republic of Germany

[Actinide generation chain, actinides cross sections, L.W. reactors, fast reactors, fast critical experiments]

Introduction

A reliable prediction of the in-pile and out-of-pile characteristics of nuclear fuel is one of the objectives of presentday reactor physics investigations. From the nuclear data point of view, the cross-sections of the dominating actinide isotopes as ^{235}U, ^{238}U, and ^{239}Pu, have been investigated over the energy range of interest for more than two decades. Especially the fast reactor development was accompanied by cross-section measurements in many laboratories. Even today the nuclear data do not match the accuracy requirements of fast reactor designers, so that many laboratories still adjust their data files to a large variety of integral experiments. In 1975 a first international specialists' meeting[1] showed large discrepancies in nuclear data and corresponding group constants for nearly all of the secondary actinide isotopes (all other actinide nuclides except the main isotopes of U and Pu). Though the accuracy requirements for these secondary isotopes are not as stringent as those for the main nuclides, improvements were clearly necessary. The usual tests of nuclear data in critical or subcritical zero power facilities is concentrated on the start-up conditions of a power reactor. The change in isotopic concentration of the fuel during burn-up, especially the build-up of secondary actinides usually is checked by post irradiation examination of spent fuel. Unfortunately, the information from these experiments is often regarded as commercial. A large effort has been spent on nuclear data measurements and evaluations especially for the cross-sections of the secondary actinide isotopes in the seventies. At many conferences the status and the needs for further improvement have been described. In May 1978, on a symposium on nuclear data problems in thermal reactor application[2], an already satisfactory accuracy of most of the cross-sections, important for in-pile and out-of-pile investigations in thermal reactors, has been reported. At Harwell in September 1978, a broad review of the nuclear data status for reactor applications has been given. For instance, in Ref. 3 the nuclear data needs for the analysis of the out-of-pile stages of various nuclear fuel cycles have been discussed. From that discussion it transpired that further improvement of nuclear data with respect to their status in 1978 was very unlikely to reduce any of the technical difficulties in fuel handling. Proper updating of the data, used in the various laboratories, has been required. At Brookhaven in November 1978[4], at Cadarache in May 1979[5] the status of the cross-sections of the secondary actinides has been summarized. Additional information can be obtained from the International Conference on fast reactor physics in Aix-en-Provence in September 1979[6]. Admittedly, only little new information can be reported in this paper. It will concentrate on the check of actinide nuclear data with special emphasis on the secondary actinide isotopes in LWRs and FBRs. Further needs for nuclear data improvements will be deduced from these tests.

Main production paths of important secondary actinides in LWRs and LMFBRs

In the generation chain of the actinides the paths of the main nuclides are well known. In order to determine the importance of nuclear data improvements of secondary actinides, the main production paths of ^{237}Np, ^{238}Pu, ^{243}Am and ^{244}Cm in PWRs and LMFBRs are listed in Table I[7].

Table I. Main Production Paths for Important Secondary Actinides. [%]

ISOTOPE	Formation	PWR 32000 MWd/t	LMFBR 85000 MWd/t	
			LWR-Pu	EQUIL.
^{237}Np	(n,γ) from ^{236}U	80	14	10
	(n,2n) from ^{238}U	20	86	90
^{238}Pu	(n,γ) from ^{237}Np	91	15	29
	(α) from ^{242}Cm	∿ 9	73	56
	(n,2n) from ^{239}Pu	< 0.1	12	15
^{243}Am	(n,γ) from ^{243}Pu (including $^{241}Pu \rightarrow {}^{241}Am \rightarrow {}^{242g}Am \rightarrow {}^{242}Pu$	99.4	95.4	97.3
	(n,γ) from ^{242m}Am	0.6	4.6	2.7
^{244}Cm	(n,γ) from ^{243}Am	99.6	99.6	99.8
	(n,γ) from ^{243}Cm	0.4	0.4	0.2

^{237}Np is important because via neutron absorption ^{238}Np is generated which decays in about 2 days to ^{238}Pu with its strong α-decay. This isotope causes special difficulties in reprocessing of spent fuel by radiolysis, and also in refabrication of reprocessed fuel. ^{243}Am is the main nuclide generating ^{244}Am by neutron capture, which decays in about 10 hours to ^{244}Cm. ^{244}Cm is, like ^{242}Cm a very strong α- and

neutron emitter.

As can be seen from Table I, the main difference between thermal and fast system is that (n,2n) processes, especially on ^{238}U, play a more important role in fast than in thermal systems. As a result the production path of ^{237}Np and therefore the production path of ^{238}Pu are changed. Also it has to be recognized that there are great differences between a fast reactor fuelled by LWR-plutonium and one operating in its equilibrium cycle.

As can be deduced from Table I, neutron capture in ^{242}Am and in ^{243}Cm are relatively unimportant. Besides the neutron reaction data of the higher plutonium isotopes also those of ^{241}Am are important, because this isotope contributes to the reactivity balance in a fast reactor. Clearly, the branching ratio leading to the ground and isomeric states of ^{242}Am have to be known sufficiently well (the accuracy requirements can be looked up e.g. in Ref. 1). Furthermore, neutron capture in ^{236}U, ^{237}Np and ^{243}Am are rather essential in leading to nuclides which are of great concern in out-of-pile fuel cycle analyses. Along with this statement goes the importance of the fission cross-sections of these isotopes. Additionally, (n,2n) processes on ^{238}U and ^{239}Pu are of concern. The requirement for accurate data for these processes is well covered by the requirements of fast reactor physics.

In the following sections we examine the accuracy of present data and methods against results obtained from post-irradiation experiments in power reactors and partly with results obtained in zero-power facilities.

Test of actinide nuclear data for LWR fuel cycle analysis

A thorough comparison of theoretical predictions with experimental results for the isotopic composition of spent fuel is very complex. The complete power-history of an operating plant has to be known. In particular the local variations of reaction rates in time around the irradiation position have to be considered very carefully. This is especially important if the isotopic compositions of higher actinides, which are rather sensitive to the neutron flux level and its variation, have to be determined. This is due to the competition between neutron reactions and decay. In order to have some conclusive results with respect to nuclear data uncertainties, some of the calculational complexities are removed by prescribing the experimental power density or flux density at the irradiation position as a function of time. If at least the dominating effective fission cross-section (i.e. of ^{235}U) is correct, from the local power density the local flux can be deduced sufficiently accurate. Often either ratios of nuclide concentrations or other relative figures (e.g. isotopic abundances), which are usually given by chemical experiments, are investigated, by which calculational uncertainties are somewhat decreased. In Table II some results from post-irradiation analyses of BWR- and PWR-fuel are given.[8,9] The figures give the deviations between theory and experiment in percent. Some of the nuclide concentrations are measured against burn-up (B), others are measured against depletion of ^{235}U (D^5), the last line gives the isotopic ratios against uranium (U). GARIGLIANO and GUNDREMMINGEN are BWRs of 150 MWe and 237 MWe, respectively. TRINO and OBRIGHEIM are PWRs of 250 MWe and 283 MWe, respectively. This comparison shows differences between theory and experiment of several percent, if empirical information is used. In the last line only the burn-up has been modified arbitrarily by 1 %, no adjustment of group constants was done. Even if empirical information is used in theory, the agreement between "theory" and experiment is sometimes not satisfactory. This can be seen in the figures for the German BWR plant GUNDREMMINGEN. The burn-up "adjustment" for TRINO gives large differences for the higher Pu and transplutonium isotopes.

Deviations sometimes are reduced by adjusting the group constants to the experiments. Darrouzet et al[7] 1978 compared theoretical results with unadjusted and adjusted nuclear data for isotopic ratios in the Ardennes PWR power plant with chemical mass determinations, shown in Table III. In adjusting the group constant data to experiments, the differences can be reduced to a few percent.

Often irradiation experiments are interpreted by use of the Oak Ridge code ORIGEN[10], which is a fundamental mode burn-up and irradiation program and in its original version it uses time independent one group

Table II. Burn-up Analysis of LWR - Spent Fuel

Reactor	^{238}Pu	^{240}Pu	^{241}Pu	^{242}Pu	^{241}Am	^{242}Am	^{243}Am	^{242}Cm	^{244}Cm
GARIGLIANO+)		D^5:0.5	D^5:0.8	D^5:1.6					
GUNDREMMINGEN+)		B:3.0	B:4.6	D^5:9.4			B:3.0	B:6.9	
OBRIGHEIM+)	B:2.3		D^5:1.0	D^5:1.0			D^5:7.0	D^5:1.3	D^5:2.8
TRINO+)	B:3.1		B:1.2	B:2.2			B:6.2		
TRINO*)		U:1.8	U:1.0	U:7.0	U:21.0	U:24.0	U:28.0	U:8.0	U:1.0

+) Theoretical prediction by using empirical information from measurements on many samples.[8]

*) Theoretical prediction with adjustment due to changing the burn-up by 1 %.[9]

Table III. Comparison of Theoretical and Experimental Isotope Ratios for Ardennes-PWR Power Plant

Isotope Ratio	Pre-Adjustment $\frac{E-C}{C}$ [%]	Post-Adjustment $\frac{E-C}{C}$ [%]
^{232}U / ^{238}U	+ 6	+ 7
^{236}U / ^{238}U	+ 7	+0.4
^{237}Np / ^{238}U	-10	- 4
^{238}Pu / ^{239}Pu	+16	- 3
^{242}Pu / ^{239}Pu	-10	- 5
^{242}Cm / ^{239}Pu	+12	+ 4
^{244}Cm / ^{239}Pu	+53	- 3

cross-sections. Part of these data were adjusted. Because this code is widely used all over the world, it is of interest to check its ability with more refined methods and with experiment. Part of the information on the revised version of ORIGEN, called ORIGEN-2 has been reported in 1978[11]. ORIGEN-2 uses time dependent group constants and has been checked with a special option of the CITATION diffusion code. Parallel to ORIGEN-2 at Karlsruhe we have developed a similar code, named KORIGEN[12]. Many of the nuclear data have been adopted from the ORIGEN-2 version, while some are based on the KEDAK nuclear data file.

In order to improve the calculational basis for out-of-pile investigations (i.e. considering more than 1000 nuclides consistently also during reactor life) a code-system, named HAMKOR, has been established[13]. With this system the neutronics of LWR-cells can be determined for any burn-up state and for any light-water lattice. HAMKOR is based on an improved version of HAMMER for the static calculations, and coupled to the burn-up and irradiation program KORIGEN. Nuclear data for the important isotopes are taken from the latest available data on the KEDAK-file, status 1979. Further sophistication and generalization of this system are underway at Karlsruhe; this includes also coupling of the burn-up routine to other cell codes and to global whole-core neutronic codes as well as the adoption of any more accurate nuclear data. Table IV gives a comparison of various methods with experiments. The experimental results, on which the figures of Table IV are based, were taken from post-irradiation analysis of the US-ROBINSON reactor[14].

The last column of Table IV shows the trend of deviations of ORIGEN-2 results in comparison to more refined calculations, which are not described in detail ("literature values" in Ref. 11).

As can be seen, the ORIGEN and KORIGEN versions show surprisingly good results up to ^{241}Am, both in comparison with each other and with experiment. The original ORIGEN version gives such relatively good agreement because of data adjustment. The good agreement of ORIGEN-2, which is mainly based on ENDFB/IV, may be fortuitious, as may be concluded from the last column. The large deviations in nuclide concentrations above ^{241}Am can easily be traced back to insufficient data in ENDFB/IV.

HAMKOR-results show large deviations from experiment for ^{238}Pu, ^{242}Am, and ^{242}Cm. Work is underway to reduce the about 5 % deviation of the ^{235}U concentration from experiment by careful investigation of all thermal power contributors, but the agreement principally is limited by the uncertainty in the burn-up determination. All other relative concentrations (they are given as ratio of the specific nuclide concentration to the concentration of the corresponding element) are sufficiently well predicted (remember that the power history has been prescribed). First of all, the nuclides with larger deviations have very low isotopic concentrations ($^{238}Pu \sim 1.6$ a/o, $^{242}Am \sim 0.3$ a/o, $^{242}Cm \sim 3.3$ a/o). The statistical errors of the relative mass determinations are about 1 % for ^{238}Pu, larger about 10 % for ^{242}Am and larger about 5 % for ^{242}Cm (these figures were communicated to the author by L. Koch, Transuranium Institute Karlsruhe). Now, various groups have undertaken an interlaboratory comparison to check the experimental accuracy of post-irradiation analysis. Preliminary results show an unsatisfactory discrepancy (e.g. for the same sample a factor of two in the ^{242}Cm content). Therefore, more effort has to be spent to assess reliable uncertainty margins. If possible, measurements, based on different methods, have to be applied to reduce systematic errors. The situation seems to be comparable to that of differential cross-section measurements some years ago, when the statistical error of a certain measure-

Table IV. Deviations (in percent) of Isotopic Compositions [a/o] between Theory and Experiment for the US-ROBINSON PWR at discharge. ($\frac{E-C}{E}$ [%])

NUCLIDE	HAMKOR (1979)	KORIGEN (1978)	ORIGEN-2 (1978)	ORIGEN (1973)	Trend of deviations for ORIGEN-2 (PWR, BWR)
^{234}U	–	-7.1	0.	7.1	up to 30 % overpred.
^{235}U	+4.9	8.4	10.4	5.8	
^{236}U	-2.9	-2.0	0.	-1.4	
^{238}U	-0.03	-0.1	-0.06	-0.03	
^{238}Pu	20.0	5.1	-3.8	15.4	up to 40 % underpred.
^{239}Pu	0.05	1.3	-1.3	-1.7	
^{240}Pu	-3.8	-1.3	8.0	4.2	up to 15 % overpred.
^{241}Pu	5.5	-4.4	-8.7	-3.6	$\pm$ 15 %
^{242}Pu	-1.3	-11.6	-2.8	1.7	$\pm$ 15 %
^{241}Am	-3.4	13.6	10.6	-5.7	up to 40 % underpred.
^{242m}Am	22.8	46.5	-31.4	factors	
^{243}Am	5.4	-23.1	-17.5	8.8	$\pm$ 5 - 10 %
^{242}Cm	-30.5	17.4	26.2	70.0	
^{243}Cm	-4.1	27.3	74.4	88.4	
^{244}Cm	-3.1	-5.3	-2.0	-7.6	up to 30 % underpred.

ment was much smaller than the discrepancy to the results of another experimentalist. In case of ^{242}Cm, comparison of HAMKOR with other post-irradiation experiments shows satisfactory agreement.

From Table IV we conclude that for most of the isotopes of interest in LWR fuel cycle analysis the nuclear data presently are accurate enough. The important exceptions are for ^{238}Pu and ^{242}Cm (with respect to HAMKOR analysis). Further investigation of these discrepancies is required. The assessment of more reliable uncertainty margins in post-irradiation experiments is necessary. Additional comparisons of theory with spent fuel experiments have to be performed to get a more transparent view of the data status. These are underway at Karlsruhe, especially for German PWRs and for PWRs with recycled plutonium fuel elements. Presently no further needs for nuclear data measurements can be made.

It should be mentioned that the spent fuel analysis is of great concern in nuclear safeguards investigations. There it is a key issue to detect reliably and early any diversion of fissile material in spent fuel. The essential plutonium content can e.g. be determined by means of the so-called isotopic correlation technique.[15] At the present time, more theoretical exploration of this method has to be undertaken. For the experimental results, better and more reliable accuracies have to be achieved, as already mentioned earlier. Up to now the technique of isotopic correlation can only be used as a supporting measure in safeguards analysis. In addition, there is no unique concept of safeguarding nuclear material, so that a request for more accurate nuclear data in this field is unlikely to be made now, see also Ref. 16.

Test of actinide nuclear data for fast reactor fuel cycle analysis

It is well known that the nuclear data for fast reactors are not of the same sufficiently good quality as for thermal reactors. This is reflected in Table V, where one group cross-sections for fast reactors are compared. These data have been provided in 1976 to the author by US and UK members of the NEACRP. A very wide spread in capture and fission data is observed. The data status is that of about 1973 and older.

Table V. Comparison of ORIGEN (US) and FISPIN (UK) One Group Cross-Sections for Fast Reactors

Isotope	ORIGEN (1973)		FISPIN (1973)	
	Capture	Fission	Capture	Fission
^{237}Np	0.76	0.36	1.87	0.34
^{238}Pu	0.22	1.38	0.44	1.15
^{239}Pu	0.5	1.85	0.51	1.82
^{240}Pu	0.41	0.35	0.59	0.38
^{241}Pu	0.43	2.49	0.59	2.64
^{242}Pu	0.34	0.28	0.38	0.30
^{241}Am	0.99	0.46	1.91	0.40
^{242}Am	0.4	1.83	0.1	3.33
^{243}Am	0.55	0.27	1.7	0.19
^{242}Cm	0.38	0.42	0.5	1.26
^{243}Cm	0.4	0.32	0.1	3.14
^{244}Cm	0.37	0.41	0.48	0.55

The discrepancies in nuclear data also show as large differencies in isotopic compositions, radiation and heat production in spent fast reactor fuel. A comparison of ORIGEN-type calculations with experimental results on the fast test reactor RAPSODIE is given in Table VI[17]. The used data are a mixture of nuclear data from various origins, some of them taken from the 1975 Karlsruhe meeting on data for actinides[1] and some of more recent communications up to 1977.

Table VI. Comparison of Calculations (ORIGEN type) with Experimental Results for RAPSODIE $(\frac{C - E}{E}\ [\%])$

ISOTOPE	BURN-UP a/o		
	1.126	4.035	1.089
^{234}U	-4	-4	-9
^{235}U	-0.1	-0.6	-0.1
^{236}U	-10	-12	-20
^{238}U	-0.6	+0.3	-0.2
^{238}Pu	-99	+2	-99
^{239}Pu	+1.5	+3	+1.6
^{240}Pu	0.09	-0.01	-0.2
^{241}Pu	+2	+5.6	+2
^{242}Pu	-9	+5	-11
^{241}Am	+39	+15	-44
^{242}Am		-96	
^{243}Am		-68	
^{242}Cm	-47	-47	-47

Even larger discrepancies can be observed for ^{238}Pu, and the americium and curium isotopes as in similar comparisons for thermal system (see Table IV).

To improve the situation, some experiments have been performed in fast critical facilities. Table VII comprises C/E ratios for fission rate ratios and $\sigma_a/\sigma_f = 1+\alpha$ obtained in the ZEBRA and SNEAK assemblies, which were already reported in 1977[18]. At the Aix-en-Provence conference in 1979 additional results were reported by Sanders et al for ^{241}Am and ^{243}Am[19]. The nuclear data for ^{241}Am were based on UK-evaluations by Lynn et al, and for ^{243}Am solely on nuclear model calculations. The agreement is satisfactory.

At the Aix-en-Provence conference in 1979 the successful in-pile measurements in PHENIX on a large variety of samples have been reported by Giacommetti[20]. The results are not yet available. After adjustment, good agreement was found with experiment. From this

analysis it can be concluded that in France and in institutions, associated with the CEA, a fairly good knowledge of the present accuracies of differential nuclear data for actinides, applied to fast power reactor experiments, exists.

Table VII. Comparison of Theoretical and Experimental Results in Fast Critical Experiments (C/E)

ISOTOPE I	ZEBRA 1975 $\sigma_f^I/\sigma_f(^{239}Pu)$	SNEAK 1975 $\sigma_f^I/\sigma_f(^{239}Pu)$	SNEAK 1975 $1+\sigma_c/\sigma_f(^{239}Pu)$
^{238}U	1.04 ± 4 %	0.95 ± 2.2 %	0.98
^{240}Pu	1.003± 5 %	0.94 ± 1.5 %	1.27
^{241}Pu	1.05 ± 3 %	1.05 ± 1.5 %	1.03
^{242}Pu	1.23 ± 5 %		
^{241}Am	1.26 ± 4 %	1.40 ± 2 %	1.95
^{243}Am	0.88 ± 4 %		
^{244}Cm	1.35 ± 8 %		

ZEBRA 1979

Isotope	σ for Cm Production	C/E	Remarks
^{241}Am	1.28±0.1	0.88±0.07	PFR Spectrum
^{243}Am	1.32±0.2	1.20±0.18	
^{241}Am	1.48±0.2	0.84±0.06	CDFR Spectrum
^{243}Am	1.99±0.2	0.87±0.09	

In 1979, the author acted as focus within an activity of the NEACRP to compare one group data for actinides (fission and capture), as used in the various laboratories. This type of benchmark comparison was based on the spectrum (for collapsing) of the NEACRP-benchmark for a 1000 MWe fast reactor.[21] The results of the benchmark were reported many times, e.g. by Lesage at the Gatlinburg Conference 1978.[22]

Tables VIII, IX and X show the one group constants provided by France (FRA), Germany (GER), Japan, UK and USA (ENDFB/IV and ENDFB/V). For completeness, values from the USSR are included, which are not strictly comparable, because they are not based on the NEACRP benchmark, but rather on a more simple benchmark (often quoted as BAKER-benchmark) of a large fast reactor; therefore due to spectrum differences the one group constants may differ to those of the NEACRP benchmark. In the tables A means: adjusted in CARNAVAL IV, the French fast reactor group constant set, M means a modification of data with respect to the UK set FGL5.

At first sight and compared with Table V, considerable improvements have been obtained in recent years. There are no longer large discrepancies as before for actinide nuclei important in in-pile and out-of-pile fuel cycle investigations. However, the differences in capture data for ^{232}Th, ^{233}Pa, $^{233,234}U$, ^{237}Np, $^{238,240,241,242}Pu$, $^{242,243}Am$ and $^{242,243,244}Cm$ are not so small that they can be neglected.

First, one has to repeat the checks already made in fast reactors, with the more recent data available now. However, it is not justified to apply the group constants, taken e.g. from Table VIII to Table X, for smaller test facilities as RAPSODIE with different neutron spectra, because most of the cross-

Table VIII. Comparison of One Group Constants for the NEACRP-LMFBR Benchmark: ^{232}Th to ^{237}Np

	CAPTURE [b]							FISSION [b]						
COUNTRY	FRA	GER	JAPAN	UK	USA		USSR*)	FRA	GER	JAPAN	UK	USA		USSR*)
BASIS	CARN IV	KEDAK	JAERI	FGL5	ENDF/B IV	ENDF/B V		CARN IV	KEDAK	JAERI	FGL5	ENDF/B IV	ENDF/B V	
^{232}Th	0.59	-	-	0.43	0.43	0.41	-	0.0097	-	-	0.0094	0.0091	0.0096	-
^{233}Pa	1.33	-	-	1.13	1.18	1.18	-	0.22	-	-	0.64	0.062	0.062	-
^{233}U	0.33	-	-	0.27	0.28	0.29	-	2.81	-	-	2.85	2.90	2.84	-
^{234}U	0.35	-	-	0.61	0.63	0.66	0.68	0.3	-	-	0.29	0.29	0.32	0.34
^{235}U	0.59^{A}	0.6	0.64	0.53	0.62	0.62	-	1.94^{A}	2.0	2.10	1.98	2.02	2.0	-
^{236}U	0.51	-	-	0.59	0.60	0.61	0.62	0.092	-	-	0.088	0.089	0.099	0.11
^{238}U	0.29^{A}	0.31	0.31	0.29	0.31	0.31	-	0.040^{A}	0.041	0.045	0.043	0.040	0.040	0.041
^{237}Np	1.44	1.64	-	1.95	1.68	1.86	1.8	0.33	0.32	-	0.31	0.31	0.32	0.32

*) not strictly comparable, see text.

Table IX. Comparison of One Group Constants for the NEACRP-LMFBR Benchmark: ^{238}Pu to ^{242}Pu

	CAPTURE [b]							FISSION [b]						
COUNTRY	FRA	GER	JAPAN	UK	USA		USSR*)	FRA	GER	JAPAN	UK	USA		USSR*)
BASIS	CARN IV	KEDAK	JAERI	FGL5	ENDF/B IV	V		CARN IV	KEDAK	JAERI	FGL5	ENDF/B IV	V	
^{238}Pu	0.54[A]	0.68	0.91	0.45	0.48	0.80	0.90	0.84[A]	1.03	1.12	1.13	1.15	1.14	1.16
^{239}Pu	0.57[A]	0.57	0.61	0.55	0.56	0.57	-	1.81[A]	1.87	1.88	1.83	1.84	1.86	-
^{240}Pu	0.55[A]	0.57	0.62	0.63	0.58	0.61	-	0.33[A]	0.36	0.37	0.35	0.36	0.36	-
^{241}Pu	0.5[A]	0.5	0.55	0.62	0.51	0.50	-	2.53[A]	2.54	2.61	2.69	2.61	2.63	-
^{242}Pu	0.63	0.5	0.41	0.39[M]	0.39	0.48	-	0.22	0.24	0.28	0.22	0.27	0.25	-

*) not strictly comparable, see text.

Table X. Comparison of One Group Constants for the NEACRP-LMFBR Benchmark: ^{241}Am to ^{244}Cm

	CAPTURE [b]							FISSION [b]						
COUNTRY	FRA	GER	JAPAN	UK	USA		USSR*)	FRA	GER	JAPAN	UK	USA		USSR*)
BASIS	CARN. IV	KEDAK	JAERI	FGL5	ENDF/B IV	V		CARN IV	KEDAK	JAERI	FGL5	ENDF/B IV	V	
^{241}Am	2.02[A]	1.93	1.69	2.01[M]	1.37	1.89	1.90	0.29	0.26	0.30	0.31	0.41	0.28	0.31
^{242}Am	0.7	0.46	-	0.11	-	0.097	0.42	3.7	3.86	-	3.33	-	3.61	3.2
^{243}Am	1.6	1.53	1.65	1.73[M]	0.86	1.20	1.8	0.2	0.2	0.23	0.19	0.17	0.22	0.20
^{242}Cm	0.59	-	-	0.51	-	-	0.46	2.05	-	-	1.23	-	-	0.16
^{243}Cm	0.5	0.18	-	0.10	-	0.27	0.39	3.39	2.46	-	2.89	-	2.77	2.5
^{244}Cm	0.85	0.65	0.66	0.49[M]	0.53	0.91	0.98	0.45	0.43	0.43	0.38	0.52	0.40	0.42

*) not strictly comparable, see text.

sections are strongly energy dependent, as can be seen from Table VII: the differences in group constants, obtained with a PFR- and a CDFR spectrum, respectively, are relatively large. Therefore, again coupling of modern data libraries to whole-core diffusion and burn-up codes (including the long-term decay phase for out-of-pile investigations), is necessary. This has been done already in Karlsruhe[23], the application of this system is underway now.

Conclusion

For thermal reactors, the present accuracy of nuclear data for the analysis of fuel cycle aspects, probably is sufficient. Further checks to integral experiments, especially on commercial power plants, have to be performed to support this statement. Updating of all data libraries including group constant libraries to the 1979 or later status is required.

For fast reactors, a careful evaluation by tracing back the observed differences between theoretical and experimental results to the basic nuclear data is required first. Additional comparisons with results from integral experiments in power reactors will show the quality of the data.

Only after this exercise for thermal and fast systems requests for new differential data measurements may be formulated.

Acknowledgment

The author is grateful to those members of the NEACRP, who provided the material presented in this paper. Helpful discussions with U. Fischer, B. Goel, M. Marzo and H.W. Wiese are gratefully acknowledged, also the careful reading of the manuscript by A. Rowe.

References

1. Transactinide Nuclear Data, Proceedings of an IAEA Advisory Group Meeting, Karlsruhe 1975, IAEA-186.

2. Proceedings of a Symposium on Nuclear Data Problems for Thermal Reactor Application, EPRI-NP 1098, BNL-NCS 25047, Brookhaven, May 22-24, 1978, published in June 1979.

3. H. Küsters, M. Lalović, H.W. Wiese, Fuel Handling, Reprocessing, and Waste and Related Nuclear Data Aspects, International Conf. on Neutron Physics and Nuclear Data for Reactors and other Applied Purposes, Harwell, UK, Sept. 1978.

4. Proceedings of the Specialists' Meeting on Nuclear Data of Plutonium and Americium Isotopes for Reactor Applications, BNL-50991, Brookhaven, Nov. 1978.

5. See Contributions to the IAEA Advisory Group Meeting on Transactinium Nuclear Data at Cadarache, May 1979

6. Proceedings of the International Conference on Fast Reactor Physics, Aix-en-Provence, Sept. 1979, not yet published.

7. M. Darrouzet et al., Secondary Actinide Formation and Decay in Light Water and Fast Breeder Reactors, Paper submitted to the 21st NEACRP-Meeting, Tokyo, 1978.

8. R. Ernstberger et al., Isotope Correlations Used in Fuel and Waste Management, Proceedings of a Symposium on the Isotopic Correlation and its Application to the Nuclear Fuel Cycle, Stresa, (1978).

9. P. Peroni, G. Guzzi, Comparison between experimental and theoretical Data for Am and Cm Build-up in the TRINO VERCELLESE PWR, Proceedings First Technical Meeting on the Nuclear Transmutation of Actinides, ISPRA, (1977).

10. M.J. Bell, ORIGEN - The ORNL Isotope Generation and Depletion Code, ORNL-4628 (1973).

11. A.G. Croff et al., Revised Uranium-Plutonium Cycle PWR and BWR Models for the ORIGEN Computer Code, ORNL/TM-6051 (Sept. 1978).

12. H.W. Wiese, Stand der im KfK verfügbaren Methoden und Daten zur Vorhersage des Verhaltens von LWR-Brennstoff im nuklearen Brennstoffkreislauf, KfK-Nachrichten 3/79, p. 76, Nov. 1979.

    U. Fischer, M. Marzo, Theoretische Analyse abgebrannter LWR-Brennstoffe auf der Basis neuerer Kerndaten und Vergleich mit Experimenten
    and
    H.W. Wiese, Einfluß einiger methodischer Verbesserungen im Abbrand- u. Zerfallsprogramm KORIGEN auf charakteristische physikalische Eigenschaften entladenen LWR-Brennstoffs, both to be published in the proceedings of the Jahrestagung für Kerntechnik, Berlin, March 1980.

13. M. Marzo, H.W. Wiese, to be published.

14. O.W. Herrmann, Private Communication, April 1979.

15. H. Küsters, M. Marzo, Isotopic Correlation Techniques - A Review, Paper presented at the 22nd Meeting of the NEACRP, Paris, October 1979.

16. T. Fuketa, Nuclear Data for Safeguards, Proceedings of the International Conference on Neutron Physics and Nuclear Data for Reactors and other Applied Purposes, Harwell, UK, Sept. 1978.

17. H. Rief, Progress Report of JCR-Ispra submitted to the 21st NEACRP-Meeting, Tokyo, 1978
    (The information given in this paper is based on an evaluation of E. Schmidt, Ispra).

18. W. Scholtyssek et al., Physics Investigations of Sodium-Cooled Fast Reactors, SNEAK Assembly 9C, KfK-2361, 1977.

19. J.E. Sanders et al., Some Aspects of Fast Reactor Operation Studied in ZEBRA, International Symposium on Fast Reactor Physics, Aix-en-Provence, Sept. 1979, paper SM-244/38.

20. A. Giacommetti et al., Mesure de sections intégrales de capture par l'irradiation PROFIL dans PHENIX, International Symposium on Fast Reactor Physics, Aix-en-Provence, Sept. 1979, paper SM-244/22.

21. L.G. Lesage et al., Proceedings of the NEACRP/IAEA International Comparison Calculation of a Large Sodium-Cooled Fast Breeder Reactor at Argonne National Laboratory on February 7-9, 1978, to be published.

22. L.G. Lesage et al., Assessment of Evaluated Nuclear Data Files via Benchmark Calculations, Proceedings of the ANS Topical Meeting on Advances in Reactor Physics, Gatlinburg, April 1978.

23. C.H.M. Broeders, not yet published.

FISSION PRODUCT DECAY HEAT FOR THERMAL REACTORS

J. K. Dickens
Oak Ridge National Laboratory
Oak Ridge, Tennessee 37830, USA

In the past five years there have been new experimental programs to measure decay heat (i.e., time dependent beta- plus gamma-ray energy release rates from the decay of fission products) following thermal-neutron fission of ^{235}U, ^{239}Pu, and ^{241}Pu for times after fission between 1 and $\sim 10^5$ sec. Experimental results from the ORNL program stress the very short times following fission, particularly in the first few hundred sec. Complementing the experimental effort, computer codes have been developed for the computation of decay heat by summation of calculated individual energies released by each one of the fission products. By suitably combining the results of the summation calculations with the recent experimental results, a new Decay Heat Standard has been developed for application to safety analysis of operations of light water reactors. The new standard indicates somewhat smaller energy release rates than those being used at present, and the overall uncertainties assigned to the new standard are much smaller than those being used at present.

(Decay heat, fission beta energy, fission gamma energy, ^{235}U, ^{239}Pu, ^{241}Pu)

Impetus for Definitive Measurements of Decay Heat

Between 1971 and 1973 the U. S. Atomic Energy Commission conducted a series of hearings on the effectiveness of Emergency Core Cooling Systems (ECCS) pertaining to the safety of light water nuclear power reactors. The results of these hearings were regulations[1] specifying acceptance criteria for the performance of the design ECCS of existing and proposed light water power reactors. Included in these regulations are specifications for several technical aspects of the determinations of the effectiveness of a design ECCS, including (Ref. 1, Appendix K) the specification of the heat generation rates from radioactive decay of fission products ("Decay Heat").

The purpose of these regulations is to ensure that the ECCS of a nuclear power plant will be able to cool the reactor in the event of one of the most serious possible accidents considered credible by the Commission, namely the Loss of Coolant Accident (LOCA). The regulations contain detailed specifications of the necessary features of the models used to analyze the LOCA and establish the adequacy of the design ECCS. Conservative assumptions must be made in the analysis of a LOCA, which specify the worst (i.e. most damaging) circumstance for each of the separate phenomena that can occur during a LOCA. A representation of part of an analysis of a typical "worst-case" LOCA is given in Fig. 1, showing the expected temperature of the cladding due to the indicated heat source.[2,3]

In this figure, the major phases of the LOCA are schematically illustrated. An unexpected pipe rupture occurs in one of the cold legs at t = 0, and the blowdown phase is initiated, lasting about 10 sec. The cladding temperature rises, due partly to the decay heat, and partly to the equalizing of the temperature gradient within the fuel. The ECCS then begins to refill the reactor and after a minute or so the core is completely covered and the cladding temperature reaches a peak. Some time later, four to six minutes in the example in Fig. 1, the cladding temperature decreases to a stable, low value, and presumably the emergency has been brought under control.

Of course, the actual scenario will depend very much on the particular reactor design and character of the LOCA that occurs. Indeed, the example in Fig. 1 is very simplified, and the results of research efforts to understand the various phenomena that occur during the refill-reflood stages are not considered in this report. The main point here is

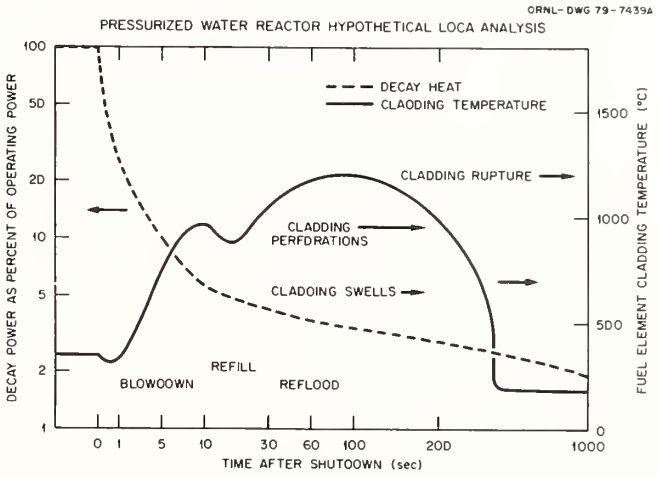

Fig. 1. Fuel element cladding temperature as a function of shutdown time for a typical "worst-case" LOCA. The time scale (abscissa) is intended only to be schematic; maximum cladding temperatures may occur earlier or later than shown depending upon assumptions made.

to suggest that the critical time period is of the order of minutes when the cladding temperature reaches the maximum allowed by the regulations, and that one should expect to bring the emergency under control within 15 min or so. Consequently, most of the research into the individual parts of a LOCA have concentrated on this time interval.

The existing regulations (Ref. 1, Appendix K) specify that decay-heat generations rates used in the design of the ECCS shall be assumed to be 1.2 times the value for infinite operating time, as given in the 1971 (revised in 1973) American Nuclear Draft Standard[4] "Decay Energy Release Rates Following Shutdown of Uranium Fueled Thermal Reactors." The factor 1.2 was selected to encompass uncertainties in the values of decay heat given in that standard. The decay-heat values and uncertainties given in that standard are shown in Fig. 2. The upper limit of the assigned uncertainty, popularly known as "A.N.S. + 20%," is used at present as the design decay-heat generation rate for a given time after shutdown.

One concern with this choice for the specification in the regulation was that the uncertainty bands shown

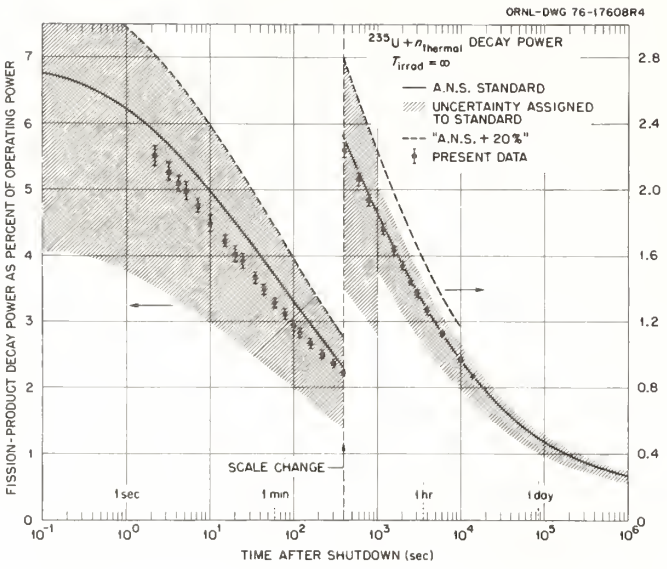

Fig. 2. The A.N.S. standard for fission-product decay heat due to thermal-neutron fission of ^{235}U (Ref. 4). The dashed curve labelled "A.N.S. + 20%" indicates the decay-heat generation rates specified in the regulations (Ref. 1) to be used in a LOCA analysis. The data points have been derived from the ORNL experimental data as described in the test.

in Fig. 2 were apparently chosen by inspection on the basis that they encompassed all of the then available data rather than a detailed evaluation and error analysis of these data. This criticism prompted two detailed evaluations of the available experimental data using more rigorous mathematical techniques. In the review by Scatena and Upham of General Electric Corporation,[5] all input data were equally weighted, and the "best fit" curve for ^{235}U was obtained by means of a polynomial regression method. These authors determined a set of recommended values for decay-heat generation that were close to the solid curve shown in Fig. 2, being larger for shutdown times less than 4 sec and for times around a day. The analysis yielded one-standard deviation (1σ) uncertainties of 2-3% in the important time interval (shutdown time < 2000 sec), and the authors recommended that using their decay heat generation rates plus twice their 1σ uncertainties should be preferred to the use of "A.N.S. + 20%." Had their suggestion been adopted the specified decay-heat generation rate would have been smaller than "A.N.S. + 20%" for shutdown times between 1 and 1000 sec, and therefore the normal operating power of the reactor would be greater than that allowed under existing regulations.

At about the same time as the release of the Scatena, Upham report, at ORNL Perry, Maienschein, and Vondy completed their analysis[6] of decay-heat data. These authors evaluated the existing data, assigned weighting factors, and obtained decay heat generation rates and uncertainties by normal statistical procedures. The decay-heat values they obtained were quite close to the values given in the A.N.S. standard; however, their 1σ deviation for most of the shutdown period of interest was $\sim$ 15%. Hence, using twice the 1σ uncertainties added to the nominal values for decay heat would result in values larger than "A.N.S. + 20%."

The major concern about the results of both of these studies was the fact that most of the experimental data being analyzed had not been obtained optimally for decay heat generation determination, and so had to be manipulated into common bases. In addition, all of the data and analyses were for thermal-neutron fission of ^{235}U; fissions from Pu in the fuel were to be treated using the same decay-heat generation rates given for ^{235}U. Clearly, these were questions that could be resolved experimentally, and so four experimental programs were initiated in the United States. All four of these programs[7-10] have completed their experimental goals, and the present status of the experimental programs is given in Table I.

The ORNL Decay-Heat Experiments

At the beginning of the present research program it was felt that the really important shutdown interval for decay-heat measurements was between 1 and 2000 sec for the reasons given in the discussion of Fig. 1. The upper time limit, 2000 sec, was deemed reasonable for a second reason. By this time after shutdown the decay heat is dominated by contributions from the longer-lived fission products which have been extensively studied and for which nuclear decay properties are presumably well known. Contributions to the decay heat for the first few minutes, however, come from hundreds of short-lived fission products, which are much more difficult to study radiochemically, and so their nuclear decay properties are not as well known. Therefore, we proposed[11] an experiment designed to emphasize the study of the contributions to the decay heat by the short-lived fission products.

The second aspect of the ORNL experimental plan that was different from the other experiments was the decision to measure differential yield spectra, gamma rays and beta rays separately, rather than an integrated total energy-release rate. The reason for this choice was the anticipated need to challenge the emerging new ability to calculate decay heat by the summation method. In the United States at least five new computer programs[12] were in various stages of development at the time of the beginning of this program. A data base is required for these calculations which includes rates-of-production and energies and branching ratios of the decay products for all fission products created during the fission process. Compilations of such data exist;[13] however, especially for short-lived nuclides, the data are incomplete and the compilations contain substantial contributions from theoretical estimations. Even with the modest energy resolution of the NaI spectrometer that was used for the ORNL gamma ray energy-release measurements it is anticipated that the gamma-ray spectral data will provide substantial assistance to evaluators of nuclear data files in improving the data bases.

As indicated in Table I, the ORNL measurements were made with the shortest irradiation times of any of the measurements. These short irradiation times enhance the contributions to the decay heat by the short-lived nuclides by reducing build up of the longer-lived nuclides during the irradiation. In addition, the short irradiations effectively eliminate uncertainties associated with sample depletion,

Table I. Decay Heat Measurements in the United States 1974-1979.

Laboratory	Type of Experiment	Fuel Elements Studied	Irradiation Times	Reference
Los Alamos	Cryogenic Calorimeter	^{235}U, ^{239}Pu, ^{233}U	20000 sec	7
Intelcom Rad Tech	Nuclear"Calorimeter"	^{235}U, ^{239}Pu	1000 sec, 20000 sec, 24 hr	8
University of California	Standard Calorimeter	^{235}U	1 hr, 4 hr, 22.35 hr	9
ORNL	Separate Beta- and Gamma-Ray Spectroscopy	^{235}U, ^{239}Pu, ^{241}Pu	1, 10, 100 sec	10

neutron capture by fission products, and the sensitivity to variations in fission rate that might occur over a long irradiation period.

In the course of developing a new standard to replace that shown in Fig. 2, it was necessary to obtain the decay-heat function f(t) defined as the rate of energy release t seconds following an instantaneous pulse of fissions,[6,14] having units of (MeV/sec)/fission. This function is easy to estimate from the ORNL data. The differential energy spectra are obtained from the experimental differential yield spectra by multiplying N(E) by E, where E is either E_β or E_γ. Then integrating these energy spectra gives the total beta-ray or gamma-ray energy release data to provide values of the total integral energy release for experimental parameters of T_{irrad}, T_{wait}, and T_{count}. The pulse function, f(t), can be determined from the total integral data if the total integral energy release is divided by the counting time, and the time t is taken to be

$$t = T_{wait} + 0.5\ (T_{irrad} + T_{count})\ . \qquad (1)$$

The difference between this estimate and an "exact" value is very small[10] if T_{wait} is > $(T_{irrad} + T_{count})$.

The pulse function, f(t), may be used to obtain a function $F(T_{wait}, T_{irrad})$ defining the energy release per fission T_{wait} seconds following an operating period of T_{irrad} sec, as follows:

$$F(T_{wait}, T_{irrad}) = \int_{T_{wait}}^{T_{wait} + T_{irrad}} f(t)\ dt\ . \qquad (2)$$

Thus, once the function f(t) has been determined, one may compute the decay-heat curves for any T_{irrad}, and in particular for $T_{irrad} = \infty$. (In actual practice, 10^{13} sec is taken to be an "infinite" period of operation.)

As mentioned above, the original experimental program anticipated that an upper limit of T_{wait} of 2000 sec would be sufficiently long so that the experimental data would mesh with calculations using compilations of radiochemical data. Preliminary gamma-ray measurements provided a surprise; the measured data agreed with calculations for T_{wait} between 50 and 800 sec, but diverged from calculations for T_{wait} between 800 and 10000 sec. So, the upper time limit was extended to 14000 sec (about 4 hr). This extension of the total time of experimental measurements has an important additional advantage, in that the ORNL data can now be compared with the standard shown in Fig. 2 with very little adjustment. The normalization, which is additive, is obtained from a summation calculation for T_{wait} = 12000 sec, which as can be observed in Fig. 2, is ≈ 0.85% of total operating power. At 2.2 sec following shutdown of $T_{irrad} = \infty$, the "experimental" datum shown as 5.5% of the total operating power includes 0.85% from calculation and 4.65% experimental. In this manner one may determine that the experimental contributions to the data points shown in Fig. 2 are 85% at 2.2 sec, 51% at 1200 sec, and 10% at 10^4 sec.

It is more instructive to compare the ORNL results with summation calculations in the pulse representation. This function, f(t), decreases with t roughly as t^{-1}. Hence for presentation purposes it has become common practice to illustrate the "pulse" function as t x f(t). This representation has the advantage of expressing the t x f(t) axis on linear graphics, but the disadvantage of magnifying an error in t. Acknowledging this defect, the beta-ray data for ^{235}U are presented in Fig. 3 in this format for comparison with summation calculation[15] and with other similar experimental data sets.[16] The present data agree very well with the earlier data for t between 15 and 500 sec, but not so well with the calculation in this time interval. For longer t the agreement with calculation is better, although there is a divergence among the experimental data sets.

The ORNL gamma-ray data for ^{235}U are presented in similar format in Fig. 4. The present data are smaller than the other experimental data,[17] although within assigned uncertainties of previous ORNL measurements. The comparison of calculation[15] with the present data is good for t between 20 and 1000 sec and for t > 5000 sec. There is a disagreement for t < 10 sec which may be indicative of incomplete information in the basic data files. The disagreement for t between 1000 sec and 5000 sec is unexpected, and suggests that further study is needed in this time interval.

As indicated in Table 1, data were obtained for ^{239}Pu in the same format as for ^{235}U. The "pulse" results, t x f(t), are compared with previous experimental data[18] and with calculations[19] for beta rays in Fig. 5 and with summation calculations[19] for gamma rays in Fig. 6. One may observe that the character of the comparison for beta-ray decay heat in Fig. 5 for ^{239}Pu is similar to that in Fig. 3 for ^{235}U. For the gamma-ray data (compare Figs. 4 and 6)

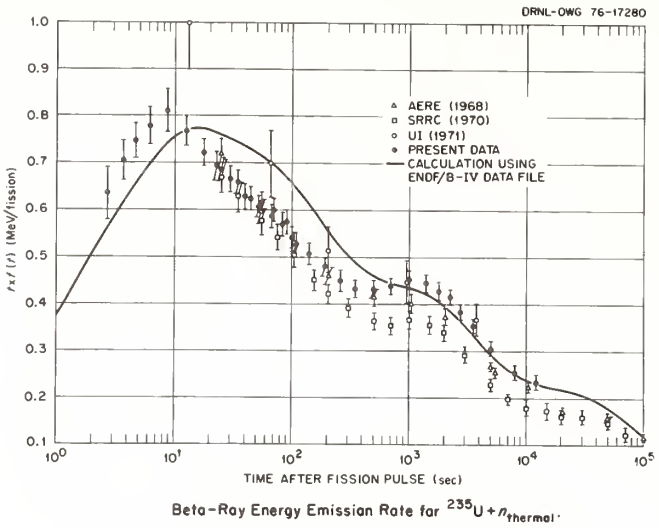

Fig. 3. Beta energy emission rate following an instantaneous pulse of thermal-neutron fissions of ^{235}U. The abscissa, t, is the time after a pulse of fissions. The ordinate is a quantity derived by multiplying the pulse function, f(t), by t as described in the text. The calculation was carried out by R. Schenter (see Ref. 15). The solid circles represent the ORNL data. The open triangles are data of McNair, et al., the open squares are data of MacMahon, et al., and the open circles are data of Tsoulfanidis, et al. (see Ref. 16).

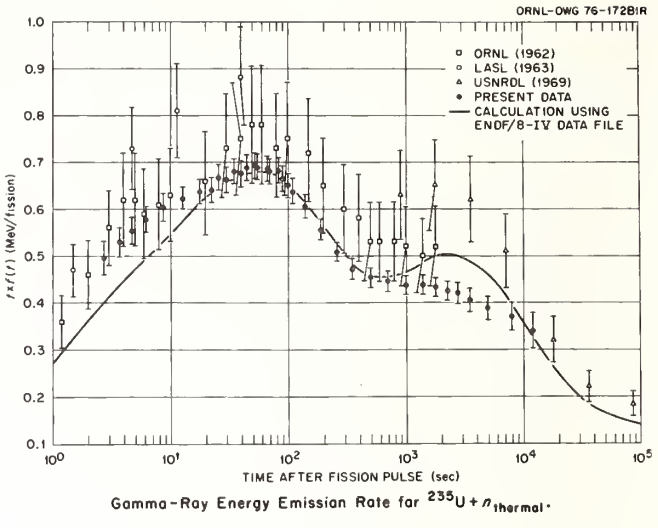

Fig. 4. Photon energy emission rate for thermal-neutron fission of ^{235}U. The solid circles represent the present ORNL data. The calculation was carried out by R. Schenter (see Ref. 15). The open squares are the data of Peelle, et al., the open circles are the data of Fisher and Engle, and the open triangles are the data of Bunney and Sam (see Ref. 17).

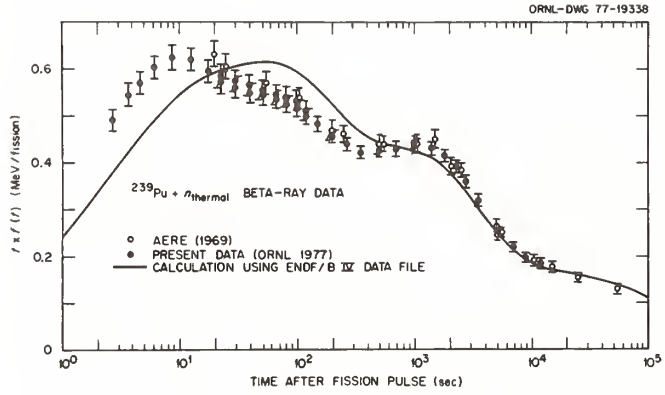

Fig. 5. Beta energy emission rate following an instantaneous pulse of thermal-neutron fissions of ^{239}Pu. The axes are the same as Fig. 3. The solid circles represent the present data, and the open circles represent the data of McNair and Keith (Ref. 18). The calculation is from Ref. 19.

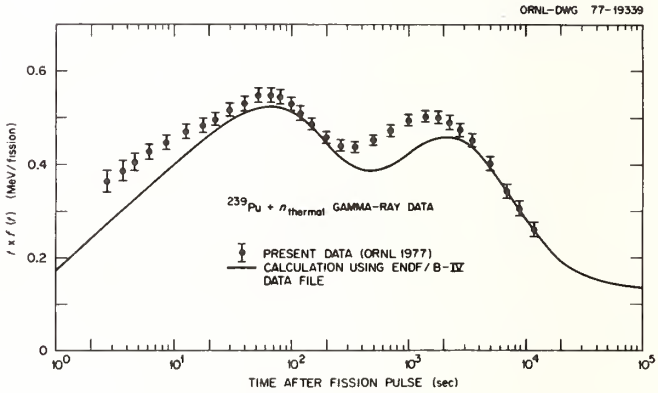

Fig. 6. Photon energy emission rate following an instantaneous pulse of thermal-neutron fissions of ^{239}Pu. The solid circle represent the present data. The calculation is from Ref. 19.

there is a definite difference; the experimental data for ^{239}Pu are $\geq$ the calculated data for all times after shutdown.

Data for ^{241}Pu were also obtained, and the ORNL experimental program is the only one to do so. The importance of ^{241}Pu may be estimated from calculations[20] indicating that for an average burnup of 32,900 Mwd/metric ton in a water reactor, the fissile Pu in the discharge is 0.74 times as great as the ^{235}U discharge, and the ^{241}Pu content is $\sim$ 1/6 of the fissile Pu. Thus, because of the larger fission cross sections, the fission rate at discharge due to Pu will be approximately equal to that due to ^{235}U, and $\sim$ 25% of the Pu fission rate will be due to fission of ^{241}Pu.

The major difficulty encountered for the ^{241}Pu experiment was in the fabrication of samples. The sample material tended to "creep" out of the sample containers. Because of the extreme biological hazard of this material, and because of the difficulty in detecting ^{241}Pu contamination, each sample after fabrication was checked twice using a special

low-energy beta-ray detection system. More than 50% of the samples had to be rejected. Because of limitations of material, fewer ^{241}Pu samples were run than were run for either ^{235}U or ^{239}Pu. Consequently, there was a loss in precision for the final data for ^{241}Pu which was not completely compensated for by improved efficiencies in data taking that had been learned from experience. The precision obtained, however, is commensurate with that needed for decay-heat application.

The data obtained for beta-ray energy-release rates are shown in Fig. 7 compared with results for ^{235}U and ^{239}Pu shown in Figs. 3 and 5. The beta-ray data are definitely larger than the beta-ray data for ^{235}U for the time interval of interest in a LOCA, becoming smaller for t > 2000 sec. For the gamma-ray data, shown in Fig. 8, the ^{241}Pu data have the same energy-release rates for t < 400 sec as those for ^{235}U. Thus, the pulse function, f(t), for ^{241}Pu is larger than that for ^{235}U in the important time period t < 500 sec.

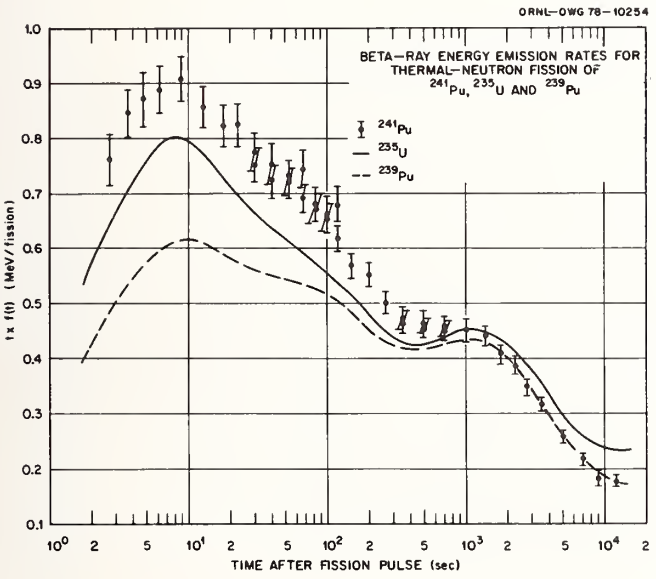

Fig. 7. Beta energy emission rate following an instantaneous pulse of thermal-neutron fissions of ^{241}Pu compared with data for ^{235}U (see Fig. 3) and for ^{239}Pu (see Fig. 5).

The "pulse" data obtained for ^{239}Pu and ^{241}Pu were integrated using, in effect, Eq. (2), to obtain the "infinite" irradiation representation, similar to that shown for the ^{235}U data in Fig. 2. Then the ratios of the $^{239}Pu/^{235}U$ data and $^{241}Pu/^{235}U$ data were obtained, and these are shown in Fig. 9. The large and consistent error bars shown in this figure indicate that there is a high degree of correlation among the data sets, since the error bars were obtained assuming independence of each of the sets of data for the three nuclides studied. It is likely, therefore, that the true uncertainties associated with the *ratios* plotted in Fig. 9 are much less than shown in this figure. However, until a detailed error analysis is completed indicating which uncertainties among the three isotopes studied are correlated, the correct 1σ uncertainties cannot be obtained; one may assume that the error bars shown are very conservative estimates of the uncertainties associated with the plotted ratios.

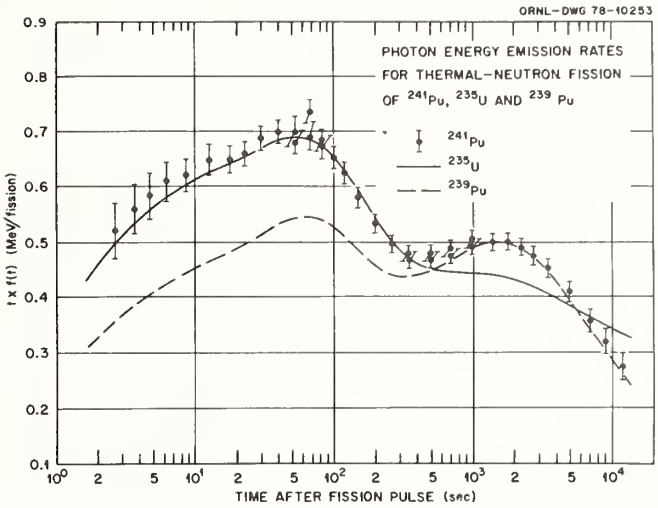

Fig. 8. Photon energy emmision rate following an instantaneous pulse of thermal-neutron fissions of ^{241}Pu compared with data for ^{235}U (see Fig. 4) and for ^{239}Pu (see Fig. 6).

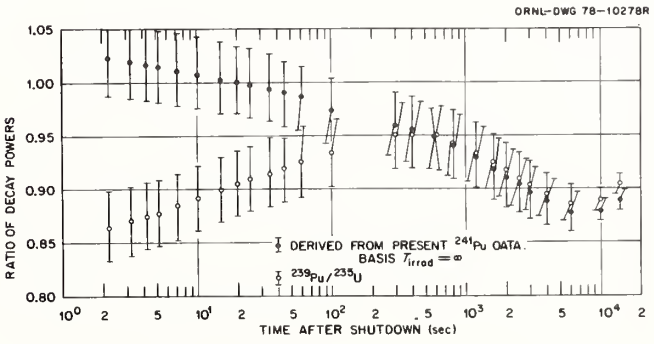

Fig. 9. Ratio of energy-released rates due to thermal-neutron fission of ^{241}Pu to that due to ^{235}U (solid points) and of ^{239}Pu to that due to ^{235}U (open points) for an infinite" irradiation.

Concerning the New A.N.S. Decay-Heat Standard

Concurrent with the new experimental programs and new calculational abilities, a new decay-heat standard[21] was initiated to replace the draft standard shown in Fig. 2. Data from the four programs given in Table 1 were used, as were data obtained from the French program in decay heat.[22] Data for ^{235}U from the four American experiments is shown in Fig. 10; all of the data, including one set from summation calculations, and the draft standard[4] data set, are shown on an infinite irradiation basis. Three of the experimental data sets and that from the summation calculation agree quite well. The University of California (UCB) experiment[9] reports data somewhat larger than data from the other experiments for T_{wait} < 400 sec. The reported uncertainties associated with the UCB data are quite large in this time region, and reflect the difficulties encountered in the experiment.

The new standard contains tabulated decay-heat energy-release rates for three nuclides, ^{235}U and

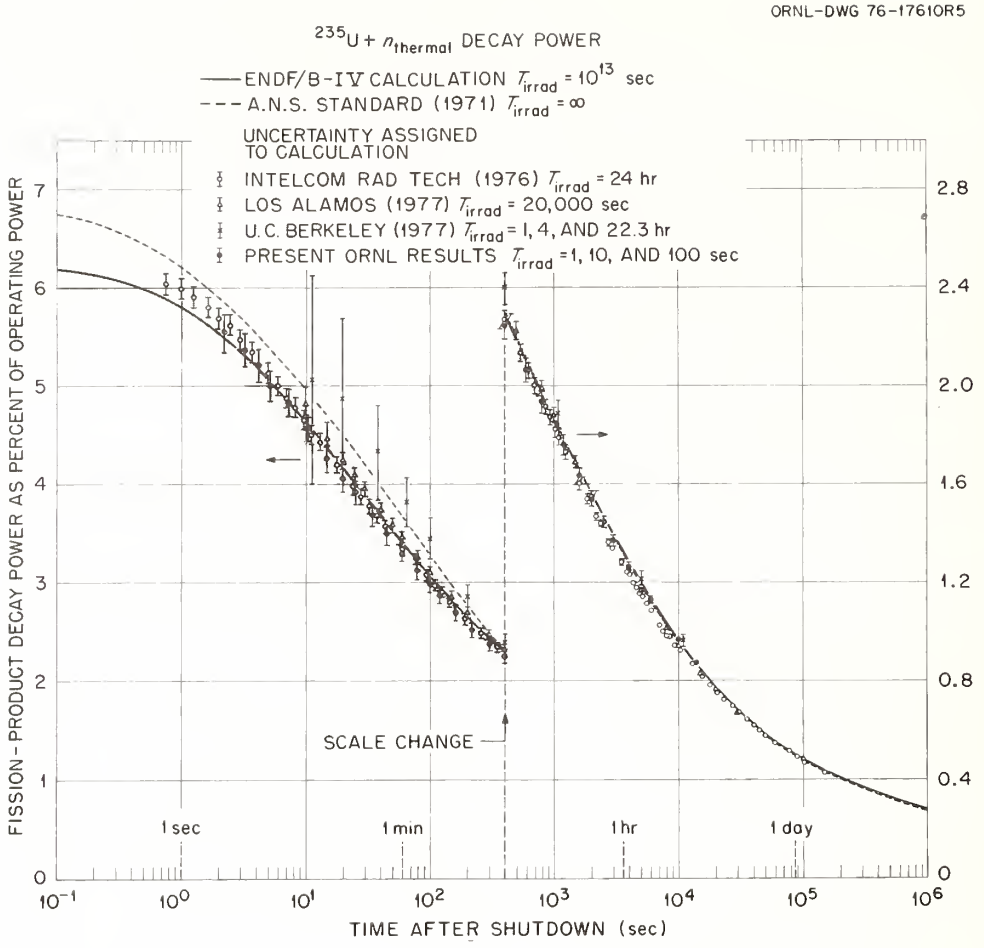

Fig. 10. Fission-product energy release following a long period of thermal-neutron fissioning of ^{235}U. The summation calculation was obtained using ORIGEN (Ref. 12) and the ENDF/B-IV data file (Ref. 13). The 1973 A.N.S. standard was obtained from Ref. 4. The data sets are from Intelcom Rad Tech (Ref. 8), Los Alamos (Ref. 7), University of California (Ref. 9), and the present results (Ref. 10); all data sets were adjusted to agree with summation calculations for data obtained at the longest time after shutdown for the particular experiment.

^{239}Pu thermal fission and ^{238}U fast fission, in both the "pulse" respresentation f(t) and the "infinite" representation $F(T_{wait}, 10^{13}$ sec). For ease in use in computer codes, the three f(t) sets have been fitted using the functional representation,

$$f(t) = \sum_{i=1}^{23} \alpha_i \, e^{-\lambda_i t} , \qquad (3)$$

with tabular values of the parameters α_i and λ_i for each of the three nuclides.

The tabular values for ^{235}U and ^{239}Pu were obtained from least-squares fitting [14,23] of the experimental data sets combined with a data set obtained from summation calculations. The experimental data were weighted according to the uncertainties assigned by the experimentalists. The weighting of the summation calculation was somewhat arbitrary, since analysis of the uncertainties associated with the separate components entering into the summation calculations yielded overall uncertainties for the calculated decay heat[24] which would have overwhelmed the experimentally obtained data with the weighting method used. For $T_{wait} > 10^5$ sec the standard relies solely on summation calculation results. For fast fission of ^{238}U the standard is determined only from summation calculations.

The standard is likely the most precise for thermal fission of ^{235}U, since there are more experimental data, and since the separate components of summation calculations (e.g. fission yields, energy releases, half lives, etc., of the fission products) are better known for ^{235}U than for the other nuclides. In Fig. 11 the results for ^{235}U in the new standard are compared with the 1971 draft standard[4] in the same format as shown in Fig. 2. The uncertainties shown for the new standard are two standard deviations, and are obtained rigorously from the least-squares analyses. That is, the uncertainties assigned to the new standard are obtained from a mathematical analysis and not a best educated guess.

For ^{239}Pu there are fewer data, and in addition there is an unexplained (an unresolved) overall normalization discrepancy between the ORNL and LASL data of $\sim$ 10%, greater than the sum of the individual experimental uncertainties of the two experiments by almost a factor of two, the LASL data being larger

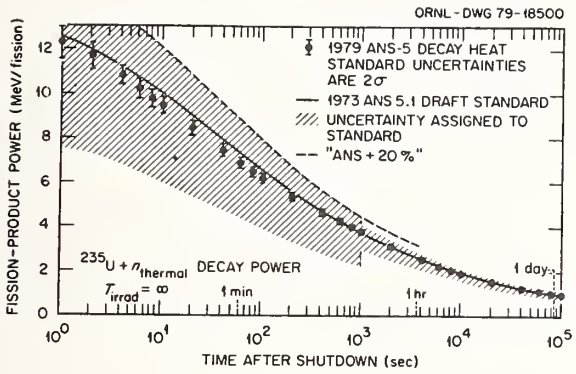

Fig. 11. Comparison of the 1973 A.N.S. standard for fission product decay heat due to thermal-neutron fission of ^{235}U given in Ref. 4 with the 1978 A.N.S. standard given in Ref. 21. Note that the uncertainties associated with the new A.N.S. standard are <u>two</u> standard deviations.

than the ORNL data. Absolute normalization of the IRT ^{239}Pu data were not available at the time of the analysis for the ^{239}Pu decay-heat curve; the most recent report indicates that the IRT data lie between the ORNL and LASL data. The major consequence of the ORNL-LASL disagreement was that the least-squares analysis gave larger 1σ uncertainties (4-5%) assigned to the ^{239}Pu decay-heat data set in the standard. However, since the decay heat from ^{239}Pu is rather less than that from ^{235}U, as indicated in Fig. 9, even with the increased uncertainties given in the standard, the overall contribution from ^{239}Pu is less than from ^{235}U, and so the old standard's prescription of using the one set of energy-release data (for ^{235}U) for all fissioning nuclides in the fuel has resulted in additional conservatism in the determination of the consequences of a LOCA.

Although decay heat from fast fission of ^{238}U was determined solely from summation calculations, it was important to include this source explicitly, because for T_{wait} < 100 sec, fast fission of ^{238}U results in more decay-heat energy release than does thermal fission of ^{235}U. In addition, calculations[25] indicate that 7-9% of the fissions in a light water reactor are due to fast-neutron fission of ^{238}U.

Further details of the experimental programs listed in Table 1, the development and complete discussion of the new standard, and several examples of its use are given in a recent review paper.[26]

What Remains to be Done

For light water reactor technology there is a definite need for experimental measurements of decay heat for fast-neutron fission of ^{238}U. As mentioned above, calculations suggest that 7-9% of the fissions in a light water reactor are from fast-neutron fission of ^{238}U, and the actual value may be larger. In addition, as shown in Figs. 3-6 there is the tendency of the summation calculations to underpredict the decay-heat pulse function, f(t), for t < 100 sec. This concern accounts for the rather large uncertainties assigned to the decay heat from fast-neutron fission of ^{238}U in the standard. For alternate fuel cycles, there is a need to experimentally determine decay heat from fast fission of ^{239}Pu and ^{241}Pu and possibly of ^{245}Cm, and further experimental work on thermal fission of ^{233}U will be valuable.

For summation calculations much experimental research needs to be done on the fission yields of the several Pu nuclides and perhaps ^{245}Cm, and much needs to be done on the decay modes and half lives of the many fission products that are created. Even many of the long-lived nuclides need to be studied, not only to provide better accuracy but in some instances to correct information thought to be valid.[27] Nuclides having short half lives need to be studied, and results of all of these studies need to be entered more rapidly into the evaluated files. In this regard, a communication from G. Rudstam[28] reports improved calculational results for beta-ray energy release in the period t < 15 sec when including specifically beta-ray experimental data for short-lived fission products recently obtained at Studsvik.

For the new A.N.S. standard, the major improvement that can be easily put into effect would be to include explicitly the decay heat from thermal fission of ^{241}Pu. Secondly, the analysis leading to the standard for thermal fission of ^{235}U might be redone in light of the final uncertainty analysis for the ORNL data. As mentioned above, in the least-squares analysis[14] the separate data sets were weighted according to the uncertainties assigned to the data by the measurers. At that time the uncertainties assigned to the ORNL data[10] had been determined most conservatively by our group assuming full correlations among the various contributions to the total uncertainties assigned to the data. The ORNL uncertainties were larger than uncertainties from either the LASL or IRT experiments when the new standard was developed, and so the latter dominated the overall normalization of the new standard for ^{235}U. Since then, a complete uncertainty analysis has been done for the ORNL data, determining all of the correlations in the various parts of this experiment, and providing a complete covariance matrix of uncertainties.[29] The consequence of the use of the more accurate set of uncertainties for the ORNL data would be that the ORNL data would have somewhat more influence in the absolute normalization of the least-squares result, and so the values of the decay heat from thermal fission of ^{235}U would be somewhat smaller in magnitude than given in the present standard. How much smaller is difficult to estimate, possibly several percent, but likely not as much as 5%.

As might be ascertained from the above discussion, I am of the opinion that the new (1978) standard for decay heat from thermal-neutron fission of ^{235}U is still somewhat too large, even if smaller than has been used in the past (see Fig. 11). Applying the new standard to the analysis of a LOCA to establish the adequacy of a design ECCS should yield a conservative result, and so therefore the new standard can be used for this purpose with confidence. (In this regard, had the ORNL data been 5-7% <u>larger</u> than the standard, rather than the other way around, I would urge much more caution in the intended use of the standard.)

According to a recent evaluation,[30] the total amount of fission product beta- plus gamma-ray energy available ∿ 1 msec after thermal fission of ^{235}U is

$\sim$ 12.7 MeV/fission. From the "experimental" results shown in Fig. 2, 10 sec following shutdown of an "infinite" operation, about 4.5% of the total operating power, or about 9.0 MeV/fission, is still available. That is, about 29% of the energy available following shutdown of an "infinite" operation is released during the first 10 sec of the shutdown. Clearly, this substantial amount of energy must be due to the decay of short-lived fission products for which there is little hard experimental information about their nuclear properties. If one assumed that this amount of energy were released by a single radionuclide, one would compute the half life of this nuclide to be about 20 sec. About half of this pseudo radionuclide would be created during *the last* 20 sec of an "infinite" operation! It must be evident that a (possibly unnoticed) power excursion in the last minute of operation can have an important effect on the consequences of a LOCA. It is also apparent that the rather large contribution to the total available decay heat at shutdown due to the last few hundred sec of operation has not been fully appreciated; nearly all of the recent experimental research has been for T_{irrad} very long compared to the shutdown times of interest in a LOCA analysis.

The ORNL experimental program has provided data suited for just this time interval, namely the decay heat during the first hundred sec after shutdown due to fission products created during the last few hundred sec prior to shutdown. The decay heat in this time interval is dominated by the short-lived fission products lacking well-measured nuclear properties, i.e. those nuclides for which "estimates" must be made of the needed nuclear properties to be included in the data files. The present experiment has provided completely separate beta- and gamma-ray spectral distributions which should provide even more information for improving the data bases used in the calculations. In fact, the optimal result of study of our experimental results will be a calculational system capable of computing the decay heat correctly and reliably not only for benchmark experiments such as the recent measurements, but also for conditions found in operating reactors.

Acknowledgment

I express my apprecation to my colleagues R. W. Peelle, T. A. Love, J. W. McConnell, J. F. Emery, K. J. Northcutt, H. Weaver, and R. M. Freestone for their able participation in performing the experiments to obtain the data; to members of the A.N.S. 5.1 Working Group, especially T. R. England, F. Schmittroth, R. E. Schenter, R. N. Oehlberg, J. Yarnell, and V. E. Schrock for their suggestions, improvements, and contributions to the ORNL program; to A. Tobias for timely correspondence, in particular his recent manuscript,[31] "Decay Heat," containing a complete history of efforts in this field from 1942 to the present which was of material assistance in the preparation of the present report; to G. Rudstam for communication of his unpublished research; and to F. C. Maienschein for suggesting the need for the measurements and especially for his continued encouragement and support.

This research was sponsored by the U. S. Nuclear Regulatory Commission, Office of Nuclear Regulatory Research, under Interagency Agreement DOE 40-551-75 and 40-552-75. The Oak Ridge National Laboratory is operated by Union Carbide Corporation for the Department of Energy under contract W-7405-eng-26.

References

1. The Code of Federal Regulations, 10 CFR Part 50 (39 FR 1003, January 4, 1974).

2. F. C. Finlayson, "Assessment of Emergency Core Cooling System Effectiveness for Light Water Nuclear Power Reactors," EQL Report No. 9, California Institute of Technology (May 1975).

3. G. Yadigaroglu, K. P. Yu, L. A. Arrieta, and R. Greif, "Heat Transfer During the Reflooding Phase of the LOCA - State of the Art," EPRI-248-1 Topical Report, Prepared by the University of California (Berkeley) for the Electric Power Research Institute (September 1975).

4. "Decay Energy Release Rates Following Shutdown of Uranium-Fueled Thermal Reactors," Proposed ANS Standard, Approved by Subcommittee ANS-5, October 1971, Revised October 1973 (now superceded by Ref. 21).

5. G. J. Scatena and G. L. Upham, "Power Generation in a BWR Following Normal Shutdown of Loss-of-Coolant Accident Conditions," NEDO-10625, General Electric Company (April 1973).

6. A. M. Perry, F. C. Maienschein, and D. R. Vondy, "Fission Product Afterheat - A Review of Experiments Pertinant to the Thermal-Neutron Fission of ^{235}U," ORNL-TM-4197, Oak Ridge National Laboratory (October 1973).

7. J. L. Yarnell and P. J. Bendt, "Calorimetric Fission Product Decay Heat Measurements for ^{239}Pu, ^{233}U, and ^{235}U, NUREG/CR-0349, LA-7452-MS, Los Alamos Scientific Laboratory (September 1978).

8. S. J. Friesenhahn, N. A. Lurie, V. C. Rogers, and N. Vagelatos, "^{235}U Fission Product Decay Heat from 1 to 10^5 Seconds," EPRI NP-180, Prepared by IRT Corporation for Electric Power Research Institute (February 1976); S. J. Friesenhahn and N. A. Lurie, "Measurements of ^{239}Pu and ^{235}U Fission Product Decay Power from 1 to 10^5 Seconds," IRT 0034-005 (Draft) IRT Corporation (undated), submitted to the Electric Power Research Institute for publication.

9. V. E. Schrock, L. M. Grossman, S. G. Prussin, K. C. Sockalingam, F. M. Nuh, C-K. Fan, N. Z. Cho, and S. J. Oh, "A Calorimetric Measurement of Decay Heat from ^{235}U Fission Products from 10 to 10^5 Seconds," EPRI NP-616, Prepared by the University of California (Berkeley) for the Electric Power Research Institute (February 1978).

10. J. K. Dickens, J. F. Emery, T. A. Love, J. W. McConnell, K. J. Northcutt, R. W. Peelle, and H. Weaver, "Fission-Product Energy Release for Times Following Thermal-Neutron Fission of ^{235}U Betwen 2 and 14000 Seconds," ORNL/NUREG-14, Oak Ridge National Laboratory (October 1977);_____, "Fission-Product Energy Release for Times Following Thermal-Neutron Fission of ^{239}Pu Between 2 and 14000 Seconds," ORNL/NUREG-34, Oak Ridge National Laboratory (April 1978);_____, "Fission-Product Energy Release for Times Following Thermal-Neutron Fission of ^{241}Pu Between 2 and 14000 Seconds," NUREG/CR-0171, ORNL/NUREG-47, Oak Ridge National Laboratory (August 1978).

11. J. K. Dickens, R. W. Peelle, and F. C. Maienschein, "Experiment for Accurate Measurements of Fission Product Energy Release for Short Times After Thermal-Neutron Fission of ^{235}U and ^{239}Pu," ORNL-TM-4674, Oak Ridge National Laboratory (May 1975).

12. M. J. Bell, "ORIGEN - The ORNL Isotope Generation and Depletion Code," ORNL-4628, Oak Ridge National Laboratory (May 1973); D. R. Marr, "A User's Manual for Computer Code RIBD-II, A Fission Product Inventory Code," HEDL-TME-75-26, Hanford Engineering Development Laboratory (January 1975); T. R. England, R. Wilczynski, and N. L. Whittemore, "CINDER-7: An Interim Report for Users," LA-5885-MS, Los Alamos Scientific Laboratory (April 1975); T. R. England, W. B. Wilson, and M. G. Stamatelatos, "Fission Product Data for Thermal Reactors - Part 2: Users Manual for EPRI-CINDER Code and Data," LA-6746-MS, Los Alamos Scientific Laboratory (1976); T. J. Trapp, S. M. Baker, A. Prichard, and B. Spinrad, "ROPEY: A Computer Code to Evaluate Reactor Fission Product Shutdown Heat and Its Uncertainties," OSU-NE-7701, Oregon State University (August 1977).

13. P. F. Rose and T. W. Burrows, "ENDF/B Fission Product Decay Data," BNL-NCS-50545 Vol. I and II, Brookhaven National Laboratory (August 1976); T. R. England and R. E. Schenter, "ENDF/B-IV Fission-Product Files; Summary of Major Nuclide Data," LA-6116-MS, Los Alamos Scientific Laboratory (October 1975); A. Tobias, "An Ordered Table of Gamma Radiation Emitted by Fission Products," RD/B/M-2356, Central Electric Generating Board (June 1972); _____, "Decay Heat Testing of the UK-ENDF/B-IV Format Fission Product Decay Data File," RD/B/N4179, Central Electric Generating Board (December 1977); W. B. Ewbank, "Evaluated Data Collections from ENDSF," Paper FB4, this conference.

14. F. Schmittroth and R. E. Schenter, Nucl. Sci. Eng. 69, 389 (1979).

15. R. E. Schenter (private communication). The calculation was carried out with the RIBD-II code (see Ref. 12) using the ENDF/B-IV data base (See Ref. 13).

16. N. Tsoulfanidis, B. W. Wehring, and M. E. Wyman, Nucl. Sci. Eng. 43, 42 (1971); A. McNair, F. J. Bannister, R. C. G. Keith, and H. W. Wilson, J. Nucl. Energy 23, 73 (1969); T. D. MacMahon, R. Wellum, and H. W. Wilson, J. Nucl. Energy 24, 493 (1970).

17. P. C. Fisher and L. B. Engle, Phys. Rev. 134, B796 (1964); L. R. Bunney and D. Sam, Nucl. Sci. Eng. 39, 81 (1970); R. W. Peelle, F. C. Maienschein, W. Zobel, and T. A. Love, "The Spectra of Gamma Rays Associated with Thermal-Neutron Fission of ^{235}U," in Pile Neutron Research in Physics, IAEA, (Vienna, 1962). See also Ref. 6 for tabulated integral values of these data.

18. A. McNair and R. L. G. Keith, J. Nucl. Energy 23, 697 (1969).

19. T. R. England, M. G. Stamatelatos, and R. J. LaBauve, "Burst Functions, Tabular Data, and Plots for Use in Generating the ANS 5.1 Decay Heat Standard," LA-UR 77-627, Los Alamos Scientific Laboratory (March 1977).

20. J. Blomeke, C. W. Kee, and J. P. Nichols, "Projection of Radioactive Wastes to be Generated by the U. S. Nuclear Power Industry," ORNL-TM-3965, Oak Ridge National Laboratory (February 1974).

21. "Decay Heat Power in Light Water Reactors," Proposed ANS Standard; Approved by Subcommittee ANS-5, June 1978; Approved by ANS Nuclear Power Plant Standards Committee, October 1978; pending approval by American National Standards Institute.

22. M. Lott, G. Lhiaubet, F. Dufreche, and R. de Tourreil, J. Nucl. Energy 27, 597 (1973); C. Fiche, F. Dufreche, and A. M. Monnier, "Measures Calorimetriques de la Puissance Residuelle Totale Emise par les Produits de Fission Thermique de ^{233}U et ^{239}Pu, CEA Rapport SEN/022, Centre d'Etudes Nucleaires de Cadarache (June 1976).

23. T. R. England, R. E. Schenter, and F. Schmittroth, "Integral Decay-Heat Measurements and Comparisons to ENDF/B-IV and V," in Nuclear Data Problems for Thermal Reactor Applications, Symposium Proceedings, June 1979, eds. P. F. Rose, S. Pearlstein, and O. Ozer, EPRI NP-1098 (BNL-NCS-25047, ENDF-270), Electric Power Research Institute (June 1979).

24. F. Schmittroth, Nucl. Sci. Eng. 59, 117 (1976).

25. C. Devillers, "Importance of Fission Product Nuclear Data for Engineering Design and Operation of Reactors," Review Paper No. 4 in Fission Product Nuclear Data, Proc. of a Panel on Fission Product Nuclear Data, Bologna 26-30 November 1973, IAEA-169 (Vienna, 1974) Vol. I, p, 83, Table X; see also B. I. Spinrad, "Evaluation of Fission Product After-Heat, Quarterly Report April 1-June 30, 1978," NUREG/CR-0399 (OSU-NE-7810) Orgeon State University (December 1978).

26. V. E. Schrock, Prog. Nucl. Energy 3, 125 (1979).

27. K. Debertin, U. Schötzig, and K. F. Walz, "Gamma-Ray Emission Probabilities and Half Lives of Selected Fission Products," in Second IAEA Advisory Group Meeting on Fission Product Nuclear Data, Petten, Netherlands, 5-9 September 1977, INDC (NDS)-87/GO+Sp (May 1978) p. 261; J. K. Dickens, Radiochem. Radioanal. Letters 39, 107 (1979).

28. G. Rudstam (private communication, 1978).

29. J. K. Dickens, T. A. Love, J. W. McConnell, and R. W. Peelle, "Fission-Product Energy Release for Times Following Thermal-Neutron Fission of ^{235}U Between 2 and 14000 Seconds," Nucl. Sci. Eng. (submitted).

30. R. Sher, S. Fiarman, and C. Beck, "Fission Energy Release for 16 Fissioning Nuclides," Stanford University (October 1976), Appendix A to the Minutes of the CSWEG Normalization and Standard Subcommittee, October 27, 1976, Brookhaven National Laboratory, B. R. Leonard, Jr., Chmn. quoted in Ref. 26.

31. A. Tobias, "Decay Heat," RD/B/N4611, Central Electricity Generating Board (July, 1979), to be published in Prog. Nucl. Energy.

NEUTRON TOTAL CROSS SECTIONS OF HYDROGEN, CARBON, OXYGEN AND IRON FROM 500 keV TO 60 MeV

D. C. Larson, J. A. Harvey, and N. W. Hill
Oak Ridge National Laboratory
Oak Ridge, Tennessee 37830, USA

The neutron total cross sections for hydrogen, carbon, oxygen, and iron have been measured from 0.5 to 60 MeV using the Oak Ridge Electron Linear Accelerator (ORELA) as the source of neutrons. The flight path was 80 m, and the repetition rate was 1000 sec^{-1}, with a burst width of 10 ns. The resulting cross sections are graphically compared with ENDF/B-V evaluations up to 20 MeV, and with selected data from 20-60 MeV.

[Neutrons, total cross sections, hydrogen, carbon, oxygen, iron, 0.5-60 MeV]

Introduction

One of the outstanding problems in fusion reactor development is radiation damage of the first wall induced by 14-MeV neutrons. In order to study these problems experimentally, the Fusion Material Irradiation Test (FMIT) facility is currently under design at Hanford Engineering Development Laboratory (HEDL), where it will be built. The facility will utilize a linac to accelerate deuterons to 35 MeV, which will then bombard a lithium target, thereby producing an intense source of neutrons. The resulting neutron spectrum will be peaked around 15 MeV, with a tail extending to ∿50 MeV. As a result of this high energy tail, shielding design studies require knowledge of neutron reaction cross sections up to ∿50 MeV. Existing neutron data at these high energies are rather sparse, and a number of new measurements are needed to reduce uncertainties of cross sections for shielding materials. The Evaluated Nuclear Data File[1] (ENDF/B), the source of neutron data for most fission reactor studies, currently has an upper limit of 20 MeV. From 20 to 60 MeV, shielding design studies have had to rely upon the few existing measurements, or predictions from optical model parameters, for their required total cross sections. In many cases, this has lead to unacceptably large uncertainties in the required cross sections, and thus to costly conservative machine designs.

As part of a program to help supply needed data for fusion device studies, we have initiated a program of measuring neutron transmission through samples of priority materials used in shielding design for FMIT and obtaining the resulting neutron total cross sections. In this paper we present results from the first of these measurements, in which we measured transmission of neutrons through carbon, oxygen, and iron. In addition, we have measured the hydrogen total cross section as a check on our technique.

Experimental Details

The Oak Ridge Electron Linear Accelerator (ORELA) was used to provide the neutrons for these measurements. Electrons from ORELA struck a dome-shaped tantalum converter 1.3 radiation lengths thick, producing bremsstrahlung. The bremsstrahlung radiation impinged on a solid block of beryllium, 61 cm long x 15 cm high x 10 cm thick, and via photonuclear processes produced a "white" spectrum of neutrons. The intensity of the gamma flash associated with the Be block is much lower than from the usual tantalum target, and thus requires less filtering material in the beam. The result is a larger flux of usable neutrons at the energies of interest in these measurements. However, due to the thickness of the target, the energy resolution is poorer than from the tantalum target. This does not affect the measurements reported in this paper, since the main interest is in the energy region above 15 MeV, where the cross sections are expected to be slowly varying with energy.

These measurements were done at a repetition rate of 1000 sec^{-1}, with a burst width of 10 ns and 3 kW of power on the target. The neutrons were detected at the end of a 79.460-m flight path by a 2-cm-thick NE110 proton recoil detector. A 12.7-cm-diameter tapered brass collimator was located at 8 m to define the beam. Since we are interested in detecting neutrons shortly (∿450 ns) after the gamma flash, we must minimize the effects of the gamma flash on the detector. This was done by using a 1.25-cm-thick uranium filter in the beam to reduce the intensity of the flash, and a gated tube base, which simultaneously defocused two dynodes of the photomultiplier tube prior to arrival of the gamma flash. The tube was turned back on ∿300 ns after the flash, awaiting arrival of the fastest neutrons. Utilizing the filter and gated tube base, effects of the gamma flash were negligible.

A neutron monitor was used to normalize the sample-in and sample-out data to the same neutron source intensity. The monitor is a ^{235}U fission chamber which views the neutron target, thus its output is proportional to the total neutron output of the ORELA target.

In order to provide a check on our results, in particular any unknown backgrounds, we measured the hydrogen cross section utilizing compensating samples of polyethylene and carbon, matched to 0.11% in the number of atoms/barn of carbon. The polyethylene sample was 10.2 cm thick with n=0.4111 atoms/barn, while the matching carbon sample was 4.8 cm thick, with n=0.4115 atoms/barn. The oxygen results were obtained from compensating samples of BeO and Be, matched to 0.18% in the number of atoms/barn of Be. The BeO sample was 7.6 cm thick, with n=0.5486 atoms/barn, while the matching Be sample was 4.4 cm thick, with n=0.5496 atoms/barn. The iron sample was 5.1 cm thick, with n=0.4296 atoms/barn. All the samples were 16.5 cm in diameter.

Alternation of the samples in and out of the beam was under control of the data-taking program. The iron, carbon and polyethylene samples were cycled in and out of the beam, together with the "open" beam, with a cycle time for all four "samples" of about 50 minutes. A total of 130 hours of beam time was used. Transmission through the BeO-Be matching set was done as a separate measurement, under identical experimental conditions, with a cycle time of about 20 minutes. A total of 95 hours of beam time was used for the BeO-Be measurement.

Neutron energies are determined by the time-of-flight method. The start signal for the time digitizer is taken from a bare phototube near the linac target, which views the gamma flash resulting from the electron burst. Stop pulses for the time digitizer are neutron or gamma-ray events in the detector at the end of the flight path. The gamma flash is observed at the remote detector in a separate measurement (with extra filters to reduce its intensity) to provide a fiducial time for determining neutron energies. One nanosecond channels

were used from 0 to 6000 ns (1 MeV neutron energy), four nanosecond channels from 6000 ns to 14000 ns (178 keV neutron energy), sixteen nanosecond channels from 14 μsec to 30 μsec, and 2000 nsec channels out to 840 μsec, the end of the looking time for a burst.

Dead Time and Background Corrections

Following a detected event, the system is dead for 1104 ns while the signal is processed, and then is alive again, waiting for another event or the end of the looking time for that burst. Multiple stops from each burst are accepted, with the average number of neutrons detected per burst ranging from 1.5 for the open beam to 1.0 for the polyethylene samples. For each channel the probability of loss of counts is calculated by summing the counts stored in the previous 1104 ns and dividing by the total number of bursts for the measurement. This gives the probability that the system accepted a count during this interval and therefore was dead at the time of the channel under consideration. This procedure implies a constant counting rate for the duration of the run, which experience has shown is a good approximation (usually 10-20%). The maximum dead-time corrections in the cross sections were 7.5% for iron at 5 MeV, 12.5% for carbon at 5 MeV, 2.4% for oxygen at 4.4 MeV, and 4.2% for hydrogen at 6.4 MeV.

Background effects in these measurements are small, except at higher energies where the count rate is low. The largest effect is from the time-independent room background. The magnitude of this background is obtained from the residual count rate at long flight times, just prior to arrival of the next neutron burst. During the measurement, this background was 0.019 cts/burst independent of sample. Following the measurement, when ORELA was turned off, the count rate was 0.017 cts/burst, or 9% lower.

The detector bias was adjusted such that neutrons above ∿500 keV would produce a signal large enough to trigger a stop. This serves to reduce effects of low energy spurious events.

To aid in background determination, four spectra are recorded for each sample.[2] Each spectrum is characterized by a different lower and upper cutoff on the recoil proton pulse height. The lower level of gate 1 was set at about 500 keV proton recoil energy, and extends to 850 keV, gate two covers from 850 keV to 1.5 MeV, gate three from 1.5 to 4.8 MeV, and gate four covers from 4.8 up to about 60 MeV. The corresponding neutron energy regions are not well defined since the recoiling protons from monoenergetic neutrons have a broad energy distribution and the pulse-height resolution of the detector is rather poor. However, this technique serves to approximately isolate some known gamma-ray backgrounds, as well as helping to identify any unknown sources of background. For the measurements reported here, only one other background was identified in addition to the time independent background. It is due to the 478-keV gamma ray, resulting from the $^{10}B(n,\alpha)$ reaction in the glass of the photomultiplier tube caused by fast neutrons moderated in the NE110 scintillator, and occurs mainly in gate two. The relative magnitudes of this background in the other three gates are measured in a separate experiment, using a ^{7}Be source, which emits the same 478-keV gamma ray. The distribution of counts among the four gates is then used to remove counts produced by this background from the measured spectrum.

Results and Discussion

Selected portions of the corrected data from each of the four bias windows were summed to form a single spectrum for each of the four samples. These spectra were normalized to the monitor counts, and converted to spectra of cross section versus energy. We now examine the individual total cross sections.

The experimental total cross section for hydrogen from 0.5 to 5.0 MeV is shown in Fig. 1, together with the ENDF/B-V evaluation.[3] Figure 2 shows the same comparison for neutron energies from 5 to 20 MeV. On the average, the experimental data are 0.7% higher than the evaluation from 0.5 to 20 MeV. Figure 3 shows our data from 20 to 60 MeV, compared to the November 1979 phase-shift analyses of nucleon-nucleon scattering data by Arndt[4] and the total cross section data of Brady *et al.*[5] at Davis. The lack of counts at energies near 60 MeV is reflected by the scatter of data points, even when averaged by five. From 20 to 60 MeV, the average deviation of the data from the evaluation is 0.6%, the data being high. The average deviation of our data and the Davis data is also 0.6%, reflecting the incorporation of the Davis data in the phase shift analysis.

Results for the carbon total cross section from 0.5 to 5 MeV are shown in Fig. 4, compared to the ENDF/B-V evaluation.[6] The data have been averaged by five in this figure. A similar comparison is shown in Fig. 5 for the energy region from 5 to 20 MeV. Averaged from 0.5 to 20 MeV, the data are 0.3% higher than the evaluation. Figure 6 shows the energy region from 20 to 60 MeV, compared to the experimental results of Auman *et al.*[7] The average discrepancy between the two measurements over the range of the Auman *et al.* data is 0.3%, with our measurement being high.

The measured results (averaged by ten) for the oxygen total cross section from 0.5 to 5 MeV are shown in Fig. 7, compared with the ENDF/B-V evaluation.[8] A similar comparison is made in Fig. 8 for energies between 5 and 20 MeV, with the data averaged by five. Averaged from 0.5 to 20 MeV, the present data are 0.2% lower than the evaluation. Figure 9 shows data in the energy range from 20 to 60 MeV, compared with the results of Auman *et al.*[7] Our data have been averaged by five, and averaged over the energy range of the Auman *et al.* results, are higher by 0.1%.

Our measured results (averaged by ten) for the iron neutron total cross section are shown in Fig. 10 from 5 to 20 MeV, compared with the ENDF/B-V evaluation[9] for iron. Comparisons below 5 MeV are not very informative, due to the large number of narrow resonances, which are mostly unresolved in our measurements. Averaging from 5 to 20 MeV, our data are 0.1% higher than the evaluated cross section. Figure 11 shows our data from 20 to 60 MeV, compared with recent preliminary data of Auman *et al.*[10] Their cross sections at 35.3 and 40.3 MeV are about 2% lower than our averaged data while their 50-MeV point is lower than our results by ∿8%. Thus the Davis data imply a different shape of the iron total cross section. Our polyethylene, carbon and iron samples were sequentially alternated in and out of the beam, which implies that a problem with the iron data should be present for hydrogen and carbon as well. However, this is not the case, as our carbon results agree well with the Davis work, and the hydrogen data agree well in this region with the known hydrogen cross section. Dead-time corrections for iron are less than 1% above 35 MeV. Careful examination of our data and backgrounds provides no insight as to the source of this discrepancy. A remeasurement of this cross section is planned.

Finally, we note that the agreement of our hydrogen cross section above 20 MeV to within 0.6% of the phase-shift analysis results and the Davis data imply that our other measured cross sections should have no significant systematic error, since they were taken under experimental conditions identical to those for

hydrogen. Indeed, we find agreement for carbon and oxygen above 20 MeV to better than 0.3% with the data of Auman *et al.* from Davis. This, together with analysis of data from each individual bias, gives us confidence that no significant corrections to the data have been overlooked, and our measurement techniques can be extended to similar measurements on other materials.

Summary and Conclusions

We have measured the neutron total cross sections for hydrogen, carbon, oxygen and iron from 500 keV to 60 MeV. Our results agree to better than 1% with ENDF/B-V evaluations up to 20 MeV, the upper energy limit of the evaluations. Above 20 MeV, the cross sections also agree to better than 1% with recent high accuracy measurements, with the exception of the iron results above 35 MeV. For iron, our results are 8% higher at 50 MeV, and imply a different shape of the cross section than obtained from the results of Auman *et al.* at Davis. This discrepancy is not understood at present. The data have been transmitted to the National Nuclear Data Center at Brookhaven National Laboratory.

Acknowledgement

Research sponsored by the U. S. Department of Energy, Office of Basic Energy Sciences, under contract No. W-7405-eng-26 with Union Carbide Corporation.

References

1. ENDF/B Summary Documentation, BNL-NCS-17541 (ENDF-201), 3rd Edition (ENDF/B-V), edited by R. Kinsey, available from the National Nuclear Data Center, Brookhaven National Laboratory, Upton, N. Y. (July 1979).
2. Details are given in "Measurement of the Neutron Total Cross Section of Fluorine from 5 eV to 20 MeV," D. C. Larson, C. H. Johnson, J. A. Harvey, and N. W. Hill, Report ORNL-TM-5612 (October 1976).
3. ENDF/B-V data file for hydrogen (MAT 1301), evaluation by L. Stewart, R. J. LaBauve, and P. G. Young (LASL), BNL-NCS-17541 (ENDF-201), 3rd Edition, edited by R. Kinsey, available from Brookhaven National Laboratory, Upton, N. Y. (July 1979).
4. Private communication from R. A. Arndt, December 1979, Solution Set CD79.
5. F. P. Brady, W. J. Knox, J. A. Jungerman, M. R. McGie, and R. L. Walraven, Phys. Rev. Lett. 25, 1628 (1970).
6. ENDF/B-V data file for ^{12}C (MAT 1306), evaluation by C. Y. Fu and F. G. Perey (ORNL), BNL-NCS-17541 (ENDF-201), 3rd Edition, edited by R. Kinsey, available from Brookhaven National Laboratory, Upton, N. Y. (July 1979).
7. M. Auman, F. P. Brady, J. A. Jungerman, W. J. Knox, M. R. McGie, and T. C. Montgomery, Phys. Rev. C 5, 1 (1972).
8. ENDF/B-V data file for ^{16}O (MAT 1308), evaluation by P. G. Young, D. G. Foster, Jr., and G. M. Hale (LASL), BNL-NCS-17541 (ENDF-201), 3rd Edition, edited by R. Kinsey, available from Brookhaven National Laboratory, Upton, N. Y. (July 1979).
9. ENDF/B-V data file for Fe (MAT 1326), evaluation by C. Y. Fu and F. G. Perey (ORNL), *ibid.*
10. C. I. Zanelli, F. P. Brady, J. L. Romero, C. M. Castaneda and D. L. Johnson, B.A.P.S. 24, 658 (1979), and private communication from F. P. Brady.

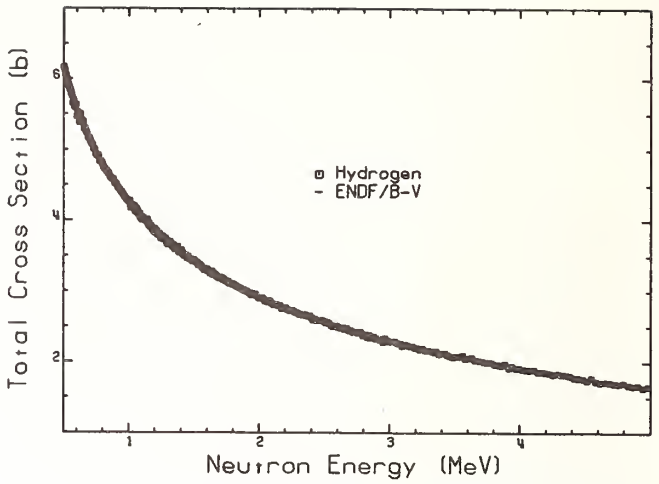

Fig. 1. Total cross section of hydrogen from 0.5 to 5 MeV, compared with ENDF/B-V.

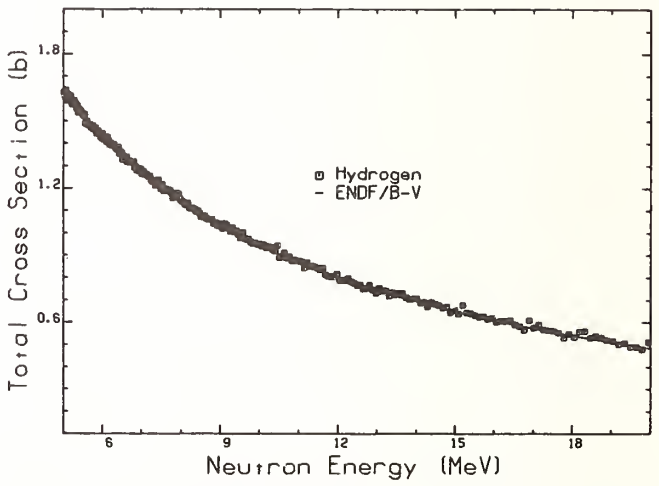

Fig. 2. Total cross section of hydrogen from 5 to 20 MeV, compared with ENDF/B-V.

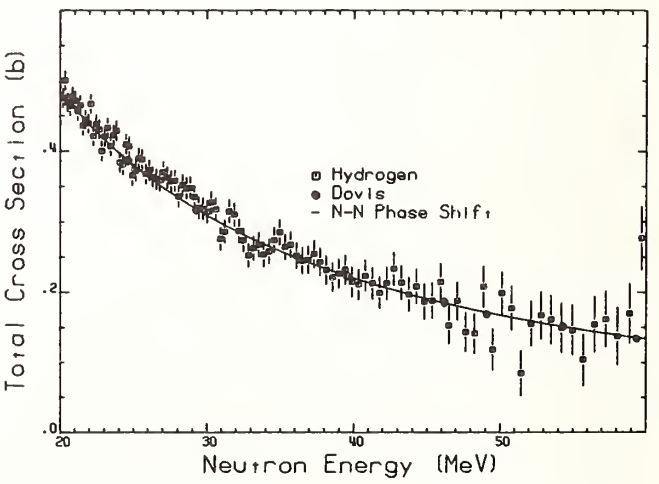

Fig. 3. Total cross section of hydrogen from 20 to 60 MeV, compared with data from ref. 5 and a recent nucleon-nucleon phase shift analysis (ref. 4).

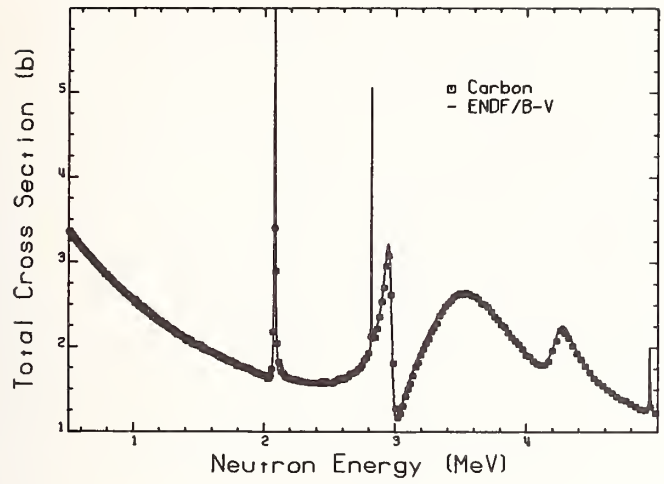

Fig. 4. Total cross section of carbon from 0.5 to 5 MeV, compared with ENDF/B-V.

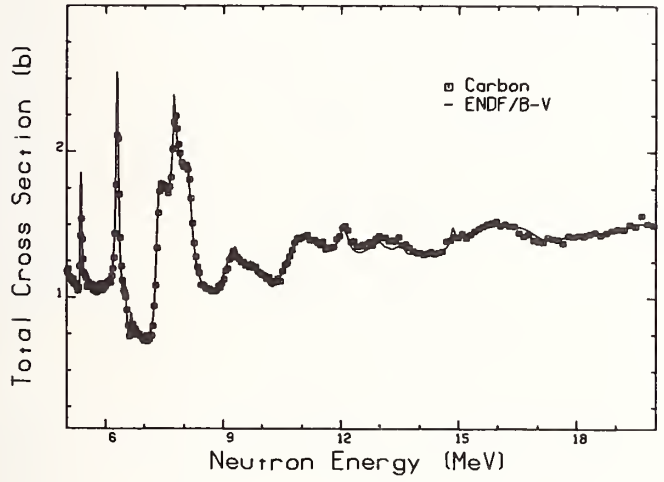

Fig. 5. Total cross section of carbon from 5 to 20 MeV, compared with ENDF/B-V.

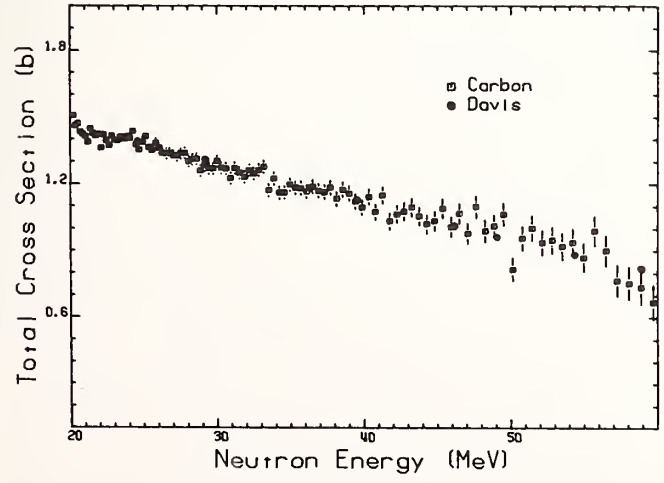

Fig. 6. Total cross section of carbon from 20 to 60 MeV, compared with data from ref. 7.

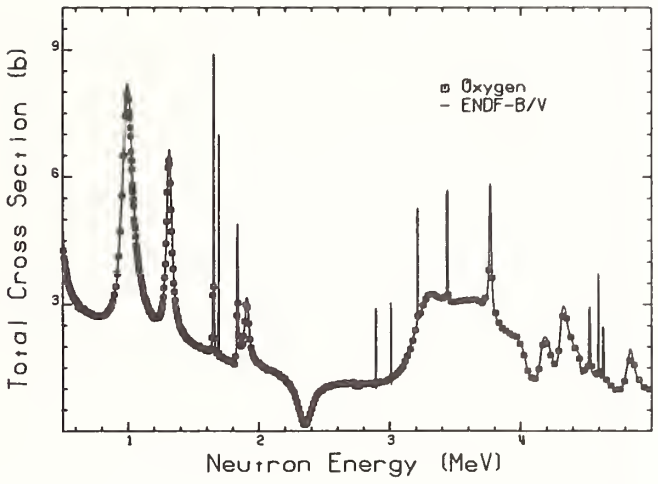

Fig. 7. Total cross section of oxygen from 0.5 to 5 MeV, compared with ENDF/B-V.

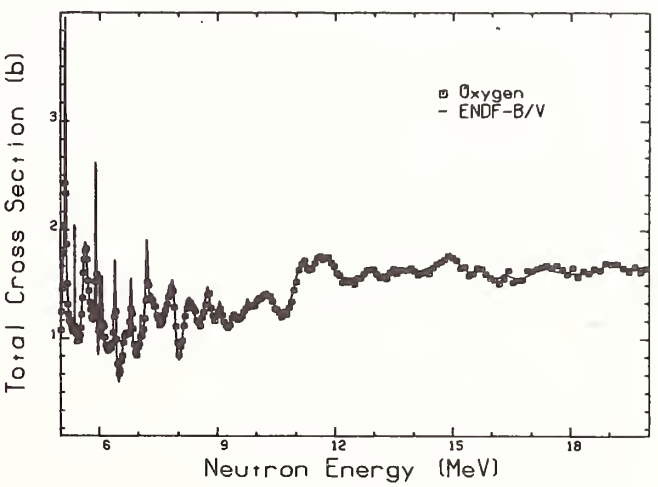

Fig. 8. Total cross section of oxygen from 5 to 20 MeV, compared with ENDF/B-V.

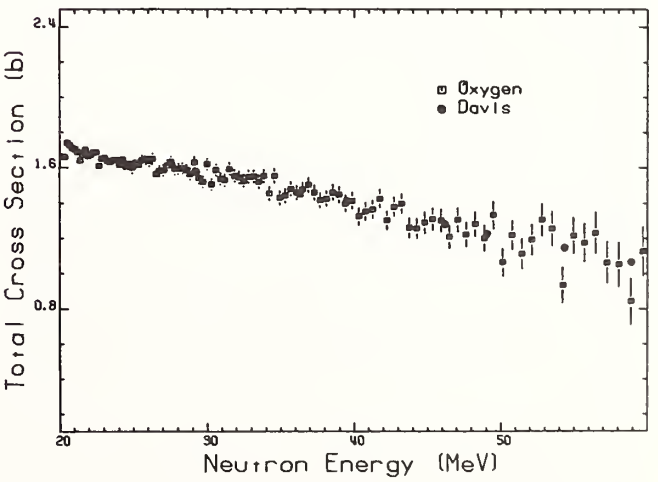

Fig. 9. Total cross section of oxygen from 20 to 60 MeV, compared with data from ref. 7.

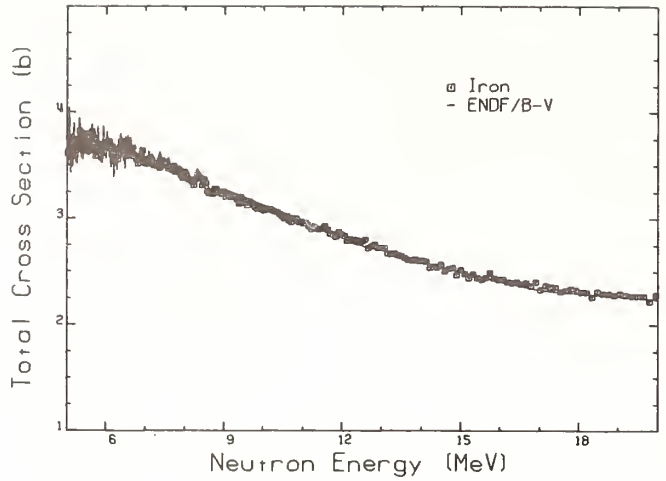

Fig. 10. Total cross section of iron from 5 to 20 MeV, compared with ENDF/B-V.

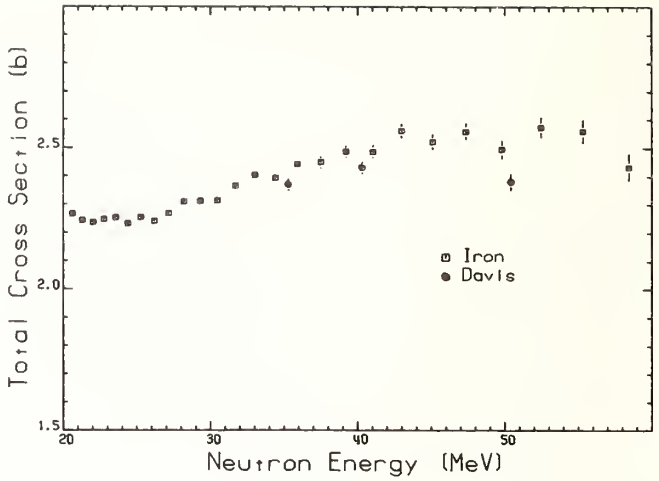

Fig. 11. Total cross section of iron from 20 to 60 MeV, compared with data from Ref. 10.

ELASTIC SCATTERING OF 14.8 MeV NEUTRONS FROM DEUTERONS

K. Gul, A. Waheed, M. Ahmad, M. Saleem Sheikh,
M. Anwar and Naeem A. Khan

Pakistan Institute of Nuclear Science & Technology (PINSTECH)
Nilore, Rawalpindi - Pakistan

The differential elastic scattering cross-sections of 14.8 MeV neutrons from deuterons have been measured between 29° and 145° in the centre-of-mass system using NE230 scintillator as a scatterer. The energies of neutrons have been measured by the time-of-flight technique. The present measurements support the deeper minimum reported by Berick et al and the measurements of Brullmann et al and Berick et al in the forward region. A value of 620 9 mb has been obtained for the total n-d elastic scattering cross-section at 14.8 MeV.

($n(^2_1H, ^2_1H)n$ reaction, E_n = 14.8 MeV, differential cross sections, total elastic scattering cross sections.)

Introduction

The measurements on fast neutron scattering from deuterons are useful for understanding strong interaction among nucleons. Measurements on elastic scattering of neutrons have been reported by several authors[1-7]. Several calculations of n-d elastic scattering have also been reported[8-10]. Two aspects of n-d elastic scattering at about 14 MeV are interesting. Firstly the measured differential scattering cross-sections in the forward region differ from exact calculations. Secondly the measurements of Berick et al[3] manifest a deeper minimum than other reported measurements. In the present measurements we have investigated these two aspects of the differential scattering cross-sections. Our measurements support the deeper minimum reported by Berick et al[3] and the measurements of Brullmann et al[5] and Berick et al[3] in the forward region.

Experimental Method and Data Analysis

The experiment was carried out using the neutron generator facility at PINSTECH. 14.8 MeV neutrons were generated through the reaction $^3_1H(d,n)^4_2He$ using deuterons of 120 keV energy. A deuterated benzene scintillator, NE230, of size 2.54 cm dia x 2.54 cm long was used as a scatterer and it was placed 12 cm from the neutron target. The neutrons were detected by a detector using a NE230 scintillator of 5.1 cm diameter and 5.6 cm length and it was placed at about 150 cm from the scatterer. The bias on the neutron detector was set at about 2.0 MeV proton equivalent energy. The neutron flux was determined by counting associated alpha particles with the help of a silicon detector. The neutron detector efficiency was measured in a separate experiment. Other relevant details of the experiment are given in our previously published work[11-12]. The efficiency measurements are compared with Monte-Carlo calculations obtained through RAWAL Monte Carlo Code[13] in Figure 1. It is now possible to calculate the neutron detection efficiencies of scintillation detectors within 5% uncertainty through Monte-Carlo calculations[14]. In the present results we have utilized the computed curve for the neutron detection efficiency. The typical time-of-flight spectra of neutrons scattered from deuterons are shown in figures 2 and 3. The spectrum shown in figure 2 was taken with a time resolution of 0.2 ns/channel. The continuum on the lower energy side of the elastic peak in figure 2 arises from deuteron and carbon break-up through charged particle emission. The spectrum shown in figure 3 was taken with a time resolution of 0.8 ns/channel. The second peak on the lower energy side arises from the neutron group leaving ^{12}C in 9.63 MeV excited state whose subsequent decay by charged particle emission results in giving a time reference signal to the time-to-pulse amplitude converter. At laboratory angles 100° the two peaks could not be resolved and necessary correction was applied for these angles. The values of required differential scattering cross-sections were taken from reference 15. In order to check that we were not losing deuterons for neutrons scattered in the forward direction, the measurements in the forward direction were also taken by taking one time reference signal from the associated alpha particle produced in the reaction $^2_1H(T,n)^4_2He$. In these measurements the elastic neutron groups from carbon and deuterons could not be resolved. These measurements were normalized with respect to measurements taken at 45° where the two elastic neutron groups were resolved. However the neutron group from deuteron contained contribution from neutrons inelastically scattered from 4.43 MeV state. The data on the scattering cross-sections of carbon for the analysis of the data was taken from references 16 and 17. The normalization constants derived at 45° from the deuteron group and carbon group agreed with each other within 1%. The differential cross-sections obtained by the two methods agreed with each other within the quoted errors. The error break-up on data is as follows:

Uncertainty in the number of deuterons	1%
Uncertainty in the neutron detection efficiency	5%
Multiple scattering error	1%
Errors on the back ground and statistics	3%
Over all error	6%
Angular resolution	1°.

Results and Discussion

The present measurements on the differential scattering cross-section are listed in table 1 and compared with previously reported measurements and calculations in figure 4. Our measurements support the deeper minimum reported by Berick et al[3] in the forward region. By combining present measurements with values at 20.4° and 13.5° from the work of Berick et al[3] and the values at 160.8°, 163.4° and 172.2° from the work of Shirato-Koori a least square fit of tenth-order Legendre Polynomial was obtained. The following values of Legendre Polynomial coefficients were obtained:

a_o = 49.35 ± 0.70, a_1 = 52.35 ± 1.46, a_2 = 59.64±1.54
a_3 = -15.97 ± 1.67, a_4 = 20.27 ±2.10, a_5 = -17.06
± 2.60, a_6 = 8.64 ± 3.02, a_7 = -8.95 ± 3.23,
a_8 = - 1.32 ± 2.78, a_9 = - 9.35 ± 2.38

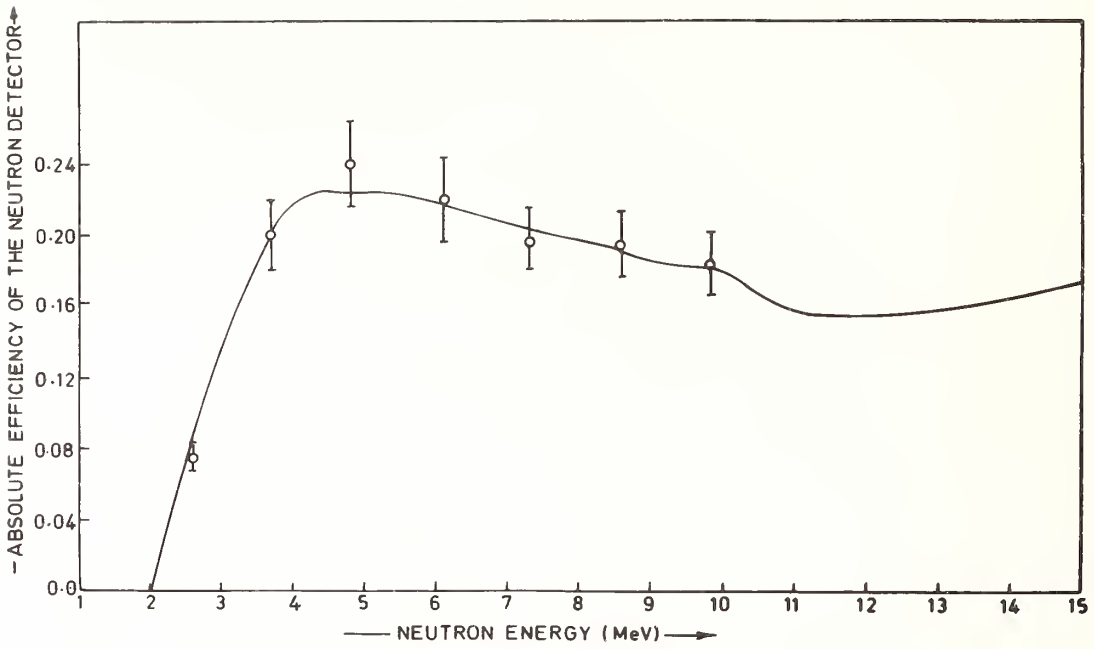

Fig.1. The neutron detection efficiency. The solid curve is Monte-Carlo calculation.

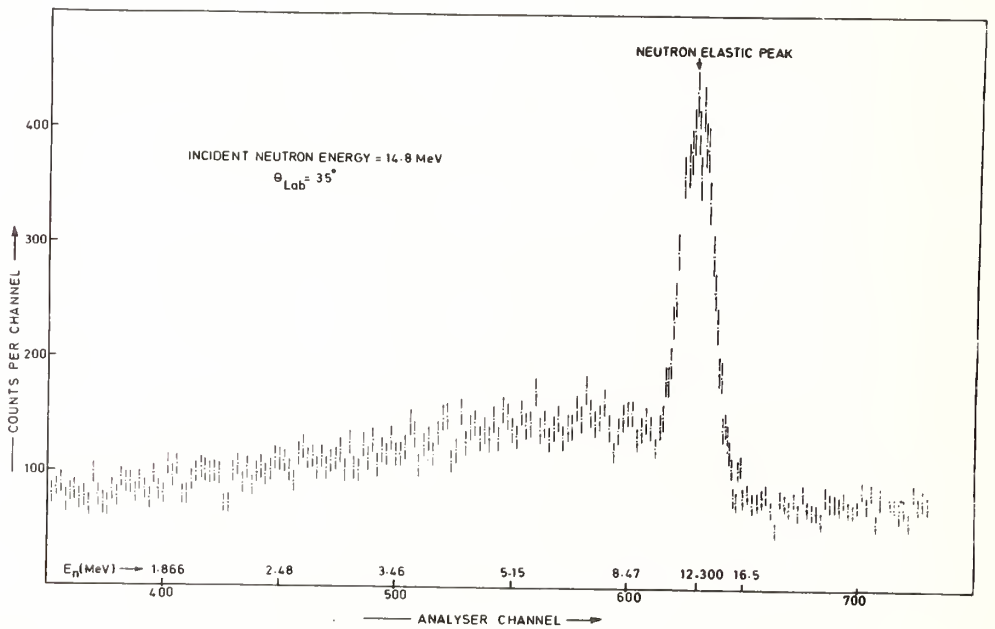

Fig.2. A neutron time-of-flight spectrum taken at 35° with time resolution of 0.2 ns/channel.

The value of total elastic scattering cross-section derived from this fit is 620±9 mb. The present results on the total n-d elastic scattering cross-section are compared with previously reported values in table II.

The theoretical curve of Aaron-Amado[8] predicts lower differential cross-sections for small scattering angles which has been attributed by them to the neglect of high momentum parts of nuclear force and higher partial waves. However it agrees with our measurements and those of Berick et al[3] in the region of minimum cross-sections. The theoretical curve of Doleschall[9] is on the other hand in better agreement in the forward region, but its minimum is comparatively shallow. By adding our previously reported inelastic scattering cross-section value of 145 mb[12] to our measured total elastic scattering cross-section, we obtain a value of 765±17 mb for 14.8 MeV neutron scattering cross-section for deuterons. This is in good agreement with recently reported value of 769±18 mb for 14.995 MeV neutrons by Davis and Barschall[18] and the measurements of Clement et al[19]

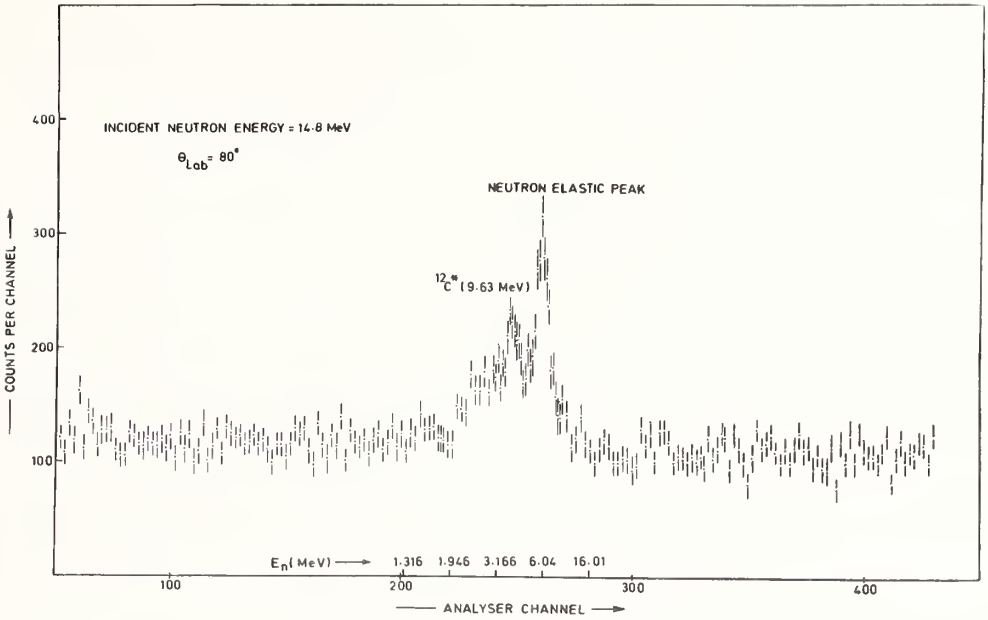

Fig.3. A neutron time-of-flight spectrum taken at 80° with time resolution of 0.8 ns/channel.

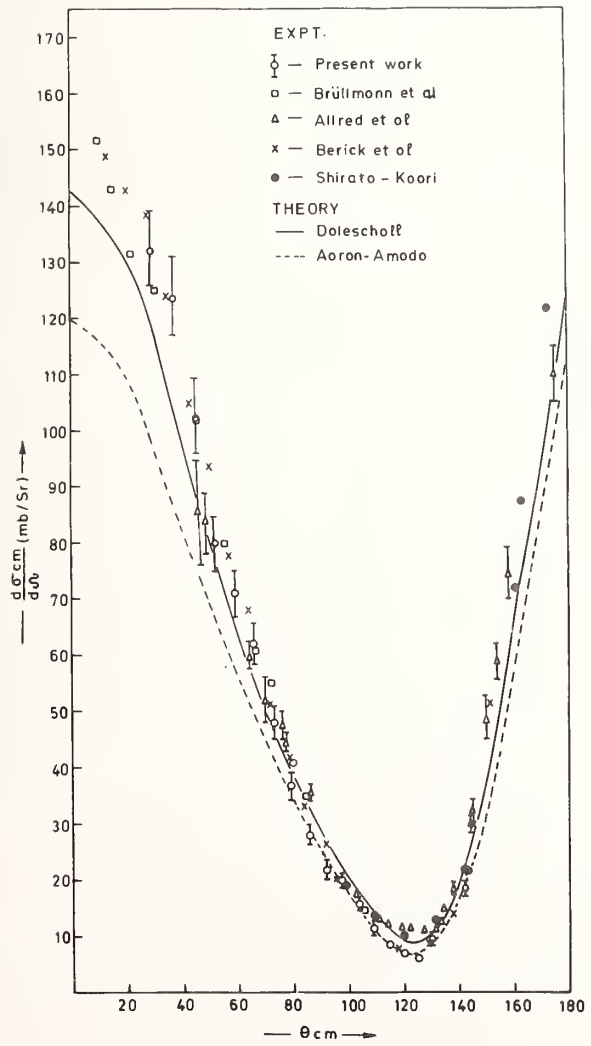

Fig.4. Comparison of present measurements with previous measurements and theoretical predictions.

Table I : The n-d elastic differential scattering cross-sections for 14.8 MeV neutrons.

θ_{cm}	$\frac{d\sigma_{cm}(\theta)}{d\Omega}$	θ_{cm}	$\frac{d\sigma_{cm}(\theta)}{d\Omega}$
28.9	132.6±7.9	92.0	21.7±1.30
37.2	124.5±7.4	98.1	20.0±1.2
44.5	102.5±6.2	103.9	15.6±0.9
51.7	79.9±4.8	109.5	11.4±0.7
58.8	71.0±4.3	114.9	8.7±0.5
65.7	61.9±3.7	120.0	7.1±0.4
72.6	48.0±2.9	124.9	6.1±0.6
79.2	36.7±2.2	129.7	11.5±1.0
85.7	27.9±1.7	142.0	17.8±2.0

Table II. A summary of theoretical and experimental total n-d elastic scattering cross-sections.

Experiment:		
Present work	14.8 MeV	620±9 mb
Brullmann et al[5]	14.1 MeV	650±40 mb
Berick et al[3]	14.3 MeV	650±6 mb
Shirato-Koori[2]	14.1 MeV	598±21 mb
Shirato-Koori[1]	14.1 MeV	623±5 mb
Allred et al[6]	14 MeV	670±100 mb
Seagrave[4]	14 MeV	610±30 mb
Theory:		
Aaron-Amado[8]	14.1 MeV	520 mb
Christian-Gammel[10]	14.1 MeV	600 mb

References

1. S. Shirato and N. Koori, in Few Particle Problems in the Nuclear Interaction ed. Ivo Slaus, Steven A. Moszkoski, Roy P. Haddock and W.T.H. Van Oers (North-Holland/American Elsevier, 1972) P. 472.

2. S. Shirato and N. Koori, Nucl. Phys. A120, 381 (1968).

3. A.C. Berick, R.A. Riddle and C.M. York, Phys. Rev. 174, 1105 (1968).

4. J.D. Seagrave, Phys. Rev. 97, 757 (1955).

5. Von M. Brullmann, H. Jung, D. Meier and P. Marmier, Helv. Phys. Acta 41, 435 (1969).

6. J.C. Allred, A.H. Amstrong and L. Rosen, Phys. Rev. 91, 90 (1953).

7. I. Basar, in Few Body Problems, Light Nuclei and Nuclear Interaction, ed. G. Paic and I. Slaus (Gordon and Breach, New York, 1968) vol. 2, p. 867.

8. R. Aaron, R.D. Amado and Y.Y. Yam, Phys. Rev. 140, B1291 (1965).

9. P. Doleschall, Nucl. Phys. A201, 164 (1973).

10. R.D. Christian and J.L. Gammel, Phys. Rev. 91, 100 (1953).

11. A. Waheed, K. Gul, M. Ahmad, S.M. Saleem and Naeem A. Khan, PINSTECH Internal Report No.5-NPD-(FNPG).

12. K. Gul, A. Waheed, M. Ahmad, M. Saleem and Naeem A. Khan, J. Phys. G: Nuclear Physics, 5, 1107 (1979).

13. K. Gul, Pinstech Internal Report, 1979, to be published.

14. D. Hermsdorf, K. Pasieka and D. Seeliger, Nucl. Instr. and Meth. 107, 259 (1973).

15. G.A. Grin, B. Vaucher, J.C. Alder and C. Joseph, Helv. Phys. Acta 42. 990 (1969).

16. D.W. Glasgow, F.O. Purser, H. Hogue, J.C. Clement, K. Stelzer, G. Mack, J.R. Boyce, D.H. Epperson, S.G. Buccino, P.W. Lisowski, S.G. Glendinning, E.G. Bilpuch, H.W. Newson and C.R. Gould, Nucl. Sci. Eng. 61, 521 (1976).

17. G. Haouat, J. Lachkar, J. Sigaud, Y. Patin and F. Cocu, Nucl. Sci. Eng. 65, 331 (1958).

18. J.C. Davis and H.H. Barschall, Phys. Rev. C3, 1798 (1971).

19. J.M. Clement, P. Stoler, C.A. Goulding and R.W. Fairchild, Nucl. Phys. A183, 51 (1972).

NEUTRON SCATTERING FROM ^{7}LI AT INCIDENT ENERGIES OF 5.1, 6.6 AND 15.4 MeV

M.Baba, N.Hayashi, T.Sakase, T.Iwasaki, S.Kamata and T.Momota
Department of Nuclear Engineering
Tohoku University
Sendai, Japan

^{7}Li double-differential neutron cross sections were measured with time-of-flight method for En=5.1, 6.6 and 15.4 MeV at six laboratory angles between 27.5° and 140°. The results were compared with the evaluated data, and the emission spectra were analysed.

[^{7}Li, σ(En,En',Ω), 5.1-, 6.6- and 15.4-MeV, σ_{el}, $\sigma_{4.6}$, $\sigma_{n,xn'}$, spectrum analysis]

Introduction

Detailed knowledge for neutron emission cross sections of ^{7}Li is important in various branchs of fusion reactor neutronics such as evaluation of tritium production, neutron shielding and radiation heating.

In the case of ^{7}Li, in addition to elastic and inelastic scattering to the first excited state, (n,nt) and (n,2n) reaction begin to contribute to continuum neutron emission above 4.5 and 10 MeV, respectively. For elastic scattering and γ-ray production cross sections, considerable effort of measurement have been taken.[1~4]

However, the data for neutron emission cross sections are very sparse, and the question about neutron spectra pointed out by Batchelor[5] and Hopkins[6] looks to be still an open question.

In this study, we have measured ^{7}Li double-differential neutron cross sections at three incident energies above (n,nt) reaction threshold. And we try to interpret the energy and angular distributions of emitted continuum neutrons applying a model for two stage sequential break-up process.

Experiment

Experimental method

The experiments were performed with a standard time-of-flight method in the same manner as it was described previously[7] The Tohoku University Dynamitron accelerator equipped with a nano-second pulsing system was used for neutron production. 5.1- and 6.6-MeV neutrons were produced via d-D reaction with a gas target. 15.4-MeV neutrons were obtained via d-T reaction using a Tritium-Titanium solid target. Energy spreads of source neutrons were about 150keV and 300keV, respectively.

The ^{7}Li sample was 99.8%-pure natural Li with a ^{7}Li isotopic content of 92.5%, which was encupsulated in a thin wall stainless steel can. Two samples with differnt sizes were used, one was 2cm in diameter and 2cm long, and the other was 2cm in diameter and 7cm long. Identical empty cans to those containing Li samples were used for sample out runs. These samples were positioned at 10cm from the neutron producing target and were suspended by a sample changer.

The neutrons emmited from the scattering sample were detected at 3.2m from the sample with a neutron detector in a massive shield. The neutron detector consisted of a 5" in diameter and 2" thick NE213 scintillator coupled to a Phillips XP2041 photomultiplier tube. The pulse-height bias was set about 0.25MeV (proton equivalent). And a zero-crossover n-γ dicriminator was employed. This circuit had a pulse-height dynamic range over 300 to cover the entire secondary neutron energy range from 0.3MeV to 15MeV with one bias setting. The relative detector efficiency was determined experimentally by counting source neutrons from d-T and p-T reaction, n-p scattered neutrons and emitted neutrons from ^{252}Cf. These results agreed well with those by calculations[8] except for the energy region near the bias energy. The uncertainty of relative efficiency was estimated to be 5%.

The cross section values were normalised to scattering cross sections of hydrogen.

A smaller NE213 scintillator of 2" in diameter and 2" thick was placed about 5m from the target at laboratory angle of 25° or 40° and served as source neutron monitor.

For the lower energy runs at 5.1- and 6.6-MeV, gas out run were also performed to check the effect of contaminant in the source neutrons. At 6.6-MeV, this effect could not be neglected completely and was taken into account in the data reduction procedure.

The measurements were made at laboratory angles of 30°,45°,60°,75°,90°and 120° for 5.1- and 6.6-MeV, and at 27.5°,40°,55°,80°,110° and 140° for 15.4-MeV, respectively.

Experimental results

A typical time-of-flight spectrum of secondary neutrons for 6.6-MeV at laboratory angle of 30° is shown in Fig.1. Back ground is already subtracted. Neutron continuum attributable to (n,nt) reaction is seen as well as discrete peaks due to elastic and inelastic scattering to the 4.6-MeV second excited state.

These time spectra were converted into energy spectra, and were corrected for detection efficiency

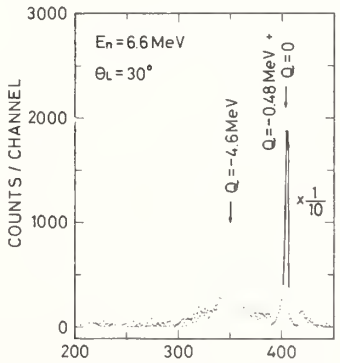

Fig.1 Back ground subtracted TOF spectrum at 30° (laboratory angle) for scattering of 6.6-MeV neutrons from ^{7}Li sample. Inelastic scattering via the 0.48-MeV first excited state was not resolved from the elastic scattering peak. The inelastic scattering group is due to the 4.6-MeV second excited state and neutron continuum.

and multiple scattering effect. The multiple scattering effect was estimated utilizing of Monte-Carlo simulation of double-differential cross sections. Then, the double-differential cross sections were obtained for neutrons with energy above 0.4MeV.

In Fig.2, double-differential cross sections at two laboratory angles are presented. For 15.4-MeV neutrons, excitation of the third level around 6.5MeV is also observed, which is consistent with the result by Morgan.[3]

From these data, we obtained

1) elastic + inelastic scattering cross sections to the 0.48-MeV first excited state.
2) inelastic scattering cross sections to the 4.6-MeV second excited state (for 6.6- and 15.4-MeV only)
3) neutron emission cross sections.

As the qouted uncertaities of data, those due to statistics, detector efficiency,normalization and Monte-Carlo statistics are considered. For the 15.4-MeV data, the uncertainty is rather large compared with that for lower energy data. This is primarily due to unfavorable signal to background ratio.

In Fig.3, the angular distribution data are shown with the results of Legendre polynomials fittings.

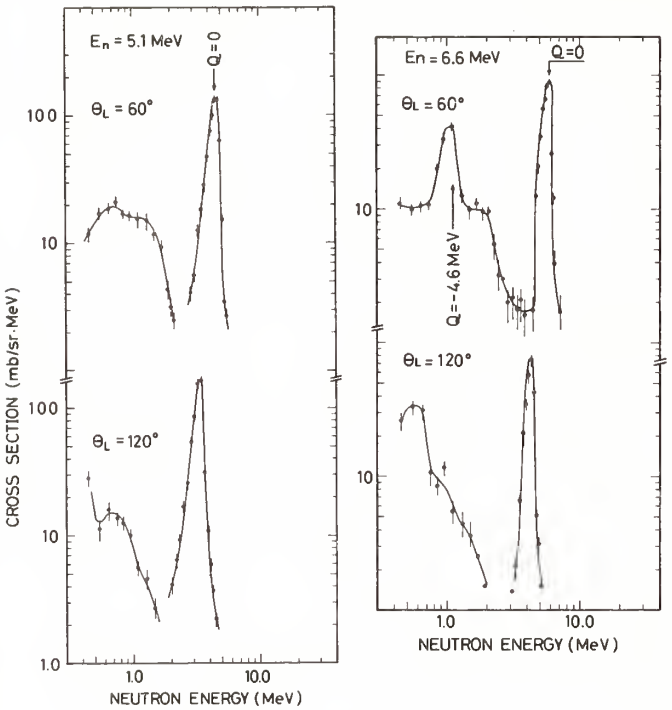

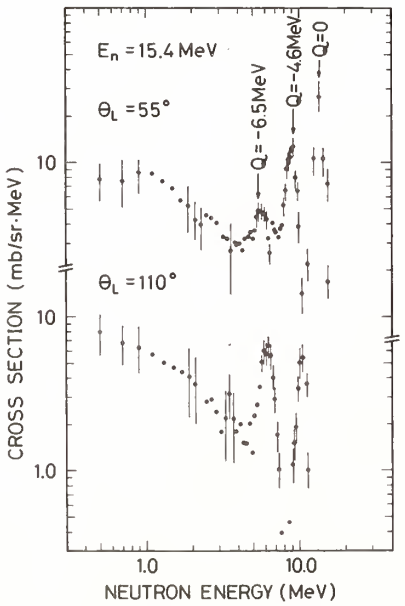

Fig.2. Double-differential cross sections at two laboratory angles for 5.1-,6.6- and 15.4-MeV incident neutrons on ^{7}Li. The cross sections are given in the laboratory system. The solid lines are for eye-guides.

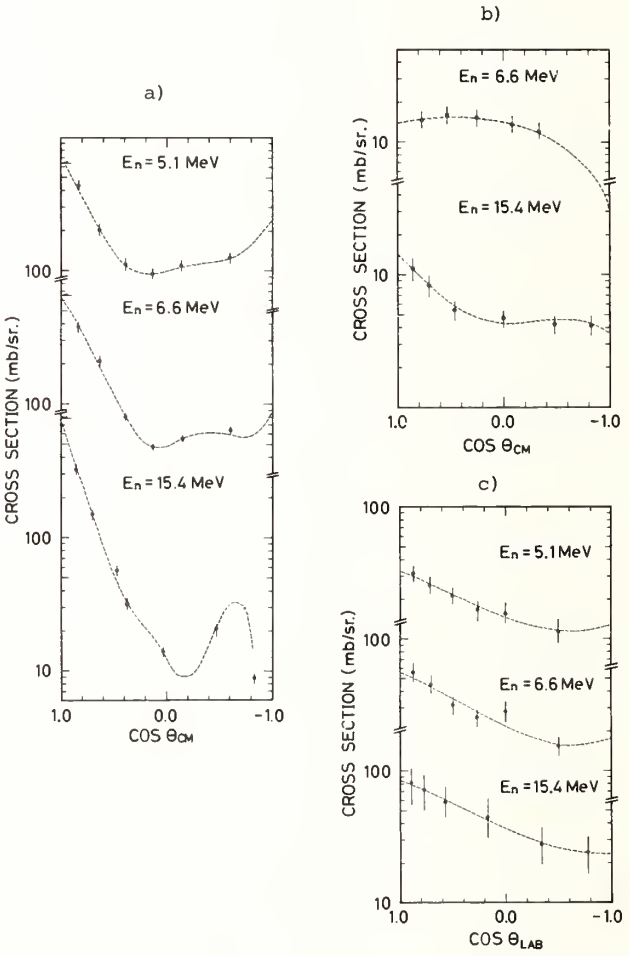

Fig.3, Angular distribution data for the scattering of 5.1-,6.6- and 15.4-MeV neutrons from ^{7}Li. Dotted lines are the results of Legendre polynomials fits to the experimental points. a) is for the sum of elastic and 0.48-MeV state inelastic scattering cross sections in the CM system. b) is for 4.6-MeV state inelastic scattering cross sections in the CM system. c) is for emitted neutrons from ^{7}Li(n,xn) reaction other than elastic and 0.48-MeV inelastic scattering, and is given in the laboratory system. For 5.1- and 6.6-MeV neutrons, only (n,nt) reaction is concerned.

Table 1. Data Comparison of ^{7}Li Neutron Cross Sections

Incident Neutron Energy (MeV)	$\sigma(n,n_0+n_1)$ (mb)		$\sigma(n,n_2)$ (mb)		$\sigma(n,xn)$ (mb)		σ(Total) (mb)	
	Present	ENDF/B-IV	Present	Ref.	Present	ENDF/B-IV	Present	ENDF/B-IV
5.1	2300±230	2104			219± 28	223	2519±258	2327
6.6	1620±159	1589	157±65	130±65[5]	342± 44	400	1960±203	2020
15.4	961±101	999	74±11	69± 4[9]	540±135	440	1421±230*	1399

*) 66mb (ENDF/B-IV value) was assumed for (n,2n) reaction

Discussion

Data comparison

In Table 1, the angle-integrated neutron cross sections for ^{7}Li by present work are compared with those given by ENDF/B-IV. For $\sigma(n,n_2)$, which is the inelastic scattering cross section to the 4.6-MeV second excited state, no data are given in ENDF/B-IV and comparison is made with other experimental data. On the whole, present results are consistent with data given by ENDF/B-IV or other experiments within experimental uncertainty. However, for the $\sigma(n,xn)$ at 15.4-MeV, if we assume $\sigma(n,2n)$ to be 66mb (ENDF/B-IV value), present result gives $\sigma(n,nt)$ to be 408mb. This is about 30% higher than ENDF/B-IV data. The larger $\sigma(n,2n)$ and/or significant contribution of (n,3n) leads to better agreement between the present results and ENDF/B-IV data for $\sigma(n,nt)$.

Present result for $\sigma(n,n_0+n_1)$ at 5.1-MeV is nearer to the data of recent measurement by Knox than that by ENDF/B-IV.

The experimental data of emission spectrum available for comparison were very sparse. Although the data by Morgan[3] are very extensive and are useful for comparison, these data are compiled as average value around 1 MeV interval for incident energies. Hence direct comparison dose not seem to be so meaningful especially for data at 5.1- and 6.6-MeV, where (n,nt) cross section might vary steeply with incident energy. Nevertheless, allowing these differences, present data at 60° or 55° and 120° or 110° are in reasonable agreement with Morgan's data at 50° and 126°, in shape and in magnitude, except those for 15.4-MeV,where present data are slightly higher.

In Fig.4, present results of energy spectra of secondary neutrons for 6.6-MeV neutrons are compared with ENDF/B-IV evaluation. In ENDF/B-IV, the energy spectra of secondary neutrons from (n,nt) and (n,2n) reaction are expressed by an angle-independent temperature model. This causes the difficulty in reproducing the structure found in experimental spectra and the energy-angle correlation.

In Fig.5, the comparison of experimental spectra for other incident energies and angles with ENDF/B-IV evaluation are shown.

Analysis of the neutron spectra

In this section, we discuss the energy spectra from $^{7}Li(n,nt)$ reaction,which plays a leading role for emission of neutron continuum in the energy region of present study.

According to Batchelor[5]and Hopkins[6], the neutron continuum resulting from $^{7}Li(n,nt)$ and $^{6}Li(n,nd)$ reaction present softer spectra compared with phase space distribution. As well, present results show similar tendency. The phase space distribution[11]

$$P(E)dE = C \cdot E^{1/2}(Emax-E)^{1/2}\,dE \qquad (1)$$

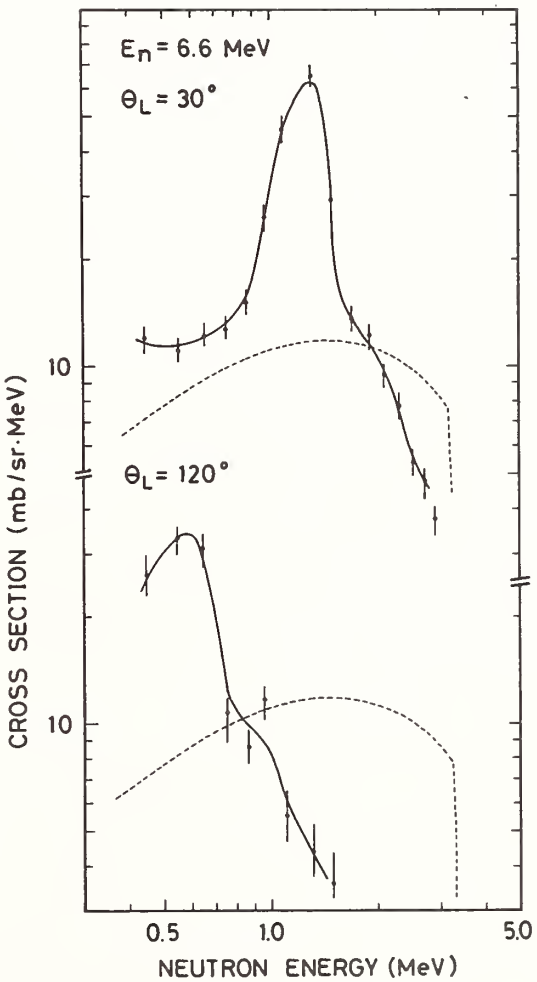

Fig.4, Comparison of experimental spectra for 6.6-MeV neutrons with the evaluation by ENDF/B-IV. Solid line are for experimental, and dash lines are for ENDF/B-IV.

is compared with experimental spectra after being transformed into laboratory system. The comparison is made in Fig.5.

Scince, the phase space distribution seems to oversimplify the mechanism, we try an improved fit taking into account the final state interactions between t and α particles. According to the data in Ref.10, for t-α interaction, we should consider up to f-wave interaction. For this purpose, we use the formulae in Ref.11 and Ref.12

$$\sigma_\ell(E) = C' \cdot \kappa_b/\kappa_a \cdot (\,|H'|\,)^2 \rho_\ell(E) \qquad (2)$$

$$\rho_\ell(E) = C'' \cdot P_\ell^{-1} \cdot \sin^2(\phi_\ell + \delta_\ell)$$

where ϕ_ℓ ; hard sphere phase shift
δ_ℓ ; nuclear phase shift
P_ℓ ; penetrability

The phase shift data for t- α interaction were taken from Ref.10. The $\rho_1(E)$ and $\rho_2(E)$ in eq. (2) show similar energy dependence with $\rho_0(E)$, and for simplification, we replace the terms for s-,p- and d-wave collectively with the phase-space modified by s-wave Coulomb interaction. Then eq.(2) for s-, p- and d-waves reduces simply to

$$P'(E)dE = C''' \cdot C_0^2(E) \cdot P(E)\,dE \qquad (3)$$

where $C_0^2(E) = 2\pi\eta/[\exp(2\pi\eta)-1]$

$$\eta = Z_\alpha \cdot Z_t / h \cdot v$$

It has been shown that eq.(3) is useful expression for neutron continuum resulting from ^{6}Li(d,n^{3}He) reactions for low energy deutrons.[13] For inclusion of f-wave final state interaction, the evaluation of trasition matrix in eq.(2) was necessary. This was made by use of DWBA. The result of eq.(2) for f-wave was added in appropriate scale to that by eq.(3).

The comparison between experimental spectra and calculated ones are shown in Fig.5. The experimental spectra for 5.1- and 6.6-MeV neutrons are fairly well reproduced by present calculation. For 15.4-MeV data, the low energy neutrons cannot be reproduced by this calculation alone. Detailed treatment of p- and d-wave terms in eq.(2) will lead to better agreement. On the other hand, as it is seen from Fig.5, the final state interaction between α and n also contribute to produce lower energy neutrons. This spectrum was calculated based upon the formula given in Ref.14, taking the level width of ^{5}He into account. By considering α-n interaction, we can reproduce almost completely the spectrum by this calculation.

Finally, in Fig.6, the labolatory angular distributions expected for neutrons which have energy distribution given by eq.(3) in the center of mass system is compared with experimental data. Isotropic distribution in the center of mass system is assumed. For the 5.1- and 6.6-MeV data, such a simple model reproduces the data fairly well. However, for 15.4-MeV neutron, experimental result shows stronger angle dependence, which will mean the necessity for inclusion of low energy neutrons.

Refinement of present analysis is interesting to identify the mechanism of neutron emission, as well as to know the energy distribution systematics.

Aknowledgment

We appreciate Messrs. I.Abe, M.Fujisawa, Y.Endo and R. Sakamoto for their cooperations.

References

1. H.H.Hogue et al., Nucl. Sci. Eng. 69, 22 (1979)

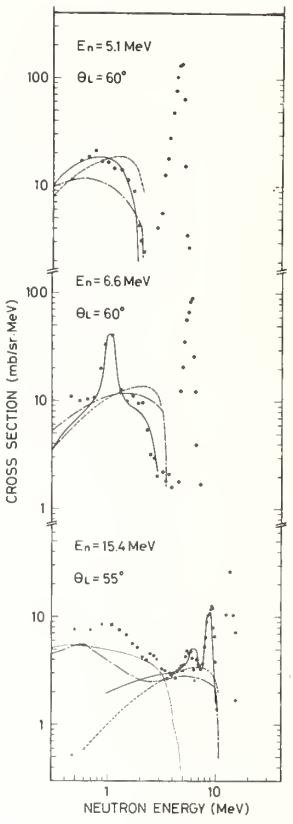

Fig.5, Comparison between the experimentally observed neutron spectra and those by evaluation or by model caculations.
experimental ; closed circle
calculation(t-α final state interaction) ; solid line
calculation(α-n final state interaction) ; dotted line
phase space ; dash line
ENDF/B-IV ; dash dotted line

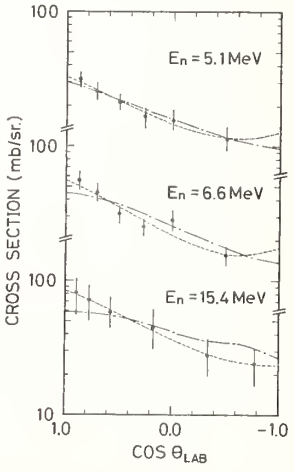

Fig.6, Comparison of angular distributions of neutron continuum from ^{7}Li(n,xn) reactions. Experimental results by closed circle, and calculated results with eq.(3) in the text by dash dotted line, Legendre polynomials fits by dotted line.

2. H.D.Knox, R.M.White and R.O.Lane, Nucl.Sci.Eng. 69,223 (1979)
3. G.L.Morgan, ORNL-TM-6247 (1978)
4. J.K.Dickens et al., Nucl.Sci.Eng. 62,515 (1977)
5. R.Batchelor and J.H.Towle, Nucl.Phys. 47,385 (1963)
6. J.C.Hopkins, D.M.Drake and H.Conde, Nucl.Phys. A107,139 (1968)
7. M.Baba et al., in Proceedings of Conference on Neutron Physics and Nuclear Data, Harwell,UK, 1978, p.198
8. V.V.Verbinski et al., Nucl.Instr.Meth. 65,8 (1968)
9. M.Hyakutake et al., J.Nucl.Sci.Tech. 11,407 (1974)
10. R.J.Spieger and T.A.Tombrello, Phys.Rev. 163, 964 (1967)
11. G.G.Ohlson, Nucl.Instr.Meth. 37, 240 (1965)
12. F.C.Barker and P.B.Tracy, Nucl.Phys. 38, 33 (1962)
13. R.E.Holland et al.,Phys.Rev. C19, 592 (1979) M.Baba et al ., NETU-27 (Internal Reprt, Department of Nucllear Engineering, Tohoku University,1978)
14. F.B.Morinigo, Nucl.Phys. A127, 116 (1969)

TOTAL CROSS SECTION MEASUREMENTS OF ^{6}Li, ^{7}Li, AND C FROM 3 TO 40 MeV

J. D. Kellie
University of Glasgow
Glasgow, Scotland

G. P. Lamaze and R. B. Schwartz
National Bureau of Standards
Washington, D.C. 20234

This paper describes the measurement of the total neutron cross sections of carbon, ^{6}Li and ^{7}Li from 3 to 40 MeV, using the pulsed beam of the National Bureau of Standards electron linear accelerator as a source of neutrons. The measured pulse width was approximately 5 ns FWHM and the neutron flight path was ∿200 m which gives an intrinsic resolution of ∿150 keV at the higher energies.

[$^{6}Li(n,n)$, $^{7}Li(n,n)$, C(n,n), total cross section, 3-40 MeV, time-of-flight]

Introduction

Neutron cross sections covering the energy range up to 15 or 20 MeV have, until recently, sufficed to cover the practical energy range of interest for neutronics calculations. Under development at present, however, is a high-flux, high energy, neutron source for materials testing: the Fusion Materials Irradiation Test (FMIT) Facility[1]. This machine will produce a significant flux of neutrons with energies up to ∿40 MeV via the thick target Li(d,n) reaction. There is thus a need for higher energy cross section data. These data would be used directly in transport calculations, as well as to verify cross section calculations which could then be used in regions where direct measurements were not available.

The present paper describes the measurement of the total neutron cross sections of carbon, ^{6}Li, and ^{7}Li up to 40 MeV, using the pulsed beam of the National Bureau of Standards electron linear accelerator as a source of neutrons. The hydrogen cross section was also measured since it is known to within ∿1% over most of the energy range of interest. A comparison between our measured hydrogen total cross section and the accepted values provides a convenient way of assessing the accuracy of the experiment. Since the carbon cross section is well known below 15 MeV[2], it acts as another check on our measurements, and new values of the carbon cross section were then obtained at higher energies.

Experimental Procedure

White source neutrons were produced at the NBS linac time-of-flight facility. A pulsed electron beam of ∿90 MeV energy and 6 μA average current (720 pps repetition rate) was incident on a composite target of 4.8 mm tungsten and 100 mm beryllium. The measured pulse width was approximately 5 ns FWHM. The samples were placed approximately 8 m from the target on a 200 m flight path. The neutron detector was a 33 cm diameter x 12.7 cm long NE211* liquid scintillator, viewed by 3 RCA 8854 photomultipliers. The photomultipliers were pulsed off during the γ-flash[3] to prevent overload and after-pulsing problems. The time-of-flight was measured digitally, using an EG&G Model TDC 100 Time Digitizer, set up to count no more than one count per machine pulse. The start pulse for the time digitizer is derived from a phototube placed near the neutron producing target. The stop signal is taken from the output of an OR gate, whose inputs are the photomultiplier anode discriminators. These discriminators were biased at a proton recoil energy of ∿1.5 MeV, which is above the tube noise and much of the gamma background. The background counting rate was measured during the experiment using a shadow bar, and amounted to ∿0.3% of the open beam counting rate. The experiment was controlled using a Datacraft 6024 Model 5 computer interfaced to the electronics via CAMAC.

Since we only counted one count per pulse, the dead-time correction could be made exactly[4], provided that the neutron flux remained constant during each "run." Consequently, samples were changed every five minutes: during any five-minute "run" the neutron flux was constant to within a few percent. At the end of each run, the number of start and stop pulses, the number of analyzed events and the monitor counts from the run were typed out and stored on magnetic tape. The time-of-flight spectrum accumulated during the run was corrected for dead-time losses and stored on magnetic tape. The next sample was then moved into position using a CAMAC controlled stepping motor.

In the experiment, the region of interest gate covered the time interval starting 1 μsec and ending 9 μsec after the γ-flash and spanned a range of neutron energies from approximately 70 MeV to 2.5 MeV. The average counting rate in the open spectra was ∿90% of the start rate, which resulted in a dead-time correction of a factor of ∿2.5 at the lowest energies measured. Consequently, if the experiment measured the cross sections accurately at energies down to ∿3.0 MeV, it is reasonable to assume that the dead-time corrections were being properly applied.

Two monitors were used. First, the electron beam current on the target was integrated and the total charge per run recorded. In addition, a BF_3 counter (shielded against the gamma-flash) monitored the neutron production. The run-to-run ratios of the two monitors agreed to better than 1% and the electron beam current was selected to normalize the data. Run lengths were chosen to obtain comparable statistical precision for both sample in and sample out.

* This particular material, and certain other commercial equipment, instruments, and materials are identified in this paper in order to adequately specify the experimental procedure. In no case does such identification imply recommendation or endorsement by the National Bureau of Standards, nor does it imply that the material or equipment identified is necessarily the best available for the purpose.

Experimental Results

A. Hydrogen

The hydrogen sample was polyethelene [(CH_2)], cut from the same material as used for our earlier hydrogen measurement.[5] Analysis at the time indicated that the ratio of hydrogen to carbon was stoichiometric to within 0.04%. The "n" value (areal density) was 1.9132 atoms/barn. A sample of high purity carbon, with the same "n" value as the carbon in the polyethelene, was used in the "open" beam.

Fig. 1 shows the percent difference between our measured data and the accepted value for the hydrogen cross section. For 20 MeV and below our data are compared to the work by Hopkins and Breit.[6] For ease in computation, above 20 MeV we compare our data to the parametrization by Binstock.[7] (Although the Binstock parametrization is only intended to apply at energies above 25 MeV, sample calculations in the range 22-30 MeV show that in this region the parameterization differs from the Hopkins-Breit results by <0.5%)

As can be seen from Fig. 1, our results differ from the accepted values by <1.5% over the range 3 MeV to 35 MeV, and are 3% high at 42 MeV. In view of this good agreement, we consider that our measurements are probably accurate to within <3% over the range 3 MeV to 40 MeV.

B. Carbon

The carbon samples were the same as used in our previous measurement, which went up to 15 MeV. The samples were pressed graphite, with <0.01% of either volatile or nonvolatile impurities, and no evidence of absorption of impurities on exposure to air. X-ray measurements of the sample showed density fluctuations were less than 1 percent. The "n" value .9569 atoms/barn, was carefully chosen to match the n value of the carbon in the polyethelene sample. Hence, by running the polyethelene, carbon, and an "open", we obtain the cross sections for hydrogen and carbon.

Our carbon results are shown in Fig. 2. Detailed comparison with the ENDF/B-V evaluation shows agreement within 2%-3% over the range 2.5 MeV-20 MeV. The statistical precision of the data is 1%, or better, between 3 and 20 MeV, and ∿3% at 40 MeV.

C. ^{6}Li and ^{7}Li

The ^{6}Li sample was obtained from Dr. C.A. Uttley of AERE, Harwell. The sample was lithium metal enriched to 95% in ^{6}Li, in a container 5.4 cm in diameter by 15.7 cm long and had a ^{6}Li "n" value of .664 atoms/barn. The ^{7}Li samples were obtained from Los Alamos Scientific Laboratory. These samples were also in metallic form and enriched to ∿100% ^{7}Li. The containers were 5.3 cm in diameter with a total length of 21 cm and a total "n" value of .7862 atoms/barn. Blank containers were supplied for both samples for the "out" runs. The lithium results are shown in Figures 3 and 4. The ^{6}Li data have been corrected for the 5% ^{7}Li content of the samples.

Conclusions

The hydrogen cross section was found to agree to within 3% of the accepted value over the entire range of interest, giving confidence in the measurement and analysis techniques. The carbon results also reproduced previous high accuracy measurements below 15 MeV to better than 3%. We therefore have confidence in our ^{6}Li, ^{7}Li and C measurements up to 40 MeV. This accuracy of 3% should be sufficient for transport and cross section calculations for the FMIT facility. All data presented here are available from the National Nuclear Data Center at Brookhaven.

References

1. R.E. Nygreh and E.K. Apperman, HEDL-TME 78-65, "FMIT Test Assemblies" (Aug. 1978).

2. H.T. Heaton II, J.L. Menke, R.A. Schrack, and R.B. Schwartz, Nucl. Sci. Eng. 56, 27 (1975).

3. G.P. Lamaze, J.K. Whittaker, R.A. Schrack, and O.A. Wasson, Nucl. Instr. and Meth. 123 (1975) 403.

4. R.B. Schwartz, R.A. Schrack, and H.T. Heaton II, "MeV Neutron Total Cross Sections," NBS Monograph 138, Appendix, National Bureau of Standards (Dec. 1973).

5. R.B. Schwartz, R.A. Schrack, and H.T. Heaton II, Phys. Lett. 30B, 36 (1969).

6. L. Stewart, R.J. La Bauve, and P.G. Young, LA-4574 (1971).

7. J. Binstock, Phys. Rev. C10, 19 (1974).

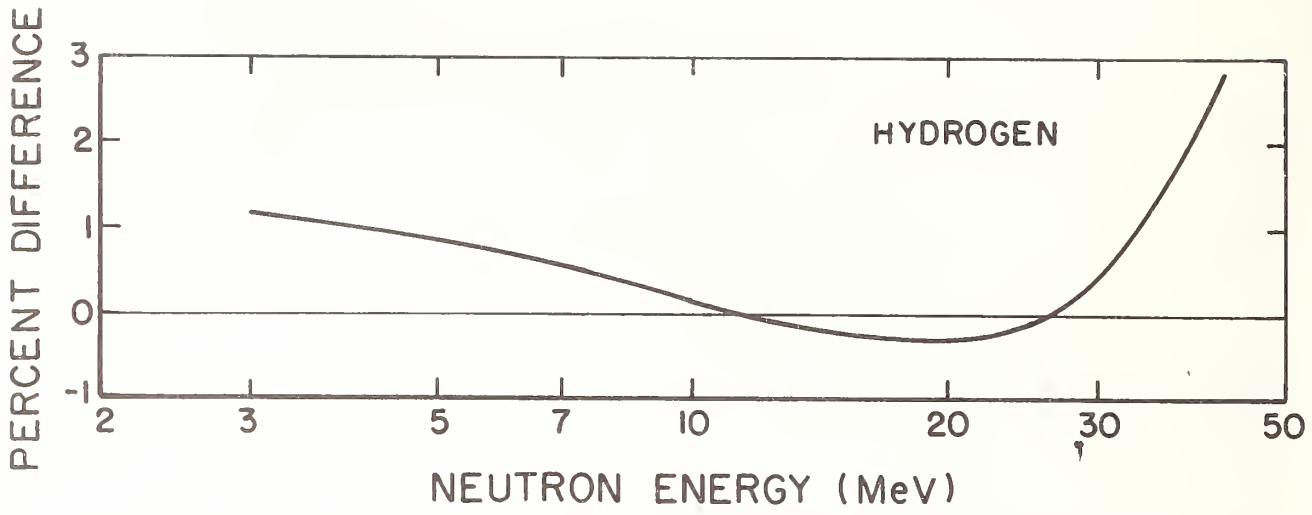

Fig. 1. Percent difference between present results and accepted values of hydrogen cross section. The accepted values are taken from Hopkins and Breit[6] below 20 MeV and from Binstock[7] above 20 MeV. The experimental curve was obtained by averaging the data over appropriate energy intervals to reduce statistical fluctuations.

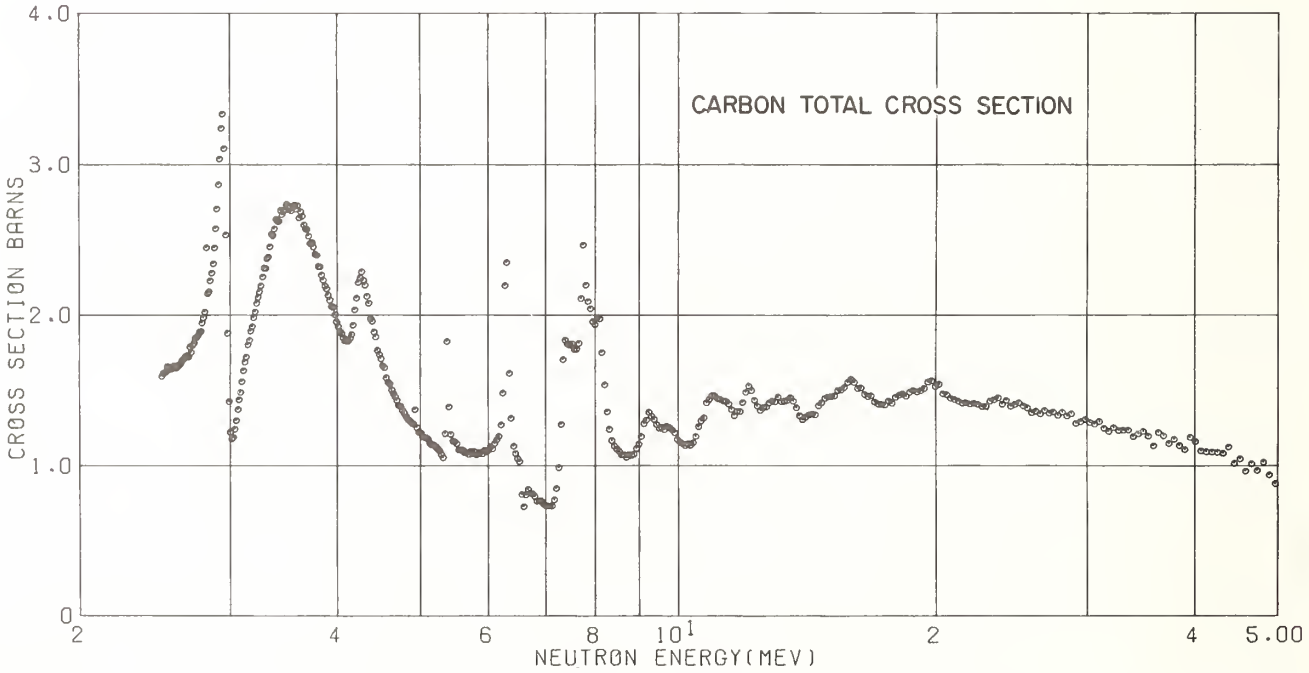

Fig. 2. The carbon total cross section obtained in this experiment. From 3 to 20 MeV, the statistical precision is better than 1%, rising to 3% at 40 MeV.

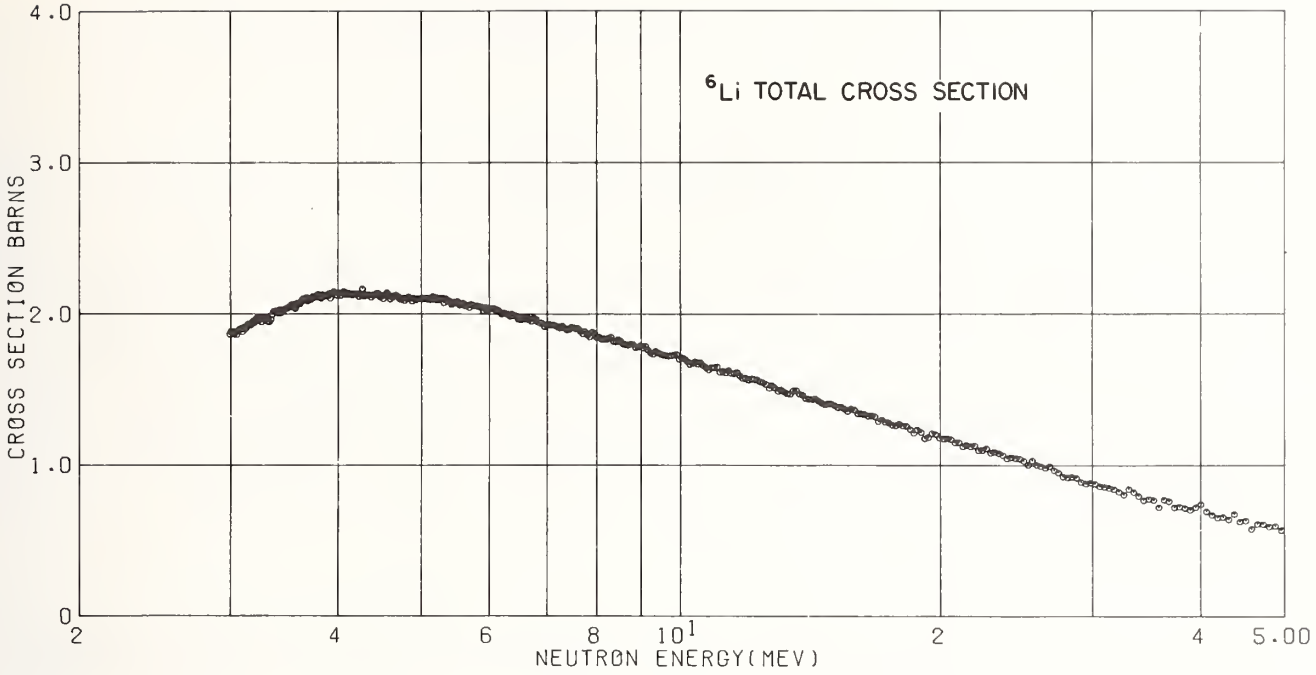

Fig. 3. The ^{6}Li total cross section obtained in this experiment. The statistical precision is ∿0.5% at 3 MeV, ∿1% at 20 MeV, and ∿3% at 40 MeV.

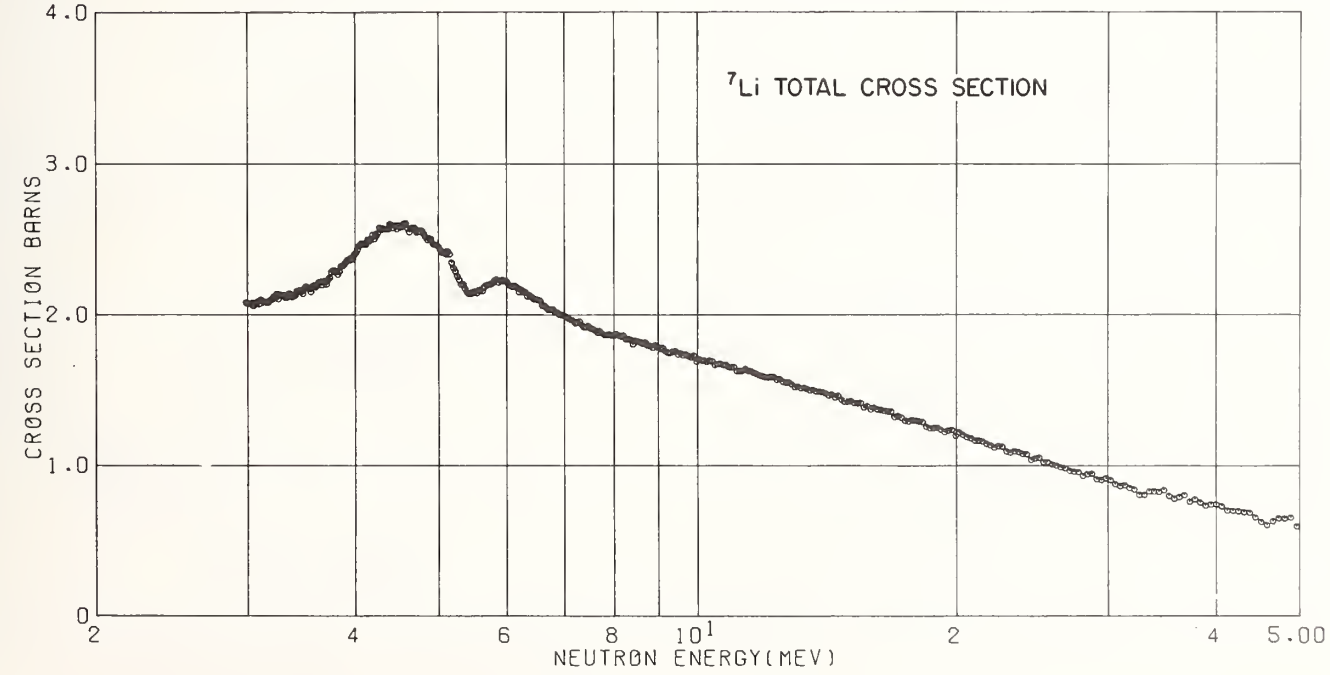

Fig. 4. The ^{7}Li total cross section obtained in this experiment. The statistical precision is ∿0.5% at 3 MeV, ∿1% at 20 MeV, and ∿3% at 40 MeV.

A COUPLED CHANNELS MODEL FOR RADIATIVE CAPTURE OF NUCLEONS BY ^{12}C.

D. L. Johnson†

University of Washington
Seattle, Washington 98195 USA

A simple model based upon coupled channels scattering calculations for nucleons on ^{12}C has been applied to the corresponding radiative capture reactions. It includes only electric dipole transitions via direct capture plus capture occurring via intermediate states consisting of only the 2+ first excited state of ^{12}C coupled to a nucleon in the s,d shell. It is shown that the shape and magnitude of measured excitation functions of the $^{12}C(p,\gamma_0)$ and $^{13}C(\gamma,n_0)$ reactions are largely reproduced for excitation energies up to about 10 MeV. Furthermore, it is shown that the excitation functions are strongly affected by competition and interference between direct capture and the indirect modes. Angular distribution data is also fairly well reproduced by the model. Implications of the success of the model will be discussed.

[Nuclear reactions, $^{12}C(p,\gamma_0)^{13}N$, $d\sigma(E_p,\Theta)/d\Omega$ E_p <9 MeV, $^{13}C(\gamma,n_0)^{12}C$, $d\sigma(E_\gamma,\Theta)/d\Omega$, E_γ<10 MeV, coupled channels model calculation, comparison to experimental data]

Introduction

There is a continuing need for development of simple nuclear models that can be applied to the understanding, prediction, and evaluation of nuclear reaction data. Here the interest was primarily in explaining data on the capture of low energy nucleons by ^{12}C.

For applied purposes, data on neutron capture by ^{12}C can be useful because, for example, (1) carbon is used in fission and fusion reactors, (2) carbon is a standard for neutron cross section measurements, (3) carbon is used in organic neutron detectors, and (4) the $^{13}C(\gamma,n)$ reaction provides a neutron source that must be considered under certain circumstances. Proton capture data may be useful for example in astrophysics.

A simple model was applied to describe the radiative capture of either neutrons or protons that was based upon coupled channels calculations which had previously been used to describe their scattering by ^{12}C. The model was very successful as will be shown and explained several complex features of experimental data.

It was somewhat surprising to see such good agreement however. Despite the successful application of the coupled channels approach to scattering, it was by no means clear that it should work as well for radiative capture. For example, weak configurations in the continuum wave functions that are neglected in the simple model might have a profound effect upon capture. The most important of these neglected configurations was expected to be that involving the giant dipole resonance of the target nucleus coupled to a single nucleon, such as is included in the so-called direct-semi-direct (DSD) capture model (Ref. 1).

The relevant structure of ^{12}C and mass 13 nuclei will be discussed. Then the data relating to capture will be described and following that, the model and its results. Finally, implications of the model will be discussed.

Relevant levels of ^{12}C and A=13 Nuclei

Radiative capture of a nucleon by ^{12}C leads to either of the mirror nuclei ^{13}C or ^{13}N. The low energy levels of these nuclei are shown in Figure 1. Shown on either side are the energy levels of ^{12}C to which each of the compound systems can decay by emission of a nucleon. Also shown are the laboratory energy scales for incident neutrons or protons which correspond to a given excitation energy in the compound system or to the threshold for inelastic scattering to a level in ^{12}C.

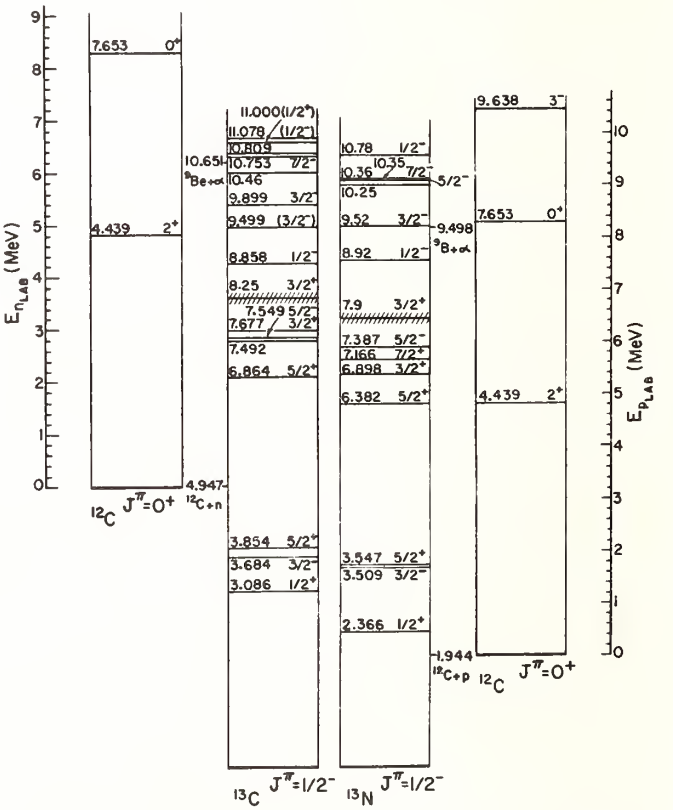

Fig. 1. Low energy level structure of A = 13 nuclei.

The proton capture reaction can be described entirely by radiative transitions to the ground state since all other states are unbound to proton decay and therefore cascade transitions cannot contribute significantly. Neutron capture can involve transitions to the three bound excited states shown, however, most of the applicable data is actually for the inverse $^{13}C(\gamma,n)$ reaction which involves only the ground state of ^{13}C. The cross section for the $^{13}C(\gamma,n_0)^{12}C$ reac-

tion is easily related by detailed balance to that of the $^{12}C(n,\gamma_0)^{13}C$ reaction. One expects a great deal of similarity in the two capture reactions because of the high degree of symmetry between the mirror nuclei.

The primary interest will be in neutron capture for incident energies less than ~ 5 MeV($E_\gamma \lesssim 9.4$MeV) and proton capture for energies less than ~8 MeV because only elastic scattering and inelastic scattering to the 2+ first excited state of ^{12}C, and radiative capture reactions are possible. Furthermore, below about 10MeV in excitation, in mass 13, the structure of the positive parity states is very simple and well understood.

Detailed shell model calculations (ref. 2) have confirmed that below ~ 10 MeV the positive parity states are composed almost entirely of the 0+ and 2+ states weakly coupled to single s,d shell nucleons, however, some mixing of configurations occurs and the 1/2+,3/2+, 5/2+, and 9/2+ states from the $(2^+ \otimes d_{5/2})$ configuration that would normally occur at ~ 8 MeV are pushed to energies greater than 10 MeV.

Capture and Photonuclear Data

There have been several measurements of the capture reaction for protons less than ~3 MeV, but only one measurement is known for the range of ~3 to 9 MeV. (Ref. 3). Figure 2 shows measured excitation functions at 90° for both the (p,γ_0) and the $(p,p'\gamma)$ (4.44MeV) reactions.

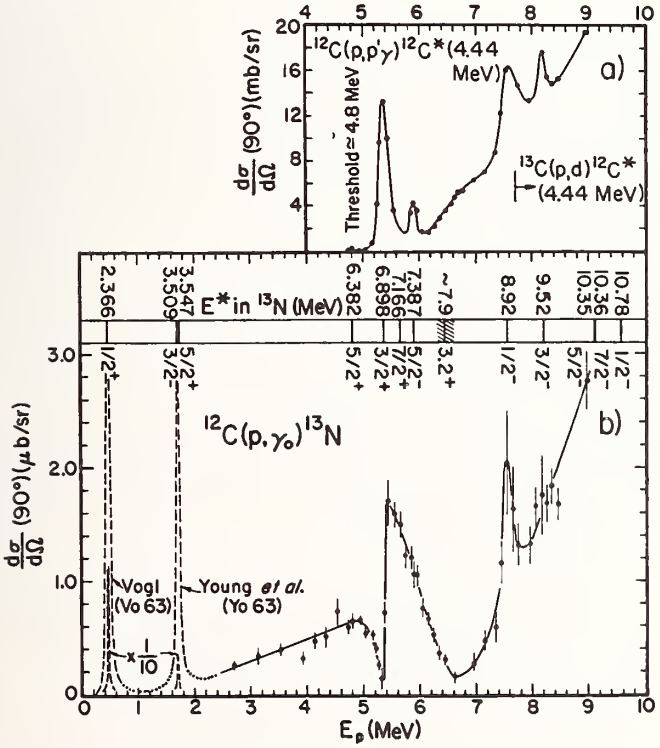

Fig. 2. Measured excitation functions of the differential cross-section at 90°. Lines are to guide the eye and are not based on theory.
a) The $^{12}C(pp'\gamma)^{12}C^*$(4.44 MeV) reaction.
b) The $^{12}C(p,\gamma_0)^{13}N$ reaction. Data from references 3, 4, and 5.

For the capture reaction data, one would expect E1 transitions to be very prominent. These would involve only 1/2+ or 3/2+ states in the compound system decaying to the 1/2 - ground state. Strong resonance effects are in fact seen that correspond to the 1/2+ state at 2.366 MeV and the 3/2+ state at 6.898 MeV in ^{13}N. Surprisingly, a minimum is seen near the only other possible E1 candidate, the broad 3/2+ state at ~7.9 MeV. A strong resonance is seen in the inelastic scattering at the lower 3/2+ state indicating that the capture reaction might also have effects associated with excitation of the 2+ state. The only other capture resonances correspond to the first 3/2- state at 3.509 MeV and the first 1/2- state at 8.52 MeV. Both of these resonances involve predominantly M1 transitions. The other compound states are not expected to be significant in capture because they would correspond to M1 multipolarity or higher and are in general rather narrow.

Since a significant capture cross-section was observed between resonances, (in particular in the wide space between ~ 3.5 to ~ 6.4 MeV in excitation), an important direct capture contribution was suggested. For direct capture, E1 radiation should predominate over higher multipoles. Thus it appears that aside from the two M1 resonances, the excitation function for capture of protons less than ~ 9 MeV is associated with E1 radiation via direct and resonant mechanisms.

There have been several measurements of the $^{13}C(\gamma,n)$ reaction at low energies. The most detailed data available at the time of this work was that of Bertozzi et al,(Ref. 6) which is shown in Figure 3. Note that the excitation function at 77° is quite similar in shape to the (p,γ_0) excitation function at 90°.

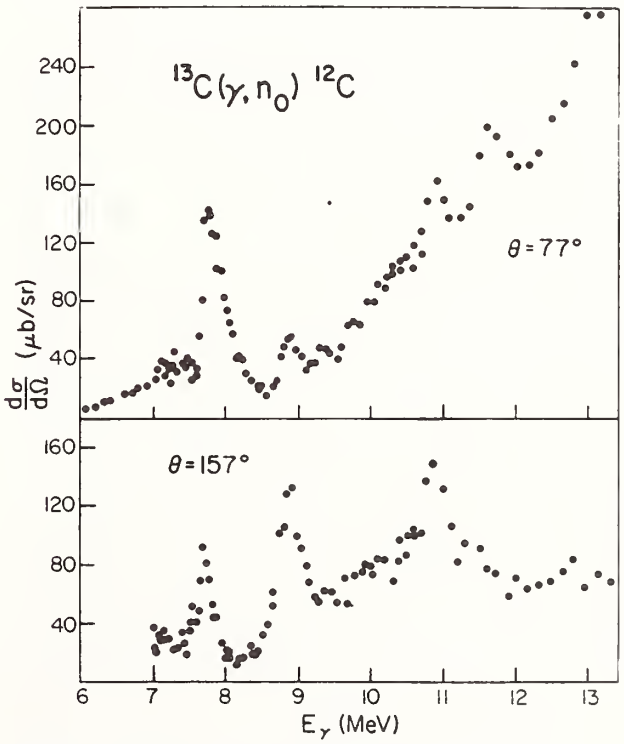

Fig. 3. Measured excitation functions of the $^{13}C(\gamma,n_0)^{12}C$ reaction. Data are taken from Bertozzi et al. (Ref. 6).

The data of Bertozzi et al, were quite useful for the theoretical comparisons to be discussed. It was known that E1 capture or photoemission involving the ground state has an angular distribution that can be described with only two terms in a Legendre expansion.

$$\frac{d\sigma}{d\Omega}(\theta) = A_o\ (1 + a_2 P_2(\cos\theta)\ ) \qquad (1)$$

Therefore it was possible to solve for the total cross section ($4\pi A_o$) and the a_2 coefficient at each energy in the excitation function where measurements at the two angles were made. Near the M1 resonance at ~9 MeV, there can be an additional $a_1 P_1(\cos\theta)$ term in the angular distribution due to E1/M1 interference. Hence, this procedure was not used for energies near the 9 MeV resonance.

The Capture Model

The capture model is briefly outlined here, details may be found in Ref. 3. The cross section for radiative capture from a continuum state to a bound state is proportional to the square of the electromagnetic matrix element between the initial continuum wave function and the final bound state wave function.

Here the electric dipole operator was used and wave functions for only the 1/2+ and 3/2+ incident channels were needed.

The initial continuum wave functions were provided by solution of a coupled channels optical model calculation of the scattering of nucleons by ^{12}C.

The incident wave function corresponding to the $J^\pi = 3/2^+$ channel can be written in the following short hand notation which represents the presence of excited core states.

$$\psi_i(3/2^+) = (0^+ \otimes d_{3/2})^{3/2^+} + (2^+ \otimes s_{1/2})^{3/2^+} + (2^+ \otimes d_{5/2})^{3/2^+} + (2^+ \otimes d_{3/2})^{3/2^+} \qquad (2)$$

For each configuration in the expansion, the coupled nucleon has a different radial wave function which varies with the incident energy. The expansion for the $1/2^+$ incident channel is analogous.

The coupled-channels scattering calculations of Mikoshiba, Tanifuji, and Terasawa (Ref. 7) have been reproduced in this work in order to generate the continuum wave functions. Their view was that the 0^+ and 2^+ states were the lowest states in the ground state rotational band of an oblate deformed ^{12}C nucleus. ($\beta = -0.5$). Excitation of the 2^+ state was treated phenomenologically via an interaction of the incident nucleon with the non-spherical part of a deformed oblate optical potential. A great deal of effort was made by Mikoshiba, et al., to reproduce the excitation functions of proton elastic and inelastic scattering cross sections and to give the correct locations for positive parity resonances below about 10 MeV in ^{13}N. In order to fit the resonant states, the real optical potential describing the interaction of a nucleon with ^{12}C was allowed to depend slightly upon the nucleon energy. In addition, a spin orbit potential and very weak spin-spin and (ℓ^2) orbital angular momentum dependent interactions were incorporated. No imaginary potential was used because all scattering channels were explicitly included. The scattering of neutrons by ^{12}C was then described using the same potential, after removing the coulomb term.

The wave function of the ground state of either ^{13}N or ^{13}C must be expanded in the same weak coupling form as the incident wave function for use in capture calculations. It has been shown (Ref. 8) that the ground state expansion includes many ^{12}C core states coupled to p-shell nucleons. The largest configurations involve the 0^+ ground state, 2+ states at 4.44 and 16.1 MeV, and 1^+ states at 12.7 and 15.1 MeV. However, only configurations involving the 0^+ and 2^+ first excited states coupled to p-shell nucleons can couple via E1 radiation to the simple continuum wave functions that have been considered. The important parts of the ground state wave function can be written as

$$\psi_f(1/2^-) = \theta_1 (0^+ \otimes P_{1/2})^{1/2^-} + \theta_2 (2^+ \otimes P_{3/2})^{1/2} + \ldots \qquad (3)$$

Here θ_1 and θ_2 are expansion coefficients which are related to the spectroscopic factor for each configuration.

The radial wave functions for each of the bound configurations were calculated using a Woods-Saxon form and a spin orbit term. The same radius, diffuseness, spin orbit, and coulomb potential parameters were used as for the coupled channels scattering calculations, however, the depth of the potential was adjusted to reproduce the binding energy of a single nucleon for each configuration. The binding energy of a nucleon coupled to the 2^+ state was taken to be 4.44 MeV more than the normal ground state binding energy.

The expansion parameters of the ground state wave function were taken from spectroscopic factors calculated by Cohen and Kurath (Ref. 8), whose results have been shown to be in good agreement with a wide variety of experimental data for p-shell nuclei. The values were $\theta_1 = 0.783$ and $\theta_2 = 1.059$, hence the probabilities for each configuration were comparable.

An example of the radiative capture mechanism is shown schematically in Figure 4. Here one sees a $d_{3/2}$ proton incident upon the 0^+ target. After collision, a compound system is formed with a wave function as in equation 2. Each of the configurations in the compound system can radiate via E1 single particle transitions to a configuration in the $1/2^-$ ground state with the core states of ^{12}C acting only as spectators. Direct capture takes place via radiative decay of the $d_{3/2}$ nucleon to a bound $p_{1/2}$ orbital. A similar process occurs for capture via the $1/2^+$ incident channel.

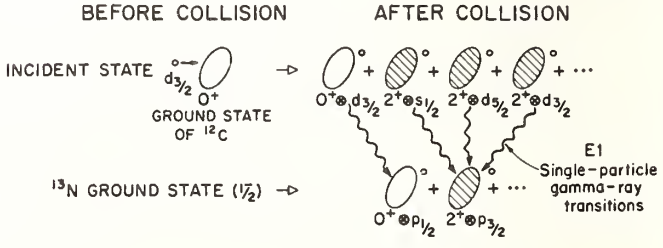

Fig. 4. Schematic diagram of the $^{12}C(p,\gamma_o)^{13}N$ reaction involving coupled-channels capture via excitation of the 2^+ first excited state of ^{12}C. Incident channel is $J^\pi = 3/2^+$.

It can be shown that the cross section for E1 capture to the ground state can be written as

$$\sigma = \frac{4K\gamma[M_{1/2^+}{}^2 + 2M_{3/2^+}{}^2]}{3\hbar v_1} \qquad (4)$$

where $M_{1/2^+}$ and $M_{3/2^+}$ are the reduced matrix elements for E1 transitions via either the $1/2^+$ or $3/2^+$ incident channels, $K\gamma$ is the photon wave number, and v_1 is the relative velocity of the incident nucleon and the target. Furthermore, because of the wave functions, each matrix element is expressed as the sum of several coherent contributions as in Figure 4. For the $3/2^+$ channel, the matrix element can be written as

$$M_{3/2^+} = \langle 3/2^+ | E1 | 1/2^- \rangle = \Theta_1 A_1 + \Theta_2 A_2 + \Theta_2 A_3 + \Theta_2 A_4 \qquad (5)$$

where Θ_1 and Θ_2 are the ground state expansion parameters and the A's are partial amplitudes for each of the E1 single particle transitions in Figure 4. For example, $A_4 = \langle 2^+ \otimes s_{1/2} | E1 | 2^+ \otimes p_{3/2} \rangle$

Interference effects may be expected between the transitions contributing to each of the reduced matrix elements.

The angular dependence was also calculated for both capture and photonuclear reactions. For pure E1 capture, the angular distribution has the form shown in equation 1. The a_2 coefficient can be expressed as

$$a_2 = \frac{2\mathrm{Re}(M_{1/2} * M_{3/2}) - M_{3/2}{}^2}{M_{1/2}{}^2 + 2\,M_{3/2}{}^2} \qquad (6)$$

This coefficient is sensitive to the ratio of capture proceeding via either the $1/2^+$ or $3/2^+$ incident channels. The first term in the numerator is related to E1/E1 interference between transitions via the two incident channels. If one ignores this term then the a_2 coefficient is bounded between $a_2 = 0.0$ (isotopic) for capture solely via $1/2^+ \rightarrow 1/2^-$ transitions and $a_2 = -0.5$ for capture solely via $3/2^+ \rightarrow 1/2^-$ transitions. The effect of the interference term could give an a_2 coefficient outside these limits.

Results

Calculations of the radiative capture cross section were made for protons up to 9 MeV and for neutrons up to 6 MeV using the model described above. The results for proton capture evaluated at 90° are compared to the experimental data between 2.7 and 9 MeV in Figure 5. The agreement is excellent except for the two M1 resonances shown in Figure 2, which are not included in the model resonance. The parameters used in the model appear to be near optimal. Some studies of the sensitivity to these parameters have been done but will not be presented here.

Results of calculations of the neutron capture cross section are shown in Figure 6. The shape is quite similar to that for proton capture, as expected, except for the low energy (p,γ) resonances that cannot occur in neutron capture.

The results of calculations of the (γ,n_0) cross section are compared to a sampling of experimental data in Figure 7. Agreement is not quite as good as for the p,γ_0 reaction, however, it is believed that small changes in the model would give excellent agreement.

To examine what determines the shape of the calculated cross section, the contributions from each of

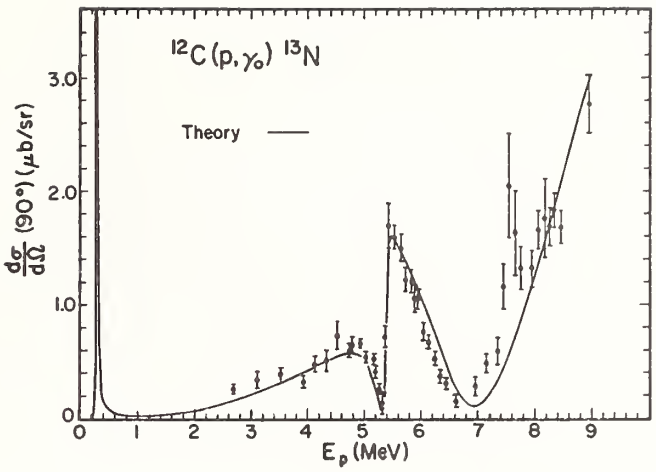

Fig. 5. $^{12}C(p,\gamma_0)^{13}N$ reaction. Comparison of calculated and measured excitation function at 90°. Data from 2.7 to 9 MeV only (Ref. 3).

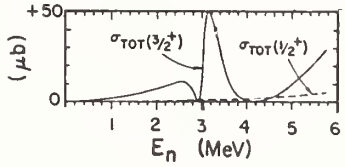

Fig. 6. $^{12}C(n,\gamma_0)^{13}C$ reaction. Calculated cross sections for $1/2^+$ and $3/2^+$ incident channels.

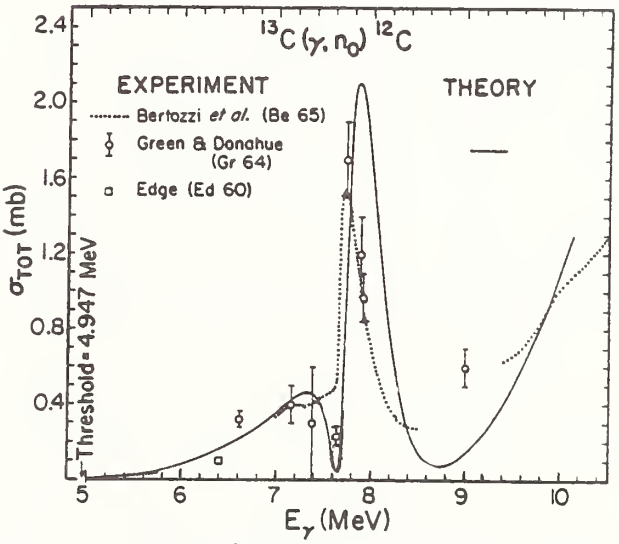

Fig. 7. $^{13}C(\gamma,n_0)^{12}C$ reaction. Comparison of calculated and measured cross-sections.

the transitions involved in the $3/2^+$ incident channel are shown separately in Figure 8 along with interference effects. The total contribution from capture via the $1/2^+$ incident channel is also shown but is small except for the low energy resonance which is predominantly direct capture via an $s_{1/2} \rightarrow p_{1/2}$ transition. Cross sections for capture via the transitions shown in Figure 4 are labeled 1 to 4. Curves labeled by two numbers correspond to the effects of interference between two transition channels.

The direct capture contribution (channel 1) is seen as a broad resonance centered near a proton energy where one expects a potential scattering resonance in the elastic $d_{3/2}$ channel. However, a strong dip is seen in this contribution due to competition effects associated with a resonance in the $(2^+ \otimes s_{1/2})^{3/2^+}$ configuration of the incident wave function. Note that

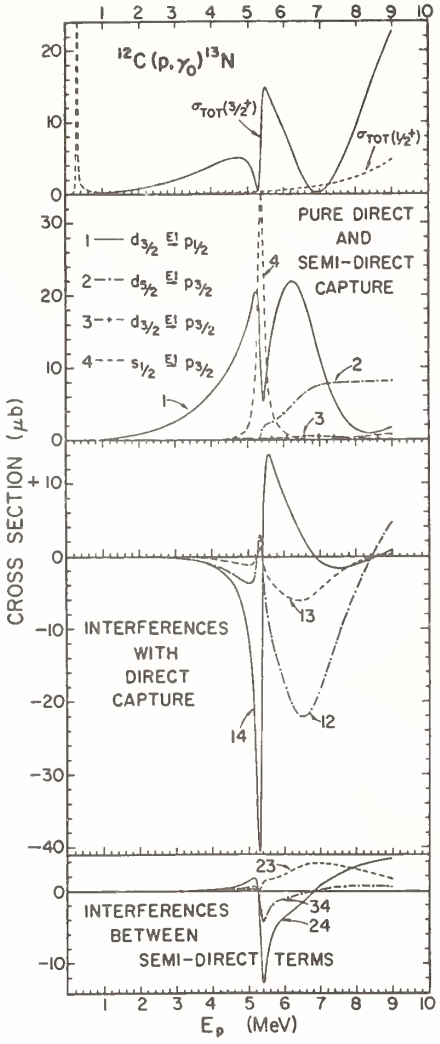

Fig. 8. $^{12}C(p,\gamma_0)^{13}N$ reaction. Shown are contributions due to pure direct capture, semi-direct capture, and the interferences between them (only capture via the $3/2^+$ incident channel is broken down).

the direct capture contribution is not at all like experimental observations.

Capture that proceeds via the inelastic configurations has a profound effect upon the shape and magnitude of the excitation function. For example, the strong interference minimum seen for protons of ~5.3 MeV is caused by interference between direct capture and capture via the $(2^+ \otimes s_{1/2})^{3/2^+} \rightarrow (2^+ \otimes p_{3/2})^{1/2^-}$ transition (channel 4). Also, the broad minimum for protons of ~ 7 MeV is due mainly to interference between direct capture and the $(2^+ \otimes d_{5/2})^{3/2^+} \rightarrow (2^+ \otimes p_{3/2})^{1/2^-}$ transition (channel 2). Furthermore, the rise in cross section at higher energies is caused predominantly by capture via the $(2^+ \otimes d_{5/2}) \rightarrow (2^+ \otimes p_{1/2})$ transition (channel 2) plus constructive interferences between it and the other inelastic capture channels. At the lowest energies, the direct mechanism dominates as might be expected.

The a_2 coefficient of the angular distribution was calculated for both the (p,γ_0) and (γ,n_0) reactions. The results are compared in Figure 9 to the values derived from the (γ,n_0) data of Bertozzi, et al.(Ref.6) described earlier. Note that the a_2 coefficient varies significantly with energy, indicating the changes in the ratio of transitions via the 1/2+ continuum channel compared to the 3/2+ channel. Since the a_2 coefficient exceeds the limits of 0 and -0.5 described earlier, it reflects the interference between the two E1 modes. The calculated a_2 coefficient is considered to be in fairly good agreement with the experimental data which are of unknown quality.

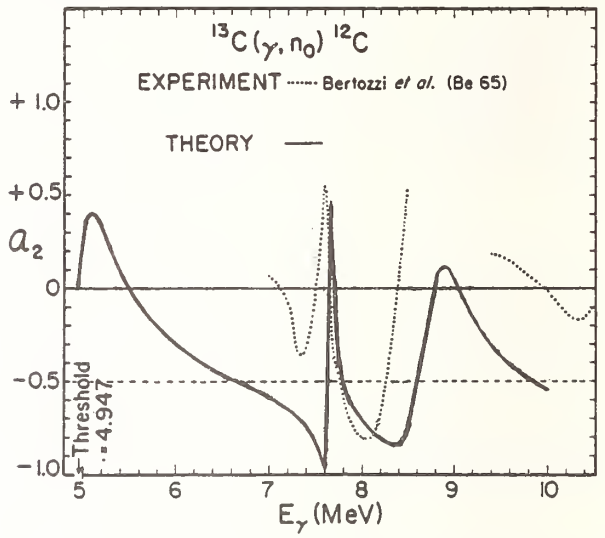

Fig. 9. $^{13}C(\gamma,n_0)^{12}C$ reaction. Comparison of calculated a_2 coefficient to experimental results.

Discussion

Considering the complexity of the competion and interference effects, it is surprising that the shape and magnitude of the experimental data are so well reproduced. It is apparent that the coupled channels calculations of Mikoshiba, et al. (Ref. 7) provide an excellent description of the important continuum wave functions.

The success of the model seems to imply that weak configurations in the continuum wave functions that were neglected are not important for capture at these low energies. One might expect a small probability for configurations such as $(1^+ \otimes s_{1/2})^{3/2^+}$ in the continuum wave function where the 1^+ state is either the 12.71 MeV (T=0) or the 15.1 MeV (T=1). Such configurations could radiate to the ground state via E1 single particle transitions just like the ones considered. However, one would not expect such configurations to become important until higher energies in the weak coupling view. Furthermore, the transition amplitudes would tend to be small because of the deep binding of the nucleon coupled to the highly excited core state in the ground state configuration.

A more important configuration for E1 capture might be expected from a configuration in the compound system having the giant dipole resonance of ^{12}C coupled to a p-shell nucleon (e.g. $(1^- \otimes p_{1/2})^{3/2^+}$). Such a configuration could radiate strongly to the ground state because of collective E1 enhancement even when only a small admixture is present in the compound system. It is explicitly included in the so-called DSD model (Ref. 1). It can be shown that at low energies, the effects of the coupled channels mechanism are dominant over the DSD mechanism because of a large overlap of radial wave functions external to the compound system which does not occur for the DSD mechanism.

Another way of viewing the simple mechanism described is from the point of view of photonuclear reactions. It is well known that for light nuclei away from closed shells, there is considerable E1 strength

below the main dipole states at ~ 20 MeV. The broad pygmy resonance in mass 13 nuclei at ~ 13 MeV is a good example of this effect. Note that the model described here predicts the lower part of the pygmy resonance to be associated primarily with the $(2^+ \otimes d_{5/2})^{3/2+}$ configuration in the continuum.

One would therefore expect that capture involving low lying excited target states might be applicable at low energies for other light targets that do not lead to closed shells. For example, the $^{17}O(\gamma,n)$ reaction at low energy (Ref. 11) shows effects very similar to those seen here including a significant resonant dip that might be explained as the effect of competition or interference between modes involving various core states. Note that a similar coupled channels model was developed by Buck and Hill (Ref. 12) to treat photonuclear reactions on closed shell nuclei. Some success was obtained for ^{16}O. A significant difference was that here a complex wave function was used for the ground state.

The model described here has similarities to the valence model (Ref. 13) in that a significant portion of the capture occurs via the direct transition and is correlated with the nucleon width. It is also similar to the DSD model (1) in that core excited states are involved, however, here the coupled single nucleons decay rather than the core state. It is also similar to a compound nuclear mechanism in which only the first stage of core excitation is involved. Note that resonances such as the first $1/2^+$ state in ^{13}N have been treated as compound nuclear effects (Ref. 14) with an underlying direct component, however, in the present model it is predominantly a direct capture resonance.

Work supported in part by the U.S.A.E.C. (at (45-1) -1388, Prog. A).

†Present address: Westinghouse Hanford Company, Richland, Washington 99352

References

1. G.E. Brown, Nucl. Phys. 57 (1964) 339.

2. H.U. Jäger, H.R. Kissener, and R.A. Eramzhian. Nucl. Phys. A171 (1971) 16.

3. D.L. Johnson, Phd. Dissertation, University of Washington (1974), unpublished.

4. J.L. Vogl, Phd. Dissertation, California Institute of Technology (1963), unpublished.

5. F.C. Young, J.C. Armstrong, and J.B. Marion. Nucl. Phys. 44 (1963) 486.

6. W. Bertozzi, P.T. Demos, S. Kowalski, F.R.Paolini, C.P. Sargent, and W. Turchinetz. Nucl. Instr. and Meth. 33 (1965) 199.

7. O. Mikoshiba, T. Terasawa, and M. Tanifuji. Nucl. Phys. A168 (1971) 417.

8. S. Cohen and D. Kurath. Nucl. Phys. A101 (1967) 1.

9. L. Green and D.J. Donahue. Phys. Rev. 135 (1964) B701.

10. R.D. Edge, Phys. Rev. 119 (1960) 1643.

11. R.J. Holt, H.E.Jackson, R.M. Laszewski, J.E. Monahan, and J.R. Specht. ANL-78-66 (ANL Physics Div. Annual Report) pg. 116.

12. B. Buck and A.D. Hill. Nucl. Phys. A95 (1967) 271.

13. J.E. Lynn. Theory of Neutron Resonance Reactions, Oxford Univ. Press. (1968) pg. 326.

14. C. Rolfs and R.E. Azuma, Nucl. Phys. A227 (1974) 291.

EVALUATION OF ^{23}Na FOR ENDF/B-V

D. C. Larson
Oak Ridge National Laboratory
Oak Ridge, Tennessee 37830, USA

Version V of the Evaluated Nuclear Data File (ENDF) for sodium is described. Major changes have been made in the total, capture, inelastic scattering and (n,2n) cross sections, as well as the elastic scattering angular distributions and gamma-ray-production files. ENDF/B-IV and V and compared where major changes were incorporated. New measurements needed to fill data gaps or resolve discrepancies among existing data sets are discussed.

[Sodium, evaluation, cross sections, neutrons]

Introduction

Since sodium is the proposed coolant in most fast breeder reactors, as well as in some conceptual fusion device designs, a precise description of sodium cross sections appropriate for technological applications is necessary. The purpose of this paper is to provide a brief summary of the cross sections included in the latest version of the Evaluated Nuclear Data File, ENDF/B-V, material number (MAT) 1311.[1] Cross sections are provided there for all major neutron-induced reactions from 10^{-5} eV to 20 MeV. The last major update of this evaluation was done by T. A. Pitterle and N. C. Paik[2] for ENDF/B-III in 1971. The energy range was extended to 20 MeV for ENDF/B-IV in 1974, with no other changes. Since 1971, much new experimental data for sodium has become available, and advances have been made in nuclear model theory. Utilizing this new information, nearly all of the cross sections were changed for ENDF/B-V. In this paper we will outline the major changes, and compare them graphically with cross sections from ENDF/B-IV.

Total Cross Section

Three significant new measurements are available for the neutron total cross section. The transmission data and accompanying analysis of Seltzer and Firk[3] provide a good description of the important resonance at 2.805 keV. Their R-matrix analysis of this resonance yielded values of J=1 for the spin and a Γ_n value of 0.376 keV. These results have been used in Version V; Version IV had values of E_R=2.85 keV and Γ_n=0.410 keV.

The thick sample measurements of Brown *et al.*[4] at RPI provide useful results near deep minima. Since sodium is present in large amounts in an LMFBR, it acts as a shielding material as well as the coolant. This requires accurate cross section values in the minima of s-wave resonances, where the neutrons most readily leak out. The third measurement which heavily impacts the evaluation for ENDF/B-V is the measurement of Larson, Harvey and Hill[5] in which the total cross section from 32 keV to 32 MeV was measured. This measurement has better energy resolution than any other available data, and a multilevel analysis of these data was used to extend the upper limit of the resolved resonance region from 160 keV in Version IV to 500 keV for Version V. Resonance energies and neutron widths obtained from fitting these data with the code SIOB[6] are presented in Table 1. In addition, the cross sections from this measurement are on the average 3-5% lower than ENDF/B-IV, resulting in improved agreement with a shielding benchmark measurement[7] of neutron transmission through thick slabs of sodium. Figure 1 compares the ORNL data, the multilevel fit used in Version V, and the ENDF/B-IV evaluation for the energy region from 190 to 270 keV. This energy range underwent the largest change from Version IV to V. Figure 2 shows the region around the 300-keV s-wave resonance. The RPI[4] and ORNL[5] data are in good agreement in the minimum, and show that the minimum is both deeper and broader than given in Version IV. We also note the p-wave resonance on top of the s-wave resonance peak. This is the first observation of this resonance, and shows that the 300-keV s-wave resonance, which has been considered[8] for energy calibration purposes, is actually a doublet.

Capture Cross Section

Two new measurements are available for capture cross sections. The measurement and analysis of capture in the 2.805-keV resonance by Wilson, Jackson, and Thomas[9] of ANL indicate that Γ_γ is in the range 0.24 eV $\leq \Gamma_\gamma \leq$ 0.40 eV. Preliminary analysis by Macklin[10] of the capture data of Musgrove, Allen and Macklin[11] at ORNL provide a value of Γ_γ = 0.385 ± 0.040 eV. These measurements are consistent with Γ_γ = 0.353 eV, which gives the measured thermal capture value of Ryves[12] of 528 mb. Thus for Version V, Γ_γ for the 2.805-keV resonance was changed from 0.47 eV to 0.353 eV. Γ_γ values for the remainder of the capture resonances up to 500 keV were obtained from the capture areas of Musgrove, Allen and Macklin,[11] and the neutron widths and J^π values were obtained from the multilevel analysis of the ORNL transmission data. The Γ_γ resonance parameters used in the Version V evaluation are presented in Table 1.

Inelastic Scattering Cross Sections

Up to an incident neutron energy of 4 MeV, there is much experimental data available describing inelastic scattering to the first excited level at 440 keV.[13-23] Most of these are low energy-resolution measurements, in which either the scattered neutron or resulting gamma ray are detected. Two high resolution measurements are available[18,23] which show much resonance structure in this cross section. This structure explains why many of the low resolution measurements are in apparent disagreement, since they have differing energy resolution, and a small error in energy calibration can cause a significant change in cross section, dependent on the nearby resonance structure. Evaluation of this cross section from threshold to 2.4 MeV was done by binning the available data into energy bins ranging from 100 keV to 500 keV, obtaining an energy averaged cross section, weighted heavily by the recent measurement of D. L. Smith[21] at ANL, and renormalizing the high resolution data sets to agree with the average. The energy averaged cross sections agree in shape, with the exception of the data of Donati *et al.*[15] where the data are shifted ∿125 keV too high in energy, and the ENDF/B-IV evaluation, based on Ref. 23, which was too large between 1.0 and 1.4 MeV. However, there was a serious problem with normalization between the various data sets, the largest difference being ∿25% around 1.1 MeV. The problem was resolved by taking the high resolution excitation function measured by Larson and Morgan[18] (which agreed well in shape with other data sets during the various averaging procedures) and

renormalizing its measured values downward by 8% (within the stated uncertainty of ±10%) to agree with the nominal value obtained from averaging the other measurements. This procedure provides the values for the evaluation of this cross section from 0.440 MeV to 2.4 MeV. From 2.4 MeV to 4.5 MeV, data of Donati *et al.*,[15] Fasoli *et al.*,[16] and Day[19] were utilized, with the data of Donati *et al.*[15] shifted down in energy by 125 keV to agree in shape with other measurements. From 4.5 to 20 MeV, the data of Refs. 24-28 were used, with the neutron inelastic scattering cross sections extracted from Dickens'[26] data by subtracting the feeding of the 440-keV level using his measured cross sections. At 17.5 MeV, the (p,p') data of Crawley *et al.*[25] were used to estimate the cross section for the 440-keV level, and DWBA calculations, assuming a deformation parameter β=0.1 were used for extrapolation of the cross section to 20 MeV. Figure 3 shows the available data, together with Version IV and V evaluations, from threshold to 2 MeV.

Evaluation of inelastic scattering to the higher excited levels was done in a manner similar to the evaluation of the 440-keV level, but no high resolution data were available. The majority of the available data were provided by the measurements of Donati,[15] (again corrected for the energy shift observed in the 440-keV data), Kinney and Perey,[28] and Dickens.[26] Nuclear model calculations, utilizing the TNG[29] code which included precompound effects, were also employed. For excitation energies $E_x \geq 6.1$ MeV, no experimental data were available, and the inelastic scattering was lumped into the continuum. Values for the continuum cross section were taken from the TNG model calculation, which included competition with the (n,p), (n,α), and (n,2n) reactions.

(n,2n) Cross Section

The (n,2n) cross section, with a threshold at 12.96 MeV, is more important for fusion than fission devices. The resulting nucleus, ^{22}Na, is radioactive with a half-life of 2.61 years, and could present troublesome maintenance problems where sodium is present. Evaluation of this cross section has been difficult because three of the four major data sets[30-33] differ significantly as shown in Fig. 4. For ENDF/B-IV the evaluation was taken from Version III (which had an upper limit of 15 MeV) and extended[34] to 20 MeV by arbitrarily scaling the 15-MeV cross section by the ratio of σ_{total}(20 MeV)/σ_{total}(15 MeV). This gives rise to the strange shape for Version IV. For Version V, we performed extensive model calculations utilizing the advanced model code TNG to provide consistency checks among cross sections for the various reactions. Neutron optical model parameters were obtained from an optical model analysis of nine sets[22,24,27,28] of elastic scattering data from 4 to 14 MeV, and the neutron total cross section.[5] Proton[35] and alpha[36] particle parameters were taken from the literature, with the strengths slightly adjusted to reproduce the (n,p) and (n,α) reactions at low neutron energies. Level density parameters were taken from Gilbert and Cameron,[37] and adjusted to reproduce experimental level density information. The compilation of Endt and Van der Leun[38] was used to obtain spins, parities and branching ratio information. The code TNG includes effects of precompound processes as well as angular momentum conservation, and allows competition between binary and tertiary reactions. Experimental data reproduced by these calculations include inelastic scattering to levels up to 5.8 MeV excitation in ^{23}Na, (n,p) and (n,pγ) activation data, (n,α) and (n,$\alpha\gamma$) activation data, a gamma-ray-production measurement for neutron energies from 400 keV to 20 MeV,[18] and a neutron production measurement at 14.6 MeV.[39] Results of these calculations, compared with experimental data, will be found in Ref. 40. The results of these calculations, fixed by the requirement of reproducing the previously mentioned reactions, are in agreement with the (n,2n) data set of Liskien and Paulsen,[30,32] as shown in Fig. 4. With the present nuclear model code used, it is not possible to reduce the calculated (n,2n) cross section to agree with the other measurements of this cross section, and still retain acceptable cross sections for the other reactions. In view of the discrepant experimental information, the evaluation of the (n,2n) cross section for Version V utilized the results of model calculations, and is shown in Fig. 4.

Elastic Scattering Angular Distributions

Based on new experimental information, the elastic scattering angular distribution file was extensively changed from 500 keV to 2 MeV. In a high resolution experiment, Kinney and Perey[41] from ORNL measured the elastic scattering in 1-keV steps from 500 keV to 2 MeV at five angles, and observed much more structure in the angular distribution than previously seen in lower resolution work. Since a maximum of 500 energies is allowed to represent angular distribution data, the data were thinned, using a code from LASL.[42] The criteria chosen for thinning the data were that from one energy to the next, the maximum RMS deviation allowed was 15%, and the maximum angle-to-angle variation allowed was 25%. This reduced the 1500 measured angular distributions from 500 keV to 2 MeV to 473, while retaining the significant structure. Figure 5 shows the thinned Legendre coefficients for a_1, a_2 and a_3, along with the Version IV coefficients. In Version IV, an excessive number of coefficients were used to describe the data (e.g., nine coefficients at 30 keV). For Version V, we refit the Version IV evaluation from 10^{-5} eV to 500 keV, using the minimum number of coefficients needed to adequately describe the angular distributions. From 4 MeV to 14 MeV, the data of Refs. 22, 24, 27 and 28 were fit with Legendre coefficients and put in the evaluation. From 14 to 20 MeV, results of optical model calculations using parameters obtained from fitting the measured data from 4 to 14 MeV were used for the evaluation.

Gamma-Ray-Production Cross Sections

Gamma-ray-production cross sections resulting from interaction of neutrons with sodium were revised for Version V, based on new experimental data. For Version IV the gamma-ray production was generated from the cross sections for neutron inelastic scattering together with the appropriate branching ratios. For incident neutron energies greater than 8 MeV, the cross sections were represented by continuum distributions taken from the 1967 evaluation of Garrison and Drake.[43] The use of branching ratios caused difficulties for some of the processing codes. In particular, for the case of sodium prior to December 1977, the LAPHNGAS code at ORNL produced processed libraries containing zero values for the gamma-ray production for incident neutrons between 8 and 9 MeV. For these reasons, and because of discrepancies between ENDF/B-IV and a benchmark gamma-ray-production measurement,[44] we felt a new evaluation was needed. A number of new measurements of gamma-ray-production cross sections for individual gamma rays at discrete incident neutron energies up to 8 MeV were available. Also, a sodium (n,xγ) measurement[18] covering the neutron energy range from 400 keV to 20 MeV, and gamma energies from 350 keV to 10.6 MeV, was available. The production cross sections for the discrete gamma rays were compared with the results of the (n,xγ) measurement and generally found to be in agreement within experimental uncertainties. Since the (n,xγ) measurement covered the complete energy range required in ENDF, these data were used directly in the Version V gamma-production file. There is good average

agreement between Version IV and Version V for all gamma rays produced by neutrons up to an incident neutron energy of 8 MeV. For higher incident neutron energies, Version V has significantly more structure in the gamma spectra, and larger cross sections for production of gamma rays. Figures 6 and 7 show a comparison of the data used for Version V with the Version IV evaluation.

Cross Section Uncertainties

Version V of ENDF/B for sodium also contains estimates of uncertainties for the cross sections. Uncertainties are given for the resonance parameters, and the total, elastic, nonelastic, inelastic, (n,2n), (n,γ), (n,d), (n,p) and (n,α) cross sections. The results given in these files are estimates of one standard deviation based on the spread of the different data sets for a given reaction, and a "best guess" in cases where there are not enough measurements to obtain an estimate in their spread.

Summary and Conclusions

In summary, significant changes have been made in the total cross section for ENDF/B-V, including the important 2.805-keV resonance, and the resolved resonance region has been extended from 160 keV to 500 keV, based on a multilevel analysis of new experimental results. The capture cross section has also benefited from new data and has been extensively revised up to 500 keV. Inelastic scattering has been lowered for the 440-keV level by 5-15% from threshold to 2.4 MeV, and modified from 2.4 to 20 MeV. Changes have also been made, based on new experimental data and model calculations, for other inelastic scattering cross sections up to an excitation energy of 5.8 MeV. The (n,2n) cross section has been increased (by a factor of $\sim$2 at 16 MeV and $\sim$4 at 20 MeV) based on results of extensive model calculations. The elastic scattering angular distribution file has been extensively modified from 500 keV to 2 MeV, in particular there is much more structure in the Legendre coefficients. Gamma-ray production has been significantly changed for incident neutron energies above 8 MeV, and uncertainties are included for all of the cross sections except the angular and energy distributions and gamma-ray production.

Further measurements would be useful for both Γ_n and Γ_γ of the 2.81-keV resonance, inelastic scattering for incident neutron energies above 8 MeV to all levels, and from threshold to 20 MeV for the 440-keV level. New data are needed to resolve the (n,2n) cross section discrepancy, and new (n,$\alpha\gamma$) activation measurements from 8-20 MeV are needed. Finally, more detailed discussions of experimental uncertainties and correlations in measurements are desperately needed in order to provide a basis for deriving meaningful uncertainty files in future evaluations.

Acknowledgements

I wish to thank C. Y. Fu for helpful discussions concerning the model calculations and for use of his model code TNG. D. M. Hetrick provided the plots for this paper. I also wish to thank F. G. Perey for advice and support during this evaluation.

Research sponsored by the U. S. Department of Energy, Office of Basic Energy Sciences, under contract No. W-7405-eng-26 with Union Carbide Corporation.

References

1. ENDF/B-V data file for ^{23}Na (MAT 1311), evaluation by D.C. Larson (ORNL), available from the National Nuclear Data Center, Brookhaven National Laboratory, Upton, N. Y. (October 1978).
2. ENDF/B-III data file for ^{23}Na (MAT 1156), evaluation by T.A. Pitterle and N.C. Paik (Westinghouse), and F.G. Perey (ORNL), Westinghouse Report WARD-3045T4B-2, Appendix A (April 1972).
3. J. Seltzer and F.W.K. Firk, Nucl. Sci. Eng. 53, 415 (1974).
4. P.H. Brown, B.L. Quan, J.J. Weiss, and R.C. Block, Trans. Am. Nucl. Soc. 21, 505 (1975).
5. D.C. Larson, J.A. Harvey, and N.W. Hill, Oak Ridge National Laboratory report ORNL/TM-5614 (October 1976).
6. G. de Saussure, D.K. Olsen, and R.B. Perez, Oak Ridge National Laboratory report ORNL/TM-6286, ENDF-261 (May 1978).
7. R. L. Macklin, private communication (1976).
8. S. Wynchank, F. Rahn, H.S. Carmada, G. Hacken, M. Slagowitz, H.I. Liou, J. Rainwater, and W.W. Havens, Jr., Nucl. Sci. Eng. 51, 119 (1973); also, G.D. James, "Neutron Energy Standards," Proceedings of Symposium on Neutron Standards and Applications, NBS 493 (1977).
9. W.M. Wilson, H.E. Jackson, and G.E. Thomas, Nucl. Sci. Eng. 63, 55 (1977).
10. Private communication from R. L. Macklin, Oak Ridge National Laboratory.
11. Private communication in letter from Tony Musgrove, March 1977.
12. T.B. Ryves and D.R. Perkins, J. Nucl. Energy 24, 419 (1970).
13. P.S. Buchanan, D.O. Wellis, and W.E. Tucker, Report ORO-2791-32 (1971).
14. J.P. Chien and A.B. Smith, Nucl. Sci. Eng. 26, 500 (1966).
15. D.R. Donati, S.C. Mathur, E. Sheldon, B.K. Barnes, L.E. Beghian, P. Harihar, G.H.R. Kegel, and W.A. Schier, Phys. Rev. C 16, 939 (1977).
16. U. Fasoli, D. Toniolo, G. Zago, and V. Benzi, Nucl. Phys. A 125, 227 (1969).
17. J.M. Freeman and J.H. Montague, Nucl. Phys. 9, 181 (1958).
18. D.C. Larson and G.L. Morgan, Oak Ridge National Laboratory report ORNL/TM-6281 (May 1978).
19. D.A. Lind and R.B. Day, Ann. Phys. 12, 485 (1961).
20. D.L. Smith, report ANL-7710, p. 15 (1971).
21. D.L. Smith, "Measurement of Cross Sections for the ^{23}Na(n,n'γ)^{23}Na Reaction near Threshold," Nucl. Sci. Eng. 64, 897 (1977).
22. J.H. Towle and W.B. Gilboy, Nucl. Phys. 32, 610 (1962).
23. F.G. Perey, W.E. Kinney, and R.L. Macklin, Proc. Third Conf. on Neutron Cross Sections and Technology, Knoxville, Tennessee, p. 191 (1971).
24. R.E. Coles, "Elastic and Inelastic Scattering of 5.0 MeV Neutrons by Sodium," report AWRE/O-3/71 (1971).
25. G.M. Crawley and G.T. Garvey, Phys. Rev. 167, 1070 (1968).
26. J.K. Dickens, Nucl. Sci. Eng. 50, 98 (1973).

27. U. Fasoli, D. Toniolo, G. Zago, V. Benzi, P.L. Ottaviani, and L. Zuffi, "Elastic and Inelastic Scattering of Neutrons by Na at 8.0, 9.7 and 14.1 MeV," report CEC(73)7 (1973).

28. F.G. Perey and W.E. Kinney, "Neutron Elastic and Inelastic Scattering Cross Sections for Na in the Range of 5.4 to 8.5 MeV," Oak Ridge National Laboratory report ORNL-4518 (1970).

29. C.Y. Fu, Paper GB2 at this Conference.

30. H. Liskien and A. Paulsen, Nucl. Phys. 63, 393 (1965).

31. H.O. Menlove, K.L. Coop, H.A. Grench, and R. Sher, Phys. Rev. 163, 1308 (1967).

32. A. Paulsen, private communication to CCDN (1965).

33. J. Picard and C. Williamson, Nucl. Phys. 63, 673 (1965).

34. Method described in a private communication from F. G. Perey.

35. J. Hellstrom, P.J. Dallimore, and W.F. Davidson, Nucl. Phys. A132, 581 (1969).

36. B.T. Lucas, S.W. Cosper, and O.E. Johnson, Phys. Rev. 144, 972 (1966).

37. A. Gilbert and A.G.W. Cameron, Can. J. Phys. 43, 1446 (1965).

38. P.M. Endt and C. Van der Leun, Nucl. Phys. A214, 1 (1973).

39. D. Hermsdorf, A. Meister, S. Sassonoff, D. Seeliger, K. Seidel, and F. Shshin, "Differential Neutron Emission Cross Sections $\sigma(E_0,E,\theta)$ for 14.6 MeV Incident Energy for Elements Be, C, Na, Mg, Al Si, P, S, Ca, Ti, V, Cr, Mn, Fe, Co, Ni, Cu, Zn, Ga, Se, Br, Zr, Nb, Cd, In, Sn, Sb, I, Ta, W, Au, Ug, Pb, and Bi," report ZfK-277, INDC(GDR)-2L (1975).

40. D. C. Larson, submitted for publication in Nuclear Science and Engineering.

41. W.E. Kinney and F.G. Perey, private communication from F. G. Perey (1976).

42. Private communication from P. G. Young at Los Alamos Scientific Laboratory.

43. J.D. Garrison and M.K. Drake, "Neutron and Gamma-Ray-Production Cross Sections for Sodium, Magnesium, Chlorine, Potassium, and Calcium, Part II, Sodium," Report NDL-TR-89-II (November 1967).

44. R.E. Maerker and F.J. Muckenthaler, Nucl. Sci. Eng. 42, 335 (1970).

Table I. ENDF/B-V Resonance Parameters.

E_R(keV)	Γ_n(eV)	Γ_γ(eV)	J	ℓ	E_R(keV)	Γ_n(eV)	Γ_γ(eV)	J	ℓ
2.81	376	0.353	1	0	298.32	2038	1.02	2	0
7.617	0.0058	0.6	2	1	299.41	130	2.56	1	1
35.39	1.6	1.9	1	1	305.20	68.3	9.70	0	2
53.22	1112	0.785	2	1	392.32	22760	9.87	1	1
117.43	26.8	4.23	1	1	430.90	4000	5.29	0	2
143.13	16.5	7.10	0	1	448.82	7026	3.52	2	2
190.06	18.2	9.30	0	2	538.57*	62770	10.14	1	0
201.15	4925	2.94	1	1	598.0*	25800	-	1	1
214.30	14280	4.64	0	1	697.0*	60000	-	4	2
236.71	65.2	1.59	2	2	727.0*	45000	-	3	1
239.05	5349	1.20	2	1	780.0*	44000	-	4	2
242.97	328	1.50	1	0					

*Outside resolved resonance region, but included in evaluation for long-range effects.

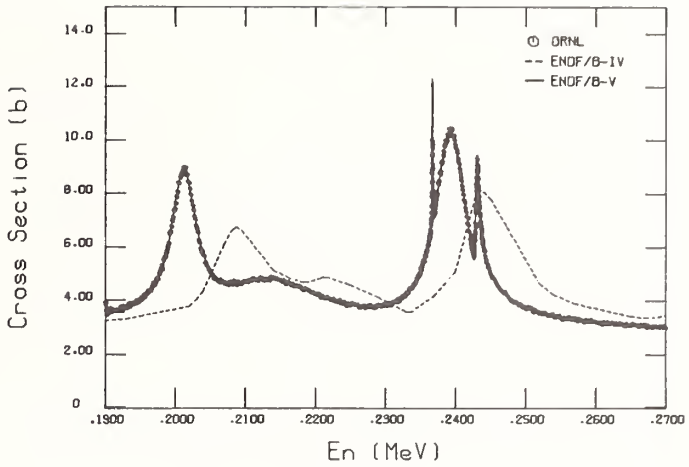

Fig. 1. A comparison among the data of Ref. 5, the ENDF/B-IV evaluation, and version V. The difference file in version V (data minus multilevel fit) is less than 5% over this energy region.

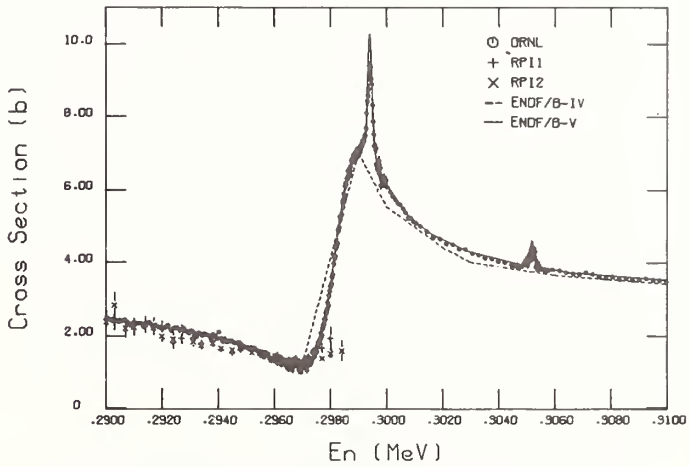

Fig. 2. A comparison among the data of Refs. 4 and 5, and versions IV and V of ENDF/B. RPI1 and RPI2 refer to two different sample thicknesses used in their measurement. This is the first reported observation of the narrow resonance at 299 keV in a transmission measurement.

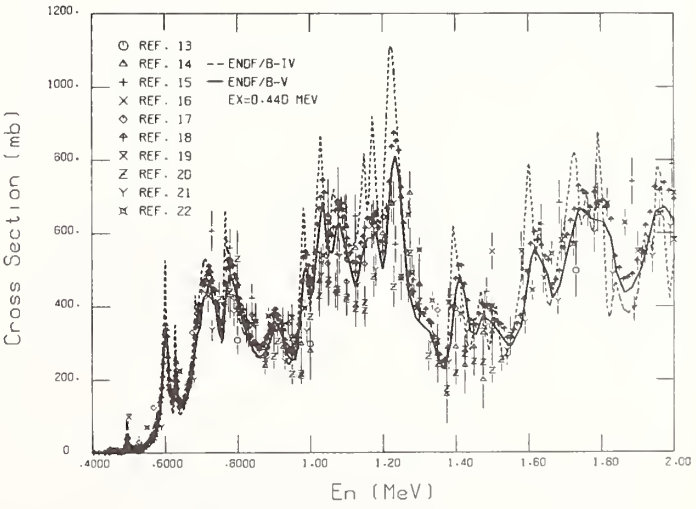

Fig. 3. A comparison of the data base for inelastic scattering from the 440-keV level with ENDF/B-IV and -V. Version IV was based on the data of Ref. 23.

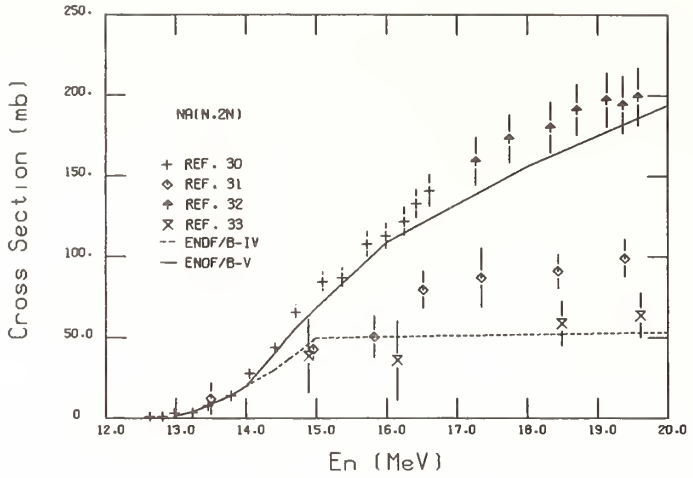

Fig. 4. A comparison of the data base for the (n,2n) reaction with ENDF/B-IV and -V. The version V cross section is based on results of extensive model calculations.

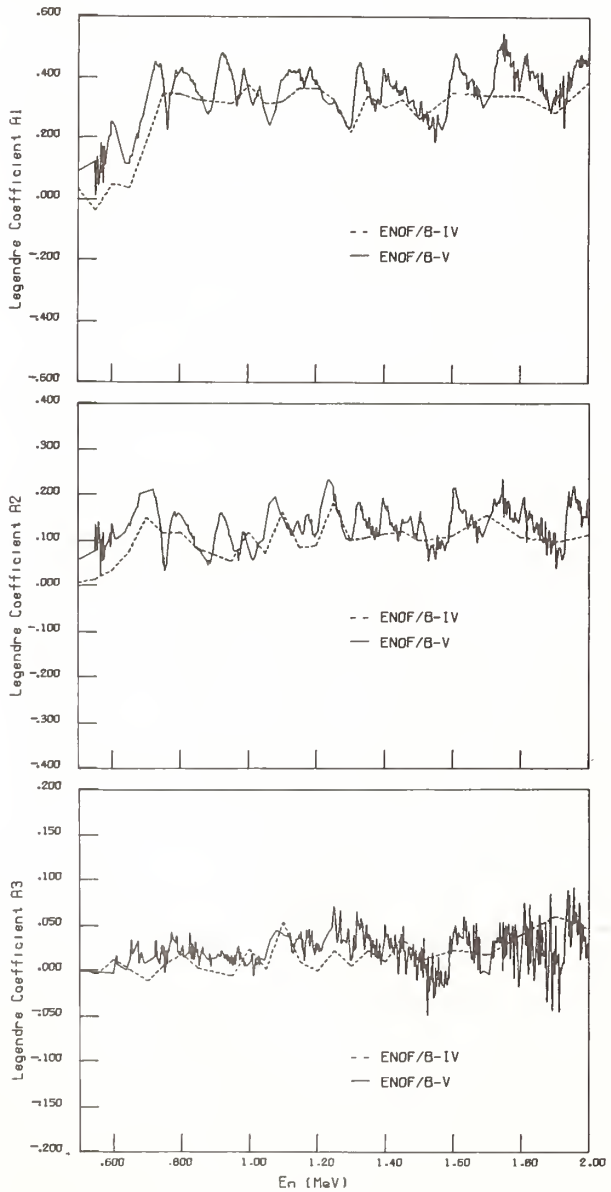

Fig. 5. A comparison of the first three Legendre coefficients, as measured by Ref. 41, with ENDF/B-IV and -V.

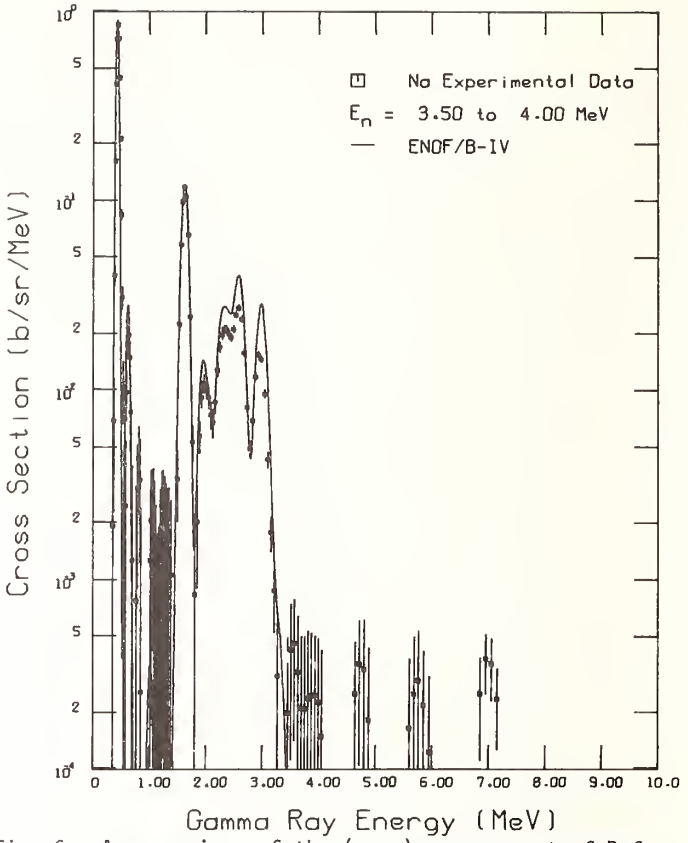

Fig. 6. A comparison of the (n,xγ) measurement of Ref. 18 with ENDF/B-IV. These experimental results were appropriately binned and used directly in version V.

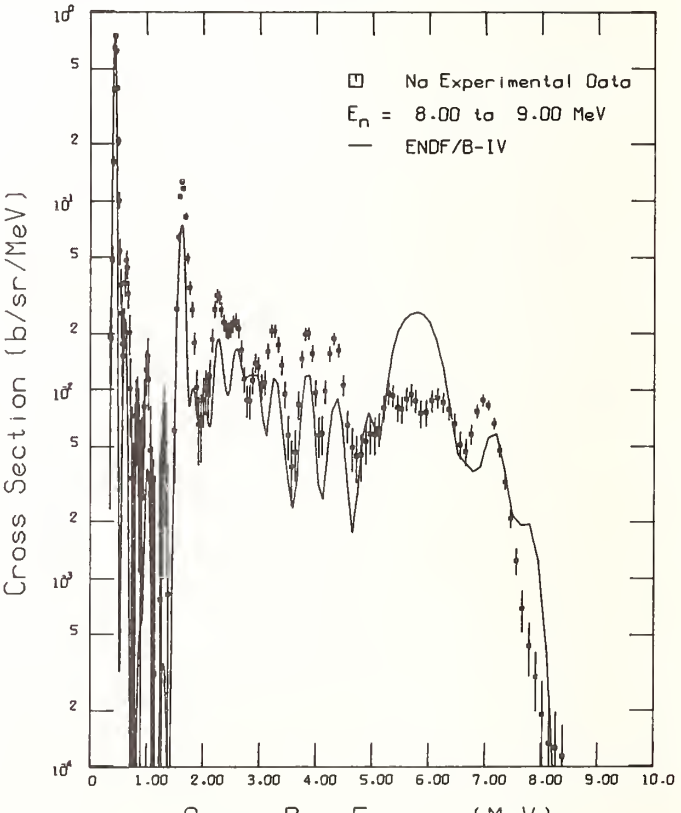

Fig. 7. A comparison of the (n,xγ) measurement of Ref. 18 with ENDF/B-IV. The large cross section around E_γ = 6 MeV in version IV results from assumptions about branching ratios for levels from E_x = 5.9 to 7.8 MeV in ^{23}Na.

SIMULTANEOUS EVALUATION OF $^{32}S(n,p)$, $^{56}Fe(n,p)$, $^{65}Cu(n,2n)$ CROSS SECTIONS

C. Y. Fu, D. M. Hetrick, and F. G. Perey
Oak Ridge National Laboratory
Oak Ridge, Tennessee 37830, USA

Previously available evaluations of cross sections and covariances were used as input for incorporating additional correlated data sets, particularly cross-section ratios. A generalized least-squares technique was employed. The output evaluations have not only updated cross sections and covariances, but also cross-reaction covariances, all of which include the additional data incorporated.

[$^{32}S(n,p)$, $^{56}Fe(n,p)$, $^{65}Cu(n,2n)$, cross-reaction covariances, ratio data.]

Introduction

Simultaneous evaluation of cross sections is required where ratio data exist. Because ratio measurements do not require absolute neutron flux determination, which is usually the largest source of uncertainties, correct use of ratio data would establish the relative magnitudes of various cross sections quite well. High-precision absolute data for one reaction would improve the absolute magnitudes of all other cross sections connected by high-precision ratios. In this paper, we consider three reactions: $^{32}S(n,p)$, $^{56}Fe(n,p)$, and $^{65}Cu(n,2n)$. Previously available evaluations of cross sections and covariances were used as part of input. Several data sets, including new absolute and relative data, were combined with the input evaluations by the least-squares technique. The output evaluations have not only updated cross sections and covariances, but also cross-reaction covariances.

Generalized Least-Squares

The use of generalized least-squares technique in nuclear data work has been widely discussed or applied by, for example: Peelle[1] in a call for better experimental data reporting, Perey[2] in the evaluation of neutron resonance energy standards, Fu and Perey[3] in the evaluation of neutron-carbon scattering standards, Dragt *et al.*[4] in capture data adjustment on the basis of integral data, Perey[5] in using ratio data for cross section evaluations, Petilli[6] and Perey[7,8] in dosimetry unfolding, Schmittroth and Schenter[9] in decay heat evaluation, and Schmittroth[10] in damage function unfolding and adjustments with a logrithmic description of *a priori* information for handling large uncertainties. We summarize the solution to the minimization of least squares for the present application following the notations of Perey.[2]

Let the vector T stand for a set of input evaluations of the cross sections with the covariance matrix M. T and M define a normal probability density function. Let the vector R be a set of new data, related to some of these cross sections, with the covariance matrix V. R and V also define a normal density function. R and T are assumed to be uncorrelated. After combining R and T, the output evaluation T' and M' are given by:

$$T' = T + A(N+V)^{-1}(R-R_T) \quad (1)$$

$$M' = M - A(N+V)^{-1}A^t \quad (2)$$

where $A = MG^t$ and $N = GA$; R_T is the vector containing calculated values for R from T and G is the matrix of partial derivatives of elements of R_T with respect to elements of T.

Input Evaluations

For $^{56}Fe(n,p)$ and $^{65}Cu(n,2n)$ cross sections, the input evaluations are those we submitted for the ENDF/B-V dosimetry file. For $^{32}S(n,p)$, the ENDF/B-IV was used together with a covariance matrix we generated on the basis of the ENDF/B-IV documentation.[11] We reproduce below a few energy points from these evaluations to provide some idea about their uncertainties and correlations.

	E(MeV)	XS(mb)	STD(%)	C matrix		
$^{56}Fe(n,p)$	10	69.3	4.0	100		
	13	112.0	2.5	33	100	
	16	81.8	2.0	19	47	100
$^{65}Cu(n,2n)$	12	475.4	6.0	100		
	14	853.0	5.3	69	100	
	16	1023.0	5.2	63	86	100
$^{32}S(n,p)$	8	324.0	10.0	100		
	12	366.0	8.0	41	100	
	16	164.0	5.0	36	69	100

C matrix represents the lower half of the correlation matrix multiplied by 100. The three cross section sets were evaluated independently and therefore their uncertainties are uncorrelated. Together they form the vector T and the covariance matrix M of Eqs. (1) and (2).

(New) Input Data Sets

We restrict ourselves to a small number of input data sets so that their impact to the output evaluations can be easily traced. Yet our selection of data sets covers all possible data types and covariances. The task of an evaluator is to transform the uncertainty estimates given by the experimenters to covariance matrices. The necessary relations for this transformation can be easily derived. Let us first consider an absolute measurement of the $^{56}Fe(n,p)$ cross sections and a ratio measurement of $^{65}Cu(n,2n)/^{56}Fe(n,p)$. Let x_{fi} be the $^{56}Fe(n,p)$ cross sections at energy i and x_{ci} be the $^{65}Cu(n,2n)$ cross sections at energy i. We may write

$$x_{fi} \equiv x_{fi}(z_{fi})$$

$$x_{ci} \equiv x_{ci}(z_{ci})$$

where z_{fi} and z_{ci}, for Fe and Cu respectively, are one of the variables associated with the data reduction at energy i. This variable may be neutron flux determination, β counting efficiencies, detector calibrations, extrapolation to zero sample thickness, half lives, or statistics, etc. The cross section ratios of $^{65}Cu(n,2n)$ to $^{56}Fe(n,p)$ may be written similarly:

$$r_i(z_{fi},z_{ci}) = x_{ci}(z_{ci})/x_{fi}(z_{fi})$$

The functions may be linearized by retaining the first two terms of a Taylor's series expansion about the mean values $\bar{x}$ and $\bar{z}$:

$$x'_{fi} \equiv \frac{x_{fi}-\bar{x}_{fi}}{\bar{x}_{fi}} = \frac{1}{\bar{x}_{fi}} \frac{\partial x_{fi}}{\partial z_{fi}} (z_{fi}-\bar{z}_{fi}) \quad . \tag{3}$$

$$r'_i \equiv \frac{r_i-\bar{r}_i}{\bar{r}_i} = \frac{1}{\bar{x}_{ci}} \frac{\partial x_{ci}}{\partial z_{ci}} (z_{ci}-\bar{z}_{ci}) - \frac{1}{\bar{x}_{fi}} \frac{\partial x_{fi}}{\partial z_{fi}} (z_{fi}-\bar{z}_{fi}) \tag{4}$$

where x'_{fi} and r'_i are introduced to simplify notations. Averaging the various products of x'_{fi} and r'_i, we have:

$$\mathrm{Cov}(x'_{fi},x'_{fj}) = C(z_{fi},z_{fj}) \tag{5}$$

$$\mathrm{Cov}(x'_{fi},r'_j) = C(z_{fi},z_{cj}) - C(z_{fi},z_{fj}) \tag{6}$$

$$\mathrm{Cov}(r'_i,r'_j) = C(z_{fi},z_{fj}) + C(z_{ci},z_{cj}) - C(z_{fi},z_{cj}) - C(z_{ci},z_{fj}) \tag{7}$$

where the C's are components (for a given z) of the "relative" covariance matrices, i.e., Cov's. For example

$$C(z_{fi},z_{cj}) = \left\langle \frac{1}{\bar{x}_{fi}} \frac{\partial x_{fi}}{\partial z_{fi}} (z_{fi}-\bar{z}_{fi}) \frac{1}{\bar{x}_{cj}} \frac{\partial x_{cj}}{\partial z_{cj}} (z_{cj}-\bar{z}_{cj}) \right\rangle . \tag{8}$$

For two ratios with the same denominator, say ^{56}Fe(n,p)/^{32}S(n,p) and ^{65}Cu(n,2n)/^{32}S(n,p), the required relation is

$$\mathrm{Cov}(r'_{fi},r'_{cj}) = C(z_{si},z_{sj}) - C(z_{fi},z_{sj}) - C(z_{ci},z_{sj}) + C(z_{fi},z_{cj}) \tag{9}$$

where the subscript s is for sulfur. Relative data can be treated as a special type of ratios as described below.

Terms of the right-hand side of Eqs. (3) and (4) are generally what the experimenters report. To construct the covariance matrices, one must use Eqs. (5) to (9) to account for correlated uncertainties. At present, it is frequently the task of an evaluator to identify whether an uncertainty component contributes to i=j only or to several i's and j's, to one reaction or to more than one reaction. We hope that the experimenters will take up this task in their data reporting in the future so that evaluators need only make minimal assumptions.

Data of Ryves *et al.*

Recently Ryves *et al.*[12] reported high-precision cross sections of ^{56}Fe(n,p) and ratios of ^{65}Cu(n,2n) to ^{56}Fe(n,p) from 14 to 19 MeV. Perey[13] has worked out the covariance matrix for these data. We discuss below the three largest uncertainty components — neutron flux, β counting efficiencies, and energies.

The neutron flux determination has an uncertainty that is systematic and is present in every term in Eqs. (5) to (7) for all i and j. The terms in Eq. (6) cancel; so do those in Eq. (7). Thus the uncertainty in neutron flux contributes only to $\mathrm{Cov}(x'_{fi},x'_{fj})$ but not to $\mathrm{Cov}(x'_{fi},r'_j)$ nor $\mathrm{Cov}(r'_i,r'_j)$.

A set of Fe foils of a fixed thickness was used for the absolute cross-section measurements and a set of Fe foils of the same fixed thickness was used for the ratio measurements. The uncertainties in the β counting efficiencies are characteristic of the β energies and the sample thicknesses. The β energies are the same for all foils of the same type, leading to a correlated component in the uncertainties. The foil thicknesses, though meant to be the same, may vary slightly, leading to a random component. The two components were assumed equal as suggested by Axton.[14] Therefore, the uncertainties in β counting efficiencies for the Fe foils used in both the absolute measurements and the ratio measurements are 50% correlated, leading to an important contribution to the term $C(z_{fi},z_{fj})$ in $\mathrm{Cov}(x'_{fi},x'_{fj})$, $\mathrm{Cov}(x'_{fi},r'_j)$, and $\mathrm{Cov}(r'_i,r'_j)$.

Ryves *et al.* also listed uncertainties in the neutron energies. Some of these uncertainties are correlated.[14] Thus an energy covariance matrix was constructed and, using linear regression,[13] transformed to cross-section or ratio covariances.

The characteristics of the resulting covariance matrices can be seen from a few representative energy points listed below.

	E(MeV)	XS(mb)	STD(%)	C matrix		
^{56}Fe(n,p)	14.67	108.1	1.1	100		
	16.55	80.1	1.5	54	100	
	18.95	53.2	1.6	50	76	100

^{65}Cu(n,2n)/^{56}Fe(n,p):

E(MeV)	Ratio	STD(%)	C matrix		
14.67	8.83	1.1	100		
16.55	13.35	1.4	26	100	
18.95	19.24	1.0	36	64	100

Cross-correlation between ^{56}Fe(n,p) and ^{65}Cu(n,2n)/^{56}Fe(n,p):

E_{ri}/E_{fj}	14.67	16.55	18.95
14.67	-19	2	2
16.55	2	-52	-42
18.95	3	-29	-27

This set of data (six absolute cross sections, ten ratios, and their covariance matrices) represents input data R and V in Eqs. (1) and (2). The resulting evaluations T' and M' were then used as T and M for incorporating the next data set which is uncorrelated with the present data set.

Data of Santry and Butler

In two separate papers,[15,16] Santry and Butler reported cross section measurements for ^{56}Fe(n,p) and ^{65}Cu(n,2n) from threshold to 20 MeV using ^{32}S(n,p) as the neutron flux monitor.[17] Thus their data should be considered as ratios of ^{56}Fe(n,p) to ^{32}S(n,p) and ^{65}Cu(n,2n) to ^{32}S(n,p). In many earlier evaluations,[11] the large body of cross section data measured by Santry and Butler with the same technique was considered as absolute data. The uncertainties in the ^{32}S(n,p) cross sections (6% from 5 to 20 MeV as estimated by Santry and Butler[18]) propagated to many other evaluated cross sections, including the input evaluations used here. We will comment on this problem below.

We converted the cross section data of Santry and Butler back into ratios and accordingly transformed their uncertainty estimates[15-18] into covariance matrices. The only assumption we had to make was that the uncertainties in the β counting efficiencies of the same type of foils are 50% correlated.

In the energy range from 12.5 to 20.3 MeV, the neutron flux was monitored by ^{32}S(n,p) reaction only

at 14.5 MeV. The neutron fluxes at other energies were calculated from the angular distribution of neutrons from the $T(d,n)^4He$ reaction. Such relative cross sections should also be treated as ratios with the 14.5-MeV cross section as the denominator. Thus we have included the data point at 14.5 MeV as ratio to sulfur but other points as ratios relative to the 14.5-MeV point of the same reaction. Let y be such a relative cross-section ratio and E_J be the fixed denominator energy, then the relations for transforming the estimated uncertainties into covariance matrices are:

$$\mathrm{Cov}(y'_{fi},y'_{fj}) = C(z_{fi},z_{fj}) - C(z_{fi},z_{fJ}) - C(z_{fj},z_{fJ}) + C(z_{fJ},z_{fJ}) \quad (10)$$

$$\mathrm{Cov}(y'_{fi},y'_{cj}) = C(z_{fi},z_{cj}) - C(z_{fi},z_{cJ}) - C(z_{fj},z_{cJ}) + C(z_{fJ},z_{cJ}) \quad (11)$$

$$\mathrm{Cov}(y'_{fi},r'_{fj}) = C(z_{fi},z_{fj}) - C(z_{fJ},z_{fj}) - C(z_{fi},z_{sj}) + C(z_{fJ},z_{sj}) \quad (12)$$

$$\mathrm{Cov}(y'_{fi},r'_{cj}) = C(z_{fi},z_{cj}) - C(z_{fJ},z_{cj}) - C(z_{fi},z_{sj}) + C(z_{fJ},z_{sj}) \quad (13)$$

Because the uncertainties of counting efficiencies for all three sample types were estimated[15-18] to be the same, the relative cross-section ratios are independent of the β counting efficiencies. Uncertainties in the angular distributions of the source neutrons were included in the diagonal elements of the covariance matrix. Since these uncertainties are relatively small compared to other uncertainties, we have not attempted an evaluation of their possible correlations.

The characteristics of the resulting data and covariances are represented by a few energy points below:

	E(MeV)	Ratio	STD(%)	C matrix		
$^{56}Fe(n,p)/^{32}S(n,p)$	8.1	0.142	3.0	100		
	10.4	0.207	2.7	49	100	
	12.1	0.283	2.9	46	51	100
$^{65}Cu(n,2n)/^{32}S(n,p)$	11.0	0.421	4.2	100		
	12.0	1.25	5.3	18	100	
	13.8	2.54	6.5	15	12	100

Cross-correlation between $^{56}Fe(n,p)/^{32}S(n,p)$ and $^{65}Cu(n,2n)/^{32}S(n,p)$:

E_{ci}/E_{fj}	8.1	10.4	12.1
11.0	16	18	16
12.0	13	14	13
13.8	10	11	11

$^{56}Fe(n,p)/^{56}Fe(n,p,E_J = 14.5)$:

E(MeV)	Ratio	STD(%)	C matrix		
12.53	1.009	5.4	100		
14.68	0.982	3.7	0	100	
19.80	0.439	5.4	0	0	100

$^{65}Cu(n,2n)/^{65}Cu(n,2n,E_J = 14.5)$:

E(MeV)	Ratio	STD(%)	C matrix		
13.58	0.898	3.0	100		
14.74	1.03	3.0	0	100	
19.80	1.06	5.8	0	0	100

Output Evaluations

The output evaluations as well as the input evaluations are shown in Fig. 1. The following changes may be worth noting:

1. The high-precision $^{56}Fe(n,p)$ cross sections and $^{65}Cu(n,2n)/^{56}Fe(n,p)$ ratios of Ryves *et al.*[12] have predominant influence in the energy range from about 12 MeV to 20 MeV to both the output $^{56}Fe(n,p)$ and $^{65}Cu(n,2n)$ cross sections even though their lowest energy data are at 14.67 MeV because of long-range correlations in the input evaluations.

2. The $^{56}Fe(n,p)/^{32}S(n,p)$ and $^{65}Cu(n,2n)/^{32}S(n,p)$ ratios of Santry and Butler[15,16] are consistent with the data of Ryves *et al.* from 14 to 20 MeV, so the $^{32}S(n,p)$ cross sections are little changed in this energy range.

3. The $^{32}S(n,p)$ cross sections are increased 6% near 12 MeV and decreased 7% near 6 MeV due mainly to the $^{56}Fe(n,p)/^{32}S(n,p)$ ratios.

4. A step-like structure is introduced to the $^{32}S(n,p)$ cross sections near 6 MeV. In the original reporting of the $^{56}Fe(n,p)$ cross sections by Santry and Butler,[13] using $^{32}S(n,p)$ as standards, the step structure was seen in their reported $^{56}Fe(n,p)$ cross sections instead. During the earlier evaluation for $^{56}Fi(n,p)$, the step structure in the Santry and Butler data was removed because it was not substantiated by other available data.

5. The dip in the $^{65}Cu(n,2n)$ cross sections near 19 MeV is due to the $^{65}Cu(n,2n)/^{56}Fe(n,p)$ ratio at 18.95 MeV. Because this dip is above the (n,3n) threshold (18.1 MeV), nuclear model analysis more advanced than that used previously[11] is required to determine the expected shape of the cross-section curve from 18 to 20 MeV.

6. Strictly speaking, the impacts of Santry and Butler's data as absolute cross sections on the input evaluations should have been removed before we could incorporate these data as ratios. Clearly we did not. However, we have qualitatively estimated the possible impacts. Except in the energy range from 10 to 12 MEV, Santry and Butler's data had marginal influence to the input evaluations. From 10 to 12 MeV, Santry and Butler's data were the only ones available for both the $^{56}Fe(n,p)$ and $^{65}Cu(n,2n)$ cross sections. It is therefore difficult to figure out what would have happened to the input evaluations if these data were not there. Nevertheless, the output evaluations from 10 to 12 MeV were predominantly influenced by the ratios. In other words, the damage done by including Santry and Butler's data as absolute cross sections in the input evaluations is rather small in the present case.

The output covariances for the same representative energy points as we tabulated above for the input evaluations are given below for comparison purposes.

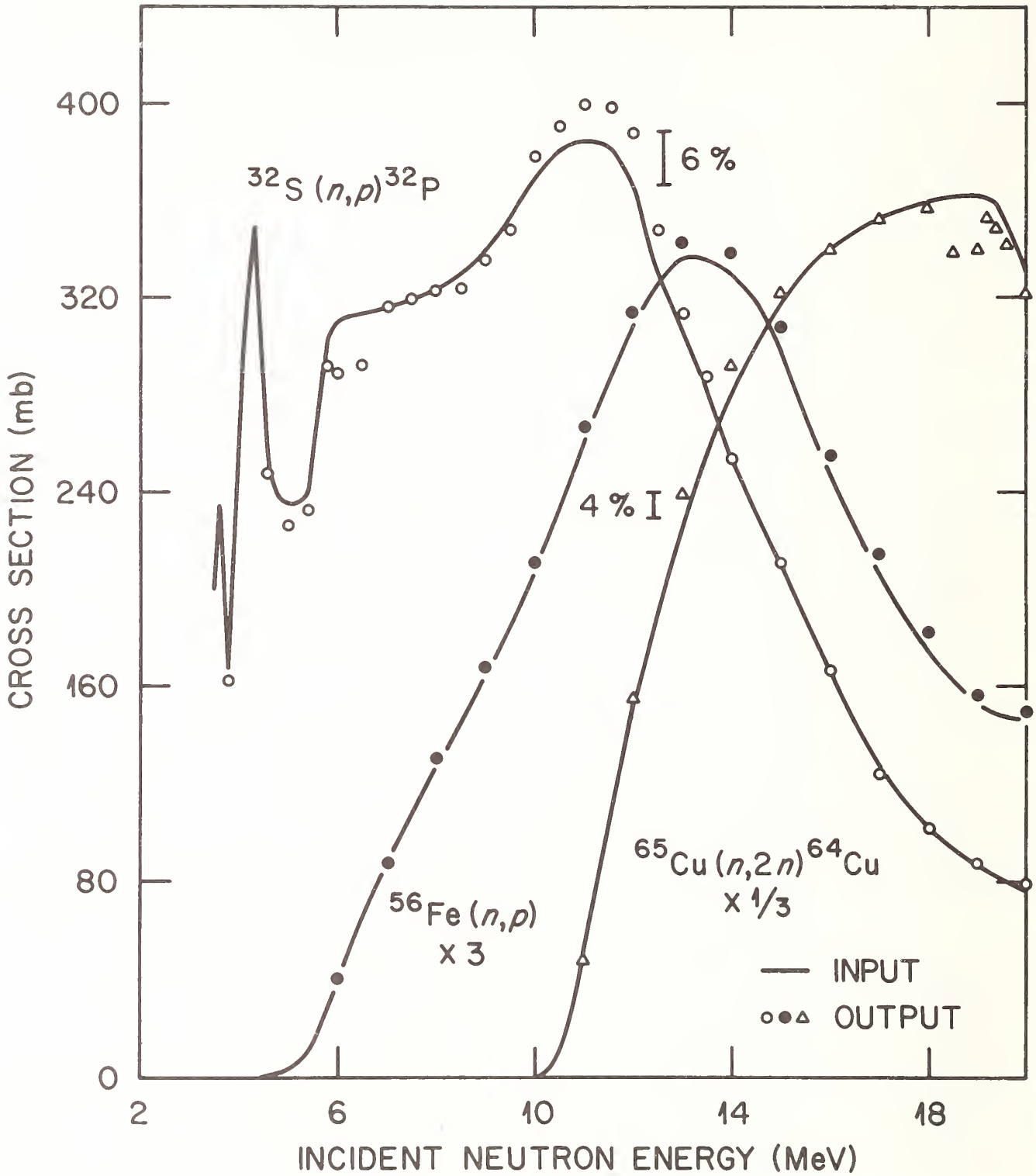

Fig. 1. Cross sections of input and output evaluations. Input evaluations and covariance matrices for $^{56}Fe(n,p)$ and $^{65}Cu(n,2n)$ are from ENDF/B-V. See text for input evaluation for $^{32}S(n,p)$. Output evaluations represent least-squares results combining input evaluations with new correlated data input, including ratios as well as absolute and relative cross sections. See text for a description of output covariances.

	E(MeV)	XS(mb)	STD(%)	C matrix		
^{56}Fe(n,p)	10	71.0	3.4	100		
	13	114.3	1.9	23	100	
	16	85.0	1.1	11	27	100
^{65}Cu(n,2n)	12	477.1	3.1	100		
	14	883.5	1.5	23	100	
	16	1022.0	1.2	19	26	100
^{32}S(n,p)	8	322.0	4.0	100		
	12	387.0	2.6	41	100	
	16	166.0	2.7	22	36	100

Cross-correlation between ^{56}Fe(n,p) and ^{65}(Cu(n,2n):

E_{ci}/E_{fj}	10	13	16
12	23	20	14
14	11	23	38
16	11	25	47

Cross-correlation between ^{56}Fe(n,p) and ^{32}S(n,p):

E_{si}/E_{fj}	10	13	16
8	41	10	5
12	27	30	15
16	6	16	13

Cross-correlation between ^{65}Cu(n,2n) and ^{32}S(n,p):

E_{si}/E_{cj}	12	14	16
8	19	8	6
12	46	18	15
16	11	23	23

Conclusions

We have utilized absolute cross sections, ratio data, and relative data in the most consistent manner in our evaluation based on generalized least-squares technique. Several other available data sets have been withheld in order to simplify the illustrations. Even so, our results form a strong basis for incorporating more data sets and other reactions.

We have also compiled experimental data and covariances for ^{63}Cu(n,2n)/^{56}Fe(n,p), ^{65}Cu(n,2n)/^{27}Al(n,p), and ^{27}Al(n,p)/^{32}S(n,p) ratios. Thus two more reactions can be easily added and at the same time strengthen the three evaluated cross sections considered herein. We intend to look into measurements using fission chambers as the neutron flux monitor, thereby initiating to incorporate two important reactions, ^{235}U(n,f) and ^{238}U(n,f), into our evaluation.

As a result of this work, a computer code[19] has been developed. The code is quite general — capable of handling large numbers of correlated evaluations, all possible data types that may be correlated, and all commonly-used ENDF/B-V covariance formats[10] and interpolation laws. (Note that evaluation and data energy grids were not the same.) This code will soon be made available for external distribution.

Acknowledgement

Research sponsored by the Electric Power Research Institute and the Office of Basic Energy Sciences, Department of Energy, under contract No. W-7405-eng-26 with Union Carbide Corporation.

One of the authors, C. Y. Fu, wishes to thank R. W. Peelle for making several constructive comments.

References

1. R. W. Peelle, Proc. NEANDC/NEACRP Specialists Meeting on Fast Neutron Fission Cross Sections of U-233, U-235, U-238, and Pu-239, Argonne, 1976, ed. W. P. Poenitz and A. B. Smith, ANL-76-90, ANL-76-90, ERDA-NDC-5/L, NEANDC(US)-199/L, p. 421.
2. F. G. Perey, Proc. Int. Conf. on Neutron Physics and Nuclear Data for Reactors and Other Applied Purposes, Harwell, England, 1978, p. 104.
3. C. Y. Fu and F. G. Perey, Atomic Data and Nuclear Data Tables 22, 249 (1978).
4. J. B. Dragt, J. W. M. Dekker, H. Gruppelaar, and A. J. Janssen, Nucl. Sci. Eng. 62, 117 (1977).
5. F. G. Perey, IAEA Meeting on Reactor Dosimetry, Vienna, 1977, proceedings unpublished.
6. M. Petilli, "The Unfolding Code DANTE and its Application," in ORNL/RSIC-40 (1976).
7. F. G. Perey, "Contributions to Few-Channel Spectrum Unfolding," Oak Ridge National Laboratory Report ORNL/TM-6267, ENDF-259 (1978).
8. F. G. Perey, "Least-Squares Dosimetry Unfolding: The Program STAY'SL," ORNL/TM-6062, ENDF-254 (1977).
9. F. Schmittroth and R. E. Schenter, Nucl. Sci. Eng. 69. 389 (1979).
10. F. Schmittroth, "Varied Applications of a New Maximum-Likelihood Code with Complete Covariance Capability," Proc. of Seminar-Workshop on Theory and Application of Sensitivity and Uncertainty Analysis, Ed. C. R. Weisbin, R. W. Roussin, H. R. Hendrickson, and E. W. Bryant, ORNL/RSIC-42 (1979).
11. N. D. Dudley and R. Kennerley, in ENDF/B-IV Dosimetry File, ed. B. A. Magurno, BNL-NCS-50446, ENDF-216 (1975).
12. T. B. Ryves, P. Kolkowski, and K. J. Zieba, Metrologia 14, 127 (1978).
13. F. G. Perey, lectures to be published as monograph on Probabilistic Analysis of Nuclear Data.
14. E. J. Axton, National Physical Laboratory, Teddington, England, private communication to F. G. Perey (1979).
15. D. C. Santry and J. P. Butler, Can. J. Phys. 42, 1030 (1964).
16. D. C. Santry and J. P. Butler, Can. J. Phys. 44, 1183 (1966).
17. D. C. Santry and J. P. Butler, Can. J. Phys. 41, 123 (1963).
18. J. P. Butler and D. C. Santry, Can. J. Phys. 41, 372 (1963).
19. D. M. Hetrick and C. Y. Fu, "BAYES: A Generalized Least-Squares Program for Updating Cross-Section Evaluations with Correlated Data Sets," ORNL/TM to be published.
20. F. G. Perey, "The Data Covariance Files for ENDF/B-V," ORNL/TM-5938, ENDF-249 (1977).

EVALUATIONS OF THE Fe58(n,γ)Fe59 AND Fe54(n,p)Mn54 REACTIONS FOR THE ENDF/B-V DOSIMETRY FILE

R. E. Schenter, F. Schmittroth,
and F. M. Mann

Hanford Engineering Development Laboratory
Richland, Washington 99352

A generalized least-squares adjustment procedure has been used to evaluate two important dosimetry reactions for the ENDF/B-V files. Calculations for the cross section adjustments were made with the computer code FERRET, where input data included both integral and differential experimental data results. For the Fe54 reaction, important ratio measurements were renormalized to ENDF/B-V evaluations of U235(n,f), U238(n,f) and Fe56(n,p). A priori curves which are required for the calculations were obtained using Hauser-Feshbach calculations from the codes NCAP (Fe58) and HAUSER*5 (Fe54). Covariance matrices were also calculated and are included in the evaluations.

(Fe58(n,γ)Fe59, Fe54(n,p)Mn54, covariance matrices, cross section evaluation)

Introduction

The Fe58(n,γ)Fe59 and Fe54(n,p)Mn54 reactions have important use as flux-fluence gradient monitors for dosimetry application in fission and fusion reactors. The radioactive reaction products Fe59 and Mn54 are sufficiently long-lived ($t_{1/2}$=45d,1yr) so that they are easily counted. Both of these reactions were previously evaluated by Schenter[1] for the ENDF/B-III and ENDF/B-IV dosimetry files. These evaluations relied on using both integral and differential experimental results.

In this paper we present the results of a re-evaluation of these reactions, where several new aspects of the evaluation process has been incorporated. The most important was use of a generalized least-squares adjustment procedure[2] to obtain an evaluated nominal cross section curve and uncertainty information in the form of a covariance matrix which linked energy points. This procedure involves calculations which use the finite element representation of the FERRET[3] data adjustment code. In addition, recent experimental results were incorporated into the evaluations and ratio data for two important experimental measurements were renormalized to ENDF/B-V data. These new evaluations have been released as part of the ENDF/B-V Dosimetry File.

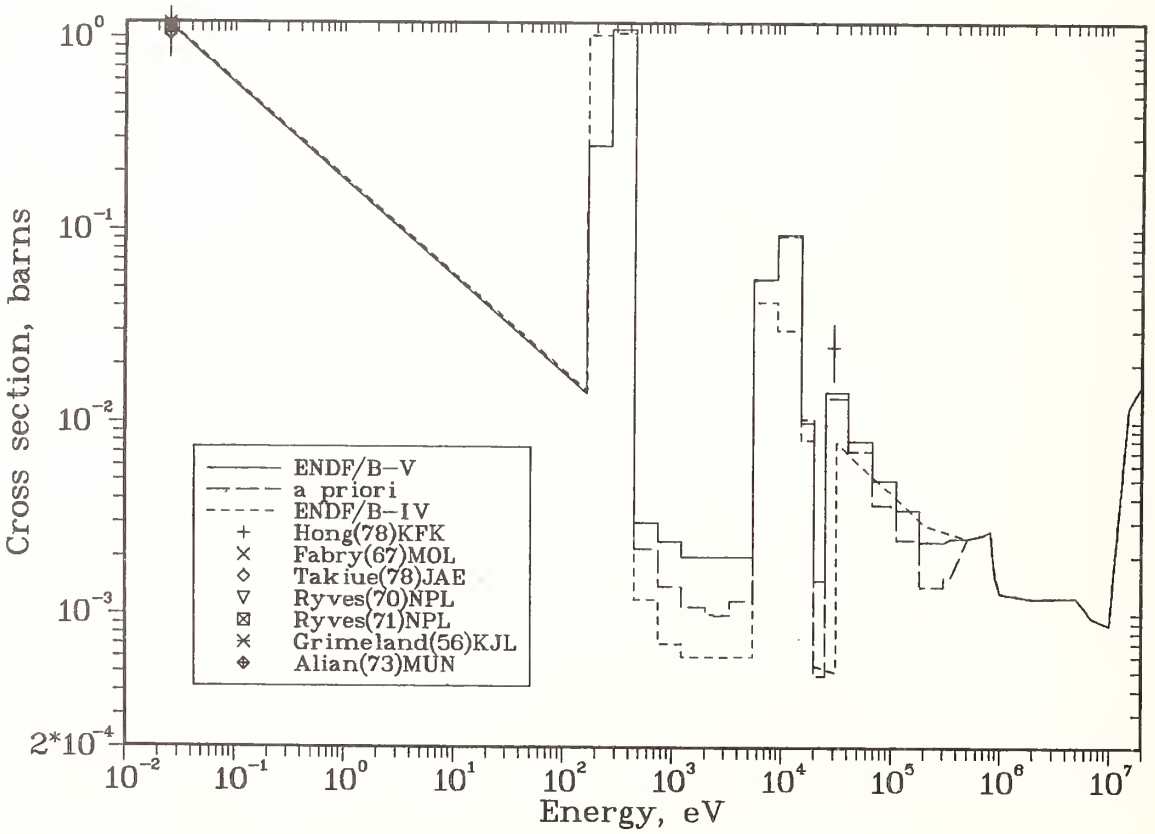

Fig. 1. Fe58(n,γ) cross section evaluations and differential data for energy range .0253eV to 20 MeV. The "a priori" curve is from ENDF/B-IV and Garg et al.[8]

Fe58(n,γ)Fe59

For ENDF/B-IV the file was mainly based on renormalizing a Hauser-Feshbach nuclear models calculation (NCAP computer code)[4] to integral results from the Coupled Fast Reactivity Measurements Facility (CFRMF)[5]. Thermal values were taken from FABRY et al[6] and resonance parameters for energies up to 32 KeV were obtained from Hockenbury et al.[7]

Figures 1-3 show the ENDF/B-V evaluation together with the ENDF/B-IV curve and differential experimental data. Input from both differential and integral data and their uncertainties were combined in the FERRET code to produce an "adjusted" continuous capture cross section curve which was used as the basis for the ENDF/B-V result. Also inputted to the calculation was an "a priori" description which combined multi-group average cross sections obtained from resonance parameters from Garg et al.,[8] for the resolved resonance region (E<300KeV) and ENDF/B-IV for the high energy (E>300KeV) region. The histogram or multi-group cross section description in the resonance region is required for the FERRET least squares calculation because following the exact resonance structure takes too many points for standard computer calculations, especially for the covariance matrix part.

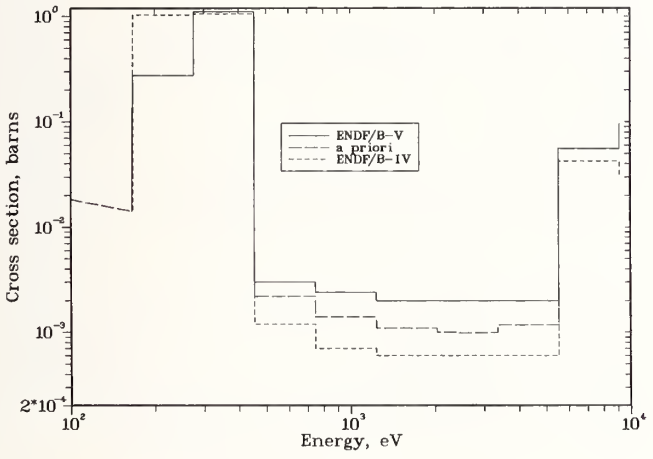

Fig. 2. Fe58(n,γ) cross section evaluations and differential datum for resolved resonance energy range. The "a priori" curve is from ENDF/B-IV and Garg et al.[8]

Results from six thermal experiments, 30 KeV point by Hong et al.,[9] and resonance parameter determinations up to 300 KeV by Hockenbury et al.,[10] Beer et al.,[11] and Garg et al.,[8] constitute the differential data input. Integral results included CFRMF[5] and resonance integral experimental measurements. As can be seen from the figures, significant differences are shown between the ENDF/B-V and ENDF/B-IV results for the energy range 220 eV to 50 KeV. The ENDF/B-V resonance integral value of 1.27b compared to 1.5b for ENDF/B-IV is in good agreement with the quoted value of 1.19±.07b given in BNL-325[12].

Fe54(n,p)Mn54

Figures 4-8 show the ENDF/B-V and ENDF/B-IV evaluations together with experimental data results and their uncertainties. For ENDF/B-IV the evaluation followed exactly the values of Smith and Meadows[13] below 6.0 MeV and smooth "eye-guide" curve was contracted which fell between previous evaluations and

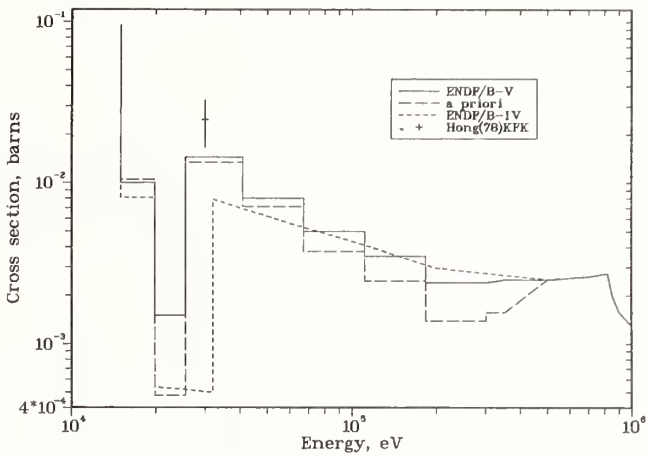

Fig. 3. Fe58(n,γ) cross section evaluations and differential datum for the resolved resonance and high energy range. The "a priori" curve is from ENDF/B-IV and Garg et al.[8]

experimental results above 6.0 MeV.

For ENDF/B-V the direct output from the FERRET code was used. Input to the calculation did not include integral data even though results of measurements exist for CFRMF, EBR-2, U235 and Cf252 fission spectra. All the differential cross section data and uncertainties (statistical and normalization errors) inputted to the calculation are shown in the figures. The two recent experiments indicated by "Smith (75) ANL-V5"[13] and "Paulsen (78) GEEL-V5"[14] were ratio measurements and were renormalized to ENDF/B-V U235 fission (E<4MeV), U238 fission (E>4MeV) for the first and Fe56(n,p) for the second. These renormalizations were substantial, making changes as much as 7% for the Smith and Meadows[13] data and as much as 13% for the Paulsen et al.[14] results.

As previously stated, the FERRET calculation requires an a priori nominal curve and covariance matrix. For this Fe54 case a nuclear models calculation using the HAUSER*5[15] code generated the nominal values. It is extremely significant, as can be seen from the figures that the HAUSER*5 calculation predicts the evaluation, since it falls within the experimental data and is surprisingly close to the adjusted curve for almost the entire energy range shown. This is further strengthened since this Hauser Feshbach calculation used no parameters adjusted to previous Fe54 cross section results.

Covariance information for this evaluation is summarized in Table I. The covariance matrix was defined on a set of eight energy intervals that span the range from .1 to 20. MeV. As indicated in Table I, final fractional uncertainties vary from 3.7% near 7 MeV to a maximum of nearly 16% in the lowest energy interval. This 16% is close to the a priori uncertainty and hence reflects the lack of data in this region.

The correlation matrix ρ_{ij} is also tabulated in Table I. Note first that neighboring energy intervals are strongly correlated, a direct consequence of strong short-range correlations that were assumed for the nuclear model calculation. Experimental data extends these correlations somewhat, particularly for the lower energies 2-10 MeV. Finally, note that all correlations are positive. Thus the uncertainties in calculated integral quantities based on this evaluation will be somewhat larger than they would be if the uncertainties in each energy interval were assumed to be statisti-

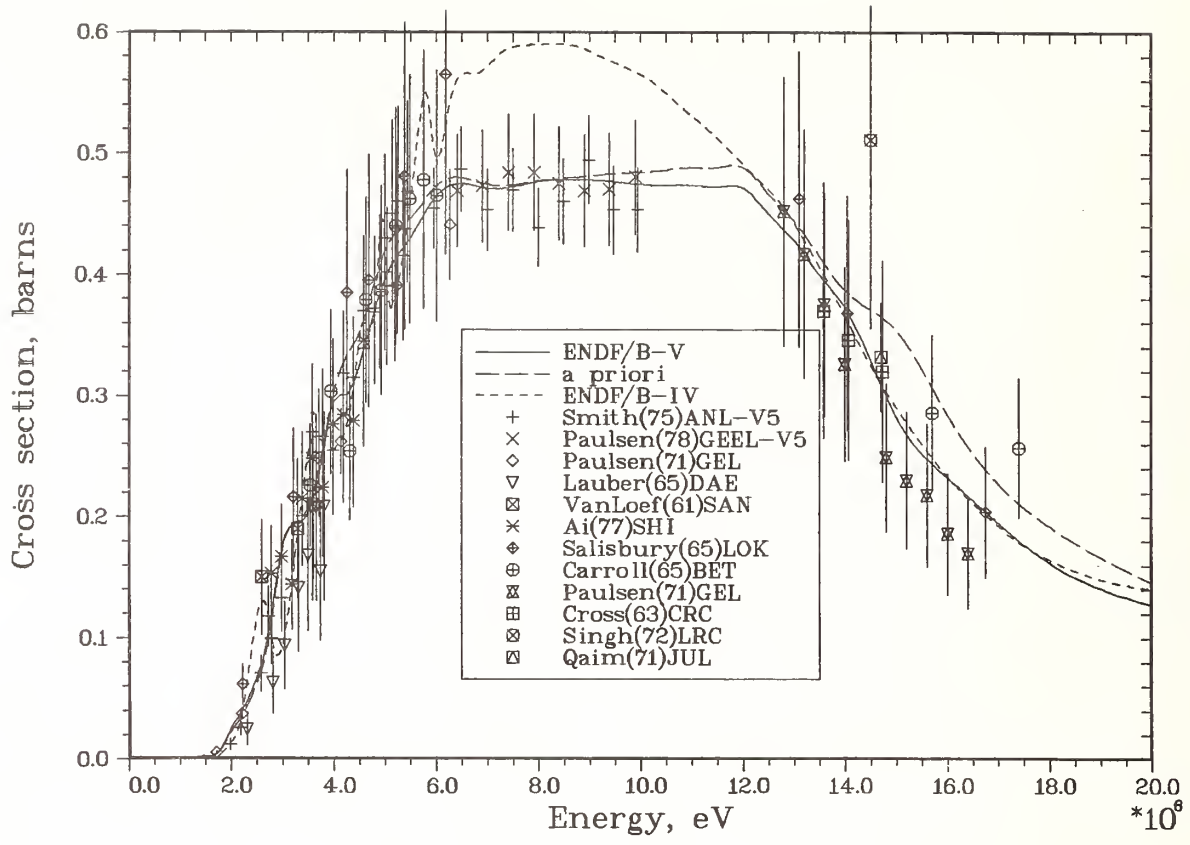

Fig. 4. Fe54(n,p) cross section evaluations and differential data, where the "a priori" curve was calculated using HAUSER*5.[15]

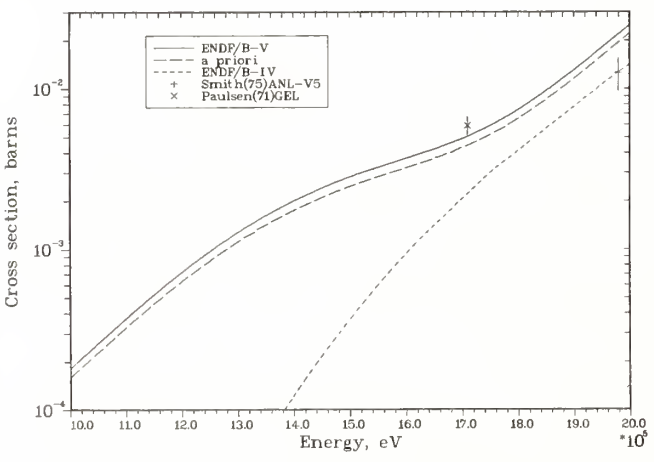

Fig. 5. Fe54(n,p) cross section evaluations and differential data, where the "a priori" curve was calculated using HAUSER*5.[15]

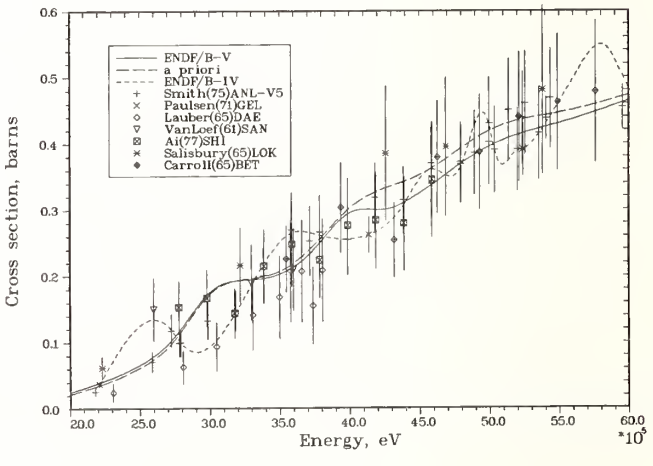

Fig. 6. Fe54(n,p) cross section evaluations and differential data, where the "a priori" curve was calculated using HAUSER*5.[15]

cally independent. If integral data had been included, anticorrelations (negative values for some of the matrix elements ρ_{ij}) would be observed. In that case the uncertainties in integral values could be reduced by a cancellation of uncertainties in contrast to this example.

It can be concluded that progress has been made with this evaluation. The changes from ENDF/B-IV to ENDF/B-V are significant, especially between 6 and 12 MeV in addition to adding the covariance information. Integral testing of this data by Magurno[16] shows good agreement with experimental results.

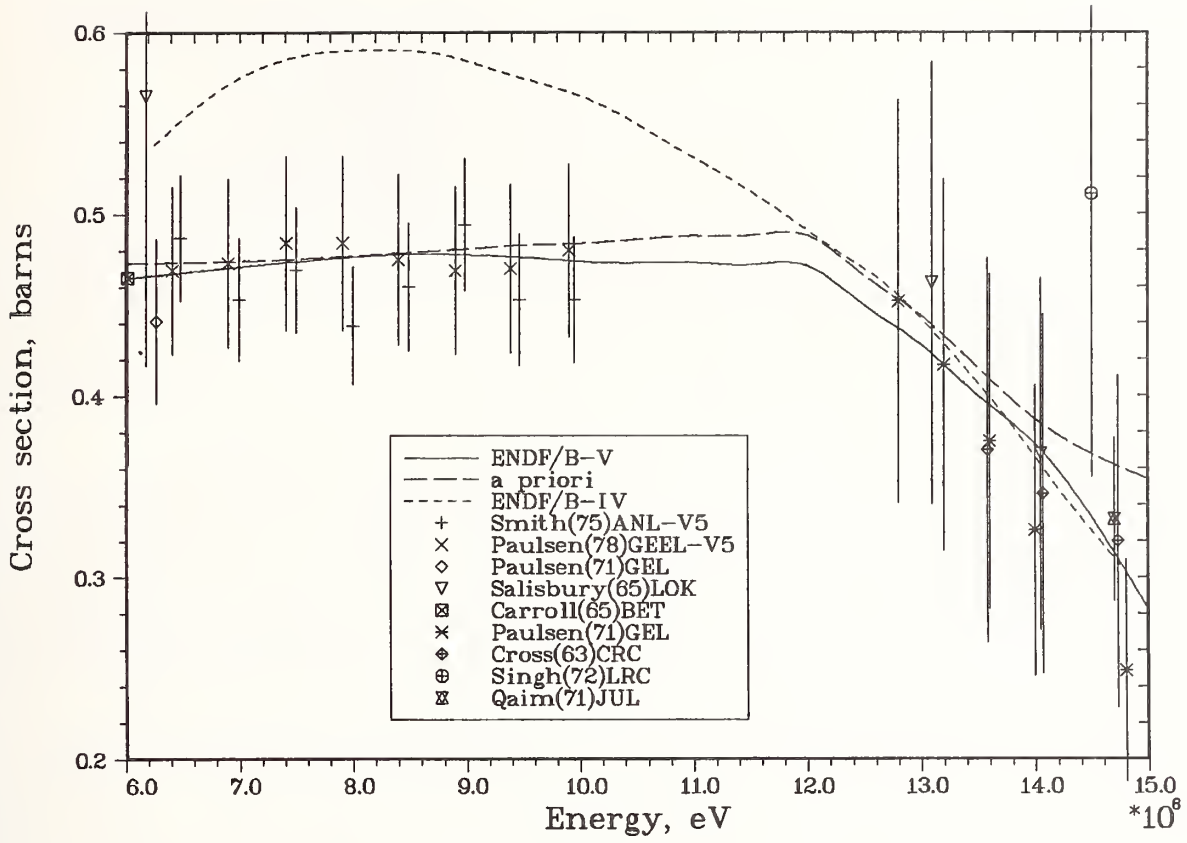

Fig. 7. Fe54(n,p) cross section evaluations and differential data, where the "a priori" curve was calculated using HAUSER*5.[15]

Table I. Multigroup uncertainties and correlations obtained for the $^{54}Fe(n,p)$ evaluation.

Energy Intervals (MeV)	0.1	1.0	2.0	4.0	6.0	8.0	12.0	16.0	20.0
Fractional Uncertainty (%)	15.6	7.2	4.7	3.9	3.7	4.4	6.5	9.2	

Correlation Matrix ρ_{ij}	i / j	1	2	3	4	5	6	7	8
	1	1.00							
	2	0.58	1.00						
	3	0.05	0.31	1.00					
	4	0.13	0.29	0.56	1.00				
	5	0.10	0.23	0.38	0.69	1.00			
	6	0.09	0.17	0.28	0.36	0.57	1.00		
	7	0.09	0.13	0.16	0.21	0.14	0.46	1.00	
	8	0.07	0.08	0.10	0.12	0.09	0.12	0.50	1.00

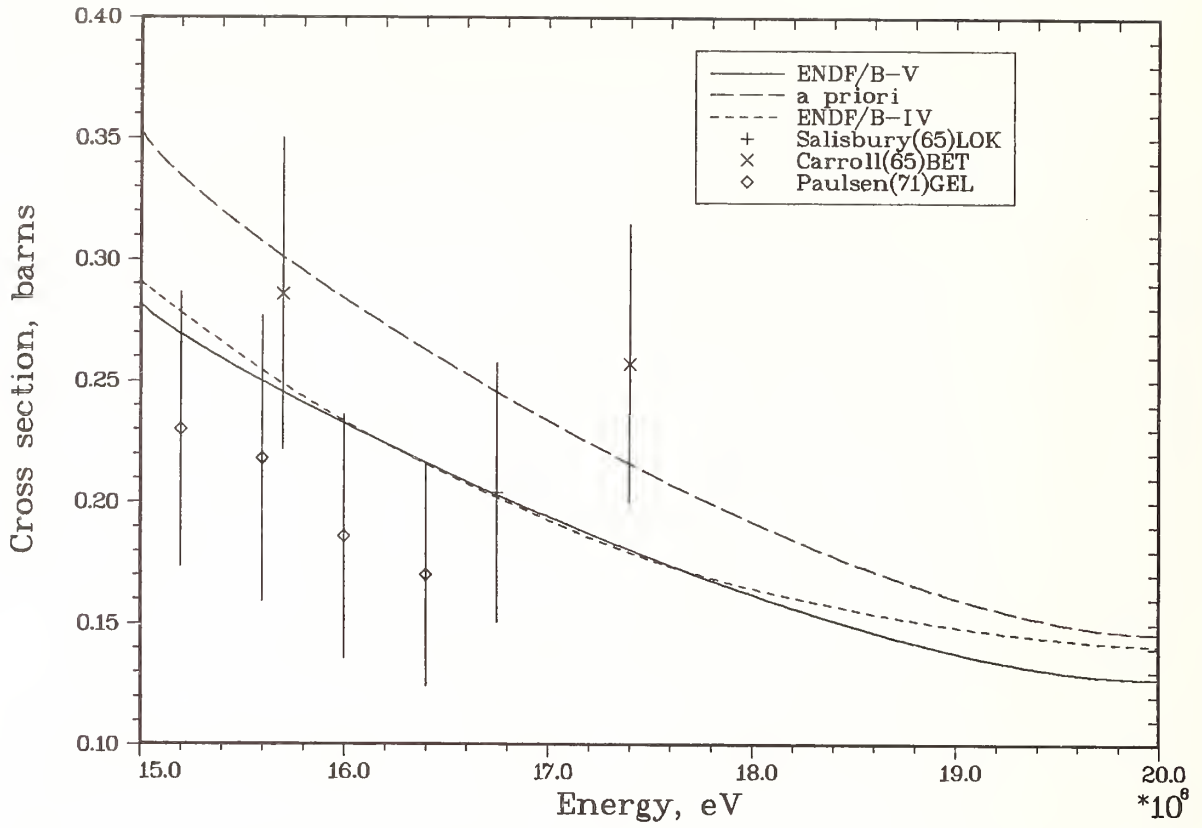

Fig. 8. Fe54(n,p) cross section evaluations and differential data, where the "a priori" curve was calculated using HAUSER*5.[15]

References

1. B.A. Magurno, "ENDF/B-IV Dosimetry File", BNL-NCS-50446, pages 74 and 88, (April 1975).
2. F. Schmittroth, "Generalized Least-Squares for Data Analysis," HEDL-TME 77-51. (March 1978).
3. F. Schmittroth, "FERRET Data Analysis Code", HEDL-TME 79-40, (Sept. 1979).
4. F. Schmittroth, "Theoretical Calculations of Fast Neutron Capture Cross Sections," HEDL-TME 71-106, (August 1971).
5. Y.D. Harker et al., EGG Report 1977, Kiamesha Lake Talk, 1972.
6. A. Fabry, et al., EANDC (E), 76J, (1967).
7. R. Hockenbury, et al., Phys. Rev. 178, 1746 (1969).
8. J.B. Garg, et al., Phys. Rev. C 18, 1141 (1978).
9. H. Hong, et al., KFK, 1978.
10. R. Hockenbury, et al., RPI Progress Report, April 1973.
11. H. Beer, et al., KFK 2337, 1976.
12. S.F. Mughabghab and D.I. Garber, "Neutron Cross Sections, Vol. I., Resonance Parameters", BNL 325, June 1973.
13. D. Smith and J. Meadows, ANL/NDM-10, 1975.
14. A. Paulsen, et al., Nucl. Sci. Eng., Oct. 1979.
15. F.M. Mann, "HAUSER*5, A Computer Code to Calculate Nuclear Cross Sections," HEDL TME 78-83, (October 1978).
16. B.A. Magurno, "Status of Data Testing of ENDF/B-V Reactor Dosimetry File", this conference.

NEUTRON ENERGY SPECTRA AND ANGULAR DISTRIBUTIONS FOR Al AND Nb(n,xn') REACTIONS AT 15.4 MeV

S. Iwasaki, M. Sugimoto, T. Tamura, T. Suzuki, H. Takahashi and K. Sugiyama
Department of Nuclear Engineering, Tohoku University
Aramaki-Aoba, Sendai, 980, Japan

Neutron energy and angular distributions from (n,xn') reactions on aluminum and niobium have been measured at an incident energy of 15.4 MeV at twelve scattering angles from 25° to 155°. From these data, angle integrated spectra have been obtained. In general, present results are consistent with those of the previous experiments in the secondary neutron energy range from 2 to 10 MeV, but some discrepancy also existed between them. Data of the ENDF/B file could not reproduce present results, particularly for niobium. Total spectra were analized by a precompound reaction model.

[(n,xn') reactions. Al and Nb, E_o=15.4 MeV, Measured $\sigma(E_o;E_n', \theta)$, θ= 25°- 155°, Total neutron spectra, Comparison]

Introduction

The secondary neutron energy and angular distributions from (n,xn') reaction on structural materials, are important nuclear data in the analysis of fusion reactor system.[1] There have been, however, few systematic study on these cross sections except the comprehensive measurements for the range of nuclei from beryllium to bismuth performed by Hermsdorf et al.[2], and significant disagreement have been found between the results of experiments and the ENDF/B-V values.[3]

In the present work, these cross sections for aluminum and niobium at 15.4 MeV have been measured utilizing the 4.5 MV pulsed Dynamitron accelerator at Fast Neutron Laboratory of Tohoku University and a time-of-flight spectrometer. These elements are important materials for the fusion applications. Each metal is typical isotope of lighter and medium weight nuclei, respectively, and has only one stable isotope. Such a single isotopic nucleus is of advantage in the comparison its cross section with theoretical estimation.

Obtained results are compared with those of previous experiments performed by Hermsdorf et al., Kammerdiener[4], and Morgan[5], and also with the ENDF evaluations.[9] Angle integrated spectra are analyzed by a simple eqilibrium plus pre-equilibrium model.

Experimental Procedure

Cylindrical samples (2 cm ϕ x 3 cm height) of aluminum and niobium metal of high purity were used. The source neutrons were provided by the T + d reaction by bombarding the titanium-tritium target on copper backing with the 1.95 MeV pulsed deuteron beam from the Dynamitron accelerator. Nickel foil of 15 mg/cm^2 was placed in front of the target in order to obtain so called 14-MeV neutrons. Actual source neutron energy was measured as 15.4 ± 0.3 MeV. The pulse width was 2 ns at half maximum.

A conventional time-of-flight spectrometer was used in the measurement of the secondary neutrons. The main detector of the spectrometer was a 5" ϕ x 2" height NE-213 scintillator which was coupled to a photomultiplier tube XP-1040. A 2" ϕ x 2" height NE-213 scintillator was placed at the angle of 30° with respect to the incident beam, and used as monitor to normalize the scattering experiments at each angle to the constant source flux. The main and monitor detector were positioned in the shielding assembly made with the mixture of Li_2CO_3 and paraffin, and water and iron, respectively. Iron shadow bar and concrete pre-collimater were used to reduce the directly incident neutrons from the source to the main detector. The main detector and shielding system were mounted on a truck which could be rotated around the sample. Schematically the present experimental set up is shown in Fig. 1

A block diagram of the electronics of the spectrometer is shown in Fig. 2. Zero crossing pulse shape analysing circuits were employed to reject gamma rays from the sample and shield assembly. Besides the conventional fixed pulse height biasing, a dynamically changing biasing technique mentioned by Brandenberger[6] was tried to improve signal to backgound ratio (S/N) of the time-of-flight spectrum. The small computer receives both flight time and pulse height signals simultaneously through the DMA bus, and selects the pulse height signals which satisfiy the predetermined bias levels (lower and upper level)depend on the flight time, and makes the time-of-flight spectrum corresponds to that pulse height signals. In the present case, lower and upper bias levels were set at 20 % and 125 % of each reference pulse height which corresponds to the maximum energy of recoil protons in the scintillator. This biasing technique provided an improvement of the S/N by about 30 %.

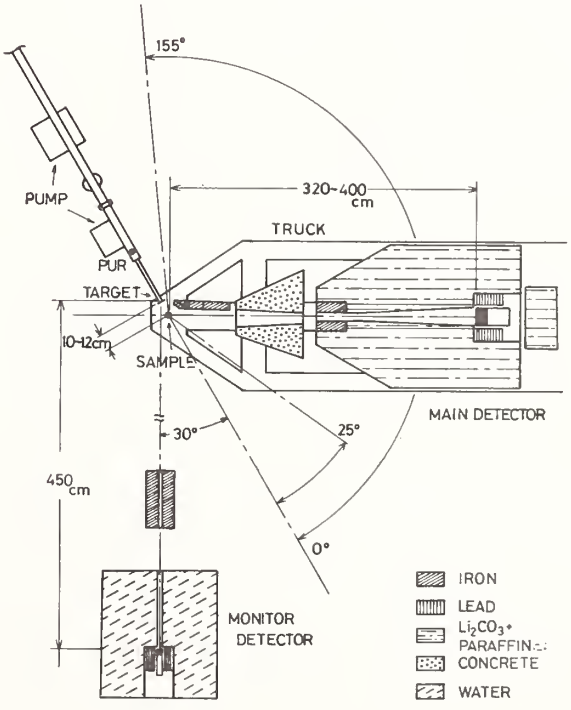

Fig. 1. Schematic diagram of the experimental arrangement.

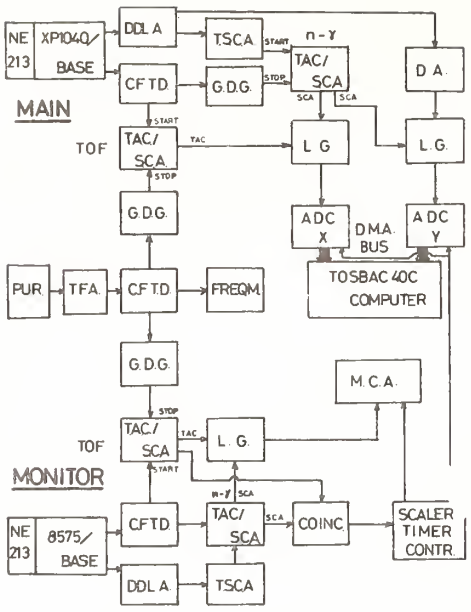

DDL.AMP:double delay line shaping amp. CFTD:const. fraction timing discri. GDG:gate and delay generator. TSCA:timing single ch.analiz. TAC:time to amplitude converter. DA:delay amp. LG:linear gate. DMA bus:direct memory access bus. PUR:beam pick up ring. TFA: timing filter amp.

Fig. 2. Block diagram of the experimental electronics.

Detection efficiency of the spectrometer was calculated by the Monte-Carlo code O5S.[7] The calculated values of the efficiency were checked by the measurement of the hydrogen scattering cross sections at several scattering angles using a polyethylene sample and carbon sample for subtraction of the effect of the carbon in the former sample, under the identical experimental condition as the measurements for aluminum and niobium. The calculated and experimental results for efficiency agreed within 11 %. The neutron multiple scattering and attenuation in the sample were corrected by Monte-Carlo calculation.

The secondary emission neutrons were measured at twelve angles from 25° to 155° with 4m flight path at forward (25°and 30°) and backward (155°) angles, and with 3.5 m at other angles. Background level for each measurement was estimated from the result of the corresponding sample-out measurement. Since the rather small sample and long flight path were used, high background level and lower statistics of the true events were obtained. For this reason the time-of-flight spectrum data were bunched to 0.5 MeV interval to obtain the energy spectra in the energy range from 2 to 13 MeV. Angular distributions for every interval were fitted by 4-th order Legendre polinomials and integrated over the solid angle. The angle integrated spectra (total differential cross sections) for 1-MeV interval were obtained from the fitted data. The uncertainty of the double differential cross sections was estimated as 7 to 17 % which included statistical, normalization,detection efficiency and other errors. Uncertainty of the total differential cross sections was also assumed as 17 to 30 %. The uncertainty value of individual data point are indicated at typical points in the Fig. 3 to 6 for the energy and angular spectra and angle integrated spectra for both, aluminum and niobium.

Results and Comparison with other data

Energy and Angular Distributions

A bird's eye view of the secondary neutron energy distributions versus scattering angles for aluminun and niobium are plotted in Fig. 3 and 4, respectively. At typical angles, other experimental results by Hermsdorf et al.[2] at 14.6 MeV, Kammerdiener[4] and Morgan [5] at 14 MeV are also presented for comparison.

In the Fig. 3 aluminum spectra show some definite structure particularly in the results of Kammerdiener. There is also an appearance of weakly excited structure for niobium spectra as shown in Fig. 4. This semi-discrete structure for the light nuclei such as aluminum have been observed in the previous experiment by Thomson [8] at 5 to 7 MeV. The light nuclei have lower density of the excited states than medium or heavy nuclei, and probably some of the states are strongly excited by inelastic scattering. The appearance of the more marked structure in the spectrum by Kammerdiener than others may be due to the difference of the energy resolution of each experiment. The experiment by Kammerdiener was a sort of high resolution one using very long flight path and ring scatterer. Hermsdorf et al. carried out their experiment using relatively a large sample and short flight path. Morgan et al. used the NE-213 scintillation spectrometer to observe the scattered neutron and analysed the data by an unfolding method. Latter two were low resolution experiments.

General trend of the present aluminum and niobium data are consistent with Hermsdorf et al. in the energy range from 2 to 10 MeV, but some deficiencies are seen in the niobium spectra in the same energy region. For both nuclei the cross sections for higher energy than 10 MeV in the present results, as well as Kammerdiener's results, are much larger than those of Hermsdorf et al.

In our results on angular distributions as shown in the Fig. 3 and 4, the secondary neutron group at higher energy exhibit pronouncedly forward peaking . Lately, these neutrons have been interpreted as a precompound component. Angular distributions of the neutron group below 4 MeV of the same figures show weak forward peaking or nearly isotropic. These feature can be interpreted as that large fraction of these neutrons are contribution of equilibrium component. On the other hand, the evaluation (ENDF/B-IV)assumes [9] the angular distribution of secondary neutrons for both nuclei as isotropic, except for only high energy neutron group of aluminum which correspond to the excitation energy of less than 3 MeV of aluminum.

Angle Integrated Spectra

Angle integrated spectra for each element are shown in Fig. 5 and 6, together with previous experimental and evaluated results. The integrated spectra by Hermsdorf et al. plotted in the figures are taken from the graphs in the ref. 3 by Hetrick et al. who had calculated the spectra in the energy range from 2 to 11 MeV from the double differential cross section data by Hermsdorf et al. in the same manner as mentioned previously. The plotted data by Kammerdiener in the Fig. 7 were taken from the figure of the ref. 10.

In the experimental results in the two figures, previously discussed structure of the spectra is disappeared by the integration and averaging process. In the energy region from 2 to 10 MeV, two experimental results for aluminum and three results for niobium are consistent with each other. Above 10 MeV, each result

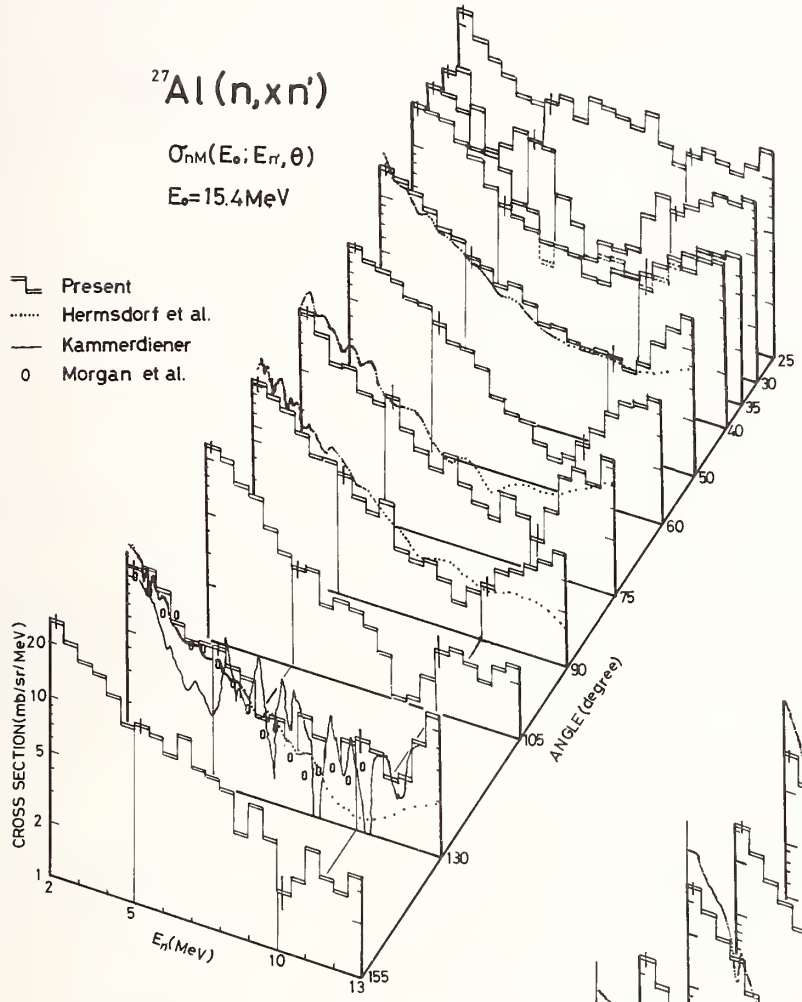

Fig. 3. The secondary neutron energy distributions versus scattering angles for aluminum.
Hermsdorf et al.[2] at 14.6MeV
Kammerdiener[4] at 14 MeV
Morgan[5] at 14 MeV

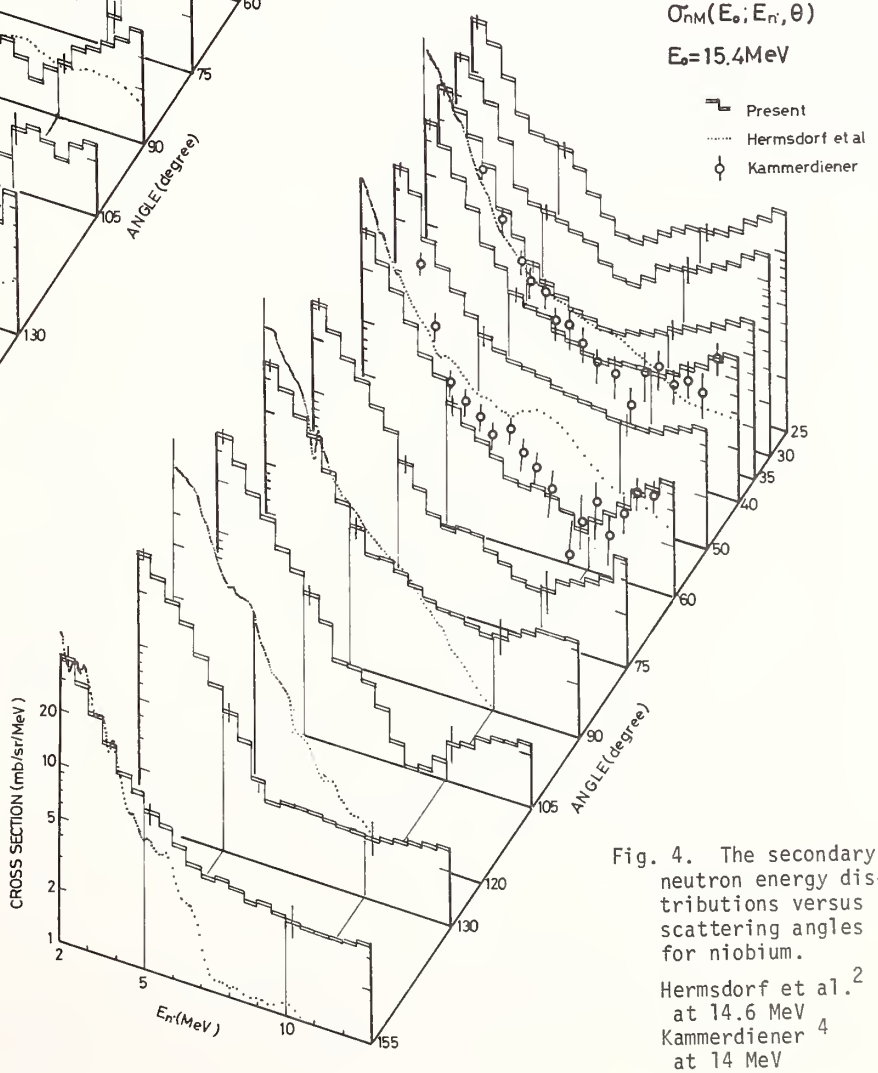

Fig. 4. The secondary neutron energy distributions versus scattering angles for niobium.
Hermsdorf et al.[2] at 14.6 MeV
Kammerdiener [4] at 14 MeV

is in contrast; present results for both nuclei, as well as Kammerdiener's result for niobium show increase of the cross section with neutron energy increase, but in contrast Hermsdorf et al.'s data show decrease.

The ENDF evaluations[9] show markedly disagreement with the experimental results. The evaluated values can not reproduce the magnitude of the cross sections nor shape of the spactra, especially for niobium. The cross section for niobium in the evaluation are much smaller than the experimental values, by a factor of 2 or more in the vicinity of 5 MeV.

The present angle integrated spectra have been analyzed by a simple precompound model.[11] In this model, it is assumed that the total spectrum shape is expressed as incoherent sum of the contribution from equilibrium and preequilibrium process. As the equilibrium spectrum, the well known simple statistical model of nuclear reaction (Fermi gas model) was adopted and for the preequilibrium component, simple exciton model was used. The inverse cross sections needed were calculated by an empirical formula given by Dostrovsky et al.[12] The level density parameter of the Fermi gas model and normalization factors of the two components were treated as free parameters. Least squares fitting procedures were performed to the total spectra for each element in the energy region from 2 to 10 MeV. Data above 10 MeV were omitted from the present analysis, because their increasing feature with increasing neutron energy have never been reproduced by any precompound model analysis. The present analysis curves are shown in the Fig. 5 and 6. Hermsdorf et al.[10] and Pearlstein[13] have performed analysis of the total spectrum for niobium, for aluminum obtained by Hermsdorf et al.[2], respectively, by means of the Blann's hybrid model (code GRUNE), the geometry dependent hybrid model (code ALICE). These results are also presented in the Fig. 5 and 6.

From these figures, it is found that present analysis as well as analysis by other authors reproduced rather well each experimental spectrum. Continuum component of the ENDF/B-IV in the niobium spectra shown in Fig. 6 is much smaller than the preequilibrium component of the analysis.

Conclusion

Double differential cross sections(energy and angular distributions) and total differential cross sections (angle integrated spectra) for (n,xn') reaction on aluminum and niobium obtained in the present work were in general consistent with the previous experimental data except with the data by Hermsdorf et al. in the secondary neutron energy range higher than 10 MeV. In this energy range, the former cross section increased, on the other hand, the latter decreased. This discrepancy is important, but the reason of this disagreement is not clear in the present stage. The ENDF evaluations for these data are found to be unsatisfactory in the interpretation of the present as well as other experimental data, particularly for niobium cross sections. From successful results of the precompound model analysis, the contribution of the precompound component were underestimated in the course of the evaluation of the cross sections for niobium.

Acknowledgment

It is a pleasure to acknowledge the help of the members of the Fast Neutron Laboratory of Tohoku University.

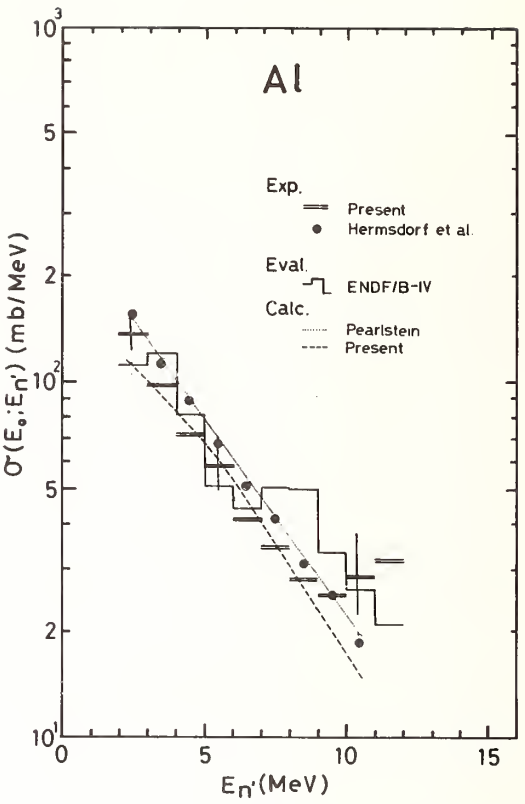

Fig. 5. Angle integrated spectrum for Al(n,xn') reaction. : Hermsdorf et al.[2], Pearlstein[13] at 14.6 MeV, Present , ENDF/B-IV[9] at 15.4MeV

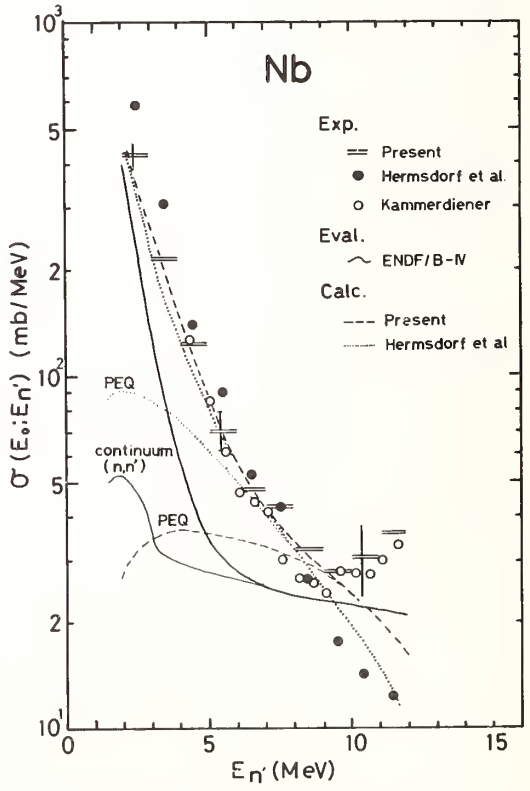

Fig. 6. Angle integrated spectra for Nb(n,xn')reaction : Present, ENDF/B-IV[9] at 15.4 MeV, Hermsdorf et al.[2,10] at 14.6 MeV, Kammerdiener[4] at 14 MeV

References

1. Discussed in the Advisary Group Meeting on Nuclear Data for Fusion Reactor Technology, Vienna, Austria, Dec. 11-15,1978
2. D. Hermsdorf, A. Meister, S. Sassonoff, D. Seeliger K. Seidel, and F. Shahin, Zfk-277(Ü) ZENTRALINSTITUT FUR KERNFORSHUNG,Dresden (1975)
3. D. M. Hetrick, D. C. Larson, and C. Y. Fu, ORNL/TM-6637 (1979)
4. J. L. Kammerdiener, UCRL-51232(1972)
5. G. L. Morgan, ORNL-TM-5072(1975)
6. J. D. Brandenberger and T. B. Grandy, Nucl. Instr. Meth. 93,495(1971)
7. R. E. Textor et al. ORNL-4160(1968)
8. D. B. Thomson, Phys. Rev. 129 1649 (1963)
9. Aluminum: ENDF/B-IV MAT 1193
   P. G. Young and D. G. Foster,Jr, LA-4726(1972)
   Niobium: ENDF/B-IV MAT 1189
   R. Howerton, A. Smith, P. Guenther and J. Whalen ANL/NDM-6(1974)
10. D. Hermsdorf, G. Kiessig, and D. Seeliger, "Kernenergie" 20, Jahrgang.Heft6, p166/1977
11. D. Hermsdorf, A. Meister, S. Sassonoff, D. Seeliger, and K. Seidel, Proc,of Consultants Meeting on the Use of Nuclear Theory in Neutron Nuclear Data Evaluation, IAEA-190, Trieste, (1975)
12. I. Dostrovsky, Z. Frankel and G. Friedlander, Phys. Rev.116 683 (1959)
13. S. Pearlstein, Nucl. Sci. Eng. 68 55 (1978)

SCATTERING OF 10 MeV NEUTRONS ON SILICON

W. Pilz, D. Schmidt, D. Seeliger and T. Streil
Technische Universitat Dresden, GDR

[Si(n,n), σ(θ) at 10 MeV, optical model, coupled channels and Hauser-Feshbach analysis.]

The elastic and inelastic differential cross sections for 10 MeV neutrons on silicon are measured. Neutrons were produced by the D(d,n) reaction in a gas target.[1] The cross sections of the neutrons emitted from higher excited states are corrected with respect to neutrons from the deuteron break-up using special computer program. Figure 1 shows the experimental arrangement.

The measurements were carried out with a multi-angle TOF-detector system consisting of 8 detectors, located between angles of 15 and 160 degrees.[2] The flight paths were about 3 meters, the energy spread about 120 keV and time resolution 3 ns.

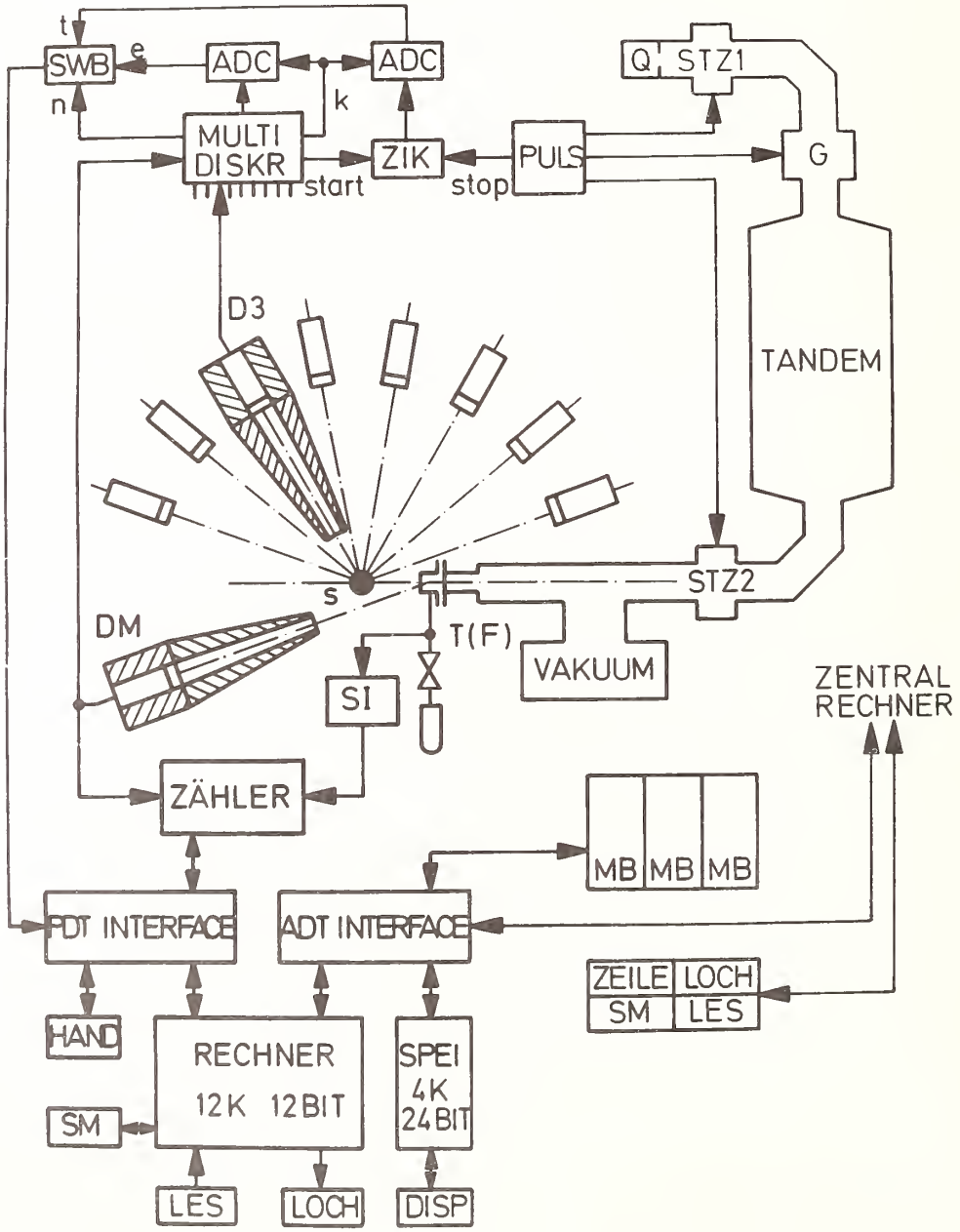

Fig. 1. The multi-angle TOF-detector system (the symbols are described in ref. [2]).

Figure 2 shows the cross sections and analysis. The measured cross sections have been corrected for geometry and multiple scattering.

The results are described by incoherent superposition of compound and direct interaction parts. For calculation of the direct part, the collective model with coupled channels method is used. The best description of elastic and two first inelastic angular distributions is obtained for an oblate deformed nucleus. Additionally, for elastic scattering an optical parameter fit gives a good agreement with results from other work.[3]

References

1. S. Mittag et al., Kernenergie 7, 235 (1979).

2. P. Eckstein et al., Nucl. Instr. Meth., in print (1979) and J. Kayser and W. Pilz, thesis, Technische Universitat, Dresden 1978.

3. A. W. Obst and J. L. Weil, Phys. Rev. C7, 1076 (1973).

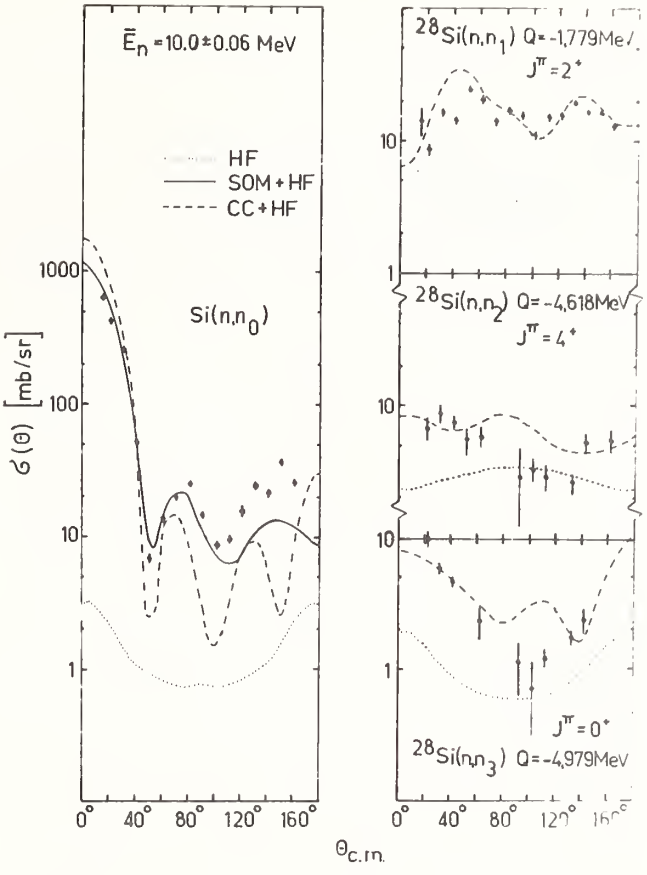

Fig. 2. Angular distributions of the elastic and inelastic (2^+, 4^+ and 0^+) scattered 10 MeV neutrons. The experimental cross sections (•) are shown with their absolute errors. The solid and dashed curves correspond to the optical model (SOM) and coupled channels calculation (CC), respectively, each plus a Hauser-Feshbach (HF) compound contribution, which is also shown separately.

DOPPLER BROADENING EFFECT TO NEUTRON RESONANCE CROSS SECTIONS FOR Ag, AgCl and Ag_2O*

H. I. Liou, R. E. Chrien and R. Moreh†
Brookhaven National Laboratory, Upton, New York 11973

The neutron capture yield of the 16.3 eV resonance in ^{107}Ag has been measured, using targets of Ag metal, AgCl and Ag_2O at room, liquid N_2 and He temperatures. The effective temperature T' defined by Lamb for weak binding, and subsequently the Debye temperature θ_D, were extracted for each case by a least squares shape fit. For Ag metal the measured θ_D values agree with both the simple Debye theory and a prediction of the Ag lattice dynamics. The θ_D values for AgCl and Ag_2O show some variations with temperature. The results for AgCl at 77.2° and 4.066°, however, agree with the inelastic scattering and calorimetric data.

(Doppler Broadening T' and θ_D, Ag metal, AgCl and Ag_2O, T=294°, 77.2°, 4.066°)

Introduction

It has long been recognized that the observed cross section is influenced by the distribution of velocities of the target atoms. Bethe and Placzek[1] derived the modification of the cross section which occurs for free atoms at a finite temperature T. By averaging over the Maxwellian velocity distribution of the gas atoms, they drived a line shape consisting of the well-known ψ function. For a solid target of crystalline materials the lattic binding effect of atoms may further influence the neutron cross sections. Many years ago Lamb,[2] by considering the normal modes of lattice oscillation in a crystal, derived a basic formalism for Doppler broadening that in principle can be computed if the detailed spectrum of phonon frequencies is known. He showed that in the weak binding case the neutron cross section has the same form as it would in a perfect gas, except that the crystal temperature T in Doppler width $\Delta = \sqrt{4k_BTE/A}$ is replaced by an effective temperature T'. This temperature T' corresponds to the average energy per vibrational degree of freedom of the lattice including zero-point energy. T' can be calculated from the detailed distribution of normal frequencies.

Applying the simple theory of Debye continuum, Lamb arrived at

$$\frac{T'}{T} = 3\left(\frac{T}{\theta_D}\right)^3 \int_0^{\theta_D/T} \left(\frac{1}{e^t-1} + 1/2\right) t^3 \, dt \, . \qquad (1)$$

The Debye theory which assumes a ν^2 dependence for the spectrum of normal frequencies up to a cut-off at θ_D is known to be inadequate to describe the specific heat data for many materials at low temperature. In study of lattice dynamics one expresses θ_D not as a constant, but as a smooth function of temperture. If an atom is bound in a lattice more strongly than in the weak binding limit, $\Delta+\Gamma >> 2\theta_D$, some fine structure appears in its broadened line shape. A more detailed model than the effective temperature theory is needed to describe this structure.

To derive neutron resonance parameters for a crystalline target, one needs to understand its structure. On the other hand, it is of interest that, if the parameters for a narrow resonance in an element are accurately known, one may be able to learn some features about lattice dynamics from the resonance line shapes for different chemical compounds at various temperatures. A number of attempts[3,4] have been made to study the Doppler broadening of resonance line shapes. Recently Bowman and Schrack[5] have studied the chemical binding effects to fission cross sections of ^{235}U and ^{239}Pu.

In the present study we did a systematic study of the resonance-broadened line shape for a set of Ag compounds at room, liquid N_2 and He temperatures. We chose to examine Ag metal, Ag_2O and AgCl through the (n,γ) reaction. Ag is a good choice for the following reasons: (1) the Ag resonances at low energy are well isolated, and their level parameters are also well known;[6] (2) the phonon frequency distribution and the specific heat data for Ag metal[7,8,9] and AgCl[10,11,12] are available for comparison; (3) the large capture width to neutron width ratio provides a good signal to background ratio in (n,γ) measurement and fulfills the weak binding condition; (4) the Doppler width for the 16.3 eV level in ^{107}Ag at room temperature dominates the natural width and our instrumental resolution width, giving a good sensitivity for its measurement. We attempt to examine how the lattice binding effect in different Ag compounds varies with temperature, and how well the simple Lamb theory applies in the weak binding case.

Experiments and Samples

The (n,γ) measurements of Ag compounds were carried out at the Brookhaven National Laboratory High Flux Beam Reactor with the fast chopper time-of-flight (TOF) spectrometer and its 21.68 m flight path. The narrow-slitted rotor was operated at a repetition rate of 1000 s^{-1}, giving a beam intensity of $\sim$ 1.5 x 10^3 E^{-1} $n/cm^2 \cdot s \cdot eV$) and a burst width of 1 μs. The target sample was clamped at end cup of a double layered cryostat, directly touching the cold finger and perpendicularly facing the incident neutron beam. A coaxial Ge(Li) detector with 10% relative efficiency was allowed to view the target in an angle of 45° through a 0.32 cm of lead shielding. The data were recorded on magnetic tape, event by event. Each event consists of one TOF parameter and one γ-ray pulse height (PH) parameter. The PH spectrum covers a wide energy range from 200 to 4000 keV.

The samples of Ag metal, Ag_2O and AgCl have a size of 5.74 cm x 5.74 cm, and n values of 0.00114 a/b for ^{107}Ag and 0.00106 a/b for ^{109}Ag. This sample thickness was deliberately chosen such that the experimental value of $n\sigma_t$ at peak of the 16.3 eV resonance is near 2 to give a good sensitivity for shape analysis. A chemical analysis indicates that the metallic target is 99.6 ± 0.2% pure. The Ag_2O crystals, being fine powders, are tightly packed in a thin Al container. Since the AgCl crystal attacks Al surface chemically, its container is made of a thin lucite frame, a front glass window, and an Al back protected with a sheet of polyethylene, so the sample can still have good thermal contact with the cold finger.

To check internal consistency, the experiments were done for 3 separate series of runs, cycling through 3 samples, each for 3 temperatures at 294, 77.2 and 4.066 degrees. The total running time for useful data amounts to 1330 hours. While individual runs for different cycles showed some variations in deduced sample effective temperatures, they are consistent within statistical fluctuation.

Method of Analysis

The background correction for a well-separated resonance in (n,γ) data is easily made by properly connecting a straight line on both sides of the resonance. Assuming a perfect resolution, the background-subtracted count in a given time-channel near the studied resonance can be expressed as

$$C(E) = S\,[1-\exp(-\delta)]\,n_R\sigma_c/\delta, \qquad (2)$$

where $\delta = n_R\sigma_r + n\sigma_r + m\sigma_q + (n\rho+m\rho')/\cos 45°$,

S = a cross section independent factor which depends only on the total number of incident neutrons and detector efficiency,

n, n_R = thicknesses for Ag element and the corresponding Ag isotope to the studied resonance,

m = thickness of oxygen or chlorine (equal to 0 in metallic Ag case),

σ_p, ρ = neutron potential scattering and γ-ray total absorption cross sections for Ag element,

σ_q, ρ' = neutron potential scattering and γ-ray total absorption cross sections for oxygen or chlorine,

$\sigma_c = \sigma_o\psi(x,s)(\Gamma-\Gamma_n)/\Gamma$,

$\sigma_r = \sigma_o[\psi(x,s) + 2kR'\,\chi(x,s)\,A/(A+1)]$,

$\sigma_o = 4\pi\lambda\bar{}^2\,(g\Gamma_n/\Gamma)\,[(A+1)/A]^2$,

$s = \Delta/\Gamma$, $\Delta = \sqrt{4k_BT'E/A}$,

$x = 2(E-E_o)/\Gamma$ and $\Gamma = \Gamma_\gamma + \Gamma_n$.

Here ψ and χ are the well known Doppler line-shape functions for the resonance and interference cross sections. Equation (2) includes the Doppler broadening according to the weak binding limit of the Lamb's theory, but ignores the multiple scattering effect that is estimated about 1% in the present study.

To deal with real count, one must also fold in resolution smearing as

$$C^*(E) = \int G(Z,E)\,C(Z)\,dZ, \qquad (3)$$

where the resolution function G follows a Gaussian form with an energy standard deviation $\Delta E(eV) = 0.001276\,E(eV)^{3/2}\Delta t(\mu s)$. The time smearing Δt contains 3 sources of uncertainties: (1) opening time of the chopper slits, (2) the analyzer channel width, and (3) the dynamic beam intensity profile on the target. From known spectrometer parameters, we estimate Δt as 0.662 μs.

With known values of Γ_γ, $g\Gamma_n$, g and ΔE, a least squares shape fit to the resonance peak can be carried out to extract the best values of S and T' (or Δ). However their true precisions depend on the accuracy of the values of ΔE and Γ_γ. To make an independent determination of ΔE and Γ_γ for the 16.3 eV resonance, our approach is to assume the correctness of the Lamb's theory for weak binding to describe metallic silver at room temperature. The corresponding T' can thus be deduced from equation (1) by means of an assumed value of θ_D, since T' is not sensitive to θ_D at large T. We obtain T'=303° for silver metal at T=294° with θ_D=226°. By applying this value to metallic silver data at room temperature, we obtain Δt=0.666 μs for a fit to the 30.4 eV resonance in ^{109}Ag where resolution width dominates over natural width, and obtain Γ_γ = 134±3 meV for a fit to the 16.3 eV resonance (an average over 3 measuring cycles). In the fit for the 16.3 eV level we adopt $g\Gamma_n$ = 2.9 meV and g = 0.25 as listed in Ref. 6. Then with these fine-tuned Δt and Γ_γ values we find T' by fitting all other data. The results averaged over 3 measuring cycles are given in Table I. In all cases of fit the χ^2 value per degree of freedom is in the order of unity. Two typical examples of the shape fit are shown in Fig. 1 for Ag metal at room temperature and for AgCl at 4.066°. The statistical fluctuation of the data is about the same size of the points plotted.

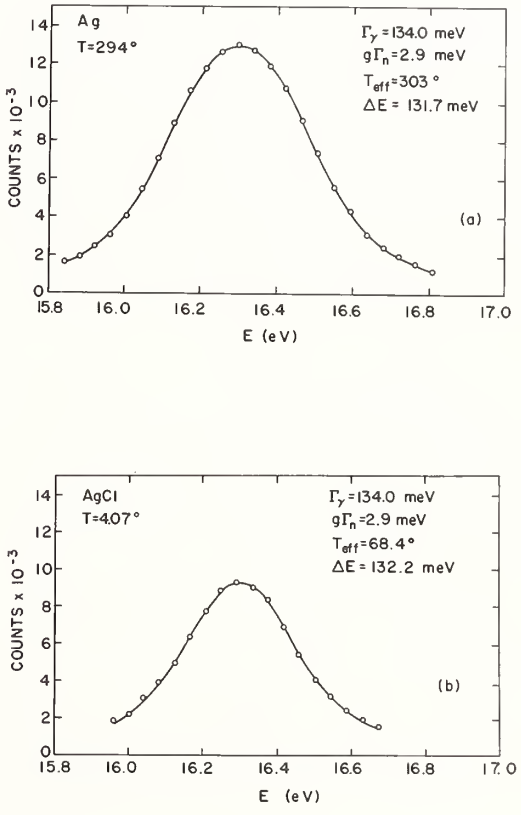

Fig. 1: This illustrates two typical examples for the least squares shape fit to the (n,γ) data at 16.3 eV resonance in ^{107}Ag. The statistical uncertainty of the data is about the same size of the points plotted.

TABLE I

T' and θ_D for Ag metal, AgCl and Ag_2O at 3 measured temperatures.

	T=294°		T=77.2°		T=4.066°	
	T'	θ_D	T'	θ_D	T'	θ_D
Ag Metal	303	226	108±6	229±25	82±7	219±19
AgCl	318±7	379±57	107±6	225±25	64±6	171±16
Ag_2O	306±7	267±83	123±7	285±25	66±10	176±27

Results and Discussion

The uncertainties of T' given in Table I are due to only the statistical fluctuations, which dominate all other systematic errors. We subsequently obtain θ_D and its uncertainty from T' and T using equation (1). The measured θ_D may vary with T because the simple Debye theory is not exactly followed. A comparison of θ_D with values derived from the specific heat and inelastic scattering data is of particular interest.

As mentioned earlier, the θ_D of Ag metal at room temperature is assumed in order to fine-tune the Δt and Γ_γ values. Figure 2 shows the present results (Δ) for Ag metal at liquid N_2 and He temperatures, compared with other measurements. Drexel's results[7] were derived from neutron inelastic scattering measurement by means of a multi-parameter fit for the distribution of phonon frequencies. '+' and 'o' represent the direct calorimeteric measurements by Eucken et al.[8] and Martin[9] respectively. It can be seen that the present results are consistent with others. The remarkable constancy of θ_D through all temperatures suggests that the metallic Ag crystal behaves well as a Debye continuum.

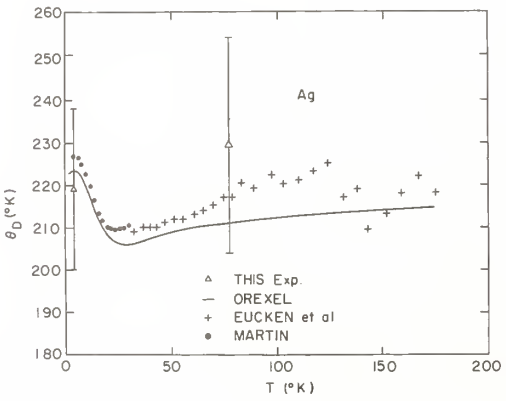

Fig. 2: A comparison of the present measured values of θ_D (Δ) for Ag metal at 77.2° K and 4.066° K with those derived from neutron inelastic scattering measurements (-), and calorimetric data (o,+).

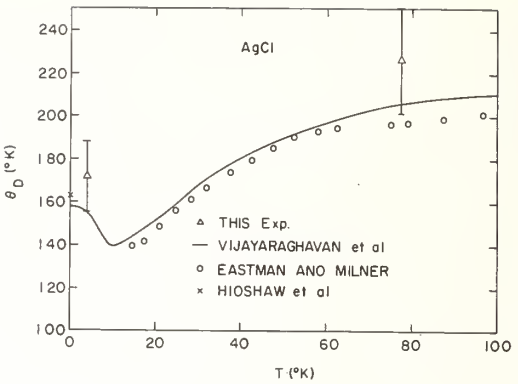

Fig. 3: A comparison of the present measured values of θ_D (Δ) for AgCl at 77.2°K and 4.066°K with those derived from neutron inelastic scattering measurements (-), calorimetric data (o), and elastic constants measurements (x).

In spite of its large uncertainty, the θ_D value of AgCl at room temperature appears anomalously high, almost 3 standard deviations away from that measured at liquid N_2 temperature. It is hard to understand with the Lamb's theory for weak binding. Figure 3 shows a comparison of our results for AgCl with other measurements at low temperature. The inelastic scattering results come from Vijayaraghavan et al.[10] 'o' represents the specific heat data of Eastman and Milner.[11] 'x' denotes a limiting value of θ_D at 0° K deduced from elastic constants measurements by Hidshaw et al.[12] Our values are a little high, but check with others within statistical uncertainty. The signficant variation of θ_D vs. T below 80° K indicates that the distribution of normal frequencies for AgCl does not follow the ν^2 law of the Debye theory.

With its large uncertainty the present value of θ_D for Ag_2O at room temperature appears reasonable, compared with the metallic silver results. However its values at liquid N_2 temperature seems abnormally high, about 2 standard deviations away from those for Ag metal and AgCl at the same temperature. Unfortunately for Ag_2O we are unaware of any other θ_D measurement. The θ_D of Ag_2O at 4° is a little lower than the value for Ag metal, but much closer to that of AgCl.

References

*Work supported by US DOE Contract EY-76-C-02-0016.
†Visitor from Negev Research Centre, Negev, Israel.

[1] H. Bethe and G. Placzek, Phys. Rev. 51, 462 (1937).

[2] W. E. Lamb, Phys. Rev. 55, 190 (1939).

[3] H. H. Landon, Phys. Rev. 94, 1215 (1954)

[4] H. E. Jackson and J. E. Lynn, Phys. Rev. 127, 461 (1962).

[5] C. D. Bowman and R. A. Schrack, Phys. Rev. C 17, 654 (1978).

[6] S. F. Mughabghab and D. I. Garber, "Neutron Cross Sections", Vol. 1, "Resonance Parameters", BNL-325, 3rd ed., Brookhaven National Laboratory (1973).

[7] W. Drexel, Z. Physik 225, 281 (1972).

[8]A. Eucken, K. Clusius and H. Woitinek, Z. Anorg. Allgem. Chem. 203, 47 (1931).

[9]D. L. Martin, Phys. Rev. 141, 576 (1966).

[10]P. R. Vijayaraghavan, R. M. Nicklow, H. G. Smith, and M. K. Wilkinson, Phys. Rev. B 4819 (1970).

[11]E. D. Eastman and R. T. Milner, J. Chem. Phys. 1, 444 (1933).

[12]W. Hidshaw, J. T. Lewis, and C. V. Briscoe, Phys. Rev. 163, 876 (1967).

MEASUREMENT OF THE $^{10}B/^{6}Li$ CROSS SECTION RATIO BELOW 1 keV

J. B. Czirr and A. D. Carlson
National Bureau of Standards
Washington, DC 20234, U.S.A.

The ratio of the $^{10}B(n,\alpha)$ and $^{6}Li(n,\alpha)$ standard cross sections has been measured from ~1 to 1000 eV with statistical uncertainties of <1%. The measurements agree with ENDF/B-V above ~20 eV, however a significant difference is observed below ~20 eV. The present measurements do not explain the discrepancy between recent ^{235}U measurements at ORNL and LLL using $^{10}B(n,\alpha)$ and $^{6}Li(n,\alpha)$, respectively, as flux monitors.

[^{10}B, $^{10}BF_3$, cross sections, flux monitors, ^{6}Li, standards.]

Recent measurements[1,2] of the ^{235}U fission cross section below 1 keV neutron energy suggest a possible discrepancy in the cross section standards - ^{10}B and ^{6}Li - used to measure the flux.

We have initiated a program at the NBS Linac to measure the ratio of these standard cross sections in the 1 to 1000 eV energy range, using the flux monitors which were used in the fission cross section measurements. The ^{6}Li detector[3] consists of a 0.67 mm thick Li-glass scintillator viewed on the ends by two 12.7 cm diameter phototubes. Only the central position of the scintillator is exposed to the neutron beam, in order to minimize neutron scattering from the phototubes and surrounding structures. The glass scintillator (NE901) contains ~2% by weight natural Li. The efficiency at thermal neutron energy is ~2.1%, so self-shielding corrections in the 1 eV to 1 keV energy range are <0.2%.

The ^{10}B detector consists of a 2.54 cm thick parallel plate ionization chamber containing enriched BF_3 at a partial pressure of 18.75 cm Hg. The efficiency of this detector is 6.3% at thermal and therefore a 0.5% correction for neutron absorption is required at 1 eV. The data were corrected for flux attenuation using the ENDF/B-V total cross sections.

The data were obtained at the 20 m station of the NBS Linac, with the accelerator operating at 300 pulses/sec and 1 μsec pulse width.

The background in both detectors was monitored throughout the measurement by the continuous presence of gold and cobalt foils covering the neutron beam area. Cadmium and lead foils were also included to reduce the overlap neutron background and gamma flash. For both detectors, the background consisted of two components - (n,α) reactions from out-of-time neutrons and gamma-ray interactions with the detector materials. A linear interpolation was used to obtain the background values between the absorber resonances for both components of the ^{10}B detector background and for the (n,α) component in the ^{6}Li detector. The gamma-induced background for the ^{6}Li detector was evaluated from the pulse-height spectrum observed at the resonance-absorber energies. This spectrum was parameterized and used to obtain a channel-by-channel background estimate. The fractional background for the ^{6}Li detector was 5% at 5 eV and 20% at 130 eV. The ^{10}B detector background was 2% and 5%, respectively.

The data were obtained in a single-event-per-beam-burst mode and corrected for the resulting deadtime. Because the detectors were at nearly the same distance from the neutron production target, the deadtime correction difference never amounted to greater than 1% of the signal rate.

The data from both detectors were collected in a two-dimensional mode using the same time digitizer and pulse-height analyzer, with subsequent tagging of the events before storage on the million word disk. Final bias levels were chosen after completion of the experiment.

The results of our measurement are listed in Table I and plotted in Fig. 1. The data have been grouped into convenient energy bins to improve the statistical precision. The observed $^{10}B/^{6}Li$ ratio is normalized using a least squares fit (for energies >20 eV) to the computed ratio based on ENDF/B-V cross sections. It can be seen that the present results agree with the energy dependence of the accepted values in the 20 to 1000 eV region. This agreement demonstrates the validity of the background subtraction techniques in this region of high and rapidly varying background values. Below 20 eV, a statistically significant departure from the ENDF/B-V ratio is observed.

Figure 2 shows a comparison of the present result with the LLL/ORNL fission cross section ratio which is normalized to 1.0 at thermal. The present measurements have been normalized to 1.0 from 1.0 to 3.9 eV.

Conclusions

We are unable to explain the discrepancy between the ORNL and LLL fission cross section measurements. It is evident that the structure observed in the present measurement is poorly correlated with that found in the fission cross section ratio. The present measurements indicate no inherent difficulties in the two flux monitors above 20 eV.

Because of the confidence we have in the corrections to the raw data, we attribute the low energy variations in the $^{10}B/^{6}Li$ ratio to unexpected variations in the effective cross sections.

Table I. Preliminary measurements of the shape of the $^{10}B/^{6}Li$ reaction rate ratio. The uncertainty shown is statistical only.

E_{min}(eV)	E_{max}(eV)	$\bar{E}$(eV)	BF_3/Li glass
1.	1.25	1.12	1.015 ± .0016
1.25	1.62	1.44	1.019 ± .0016
1.62	2.17	1.90	1.016 ± .0016
2.58	3.23	2.90	1.011 ± .0020
3.23	3.90	3.57	1.017 ± .0024
6.99	9.26	8.12	1.008 ± .0022
9.26	12.84	11.05	1.001 ± .0021
12.84	25.91	19.37	1.000 ± .0016
25.91	30.89	28.39	.993 ± .0036
30.89	48.51	39.70	.997 ± .0024
48.51	75.84	62.17	.996 ± .0027
75.84	92.60	84.22	.999 ± .0048
177.0	247.2	212.0	.987 ± .0042
247.2	311.4	279.3	.998 ± .0052
311.4	409.8	360.6	.986 ± .0054
409.8	610.3	510.1	.986 ± .0044
610.3	963.4	786.9	.988 ± .0044

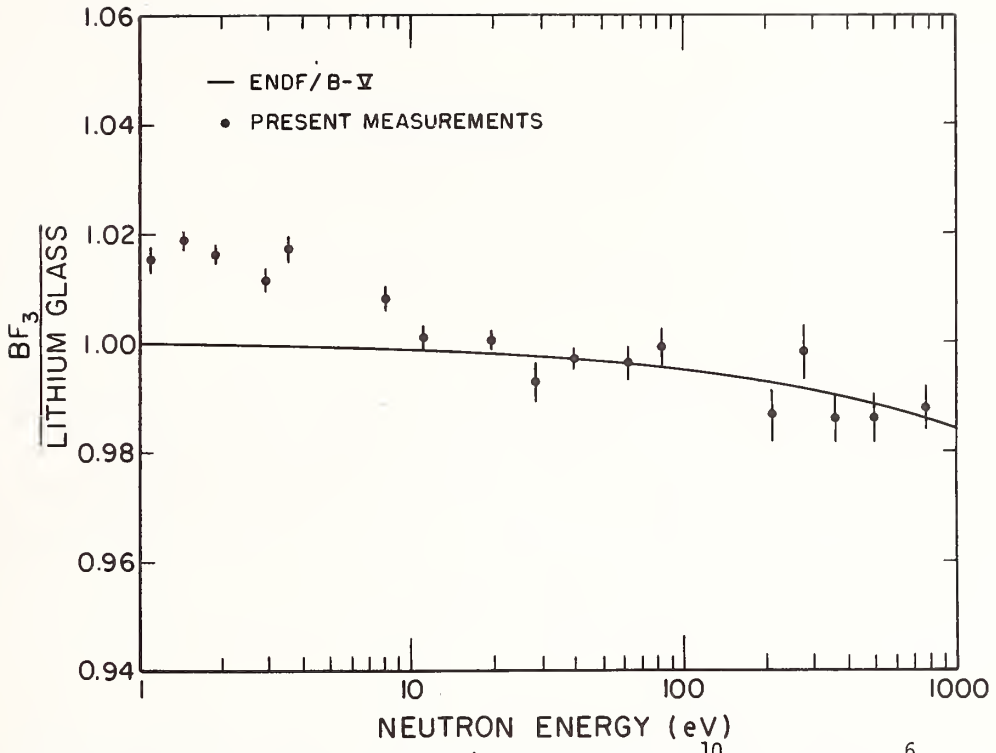

Fig. 1. Measurements of the ratio of the (n,α) cross section of $^{10}BF_3$ to that of ^{6}Li glass compared with ENDF/B-V. For convenience the ENDF/B-V ratio has been normalized to 1.0 at 1 eV. The error bars on the points indicate the statistical uncertainties of the data.

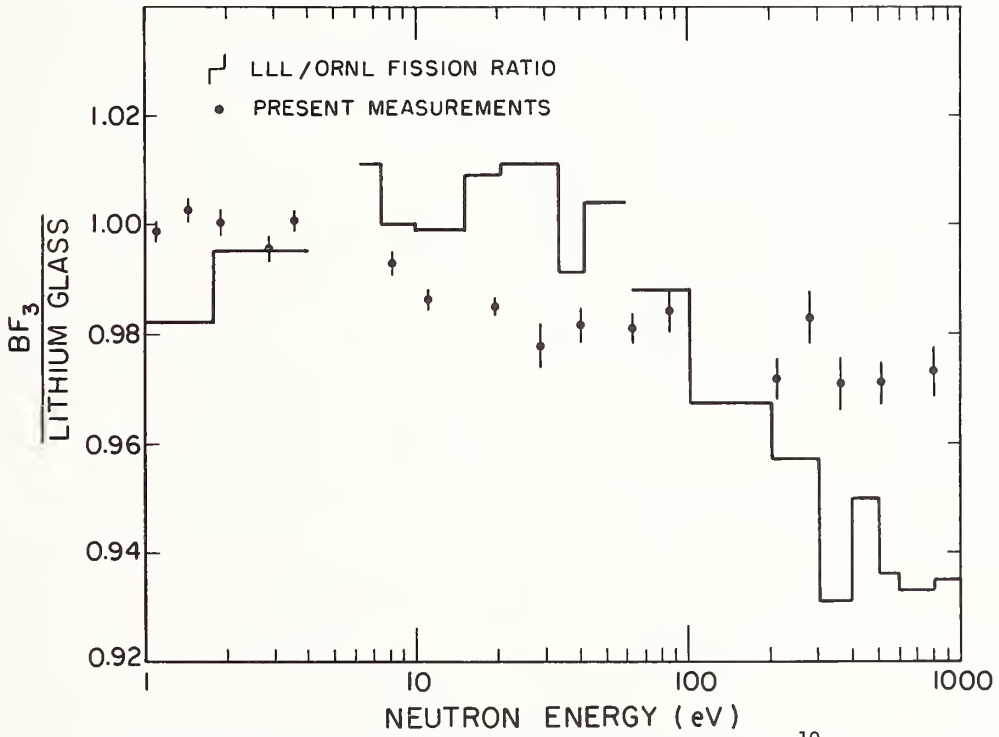

Fig. 2. Present measurements of the ratio of the (n,α) cross section of $^{10}BF_3$ to that of ^{6}Li glass compared with the LLL/ORNL fission cross section ratio.

References

1. J. B. Czirr and G. W. Carlson, Nucl. Sci. Eng. 64, 892 (1977).

2. Private communication from R. Gwin, Oak Ridge National Laboratory, 1977.

3. J. B. Czirr and G. S. Sidhu, Nucl. Sci. Eng. 60, 383 (1976).

THE NEUTRON TOTAL CROSS SECTION OF SINGLE CRYSTAL SILICON AT 21°K

R. M. Brugger
Research Reactor Facility
University of Missouri
Columbia, Missouri 65201 USA

R. G. Fluharty, P. W. Lisowski and C. E. Olsen
Los Alamos Scientific Laboratory*
Los Alamos, New Mexico 87545 USA

The neutron total cross section of a single crystal of Si has been studied over the energy range 0.003 eV to 50 eV at the Weapons Neutron Research Facility (WNR). The neutron energies were determined by time of flight. The 28.77 cm long Si sample was held at three temperatures, 296°K, 77°K, and 21°K. The 21°K temperature was obtained by filling an encircling cryostat with liquid H_2. The region of greatest interest is below 1 eV where Bragg scattering from the perfect crystal is small and where thermal diffuse scattering can be reduced by cooling the Si. Near 0.05 eV the cross section dips to less than 1/5 its value at energies greater than 1 eV. This feature has allowed single crystals of Si to be used very successfully as thermal neutron band pass filters. Our data at 296°K and 77°K agree with previous measurements. Very little structure caused by Bragg scattering is observed. Our measured cross sections for 21°K are somewhat below the 77°K data but not enough lower to justify cooling a Si filter to 21°K to dramatically improve its transmission.

[Si(n,n), total cross section, 0.003 - 50 eV, single crystal, 2 96, 77, 21°K]

Introduction

Fission reactors are intense sources of thermal neutrons which are being used extensively for materials studies.[1] Unfortunately these thermal neutrons are accompanied by fast neutrons and gamma rays which produce a background in many experiments in addition to being a hazard to personnel. Filters are needed that will pass bands of thermal neutrons but reject the fast neutrons and gamma radiation. Some single crystals act as thermal neutron band pass filters and are being used.[2] Silicon has recently found application as such a filter.[3,4,5] Presented in this paper are new total neutron cross section data which will allow experimenters to evaluate and to select the most effective parameters for the design of single crystal silicon filters.

Previous cross section measurements[3,4] of single crystal silicon have been made at only a few neutron energies at room temperature (RT) or liquid nitrogen temperature (LNT). Data over a wider energy range with better resolution were needed for evaluation and design. The cross sections presented here provide that breadth and resolution.

One previous cross section point[4] was obtained at 0.073 eV at liquid helium temperature (LHeT) but with some experimental uncertainty in the measurements. Since this one point indicated that a silicon filter cooled to near LHeT would be much more effective than one cooled to near LNT, more data near LHeT were needed. Such data are presented in this paper as the cross section of single crystal silicon at liquid hydrogen temperatures (LHT).

The experiment is described in the next two sections, the data in the fourth section, and the results are discussed in the final section.

Sample

The sample was one single crystal of silicon provided by the Electro Products Division of the Monsanto Company. This crystal is 7.6 cm diameter by 28.77 cm long. One of the symmetry directions of the crystal is along the axis of the cylinder. The crystal is dislocation free and was made by the Czochralski process.

This crystal was inserted into the center of an annulus formed by the liquid nitrogen (or liquid hydrogen) jacket of a cryostat. The ends of the annular hole were sealed with thin windows of stainless steel so that helium gas could be added to provide heat conduction from the crystal to the annular liquid hydrogen jacket. Thermocouples were attached to the crystal to measure the temperature.

Experiment

The Weapons Neutron Research (WNR)[6] facility at the Los Alamos Scientific Laboratory (LASL) was used as the source of neutrons for the total cross section measurements. The WNR produced pulses of moderated neutrons using a 3 μs wide 800 MeV proton pulse at 60 Hz incident on a tantalum target with a heterogenously poisoned H_2O moderator. Cadmium was used as the poison in the moderator to suppress upscattering. An off-center flight path observed the "slab" geometry neutron moderator. The neutron energies were determined by time-of-flight methods. The experimental arrangement is shown in Fig. 1. A collimator with a 1 cm^2 hole was

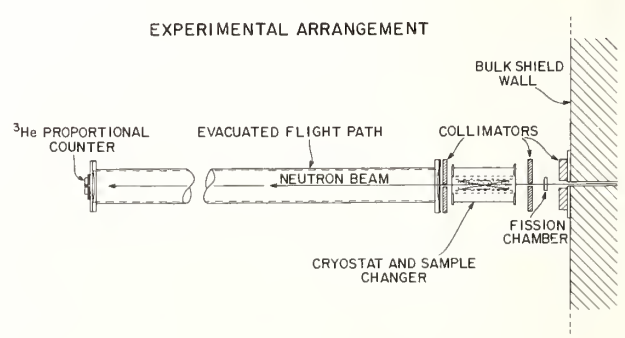

Fig. 1. Experimental arrangement of apparatus outside the bulk shield.

placed at the outer edge of the bulk shield, 3 meters from the moderator. A ^{235}U fission chamber was placed in the neutron beam after the first collimator to monitor the neutron flux. A second collimator was placed after the fission chamber to eliminate any effect of the sample position on the flux monitor. The silicon sample in the cryostat was placed on a remote-control changer mechanism positioned about 25 cm from the first collimator. A third collimator was located downstream from the cryostat to ensure that the neutron detector viewed only the silicon sample and no part of the cryostat. The neutron detector was an 0.6 cm diam 300 Atm ^{3}He proportional counter placed at 11 m from the moderator center at the end of an evacuated flight path.

The sample changer mechanism was a platform that could be raised and lowered so that data could be taken with the sample "in" and with the sample "out". The sample "out" position had two sheets of aluminum to simulate the windows on the cryostat. No correction was made for the difference in paths of vacuum, helium, and air.

Data were collected for repetitive sets of sample "in" and sample "out". Each "in" and "out" lasted about ten minutes to obtain good statistics. For the low temperature runs, thermocouples monitoring the sample temperature were read between each set of data. Room background was measured by placing either a 0.08 cm Cd sheet or a 5.6 cm thick boron loaded paraffin block in the beam. In each case, in the regions of interest, the backgrounds were negligible. The data were collected and stored on magnetic tape using a Modcomp IV computer via a CAMAC interface. Data reduction consisted of correcting both sample-in and sample-out spectra for dead-time losses, combining the data into bins of constant (5%) energy resolution, and converting to total cross section as a function of neutron energy.

Data

Figure 2 represents the data of this experiment. The data extend from 0.003 eV to 50 eV and cover the window which is important as a band pass filter. At 50 eV the scattering approaches free-atom scattering. Our measured cross sections at 50 eV are

$\sigma_{RT} = 2.13 \pm 0.02b$,

$\sigma_{LNT} = 2.11 \pm 0.02$ b,

and $\sigma_{LHT} = 2.10 \pm 0.04b$.

These are in good agreement with the $\sigma_{FA} = 2.16$ b quoted by Willis.[7] This agreement lends confidence that the cross sections are being measured accurately, for example; that the number of atoms/cm^2 in the beam is known, that dead time corrections are being made correctly, and that backgrounds are understood.

At the low energy end of the data, the σ_{RT} appears to extrapolate to data extending up to 0.002 eV from BNL-325 for RT powdered Si. The σ_{LBT} abd σ_{LHT} data approach but are slightly higher than the 1/v-line representing the absorption cross section of Si. This behavior is as expected and lends confidence that the cross sections are being accurately measured at the low energy end.

The data show the expected broad dip near thermal energies and the σ_{LNT} and σ_{LHT} cross sections are lower than the σ_{RT} cross section. Little structure is observed in the cross section indicating that Bragg scattering is small. These data at RT and LNT are consistent with the previous data. Our RT data for E = 0.1 eV is somewhat higher than data obtained by Shull.[8]

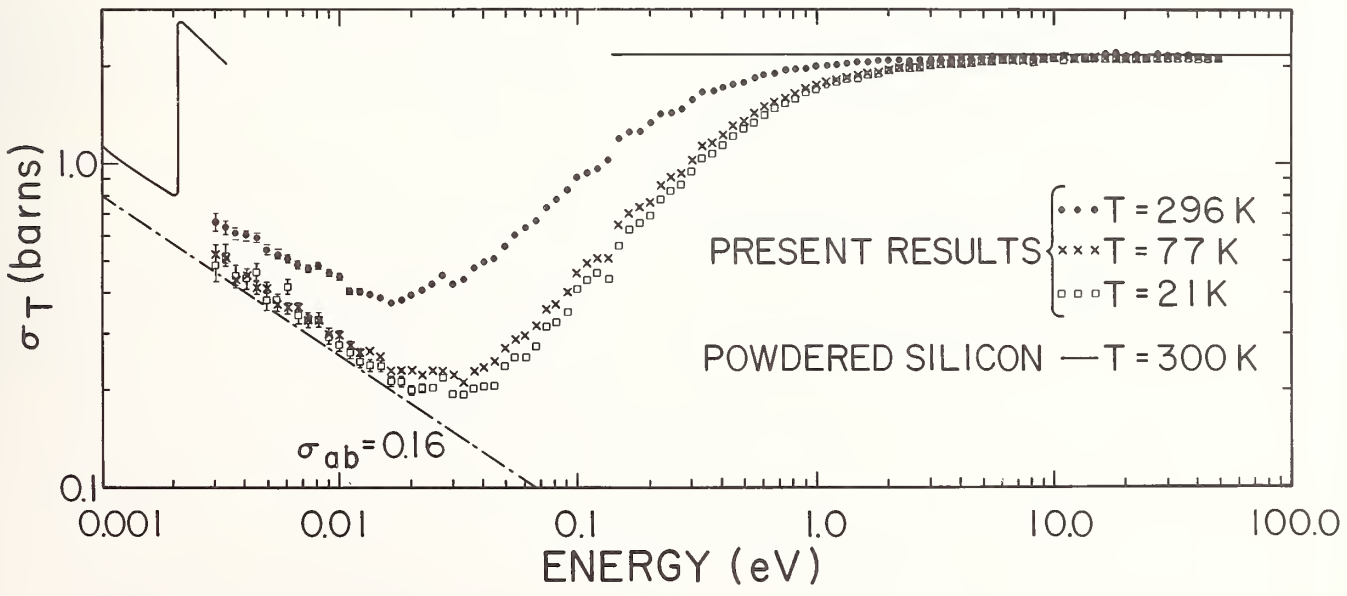

Fig. 2. Results of the present experiment. The solid lines represent data for powdered silicon. The dashed line shows the 1/v silicon absorption cross section.

The LHT data in Fig. 2 is not consistent with the previous cross section point measured by Brugger and Yelon [4] at 0.073 eV and LHeT. While the present data shows a cross section of about 0.25b, the previous point was 0.1 b. The previous point is described as "not of high accuracy" because the sample was only 5 cm across and the sample could not be cycled into and out of the beam to get "in" and "out" data. A change in the beam intensity during the experiment could have produced a poor measurement.

Conclusions

The cross sections measured in this experiment provide high resolution data over the full range of neutron energies needed to evaluate silicon single crystal band pass filters. The RT and LNT data agree with previous measurements. Little structure is evident. The cross sections at LHT are only slightly lower than the cross sections at LNT. Thus a silicon single crystal cooled to LHT or LHeT will be only a little better as a filter than one cooled to LNT. The extra effort to cool below LNT is not justified.

Acknowledgments

The authors thank the Monsanto Co. for providing the single crystal silicon sample. One of the authors (RMB) is very appreciative of the opportunity provided by LASL to make these measurements. This work was performed under the auspices of the U.S. Department of Energy.

*Work performed under auspices of U.S. Dept. of Energy.

References

1. Neutron Research on Condensed Matter; A Study of the Facilities and Scientific Opportunities in the Unites States, National Academy of Science (1977).

2. B. N. Brockhouse, Rev. Sci. Instr. 30 (1959) 135; V. P. Duggal and C. L. Thaper, Rev. Sci. Instr. 33 (1962) 49; ed P. H. Egelstaff, Thermal neutron scattering (Academic Press, London, 1965) p. 130; S. Menardi, R. Haas and W. Kley, in Inelastic scattering of neutrons in solids and liquids, vol. I (IAEA, Vienna, 1963) p. 139.

3. Robert M. Brugger, "A Single Crystal Silicon Thermal Neutron Filter" Nucl. Inst. & Meth. 135, 289 (1976).

4. Robert M. Brugger and William Yelon "Use of Single Crystal Silicon as a Thermal Neutron Filter," Proceedings of the Conference on "Neutron Scattering," Gatlinburg, Tennessee (June 6-10, 1976).

5. Y. Hanaguchi, private communications.

6. G. J. Russell, P. A. Seeger, and R. G. Fluharty, "Parametric Studies of Target/Moderator Configuration for the Weapons Neutron Research (WNR) Facility," Los Alamos Scientific Laboratory Report LA-6020 (March 1977). G. T. Russell, "Initial Target/Moderator Configuration for the Weapons Neutron Research Facility," Trans. Amer. Nucl. Soc. 27 861 (1977).

7. B. T. M. Willis, Chemical Applications of Thermal Neutron Scattering, Oxford University Press (1973).

8. Cliff Shull, private communications.

A COMPARISON OF (n,α) CROSS SECTION MEASUREMENTS FOR $^{10}BF_3$ AND SOLID ^{10}B FROM 0.5 TO 10,000 eV

A. D. Carlson, C. D. Bowman, J. W. Behrens and R. G. Johnson
National Bureau of Standards
Washington, D.C. 20234, USA

J. H. Todd
Oak Ridge National Laboratory
Oak Ridge, Tennessee, 27830, USA

The (n,α) cross sections of $^{10}BF_3$ gas and solid ^{10}B are compared in order to study possible influences of binding effects on reaction cross sections. It is shown that for $^{10}BF_3$ a deviation from a 1/v cross section of 8% is expected. The ratio of the measured cross sections does not show this deviation.

[Cross sections, molecular binding, neutron reactions, neutron standards, phonons, $^{10}BF_3$.]

Introduction

It is generally assumed that atomic binding in gases, liquids, and solids has no observable influence on neutron nuclear reaction cross sections except for small changes in the broadening of neutron resonances. By nuclear reactions, we exclude measurements of neutron scattering for which there exists a very extensive literature of both theoretical and experimental studies. During the past year the NBS has looked at the possible influences of physical state, atomic binding, etc., on neutron reaction cross sections primarily with regard to improving the accuracy of the 1/v cross section standards $^{10}B(n,\alpha)$, $^{6}Li(n,\alpha)$, and $^{3}He(n,p)$. A literature search revealed only two papers on the subject: a 1947 paper by Steinwedel and Jensen[1] comparing the classical and quantum mechanical effects of atomic binding on nuclear cross sections and a 1937 paper by Lamb[2] concerning the effects of molecular vibrations on the neutron capture cross section for hydrogen. The purposes of this paper are to give a physical basis for expecting differences arising from atomic binding and physical state, and to describe results of an experiment expected to show differences.

Physical Basis

The physical basis for expecting effects on 1/v cross sections in this paper arises solely from the influence of binding on the energy available for the nuclear reaction in the center of mass. The 1/v cross section can be derived from the Breit-Wigner formula

$$\sigma_{n\alpha} = \frac{\pi \lambda^2 g \Gamma_n \Gamma_\alpha}{(E-E_0)^2+\Gamma^2/4} \qquad (1)$$

using the usual notation[3] with all energies taken in the center of mass. If no resonances are close by, $(E-E_0)^2$ is usually very much larger than $\Gamma^2/4$ and for small values of E is essentially constant. For an exoergic reaction Γ_α is nearly constant. However Γ_n can be written in terms of the reduced width[4] γ_n as $(2kR)\gamma_n$ (for $\ell = 0$ neutrons), effectively separating the conditions outside the nucleus from the properties of the interior. Therefore from Eq. (1), $\sigma_{n\alpha}$ is proportional to 1/k (where k is the neutron wave number). Written as a function of the center-of-mass energy $\sigma_{n\alpha} = \frac{\text{constant}}{\sqrt{m_r E_{cm}}}$ where m_r is the reduced neutron mass, where we draw attention to the importance of properly accounting for the center-of-mass energy. Figure 1 shows the six normal modes[4] of oscillation of the BF_3 molecule which is a case of particular interest. All but ν_1 involve the ^{10}B nucleus at the center. The normal modes ν_{3a} and ν_{3b} are degenerate as are ν_{4a} and ν_{4b}. The energies of these normal modes for $^{10}BF_3$ are given in Table I.[5]

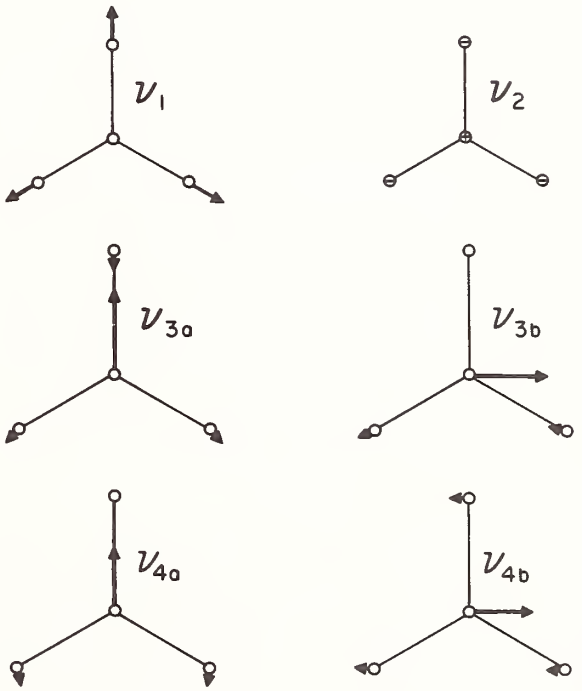

Fig. 1. The normal modes of the planar centrosymmetric molecule BF_3. Note that only ν_1 does not involve the boron nucleus. The modes ν_{3a} and ν_{3b} are degenerate as are the modes ν_{4a} and ν_{4b}.

Table I. Fundamental energies of the $^{10}BF_3$ molecule

Mode	$\hbar\omega$(eV)
ν_1	0.109
ν_2	0.088
ν_3	0.183
ν_4	0.059

Restricting our attention to the ν_2 mode, consider the classical picture of a reaction of a neutron with the ^{10}B nucleus in the ground state (zero energy classically). The compound nucleus recoils initially with an energy of $E_n\ m/(M_B+m)$ where M_B is the mass of the boron nucleus and m is the mass of the neutron. In its equilibrium position the forces are balanced so that the net molecular force on $^{10}BF_3$ is zero. The forces are proportional to displacement for a harmonic oscillator, $F \propto x$, so that for small x the forces are small. The compound nucleus therefore initially recoils as if it were free. As the displacement becomes larger the molecular binding forces come into play. The resulting motion can be pictured as the translation of the molecule center of mass with the molecular vibration superimposed on it. The translational energy of the molecule E_r is given by

$E_r = E_n\ m/M+m$ where M is the mass of the molecule.

The vibrational energy E_{vib} is

$$E_{vib} = E_n m/(M_B+m) - E_n m/(M+m) = \frac{3E_r M_F}{M_B+m} \qquad (2)$$

In the classical case where the neutron energy is large enough to knock the ^{10}B nucleus free of the molecular binding, kinetic energy also will be imparted to the fluorine atoms in an amount depending on the potential energy binding the relative masses and the neutron energy. However the total recoil energy remains $E_n\ m/(M_B+m)$. Note that since BF_3 is a centrosymmetric molecule, with B located at the center of mass of the molecule, no energy of rotation can be imparted as long as the molecule initially is in its ground state. Whether or not, the recoil energy is sufficient to destroy the molecule the recoil energy is always given by $E_n\ m/(M_B+m)$ so that the energy in the center of mass system is unchanged.

When E_r is large compared with $\hbar\omega$, the quantum mechanical picture is very nearly the same. Consider the case of ν_2 again when the neutron strikes the ^{10}B molecule while moving perpendicular to the plane of the molecule. When the molecule is in the ground state, the probability of a transition from the ground state to state k, P(k,0) is given by the Poisson distribution[6]

$$P(k,0) = \frac{Z^k e^{-Z}}{k} \qquad (3)$$

where Z is given by

$$Z = \frac{E_r}{\hbar\omega}\frac{3M_F}{M_B+m} \qquad (4)$$

The average amount of vibrational energy is $\bar{E}_{vib} = \hbar\omega Z = E_r\ 3M_F/(M_B+m)$ and when we add to this the average translational energy E_r, the sum of these is the compound nucleus recoil energy $E_n m/(M_B+m)$ in exact correspondence with the result from classical mechanics.

An important deviation between classical and quantum mechanics appears to develop however when the neutron energy is lower than that necessary to excite the first vibrational state.

$$E_n < \hbar\omega \frac{(M_B+m)}{m}\frac{(M+m)}{3M_F} \qquad (5)$$

For the lowest lying vibrational mode of $^{10}BF_3$, the ν_4 mode, this energy is about 0.8 eV. Therefore below this energy no vibrational excitations are possible when the molecule is in its ground state* and the molecule will recoil as an absolutely rigid unit when struck by a neutron. The energy in the center of mass E_{cm} is therefore $E_n(M/M+m)$ rather than $E_n(M_B/M_B+m)$ as at higher energies. Since E_{cm} is higher in the former case, the $1/m_r v$ dependence requires that the measured cross section be lower than the free atom cross section by the fraction f given by

$$f = \left(\frac{M+m}{M_B+m}\ \ \frac{M_B}{M}\right) \qquad (6)$$

For $^{10}BF_3$ this fraction is 0.92 and implies a rise in the $^{10}BF_3$ cross section by 8% between low and high neutron energies compared to the free atom cross sections.

In most molecules the collision of the neutron will excite rotations as well as the translations and vibrations discussed already. For BF_3 the equilibrium position of the ^{10}B nucleus lies at the molecular center of mass. Classically for an unexcited molecule no angular momentum can be transferred. However, the quantum mechanical zero point vibration in the ground state allows a small displacement from the molecular center of mass which permits the transfer of rotational energy. The amplitude of this vibration can be estimated from the force constants for the molecule. Since the ^{10}B nucleus is much lighter than the combination of three fluorine nuclei against which it oscillates, the fluorine nuclei stay relatively fixed and most of the motion is associated with the boron atom. For a force constant[5] of 8.83×10^5 dynes/cm and the energy $\hbar\omega = 0.059$ eV, the required displacement is 0.046×10^{-8} cm.

The probability for inducing a change in the angular momentum can be calculated.[8] For a molecule with zero angular momentum (j=0) the probability for a transition to a higher state j is given by

$$P(j,0) = \frac{\pi}{2a}(2j+1)\ J^2_{j+1/2}(a) \qquad (7)$$

where J is the Bessel function of half integral order and a is the angular momentum in units of $\hbar$. For a neutron of energy 0.06 eV, the quantity a = 0.25. The quantity 1 - P(0,0) gives the probability for excitation to all higher states. For a = 0.25, Eq. (7) gives 1 - P(0,0) = 0.02. Therefore a transition will occur in only 2% of the collisions and a further study of Eq. (7) shows that nearly always the change is by only one quantum. The moment of inertia for BF_3 around an axis passing through the center of the molecule and perpendicular to the plane of the molecule is 52.48×10^{-40} gm cm^2. The rotational constant is found to be 0.000066 eV.

---

* Calculations using the prescription of Jackson[7] show that the BF_3 molecule is in its ground state 52% of the time and in an excited ν_4 mode 42% of the time. It is expected that this may change the effect by as much as a factor of two.

On the average therefore only .02 x .000066 ≃ 1 x 10^{-6} eV is transferred per collision so that this mode of energy exchange can be neglected for BF_3 and in general for centrosymmetric molecules. The recoil energy is greater by about 10^4. For non-centrosymmetric molecules, the impact parameter a is much larger and a significantly greater amount of rotational energy can be transferred. Steinwedel and Jensen[1] show that for a diatomic molecule averaged over all directions of the incoming neutron the classical calculation gives $E_{rot}/E_{vib} = 2$. In general therefore significant energy transfer can take place for gaseous molecules below the energy limit of equation 5, so that while the molecule may be rigid, extra energy can be transferred to rotations.

For solids and liquids the molecules are confined by its neighbors to a fixed position and therefore no energy is transferred to translation. For crystalline solids, the recoil energy is taken up by phonons. Lipkin[9] has proved that for nuclear γ-ray absorption or emission on crystalline solids, the average energy transferred to phonons is equal to the recoil energy E_γ. In the case of γ-rays the energy E_γ is always very much greater than the energy of the lowest phonons. This however is not always the case for neutrons as Lipkin points out. However in general this is not a significant limitation in crystallinesolids since the phonon spectrum extends to zero energy[10]. In liquids and perhaps in some solids such as amorphous materials, where there are no long range correlations, phonons cannot exist and the situation is less clear. However the comparison of $^{10}BF_3$ with solid ^{10}B in some form appears to be worthwhile.

Experiment

The ORELA group at ORNL has constructed and used two ^{10}B-loaded-detectors for flux measurement. The geometry of the two is the same and is shown in Fig. 2.

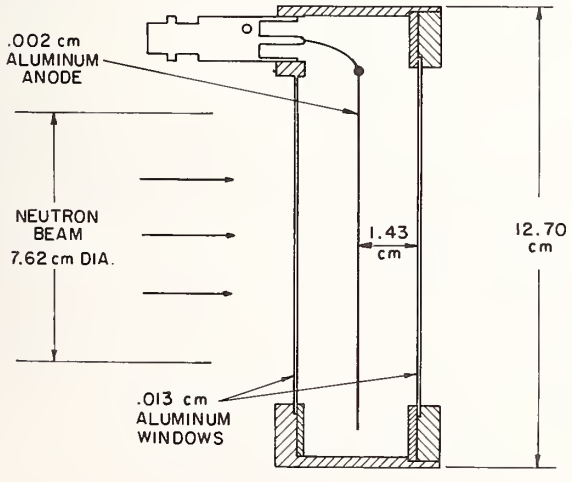

Fig. 2. Geometry for the BF_3 and evaporated boron counters. The central electrode is coated with boron on both sides for the evaporated boron measurement. For BF_3 studies the second detector is filled with BF_3 gas and the center electrode is bare metal.

One detector contains $^{10}BF_3$ at a pressure of 18.75 cm and argon at a pressure 56.25 cm and the other has ^{10}B deposited by vacuum evaporation on both sides of the central electrode and is filled with 7.6 cm of CH_4 and 68.4 cm of argon. These detectors were used for a comparison of the cross sections of $^{10}BF_3$ and solid ^{10}B, which may be in an amorphous state. While the detectors have the same geometry, the counter characteristics are significantly different. The pulse height spectrum for the solid boron shows the ^7Li and α-particle peaks clearly separated from each other and from the low level electronic noise. For the $^{10}BF_3$ detector these two peaks cannot be resolved and the isolation is not complete from electronic noise and from other sources of small pulses such as γ-rays. Any gamma ray background is difficult to eliminate by bias on the pulse height spectrum.

Care must therefore be taken in the design of the experiment to reduce and measure background. The detectors were arranged in the configuration shown in Fig. 3.

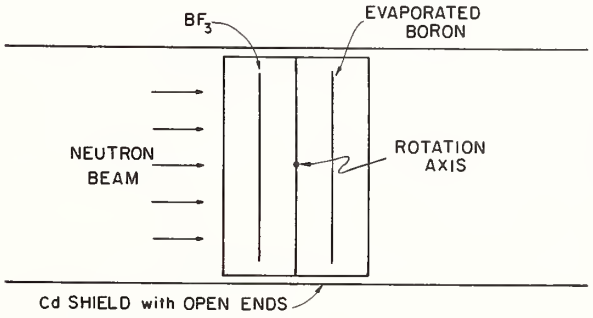

Fig. 3. Positioning of the detectors. The detectors were placed against one another and mounted on an axis which passed between the detectors and across the diameter. By rotating the detectors about this axis by 180°, the detector positions were transposed. The detectors were placed inside a 50-cm long Cd tube with open ends to reduce neutron background.

By placing the detectors directly against each other, both are in very nearly the same background field. Measurements were made of the counting rate as a function of neutron energy for both detectors as shown in Fig. 3. The detectors were then reversed and the measurements repeated. The ratio of the cross sections was determined by taking the geometric mean of the two counting rate ratios. By this means the effect of neutron background is almost completely eliminated. The method does not however eliminate γ-ray background which will be different for solid B and BF_3 owing to the differences in pulse height spectra. The background was therefore measured using Au, Co, and Na filters. The results are given in Table II.

The data were collected in an on-line computer which sorted the data as it was received into a two-dimensional array. The data were sorted according to pulse height and time-of-flight into 5X10^5 channels for each detector. This procedure allowed the choice of bias to be made at the completion of the experiment. The same time-interval meter

Table II. Background measurements.

Filter	Energy (eV)	% Background B	% Background BF_3
Au	4.9	1.0	1.7
Co	132	1.7	4.9
Na	2850	2.1	5.5

was used for both detectors on a first come--first served basis. Even though deadtime effects were about 70% for the lower neutron energies, no deadtime corrections were required in deriving the cross section ratio from the data for this collection method. Table III is a summary of the operating parameters for the experiment.

Table III. Experiment parameters.

Flight path length	21.37 meters
Electron power	4 kW
Pulse rate	300 pps
Pulse width	1 μsec
Channel width	1/2 μsec
Lead γ-flash filter	1.4 cm
Resonance filters	Au, Co, Na

Results

The results of the experiment are shown in Fig. 4 where the ratio of BF_3 to solid boron is given as a function of neutron energy. The uncertainties shown in the figure arise from counting statistics alone. The authors are aware of no systematic uncertainty except for γ-ray background in the BF_3 detector. The size of the uncertainty of this background is thought to be about 1/3%. The ratio is found to be constant to within about 1%. An experiment[11] performed with the same statistical accuracy at the ORELA facility at ORNL using the same detectors gave a similar result.

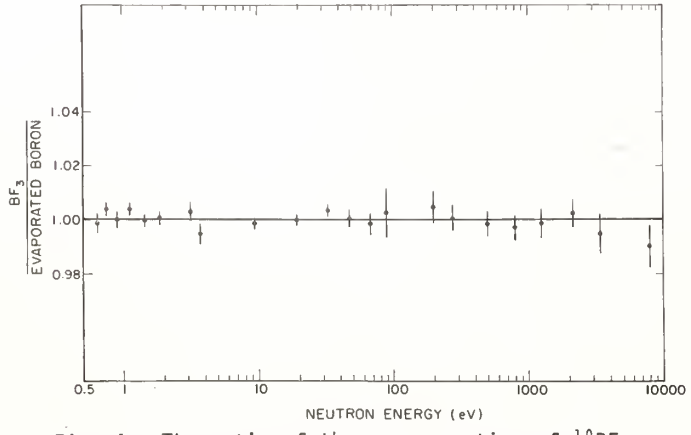

Fig. 4. The ratio of the cross section of $^{10}BF_3$ and evaporated boron. The bars on the points show the statistical uncertainties of the data.

The experiment did not show an 8% difference between solid B and BF_3 as predicted. Therefore either the 8% effect is not present or else the solid B exhibits essentially the same change as BF_3.

Summary

It is shown that for neutrons less than about 0.8 eV, the $^{10}BF_3$ molecule should behave as a rigid body. This is expected to lead to an 8% increase in the observed $\sigma_{n\alpha}$ relative to the free atom cross section. The effect is not expected to be present in crystalline boron solids. The ratio of the cross sections was measured with an accuracy better than 1% and found to be constant over the energy range from 0.5 to 10,000 eV. Therefore, either the expected effect actually is not present or else the evaporated ^{10}B shows the same 8% change as BF_3. Since $^{10}BF_3$ has probably been used over the years much more for eV flux measurement than any other boron detector, an understanding of the effect of binding of the BF_3 on the $^{10}B(n,\alpha)$ cross section is essential for assuring a firm basis for eV cross section measurements.

Acknowledgments

The authors are grateful for the interest shown in the work by Dr. R. Gwin and Dr. L. W. Weston of the Oak Ridge National Laboratory and for providing us with results from an experiment similar to this carried out at ORELA. We also acknowledge the encouragement and helpful comments of Dr. J. B. Czirr.

References

1. V.H. Steinwedel and J.H.D. Jensen, Zeitschrift für Naturforschung, 2a, 125 (1947).

2. W.E. Lamb, Phys. Rev. 51, 187 (1937).

3. J.E. Lynn, The Theory of Neutron Resonance Reactions (Clarendon Press, London, England, 1968).

4. J.M. Blatt and V.F. Weisskopf, Theoretical Nuclear Physics (John Wiley and Sons, New York, 1960)

5. G. Herzberg, Infrared and Raman Spectra of Polyatomic Molecules (D. Van Nostrand Company, New York, NY, 1945).

6. V.S. Letokhov, Phys, Rev. 12, 1954 (1975); C.D. Bowman and R.A. Schrack, The Influence of Vibrations of Gas Molecules on Neutron Reaction Cross Sections. Accepted by Phys. Rev. (Sept. 1979).

7. D. Jackson, Los Alamos Scientific Laboratory Report LA-6025-MS, 1975.

8. V.S. Letokhov and V.G. Minogin, Soviet Physics, JETP 42, 800 (1976).

9. H.J. Lipkin, Ann. Phys. 9, 332 (1960).

10. C. Kittel, Introduction to Solid State Physics (John Wiley and Sons, Inc., New York, 1967).

11. L.W. Weston (private communication, 1979).

PERTURBATIONS OF NUCLEAR CROSS SECTIONS ASSOCIATED WITH CHANGES IN MOLECULAR VIBRATIONAL ENERGY

C. D. Bowman and R. A. Schrack
National Bureau of Standards
Washington, D. C. 20234

Abstract

The change in molecular vibration energy upon absorption of a neutron by a nucleus bound in a free molecule can influence resonance shape and other aspects of neutron reaction cross section. A formalism is developed for centrosymmetric molecules such as UF_6 which allows a calculation of the displacement in resonance energy and the dispersion in resonance shape arising from molecular transitions. The calculations have been applied to the 6.67 eV resonance in ^{238}U. Comparison with measurements of $^{238}U_3O_8$ and $^{238}UF_6$ indicate satisfactory agreement. Implications of these effects for other systems are discussed.

(Cross section, molecules, neutron reactions, neutron time-of-flight, UF_6, vibration)

Introduction

When a neutron strikes a nucleus bound in a free molecule, the molecule will recoil with the possibility of changing its vibrational and rotational state. The energy available tothe compound nucleus is therefore not that obtained simply by conserving energy and momentum in the neutron-nuclear collision since energy conservation must include the change in the molecular excitation. The possibility and necessity of taking such effects into account apparently has not been studied previously for low energy neutron fission and capture reactions. However, the similar effect for γ-ray absorption has been theoretically studied in detail by V. S. Letokhov [1] for centro-symmetric molecules such as SF_6. Rotational transitions are not induced by neutron absorption by the central nucleus so that the calculation is significantly simplified by restricting the study to centrosymmetric molecules. We report here a calculation of the resonance shape for the 6.67 eV resonance in $^{238}UF_6$ and compare the calculation with a measurement of the ratio of gas to solid $^{238}U_3O_8$ carried out at the NBS linear accelerator.

Theory

The relative probability P_{ba} for a molecular transition from an initial state a to a final state b upon collision of a neutron with a molecule is given by the expression

$$P_{ba} = |\langle\psi_b^*(\vec{R}) \mid e^{-i\vec{K}\cdot\vec{R}}|\psi_a(\vec{R})\rangle|^2 \qquad (1)$$

where $\vec{K}$ is the wave number associated with the neutron and molecular center-of-mass motion and $\vec{R}$ is the position of the nucleus struck by the neutron. The vector R can be written $\vec{R} = \vec{R}_0+\vec{r}+\vec{u}$ where $\vec{R}_0$ is the vector from the origin to the center of mass of the molecule, $\vec{r}$ is the vector from the molecular center-of-mass to the equilibrium position of the nucleus and $\vec{u}$ is the vector from the equilibrium position of the nucleus to its instantaneous position. Assuming the separation of translational and vibrational variables, the matrix element of Eq. (1) can be written

$$\langle\psi_b^*(R)|e^{-i\vec{K}\cdot\vec{R}}|\psi_a(R)\rangle = \langle T_b^*|e^{-i\vec{K}\cdot\vec{R}_0}|T_a\rangle$$

$$\langle\psi_b(\vec{r},\vec{u})|e^{-i\vec{K}\cdot(\vec{r}+\vec{u})}|\psi_a(\vec{r},\vec{u})\rangle \qquad (2)$$

where T_a and T_b are the wave function for the initial and final molecular translation, and $\psi(\vec{r},\vec{u})$ describes the molecular vibration and rotation.

For a centrosymmetric molecule, one nucleus is located at the center of mass which has $\vec{r} = 0$ always. If the neutron strikes this nucleus, which in the case of UF_6 would be the uranium nucleus, the vector $\vec{r}$ may be neglected. Furthermore, changes in rotational state of the molecule can be neglected since the uranium is always very near the center of mass of the molecule. The transition probability required in this case reduces to the calculation of the matrix element

$$\langle\psi_b^*(\vec{u})|e^{-i\vec{K}\cdot\vec{u}}|\psi_a(\vec{u})\rangle$$

The vibrations of the nucleus can be expressed as a product of the various modes ψ_ℓ including all degeneracies. We assume a harmonic oscillator approximation for the vibration and write the harmonic oscillator wave functions [2] in terms of the Hermite polynominals as

$$\psi_{m_\ell} = N_{m_\ell} e^{-\alpha Q^2/2} H_{m_\ell}(\sqrt{\alpha_\ell} Q) \ . \qquad (3)$$

In Eq. (3), the vector $\vec{u}$ has been rewritten in terms of the normal modes as $\vec{u}_\ell = Q_\ell\vec{\rho}_\ell$ when ρ_ℓ is the ℓ^{th} normal molecular coordinate and Q_ℓ is the associated displacement amplitude. The smallest energy quantum of the ℓ^{th} normal mode $\hbar\omega_\ell \equiv \hbar^2\alpha_\ell$ and m_ℓ is the order of the ℓ^{th} vibrational mode. For the ground state m = 0, and for the first excited state of the vibrational mode m = 1, etc. The normalization constant N_{m_ℓ} is defined as $[2^{m_\ell} m_\ell !(\pi/\alpha_\ell)^{1/2}]^{-1/2}$. Therefore the required matrix element becomes

$$\langle\psi_b^*(\vec{u})|e^{-i\vec{K}\cdot\vec{u}}|\psi_a(\vec{u})\rangle =$$

$$\Pi_{m_\ell}\langle\psi^*_{m_\ell}(Q_\ell)|e^{-i\vec{K}\cdot\vec{\rho}_\ell Q_\ell}|\psi_{m_\ell}(Q_\ell)\rangle \qquad (4)$$

The average energy δ transferred into molecular excitation for an initial state j assuming only one normal mode is

$$\delta_j = \sum_{k=0}^{\infty} P(k,j)\,\hbar\omega(k-j) \ . \qquad (5)$$

The influence of vibrational energy increments such as these on cross sections was first pointed out by Lamb [2] who carried out a calculation for energy increments associated with photon exchange. These concepts were further developed by many authors and for neutron energies less than 1 eV by Bowman and Schrack [3]. Following these papers, we find that the transfer in molecular vibration energy therefore influences the neutron cross section through two terms: the energy dependent neutron width and the resonance denominator. To a small degree it also influences the total width since Γ_n represents one component of the total width.

However, this term is small in almost all practical cases and will be neglected for the purposes of this work. For the resolved resonance region of heavy nuclei, the influence on the neutron width is small and will be neglected here.

The calculation of the effects for a practical case are significantly complicated by several factors. First, there usually are several normal modes present which compete with one another in the energy exchange process. Second, these normal modes also have degeneracies which must be taken into account. Third, for room temperature systems, most molecules are in some state of excitation other than ground state. Fourth, in practice the direction of oscillation of any particular normal mode is randomly oriented to the direction of neutron motion. In the following calculation all of these factors are included for the purpose of predicting the shape of the 6.67 eV resonance ^{238}U.

Application to $^{238}UF_6$

The molecule $^{238}UF_6$ is a solid at standard temperature and pressure, but is in a gaseous state at reduced pressure. The molecule has six normal modes. The two of these which involve the uranium nucleus are shown in Fig. 1 and are usually identified as the ν_3 and ν_4 modes as indicated in the figure. Since the other four modes do not involve an oscillation of the uranium nucleus, the collision of a neutron with the ^{238}U nucleus does not excite or deexcite these modes.

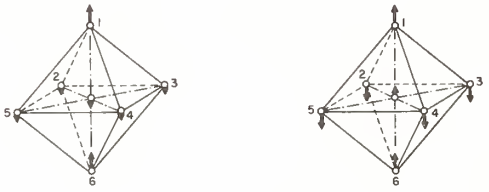

ν_3 ν_4

Figure 1. UF_6 molecules showing the atomic motions for the ν_3 and ν_4 normal modes. The numbered points indicate the positions of the flourine atoms.

The required probability for a transition from one condition of molecular vibration to another may be rewritten

$$P = |\langle\psi_b^*(\vec{u})|e^{-i\vec{k}\cdot\vec{u}}|\psi_a(\vec{u})\rangle|^2 = \Pi_{jk_\ell}|S_{k_\ell,j_\ell}|^2 \qquad (6)$$

where the product over ℓ includes all normal modes and their degeneracies. For the normal modes each with its three-fold degeneracy of concern here, we denote the initial state by $(j_1j_2j_3,j_1'j_2'j_3')$ and final state by $(k_1k_2k_3,k_1'k_2'k_3')$. The unprimed indices are associated with ν_3 and the primed with ν_4. The probability for a transition from an initial state to some final state, therefore, can be written from Eq. (6) and (3) as:

$$P\left(j_1j_2j_3,j_1'j_2'j_3';k_1k_2k_3,k_1'k_2'k_3'\right) = \prod_{n,\ell} W_{n,\ell}\left(L_{j_{n,\ell}}^{k_{n,\ell}-j_{n,\ell}}\left(Z_{n,\ell}\right)\right)^2$$

$$\text{where } W_{n,\ell} = \frac{j_{n,\ell}!}{k_{n,\ell}!}\, e^{-Z_{n,\ell}}\, Z_{n,\ell}^{k_{n,\ell}-j_{n,\ell}} \qquad (7)$$

ℓ is the index on the normal modes, n is the index on the degeneracy, and L are the Laguerre functions defined by

$$L_j^{k-j}(Z) = \sum_{\nu=0}^{j}(-1)^\nu \frac{k!}{(j-\nu)!}\,\frac{1}{(k-j+\nu)!}\,\frac{Z^\nu}{\nu!} \qquad (8)$$

The $Z_{n,\ell}$ quantities are proportional to $(\vec{K}\cdot\vec{p})^2$ and are important parameters for determining the probability of molecular transitions. In general they depend on the molecule geometry, force constant, atomic masses and are not easy to evaluate. For a linear triatomic molecule XY_2 Letokhov (1) gives

$$Z = \frac{2Er}{\hbar\omega}\,\frac{m_X}{M_Y} \qquad (9)$$

where Er is the molecular recoil. For the purposes of this paper we estimate Z by viewing the ν_3 and ν_4 modes as approximations to the normal mode of a linear triatomic molecule. Adjustments in these estimates then can be made to improve the fit to the data. Our estimated values of $Z_3 = .075$ and $Z_4 = 0.23$ are used througout the remainder of this paper.

The P quantities of equation (7) must then be averaged over all orientations of the molecule since the molecules are in general randomly oriented. The angle-averaged quantity $\bar{P}$ is a somewhat complicated expression(4) which however can be used to quickly calculate specific transitions of interest. Three examples are given below all starting from the same intial state (100,000)

$$\bar{P}(000,000;100,000) = \frac{Z_3}{3}\, e^{-(Z_3+Z_4)}$$

$$\bar{P}(100,000,100,000) = (1-\tfrac{2}{3}Z_3)\, e^{-(Z_3+Z_4)} \qquad (10)$$

$$\bar{P}(200,000,100,000) = Z_3 e^{-(Z_3+Z_4)}\left[2/3 - \frac{6}{15}Z_3 + \frac{1}{14}Z_3^2\right]$$

This method of solution is practical for weakly excited molecules, small changes in excitation energy and values of $Z < 0.5$ and therefore is suitable for the problem at hand. The calculation was carried through by weighting the various initial states with the initial thermal probabilities, calculating the transition probabilities to states of lower, higher or the same state of excitation and summing together all transitions representing the same energy change. The results are summarized in Table I.

The results of Table I now must be converted into a form easily compared with the experiment. The experimental resonance shape would be the sum of resonance shapes weighted by the transition probabilities and displaced in energy by the appropriate value for ΔE. Before this can be done, however, the appropriate form for the resonance shape must be selected.

If the target molecule were rigid and at rest, the resonance shape would be the unbroadened Breit-Wigner shape shifted upward by the amount of recoil energy given by $E/(m_u + 6m_f)$ for UF_6. However, the molecules are in thermal motion so that the shape of the resonance must be modified to the Doppler-broadened shape for a rigid molecule as prescribed by Bethe(5). A resonance shape taking account of molecular vibration was calculated beginning with the Doppler-broadened resonance shape defined by Bethe for the rigid molecules which were displaced by the energies in the table, weighted by the probability factors of the table and added together. To facilitate a comparison

Table I

Transition*	Probability	ΔE(eV)
No change	.683	--
$\nu_4^{\uparrow}$	.205	.023
$\nu_4^{\downarrow}$	.068	-.023
$\nu_3^{\uparrow}$	.033	.078
$\nu_3^{\downarrow}$	0.00	-.078
$\nu_4^{\downarrow}\nu_3^{\uparrow}$	0.01	.055

*The upward directed arrow implies excitation of the molecule to a higher lying state and the consequent absorption of energy by the molecule. The downward directed arrow implies deexcitation and energy release from the molecule. For the bottom row two normal modes change simultaneously.

with experiment, this resonance shape was then compared with the shape which one would obtain in a solid uranium oxide target as prescribed by Jackson and Lynn[6]. The ratio of the U_3O_8 to the UF_6 case is shown as the upper solid line in Fig. 2. The dashed line of the figure shows a calculation of the shape for U_3O_8 divided by the prediction for a rigid molecule of UF_6. The differences with the solid indicated by the dashed line are due to recoil and Doppler broadening associated with the larger gas target mass (A = 352). The position and shape of the resonance in the solid is shown at the bottom of the figure.

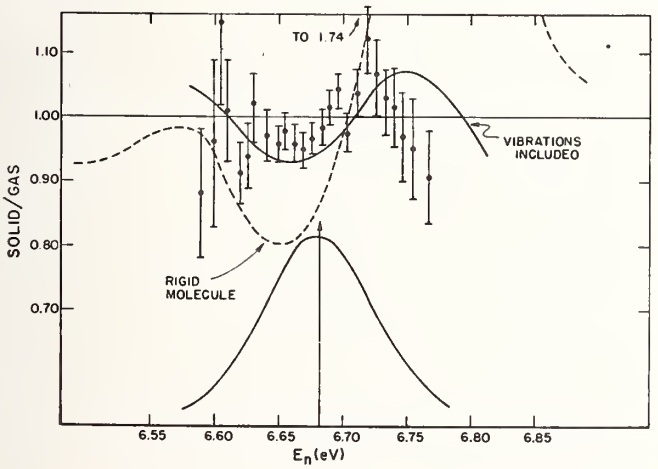

Figure 2. The points show the ratio of the measured resonance shape of a gas to that for a solid. The upper solid line is the results of the calculation of this ratio with vibrational transitions included. The dashed line is the same ratio under the assumption of a rigid molecule. The lower solid line is included to show the shape and position of the 6.67 eV resonance in ^{238}U.

The Experiment

To compare the prediction with experiment, measurements of the total cross section for U_3O_8 and for an equivalent thickness of UF_6 were carried out. The U_3O_8 sample was prepared by mixing a small portion of U_3O_8 with aluminum powder which yielded a thickness of 8.56×10^{-5} atoms/barns corresponding to a peak transmission of 0.5 at the 6.67 eV resonance.

A UF_6 gas sample was prepared by filling a steel container 30 cm long with UF_6 gas at a pressure of 72 Torr. At this pressure and at room temperature all the UF_6 will exist in the gas phase. Also, this pressure yielded approximately the same thickness of ^{238}U as the solid sample.

The measurements were made on the NBS Linac using a neutron flight path from neutron source to detector of 69 meters. The samples were placed 5 meters from the neutron source. The samples were 8 inches in diameter and the collimated neutron beam was 6 inches in diameter at the sample. The detector was a 5 inch diameter, 1 inch thick slab of 6% enriched lithium glass directly attached to an 8854 photomultiplier. The beam is collimated to 4 inches at the detector. The flight tube contains appropriate collimators to prevent inscattering. The linac was operated at 126 MeV with an average electron current of 18 μA, 360 pulses per second, with a pulse width of about 60 nanoseconds. The neutrons were generated in a tungsten target with an external moderator of polyethylene 1-inch thick. The neutron pulse width has a total width of approximately 6 meV at 6.6 eV. The data was collected using a time interval meter having 256 nanoseconds resolution, which represents about 2 meV resolution at 6.6 eV neutron energy. The observed FWHM of the 6.6 eV line in ^{238}U was 111 meV, (about 36 channels). Linac runs of about 20 hours produced about 7000 counts per channel at 6.6 eV. For analysis the data was grouped eight channels at a time.

Transmission measurements were completed and transformed to cross sections. The ratio of the solid to the gas was then calculated and the results plotted in Fig. 2. The uncertainties shown are derived from the statistical uncertainty of the two transmissions. The shift in energy between the two measurements is less than two millivolts. The agreement between theory and experiment is not perfect but is satisfactory in view of the approximations in the application of Eq. 7. The large difference compared with the result for a rigid molecule (dashed curve) clearly shows the necessity of taking vibrational transitions into account. It is probable that an improved fit could be obtained by adjustments of Z_3 and Z_4. We believe, however, that these parameters are very nearly the actual values. The possibility of adjustment of these parameters was not included in this paper and is a subject for further study.

Summary

In this paper we believe we have demonstrated for the first time the necessity of taking into account the change in internal excitation of a free molecule upon absorption of a neutron. The calculation is, of course, distinctly different from that required for slow neutron inelastic scattering measurements. The effect depends approximately on the ratio of the mass of peripheral nuclei to the central nucleus for centrosymmetric molecules. For this reason the effect for other molecules can be much larger than for UF_6.

A thorough exploration of this class of phenomena should include a study of non-centrosymmetric molecules including diatomic molecules where the full treatment must include both vibrations and rotations and the interactions between them. Qualitatively it appears that induced transitions might be significantly higher for such molecules.

The phenomena discussed here might find practical applications in the design and operation of very high temperature gas-fueled reactors for understanding of reactor reactivity and the Doppler coefficient. For the conventional fuel cycle it might find application in criticality evaluations of isotope enrichment facilities. There also are interesting practical possibilities associated with the control by various means of the initial state of the molecule.

Acknowledgements

The authors wish to acknowledge helpful discussions with D. Jackson and R. S. McDowell of the Los Alamos Scientific Laboratory on the properties of the UF_6 molecules. We also wish to thank J. C. Browne of the Lawrence Livermore Laboratory (LLL) and R. G. Johnson of the University of Pennsylvania for their help in attempting a comparison of capture for the gas and solid ^{238}U carried out at the LLL linac.

References

1. V. S. Letokhov, Phys. Rev. A, 1954 (1975).
2. W. E. Lamb, Jr., Phys. Rev. 55, 190 (1939).
3. C. D. Bowman and R. A. Schrack, Phys. Rev. C 17, 654 (1978).
4. C. D. Bowman and R. A. Schrack, "The Influence of Vibrations of Gas Molecules on Neutron Reaction Cross Sections", Proceedings of an International Conference "Neutron Physics and Nuclear Data." Harwell Sept. 1978 p. 736.
5. H. Bethe, Rev. Mod. Phys. 9, 140 (1937).
6. H. E. Jackson and J. E. Lynn, Phys. Rev. 127, 461 (1962).

THE RATIO OF THE $^{10}BF_3$ AND $^3He(n,p)$ CROSS SECTIONS BETWEEN 0.025 eV AND 25,000 eV

C. D. Bowman and J. W. Behrens
National Bureau of Standards
Washington, D.C. 20234, USA

R. Gwin and J. H. Todd
Oak Ridge National Laboratory
Oak Ridge, Tennessee 37830, USA

The $^{10}BF_3(n,\alpha)$ and $^3He(n,p)$ cross sections have been compared in the energy range from 0.025 to 25,000 eV. Measurements at NBS using filtered beams gave results at 2 and 25 keV. At the Oak Ridge National Laboratory using the ORELA facility measurements were completed between 0.025 and 10,000 eV. Normalizing the ratio of BF_3/He to 1 at 0.03 eV, the ratio increases by 1% at 10 eV, by 2% at a few hundred eV, by 4% at 2 keV, and by 16% at 25 keV. The large deviations at the higher energies are expected purely from the nuclear parameterization of the cross sections. However, the deviations from 1/v in the ratio below 100 eV are surprising and perhaps might have their origin in the molecular binding for ^{10}B in the $^{10}BF_3$ system.

[$^{10}BF_3$, cross sections, eV neutrons, ^3He, ratio, standards.]

Introduction

The low energy reaction cross sections of ^3He, ^6Li, and ^{10}B have long been used as neutron flux measurement standards at low energies owing to their 1/v cross sections. For the energy region below 1 eV these cross sections have been verified to have an almost pure 1/v cross section by measurements of the total cross section.[1-3] Since the scattering portion of the reaction is small and essentially constant, corrections for scattering can be made with sufficient accuracy to demonstrate a 1/v cross section for them to a nominal accuracy of ±1%.

At higher energies the reaction cross section decreases and scattering corrections reduce the effectiveness of total cross section measurements for measuring the (n,α) cross section. It, therefore, becomes necessary to measure the neutron flux to obtain a reaction cross section. For this purpose a black detector which absorbs a constant fraction of all neutrons striking it may be used. However, the efficiency of such detectors can only be obtained by calculation, and the usefulness of these detectors for accuracy below a few percent is doubtful. The black detectors usually are not easy to use either, so that in spite of the potential inaccuracy, ^{10}B, ^6Li, and ^3He are used up to 100 keV for monitoring neutron flux. The cross sections for ^6Li and ^{10}B have been carefully studied at higher energies in recent years[4,5] and the shape of these cross sections between 1 and 100 keV probably are known to 1-2%. However in the region from 1-1000 eV where all three reactions have been extensively used, essentially no cross section measurements have been made. The purpose of this paper is to compare the reactions $^3He(n,p)$ and $^{10}BF_3(n,\alpha)$ with the purpose of gaining information about the adherence of these cross sections to a 1/v shape below a few keV.

Reactor Measurements at NBS

The NBS 10-MW reactor has filtered beams[6] of energies 2 and 25 keV obtained using Si and Fe filters, respectively. In addition to the filters, resonant scatterers are used in the through-tubes which run beside the reactor core to scatter neutrons of the desired energy into the beam. The method gives neutron beams of greater spectral purity and lower in-beam gamma-ray background than beam tubes which terminate at or near the reactor core. Both factors should be helpful in carrying out a high accuracy ratio measurement.

Identical proportional counters were used for these measurements whose parameters are summarized in Table I. Three tubes were used altogether--two containing BF_3 and one containing ^3He. The pressures were adjusted so that the neutron efficiency in both $^{10}BF_3$ and ^3He detectors were nominally the same. At these pressures the attenuation of a 0.025 eV neutron beam moving perpendicular to the axis and across the 5-cm diameter of the tube is about 8%.

Table I. Detector parameters.

Diameter	5 cm
Active length	30.5 cm
Pressure	
^3He	69 Torr
BF_3#1	100 Torr
BF_3#2	85 Torr
High voltage	1500 volts
Wall thickness	0.084 cm
Wall material	stainless steel
^{10}B enrichment	96%
Neutron beam diameter	
Thermal	1.25 cm
2 keV	∿1.25 cm
25 keV	∿2.5 cm

The detectors were arranged in the geometry shown in Fig. 1 with the beam traversing the diameter of both detectors. Counting rates were determined and the positions of the counters were then reversed. Counting rates were again determined in this second arrangement. The geometric mean of these two ratios

is then taken. This procedure yields a cross section ratio which is self-correcting for backgrounds to a very high degree as is demonstrated in the following relationships.

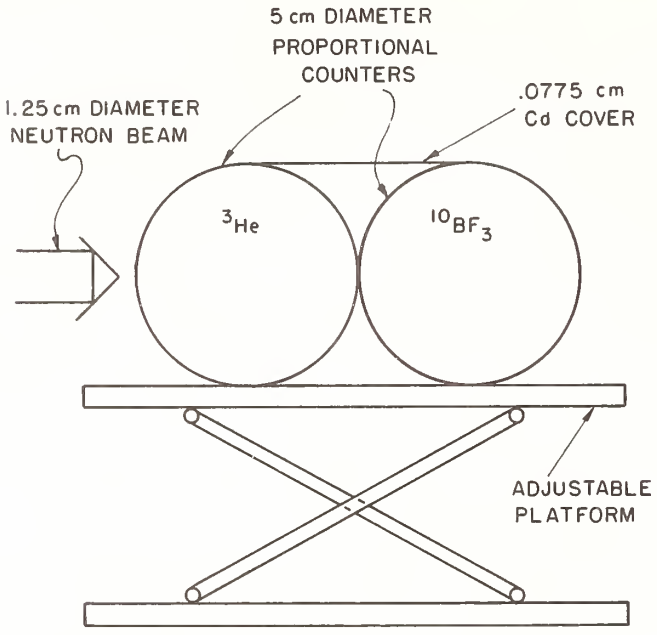

Fig. 1. The detector-beam arrangement for the 2 keV measurements. A 1.25-cm diameter neutron beam passes across the 5-cm diameter ^{3}He and BF_3 tubes. The tubes are surrounded by Cd and rest on an adjustable platform. The detector positions are interchanged for the second part of the measurement.

Assume that the first measurement is done with the beam first passing through the ^{10}B counter. The rate in the ^{10}B and ^{3}He counters, R_B and R_{He} respectively, is given as

$$R_B = \phi(1-T_B)+b_1\varepsilon_B$$
$$R_{He} = \phi T_B(1-T_{He})+b_2\varepsilon_{He} \quad (1)$$

where ϕ is the neutron current, T_B and T_{He} are the transmissions across the 5-cm diameter of the ^{10}B and ^{3}He counters, b_1 and b_2 are the background neutron intensities at counter positions 1 and 2 and ε_B and εHe are the efficiencies for background detection for the ^{10}B and ^{3}He counters. When the counter positions are switched, the counting rates R'_B and R'_{He} are given by

$$R'_B = \phi\, T_{He}(1-T_B)+b_2\varepsilon_B$$
$$R'_{He} = \phi\,(1-T_{He})+b_1\varepsilon_{He} \quad (2)$$

The geometric mean of the ratios of these rates is

$$\left(\frac{R_B\,R'_B}{R_{He}\,R'_{He}}\right)^{\frac{1}{2}} = \frac{\sinh\,(n\sigma/2)B}{\sinh\,(n\sigma/2)He}\,F \simeq \frac{(n\sigma)_B}{(n\sigma)_{He}}\,F \quad (3)$$

with the background correction factor F given by

$$F^2 = \frac{1+\dfrac{b_1\varepsilon_B}{\phi(1-T_B)}+\dfrac{b_2\varepsilon_B}{\phi(1-T_B)T_{He}}}{1+\dfrac{b_1\varepsilon_{He}}{\phi(1-T_{He})}+\dfrac{b_2\varepsilon_{He}}{\phi(1-T_{He})T_B}} \quad (4)$$

Even for significant differences in the backgrounds at positions 1 and 2 and for significantly different transmissions, the factor F is very close to unity. For example, if the background intensities at positions 1 and 2 differed by a factor of two

$b_1/\phi = .1$, $b_2/\phi = 0.2$ and if the absorption of the two counters for neutrons also differed by a factor of two ($T_B = .95$, $T_{He} = .9$ at thermal) the value of F for two pure 1/v cross sections at 2 keV assuming a background at 8 keV is less than 1 part in 10^6. If the boron cross section drifts away from a 1/v dependence by 10% in the energy interval between 2000 eV and 8000 eV, the value for F with the previously stated conditions differs from unity by 5 parts in 10^3. Both of these are extreme cases; the transmission for the $^{10}BF_3$ and ^{3}He detectors at thermal are the same within 10% and the backgrounds at the two positions are not expected to differ by more than 10%. With a Cd cover on the tubes, the background rate at the 2 keV beam with the detectors just out of the beam was found to be 10% of that with the counters in the beam. The 2 keV beam was contaminated with 6% of its neutrons at energies higher than 8 keV. A Cd filter eliminated any thermal neutrons in the beam. We believe that the influence of background for the 2 keV measurement on the cross section ratio is less than 0.1%.

The ratio next was measured using thermal neutrons with a Cd ratio of 2000/1 from the NBS thermal column. A beam diameter of 7.25 cm was used with the detectors in the same geometry as in Fig. 1. The bias levels on the detectors were maintained at the same level for the 2 keV and .025 eV measurements using a ^{252}Cf neutron source.

For the 25 keV measurements different procedures were necessary since the 1/v cross sections are lower at 25 keV and the room background in the vicinity was somewhat higher. The in-beam background for the 25 keV beam is 3% with the lowest energy contaminant neutrons occurring at 74 keV. To achieve a better signal to background ratio, only one detector at a time was placed with Cd cover in the beam. The axis of the detector was centered and aligned parallel to the axis of the beam so that the beam traveled along the full length of the detector volume. The counting rates with the detector outside of the beam were 5% of that in the beam. The $^{10}BF_3$ and ^{3}He counters were alternately placed in the beam and counts were taken for about 200 seconds. Fluctuations of less than 1% in reactor power with a period of about 30 seconds were thus averaged over about six cycles. The ratio of $(n\sigma)B/(n\sigma)He$ was measured four times with the results 1.037, 1.035, 1.043, and 1.043 for an average value of 1.040 $\pm$ .003. The sensitive length of the detectors varies slightly according to the length of the central wire. Construction accuracy is believed to be better than $\pm$ 3 mm so that this uncertainty was taken to be $\pm$ 1%. Since the cross section shapes for both detectors were very nearly the same, the 5% backgrounds are expected to cancel in the ratio so that the background effect on the ratio is much less

than 1%. The final values of these ratios as a function of energy are given in Table II.

Table II. Ratio* of $(n\sigma)_B/(n\sigma)_{He}$

Energy (eV)	$(n\sigma)_B/(n\sigma)_{He}$
0.025	1.
2000	1.045 ± .002
25000	1.16 ± .01

*Normalized to 1 at 0.025 eV

Linac Measurements

The linac measurements were carried out at the ORELA facility at the Oak Ridge National Laboratory. Measurements were made at a 20 meter flight station with an accelerator pulse rate of 25 per second. Overlap of neutrons from one pulse to the next occurs at 0.0013 eV so that little effect is expected. However since both cross sections have nearly the same shape and the same absorption, even if significant overlap had been present, there would be little effect on the measurement of cross section ratio.

The measurements were made with the two detectors placed one behind the other. The detectors were then interchanged for a second measurement. The cross section ratio was found by taking the geometric mean of the two measured ratios. The background counting rate for the detectors when located close to but outside of the neutron beam was less than 1% of that in the beam. The background in the beam at 4 eV and at 2000 eV measured with resonance filters was found to be less than 1%. The ratio of these rates for different energy bands were taken starting near thermal and extending to 10,000 eV. Since the transmission was nearly the same for both detectors and was always greater than 0.92, no corrections were made for self-protection. The uncertainty in this method assuming a 10% difference in $n\sigma$ for the two detectors is less than 0.2% in the ratio.

The data from the linac run is shown in Fig. 2 as the dots. The vertical bars on the points represent the statistical uncertainty (1σ) in the points which dominate the other contributions to the uncertainties. The results from the filtered beams listed in Table II are shown by the squares. The solid line is a fit by eye to the linac and filtered beam data. These results are in good agreement. The dashed line is the ratio determined from ENDF/B-5.

Unpublished measurements of this ratio using an electron linac as a pulsed neutron source have been reported by Lopez et al.[7] Their results were normalized at 400 eV which appears to be significantly different from a normalization at thermal energy. The triangles show a few representative points of these data renormalized upward by a factor of 1.02. Their results are in good agreement with the present data.

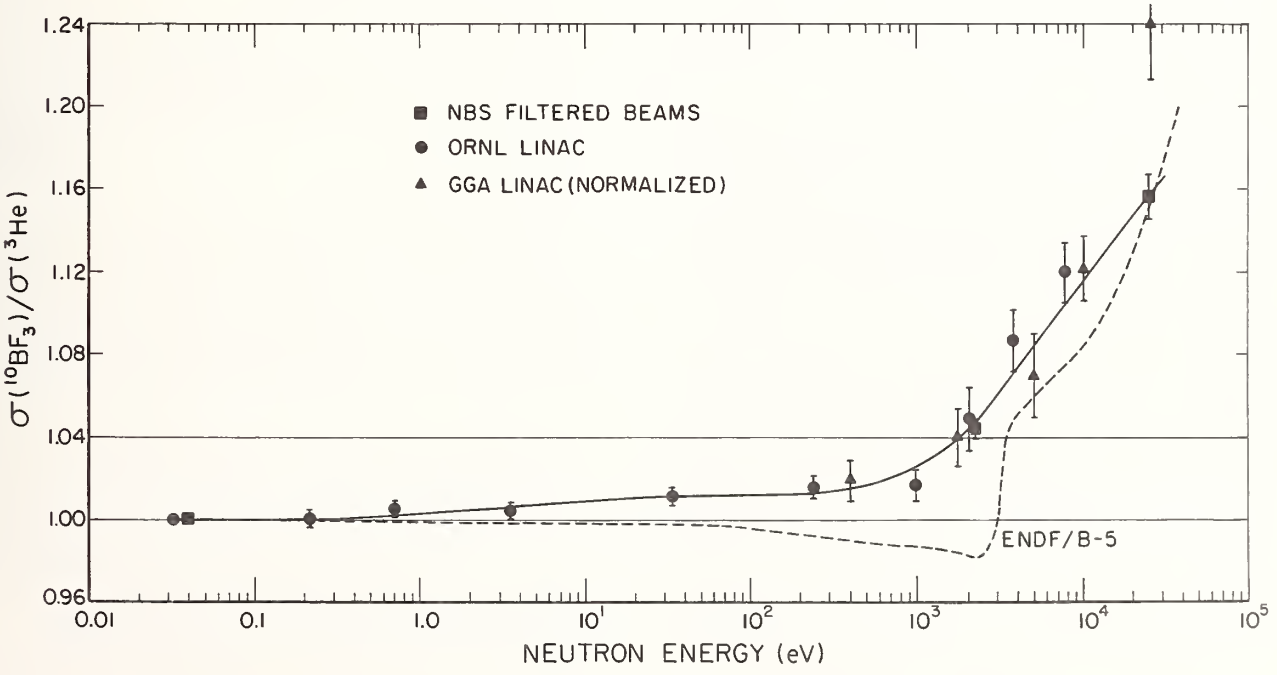

Fig. 2. The ratio of $\sigma(^{10}BF_3)/\sigma(^3He)$ normalized to 1 at 0.025 eV. A few representative points from the GGA linac unpublished results are included. The solid line is an eye guide through the data. The dashed line is the ratio from ENDF/B-5.

Both the filtered beam and the linac experiments at ORNL indicate a difference in the ratio between 0.025 eV and 2000 eV of a little over 4%. As the energy increases, this difference increases and at 25 keV the difference is 16%. Either $^{10}BF_3$ or ^{3}He or both account for these differences from a 1/v shape. In the higher energy region where the differences are largest, these deviations arise from the proximity of resonances. However in the region below 100 eV, it is not clear that nearby levels can cause deviations as large as observed. The possibility of a deviation from a 1/v cross section between 1 and 300 eV arising from the molecular binding of the $^{10}BF_3$ is discussed elsewhere.[8]

In order to achieve the accuracy goal of 1% for these standards for the energy region of Fig. 2, it is clear that absolute cross sections must be measured for each of the three nuclei used as 1/v flux monitors.

Acknowledgment

The authors gratefully acknowledge the loan by Dr. Robert B. Schwartz of the detectors used in these experiments and his advice in the use of the NBS filtered beams.

References

1. G.J. Safford, T.I. Taylor, B.M. Rustad, and W.W. Havens, Jr. Phys. Rev. 119, 1291 (1960).

2. W.W. Havens, Jr. and L.J. Rainwater, Phys. Rev. 70, 154 (1946).

3. J. Als-Nielsen and O. Dietrich, Phys. Rev. 133 B925 (1964).

4. G.P. Lamaze, R.A. Schrack, and O.A. Wasson, Nucl. Sci. Eng. 68, 183 (1978).

5. R.A. Schrack, G.P. Lamaze, and O.A. Wasson, Nucl. Sci. Eng. 68, 189 (1978).

6. R.B. Schwartz, "Calibration and Use of Filtered Beams" in Neutron Standards and Applications (NBS Special Publication 493, 1977) p. 250.

7. W.M. Lopez, M.P. Fricke, D.G. Costello and S.J. Friesenhahn, Neutron Capture Cross Sections of Tungsten and Rhenium, (Gulf General Atomic Report No. GA-8835, p. 59, 1968).

8. A.D. Carlson, C.D. Bowman, J.W. Behrens, and J.H. Todd, "A Comparison of (n,α) Cross Section Measurements for $^{10}BF_3$ and Solid ^{10}B from 1 to 10^4 eV." Proceedings of the International Conference on Nuclear Cross Sections for Technology, Univ. of Tennessee, Knoxville, Tennessee, USA, Oct. 22-26, 1979.

MEASUREMENTS OF THE TOTAL NEUTRON CROSS-SECTIONS OF Be, Ni AND Cu AT ROOM AND LIQUID NITROGEN TEMPERATURES IN THE ENERGY RANGE FROM 2.2 eV TO 2.2 MeV

M.Adib, A.Abdel-Kawy, R.M.A.Maayouf, Y.Eid, G.Shuriet, and I.Hamouda
Reactor and Neutron Physics Department, Atomic Energy Establishment, Cairo, Egypt

The total neutron cross-sections of Be, Ni and Cu are measured using two time-of-flight spectrometers installed in front of two of the horizontal channels of the ET-RR-1 reactor. The measurements were carried out in the energy range from 2.2 eV 2.2 meV at room temperature and at liquid nitrogen temperature for neutron energies below 5 meV. The coherent scattering cross-sections of these elements were determined from the Bragg cut-offs observed in the behaviour of the total cross-sections at cold neutron energies. The incoherent cross-sections of Be, Ni and Cu were obtained from the analysis of the total neutron cross-section data beyond the Bragg cut-off. The one phonon annihilation process was estimated at long neutron wavelengths and was found to be in reasonable agreement with the results of calculations.

(σ_T, 2.2 eV - 2.2 meV, BeNiCu, coherent and incoherent scattering, Bragg cut-off)

Introduction

The total neutron cross-section for neutron energies below 1 eV can be expressed as :

$$\sigma_t = \sigma_a + S + s + \sigma(S) + \sigma(s)$$

where σ_a - the absorption cross-section,
S and s - are the coherent and incoherent elastic scattering cross-sections respectively,
$\sigma(S)$ and $\sigma(s)$ - are the coherent and incoherent inelastic scattering cross-sections respectively.

The coherent scattering amplitude b_{coh} can be determined from the values of the Bragg cut-offs observed in the measured total cross-sections at low neutron energies.

Beyond the Bragg cut-off λ_c the coherent scattering cross-section S is zero. Besides, at liquid nitrogen temperature $\sigma(S)$ and $\sigma(s)$ are negligible; consequently, the incoherent scattering cross-section can be obtained from the measured data by substracting the contribution of the absorption cross-section beyond λ_c.

The present work deals with total neutron cross-section measurements carried out for Be, Ni and Cu in the energy range from 2.2 eV-2.2 meV, as well as with the determination of their coherent and incoherent scattering cross-sections.

The one phonon annihilation process for Be, Ni and Cu is also estimated at room temperature following the procedure reported by Cassels[1].

Experimental Details

The measurements were performed using two TOF spectrometers, installed infront of two of the horizontal channels of the ET-RR-1 reactor.

In the energy range from 2.2 eV to 5 meV, the measurements were carried out with one of the spectrometers having a rotor with a straight slit 1x25 mm^2 while the spectrometer's flight path was 8.1m. Below 5 meV, the measurements were performed using the second spectrometer with a rotor having a cigar shape slit and flight path 4.2 m. The rotation rate of the rotors could be controlled in the range from 800 rpm to 3600 rpm within accuracy 0.14%. $^{10}BF_3$ and ^3He gas filled neutron detectors were used during the measurements along with a 400-channel time analyser with channel widths varying between 24.4 μs-97.6 μs. Both the TOF spectrometers are described in details elsewhere [2,3,4].

The Be, Ni and Cu samples were prepared from spec. pure fine powders.

Results & Discussion

Beryllium

Fig.1 shows the dependence of the total cross-section on both wevelength and energy for Be at room temperature, as measured in the energy range from 2.2 eV-2.2 meV, along with the cross-sections, measured at liquid nitrogen temperature, for neutrons below 5 meV. The measured behaviour of the Be cross-section, in the energy range from 2.2 eV-60 meV, was found to fluctuate near a constant value of $\sigma_t = (5.9 \pm 0.2)$ b. This value is in good agreement with the value (6.0 ± 0.1) b.reported in the BNL-325[5].

The coherent scattering amplitude of Be was calculated from the Bragg cut-offs, observed in the total cross-section, and found to be $b_{coh} = (7.7 \pm 0.8)$ F. Consequently, the coherent scattering cross-section of Be S=(7.5 ± 1.5) b. These values are in good

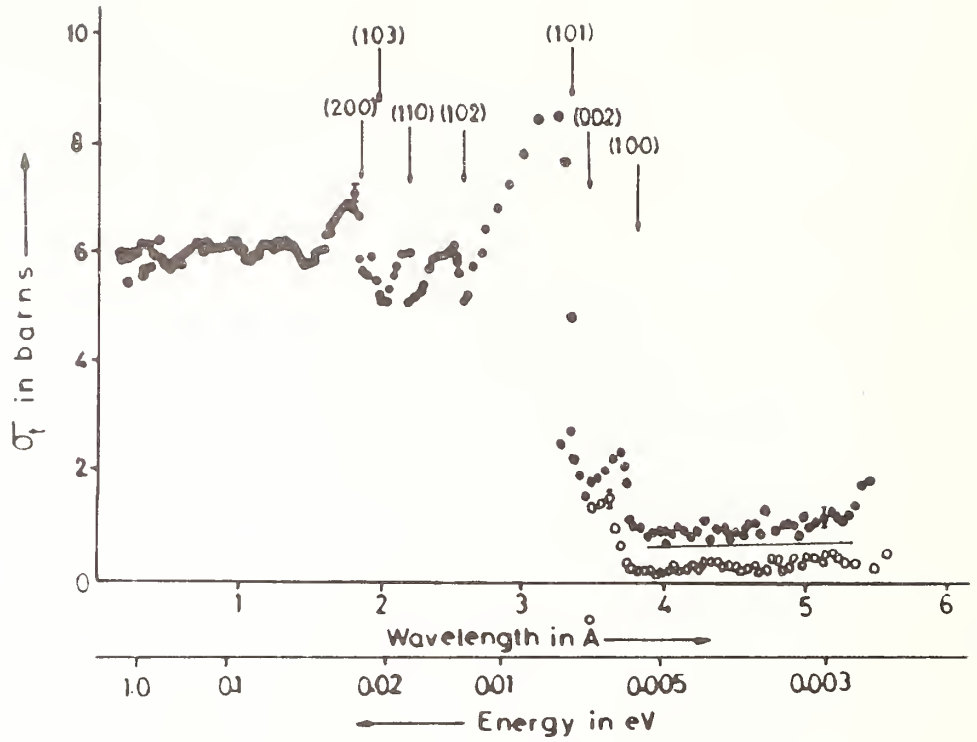

Fig. 1. Total cross-section of beryllium vs wavelength and energy.
● - measurements at room temperature.
o - measurements at liquid nitrogen temperature.

agreeement with the values 7.74 F and 7.53 b. reported in reference 6.

The total neutron cross-section of Be at liquid nitrogen temperature (see fig. 1) is fluctuating around a constant value (0.27 ± 0.11) b. This value corresponds to the Be incoherent scattering cross-section since it has a negligible absorption cross-section. The straight line in fig. 1 shows the calculated total cross-section of Be at room temperature considering only the one phonon annihilation process. It is slightly lower than the observed total cross-section of Be at room temperature. Such disagreement may be attributed to the Fe impurities present in the used Be sample.

Nickel

The total cross-section data of Ni in the energy range 2.2 eV-0.06 eV were fitted using the least square method and was found to be :

$$\sigma_t=(17.5\pm0.2)+(0.652\pm0.007)E^{-1/2} \quad b.$$

E, in eV, which is in good agreement with the expression:

$$\sigma_t=(17.4\pm0.2)+(0.79\pm0.10)E^{-1/2} \quad b.$$

reported by Bendt and Ruderman[7].

The coherent scattering amplitude and cross-section for Ni were determined from the observed Bragg cut-offs and found to be:

$b_{coh}=(10.4\pm0.3)$ F and

S $=(13.6\pm0.8)$ b. respectively.

These values are in good agreement with the values 10.3 F and (13.2±0.2) b reported previously[5,6].

At liquid nitrogen temperature the total cross-section of Ni follows the expression:

$$\sigma_t=(3.3\pm0.2)+(0.75\pm0.06)E^{-1/2} \quad b.$$

which yields a value of (3.3±0.2) b.for the incoherent elastic scattering cross-section This value is in good agreement with the value of (4.1±1.2) b. reported by Bendt and Ruderman[7] for Ni incoherent scattering cross-section at room temperature.

The solid line in Fig. 2 represents the calculated total neutron cross-section of Ni at room temperature, while the dashed one represents the calculated total cross section at liquid nitrogen temperature.

Cupper

The expression obtained for Cu total neutron cross section (Fig.3) at thermal neutron energies was found to be :

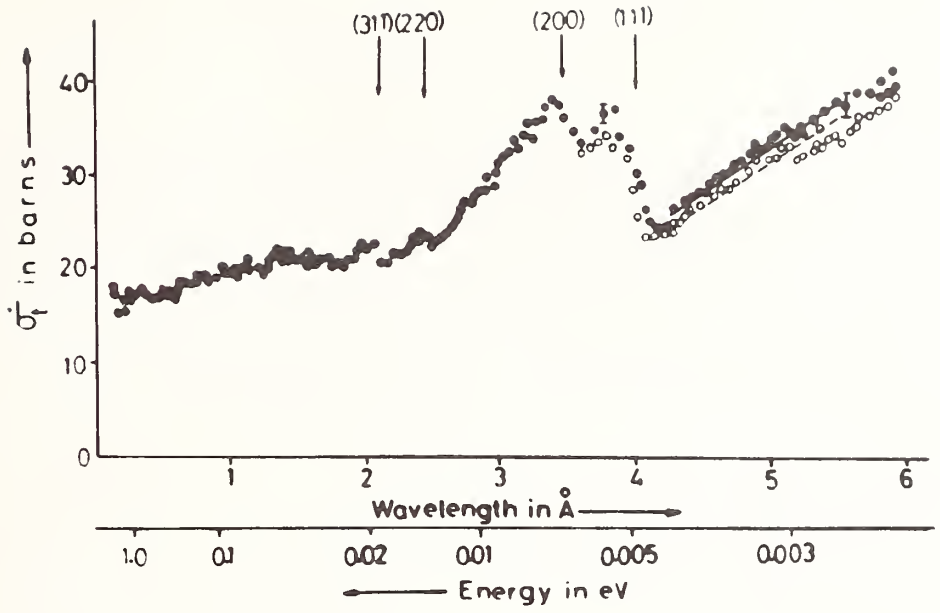

Fig. 2. Total cross-section of nickel vs wavelength and energy.
● - measurements at room temperature.
o - measurements at liquid nitrogen temperature.

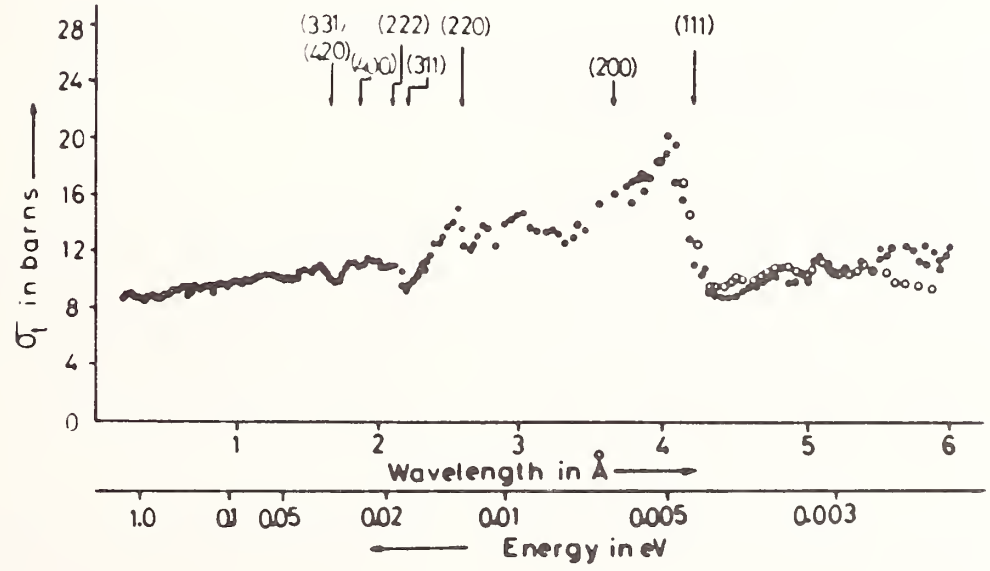

Fig. 3. Total cross-section of cupper vs wavelength and energy.
● - measurements at room temperature.
o - measurements at liquid nitrogen temperature.

$$\sigma_t=(7.4\pm0.6)+(0.37\pm0.12)E^{-1/2} \quad b.$$

which is in good agreement with that reported by Bendt and Ruderman[7], as :

$$\sigma_t=(8.2\pm0.2)+(0.54\pm0.05)E^{-1/2} \quad b.$$

The coherent scattering amplitude and cross-section for Cu were found to be $b_{coh}=(7.7\pm0.4)$ F and $S=(7.5\pm0.8)$ b. respectively, which are in good agreement with the values 7.9 F and 7.8 b. reported previously[5,6].

At liquid nitrogen temperature and beyond λ_c the total cross-section follows the expression:

$$\sigma_t=(1.98\pm0.09)+(0.54\pm0.03)E^{-1/2} \quad b.$$

This gives a value of (1.98±0.09) b. for the incoherent elastic scattering cross-section which is in agreement with the value of (1.9±0.6) b. reported by Bendt and Ruderman[7].

The contribution established by the one phonon annihilation process in the total cross-section at room temperature is higher than at liquid nitrogen temperature by about 0.3 b. That is why the obtained total cross-section data of Cu beyond λ_c at both room and liquid nitrogen temperatures agree within the statistical errors of the measurements which are not less than 0.4 b.

References

1. G.M.Cassels, Proc. Roy. Soc. A 208, 527 (1951).

2. I.Hamouda, et al., Proc. of the Fifth Arab Scientific Conference, Bagdad, March 27-31 (1966).

3. I.Hamouda, R.Maayouf, M.Salama,M.Abu-El-Ela, V.Nesterenko and A.Stupak, Nucl. Inst. & Meth. 40, 153 (1966).

4. M.Adib, et al., Arab Jour. of Nucl. Sci. and Applications, 9, 155 (1976).

5. D.J.Hughes and J.A.Harvey, Neutron Cross Sections, BNL-325, 2 nd Ed. (1958), Supplement (1960), Supplement 2, (1966).

6. G.E.Bacon, Neutron Diffraction, Oxford Press, (1962).

7. P.J.Bendt and I.W.Ruderman, Phys. Rev. 77, 575 (1950).

CHEMICAL DEPENDENCE OF URANIUM FISSION

R. A. Schrack and C. D. Bowman
National Bureau of Standards
Washington, DC 20234, USA

A difference on the order of 4% in the delayed neutron yield from ^{235}U after fission induced by thermal neutrons has been previously reported for samples of U_3O_8 and UO_2. Both theoretical calculations and experimental checks have been made in an attempt to verify the effect. The calculation of the effect of phonon distribution on fission cross section using an Einstein model of the lattice phonon distribution shows no significant dependence on the chemical state. Experimental measurements of the fission fragment yield from thermal-induced fission of ^{235}U in UO_2 and U_3O_8 were made. The relative fission fragment yield was: UO_2/U_3O_8 = .9972±.0003 where the error is from the counting statistics only. A second experiment was carried out that compared the delayed neutron yield after irradiations in a thermal neutron flux. A relative yield of UO_2/U_3O_8 = .9914±.012 was obtained. Neither theory nor experiment would thus support a chemical dependence on the order of the previously reported experiment.

[Chemical dependence, delayed neutrons, fission yield, thermal neutrons, ^{235}U, UO_2, U_3O_8.]

Introduction

A difference on the order of 4% in the delayed neutron yield from ^{235}U after fission induced by thermal neutrons has been reported for samples of U_3O_8 and UO_2.[1] Differences in yield of this magnitude are not only interesting from the viewpoint of the underlying physical phenomena but have major commercial and safeguard implications because of the use of neutron-induced delayed neutron yield to measure ^{235}U concentration in commercial power reactor fuel rod scanners. We have carried out theoretical calculations to determine if the difference in phonon distributions between the two chemical states could account for the observed effect.[2] Using the Einstein approximation for the phonon distribution, we have calculated the fission cross section for ^{235}U in the thermal energy region. The calculated cross section changed by less than .015% when the phonon energy was changed from 11 to 17 millielectron volts, covering the range of energy that would be expected for phonon distributions characteristic of the uranium and uranium oxide lattices,[3,4,5] Measurements were also undertaken for the purpose of reproducing the results of the earlier work.

Measurements

To see if the observed effect was related to the fission process, we utilized the NBS double fission chamber.[6] Two foils can be placed back to back in this chamber and relative fission yields measured in very nearly the same geometry. The chamber is rotated 180° in the beam for half the measurements to compensate for any differences in neutron flux and geometry. The uranium oxide deposits are about 500 $\mu g/cm^2$ thick, covering an area of about 1 cm^2 in the center of the backing disks. The backing disks are platinum, about .0127 cm thick. The uranium is enriched to 99.7% ^{235}U.

Two fission foils of UO_2 were chosen that were of approximately equal mass. One of the foils was baked at 600° for several hours to convert it to U_3O_8. The foils were then placed in the chamber and the relative fission yield measured in the external thermal neutron beam of the NBS reactor. The ratio of U_3O_8 to UO_2 yield obtained was:

$$.9794 \pm .00085$$

$$.9795 \pm .00029$$

with a weighted average of: $.97948 \pm .00027$.

The other UO_2 foil was then removed and baked in the same manner as the first, and the yield ratio of the two foils was obtained to measure the relative amount of ^{235}U in the foils. The yield ratios obtained were:

$$.9774 \pm .00022$$

$$.9763 \pm .00025$$

$$.9763 \pm .00025$$

with a weighted average of $.9767 \pm .00014$.
The first result is divided by the second to eliminate the effect of the mass difference. We obtain a relative yield:

$$\frac{UO_2}{U_3O_8} = \frac{.97670 \pm .00014}{.97948 \pm .00027} = .9972 \pm .00032.$$

The errors are from counting statistics only. Systematic errors are not known but might be large enough to cover the observed yield difference of .28%. The α-particle yield was measured before and after the second baking to determine if any material was lost in the process.

The ratio of the α-particle yield before and after the second baking is $1.0011 \pm .002$. The error is unfortunately too large to determine if there was a mass loss in handling the foils large enough to explain the difference. Other systematic errors, such as change in shape or orientation of foil, have not been formally investigated, but previous experience indicates that .1% changes for measurements of the same foil are not unusual. Although the results of this experiment do not preclude a small effect, it does appear to rule out a fission yield difference between UO_2 and U_3O_8 of 4%.

It has been suggested that the difference in delayed neutron yield might be associated with the fission product distribution or decay mode rather than the total yield of fission products. To test this possibility a second set of experiments was performed to measure the delayed neutron yield from UO_2 and U_3O_8 after irradiation in the thermal column of the NBS reactor.

To insure that no differences in isotopic abundance or impurities affect the result, we produced the UO_2 sample by chemical reduction of U_3O_8. The U_3O_8 sample used was NBS standard sample U-930, which is 93.2% ^{235}U enriched. Approximately 100 mg of

U_3O_8 was heated in a microbalance furnace in an atmosphere of 5% H and 95% N. Figure 1 shows the change in weight as a function of furnace temperature. The reaction $4H + U_3O_8 \rightarrow 3UO_2 + 2H_2O$ proceeded to completion, and the expected weight change for stochiometric conversion was obtained within 0.1%.

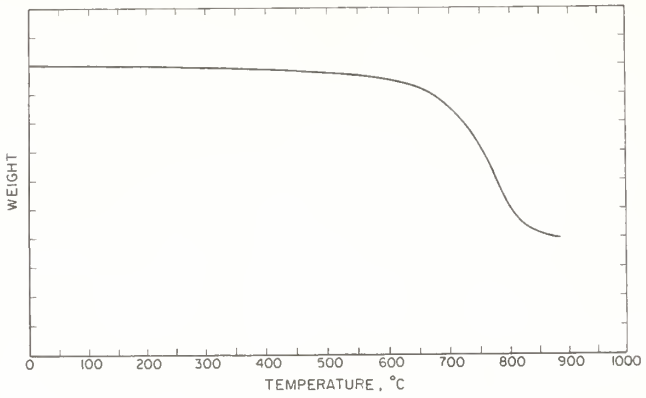

Fig. 1. Reduction of U_3O_8 to UO_2 in 5% H atmosphere. The change in weight as a function of microbalance furnace temperature is shown. The rate of temperature increase was 20°C/min.

Fourteen samples were prepared, seven each of U_3O_8 and UO_2 of about 2 mg. After careful weighing, the samples were wrapped in aluminum foil and sealed in quartz tubes. The quartz tubes were evacuated and the sample end of the tube immersed in liquid nitrogen during the sealing process to avoid any possible modification of the chemical state.

Samples of alternate chemical state were then irradiated sequentially in the thermal column of the NBS reactor. Flux levels in the reactor are constant to about 1%. The samples were irradiated for 100 seconds. After a delay of 100 seconds, the neutron yield was counted for 100 seconds. All timing was done by automatically operated circuits. Approximately 60,000 counts were recorded during the 100-second counting period. The experiment was repeated on a suceeding day. The mean values of the ratios of delayed neutron yields from UO_2 to U_3O_8 for the two experiments are:

$$.9910 \pm .013$$

$$.9914 \pm .011$$

or an average of

$$UO_2/U_3O_8 = .9912 \pm .012$$

where the error given is the standard deviation of the mean of the measurement set.

Table I compares the experimental conditions of this experiment and the previously reported work of Lukens and Bramblett.[1] The irradiation time t_i is the time period spent in the reactor thermal column; the delay time t_d is the time from the end of the irradiation period to the beginning of the counting period, delayed neutron yield is then counted for the time period t_c. The longer times used in our experiment enhanced the importance of the longer lived ^{87}Br precursor-delayed neutron group.

Table I. Comparison of time periods.

Experiment	Sample weight mg.	Neutron Flux n/sec/cm^2	t_i (sec)	t_d (sec)	t_c (sec)
Lukens and Bramblett	3-25	2.5×10^9	30	30	50
NBS	1-2	1.6×10^{11}	100	100	100

Table II shows the distribution in yield detected from the different neutron groups for the two experiments. Lukens and Bramblett suggested that their results might have been a result of a change in the branching ratio of ^{87}Kr to neutron stable and neutron-emitting states. It would seem that if such a shift in branching ratio were the cause of the reported difference in yield our experiment would be more than twice as sensitive as the Lukens and Bramblett experiment.

Table II. Comparison of neutron group contributions.

Delayed Neutron Group	Precursor	Percent Neutrons Contributed NBS	Lukens and Bramblett
1.	^{87}Br	.55	.19
2.	^{137}I, ^{88}Br	.45	.79
3.	^{138}I	0	.02

Summary

Within the accuracy of the experimental results reported here, no difference was observed in either fission rates or delayed neutron yield from the two chemical states of $^{235}UO_2$ and $^{235}U_3O_8$ for thermal neutron-induced fission.

Acknowledgments

We would like to acknowledge the contributions of a large number of people to the experimental work reported here. The delayed neutron counting experiment was carried out using a detector system designed and constructed by James E. Bond. The assistance of David M. Gilliam in preparing fission foils and assistance in carrying out the double fission chamber experiment is gratefully acknowledged. We are indebted to Bert M. Coursey for careful preparation and analysis of sample weights. We would also like to acknowledge the assistance and advice of James A. Grundl, George P. Lamaze, Val Spiegel, and Wilfrid B. Mann during various phases of the experiments. This work was supported in part by the Nuclear Regulatory Commission.

References

1. H.R. Lukens and R.L. Bramblett, "Observation of a Difference in Yields of Delayed Neutron Emitters from U_3O_8 and UO_2," Nucl. Sci. Eng. Vol. 61 pp. 426-428 (1976).

2. C.D. Bowman and R.A. Schrack, "Effects of Phonon Transfer on Near-Thermal Neutron Fission Cross Sections," Phys. Rev. Vol. 17, No. 2 pp. 654-663 (1978).

3. H.E. Jackson and J.E. Lynn, "Resonant Absorption of Neutrons by Crystals," Phys. Rev., Vol. 127, pp. 461-468 (1962).

4. J.A. Young, "Neutron Scattering from Uranium Dioxide," Nukleonik, Vol. 12, pp. 205-208 (1969).

5. C. LaJeunesse, W.E. Moore, and M.L. Yeater, "Low Energy Neutron Interactions with Uranium Carbide," Nucl. Sci. Eng. Vol. 47, pp. 349-364 (1972).

6. J.A. Grundl et al., "Measurement of Absolute Fission Rates," Nucl. Tech., Vol. 25, pp. 237-257 (1975).

ADVANCED CONVERTER REACTORS

Paul R. Kasten
Oak Ridge National Laboratory
Oak Ridge, Tennessee 37830, USA

ABSTRACT

Advanced converter reactors (ACRs) of primary U.S. interest are those which can be commercialized within about 20 years, and are: Advanced Light-Water Reactors, Spectral-Shift-Control Reactors, Heavy-Water Reactors (CANDU type), and High-Temperature Gas-Cooled Reactors. These reactors can operate on uranium, thorium, or uranium-thorium fuel cycles, but have the greatest fuel utilization on thorium type cycles. The water reactors tend to operate more economically on uranium cycles, while the HTGR is more economical on thorium cycles. Thus, the HTGR had the greatest practical potential for improving fuel utilization. If the U.S. has 3.4–4 million tons U_3O_8 at reasonable costs, ACRs can make important contributions to maintaining a high nuclear power level for many decades; further, they work well with fast breeder reactors in the long term under symbiotic fueling conditions. Primary nuclear data needs of ACRs are integral measurements of reactivity coefficients and resonance absorption integrals.

[Advanced converters, thorium reactors, fuel cycles, denatured uranium-thorium fuel cycles, thorium reactor introduction, nuclear data needs.]

1. Introduction

The term, "advanced converter reactors," is a generic term which is utilized to indicate a reactor system which has improved fuel utilization characteristics relative to that of present Light-Water Reactors (LWRs). Through the years, many advanced converter systems have been proposed and worked on, including aqueous homogeneous (D_2O) reactors, molten-salt fueled graphite-moderated reactors, organic-cooled heavy-water reactors, organic-cooled and moderated reactors, sodium-cooled graphite-moderated reactors, and sodium-cooled hydride-moderated reactors. However, only a relatively few advanced converter types can be applied commercially within the next approximately 20 years from a practical viewpoint; these include Advanced LWRs (ALWRs) such as LWRs using thorium as the fertile material (including Light-Water Breeder Reactors [LWBRs]), Spectral-Shift-Control Reactors (SSCRs), Heavy-Water Reactors (HWRs), Advanced Gas Reactors cooled with CO_2 (AGRs), and High-Temperature Gas-Cooled Reactors (HTGRs). Further, although applied in the United Kingdom, AGRs are not considered practical in the U.S. because of their high capital cost. Thus, only ALWRs, SSCRs, HWRs, and HTGRs are given serious consideration as advanced converters in the U.S., and these are discussed below. However, not all of these have the same likelihood of being applied in the U.S.

The general order of this presentation will be: (1) a brief description of the reactor systems; (2) a brief description of reactor fuel cycles which can be utilized; (3) the nuclear and economic performance of various fuel cycles in the ACRs as measured against reference LWRs; (4) general comments on nuclear cross section needs for the ACRs; and (5) overall conclusions.

2. Brief Discussion of the Advanced Converters Considered Here

2.1 Advanced Light-Water Reactors (ALWRs)

ALWRs are variants of present-day LWRs and thus a brief review of the latter is given first. LWRs refer to either Pressurized Water Reactors (PWRs) or Boiling Water Reactors (BWRs), both of which are operating commercially in the U.S. LWRs basically consist of reactor cores contained in steel pressure vessels, and utilize low-enriched UO_2 pellet fuels contained in Zircaloy tubular cladding. High-pressure water and steam is used as the coolant. Reactivity control is by movable neutron-absorbing mechanically-driven control elements; further, burnable poisons (plus soluble poisons in the case of PWRs) are utilized to extend reactivity control and obtain better fuel utilization. LWRs are highly developed and there is a wide resource of test and operating experience on these systems.

ALWRs include a number of variants from standard LWRs. A simple variant is that associated with increased fuel exposure (i.e., increasing the average fuel exposure from approximately 30 MWD(th)/kg heavy metal to about 50 MWD(th)/kg heavy metal). In this case, the ALWR system is essentially the same as the LWR, with modification to accommodate the higher fuel exposure. Another ALWR is one uniformly utilizing thorium as the fertile material; again, the ALWR system is essentially the same as the LWR, with modifications to accommodate thorium-uranium fueling instead of uranium fueling.

A more complex ALWR is the LWBR. This is a PWR-type system which has a novel seed-blanket fuel design utilizing the thorium fuel cycle. The fuel basically consists of a seed fissile region surrounded by a blanket thorium region in a modular type arrangement. Further, the seed region is movable, permitting changes in neutron leakage to the blanket region when the seed assembly is moved, thus providing reactivity control through changes in neutron absorption by thorium. Otherwise, the LWBR basically uses PWR technology, except that the core operates with a relatively high power density in the seed regions and with a relatively low power density in the blanket regions. However, the LWBR has more complicated reactivity control mechanisms. The LWBR concept is presently being demonstrated in the Shippingport Reactor in Pennsylvania.

2.2 Spectral-Shift-Control Reactors (SSCRs)

SSCRs consist basically of a PWR with the conventional soluble boron reactivity control system replaced with a system which controls the amount of D_2O in H_2O (spectral shift control). The latter system controls reactivity by changing the neutron spectrum through the addition of heavy water to LWR coolant in a manner analogous to the use of soluble boron in the conventional PWR. Since light water is a better moderator of neutrons than heavy water, the introduction of heavy water shifts the neutron spectrum in the reactor to higher energies and results in the preferential absorption of neutrons in fertile materials. In contrast to the conventional PWR, where absorptions in control absorbers is unproductive, the absorption of excess neutrons in fertile material breeds additional fissile material, increasing the conversion ratio of the system and decreasing the annual makeup requirements. Over the cycle, the spectrum is thermalized by decreasing the D_2O to H_2O ratio in the coolant.

2.3 Heavy-Water Reactors (HWRs)

The HWRs considered here are of the CANDU type which have been commercialized in Canada. The CANDU reactors utilize fuel bundles within pressure tubes which separate the heavy-water coolant from the heavy-water moderator. The pressure within the coolant system is comparable to that of LWR pressures, whereas the pressure within the calandria vessel is relatively low. The fuel elements are quite short, roughly two feet in length, and the system employs continuous on-line refueling rather than periodic refueling as in LWRs. The on-line refueling scheme reduces excess reactivity requirements. However, there is a large inventory of heavy-water moderator which adds to the costs and the thermal efficiency is relatively low because of the low temperature at which the moderator operates. The reactor operates effectively with natural uranium fuel and also slightly enriched uranium fuel.

2.4 High-Temperature Gas-Cooled Reactors (HTGRs)

HTGRs use unique fuels involving coated fuel particles bonded together by a graphite matrix into a fuel rod; the coatings on the individual fuel particles provide fission product containment. The fuel rods are loaded into holes in hexagonal graphite fuel blocks, with these blocks also containing hexagonal arrays of channels for coolant flow. HTGRs operate at high coolant temperatures, leading to high thermal efficiencies - about 40% relative to about 35% in LWRs and 30% in HWRs. HTGRs have a relatively low core power density, a large heat capacity associated with the graphite moderator, and a large core volume contained within a prestressed concrete reactor vessel (PCRV). Helium is used as the coolant. The above fuel description is for U.S. fuel designs; however, HTGR designs based on use of pebble-bed type fuel are being developed in the Federal Republic of Germany (FRG).

3. Brief Description of Reactor Fuel Cycles

All of the advanced converter reactors (ACRs) can operate on various fuel cycles. In general, the uranium fuel cycle is the reference cycle in water reactors; however, thorium fuel cycles and mixed thorium-uranium fuel cycles can be employed. In general, the term "fuel cycle" implies all operations, processes, and reactor exposures associated with the fuel from the time of its initial purchase to the time of its sale or recycle. "Fuel cycle" includes the conversion of natural uranium to a fuel form or to UF_6 for feed to an enrichment plant. After the desired enrichment, the fuel is chemically converted to the desired form, followed by fabrication; after exposure in the reactor, the fuel is stored/cooled until the high activity fission products decay to a satisfactory level for shipping, and sent to a reprocessing plant for fuel recovery (alternatively, the fuel can be stored without reprocessing); after reprocessing, the fuel is either sold, recycled, stored, partially discarded, or a combination of the above. If thorium is utilized, it is introduced in the fuel preparation step and then follows the recycle stages indicated above.

The term "uranium fuel cycle" implies the above steps, and also that ^{238}U is employed as the fertile material; the term "thorium fuel cycle" is analogous to the above, but with ^{232}Th used as the fertile material. Mixed uranium-thorium fuel cycles imply the use of ^{238}U and ^{232}Th as fertile material with various fissile fuels, or the use of ^{233}U with ^{238}U, or of Pu with ^{232}Th. All reactors can utilize the above fuel cycles, but not all cycles have the same performance in a given reactor, nor does a given fuel cycle have the same performance in various reactor types.

The nuclide chains associated with bred fuel and higher isotope productions for the thorium cycle and the uranium cycle are completely analogous. However, there are important differences in neutron cross sections, nuclear constants, and decay rates associated with the corresponding nuclides. Further, since the thorium cycle requires ^{235}U to initiate the cycle, both uranium and thorium fuel cycles are basically dependent upon the mining of natural uranium for the initial fissile fuel used to charge a reactor.

In thermal reactors such as LWRs, the uranium cycle is normally utilized, with use of slightly-enriched uranium as the initial fuel material. However, the thorium cycle could also be employed, with ^{235}U (as highly enriched uranium) plus thorium as the initial fuel. For either fuel cycle, the bred fuel can be stored, sold to another user, or recycled. Since Pu is a valuable fuel for fast reactors, the uranium fuel cycle in LWRs often considers bred Pu to be stored for future use. Under such circumstances, the uranium cycle operates on what is termed the first cycle or the open cycle. For thorium fuel cycles, the bred ^{233}U has a relatively high value in thermal reactors, and is often considered to be recycled.

In addition to the features of fuel cycles discussed above, there are variations which might be introduced because of weapons proliferation concerns. Thus, while the standard recycle process in LWRs treats the separation of Pu from other fuel and fission products and the recycle of Pu with ^{238}U or natural uranium, proliferation concerns may lead to restrictions on reprocessing such that separation of Pu from fission products (or radioactivity) is not permitted; alternatively, reprocessing may not be permitted. Another variant would be to coprocess Pu with uranium while retaining reactivity within the fuel materials. Similar types of fuel cycle variations can be associated with the thorium cycle, with ^{233}U being diluted with ^{238}U to give denatured uranium, or with retention of reactivity with ^{233}U at all times, or a combination of the above. The influence of the above variations in the fuel cycles, which are basically variations in the reprocessing and refabrication end of the fuel cycle, do not have a significant effect on the nuclear performance of the reactor per se, since the neutron poisoning added by the radioactive components would not be significant from a nuclear performance viewpoint. However, the above variants could influence the cost of fuel refabrication significantly, making it more difficult for fuel recycle to compete with the "stowaway" cycle. This is not considered below, but is pointed out here as a factor to consider, with the specific economic penalty a function of the reactor fuel and the conditions which have to be met. In general, the addition of radioactivity to fissile fuel would affect the uranium cycle more than thorium cycle since ^{233}U already has significant activity because of daughter products resulting from ^{232}U present in the ^{233}U.

The relative desirability of thorium, uranium, or mixed fuel cycles in a given reactor type is dependent on a number of factors such as the nuclear constants associated with the pertinent materials compositions, the unit cost of fissile fuel used to inventory the reactor initially, the unit cost of makeup fuel, the unit cost of fuel recycle, the physical and chemical properties of the fuel material, the economic bases and

ground rules which apply, and proliferation resistance perceptions. These factors are included in the evaluations given below.

4. Nuclear and Economic Performance of Various Fuel Cycles

4.1 General Performance of Advanced Converters

As indicated above, the nuclear and economic performance of reactor systems as a function of fuel cycle are related; i.e., power cost is influenced by fuel conversion ratio, with costs increasing as the conversion ratio increases beyond a certain point. At the same time, increasing the conversion ratio improves fuel utilization. Thus, improving fuel utilization does not always correspond to improving economics. This is illustrated in Fig. 1 which shows the fuel cycle costs for HWR thorium systems (CANDU type) initially fueled with uranium containing 93% ^{235}U mixed with thorium; results are given for two sets of fuel recycle costs and for two specific power levels in the fuel for various U_3O_8 ore costs. [1] As shown, the results for the HWR-Th system examined indicate that the economic conversion ratio would be about 0.8. In the following, the fuel conversion ratios of the reactor systems studied correspond to the values near the minimum fuel cycle costs for the economic parameters considered.

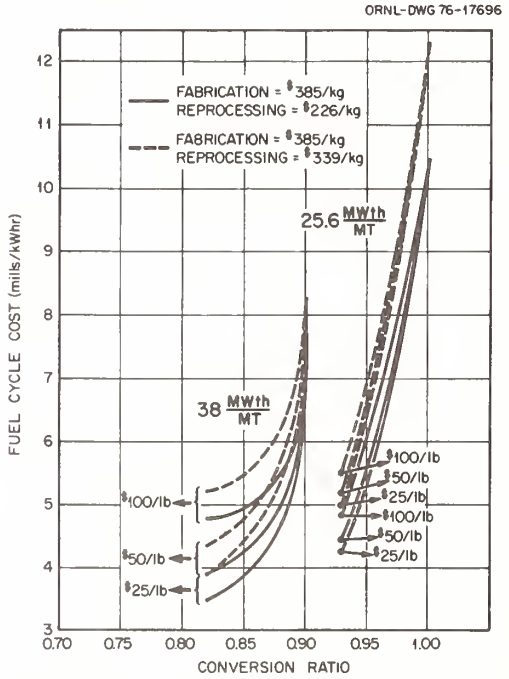

Fig. 1. Fuel Cycle Cost for CANDU-Thorium Concept Having 93% ^{235}U Topping.

In order to compare the fuel utilization and economic performance of various advanced converters, a number of economic and power growth ground rules have to be considered, and these are discussed below. Also, as indicated previously, the results will compare the standard thorium fuel cycle with the standard uranium cycle. [1]

First, let us consider the nuclear power growth scenario given in Fig. 2. It assumes a nuclear power growth of 15 GW(e)/yr during the period 1970–2000. After the nuclear power capacity reaches 450 GW, it is maintained at that level until reduction is necessary because of limitations in U_3O_8 resources, consistent

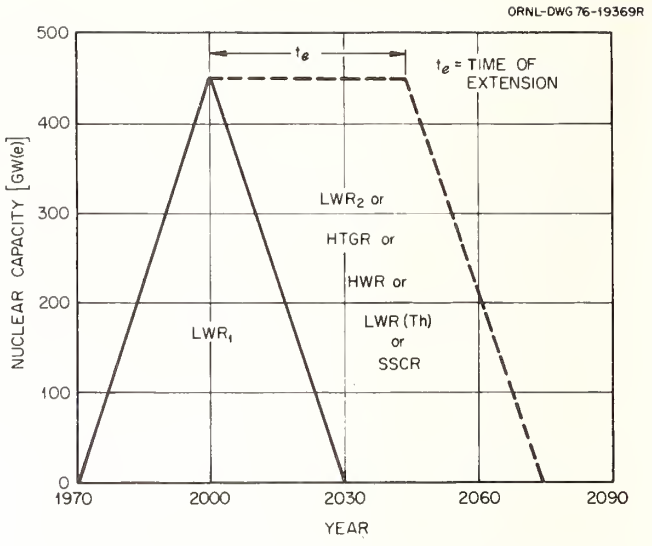

Fig. 2. Thermal Reactor Power Growth Scenario [initial growth of 15 GW(e)/yr; LWR$_2$, LWR(Th), HWR, or HTGR introduced in 2000]. The t_e is illustrative only and varies with different reactor types introduced.

with a 30-year lifetime for all reactors that are built. The available U_3O_8 resource is considered to be either 2.3 or 3.2 Tg (2.5 or 3.5 million short tons) U_3O_8.

In these studies, reference LWRs operating on the uranium fuel cycle are used initially; these are termed LWR$_1$s, as given in Fig. 2. Reactors built after the year 2000 are either additional LWRs operating on the uranium cycle (termed LWR$_2$s for ease of identification), LWRs operating on the thorium cycle [LWR(Th)s], SSCRs, HWRs, or SC-HTGRs. The latter three reactors use the thorium fuel cycle in these studies. (These reactors can be operated on either the thorium or uranium fuel cycle; however, the best fuel utilization will be obtained with the thorium cycle; the economic performance tends to be better on the thorium cycle for HTGRs, and tends to be better on the uranium cycle for HWRs and SSCRs). After the year 2000, LWR$_1$s are withdrawn from use as their 30-year lifetime (21 full-power years) is attained and replaced with a second type reactor chosen from the available types considered above. The power capacity is maintained at 450 GW(e) for a period of time, t_e, no new reactors are built, and those in use operate until the end of their 30-year lifetime. (Figure 2 serves as an illustration of what t_e signifies, and the time given should not be taken literally.)

The power growth scenario of Fig. 2, along with the estimated lifetime U_3O_8 requirements of the various reactors, is used to calculate the energy that can be generated for each type of new reactor used. This calculation assumes that a given reactor operates 21 full-power years over its lifetime, the uranium tails from enrichment plants are 0.2% ^{235}U, and 1.1 Gg (1200 tons) of fissile plutonium generated by LWR$_1$s is stored for future use in FBRs. That amount of plutonium permits a significant breeder economy to develop eventually.

In measuring the improved fuel utilization of a new reactor, it is important to factor in the time of introduction of the new reactor and the amount of U_3O_8 resource available to it. This is done here by measuring the energy generation of combined reactor systems against the energy that could be generated if

no new reactors were introduced. Thus, the energy generated by LWR_1s plus LWR_2s is the reference energy generation, based on the use of LWRs with uranium and plutonium recycle in which the entire ore resource is utilized (except for the plutonium stored for FBRs). The corresponding energy generation when new reactors are introduced after the year 2000 is also calculated and compared with the reference energy generation. The resulting comparisons are termed the relative energy generation (REG), and are given in Table 1 for the various reactor combinations and U_3O_8 resource levels. [2] Table 1 results are based on thorium fuel cycle use in the second reactor, on reference designs, and on fuel conversion ratios that correspond to economic operation based on estimated unit fuel recycle costs for the above reactors. The fuel utilization results also consider the reactor thermal efficiencies as given in Table 1.

In the power growth scenario of Fig. 2 and up to time t_e, new reactors are always being built at 15 GW(e)/year (including replacement reactors); thus, the higher the value of t_e, the longer the time available for FBR development without a closeout of the nuclear power industry.

Table 1. Relative Energy Generation and Extension Time for Assumed Power Growth Scenario as a Function of Reactor Use and U_3O_8 Resource (HTGR is SC-HTGR)[2]

Reactor Use	Fuel Conversion Ratio for Second Reactor	Second Reactor Thermal Efficiency (%)	Relative Energy Generation (REG) and Extension Time (t_e) for two U_3O_8 Resource Levels in Tg (tons)			
			2.3 (2.5×10^6)		3.2 (3.5×10^6)	
			REG	t_e (years)	REG	t_e (years)
LWR_1 + LWR_2	0.60	33	1	8.6	1	25
LWR_1 + LWR(Th)	0.68	33	1.12	13.4	1.16	34
LWR_1 + SSCR(Th)	0.74	33	1.14	14.2	1.25	40
LWR_1 + HTGR(Th)	0.82	39	1.20	16.5	1.42	48
LWR_1 + HWR(Th)	0.82	30	1.15	14.7	1.31	43

The results in Table 2 illustrate that use of the thorium fuel cycle rather than the uranium cycle permits a significant increase in energy generation, even though thorium reactors are not introduced until the year 2000. At the same time, there is a difference in the relative energy generation associated with the different reactor types, and also with the U_3O_8 resource base. The higher the U_3O_8 base, the more ore is available for fueling advanced converters and the greater the relative energy contribution of advanced converters.

Table 2 gives the economic benefits associated with the various combinations of reactors for the assumed power growth scenario, the economic and cost bases given in ref. 1, a 7.5%/year discount factor on benefits, a U_3O_8 price of \$220/kg (\$100/lb), and a uranium enrichment (separative work) price of \$150/SWU. The economic benefits were calculated relative to the power cost of the LWR (U-Pu recycle) system for designs with economic fuel conversion ratios. Fuel recycle was assumed after the year 2000. The specific unit reactor and fuel recycle costs considered are given in ref. 1, the capital costs of HTGRs were considered to be the same as those of LWRs based on estimates by UE&C.

For the specific designs and economic bases considered, the SC-HTGR gave the best fuel utilization and economic performance of the thorium-fueled reactors. Use of different bases, however, could change the results.

Table 2. Discounted Benefits of Various Thorium-Fueled Reactors Relative to LWR (U-Pu Recycle) Systems

Reactor System	Discounted Benefits, $\$10^9$ for each U_3O_8 Resource in Tg (tons)	
	2.3 (2.5×10^6)	3.2 (3.5×10^6)
LWR_1 + LWR_2	reference value = 0	
LWR_1 + LWR(Th)	negative benefit	
LWR_1 + SSCR(Th)	~0.5	~1.0
LWR_1 + HWR(Th)	1.1	1.5
LWR_1 + SC-HTGR(Th)	6.4	8.7

While the above results summarize economic performance of advanced converters based on use of the thorium fuel cycle, comparative results have also been obtained for the uranium cycle. [1] These more detailed results confirm the results cited previously, namely, that in water reactors the uranium cycle tends to be more economic than the thorium cycle; only the thorium cycle is considered in HTGRs since, based on earlier studies, that cycle is economically preferred to the uranium cycle.

4.2 Light-Water Breeder Reactors (LWBRs)

By going to Advanced Light-Water Reactors (ALWRs) such as the seed-blanket LWBR (having major changes in core design relative to present LWRs), more significant improvements in fuel utilization can be achieved than considered previously. The major core design change to improve performance corresponds to effective removal of neutron poisons from the core region during the fuel exposure cycle. This can be done by seed-blanket type control, in which relative neutron absorptions in fertile material are varied during the cycle. However, use of seed-blanket core designs leads to lower average core power densities, larger reactor vessels for a given power capacity, and thus higher capital costs. Further, the seed-blanket fuel elements would have higher unit fuel fabrication costs because they require more complex fuel loading, and the cost of recovering the ^{233}U in the blanket rods does not justify that recovery at the recovery rates needed in an LWBR. As a result, it is not assured that the envisioned improved fuel utilization performance associated with control-poison removal corresponds to practical core designs; based on the power growth scenario given in Fig. 2 and use of prebreeders to fuel LWBRs, the penalty associated with use of such reactors at U_3O_8 costs of \$100/lb is estimated to be well over \$100 billion.

4.3 Denatured-Uranium-Thorium (DUTH) Fuel Cycles

The above considered the standard thorium cycle, which recycles bred ^{233}U. The present U.S. emphasis on maintaining high proliferation resistance in nuclear fuel cycles indicates that the ^{235}U in thorium cycles would be replaced by denatured uranium (that is, uranium having an enrichment low enough that effective weapons could not be made directly from such material). Under such circumstances, DUTH fuels would be employed rather than highly enriched uranium-thorium (HEUTH) fuels, with the enrichment of the denatured uranium

being about 20% ^{235}U. The ^{233}U bred in such systems could be denatured in situ by the appropriate presence of ^{238}U along with the thorium. However, high levels of radioactivity will be associated with the decay products of ^{232}U, which will be generated along with the ^{233}U, and this activity may be sufficient to permit recycle of ^{233}U (along with attendant ^{232}U) under certain circumstances without denaturing. If all uranium has to be denatured, use of the DUTH fuel cycle rather than the HEUTH cycle will degrade the fuel utilization of the reactor. However, the decrease in performance is inherently small in water reactors, and it can be made relatively small in HTGRs with proper reactor physics design. [2] Thus, the results for the DUTH fuel cycles are reasonably close to the fuel utilization performances associated with the previous results, so long as plutonium produced in the DUTH cycles is also recycled. However, the continued use of DUTH fuel cycles in thermal reactors does have implications relative to the ratio of thermal to fast reactors in the long term. The discussion below assumes that highly concentrated fissile fuel can be recycled so long as high activity is inherently associated with it. Thus, the thorium fuel cycles would utilize DUTH fuel for the initial and makeup fuel, but recycle fuel would primarily be ^{233}U and thorium. Since only small quantities of plutonium would be discarded from such HTGRs, the fuel utilization performance would be close to that for the HEUTH cycle (mined U_3O_8 requirements would be less than 10% more than the requirements for the HEUTH cycle), based on core designs that give fuel conversion ratios of about 0.8. The appropriate requirements are considered below.

The above considered only thermal reactors. In fast breeder reactors, use of the DUTH fuel cycle leads to significantly lower nuclear performance than the U-Pu cycle. However, incorporating thorium only in the blanket of a fast reactor does not lead to significant changes in nuclear performance, and the ^{233}U that is produced is the most efficient fissile material for thermal reactors, thus leading to good fueling interactions between fast and thermal reactors. Further, the ^{233}U produced could be denatured if desired, which permits fast breeder reactors to provide a long-term source of low-enriched uranium for a limited number of reactors.

Another way of showing the impact of advanced converters on permissible nuclear power level is that given by Till, et al. [3] In Till's study, an ore resource of 3.7 million tons U_3O_8 was assumed, and power growth scenarios calculated which yield about the maximum amount of energy from that ore resource for the reactor systems considered. Figure 3 shows (1) the nuclear power capacity which is permissible with 3.7 million tons U_3O_8 when LWRs are employed on once-through uranium fuel cycles; (2) the nuclear power growth potential for LWR uranium systems with uranium recycle plus the additional growth possible from plutonium recycle; (3) the nuclear power capacity under similar circumstances when LWR once-through reactors are used along with advanced converter reactors operating on the DUTH cycle with ^{235}U makeup and recycle of the bred ^{233}U; and (4) the nuclear power capability if oxide-fueled LMFBRs were also used. Overall, the results illustrate that there is some flexibility in nuclear power growth afforded by the better fuel utilization of advanced converters. While advanced converters do not provide the fuel utilization flexibility of fast breeder reactors, they may be an important means in maintaining a high nuclear power level if LMFBRs cannot compete economically for many decades.

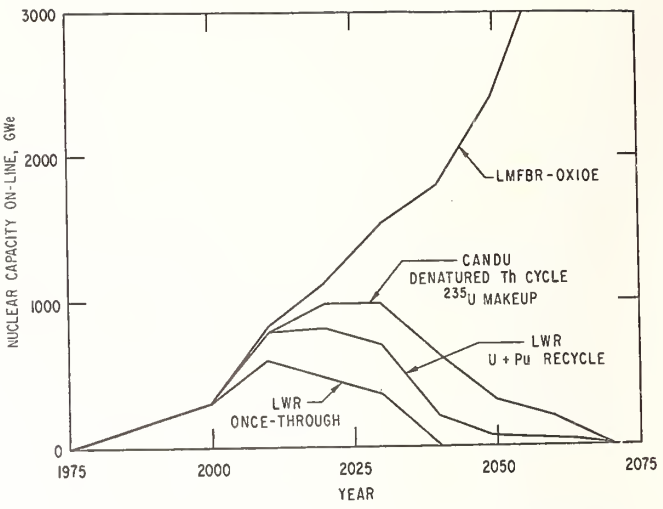

Fig. 3. Comparison of Nuclear Power Growth Potential for Converter Reactor Scenarios and LMFBR Scenario (Resource Base = 3.7 million ST U_3O_8)

4.4 Practical Introduction of Thorium Fuel Cycles

The above results indicate that early introduction of economic thorium fuel cycles is best accomplished by commercial introduction of HTGRs, and a practical scenario for such introduction is given by Kasten. [2] The scenario considers LWRs, HTGRs, HWRs, and FBRs, with HTGRs or HWRs introduced in the year 2000, and FBRs in 2020. The nuclear power level is considered to be 300 GW(e) in 2000, and remains at 800 GW(e) after 2050. Overall, use of HTGRs rather than LWRs after the year 2000 led to a 20 to 30% reduction in mined U_3O_8 requirements (>1 million tons of U_3O_8), and the economic impact of HTGR use could be significant, since the U_3O_8 saved would be the highest cost resource. Finally, the ratio of thermal to fast reactors could be significantly higher if HTGRs were used rather than LWRs in the long term.

Use of HWRs on uranium fueling would provide only slightly less fuel utilization than the HTGR (using thorium) up to the year 2040, if the HWR replaced the HTGR. However, in converting the HWR to ^{233}U/Th fueling after the year 2040, the HWR is estimated to require an additional 0.5 million tons U_3O_8 in mined uranium. Thus, the potential advantages of the HTGR over the HWR are its better economic performance (due to capital cost and fuel utilization factors), its smaller amount of U_3O_8 needed to convert to ^{233}U fueling in symbiotic systems, its higher thermal efficiency, and the versatile application of HTGR component technology.

5. Comments on Nuclear Cross Section Needs for Advanced Converters

Improvements in the accuracy of nuclear cross sections is generally desirable, and that holds true for those nuclear values applicable to the various fuel cycles in advanced conveter reactors. However, needed accuracy improvements in certain nuclear cross sections is more important than in others, and is dependent upon the practicality of the reactor system being considered. In this section, some general remarks on reactor physics quantities will be first summarized, followed by comments on cross section needs.

Of the reactor physics features of thorium and uranium fuel cycles in advanced converters, the most important are the fuel conversion ratio, the critical mass requirements of the reactor, and the reactivity coefficients of the reactor. These quantities are directly related to the absorption and fission cross sections of the heavy metal nuclides and to the η values (η = neutrons produced per neutron absorbed) of the fissile materials. In particular, the potential fuel conversion ratio associated with a given fissile fuel is given by $(\eta - 1)$, while the minimum reactor critical mass is roughly inversely proportional to $(\eta - 1)\sigma_a$, where σ_a is the microscopic neutron absorption cross section of the fuel. The value of η as a function of neutron energy for the various fissile fuels shows that in advanced converter reactors the thorium fuel cycle has a higher potential fuel conversion ratio than the uranium cycle. At the same time, the critical mass of a reactor system is dependent upon the fissile composition of the fuel, and breeding of plutonium in uranium fuels tends to decrease the critical mass of thermal reactors. Alternatively, breeding ^{233}U into a system fueled initially with ^{235}U does not change the critical mass of thermal reactors. Finally, the temperature coefficient of reactivity is different for the various fissile fuels.

The nuclear behavior of fertile material also influences the nuclear performance of converter reactors and that behavior is different for ^{238}U and ^{232}Th in both resonance-capture cross section and in fast-fission effects. The thorium thermal cross section is significantly higher than that of ^{238}U, which changes the amount of fertile material which is needed in a thorium system. Alternatively, the ^{238}U has a higher resonance integral than does thorium, which influences the resonance absorptions in fertile material as a function of fuel cycle. Further, the fast effect in thorium systems is significantly less than the fast effect in uranium systems. Also, the effective cross sections for thorium and uranium and their dependence on temperature have an important influence on the temperature coefficient of reactivity.

Another important reactor physics effect on practical use of fuel cycles is the effect of heterogeneity on criticality conditions and on reactivity coefficients. As the fuel becomes more heterogeneous (in a nuclear sense and relative to fertile material), the fuel enrichment required for criticality tends to decrease. Thus, when the fertile fuel is very "heterogeneous" as in the light water or heavy water reactors having relatively high fertile material concentrations, the fuel enrichment tends to be relatively low. This leads to use of uranium for which the unit costs of fissile fuel are relatively low compared with the high unit cost of fissile fuel when thorium fuel cycles are employed. Conversely, in systems which are relatively homogeneous in a nuclear sense, such as in high-temperature gas-cooled reactors, the fuel enrichment utilized in the uranium cycle is relatively high, which means that the unit costs of fissile fuel for both the uranium and thorium fuel cycles are more nearly the same. From an economic viewpoint, this tends to make the thorium cycle the preferred cyle in the more "homogeneous" systems and the uranium cycle the preferred system in the more "heterogeneous" systems.

Additional factors which influence the economic use of fuel cycles are the unit costs of fuel fabrication and of fuel recycle; the higher those unit costs, the higher the desired fuel burnup before discharge. Increasing the fuel burnup increases the desirability of having a system with an inherently higher fuel conversion ratio, which influences the choice of fuel cycle. Both the relatively high fuel recycle unit costs and the relatively high nuclear homogeneity of of the fuel in HTGRs cause the thorium cycle to be preferred in that reactor system. However, in water reactors, the uranium fuel cycle appears to be preferred economically. Thus, the need for specific nuclear cross sections is influenced by the practical application of both reactor type and of fuel cycle.

While it is advantageous to have improved nuclear cross sections for reactors, both basic cross section data and calculational methods are applied in practical use. Further, the physics calculation costs often limit core analyses to those methods which are less rigorous than might be desired. As a result, present cross section values for thermal reactors generally appear reasonably adequate when used with production type calculational models. For example, Quan, et al., [4] looked at the sensitivity of present nuclear data relative to fuel cycle costs of extended-burnup fuel cycles in LWRs. In general, sensitivities are comparable to or smaller than those for reference fuel cycles. Also, Hardy, et al., [5] have performed integral testing of Th-^{233}U and Th-^{235}U data for thermal reactors and found that existing experiments provide a reasonable, consistent picture with regard to calculated reactivities based on present nuclear cross sections. However, specific integral parameter measurements in simple geometries are limited in number, and do not provide an adequately consistent basis for refining the nuclear data needs of thorium systems. In general, the basic need is for well-defined, integral-type experiments which measure average values of cross sections useful in practical reactor calculations, particularly integral measurements of reactivity coefficients. Further, it appears useful to improve the accuracy of the prompt fission neutron spectra for ^{233}U (primary) and for ^{235}U (secondary) [6], particularly for those systems which have high neutron leakage effects such as the seed-blanket LWBR. Also, for thorium systems, improved cross sections appear needed for ^{233}Pa in the resonance energy region. From the viewpoint of useful shielding source data, information on the (n,γ) reaction on thorium would be useful for those reactor systems using thorium blankets.

For HTGRs, there are two fuel heterogeneity levels; the fuel rods are in hexagonal lattices with each fuel rod containing separated, coated fissile and fertile particles within a graphite matrix. The double heterogeneity increases the complexity of the core calculations and the difficulty in getting correlation between experimental and calculated measurements. More experimental integral measurements are needed in carefully controlled experiments in order to determine the adequacy of calculated effective cross sections; this is particularly true for reactivity coefficients (e.g., Doppler coefficients), and for effective neutron capture cross sections for fertile material in the resonance energy region.

Overall, the basic cross section data appear better known than the ability to translate the values to effective cross sections useful in practical core calculations involving complex fuel geometries and materials. This is particularly true for thorium systems, and for reactor types such as HTGRs and LWBRs. Integral measurements of effective reactivity coefficients and of effective resonance absorption and fission integrals (including neutron absorption in complex control assemblies) are most needed.

6. Conclusions

Advanced converters provide a means of improving fuel utilization in thermal reactors using either uranium or thorium fuel cycles. Thorium cycles give the highest potential fuel utilization, but not all reactor types operate economically on that cycle. Use of a mixed uranium-thorium (DUTH)fuel cycle permits the bred ^{233}U to be "denatured" in situ, which may give that cycle significant proliferation resistance even with recycle of bred ^{233}U.

Important factors relative to the use of various advanced converters and fuel cycles are the U_3O_8 resource levels available at reasonable costs, the nuclear power growth, and applicable economic factors and ground rules. Based on once-through fueling, the thorium cycle is the most economic cycle in HTGRs and the uranium cycle is most economic in water reactors (ALWRs, HWRs, SSCRs). With recycle, thorium cycles gain relative to uranium cycles, and at high enough U_3O_8 costs will compete economically with uranium cycles. Based on the economic cost factors employed here, the HTGR operated on the thorium cycle had the lowest power cost of the advanced converters studied.

In general, advanced converters can be a significant advantage in maintaining a viable nuclear option with limited U_3O_8 resources, and that advantage is greatest when the thorium cycle is employed. However, the thorium cycle is the economically preferred cycle primarily in the HTGR. Further, it is important to commercialize the thorium cycle at an early date to realize the potential fuel utilization advantages. Thus, the HTGR appears to be the preferred advanced converter for improved fuel utilization prior to or working with fast breeder reactors. At the same time, the capital cost of the HTGR cannot be more than about 10% higher than that of LWRs in order to maintain the above features.

All the advanced converters can operate as breakeven breeders, but such operation is too expensive to justify that mode of operation.

If U_3O_8 resources at reasonable costs are $3.5-4 \times 10^6$ tons, advanced converters can make important contributions to maintaining a high nuclear power level for many decades; however, they do not replace the long-term need for fast breeder reactors. At the same time, if symbiotic fueling between fast and thermal reactors is desired because of economic and proliferation resistance factors, it is important to have advanced converters prior to as well as working with FBRs. Based on present information, the HTGR is the preferred advanced converter.

The basic nuclear data needs of advanced converters are not clearly identified at this time. However, there are some specific nuclear values which appear to need improvement, such as the fission spectrum of ^{233}U and the ^{233}Pa resonance absorption cross section. A greater need is for integral type cross section measurements useful in determining the calculational models needed to translate basic nuclear data to reactor characteristics. In this latter area, important HTGR measurements are integral values of reactivity coefficients and of resonance absorption characteristics of fertile material.

References

1. P. R. Kasten, F. J. Homan, et al., Assessment of the Thorium Fuel Cycle in Power Reactors, report ORNL/TM-5565, Oak Ridge National Laboratory, January 1977.

2. P. R. Kasten, Gas-Cooled Reactors — The Importance of Their Development, report ORNL-5515, Oak Ridge National Laboratory, June 1979.

3. Y. I. Chang, C. E. Till, et al., Alternative Fuel Cycle Options: Performance Characteristics and Impact on Nuclear Power Growth Potential, report RSS-TM-4, Argonne National Laboratory, July 19, 1977.

4. B. Quan, C. Chen, et al., "Sensitivity of Alternative LWR Fuel Cycles to Data Uncertainties," TANSAO 32, 762 (1970).

5. J. Hardy, Jr., J. J. Ullo, N. M. Steen, "Integral Testing of Thorium and ^{233}U Data for Thermal Reactors," TANSAO 28, 714 (1978).

6. N. M. Steen, "Status of Nuclear Data for Th^{232} and U^{233}," TANSAO 28, 712 (1978).

Acknowledgment

Research sponsored by the U.S. Department of Energy, Division of Nuclear Power Development, under contract W-7405-eng-26 with Union Carbide Corporation.

DENATURED FUEL CYCLES

C. E. Till
Argonne National Laboratory
Argonne, Illinois 60439

This paper traces the history of the denatured fuel concept and discusses the characteristics of fuel cycles based on the concept. The proliferation resistance of denatured fuel cycles, the reactor types they involve, and the limitations they place on energy generation potential are discussed. The paper concludes with some remarks on the outlook for such cycles.

(denatured fuel, nuclear proliferation, once-through cycles, ^{233}U based cycles, denatured Pu)

The history of the concept of denaturing nuclear fuel goes all the way back to the early efforts that were made to find acceptable ways of handling nuclear energy in the postwar world. It first appears in the "Report on the International Control of Atomic Energy," commonly referred to as the Acheson-Lilienthal Report.[1] This report was released March 28, 1946. The report was the work of a board of consultants to the Department of State. This board of five members, chaired by Mr. David E. Lilienthal, chairman of the Tennessee Valley Authority, and including Dr. J. Robert Oppenheimer, were charged with considering "the problems arising as to the control of atomic energy" and "to study the subject of controls and safeguards necessary to protect this Government ..."

The report brings in the concept of denaturing with the following sentence, "^{235}U and plutonium can be denatured; such denatured materials do not readily lend themselves to the making of atomic explosives, but they can still be used with no essential loss of effectiveness for the peaceful applications of atomic energy." The report does not define the denaturant, and is in fact somewhat enigmatic on the whole subject. For it goes on to say that "... another case of an operation that we would regard as safe ... is the development of power from the fission of denatured ^{235}U and plutonium in high power-level reactors. Such power reactors might operate in the range from one hundred thousand to one million kW. If these fissionable materials are used in installations where there is no additional uranium or thorium they will not produce further fissionable material. The operation of the reactors will use up the material." The last two sentences particularly, leave the reader wondering about the nature of the denaturant contemplated.

A clarifying press release was issued April 9, 1946. The release first noted that after consultation with the Department of State, Major General L. R. Groves called together a group, representative of the outstanding scientists connected with the Manhattan Project during the development of the atomic bomb, and stated that the group had just completed a conference in which the measure of safety afforded by the use of denaturants was discussed. Their report read as follows:

"The possibility of denaturing atomic explosives has been brought to public attention in a recent report released by the State Department on the international control of atomic energy. Because, for security reasons, the technical facts could not be made public, there has been some public misunderstanding of what denaturing is, and of the degree of safety that it could afford. We have thought it desirable to add a few comments on these points. The report released by the State Department proposes that all dangerous activities in the field of atomic energy be carried out by an international authority, and that operations which by the nature of the plant, the materials, the ease of inspection control, are safe be licensed for private or national exploitation. The report points out the possibility of denaturing explosive materials so that they do not readily lend themselves to the making of atomic explosives may contribute to the range of licensable activities, and to the overall possibility of the proposed controls. The report does not contend, nor is in fact true, that a system of control based solely on denaturing could provide adequate safety."

"As the report states, all atomic explosives are based on the raw materials uranium and thorium. In every case the usefulness of the materials as an atomic explosive depends to some extent on different properties than those that determine its usefulness for peacetime applications. The existence of these differences makes denaturing possible. *In every case denaturing is accomplished by adding to the explosive an isotope, which has the same chemical properties.*+ These isotopes cannot be separated by ordinary chemical means ..."

"For the various atomic explosives the denaturing has a different effect on the explosive properties of the materials. In some cases denaturing will not completely preclude making atomic weapons, but will reduce their effectiveness by a large factor. The effect of the denaturant is also different in the peacetime applications of the materials. Further technical information will be required, as will also a much more complete experience of the peacetime uses of atomic energy and into economics, before precise estimates of the value of denaturing can be formulated. But it seems to us most probable that within the framework of proposals advanced in the State Department report denaturing will play a helpful part."

So it is clear that it was isotopic denaturing, the same as is being considered once again today, that the authors had in mind. With the failure of the internationalization proposals over the next year or two, however, the concept of denaturing seems to have faded into the background as nuclear energy development proceeded.

Some 30 years later, in 1976, the notion was picked up again and expanded upon by Theodore Taylor and others at Princeton. First in their influential articles in the bulletin of Atomic Scientists,[2] and later in a monograph entitled, "Nuclear Proliferation,"[3] they proposed an international reactor deployment system wherein the main fissile material would be ^{233}U, bred from thorium, and diluted with the naturally abundant isotope ^{238}U to such an extent as to make the mixture unsuitable for weapons without isotope separation. At maturity the system would consist of two classes of facilities: national reactors and a few international fuel cycle support centers. The national reactors "would operate on a fresh fuel mix of something like one part ^{233}U, six parts ^{238}U and 10 to 60

*This work performed under the auspices of the U.S. Department of Energy.
+Italics mine.

parts thorium. The six to one ratio ^{238}U to ^{233}U would probably be sufficient for practical purposes to denature the ^{233}U, so that the denatured uranium, both in the fresh fuel assemblies and the spent fuel would not be suitable for weapons material. There would be some plutonium in the spent fuel produced by neutron capture in the ^{238}U diluent but only somewhere between a fifth and a tenth as much as present fuels, and less a tenth as much in plutonium breeder fuel, for the same amount of power.

The international fuel cycle support center would reprocess all spent fuel from national reactors and would undertake all fabrication and denaturing of fresh fuel assemblies to be sent to the national plants."

The authors also however go on to note, "Since it is unlikely that the current types of nuclear power plants could breed sufficient amounts of ^{233}U to allow them to be self-sustaining on a thorium cycle if the recycle ^{233}U is denatured with ^{238}U, the internationally controlled centers at which the fuel is reprocessed would also have to provide some additional source of ^{233}U." And that "one possibility is fast breeder reactors that use plutonium extracted from the converter reactor fuels in their cores and thorium as the fertile materials in the breeding blankets. Such reactors could produce more ^{233}U than the plutonium they consume. All recycled plutonium could in this fashion consumed on site at the centers, avoiding the need for any national access to plutonium free from fission products."

On April 7, 1977, the Presidential nuclear power policy statement was released. It had as its third point, "We will redirect funding of the U.S. Research and Development programs to accelerate our research into alternative nuclear fuel cycles which do not involve direct access to materials usable in nuclear weapons." The studies set under way by new policy, in effect defined "alternative nuclear fuel cycles" by the presence of denaturing. Alternative cycles in these studies were of two types. One type were variants based on ^{233}U/thorium cycles, and the other, variants of the current ^{235}U once-through cycle.

The possibility of plutonium denaturing was also implied in the Acheson-Lilienthal report, and has been raised again from time to time over the past year or two. Plutonium denaturing though has not received the attention that fissile uranium denaturing has been given. The reason is quite simple. Reactor produced plutonium is always a mixture of the fissile isotopes, ^{239}Pu and ^{241}Pu, and the fertile isotopes, ^{240}Pu and ^{242}Pu. The proportions of each are set largely by the reactor performance and fueling requirements, and in practical situations the fissile fraction will predominate. While high concentrations of ^{240}Pu in particular make the material less desirable for weapons purposes, it appears to be impossible to rule out its usefulness on the basis of normal reactor ^{240}Pu concentrations. Further, increasing the amount of ^{240}Pu and ^{242}Pu by selective repetitive recycle sharply limits the amount of such fuel and thus its applicability. A variant of the idea is to decrease the usability by attempting to increase the ^{238}Pu content -- the latter is a minor constituent of reactor-produced plutonium that has the property of relatively high heat generation. However, it is not produced in appreciable fractions in fast breeder fuel cycles, and as the great incentive for using plutonium derives from its use in the breeder it is difficult to assign high importance to the plutonium denaturing ideas.

Uranium-denatured fuel cycles have been examined extensively in the studies of the past year or so. Their general characteristics can be divided into three general classes. First, their proliferation resistance, second, the reactor types they involve, and third, their energy generation potential.

A. Proliferation Resistance

The entire reason for considering denatured fuel cycles is based on the hope of improving proliferation resistance. It is important therefore that the relative effectiveness for many decades in the future of isotopic denaturing for this purpose be rigorously examined. The fact that the fissile uranium isotopes can be mixed with the fertile isotope ^{238}U such that isotopic separation techniques are required to separate fissile material from fresh reactor fuel is considered to be the key property. As isotope separation techniques, for the present at least, are considered to be more difficult than chemical reprocessing techniques, an increase in proliferation resistance may be assigned. The degree of the increase is the important point. Centrifuge techniques are coming on the scene now and more advanced isotopics separation technologies are probable in the future. Whether, in the face of this, a significant advantage should be assigned to denaturing is the real question. In any event, the situation differs somewhat for the two basic denatured cycles.

Once-Through Cycles: In the once-through cycle, ^{235}U contents are no more than a few percent of the ^{238}U content in the fresh fuel, so that the isotopic denaturing present is more than sufficient. Problems exist, however, at both the front and back ends of the cycle. For LWR's, or in fact for any converter reactor except the heavy water reactor, enrichment facilities are required (and even heavy water reactors would benefit from enrichment). The presence of the enrichment facility gives the capability for separation of pure ^{235}U. Also, at the other end of the cycle, spent fuel, containing plutonium, accumulates and the burden is placed on arrangements for satisfactory retrieval (if in a sensitive location), safeguarding and storage of continuously increasing amounts of such fuel. Although spent fuel initially is highly radioactive, its activity decreases as time passes and after a period of years it becomes fairly accessible.

^{233}U Based Cycles: In any cycle that uses artificially created fissile isotopes to fuel reactors, reprocessing remains an essential component of the cycle and the ^{233}U cycle is no exception. The denaturant concentrations discussed in most studies involve ^{238}U contents about seven times the ^{233}U content. The uranium is then mixed with thorium. For startup, where ^{235}U is used, the denaturant concentration is normally taken to be four parts ^{238}U to one part ^{235}U. In converter reactors these mixtures allow thorium to remain the main fertile species in the fuel. Reactor operation produces ^{233}U from thorium but also produces plutonium from the ^{238}U denaturant. In the case of ^{233}U, some small amount of additional proliferation resistance may be assigned due to the presence of radiation from the decay of the ^{232}U that is always present in such fuel. However, the important point is that the reprocessing step remains a requirement in this cycle.

Further, the combination of the increased mass difference between $^{233}U/^{238}U$ and $^{235}U/^{238}U$, the smaller critical mass of ^{233}U than ^{235}U, and the feed materials starting at a 12% fissile level instead of a 3 or 4% fissile level, makes the separation of equivalent amounts of weapon usable material in the ^{233}U

cycle is at least an order of magnitude easier than it would be starting from current LWR fuel.

B. Reactor Types

The types of reactor that can effectively use denatured cycles follow directly from the basic nuclear properties of ^{235}U and ^{233}/Th: Thermal reactors are implied. This is not to say that fast reactors could not operate on a ^{233}U/Th cycle. In principle, of course, they could, but the basic nuclear properties of ^{233}U and thorium sharply limit breeding properties in a fast reactor, and the incentive to undertake the effort to develop and deploy the fast breeder under these circumstances would be correspondingly limited. Further, a fast breeder ^{233}U/Th cycle would require reprocessing efforts of a very similar kind to those required for the plutonium/^{238}U cycle. In effect, the only real change would be the substitution of ^{233}U for plutonium, but still in a very similar cycle and any gain from the viewpoint of non-separability of fissile material would certainly be small, and in all likelihood it would be non-existent.

Once-through cycles are still less suited to any version of the fast reactor that has yet been shown to be feasible. The higher initial enrichments of the fast breeder, compared to thermal reactors, and the correspondingly higher fissile contents discharged in spent fuel give net fuel utilizations that are much worse than those for the present day LWR, much less for any improved version. Mixes of reactor types that include some fast breeders and some thermal reactors operating on alternative cycles, termed "symbiotic cycles," are possible and from one class of suggested means for balancing energy production requirements and non-proliferation goals. But if denatured cycles alone are considered, unless there are breakthroughs in fuel irradiation technology, it is almost certain that thermal reactors alone are involved.

In thermal reactors once-through cycles tend to rule out thorium use. A once-through cycle implies ^{235}U fissile fueling, with thorium as the main fertile element in place of ^{238}U. The higher neutron absorption of thorium, a fundamental nuclear property, requires higher initial enrichments to maintain reactor operation. In any calculation of the resulting fuel utilization in practical thermal reactor types that I am aware of, the resulting fuel utilization is invariably worse than for the corresponding $^{235}U/^{238}U$ once-through cycle. The reason is the same as in the fast reactor case, although to lesser degree. In both the fissile contents in the discharged fuel remain high and too much fissile material is discarded in the spent fuel.

The reference to breakthroughs in fuel technology was made for the following reason. The only way that the once-through cycle even in concept could overcome the limitations just described would be through breakthroughs in fuels and materials technology to allow extremely long fuel burnups. The same principle would hold for both thermal reactors using thorium as its fertile material or a fast reactor fueled with ^{235}U and using ^{238}U as its fertile material. Very long burnups could in principle convert substantial quantities of fertile material to fissile (thorium to ^{233}U to plutonium in the fast reactor case) and then burn a large amount of it in place. Enough would have to be burned in place to make up for the large amount of fissile that would be discarded in the spent fuel. In either a fast or a thermal reactor version the basic design problem would be similar. First, the conversion or breeding properties would need to be as high as possible (to efficiently convert fertile to fissile) and second, the burnups or reactor residence times would need to be as long as possible in order to extract sufficient energy from the bred fissile that the effects both of high initial inventory requirements and high fissile contents in the spent fuel would be overcome. These two design requirements tend to conflict. Further, in the fast reactor case at least, the irradiations that the fuel would have to undergo are far out of the range of any existing experimental data indicating feasibility.

Thus apart from reactor concepts based fundamentally on speculations of very long burnups, the only way that substantial gains in fuel utilization are possible is by reprocessing. This is specifically true for the ^{233}U/thorium cycle in thermal reactors.

With such reprocessing, substantial gains in fuel utilization over the current once-through cycle are possible. Net ^{235}U consumptions half of those of the current once-through cycle are probably easily achievable, and consumptions down to a quarter of the current once-through cycle are possible, at least in principle. In all these denatured fuel reactor designs there is a trade-off between fuel utilization, on one hand, and inventory and burnup on the other, and therefore in the amount of reprocessing required annually. In all, reprocessing is fundamental.

C. Energy Generation Potential

The most fundamental point of concern about the alternative cycles is the limitation they impose on the amount of energy that can be produced by nuclear power. Denatured cycles are net consumers of fissile material and their use alone implies a net drain on the world supply of fissile material. Put another way, the amount of nuclear power production possible is more or less directly dependent on the world supply of natural uranium. Thus in a fundamental sense, the alternatives to the reference uranium-plutonium cycle can be said to reflect alternative views of the necessary or desirable role of nuclear power. If a fairly limited role for nuclear power is envisaged denatured cycles may well suffice. On the other hand, if the magnitude of nuclear power production is not to be limited by the uranium resource base, true breeding is necessary and the uranium-plutonium cycle is almost undoubtedly required.

Another general point, useful to keep in mind, is that the three main reactor deployment possibilies -- the once-through cycle, the denatured ^{233}U/Th cycle, and the breeder reactor -- are, by their inherent characteristics, explicitly suited to one or other quite specific scenario for the future of nuclear power. Each reactor deployment strategy will suffer by comparison when applied to an energy scenario that is specifically suited to one of the other alternatives. It is important in assessing the meaning of comparisons of the resource utilization efficiency of various alternative reactor development strategies that this be understood. Simply, the breeder shows to best advantage in scenarios that contemplate exponential rises in nuclear electrical energy production and an essentially unlimited future; the denatured ^{233}U/Th cycles show to best advantage in scenarios that contemplate a leveling off in nuclear power production after a period that can include a relatively rapid rise, and once-through cycles are suited to scenarios that contemplate nuclear power production as a passing phase, possibly of considerable length, but nevertheless eventually phasing out.

The scenario that is seen in some recent policy-related papers is the second one, that is, the denatured cycle nuclear power leveling-off scenario. The characteristics of thermal reactors using denatured $^{233}U/Th$ cycles, i.e., rather high initial inventory requirements, but not as high as the fast breeder, and relatively small refueling requirements, are specifically suited to this scenario. Put another way, if one wishes to make a case for these cycles, the scenario for nuclear power that one should chose is such a plateau scenario. The breeder, when applied to this scenario, suffers greatly in the comparison, as a relatively rapid rise in nuclear capacity penalizes the breeder through its high inventory requirement and a short time period for rising capacity does not allow time for the breeding characteristics of the system to be of much help. Further, when sufficient time has passed that the doubling characteristics of the breeder are starting to become important such a scenario contemplates a leveling off of nuclear power production so the excess fissile material generated by the breeder is of little importance.

D. Outlook for Denatured Cycles

The rationale for denatured cycles rests on their possible application to increase in proliferation resistance. Most I think would agree that isotopic separation at the moment is more difficult, and may remain somewhat more difficult in the long run, than chemical reprocessing. For this reason the fissile content of denatured fuel is likely to be somewhat less accessible than plutonium contained in uranium. The magnitude of this difference and the importance to be assigned to it, however, is of course, the difficult point. I think most now would agree that insofar as the fresh fuel is concerned, standard LWR fresh fuel should be assigned somewhat more proliferation resistance than ^{233}U denatured fuel and it in turn somewhat more than plutonium/^{238}U. The differences, however, taking into account the entire fuel cycle, are probably not very significant when compared to alternative institutional arrangements for nuclear power deployment. This last statement would not be agreed to by everyone, but I think one would find nearly unanimous agreement to it in the reactor technical community.

Denatured cycles, if they are to lead to significant improvements in uranium resource usage over the present once-through cycle, must have reprocessing for any reactor types that have currently been shown to be feasible. Without reprocessing, fundamental breakthroughs in fuels and material technology to allow extremely long fuel burnups would be required for even conceptual feasibility. As long as reprocessing is present in any case, the denatured cycles offer little obvious advantage over Pu/^{238}U cycles.

The denatured cycles all impose a penalty on the amount of energy that can be produced from given uranium resources. The denatured cycles themselves are consumers of fissile material and their use alone implies a net drain on the world supply of fissile material. Thus they reduce the energy generation potential and to make up for this they must have a very substantial advantage in proliferation resistance. Because this does not appear to be the case, the future of the denatured cycle based on ^{233}U thorium does not appear to me to be very bright. My suspicion is that the thorium cycle, when and if it arrives, will come because of its technical merits and the wish to utilize the thorium resources rather than on the basis of superior proliferation resistance. The current once-through cycle, of course, will continue for some time. But even with postulated improvements in the LWR, and reduction in the isotopic tails assays, the period over which the once-through can satisfy world nuclear energy needs is likely to be of the order of the lifetime of existing reactors, unless large new supplies of uranium are discovered. Thus although it may still be too early to say for certain, there is little to point to that would suggest any gathering momentum in the direction of denatured cycles.

References

1. D. E. Lilienthal, C. I. Barnard, J. R. Oppenheimer, C. A. Thomas, and Winne, A Report on the International Control of Atomic Energy, Department of State Publication 2498 (March 16, 1946).

2. H. A. Feiveson, T. B. Taylor, F. von Hippel, and R. H. Williams, The Plutonium Economy, The Bulletin of the Atomic Scientists (Dec. 1976).

3. T. Greenwood, H. A. Feiveson, and T. B. Taylor, Nuclear Proliferation, 1980's Project/Council of Foreign Relations, McGraw Hill (1977).

THE USE OF THORIUM IN FAST BREEDER REACTORS

D. E. Bartine
Oak Ridge National Laboratory
Oak Ridge, Tennessee 37830, USA

Recently several fuel cycles involving thorium have been suggested for use in fast breeder reactors. These cycles involve the use of thorium in fuels containing ^{233}U and fissile plutonium and the use of both internal and conventional thorium blanket elements. Studies were performed in the Engineering Physics Division at ORNL to determine the performance of fast breeder reactors utilizing such cycles. In addition, there is a current effort toward analyzing reaction rates, spectra, and integral measurements of prototypic fast reactor configurations involving thorium. These experiments were performed at the PROTEUS facility of the EIR laboratory at Würenlingen, Switzerland, and at the Tower Shielding Facility at ORNL. The analysis of these experiments provides insight regarding data needs for fast reactor applications involving the thorium cycle.

Results of the fast breeder fuel cycle analysis indicate a significant penalty from replacing Pu/UO_2 fuel with $U\text{-}233/ThO_2$ fertile blanket elements. Preliminary analysis of the experiments indicates improved agreement with neutron spectra involving deep penetration in ThO_2 radial blankets by utilizing ENDF/B-V thorium cross section data as compared with ENDF/B-IV. However, thorium capture rates now appear significantly underpredicted.

[Thorium, fast reactors, symbiosis, integral and critical experiments, cross sections.]

Introduction

Interest in the use of thorium in fast breeder reactors (FBR's) has increased in recent years, primarily due to the fissile advantages of uranium-233 as a thermal reactor fuel and to potential capital cost advantages for thermal reactors over FBR's. This perceived capital cost differential makes a symbiotic fast-thermal reactor system based on the thorium fuel cycle in which fast reactors would produce excess fuel for consumption in thermal reactors, more desirable than in an all-fast reactor plutonium cycle system.

A series of studies were performed at ORNL as part of the NASAP studies[1] to characterize the behavior of various reactor types on the thorium fuel cycle, both separately and as part of fast-thermal symbiotic systems. In addition, experiments have been conducted at ORNL and at the EIR in Switzerland and analyzed at ORNL to determine the ability of the current cross section data to predict reaction rates and neutron spectra in the presence of thorium in FBR's.[2,3]

This paper presents an overview rationale for the use of thorium in symbiotic systems along with some results from the ORNL studies and then briefly comments on the status of the current thorium cross section data as inferred from the experimental analysis presented by the two following papers and the possible effects of this data on the symbiotic calculations performed at ORNL.

Thorium Performance in FBR's

Basically, the properties of the two fissile materials which can be bred in fast reactors favor use in systems with different energy spectra. Fissile plutonium (bred from uranium-238) is the best fissile material in a fast reactor spectrum. Uranium-233 (bred from thorium-232) is the best fissile material in a thermal reactor spectrum. This leads one to investigate the possibility of using fissile plutonium as a fuel in fast reactors which contain thorium-232. The uranium-233 produced would then be used to fuel thermal reactors. This symbiotic system could also be economically advantageous, since thermal reactors may have a capital cost advantage over fast reactors. If this is the case, economics would lead to maximizing the number of thermal reactors in the fast-thermal mix, while retaining sufficient fast reactors to satisfy anticipated electrical growth rate demands. Table 1 indicates the performance of a typical homogeneous FBR with various fissile-fertile material combinations. It is clear that replacing the traditional plutonium-uranium cycle with fissile uranium-233 and fertile thorium-232 results in a fairly severe decrease in the calculated breeding ratio. Specifically, in replacing plutonium with uranium-233 as fuel, the breeding gain for the system is about cut in half (breeding ratio reduced ~20 points). Additionally, replacing the uranium-238 with thorium-232 as the fertile material in the fuel elements further reduces the breeding gain (breeding ratio reduced ~15 points). Significantly, the blanket composition does not strongly effect system performance (replacing uranium-238 in the axial and radial blankets reduces the breeding ratio ~5 points). It should be pointed out that these calculations were performed with ENDF/B-IV cross sections and that most calculations of uranium-238 capture[4] tend to overpredict plutonium breeding by 5-10% compared with measurement.

ORNL-DWG 77-15104

TABLE 1. FBR BREEDING RATIOS FOR VARIOUS FISSILE AND FERTILE MATERIAL COMBINATIONS

CORE	AXIAL BLANKET	RADIAL BLANKET	BREEDING RATIO (BOL)
$Pu/^{238}UO_2$	$^{238}UO_2$	$^{238}UO_2$	1.42
$Pu/^{238}UO_2$	$^{238}UO_2$	ThO_2	1.39
$^{233}U/^{238}UO_2$	$^{238}UO_2$	ThO_2	1.14
$^{233}U/^{238}UO_2$	ThO_2	ThO_2	1.12
(20%) $^{233}U/^{238}UO_2 + ThO_2$	ThO_2	ThO_2	1.05
(40%) $^{233}U/^{238}UO_2 + ThO_2$	ThO_2	ThO_2	1.03
$^{233}U/ThO_2$	ThO_2	ThO_2	1.02

Heterogeneous reactor core configurations (using fertile elements as "internal blankets" within the core) can significantly improve the fissile balance, as indicated in Fig. 1. The uranium-thorium cycle is essentially break-even for the homogeneous system, while the heterogeneous system creates a modest surplus of uranium-233. Using plutonium-uranium fuel elements and thorium blanket assemblies also shows a modest fissile gain for uranium-233 for a homogeneous system. The corresponding heterogeneous system indicates a large gain in fissile uranium-233, but is operating at a plutonium deficit of about half the uranium-233 gain. This deficit would need to be made up by plutonium produced in other reactors in the system (thermal or fast), or possibly by substituting uranium-238 fertile assemblies for some of the thorium-232 assemblies in the core, which is possible with the flexibility inherent in the heterogeneous design. The plutonium-thorium cycles show large uranium-233 production coupled with large plutonium usage as expected, since the cycle is fueled with plutonium while breeding uranium-233. The homogeneous plutonium-thorium cycle produces about as much uranium-233 as the heterogeneous plutonium-uranium fuel, thorium blanket case, but has about twice the plutonium deficit. The heterogeneous plutonium-thorium case shows the same trends as the homogeneous, but with increased uranium-233 production and a slightly greater plutonium deficit. Overall, the FBR with plutonium-uranium fuel and thorium blankets seems to have the most promise for a net fissile producer, especially in the heterogeneous mode if the plutonium deficit can be made up by other reactors in the system.

ORNL-DWG 78-22762

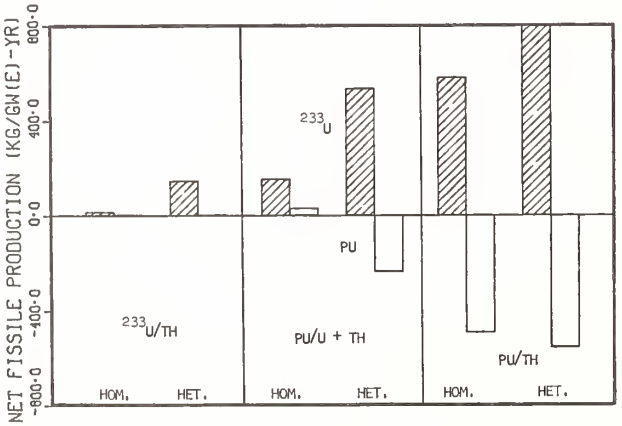

Fig. 1. Fissile balance for three homogeneous and heterogeneous oxide FBR systems.

Symbiotic Systems

To illustrate how such a system might be structured, consider a mix of fast reactors operating in conjunction with a mix of thermal reactors.[4,5] The fast reactors are all fueled with plutonium oxide, but contain varying fertile materials (uranium oxide, thorium oxide, or a mixture). The thermal reactors are fueled with uranium-233 and can also contain either uranium-238 or thorium-232 as fertile material. The overall system comprising these reactors will be characterized by two fundamental parameters--the thermal/fast support ratio and the growth rate. Figure 2 illustrates a generalized operational envelope for such a system, indicating the constraints under which the fissile mass flows are "balanced" so that the thermal/fast support ratio remains constant as the total system power increases or decreases, as indicated by the growth rate. Point A represents an all-fast plutonium-uranium system which has the highest potential system growth rate, since it has the highest breeding gain (produces excess plutonium) but supports no thermal reactors since it produces no uranium-233. Point C represents a system containing only plutonium-thorium FBR's coupled with thermal reactors. This situation gives the maximum thermal/fast ratio within the operating envelope since it produces the most uranium-233 but has a negative growth rate (system power declining) due to a deficit of plutonium. Point B represents a system with fast reactors containing plutonium-uranium fuel and thorium blanket assemblies coupled with thermal reactors to give a mixture which allows some limited growth, and also allows a reasonable thermal/fast support ratio. The lines connecting points A, B, and C define the operational envelope. Any point on these lines corresponds to a given mixture of the two FBR's represented by the line end points. For example, the line A-B represents a mixture of plutonium-uranium FBR's (A) and plutonium-uranium fueled, thorium blanketed FBR's (B). As the point A is approached, the number of type "A" reactors increases relative to type "B." The reverse is true as one approaches point B.

It is important to note that the envelope formed by lines AB, BC, and AC represents the range of FBR mixes under which this system is stable. Every point within the envelope corresponds to a given mixture of type A, B, and C FBR's and has a defined system growth rate and thermal/fast support ratio. The units shown on Fig. 2 are arbitrary and intended only to give a feeling for the way the system parameters interact. To determine specific values it is also necessary to specify the associated thermal reactor mixture. For example,[6] if conventional LWR's are used, thermal/fast support ratios vary from ∿0.5 at 0 growth up to 1.5. On the other hand, if advanced converter systems are utilized such as the high temperature gas-cooled reactor (HTGR) or the pebble bed reactor (PBR), support ratios can vary from ∿2 at 0 growth up to ∿6.

ORNL-DWG 78-6735 R

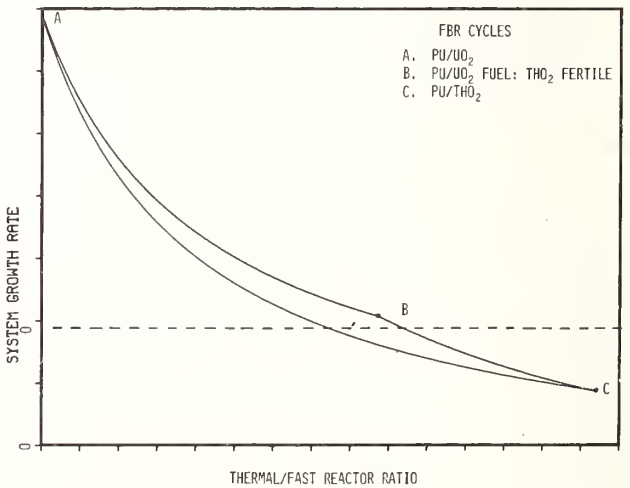

Fig. 2. Typical operating envelope for a system comprising a mixture of heterogeneous FBR's and thermal reactors.

Thorium Cycle Disadvantages

However, several disadvantages should also be pointed out for the use of thorium in FBR's. The plutonium-uranium fuel cycle is much nearer commercialization, and in order to insure that the projected benefits are worth the increased research and development (R&D) requirements and the resulting increased complexity of operating both PUREX and THOREX reprocessing cycles, it will probably be necessary to commit the R&D required to commercialize advanced converters. This is more difficult in view of the limited growth capability of a mixed fast-thermal system as opposed to an all-fast system, although it is not certain that the growth rate represented by an all-fast system will be required.

Thorium Cross Sections

Several thorium cross sections are important in fast reactor evaluation:

capture	- for breeding estimation;
fission	- for power determination;
(n, 2n')	- for uranium-232 production;
γ production	- for heating, especially at core/blanket interfaces;
inelastic	- for determining the neutron spectrum which in turn determines reaction rates and the blanket leakage spectrum for shielding calculations.

The Engineering Physics Division at ORNL has been investigating the status of thorium cross sections for FBR application. A GCFR thorium radial blanket integral experiment has been performed at the Tower Shielding Facility (TSF) at ORNL which measured neutron spectra, Bonner ball response to neutrons, and gamma heating. In addition, ORNL has been involved in a cooperative analysis of a simulated GCFR-core lattice measurements involving thorium at the PROTEUS facility at the EIR, Switzerland. Reaction rates were measured, (especially for thorium and uranium-233), as were neutron spectra. The ORNL and EIR experiments are described in detail in the following two papers,[2,3] respectively, so only a brief overview of selected results will be presented here.

The neutron spectrum emerging from two- and three-row blanket configurations at the TSF was measured down to ~0.1 MeV. Good agreement with the measured spectra was obtained when ENDF/B-V thorium-232 data was used instead of ENDF/B-IV. However, agreement with Bonner ball measurements decreased with decreasing energy. The most significant result of the analysis of the EIR data is that changing from ENDF/B-IV thorium to ENDF/B-V worsened the calculated/experimental ratio for thorium capture/plutonium fission from about 0.95 to about 0.88. It should be noted that the neutron spectra peaks from about 1 kev to 1 MeV, and the most important region for capture in thorium in FBR's is from 10 kev to 100 kev. Also, the EIR measurements cited here were taken in lattices dominated by plutonium and uranium oxide, so the measurements represent infinite dilute spectra.

Thus, initial results seem to indicate that improvements to the current cross sections could increase thorium capture rates and thus improve the breeding performance in FBR's of thorium-232 relative to that of uranium-238. However, further work will be necessary to clarify this situation. Sensitivity studies will be performed on the lower-energy Bonner ball results to determine if the observed disagreement indicates that the thorium capture cross section might be too low. Analysis of EIR results in a thorium-dominated spectrum will be performed to investigate the effects of resonance self-shielding.

Conclusions

The use of fissile uranium-233 and fertile thorium-232 in FBR's results in significantly lower breeding ratios than those achieved with the conventional plutonium-uranium fuel cycle. However, replacing uranium-238 radial blanket elements with thorium-232 assemblies doesn't cause a major perturbation and results in the production of uranium-233, which is an excellent fuel for thermal reactors. This makes possible the creation of fast-thermal symbiotic reactor systems, which have the potential advantage of lower system capital costs at the expense of potential system growth rate.

Analysis of recent experimental measurements at ORNL at EIR, Switzerland, indicate the possibility of increased thorium breeding in FBR's due to improved cross section data. Additional investigation is required in order to verify this possibility, specifically in the area of resonance self-shielding effects.

Acknowledgment

Research sponsored by the Reactor Research and Technology Division, U. S. Department of Energy under contract W-7405-eng-26 with the Union Carbide Corporation.

References

1. Interim Assessment of the Denatured ^{233}U Fuel Cycle: Feasibility and Nonproliferation Characteristics, ed. by L. S. Abbott, D. E. Bartine, T. J. Burns, ORNL-5388 (December 1979).

2. D. T. Ingersoll, "Deep Penetration Integral Experiment for a Thorium Blanket Mockup," paper presented at International Conference on Nuclear Cross Sections for Technology, October 22-26, 1979.

3. J. R. White, et al., "Analysis of a Swiss Thorium Blanket Integral Experiment," paper presented at International Conference on Nuclear Cross Sections for Technology, October 22-26, 1979.

4. Sensitivity Analysis of TRX-2 Lattice Parameters with Emphasis on Epithermal ^{238}U Capture, EPRI NP-346 (March 1977).

5. C. R. Weisbin, et al., Application of FORSS Sensitivity and Uncertainty Methodology to Fast Reactor Benchmark Analysis, ORNL/TM-5563 (December 1976).

6. T. J. Burns and J. R. White, Preliminary Evaluation of Alternative Fuel Cycle Options Utilizing Fast Breeders, ORNL-5389 (October 1978).

DEEP PENETRATION INTEGRAL EXPERIMENT FOR A THORIUM BLANKET MOCKUP

D. T. Ingersoll and F. J. Muckenthaler
Oak Ridge National Laboratory
Oak Ridge, Tennessee 37830, USA

An integral experiment has been performed for verification of radiation transport methods and nuclear data used for design of the radial shield for the gas-cooled fast breeder reactor (GCFR). The experiment included a thorium oxide blanket mockup and several shield configurations. The blanket measurements were needed to reduce uncertainties in the cross-section data used for calculating neutron transmission through a thorium blanket and to bound the uncertainties in calculated gamma-ray heating rates within the blanket.

Measured neutron spectra and integral flux data are compared to 1D calculations of the transmitted flux. Calculations using ENDF/B-IV and ENDF/B-V data for thorium are compared and show the version V data to be superior above 1 MeV. The experiment, which is primarily sensitive to the total removal cross section, also showed V to be an improvement below 1 MeV, but still discrepant from the measurements.

[Thorium, total cross section, integral experiment, GCFR, blanket, neutron transmission.]

Introduction

The design of reactor shielding is a complex effort involving intimate relationships between radiation transport, thermomechanical forces, material properties, and economics. To aid the shield designer in achieving the optimum compromise of these considerations, several analytic tools have been developed such as discrete ordinates and Monte Carlo codes. For advanced reactors, where little operating experience is available, verification of these design methods and the design-based data is important. Integral experiments perform this function by (1) providing data against which the methods and data can be tested or (2) providing direct verification of the effectiveness of the final design.

An integral experiment was designed for the verification of radiation transport methods and nuclear data used for the design of the radial shield for the proposed 300 MW(e) gas-cooled fast breeder reactor (GCFR).[1] The scope of the experiment was chosen to include a thorium oxide radial blanket mockup as well as several shield configurations. The blanket measurements are needed to reduce the large uncertainties which exist in the cross-section data required for calculating neutron transmission through a thorium blanket, hence reducing the uncertainties in the calculated source terms for the radial shield. Similarly, the shield measurements are needed to reduce the uncertainties in the calculated radiation damage to the prestressed concrete reactor vessel. Additionally, the measurements are intended to bound the uncertainties in calculated gamma-ray heating rates within the blanket and shield. Although designed specifically for the GCFR, the experiment provides generic data regarding deep penetration in ThO_2 and common shield materials, which also benefits LMFBR designers.

The experiment is currently being analyzed using primarily one- and two-dimensional discrete ordinates methods. The purpose of this paper is to describe the experiment and measurements, and to present significant results from the analysis of the blanket configurations.

Experiment Design

The experiment was performed at the ORNL Tower Shielding Facility (TSF), and consisted of measurements behind one-dimensional mockups of a GCFR-type radial blanket and radial shield. Both integral and spectral measurements were made of the neutron and gamma-ray flux transmitted through successive material configurations and compared to corresponding calculations of the radiation transport. The collimated neutron source from the TSF reactor[2] was first directed through a spectrum modifier to produce a neutron energy distribution typical of a GCFR. The modified source then penetrated the experimental assemblies which consisted of 150- by 150-cm slabs of blanket and shield material placed perpendicular to the neutron beam centerline. Figure 1 shows the experimental geometry for the case of a three row ThO_2 blanket mockup. One of the three 15-cm-thick slabs of ThO_2 (density of 7.2 g/ml) was fabricated as two 7.5 cm-thick slabs in order to make measurements in 1/2-row increments. The concrete shown in Fig. 1 which surrounds the configuration provides a biological shield for the TSF personnel, while the lithiated paraffin minimizes the contribution of neutrons

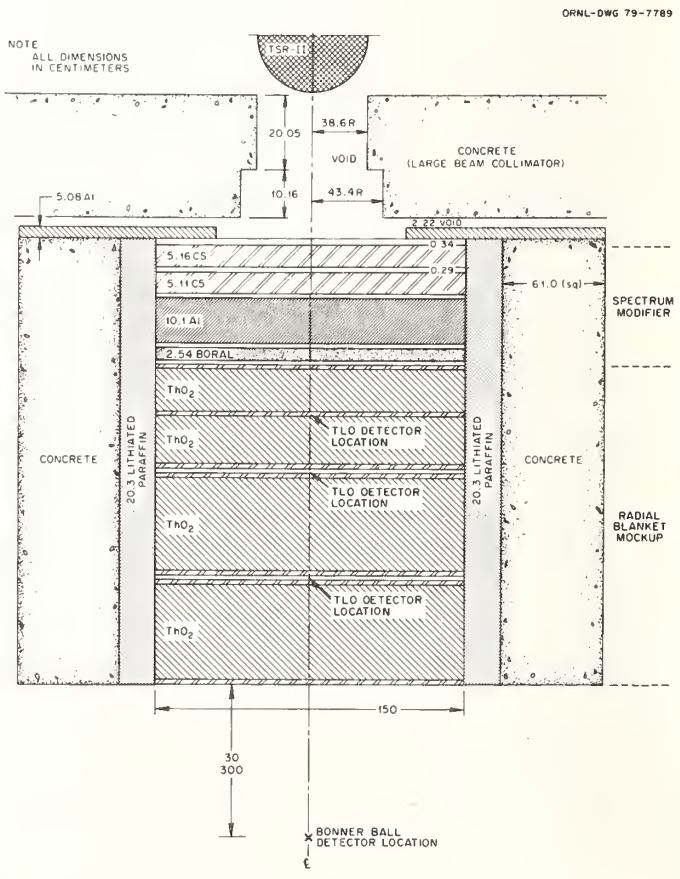

Fig. 1. Plan view of ThO_2 blanket configuration.

which reflect from the concrete back into the test assembly.

In addition to the ThO_2, measurements were made behind 30 cm of UO_2 and numerous arrangements of shielding material consisting of up to 95 cm of stainless steel, graphite, and boronated graphite. The measurements were made using Bonner balls (BB) for integral neutron flux measurements, NE-213 and hydrogen counters for fast neutron spectra measurements, NE-213 for gamma-ray spectra measurements, and thermoluminescent dosimeters (TLD) for gamma-ray heating measurements. All detectors were positioned on the reactor beam centerline, and were located behind the configurations except for the TLDs which were sandwiched between the blanket and shield slabs.

Analysis

Complete analysis of the blanket and shield measurements will consist of one-dimensional (1D) fine-group and two-dimensional (2D) semifine-group transport calculations of the neutron and gamma-ray fluxes throughout the experimental configurations. The calculated fluxes are used with energy-dependent response functions to predict the observed data from the BB and TLD measurements, and are compared directly to the reduced data from the spectrometer measurements. Since the analysis of the full experiment is currently in progress, results based only on the 1D calculations of the blanket mockups will be presented here. There is much information to be learned from the 1D analysis, however, since the slab design of the experiment intentionally lends itself well to 1-D methods. Also, results from the blanket measurements are of immediate interest since they provide a comparison of the adequacy of thorium data for deep penentration problems typical of reactor physics and shield design calculations.

Analytic Approach

The one-dimensional calculations were performed using the ANISN discrete ordinates transport code.[3] Coupled neutron-gamma-ray cross sections with 171-neutron and 36-gamma-ray energy groups and a P_3 order of expansion were specially prepared for this analysis from the ORNL Vitamin C cross section library[4] and from ENDF/B-V data files for thorium-232. The cross sections were processed using the AMPX-II code system[5] which performed the necessary resonance self-shielding, the neutron-gamma-ray coupling, and the reformatting required to produce an ANISN cross section tape.

The neutron source spectrum was obtained by interpolation of the previously determined 51-group S_{16} angular source[2] on a per unit lethargy basis for each of the 8 forward-directed angles. A similar procedure was used to obtain fine-group response functions from the 51-group Bonner ball responses[6] and the 51, 25-group TLD responses. The experimental configurations were modeled from the TSF boundary source through the spectrum modifier and the blanket slabs. A symmetric S_{16} quadrature was used and mesh intervals were made less than 1 cm.

Calculation of Observed Data

The observed responses of the Bonner balls and the TLDs were determined by folding the calculated fluxes with the corresponding detector response functions. Since the 1D slab geometry does not account for the geometric attenuation of the flux, an absolute comparison between the calculated and measured data can not be made. It is possible, however, to draw several conclusions from the relative comparisons.

The spectrometer pulse height data were converted in a data-reduction process to yield spectra data which could be compared directly to the calculated flux spectra, except for the normalization limitation described above. However, before comparing the calculated and measured spectra, it was appropriate to first smooth the calculation with the approximate resolution of the spectrometer. Also, since the detectors were located several meters behind the configurations, it was felt that the neutron leakage for the forward-most angle at the exit of the calculation was a better approximation to the observed flux. Therefore, all of the calculated results presented below are given as the forward angle leakage.

Results

A comparison of the calculated leakage and the NE-213 neutron flux measurement is given in Fig. 2 for the case of the full UO_2 blanket mockup. With the calculation normalized to give the same integrated flux as the measurement between 3 and 12 MeV, it is apparent that the agreement in the spectral shape is excellent. The only significant discrepancy is between 2 and 4 MeV, but this discrepancy merely suggests that the actual detector had a poorer resolution in this energy range than was used to smooth the calculation. The normalization of the calculated spectrum is substantiated, in part, by a comparison of calculated and measured Bonner ball responses where the detectors were located at the same position as the NE-213 detector. It was found that the calculated-to-measured ratio (C/E) for each of the 3 Bonner balls agreed within 5% with the other balls, and agreed within 25% with the scale factor used to normalize the calculated spectrum in Fig. 2. The fact that the 3 Bonner ball C/E's agreed with each other suggests that the entire energy spectrum was predicted well by the calculations.

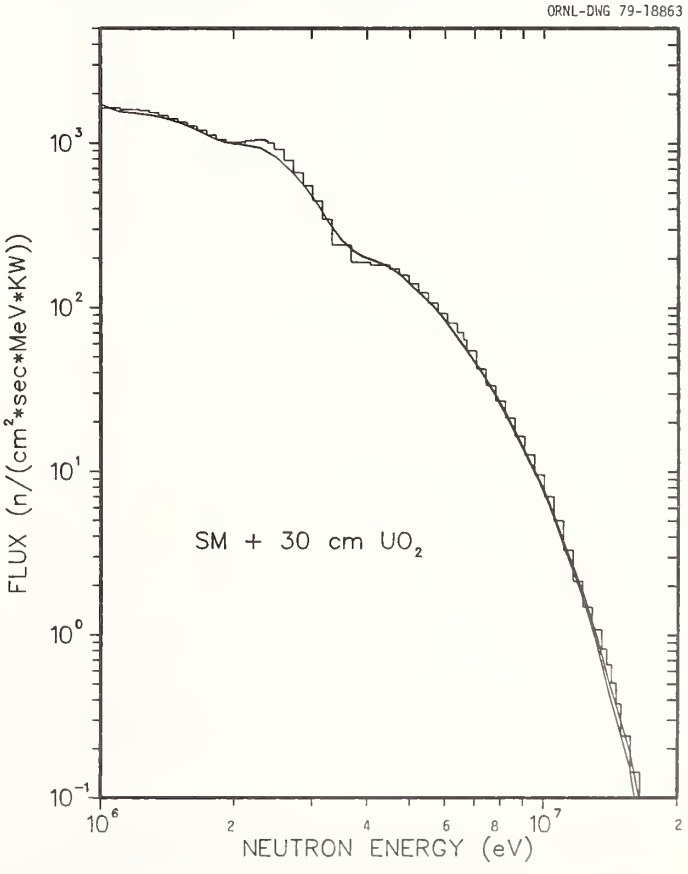

Fig. 2. Comparison of measured (double line) and calculated (histogram) neutron spectrum through a 2-row UO_2 blanket mockup.

Figures 3 and 4 give comparisons of calculated and measured spectra behind a 30-cm-thick ThO_2 blanket mockup. As before, the calculations were normalized based on the integrated flux between 3 and 12 MeV. The calculations shown in Fig. 3 used cross sections which were derived entirely from ENDF/B-IV data, and is in general agreement with the measured spectrum except below 4 MeV. However, the calculation shown in Fig. 4 used thorium data from ENDF/B-V, and predicts the observed spectrum exceedingly well. Similar results, to a greater degree, are shown in Figs. 5 and 6 which compare measurements behind 45 cm of ThO_2 to the corresponding calculations based on ENDF/B-IV and -V thorium data. It is also apparent from the 45-cm case that both sets of data underpredict the observed spectra by 30-40% in the range of 11 to 14 MeV.

As with the UO_2 case presented above, the scale factors used to normalize the calculated spectra in Figs. 3 - 6 were compared to the C/E values determined for the 3 Bonner balls. For the calculations utilizing ENDF/B-V thorium data, the agreement between the scale factors and the C/E's ranged from 10% for the 10" BB to 25% for the 3" BB. The calculations utilizing ENDF/B-IV Th data showed agreements ranging from 15% for the 10" BB to 35% for the 3" BB. The reasonably good agreement between the spectra scale factors and the 10" BB C/E values gives credence to the comparisons in Figs. 3 - 6; however, the disagreement in C/E values among the Bonner balls suggests that the lower energy spectrum is not predicted as well as the higher energies.

One result from the 1D analysis which is independent of the normalization and which also suggests that the low energy neutron transport through ThO_2 is not predicted well, is a comparison of measured and calculated attenuation factors for a single slab of ThO_2. This was determined by calculating the ratio of a detector response for the 30 cm ThO_2 case and the 45 cm case. The results for the Bonner balls and the integrated NE-213 flux are given in Table 1. Also given in Table 1 are the percent differences between the calculated and measured attenuations, which vary from 5% to 18% for calculations utilizing ENDF/B-V thorium, and vary from 11% to 23% for ENDF/B-IV thorium. Both sets of data yield an underprediction of the lower energy neutron attenuation as measured by the 3" BB, but it appears that the ENDF/B-V thorium data reduces the observed discrepancies.

Table 1. Neutron Attenuation Through 15 cm of Thorium Oxide

	ATTENUATION[a]		
DETECTOR	MEASURED	ENDF/B-IV	ENDF/B-V
3" BB (epithermal)	3.70	2.85 (23)[b]	3.04 (18)
6" BB (total)	4.24	3.46 (18)	3.69 (13)
10" BB (fast)	4.39	3.92 (11)	4.19 (5)
NE-213 (3-12 MeV)	6.15	5.10 (17)	5.42 (12)

[a] Ratio of detector response with 30 cm ThO_2 to 45 cm ThO_2.

[b] Calculated using leakage for forward-most angle only. Number in parentheses give percent deviation from measured attenuation.

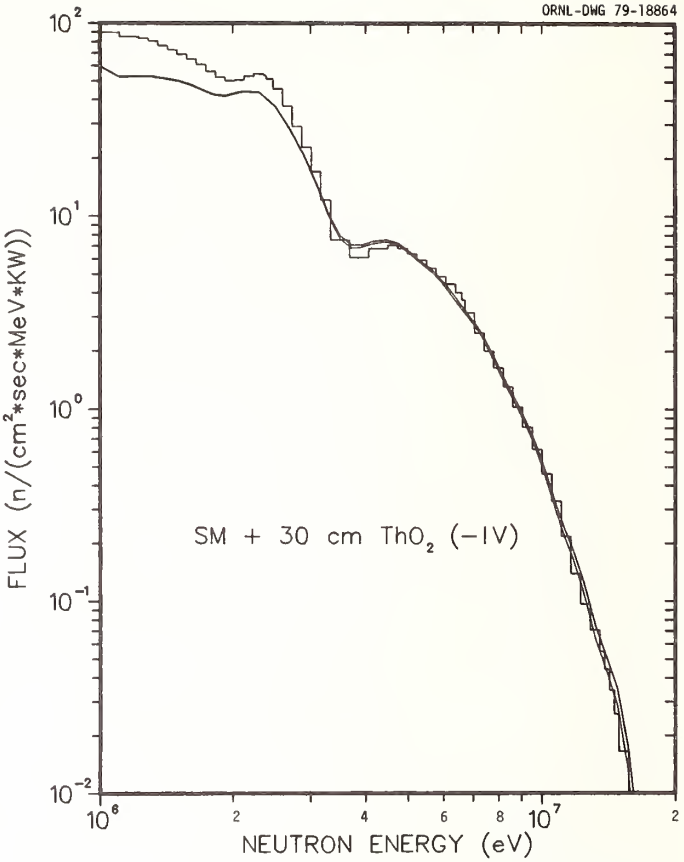

Fig. 3. Comparison of measured and calculated neutron spectrum through a 2-row ThO_2 blanket mockup. Calculation used ENDF/B-IV Th data.

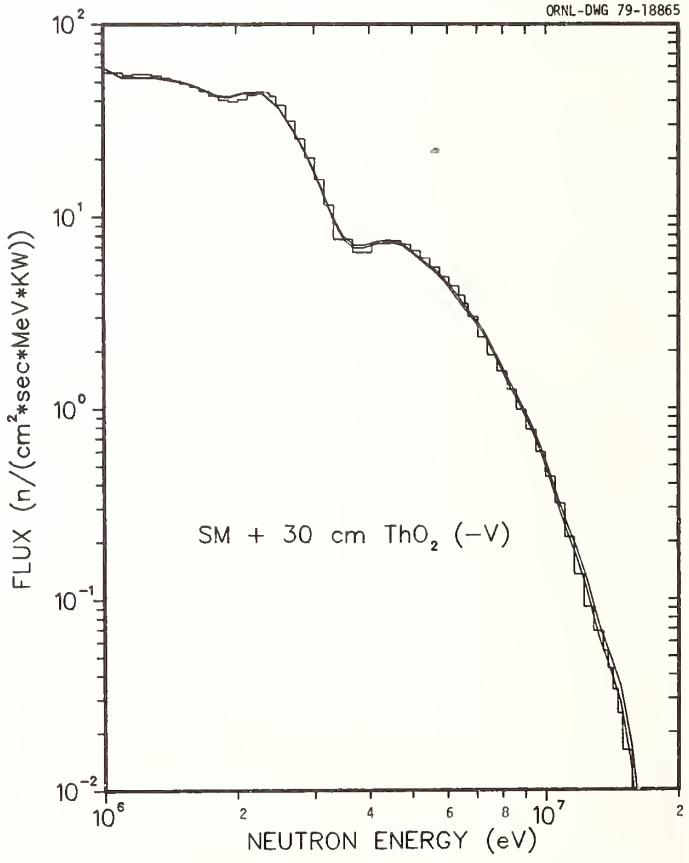

Fig. 4. Comparison of measured and calculated neutron spectrum through a 2-row ThO_2 blanket mockup. Calculation used ENDF/B-V Th data.

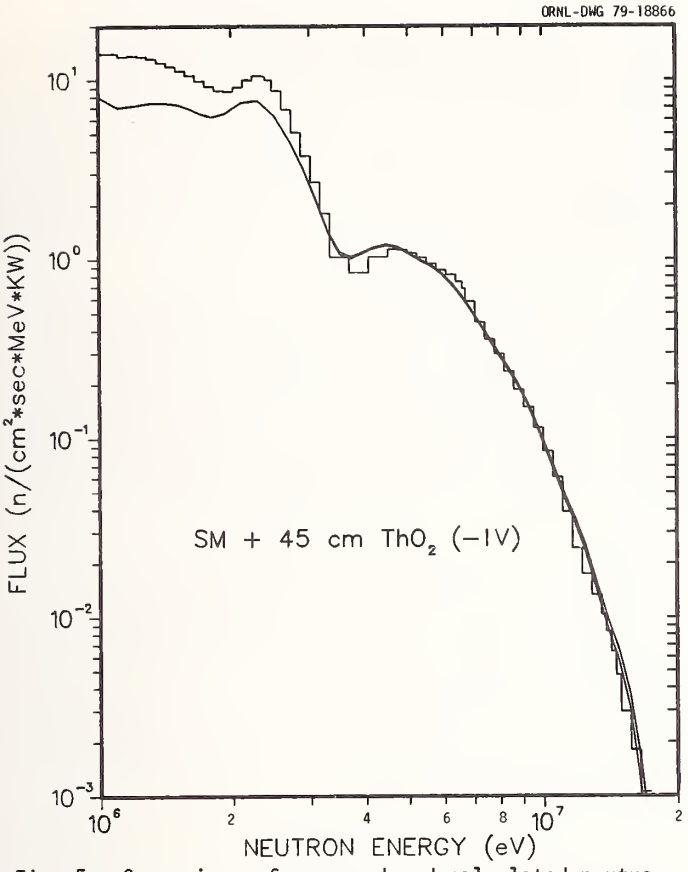

Fig. 5. Comparison of measured and calculated neutron spectrum through a 3-row ThO_2 blanket mockup. Calculation used ENDF/B-IV Th data.

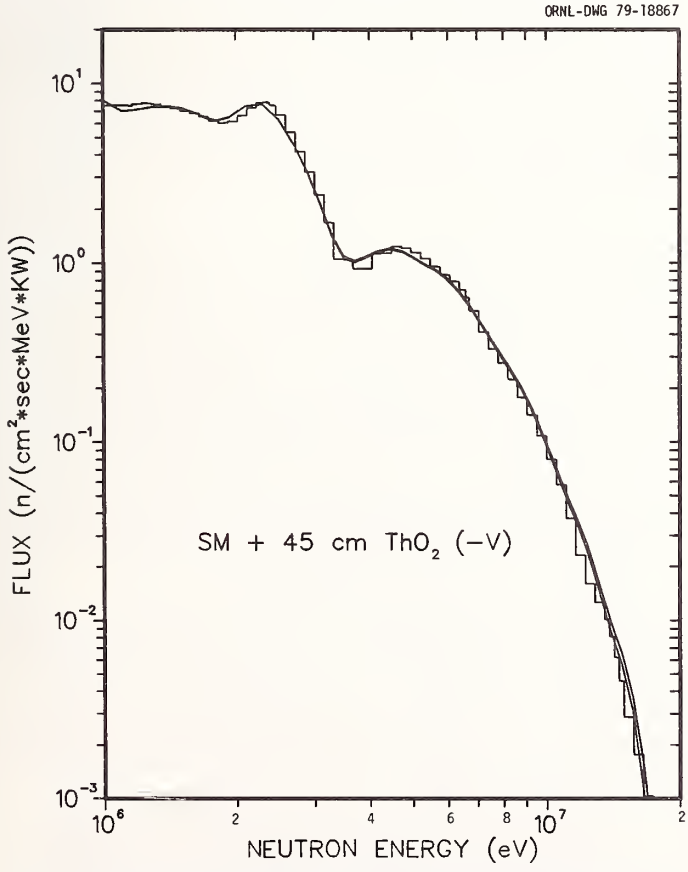

Fig.6. Comparison of measured and calculated neutron spectrum through a 3-row ThO_2 blanket mockup. Calculation used ENDF/B-V Th data.

Conclusions

Any meaningful interpretation of the experimental results which have been analyzed thus far requires a familiarity with the relevant nuclear data: the thorium-232 total neutron cross section. Figure 7 compares the total macroscopic cross section for ThO_2 resulting from ENDF/B-IV-derived data for both thorium and oxygen, and from ENDF/B-V-derived thorium data mixed with version IV oxygen data. Since no significant changes were made to the oxygen evaluation for ENDF/B-V, the two mixtures given in Fig. 7 represent version IV and V, respectively. The most striking difference is the almost uniform 7-9% increase in the total cross section between 1 eV and 100 keV for ENDF/B-V, which largely explains the differences observed in Table 1 between the two calculations. The newer thorium evaluation also increased the total cross section by a few percent between 1 and 3 MeV and between 5 and 8 MeV which contributes to the spectral differences observed in Figs. 3 - 6.

It can, therefore, be concluded that based on the initial results from this integral experiment, the ENDF/B-V evaluation of the thorium-232 total cross section is a significant improvement over the previous ENDF/B-IV evaluation. Furthermore, the new total cross section appears adequate above 1 MeV for calculating deep penetration in ThO_2, which is the dominant concern for most shielding requirements. However, additional investigation of the total cross section at lower energies appears to be needed. It is expected that the remaining analysis of the blanket measurements will better identify the source of the observed discrepancies, and will provide additional information on the adequacy of thorium gamma-ray production cross sections.

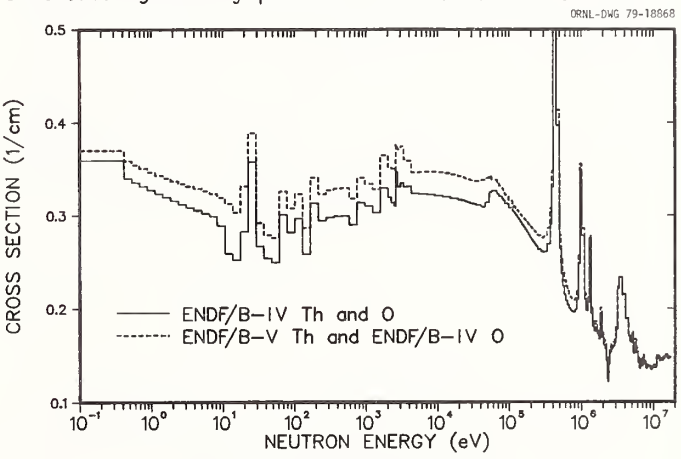

Fig. 7. Comparison of ENDF/B-IV and ENDF/B-V macroscopic total cross section for ThO_2.

References

1. General Atomic Co. Project Staff, General Atomic Company Report GA-A-13045 (1974).
2. R. E. Maerker, F. J. Muckenthaler, ORNL/TM-5183 (1976).
3. W. W. Engle, Jr., Oak Ridge Gaseous Diffusion Plant Report K-1693 (1967).
4. R. W. Roussin, et al., ORNL/RSIC-37 (1978).
5. N. M. Greene, et al., ORNL/TM-3706 (1976).
6. R. E. Maerker, et al., ORNL-4880 (1974).
7. C. E. Clifford, et al., ORNL-5161 (1977).

Research sponsored by the Reactor Research & Technology Division, U. S. Department of Energy, under Contract W-7405-eng-26 with the Union Carbide Corporation.

ANALYSIS OF A SWISS THORIUM BLANKET INTEGRAL EXPERIMENT

J. R. White and D. T. Ingersoll
Oak Ridge National Laboratory
Oak Ridge, Tennessee 37830, USA

U. Schmocker and K. Gmür
Swiss Federal Institute for Reactor Research
CH-5303 Würenlingen, Switzerland

A detailed postanalysis of the ThO_2 axial blanket experiment (CORE 14) performed at the PROTEUS critical facility is presently being completed at ORNL. The purpose of the analysis is to compare measured reaction rates along the axial centerline of the test zone with results calculated utilizing various data libraries. In particular, the analysis is investigating the adequacy of the available thorium data. The cross section data supplied by EIR is compared to ENDF/B-4 data collapsed to the broad-group level via the AMPX modular code system. Furthermore, a comparison of C/E values using ENDF/B-4 and new ENDF/B-5 thorium data is given. Finally, some theory and modeling questions are investigated. Detailed results from the above analyses are presented which support the conclusion that the presently available ^{232}Th data appears inadequate for accurate GCFR fuel cycle studies.

(Integral experiment, GCFR, thorium, capture cross section, ENDF/B-5.)

Introduction

The current interest in proliferation-resistant fuel cycles has generated several questions concerning the adequacy of the basic nuclear data available for the alternate ^{232}Th and ^{233}U fuels. A cooperative program between the U.S. and Switzerland is trying to quantify some of the uncertainties associated with the more important ^{232}Th and ^{233}U neutron reactions. The U.S. program includes the postanalyses of a series of Swiss integral experiments[1] designed to validate neutron physics data for thorium-bearing GCFR lattices. The experiments included several configurations utilizing UO_2, ThO_2, and Th-metal pins in prototypic GCFR core and axial blanket mockups.

The PROTEUS critical facility located at the EIR laboratory in Würenlingen, Switzerland, is a hybrid reactor consisting of a central GCFR-type pin lattice which is driven critical by annular thermal drivers. A cross-sectional view of the PROTEUS fast-thermal critical facility is shown in Fig. 1. Reaction rate and neutron spectrum measurements are made at the center of the test zone core and axial blanket regions. The

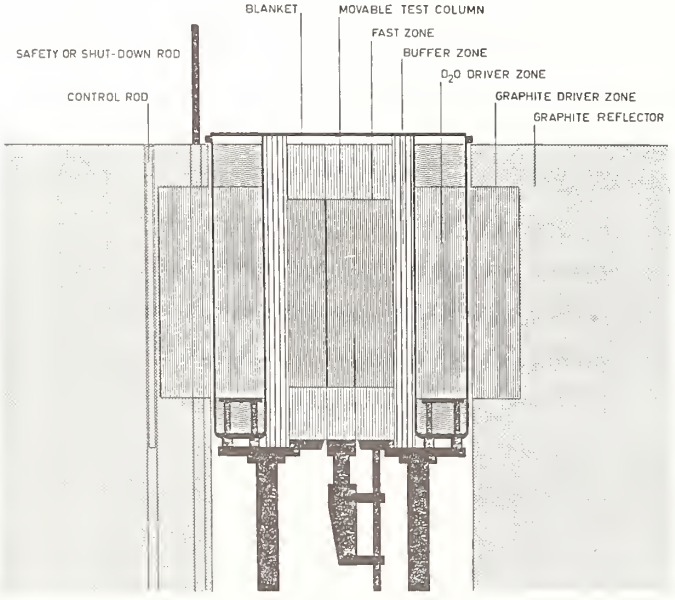

Fig. 1. Cross-sectional view of the PROTEUS fast-thermal critical facility.

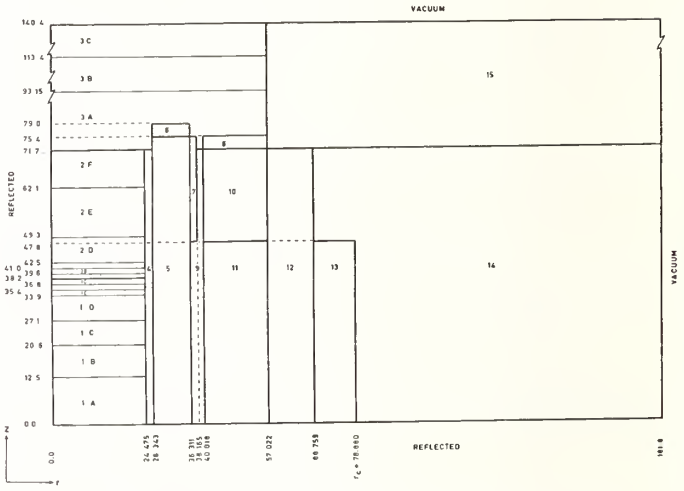

Fig. 2. Two-dimensional calculational model of the CORE 14 configuration.

measurements are compared to calculated detector responses as a test of the accuracy of the nuclear data, multigroup processing, and analytic methods.

The preliminary results of the ORNL analysis of the ThO_2 axial blanket experiment (CORE 14) performed at PROTEUS are reported here. The purpose of the analysis is to compare experimentally-determined reaction rates along the axial centerline with results calculated using various data libraries and calculational methods. In particular the analysis is trying to address the adequacy of the available thorium data for use in accurate fast reactor studies.

The two-dimensional geometric model for the CORE14 configuration is displayed in Fig. 2. The detail along the vertical centerline is to account for the axial variation of the broad-group cross sections. This fine detail in the fast region is especially important in the vicinity of the region 1/region 2 interface ($PuUO_2$ core/ThO_2 axial blanket) where large changes in spectra and resonance shielding effects occur.

The reference cross section data utilized in the 2-D computations were supplied by EIR. This 10-group P_0 library was originally derived from the British FGL5[2] fine-group adjusted data set. However, the ^{232}Th and ^{233}U data (37 groups plus shielding factors) included in the Swiss version of FGL5 were derived from

the ENDF/B-4 based LIB-IV[3] library. To further address the adequacy of ENDF/B data, fast region cross sections were generated using the AMPX[4] cross section processing system. Two data libraries were processed, one containing all ENDF/B-4 data[5] and the other containing all ENDF/B-4 data with the exception of ENDF/B-5 thorium (referred to as ENDF/B-45). These two fast region data sets were then coupled with EIR data for the subsequent 2-D DOT-IV[6] transport calculations.

Calculational Results

Data Comparisons

Two-dimensional DOT-IV P_0S_6 transport calculations were performed utilizing the three data sources just described. In addition, one-dimensional fine-group P_3S_4 calculations were used in the spectral and spatial collapse of the ENDF/B data to the 10-group level. Several interesting observations can be made from this calculational data base.

Table I compares the calculated-to-measured (C/E) values of several important central reaction rate ratios determined using EIR-supplied and ENDF/B-4 data. Fair agreement between the two data sets is achieved for all but the (N2N)2/C2 ratio. The important C2/F9 and F2/F9 ratios are consistently underpredicted by 4–7 percent and 10–12 percent respectively. The C2/C8 ratio, although well predicted with EIR data, is quite low relative to the measured value when the ENDF/B-4 library is utilized. This difference in the calculated C2/C8 ratio can be attributed to a decreased ^{232}Th capture rate and an increased ^{238}U capture rate with ENDF/B-4 data.

This comparison is more clearly shown in Table II where the percent difference between the individual reaction rates calculated using EIR and ENDF/B-4 data is tabulated. In most cases there is only a ±3% difference in the individual central reaction rates. This is not surprising for the ^{232}Th and ^{233}U data since, as previously mentioned, the cross sections included in the Swiss version of FGL5 for these nuclides were derived from ENDF/B-4 data. However, a slightly higher ^{238}U capture rate using the ENDF/B-4 data was expected since the C8/F9 ratio is known to be overpredicted with ENDF/B-4 data.[7]

A final point of interest in this initial data comparison is the large difference in the calculated thorium (n,2n) reaction rate between the EIR and ENDF/B-4 data. This discrepancy is not clearly understood since the data have the same origin. In spite of this fact, there was a 24 percent increase in the thorium (n,2n) cross section in the 10-group ENDF/B-4 library relative to EIR-supplied data. Since this is a high energy threshold reaction, the calculated thorium (n,2n) reaction rate is very sensitive to data and calculational methods. However, this uncertainty in the (n,2n) reaction rate is an important consideration since the (n,2n) reaction in thorium is a main production route to ^{232}U and its highly radioactive decay chain.[8]

Table I. Comparison of Calculated Reaction Rate Ratios at the Center of CORE 14 Using EIR and ENDF/B-4 Data

Reaction Rate Ratio	Measured Value	Calculated*-to-Measured Value (C/E)	
		EIR Data	ENDF/B-4 Data
C2/F9	0.2026 ± 1.7%	0.956	0.934
C8/F9	0.1338 ± 1.0%	0.977	1.013
C2/C8	1.506 ± 1.4%	0.983	0.927
F2/F9	$8.061^{*}\ 10^{-3}$ ± 2.0%	0.882	0.901
(N2N)2/C2	$6.93^{*}\ 10^{-3}$ ± 2.6%	0.987	1.287

*2-D P_0S_6 transport calculations (ENDF/B data was collapsed using 1-D buckling search approximation.)

Table II. Detailed Central Reaction Rate Comparisons Using EIR and ENDF/B-4 Data

Reaction Rate	$\left(\frac{\text{ENDF/B-4} - \text{EIR}}{\text{EIR}}\right)^{*}100$
C2	− 3.10
F2	1.31
(N2N)2	26.74
F3	− 2.23
C8	2.80
F8	− 2.55
F9	− 0.85

The second data comparison to be made is the contrast between the presently available ENDF/B-4 thorium data and the more recent ENDF/B-5 thorium evaluation. Table III displays the results of this comparison, giving both the 1-D and 2-D central C/E values. The most important observation here is the large decrease in the C/E values for C2/F9 and C2/C8 when going from ENDF/B-4 to ENDF/B-5 thorium data. Since differences in the core center flux spectra are negligible, this decrease is due solely to the reduction of the ^{232}Th capture cross section in the ENDF/B-5 data files. Figure 3 displays the normalized capture rate as a function of energy for the 1-D, 171-group infinite slab calculations using ENDF/B data. A decrease (7.2% overall) in the ENDF/B-5 thorium capture rate is apparent for most of the energies of interest. Thus, these preliminary results seem to question the validity of the new ENDF/B-5 thorium capture data above 100 eV. Since the C/E values with ENDF/B-4 data are already low (C2/F9 = 0.95 and C2/C8 = 0.93), the new ENDF/B-5 data seems to have been adjusted in the wrong direction.

In contrast to the capture cross sections, the recent ENDF/B-5 evaluation seems to have improved the thorium fission and (n,2n) data relative to ENDF/B-4. An increase of approximately 5 percent in the central ^{232}Th fission rate and a decrease of about 6 percent in the (n,2n) reaction rate are observed with ENDF/B-5 data in the $PuUO_2$ fast lattice spectrum. This brings the calculated ^{232}Th fission rate into fair agreement with experiment with C/E value for F2/F9 of about 0.95. However, although adjusted in the proper direction, the ^{232}Th (n,2n) reaction rate is still significantly overpredicted with ENDF/B-5 data.

Table III. Comparison of Central C/E Values Using ENDF/B-4 and ENDF/B-5 Thorium Data.

Reaction Rate Ratio	Calculated*-to-Measured Value (C/E)			
	2-D, 10-group model		1-D, 171-group model	
	ENDF/B-4 Data	ENDF/B-45 Data	ENDF/B-4 Data	ENDF/B-45 Data
C2/F9	0.947	0.878	0.987	0.918
C8/F9	1.022	1.022	1.079	1.081
C2/C8	0.932	0.864	0.920	0.854
F2/F9	0.897	0.948	0.827	0.872
(N2N)2/C2	1.261	1.281	1.113	1.126

*ENDF/B data was collapsed using 1-D infinite slab approximation.

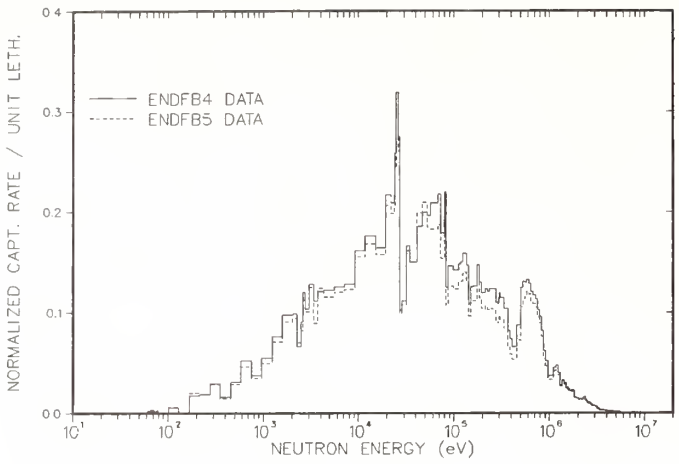

Fig. 3. Thorium-232 capture rate as a function of energy at the center of CORE 14.

Up to this point comparisons among the various data sources have been restricted to the center of CORE 14. This is because the spectrum at the core center is known more accurately and is also less sensitive to methods and geometric modeling effects. Therefore, variations from experimental results at the core center are mainly due to data discrepancies, while differences in the axial blanket regions can be a combination of many effects. However, as a test of the overall ability of the present methods, comparisons of calculated and measured axial profiles of several important reaction rates were performed.

In general, agreement of the axial profiles with experiment is excellent for the threshold ^{232}Th and ^{238}U fission rates, fair for the ^{232}Th capture and ^{233}U fission rates, and quite poor for the ^{239}Pu fission and ^{238}U capture rates. The disagreement in the last two cases has been attributed to the resonance shielding effect and resultant large variation in the cross sections near the $PuUO_2$ core/ThO_2 blanket interface. These discrepancies are probably due more to model and method uncertainties than to data uncertainties.

Also, generally speaking, the two ENDF/B data sets give quite similar results and these compare more favorably with experiment than the EIR data. Figure 4, for example, indicates that ENDF/B-5 thorium data predicts the axial ^{232}Th capture rate profile slightly better than the other data. However, the calculated values near the core/blanket interface (38.2 cm) are still too high relative to the central reaction rate.

Comparison of 1-D and 2-D Results

The final point to be made from Table III is the large variation of the C/E values from the 2-D, 10-group calculation to the 1-D, 171-group infinite slab results. The 2-D calculation uses data collapsed from the 1-D fine-group model. Therefore, if the spectra in the two calculations are similar, then the reaction rates should also be similar. Figure 5 displays the spectra in the important energy range at core center for the ENDF/B-4 data calculations. The fine-group spectrum from the 1-D infinite slab calculation is collapsed to the broad-group structure for ease of comparison.

There is an obvious shift to a softer spectrum in the fine-group calculation. The effect of this

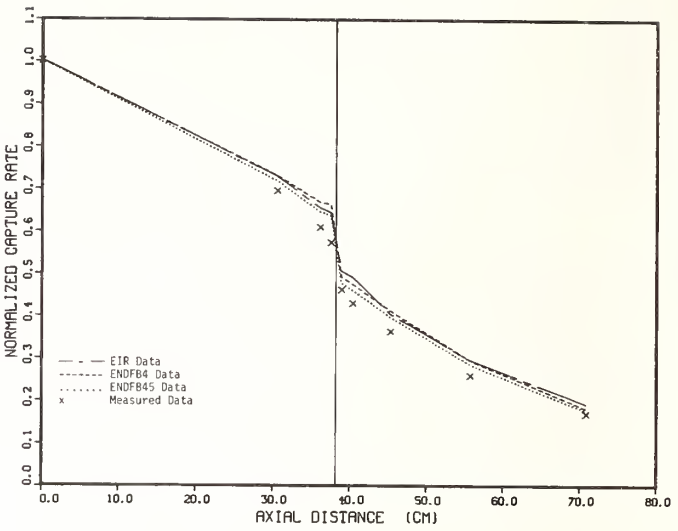

Fig. 4. Axial profile of the ^{232}Th capture rate in CORE 14.

spectral change is displayed in Table IV. For example, since the ^{239}Pu fission rate changed only slightly, the C2/F9 ratio should have increased about 4 percent in the 1-D calculation. This is the result observed in Table III. Thus, the infinite slab calculation used to perform the cross section collapse has a characteristic spectrum different from the 2-D model and, therefore, represents an approximation in the CORE 14 analysis effort.

Sensitivity to the 1-D Weighting Spectra

Due to the disagreement in the results from the 1-D and 2-D models, an attempt was made to investigate the sensitivity of the central reaction rate ratios to the 1-D weighting spectrum utilized in the collapse to a broad-group library. The 1-D infinite slab geometry in the XSDRNPM[3] module of the AMPX system was modified to include a buckling correction to account for the finite radius of the central fast region of CORE 14. In addition, a buckling search calculation for a critical system was performed. These finite geometry calculations resulted in an increased fast leakage and a decreased downscatter source, which, when combined, produces a

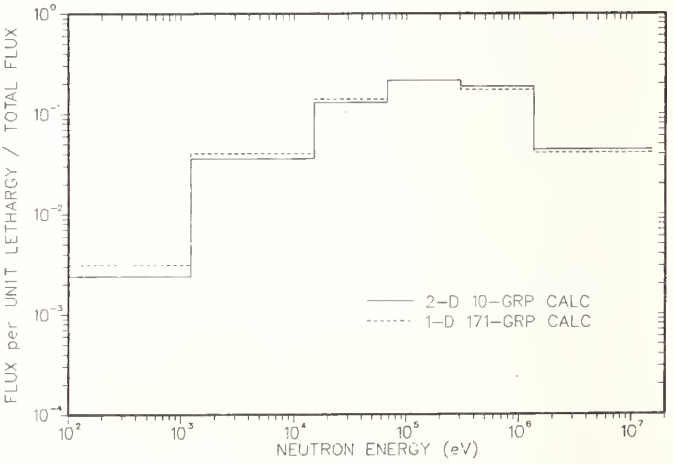

Fig. 5. Comparison of 1-D infinite slab and 2-D flux spectra at core center.

Table IV. Detailed Reaction Rate Comparison Between 1-D and 2-D Models With Infinite Slab 1-D Approximation.

Reaction Rate	$\left(\frac{1D - 2D}{2D}\right)$ *100
C2	4.19
F2	−7.86
(N2N)2	−7.88
F3	0.06
C8	5.53
F8	−7.83
F9	−0.06

harder neutron spectrum relative to the infinite slab geometry. Figure 6 compares the flux spectra from the infinite slab, buckling correction, and buckling search one-dimensional approximations. As can be seen, the buckling correction spectrum varies significantly from the infinite slab calculation. On the other hand, the buckling search and infinite slab calculations are quite similar with the former producing the slightly harder spectrum. Investigation of Fig. 5 indicates that this type of spectral change is what is needed to bring the 1-D and 2-D calculations into better agreement.

The first half of Table V displays the central C/E values from the three 1-D model approximations. If the cross sections collapsed using these different approximations are utilized in the 2-D calculations, the 2-D C/E values in the second half of Table V result. As would be expected, the sensitivity of the C/E values to the 1-D weighting spectrum is much greater in the 1-D calculations than the 2-D calculations. However, there is still a significant difference between the 2-D results when using the infinite slab and buckling corrected weighting spectra. This indicates the importance of having the correct weighting function in the collapse of a fine-group data set to a broad-group library.

The most important observation from Table V is the good agreement of the central C/E values in the 1-D and 2-D geometries when using the critical flux spectrum from the buckling search calculation as the weighting function for the cross section collapse. Obviously, this is the best 1-D approximation for the CORE 14 analysis, since good agreement between the 1-D and 2-D models is obtained. Thus, this approximation should have been used for all the data comparisons previously described. However, Table V also shows good agreement between the 2-D central reaction rate ratios using the infinite slab and buckling search approximations. Thus, the previous conclusions concerning the ENDF/B-4 and ENDF/B-5 thorium data comparisons are still valid. The trends in the comparisons are the same, only the absolute numbers will change slightly.

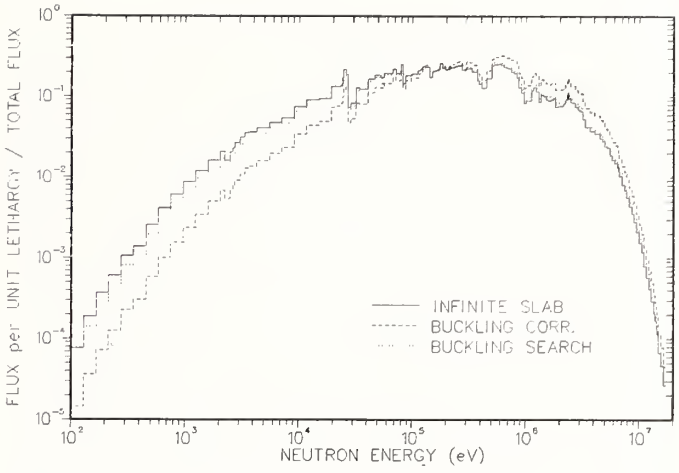

Fig. 6. Comparison of flux spectra at core center for various 1-D model approximations.

Theory Comparisons

In addition to the analyses described above, the effect of some theory approximations were also investigated. A comparison of diffusion theory versus transport theory methods showed that the two theories gave very similar central C/E values. However, recent Swiss analysis has shown that the axial profiles of several of the important reaction rates were slightly improved with transport theory methods.

The reference transport calculations were performed using a P_0 cross section expansion and an S_6 symmetric quadrature approximation. However, P_3S_6 and P_3S_4 calculations were also performed. Comparison of these last two theory variations showed no observable differences in either the central or axial profiles of the calculated reaction rates. Therefore, the C/E values are not sensitive to the quadrature approximation utilized.

On the other hand, the P_3 cross section expansion showed some interesting differences from the reference P_0 calculation. Although central C/E values were unchanged, the variation in the axial distribution of the reaction rates was quite apparent. A harder flux spectrum as well as an increased flux magnitude relative to core center were observed in the axial blanket region for the P_3 cross section expansion. These effects are due to increased leakage from the core due to the better scattering approximation associated with the P_3 expansion.

Table V. Sensitivity of Important Central C/E Values to the 1-D Weighting Spectra.

Central Ratio	1-D C/E Values			2-D C/E Values		
	Infinite Slab	Buckling Search	Buckling Correction	Infinite Slab	Buckling Search	Buckling Correction
C2/F9	0.987	0.928	0.722	0.947	0.934	0.884
C8/F9	1.079	1.023	0.808	1.022	1.013	0.975
C2/C8	0.920	0.913	0.899	0.932	0.927	0.911
F2/F9	0.827	0.926	1.386	0.897	0.901	0.915
(N2N)2/C2	1.113	1.334	2.646	1.261	1.287	1.425

Summary and Conclusions

In summary, the analysis of the CORE 14 ThO_2 axial blanket experiment has produced the following results:

1. The EIR and ORNL ENDF/B-4 data libraries produce similar central reaction rates (±3% difference) except for the significantly higher ^{232}Th (n,2n) rate obtained using ORNL ENDF/B-4 data.

2. Both libraries underpredict the central ^{232}Th capture and fission rates with C/E values of 0.93–0.96 and 0.88–0.90 for C2/F9 and F2/F9, respectively.

3. ENDF/B-5 thorium data produce significantly lower capture rates (–7%) and better fission and (n,2n) rates (+5% and –6%, respectively) relative to ENDF/B-4 data.

4. The central C/E values were insensitive to the theory and modeling approximations investigated, however, the weighting spectrum utilized in the cross section collapse must be properly matched to the calculated broad-group spectrum.

Two main conclusions can be drawn from these results. First, one can conclude that since the central C/E values are insensitive to theory and modeling approximations, a comparison of calculated and measured reaction rate ratios at the center of the CORE 14 configuration is a true measure of the adequacy of the nuclear data in the energy range of interest. Thus, from the C/E values obtained in this study, one can only conclude that the present thorium data appears inadequate for accurate GCFR fuel cycle analysis. Although the more recent ENDF/B-5 ^{232}Th fission data appears satisfactory, the discrepancies in the observed ^{232}Th capture rate in a $PuUO_2$ fast lattice spectrum is greatly exaggerated with ENDF/B-5 data. In addition, the ^{232}Th (n,2n) cross section uncertainties in both ENDF/B data sets appear to be extremely large. This all indicates that relatively large uncertainties must be associated with many of the results obtained from a wide variety of recent fast reactor alternate fuel cycle studies.

Finally, it should be stressed that the above conclusions are based only on the core center results from the CORE 14 analysis. This analysis was primarily concerned with infinitely dilute thorium data in a $PuUO_2$ fast spectrum. However, analyses of other PROTEUS experimental configurations which provide more information about ^{232}Th data in a thorium-bearing lattice are planned. When these latter analyses are complete a more detailed set of conclusions regarding the adequacy of thorium cross section data will be possible.

Acknowledgment

Research sponsored by the U. S. Department of Energy under contract W-7405-eng-26 with Union Carbide Corporation Nuclear Division.

References

1. U. Schmocker et al., "Critical Experiments in a Zero-Power Fast Reactor Lattice with Breeder Zones of Thorium and Uranium," presented at International Symposium on Fast Reactor Physics, Aix-en-Provence, France (September 1979).

2. J. Rowlands et al., "The Production and Performance of the Adjusted Cross Section Set FGL5," Proc. Int. Symp., Physics of Fast Reactors, Tokyo (1973).

3. R. B. Kidman et al., LIB-IV, A Library of Group Constants for Nuclear Reactor Calculations, Los Alamos Scientific Laboratory, LA-6200-MS (1976).

4. N. M. Green et al., AMPX: A Modular Code System for Generating Coupled Multigroup Neutron-Gamma Libraries from ENDF/B, Oak Ridge National Laboratory, ORNL/TM-3706 (March 1976).

5. R. W. Roussin et al., The CTR Processed Multigroup Cross-Section Library for Neutronics Studies, ORNL/RSIC-37 (1978).

6. W. A. Rhoades et al., The DOT-IV Two-Dimensional, Discrete-Ordinates Transport Code with Space-Dependent Mesh and Quadrature, ORNL/TM-6529 (August 1978).

7. P. J. Collins et al., "A Comparison Between Physics Parameters in Conventional and Heterogeneous LMFBRs Using Results from ZPPR," Proc. Advances in Reactor Physics, Gatlinburg, CONF-780401, p. 207 (1978).

8. L. S. Abbott, D. E. Bartine, and T. J. Burns, Interim Assessment of the Denatured ^{233}U Fuel Cycle: Feasibility and Nonproliferation Characteristics, Oak Ridge National Laboratory, ORNL-5388 (December 1978).

DATA NEEDS FOR FUEL HANDLING AND WASTE MANAGEMENT ASPECTS OF THORIUM FUEL CYCLES

S. Nair and H.F. Macdonald
Berkeley Nuclear Laboratories
Central Electricity Generating Board
Berkeley, Glos. GL13 9PB, UK

The cross-section data needs for strategies employing various feed fuels in a thorium-fuelled HTR have been examined from the viewpoint of fuel handling and high-level waste management. The important nuclides and their major production routes have been identified and tentative accuracy requirements are suggested for some key spectrum-averaged cross-sections not covered by the requirements for reactor physics calculations.

[Thorium HTR fuel cycles, fuel handling, high-level waste management, cross-section accuracy requirements.]

Introduction

The use of thorium fuels in power reactors has been proposed both as an alternative to plutonium production and as a potential energy source in itself. An important consideration in a comprehensive assessment of any such fuel cycle would be the identification of the novel radiological protection aspects arising from the use of thorium. In this paper we have examined the cross-section data needs for strategies employing various feed fuels in a thorium-fuelled High Temperature Reactor (THTR) from the viewpoint of fuel handling and transport, and long-term high-level waste management.

Definition of the fuel cycles

Most thorium-based fuel cycle strategies fall into two groups, namely, those designed to be based eventually entirely on thorium (once sufficient ^{233}U has been bred) and those designed to use thorium as a complement to uranium. The examples of these strategies considered here are depicted schematically in figures 1(a) and 1(b) respectively. The effects of using high and low ^{235}U-enrichment UO_2/ThO_2 fuel in strategy 1(b) was also investigated, as was recycling of uranium and, where appropriate, plutonium. A perspective on the results obtained was achieved by comparison with a reference fuel cycle using UO_2 fuel of low ^{235}U-enrichment. Details of the fuel cycles considered are given in table I and in figures 1(a) and 1(b).

Calculational methods

The calculations utilised the CEGB reactor inventory code RICE[1,2] in conjunction with the WIMS reactor physics code[3]. Full details are given elsewhere[4].

Identification of the critical nuclides

Fuel handling and transport

A detailed study[5] of the cycles described above lead to the following conclusions:

(i) the requirements for decay heat removal and γ shielding of spent fuel are largely independent of fuel type being dominated by fission product decay.

(ii) significant differences were found for the neutron emissions; the results are presented in figure 2. The neutron emissions from cycle HTR1, THTR20 and 21 spent fuels are dominated by the spontaneous fissions of $^{242,244}Cm$ for up to three years after discharge from the reactor. In contrast, cycle THTR10, 11, 30 and 31 spent fuels exhibit much reduced neutron emission rates. Up to 80% of the emitted neutrons are produced by (α,n) reactions on oxygen and Be, B, F, Li, Na, Mg and Al impurities in the fuel. The α particles are produced mainly by the decay of ^{238}Pu.

(iii) the γ emissions from cycle THTR21 and 31 unirradiated fuels can also be an important consideration. Results are presented in figure 3, which shows the temporal variation of the hard γ emissions from the uranium, plutonium and thorium isotopes incorporated in the unirradiated fuel. These arise from the decay of ^{208}Tl and ^{212}Bi, the latter being produced by ^{232}U decay in the fuels. Similar conclusions applied for cycle THTR10 and 11 unirradiated fuels.

Waste management

The important parameters of interest from the viewpoint of high-level waste (HLW) disposal are the α activity and biological toxicity of the separated HLW over a geological timescale. The biological toxicity, T_i, of isotope i may be expressed by the relation:

$$T_i = \frac{Q_i}{(MPC_w)_i} \quad , \qquad (1)$$

where Q_i is the isotopic activity and $(MPC_w)_i$ is the corresponding maximum permissible concentration in water for the critical organ as defined by ICRP[6,7]. The overall biological toxicity, T is then given by:

$$T = \sum_{\substack{\text{isotope } i \\ \text{in waste}}} T_i = \sum_i \frac{Q_i}{(MPC_w)_i} \quad . \qquad (2)$$

The validity of this method of assessing relative toxicity has been critically reviewed by [8].

The conclusions from the present study[4] may be summarised as follows:

(i) the α activity and biological toxicity of the separated HLW after 99.9% extraction of thorium, uranium and plutonium are dominated by the same isotopes in all cases.

(ii) the differences in actinide HLW toxicities for the first 500-800 years after reprocessing are masked by the much greater fission product toxicity, which is similar for all the fuel cycles considered.

(iii) the results of the toxicity calculations for the actinide component of the HLW from cycles HTR1, THTR10 and 20 are presented in figure 4 for both water-soluble and insoluble chemical forms. The toxicities of cycle THTR10, 11, 30 and 31 waste are dominated by the daughters of ^{231}Pa decay for timescales in the range 10^3-10^5 years after reprocessing. The corresponding isotopes for cycles THTR20 and 21 are $^{241,243}Am$ for times in the range 10^3-10^4 years. The dominant isotopes for subsequent time periods up to 10^6 years are ^{226}Ra, formed by ^{242}Cm and ^{238}Pu decay, and the daughters of ^{237}Np decay, for all the fuel cycles considered.

Cross-section data requirements

The major production routes for which reactor spectrum-averaged cross-sections are required are shown in figure 5 for the various critical nuclides. The accuracy requirements for the capture and fission cross-sections of ^{232}Th, $^{233,234,235,236,238}U$ and $^{239,240,241}Pu$, which determine the inventories of ^{237}Np and ^{241}Am, are covered by those for reactor physics calculations and will not be considered further. A sensitivity study was made to assess the changes in the critical nuclide inventories for correlated and uncorrelated changes in the remaining key cross-sections. The results were used to determine the accuracy requirements for these cross-sections, the aim being to predict the ^{231}Pa, ^{232}U, ^{237}Np, ^{243}Am and $^{242,244}Cm$ inventories to within ±25%. This target was considered realistic in the light of errors always present in non-nuclear parameters such as fuel rating and irradiation history that are also important in inventory predictions.

The tentative cross-section accuracy requirements are listed in table II. Also given are suggested requirements for various (α,n) reactions on light elements.

Conclusion

A preliminary study has been made of the cross-section data needs for a radiological assessment of various thorium-fuelled HTR fuel cycle scenarios. The important nuclides and their major production routes have been identified and tentative accuracy requirements are suggested for various cross-sections not covered by the stricter requirements for reactor physics calculations.

Acknowledgement

This paper is published by permission of the Central Electricity Generating Board.

TABLE II: Tentative cross-section accuracy requirements

(Reactor spectrum-averaged cross-sections)

Reaction	Required accuracy
$^{231}Pa(n,\gamma)$	± 15%
$^{237}Np(n,\gamma)$	± 20%
$^{242}Pu(n,\gamma)$	± 10%
$^{241}Am(n,\gamma)$	± 10%
$^{243}Am(n,\gamma)$	± 10%
$^{232}Th(n,2n)$	± 20%
$^{233}U(n,2n)$	± 15%
$^{238}U(n,2n)$	± 20%
(α,n) thick target yields on elemental O, Be, B, F, Li, Na, Mg, Al. *	± 20% (E_α = 5-6 MeV)

*Some of these requirements may be relaxed or even deleted if fuel impurity levels can be shown to be low enough to make negligible contribution to the total (α,n) emission.

TABLE I: Listing of fuel cycles considered

Cycle	Feed fuel composition	Comment
HTR1	10% ^{235}U-enriched UO_2 fuel	Reference cycle.
THTR10	3.5% UO_2/96.5% ThO_2	U bred in CFR Th blanket.
THTR11	4.5% UO_2/95.5% ThO_2	U recycled from THTR10.
THTR20	65% UO_2/35% ThO_2	12% ^{235}U enrichment.
THTR21	53% UO_2/1% PuO_2/46% ThO_2	U & Pu recycled from THTR 20.
THTR30	5% UO_2/95% ThO_2	94% ^{235}U-enrichment.
THTR31	5% UO_2/95% ThO_2	U recycled from THTR 30.

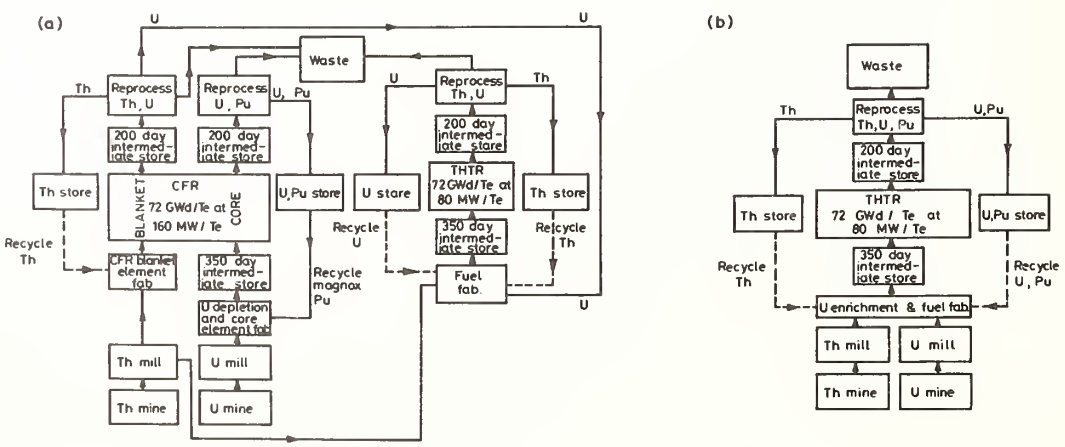

Fig. 1 Pictorial Representation of the Fuel Cycles Considered

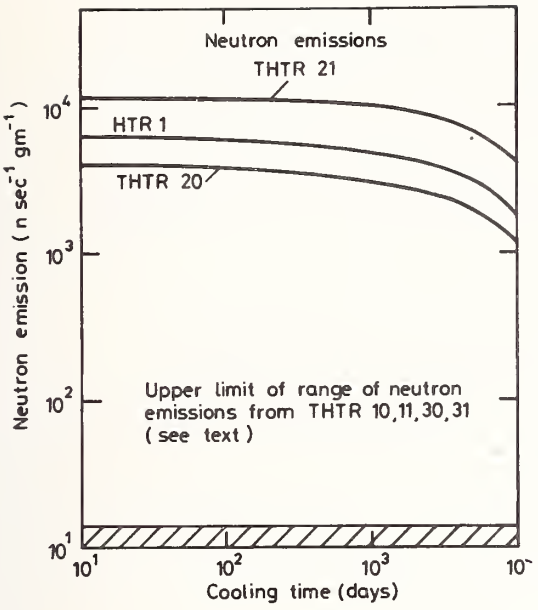

Fig. 2 The neutron emissions from the spent THTR fuels.

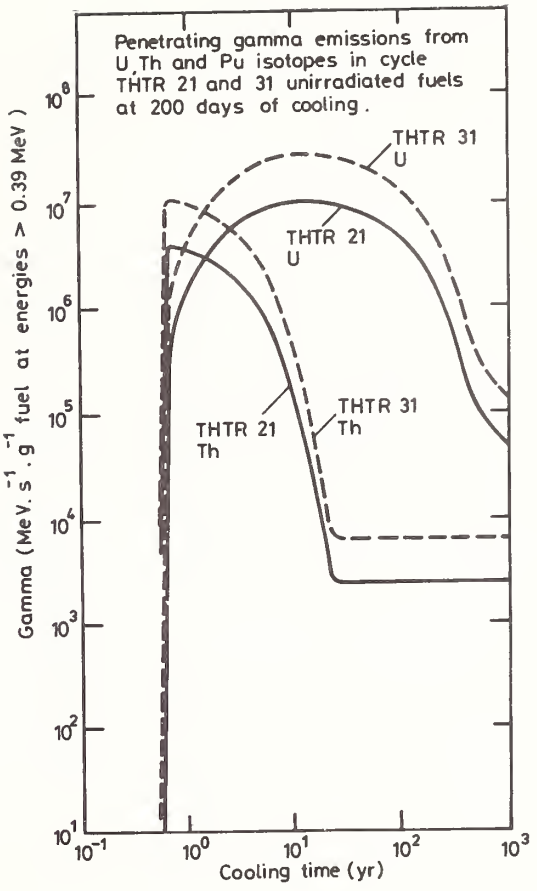

Fig. 3 Gamma emissions at energies >0.39 MeV from uranium, thorium and plutonium isotopes in cycle THTR21, 31, unirradiated fuels.

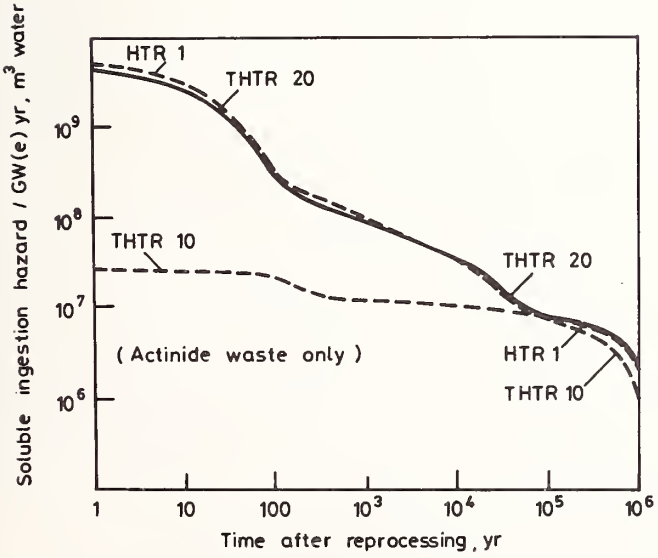

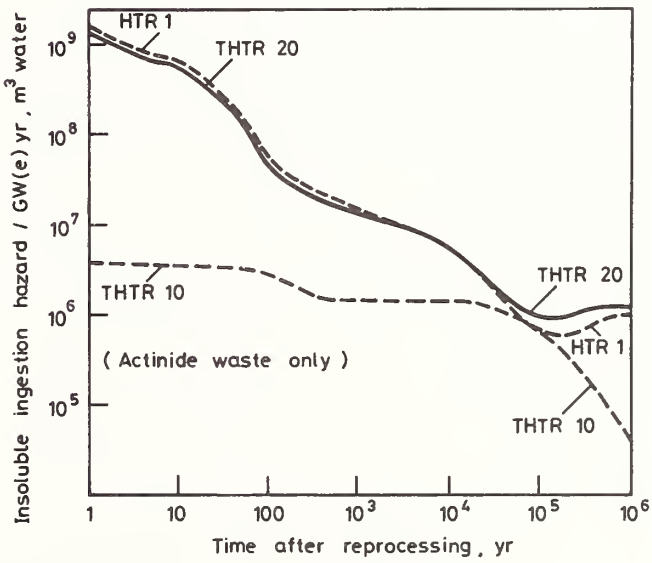

Fig. 4 A comparison of the toxicities of separated high-level waste from cycles HTR1 and THTR10 and 20.

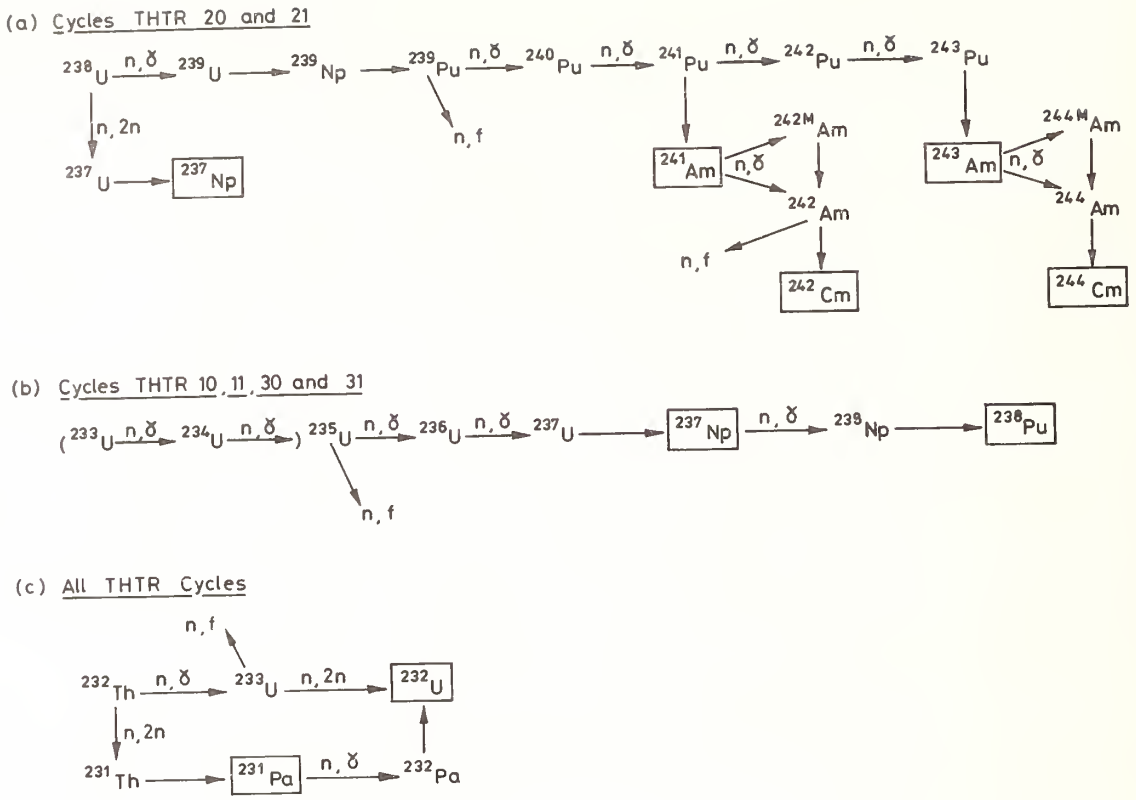

Fig. 5 The major production routes for the radiologically-significant isotopes.

References

1. S. Nair, CEGB report RD/B/N4138 (1977).
2. S. Nair and M.J. Henning, CEGB report RD/B/N4079 (1978).
3. J.R. Askew, F.J. Fayers and P.B. Kemshell, J.Br.Nucl.Eng.Soc. 5, 564 (1966).
4. S. Nair, CEGB report RD/B/N4124 (1977).
5. H.F. Macdonald and S. Nair, Nucl.Tech.42,353(1979).
6. ICRP Publication No. 2 (1959), Pergamon Press.
7. ICRP Publication No. 6 (1962), Pergamon Press.
8. H.A.C. McKay and B. Verkerk, CEC report EUR 5801 e, Chapter 4 (1977).

NEUTRON SCATTERING CROSS SECTIONS from (n,n') and (n,n'γ) METHODS - A COMPARISON

F. D. McDaniels*, G. P. Glasgow†, and M. T. McEllistrem
University of Kentucky, Lexington, Kentucky 40506, USA

Neutron inelastic scattering cross sections can be obtained conveniently from (n,n'γ) yields provided a good normalization standard is available. Measurements from independent neutron and γ-ray detection experiments are compared to confirm the use of the ^{56}Fe(n,n'γ) ^{56}Fe - 846.7-keV production cross section as a normalization standard.

[^{56}Fe(n,n'γ)^{56}Fe compilation; (n,n') and (n,n'γ) results compared for Zr, Mo, and Sm isotopes]

Introduction

Neutron scattering measurements to separate levels of a target nucleus are made either directly through detection of scattered neutrons, (n,n') measurements, or indirectly through detection of subsequent γ-rays, (n,n'γ) detection. In neutron detection the pulsed - and bunched - beam techniques provide level separations[1], and in γ-ray detection similar methods reduce backgrounds.[2] For experiments in which the scattering cross sections $\sigma_{n'}$ are a principal concern, and for nuclei with large level separations, neutron detection is the method of choice because of two key advantages: 1) observed scattering yields directly reflect $\sigma_{n'}$ for individual levels, and 2) many scattering cross sections are known with enough accuracy, $\lesssim \pm 2\%$, to serve as convenient normalization standards. These include neutron total cross sections measured with white source techniques at electron linear accelerators[3] and with monoergic beam techniques at electrostatic accelerators.[4]

But current neutron detection methods also have severe problems and disadvantages. Most serious is that the resolving power $R \equiv E/\Delta E \lesssim 100$ always, and usually $R \lesssim 70$. It is rare, therefore, to see a neutron detection experiment in which $\sigma_{n'}$ are reported for more than a few levels, except for a few cases near closed shells, like the Zr isotopes.[5] The (n,n'γ) methods have the major advantage of greatly expanding the number of levels separately studied, even in the Zr isotopes;[6] but most importantly they extend the range of nuclei which can be studied, since in practice one usually has $R > 1000$. The resolving power advantage also improves detection sensitivity by a factor of 3 to 4, in comparison to neutron detection.

The $\sigma_{n'}$ from γ-ray detection have been received with less confidence than those from neutron detection, because of key disadvantages of the γ-ray method: 1) the need for accurate decay scheme and branching ratio knowledge which enables the conversion from γ-ray production cross sections (σ_γ) to $\sigma_{n'}$, through corrections for γ-ray cascades, and 2) the lack of a convenient, high accuracy (n,n'γ) standard for normalization. We will attempt to address the latter problem to some extent, and compare some $\sigma_{n'}$s measured both with neutron and γ-ray detection.

Normalization

The straightforward way of normalizing γ-ray yields to σ_γ-values involves measuring the neutron flux incident on a scattering sample using calibrated neutron detectors, and the γ-ray detection efficiency as a function of γ-ray energy using standard sources. Most experiments, in order to have good sensitivity to weak transitions, use substantial scattering samples located close to the neutron source - typically the source-to-sample distance $d \lesssim (3\text{-}4)\ell$, where ℓ represents the maximum linear dimension of the sample. Since the anisotropy of neutron source reactions is energy dependent, determining the flux incident on all parts of the scattering sample over a large range of incident neutron energies is reasonably difficult. The γ-ray yields obtained from a scattering sample in an experiment must subsequently be corrected for geometry and other effects associated with sample-size.[1,7]

A secondary normalization method is that of normalizing detected γ-ray yields to those for an (n,n'γ) reaction of known σ_γ. This is convenient if a good standard σ_γ is available, and in addition appropriate choices of sample-sizes can lead to approximate cancellation of corrections for sample-size. The correction uncertainties are thus reduced, at the expense of introducing the uncertainty in the "known" σ_γ.

The yields of the 846.7-keV $2_1^+ \rightarrow 0^+$ transition of the ^{56}Fe(n,n'γ)^{56}Fe reaction have been measured perhaps more often than those for transitions in most other nuclei combined; it is a strongly excited, well separated line, the atomic density is larger for Fe than for other elements, and ^{56}Fe is 91.7% abundant. Measurements of σ_γ for this line exist from numerous experiments spanning at least 25 years, and over the incident neutron energy range from 1 to 14 MeV. In spite of the many measurements of σ_γ, early compilations of them were quite discouraging. Examination of some of these compilations showed, however, that they included results measured at different observation angles, sometimes normalized per atom of Fe and sometimes per atom of ^{56}Fe, and for widely differing incident neutron energy spreads.

Compilation - ^{56}Fe(n,n'γ)^{56}Fe

A special compilation of σ_γ - values for this line has been prepared and updated at the University of Kentucky for several years. The values compiled are for differential production cross sections at 90° laboratory angle. Many good measurements have been reported for this or nearby angles, and it is a convenient angle for use with a well shielded Ge(Li) detector. All measurements included in the compilation met the following criteria:

a) All measurements transformed to γ-ray differential production cross sections at 90° laboratory angle.
b) The σ_γ are normalized as isotopic cross sections, per atom of ^{56}Fe.
c) Measurements correspond to an incident energy spread between 50 and 100 keV over the incident energy range between 2.0 and 4.0 MeV. Tests made by energy averaging the high resolution results of Voss et.al.[8] showed average values which were little dependent upon the

averaging interval ΔE for 50 keV $\lesssim \Delta E \lesssim$ 100 keV.

d) All measurements are carefully corrected for the effects of sample-size, either through empirical test or calculations.

Even with these restrictions, many measurement sets are available for inclusion in the compilation. Some older data sets were omitted when:

1) They deviated systematically two standard deviations or more above or below the compilation of included values, and
2) They were noted in other publications as being in substantial disagreement with other measurements.

The compilation is shown in Fig. 1, which includes a least-squares-fitted curve to the measurements over the incident energy interval from 2.0 to 4.0 MeV. The fit is calculated as a sequence of curves, each fitted to the form: $A + BE_n + CE_n^2$, where E_n is the incident energy and A, B, C are fitting constants; each curve is least-squares-fitted to all measurements in a 0.5 MeV interval to determine the three constants, together with the constraint that the curves join each other smoothly at the end points of the fitting intervals. The combined curve is that shown in Fig. 1.

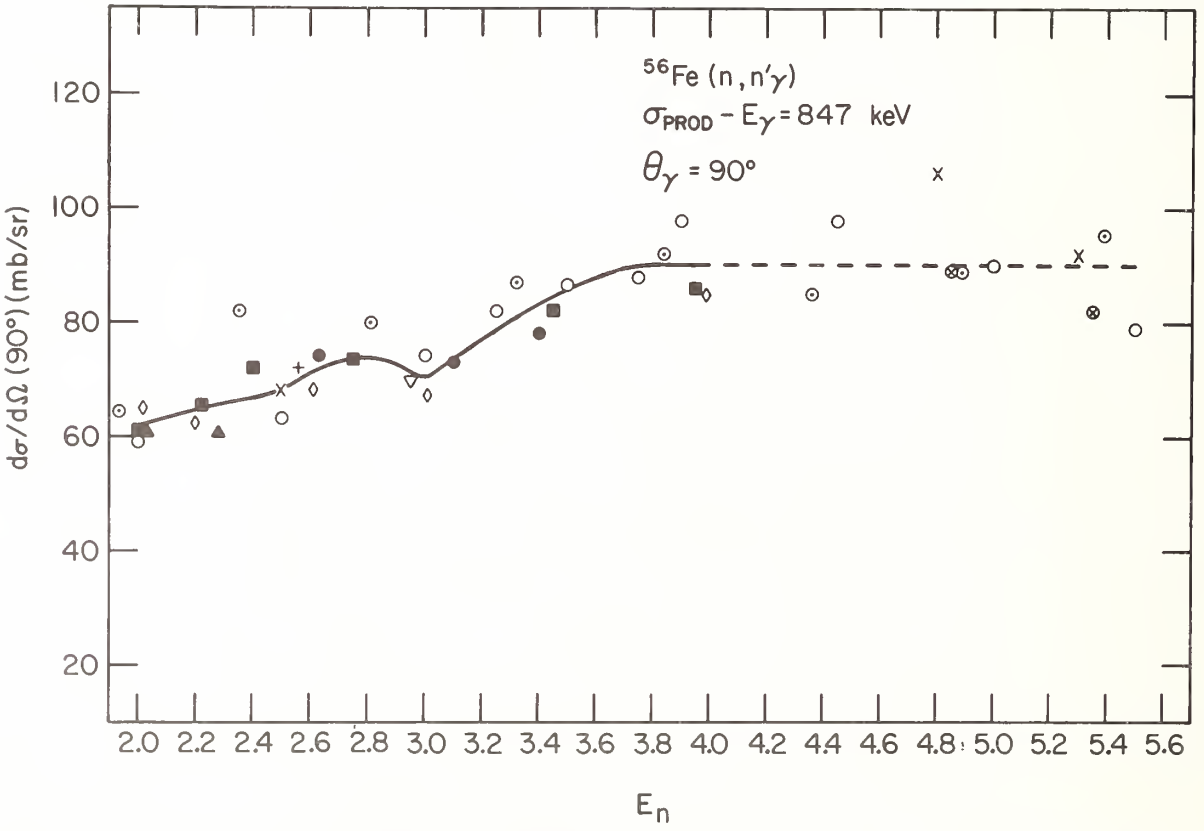

Fig. 1. Differential γ-ray production cross sections for the 847-keV transition in ^{56}Fe. Some measurements were corrected to 90° from an observation angle of 125° using measured anisotropies. All measurements correspond to an incident energy spread between 40 and 90 keV. The rms deviation of points from the fitted curve is ±4%. More than 80% of them lie within ±5.5% of the fitted curve. Symbols are identified in Ref. 10.

Above 4.0 MeV the data are too sparse and insufficiently consistent to encourage a compilation effort. Values of σ_γ taken from this curve are assigned an uncertainty of ± 7%, based on uncertainties reported from individual measurements and the internal consistency of the measurements. About 80% of them lie within 5.5% of the fitted curve. This curve provides values for use in normalizing yields in (n,n'γ) experiments.

Comparisons from Neutron and γ-ray Detection

During the last 5 or so years we have had occasion to study neutron scattering from many nuclei using both neutron and γ-ray techniques. The latter technique allows us to separate scattering to levels not resolvable in neutron detection.[6,8] In all cases so far, at least a few well separated levels have been observed in both types of experiments, so that comparisons of the two methods are possible. The neutron and γ-ray detection experiments, though carried out in the same laboratory, were done at completely different times, and normalized to different cross sections used as standards. The neutron detection experiments were normalized both to the (n,p) scattering cross section[9] and to the total cross section of C.[3]

Zrisotopes

A recent study of ^{92,94}Zr presented several comparisons of pairs of (n,n') cross sections, from (n,n') and (n,n'γ) techniques. In all 18 pairs of cross sections were examined,[6] at incident neutron energies of 2.75, 3.20 and 3.50 MeV. At each incident energy the results of each technique can be summed, to give an overall comparison which reflects normalizations of the two methods. The deviations of the (n,n') and (n,n'γ) sums are 4%, 2%, and 5% respectively[6], well within the assigned 7% uncertainty of the Fe compilation above. Comparisons of cross section pairs for individual levels produced average deviations of 10%, 13%, and 13% respectively. Thus uncertainties for individual lines - background subtractions, statistics, peak

separations are considerably more important now than normalization uncertainties. The errors reported[6] on individual inelastic scattering cross sections are ∿ ± 10%.

^{152}Sm

A recent study of neutron scattering in the Sm isotopes presents one comparison[8], that for scattering to the 4_1^+ state of ^{152}Sm, where the deviation of the values from the two methods is 5%.

Mo isotopes

Finally a comparison of several cross sections for the Mo isotopes is presented in Table I below.

Table I. Comparison of σ(n,n') from γ-ray and neutron detection.

E_n	Isotope	Level Energy	(n,n')	(n,n'γ)	% Difference
2.50	^{92}Mo	1.509	917	830	10
	^{94}Mo	0.871	641	607	5.5
2.75	^{100}Mo	0.535/9.694	441	438	0.7
3.50	^{92}Mo	1.509	577	577	0
		2.281	257	220	15.5
		2.517/2.525	164	140	5.3
		2.849	170	158	7.3

The top part of Table I presents cross sections and comparisons for scattering to the first excited 2^+ states of three even A Mo isotopes (and includes the 0^+ state of ^{100}Mo). The average deviation is 5.5%. The bottom four rows present values for several levels of semi-magic ^{92}Mo, which show an average deviation of 7%. Individual level deviations in these Mo comparisons suggest, as in the Zr isotopes, that errors which may vary from group to group or peak to peak are now more important than the overall normalization errors. All of the comparisons cited above suggest that the method of normalizing (n,n'γ) yields is effective within the incident energy range from 2 to 4 MeV, and that (n,n'γ) methods provide reliable neutron inelastic scattering cross sections when the level and decay schemes of the target nucleus are well determined.

Acknowledgement

This work was supported by the National Science Foundation and the University of Kentucky Graduate School.

References

* Now at Dept. of Physics, North Texas State University, Denton, Texas.

† Now at Mallinckrodt Institute of Radiology, Washington University, St. Louis, Missouri.

1. D. W. Glasgow et.al., Nucl. Instrum. Methods 114, 541 (1976).

2. J. P. Fouan and J. P. Passerieux, Nucl. Instrum. Methods 62, 327 (1968); J. D. Brandenberger, ibid. 69, 271 (1969).

3. R. D. Schwartz, R. A. Schrack, and H. T. Heaton, National Bureau of Standards Monograph No. 138 (U.S. GPO, Washington, D.C., 1964).

4. R. E. Shamu et.al., Phys. Let. 61B, 29 (1976).

5. P. Guenther, A. Smith, and J. Whalen, Phys. Rev. C 12, 1797 (1975).

6. G. P. Glasgow, F. D. McDaniel, J. L. Weil, J. D. Brandenberger, and M. T. McEllistrem, Phys. Rev. C 18, 2520 (1978).

7. D. E. Velkley, D. W. Glasgow, J. D. Brandenberger and M. T. McEllistrem, Nucl. Instrum. Methods 129, 231 (1975)

8. D. F. Coope, S. N. Tripathi, M C. Schell, J. L. Weil, and M. T. McEllistrem, Phys. Rev. C 16, 2223.

9. J. C. Hopkins and G. Breit, Nuclear Data Tables A9, 137 (1971).

10. The symbols of Fig. 1, followed by the appropriate references, are: (†) R. B. Day, Phys. Rev. 102, 767 (1956); (▽) M. Hosoe and S. Suzuki, Jour. Phys. Soc. Japan 14, 699 (1959); (■) Bull. Nucl. React. Des. (USSR) 254 (1962); (●) J. H. Montague and E. B. Paul, Nucl. Phys. 30, 93 (1962); (◊) W. B. Gilboy and J. H. Towle, Nucl. Phys. 64, 130 (1965); (▲) A. Jacquot and C. R. Rosseau, Nucl. Phys. 84, 239 (1966); (○) W. E. Kinney and F. G. Perey, ORNL-4249 (1968); (⊗) J. K. Dickens, G. L. Morgan, and F. G. Perey, ORNL-4798 (1972); (×) J. Lachkar, J. Sigand, Y. Patin, and G. Aaonat, Nucl. Sci. Eng. 55, 168 (1974); (⊙) V. J. Orphan, C. G. Hoot, and V. C. Rogers, Nucl. Sci. Eng. 57, 309 (1975).

DOUBLE DIFFERENTIAL NEUTRON SCATTERING CROSS SECTIONS FOR Fe, Cu, Ni and Pb BETWEEN 8 AND 12 MeV

A. Beyerle, C. Gould, W. Seagondollar and P. Thambidurai
North Carolina State University
Raleigh, NC 27607 USA
and
Triangle Universities Nuclear Laboratory
Duke Station, Durham, NC 27706 USA

S. El-Kadi, G. Glendinning, C.E. Nelson, F.O. Purser and R.L. Walter
Duke University and Triangle Universities Nuclear Laboratory
Duke Station, Durham, NC 27706

Neutron emission spectra have been measured for iron, nickel, copper, and lead at incident neutron energies from 8-12 MeV. The TUNL time-of-flight system has been used to obtain data at about 5 scattering angles for each incident energy down to an emitted neutron energy of less than 500 keV. The experimental procedure and progress toward converting the yields to double-differential cross sections will be reviewed.

(Fe(n,n'), Ni(n,n'), Cu(n,n'), Pb(n,n'), 8-12 MeV, θ_{lab} 40°-145°, measure time-of-flight spectra)

Introduction

Measurements of the spectra of neutrons emitted following neutron bombardment of nuclei are of both theoretical and experimental interest. Information on nuclear level densities can be extracted from an analysis of the spectral shapes. In addition, the cross sections are of importance in design calculations for fusion reactor blanket and wall structures. There have been many measurements of neutron evaporation spectra at ∿14-MeV bombarding energy[1] and at energies below 7.5 MeV[2]. There have been relatively few studies in the 8- to 14-MeV region however.[3,4] In this energy range (n,2n) channels are becoming energetically accessible, and preequilibrium effects may cause the neutron angular distributions, predominantly isotropic at lower energies, to become forward peaked. Thus extrapolations of spectral shapes from higher and lower energy data may not necessarily be reliable. Even at 14 MeV, discrepancies exist between several sets of measurements.[5]

In order to complement theoretical predictions of neutron emission cross sections, we have recently undertaken a program of (n,n') measurements on medium mass to heavy nuclei, with particular emphasis on inelastic scattering to the continuum region. Our first experiments concentrated on neutron emission spectra measurements for natural iron, nickel, copper and lead following 7.5-MeV, 10- and 12-MeV neutron bombardment. Here we report on our data acquisition and analysis procedures, and review our progress in converting the data to absolute double differential inelastic scattering cross sections.

Experimental Procedure

The present TUNL neutron time-of-flight system is reviewed in a separate contribution to this Conference.[6]

Source neutrons are produced with the $^3H(p,n)^3He$ or $^2H(d,n)^3He$ reactions using a 3.0 cm-long gas cell pressurized to two atmospheres of tritium or deuterium. The neutrons from the cell are scattered from cylindrical samples, suspended vertically 7.8 cm beyond the end of the cell and are detected in either of two massively shielded liquid scintillators via the time-of-flight (TOF) method. For the continuum neutron studies described here, the proton or deuteron beams from the TUNL FN Tandem Van de Graaff accelerator were pulsed and bunched into about 2 ns bursts at a repetition rate of 1 MHz with typical beam currents on target of 1.5 μA. The neutron flight paths were 2.76 and 3.73 m respectively for the two detectors, permitting detection of neutrons below 300 keV in energy without overlap from previous beam bursts. The neutron detectors were biassed near the pulse height minimum between the 26- and 59-keV γ rays from our ^{241}Am source, corresponding to a threshold neutron energy of ∿300 keV. The detection efficiency of the scintillators was measured in separate experiments from threshold to ∿20 MeV using the $^3H(p,n)$, $^2H(d,n)$, $^3H(d,n)$ reactions and the absolute cross sections of Liskien and Paulsen[7] and Drosg[8].

The data at 7.5 MeV were taken with the $^2H(d,n)$ reaction. This corresponds to a deuteron energy which is below threshold for deuterium gas breakup and therefore this neutron source is strictly monoenergetic apart from ^2H breakup in the cell and entrance foil. At higher energies the D+d gas breakup cross section relative to the monoenergetic cross section rises more rapidly than for the $^3H(p,n)$ reaction. As discussed in Ref. 9, the $^3H(p,n)$ source is a factor of 3 better in this respect than the $^2H(d,n)$ reaction. Therefore, the 10- and 12-MeV data were taken with the $^3H(p,n)$ reaction. Background neutrons from (p,n) reactions in the cell material and beam stop are also present but, as in the case of the D+d experiment, can be taken into account by performing a gas-out measurement. These background contributions were large for the T+p experiments, even with the use of a ^{58}Ni beam dump. For the D+d experiments a tantalum beam dump was used and the backgrounds were much lower. The entrance foil in all experiments was of 3.5 μm molybdenum.

At 7.5 MeV the samples were in the form of small solid cylinders 3.0 cm high and 2.0 cm in diameter. At 10 and 12 MeV hollow cylindrical samples were used of height 4.5 cm, 3.0 cm outside diameter and 1.3 cm inside diameter.

Neutron angular distributions were typically measured at five angles from 40° to 145° at each energy. At each angle four TOF spectra were accumulated. These corresponded to (1) gas in, sample in, (2) gas out, sample in, (3) gas in, sample out, (4) gas out, sample out. Here 'gas in' refers to deuterium or tritium gas in the cell. 'Gas out' refers to the hydrogen isotope having been removed and replaced by an equal pressure of helium. This simulates energy loss effects. These four spectra were normalized to the integrated charged particle beam on target. Fig. 1 shows TOF spectra for the scattering of 10-MeV neutrons from iron at 100°. The neutron elastic scattering peak is visible in about channel 700 only in spectrum 1. The sample out backgrounds in spectra 3 and 4 are relatively flat. The contribution of the (p,n) background in spectrum 2 is

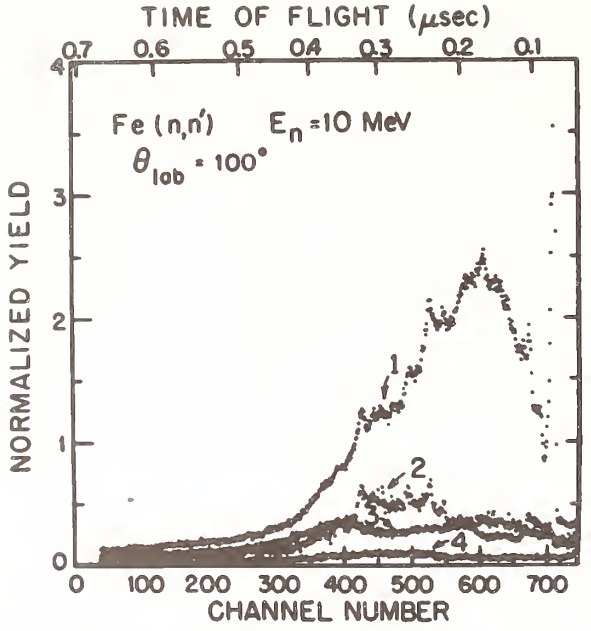

Fig. 1 Four neutron scattering spectra.
1) Tritium in cell, sample in place
2) Helium in cell, sample in place
3) Tritium in cell, sample removed
4) Helium in cell, sample removed

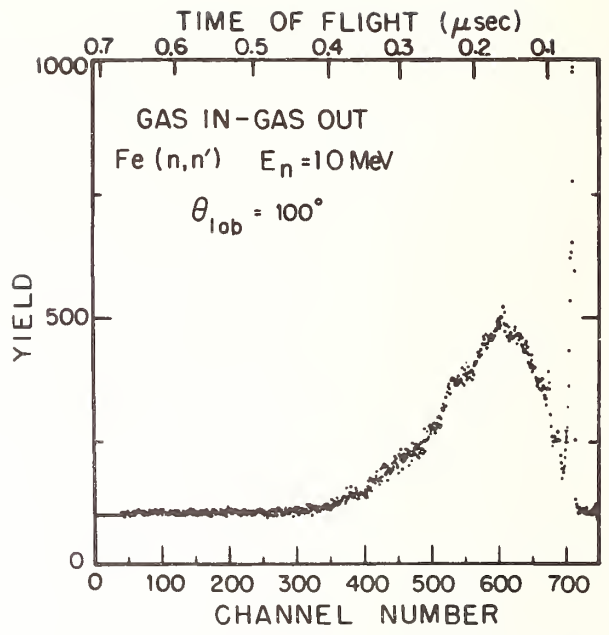

Fig. 2 Difference spectrum from Fig. 1 (1-3)-(2-4). This spectrum is biased by 100 counts.

structured because of resonances in the elastic scattering cross section of iron. The background associated with (p,n) reactions in the cell material is eliminated by forming the difference (1-3)-(2-4). This is the final TOF spectrum and is shown in Fig. 2. Most of the structure between channels 400 and 550 is removed and the final spectrum is relatively smooth. Scattering of tritium-gas breakup neutrons is still present in this spectrum and is not removed by subtracting the 'gas out' spectra. The contribution of these neutrons to the continuum yield is taken into account later in the analysis.

Experimental Results

The final time of flight spectra are transformed to energy spectra, folding in the detector efficiency. Figures 3-5 show energy spectra for iron, nickel, copper and lead scattering at ∿125° for incident neutron energies of 7.5, 10 and 12 MeV. These spectra are arbitrarily normalized and are not corrected for attenuation effects or for multiple scattering. The spectra for copper are relatively structureless at all energies. At 7.5 MeV the iron, nickel and lead spectra show fairly pronounced structure but at 12 MeV all spectra are fairly smooth. The fluctuations below ∿2 MeV for the iron and nickel data at 12 MeV are an artifact of the data due to a slight energy shift between the gas-in and gas-out runs. As in Ref. 2, there is some evidence for collective enhancement in the region of the 3^- states of the even-even nuclei.

Fig. 6 shows the angular distributions for the scattering of 10-MeV neutrons from iron. The spectral shapes are almost identical apart from the effects of the highly anisotropic elastic scattering peak.

Multiple scattering corrections will be made with the code EFFIGYC, discussed in a separate contribution to this conference[10]. This code takes as input known source cross sections, differential cross sections to 'discrete groups', and parameters describing the time-of-flight system. It then determines through Monte Carlo simulation the energy distribution of continuum scattering processes that reproduces the observed TOF spectra. In this manner a cross section for scattering to the continuum is developed. In addition to calculation of attenuation, multiple scattering, and finite geometry effects, EFFIGYC removes the effects of source gas breakups.

Preliminary results indicate that at the lower energies, the dominant corrections are due to attenuation in the samples. This does not greatly distort the spectral shapes and the uncorrected energy spectra can then be used to extract nuclear temperatures. Assuming the emission spectra have the form $(N(E) \propto E \exp(-E/kT)$ (see Ref. 11), plotting $\ell n\ N(E)/E$ against E yields a straight line whose slope is $-1/kT$. Fig. 7 shows such a plot for the iron scattering data at 10 MeV. The excess yield at 45° below 3 MeV is due to the scattering of the tritium gas breakup neutrons. Fitting to the regions between 0.5 and 4.5 MeV at the other angles yields the straight lines shown. The average temperature found from these lines is 1.00±0.05 MeV, in agreement with values obtained from lower energy neutron scattering.[4] The expected variation of the apparent temperature[12] with scattering angle is negligible. More detailed comparisons of spectral shapes with theoretical predictions will be made once the experimental spectra have been fully corrected with the code EFFIGYC.

Summary

The TUNL neutron time of flight system is being used to measure neutron emission spectra for medium mass to heavy nuclei bombarded by neutrons in the 7.5-14 MeV region. Preliminary results indicate that emission spectra can be measured down to ∿500 keV emitted neutron energy with the D+d and T-p source reactions. Statistical accuracies of ~5% are obtained in the experiment. Overall accuracies of ∿10% are expected for final double differential cross section data once corrections for multiple scattering and source gas breakup have been made.

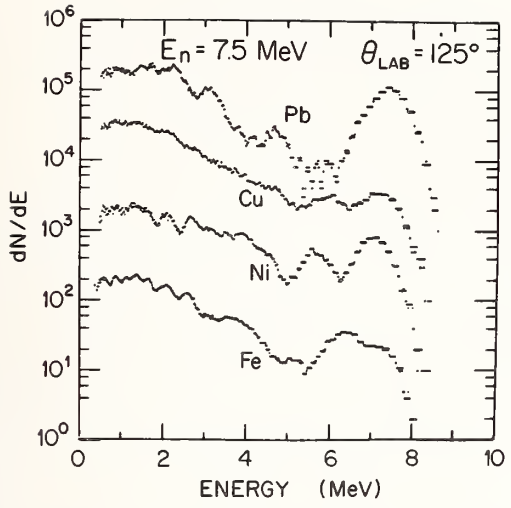

Fig. 3 Energy spectra for neutron scattering from Fe, Ni, Cu, Pb at 125° for an incident neutron energy of 7.5 MeV. The vertical scale is arbitrarily normalized and is in counts per 20 keV energy interval.

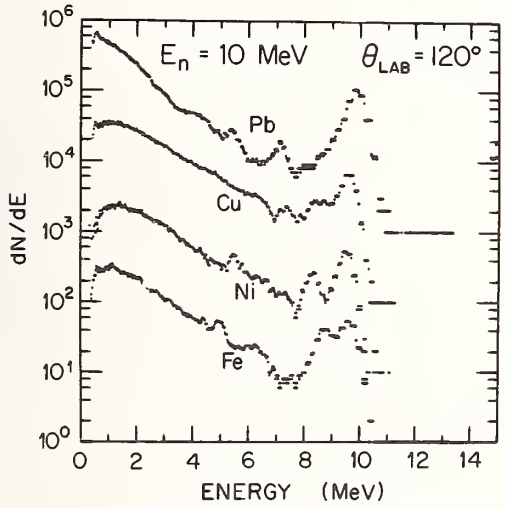

Fig. 4 As Fig. 3 except at 120° for 10 MeV incident neutron energy.

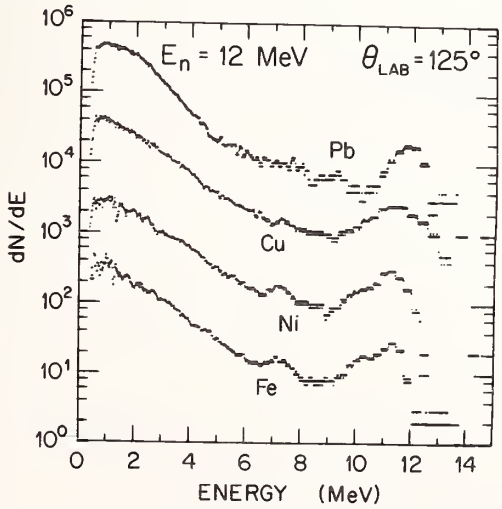

Fig. 5 As Fig. 3 except for 12 MeV incident neutron energy.

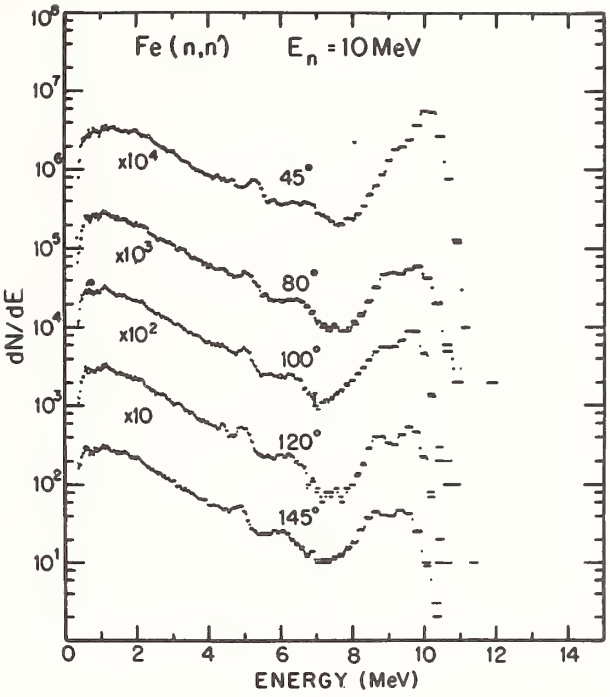

Fig. 6 As Fig. 3 except Fe scattering at 10 MeV for five different laboratory scattering angles.

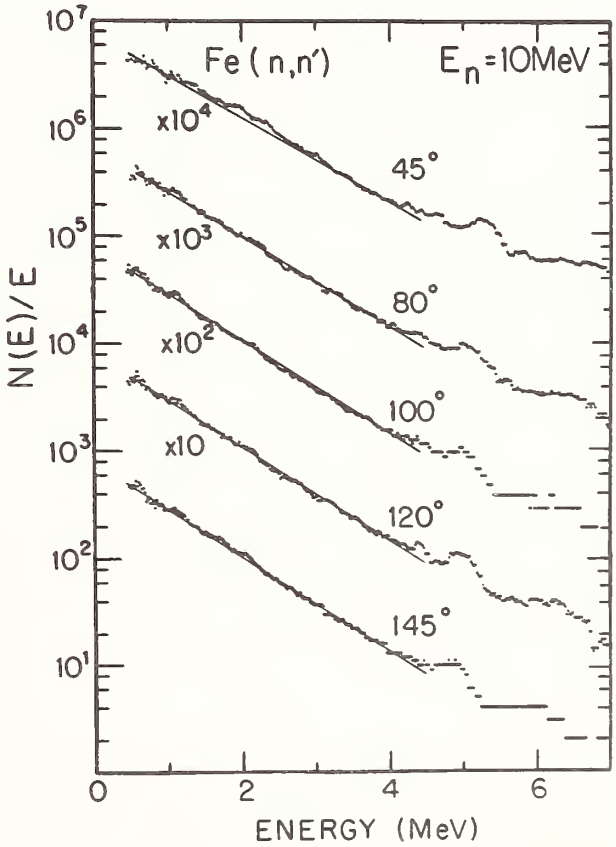

Fig. 7 Plots of log (N(E)/E) for neutron scattering from iron at 10 MeV. Nuclear temperature is extracted from the slopes of these plots. Average temperature is $\bar{T}$=1.00±0.05 MeV.

Acknowledgment

This work was supported in part by the U.S. Department of Energy.

References

1. D. Hemsdorf, et al., Zentralinstitut für Kernforschung Rossendorf Bei Dresden, ZfK-277 (Ü), (1975).

2. J.H. Towle and R.O. Owens, Nucl. Phys. A100, 257 (1967).

3. D.M. Drake et al., Nucl. Sci and Eng. 63, 401 (1977).

4. N.S. Biryukov, et al., Yad. Fiz. 19, 6 (1974), translated in Sov Jour Nucl Phys. 19, 608 (1974).

5. G. Stengl, M. Uhl, H. Vonach, Nucl. Phy. A290, 109 (1977).

6. L.W. Seagondollar et al., contribution EC10 to this Conference.

7. H. Liskien and A. Paulsen, Nuclear Data Tables, A11, 569 (1973).

8. M. Drosg Nucl. Sci and Eng. 67 190 (1978).

9. M. Drosg et al., Nucl. Inst. and Meth. 140, 515 (1977).

10. H. Hogue and A. Beyerle, contribution EC1 to this Conference.

11. J.M. Blatt and V.F. Weisskopf, Theoretical Nuclear Physics (Wiley, NY, 1952).

12. S. Grimes, et al., Phys. Rev. C3, 645 (1971).

ELASTIC NEUTRON SCATTERING FROM ^{63}Cu, ^{65}Cu, ^{54}Fe and ^{56}Fe FROM 8 TO 12 MeV

S. El-Kadi, R. Pedroni, G. Glendinning, C.E. Nelson, F.O. Purser, and R.L. Walter
Dept. of Physics, Duke University, Durham, NC, 27706, USA
and
Triangle Universities Nuclear Laboratory, Duke Station, NC, 27706, USA

A. Beyerle, C. Gould and W. Seagondollar
Dept. of Physics, North Carolina State University, Raleigh, NC, 27650, USA
and
Triangle Universities Nuclear Laboratory, Duke Station, NC, 27706, USA

Elastic scattering cross sections have been measured for 8 to 12 MeV neutrons for ^{63}Cu, ^{65}Cu, ^{54}Fe and ^{56}Fe using the TUNL time-of-flight facility. The measurements are compared to earlier data and to optical model calculations.

[$^{63,65}Cu$ and $^{54,56}Fe$(n,n), differential cross section, 8-12 MeV, optical model comparison.]

Introduction

During the past few years, the neutron time-of-flight group at Triangle Universities Nuclear Laboratory (TUNL) has concentrated on differential cross-section measurements for elastic and discrete inelastic scattering for targets $A \leq 16$. The energy range typically was 8 to 15 MeV, a region important in the development of fusion-energy sources. Recently, we extended these measurements to the medium weight isotopes $^{54,56}Fe$ and $^{63,65}Cu$, elements which also will enter into the design of such devices.

In this paper we report on the progress made in determining the elastic scattering cross sections for these isotopes. The final uncertainties to be assigned to the data and all the normalization errors have not been fully assessed yet, and therefore the data are still subject to small adjustments.

Experimental Procedure and Data Processing

At TUNL, a direct extraction negative ion source produces a beam of negative deuterium ions which is chopped and bunched by a standard High Voltage Engineering Corporation pulsing and bunching system prior to injection into the FN tandem Van de Graaff accelerator. The accelerated deuteron beam is transported to a deuterium gas cell via an all metal and ceramic beam line which is maintained at a vacuum of approximately 10^{-7} Torr by a combination of diffusion pumps, a titanium sublimation pump, and liquid nitrogen traps. The deuteron beam bursts at the target are about 1.5 ns wide and the average current is about 2 μA.

Source neutrons were obtained from the $^{2}H(d,n)^{3}He$ reaction using 3 bar of high purity deuterium gas in a 3.2 cm long tantalum lined cylindrical cell isolated from the vacuum system by a 5.8 mg/cm^2 Havar Foil. An overview of the system is given in the paper of Seagondollar et al.[1] contained in these proceedings.

The flight paths of the two detectors were set at the maximum permissible amount approximately 4 m and 6 m. The detectors are made from NE218, and a bias of about 1.9 MeV neutron energy was used throughout. The efficiency function was determined by using known $^{3}H(p,n)$ and $^{2}H(d,n)$ reaction cross sections.

The physical data of the cylindrical scattering samples are given in table I. These samples were supported with thin stainless steel wire.

Table I. Scattering sample properties.

Sample	Radius (cm)	Height (cm)	Mass (gm)	Purity (%)
^{54}Fe	0.95	2.40	50.9	97.6
^{56}Fe	0.95	2.91	63.4	99.9
^{63}Cu	1.00	2.97	82.1	99.9
^{65}Cu	1.00	2.94	84.6	99.7

Representative 10 MeV time-of-flight spectra for ^{54}Fe at 40° and 100° are shown in fig. 1. The prominent peak is due to elastic scattering and the neighboring peak is due to the first excited state at 1.41 MeV. The spectra have been offset by 100 counts per channel to facilitate the data analysis. To measure the neutron background, a sample-out count was taken with a bare wire in place of the sample. To minimize accelerator time, no background measurements were taken with the deuterium gas removed from the cell.

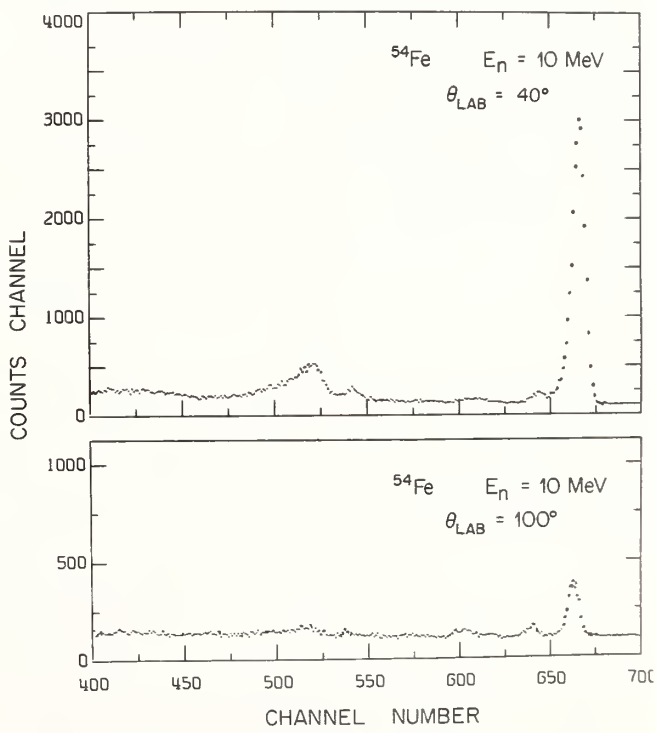

Fig. 1. Time-of-flight spectra for ^{54}Fe. Time resolution is approximately 3 ns (FWHM). Both spectra are offset by 100 counts/channel.

The differential elastic scattering cross-section measurements were performed at the three energies 8.0, 10.0 and 12.0 MeV, and at angles from 30° to 155° in 5° increments. At 8.0 MeV the cross-section measurements for the odd angles were performed with the 4 m detector and the even angles were performed with the 6 m detector. At 10.0 MeV and 12.0 MeV we used the longer flight path detector to measure the cross sections at forward angles. The differential cross sections were normalized to the accurately known n-p scattering cross-sections. This was accomplished by measuring the number of neutrons scattered by a polyethylene sample.

The normalized cross sections were corrected for the effects of finite neutron source, sample size, and multiple scattering. These corrections were performed by a Monte Carlo calculation using the program EFFIGY described in the paper by Hogue and Beyerle[2] in these proceedings. This program takes into account the anistropy of the incident flux from the $^{2}H(d,n)^{3}He$ source reaction, the attenuation of this flux in the sample, the effects of multiple scattering in the sample, and the angular resolution of each detector. With the samples sizes mentioned above and with a gas target to scatterer distance of about 8 cm, multiple scattering and finite size effects are substantial. Figure 2 shows a calculation of the ratio of multiple scattered neutrons detected to singly scattered neutrons for ^{63}Cu at 8.0 MeV. As can be seen, at the scattering minimum around 55°, approximately 45% of the neutrons detected are multiple scattered.

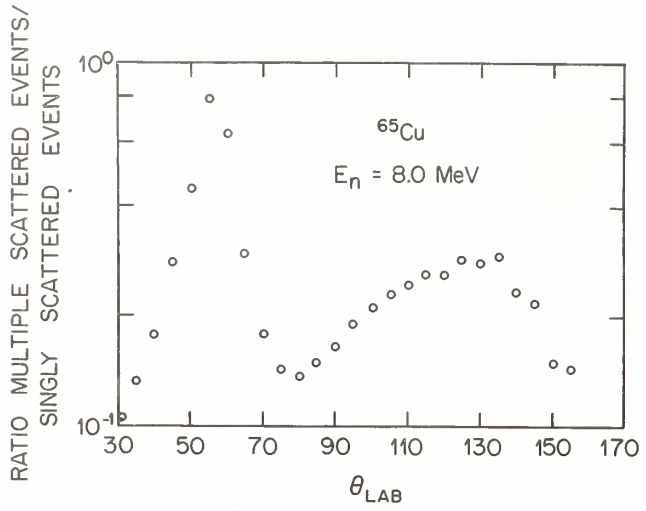

Fig. 2. Results of Monte Carlo calculation.

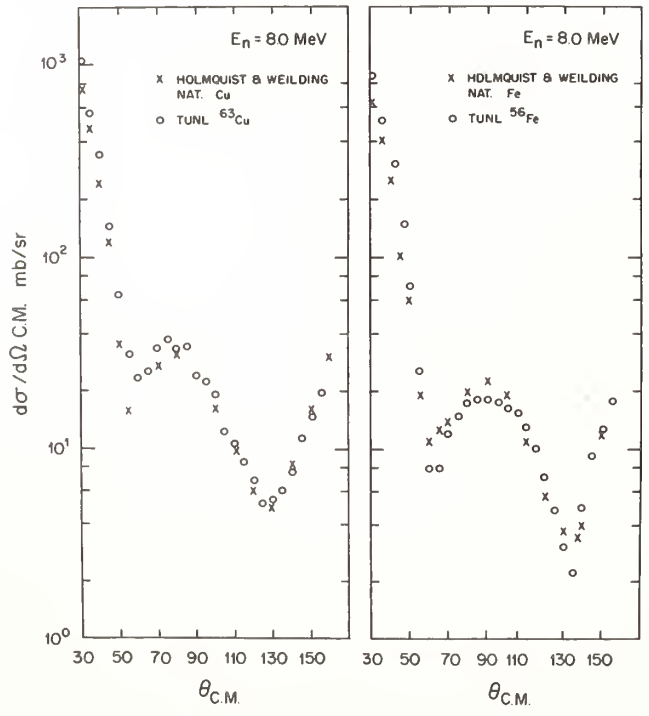

Fig. 3. Comparison of present results to previous work.[3]

Figure 3 shows our corrected 8.0 MeV data for ^{53}Cu and ^{56}Fe compared to an earlier measurement of natural copper and natural iron by Holmquist and Weilding[3]. The agreement with their data is quite good except in the forward scattering peak where our results are somewhat higher.

Optical Model Comparison

Due to time limitations, a comprehensive optical model analysis has not been completed. Our ^{63}Cu and ^{56}Fe data are shown in fig. 4 and 5 along with an optical model prediction obtained using the parameter set reported by Wilmore and Hodgson[4]. A standard

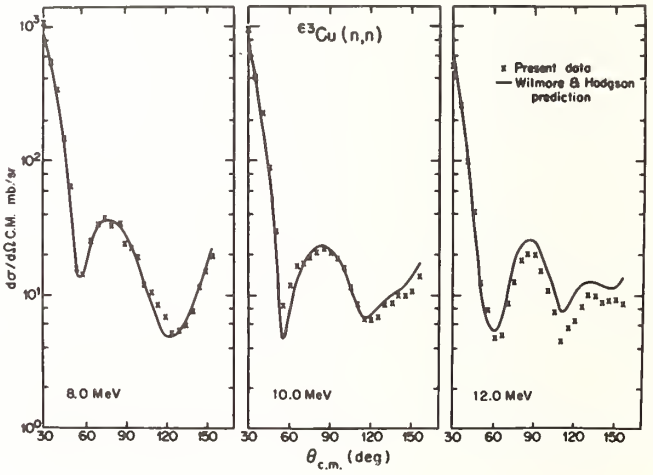

Fig. 4. Present results compared to optical model predictions based on Wilmore and Hodgson parameters.[4]

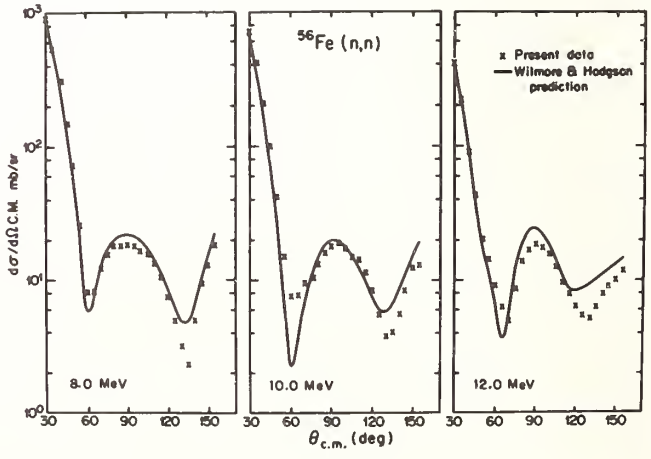

Fig. 5. Same as fig. 4.

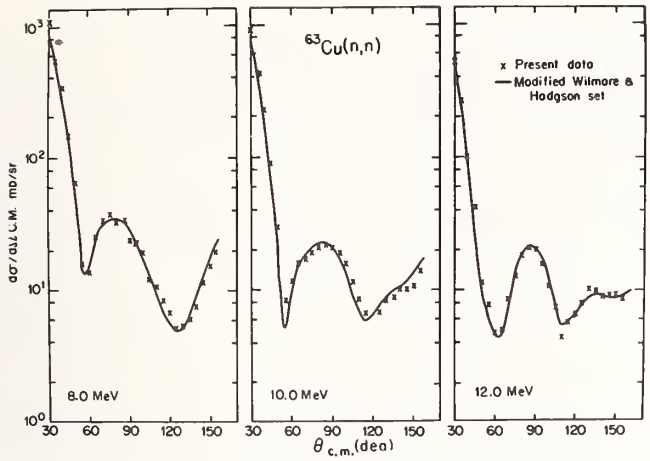

Fig. 6. Present results compared to optical model search on V_o and W_o.

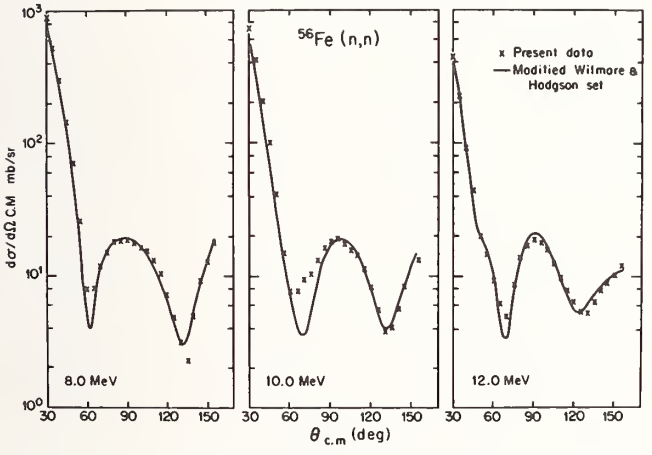

Fig. 7. Same as fig. 6.

spin-orbit term of V_s=6.2 MeV, r_s=1.1 fm, and a_s=0.75fm has been added. This term was not included in the work of ref. 4. The agreement is already quite good even without varying any of the parameters. We took the straightforward step of allowing the real well depth and imaginary well depth to vary. The search results indicated some improvement in the fits with very small changes in V_o and moderate changes in W_d. These calcu- are shown in fig. 6 and 7 respectively. As can be seen for this modest search, the data are reasonably well fit; however, the calculations do fall below the data in the region of the first minimum in the case of the ^{56}Fe at 8 and 10 MeV.

The agreement of the Wilmore and Hodgson predictions for ^{65}Cu were similar to that for ^{63}Cu, and for ^{54}Fe were similar to that for ^{56}Fe. In addition, the optical model searches for ^{63}Cu and ^{54}Fe followed closely the features of the searches for the ^{65}Cu and ^{56}Fe, respectively.

Compound elastic scattering calculations have not been conducted by us for these isotopes. Holmquist[5] tabulated the results of calculations for many elements and reported the energy dependence of the total compound elastic cross section for copper and iron between 1.5 and 8 MeV. Based on these values, the compound elastic scattering contribution will be too low to affect the present optical model search conclusions.

All the optical model calculations mentioned above were performed using the computer code GENOA obtained from Perey[6]. We intend to use the global feature of this code to search simultaneously three such sets of data for all four isotopes to obtain the best overall description for neutron scattering in the region 8 to 12 MeV. However, before we initiate these searches, all the cross-section values will be checked and proper uncertainties will be assigned to the data.

Conclusion

We have obtained the differential cross sections for elastic scattering for two isotopes each of Cu and Fe from 8 to 12 MeV. However, our optical model fitting of these data sets has not been completed, and we are not yet able to specify the details of the systematics of the optical model parameters. On the other hand, it does appear that most of the data for all four isotopes can be described reasonably well with only slight changes from the global parameters of Wilmore and Hodgson.

We have not completed our analysis of the inelastic data for the first excited states for these isotopes. These data are being analyzed using a peak fitting routine, but it has been difficult so far to assess the background uncertainties. In general, the preliminary results show that the cross sections range from a few mb/sr around 90° to perhaps 10 mb/sr at forward angles.

Acknowledgement

Research sponsored by the U.S. Department of Energy.

References

1. W. Seagondollar et al. (these proceedings).

2. H. Hogue and A. Beyerle (these proceedings).

3. B. Holmquist and T. Weilding, A.B. Atomenergi, Studsvik, Sweden, Report AE-303 (1967); BNL 400, TID-4500 (1970) EANDC(US)-138 "U" .

4. D. Wilmore and P.E. Hodgson, Nucl. Phys. 55, 673 (1964).

5. B. Holmquist, Arkiv För Fysik 38, 403 (1968).

6. F. Perey (private communication).

ELASTIC AND INELASTIC SCATTERING OF 24 MeV NEUTRONS FROM EVEN ISOTOPES OF Ni

Y. Yamanouti*, J. Rapaport, S.M. Grimes**, V. Kulkarni, R.W. Finlay,
D. Bainum***, P. Grabmayr and G. Randers-Pehrson
Physics Department
Ohio University
Athens, Ohio 45701, USA

Differential cross sections for the scattering of 24 MeV neutrons from ^{58,60}Ni were measured as part of a continuing study of nucleon scattering from single-closed-shell nuclei. Measurements were taken every 5° from 15° to 150° using the Ohio University time-of-flight spectrometer. Inelastic excitation of the first 2^+ and 3^- states was measured simultaneously with the elastic scattering in each case. Results are analyzed in terms of a global nucleon-nucleus optical model potential, DWBA and coupled-channel calculations using collective model.

[Global optical potential, elastic scattering, inelastic scattering, neutron, 24 MeV, ^{58,60}Ni, DWBA, coupled-channel, deformation parameter, differential cross sections]

Introduction

Neutron scattering experiments in the energy range from 11 to 26 MeV have been carried out to investigate the energy and isospin dependence of the nuclear optical-model potential[1-5]. These experiments are indispensable to get deeper understanding of the systematics for the nucleon-nuclear optical potential. This work is one of several in a series of neutron scattering studies in the mass region where neutron scattering data are not available.

The reaction mechanism of nucleon scattering in this energy range is generally described by the DWBA[6] and/or the coupled-channel formalism[7].

In this paper the measured differential cross sections have been analyzed in terms of a global nucleon nucleus optical model potential, the DWBA and the coupled-channel formalism. The deformation parameters obtained in the (n,n') reaction are compared with those obtained in the (p,p') reaction.

Experiment

The 24 MeV pulsed neutron beam was obtained from the Ohio University 11 MeV Tandem Van de Graaff Accelerator. Monoenergetic neutrons were generated by the ^{3}H(d,n)^{4}He reaction.

Scattered neutrons were observed by a very large NE224 liquid scintillator detector[8] 28.6 cm thick by 18.2 cm in diameter which was viewed by two RCA 4522 photomultipliers from the front and rear faces. Protons generated at the point of interaction travel to the rear and front faces of the scintillator where they generated time signals t_1 and t_2, respectively. The total flight time is related to t_1 and t_2 in a term proportional to $(t_1 - \alpha\, t_2)$. Time-of-flight spectra by the very large detector were observed with $\alpha = 0.4$. A small 5.1 cm thick by 5.1 cm in diameter NE102 scintillation detector was used as a neutron flux monitor. Pulse shape discrimination was employed to eliminate gamma-ray events from the time-of-flight spectra for these neutron detectors.

The enriched ^{58,60}Ni samples were all right cylinders. Dimension, mass and isotopic abundance of the scattering samples are listed in table 1.

* Permanent address: JAERI, Japan
** Permanent address: Lawrence Livermore Laboratory, Livermore, California
*** Permanent address: Emporia State University, Emporia, Kansas

Experimental Results

Experimental yields were calculated by fitting the peaks of interest with line shapes of an Hermite polynomial expansion superimposed on a residual linear background. The analysis of the time-of-flight spectra was done using the least-square curve-fitting program PEAKFIT[9]. The relative efficiencies for the neutron detector were calculated with the code DETEFF[10]. The resulting differential cross sections were corrected for finite angular geometry, multiple scattering and neutron flux attenuation in the sample using the Monte Carlo code MULTISCAT[11].

In this experiment measurements were made for the elastic scattering and the inelastic scattering leading to the excited states at 1.454 MeV (2^+) and 4.472 MeV (3^-) in ^{58}Ni, and 1.332 MeV (2^+) and 4.045 MeV (3^-) in ^{60}Ni, respectively. The cross sections for the 3^- for ^{58}Ni and ^{60}Ni may include the contribution from adjacent states around the 3^- states because of the insufficient energy resolution of the time-of-flight method. In this paper the "3^-" cross sections were assumed to have the contribution from only the 3^- state. The measured cross sections obtained in this experiment are shown in figures 1-4 together with theoretical cross sections.

Analysis

Optical Model Potentials

A local optical model potential was used in the analysis of the neutron scattering data. The form of the potential used in this evaluation is similar to the global optical potential parameter set A in ref. [12], and these optical potential parameters were used as initial set of the parameter searches. The data were fitted with the optical potential search code GENOA[13]. In the first step the optical potential parameters were searched to get the individual best fit on each of ^{58}Ni and ^{60}Ni. The best fit optical potential parameters obtained in the searches are given as set A in table 2. In the second step, searches for all the potential parameters except spin orbit part were performed by fitting the two sets of elastic scattering simultaneously to see the isospin dependence of the optical potentials. The geometrical parameters obtained from the individual best fit searches for ^{58}Ni and ^{60}Ni were averaged for the starting parameters of the second step.

In the Lane model[14] the neutron optical potential has isoscalar and isovector parts in the form $U = U_o - U_1\varepsilon$, where $U = V + iW$ and $\varepsilon = (N-Z)/A$. The starting values for the isoscalar and isovector strengths were taken as those of the global optical potential parameter set A[12].

The results of these searches are given as set B in table 2. The best fit isovector strengths for the real and imaginary potentials were $V_1 = 21.67$ MeV and $W_1 = 10.01$ MeV, respectively.

DWBA Calculations

Collective-model calculations were made for the experimental cross sections by using the DWBA code DWUCK 4[15]. The individual best fit optical potential parameter set A in table 2 was used in the DWBA calculations. The deformation parameters obtained in the calculations are listed in table 3. The results obtained by the DWBA calculations are shown in figures 1-4. The experimental cross sections were well reproduced by the DWBA calculations.

Coupled-Channel Calculations

The experimental cross sections were analyzed by the coupled-channel formalism by using the code CHUCK 3[16]. In the coupled-channel calculations, the individual best fit optical potential parameter sets were adjusted to preserve the fit to the elastic scattering cross sections. It was sufficient to reduce only the imaginary potential depths W_V and W_D by 10%. The coupled-channel calculations based on the vibrational model were carried out with the $0^+ - 2^+ - 3^-$ coupling scheme. The coupling between the 2^+ and 3^- states was taken into account in addition to the couplings to the ground state. The deformation parameters β_2 and β_3 were chosen to get best fit to the experimental cross sections for the 2^+ and 3^- states, respectively. The results obtained in the coupled channel calculations are shown in figures 1-4 together with the experimental cross sections and the DWBA predictions. The results are in good agreement with the experimental cross sections. The deformation parameters obtained in the coupled-channel calculations are listed in table 3 together with the deformation parameters obtained in the (p,p') reaction[17-21] for comparison.

Discussion

In table 3 it is noticed that the present β_2 parameter obtained in the (n,n') reaction is systematically smaller than those obtained in the (p,p') reaction. Madsen, Brown and Anderson presented numerical relationships between the deformation parameters $\beta_{nn'}$ and $\beta_{pp'}$ from the microscopic effective-charge theory[22]. The model ratios $\beta_{pp'}/\beta_{nn'}$ are given to be 1.21 and 1.19 for ^{58}Ni and ^{60}Ni, respectively by using the eqs. (13) and (14) in ref. 22. While the experimental ratios $\beta_{pp'}/\beta_{nn'}$ obtained by the DWBA were 1.21 and 1.32 for ^{58}Ni and ^{60}Ni, respectively. These experimental results satisfy the inequality relationship $\beta_{nn'} < \beta_{pp'}$, which is expected for the single-closed-shell nuclei (neutron vibrational nuclei).

Conclusion

Accurate measurements of experimental neutron cross sections for the elastic and the inelastic scattering leading to the first 2^+ and 3^- states for ^{58}Ni and ^{60}Ni are presented. Prior to this work no neutron scattering data at this energy and range of nuclei were available. Isospin dependent optical model potential parameters are presented as well as the individual best fit optical potential parameters.

The DWBA and coupled-channel calculations resulted in a good agreement to the experimental cross sections for ^{58}Ni and ^{60}Ni at 24 MeV.

The comparison between (n,n') and (p,p') data shows that $\beta_{pp'}$ is systematically larger than $\beta_{nn'}$ by approximately 20% or more. This difference between $\beta_{nn'}$ and $\beta_{pp'}$ is explained by the predictions based on the microscopic effective-charge theory.

The authors wish to thank Dr. R.D. Koshel for the helpful discussions.

References

1. J.C. Ferrer, J.D. Carlson and J. Rapaport, Nucl. Phys. A275 (1977) 325
2. J. Rapaport, J.D. Carlson, D. Bainum, T.S. Cheema and R. W. Finlay, Nucl. Phys. A286 (1977) 232
3. J. Rapaport, T.S. Cheema, D.E. Bainum, R.W. Finlay and J.D. Carlson, Nucl. Phys. A296 (1978) 95
4. D.E. Bainum, R.W. Finlay, J. Rapaport, M.H. Hadizadeh and J.D. Carlson, Nucl. Phys. A311 (1978) 492
5. J. Rapaport, T.S. Cheema, D.E. Bainum, R.W. Finlay and J.D. Carlson, Nucl. Phys. A313 (1979) 1
6. R.H. Bassel, G.R. Satchler, R.M. Driska and E. Rost, Phys. Rev. 128 (1962) 2693
7. T. Tamura, Rev. Mod. Phys. 37 (1965) 679
8. J.D. Carlson, R.W. Finlay and D.E. Bainum, Nucl. Instr. Meth. 147 (1977) 353
9. S. Grimes, P. Grabmayr, J. O'Donnell and R. Moyer, private communication
10. S.T. Thornton and J.R. Smith, Nucl. Instr. 96 (1971) 551
11. W.E. Kinney, Nucl. Instr. 83 (1970) 15; and private communication
12. J. Rapaport, V. Kulkarni and R.W. Finlay, to be published in Nucl. Phys.
13. R.G. Perey, private communication
14. A.M. Lane, Nucl. Phys. 35 (1962) 676
15. P.D. Kunz, University of Colorado, unpublished
16. P.D. Kunz, University of Colorado, unpublished
17. M.J. Throon, Y.T. Cheng, A. Goswami, O. Nalcioglu, D.K. McDaniels, L.W. Swenson, N. Jarmie, J.H. Jett, P.A. Louoi, D. Stupin, G.G. Ohlsen, G.C. Salzman, Nucl. Phys. A283 (1977) 475
18. S.F. Eccles, H.F. Lutz and V.A. Madsen, Phys. Rev. 141 (1966) 1959
19. P.J. Van Hall, J.P.M.G. Melssen, S.D. Wassenaar, O.J. Poppema, S.S. Klein and G.J. Nijgh, Nucl. Phys. A291 (1977) 13
20. O. Karban, P.D. Greaves, V. Hnizdo, J. Lowe and G.W. Greenlees, Nucl. Phys. A147 (1970) 461
21. N. Lingappa and G.W. Greenlees, Phys. Rev. C2 (1970) 1329
22. V.A. Madsen, V.R. Brown and J.D. Anderson, Phys. Rev. C12 (1975) 1205

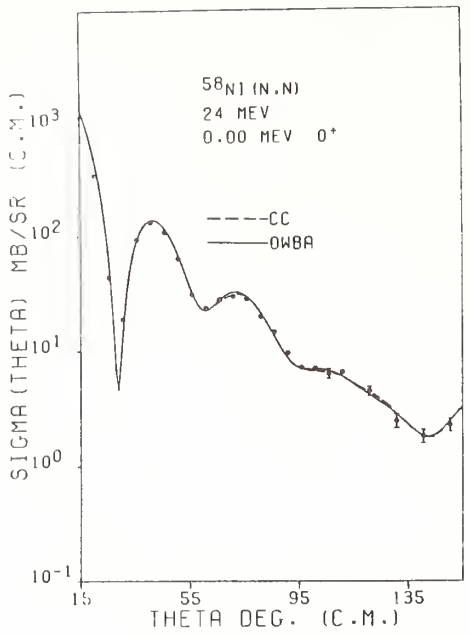

FIGURE 1

DWBA and coupled-channel fits to the elastic scattering of 24 MeV neutrons for ^{58}Ni using $0^+ - 2^+ - 3^-$ coupling.

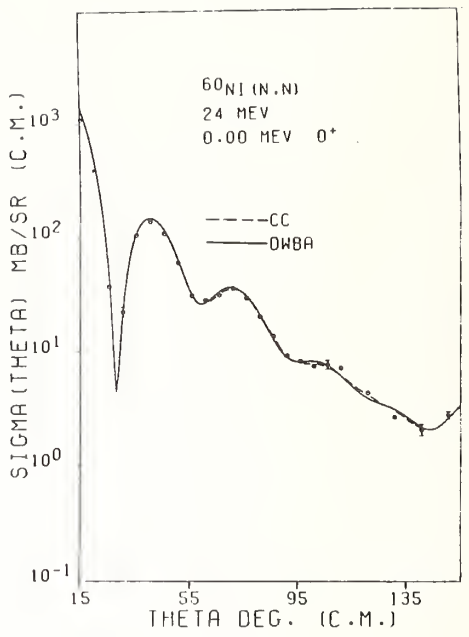

FIGURE 3

DWBA and coupled-channel fits to the elastic scattering of 24 MeV neutrons for ^{60}Ni using $0^+ - 2^+ - 3^-$ coupling.

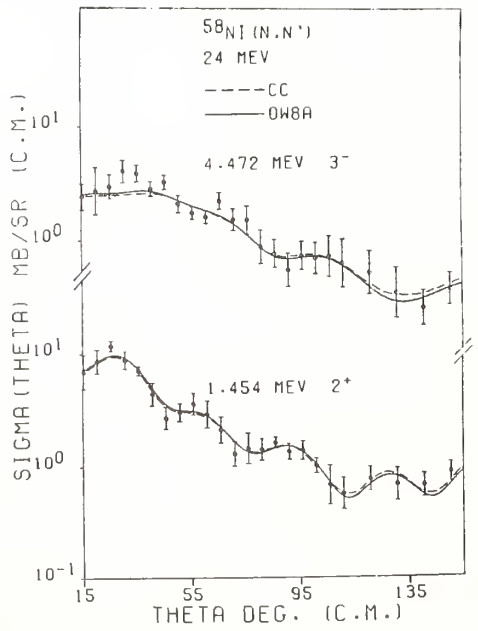

FIGURE 2

DWBA and coupled-channel fits to the inelastic scattering of 24 MeV neutron from 2^+ and 3^- states of ^{58}Ni using $0^+ - 2^+ - 3^-$ coupling.

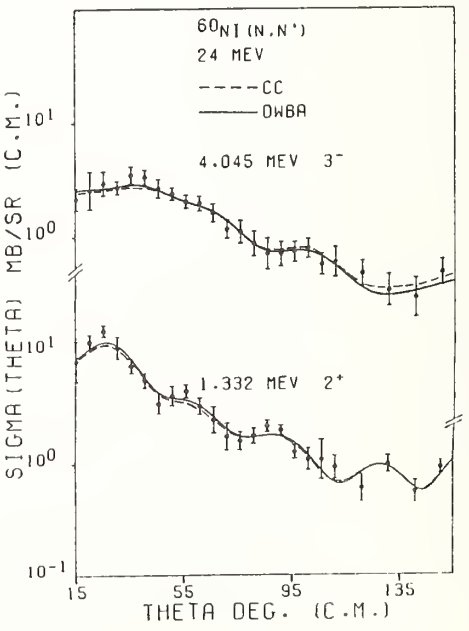

FIGURE 4

DWBA and coupled-channel fits to the inelastic scattering of 24 MeV neutrons from 2^+ and 3^- states of ^{60}Ni using $0^+ - 2^+ - 3^-$ coupling.

TABLE 1

Dimension, Mass and Enrichment of Scattering Samples*

Sample	Diameter (cm)	Height (cm)	Mass (g)	Enrichment (%)
^{58}Ni	1.541	2.41	34.493	99.935
^{60}Ni	1.546	2.41	38.678	99.79
^{60}Ni	2.00	2.08	57.434	99.62

*The samples were obtained on loan from the Isotope Division, Oak Ridge National Laboratory.

TABLE 2

Best Fit Optical Potential Parameters†

	^{58}Ni		^{60}Ni	
	set A	set B	set A	set B
V_R	44.80	45.36	44.75	44.81
V_R	1.194	1.190	1.191	1.190
a_R	0.615	0.625	0.646	0.625
W_V	2.181	2.096	2.315	2.096
W_D	5.301	5.184	4.661	4.860
r_I	1.219	1.233	1.232	1.233
a_I	0.707	0.737	0.762	0.737
V_{SO}	6.2	6.2	6.2	6.2
r_{SO}	1.01	1.01	1.01	1.01
a_{SO}	0.75	0.75	0.75	0.75
σ_T	2.36	2.42	2.49	2.44

set A: individual best fits

set B: best fits obtained with the average geometry and simultaneous fitting to two sets of elastic scattering

† Potential depths in MeV, geometrical parameters in fm, total cross sections in barn

TABLE 3

Deformation parameters of ^{58,60}Ni from (n,n') and (p,p') experiments

Reaction	Incident Energy (MeV)	Analysis	^{58}Ni β_2	^{58}Ni β_3	^{60}Ni β_2	^{60}Ni β_3	Reference
(n,n')	24	cc	0.175	0.16	0.185	0.16	present work
	24	DWBA	0.190	0.164	0.202	0.163	present work
(p,p')	15	DWBA	0.234	0.141	0.247	0.186	17
(p,p')	18.6	cc	0.21	0.19	0.30	0.22	18
	18.6	DWBA	0.24	0.19	0.30	0.22	18
(p,p')	20.4	DWBA	0.24	--	0.27	--	19
	24.6	DWBA	0.22	0.19	0.25	0.19	19
(p,p')	30.3	cc	0.18	0.165	--	--	20
(p,p')	40	cc	0.183	0.173	0.203	0.174	21

MEASUREMENT OF DIFFERENTIAL ELASTIC AND INELASTIC SCATTERING CROSS SECTIONS WITH 14 MeV NEUTRONS ON BARIUM AND CHROMIUM *

G. Winkler, K. Hansjakob and G. Staffel

Institut fuer Radiumforschung und Kernphysik
A-1090 Vienna, Austria

The elastic scattering of 14 MeV neutrons has been measured at angles from 20° to 130° with an accuracy of about 10%, the high energy part of the inelastic neutron spectrum has been measured as a function of θ and $E_{n'}$ in the region of θ = 20° - 130° and $E_{n'}$ = 4 - 12 MeV with an energy resolution $\leq$ 0.5 MeV, on elemental Barium and Chromium, using time-of-flight techniques. The cross sections for forming the first 2^+ level of ^{138}Ba and ^{52}Cr and the 3^- level of ^{52}Cr(4.56 MeV) have been measured. The results are compared with optical and statistical model calculations. The knowledge of the neutron interaction with Barium is important due to its use in reactor shielding, Chromium is expected to be an important structural material in fusion reactors.

(Nuclear reactions, 14 MeV Ba(n,n), Cr(n,n), $\sigma(\theta)$ Ba(n,n'), Cr(n,n'), $\sigma(E_{n'},\theta)$, $E_{n'}$ = 4 to 12 MeV, ^{138}Ba(n,n'), ^{52}Cr(n,n'), discrete levels, θ_{lab} = 20° to 130°, optical and statistical model)

Introduction

The measurements reported in the present work were undertaken as the first part of a program to determine energy and angular differential cross sections for elastic and inelastic scattering of 14 MeV neutrons on elements of practical importance in shielding and structural materials. The measurements were carried out with the fast neutron generator of Cockcroft-Walton-type at the IRK, Vienna, using the pulsed-beam time-of-flight (TOF)technique. In the case of Barium, which occurs in the form of barite as a constituent of heavy concrete, no differential scattering cross sections in the energy region considered have been previously reported. The results are compared with calculations based on the optical and statistical model of nuclear reactions.

Experimental Apparatus

The scattering geometry is shown schematically in Figure 1. The accelerator room is about 6.5 m x 6.8 m wide and 5.2 m high. Source neutrons in the 14 MeV region were produced via the ^{3}T(d,n)^{4}He reaction by a pulsed deuteron beam (FWHM of the deuteron pulse 0.8 - 1.0 ns)[1] with an energy of about 220 KeV at a repetition rate of 2.5 and 5.0 MHz. The average beam current at the target was about 4 - 7 μA. Solid state Tritium-Titanium-Copper targets were used in a low mass aluminum target assembly.

The position of the target and of the neutron detector was fixed. The axis of the access channel for the detection of scattered neutrons was defined by the axis of a cylindrical collimator consisting of three parts which had been carefully aligned: the section with the detector shielding, the section through the shielding wall (doped with boric acid), and an additional paraffin collimator to reduce the acceptance angle and thereby reducing the influence of scattering by air molecules. A hole had been broken through the opposite wall of the accelerator room to keep wall backscattering as low as possible. The angle between the deuteron beam axis and the collimator axis was 167°. The scattering angle was defined by the position of the scattering sample along the access channel axis. The normal distance from the beam spot on the tritium target to the access channel axis (position of the sample center for 90° scattering angle) was 34.7 $\pm$ 0.2 cm. The variation of the scattering angle in the course of the measurements was achieved by moving the sample along the access channel axis by means of a precision positioning system consisting of an optical bench 2 meters long, a carrier combined with a transverse, a vertical motion unit and an inclining and rotating table. In this way the different degrees of freedom of the sample could be adjusted independently and the symmetry axis of the sample set perpendicular to the scattering plane defined by the neutron source and the access channel axis. This simplified the geometrical conditions and made analytically calculated corrections for finite dimensions, absorption, and multiple scattering of the sample, possible. The direction of the optical bench, the position of the sample center and the stability of the collimator was determined by a laser beam aligned with the access channel axis, which could be split into a second parallel beam along the optical bench.

The neutron detector consisted of a NE 213 cylindrical liquid scintillator cell (12.7 cm diameter, 5.1 cm thick) mounted on a Phillips XP2041 fast photomultiplier. In addition, it was shielded by a 5 cm thick and 60 cm long quadrangular lead cage (with the scintillator cell in the center) to reduce the uncorrelated gamma-background. The flight path from the 90°-position to the center of the detector scintillator was 734 $\pm$ 1.5 cm. This enabled an energy resolu-

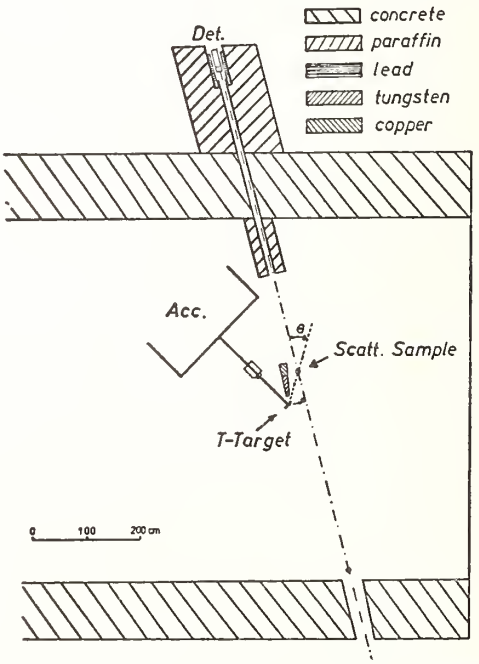

Fig. 1. Schematic view of scattering geometry

* Work supported by the European Community through Euratom

tion of about 450 KeV for 14 MeV neutrons, taking into account an overall time resolution of about 1.6 ns of the detector electronics and a flight path uncertainty of about 5 cm due to the scintillator thickness. The energy spread for the incident neutrons due to the neutron source was about 120 KeV, FWHM. The entrance aperture of the collimator and the air volume close to the collimator entrance was shielded against direct source neutrons by a conic shadow bar of 31 cm tungsten combined with 25 cm copper.

A second neutron detector consisting of a small plastic scintillator (2.0 cm diameter, 0.2 cm thick) coupled to a Phillips 56 AVP photomultiplier, which was positioned at backward angles relative to the deuteron beam at a distance of 1.0 m from the Tritium-Target, viewed the primary neutron source directly and served as a monitor for normalizing the incident neutron fluence.

Experimental Procedures

Samples. The experiments were very low in intensity due to the geometrical conditions. Therefore a good compromise had to be worked out between a tolerable net count rate and several effects that reduce the quality of the experiment and increase with the size of the sample. Detailed investigations were carried out to determine which sample shape would be best for the given scattering geometry. The following facts limiting the lateral dimensions of the sample were considered:

(1) The angular resolution, which must not exceed a few degrees to resolve the structure in $d\sigma/d\Omega(\theta)$,
(2) The spread of the path lengths due to scattering events at different points of the sample, which should not exceed the detector thickness appreciably,
(3) The spread in energy due to the source characteristics,
(4) The absorption and multiple scattering events in the sample, which decrease and/or increase the number of scattering events in the measured TOF-spectrum.

The dimensions of the sample perpendicular to the scattering plane have less influence on the angular resolution, path jitter and multiple processes than the lateral dimensions. It turned out that a plane rectangular slab with an approximate length of 12 cm and lateral dimension of 4 cm would be a good choice. The effects (1) to (4) depend on the orientation of the sample and also change with the scattering angle (here the position of the sample). The two favored positions of a rectangular sample relative to the incident neutron beam, (called tangential (t) and normal (n)) are shown in Figure 2. Obviously the spread in path length becomes a minimum in the tangential position. In that position the sample can be considered as a part of the tangent plane of an ellipsoid with its foci at the neutron source and the neutron detector, respectively. As a compromise between all the effects (1) to (4) the sample was used for scattering angles up to 75° in the normal position, for larger scattering angles in the tangential position. The thickness of the polyethylene covered Barium samples was 1.67 cm for measuring the elastic scattering and the inelastic scattering to the 2^+ level of ^{138}Ba, 4.0 cm for measuring the neutron spectra between 4 and 12 MeV. The thickness of the Chromium samples was 0.4 and 0.8 cm.

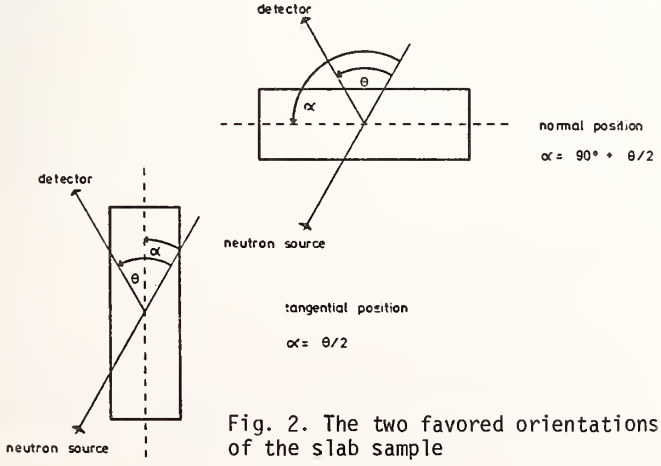

Fig. 2. The two favored orientations of the slab sample

Detector calibration. The efficiency of the main neutron detector was calibrated by measuring the scattering of neutrons from hydrogen in polyethylene samples with the same dimensions as used for the Ba- and Cr-samples, but thicknesses of 0.1, 0.2, 0.4 and 0.6 cm.[5] Separate runs with a graphite scatterer were necessary to correct for the background stemming from the carbon in polyethylene. Efficiency points at 13 - 14 MeV neutron energy were based on carbon scattering only. Thus all cross sections were determined relative to the well known H(n,n) and C(n,n) cross sections.[2,3,4]

The neutron fluence monitor detector was calibrated to absolute yields by irradiating small pure aluminum foils at definite distances from the target and measuring the ^{24}Na-activity induced by the $^{27}Al(n,\alpha)^{24}Na$ reaction, the cross section of which is well known in the 14 MeV region.[6] The relative dependence of the neutron fluences on the different sample positions (averaged over the sample surface), were measured by activating pure Aluminum sheets of the same size and in the same position as the scattering samples.

Electronics and data aquisition. A simplified block diagram of the electronics for the main neutron detector and the neutron flux monitor is shown in Fig. 3. A fast negative stop pulse for all TOF-timing was derived from the capacitive beam pick-off signal by a zero-crossing discriminator. Also, streched signals were available from a trigger (T) to automatically correct for a stop-efficiency less than 100%, by running the timing signals from the main detector as well as those from the monitor over a coincidence (K) with these streched pick-off signals prior to further processing. The electronics used with the main neutron detector involved three circuits, each of which fed an ADC:

(1) The pulse shape discrimination circuit,[7] which provided a separation of gamma and neutron pulses due to the different decay times of the light-output in the scintillator,
(2) The slow analog circuit which processed the recoil-energy information and
(3) The TOF-circuit, using a constant-fraction trigger.

If all conditions applied to the signals were met, a tripple coincidence provided a common gate signal for the three ADC's. A common ADC-busy signal prevented the acceptance of pulses from the detector via the above mentioned veto-coincidence during the ADC-busy time. The total dead-time was counted by overlapping it with pulses from a 1 MHz oscillator. The same dead-time was also applied to the monitor circuit by means of coincidence, thus securing an automatic dead-time compensation. The three ADC's providing the PSD-cross-over time spectra, the energy-loss, and time-of-flight information of each event, were interfaced to an on-line PDP 11/10 computer for data storage, on-line display and analysis. [8]

Data for the elastic scattering and the inelastic scattering to discrete levels were taken in steps of 5° for scattering angles from 20° to 130°, employing a beam-pulse separation of 200 ns. To measure the inelastic cross sections $d^2\sigma(n,n')/dE_{n'}d\Omega$ for the high energy part of the inelastic neutron spectra (i.e.

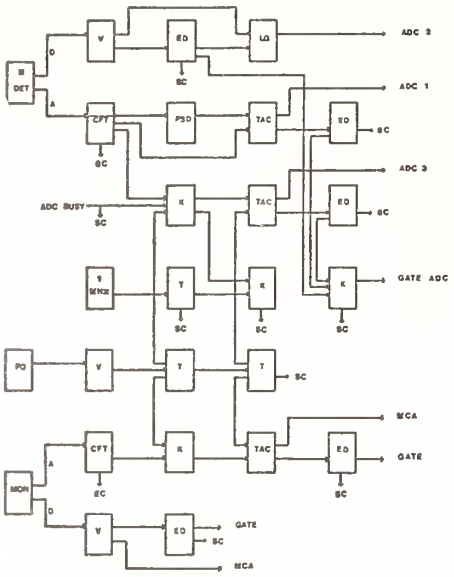

Fig. 3. Block diagram of the electronics (A...path of neg. fast anode signal, B...path of pos. linear signal from the 13th dynode, PO...beam-pick-off, V...amplifier, K...Coincidence, ED...pulse height selector, T..trigger, CFT...constant fraction trigger, LG...linear gate, SC...scaler, TAC...time-amplitude-converter)

for $4 \leq E_n' \leq 12$ MeV) data were taken from 20° to 130° in steps of 5° with a beam-pulse separation of 400 ns. To obtain an accuracy of about 10% for the differential elastic cross-section, it was necessary to get a statistical uncertainty of about 5 - 7%. This required an effective beamtime of about 300 hours for the Ba, Cr and calibration runs, each. Twelve scalers controlled by the on-line computer were included at critical points of the electronics set-up to signal electronic instabilities.

Data reduction

Multiparameter analysis was done off-line using the program MPASW.[9] The first step in data reduction was generating TOF-spectra including all events produced by neutrons with a pulse-height above 1.5*Cs (compton edge which resulted from ^{137}Cs gamma rays interacting in the scintillator). The separation between gamma- and neutron pulses was performed by a two dimensional sorting pulse-height versus pulse shape information(Fig. 4). The background was substracted

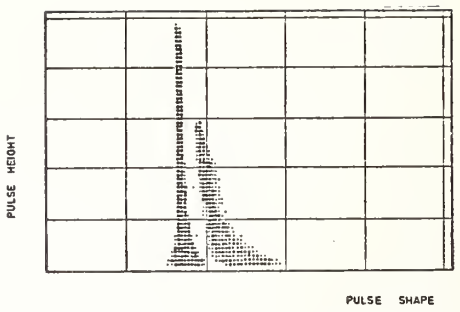

Fig. 4. Two dimensional spectrum: pulse height versus pulse shape cross-over. (The thickness of the point is proportional to the number of counts).

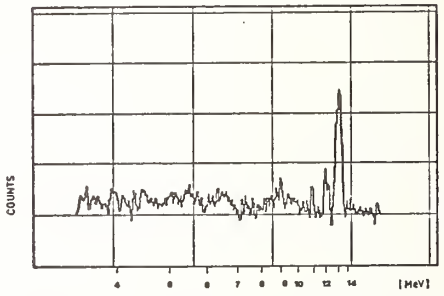

Fig. 5. Background subtracted neutron TOF-spectra (bias 1.5*Cs) for Chromium, $\theta_{lab} = 70°$

from these TOF-spectra after normalization (Fig. 5) The elastic cross sections were determined by direct integration over the elastic peaks in the TOF-spectra. For the determination of the inelastic scattering cross sections $d^2\sigma/dE_n'd\Omega$ ($4 \leq E_n' \leq 12$ MeV) the spectra were transformed to energy spectra in the C.M.-system, divided by the efficiency and corrected for absorption in the sample. As the incident neutron energy varied between 13.6 und 14.6 MeV, depending on the sample position, the energy spectra were transformed to an incident neutron energy $E_n = 14.1$ MeV, and were integrated over 0.5 MeV energy bins. An analytical approach was used for the estimation of absorption and multiple scattering effects.[10] In estimating double scattering for the inelastic case, for every energy bin E_x the probability was computed for events being scattered first to an energy bin E_1, and then being scattered to the energy bin E_x with $E_1 > E_x$. When comparing the probabilities $W(E_n \rightarrow E_x)$ and $W(E_n \rightarrow E_1, E_1 \rightarrow E_x)$ double scattering effects were found to be less than 1%. Nonelastic cross sections were computed by the code STAPRE.[11] Fig. 6 shows an example of the estimated correction

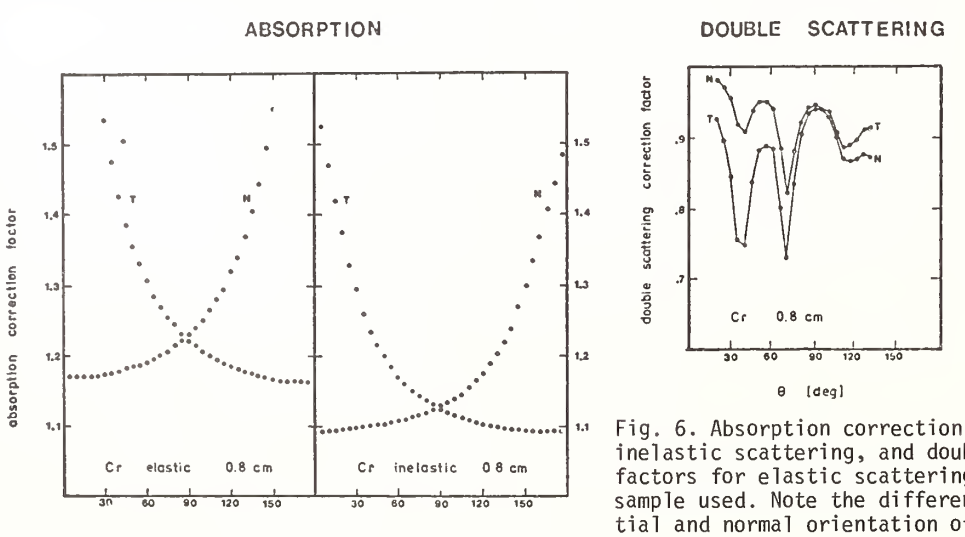

Fig. 6. Absorption correction factors for elastic and inelastic scattering, and double scattering correction factors for elastic scattering in the case of the Cr-sample used. Note the difference between the tangential and normal orientation of the sample.

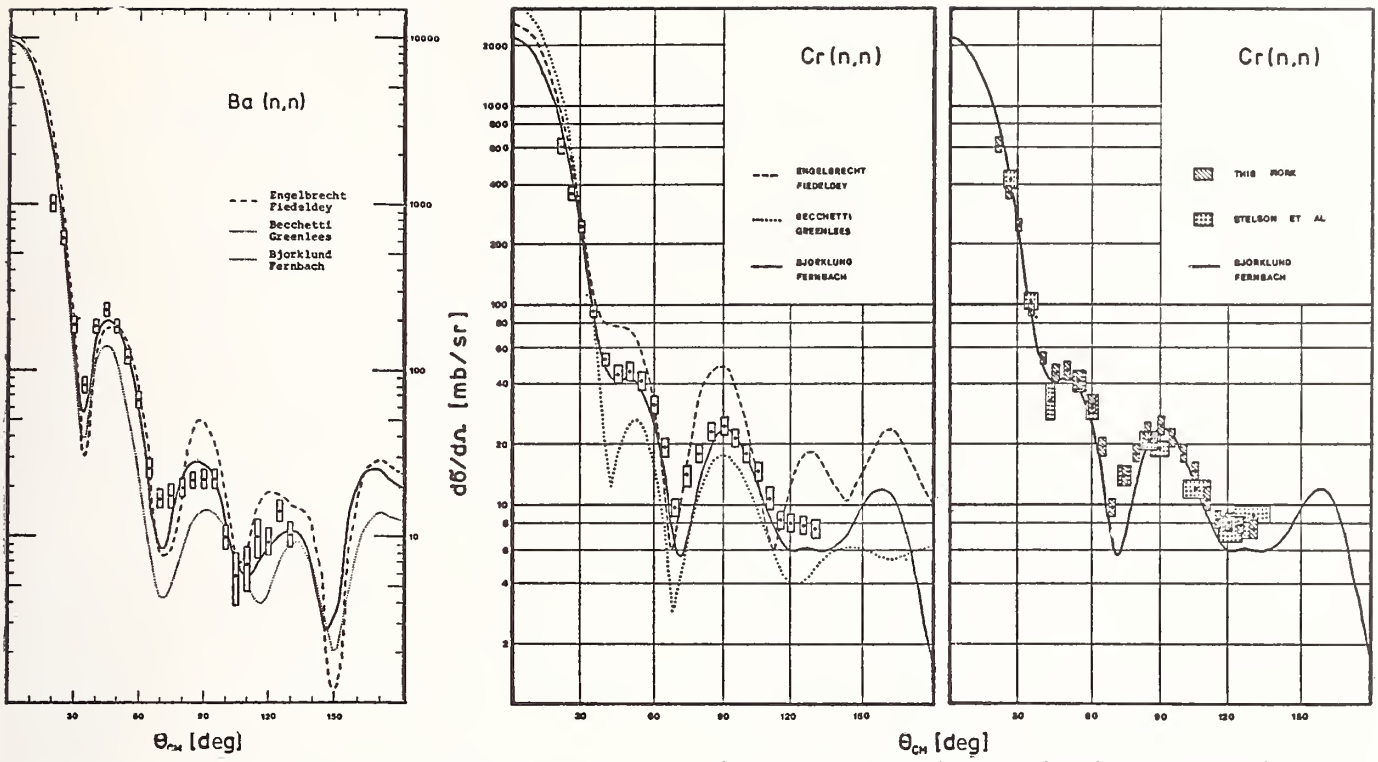

Fig. 7. The results for the elastic scattering cross section of natural Barium and Chromium compared with optical model calculations using different model parameter sets (full, dashed and dotted lines). The results measured in the present work are also compared with previously reported measurements by Stelson et al.[20]

factors for absorption, and the correction for double scattering as applied to the case of the elastic scattering. In a few instances the corrections for absorption and multiple scattering were compared with results from a Monte Carlo calculation done at the PTB Braunschweig,[12] which simulated the experiment. The agreement was better than 25% for corrections up to 30%. Corrections for air-absorption were done, when necessary, to account for large differences in the flight-path between the calibration runs and the sample runs using data from Refs. 13 and 14.

Results

The experimental results obtained for the elastic scattering cross section of natural Barium and Chromium are shown in Figure 7, indicating uncertainties and the angular resolution. The overall accuracy obtained was about 10%. The results are compared with a calculation based on the optical model of nuclear reactions using the computer code ABACUS II.[15] The results of the calculation are illustrated for the commonly used optical potentials of Becchetti and Greenless,[16] Engelbrecht and Fiedeldey,[17] and Bjorklund and Fernbach,[18] assuming an incident neutron energy of 14.1 MeV. Calculations using the actual angle dependent incident neutron energies do not show deviations of more then 5% from these results. The best agreement between experimental and calculated results is achieved using the optical model parameters of Bjorklund and Fernbach in the angular range 25° to 130°.

The results for the inelastic scattering cross section to the first 2^+ level of ^{138}Ba(1.44 MeV) are shown in Fig. 8. The experimental accuracy was between 10 and 20%. The calculations were done using the coupled-channel optical model code JUPITOR I[19] which used the potential of Bjorklund and Fernbach that best reproduces the elastic scattering results. Good agreement between calculation and experiment is achieved assuming the deformation parameter to be $\beta = 0.13 \pm 0.02$.

Inelastic scattering cross sections for the first 2^+ level in ^{52}Cr(1.43 MeV) and for the 3^- level

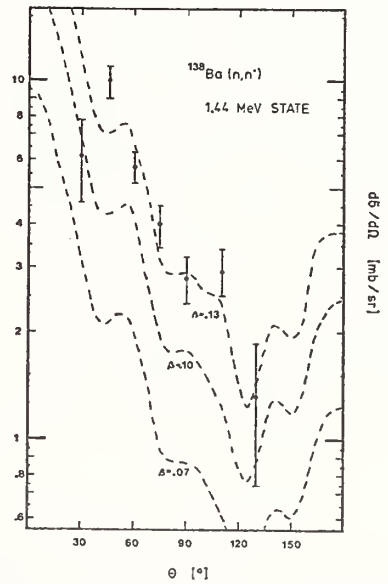

Fig. 8. The cross section for inelastic scattering to the first 2^+ level of ^{138}Ba. The dashed lines represent results from a coupled-channel optical model calculation.

(4.56 MeV) are shown in Figure 9. The calculated values are from a DWBA calculation taken from a work by Stelson et al.[20] The deformation parameters assumed were $\beta = 0.21$ for the 1.43 MeV level and $\beta = 0.18$ for the 3^- level in good agreement with $\beta = 0.23$ derived from inelastic scattering of protons.[21]

Double differential inelastic cross sections for $4 \leq E_{n'} \leq 12$ MeV were determined with an accuracy of 10 - 20%. Angle-integrated inelastic cross sections derived from these data are shown in Figure 10. They are compared with statistical model calculations done with the code STAPRE,[11] using the Hauser-Feshbach-formalism[22] and taking into account preequilibrium

emission on the basis of the exciton model.[23] Transmission coefficients were calculated by means of the optical model code ABACUS II.[15] There is a good agreement between experimental and calculated data.

Acknowledgement

The authors are indebted to Prof. Dr. H. Vonach for his advice and continuing interest in the course of this work.

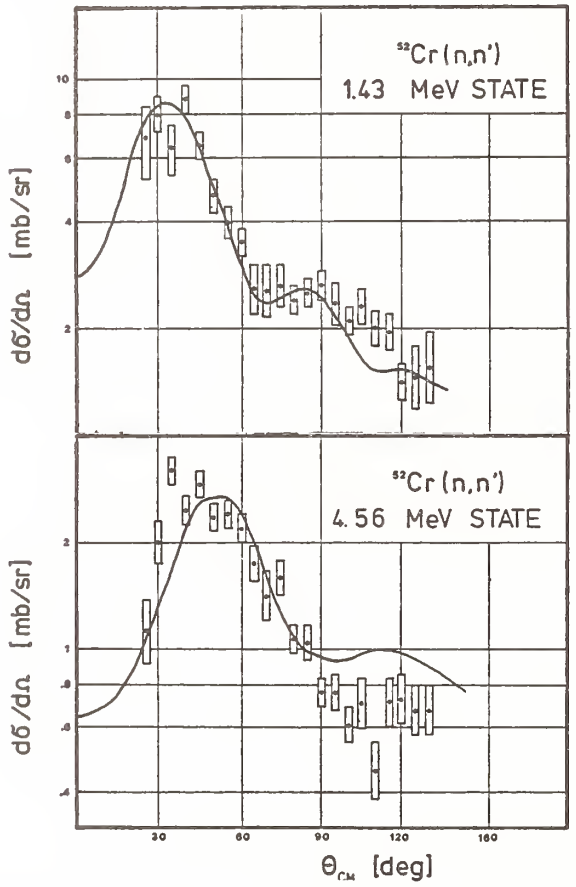

Fig. 9. The cross section for inelastic scattering to the first 2^+ level and the 3^- level (4.56 MeV) of ^{52}Cr. The full lines represent results from a DWBA-calculation by Stelson et al.[20]

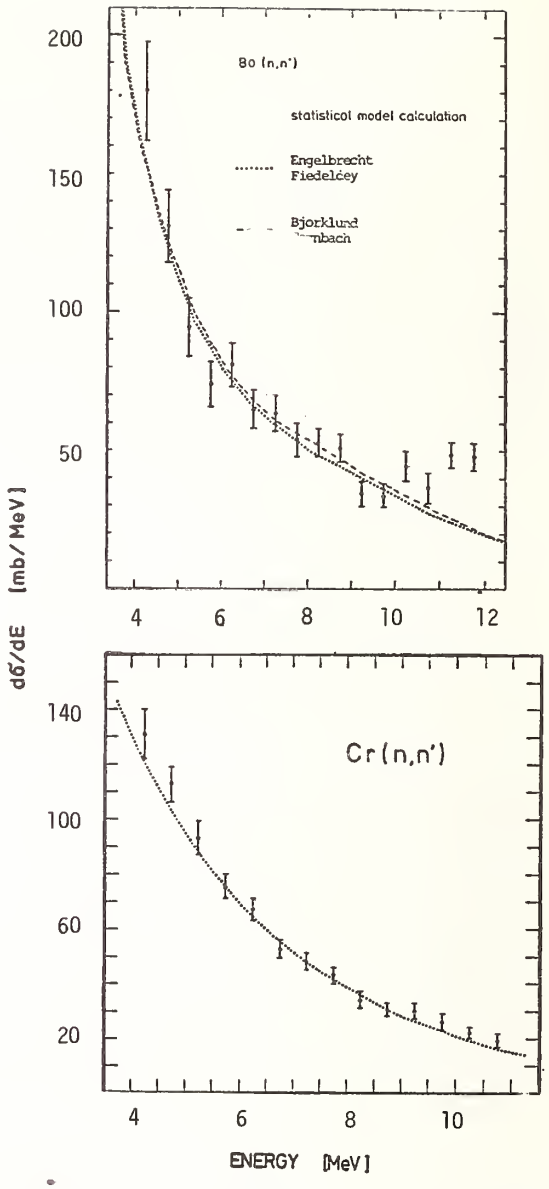

Fig. 10. Experimental angle-integrated cross section for inelastic scattering versus the energy of the inelastically scattered neutrons for Barium and Chromium, compared with results from a optical-statistical model calculation using two different sets of optical model parameters (dashed and dotted lines).

References

1. G. Stengl, Sitzungsber. Oesterr. Akad. Wiss., mathem.-naturw. Klasse, Abt. II, 185(1976)291
2. J.C. Hopkins and G. Breit, Nuclear Data Tables A9(1971)147, Academic Press, New York-London
3. G. Haouat, J. Lachkar, J. Sigaud, Y. Patin and F. Cocu, Nucl. Sci. Eng. 65(1978)331
4. O.W. Glasgow, F.O. Purser, H. Hogue, J.D. Clement, K. Stelzer, G. Mack, J.R. Boyce, D.H. Epperson, S.G. Buccino, P.W. Lisowski, S.G. Glendinning, E.G. Bilpuch, H.W. Newson and R.C. Gould, Nucl. Sci. Eng. 61(1976)521
5. G. Staffel, Thesis, University of Vienna (1979)
6. H. Vonach, M. Hille, G. Stengl, W. Breunlich and E. Werner, Z. Phys. 237(1970)155
7. P. Sperr, H. Spieler, M.R. Maier and D. Evers, Nucl. Instr. Meth. 116 (1974)55
8. S. Tagesen, Proc. of the 2nd Symp. on CAMAC, Brussels, Oct. 1975, EUR 5485 d-e-f (1976), p. 267
9. R. Fischer, Program library of the IRK for process control computers (1978)
10. K. Hansjakob, Thesis, University of Vienna (1979)
11. B. Strohmaier, M. Uhl and W.K. Matthes, Nucl. Sci. Eng. 65(1978)368
12. B.R.L. Siebert, private communication
13. G.I. Crawford, S.J. Hall, J. McKeown, J.D. Kellie and D.B.C.B. Syme, Nucl. Instr. Meth. 109(1973)479
14. O.G. Foster and O.W. Glasgow, Phys. Rev. C3(1971)576
15. E.H. Auerbach, ABACUS II, BNL-6562, Revised Version, Brookhaven National Laboratory (1962)
16. F.O. Becchetti and G.W. Greenless, Phys. Rev. 182(1969)1190
17. C.A. Engelbrecht and H. Fiedeldey, Ann. Phys. 42(1967)262
18. F. Bjorklund and S. Fernbach, Phys. Rev. 109(1958)1295
19. T. Tamura, ORNL-4152, Oak Ridge National Laboratory (1967); H. Rebel and G.W. Schweimer, KFK 1333, Kernforschungszentrum Karlsruhe (1971)
20. P.H. Stelson, R.L. Robinson, H.J. Kim, J. Rapaport and G.R. Satchler, Nucl. Phys. 68(1965)97
21. J.Beneviste, A.C. Mitchell and C.B. Fulmes, Phys. Rev. 133(1964)B317
22. W. Hauser and H. Feshbach, Phys. Rev. 87(1952)366
23. J.J. Griffin , Phys. Lett. 17(1966)478; C.K. Cline and M. Blann, Nucl. Phys. A172(1971)225

DETERMINATION OF THE CAPTURE WIDTH OF THE 27.7 keV s-WAVE RESONANCE IN ^{56}Fe

K. Wisshak and F. Käppeler
Kernforschungszentrum Karlsruhe GmbH
Institut für Angewandte Kernphysik
P.O.B. 3640, D-7500 Karlsruhe
Federal Republic of Germany

The capture width of the 27.7 keV s-wave resonance in ^{56}Fe has been determined using a setup completely different from previous experiments. A pulsed 3 MV Van de Graaff accelerator and the ^{7}Li(p,n) reaction served as a neutron source. Capture gamma rays were observed by a Moxon-Rae detector and gold was used as a standard. The samples were positioned at a flight path of only 7.6 - 8.0 cm. This allowed the use of very thin samples avoiding large multiple scattering corrections. Three metallic discs enriched in ^{56}Fe were used with a thickness between 0.6 and 0.15 mm. Capture events in the detector due to resonance scattered neutrons were discriminated by time-of-flight. The result for the capture width is Γ_γ = 0.99 with a statistical uncertainty of 1.3 % and a systematic uncertainty of ∿5 %.

[^{56}Fe(n,γ), capture cross section, 10-60 keV, multilevel analysis, Γ_γ of s- and p-wave resonances]

Introduction

The experimental determination of the capture widths of s-wave resonances in structural materials is complicated by the fact that the ratio of neutron to capture width is typically of the order 10^3. This caused two main difficulties in previous experiments, large corrections for multiple scattering and self-shielding as well as severe problems with the neutron sensitivity of the respective capture gamma ray detectors.

Both effects required sizeable corrections to the observed capture yield and introduced large systematic uncertainties. For the 27.7 keV resonance in ^{56}Fe, one of the most important s-wave resonances in structural materials, the experimental values for the capture width vary between 1.6 and 0.7 eV [1-5].

As proposed earlier[6], in the present investigation of the 27.7 keV resonance in ^{56}Fe the difficulties mentioned above have been avoided by an experimental setup completely different from all previous measurements. A flight path of 8 cm between neutron target and sample was chosen which was much shorter than the distance between sample and the capture gamma ray detector (16 cm). This geometry was enabled by using kinematically collimated neutrons from the ^{7}Li(p,n)-reaction in the energy range from 10 to 60 keV in conjunction with a very fast pulsed proton beam.

The main advantages of this experimental arrangement are the following:

1. The high neutron flux at the sample position obtained with the short flight path allowed the use of very thin samples with thicknesses between 0.15 and 0.6 mm. Consequently this reduced the correction for multiple scattering events considerably.
2. The distance between sample and detector is a factor of two larger than the flight path of the primary neutrons. In addition the immediate surrounding of the sample to a distance of at least 8 cm in all directions (corresponding to the flight path) was free from any material. Therefore, in the time-of-flight spectra capture of sample scattered neutrons in the detector or in the surrounding materials appear with a long delay with respect to prompt capture. These events are clearly discriminated in the spectra and do not contribute to the area of the 27.7 keV resonance.
3. The limited energy range of the neutron spectrum from 10 to 60 keV guarantees that no other s-wave resonance in ^{56}Fe contributes to the background.
4. The good timing properties of accelerator and detector allowed for an overall time resolution of 1.2 ns. Thus a flight path of about 8 cm is sufficient to unambiguously separate the 27.7 keV resonance in ^{56}Fe from the neighboring p-wave resonances.

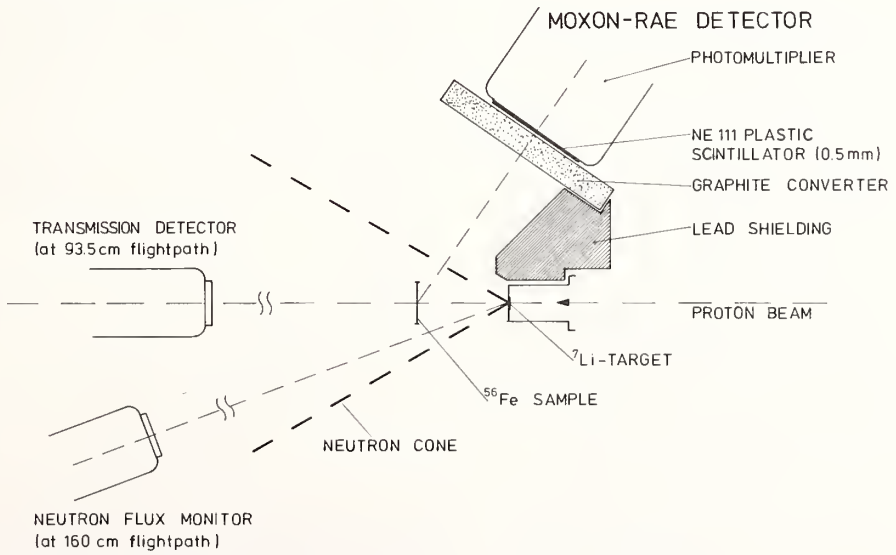

Fig. 1. Schematic setup for the capture cross section measurement on ^{56}Fe.

Measurements

The scheme of the experimental setup is shown in Fig. 1. The proton beam from the Karlsruhe 3 MV Van de Graaff accelerator hits a water cooled lithium target producing kinematically collimated neutrons. The sample is located at a flight path of ∿8 cm. Beside of three very thin copper wires fixing the sample in its position the immediate surrounding of the sample to a distance of the neutron flight path is free from any material.

A Moxon-Rae detector situated at a backward angle of 120 deg outside the neutron cone is used for the detection of capture gamma rays. The distance from the detector to the sample is 16 cm which is a factor of two larger than the primary flight path. With this geometry a complete discrimination of the background due to capture of scattered neutrons is achieved via time-of-flight. Four samples were used in each run and cycled in equal intervals into the measuring position:

1) The ^{56}Fe sample: All samples were metallic discs 38.2 mm in diameter and enriched in ^{56}Fe to 99.93 %. In the course of the measurement, three different samples were used with thicknesses of 0.6 mm ($5.282 \cdot 10^{-3}$ A/b), 0.3 mm ($2.653 \cdot 10^{-3}$ A/b) and 0.15 mm ($1.375 \cdot 10^{-3}$ A/b). Compared to previous measurements [1,2,4,5] our samples were thinner by factors of 3 to 10.
2) The ^{197}Au sample: In all measurements gold was used as a standard cross section. The sample thickness was 0.25 mm ($1.358 \cdot 10^{-3}$ A/b).
3) The scattering sample: A graphite sample was used as a pure scatterer. The thickness of the sample was adjusted such that the scattering yield $N\sigma_{el}$ is the same as for the gold sample.
4) No sample: An empty position in the sample changer frame was also measured.

Since in the Li(p,n) reaction at energies just above the reaction threshold even small energy modulations cause strong variations in neutron intensity, precautions had to be taken to ensure that all samples were irradiated by the same neutron flux. Therefore a time-of-flight spectrum was recorded from a lithium glass transmission detector at a flight path of 93.5 cm. A second lithium glass detector was positioned at an angle of about 20° to the beam axis, which served as an additional neutron flux monitor.

To demonstrate the experimental signal to background ratio Fig. 2 shows the time-of-flight spectrum measured with the thinnest ^{56}Fe sample. As can be seen the time resolution was sufficient to separate the 27.7 keV resonance uniquely from the neighboring p-wave resonances.

Determination of the Capture Widths

The calculation of the capture widths from the experimental capture yields was performed using the FANAC code of Fröhner [7]. This code is based on level statistics using a Reich-Moore formalism and level level interference for s-waves. p-waves are treated as single levels with doppler broadening. This program is especially well suited to fit the present data because it takes into account that at the very short flight paths used multiple scattering events are slightly delayed in time and consequently are shifted to lower energies in the TOF spectra.

The calculations were performed in two steps: First, except the resonance energies only the capture width of the 27.7 keV resonance was taken as a free parameter. For all other parameters like the neutron width of the 27.7 keV resonance or neutron and capture

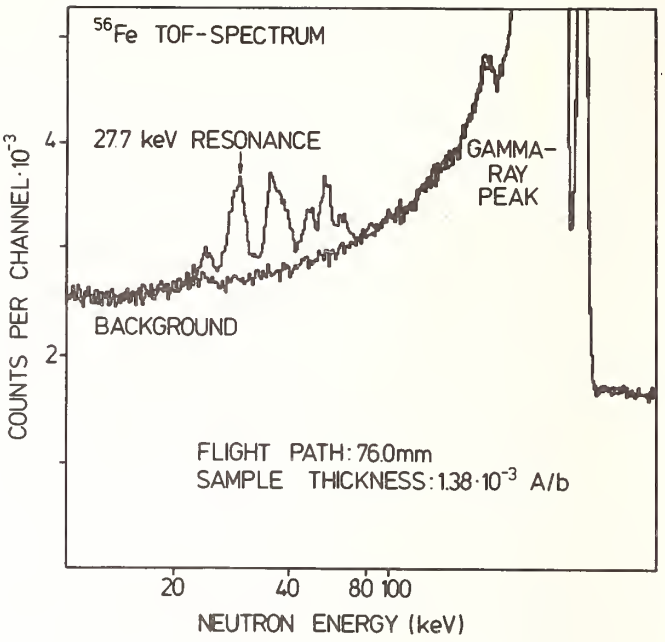

Fig. 2. Experimental TOF-spectrum of the ^{56}Fe sample (sample thickness 0.15 mm) and the corresponding background.

widths of other s-wave and p-wave resonances fixed values were taken from literature. Here, two different data sets were used from Fröhner[3,7] and Perey et al.[8], the first of which described the p-wave resonances slightly better. The so determined resonance energies were taken as fixed parameters for the final fits. Now the smaller values of Γ_n and Γ_γ of the p-wave resonances and Γ_γ of the 27.7 keV s-wave resonance were determined by the fit. This procedure gave a slightly better description of the p-wave resonances and changed the value for the capture width of the 27.7 keV resonance by less than 1 %.

Results

The results for the capture width of the 27.7 keV resonance obtained with different samples and different sets of fixed parameters are compiled in Table I. The uncertainties given are the statistical uncertainties only. Fig. 3 shows the final fit to the capture yield measured with the 0.15 mm thick sample. The dashed line indicates the contribution due to multiple

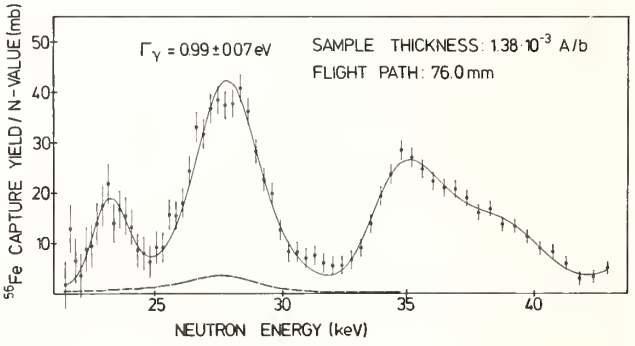

Fig. 3. FANAC fit to the capture yield measured with the sample of 0.15 mm thickness. The dashed line indicates the component due to multiple scattering in the sample. The uncertainty given for Γ_γ is the total statistical and systematic uncertainty.

Table I. Results for the capture width of the 27.7 keV s-wave resonance in ^{56}Fe

Sample thickness (mm)	0.15		0.3		0.6	
Flight path (mm)	76.0		80.0		79.5	
	E_{res} (keV)	$g\Gamma_\gamma$ (eV)	E_{res} (keV)	$g\Gamma_\gamma$ (eV)	E_{res} (keV)	$g\Gamma_\gamma$ (eV)
Fixed parameters from Fröhner	28.0	0.99 ± 0.027	28.0	1.00 ± 0.023	27.5	0.98 ± 0.020
Fixed parameters from Perey et al.	27.9	1.02 ± 0.027	28.0	1.03 ± 0.023	27.5	1.00 ± 0.020

scattering events which amount to only ∿8 % of the observed yield. In spite of the fact that the systematic uncertainties are quite different for different sample thicknesses no systematic effect was found in the data. Using the fixed parameters from Fröhner[3,7] we obtained an average mean value Γ_γ = 0.99 eV with a statistical accuracy of 1.3 %. A systematic difference of about 1.5 % is observed in the results obtained with the data set of Perey et al. [8]. This difference is correlated with the higher value of Γ_n = 1.52 keV for the 27.7 keV resonance compared to the width of 1.4 keV quoted by Fröhner.

The results for the p-wave resonances are given in Table II. This Table lists the mean values from the three measurements together with their statistical accuracy. Finally, it has to be mentioned that in spite of the short flight path used the energy of the 27.7 keV resonance could be determined with an accuracy of ∿1 % (see Table I). For the p-waves the experimental resonance energies agreed within 2 % to the values given in Table II.

Discussion of Uncertainties

A detailed evaluation of the systematic uncertainties of the measured capture yield has been performed. This includes the uncertainties in the measured flight paths, in the background subtraction and differences in neutron beam intensity. It also considers gamma ray self absorption and multiple scattering in the gold sample as well as an uncertainty of 2.5 % for the capture cross section of gold taken from ENDF/B-IV. The resulting systematic uncertainty is 3.8 %, 4.6 % and 6.7 % for the 0.6, 0.3 and 0.15 mm thick sample.

An additional systematic uncertainty may arise from the detector efficiency. The present results are based on the assumption of a linear increase of the detector efficiency with gamma energy. However, for a pure graphite converter, as it was used in this experiment, theoretical calculations[9,10] indicate slight nonlinearities. As long as the capture gamma ray spectra are similar, this effect cancels out in the measurement of cross section ratios. But in case of ^{56}Fe one deals with a spectrum which is certainly harder than that of ^{197}Au[11]. A preliminary estimate yielded a possible correction of the order of only 5 %. This is supported by the fact that our results for the p-wave resonances agree well with the data of other authors[3,5], although some of these resonances have even harder capture gamma ray spectra than the 27.7 keV resonance[12].

Table II. Results for the capture widths of p-wave resonances in ^{56}Fe.

Resonance energy (keV)	$g \cdot \frac{\Gamma_\gamma \cdot \Gamma_n}{\Gamma}$ (eV)
22.8	0.160 ± 0.008
34.3	0.526 ± 0.015
36.7	0.325 ± 0.014
38.4	0.305 ± 0.014

Conclusions

In the present investigation of the capture width of the 27.7 keV resonance in ^{56}Fe difficulties of previous experiments have been avoided using a completely different experimental setup. Data were recorded from very thin samples (0.6, 0.3, 0.15 mm) but still with a statistical accuracy of 2-3 %. The final result is a weighted average of Γ_γ = 0.99 eV with a statistical uncertainty of 1.3 %. The total systematic uncertainty is 5-7 %.

This result is significantly lower than most of the existing data but slightly larger than the final result of Gayther et al.[13] who obtained Γ_γ=0.85 +0.09 from a measurement with natural iron samples of 6.0, 2.0 and 0.5 mm thickness. Recently, another experiment using a Van de Graaff accelerator and a Moxon-Rae detector has been performed by Allen et al. [14] .However, due to the limited time resolution a flight path of 30 cm was necessary to separate the 27.7 keV resonance from the neighboring p-wave resonances. Consequently, a much heavier sample of 2 mm thickness had to be used to obtain a sufficient effect to background ratio. The result of this measurement is Γ_γ = 0.76 ± 0.11 which is significantly lower than our value.

Acknowledgements

The authors would like to thank Dr. F. Fröhner for helpful discussions and for his assistance in the calculations with the FANAC code. The continuous and strong support of the Van de Graaff crew in providing the neutron beam is gratefully acknowledged.

References

1. R.W. Hockenbury, Z.M. Bartolome, J.R. Tatarczuk, W.R. Moyer, and R.C. Block, Phys. Rev. 178, 1746 (1969).

2. A. Ernst, D. Kompe, and F.H. Fröhner, Proceedings of the Int. Conference on Nuclear Data for Reactors, Helsinki 1970 (Intern. Atomic Energy Agency, Vienna, 1970) Vol. 1., p. 619.

3. F.H. Fröhner, Proceedings of a Specialists' Meeting on Neutron Data of Structural Materials for Fast Reactors, Geel, Belgium 1977, ed. by K.H. Böckhoff (Pergamon Press 1979) p. 138.

4. B.J. Allen and A.R. de L. Musgrove, Proceedings of a Specialists' Meeting on Neutron Data of Structural Materials for Fast Reactors, Geel, Belgium, 1977, ed. by K.H. Böckhoff(Pergamon Press 1979) p. 447.

5. D.B. Gayther, B.W. Thomas, B. Thom, and M.C. Moxon, Proceedings of a Specialists' Meeting on Neutron Data of Structural Materials for Fast Reactors, Geel, Belgium, 1977, ed. by K.H. Böckhoff (Pergamon Press 1979) p. 547.

6. F. Käppeler, "Annual Report Teilinstitut Kernphysik, July 1, 1977 - June 30, 1978", KfK 2686, Kernforschungszentrum Karlsruhe (1978) p. 24.

7. F.H. Fröhner, "FANAC - A Shape-Analysis Program for Resonance Parameter Extraction from Neutron Capture Data for Light and Medium-Weight Nuclei", KfK 2145, Kernforschungszentrum Karlsruhe, (1977).

8. F.G. Perey, G.T. Chapman, W.E. Kinney, and C.M. Perey, Proceedings of a Specialists' Meeting on Neutron Data of Structural Materials for Fast Reactors, Geel, Belgium, 1977, ed. by K.H. Böckhoff (Pergamon Press 1979) p. 530.

9. K.V.K. Jyengar, B. Lal, and M.L. Ihingan, Nucl. Instr. Meth. 121, 33 (1974).

10. S.S. Malik and C.F. Majkrzak, Nucl. Instr. Meth. 130, 443 (1975).

11. J.E. Lynn, Proceedings of a Specialists' Meeting on Neutron Data of Structural Materials for Fast Reactors, Geel, Belgium, 1977, ed. by K.H. Böckhoff (Pergamon Press 1979) p. 339.

12. G. Rohr, private communication.

13. M.C. Moxon, private communication.

14. B.J. Allen, D.D. Cohen, and F.Z. Company, private communication.

TOTAL NEUTRON CROSS SECTION MEASUREMENTS ON ^{54}FE, ^{56}FE AND ^{57}FE

E.M.R. CORNELIS
University of Antwerp, R.U.C.A.,
B-2020 Antwerp, Belgium

C.R. JUNGMANN
CEC - JRC, Central Bureau for Nuclear Measurements
B-2440 Geel, Belgium

L. MEWISSEN and F. POORTMANS
S.C.K.-C.E.N., B-2400 Mol, Belgium

High resolution total neutron cross section measurements have been performed on samples of enriched isotopes (on loan from ORNL) of ^{54}Fe, ^{56}Fe and ^{57}Fe in the energy range from 35 keV up to 2 MeV. The experiments were made on a 200 meter flight path at the GELINA facility using a plastic scintillator (NE 110) as neutron detector. The R-matrix multi-level code FANAL[1] was used to fit the broad s-wave resonances and the multi-level Breit-Wigner code SIOB[2] to fit the narrow $\ell > 0$ resonances. The analysis is completed for ^{54}Fe and ^{56}Fe up to a neutron energy of 300 keV.

(σ_T, time-of-flight, ^{54}Fe, ^{56}Fe, ^{57}Fe, R-matrix, Breit-Wigner resonances)

Introduction

The cross sections of structural materials have considerable impact on important parameters of fast reactors such as critical enrichment, breeding gain and Doppler coefficient. Furthermore, total neutron cross section and resonance parameters provide important information about compound nucleus formation in the mass range A = 40-70, where the s-wave strength function has a maximum.

We have started at the CBNM a series of experiments on Fe and Cr isotopes. The present report will discuss the results from an analysis of transmission experiments on ^{54}Fe and ^{56}Fe below 300 keV.

Experimental Details

The experiments were performed at the 150 MeV electron linac of the CBNM. Operating conditions of the linac were 4 ns beam burst and 800 Hz repetition rate. A 400 mg/cm^2 ^{10}B filter was placed in the beam for absorption of low-energy neutrons. An automatic sample changer was installed on a 100 meter flight station and the transmission detector was mounted at a distance of 197.85 meters from the pulsed neutron source.

The samples were prepared from oxide powder (Fe_2O_3) canned in aluminium tubes with windows of 0.3mm thick. The sample diameters were 35 mm and the thicknesses were :

^{54}Fe (97.68%)	6.98 10^{-2}	Fe atoms/barn
^{56}Fe (99.93%)	7.81 10^{-2}	Fe atoms/barn
^{57}Fe (91.69%)	5.11 10^{-2}	Fe atoms/barn

A neutron monitor was used to normalize the sample-in and sample-out data to the same neutron source intensity. The alternation of sample-in and out of the beam was under the control of the data-taking system.

The transmission detector was a plastic scintillator NE-110, with viewed side on by four photomultipliers type RCA 4516 (diameter of 0.75 These photomultipliers have very low noise so that above 20 keV neutron energy no coincidence operation was required. In order to optimise signal to background ratio, we divided the pulse-height into four windows and stored only those time-of-flight events when the pulse-height was within the required window. The time-of-flight analyzer consisted of a time digitizer with minimum channel width of 4 ns[3] interfaced via a double data buffer (2 x 128 words, each 32 bits) to a computer HP 2113-E with 96 K words of memory available for data storage. The data-taking system could handle a count rate of more than 10^4 events per second and the dead time after each event was only 300 ns.

The total background in the experiment was low; typical values were : 0.5% at 1 MeV, 0.3% at 500 keV, 3% at 100 keV and 16% at 40 keV. The background consisted of two components : a constant room background, determined for each pulse-height window at long flight times, and an exponentially decaying background due to gamma rays produced in the neutron target and surrounding moderator. This last component was measured by eliminating the beam neutrons using a 16 cm thick polyethylene filter.

The time-of-flight resolution was determined by fitting narrow resonances in Fe and S. At present, our resolution is not known to better than 20%, and we have planned additional experiments to improve the situation. Typical neutron resolutions were 80 eV at 100 keV and 1.1 keV at 1 MeV.

Analysis

Background and dead time correction as well as the reduction to transmission has been performed using the ANGELA[4] procedure, a system program for the off-line reduction of nuclear data at the CBNM.

Parametrisation of the transmission was performed using two shape-fitting procedures : The SIOB-code, developed at Oak Ridge by de Saussure et al[2], uses a multi-level Breit-Wigner formalism and gives satisfactory results for isolated and weakly interfering resonances. The FANAL-code by Fröhner[1] from K.F.K. Karlsruhe, uses a R-matrix formalism for the s-wave resonances and correctly takes into account strong interferences. The original FANAL-code which describes the Doppler-broadened p-wave resonances with a gaussian shape, yielded higher neutron widths for p-wave resonances than SIOB in identical conditions. The FANAL-code has therefore been modified to include single level Breit-Wigner formula for $\ell > 0$ resonances. Doppler broadening was calculated using the complex error integral. This description is acceptable below roughly 300 keV because p-wave resonances are well separated and have small neutron widths so that level-level interference in negligible.

In those cases where p-wave resonances have been

TABLE I

FE-54 S-WAVES PRESENT WORK				PANDEY ET AL		BOWMAN ET AL		BEER ET AL	
EO (KEV)	ΔEO (KEV)	GN (KEV)	ΔGN (KEV)	EO (KEV)	GN (KEV)	EO (KEV)	GN (KEV)	EO (KEV)	GN (KEV)
52.654	.007	1.978	.001	52.62	1.95	52.5	2.1	52.78	2.16
71.805	.005	1.678	.001	71.75	1.54	72.0	1.6	71.86	1.77
98.664	.004	.511	.005	98.66	0.55	98.0	0.4	98.5	0.51
130.092	.008	3.47	.01	130.1	3.34	130.0	1.27	129.6	3.0
147.328	.009	3.78	.015	147.4	3.38	146.	1.51	147.1	2.75
174.033	.009	1.59	.03	174.2	3.68	173.	4.8	173.9	2.8
188.581	.041	53.17	.1	192.2	40.0	188.5	38.0	191.2	42.4
223.394	.004	1.08	.08	223.5	.73	223.0	1.9	222.8	1.57
244.107	.016	19.48	.07	246.8	19.7	244.5	13.0	245.7	24.6
257.070	.005	.37	.01	256.0	3.36	-	-	-	-
291.852	.006	.89	.01	292.4	1.1	-	-	-	-

analysed with SIOB and the modified FANAL-code (^{54}Fe from 50 keV to 215 keV), the results are in good agreement.

Both codes use a picket fence model to take into account the contributions of far-away s-wave resonances outside the analysis region. It is well known that their contribution to the phase-shift affects the fitted value of the potential scattering radius considerably.

We tried to reduce this effect by explicitly introducing all known s-wave resonances up to 400 keV. Fairly realistic values for the potential scattering radius were found.

In order to obtain a good overall fit in both interference minima and peak maxima, we had to introduce a potential scattering radius for oxygen of 5.17 fm. The analysis is completed from 40 keV to 300 keV.

The resonance energies listed in the tables are based on the work of Pandey et al[5]. Meanwhile our flight path has been calibrated using well known resonance energies[9] in ^{32}S but these data have not yet been analysed.

Results

^{54}Fe

Strong level-level interference between s-wave resonances complicates the spectrum of ^{54}Fe. Nevertheless the R-matrix calculation is able to reproduce this behaviour fairly well. In figure I the experimental and fitted total cross-sections for the oxide sample are plotted from about 100 keV to 300 keV. Only where deviations are larger than the statistical fluctuations can the fitted curve be seen. A few isolated s-wave resonances have been analysed with both codes and the results agree. The assignment of s-waves was taken from the work of Pandey et al[5] and the goodness of the fits reconfirm this choice.

In table I our results are compared with those of Pandey et al[5], Beer et al[6] and earlier work of Bowman et al[7]. All our resonance parameters quoted in this table were obtained with the R-matrix fit.

On the average, there is best agreement with the work of Pandey et al[5], with a striking disagreement in the resonance width of the resonance at 257 keV. This resonance shows strong interference with the resonance at 244 keV, and visual inspection of the plotted spectra favours our value of .37 keV against 3.36 keV for the neutron width quoted in ref. 5. A comparison of the results for s-wave resonances from various laboratories can best be made through the s-wave strength function, taken in the same energy interval

TABLE II

FE-56 S-WAVES PRESENT WORK				PEREY ET AL (EVALUATION)		
EO (KEV)	ΔEO (KEV)	GN (KEV)	ΔGN (KEV)	EO (KEV)	GN (KEV)	ΔGN (KEV)
73.934	.002	0.588	.004	73.98	0.535	.010
83.513	.005	1.210	.010	83.65	1.250	.050
129.721	.002	0.576	.004	129.80	0.500	.050
140.266	.005	2.610	.010	140.40	2.700	.100
169.053	.003	0.950	.007	169.00	1.000	.100
187.538	.006	3.525	.015	187.60	3.600	.100
220.346	.004	1.230	.010	220.50	1.150	.050
244.708	.004	0.450	.005	245.00	0.600	.020
276.790	.011	3.630	.020	276.60	4.000	.300

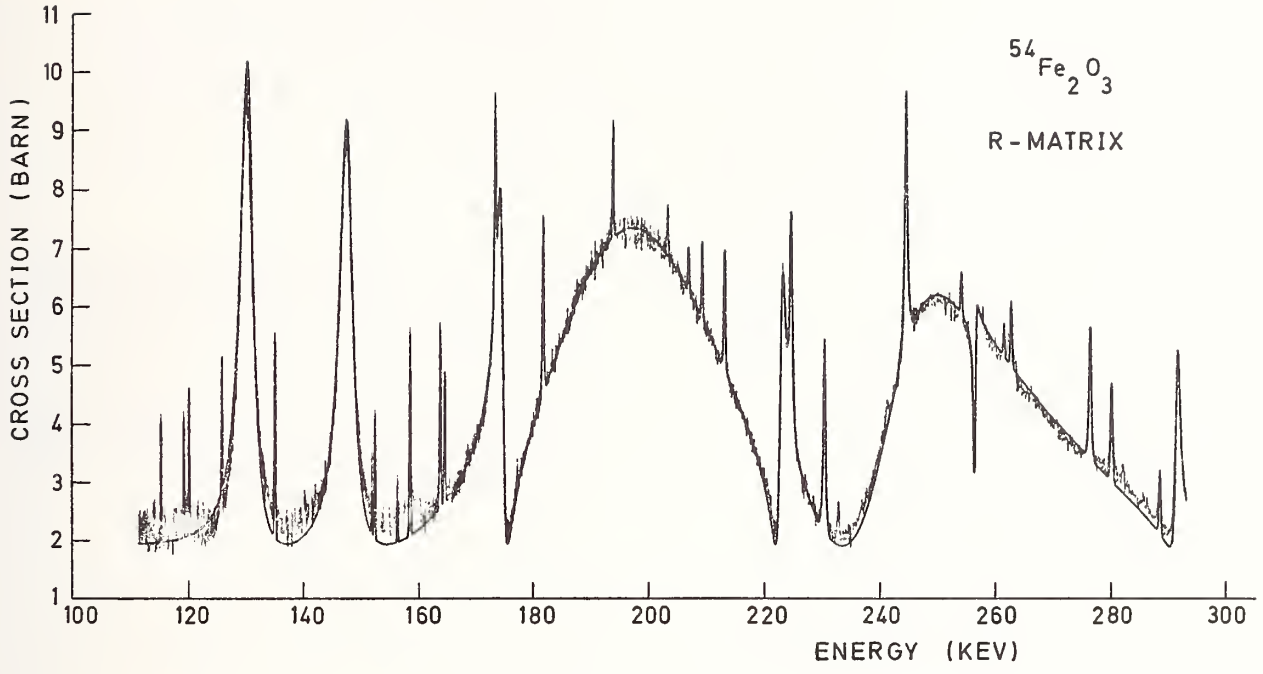

Fig 1 : Total cross section of $^{54}Fe_2O_3$, data were fitted using a R-matrix formula for s-waves and a single Breit-Wigner formula for p-waves; s-wave resonances up to 400 keV taken into account explicitly; fitted channel radius was a= 5.5 fm.

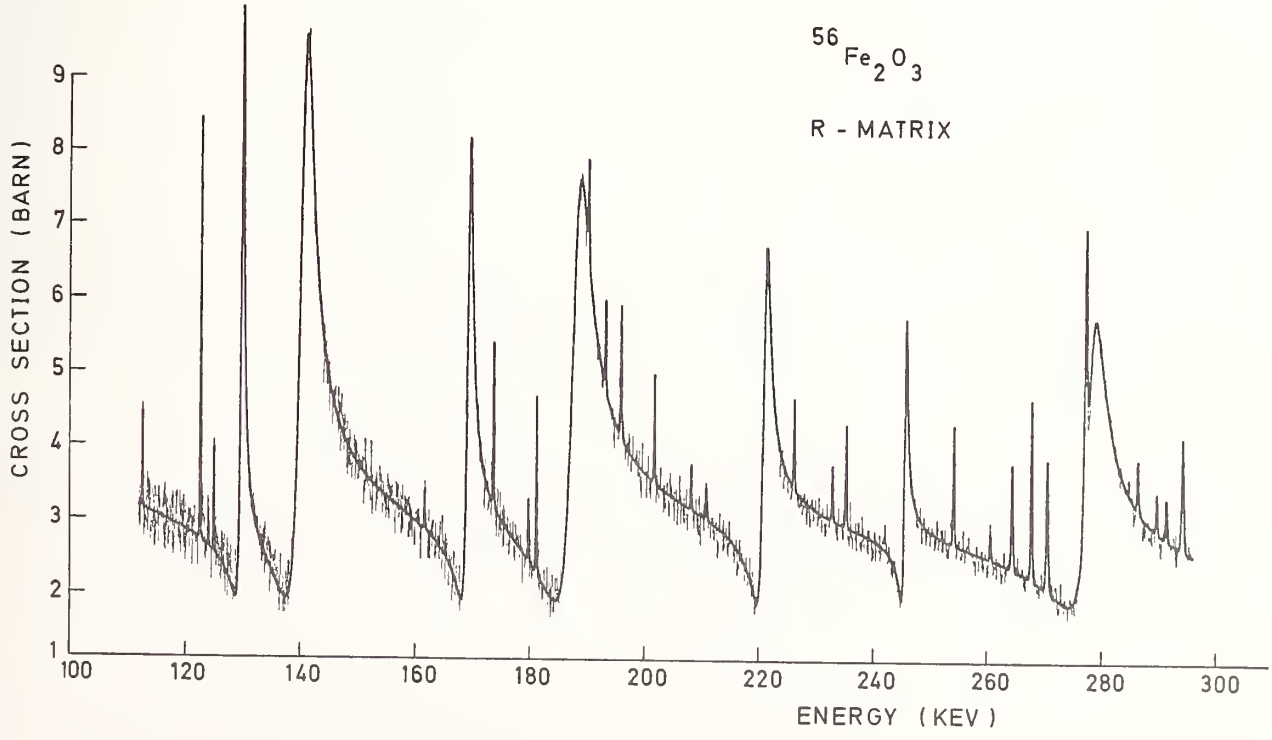

Fig 2 : Total cross section of $^{56}Fe_2O_3$, same fitting conditions as fig 1. Fitted channel radius a= 5.0 fm.

(52 keV - 292 keV) and ignoring the large statistical error due to the small number of resonances :

Duke [7]	$S_0 = 6.4\ 10^{-4}$	(9 resonances)
K.F.K.[6]	$S_0 = 7.9\ 10^{-4}$	(9 resonances)
O.R.N.L.[5]	$S_0 = 7.7\ 10^{-4}$	(11 resonances)
present work	$S_0 = 7.5\ 10^{-4}$	(11 resonances)

As no spin and parity assignment has been undertaken for the resonances with $\ell > 0$, all narrow resonances have been analysed using a g-value of 1. Our results for p-wave resonances are still preliminary because of uncertainties in the resolution width, but individual resonance widths seem, in general, to be lower than those of Pandey et al[5].

In the region from 50 keV up to 290 keV, we find a p-wave strength function

$$S_1 = .45\ 10^{-4} \qquad (34 \text{ resonances})$$

as compared to the value

$$S_1 = .43\ 10^{-4} \qquad (23 \text{ resonances})$$

for the corresponding data set of reference 5.

^{56}Fe

For this isotope, the fits are better than for ^{54}Fe. S-wave resonances are perfectly described by the R-matrix formalism as can be seen in figure 2.

In table II we compare our result with the evaluation of Perey et al[8], which is mainly based on the results from reference 5. With this limited sample, we find a s-wave strength function of

$$S_0 = 1.9\ 10^{-4} \qquad (9 \text{ resonances})$$

which compares favourably with the value

$$S_0 = 2.0\ 10^{-4} \qquad (9 \text{ resonances})$$

using the values quoted by Perey et al[8]. Also in this case, the results were taken from the R-matrix fit.

For the p-waves, we inserted the g-values corresponding to the spins and parities as assigned by Perey et al[8]. For this isotope, we find systematically slightly higher neutron widths for p- and d-wave resonances than those of the Perey-evaluation[8].

Using the same sample (resonances from 40 keV up to 300 keV), our results for the p- and d-wave strength functions compare as follows with this evaluation :

	Perey et al.[8]	Present work	
S_1	$.20\ 10^{-4}$	$.26\ 10^{-4}$	(20 resonances)
S_2	$2.0\ 10^{-4}$	$3.1\ 10^{-4}$	(16 resonances)

Both our results are preliminary.

References

1. F.H. Fröhner, report K.F.K. 2129 (1976)
2. G. de Saussure, D.K. Olsen and R.B. Perez, Report ORNL/TM-6286, 1978
3. S. de Jonge, to be published
4. C. Bastian, The ANGELA system (to be published as a EUR report)
5. M.S. Pandey, J.B. Garg, J.A. Harvey and W.M. Good, in Proceedings of the Conference on Nuclear Cross Sections and Technology, Washington, D.C. USA, 1975 ed. by R.A. Schrack and C.D. Bowman (NBS Special Publication 425 Vol. II, 1975) p. 748
6. H. Beer and R.R. Spencer, report K.F.K. 2063(1974)
7. D.D. Bowman, E.G. Bilpuch and H.W. Newson, Annals of Physics 17, 319 (1962)
8. F.G. Perey, G.T. Chapman, W.E. Kinney and C.M. Perey C.M. Perey, in Proceedings of the Specialists' Meeting on Neutron Data of Structural Materials for Fast Reactors, Geel, Belgium 1977, ed. by K.H. Böckhoff (Pergamon Press, 1978) p. 530
9. G.D. James, in the Proceedings of the International Specialists' Symposium on Neutron Standards and Applications (N.B.S. Gaithersburg, March 1977) NBS Special Publication 493, ed. by C.D. Bowman and A.D. Carlson 1977, p. 319.

NEUTRON CAPTURE CROSS SECTION MEASUREMENTS OF ^{56}Fe

A. Brusegan, F. Corvi, G. Rohr, R. Shelley and T. van der Veen
CEC-JRC, Central Bureau for Nuclear Measurements
B-2440 Geel, Belgium

High resolution capture cross section measurements have been carried out on an enriched sample of ^{56}Fe at the Geel linear electron accelerator. The data have been analysed up to 100 keV and the deduced capture areas and relevant resonance parameters are given. Special emphasis has been given to problems connected with the weighting method and the capture data normalization.

[$^{56}Fe(n,\gamma)$, 1-100 keV, E_o, A_γ, Γ_n, Γ_γ .]

Introduction

According to the European Category 1 [1]request list and Filip et al.[2] the iron neutron capture cross section in the range 1 - 100 keV is required with a 5 - 10% accuracy. A working group on differential data convened at the Geel 1977 meeting[3] estimated that $\sigma(n,\gamma)$ for Fe in the range 100 eV to 1 MeV is, at present, only accurate to ± 20%. Also in view of the amount of work already spent on such an element in the past 20 years, it is therefore clear that the final goal can only be achieved through a major improvement in the state-of-the-art of resonance neutron capture measurements. It is the opinion of the authors that this can be obtained, if at all, by careful consideration of the various steps incorporated in the experimental procedure rather than by refining the technique of analysis of neutron resonances. The most important of such steps will be briefly reviewed in the following section after a short description of the experimental set up.

Experimental Method

Apparatus

The measurements were performed at a 60m flight-path station at the Geel linear electron accelerator operated at 4ns burst width and 800 hertz repetition frequency. The capture detectors consisted of two deuterated benzene (C_6D_6) liquid scintillators encapsulated in thin aluminium containers of 10.2 cm diameter and 7.6 cm height. The detectors which were 10 cm apart and placed perpendicularly to the neutron beam, were coupled to two 5" photomultipliers with flat quartz windows. The system, which was placed about 1.8 m above the concrete floor, was completely unshielded and supported only by a light aluminium frame. The sample, on loan from ORNL, consisted of iron oxide enriched to 99.93% ^{56}Fe, packed in an aluminium container of 8 cm diameter and 0.3 mm thick wall. The sample thickness was 0.015 atoms/barn.

For each detected event, the amplitude information was analysed over 256 channels and the time-of-flight over 16 K. Via a satellite computer the information was then stored in listing mode on a disk connected to the IBM 370/138 main computer.4 On this disk 2 files were defined each with a capacity of 3.4 million events working in ping-pong mode : whenever one file was filled, data were sorted out and weighted according to the associated pulse height in order to achieve a detector response proportional to the total energy released in the capture reaction. Three types of time-of-flight spectra were recorded : unweighted, weighted (see fig.1) and weighted squared, the latter for calculating the statistical error. An average weight $\bar{w}$ corresponding to the ratio between weighted and unweighted areas, can be defined for each resonance.

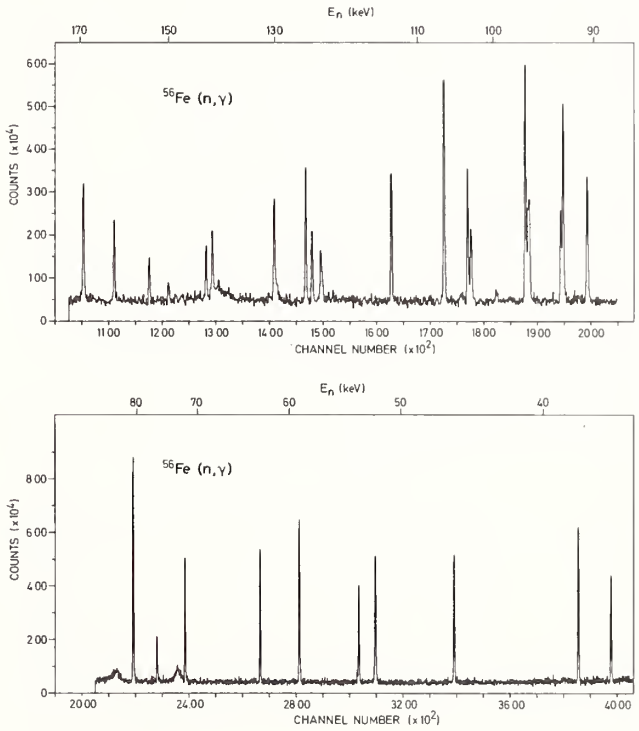

Fig. 1 : Time-of-flight spectrum of the relative yield of ^{56}Fe resonance neutron capture between 35 and 170 keV.

Weighting Method

The validity of the main assumption of the weighting method[5], i.e. a detector response independent of the particular γ-ray decay mode, depends entirely on a correct evaluation of the weighting function W(E). This has been calculated by means of a Monte Carlo based computer code initially developed at Cadarache[6] and later modified for the geometry of our detector system in collaboration with Karlsruhe.[7] This programme takes into detailed account the composition of the detector and all surrounding materials. Further improvements have recently been made on this programme, in particular, the energy loss of electrons in the scintillator has been increased by using newly available data from Atomic Data[8].

The new W(E), so calculated, results in a decrease of 18% at 8 MeV as compared to the old W(E) (normalized to the same value at 1 MeV).

Structural materials such as Fe, Cr and Ni represent a particularly severe test for the weighting method because of two reasons: firstly, their capture γ-ray spectra are much harder than those of elements such as Ag or Au, which are normally used for calibration. Secondly, the shape of the capture spectra of different resonances belonging to the same isotope can vary widely due to Porter Thomas fluctuations, since the high energy part is made of few γ-rays of high average intensity. This is illustrated in Figure 2, where the mean value of the average weight $\bar{w}$ is plotted vs A for various nuclei. The error bar associated to each isotope gives the $\pm 1\sigma$ deviation of the $\bar{w}$ values distribution for different resonances. The total number of resonances considered is given in brackets near the isotopic symbol.

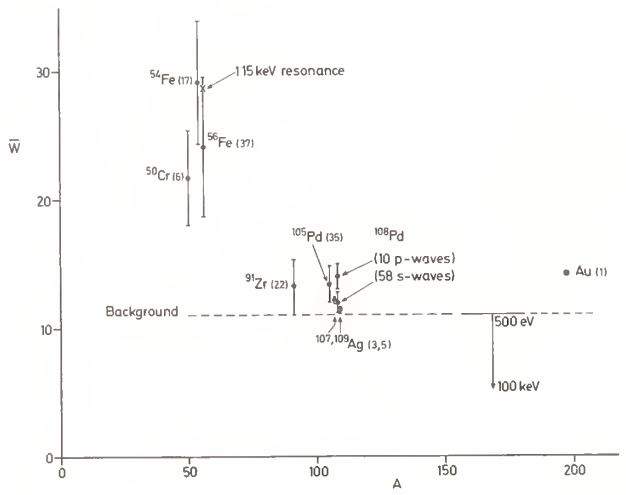

Fig. 2. Experimental mean values of $\bar{w}$ averaged over many resonances for various nuclides (arbitrary units).

In order to test the weighting function thermal capture measurements were performed on a number of targets, with widely varying binding energy B.E. and spectral shape but with high (except for Fe) and well known $\sigma_{th}(n,\gamma)$, in order to minimize background and multiple scattering effects. The results are listed in Table I: the sum of photon intensities above 6 MeV, listed in the second column[9], is representative of the hardness of the capture spectrum. In column 3 are given the assumed thermal capture cross sections, taken from ref. 10, and in column 4 the average weights $\bar{w}_{th}$ calculated with the old W(E). The detector efficiency ϵ given in the fifth and sixth columns for the old and new W(E) respectively, is defined as the ratio between the thermal "weighted" counting rate C_w and the product of B.E. and capture probability P_γ. This ratio is normalized to unity for Ag and for a correct W(E) should not vary for different target nuclei. This is not really satisfied even for the new w(E) and in particular there is a contradiction between the values obtained for Fe and ^{50}Cr and that for ^{53}Cr. We thus believe that further investigation is needed in order to confidently apply the weighting method to structural materials. For this reason, any calibration of the data to Ag or Au saturated resonances was avoided in the present work. Rather, the data were normalized to the 1.15 keV resonance of ^{56}Fe, as explained in the next section: this resonance has a capture γ-ray spectrum very similar to the thermal one, i.e. $\bar{w} = \bar{w}_{th}$. A correction for the spread in spectral shapes between different ^{56}Fe resonances was calculated by linear interpolation in the following way: based on the results of Table I for the old w(E), which was the one actually used in the measurements, an average deviation of 10% between Ag and the 1.15 keV resonance was assumed. Then for a resonance E_x of average weight $\bar{w}(E_x)$ the relative change in the capture area $\Delta A_\gamma/A_\gamma$ was given as

$$\Delta A_\gamma/A_\gamma = 0.10 \times [\bar{w}(1.15)-\bar{w}(E_x)]/[\bar{w}(1.15)-\bar{w}(Ag)]$$

For the various resonances considered, this correction ranged from - 4% to + 8%. This correction and its uncertainty, estimated to ± 50%, is included in the results of Table III.

Data Normalization

The isotope ^{56}Fe has the nice feature of having at low energy, namely at 1.15 keV, a well isolated resonance which is dominated by capture. This fact can be exploited to normalize the capture measurements to transmission data. Unfortunately there is a large spread in the values of Γ_n given in the literature for this resonance, as can be seen from Table II. To clarify the situation, a transmission measurement on a 2 mm thick natural iron metallic sample was performed. The detector consisted of a 3 mm thick ^{10}B slab viewed by two NaI(Tl) crystals

Table I. Test of the weighting function at thermal neutron energy

Target	ΣI_γ E > 6 MeV (%)	$\sigma_{th}(n,\gamma)$ (barn)	$\bar{w}_{th}$ (old)	$\epsilon = C_w/(B.E.)\cdot P_\gamma$ Old W(E)	New W(E)
Ag	4	63.6 ± 0.6	10.9	1.00	1.00
Au	16	98.8 ± 0.3	13.5	1.018 ± 0.01	0.997 ± 0.01
Fe	66	2.55 ± 0.03	28.9	1.082 ± 0.03	1.045 ± 0.03
^{50}Cr	71	15.9 ± 0.2	23.1	1.093 ± 0.02	1.063 ± 0.02
^{53}Cr	82	18.2 ± 1.5	26.1	1.24 ± 0.09	1.19 ± 0.08

of 10.2cm diameter and was placed at 50m from the Linac target.

Table II. Summary of experimental results for the 1.15 keV resonance of ^{56}Fe.

Author	Year	Type of measurement	Γ_n (meV)	Γ_γ (meV)
Block[12]	1964	Transmission	68±6	600±60
Moxon[13]	1965	Transmission	52±5	560
Hockenbury[14]	1968	Capture	86±21	(600) [a]
Julien[15]	1969	Transmission	62±4	570±60
Gayther[16]	1979	Capture	53±7	615±26
Present work		Transmission	58±4	610±60
Present work		Capture (thermal calibration)	56±6	(610) [a]

a) Assumed Γ_γ value, used to derived Γ_n.

The data were analyzed with the shape fitting programme SIOB[11]: a plot of the fitted transmission is given in Figure 3. From this a value of Γ_n = 58±4 meV was obtained.

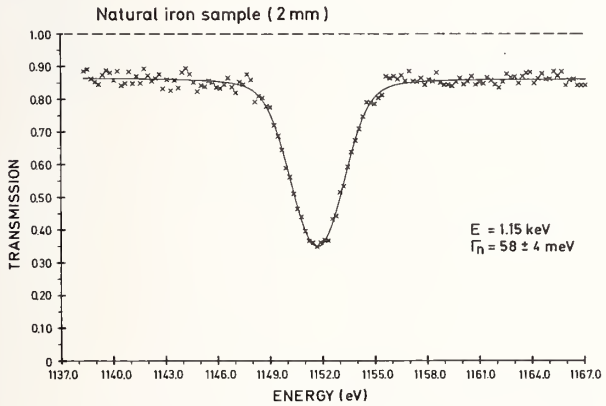

Fig. 3. Transmission of a 2mm thick Fe metallic sample in the region of the 1.15 keV resonance. The fitted curve (continuous line) was obtained with the SIOB programme.

A second approach used was to measure capture from the 1.15 keV resonance down to thermal energy for a 1mm thick natural metallic sample and to normalize to the thermal value $\sigma(n,\gamma)$ = 2.55±0.03b. A correction for the difference in B.E. of the other Fe isotopes was introduced. This measurement was performed on a 12m flight path and a BF_3 detector was used to measure the relative flux. A spectrum of the relative capture yield is shown in Figure 4: the background refers to a run done with an equivalent scatterer of graphite. This measurement was performed twice, with and without shielding around the detector, and a consistent value of Γ_n = 56±6 meV was found, giving good agreement with the previous measurement. The transmission value and its error were taken for normalizing our capture data.

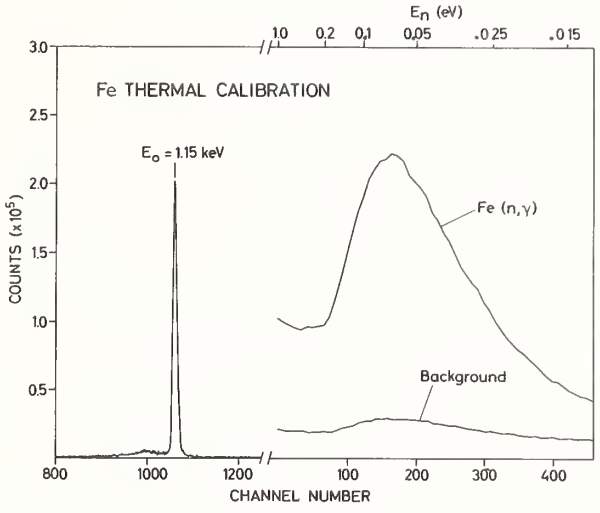

Fig. 4. Thermal energy calibration of the 1.15 keV resonance using a 1mm thick Fe metal sample. The background is measured with an equivalent scatterer of graphite.

Neutron Flux

The energy dependence of the neutron flux was measured with a 0.5mm thick Li-glass detector type NE 912 enriched to 95% ^6Li, situated in air and viewed by two 5 inch photomultipliers placed outside the neutron beam and perpendicular to its axis. The $\sigma_{tot.}$ and $\sigma(n,T)$ cross sections for ^6Li, needed to calculate the detector efficiency, were taken from ref. 17. The experimental neutron flux per unit energy interval $\Phi(E)$ deduced after correction for the efficiency could be fitted with the following expression

$$\Phi(E) = K\, E^{[a(E)-1.5]}$$

where $a(E) = 0.598+0.364\cdot10^{-3}\sqrt{E}-0.523\cdot10^{-6}E$ and the energy E is in eV.
Since the data were normalized at the 1.15 keV resonance, the uncertainty in the neutron flux was estimated to vary from 0 at 1 keV to ± 5% at 100 keV. This uncertainty is included in the errors given in Table III.

Results

A modified version of the TACASI code was employed to deduce resonance parameters, either Γ_γ or Γ_n whichever is the lower, from capture areas. This code takes into account Doppler, resolution and multiple scattering corrections, the latter by means of a Monte Carlo routine. The results are listed in Table III aside the Perey[18] evaluation and the Harwell preliminary data[19].

Apart from the usual resonance parameters it was thought useful to introduce in the second column the value of $\bar{w}$ associated to each resonance

in order to give information about its spectral shape.

The values of J, l and Γ_n or Γ_γ (which ever is the larger) from ref. 18 were taken as fixed input parameters in the TACASI programme.

The given uncertainties are composed of the statistical plus three types of systematic errors: a 5% uncertainty in the 1.15 keV capture area normalization, the uncertainty due to difference in spectral shape and the uncertainty on flux.

A comparison with refs. 18 and 19 shows that the present data, while being in good agreement with Harwell's preliminary results are systematically about 15% lower than the Oak Ridge values.

Table III. Resonance parameters of ^{56}Fe between 1 and 100 keV.

		PRESENT RESULTS			OAK RIDGE EVALUATION [18]					HARWELL [19]
E_o (keV)	$\bar{w}$	$g\Gamma_n\Gamma_\gamma/\Gamma$ (eV)	Γ_n (eV)	Γ_γ (eV)	$g\Gamma_n\Gamma_\gamma/\Gamma$ (eV) a)	Γ_n (eV)	Γ_γ (eV)	J	l	$g\Gamma_n\Gamma_\gamma/\Gamma$ (eV) b)
1.152	28.7	$(53.\pm4.)\times10^{-3}$	$(58.\pm4.)\times10^{-3}$		$(55.\pm3.8)\times10^{-3}$	$(60.\pm4.)\times10^{-3}$	0.6±0.06	1/2	1	$(49.\pm7.)\times10^{-3}$ c)
2.352	17.7	$(0.54\pm0.1)\times10^{-3}$	$(0.27\pm0.05)\times10^{-3}$		$(0.4\pm0.12)\times10^{-3}$	$(0.2\pm0.06)\times10^{-3}$	0.84	3/2	2	0.5×10^{-3}
12.46	14.8	$(2.3\pm0.4)\times10^{-3}$	$(2.3\pm0.4)\times10^{-3}$		2.3×10^{-3}	$(2.3\pm0.3)\times10^{-3}$	0.54	1/2	1	
17.76	28.6	$(17.\pm2.)\times10^{-3}$	$(17.\pm2.)\times10^{-3}$		$19.\times10^{-3}$	$(19.\pm2.)\times10^{-3}$	0.54	1/2	1	
20.18	23.2	$(7.8\pm1.2)\times10^{-3}$	$(3.9\pm0.6)\times10^{-3}$		9.4×10^{-3}	$(4.7\pm0.5)\times10^{-3}$	0.84	3/2	2	
22.80	23.4	0.17±0.03	0.24±0.04		0.18	0.27±0.06	0.54	1/2	1	0.17
27.68	24.4	0.80±0.20		0.80±0.20		1520.±30.	1.4±0.1	1/2	0	0.85±0.09 c)
34.24	35.8	0.54±0.08		0.46±0.08	0.64±0.05	0.79±0.3	0.54	3/2	1	0.52
36.73	21.2	0.23±0.03	0.086±0.01		0.28±0.02	0.11±0.01	0.84	5/2	2	0.24
38.42	29.3	0.34±0.05	0.25 ±0.035		0.4	0.32±0.08	0.54	3/2	1	0.33
46.06	18.9	0.45±0.06		0.48±0.06	0.5	10.0±3.0	0.53±0.05	1/2	1	0.47
52.14	24.0	0.68±0.08		0.35±0.04	0.81	12.0±1.0	0.42±0.04	1/2	1	
53.57	18.8	0.33±0.07		0.51±0.09	0.4	1.0±0.4	0.67±0.17	1/2	1	
53.70	29.6	0.032±0.01	0.034±0.01							
59.23	30.5	0.74±0.1		0.42±0.05	0.87	4.0±0.5	0.49±0.05	3/2	1	
63.47	17.5	0.55±0.1		0.41±0.075	0.65	0.8±0.16	0.55±0.13	3/2	1	
72.98	37.2	0.61±0.09		0.62±0.09	0.7	20.±4.	0.72±0.07	1/2	1	
74.00	29.2	0.57±0.07		0.57±0.07	0.73	535.±10.	0.73±0.07	1/2	0	
77.07	25.4	0.27±0.04		0.29±0.04	0.3	3.6±0.5	0.33±0.03	1/2	1	
80.84	20.5	1.75±0.2		0.63±0.085	2.04	7.0±0.7	0.74±0.08	5/2	2	
83.69	18.4	0.94±0.13		0.94±0.13	1.28	1250.±50.	1.28±0.13	1/2	0	
90.33	20.9	0.73±0.1		0.37±0.05	0.89	14.±1.	0.46±0.05	3/2	1	
92.70	21.7	0.93±0.2		0.66±0.12	0.93	1.6±0.3	0.65±0.11	3/2	2	
92.93	23.5	0.40±0.1	0.32 ±0.08		0.53	0.52±0.15	0.54	3/2	1	
96.22	26.3	0.55±0.2	0.22 ±0.08		1.26	0.67±0.40	1.1 ±0.9	5/2	2	
96.37	21.6	0.38±0.1		0.51±0.15	0.3	1.3 ±1.1	0.4 ±0.3	1/2	1	
96.62	23.6	1.06±0.2		0.68±0.12	0.7	2.5 ±0.3	0.4 ±0.2	3/2	1	

a) 10% error unless given

b) Γ_γ assumed to be 1eV

c) Values from ref.16.

Conclusions

A serious systematic discrepancy is apparent between the present results and the Oak Ridge ones. It is believed that this arises from a different way of normalizing the capture data. More work is therefore needed in order to fulfill the ± 5% accuracy request. On the other hand, the excellent agreement with Harwell's preliminary values is very promising. It is particularly rewarding to notice the agreement between the Γ_γ values of the 27.7 keV resonance, a fact which indicates a very low neutron sensitivity of our detector system, comparable to that measured at Harwell for the liquid scintillator tank[16]. Our plans for the future include extension of measurements and analysis up to 400 keV, a precise assessment of the neutron flux also up to this energy, a continued investigation on the weighting method and a measurement of the neutron sensitivity. Also, R matrix multilevel codes such as FANAC[20] and REFIT[21] will be implemented. For all these reasons the present results should be considered as preliminary.

Acknowledgement

The authors are indebted to B.B. Thom, A.E.R.E., Harwell for performing calculations of the weighting function with a different programme.

References

1. C.G. Campbell, NEACRP-A-314, NEANDC-110"A".
2. A. Filip et al., Neutron Data of Structural Materials for Fast Reactors, Geel, 1977, ed. by K.H. Böckhoff, Pergamon Press, p. 3.
3. Neutron Data of Structural Materials for Fast Reactors, Geel, 1977, ed. by K.H. Böckhoff, Pergamon Press, p. 795.
4. T. Babeliowsky, C. Cervini, A. De Keyser, An acquisition system for two parameter measurements with a high data rate (to be published).
5. R.L. Macklin and J.H. Gibbons, Phys. Rev. 159, 1007 (1967).
6. C. Le Rigoleur and A. Arnaud, Proceedings of NEACRP-NEANDC Specialist Meeting, Karlsruhe, 1973, Report KFK 2046 (1975).
7. F. Hensley, private communication.
8. L. Pages et al. Atomic Data 4, 1-127 (1972).
9. Groshev et al., Nuclear Data A3, 367 (1967)
" " A5, 1 (1968)
" " A5, 243 (1969)
10. S.F. Mughabghab and D.J. Garber, Neutron Cross Sections, I, Report BNL 325 (1973).
11. G. de Saussure, D.K. Olsen and R.B. Perez, Report ORNL/TM-6286 (1978).
12. R.C. Block, Phys. Letters 13, 234 (1964).
13. M.C. Moxon, Study of Nuclear Structure with Neutrons, Antwerp, 1965, paper 88.
14. R.W. Hockenbury et al., Phys. Rev. 178, 1746 (1968).
15. J. Julien et al., Nucl. Phys. A132, 129 (1969).
16. D.B. Gayther and M.C. Moxon, private communication.
17. H.H. Knitter and C. Butz-Jörgensen, Report EUR 5276 (1976).
18. F.G. Perey et al., Neutron Data of Structural Materials for Fast Reactors, Geel, 1977, ed. by K.H. Böckhoff, Pergamon Press, p. 530.
19. D.B. Gayther et al., Neutron Data of Structural Materials for Fast Reactors, Geel, 1977, ed. by K.H. Böckhoff, Pergamon Press, p. 547.
20. F.H. Fröhner, Report K.F.K. 2129 (1976).
21. M.C. Moxon, Neutron Data of Structural Materials for Fast Reactors, Geel, 1977, ed. by K.H.Böckhoff, Pergamon Press, p. 644.

FAST-NEUTRON TOTAL AND SCATTERING CROSS SECTIONS OF Cr, Fe and ^{60}Ni*

A. B. Smith, P. T. Guenther and J. F. Whalen
ARGONNE NATIONAL LABORATORY
9700 South Cass Avenue
Argonne, Illinois 60439, USA

Neutron total cross sections are measured with broad resolutions (50-100 keV) from ≈1.0-4.5 MeV at intervals of $\lesssim$50 keV and to accuracies of ≈1% using a variety of sample thicknesses. Differential elastic-scattering cross sections are measured at $\gtrsim$10 scattering angles distributed between 20-160 deg. from ≈1.5-4.0 MeV at intervals of $\lesssim$50 keV. Angle-integrated elastic scattering cross sections are deduced from the measured values to accuracies $\gtrsim$5%. Inelastic-neutron-scattering cross sections are determined up to incident neutron energies of 4.0 MeV, at scattering angles distributed between 20-160 deg., and for 5 observed excitations in Cr, for 7 in Fe and for 6 in ^{60}Ni. The experimental results are discussed in terms of conventional optical-statistical models with attention to cross section fluctuations and in the context of direct-scattering processes. The experimental and calculational results are compared with the corresponding evaluated quantities given in the ENDF/B file with attention to regions of agreement and inconsistency.

[Nuclear Reactions, Cr, Fe and ^{60}Ni, measured σ_T and σ_{SCAT} 1-4.5 MeV, Model interpretation.]

I. INTRODUCTION

The fast-neutron data of the primary constituents of stainless steel remain remarkably deficient and fall far short of meeting the stated need.[1] This is despite of the fact that many of the data needs in this area can be met with relatively modest applications of existing measurement systems and techniques. These observations stimulated new interest in structural-material measurements at Argonne. This report outlines results obtained in this renewed effort.

The objective was the measurement of energy-averaged neutron total and scattering cross sections of chromium, iron and nickel providing the neutron elastic-and inelastic-scattering cross sections to the requested accuracies of ≈5% over the energy range 1-5 MeV. The procedure was the measurement of broad-resolution neutron total and elastic-scattering cross sections to accuracies that imply a non-elastic cross section to an uncertainty of ≈5%. Concurrently, neutron inelastic-scattering cross sections were sought consistent with the non-elastic cross section and to the same accuracies. This procedure implies energy-averaged total neutron cross section accuracies of ≈1% and neutron elastic-scattering cross sections to accuracies of ≲5%. Generally, the detailed aspects of this work are given in the Laboratory reports of Refs. 2-5.

II. MEASUREMENT METHODS

A. Samples

All measurement samples were fabricated into cylinders from high-chemical-purity metal. The Cr and Fe samples consisted of elemental material while the Ni sample was essentially 100% enriched in the isotope ^{60}Ni. All scattering samples were approximately 2 cm in diameter and 2 cm long. The Cr and Fe total-cross-section samples varied in length so as to provide a number of transmissions over the range of 20-80%. The ^{60}Ni total cross sections were determined using the above scattering sample.

B. Neutron Total Cross Sections

The neutron-total-cross-section measurements were made using the monoenergetic-source facilities at the Argonne National Laboratory Fast Neutron Generator. The neutron source was produced by a proton burst of ≈1 nsec duration incident on a lithium metal film at a repetition rate of 2 MHz. The energy of the resulting neutrons was governed by the proton energy and the neutron-energy resolution was controlled by the thickness of the lithium-target film. A shield and associated collimator around the source were used to obtain a neutron beam ≈1 cm in diameter at a zero-degree source-reaction angle. The samples were placed upon a wheel so that they rapidly rotated through the beam. The neutron detector was a proton-recoil scintillator placed on the neutron-beam axis approximately 5 m from the neutron source. Conventional time-of-flight techniques were used to obtain the velocity spectra of neutrons arriving at the detector. Backgrounds and source perturbations were small and easily determined from an analysis of the velocty spectra. A random signal was introduced into the data acquisition system in order to precisely determine dead-time corrections. In-scattering corrections were estimated and found to be negligible. The neutron transmissions through the samples followed directly from the observed detector responses. The total cross sections were calculated from the transmissions in the conventional manner[6].

C. Neutron Scattering Measurements

The neutron scattering measurements were made using the Argonne National Laboratory 10-angle, pulsed-beam time-of-flight system using the above pulsed ^{7}Li(p,n)^{7}Be source. The mean incident-neutron energy at the scattering sample was known to ≈10 keV. The scattering samples were placed ≈13 cm from the neutron source at a zero-degree reaction angle. Proton-recoil scintillators were placed at flight paths of 5 to 5.5 m. The flight paths extended over a scattered-neutron angular range of 20 to 160 deg. The scattering angles were determined to a relative $\lesssim$0.5 deg. accuracy

*This work supported by the U. S. Department of Energy.

and to an absolute accuracy of ≲1.0 deg. The relative energy dependencies of the scattered-neutron-detector sensitivities were determined by observation of neutrons scattered from hydrogen (polyethylene) at selected angles and a fixed incident energy or from measurements of the neutron spectrum emitted during the spontaneous fission of ^{252}Cf[7]. The normalizations of the relative-detector sensitivities were determined by observing neutrons scattered from hydrogen (polyethylene) at selected energies and angles. Thus all scattering cross sections were determined relative to well known H(n,n) cross sections[8]. The measured velocity spectra were reduced to cross sections and corrected for angular resolution, sample attenuation and multiple-event effects[7]. Concurrent determinations of the elastic scattering cross sections of carbon verified the fidelity of the measurement system. In the case of ^{60}Ni there were some ancillary measurements of the (n;n', gamma) cross sections using conventional GeLi detector techniques[3].

III. EXPERIMENTAL RESULTS

A. Neutron Total Cross Sections

The objective of the total cross section measurements was the determination of precise energy-averaged magnitudes comparable with the subsequently measured scattering cross sections, model predictions and evaluations. Resolution of detailed resonance structure was explicitly avoided. The measured energy range varied somewhat from sample to sample but generally extended from 1.0 - 4.5 MeV with mesurements made at intervals of ≲50 keV with incident resolutions of >50 keV. The Cr and Fe measurements envolved at least four sample thicknesses. The experimental values for a given sample thickness were averaged over incident energy intervals of 100 - 200 keV to obtain average values with a statistical accuracy of ≈1%. The energy-averaged results were appreciably dependent upon sample thickness. The results obtained with the thicker samples were very much lower than those obtained with the thin samples due to the appreciable self shielding of the samples. The results obtained with the various sample thicknesses were extrapolated to the zero-thickness value to obtain the "true" energy-averaged cross sections. In the case of Fe carefully-measured high resolution results have been obtained by Harvey et al.[9]. In this unusual case the resolution is sufficient to resolve the structure well into the MeV range and thus the average of the high resolution results should be consistent with the present broad-resolution values. The agreement is generally within ≈1% as illustrated in Fig. 1A. On the average, both of the measured sets of values tend to be systematically larger than a corresponding average constructed from the ENDF/B-IV file. A somewhat similar trend was observed in the comparison of the measured and evaluated neutron total cross sections of Cr shown in Fig. 1B. These comparisons suggest that experimenters have not generally given proper consideration to the interplay of resolution, sample thickness and resonance structure and that, as a consequence, the neutron-total-cross-section data base in the highly fluctuating structural region may be systematically distorted to too low values in the MeV range with consequent impact upon the evaluated files. Similar problems are known to occur in other mass-energy regions.

The ^{60}Ni neutron total cross sections measurements had to be confined to a single and relatively thick sample. As a consequence the measured values are systematically lower than an equivalent average constructed from the better resolution results of Clement et al.[10] at lower energies as illustrated in Fig. 1C. Numerical estimates suggest that the present values are distorted by 5-10% (or in the extreme, 20%) toward too low values at energies below 1 MeV. This distortion rapidly decreases as the energy increases. There is no comparable ENDF/B file, but optical models based upon high-energy scattering measurements generally predict higher neutron total cross sections in this mass region near 1 MeV. The discrepancies may be due, in part, to shortcomings in the models or physical behavior such as fluctuations, "doorways"[11], etc., that are not consistent with the underlying precepts of the optical model. However, the model-measurement discrepancy has been widely observed and an extreme example is shown in Fig. 1C. Such discrepancies tend to be consistent with shortcomings in the experimental determinations of energy-averaged neutron total cross sections in this mass-energy region.

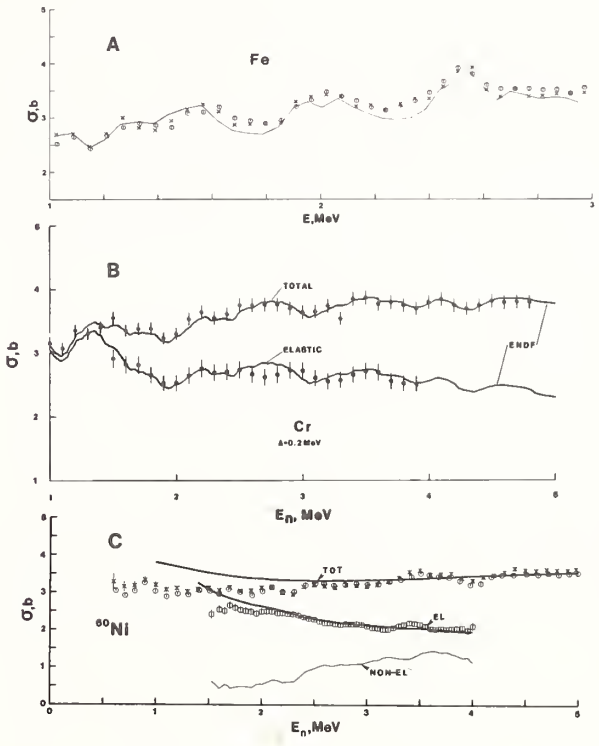

Fig. 1. Neutron cross sections of: A Iron, present total-cross-section results (O), equivalent average of the Ref. 9 values (X), and ENDF-IV (curve). B. Chromium, present total (O) and elastic-scattering (□) results, and ENDF-IV (curves). C. ^{60}Ni, Present total (O) and elastic scattering (□) results, equivalent average of total cross sections of Ref. 10 (X), and results of model calculations (heavy curves).

B. Neutron Elastic Scattering

Elastic neutron scattering cross sections were measured at incident energy intervals of ≤50 keV from 1.5 to 4.0 MeV with incident-energy resolutions of ≈20-60 keV. The objective was an angle-energy scope that would well define the elastic scattering cross sections to an intermediate energy resolution. The individual differential scattering cross sections were generally determined to 5 to 8% accuracies. Statistical uncertainties contributed 1-3% to the overall uncertainties. Correction procedures, including those for effects due to angular uncertainties, made a similar small contribution. The largest contribution to the overall uncertainty came from the calibration of the detector efficiency (typically 3 to 5%). The uncertainty in the H(n,n) standard was a small factor (i.e. ≲1%).

Despite the relatively-broad incident-energy resolutions, considerable variation in the distributions with energy was discernable throughout the measured energy range. Any single distribution was not necessarily representative of the more general energy-averaged behavior. A better representation of the average behavior was obtained by averaging the measured values over 200-keV intervals with results as illustrated in Fig. 2. With these 200-keV averages, the behavior of the distributions varies reasonably smoothly with energy, and is comparable with predictions of the energy-averaged models.

The 200-keV averages of the present results were least-square fitted with a Legendre polynomial expansion from which the angle-integrated elastic-scattering cross sections were derived. The accuracies of the latter were generally 3-5%, i.e. essentially dominated by the uncertainties associated with detector calibrations. Representative elastic-scattering cross sections are shown in Fig. 1B-C. The angle-integrated elastic scattering cross sections fluctuate with energy in a manner consistent with the fluctuations of the neutron total cross sections. Together the two sets of cross sections yield the non-elastic cross sections. The non-elastic cross sections were generally known to ≈5% and consistent with the directly-measured neutron inelastic scattering cross sections above 1.5-2.0 MeV.

C. Neutron Inelastic Scattering

Differential-neutron-inelastic-scattering cross sections were determined concurrently with the elastic-scattering values. Scattered neutrons were observed corresponding to levels in Cr at 1.433 ± 0.009, 2.377 ± 0.008, 2.665 ± 0.005, 2.778 ± 0.007 and 2.970 ± 0.006 MeV; in Fe at 0.853 ± 0.050, 1.389 ± 0.030, 2.097 ± 0.022, 2.579 ± 0.035, 2.677 ± 0.014, 2.974 ± 0.011 and 3.152 ± 021 MeV; and in ^{60}Ni at 1.342 ± 0.013, 2.168 ± 0.010, 2.304 ± 0.026, 2.509 ± 0.022, 2.636 ± 0.019 and 3.164 ± 0.041 MeV. These observed excitation energies are averages of a number of independent measurements and the uncertainties are RMS deviations from the mean. The presently observed excitations correspond reasonably well to previously reported levels as summarized in the compilations of Ref. 12.

Angle-integrated neutron inelastic-excitation cross sections were determined by least-square fitting no fewer than four differential values at each energy with Legendre-polynomial series. The uncertainties in the differential-cross section values ranged from a minimum of ≈5% for prominent and well-resolved neutron groups at favorable energies to ≳20% for less well resolved and/or low-intensity neutron groups. There was a similar spread in the uncertainties of angle-integrated cross sections ranging upward from a minimum of ≈5%.

A major feature of the inelastic process is the prominent excitation of the first, 2+, levels. These levels are either vibrational (as in ^{60}Ni[12]) or rotational (as in ^{56}Fe[13]). The differential cross sections for the excitation of these levels fluctuate with energy in a manner analogous to that of the elastic scattering cross sections. In order to remove these fluctuations the measured inelastic-scattering distributions were averaged over ≈200 keV incident-neutron energy intervals in the same manner as for the elastic-scattering distributions. The resulting averages behaved in a relatively smooth manner. Furthermore, there was a trend from distributions symmetric about 90 deg. at lower energies to those that were somewhat peaked forward at upper energies in a manner that could be expected as the result of increasing contributions from direct-inelastic processes. Cross sections for the excitation of higher-lying levels also fluctuated, and averaging procedures were used to obtain the energy-averaged behavior in the same fashion as outlined above for the first, 2+, levels. Scattered neutron distributions resulting from the excitation of these higher-lying levels were generally essentially symmetric about 90 deg.

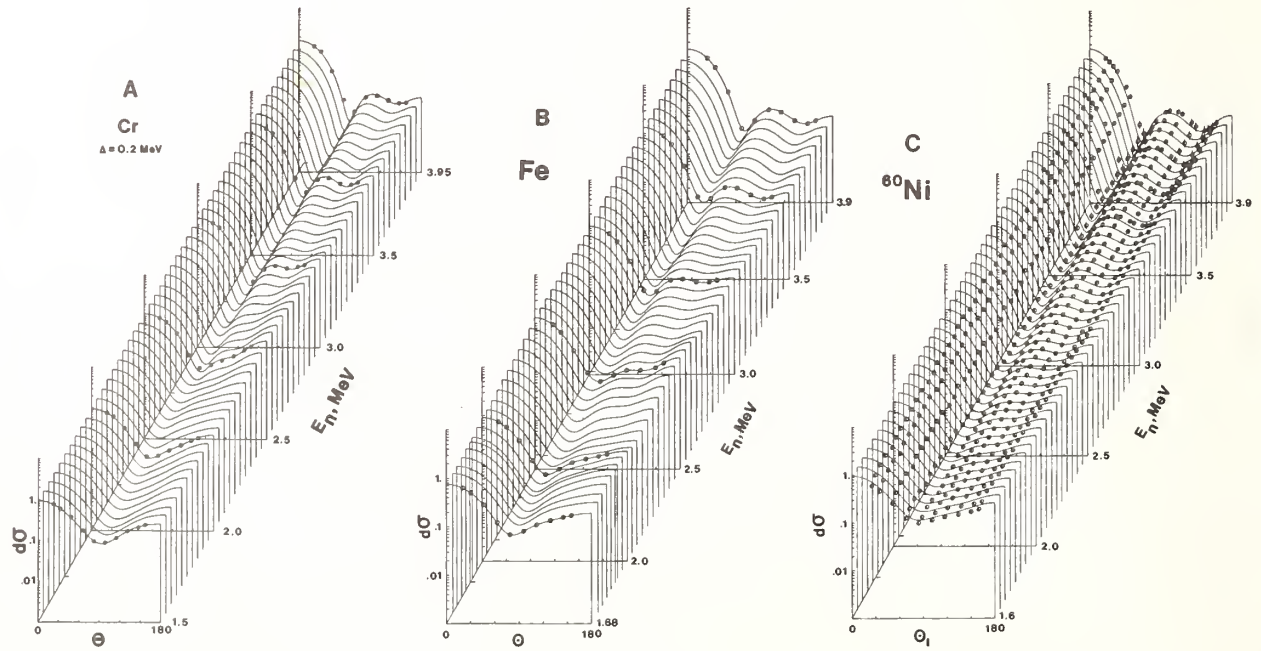

Fig. 2. Measured differential elastic scattering cross sections of chromium (A), iron (B), and ^{60}Ni (C). The present experimental results are indicated by data points. Curves denote the results of fitting Legendre expansions to the chromium and iron data and the results of model calculations in the case of ^{60}Ni. All data have been averaged over 200 keV increments.

The above direct-neutron measurements extended to within ≈0.8 MeV of threshold. In the case of ^{60}Ni, (n,n',γ) techniques were used to extend the measured cross sections for the excitation of the prominent 1.342 MeV level to threshold. The measured relative (n;n',γ) results were normalized to the directly measured (n;n') values near 2.0 MeV.

The angle-integrated neutron inelastic scattering cross sections derived from the measurements are shown in Fig. 3. There are a number of previously reported results some of which are indicated in these figures. The agreement with the present results varies from good to very poor. Many of these previous results consist of isolated or a few experimental values. The validity of comparisons of isolated values is questionable in view of the fluctuations in the cross sections and unavoidable variations in experimental energy scales and resolutions. Additional discussions of data comparisons are to be found in Refs. 3 to 5.

Many of the present neutron-inelastic-scattering results can be compared with values given in the ENDF/B-IV files, corrected to isotopic quantities where necessary. The comparisons, indicated in Fig. 3 suggest that portions of the differential inelastic scattering files are discrepant with the present results by 15-20% or more. Some of these discrepancies appear in the largest inelastic excitation cross sections (e.g. the 2+ level of iron) and amount to 5-10% (or larger) discrepancies between measured and evaluated total neutron inelastic-scattering cross sections. The present inelastic-scattering results are further supported by their consistency with the above non-elastic cross sections to within ≈5%, i.e. to within the experimental uncertainties.

IV. INTERPRETATION

The theoretical interpretations sought to: a) establish spherical optical potentials providing an acceptable description of the energy-averaged neutron cross sections in this mass-energy region of strong fluctuations, and b) explore the effect of direct-inelastic processes in the neutron interaction. The scope and detail of the present experiments provides a suitable foundation for such investigations.

The spherical optical potential was entirely based upon the 200 keV averages of the measured differential elastic-scattering cross sections. The averaging increment was a compromise between a representation consistent with the concept of the optical model and the excited-level spacing influencing the compound-elastic component. The initial step in the deduction of the potential was a 6-parameter (real and imaginary strengths, radii and diffusenesses) Chi-square fit of a conventional surface-absorption optical potential to each of the measured elastic-scattering distributions. The compound-elastic contributions were calculated using the Hauser-Feshbach formula with width-fluctuation corrections[14,15]. The initial fitting procedures reasonably defined real and imaginary radii and diffusenesses. These four-parameters were then fixed for subsequent and more detailed two-parameter (real and imaginary strengths) Chi-square fitting procedures. The latter included the enhancement of compound-nucleus components using the formalism of Hofmann et al.[16]. The level-density-distribution of Gilbert and Cameron[17] was used for the description of levels with excitations of ≥3.0 MeV. The resulting V (real strength) and W (imaginary strength) followed a general linear energy dependence. Superimposed on these general trends were relatively small (≈ ± 1 MeV) fluctuations with a periodicity of ≈0.5 MeV. These fluctuations reflected those of the underlying data bases. The fluctuations were not characteristic of a general energy-averaged behavior and were ignored in the resulting "general potentials" derived for each target. These "general potentials" were the basis for subsequent comparisons of measured and calculated values and the investigation of direct-vibrational processes. The numerical potential parameters are given in Refs. 3-5. It must be stressed that these potentials are pragmatic parameterizations of the particular experimental results and are not "global" or even "regional". Indeed, there are pronounced differences between the potentials. These differences may well be rooted in the nature of the cross section fluctuations inherent to each target. However, the "general potentials"

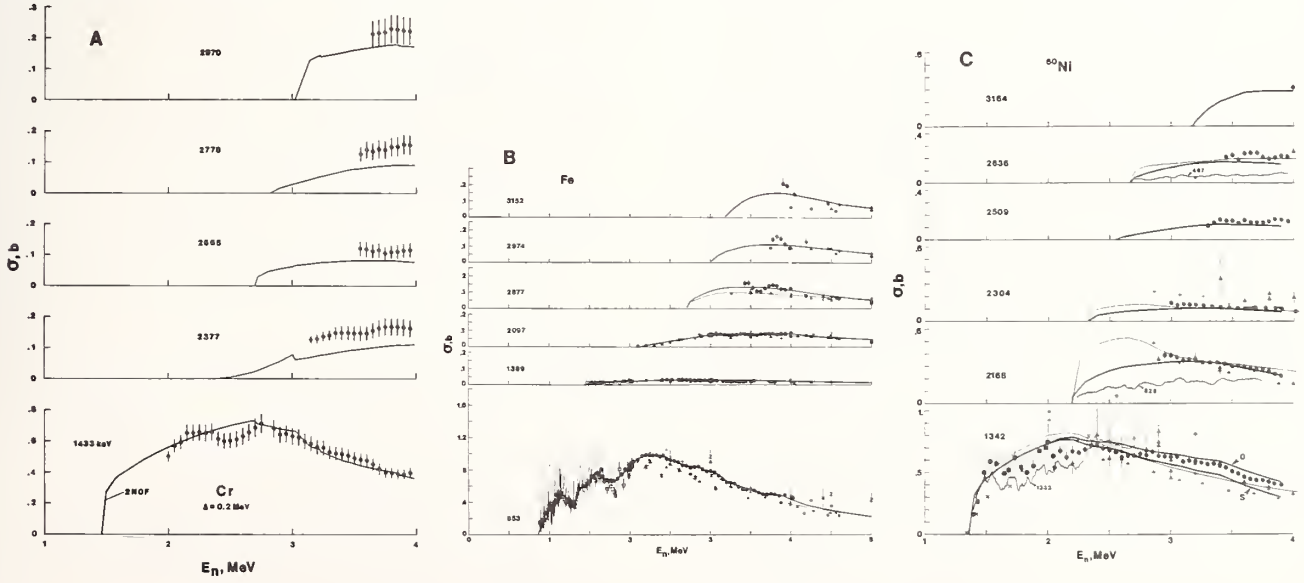

Fig. 3. Measured inelastic-neutron-excitation cross sections of Cr (A), Fe (B) and ^{60}Ni (C). The present results are indicated by solid data points. Corresponding ENDF-IV values are noted by dotted (Fe and ^{60}Ni) and solid (Cr) curves. Spherical (S or no notation) and deformed (D) model results for ^{60}Ni are indicated by solid curves.

provide an acceptable description of measured neutron-elastic-scattering cross sections of each target as illustrated in Fig. 2C. Differences between measured and calculated results were generally small and ramdom in nature as might be expected from the residual fluctuations and doorway configurations[11].

Comparisons of measured and calculated neutron total cross sections follow the same general trends as those of the angle-integrated elastic-scattering cross sections. In addition to the effects of fluctuations and doorway levels there were the problems of experimental sample-size perturbations outlined above. The differences between measured and calculated values were generally within the range of estimated experimental perturbations alone. The inability of optical potentials based upon higher-energy elastic scattering to describe neutron total cross sections near 1.0 MeV in this mass region has long been observed. As outlined above, much of this discrepancy may be experimental in origin, but there may also be a shortcoming in the concept of a simple spherical optical potential. In either event, there remains an uncertainty in energy-averaged neutron total cross sections in this mass-energy region of ≈10% in a number of nuclides.

The neutron-inelastic-scattering cross sections calculated using the spherical "general potentials" were qualitatively descriptive of the measured values (as illustrated in Fig. 3C) but there were quantitative discrepancies. The calculated excitation of the first, 2+, levels tend to be larger than the measured values below ≈2.5 MeV and smaller above ≈3.0 MeV. These differences are ≈10-30%. In addition, the calculated angular distributions of scattered neutrons do not show the forward peaking observed at higher energies. Some of the comparisons between measured and calculated excitation cross sections do suggest reconsideration of some previously assigned J-Π values (see Refs. 4-5).

At higher incident energies (e.g. $\gtrsim$3.0 MeV) the above spherical interpretations have three shortcomings: a) the calculated excitations of the first, 2+, levels are systematically smaller than the measured values, b) measured neutron distributions resulting from the excitation of the first, 2+, levels are not symmetric about 90 deg. as predicted by theory, and c) the measured elastic-neutron distributions deviate systematically from the calculated values as 4.0 MeV is approached. It is difficult to attribute these shortcomings entirely to fluctuations and/or the level-density approximation employed in the calculations. However, qualitatively the above features are characteristic of direct-inelastic processes. Coulomb-excitation, (γ,n) and stripping studies indicate that the first excited, 2+, levels are rotational (e.g. ^{56}Fe) or vibrational (e.g. ^{60}Ni) states. The effects of these direct interactions were estimated using a coupled-channels calculation, coupling the ground (0+) and first-excited state assuming the β_2 values of Ref. 18. In doing so it was assumed that direct and compound-nucleus processes were approximately separable and that the latter could be reasonably calculated using transmission coefficients derived from the spherical potential. The "general potentials" were used for the direct calculations except for the imaginary strengths which were adjusted to improve the description of the observed differential elastic-scattering distributions. The direct calculations were an approximation in that they did not derive transmission coefficients directly from the deformed potential nor was there an attempt made to explictly Chi-square fit the measured elastic distributions using the deformed potential. Such procedures would have been very costly and deceptive if applied to only a few measured distributions.

The coupled-channels results mitigated the shortcomings of the spherical calculations. The calculated distributions of neutrons resulting from the excitation of the first, 2+, level were peaked forward in the manner of the measured values. The inelastic cross section magnitudes and the neutron differential-scattering distributions were in much better agreement with the measured values than those obtained from the spherical calculations (as illustrated in Fig. 3C). Thus the comparisons of measured and calculated values suggest that direct-inelastic processes are significant in the present energy range. In particular they account for facets of the interaction not consistent with the spherical optical-statistical model. Consideration of direct-inelastic interactions does result in modifications of potential parameters relative to the spherical model (e.g. 30% reduction in imaginary strength.

REFERENCES

1. WRENDA 74, IAEA Report, INDC(SEC)-38/U (1974).
2. A. Smith and J. Whalen, Argonne Natl. Lab. Report, ANL/NDM-33 (1977).
3. A. Smith et al., Argonne Natl. Lab. Report, ANL/NDM-44 (1979).
4. A. Smith and P. Guenther, Argonne Natl. Lab. Report, ANL/NDM-47 (1979).
5. P. Guenther et al., Argonne Natl. Lab. Report, to be published.
6. D. Miller, Fast Neutron Physics, Vol.-II, Inter. Sci. Pub., New York (1963).
7. P. T. Guenther, University of Ill. Thesis (1977).
8. J. Hopkins and G. Breit, Nucl. Data, A9 137 (1971).
9. J. A. Harvey et al., Data available from the NNDC.
10. Clement et al., Data available from the NNDC.
11. S. Cierjacks and I. Chouky, Proc. Conf. Neut. Data of Structural Materials for Fast Reactors, Pergamon Press, London (1979).
12. Nuclear Data Sheets for the respective masses.
13. H. E. Jackson, Priv. Com. (1979).
14. W. Hauser and H. Feshbach, Phys. Rev., 87 366 (1952).
15. P. A. Moldauer, Phys. Rev., C11 426 (1978).
16. H. Hofmann et al., Ann. Phys. (NY), 90 403 (1975).
17. A. Gilbert and A. Cameron, Can. Jour. Phys., 43 1446 (1965).
18. P. Stelson and L. Grodzins, Nucl. Data, A1 21 (1965).

NEUTRON RESONANCE PARAMETERS OF ^{79}Br AND ^{81}Br up to 15 keV

Makio OHKUBO, Yuuki KAWARASAKI and Motoharu MIZUMOTO

Japan Atomic Energy Research Institute, Tokai-mura, Ibaraki-ken, Japan

Resonance parameters of separated isotopes of bromine were measured using TOF spectrometer of Japan Atomic Energy Research Institute linear accelerator. Transmission and capture measurements were made with ^{6}Li-glass and Moxon-Rae detectors, on separated isotopes (~98%) of ^{79}Br and ^{81}Br. Resonance analyses were made on transmission data with an area analysis code, and on capture data with a Monte-Carlo program CAFIT. For ^{79}Br $g\Gamma_n^0$ values for 156 levels below 10 keV are obtained, and for ^{81}Br 100 levels below 15 keV. Strength functions are obtained: for ^{79}Br $S_0=(1.27 \pm 0.14) \times 10^{-4}$ below 10 keV, and for ^{81}Br $S_0=(0.86 \pm 0.14) 10^{-4}$ below 15 keV. Intermediate structures are observed in the resonances of ^{81}Br showing clusters of levels at 1.2, 10, 11.5 and 14 keV, where the sum of $g\Gamma_n^0$ vs. neutron energy shows steep rises.

[^{79,81}Br(n,n),(n,γ),50eV~15 keV, resonance parameters, E_o, $g\Gamma_n^0$, Γ_γ, Γ, g, S_0, $\bar{D}$]

Introduction

Neutron cross sections of bromine are of importance as one of the fission products. Resonance parameters of these nuclides were rather poor; isotopic assignments of resonances had not been made except lowest 10 levels, though 157 levels of natural bromine have been observed in the energy region below 4 keV.[1,2,3] In order to obtain precise resonance parameters of these nuclides, transmission and capture measurements were made on separated isotopes of ^{79}Br and ^{81}Br using the TOF spectrometer of the Japan Atomic Energy Research Institute linear accelerator.

Measurements and Analyses

Measurements were mainly made at the 47-m station of the JAERI linac TOF facility.[4,5] Neutrons were produced by bombarding a tantalum target with an electron beam of 120 MeV energy and 2 A peak current. The beam pulse width was 30 or 80 nsec with repetition rate 300 pps. Neutrons were traversed to the 47-m station via evacuated flight tubes,and were collimated to have the beam diameter of either 7 cm for capture measurement on thin samples or 3.5 cm for transmission measurements on thick samples. A ^{6}Li-glass and a Moxon-Rae detectors were used for transmission and capture measurements.[5] Neutron flux on the samples was detected with a ^{6}Li-glass transmission type flux monitor, placed 1.1 m upstream in the neutron beam. Flight path distance was 47.08 m from the neutron source to the capture sample. Additional transmission measurements of ^{81}Br were performed at the 190-m station to achieve a better resolution, and for these measurements another ^{6}Li-glass scintillators were employed.

Samples used were separated isotopes of ^{79}Br(98.61%) and ^{81}Br(97.81%) in chemical form NaBr, loaned by ORNL isotope pool. Three kinds of sample thicknesses were adopted, 2 mm, 10 mm and 30 mm for each isotope. For 2 mm sample, NaBr powder was sandwiched with two 1 mm thick aluminum to have the dimension 120 mm x 90 mm. To keep uniformity in thickness a block guage was used to make the sample. These were for capture measurements, and were set at the sample position inclined to 45 deg. to the neutron beam. For thick sample, the NaBr powder was packed in aluminum cylinders to have the dimension 40 mm diameter and 10 mm and 20 mm thicknesses. They were set in the collimated beam of 35 mm diameter.

A time analyzer used was a TMC-4096, with a TOF unit of a minimum channel width 31.25 ns which was made at this laboratory. The accumulated data were sent in a disk-file of the FACOM-230/75 at the computer center of JAERI. Resonance analyses and plottings were made with the FACOM-230/75 in remote batch operation, using FACOM-U-200 computer as a terminal station installed at the linac laboratory.

Transmission raw data with open beam and corresponding capture data for ^{79}Br and ^{81}Br are shown in fig.1, which were measured with channel width of 31.25 nsec. From these data isotopic identification of resonances are clearly made even in the region of the 2.85 keV sodium resonance. For transmission analyses, area analysis program modified from the Harvey-Atta program was used. Neutron capture yields were obtained by dividing the capture spectra by the neutron flux and the efficiency of the Moxon-Rae detector. Effective background in capture counts for NaBr was estimated from the capture counts for a sample of Na_2CO_3 powder packed in the same manner as that of the NaBr. Capture yields for resonances were analysed by a program CAFIT, in which multiple scattering correction is made by the Monte-Carlo method. Γ values were obtained for assumed values of $g\Gamma_n^0$ for two possible spin states (J=1 or 2) of the compound nucleus.

Results

For 156 resonances of ^{79}Br below 10 keV and 100 levels of ^{81}Br below 15 keV, parameters are obtained and listed in table 1 and 2, where $g\Gamma_n^0$ values in the region from 2.5 to 3.9 keV are taken from those of Garg et al.[2] Cumulative number of levels vs.neutron energy are shown in fig.2A for ^{79}Br, and in fig.2B for ^{81}Br. Level selections with several cut-off values in $g\Gamma_n^0$ are performed to see the level strength distribution over neutron energy. Ordinary level spacings are obtained from the curves,which correspond to cut-off value of zero, to be

^{79}Br: $\langle D \rangle = 45 \pm 6$ eV below 3.5 keV

^{81}Br: $\langle D \rangle = 70 \pm 16$ eV below 2.5 keV

Cumulative sum of $g\Gamma_n^0$ versus neutron energy are shown in fig.3a for ^{79}Br and in fig.3b for ^{81}Br. The gradient of the staircase plots is reasonably well approximated by a straight line for ^{79}Br, but it clearly shows sharp rises at 1.2, 10, 11.5 and 14 keV and probably at 4 keV for ^{81}Br. The intermediate structures of level distributions are due to the existence of level clusters at these energies, as also seen in fig.1. It is to be noted that the number of levels with $g\Gamma_n^0$ values between 3 and 7 meV seems to be much

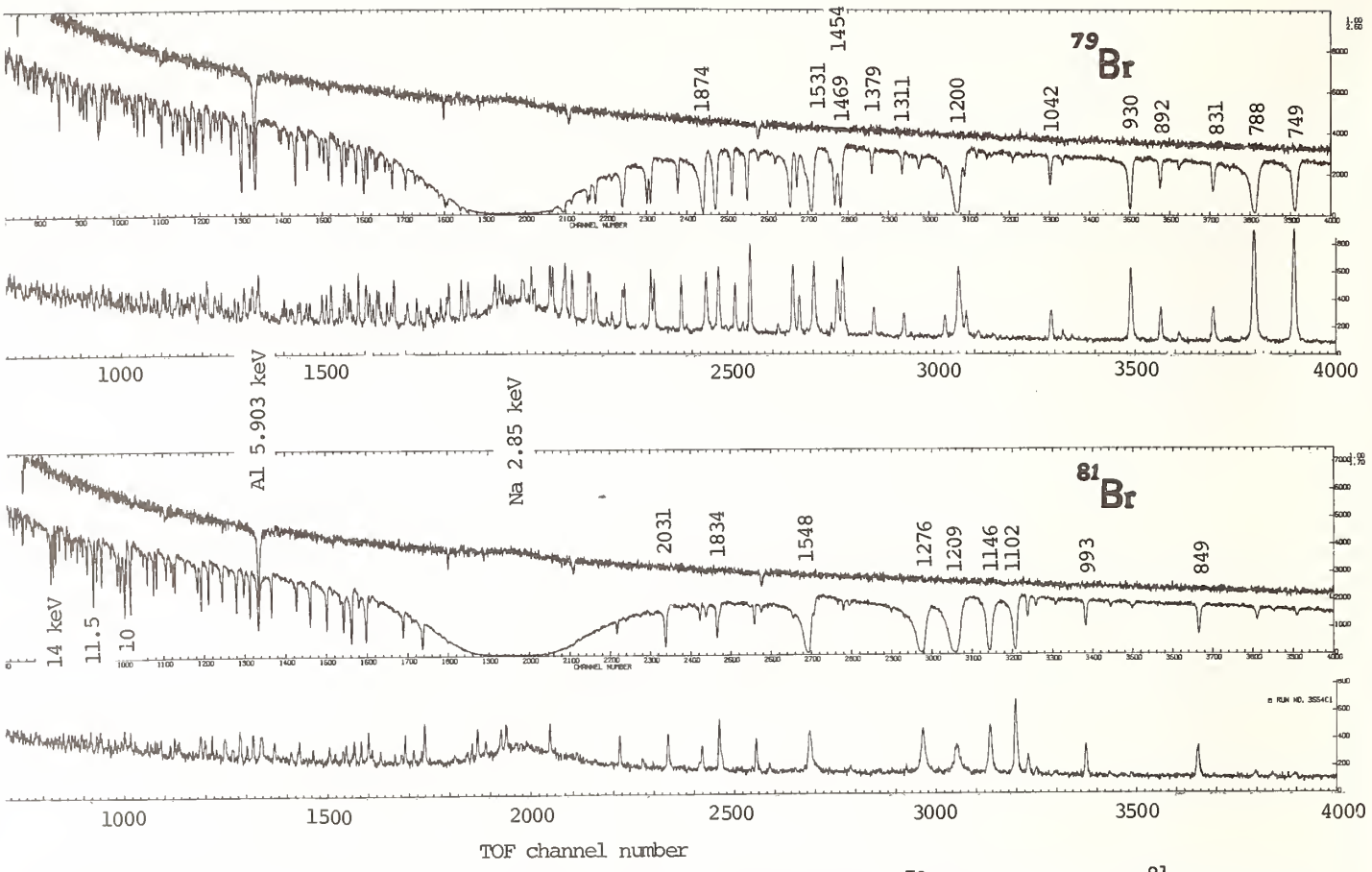

Fig.1 Transmission and corresponding capture counts vs. TOF channel for ^{79}Br(upper half) and ^{81}Br(lower half), in the energy region from 750 eV to 16 keV. Open beam are also shown with the transmission data.

smaller than expected in a Porter-Thomas distribution. The s-wave strength function for ^{79}Br is obtained from fig.3(A) as ,

^{79}Br; $S_0 = (1.27 \pm 0.14)10^{-4}$ below 10 keV

For ^{81}Br local strength functions seem to have two values; one is 0.54×10^{-4} between level clusters, and the other 3×10^{-4} in the region of the level clusters. However if the intermediate structures are neglected, the strength function is

^{81}Br; $S_0 = (0.86 \pm 0.14)10^{-4}$ below 15 keV

In the energy region below 4 keV, S_0 are $(1.4 \pm 0.2) \times 10^{-4}$ and $(1.0 \pm 0.2)10^{-4}$ for ^{79}Br and ^{81}Br respectively, which are consistent with the value obtained for natural bromine[2] $S_0 = (1.2 \pm 0.18)10^{-4}$ below 4 keV.

The observed strength functions for both isotopes are consistent with the trend in the mass dependence of strength functions in the mass region of A=80.

The radiation width are obtained for 17 levels of ^{79}Br below 2 keV, and the average value $\langle \Gamma_\gamma \rangle$ is obtained to be $\langle \Gamma_\gamma \rangle = 293 \pm 20$ meV

Level spacing distribution between two arbitrary levels are examined in the energy region from 9 to 15 keV of ^{81}Br, where three level clusters are observed. Then spacings of 943 ± 5 eV appear much frequently than in the case of random level distribution.

Acknowledgement

Authors wish to thank Dr.G.Rogosa and U.S.Department of Energy for help in procuring the separated isotope samples. They are deeply indebted to Dr.A.Asami for his encouragement and support to this work. They also thank Mr.T.Shoji for the construction of the TOF unit, and operation crew for the operation of linac.

References

1) BNL-325 3rd ed. vol 1, Resonance Parameters.
2) J.B.Garg,W.W.Havens,and J.Rainwater;Phys.Rev.136 (1964)B177
3) J.Julien, S.D.Baros, V.D.Huyne, G.Lepoittevin, J.Morgenstern, F.Netter, et C.Samour; Nucl.Phys.66(1965)433
4) H.Takekoshi ed. JAERI-Report 1238(1975)
5) M.Ohkubo and Y.Kawarasaki; JAERI-M-7545(1978)

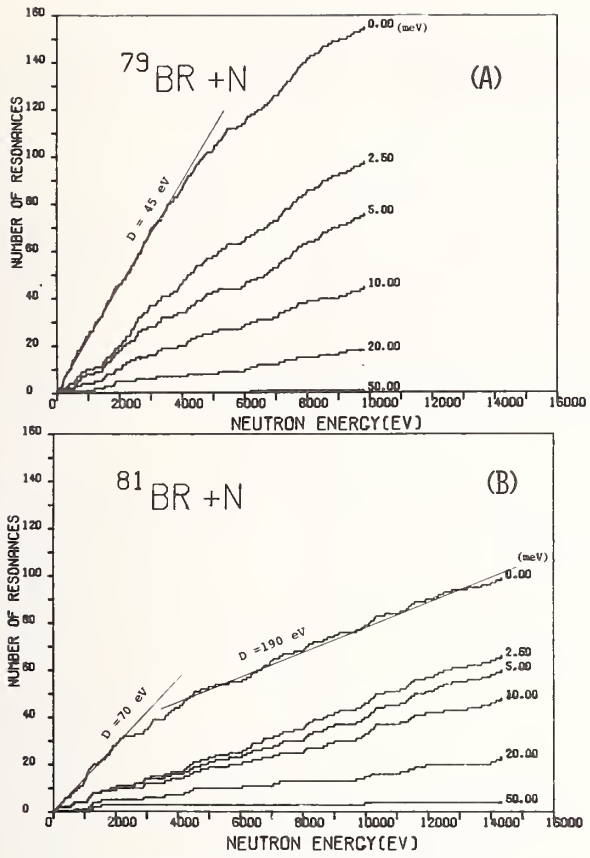

Fig.2 Cumulative number of levels vs. neutron energy for ^{79}Br (A), and ^{81}Br (B).

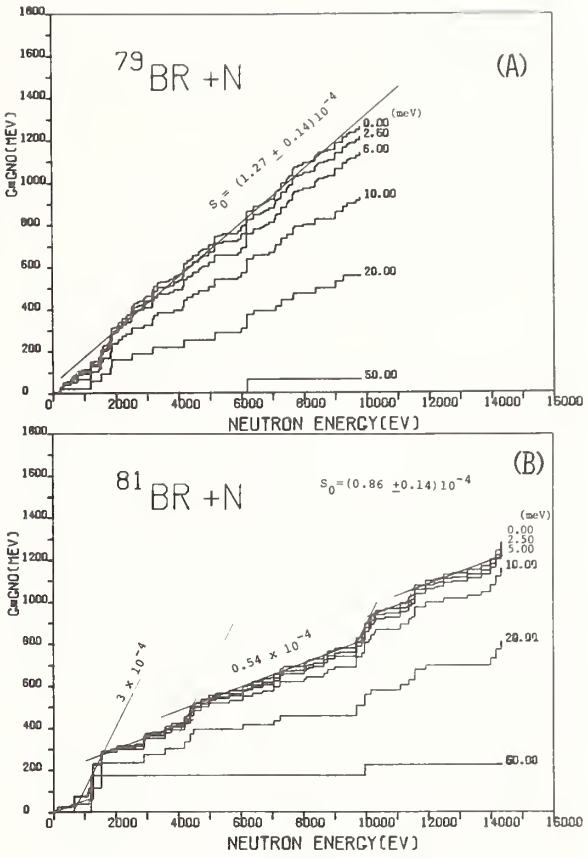

Fig.3 Cumulative values of $g\Gamma_n^0$ vs. neutron energy for ^{79}Br (A) and ^{81}Br (B).

Table 1 Resonance Parameters of ^{81}Br

	Energy (eV)	DE	$g\Gamma_n^0$	D($g\Gamma_n^0$)		Energy (eV)	DE	$g\Gamma_n^0$	D($g\Gamma_n^0$)		Energy (eV)	DE	$g\Gamma_n^0$	D($g\Gamma_n^0$)
	101.1	.04	10.			2944.	1.5	11.	2.		8038.	1.3	13.	1.
	135.5	.05	14.			3060.	1.5	1.4	0.6	70	8106.	1.4	10.	1.
	204.9	.1	0.41	.04		3121.	1.6	2.8	0.4					
	255.3	.1	0.058	.01		3163.	1.6	0.5	0.1		8182.	1.4	5.0	1.0
	336.4	.1	0.069	.01		3202.	1.7	0.1	0.05		8329.	1.4	7.	1.
	369.2	.1	0.083	.01	40	3586.	2.0	28.	4.		8666.	1.5	17.	2.
	560.0	.15	0.32	.05							8773.	1.5	18.	2.
	578.4	.15	10.5	1.		3610.	2.5	0.5	0.1		9011.	1.6	12.	1.
	668.4	.15	40.	4.		3694.	2.1	1.0	0.5		9163.	1.6	4.	0.5
10	771.6	.2	0.07	.01		3782.	2.1	12.5	2.5		9704.	1.8	48.	4.
						3890.	2.2	0.2	0.1		9881.	1.8	18.	2.
	849.8	.2	0.9	.1		4056.	2.4	1.0	0.3		9964.	1.8	52.	5.
	959.	.5	0.15	.1		4156.	2.4	1.0	0.3	80	10109.	1.9	13.	1.5
	993.7	.3	0.83	.1		4199.	2.5	32.	4.					
	1038.	.3	0.15	.05		4289.	2.6	3.0	0.5		10165.	1.9	22.	2.
	1068.7	.3	0.22	.03		4382.	2.6	37.	5.		10278.	1.9	13.	1.
	1082.1	.3	0.5	0.1	50	4488.	2.7	23.	3.		10320.	1.9	13.	1.
	1102.1	0.3	17.0	1.0							10622.	2.0	8.	1.
	1146.3	.3	20.	2.							11113.	2.1	25.	2.
	1209.3	.4	60.	6.		4529.	2.8	1.2	0.5		11310.	2.2	5.	0.5
20	1275.9	.4	55.	5.		4725.	0.6	17.	2.		11386.	2.2	24.	2.
						4975.	0.6	18.	2.		11457.	2.2	10.	1.
	1440.	.7	0.1	0.1		5197.	0.9	9.0	1.0		11564.	2.2	48.	5.
	1547.7	.5	60.	6.		5642.	0.8	14.	1.5	90	11922.	2.4	22.	2.
	1666.	.6	0.1	0.1		6075.	0.8	20.	2.					
	1708.	.6	1.4	0.2		6207.	1.2	6.	1.		12197.	2.4	8.	1.
	1824.	1.	0.5	0.1		6348.	1.5	2.5	0.4		12326.	2.5	5.	0.5
	1834.	.7	8.	1.		6374.	0.9	13.	1.5		12507.	2.5	18.	2.
	1897.	.7	1.0	0.1	60	6547.	1.2	1.7	0.3		12769.	2.6	6.	1.0
	1908.	.7	0.3	0.1							13266.	2.7	15.	1.5
	2031.5	.8	13.	1.5		6705.	1.0	11.	1.		13708.	2.9	17.	1.5
30	2097.	1.0	0.1	0.1		6752.	1.0	3.5	0.5		13998.	3.0	32.	3.
						6950.	1.5	2.0	0.5		14169.	3.1	42.	3.
	2140.	.9	0.3	0.1		6964.	1.5	1.0	0.5		14346.	3.1	36.	3.
	2250.	1.	1.7	0.2		7061.	1.1	20.	2.	100	16430.	3.8	10.	2.
	2618.5	1.2	6.5	1.		7259.	1.1	24.	2.					
	2907.	1.4	40.	10.		7359.	1.2	9.	1.					
						7716.	1.3	3.	0.5					

Table 2 Resonance Parameters of ^{79}Br

	Energy(eV)	DE	$g\Gamma_n^0$	$D(g\Gamma_n^0)$	Γ	$D(\Gamma)$	Γ_γ	$D(\Gamma_\gamma)$	g
	* 35.8	0.1	4.5	0.45					
	53.6	0.02	1.7	0.1					
	158.0	0.2	0.0_3	0.0_1					
	189.3	0.1	2.0	.2	310.	50.	240.	30.	3/8
	192.4	.1	0.13	.02					
	211.	0.1	0.043	.01					
	$2^{38}.5$	0.13	23.	2.	$8_5$0.	5^0.	300.	30.	5/8
	294.1	0.2	1.5	0.3	330.	50.	260.	30.	3/8
	318.3	0.2	19.	2.0	850.	50.	280.	30.	5/8
10	394.4	0.3	3.2	0.2	420.	50.	260.	30.	3/8
	463.	0.5	0.004	.001					
	467.9	0.4	1.3	0.2	300.	50.			
	482.5	0.4	1.5	0.2	300.	50.	230.	20.	3/8
	490.3	0.5	0.0_6	0.02					
	564.7	0.5	12.	1.5	700.	50.	260.	20.	5/8
	604.0	0.5	7.7	0.5	750.	50.	270.	30.	3/8
	637.6	0.6	1.8	0.3					
	646.1	0.6	8.0	0.8	600.	60.	240.	30.	5/8
	749.4	0.2	5.8	0.6	800.	100.	360.	50.	3/8
20	788.0	0.2	13.0	1.5	920.	70.	290.	30.	5/8
	831.6	0.2	0.8	0.1					
	870.2	0.5	0.13	0.02					
	892.5	0.3	0.75	0.1					
	930.4	0.3	5.5	0.5	750.	100.	260.	30.	3/8
	$10^{24}.5$	0.5	0.1	0.0^5					
	1042.8	0.3	0.9	0.1					
	1164.7	0.3	0.16	0.02					
	1186.8	0.3	0.6	0.1					
	$1^{20}0.3$	0.3	3_6.	2.	$2_6$00.	$3^0$0.	$3^2$0.	3^0.	5/8
30	1228.0	0.4	0.45	0.05					
	1311.8	0.5	0.75	0.1					
	1379.5	0.5	1.1	0.1					
	1454.8	0.5	14.	1.	1800.	200.	420.	40.	3/8
	1469.6	0.5	7.5	0.5					
	1484.4	0.5	0.15	0.05					
	1531.5	0.5	34.	3.	2700.	300.	330.	30.	5/8
	1571.3	0.6	1.8	0.2					
	1590.0	0.6	17.	1.	1300.	200.	300.	30.	5/8
	1634.	0.8	0.3	0.1					
40	1721.3	0.6	6.5	0.6					
	1744.	0.8	0.17	0.03					
	1771.5	0.7	8.5	1.					
	1803.	1.0	0.05	0.05					
	1829.1	0.7	30.	4.	2300.	300.	360.	40.	5/8
	1874.5	0.7	38.	4.					
	1969.0	0.8	5.4	0.5					
	2081.	0.9	10.	1.					
	2096.	0.9	11.	1.					
	$2^{19}9.$	1.0	3.	0.5					
50	2209.	1.0	16.	2.					
	2261.	1.0	0.5	0.1					
	2340.	1.0	10.	1.5					
	2370.	1.0	3.	1.					
	2380.	1.0	4.	1.					
	2467.	1.2	2.5	0.5					
	2506.	1.2	9.	2.					
	2518.	1.2	29.	6.					
	2579.	1.2	8.	1.					
	2595.	1.2	7.	1.					
60	2691.	1.3	1.2	0.2					
	2709.	1.3	6.	1.					
	2729.	1.3	0.5	0.1					
	2759.	1.3	1.3	0.2					
	2770.	1.4	3.2	0.6					
	2850.	1.4	0.06	0.0_2					
	2897.	1.4	12.	4.					
	2927.	1.4	2.7	0.6					
	2958.	1.5	4.	2.					
	297^0.	1.5	2.	1.					
70	3009.	1.5	0.1	0.04					
	3102.	1.6	0.15	0.05					
	3167.	1.6	30.	4.					
	3222.	1.7	16.5	3.					
	3327.	1.8	5.	0.8					
	3346.	1.8	13.	2.					
	3401.	2.	2.	0.4					
	3437.	2.	0.5	0.2					
	3490.	2.	0.1	0.1					
	3509.	2.	1.0	0.3					
80	3528.	2.1	0.5	0.2					

	Energy(eV)	DE	$g\Gamma_n^0$	$D(g\Gamma_n^0)$
	3625.	2.1	2.5	1.
	3718.	2.1	7.5	2.
	3743.	2.2	0.5	0.1
	3859.	2.2	12.5	2.5
	3895.	2.2	2.5	0.5
	3937.	2.2	3.5	1.
	4002.	2.5	0.2	0.1
	4025.	2.4	4.	0.5
	4049.	2.4	4.2	0.5
90	4096.	2.4	1.	0.2
	4140.	2.	15.	3.
	4183.	2.5	33.	5.
	4279.	2.5	13.	2.
	4342.	2.6	0.5	0.2
	4378.	2.6	3.	0.5
	4407.	2.6	5.	1.
	4461.	2.7	16.	1.
	4530.	3.	1.0	0.3
	4573.	3.	0.5	0.2
1_00	4645.	2.8	16.	1.
	4714.	2.8	7.	1.
	4775.	3.	6.	1.
	4966.	3.2	18.	5.
	5016.	3.2	2.	0.3
	5023.	3.3	1.	0.3
	5123.	3.4	3.	0.5
	5158.	3.4	35.	5.
	5263.	3.5	4.	0.5
	5299.	3.5	1.	0.2
110	5353.	4.	1.0	0.3
	5398.	3.6	4.	0.5
	5431.	3.7	4.	0.5
	5752.	3.9	1.	0.3
	5900.	5.	10.	5.
	6000.	4.3	20.	5.
	6032.	4.5	6.	1.
	6070.	4.5	2.	0.5
	6180.	4.5	66.	10.
	6320.	4.5	4.	0.5
120	6398.	4.6	20.	3.
	6555.	5.	1.	0.2
	6623.	4.8	8.	1.
	6722.	5.0	8.	1.
	6792.	5.2	6.	1.
	6863.	6.	2.	0.5
	6897.	5.3	10.	2.
	7075.	5.4	16.	2.
	7100.	5.5	20.	3.
	7165.	5.6	5.	1.
130	7222.	5.7	3.	1.
	7282.	5.8	30.	5.
	7335.	5.8	1.	0.5
	7457.	5.8	18.	2.
	7499.	6.0	7.	1.
	7544.	6.0	9.	2.
	7606.	6.1	2.	0.5
	7662.	6.2	30.	5.
	7704.	6.3	10.	2.
	7767.	7.	1.	0.5
1_40	784^2.	6.4	6.	1.
	7952.	6.4	3.	1.
	7988.	6.6	10.	2.
	8080.	6.6	2.	0.5
	8228.	6.9	5.	1.
	8367.	7.0	25.	4.
	8430.	7.1	8.	2.
	8480.	7.2	8.	2.
	8665.	7.4	6.	2.
	8786.	7.6	8.	2.
150	9009.	7.8	33.	5.
	9264.	8.2	26.	4.
	9403.	8.4	15.	3.
	9479.	8.5	7.	1.
	9685.	8.7	13.	2.
	9808.	8.9	14.	2.
	9920.	9.1	7.	2.

* data from reference 1.

CROSS SECTION ADJUSTMENT APPLIED TO ESTIMATION OF UNCERTAINTY IN THE BREEDING RATIO OF AN LMFBR

J. H. Marable, C. R. Weisbin, and G. de Saussure
Oak Ridge National Laboratory
Oak Ridge, Tennessee 37830, USA

Eleven fast-reactor benchmark experiments and two neutron-field benchmark experiments were applied to a least-squares adjustment of a 26-group cross section library based primarily on ENDF/B-IV. The covariance data includes correlations between cross sections for different energies, reactions, and materials, and between integral experiments, and covariances of calculational bias factors due to specific modeling and calculational procedures. The results of the adjustment are applied to the determination of the uncertainties in the multiplication factor and in the breeding ratio of a large LMFBR design model fixed by the Large Core Code Evaluation Working Group (LCCEWG).

[least-squares adjustment, group cross sections, fast reactors, integral experiments, LMFBR, breeding ratio, uncertainty analysis, sensitivity analysis, calculational bias uncertainties]

Introduction

The significance of nuclear data uncertainties to LMFBR design performance parameters and the resulting economic implications have been generally recognized.[1] Uncertainties in calculated performance parameters may necessitate excessive and expensive design margins. In order to reduce these uncertainties, integral experiments are often introduced. Using recent developments in sensitivity and uncertainty analysis, this study applies a large data base of fast reactor benchmark sensitivities, of nuclear data uncertainties, of integral experiment measurements and uncertainties, and of computed results for integral experiments and design parameters to calculate the uncertainty in the criticality and breeding ratio of a representative design model of a large LMFBR. The analysis includes the capability to handle methods uncertainties and the results of related data adjustments, based essentially upon ENDF/B-IV, are also reported.

Methods Biases

In order to include calculational uncertainties in the least-squares adjustment, bias factors are introduced. These bias factors b are calculation-B-to-Calculation-C ratios, where calculation B is supposedly based on a more precise calculational technique or on a more realistic model than is calculation C. Conceptually, a chain of calculations is envisioned

$$A \rightarrow B \rightarrow C \rightarrow \ldots \rightarrow Y \rightarrow Z$$

where A corresponds to the real reactor being considered and Z represents the model actually calculated along with the accompanying approximating techniques. The other members of the chain B, C, ..., Y correspond to intermediate models and calculational techniques. All calculations of the chain are based on the same evaluated nuclear data file. The response R(A) for the real reactor (and the nuclear data base) may be obtained from the calculated response R(Z) by applying the bias factors in turn, R(Y)/R(Z),...,R(A)/R(B).

Consider now the uncertainty in R(A) due to calculational and modeling uncertainties only. Presumably there is no uncertainty in R(Z) since that is exactly what is calculated. Hence the uncertainty in R(A) is the accumulation of the uncertainties of the individual bias factors.

Adjustment Procedure

The least-squares adjustment including calculational uncertainties is based on the following formula

$$x_a = x_e + P(x_c - x_e)$$

where x is a vector whose components are integral experiment values I_n, bias factors b_k, and discretized nuclear data (i.e., group cross sections) σ_m, respectively; i.e.,

$$x = \{I_1, \ldots I_N, b_1, \ldots b_K, \sigma_1, \ldots \sigma_M\} \quad .$$

Subscripts a, e, c refer to the adjusted, experimental, and calculated values, respectively. P is a projection operator in this N+K+M dimensional space given by

$$P = B\, s^T\, G^{-1}\, s$$

where B is the covariance matrix for the evaluated values of the components of x, s is a generalized sensitivity matrix (superscript T indicates the transpose)

$$s = \left[-1 \vdots \beta \vdots S \right]$$

consisting of three submatrices: the negative unit matrix and the relative sensitivities β and S of the calculated integral quantities with respect to b and the nuclear data σ, respectively. G is given by

$$G = s\, B\, s^T \quad .$$

Integral Experiments

The integral experiments used in this study were k_{eff} and central reaction rate ratios for four CSEWG fast benchmark critical assemblies,[2] and two reaction rate ratios in a clean benchmark neutron field. The facilities in which the measurements were made include critical assemblies of interest to the designer of a demonstration size reactor as well as those of interest to the designer of a large commercial power plant. The ZPR-6/7 and ZPR-6/6A have spectra characteristic of large, dilute mixed-oxide assemblies. The ZPR-3/48 and ZPR-9/31 are similar to the above two but are carbide rather than oxide assemblies. The ^{235}U fueled ZPR-6/6A was included because ^{235}U fission is used as a standard for cross sections in a number of important materials including ^{239}Pu and ^{238}U. Two benchmark experiments were carried out in the Intermediate Energy Standard Neutron Field (ISNF)[3] of the National Bureau of Standards (NBS). The spectrum of this facility is that resulting from the slowing down in carbon of neutrons from the thermal fission of ^{235}U. The lower energy region of this spectrum is modified by the use of a boron shell.

These thirteen integral experiments are listed in Table I with the experimental values, standard deviations, and calculated values, calculation-to-experiment (C/E) ratios, references. Not shown are correlations which were evaluated by Collins and Lineberry[4] for the fast reactor integral experiments and by J. J. Wagschal, R. E. Maerker and D. M. Gilliam[5] for the ISNF experiments.

Table I. Integral Experiment Values and Standard Deviations.[a]

Assembly and Response	Measured Value	Std. Dev. (%)	Calc. Value	C/E
ZPR-6/7:				
k	1.000	0.1	0.9847	0.985
$^{28}f/^{49}f$	0.02422	2.9	0.02339	0.966
$^{28}c/^{49}f$	0.1422	2.3	0.1526	1.073
ZPR-3/48:				
k	1.000	0.1	0.9914	0.991
ZPR-9/31:				
k	1.000	0.1	0.9888	0.989
$^{25}f/^{49}f$	1.036	2.4	1.0142	0.979
$^{28}f/^{49}f$	0.0300	2.6	0.0287	0.958
$^{28}c/^{49}f$	0.1230	2.3	0.1313	1.067
ZPR-6/6A:				
k	1.000	0.1	0.9853	0.985
$^{28}f/^{25}f$	0.02388	2.8	0.02228	0.933
$^{28}c/^{25}f$	0.1378	2.7	0.1419	1.030
ISNF:				
$^{49}f/^{25}f$	1.155	1.3	1.119	0.968
$^{28}f/^{25}f$	0.0920	.62	0.0855	0.929

[a]These data are from References 4-10.

Sensitivity Coefficients

Sensitivity coefficients for the benchmark fast reactor criticals for reactions other than ^{238}U inelastic were obtained from the sensitivity data library[11-13] distributed by the Radiation Shielding Information Center (RSIC). These sensitivities were calculated at Oak Ridge National Laboratory using the FORSS sensitivity code system[14] and at the Argonne National Laboratory using the VARI-1D code.[15]

Nuclear Data and Bias Factors

The nuclear data used for the calculations of the integral experiments and for the adjustment reported here are based on ENDF/B-IV nuclear data evaluations with one exception — the ^{238}U inelastic cross section data were taken from the ENDF/B-V evaluation[16,17] because evaluated covariances were available for this version only. The data included for adjustment include $\bar{\nu}$, σ_f, and σ_c of ^{235}U, ^{238}U, ^{239}Pu, σ_c of ^{240}Pu, σ_{el} of O, σ_{in} (Version V) of ^{238}U, and ^{235}U and ^{239}Pu fission spectrum parameters. Several nuclear data with relatively small sensitivities were not included in the adjustment although some of these data may have relatively large uncertainties.

The covariances for the cross sections and for $\bar{\nu}$ are based on a 26-energy-group structure.[18] However, the ^{239}Pu and ^{235}U fission spectra were each described by two parameters, the mean energy $\bar{E}$ of the fission neutrons and the relative root-mean-square width M of the spectrum about the mean, explicitly given by

$$M = \left[\int \frac{(E - \bar{E})^2 \chi(E) dE}{\bar{E}^2} \right]^{\frac{1}{2}}$$

where $\chi(E)$ is the fission spectrum. For these two fission spectra the relative uncertainties in $\bar{E}$ were evaluated by Peelle[19] as 2%. The uncertainties in M were evaluated as 5% uncorrelated to $\bar{E}$.[20] The covariance files for the ENDF/B-V ^{238}U inelastic cross sections were represented by grouping 26 levels and the continuum into ten sets with a 26x26 covariance submatrix for each set.[21,22]

The totality of covariances used in the adjustment (taken from References 3, 4, 6, 10, 19, 20, and 22-26) form a large matrix, which is represented schematically in Fig. 1. The covariances of the integral experiments, as described in the previous subsection, are represented by the first box. The second box along the diagonal represents the covariances of the calculational and modeling biases. Starting in the third row and third column, each box represents a 26x26 cross section covariance matrix up to and including the oxygen elastic cross section covariance. The next box on the diagonal represents the 4x4 covariance matrix of fission spectrum parameters $\bar{E}$ and M for ^{239}Pu and ^{235}U, and the next to last row and column represent the ten sets of ^{238}U inelastic levels. The last box represents the nuclear data uncertainties associated with the flux ϕ of the ISNF dosimetry field. Bias factor uncertainties used are given in Table II.

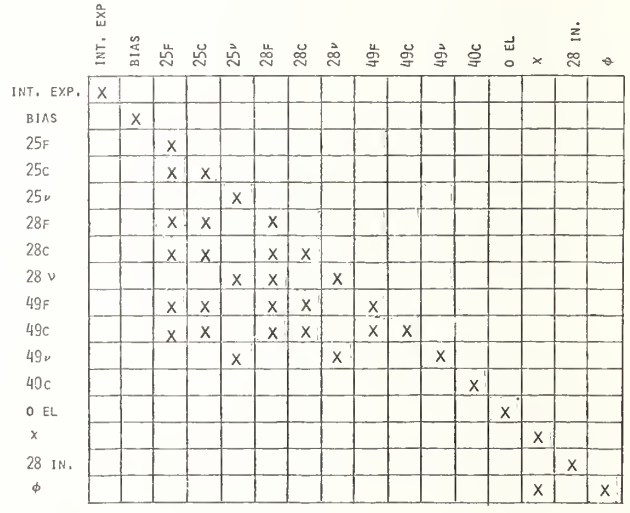

Fig. 1. Covariance Data for Fast Reactor Applications. The matrix is symmetric, but the upper half is left blank for simplicity of presentation. Below the principal diagonal a blank box represents an unknown covariance to which we have assigned zero values.

Table II. Bias Factor Relative Standard Deviations[a]

Assembly	Response	Relative Standard Deviations for Various Effects: Plate Streaming[b] (%)	Hompgeneous/ Heterogeneous[b] (%)	Unit Cell Non-normality[b] (%)	Cross Section Processing[c] (%)
ZPR-6/7	k	0.03	0.2		0.4
	$^{28}f/^{49}f$	0.12	0.5	1.1	0.8
	$^{28}c/^{49}f$	0.05	0.3	0.1	0.9
ZPR-3/48	k	0.03	0.2		0.4
ZPR-9/31	k	0.03	0.2		0.4
	$^{25}f/^{49}f$	0.04	0.2		0.8
	$^{28}f/^{49}f$	0.12	0.5		0.8
	$^{28}c/^{49}f$	0.05	0.3		0.9
ZPR-6/6A	k	0.03	0.2		0.4
	$^{28}c/^{25}f$	0.05	0.3		0.9
	$^{28}f/^{25}f$	0.12	0.5		0.8

[a]Bias factors corresponding to different responses or different effects are assumed to be uncorrelated. Those corresponding to the same response (but in different assemblies) and the same effect are assumed fully correlated.

[b]These data are taken from McKnight and Collins.[23]

[c]These data are from Weisbin *et al.*[6]

Table III. Effect of Adjustment on Integral Values and their Uncertainties

Response	Facility	$\frac{C - E^a}{C}$ (%)	$\frac{A - E^a}{C}$ (%)	Std. Dev. Exp. (%)	Std. Dev. Calc. (%)	Std. Dev. Adj. (%)	S.D. Ratio (Adj./Exp.)	S.D. Ratio (Adj./Calc.)
k	ZPR-6/7	-1.555	-0.043	0.1	3.7	0.1	0.95	0.03
	ZPR-3/48	-0.869	0.019	0.1	3.6	0.1	0.98	0.03
	ZPR-9/31	-1.134	0.037	0.1	3.7	0.1	0.94	0.03
	ZPR-6/6A	-1.493	-0.007	0.1	2.6	0.1	1.00	0.04
$^{28}f/^{49}f$	ZPR-6/7	-3.551	-2.146	2.9	5.6	2.0	0.70	0.36
	ZPR-9/31	-4.392	-2.477	2.6	6.0	2.1	0.79	0.34
$^{28}f/^{25}f$	ZPR-6/6A	-7.178	-2.815	2.8	4.3	1.8	0.63	0.41
	ISNF	-7.628	-0.172	0.62	3.2	0.6	0.97	0.19
$^{28}c/^{49}f$	ZPR-6/7	6.810	0.850	2.3	8.9	1.5	0.67	0.17
	ZPR-9/31	6.296	1.830	2.3	9.5	1.5	0.67	0.16
$^{28}c/^{25}f$	ZPR-6/6A	2.880	-2.495	2.7	7.7	1.8	0.67	0.23
$^{25}f/^{49}f$	ZPR-9/31	-2.147	-1.632	2.4	6.2	1.4	0.57	0.22
$^{49}f/^{25}f$	ISNF	-3.259	-1.034	1.3	5.1	1.0	0.82	0.21

[a]The calculational biases are included in the calculated values (C) and the adjusted calculational biases are included in the adjusted values (A).

The Adjustment

Table III summarizes the adjustment of the integral parameters. The adjusted data bring the calculated values closer to the experimental values and reduce the estimated standard deviations.

It can be seen from Table III that the adjustments of the integral responses are fully consistent with the measurements: all differences between adjusted values and measurements are smaller than the combined standard deviation of the experiment and the adjusted calculation. Similarly, all differences between adjusted values and calculated values (based on the adjusted group cross sections) are less than the combined standard deviations of the adjustment and the calculation, except for the ^{238}U to ^{235}U fission ratio in the ISNF neutron field. This exception may be associated with the change in the ^{235}U fission spectrum. This consistency in the adjustment is also reflected in the overall χ^2 per degree of freedom which is 1.2. Self-shielding factors, which may be significant for ^{238}U capture, have not been included as adjustment.

The adjustment of the group cross sections of some of the most important reactions is summarized in Tables IV through VII. Each adjustment is small compared to a standard deviation except for $\bar{E}$ of ^{235}U (Table VII), for which adjustment is 1.6 standard deviations, and for ^{238}U capture between 0.5 and 40 keV (Table VI) and ^{235}U fission between 9 and 500 keV (Table V). For these latter two the adjustments are of the order of one standard deviation.

The significant reduction in standard deviation for ^{239}Pu $\bar{\nu}$ suggests the possibility of using an adjustment to improve the evaluation of some group cross section, or some nuclear parameter, for use outside the adjustment. In principle, this should be possible. However, it has not yet been shown that adjusted cross sections incorporating integral experiments will result in more reliable calculations if applied to situations quite remote from the integral experiments. Neither has it been shown that one can make more reliable predictions by selecting a part of the adjusted results on the basis of some criterion, such as the ratio of adjusted to unadjusted standard deviations.

The LMFBR Design Model

The large fast breeder design chosen for this study is based on the model specified in the first problem issued by the Large Core Code Evaluation Working Group (LCCEWG).[27] This is a 1200 MWe conventional plutonium-oxide fueled LMFBR with two core zones and a blanket of depleted uranium. The performance parameters are the multiplication factor k and the breeding ratio, which for this static model (mid-equilibrium cycle) is defined as fertile captures in the reactor divided by fissile absorptions in the reactor. The fertile nuclides here are ^{238}U and ^{240}Pu, and the fissile nuclides are ^{235}U, ^{239}Pu and ^{241}Pu.

Folding the LCCEWG sensitivities with adjusted covariance matrix gives the effect of the adjustment on the calculated uncertainties of the LMFBR performance parameters, as indicated by the results presented in Table VIII. These results indicate that a design goal of 1/2 percent in k and 2 percent in breeding ratio should be attainable with present calculational methods if one incorporates the results of integral experiments. In calculating the standard deviations and the adjustment changes shown in Table VIII, it was assumed that the cross-section-processing and the homogeneous-to-heterogeneous bias factors used in the adjustment for k

Table IV. Adjustments to $^{239}Pu\ \bar{\nu}$

Upper Energy	Change (%)	Std. Oev. Old (%)	Std. Oev. New (%)
17.33 MeV	-0.39	1.47	1.30
10.00	-0.19	0.97	0.90
6.07	-0.37	1.42	1.26
3.68	-0.18	0.99	0.93
2.23	0.00	0.59	0.57
1.35	0.21	0.44	0.33
0.82	0.31	0.52	0.29
0.50	0.45	0.79	0.44
0.30	0.45	0.79	0.44
0.18	0.45	0.79	0.44
0.11	0.45	0 79	0.44
67.38 keV	0.45	0.79	0.44
40.87	0.45	0.79	0.44
24.79	0.45	0.79	0.44
15.03	0.45	0.79	0.44
9.12	0.45	0.79	0.44
5.53	0.45	0.79	0.44
3.36	0.45	0.79	0.44
2.04	0.45	0.79	0.44
1.23	0.45	0.79	0.44
0.75	0.45	0.79	0.44
0.45	0.45	0.79	0.44
0.28	0.45	0.79	0.44
0.17	0.45	0.79	0.44
0.10	0.45	0.79	0.44
0.4 eV	0.42	0.83	0.61

Table V. Adjustments to ^{235}U Fission

Upper Energy	Change (%)	Std. Oev. Old (%)	Std. Oev. New (%)
17.33 MeV	1.4	4.0	3.9
10.00	1.8	3.5	3.2
6.07	2.0	3.0	2.6
3.68	2.1	3.0	2.4
2.23	1.2	2.3	1.9
1.35	-0.1	2.3	2.0
0.82	-2.0	3.5	3.2
0.50	-2.2	2.9	2.5
0.30	-2.4	2.8	2.5
0.18	-2.1	3.3	3.0
0.11	-2.7	2.7	2.2
67.38 keV	-2.8	3.0	2.4
40.87	-3.0	3.0	2.2
24.79	-3.4	3.7	2.9
15.03	-3.5	3.9	3.1
9.12	-3.7	5.0	4.1
5.53	-3.7	5.0	4.1
3.36	-3.9	5.6	4.7
2.04	-4.0	5.8	4.9
1.23	-2.5	3.7	3.1
0.75	-1.4	3.2	2.9
0.45	-1.4	3.1	2.8
0.28	-1.4	3.1	2.8
0.17	-1.4	3.2	2.9
0.10	-0.8	1.9	1.7
0.41 eV	-0.0	0.3	0.3

Table VI. Adjustments to ^{238}U Capture

Upper Energy	Change (%)	Std. Oev. Old (%)	Std. Dev New (%)
17.33 MeV	1.1	127.0	127.0
10.00	-2.3	84.1	73.5
6.07	9.2	51.8	49.1
3.68	6.5	26.8	25.8
2.23	1.1	16.2	13.8
1.35	-7.6	23.9	16.3
0.82	-5.5	17.5	12.5
0.50	-3.7	13.1	8.6
0.30	-3.0	13.5	10.5
0.18	-2.0	10.3	8.0
0.11	-4.8	8.8	6.8
67.38 keV	-3.0	4.7	3.9
40.87	-7.6	9.9	7.8
24.79	-12.0	11.5	7.4
15.03	-14.0	14.9	10.5
9.12	-12.7	13.2	9.2
5.53	-7.5	9.0	7.1
3.36	-9.8	11.4	9.3
2.04	-12.3	12.3	10.2
1.23	-8.4	8.0	6.6
0.75	-6.9	8.1	7.2
0.45	-9.1	13.5	12.5
0.28	-5.2	7.7	7.1
0.17	-3.3	4.9	4.6
0.10	-0.0	0.0	0.0
0.41 eV	0.0	3.2	3.2

Table VII. Adjustments to Fission Spectra Parameters.

Parameter	Change (%)	Std. Dev. Old (%)	Std. Dev. New (%)
$\bar{E}^{49}$	0.21	2.0	1.71
M^{49}	-1.38	5.0	4.30
$\bar{E}^{25}$	3.26	2.0	1.37
M^{25}	-2.67	5.0	4.81

Table VIII. Performance Parameters, Standard Oeviations, and Effects of Adjustment for the LCCEWG Model.

Performance Parameter	Calculated Value Based on Evaluated Data	Change in Calculated Value due to Adjustment (%)	S.O.'s based on Evaluated Nuclear Oata and Methods Biases (%)	S.O.'s based on Adjustment Including Integral Experiments (%)
k	1.000	1.5	3.1	0.3
B.R.	1.15	-5.5	7.2	1.9
B.R. (critical)	1.15	-2.5	3.4	1.7

and for $^{28}c/^{49}f$ of the plutonium assemblies applied to k and to the breeding ratio, respectively, in the LCCEWG LMFBR design.

Conclusions

The above results support previous conclusions that good clean integral experiments are required for accurately predicting large LMFBR physics performance. Moreover, the associated data adjustments suggest problem areas in which nuclear data, group cross section preparation, and a consistent treatment of the resonance region may need further study. (A more detailed report of this work has been submitted to Nuclear Science and Engineering.)

Acknowledgements

The authors acknowledge and thank the many members of the ORNL staff, in particular, G. W. Cunningham, F. Difilippo, B. R. Diggs, W. E. Ford, T. B. Fowler, C. Y. Fu, R. Gwin, D. C. Larson, R. B. Perez, L. W. Weston, J. E. White, and R. Q. Wright. This work would not have been possible without the encouragement of F. C. Maienschein, and the support of the Division of Reactor Research and Technology of the U.S. Department of Energy under contract no. W-7405-eng-26 with Union Carbide Corporation.

References

1. P. Greebler et al., in Proceedings of the International Conference Nuclear Data for Reactors, Helsinki, International Atomic Energy Agency, Vienna 1970).

2. "Cross Section Evaluation Working Group Benchmark Specifications," ENDF-202, Brookhaven National Laboratory (1974).

3. D. M. Gilliam, in Proceedings of the International Specialists Symposium on Neutron Standards and Applications (NBS Special Publication 493, 1977) p. 299.

4. P. J. Collins and M. J. Lineberry, in Proceedings of RSIC Seminar and Workshop, "Theory and Application of Sensitivity and Uncertainty Analysis," Oak Ridge, TN, 1978. [See also P. J. Collins et al. in Proceedings of the International Symposium on Fast Reactor Physics, Aix-en-Provence, IAEA-SM-244, 1979.]

5. J. J. Wagschal, R. W. Maerker and D. M. Gilliam, to be published in Trans. Am. Nucl. Soc. 33 (1979).

6. C. R. Weisbin et al., Oak Ridge National Laboratory Report, ORNL-5517 (ENDF-276) (1979).

7. R. D. McKnight, Nucl. Sci. Eng. 62, 309 (1977). [See also R. D. McKnight, ZPR-TM-214, Argonne National Laboratory, 1975).

8. P. J. Collins and D. N. Olsen, Argonne National Laboratory, private communication to C. R. Weisbin concerning revisions to data in Ref. 7 (1979).

9. R. D. McKnight, ZPR-TM-281, Argonne National Laboratory (1977).

10. J. A. Mormon, Argonne National Laboratory, private communication to P. J. Collins, Argonne National Laboratory, Idaho, 1979.

11. C. R. Weisbin et al., Brookhaven National Laboratory Report BNL-NCS-24853 (ENDF-265) (1978).

12. "SENPRO: Compilation of Multi-Group Sensitivity Profiles in SENPRO Format for Fast Reactor Core and Shield Benchmarks and Thermal Reactor Benchmarks," RSIC Data Library Collection DLC-45B/SENPRO (1978).

13. E. M. Bohn, I. K. Olson and K. E. Freese, ZPR-TM-240, Argonne National Laboratory (1976).

14. C. R. Weisbin et al., Oak Ridge National Laboratory, ORNL/TM-5563 (1976).

15. W. M. Stacey, Jr. and J. P. Regis, FRA-TM-57 Argonne National Laboratory (1973).

16. R. Kinsey, BNL-17541 (ENDF-201), Third Edition, Brookhaven National Laboratory (1979).

17. W. Poenitz et al., ANL-NDM-32, Argonne National Laboratory (1977).

18. J. H. Marable and C. R. Weisbin, in Proceedings American Nuclear Society Topical Meeting, Gatlinburg, TN, 1978, p. 231.

19. R. W. Peelle, private communication (April 1978).

20. J. L. Lucius and J. H. Marable, Trans. Am. Nucl. Soc. 32, 731-2 (1979).

21. Memo from D. K. Olsen and G. de Saussure to C. R. Weisbin, R. W. Peelle and F. G. Perey, SUBJECT: ^{238}U Inelastic Scattering Covariance Matrix, Intra-Laboratory Correspondence, Oak Ridge National Laboratory (February 1978).

22. J. D. Drischler and C. R. Weisbin, ORNL-5318 (ENDF-235) Oak Ridge National Laboratory (1977) (revision to be published).

23. R. D. McKnight and P. J. Collins, Appendix III of the Minutes of the Data Testing Subcommittee of the Cross Section Evaluation Working Group, held October 24-26, 1978, Brookhaven National Laboratory.

24. E. T. Tomlinson, G. de Saussure and C. R. Weisbin, EPRI NP-346 (ENDF-252) (1977).

25. "Summary Documentation of LASL Nuclear Data Evaluations for ENDF/B-V," P. G. Young, Ed., LA-7663-MS (1979).

26. B. L. Broadhead, Trans. Am. Nucl. Soc. 30, 590 (1978).

27. E. Kujawski and H. S. Bailey, Nucl. Sci. Eng. 64, 90 (1977).

RELATIVE CONSISTENCY OF ENDF/B-IV AND -V WITH FAST-REACTOR BENCHMARKS

Y. Yeivin,[+] J. J. Wagschal,[+] J. H. Marable and C. R. Weisbin
Oak Ridge National Laboratory
Oak Ridge, Tennessee 37830 USA

[+]On leave from the Racah Institute of Physics, Hebrew University, Jerusalem, Israel

The consistency of eleven selected fast-reactor and two neutron-field integral experiments with the ENDF/B-IV and -V libraries was examined by considering contributions to chi-square. Integral measurements least consistent with each given library were identified one at a time, and the particular cross sections which were significantly adjusted at each step were also identified. The results of this analysis demonstrate that, with respect to twelve out of the thirteen integral measurements considered, ENDF/B-V is a marked improvement over Version IV in the sense that (a) the integral data are significantly more consistent with Version V than with Version IV, (b) fewer cross sections need to be adjusted to achieve agreement between all the experimental data and the corresponding values calculated by Version V, and (c) the necessary adjustments are smaller.

[least-squares adjustment, group cross sections, fast reactors, integral experiments, chi-square, data testing, data consistency, ENDF/B-IV, ENDF/B-V]

Introduction

The motivation and plan for a large-scale undertaking at ORNL to produce an adjusted cross-section library for fast-reactor core-physics analysis has been elaborated in a recently published report.[1] Although some consider the ideal ultimate product of adjustment to be an improved basic data (energy-point) library, the more immediate and practical goal here is the generation of a multigroup cross section and covariance library to estimate core physics performance with a minimum of data-related bias and to quantify performance uncertainties. In the last decade adjusted multigroup libraries have been used extensively by reactor designers throughout the world, and many now consider that least-squares adjustment of group constants is a most practical way to extrapolate measured performance-parameters to similar systems. For other than a very restricted use of the adjusted library, the quality of the input data is critical, and therefore the emphasis here is on using carefully analyzed integral data (including uncertainties and correlations) and on adjusting cross sections for which evaluated uncertainty files are available.

Unless convincingly demonstrated, the validity of *any* adjusted nuclear data library can be challenged. Nevertheless, the adjustment procedure can point to cross sections and integral data which deserve re-examination, as well as to modeling and calculational methods inadequacies. With this in mind, procedures were developed to analyze the consistency of the data used to adjust the cross sections. The first such procedure to be applied was originally intended to identify definitely irregular integral data (in a comparative sense to be discussed). A similar procedure has been successfully applied in the past to achieve improved agreement between measured data and corresponding calculated values.[2]

This procedure turned out to be a very practical and effective tool for "data testing," and the purpose of the present paper is to report preliminary results of the application of this procedure to data testing of ENDF/B-V. Since this procedure has also been applied to ENDF/B-IV data, we are able to present a comparison of these two libraries. In fact, much more can be gained from a comparative analysis of two or several libraries than from data testing of just one given library, be it even the latest and supposedly the "best."

In what follows we shall briefly outline the theoretical basis for our analysis, specify our input data, describe the results and present a partial analysis.

Procedure

Our starting point is the observation that the quantity which, in the context of least-squares adjustment, is referred to as χ^2, is acually a measure of the consistency between the measured and calculated values of the integral parameters. In other words, if the row $r^t = (r_1, r_2, \ldots, r_n)$ is the transpose of the column vector of the experimental responses (integral data), $\bar{r} = \bar{r}(\sigma)$ the corresponding vector of calculated responses (the vector σ is the given cross-section library), and $d = r - \bar{r}$, i.e., the vector of the deviations between the two, and if C_d is the covariance (uncertainty) matrix of the deviations d, then our statement is simply the identity

$$\chi^2 = d^t C_d^{-1} d. \qquad (1)$$

To derive this identity we note that χ^2, by definition, is the minimum of the quadratic form

$$Q(\sigma') = (r-r')^t C_r^{-1}(r-r') + (\sigma-\sigma')^t C_\sigma^{-1}(\sigma-\sigma'), \qquad (2)$$

where

$$r' = \bar{r}(\sigma') = \bar{r} + S \cdot (\sigma'-\sigma) . \qquad (3)$$

A common notation was used for all quantities in Eqs. (2) and (3): C_σ is the covariance matrix of the given cross-section library, C_r the measured response covariance, and S is the sensitivity matrix of the responses ($S_{ij} = \partial r_i/\partial \sigma_j$). The components of the vector σ' which minimizes $Q(\sigma')$, Eq. (2), are the adjusted cross section, and are given by

$$\sigma' = \sigma + C_\sigma S^t (C_r + S C_\sigma S^t)^{-1} d \quad . \qquad (4)$$

When this result, with Eq. (3), is used to eliminate σ' and r' from Eq. (2), the latter equation reduces to

$$\chi^2 = d^t (C_r + S C_\sigma S^t)^{-1} d \ , \qquad (5)$$

and it only remains to show that $C_r + S C_\sigma S^t$ *is* C_d. This is almost trivial, since obviously $C_d = C_r + C_{\bar{r}}$, and Eq. (3) implies that indeed $S C_\sigma S^t$ is $C_{\bar{r}}$.

Thus, χ^2 measures the global, overall consistency of a given set of differential and integral data. However, underrating a complete set of data because of relative inconsistency might be premature, since even one single integral datum might significantly degrade

its overall consistency. It is therefore desirable to check whether perhaps only just few integral data are irregular, in the sense that their inclusion significantly increases χ^2, but most of the data are still definitely consistent with the cross sections. However studying partial sets of integral data for consistency would only make sense, of course, if a definite scheme is devised for systematically ordering the data to obtain a consistency-wise optimal sequence.

Now, a very simple, and seemingly adequate procedure to determine this optimal sequence would be to order the integral data by their *individual* consistencies, i.e., by the values of the χ^2's obtained for each datum as if it were the only integral datum. We note in passing that these individual consistencies are just the squares of the above-defined deviations d_i, measured in terms of their respective standard deviations. We also note that because the deviation covariance matrix C_d is nondiagonal (and would generally still be nondiagonal even if both C_r and C_σ were diagonal!) the joint consistency, i.e., the joint χ^2, of a set of integral data is not equal to the sum of the respective individual consistencies. Still one might hope that this would not affect the optimal order of the integral data. Unfortunately, this is definitely not the case, and another algorithm had to be formulated to produce the optimal sequence.

The following procedure was eventually adopted: Starting from the complete set of n integral data, we eliminate the first datum and evaluate χ^2 for the remaining n-1 data, which we denote by $\chi^2_{n-1}(1)$. Then the second datum is eliminated from the complete set, and $\chi^2_{n-1}(2)$ is evaluated. After this sequence is repeated for all n data, the datum m_n for which

$$\chi^2_{n-1}(m_n) = \min \{\chi^2_{n-1}(m)\} \qquad (6)$$

is obviously the least consistent datum, and thus the last element in the optimal sequence. This procedure is now applied to the remaining n-1 "more consistent" data, and the m_{n-1} datum is determined as the one for which

$$\chi^2_{n-2}(m_{n-1}|m_n) = \min \{\chi^2_{n-2}(m|m_n)\}, \qquad (7)$$

where $m = 1,2,\ldots,m_{n-1},m_{n+1},\ldots,n$. The procedure is now repeated to determine m_{n-2}, m_{n-3},... and so on, down to m_1.

Now, χ^2 is certainly a valid measure of the consistency between the experimental integral data and the calculated values of the corresponding integral parameters, and thus essentially measures the consistency between the integral data and the cross-section library used to calculate the integral parameters. However, it is too often applied in a rather cavalier fashion. In common usage, if χ^2/n ("χ^2 per degree of freedom") is less than or equal to about unity, an adjustment is considered satisfactory and valid. Not only is this too vague, it may also be misleading. For a given n, any value of χ^2 (or of χ^2/n) corresponds to a definite probability p, the *a priori* probability that χ^2 (considered as a random variable) would fall at or above that value. It is this probability which is the proper measure of consistency. Thus, if for instance $p(\chi^2) = 0.7$, we say that the data are consistent at the 70% level. Furthermore, $p(\chi^2)$ depends on n:$p((\chi^2/n)=1)$ is 0.32 for n = 1, 0.44 for n = 10, and tends to 0.5 only as $n \to \infty$. This is very relevant to our analysis, since we shall evaluate χ^2 for data subsets of all orders, from 1 up to the order of the complete set, and $p(\chi^2)$ is particularly sensitive to n for the smaller values of n. Thus, even if all the data in a given set are equally consistent with the cross sections, we shall still expect χ^2_m/m to increase with m.

The analysis of a given set of differential and integral data, with respect to consistency, thus consists of generating the optimal sequence, and then plotting $p(\chi^2_m)$ as a function of m. The less consistent data will appear at the end of the sequence, and the p curve will decrease as m approaches n. Such analysis should obviously identify significantly less-consistent data, if any, and should also indicate the "level of consistency" of the data subsets.

So far we have elaborated on how the less-consistent experimental integral data can be clearly identified, and how each datum can be even assigned a quantitative consistency index. There still remains the question of identifying the "less-consistent" cross sections in the given library. An advantage of our procedure is that, simultaneously with the optimal ordering of the integral data, it actually adjusts the cross sections by each subset of integral data along the optimal sequence. Thus, at each step we may examine the corresponding adjustment and determine what cross sections, at which energies, need to be modified and to what extent.

We expect that for the more consistent subsets, only marginal adjustments will be necessary to further improve the agreement between the experimental and calculated values of the integral parameters. But as each of the definitely less-consistent data is added, more significant adjustments of particular differential parameters will be needed to compensate for the discrepancies of these data.

The procedure for input-data analysis that we have described actually identifies both the integral *and* differential data which deserve re-examination and further study. It should furthermore, indicate the specific differential parameters which are related to the irregularity of each particular less-consistent integral datum.

Input Data

The measured values and their uncertainties, the calculated values using ENDF/B-IV data, sensitivities and covariances are described in the preceding paper by J. H. Marable, C. R. Weisbin and G. de Saussure.[3] The Version V calculated values are described in an ORNL internal status report by R. Q. Wright et al.[4] and in a paper by J. J. Wagschal, B. L. Broadhead and R. E. Maerker.[5] Table I lists the integral experiments, their measured values and the deviations of the calculated values (IV and V) from the measured values. The same covariances and sensitivities were used in this work for the analysis of ENDF/B-IV and the preliminary analysis of Version V.

Results and Discussion

Before reporting on the actual results of the present analysis, it is instructive to briefy consider "conventional" data testing, and at the same time to also acquire some feeling for the evolvement of the ENDF/B libraries. To this end we consider Fig. 1 in which plots are given of "calculated reactivity vs. critical assembly," corresponding to calculations based on the Bondarenko multigroup library and the five ENDF/B versions. The Version V reactivities were calculated at ORNL;[4] all other reactivities were calculated at HEDL.[6] Along the abscissa the order of the U-fueled and then that of the Pu-fueled assemblies is determined by the core fractions of the respective fissile isotope. These fractions are also plotted in the figure. The "curves," i.e., the segments connecting the points which represent the calculated reactivities, only serve to identify the sets of calculated

Table I. Experimental and Calculated Values of Integral Parameters By Which ENDF/B Libraries Were Adjusted

Exp. No.	Assembly	Integral Parameter	Measured Value	(E/C)-1 (%) Version IV	Version V
1	ZPR-6/7	k	1.000	1.555	-0.190
2		28f/49f	0.02422	3.551	-0.498
3		28c/49f	0.1422	-6.810	-6.720
4	ZPR-3/48	k	1.000	0.869	-0.882
5	ZPR-9/31	k	1.000	1.134	-0.705
6		25f/49f	1.036	2.147	5.930
7		28f/49f	0.0300	4.392	0.402
8		28c/49f	0.1230	-6.296	-3.940
9	ZPR-6/6A	k	1.000	1.493	0.472
10		28c/25f	0.1378	-2.880	-3.190
11		28f/25f	0.02388	7.178	2.040
12	ISNF	49f/25f	1.155	3.259	1.490
13		28f/25f	0.0920	7.628	2.970

values pertaining to a given library. They have no meaning other than to serve as an eye guide. This refers to all the following graphs as well since we deal everywhere with discrete sets of points. Such a graphic representation of calculated reactivities already has an advantage over the common tabular representation, in that certain regularities (and irregularities) appear at a glance, which are almost impossible to infer from a table. As an example, we note the great similarity of the Version V k plot to the core-^{239}Pu-percentage plot (over the ZPR-6/7, 3/56B, 9/31 and 3/48 points), which seems to indicate that these measurements are highly consistent with each other, and that perhaps a relatively simple and small modification of the ^{239}Pu file would result in agreement between calculation and experiment. As another example we note that the reactivity of ZPR-3/11 seems "irregular." The main reason for presenting this figure, however, is to illustrate the development of the ENDF/B libraries. The Bondarenko and Version II libraries are rather poor. The qualities of the other libraries are definitely better, but rather similar. Certainly, on the basis of these data, Version V cannot be judged as better than Version IV.

A flaw of "conventional" analysis, at least with respect to consistency of integral and differential data, is that it fails to take account of the joint standard deviations (which we discussed under "Procedure") of the r-$\bar{r}$ deviations which are the appropriate units in which these deviations should be measured. Figure 2 shows the properly measured deviations for the Version IV and Version V calculations. The better quality of ENDF/B-V is already indicated. The relative inconsistency of Exp. 11 (^{28}f/^{25}f in ZPR 6/6A) and Exp. 13 (same ratio in ISNF) with ENDF/B-IV is obvious. However, not very much can be said with any certainty regarding the other experiments. In any case, since the limitations of this individual consistency analysis were already discussed, we shall now proceed to present the results of our proposed analysis. It will indeed show that, except for the obvious irregularity of Exps. 11 and 13 with respect to ENDF/B-IV, any other tentative conclusion that we might be tempted to draw from Fig. 2 would be wrong.

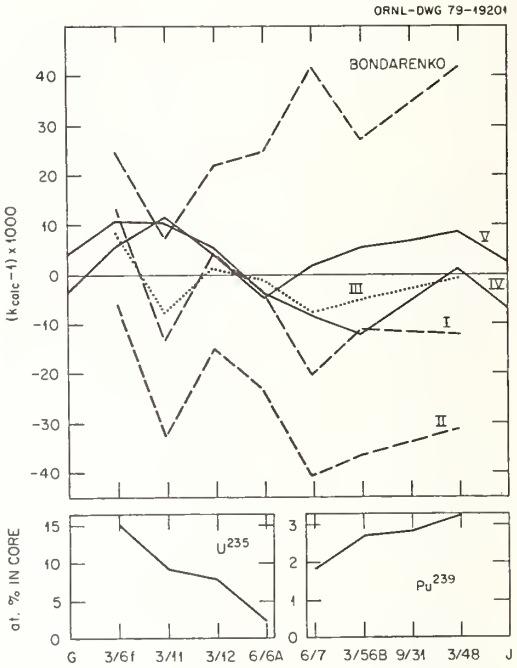

Fig. 1. Calculated reactivities using ENDF/B-I through -V.

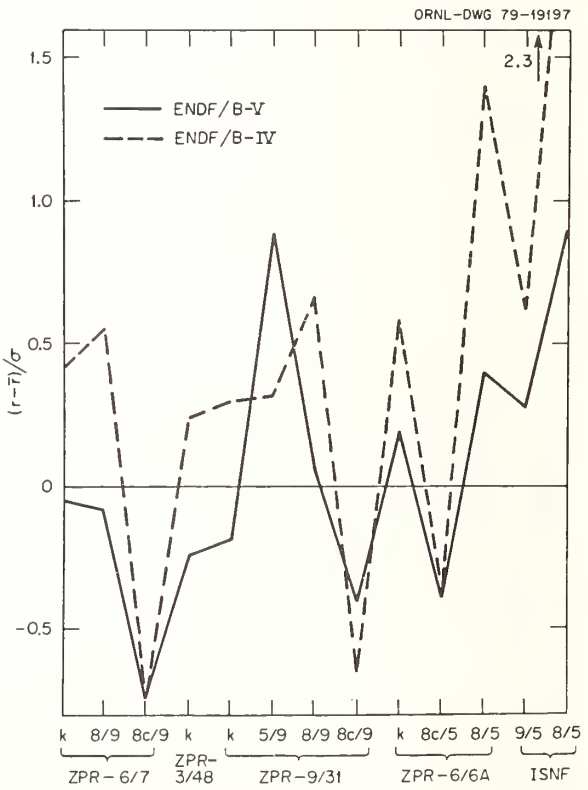

Fig. 2. Differences between measured and calculated performance parameters in units of combined standard deviations (σ).

Figure 3 shows (a) the "χ^2/n vs. n" plots for our 13 input data evaluated for ENDF/B-IV and V, (b) "equi-p" curves in (χ^2/n,n) plane, and (c) the two "p vs. n" plots corresponding to the respective χ^2/n plots. We note that the two optimal sequences are quite different. While the integral data least consistent with ENDF/B-IV, in order of decreasing consistency, are experiments 1, 11, 13, 12 and 10, the five experiments least consistent with Version V are 12, 8, 1, 3 and 6. The only datum common to the two sets is Exp. 1 (k of ZPR-6/7). We also note that the p curves drop rather dramatically towards the end of the sequence, so that in each case the last data in the sequence are definitely less consistent with the respective library than the first eight, which in both cases show a remarkably constant consistency. Most importantly, it is clear that ENDF/B-V is significantly more consistent with our integral data than Version IV. However, this strong statement should be stated with a certain reservation. while it is true for *almost* all the integral data, when the complete set of 13 data is considered, it turns out to be about equally consistent with the two libraries at the (rather unexciting) level of $\simeq$ 30%. Further scrutiny of the curves shows that Version V is even marginally less consistent with the data than Version IV. This, we believe, is "accidental." But it serves to emphasize that testing *complete* sets only of relatively many data for consistency may indeed by an oversimplification.

So far we have identified less consistent integral data, let us now identify some differential data that deserve re-examination. The contribution to χ^2 of the cross section of isotope i for reaction k is obtained from the term $(\sigma-\sigma')^t C_\sigma^{-1}(\sigma-\sigma')$ in Eq. (2) by setting all other elements of the adjustment vector $(\sigma-\sigma')$ not pertaining to the particular cross section equal to zero. The more significant differential data contributions to χ^2, as more and more integral data are added along the optimal sequence, are plotted in Figs. 4 and 5 for ENDF/B-IV and V respectively. It is seen that

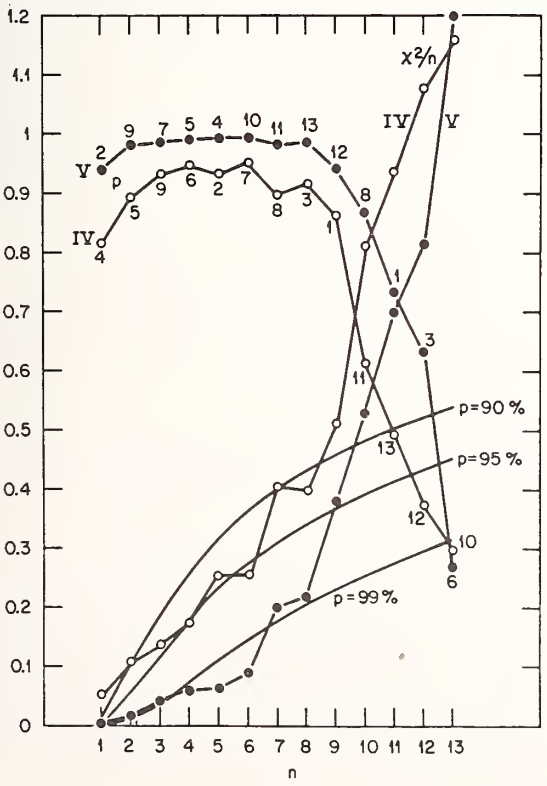

Fig. 3. χ^2/n and associated probability p as a function of the number of performance parameter n. The experiment ID numbers correspond to those in Table I.

significant contributions appear only with the addition of the less consistent data, and that generally these appear one at a time. In other words, there is a distinct relation between each irregular datum and a *particular* cross section.

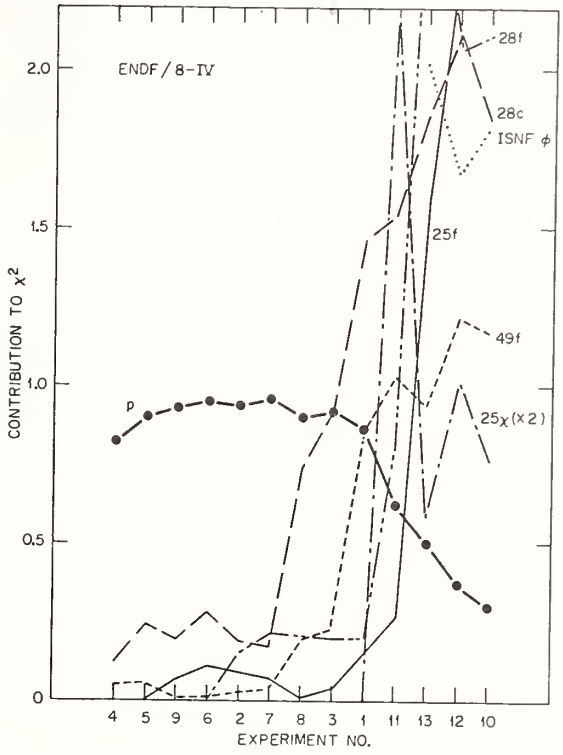

Fig. 4. ENDF/B-IV differential data contributions to χ^2 as a function of the ID number of the experiment added.

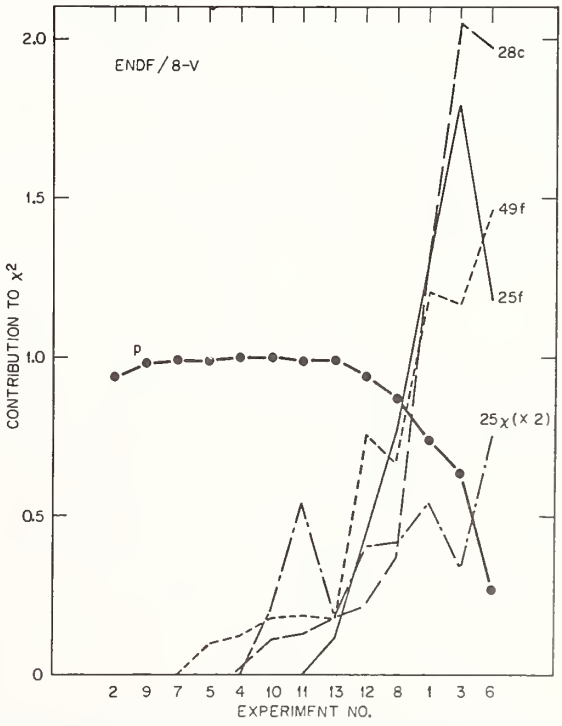

Fig. 5. ENDF/B-V differential data contributions to χ^2 as a function of the ID number of the experiment added.

The inclusion of Exp. 11 ($^{28}f/^{25}f$ in ZPR-6/6A), for example, in the ENDF/B-IV data testing optimal sequence resulted in a sharp drop of the "p-curve" to the 60% level (Fig. 3; also reproduced in Fig. 4). This drop is accompanied by a sharp rise in the ^{235}U fission spectrum contribution to χ^2 ($^{25}\chi$ line by No. 11 in Fig. 4). The ^{235}U fission spectrum was indeed changed in Version V, and Exp. 11 is now "regular." The inclusion of this $^{28}f/^{25}f$ ratio in ZPR-6/6A now leaves us at the extremely high consistency level ($\sim$ 98%) with Version V data. A closer look at the Version V "p-curve", however, shows a slight change in the slope when the now "regular" No. 11 is added. Once again this is associated with the ^{235}U fission spectrum of which the contribution to χ^2 ($^{25}\chi$ line by No. 11 in Fig. 5) is now much smaller, and indeed the actual change in the mean energy of the fission spectrum adopted for ENDF/B-V was less than the calculated adjustment to the -IV fission spectrum. It is also worth mentioning that the ISNF flux spectrum, which is dominated above the ^{238}U fission threshold by the ^{235}U thermal fission spectrum no longer contributes significantly to χ^2.

From the preceding discussion it is clear by now that an irregular datum with respect to a given differential data library may turn out to be regular with respect to another cross-section library. This will usually point to a particular cross section that deserves attention rather than to the elimination of this datum. However, if the same datum appears again and again as irregular, with different libraries, the measurement may be dubious. Careful judgment should be exercised before a datum, if any, is to be eliminated.

Concluding Remarks

The significant undertaking at ORNL to produce an adjusted cross section library for fast-reactor core physics is proceeding. The library will be based on ENDF/B-V, and sensitivities and covariances for these data are being developed. They will be used in meaningful data testing as outlined in this paper. Based on our preliminary data testing of ENDF/B-V we conclude that with respect to twelve out of thirteen integral measurements considered, ENDF/B-V is a marked improvement over Version IV in the sense that (a) the integral data are significantly more consistent with Version V than with Version IV, (b) fewer cross sections need to be adjusted to achieve agreement between all the experimental data and the corresponding values calculated by Version V, and (3) the necessary adjustments are smaller.

Acknowledgements

The authors acknowledge and thank the many members of the ORNL staff, in particular, J. L. Lucius, J. D. Drischler, R. Q. Wright, W. E. Ford III, G. de Saussure, and F. G. Perey. Two of us (Y. Yeivin and J. J. Wagschal) are greatful for the opportunity to work on this project at the ORNL Engineering Physics Division and for the corresponding support.

Research sponsored by the U. S. Department of Energy under contract W-7405-eng-26 with the Union Carbide Corporation.

References

1. C. R. Weisbin et al., ORNL-5517 (1979).
2. A. Pazy et al., Nucl. Sci. Eng. 55, 280 (1974).
3. J. H. Marable, C. R. Weisbin, and G. de Saussure, this conference.
4. R. Q. Wright et al., UCND internal correspondence, October 1979.
5. J. J. Wagschal, B. L. Broadhead, and R. E. Maerker, this conference.
6. R. W. Hardy, R. E. Schenter, and R. E. Wilson, Nucl. Sci. Eng. 57, 222 (1975).

A TEST OF ENDF/B LIBRARY IN THE CRITICALITY PREDICTIONS OF FAST ASSEMBLIES

V.K. Shukla and S.B. Garg
Bhabha Atomic Research Centre
Trombay, Bombay-400085, India

A criticality analysis has been carried out of several fast neutron multiplying assemblies using the 27-group cross-section set and resonance self-shielding factors which have been derived from version III and IV of ENDF/B library. These assemblies utilize metallic, oxide and carbide fuels of uranium and plutonium and represent very soft to very hard neutron spectra. The analysis indicates that fission and scattering cross-sections of uranium and its isotopes need updating in the MeV energy range.

[27-group set, self-shielding factors, spherical model, diffusion theory, transport theory k_{eff} .]

Introduction

A 27-group cross-sections set[1] (Garg set) and the resonance self-shielding factors have been generated[2] for several elements from ENDF/B library. The energy group structure of this set is identical to that of the 26-group ABBN set[3] but with an additional group in the energy range 10.5 to 15.0 MeV mainly to account for the (n,2n), (n,p) and (n,α) reactions which assume significance in hard spectra fast reactors or fission-fusion systems. This set was used to analyse[4] some 20 uranium and plutonium based fast critical assemblies. Some of these assemblies were amongst those recommended by the Cross-Section Evaluation Working Group[5]. These assemblies represent very soft to very hard neutron spectra in carbide, oxide and metallic fuels of uranium and plutonium. Thus they provide a good testing bed for the newly generated cross-section set in the keV and MeV energy range. In the above-mentioned analysis the resonance self-shielding in cross-sections was not taken into account. It was observed that the hard spectra fast systems could be predicted well with this set even without accounting for the resonance self-shielding effects in cross-sections. However, the importance of the resonance self-shielding was found to be significant in the case of soft spectra cores. To account for this effect the analysis has been carried out for some selected fast assemblies using the usual self-shielding factor method of generating the self-shielded cross-sections. The selected assemblies are GODIVA, TOPSY, VERA-1B, ZPR-3-11, ZPR-3-12, ZEBRA-2, ZPR-6-6A, JEZEBEL, ZEBRA-3, SNEAK-7B, ZPR-3-48, ZPR-3-50, ZPR-3-53 and ZPR-6-7.

Description of Critical Assemblies

The fourteen assemblies selected for this analysis include seven uranium based and seven plutonium based fast critical assemblies. The general characteristics of these assemblies are given in Table II.

The composition, dimension and other relevant details of these assemblies are given by Hardie et al[6], Mills[7] and Benzi et al[8].

Method of Calculation

The 27-group infinite dilution cross-section set and the resonance self-shielding factors for various reactions at some specified background potential scattering cross-sections have been derived[1,2] from the basic nuclear data library ENDF/B, The ENDF/B version III has been used in the case of actinides whereas version IV has been used for coolant and structural elements.

The self-shielded multigroup cross-secions of constituent isotopes in a mixture depend on its composition. These have been calculated for different isotopes in the mixtures by the usual method of iteration on the potential scattering cross-sections. Most of the cross-sections used in the neutronics calculations are not very sensitive to the neutron spectrum within a group but the elastic slowing down and group to group cross-sections are. The elastic slowing down and group to group cross-sections for constituent isotopes are, therefore, modified according to the spectrum calculated by one dimensional diffusion theory. This process is iterated to obtain a converged value of multiplication factor. All this has been done using the code 1DX[9]. These 27-group self-shielded cross-sections have been used to calculate the k_{eff} values of some of the assemblies, as mentioned in Table II, by one dimensional transport theory using the code [illegible]-DTF-IV[10]. For the other assemblies the diffusion to transport corrections have been applied as reported by Hardie et al. The final values of k_{eff} reported in this paper have been obtained after applying heterogeneity and 1D to 2D corrections as given in the same reference.

Discussion of Results

The k_{eff} values of different assemblies as calculated by this 27-group set are compared in Table I with those obtained by other cross-section sets.

TABLE I Intercomparison of k_{eff} Values

Sr. No.	Assembly	Fuel	27-Group k_{eff}	Reference k_{eff}	ABBN-70 k_{eff}	UKNDF-70 k_{eff}
1	GODIVA	U	1.0057	0.9912	1.0133	1.01587
2	TOPSY	U	1.0232	0.9907	-	-
3	VERA-1B	UC	1.0014	1.0026	-	-
4	ZPR-3-11	U	0.9983	0.9924	-	-
5	ZPR-3-12	UC	1.0006	1.0017	-	-
6	ZEBRA-2	UC	0.9987	0.9902	-	-
7	ZPR-6-6A	UO_2	0.9982	0.9988	1.00026	1.00050
8	JEZEBEL	Pu	0.9990	0.9891	0.99518	0.99185
9	ZEBRA-3	Pu	1.0026	0.9816	0.96530	0.93683
10	SNEAK-7B	PuO_2	1.0098	0.9893	-	-
11	ZPR-3-48	PuC	0.9970	0.9997	0.96663	0.95159
12	ZPR-3-50	PuC	0.9936	0.9940	-	-
13	ZPR-3-53	PuC	0.9964	1.0008	-	-
14	ZPR-6-7	PuO2	1.0053	0.9926	0.97325	0.95254

In this Table, the reference values are those obtained by Hardie et al for all the assemblies except GODIVA, TOPSY and JEZEBEL. The reference values of GODIVA and TOPSY are taken from Mills and that of JEZEBEL from Benzi et al. Hardi et al have calculated the k_{eff}'s of these assemblies using different versions of ENDF/B but we are referring to those obtained with version III for

TABLE II. Description of the Critical Assemblies

Sr. No.	Assembly	Fuel Type	Core Volume (litres)	Fissile to Fertile Ratio	Reflector Material	Reflector Thickness (cms)	Mode of Investigation	Remarks
1	GODIVA	U	2.8	15.38	-	-	S_{16}	A bare core assembly with a very hard neutron spectrum. It is suitable for testing the cross-sections of ^{235}U and ^{238}U in the high energy range.
2	TOPSY	U	0.93	15.53	^{238}U	22.86	S_{16}	An assembly with a spectrum softer than that of GODIVA. It tests the cross-sections of ^{235}U and ^{238}U in the high energy region.
3	VERA-1B	U	30	12.5	^{238}U + Structural Elements	39.45	S_{16}	An assembly with a graphite content and a reasonably hard neutrom spectrum. It is good for testing the MeV energy cross-sections of ^{235}U and ^{238}U.
4	ZPR-3-11	U	140	0.13	^{238}U + Structural Elements	30.0	Diffusion	An assembly with a graphite content which produces slightly soft neutron spectrum. The objective is to test the high energy cross-sections of ^{235}U and ^{238}U.
5	ZPR-3-12	U	100	0.26	^{238}U + Structural Elements	30.5	S_{16}	An assembly similar to ZPR-3-11. The higher content of fissile material is compensated by graphite which is added to soften the spectrum. The objective is the same as in ZPR-3-11.
6	ZEBRA-2	U	430	0.16	^{238}U + Structural Elements	31.70	S_4	The core contains graphite and produces spectrum similar to that of a large carbide power reactor. Self-shielding effects are to be tested.
7	ZPR-6-6A	U	4000	0.20	^{238}U + Structural	33.81	Diffusion	It represents a current large oxide system cooled by sodium. It is suitable for testing the resonance self-shielding effects.
8	JEZEBEL	Pu	1.1	21.23	-	-	S_{16}	A bare core assembly with a very hard neutron spectrum. It is good for testing the cross-sections of ^{239}Pu in the higher energy range.
9	ZEBRA-3	Pu	60	0.116	^{238}U + Structural Elements	30.50	S_4	A hard spectrum system. It tests the cross-sections of ^{239}Pu, ^{240}Pu and ^{238}U in the MeV energy range.
10	SNEAK-7B	Pu	310	0.143	^{238}U + Structural Elements	30.0	Diffusion	A mixed-oxide fuel system. Suitable for testing the resonance self-shielding effects of cross-sections
11	ZPR-3-48	Pu	410	0.222	^{238}U + Structural Elements	30.0	Diffusion	A mixed-carbide system with additional graphite to obtain soft spectrum characteristics of a large fast reactor cooled by sodium. Resonance self-shielding effects are to be tested.
12	ZPR-3-50	Pu	350	0.222	^{238}U + Structural Elements	40.34	Diffusion	A mixed carbide system with additional graphite content to obtain softer spectrum characteristics of a large power reactor. Good for testing resonance self-shielding effects.

TABLE II (Continued)

Sr. No.	Assembly	Fuel Type	Core Volume (litres)	Fissile to Fertile Ratio	Reflector Material	Reflector Thickness	Mode of Investigation	Remarks
13	ZPR-3-53	Pu	220	0.625	^{238}U + Structural Elements	37.33	S_4	An assembly with a larger content of graphite to yield soft spectrum. Suitable for testing resonance self-shielding effects
14	ZPR-6-7	Pu	3100	0.154	^{238}U + Structural Elements	33.81	Diffusion	A mixed-oxide system to yield spectrum of current large fast reactors cooled by sodium. Suitable for testing resonance self-shielding effects.

our comparison because we have derived the cross-sections of all the actinides using version III of ENDF/B. The values of k_{eff} referred as ABBN-70 and UKNDF-70 are those obtained by Cuculeanu et al in a recent analysis[11] carried out by using two sets of cross-sections; one the 26-group Russian set (version 1970) and the other set derived from British Nuclear Data File (UKNDF) version 1970.

It is seen from this Table that the k_{eff} values obtained by this 27-group set agree reasonably well with the experiments for all the assemblies except TOPSY. Both GODIVA and TOPSY are hard neutron spectra uranium fuelled assemblies with the difference that TOPSY is uranium reflected whereas GODIVA is a bare core. By intercomparing the results of these two assemblies it appears that the scattering cross-sections of ^{238}U are not known accurately in the MeV energy range. The fission cross-sections of ^{235}U and ^{238}U, as reported in ENDF/B, also appear to be higher in the MeV energy range. All the plutonium fuelled assemblies are predicted within 0.5% as compared to the experiments except SNEAK-7B where the disagreement is about 1.0%. Hardie et al have indicated in their analysis[6] that the scattering and capture cross-sections of iron produce more negative reactivity worths in version IV of ENDF/B as compared to version III. We have also tested the ENDF/B version III iron cross-sections in ZPR-3-48 assembly and found that it increases the predicted k_{eff} by about 0.25% which improves the agreement with experiments. However, the effect is found to be small.

Conclusions

The present study limited to the criticality analysis of the fast critical assemblies covering a very wide range of neutron spectra and fuelled with plutonium and uranium in their metallic, carbide and oxide forms indicates that the 27-group Garg set is adequate for the criticality predictions of fast assemblies. However, the criticality predictions in the hard spectrum uranium assemblies can be further improved if the fission cross-sections of these isotopes are slightly reduced in the MeV energy range. Inadequate knowledge of inelastic scattering cross-section of ^{238}U in the MeV energy range combined with higher fission cross-sections tend to overpredict the reactivity in the uranium assemblies reflected by ^{238}U as is seen in TOPSY. The iron cross-sections in version III give marginally superior k_{eff} values compared to those obtained with version IV of ENDF/B. Overall, the present 27-group cross-section set appears to be adequate for the criticality predictions of a variety of fast assemblies.

References

1. S.B. Garg, INDC(IND)-21/G + SP (1977).
2. S.B. Garg, BARC-1002 (1979).
3. L.P. Abagyan et al, Group Constants for Nuclear Reactor Calculations, Consultants Bureau, New York (1964).
4. S.B. Garg and V.K. Shukla, INDC(IND)-22/G + SP (1977).
5. BNL-19302, Cross-Section Evaluation Working Group Benchmark Specifications (1974).
6. R.W. Hardie et al, Nucl. Sci. Engg. 57, 222 (1975).
7. C.B. Bills, Nucl. Appl. 5, 214 (1968).
8. V. Benzi et al, ANL-7320 (1966).
9. R.W. Hardie and W.W. Little Jr., BNWL-954 (1969).
10. K.D. Lathrop, LA-3373 (1965).
11. V. Cuculeanu et al., INDC(RUM)-9/GV (1979).

BASIC NUCLEAR DATA AND THE FAST REACTOR SHIELDING DESIGN FORMULAIRE PROPANE Do

J. C. Estiot, M. Salvatores, J. P. Trapp
DRNR/SEDC/SPNR/LPR
CEN/CADARACHE - Boîte Postale N°1
13115 - SAINT-PAUL-LEZ-DURANCE
(France)

This paper presents a calculational scheme -formulaire PROPANE- to calculate the deep neutron penetration in the fast reactor shield. The emphasis is put on the multigroup data and method approximations. The performances of this formulaire are presented.

[Neutron propagation - Multigroup data - Method approximations].

Introduction

The main purposes of the PROPANE "formulaire" to reduce the design calculation cost with a good accuracy with regard to the reference method (± 10%) [1] ;

. to be the basis for the cross-sections adjustements using integral experiments ;

. to assess the uncertainties on design parameters due to cross-sections uncertainties and their correlations.

The new version PROPANE Do, is presented, the emphasis is put on : method approximations, multigroup data, and spatial weighting procedures.

The improvement of PROPANE due to the multigroup scheme optimization and the improvement of the basic nuclear data (successively 26 - 39 - 45 groups) is also shown.

Finally, the PROPANE "formulaire" is tested by the analysis of two deep penetration problems : HARMONIE, Na configuration, and ORNL/TSF experiment, against a reference calculation performed with the 113 group BABEL library [1].

Reference library : BABEL

The multigroup BABEL library [1], based on the ENDF/B.4 nuclear data file, has a 113 group structure. The MC2.2 code [6] was used to collapse the original fine group structure (2000) to 113 groups; these procedure allows use of an appropriate fine neutron spectrum adapted to each propagation medium : stainless-steel Sodium mixture (50% - 50% v/o), pure stainless-steel, pure Sodium, pure Iron.

The BABEL-VITAMINE C [2] comparison has been done on TSF geometry given in the simplified diagram 1 [7] .

The following table shows the calculation experiment ratio for the Bonner-Ball detector in various positions.

Table I. Calculation/Experiment.

	VITAMINE C 171 groups	BABEL 113 groups
46cm SS + 460cm Na		
+ 0. cm C.S.	0.663	0.730
+15.41 cm C.S.	0.828	0.910
+30.85 cm C.S.	1.275	1.025
+41.11 cm C.S.	0.877	0.635
+51.40 cm C.S.	0.735	0.561
+61.68 cm C.S.	0.757	0.570

The performances of the two structures VITAMINE C and BABEL are very similar in spite of about sixty groups reduction.

Do Version of the "formulaire" PROPANE

Multigroup structure

The choice of multigroup structure satisfies three criteria :

. calculation accuracy : ±15% on regard to the refernce method (113 groups) ;

. energy limits consistent with the core design formulaire CARNAVAL ;

. group number as small as possible.

The sensitivity profiles applied to the shielding Benchmark calculation [1], [3], (diagram 2), (Figure Ia and Ib), show the energy ranges where the fine structure must be closely respected ; particularly the Sodium (300 KeV) and Iron (24 KeV) windows. Howeover, below 1 KeV, the structure must be adequate to treat the slowing down to the thermal energy.

The optimized structure includes 45 groups and it is given in appendix.

Weighting Procedure

The weighting functions are the neutron fluxes calculated by the reference method (113G/S16/P3) on the Benchmark geometry on each spatial zone according to :

$$\Phi_g = \sum_{I1}^{IN} \phi_g(I).\Delta V(I) \Big/ \sum_{I1}^{IN} \Delta V(I)$$

where $\Delta V(I)$ refers to the volumn of the mesh interval I.

The choice of spatial zones is very important as shown in Table III where are given the discrepancies between 113 Groups and 45 Groups calculations with various weighting functions for the total flux in the Benchmark geometry at several penetrations :

Table II. $E = [\phi(113/S4/P1)-\phi(45/S4/P1)] / [\phi(113/S4/P1)]$
(percentage values)

	Distance to the center	CASE 1 1zone PNL + 1zone Na	CASE 2 5zonesPNL 10zonesNa 1z.H.Exch 1zone Na	CASE 3 3zonesPNL 3zones Na 1z.H.Exch 1zone Na	CASE 4 3zonesPNL 4zones Na 1z.H.Exch 1zone Na
TOTAL FLUX	337cm	6.6	3.5	4.6	4.6
	415 (ExitPNL)	11.4	6.6	5.8	5.8
	650	10.3	4.6	2.2	2.2
	915 (H.Exch)	-40.8	0.6	-19	-11

Spatial zones must be narrow enough at the vicinity of the interface between two media (see cases 1 and 2) ; in the pure Sodium, a sufficicent number of spatial zones is necessary when the penetration exceeds 2.5 meters (see cases 3 and 4).

Method Approximations

Table III shows the discrepancies introduce by the method approximations : angular quadrature (S_N) and anisotropy treatment (P_n)

Table III. $E = [\phi(45G/S16/P3-\phi(45G/Sn/Pn)]/ [\phi(45G/S16/P3)]$
(percentage values)

Penetration position (see Benchmark geometry)	FLUX ≥ 111KeV			EQUIV. THERMAL FLUX		
	S16 P1	S4 P1	S4 P3	S16 P1	S4 P1	S4 P3
337cm	3.4	5.6	2.3	0.3	2.4	1.3
415cm	10.1	14.1	6.1	2.4	6.4	4.4
650cm				3.7	9.4	6.4
915cm				4.6	13.2	9.2
998cm				5.0	14.8	9.6

It appears that approximations : S4 and P3 give a reasonable accuracy (similar conclusions may be seen in 113 groups calculations).

The spatial meshes are :
. 3 cm in SS-Na or Fe-Na mixtures,
. 5 cm in pure Na,
. 1.5 cm in pure Iron or stainless-steel.

PROPANE Do Performances

Table IV shows the discrepancies between PROPANE Do and the reference method on the Benchmark geometry.

Table IV. $E = [\phi(113/S16/P3-\phi(45/S4/P3)] / [\phi(133/S16/P3)]$
(percentage values)

	TOTAL FLUX	FLUX ≥ 820 KeV	FLUX ≥ 111 KeV	EQUIVALENT THERMAL FLUX
337 cm	6.5	- 5.1	2.3	6.5
415 cm	10.2	-19.7	6.2	10.0
650 cm	9.2			12.9
950 cm	- 1.8			3.2

Then the PROPANE Do "formulaire," allows calculation of the neutron propagation in a representative fast reactor configuration with a good accuracy and a shorter computer time with respect to the reference method.

PROPANE Successive Versions Review

Discrepancies between 26 groups structure and the reference method (100 groups) on the Benchmark calculation being too large, an optimization was made for this structure : PROPANE Co with 39 groups. The change from DLC2 to BABEL structure led to the 45 groups structure.

So, since 1975, four successive versions have been performed :
. PROPANE 0 : 26 groups based on DLC2 structure and ENDF/B2 [4]
. PROPANE Bo : 26 groups based on DLC2 structure and ENDF/B2, and ENDF/B4 for Na and Fe
. PROPANE Co : 39 groups found on the same library than the former
. Finally PROPANE Do : 45 groups found in BABEL 113 groups structure and ENDF/B4 data file.

Table V shows the respectives performances of these versions :

Table V. Discrepancies between PROPANE (0, Bo, Co, Do) and the respective reference method (100-113G/S16/P3) in percentage.

		PROPANE 0	PROPANE Bo	PROPANE Co	PROPANE Do
TOTAL FLUX	289 cm	9.9	6.5	4.0	2.4
	337 cm	10.	10.5	8.5	6.5
	425 cm	29.0	9.0	14.0	10.5
	650 cm	50.7	9.0	13.0	9.2
	915 cm	25.1	-137.0	- 31.8	- 1.8

The last version reduces significantly all the discrepancies of the reference method and their spatial fluctuations.

Uncertainty Matrices For Basic Nuclear Data

The knowledge of the uncertainties on basic nuclear data and their correlations although incomplete allows an estimate of the standard deviations of integral responses owing to these uncertainties.

The preliminary data for Fe and Na of [5], were used to produce data in the PROPANE Do 45 energy group structure.

These data will allow an adjustment of the multi group cross section and a recalculation of new dispersion matrices.

PROPANE Do Tests

We have tested the"formulaire"in the analysis of two deep penetration problems :
. HARMONIE Na configuration (diagram 3),
. ORNL/TSF Na experiment (diagram 1).[7]

Table VI gives the results for HARMONIE configuration :

Table VI. Discrepancies between PROPANE and Reference method.

$E(\%) = [\phi 113/S16/P3 - \phi(45/S4/P1)] / \phi(113/S16/P3)$

DISTANCE IN Na (cm)	TOTAL FLUX	EQUIVALENT THERMAL FLUX
20	0	0
30	0.6	0.01
70	2.7	2.4
170	6.1	7.0
270	6.7	11.0

Table VII gives together the discrepancies between PROPANE Do and the reference method for the geometry given in diagram 1 and the calculation-experiment ratio for the two calculations.

Table VII.

	E(%)=[φ(113/S16/P3) -φ45/S45/S4/P3]/ Ref.		CALCULATION TO EXPERIMENT		DISTANCE
	TOTAL FLUX	EQUIVAL. THERMAL FLUX	113G/S16 P3	PROPANE S4/P3	
End SS	7.6	- 0.1			46cm SS+ 460cm Na+
240cm Na	18.0	10.4	0.73 0.91	0.71 0.89	0cm CS 15.4cmCS
460cm Na	9.7	4.7	1.025 0.635	0.88 0.31	30.85cmCS 41.11cmCS
35cmCS	19.0	- 4.	0.56	0.25	51.40cm
60cmCS	55	50	0.57	0.25	61.68cm

Discrepancies between "formulaire" and the reference method are small till the end of the Sodium tank ; however in the Carbon steel penetration they become important. A spatial cross-sections weighting in this area would allow to reduce these discrepancies.

Conclusion

The PROPANE Do, the last non adjusted version of the"formulaire"is founded on the BABEL Library (113 groups) and the ENDF/B4 nuclear data file.

PROPANE Do allows calculation of the flux and the design responses of a fast reactor representative geometry with an accuracy near: ± 10% with regard to the reference method and a reduction of computing time (about a factor 5). The PROPANE Do performances have been tested on two experimental configurations like HARMONIE and TSF ; the results are consistent with the purpose.

The analysis of integral experiment made jointly by CEA and CNEN on pure Na and stainless-steel-Sodium mixture will allow adjustmemt of the cross-sections of Na, Fe, Ni and Cr. This last version will constitute the PROPANE 1 formulaire.

Diagram 1. TSF geometry

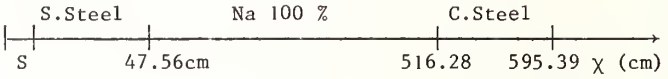

Diagram 2. Benchmark Geometry [4]

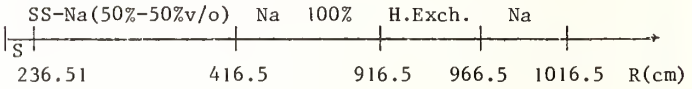

Diagram 3.

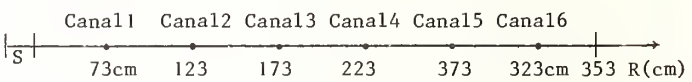

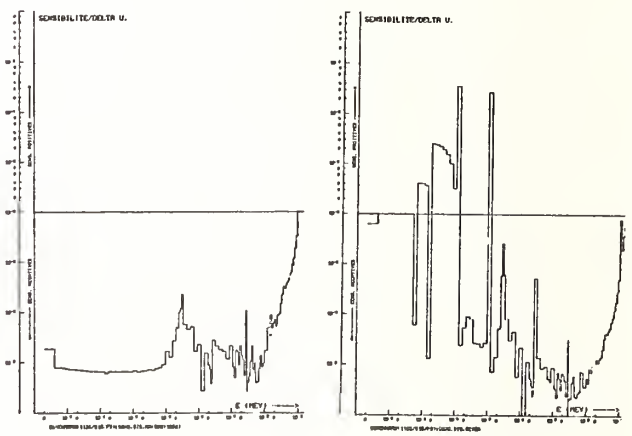

Figure 1a Figure 1b

Figure 1. Sensitivity profiles to Na and stainless-steel cross-sections on Sodium activation on heat exchanger.

Appendix

PROPANE Do

ENERGY RANGE	NUMBER OF ENERGY GROUPS IN: BABEL	PROPANE Do
14.19 MeV 1.35 MeV	33	5
1.35 MeV .333 MeV	10	6
333 KeV 273 KeV	6	3
273 KeV 26. KeV	14	8
26. KeV 2 KeV	17	9
2 KeV Thermal	33	14

References

[1] JC. Estiot, V. Rado, M. Salvatores, JP. Trapp ; Conséquence des incertitudes sur les données de base dans les calculs de protection, Conférence Internationale sur la Physique Neutronique et les Données Nucléaires pour les Réacteurs et Autres Applications, Harwell, 25-29 Septembre 1978.

[2] CR. Weisbin and al., ORNL/TM-5142, 1975

[3] JY. Barré ; Fast Reactors, Definition of a standard configuration for the comparison of shielding calculations, Proceedings of the Specialists' Meeting on Differential and Integral Nuclear Data Requirements for Shielding, NEA/IAEA, Vienne, 1976.

[4] F. Bouteau, P. Caumette, C. Devillers, A. Khairallah ; Formulaire de propagation des neutrons dans les milieux Acier-Sodium pour les protections de la filière rapide, Réunion de Spécialistes des Etudes de Sensibilité et des Expériences-Repères sur les Protections, Paris, 7-10 Octobre 1975.

[5] JD. Drischler, CR. Weisbin, ORNL-4318.

[6] H. Henkyson and al. ANL-8144, 1976

[7] RE. Maerker, FJ. Muckentmaler, CE. Clifford ; Measurements and calculations of the ORNL CRBR upper axial shield experiment, ORNL-5259.

-oOo-

NUCLEAR DATA FOR SHIELDING CALCULATIONS : Na CROSS-SECTION ADJUSTMENT USING PROPAGATION EXPERIMENTS

J.C. Estiot, M. Salvatores, J.P. Trapp
DRNR/SEDC/SPNR/LPR
C.E.N. Cadarache - B.P. N°1
13115 - Saint Paul Lez Durance - FRANCE

A. De Carli, V. Rado
C.N.E.N. Casaccia
S.P. Anguillarese - Km 1+300
00060 - Casaccia (Roma) - ITALIE

This paper presents an analysis of the propagation experiments in sodium, performed both with Tapiro and Harmonie source reactors. The neutron source in both experiments was varied by replacing the normal reflectors with a buffer for fast reactor blanket simulation. A satisfactory consistency was found between the two series of experiments. The resulting E-C/C values were used in an attempt to adjust sodium cross-sections. There is evidence for a slight decrease (≃ 5 + 7%) in the total cross-section of sodium below ≃ 100 KeV and a significant (≃ 20%) decrease in all the inelastic cross-sections above ≃ 2 MeV.

[Sodium propagation experiments, Na cross-section adjustment]

Introduction

The extensive series of neutron propagation experiments in sodium at Tapiro and Harmonie are briefly reviewed. The analytical methods used in the calculation are presented and the resulting E-C/C values are given for all the response functions considered. In view of the satisfactory consistency found among the different series of experiments, a statistical adjustment was attempted. The preliminary ORNL data on Na cross-section uncertainties and correlations were used. The results so far obtained, and their reliability are discussed.

Experimental configurations

The complete description of the Harmonie and Tapiro facilities are given in[1]. The following table summarizes the main characteristics of the propagation experiments in sodium performed with both reactors (plates 1 and 2):

	HARMONIE	TAPIRO
Size of the sodium thank	3x3x3 (m^3)	1x1x2 (m^3)
Mesh of the measurements on the central axis	50 cm	20 cm
Reflector surrounding the core	Stainless steel	Copper

Spectrum converter

Both at Tapiro and Harmonie a typical fast breeder blanket (UO2-Na) has been inserted between the reflector and the sodium tank, in order to get a source spectrum feeding the sodium tank close to the spectrum at the blanket/shielding interface of a power reactor. The thickness of this converter zone in both cases is ≃ 25 cm. Plate 3 gives as on example the Tapiro assangement.

The blanket composition is given in table I :

TABLE I

Isotopes	N/cm^3 ($x10^{24}$)	Isotopes	N/cm^3 ($x10^{24}$)
Na	$1.0\ 10^{-2}$	Fe	$5.4\ 10^{-3}$
U5	$4.1\ 10^{-5}$	Ni	$7.8\ 10^{-4}$
U8	$9.7\ 10^{-3}$	Cr	$1.4\ 10^{-3}$
O	$1.9\ 10^{-2}$		

Measurements and accuracies :

Five integral detectors are used in all the experimental configurations : Na/Cd, Mn/Cd, Au/Cd, Rhodium and Sulfur. Experimental accuracies are : ±5% for Na/Cd, Mn/Cd and Au/Cd ; ±15% for Sulfur and Rhodium.

Spectrum measurements are made with protron recoil technique (9.6 KeV - 1.3 MeV) between the reflector (or blanket) and the sodium tank.

Experimental analysis

Neutron source

Plates 4 and 5 show the 2D schematization used to calculate the neutron source (Part 1) to propagate in the sodium medium (Part 2). Monte Carlo 3D calculations (code Morse) are also performed to calculate the neutron spectrum at the end of the blanket (or the reflector). The comparison between the two calculationnal approaches and measurements shows a good agreement within the experimental uncertainties. Figures 1 and 2 show the calculated neutron spectrum at the of the sodium thank for both Tapiro and Harmonie.

Uncertainties due to the neutron shell source

Sensitivity studies of the Na/Cd activities ratio between to measurements (canal 1/ canal 3) to the neutron source spectrum show

that the effects of the uncertainties in the spectrum are fairly small and the same can be said for the uncertainties due to the angular distribution of the neutron shell source. It was found that for the activity ratio between canal 1 and canal 3, the change of the Na/Cd response is ≃ 1.4% for the Na/Cd detector and ≃ 2.8% for the Sulfur, in drastic conditions, i.e. the elimination of one of the forward angular components of the source.

Weighting procedure

An appropriate weighting procedure has been used to collapse the sodium cross-sections and the detectors cross-sections from the original 113 group Babel library to 45 groups. Comparison between the reference method in which the Babel library[2] (113 group, S16, P3) is used and the Propane calculation[3] (45 group, S4, P3) using two spatial zones of cross-sections weighting show discrepancies lower than 6% after three meters of sodium for the Na/Cd response and similar values for the other response.

It has been checked that the weighting procedure has negligeable effects on the detectors responses as expected from the optimization of the Propane multigroup structure.

Spatio angular tests

Extensive test have been performed, with 2D or 1D calculations to optimize the spatio angular meshs size :

A 5 cm spatial mesh was found to be appropriate for flux convergence,

S4 angular approximation is adequate for low energies but S16 is necessary at high energies (Sulfur and Rhodium response calculation).

Boundaries conditions

The correct treatment of experimental boundaries conditions - the concrete for Tapiro, the stainless steel walls and the wood for Harmonie - is necessary particularly at the end of the sodium tank. Moreover, the sodium impurities - especially the hydrogen - must be carefully taken into account. The uncertainty in the amount of these constituents will increase the global experimental uncertainty by 5 to 10%.

1D calculation

The 1D model needed for sensitivity calculation is choosen to get the geometry (leakage) factors (C_{1D}/C_{2D}) as close to one as possible. This leads to choose :

The spherical geometry

The 1D shell source is derived from the DOT source weighted on the whole radial distribution (i.e. on the outer edge of the blanket or reflector).

Calculation to experiment deviation

Table II presents the discrepancies between experiment and 2D calculations for ratio responses in two positions :

TABLE II - (E-C)/C en (%)

			Na/Cd	Mn/Cd	Au/Cd	Rhodium	Sulfur	Pos.
HARMONIE	With blanket		- 17.2	- 23.7	No result	No result	- 28.9	1/3
			- 7.9	- 27.9			-	3/6
	Without blanket		- 23.1	- 29.9	- 6.7	- 11.2	-	1/3
			- 13.8	- 30.0	- 7.0	-	-	3/6
TAPIRO	With blanket		- 41.2	- 48.3	- 27.0			1/6
						- 36.8		1/4
							- 15.0	1/2
	Without blanket		- 41.1	- 49.8	- 29.0			1/6
						- 32.5		1/4
							+ 4.8	1/2

Harmonie	Tapiro
Position1 : 20cm in Na	Position1 : 20cm in Na
Position3 : 120cm " "	Position2 : 35cm " "
Position6 : 270cm " "	Position4 : 50cm " "
	Position6 : 120cm " "

The results between the detectors and also between the two installations appear to be fairly consistent.

Sensitivity analysis

Figures 3 to 6 show the sensitivities profiles of the integral responses to sodium total cross-sections in various positions in the propagation medium. One note a large consistency between the sensitivity profiles corresponding to the same detector in the two facilities for a similar propagation length. The displacement to the low energies between the two positions (1/3 and 3/6) for Harmonie experiment is very important. This is very interesting because the whole energy area is covered by the experiment. At high energy (Sulfur and Rhodium) we observe that about 60% of the sensitivity coefficient to the total cross-section is due to the inelastic cross-section. At lower energies, the elastic cross-section contributes 90% to the sensitivity coefficient.

The change in the source spectrum obtained by the introduction of the blanket between the core and the sodium thank is more significant in the case of Harmonie than in Tapiro. This allows multiplication by a factor 4 of the ratio of the small sensitivities to the inelastic sodium cross-section in the position 1/3 for Na/Cd and by a factor 20 in the position 3/6.

Experimental and calculation uncertainties

The uncertainties values introduced in the adjustment procedure were :

± 15% for all low energy detectors in Harmonie

± 20% for high energy detectors in Harmo-

nie and Tapiro
± 25% for low energy detectors in Tapiro.

These uncertainties values take into account the actual experimental uncertainties, the comparison (impurities) uncertainties, and the uncertainties related to the calculation 2D modeling, SN, mesh size effects and source calculation.

Adjustment procedure and results

Even if the uncertainties, indicated in the previous paragraph, are fairly significant, the results of Table II relative to the (E-C)/C values show that is possible to reduce the calculation to experiment deviation. For this purpose we used the typical statistical adjustment procedure[4]. For the cross-sections uncertainties and their correlations we used the ORNL data[5] in the Propane multigroup structure[3]. In Table III, we show the standard deviations obtained with these uncertainties. It is obvious that the large adjustment is not possible in the present state of uncertainties evaluation. In fact, an attempt to gain consistency between experiments and basic data gave the results indicated in the same table. The (E-C)/C values are actually reduced for all parameters and the cross-sections adjustment are in range of allowed values. It is interesting to note that the X^2 test gave a 37% confidence level to this particular adjustment.

Conclusions

An extensive analysis of several neutron propagation experiments in sodium has been performed. This analysis has shown a satisfactory consistency between the experiments in different installations, in spite of modelling difficulties which need further studies. However, it was possible to use a large amount experimental informations to attempt a sodium cross-sections adjustment.

The present results indicate for the σ_t a slight overestimation from 5 to 7 percent below 100 KeV, and a significant overestimation (≃ 20%) for the inelastic cross-sections above 2 MeV.

TABLE III - Adjustment results

Experiment			St* Dev (%)	E-C/C (%) Before Adjustment	E-C/C (%) After Adjustment	Original total uncertainty (%)	$\Delta\sigma_{tot}/\sigma_{tot}$ (%)	$\Delta\sigma_{inel}/\sigma_{inel}$ (%)	En
HARMONIE	With blanket	S 1/3	55.5	- 28.9	0.3				14 MeV
		Na 1/3	4.4	- 17.2	- 9.0	± 3.3	- 1	- 20	2 MeV
		Na 3/6	13.7	- 7.9	+ 10.3				
		Mn 1/3	5.9	- 23.7	- 11.5	± 2.7	- 2	- 10	
		Mn 3/6	13.3	- 27.9	- 8.4				0.8 MeV
	Without blanket	Rh 1/3	13.2	- 11.2	+ 1.4				
		Na 1/3	4.5	- 23.1	- 15.0	± 4.5	- 2.5		
		Na 3/6	13.6	- 13.8	+ 4.4				0.1 MeV
		Mn 1/3	5.8	- 29.9	- 18.0				
		Mn 3/6	13.3	- 30.0	- 10.4				
		Au 1/3	5.3	- 6.7	+ 1.4	± 8.0	- 5.5		
		Au 3/6	15.3	- 7.0	+ 11.9				2 KeV
TAPIRO	With blanket	S 1/2	5.7	- 13.0	- 9.9				
		Rh 1/4	7.5	- 36.8	- 29.8	± 7.0	- 7		
		Na 1/6	3.7	- 41.2	- 34.3				
		Mn 1/6	6.2	- 48.3	- 35.6				10 eV
	Without blanket	S 1/2	5.4	+ 4.8	- 7.7				
		Rh 1/4	6.6	- 32.5	- 26.1				
		Na 1/6	4.8	- 31.4	- 24.2	± 7.0	- 5.0		
		Mn 1/6	6.1	- 48.5	- 35.9				
		Au 1/6	3.8	- 29.0	- 22.0				Thermal

* Integral parameters standard deviations obtained with original uncertainties on Na cross-sections derived from[5].

Reference

1. J.C. Estiot, A. De Carli and J.P. Trapp, Results of neutron propagation in steel sodium mixtures with various source spectra on Harmonie and Tapiro, Knoxville April 1977.

2. J.C. Estiot, V. Rado, M. Salvatores and J.P. Trapp, Conséquences des incertitudes sur les données de base dans les calculs de protection, Harwell Sept. 1978.

3. J.C. Estiot, M. Salvatores and J.P. Trapp, Basic data and the fast reactor shielding design formulaire Propane Do, Knoxville Oct. 1979.

4. A. Gandini and M. Petilli, Amara : code using the Lagrange's multipliers methods for nuclear data adjustment, RT/TI (73) 39.

5. J.D. Drischler and C.R. Weisbin, Compilation of multigroup cross-sections covariance matrices for several important reactor materials, ORNL-5318.

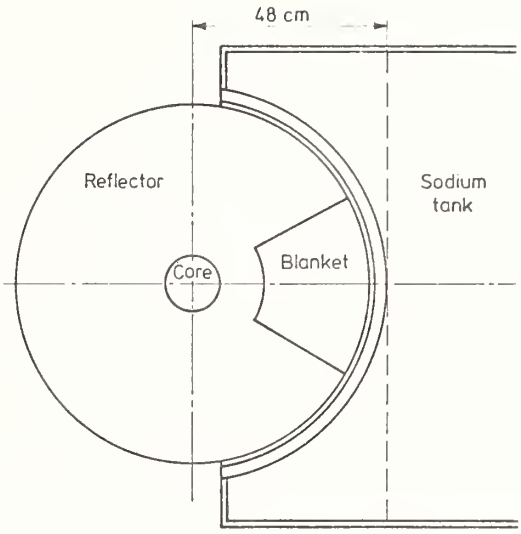

Plate 3

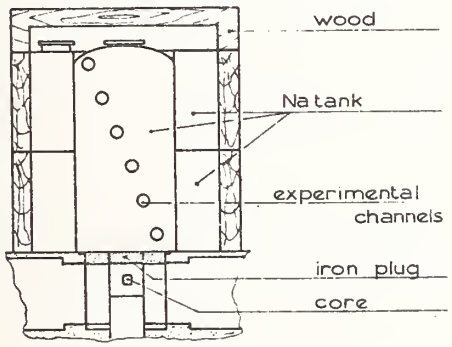

Plate 1 - Harmonie reactor

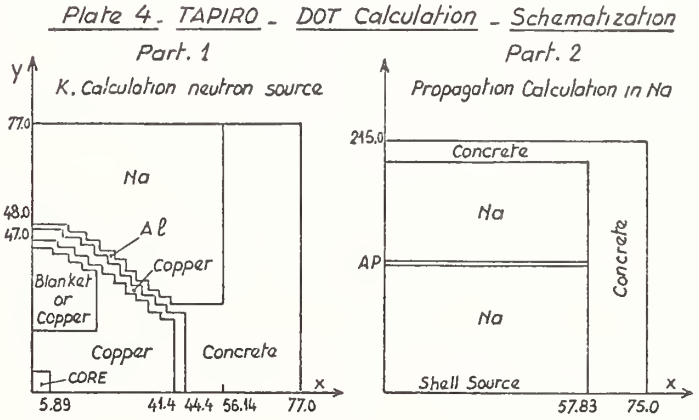

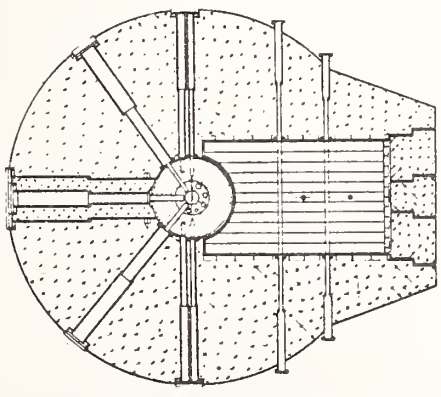

Plate 2 - Tapiro reactor

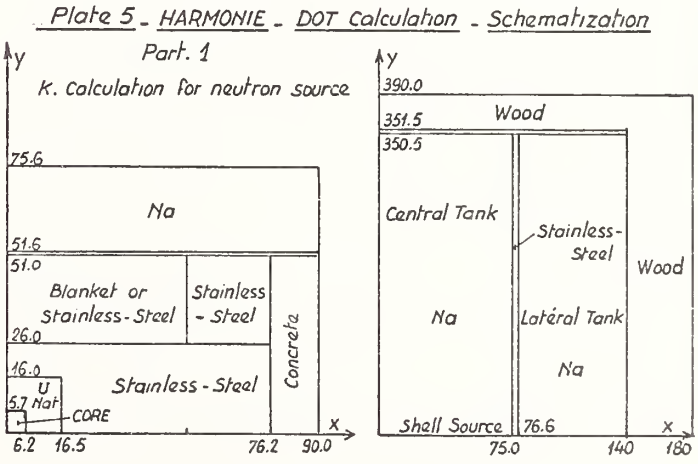

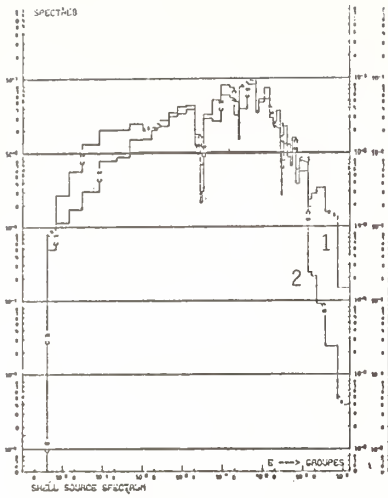

FIGURE 1
1 - Harmonie with blanket
2 - Harmonie without blanket

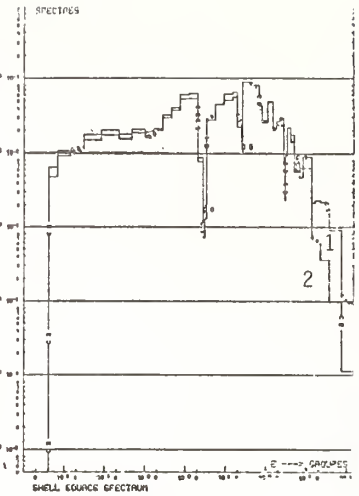

FIGURE 2
1 - Tapiro with blanket
2 - Tapiro without blanket

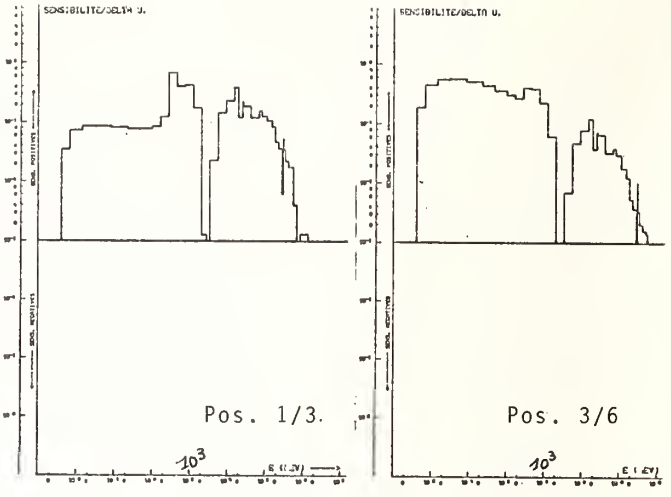

FIGURE 4
Harmonie - Sentivity to Na cross-sections for Mn/Cd detector

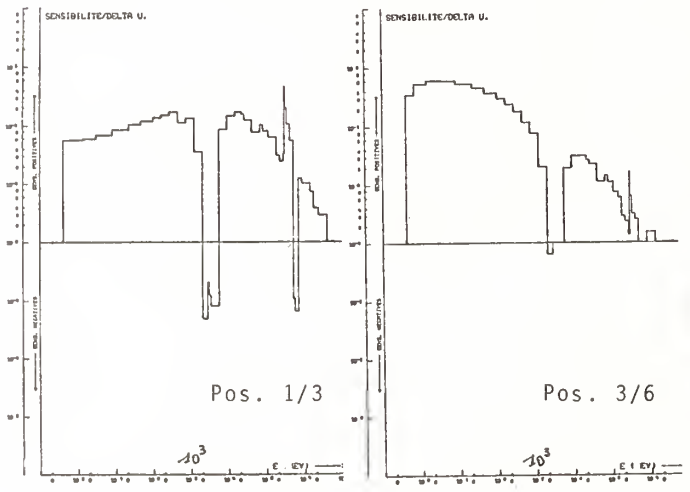

FIGURE 3
Harmonie - Sensitivity to Na cross-section for Na/Cd detector

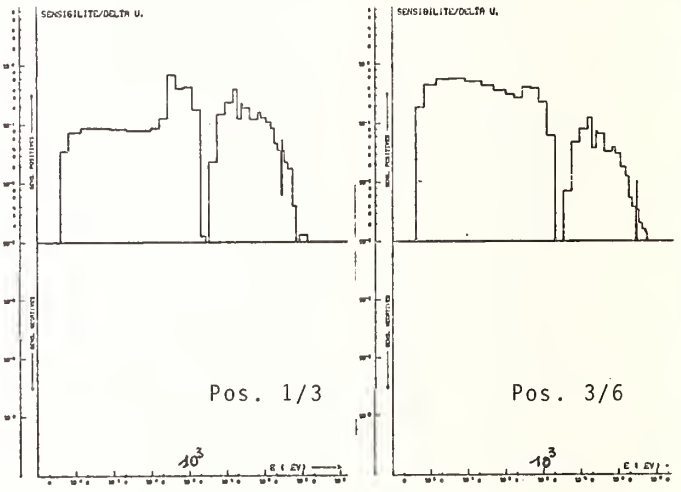

FIGURE 5
Harmonie - Sensitivity to Na cross-sections for Au/Cd detector

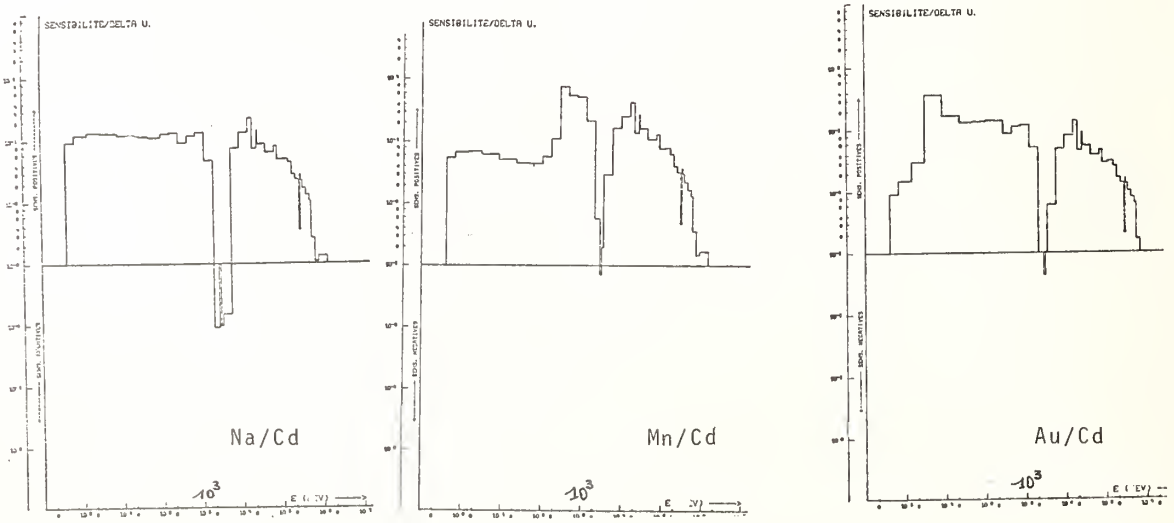

FIGURE 6
Tapiro - Sensitivity to Na cross-sections for detectors in position 1/6

ON THE DISCREPANCY BETWEEN DIFFERENTIAL AND INTEGRAL RESULTS FOR THE $^{63}Cu(n,\alpha)^{60}Co$ CROSS SECTION*

G. WINKLER,** D. L. SMITH and J. W. MEADOWS
Argonne National Laboratory
Argonne, Illinois 60439

The threshold-reaction $^{63}Cu(n,\alpha)^{60}Co$ is of special importance in reactor dosimetry for long-term fast-flux integration. The inconsistency in the available differential and integral data base has limited the applicability of that reaction as a reliable monitor. The availability of results from a recent measurement of the excitation function for the reaction $^{63}Cu(n,\alpha)$ at ANL prompted a further investigation of this problem. The implications of the new data are discussed.

[$^{63}Cu(n,\alpha)^{60}Co$, excitation function, ^{235}U-fission spectrum averaged cross sections, reactor dosimetry, fluence monitor, threshold reactions.]

Introduction

The threshold-reaction $^{63}Cu(n,\alpha)^{60}Co$ is very suitable for long-term fast neutron flux integration for the response range $E_n > 4.7$ MeV. Its importance in reactor dosimetry programs, especially for light water reactor pressure vessel surveillance has been indicated in several articles.[1] As was noted in several review papers (see e.g. Refs. [2,3]) this reaction represented a typical example of differential-integral inconsistencies. The ^{235}U thermal neutron fission spectrum averaged cross section as obtained from integral measurements was ~40% higher than the value calculated from existing differential data. To solve this discrepancy a new effort was undertaken to remeasure the excitation function from threshold to about 10 MeV, the region of most significant response in a fission spectrum. Averaged cross sections have been derived based on the results from this work. These are compared with a new evaluation of reported experimental integral data.

Measurement and Evaluation of the $^{63}Cu(n,\alpha)^{60}Co$ Excitation Function

The $^{63}Cu(n,\alpha)^{60}Co$ cross section has been measured from ~3 MeV to 10 MeV by activation relative to the well known $^{238}U(n,f)$ cross section using a fission chamber as neutron fluence monitor. The reactions $^{7}Li(p,n)^{7}Be$ and $D(d,n)^{3}He$ served as source reactions. The induced ^{60}Co activity was measured with a high-sensitivity detector configuration using two 3- × 3-in. NaI(Tl)-detectors to surround the sample. The counting was performed in an extremely low background facility. Details of this measurement will be published elsewhere.[4] The new results differ significantly from the previously reported data[5] (which were the basis for the ENDF/B-IV evaluation) in the region near threshold below 6 MeV, and around 10 MeV. Below 5 MeV the new measured values agreed very well with the ENDF/B-V[6] evaluation.

For the calculation of the ^{235}U fission spectrum averaged cross section $\langle\sigma\rangle_{U5}$ an estimate had to be made for neutron energies above 10 MeV. Figure 1 shows the excitation function for the $^{63}Cu(n,\alpha)^{60}Co$ reaction, which was used to calculate the fission spectrum averaged cross section $\langle\sigma\rangle^{Cu}_{U5}$ (solid line). Table I provides numerical values. Below 5 MeV the ENDF/B-V representation was taken. Between 5 MeV and 10 MeV, the results of our recent measurements were used. Above 13 MeV the ENDF/B-V representation was chosen as it is close to the result of a precise 14 MeV measurement;[7] our estimate assumes that the shape of the original Paulsen[5] data is correct in this energy region. The interpolation between 10 and 13 MeV is guided by an evaluation by Benzi et al.[8] Table II summarizes the effect of uncertainties in the assigned cross section and in the energy scale on the calculation of $\langle\sigma\rangle^{Cu}_{U5}$. An additional error in the calculated $\langle\sigma\rangle^{Cu}_{U5}$, which arises from the uncertainty in the chosen fission neutron spectrum representation, was estimated to be 4.5%. It was obtained from the variation of the result observed when using different spectrum representations (see Table III). These three error contributions were added quadratically.

TABLE I. The estimated $^{63}Cu(n,\alpha)^{60}Co$ cross section as used in the present work for the energy region where it differs from ENDF/B-V.

E_n (MeV)	σ (mb)	E_n (MeV)	σ (mb)
5.0	1.48	9.0	25.6
5.5	3.15	9.9	30.0
6.0	5.5	10.3	31.9
6.5	9.0	11.0	36.5
7.0	11.8	11.5	39.6
7.5	15.0	12.0	43.0
8.0	18.4	12.5	44.6
8.3	20.6	12.75	45.1
8.5	22.0	13.0	45.52
8.7	23.8		

Interpolation law:

5.0 - 8.0 MeV σ linear in E_n
8.0 - 13.0 MeV log σ linear in E_n

TABLE II. Effect of the uncertainties in the normalization of the $^{63}Cu(n,\alpha)^{60}Co$ cross section ($\Delta\sigma$) and of the uncertainty in the definition of the neutron energy scale (ΔE_n)on the uncertainty of the calculated fission spectrum averaged cross section $\langle\sigma\rangle_{U5}$, given for the present evaluation and the ENOF/B-V Watts - representation of the ^{235}U fission spectrum.

E_n(MeV)	Response in U-5 Spectrum (%)	Normalization $\frac{\Delta\sigma}{\sigma}$ (%)	Normalization $\frac{\Delta\langle\sigma\rangle}{\langle\sigma\rangle}$ (%)	Energy scale ΔE_n (MeV)	Energy scale $\frac{\Delta\langle\sigma\rangle}{\langle\sigma\rangle}$ (%)
2.1 - 3.8	0.8	50[a]	0.4	--	negligible
3.8 - 5.0	7.4	8[b]	0.6	0.025	0.360
5.0 - 6.5	28.6	7.2[b]	2.1	0.020	0.663
6.5 - 10.0	53.9	6.7[b]	3.6	0.018	0.386
10.0 - 14.0	8.9	20	1.8	--	negligible
14.0 - 20.0	0.4	10	negligible	--	negligible
total response range	100.0		8.5		1.4

[a] estimate
[b] based on recent experimental data

Our final result (determined using the present differential cross section data and the ENDF/B-V Watts spectrum representation for the ^{235}U thermal neutron fission spectrum) for the calculated spectrum averaged cross section for the reaction $^{63}Cu(n,\alpha)^{60}Co$ is

$$\langle\sigma\rangle^{Cu}_{U5,calc.} = 0.507 \pm 0.049 \text{ mb } (\pm 9.7\%)$$

* Work supported by the U. S. Department of Energy.
** Permanent Address: Institut fuer Radiumforschung und Kernphysik, Boltzmanngasse 3, A-1090 Vienna, Austria.

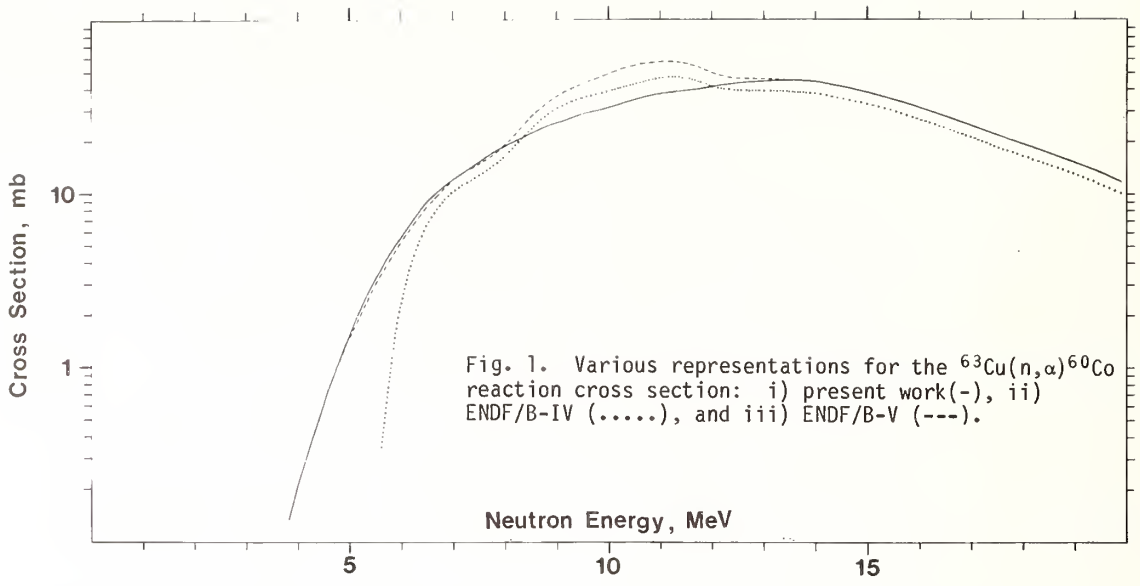

Fig. 1. Various representations for the $^{63}Cu(n,\alpha)^{60}Co$ reaction cross section: i) present work(-), ii) ENDF/B-IV (.....), and iii) ENDF/B-V (---).

Figure 2 demonstrates the change of the response in a fission spectrum when two other cross section evaluations are used for this reaction (ENDF/B-IV yields 0.364 mb, and ENDF/B-V yields 0.557 mb for $\langle\sigma\rangle^{Cu}_{U5,calc}$).

Reevaluation of the Experimental Integral Data Base for $^{63}Cu(n,\alpha)^{60}Co$

Concept. The average cross section for the reaction $^{63}Cu(n,\alpha)^{60}Co$ (denoted as Cu in the following) in a pure ^{235}U-fission spectrum (U5) may be expressed by the following identity

$$\langle\sigma\rangle^{Cu}_{U5} = \frac{\dfrac{\langle\sigma\rangle^{Cu}_{U5}}{\langle\sigma\rangle^{X}_{U5}}}{\dfrac{\langle\sigma\rangle^{Cu}_{\phi}}{\langle\sigma\rangle^{X}_{\phi}}} \times \frac{\langle\sigma\rangle^{Cu}_{\phi}}{\langle\sigma\rangle^{X}_{\phi}} \times \langle\sigma\rangle^{X}_{U5} \qquad (1)$$

The upper indices denote the type of reaction (Cu and some other threshold reaction, X, respectively), the lower indices denote the neutron field (U5 and some other arbitrary neutron field, ϕ, respectively).

Equation (1) may be rewritten as

$$\langle\sigma\rangle^{Cu}_{U5} = \frac{R^{Cu,X}_{U5}}{R^{Cu,X}_{\phi}} \times R^{Cu,X}_{\phi} \times \langle\sigma\rangle^{X}_{U5} \qquad (2)$$

where the quantities R are reaction rate ratios,

or $$\langle\sigma\rangle^{Cu}_{U5} = D^{Cu,X}_{U5,\phi} \times R^{Cu,X}_{\phi\ exp} \times \langle\sigma\rangle^{X}_{U5} \qquad (3)$$

where the double ratio $D^{Cu,X}_{U5,\phi} = \beta$ can be interpreted as a spectrum shape adjustment factor, $R^{Cu,X}_{\phi\ exp}$ can be taken as the experimental reaction rate ratio measured in a certain neutron field ϕ (e.g. in a reactor) in a specific experiment and $\langle\sigma\rangle^{X}_{U5}$ can be considered the cross section of a reference reaction in a U5-spectrum.

Equation (3) was used to renormalize the existing experimental data base. We selected a set of reference threshold reactions whose response ranges bracket the response range of $^{63}Cu(n,\alpha)^{60}Co$. The

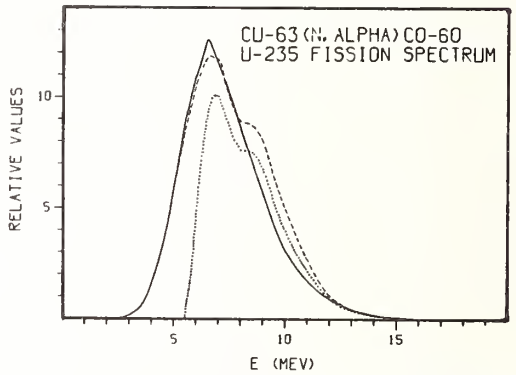

Fig. 2. Plots of $\sigma\phi$ for various representations of the $^{63}Cu(n,\alpha)^{60}Co$ differential cross section and the ENDF/B-V Watts representation for the pure ^{235}U therma neutron fission spectrum. The response functions show are: i) present evaluation (-), ii) ENDF/B-IV (....), and iii) ENDF/B-V (---).

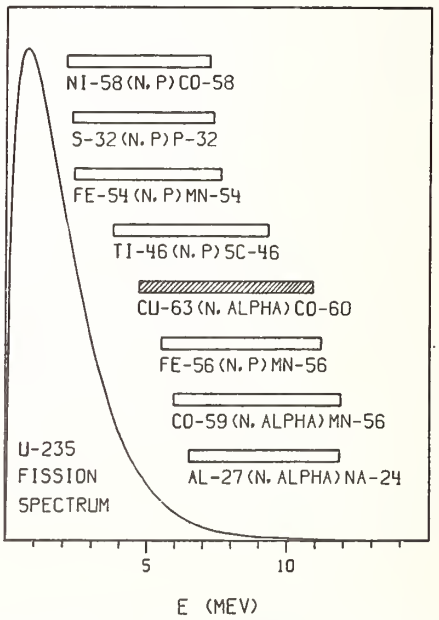

Fig. 3. The threshold reactions that were used for renormalizing the existing integral data, and their respective response ranges in a ^{235}U fission spectrum.

TABLE III. Calculated ^{235}U-Fission Spectrum Averaged Cross Sections $\langle\sigma\rangle_{U5}$(mb) and Cross Section Ratios $R^{Cu,X}_{U5} = \langle\sigma\rangle^{Cu}_{U5}/\langle\sigma\rangle^{X}_{U5}$ Obtained Using Different Spectrum Representations: ENOF/B-V Watts, NBS Segments Adjusted,[23] NBS Reference Maxwellian ($E_{Average}$ = 1.97 MeV), and ENOF/B-IV Maxwellian ($E_{Average}$ = 1.98 MeV). For the Differential Cross Section Data, the ENOF/B-V Version was Used for the Threshold Reactions $^{58}Ni(n,p)^{58}Co$ Through $^{27}AL(n,\alpha)^{24}Na$, Which were Used in the Renormalization of the Existing Experimental Integral Data for $^{63}Cu(n,\alpha)^{60}Co$. The Values Given for the Reaction $^{63}Cu(n,\alpha)^{60}Co$ are Based on an Estimate of the Differential Cross Section. The Response Ranges Given were Derived Using the ENOF/B-V Watts Spectrum Representation.

			FISSION SPECTRUM REPRESENTATION[d]										
			ENOF/B-V Watts		NBS Segments Adjusted		NBS Reference Maxwellian		ENOF/B-IV Maxwellian				
Threshold Reaction	Category Status	5% - 95% Response Range (MeV)	$\langle\sigma\rangle_{U5}$	$R^{Cu,X}_{U5}$	$\langle\sigma\rangle_{U5}$	$R^{Cu,X}_{U5}$	$\langle\sigma\rangle_{U5}$	$R^{Cu,X}_{U5}$	$\langle\sigma\rangle_{U5}$	$R^{Cu,X}_{U5}$	$\Delta\langle\sigma\rangle^{a}_{U5}$(%)	$\langle\sigma\rangle^{c}_{U5}$ Exp.	
$^{58}Ni(n,p)$	I-Cand.	2.13- 7.20	104.9*	0.004836	100.9	0.004875	99.72	0.005204	100.6	0.005269	5.0	108.5	± 5.%
$^{32}S(n,p)^{b}$	I-Cand.	2.29- 7.35	66.80*	0.007594	64.09	0.007679	63.30	0.008197	63.87	0.008300	5.5	66.8	± 5.5%
$^{54}Fe(n,p)$	I-Cand.	2.35- 7.59	80.98*	0.006265	77.80	0.006323	76.88	0.006749	77.63	0.006829	5.2	79.7	± 6.1%
$^{46}Ti(n,p)$	II	3.75- 9.3	11.16*	0.04546	10.81	0.04550	10.88	0.04769	11.05	0.04797	8.6	11.8	± 6.4%
$^{56}Fe(n,p)$	I	5.48-11.17	1.035*	0.4901	1.005	0.4895	1.072	0.4840	1.096	0.4837	7.3	1.035	± 7.2%
$^{59}Co(n,\alpha)$	I-Cand.	5.95-11.90	0.1496	3.391	0.1447*	3.399	0.1604	3.235	0.1645	3.222	10.2	0.143	± 7.0%
$^{27}AL(n,\alpha)$	I	6.48-11.85	0.7187*	0.7059	0.6927*	0.7107	0.7798	0.6654	0.8008	0.6620	11.4	0.705	± 5.7%
$^{63}Cu(n,\alpha)$	II	4.67-10.90	0.5073*	1.0	0.4919*	1.0	0.5189	1.0	0.5301	1.0	9.7	0.500	± 11.2%

[a]Estimated uncertainty of the calculated Spectrum averaged cross sections when using the ENOF/B-V Watts ^{235}U-fission spectrum representation, including also uncertainties in the differential cross sections.

[b]Presently in ENOF/B-IV only.

[c]Evaluated experimental data taken from a recent review of microscopic integral cross section data by Fabry et al.[10]

[d]A star indicates which of the calculated cross sections is closest to the evaluated experimental integral data in the last column. A star in both columns indicates both values are equally close.

set was limited so that all response ranges (5% - 95% response in a U5 fission spectrum) were above 2 MeV. In this region the neutron fields of most of the irradiation facilities used for integral experiments exhibit spectra with shapes rather close to a pure U5-spectrum. The list of reactions selected appears in Fig. 3 (or Table III), with the respective response ranges indicated. Figure 4 demonstrates the similarity of the response for three obviously different fast-neutron spectra in the case of the $^{63}Cu(n,\alpha)^{60}Co$ reaction. The double ratio β should therefore be approximately 1 (exactly 1 for $\phi \equiv U5$). There are two possible choices of data sets to be used for the $\langle\sigma\rangle^{X}_{U5}$ integral reference cross sections:

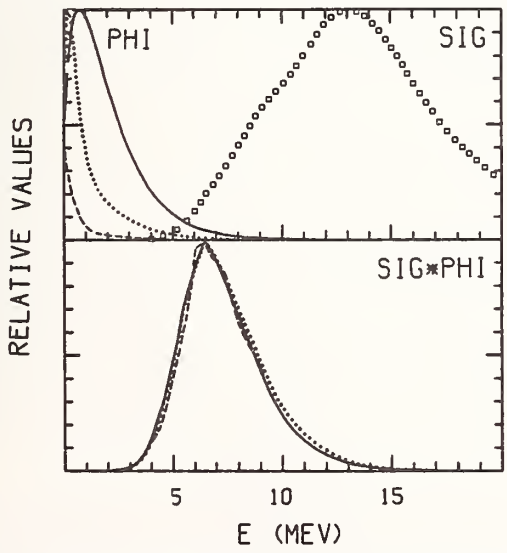

Fig. 4. Present estimation of the $^{63}Cu(n,\alpha)^{60}Co$ cross section (□ □ □□), and the spectra σ and response function σφ for $^{63}Cu(n,\alpha)^{60}Co$ applicable for three noticeable different fast neutron spectra i) pure ^{235}U thermal fission (-), ii) the YAYOI fast reactor (.....) and iii) the Mol ∑∑ facility (---). Note the similarity of the response functions. This implies that the $^{63}Cu(n,\alpha)^{60}Co$ reaction is sensitive only to the high-energy portions of these spectra and that they are all quite similar in shape.

calculated values based on evaluated differential data for the reaction X, or values from evaluated experimental integral data. Since all the reactions considered in Fig. 3 (or Table III), with the exception of $^{46}Ti(n,p)^{46}Sc$, are Category I reactions or Category I candidates (see ref. 9 for a definition) and since ENDF/B-V seems to give a reasonably reliable representation of the real U5-spectrum (at least for the higher energy region considered here), we decided to use $\langle\sigma\rangle^{X}_{U5}$ cross sections based on differential data and the ENDF/B-V Watts spectrum representation of the U5 spectrum as the reference cross sections. The information in Table III offers some justification for this choice. Calculated $\langle\sigma\rangle^{X}_{U5}$'s dependent on different spectrum representations are compared in Table III and the results of a recent evaluation of experimental in-

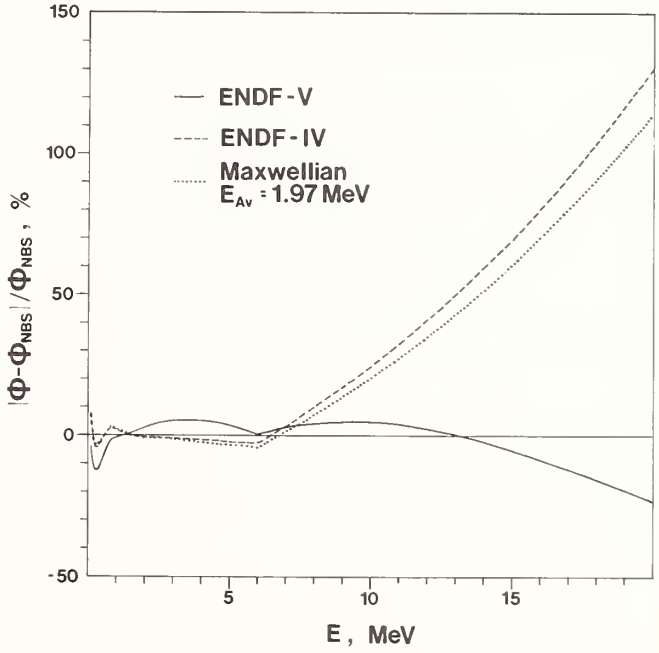

Fig. 5. Comparison of various representations of the ^{235}U-fission neutron spectrum. $[\int_0^\infty \phi(E)dE = 1$ for all representations of $\phi(E)]$.

tegral data by Fabry et al.[10] are also presented. The agreement between calculated values for $\langle\sigma\rangle_{U5}$ using the ENDF/B-V Watts spectrum representation and Fabry's values is better than 6% for all reference reactions considered, (better than 5% if $^{46}Ti(n,p)^{46}Sc$ is excluded). We included the reaction $^{46}Ti(n,p)^{46}Sc$, because considerable data were available for this reaction, and its inclusion turned out not to bias our evaluated result. The change of $\langle\sigma\rangle^{X}_{U5}$ with different representations of the U5-spectrum can be explained by differences in the spectral shapes of the various representations as shown in Fig. 5. To investigate the degree to which the spectral shape correction factor, β, might be expected to deviate from 1.0, double reaction rate ratios were calculated for several obviously different reference neutron spectra and for various representations of the U5-fission spectrum. The values obtained for β did not deviate from unity by more than 10% as seen in Table IV. Table V shows $\langle\sigma\rangle^{Cu}_{\phi}$ values calculated for various neutron fields based on our estimate of the $^{63}Cu(n,\alpha)^{60}Co$ differential cross section. Since there is clearly a non-negligible effect on β attributed to uncertainty in knowledge of the pure U5 spectrum, no attempt was made to calculate and use β-values for the renormalization according to equation (1)-(3), even in instances when there was some information available about the neutron spectrum used in a specific measurement. The β-values were taken as 1.0 and the uncertainty of this assumption was estimated by considering the spread of double reaction rate ratios that can be calculated using the reported reaction rates or integral cross sections for $^{63}Cu(n,\alpha)^{60}Co$ and the others of the list of the chosen reference reactions (to the extent that there were values available from specific data sets). This survey also provided a test of the spectral purity (relative to a U5-fission spectrum) for the spectra relevant to the various data sets considered in this evaluation.

TABLE IV. Calculated Double Ratios $C^{Cu,X}_{U5,\phi} = R^{Cu,X}_{U5}/R^{Cu,X}_{\phi}$. These are Ratios of the Spectrum Averaged Cross Sections of the Reaction $^{63}Cu(n,\alpha)^{60}Co$ to the Reaction Specified in a Pure ^{235}U Thermal Neutron Fission Spectrum (Given by the ENDF/B-V Watts Representation) Relative to the Ratios for the Same Reaction Pair in Several Reference Neutron Fields.[23] For the Differential Cross Sections, the ENDF/B-V Version was Used for $^{58}Ni(n,p)^{58}Co$ Through $^{27}AL(n,\alpha)^{24}Na$ Except for $^{32}S(n,p)$, where only ENDF/B-IV is available, and for the Reaction $^{63}Cu(n,\alpha)^{60}Co$ the New Evaluation was Used.

Threshold Reaction	Spectrum Representation							
	BIG 10	MOL-⅀⅀	CFRMF	YAYOI	NBS Segm. Adj.	NBS Ref. Maxw.	ENDF/B-IV Maxw.	ENDF/B-V Watts
$^{58}Ni(n,p)$	0.9281	1.056	0.9591	0.9798	0.9920	0.9294	0.9178	1.0
$^{32}S(n,p)$	0.9140	1.042	0.9458	0.9741	0.9890	0.9264	0.9150	1.0
$^{54}Fe(n,p)$	0.9139	1.032	0.9444	0.9732	0.9908	0.9281	0.9174	1.0
$^{46}Ti(n,p)$	0.9269	0.9640	0.9463	0.9725	0.9990	0.9531	0.9476	1.0
$^{56}Fe(n,p)$	1.019	1.017	1.015	1.007	1.001	1.013	1.013	1.0
$^{59}Co(n,\alpha)$	1.076	1.024	1.046	1.031	0.9975	1.048	1.052	1.0
$^{27}AL(n,\alpha)$	1.097	1.023	1.058	1.040	0.9940	1.061	1.066	1.0
Average	0.9821	1.035	0.9878	0.9968	0.9954	0.9800	0.9755	1.0

TABLE V. Calculated Spectrum Average Cross Sections $\langle\sigma\rangle\phi$ (mb) for Different Reference Reactor Spectra ϕ and for the Pure ^{235}U Thermal Neutron Fission Spectrum (U5) Using the ENDF/B-V Watts Representation

Threshold Reaction	Reference Neutron Fields				U5 ENDF/B-V Watts	Differential Data From
	8IG 1D	MDL-⅀⅀	CFRMF	YAYDI		
$^{58}Ni(n,p)$	16.D1	23.18	23.52	55.13	1D4.9	ENDF/B-V
$^{32}S(n,p)$	1D.D4	14.57	14.77	34.9D	66.8D	ENDF/B-IV
$^{54}Fe(n,p)$	12.17	17.5D	17.88	42.27	8D.98	ENDF/B-V
$^{46}Ti(n,p)$	1.7D1	2.252	2.469	5.821	11.16	ENDF/B-V
$^{56}Fe(n,p)$	D.1735	D.22D3	D.2457	D.5592	1.D35	ENDF/B-V
$^{59}Co(n,\alpha)$	D.D2648	D.D32D7	D.D3658	D.D8279	D.1496	ENDF/B-V
$^{27}AL(n,\alpha)$	D.1297	D.1539	D.1778	D.4D1D	D.7187	ENDF/B-V
$^{63}Cu(n,\alpha)$	D.D8342	D.1D62	D.1186	D.2721	D.5D73	This Work

Results. Table VI summarizes the results from the evaluation procedure. In addition to the original $^{63}Cu(n,\alpha)^{60}Co$ cross sections, the table includes the original results reported for other reactions (X) from our list of reference reactions (Table III) as far as there were values available for each individual author. For each author all possible ratios $R^{Cu,X}_{exp}$ were formed and multiplied by $\langle\sigma\rangle^{X}_{U5}$ (calculated using the ENDF/B-V spectrum representation) to get as many renormalized cross sections for $^{63}Cu(n,\alpha)^{60}Co$ as there were data available for the reference reactions. The averages of these various values are given in column 4 as averaged renormalized $\langle\sigma\rangle^{Cu}_{U5}$ derived from specific authors. The assigned uncertainty includes essentially three contributions which were added in quadrature: δ_1 was obtained from the scattering of the renormalized values for $\langle\sigma\rangle^{Cu}_{U5}$ based on different reference reactions (in cases where more than two reference reactions could be used); otherwise the estimated uncertainties $\Delta\langle\sigma\rangle_{U5}$ from column 12 in Table III were applied; δ_2 accounts for the error in the originally reported $\langle\sigma\rangle^{Cu}_{exp}$ for the reaction $^{63}Cu(n,\alpha)^{60}Co$, which shows up in an uncertainty in $R^{Cu,X}_{\phi\ exp}$; δ_3 accounts for possible deviations of β from unity; this was taken as 10% for most cases. A larger error was assumed wherever the spread of the double ratios indicated a larger uncertainty. For Fabry's work,[18] an uncertainty of only 4% was assumed. For this latter author a spread of this magnitude was obtained when considering the double ratios from all his reported reactions except for $^{63}Cu(n,\alpha)^{60}Co$. If this copper reaction is considered, we obtain a spread of about 8.5%. Apparently, the cross sections reported by Fabry[18] are relatively consistent among one another except for the value for $^{63}Cu(n,\alpha)^{60}Co$. Since this was the only investigation involving measurements with a Uranium converter (which provides a spectrum which is indeed very close to a pure ^{235}U thermal neutron fission spectrum) the 4% uncertainty was retained. Care was taken to consider only those measurements for a given facility which were apparently all made under the same conditions. If for a specific author, one reaction provided a double ratio which was off from 1.0 more than 25%, this reaction was not considered in the evaluation. If such deviations were observed for more than one reaction or for the standard reaction used by a specific work, this work was not included in the evaluation or in Table VI (Refs. 21 and 22). The

TABLE VI. The Experimental Fission Spectrum Averaged Cross Sections for the Reaction $^{63}Cu(n,\alpha)$ as Taken from the Literature and the Averaged Renormalized Values as Derived from Experimental $\langle\sigma\rangle$-Ratios to Other Reactions.

$\langle\sigma\rangle^{exp}$ (mb) for $^{63}Cu(n,\alpha)$	Reference	$\langle\sigma\rangle_{exp}$ (mb) for Other Reactions	Averaged Renormalized $\langle\sigma\rangle_{U5}$ for $^{63}Cu(n,\alpha)$	Error Contributions (%)		
				δ_2	δ_2	δ_3
0.54 ± 0.07	Nilsson 1963[11]	$^{58}Ni(n,p)$ 101	0.561 ± 0.095	5	13	10
0.42	Hogg + Weber 1963[12]	$^{27}AL(n,\alpha)$ 0.57	0.535 ± 0.091	8.5	10[a]	10
		$^{58}Ni(n,p)$ 90 ± 1[b]				
		$^{54}Fe(n,p)$ 65 ± 1.5[b]				
		$^{46}Ti(n,p)$ 9.0 ± 0.1[b]				
		$^{56}Fe(n,p)$ 0.71				
0.45 ± 0.05	Clare + Martin 1964[13]	$^{54}Fe(n,p)$ 56	0.479 ± 0.077	5	11	10
0.44	Lloret 1965[14]	$^{58}Ni(n,p)$ 90.6	0.537 ± 0.086	7	10[a]	10
0.52 ± 0.04	Fabry + Deworm 1966[15]	$^{56}Fe(n,p)$ 68.5 ± 3.8	0.587 ± 0.112	7	7.7	16
		$^{46}Ti(n,p)$ 10.4 ± 0.05				
0.382 ± 0.036	Nasyrov 1968[16]	$^{58}Ni(n,p)$ 96 ± 13	0.445 ± 0.080	6	9.5	14
		$^{54}Fe(n,p)$ 67 ± 9				
		$^{46}Ti(n,p)$ 9.30 ± 0.73				
		$^{56}Fe(n,p)$ 0.96 ± 0.09				
		$^{27}AL(n,\alpha)$ 0.58 ± 0.0[c]				
0.10/0.090/ 0.086/0.049[c]	Oudey + Heinrich 1970[17]	$^{58}Ni(n,p)$ 23/22/2010[c]	0.509 ± 0.086	9	11	10
		$^{54}Fe(n,p)$ 16/16/13/7.3[c]				
		$^{46}Ti(n,p)$ 2.0/2.0/1.7/0.93[c]				
0.66 ± 0.06	Fabry 1970, 1972[18]	$^{58}Ni(n,p)$ 120 ± 6	0.592 ± 0.061	2.7	9.1	4
		$^{32}S(n,p)$ 73 ± 3				
		$^{54}Fe(n,p)$ 89 ± 5				
		$^{46}Ti(n,p)$ 13.0 ± 0.6				
		$^{56}Fe(n,p)$ 1.15 ± 0.04				
		$^{27}AL(n,\alpha)$ 0.78 ± 0.03				
0.402	McElroy et al., 1972[19]	$^{58}Ni(n,p)$ 81.1	0.500 ± 0.075	5.2	10	10
		$^{32}S(n,p)$ 52.6				
		$^{54}Fe(n,p)$ 61.0				
		$^{46}Ti(n,p)$ 9.21				
		$^{56}Fe(n,p)$ 0.902				
		$^{27}AL(n,\alpha)$ 0.591				
0.484 ± 0.034	Kobayashi et al., 1976[20]	$^{58}Ni(n,p)$ 102	0.522 ± 0.063	5.6	7	8
		$^{27}AL(n,p)$ 0.644				
		$^{46}Ti(n,p)$ 10.9 ± 0.59				
		$^{59}Co(n,\alpha)$ 0.131 ± 0.0061				

[a] Assumed error.

[b] Standard deviations only.

[c] Values for different rows of the EBR-2.

weighted average of the averaged renormalized integral cross sections for the reaction $^{63}Cu(n,\alpha)^{60}Co$ is:

$$\langle\sigma\rangle^{Cu}_{U5\ eval.} = 0.534 \pm 0.015$$

The error given is the standard deviation of the weighted average.[24] The result is illustrated and compared with the calculated value based on the new differential cross section data of this work in Fig. 6. If the renormalization of the integral data is accomplished in the same way as outlined above, except that the evaluated integral cross sections of Fabry et al.[10] for the reference reactions (as given in column 13 of Table III) are used instead of the values of column 4 of Table III, then the result for the weighted average of the averaged renormalized integral cross sections for the reaction $^{63}Cu(n,\alpha)^{60}Co$ would be:

$$\langle\sigma\rangle^{Cu}_{U5\ eval.} = 0.540 \pm 0.016$$

which is only 1.1% larger than the value resulting from the renormalization procedure based on differential data.

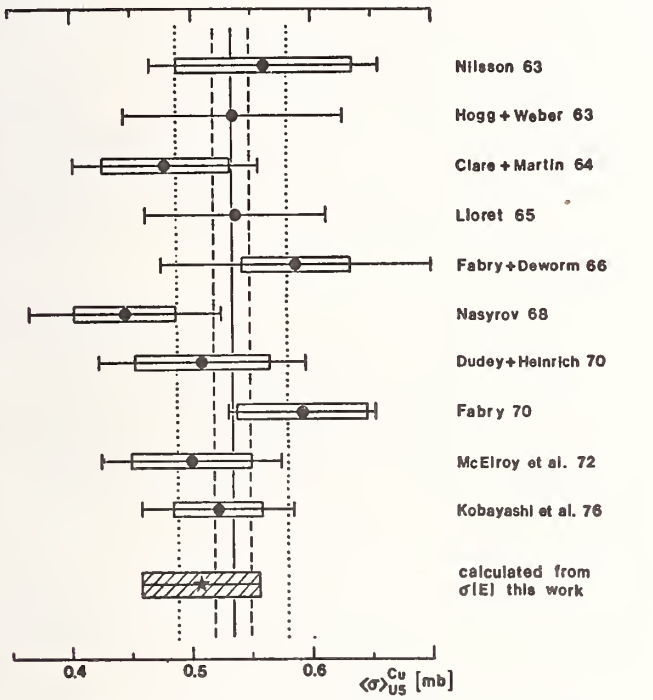

Fig. 6. Results of the evaluation of the experimental integral data base for the reaction $^{63}Cu(n,\alpha)^{60}Co$, compared with the calculated result based on the representation of the differential cross section used in the present work. The full vertical line shows the weighted average of the renormalized ^{235}U fission spectrum averaged cross sections $\langle\sigma\rangle^{Cu}_{U5}$ from the literature; the dashed lines show the standard deviation of the weighted average, and the dotted lines the standard deviation of the whole data set.

Conclusions

Comparing the ^{235}U thermal neutron fission spectrum averaged cross section for the reaction $^{63}Cu(n,\alpha)^{60}Co$, as derived from a new measurement of the excitation function from threshold to ~10 Mev, with the result of a reevaluation of the integral experimental data, shows that the discrepancy between differential and integral data for the reaction $^{63}Cu(n,\alpha)^{60}Co$ has been eliminated. In fact the reaction $^{63}Cu(n,\alpha)^{60}Co$ now fulfills the condition for a Category I reaction.

The Watts representation of the ^{235}U fission spectrum as given by ENDF/B-V seems to work very well in the energy region investigated (2.5 - 11.0 MeV). For the higher energy region (above 6 MeV) possibly the NBS segment-adjusted representation might give better consistency overall.

The authors are of the opinion that when dealing with threshold reaction data it is preferable to use only data of other threshold reactions as references so that the response ranges will not differ too much. Global renormalizations (which also include nonthreshold reactions) as used by Fabry[18] are afflicted with the problem that they are more sensitive to lower energy parts of the neutron spectrum than to the response region of the threshold reactions, a fact that has been pointed out by Kobayashi et al.[20].

References

1. Proceedings of the Second ASTM-EURATOM Symp. on Reactor Dosimetry, Dosimetry Methods for Fuels, Cladding, and Structural Materials, held at Palo Alto, California, Oct. 3-7, 1977. NUREG/CP-0004, Vols. 1, 2, and 3; see contributions by W. N. McElroy et al., Vol. 1, p. 17, A. Alberman et al., Vol. 1, p. 145, C. G. Martin, Jr., Vol. 1, p. 229, G. Bartholomé et al., Vol. 1, p. 285, L. Steward, Vol. 2, p. 843, F. J. Rahn et al., Vol. 3, p. 1069, and L. S. Anderson, Vol. 3, p. 1093.
2. M. F. Vlasov, A. Fabry, and W. N. McElroy, "Status of neutron cross sections for reactor dosimetry," INDC (NDS)-84/L+M, Nuclear Data Section, IAEA, Vienna (1977) or Proc. Int. Conf. Interactions of Neutrons with Nuclei, July 6-9, 1976, Lowell, Massachusetts, USA, CONF-760715, Vol. 2, p. 1186.
3. W. L. Zijp, "On the consistency between integral and differential cross section data, Proc. Advisory Group Meeting on Nuclear Data for Reactor Dosimetry," Vienna, 13-17 Nov. 1978, INDC (NDS)-103/M, Nuclear Data Section, IAEA, Vienna (1979).
4. G. Winkler, D. L. Smith, and J. W. Meadows, to be published.
5. A. Paulsen, Nucleonik 10, 91 (1967); see also H. Liskien and A. Paulsen, Nukleonik 8, 315 (1966) and A. Paulsen, Z. Phys. 205, 226 (1967).
6. Evaluated Neutron Data Files ENDF/B-IV and ENDF/B-V, National Nuclear Data Center, Brookhaven National Laboratory, Upton, New York (1976 and 1979); ENDF/B-IV Dosimetry File, ed. B. A. Magurno, BNL-NCS-50446, Brookhaven National Laboratory (1975).
7. G. Winkler, Nucl. Sci. Eng. 67, 260 (1978).
8. V. Benzi, N. Iliescu, E. Menapace, M. Motta, and M. Vaccari, Evaluation accepted as DFN 68I of the UK Nucl. Data Library, documented in CEC(74)5 and CEC(74)9, Oct. and Dec. 1974, Commitato Nazionale Energia Nucleare, Centro di Calcolo, Bologna.
9. M. F. Vlasov, editor, IAEA Consultants Meeting on Integral Cross Section Measurements in Standard Neutron Fields, held at Vienna, Nov. 15-19, 1976, INDC (NDS)-81/L+M, Nuclear Data Section, IAEA, Vienna (1978).
10. A. Fabry, W. N. McElroy, L. S. Kellogg, E. P. Lippincott, J. A. Grundl, D. M. Gilliam, and G. E. Hansen, "Review of Microscopic Integral Cross Section Data in Fundamental Reactor Dosimetry Benchmark Neutron Fields", Contribution to "Neutron Cross Sections for Reactor Dosimetry", IAEA-208, Vol. I., p. 233, Nuclear Data Section, IAEA, Vienna (1978).
11. R. Nilsson, Neutron Dosimetry (Proc. Symp. Harwell, 1962), 2, IAEA Vienna (1963)275.
12. C. H. Hogg, L. D. Weber, Symp. on Radiation Effects on Metals and Neutron Dosimetry (Proc. Symp. Los Angeles, 1962), American Society for Testing Materials (1963) 133.
13. M. D. Clare and W. H. Martin, J. Nucl. Energy A/B 18 (1964) 703.
14. R. Lloret, EANDC(E)-57U, p. 172 (1965).
15. A. Fabry and J. P. Deworm, EANDC(E)-66U, p. 125 (1966).
16. F. Nasyrov, Atomnaya Energiya 25 (1968) 437, engl. transl. Soviet J. At. Energy 25 (1968) 1251.
17. N. D. Dudey and R. R. Heinrich, Flux-Characterization and neutron-cross-section studies in E3R-II, ANL-7629, Argonne National Laboratory (1970).
18. A. Fabry, M. Decoster, G. DeLeeuw, S. DeLeeuw, J. C. Schepers, and P. Vandeplas, Highlights in the Belgian Contribution to Clean Integral Measurements for Fast Neutron Physics, Proceedings of the Russian-Dutch-Belgian meeting on Fast Reactor Physics, Melekess, 23-27 February (1970); A. Fabry, "Evaluation of Microscopic Integral Cross Sections Averaged in a ^{235}U Thermal Fission Neutron Spectrum", BLG-465, Centre d'Etude de l'Energie Nucleaire, Bruxelles, (1972).
19. W. N. McElroy, R. J. Armani and E. Tochilin, Nucl. Sci. Eng. 48 (1972) 51.
20. K. Kobayashi, I. Kimura, M. Nakazawa and M. Akiyama, Journal of Nuclear Science and Technology 13 (1976) 531.
21. R. S. Rochlin, Nucleonics 17, No. 1 (1959) 54.
22. R. L. Ritzman, R. Lieberman, J. F. Kirchner and D. N. Sunderman, Symp. on Radiation Effects on Metals and Neutron Dosimetry (Proc. Sym. Los Angeles, 1962), American Society for Testing Materials (1963)141.
23. J. Grundl and C. Eisenhauer, "Benchmark Neutron Fields for Reactor Dosimetry", Contribution to Neutron Cross Sections for Reactor Dosimetry, IAEA-208, Vol. I. p. 53, Nuclear Data Section, IAEA, Vienna (1978).
24. S. Wagner, Auswertung von Beobachtungen, in F. Kohlrausch, Praktische Physik, Bd. 1, 22. Aufl., p. 41, G. Lautz and R. Taubert, Eds., Teubner, Stuttgart (1968).

VITAMIN E: A MULTIPURPOSE ENDF/B-V COUPLED NEUTRON-GAMMA CROSS SECTION LIBRARY

J. Barhen, D. G. Cacuci, W. E. Ford III, R. W. Roussin, J. J. Wagschal[†], C. R. Weisbin, J. E. White, R. Q. Wright

Oak Ridge National Laboratory
Oak Ridge, Tennessee 37830, USA

[†]On leave from The Hebrew University, Jerusalem, Israel.

The U. S. Department of Energy (DOE) Office of Fusion Energy (OFE) and the Division of Reactor Research and Technology (DRRT) jointly sponsored the development of a coupled fine-group cross section library [VITAMIN-C]. The experience gained in the generation, validation and utilization of the VITAMIN-C library along with its broad range of applicability has led to the request for updating this data set using ENDF/B-V. Additional support in this regard has been provided by the Defense Nuclear Agency (DNA) and by EPRI in support of weapons analyses and light water reactor shielding and dosimetry problems, respectively. The rationale for developing the multipurpose ENDF/B-V based VITAMIN-E library is presented, with special emphasis on new models used in the data generation algorithms. The library specifications and testing procedures are also discussed in detail. The distribution of the VITAMIN-E library is currently subject to the same restrictions as the distribution of the ENDF/B-V data.

[Multigroup Cross Section Libraries, ENDF/B-V, Fusion Neutronics, LMFBR Analysis, LWR Shielding and Dosimetry, Weapons Applications]

Introduction

The U.S. Department of Energy (DOE) Office of Fusion Energy (OFE) and the Division of Reactor Research and Technology (DRRT) jointly sponsored the development of a coupled fine-group cross section library.[1-4] This 171-neutron, 36-gamma-ray group library was based upon ENDF/B-IV and was intended to be applicable to fusion reactor neutronics and LMFBR core and shield analysis. Versions of the library are available from the Radiation Shielding Information Center (RSIC) at the Oak Ridge National Laboratory in both AMPX (DLC-41/VITAMIN-C) and CCCC (DLC-53/VITAMIN-4C) formats. Computer codes for energy group collapsing, interpolation on Bondarenko factors for resonance self-shielding and temperature corrections, and various other useful data manipulations are also available via the PSR-63/AMPX-II and PSR-117/MARS packages.

VITAMIN-C has been utilized in a variety of projects at ORNL[5-7] and at other organizations.[8-10] The experience gained in the generation, validation, and utilization of this library along with its broad range of applicability has led to the request for updating this data set using ENDF/B-V. Additional support in this regard has been provided by the Defense Nuclear Agency (DNA) and by the Electric Power Research Institute (EPRI) in support of weapons analyses and light water reactor shielding and dosimetry problems, respectively. The purpose of this paper is to provide detailed specifications and rationale for the proposed ENDF/B-V update (designated VITAMIN-E) to the VITAMIN-C library, emphasize the changes made to upgrade the data generation algorithms, and discuss the various testing procedures.

Specifications for VITAMIN-E

Materials/Temperatures/Background Cross Sections

All materials on the ENDF/B-V General Purpose file will be processed at 0°, 300°, 900°, and 2100°K. There is a possibility that future Doppler calculations may require higher temperatures for certain selected materials, but this will be treated later on a case-by-case basis. The selection of background cross sections σ_B was modified from VITAMIN-C based upon experience[1,11] and extended to include values of $\sigma_B = 0$ (actually $\sigma_B = 10^{-6}$ is used to avoid problems taking logarithms) and $\sigma_B = 10^{10}$, corresponding to pure concentration and infinite dilution, respectively. The special purpose files (e.g., actinide, dosimetry, activation, etc.) will be processed at room temperature and infinite dilution. The ENDF/B-V fission product library has also been updated; accordingly, the DLC-38/ORYX-E library[12] will be updated with fine-group fission-product cross sections. The ORYX data can be collapsed to the group quantities required by ORIGEN[13] to obtain lumped fission products for fuel calculations. Additional materials not in this issue of ENDF/B include Ar, Ga, and Sn. These will be taken from the ENDL library.[14] All reactions will be processed, including the covariance files.

Group Structure

For the intended range of application (LMFBR core physics and shielding, LWR shielding and dosimetry, weapons analyses, fusion blanket technology), a 174-neutron/37-gamma-ray group structure was adopted. This structure was obtained from the favorably received 171/36 VITAMIN-C specification[2] by making only minor adjustments to formally include energy boundaries of the DNA broad group library[15] and to extend the energy range to ∿ 20 MeV. Synthesis with higher energy libraries (> 20 MeV), primarily for CTR applications, will be performed in a separate step as done previously.[16] Finally, the group boundaries include the break points used to describe the multi-region weighting function. The gamma-ray energy group structure has been extended to 20 MeV and a single minor change to one energy boundary (75 keV → 70 keV) was made, for compatibility with the DNA gamma-ray group structure.

Weighting Function

Several considerations enter into the selection of a smooth weighting function, W(E), to represent the neutron flux spectrum. Experience in Cooperative Processing Methods Testing has shown that the use of a more realistic smooth weighting function would help in assuring computation of proper group constants. In particular, below ∿ 25 keV the weighting function used previously was 1/E while we know that typical LMFBR spectra in this energy range are roughly constant and do not increase with decreasing energy. Similarly, the point at which the 1/E spectrum was joined to the fission spectrum was 821 keV in the VITAMIN-C library, while testing has shown that a higher value might be more reasonable. One must be quite careful with these types of arguments however, since for "typical" shielding situations the flux spectrum is often 1/E and sometimes even $1/E^n$, where $n > 1$. Also, it is perceived that the use of any particular reactor-dependent weighting function may detract from the generality of the resulting shielding factor library. Finally,

built-in spectral corrections (e.g., elastic removal) are intended to account for some of these effects and the associated theories are currently based on a 1/E model.[17] It is also recognized that in special circumstances other sets of weighting functions may be required.

Thus, the weighting function specified in Table I obviously represents a set of compromises which hopefully can provide adequate accuracies over the range of intended applications. Basically, the energy at which the fission spectrum can be smoothly joined to the 1/E spectrum (i.e., where flux/lethargy is constant) is found to be equal to 3/2 of the fission spectrum temperature (taken here as $\theta \simeq 1.4$ MeV). To provide consistency with the selected energy group boundaries, the (1/E)/fission spectrum cutpoint was raised to 2.1225 MeV, a boundary equal to 3/2 θ (θ = 1.415 MeV). Below this energy and above 0.414 eV, the W(E) spectrum is assumed to be 1/E with the knowledge that elastic removal corrections may be used to improve estimates of flux shapes. Shielding and thermal reactor problems also favor this shape. It should also be noted whereas the Maxwellian temperature in the thermal group was fixed at 300°K for the VITAMIN-C library, it will be temperature dependent in the VITAMIN-E library. For the 0° temperature, the smooth flux spectrum temperature is still set at 300°K. However, for the 300°, 900°, and 2100°K cases the spectrum temperature will be changed to the respective temperatures. The cutpoint for the Maxwellian and 1/E shapes is fixed at 0.414 eV independent of temperature (the original 5kT guideline was only nominal).

The weighting function for the gamma ray interaction cross sections is to be constant in energy.

Table I. Specification of neutron interaction weighting function

Functional Form	Energy Limits	Group Range
1) Maxwellian Thermal Spectrum $W_1(E) = C_1 E e^{-E/kT}$	10^{-5} eV to 0.414 eV	173-174
2) "1/E" Slowing-Down Spectrum $W_2(E) = C_2/E$	0.414 eV to 2.12 MeV	48-172
3) Fission Spectrum (θ=1.415 MeV) $W_3(E) = C_3 E^{1/2} e^{-E/\theta}$	2.12 MeV to 10.0 MeV	16-47
4) "1/E" Spectrum $W_4(E) = C_4/E$	10.0 MeV to 12.52 MeV	11-15
5) Velocity Exponential Fusion Peak (E_p = 14.07 MeV) (kT = 0.025 MeV) $W_5(E) = C_5 \exp -\left\{\frac{5}{kT}(E^{1/2}-E_p^{1/2})^2\right\}$	12.52 MeV to 15.68 MeV	5-10
6) "1/E" Spectrum $W_6(E) = C_6/E$	15.68 MeV to 19.64 MeV	1-4

Legendre Order of Scattering

The neutron group-to-group transfer matrices for the following materials are being expanded to P_8 : H^1, H^2, H^3, He^3, He^4, Li^6, Li^7, Be^9, B^{10}, B^{11}, C, N^{14}, O^{16}, Na^{23}, Mg, Al, Si, K, Ca, Ti, Cr, Mn^{55}, Fe, Co^{59}, Ni, Cu, Mo Pb, Ta^{181}, Ta^{182}, W^{182} to W^{186}. All other materials are being processed with a P_3 expansion.

The photon-interaction expansion is truncated at P_5.

Convergence Parameter Requirements

To improve accuracy the tolerance on resonance reconstruction has been reduced from 1% in VITAMIN-C to 0.5% in VITAMIN-E and that for linearization from 0.5% to 0.2%. The linearization tolerance was reduced below 0.5% without significant computational penalty. Thinning and integration convergence parameters were specified as 0.2% and 0.1%, respectively. The cumulative uncertainty is a complex combination of all of these approximations; there is currently no methodology used to systematically combine these various sources of error.

Processing Codes System

The upgraded self-consistent processing codes system has been tested as part of the CSEWG Data Testing Process. Multigroup neutron cross sections are being generated with the updated MINX module[18] and photon production and interaction cross sections are being generated with the LAPHNGAS and SMUG modules of the AMPX-II system.[19] Covariance files are being processed with PUFF[20,21] This system was chosen because of its successful performance in the generation of VITAMIN-C, the experience obtained by ORNL and General Electric as part of the preliminary ENDF/B-V Data Testing, and the improvements to the modules as described in the following section.

Output Formats

Multigroup BRKOXS, ISOTXS, AMPX master, and MATXS libraries are being produced. The pointwise files generated from ENDF/B-V in the process of preparing VITAMIN-E are also available. The covariance files will be output in COVERX format.[22] Special purpose files of elastic removal f-factors will also be provided.

Handling Codes for the Library

Two different sequences of handling codes for retrieving, manipulating, converting, editing, collapsing, self-shielding, etc., the libraries are available depending upon whether one needs to work in the CCCC or AMPX code systems. Codes for handling AMPX format are available in PSR-63/AMPX-II, and codes for handling CCCC format are available in PSR-117/MARS. Both computer code packages are available from RSIC. The various programs and functions are listed in Table II.

Table II. Handling codes from the AMPX and MARS packages of software support

AMPX Module	CCCC Computer Code	Function
AIM	BINX, LASIP-III	BCD-to-binary (or vice-versa) conversion
AJAX	LINX, I2I, B2B	Merging and deleting operations
CHOX		Combining neutron and gamma-ray files
CHOXM		Combining self-shielding factors, neutron files, and gamma-ray files
MALOCS	CINX	Energy group collapsing
BONAMI-2	SPHINX	Compute system-dependent shielded cross sections
NITAWL	I2O	Prepare working libraries for use in transport calculations
RADE		Perform tests on multigroup libraries

A new program has been written[23] to provide a conversion capability between the AMPX-master and MATXS formats.

Upgrading of the Data Processing System

The processing codes system has been upgraded by updating individual modules as described below.

Resonance Reconstruction/Linearization/Doppler Broadening

New editions[24,25] of the LINEAR and SIGMA-1 programs have been installed. In the new SIGMA-1 version, particular care is taken to include a sufficient number of points on the Doppler broadened file, so that linear interpolation is accurate to within a fixed input criterion. In addition, the program allows now for proper broadening of threshold reactions to controlled thermonuclear reactor temperatures.

In future releases of the VITAMIN-E library, the resonance profile reconstruction algorithm will also be upgraded by replacing the standard RESEND techniques by the newly-developed RECENT code.[26]

Finally, by optimizing the computational flow, i.e., thinning the 0°K data before broadening, enormous amounts of computer time are saved.

Unresolved Resonances Treatment

The treatment of the unresolved resonance region in MINX has been updated by replacing the standard UNRESR module with a new treatment largely based on the sophisticated techniques developed by Hwang[27] and implemented in the MC^2-2 code[28] for computing flux-weighted effective pointwise cross sections. These techniques were extended at ORNL to allow for the computation of effective pointwise current weighted total cross sections[29], and more generally for the computation of higher order effective pointwise cross sections required for the consistent computation of the shielded scattering matrices.[30] Notice that these algorithms[27-30] include processing of competitive widths, interference scattering, within sequence and sequence-sequence overlap corrections.

The numerical procedure employed in MINX to obtain the infinitely dilute group averaged cross section in the unresolved energy region has also been improved.[31]

Elastic Removal

In the current version of MINX fully shielded scattering transfer matrices are generated as functions of the temperature T and the Bondarenko parameter σ_B

$$\sigma_{e,\ell}^{g\to h}(\sigma_B,T) = \frac{\int_g W_\ell(E)\,\dfrac{\sigma_e(E,T)}{[\sigma_B+\sigma_t(E,T)]^{\ell+1}}\,A_\ell^h(E)\,dE}{\int_g \dfrac{W_\ell(E)}{[\sigma_B+\sigma_t(E,T)]^{\ell+1}}\,dE} \qquad (1)$$

$A_\ell^h(E)$ denotes the integral of the scattering transfer probability moment over group h.

Particular care has to be exercised in the unresolved resonance region, where Eq. (1) becomes

$$\sigma_{e,\ell}^{g\to h}(\sigma_B,T) = \frac{\int_g W_\ell(E^*)A_\ell^h(E^*)\bar{\sigma}_{e,\ell}(E^*,\sigma_B,T)\prod_{k=0}^{k=\ell}\dfrac{1}{\sigma_B+\bar{\sigma}_{t,k}(E^*,\sigma_B,T)}\,dE^*}{\int_g W_\ell(E^*)\prod_{k=0}^{k=\ell}\dfrac{1}{\sigma_B+\bar{\sigma}_{t,k}(E^*,\sigma_B,T)}\,dE^*} \qquad (2)$$

The higher order effective pointwise cross sections are defined as

$$\bar{\sigma}_{x,\ell}(E^*,\sigma_B,T) = \frac{\int_{\Delta E}\dfrac{\sigma_x(E,T)dE}{[\sigma_B+\sigma_t(E,T)]^{\ell+1}}}{\int_{\Delta E}\dfrac{dE}{[\sigma_B+\sigma_t(E,T)]^{\ell+1}}} \qquad (3)$$

In the above expressions $W_\ell(E)$ describes the slow varying broad energy behavior of the weighting function. E* denotes the energy point, contained in the interval ΔE at which average resonance parameters are specified. The computational procedure is based upon the transformation

$$\sigma_B+\sigma_t(E,T) = \sigma_p + \sum_\lambda x_\lambda(E,T) \qquad (4)$$

where x_λ refers to resonance component λ (i.e., resonance i in sequence ν) of the total cross section, expressed in terms of the usual symmetric and anti-symmetric line shape functions

$$x_\lambda = \sigma_{o,\lambda}[\psi_\lambda+a_\lambda\chi_\lambda] \qquad (5)$$

According to the ENDF specifications, the "effective" potential cross section σ_p includes the smooth corrections contributions (σ_{F3}^x) from scattering, fission (if relevant), and capture, but not from the competitive reaction

$$\sigma_p = \sigma_{pot}(E^*) + \sum_{x\neq comp}^{x}\sigma_{F3}^x(E^*) + \sigma_B \qquad (6)$$

Since existing spectral correction procedures [TDOWN[17,32], SPHINX[33], BONAMI-2[19], etc.] are based on elastic removal treatments, elastic removal shielding factors will be provided with VITAMIN-E. These are computed according to the standard definition

$$f_{er}^g(\sigma_B,T) = \frac{\sigma_{er}^g(\sigma_B,T)}{\sigma_{er}^g(\infty,o)} \qquad (7)$$

where the shielded elastic removal cross section is obtained from the shielded outscatter matrix

$$\sigma_{er}^g(\sigma_B,T) = \sum_{h>g}\sigma_{el,\ell=0}^{g\to h}(\sigma_B,T) \qquad (8)$$

The elastic removal shielding factors will be stored on special purpose files.

Temperature-Dependent Thermal Weighting

A change was made in MINX to permit the smooth energy weighting Maxwellian in the thermal range to be temperature dependent.

Computation of Analytical Bounds for the Cross Section Self-Shielding Factors

A fundamental problem regarding the applicability of the shielding factor method is to determine the limits of the range of values within which a cross section shielding factor is restricted, and whether these limits are physically meaningful. Using functional analysis techniques, a general methodology for computing strict upper and lower bounds for self-shielding factors has been developed.[34,38] The complete range of f-factors computed by cross section processing codes was addressed, and ENDF/B specified cross section

discontinuities were taken into account. The resulting formalism was implemented into BRINE[35], a stand-alone module easily incorporable into existing cross section processors. BRINE is being used to check the VITAMIN-E shielding factors.

Formats

The code system was upgraded to handle Version V formats. Major new features included the processing of competitive widths, uncertainty files and energy-dependent Watt fission spectra. Note that, as in VITAMIN-C, only the 1-MeV spectrum will be placed in the VITAMIN-E library, since MINX does not currently process fission matrices.

Photon Production Processing

Experience with ENDF/B-IV gamma ray production processing led to linearization and normalization of the weight function to help improve the precision of the LAPHNGAS calculation.

A coding change was made to the LAPHNGAS code to allow better precision when an input weighting spectrum is used (the case for VITAMIN-E). The change improves the integration scheme by incorporating the weighting function energy grid into the energy grid used by LAPHNGAS to calculate the group averaged multiplicities or gamma ray production cross sections.

A feature was also added to LAPHNGAS to allow calculation of multigroup multiplicities for materials without resonance parameters.[19] This permits self-shielding of gamma ray production cross sections, e.g., from capture, using the Bondarenko scheme.

Processing ENDF/B-V Uncertainty Data Into Multigroup Covariance Matrices

A capability for processing ENDF/B-V uncertainty data into multigroup covariance matrices has been developed[21] and implemented in the PUFF-II module. Specifically, the new module allows processing of all "NI-type" uncertainty relationships[36], required to describe explicitly the various components of the covariance matrix. In addition, explicit cross reaction and cross material relationships and derived uncertainties can be treated. Finally, the infinitely dilute cross section covariances due to uncertainties in the resolved resonance parameters can be computed.

First Order Data Checks

Processed VITAMIN-E data are undergoing an extensive series of first order data checks.

The RADE module of the AMPX-II system[19] is used to check each AMPX master data set for partial cross section consistencies. The BRINE module[35] is used to check the shielding factors against analytically computed upper and lower bounds. Finally, plots of point versus multigroup data for specified materials and reactions are being produced.

Testing Program and Anticipated Schedule

The testing program will be intimately associated with feedback from sponsor application and participation in various cooperative national testing programs. Anticipated application includes continued analysis of the OFE integral experiments, analysis of LMFBR critical experiments and Large Plant Design Studies, analysis of experiments relevant to pressure vessel surveillance, and weapons related applications. Benchmark validation will include cooperative testing in the framework of the CSEWG Data Testing Subcommmittee, the CSEWG Processing Methods Testing Subcommittee, ANS-6.1.2 (LWR Shield Standard Cross Sections), and the OFE Validation Group.

In order to initiate the testing procedures, some of the more important materials for the above-mentioned applications are being processed with high priority. Of particular importance is a comprehensive feedback to CSEWG's fast reactor benchmark program, in order to address the following questions: How do Version V data compare to experiment, as compared to Version IV data? If major changes were observed, could one trace their origin? Are there still outstanding discrepancies?

For the initial phase of testing, the available VITAMIN-E data have been augmented, where necessary, with multigroup data generated in adherence to the VITAMIN-E specifications using preliminary ENDF/B-V evaluations and with VITAMIN-C data. The cross section sets were then collapsed to a 100-group structure, and were used to calculate performance parameters of CSEWG fast reactor benchmarks.

Specifically, the effective multiplication factors and central core reaction rate ratios were calculated for the Pu-fueled JEZEBEL, ZPR-3/48, -3/56B, -9/31, and -6/7 benchmarks and for the U-fueled GODIVA, ZPR-3/6F, -3/12, -3/11, and -6/6A benchmarks. Results indicate[37] a general improvement in the ratio of the calculated/experimental values of the parameters calculated with VITAMIN-E data versus parameters calculated with the ENDF/B-IV based VITAMIN-C library.

Our current estimate of the VITAMIN-E schedule is that the first release of the complete library will not be available until mid-1980, although preliminary issues will be used in the context of CSEWG testing and cooperative nuclear data and methods development. Extensions to the current effort will include the dosimetry, activation and gas production data, kerma factors, response functions, and delayed neutron data. Processing refinements and library improvements are thus expected to continue for at least 2-3 more years.

Acknowledgements

Research sponsored jointly by EPRI under Interagency Agreement RTS 78-143, DNA under Interagency Agreement No. 40-65-65, and DRRT-USDOE under contract no. W-7405-eng-26 with Union Carbide Corporation.

The authors gratefully acknowledge support provided by DRRT, OFE, EPRI and DNA.

The authors also acknowledge the invaluable support of the following individuals in various phases of this undertaking: R. G. Alsmiller, Jr., D. Autun (DNA), D. E. Bartine, L. A. Berry, B. Broadhead, T. J. Burns, J. D. Smith, W. E. Engle, G. F. Flanagan, P. Hemmig (DOE-DRRT), D. T. Ingersoll, J. Lewellen (DOE-DRRT), R. E. Maerker, E. M. Oblow, O. Ozer (EPRI), J. V. Pace, F. G. Perey, R. Protsik (GE), R. T. Santoro, D. L. Selby, and L. Simmons (SAI).

References

1. R. W. Roussin et al., ORNL-RSIC-41, 107 (1978).
2. C. R. Weisbin et al., ORNL/TM-5142 (ENDF-224) (1975).
3. R. W. Roussin et al., ORNL-RSIC-37 (1978).
4. C. R. Weisbin et al., Proceedings of the Fifth International Conference on Reactor Shielding, Science Press, Princeton, NJ (1977).

5. D. L. Selby and G. F. Flanagan, ORNL-5314 (1978).

6. T. J. Burns and J. R. White, ORNL-5389 (1979, in preparation.

7. Y. Seki et al., Trans. Am. Nucl. Soc. 28, 662 (1978).

8. N. Hertel and B. Wehring, ORNL-RSIC-41, 181 (1978)

9. L. Green, WFPS-TME-79-015 (1979).

10. D. Berwald, Thesis, University of Michigan (1977).

11. R. B. Kidman and R. E. MacFarlane, LA-6260-MS (1976).

12. ORYX-E ORIGEN Yields and Cross Sections, DLC-38 RSIC, Oak Ridge National Laboratory (1976).

13. M. J. Bell, ORNL-4628 (1973).

14. R. J. Howerton, M. H. MacGregor, UCRL-50400, 15 (1978).

15. D. E. Bartine et al., ORNL/TM-4840 (1977).

16. R. G. Alsmiller, Jr. and J. Barish, ORNL/TM-6486 (1978).

17. C. L. Cowan, E. Kujawski, R. Protsik, ORNL-RSIC-41, p. 37 (1978).

18. C. R. Weisbin et al., LA-6486-MS (1976).

19. N. M. Greene et al., ORNL/TM-3706, revised, December 1978.

20. C. R. Weisbin et al., ORNL/TM-4847 (ENDF-218) (1975)

21. J. D. Smith et al., Trans. Am. Nucl. Soc. 33 (1979).

22. J. D. Drischler and C. R. Weisbin ORNL-5318 (ENDF-235) (1977).

23. J. L. Lucius, RSIC-FORSS Seminar Workshop, August, 1978.

24. D. E. Cullen, UCRL-50400, 17, Part A, Rev. 1, (1978)

25. D. E. Cullen, UCRL-50400, 17, Part B, Rev. 1, (1978)

26. D. E. Cullen, UCRL-50400, 17, Part C, in print (1979).

27. R. N. Hwang, Nucl. Sci. Eng. 52, 157 (1973).

28. H. Henryson, II, B. J. Toppel, C. G. Steinberg, ANL-8144 (1976).

29. J. Barhen and D. G. Cacuci, Trans. Am. Nucl. Soc. 32, 310 (1979).

30. D. G. Cacuci and J. Barhen, in Memorandum from C. R. Weisbin to CSEWG, CEWG, January, 1979.

31. D. G. Cacuci, ORNL-Intralaboratory correspondence dated 10/27/78.

32. C. L. Cowan, B. A. Hutchins, J. E. Turner, GEAP-13740 (1971).

33. W. J. Davis, M. B. Yarbrough, A. B. Bortz, WARD-XS-3045 (1977).

34. J. Barhen and D. G. Cacuci, Trans. Am. Nucl. Soc. 33 (1979).

35. M. A. Bjerke, J. Barhen and D. G. Cacuci, ORNL-CSD-TM-104, 1979, in preparation.

36. F. G. Perey, ORNL/TM-5938 (ENDF-249) (1977).

37. Y. Yeivin et al., Proceedings of International Conference on Cross Sections in Technology, Knoxville, TN, October 1979.

38. D. G. Cacuci, ORNL-RSIC-41, p. 227 (1978).

VERIFICATION OF PHOTON-PRODUCTION PROCESSING TECHNIQUES

R. J. Barrett,[+] W. E. Ford III,[++] Y. Gohar,[+++]
T. S. Bohn,[++++] R. E. MacFarlane,[+] and R. M. Boicourt[+]

+ Los Alamos Scientific Laboratory
Los Alamos, NM 87545, USA
++ Oak Ridge National Laboratory
Oak Ridge, TN 37830, USA
+++ Argonne National Laboratory
Argonne, IL 60439, USA
++++ EGG-Idaho, Inc.
Idaho Falls, ID 83401, USA

Several laboratories have independently developed computer codes which use evaluated data from the ENDF/B file to produce group-averaged cross sections and transfer matrices for neutron-induced photon production. There have been several instances in which these codes have produced discrepant data sets, thereby casting doubt on the validity of all the codes. For a series of specified test cases, the results from three of these codes (NJOY, LAPHNGAS, and MACK-IV) were systematically compared with each other and with hand calculations. Several shortcomings in the codes have been discovered and repaired. One major difference of philosophy has been resolved. Consequently, the codes have arrived at substantial agreement on all of the nearly 1200 nonzero group constants calculated in the study.

(Photon-production, multigroup, code comparison, ENDF/B-IV)

Introduction

For several years, the LAPH[1] series of codes were the most widely used photon-production processors of ENDF/B data.[2] Versions of LAPH are in use at the Los Alamos Scientific Laboratory (LASL) [LAPH, LAPHANO] and General Atomic (GA) [LAPHANO]. Discrepancies in the LASL version of LAPHANO were reported by Seamon[3] at the September 1975 meeting of the Shielding Subcommittee (SSC) of the Cross Section Evaluation Working Group (CSEWG). Seamon's report included sample data from LAPHANO and comparisons with hand calculations. Several specific code modifications were also suggested to rectify the discrepancies.

Extensive modifications were made to the LAPHANO code at the Oak Ridge National Laboratory (ORNL) to give the LAPHNGAS code.[4] LAPHNGAS was incorporated into the AMPX system--a modular system for producing coupled multigroup neutron-gamma cross section sets from ENDF/B data.*

In recent years, a number of other codes (NJOY,[5]** MACK-IV[6]) have gained the capability of processing photon-production data into transfer matrices in several Legendre orders. Because these codes were not related to LAPH, the opportunity was now available for intercomparison of independent codes and methods, as well as comparison of each code with selected hand calculations.

Under the auspices of the Shielding Subcommittee, the authors have compared calculated photon-production data from NJOY, MACK-IV, the LASL version of LAPHANO, the ORNL LAPHNGAS, and a late 1977 version of LAPHNGAS from the EG&G-Idaho version of the AMPX system. For the purpose of this paper, only NJOY, MACK-IV, and the ORNL LAPHNGAS will be discussed. The corrections made to LAPHNGAS as a result of this study are applicable in general to all LAPH-series codes. In the following discussions, it is assumed that the reader is familiar with the ENDF terminology described in Ref. 2.

Methodology

The scope of the study, summarized in Table I, was similar to the work of Seamon,[3] except for the fact that higher order matrices were calculated for ^{12}C, ^{14}N, and ^{16}O. Isotopes and reactions were chosen to represent a variety of ENDF interpolation schemes. Photon-production data for both discrete and continuum photons were calculated using both multiplicities (MF12) and photon-production cross sections (MF13). In addition, a reasonably complex cascade of transition probability arrays was processed for ^{23}Na. (To illustrate the complexity of the ^{23}Na transition probability data, the MT60 cascade is depicted in Fig. 1.) The LASL 30-neutron and 12-photon energy group structures were used in this study. All calculations were repeated with both a constant and a 1/E neutron flux weighting for all Legendre orders. These simple weight functions were chosen to facilitate hand calculations. A total of 1168 nonzero matrix elements were compared.

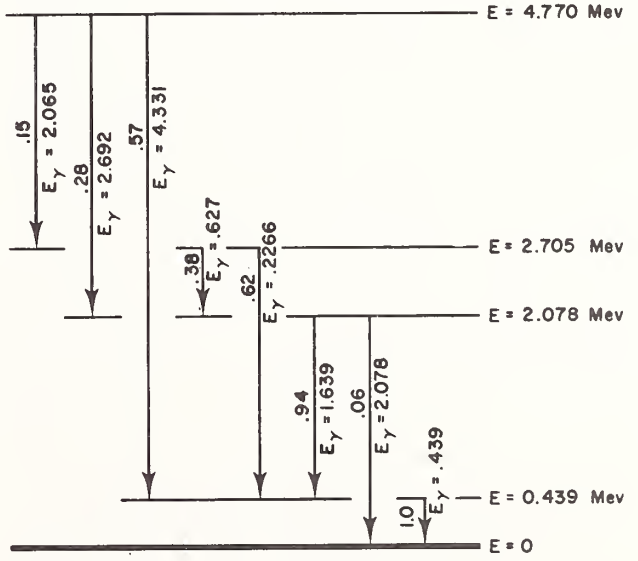

Fig. 1. Photon transition probabilities for ^{23}Na, MT = 60.

*The AMPX system is distributed by the Radiation Shielding Information Center (RSIC) in the package identified as PSR-63/AMPX-II.

**NJOY is a comprehensive computer code package for producing pointwise and multigroup neutron and photon cross sections from ENDF/B evaluated nuclear data.

TABLE I

ISOTOPES AND REACTIONS CONSIDERED IN THIS STUDY

Isotope	ENDF/B-IV MAT	MT	Photon Production Data MF=12/13	LF[a]	E_{INT}[b]	E_{INT}[b]	$E_{\gamma,INT}$[b]	MF = 15 Legendre Order
C-12	1274	51	13	DISC	2	-	-	P4
N-14	1275	102	12	DISC	2	-	-	P2
O-16	1276	4	13	DISC	2	-	-	P6
		22	13	DISC	2	-	-	P0
F	1277	3	13	CONT	1	2,4	1	P0
		4	13	DISC	2,4	-	-	P0
		102	13	CONT	5	1	1,2	P0
		107	13	DISC	2,4	-	-	P0
NA-23	1156	55	12	TPA	-	-	-	P0
		60	12	TPA	-	-	-	P0

[a] Photon distributions are discrete (DISC) or continuous (CONT) or the neutron energy dependence is represented by means of transition probability arrays (TPA).

[b] Interpolation scheme used in the evaluated data; that is, INT = 1, 2, 4, and 5 specifies constant, linear-linear, log-linear, and log-log interpolation schemes, respectively.

The calculations were performed on ENDF/B-IV evaluated data, which had been linearized, resonance-reconstructed and Doppler-broadened to 300 K using the NJOY code at LASL. The purpose of this preprocessing was to minimize the possibility of discrepancies arising from code differences not directly related to photon-production processing. Calculated matrices from all the laboratories were automatically sorted and compared at LASL. Side-by-side listings of all the calculated data were provided to all participants. In addition, the percentage difference by which each code deviated from the NJOY result was calculated and displayed. Discrepancies of less than 0.1% were set equal to zero. Cases in which the magnitude of the difference between two calculated cross sections was less than 1.0×10^{-6}b were similarly disregarded. The choice of NJOY as the standard of comparison was completely arbitrary.

Conclusions

The first round of comparisons showed agreement (to within 1%) among the three codes for only 77% of the 1168 numbers calculated, a fact which reinforced our motivation for doing the study. Hand calculations performed on a representative sample of discrepant matrix elements suggested several improvements, and progress in the form of code modifications came quickly. The remaining discrepancies (involving 4% of the calculated numbers) are due in part to differences in interpretations of the ENDF/B-IV format or to minor differences in the calculational techniques used by the codes.* Three of these differences bear mentioning.

The most serious ambiguity exists in the processing of continuous energy spectra which are expressed in ENDF/B as normalized probability distributions $g(E_\gamma \leftarrow E_i)$ at selected neutron energies E_i. The codes under study employ different methods for interpolating to determine the photon spectra at intermediate neutron energies. The problem is illustrated in Figs. 2(a) and (b). At the lower neutron energy E_i, the photon endpoint energy is E_γ^i; at the higher neutron energy $E_i + 1$, the photon endpoint energy is E_γ^{i+1}. At the intermediate neutron energy E_i', the NJOY and LAPHNGAS codes interpolate in such a way [Fig. 2(a)] as to give photon yields (dashed line) for photon energies up to E_γ^{i+1}, whereas the interpolation method used by MACK-IV [Fig. 2(b)] gives photon yields only up to an energy of E_γ^i. Because the resulting intermediate distributions are normalized, the NJOY/LAPHNGAS method gives more

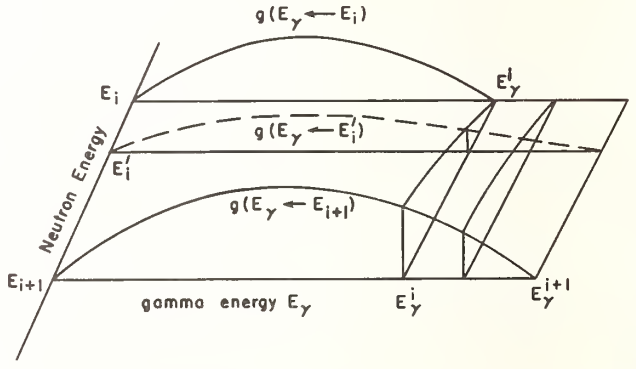

Fig. 2(a). NJOY/LAPHNGAS approach for interpolation of normalized probability distributions.

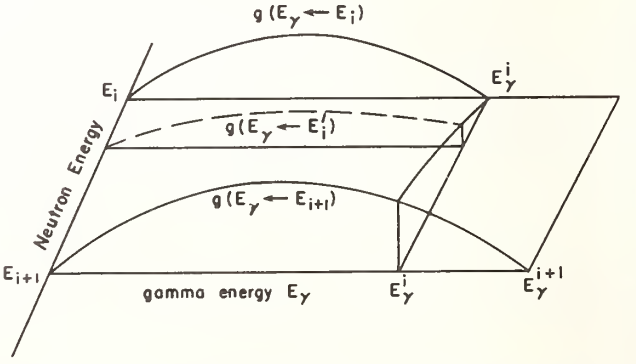

Fig. 2(b). MACK-IV approach for interpolation of normalized probability distributions.

*In addition, there are differences due to evaluation errors.

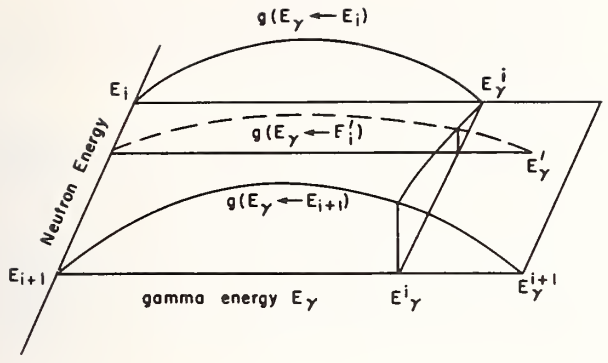

Fig. 3. Illustration of the proposed approach to interpolation of normalized probability distributions where E'_γ is defined from given TAB1 data.

photons in higher energy groups and the MACK-IV method gives fewer photons in the same energy groups.

Neither the NJOY/LAPHNGAS nor the MACK-IV method gives a physically correct result. The endpoint energy for the intermediate photon spectrum should be somewhere between E'^{i}_{γ} and E'^{i+1}_{γ}. However, the current formats and procedures for ENDF/B-IV do not allow for an interpolation scheme that would produce the physically reasonable result.

A quick remedy for this ambiguity is to introduce a TAB1 record that gives the photon endpoint energy as a function of neutron energy. As shown in Fig. 3, the new data, which are compatible with current ENDF formats and which employ standard ENDF interpolation schemes, would allow a more reasonable method of interpolation.

A further source of difficulty with the normalized probability distributions is the use of this format to represent discrete photons. Figure 4 depicts the spectrum for MT = 102 in fluorine. Differences in the approach to interpolation, described above, led to a discrepancy (MACK-IV results versus NJOY/LAPHNGAS results) of 13% in photon production from neutron group 9 to photon group 2 and 100% from neutron group 9 to photon group 1. Similar difficulties were encountered in several neutron groups for this reaction. The effects of these discrepancies on the photon energy per neutron group were caluclated at ANL and found to be as high as 14%. These discrepancies, which can be significant for many applications, demonstrate the difficulties that can result from the use of file 15 to represent discrete photons.

A second difference involves the way in which the energies of certain discrete photons are calculated. The ENDF/B format calls for the photon energy E_γ to be calculated from the target atomic mass ratio AWR and the neutron energy E_n according to the formula

$$E_\gamma = E'_\gamma + \frac{AWR}{AWR+1} \times E_n \ ,$$

where E'_γ is the discrete photon energy quoted in the ENDF file. The MACK-IV and NJOY codes calculate E_γ at each neutron energy within a group, whereas LAPHNGAS calculates one value of E_γ using the group-average neutron energy $\bar{E}_n$. The latter procedure can distort the average photon secondary energy by placing discrete photons in the wrong energy group. This difference is known to have caused a discrepancy in two of the 1168 nonzero group constants produced in this study--photon production from neutron group 5 to photon group 1 for

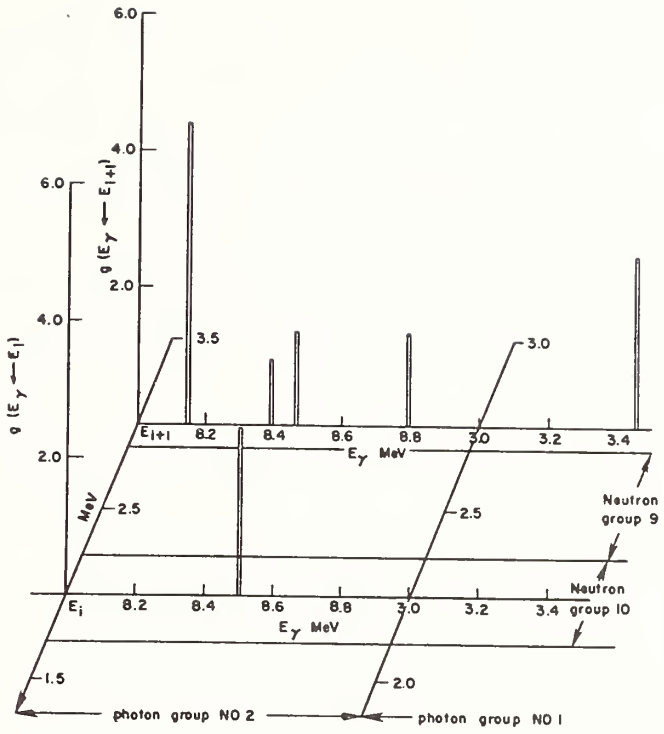

Fig. 4. Representative normalized probability distribution functions $g(E_\gamma \leftarrow E_i)$ for fluorine (MAT1277, MT102).

radiative capture (MT = 102) in nitrogen for both constant and 1/E weighting.

Finally, there is a difference in the method of interpolating a function that is a product of two or more variables for which interpolation schemes are specified in ENDF. The MACK-IV code uses the highest interpolation scheme, while NJOY and LAPHNGAS use linear interpolation and disregard the interpolation schemes associated with the components of the product. When 1/E weighting is used, this difference in algorithm causes a maximum discrepancy of 0.5% for photon production from radiative capture (MT = 102) in nitrogen.

With the exceptions noted above, the three codes compared in this study are now in substantial agreement on the processing of ENDF/B-IV evaluated photon production data. Because no format changes in this area are contemplated for ENDF/B-V, the same statement should be true for that data file.

Acknowledgements

The authors wish to acknowledge the constant encouragement and assistance of the Shielding Subcommittee Chairman, Dr. R. W. Roussin and the constructive discussion of Dr. H. Henryson II, of the Applied Physics Division, Argonne National Laboratory. Ms. B. R. Diggs contributed significantly to the ORNL LAPHNGAS calculational effort. Research sponsored by the U. S. Department of Energy.

References

1. D. J. Dudziak, A. H. Marshall, and R. E. Seamon, "LAPH; A Multigroup Photon Production Matrix and Source Vector Code for ENDF/B," Los Alamos Scientific Laboratory report LA-4337 (May 1970).

D. J. Dudziak, R. E. Seamon, and D. V. Susco, "LAPHANO: A P_0 Multigroup Photon-Production Matrix and Source Vector Code for ENDF," Los Alamos Scientific Laboratory report LA-4750-MS (January 1972).

2. D. Garber, C. Dunford, and S. Pearlstein, "Data Formats and Procedures for the Evaluated Nuclear Data File, ENDF," Brookhaven National Laboratory report BNL-NCS-50496 (ENDF-102) (1975).

3. R. E. Seamon, "Processing Photon Production Data with the LAPHANO Code," a report presented to the Shielding Subcommittee of the Cross Section Evaluation Working Group (CSEWG), Los Alamos, September 25, 1975.

4. N. M. Greene, J. L. Lucius, L. M. Petrie, W. E. Ford III, J. E. White, and R. Q. Wright, "AMPX: A Modular Code System for Generating Coupled Multigroup Neutron-Gamma Libraries from ENDF/B," ORNL/TM-3706 (March 1976).

5. R. E. MacFarlane, R. J. Barrett, D. W. Muir, and R. M. Boicourt, "The NJOY Nuclear Data Processing System; User's Manual," Los Alamos Scientific Laboratory report LA-7584-M (December 1978).

6. M. A. Abdou, Y. Gohar, and R. Q. Wright, "MACK-IV, A New Version of MACK: A Program to Calculate Nuclear Response Functions from Data in ENDF/B Format," Argonne National Laboratory report ANL/FPP-77-5 (1978).

THE MATXS-TRANSX SYSTEM AND THE CLAW-IV NUCLEAR DATA LIBRARY

R. J. Barrett and R. E. MacFarlane
Los Alamos Scientific Laboratory, University of California
Theoretical Division
Los Alamos, New Mexico 87545 U.S.A.

A new system for post-processing multigroup cross sections has been developed. The MATXS interface format stores group-averaged cross sections and scattering matrices for all reactions of interest for neutron transport, photon production, and photon transport, including kerma factors, thermal upscatter matrices, and self-shielded cross sections. The TRANSX code can produce a variety of working libraries for transport calculations from a single MATXS file. TRANSX capabilities include group collapsing, material mixing, coupling of neutron and photon matrices, transport corrections, interpolations of self-shielding data, calculation of fission vectors, and creation of flexible user-specified response functions. Using the MATXS-TRANSX system, we have produced the CLAW-IV library, a 73-isotope coupled set in 30-neutron and 12-photon groups. The library, available from RSIC, includes prompt and steady-state transfer tables in FIDO format, prompt and total fission spectra, and a table of useful response functions including heating and gas production.

(Processed cross-section library, neutron and photon transport, prompt and delayed nuclear activities, ENDF/B-IV)

MATXS

The wide variety of calculational problems associated with thermal and fast reactors, CTR, shielding, and weapons has led to an increasing diversity in requirements for group-averaged nuclear data sets. The need for coupled or uncoupled transfer tables, with prompt or steady-state fission vectors, with special activity edit cross sections such as "tritium production" and "isotope depletion" has led to a proliferation of data sets tailored for solving a specific problem with a particular type of code. There is clearly a need for generalizing the methods used for producing, exchanging, and accessing multigroup data sets.

Currently the most widely used standards for the exchange of nuclear data are those defined by the Committee for Computer Code Coordination (CCCC).[1] These interface files and their associated codes, developed primarily in support of the fast reactor program, have done much to improve the situation. However, they are not flexible enough to serve as a general system. For example, the fixed set of allowed reactions gives very little latitude for defining activity edit cross sections or for including sufficiently detailed cross sections for sensitivity analysis. There is no provision for thermal kernels or for self-shielding of elastic removal. The system is not easily expanded to meet new demands.

We have developed the MATXS format, which is similar in many ways to the CCCC-ISOTXS file and incorporates some of that file's useful features; e.g., efficient storage of banded matrices. The principal advantages of MATXS are

A. Various kinds of nuclear data are separated into "data-types." These "data types" include neutron scattering, gamma production, photon scattering, thermal matrices, and coupled sets. New types are easily added.

B. For any "data type," all vector or matrix cross sections may be included, or any other data that can be written as a vector (kerma factors, ν), or as a matrix (delayed yields).

C. Any combination of incident and exit particles is allowed (including coupled sets and charged-particle production).

Currently, the MATXSR module of the NJOY[2] system can produce a MATXS file containing neutron-scattering, gamma-production, and photon-interaction cross sections, as well as thermal upscatter matrices and resonance self-shielding data.

TRANSX

TRANSX is a utility code that reads a cross-section library in MATXS format and produces transport tables suitable for use in discrete-ordinates (S_N) transport codes such as ONETRAN[3] and ANISN.[4]

The tables can be printed and/or written to an output unit in various forms including FIDO format (zeroes are stripped out using a repeat count), or ANISN format (same as FIDO except a factor of $2\ell + 1$ is included in the scattering matrices). The user can request either direct or adjoint tables in either materialwise or groupwise ordering. Groupwise ordering allows S_N calculations with very large group structures.

The code will produce tables for neutron transport (NN), photon transport (GG), or coupled sets where both neutrons and photons are transported simultaneously. Microscopic and macroscopic mixtures can be generated. Thermal upscatter is allowed, and all neutron reactions and photon production can be self-shielded.

A flexible capability is included for producing cross sections for response function edits. Any linear combination of cross sections from the MATXS file can be requested. As will be seen below, this allows the user to obtain complex quantities like helium production or steady-state heating.

The fission matrices on the MATXS file are converted into the vectors $\nu\sigma_f$ and χ for the transport tables. Either prompt or steady-state vectors can be selected. For the latter, delayed neutron contributions are added. The fission spectrum is calculated using flux weighting and includes mixture effects. A special option is included to handle the partial fission reactions (n,n')f, (n,2n)f, and (n,3n)f at high energies. The scattering part of the reaction is removed from fission and added to the scattering matrix. The fission part is included in χ, and the $\nu\sigma_f$ is reduced appropriately. This option provides a better account of the incident energy dependence of fission.

TRANSX allows several transport correction options. In general, S_N codes require a different total cross section and different in-group scattering cross sections than P_N codes.[5] The following four approximations are available.

$$\sigma^{SN}_{n,g\to g} = \sigma^{PN}_{n,g\to g} - \sigma_{ntg} + \sigma_g \quad ; \quad 0 \leq n \leq N$$

$$\sigma_g = \begin{cases} \sigma_{0tg} & \text{CONS.P} \\ \sigma_{N+1,tg} - \sigma_{N+1,g\to g} & \text{DIAG} \\ \sigma_{N+1,tg} - \sum_{g'} \sigma_{N+1,g\to g'} & \text{BHS} \\ \sigma_{N+1,tg} - \sum_{g'} \sigma_{N+1,g'\to g}\phi_{N+1,g'}\ \phi_{N+1,g} & \text{INFLO} \end{cases}$$

They are consistent P, diagonal, Bell-Hansen-Sandmeier, and inflow. The angular dependence of the total cross section can be important when self-shielding is present or when collapsing cross sections using a detailed angular flux from a previous S_N calculation.

TRANSX can collapse to a subset group structure using the weight function from the library, a read-in weight function, or a flux computed internally by the B_0 or B_1 approximation. The weight function is the reaction rate $\sigma_g \times \phi_g$, and it is used as the starting guess for the flux calculation (if any). Also note that a one-to-one "collapse" with a realistic input weight function given will result in improved fission spectra and inflow transport corrections.

Heterogeniety options are available for buckled homogeneous mixes, lumps described by a constant escape cross section, cylindrical rods in square or hexagonal lattices, and multi-region slab cells. Escape cross sections are based on standard two-region equivalence relations, but the Dancoff corrections use neutron optical path lengths computed for the exact multi-region cell. The background cross section due to other isotopes can be specified or obtained by iteration on the total cross section.

Mixes are identified by the density or fraction of the library nuclides to be used, by temperature, by background cross section (σ_0), and by spatial region. In addition, thermal groups can be requested with a choice of bound scatterers from the library.

CLAW-IV

Basic data from the evaluated nuclear data file (ENDF/B-IV)[6] were used for all materials in the library except Li-6A, Be-9A, and C-12A, which were based on the local LASL evaluations.[7-9] The NJOY code system was used to process the cross sections. The point cross section linearization and resonance reconstruction tolerance was 0.5%, and all cross sections were Doppler broadened to 300 K. Cross sections were averaged over the LASL 30-neutron and 12-photon energy groups using a fusion-fission-1/E-thermal weight function. Neutron-transport, photon-production, and photon-transport data in five Legendre orders were all stored on the same computer file in MATXS format. The final processing step involved several runs with the TRANSX code, which translated MATXS files into the formats used in S_N codes.

The library described here consists of several computer files, as detailed below.

TRANSFER TABLES

Coupled sets of P_3 transfer tables were transport-corrected with the "inflow" approximation. The $\nu\sigma_f$ vector was calculated by summation of the full square fission matrix

$$\nu\sigma_{f,g} = \sum_{g'} \sigma_{f,g\to g'} \quad .$$

The absorption cross section ($\sigma_{a,g}$) is simply a neutron balance, calculated from the total cross section and the P_0 transfer matrix according to the equation,

$$\sigma_{a,g} = \sigma_{t,g} - \sum_{g'} \sigma_{0,g\to g'} \quad .$$

For the more important fissile nuclides, the partial fission reactions (n,f), (n,n'f), and (n,3nf) are given in ENDF/B-IV in addition to the fission total. Because the neutrons emitted prior to fission have a quite different energy distribution from those emitted during fission, we have separated them from the $\nu\sigma_f$ and vectors and added them to the transfer matrix.

Separate files are given for prompt and steady-state data (see below). Both files are in FIDO format. The $2\ell + 1$ factor is not included, and a header card is included for each table.

PROMPT TRANSFER TABLES

The reference set of transfer tables consists of 73 isotopes, elements, and mixtures as specified in Table I. In this set, only the prompt secondary neutrons from fission are included in $\nu\sigma_f$, and only prompt photon production is included in the transfer matrix. Photon production data are not available in ENDF for all isotopes, and the photon-production portion of the transfer matrix is non-zero only for those materials specified in Table II. Photon interaction data for plutonium were used in the tables for all isotopes of americium, curium, and californium.

STEADY-STATE TABLES

For several isotopes (Table II), there is information available concerning the yield and energy distribution of delayed neutrons from fission and delayed photons from fission and other reactions. A separate set of coupled group-to-group transfer tables, which includes the delayed contribution, has been generated for use in steady-state neutronics calculations. Delayed neutron yields were calculated from data supplied in ENDF.

Delayed photon yields and spectra from the fission reaction have been calculated as a function of cooling time by CINDER[10] and related codes[11] for inclusion in the ENDF system. Using the FITPULS[12] program, we have calculated photon-group-averaged constants (α and λ) and deduced the photon yield,

$$Y_g = \sum_{i=1}^{n} \frac{\alpha_{i,g}}{\lambda_{i,g}} \quad ,$$

for infinite cooling time.

For reactions other than fission, a select group of discrete photons were included. Selection of these photons from among the hundreds of potential candidates was based on a combination of half-life, photon energy, and the importance of the isotope.

RESPONSE FUNCTIONS

For each material contained in the prompt transfer tables (Table I), the following reponse functions have been calculated.

A. PHEAT. Prompt local heat deposition (in Joule-barns) for both neutrons and photons was calculated by the energy balance method.

B. THEAT. The total heat deposition is defined as the sum of the prompt heat described above and the delayed heating from beta decay. For the fission reaction, the average delayed heat was taken from Sher, Fiarman, and Beck[13] Other reactions were included only for materials of significant im-importance in a wide variety of calculations.

C-G. HPROD, DPROD, TPROD, BPROD, APROD. The production of hydrogen, deuterium, tritium, helium-3, and helium-4, respectively.

H. PARAB. Parasitic absorption includes all reactions in which the incident particle is not re-emitted.

I. DEPLET. The depletion cross section is the probability that the target nucleus will be transformed to another species.

J-L. N2N, N3N, NGAM. The (n,2n), (n,3n), and (n,γ) cross sections, respectively.

M-N. FISSN, NUSIGF. The fission cross section and $\nu\sigma_f$, respectively,

O. TOTAL. The total cross section, σ_t.

For ease in editing, the response functions are given in 6E12.5 format. The table for each material starts with a title card (e.g., "AL-27 EDITS"). Seven cards follow for each response function, for a total of 106 cards per material.

FISSION SPECTRA

Both prompt and steady-state (prompt plus delayed) fission neutron spectra (χ-vectors) are available in 6E12.5 format for the 26 materials listed in Table III. The prompt spectra were generated from the fission transfer matrix according to the formula

$$\chi_g = \sum_{g'} \sigma_{f,g'\to g} \times \phi_{g'} \Big/ \sum_{g} \sum_{g'} \sigma_{f,g'\to f} \times \sigma_{g'} \quad ,$$

where ϕ_g is the group-averaged, P_0 weighted flux for group (g).

The steady-state spectra were obtained by factoring in the delayed neutron yield (ν_d) and spectrum (χ).

The χ vectors are given in 6E12.5 format. The data for each isotope is preceded with a title card (e.g., "U-235 CHI"), and followed by seven cards of data. Photon groups contain zeroes.

CONCLUSIONS

The MATXS-TRANSX system promises to provide a flexible and convenient tool for neutronics analysis as demonstrated by this sample coupled library that should be useful for many problems where self-shielding can be ignored.

REFERENCES

1. R. D. O'Dell, "Standard Interface Files and Procedures for Reactor Physics Codes, Version IV," LA-6941-MS (Sept. 1977).

2. R. E. MacFarlane, R. J. Barrett, D. W. Muir, and R. M. Boicourt, "The NJOY Nuclear Data Processing System: User's Manual," LA-7584-MS (ENDF-272) (Dec. 1978).

3. T. R. Hill, "ONETRAN: A Discrete Ordinates Finite Element Code for the Solution of the One-Dimensional Multigroup Transport Equation," LA-75590-MS (June 1975).

4. W. W. Engle, Jr., "A User's Manual for ANISN, A One-Dimensional Discrete Ordinates Transport Code with Anisotropic Scattering," ORGDP-K-1693 (March 1967).

5. G. I. Bell, G. E. Hansen, and H. A. Sandmeier, Nucl. Sci. Eng. 28, 376 (1967).

6. D. Garber, C. Dunford, and S. Pearlstein, "Data Formats and Procedures for the Evaluated Nuclear Data File, ENDF," BNL-NCS-50496 (ENDF-102) (Oct. 1075).

7. L. Stewart and P. G. Young, "Trans. Am. Nucl. Soc. 23, 22 (1976).

8. C. I. Baxman, G. M. Hale, and P. G. Young, "Applied Nuclear Data Research and Development: January 1 - March 31, 1976," LA-6492-PR (1976).

9. C. I. Baxman and P. G. Young, "Applied Nuclear Data Research and Development: January 1 - March 31, 1977," LA-6893-PR (1977).

10. T. R. England, R. Wilczynski, and N. L. Whittemore, "CINDER-7: An Interim Report for Users," LA-5885-MS (April 1975).

11. M. G. Stamatelatos and T. R. England, "FPDCYS and FPSPEC, Computer Programs for Calculating Fission-Product Beta and Gamma Multigroup Spectra from ENDF/B-IV Data," LA-NUREG-6818-MS (May 1977).

12. R. J. LaBauve, T. R. England, D. C. George, and M. G. Stamatelatos," The Application of A Library of Processed ENDF/B-IV Fission-Product Aggregate Decay Data in the Calculation of Decay Energy Spectra," LA-7483-MS (Sept. 1978).

13. Rudolph Sher, Sidney Fiarman, and Curt Beck, Stanford University, "Fission Energy Release for 16 Fissioning Nuclides," personal communication (Oct. 1976).

TABLE I. Materials in Prompt Transfer Tables

Material	γ-Production	Material	γ-Production	Material	γ-Production
H-1	X	V	X	U-235	X
H-2	X	Cr	X	U-236	
H-3		Mn-55	X	U-237	X
He-3		Fe	X	U-238	X
He-4		Co-59	X	U-239	X
Li-6	X	Ni	X	Np-237	
Li-6A	X	Cu	X	Pu-238	
Li-7	X	Zirc2		Pu-239	X
Be-9	X	Nb-93	X	Pu-240	X
Be-9A	X	Mo	X	Pu-241	
B-10	X	Rh-103		Pu-242	
B-11		Ag-107		Am-241	
C-12	X	Ag-109		Am-243	
C-12A	X	Cd		Cm-244	
N-14	X	Ta-181	X	Cm-245	X
O-16	X	W	X	Cm-246	X
F-19	X	Re-185		Cm-247	X
Na-23	X	Re-187		Cm-248	X
Mg	X	Au-197		Cf-249	X
Al-27	X	Pb	X	Cf-250	X
Si	X	Th-232		Cf-251	X
Cl	X	Pa-233		Cf-252	X
K	X	U-233		STANLS	X
Ca	X	U-234		CONCRT	X

TABLE II. Materials Included in the Steady-State Transfer Tables

Be-9	Fe	Mo	Pu-239
Be-9A	Ni	Th-232	Pu-240
B-11	Cu	U-233	Pu-241
Na-23	Nb-93	U-235	STANLS
Cr		U-238	CONCRT

TABLE III. Materials for which Fission Neutron (χ) Vectors Are Given

Th-232*	U-238*	Pu-241*	Cm-247
Pa-233	U-239	Am-232	Cm-248
U-233*	Np-237	Am-241	Cf-249
U-234	Pu-238	Am-243	Cf-250
U-235*	Pu-239*	Cm-244	Cf-251
U-236	Pu-240*	Cm-245	Cf-252
U-237		Cm-246	

* Denotes isotopes for which steady-state spectra are given.

ENDF/B-IV AND V CROSS SECTION LIBRARIES FOR THERMAL POWER REACTOR ANALYSIS

R. E. MacFarlane
Los Alamos Scientific Laboratory, University of California
Theoretical Division
Los Alamos, New Mexico 87545 USA

The NJOY processing system has been used to produce thermal reactor cross-section libraries from ENDF/B-IV and V evaluations for the fuel cycle codes EPRI-CELL and EPRI-CPM, for the continuous-energy Monte Carlo code MCNP, and for the Los Alamos discrete-ordinates transport codes. This consistent data source has allowed the approximate methods (equivalence theory, B_1, integral transport, P_L-S_N) to be compared with accurate Monte Carlo results. So far, this has resulted in improved methods for space-and-energy self-shielding in the resonance range (e.g., the NJOY flux calculator, epithermal disadvantage factors for EPRI-CELL, shielded elastic removal), it has shown why the newest ENDF-based libraries initially gave results worse than the old libraries, and it has pointed out problems for future study such as resonance interference effects at high burnup. Finally, the results are compared to various criticality benchmarks to evaluate the performance of ENDF/B-V for thermal reactor analysis and to establish the biases introduced by the approximate methods used in the fuel cycle codes.

(Thermal reactor cross sections, ENDF/B-V)

Evaluated Nuclear Data

The fifth version of the Evaluated Nuclear Data Files (ENDF/B-V) has recently been released.[1] It shows improvements in both scope and quality due to the inclusion of new experimental data, to the expanded use of nuclear models, and to the dedicated work of the members of the Cross Section Evaluation Working Group (CSEWG) and the U. S. National Nuclear Data Center. In addition to many updated evaluations, ENDF/B-V includes new materials (e.g., ^{15}N, ^{231}Pa, ^{253}Es), new data types (e.g., gas production, isomer production, and components of energy release in fission), improved representations (e.g., Watt fission spectra, Adler-Adler multilevel resonance representations), and expanded data covariance and photon production files.

Except in its early years, the development of ENDF/B has been most responsive to the needs of its major supporter, the U. S. Fast Reactor Program. The impact of ENDF/B-III and IV on thermal power reactor design and operation has been minimal; various proprietary adjusted cross-section libraries have dominated the field. This situation has begun to change with the advent of the Electric Power Research Institute (EPRI). The existing sets are not always adequate for analyzing the new ideas such as ^{233}U-fueled reactors, thermal breeders, and advanced converters that are so active these days. Even more important is the problem of regulatory accountability. It is becoming increasingly desirable for everyone--vendors, utilities, fuel management companies, and regulatory agencies--to be able to trace their calculations back to a single reference data base without the problems of proprietary rights. Many people in the power reactor industry think that ENDF/B-V could become this standard.

Neutron Cross-Section Processing

For these reasons and others, EPRI has sponsored the development of the Advanced Recyle Methodology Program (ARMP)[2] whose main cross-section-producing components are the reactor cell codes EPRI-CELL and EPRI-CPM. CELL was developed by Nuclear Associates, International (NAI) and uses the B_1 method of GAM[3] and the integral transport method of THERMOS[4] to produce coarse-group cell-averaged cross sections. Its library is an adjusted set based on ENDF/B-I and II. CPM was developed by AB Atomenergi, Studsvik, Sweden, and uses collision probability methods similar to WIMS[5] with a library adjusted from ENDF/B-III to give agreement between CPM and CELL.

With the hope that ultimately no adjustments will be required, EPRI has sponsored the development of new libraries for CELL and CPM based on ENDF/B-IV and V and using the NJOY nuclear data processing system.[6] This code system operates directly from the ENDF/B files. It first reconstructs resonance shapes and linearizes all cross sections, then Doppler broadens them to all desired temperatures, and then adds unresolved self-shielded cross sections where required. Next thermal scattering data is added. Inelastic cross sections and energy-to-energy-by-angle scattering matrices can be produced from ENDF/B scattering functions $S(\alpha,\beta)$ (e.g., H in H_2O, D in D_2O, and graphite) or the free gas model. Elastic coherent or incoherent cross sections by energy and angle can be produced for hexagonal crystals (C,BeO) as well as for polyethyline and zirconium hydride. The result is a pointwise-ENDF (PENDF) file that can be saved as the starting point for several subsequent procedures. For multigroup codes, the GROUPR module of NJOY is used to average the PENDF cross sections. The results can then be reformatted using the POWR module into the proper forms for the CELL and CPM library maintenance programs, or the MATXSR module can be used to produce a file called MATXS appropriate for later coupling to discrete-ordinates transport codes such as ONETRAN[7] and its diffusion-accelerated successor ONEDA. Alternately, the PENDF file can be processed with the ACER module into a form acceptable to the Los Alamos continuous-energy Monte Carlo neutron and photon code MCNP.[8]

The multigroup codes account for resonance self-shielding using the background cross-section method.[9] For an accurate representation of the broad and intermediate resonances important for resonance absorption in thermal reactors, GROUPR uses a detailed pointwise calculation of the flux in an homogeneous mixture of the heavy absorber (e.g., ^{238}U) with a light moderator. The moderator can be real, (i.e., ^{1}H, ^{16}O), the ideal moderator that gives a 1/E source, or a combination of the two. Equivalence relations based on an infinite two-region model can then be used to obtain shielded cross sections[9] for CELL, CPM, or ONEDA.

This library generation process has been carried out using ENDF/B-IV and V for the four codes, EPRI-CELL, EPRI-CPM, ONEDA, and MCNP.

Initial ENDF/B Library Testing

As a first test, the ENDF/B-IV libraries were used to analyze the CSEWG benchmark[10] assembly BAPL-UO2-1. This is a simple light-water triangular lattice with a pitch of 1.558 cm fueled by aluminum-clad enriched uranium pins 1.15 cm in diameter. The calculated integral parameters are compared with results obtained using the standard NAI and Studsvik libraries in Table I. The lack of agreement is very disappointing.

The largest difference here is clearly the prediction of ^{235}U resonance absoption using the ENDF-based CELL library (note ρ_{28} and σ_{a3}).

EPRI-CELL Epithermal Disadvantage Factor

A study of the CELL code has shown that it implicitly assumes that the flux in the fuel is equal to the flux in the moderator when preparing cell average cross sections for its epithermal B_1 calculation. On the contrary, near a resonance, the fuel flux is expected to be depressed, putting the fuel at a relative "disadvantage" in competing for absorptions. A correct accounting for this effect would require separate detailed calculations for each different set of cell dimensions, and hence problem-dependent libraries. However, for many purposes, it is possible to define a simple disadvantage factor based on two-region equivalence theory.

Following the notation of Ref. 9, the fluxes in fuel f and moderator m are given by

$$V_f\Sigma_f\phi_f = (1-P_f)V_fS_f + P_mV_mS_m \quad , \quad \text{and} \tag{1}$$

$$V_m\Sigma_m\phi_m = P_fV_fS_f + (1-P_m)V_mS_m \quad , \tag{2}$$

where V is volume, Σ is macroscopic total cross section, ϕ is flux, and S is source. The escape probabilities are assumed to satisfy the reciprocity relation $V_m\Sigma_mP_m = V_f\Sigma_fP_f$, and the fuel escape probability is represented by the Wigner rational approximation

$$P_f = \frac{\Sigma_e}{\Sigma_e + \Sigma_f} \quad , \tag{3}$$

where Σ_e is an effective escape cross section. Assuming further that all fuel resonances are narrow with respect to moderator scattering ($S_m = \Sigma_m/E$) and using the intermediate-resonance approximation for fuel scattering [$S_f \simeq \lambda\Sigma_p|E+(1-\lambda)\Sigma_p\phi_f$], the fuel and moderator fluxes become

$$\phi_f = \frac{\Sigma_e + \lambda\Sigma_p}{\Sigma_e + \lambda\Sigma_p + \Sigma_a}\,\frac{1}{E} \quad , \quad \text{and} \tag{4}$$

$$\phi_m = (1-\beta)\,\frac{1}{E} + \beta\phi_f \quad , \tag{5}$$

where $\lambda\Sigma_p$ is an effective potential scattering and

$$\beta = \frac{V_f\Sigma_e}{V_m\Sigma_m} \quad , \tag{6}$$

Table I. Comparison of Integral Parameters of BAPL-UO2-1 for ENDF/B-IV and Standard Libraries Using Standard Codes

Integral Parameter[a]	Standard CELL	Standard CPM	ENDF/B-IV CELL	ENDF/B-IV CPM
k_∞	1.1330	1.1363	1.1020	1.1228
k_{eff}	0.9978	0.9970	0.9701	0.9850
ρ_{28}	1.374	1.360	1.613	1.471
δ_{25}	0.0856	0.0840	0.0883	0.0819
δ_{28}	0.0700	0.0716	0.0734	0.0724
σ_{a3}	1.874b	1.911b	2.246b	2.073b
σ_{f3}	25.48b	24.97b	25.99b	24.31b

[a] ρ_{28} is ^{238}U epithermal to thermal capture ratio.
δ_{25} is ^{235}U epithermal to thermal fission ratio.
δ_{28} is ^{238}U to ^{235}U fission ratio.
σ_{a3} and σ_{f3} are ^{238}U absorption and ^{235}U fission for the 0.625 eV to 5.53 keV group.

is an heterogeniety parameter (β =1 gives the close-packed limit where $\phi_f = \phi_m$ as assumed in CELL, while β = 0 gives an isolated rod with $\phi_m = 1/E$; β = 0.407 is appropriate for the BAPL-UO2-1 cell).

It is now easy to define disadvantage factors for the fuel and moderator regions based on flux and volume weighting:

$$D_f = \frac{V_f\phi_f}{V_f\phi_f + V_m\phi_m} = \frac{V_f}{V_f + V_m}\,\frac{1}{1 + d\Sigma_a} \quad , \tag{7}$$

where d can be called the "disadvantage coefficient" (d = 0.357 cm for BAPL-1),

$$d = \frac{(1-\beta)V_m}{(V_f+V_m)\ (\lambda\Sigma_p+\Sigma_e)} \quad . \tag{8}$$

Equation (7) clearly leads to a reduction in fuel cross sections for an energy group containing a large absorption resonance. The moderator factor is given by

$$D_m = \frac{V_m\phi_m}{V_f\phi_f + V_m\phi_m} = \frac{V_m}{V_m + V_f}\,\frac{1 + \frac{V_f + V_m}{V_m}\,d\Sigma a}{1 + d\Sigma a} \quad . \tag{9}$$

Coding to implement this correction has been added to EPRI-CELL for use with ENDF/B-IV and V libraries. Table II shows a comparison of the modified CELL with MCNP, ONEDA, and EPRI-CPM for a simplified infinite model of BAPL-UO2-1 using ENDF/B-IV libraries. The new method together with consistent libraries clearly reduces the absorption discrepancy between the codes (note that this CPM library has not been adjusted).

Since the MCNP calculation is nearly a correct solution to this problem, the results in Table II cast severe doubt on the validity of the original CELL and CPM libraries. It is suspected that the original NAI

Table II. Comparison of EPRI-CELL With Disadvantage Factor Against Several Other Codes for Infinite BAPL-1[a] Using ENDF/B-IV

Parameter	CELL	CPM	ONEDA[b]	MCNP
k_∞	1.1273	1.1241	1.1241	1.1298
ρ_{28}	1.1422	1.424	1.443	1.427
δ_{25}	0.0826	0.0797	0.0827	0.0826
δ_{28}	0.0683	0.0685	0.0682	0.0689
$^{235}\sigma_f$	1.281	1.297	1.297	1.302
	1.646	1.670	1.672	1.685
	25.54	24.32	25.35	25.58
	366.1	367.0	366.8	369.4
$^{238}\sigma_a$	0.452	0.436[c]	0.459	0.458[d]
	0.250	0.254	0.253	0.266
	2.061	2.063	2.075	2.049
	1.791	1.795	1.793	1.800

[a] Infinite cylinder (zero buckling) with white boundary conditions on outer radius.

[b] P_3, S_8, 20 fine mesh intervals, CPM 69-group structure.

[c] n,2n subtracted.

[d] No unresolved self-shielding.

resonance absorption shielding factors were produced incorrectly and do not reflect the ENDF/B evaluation used at that time.[11]

Part of the remaining discrepancy in ^{238}U resonance absorption is probably due to the rather coarse group structure used in CPM and ONEDA. Two other differences between CPM and CELL are yet to be explained: the CPM ^{235}U resonance fission is too low, and the CPM transport cross section is larger than the EPRI-CELL value. The first has little impact except on δ_{25}, but the second causes CPM to predict low values of k_{eff}.

Resonance Overlap and Scattering

Comparisons between the fine-group cross sections used in the CELL and MCNP runs described above show that the resonance interference correction used in CELL does not represent ^{235}U fission well (the results quoted here did not use this option). Resonance interference should become more important at high burnup, and methods to correct for it should be studied. Similar comparisons show that it is important to self-shield resonance scattering from ^{238}U in the fuel pin.[9] Since neither CELL nor CPM allows for this effect, the ENDF/B-IV and V libraries were prepared containing elastic scattering matrices using 50 barns of background cross section for ^{238}U and ^{232}Th but infinite dilution for all other materials. This problem also needs further study.

Thermal Lattices Using ENDF/B-V

As an example of the application of ENDF/B-V to thermal reactor analysis, results for the integral parameters of several lattices are given in Table III. These numbers are generally closer to experiment than the same numbers obtained using ENDF/B-IV. However, the models are fairly crude when compared to full-core Monte Carlo, and these results shouldn't be interpreted as "benchmarks" of ENDF/B-V. They do show that the quality of the results produced by EPRI-CELL and EPRI-CPM is close to that required for engineering studies of reactor fuel cycles. Additional "tuning" of the approximate methods by comparison with Monte Carlo and, perhaps, some small cross-section adjustments, should produce an accurate tool for many practical problems.

This positive result combined with the reasons discussed above (i.e, up-to-date evaluations, open access, analysis of advanced systems, regulatory accountability) provide a strong case for working toward a wide application of ENDF/B-V in the thermal power reactor industry.

Acknowledgments

Thanks are gratefully extended to Odelli Ozer (EPRI), M. Becker (RPI), and H. Henryson, Jr. (ANL) for many helpful conversations; to R. Q. Wright, V. Baker, and M. Williams at ORNL for their interaction on EPRI-CELL; to R. Prael (LASL) for his help with Monte Carlo processing theory and for the MCNP results reported here; and to R. M. Boicourt (LASL) for technical support.

References

1. Information and tapes for ENDF/B-V can be obtained from the National Nuclear Data Center, Brookhaven National Laboratory, Upton, NY 11973.

2. Additional information on ARMP can be obtained from the Electric Power Research Institute, P. O. box 10402, Palo Alto, CA 94304

3. G. D. Joanou and J. S. Dudek, "GAM-I: A Consistent P_1 Multigroup Code for the Calculation of Fast Neutron Spectra and Multigoup Constants," GA-1850 (1961).

4. H. C. Honeck, "THERMOS, A Thermalization Transport Theory Code for Reactor Lattice Calculations," BNL-5826 (1961).

5. J. R. Askew, F. J. Fayers, and P. B. Kemshell, J. Brit. Nucl. En. Soc. 5, 564 (1966).

6. R. E. MacFarlane et al., "The NJOY Nuclear Data Processing System: User's Manual," LA-7584-M (1978).

7. T. R. Hill, "ONETRAN: A Discrete Ordinates Finite Element Code for the Solution of the One-Dimensional Multigroup Transport Equation," LA-5990-MS (1975).

8. "MCNP - A General Monte Carlo Code for Neutron and Photon Transport," LA-7396-M (1978).

9. R. E. MacFarlane, "Data Processing for Power Reactor Fuel Cycle Codes," in Symposium Proceedings: Nuclear Data Problems for Thermal Reactor Applications, NP-1098 (ENDF-270) (1979).

10. "Cross Section Evaluation Working Group Benchmark Specifications," BNL19302 (ENDF-202) (1974).

11. O. Ozer, Electric Power Research Institute, personal communication (August 1979).

Table III. EPRI-CELL ENDF/B-V Results for Some CSEWG Thermal Benchmarks

Parameter[a]	TRX-2	TRX-1	BAPL-3	BAPL-1
k_∞	1.1590	1.1761	1.1287	1.1364
k_{eff}	0.9987	1.0001	1.0033	1.0015
ρ_{28}	(0.830±0.015)	(1.1311±0.02)	(0.906±0.01)	(1.39±0.01)
	0.8405	1.341	0.9192	1.417
δ_{25}	(0.0608±0.0007)	(0.0981±0.001)	(0.052±0.001)	(0.084±0.002)
	0.0596	0.0972	0.0520	0.0833
δ_{28}	(0.0667±0.002)	(0.0914±0.002)	(0.057±0.003)	(0.078±0.004)
	0.0689	0.0968	0.0527	0.0747

[a] Experimental numbers in parentheses.

FINITE ELEMENT BASIS USED IN CONSISTENT NUCLEAR DATA EVALUATION

F. Schmittroth
Hanford Engineering Development Laboratory
Richland, Washington 99352, USA

A method for the consistent evaluation of nuclear cross sections and other data is presented. The method allows the simultaneous inclusion of nuclear model calculations, microscopic and integral measurements, and the results of previously adjusted multigroup cross sections in a consistent evaluation. Complete covariance information is retained throughout the analysis.

[evaluation, cross section, covariance.]

Introduction

The evaluation of nuclear data often depends on the incorporation of diverse but related measurements, e.g. the simultaneous use of integral reaction rate measurements and microscopic cross section measurements. The evaluation of fission-product decay heat is a second example. Different integral experiments that represent samples irradiated for differing time intervals all provide an indirect measurement of the decay heat from a fission pulse. The evaluation method described here provides a consistent way to include the results of differing but related measurements. It utilizes a finite element basis representation that is especially suited for describing nuclear data that are well represented by continuous functions. Generalized least-squares methods are incorporated that allow the use of complete covariance information.

Finite Element Basis

Basis functions

Let the continuous function f(E) represent the desired evaluated function, e.g. a nuclear cross section as a function of the incident particle energy E. We then assume that f(E) can be approximated by the following sum of finite element basis functions $\{\Delta_i(E)\}$:

$$f(E) \simeq f_N(E) = \sum_{i=1}^{N} X_i \Delta_i(E). \qquad (1)$$

The choice of the basis functions $\{\Delta_i(E)\}$ is the key element in the method, and they are defined as follows. One first selects a set of mesh points $\{\varepsilon_0, \varepsilon_1, \ldots, \varepsilon_N, \varepsilon_{N+1}\}$ of the independent variable E. [Henceforth, E and f(E) will be described as energy and cross section solely for convenience in the discussion.] Once the energy mesh $\{\varepsilon_i\}$ is fixed, the i-th basis function is described by

$$\Delta_i(E) = \begin{cases} 0 & \varepsilon_{i+1} \leq E \leq \varepsilon_{i-1} \\ 1 & E = \varepsilon_i \\ \text{Defined by straight line interpolation} & \varepsilon_{i-1} < E < \varepsilon_{i+1} \end{cases} \qquad (2)$$

This triangle or "roof" function $\Delta_i(E)$ is clearly just a triangle of unit height whose vertex is at ε_i and whose legs terminate at ε_{i-1} and ε_{i+1}. It is obviously continuous. It therefore follows that the approximation [Eq. (1)] of f(E) by a sum of these triangle functions is piecewise linear and continuous.

This representation is a prime element in the determination of the scope of the method. Virtually any function that can be conveniently described by a continuous series of line segments is a potential candidate for the techniques described here. One of the severest limitations is the need to keep the number of mesh points $\{\varepsilon_i\}$ manageable. Cross sections with many sharp resonances are thus eliminated; although, energy-averaged resonant cross sections are manageable. Nevertheless, there is no intrinsic smoothness limitations as with low-order polynomial expansions for example. And the arbitrary choice of the mesh points $\{\varepsilon_i\}$ allows the user a great deal of flexibility in tailoring the representation to the application. A high mesh density need be used only where the cross section f(E) is rapidly varying.

Interpretation of the Coefficients $\{X_i\}$

As is well known in finite-element theory,[1] the expansion coefficients $\{X_i\}$ have a trivial but very convenient interpretation. Direct substitution into Eq. (1) will verify that

$$f_N(\varepsilon_i) = X_i \qquad (3)$$

Thus the value of X_i has a direct physical interpretation.

Covariance properties

In the same way as for the parameters $\{X_i\}$, the covariance properties of the $\{X_i\}$ are easily related to the covariance properties of f(E). In general, one has

$$\text{Cov}\,[f_N(E), f_N(E')] = \sum_{ij} \text{Cov}\,(X_i, X_j)\, \Delta_i(E)\, \Delta_j(E') \qquad (4)$$

for the covariance of $f_N(E)$ with $f_N(E')$. As before, it immediately follows that

$$\text{Cov}\,[f_N(\varepsilon_i), f_N(\varepsilon_j)] = \text{Cov}\,(X_i, X_j), \qquad (5)$$

so that the covariance term $\text{Cov}\,(X_i, X_j)$ also has a very simple and direct connection to the function being evaluated.

The finite set of discrete parameters $\{X_i\}$ generates an approximate representation of f(E) for all energies E. Likewise, the discrete covariance matrix $\{\text{Cov}\ (X_i,X_j)\}$ approximates Cov [f(E), f(E′)] for all E and E′. For energies E between two mesh points ε_i and ε_{i+1}, the approximating function $f_N(E)$ represents a straight-line interpolation between the values $f_N(\varepsilon_i)$ and $f_N(\varepsilon_{i+1})$. The situation is a bit more complicated for the covariance representation given in Eq. (4). First write

$$\text{Cov}\ (X_i, X_j) = \sigma_i\sigma_j\rho_{ij}, \tag{6}$$

where σ_i is the standard deviation of X_i.

Next assume that the correlation matrix depends only on the separation of ε_i and ε_j:

$$\rho_{ij} = \rho(\varepsilon_i - \varepsilon_j). \tag{7}$$

Then if $\rho(\varepsilon)$ is a slowly varying function and if σ_i varies slowly with respect to i, Eq. (4) can be approximated by

$$\text{Cov}\ [f_N(E), f_N(E')] \simeq \sigma(E)\sigma(E')\rho(E - E'), \tag{8}$$

where

$$\sigma(E) = \Sigma_i\ \sigma_i\ \Delta_i(E). \tag{9}$$

Under these moderately weak restrictions, Eq. (8) shows that the covariance representation given by Eq. (4) is relatively basis independent. If the correlation function $\rho(\varepsilon)$ in Eq. (7) is rapidly varying relative to the distance $|\varepsilon_i - \varepsilon_j|$ between adjacent mesh points, then the covariances described by Eq. (4) are more basis dependent.

Equation (4) provides a very convenient way to obtain a discrete parameterization of the covariance of continuous functions. In some ways, it is more suitable than the file 33 covariance formats[2] in the Evaluated Nuclear Data File (ENDF/B).[3] In ENDF/B for smoothly varying functions (file 3 data), one selects a set of energy intervals such that cross section values within an interval are completely correlated with a constant covariance. This artificial behavior is less with the covariance representation of Eq. (4).

Least Squares

The utility of the finite element representation described above resides in its very easy interface with existing least-squares algorithms. Here we review a particular method described elsewhere[4,5] and particularly suitable in cross section evaluations. The first step is to define a least-squares model equation

$$\vec{f}_m = A\vec{X} \tag{10}$$

that relates a vector $\vec{f}_m$ of measurements to a vector of least-squares parameters $\vec{X}$ that are to be determined. Consider a set $\{f_{m\alpha}\}$ of microscopic cross section measurements at a set $\{E_\alpha\}$ of corresponding incident particle energies. Then for each measurement α in the set, Eq. (1) becomes

$$f_{m\alpha} = \sum_{i=1}^{N} \Delta_i(E_\alpha)\ X_i\ , \tag{11}$$

which is in the desired least-squares form. The elements of the design matrix A are given by

$$A_{\alpha i} = \Delta_i(E_\alpha)\ . \tag{12}$$

The least squares solution[5] is now defined as the minimum of

$$S^2_r = (\vec{f}_m - A\vec{X})^t M_f^{-1}\ (f_m - A\vec{X}) + (\vec{Z} - \vec{Z}_o)^t\ M_{Zo}^{-1}\ (\vec{Z} - \vec{Z}_o) \tag{13}$$

where

$$Z_i = \ln(X_i)\ , \tag{14}$$

and

$$Z_{oi} = \ln(X_{oi})\ . \tag{15}$$

The second term in Eq. (13) casts the least-squares problem into a data-adjustment format[6,7] whereby one utilizes the set of measurements $\vec{f}_m$ to adjust a set of previously known values $\vec{X}_o$. These prior values $\vec{X}_o$ could come from a nuclear model calculation for instance. Any uncertainties and correlations that arise from such a model calculation are included in the fractional covariance matrix M_{Zo} to ensure a proper weighting. For example, a nuclear model calculation that was expected to predict the energy dependence of the cross section accurately but not its magnitude would give a covariance matrix M_{Zo} that contained strong correlations but large uncertainties. The logarithms in Eqs. (14) and (15) ensure that the cross section values $\{X_i\}$ are never negative. As noted before, Eq. (3) shows that the values of the least-squares parameters $\{X_i\}$ can be directly interpreted as the cross section values themselves. Likewise [see Eq. (5)], the matrix elements Cov (X_i,X_j) can be directly identified with the cross section covariances.

The fractional and absolute covariance matrices are related by

$$(M_Z)_{ij} = \frac{\text{Cov}\ (X_i,X_j)}{X_i\ X_j}\ . \tag{16}$$

Finally, any uncertainties and correlations in the experimental measurements $\vec{f}_m$ are given a proper weighting by the covariance matrix M_f.

The actual algorithm used to obtain a minimum for Eq. (13) as well as the calculation of final uncertainties and correlations in the adjusted least-squares parameters has been described elsewhere.[5]

Features

Integral data

Some features of the present method are easier to discuss in the context of specific examples. Two examples, a cross section evaluation and a fission-product decay-heat evaluation are presented elsewhere in this conference. Both examples have the potential

for integral measurements of the form

$$f_{m\alpha} = \int_{E_{L\alpha}}^{E_{U\alpha}} R_\alpha(E') \, f(E') \, dE' \qquad (17)$$

where α indexes a particular integral measurement corresponding to an integration of the microscopic function f(E) with some response function $R_\alpha(E)$. For a cross section evaluation, the integration can represent an integral reaction rate measurement. For decay heat, the integration represents an integration over the irradiation time of the sample. In either case, one can insert Eq. (1) into Eq. (17) to obtain the standard least-squares model equation, Eq. (10). The elements of the design matrix are given by

$$A_{\alpha i} = \int_{E_{L\alpha}}^{E_{U\alpha}} R_\alpha(E') \, \Delta_i(E') \, dE'. \qquad (18)$$

Once they are calculated for a particular set of basis functions $\{\Delta_i(E)\}$, the least-squares formalism applies exactly as before.

The integral in Eq. (17) could also represent the calculation of a multigroup cross section. Then one could use any available set of multigroup cross section values as "measurements" to adjust the microscopic cross section f(E).

Sequential adjustment and partitioning

Two other features, sequential adjustment and partitioning, have been described elsewhere.[5,7] They are reviewed here only briefly in the context of the present examples. If all integral and microscopic measurements are lumped into a single measurement reactor $\vec{f}_m$, then the covariance matrix M_f can become unmanageably large. Fortunately, the least-squares method allows the sequential addition of data in a step-by-step adjustment of the microscopic values as long as the individual data sets are statistically independent. Each independent measurement of the cross section, whether an integral measurement or a set of microscopic measurements can be added one at a time. The same is true for the decay heat problem. Similarly, the covariance matrix for the parameter vector $\vec{X}$ can also become unwieldy. Decay heat measurements can include separate measurements of the beta, gamma, and total decay heat. One can partition the parameter vector into two subvectors, one representing the beta decay heat curve and one for the gamma. As for the measurement vector $\vec{f}_m$, this partitioning of the parameter vector can save large amounts of computer time and storage. A complete cross section evaluation could pose a similar example. Various parameter partitions could represent various partial cross sections. Then it would be possible to include measurements of the total cross section in the evaluation of the partial cross sections.

Summary

It was shown how a very simple set of "triangle" basis functions taken from finite element theory can be used to model nuclear cross sections and other nuclear data that are well represented by continuous functions. Furthermore, this representation was imbedded in a generalized least-squares method that allows a complete accounting of important data uncertainties and correlations.

References

1. W. J. Strang and G. J. Fix, An Analysis of the Finite Element Method, Prentice Hall (1973).

2. F. G. Perey, "The Data Covariance Files for ENDF/B-V," ORNL/TM-5938, Oak Ridge National Laboratory (July 1977).

3. The Evaluated Nuclear Data File (ENDF/B) is maintained by and may be obtained from the National Nuclear Data Center (NNDC) at Brookhaven National Laboratory, Upton, New York.

4. F. Schmittroth, "Generalized Least-Squares for Data Analysis," HEDL-TME 77-51, Hanford Engineering Development Laboratory (March 1978).

5. F. Schmittroth, Nucl. Sci. Eng. ,72, 19 (1979).

6. A Gandini, "Nuclear Data and Integral Measurement Correlation for Fast Reactors Part 2: Review of Methods," RT/FI(73)22, Comitats Nazionale per l'Energia Nucleare (1973).

7. J. B. Dragt, "Statistical Considerations on Techniques for Adjustment of Differential Cross Sections with Measured Integral Parameters," in M. Bustraan et al., "STEK, The Fast-Thermal Coupled Facility of RCN at Petten," RCN-122, p. 85, Reactor Centrum Nederland (1970).

EFFECT OF RESONANCE INTERERENCE BETWEEN U-238 AND CS-133 ON ISOTOPIC CORRELATION OF FISSION PRODUCT

H. Takano, Y. Ishiguro and S. Matsuura
Japan Atomic Energy Research Institute
Tokai-mura, Ibaraki-ken, Japan

Interference effect between resonances of ^{238}U and ^{133}Cs was calculated for the spent fuel rod of Japan Power Demonstration Reactor I (JPDR-I). The resonance interference effect reduces resonance integral af ^{133}Cs by 4-15 percent. The main reduction is caused by the resonance interference between the 5.9 eV level of ^{133}Cs and 6.67 eV level of ^{238}U. The interference effect depends considerably on bath the concentration of ^{133}Cs and the void fraction of coolant water, but its dependence on temperature variation of fuel rod is small. The effective resonance integral af ^{133}Cs becomes small by about 5 percent when the void fraction of coolant water is changed from zero to 45 percent. It is concluded that the value of five percent is very important correction factor which proves a linear correlation between activity ratio $^{134}Cs/^{137}Cs$, neutron capture product to direct fission product, and burnup.

[^{133}Cs, ^{238}U, resonance interference effect, spent fuel, JPDR-I reactar, resanance integral, fission product, burnup.]

Introduction

Activity ratias between product of neutron capture and direct fissian have been considered as a good indicator of burnup.[1] The activity ratio such as $^{134}Cs/^{137}Cs$ depends on spatial distribution of neutron spectrum or void fraction during operatian. By calculating accurately the spatial variations, a linear correlation between activity ratia and burnup was found[1]. In the calculation, hawever infinitely dilute resonance integrals were assumed far resonance integral af fission products. This treatment is valid for the case where mutual resanance shielding effect is not very important among related nuclei. In the present paper, the resonance interference effect between ^{133}Cs and ^{238}U is calculated and the effect of interference on isotopic correlation of fission praduct is studied.

Calculational Method

Doppler-broadened Cross Sectian

Resonance cross sections of ^{133}Cs and ^{238}U were calculated with the TIMS[2] code by using the resanance parameters of ENDF/B-IV. Comparisan of the capture cross sections for the temperature 743°K is shown far a typical energy range in Fig. 1. It can be found from this figure that several important resonances of ^{133}Cs and ^{238}U are overlapping. Thus, the effective resanance integral of ^{133}Cs should be calculated by considering mutual shielding effect by ^{238}U.

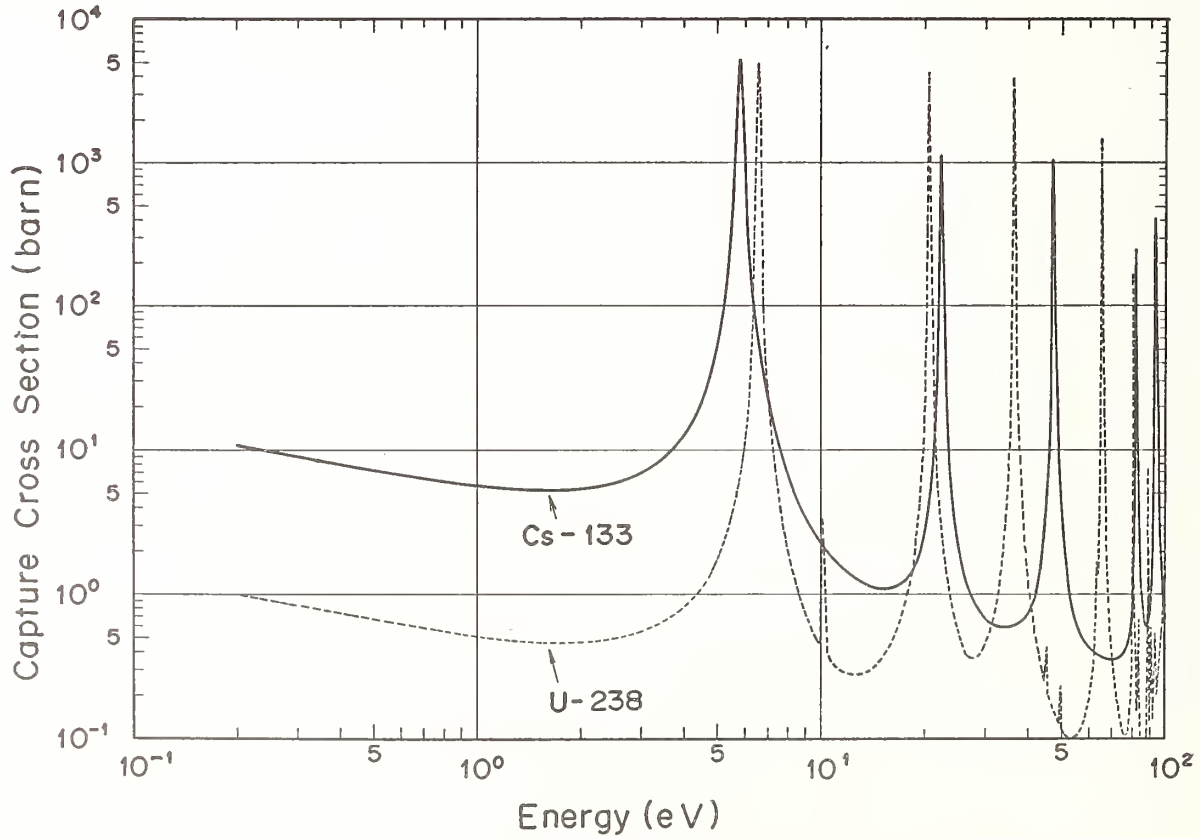

Fig. 1 Capture cross sections of Cs-133 and U-238 calculated with the TIMS code

Effective Resonance Integrol

The neutron spectrum wos colculoted for the spent fuel rod of Japan Power Demonstration Reactor (JPDR-1), which is a BWR. The calculations were performed with the TIMS code[2] which solves numericolly the neutron slowing down equotion using the RABBLE code method[3]. The cylindricol cell model used in the present colculotion is shown in Fig. 2. Toble I lists the otomic number densities in eoch region cell. The colculoted neutron spectro ore shown in Fig. 3. The spectro depend on the void froction of coolont woter ond olso on temperoture.

The effective ond infinitely dilute copture cross sections colculoted for the twenty-five - group structure[4] ore compored in Fig. 4. From this figure, it con be found thot the resononce integrol of ^{133}Cs is moinly reduced by the resononce interference between the 5.9 eV level of ^{133}Cs ond 6.67eV of ^{238}U. Furthermore, the interference effect depends considerobly on both the void froction of coolont woter ond the concentrotion of ^{133}Cs, os seen in Fig. 5. It should be noticed thot the copture resononce integrol for the 5.9 eV level occounts for obout 75 percent of totol one of ^{133}Cs. Therefore, the mutuol resononce shielding effect for the 5.9 eV resononce is very importont. The copture shielding foctors colculoted for the energy ronge of 10 to 4.65 eV ore chonged between 0.94 ond 0.8 depending on void froction of coolont woter ond concentrotion of ^{133}Cs. This meons thot the effect of the mutuol resononce interference on the totol resononce integrol ore obout 4 - 15 percent.

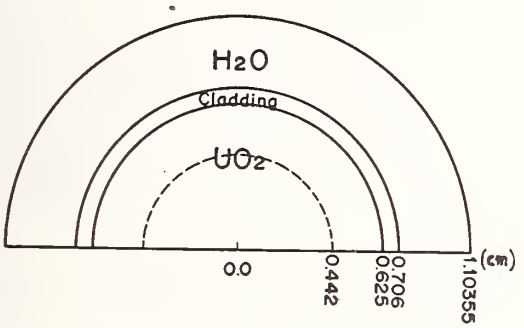

Fig. 2 Cylindricol cell model for the spent fuel rod in JPDR-1

Toble 1. Atomic number densities (otoms/born)

Region / Nuclide	Fuel	Clodding	Moderotor
^{235}U	6.0593×10^{-4}		
^{238}U	2.2457×10^{-2}		
^{133}Cs	3.0×10^{-5}		
O	4.6451×10^{-2}		2.5274×10^{-2}
Zr		4.2721×10^{-2}	
Fe		1.1856×10^{-4}	
Ni		4.5680×10^{-5}	
Cr		8.016×10^{-5}	
H			5.0548×10^{-2}

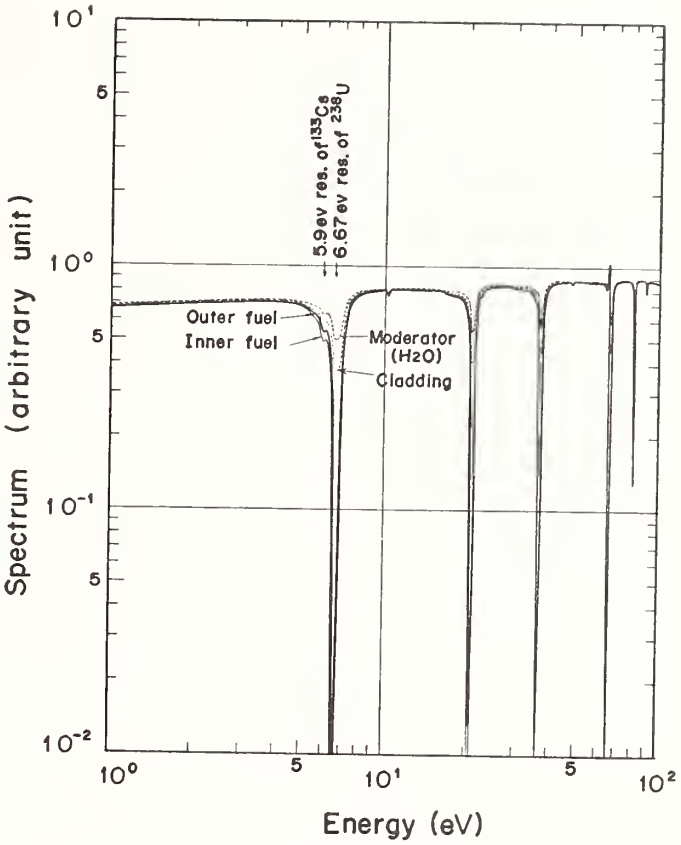

Fig. 3 Neutron spectrum colculoted with the TIMS code for the cose; the steom void froction = 25 percent, the density of Cs^{133} = 5 percent of ^{235}U density ond the fuel temperoture = 743 °K.

In Fig. 5, the shielding foctor is shown to be reduced by obout 7 percent when the void froction of coolont woter is chonged from zero to 45 percent. Then, the totol effective copture resononce integrol becomes smaller by about five percent. The five percent is o very importont correction foctor which proves o liveor correlotion between the octivity rotio $^{134}Cs/^{137}Cs$ ond burnup, as described in the next section.

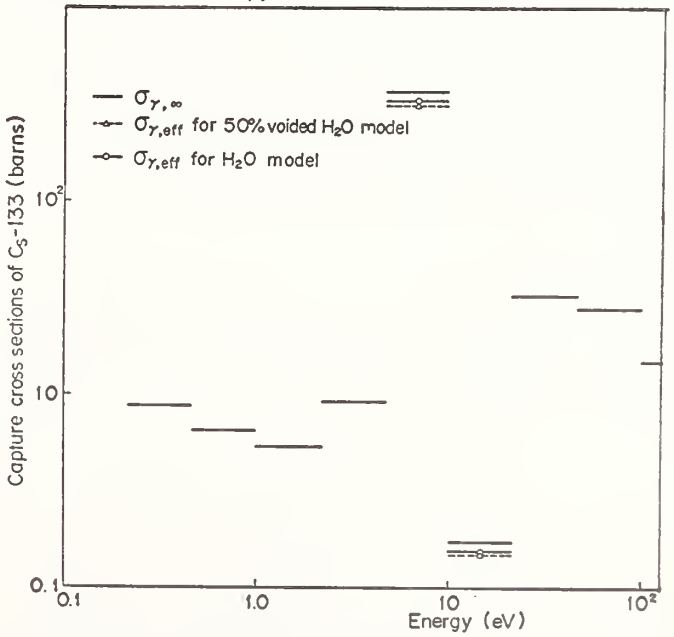

Fig. 4 Comporison of effective copture cross sections of ^{133}Cs

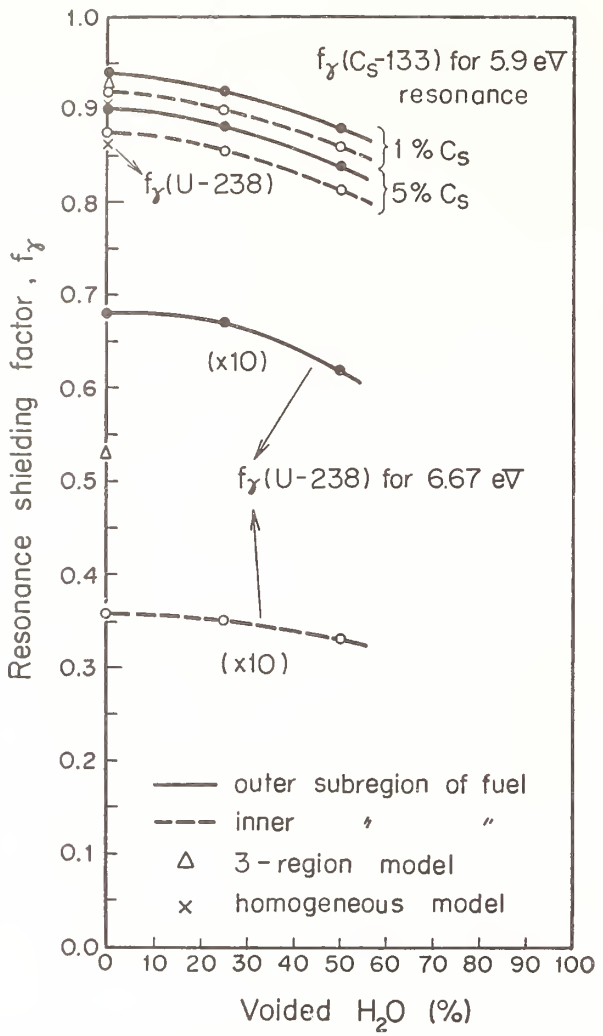

Fig. 5 Resonance copture shielding factors of ^{133}Cs and ^{238}U as function of the steam void fraction

Uncertointy in Resononce Parometers

In the BNL-325,[5] the evaluated resonance porometers are Eo = 5.9± 0.04 (eV), Γ_n = 5.4± 0.4 (meV) ond Γ_r=115±20(meV) for ^{133}Cs, and Eo=6.67±0.02(eV), Γ_n=1.52±0.02 (meV) and Γ_r =26±2 (meV) for ^{238}U, respectively. When the resonance porometers are changed by the given errors, the maximum change of the capture resonance integral and shielding foctor for ^{133}C is about 13 and 14 percent, respectively.

Temperoture Dependence

The Doppler-broadened cross sections of ^{133}Cs and ^{238}U were colculated for the temperatures T=300 and 1100°K. The copture shielding factor of ^{133}Cs for T=1100°K becomes larger than that for T=300°K by only one percent.

Isotopic Correlation of Fission Product

The activity ratios of fission products $^{134}Cs/^{137}Cs$ and $^{154}Eu/^{137}Cs$ have been studied[1] in their relation to burnup. The study showed that the activity ratios of the fission products can be expressed by a linear function of burnup, provided that corrections are made for differences in irradiation history and for spatial variations in the neutron spectrum. When the power distribution in a core shifts during irradiation, the short-lived and long-lived nuclides come to differ in their distribution : The long-lived nuclides such as ^{137}Cs ond ^{154}Eu retain their whole irradiation history, while the short-lived ^{134}Cs reflects in the behovior mostly the more recent history. The effect of this irradiation history on the correlation between the octivity ratio and burnup wos studied in detail in Ref.(1). In the present paper, the effect of spatial varriation of neutron spectrum on the correlation is described.

A typical characteristic of the BWR is the spatial variation of neutron spectrum in the core due to steam void formation and the existence of the woter gap. The omount of accumuloted ^{137}Cs depends mainly on the time integration of the neutron flux ; besides the formation of ^{134}Cs depends on the neutron capture cross section of ^{133}Cs. If the neutron flux does not change during irradiation and the half-lives of the fission products are long enough compared with the irradiation time, the octivity of a direct fission product N_{137} and that of o neutron capture product N_{134} ore described by

$$N_{137} \propto \bar{\Sigma}_f \cdot \Phi \qquad (1)$$

$$N_{134} \propto \bar{\Sigma}_f \cdot \tilde{\sigma}_\gamma^{133} \Phi^2 \qquad (2)$$

where Φ is the totol neutron ϕ multiplied by irradiation time, $\bar{\Sigma}_f$ the spectrol averaged fission cross section of the fuel rod ond $\tilde{\sigma}_\gamma^{133}$ the spectral averaged neutron copture cross section of ^{133}Cs.

Considering that these nuclides are formed seporately with epithermol ond thermol neutrons, the rotio N_{134}/N_{137} is expressed for a given burnup volue, i.e. for constont $\bar{\Sigma}_f \cdot \Phi$ by

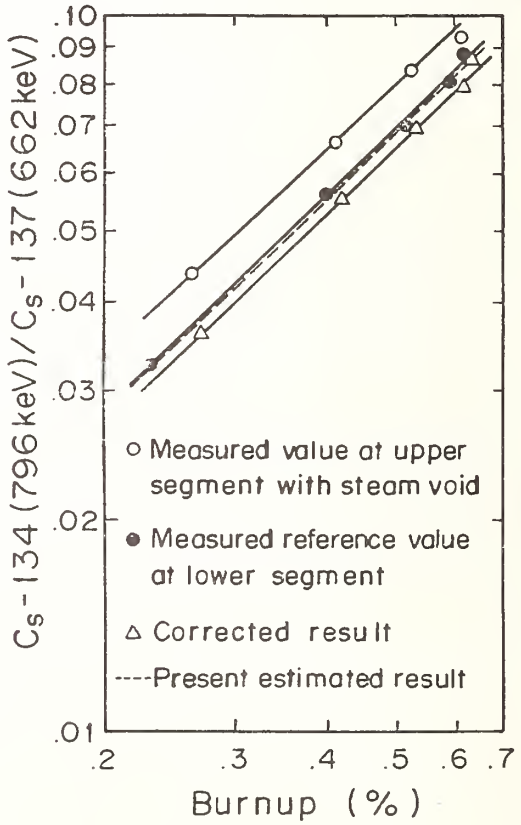

Fig. 6 Activity ratio $^{134}Cs/^{137}Cs$ plotted against burnup

$$\frac{N_{134}}{N_{137}} \propto \frac{\tilde{\sigma}^{133}_{\gamma,th}}{\bar{\Sigma}_{f,th}} \frac{1+\dfrac{\tilde{\sigma}^{133}_{\gamma,ep}\phi_{ep}}{\tilde{\sigma}^{133}_{\gamma,th}\phi_{th}}}{1+\dfrac{\bar{\Sigma}_{f,ep}\phi_{ep}}{\bar{\Sigma}_{f,th}\phi_{th}}} \quad (3)$$

where the subscripts ep and th stond for the epithermal ond thermol energy regions, respectively. The copture crass sectian is obtained by

$$\tilde{\sigma}^{133}_{\gamma,ep} = \frac{RI}{\int_{E_{c,th}}^{E_{c,ep}} \frac{1}{E}\,dE} \quad (4)$$

where RI stonds for the resonance integral in the epithermal region, ond E_c the cut-off energy. In a BWR, $\bar{\Sigma}_{f,ep}/\bar{\Sigma}_{f,th}$ is about 0.1, $\tilde{\sigma}^{133}_{\gamma,ep}/\tilde{\sigma}^{133}_{\gamma,th}$ is 2.6 and ϕ_{ep}/ϕ_{th} ranges from obout 1 to 2. Thus, the ratio of N_{134}/N_{137} varies with ϕ_{ep}/ϕ_{th} even for the same burnup. According ta Eq.(3), the ratio of a given value $(N_{134}/N_{137})_i$ to the reference $(N_{134}/N_{137})_o$ is expressed by

$$C_i = \left(\frac{N_{134}}{N_{137}}\right)_i \Big/ \left(\frac{N_{134}}{N_{137}}\right)_o = \frac{\left[1+\dfrac{\tilde{\sigma}^{133}_{\gamma,ep}\phi_{ep}}{\tilde{\sigma}^{133}_{\gamma,th}\phi_{th}}\right]_i \left[1+\dfrac{\bar{\Sigma}_{f,ep}\phi_{ep}}{\bar{\Sigma}_{f,th}\phi_{th}}\right]_o}{\left[1+\dfrac{\tilde{\sigma}^{133}_{\gamma,ep}\phi_{ep}}{\tilde{\sigma}^{133}_{\gamma,th}\phi_{th}}\right]_o \left[1+\dfrac{\bar{\Sigma}_{f,ep}\phi_{ep}}{\bar{\Sigma}_{f,th}\phi_{th}}\right]_i} \quad (5)$$

Division by C_i canverts the measured octivity ratio into the value under the some neutron spectrum at the reference point.

Colculation by the FLARE cade[6] indicoted that the void fraction in the JPDR-I core distributed fram 0 ta 45 percent in the verticol direction. The neutran flux ratio ϕ_{ep}/ϕ_{th} at the fuel rod pasitian increased with vaid froctian from 1.1 ta 1.7.[7] In this calculatian, the values af 5.53 KeV and 0.625 eV were taken far $E_{c,ep}$ and $E_{c,th}$, respectively. By using the correction factor C_i the measured ratio $^{134}Cs/^{137}Cs$ was reduced ta the value for the neutran spectrum at the reference paint in lower segment of fuel rad. The result is shawn in Fig. 6 with the triangular symbals. The carresponding values for the upper and lawer segments have came much claser ta each other, though o small difference still remains.

In this carrectian calculatian, the capture cross sectian $\tilde{\sigma}^{133}_{\gamma,ep}$ was assumed as the infinitely dilute one. However, the effective capture cross section $\tilde{\sigma}^{133}_{\gamma,ep}$ is reduced by 5 percent in the variation of the steam void fractian os described above. The overcorrection produced by using the infinitely dilute cross sectian can be corrected by considering the mutual shielding effect depending on the steam void fraction. The result is shown alsa in Fig. 6.

The present result means that nan-destructively measured activity rotio $^{134}Cs/^{137}Cs$ is a good indicator, provided that the irrodiation history and the steam void fraction are accurotely given. Conversely, a diagonostic estimation of the vaid distributian in BWR-type reactor moy be possible by finding the relationship between the activity rotio $^{134}Cs/^{137}Cs$ ond resonance shielding effect af ^{133}Cs.

Conclusion

It was found that the resonance integral of ^{133}Cs was considerably reduced by the resanance interference effect between ^{133}Cs ond ^{238}U. The amount of the reduction depends on the slawing dawn pawer of maderatar materials, for example, on the steam void fraction in BWR-type reactor. Hence, when integrol properties for the fission products with lorge resonance such os ^{133}Cs are studied for BWR or gas cooled reoctors, the resonance shielding effect should be considered far the calculation of resonance integral.

References

1. S. Matsuura, H. Tsuruta, and T. Suzuki, et al., J. Nucl. Sci. Technal., 12[1], 24 (1975).
2. H. Takano, et al., ta be published. For exomple, this cade abstract is described in JAERI 1255 (1978).
3. P.H. Kier and A. A. Robba, ANL 7323 (1967)
4. L.P. Abagjan, et al., "Graup Canstants for Nucleor Reactar Colculatian", Cansultant Bureau, New Yark (1964).
5. S.F. Mughabghab and D. I. Garber, BNL-325 third ed., Val. I, 1973.
6. D. L. Delp., et al., GEAP-4598, (1964)
7. H. Ezure.: Private communication.

NEUTRON CROSS SECTIONS FOR FUSION

R. C. Haight
Lawrence Livermore Laboratory
Livermore, California 94550 USA

First generation fusion reactors will most likely be based on the $^{3}H(d,n)^{4}He$ reaction, which produces 14-MeV neutrons. In these reactors, both the number of neutrons and the average neutron energy will be significantly higher than for fission reactors of the same power. Accurate neutron cross section data are therefore of great importance. They are needed in present conceptual designs to calculate neutron transport, energy deposition, nuclear transmutation including tritium breeding and activation, and radiation damage. They are also needed for the interpretation of radiation damage experiments, some of which use neutrons up to 40 MeV. In addition, certain diagnostic measurements of plasma experiments require nuclear cross sections. The quality of currently available data for these applications will be reviewed and current experimental programs will be outlined. The utility of nuclear models to provide these data also will be discussed.

(Fusion, E_n=14 MeV, tritium breeding, neutron transport, radiation damage, neutron heating, activation, dosimetry)

Introduction

The goal of producing power with fusion reactors is now nearly in sight. Although one is continually reminded of how difficult the fusion reaction is to control, the progress of the past decade has been remarkable. The Tokamak concept of a magnetically confined plasma has matured and been tested in large-scale experiments to produce high temperature plasmas up to tens of keV; the magnetic mirror approach has evolved through new schemes to stabilize the plasma and radically new containment schemes such as the tandem mirror; and inertial confinement, with laser, electron or ion beam drivers, has been a product almost entirely of the 1970's.

System studies for fusion reactors have also progressed greatly during this time. Tokamak, mirror and inertial-confinement reactors all have been designed and extensively evaluated. From these studies, problem areas have been identified and several have been either solved through technical advances or obviated by changes in reactor design. In addition, novel opportunities afforded by fusion have emerged in the areas of material selection, isotopic tailoring, utilization of fast (14-MeV) neutrons, and applications of very high quality heat.

We have seen remarkable changes also in the status of nuclear data. For, in 1970 we had ENDF/B-II, ORELA was just coming on line, and pre-equilibrium particle emission was a concept in its infancy.

In this decade the needs for nuclear data for fusion have increased and broadened as a result of the progress in plasma devices and reactor concepts. Summaries of the status of and needs for nuclear data are *de rigueur* at cross section conferences. A selection of recent summaries is given in Table I. In addition, other recent reviews such as those on threshold reactions (e.g. Ref. 8), neutron dosimetry (e.g. Ref. 9), and data for radiation damage (e.g. Ref. 10) are directed to a great extent by fusion applications.

This review will cover certain neutron data currently perceived as important for fusion. Because the data needs have been well summarized previously (Table I), certain areas where the data needs are greatest will be discussed here. Many of these areas are now under active investigation, some with new techniques, and the considerable progress in the past few years will be illustrated. Experimental data will be emphasized here with occasional reference to nuclear theory and evaluation which are the central subjects of other reviews at this conference.

Why Neutrons?

The first generation fusion reactor, that is, the one with least demanding plasma requirements, will be based on the fusion reaction,

$$D + T \rightarrow n\ (14.1\ MeV) + \alpha\ (3.5\ MeV)$$

Somewhat more stringent plasma parameters must be met by the second generation reactors that will burn deuterium:

$$D + D \rightarrow n + {}^{3}He$$

and

$$D + D \rightarrow p + T$$
$$T + D \rightarrow n\ (14.1\ MeV) + \alpha$$

Table I. Neutron Data for Fusion - Some Previous Reviews[1-7]

1974	U.S. Nuclear Data Committee, CTR Subcommittee - USNDC-CTR-1
1975	D. Steiner - Cross Sections & Techn. Conf. - Washington
1975	S. M. Qaim, R. Wölfle, G. Stöcklin - Debrecen, Hungary
1976	C. Maynard - Int. Conf. Neutrons & Nuclei - Lowell
1977	Symposium on Neutron Cross Sections 10-40 MeV - Brookhaven
1978	O. N. Jarvis - Neutron Physics & Nuclear Data - Harwell
1978	IAEA Advisory Group Meeting on Nuclear Data for Fusion - Vienna

In both types of reactors, then, copious numbers of 14-MeV neutrons will be produced. (Third and later generation fusion reactors may use fuels that produce few neutrons and for them this present report would not be necessary.)

To capture the energy carried by the neutrons or to use them for other purposes, a blanket surrounds the plasma (Fig. 1). The constituents of the blanket vary with design but can be grouped into materials for structure, tritium breeding (always lithium, perhaps isotopically enriched), shielding, neutron multiplication, and those for controlling the plasma itself. The time-dependent list of materials (slowly varying) may be found in Refs. 1-4 and 6-7, and may be summarized as elements (and selected isotopes) with Z = 1, 3-9, 11-14, 20, 22-30, 39-42, 50, 73-74, and 82 with the addition of Z = 90-98 and fission products for fusion-fission hybrid reactors.

The special neutron data requirements for fusion reactors result from the large number of fusion neutrons and their energy. Compared with a fission reactor of equal nuclear power, a D-T fusion reactor produces seven times as many net primary neutrons:

Fusion: 1 n/17.6 MeV → $3.6 \cdot 10^{11}$ n/Joule

Fission: $(\bar{\nu}-1)$/200 MeV → $\gtrsim 0.5 \cdot 10^{11}$ n/Joule

And in the D-T fusion reaction 80% of the energy is carried by the neutrons compared to 2 to 3% in the fission reaction. These differences are enormous.

The neutron environments for fast-fission and fusion reactors are compared in more detail in Fig. 2. Here the neutron flux spectrum at the first wall of the standard blanket[11] (consisting of a niobium first wall and a mostly lithium breeding region) is plotted along with that of two EBR-II spectra.[12] This comparison shows similarities and the differences. On the favorable side is that below about 5 MeV, the EBR-II spectra bracket the fusion reactor spectrum. That means that much of the current experience with fission reactors can be adapted to fusion below 5 MeV neutron energy.

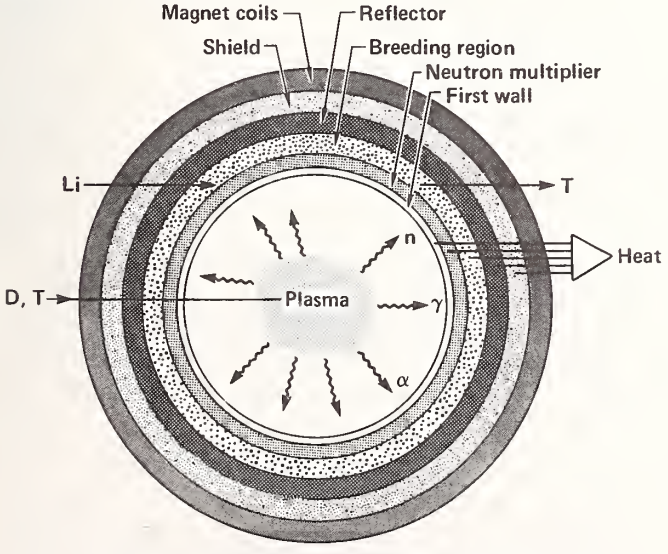

Fig. 1. Schematic view of the simplest D-T fusion reactor showing the essential elements for neutronics. For a D-D fusion reactor, the lithium-containing breeding region would be replaced by a non-breeding heat-exchange region.

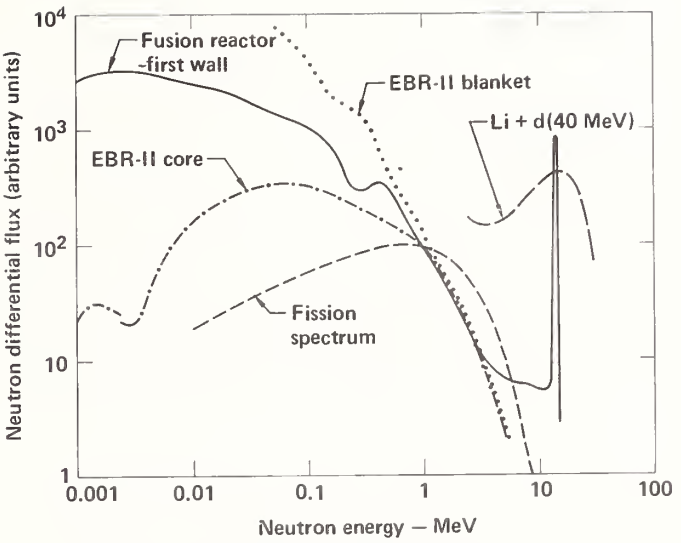

Fig. 2. Neutron flux spectra, arbitrarily normalized, at the first wall of the "standard blanket" (solid line). For comparison, two spectra of the EBR-II reactor are shown together with the spectrum for 0° neutrons from 40-MeV deuterons on a thick natural lithium target, representative of the Fusion Materials Irradiation Test facility, FMIT, now under construction.

In contrast, the effects of neutrons above 5 MeV will be far greater in fusion reactors. The areas where the differences are most marked are in

- tritium breeding (for D-T reactors)
- fast neutron transport, especially in light isotopes
- radiation damage
- neutron heating
- activation and dosimetry

These areas will now be discussed in turn. Finally, the special requirements for certain radiation damage facilities in the area of neutron transport for $E_n > 15$ MeV will be treated.

Tritium Breeding

For a D-T fusion reactor economy, tritium must be available in large quantities, and, in nearly every systems study, the tritium is envisaged to be bred in the reactor itself by reactions of the neutrons with lithium. Of crucial importance then is whether the breeding ratio (BR = tritium atoms formed for each one burned) is greater than unity so that the cycle is self-sustaining. For the standard blanket referred to earlier (a favorable case), the breeding ratio (calculated with ENDF/B-IV and the TARTNP Monte Carlo code[13]) is:

Reaction	BR
^{6}Li(n,t)	0.97
^{7}Li(n,n't)	0.57
Total	1.54

These ratios will be reduced by additional structural elements in the blanket; by penetrations for the neutral beam injectors, divertors and pumping ports; and by any intervening materials necessary for plasma containment. As a result the breeding ratio could be perilously close to 1.

How accurate then, are the data on which the calculation based? The most important cross section data for this mostly lithium blanket are those of ^{7}Li, both the (n,n't) cross section itself and the energy distribution of the emitted neutron. The published data for the former are illustrated in Fig. 3. If this cross section is considered uncertain by 25% (a rather large uncertainty but one that has recently been suggested[21]), then the breeding ratio for the standard blanket is uncertain by 10% which could be a very important uncertainty.

The energy spectrum of the emitted neutron in the $^{7}Li(n,n't)$ reaction is important because the emitted neoutron could induce another $^{7}Li(n,n't)$ reaction (Q = -2.47 MeV) if its energy is above 2.82 MeV (accounting for center-of-mass effects). Recent measurements of partial or complete spectra of the emitted neutrons have been made at Ohio University with monoenergetic neutrons ($4 < E_n < 7.5$ MeV),[22] Triangle Universities Nuclear Laboratory ($7 < E_n < 14$ MeV),[23] and Los Alamos (E_n = 6, 10, 14 MeV)[24] and with a white neutron source at the Oak Ridge National Laboratory ($1 < E_n < 20$ MeV).[25] Figure 4 gives the data at E_n = 10 MeV from Ref. 24 and compares them with the ENDF/B-IV evaluation. (For this material the ENDF/B-V evaluation is identical.) Clearly, some improvements in the evaluation are indicated for the non-elastic neutron emission spectrum. Examples of the elastic and discrete inelastic cross section data are shown in Figs. 5 and 6.

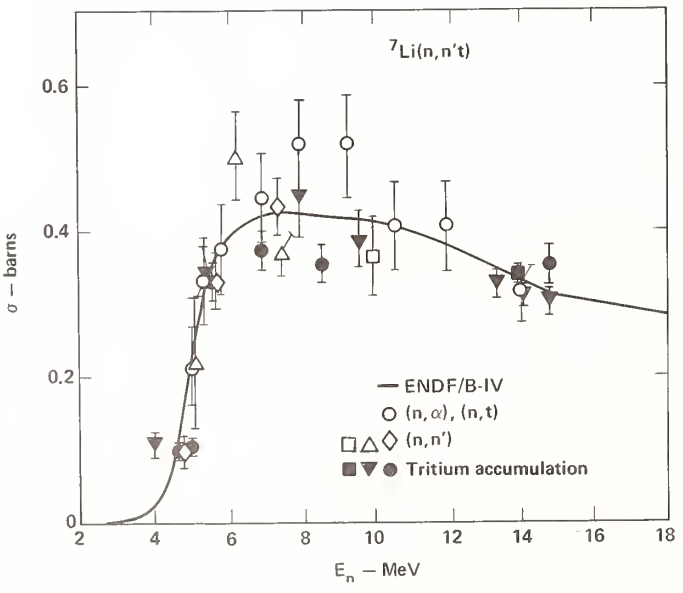

Fig. 3. Cross section for $^{7}Li(n,n't)$. Experimental values are deduced from tritium accumulation (Ref. 14 solid circles, Ref. 15 solid square, Ref. 16 solid inverted triangles); from tracks in photographic emulsion (Ref. 17 open circles); and from neutron emission spectra (Ref. 18 open triangles, Ref. 19 diamonds, Ref. 20 open squares). The solid curve is from ENDF/B-IV.

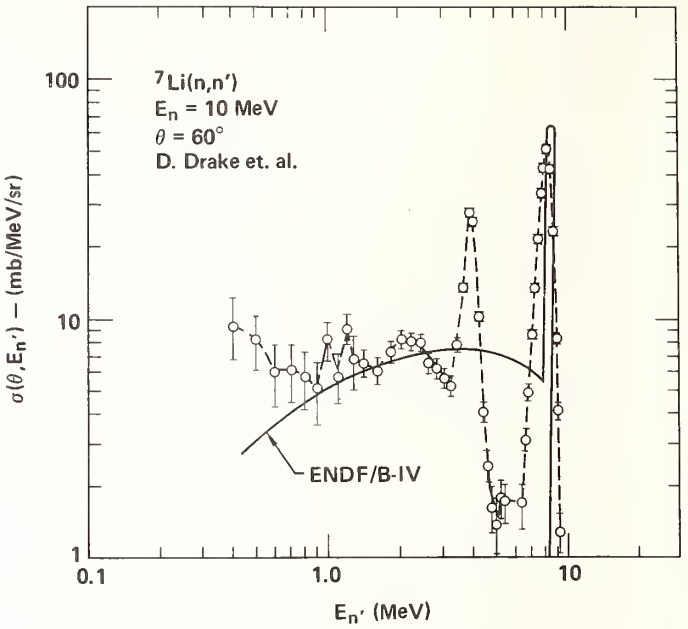

Fig. 4. Spectrum of neutrons emitted at 60° from 10-MeV neutron bombardment of ^{7}Li. Data are from Ref. 24.

This problem in the evaluated neutron emission spectra also manifests itself in integral experiments such as the LLL pulsed spheres (Ref. 26). On the other hand in lithium assemblies where the tritium is measured directly,[27] these errors in the evaluated neutron emission data could be compensated by changes in the (n,n't) cross section. Even if the large lithium assemblies can be calculated correctly, reactor blankets will contain more structural members, and the relative importance of the cross section and emission spectra likely would be different. Thus additional uncertainties are present. Because of these problems and because of the importance of the reactions in ^{7}Li, both the evaluation and the (n,n't) cross section data require substantial improvement.

The $^{6}Li(n,t)$ cross section on the other hand has received much attention as a standard cross section, and its values are quite well determined in the important region below a few MeV (notwithstanding the continuing debate over values near the 250-keV resonance). The global R-matrix analysis of Hale and Dodder[28] has significantly narrowed the range of uncertainty of this cross section. For most fusion reactor purposes, the $^{6}Li(n,t)$ cross section is considered known.

If the breeding ratio in a realistic design is close to unity, one could add neutron-multiplying materials to the blanket. For example, beryllium, uranium and thorium are often suggested. The (n,2n) reaction on each of these, and the (n,3n) and (n,f) reactions on the last two give the required extra neutrons. The penalty of course is a more complex and perhaps a more costly design.

Neutron Transport in Light Isotopes

The neutron scattering measurements on ^{7}Li are only part of recent progress in understanding neutron reactions on light isotopes of importance to fusion. Elastic and inelastic scattering of neutrons by ^{9}Be ($7 < E_n < 15$ MeV),[29] and ^{11}B and ^{13}C ($4.8 < E_n < 6$ MeV)[30] have been investigated. These studies have provided useful data directly and they

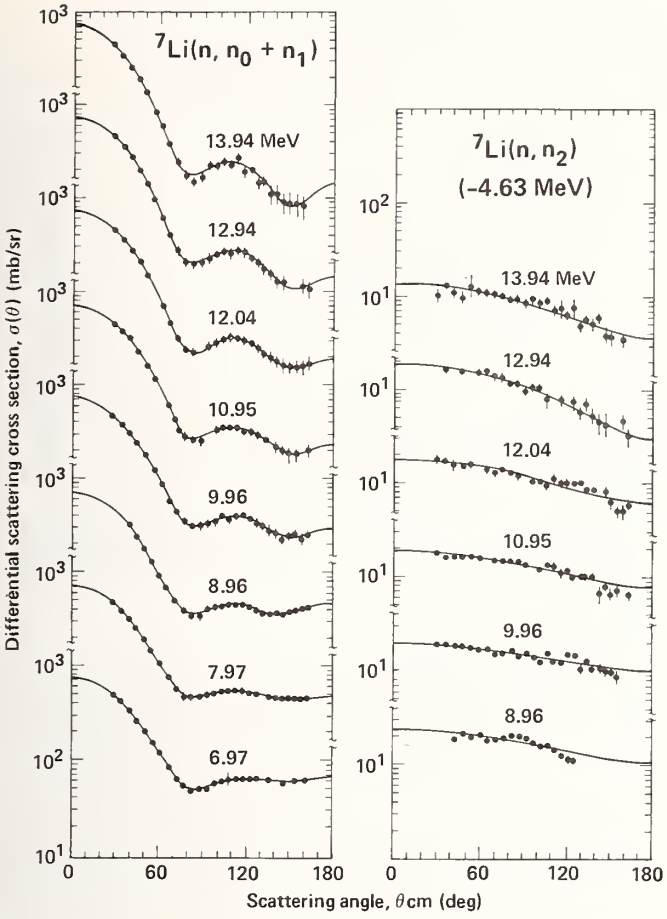

Fig. 5. Angular distribution of neutrons scattered from ^{7}Li. The left graph gives the sum of the elastic and 0.478 MeV-state cross sections; the right graph is for the 4.63 MeV state in ^{7}Li. The solid lines are Legendre polynomial fits. This figure is taken from Ref. 23.

have yielded insights into the possibilities of extending the optical model to such light nuclei[29] and into the resonance properties of these nuclei.[30]

To guide these monoenergetic measurements, extremely high-resolution total cross sections are available from white source measurements with a Van de Graaff-based ^{9}Be(d,n) source (Fig. 7). The total cross sections, of direct interest also in neutron transport, have been reported for ^{9}Be, ^{10,11}B, and ^{12,13}C from 1 to 20 MeV.[31]

Neutron Emission for Structural Materials

Neutron emission cross sections and spectra have been investigated for many years. Because of the importance of these data for neutron transport, reliable data are required. Of the recent measurements of these quantities, those of Hermsdorf et al.[32] at E_n = 14.6 MeV stand out for their comprehensiveness. They included Be, C, Na, Mg, Al, Si, P, S, Ca, Ti, V, Cr, Mn, Fe, Co, Ni, Cu, Zn, Ga, Se, Br, Zr, Nb, Cd, In, Sn, Sb, I, Ta, W, Au, Hg, Pb and Bi. These data have been used to assess nuclear reaction model calculations[33] and the accuracy of ENDF/B-V data.[34] To this author, the data of Ref. 32 would have been more useful if the reported spectra had included also the elastic scattering peak.

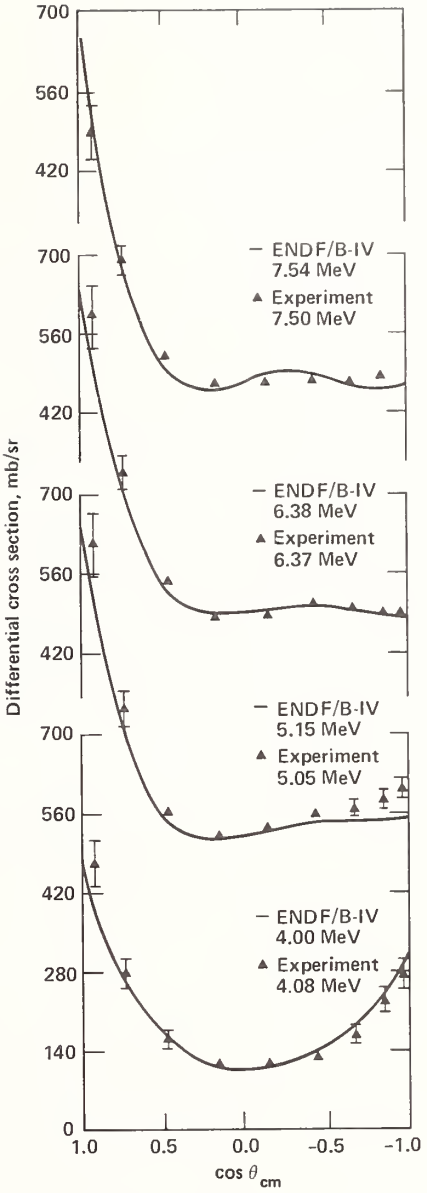

Fig. 6. Angular distribution of neutrons scattered elastically from ^{7}Li. The experimental data are from Ref. 22 from which this figure is taken.

Radiation Damage

Because of the large numbers of neutrons and their energy spectrum, the problem of radiation damage in fusion reactor materials is expected to be much more severe than that in fission reactors, perhaps by one to two orders of magnitude (see Introduction). Two new facilities have been created specifically to study radiation damage by fast neutrons, the Rotating Target Neutron Source RTNS-II facility at Lawrence Livermore Laboratory, and the Fusion Materials Irradiation Test facility at Hanford, Washington. The former, producing neutrons between 14 and 15 MeV, has been in operation for a year. The spectrum of the latter is a broad d + Li spectrum (Fig. 2); it is planned to be available for experiments by 1984.

(It should be noted here that many features of neutron-induced radiation damage can be simulated with charged-particle beams. For example the primary

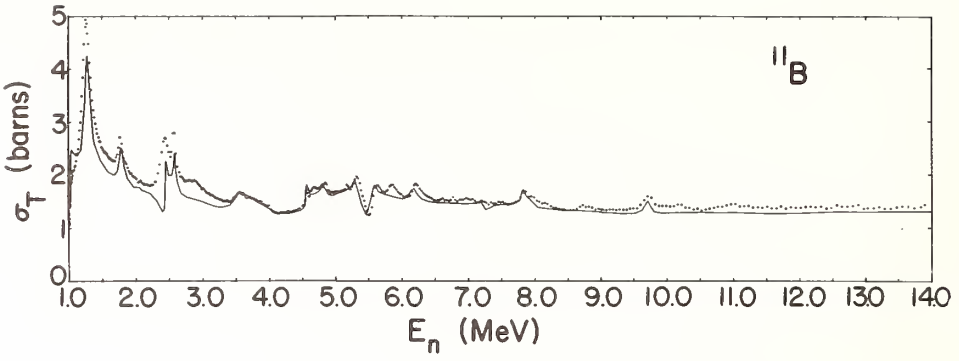

Fig. 7. Total cross section of ^{11}B as measured with a $^{9}Be(d,n)$ white neutron source using a Van de Graaff to accelerate the deuterons to 15 MeV. This figure is taken from Ref. 31. The solid line represents the ENDF/B-IV data.

recoil energy spectrum for 16-MeV protons incident on a material has been shown to be very similar to that for 14-MeV neutrons incident on the same material.[35] The beam intensities from existing accelerators induce the damage more rapidly than do available neutron fluxes and consequently the studies can progress quickly. The nuclear data needs for radiation damage thus include cross sections for charged particles as well as for neutrons.)

At present the nuclear cross sections of importance are for (1) all those interactions that lead to a recoiling heavy atom that then creates displacement damage by disordering other lattice atoms as it slows down, (2) transmutation reactions that produce hydrogen or helium; (3) transmutations that result in heavy atom impurities.

Data for Displacement Damage

The damage cross section depends on the energy of the recoiling heavy nuclei and on the efficiency of transmitting that energy into displacements. The energy spectrum of the recoiling heavy nucleus is typically calculated from the elastic scattering cross section and angular distribution and from the non-elastic cross section. If there are data or estimates on the energy and angular distribution of the emitted neutrons and other light particles, then the non-elastic component can be considerably refined (Fig. 8).

In most of the energy regions of interest to fusion, the optical model with appropriate parameters describes adequately the angular distribution for elastic scattering. Where the optical model encounters difficulties, usually at back angles, the differential cross section is usually relatively small. For iron, the backward elastic scattering accounts for the bump in Fig. 8 near 0.9 MeV. Although the several popular parameter sets do give somewhat different angular distributions, most of the differences are small compared with the present needs of radiation damage studies where knowledge of the damage energy spectrum to better than 20% is usually not needed.

Much of the damage results from non-elastic interactions (Fig. 9). To calculate these effects, the usual assumption is that the emitted light particles are isotropic in the center of mass. This assumption errs on the side of a too large calculated dose since direct and pre-equilibrium processes are characterized by forward-peaked light particles and less recoil energy. Because the pre-equilibrium particles represent only about 10% of the emitted particles for E_n = 14 MeV,[37] these effects are small compared with today's requirements for radiation damage studies. At higher incident neutron energies, the fraction of pre-equilibrium particles is higher and the effects may be important.

Hydrogen and Helium

The hydrogen and helium produced by (n,p), (n,d) and (n,α) reactions is a major concern for radiation damage. For typical reactors, in a year of operation a stainless steel first wall will be transmuted into several hundred ppm each of hydrogen and helium. At these levels, significant effects on material are likely for stainless steel. Other materials will of course have different responses to hydrogen and helium, and the responses will depend on temperature and the combined effects with displacement damage.

To guide the present radiation damage experiments, hydrogen and helium production cross sections must be known. They are being measured by several new techniques, gas accumulation (helium only) and charged-particle detection. Where they can be compared (Table II), the results agree well.

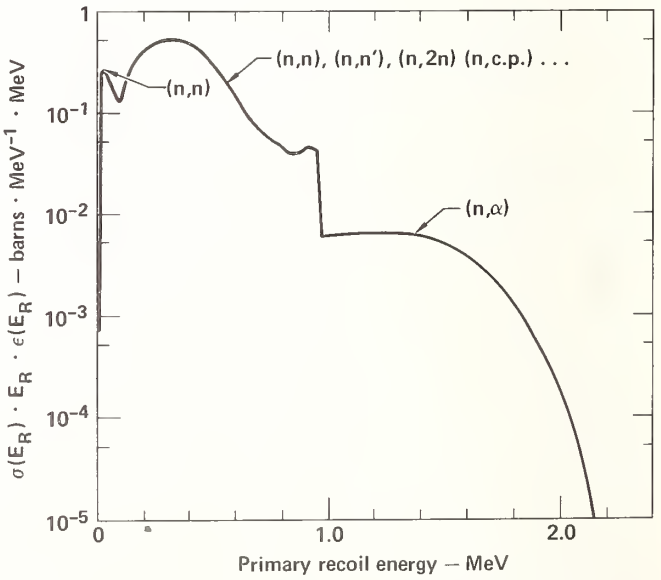

Fig. 8. Damage energy spectrum for 14-MeV neutrons on iron. Calculation from Ref. 36.

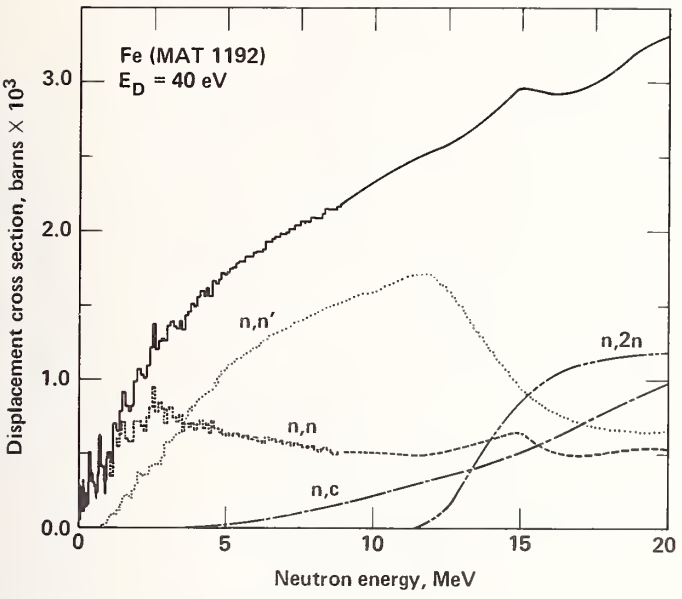

Fig. 9. Displacement cross section as a function of neutron energy showing the relative importance of elastic, inelastic and other reaction channels. This calculation is adapted from Ref. 10.

Table II. Helium production cross sections (mb at $E_n \cong 15$ MeV).

	Helium Accumulation[a]	Charged-Particle[b] Detection
Al	143 ± 7	121 ± 25
Ti	38 ± 3	34 ± 7
V	18 ± 2	17 ± 3
Fe	48 ± 3	43 ± 7
Ni	98 ± 6	97 ± 16
Cu	51 ± 3	42 ± 7
Nb	17 ± 5	14 ± 3

a. Ref. 38

b. Ref. 39

The helium accumulation measurement is by mass spectrometry after the sample has been exposed to a large neutron fluence such as that now practical at 14-15 MeV with the rotating target neutron source. For higher neutron energies, cyclotron-produced neutrons via the Be(d,n) reaction are used.[38]

The charged particles from neutron induced reactions are now detected cleanly by magnetic quadrupole spectrometers[40] that focus the charged particles (p,d,α...) from the foil when they are born to a detector removed from the intense radiation field of the source (Fig. 10). These measurements provide information on hydrogen as well as on helium production and the charged-particle spectra and angular distributions. These latter data are useful in identifying the reaction mechanisms such as in quantitative studies of second-chance proton emission (Fig. 11).[41] The spectra are also useful in validating nuclear reaction model codes that can predict the cross sections at different neutron energies where the measurements may be more difficult.

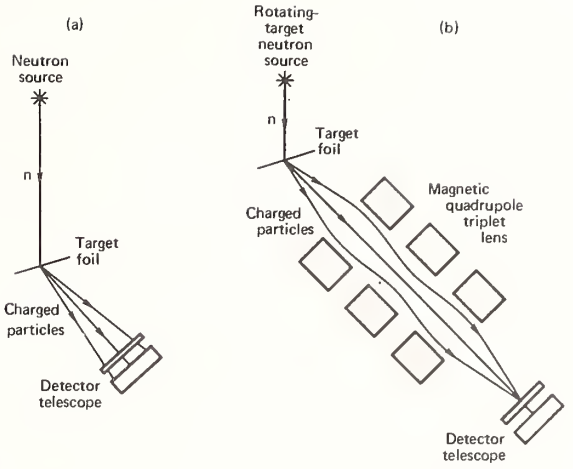

Fig. 10. Measurement techniques for (n, charged particle) reactions. (a) Traditional arrangement. (b) A magnetic quadrupole focuses the charged particles from the target foil onto the detector telescope. Unless the detector telescope can be shielded well from the neutron source, method (b) gives much cleaner data.

At higher neutron energies, the (n,charged particle) cross sections are being measured with the apparatus diagrammed in Fig. 12.[42] To date, measurements have been performed on C, N, and O at 27.4, 39.7 and 60.7 MeV.[43] Because the detectors could be well shielded from the Li(p,n) neutron source used in these studies, the schematic arrangement of Fig. 10a was preferred.

Burnup

In many proposed reactor concepts the neutron fluence is so high at the first wall that, after several years, a significant amount of material will be transformed from one element into another. Consequently the properties of the material will change but in ways that at present can only be simulated by doping the irradiated samples. Many of the relevant nuclear cross sections for burnup are reasonably well known since they are large cross sections. Others are being measured via the (n,p) spectral measurements and by the (n,α) and helium accumulation studies already mentioned. The more significant uncertainty is in the response of a material to such severe damage.

Neutron Heating

The energy of the fusion neutrons is converted to heat by a variety of processes that may be grouped into three classes according to the interaction of the neutron with the material:

1. Prompt (n,xγ) and (n,conversion electron) processes.

2. Beta-decay and the accompanying energy release.

3. Processes resulting in a moving nucleus, such as a recoiling heavy nucleus or a proton, deuteron, alpha particle, etc.

Clearly many interactions will fall into more than one class, such as the (n,pγ) reaction which will contribute directly or indirectly to all three.

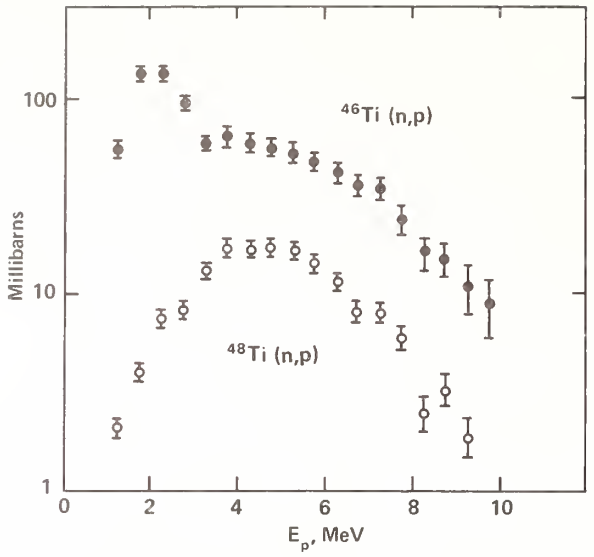

Fig. 11. Proton emission spectra from 15-MeV neutron bombardment of ^{46}Ti and ^{48}Ti. The large peak at low energies in the ^{46}Ti spectrum is from (n,n'p) reactions. Data are from Ref. 41.

Neutron data for (n,xγ) processes have undergone an extremely rapid improvement in the past decade, due in large measure to studies up to 20 MeV with white neutron souces.[25,44] Materials investigated include the following important fusion reactor materials: Li, ^{7}Li, C, N, F, Mg, Al, Si, Ca, V, Cr, Fe, Ni, Cu, Nb, Mo, Sn, Ta, W, Au and Pb. Although there are still gaps in isotopic data that could be important for reactors with large burnup of structural or other materials, much of the data needed for near term applications is available now. The cross section for prompt conversion electron production may be important for thin layers or coatings. It is usually obtained from the (n,xγ) cross sections and the multipolarities of gamma rays, with most multipolarities being assumed rather than measured.[45]

Beta decay will be a source of after-heat and nuclides produced by (n,2n) and (n,p) reactions--of little importance in fission reactors--will likely be dominant here. The accuracy of the data has not been assessed. However, except for hybrid reactors, the after-heat problem will probably be less severe because many of the radioactive species are short-lived and there are few beta-decay chains similar to those of fission products.

Prompt processes that result in a recoiling heavy nucleus or an energetic light charged particle deposit energy locally, that is very near the initial point of interaction. The kinetic energy of the charged particles deposited in a unit mass per unit neutron fluence is given the name KERMA factor (kinetic energy released in materials) and has the units of rads · cm^2/neutrons or Gy · cm^2/neutron (Gy = 1 Gray = 1 Joule/kg = 100 rads). Tabulations of KERMA factors have been published[46] and are based on evaluated cross section data and on estimates, some from measured data, on the energy and angular distribution of the emitted particles. KERMA factors are important in fusion in two areas: they can be used to calculate the energy deposited by protons and heavier charged particles; and with proper dosimeters of different neutron/gamma relative sensitivities, one can use KERMA factors to infer and separate the absorbed dose from gamma rays and that from neutrons.

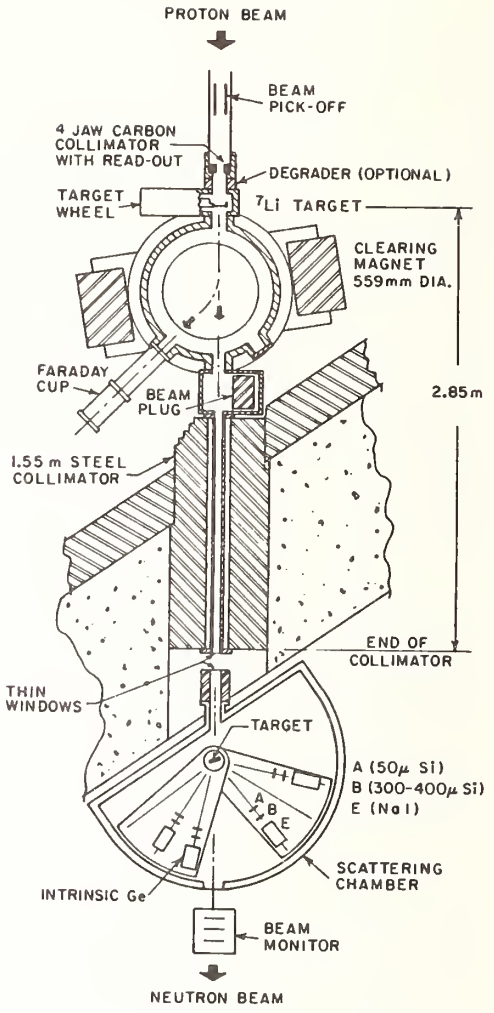

Fig. 12. Schematic view of the neutron production target and the detectors for measuring (n,charged particle) cross sections and spectra at neutron energies up to 60 MeV (Ref. 42).

The measurement of the spectra of light charged particles gives part of KERMA and for many materials it gives the majority. For example, using the recent data for charged particle emission from iron at E_n = 15 MeV,[47] we find

Reaction	KERMA factor
n,p	$0.199 \cdot 10^{-11}$ Gy · cm^2 · neutron^{-1}
n,d	0.007
n,α	0.065
Recoil	0.072 (estimated
Total	0.343

This value is compared to the tabulated value[46] of $0.469 \cdot 10^{-11}$. The measurements of (n,charged particle) cross section and spectra at E_n = 14 to 15 MeV[41,47] have provided important information on KERMA for medium weight nuclei (Al to Nb). Measurements on light nuclei (^{7}Li, ^{11}B and C) are now in progress.

Activation and Dosimetry

This subject is discussed in detail by D. L. Smith elsewhere in this conference[48] and will be treated only briefly here. Cross sections for producing radioactive nuclides are needed for reactor

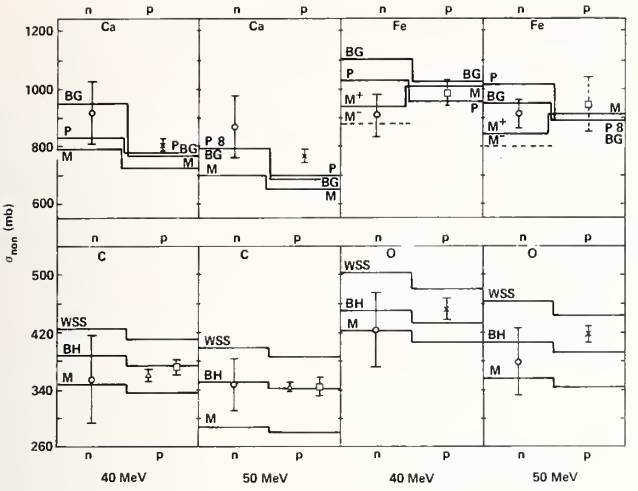

Fig. 13. Non-elastic cross sections for neutrons and protons from Ref. 57. The experimental points are denoted by the points with error bars. Theoretical values are from the optical model parameters of Becchetti and Greenlees,[58] Patterson et al.,[59] Menet et al.,[60] Bassel and Herling,[61] and Watson et al.[62]

systems studies, for diagnosing fusion experiments, and for fluence monitors for radiation damage experiments.

Reactor systems studies have pointed out that after shutdown of a fusion reactor, the inventory of radionuclides could be more than 10^9 Ci. There is often the design flexibility to substitute materials with shorter-lived or lower residual activity, however. Some recent studies (e.g. Ref. 49) suggest ferrite steel, for example, to eliminate the ^{58}Co and ^{60}Co produced from nickel-based alloys. The validity of the conclusions rests, of course, on the adequacy of the nuclear data base. It is not obvious to this author that the activation data base has been tested sufficiently. The often used compilation of Alley and Lessler,[50] for example, while giving reasonable values for many cross sections, contains many errors. Recently this compilation has been substantially corrected and updated.[51]

Long-lived activation products are a particular area deserving further study since they could present a serious waste disposal problem. For example the ^{93}Nb(n,2n)^{92}Nb reaction produces a $3.6 \cdot 10^7$ year activity that was unknown until 1972.[51] The half-life was measured accurately only in the past two years.[52,53] Another long-lived isotope is ^{59}Ni($t_{1/2}$ = 80,000 years), which decays with a small probability by internal bremsstrahlung during electron capture. This decay branch is important in the decommissioning of light water reactors now and could also be important in fusion reactors using nickel alloys. Other long-lived species such as ^{26}Al($7.2 \cdot 10^5$ yr), ^{53}Mn($3.7 \cdot 10^6$ yr), and ^{94}Nb($2.0 \cdot 10^4$ yr) may be important. Perhaps other species, not yet known because of their long half-lives, will also be produced. Although no systematic study is underway now, it would be straightforward to irradiate candidate materials for many months in an intense 14-MeV flux and then, by chemical and isotopic separation, to search for long-lived products.

Diagnostic measurements for present-day fusion experiments include nuclear activation techniques. For example laser fusion experimenters often use the ^{28}Si(n,p)^{28}Al reaction to infer the radius of the

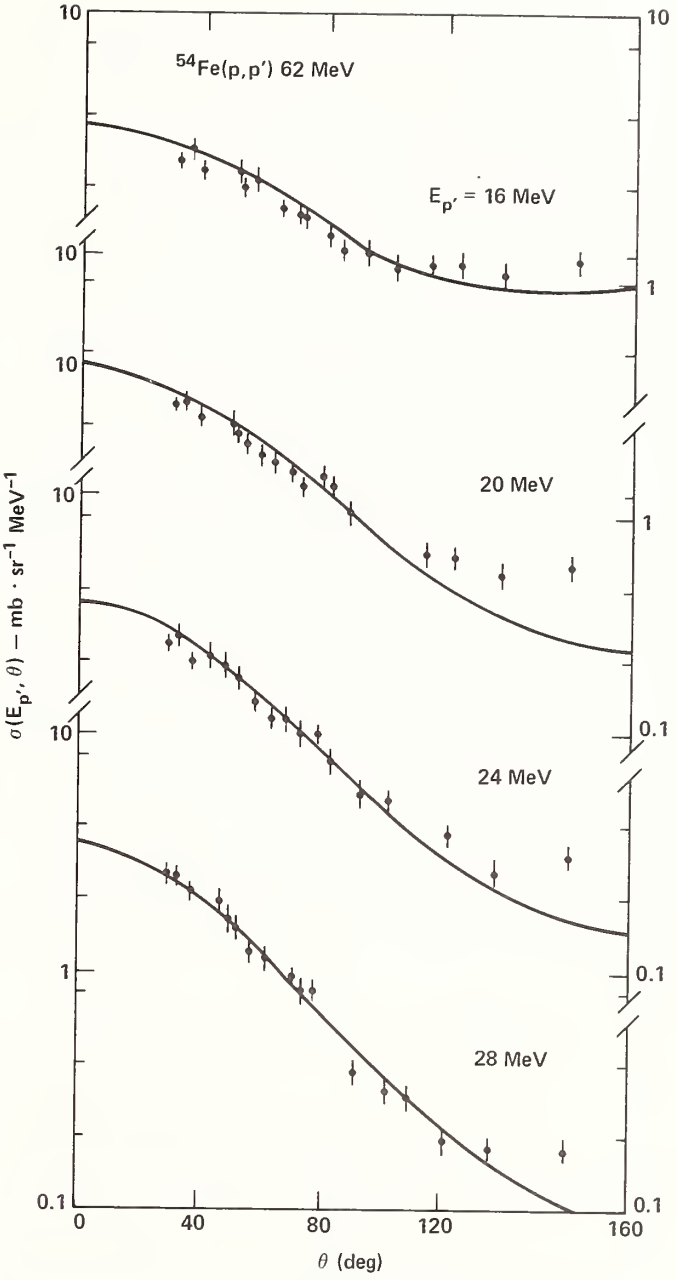

Fig. 14. Angular distribution of protons from 62-MeV proton bombardment for several outgoing proton energies. Experimental data are from Ref. 64; theoretical (systematic) curves are from Ref. 63, from which this figure is adapted.

glass microballoon at the time of fusion neutron production. For both laser and magnetic fusion, the activation of different materials with thresholds near 14 MeV can in principle give information on the ion energies.

The interpretation of radiation damage experiments also depends on knowledge of the neutron fluence and its energy spectrum. At 14 MeV, the ^{93}Nb(n,2n)^{92m}Nb (10 day) activation is commonly used and well known. Dosimetry for d + Li and D + Be sources requires cross sections for neutron energies up to 40 MeV, and many of these quantities have not been measured. A systematic study for $7.5 < E_n < 28$ MeV for Al, Sc, Ni, Y, Zr, Ag, Eu, Tm, Lu, Au and Tl provides much of the experimental information for these cross sections.[48]

Neutron Transport and Shielding, $E_n > 15$ MeV

A new dimension to the shielding problem has evolved with the design of the Fusion Materials Irradiation Test (FMIT) facility, which will be a very intense source of d + Li neutrons with a spectrum that will extend to at least 40 MeV. In support of the design of this facility total cross sections have been measured[55,56] together with removal cross sections,[57]

$$\sigma_{removal} \equiv \sigma_{total} - \int_{\theta=0}^{25°} \sigma_{elastic}\, d\Omega \quad .$$

The deduced non-elastic cross sections for neutrons are compared with optical model values and with measured values for protons in Fig. 13.

At these higher neutron energies, the importance of pre-equilibrium processes is greatly enhanced. The angular distributions of the emitted pre-equilibrium neutrons are now being obtained by empirically fitting (p,n) and (p,p') data where systematic features have been found.[63] An example of the quality of the fit is given in Fig. 14.

Finally, total cross sections up to 200 MeV are being measured at the WNR facility at LAMPF.[65] This facility, only recently completed, should have the capability to provide any total cross section data now needed for the d-Li neutron source.

Charged-Particle Data to Support Neutron Data

It should not be forgotten that nuclear model studies with protons can be used to clarify the calculation of neutron interactions. Although recent progress in charged particle reactions will not be reviewed here, the following areas of relevance should be noted:

- Optical model for σ_{total}, $\sigma_{non\text{-}elastic}$, $\sigma_{compound}$, etc.
- Statistical model for particle emission in (n,p), (n,α), (n,2n), etc. reactions. Proton-induced reactions such as (p,p'), (p,α) and (p,γ) give essential information on level densities, transmission factors, and gamma-ray strength functions.
- Pre-equilibrium particle emission as noted in the preceeding section.
- Direct reactions with or without channel coupling.

The flexibility of proton beams and the relative ease of performing clean experiments has led and will continue to lead to a greatly improved understanding of these areas.

Radiation damage studies with protons and other charged particles are advancing an understanding in the area of materials studies.

Finally, charged-particle cross sections are needed in the design of high-current accelerators. Reactions of deuterons on Cu, Au, and other accelerator materials are needed now.

Conclusion

The progress toward fusion energy in the 1970s has included significant advances in nuclear data, neutron source facilities, and measurement techniques. At the same time, the approach of controlled fusion toward demonstration reactors makes the needs for nuclear data even more urgent. The additional requirements of FMIT have directed our attention to an area of nuclear data where our knowledge until the past year was completely inadequate.

In the future, we can look forward to many more requests for neutron data for fusion. Basic data such as the ^{7}Li(n,nt) cross section need to be pinned down. The region of incident neutron energies between 8 and 14 MeV, while now under attack, will continue to provide a challenge. Filling the data requirements above 15 MeV for FMIT will be a very large task and one in which the priorities will likely be revised often.

For all of these needs, nuclear models will undoubtedly be used to provide many of the requested cross sections, either through analysis of systematics or by detailed calculations. Thus our fundamental understanding of the underlying models must continue to improve. Empirical determination of the model parameters will also be essential.

The fusion demonstration reactor may or may not show nuclear fusion to be acceptable economically, politically, and socially. In any event, nuclear data will be needed for the technical designs and assessments of this and succeeding reactors. Someday, if the plasma physics is favorable, fuel cycles producing few neutrons may become a practicality. Before then, however, neutron data are essential to the development of fusion power.

Acknowledgment

I am indebted to many people for assistance in the preparation of this review. In particular, the following are due special thanks: J. Romero, C. Kalbach-Walker, G. Glendinning, R. Walter, F. Mann, D. Larson, R. Lane, H. Knox, P. Young, P. Lisowski, G. Auchampaugh, D. Drake, D. Smith, M. Guinan, J. Kinney, C. Logan, R. Howell, M. Singh, R. J. Howerton, R. W. Bauer, S. M. Grimes, and J. G. Woodworth.

This work was performed under the auspices of the U.S. Department of Energy by Lawrence Livermore Laboratory under contract no. W-7405-ENG-48.

References

1. The Status of Neutron-Induced Nuclear Data for Controlled Thermonuclear Research Applications: Critical Reviews of Current Evaluations," D. Steiner, coordinator. U.S. Nuclear Data Committee, Controlled Thermonuclear Research Subcommittee report USNDC-CTR-1 (1974).

2. D. Steiner, "Nuclear Data Needs for Fusion Reactor Design," Proc. Conf. Nuclear Cross Sections and Technology (NBS Special Publication 425, Washington, 1975) 646.

3. S. M. Qaim, R. Wölfle and G. Stöcklin, "Nuclear Data for Fusion Reactors," Atomki Közlemények 18, 335 (1976). Proc. Symp. on Fast Neutron Interactions and on the Problems of High Current Neutron Generators, Debrecen Hungary (1975).

4. C. W. Maynard, "Neutrons and Fusion," Proc. Int. Conf. on the Interactions of Neutrons with Nuclei, CONF-760715-P1, (Lowell, Mass. 1976) 789.

5. "Symposium on Neutron Cross Sections from 10 to 40 MeV," ed. M. R. Bhat and S. Pearlstein, Brookhaven National Laboratory report BNL-NCS-50681 (Brookhaven N.Y., 1977).

6. O. N. Jarvis, "Nuclear Data for Fusion Reactors," Proc. Int. Conf. on Neutron Physics and Nuclear Data for Reactors and Other Purposes, (OECD/AEN Harwell, 1978) 1073.

7. IAEA Advisory Group Meeting on Nuclear Data for Fusion Reactor Technology, ed. A. Lorenz and D. W. Muir, INDC (NDS)-101/LF Vienna (1978).

8. S. M. Qaim, "Recent Advances in the Study of Some Neutron Threshold Reactions," Proc. Int. Conf. on Neutron Physics and Nuclear Data for Reactors and Other Purposes, (OECD/AEN, Harwell, 1978) 1088.

9. D. L. Smith, "Neutron Dosimetry for Radiation Damage in Fission and Fusion Reactors," this conference.

10. D. G. Doran, R. R. Heinrich, L. R. Greenwood, and H. Farrar, IV, "MFE Damage Analysis Program Nuclear Data Needs," Symp. on Neutron Cross Sections from 10 to 40 MeV, Brookhaven National Laboratory report BNL-NCS-50681 (1977) p. 321.

11. D. Steiner, "Analysis of a Bench-Mark Calculation of Tritium Breeding in a Fusion Reactor Blanket: The United States Contribution," Oak Ridge National Laboratory Report ORNL-TM-4177 (1973).

12. W. N. McElroy and H. Farrar IV, "Helium Production in Stainless Steel and its Constituents as Related to LMFBR Development Programs," in Proc. Int. Conf. on Radiation-Induced Voids in Metals, ed. J. W. Corbett and L. C. Ianniello, Albany N.Y. (USAEC, 1971) p. 187.

13. E. F. Plechaty and J. Kimlinger, Lawrence Livermore Laboratory, private communication.

14. F. Brown, R. H. James, J. L. Perkin, and J. F. Barry, J. Nucl. Energy A/B 17, 137 (1963).

15. A. R. Osborn and H. W. Wilson, private communication, AWRE (1961).

16. M. E. Wyman and M. M. Thorpe, Los Alamos Scientific Laboratory report LA-2235 (1958).

17. L. Rosen and L. Stewart, Phys. Rev. 126, 1150 (1962).

18. R. Batchelor and J. H. Towle, Nucl. Phys. 47, 385 (1963).

19. J. C. Hopkins, D. M. Drake and H. Conde, Nucl. Phys. 107, 139 (1968).

20. J. A. Cookson, D. Dandy, and J. C. Hopkins, Nucl. Phys. A91, 273 (1967).

21. C. A. Uttley, private communication (1979); M. T. Swinhoe et al., this conference.

22. H. D. Knox, R. M. White and R. O. Lane, Nuclear Sci. and Eng. 69, 223 (1979).

23. H. H. Hogue, P. L. von Behren, D. W. Glasgow, S. G. Glendinning, P. W. Lisowski, C. E. Nelson, P. O. Purser, and W. Tornow, Nucl. Sci. Eng. 69, 22 (1979).

24. D. Drake, et al., private communication (1979).

25. G. L. Morgan, "Cross Sections for the ^{7}Li(n,xn) and ^{7}Li(n,n'γ) Reactions Between 1 and 20 MeV," Oak Ridge National Laboratory report ORNL/TM-6247 (1978).

26. R. J. Howerton, Lawrence Livermore Laboratory, private communication (1979); calculation with a similar library shows the same problem: R. J. Howerton, "Data Testing Results for the LLL Evaluated Nuclear Data Library (ENDL-78)," Vol. 15 part E of Lawrence Livermore Laboratory report UCRL-50400, An Integrated System for the Production of Neutronics and Photonics Calculational Constants (1979).

27. C. Maynard, "Integral Experiments for CTR Nuclear Data," Symposium on Neutron Cross Sections from 10 to 40 MeV, ed. M. R. Bhat and S. Pearlstein, Brookhaven National Laboratory report BNL-NCS-50681 (Brookhaven N.Y., 1977).

28. G. M. Hale, "R-Matrix Analysis of Light Element Reactions for Fusion Applications," this conference.

29. H. H. Hogue, P. L. von Behren, D. H. Epperson, S. G. Glendinning, P. W. Lisowski, C. E. Nelson, H. W. Newson, P. O. Purser, and W. Tornow, Nucl. Sci. Eng. 68, 34 (1978).

30. R. O. Lane, "Study of Structure of Nuclei with Neutrons and Nuclear Data Measurements for MFE," Ohio University report COO-2490-10 (unpublished, 1979).

31. G. F. Auchampaugh, S. Plattard, and H. W. Hill, Nucl. Sci. Eng. 69, 30 (1979).

32. D. Hermsdorf, A. Meister, S. Sassonoff, D. Seeliger, K. Seidel, and F. Shahin, Zentralinstitut für Kernforschung Rossendorf bei Dresden report ZfK-277(U), INDC(GDR)-2/L (1975).

33. S. Pearlstein, Nucl. Sci. Eng. 68, 55 (1978).

34. D. M. Hetrick, D. C. Larson, and C. Y. Fu, "Status of ENDF/B-V Neutron Emission Spectra Induced by 14-MeV Neutrons," Oak Ridge National Laboratory report ORNL/TM-6637 (1979).

35. C. M. Logan, J. D. Anderson, and A. K. Mukherjee, J. Nuclear Materials 48, 223 (1973).

36. J. Kinney and M. Guinan, private communication, LLL (1979).

37. L. F. Hansen, S. M. Grimes, R. J. Howerton, and J. D. Anderson, Nucl. Sci. Eng. 61, 201 (1976).

38. H. Farrar, IV and D. W. Kneff, Trans. Am. Nucl. Soc. 28, 197 (1978).

39. R. C. Haight, S. M. Grimes, K. R. Alvar and H. H. Barschall, Trans. Am. Nucl. Soc. 30, 164 (1978).

40. K. R. Alvar, H. H. Barschall, R. R. Borchers, S. M. Grimes, and R. C. Haight, Nucl. Instr. Meth. 148, 303 (1978).

41. S. M. Grimes, R. C. Haight, and J. D. Anderson, Nucl. Sci. Eng. 62, 187 (1977).

42. J. L. Romero, T. S. Subramanian, F. P. Brady, N. S. P. King and J. F. Harrison, "A Facility for Neutron-Induced Charged Particle Reactions in the Energy Range E_n = 20-60 MeV," Symp. on Neutron Cross Sections from 10 to 40 MeV, Brookhaven National Laboratory report BNL-NCS-50681 (1977) p. 247.

43. T. S. Subramanian, J. L. Romero, F. P. Brady, et al., Bull. Am. Phys. Soc. 23, 12 (1978); 23, 943 (1978); and 24, 593 (1979).

44. J. K. Dickens, G. L. Morgan, G. T. Chapman, T. A. Love, E. Newman, and F. G. Perey, Nucl. Sci. Eng. 62, 515 (1977).

45. S. T. Perkins, R. C. Haight, and R. J. Howerton, Nucl. Sci. Eng. 57, 1 (1975).

46. R. S. Caswell, J. J. Coyne, and M. L. Randolph in Neutron Dosimetry for Biology and Medicine, International Commission on Radiation Units and Measurements, ICRU Report 26 (1977) pp. 78-90.

47. S. M. Grimes, R. C. Haight, K. R. Alvar, H. H. Barschall, and R. R. Borchers, Phys. Rev. C19, 2127 (1979).

48. D. L. Smith, "Neutron Dosimetry for Radiation Damage in Fission and Fusion Reactors," this conference.

49. M. Monsler, J. Maniscalco, J. Blink, J. Hovingh, W. Meier, and P. Walker, "Electric Power from Laser Fusion: The HYLIFE Concept," Proc. of 13th IECEC Conf., Aug. 20-25, 1978, San Diego p. 2164, Vol. 1.

50. W. E. Alley and R. M. Lessler, Nucl. Data Tables, 11, 621 (1973).

51. J. D. Knight, Los Alamos Scientific Laboratory report LA-DC-72-209 (1972).

52. T. Makino and M. Honda, Geochim. Cosmochim. Acta 41, 1521 (1977).

53. D. R. Nethaway, A. L. Prindle, and R. A. Van Konynenburg, Phys. Rev. C17, 1409 (1978).

54. B. P. Bayhurst, R. J. Prestwood, J. B. Wilhelmy, N. Jarmie, B. H. Erkkila, and R. A. Hardekopf, Phys. Rev. C12, 451 (1975).

55. C. I. Zanelli, F. P. Brady, J. L. Romero, C. M. Castaneda, and D. L. Johnson, Bull. Am. Phys. Soc. 24, 658 (1979).

56. D. C. Larson, ORNL private communication (1979).

57. P. P. Urone, F. P. Brady, C. L. Castaneda, M. Johnson, G. A. Needham, J. L. Romero, and J. Ullman and D. L. Johnson, Bull. Am. Phys. Soc. 24, 657 (1979) and Crocker Nuclear Laboratory report UCD-CNL-192 (Davis, CA, 1979) p. 154.

58. F. D. Becchetti and G. W. Greenlees, Phys. Rev. 182, 1190 (1969).

59. D. M. Patterson, P. R. Doering, and A. Galonsky, Nucl. Phys. A263, 261 (1976).

60. J. J. H. Menet, E. E. Gross, J. J. Malanify, and A. Zucker, Phys. Rev. C4, 1114 (1971).

61. R. Bassel and G. Herling, quoted in Crocker Nuclear Laboratory report UCD-CNL-192 (Davis, CA, 1979) p. 164.

62. B. A. Watson, P. P. Singh and R. E. Segel, Phys. Rev. 182, 977 (1969).

63. C. Kalbach-Walker, private communication (1979).

64. F. E. Bertrand and R. W. Peelle, Phys. Rev. C8, 1045 (1973).

65. P. W. Lisowski et al., this conference.

SHIELDING OF FUSION REACTORS

R. G. Alsmiller, Jr.
Oak Ridge National Laboratory
Oak Ridge, Tennessee 37830, USA

The blanket and shield assemblies of fusion reactors will contain a significant number of very sizable penetrations (neutral beam injection ducts, pumping ports, etc.). The combination of high-energy neutrons and large penetrations will introduce severe design problems that are quite different from those encountered previously. Fusion reactors with their penetrations are very complex geometric structures and in calculating nuclear effects (heating, activation, etc.) tradeoffs must be made between computing efficiency and the accuracy in the geometric modeling. The types of problems that arise due to large penetrations will be illustrated by the calculations that have been carried out to aid in the design of the shielding for the neutral beam injectors of the Tokamak Fusion Test Reactor being built at Princeton University.

(shielding, fusion, neutrons, photons, neutral beam injection, nuclear heating, photon dose rate)

Introduction

Fusion reactors will, in general, operate on a D-T cycle and thus will produce 14-MeV neutrons. In many of the reactors under consideration, the plasma will be ignited by the injection of high-energy deuteron beams. To accommodate neutral beam injectors there will be sizable penetrations through the shield-blanket assemblies, and the neutrons produced in the plasma will stream through these penetrations into the neutral beam injectors and out of the injectors into the reactor building. Fusion reactors with their neutral beam injectors are very complex geometric structures and the combination of high-energy neutron streaming and complex geometry severely strain the available shield design methods. In this paper, some of the problems that arise in the shielding of fusion reactors are described and discussed.

To illustrate the various shielding problems that occur, the calculations that have been carried out at the Oak Ridge National Laboratory to aid in the design of the shielding of the Tokamak Fusion Test Reactor (TFTR)[1] being built at Princeton University will be used.* The TFTR will have a lower neutron intensity and a lower duty factor than a power producing reactor, will have no blanket region for tritium breeding, and will not use superconducting coils, so it is quite different from a commercial reactor. Nevertheless, the shielding problems that occur in the design of the TFTR are similar, but less severe, than those that will occur in the design of a commercial reactor.

Nuclear Heating in the Cryopanels of a Neutral Beam Injector+

The TFTR plasma will be ignited by neutral beam injection.[1,3] The vacuum in the neutral beam injectors will be maintained by cryopumps[4,5,6] and thus for design purposes it is necessary to know the nuclear heat load on the cryopanels in the injectors. In this section the methods that were used to calculate this nuclear heating for the TFTR injectors will be described and the results discussed.

In Fig. 1a, a schematic of the TFTR with its four neutral beam injectors is shown, and in Fig. 1b, an

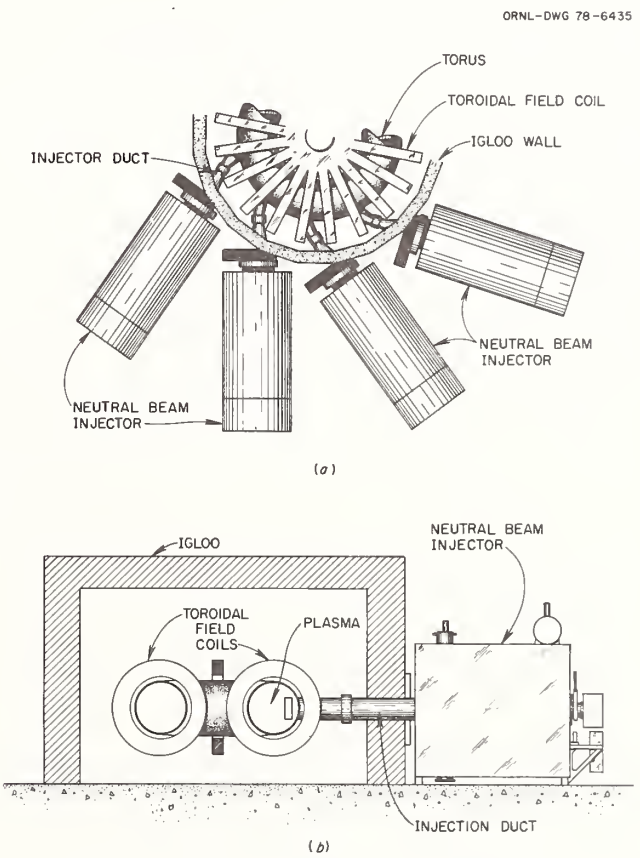

Fig. 1. Plane (a) and elevation (b) views of the neutral beam injectors and their locations relative to the igloo wall and the TFTR torus.

elevation view of one of the injectors showing its location relative to the igloo is shown. In Fig. 2a, a schematic diagram of a neutral beam injector is shown. The neutral beam injector components are housed in a box-shaped vacuum vessel ($\sim 50\ m^3$) constructed primarily of stainless-steel type 316 (SS-316). The inner vertical walls of the vessel are lined with cryocondensation vacuum pumping panels having a total active pumping area of $\sim 30\ m^2$. The vacuum enclosure contains three deuteron sources and ion neutralizing tubes that are mounted horizontally. Each source directs deuterons into the plasma through a common bending magnet.

*These calculations represent the work of R. T. Santoro, R. A. Lillie, J. M. Barnes, J. Barish and M. M. H. Ragheb as well as myself.

+The results presented in this section are taken from Ref. 2.

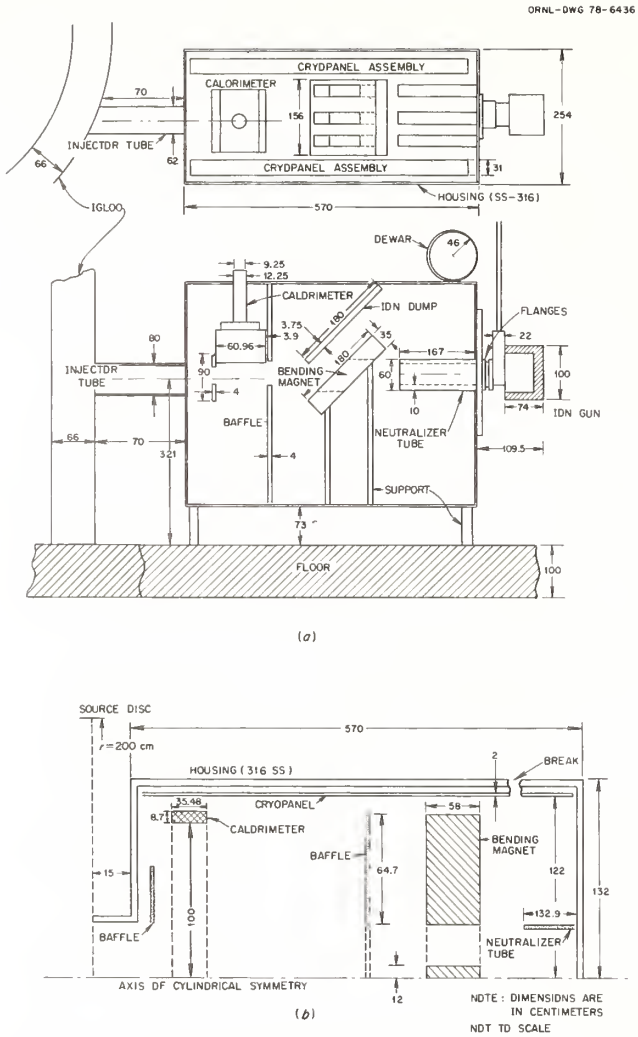

Fig. 2. Three-dimensional (a) and two-dimensional (b) calculational models of the neutral beam injector and its various components.

The bending magnet removes any charged deuterons that remain in the beams following neutralization and deflects them into the ion dump. The calorimeter shown in the out-of-beam position is used to make diagnostic tests on the beams when it is lowered into the beam path. The important point to be noted is that the hole through the igloo to accommodate neutral beam injection is large, $\sim$ 62x80 cm^2, and the cryopanels are, because of this hole, exposed to neutrons produced in the plasma.

In Fig. 2b, a two-dimensional model of the injector that is used in some of the calculations is shown. In the two-dimensional representation most of the injector components are still represented, but as the figure indicates, considerable geometric distortion has been introduced.

The geometry of the TFTR with its injector is very complex and must be simplified in order to carry out shielding calculations. In the calculations discussed here, the transport was carried out in several steps. A very brief description of the procedure will be given here, but the interested reader will find all of the details given in Ref. 2. A neutron and photon source, i.e., an energy, angular and spatial distribution of neutrons and photons produced by neutron interactions, was calculated at the outside of the igloo taking into account a single neutral beam injector penetrations, but no neutral beam injector. This source was obtained using the two-dimensional discrete ordinates code, DOT[7], but did not account for the 14-MeV neutrons that stream directly from the plasma through the injector penetration. These 14-MeV neutrons were treated in a separate calculation using the Monte Carlo code, MORSE[8]. A significant point to be noted is that in calculating the source at the outside of the igloo the toroidal field coils were neglected. In all of the calculations the neutron source from the plasma was taken to be that at strong post-compression, the condition at which it is expected that the neutron yield will be the largest.[9]

With this source at the outside of the igloo, plus the 14-MeV neutrons that stream directly from the plasma through the injector penetration, a transport calculation using a three-dimensional representation of the injector geometry (see Fig. 2a) was carried out using MORSE.[8] In the three-dimensional calculations the source at the igloo surface obtained from DOT was processed by the code DOMINO[10], that converts a DOT source into a source that can be sampled from by the Monte Carlo code MORSE.[8] After the neutron and photon fluxes per unit energy were obtained at various points on the cryopanels, the nuclear heating in the cryopanels were calculated using kerma factors generated by MACK[11] and SMUG.[12]

Calculations have also been carried out using a two-dimensional representation of the source and the injector. The two-dimensional model allows the use of deterministic methods rather than statistical methods and thus will provide the heating rate at all positions of interest rather than as a few selected positions as in the Monte Carlo calculations. Furthermore, this two-dimensional model will be used in the next section of this paper where calculations throughout the reactor building are needed. To carry out the two-dimensional calculation, the source at the igloo surface was converted by using DOMINO and MORSE into a source over a 200 cm radius disk (see Fig. 2b) that was suitable for use in a two-dimensional r-z DOT calculation with the z-axis being the axis of the injector. As stated above, this source does not account for the 14-MeV neutrons that stream directly from the plasma into the injector. In the two-dimensional calculations these 14-MeV neutrons were treated using an analytic first collision source calculated by GRTUNCL[13*]. It is important to note that the source disk (see Fig. 2b) is normal to the axis of the injector and the neutron and photon energy and angular distributions over this disk must exhibit cylindrical symmetry with respect to the injector axis. Thus, in the two-dimensional injector calculation the source distribution of the neutrons and photons must be approximated as well as the injector geometry. With this source the neutron and photon fluxes per unit energy were calculated using DOT and the geometry shown in Fig. 2b. The heating rates in the cryopanels were calculated from these fluxes using the kerma factors as in the three-dimensional calculations.

In Fig. 3, the positions in the injector at which heating rates have been calculated on the basis of the three-dimensional model of the injector are shown. In Tables 1 and 2 the instantaneous heating rates, i.e., the heating rates during a D-T pulse that produces $7 \cdot 10^{18}$ neutrons/s, in the stainless steel of the cryopanels at position B and E are shown. In the tables,

*This code is undocumented, but a brief description of the method used in the code is given in Ref. 14.

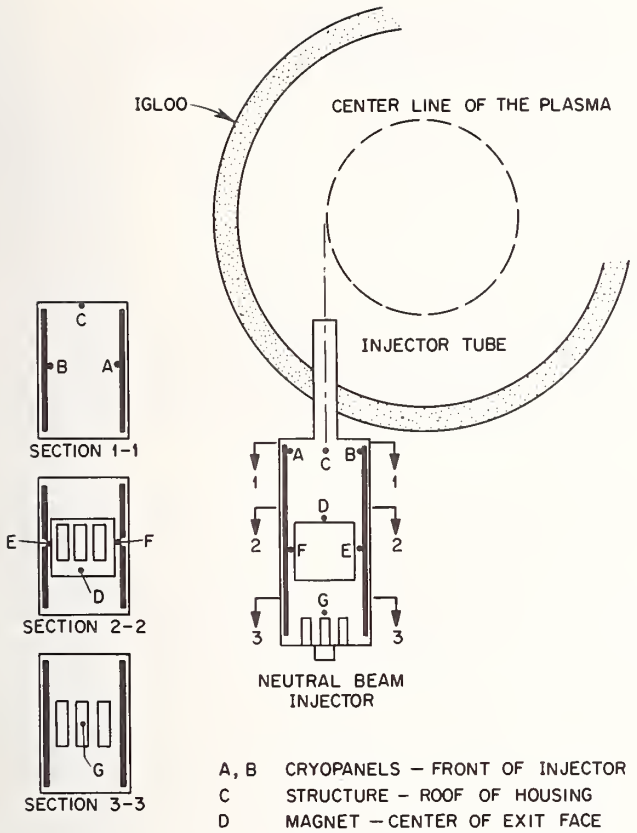

Fig. 3. Location of the detectors in the three-dimensional calculational model relative to the injector duct and igloo wall.

Table I. Nuclear Heating Rates in the Cryopanel at Detector Location B

	Nuclear Heating Rates (Watts/cm³)		
	Type 316 Stainless Steel		
	Neutron	Gamma Ray	Total
MORSE[a]			
Injector Port	7.80×10^{-4} (0.113)	1.19×10^{-3} (0.144)	1.98×10^{-3} (0.096)
Igloo Wall	3.77×10^{-5} (0.201)	3.55×10^{-3} (0.205)	3.59×10^{-3} (0.187)
Total	8.18×10^{-4} (0.231)	4.74×10^{-3} (0.251)	5.57×10^{-3} (0.210)
DOT[b]	2.09×10^{-4}	1.09×10^{-3}	1.30×10^{-3}
MORSE/DOT Ratios[c]	3.0-4.8	3.3-5.4	3.4-5.2

[a] Three-Dimensional Calculation
[b] Two-Dimensional Calculation
[c] (H(MORSE) × (1-fsd))/H(DOT) - (H(MORSE) × (1+fsd))/H(DOT)
fsd = fractional standard deviation

Table II. Nuclear Heating Rates in the Cryopanel at Detector Location E

	Nuclear Heating Rates (Watts/cm³)		
	Type 316 Stainless Steel		
	Neutron	Gamma Ray	Total
MORSE[a]			
Injector Port	4.60×10^{-6} (0.207)	4.33×10^{-5} (0.298)	4.80×10^{-5} (0.272)
Igloo Wall	5.00×10^{-6} (0.679)	1.48×10^{-5} (0.266)	1.98×10^{-5} (0.242)
Total	9.60×10^{-6} (0.710)	5.81×10^{-5} (0.399)	6.78×10^{-5} (0.364)
DOT[b]	2.49×10^{-6}	1.32×10^{-5}	1.50×10^{-5}
MORSE/DOT Ratios[c]	1.1-6.6	2.6-6.2	2.9-6.2

[a] Three-Oimensional Calculation
[b] Two-Oimensional Calculation
[c] (H(MORSE) × (1-fsd))/H(DOT) - (H(MORSE) × (1+fsd))/H(DOT)
fsd = fractional standard deviation

the heating rates due to neutrons and gamma rays are given separately, and in the case of the three-dimensional calculations the contributions due to radiation that streams through the injector port and leaks through the igloo wall are given separately. At both positions, the contribution to the heating rate from the injector port and the igloo wall are very approximately comparable. The heating rate changes by approximately two orders of magnitude as one goes from point B to E because of geometric effects and because the position E is partially shielded by the magnet. The MORSE-to-DOT ratio indicates that the two-dimensional model underestimates the heating rates by a significant amount.

In Fig. 4, the heating rate is shown as a function of distance along the cryopanel. The curves are the results obtained from the two-dimensional model and the points at locations A and E are from the three-dimensional model. This figure indicates rather dramatically how the results from the two- and three-

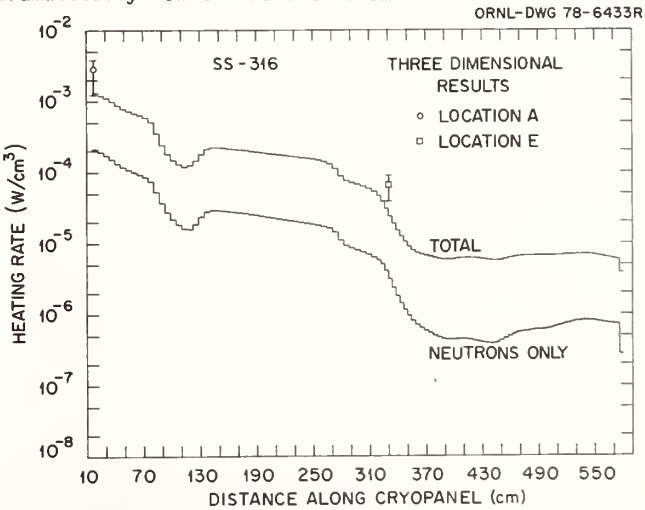

Fig. 4. Nuclear heating rate in SS-316 as a function of distance along the cryopanel. The histograms show the results from the two-dimensional model.

dimensional models can be used to complement each other. In Ref. 2 results similar to those in Tables I and II and Fig. 4 for other locations and for cryopanel materials other than SS-316 are given.

The heating rates calculated here are small and are not expected to have a serious impact on the cryogenics of the panels. This result is, however, very dependent on the relatively low neutron intensity and low duty factor (.5 s pulse every 300 s) of the TFTR and may be expected to be substantially different when a power producing reactor is considered.

Shielding Calculations for the TFTR Test Cell*

In Fig. 5, a schematic diagram of the TFTR test cell with a single neutral beam injector (two-dimensional model) is shown. To determine the biological dose rate outside of the test cell would be relatively straightforward if the injectors and the penetrations through the igloo to accommodate neutral beam injection were not present. In this section the methods that were used to estimate the biological dose rates outside of the test cell when the neutral beam injectors are present are presented and the results discussed.

In Fig. 5, the toroidal field coils are not shown and were not included in the calculations. The poloidal field coils are not shown, but were included in the calculations. Also note that the TFTR floor is not included in the calculations. The injector is shown with concrete shielding around the sides and the back, but calculated results have been obtained with this shielding both present and absent. The problem of interest here is to determine what shielding around the injector is required to reduce the biological dose rate outside of the test cell to an acceptable level.

In order to use deterministic, i.e., discrete ordinates methods, rather than statistical methods, the geometry in Fig. 5 has been modeled as two two-dimensional geometries. In fact, one of the reasons for developing the two-dimensional calculational model of the injector discussed in the previous section was because such a model was needed for the present calculations. In the first geometry, the neutral beam injectors and the penetrations through the igloo are ignored and cylindrical symmetry about the vertical axis in Fig. 5 is assumed. The neutron and photon transport calculations in this geometry are carried out using DOT[7] and the dose rates are obtained outside of the test cell using available flux-to-dose rate conversion factors.[16,17] The neutron source from the plasma used in this calculation is the same as that used in the previous section.

In the second geometry, cylindrical symmetry about the horizontal axis in Fig. 5 is assumed and the neutron and photon source was taken to be the same as that used in the two-dimensional injector calculations (see source disk in Fig. 2b) in the previous section. It should be noted that the fact that the injector is not normal to the igloo wall is being ignored except that tangential injection was taken into account in determining the neutron and photon source. The transport calculations in this geometry were carried out with DOT and the dose rate calculations were carried out using flux-to-dose rate conversion factors.

In Fig. 6, the dose equivalent rate on the test cell roof is shown as a function of distance from the roof centerline. The results are given in units of mrem/pulse when there are $7 \cdot 10^8$ neutrons/s during a

*The results presented in this section are taken from Ref. 15.

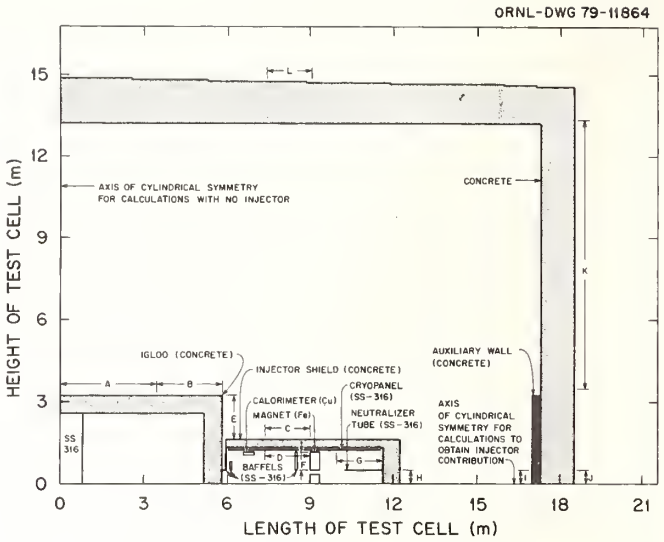

Fig. 5. Schematic diagram of the TFTR test cell and a neutral beam injector. (The diagram is drawn to scale)

0.5 s pulse. The curve labeled "without injector" shows the results from the first geometry described above and is the result when all injectors and all igloo penetrations are ignored. The curves labeled "shielded injector" and "unshielded injectors" were obtained in the second geometry described above and represent the dose equivalent rate on the roof when the injector shielding (.305 m of concrete on the sides and .61 m of concrete on the back) is present and absent, respectively. To a first approximation, the dose equivalent rate on the roof when a single injector is present is obtained by adding the curve without injector to either the shielded or unshielded injector curve. The addition gives only an approximate answer due to the fact that injection is tangential and thus the positions on the roof given in the two geometries are only approximately comparable. Furthermore, only a single injector has been considered. In the TFTR design the four neutral beam injectors are located on the same side of the reactor so the dose equivalent rate on the roof above the neutral beam injector cluster is very approximately the sum of the dose rate "without injector" plus four times the contribution to the dose rate from the shielded or unshielded injector.

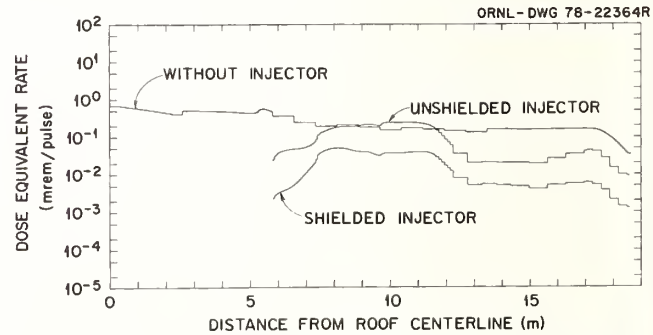

Fig. 6. Dose equivalent rate on the TFTR test cell roof as a function of distance from the roof centerline.

In Fig. 7, the dose equivalent rate outside of the test cell wall as a function of distance from the injector centerline is shown. The labels on the curves have the same meaning as in Fig. 6. The dose rate "without injector" is reduced considerably at small distances by the presence of the auxiliary wall.

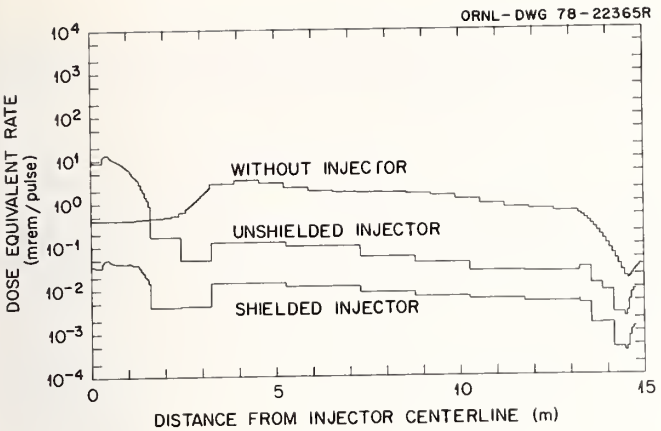

Fig. 7. Dose equivalent rate outside of the TFTR test cell wall as a function of distance from the injector centerline.

For the unshielded injector, the dose rate outside of the wall peaks near the injector centerline as the result of 14-MeV neutrons that stream directly from the plasma region through the injection duct and the injector. Above approximately 1.5 m the contribution to the dose rate from the unshielded injector is small. The dose rate from the shielded injector is small compared to the dose rate "without injector" at all distances.

Photon Dose Equivalent Rate From Induced Activity*

The induced activity in fusion reactor assemblies will determine the extent to which remote maintenance is required and thus accurate calculations of the photon dose rate from induced activity are very desirable. The induced activity in the components of a neutral beam injector is determined to a considerable extent by the neutrons that stream from the plasma through the injector port. To illustrate induced activity calculations, the results that have been obtained of the induced activity in a TFTR neutral beam injector and in the TFTR test cell will be described.

The geometry considered here is the same as that shown in Fig. 5 and the geometric models used here are in all details those described in the previous section. In fact, the starting point of the calculations described here were the scalar neutron flux per unit energy as a function of position in the test cell obtained from the calculations described in the previous section.

From these scalar neutron fluxes per unit energy, the number of radioactive nuclei produced as a function of position throughout the test cell were determined by multiplying the flux by macroscopic activation cross sections and integrating over energy. The activation cross sections were obtained from the MONTAGE library of D. W. Muir.[19] In those cases where a produced radioactive nucleus has a metastable state with a half-life that is substantially different from that of the ground state it was arbitrarily assumed that half of the production is to the ground state and half of the production is to the metastable state since the experimental data giving the production into the separate states is not generally available. Sixty-five residual nuclei with half-lives between 10 min. and 50 years were considered in the calculations. The photon spectra from the decay of these nuclei was taken from the Evaluated Nuclear Structure Data Files of the Nuclear Data Project at ORNL.[20]

In the calculation, the change in the nuclear densities due to neutron interactions and the destruction of radioactive nuclei by interaction with neutrons were neglected. The photon transport calculations were carried out with the Monte Carlo code MORSE. The geometries used are two-dimensional so discrete ordinates methods could have been used, but to take into account the pulsed nature of the source and the time-dependent decays, Monte Carlo methods are more suitable. The advantage of Monte Carlo methods lies in the fact that photons are tracked from birth-to-death so it is possible when a photon contributes to the dose rate at any position to know which radioactive nuclear specie gave rise to this photon. This fact makes it possible to carry out all transport calculations before introducing any time dependence and greatly facilitates the treatment of a variety of pulse repetition sequences and times after the last pulse. The photon fluxes were converted to dose equivalent rates using the flux-to-dose equivalent rate conversion factors given by Claiborne and Trubey.[21]

Calculations have been carried out in each of the two geometries considered in the previous section. In the case of the injector geometry it is necessary to consider, in addition to the activation photons produced in the injector structure, those activation photons that are produced inside the igloo and stream through the penetration in the igloo into the injector. This photon source for the injector calculation was obtained from the photon flux inside the igloo that existed in the calculations with no injector. The energy, angular and spatial distribution of the outgoing photons at the inside surface of the igloo in the vicinity of the penetration but with no penetration through the igloo was calculated. The direction cosines of these photons were then changed to correspond to tangential injection and these photons were then transported using Monte Carlo methods through the penetration in the igloo into the injector. To account for edge effects, i.e., to account for the fact that photons may travel some distance through the igloo concrete before entering the penetration, the photon source inside the igloo was taken over an area that was four times the area of the actual penetration.

The TFTR pulse length was taken to be 0.5 s and the time between pulses was taken to be 300 s. The total neutron source strength was, as before, assumed to be $7 \cdot 10^{18}$ neutrons/s.

Since the calculations are carried out using Monte Carlo methods, the dose rates are obtained not at a point, but averaged over a spatial interval. In Fig. 5 the letters A-L give the position at which the dose rates have been calculated and the arrows with the letters indicate the spatial intervals over which the dose rates are averaged. The position E is just outside of the igloo and the position F is on the face of the magnet inside the injector. In Figs. 8 and 9 the dose equivalent at positions E and F (see Fig. 5) as a function of time after the last pulse are shown for the case of 100 pulses each day for 10 consecutive days. Also shown in the figures are the contributions to the dose rates from the various residual nuclei. The solid lines show the dose equivalent rates for the case of the test cell with no injector and the dashed lines show the contributions of the injector. The two geometries are such that at a given postion the two contributions may be added to obtain the total contribution. It should be noted, however, that inside the injector

*The results presented in this section are taken from Ref. 18.

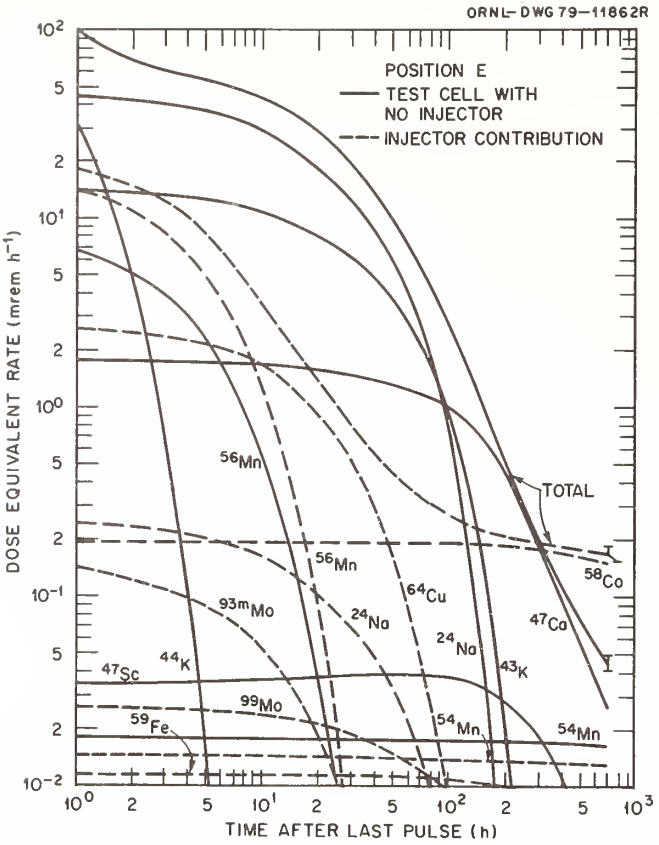

Fig. 8. Dose equivalent rate vs time after the last pulse for 100 pulses per day for ten consecutive days. (See Fig. 5 for the location of position E.)

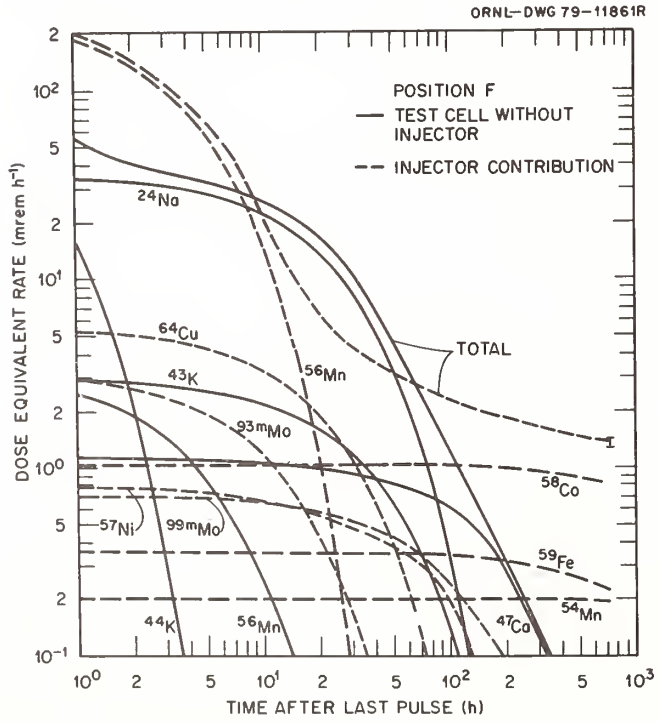

Fig. 9. Dose equivalent rate vs time after the last pulse for 100 pulses per day for ten consecutive days. (See Fig. 5 for the location of position F.)

the dose rate obtained from the calculation without the injector is an upper limit because in the transport calculations the injector structure was not present to attenuate the photons.

At position E the total dose equivalent rate is for most of the times considered due almost entirely to the contribution from the "test cell without injector," At the very largest times considered the total dose equivalent rate is dominated by the injector contribution due to the contribution from ^{58}Co. The total dose equivalent rate at the early times after the last pulse is due in a large part to ^{24}Na.

At position F the injector contribution dominates the total dose equivalent rate at the early times after the last pulse and at the largest times considered.

Calculated results at the other positions shown in Fig. 5 and for other pulse repetition sequences are given in Ref. 18.

Acknowledgement

Research sponsored by the U.S. Department of Energy, Division of Development and Technology, Office of Fusion Energy under Contract No. W-7405-eng-26 with Union Carbide Corporation.

References

1. Tokamak Fusion Test Reactor - Final Design Report, PPPL-1475, Princeton Plasma Physics Laboratory (1978).

2. R. T. Santoro et al., Nucl. Sci. Eng. 70, 225 (1979).

3. L. C. Pittenger et al., in the Proceedings of the Seventh Symposium on Engineering Problems of Fusion Research, Knoxville, TN, USA, 1977, Vol. I, p. 555.

4. L. R. Pedrotti, in Proceedings of the Seventh Symposium on Engineering Problems of Fusion Research, Knoxville, TN, USA, 1977, Vol. II, p. 1001.

5. L. E. Valby, in Proceedings of the Seventh Symposium on Engineering Problems of Fusion Research, Knoxville, TN, USA, 1977, Vol. II, p. 1040.

6. R. R. Stone and J. M. Hanghian, in Proceedings of the Seventh Symposium on Engineering Problems on Fusion Research, Knoxville, TN, USA, 1977, Vol. II, p. 1425.

7. W. A. Rhoades and F. R. Mynatt, "The DOT III Two-Dimensional Discrete Ordinates Code," ORNL/TM-4280, Oak Ridge National Laboratory (1973).

8. M. B. Emmett, "The MORSE Monte Carlo Radiation Transport System," ORNL-4972, Oak Ridge National Laboratory (1975).

9. B. Pritchard, Princeton Plasma Physics Laboratory, private communication, 1977.

10. M. B. Emmett, C. E. Burgart, T. J. Hoffman, "DOMINO, A General Purpose Code for Coupling Discrete Ordinates and Monte Carlo Radiation Transport Calculations," ORNL-4853, Oak Ridge National Laboratory 91973).

11. M. A. Abdou, C. W. Maynard, R. Q. Wright, "MACK - A Computer Program to Calculate Neutron Energy Release Parameters (Fluence-to-Kerma Factors) and Multigroups Neutron Reaction Cross Sections from Nuclear Data in ENDF Format," ORNL/TM-3994, Oak Ridge National Laboratory (1973).

12. N. M. Greene et al., "AMPX: A Modular Code System for Generating Coupled Multigroup Neutron-Gamma Libraries from ENDF/B," ORNL/TM-3706, Oak Ridge National Laboratory (1976).

13. R. S. Childs and J. V. Pace, III, Oak Ridge National Laboratory, private communication, 1978.

14. R. A. Lillie, R. G. Alsmiller, Jr. and J. T. Mihalczo, Nucl. Tech. 43, 373 (1979).

15. R. T. Santoro et al., "Shielding Calculations for the TFTR Neutral Beam Injectors," ORNL/TM-6949, Oak Ridge National Laboratory (1979).

16. NCRP Report No. 38, Protection Against Neutron Radiation, National Council on Radiation Protection and Measurements (1971).

17. H. C. Claiborne and D. K. Trubey, Nucl. Tech. 450 (1970).

18. R. G. Alsmiller, Jr. et al., "Dose Rates From Induced Activity in the TFTR Test Cell," ORNL/TM-6904, Oak Ridge National Laboratory (1979).

19. D. W. Muir, "DLC-33 Data Library MONTAGE," Radiation Shielding Information Center, Oak Ridge National Laboratory (1975).

20. D. J. Garber and C. Brewster, "ENDF/B Cross Sections," BNL-17100 (ENDF-200) Second Edition (1975).

21. H. C. Claiborne and D. K. Trubey, Nucl. Tech. 8, 450 (1970).

TRITIUM BREEDING IN FUSION

M.T. Swinhoe * (in collaboration with C.A. Uttley)
A.E.R.E. Harwell
Didcot, Oxfordshire, England.

Commercial DT fusion reactors need a breeding ratio (BR) of at least unity. The accuracy of BR calculations is limited by data uncertainties, especially the $^{7}Li(n,n'\alpha t)$ cross-section. A recent absolute measurement of this cross-section (4-14 MeV) is described. These results and other experimental evidence for a discrepancy in the ENDF/B evaluated cross-section are presented. The effect of the new measurements on various reactor blanket designs is also discussed.

[DT fusion tritium breeding ratio, ^{6}Li, ^{7}Li, breeding blankets, activation, $^{27}Al(n,\alpha)$, ENDF/B, LiOH, liquid scintillator, quenching, integral and differential experiments]

* University of Birmingham, Edgbaston, Birmingham, England.

Introduction

DT fusion is a viable power producing system only if a tritium supply is assured. One of the most obvious ways of obtaining tritium is to utilise the produced neutrons and generate the necessary tritium from lithium, the material with the highest (n,t) cross-section. The energy of the 14 MeV neutrons has to be converted into a useful form (eventually electricity), and for magnetically confined systems the neutrons must be prevented from damaging and heating the superconducting magnet coils. These three functions, tritium breeding, energy conversion and shielding are normally designed to be carried out by a region of the fusion reactor between the first wall and the coils, called the blanket.

In order that these three tasks are carried out successfully simultaneously, the constraints on blanket design are quite complex as shown in Figure 1.

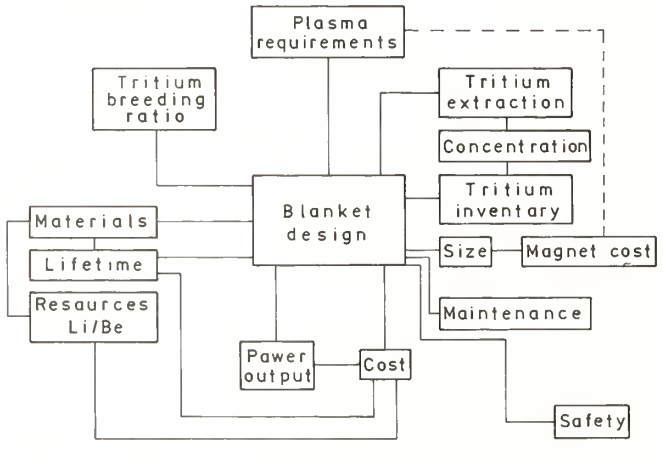

Figure 1. Constraints on blanket design.

In addition to the technical requirements of an operational reactor system, there is the problem of achieving the desired effective tritium breeding ratio. It is necessary that the breeding ratio should not be less than one, but on the other hand, neither should too much tritium be produced. It may be the least offensive of the common radionuclides, but too much is still more than enough. Table 1 shows the doubling time (that is the time taken to double the tritium inventory) versus tritium breeding ratio for a liquid lithium blanket system. This demonstrates how sensitive the doubling time is to a small change in the breeding ratio. In an operating system it may be necessary to install some kind of control system to vary the tritium breeding rate, remembering that it is always easier to reduce it than increase it. Once an ideal breeding ratio has been decided, (depending on the expected growth rate of the DT fusion programme

Table I. Doubling time versus breeding ratio.

Breeding ratio	Doubling time days
1.0	∞
1.05	180
1.1	90
1.3	30
1.5	18

etc) then the problem is to calculate it for any particular reactor type.

The uncertainty in the calculated breeding ratio for any blanket depends on neutronics calculation uncertainty, design uncertainty and data uncertainty. An example of neutronics uncertainty is given by the calculations performed on the UWMAK-III system [1] which give a difference of 22% between a 1-dimensional breeding ratio calculation (1.37) and a 2-dimensional calculation (1.07). Difficulties of this type can usually be overcome by the use of 3-dimensional Monte Carlo codes when sufficient computer time is available.

The design uncertainty is the difference between a calculation of the breeding ratio of an infinite cylinder with homogeneous zones, and a calculation of a real reactor system with coolant channels, tritium extraction system, ducts for injectors and divertors, and magnet shields, all of which need to be accessible and maintainable. One calculation of the change from a thin homogeneous to a cellular blanket [2] showed a change in breeding ratio from 1.16 to 0.99, although it was possible to regain some breeding by the addition of graphite in the intercellular regions [3].

The third contribution to the uncertainty in breeding ratio calculations is the uncertainty in the basic data used. The significance of any particular cross-section error depends strongly on the design of the reactor we are considering. Table II. shows the effect of uncertainties in some important cross-sections on the calculations of the breeding ratios of several reactor types. [4, 5] The uncertainty shown in the breeding ratio is due to the estimated uncertainty in each of the cross-sections, except for the final row where the 7% difference in breeding ratio is due to the difference in the representation of the secondary neutron spectrum of $^{7}Li(n,n'\alpha t)$ between UKNDL and

Table II. Effects of cross-section uncertainties on some blanket designs.[4, 5]

Cross-section	% change in breeding ratio			
	ORNL (Nb)	ORNL (V)	LASL	PPPL
$^{6}Li(n,\alpha)$	0.13	0.06	0.19	0.03
$^{7}Li(n,n'\alpha t)$	5.86	5.91	2.44	1.95
C(n,n)			-0.58	
Be(n,2n)			2.33	1.23
F				-2.30
Secondary spectrum of $^{7}Li(n,n'\alpha t)$	7.00			

ENDF/B-III. The most significant uncertainties are due to the cross-section and secondary neutron spectrum of the $^{7}Li(n,n'\alpha t)$ reaction. The uncertainty on the cross-section of this reaction was estimated at ± 20% from the existing data, shown in Figure 2. It was for this reason that we undertook the measurement

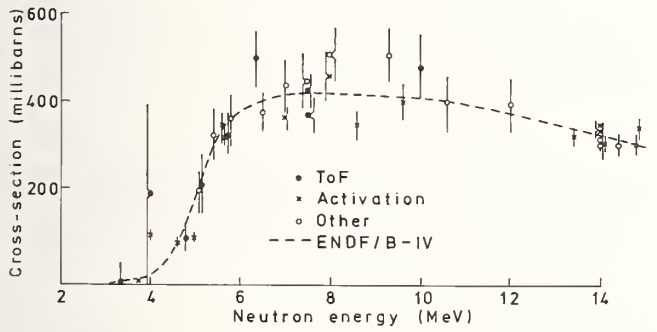

Figure 2. Original data on the $^{7}Li(n,n'\alpha t)$ cross-section.

of this cross-section, and I would like to describe briefly the experimental method, and the results of other recent experiments which give information on this cross-section before discussing the effect of our results on a few reactor blanket designs.

Measurements

^{7}Li cross-section

An activation method was used to measure the cross-section, in which the tritium produced by an irradiation in a measured neutron dose was subsequently counted by a liquid scintillation technique.

Irradiations. Figure 3 shows the geometry for the irradiations using the D(d,n) neutron source reaction on the Tandem accelerator at Harwell to produce neutrons from 4.7 to 12 MeV. The target was a 10 cm long, 2 atmosphere gas cell with a thin entrance window. The use of this reaction necessitated an 8% correction for deuteron break-up neutrons (d(d,np)d) on the 12 MeV irradiation. The irradiations lasted for approximately 24 hours. The lithium samples were enclosed in an aluminium case, and aluminium foils were used as a check on the measured neutron dose by determining the $^{27}Al(n,\alpha)$ cross section. The whole assembly was contained in a 1 mm thick cadmium case to prevent thermal neutrons producing tritium via the $^{6}Li(n,\alpha t)$ reaction.

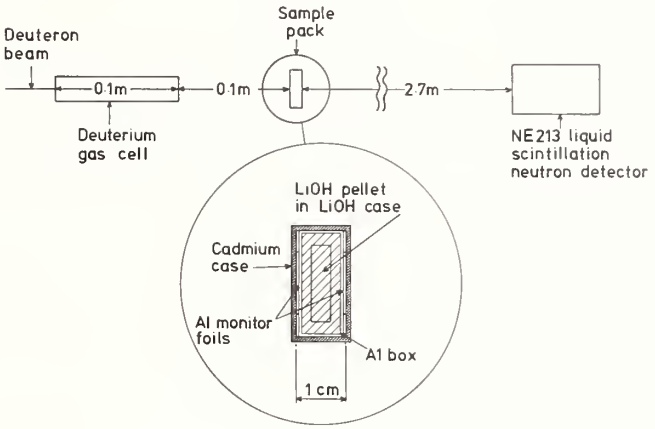

Figure 3. Irradiation geometry.

Neutron measurements. The neutron dose was measured with an NE213 liquid scintillation detector which was calibrated using the associated particle method.[6] The efficiency for three different discriminator levels is shown in Figure 4. as a function of neutron energy which were used to measure

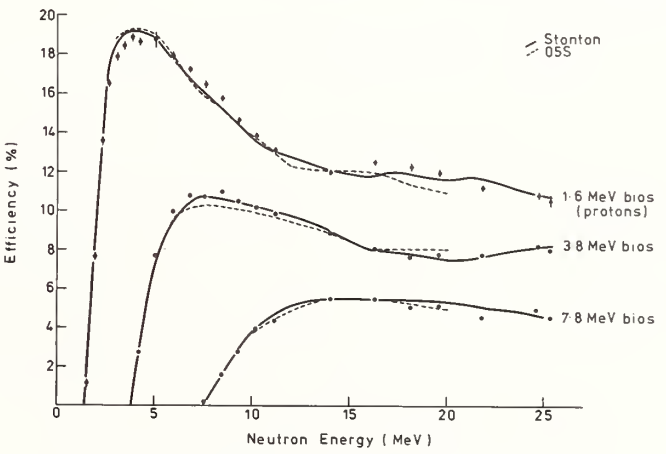

Figure 4. NE213 detector efficiency for three proton biases.

the primary neutron dose with an uncertainty of less than ± 2%. The observed dose was corrected for the measured transmission of the sample pack, and together with the ^{24}Na activity induced in the ^{27}Al monitor foils (measured using a calibrated Ge(Li) detector in the chemistry division at Harwell) this gave the cross-section for the $^{27}Al(n,\alpha)^{24}Na$ reaction. The results are shown in Figure 5. which includes results from previous experiments and the ENDF/B IV evaluated curve. The agreement between the present results and the previous data confirms the detector calibration for flux measurement. At 14.1 MeV the cross-section of the $^{7}Li(n,n'\alpha t)$ reaction was measured relative to the $^{27}Al(n,\alpha)$ reaction cross-section using a 500 keV Cockcroft-Walton generator. A value of 122±2 mb was assumed for the $^{27}Al(n,\alpha)^{24}Na$ cross-section at 14.1 MeV relative to which a nickel foil irradiated concurrently gave a value of 382±15 mb for the $^{58}Ni(n,p)$ cross-section.

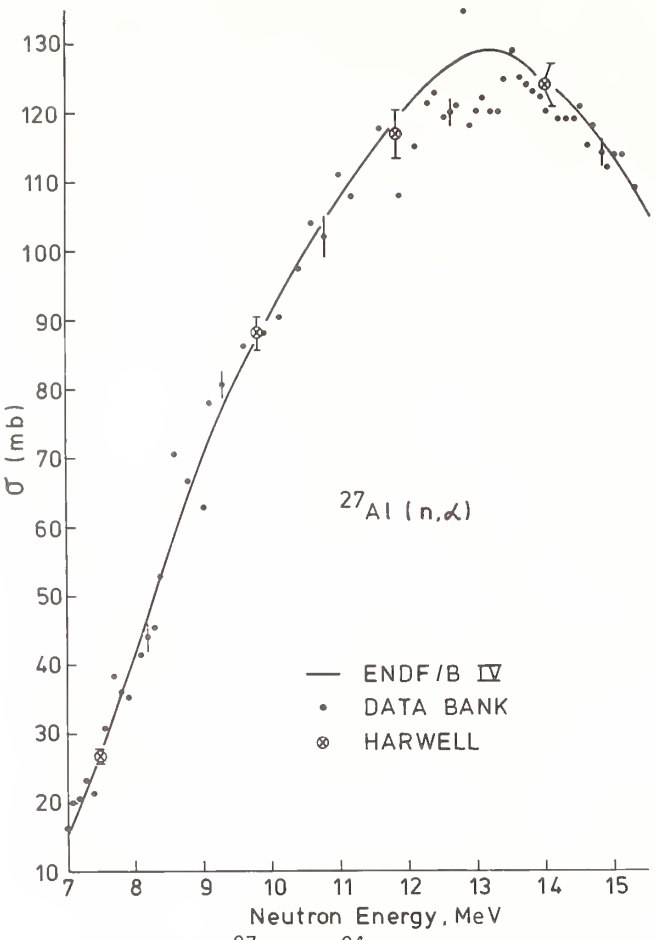

Figure 5. $^{27}Al(n,\alpha)^{24}Na$ cross-section.

Tritium Measurement. Lithium hydroxide enriched to 99.5% in ^{7}Li was used as the sample material, (Figure 6) and pellets in the form of compacted discs were made by compressing the LiOH powder without a binder. These pellets were stable in that their weight did not increase, and chemical analyses showed them to be almost pure LiOH. This material was also used because the tritium is stored as LiOT and so goes into solution on chemical processing. [7,8] A case of t he same material was used to compensate for the loss of recoil tritons which are formed with an energy of several MeV. The multiple scattering correction factor was calculated from the composition of the sample, using a Monte Carlo technique, and increased to 5% at 14 MeV.

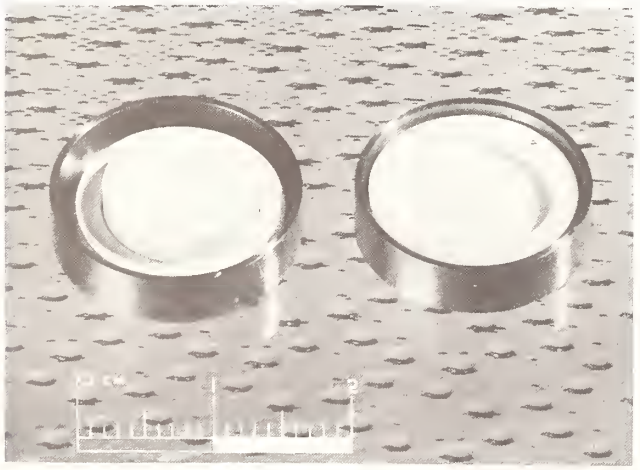

Figure 6. Lithium hydroxide pellet assembly.

In order to extract the tritium from the pellet a method based on that of Dierckx[9] was used. The pellet is first slowly dissolved in dilute acetic acid (Figure 7) which converts the tritium into tritiated

$$LiOH\,(T) + CH_3COOH \rightarrow CH_3COOLi + H_2O\,(T)$$
$$CH_3COOLi + HF \rightarrow LiF + CH_3COOH$$

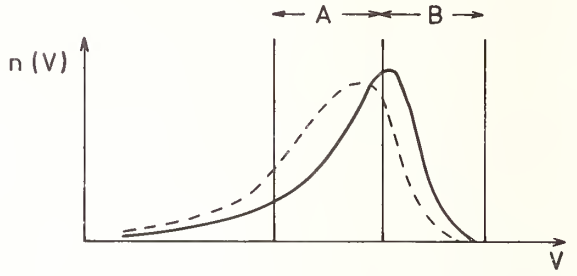

Figure 7. (a) Chemistry involved in tritium counting.
(b) Effect of quenching on spectrum.

water. The associated lithium acetate in solution prevents good mixing of the scintillator with the solution and so the lithium is deposited as lithium fluoride. The scintillator Dimilume (Packard Instruments Ltd) is added for counting and all the processing was carried out in the counting vial. The liquid scintillation counting was carried out using a Packard Liquid Scintillation Spectrometer in the Industrial Physics group at Harwell.

Small differences in the amounts of chemicals alter the beta counting efficiency of each sample. This is due to extra paths for energy to be lost between deposition by the beta and photon production. The efficiency for each sample was measured by the external standard channels ratio technique.

The quenching gives a characteristic shape to the spectrum for any degree of quenching. (Figure 8) The method involves calibration of the tritium counting efficiency as a function of the quench by using standard tritiated water (or tritiated hexadecane) in solutions of unirradiated pellets. The quench of any particular sample is measured as the ratio of the counts in two windows on the spectrum

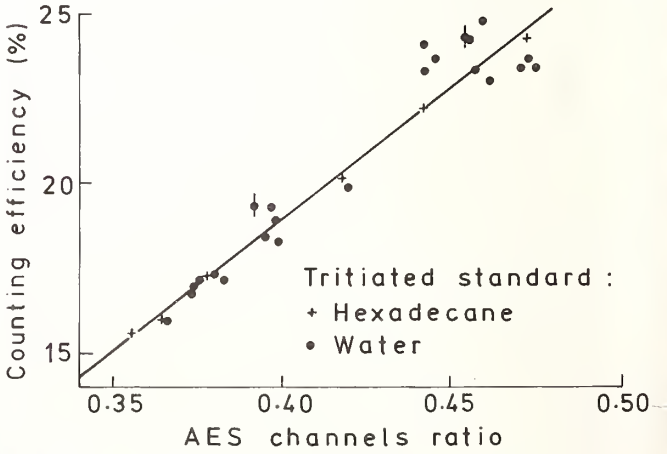

Figure 8. Tritium counting efficiency versus AES ratio.

of an external gamma source. Figure 8 shows the result; a plot of efficiency versus channels ratio,

enabling the efficiency of any sample to be determined once the channels ratio has been measured. The straight line fitted to the points is closer to those points measured using hexadecane because this material does not evaporate significantly at room temperature which facilitates accurate dispensing. The background count-rate was found by processing unirradiated samples in the same way.

Results. Figure 9 shows the final results for the cross-section together with previous data from activation experiments. The uncertainty on the present measurement is approximately + 5%. The results are uniformly 26% lower than the ENDF/B IV evaluated curve.

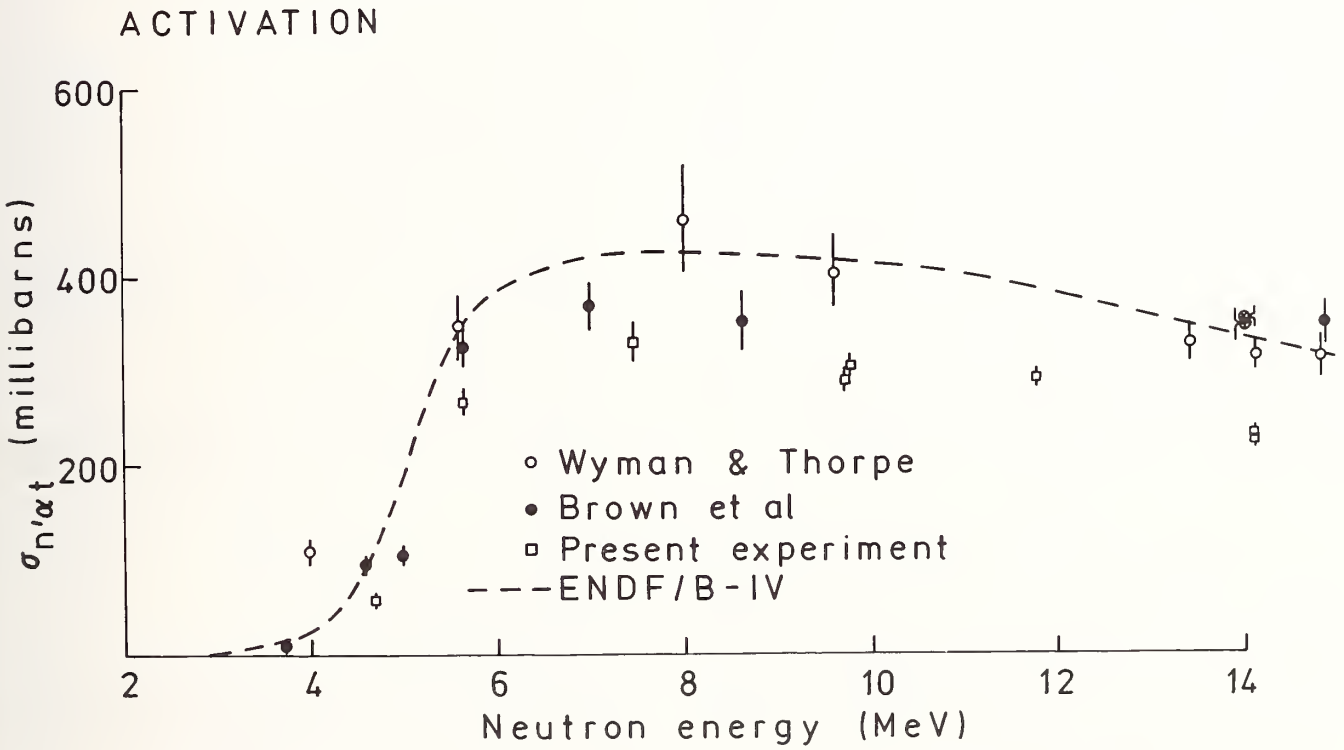

Figure 9. Results of the present experiment compared with previous values obtained by activation.

^{6}Li Cross-section Measurement

In order to check for systematic effects in the tritium measuring system, the ^{6}Li thermal cross-section, which is known to an accuracy of about ½%, was measured in a reactor irradiation.

Pellets with ^{6}Li/^{7}Li ratios of (0.6±0.005)% and (0.94±0.008)% were used in order that the self-shielding correction should be small. The self-shielding calculation was carried out using Monte-Carlo calculated collision probabilities, with an overall uncertainty of + 3%. The ^{6}Li cross-section was determined by measuring the tritium activity produced with and without a cadmium cover on the pellet assembly in order to subtract the effect of fast neutrons. The thermal flux at the point of irradiation in the GLEEP reactor is known to an accuracy of + 2% by periodic measurements using gold foil activation. The tritium counting was carried out in exactly the same way as for the main experiment and the results gave 970±42b for the high concentration pellet and 936±40b for the lower concentration pellet. As the accepted value is 936±4b [10] this is confirmation that no significant systematic errors are present in the method of sample preparation for β-counting.

Other Evidence

Integral Experiments

Before we discuss the consequences of such a change in the ^{7}Li cross-section, other evidence for a discrepancy between measurements and evaluation should be examined.

There have been three recent integral experiments on lithium assemblies in which tritium production has been directly measured. The experiments, at Jülich, [11] Karlsruhe, [12] and Los Alamos [13] are basically similar, but have sufficient differences to exclude obvious systematic errors. There were two natural lithium metal blankets (one a cylinder and one a sphere) and a ^{6}LiD sphere. All used a DT 14 MeV neutron source at the centre of the assembly and the source strength was determined by activation of threshold detectors or counting of the alpha particles associated with the neutron production. The tritium measurements were carried out in two ways. In Jülich and Karlsruhe the tritium was produced in samples of Li_2CO_3 and measured using a similar technique to the present experiment. In the Los Alamos experiment the samples were lithium hydride and the tritium counting was carried out in a gas proportional counter. The calculations in each case used the ENDF/B III data file for the lithium-7 cross-

section and the calculation was carried out using a variety of discrete ordinates codes and Monte Carlo codes in 1 and 3-D geometry. The results are shown in Figure 10. On the left is the radial distribution of the secondary spectrum.

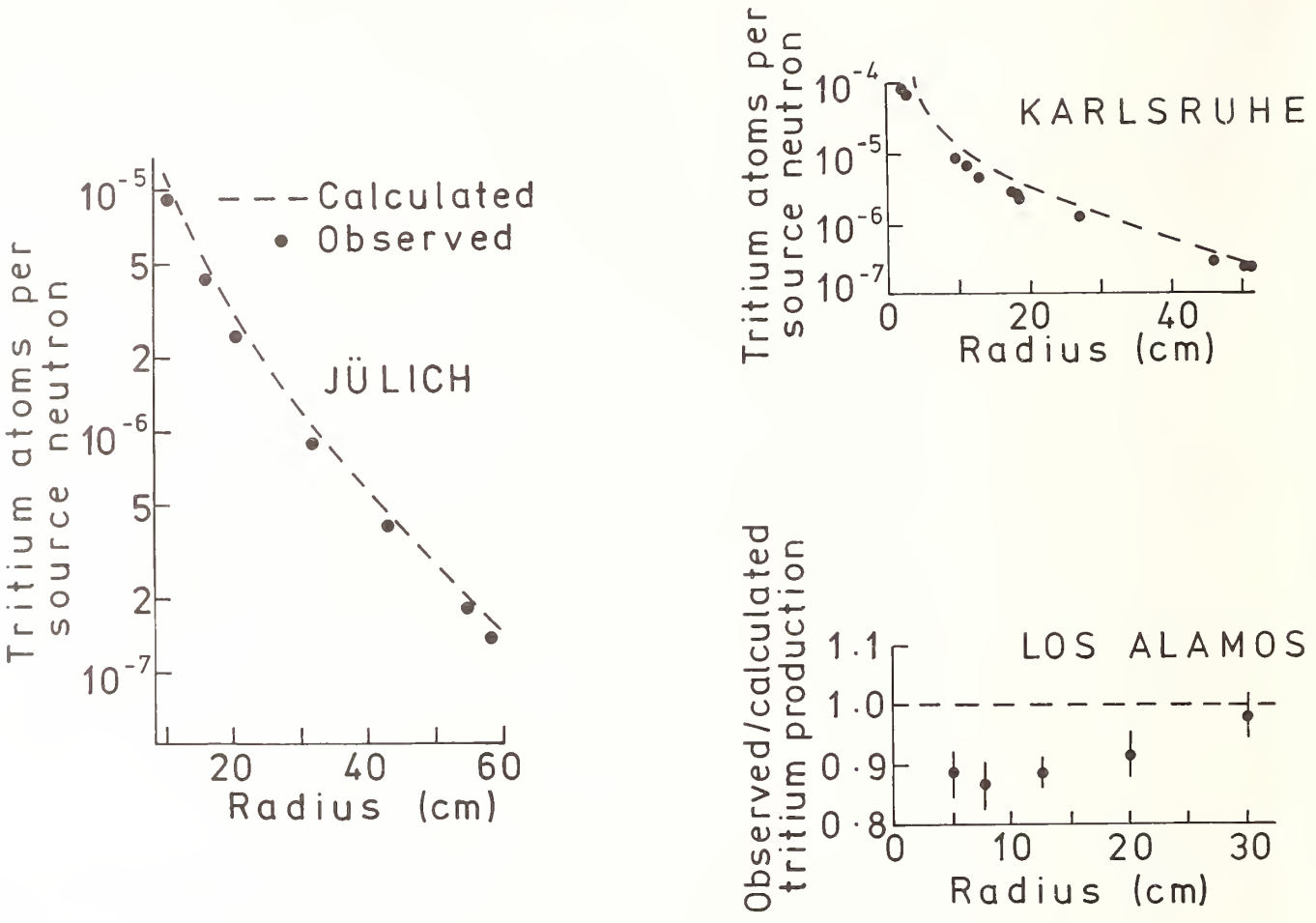

Figure 10. Results of tritium production measurements on integral assemblies.

of tritium production in ^{7}Li in the Jülich blanket showing that the measurements are significantly below the calculation. On the top right is the same information for the Karlsruhe blanket, except in this case the tritium production is in natural lithium. The paper reporting this result states that the measurements are 35% below the calculation with a standard deviation of 5.1%. In the bottom right the ratio of measured to calculated tritium production in ^{7}Li is shown for the Los Alamos assembly, again demonstrating measured values considerably lower than calculated. Two of the papers mention the discrepancy as due to the $^{7}Li(n,n'\alpha t)$ cross-section, and the Karlsruhe report suggests that the ^{7}Li cross-section as given in ENDF/B should be reduced.

A recent consistency analysis [14] performed on an older tritium production integral experiment of Wyman [15] suggested that a 13% reduction in the $^{7}Li(n,n'\alpha t)$ cross-section at 14 MeV would give a better representation of the experiment.

One usual problem with cross-section adjustments suggested by lithium integral experiments is the uncertainty of the calculated spectrum due to the uncertainty of the energy distribution of the secondary neutrons from the $^{7}Li(n,n'\alpha t)$ reaction. However since one of the integral experiments was carried out using a ^{6}Li assembly, the tritium production rate in a ^{7}Li probe is almost independent

Differential Experiments

Although there have been no recent differential measurements of the tritium production cross-section of ^{7}Li, there have been two recent measurements of the elastic cross-section; at Triangle Universities Nuclear Laboratory [16] and Ohio University, [17] using ^{7}Li and natural lithium respectively. In the energy range 4 - 14 MeV the reactions with significant cross-sections are elastic scattering, inelastic scattering to the 1st excited state (higher levels are unstable with respect to particle emission) and tritium production. Other reactions such as (n,2n) begin to become significant and reach a total of 65 mb at 14 MeV. The total cross-section is reasonably well known in this energy region and so from the new measurements, which were in fact elastic + inelastic to the first excited state we can calculate the expected value for the $(n,n'\alpha t)$ cross-section. The results from both measurements are shown in Figure 11. The total cross-section was taken from ENDF/B IV and this evaluation was also used for the (n,2n) and other reactions needed to correct the Triangle Universities' data; the Ohio data does not go high enough in energy to be affected by these other reactions.

The measurements from TUNL show better agreement with the present values than the ENDF/B evaluated curve, but the Ohio results show a marked disagreement

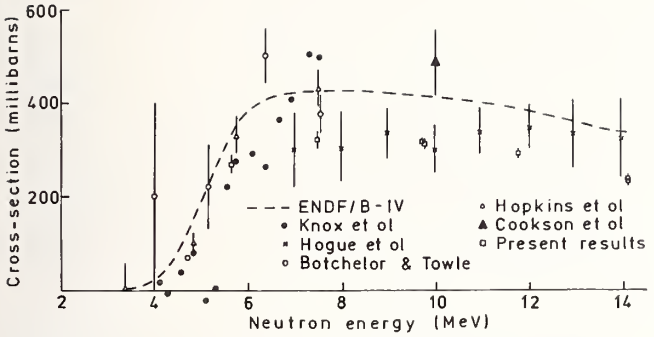

Figure 11. $^{7}Li(n,n'\alpha t)$ cross-section derived from elastic cross-section measurements.

at the higher end of their energy range. The 25% difference in $(n,n'\alpha t)$ cross-section between TUNL and Ohio data is due to only a 6% difference in the elastic scattering cross-section measurements of the two groups and serves to illustrate the difficulty of determining the $(n,n'\alpha t)$ cross-section in this way.

Another recent differential experiment of a more restricted character has also been carried out recently at ORNL.[18] (Figure 12). It is a measurement

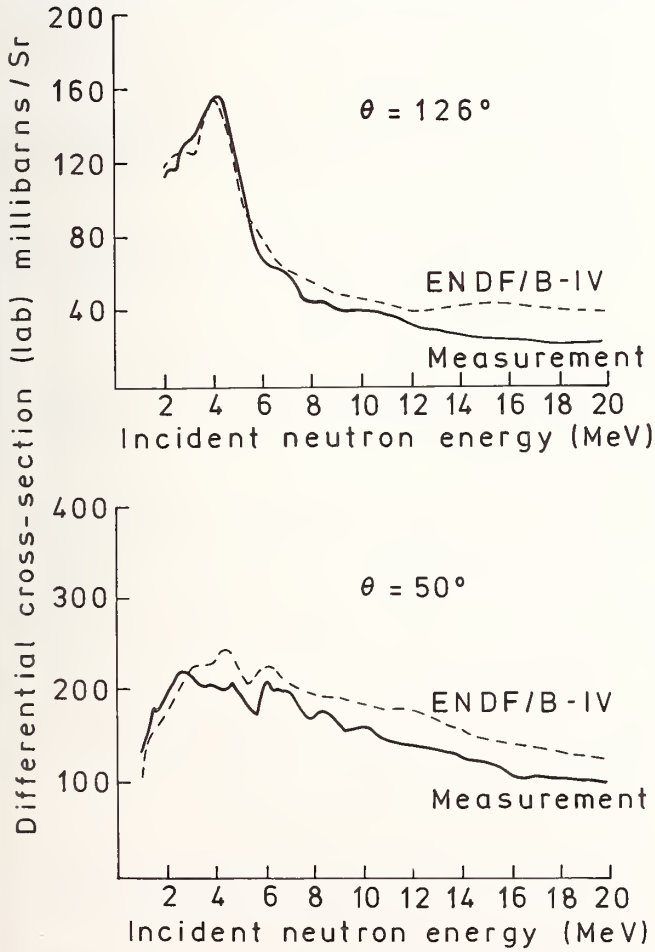

Figure 12. $^{7}Li(n,xn')$ differential cross-section measurement. [18]

of the differential cross-section for $^{7}Li(n,xn)$ processes at two angles. The data extend from 2 to 20 MeV incident neutron energy and includes all secondary neutrons above a 0.76 MeV bias. A comparison with the ENDF/B values (given in the report) over the incident neutron energy range 6-14 MeV where $^{7}Li(n,n'\alpha t)$ is the predominant reaction, shows that the results are approximately 20% lower than the evaluation.

Implications

The importance of the present experiment depends on the effect of the cross-section changes, indicated above, on various fusion reactor blanket designs. The change in cross-section amounts to 1.3 standard deviations of the previous uncertainty associated with the $^{7}Li(n,n'\alpha t)$ reaction. Previous precise uncertainty analyses have been carried out using perturbed data sets and sensitivity analysis to calculate the effect of a change of 1 standard deviation in the cross-section. To calculate the effect of the present measurement is a simple extension of these results, and this has been done for some blankets. However, for those blankets without such uncertainty analysis an approximation was made that the ^{7}Li breeding rate decreased in the same proportion as the cross-section. This is equivalent to the assumption that the flux distribution in the blanket is not affected by the cross-section change. This would be expected to be valid when the ^{7}Li reaction rate is a small part of the total reaction rate. (In fact this method agrees well with those cases which have been calculated precisely).

The results for seven blanket designs are shown in Table III. The particular designs were chosen to be

Table III. Effect of present cross-section change on various reactor blankets.

Breeder or reactor type	Original B.R	New B.R	% loss in breeding gain
Liquid metal (ORNL (Nb))	1.49	1.38*	22 %
Lithium oxide	1.15	1.06	60 %
Li_7Pb_2/Li_2O	1.08	1.03	63 %
$LiAlO_2$ (Be) (UWMAK-II)	1.07	1.07	0 %
LiAl (30 % ^{6}Li)	1.07	1.04	43 %
Molten salt (PPPL)	1.05	1.02*	60 %
Theta pinch (Be) (LASL)	1.04	1.01*	75 %

* Results from sensitivity analysis

representative of the range of designs which have been proposed to meet the constraints mentioned earlier. The first is a standard lithium metal blanket.[4] (The references refer to those publications in which calculations were carried out, not necessarily the original design publication). The second uses lithium oxide as a breeding material in a Wisconsin design.[19] The third is a system of lithium lead and lithium oxide in a cellular design [3] for a Culham conceptual reactor. The lead of course is a neutron multiplier. The next two systems are again from Wisconsin; lithium aluminate in UWMAK-II [20] and a LiAl blanket.[20] The next is a Flibe (molten salt) system [4] from Princeton and finally there is a lithium/beryllium theta-pinch reactor design [4] of Los Alamos. As the table shows, the change in breeding gain is very significant for most systems, especially those designs

which have low breeding ratios initially. Designs which are totally dependent on ^{6}Li breeding and therefore immune to changes in the ^{7}Li cross-section, i.e. 'thermal' systems, usually rely on the use of beryllium as a neutron multiplier. This may not be possible because the world's supply may prevent its use in reactor programs based on some designs, [22] and also recent measurements [23] imply a reduced effectiveness for beryllium on the tritium breeding ratio.

The changes shown in the table are those produced by a change in the $^{7}Li(n,n'\alpha t)$ cross-section. However there is still an error on the calculated breeding ratio due to cross-section uncertainties, including a 5% error on the present $^{7}Li(n,n'\alpha t)$ measurement. It is estimated that these uncertainties would produce a 6.5% error on the calculated breeding ratio of a lithium metal blanket system when the effect of the ^{7}Li secondary neutron spectrum is also included.[24]

In addition to this uncertainty, none of the blanket calculations mentioned above has given a realistic allowance for voids in the blanket which are required for practical systems (divertors, injectors etc.). It may be possible in some systems to regain some of the lost breeding gain by enrichment of the lithium in ^{6}Li, although this would add to the cost and the amount of lithium required.

Finally, these measurements, together with the supporting evidence, show that further determinations of the $^{7}Li(n,n'\alpha t)$ cross-section are essential. The value is particularly important at 14 MeV where many laboratories are able to carry out experiments.

References

1. Y.Gohar, C.W. Maynard and E.T. Cheng. Neutronic and photonic analysis of the UWMAK-III blanket and shield in non-circular toroidal geometry in Proc. of Technology of Controlled Nuclear Fusion. Washington 1976 CONF-760935 p.833.

2. L.J.Baker. Some implications of a cellular structure in minimum thickness fusion reactor blankets. 10th Symposium on Fusion Technology. Padova 1978.

3. G.Constantine. Possible improvements to a basic cellular thin blanket fusion reactor configuration. 10th Symposium on Fusion Technology. Padova 1978.

4. R.G.Alsmiller, Jr., R.T.Santoro, J.Barish and T.A.Gabriel. Comparison of the cross-section sensitivity of the tritium breeding ratio in various fusion-reactor blankets. Nuc.Sci. and Eng. 57 (1975) p.122

5. D.V.Markovskii, G.E.Shatalov and G.B.Yan'Kov. Influence of neutron constants on the neutronics of a thermonuclear reactor blanket. IAE 2579(1975)

6. J.A.Cookson, M.Hussain, R.B.Schwartz and C.A.Uttley Absolute calibration of neutron detectors in the 10-30 MeV range. Proc.Conf.on Nucl.Cross-sections and Technology Washington 1975 NBS SP 425 p.66 and J.L.Fowler, J.A.Cookson, M.Hussain, R.B. Schwartz, M.T.Swinhoe, C.Wise and C.A.Uttley. Efficiency calibration of scintillation detectors in the neutron energy range 1.5 to 25 MeV by the associated particle technique. (to be published)

7. P.Van Urk. Tritium recoil reactions in solids. PhD thesis (1970) I.K.O. Amsterdam.

8. M.Kudo, K.Tanaka, J.Amano. Chemical behaviors of tritium produced by the $^{6}Li(n,\alpha t)$ reaction in lithium oxide. J.Inorg.Nucl.Chem. 40 (1978) p.363

9. R. Dierckx. Direct tritium production measurement in irradiated lithium. Nuc.Instr. and Meth. 107 (1973) p.397

10. See reference 13.

11. R.Herzing, L.Kuypers, P.Cloth, D.Filges, R.Hecker and N.Kirch. Experimental and Theoretical Investigations of tritium production in a controlled thermonuclear reactor blanket model. Nuc.Sci. and Eng. 60 (1976) p.169 and L.Kuypers. Experimental model studies for a fusion reactor blanket. PhD thesis (1976) Eindhoven.

12. H.Backmann, U.Fritscher, F.W.Kappler, D.Rusch, H.Werle and H.W.Wiese. Neutron spectra and tritium production measurements in a lithium sphere to check fusion reactor blanket calculations. Nuc. Sci. and Eng. 67 (1978) p.74 and U.Fritscher, F.Kappler and D.Rusch. Tritium production measurement in a lithium metal sphere with new techniques in neutron source strength determination. Nuc. Instr. and Meth. 153 (1978) p.563

13. A.Hemmendinger, C.E.Ragan, E.R.Shunk, A.N.Ellis, J.M.Anaya and J.M.Wallace. Tritium production in a sphere of ^{6}LiD irradiated by 14 MeV neutrons LA-7310 (1978) and A.Hemmendinger, C.E.Ragan and J.M.Wallace. Tritium production in a sphere of ^{6}LiD irradiated by 14 MeV neutrons. Nuc.Sci. and Eng. 70 (1979) p.274

14. W.A.Reupke and D.W.Muir. Neutronic data consistency analysis for lithium blanket p.861 same Conf. as ref. 1 and Consistency analysis of fusion reactor neutronics data: tritium production TANS 23 (1976) p.21

15. M.E.Wyman. An integral experiment to measure the tritium production from ^{7}Li by 14 MeV neutrons in a lithium deuteride sphere. LA-2234 (1972)

16. M.M.Hogue, P.L.von Behren, D.W.Glasgow, S.G.Glendinning, P.W.Lisowski, C.E.Nelson, F.O.Purser, W.Tornow, C.R.Gould and L.W.Seagondollar Elastic and inelastic scattering of 7 to 14 MeV neutrons from ^{6}Li and ^{7}Li. Nuc.Sci.and Eng. 69 (1979) p.22

17. H.D.Knox, R.M.White and R.O.Lane. Differential neutron scattering cross-sections of ^{6}Li and ^{7}Li for neutrons of 4 to 7.5 MeV energy. Nuc.Sci.and Eng. 69 (1979) p.223

18. G.L.Morgan. Cross-sections for the $^{7}Li(n,xn)$ and $^{7}Li(n,n'\gamma)$ reactions between 1 and 20 MeV. ORNL-TM-6247 (1978)

19. E.T.Cheng, M.M.H. Ragheb, R.W.Conn. Neutronics and photonics studies for the University of Wisconsin laser fusion reactor blanket. TANS 26 (1977) p.504

20. E.T.Cheng, R.W.Conn. The influence of design variations on controlled thermonuclear reactor blanket neutronic performance using variational techniques. Nuc.Sci.and Eng. 62 (1977) p.601.

21. E.T.Cheng. Application of generalised variational principles to fusion reactor neutronics studies. TANS 27 (1977) p.802

22. A.P.Fraas. Comparative study of the more promising combinations of blanket materials, power conversion systems and tritium recovery and containment systems for fusion reactors. ORNL-TM-4999 (1975)

23. T.K.Basu, V.R.Nargundkar, P.Cloth, D.Filges and S.Taczanowski. Neutron multiplication studies in beryllium for fusion reactor blankets. Nuc.Sci. and Eng. 70 (1979) p.309

24. D.Steiner and M.Tobias. Cross-section sensitivity of tritium breeding in a fusion reactor blanket: Effects of uncertainties in cross-sections of ^{6}Li, ^{7}Li and ^{93}Nb. Nuc.Fus. 14 (1974) p.153.

CHARGED PARTICLE CROSS SECTION REQUIREMENTS FOR ADVANCED FUSION FUEL CYCLES

Geoffrey W. Shuy and Robert W. Conn
University of Wisconsin, Nuclear Engineering Department,
Madison, Wisconsin 53706, USA

Charged particle cross sections required for advanced fusion fuel cycle calculations are discussed. Reactions important for the d-d, d-^{3}He, d-^{6}Li, p-^{6}Li and p-^{11}B cycles are described. The importance of nuclear elastic scattering is emphasized. Important fusion cross sections and the energy range where data is required are identified. Of particular interest for the propagating p-^{6}Li cycle is the ^{6}Li(^{3}He,p)^{8}Be reaction where the ^{8}Be can be in different energy states. The reactivity of the catalyzed d-d reaction at T_i = 75 keV can be increased by 25% at T_e = 50 keV to 75% at 100 keV relative to the reactivity neglecting nuclear elastic scattering. The result is due to fusion events between fast deuterons produced by elastic scattering with the background ions. The fraction of energy given to electrons is likewise influenced by nuclear elastic scattering. The fraction of a 14.5 MeV proton's energy given to electrons at 100 keV decreases from 85% when only coulomb scattering is assumed to 50% when coulomb plus nuclear scattering is included.

[Fusion, d-d, d-^{3}He, d-^{6}Li, p-^{6}Li, p-^{11}B fuel cycles; charged particle cross section needs; fusion reactivity]

Introduction

Fusion devices utilizing the d-t-Li cycle will certainly be the first to demonstrate energy breakeven and also very likely will be the first cycle for commercial fusion reactors. Nevertheless, fusion reactors with tritium fuel should be viewed as an intermediate step in fusion power development. The ultimate goal is to achieve a reactor based on either hydrogen or deuterium to insure both an inexhaustible fuel supply and systems with minimum radioactivity. To preserve this potential, it is essential to maintain efforts to develop advanced fuel cycle fusion power based on d-d, d-^{3}He, d-^{6}Li or proton based cycles such as p-^{11}B and p-^{6}Li. Minimizing the plasma deuterium content is a key to a minimum neutron producing reactor. A proper determination of the potential of each cycle requires cross section data for the basic reactions and for nuclear elastic and inelastic scattering among the nuclei with A less than 12.

Required Nuclear Data

The nuclear data required to analyze advanced fuels include fusion reaction cross sections, reaction rate parameters such as $\langle\sigma v\rangle$, reaction probabilities for fast fusion products to react with various elements in the background plasma, and nuclear elastic and inelastic cross sections to determine the energy transfer from the energetic fusion products to the background ions and electrons. The reaction rate, R, for two reacting species, a and b, is

$$R = \int d\bar{v}_a \int d\bar{v}_b \; f_a(\bar{v}_a) f_b(\bar{v}_b) \sigma(u) u \qquad (1)$$

where R is the number of reactions per unit volume per unit time, f_a and f_b are the distribution functions, σ is the reaction cross section, and u is the relative velocity, $u = |\bar{v}_a - \bar{v}_b|$. It is convenient to write R as $n_a n_b \langle\sigma v\rangle$, where the density of species a and b (n_a and n_b) are found from

$$n_i = \int f_i(\bar{v}_i) d\bar{v}_i \qquad (i = a,b). \qquad (2)$$

The reaction rate parameter, $\langle\sigma v\rangle$, depends on the form of the normalized distribution functions $\hat{f}_i(\bar{v}_i) = \frac{1}{n_i} f_i(\bar{v}_i)$:

$$\langle\sigma v\rangle = \int d\bar{v}_a \int d\bar{v}_b \; \hat{f}_a(\bar{v}_a) \hat{f}_b(\bar{v}_b) \sigma(u) u. \qquad (3)$$

If $\hat{f}_i(\bar{v}_i)$ is the Maxwellian distribution,

$$\hat{f}_i(\bar{v}_i) = \left(\frac{m_i}{2\pi KT}\right)^{3/2} \exp(-m_i v_i^2/2KT), \qquad (4)$$

the integral in Eqn. (3) can be expressed as:

$$\langle\sigma v\rangle = 4\pi \int_0^\infty u^2 du \left(\frac{\mu}{2\pi KT}\right)^{3/2} \exp\left(\frac{-\mu u^2}{2KT}\right) \sigma(u) u, \qquad (5)$$

where μ is the reduced mass. Using $E = \frac{1}{2}\mu u^2$, Eqn. (5) becomes

$$\langle\sigma v\rangle = \sqrt{\frac{8}{\pi\mu}} \left(\frac{1}{KT}\right)^{3/2} \int_0^\infty E\sigma(E) \exp(-E/KT) dE. \qquad (6)$$

The ion temperature in advanced fuel cycle fusion plasmas may reach 500 keV. One clearly would like to know the reaction cross section, $\sigma(E)$, up to an energy of at least 4KT (or 2 MeV in the most extreme case) to analyze fusion reactions among species with a Maxwellian distribution. In addition, nuclear scattering events between energetic fusion products and the background Maxwellian can transfer significant energy (>1 MeV) to the struck particle thereby promoting it to higher energy where it is typically more reactive. In short, cross sections are required not just to an energy of 4-5 KT but to the energy of fusion reaction products. The p-^{6}Li cycle is particularly useful to demonstrate this point.

The primary reactions of this fuel cycle are

$$p + {}^6\text{Li} \rightarrow {}^3\text{He}(2.3\text{ MeV}) + \alpha(1.7\text{ MeV}) \qquad (7)$$

$$^3\text{He} + {}^6\text{Li} \rightarrow p(11.3\text{ MeV}) + 2\alpha(2.813\text{ MeV}) \qquad (8a)$$

$$\rightarrow p + {}^8\text{Be(various nuclear levels)} \qquad (8b)$$

$$\rightarrow d(.088\text{ MeV}) + {}^7\text{Be}(.026\text{ MeV}) \qquad (8c)$$

Secondary and tertiary reactions include:

$$d + {}^6\text{Li} \begin{cases} n + {}^7\text{Be}(.42\text{ MeV}) & (9a) \\ p(4.4\text{ MeV}) + {}^7\text{Li}(.63\text{ MeV}) & (9b) \\ p(1.6\text{ MeV}) + t + \alpha & (9c) \\ n + {}^3\text{He} + \alpha & (9d) \\ 2\alpha(11.2\text{ MeV}) & (9e) \end{cases}$$

$$d + {}^3He \rightarrow p(14.6\ MeV) + \alpha(4.7\ MeV) \quad (10)$$

$$d + d \begin{cases} \rightarrow n + {}^3He(.82\ MeV) & (11a) \\ \rightarrow p(3MeV) + t(1.01\ MeV) & (11b) \end{cases}$$

$$d + {}^7Be \rightarrow p(11.2\ MeV) + 2\alpha(2.8\ MeV) \quad (12)$$

$$d + t \rightarrow n + {}^4He(3.5\ MeV) \quad (13)$$

$$t + {}^3He \begin{cases} \rightarrow d(9.6\ MeV) + \alpha(4.8\ MeV) & (14a) \\ \rightarrow p + n + \alpha & (14b) \end{cases}$$

$${}^3He + {}^3He \rightarrow 2p(5.7\ MeV) + \alpha(1.4\ MeV) \quad (15)$$

$${}^3He + {}^7Be \rightarrow 2p(4.5\ MeV) + 2\alpha(1.1\ MeV) \quad (16)$$

$$t + {}^7Be \rightarrow p(4.2\ MeV) + 2\alpha \quad (17)$$

$$d + {}^7Li \rightarrow n + 2\alpha(2.52\ MeV) \quad (18)$$

In addition, there are at least thirty side reactions and thirteen $^6Li + {}^6Li$ exothermic reactions which produce elements from H to ^{12}C and neutrons. Many of the fusion reaction products are energetic and may react with elements in the background plasma prior to completely slowing down (fast fusion or two-component fusion events). Including these fast fusion events is crucial, particularly for cycles that are either propagating or chain events. Some important propagating fusion reaction sequences in the p-^6Li cycle (the fast particle has a bar over the element's designation) include

$$\left\{ \begin{array}{l} \bar{p} + {}^6Li \rightarrow {}^3\overline{He} + \alpha \\ {}^3\overline{He} + {}^6Li \rightarrow \bar{p} + 2\alpha \\ \bar{p} + {}^6Li \rightarrow {}^3\overline{He} + \alpha \\ \vdots \end{array} \right\} (19) \qquad \left\{ \begin{array}{l} \bar{p} + {}^6Li \rightarrow {}^3\overline{He} + \alpha \\ {}^3\overline{He} + d \rightarrow \bar{p} + \alpha \\ \bar{p} + {}^6Li \rightarrow {}^3\overline{He} + \alpha \\ \vdots \end{array} \right\} (20)$$

$$\left\{ \begin{array}{l} \bar{p} + {}^6Li \rightarrow {}^3\overline{He} + \alpha \\ {}^3\overline{He} + {}^6Li \rightarrow \bar{d} + {}^7Be \\ \bar{d} + {}^6Li \rightarrow \bar{p} + {}^7Li \\ \bar{p} + {}^6Li \rightarrow {}^3\overline{He} + \alpha \\ \vdots \end{array} \right\} (21) \qquad \left\{ \begin{array}{l} \bar{p} + {}^6Li \rightarrow {}^3\overline{He} + \alpha \\ {}^3\overline{He} + {}^6Li \rightarrow \bar{d} + {}^7Be \\ \bar{d} + {}^7Be \rightarrow \bar{p} + 2\alpha \\ \bar{p} + {}^6Li \rightarrow {}^3\overline{He} + a \\ \vdots \end{array} \right\} (22)$$

and there are many others.

Nuclear elastic scattering of the energetic products with the background plasma produces additional energetic particles which can undergo fast fusion and further propagate the reaction. Therefore, the reaction cross section for the various channels and nuclear elastic scattering cross sections are required up to about 20 MeV.

In general, the nuclear scattering cross section is 1 barn or greater when the incident energy is in the range, 1 to 15 MeV. As an example, the proton-deuterium nuclear elastic scattering cross section is shown in Fig. 1 as a function of proton energy. The coulomb scattering cross section has been subtracted prior to plotting the result.

The average energy transfer per collision is large. For example, counting only collisions which transfer 1 MeV or more, a 3 MeV proton in a deuterium plasma with a 75 keV ion temperature is found to transfer ~30% of its energy to the energetic deuterons when the electron temperature is 60 keV. This fraction increases to ~50% when T_e is 100 keV. The fast fuel ions produced from this process undergo fusion while slowing down thereby enhancing the reactivity and the effect of propagating reaction. In Figs. 2 and 3, we show the fraction of energy transferred from fast alphas and fast protons to produce energetic deuterons with an energy greater than 1 MeV. The effect is smaller for alphas at 3 to 4 MeV than for protons at either 3 MeV or 14.5 MeV because of the larger coulomb cross section for alphas.

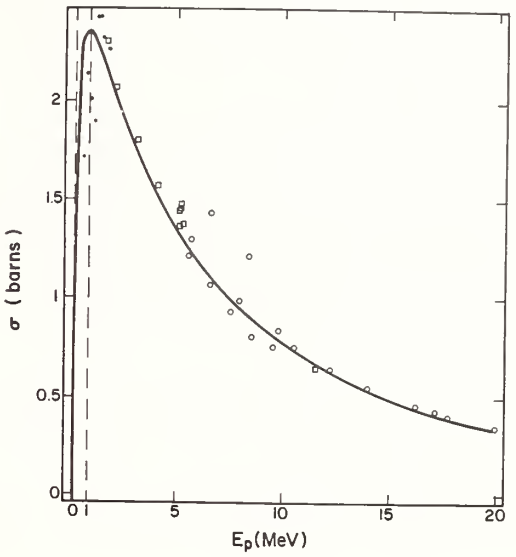

Fig. 1. The elastic scattering cross section for protons with deuterons after subtracting the coulomb scattering from the angular distributions.

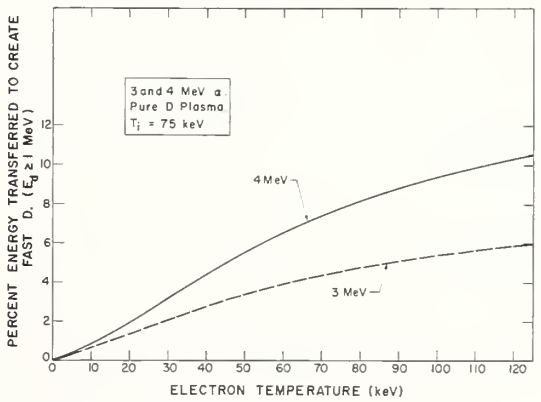

Fig. 2. Percentage of initial energy transferred from fast alphas to produce energetic (>1 MeV) deuterons.

The catalyzed d-d fuel cycle can be used to elaborate on the role of nuclear elastic scattering and propagating effects. The major reactions for this cycle are:

$$d + d \begin{cases} \rightarrow n(2.45\ MeV) + {}^3\overline{He}(.87\ MeV) & (23a) \\ \rightarrow \bar{p}(3.01\ MeV) + \bar{t}(1\ MeV) & (23b) \end{cases}$$

$$d + t \rightarrow n(14.06\ MeV) + \bar{\alpha}(3.5\ MeV) \quad (24)$$

$$d + {}^3He \rightarrow \bar{\bar{p}}(14.68\ MeV) + \bar{\alpha}(3.67\ MeV). \quad (25)$$

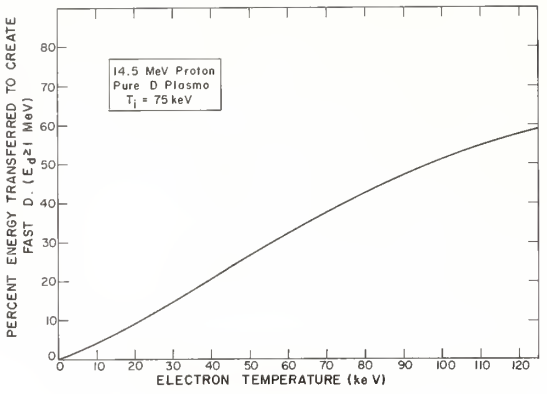

Fig. 3. Percentage of energy transferred from a fast proton to produced deuterons with an energy exceeding 1 MeV.

The overbars denote fast charged particles. Nuclear elastic events such as

$$\bar{p} + d \rightarrow p + \bar{d} \qquad (26)$$

$$\bar{\alpha} + d \rightarrow \alpha + \bar{d} \; . \qquad (27)$$

promote fast deuterons from the background Maxwellian distribution. Some of the propagating sequences in this cycle are:

$$\left\{ \begin{array}{l} d + d \rightarrow \bar{p} + \bar{t} \\ \bar{p} + d \rightarrow \bar{d} + p \\ \bar{d} + d \rightarrow \bar{p} + \bar{t} \\ \vdots \end{array} \right\} \qquad (28)$$

$$\left\{ \begin{array}{l} d + d \rightarrow \overline{^3He} + n \\ \overline{^3He} + d \rightarrow \bar{\bar{p}} + \bar{\alpha} \\ \bar{\bar{p}} + d \rightarrow \bar{d} + p \\ \bar{d} + d \rightarrow {}^3He + n \\ \vdots \end{array} \right\} \qquad (29)$$

$$\left\{ \begin{array}{l} d + \bar{d} \rightarrow \bar{t} + \bar{p} \\ \bar{t} + d \rightarrow \bar{\alpha} + n \\ \bar{\alpha} + d \rightarrow \bar{d} + \alpha \\ \bar{d} + d \rightarrow \bar{t} + p \\ \vdots \end{array} \right\} \qquad (30)$$

$$\left\{ \begin{array}{l} d + d \rightarrow \overline{^3He} + n \\ \overline{^3He} + d \rightarrow \bar{\alpha} + \bar{\bar{p}} \\ \bar{\alpha} + d \rightarrow \bar{d} + \alpha \\ \bar{d} + d \rightarrow {}^3He + n \\ \vdots \end{array} \right\} \qquad (31)$$

and there are more. As an example, the propagating sequence indicated in set (28) produces fast protons; the fast proton promotes the deuteron out of the thermal bath; the energetic deuteron then reacts before slowing down, producing a fast proton; and so on.

The inclusion of these effects increases the reactivity of the catalyzed d-d cycle at T_i = 75 keV by 25% when T_e is 50 keV and by 75% when T_e is 100 keV. The results are shown in Fig. 4. These increases are measured relative to a standard calculation in which propagating reactions are neglected.

An additional effect is that nuclear knock-on events alter the fraction of energy given to electrons and ions by energetic fusion products. The energy transferred to electrons by various fast particles (a 4 MeV alpha, a 3 MeV proton, and a 14.5 MeV proton) is shown in Fig. 5, 6 and 7 as a function of electron temperature. The dashed curve in each figure is the fraction of the initial energy received by electrons when only the coulomb interaction is assumed. The dash-dot curves in each figure give the analogous result when both coulomb and nuclear elastic scattering are included. Finally, the solid curve properly includes the effect of fast ion production by nuclear scattering and the subsequent slowing down of those ions with background ions and electrons. The background plasma in all cases is electrons and deuterium ions. The ion temperature is fixed at 7.5 keV. The difference in the results is small for the 4 MeV alphas but substantial for both the 3 MeV and 14.5 MeV protons, and the differences become more important as the electron temperature increases. Accounting for both nuclear elastic scattering and subsequent slowing down of knock-on ions, a 14.5 MeV proton in a 75 keV ion temperature deuterium plasma will transfer 79% of its energy to 50 keV electrons compared to 93% when only coulomb scattering is assumed. At an electron temperature of 100 keV, the percentage of energy transferred to electrons decreases to 51% compared to 85% with coulomb interactions only. The effect is clearly important to a plasma energy balance calculation. Overall, the net result is that lower $n\tau_E$ values are required to meet either the Lawson or ignition condition for the catalyzed d-d cycle.

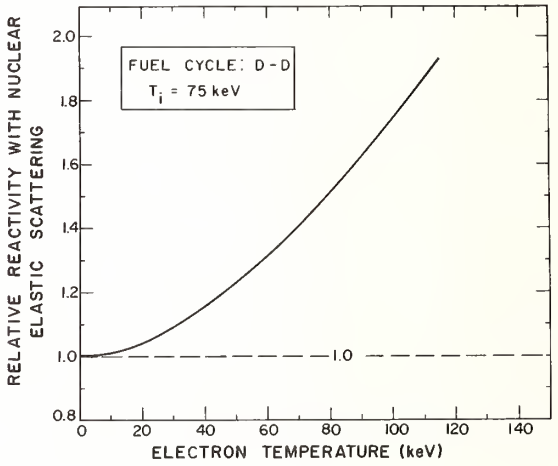

Fig. 4. Increase in d-d reactivity due to promotion and propagation effects measured relative to the reactivity of a pure Maxwellian at T_i = 75 keV.

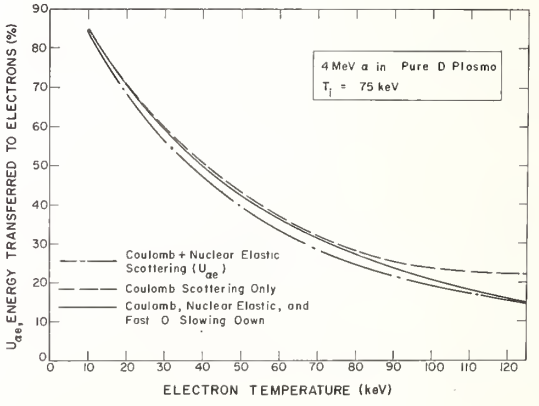

Fig. 5. Calculations of the fraction of energy given to electrons by a 4 MeV alpha. The solid curve includes all effects properly.

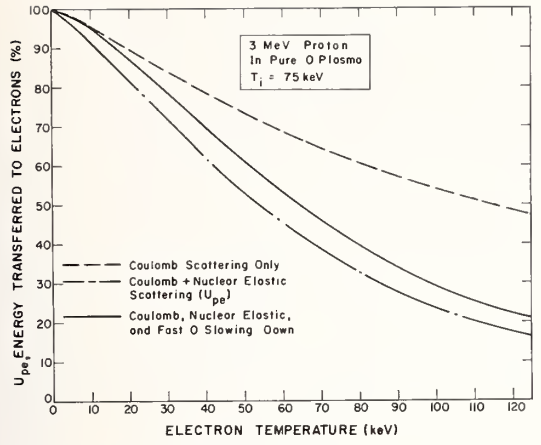

Fig. 6. Fraction of energy given to electrons by a 3 MeV proton.

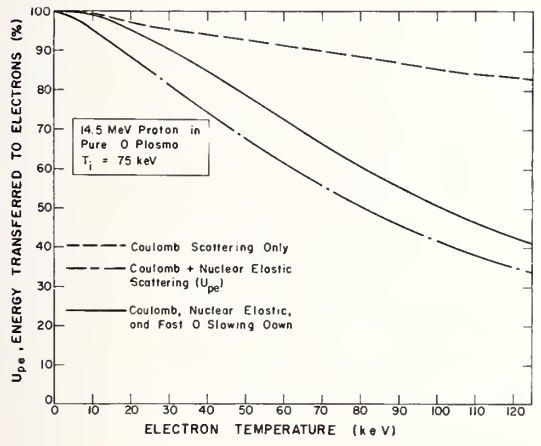

Fig. 7. Fraction of energy given to electrons by a 14.5 MeV proton.

The examples, while not inclusive, show the need in the analysis of advanced fusion fuel cycles for reaction cross section data to various final channels and for nuclear elastic and inelastic scattering cross sections up to about 20 MeV.

Status of Nuclear Data for Advanced Fusion Fuel Cycle Analysis

The literature has been examined through October 1979. The list of references in this paper is a partial one because of the very large number of works reported. All data for a given reaction were examined for consistency. In general the uncertainties or inconsistencies ranged from 10% to as much as an order of magnitude. Cross sections for some of the reaction branches have either been partially measured or not measured at all. In the reactions of ^{3}He-^{6}Li and d-^{7}Be, for example, the total reaction cross section may be 10 to 50 times larger than reported values. For other reactions, such as ^{3}He with ^{7}Be, data do not exist.

The status of the nuclear data is summarized in matrix form in Tables 1, 2, and 3. The asterisk (*) indicates the reaction is important for fusion fuel cycle analysis; the check (√) indicates the data for that reaction are reasonably consistent; while the cross (X) indicates the existing data are either inconsistent or have large error bars. References are given in the parentheses. The numbers followed by MeV give the energy range over which data have been measured. A literature search for nuclear inelastic cross sections is in progress and is not included in this paper. Comments are as follows:

1. The d-d Reactions

$$d + d \rightarrow n + {}^3He \qquad Q = 3.269 \text{ MeV} \qquad (33)$$

$$d + d \rightarrow p + t \qquad Q = 4.033 \text{ MeV} \qquad (34)$$

Liskien and Paulsen[461] have summarized and evaluated the cross section measurements for E_d = 0.13 - 10 MeV. The data and evaluation are shown in Fig. 8. This is adequate for fusion fuel cycle analysis.

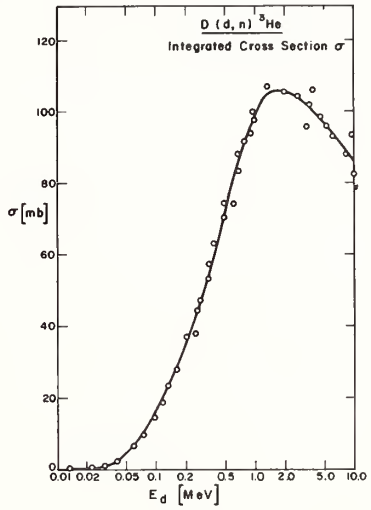

Fig. 8. Data and evaluation for the d-d reaction.

2. The p-t Reaction

$$t + p \rightarrow n + {}^3He \qquad Q = -.764 \text{ MeV} \qquad (35)$$

Cross section measurements have been evaluated by Liskien and Paulsen.[462] The angular distribution measurements are inconsistent with one another. Most of the integrated cross section measurements are within 15% of the recommended values. Experimental and recommended values for E_p = 1.0-10 MeV are shown in Fig. 9. This data is adequate for fusion fuel cycle analysis.

3. The d-t Reaction

$$t + d \rightarrow n + \alpha \qquad Q = 17.590 \text{ MeV} \qquad (36)$$

There has been only one measurement since 1960. The cross section measurements have been evaluated[463] and indications are that a number of reported angular distributions are not satisfactory at energies above 5 MeV. Most of the integrated cross section measurements are within 10% of the recommended values. In general, the data is adequate for fusion fuel cycle analysis.

TABLE

	p	d	t	^{3}He	^{4}He
d	ELASTIC (1 - 20) σ (E, θ) 0.2 - 30. MeV ✱ ✓ REACTION (———) ———	ELASTIC (46 - 49) σ (E, θ) 2. - 20. MeV ✱ ✓ REACTION (50 -90) σ (E) or σ (E, θ) 0.013 - 14. MeV	S	S	ELASTIC (164 - 178) σ (E, θ) 0.3 - 20. MeV ✱ ✓ REACTION (———) ———
t	ELASTIC (21 - 30) σ (E, θ) 0.05 - 8.3 MeV ✱ ✓ REACTION (31 - 45) σ (E) or σ (E, θ) 1.0 - 10. MeV	ELASTIC (91 - 93) σ (E, θ) 0.013 - 10. MeV ✱ ✓ REACTION (94 - 112) σ (E) or σ (E, θ) 0.01 - 15. MeV	ELASTIC (141 - 142) σ (E, θ) 1.58 - 2. MeV ✘ REACTION (143 - 146) σ (E) or σ (E, θ) 0.04 - 2.2 MeV	S	ELASTIC (179 - 182) σ (E, θ) 1.2 - 18.2 MeV ✱ ✘ REACTION (———) ———
^{3}He	ELASTIC (126 - 140) σ (E, θ) 0.1 - 20. MeV ✱ ✓ REACTION (———) ———	ELASTIC 113 - 116 σ (E, θ) 0.38 - 20. MeV ✱ ✓ REACTION (117 - 125) σ (E) or σ (E, θ) 0.25 - 15. MeV	ELASTIC (147 -148) σ (E,θ) 5. - 19. MeV ✘ REACTION 149 - 154 σ (E) or σ (E, θ) .15 - 1.9 MeV	ELASTIC (155 - 158) σ (E, θ) 5. - 20. MeV ✱ ✓ REACTION (159 - 163) σ (E) or σ (E, θ) 0.06 - 2.2 MeV	ELASTIC (183 - 190) σ (E, θ) 1.72 - 20. MeV ✱ ✘ REACTION (———) ———

TABLE 2

	p	d	t	^{3}He	^{4}He
^{6}Li	ELASTIC (191 - 196) σ (E, θ) 0.5 - 16. MeV ✱ ✓ REACTION (197 - 210) σ(E, θ) 0.14 - 12. MeV	ELASTIC (211 - 213) σ (E, θ) 2. - 7. MeV ✱ ✓ REACTION (213 - 225) σ(E, θ) 0.1 - 1. MeV	ELASTIC (———) No measurement ✘ REACTION (226 - 230) σ (E, θ) 0.3 - 20. MeV	ELASTIC (231) σ (E, θ) 8. - 20. MeV ✱ ✘ REACTION 232 - 245 σ(E, θ) or σ (E) 1.2 - 4.2 MeV	ELASTIC (246 - 250) σ(E, θ) 2. - 7.5 MeV REACTION (———) ———
^{7}Li	ELASTIC (251 - 254) σ(E, θ) 0.4 - 20. MeV ✘ REACTION (255 - 285) σ(E, θ) or σ(E) 0.8 - 15. MeV	ELASTIC (286) σ(E, θ) 0.4 - 1.8 MeV ✘ REACTION (287 - 300) σ(E) or σ (E, θ) 0.6 - 2.6 MeV	ELASTIC (———) No measurement ✘ REACTION (301 - 310) σ (E, θ) 0.23 - 2.5 MeV	ELASTIC (311) σ (θ) 11. MeV ✘ REACTION (312 - 325) σ(E, θ) 0.8 - 6. MeV	ELASTIC (326 - 330) σ (E, θ) 1.6 - 20. MeV REACTION (———) ———
^{7}Be	ELASTIC (———) No measurement ✘ REACTION (———) ———	ELASTIC (———) No measurement ✱ ✘ REACTION (331-332) σ (E, θ) 0.8 - 1.7 MeV	ELASTIC (———) No measurement ✘ REACTION (306) No measurement $\langle\sigma v\rangle$ Estimated	ELASTIC (———) No measurement ✱ ✘ REACTION (306) No measurement $\langle\sigma v\rangle$ Estimated	ELASTIC (———) No measurement REACTION (———) ———

TABLE 3

	p	d	t	^{3}He	^{4}He
^{9}Be	ELASTIC (333 - 340) $\sigma(E,\theta)$ 0.2 - 10. MeV ✓ REACTION (341 - 345) $\sigma(E,\theta)$ 0.028 - 2.0 MeV	ELASTIC (346 - 350) $\sigma(E, 90^0)$ 0.4 - 7. MeV ✓ REACTION (351 -370) $\sigma(E)$ or $\sigma(E,\theta)$ 0.15 - 19. MeV	ELASTIC (371, 372) $\sigma(E,\theta)$ 0.6 - 2.1 MeV ✓ REACTION (371, 372) $\sigma(E,\theta)$ 0.52 - 2.1 MeV	ELASTIC (373 - 375) $\sigma(E, 45^0)$ or $\sigma(E,90^0)$ 1.2 - 20. MeV ✗ REACTION (376 - 380) $\sigma(E,\theta)$ 1.6 - 20. MeV	ELASTIC (381 - 384) $\sigma(E,\theta)$ 1.4 - 20. MeV REACTION (—) —
^{10}B	ELASTIC (385 - 387) $\sigma(E,\theta)$ 0.15 - 10.5 MeV ✗ REACTION (388 - 390) $\sigma(E,\theta)$ 0.06 - 6.3 MeV	ELASTIC (391 - 393) $\sigma(E,\theta)$ 1. - 16. MeV ✗ REACTION (394 - 415) $\sigma(E)$ or $\sigma(E,\theta)$ 0.14 - 12. MeV	ELASTIC (416 - 418) $\sigma(E,\theta)$ 1.5 - 3.3 MeV ✗ REACTION (416) $\sigma(E)$ 0.8 - 2.0 MeV	ELASTIC (419 - 423) $\sigma(E,\theta)$ 4. - 20. MeV ✗ REACTION (424 - 430) Excitation function 2. - 19. MeV	ELASTIC (431 - 433) Excitation function 2. - 20. MeV REACTION (—) —
^{11}B	ELASTIC (—) No data reported * ✗ REACTION (434 - 440) $\sigma(E)$ or $\sigma(E,\theta)$ 0.17 - 10. MeV	ELASTIC (—) No data reported ✗ REACTION (441 - 453) $\sigma(E)$ or $\sigma(E,\theta)$ 0.3 - 10. MeV	ELASTIC (—) No data reported ✗ REACTION 454, 455 $\sigma(E,\theta)$ 1.0 - 2.1 MeV	ELASTIC (—) No data reported ✗ REACTION (456 - 460) Excitation function or $\sigma(E)$ 0.9 - 18. MeV	ELASTIC (—) No data measurered below 27. MeV REACTION (—) —

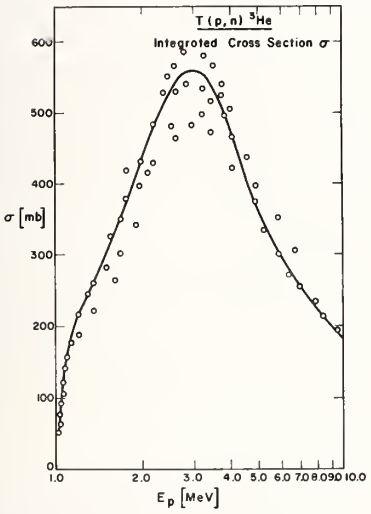

Fig. 9.

4. The d-^{3}He Reaction

$$^3He + d \rightarrow p + \alpha \qquad Q = 18.35 \text{ MeV} \qquad (37)$$

There have been no measurements since 1960. A pronounced resonance occurs at E_d = 430 keV with Γ ~ 450 keV. The experimental data disagree in the neighborhood of this resonance (~25%). However, analysis by Hale(464) suggests that the recommended values are very good. Thus, the cross sections are adequate for fusion fuel cycle analysis.

5. The ^{3}He-^{3}He Reactions

$$^3He + {}^3He \rightarrow p + {}^5Li \qquad Q = 10.890 \text{ MeV} \qquad (38)$$
$$\hookrightarrow p + \alpha$$

$$^3He + {}^3He \rightarrow 2p + \alpha \qquad Q = 12.860 \text{ MeV} \qquad (39)$$

A study of the proton spectrum indicates that the reaction proceeds mainly via a direct mechanism and the ^{5}Li channel. However, the branching ratio is not firmly established, particularly at low energy.

6. The p-^{6}Li Reaction

$$^6Li + p \rightarrow {}^3He + \alpha \qquad Q = 4.023 \text{ MeV} \qquad (40)$$

The cross section measurements for E_p = .14-3 MeV by Elwyn et al.(197) appear to be definitive. The earlier measurements are inconsistent with one another as shown in Fig. 10. Cross section measurements for E_p = 3 to 12 MeV have been made recently by Gould et al.(198) The measurements for E_p = 62 to 188 keV deviate from an S-wave Gamow plot above ~130 keV.

7. The d-^{6}Li Reactions

$$d + {}^6Li \rightarrow n + {}^7Be \qquad Q = 3.380 \text{ MeV} \qquad (41)$$
$$\rightarrow p + {}^7Li \qquad Q = 5.026 \text{ MeV} \qquad (42)$$
$$\rightarrow p + t + \alpha \qquad Q = 2.561 \text{ MeV} \qquad (43)$$
$$\rightarrow n + {}^3He + \alpha \qquad Q = 1.796 \text{ MeV} \qquad (44)$$
$$\rightarrow 2\alpha \qquad Q = 22.374 \text{ MeV} \qquad (45)$$

The recent measurements for E_d = .1-1 MeV by Elwyn et al.(214) are definitive. Other measurements differ sharply with one another, even in recent experiments.(218) Cross section measurements for E_d > 1 MeV are needed for a complete analysis.

8. The ^{3}He-^{6}Li Reactions

$$^6Li + {}^3He \rightarrow p + {}^8Be(g.s.) \qquad Q = 16.787 \text{ MeV} \qquad (46)$$
$$\hookrightarrow 2\alpha$$
$$\rightarrow p + {}^8Be(2.94) \qquad Q = 13.847 \text{ MeV} \qquad (47)$$
$$\hookrightarrow 2\alpha$$
$$\rightarrow p + {}^8Be(11.4) \qquad Q = 5.387 \text{ MeV} \qquad (48)$$
$$\hookrightarrow 2\alpha$$

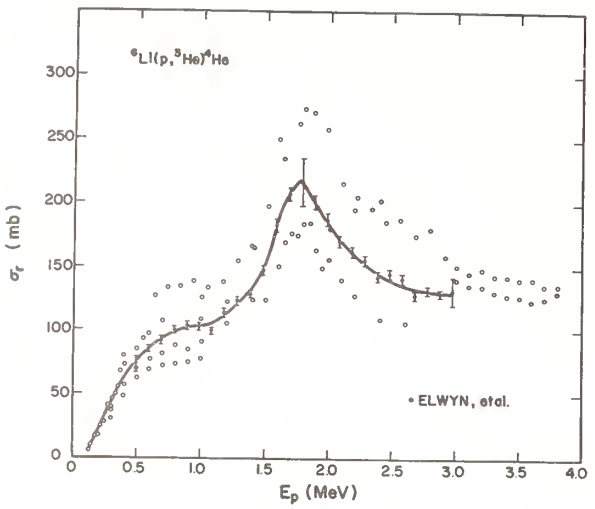

Fig. 10

$$\rightarrow p + {}^8Be(16.63) \quad Q = .157 \text{ MeV} \quad (49)$$
$$\quad \hookrightarrow 2\alpha$$
$$\rightarrow p + {}^8Be(16.92) \quad Q = -.1325 \text{ MeV} \quad (50)$$
$$\quad \hookrightarrow 2\alpha$$
$$\rightarrow p + {}^8Be(17.64) \quad Q = -.853 \text{ MeV} \quad (51)$$
$$\rightarrow p + 2\alpha \quad Q = 16.88 \text{ MeV} \quad (52)$$
$$\rightarrow \alpha + {}^5Li \quad Q = 14.91 \text{ MeV} \quad (53)$$
$$\quad \hookrightarrow p + \alpha$$
$$\rightarrow d + {}^7Be \quad Q = .1126 \text{ MeV} \quad (54)$$
$$\rightarrow d + {}^7Be(.43) \quad Q = -.317 \text{ MeV} \quad (55)$$
$$\rightarrow 2p + {}^7Li \quad Q = -.468 \text{ MeV} \quad (56)$$

A measurement is in progress by A. Elwyn et al. at the Argonne National Laboratory.(465) The earlier measurements are not complete. At least 5 nuclear levels in ^{8}Be can be excited. It is expected that the reaction cross section to all branches will be at least a factor of 10 larger than those now known. For example, at $E_{^3He}$ = 3.5 MeV, Gould et al.(245) measured $\sigma_r \approx$ 10-12 mb for the ^{8}Be(g.s.) branch, $\sigma_r \approx$ 55 mb for the ^{8}Be(2.94 MeV) branch, and estimated $\sigma_r \approx$ 42 mb for the continuum breakup reaction, Elwyn et al. indicates values could be $\sigma_r \approx$ 30-50 mb for the ^{8}Be(16.63 MeV) branch, $\sigma_r \approx$ 20-40 mb for the ^{8}Be(16.9 MeV) branch and $\sigma_r \approx$ 400 mb for the d + ^{7}Be branch.

9. The d-^{7}Be Reactions

There have been no measurements since 1960. d + ^{7}Be reacts via the same compound nucleus as ^{3}He + ^{6}Li. Therefore, it will have the same reaction channels as ^{3}He + ^{6}Li except for eqns. (54) and (55). Since the existing data are only for the eqn. (46) and (47) branches, measurements for each branch stated above are required. However, a standard 9-nucleon R-matrix calculation can give good estimated values, provided that the cross sections of each branch of ^{3}He + ^{6}Li reaction are given.

10. The p-^{11}B Reactions

$$^{11}B + p \rightarrow \alpha + {}^8Be \quad Q = 8.590 \text{ MeV} \quad (57)$$
$$^{11}B + p \rightarrow 3\alpha \quad Q = 8.682 \text{ MeV} \quad (58)$$

The most recent cross section measurements for E_p = 0.08-1.4 MeV by Davidson et al.(434) appear to be definitive. There are 7 pronounced resonances in the range, E_p = .1-5 MeV. The energy of the resonances, the cross sections at each resonance peak, and the width of each resonance are summarized in Table 4. The cross sections are uncertain above 2 MeV and should be measured again.

Table 4

Parameters for p-^{11}B Resonances

Resonance Energy E_p (MeV)	Cross Section at Resonance Peak (mb)	Resonance Width Γ (keV)
.172	28	10
.64	800	300
1.39	180	1160
1.98	113 - 132	100
2.62	200 - 347	320
3.75	200 - 348	1100
4.93	130 - 210	180

Conclusions

As described in the previous sections, propagating effects in an advanced fusion fuel cycle analysis are important. Data for both nuclear reactions and nuclear elastic scattering up to 20 MeV are required. For example, with the inclusion of propagating effects, the reactivity of the catalyzed d-d reaction at T_i = 75 keV can be increased from 25% at T_e = 50 keV to 75% at 100 keV relative to the reactivity neglecting nuclear elastic scattering. The result is due to fusion events between fast deuterons produced by elastic scattering and the background ions. The fraction of energy given to electrons is likewise influenced by nuclear elastic scattering. The fraction of a 14.5 MeV proton's energy given to electrons at 100 keV decreases from 85% when only coulomb scattering is assumed to 50% when coulomb plus nuclear scattering is included.

In addition, charged particle cross sections required for advanced fusion fuel cycle calculations have been discussed. Reactions important for the d-d, d-^{3}He, d-^{6}Li, p-^{6}Li and p-^{11}B cycles have been described. The importance of nuclear elastic scattering has been emphasized. Important fusion cross sections and the energy range where data is required have been identified.

Acknowledgement

The authors acknowledge valuable discussions with Prof. H. H. Barschall on many aspects of this paper. This research has been supported by a contract with TRW, Inc. and the Electric Power Research Institute.

References

1. Taschek, Phys. Rev. 61 (42) 13.
2. Sherr et al., Phys. Rev 72 (47) 662.
3. Kocher and Clegg, Nucl. Phys. A132 (69) 455.
4. Wilson et al., Nucl. Phys. A130 (69) 624.
5. Kikuchi et al., J. Phys. Soc. Japan 15 (60) 9.
6. Kerman, Phys. Rev. 107 (57) 200.
7. Kiceleva et al., Ukr. Fiz. Zh. 4 (71) 83.
8. Cahill et al., Phys. Rev. C4 (71) 83.
9. Cadwell and Richardson, Phys. Rev. 98 (55) 28.
10. Allred and Rosen, Phys. Rev. 79 (50) 227.
11. Karr et al., Phys. Rev. 81 (51) 37, 78 (50) 292.
12. Allred et al., Phys. Rev. 88 (52) 433.
13. Simpson, Thesis, Rice Univ., Houston (65).
14. Grötzschel et al., Nucl. Phys. A176 (71) 261.
15. Brolley Jr. et al., Phys. Rev. 117 (60) 1307.
16. Mather, Phys. Rev. 88 (52) 1408.
17. Heither et al., Proc. Roy. Soc. A190 (47) 180.

References (cont.)

18. Brown et al., Phys. Rev. 88 (52) 253.
19. Tuve et al., Phys. Rev. 50 (36) 806.
20. Bunker et al., Nucl. Phys. A113 (68) 461.
21. Balashko et al., Zh. Eksp. Teor. Fiz. 36 (59) 1937, JETP (Soviet Physics) 9 (59) 1378.
22. Baumann, J. Phys. Rad. 18 (57) 337.
23. Jarmie et al., Phys. Rev. 130 (63) 1987.
24. Balashko et al., JETP 19 (64) 1281.
25. Kurepin, Trudy of the Lebedev Phys. Inst., Vol. 33 (65) p.1 (Transl. by Consultant Bureau, N.Y. 66).
26. Jarmie and Allen, Phys. Rev. 114 (59) 176.
27. Hemmendinger et al., Phys. Rev. 79 (49) 1137.
28. Ennis and Hemmendinger, Phys. Rev. 95 (54) 772.
29. Brolley et al., Phys. Rev. 117 (60) 1307.
30. Classen et al., Phys. Rev. 82 (51) 589.
31. Seagrave, Proc. Conf. on Nuclear Forces and the Few Nuclear Problem , London (59) Vol. II, p.583.
32. Macklin and Gibbons, EANDC-50-S, Vol. I (65).
33. Willard et al., Phys. Rev. 90 (53) 865.
34. Jarmie and Seagrave LA-2014 (56).
35. Gibbons and Macklin, Phys. Rev. 114 (59) 571.
36. Batchelor et al., Rev. Sci. Instr. 26 (55) 1037.
37. Costello et al., Nucl. Sci. Eng. 39 (70) 409.
38. Vlasov et al., JETP 1 (55) 500.
39. Coon, Phys. Rev. 80 (50) 488.
40. Sayres et al., Phys. Rev. 122 (61) 1853.
41. Seagrave et al., Phys. Rev. 119 (60) 1981.
42. Bogdandov et al., JETP 9 (59) 440.
43. Stewart et al., Bull. Am. Phys. Soc. 1 (56) 93.
44. Wilson et al., Nucl. Phys. 27 (61) 421.
45. Goldberg et al., Phys. Rev. 122 (61) 1510.
46. Theus et al., Nucl. Phys. 80 (66) 273.
47. Bacher and Tombrello, Nucl. Phys. A113 (68) 557.
48. Wilson et al., Nucl. Phys. A126 (69) 193.
49. Cahill et al., CEN-Saclay Annual Report CEA-N 844 (67) 121.
50. Goldberg, Progress in Fast Neutron Physics (U. of Chicago Press 63).
51. Arnold et al., Phys. Rev. 93 (54) 483.
52. Booth et al., Proc. Phys. Soc. (London) A69 (56) 265.
53. NcNeill and Keyser, Phys. Rev. 81 (51) 602.
54. Ganeev et al., Atomnaya Energiya Suppl. 5 (57)21.
55. Preston, et al., Proc. Roy. Soc. (London) A226 (54) 206.
56. Chagnon and Owen, Phys. Rev. 101 (56) 798.
57. Hunter and Richards, Phys. Rev. 76 (49) 1445.
58. Ref. 40
59. Brolley et al., Phys. Rev. 107 (57) 820.
60. Blair et al., Phys. Rev. 74 (48) 1599.
61. - 70. Not Used
71. Schulte et al., Nucl. Phys. A192 (72) 609.
72. Goldberg et al., Phys. Rev. 119 (60) 1992.
73. Thornton, Nucl. Phys. A139 (69) 25.
74. Brolley et al., Phys. Rev. 107 (57) 820.
75. Eliot et al., Proc. Roy. Soc. (London) 216 (53) 57.
76. Ref. 46
77. Kane, Nucl. Phys. 10 (59) 429.
78. Fuller et al., Phys. Rev. 108 (57) 91.
79. Volkov et al., Stomnaya Energiya Suppl. 5 (57)13.
80. Milone and Ricamo, Nuovo Cim. 22 (61) 116.
81. Cranberg et al., Phys. Rev. 104 (56) 1639.
82. Kerr and Anderson, Bull. Am. Phys. Soc. 13 (68) 564.
83. Daehnick and Fowler, Phys. Rev. 111 (58) 1309.
84. Ref. 43
85. Wilson et al., Bull. Am. Phys. Soc. 5 (60) 410.
86. Brill et al., Atomnaya Energiya 16 (64) 141.
87. Bame et al., Rev. Sci. Instr. 28 (57) 997.
88. Fowler and Brolley, Rev . Mod. Phys. 28 (56) 103.
89. Ref. 34
90. Defacio, Proc. 3rd Int. Symp. on Polarization Phenomena in Nuclear Reactions (71) 534 (U. of Wisconsin Press).
91. Stratton et al., Phys. Rev. 88 (52) 257.
92. Brolley et al., Phys. Rev. 120 (60) 905.
93. Allred et al., Phys. Rev. 88 (52) 425.
94. Conner et al., Phys. Rev. 88 (52) 468.
95. Ref. 51
96. Davidenks et al., J. Nucl. Energy 2 (57) 258 .
97 Balabanov et al., Atomnaya Energiya Suppl. 5 (57) 43.
98. Argo et al., Phys. Rev. 87 (52) 612.
99. Kobzev et al., Sov. J. Nucl. Phys. 3 (66) 774.
100. Bame and Perry, Phys. Rev. 107 (57) 1616.
101. Allen and Jarmie, Phys. Rev. 111 (58) 1129.
102. Hemmendinger and Argo, Phys. Rev. 98 (55) 70.
103. Galonsky and Johnson, Phys. Rev. 104 (56) 421.
104. Stewart et al., Phys. Rev. 119 (60) 1649.
105. Brill et al., Atomnaya Energiya 16 (64) 141.
106. Stratton and Freir, Phys. Rev. 88 (52) 261.
107. Goldberg et al., Phys. Rev. 122 (61) 164.
108. Simmons and Malanify, Bull. Am. Phys. Soc. 13 (68) 564.
109. Bretscher and French, Phys. Rev. 75 (49) 1154.
110. Allan and Poole, Proc. Roy. Soc. (London) A204 (50) 500.
111. Brolley et al., Phys. Rev. 82 (51) 502.
112. Paulsen and Liskien, Nucl. Phys. 56 (64) 394.
113. Brown et al., Phys. Rev. 96 (54) 80.
114. Tombrello et al., Phys. Rev. 154 (67) 935.
115. King and Smythe, Nucl. Phys. A183 (72) 657.
116. Baker et al., Nucl. Phys. A184 (72) 97.
117. Jarmie et al., LA-2014 (57).
118. Carlton, Thesis, U. of Georgia (70) Phys. Abst. 67885 (71).
119. Gruebler et al., Nucl Phys. A176 (71) 631.
120. Stewart et al., Phys. Rev. 119 (60) 1649.
121. Kunz, Phys. Rev. 97 (55) 456.
122. Bonner et al., Phys. Rev. 88 (52) 473.
123. Frier and Halmgren, Phys. Rev. 93 (54) 825.
124. Yarnel et al., Phys. Rev. 90 (53) 292.
125. Jarmie and Jett, Phys. Rev. C10(74) 145.
126. Hutson et al., Phys. Rev. C4 (71) 17.
127. Vanetsian and Fedchenko, Soviet J. of Atomic Energy 2 (57) 141.
128. Lovberg, Phys. Rev. 103 (56) 1393.
129. Igo and Leland, Phys. Rev. 154 (67) 950.
130. Brolley and Fowler, Fast Neutron Physics (60).
131. Rosen, Nuclear Forces and the Few Nuclear Problem (Pergamon 60) p. 481.
132. Brolley et al., Phys. Rev. 117 (60) 1307.
133. Sweetman, Phil. Mag. 46 (55) 358.
134. Artemov et al., JETP 10 (60) 474.
135. Clegg et al., Nucl. Phys. 50 (64) 621.
136. McDonald et al., Phys. Rev. 133 (64) B1178.
137. Tombrello et al., Nucl. Phys. 39 (62) 541.
138. Drigo et al., Nuovo Cim. 42B (66) 363.
139. Famularo et al., Phys. Rev. 93 (54) 928.
140. Kavanagh and Parker, Phys. Rev. 143 (66) 779.
141. Holm and Argo, Phys. Rev. 101 (56) 1772.
142. Frank and Grammel, Phys. Rev. 100 (55) 973A.
143. Agnew et al., Phys. Rev. 84 (51) 862.
144. Jarmie et al., Los Alamos Report 2014 (57).
145. Jarmie and Allen, Phys. Rev. 111 (58) 1121.
146. Strelenikov et al., Izv. Akad. Nauk USSR (Ser. Fiz.) 35 (71) 165.
147. Ivanovich et al., Nucl. Phys. A110 (68) 441.
148. Bacher et al., Nucl. Phys. A119 (68) 360.
149. Kuhn and Schlenk, Nucl. Phys. 48 (63) 353.
150. Moak, Phys. Rev. 92 (53) 383.
151. Youn et al., JETP 12 (61) 163.
152. Smith et al., Phys. Rev. 129 (63) 785.
153. Leland et al., Bull. Am. Phys. Soc. 10 (65) 51.
154. Kuhn and Schlenk, Joint Inst. Nucl Res. USSR Report No. P1197 (63).
155. Ref. 147 & Ref. 148

156. Tombrello and Bacher, Phys. Rev. 130 (63) 1108.
157. Jenkin et al., Phys. Rev. C1 (70) 1622.
158. Bacher et al., Bull. Am. Phys. Soc. 13 (68) 1366.
159. Dwarakanath, Phys. Rev. C9 (74) 805.
160. Dwarakanath and Winkler, Phys. Rev. C4 (71)1532.
161. Dwarakanath, Thesis, Caltech (69) Phys. Abstr. 39101 (70).
162. Slobodrian et al., Nucl. Phys. A194 (72) 577.
163. Good et al., Phys. Rev. 94 (54) 87.
164. Lauritsen et al., Phys. Rev. 92 (53) 1501.
165. Guggenheimer et al., Proc. Roy. Soc. A190 (47) 196.
166. Burge et al., Proc. Roy Soc. A210 (51) 534.
167. Galonsky et al., Phys. Rev. 98 (55) 586.
168. Alfred et al., Phys. Rev. 82 (51) 786.
169. Freemantle et al., Phil. Mag. 45 (54) 1090.
170. Artemov and Vlasov, JETP 12 (61) 1124.
171. Stewart et al., Phys. Rev. 128 (62) 707.
172. Rothe et al., Bull. Am. Phys. Soc. 8 (63) 537.
173. Ohlsen and Young, Nucl. Phys. 52 (64) 134.
174. Senhouse and Tombrello, Nucl. Phys. 57 (64)624.
175. Matons and Browne, Phys. Rev. 136 (64) B399.
176. Fukunaga et al., J. Phys. Soc. Japan 22 (67) 28.
177. Mani and Tarratts, Nucl. Phys. A107 (68) 624.
178.* Jett et al., Phys. Rev. C3 (71) 1769.
180. Allen and Jarmie, Phys. Rev. 111 (58) 1129.
181. Brolley et al., Nuclear Forces and the Few Nuclear Problem Vol. II, p. 455.
182. Tombrello and Phillips, Phys. Rev. 122(61)224.
183. Miller and Phillips, Phys. Rev. 112 (58) 2048.
184. Barnard et al., Nucl. Phys. 50 (64) 629.
185. Tombrello and Parker, Phys. Rev. 130 (63) 1112.
186. Spiger and Tombrello, Bull. Am. Phys. Soc. 9 (64) 703.
187. Chuang, Nucl. Phys. A174 (71) 399.
188. Spiger and Tombrello, Phys. Rev. 163 (67) 964.
189. Dunnil et al., Nucl. Phys. A93 (67) 201.
190. Ivanovich et al., Nucl. Phys. A110 (68) 441.
191. Harrison, Nucl. Phys. A92 (67) 253 and 260.
192. Harrison and Whitehead, Phys. Rev. 132 (63)2607.
193. Fasoli et al., Nuovo Cim. 34 (64) 1832.
194. Merchez et al., J. Physique 29 (68) 969.
195. Bashkin and Richards, Phys. Rev. 84 (51) 1124.
196. McCray, Phys. Rev. 130 (63) 2034.
197. Elwyn, Holland, Davids et al., accepted by Phys. Rev. C, to be published.
198. Gould et al., Nucl. Cross Section and Tech. NPP 425, 697.
199. Spinka et al., Nucl. Phys. A164 (71) 1.
200. Bowersox, Phys. Rev. 55 (39) 323.
201. Marion et al., Phys. Rev. 104 (56) 1402.
202. Field and Kunze, Nucl. Phys. A96(67) 513.
203. Beavmevielle, CEA-R-2624 (64).
204. Hub et al., Z. Phys. 252 (72) 332.
205. Varnagy et al., Nucl. Int. Methods 119 (74) 451.
206. Hooton and Ivanovich, AERE-R-7761 (74).
207. Johnston and Sargood, Nucl. Phys. A224 (74) 349.
208. Jeronymo et al., Nucl. Phys. 43 (63) 424.
209. Kibler, Phys. Rev. 152 (56) 932.
210. Gemeinhardt et al., Zeit, für Physik 197 (66) 58.
211. Paul and Lieb, Nucl. Phys. 53 (64) 465.
212. Bruno et al., J. Physique C1 (66) 85.
213. Black et al., Phys. Lett. 30B (69) 100.
214. Elwyn et al., Phys. Rev. C16 (77) 1744.
215. Risler et al., Nucl. Phys. A286 (77) 115.
216. Schier, et al., Nucl. Phys. 88 (66) 373.
217. McClenahan and Segal, Phys. Rev. C11 (75) 370.
218. Ruby et al., Nucl. Sci. Eng. 71 (79) 280.
219. Baggett et al., Phys. Rev. 85 (52).
220. Slattery et al., Phys. Rev. 108 (57) 809.
221. Bertrand et al., Saclay Report CEA-R-3428.
222. Whaling et al., Phys. Rev. 75 (49) 688.
223. Sawyer and Phillips, LA-1578.
224. Hirst et al., Phil. Mag. 45 (54) 762.
225. Elwyn et al., Phys. Rev. C19 (79) 592.
226. Pepper et al., Phys. Rev. 85 (52) 155.
227. Serov, et al., Soviet J. At. En. 12 (62) 1.
228. Valter, et al., Soviet J. At. En. 10 (61) 574.
229. Abramovich et al., Izv.Akad. Nauk SSSR (Ser. Fiz) 37 (73) 1967.
230. Ciric et al., Fizika (Yugoslavia) 4 (72) 40 and 193.
231. Ludecke et al., Nucl. Phys. A109 (68) 676.
232. Holmgren, Nuclear Research with Low Energy Accelerators, p. 213.
233. Mazari et al., Proc. 2nd Int. Conf. on Nuclidic Masses (63).
234. Reimann et al., Phys. Rev. Lett. 18 (67) 246.
235. Baker et al., Nucl. Phys. A184 (72) 97.
236. Reinmann et al., Can. J. Phys. 46 (68) 2241.
237. Treado et al., Bull. Am. Phys. Soc. 16 (71)1186.
238. Gagne et al., Bull. Am. Phys. Soc. 15 (70) 1695.
239. Vignon et al., J. Physique 30 (69) 913.
240. Tompson and Tripard, Phys. Rev. C5 (72) 1174.
241. Livesey and Piluso, Can. J. Phys. 52 (74) 1167.
242. Guichard et al., Nature 272, No. 5649 (78) 155.
243. Ref. 231 and Ref. 217
244. McClenahan, Thesis, Northwestern U. (74).
245. Gould and Boyce, Nucl. Sci. and Eng. 60 (76) 477.
246. Dearnaley et al., Nucl. Phys. 36 (62) 71.
247. Barnes et al., Bull. Am. Phys. Soc. 7 (62) 111.
248. Singh and Gemmell, Bull. Am. Phys. Soc. 10 (65) 538.
249. Meyer et al., Nucl. Phys. A101 (67) 114.
250. Balakrishnan et al., Nuovo Cim 1A (71) 205.
251. Warren et al., Phys. Rev. 91 (53) 917.
252. Malmberg, Phys. Rev. 101 (56) 114.
253. Kinsey and Stone, Phys. Rev. 103 (56) 972.
254. Gogny and Jean, Compt. Rend. 260 (65) 510.
255. Heydrenburg et al., Phys. Rev. 74 (48) 405.
256. Conrad et al., Nature 45 (58) 204.
257. Cavallaro et al., Nucl. Phys. 36 (62) 597.
258. Maxson, Phys. Rev. 128 (62) 1321.
259. Miller et al., Nucl. Phys. 54 (64) 155.
260. Madsen and Vedelsby, Nucl. Phys. 55 (64) 477.
261. Johnson et al., Phys. Rev. 77 (51) 413.
262. Taschek and Hemmendinger, Phys. Rev. 74 (48) 373.
263. Willard and Perston, Phys. Rev. 81 (51) 480.
264. Cranberg, LA-1654 (54).
265. Batchelor, Proc. Phys. Soc. A68(55)452.
266. Batchelor and Morrison, Proc. Phys. Soc. A68 (55) 1081.
267. Marion et al., Phys. Rev. 100 (55) 91.
268. Macklin and Gibbons, Phys. Rev. 109 (58) 105.
269. Newson et al., Phys. Rev. 108 (57) 1294.
270. Jarmie and Seagrave, LA-2014 (56).
271. Bogdanov et al., Soviet J. At. En. 3 (59) 907.
272. Gibbons and Macklin, Phys. Rev. 114 (59) 571.
273. Hisatake et al., J. Phys. Soc. Japan 15 (60)741.
274. Bevington et al., Phys. Rev. 121 (61) 871.
275. Nilsson, Ark. Fys. 19 (61) 289.
276. Borchers and Poppe, Phys. Rev. 129 (63) 2679.
277. Bair et al., Nucl. Phys. 53 (64) 209.
278. Buccino et al., Nucl. Phys. 53 (64) 375.
279. Austin, Bull. Am. Phys. Soc. 7 (62) 269.
280. Bergstroem et al., Ark. Fys. 34 (67) 153.
281. Lefevre and Din, Austr. J. Phys. 22 (69) 669.
282. Peetermans, Thesis, U. of Liege.
283. Elbakr et al., Nucl. Inst. Meth. 105 (72) 519.
284. Meadows and Smith, ANL-7938 (72).
285. Presser and Bass, Nucl. Phys. A182 (72) 321.
286. Ford, Phys. Rev. 136 (64) B953.
287. Sellschop, Phys. Rev. 119 (60) 251.
288. Chase et al., Phys. Rev. 127 (62) 859.
289. Schilling et al., Nucl. Phys. A263 (76) 389.
290. Kavanagh, Nucl. Phys. 15 (60) 411.
291. Bagget et al., Phys. Rev. 85 (52) 434.
292. McClenahan et al., Phys. Rev. C11 (75) 370.
293. Parker, Phys. Rev. 150 (66) 851.
294. Bashkin, Phys. Rev. 95 (54) 1012.

295. Valkovic et al., Nucl. Phys. A96(67) 241.
296. Garnir et al., Bull. Soc. R. Sci., Liege (Belgium) 42 (73) 195.
297. Crews, Phys. Rev. 82 (51) 100.
298. Serov et al., Soviet J. At. En. 12 (62) 1.
299. Valter et al., Soviet J. At. En. 10 (61) 574.
300. Arnold, In Proceedings, Cluster, Winnipeg (78) B8.
301. Valter et al., Soviet J. At. En. 10 (61) 577.
302. Seltz and Magnac-Valette, Compt. Rend. 251 (60) 2006.
303. Serov and Guzhovskii, Atomnaya Energiya 12 (62) 5.
304. Ciric et al., Fizika (Yugoslavia) 7, Suppl. 1 (77) 39.
305. Subotic et al., Fizika (Yugoslavia) 9, Suppl. 1 (77) 44.
306. Fowler, Caughlan and Zimmerman, Ann. Rev. Astro. & Astrophys. 13 (75) 69.
307. Middlton and Pullen, Nucl. Phys. 51 (64) 50.
308. Hunchen et al., Nucl. Phys. 58 (64) 417.
309. Jelley et al., Phys. Rev. C11 (75) 2049.
310. Hardekopf, Bull. Am. Phys. Soc. 21 (76) 551.
311. Scheklinski et al., Nucl. Phys. A153 (70) 97.
312. Paul et al., Phys. Rev. 137 (65) B493.
313. Ling, et al., Nucl. Phys. A108 (68) 221.
314. Ling and Blatt, Nucl. Phys. A174 (71) 375.
315. Lin and Chin, J. Phys. (Taiwan) 10 (72) 76.
316. Cocke, Nucl. Phys. A110 (68) 321.
317. Din and Weil, Nucl. Phys. 86 (66) 509.
318. Dixon and Edge, Nucl. Phys. A156 (70) 33.
319. Dixon, Thesis, U. South Carolina (70).
320. Duggan et al., Nucl. Phys. 46 (63) 336.
321. Serov and Guzhovskii, Atomnaya Energiya 12 (62) 5.
322. Stanojevic et al., Fizika 3 (71) 99.
323. Sanada et al., J. Phys. Soc. Japan 26 (69) 853.
324. Wolicki and Meyer, Bull. Am. Phys. Soc. 6 (61) 415.
325. Orihara et al., Nucl. Phys. A139 (69) 226.
326. Cusson, Nucl. Phys. 86 (66) 481.
327. Bingham, Thesis, Florida State U. (70).
328. Bingham et al., Nucl. Phys. A175 (71) 374.
329. Bohler et al., Nucl. Phys. A179 (72) 504.
330. Kelleter et al., Nucl. Phys. A210 (73) 502.
331. Spear, Australian J. Phys. 12 (59) 99.
332. Kavanagh, Nucl. Phys. 18 (60) 492.
333. Mashkarov et al., Izv, Akad. Nauk SSSR (Ser. Fiz.) 37 (73) 1729.
334. Kiss, et al., Nucl. Phys. A282 (77) 44.
335. Kild and Crinean, Australian J. Phys. 27 (74)663.
336. Yasue et al., J. Phys. Soc. Japan 36 (74) 1254.
337. Dearnaley, Phil. Mag. 1 (56) 821.
338. Mozer, Phys. Rev. 104 (56) 1386.
339. Mo and Hornyak, Phys. Rev. 187 (69) 1220.
340. Rohrer and Brown, Nucl. Phys. A210 (73) 465.
341. Bertrand et al., Comm. A L'energie Atomique, RPT. CEA 3575 (68).
342. Montague et al., Nucl. Phys. A199 (73) 457.
343. Sierk and Tombrello, Nucl. Phys. A210 (73) 341.
344. Tu and Hornyak, Bull. Am. Phys. Soc. 14 (69) 489.
345. Votava, Thesis, U. North Carolina (72).
346. Djaloeis et al., Nucl. Phys. 15 (72) 266.
347. Powell et al., Nucl. Phys. A147 (70) 65.
348. Lombard and Friedland, Z. Phys. 249 (72) 349.
349. Machali et al., Nucl. Phys. A112 (68) 654.
350. Renken, Phys. Rev. 132 (63) 2627.
351. Ralph and Dunnam, Phys. Rev. 120 (60) 249A.
352. Bardes and Owen, Phys. Rev. 120 (60) 1369.
353. Evans et al., Phys. Rev. 75 (49) 1161.
354. Kotlay, Acta. Phys. Acad. Sci. Hung. 16 (63)93.
355. Siemssen et al., Nucl. Phys. 69 (65) 209.
356. Canavan, Phys. Rev. 87 (52) 136.
357. Biggerstaff et al., Nucl. Phys. 36 (62) 631.
358. De Jong et al., Physica 18 (52) 676.
359. Dolinov and Melikov, Vest. Mosk. Univ. Fiz. Astron., P116 (66).
360. Ambrossino et al., J. Physique C1 (66) 62.
361. Farouk et al., Z. F. Phys. 201 (67) 52.
362. Juric, Phys. Rev. 98 (55) 85.
363. McCrary et al., Phys. Rev. 108 (57) 392.
364. Read and Calvert, Proc. Phys. Soc. 77 (61) 65.
365. Read et al., Nucl. Phys. 23 (61) 386.
366. Bondouk et al., Ann. Der. Phys. 32 (75) 255.
367. Friedland et al., Z. Phys. 267 (74) 97.
368. Sledzinska et al., Acta. Phys. Polonica 88 (77) 277.
369. Tanaka, J. Phys. Soc. Japan 44 (78) 1405.
370. Zwieglinski et al., Nucl. Phys. A250 (75) 93.
371. Cohen and Herling, Nucl. Phys. A141 (70) 595.
372. Nam and Osetinskii, Soviet J. Nucl. Phys. 9 (69) 279.
373. Earwaker, Nucl. Phys. A90 (67) 56.
374. Bondouk et al., Rev. Roumaine Phys. 19 (74) 653.
375. McEver et al., Nucl. Phys. A178 (72) 529.
376. Taylor et al., Nucl. Phys. 15 (72) 31.
377. Artemov et al., Yadernaya Fiz. 1 (65) 1019.
378. Dorenbusch and Browne, Phys. Rev. 131 (63) 1212.
379. Ehlers, Thesis, Washington State U. (70).
380. Moazed and Holmgren, Phys. Rev. 166 (68) 977.
381. Goss, Thesis, Ohio State U. (70).
382. Goss et al., Phys. Rev. C7 (73) 1837.
383. Taylor et al., Nucl. Phys. 65 (65) 318.
384. Saleh, et al., Ann. Der Physik 31 (74) 76.
385. Overley, Thesis, Caltech (60).
386. Overley and Wahling, Phys. Rev. 128 (62) 315.
387. Boerli et al., Fizika (Yugolsavia) 2 (70) 19.
388. Jenkin et al., Nucl. Phys. 50 (64) 516.
389. Segel et al., Phys. Rev. 145 (66) 736.
390. Szabo et al., Nucl. Phys. A195 (72) 527.
391. Stocker and Browne, Phys. Rev. C9 (74) 102.
392. Lombaard, et al., Z. Phys. 219 (69) 124.
393. Busch et al., Nucl. Phys. A223 (74) 183.
394. Comsan et al., Atomkernergie 13 (68) 415.
395. Assimakopoulos and Gangas, Nucl. Phys. A108 (68) 497.
396. Black et al., Phys. Rev. Lett. 25 (70) 877.
397. Friedland and Verleger, Z. Phys. 211 (68) 373.
398. Rendic et al., Bull. Am. Phys. Soc. 16 (71)1153.
399. Roy et al., Nuovo Cim. 6 (73) 374.
400. Becker, Phys. Rev. 119 (60) 1076
401. Breuer, A. Phys. 178 (64) 268.
402. Marion and Weber, Phys. Rev. 103 (56) 1408.
403. Longequeue et al., Compt. Tend. 264 A/B (67)1032.
404. Legge, Nucl. Phys. 26 (61) 608.
405. Purser and Wildenthal, Nucl. Phys. 44 (63) 22.
406. Paris et al., Physica 20 (54) 573.
407. Poore et al., Nucl. Phys. A92 (67) 97.
408. Burke et al., Phys. Rev. 93 (54) 188.
409. Croissiaux, Ann.der Phys. 5 (60) 409.
410. Endt, et al., Physica 18 (52) 423.
411. Harrison et al., Phys. Rev. 117 (60) 532.
412. Lee and Siemssen, Bull. Am. Phys. Soc. 10 (65) 510.
413. Ahmad et al., 4th AINSE Nucl. Phys. Conf., Sydney (72) p. 76.
414. Arena et al., Lett. Nuovo Cim. 5 (72) 879.
415. Black et al., Phys. Rev. Lett. 25 (70) 877.
416. Holmgren et al., Nucl. Phys. 48 (63) 1.
417. Gerardin et al., Nucl. Phys. A169 (71) 521.
418. Herling et al., Phys. Rev. 178 (69) 1551.
419. Duggan et al., Nucl. Phys. A151 (70) 107.
420. Buffa and Brussel, Nucl. Phys. A195 (72) 545.
421. Nusslin and Braun-Munzinger, Z. Phys. 240 (70) 217.
422. Patterson et al.,Proc. Phys. Soc. 90 (67) 577.
423. Squier et al., Nucl. Phys. A119 (68) 369.
424. Bell et al., Nucl. Phys. A179 (72) 408.
425. Kuan et al., Nucl. Phys. 60 (64) 509.
426. Bell et al., Nucl. Phys. A193 (72) 385.
427. Patterson et al., Proc. Phys. Soc. 85 (65) 1085.
428. Schiffer et al., Phys. Rev. 104 (56) 1064.

429. Patterson et al., Proc. Phys. Soc. 88 (66) 641.
430. Singh, Nucl. Phys. A155 (70) 453.
431. Gallmann et al., Nucl. Phys. A123 (69) 27.
432. David et al., Nucl. Phys. A182 (72) 234.
433. Mo and Weller, Phys. Rev. C8 (73) 972.
434. Davidson et al., Caltech Report LAP-165 (78).
435. Weaver et al., UCRL-74938 (73).
436. Anderson et al., Nucl. Phys. A223 (74) 286.
437. Fowler et al., Ann. Rev. Astron. Astrophys. 5 (67) 525.
438. Segel et al., Phys. Rev. B139 (65) 818.
439. Symons et al., Nucl. Phys. 46 (63) 93.
440. Dehnhard, Rev . Mod. Phys. 37 (65) 450.
441. Chase et al., Phys. Rev. 166 (68) 997.
442. Williams et al., Phys. Rev. 144 (66) 801.
443. Olness and Warburton, Phys. Rev. 166 (68) 1004.
444. Buechner et al., Phys. Rev. 79 (50) 262.
445. Elkin, Phys. Rev. 92 (53) 127.
446. Fortune and Vincent, Phys. Rev. 185 (69) 1401.
447. Friedland and Verleger, Z. Phys. 222 (69) 138.
448. Breuer, Z. Phys. 178 (64) 268.
449. Kavanagh and Barnes, Phys. Rev. 112 (58) 503.
450. Weller and Blue, Nucl. Phys. A211 (73) 221.
451. Din et al., Nucl. Phys. A93 (67) 190.
452. Almond and Risser, Nucl. Phys. 72 (65) 436.
453. Thornton et al., Nucl. Phys. A198 (72) 397.
454. Silverstein and Herling, Phys. Rev. 181 (69) 1512.
455. Ciric et al., Fizika (Yugoslavia) 9, Suppl. 1 (77) 39.
456. Black et al., Nucl. Phys. A153 (70) 233.
457. Holmgren et al., Phys. Rev. 114 (59) 1281.
458. Hahn and Ricci, Nucl. Phys. A101 (67) 353.
459. Mante et al., Paper 8B6, Asilomar (73).
460. Brill, Soviet J. Nucl. Phys. 1 (65) 37.
461. Liskien and Paulsen, Report EANDC (E) - 143 "L" (72).
462. Liskien and Paulsen, Report EANDC (E) - 152 "L" (72).
463. Liskien and Paulsen, Report EANDC (E) - 144 "L" (72).
464. G. M. Hale and D. C. Dodder, "R-Matrix Analysis of Light-Element Reactions for Fusion Applications", Presented at the International Conference on Nuclear Cross Sections for Technology, Knoxville, TN, Oct. 79.
465. A. Elwyn et al., private communication.

*179. Hemmendinger, Bull. Am. Phys. Soc. 1 (56) 96.

MEASUREMENT AND ANALYSIS OF NEUTRON SPECTRA IN SOME ASSEMBLIES OF REACTOR MATERIALS

Itsuro Kimura

Research Reactor Institute, Kyoto University
Kumatori-cho, Sennan-gun, Osaka-fu
590-04, Japan

In order to assess group constants for reactor materials, energy spectra of neutrons from about 1 keV to a few MeV in some sample assemblies have been measured by the linac-time-of-flight method and the results are compared with those theoretically predicted by one-dimensional transport calculation. In addition to the ordinary large bulk pile system, a smaller pile surrounded by a reflector and a slab scattering method have been investigated by introducing the sensitivity coefficients of group constants to neutron spectrum. Typical results for some reactor materials taken at the Research Reactor Institute, Kyoto University are shown.

(Neutron spectrum, time-of-flight, group constants, sensitivity coefficient, transport calculation)

Introduction

Since an electron linear accelerator became a powerful tool of an intense pulsed neutron source for the neutron time-of-flight spectroscopy, a large number of groups have carried out the assessment of neutron cross sections or group constants of reactor materials through measurement and analysis of neutron spectra in sample piles of them. At first, this method started in the thermal neutron region, by which various models of thermal neutron scattering were investigated. Thermal neutron spectra in multiplying media were also measured and the results were compared with those theoretically predicted. On the other hand the spectra of fast neutrons penetrating reactor materials were studied by several workers. Recently similar works have been achieved for the 14 MeV neutrons from the standpoint of the neutronics of a fusion reactor blanket. A little more than ten years ago the measurement of fast and intermediate neutrons in materials for fast breeder reactors was begun and since then many works have been performed [1-10].

Beyond other integral methods, such as critical experiments, for the assessment of group constants of reactor materials, this method has less ambiguity, because a sample has simpler geometry and has homogeneous pure constituent. Moreover, among various methods of fast and intermediate neutron spectroscopy, the time-of-flight method with an electron linear accelerator covers wider range of energy without any big technical problem.

In this paper, the experimental and theoretical works of neutron spectra in some reactor materials, which have been carried out by the author and his collaborators at the Research Reactor Institute (KURRI) and the Department of Nuclear Engineering of Kyoto University and Japan Atomic Energy Research Institute, are reviewed. In addition to the common method of a large bulk sample pile or assembly, a method using a small sample pile surrounded by a reflector and a slab scattering method are introduced. Both methods are aimed to save the quantity of sample material. The latter can be regarded as a method between a large bulk pile experiment and a smaller scatterer experiment which was performed by Verbinski et al.[11] before.

In order to compare these methods with each other, we have studied the sensitivity coefficients of group constants to neutron spectrum.

Experimental Arrangement and Procedure

Sample Piles and Slabs

The sample piles and slabs, which we have experimentally and theoretically studied, are listed in Table I.

As the sample, we have mainly chosen structural materials of fission reactors, but some other materials such as thorium and those for a fusion reactor have been also selected.

The shapes of sample piles can be classified to three types: (1) a cube or a rectangular parallelepiped, (2) a sphere, and (3) a polyhedron (14-hedron). For the case of an iron pile surrounded by a lead reflector, the pile was composed of 2.5cm cubes of iron to simulate a sphere 35cm in diameter.

Each pile has a cylindrical or cubic lead photoneutron target at the center and a reentrant hole from which we can take position and angular dependent neutron flux beam to the flight tube. When we measure background counts, a plug in the bottom of the reentrant hole is removed. In order to measure angular distribution of neutrons around the target, we can set activation wires or foils, such as Ni and Au radially in the pile.

Table I Sample piles and slabs at KURRI

Name	Purity of sample	Shape and size	Position and direction mainly measured
Borated graphite* (Standard)	2.6 % boron in graphite	Rectangular parallelepiped 70 cm x 70 cm x 80 cm	r=22.5 cm, μ=0.0 r=30 cm, μ=$\pm$0.66
Iron pile*	Soft steel, SS-41	Rectangular parallelepiped	r=22.5 cm, μ=0.0 r=29.5 cm, μ=$\pm$0.68
Iron slab	Soft steel, SS-41	Plate, 14 cm thick	r=74 cm, μ=$\pm$0.86
Iron sphere surrounded by lead	Soft steel, SS-41 Lead, 99.9 %	Iron : simulated sphere 35 cm in diameter Lead : cube, 70 cm x 70 cm x 70 cm	r=12.5 cm, μ=0.0 r=22.5 cm, μ=0.0
Stainless steel*	SUS-304	Cube 76 cm x 76 cm x 76 cm	r=25.5 cm, μ=0.0 r=34.5 cm, μ=$\pm$0.68
Iron oxide	99.2 % Fe_2O_3	Powder packed into a spherical vessel of 60 cm in diameter	r=15 cm, μ=0.0
Aluminum*	99.5 % Al (A 1050P)	Cube 70 cm x 70 cm x 70 cm	r=15 cm; 30 cm, μ=0.0 r=21.2 cm, μ=$\pm$0.7
Alumina	99.5 % Al_2O_3	Same as iron oxide	r=15 cm, μ=0.0
Lead*	99.9 % Pb	Cube 70 cm x 70 cm x 70 cm	r=20 cm, μ=0.0 r=2; 10; 20; 30 cm, μ=1.0
Zirconium	99.6 % Zr	Same as iron oxide	r=15 cm, μ=0.0
Thorium slab	99.5 % Th	Plate, 5 cm thick	r=76 cm, μ=0.86
Thoria	99.9 % ThO_2	Same as iron oxide	r=15 cm, μ=0.0 r=20 cm, μ=-0.64
Lithium pile	99.8 % Li	Rectangular parallelepiped 60 cm x 50 cm x 40 cm	r=15 cm, μ=0.0
Lithium slab	Same above	Plate, 10; 20 cm thick	r=81 cm, μ=$\pm$0.83
Lithium fluoride	98.1 % LiF	Same as iron oxide	r=15 cm, μ=0.0
Titanium	99.4 % Ti	14-hedron, in which a sphere 104 cm in diameter inscribes	r=25 cm, μ=0.0 r=35 cm, μ=$\pm$0.7
Polytetrafluoro-ethylene pile	99.9 % $(CF_2)_n$	14-hedron, in which a sphere 90 cm in diameter inscribes	r=19 cm, μ=0.0 r=30 cm, μ=$\pm$0.79
Polytetrafluoro-ethylene slab	Same above	Plate, 14 cm thick	r=65 cm, μ=0.75
Barytes concrete	- - - -	Cube 50 cm x 50 cm x 50 cm	r=18.2 cm, μ=0.27

Pulsed Neutron Source

Fast neutron pulses are generated with the electron linear accelerator of KURRI. The typical operating conditions of the accelerator are as follows: electron energy; about 30 MeV, repetition rate; 166 pps, pulse width; 30 or 100 ns, target current; about 300 mA.

The cylindrical lead photoneutron target 5cm in diameter and 5cm long is cooled by air. The spectrum of the neutrons emitted from the target was measured by the time-of-flight method. Figure 1 shows the neutron spectra from the lead target and the tantalum target that is cooled by water. The shape of the photoneutron spectrum above 1.5 MeV for the lead target was measured previously and it was shown to be a composite of two Maxwellians [8]. The angular distibution of the neutrons from the lead target shows isotropic as seen in Fig. 2, which was measured by making use of the $^{27}Al(n,\alpha)^{24}Na$ reaction. For the piles shown as * in Table I, we used a cubic lead photoneutron target, 5cm x 5cm x 5cm.

For the slab scattering experiment, we have used a water cooled tantalum target.

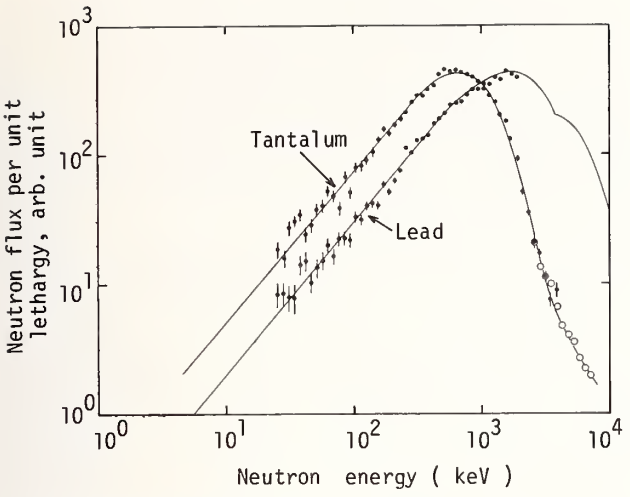

Fig. 1 Spectra of neutrons emitted from lead and tantalum targets.
(♦ ^{6}Li glass, o NE-213)

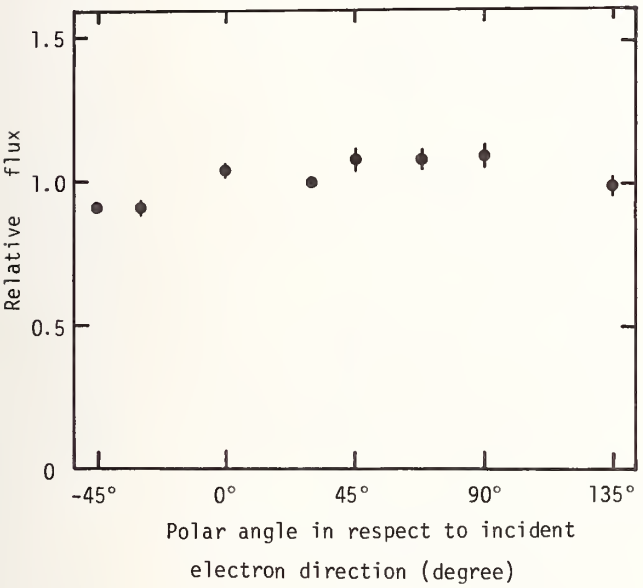

Fig.2 Angular distribution of photoneutrons from the lead target measured by ^{27}Al (n , α) ^{24}Na

Collimators and Flight Tube

The general configuration of collimators and an evacuated neutron flight tube is depicted in Fig 3. The total distance between the electron beam center and the front surface of a neutron detector is about 22m. For the photoneutron spectrum measurement a 45m flight path was used. The geometry for the slab scattering experiment is shown in Fig.4, where we use the same collimators and the flight tube as the case of a sample pile.

In order to eliminate gamma flash in the early part of time analysis, a natural uranium plate of 1cm or 2cm thick is used as a X-ray filter.

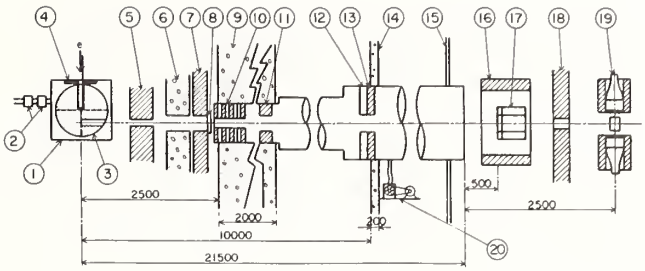

Fig. 3 Experimental arrangement for the case of the measurement of thoria (Numbers which show distance in the figure are in mm)
(1) Hood, (2) Blower and filter, (3) Thoria pile, (4) Aluminum electron collimator, (5) Lead pre-collimator (250 mm thick, 22 mm ø), (6) Heavy concrete, 400 mm t, (7) Lead shield, 300 mm t, (8) Uranium filter, (9) Concrete wall, (10) Lead and B_4C collimator (lead 47 mm t and B_4C 47 mm t) x 4, 50 mm ø, (11) Lead collimator, 200 mm t, (12) B_4C collimator, 80 mm t, 160 mm ø, (13) Lead collimator, 60 mm t, 160 mm ø, (14) Concrete wall, (15) Wall of hut, (16) Lead shield for detector, (17) ^{6}Li glass scintillation counter bank (This is removed when the ^{10}B-vaseline-plug-NaI(Tl) detector is used), (18) Lead shield, 150 mm thick, (19) ^{10}B-vaseline-plug-NaI(Tl) detector, (20) Rotary vacuum pump.

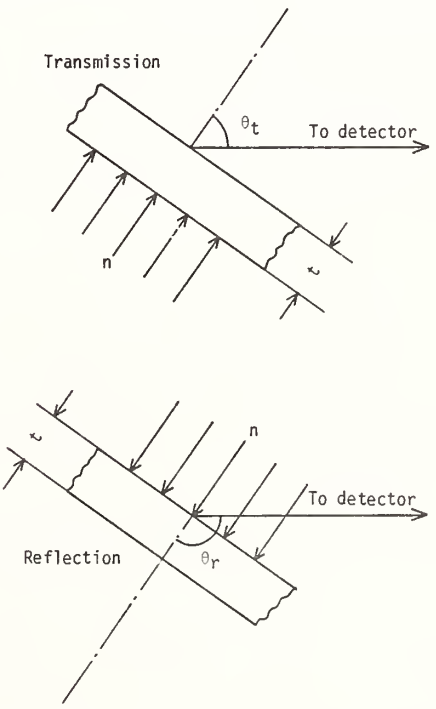

Fig. 4 Configurations of slab scattering experiment

Neutron Detectors and Electronics

As the neutron detector, we use a bank of three ^{6}Li glass scintillation counters of type NE 912, 12.7cm in diameter and 1.27cm thick and a ^{10}B-vaseline-NaI(Tl) counter. The structure and the electronic circuit of these detectors are given elsewhere [12]. The detection efficiencies of

them were experimentally determined by making use of a standard neutron spectrum field with a borated graphite pile[13]. A ^{235}U fission chamber and a BF_3 counter are used for neutron monitor.

The electronic circuit for the neutron time-of-flight analysis is described elsewhere [8].

Measurements of Spatial Distributions of Neutrons

Nickel wire of 1mm in diameter and gold foils of 3mm in diameter and 0.05mm thick are used for the measurement of spatial distribution of neutrons around the photoneutron target by the $^{58}Ni(n,p)^{58}Co$ and $^{197}Au(n,\gamma)^{198}Au$ reactions. The induced activities of both ^{58}Co and ^{198}Au are measured with a Ge(li) detector.

Sensitivity of Group Constants to Neutron Spectrum

For the purpose of the assessment of the group constants by neutron spectrum, it is desirable that the neutron flux spectrum is as sensitive to group constants as possible. In order to deal with the problem quantitatively, we define the sensitivity coefficient of group constants to angular neutron flux S_x^g as

$$S_x^g = \frac{\Delta\Phi_g}{\Phi_g} \Big/ \frac{\Delta\Sigma_x}{\Sigma_x} = \frac{\Sigma_x}{\Phi_g} \frac{\Delta\Phi_g}{\Delta\Sigma_x} .$$

In stationary state, the neutron transport equation is given by

$$A[\Sigma(\rho)]\Phi(\rho) = S(\rho) ,$$

where

A : operator of neutron transport,
S : external neutron source,
Φ : angular neutron flux,
ρ : variables in phase space.

As Oblow et al.[14] show, the sensitivity coefficient can be given by

$$S_{x(\rho)}^{\Phi_g} = -\frac{\Sigma_{x(\rho)}}{\Phi_g} \int \Phi^*(\xi) \frac{dA[\Sigma(\xi)]}{d\Sigma(\rho)} \Phi(\xi) d\xi ,$$

where

$$A^*[\Sigma(\rho)]\Phi^*(\rho) = \delta(\rho-\rho_0) .$$

We made a computer code DTF-IV-KANDO for the calculation of the sensitivity coefficient from DTF-IV[15] and have performed numerical calculation. We also made a similar code from ANISN[16]. Some results for iron are shown below. In these cases, we have chosen:

(1) 26 group constants by Abagyan et al.[17]
(2) Observed groups, g's
fifth group --- 0.8 MeV ∿ 1.4 MeV
tenth group --- 21.5 keV ∿ 46.5 keV

At first, the sensitivity coefficients to the angular neutron flux at the position r=12.5cm and the direction μ=0 in spherical piles of iron, have been investigated. Figure 5 shows the variation of the sensitivity coefficients and the neutron fluxes when the radius of the spherical pile is changed. The sensitivity coefficients to the fifth group are generally almost constant for R>42cm, however those to the tenth vary apparently even at R=100cm.

For the iron sphere with the radius of 54cm, the sensitivity coefficients for dif-

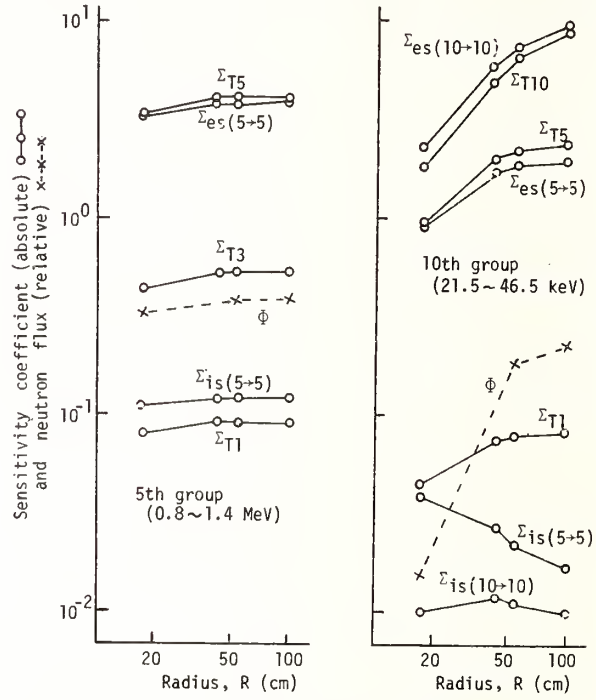

Fig. 5 Sensitivity coefficient and neutron flux at r=12.5cm, μ=0 versus radius of iron sphere

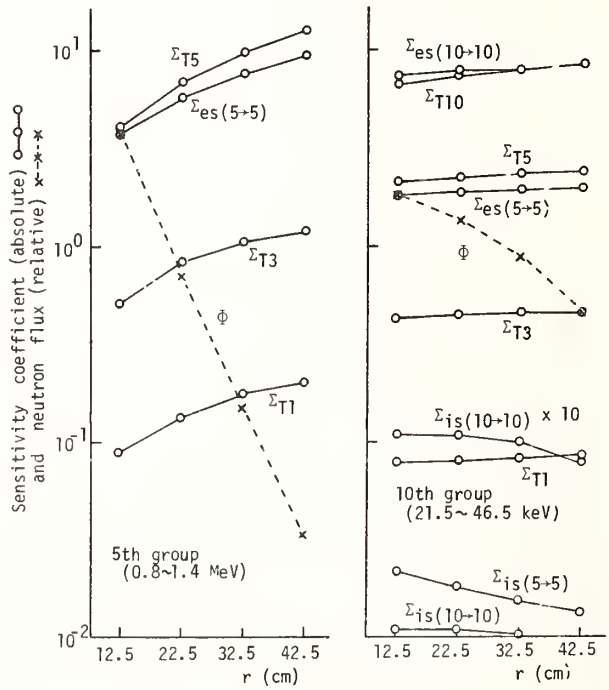

Fig. 6 Sensitivity coefficient and neutron flux versus position r in spherical iron pile, R=54cm. (μ=0)

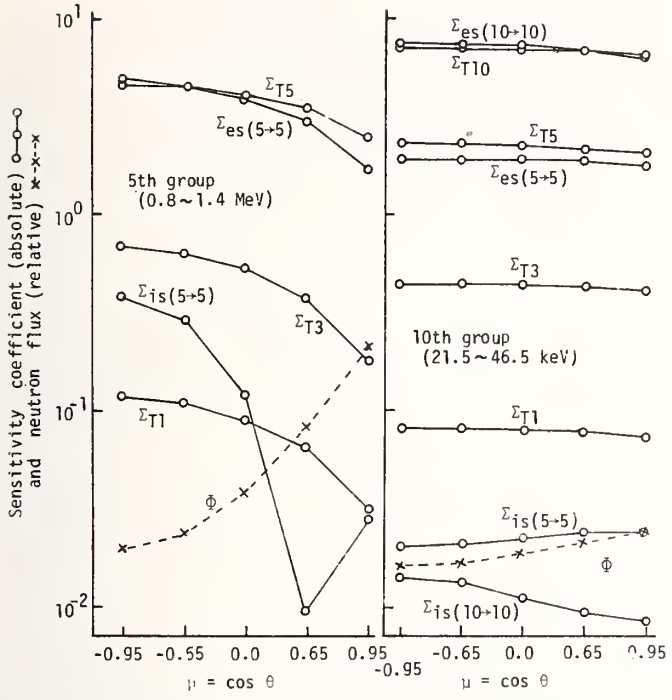

Fig. 7 Sensitivity coefficient and neutron flux versus direction cosine μ in spherical iron pile, R=54cm. (r=12.5cm)

ferent positions and for different directions are shown in Fig. 6 and Fig. 7, respectively. For both cases, the sensitivity coefficients to the fifth group depend on position and direction much more than those to the tenth.

The effect of the spectrum of the neutron source can be seen in Table II, where the sensitivity coefficients for the photoneutrons and the 14 MeV neutrons are compared. Remarkable difference can be found only for the first group, where neutron spectra entirely differ from each other.

The sensitivity coefficients for the slab scattering method have been calculated

Table II Sensitivity coefficients for different source spectra. Iron sphere (R=54cm) for r=22.5cm μ=0.

Energy group, g	Σ being varied	Sensitivity coefficient	
		Photoneutrons	14MeV neutrons
5	$\Sigma_{T\cdot1}$	-0.143	-2.64
	$\Sigma_{T\cdot3}$	-0.839	-0.649
	$\Sigma_{T\cdot5}$	-6.84	-5.96
	$\Sigma_{es(5\to5)}$	5.74	5.08
	$\Sigma_{is(5\to5)}$	-0.002	-0.0253
10	$\Sigma_{T\cdot1}$	-0.082	-1.80
	$\Sigma_{T\cdot3}$	-0.425	-0.390
	$\Sigma_{T\cdot5}$	-2.31	-2.25
	$\Sigma_{T\cdot10}$	-7.45	-7.45
	$\Sigma_{es(5\to5)}$	1.95	1.89
	$\Sigma_{es(10\to10)}$	7.98	5.57
	$\Sigma_{is(5\to5)}$	-0.018	-0.0176
	$\Sigma_{is(10\to10)}$	-0.011	-0.0108

$\Sigma_{T\cdot i}$: Total cross section of i-th group,
Σ_{es} : P_0 component of slowing-down cross section,
Σ_{is} : P_1 component of in-scattering cross section.

and the result is compared for the cases of transmission and reflection in Table III. The dependences of the coefficients on thickness of a slab and direction are depicted in Fig. 8 and Fig. 9, respectively. For the direction of μ=0.65, most of the coefficients increase with thickness, however they are generally almost constant for different angles.

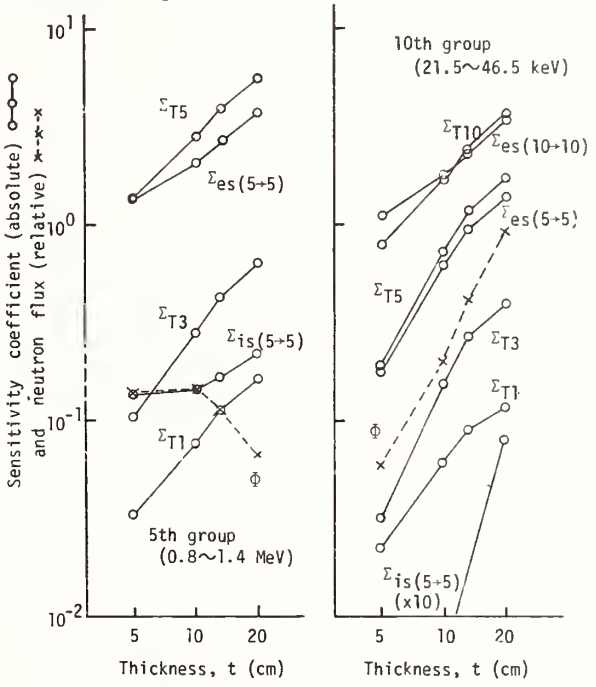

Fig. 8 Sensitivity coefficient and neutron flux versus thickness of iron slab. Angular cosine is 0.65.

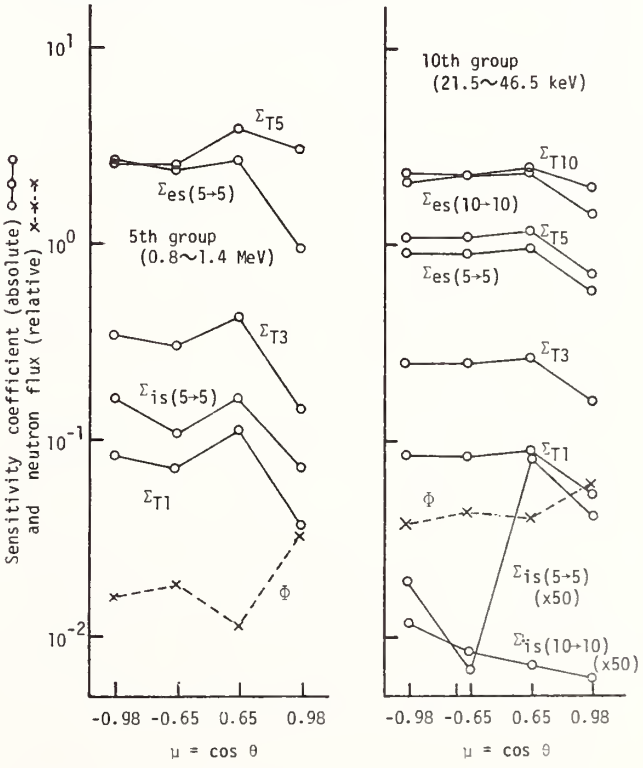

Fig. 9 Sensitivity coefficient and neutron flux versus angular cosine μ for slab scattering experiment of iron plate 14 cm thick.

Table III Sensitivity coefficients for slab scattering experiment of iron plate 14 cm thick. Angular cosines μ for transmission and reflection are 0.65 and -0.65 respectively.

Energy group, g	Σ being varied	Sensitivity coefficient	
		Transmission	Reflection
5	$\Sigma_{T\cdot1}$	-0.113	-0.073
	$\Sigma_{T\cdot3}$	-0.426	-0.305
	$\Sigma_{T\cdot5}$	-3.854	-2.495
	$\Sigma_{es(5\to5)}$	2.695	2.398
	$\Sigma_{is(5\to5)}$	0.166	-0.111
10	$\Sigma_{T\cdot1}$	-0.0883	-0.0822
	$\Sigma_{T\cdot3}$	-0.264	-0.247
	$\Sigma_{T\ 5}$	-1.151	-1.078
	$\Sigma_{T\cdot10}$	-2.417	-2.242
	$\Sigma_{es(5\to5)}$	0.955	0.900
	$\Sigma_{es(10\to10)}$	2.327	2.232
	$\Sigma_{is(5\to5)}$	0.00160	0.000133
	$\Sigma_{is(10\to10)}$	0.00140	-0.00163

$\Sigma_{T\cdot i}$: Total cross section of i-th group,
Σ_{es} : P_0 component of slowing-down cross section,
Σ_{is} : P_1 component of in-scattering cross section.

Theoretical Calculation of Neutron Spectrum

Configuration and Assumption

In the theoretical calculation each pile is assumed to be a sphere. We assume uniform and isotropic photoneutron source in the part of spherical lead target.

In typical calculation, space mesh and number of angular quadrature points are taken to be 1cm and 8/16 respectively. For the case of slab scattering experiment, we assume parallel beam source and slab geometry.

Computer Codes and Group Constants

Canculations have been performed by both DTF-IV[15] and ANISN[16] for both pile and slab geometries.

As the neutron group constants to be assessed, we have selected the 70 group JAERI-FAST constants (J-F)[18], the 26 group constants compiled by Abagyan et al. (ABBN)[17] and the 100 group constants compiled from ENDF/B library[19].

Neutron Spectra of Some Reactor Materials

Borated Graphite

The borated graphite pile has been utilized as the standard neutron spectrum field for the calibration of neutron detectors[13]. Whenever we change the configuration and the alignment of the neutron collimator system and the detector arrangement, we make it a rule to calibrate the detection efficiency.

Iron

The neutron spectra in the iron pile were investigated before and the result was given in the previous paper8. Recently the data measured by the authors were used to evaluate the JENDL-1 library by Otake et al. 20.

The significance to study the neutron spectrum in the small iron pile surrounded by the lead reflector was described else-

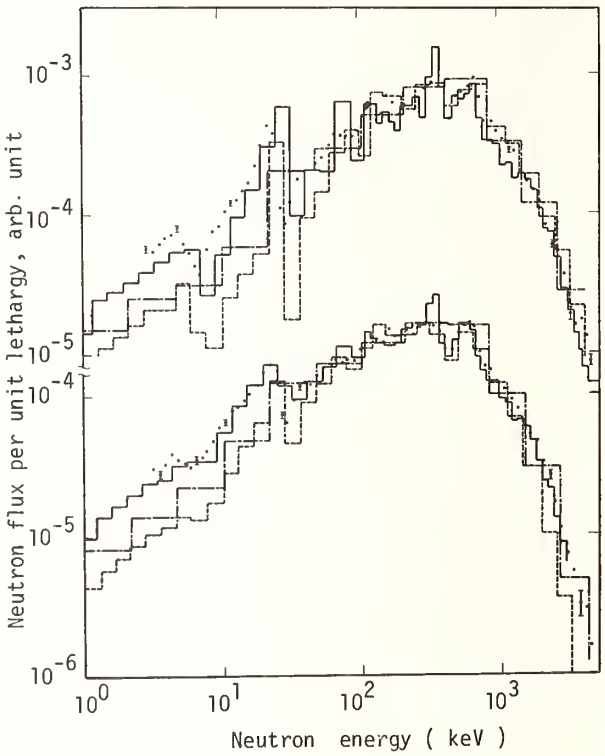

Fig. 10 Neutron spectra for iron sphere with lead reflector. Top : in iron sphere, r = 12.5cm, μ = 0, bottom : in lead reflector, r = 22.5cm, μ = 0. ϕ measured, ⌐ calculated by ANISN /DLC-2D, ⌐ DTF-IV/ABBN, ⌐ DTF-IV/JAERI-FAST.

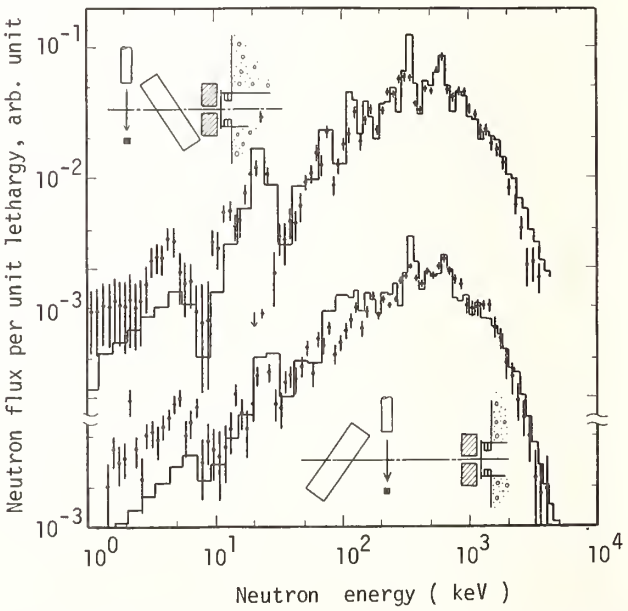

Fig. 11 Spectra of neutrons scattered by iron slab 14cm thick.
ϕ measured, ⌐ calculated by ANISN(P8S16)/ DLC-2D

where10. As seen in Fig.10, the measured spectra in the iron pile and in the lead reflector agree with those predicted by ANISN/DLC-2D satisfactorily.

The spectra of the neutrons scattered by an iron slab 14cm thick have been measured and the results are compared with those analyzed, as shown in Fig. 11. A spherical shell geometry has been assumed in this calculation.

Stainless Steel

As seen in the previous paper[8], the measured spectra agree with the predicted

Aluminum

The spectra of neutrons in the aluminum cube were measured and calculated. The result for r=15cm and μ=0 is shown in Fig. 12. General agreement can be seen between the measured and the predicted by ANISN/DLC-2D. The calculated spectra by DTF-IV/ABBN and by DTF-IV/JAERI-FAST show higher and lower values below several ten keV respectively. At the two peaks between 10 keV and 100 keV, the experimental points are considerably smaller than the predicted by ANISN/DLC-2D. Similar tendency was shown by Golay et al. before[21].

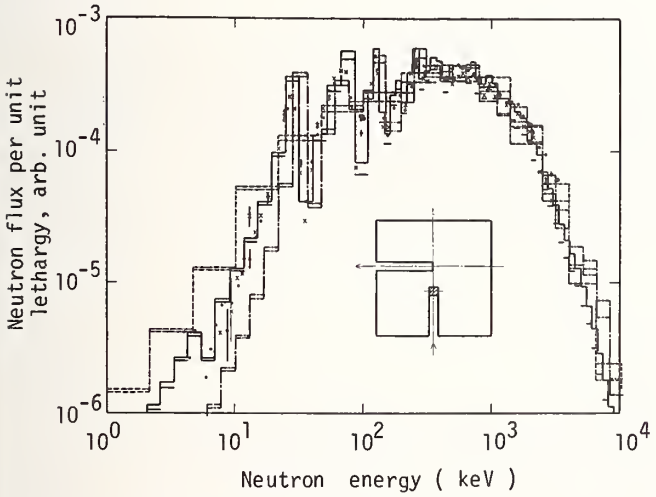

Fig. 12 Neutron spectrum in aluminum pile, r = 15cm, μ = 0 .
* measured with ^{10}B-V-Na(Tl), ϕ measured with ^{6}Li glass, calculated by DTF-IV/J-F, ANISN/DLC-2D, DTF-IV/ABBN.

Zirconium

The neutron spectrum in the spherical pile of zirconium was investigated and the result is depicted in Fig. 13. In the calculation we used the group constants for zircalloy instead of pure zirconium. Between 20 keV and 200 keV the measured values are larger than that theoretically predicted by DTF-IV/ENDF/B-IV almost by twice. The reason of this disagreement should be investigated in future.

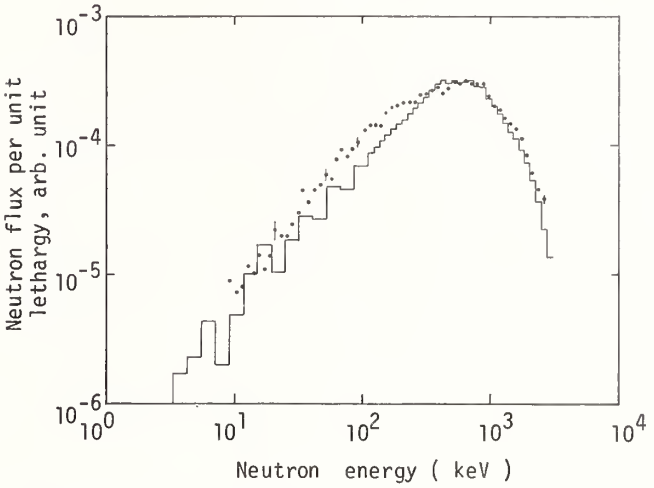

Fig. 13 Spectrum of neutrons in spherical pile of zirconium, r = 15cm, μ = 0.
ϕ measured, calculated by DTF-IV(P8S8)/ENDF/B-IV

Thorium Slab

Figure 14 shows the spectrum of the neutrons scattered by a thorium slab 5cm thick. Good agreement can be seen between the measured and the predicted by ANISN/DLC-2D. The calculated spectrum by DTF-IV/JAERI-FAST also agrees with the measured below about 2 MeV, however above this energy the former becomes larger than the latter. This disagreement is thought to be mainly due to the former was calculated with the assumption of the spherical symmetry system. The experimental error increases rapidly with decreasing energy below 100 keV.

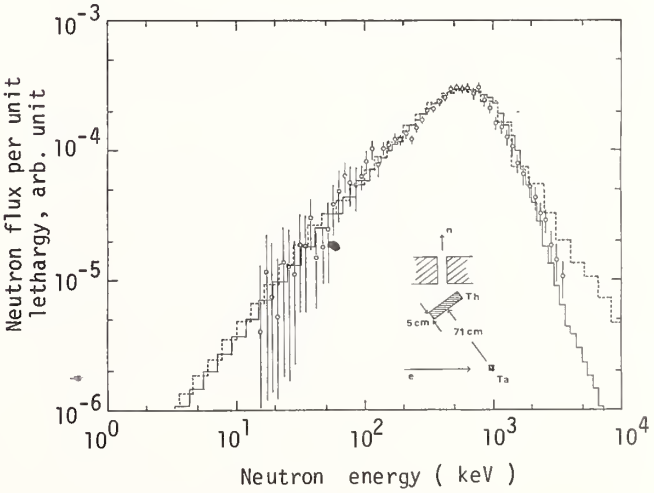

Fig. 14 Spectrum of neutrons scattered by thorium slab 5cm thick.
ϕ measured, ANISN(P8S16)slab/ENDF/B-IV DTF-IV(P1S8) spherical shell/JAERI-FAST.

Thoria Pile

The experimental and theoretical study of the neutron spectrum in a spherical thoria pile was carried out and the result was published before[9]. Recently Kobayashi recalculated the spectrum by making use of his revised constants[22],JF-II-K, which is given in Fig.15. This result as shown in Fig.16. becomes closer to the measured than the original, however the measured value still exceeds the predicted by about 20% around 10keV.

Most recently this thoria pile was sent to the Gaerttner Linac Laboratory, Rensselaer Polytechnic Institute (RPI) and the neutron spectrum in it has been cooperatively investigated by RPI and KURRI.

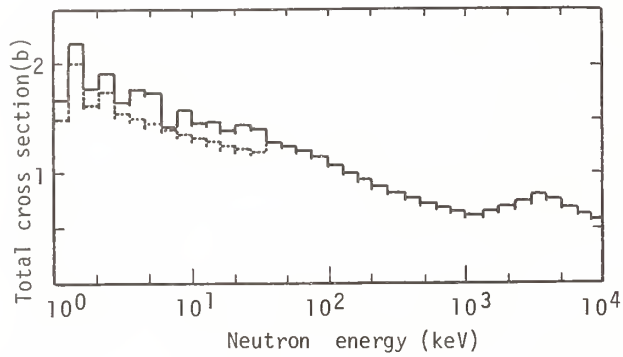

Fig. 15 Total cross section of original JAERI-FAST II and revised constants JF-II-K for thorium[22].
JF-II-K, JAERI-FAST II

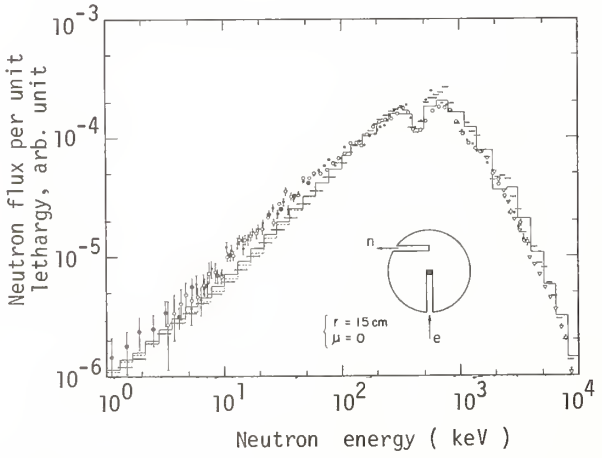

Fig. 16 Spectrum of neutrons in spherical pile of thoria[22].
^{6}Li glass, ^{10}B-V-NaI(Tl), NE-213
DTF-IV(P1S8)/JF-II-K, DTF-IV(P1S8)/JF-II, ANISN(P8S8)/DLC-2D.

Lithium

The neutron spectrum in a metallic lithium pile was measured and calculated, and the results are shown in Fig. 17. General agreement can be seen between them, but since the leakage of neutrons is considerably large for this lithium pile because of its longer shape and the angular distribution of fast neutrons around the photoneutron target shows forward peaking in this case, improvement of the calculational model should be performed in future.

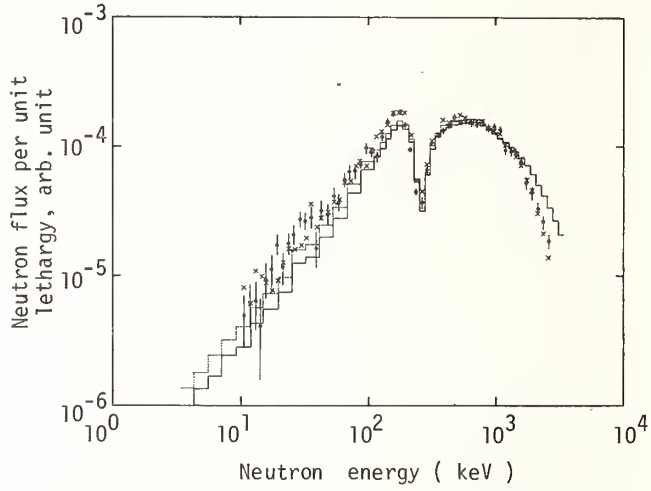

Fig. 17 Spectrum of neutrons in lithium pile, r = 15cm, μ = 0 .
measured with ^{10}B-V-NaI(Tl), measured with ^{6}Li glass, and calculated by DTF-IV(P8S8)/ENDF/B-IV for R = 30cm and 35cm, respectively.

Lithium fluoride

Powder of lithium fluoride, LiF was packed into a spherical vessel of 60cm in diameter, and the angular flux spectrum of the neutrons of r=15cm and μ=0 was measured. The result is compared with the predicted in Fig. 18. Discrepancy is remarkable at three places: (1) higher energy half of the 250 keV dip, (2) dip about 100 keV and (3) dip about 50 keV.

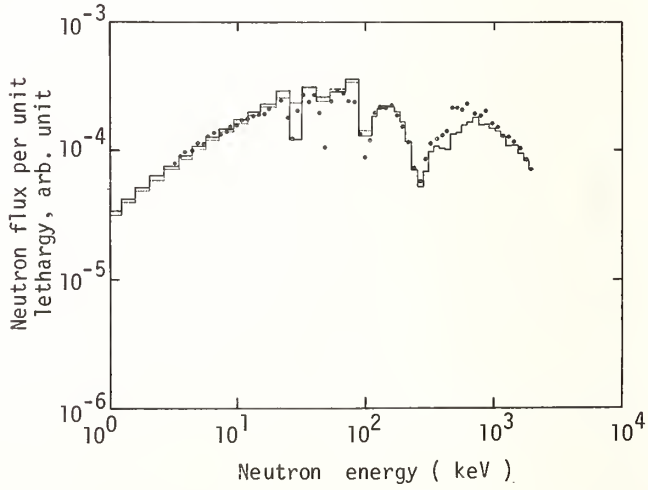

Fig. 18 Spectrum of neutrons in spherical pile of lithium fluoride, LiF, for r = 15cm, μ = 0 .
measured, and calculated by ANISN(P8S8)/ENDF/B-IV without and with correction of self-shielding,respectively.

Polytetrafluoroethylene

The spectrum of the neutrons in the polytetrafluoroethylene, $(CF_2)_n$, pile was measured and theoretically calculated, and the results are depicted in Fig. 19. The experimental values are higher than the predicted by almost 50% from 250keV to 700keV. At the three dips, the predicted values show much shallower than the measured. Since both tendencies can be also seen in the neutron spectrum in the lithium fluoride pile, we may suspect the nuclear data for fluorine. A trial to revise the group constants for fluorine with respect to the Sugi and Nishimura's report[23] has slightly improved the disagreement in several hundred keV, but we cannot get good agreement there yet. For the polytetrafluoroethylene pile, the forward peaking of angular distribution of photoneutrons has been also recognized, therefore more sophisticated calculation should be done in future.

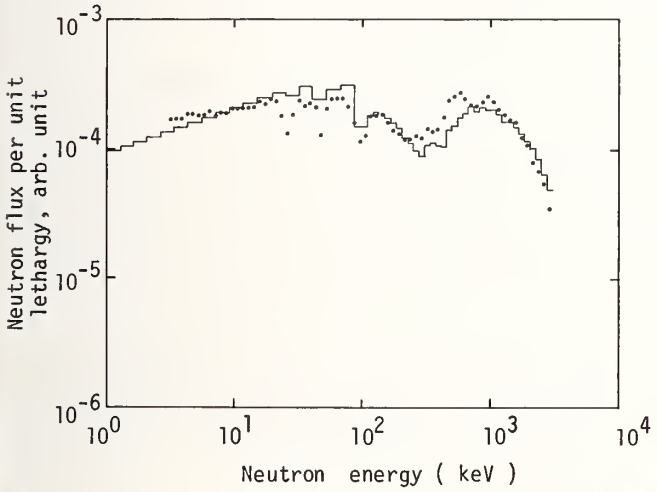

Fig. 19 Neutron spectrum in polytetrafluoroethylene pile, r = 19cm, μ = 0 .
♦ measured, ⌐⌙ calculated by ANISN(P8S8)/ ENDF/B-IV

Titanium

Metallic powder of titanium was packed into a 14-hedron vessel and the angular neutron flux spectra for three cases were measured and analyzed. As seen in Fig. 20, the measured values are remarkably higher than the calculated by DTF-IV/ENDF/B-IV between 20 keV and 150 keV. The reason of this disagreement should be investigated.

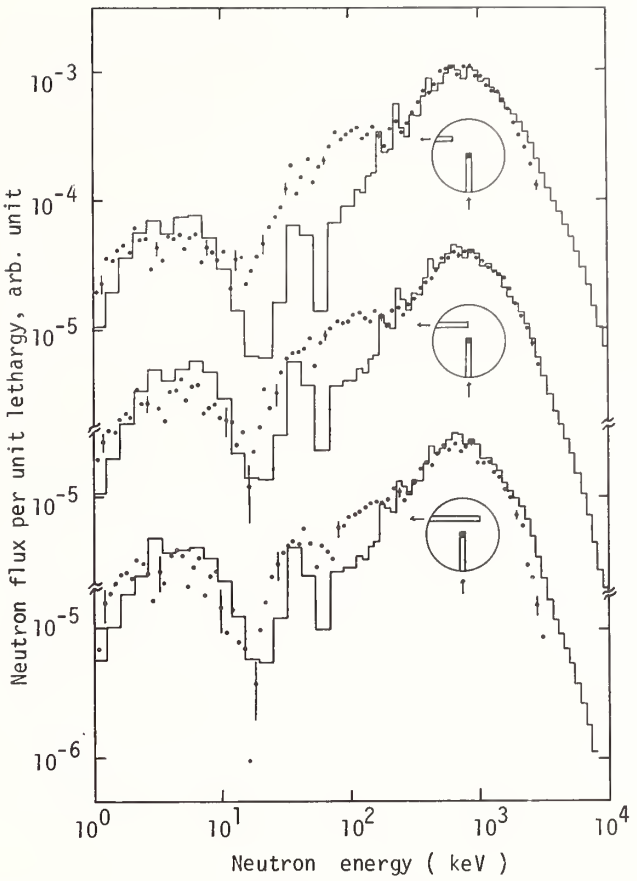

Fig. 20 Neutron spectrum in titanium pile.
Top : r = 35cm, μ = +0.7, middle : r = 25cm, μ = 0, bottom : r = 35cm, μ = -0.7 .
♦ measured, ⌐⌙ calculated by DTF-IV(P8S8)/ ENDF/B-IV.

Conclusion

1. At KURRI, spectra of fast and intermediate neutrons in more than ten piles of reactor materials have been investigated to assess group constants. The borated graphite pile was utilized as the standard neutron field for detector calibration.

2. Possibility to use a small sample pile surrounded by a reflector and a slab scattering method was shown by making use of the sensitivity coefficients of group constants to neutron spectrum.

3. The measured neutron spectra in the small iron pile surrounded by the lead reflector and scattered by the iron slab agree those predicted by ANISN/DLC-2D, as well as the case of the large iron pile.

4. The measured neutron spectrum in the aluminum pile also agrees that calculated by ANISN/DLC-2D except at two peaks.

5. However, agreement is rather poor between the measured and the calculated neutron spectra in the zirconium pile. In this calculation the group constants for zircalloy were used.

6. The observed spectrum of the neutrons scattered by the thorium slab agrees with the predicted, but the error increases rapidly below 100 keV.

7. The experimental value of neutron spectrum in the thoria pile exceeds the calculated by 20%, even we use the new constants revised by Kobayashi.

8. Agreement is rather poorer for the measured and the predicted neutron spectra in the lithium pile. On the contrary, the measured neutron spectrum in the lithium fluoride pile generally agrees that calculated except in three regions.

9. From the fact that the observed neutron spectrum in the polytetrafluoroethylene pile disagrees the calculated at three resonant dips and between 250 keV and 700 keV, we may suspect the group constants for fluorine.

10. The group constants for titanium also may have problem, because the measured neutron spectrum in the titanium pile is considarably higher than the predicted between 20 keV and 150 keV.

11. The following improvements should be carried out in future:
(1) Modification of calculational model for the case of forward neutron peak such as lithium and polytetrafluoroethylene.
(2) Comparison of the measured and the predicted neutron spectra by absolute values.
(3) Revision of group constants by making use of the sensitivity coefficients.

Acknowledgments

This study has been supported by the Grant in Aid for Fundamental Research of the Ministry of Education in Japan and the Visiting Researcher Program of KURRI.

The collaborators with the author are Prof. Hiroshi Nishihara and Mr. T. Mori of Department of Nuclear Engineering, Kyoto University, Messrs. Shu A. Hayashi, K.Kobayashi and S. Yamamoto of KURRI and Dr. M. Nakagawa of JAERI.

The author would like to acknowledge the continuing support of Prof. T. Shibata, Director of KURRI and the cooporation of Mr. Y. Fujita.

References

1. M. S. Coates et al., AERE-R 5364(1968).

2. A. E. Profio, H. M. Autunez, and D. L. Huffman, Nucl. Sci. Eng. 35, 91(1969).

3. R. J. Cerbone, GA-9149, Vol.1 (1969).

4. T. Nanjyo et al., Annu. Repts. Res. Reactor Inst., Kyoto Univ. 4, 25(1971).

5. B. K. Malaviya et al., Nucl. Sci. Eng. 47, 329(1972).

6. N. N. Kaushal et al., ibid. 49, 330 (1972).

7. A. J. H. Goddard, J. G. Williams and H. Lichtblau, Annals Nucl. Sci. Eng. 1, 139(1974).

8. I. Kimura et al., in Proc. of Conf. of Nucl. Cross Sections and Technology, Washington, D. C., 1975, ed. R. A. Schrack and C. D. Bowman (NBS Special Publication 425, 1975)p. 184.

9. H. Nishihara et al., J. Nucl. Sci. Technol. 14, 32(1977).

10. I. Kimura et al., ibid. 15, 183(1978).

11. V. V. Verbinski et al., Nucl. Instr. Meth. 52, 181(1967).

12. I. Kimura and S. Yamamoto, KURRI-TR-89 p. 108(1971).

13. I. Kimura et al., Nucl. Instr. Meth. 137, 85(1976)

14. E. M. Oblow et al., Nucl. Sci. Eng. 59, 189(1976).

15. K. D. Lathrop, LA-3373(1965).

16. W. W. Engle, Jr., K-1693(1967).

17. I. I. Bondarenko, Group Constants for Nuclear Reactor Calculations, (Consultants Bureau, New York, 1964).

18. S. Katsuragi et al., JAERI-1109(1966).

19. Magnetic Tapes from Radiation Shielding Information Center, ORNL.

20. I. Otake, in Neutron Data of Structral Materials for Fast Reactors, ed. K. H. Köckhoff (Pergamon Press, 1979) p. 105.

21. M. W. Golay et al., Trans. Am. Nucl. Soc. 14, 836(1971).

22. K. Kobayashi, Fundamental Study of Neutron Cross Section Related to Thorium Fuel Cycle, Thesis to Kyoto University (1978).

23. T. Sugi and K. Nishimura, Evaluation of Neutron Cross Sections for 19F in the Energy Range from 100 keV to 20 MeV, JAERI-M 7253 (1977).

NEUTRON TRANSPORT IN STRUCTURAL MATERIALS AND SHIELDING DESIGN

M. Salvatores
DRNR/SEDC/SPNR/LPR
C.E.N. Cadarache - B.P. N°1
13115 - Saint Paul Lez Durance - FRANCE

In this paper the recent development in integral Benchmark experiments and their analysis is reviewed. The main problems related to data and method assesment are also briefly reviewed. In particular, the basic data processing and multigroup structure optimization and the effects of the basic data uncertainty evaluation are stressed.

The representativity of an integral experiment from the designer point of view is indicated. Moreover a procedure to deduce design oriented bias factors is outlined. Cross section adjustments are indicated as a useful tool to reduce these bias factors and their uncertainties.

[Neutron transport, shielding, bias factors]

Introduction

The neutron transport calculation in structural materials and sodium plays an important role in the shielding design of a fast neutron power plant.

In particular, the neutron transport is directly connected to the damage in steel, secondary heat exchanger activation, external biological dose-rates, demountable structure activation, corrosion product formation, out of core neutron monitoring devices, gas (He, ^{3}H) production etc. Some of these parameters are of high relevance in the plant design, in particular the damage in steel and the secondary sodium activation.

The calculational methods used and the system geometric modeling, are relevant sources of errors, together with the basic data and the processing procedures used to reduce the basic nuclear data file data to a multigroup form suitable for calculation.

The resulting uncertainties, associated to the shielding calculations, can be fairly large. A cooperative effort of the NEA agency in cooperation with IAEA has resulted in a number of specialist meetings[1,2] aimed to the quantitative assessement of these uncertainties on a common basis, their impact on shielding design and to the definition of Benchmark experimental programs to reduce these uncertainties.

Since the cost of reducing uncertainties by improving methods and/or data is balanced by the benefits obtained from a reduction in the cost of the plant, we shall try in this paper to relate sensitivity and experiment analysis to actual shield design and optimization.

We will use the concept of "bias factors" or "safety factors" with their associated uncertainties[3].

In fact, in this way, we will try to follow the practical approach of a designer both for the actual design or for optimization studies, when he tries to assess quantitatively the data and methods uncertainty consequences. In other words, the integral experiment analysis of neutron propagation in structural material, should be seen in the context of the assessement of data, methods and procedures to be used together with appropriate bias factors, for the calculation of the various parameters of interest in the shielding of a power plant.

In this paper, we will briefly review a number of significant integral experiments of neutron propagation in different media.

The present state of basic data will be outlined together with an analysis of some of the methods used to reduce these basic data to multigroup libraries.

This analysis, related to the data, will be compared to a similar short analysis of the problems related to the calculational procedures, in particular for integral experiment analysis. Sentivity methods will provide a further tool to assess the feasibility of basic data and methods improvement, using the experimental results.

As a result, a number of tentative bias factors will be indicated for some quantities of major interest in fast reactor shielding design. This study will be centered on the integrated stainless steel shield configurations, represented by a well known Benchmark geometry[4], represented in Appendix, and the conclusions of this report are applicable mainly to this type of shield design. New and optimized shield design and the use of less conventional materials, would impose the planning of a consistent set of new "ad hoc" integral experiments.

Integral experiments

In the last few years a number of significant integral experiments have been performed in many leading laboratories for shielding data and methods assessment. Apart from a number of special purpose mock-up experiments to experimentally verify the calculation of specific configurations, there has been a fairly widespread tendency to perform simplified, "Benchmark" type experiments, often related to the neutron propagation in single material media.

We will consider only the most recent experiments. Among them we will quote the experiments indicated in the table on the following page :

Experiment	Propagation in:	Source type	Dimensions (cm)	Type of measurements
TSF[5]	Pure Na (with thick steel plates at both ends)	TSR-II reactor with "large" collimator	Several configuration up to 450 cm propagation in Na	Integral flux with Bonner Ball
YAYOI[6]	Pure Na (with iron layers)	YAYOI source reactor	≃ 100 x 100 x 180 (including iron plate at different positions)	In(n,n') Au(n,γ), LiF_6 TLD
HARMONIE[7]	Pure Na	HARMONIE source reactor with and without blanket type buffer	300 x 300 x 300 block	Au(n,γ), Mn(n,γ), Na(n,γ), Rh(n,n'), S(n,p) and proton recoil at selected positions
TAPIRO[7]	Pure Na	TAPIRO source reactor with and without blanket type buffer	100 x 100 x 150 block	see HARMONIE
ASPIS[8]	Pure Fe	Fission plate converter	≃ 190 x 190 x 140 block	Proton recoil spectra at several penetrations. Au(n,γ), Rh(n,n'), In(n,n'), S(n,p)
YAYOI[9]	Pure Fe	YAYOI source reactor	≃ 94 x 94 x 70	In(n,n'), Au(n,γ) etc
ORNL[10]	Pure Fe (or SS slabs)	Tightly collimated source	≃ 150 x 150 x 100 (≃ 150 x 150 x 40)	Bonner Ball and other spectrometers
EURACOS[11]	Pure Fe	Converter plate	≃ 150 x 150 x 100	S(n,p), Au(n,γ), Dy(n,γ
PROTEUS[12]	Pure Fe	PROTEUS source reactor	Cylinder R = 60, z = 80	Rh(n,n'), In(n,n'), S(n,p) and proton recoil
TAPIRO[7]	SS/Na mixtures : 75/25, 50/50, 25/75 v/o	TAPIRO source reactor with blanket type buffer	100 x 100 x 150	Au(n,γ), Mn(n,γ), Na(n,γ), Rh(n,n'), S(n,p) and proton recoil (1 position)

From the previous table, three main types of measurements can be individuated, namely activation measurements, integral spectrum measurements (Bonner Ball), and differential spectrum measurements. No unique technique has been adopted to define the source, calculation and experiment playing complementary roles.

Basic data

The main data involved both in the shielding design of a fast power plant and the analysis of the above mentioned integral experiments, are the sodium and the stainless steel data by isotope. A recent comprehensive review of data needs for shielding calculation can be found in reference 13. Here, we will recall only the principal features of the present state of basic data assessment from the user point of view. The present major basic data files (e.g. ENDF/B and UKNDL) include detailed compilations for all the isotopes of interest. Extensive sensitivity analysis have indicated that specific partial cross sections in selected energy ranges are of particular interest, and that their uncertainties are responsible for significant uncertainties in design parameters[14]. Total cross sections minima play of course a major role in deep penetration calculations, but the quality of inelastic cross sections will also affect significantly the basic data set performances. However, it has been stressed[15] that any future request for high accuracy measurements and for extensive re-evaluation, should include the request for evaluated uncertainty assessment and their correlations. The effects of these uncertainty matrices has been stressed but the only comprehensive effort in this field has been, with the exception of the Schmidt compilation[16], the compilation in the framework of the ENDF/B file evaluation[17]. Preliminary data released by ORNL in the form of 15 energy groups correlation matrices for iron and sodium[18] have been welcome as a first step for a better understanding of the role played by data uncertainties in shielding calculations. We will see some of the practical implications of these data in the integral experimental result exploitation in one of next paragraphes. A more complete compilation has to be found in the ENDF/B version 5

files which are at present not generally available outside the US. The need for the development and the use of such "error files" will certainly be a significant point in future improvements of shielding calculation accuracy.

The reduction of the basic data to multigroup data, introduces approximations which can be fairly important. The multigroup structure should also be optimized to include the main features of the most important cross sections. Usually, sensitivity studies are used for this purpose and several group structures has been proposed so far both at the level of hundred groups or more (DLC-2 100 group structure, Eurlib 100 group, Vitamin-C/E 171 group or the Babel 113 group[26]) and the few group structures like the Propane 45 group[20]. As far as the weighting procedure, it is generally agreed that collision density weighting (i.e. with a flux $\phi \simeq (E\Sigma_t)^{-1}$) should be used to reduce the data to the typical $\simeq$ 100 group schemes. But more elaborate procedures are necessary to take properly into account the self-shielding effects and the resonance interaction effects in mixture of several isotopes with resonance cross sections. The self-shielding factors method has been proposed, but the ultrafine group flux weighting procedure of such codes as the MCC-2[19], seems to be particulary valuable if these codes are equipped with full P_n capabilities for appropriate weighting of higher order scattering moments. More work is still needed in this area to clarify for deep penetration problems the relevance of algorithms already well known in data processing for core purposes, and no systematic study has been performed up to now to establish the magnitude of errors introduced in the weighting procedure. For the successive reduction of the multigroup data, from approximately one hundred to a smaller number, the space collapsing procedures and the optimization of the few group schemes, allow to reproduce the integral parameters calculated at the many group level, to a few percent[20].

Calculation methods and integral experiment analysis

It is usually assumed that the degree of sophistication in shielding calculations varies according to their scope.

Generally, design related calculations will benefit from semplified procedures and methods, as they are defined in shielding "formulaires". A typical example is described in reference 20.

The integral experiment analysis will involve sophisticated methods to avoid as far as possible to introduce method bias factors in the attempt to improve the knowledge of the basic nuclear data.

Two dimensional analysis are usually performed, based on the widespred S_N approximation with "ad hoc" choices of space-angular mesh grids[5,21,22]. The finite difference scheme and acceleration technique choice will also influence the degree of confidence of the experiment analysis. The Benchmark integral experiments for data improvement, which are the main subject of the present paper, do not need in general Monte-Carlo calculations, which are mainly used in mock-up type integral experiment analysis.

As it was mentioned in the previous paragraph, the reduced energy group schemes ($\simeq$ 10-50 groupes) which are used in the multidimensional analysis, impose special space dependent group collapsing procedures[20,6], which can strongly influence the calculations. This is applicable to detector cross sections too, in particular threshold detectors. Obviously, the few group optimized structures are best suited to point out the spatial regions of strong spectrum variation.

A powerful tool in the integral experiment analysis is the sensitivity analysis which uses the methods of the generalized perturbation theory[23]. Outstanding examples of the the use of this type of analysis, are the detection of the strong importance of the $\simeq$ 300 Kev minimum in sodium by Oblow and Weisbin[24], and the sensitivity analysis to exploit detailed spectral informations performed by Mc Craken[25], with the use of a special adjoint source calculation.

Sensitivity analysis is used to point out cross sections and energy ranges of special interest, to perform the so-called uncertainty analysis and to perform consistency analysis or cross section adjustments. Examples of these procedures related to specific experiments will be considered in a later paragraph.

Recent developments in perturbation theory which are of interest in shielding data improvement, are the higher order perturbation methods[26] which can allow to take into account non-linear effects.

Integral experiments and shielding design parameters

In this section we will examine the following problems :

- design integral parameters and their experimental counterpart
- representativity of the integral experiments
- relative sensitivity to cross section uncertainties of both design parameters and integral experiment responses
- reduction of the C/E of the integral experiment to design bias factors
- role of cross section adjustments.

Design integral parameters and their experimental counterpart

We will try first to outline what are the integral response functions measured in the integral experiments that better reproduce the reference integral parameters. This will be done mainly in terms of attenuation in specific media, e.g. thermal equivalent flux in Na both in the reference configuration and in the integral experiments. In figure 1 the total flux attenuation in the reference configuration is compared respectively to the Bonner Ball detector response (as used in the TSF at ORNL[5]) and to the $Mn(n,\gamma)$ and $Na(n,\gamma)$ responses (as used in the Harmonie and Tapiro experiments[7]).

In figure 2 the ϕ_{theq} attenuation is com-

pared to the Au(n,γ) response in the appendix reference configuration. These trends are confirmed in the integral experiment configurations, see figs 3-4, i.e. the Au(n,γ) response is fairly well representative of the thermal equivalent flux attenuation both in the reference and in typical integral experiments, and the same can be said of the Mn(n,γ) (and Bonner Ball) response and the total flux. Finally the Rh(n,n') is known to be fairly well representative of the damage function in stainless steel.

This is not, of course, a unique choice but it is intended to represent common trends in integral experiment parameters and their reference counterparts.

Representativity of integral experiments

Attenuation. To assess the representativity of an integral experiment it is necessary to verify that the source used in the integral experiment will not be responsible for a neutron propagation too different from the reference situations. A typical case is of course the neutron propagation in sodium. In Fig. 5 several spectra are shown relative to possible neutron source spectra to be found in actual design configurations. The curve 1 and 2 are representative of the spectra that can be found in the integrated shield design, described in the introduction, and located behind the lateral shield at two different heights, central plane, z = 0 (curve 1) and fuel assembly upper limit, z ≃ 200 cm (curve 2). The curve 3 is representative of the source spectrum that will be found behind an integrated B_4C lateral shield (at z = 0.). These spectra will produce the following attenuations in 250 cm of sodium :

Attenuation on :	Source of curve 1 behind SS/Na shield	Source of curve 2 behind SS/Na shield	Source of curve 3 behind B_4C shield
$\phi_{th\ eq}$	0.01	0.02	0.133
ϕ_{total}	0.0023	0.007	0.011

Similar attenuations have been found in many typical integral experiments in Na :

Attenuation on :	HARMONIE		HARMONIE with blanket	
	250 cm in Na	120 cm in Na	250 cm in Na	120 cm in Na
Au (n,γ)	0.008	0.15	0.012	0.23
$\phi_{th\ eq}$	0.011	0.20	0.018	0.30

Attenuation on :	ORNL TSF	TAPIRO with blanket	YAYOI
Bonner Ball response	0.017*	-	-
Au(n,γ)	-	0.07	0.08
$\phi_{th\ eq}$	-	0.094	-

* Deduced from two separate experiments

These attenuations are related to neutron propagation starting from different sources. In Fig. 6 we show typical source sentivities related to ≃ 120 cm and 250 cm propagation, i.e. the sensitivities to the source spectrum of the following integral parameters

$$a_1 = \phi_{tot1}/\phi_{tot2}$$

$$a_2 = \phi_{tot2}/\phi_{tot3}$$

where $\phi_{tot\,i}$ is the total flux defined at penetration i (i=1 0., i=2 120. and i=3 250 cm in sodium). These sensitivities, when folded with different source spectra (see Fig.7 for the case of Harmonie), give rise to the different attenuations shown in the previous table.

From these sensitivities it is evident that uncertainties in the source values both experimental and/or calculated (± 20% in typical cases), will not influence the calculated attenuation on the main integral parameters.

In conclusion, we see that the experimental configurations are fairly well representative of the reference (design) configurations of neutron propagation in sodium.

We will now consider the propagation in stainless steel/sodium media. Typical attenuations found are as follows :

Attenuation on :	Inside lateral shield (100cm)	End of axial SS/Na shield (80/20 v/o) (100 cm)
ϕ_{tot}	0.0013	5.45x10-4
SS damage	0.0014 (*)	6.6 x10-3(*)
$\phi_{th\ eq}$	0.002	8.4 x10-4

* Relative to ≃ 60 cm propagation

Integral experiment configurations give the following results :

Attenuation on :	TAPIRO SS/Na 50/50 v/o exper. (≃ 100 cm propag)	TAPIRO SS/Na 75/25 v/o exper. (≃ 100 cm propag)	ASPIS Fe experim. (≃ 100 cm propag.)	SS theor. config. (≃ 100 cm) (**)
Mn(n,γ) response	0.001	0.00029	0.017	7.5×10^{-5}
Rh(n,n') response	0.0027(*)	0.0013(*)	0.013(*)	-
Au(n,γ) response	0.0025	0.00067	0.025	1.7×10^{-4}
ϕ_{tot}	0.0006	0.00016	0.0013	4.8×10^{-5}
$\phi_{th\ eq}$	0.0020	0.00061	0.024	1.4×10^{-4}

* Relative to ≃ 60 cm propagation
** Pure stainless steel theoretical configuration

Here again we can notice the representativity of the Tapiro experiments.

In Figs 8-9 we show the source sensitivity profiles for all the above configurations,

that confirm that similar sensitivities are found in the Tapiro experiment and in the reference design configuration. On the contrary, stainless steel and iron blocks will show largely different sensitivity profiles.

Cross section sensitivity. We will now consider the representativity of the integral experiment from the point of view of the sensitivity to cross section and their uncertainties. The preliminary ORNL data for iron and sodium covariance matrices[18] were considered in the form of the 45 multigroup energy structure of the Propane shielding "formulaire[20]." In the following tables we present the standard deviation on relevant integral parameters related both to design and to integral experiments for neutron propagation in sodium (table I) and in stainless steel/sodium mixtures (table II).

TABLE I. Neutron propagation in sodium
Sensitivity to sodium cross sections

	Standard deviation (rel. values)
Au(n,γ) response (120 cm attenuation)	0.05
Au(n,γ) response (240 cm attenuation)	0.15
$\phi_{th\ eq}$ (450 cm attenuation)	0.42
$\phi_{th\ eq}$ (250 cm attenuation)	0.15

In this table, the last two responses are relative to the reference configuration of the appendix and they correspond roughly to the $\phi_{th\ eq}$ on the secondary heat exchanger due to the neutron penetration through the upper axial shield and to the lateral shield, respectively.

TABLE II. Standard deviation (rel. values)

	Reference lateral shield (≃ 180 cm propag.)	TAPIRO SS/Na 50/50 v/o conf. (≃ 100 cm propag.)	ASPIS Fe experiment (≃ 100 cm propag.)	SS theor. config. (≃ 100 cm propag.)
ϕ_{tot} response	0.10	0.04	0.09	0.05

Neutron propagation in stainless steel. Sensitivity to iron cross sections

In Fig. 10 the corresponding sensitivity profiles of the reference and Tapiro configurations are compared. The two profiles are very similar and scaled by a factor due to the different penetrations (≃ 100 cm in the Tapiro experiment and 180 cm in the reference lateral shield case).

Iron and steel block sensitivities are shown in Fig. 11. It is evident in this case that very different profiles will be found in such experiments;which could be used to check the results (and possible adjustments) obtained in a steel/sodium experiment.

In conclusion, from all these data it is clear that the integral experiments can be a useful source of information on the quality of data, but that the present state of the preliminary uncertainty evaluations, allows only a limited amount of the possible C/E discrepancies, to be explained with data uncertainties. This situation poses the problem of the confidence in these new evaluated uncertainty data and of their careful future improvement.

Reduction of the C/E of the integral experiments to design bias factors

Using the discussions of the previous paragraphs, it is possible to outline a tentative procedure to correlate the experimental C/E for selected measured parameters to specific design parameters.

Thermal equivalent flux and total flux in sodium

The E-C/C values of the Au(n,γ) response can be used. The standard parameter which represent the propagation in sodium, is the inverse of the attenuation of the above mentioned response, i.e. Au(n,γ)position2/An(n,γ)position1, position 1 being at zero penetration. This parameters "a" can vary in a single experiment (decreasing with increasing penetration) and from experiment to experiment, as a function of the source spectrum and geometry.

Available experimental data could than be used to find bias factors for the $\phi_{th\ eq}$, and their uncertainties. The ratios considered are fairly independent of detector cross sections. Only self-shielding and spatial weighting give rise to differences to the detector cross sections in positions 1 and 2, and these are small effects (see previous paragraph). Moreover, we have already seen that these ratios are only slightly influenced by experimental source uncertainties (up to ≃ 30% in spectrum or angular definition,gives rise to ≃5% in the ratio).

In Fig. 12 the (E-C)/C and their associated uncertainties for the same response (Au(n,γ)) in different integral experiment configurations at the same penetration (≃ 120 cm in Na), are used to deduce for the $\phi_{th\ eq}$ in the reference configuration (and at the same penetration), a bias factor of 1.22±0.15.

A futher example is shown in Fig. 13. In this case we considered the total flux, and we used the Mn(n,γ) response in Harmonie and Tapiro and the Bonner Ball response in the TSF experiment. Bias factors of 1.30±0.15 and 1.45±0.15 could be deduced for penetrations of 250 and 300 cm in sodium.

Total flux and steel damage in sodium/steel mixtures

Preliminary results in the Tapiro SS/Na 50/50 experiment give the trends indicated in Fig. 14, where the values are relative to the Na(n,γ) and Rh(n,n') experimental responses. Bias factors could be deduced from the complete set of measurements in the different mix-

tures, as function of the stainless steel percentage both for the total flux and for the steel damage response function.

However, it would be more complicated to extrapolate these bias factors to larger penetrations and to different media, or to the locations where the geometrical modeling would play a major role. At this regard, it is useful to remind that the bias factors have to be applied to design calculations that have the same degree of approximation of the experimental analysis calculations. In fact, since all the bias factors are deduced from two dimensional calculations, usually in 45 energy groups S_8 P_3 with ad-hoc spatial cross section weighting (see paragraph above), supplementary uncertainties have to be applied to design calculations when a simplified "formulaire" is used[20].

The role of cross section adjustments

Large bias factors, the need to extrapolate to different situations (i.e. with much larger penetrations) and the use of experimental responses instead of the actual design parameters, advice to a careful use of experiments to assess bias factors and indicate that the improvement of the basic data is still strongly needed. Cross section adjustment procedures, based, when possible, on a consistent method[21] can give significant indications for evaluated data and uncertainties modifications.

The present evaluations do not allow large adjustments to the integral parameters due to data, as we have seen in a previous paragraph. Some attempts have been made for iron and sodium[21,22,24,25].

The iron inelastic cross sections, both derived from ENDF/B-IV and from UKNDL were found to be too high, i.e. too much degradation has been calculated at high energies (> 5 Mev)[21,22,24,25]. No definite conclusion has been drawn on the contrary for the same cross section between 1 and 5 Mev. It is necessary to stress, however, that the adjustment attempts have been made independently and on separate integral experiments.

The sodium total cross section seems to be responsible at least in part for the somewhat low C/E found in the Yayoi, Tapiro and Harmonie sodium experiments[6,7,22]. But the adjustments obtained[22], are only in part in agreement with the adjustment attempted at ORNL on the TSF experiments[5]. Further light will be thrown by new analysis of the already existing experiments, hopefully in the framework of more cooperative efforts.

However, once significant adjustments will be derived, a bias factors assessement procedure can be used such as the one previously outlined. The residual (i.e. after adjustments) (E-C)/C should be used with their associated uncertainties.

Conclusions

The analysis of integral experiments of neutron propagation in simple media of interest for fast reactor shielding, can throw light on the transport methods and on the basic cross sections used. Some general trends can also be used to assess design oriented bias factors and some possible cross section adjustments.

In this delicate task, more experimental evidence, together with methods and data intercomparison, is still needed.

Acknowledgments

This work resumes some of the results obtained and some of the ideas developed in the course of a joint CNEN (Italy)/CEA (France) effort on fast reactor shielding. Moreover, the author gratefully acknowledges the many fruitful discussions with G. Palmiotti.

References

1. Proceedings of the Spec. Meet. on sensitivity studies and shielding Benchmark, OECD Paris 1975.

2. Proceedings of the Spec. Meet. on differential and integral nuclear data requirements for shielding, NEA/IAEA, Vienna 1976.

3. V. Herrnberger et al, Required target accuracies, in Ref. 1.

4. J.Y. Barré, Fast reactors : definition of a standard configuration for the comparison of shielding calculations, see Ref. 2.

5. R.E. Maerker et al, Measurements and calculations of the ORNL CRBR upper axial shield experiment, ORNL-5259 (1977).

6. Y. Oka et al, Two dimensional shielding Benchmark for sodium and iron at Yayoi, Proc. fifth Int. Conf. on Reactor Shielding, Knoxville 1977.

7. J.C. Estiot et al, Use of integral data for the prediction of the penetration in iron sodium mixtures, Ibidem.

8. M.D. Carter and A. Packwood, The Winfrith Benchmark experiment in iron. Experimental results, in Ref. 1.

9. S. An et al, Iron shielding Benchmark Experiments at Yayoi, in Ref. 1.

10. R.E. Maerker and F.J. Muckenthaler, Final report on a Benchmark experiment for neutron transport through iron and stainless steel, ORNL-4892 (1974).

11. G. Perlini, First measurements at EURACOS-II, NEA spec. Meet. on the analysis of shielding Benchmarks, Paris Nov. 1977.

12. K. Gmür et al, The PROTEUS iron shielding Benchmark experiment, ibidem.

13. J. Butler, Nuclear Data for shielding, Proc. Int. Conf. on neutron physics and Nuclear Data, Harwell, Sept. 1978.

14. M. Salvatores, Design sensitivity and un-

certainty analysis of fast breeder reactor shiedl, in Ref. 2.

15. J. Butler, The evolution of shielding methods and data, Proc. fifth Int. Conf. on Reactor Shielding, Knoxville 1977.

16. J.J. Schmidt, Neutron cross-sections for fast reactor materials - Part I : evaluation, KFK-120 (EANDC-E-35U) (1966).

17. F.G. Perey, The data covariance files for ENDF/B-V, ORNL-5938 (1977).

18. J.D. Drieschler and C.R. Weisbin, Compilation of multigroup covariance matrices for several important reactor materials, ORNL-5318 (1977).

19. H. Henryson II et al, MC^2-2 - A code to calculate fast neutron spectra and multigroup cross sections, ANL-8144 (1976).

20. J.C. Estiot et al, Theese Proceedings.

21. A. d'Angelo et al, Nucl. Sci. Eng. 65, 477 (1978).

22. A. de Carli et al, Theese Proceedings.

23. A. Gandini, Nucl. Sci. Eng. 67, 91 (1978).

24. E. Oblow and C.R. Weisbin, Fast reactor shield sensitivity studies for steel-sodium systems, Proc. Fifth Int. Conf. on Reactor Shielding, Knoxville 1977.

25. M.M. Chestnutt and A.K. Mc Cracken, The use of error files in uncertainty analysis and data adjustments, ORNL/RSIC-42 (1979).

26. A. Gandini, First and higher order perturbation techniques and their application, ibidem.

27. J.C. Estiot et al, Consequences des incertitudes sur les données de base dans les calculs de protection, Proc. Int. Conf. on neutron physics and nuclear data, Harwell, Sept. 1978.

Appendix

Benchmark 1D geometry for fast reactor shield

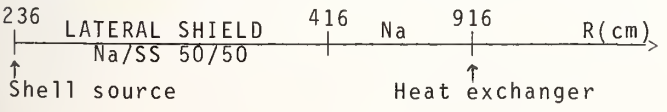

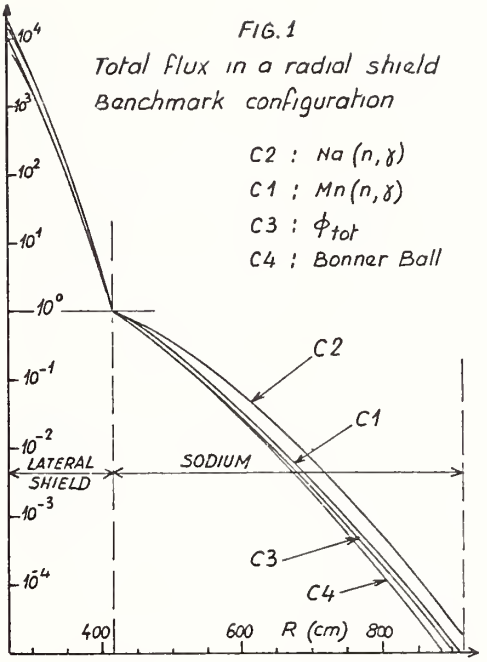

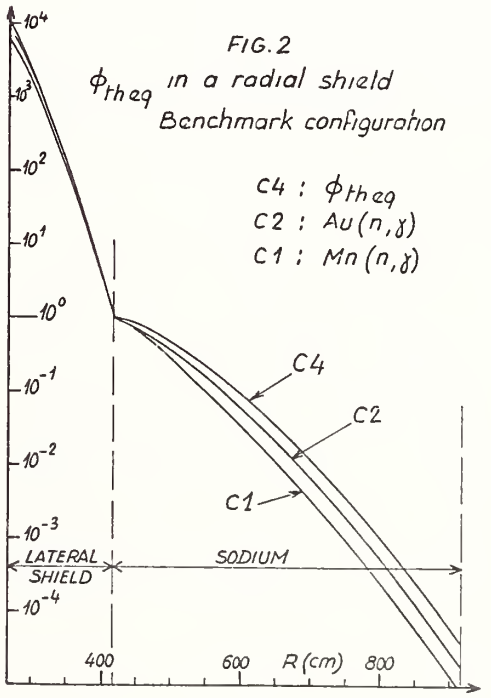

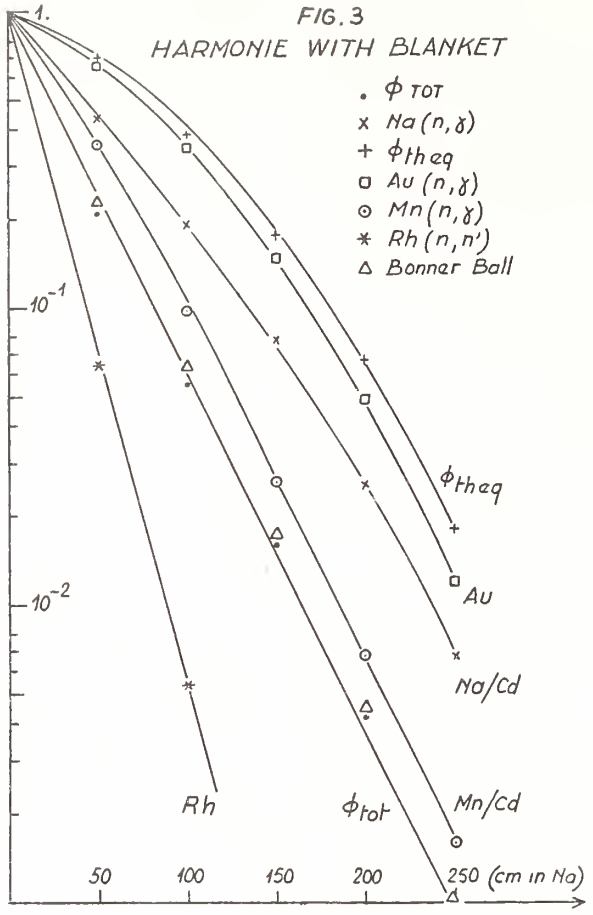

FIG. 3
HARMONIE WITH BLANKET

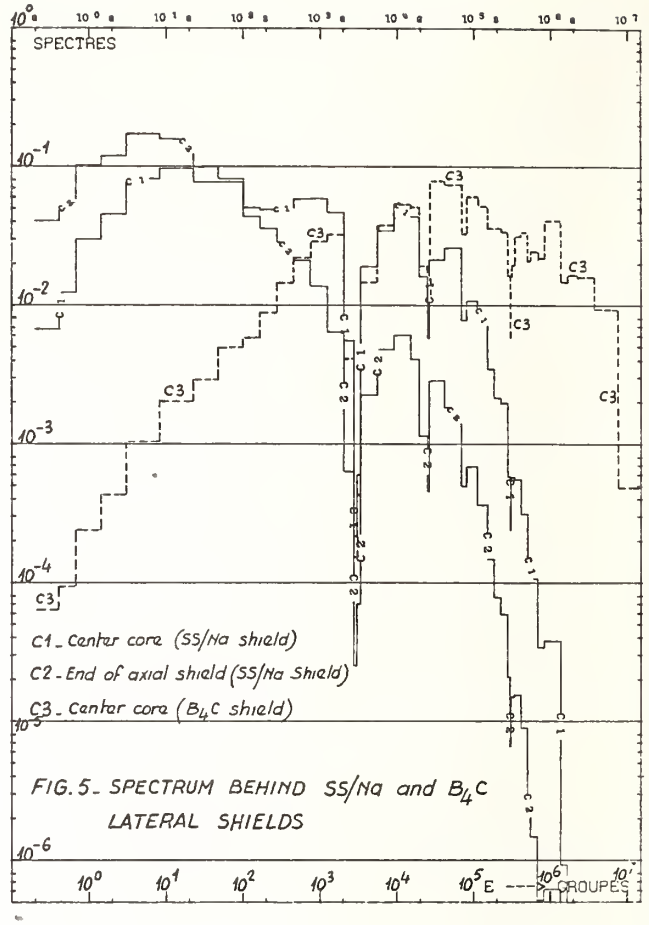

FIG. 5 - SPECTRUM BEHIND SS/Na and B_4C LATERAL SHIELDS

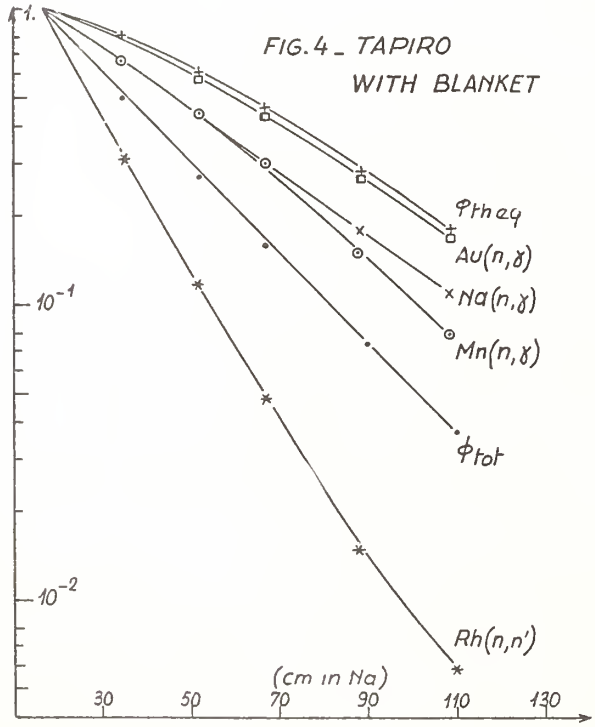

FIG. 4 - TAPIRO
WITH BLANKET

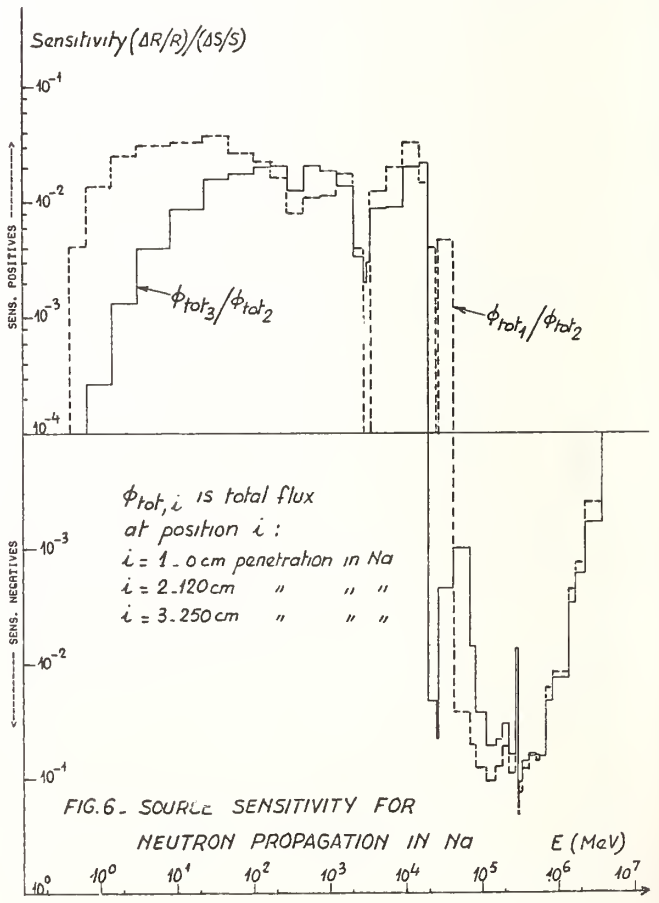

FIG. 6 - SOURCE SENSITIVITY FOR
NEUTRON PROPAGATION IN Na

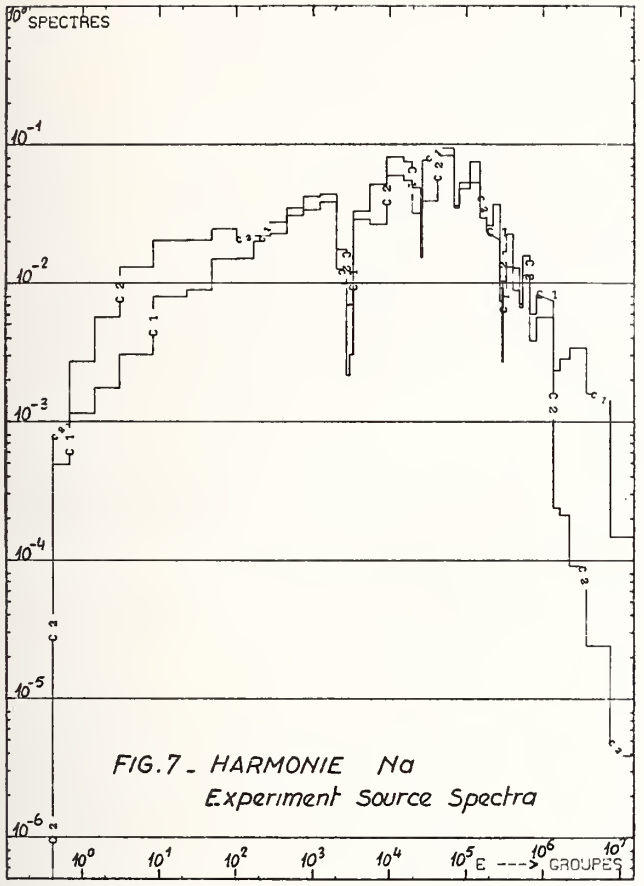

FIG. 7 - HARMONIE Na Experiment Source Spectra

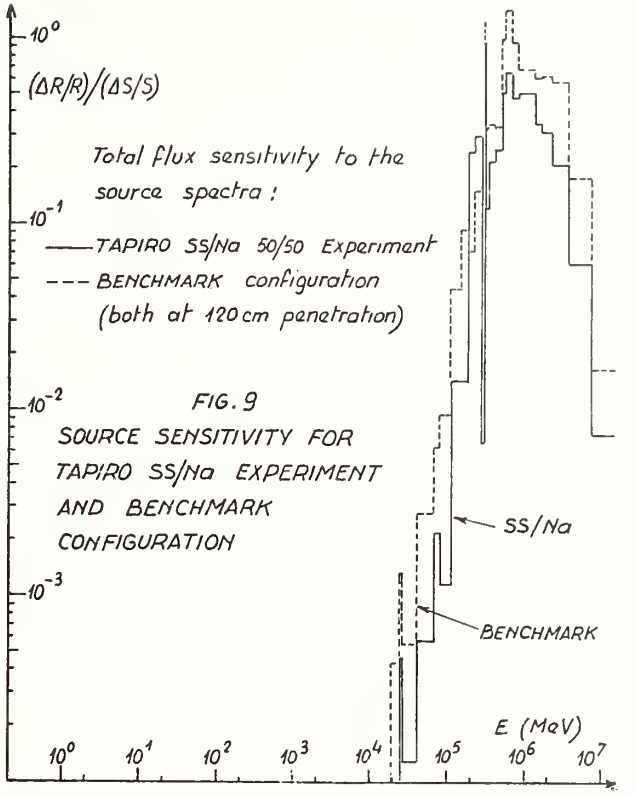

FIG. 9 SOURCE SENSITIVITY FOR TAPIRO SS/Na EXPERIMENT AND BENCHMARK CONFIGURATION

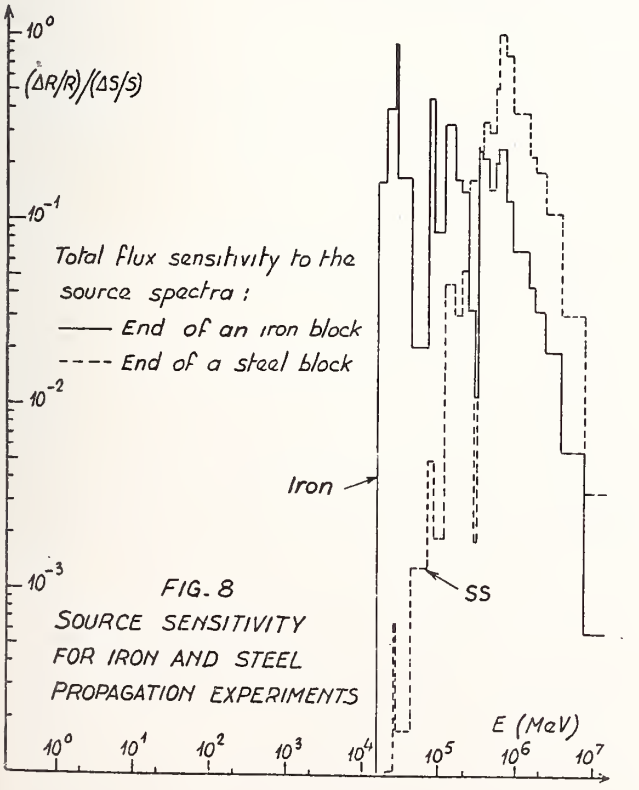

FIG. 8 SOURCE SENSITIVITY FOR IRON AND STEEL PROPAGATION EXPERIMENTS

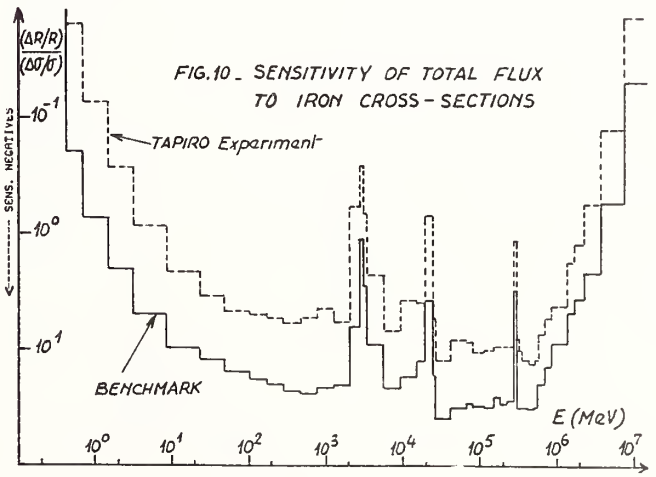

FIG. 10 - SENSITIVITY OF TOTAL FLUX TO IRON CROSS-SECTIONS

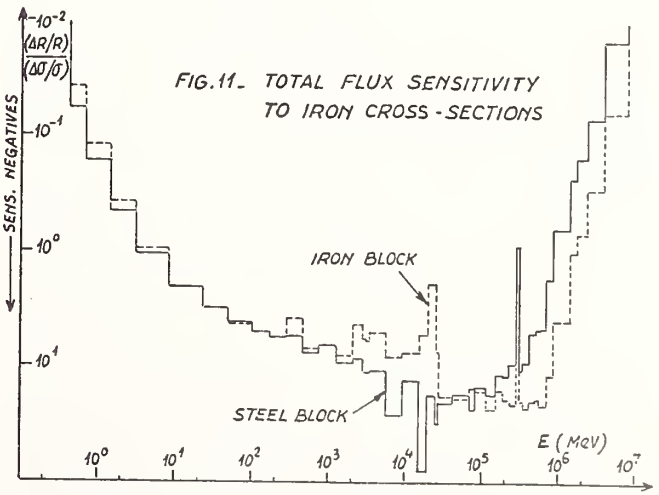

FIG. 11 - TOTAL FLUX SENSITIVITY TO IRON CROSS-SECTIONS

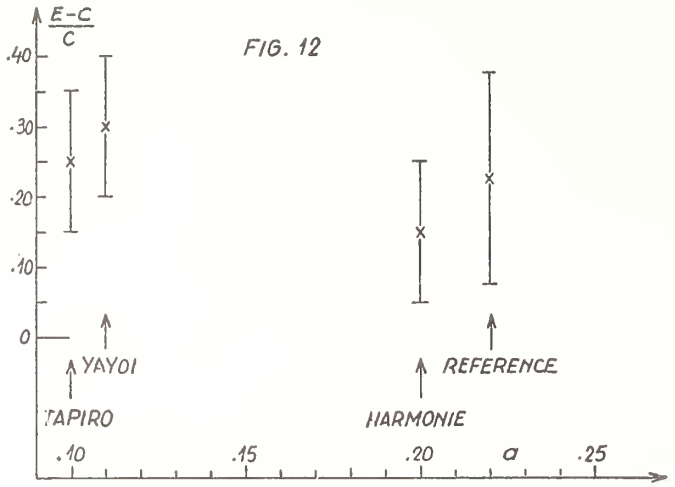

FIG. 12

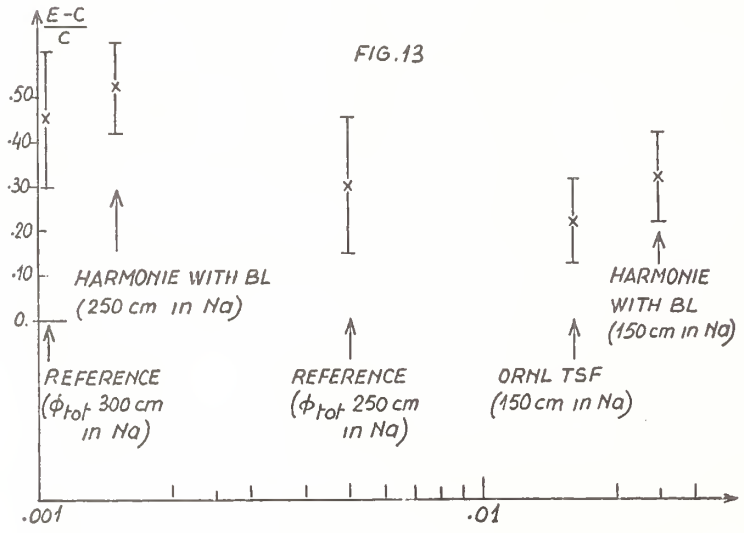

FIG. 13

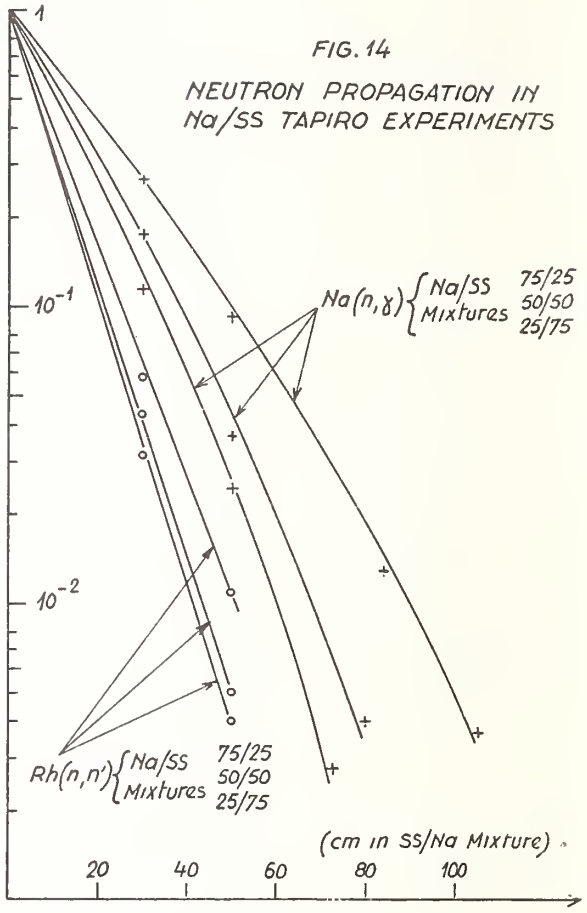

FIG. 14

NEUTRON PROPAGATION IN Na/SS TAPIRO EXPERIMENTS

NEUTRON DOSIMETRY FOR RADIATION DAMAGE IN FISSION AND FUSION REACTORS

Donald L. Smith
ARGONNE NATIONAL LABORATORY
9700 South Cass Avenue
Argonne, Illinois 60439, USA

The properties of materials subjected to the intense neutron radiation fields characteristic of fission power reactors or proposed fusion energy devices is a field of extensive current research. These investigations seek important information relevant to the safety and economics of nuclear energy. In high-level radiation environments, neutron metrology is accomplished predominantly with passive techniques which require detailed knowledge about many nuclear reactions. The quality of neutron dosimetry has increased noticeably during the past decade owing to the availability of new data and evaluations for both integral and differential cross sections, better quantitative understanding of radioactive decay processes, improvements in radiation detection technology, and the development of reliable spectrum unfolding procedures. However, there are problems caused by the persistence of serious integral-differential discrepancies for several important reactions. There is a need to further develop the data base for exothermic and low-threshold reactions needed in thermal and fast-fission reactor dosimetry, and for high-threshold reactions needed in fusion-energy dosimetry. The unsatisfied data requirements for fission reactor dosimetry appear to be relatively modest and well defined, while the needs for fusion are extensive and less well defined because of the immature state of fusion technology. These various data requirements are examined with the goal of providing suggestions for continued dosimetry-related nuclear data research.

[Neutron dosimetry, radiation damage, fission, fusion, reactors, radioactivity, cross sections.]

Introduction

The widely-publicized incident at the Three-Mile-Island plant has taught us that the costs inflicted by a malfunctioning nuclear reactor are very high. The expense of bringing the facility back on line and of purchasing power from other sources during the interim period must be added to the inestimable effect of shaken public confidence in nuclear energy. Electric utilities must have reactors which will operate safely and reliably for many years. Extensive research and development is needed to meet this requirement because of the existence of complex engineering problems, unprecedented materials science phenomena and uncertainties resulting from incomplete quantitative understanding of fundamental atomic and nuclear processes.

An understanding of the scale of nuclear reactor parameters is necessary before one can truly appreciate the magnitude of this issue. Some statistics on operating power reactors may help to provide perspective: The core power density for a commercial light-water reactor (LWR) is ~30-100 KW/liter. This is ~60-200 times larger than for a 100 W light bulb. Most units under construction in the U.S. will produce $\gtrsim$1000 MWe. Operating pressures of >1000 psi for a boiling-water reactor (BWR) and >2000 psi for a pressurized-water reactor (PWR) must be withstood by the pressure vessel (PV). Operating temperatures of several hundred degrees centigrade are typical. PVs are enormous: ~10-15 meters high by ~5-7 meters diameter with steel walls ~20 centimeters thick. Commercial nuclear plants are productive (~2 x 10^8 U.S. dollars of electricity per year) but very capital intensive (~2 x 10^9 U.S. dollars to build a plant). Structural components of reactors experience radiation damage in addition to conventional wear produced by high temperatures and pressures. In one full-power year, the interior of the PV receives a neutron dose $\lesssim 10^{18}$ n/cm^2 (>1 MeV). Measurable property changes have been observed for PV steel at fluences >10^{19} n/cm^2 (>1 MeV), but this depends on the spectrum and the operating temperature history as well as on material properties. Ten nuclear plants in the U.S.A. are >10 years old. The issue of reactor lifespan is of a paramount social and economic importance.

The scope of this paper is very broad; it encompasses operating problems for thermal power reactors (e.g. LWRs), developmental problems for fast breeder reactors and conceptual problems for controlled fusion reactors. This review is an overview of the field. The primary goal is to aquaint nuclear data people with some nuclear data needs for reactor dosimetry. The motivations for dosimetry transcend damage problems and include other important topics (fuel burnup, shielding, etc.). There have been major advances in data development and neutron metrology during the last decade. This is evident from the dramatic change in accuracy expectations for fast reactor metrology (see Fig. 1). Published references on the subject are extensive. This paper will not attempt to credit all sources of material used in the review, but will list mostly those references considered useful to readers who might wish to pursue certain aspects of the subject in more detail.

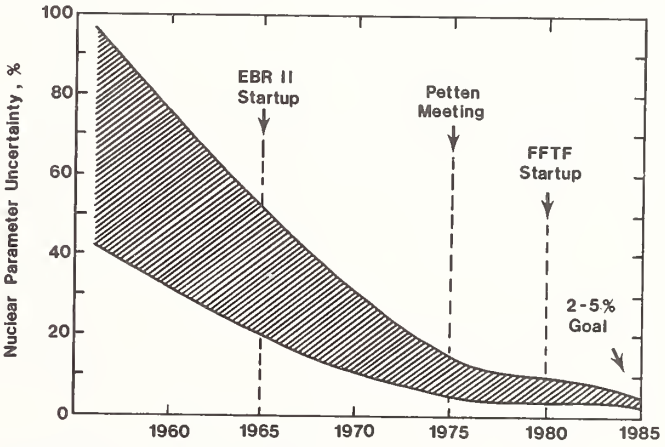

Fig. 1. Chronology of accuracy expectations for U.S. fast reactor neutron metrology [after McElroy et al., Ref. 1].

Fundamentals of Neutron Dosimetry

Concepts

There is no simple relationship between materials damage and the neutron dose. Nevertheless, a review of the field should begin with a consideration of the fundamentals of neutron metrology. Awareness of the characteristics of reactor neutron spectra is needed in order to understand damage phenomena. Figure 2 provides qualitative insight. Since wide dynamic ranges of energy and flux are encountered, logarithmic scales

and the parameter lethargy μ, defined as $\ell n(E/E_0)$, are often used when discussing reactor spectra. Neutron flux, represented by $\phi(E,t)$ or $\Phi(t)$, refers to neutron intensity in units of $n/cm^2/sec/MeV$ or $n/cm^2/sec$ (if all energies are considered). Fluence refers to the time integrals of these quantities and is expressed in dose units. Reactor people usually refer to (nv) or (nvt) which are the energy differential flux and fluence, respectively, for neutron density n and velocity v (e.g. Ref. 3). Often the variable t is dropped and $\phi(E)$ or Φ is used when referring to the neutron spectrum or its energy integral. The function $\phi(\mu)$ is equivalent to $E\phi(E)$. Group fluxes or fluences refer to total neutron intensity in an energy interval $\Delta E\phi(E)$, or lethargy interval $\Delta\mu\phi(\mu)$. An energy dependent process is represented by $\omega(E)$. The response R of ω in spectrum ϕ is the product $\omega\phi$. The observable I is an integral quantity

$$I = \int_0^\infty R(E)dE = \int_0^\infty \omega(E)\phi(E)dE \quad . \qquad (1)$$

The function ω may be a reaction differential cross section σ in which case I is a reaction rate. I is then related to the spectrum average cross section $\bar{\sigma}$ ($I = \Phi\bar{\sigma}$). If ω is a damage function, then I is the observed damage rate associated with integrated flux Φ.

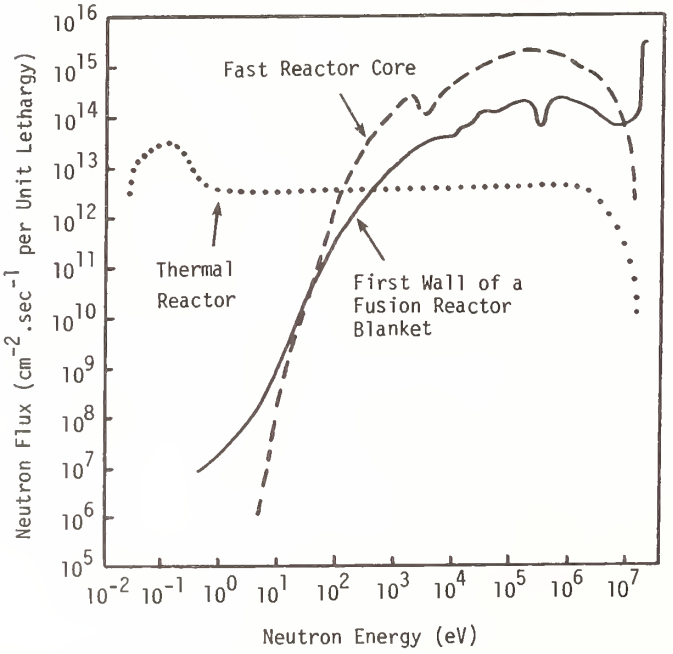

Fig. 2. Characteristic reactor neutron spectra [after Qaim, Ref. 2].

Dosimeter cross sections σ can be categorized as threshold or nonthreshold, activation or nonactivation, and fission or nonfission. Threshold reactions respond to flux above the threshold energy E_t, and the truncated average cross section $\bar{\sigma}_t$ is defined by

$$\bar{\sigma}_t = \int_{E_t}^\infty \sigma(E)\phi(E)dE \Big/ \int_{E_t}^\infty \phi(E)dE \quad . \qquad (2)$$

The 90% response range is the energy interval which contributes 90% to I in Eq. (1). Figure 3 shows 90% response ranges for several reactions in a spectrum like that which will be used for fusion material testing.

Non-threshold reactions may respond mainly to the lower energies of the spectrum (e.g. the 1/v and resonance region for capture reactions) or to most of the spectrum (e.g. U-235 or Pu-239 fission). Flat response reactions such as Pu-239 fission are insensitive to the spectrum shape above ~10 keV and are ideal flux integrators for fast-neutron spectra. This feature is used in calibrating fast reactors relative to absolute Cf-252 sources. Neutron metrology in the lower-energy regions of reactor spectra is hindered by resonance phenomena. Dosimetry differential cross sections there are not well known and uncertainties in flux depression factors (because of resonances in the total cross section) obscure the true reaction rates. The need to improve this state of affairs is motivation for further nuclear data research in the resonance region.

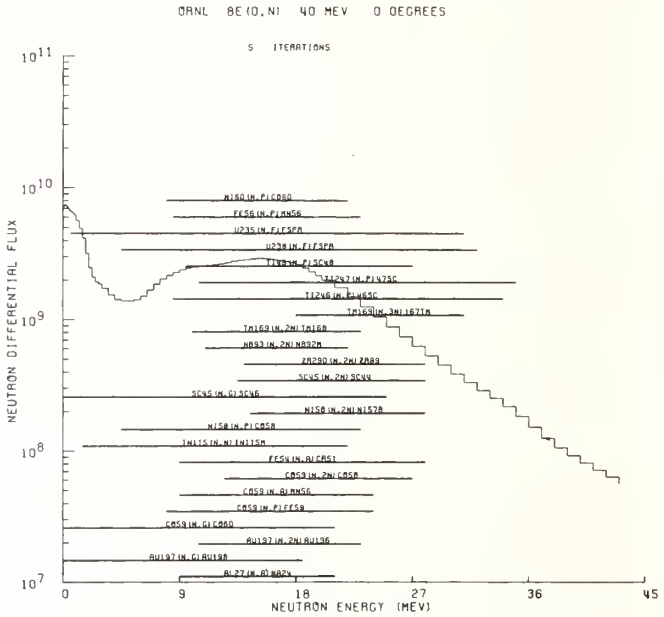

Fig. 3. Response ranges for several dosimetry reactions in a d + Be neutron spectrum [after Greenwood, Ref. 4].

Threshold reactions are useful spectral indicators. Two fundamental problems plague fission reactor dosimetry: One is a lack of suitable threshold reactions for the region 1 keV to 0.5 MeV. It is possible to shift the response range of nonthreshold reactions to higher energies by encapsulating monitor foils in Cd or B. It is not possible to shift the response to lower energies. The second problem is that above ~2 MeV all fission-based spectra have similar shapes and produce similar truncated responses for most threshold reactions (e.g. Fig. 4). Various threshold reactions provide redundant information about spectra because the response ranges overlap to a considerable degree in the MeV region. Another problem affects dosimetry for fusion reactor applications: Response ranges for threshold reactions are much broader for these spectra then they are for fission spectra. This affects the reliability of spectrum unfolding procedures.

Activation reactions are more widely used for dosimetry than nonactivation reactions. Long-half-life activation reactions ($\gtrsim$months) are essential for power reactor dosimetry since access is generally possible only during complete shutdown for refueling. Test reactors and critical assemblies are more accessible and shorter half-life monitors ($\gtrsim$minutes) are also useful for them (e.g. Ref. 5).

Fission reactions are very important for dosimetry because the cross sections are relatively well known and these processes can be used in active (fission chamber) measurements at low power and passive (fission products) applications at high power. Fission products offer a wide range of decay half lives which can be used for dosimetry purposes. Fission is beset by problems such as burn-in (growth of parasitic fissionable isotopes by capture) at high power and photofission. These effects complicate the interpretation of measured integral data (see Table I and Refs. 6-8).

Photofission corrections can be estimated with the aid of graded gamma-ray shields, but burn-in effects cannot be avoided. A subtle problem for threshold fission reactions is that the thresholds are poorly defined and the cross sections for the so-called "subthreshold" region are not well known.

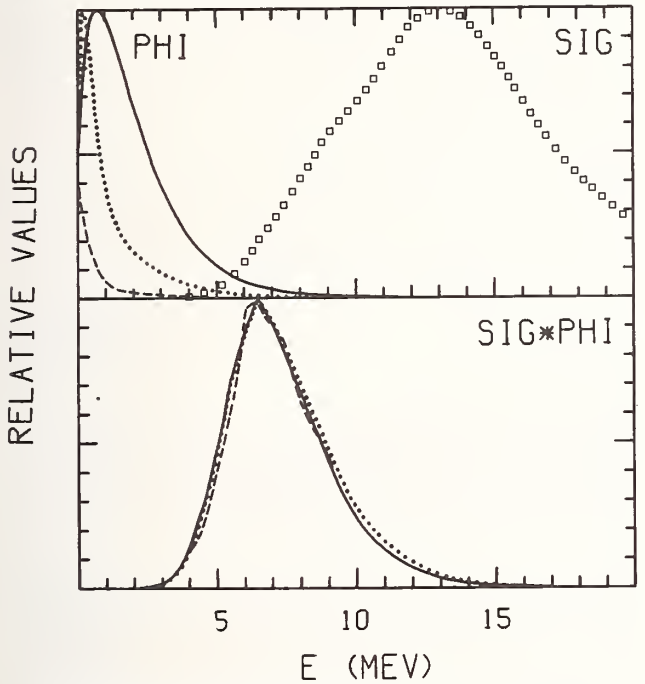

Fig. 4. Response function shapes for three different fission-driven spectra are nearly the same for a high threshold reaction.

Table I. Relative importance of photo fission at inner surface of pressure vessels. Cd is used to cover foil packets [after Bowman et al., Ref. 8].

	PWR			BWR		
Detector	Cd gammas	Reactor gammas	Reactor Neutrons	Cd gammas	Reactor gammas	Reactor Neutrons
U-235	3.80(-5)	1.08(-2)	1	6.09(-5)	2.91(-2)	1
U-238	1.90(-3)	0.476	1	2.28(-3)	0.962	1
Th-232	5.06(-3)	0.968	1	6.03(-3)	1.95	1

Spectrum Unfolding

Measurement of a series of spectrum sensitive observables I_i provides information which can be used to estimate the spectrum shape. It is necessary to solve the problem

$$I_i = \sum_{j=1}^{m} \phi_{ij}\, \sigma_{ij}\, \Delta E_j \qquad (i = 1, \ldots n) \quad . \qquad (3)$$

This is a version of the Fredholm integral problem of the first kind. Usually $m > n$ so no unique solution for ϕ exists. What is sought is a solution consistent with a preconceived form which is often based upon reactor Physics calculations. Various schemes for unfolding spectra from measured reaction rates and assumed differential cross sections have been developed. These have been discussed by Oster (Ref. 9) and Zijp et al. (Ref. 10) among others. The IAEA sponsored a critical comparison of several commonly used spectrum unfolding codes such as SAND-II, Crystal Ball, RFSP-Julich, etc. (see Refs. 9-11). The conclusion from this effort was that these various codes yield rather similar results provided that: i) the requisite trial spectrum does not differ substantially from the final solution, ii) the uncertainties in the integral quantities I_i are moderate, iii) the differential cross sections σ_i are realistic, and iv) the dosimeter response functions cover the spectrum well. As indicated above, it is generally not possible to cover spectra as well as desired with the response functions of available dosimeters. The energy region $\gtrsim$1 MeV is manageable for fission spectra. The lower limit for accurate spectrum unfolding is ~5 MeV for fusion-like spectra. Measurements $\lesssim$1 keV are complicated by resonance phenomena. Stallman and Kam (Ref. 12) have reported success in the use of linear programming techniques to generate artificial response functions with desired properties from combinations of the natural response functions of several dosimeter reactions. This "window function" method was conceived to deal with the region $\lesssim$1 keV. The gap from ~1 keV to ~0.5 MeV is problematic for fission spectrum dosimetry as indicated above.

Since spectrum unfolding methods do not usually yield unique results, it is reasonable to ask how one can deduce the most likely spectrum representation and estimate its uncertainty from available integral data and evaluated differential dosimetry cross sections. F. Perey addressed this problem and developed a least-squares procedure which answers this question in a rigorous manner (Ref. 13). A variation of this approach can also be used for performing unbiased evaluations of cross section data. The method uses techniques of matrix algebra and covariance matrices must be provided for the trial spectrum, for the differential cross sections, and for the integral reaction rates. This requirement is both a source of strength and of weakness in this approach. The strength lies in the fact that all uncertainties in the unfolding procedure are properly considered and the unfolded spectrum is the best estimate (in the least-squares sense) which the available information can provide. The weakness is that it is very difficult to provide realistic covariance matrix elements (especially off diagonal elements representing cross correlation effects). Use of inadequate matrix elements can thwart the process and lead to unreasonable results. It is generally accepted that the Perey formalism is a logical way to proceed - for the long run. Steps are being taken to implement it (e.g. inclusion of covariance matrices in ENDF/B-V). Experience gained over the next few years should establish whether it is a practical approach. In the meantime, it is likely that many other methods will continue to be used.

Neutron Damage Phenomenology

Determination of neutron flux (or fluence) and spectral shapes is only part of damage analysis. A fundamental understanding of microscopic and macroscopic damage phenomena is required to extrapolate results from damage studies in test facilities to the environment of power reactors.

The basic mechanisms of neutron damage have been discussed in several papers (e.g. Refs. 2, 14-19). Neutrons with energies of a few eV can rupture chemical bonds and participate in a few exothermic reactions, such as $^{58}Ni(n,\gamma)^{59}Ni(n,\alpha)^{56}Fe$ which produces gas in reactor structural materials. Above 40 eV, scattered neutrons can impart sufficient energy to Fe atoms in steel to displace them from the lattice. At ~1 MeV, neutrons can impart ~1000 times more recoil energy to Fe atoms than is needed to eject them from the lattice. Spectra of these recoil or primary knock-on atoms (PKA) can be calculated from a knowledge of neutron cross sections. The PKA propagate through the lattice producing more displacements until the available energy is exhausted. High-energy neutrons produce copious displacements. The term displacements per lattice atom (DPA) is used and DPA cross sections are calculated using models (e.g. the model of Kinchin-Pease, of Thompson-Wright and of Linhard). Analysis of this cascade process requires methods from atomic, molecular, and solid-state Physics. DPA cross sections determined

using various methods agree reasonably well for most important reactor materials.

DPA cross sections increase with neutron energy and may be >1000 barns in the MeV region (see Figs. 5 and 6B). During long periods of service it is very likely that most of the atoms of components located in high flux regions of a power reactor will experience displacement. Fortunately, most displacements are not permanent and much of the damage is eliminated by rearrangement of the lattice - especially at elevated temperatures (annealing). However, there are neutron-induced processes which hinder the annealing of displacement damage. All transmutation reactions produce some displacement by recoil, but the more important effect is a weakening of the lattice by introduction of foreign atoms. Even more serious are the hydrogen- and helium-producing reactions which become important at higher energies. The presence of gas in the lattice encourages the growth of voids produced by displaced atoms. This promotes swelling, creep and embrittlement of the material (Fig. 6C). Fracture resistance at elevated temperatures is reduced (Fig. 6A). The

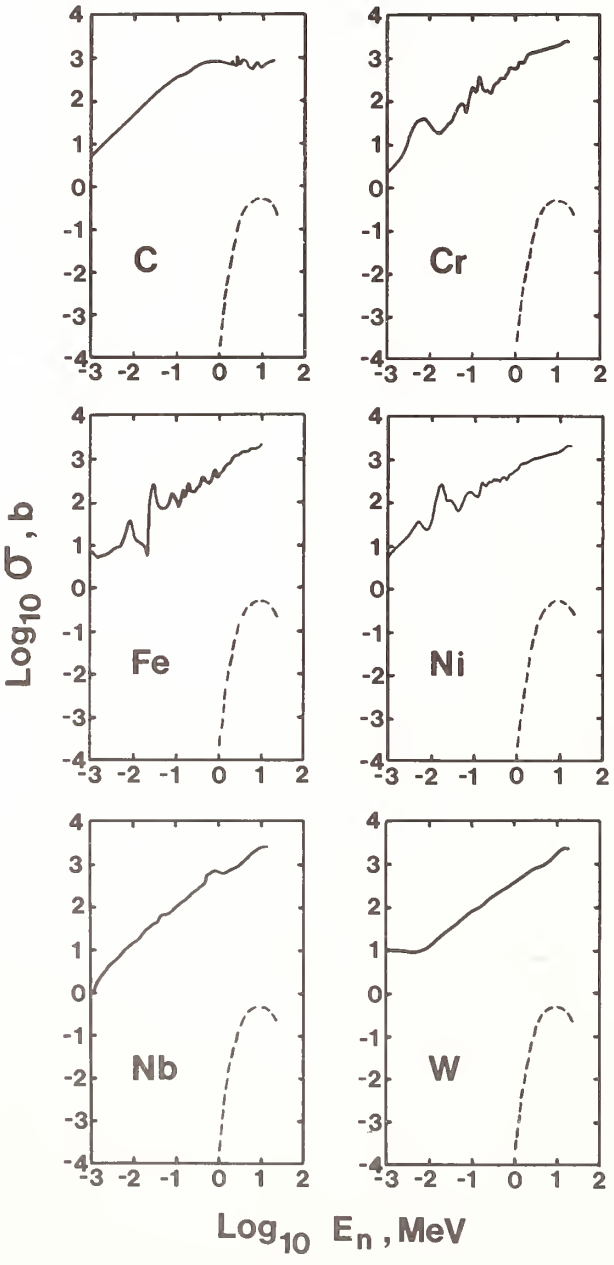

Fig. 5. Typical atomic displacement cross sections. Dashed line shows the $^{58}Ni(n,p)^{58}Co$ cross section for comparison. [after Zijp et al., Ref. 16].

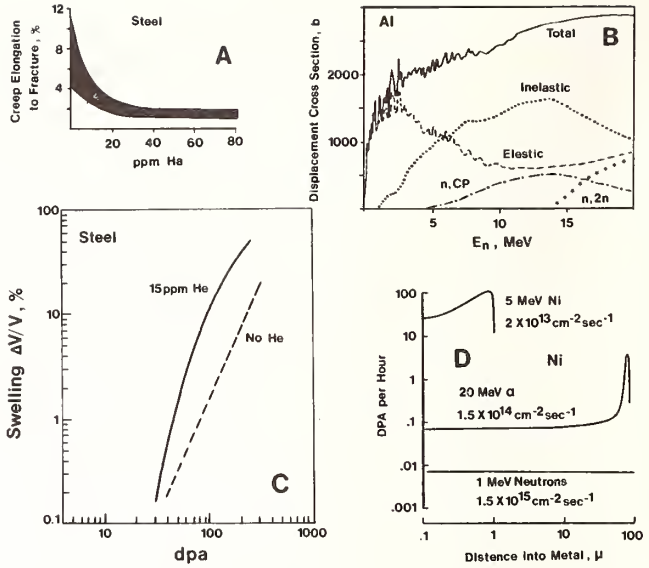

Fig. 6. Several aspects of damage phenomenology: A - Fracture resistance of steel is reduced by He [after Ullmaier et al., Refs. 20-21], B - Contributions to neutron-induced atomic displacements from various processes [after Doran et al., Ref. 19], C - Swelling vs. atomic displacement is affected by He [after Johnston et al., Ref. 22], D - Radiation damage produced by ion beams occurs near the surface whereas neutrons produce a more uniform effect throughout the volume [after Ullmaier and Schilling, Ref. 20].

presence of helium is more serious than hydrogen because hydrogen migrates out of the lattice at elevated temperatures while helium is more likely to be trapped. In reactor PVs where temperatures are lower, hydrogen production may be a significant problem.

The DPA parameter appears to be more useful for damage correlation than other common indicators (e.g. fluence >0.1 MeV or >1 MeV). However, the connection between DPA and macroscopic damage is neither simple nor well understood. Considerable research is being devoted to this problem. Gas production data files have been developed within the ENDF system. A library of DPA cross sections has been published in Europe (Ref. 16). Many irradiation experiments have been performed on reactor materials to study macroscopic damage. Ion beams readily produce atomic displacements, but the observed damage consists mainly of blistering and erosion near the surface owing to range limitations (Fig. 6D). Neutron irradiations under accelerated conditions in the core of test fast reactors such as EBR-II (U.S.A.) provide results which are not easily related to what might be expected in other environments (e.g. the PV of a LWR or the first-wall of a fusion reactor). This area of research will continue to be of paramount importance in the future.

Figures 5 and 6 show that effective thresholds for atomic displacements are relatively low, and the important damage response region for fission reactors (~50 keV to ~5 MeV) is only partially covered by activation dosimetry reactions. Effort is being directed toward developing the $^{103}Rh(n,n')^{103m}Rh$ and $^{93}Nb(n,n')^{93m}Nb$ reactions as activation dosimeters because they have low thresholds (~40 keV and ~30 KeV respectively). The response functions resemble those for DPA cross sections (Fig. 7). ^{103}Rh is better known, but a short half life (~56m) limits its application to low-power research reactors. ^{93}Nb is not well developed but has potential for power reactor applications because of a long half life (~13.6y). Further development of the data base for these reactions is an important task for the nuclear data community.

Damage Dosimetry Requirements and Programs

A review of all dosimetry-related requirements is beyond the scope of this paper. Here, an attempt will

be made to indicate some of the current damage dosimetry interests for the LWR industry, for fast-reactor development and for controlled fusion technology.

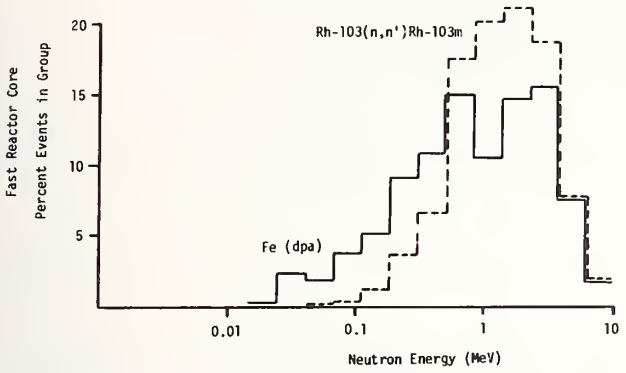

Fig. 7. Comparison of the response of Fe DPA and $^{103}Rh(n,n')^{103m}Rh$ in a fast reactor spectrum [after Sanders, Ref. 23].

LWR Industry

A major concern is longevity of the PV. The PV must last for the 40-year design life of the reactor. It has been proposed that in-situ annealing of the PV be used to remove some damage effects in welded joints of older units where the concentration of Cu and S is known to be high. Apparently, no attempt has been made yet to attempt this difficult task. Regulatory quidelines for PV surveillance (PVS) were established without a detailed understanding of damage phenomena. They may be excessively conservative, yet the results of periodic mechanical tests on specimens of irradiated PV steel must conform to these guidelines if the unit is to remain in operation. This is an important economic consideration. Dosimetry practices at most power reactors are of pre-1970 vintage and a factor of two improvement in dosimetry accuracy could be achieved using current fast-reactor techniques. Improvement of cross section data for the resonance region is required in order to better estimate resonance self-shielding in dosimeter packets. Furthermore, more accurate cross section data for some long-half-life, threshold activation monitors such as $^{54}Fe(n,p)^{54}Mn$, $^{63}Cu(n,\alpha)^{60}Co$ and $^{93}Nb(n,n')^{93m}Nb$ are required since studies have shown the MeV region to be important for PV damage effects (Fig. 8). Considerable effort is being devoted to improving computational methods (see Table II) for flux determination in LWRs. Benchmark measurement programs such as the one at Oak Ridge (U.S.), have been undertaken to test computational and experimental dosimetry methods. Other research programs are underway at selected controlled-environment power reactors (e.g. Browns Ferry-III in the U.S.). Additional material on LWR dosimetry can be found in Refs. 26-31.

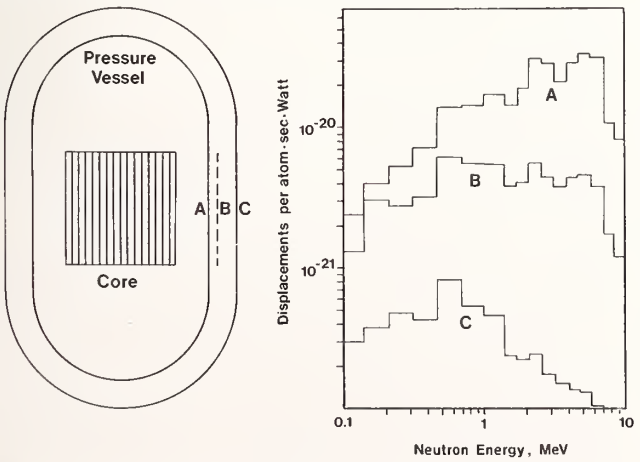

Fig. 8. DPA profiles for the PV of a LWR [after Takeuchi et al., Ref. 24].

Table II. Calculated fluxes for a PWR and BWR [after Simmons, Ref. 25].

	PWR			BWR		
Location	Flux* >0.414 eV	Flux >100 keV	Flux >1 MeV	Flux* >0.414 eV	Flux >100 keV	Flux >1 MeV
Core center	2.59(14)	1.32(14)	6.14(13)	3.08(14)	1.58(14)	7.73(13)
Core boundary	5.35(13)	2.74(13)	1.39(13)	9.33(13)	4.74(13)	2.18(13)
Pressure vessel inner surface	8.03(9)	4.56(9)	2.52(9)	6.55(10)	3.47(10)	1.77(10)
Pressure vessel outer surface	2.65(9)	1.47(9)	3.57(8)	1.38(10)	6.82(9)	9.35(8)

*Cadmium cutoff

Fast-reactor Development

The development of modern dosimetry techniques is being sponsored mostly under the auspices of fast reactor programs. Much of the support for cross section determination comes from this source as well. Engineering studies have been in progress for several years at various benchmark and critical facilities and at materials testing facilities (e.g. EBR-II in the U.S.). Damage research in the next decade will be concentrated at several new facilities such as FFTF (U.S.), PFR (U.K.) and Phenix and Super-Phenix (France). Core damage phenomena (swelling, creep, etc.) are undoubtably a very great concern for fast reactors since high fuel burnups (long fuel cycles) are important for efficiency. Alteration of core configurations by swelling and creep can affect efficiency and might lead to safety problems since fast-reactors are not designed to operate in the most reactive configuration. Improvements in dosimetry methodology are required in all facets of the field to meet the accuracy goals of Fig. 1. These primarily involve refinements of existing techniques and increases in accuracy of the data base <10 MeV for neutron reactions which have already been studied.

Controlled Fusion Technology

The design of fusion reactors is speculative since breakeven (feasibility) of controlled fusion has not been demonstrated. Most materials damage studies are formulated under the assumption that a demonstration facility will be a Tokamak; however, fission-fusion hybrids, laser fusion machines, and ion beam devices are being considered as alternatives. Damage to the "first wall" of the blanket is of primary concern. It is anticipated that the first wall will experience a power loading of ~1-3 MW/m^2 due primarily to fast neutrons ($\gtrsim 10^{14}$ n/cm^2/sec). Approximately 75% of the neutrons will have energies >100 keV and 80% will be below 13.5 MeV. The average energy for this degraded "14-MeV" spectrum is considerably higher than in a fast reactor spectrum. Although the atomic displacement rate is expected to be similar to the core of a fast reactor, damage rates an order of magnitude greater are anticipated because of larger gas production rates. A major goal is the design of radiation-resistant materials for the first wall. Materials testing for fusion applications will take place at fission test reactors (e.g. FFTF), but this will have to be supplemented by measurements at higher energies. Programs are now being conducted at 14-MeV facilities (e. g. the RTNS at Livermore in the U.S.). The U.S. intends to build a high-energy test facility (FMIT) based on the d + Li reaction. It will provide a spectrum similar to the one shown in Fig. 3 with total neutron output ~10^{16} n/sec. Dosimetry for the region 10 - 15 MeV will involve some extrapolation of the existing data base for fission reactors. Proper utilization of a d + Li test facility will require extension of dosimetry techniques to ~40 MeV. The opening of many uninvestigated nuclear reaction channels will necessitate expansion of our quantitative knowledge of nuclear processes far beyond current limits. Since the current level of research support for fusion energy nuclear data development is low,

it is difficult to speculate on how this might be accomplished. The reader is referred to the proceedings of a 1977 symposium at Brookhaven, U.S.A., and other selected references for more information on this subject (Refs. 32-36).

Dosimetry Techniques

Dosimetry techniques are categorized as active or passive, nuclear reaction or direct damage, activation or nonactivation, high flux or low flux, differential or integral, and flux measurement or fluence measurement. A requirement for most methods is accurate characterization of dosimetry materials (e.g. Ref. 37). Accurate assay of fissionable materials is crucial for other areas of fission reactor development as well. A comparison of fission standard materials used in several laboratories in the U.S. and Europe has been carried out under the auspices of the Interlaboratory Reaction Rate (ILRR) program (see Ref. 38). Nuclear data people should not overlook the fact that dosimetry materials must survive the high temperature environments of power reactors where some materials will melt or vaporize and could be lost without proper encapsulation (e.g. see Refs. 6 and 27).

Active Dosimetry

This term applies to on-line measurements with electronic instrumentation. An obvious advantage of active dosimetry is the ability to detect rate variations. Disadvantages include the possibility of instrument failure, flux level limitations (for most methods) and complexity. Discussion of time-of-flight techniques will be avoided here, though they are useful for measuring the thick-target spectra which are employed in fusion research.

Fission chambers are widely used. They are compact and the cross sections for several fission reactions are well known. Measurement procedures are not difficult. Flux limitations ($\lesssim 10^{10}$ n/cm^2/sec) restrict these detectors to moderately low-power applications. Fission detectors provide only integral reaction rate data (e.g. see Ref. 39).

Differential spectrometry is only possible at quite low fluence levels ($\lesssim 10^7$ n/cm^2/sec). Proportional counters based upon n-p scattering or the ^{3}He(n,p)^{3}H reaction, and solid state detectors based upon both these reactions and the ^{6}Li(n,t)^{4}He reaction as well are used (e.g Refs. 40-44). Differential measurements require great care and experience, but are worth the effort since they provide spectral information in the region from 10 keV to $\lesssim$5 MeV which is difficult to investigate by other means. Figure 9 shows the quality of data which can be obtained from such measurements. Accuracies of ~5-10% for 0.01 < E_n < 2 MeV and ~10-15% for E_n > 2 MeV are possible using differential techniques. Discrepancies have been observed in measurements involving the ^{6}Li(n,t)^{4}He reaction which lead to underestimation of neutron fluence ~40-80 keV and ~200-300 keV. Inexact knowledge of the cross section may be responsible.

Self-powered neutron detectors (SPND) are used for measurements at full power in LWRs. The SPND probe is charged with rhodium. Neutrons are captured by ^{103}Rh and energetic beta rays are emitted during the decay of ^{104}Rh. These betas penetrate the insulation to the sheath of the probe; electrons then flow up from ground through a leadwire to neutralize the emitter. This generates a measurable current. These devices are in commercial use, but suffer from several problems including the effects of Rh depletion (it converts to Pd) and radiation degradation of the insulation (see Ref. 45).

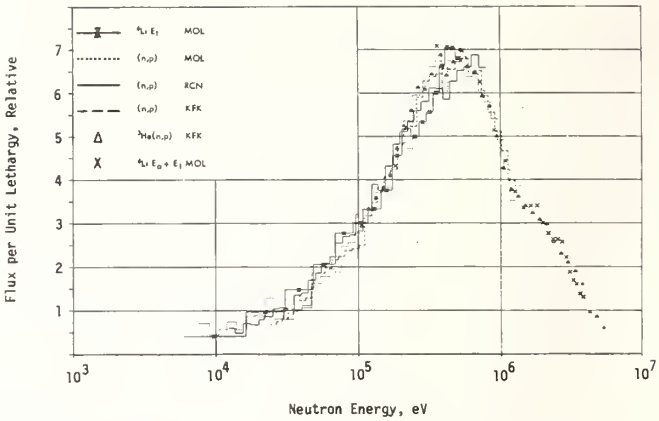

Fig. 9. Some differential spectrometry results for the Mol Sigma-Sigma field [after Fabry et al., reproduced from Ref. 41 with permission from the Am. Nucl. Soc.].

Passive Dosimeters

Passive dosimeters offer many advantages for research and for routine dosimetry in power reactors. They can be used at flux levels covering a dynamic range of over ten decades. They can be made compact and require no attention during irradiation. Activation-detector dosimetry is more widely used than any other method and it offers great versatility. The development of instruments for high resolution photon spectroscopy (Li and Ge diodes) has revolutionized activation counting. Older methods involving the use of NaI (Tℓ) gamma-ray detectors and beta detectors are on the decline. Attention will be directed in this paper toward less-well-known dosimetry techniques, several of which were introduced recently.

Solid-State Track Recorders (SSTR) and Nuclear Research Emulsion (NRE) techniques have been used for many years. They offer several features which insure that they will continue to be useful for LWR, FBR and Fusion dosimetry applications. These recorders measure dose and are not rate sensitive. Once exposed, they provide a permanent record of the irradiation. SSTR recorders provide an enormous sensitivity range. Manual and automated scanning techniques have been developed and track densities in the range 1 to 10^8 tracks/cm^2 can be handled. By properly selecting the recorder materials it is possible to discriminate between various events (e.g. alpha particles and fission fragments). SSTRs can be doped with various sensor materials including fissionable isotopes and (more recently) alpha emitters. NREs have been in use longer than SSTRs. NRE recorders offer the possibility of measuring the angular dependence of neutron flux. No other reactor dosimetry technique offers this feature. NRE dosimetry is limited to fluences $\lesssim 3 \times 10^9$n/cm^2. The reader is referred to Refs. 5 and 46 for more information on this subject.

One of the most promising techniques to be developed during recent years is the helium-accumulation fluence monitor (HAFM). High sensitivity mass spectrometry and isotopic dilution methods are used to detect helium produced by (n,α) reactions in sealed dosimeter capsules. The detection range for the apparatus is from ~10^9 to ~10^{18} He atoms. Measurements can be made with an accuracy < 2% if >10^{11} He atoms are present. Initially, only the ^{6}Li(n,t)^{4}He and ^{10}B(n,α)^{7}Li reactions were employed, but the method is being extended to other (n,α) reactions (e.g. to F, Fe, Ni, etc.). All early capsules were made of vanadium because of its low (n,α) cross section and its ability to contain He. Techniques involving other encapsulation materials (e.g. Au) and the measurement of He trapped in bare solid

wires are under current investigation. One of the most exciting features of HAFM dosimetry is the possibility for measurement of He buildup which is closely related to observed macroscopic damage. At present, only one group (at Rockwell International Corp., California, U.S.A.) has a laboratory equipped for these measurements. Exploitation of this promising nonactivation technique should be more widespread (see Ref. 47). Of interest to nuclear data people is the requirement for accurate differential (n,α) cross section data which this method imposes.

Effort is being devoted to develop so-called "direct damage" sensors because they possess response ranges closely related to the atomic displacement cross sections. Research on the alteration of physical properties of quartz by neutrons has been conducted at Mol (Belgium). The effect of neutrons on p-i-n diodes has also been considered for dosimetry purposes. Neither approach is widely used at this time. The French have developed the graphite damage monitor (GAMIN) and (more recently) a variation involving tungsten. The change in resistance of precision graphite (or tungsten) resistors following neutron irradiation is measured. Information about the sample temperature during irradiation is also needed. Damage dosimetry information is deduced from measured resistance changes and from a knowledge of the fission-neutron equivalent fluence above ~1 MeV deduced from $^{58}Ni(n,p)^{58}Co$ activation monitors included in the dosimetry package. DPA cross sections for major components of steel (Fe, Ni and Cr) are bracketed by those for carbon and tungsten (See Fig. 5). The French method therefore provides upper and lower estimates for structural materials damage (Refs. 15, 48-50).

Another direct damage technique is based on the change in the thermocouple properties of neutron irradiated wires (Fig. 10). This technique is being investigated at Mol. One version involves measurements on a uniform wire which has received various neutron doses as a function of position along the wire. The irradiated wire is inserted into a furnace with a sharp gradient. Net currents are produced as damaged portions of wire pass through the region with a large temperature gradient. The sharper the gradient, the better the resolution for measuring damage versus position. Interpretation is complicated by the fact that some types of damage are annealed out of the wire while it is in the furnace. This fact can also be put to good use if the apparatus is properly calibrated (see Ref. 51).

Dosimetry Cross Section Data Development

This section considers methods for improving the dosimetry cross section data base. Progress toward this goal is being achieved as a result of work in four distinct areas: i) differential measurements, ii) theoretical calculations, iii) integral measurements in benchmark fields, and iv) evaluations. The accuracy of the cross section data required for most fission reactor applications has improved remarkably over the last decade. Each of these distinct activities can claim a share of the credit for this progress.

Differential Measurements

Techniques and problems associated with differential dosimetry cross section measurements at energies >100 keV were reviewed in 1976 (Ref. 52). It was concluded that an accuracy goal of ~5% for the energy range 0.1-20 MeV (except for a gap from 10-14 MeV) is feasible for most activation reactions, but that it will be quite a while before this goal is achieved. The future is more uncertain for nonactivation reactions and for energies <0.1 MeV and >20 MeV. It is necessary to direct measurement effort toward energy regions which are important for major applications. This fact is illustrated in Fig. 11. For threshold reactions the first eight MeV above threshold are important in fission reactor applications. The sensitivity of integral quantities to differential data merits detailed investigation so that relevant differential measurement programs can be undertaken. Smith (Ref. 53) and Mannhart (Ref. 54) have addressed this problem. Several integral-differential discrepancies were eliminated during the last decade as a result of various independent broad-energy-scope differential measurement programs with accuracies $\lesssim$10%. It is anticipated that carefully conducted differential measurements will continue to serve this purpose in the future.

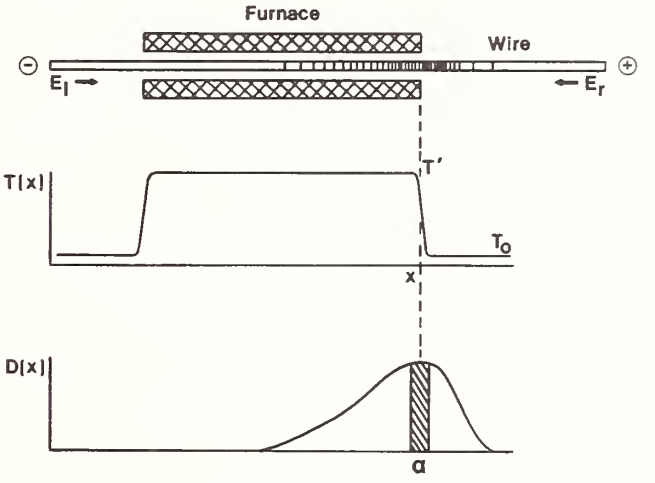

$$E = E_r - E_l = F\{D[x], T', T_o, \cdots\} \neq 0 \text{ if } D[x] > 0$$

Fig. 10. Basic concept of thermocouple neutron dosimetry [after Mathieu et al., Ref. 51].

Theoretical Calculations

In fission reactor applications, model calculations are important for interpolation between experimental data points (especially from ~10-14 MeV) and for extrapolations from 15 to 20 MeV and to threshold. As a general rule, computations for energies from 0.1 to 20 MeV cannot be trusted to much better than ~20% unless they are guided by experimental data. The role of theory in high-energy dosimetry data development (20-40 MeV) will be much greater than for lower energies. It is too early to speculate on how successful this approach will be (see Refs. 32-33). The energy region <1 keV should also be a fertile one for theoretical work since differential measurements are difficult in this region.

Integral Benchmark Fields

The quality of integral measurements is not always superior to corresponding differential ones. A survey of integral measurements for the Cf-252 neutron field indicates that there are sizeable differences between reported spectrum average cross sections for several important reactions (e.g. for (n,p) reactions on Ti-46, 47, 48). Furthermore, integral studies have not been particularly successful in distinguishing between shape and normalization effects in differential cross sections (e.g. Fig. 12). One is led to the conclusion that it will not be possible to develop the cross section data base for dosimetry applications to stated accuracy goals (e.g. Fig. 1) by means of benchmark integral studies alone as has been implied by some members of the integral community (see Fig. 13). Nevertheless, the importance of research at well-characterized integral facilities must not be discounted. These facilities are especially useful for development of metrology and computational techniques

required for development of nuclear energy sources. Good quality spectrum average cross section measurements have been very helpful in pointing out deficiencies in differential data (e.g. the (n,p) reaction on Ti-48). Interlaboratory cooperation (e.g. the ILRR and IAEA sponsored programs) has been valuable in upgrading the overall quality of integral data. The topic of benchmark fields has been reviewed by Grundl and Eisenhauer (Ref. 3), so only a few items of interest will be mentioned here.

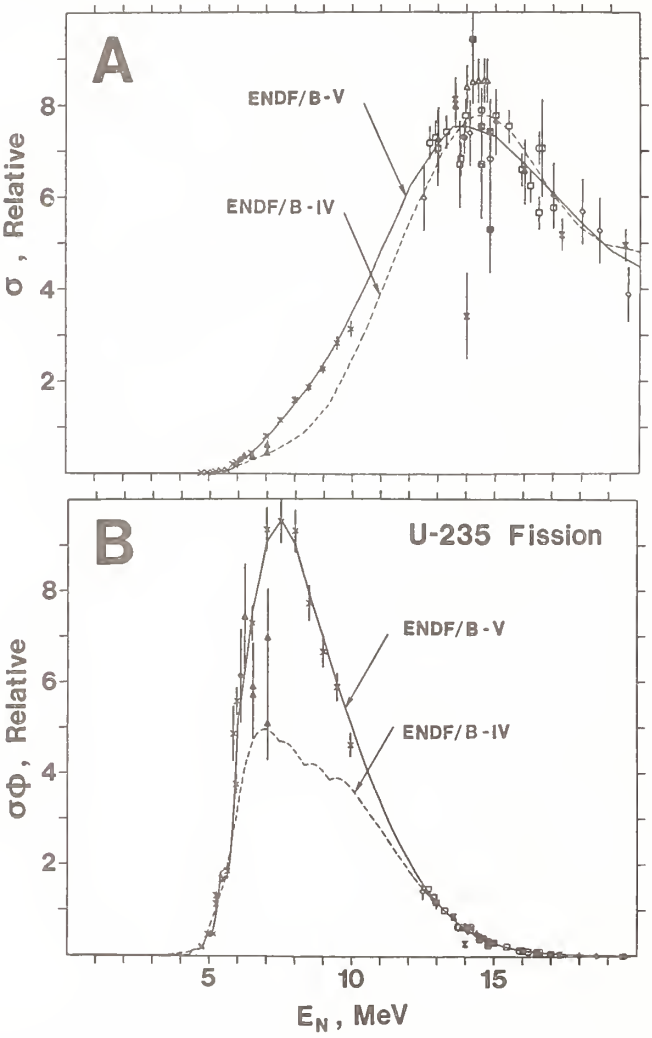

Fig. 11. Cross sections for $^{48}Ti(n,p)^{48}Sc$: A - normal, B - weighted by a fission spectrum.

Table III provides information about integral facilities which are generally accepted as benchmark fields for nuclear data development. Figure 14 shows the approximate spectral shapes for most of these fields. The redundancy of several of these fields is apparent. The available detector response ranges are limited. However, this is an advantage for investigating threshold reactions since the truncated average cross sections for several of these fields are quite similar. It is sometimes possible to compare the results of measurements at various facilities without regard to absolute fluence normalization by considering reaction rate ratios.

The best known field is that of Cf-252 spontaneous fission. This field has the advantage that absolute source strengths can be measured readily. The spectrum is not well known <0.25 MeV or >8 MeV. None of the benchmark fields in Table III are of much value for investigations above ~10 MeV except for d + Be.

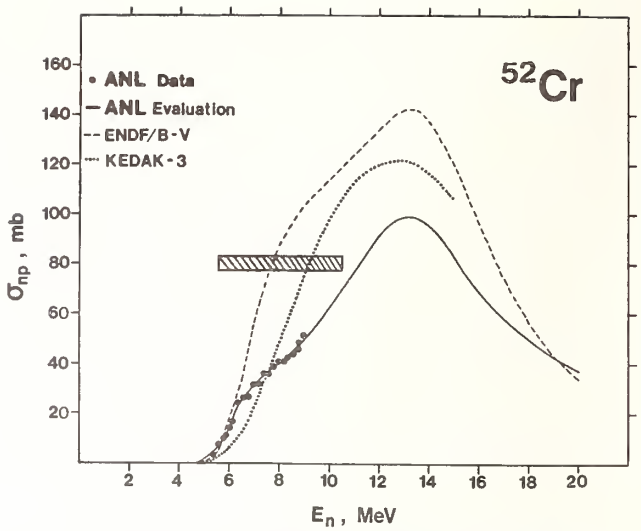

Fig. 12. Integral measurements in a fission spectrum do not sense much difference between the ANL and Kedak-3 evaluations. Experimental data support the ANL evaluation. Dashed bar shows the fission spectrum 90% response range.

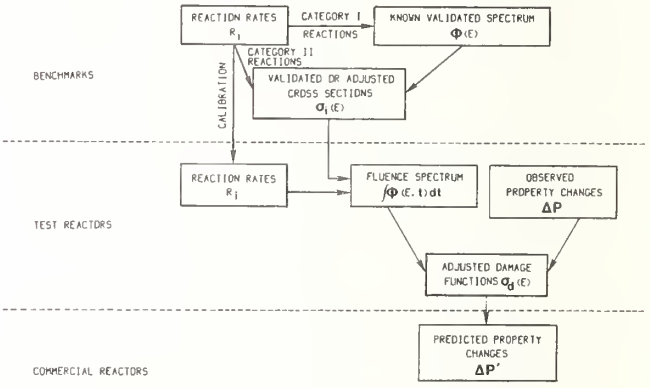

Fig. 13 The integral approach to dosimetry data development [after Fabry et al., Ref. 55).

Table III. Benchmark fields for dosimetry cross section development [after Grundl and Vlasov, Refs. 3 and 56].

Benchmark Neutron Field	Average Energy	Energy Range for Data Testing	Available Fluxes	Status of Group-Flux Spectrum Characterization
^{252}Cf spontaneous fission neutrons	2.13 MeV	0.1 to ~18 MeV	~(1-3)x10^9 n/sec	±13%, E<0.25 MeV ±2%, 0.25<E<8 MeV ±9%, 8<E<12 MeV ±10%, 12<E<15 MeV
^{235}U pure thermal fission neutrons	1.97 MeV	0.1 to ~18 MeV	≤1x10^{13} n/cm^2/sec	±15%, E<0.25 MeV ±2-5%, 0.25<E<8 MeV ±5%, 8<E<12 MeV ±10%, 12<E<15 MeV
Near 1/E (ISNF/CV)	0.75 MeV	0.4 eV to 0.1 MeV	~1.6x10^9 n/cm^2/sec	±5% over range
Sigma-Sigma	0.76 Mev	0.01 to ~18 MeV	~7x10^8 n/cm^2/sec	±15%, E<0.1 keV ±5%, 0.1 keV <E<2 MeV ±5%, E>2 MeV
ISNF	~1 MeV	0.008 to ~18 MeV	~0.8x10^9 n/cm^2/sec	±5%, E < ~2 MeV ±2-5%, 2<E<12 MeV
Big Ten	0.58	0.01 to ~18 MeV	10^9-10^{11} n/cm^2/sec	±5%, 0.05<E<2 MeV ±5%, E>2 MeV
CFRMF	0.76	0.01 to ~18 MeV	<10^{11} n/cm^2/sec	±15%, E<0.01 MeV ±5%, 0.01<E<2 MeV ±5-10%, E>2 MeV
YAYOI	1.5	0.01 to ~18 MeV	<10^{12} n/cm^2/sec	±5-20%, 0.01<E<18 MeV
Tapiro	1.5	0.01 to ~18 MeV	~1x10^{13} n/cm^2/sec	±5-20%, 0.01<E<18 MeV
Accelerator d + Be	~0.4 Ed	1 to ~30 MeV	<1 x 10^{12} n/cm^2/sec	±10-30%, 1<E<30 MeV

The field from pure thermal neutron fission of U-235 is less well known, but knowledge of the spectrum of this field is extremely important since it is used not only for cross section validation, but also in reactor transport calculations. The Cf-252 and U-235

spectra have been evaluated in a very important study by Grundl and Eisenhauer (Ref. 57). The results of their work appear to have been confirmed by most integral tests during the last four years although there has been some dissent (e.g. Ref. 58). Various representations of the U-235 fission spectrum which have been used during the last few years differ considerably from each other above ~7 MeV (see Fig. 15). The recent ENDF/B-V evaluation (a Watts function) does not differ seriously from the NBS evaluation of Grundl and Eisenhauer. Uncertainty in the shape of the U-235 fission spectrum has led to considerable confusion in the area of differential-integral data comparisons-especially for high threshold reactions. For the same reason, fission reactor spectra are poorly known at high energies. Fission spectrum measurements are useless for testing high threshold differential data, but good quality differential cross section determinations for these reactions may eventually help to define fission spectra above 10 MeV to suitable accuracy.

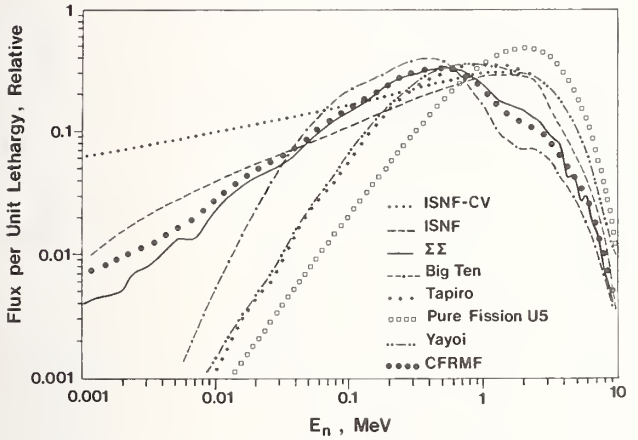

Fig. 14. Approximate spectral shapes for several integral benchmark fields [most of this material comes from Fabry, Ref. 55].

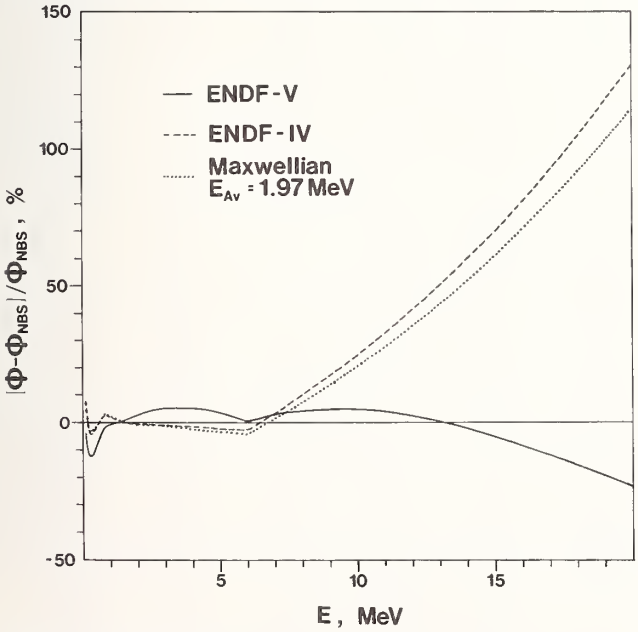

Fig. 15. Several representations of the U-235 fission spectrum plotted relative to the NBS evaluation from Ref. 57.

Nearly pure U-235 spectra can be obtained by using small enriched uranium converters in reactor thermal column cavities; the thermal neutrons are excluded by Cd shields (Fig. 16A). Tailored cavity spectra can be generated by using scatterers of carbon, boron or cadmium (Fig. 16B). The geometries and scattering cross sections for these cavities are well known so their spectra can be calculated reliably using transport methods. Other reactor benchmarks do not possess these advantages. The geometries are more complex and scattering in Fe and U produce uncertainties because of inaccurate knowledge of the cross sections. Uncertainties in uranium inelastic scattering have been a major source of difficulty in characterizing these fields (e.g. see the effect of changes in U-238 inelastic scattering on CFRMF in Figs. 17 and 18).

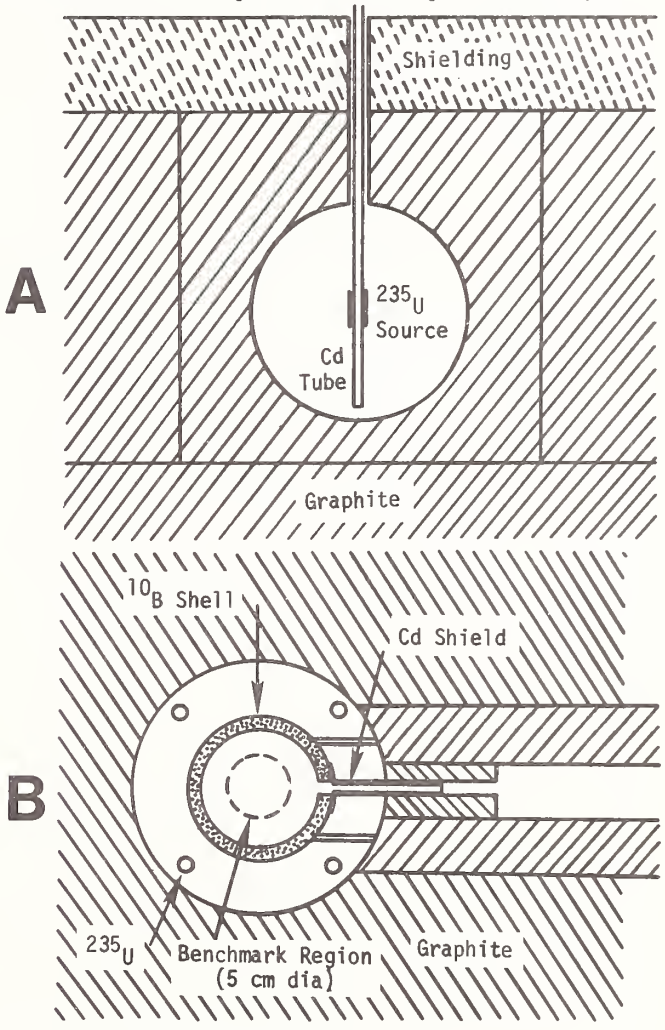

Fig. 16. Representative cavity benchmark fields: A - The U-235 field at Mol, B - the NBS ISNF [after Grundl and Eisenhauer, Ref. 3].

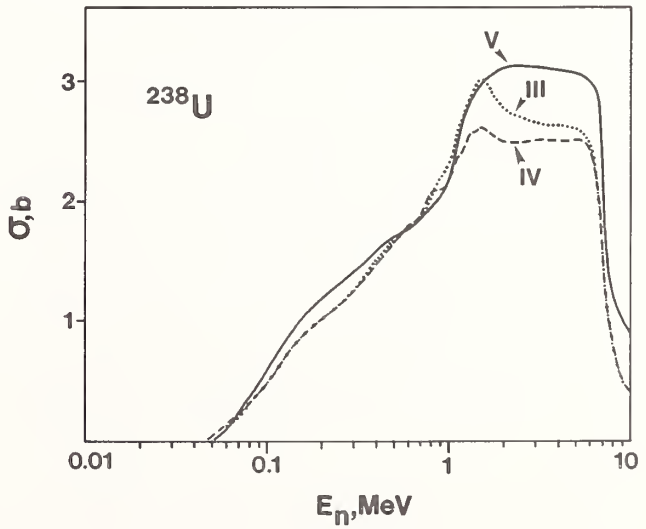

Fig. 17. Three generations of ENDF evaluations for U-238 inelastic scattering [Ref. 59].

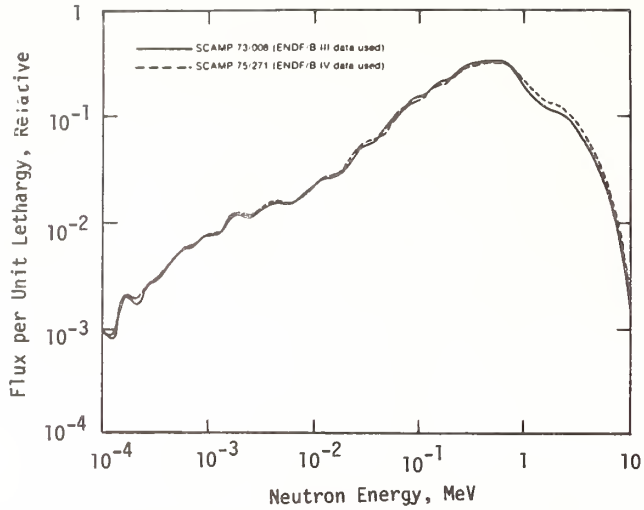

Fig. 18. Change in the CFRMF neutron spectrum produced by converting from ENDF/B-III to IV cross sections. Most of the effect is due to U-238 inelastic scattering [after Rogers, Ref. 38].

Data testing in the integral fields produced by bombarding thick Be targets with deuterons is underway on a limited scale for fusion applications. The opportunity to use pulsed beams and time-of-flight methods to measure spectrum shapes is an important feature of this work. This effort should be encouraged so that the methodology can be developed, however the results will continue to be affected for the forseable future by the totally inadequate knowledge of differential cross sections above 20 MeV (Refs. 32, 60).

Evaluations

The widespread availability of comprehensive differential data evaluations such as those provided by ENDF (U.S.A.) and KEDAK (F. R. Germany) has eliminated several discrepancies which could be traced to use of inconsistent differential cross sections. Evaluations of integral cross sections are also useful, but far less work has been done in this area. Continued evaluation effort should be encouraged. It is hard to find people who are willing and able to perform these evaluations. More international collaboration is recommended and cooperation between theorists and experimentalists is essential.

Some Remarks on the Status of Cross Section Data for Dosimetry

Four categories of nuclear data are of interest for dosimetry applications. These are: i) radioactive decay data, ii) fission mass yield data, iii) differential cross section data, and iv) integral cross section data. There are many lists of reactions considered important as dosimeters. The compiled list of all separate lists is intractable. Table IV represents an attempt to produce a list of those reactions which appear most often on other lists. This is still a very long list and the ENDF/B Dosimetry File is a small subset (39%). The number of reactions which are thought to be adequately known for applications (Category I or I Candidate) is smaller still (18%). Reactions with thresholds >10 MeV are of marginal interest for fission applications, yet they constitute ~25% of the list. If one accepts this list as the goal for nuclear data development, then <20% of the needed work has been accomplished. Actually the situation is worse than this when the need to advance to ~40 MeV is considered.

The list of requisite decay data for dosimeter applications is also impressive (Table V). If one arbitrarily assumes that decay half lives should be

Table IV. Reactions useful for neutron dosimetry. Approximate effective threshold energies E_t (MeV) are shown where applicable.

Reaction		E_t	Reaction		E_t	Reaction		E_t
Li-6(n,total He)	*	-	Fe(n,total He)		1	In-115(n,G)In-116m	*	-
B-10(n,total He)	*	-	Co-59(n,G)Co-60	*IC	-	I-127(n,G)I-128		-
F-19(n,2n)F-18		10.9	Co-59(n,A)Mn-56	*IC	5	I-127(n,2n)I-126	*	9.3
Na-23(n,G)Na-24	*	-	Co-59(n,2n)Co-58	*	10.6	La-139(n,G)La-140		-
Na-23(n,2n)Na-22		13	Co-59(n,3n)Co-57		19.1	Oy-164(n,G)Oy-165		-
Mg-24(n,p)Na-24		5	Co-59(n,4n)Co-56		30.5	Tm-169(n,2n)Tm-168		8
Al-27(n,total He)		4.9	Co-59(n,p)Fe-59		2.5	Tm-169(n,3n)Tm-167		14.9
Al-27(n,p)Mg-27	*	2.3	Ni-58(n,p)Co-58	*IC	0.3	Tm-169(n,4n)Tm-166		23.6
Al-27(n,A)Na-24	*I	4.9	Ni-58(n,2n)Ni-57	*I	12.5	Lu-175(n,2n)Lu-174		7.7
P-31(n,p)Si-31		1.5	Ni-58(n,3n)Ni-56		22.9	Lu-176(n,3n)Lu-174		14
S-32(n,p)P-32	*IC	1.5	Ni-60(n,p)Co-60	*	3.3	Lu-175(n,G)Lu-176m		-
S(n,total He)		1.5	Ni-60(n,2n)Ni-59		11.6	Lu-176(n,G)Lu-177m		-
Cl-35(n,G)Cl-36		-	Ni(n,total He)		<0.5	Ta-181(n,G)Ta-182		-
Cl-35(n,A)P-32		3	Cu-63(n,G)Cu-64	*	-	W-186(n,G)W-187		-
A-40(n,G)A-41		-	Cu-63(n,A)Co-60	*	3.0	Au-197(n,G)Au-198	*I	-
Sc-45(n,G)Sc-46	*	-	Cu-63(n,2n)Cu-62	I	10.9	Au-197(n,2n)Au-196		8.5
Sc-45(n,2n)Sc-44m		11.9	Cu-65(n,2n)Cu-64	*	10.1	Au-197(n,3n)Au-195		16
Ti-46(n,2n)Ti-45		13.2	Cu(n,total He)		2.5	Au-197(n,4n)Au-194		25
Ti-46(n,p)Sc-46	*	2.5	Zn-64(n,p)Cu-64		1	Au-197(n,5n)Au-193		30.1
Ti-47(n,p)Sc-47	*	1	Y-89(n,2n)Y-88		11.5	Hg-199(n,n')Hg-199m		0.53
Ti-47(n,n-p)Sc-46	*	10.8	Y-89(n,3n)Y-87		21.2	Th-232(n,f)F.P.	*	<0.5
Ti-48(n,p)Sc-48	*	4.5	Zr-90(n,p)Y-90m		4.5	Th-232(n,G)[Pa-233]	*	-
Ti-48(n,n-p)Sc-47	*	11.7	Zr-90(n,2n)Zr-89		12	U-234(n,f)F.P.		<0.1
Cr-50(n,G)Cr-51		-	Zr-90(n,3n)Zr-88		21.3	U-235(n,f)F.P.	*IC	-
V-51(n,G)V-52		-	Nb-93(n,n')Nb-93m		0.03	U-236(n,f)F.P.		-
Mn-55(n,G)Mn-56		-	Nb-93(n,2n)Nb-92m		9	U-238(n,G)[Np-239]	*IC	-
Mn-55(n,2n)Mn-54	*	10.5	Rh-103(n,n')Rh-103m	IC	0.04	U-238(n,2n)U-237		6
Fe-54(n,A)Cr-51		1	Ag-107(n,2n)Ag-106m		9.7	U-238(n,f)F.P.	*I	<0.5
Fe-54(n,p)Mn-54	*IC	0.8	Ag-107(n,3n)Ag-105		17.5	Np-237(n,f)F.P.	*I	<0.1
Fe-56(n,p)Mn-56	*I	3.7	Ag-109(n,G)Ag-110m		-	Pu-239(n,f)F.P.	*I	-
Fe-58(n,G)Fe-59	*	-	In-115(n,n')In-115m	*IC	0.34	Am-241(n,f)F.P.		-

*-ENOF/8 Dosimetry File / I-Category I / IC-Category I Candidate / [...]-Useful Product

Table V. Decay data required for dosimetry applications: L - (Ref. 61), H - (Helmer and Greenwood, Ref. 38). Half life uncertainties ≥0.5% and principle gamma-ray branch uncertainties ≥1% are underlined. Bracketed isotopes are fission products.

Activity		$t_{1/2}$		E_G, MeV	I_G	
F-18	L	109.72m	(0.05%)	0.511 (8eta +)	1.94	(0.2%)
Na-22	L	2.602y	(0.08%)	1.275	0.9993	(0.02%)
Na-24	H	15.00h	(0.1%)	1.3686	0.99993	(0.002%)
Mg-27	H	9.462m	(0.1%)	0.8438	0.717	(0.7%)
Si-31	L	2.62h	(0.4%)	1.2662	0.0007	(?)
P-32	L	14.282d	(0.04%)	Beta -	<0.0001	
Cl-36	L	3.00(5)y	(0.7%)	8eta -, EC	---	
A-41	L	1.827h	(0.4%)	1.2936	0.9916	(0.02%)
Sc-44m	L	2.442d	(0.2%)	0.2712	0.866	(0.2%)
Ti-45	L	3.08h	(0.3%)	0.7196	1.54(-3)	(7.8%)
Sc-46	H	83.9d	(0.4%)	0.8893	0.99984	(0.002%)
Sc-47	H	3.40d	(0.9%)	0.1594	0.690	(3.6%)
Sc-48	H	43.8h	(0.2%)	0.9834	0.99987	(0.002%)
Cr-51	H	27.700	(0.04%)	0.3201	0.0983	(1.4%)
V-52	H	3.75m	(0.3%)	1.4341	1.00	(1%)
Mn-54	H	312.5d	(0.2%)	0.8348	0.9997	(0.02%)
Mn-56	L	2.5785h	(0.02%)	0.8468	0.9887	(0.04%)
Ni-56	L	6.10d	(0.3%)	0.1584	0.988	(0.1%)
Co-57	L	271.65d	(0.05%)	0.1221	0.856	(0.5%)
Ni-57	L	35.99h	(0.3%)	1.3776	0.776	(1%)
Co-58	H	70.85d	(0.2%)	0.8108	0.9944	(0.01%)
Fe-59	H	44.6d	(0.2%)	1.0992	0.561	(1.8%)
Ni-59	L	7.5(4)y	(17%)	EC	---	
Co-60	H	5.271y	(0.04%)	1.3325	0.99980	(0.003%)
Cu-62	L	9.73m	(0.2%)	0.511 (Beta +)	1.956	(<0.5%)
Cu-64	H	12.702h	(0.03%)	0.511 (Beta +)	0.38	(5.3%)
Y-87	L	80.3h	(0.4%)	0.4848	0.92	(1.1%)
Y-88	L	106.61d	(0.02%)	1.8360	0.9934	(0.07%)
Zr-88	L	83.4d	(0.4%)	0.3937	0.973	(0.1%)
Zr-89	L	78.43h	(0.1%)	0.9092	0.9901	(0.04%)
Y-90m	L	3.19h	(0.3%)	0.4795	0.91	(4.3%)
Nb-92m	L	10.14d	(0.3%)	0.9344	0.992	(0.2%)
Nb-93m	L	13.6y	(2.2%)	IC	---	
[Zr-95]	H	64.1d	(0.5%)	0.7567	0.546	(0.9%)
[Zr-97]	H	16.88h	(0.4%)	0.7433	0.929	(0.3%)
Rh-103m	L	56.116m	(0.02%)	IC	<0.00068	
[Ru-103]	H	39.43d	(0.3%)	0.4971	0.89	(1.1%)
Ag-105	L	41.29d	(0.2%)	0.443	0.12	(8.3%)
Rh-106m	L	130m	(1.5%)	0.512	0.864	(0.5%)
[Rh-106]	H	30.0s	(0.7%)	0.512	0.205	(1%)
[Ru-106]	L	368.2d	(0.3%)	Beta -	---	
Ag-110m	L	252.2d	(0.1%)	0.6577	0.944	(0.1%)
In-115m	H	4.486h	(0.09%)	0.3362	0.459	(0.2%)
In-116m	H	54.2m	(0.2%)	1.2935	0.848	(0.6%)
I-126	L	13.02d	(0.5%)	0.3886	0.35	(8.6%)
I-128	L	24.99m	(0.08%)	0.4429	0.16	(12.5%)
[Te-132]	H	77.9h	(0.6%)	0.2282	0.89	(5.6%)
[Cs-137]	H	30.03y	(0.5%)	0.6616	0.853	(0.5%)
[La-140]	H	40.26h	(0.05%)	1.5962	0.9540	(0.08%)
[Ba-140]	H	12.789d	(0.05%)	0.5374	0.244	(1.2%)
[Ce-141]	H	32.50d	(0.2%)	0.1454	0.49	(4.1%)
[Ce-143]	H	33.0h	(0.6%)	0.2933	0.47	(8.5%)
[Pr-144]	H	17.28m	(0.3%)	0.6965	0.01342	(1%)
[Ce-144]	H	284.4d	(0.1%)	0.1335	0.110	(1.8%)
Oy-165	L	2.334h	(0.3%)	0.095	0.036	(11.1%)
Tm-166	L	7.70h	(1%)	2.0527	0.2	(10%)
Tm-167	L	9.25d	(0.2%)	0.2078	0.41	(2.4%)
Tm-168	L	93.1d	(0.1%)	0.198	0.50	(6%)
Lu-174	L	3.31y	(1.5%)	1.242	0.06	(?)
Lu-176m	L	3.684h	(0.2%)	0.088	0.087	(10.3%)
Lu-177m	L	160.1d	(0.1%)	0.105	0.12	(8.3%)
Ta-182	L	115.0d	(0.2%)	1.1213	0.351	(1.4%)
W-187	L	23.85h	(0.3%)	0.4796	0.21	(?)
Au-193	L	17.5h	(1.1%)	0.256	0.07	(?)
Au-194	L	39.5h	(1.3%)	0.328	0.61	(9.8%)
Au-195	L	182.9d	(0.3%)	0.099	0.11	(?)
Au-196	H	6.1d	(1.6%)	0.3557	0.877	(2.3%)
Hg-199m	L	42.6m	(0.5%)	0.158	0.523	(1%)
Pa-233	L	26.95d	(0.2%)	0.3119	0.37	(5.4%)
U-237	L	6.752d	(0.3%)	IC	---	
Np-239	L	2.355	(0.2%)	0.2776	0.143	(1.4%)

known to better than 0.5%, and the yield of the principle decay gamma ray should be known to better than 1%, then it is clear that much work remains to be done in this area too.

Knowledge of mass yields for fission reactions is important for passive applications of fission dosimeter reactions. The subject has been reviewed in articles by Maeck et al., Gilliam et al. and Kellogg et al. (Ref. 62). Fission mass yields are important for reactor application other than dosimetry and they have been investigated in both integral and differential experiments. The accuracies of fission yield results are no better than the accuracies for relevant decay data (see Table V). Mass yield accuracy requests are ~2% while the accuracy of the data base is presently ~5-10%. Clearly, much work is needed in this area to meet the stated objectives.

The available literature was surveyed to see how many of the ENDF/B Dosimetry File reactions (Table IV) have been investigated in the benchmark fields listed in Table III. The results of this survey appear in Table VI. Notice the limited data available for (n,2n) reactions. It is also evident that there has been only limited data testing in the NBS ISNF and ISNF/CV fields. These facilities are suitable for testing capture data and should be used for this purpose.

Table VI. An inventory of spectrum average cross section measurements in benchmark fields.

Reaction	Cf-252	U-235	1/E (ISNF/CV)	Sigma-Sigma[b]	ISNF	Big-10	CFRMF	YAYOI	Tapiro	Accelerator d+Be
Li-6(n,total He)						•	•			
B-10(n, total He)						•	•			
Na-23(n,G)Na-24	•									
Al-27(n,p)Mg-27	•	•		•		•	•	•	•	
Al-27(n,A)Na-24	•	•		•		•	•		•	•
Sc-45(n,G)Sc-46				•		•	•			•
Ti-46(n,p)Sc-46 [a]	•	•		•		•	•	•		•
Ti-47(n,n-p)Sc-46 [a]	•	•		•		•	•	•		•
Ti-47(n,p)Sc-47 [a]	•	•		•		•	•	•		•
Ti-48(n,n-p)Sc-47 [a]	•	•		•		•	•	•		•
Ti-48(n,p)Sc-48	•	•		•		•	•	•		•
Mn-55(n,2n)Mn-54	•	•								
Fe-54(n,p)Mn-54	•	•				•	•	•	•	•
Fe-56(n,p)Mn-56	•	•		•		•		•		•
Fe-58(n,G)Fe-59						•	•			
Co-59(n,G)Co-60	•					•	•		•	•
Co-59(n,2n)Co-58	•	•								•
Co-59(n,A)Mn-56	•	•						•	•	•
Ni-58(n,2n)Ni-57		•						•		•
Ni-58(n,p)Co-58	•	•		•		•	•	•	•	•
Ni-60(n,p)Co-60	•									•
Cu-63(n,G)Cu-64	•	•		•		•	•			
Cu-63(n,A)Co-60		•						•	•	
Cu-65(n,2n)Cu-64										
In-115(n,n')In-115m	•	•		•		•	•		•	•
In-115(n,G)In-116	•	•		•		•	•			
I-127(n,2n)I-126		•								
Au-197(n,G)Au-198	•	•		•		•	•		•	•
Th-232(n,f)F.P.	•	•		•				•		
Th-232(n,G)[Pa-233]		•								
U-235(n,f)F.P.	•	•		•	•	•	•		•	•
U-238(n,f)F.P.	•	•		•	•	•	•	•	•	•
U-238(n,G)[Np-239]		•		•	•	•	•			•
Np-237(n,f)F.P.	•	•		•		•	•			
Pu-239(n,f)F.P.	•	•		•	•	•	•			

[a] Activation measurements usually produce cross sections for Ti(n,X)Sc-46 or Ti(n,X')Sc-47 rather than individual components.

[b] Quite similar Sigma-Sigma type facilities are found at Mol (Belgium), NISUS (U.K.) and ITN (Romania). This is a composite list for these laboratories.

A comparison of integral cross sections with those calculated using differential data provides an overall indication of the status of the available data base. Table VII provides information on the reactions in the ENDF/B Dosimetry File. Values in this table are based entirely on ENDF/B-V. It is seen that ~29% of the reactions satisfy dosimetry goals, ~34% are known to not satisfy dosimetry goals, and a lack of integral data makes it impossible to reach a conclusion for ~37% of these reactions.

Table VII. Comparison of integral and differential cross sections using ENDF/B-V data [after Magurno, Ref. 63].

Reaction		Sig Avg$_{CALC}$* (mb)	Sig Avg$_{CALC}$** (mb)	Difference***
Li-6(n, total He)		453.10	---	---
B-10(n, total He)		483.36	---	---
Na-23(n,G)Na-24		0.268	---	---
Al-27(n,p)Mg-27		4.26	3.86±0.25	+9.4%
Al-27(n,A)Na-24	I	0.720	0.705±0.040	+2.1%
Sc-45(n,G)Sc-46		5.27	---	---
Ti-46(n,p)Sc-46		11.18	11.80±0.75	-5.5%
Ti-47(n,n-p)Sc-46		0.0084	---	---
Ti-47(n,p)Sc-47		22.48	19.0±1.4	+15.5%
Ti-48(n,n-p)Sc-47		0.0014	---	---
Ti-48(n,p)Sc-48		0.282	0.300±0.018	-6.4%
Mn-55(n,2n)Mn-54		0.202	0.244±0.015	-21%
Fe-54(n,p)Mn-54	IC	81.08	79.7±4.9	+1.7%
Fe-56(n,p)Mn-56	I	1.04	1.035±0.075	+0.5%
Fe-58(n,G)Fe-59		1.64	---	---
Co-59(n,G)Co-60	IC	6.02	---	---
Co-59(n,2n)Co-58		0.183	---	---
Co-59(n,A)Mn-56	IC	0.150	0.143±0.010	+4.7%
Ni-58(n,2n)Ni-57	I	0.0028	0.0058±0.0003	-107%
Ni-58(n,p)Co-58	IC	105.1	108.5±5.4	-3.2%
Ni-60(n,p)Co-60		2.61	---	---
Cu-63(n,G)Cu-64		9.31	9.30±1.40	+0.1%
Cu-63(n,A)Co-60		0.558	0.500±0.056	+10.4%
Cu-65(n,2n)Cu-64		0.309	---	---
In-115(n,n')In-115m	IC	179.5	189±8	-5.3%
In-115(n,G)In-116		123.68	134.5±6.0	-8.7%
I-127(n,2n)I-126		1.22	1.05±0.065	+13.9%
Au-197(n,G)Au-198	I	76.60	83.5±5.0	-9.0%
Th-232(n,f)F.P.		75.10	81.0±5.4	-7.9%
Th-232(n,G)[Pa-233]		91.10	---	---
U-235(n,f)F.P.	IC	1233.71	1203±30	+2.5%
U-238(n,f)F.P.	I	304.7	305±10	-0.1%
U-238(n,G)[Np-239]	IC	69.37	---	---
Np-237(n,f)F.P.	I	1350.00	1312±50	+2.8%
Pu-239(n,f)F.P.	I	1790.66	1811±60	-1.1%

* Differential cross sections and Watts U-235 thermal fission neutron spectrum from ENOF/B-V.

** Supplied to B. Magurno (BNL) by W. McElroy (HEOL). Values come from an evaluation by A. Fabry of integral data for a pure U-235 thermal fission neutron spectrum.

*** Difference = (Sig Avg$_{CALC}$ - Sig Avg$_{MEAS}$)/Sig Avg$_{CALC}$ expressed in percent. Values underlined indicate discrepancies exceeding 5% (or 10% for high threshold).

Conclusions

Damage dosimetry accuracy requirements have become stringent. Uncertainties in basic nuclear data will probably prevent realization of stated goals for the near term. Greater emphasis on quality rather than quantity of data is needed. It will be necessary to reduce the lists of requested cross section data rather than to expand them as has been the past trend. This should be possible if users assess their needs carefully and refrain from asking for every conceivable type of information which might be related to their specific application - and focus on important requirements.

Acknowledgements

The author gratefully acknowledges the support of those individuals who supplied material upon request and offered suggestions relevant to this review. This work was sponsored by the U. S. Department of Energy.

REFERENCES

1. W. N. McElroy et al., Proc. 2nd ASTM-EURATOM Symp. Reactor Dosimetry, Palo Alto, Calif., Oct. 3-7, 1977, p. 17, NUREG/CP-0004 (Vol. 1).
2. S. M. Qaim, IAEA-Advisory Group Meeting on Nucl. Data for Fusion Reactor Technology, Vienna, Austria, 11-15 Dec., 1978.
3. J. Grundl and C. Eisenhauer, Neutron Cross Sections for Reactor Dosimetry (Vol. I), p. 53, IAEA-208, Proc. IAEA Consultants' Mtg. on Integral Cross Sections and Std. Neutron Fields for Reactor Dosimetry, Vienna, Austria, 15-19 Nov., 1976. Also, ibid. Ref. 1 (Vol. 2), p. 1177.
4. L. R. Greenwood, Argonne National Laboratory, Private Communication (1979).
5. H. Farrar, IV and E. P. Lippincott, ibid. Ref. 1 (Vol. 2), p. 725. Also, Proc. 1st ASTM-EURATOM Symp. on Reactor Dosimetry, Petten, Holland, 22-26 Sept. 1975, EUR 5667ef (Part I), p. 675.
6. E. P. Lippincott and J. A. Ulseth, ibid. Ref. 1, p. 271.
7. G. L. Simmons et al., EPRI NP-1056, Electric Power Research Institute, Palo Alto, Calif. (April 1979).
8. C. D. Bowman et al., ibid. Ref. 1 (Vol. 2), p. 1365.
9. C. A. Oster, ibid. Ref. 1 (Vol. 3), p. 1365.
10. W. L. Zijp et al., ibid. Ref. 1 (Vol. 3), p. 1333.

11. C. Ertek et al., ibid. Ref. 1 (Vol. 3), p. 1385.

12. F. W. Stallman and F. B. K. Kam, ibid. Ref. 1 (Vol. 3), p. 1411.

13. F. G. Perey, DRNL/TM-6D62, Dak Ridge National Laboratory, Oak Ridge, Tennessee (Dctober 1977). Also, ibid. Ref. 1 (Vol. III), p. 1449.

14. A. Alberman et al., ibid. Ref. 1, p. 145, Also Nucl. Technology 36, 336 (1977).

15. J. P. Genthon et al., EUR-5274 d,e,f,n, C8NM, Geel, Belgium (1975).

16. W. L. Zijp et al., ECN-36, Netherlands Energy Research Foundation, Petten, Holland (Feb. 1978).

17. S. Ganesan, Reactor Research Centre, Kalpakkan 603102, Tamil Nadu, India, private communication (notes from lectures given in 1976).

18. B. Goel, Nucl. Sci. Eng. 69, 99 (1979).

19. D. G. Doran et al., invited paper, Proc. Radiation Effects in Breeder Reactor Structural Materials, Scottsdale, Arizona, June 1977, Amer. Met. Soc. of AIME, New York (1977).

2D. H. Ullmaier and W. Schilling, Proc. Int. Course on Physics of Modern Materials, ICTP Trieste, June 1979 (to be published in 1979 by IAEA).

21. A. A. Sagues et al., ibid. Ref. 19, p. 367.

22. W. G. Johnston et al., J. Nucl. Materials 48, 330 (1973).

23. J. E. Sanders, U.K.A.E.A., Reactor Physics Division, A.E.E.-Winfrith, private communication. Document based on a lecture given at the Nuclear Data Forum, London, (Dec. 1978).

24. K. Takeuchi et al., ibid. Ref. 1, p. 257.

25. G. L. Simmons, ibid. Ref. 1 (Vol. 2), p. 627.

26. F. J. Rahn et al., EPRI NP-38D-SR, Electric Power Research Institute, Palo Alto, California (April 1977). Also, ibid. Ref. I (Vol. 3, p. 1D69.

27. G. C. Martin, Jr., ibid. Ref. 1, p. 229.

2B. G. Bartholome et al., ibid. Ref. 1, p. 2B5.

29. S. L. Anderson, ibid. Ref. 1 (Vol. 3), p. 1069.

3D. E. B. Norris and J. S. Perrin, ibid. Ref. 1 (Vol. 3), p. 11D9.

31. R. Odette et al., ibid. Ref. 1 (Vol. 3), p. 1123.

32. Symposium on Neutron Cross Sections from 1D to 4D MeV, Brookhaven National Laboratory, U.S.A., May 3-5, 1977, BNL-NCS-5D681. Many papers.

33. M. R. Bhat, BNL-NCS-25295, Brookhaven National Laboratory (1979).

34. A. B. Smith et al., invited paper at the NEANDC Meeting held in Oak Ridge, Tennessee, U.S.A., April 3-7, 1978. Text available from authors at Argonne National Laboratory, Argonne, Illinois, U.S.A.

35. R. A. Konynenberg, UCRL-51393, Rev. 1, Lawrence Livermore Laboratory, Livermore, California, U.S.A.

36. The Fusion Reactor Materials Program Plan, Section 11 - Damage Analysis and Fundamental Studies, DDE/ET-DD32/2, U.S. Dept. of Energy, Washington, D.C., U.S.A. (July 1978).

37. H. L. Adair, J. Van Audenhove et al., ibid. Ref. 1 (Vol. 2), p. 975; (Vol. 3) p. 987 and p. 1DD3.

38. Interlaboratory Reaction Rate Program, 11th Progress Report, HEDL-TME 77-34, UC-79b,d, compiled by W. McElroy, Hanford Eng. Dev. Laboratory, Richland, Washington, U.S.A. (March 1978). Many papers.

39. J. A. Grundl et al., Nucl. Tech. 25, 237 (1975).

40. G. DeLeeuw-Gierts and S. DeLeeuw, ibid. Ref. 1 (Vol. 2) p. 591. Also, ibid. Ref. 38.

41. A. Fabry et al., ibid. Ref. 39, p. 349.

42. E. Bennett, Nucl. Sci. Eng. 27, 16 (1967).

43. E. J. Dowdy, ibid. Ref. 39, p. 381.

44. J. W. Rogers et al., ibid. Ref. 39, p. 330.

45. H. D. Warren et al., ibid. Ref. 1 (Vol. 2), p. 775.

46. J. H. Roberts and R. Gold, ibid. Ref. I (Vol. 2), p. 739.

47. H. Farrar, IV et al., ibid. Ref. 1 (Vol. 2), p. 725. Also, see Proc. 1st Topical Mtg. on Fusion Reactor Materials, Miami Beach, Florida, U.S.A. (January 1979).

48. J. P. Genthon et al., Nucl. Inst. and Meth. 131, 1 (1975).

49. A. Alberman et al., Contrib. paper, 3rd ASTM-EURATOM Symp. on Neutron Oosimetry for Reactors, Ispra, Italy, October 1979.

50. J. P. Genthon et al., EUR 5795 e,n, ECN, Petten, Holland (1977).

51. F. Mathieu et al., ibid. Ref. 1 (Vol. 2), p. 789.

52. D. L. Smith, ibid. Ref. 3, p. 321.

53. D. L. Smith, ANL/NDM-3D, Argonne National Laboratory, Argonne, Illinois, U.S.A. (March 1977).

54. W. Mannhart, RSIC Seminar-Workshop on Theory and Applic. of Sensitivity and Uncertainty Analysis, Oak Ridge, Tenn., Aug. 22-24, 1978. Text of paper available from author at PTB-Braunschweig, F. R. Germany.

55. A. Fabry et al., Proc. 1st ASTM-EURATOM Symp. on Reactor Dosimetry, Petten, Holland, 22-26 Sept. 1975, EUR 5667 e,f.

56. Summary Report, ibid. Ref. 3, ed. M. F. Vlasov.

57. J. Grundl and C. Eisenhauer, Conf. on Nucl. Cross Sections and Technology, Washington, D. C., March 3-7, 1975, NBS Special Publ. 425, p. 25D.

58. W. N. McElroy et al., ibid. Ref. 3, p. 147.

59. Evaluated Nuclear Data File, Brookhaven National Laboratory, Brookhaven, N.Y., U.S.A.

60. L. R. Greenwood et al., Nucl. Tech. 41, 1D9 (1978).

61. Table of the Isotopes, 7th Edition, ed. by C. M. Lederer and V. S. Shirley, Lawrence Berkeley Laboratory, published by John Wiley and Sons, Inc., New York (1978).

62. Articles on the status of fission mass yields in Ref. 1 (Vol. 3): W. J. Maeck et al., p. 983, p. 1267 and p. 1279; D. M. Gilliam et al., p. 1289; L. S. Kellogg et al., p. 1307.

63. B. A. Magurno, Brookhaven National Laboratory, private communication, (1979).

DISCUSSION OF INTEGRAL EXPERIMENT C/E DISCREPANCIES*

L. G. LeSage and R. D. McKnight
Argonne National Laboratory
Argonne, Illinois 60439

Calculation-to-experiment discrepancies for several key integral parameters measured in ZPR fast critical assemblies are examined. Discussion includes a brief review of experimental and calculational methods and an estimate of their uncertainties. Comparison of the bias between the calculated and experimental values with their combined estimated uncertainties is used to infer nuclear data deficiencies. Several of these C/E discrepancies indicate probable errors in the ENDF/B-IV nuclear data files.

[Keywords: integral experiments, ZPR critical assembly, ENDF/B-IV, delayed neutron data, eigenvalue, reaction rate ratios, reactivity worths, ^{238}U Doppler.]

INTRODUCTION

The purpose of this paper is to compile a list of some of the key calculation-to-experiment (C/E) discrepancies from the ZPR fast critical facilities at Argonne National Laboratory, to discuss the possible sources of these discrepancies and to identify those experiments that suggest deficiencies in the nuclear data. The experimental results will be limited to those from the ZPPR facility at ANL (Idaho) and the ZPR-6 and -9 facilities at ANL (Illinois). With only a few exceptions (which are noted) the calculations presented are based on ENDF/B-IV nuclear data. The parameters considered include the eigenvalue, three key central reaction rate ratios, three small sample central reactivity worths and the ^{238}U Doppler reactivity worth. These particular parameters were chosen for several reasons. Both experimental and calculated values are available for a series of clean assemblies, and they are largely material- or spectral-dependent quantities rather than configuration-dependent (e.g., large-region sodium void reactivities).

In going through an exercise such as this the deficiencies in experiments and calculations are once again brought home. These will be pointed out, and areas where additional work is in-progress, planned or needed will be identified. Very little new data is presented in this paper. Nearly all the results have been published previously, although in some cases the values have been adjusted slightly so as to correct all results for a consistent set of effects (e.g., transport correction, streaming correction, etc.).

The methodology used to identify the experiments that suggest nuclear data deficiencies is as follows. The uncertainties in the results due to experimental methods and calculational methods are examined in a generic way with emphasis on the work which has been done recently to either validate or set limits on these uncertainties. Pessimistic assumptions are used in order to scope the range of possible uncertainties. If the total discrepancy in the parameter is significantly more than that which can be ascribed to the combined experimental and calculational methods, a deficiency in the nuclear data is suggested. For some parameters this will be the case, while for others the total discrepancy could be explained by the uncertainties in the experimental and/or calculational methods. For these cases nuclear data may be contributing to the C/E discrepancies but it is less certain. Further, it is clear that a C/E of unity for a parameter does not prove that the nuclear data is correct, but could result from cancellation of errors.

It is also important to be clear regarding what this paper does not attempt to do. It is not a detailed reevaluation of the uncertainties in the individual C/E values. The uncertainties are discussed generically in the text but are not listed for the individual values in the tables of C/E's. Further, this paper does not attempt to indicate which individual cross sections are contributing to the C/E discrepancies. It does attempt to assess the degree to which the integral experiment results are or are not in agreement with predictions based on ENDF/B-IV nuclear data.

POSSIBLE SOURCES OF DISCREPANCIES

The possible sources of calculation-to-experiment (C/E) discrepancies for fast integral experiments and calculations are outlined in Table I. Three general categories (i.e., experimental methods, calculational methods, and nuclear data) are used, however, the distinction between experimental methods and calculational methods must be defined. In general, the experimental methods include only the "as-built" or "as performed" experiment, and calculated experimental corrections, such as corrections for local effects, are included in the calculational methods. For the reaction rate ratio measurements both the measurement of point absolute reaction rates using foils and the derivation of the cell-average reaction rates are included in the experimental methods, since the cell averaging is largely based on additional experiments.

The data processing and cross section homogenization subtitle (under calculational methods) includes all the calculations required to convert the data on the nuclear data files to broad group cross sections used in the reactor calculation. Specifically this includes the homogenization of the heterogeneous platelet unit cell in such a manner that the resultant broad group cross sections preserve the integral properties of the unit cell such as k_∞, leakage, and cell-average reaction rates.

The calculation of the experimental modeling is important for the ^{238}U Doppler and the small sample reactivity worth measurements since moderately large samples are used, resulting in local flux distortions of a few percent. The experiment modeling calculation is relatively unimportant for the foil reaction rate measurements.

The reactivity scale conversion factor has been included as part of the nuclear data category since it is determined by the delayed neutron parameters; here

*Work performed under the auspices of the U. S. Department of Energy.

TABLE I. Possible Sources of Calculation-to-Experiment Discrepancies

	Eigenvalue (k_{eff})	Reaction Rate Ratios	Small Sample Reactivity Worths	^{238}U Doppler Reactivity
Experimental Methods	-Knowledge of Core Loading and Configuration	-Measurement of Absolute Point Reaction Rates and Ratios from Foil Irradiation	-Reactivity Measurement	-Reactivity Measurement and Temperature Measurement
	-Reactivity Measurement	-Cell-Averaging of Reaction Rates		-Sample Expansion and Capsule Doppler
Calculational Methods	-Data Processing and Cross Section Homogenization	-Data Processing and Cross Section Homogenization	-Data Processing and Cross Section Homogenization (Must Consider Adjoint as Well as Flux)	-Data Processing and Cross Section Homogenization (Must Consider Adjoint as Well as Flux)
	-Global Core Calculation	-Global Core Calculation	-Global Core Calculation	-Global Core Calculation
	·Geometrical Approximation (Cylindricalization)	-Experiment Modeling (Calculation of Local Distortions)	-Experimental Modeling (Calculation of Local Distortions	-Experimental Modeling (Calculation of Local Distortions
	·Transport Effects			
Nuclear Data	-Nuclear Data of Constituent Materials	-Direct: Primary Foil Reaction Cross Section Data	-Direct: Primary Sample Cross Section Data	-Direct: ^{238}U Resonance Parameters
	-Reactivity Scale Conversion Factor (Delayed Neutron Data)	-Indirect: Effect of Cross Sections on Reactor Spectrum	-Indirect: Effect of Cross Sections on Reactor Flux and Adjoint Spectra	-Indirect: Effect of Cross Sections on Reactor Flux and Adjoint Spectra
			-Reactivity Scale Conversion Factor (Delayed Neutron Data)	-Reactivity Scale Conversion Factor (Delayed Neutron Data)

we distinguish between two components of the delayed parameters: the total delayed fraction, β_{eff}, and the relative delayed fractions and decay constants (a_i,λ_i). It is possible to measure both the effective delayed neutron fraction, β_{eff}, and the relative yields and the decay constants in the critical assemblies and to use these values in the reactivity determinations. In practice, however, the β_{eff} is always derived from the nuclear data files and this is the most important of the delayed neutron parameters used in the reactivity scale conversion factor. Alternately, values of the relative yields and decay constants have been derived and used from both the nuclear data files and from integral measurements, but the results appear to be relatively insensitive to the choice. This point is currently being investigated further.

SUMMARY OF C/E DISCREPANCIES

A brief summary of typical C/E values obtained using ENDF/B-IV nuclear data to calculate eigenvalue, central reaction rate ratios, material reactivity worths, and ^{238}U Doppler reactivity is given in Table II. Included for each parameter are the range, mean and standard deviation of the individual C/E values (which are listed in Tables A.1-A.5 of the Appendix) for a series of ZPR fast critical assemblies. As noted below, this list of assemblies spans a wide range of size, composition, fuel type, and energy spectrum. No attempt has been made to weight individual values in the determination of these mean and 1σ values. These mean values do not have a specific physical interpretation but simply represent typical values and are provided as an aid to the present discussion.

Table II. Summary of C/E Values for Eigenvalue Central Reaction Rate Ratios and Reactivity Worths, and ^{238}U Doppler Reactivity Worth in Selected ZPR Fast Critical Assemblies

Integral Parameters	Range of C/E Values	Mean ± Standard Deviation of C/E Values
Eigenvalue	0.9790 - 1.0012	0.9877 ± 0.0069
Central Reaction Rate Ratios		
c^{28}/f^{49}	1.048 - 1.092	1.077 ± 0.013
f^{25}/f^{49}	0.979 - 1.036	1.016 ± 0.020
f^{28}/f^{49}	0.909 - 0.988	0.947 ± 0.026
Central Reactivity Worths		
$\rho(^{239}Pu)$	1.08 - 1.28	1.16 ± 0.05
$\rho(^{235}U)$	1.12 - 1.33	1.19 ± 0.05
$\rho(^{10}B)$	0.94 - 1.17	1.05 ± 0.06
^{238}U Doppler	0.827 - 0.966	0.903 ± 0.056

EXPERIMENTAL METHODS

This section includes a brief description of each of the four types of experiments evaluated in this paper. Discussions of the experimental uncertainties are included in later sections.

The measurements accompanying the eigenvalue C/E determination are straight forward. At a point very near critical a precise determination of the actual loading and configuration of the assembly is made. Usually this occurs with at least one of the operational control rods partially inserted. Since the reference critical configuration is quoted with all operational control rods removed a small correction to account for the supercriticality of the reference system is made, and the reference k_{eff} is slightly greater than 1.0. Other small reactivity adjustments are made to correct the system to a reference temperature and to correct for the fact that the apparent critical condition in a plutonium fueled assembly is actually slightly subcritical due to the relatively large ^{240}Pu neutron source.

All of the reaction rate ratio C/E values discussed herein pertain to unit cell average values measured at a location in the core where the spectrum is essentially asymptotic. Measurement of cell average values eliminates the uncertainties concerning the flux distortion effects of the cavity and the counters when fission chambers are used. There are several steps in the measurement of the cell-averaged capture and fission rate ratios. First, foils of uranium and/or plutonium are irradiated at various locations throughout the unit cell. From this foil data absolute reaction rates are determined either with a carefully calibrated foil counting system or by ratioing to calibrated absolute in-core fission

chambers.* The reaction rate ditributions in the unit cell are also obtained from the foil data. Integrating foils which span the plate thickness are used to measure the average reaction rate through a thick plate. Next the absolute cell-averaged reaction rate for each reaction is determined from the absolute reaction rates, the reaction rate distribution and the material atomic number densities for each region of the unit cell. Cell-averaged reaction ratios are determined by ratios ratioing cell-averaged reaction rates.

The small sample reactivity worths are determined from the change in system reactivity when the reactivity sample is either inserted or removed from a small cavity in the core (near the core center). The samples are oscillated for a period of time so that the effects of reactivity drifts caused by core temperature changes are cancelled. System reactivity changes are measured either by an inverse kinetics algorithm or by the change in position of a calibrated autorod, which has itself been calibrated by an inverse kinetics or by a period technique. Because the reactivity measuring system is very precise (with a reproducibility of about ±0.002 Ih) it is possible to use very small reactivity samples which result in no gross perturbation of the core fluxes. The reactivity samples are usually small cylinders approximately 2 inches long which are positioned in the core so as to span a 2-inch unit cell. In other cases all or part of one of the core constituent plates is removed and its worth measured. The difference between these two techniques is discussed in a later section of this paper.

The ^{238}U Doppler reactivities are measured in the same way as the small sample reactivity worths. The Doppler reactivity is, however, the change in worth of a ^{238}U oxide sample induced by a temperature change in the sample. In actual practice the change in worth between Doppler sample and a fixed system reference configuration is measured. The difference is measured with the Doppler sample at various temperatures so that the difference of the differences represents the reactivity worth associated with the Doppler effect. The oxide Doppler samples are encapsulated in inconel cans 12 inches long and 1 inch in diameter. They are heated electrically (externally) and an elaborate system is included to maintain temperature stability in the samples and prevent escape of heat to the surrounding core region. The Doppler results must be corrected for thermal expansion of the sample and for a small Doppler effect in the capsule material itself. These corrections have been checked experimentally.

ANALYTICAL METHODS

The standard ZPR critical assembly analysis methods employed by ANL are diagrammed in Fig. 1. The basic nuclear data (ENDF/B) are processed by the ETOE-II/MC^2-II/SDX codes.[1,2,3] ETOE-II reformats the ENDF/B data into libraries for MC^2-II and SDX; MC^2-II is a zero-dimensional ~2000 ultra fine energy group slowing down code which is used to produce a ~200 fine group library for SDX (which excludes the contributions from heavy element capture and fission resonances); SDX is a one-dimensional cell homogenization code which collapses in space and energy from the ~200 fine group level to produce ~10

*These are the methods primarily used at the ZPR facilities at ANL to make reaction rate ratio measurements. Other calibration techniques based on the method of thermal calibration or on radiochemistry have been used, primarily as checks on this technique.

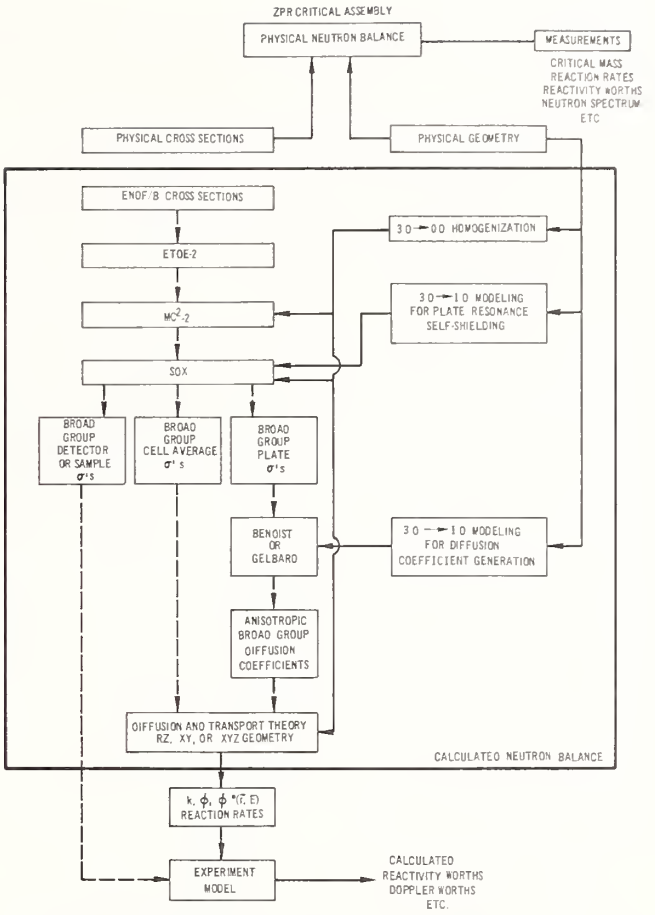

Fig. 1. Diagram of ZPR Critical Assembly Analysis Methods.

to 30 broad group cell-averaged cross sections. As depicted in Fig. 1, SDX produces three types of broad group cross sections for use in ZPR analysis:

a. "Cell-average" cross-sections which include the effects of plate spatial self-shielding and platewise resonance energy self-shielding in such a way that unit cell-average reaction rates are preserved in a calculation in which the unit cell composition is homogenized.

b. "Detector" cross-sections which include resonance energy self-shielding but do not include the plate spatial self-shielding effects.

c. "Plate" cross-sections which are used in the generation of broad group cell anisotropic diffusion coefficients.

Broad group cell anisotropic diffusion coefficients are generated using either the Benoist method[4] or the Gelbard method.[5] The above steps in the ZPR analysis procedures are depicted with dashed lines in Fig. 1 and together represent the nuclear data processing. An extensive validation by Wade et al.,[6] has shown that these cross sections and diffusion coefficients do (to within a few tenths of a percent) conserve reaction and leakage rates in the asymptotic part of the core. This validation study of the ETOE-II/MC^2/SDX homogenization path was based on detailed comparisons against results produced by high precision Monte Carlo calculations of the ZPR unit cells. These calculations were produced by the VIM continuous-energy Monte Carlo code[7] employing the ENDF/B basic data. The

validation effort has systematically progressed from homogeneous, zero-leakage tests through models of infinite arrays of heterogeneous plate or pin-calandria cells subject to an imposed buckling, and from typical LMFBR compositions stressing the ~100 keV range through steam-flooded GCFR compositions which exhibit a substantial sensitivity to the ~100 eV epithermal range. The result of the validation tests has been to foster a high degree of confidence in the correctness of methods and codes for predicting reaction and leakage rates in plate and pin calandria unit cells located in an asymptotic spectrum.

The resultant broad group nuclear data is used in either diffusion theory (with and/or without anisotropic diffusion coefficients) or transport theory calculations of the reactor model. Generally, RZ models are used to analyze the critical mass experiment, central and axial traverses of reaction rates and small sample worths, and large region perturbation experiments (e.g., sodium-void or steam entry measurements). Analysis of a core containing simulated control rods or control rod positions utilizes an RZ model of the assembly to obtain region- and group-dependent bucklings for use with a detailed XY model. This method has been found to give excellent agreement with three-dimensional (XYZ) modeling. Generally, XY models are used to analyze the reaction rate and small sample reactivity worth radial traverse measurements. Finally, the calculation of some of the measurements discussed herein require additional modeling (of the sample and its environment) and analysis to determine "sample size effects" or local "flux correction factors".

EIGENVALUE DISCUSSION

The results presented in Table II indicate an approximate eigenvalue discrepancy of -1.2% based on ENDF/B-IV calculations. The absolute δk uncertainty in the experimental critical configuration has recently been under evaluation by Collins.[8] When all identifiable contributions to this uncertainty are carefully considered and combined the total experimental uncertainty in the "as-built" critical configuration is less than 0.1% δk. This value is consistent with values determined independently in foreign programs.

The uncertainty associated with the eigenvalue calculation is more difficult to assess. Consider the corrections or adjustments which would be necessary to refine a calculated eigenvalue obtained from a diffusion theory calculation of a homogeneous* model. These corrections are a strong function of the particular assembly, however, the following values which are appropriate for ZPR-6 Assembly 7 will illustrate the nature of these corrections and approximate uncertainties.

Correction	Value ± 1σ, in δk
Cell Homogenization (Including Plate Heterogeneity)	+0.0162 ± 0.0010
Streaming	-0.0030 ± 0.0003
Transport Effects (Including S_n and P_n order; Spatial and Energy Mesh)	+0.0018 ± 0.0005
Geometry 2D → 3D	0.0000 ± 0.0005
Total	+0.0150 ± 0.0013

Although the overall corrections are large (typically ~1-2% δk), the overall uncertainty in eigenvalue resulting from these corrections is relatively small (~0.2% δk). This estimate in the uncertainty in the calculated eigenvalue is valid for a clean, simple benchmark assembly such as ZPR-6 Assembly 7, and is reasonable for most of the assemblies (see Appendix) considered herein. These estimates are derived largely from the Monte Carlo-based validation of the ENDF/MC^2-II/SDX cell homogenization path.[4]

Another estimate of the overall uncertainty in the calculated eigenvalue can be obtained by comparison of a "transport/streaming" corrected diffusion theory solution with a detailed three-dimensional Monte Carlo calculation. An explicit (i.e., plate-by-plate) VIM Monte Carlo calculation has been made for ZPR-9/32. The VIM Monte Carlo calculation eliminates the data processing and cell homogenization uncertainties (since ENDF data is used directly in the form of continuous energy cross sections and each individual plate in the assembly is explicitly modeled). The corrections for the diffusion calculation for this assembly are large (~1.7% δk heterogeneity, ~0.2% δk streaming, and ~1.1% δk transport) and the resultant C/E on eigenvalue is 1.0004. The VIM Monte Carlo C/E is 0.9950 ± 0.0024 (1σ). This bias of 0.5% between the eigenvalue C/E's is a reasonable estimate of the overall calculational uncertainties for a small leaky assembly such as ZPR-9/32. Monte Carlo calculations of some of the larger clean benchmark assemblies are planned so as to obtain additional insight into the calculational uncertainty.

It is seen that the overall bias in eigenvalue C/E of ~1.2% is large compared to the experimental and calculational uncertainties (~0.1% and 0.2 - 0.5% δk, respectively). These results suggest that nuclear data (i.e., ENDF/B-IV) is contributing to the eigenvalue underprediction.

REACTION RATE RATIO DISCUSSION

The C/E values for reaction rate ratios can be useful in testing the quality of some of the principal nuclear data used in fast reactor design because the calculation of these quantities is most sensitive to only two directly involved reaction cross sections. As shown in Table II, typical C/E values for c^{28}, f^{25}, and f^{28} relative to f^{49} are ~1.08, 1.02, and 0.95, respectively. As before, we shall review the experimental and calculational uncertainties in these C/E values to ascertain the likelihood of a discrepancy due to ENDF/B-IV nuclear data. In this case, however, the burden (or complexity) has been largely bundled into the experimental measurement. Namely, through distribution of activation foils throughout the unit cell, the cell-average reaction rates are measured directly; and these are exactly the reaction rates calculated using cell-averaged cross sections. As discussed above (and described in detail in Ref. 6), the ENDF/MC^2-II/ SDX cell homogenization path has been shown to preserve cell average reaction rates to within ±1%. The experimental uncertainties in measured cell-average reaction rate ratios of c^{28}, f^{25}, and f^{28} relative to f^{49} are ~3.0%.

A few additional points should be considered with regard to these experimental uncertainties. Inter-laboratory comparisons of fission foil masses between ANL (Illinois), ANL (Idaho) and NBS have yielded excellent agreement (almost always better than 1%).[9] However, a current (in-progress) intercomparison within ANL between the experiments groups of ZPR (Illinois), ZPPR (Idaho) and FNG (Illinois) indicate a small discrepancy in the c^{28} measurements. Plans are underway to intercompare ^{238}U capture rate measurements between ANL and one or more foreign laboratories. At the present time, the uncertainty in the ZPR integral measurements of c^{28}/f^{49} is set at an upper

*That is, a model in which the cross sections had been generated for a homogeneous composition as opposed to a heterogeneous unit cell.

limit of ±4%. Finally, a current VIM Monte Carlo analysis[10] of the unit-cell reaction rate measurements indicates that the measurements might be neglecting axial edge effects (of structural materials) and thereby overpredicting f^{28}/f^{49} by up to 4-5%. This effect will be evaluated further.

Combining these overall experimental and calculational uncertainties together for central reaction rate ratios, the following conclusions may be stated:

a. There does not appear to be a discrepancy in the f^{25}/f^{49} ratio. The C/E bias of +1.7% is well within overall uncertainties of ~3%.

b. The C/E bias of -5.3% for the f^{28}/f^{49} ratio appears to be significant. However, this threshold ratio is also very sensitive to other nuclear data (than σ_f^{28} and σ_f^{49}). Furthermore,if the measured values are decreased by 4-5% due to edge effects (thereby raising the C/E by that amount), the discrepancy would almost vanish).

c. The consistent overprediction of the c^{28}/f^{49} ratio by ~7.7% using ENDF/B-IV data is large compared to the combined experimental and calculational uncertainties (perhaps ±4-5%).

SMALL-SAMPLE REACTIVITY WORTH DISCUSSION

The discrepancy between the measured and calculated small sample central reactivity worths is well known. Bohn studied this discrepancy for three ZPR critical assemblies, ZPR-6/6A, ZPR-6/7 and ZPR-3/48. Much of the following discussion is based on his study.[11]

The experimental and calculated uncertainties for the three small-sample reactivity worth materials are similar enough to allow a combined generic discussion. The only significant source of experimental uncertainty is the reactivity measurement itself. Since the system perturbation is small due to the small sample size, the point kinetic model introduces essentially no error. Comparisons have been made between period and inverse kinetics techniques, and they are in excellent agreement. This simply means that the algorithms for the two methods have been properly (or at least consistently) coded. The error in these measurements, then, is primarily that associated with counting statistics and curve fitting, and these are very small. The error in the reactivity measurements is, therefore, assumed to be no more than 1.0%.

All of the problems associated with experimental modeling are considered part of the calculational uncertainty. Bohn considered both a flux distortion factor and a sample size correction factor. The calculated corrections for flux distortion were in the range of 1-2%. The calculated sample size correction factors were 1-3%, and they agreed with the measured factors that were available. Based on these values Bohn concluded that these factors could account for only 1-2% of the central worth C/E discrepancy. More recent experimental evidence indicates that the worth of the fissile material in the fissile plate itself may be from 1 to 5% more than the worth of the fissile material in the cylindrical samples normally used in the small-sample worth measurements. If this correction is verified, it would have an impact on the interpretation of the central worth C/E discrepancy. This effect is apparently due to the relatively large spatial variations in the flux and adjoint within the unit cell due to its plate structure. Measurements are currently underway at ZPR-9, as part of the Diagnostic Core Program, to experimentally evaluate the effects of local distortions on small sample worth values.

The calculations also contribute to the uncertainty through the global flux and ajoint calculations. A misprediction of flux or adjoint spatial shape can affect the reactivity normalization (perturbation denominator) which directly affects the calculated worth value. Bohn evaluated the radial and axial fission rate shapes in two of the assemblies, ZPR-6/6A and ZPR-6/7, and determined that they were predicted very well. He further considered the measured shape of a ^{239}Pu worth sample in ZPR-6/7 and of a ^{252}Cf neutron source sample in ZPPR-3. Both of these shapes were well-predicted indicating that the calculated radial shape of the adjoint flux was not seriously in error. Based on these results he concluded that the spatial flux distributions and fission rate shapes did not contribute significantly to the central C/E worth discrepancy for the cores considered. Evidence from ZPPR indicates that spatial fission rate shapes may be overpredicted by up to 2-3% in the outer regions of the core relative to the core center for large (i.e., ZPPR-9 and ZPPR-10) assemblies.[12] This suggests that the uncertainty due to the spatial flux and adjoint calculations should be somewhat larger for the larger-sized assemblies.

The data processing and cross section homogenization procedures may also introduce an uncertainty into the calculated small sample worth. It has been shown by Wade, as discussed in the previous paragraphs, that the homogenization procedures used for the ZPR analysis do produce accurate flux weighted broad group cross sections. These cross sections preserve eigenvalue, reaction rates and leakage. The proper way to generate effective broad group cross sections for use in small sample worth calculations is to use both flux and adjoint weighting. This is not done in normal ZPR analysis. Wade and Bucher have shown, however, that this does not introduce a significant error for fissile and absorber sample worths but that the effect can be appreciable for scattering samples.[13] Since only fissile and absorber samples are included in this study no significant contribution to the calculational uncertainty is predicted.

If the experimental uncertainty is taken as 1%, the uncertainty due to experimental modeling as 5% and the uncertainty due to global flux and adjoint shapes as 2%, then an upper limit for th combined experimental and calculational uncertainty is ~8%. This is small compared to the fissile worth C/E discrepancies but is larger than the boron C/E discrepancy.

The three possible ways nuclear data errors can affect the central worth C/E values are shown in Table I. The delayed neutron data used in fast reactor analysis has long been suspect, but most studies conclude that there is no solid evidence that the values should be changed to eliminate the central worth discrepancy.[11,14] Reduced uncertainty in the delayed neutron data would be useful, however. The effective delayed neutron fraction, β_{eff}, can be measured in the critical assemblies. C/E values in the range of 0.9 to 1.0 are normally obtained. This is in the direction to reduce the central worth discrepancy. It is difficult to access the accuracy of the integral β_{eff} measurements, however, due to (1) an apparent difference of about 5% between two different measurement techniques and (2) limited experience with both techniques. Additional central worth and integral β_{eff} measurements have recently been made or are being planned as part of the Diagnostic Core Program on ZPR-9 and ZPR-6. Simple-composition

cores for which the only fissionable isotope is either ^{235}U or ^{239}Pu (i.e., no ^{238}U) are part of this program as is a core with a very high concentration of ^{238}U. The objective is to experimentally isolate, as much as possible, the effects of ^{239}Pu, ^{235}U and ^{238}U nuclear data on the small sample worth and β_{eff} C/E discrepancies.

Bohn has shown that reasonable adjustments in the cross section data, primarily for ^{238}U capture and inelastic scattering, can result in an appreciable reduction (up to 10%) in the central worth C/E discrepancy.[11] The adjusted cross section sets (e.g., FGL5 from the U.K. and CARNAVAL-III and -IV from France) also demonstrate that the central worth discrepancy can be largely removed by suitable cross section adjustments.

The conclusion from this discussion is that the fissile central worth discrepancies are large compared to all identifiable experimental and calculational uncertainties. Further, significant changes in the calculated integral values can result from reasonable, although not necessarily a priori justifiable, changes in the nuclear data.

Specific comments regarding the individual small-sample worth measurements list in Table A.4 are:

a. ZPR-9/32 was a small, relatively hard spectrum, leaky assembly. The spatial flux shapes were not well predicted. The abnormally high central worth C/E's for this core are believed to be largely caused by a perturbation denominator normalization problem resulting from the misprediction of the flux shapes.

b. ZPR-6/6A and ZPR-9/33 are the only ^{235}U fueled assemblies. The lower C/E values for these assemblies are consistent with previous observations for uranium-fueled assemblies.

^{238}U DOPPLER REACTIVITY WORTH DISCUSSION

The ^{238}U Doppler measurements have many common features with the small sample worth measurements. It is interesting that there is such a large difference in the C/E's for these two types of measurements. The possible implication of this difference will be addressed, but first the experimental and calculational uncertainties for the Doppler measurements must be discussed.

For the Doppler measurement, there is an uncertainty in the determination of the average temperature in the experimental sample, and there are corrections for thermal expansion of the sample and for a Doppler effect associated with the Inconel capsule. The temperature uncertainty is very small and the two corrections are only a few tenths of a percent each, for the ^{238}U Doppler measurements, so that their uncertainty is also very small. Therefore, the Doppler experimental uncertainty is essentially the same as for the small sample worths, aproximately 1%.

Detailed estimation of the Doppler calculational uncertainty is complicated and will not be addressed in this paper. It is clear, however, that it must be at least as large as for the small sample worth measurements and is probably somewhat larger. The Doppler samples are larger so that the local perturbations are larger. Further, there are additional effects that must be calculated. These include items such as the sample/core hot/cold resonance interaction effects. An analytical study of the effects of Doppler broadening of the scattering resonances is in progress. These additional corrections add to the total calculational uncertainty.

A strong case for nuclear data error can not be made from the ^{238}U Doppler measurements. The C/E discrepancy of approximately 10% is not large with respect to the maximum combined experimental and calculational errors.

It should be noted that if there are nuclear data errors (as for example in the delayed neutron data) that affect the reactivity normalizations, then these errors would affect equally the small sample central worth values and the Doppler values. The fact that the C/E's for these two measurements are significantly different doesn't rule out errors in the delayed neutron parameters. It does strongly imply additional discrepancies between these two measurements, however.

Two explanations for the inconsistency between the Doppler and small sample worth measurements are suggested. One is that there are discrepancies in the ^{238}U resonance parameters relative to the capture and fission cross sections of the fissile materials. Another is that the low-energy real and/or adjoint spectra in the critical assemblies are being underpredicted relative to the core average real and adjoint spectra. The possibility of this effect is also suggested by the lower C/E for the ^{10}B central worths (~1.05) which is also a low energy indicator, but not as strong a one as the Doppler worth.

Neutron energy spectrum measurements are made in the ZPR critical assemblies by means of proton recoil spectroscopy, but their low energy cut-off is in the Doppler range, at a few keV, and their experimental uncertainty increases appreciably near their low energy cutoff. The spectrum measurements, therefore, do not provide a good measure of the Doppler range spectrum. It has been calculated that, for a typical fast reactor spectrum, about 80% of the sodium capture occurs in the 3 keV resonance. This is clearly in the ^{238}U Doppler energy range of approximately 1 to 25 keV. A measure of the ratio of sodium capture to ^{235}U fission would be a good index of low energy to total real flux, and would provide another check on the low energy spectrum. Techniques for this measurement are being developed, and measurements are planned for the Diagnostic Core Program.

Specific comments regarding the individual Doppler measurements listed in Table A.5 are:

a. The three Doppler measurements in relatively hard neutron energy spectra, ZPR-9/31, ZPPR-2 (Na-voided), and GCFR-II, have significantly lower C/E values. This implies an underprediction of the Doppler range flux in these assemblies relative to the other assemblies.

b. Calculational techniques used to predict the ZPPR Doppler measurements are somewhat different than those used to predict the other cores (see footnote b of Table A.5). Initial comparison calculations indicate little difference in the calculated results but a more thorough check is planned.

NEACRP INTERNATIONAL COMPARISON CALCULATIONS

All of the calculations discussed thus far have been based on ENDF/B-IV nuclear data (and ANL/ZPR analysis methods). It is interesting to know how these calculations might compare with calculations

based on other nuclear data files. The results of the NEACRP international comparison calculation of a large sodium-cooled fast breeder reactor make it possible to relate ENDF/B-IV calculations to results obtained with other nuclear data files used throughout the world.[15] Sixteen solutions to this NEACRP benchmark model were obtained from ten participating countries. Of these sixteen solutions, ten used evaluated nuclear data files (i.e., non-adjusted data sets) including four solutions based on ENDF/B-IV; six used adjusted data sets. A detailed comparison of the NEACRP benchmark calculation is given in Ref. 15.

Several points are noteworthy about the benchmark results. The benchmark calculations have no corresponding measured or experimental values for comparison. The mean values calculated from the sixteen submitted solutions lack physical meaning; however, the spread of the solutions (as indicated by the standard deviation) is of interest. Since the calculational model was precisely defined, the source of these differences should lie in the multigroup data used by each participant. Furthermore, the comparison of the ENDF/B-IV results with adjusted data set results is interesting because as the end result of the adjustment process the C/E discrepancies discussed above (eigenvalue, c^8/f^9, and fissile central reactivity worths) are not observed (or are small) with the adjusted data sets.

For the present discussion, we shall compare some of the ANL results with the adjusted data set results of Winfrith (UKAEA) and Cadarache (France). These particular sets were chosen somewhat arbitrarily, because they are well-known and extensively tested against critical experiments. These results are shown in Table III. The UKAEA solution used the FGL5 nuclear data file; the CADARACHE-1 and CADARACHE-2 solutions used the CARNAVAL-III and -IV data files, respectively. The mean value and the standard deviation of the results (of all sixteen submitted solutions) are presented in the top two lines of Table III. In the remainder of the table, the percent differences from the mean value for each parameter and solution are listed.

The 1σ spread in calculated eigenvalue for the benchmark model is 1.3%. The ENDF/B-IV (ANL solution is 1.2% below the mean, while the CARANAVAL-III and -IV and FGL5 solutions are well above the mean. The CARNAVAL-III and FGL5 eigenvalues are almost 4% higher than ENDF/B-IV. There is a similar, though slightly larger, spread in values of k_∞. This eigenvalue bias between ENDF/B-IV and the adjusted data sets is much greater than the bias between the calculated eigenvalues among these participants. However, integral information used by participants in testing their data files has been obtained in cores much smaller than the NEACRP 1250 MWe reactor benchmark.

There is a 1σ spread of ~4% in the reaction rate ratios c^{28}/f^{49} and f^{28}/f^{49}. The CARNAVAL-III and FGL5 values for c^{28}/f^{49} are 3.4% and 4.2%, respectively, below the ENDF/B-IV value. The CARNAVAL-IV value is 1.1% smaller than the CARNAVAL-III value. This bias between ENDF/B-IV and the adjusted data sets for c^{28}/f^{49} is almost totally due to the differences in σ_c^{28}. One-group-averaged values of σ_c^{28} for the NEACRP benchmark for FGL5, CARNAVAL-III and -IV were 5.1, 4.7, and 3.7% smaller than ENDF/B-IV. The ENDF/B-IV values for f^8/f^9 are similar to both the CARNAVAL-III and -IV results, but 7% smaller than the FGL5 value.

It was expected that the central worth values of plutonium calculated by the adjusted sets would be ~16% lower than the ENDF/B-IV values. This would be consistent with the central worth C/E discrepancies obtained with ENDF/B-IV-based calculations and the elimination of the discrepancy with FGL5 and CARNAVAL based calculations. In fact, the central worths calculated by the adjusted sets were from 5.1% to 6.9% higher than the ENDF values. This apparent inconsistency can be partially explained by differences in the β_{eff} values (the CARNAVAL-III values were 5.5% higher and the FGL5 values were 7.0% higher than ENDF/B-IV) combined with differences in the calculated spatial flux shapes which result in differences in central reactivity normalization of up to 10%. An unexplained 5-10% inconsistency remains, however.

The 1σ variation of the ^{238}U Doppler values is ~11%. The differences between ENDF/B-IV and the adjusted sets range from 1-5%, with the largest difference (7.5%) being between the CARNAVAL-III and -IV solutions.

The results of the NEACRP exercise demonstrate the degree of variation in the integral parameters that results from reasonable variations in the nuclear data. It is a measure of the differences in the nuclear data files and/or processing codes in the participating countries. It is related to, but not a measure of, the uncertainty in the calculation of LMFBR parameters. The brief review included in this paper was intended to illustrate the differences observed between ENDF/B-IV calculations and calculations based on other nuclear data files for the NEACRP benchmark model.

TABLE III. Comparison of NEACRP Benchmark Calculations Using the ENDF/B-IV, CARNAVAL-III, CARNAVAL-IV, and FGL5 Nuclear Data Files

		k_{eff}	k_∞(IC)	c^8/f^9	f^8/f^9	$\rho(^{239}Pu)$	$\rho(^{10}B)$	^{238}U Doppler
Mean[a]		1.005	1.124	0.166	0.0222	118.7	-78.2	-0.00729
Std. Deviation (%)		1.29	1.83	3.74	3.97	3.71	-5.50	10.84
Solution	Nuclear Data File	$\Delta k \times 10^2$		Percent Difference Relative to the Mean[a]				
ANL	ENDF/B-IV	-1.205	-1.578	0.37	-1.43	-0.9	-5.0	-1.46
CADARACHE-1	CARNAVAL-III	1.615	2.814	-3.43	-2.34	4.2	5.3	3.48
CADARACHE-2	CARNAVAL-IV	0.765	-	-2.34	-1.12	6.0	6.0	-4.07
UKAEA	FGL5	1.723	2.695	-4.24	5.92	4.7	2.9	-0.09

[a]This value represents the mean of all sixteen submitted solutions.

SUMMARY AND CONCLUSIONS

This paper has reviewed the status of calculation-to-experiment discrepancies for several key integral measurements from the ZPR fast critical facilities at ANL. Discussion of the C/E bias for each parameter has included a brief review of the measurement and calculational methods, including estimates of their uncertainties. The uncertainties were considered generically, and generally-pessimistic assumptions were made in order to scope the possible range of uncertainties. Comparison of the combined uncertainties with the C/E bias has been used to infer possible nuclear data deficiencies.

For most of the parameters considered, a rather consistent C/E bias is observed. Specifically, for eigenvalue, c^{28}/f^{49}, f^{28}/f^{49}, $\rho(^{239}Pu)$, $\rho(^{10}B)$, and ^{238}U Doppler worth, the C/E bias is greater than the 1σ variation in the C/E's. The ratio of C/E bias to its 1σ spread is ~2 for eigenvalue, ~3 for fissile reactivity worths, and ~6 for c^{28}/f^{49}. For the other cases considered, the C/E discrepancies were not large compared to the combined experimental and calculational uncertainties. For the purposes of the simple exercise attempted in this paper no clear-cut conclusions can be drawn from these cases.

A review of each of the integral parameters yielded the following conclusions.

Eigenvalue

- The experimental uncertainties in the measured critical mass and configuration are very small (<0.1% δk).
- Estimated calculational uncertainties range from ~0.2 to 0.5% δk.
- ENDF/B-IV nuclear data is a likely contributor to the general underprediction of eigenvalue (by ~1.2% δk).

Reaction Rate Ratios

- The consistent overprediction by ~8% of c^{28}/f^{49} is greater than combined experimental and calculational uncertainties (~4 to 5%).
- The fission ratio f^{25}/f^{49} is well predicted, however, the threshold ratio, f^{28}/f^{49}, is underpredicted by ~5%.

Central Reactivity Worths

- The traditional C/E discrepancy for central reactivity worths (1.15 - 1.20 for ^{239}Pu and ^{235}U; 1.05 for ^{10}B) is apparent.
- The C/E bias for the fissile sample reactivity worths is large compared to the combined experimental and calculational uncertainties (~8%).

^{238}U Doppler Worth

- The C/E bias for ^{238}U Doppler worth (~10%) is not large compared to possible experimental and calculational uncertainties.

Finally, a brief comparison of the calculated values obtained with ENDF/B-IV and the calculated values obtained with other nuclear data files has been made using the recent NEACRP benchmark calculations. These comparisons indicate reasonable adjustments in nuclear data can be made that reduce C/E discrepancies in several integral results (e.g., eigenvalue and c^{28}/f^{49}).

In this paper a broad range of experimental results was considered to achieve a limited objective -- that of determining the degree to which the ZPR integral experiments indicate error in the ENDF/B-IV nuclear data base. Based on the comparisons for several of the parameters it appears that there are either significant errors in the nuclear data, unidentified errors in the experimental or calculational methods, or both. In several cases additional calculations or experiments are suggested (some are planned) which should further isolate the sources of the C/E discrepancies.

REFERENCES

1. B. J. Toppel, H. Henryson II, and C. A. Stenberg, "ETOE-II/MC^2-2/SDX Multigroup Cross Section Processing," RSIC Seminar Workshop on Multigroup Cross Sections, ORNL, March 14, 1978.
2. H. Henryson II, B. J. Toppel, and C. G. Stenberg, "MC^2-II A Code to Calculate Fast Neutron Spectra and Multigroup Cross Sections," ANL-8144 (ENDF 239), (June 1976).
3. W. M. Stacey et al., "A New Space-Dependent Fast-Neutron Multigroup Cross-Section Preparation Capability," Trans. Am. Nucl. Soc., 15, 292 (1972).
4. P. Benoist, "Streaming Effects and Collision Probabilities in Lattices," Nucl. Sci. Eng., 34, 285, (1968).
5. E. M. Gelbard et al., "Calculations of Void Streaming in the Argonne Gas-Cooled Fast Reactor Critical Experiments," Proc. ANS National Topical Meeting on Improved Methods for Analysis of Nuclear Systems, Tucson, Arizona, March 28-30, 1977 (published in Nucl. Sci. Eng., 64, p. 624, October 1977).
6. D. C. Wade, "Monte Carlo-based Validation of the ENDF/MC^2-II/SDX Cell Homogenization Path," ANL-79-5 (April 1979).
7. E. M. Gelbard and R. E. Prael, "Monte Carlo Work at Argonne National Laboratory," Proc. of NEACRP Meeting of a Monte Carlo Study Group, ANL-75-2, Argonne National Laboratory (1975).
8. P. J. Collins and D. N. Olsen, private communication (1979).
9. D. M. Gilliam, R. J. Armani, D. Maddison, and R. J. Forrester, private communication (1978).
10. R. H. Johnson, J. A. Morman, and D. C. Wade, private communication (October 1978).
11. E. M. Bohn, "The Central Worth Discrepancy in Three Fast Reactor Benchmark Critical Assemblies," ANL-75-14 (June 1975).
12. M. J. Lineberry et al., "Experimental Studies of Large Conventional LMFBR Cores at ZPPR," Proc. of IAEA Symposium on Fast Reactor Physics, Aix-en-Provence, France (September 1979).
13. D. C. Wade and R. G. Bucher, "Conservation of the Adjoint by Use of Bilinear-Weighted Cross Sections and Its Effect on Fast Reactor Calculations," Nucl. Sci. Eng., 64, 517, (October 1977).
14. R. E. Kaiser and S. G. Carpenter, private communication (February 1977).

15. L. G. LeSage et al., "Proceedings of NEACRP/IAEA Specialists Meeting on the International Comparison Calculation of a Large Sodium-Cooled Fast Breeder Reactor at Argonne National Laboratory on February 7-9, 1978, NEACRP Report to be published.

APPENDIX

The following tables provide C/E values for a series of ZPR fast critical assemblies. Although data from a considerably longer list of assemblies is available, these selected assemblies span a wide range of size, composition, fuel type, and energy spectrum. Note that of the assemblies listed in Table A.1, the first two are ^{239}Pu-fueled carbide systems; the next eight are typical LMFBR ^{239}Pu-fueled oxide systems; next is a GCFR assembly; and the last two are ^{235}U-fueled assemblies. Assemblies such as heterogeneous systems (e.g., the ZPPR-7 and -8 programs) and hypothetical accident configurations (e.g., ZPPR-5 and the meltdown configurations of ZPR-9/32) were specifically not included. Such assemblies were not omitted because their C/E values are significantly different (which, in general, they are not). However, because such systems typically require slightly different analytical methods and/or modeling (which is often one of the motives for such programs), the comparison and analysis of their C/E values is more intricate.

Similar considerations were applied to the lists of experiments included. In addition to the eigenvalue, only experiments which were primarily spectral-dependent were included, and individual experiments for which there was some complicating feature (e.g., a simulated control rod near the experimental location) were omitted.

TABLE A.1. Critical Assembly Characteristics

Reactor/Assembly[a]	Fuel Material[b]	Core Volume(ℓ)[c]	Number of Core Zones	Simulated CR's amd CRP's[d]	Comments
ZPR-3/48	Pu/DU Carbide	415	1	None	Early Pu Benchmark
ZPR-9/31	Pu/DU Carbide	1000	1	None	Pu Carbide Benchmark
FTR-EMC	Pu/DU Oxide	1060	2	CR/CRP	FFTF Mockup
ZPR-6/7	Pu/DU Oxide	3100	1	None	Clean Pu Benchmark
ZPPR-2	Pu/DU Oxide	2400	2	None	Clean Pu Benchmark
ZPPR-3/1B	Pu/DU Oxide	2400	2	CRP	GE Demo Design
ZPPR-4/1	Pu/DU Oxide	2500	2	CRP	CRBR Mockup
ZPPR-9	Pu/DU Oxide	4600	2	None	Large Benchmark
ZPPR-10A	Pu/DU Oxide	5100	2	CRP	Large Benchmark
ZPPR-10B	Pu/DU Oxide	5100	2	CR/CRP	Large Benchmark
ZPR-9/32	Pu/DU Oxide	560	1	None	NRC Safety Cores
GCFR-II	Pu/DU Oxide	1250	1	None	GCFR Benchmark
ZPR-6/6A	EU/DU Oxide	4000	1	None	Clean U Benchmark
ZPR-9/33	EU/Fe Metal	4300	1	None	STF Design Support

[a] ZPR-9/31 and GCFR-II had the hardest neutron energy spectra. The spectra in ZPR-3/48 and ZPR-9/32 were moderately hard. The other assemblies had typical LMFBR spectra or spectra with about the same average neutron energy.

[b] EU and DU refer to enriched and depleted uranium, respectively.

[c] Core volumes include simulated in-core control rods, control rod positions and test loops.

[d] CRP in this column means the assembly contained simulated control rod positions. CR/CRP means it contained both simulated control rods and simulated control rod positions.

Table A.2. C/E Values for Eigenvalue

Reactor/Assembly	C/E[a]
ZPR-3/48	0.9941
ZPR-9/31	0.9905
ZPR-6/7	0.9828
ZPPR-2	0.9849
ZPPR-3/1B	0.9858
ZPPR-4/1	0.9840
ZPPR-9	0.9835
ZPPR-10A	0.9841
ZPPR-10B	0.9854
ZPR-9/32	1.0004
GCFR-II Reflected	1.0012
ZPR-6/6A	0.9843
ZPR-9/33	0.9790
Range	0.9790 - 1.0012
Mean ± 1σ	0.9877 ± 0.0069

[a]All values include calculated or estimated corrections for heterogeneity, streaming, and transport effects.

Table A.3. C/E Values for Central Reaction Rate Ratios

Reactor/Assembly[a]	c^{28}/f^{49}	f^{25}/f^{49}	f^{28}/f^{49}
ZPR-9/31	1.066	0.979	0.961
ZPR-6/7[b]	1.072	1.036	0.969
ZPPR-4/1			
Inner Core	1.048	-	-
Outer Core	1.080	-	-
ZPPR-9			
Inner Core	1.086	1.024	0.938
Outer Core	1.091	1.028	0.971
ZPPR-10A			
Inner Core	1.071	1.028	0.929
Outer Core	1.082	1.026	0.922
ZPPR-10B			
Inner Core	1.072	1.022	0.935
Outer Core	1.090	1.021	0.909
GCFR-II Reflected	1.088	0.984	0.988
Range	1.048-1.092	0.979-1.036	0.909-0.988
Mean ± 1σ	1.077±0.013	1.016±0.020	0.947±0.026

[a]Values for ZPPR assemblies represent average of several measurements throughout the region indicated.

[b]Values for ZPR-6/7 have been revised (based on current study of Collins and Olsen[8]) from previous published values.

Table A.4. C/E Values for Central Reactivity Worths

Reactor/Assembly[a]	$\rho(^{239}Pu)$	$\rho(^{235}U)$	$\rho(^{10}B)$
ZPR-3/48	1.17	1.17	1.03
ZPR-9/31	1.18	1.21	1.03
ZPR-6/7	1.19	1.17	1.12
ZPPR-4/1	1.15	1.18	1.06
ZPPR-9	1.13	1.18	1.05
ZPPR-10A	1.14	1.18	1.05
ZPR-9/32[b]	1.28	1.33	1.17
GCFR-II Reflected	1.16	1.19	1.00
ZPR-6/6A[c]	1.08	1.13	0.94[d]
ZPR-9/33[c]	1.12	1.15	1.08
Range	1.08 - 1.28	1.12 - 1.33	0.94 - 1.17
Mean ± 1σ	1.16 ± 0.05	1.19 ± 0.05	1.05 ± 0.06

[a]The values do not include flux correction factors or sample size correction factors, except for the ZPPR values which do include sample size corrections. These are typically ~1-2% effects.

[b]These values are calculated higher than usual because of a significant misprediction of the spatial flux distribution (as shown by reaction rate C/E profiles) in this small, leaky assembly.

[c]These assemblies are ^{235}U-fueled. The fissile sample or C/E values have been observed to be slightly smaller in U-fueled cores (than in Pu-fueled cores).

[d]The experimental uncertainty was unusually large (~13%) for this measurement. Typical values are ~1-2%.

Table A.5. C/E Values for ^{238}U Doppler Worth

Reactor/Assembly[a,b]	C/E[c]
ZPR-9/31	0.874
FTR-EMC	0.966 (ENDF/B-III)
ZPPR-2	0.932
ZPPR-2 Na-Voided	0.863
ZPPR-3	0.954
GCFR-II Reflected	0.827
Range	0.827 - 0.966
Mean ± 1σ	0.903 ± 0.056

[a]Based on measurements over the temperature range 300-1100°C.

[b]Calculations of the ZPR measurements used integral-transport theory (MC^2-II/RABANL) treatment; ZPPR results used equivalence theory (MC^2-II/SDX) treatment.

[c]Calculations based on ENDF/B-IV except as noted.

CROSS SECTIONS FOR FAST NEUTRON CAPTURE ON Se, Cd AND Os ISOTOPES

M. Herman and A. Marcinkowski
Institute of Nuclear Research
00-681 Warsaw, Poland

Activation capture cross sections were measured for Se, Cd and Os isotopes in the neutron energy range from 0.5 MeV to 1.3 MeV. The results of measurements are compared with statistical model calculations.

[(n,γ), cross sections on Se, Cd, Os, 0.5-1.3 MeV, statistical model analysis.]

Introduction

In fast breeder reactor calculations data on cross sections of about 150 fission product nuclei are important. The required accuracies are generally stated to be of the order of 10%. Since for majority of these nuclei measured values of cross sections do not exist one has to resort to statistical model calculations. Such calculations have been compared against capture cross sections measured by the activation method. Special care has been devoted to a consistent parametrization of the calculations.

Experiment

Activation cross sections for fast neutron capture were measured at four neutron energies in the 0.5 MeV to 1.3 MeV range on ^{78}Se, ^{80}Se, ^{82}Se, ^{114}Cd, ^{116}Cd, ^{190}Os and ^{192}Os. Enriched samples of ^{190}Os (98.06%), supplied by the IAEA, as well as high purity natural materials have been irradiated with neutrons from the ^{3}H(p,n)^{3}He reaction. Tritium absorbed targets were bombarded with protons from a 3 MeV Van de Graaff accelerator.

The product nuclei were identified by their characteristic γ-decays. The induced γ-activities were measured with a 60 cm^3 Ge(Li) spectrometer. The relative detection efficiency of the crystal has been determined with help of radioactive sources ^{75}Se, ^{113}Ba and ^{226}Ra. The decay data of the investigated nuclei, adopted in the analysis of the reaction yields were taken from Nuclear Data Sheets.[1]

The measured reaction yields were referred to the capture cross section of ^{115}In taken from ref.[2] In order to control the possible effect of the low energy background neutrons a simultaneous reference was made to the cross section of the ^{115}In(n,n')^{115m}In threshold reaction.[3] In Fig.1 are presented the measured capture cross sections for population of following residual states ^{79m}Se (3.9 min), ^{81m}Se (57 min), ^{83g}Se (22.5 min), ^{115g}Cd (53 h), ^{117g}Cd (2.5 h), ^{117m}Cd (3.4 h), ^{191}Os (15.4 d) and ^{193}Os (31 h). These cross sections have been corrected for the attenuation of the γ-rays in the samples and for summing of cascading γ-rays in the Ge(Li) detector. The attached errors contain statistical and systematic uncertainties including the uncertainty of the standard cross section.

Model calculations

The statistical model according to the Hauser-Feshbach formulation was adopted. Angular momenta and complete γ-ray cascade calculation were included in the formalism. Only neutron and radiative channels were assumed to be relevant for comparison of the theoretical prescription with the present experiment. The population of known excited levels of nuclei was treated independently and for excitation energies surpassing the highest known level the level density, according to Gilbert and Cameron[4] was used. The code used for the calculations was EMPIRE.[5] The choice of the model parameters in the calculations follow the method outlined by Reffo.[6] The values of the level density parameter a adopted for the investigated compound nuclei follow the overall systematics obtained by fitting the resonance

Table I. Level density parameters for the investigated nuclei.

Neutron number	a		T		U_x	
	syst.	adopted	syst.	adopted	syst.	calculated
45	13.3	13.3	0.80	0.80	5.9	5.89
47	13.2	13.6	0.77	0.78	5.1	5.69
49	11.5	11.0	0.65	0.65	2.9	2.28
67	17.2	18.0	0.60	0.63	5.1	5.08
69	17.1	18.2	0.60	0.62	5.0	4.96
115	23.0*	24.0	0.52*	0.50	4.7	4.24
117	21.6*	23.5	0.50*	0.50	3.9	4.37

* taken from local systematics [6,7]

schemes of nuclei.[6,7] Also the nuclear temperature T was choosen in accordance with the systematic behaviour outlined in ref.[6] The pairing energies Δ were those of Gilbert and Cameron.[4] Once a, T and Δ have been fixed the remaining level density parameter U_x, which is the energy of the matching point of the low energy and high energy level density formulas, and E_0, defining the normalization of the low energy level density formula, can be calculated.[6] In order to define the spin dependence of the level density the spin cut-off parameter σ^2 was determined by assuming the average over angular momentum projections of single particle states near the Fermi energy to be $\langle m^2 \rangle = 0.24\ A^{2/3}$ or, at excitation energies below U_x, by extrapolating the formula

$$\sigma^2 = \frac{1}{N} \sum_{i=1}^{N} \left(J_i + \frac{1}{2} \right)^2 \qquad (1)$$

where N is the number of known excited levels in the nucleus.[6]

The radiative widths were calculated according to the Brink-Axel suggestions[8], with the giant dipole resonance parameters measured for the individual cases, or when such data were lacking, with parameters taken from systematics mentioned in ref.[6]

The optical model transmission coefficients were calculated for the Moldauer potential.[9] Width fluctuaction effects have been accounted for according to the method of Tepel et al.[10]

Results

The comparison of the model calculations with experiment presented in Fig.1 reveals that a good theoretical description of the measured excitation curves may be obtained when using the overall systematics for the level density parameters. In case of the heaviest Os nuclei there was a need to call for a local systematics, which account for isotopic effects. The consistency of the used parameters is shown in Table 1, where the level density parameters, as extracted from the present experiment are compared with the average trends estimated in the frame of a rigorous methodology.[6] All parameters obtained in the present experiment lie within the uncertainty limits assigned to the systematics, i.e. within 15% of a, 15% of T and 25% of U_x.

References

1. R.C. Auble, NDS 25, 315(1978); J.F. Lemming, NDS 15, 257(1975); D.C. Kocher, NDS 15, 169(1975); NDS 9, 479 (1973).
2. F. Schmittroth, BNL-NCS-5044, 158(1975), ENDF/B-III MAT.6416 .
3. R. Sher, BNL-NCS-50446, 150(1975), ENDF/B-III MAT.6406 .

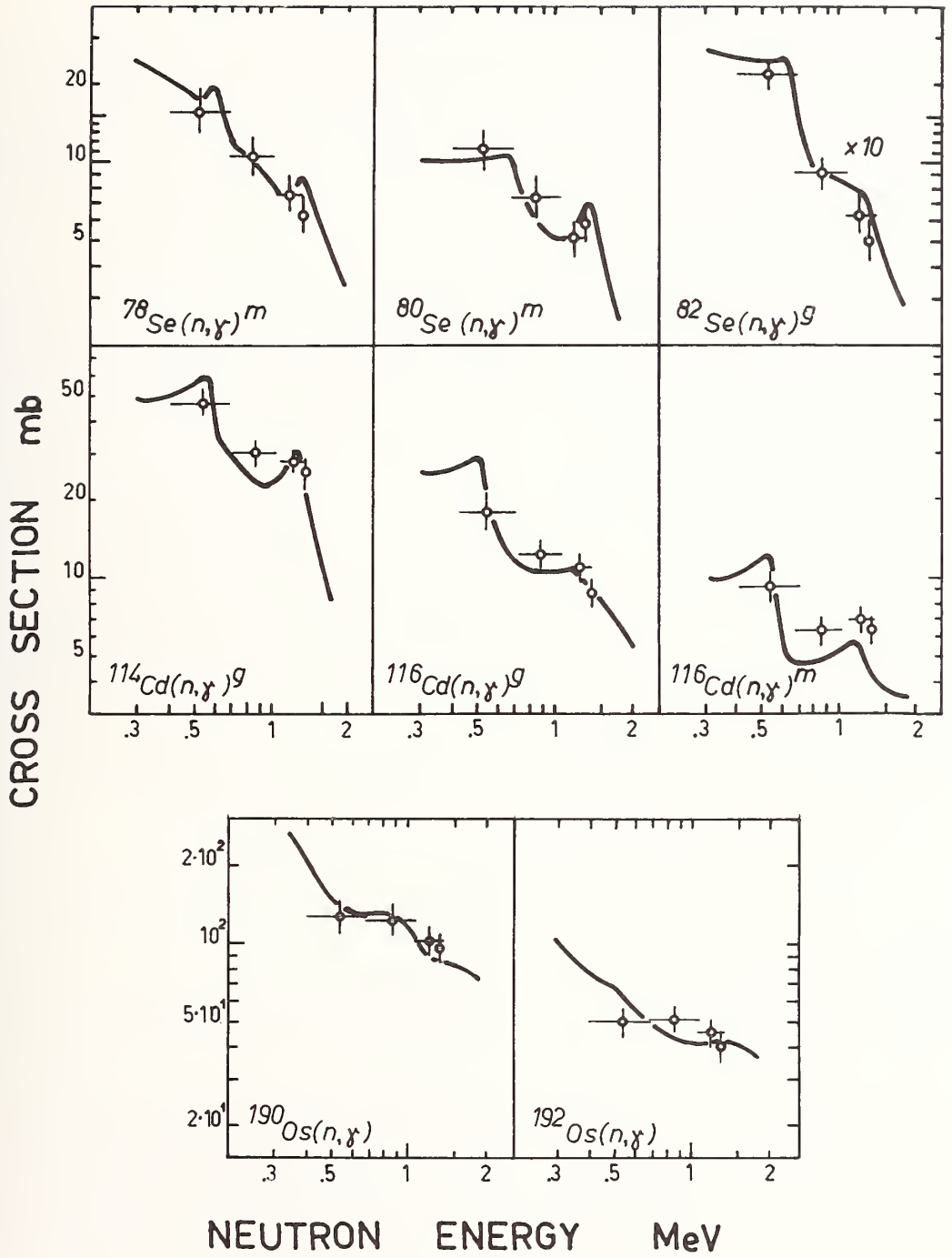

Fig. 1. Capture cross sections compared with the prescription of the statistical model.

4. A. Gilbert and A.G.W. Cameron, Can.J. Phys. 43, 1446 (1965).
5. M.Herman and A. Marcinkowski, unpublished.
6. G. Reffo, CNEN Report RT/FI(78)11 (1978) and IAEA Winter Courses on Nuclear Physics and Reactors, Trieste, Feb.1978.
7. F. Fabbri, G. Reffo, M. Herman and A. Marcinkowski, Second International Symposium on Neutron Induced Reactions, Smolenice, June, 1979, contributed paper.
8. P.Axel, Phys.Rev. 126, 671 (1962).
9. P.A. Moldauer, Nucl.Phys. 47, 6 (1963).
10. J.W. Tepel, H.M. Hofmann and H.A. Weidenmüller, Phys.Lett. 49B, 1 (1974).

OPTICAL MODEL CALCULATIONS OF NUCLEON INTERACTIONS WITH ^{93}Nb, FROM 10 keV up to 50 MeV

Ch. Lagrange*
Los Alamos Scientific Laboratory, University of California
Theoretical Division
Los Alamos, New Mexico 87545, USA

The neutron spherical optical potential is determined following the SPRT method by a fit to strength functions, scattering radius, total cross section and neutron elastic scattering data. Comparison to the potential obtained with existing proton scattering data, (p,p) (p,n), provides a basis for the determination of the complex symmetry term of the optical potential. Calculations using the J.L.M. optical model will be also presented and discussed.

[Optical potential, ^{93}Nb, isobaric analog, (p,p) and (p,n) reactions, n-scattering]

Introduction

Optical model calculations are currently used to predict neutron cross sections in the mass number region A = 90-100 in cases where no experimental data are available. For this purpose a good knowledge of the optical model parameterization as well as limitations or failures of the model are required. In this context, as many nucleon-nucleus experimental data exist for ^{93}Nb in a broad energy range (10 keV-50 MeV), the "empirical" determination of the energy and isospin dependences of the potential strengths obtained for this nucleus are presented. These determinations are based on a fit to all available nucleon-nucleus experimental data. Since the usual model employed here is a gross approximation of the reaction mechanism, comparisons are made with results obtained by using a more fundamental "microscopic" optical potential developed by Jeukenne, Lejeune, and Mahaux[1] (J.L.M. model).

Neutrons-^{93}Nb Optical Potential

The optical potential U has the following standard form:

$$U(r) = -Vf(r,a_R,R_R) - iW_v f(r,a_v R_v) + 4ia_D W_D \frac{d}{dr} f(r,u_D,R_D) + 2V_{so} \lambda_\pi^2 \frac{1}{r}\frac{d}{dr} f(r,a_{so},R_{so}) \vec{\ell} \cdot \vec{S} \qquad (1)$$

in which $f(r,a_i,R_i)$ is the Woods-Saxon form factor and $R_i = r_i A^{1/3}$.

The optical model determination was carried out in two stages. The first one consisted of a search to obtain a reasonable fit to the experimental values of the s and p-wave strength functions (S_0,S_1), the s-wave scattering length (R'), the average total cross sections from 10 keV up to 15 MeV, and the elastic scattering data obtained at 7 MeV by Etemad[2] and at 8.05 MeV by Holmqvist and Wielding[3] (SPRT method[4]). The parameterization so obtained was presented[5] at the National Soviet Conference on Neutron Physics (KIEV, June 9-13, 1975). In this parameterization we have made use of a surface absorption term only. The second more recent step, consisted in a comparison of our calculated elastic scattering cross section to experimental results obtained by Ferrer et al.[6] for 11.0 MeV neutrons. The best fit required a greater surface absorption, and a greater spin orbit term, i.e., $W_D = 3.4 + 0.41\ E_n$ ($E_n \leqslant 11$ MeV), $W_D = 7.91\ E_n$ ($E_n \geqslant 11$ MeV) instead of $W_D = 3.4 + 0.37\ E_n$ ($E_n < 8$ MeV), $W_D = 6.36\ E_n \geqslant 8$ MeV and $V_{so} = 7.7$ instead of $V_{so} = 6.2$.

Protons-^{93}Nb Optical Potential

The dependence of the optical potential on the asymmetry: $\eta = (\frac{N-Z}{A})$, may be written as:

$$U(r) = U_0(r) \pm U_1(r)\ \eta \qquad (2)$$

where the upper and lower signs refers to neutrons and to protons respectively. The determination of the isovector component strengths of the optical polential was obtained by a least squares search on 22.2 MeV protons elastic scattering data.[7] The resulting values for the real and surface imaginary components are the following:

$$V_1 = 17.0 \text{ MeV}, \quad W_{D1} = 8.5 \text{ MeV} \quad .$$

In these calculations the Coulomb correction term was estimated as $0.417\ Z/A^{1/3}$, and the reduced Coulomb radius used was 1.18 fermi. We also made a search on the spin-orbit potential depth, and found the following value of $V_{so} = 6.4$ MeV. This seems to corroborate the conclusion obtained from analysis of analyzing powers in charge exchange reactions.[8] The asymmetry dependence of the spin-orbit potential is of an opposite sign than that of the central real potential. In order to test the global consistency of the adopted parameterization, comparisons of calculated values with experimental data[9] of proton polarization were made at 10.5 MeV and 19.5 MeV. Very good agreement was obtained at both energies.

Analyses of (p,n) isobaric analog transition data

The most direct manner of studying the nucleon isospin interactions is between isobaric analog states (IAS). Comparisons of calculated values with experimental data of (p,n) IAS angular distributions between 18 MeV and 50 MeV were made as to test the validity of the isovector components of the optical potential previously determined. The calculations agreed fairly well with the experimental data[10] in the proton energy

---

*Permanent address: C.E. de Bruyères-le-Châtel, CEA, France.

range 18-22 MeV. As can be seen from Fig. 1 it was not the case for 49.4 protons.[11]

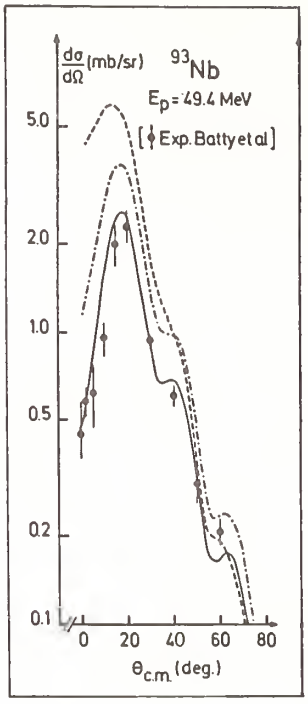

Fig. 1. Comparisons of coupled channels calculations with (p,n) IAS differential cross section data. The dashed curve has been obtained with previously determined parameter set. The dot-dashed curve has been obtained with the same parameters modified as to take into account competition between volume and surface absorption. The solid curved differs from the dot-dashed one only in the energy dependence of the real isovector term.

The modifications required for the previously determined potential to obtain a good agreement with these experimental data concern the energy dependence of the isoscalar imaginary potential for nucleon energies (E) greater than 11.0 MeV:

$$W_V = 0.16\,E - 1.76,\quad W_D = 9.67 - 0.16\,E$$ instead of $W_V = 0$, $W_D = 7.94$; and the energy dependence of the real isovector term:

$$V_1 = 20.3 - 0.15E \text{ instead of } V_1 = 17.0 \quad .$$

CALCULATIONS OF NEUTRON CROSS SECTIONS WITH THE J.L.M. MODEL

It is not unrealistic to expect that the use of a microscopic optical potential will be able to help in the prediction of neutron cross sections. In this context we investigate the use of the J.L.M. microscopic optical potential model. The reason of this choice is that their numerical results, in the energy domain 10-160 MeV, were parameterized in an analytical form. We use the formula (A.1) of their work,[1] and the nucleon density obtained from Hartree-Fock, Bogolyubov calculations of J. Dechargé.[12] Tests of this model in the energy domain 10 keV-50 MeV indicates the need of a modification of their calculated Fermi energy. The following modification was suggested to us by A. Lejeune:[13]

$$\varepsilon_F = -16 \text{ MeV}$$

instead of

$$\varepsilon_F(\rho) = \rho(-510.8 + 3222\,\rho - 6250\rho^2) \quad \text{(formula 27 of Ref. 1.)}$$

in which ρ is the target nucleon density distribution. The microscopic model does not include a spin orbit potential so we add a spin orbit potential of the form:

$$U_{so}(r) = -\frac{1}{3}\,\pi\,V_{so}\,\frac{1}{r}\,\frac{d}{dr}\left[\rho_U + 2\,\rho_L\right]\vec{\ell}\cdot\vec{\sigma} \qquad (3)$$

where ρ_U and ρ_L refers respectively to unlike (or like) nucleon target density distributions.

The parameters of the model are N_R, and N_I, the renormalization factors of the real and imaginary potentials, t_R, and t_I, the ranges of the effective interaction (Gaussian form factor) for the real and imaginary potentials, and V_{so} the strength of the spin orbit potential. These parameters were determined following the SPRT[4] method. The agreement obtained for the strength functions (S_0, S_1) and scattering radius is shown in Table I.

Table I. s,p Wave Strength Functions and Scattering Radius R' for ^{93}Nb

	$S_0 \times 10^4$	$S_1 \times 10^4$	R'(fm)
EVALUATION ^{14} B.N.L. 325	0.32±0.11	$4.4^{+2}_{-1.2}$	6.7±0.1
CALCULATION J.L.M. - MODEL	0.459	5.0	6.64
CALCULATION CONVENTIONAL-MODEL	0.433	4.566	6.628

Calculated values of neutron total cross sections from 10 keV to 11.0 MeV are in good agreement (within 5%) with experimental data. Comparisons at 11.0 MeV between measured and calculated elastic scattering neutron cross sections are shown in Fig. 2.

The agreement obtained by using the J.L.M. model is quite good, considering that the number of free parameters is less than in conventional model calculations. The so determined parameters are the following:

$$N_I = 0.43 + 0.003E \quad , \quad N_R = 0.93 + 0.02E \quad ,$$

$$V_{so} = -61 \text{ MeV fm}^5 \quad , \quad t_R = t_I = 1.4 \text{ fm} \quad .$$

where E is the incident nucleon energy.

It is notable that the renormalization factor here obtained for the real potential is in agreement with values obtained previously by Lejeune and Hodgson[15] in their calculations of nucleon differential cross sections for various nuclei (^{12}C-^{209}Bi) in the energy range 5.0 - 70 MeV. On the whole these results are encouraging since that the same agreement was obtained

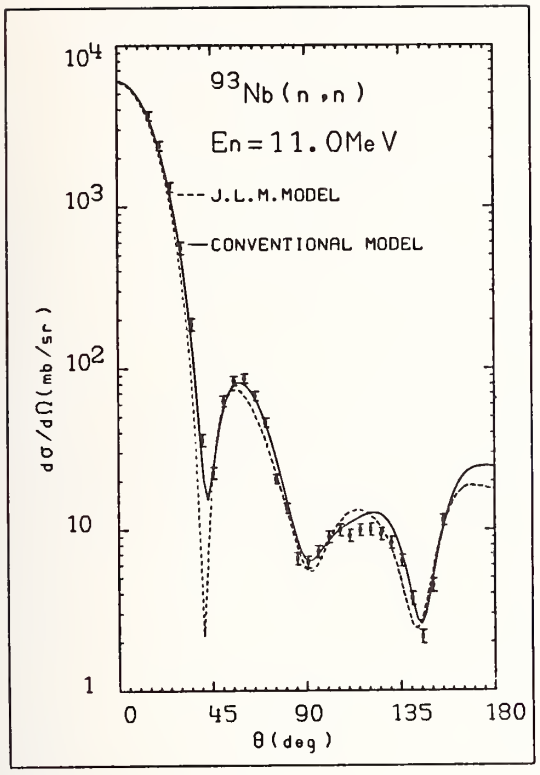

Fig. 2. Neutron differential elastic scattering cross sections.

by us for ^{208}Pb, using the same range of the effective interaction and different renormalization factors.

Reaction cross sections for sub-Coulomb protons

It was pointed out by Johnson et al.[16] that conventional optical model analyses of (p,n) cross sections, in energy region where these cross sections are nearly equal to the total absorption cross sections, could lead to anomalous energy or mass dependences of the optical potential parameters. To test our conventional optical model parameter determinations, comparisons of our calculated protons-reaction cross sections with those obtained by using optical model parameters determined by Johnson et al.[16] as fixed from the least square fits to their (p,n) experimental data, are shown in Table II.

Table II. Calculations of Reaction Cross Sections for p + ^{93}Nb

Ep (MeV)	σ_R (mb) (1)	σ_R (mb) (2)	σ_R (mb) (3)
2.5	0.185	0.159	0.157
3.0	1.106	1.153	1.102
4.0	10.74	12.64	10.50
5.0	45.32	55.12	45.77
6.0	131.8	151.5	136.0
7.0	286.1	302.3	288.3

(1) Optical model parameters of Johnson et al.[16]
(2) Optical model parameters from our determination.
(3) Same as (2) with modifications as explained above.

From the results shown in Table II column 1 and 2 it appears that our "a priori" determination is within 20% the results obtained by Johnson et al.[16] A most "puzzling" result is presented in Column 3. It was obtained by assuming, first that the real Coulomb correction term was in our "conventional" calculations underestimated by a factor 1.2 (this factor is quite reasonable considering "microscopic" calculations of Ref. 1), and second, that the strength of the absorptive term was the same for protons and neutrons. This last result is not as surprising as it could appear, knowing that in our "conventional" calculations we have not taken into account an imaginary Coulomb correction term, currently calculated in the "microscopic" model of the optical potential. From the "microscopic" calculations of Jeukenne, Lejeune, and Mahaux it appears that such a term has in general an opposite sign than the "conventional" absorptive term, and is also greatly energy dependent[1] (greater at lower energies than at higher energies). The "conventional" value presented here can be understood as an "effective" difference between nuclear absorptive term and Coulomb correction absorptive term. It is perhaps the first time such a "failure" of the "conventional" model is reported so clearly. We have presented a good fit to neutron data and proton data at higher energies, and for these reasons have a great confidence in these considerations. More fundamental "microscopic" calculations of the optical potential are urgently needed for proton cross sections in sub-Coulomb energy region.

ACKNOWLEDGMENTS

The author would like to thank the Los Alamos Scientific Laboratory for its kind hospitality. Useful discussions with Phil Young and Ed Arthur are greatfully acknowledged. We thank C. H. Johnson for sending his results previous to publication and A. Galonsky and D. Flynn for stimulating discussions.

References

1. J. P. Jeukenne, A. Lejeune, and C. Mahaux, Phys. Rev. C16, 80 (1977).
2. M. A. Etemad, Report AE-482 (1973).
3. J. B. Holmqvist and T. Wiedling, Report AE-430 (1971).
4. J. P. Delaroche, Ch. Lagrange, and J. Salvy, Nucl. Theory in Neutron Nuclear Data Evaluation, IAEA-150 (1976).
5. Ch. Lagrange, Proc. Nat. Soviet Conf. on Neutron Physics, Kiev (1975), Neitronaia Fysika (1976).
6. J. C. Ferrer, J. D. Carlson, and J. Rapaport, Nucl. Phys. A275, 325 (1977).
7. C. B. Fulmer, Phys. Rev. 125, 631 (1962).
8. J. Gosset, Thèse d'État Université de Paris.
9. L. Rosen, J. G. Beery, and A. S. Goldhaber, Annals of Physics 34, 96 (1965).
10. C. Wong, J. D. Anderson, J. C. Davis, and S. M. Grimes, Phys. Rev. C5, 581 (1972).
11. C. J. Batty, B. E. Bonner, E. Friedman, C. Tschalär, L. E. Williams, A. S. Clough, and J. B. Hunt, Nucl. Phys. A116, 693 (1968).
12. J. Dechargé, private communication.

13. A. Lejeune, private communication.

14. S. F. Mughaghab and G. I. Garber, BNL-325, Third edition, Volume 1 (EANDC(US) 183 "L") (INDC(US) 3816).

15. A. Lejeune and P. E. Hodgson, Nucl. Phys. A295, 301 (1978).

16. C. H. Johnson and R. L. Kernell, Phys, Rev. C2, 635 (1970).
C. H. Johnson, A. Galonsky, and R. L. Kernell, Phys. Rev. Lett 39, 1606 (1977).
C. H. Johnson, A. Galonsky, and R. L. Kernell to be published in Phys. Rev. C.

NEUTRON RESONANCE PARAMETERS FOR PALLADIUM ISOTOPES

P. STAVELOZ
IWONL bursary and S.C.K./C.E.N., B-2400 Mol, Belgium

E. CORNELIS
University of Antwerp, R.U.C.A., B-2020 Antwerp, Belgium

L. MEWISSEN and F. POORTMANS
S.C.K./C.E.N., B-2400 Mol, Belgium

G. ROHR, R. SHELLEY and T. VAN DER VEEN
C.E.C.-JRC, Central Bureau for Nuclear Measurements
B-2440 Geel, Belgium

We have undertaken a systematic study of neutron resonance parameters for the isotopes Pd-104,105,106,108 and 110 (enriched isotopes on loan from ORNL) in response to requests for such data on important fission products. Various neutron time-of-flight experiments have been performed at GELINA - capture, elastic scattering and total cross section measurements. Parity assignments are made on the basis of low-bias to high bias ratios deduced from capture gamma ray spectra. The resonance parameter analysis is completed for Pd-105 and partial results are available for Pd-106,108 and 110.

[NUCLEAR REACTIONS Pd(n,n), Pd(n,γ), E = 10eV - 40keV, measured $\sigma_{n,T}$, $\sigma_{n,\gamma}$, $\sigma_{n,n}$, resonance parameters deduced, enriched targets Pd-104,105,106,108,110]

Introduction

Neutron data for Pd isotopes are of particular interest as they are important fission products formed in fission reactors. During the last years, various results have been published : capture cross sections in the unresolved resonance region[1] for ^{105}Pd, neutron widths from transmission data[2,3] of ^{105}Pd up to 1.5keV, capture and transmission data[4] on ^{107}Pd up to 660 eV. Capture cross section measurements above 2.6 keV for all stable isotopes were measured at ORELA[5].

We have performed transmission experiments for all stable isotopes ^{104,105,106,108,110}Pd in the resolved resonance region, up to 2 keV for ^{105}Pd and up to approximately 40keV for the even isotopes. Elastic scattering and capture experiments were performed on ^{105}Pd and ^{108}Pd and are planned for the other isotopes. Parity assignments of resonances were made on the basis of low-bias to high bias ratios deduced from capture gamma ray spectra for the isotopes ^{108}Pd and ^{110}Pd, and are in preparation for the other isotopes.

The work for the important fission product ^{105}Pd is completed and resonance parameters are obtained for the resonances below 2keV from the analysis of transmission, scattering and capture data. As stated above, a few additional experiments are planned for the even isotopes and the results reported here are mostly from the analysis of the transmission data.

Measurements

The experiments were performed on the neutron time-of-flight spectrometer of the 150 MeV Linac of CBNM. Operating conditions were 4 nsec beam burst and minimum channel width of 4 nsec for the capture experiments and 10 nsec for the transmission and scattering experiments. The samples were prepared from metallic, highly enriched isotopes which we have on loan from Oak Ridge National Laboratory.

Capture experiments

Capture data for ^{105}Pd and ^{108}Pd were taken at a 60 meter flight path. The sample thicknesses were respectively 8.94 10^{-4} atoms/barn (97.38%) for ^{105}Pd and 2.50 10^{-3} atoms/barn (98.88%) for ^{108}Pd.

The capture detection system consisted of a pair of cylindrical deuterated liquid scintillators (C_6D_6) each with a diameter of 4 inches and a length of 3 inches, the faces of which were in optical contact with EMI photomultipliers (2823 QKB). Using a bias of 0.1 MeV in amplitude, the data have been taken in two parameters, 14 time-of-flight and 8 amplitude bits, using a data acquisition system developed at CBNM.[6] A weighting over 256 amplitude channels was applied to achieve a detector response proportional to the total energy released in the capture process. The weighting factors used have been calculated by means of a Monte Carlo based computer code originally developed at Cadarache[7] and later modified for our detector system in collaboration with Karlsruhe[8]. The neutron flux was measured using the same C_6D_6 detector system by replacing the Pd sample with a ^{10}B slab. Absolute calibration was obtained by the black resonance technique using resonances in Ag below 72 eV. The thickness of the Ag sample was 5.87 10^{-3} atoms/barn.

Elastic scattering experiments

The scattering experiments were performed with six ^{3}He high pressure gaseous scintillators as neutron detectors. The scattering cross sections were measured using lead and carbon as standard scattering samples. Data were taken only for ^{105}Pd and ^{108}Pd using the same sample thicknesses as for the capture measurements.

Transmission experiments

Four ^{3}He high pressure gaseous scintillators were installed as transmission detector at 30 meters for ^{105}Pd and at 60 meters for the even isotopes ^{104,106,108,110}Pd. The samples were cooled by liquid nitrogen. The sample thicknesses were : 8.32 10^{-3} for ^{104}Pd (95.25%), 1.096 10^{-2} for ^{105}Pd (97.38%), 1.048 10^{-2} for ^{106}Pd (98.48%), 2.50 10^{-3} for ^{108}Pd (98.88%) and 6.06 10^{-3} for ^{110}Pd (97.73%).

p-wave assignment of neutron resonances

Excited states at low energy of the uneven compound nuclei ^{105,107,109}Pd are predominantly of positive parity permissible for E1 transitions from p-wave resonances. So it is to be expected that the capture gamma ray spectra for p-wave resonances show

more high energy transitions to low lying states than for the s-wave resonances. Not much information is known on the energies and spin and parity of low-lying states in the compound nucleus ^{111}Pd, but we suppose that the overall picture will be the same as for the other Pd isotopes

To make a parity assignment of neutron resonances we compare, in the capture data, the resonance areas of the time-of-flight data taken with a high bias for the gamma rays (binding energy minus 1 MeV) to the resonance data taken with a low bias. Up to now we performed such measurements for ^{108}Pd using a C_6D_6 scintillator (low bias 0.1 MeV) and a 7" x 6" NaI(Tl) scintillator (low bias 0.55 MeV) as capture detectors and for ^{110}Pd using the NaI(Tl) scintillator. The results with the C_6D_6 were communicated at the Harwell Conference [9]. The data taken with the NaI(Tl) detector are not yet analysed.

Analysis

The transmission data were analysed with the multi level Breit-Wigner fitting routine SIOB[10].

The scattering data were corrected for multiple interaction effects using a Monte-Carlo computer code. An area analysis on the corrected data yields Γ_n as a function of Γ_γ.

The capture data have been analysed using a modified Tacasi area analysis programme[11] which includes corrections for Doppler and resolution effects. The influence of multiple scattering on the capture area is taken into account by means of a Monte Carlo routine.

Results

^{105}Pd

Resonance-parameter analysis was performed up to 2keV where the resonances start overlapping each other more and more. Preliminary results,only from the analysis of the transmission data, were communicated at the Harwell conference [9]. The final results reported here are from the complete analysis of capture, elastic scattering and transmission data and are corrected for the contribution of strong resonances in the even isotopes and appearing in the ^{105}Pd data (enrichment of the ^{105}Pd sample was 97.38%). Neutron widths were determined for 200 resonances and the capture widths for 71 of them.

The average capture width was determined as :

$$\langle\Gamma_\gamma\rangle = 150 \text{ meV} \pm 1 \text{ meV (stat. error)} \pm 8 \text{ meV (syst. error)}$$

The contribution from p-wave resonances to the strength function can be neglected in this energy-range so that the s-wave strength function can be determined from the data :

$$S_o = \frac{\Sigma\, g\Gamma_n^o}{\Delta E} = 0.63 \pm 0.07 \times 10^{-4} \text{ (200 resonances below 2051 eV)}$$

The level spacing has been determined using a method [12] which separates large s-wave resonances from smaller ones and from resonances with higher angular momentum ($\ell \geq 1$) by means of the Bayes theorem. The number of s-wave resonances lost in this procedure has been estimated assuming a Porter Thomas distribution of the reduced neutron widths. For ^{105}Pd this yields a value of

$$D = (10.0 \pm 0.5) \text{ eV}.$$

The capture cross section measurements in the unresolved resonance range performed at R.P.I. were normalised to the resonance capture area of the 55.2eV resonance with a neutron width of $2g\Gamma_n = 6.9$. We find $2g\Gamma_n = 6.70 \pm 0.04$ meV (st. error) for that resonance which is in good agreement with ref. 1 but larger than the value 6.36 ± 0.12 meV of ref. 2.

^{106}Pd

The neutron widths were determined from the transmission data for 172 resonances up to 20 keV. In fig.1 is shown the cumulative sum of reduced neutron widths ($\Gamma_n/\sqrt{E_o}$) versus neutron energy. As can be seen on that figure, the strength function is roughly two times larger below 4 keV than above that limit.

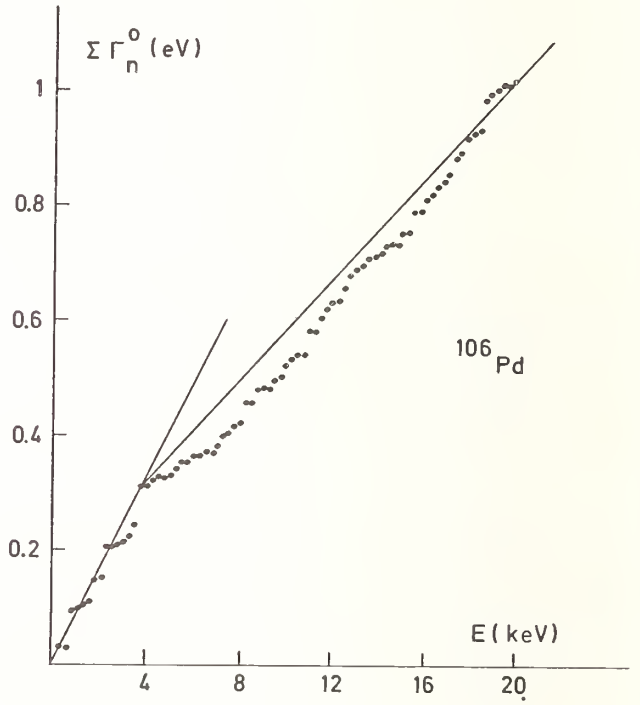

Fig 1 : ^{106}Pd cumulative sum of reduced neutron widths versus neutron energy

We did not perform, up to now, a parity-assignment of the neutron resonances. However, below 4 keV, more than 80% of the strength is due to strong s-wave resonances which can be identified by their strong resonance-potential interference term in the total cross section. So we conclude that the structure is probably in the s-wave strength function.

^{108}Pd

The results for the s-wave strength function $S_o = 0.78\,^{+\,0.19}_{-\,0.15}\,10^{-4}$ and for the average capture width $\langle\Gamma_\gamma\rangle = 76.8$ meV $\pm$ 2.8 meV (stat. error) $\pm$4 meV (syst. error) were already communicated at the Harwell Conference[9]. We did additional experiments for the parity assignment of the resonances using a Na I scintillator for the capture spectra measurements but

these data are not yet analysed. Transmission experiments with a thick sample will be started soon and should allow the determination of neutron widths up to 30 keV.

^{110}Pd

Neutron widths were deduced from the shape-analysis of the transmission experiments for 121 resonances up to 40 keV. However because of resolution and Doppler effect, the analysis above 25 keV was only possible for 16 broad resonances. The data show a very pronounced structure in the strength functions as can be seen from figures 2 and 3.

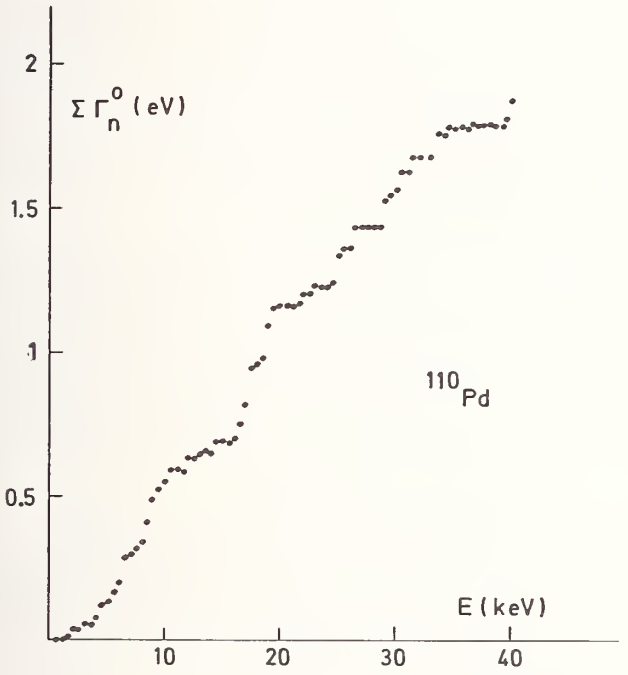

Fig 2 : ^{110}Pd, cumulative sum of reduced neutron widths versus neutron energy

In figure 3 we show the strength function over intervals of 4 keV. There are fluctuations of as large as a factor of 7. Although the strength function has a minimum below 4 keV, we have detected 26 resonances in that energy range which means that the error on the strength function is approximately 30% for that energy interval. At higher energies, and especially above 25 keV, the data are poor. However, we are quite confident that we have analysed a large fraction of the resonances contributing significantly to the strength function and that we may state that the error on the strength function for each interval of 4 keV is much smaller than the magnitude of the structure. We have not yet completed our low bias to high bias ratio capture experiments, but for the same reason as in the ^{106}Pd case, we believe that the structure is in the s-wave strength function.

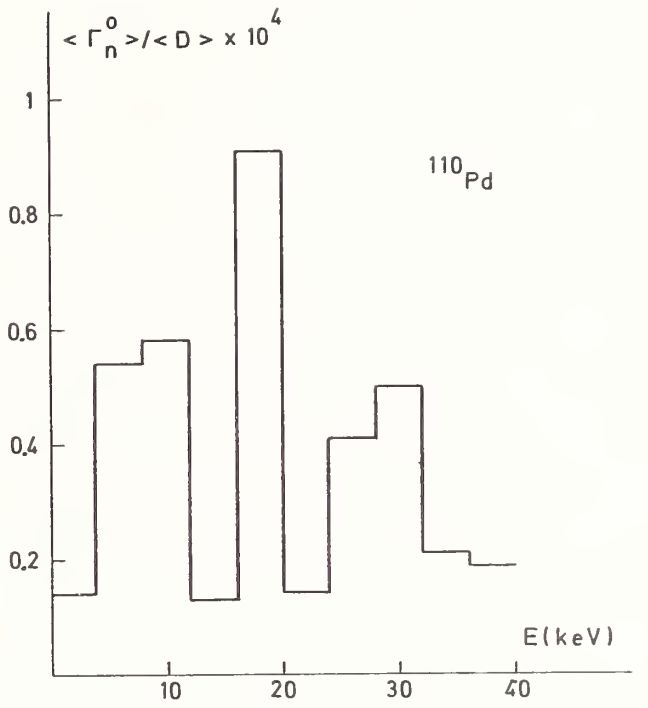

Fig 3 : ^{110}Pd, "Strength Function" averaged over energy intervals of 4 keV, s- and p-wave resonances

Conclusions

Resonance parameters and their average properties were obtained for the important fission product ^{105}Pd from capture, scattering and transmission data. The work for the even isotopes is not completed yet but preliminary results show very pronounced intermediate structure effects in the strength function.

Acknowledgement

Thanks are due to the sample preparation group of CBNM for preparing the metallic Pd samples, to the electronic and mechanical workshops of CBNM and S.C.K. for technical support, and to the linac operation group.

References

1. R.W. Hockenbury, H.R. Knox and N.N. Kanshal, in Proceedings of the Conference on Nuclear Cross Sections and Technology, Washington, D.C. USA, 1975, ed. by R.A. Schrack and C.D. Bowman (NBS Special Publication 425, Vol. II, 1975) p. 905

2. A.V. Popov, K. Trzeciak, Khvan Cher Gu, Report SINR, 83 - 11013, 1977

3. Hvan Cher Gu, A.B. Popov, K. Trzeciak, in Proceedings of the Conference on Neutron Physics and Nuclear Data, Harwell, 1978 (OECD Publication 1978) p. 327

4. V.N. Singh, R.C. Block and Y. Nakagama, Nuclear Science and Engineering, 67, 54 (1978)

5. R.L. Macklin, J. Halperin and R.R. Winters, Nuclear Science and Engineering, 71, 182 (1979)

6. T. Babeliowsky, C. Cervini and A. De Keyser, "A data acquisition system for weighted multi-parameter measurements", in preparation

7. C. Le Rigoleur and A. Armand, Proceedings of NEACRP/NEANDC Specialists' Meeting at Karlsruhe, published in KFK 2046 (1975)

8. F. Hensley, private communication

9. P. Staveloz, E. Cornelis, L. Mewissen, F. Poortmans, G. Rohr, R. Shelley and T. van der Veen, in Proceedings of the Conference on Neutron Physics and Nuclear Data, Harwell, 1978 (OECD Publication, 1978) p. 701

10. G. de Saussure, D.K. Olsen and R.B. Perez, Report ORNL/TM - 6286, 1978

11. F.H. Fröhner, Report GA - 6906 (1966)

12. G. Rohr and L. Maisano, Specialists' Meeting of Neutron Cross Sections of Fission Product Nuclei, CNEN, Bologna, December 1979, to be published

RESONANCE PARAMETERS OF ^{96}Zr BELOW 40 keV

C. Coceva, P. Giacobbe and M. Magnani
Comitato Nazionale Energia Nucleare
Via Mazzini 2, Bologna, Italy

Time-of-flight neutron transmission measurements on ZrO_2 enriched samples, performed with high resolution, allowed evaluation of energy, spin, parity and neutron width of fourteen ^{96}Zr resonances below 40 keV. Accurate single-level analysis was carried out. Strength function estimate is significant only for p-wave, owing to the limited number of resonances.

[Zr(n,total) cross section, 0.3-40 keV, single level analysis, E_o, ℓ, J, Γ_n.]

Introduction

Measurements available in the literature of resonance parameters of the various Zr isotopes often show considerably discrepant results (see, for ^{96}Zr, refs 1, 2,3). This is particularly inconvenient for an element such as zirconium, which is of great importance for reactor technology and of considerable interest as it lies near the minimum of the s-wave neutron strength function and at the 3p maximum of the p-wave strength function, as predicted by the optical model.

A contribution to reliable determination of ^{91}Zr parameters was given in a previous work[4] based on transmission, capture cross section and gamma-ray spectra measurements. The present work on ^{96}Zr is only concerned with time-of-flight transmission measurements. These were performed at the Geel electron linac within the frame of a CNEN-Euratom cooperation programme which included also capture experiments whose analysis is in progress.

Measurement

Time-of-flight measurements were performed on a 100 m flight path using three ZrO_2 enriched samples having thicknesses of 7×10^{-3}, 6.1×10^{-3} and 0.9×10^{-3} at/barn, and ^{96}Zr enrichments 61%, 57% and 85%, respectively. Several measurements were made with each sample under different experimental conditions and over different energy ranges. The neutron transmission was measured up to 130 keV; however, the small size of the samples at disposal (14.95 g total oxide weight) prevented the obtaining of good data statistics above 40 keV within a reasonable time.

The electron pulse width was 22 ns. The neutron detector consisted of a 1.5 cm thick ^{10}B plug, viewed by two 10x10 cm NaI(Tl) crystals. Automatic gain control amplifiers were used in order to ensure that detection efficiency be not affected by gain variation of the multiplier phototubes. This enables the setting of a rather narrow window at the 480 keV γ-ray peak, thus improving the signal-to-background ratio, and allows reliable determination of the background by means of runs with black resonances.

Data analysis

Transmission spectra were analyzed with the shape-analysis computer programme described in ref. 6, using single-level formalism. The programme can simultaneously treat several spectra with different thickness and enrichment. The analysis of neutron resonances was interrupted at 40 keV because the presence of many resonances of other Zr isotopes would have prevented reliable resonance parameter estimates above this energy. The resonances did not display any multilevel effect, at least within the statistics and resolution limits of the experiment.

Accurate analysis of the transmission data requires an exact description of the resolution function. On the basis of ref. 5, the contributions to the resolution function coming from: a) the spread of the neutron burst generated by the particular moderator used, b) the inclination of the flight path with respect to the moderator face and c) the neutron path distribution in the detector, were determined; the last contribution was calculated with the same Montecarlo routine described in ref. 5. The overall effect may be expressed as a function of an effective distance d as:

$$f(z) = \frac{z^{\nu/2-1}}{2^{\nu/2}\,\Gamma(\nu/2)}\, e^{-z/2} \qquad (1)$$

with

$$d = a_1 z + a_2 z^2 + a_3 z^3 \qquad (2)$$

In fig. 1 the function calculated for 3-30 keV energy is represented, and the values of the parameters ν, a_1, a_2, a_3 are given. For any neutron energy, this function of length may be converted into a function of flight-time and folded with the electron pulse

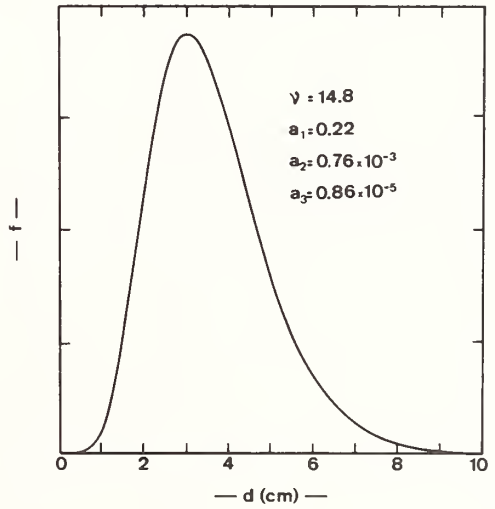

Fig. 1 - Resolution function resulting from the contribution of the neutron burst spread, of the flight-path inclination and of the neutron path distribution in the detector. Giving an "effective distance" d in abscissa, the same function holds in a wide energy range: in this case from 3 to 30 keV. The values of the parameters to be introduced in eqs. (1) and (2) are shown.

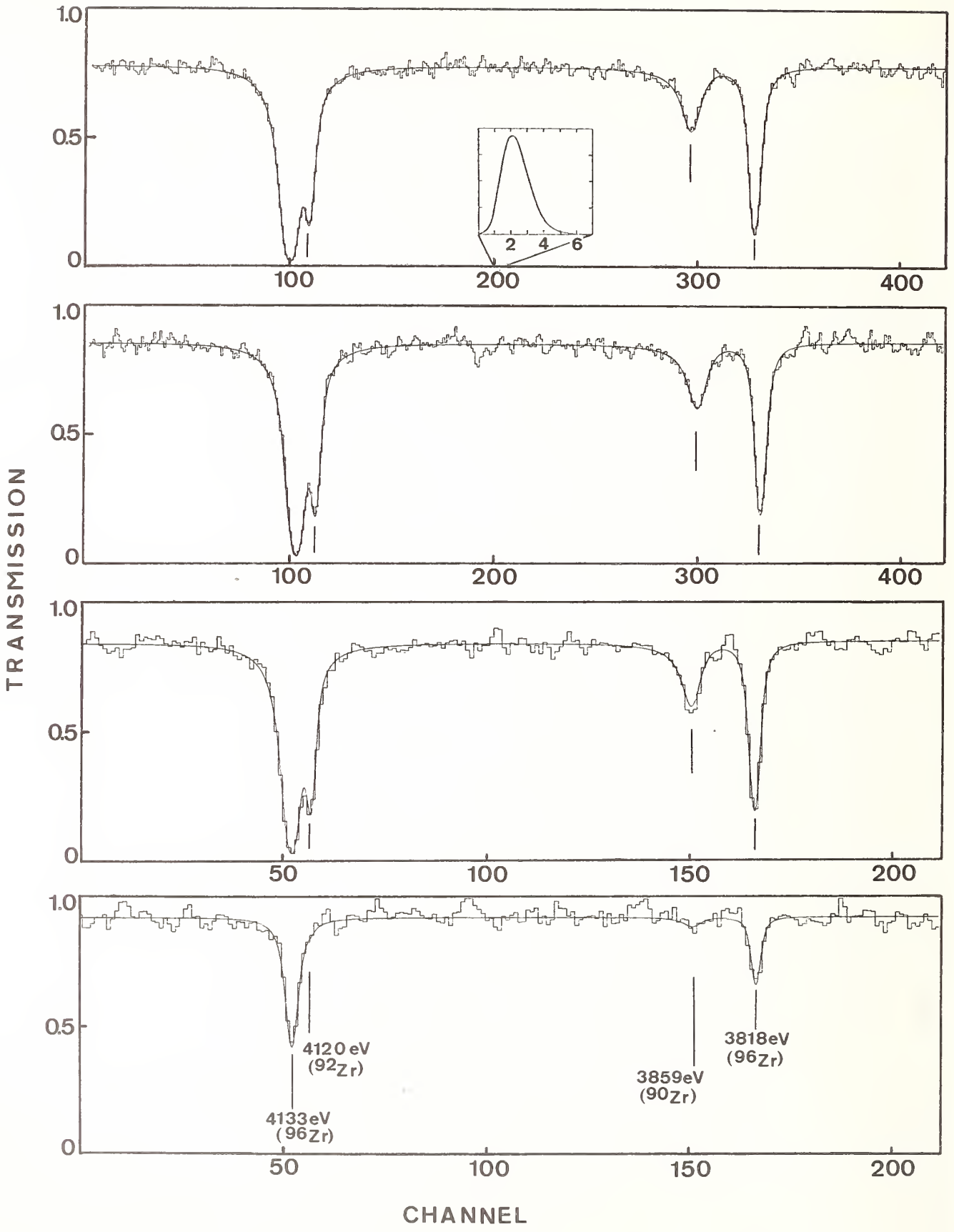

Fig. 2 - Example of a simultaneous fit of four transmission spectra referring to different samples in the same energy interval at about 4 keV. The channel width is 20 ns in the first two spectra and 40 ns in the last two. The complete resolution function at a particular time-of-flight is represented in the first spectrum.

Table I. Resonance parameters of ^{96}Zr below 40 keV

E_o (eV)	$g\Gamma_n$ (eV) present work	$g\Gamma_n$ (eV) ref.3	ℓ pres. work	ℓ ref.3	g pres. work	g ref.3	Γ_n (eV)	
301.1	0.215 ± 0.002	0.141	1	1	1	(1)	0.215	a)
3818	3.93 ± 0.06	2.85	1	1	1	1	3.93	
4133	14.9 ± 0.2	11.8	1	1	2	2	7.45	
5443	25.3 ± 0.5	17.4	0	0	1	1	25.3	
5971	11.6 ± 0.6	7.5	1	1	2	(2)	5.8	
9004	9.9 ± 0.4	8.8	1	1	1	(2)	9.9	
13278	6.0 ± 0.4	3.4	1	1	1		6.0	
15138	9.2 ± 0.5	3.9	1	1	(1)		(9.2)	
15419	66.1 ± 1.5	39	0	0	1	1	66.1	
17779	16.1 ± 1.0	12.4	1	1	(1)	2	(16.1)	
24687	13.6 ± 1.5	7.3	0	0	1	1	13.6	
29830	584 ± 12	304	1	1	2	1	292	
35177	67.3 ± 5.0	31		0	(1)	1	(67.3)	
35880		14		1				
36666	141 ± 6	80	1	1	2	(2)	70.5	

a) measured $\Gamma_\gamma = 0.258 \pm 0.015$ eV.

shape. The electron pulse shape is approximated by a trapezium 22 ns f.w.h.m.- In ref. 6 this procedure is discussed also with reference to a correct determination of resonance energy. An example of the resolution function is given in Fig. 2 for a specific time-of-flight. For the first resonance at 301 eV the results were obtained also from the analysis of transmission spectra of three metallic samples having thicknesses in the range 0.023-0.14 at/barn. Such samples allowed highly precise resonance parameter determination.

For oxide-sample spectra analysis an effective temperature of 317°K was assumed, according to ref. 4.

Results

The analysis allowed determination of energy, spin, parity and neutron width of fourteen resonances below 40 keV. For the 301 eV resonance the gamma width, too, was evaluated.

Comparison of these results with the values reported in the literature must be made essentially with reference to the most recent work by Musgrove et al.[3]. Energy values are almost coincident. The same holds for parity assignments, except for the 35.18 keV resonance, for which we could not confirm the $\ell=0$ assignment. As for spin, three tentative assignments of ref. 3 were confirmed and two new assignments given. Discrepancies concern the 9.0 , 17.8 and 29.8 keV resonances.

For neutron widths, on the contrary, the estimates of the present work are systematically higher than those of ref. 3 and by a large amount. It is possible that the analysis routine plays a major rôle in producing such discrepancies; this point should be carefully examined in connection with data evaluation.

Complete results are given in Tab. I. For calculating the p-wave reduced width a radius $R = 7.1$ fm was assumed.

The small number of s-wave resonances does not allow a meaningful estimate of the strength function. Taking correctly into account the Porter-Thomas neutron width fluctuations and those of the resonance spacings, one would get

$$S_o = (0.39^{+1.11}_{-0.17}) \times 10^{-4} ,$$

where the indicated 68% confidence limits are too large to be significant. For p-wave, the ten assigned resonances give as 68% confidence limits:

$$S_1 = (11.6^{+9.5}_{-3.7}) \times 10^{-4}$$

The lower limit is higher than the value $S_1 = 7.4$ given in ref. 3. The estimated S_1 value is much higher than predicted by conventional optical model calculations, but in good agreement with the calcula-

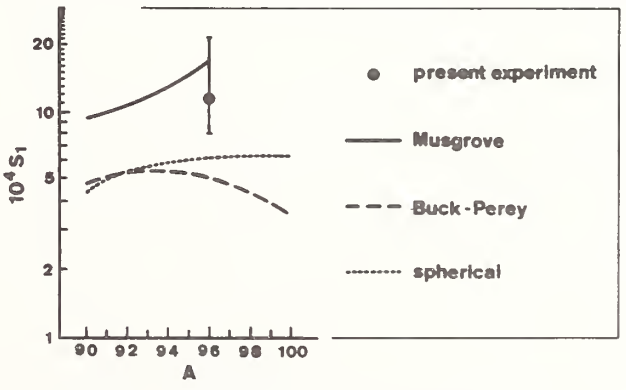

Fig. 3 - Comparison of the measured ^{96}Zr p-wave strength function with some optical model calculations: a) potential including an imaginary isospin term[7] (solid line), b) potential including collective and spin-orbit coupling[10] (dashed line), c) spherical potential[10] (dotted line).

tions reported in ref. 7 performed with an optical potential characterized by the introduction of an imaginary isospin term[8,9]. In Fig. 3 the result of the present experiment is compared with the curve given in table 6b of ref. 7 valid for the even-A Zr isotopes and with two typical optical-model predictions[10].

Acknowledgements

The authors are grateful to R. Simonini for his Montecarlo calculations of the resolution function.

References

1. S.S. Moskalev, H.V. Muradyan and Yu.V. Adamchuk, Nucl. Phys. 53, 667 (1964).

2. W.M. Good and H. Kim, Phys. Rev. 165, 1329 (1968).

3. A.R. de L. Musgrove, W.M. Good and J.A. Harvey, AAEC/E415 Report, 1977.

4. A. Brusegan, F. Corvi, G. Rohr, C. Coceva, P. Giacobbe and M. Magnani, in Proceedings of the International Conference on Neutron Physics and Nuclear Data for Reactors and other Applied Purposes, Harwell, September 1978, p. 706.

5. A. Bignami, C. Coceva and R. Simonini, EUR 5157 e Report, 1974.

6. P. Giacobbe and M. Magnani, RT/FI(79)17 and NEANDC(E)208'L' Report, 1979.

7. A.R. de L. Musgrove, B.J. Allen, J.W. Boldeman and R.L. Macklin, in Proceedings of the International Conference on Neutron Physics etc., Harwell, September 1978, p. 449.

8. F. Perey, Phys. Rev. 131, 745 (1963).

9. H. Tellier and C.M. Newstead, in Proceedings of the Third Conference on Neutron Cross Sections and Technology, Knoxville, March 1971, p. 680.

10. B. Buck and F. Perey, Phys. Rev. Lett. 8, 444 (1962).

NEUTRON CAPTURE CROSS SECTIONS OF Y, Nb, Gd, W AND Au BETWEEN 0.5 AND 3.0 MeV

G. Grenier, J.P. Delaroche, S. Joly, Ch. Lagrange, J. Voignier
Service de Physique Neutronique et Nucléaire
Centre d'Etudes de Bruyères-le-Châtel
B.P. n° 561
92542 MONTROUGE CEDEX, France

Absolute neutron capture cross section measurements for Y, Nb, Gd, W and Au as well as for the following isotopes ^{155}Gd, ^{156}Gd, ^{157}Gd, ^{158}Gd, ^{182}W, ^{183}W, ^{184}W, ^{186}W were carried out in the 0.5 MeV - 3.0 MeV energy range. For most of these isotopes, available data were scarce and discrepant. In the present work the capture cross sections were determined through direct γ-ray spectrum emitted by the samples (integrated spectrum method)[1] and compared with statistical model calculations involving transmission coefficients deduced from spherical or deformed optical potential analyses.

[Y, Nb, Gd, W and Au(n,γ), 0.5 - 3 MeV, statistical model calculations].

Introduction

Fast neutron capture spectra and cross sections are important for the understanding of nuclear reaction mechanisms and for various applications in nuclear technology.

Moreover, systematic capture cross sections in the mass region $90 < A < 200$ for neutrons in the energy range from 0.5 to 3.0 MeV test the validity of statistical model calculations.

Two main techniques are used in neutron capture cross section measurements. The first is the activation method which was historically the first means of measurement in the MeV energy range. Although this method is technically easy to use, it is limited to final nuclei having suitable lifetimes and well-known decay schemes. An other of its disadvantages, is its high sensitivity to all secondary neutrons produced in the surrounding materials.

In the second method, one detects prompt γ-rays with large liquid scintillators, Moxon-Rae and Maier-Leibnitz detectors. In this method, the γ-ray detector efficiency must be independent of the cascade. This independence is obtained by :

- an efficiency near 100% in large liquid scintillators,
- the principle of detection in Moxon-Rae detectors and,
- a weighting function associated with each pulse in Maier-Leibnitz detectors.

The main uncertainty for large liquid detectors is due to high thresholds used. Moxon-Rae detectors are easy to use but they have low efficiencies. Maier-Leibnitz counters are generally used up to 1 MeV but at higher neutron energy events due to (n,n',γ) reaction cause problems with the weighting functions.

In the present work, capture cross sections for neutrons in the energy range from 0.5 to 3.0 MeV were determined from the direct γ-ray spectrum. The γ-rays were detected by a NaI scintillator surrounded by an annular NaI detector. Because the solid angle was small, the probability of detection of more than one γ-ray of the cascade is small and the energy distribution of the capture γ-rays can be measured. Moreover, γ-ray strength functions can be investigated.

Absolute neutron-capture cross sections for Y, Nb, Gd, W and Au as well as for the following isotopes ^{155}Gd, ^{156}Gd, ^{157}Gd, ^{158}Gd, ^{160}Gd, ^{182}W, ^{183}W, ^{184}W, ^{186}W were measured with this method.

Results are compared with previous data and with statistical model calculations involving transmission coefficients deduced from spherical or deformed optical potential analyses.

Experimental procedure

The integrated spectrum method used has been described in some detail elsewhere[1] and is summarized briefly below. The pulsed and bunched beam of the 4 MV Van de Graaff accelerator of the Centre d'Etudes de Bruyères-le-Châtel was used.

Neutrons in the energy range from 0.5 to 3.0 MeV were produced by the $^{7}Li(p,n)^{7}Be$ and $T(p,n)^{3}He$ reactions. The targets consisted of metallic lithium or tritium adsorbed in titanium on tantalum or gold backings. The spectrometer was used in the anti-Compton (AC) and first escape modes (PE) simultaneously. The γ-ray detector efficiency as a function of γ-ray energy was determined by calibrated-radioactive sources and by nuclear reactions. The same sources and reactions were used to build the response matrices (AC and PE modes) of the spectrometer. The neutron flux was measured by a directional long counter.

Measurements and data processing

Pulse-height spectra (AC and PE) were recorded with appropriate gating windows on the time-of-flight (TOF) spectra. The pulse-height spectra were then corrected for time independent events. In addition, data were recorded event by event on magnetic tape so that different TOF windows could be set in subsequent analyses. The net pulse-height spectra were converted to γ-ray distributions using a least-squares unfolding method[2].

A general method which can be used to determine the number of captures requires the knowledge of the γ-ray distribution per capture. Using the statistical model, the distribution $\nu(U,E_\gamma)$ of capture γ-rays emitted by levels at energy U can be calculated from the level density distribution $\rho(U)$ and the γ-ray strength function $f(E_\gamma)$. The total spectrum $\nu(E_\gamma)$ has been calculated using the procedure described in references [3-5]. The level densities were determined according to Dilg et al.[6]. The function $f(E_\gamma)$ was obtained by the best fit between experimental and computed γ-ray distributions containing only capture events. Then the strength function was extrapolated to zero energy to obtain the final γ-ray distribution per capture.

The number of captures is the ratio, R, between

the experimental γ-ray spectrum, $S(E_\gamma)$, and the computed γ-ray distribution per capture $\nu(E_\gamma)$:

$$R = \int_{E_{min}}^{E_{max}} S(E_\gamma)\, dE_\gamma \Big/ \int_{E_{min}}^{E_{max}} \nu(E_\gamma)\, dE_\gamma$$

where E_{max} is the sum of the neutron binding energy, B_n, and the kinetic energy in the center-of-mass system and E_{min} is the threshold chosen for the capture γ-ray spectrum.

In the other method, the number of captures, R', is given by the principle of energy conservation :

$$R' = \frac{1}{E_{max}} \int_{o}^{E_{max}} E_\gamma \cdot S(E_\gamma)\, dE_\gamma$$

The observed spectrum must be extrapolated to zero energy. So, this method is more useful to low energy region.

In both methods, assuming that the angular distribution of capture γ-rays is isotropic, the capture cross section is given by :

$$\sigma_{n\gamma} = 4\,\pi\, R/N\, \emptyset$$

where N : is the number of nuclei in the sample
$\emptyset$: is the average neutron flux per cm^2.

Several corrections are required to obtain absolute cross sections :

- γ-ray attenuation in the sample,
- attenuation of neutrons in the sample,
- multiple scattering of neutrons in the sample,
- transmission of neutrons through the sample and through the air between the sample and the long counter, and,
- neutron source anisotropy.

Except for the transmission of neutrons (obtained experimentally) all the other corrections were calculated by a modified version of the Monte Carlo programme of D.L. Smith[6].

Statistical model calculations

The present measurements are now compared to some statistical model (SM) calculations. The de-excitation modes practically available to the compound nuclei are elastic and inelastic scattering and capture. The compound nucleus cross sections have been determined from separate spherical or deformed optical model calculations performed over a large energy range (10 keV-15 MeV). In view of SM studies, the useful parameters other than transmission coefficients (deduced from Optical Model calculations) are the average radiation widths and level densities as explained in the companion contributed paper to this Conference by Delaroche et al. In table I the level density parameters of gadolinium isotopes are shown as an example of results obtained from a method close to that of Gilbert and Cameron[8].

Results and discussion

Results are compared with previous data and with statistical model calculations in figs. 1 through 14.

- Yttrium capture cross sections versus neutron energy are shown in fig. 1. All cross sections above 0.5 MeV are obtained by activation. We agree very well with values of Stupegia[9] and Korovela[10]. The solid curve represents a calculation made by Thomet[15] in 1975. The ENDF/BIV evaluation is systematically too high.

Table I. Gadolinium isotopes level density parameters E_o, T, a^{-1} and E_x for the level density laws : $E < E_x$, $\rho_1(E) \sim exp\ [E-E_o)/T]$, $E > E_x$, $\rho_2(E) \sim exp\ [a(E-\delta)]^{1/2}$ The pairing parameters δ are from Cook et al.[7].

Nucleus	E_o(MeV)	T(MeV)	a(MeV^{-1})	E_x(MeV)
^{152}Gd	0.100	0.520	21.000	5.682
^{153}Gd	-1.100	0.513	21.773	4.643
^{154}Gd	-0.050	0.526	21.300	5.856
^{155}Gd	-1.200	0.533	21.294	4.941
^{156}Gd	-0.150	0.546	21.497	6.520
^{157}Gd	-0.950	0.535	20.459	4.809
^{158}Gd	-0.200	0.565	20.773	6.703
^{159}Gd	-0.900	0.537	21.364	5.373
^{160}Gd	-0.100	0.546	20.200	5.840
^{161}Gd	-0.650	0.520	19.426	4.124

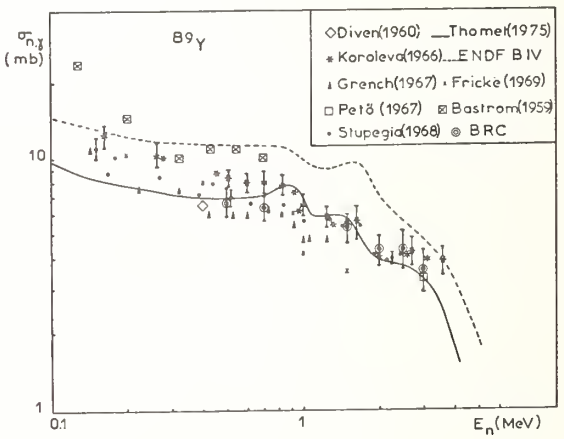

Fig. 1 . Neutron capture cross section for $^{89}Y(n,\gamma)$.

- Niobium capture cross sections are presented in fig. 2. Most results for niobium were obtained by a prompt γ-ray method. Our results are in good agreement with recent data of Macklin[21] and those of Poënitz[22] up to 1.2 MeV. Above this energy our values are higher than those of Poënitz (≃ 15% at 2 MeV). Calculations of Lagrange fit very well all recent experimental data.

- Capture cross sections of the isotopes ^{155}Gd, ^{156}Gd, ^{157}Gd, ^{158}Gd and ^{160}Gd, as well as natural gadolinium are shown in figs. 3 through 8. With the exception of ^{158}Gd, there are no data in the energy range from 0.5 to 3 MeV for other isotopes of gadolinium. Other results for ^{158}Gd obtained by the activation method and our values are in agreement, except our datum at 0.5 MeV which appears to be too high.

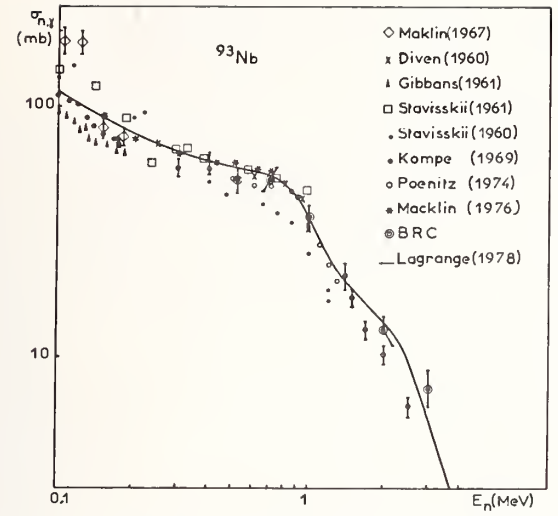

Fig. 2 . Neutron capture cross section for $^{93}Nb(n,\gamma)$.

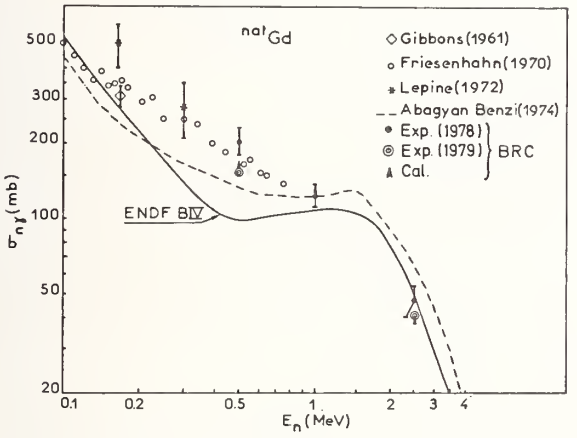

Fig. 3 . Neutron capture cross section for $^{nat}Gd(n,\gamma)$.

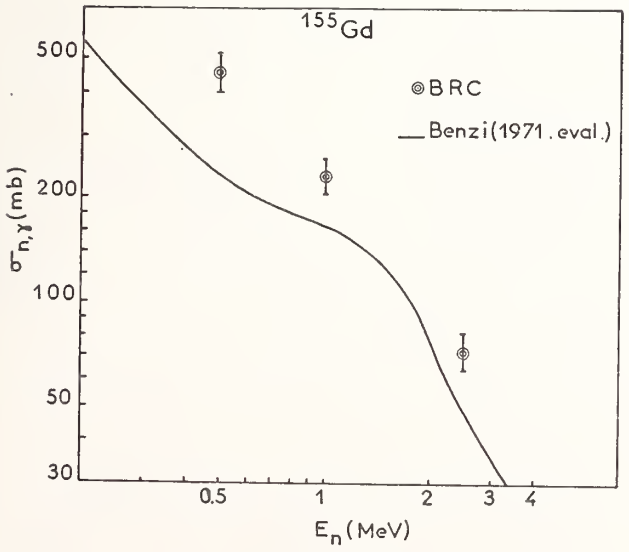

Fig. 4 . Neutron capture cross section for $^{155}Gd(n,\gamma)$.

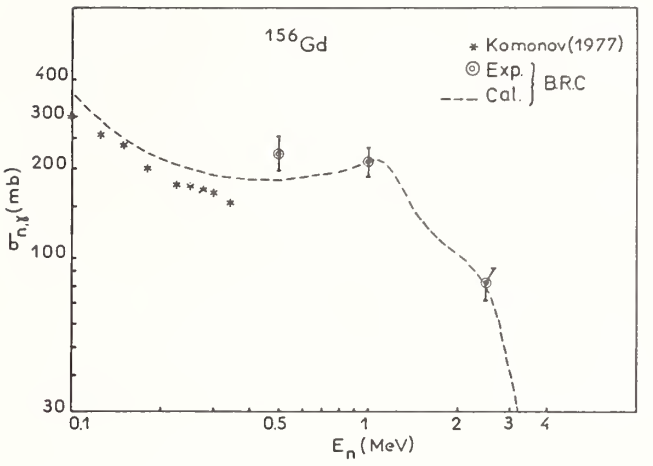

Fig. 5 . Neutron capture cross section for $^{156}Gd(n,\gamma)$.

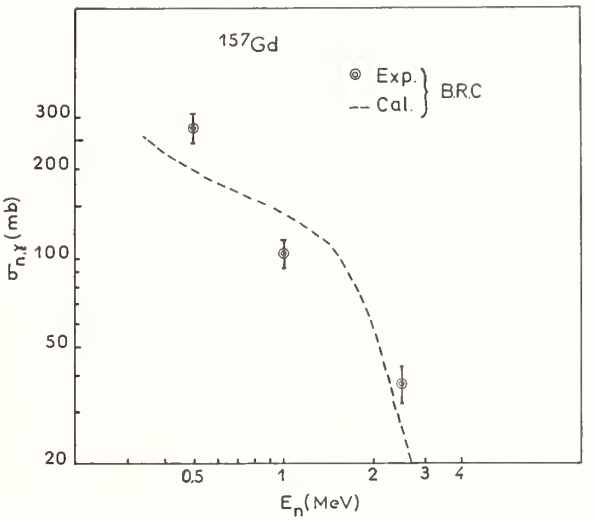

Fig. 6 . Neutron capture cross section for $^{157}Gd(n,\gamma)$.

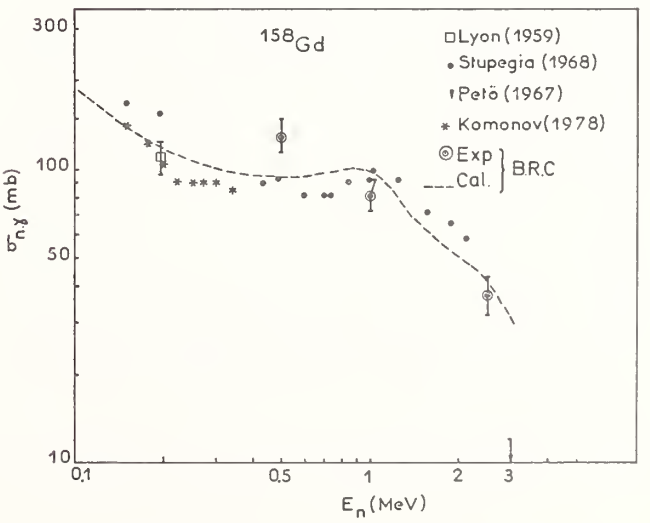

Fig. 7 . Neutron capture cross section for $^{158}Gd(n,\gamma)$.

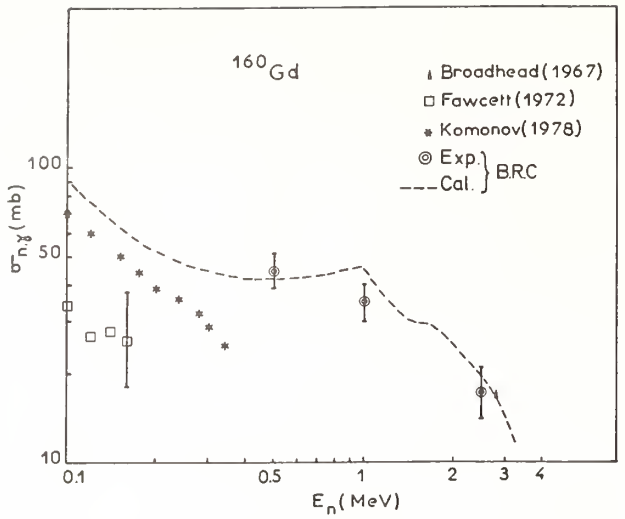

Fig. 8 . Neutron capture cross section for $^{160}Gd(n,\gamma)$.

Our experimental results are again in good agreement with calculations made at BRC but the Komonov values[25] seem systematically lower. For ^{155}Gd preliminary SM calculations have been made. In contrast with the other cases, it has not been possible to reproduce even roughly, the energy variation or the magnitude of the measured capture cross sections. This discrepancy is still not understood. However, it seems that the problem concerns the lack of precise knowledge of the excited states.

- Capture cross sections of the isotopes of ^{183}W, ^{184}W, ^{185}W, ^{186}W, and natural tungsten are presented in figs. 9 through 13. The status for the tungsten isotopes is similar to that for gadolinium. With the exception of ^{186}W there are no data above 0.5 MeV. For ^{186}W a lot of activation data are available. As with gadolinium Komonov values[33] are too low. Our results are in good agreement with other data. Calculations are also very consistent with most of the data. For natural tungsten we agree at 0.5 MeV with the Fricke values[34] which are the most recent data. Our experimental results and calculations show a large discrepancy with the Devaney evaluation[35].

- Results concerning the capture cross section of gold are given in fig. 14. The capture cross section of gold is a standard, so the comparison between our results and previous data is important. Our values are in good agreement with recent activation measurements of Paulsen[40] and Lindner[41]. These values agree also with prompt γ-ray measurements of Poënitz[42], except at 2.5 MeV where our result is 15% lower than his. Our results and other recent data are also well consistent with statistical model calculations (solid curve)[44].

References

1. S. Joly, J. Voignier, G. Grenier, D. Drake and L. Nilsson, Nucl. Instr. Methods 153, 493 (1978).
2. J.L. Trombka, in Proc. Symp. Applications of Computers to Nuclear and Radiochemistry, Gathinsburg Tennessee, October 17-19, 1962 National Academy of Sciences (1962).
3. N. Starfelt, Nucl. Phys. 53 (1964) 397.
4. E.S. Troubetzkoy, Phys. Rev. 122 (1961) 212.
5. G.A. Bartholomew et al., Advances in Nucl. Phys. 7 (1973) 229.

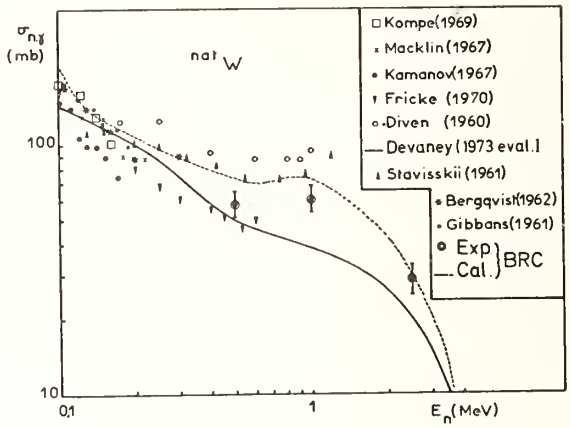

Fig. 9 . Neutron capture cross section for $^{nat}W(n,\gamma)$.

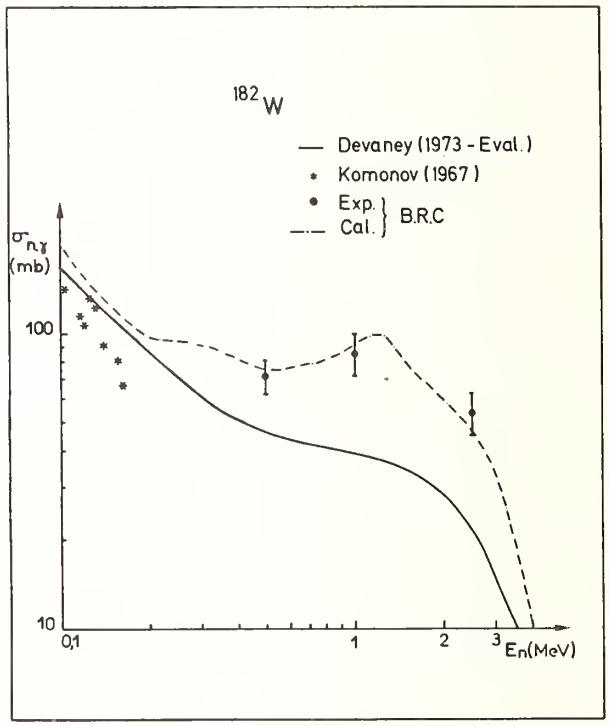

Fig. 10 . Neutron capture cross section for $^{182}W(n,\gamma)$.

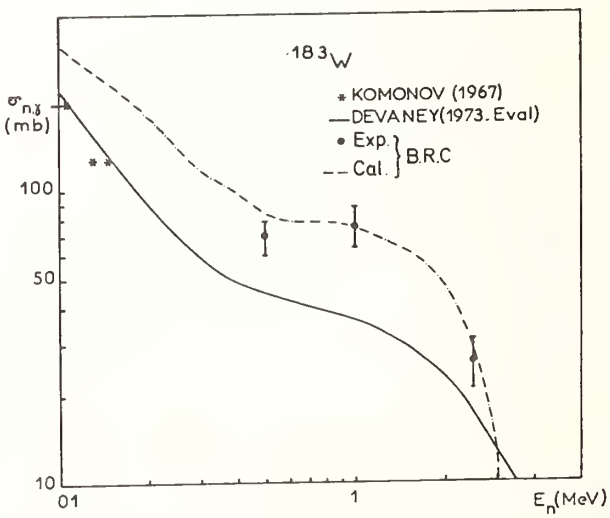

Fig. 11 . Neutron capture cross section for $^{183}W(n,\gamma)$.

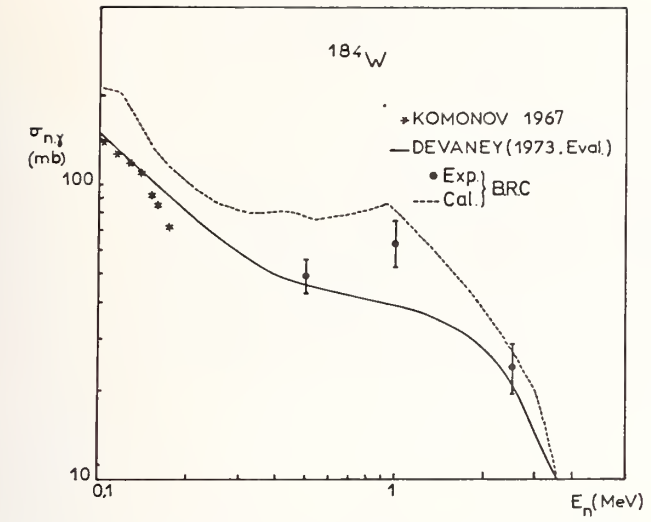

Fig. 12 . Neutron capture cross section for $^{184}W(n,\gamma)$.

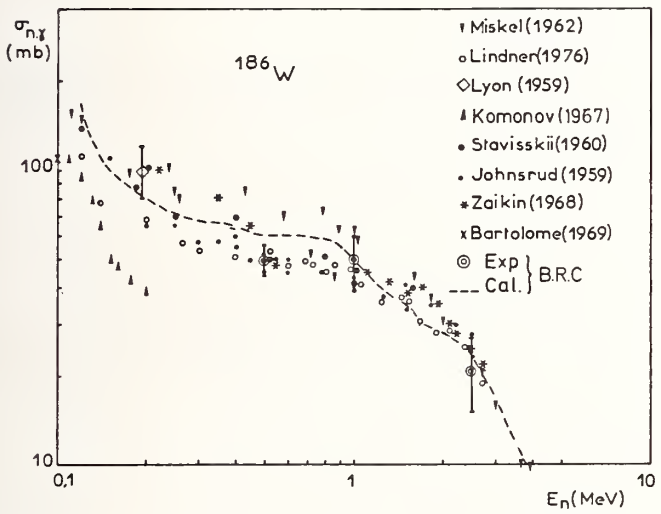

Fig. 13 . Neutron capture cross section for $^{186}W(n,\gamma)$.

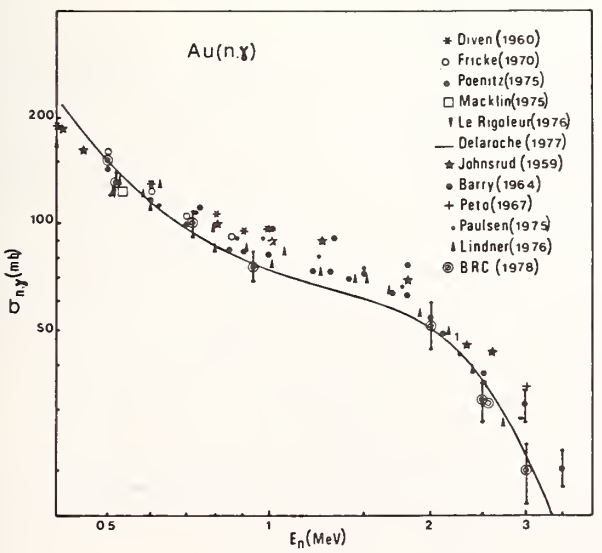

Fig. 14 . Neutron capture cross section for Au(n,γ).

6. D.L. Smith, ANL/NDM-17 (1975), Argonne National Laboratory, Argonne.
7. D.L. Cook et al., Aust. J. Phys. 20, 477 (1967).
8. A. Gilbert and A.G. Cameron, Can. J. Phys. 43,1446 (1965).
9. D.C. Stupegia et al., J. of Nucl. Energy, Vol. 22, p. 267-281 (1968).
10. V.P. Koroleva et al., Conf. Internationale sur les données nucléaires, Paris (1966), p. 473.
11. B.C. Diven et al., Phys. Rev. 120 (1960) 556.
12. H.A. Grench et al., Nucl. Phys. 194 (1967) 157.
13. M.P. Fricke et al., Phys. Lett. 29B (1969) 393.
14. N.A. Bastrom et al., Report WADC-TN 59-107, p. 126 (1959).
15. P. Thomet, Conf. Kiev (1975) Vol. 1 p. 252.
16. Y.Y. Stavinski et al., J. Nucl. Energy A316 (1962) 496.
17. Y.Y. Stavinski et al., Atomnaya Energiya 10 (1961) 264 - Atom. Energy 10 (1962) 255.
18. J.H. Gibbons et al., Phys. Rev. 122 (1961) 182.
19. D. Kompe, Nucl. Phys. A133 (1969) 513.
20. R.L. Macklin et al., Phys. Rev. 159 (1967) 1007.
21. R.L. Macklin, Nucl. Sci. and Eng. 59 (1976) 12.
22. W.P. Poënitz, Report ANL/NDM-8 (1974).
23. Ch. Lagrange, Internal. Report.
24. V. Benzi et al., Report DOC CEC (71) 9 (1971)
25. V.N. Komonov et al., Conf. Kiev (1977) Vol. 2 p. 206.
26. W.S. Lyon et al., Phys. Rev. 114 (1959) 1619.
27. G. Petö et al., J. of Nucl. Energy 21 (1967) 797.
28. Broadhead et al., A.R.I. 18, 279 (1967).
29. L.R. Fawcett et al., Nucl. Sci. and Eng. 49 (1972) 317.
30. S.J. Friesenhahn et al., Nucl. Phys. A146 (1970) 337.
31. J. Lepine et al., Nucl. Phys. A196 (1972) 83.
32. L.P. Abayan et al. "Benzi", Rep. INDC (CCP) 39/2 (1974) p. 102.
33. V.N. Komonov et al., Soviet J. of Nuclear Physics Vol. 4 n° 2 (1967) p. 204.
34. M.P. Fricke et al., Report IAEA-CN-26/43 (1970) p. 265.
35. J.J. Devaney, Report Los Alamos Laboratory LA 5221 (1973).
36. L. Bergqvist, Nucl. Phys. 39 (1962) 353.
37. A.E. Johnsrud et al., Phys. Rev. 114 927 (1959).
38. J.F. Barry, J. of Nuclear 18 491 (1964).
39. R.L. Macklin, Phys. Rev. 11 1270 (1975).
40. A. Paulsen et al., Atomkernenergy 26 80 (1975).
41. M. Lindner et al., Nucl. Sci. and Eng. 59 381 (1976).
42. W.P. Poënitz, Nucl. Sci. and Eng. 57 300 (1975).
43. C. Le Rigoleur et al., CEA-R-4788 (1976).
44. J.P. Delaroche, to be published.

NEUTRON RADIATIVE CAPTURE AND TRANSMISSION MEASUREMENTS OF ^{147}Sm AND ^{149}Sm

M. Mizumoto, M. Sugimoto*, Y. Nakajima,
Y. Kawarasaki, Y. Furuta and A. Asami
Japan Atomic Energy Research Institute,
Tokai-mura, Ibaraki-ken, Japan

The neutron capture and transmission of ^{147}Sm and ^{149}Sm were measured at the 55 m time-of-flight station of the Japan Atomic Energy Reasearch Institute Electron Linear Accelerator. Measurements were carried out with a large liquid scintillation detector, a ^{6}Li glass detector and a ^{10}B-NaI detector using enriched samples of ^{147}Sm (98.34 %) and ^{149}Sm (97.72 %). The average capture cross sections were deduced from 3.3 to 300 keV with an estimated accuracy of 5 to 15 %. The transmission data were analyzed with a multi-level Breit Wigner formula to obtain neutron widths of resonances up to 2 keV for ^{147}Sm (212 resonances) and 520 eV for ^{149}Sm (157 resonances). The S-wave strength functions and average level spacings were found to be $10^4S_0 = 4.8 \pm 0.5$, $\bar{D} = 5.7 \pm 0.5$ eV for ^{147}Sm and $10^4S_0 = 4.6 \pm 0.6$, $\bar{D} = 2.2 \pm 0.2$ eV for ^{149}Sm.

[$^{147,149}Sm(n,n),(n,\gamma)$, 1.5 eV-300 keV, resonance parameters, E_0, Γ_n, S_0, $\bar{D}$, average capture cross sections.]

Introduction

The accurate neutron cross sections of ^{147}Sm and ^{149}Sm isotopes are of practical importance for the design of fast power reactor. These two isotopes contribute about 6 % to total capture rate of all fission products[1]. Average capture cross sections with an accuracy of 20 % in the neutron energy range below 200 keV have been requested by various groups[2]. In spite of importance of these isotopes, relatively few measurements[3~5] have been performed to obtain average capture cross section in the keV region. Average values of resonance parameters, such as strength function average radiation width and level spacing, are also useful to describe the average cross section in the unresolved resonance region. Several measurements have been made to determine resonance parameters in the resolved region[6~7]. Gruppelaar[8] pointed out that the calculated capture cross sections of ^{147}Sm and ^{149}Sm based on the systematics of average parameters in the keV region could not represent the experimental capture data. In the present experiment, the neutron capture and transmission were measured to obtain accurate capture cross sections and average resonance parameters. The discrepancy between calculated and experimental capture data was studied using these results.

Experimental Procedure

Measurements were carried out with the neutron time-of-flight method. Neutrons were produced by a pulsed electron beam of 120 MeV which was stopped in a laminated water-cooled Ta target. The neutrons were moderated by a 5 cm thick boron loaded polyethylene plate. The linac was operated at 150 pps or 300 pps with electron burst widths of 80 nsec or 30 nsec, respectively. The neutron beam was collimated to 4 cm diameter at the sample position.

Capture cross sections were measured with a large liquid scintillator tank of 3500 l at a flight path of 51.946 m from the neutron producing target. Neutron transmissions were measured with an 11.1 diameter x 0.635 cm thick ^{6}Li glass scintillation detector at 56.319 m and with a ^{10}B-NaI detector at 55.981 m. These two detectors were also served as neutron flux detectors for capture experiments. The relative efficiencies of flux detectors were carefully estimated with the Monte Carlo method using the evaluated $^{6}Li(n,\alpha)$ and $^{10}B(n,\alpha\gamma)$ cross sections[9]. Beam filters were inserted permanently in the neutron beam; 8 mm metallic Na encapsulated in an aluminum container to normalize backgrounds at the 2.85 keV resonance, 5 mm boron nitrate to absorb low energy neutrons and 8 mm lead to reduce the γ-flash. Time dependent background was determined by inserting, in the beam, notch filters consisting of thick Al (or Al_2O_3) and Co which have black resonances at 440 keV, 88.5 keV, 34.7 keV and 132 eV. The capture and neutron flux (transmission) time-of-flight spectra were measured in alternate cycle with sample and notch filters in and out of the neutron beam, and were taken on an on-line computer with 8192 time channels and minimum channel width of 25 nsec. Detailed description of the experimental procedure was given elsewhere[10].

The samples of ^{147}Sm and ^{149}Sm were oxide powder contained in aluminum cans. The diameter of the sample was 6 cm. Sample thicknesses and isotopic compositions shown in Table I.

Table I. Isotopic compositions and thicknesses of samples

Isotope	Isotopic abundance (%)	Thickness Thick (atoms/barn)	Thin (atoms/barn)
^{147}Sm	98.34	0.00393	0.000962
^{149}Sm	97.72	0.00393	0.00114

Analysis

Resonance Parameters

The transmission data for two different sample thicknesses were fitted simultaneously in the neutron energy range from 1.5 to 200 eV for both ^{147}Sm and ^{149}Sm. A multi-level Breit Wigner formula incorporated in a least squares fitting program SIOB[11] was used. Above 200 eV, only thick sample data were analyzed due to poor statistics in the thin sample data. Example of experimental and calculated transmission data is shown in Fig. 1. Neutron widths $2g\Gamma_n$ of 212 resonances for ^{147}Sm and of 157 resonances for ^{149}Sm were obtained below 2 keV and 520 eV, respectively. Radiation widths Γ_γ were assumed constant to be 70 ± 6 meV (^{147}Sm) and 62 ± 5 meV (^{149}Sm). These values were obtained from capture cross section data in several tens eV region, using the Monte Carlo area analysis code TACASI[12]. The statistical factor g, assuming that observed resonances were all S-wave, was taken from reference[13], otherwise g = 0.5l was assumed.

The cumulative number of resonances below neutron energy E_n are plotted in Figs. 2a and 2b. Considerable fraction of weak resonances are missed at higher energy.

The plots of $\Sigma g\Gamma_n^0$ are given in Figs. 3a and 3b. These plots are insensitive to missed weak levels.

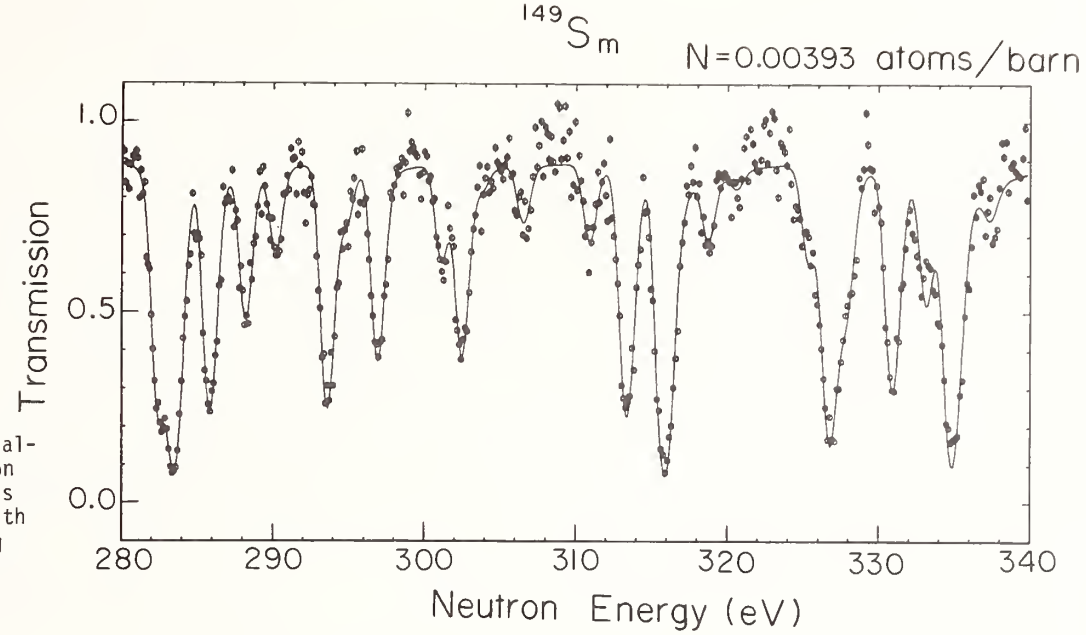

Fig. 1.
Example of resonance analysis of the transmission data. The solid line is the calculated curve with a least squares fitting program.

The slopes give the values of the S-wave strength functions. Figs. 4a and 4b show histograms of the observed $(g\Gamma_n^0\ meV)^{1/2}$ values for ^{147}Sm and ^{149}Sm to estimate number of missing levels. The theoretical Porter-Thomas distribution for two merged population were used to fit above the region where $(g\Gamma_n^0\ meV)^{1/2} > 0.5$.

Average Capture Cross Sections

In the region above a few keV neutron energy, where individual resonances could not be resolved, average capture cross sections were deduced. The time dependent backgrounds were determined using a lead scatterer and notch filters. The normalization of the capture cross sections was made by the saturated resonance technique Three resonances 3.496, 18.32 and 29.74 eV for ^{147}Sm and 4.940, 6.428 and 14.89 eV for ^{149}Sm were used for this purpose, resulting that agreement was good within 3 %. Capture probabilities for these resonances were calculated by the Monte Carlo program MCRTOF[14]. The resonance selfshielding and multiple scattering corrections due to finite sample thickness were estimated by a similar way employed by Macklin[15]. The combined correction factors were less than 12 % for our samples in the whole region. Major sources of uncertainty in this experiment were determination of the background (2.7 to 12 %) and normalization (4 %). The statistical uncertainties were from 0.4 % to 2 % after the data were averaged over suitable energy interval. Overall uncertainty in capture cross sections were estimated to range from 5 % at 3.3 keV to 15 % near 300 keV.

Results and Discussions

Resonance Parameters

From the present experiments, the resonance parameters were obtained for ^{147}Sm and ^{149}Sm to about twice higher energy than they were previously known. Results of resonance parameters for ^{147}Sm were reported by Eiland et al.[7](below 1.2 keV) and Karzhavina and Popov[6]

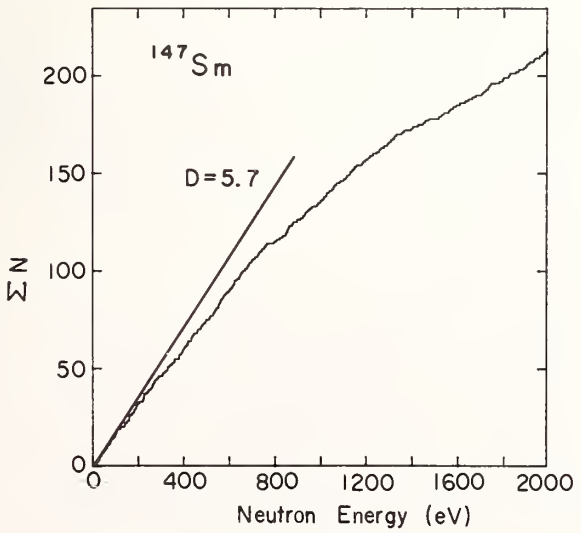

Fig. 2a. The cumulative numbers of observed level vs energy for ^{147}Sm.

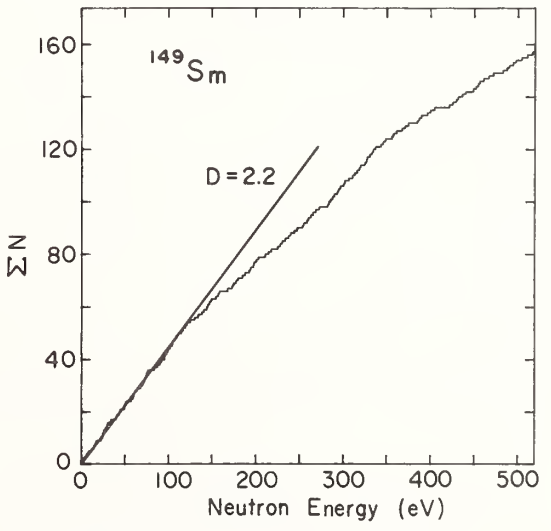

Fig. 2b. The cumulative numbers of observed level vs energy for ^{149}Sm.

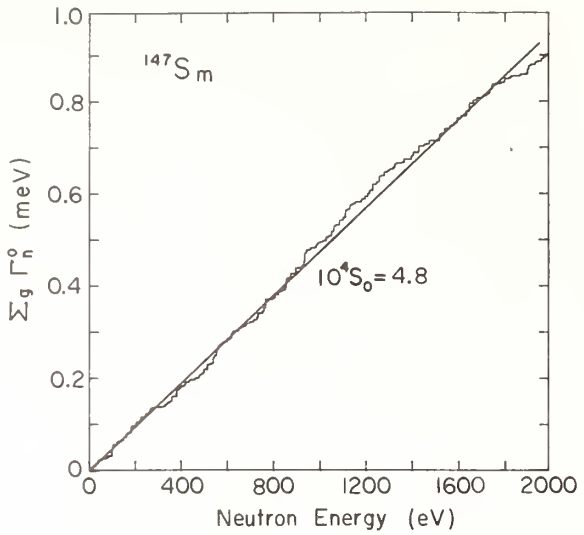

Fig. 3a. $\Sigma g\Gamma_n^0$ vs energy for level in ^{147}Sm.

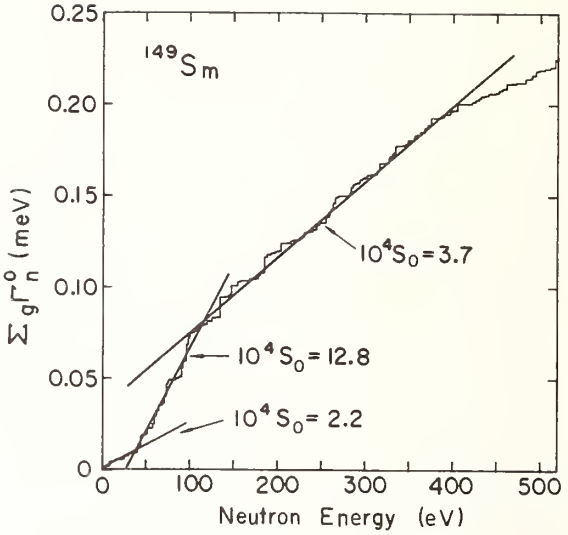

Fig. 3b. $\Sigma g\Gamma_n^0$ vs energy for level in ^{149}Sm.

(below 240 eV). Our resonance energies are systematically lower than Ref. 7, but are in good agreement with Ref. 6. The overall agreement between Γ_n values seems to be good. Our values $10^4S_0 = 4.8 \pm 0.5$ ($0 < E_n < 1.8$ keV) were compared with values $10^4S_0 = 4.3 \pm 1.3$ given by Ref. 7 and $10^4S_0 = 3.7 \pm 0.8$ by Ref. 6. On the other hand, our level spacing $\bar{D} = 5.7 \pm 0.5$ eV are considerably smaller than previous values, 7.42 ± 0.5 eV[7] and 7.20 ± 0.9 eV[6], partly because the different method of missing level analysis was used. As already pointed out by Karzhavina and Popov, the S-wave strength function for ^{149}Sm shows an apparent energy dependence represented by three full line in Fig. 3b,

$10^4S_0 = 2.2 \pm 0.8$ ($0 < E_n < 40$ eV)
$10^4S_0 = 12.8 \pm 3.1$ ($40 < E_n < 115$ eV)
$10^4S_0 = 3.7 \pm 0.6$ ($115 < E_n < 400$ eV).

The mean slope yields the S-wave strength function to be $10^4S_0 = 4.6 \pm 0.6$ ($0 < E_n < 400$ eV). The level spacing $\bar{D}$ obtained from Fig. 4b is 2.2 ± 0.2 eV. Our results were in good agreement with $10^4S_0 = 5.1 \pm 0.9$, $\bar{D} = 2.3 \pm 0.3$ eV given in Ref. 6.

Average Capture Cross Sections

The average capture cross sections are shown in Figs. 5a and 5b. Several previous experimental[3~5] and evaluated data[6] available for comparison are also shown in the figures. The present data on ^{147}Sm (see Fig. 5a) agree relatively well with the 24 keV data of Macklin et al.[3] and the evaluated data[8,16], but differ largely in both magnitude and shape from the data of Kononov et al.[5]. On the contrary, in the case of ^{149}Sm (see Fig. 5b), the data from Refs. 5 and 6 are in good agreement with our data, while evaluated data[16] and data from Ref. 3 are smaller by more than 30 %. The calculated capture cross sections by Gruppelaar[8] are slightly higher than JENDL-1[16], representing reasonably good agreement with our data of ^{147}Sm, but giving still appreciably lower values compared with our data of ^{149}Sm.

Table II shows the average parameters which were deduced from the evaluations[8,16], as well as our final values. These four parameters are most important for

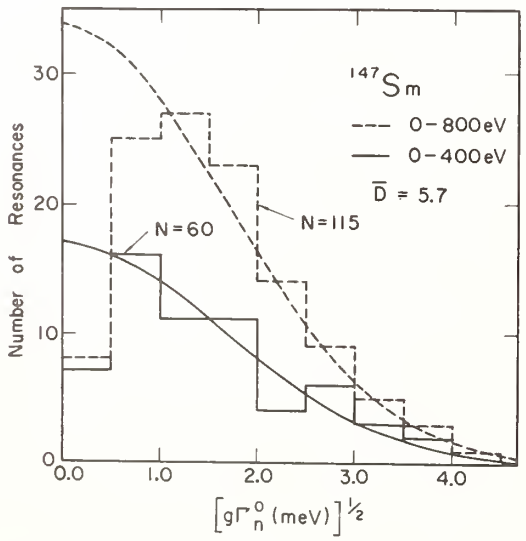

Fig. 4a Histogram of observed $(g\Gamma_n^0\ meV)^{1/2}$ values for ^{147}Sm.

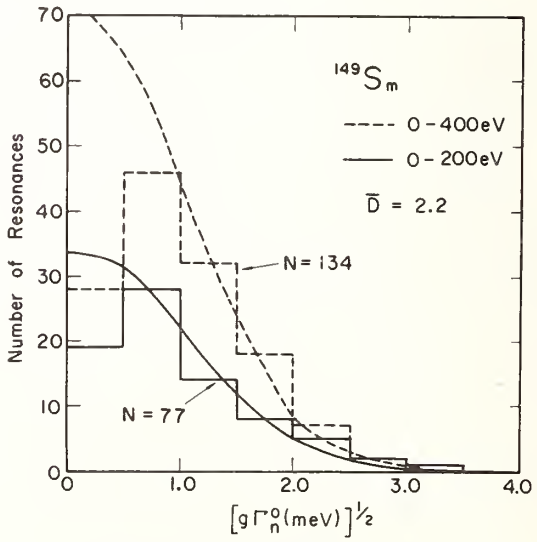

Fig. 4b Histogram of observed $(g\Gamma_n^0\ meV)^{1/2}$ values for ^{149}Sm.

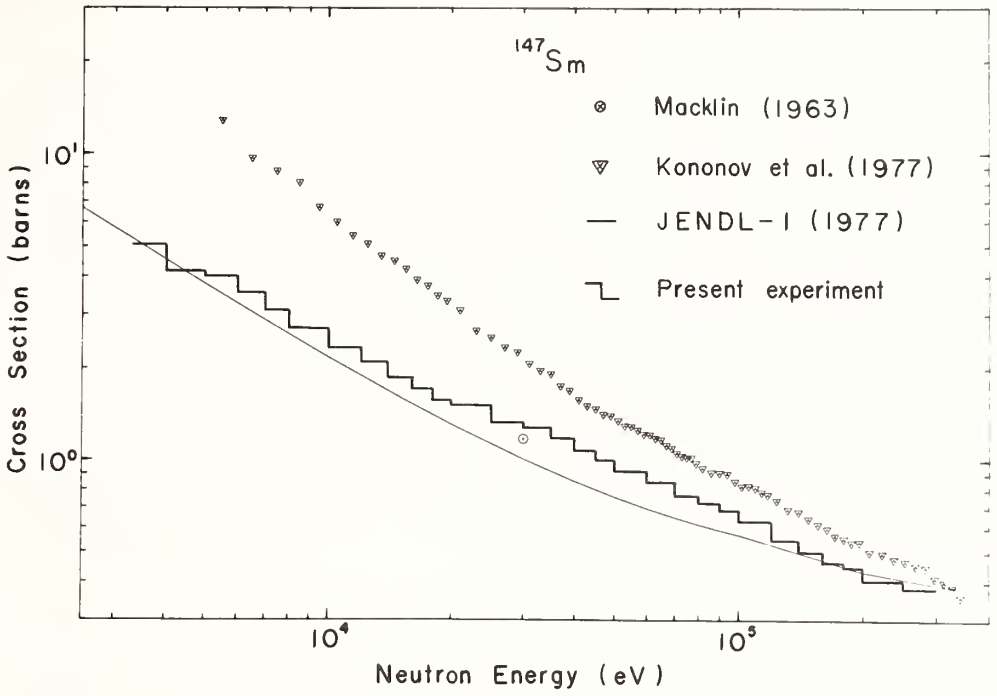

Fig. 5a.
The neutron capture cross sections of ^{147}Sm in the neutron energy range from 2.5 to 400 keV.

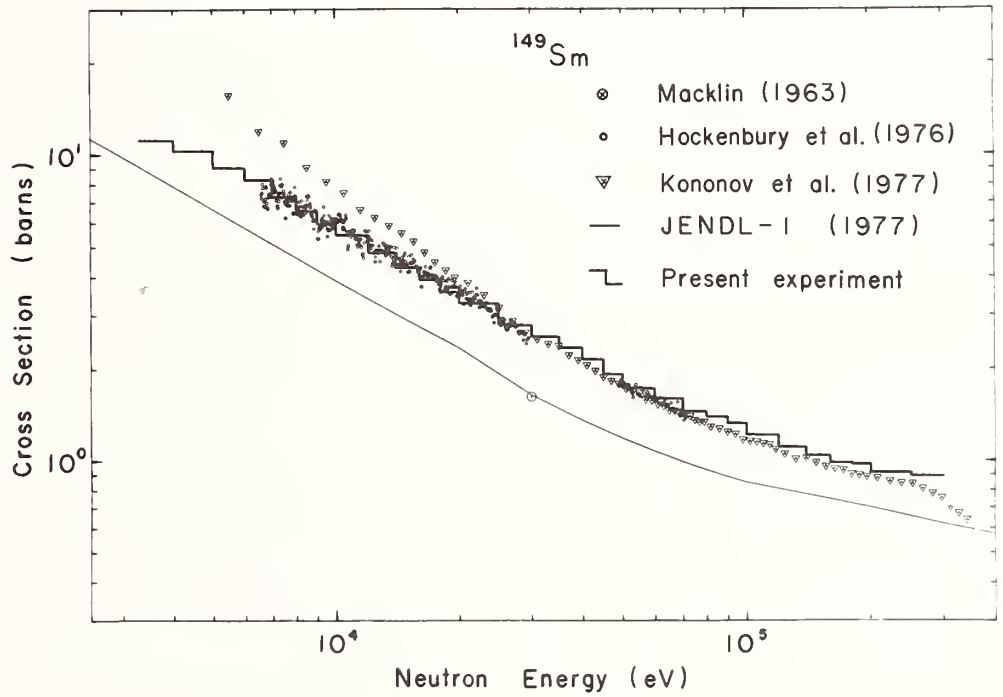

Fig. 5b.
The neutron capture cross sections of ^{149}Sm in the neutron energy range from 2.5 to 400 keV.

calculating average capture cross sections in the keV region based on the statistical model. The values of the present experiment are only from resonance analysis since it is rather difficult to fit our average capture cross sections with usual average model parameters. Furthermore, the S-wave strength function for ^{149}Sm have distinct energy dependence and are not uniquely determined. Our missing level analysis to obtain the level spacings depends on the S-wave strength functions through the assumed Porter-Thomas distribution. It is likely that the other average parameters in the keV region also may not be the same as the values in the resolved resonance region. New interpretations and further measurements will be needed to understand the discrepancy between the experimental and calculated data in these isotopes.

Acknowledgment

Authors wish to thank Dr. G. Rogosa and the U.S. Department of Energy for help in procuring the separated isotope samples, and Professor K. Sugiyama (Tohoku University) for helpful discussions and comments. They also thank Mr. T. Shoji for technical assistance and

Mr. T. Nakagawa for valuable discussions concerning the resonance analysis. They were very grateful to Drs. G. de Saussure, D. K. Olsen and R. B. Perez for providing the multi-level transmission fitting code SIOB. The contribution of the operation crew of linac is acknowledged.

Table II. The average parameters of ^{147}Sm and ^{149}Sm.

		JENDL-1	RCN-2	Present
^{147}Sm	$\bar{D}$ (eV)	4.26	6.3	5.7
	Γ_γ (meV)	67	100	70
	$S_0 \times 10^4$	4.02	4.3	4.8
	$S_1 \times 10^4$	0.53	1.8	
^{149}Sm	$\bar{D}$ (eV)	1.63	2.0	2.2
	Γ_γ (meV)	61	76	62
	$S_0 \times 10^4$	3.8	5.1	4.6
	$S_1 \times 10^4$	0.54	1.8	

* On leave from Department of Nuclear Engineering, Tohoku University.

References

1. Y. Kikuchi et al., Fission Product Fast Reactor Constant System of JNDC, JAERI-1248 (1976).

2. R. M. Lessler (Editor), WRENDA 76/77, World Request List for Nuclear Data, INDC (SEC) -55/ URSF (1976).

3. R. L. Macklin, J. H. Gibbons and T. Inada, Nature 197, 370 (1963).

4. R. W. Hockenbury et al., Reports to the ERDA Nuclear Data Comittee ERDA/NDC-3/U (1976) 255: data from NEA data center, Saclay.

5. V. N. Kononov et al., in Proceedings of the Fourth All Union Conference on Neutron Physics, Kiev, 1977.

6. E. N. Karzhavina and A. B. Popov, Sov. J. Nucl. Phys. 15, 225 (1972).

7. H. M. Eiland, S. Weinstein and K. W. Seemann, Nucl. Sci. Eng. 54, 286 (1974).

8. H. Gruppelaar, Tables of RCN-2 Fission Product Cross Section Evaluation volume 2 (13 nuclides) ENC-33 (1977).

9. S. Igarasi et al., Japanese Evaluated Nuclear Data Library, Version-1, JENDL-1, JAERI 1262 (1979).

10. M. Mizumoto et al., J. Nucl. Sci. Technol. 16, 711 (1979).

11. G. de Saussure, D. K. Olsen and R. B. Perez, SIOB: A Fortran Code for Least Square Shape Fitting Several Neutron Transmission Measurements using the Breit-Wigner Multilevel Formula, ORNL/ TM-6286 (1978).

12. F. H. Fröhner, TACASI: A Fortran IV Code for Least Square Area Analysis of Neutron Resonance Data, GA-6906 (1966).

13. B. Cauvin et al., in Proceedings of the Third Conference on Neutron Cross Sections and Technology, Knoxville, CONF-710301, p785 (1971).

14. M. Ohkubo, MCRTOF: A Monte Carlo Program for Multiple Scattering of Neutrons in Resonance Energy Region, JAERI-M 7988 (1978).

15. R. L. Macklin, Nucl. Instrum. and Methods 26, 213 (1964).

16. S. Iijima et al., J. Nucl. Sci. Technol. 14, 161 (1977).

CALCULATION OF NEUTRON CROSS SECTIONS FOR TUNGSTEN ISOTOPES

E. D. Arthur
Los Alamos Scientific Laboratory
Theoretical Division
Los Alamos, New Mexico 87545 U.S.A.

C. A. Philis
C. E. de Bruyéres-le-Châtel, CEA
Montrouge, France

Neutron-induced cross sections on tungsten isotopes have been calculated in the energy range between 0.2 and 20 MeV using preequilibrium-statistical model techniques. The success of these calculations, which form part of an effort to improve the evaluated neutron and gamma-ray production cross sections for tungsten appearing in ENDF/B, depends strongly on the determination of consistent input parameter sets applicable over the entire range of interest. For example, neutron optical model parameters have been derived through a simultaneous analysis of total cross sections, resonance data, and angular distributions. These parameters, when used in multistep Hauser-Feshbach calculations, produce good agreement with varied experimental data such as neutron inelastic scattering excitation functions and (n,2n) cross sections. Likewise, gamma-ray strength functions have been determined through fits to neutron capture data that produce calculated results that compare well to measured gamma-ray production cross sections. A description of the techniques used in such parameter determinations as well as comparison of calculated results to experimental data will be presented.

[Neutron Cross-Section Calculations, $^{182,183,184,186}W$, 0.2-20 MeV, $\sigma(E)$, Hauser-Feshbach, Preequilibrium, Coupled-Channel Methods]

Preliminary calculations of neutron-induced cross sections on tungsten isotopes have been made using preequilibrium statistical model techniques from 0.2 to 20 MeV. This effort comprises part of a new tungsten evaluation[1] which hopefully will correct problems in the present ENDF/B evaluation arising from energy imbalance at several energies.

The determination of neutron optical parameters plays an important role in the present calculations since parameters are needed which realistically describe low energy neutron emission such as in (n,2n) reactions while also producing reasonable values for compound nucleus formation cross sections at higher energies. To produce such parameters, we adopted the following approach. Since the tungsten isotopes are deformed, we determined the direct inelastic cross section from scattering off low lying collective states through use of coupled-channel calculations. This cross section was then subtracted from evaluated values of the experimental total cross section and an effort was made to fit this remainder using the spherical-optical model with realistic parameter values. By doing so, we sought to separate compound and direct reaction effects so that reaction cross sections determined from these optical parameters would in fact represent mainly the compound nucleus formation cross section. In this manner, Hauser-Feshbach calculations could be made without having to adjust the formation cross section to account for direct effects not included in the reaction mechanism.

To determine direct inelastic scattering cross sections from the 2^+ and 4^+ rotational states of the even tungsten isotopes, we used the JUPITOR[2] coupled channel program along with deformed neutron optical parameters and β_2, β_4 values determined by Delaroche.[3] We then took recent evaluations of the $^{182,184,186}W$ total cross sections based mainly on new measurements of Guenther[5] as well as those of Foster[6] and subtracted these calculated direct inelastic scattering contributions. For ^{183}W we used an average of the evaluated total cross sections for ^{182}W and ^{184}W and subtracted contributions from direct inelastic scattering to the $1/2^-$, $3/2^-$, $5/2^-$, and $7/2^-$ levels. As an example, the subsequent spherical optical parameters determined for ^{184}W are shown in Table I.

Along with this effort, we also extracted approximate gamma-ray strength functions from fits to $^{182,183,184,186}W(n,\gamma)$ cross sections. In doing so, we assumed a giant dipole resonance form consisting of one Lorentz shape whose width and location were adjusted to approximate the double Lorentz shape which exists because of deformation effects. We did not attempt, for these preliminary calculations, to include refinements such as the pygmy resonance and/or dip occuring for $\varepsilon_\gamma \sim 6$ MeV in the shape of the strength function. Our present gamma-ray strength functions enabled us to describe effectively gamma-ray competition to neutron emission, which is important especially around the (n,2n) reaction threshold.

To test our choice of neutron optical model and gamma-ray strength function parameters, we performed two sets of calculations, one for incident neutron energies below 5 MeV and one for energies from the (n,2n) threshold up to 15 MeV. The latter calculations also provided information concerning the suitability of the Gilbert-Cameron level density parameters[7] used throughout the calculations. Figure 1 illustrates results obtained for ^{184}W from optical model and width-fluctuation corrected Hauser-Feshbach calculations using the optical parameters of Table I. For the calculations of the total cross section and the excitation cross

Table I. Spherical Optical Model Parameters for n + ^{184}W

	r(fm)	a(fm)
V(MeV) = 55.2-0.13E	1.1	0.45
W_{SD}(MeV) = 5.2+0.23E	1.409	0.4
Above 6 MeV		
W_{SD}(MeV) = 6.6		
V_{SO}(MeV) = 6.2	1.01	0.75

sections for the 0.11 MeV (2^+) and the 0.365 MeV (4^+) states, we added the appropriate direct inelastic scattering contribution (as obtained from JUPITOR) to the Hauser-Feshbach or spherical optical model results. The elastic cross section includes both contributions from the shape elastic and compound elastic cross sections. Figure 2 compares calculated (n,2n) results to the experimental $^{182,183,184,186}W(n,2n)$ cross sections measured by Frehaut[8] from threshold to 14 MeV. Here the multistep Hauser-Feshbach code GNASH[9] was used along with preequilibrium corrections based on the Kalbach[10] exciton model. The agreement with these differing types of data confirms several things, particularly the low and high energy behavior of the neutron transmission coefficients as well as the value of the gamma-ray strength functions. Finally, in Figure 3 we compare our neutron emission spectrum obtained by a combination of calculated results from $^{182,183,184,186}W$ with measurements on natural tungsten by Hermsdorf et al.[11] This comparison provides a further check on our calculation, particularly with regard to preequilibrium corrections applied above 10 MeV.

Thus, our preliminary efforts to determine and verify neutron and gamma-ray parameters have led to values which appear to satisfactorily reproduce the majority of neutron-induced reaction data for tungsten isotopes.

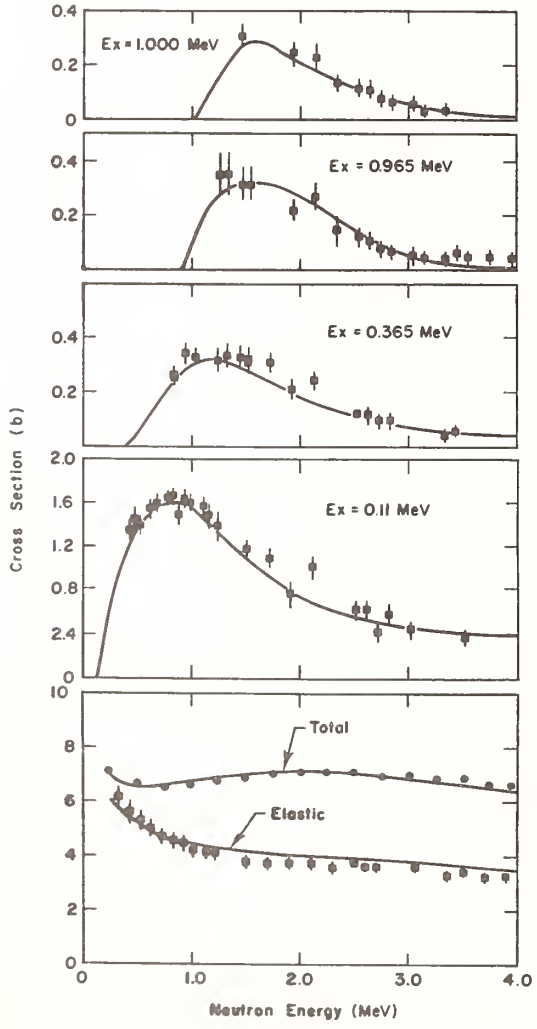

Fig. 1. Calculated values for the total, elastic, and certain inelastic scattering cross sections are compared to the Guenther (Ref. 5) data for ^{184}W.

REFERENCES

1. In collaboration with A. B. Smith, Argonne National Laboratory.

2. T. Tamura, "Computer Program JUPITOR for Coupled Channel Calculations," ORNL-4152 (1967).

3. J. P. Delaroche et al., "Study of Even-Even Tungsten Isotopes by Neutron Scattering," Proc. of the National Conf. on Neutron Physics, Kiev (1977).

4. A. B. Smith, Argonne National LAboratory, personal communication (1978).

5. P. A. Guenther and A. B. Smith, Bull. Am. Phys. Soc. 23, 944 (1978).

6. D. G. Foster and Dale W. Glasgow, Phys. Rev. C3, 576 (1971).

7. A. Gilbert and A. G. W. Cameron, Can. J. Phys. 43, 1446 (1965).

8. J. Jary and J. Frehaut, "Systematique des Sections Efficaces de Reaction (n,2n) pour des Series d'Isotopes Separes," Proc. Int'l. Conf. on Neutron Physics and Nuclear Data for Reactors and Other Applied Purposes, Harwell (1978).

9. P. G. Young and E. D. Arthur, "GNASH - A Preequilibrium Statistical Model Code for Calculation of Cross Sections and Spectra," LA-6974 (1977).

10. C. Kalbach, Z. Phys. A283, 401 (1977).

11. D. Hermsdorf et al., Kernenergie 19, 241 (1976).

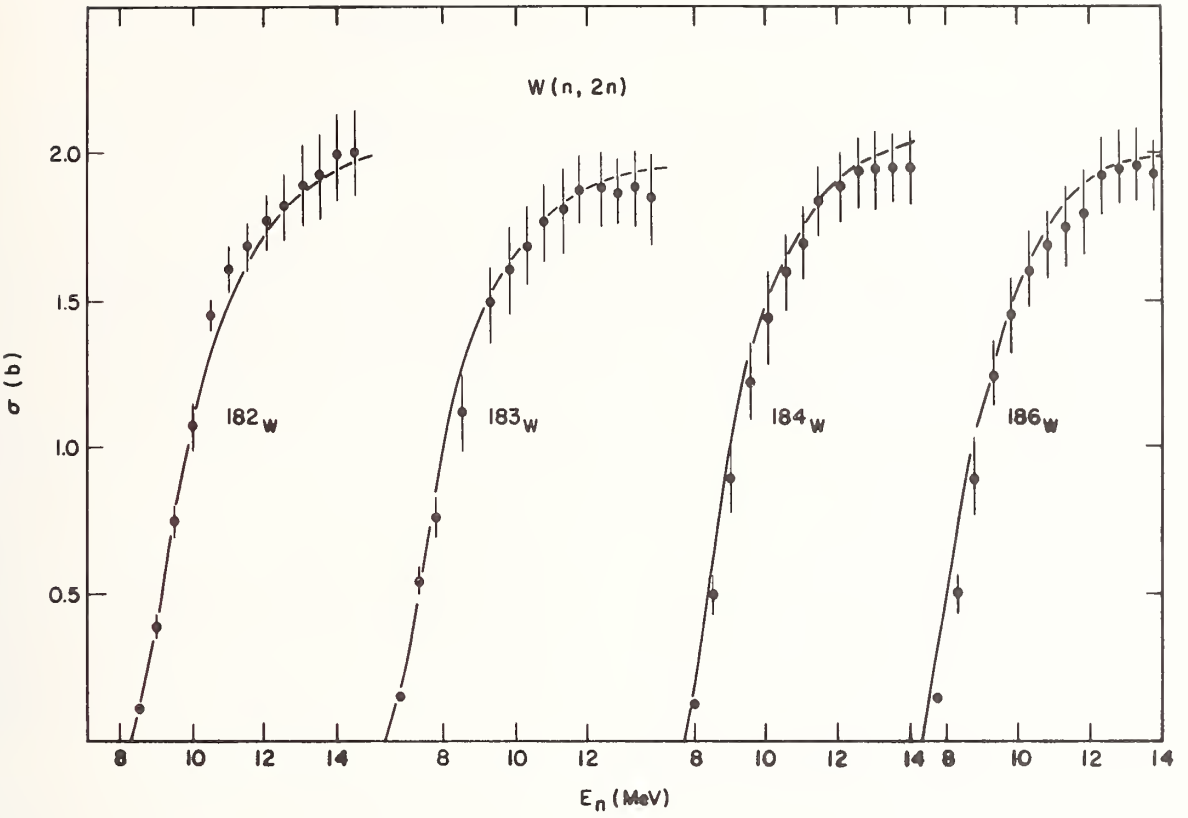

Fig. 2. Calculated $^{182,183,184,186}W(n,2n)$ cross sections are compared to the Frehaut (Ref. 8) results.

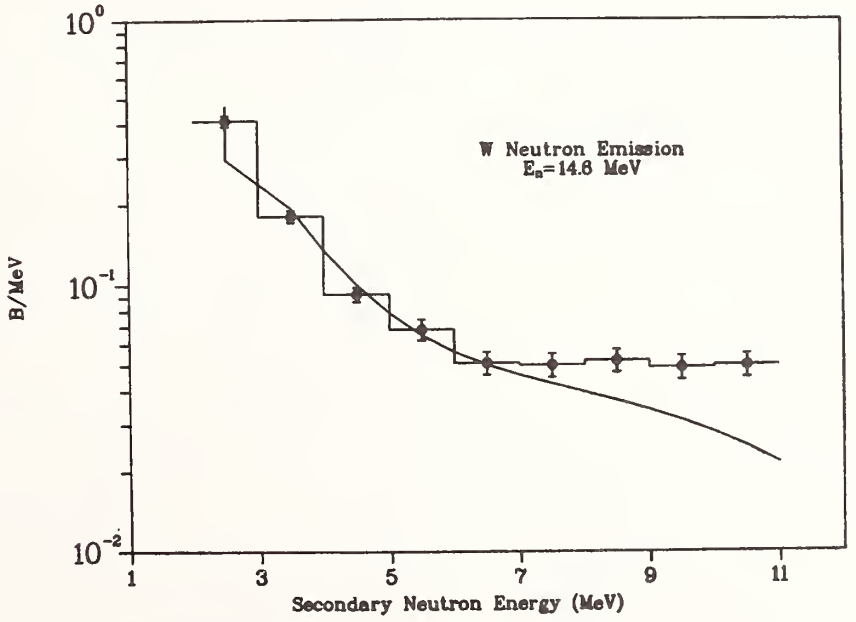

Fig. 3. A comparison of calculated and experimental (Ref. 11) values for the neutron emission spectra induced by 14.5 MeV neutrons.

COHERENT OPTICAL AND STATISTICAL MODEL ANALYSIS OF ^{182,183,184,186}W NEUTRON CROSS SECTIONS

J.P. Delaroche, G. Haouat, J. Lachkar, Y. Patin, J. Sigaud, and J. Chardine

Service de Physique Neutronique et Nucléaire
Centre d'Etudes de Bruyères-le-Châtel
B.P. n° 561
92542 MONTROUGE CEDEX, France

Previously reported s- and p- wave strength functions, potential scattering radii and total cross sections along with scattering data below 15 MeV have been analysed in the frame of coupled channel formalism. Potential parameters, deformation parameters and transmission coefficients have been obtained. Statistical model calculations involving the above transmission coefficients have been performed in order to determine compound elastic and inelastic scattering cross sections as well as capture cross sections. These optical and statistical model calculations yield good agreement with most of the available cross section measurements.

[W isotopes, potential scattering radii, s- and p- wave strength functions, total cross sections, elastic and inelastic scattering cross sections, optical and statistical model calculations, energy range 10 keV - 15 MeV.]

Introduction

The element tungsten is an important structural material for nuclear technology. For this reason and as parts of fundamental nuclear physics studies, neutron scattering and reaction cross sections for these nuclei have been measured in the last decade. No one has recently analysed tungsten data in order to check the nuclear reaction models over a large energy range (10 keV - 15 MeV). This has been achieved by using the coupled channel formalism and statistical model.

Analysis

Coupled channel analysis. Lying at the rotational edge of the A = 190-200 transitional region[1], the W nuclei may be assumed in a first approximation to be permanently deformed. The deformed optical potential, unique for all the isotopes, has been varied from one isotope to the other through the deformation parameters β_2 and β_4, the asymmetry term $\varepsilon = (N-Z)/A$ and the A-dependence of potential radii. The neutron optical potential has been determined basically from (i) potential scattering radii[2] R', (ii) s- and p- wave strength functions[2,3] S_0 and S_1, and (iii) energy variations of the total cross sections measured by Whalen et al.[4], Martin[5] and Glasgow et al.[6]. The differential elastic and inelastic scattering cross sections from ^{182,183,184,186}W measured at BRC for 3.40 MeV incident energy have been used in order to optimize the parameterization[7]. In our analysis the optical potential has the following form :

$$U=-Vf(r,a_V,R_V)+4ia_D W_D \frac{d}{dr}f(r,a_D,R_D)-iW_V f(r,a_V,R_V) + 2\lambda_\pi^2 V_{so}\, \vec{\ell}.\vec{s}\, \frac{1}{r}\frac{d}{dr}f(r,a_{so},R_{so}), \quad (1)$$

where $f(r,a_i,R_i) = [1 + \exp(r-R_i)/a_i]^{-1}$ and $R_i = r_i A^{1/3}[1+\Sigma_{\lambda=2,4}\beta_\lambda Y_\lambda^o(\Omega')]$ in the intrinsic coordinate frame. The volume absorption W_V is generally neglected at incident energy E below 10 MeV ; its strength has been estimated from the analysis of elastic and inelastic scattering of protons from ^{182,184,186}W measured at 16 MeV incident energy[8]. The coupling basis ($0^+,2^+,4^+$) for the even isotopes and the equivalent basis ($1/2^-$, $3/2^-$, $5/2^-$, $7/2^-$, $9/2^-$) for ^{183}W sample were used in the coupled channel (CC) calculations. The coupling form factors $U_{\Lambda\neq o}$ in the expansion of the optical potential (1) :

$$U(r,\Omega')=\Sigma_\Lambda U_\Lambda(r)Y_\Lambda^o(\Omega') \ , \quad \Lambda = 0,2,4,6,8$$

were assumed to be complex. The code ECIS 78[9] was used to perform calculations for scattering from ^{183}W and to estimate the spin-orbit deformation effects. The latter were found negligible. A modified form[10] of Tamura's code JUPITOR-1[11] was used in most of the calculations. Compound nucleus effects, still important at 3.40 MeV incident energy, were included. An outline of the statistical model (SM) calculations is given below.

Statistical model calculations. The only de-excitation modes available to the compound tungsten nuclei at the incident energies considered (i.e. $E \lesssim 4$ MeV) are elastic and inelastic scattering and capture. The neutron transmission coefficient values have been chosen identical for all the open channels and assumed equal to those of the ground state channels. These hypotheses, though not well justified, are widely assumed in SM studies. The coherence between optical model (OM) and SM calculations has been reached by using in the SM calculations the neutron transmission coefficient values deduced from the coupled channel analysis. The SM calculations were performed by using Lagrange's et al. code HELMAG[12] which has been modified in order to include the modern SM theories[13]. These significantly influence the elastic and inelastic scattering cross sections calculated in the A = 90 - 100 mass region[14] When compared with Dresner's formalism[15] the more modern SM theories[13] improve the fits to the tungsten cross sections measured below $\sim$ 3 MeV, that is by enhancing the inelastic scattering cross sections while lowering the elastic scattering cross sections. At incident energies higher than $\sim$ 3 MeV both theories tend to produce similar results for inelastic scattering. The possibility for interference between direct and compound mechanisms was ignored. We believe that such a study in the W mass region remains premature, considering the lack of enough accurate cross section measurements at low energy and/or near thresholds of inelastic scattering channels.

The SM calculations require the knowledge of level densities ρ, both for target (ρ_T) and compound system (ρ_{CN}). The level density ρ_{CN} has been used in the determination of the transmission coefficients for the radiation channel. Each level density contains a discrete portion and a continuum parameterized by following a procedure close to that formulated by Gilbert and Cameron[16]. More than 12 discrete levels for each nucleus have been explicitely used in the SM calculations. The adopted level density parameter "a" values are consistent with those determined from the experimental values of the averaged s-wave level spacings, $\langle D \rangle^2$. The adopted gamma-ray widths $\langle \Gamma_\gamma \rangle$ at very

low incident energy are within the experimental uncertainties[2].

Discussion

The optical potential and deformation parameters are gathered in Tables I and II respectively.

Table I. Tungsten isotopes. Neutron optical potential parameters. Strengths in MeV ; geometry parameters in fm ; incident energy E in MeV.

$$V = 49.90 - 16\left(\frac{N-Z}{A}\right) - 0.25E \; ; \; r_V = 1.26 \; ; \; a_V = 0.63$$

$$W_D = \begin{cases} 4.93 - 8\left(\frac{N-Z}{A}\right) + 1.3E^{1/2}, & E \leq 9 \text{ MeV} \\ 8.83 - 8\left(\frac{N-Z}{A}\right) - 0.10(E-9), & E \geq 9 \text{ MeV} \end{cases} \qquad r_D = 1.28 \; ; \; a_D = 0.47$$

$$W_V = \begin{cases} 0, & E \leq 9 \text{ MeV} \\ 0.20E - 0.80, & E \geq 9 \text{ MeV} \end{cases} \qquad r_V = 1.26 \; ; \; a_V = 0.63$$

$$V_{so} = 6.00 \; ; \; r_{so} = 1.26 \; ; \; a_{so} = 0.63$$

Table II. Deformation parameters and estimated uncertainties determined from the present analyses.

Nucleus	β_2	β_4
^{182}W	0.223 ± 0.007	-0.054 ± 0.006
^{183}W	0.220 ± 0.012	-0.075 ± 0.010
^{184}W	0.209 ± 0.009	-0.056 ± 0.006
^{186}W	0.203 ± 0.006	-0.057 ± 0.006

The potential parameterization contains energy dependences and geometries which are commonly accepted. The deformation parameters, shown with estimated uncertainties, are close to those calculated by Möller et al. in nuclear structure studies[17]. With that respect, note that the sign of the deformation parameters β_4 has been determined unambiguously from the neutron data. These results support the use of neutron cross sections in nuclear structure investigations.

We met some unexpected difficulties while making the potential parameter search : it was not possible to adequately reproduce the total cross sections measured by Whalen et al.[4] and Martin[5] at incident energies below ∿ 2 MeV. The impossibility for our OM calculations to reproduce to within ∿ 5% accuracy these data is still not understood. Since our analysis was completed, new σ_T measurements have been performed by Whalen[18] in the energy intervall 300 keV - 5 MeV. The comparison of OM calculations and these new data shows that most of discrepancies previously observed vanish. The measured and calculated angular distributions at E = 3.40 MeV for $^{183,184}W$ samples are shown in Figs. 1 and 2 respectively. The compound nucleus components are included in the curves and, for ^{184}W, contribute approximately 1%, 15% and 50% of the

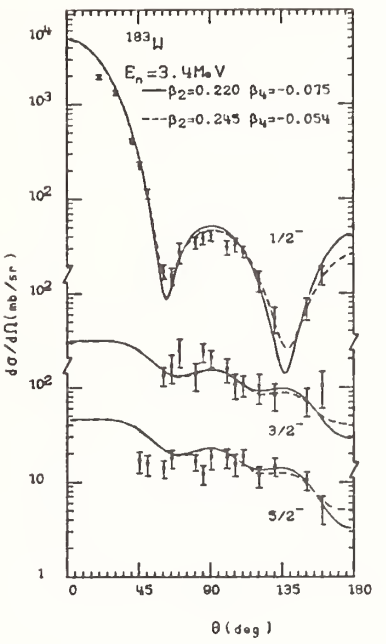

Fig. 1. Elastic and inelastic scattering cross sections for the ground state ($1/2^-$) and first excited states ($3/2^-$, $5/2^-$) of ^{183}W. Full and dotted lines represent calculations including CC and SM contributions for two sets of deformation parameters (β_2, β_4). Experimental data (present work), see Ref.7.

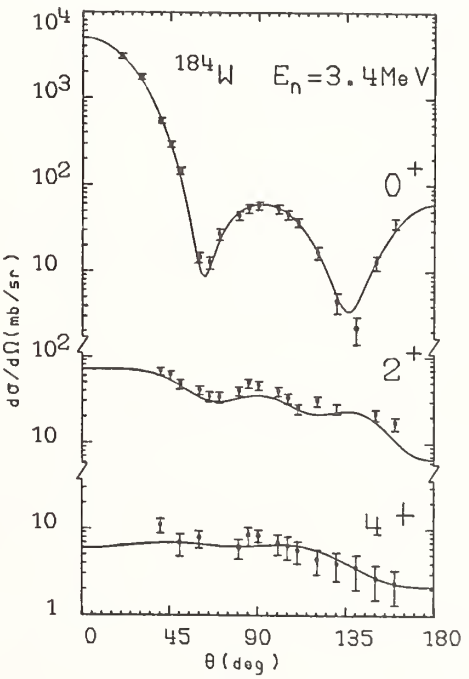

Fig. 2. Elastic (0^+) and inelastic scattering cross sections to the first 2^+ and 4^+ states of ^{184}W. Full lines represent calculations including CC and SM contributions. Experimental data (present work), see Ref.7.

calculated $\sigma(0^+)$, $\sigma(2^+)$ and $\sigma(4^+)$ cross sections respectively. The fits obtained are good, with comparable quality for all the measurements. Fig.3 shows measured[19] and calculated elastic and inelastic scattering

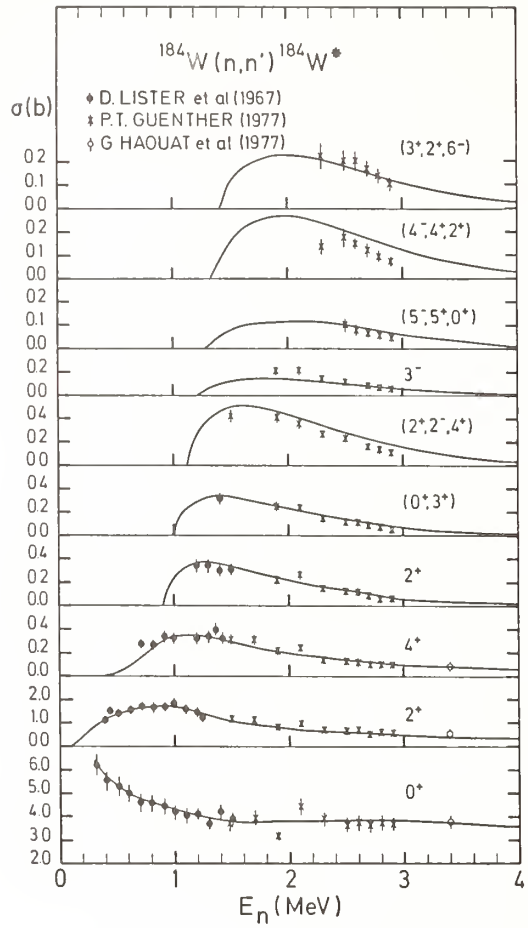

Fig. 3. Excitation functions for the elastic (0^+) and some inelastic scattering cross sections of ^{184}W. Curves are CC and/or SM calculations described in the text.
●, x Ref.19 ; o (present work) Ref.7.

excitation functions for ^{184}W. The curves result from OM and/or SM calculations. The satisfactory agreement for that nucleus and similar agreement for $^{182,186}W$ confirm the reliability of our model parameterizations. Calculations and new measurements of capture cross sections performed at BRC below 3 MeV are compared by Grenier et al. in a companion contributed paper to this Conference. A recent study by Jary[20] devoted to (n,2n) cross sections measured by Frehaut[20] at incident energies below 15 MeV, and based on the present work, leads also to reasonable agreement between calculations and measurements. Finally, similar conclusions are obtained for the available elemental tungsten cross sections[6,21] as shown in Fig.4.

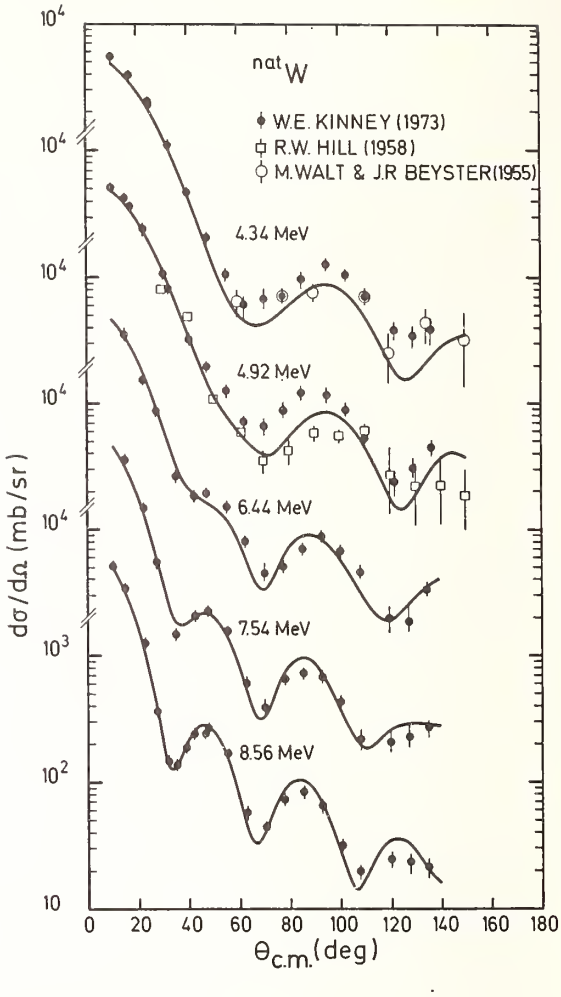

Fig. 4. Differential cross-sections for natural tungsten between 4.34 MeV and 8.56 MeV. Data (Ref.21) and CC calculations are for an energy resolution of ≃ 120 keV.

Conclusion

Data on the scattering by $^{182,183,184,186}W$ of neutron in the energy range 10 keV to 15 MeV, have been reviewed and compared with optical and statistical model calculations. An overall agreement between data and calculations is obtained. The optical model analysis has provided deformation parameters β_2 and β_4 for each isotope. These values are close to those calculated by Möller et al., indicating that neutrons can be used as probes of nuclear structure.

References

1. K. Kumar, and M. Baranger, Nucl. Phys. A122, 273 (1968).

2. S.F. Mughabghab, and D.I. Garber, BNL-325 (1973), 3rd ed., Vol. 1.

3. A.R. de L. Musgrove, AAEC/E277 (1973).

4. J. Whalen, and J. Meadows, ANL-7210 (1966).

5. R.C. Martin, Ph.D. Thesis (1967), unpublished.

6. W. Glasgow, and D.G. Foster, Phys. Rev. C3, 604 (1971).

7. J.P. Delaroche, G. Haouat, J. Lachkar, Y. Patin, J. Sigaud, and J. Chardine, to be submitted for publication.

8. T. Kruse, W. Makofske, H. Ogata, W. Savin, M. Slagowitz, M. Williams, and P. Stoler, Nucl. Phys. A169, 177 (1971).

9. J. Raynal, unpublished.

10. Ch. Lagrange, and N. Mondon, unpublished.

11. T. Tamura, ORNL-4152 (1967).

12. Ch. Lagrange, and B. Duchemin, unpublished.

13. P.A. Moldauer, Phys. Rev. C11, 426 (1975) ; C12, 744 (1975) ; C14, 764 (1976).
J.W. Tepel, H.M. Hofmann, and H.A. Weidenmüller, Phys. Lett. 49B, 1 (1974).
H.M. Hofmann, J. Richert, J.W. Tepel, and H.A. Weidenmüller, Ann. Phys. 90, 403 (1975).

14. Ch. Lagrange, in Proceedings of a Specialists' Meeting held at the Central Bureau of Nuclear Measurements, Geel, Belgium, 5-8 December 1977, ed. by K.H. Böckhoff (Pergamon Press, 1978) p. 756.

15. L. Dresner, ORNL-CF-57-6-2 (1957).

16. A. Gilbert, and A.G.W. Cameron, Can. J. Phys. 43, 1446 (1965).

17. P. Möller, S.G. Nilsson, and J.R. Nix, Nucl. Phys. A229, 292 (1974).

18. J. Whalen, to be published.

19. D. Lister, A. Smith, and C. Dunford, Phys. Rev. 162, 1077 (1967).
P.T. Guenther, Ph. D. Thesis (1977), unpublished.

20. J. Jary, unpublished ; J. Frehaut, unpublished.

21. W.E.Kinney, and F.G. Perey, ORNL-4803 (1973) ; M. Walt, and J.R. Beyster, Phys. Rev. 98, 677 (1955) ; R.W. Hill, Phys. Rev. 109, 2105 (1958).

THE NEUTRON CAPTURE CROSS SECTIONS OF NATURAL Yb, ^{170}Yb, ^{175}Lu AND ^{184}W IN THE ENERGY RANGE FROM 5 TO 200 keV FOR THE ^{176} Lu-CHRONOMETER

H. Beer, F. Käppeler, and K. Wisshak
Kernforschungszentrum Karlsruhe GmbH
Institut für Angewandte Kernphysik
P.O.B. 3640, D-7500 Karlsruhe
Federal Republic of Germany

The neutron capture cross sections of natural Yb, ^{170}Yb, ^{175}Lu and ^{184}W have been measured in the keV neutron energy range with a pulsed Van de Graaff accelerator using the kinematically collimated neutron beam from the ^{7}Li(p,n) and the T(p,n) reaction. Prompt capture gamma rays were registered by a Moxon-Rae detector. All measurements were performed in a single run relative to the ^{197}Au cross section as a standard. The cross sections of ^{175}Lu and ^{170}Yb were used to investigate the ^{176}Lu-cosmic clock.

[Yb(n,γ), ^{170} Yb(n,γ), ^{175}Lu(n,γ), ^{184}W(n,γ), capture cross sections, E_n = 5-200 keV, nucleosynthesis, ^{176}Lu-cosmochronometer]

Introduction

The neutron capture cross sections of ^{170}Yb and ^{175}Lu in the keV energy range are of particular importance to s-process nucleosynthesis as they can provide information for the only s-process cosmochronometer ^{176}Lu. All relevant quantities for the s-process are normally accessible to laboratory measurements as mostly stable isotopes along the valley of stability are involved. In addition for a calculation of the ^{176}Lu clock only cross section ratios are needed. In the present investigation all measurements were carried out in a single run relative to the ^{197}Au cross section to minimize systematic uncertainties. This allows to combine the present results with the cross sections of our recent activation measurements[1] for the ^{176}Lu chronometer where also ^{197}Au was used as a standard. The experimental technique was designed with special emphasis on an optimum signal-to-background ratio. In this way relatively thin samples could be used to avoid large corrections for multiple scattering and self-shielding. As for the investigated cross sections a smooth energy dependence is expected and as average cross sections are the quantities relevant to the astrophysical s-process no particular effort is necessary to obtain a high energy resolution. Therefore a Moxon-Rae system with short flight path and good time resolution was found to be adequate for the measurements.

Experimental Method

The neutron source and the experimental set up are almost the same as reported in Ref.[2] Therefore only a brief description of the experiment is given here. The measurements were carried out at the Karlsruhe pulsed Van de Graaff accelerator. Neutrons were generated via the ^{7} Li(p,n) and T(p,n) reactions with proton energies at 20 and 100 keV above threshold, respectively, to obtain a kinematically collimated neutron beam in the entire energy range from 5 to 200 keV. Neutron energies were measured by the time-of-flight technique; in spite of the very short flight paths of ∿68 mm the overall time resolution of 1.2 ns allowed for a reasonable energy resolution. Table I summarizes some important parameters of the experiment. The prompt capture gamma rays of the samples were recorded with a Moxon-Rae detector located at a backward angle of 120° with respect to the beam axis completely outside the neutron cone. A set of 7 samples was mounted on the light weight aluminium frame of a sample changer. The cycle time was determined by a beam current integrator and controlled by a ^{6} Li-glass monitor. Besides the Lu, the nat. Yb, the ^{170}Yb, the ^{184}W and the ^{197}Au reference sample, an empty Al canning and a graphite scattering sample were used to correct for background events. In Table II a compilation of the sample data is given. An example for a TOF-spectrum is shown in Fig. 1 to demonstrate the signal-to-background ratio for our thinnest sample.

Table I. Experimental parameters

Neutron reaction	^{7}Li(p,n)	T(p,n)
Beam current	20 μA	10 μA
Repetition rate	2.5 MHz	2.5 MHz
Pulse width	700 ps	700 ps
Max. proton energy	1.90 MeV	1.12 MeV
Time resolution	1.2-1.3 ns	1.2-1.3 ns
Flight path	67 mm	69 mm
Energy range	5-90 keV	50-200 keV

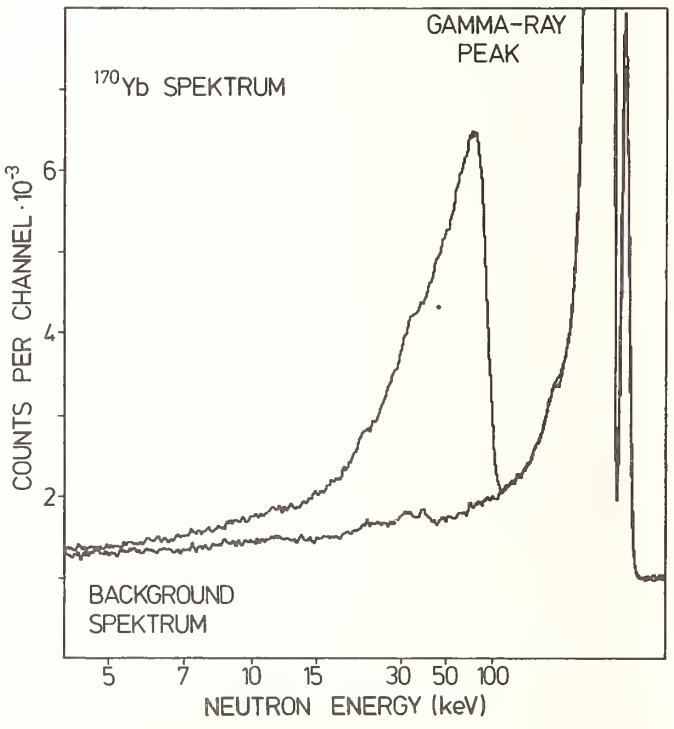

Fig. 1. Experimental TOF spectrum for the ^{170}Yb sample and the corresponding background spectrum.

Table II. Sample characteristics

Sample	Chemical composition	Isotopic composition (%)	Weight (g)	Thickness (at/b) x 10^4	(MS•SS)
^{170}Yb	Yb_2O_3	(168)0.02, (170) 78.78 (171)10.54, (172) 4.85, (173)2.08 (174)3.05, (176) 0.68	1.704	7.467	1.01
Yb	Yb_2O_3	natural	5.345	23.113	1.03
Lu	Lu_2O_3	natural	5.294	22.668	1.03
^{184}W	WO_3	(180)<0.05,(182)1.91,(183)1.87 (184)94.3,(186)1.91	3.245	11.235	1.02
^{197}Au	metallic	-	6.666	28.833	1.04
C	graphite	natural	1.010	71.641	-

Data Analysis

After background subtraction the capture cross section σ can be calculated from the TOF spectra on the basis of eq. (1):

$$\frac{C_x}{C_{Au}} = \frac{N_x}{N_{Au}} \cdot \frac{(MS\cdot SS)_x}{(MS\cdot SS)_{Au}} \cdot \frac{\sum \sigma_i H_i E_{B,i}}{\sigma_{Au} E_{B,Au}} \qquad (1)$$

where C denotes the background subtracted count rates, (MS•SS) the corrections for multiple scattering and self-shielding and N the sample thickness in atoms per barn. The subscripts x and Au refer to the sample under investigation and the gold reference sample. The index i stands for the various isotopes of the sample. H designates the isotopic abundance and E_B is the sum of neutron separation energy and neutron kinetic energy. The correction factors (MS•SS) were determined by the computer code SESH [3]. The isotopic impurities in the ^{170}Yb and ^{184}W sample were taken into account using the data of Shorin et al.[4] and Bartolome et al.[5], respectively. The cross sections were calculated in energy increments corresponding to the time resolution of the Moxon-Rae detector. However, in the low energy region larger energy intervals were chosen to improve statistics.

Results

In Fig. 2 the cross sections determined from the measurement with the $^7Li(p,n)$ reaction are plotted. For Lu no serious discrepancies were found relative to previous results[6,7,8], whereas our ^{184}W cross section is about 20 % higher than the one reported by Bartolome [5].

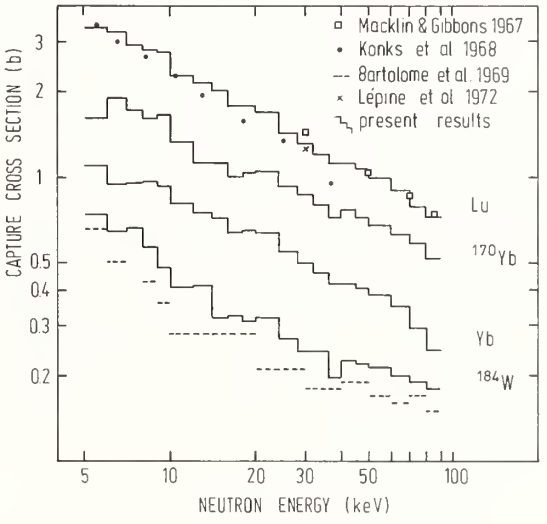

Fig. 2. Experimental results for the present capture cross section measurements in the energy range 5 to 90 keV (histogram) compared to previous data.

Discussion

In the mass region around ^{176}Lu fast and slow neutron capture are the main mechanisms for the synthesis of the chemical elements in stellar systems. Slow neutron capture (s-process) forms the elements step by step along the valley of stability as it is shown in Fig. 3 by the solid line. Fast or rapid neutron capture (r-process) is assumed to take place on the neutron rich side of nuclear matter. After the neutron flux has terminated the synthesized nuclei decay back to the valley of stability as is indicated by dashed arrows in Fig. 3. ^{176}Lu is shielded against r-process contributions by its isobar ^{176}Yb. This means that ^{176}Lu was formed only by the s-process. Therefore it is possible from s-process systematics to calculate how many ^{176}Lu was originally created. The comparison of that original abundance, $N^*(^{176}Lu)$ with the abundance $N(^{176}Lu)$ observed in the solar system offers then the possibility to evaluate the age of ^{176}Lu - and herewith the age of the s-process - from the ^{176}Lu half life $T_{1/2} = 3.6 \times 10^{10}$ y. Although the production rate of s-process matter cannot be expected to be uniform in time, Schramm and Wasserburg[9] have shown that such fluctuations can be neglected if a long lived isotope like ^{176}Lu is used as a clock. Therefore in this case the mean s-process age

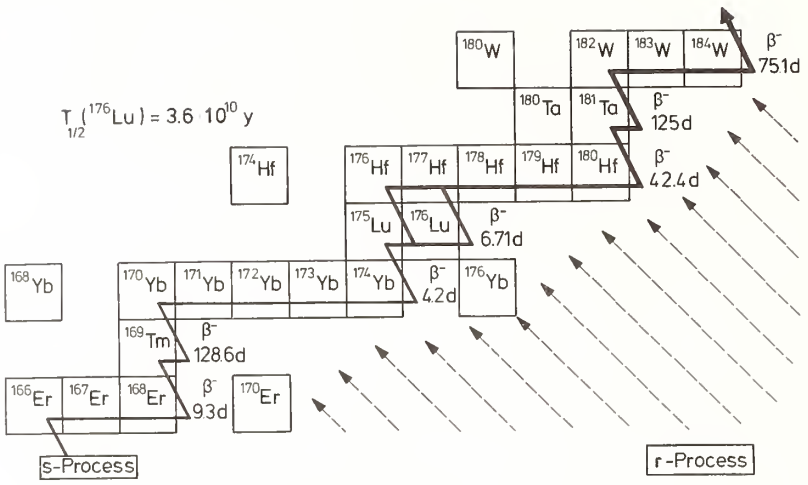

Fig. 3. The s-process synthesis path in the vicinity of ^{176}Lu (solid) line). Possible r-process contributions are indicated by dashed arrows.

T is given simply by:

$$R \doteq \frac{N^*(^{176}Lu)}{N(^{176}Lu)} = e^{\lambda T} \qquad (2)$$

$$N^*(^{176}Lu) = B \cdot N(176) \qquad (2a)$$

where λ denotes the decay rate of ^{176}Lu. The factor B takes into account that only a fraction B of the total amount of synthesized nuclei with mass number 176 is formed in the ground state of ^{176}Lu. The residual part populates the 3.68 h isomeric state in ^{176}Lu which decays immediately to ^{176}Hf. From eq. (2), the mean s-process age T can be evaluated if the ratio R is known. The branching ratio B is determined by the probability for populating the ground-state via neutron capture in ^{175}Lu:

$$B = \frac{\sigma^g(^{175}Lu)}{\sigma(^{175}Lu)} = 1 - \frac{\sigma^m(^{175}Lu)}{\sigma(^{175}Lu)} \qquad (3)$$

$\sigma^m(^{175}Lu)$, $\sigma^g(^{175}Lu)$ and $\sigma(^{175}Lu)$ are the Maxwellian averaged capture cross sections to the isomeric state and the groundstate in ^{176}Lu as well as the total neutron capture cross section in ^{175}Lu.

The total abundance N(176) at mass number A=176 must be derived from s-process systematics. Assuming an exponential flux distribution for the s-process with a time integrated average flux τ_0 , one obtains the following relation between the abundance N(A) and

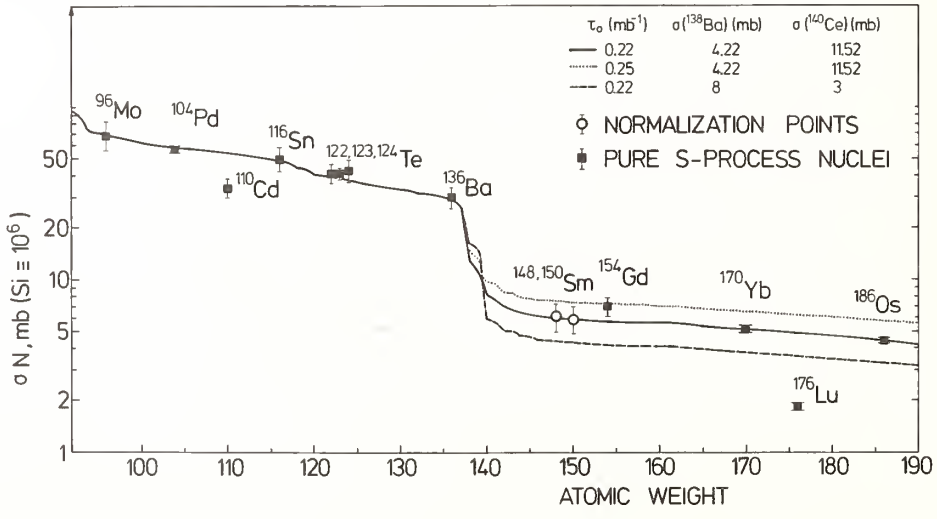

Fig. 4. The product of the Maxwellian averaged capture cross section σ times the s-process abundance N is plotted as a function of atomic number between ^{96}Mo and ^{190}Os. The sensitivity with respect to the cross sections of ^{138}Ba and ^{140}Ce is demonstrated by the dashed line, whereas the dotted curve illustrates the influence of the flux distribution constant τ_0.

the respective average capture cross section $\sigma(A)^{10}$:

$$\sigma(A)N(A) = \sigma(A-1)\ N(A-1)\ (1 + \frac{1}{\tau_0\sigma(A)})^{-1} \qquad (4)$$

By means of this formula the product $\sigma(A)N(A)$ can be extrapolated from ^{170}Yb, a stable s-process nucleus in the vicinity of ^{176}Lu, to mass number A=176. $N^*(^{176}Lu)$ is then calculated using the experimental average capture cross section of ^{176}Lu.

The average flux τ_0 was determined in the mass range about A = 140 where the magic neutron number 82 causes very small capture cross sections. In that range the σN-values calculated with eq. (4) are most sensitive to τ_0. With our capture cross section measurements on ^{138}Ba and ^{140}Ce τ_0 was determined to 0.22 mb^{-1} . Fig. 4 shows an analysis of the σN curve between ^{96}Mo and ^{190}Os. The Sm isotopes 148 and 150 were used as normalization points. Obviously, the calculated curve is in excellent agreement with the empirical value determined with our ^{170}Yb cross section. This is also true for another result on ^{170}Yb[11] and for ^{186}Os, for which a cross section was reported recently [12]. As our analysis of the capture cross sections of ^{170}Yb and ^{175}Lu is not yet completed only a preliminary estimate for the mean age T can be given at present. From the calculated curve of Fig. 4 $N\sigma(176)$=5.2 mb (Si = 10^6) can be extrapolated for A = 176. The total capture cross section of ^{175}Lu and the partial capture cross section to ^{176m}Lu yield a branching ratio B = 0.4. With the capture cross section of ^{176}Lu and the Lu-abundance we obtained R = 1.08. According to eq. (2) this corresponds to a mean age for the s-process T = (9 + 4) x 10^9 y from now. However, this number has to be taken with caution, as it depends sensitively on the cross section of ^{175}Lu and might change after the final analysis of our measurements.

Acknowledgement

We appreciate it very much that Drs. Allen and R.R. Winters provided us with their results on ^{170}Yb ^{186}Os prior to publication.

References

1. H. Beer, F. Käppeler, this conference.
2. K. Wisshak, F. Käppeler, Nucl. Sci. Eng. 66 363 (1978), Nucl. Sci. Eng. 69, 39 (1979) this conference.
3. F.H. Fröhner, GA-8380, Gulf-General Atomic (1968).
4. V.S. Shorin, V.N. Kononov, E.D. Poletaev, Yad. Fiz. 20, 1092 (1974).
5. Z.M. Bartolome, R.W. Hockenbury, W.R. Moyer, J.R. Tatarczuk, R.C. Block, Nucl. Sci. Eng. 37, 137 (1969).
6. R.L. Macklin, J.H. Gibbons, Phys. Rev. 159, 1007 (1967).
7. V.A. Konks, Yu. P. Popov, Yu. I. Fenin, Yad. Fiz. 7, 493 (1968).
8. J.R.D. Lêpine, R.A. Douglas, H.A. Maia, Nucl. Phys. A 196, 83 (1972).
9. D.N. Schramm, G.J. Wasserburg, Astrophys. J. 162, 57 (1970).
10. R.A. Ward, M.J. Newman, D.D. Clayton, Astrophys. J. Supp. 31, 33 (1976).
11. B.J. Allen, D.D. Cohen, Aust. J. Phys. (to be published).
12. R.R. Winters, R.L. Macklin, J. Halperin, Phys. Rev. C. (to be published).
13. A.G.W. Cameron, Space Sci. Rev. 15, 121 (1973).

STELLAR NUCLEOSYNTHESIS AND THE 24-keV NEUTRON CAPTURE CROSS SECTIONS OF SOME HEAVY NUCLEI*

Thomas Bradley, Z. Parsa
New Jersey Institute of Technology, Newark, New Jersey 07102
and
M. L. Stelts and R. E. Chrien
Brookhaven National Laboratory, Upton, New York 11973

The neutron capture cross sections of ^{112}Sn, ^{130}Ba, ^{146}Nd, ^{148}Nd, ^{186}W, ^{190}Os and ^{192}Os at 24 keV neutron energy were measured with respect to ^{197}Au by activation in a 24 keV neutron beam at the Brookhaven High Flux Beam Reactor. The reliability of this technique was verified by remeasuring the cross section of ^{186}W and comparing it to previous measurements. This continuing series of measurements will provide a more reliable data base for nucleosynthesis calculations.

(Activation cross sections at 24 keV; stellar nucleosynthesis on ^{112}Sn, ^{130}Ba, ^{146}Nd, ^{148}Nd, ^{186}W, ^{190}Os and ^{194}Os)

Introduction and Background

The importance of neutron capture cross sections in stellar nucleosynthesis was first emphasized in 1946. At this time Alpher, Bethe and Gamow[1] demonstrated the approximately inverse relationship between elemental abundances and their capture cross sections at stellar temperatures. Since then it has been concluded that buildup of heavy nuclei is accomplished by neutron capture via either the slow (s) process in normal stars or the rapid (r) process in supernovae. The s process occurs inside of stars at a temperature of about 20-30 keV.

A reactor spectrum can be filtered through a ^{56}Fe-Al filter to provide a source of neutrons at an energy corresponding approximately to these stellar temperatures. Such a beam is available with sufficient intensity ($\sim 4 \times 10^7$ n/sec) to allow measurement of the activation cross section with natural samples.

Experimental Technique

The source of neutrons used in this series of measurements was the 24.3 keV filtered beam facility at the High Flux Beam Reactor at Brookhaven National Laboratory. This energy is obtained by use of an iron-aluminum filter made of 12" of ^{56}Fe and 7" of Al.[2] This is the energy equivalent to neutrons in equilibrium with their surroundings at 2.8×10^{8}° K. This is a good approximation to the internal temperature inside a red giant.

The measurements were done in the following manner: Since the neutron capture cross section of gold at 24 keV neutron energy is well known (621 ± 3 mb), averaged over the iron-filtered spectrum, all cross sections were measured relative to gold. A sample packet, with dimensions slightly larger than the $(2.5\ cm)^2$ beam, was prepared consisting of $\sim 0.2\ gm/cm^2$ Au and $\sim 1\ gm/cm^2$ of the sample sandwiched between two sheets of $0.022\ gm/cm^2$ cadmium. Thus the samples were irradiated simultaneously in a geometry that minimized any variation of the flux over the beam area. The cadmium was used to shield the sample from any thermal neutrons returning from the room. After irradiations of about one day the sample was removed from the beam and the activity measured with a Ge(Li) detector. Because of the high neutron current and the excellent γ-ray resolution of Ge(Li) detectors it was possible to use natural samples rather than separated isotopes.

After irradiation, the sample packet (without Cd) was placed in a fixed geometry about 12 cm away from a Ge(Li) detector, which detected the gamma rays emitted from the sample (Fig. 1). This relatively large distance was to insure that the geometrical efficiency would not change due to slight differences in the positions of the samples. The relative efficiency calibration of the detector used was obtained by placing previously calibrated ^{226}Ra[3] and ^{182}Ta[4] sources in the same fixed geometry as that of the samples. The relative efficiency curve thus obtained is shown in Fig. 2. The detector was surrounded with bismuth and lithium loaded polyethelene to shield from γ- and n-backgrounds, respectively.

The signal from the detector, after being shaped and amplified was digitized and the spectra stored in a computer memory. A representative spectrum obtained by this method can be seen in Fig. 3.

The length of the time necessary to accumulate sufficient data was dependent upon the abundance of the isotope, its half life, and the level of activation obtained. This varied from several hours for ^{148}Nd to over a week for ^{112}Sn.

Data Analysis

During irradiation of the target nuclei, the total number of activated nuclei is dependent on both the rate of activation and the rate of decay. Thus the number of activated nuclei at any time t is:

$$N_2(t) = \phi\, \sigma\, N_1[1-e^{-\lambda t}]/\lambda \qquad (1)$$

where ϕ is the neutron flux, σ the neutron capture cross section, N_1 is the number of target nuclei at the beginning of the irradiation and λ is the decay constant. However, since the cross sections of the various nuclei are to be found with respect to the gold cross section, absolute flux measurements are not necessary. Thus, when Eqn. (1) is solved for a relative σ it becomes:

$$\sigma_B = \sigma_A \frac{N_{2_B}}{N_{2_A}} \frac{\lambda_B}{\lambda_A} [1-e^{-\lambda_A t_I}]/[1-e^{-\lambda_B t_I}] \qquad (2)$$

where A signifies the nucleus used as a standard and B is the nucleus whose cross section is to be calculated. In this case t_I is the irradiation time. The gold cross section is taken to be 621 millibarns.[5]

The numbers of activated nuclei at the end of the irradiation period (N_{2A}+N_{2B}) are given by the following equation:

$$N_2 = \frac{C}{\varepsilon f(1-e^{-\lambda t_c})F}$$

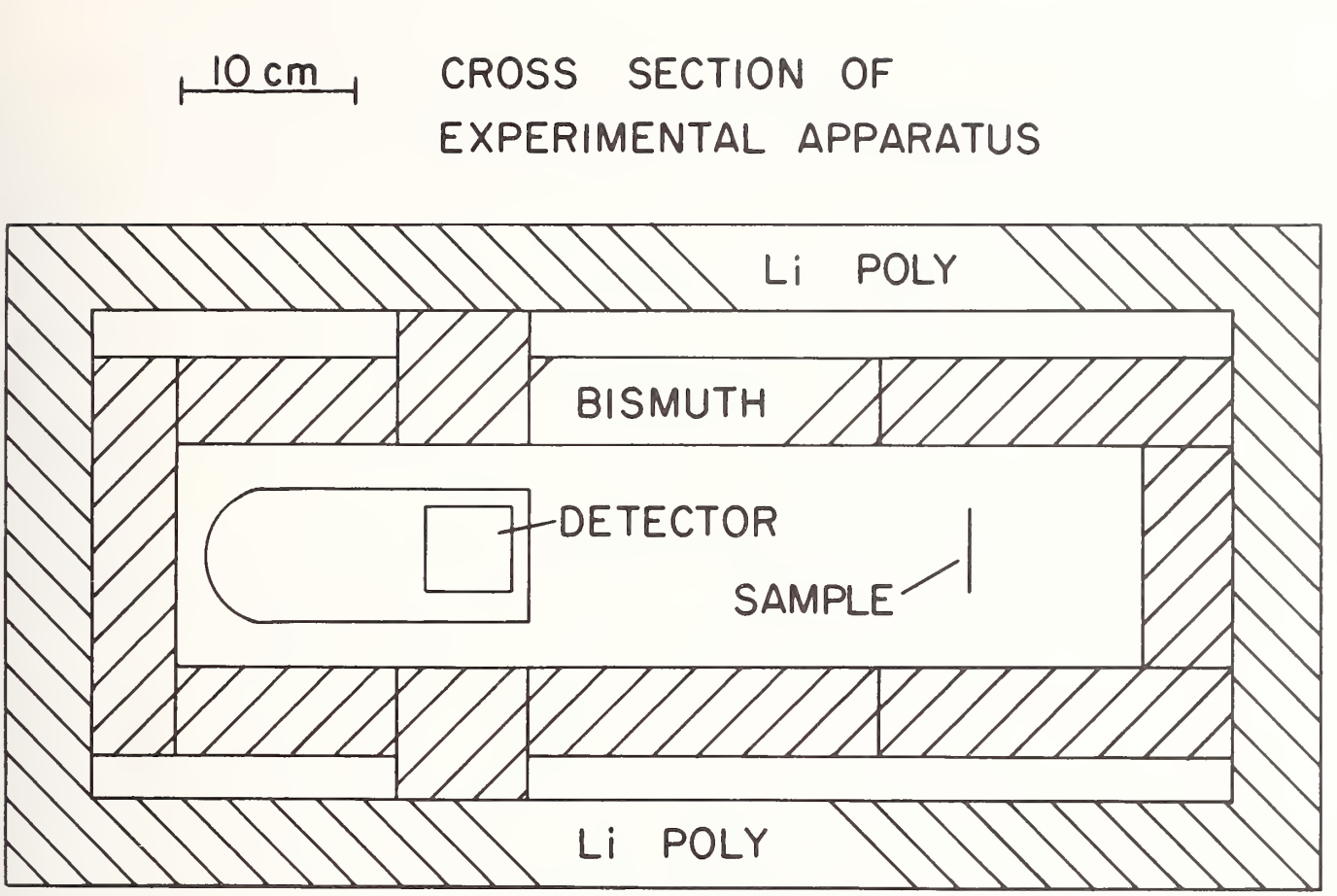

Fig. 1: Shielding and γ-ray source geometry used in conjunction with the Ge(Li) detector.

where C is the total number of gamma rays of a particular energy counted over a period of time t_c corrected for decay after irradiation, ε is the relative detector and geometrical efficiency of the sample gamma-ray line versus the gold line, f is the branching ratio and internal conversion of the emitted photon (listed in Table 1), and F is the correction for the self-absorption within the sample. Corrections for neutron attenuation and multiple scattering are negligible. No corrections for dead time were necessary when the sample and gold were counted simultaneously. For those cases where the gold and sample were counted separately, dead time corrections of $\lesssim$ 5% were applied.

24 keV Neutron Capture Results

The results for each nuclide are listed in Table 1. Also given are the γ-ray lines used to determine the cross section with the γ-ray branching ratios (per decay), f, for each γ-ray. In the case of ^{112}Sn and ^{190}Os the γ-ray results from a 100% decay of an isomeric level populated by β decay. For these nuclei f = 1/1+α, where α is the electron conversion coefficient. Comments on each nuclei measured follow.

Due to the low natural abundance of ^{112}Sn(1%) and the relatively long half life (115 days) of ^{113}Sn, the sample was counted for about two weeks to achieve good counting statistics.

For ^{146}Nd, due to a low count rate, several measurements of the strength of the 531 keV line were made over about a week and then were folded together.

Since the 24 keV cross section of ^{186}W has been previously measured[8] to an accuracy of better than 10% it was used as a check on the reliability of the technique. Our measured 24 keV cross section is 247 ± 12, in excellent agreement with the evaluation based on previous data of 250 ± 20.

The cross section measured for ^{190}Os is the total capture cross section ($\sigma_T = \sigma_{\text{Excited State}} + \sigma_{\text{Ground State}}$). For the osmium isotopes it was necessary to also correct for γ absorption in the Al container of the powdered sample.

Discussion and Analysis of Results

Since most compilations of cross sections data for stellar nucleosynthesis are done at 30 keV it is necessary to extrapolate the 24 keV measurements to this energy. What is usually done at this point is to simply assume that the absorption cross section in this area follows a strictly 1/v dependence. If that assumption is made here, the measured results should be multipled by .90 to obtain the equivalent 30 keV cross section.

However, it is possible to get a more precise correction factor for each nuclide from its resonance parameters and strength functions.[9] More exactly, what is done is to calculate each isotopic cross section as well as possible at 24 and 30 keV. The ratio of these values is then the correction factor which the measured cross section should be multipled by to obtain the corresponding 30 keV cross section. This allows for a deviation from the 1/v trend due to p-wave capture. The equation used, which was adapted from Ref. 10 may be expressed as follows:

$$\sigma = 2\pi^2 \lambda^2 \sum_{\ell,J} g_J \frac{\langle \Gamma_n \rangle}{D_J} \frac{\langle \Gamma_\gamma \rangle}{\langle \Gamma \rangle} F \left(\frac{\Gamma_\gamma}{\Gamma_n}\right) \qquad (4)$$

where D_J is the level density of each resonance spin

g_J = statistical weighting factor = $\frac{(2J+1)}{2(2I+1)}$

$\langle\Gamma_n\rangle$ = average neutron level width

= $S_0 D_J(E_n)^{1/2}$ for s-wave capture

= $S_1 D_J(E_n)^{1/2}(1 + (\frac{1}{\kappa R})^{-1}$ for p-wave capture

(S_0 and S_1 are s and p wave strength functions)

$\langle\Gamma_\gamma\rangle$ = average radiative capture width

$\langle\Gamma\rangle = \langle\Gamma_n\rangle + \langle\Gamma_\gamma\rangle$ = total level width

F = fluctuation factor, defined by Lynn.[11]

The correction factors thus obtained and the resultant 30 keV cross sections are listed in Table 2. These 30 keV cross sections, however, do not take into account possible fluctuations in level spacing. Due to the fact that the half width of the filtered beam used is 1.9 keV, there may be relatively few resonances within this width for some of the nuclei. The effect this would have is to increase the error of the extrapolated results for the nuclei with large level spacing.

Table 1

Nuclide	$\sigma(\Delta\sigma)$ mb	E_γ (keV)	$f = (\frac{1}{1+\alpha})f_d$
^{112}Sn	228(25)	392.7	.617 ± .012
^{130}Ba	755(54)	496	.47 ± .01 *
		373	.141 ± .005*
		216	.22 ± .01 *
^{146}Nd	87.7(6.0)	531	.12 ± .005†
^{148}Nd	126.8(8.0)	423.5	.11 ± .01 †
		211	.31 ± .01 †
		114.3	.22 ± .01 †
^{186}W	247(12)	685.8	.266 ± .001†
		479.8	.209 ± .001†
^{190}Os	358(38)	129.4	.225 ± .005
^{192}Os	156(16)	460.5	.039 ± .0005†
		138.9	.043 ± .0005†

† Measured γ intensity from Table of Isotopes.[6]
* Measured γ intensity from ref. 7.

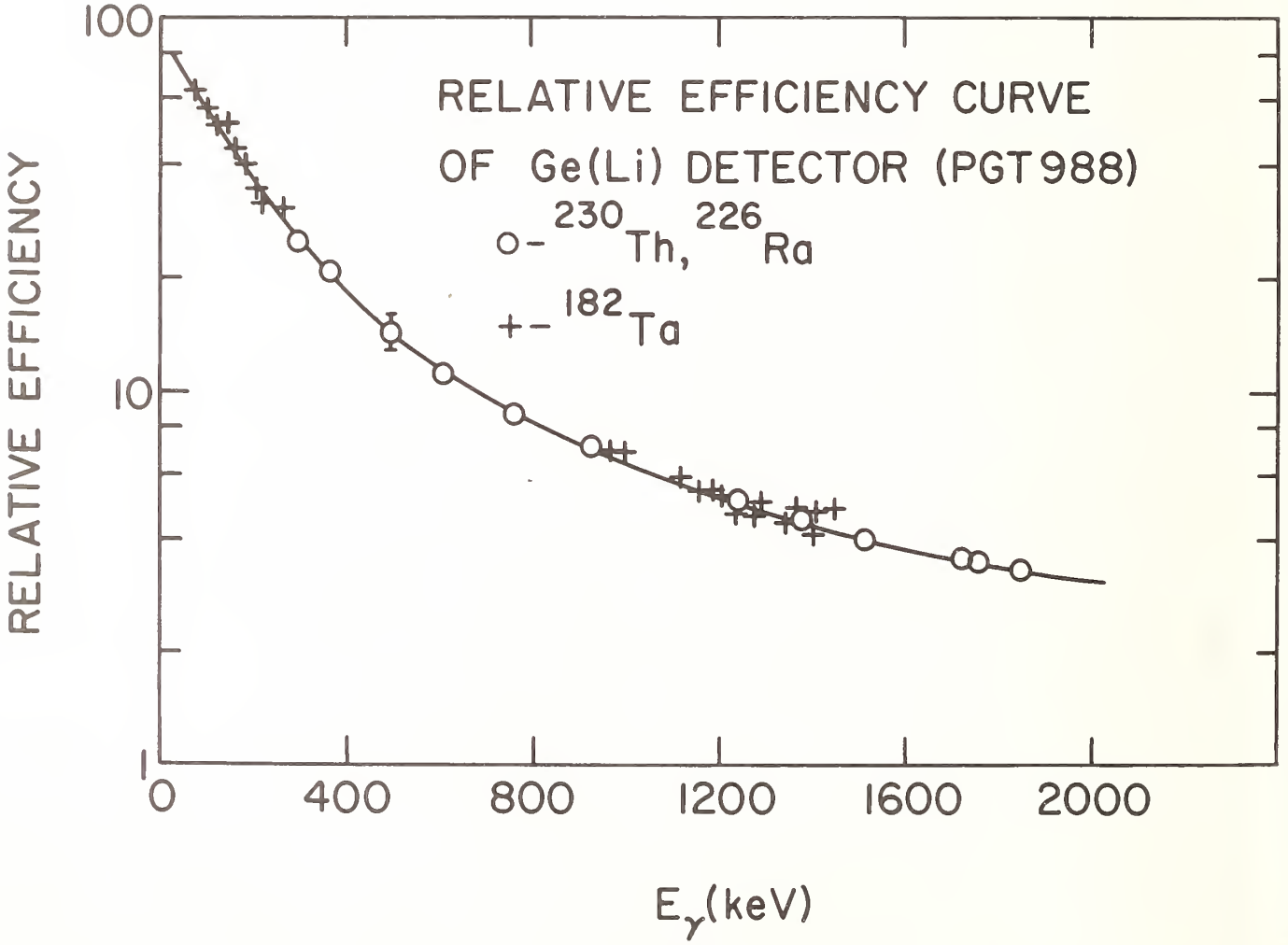

Fig. 2: Composite efficiency curve obtained from ^{226}Ra and ^{182}Ta sources.

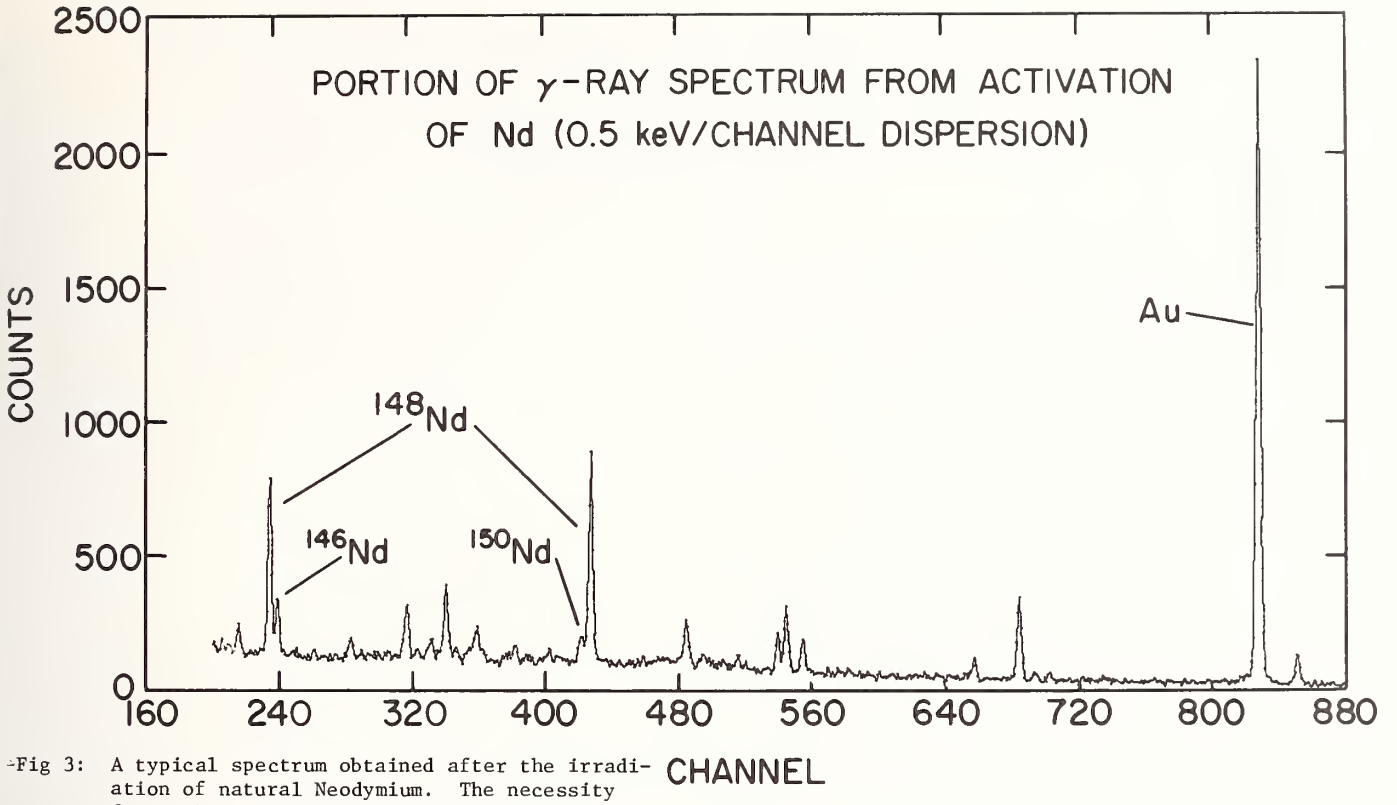

Fig 3: A typical spectrum obtained after the irradiation of natural Neodymium. The necessity for high resolution techniques can be seen from the numerous decay lines present.

Table 2

Nuclide	24 keV Measured σ	Correction Factor	30 keV Extrapolated σ	Previous Value
^{112}Sn	228 ± 25	.886	202 ± 24	180†
^{130}Ba	755 ± 54	.922	715 ± 58	2000†
^{146}Nd	88 ± 6	.853	75 ± 7	110 ± 25
^{148}Nd	127 ± 8	.785	99.4± 14	110 ± 20
^{186}W	247 ± 12	.893	221 ± 12	220 ± 20
^{190}Os	359 ± 38	.890	320 ± 36	230
^{192}Os	156 ± 16	.904	144 ± 15	200

† Semi-empirical estimate from Allen et al.[12]

Conclusion

The proven reliability of this technique in addition to the improvement in the accuracy of these measurements over previous ones, shows that these measurements plus future similar measurements will improve the data base for calculations in stellar nucleosynthesis.

References

*Research supported under contract EY-76-C-02-0016 with the Division of Basic Energy Sciences, U. S. Department of Energy.

[1] R. A. Alpher, H. A. Bethe, and G. Gamow, Phys. Rev. 73, 803 (1948).

[2] R. C. Greenwood and R. E. Chrien, Nuclear Instruments and Methods 138, 125 (1976).

[3] V. Zobel, J. Eberth, U. Eberth, E. Eube, Nuclear Instruments and Methods 71, 261 (1970).

[4] D. H. White, R. H. Birkett, T. Thomson, Nuclear Instruments and Methods 71, 261 (1970).

[5] K. Rimawi and R. E. Chrien, Nuclear Cross Section and Technology 145, 920 (1975).

[6] C. M. Lederer, V. S. Shirley, Table of Isotopes, Vol. 7, John Wiley and Sons, Inc. N.Y. (1978).

[7] R. J. Gehrke, R. G. Helmer, C. W. Reich, R. C. Greenwood, R. A. Anderl, Phys. Rev. C 14, 1898 (1976).

[8] M. D. Goldberg, S. F. Mughabghab, S. N. Purohit, B. A. Magurno, V. M. May, Neutron Cross Sections, Vol. 2C, Supplement 2 (1966).

[9] D. I. Garber, R. R. Kinsey, Neutron Cross Sections, Vol. I. (1976).

[10] R. E. Chrien, G. W. Cole, J. L. Holm and O. A. Wasson, Phys. Rev. C 9, 1629 (1974).

[11] J. E. Lynn, The Theory of Neutron Resonance Reactions, p. 228, Clarendon Press, N.Y. (1968).

[12] B. J. Allen, J. H. Gibbons, R. L. Macklin, Advances in Nuclear Physics 4, 205 (1971).

THE MEASUREMENT OF MAXWELLIAN AVERAGED CAPTURE CROSS SECTIONS FOR ^{138}Ba, ^{140}Ce, ^{175}Lu and ^{176}Lu WITH A SPECIAL ACTIVATION TECHNIQUE

H. Beer and F. Käppeler
Kernforschungszentrum Karlsruhe GmbH
Institut für Angewandte Kernphysik
P.O.B. 3640, D-7500 Karlsruhe
Federal Republic of Germany

The capture cross sections of ^{138}Ba, ^{140}Ce, ^{176}Lu, and the capture cross section of ^{175}Lu to the 3.68 h isomeric state in ^{176}Lu have been determined at 30 keV neutron energy using the activation technique. Neutrons were generated via the $^{7}Li(p,n)$ reaction just above the reaction threshold at a 3 MV pulsed Van de Graaff accelerator. The neutron beam was kinematically collimated with an energy spectrum similar to a Maxwellian distribution, so that the activation measurements yielded directly Maxwellian averaged capture cross sections.

[$^{138}Ba(n,\gamma)$, $^{140}Ce(n,\gamma)$, $^{175}Lu(n,\gamma)^{176m}Lu$, $^{176}Lu(n,\gamma)$, capture cross sections, E_n=30 keV, s-process synthesis]

Introduction

Accurate capture cross sections are often a prerequisite for a meaningful analysis of stellar s-process nucleosynthesis. In theoretical studies this has been emphasized especially for the small cross sections of ^{138}Ba and ^{140}Ce [1] and the branching ratio at ^{176}Lu which is of importance for the ^{176}Lu cosmic clock [2]. In view of these requests we developed a special activation technique. With a pulsed 3 MV Van de Graaff accelerator, we were able to produce a neutron spectrum similar to a Maxwellian energy distribution for a thermal energy of kT ∿ 30 keV via the $^{7}Li(p,n)$-reaction. The corresponding temperature of 3.5×10^{8} °K is expected for the s-process environment. In this neutron spectrum cross section measurements were performed for the reactions $^{138}Ba(n,\gamma)^{139}Ba$, $^{140}Ce(n,\gamma)^{141}Ce$, $^{175}Lu(n,\gamma)^{176m}Lu$, and $^{176}Lu(n,\gamma)^{177}Lu$. The capture cross section of ^{175}Lu to the short lived isomeric state ^{176m}Lu can be measured only by activation.

Beside the special neutron spectrum, the activation technique used is characterized by the following features:

- The activation samples were placed very close to the neutron target in a comparably high flux. Thus it was possible to measure the small cross sections of ^{138}Ba and ^{140}Ce accurately even with small amounts of sample material. In each case, only thin samples were used to minimize corrections for scattering or self absorption effects.
- The method is so sensitive that no high isotopic enrichments are required. This allows even the investigation of the rare isotope ^{176}Lu with a natural Lu-sample.
- All measurements are carried out with a ^{197}Au foil as a standard which is activated simultaneously. In this way most systematic uncertainties can be avoided.
- The neutron flux during the activation is recorded continuously to account for the exact activation history.
- All samples are counted with a calibrated, high resolution Ge(Li)-detector to achieve the best signal-to-background ratio.

Experimental Method

The neutron activation consists of two steps: neutron irradiation of a suitable sample and absolute counting of the induced activity.

Fig. 1 illustrates how the irradiations were carried out. Kinematically collimated neutrons were produced via the $^{7}Li(p,n)$ reaction with protons 25 keV above the reaction threshold.

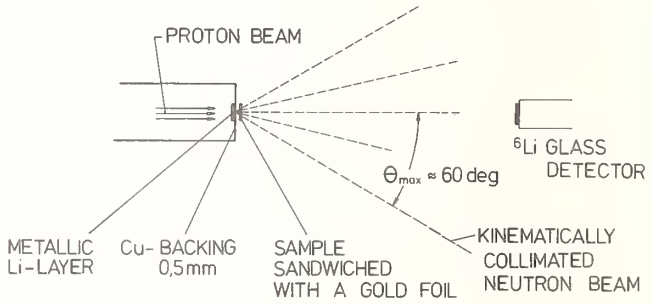

Fig. 1. Scheme of the experimental technique.

The neutron spectrum obtained in this way from thick metallic Li targets exhibits a maximum neutron energy of 106 keV and can be well characterized by a Maxwellian distribution for a thermal energy kT = 23.4 keV (Fig. 2).

In this neutron field the sample and a gold reference sample were irradiated in a back-to-back geometry. The irradiation history was recorded in a Nova 2 computer. Beside the total irradiation time also the time dependence of the neutron yield was measured. For this purpose the integral count rate of the ^{6}Li glass detector was stored in intervals of 40 sec. Due to the high neutron yield obtained (10^{8} - $10^{9} s^{-1}$) relatively thin samples could be used. All measurements were made with natural samples, mostly in form of metal foils. The sample diameter was 6 mm. In Table I the total and the effective sample thicknesses are given for the investigated isotopes.

Table I. Sample characteristics of the investigated isotopes (all natural composition)

Sample	Thickness (mg/cm²)	Investigated isotope	Eff. Thickness (at/b)
Ba	339	^{138}Ba	$7.46 \cdot 10^{-4}$
Ce	132	^{140}Ce	$5.05 \cdot 10^{-4}$
Lu	31.6	^{175}Lu	$1.06 \cdot 10^{-4}$
	396	^{176}Lu	$0.353 \cdot 10^{-4}$
Au	112	^{197}Au	$3.42 \cdot 10^{-4}$

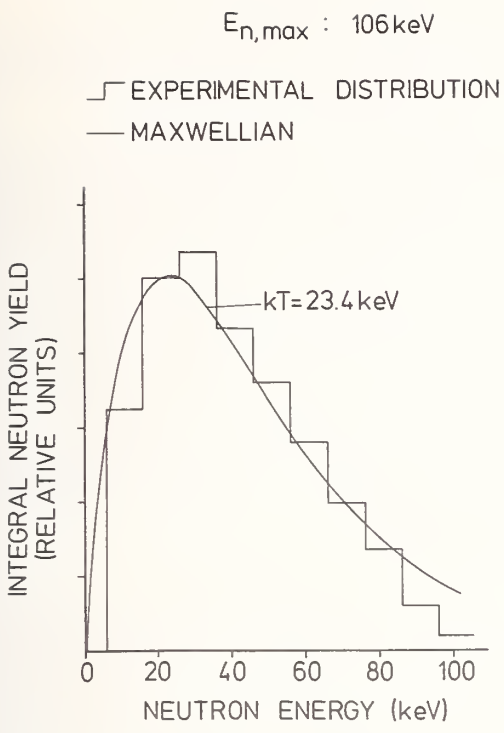

Fig. 2. The measured, integral neutron yield (histogram) from the $^{7}Li(p,n)$ reaction for a maximum neutron energy of $E_{n\ max}$ = 106 keV corresponding to a proton energy of 25 keV above reaction threshold. A least squares fit with the Maxwellian distribution (solid line) yields a thermal energy kT = 23.4 keV.

The induced activity in the respective sample and in the gold reference sample was counted with a calibrated high resolution Ge(Li) detector. The gamma ray spectra from the decay of the samples were recorded in subsequent time intervals which were considerably shorter than the respective half lives. This mode of registration allows to select an optimum counting time from the signal-to-background ratios of the relevant gamma ray lines, and it also provides a check for the background subtraction via the well known half life of the sample activity.

Analysis

For a particular gamma ray line the number of events C registered in the Ge(Li) detector during the activity determination is given by the expression

$$C = A \cdot K_\gamma \cdot \varepsilon_\gamma \cdot f_\gamma \cdot (1 - e^{-\lambda T_M}) \cdot e^{-\lambda T_W} \qquad (1)$$

where ε_γ is the Ge(Li) efficiency, f_γ the relative gamma intensity per decay for the investigated line, and λ is the decay rate. T_W is the time interval between irradiation and activity measurement and T_M stands for the Ge(Li) measuring time. K_γ gives the correction factor for gamma self-absorption in the sample.

The number of activated nuclei, A, can be written as

$$A = \phi_T N \sigma f_B \qquad (2)$$

Here, $\phi_T = \int \phi(t)dt$ is the time integrated neutron flux, N the sample thickness in at/b, and σ the capture cross section. The factor

$$f_b = \int_0^{T_B} \phi(t)\, e^{-\lambda(t-T_B)} dt \Big/ \int_0^{T_B} \phi(t)\, dt \qquad (3)$$

accounts for the decay of activated nuclei during the irradiation time T_B.

As the measurements are carried out relative to ^{197}Au as a standard, the neutron flux ϕ_T cancels out to first order:

$$\frac{A_i}{A_{Au}} = \frac{\sigma_i}{\sigma_{Au}} \frac{N_i}{N_{Au}} \frac{f_{B_i}}{f_{B_{Au}}} \qquad (4)$$

The cross section σ_i determined from eq. (4) represents an average over the neutron spectrum used during the irradiation:

$$\bar{\sigma}_{exp} = \int \sigma(E)\ \phi(E)dE / \int \phi(E)\ dE \qquad (5)$$

As in our mesurements the neutron spectrum $\phi(E)$ (see Fig. 2) is very similar to a Maxwellian distribution

$$\phi_{Maxw.}(E) \sim E\ e^{-E/kT} \qquad (6)$$

with kT = 23.4 keV, our measurements represent already proper Maxwellian averaged cross sections for that particular temperature:

$$\frac{\langle \sigma v \rangle}{v_T} = \frac{2}{\sqrt{\pi}} \int_0^\infty \sigma(E)\ E\ e^{-E/kT}\ dE \Big/ \int_0^\infty E\ e^{-E/kT} dE \sim \frac{2}{\sqrt{\pi}} \bar{\sigma}_{exp} \qquad (7)$$

In this expression v_T is the most probable thermal velocity and $2/\sqrt{\pi}$ is a normalization factor introduced by the definition of $\langle \sigma v \rangle / v_T$ [3].

Results

In Table III the results are shown for all isotopes together with the respective half lives, the detected gamma ray energies and intensities. The information on half lives and decay schemes was taken from Nuclear Data Sheets (Status 6/79). Only the relative gamma intensity for the 88 keV line in the decay of $^{176\ m}Lu$ is taken from a recent measurement of Morel[4]. The quoted uncertainties arise mainly from the ENDF/B-IV Au-standard (2.5 %), the gamma self absorption in the sample (0.4 - 2 %), the decay scheme of the activated nuclides (0.8 - 4 %) and the irradiation history (<3 %). Columns five and six give the thermal energies kT and the respective experimental Maxwellian averaged cross sections. An extrapolation to the "normal" distribution for kT=30 keV is included in column seven for those cases where the energy dependence of the cross sections was known [5].

Discussion

A comparison of our data with existing values is made in the last two columns of Table II. Especially for the Ce and Ba isotopes the results reported in the literature show large discrepancies, demonstrating the difficulties encountered in the measurement of small cross sections. Here, the advantages of our improved activation technique are outstanding: high neutron flux, small samples, no corrections for scattered neutrons, high resolution gamma spectrocopy and a well-known neutron spectrum which yields Maxwellian averaged cross sections with only minor corrections. Especially neutron scattering caused large corrections in the recent measurements of Musgrove et al.[6] As far as the results of Sidappa et al.[7] are concerned, we find in all cases discrepancies of a factor of 2 or even more which may be due to moderation effects in the perspex sample cannings. Also, a severe discrepancy was found for ^{140}Ce with respect to the cross section of Ref. [3]

For ^{176}Lu the result of Macklin and Gibbons[8] is 30 % higher than our result. This relatively large

Table II. The relevant decay parameters and the resulting Maxwellian average cross sections

Reaction	Half life	Detected gamma transition (keV)	Relative intensity per decay (%)	Fitted thermal energy kT (keV)	Experimental average cross section (mb)	Extrapolated average cross section for kT = 30 keV (mb)	Other work (mb)
$^{138}Ba(n,\gamma)^{139}Ba$	82.7 m	165.85	23	23	4.55 ± 0.23	4.22 ± 0.25	8 ± 2 [a] 11 ± 1.5 [b] 3.9 ± 0.8 [c]
$^{140}Ce(n,\gamma)^{141}Ce$	32.51 d	145.44	48.44 ±0.41	24	12.63 ± 0.57	11.52 ± 0.57	3 ± 3 [a] 23 ± 4 [b] 7.7 ± 0.9 [c]
$^{175}Lu(n,\gamma)^{176m}Lu$	3.68 h	88.35	8.86 ±0.25	24	906 ± 54		
$^{176}Lu(n,\gamma)^{177}Lu$	6.71 d	208.36	11.0 ± 0.4	24	1925 ± 95	1718 ± 85	2250±200 [d]
$^{197}Au(n,\gamma)^{198}Au$	2.69 d	411.79	95.52± 0.06	accepted standard value for kT = 30 keV : 610 ± 15 [e]			

[a] Ref. [3], [b] Ref. [7], [c] Ref. [6], [d] Ref. [8] [e] ENDF/B-IV

value (with respect to ^{175}Lu) was interpreted in terms of theoretical arguments. However, another explanation might be that there is a shape problem in the data. If we extrapolate our cross section to higher energies using the energy dependence reported by Benzi et al.[5] we find agreement with the data of Macklin and Gibbons above ∼100 keV.

Acknowledgement

We are grateful to Dr. J. Morel for providing us with his results on the ^{176m}Lu decay prior to publication.

References

1. R.A. Ward, M.J. Newman, Astrophys. J. 219, 195 (1978).

2. J. Audouze, W.A. Fowler, D.N. Schramm, Nature Phys. Sci. 238, 8 (1972).

3. B.J. Allen, J.H. Gibbons, R.L. Macklin, Adv. in Nucl. Phys. 4, 205 (1971).

4. J. Morel, LMRI-77-43/MJ (private communication).

5. V. Benzi, R. d'Orazi, G. Reffo, M. Vaccari, C.N.E.N. Report RT/F.1 (72) 6.

6. A.R. de L. Musgrove, B.J. Allen, R.L. Macklin, Aust. J. Phys. 32, 213 (1979).

7. K. Siddappa, M.S. Murty, J.R. Rao, Nuovo Cimento 18A, 48 (1973).

8. R.L. Macklin, J.H. Gibbons, Phys. Rev. 159, 1007 (1967).

NUCLEAR DEVELOPMENT NEEDS FOR FUSION-FISSION HYBRID REACTORS

D. L. Jassby
Plasma Physics Laboratory, Princeton University
Princeton, New Jersey 08544 USA

A fusion-fission (hybrid) reactor consists of a D-T or D-D fusion-neutron source surrounded by a neutron-absorbing "blanket" containing fertile materials (Th-232, U-238, Li-6, Li-7). The hybrid reactor's basic attraction derives from its ability to perform certain practical functions—notably power multiplication and fissile breeding—without requiring either start-up or make-up fissile feed. Apart from the development of an adequate fusion-neutron generator, development needs for the hybrid reactor include (1) improved information on neutron cross sections at energies of 3 to 16 MeV, in nuclides of thorium, protactinium, uranium, neptunium, and plutonium, and on secondary gamma-ray spectra due to inelastic neutron scattering and (n, xn) events in these nuclides; (2) cross-section sensitivity analyses of breeding performance; (3) resolution of compatibility problems among potential fuels, claddings, and coolants; (4) more extensive data on coolant flow and heat transfer properties, for analyzing severe thermal hydraulics problems arising from sharp gradients in heat production; (5) quantitative information on the adverse effect of cyclic power operation on fuel-clad interaction and mechanical properties; (6) determination of radiation damage effects on candidate blanket materials. Because the basic source of neutrons in a hybrid reactor operates independently of the means by which these neutrons are utilized, many blanket development requirements can be satisfied simultaneously by testing in separate and independent blanket modules of a fusion test reactor.

[Fusion, fission, hybrid blanket, tokamak, cross-section data, heat transfer.]

Introduction

A fusion-fission hybrid reactor consists of a D-D or D-T fusion plasma with a (sub-critical) blanket of fertile material surrounding the plasma chamber to capture the fusion neutrons (see Fig. 1). These neutrons may be multiplied by fission or (n, xn) processes, or may be captured in the fertile material to produce fissile fuel. In most conceptual designs, some optimal combination of energy multiplication and fuel production rate is sought.[1-3] Beyond the fertile blanket and reflector is a neutron and gamma-ray shield which protects other reactor components from radiation damage and activation. Lithium is distributed in various regions of the blanket to breed tritium for replenishment of the burned tritium.

The fusion-neutron source is referred to as the "fusion driver" of the hybrid. This paper is concerned only with fusion drivers operating on the D-T cycle: About 99% of the neutrons have nominally 14.1 MeV energy (from the D-T reaction), while about 1% have various energies between 2 and 8 MeV (from the D-D and T-T reactions). Table I lists the principal nuclear reactions for hybrid reactors.

Table I. Principal Nuclear Reactions for Hybrids

Fusion Reactions

1. $D + T \rightarrow n\ (14.1\ MeV) + {}^{4}He\ (3.5\ MeV)$
2. $D + D \rightarrow n\ (2.45\ MeV) + {}^{3}He\ (0.82\ MeV)$

Tritium Breeding

1. $n + {}^{6}Li \rightarrow T + {}^{4}He + 4.8\ MeV$
2. $n + {}^{7}Li \rightarrow T + {}^{4}He + n - 2.8\ MeV$

Fissile Breeding

1. $n + {}^{232}Th \rightarrow {}^{233}Th \xrightarrow[22m]{\beta^-} {}^{233}Pa \xrightarrow[27d]{\beta^-} {}^{233}U$
2. $n + {}^{238}U \rightarrow {}^{239}U \xrightarrow[24m]{\beta^-} {}^{239}Np \xrightarrow[2.4d]{\beta^-} {}^{239}Pu$

Interaction of the 14 MeV neutrons with the fertile materials in the blanket can result in large neutron multiplication and energy multiplication, M. Both uranium and thorium exhibit significant (n, 2n), (n, 3n), and (n, fission) reaction cross sections with 14 MeV neutrons, as indicated in Fig. 2. The number of neutrons released per fission reaction increases significantly with neutron energy, for both fissile and fissionable nuclides (see Fig. 3). The performance characteristics of typical uranium and thorium blankets[1-3] are given in Table II.

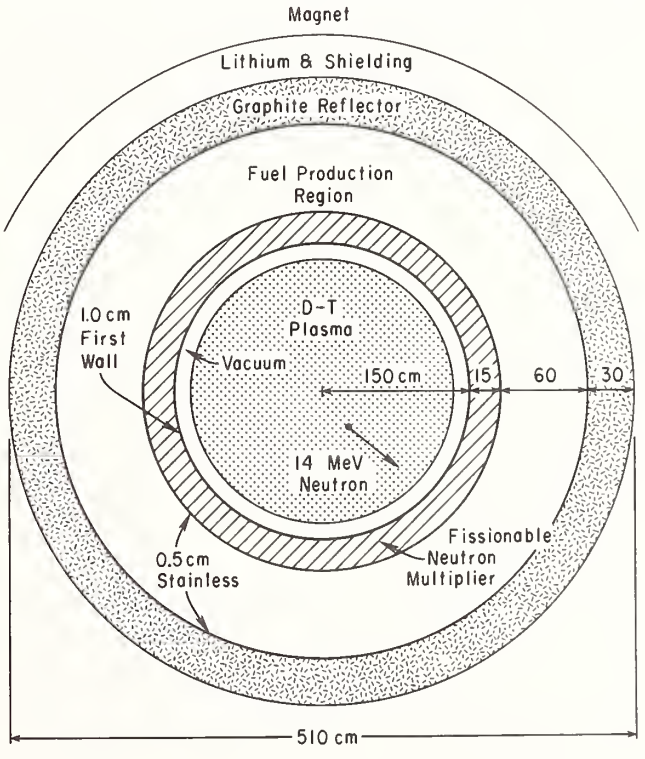

Fig. 1 Schematic diagram of the major components of a fusion-fission (hybrid) reactor utilizing a magnetically confined fusion plasma. Not to scale. 803178

For a uranium-based hybrid blanket, M may be 10 or more, partly as a result of fission of U-238 by fast neutrons. The Pu-239 production rate can be as high as 8 kg/yr per MW of fusion power (0.7 - 1 kg/yr per MW_t). With a thorium-based hybrid blanket, M ~ 3 and a U-233 production rate of up to 3.5 kg/yr per MW of fusion power (typically 1.5 kg/yr per MW_t) is possible. Fissile breeding performance is also very sensitive to the method by which a global TBR (tritium breeding ratio) of at least unity is obtained.

For any hybrid application, no start-up or make-up fissile fuel is required. The intial fuel loading can be entirely depleted uranium or thorium. It has been determined that with chemical reprocessing, the fuel-producing hybrid can provide make-up fuel for 4 to 10 LWR's (light-water reactors), or for as many as 20 HTGR's, each having the same thermal power as the hybrid. [4-5] By way of comparison, the LMFBR is capable of supporting at most a single LWR of the same power rating. [6]

This paper is concerned generally with the nuclear development needs for hybrid reactors, and in particular with cross-section data needs. The development requirements for the fusion neutron source are mentioned only briefly. Some of the information presented here reflects presentations that were made in the Third US-USSR Symposium on Fusion-Fission Reactors [7] that was held at Princeton in January 1979. During 1978-79, a thorough study of hybrid blanket data and development requirements was carried out by the Westinghouse Fusion Power Systems Department, [8] under the auspices the Electric Power Reseach Institute. That study also defined a blanket development plan that would provide the necessary data base to implement hybrid test reactors.

Motivation For Fusion-Fission Reactors

There are at least 5 potential applications of hybrid reactors:

(1) Power Multiplication. The addition of a depleted uranium or thorium blanket to a fusion reactor can result in a large increase in thermal power production (a factor of 3 to 30) for a relatively much smaller increase in total plant cost.

(2) Fissile Production. By special tailoring of the thickness and composition of the blanket regions, a hybrid reactor can be made to produce a large rate of fissile fuel per unit power production (see Table II).

(3) Net Tritium Production. Hybrid reactors with neutron multipliers can be used to achieve global tritium breeding ratios of 2 or more, thus producing considerable tritium for sale. This excess tritium could enable the deployment of a system of nonbreeding D-T reactors.

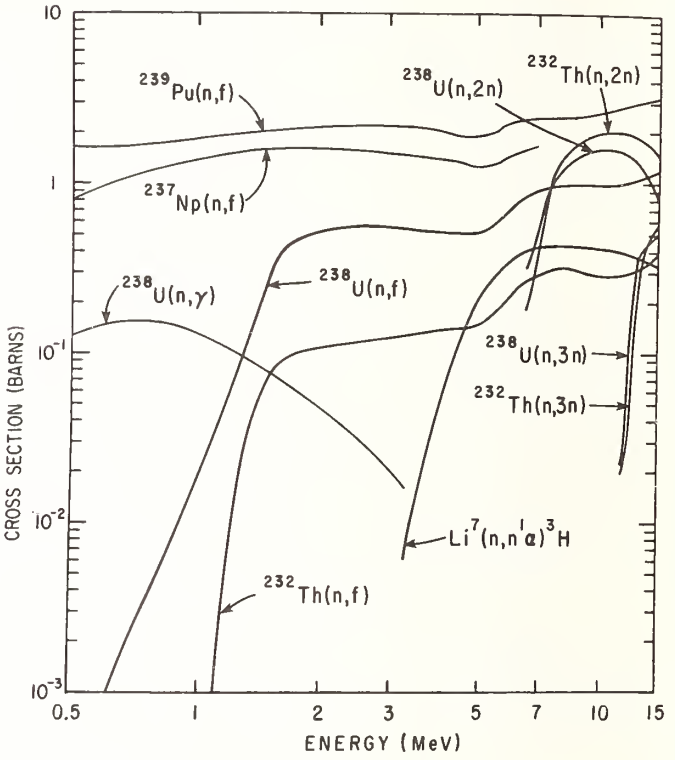

Fig. 2. High-energy neutron cross sections of various nuclides of interest for hybrid reactor blankets. 803179

Table II.

Performance of Hybrid Reactor Blankets

A. Hybrid Blankets Designed to Maximize Power Production

(Favored Candidate Fuels Are UC, U_3Si, U-Mo)

Fissile Concentration	0.5 to 2.0%
Energy Multiplication of Incident 14 MeV Neutrons	10 to 50
Net Fuel Production (Pu-239)	0 to 0.3 kg/MW_t-yr
Tritium Breeding Ratio	1.0

B. Hybrid Blankets Designed to Maximize Fuel Production

	Uranium Blanket	Thorium Blanket
Fissile Concentration	≲0.01	≲0.01
Tritium Breeding Ratio	1.0	1.0
Fissile Production (atoms per fusion neutron)	1.5 - 2	0.5 - 0.9
Blanket Energy Multiplic.	8 - 14	2 - 3
Net Fuel Produc.(kg/MW_t-yr)	0.7 - 1.0	0.8 - 2.5

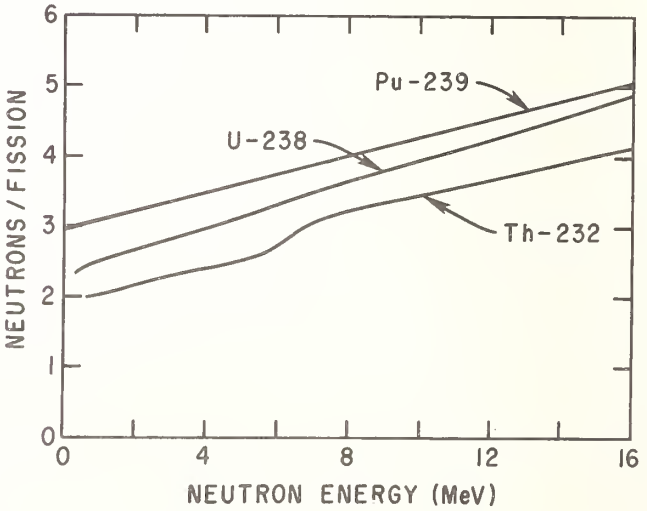

Fig. 3. Neutrons released per fission (ν), as a function of neutron energy. 803176

(4) Actinide Burning. Long-lived actinide "waste" nuclides (Np, Am, and Cm) from thermal convertor reactors can serve as both power multipliers and neutron multipliers when bombarded by high-energy neutrons (see Fig. 2). Hence actinides placed in the front end of a fusion reactor blanket can result in a hybrid which performs applications (1), (2), or (3), while simultaneously eliminating the actinide waste products of thermal reactors.

(5) Chemical Fuel Production. In analyses of chemical fuel ("synfuels") production in pure fusion reactors, it is found that a majority of the thermal energy deposited in the blanket by fusion neutrons is dissipated in the lithium breeding region.[9] This problem can be alleviated by breeding tritium in separate modules, but then a powerful neutron multiplier must be used to ensure a global TBR exceeding unity. If the breeding modules make use of a fissionable multiplying layer for the neutron multiplier, the large power produced in that layer can be used to generate whatever electricity is needed by the fusion driver and by the synfuels production processes in the other modules, thus permitting all the fusion neutrons incident on the synfuels modules to be used solely for the generation of very high temperatures ($\gtrsim 1000^{o}C$).

Preferred Hybrid Objectives

By the mid-1970's, the majority view of the role of hybrids had become that the principal purpose of the hybrid should be the production of fissile fuel for use in thermal converter reactors, while at the same time the hybrid should produce at least enough electricity to drive the reactor subsystems and to be self-sufficient in tritium.[1-3] The validity of this majority view (to which there are important exceptions[10]) evidently depends on the deployment of very large numbers of thermal converters whose fuel needs cannot be satisfied by the mining and enrichment of uranium ore. This assumption has become increasingly open to doubt, at least as far as the U.S. reactor market is concerned. Other serious difficulties involved with the fissile breeding objective are the achievement of economically attractive fissile production rates together with adequate tritium breeding, and the large cost of chemical reprocessing of the bred fuel.

In this author's view, power multiplication with minimal or zero net fissile production will become the most important role of the hybrid. In a power-producing hybrid, a highly moderated blanket (using water or graphite moderator) is fueled with depleted uranium or thorium. Within 2 years of irradiation by a reasonable fusion-neutron wall loading, the fissile concentration in the blanket will build up to an equilibrium value of 0.5 to 2.0%. This type of hybrid has the following advantageous features:

- No mining or enrichment of uranium is required.
- No reprocessing is required (once-through cycle).
- The blanket can be highly subcritical.
- Spent LWR fuel can be used after removal of fission products and recladding.
- Blanket technology and fuel cycle can be similar to those of the LWR, CANDU, or MAGNOX systems.
- Lithium can be used for spatial power flattening,[11] and tritium self-sufficiency is readily achieved.

Near-Term Fusion Drivers

An economic hybrid reactor requires a cost-effective fusion driver. That requirement means typically a fusion plasma with a power gain Q_p (= fusion power/heating power) exceeding 1 or 2, and capable of sustained high-duty-factor operation. Figure 4 shows the record values of Q_p that have been achieved in the most successful types of experimental fusion devices.[12] (Beam/solid-target fusion-neutron generators, not shown in Fig. 4, operate continuously and have $Q_p = 0.002$.)

In this author's opinion, only some version of the tokamak fusion driver is capable of meeting these goals in the next few decades. This perceived superiority of the tokamak is based on demonstrated performance to date, the probability of vastly improved performance to be demonstrated in the numerous advanced tokamaks recently comissioned or under construction, and the much poorer (or in most cases, hopelessly poorer) performance of all other magnetic confinement and inertial confinement fusion schemes. In the long run, one might well find fusion drivers superior to the tokamak. Nevertheless, the discussion below will assume, when a fusion driver must be identified, that we are concerned only with tokamaks. Most of the discussion, particularly involving cross sections, applies to hybrids with any type of fusion driver.

Figure 5 shows a trimetric view of a conceptual tokamak hybrid reactor.[3]

Optimal Hybrid Blankets

Front-End Multiplier

The "optimal blanket" for any specific hybrid application is a matter of considerable controversy. If the hybrid is to serve a purpose other than power production with zero net fuel production, and if the hybrid must be self-sufficient in tritium, then the optimal blanket should probably have a fast-neutron fissionable multiplier at the front face (i.e., exposed to the fusion neutrons). A multiplying layer 10 to 20 cm thick (see Fig. 1) will ensure an adequate neutron population for both fissile and tritium breeding, as well as adequate power production for driving the reactor subsystems.[13] A front-end multiplying layer maximizes the exploitation of 14 Mev neutrons, by producing many more neutrons in a unique fashion:

- Fissioning of non-fissile materials.
- Achieving higher υ in the fissioning of fissile materials (see Fig. 3).
- Making available the high-threshold (n, 2n) and (n, 3n) reactions (see Fig. 2).

This type of blanket results in the largest usable output of fissile fuel or tritium per unit capital cost (but not per unit energy!). Moderating materials should be avoided in the front end of a fuel-producing hybrid, as moderation reduces the exploitation of 14 MeV neutrons, and the generated fuel, either Pu-239 or U-233, is burned up at an excessive rate.

Heavy Actinide Multipliers

The choice of a fast-fission front-end multiplier leads to the consideration of fissionable heavy actinide "wastes" to serve as the high-gain multiplier material. The advantages are that one circumvents the time (several years) to build up Pu-239 to a large equilibrium value in the multiplier, and the burn-up of the actinides obviates their long-term disposal. The production of actinides in LWR's is approximately 7 kg per 1000 MW_t-year,[14] or about 1 ton per year from present U.S. LWR's. These nuclides consist of Np-237 (75%), Am-241 and Am-243 (20%), and Cm-242 and Cm-244 (5%).

Choice of Coolant

Water, steam, helium, liquid metals, and molten salts have been analyzed as potential coolants for the blankets of hybrid reactors.[1-3,7] Pressurized water is probably the preferred coolant for power-producing hybrids, whereas helium is preferred for fuel-producing hybrids. The disadvantages of the various candidate coolants are listed in Table III. Each type of coolant has definite advantages in one situation or another, so that despite the drawbacks, each coolant continues to have enthusiastic adherents.

Table III.
Drawbacks of Candidate Blanket Coolants

A. Water

1. Temperature limited to 350°C.
2. Strong neutron moderation results in excessive burn-up of Pu-239 or U-233 (in fuel-producing hybrids).
3. Possibility of water-lithium accidents.

B. Steam

1. Requires high pressure and thick piping, resulting in serious degradation of neutron energy spectrum.

C. Helium

1. Requires large pumping power (3% of thermal power).
2. Relatively scarce resource.

D. Liquid Metals

1. Difficult to flow across magnetic fields.
2. Fire hazard.
3. Chemically active.

E. Molten Salts

1. Limited neutron multiplication.
2. Corrosive.
3. Electrochemical effects.

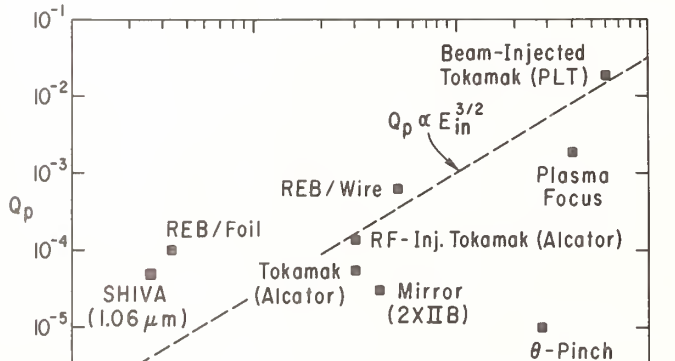

Fig. 4. Record values of fusion energy multiplication Q_p versus energy injected into the plasma (tokamak or mirror devices) or delivered to the pellet or wire. For systems that have used only deuterium, the equivalent Q_p for D-T fuel is given. 793206

Summary of Nuclear Development Needs

(1) Improved neutron cross sections, and secondary neutron and gamma-ray spectra for heavy elements, at neutron energies of 3 to 16 MeV.

(2) Testing of blanket neutronics models against integral experiments.

(3) Cross-section sensitivity analyses for fuel and power production.

(4) Techniques for maximizing blanket coverage of the fusion neutron source.

(5) Solution of thermal hydraulics problems, especially with high-gain multiplying layers at the front face.

(6) Alleviation of the effects of thermal cycling.

(7) Minimization of the first-wall thickness and blanket structural material.

(8) Compatibility among fuels, claddings, and coolants.

(9) Radiation damage data—DPA and gas production in compounds of heavy elements.

Nuclear Data Needs for Hybrid Blankets

Here we address only those nuclear data needs that are peculiar to hybrid reactor blankets. In addition, there are many data needs, particularly involving structural materials, that are common to both pure fusion and hybrid reactors, but these needs are discussed elsewhere in these Proceedings.

Sensitivity studies indicate that knowledge of the relevant cross sections to ±10% may result in estimates of breeding performance and power production with about 5% accuracy.[15] Attempts to obtain more accurate determinations cannot be justified, because of the large remaining uncertainties which have nothing to do with cross sections.

For U-238, uncertainties in (n,f), (n,γ), and (n, 2n) cross sections are documented, but (n, 3n) cross sections, secondary neutron spectra, and fission spectra are not well

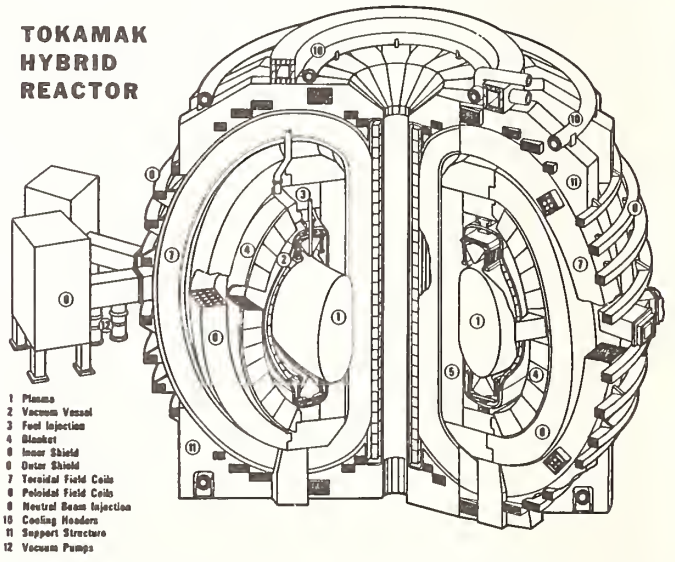

Fig. 5. Trimetric view of a tokamak hybrid reactor conceptual design by Westinghouse Electric Corp. (Dec., 1977), published in Ref. 3, p. 134. Diameter of plasma in horizontal midplane is 2.5 m.

Table IV.

Specific Cross-Section Data Needs For Hybrid Reactors

(Uncertainties Need To Be Reduced To ±10% In The Energy Ranges Indicated.)

Nuclide	Neutron Energy (MeV)	Reactions Needing Improved Data	Comments
Li-7	3 - 15	$(n, n'\alpha)^3H$ & (n, 2n)	Data needed to determine spatial lithium distribution for tritium self-sufficiency.
Zr-90	5 - 15	(n, 2n) & (n, 3n)	Favorable cladding & structural material.
Bi-209	5 - 15	various	Used specifically for neutron multiplication.
Th-232	0.1 - 3	(n,γ)	Present uncertainty is ± 15%.
Pa-231	1 - 5	(n,γ) & (n, fission)	U-232 product has highly active decay products, increasing reprocessing cost.
Pa-233	3 - 15	(n, fission)	Intermediate nuclide in U-233 production. $T_{1/2}$ = 27 days.
U-233	6 - 15	(n, 2n)	U-232 product has highly active decay products.
Pu-240, Pu-241	3 - 15	(n, fission) & (n,γ)	Formed by successive (n, 2n) reactions.
Th-232, U-232, U-238, Pu-240, Pu-241	6 - 15	(n, 2n) & (n, 3n)	Present uncertainties are ± 15 to 20% for (n, 2n), and ± 30 to 35% for (n, 3n).

Table V.

Nuclear Data Needs for Burning Actinide "Wastes"

- ν and fission neutron spectra at E_n = 3 to 15 MeV.
- (n, 2n) and (n, 3n) cross sections at E_n = 6 to 15 MeV.
- Secondary neutron spectra for (n, 2n) and (n, 3n) reactions.
- (n,γ) cross sections at E_n = 3 to 15 MeV.
- Inelastic scattering cross sections.

The cross-section data is needed with 10% uncertainties.

known. Nuclear data for the many isotopes (15-20) of uranium, neptunium, and plutonium found in a uranium blanket are required for time-dependent calculations, and data gaps exist.

General Nuclear Data Needs

(1) Secondary neutron emission spectra and angular distributions, to fill large gaps in data for (n, fission), (n, 2n), (n, 3n) reactions in nuclides of Th, Pa, U, Np, and Pu, at neutron energies in the range 5 to 15 MeV. This information is need for determining spatial distributions of fissile breeding and power production.

(2) Secondary gamma-ray emission spectra for inelastic scattering in nuclides of Th, Pa, U, Np, and Pu, at neutron energies of 5 to 15 MeV.

(3) Specification of estimated errors in cross sections and secondary neutron and gamma spectra for primary neutron energies of 3 to 15 MeV. This information is needed for cross-section sensitivity studies for specific hybrid reactor blanket designs.

Table IV gives specific cross-section data needs. Table V lists the nuclear data needs for the burning of the heavy actinides (Np, Am, Cm) in hybrid blankets.

In "pure fusion" reactors with blankets fueled with natural lithium (92.6% ^{7}Li), the ^{7}Li(n, n'α)reaction, which has a threshold of 2.8 MeV, can contribute up to 30% of the total tritium breeding. In hybrid reactors, on the other hand, most of the higher energy neutrons are exploited for (n, xn) and (n,f) reactions in fissionable material, so that ^{7}Li will contribute 10% or less of the total tritium breeding. Hence accurate knowledge of the cross section for the ^{7}Li(n,n'α) reaction is not nearly so critical for hybrid reactors as for pure fusion reactors.[16]

Computational Modeling of Blanket Neutronics Performance

While little new basic methods development is required, significant code development effort is necessary, particularly for 2-dimensional neutronics models. There are still serious limitations to these codes for fusion neutron applications, such as the omission of (n, 3n) reactions. Multi-dimensional neutronics codes treating toroidal geometry need further development. These codes must incorporate a toroidal neutron source, curved surfaces and penetrations. There is a general consensus that 3-D streaming problems can be handled with existing Monte Carlo codes. These and related matters are discussed in a paper by Chapin et. al., on tokamak blanket neutronics requirements.[17]

Cross-section sensitivity studies for specific hybrid blanket designs are needed to determine how uncertainties in the available data affect uncertainties in fissile breeding and power production.

Experimental Tests

Tests of code predictions against experimental data are needed, because of the many sources of uncertainties[18] in the modeling, as illustrated in Fig. 6:

- Heterogeneous blankets aggravate the effect of data uncertainties.
- Geometrically restricted blankets and the effects of large penetrations tax geometric models.
- The spatially asymmetric plasma neutron source and blanket regions result in a strong poloidal flux variation at the blanket face.
- Neutron scattering and energy degradation by the vacuum vessel and other nonblanket components give rise to uncertainties in the incident neutron spectrum and angular flux. As indicated in Fig. 7, the neutron spectrum just outside the vacuum vessel is likely to have a large flux component below 5 MeV.

To reduce uncertainties in the predictions of blanket performance, integral experiments are needed with calibrated fusion-neutron sources:

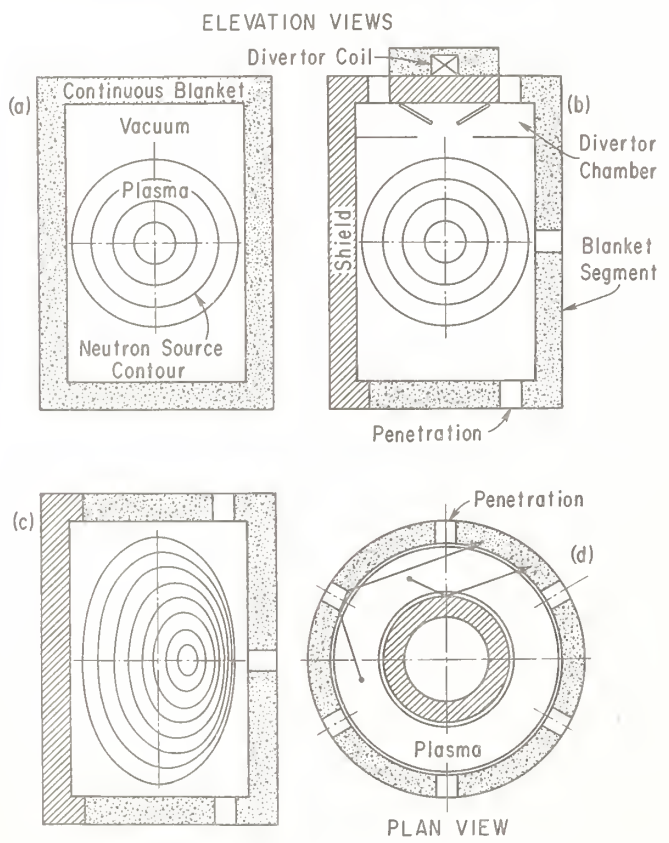

Fig. 6. Elevation and plan view of tokamak blanket arrangements. (a) No geometric uncertainties peculiar to the reactor. (b) Uncertainty introduced by finite geometry of heterogeneous blanket segment. (c) Uncertainty introduced by asymmetric neutron source. (d) Uncertainty introduced by neutron scattering phenomena. 803006.

(1) Spherical lattices with internal point-neutron sources. Many such experiments have been completed at LLL, LASL, JULICH, and JAERI. Benchmark experiments with uranium and thorium spheres and cylinders have been reviewed in Refs. 19-21. Sphere radii ranged from 6 cm for U-235 to 50 cm for U-238. Other recent measurements with Th-232, U-238, and Pb-208 assemblies have been made.[22,23] Agreement between experimental and calculated results for U-238 is adequately close to give confidence in estimating beginning-of-life performance, as would be appropriate for early testing in a tokamak reactor program.

(2) Blanket module mock-up experiments with an external point neutron source (e.g., RTNS-II[24]).

(3) Prototypical reactor blanket modules with a toroidal neutron source and reactor-characteristic spectrum (see Fig. 7). A tokamak neutron source, such as the TFTR, is required.[25]

A fusion-neutron fluence of 10^{13} n/cm^2 over an area of at least 1000 cm^2 is needed for satisfactory measurements of neutron flux and spectra, reaction rate profiles, spatial distribution of tritium and fissile breeding, and activation.

Induced Radioactivity

Development is needed of radioactivity and afterheat codes treating nuclides of Th, Pa, U, Np, and Pu, when irradiated by the mixed fusion and fission neutron spectrum of a hybrid blanket.

Thermal and Materials Development Requirements

Table VI summarizes the hybrid blanket development requirements, other than neutronic matters, as viewed by the participants in a recent symposium on fusion-fission reactors.[7]

The significant multiplication of the fusion neutron energy by fission can produce power densities in the blanket media as large as 500 W/cm^3. Since the blankets of hybrid reactors are designed to be highly subcritical, the power density gradient in the blanket can be quite steep,[1-3] as shown in Fig. 8. This steep power gradient can lead to steep temperature gradients, differential thermal expansion, and radiation-induced swelling with resulting stress in the blanket materials. The energy multiplication of the hybrid blanket also worsens the thermal cycling problems associated with the transient response of the blanket to the pulsed nature of the tokamak fusion generator (see Fig. 9).

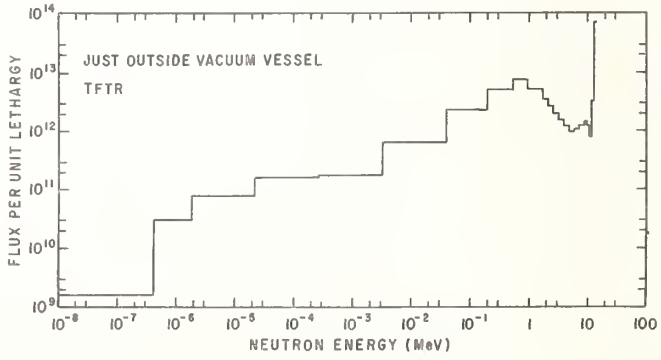

Fig. 7. Calculated neutron spectrum just outside the TFTR toroidal stainless-steel vacuum vessel, between toroidal-field coils. 793009

Thermal Hydraulics

Figure 8 shows the enormous radial variation in power density that can be expected in a hybrid reactor blanket if no measures are taken to flatten power production.[26] The steep fall-off in power production is characteristic both of moderated, single-layer, power-producing blankets, and of blankets with an unmoderated "multiplying region" up front, followed by a breeding region. In fact, power density can be made spatially more uniform by placing lithium in strategic locations to soak up thermal neutrons which would otherwise cause fission.[11] This latter technique also contributes to the achievement of TBR ≥ 1.

Structural Design

The blanket performance is quite sensitive to the amount of structural material located in the breeding zones, and to the thickness of the structural wall between the

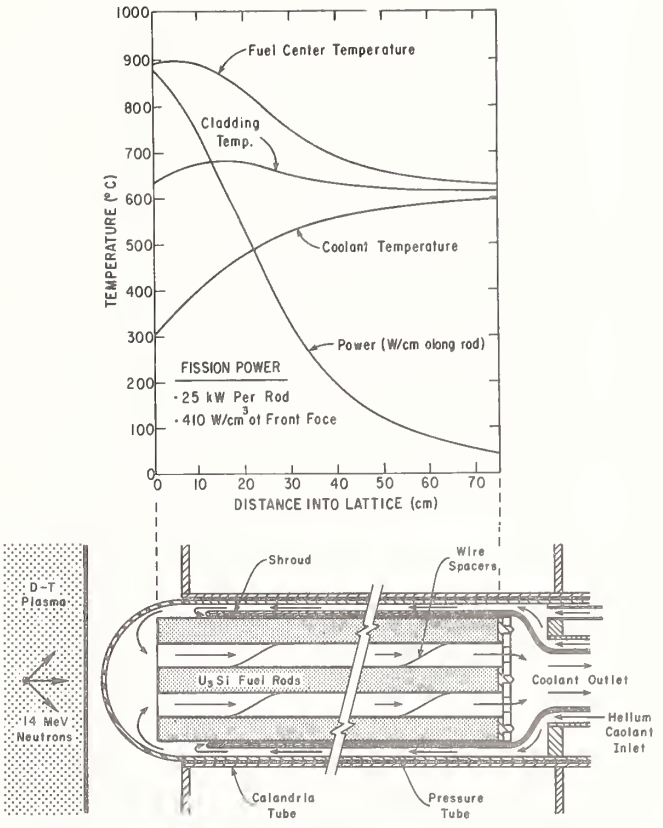

Fig. 8. Tops graphs give the power and temperature distributions in the fuel assembly shown below in longitudinal section. [From W. Pettus, Babcock & Wilcox Co. LRC-9081, July 1979.]

Table VI

Results from Blanket Engineering Development Questionnaire*

3rd USA-USSR Symposium on Fusion-Fission Reactors[7]

Q. What are the development requirements for your preferred blanket(s)? Indicate "developed" if you feel sufficient information is available from the fission program or elsewhere to proceed with reasonable confidence, "being developed" if the needed information is expected to be provided by an existing program, or "needs development" if work will have to be done specifically for hybrids.

Development Requirements	Developed	Being Developed	Needs Develop.
Fuel Fabrication	71%	--	29%
Fuel Irradiation Capab.	6%	18%	76%
Fuel Reprocessing	59%	6%	47%
Fuel-Clad Interaction	41%	6%	41%
Clad Irradiation Capab.	18%	6%	76%
Clad-Coolant Interaction	35%	12%	53%
Coolant Chemistry	47%	18%	41%
Coolant Thermal-Hydraulics	47%	6%	53%
Blanket Designs	6%	6%	88%
Remote Handling & Maint.	18%	--	82%
Power Conversion System	76%	6%	24%
Waste Handling & Disposal	47%	6%	47%
Safety Aspects	18%	6%	76%

Other Blanket Engineering Development Requirements

-Thermal-mechanical fatigue analysis and data.

-Reliable remote vacuum and pressure seals.

-Acceptable interaction with pulsed magnetic fields.

-Methods of minimizing blanket structural material.

-Blanket instrumentation.

* Questionnaire was conducted by K. R. Schultz of General Atomic Company, January 1979.

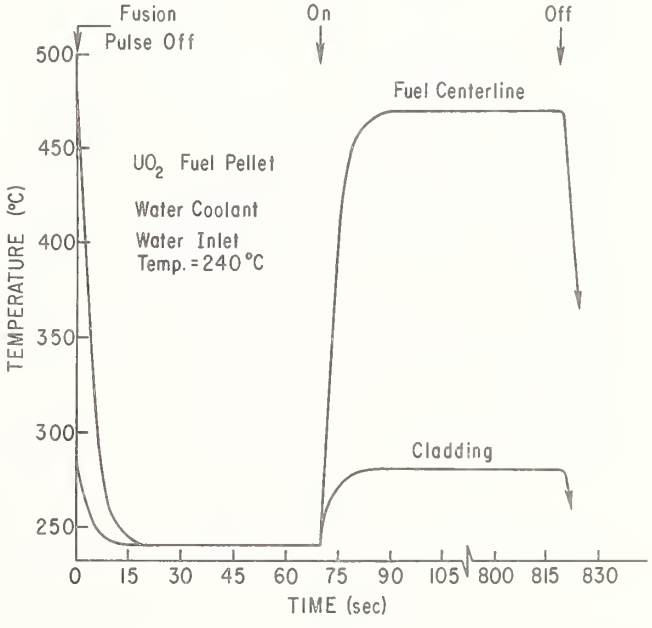

Fig. 9. Typical response of water-cooled UO_2 fuel pellet and cladding in the blanket of a tokamak hybrid reactor. [Modified from Westinghouse Electric Corp. Report for EPRI Contract No. RP-1347 (1979).] 803175

plasma and the blanket.[27] For fuel-producing hybrids, it is important to minimize the amount of structure and coolant materials in the blanket, as well as the thickness of the wall between plasma and blanket, in order to minimize neutron attenuation and softening of the neutron spectrum. Practical variations in these structures can have a larger effect on breeding performance than the present cross-section uncertainties.

The need to remove bred fuel implies the need for a blanket structural design that can be readily disassembled and reassembled.[27] Again, these requirements are greatly relaxed for power-producing hybrids with zero net fissile production.

Materials Compatibility Issues Peculiar to Hybrid Reactors

There are several features of hybrid reactor blankets that are generally absent from fission reactors, and that require considerable investigation before any design can be qualified for practical use.

(1) Cyclic Heating. The mechanical and thermal interactions of fuel, cladding, coolant and structure under pulsed heating, such as illustrated in Fig. 9.

(2) Strong Magnetic Fields. Electrochemical corrosion mechanisms, in the case of molten salt coolants flowing across strong magnetic fields.

(3) Lithium Compounds & Tritium Breeding. A vastly improved materials data base is need for solid lithium compounds. Tritium migration in candidate hybrid blankets under expected operating conditions must be investigated. The chemistry of molten salts containing both thorium and lithium, for example, needs to be studied. (Note that there has been considerable experience with lithium and tritium obtained with the heavy-water reactors at SRL and with the N-reactor at HEDL.)

PLAN VIEW OF A TOKAMAK BLANKET TEST REACTOR

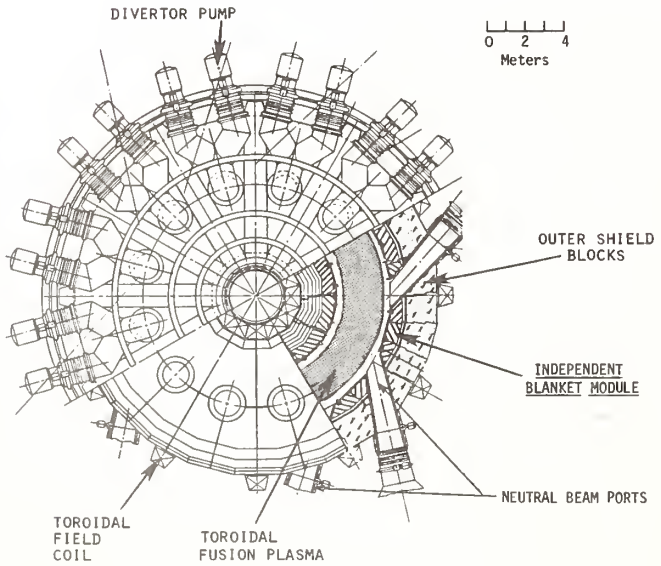

Fig. 10. A tokamak blanket test reactor will enable simultaneous testing of separate, independent blanket modules using the same fusion-neutron source. 803177

(4) Mixed Fusion/Fission Neutron Spectrum. The neutron spectrum in the blanket will vary from thermal to 15 MeV, and will have a strong spatial variation. The effect of radiation damage by this unusual spectrum on the degree of compatibility among fuels, clad, and coolant must be investigated.[8] DPA and gas production rates (hydrogen, helium, tritium) in fuel pins of Th, U, Np, and Pu compounds, irradiated by a mixed fusion/fission neutron spectrum, need to be measured. The degradation in mechanical properties of fuel pins and candiate blanket structures must be assessed.

Relevant tests could be performed in EBR-II at present, in the FFTF beginning in 1981, and in the FMITF beginning in 1984. While EBR-II and the FFTF have relatively small neutron populations at energies above about 6 MeV, the neutron spectrum incident on a hybrid blanket in a tokamak reactor will actually be much softer than a fusion spectrum (~14 MeV), because of attenuation and moderation of fusion neutrons in the "first wall," and because of scattering around the torus (see Fig. 7).

Development Venue of Hybrid Blanket Modules

What is the future of hybrid reactors in the next 30 years? This question can be answered from the following considerations:

First, no government or group of organizations is going to rush out to fund the development of a hybrid pilot plant dedicated to the production of nuclear fuel. For the next several decades at least, the likely commercial market for fissile fuel can be met by uranium ore resources with relatively well-known economics.

Second, any fusion test reactor is going to cost at least 1 billion dollars. Hence only a very few test reactors can be built, and each must be exploited to the utmost.

Third, D-T fusion energy has the unique feature among man-made energy sources that the region of energy utilization (the blanket) is decoupled from the region of energy production (the fusioning plasma). As illustrated in Fig. 10, a single fusion neutron source can be used for the simultaneous testing of many independent blanket module assemblies, having a variety of purposes, without affecting the fusion neutron source in any way. In addition to non-hybrid blanket modules for tritium production, synfuels production, or whatever, one or more hybrid blanket modules can be installed for fissile breeding, one or more for fuel-self-sufficient energy-multiplication, and one or more for actinide burning.

Thus many blanket development requirements can be satisfied by testing in separate blanket modules, with lateral dimensions of the order of 2 m x 2 m, and radial depth of 1 m. Shortcomings in blanket design can be tolerated, simply because retrofitting with blanket modules of improved design can be made at relatively little cost, and with no effect on the driving neutron source. These characteristics of a fusion test facility will permit systematic trial-and-error selection of materials, coolants, and configurations for hybrid and other fusion reactor blankets, without elaborate and separate materials testing or thermal hydraulics programs.

The level of individual blanket performance in one or more test reactors, which would be operated in the 1990's, and the perceived future market for hybrid-generated electricity or process heat or nuclear fuel, will determine whether hybrid reactors for any purpose are deployed in the early 20th century.

Acknowledgment

This work was supported by the U.S. Department of Energy, Office of Fusion Energy, Contract No. EY-76-C-02-3073.

References

1. Proceedings DCTR Fusion-Fission Energy Systems Review Meeting (Germantown, MD, 1974), ed. by S.L. Bogart, Report ERDA-4 (1975).

2. Proceedings US-USSR Symp. on Fusion-Fission Reactors (Lawrence Livermore Lab., 1976), ed. by C. Taylor, CONF. 760733.

3. Proceedings 2nd MFE Fusion-Fission Energy Systems Review Meeting (Washington, D.C., 1977), ed. by S. L. Bogart, CONF. -771155.

4. R.P. Rose, et al.,in Proc. 7th Intern. Conf. Plasma Physics and Controlled Nuclear Fusion (Innsbruck, Austria, 1978) 3, IAEA, Vienna (1979) 419.

5. J. A. Maniscalco, L. F. Hansen, and W. O. Allen, in Proc. 3rd Topical Meeting on the Technology of Controlled Nuclear Fusion (Santa Fe, New Mexico, 1978) 159.

6. R.N. Kostoff, "Status and Prospects of Advanced Fissile Fuel Breeders," U.S.DOE Report CONF.-790103 (Jan., 1979).

7. Proceedings Third US-USSR Symp. on Fusion-Fission Reactors (Princeton, N.J., 1979), to be published; see also D.L. Jassby, ed., "Workshop Summaries," Princeton Plasma Physics Lab. Rep. PPPL-1550 (July, 1979).

8. J.W.H. Chi and R.P. Rose, in Proc. 8th Symp. Engin. Problems of Fusion Research (San Francisco, 1979), paper 29-01, to be published.

9. L. Rovner, et al., "Study of Chemical Production," General Atomic Co. Report GA-A15371 (April 1979).

10. F.H. Tenney, et al., "A Systems Study of Tokamak Fusion Reactors", Princeton Plasma Physics Lab. Report PPPL-1450 (Nov. 1978); W.G. Pettus, R.G. Mills, and E. Greenspan, "Characteristics of a Gas-Cooled Water-Moderated Blanket Using U_3Si Fuel," to be published in Proc. 3rd US-USSR Symp. on Fusion-Fission Reactors.

11. E. Greenspan, et al., Trans. Am. Nucl. Soc. 30 (1978) 55.

12. D.L. Jassby, "Maximum Neutron Yields in Experimental Fusion Devices", Princeton Plasma Physics Lab. Report PPPL-1515 (Jan., 1979).

13. S.F. Su, G.L. Woodruff, and N.J. McCormick, Nucl. Tech. 29 (1976) 392.

14. "Fusion-Driven Actinide Burner Design Study", EPRI Report EPRI-ER-451, by Westinghouse Electric Corp. (May, 1977); H.C. Claiborne, "Neutron-Induced Transmutation of High-Level Radioactive Wastes," Oak Ridge Nat. Lab. Report ORNL-TM-3964 (Dec., 1972)

15. See, for example, B.R. Leonard, Jr., et al., in Nuclear Cross Sections and Technology, NBS Spec. Publ. 425, Vol. II (1975) 680.

16. H. Bachmann, et al., Nucl. Sci. Eng. 67 (1978) 74; A. Hemmendinger, C.E. Ragan, and J.M. Wallace, Nucl. Sci. Eng. 70 (1979) 274.

17. D.L. Chapin, G. Gibson, and L. Green, "Neutronic Analysis Requirements for Fusion Hybrid Reactor Blankets," Westinghouse Electric Corp. Report WFPS-TME-79-011 (Feb., 1979).

18. D.L. Jassby, et al., Trans. Am. Nucl. Soc. 33 (1979) 63.

19. B. R. Leonard, Jr., Addendum No. 4 of Proc. Magnetic Fusion Energy Blanket and Shield Workshop, (Brookhaven, NY, 1976), ERDA-76/117/1, pp. 66-79 (1976).

20. C. W. Maynard in Symp. on Neutron Cross-Sections from 10-40 MeV, BNL-NCS-50681, (July, 1977) 375.

21. M. H. Bhat, "Evaluated Files of Nuclear Cross-Sections for Fusion Reactor Calculations," Brookhaven Report BNL-NCS-25295 (1979).

22. J. W. Weale, et al., private communication (1979).

23. L. F. Hansen et al., "Neutron and Gamma-Ray Spectra from 232-Th, 235-U, 238-U, and 239-Pu After Bombardment with 14-MeV Neutrons," Nucl. Sci. Eng., 72 (1979) 35.

24. L. Green, Trans. Am. Nucl. Soc. 32 (1979) 59; L.F. Hansen, et al., private commun. (Sept. 1979).

25. D.L. Jassby, C.S. Caldwell, et al., "TFTR Fusion Blanket Experiments", Final Report for EPRI Contract No. TPS79-705 (Jan., 1980).

26. W.G. Pettus, "A Spectral-Shift Blanket Concept for Hybrid Reactor Applications", Babcock & Wilcox Co. Report LRC-9081 (July, 1979).

27. K.R. Schultz, in Proc. 5th Intern. Conf. on Structural Mechanics in Reactor Technology (Berlin, Germany, 1979), to be published.

BURNING NUCLEAR WASTES IN FUSION REACTORS*

Heiner W. Meldner and W. Michael Howard
University of California, Lawrence Livermore Laboratory, Livermore, California 94550 USA

We have studied actinide burn-up in ICF reactor pellets; i.e. 14 MeV neutron fission of the very long-lived actinides that pose storage problems. A major advantage of pellet fuel region burn-up is safety: only milligrams of highly toxic and active material need to be present in the fusion chamber, whereas blanket burn-up requires the continued presence of tons of actinides in a small volume. The actinide data tables required for Monte Carlo calculations of the burn-up of ^{241}Am and ^{243}Am are discussed in connection with a study of the sensitivity to cross section uncertainties. More accurate and complete cross sections are required for realistic quantitative calculations.

[Actinide burn-up, fusion pellets, neutron spectra, $^{241,243}Am$, ^{237}Np, neutron cross sections]

I. Introduction

A major factor in the present nuclear power debate is the disposal of long-lived radioactive isotopes of high dose rates. In this paper we discuss possible solutions of this problem utilizing the future technology of fusion reactors.

A significant amount of work has been done on the design of laser driven inertially confined fusion pellets and on the use of such pellets in conceptual fusion power reactors. We discuss here a scheme whereby the radioactive wastes from fission reactors can be burned up during the early development of fusion reactors, even before fusion plants become economically competitive with fission power sources.

Using the high energy neutrons from fusion reactors for burning up radioactive wastes has been discussed for many years. However, we believe that only the inertial confinement fusion (ICF) approach satisfies the necessary practical safety criteria. This is because our proposed ICF scheme does not require a near critical assembly of highly toxic amounts of nuclear materials. This is in contrast to the use of magnetically confined fusion or other methods using blanket burn up. The type of future fusion reactor technology which we have in mind for our proposal is that of the HYLIFE concept proposed by LLL[1].

There are two major categories of high level radioactive waste from fission reactors: fission products and actinides. All fission products that contribute significantly to the hazard potential have half lives of order 30 years or less, i.e., their contribution to the radioactivity drops on that relatively short time scale although they dominate during the first 200 years or so of storage because of their abundance in nuclear wastes[1]. The truly long term hazard potential is determined by actinides, some of which have half lives of over 10^6 years. The major actinides in question are: ^{244}Cm, ^{238}Pu, ^{242}Cm, ^{241}Am, ^{243}Am, ^{240}Pu, ^{239}Pu, and ^{237}Np. The Cm and Pu isotopes have power source applications and will therefore normally be separated and (commercially) used. The fission cross sections for $^{241,243}Am$ and ^{237}Np are very low for typical fission spectrum neutrons. As a consequence, these isotopes are essentially useless and accumulate in abundance in fission reactors. They are therefore the standard test materials for the evaluation and comparison of potential long-term waste management concepts[2,3,4]. In this paper we describe a transmutation or "actinide burning" method which we had proposed several years ago[5] as a major alternative to blanket burn-up[3] methods.

* Work performed under the auspices of the U. S. Department of Energy by the Lawrence Livermore Laboratory under Contract No. W-7405-ENG-48.

We know of only one actual publication about Monte Carlo Calculations of pellet center neutron reactions on heavy elements in the fusion fuel region[6].

The (computer) design of reactor-size fusion pellets[7] has now been sufficiently finalized for quantitative transmutation studies. The relevant features of a "standard" fusion reactor pellet in its imploded configuration are described in Section 2. The corresponding neutron spectra are discussed in Section 3 along with the results for transmutation of the three isotopes in question using both the "standard" and a somewhat burn-up optimized pellet. We conclude in Section 4 with a brief discussion of the required actinide data and some results of our sensitivity analysis.

2. Fusion Reactor Pellets

Several high-gain reactor pellet designs have been published recently by Lindl[8]. The calculations here are based on a relatively conservative design, also by Lindl, with a gain on the order of 300.

The imploded configuration of such a target as shown in Fig. 1 is a schematic representation simplified to two homogeneous regions. However, it was carefully matched to the implosion-explosion characteristics of the full design, especially with respect to neutronics and other energy transport features.

The only high-atomic-number, Z, material in the composite material tamper is 6 mg of ~99.9% pure ^{208}Pb. This choice minimizes accumulative neutron activation.

The imploded configuration of this standard pellet is reached after using ~6 MJ of laser or "beam" energy and the resulting thermonuclear yield is 1800 MJ. The same pellet configuration with its imploded density doubled, as indicated in Fig. 1, serves as an example of a more transmutation optimized design. The actinides are admixed to the fuel by Raleigh Taylor instability effects at the inner tamper surface.

3. Monte Carlo Calculation of Neutron Reactions in the Explosion

Realistic computations of neutron spectra and reactions require careful consideration of the rapidly disassembling burning fuel. The broadening resulting from fast ions is, for example, quite significant[4,8]. A plasma of thermal electrons and ions, x-rays and thermonuclear reaction products was evolved in time with Lagrangian thermonuclear burn and explosion calculations (see for example reference

10). Non-thermal charged particle transport and reactions were also included. The electrons and ions are assumed to be Maxwellian, but with different effective temperatures. Neutrons were Monte Carlo transported and the cross sections were taken from reference 10.

A transfer matrix formed from the 1978 evaluated-nuclear-data library (ENDL) neutron cross sections is used to calculate the neutron transport, reactions, and redistribution of neutrons among energy groups. Figure 1 shows the time-integrated neutron spectra for the fuel region of pellets in which the fuel density times the fuel radius R equals 5.0 g/cm^2. The amount of downscattering is noticeably different from some published estimates[12] that did not involve the detailed explosion simulations and extensive Monte Carlo calculations performed here. The high-energy (>15 MeV) neutrons contribute noticeably to the burn up by fast fission.

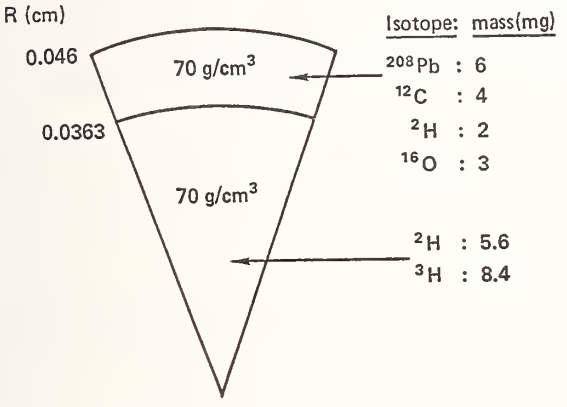

Fig. 1. Imploded configuration of a reactor-size fusion pellet. In the standard case, compression results in a density of 70 g/cm^3 for both the deuterium-tritium (DT) fuel and the tamper, i.e., ρR = 2.5 g/cm^2 and the yield is ~1800 MJ (0.43 tons of explosive). Increasing ρR to 5.0 g/cm^2 by doubling tamper and fuel density improves burnup considerably as discussed in the text (cf., Fig. 4).

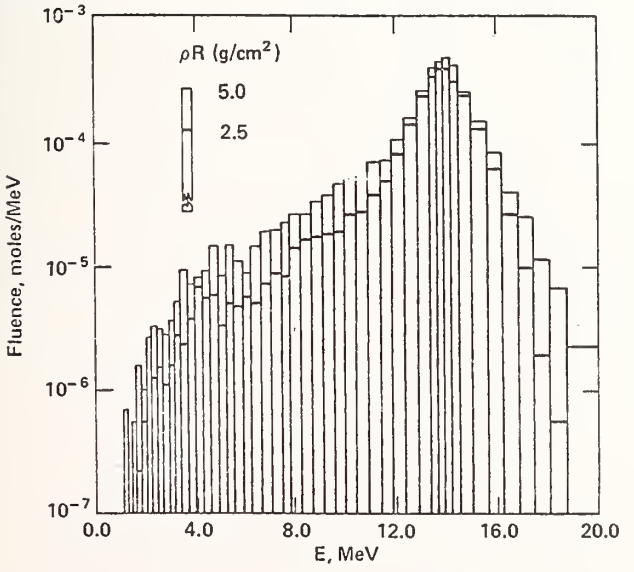

Fig. 2. Neutron spectra for the ρR = 2.5 and 5.0 g/cm^2 pellets as indicated.

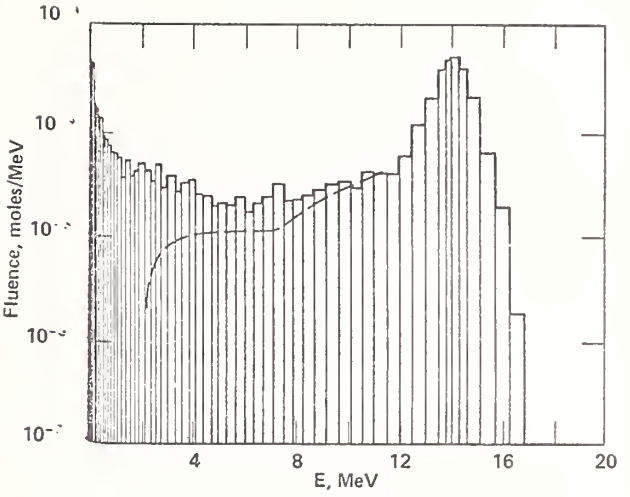

Fig. 3. Neutron spectra for a ρR = 5 g/cm^2 pellet with admixture of 12 mg of ^{241}Am. The dashed line indicates the shape of the spectrum without fission contributions. (cf., Figure 2).

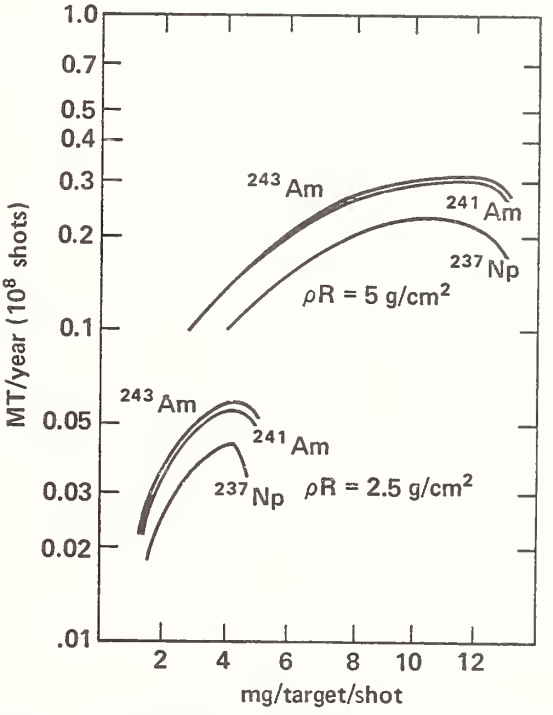

Fig. 4. Metric tons of actinides burned up per year as function of their admixture to the DT fuel. The scale refers to 10^8 explosions/year roughly corresponding to a reactor power output of about one GW.

Figure 4 depicts our burn-up results. The nonelastic reactions explicitly followed for each isotope in question are (n, n'), (n, 2n), (n, 3n), (n, 4n), (n, γ) and (n, fission). The actual loss per target seed is plotted in Fig. 4 as metric tons burned up for 10^8 shots. The curves turn over because increased admixture of high Z material to the fuel eventually squelches the thermonuclear bootstrapping by absorptive processes. The limits in the ratio of burned to admixed actinides as depicted in Fig. 4 indicate how a few milligrams of active material will accumulate from each shot. In addition some fission products will also accumulate. The

longest lived fission products from Am fission at thermonuclear neutron energies are ^{129}I($\tau = 1.57 \times 10^7$y), ^{135}Cs($\tau = 2 \times 10^6$y), ^{99}Tc($\tau = 2 \times 10^5$y) and ^{107}Pd($\tau = 6.5 \times 10^6$y).[13] These isotopes will be produced at a level of a few percent of the original admixture, as will ^{242}Am from neutron capture on ^{241}Am. Insignificant amounts ($\lesssim$ 0.1%) of ^{243}Am will be produced by neutron capture on ^{241}Am. Neutron reactions on the fission fragments $(n,2n)$ being the most important will also be of some importance in rearranging the fission fragment distribution. These quantities are, however, similar to the amounts of tritium and activated first wall/structure material produced per explosion in any ICF reactor. The complications of reprocessing unburned actinides therefore do not significantly change the operational hazard potential relative to a "pure fusion" plant. This is in marked contrast to any hybrid and/or blanket burn-up device. Continuous separation of fission products and heavy radioactive materials would seem to be straightfoward with the proposed remote systems of HYLIFE-type reactor concepts[1]. The liquid Li current continuosly removes actinides and fission products, is a mediun to breed the tritium necessary for self-sufficiency, and serves as a convector fluid and first wall shield for neutrons, x-rays and debris.

Although exact estimates are not possible without specifying the type of reactor and initial waste reprocessing involved, we conclude that our results demonstrate how just one ICF power plant could safely take care of the actinide waste of about 10 power equivalent fission reactors.

4. Sensitivity Results and Conclusions

Table I lists actinide neutron reaction data used in the present work. Our sensitivity studies for this type of input have not been completed. One result is that a 20% shift in the $^{241}Am(n,f)$ cross section for all energies produces a 17% change in the amount of material burned up. We found large discrepancies in the published fission cross sections for neutron energies below 100 keV; our results, however, are quite insensitive to the low energy part of the input. Example: reducing all $^{241}Am(n,f)$ cross sections below 100 keV to 10 mb gives changes of less than one percent. The reaction data for high energy neutrons ($\gtrsim$12 MeV) are clearly the major factors determining the burn up characteristics. In addition, more detailed information on fission product yield is of great interest here, in particular for ^{243}Am and ^{237}Np.

These calculations suggest that although many orders of magnitude may be gained in dose rate, relative to the initial ^{241}Am, long-lived fission products will result. However, these isotopes can be dealt with in a more conventional manner, for example, by exposure to thermal neutrons.

ACKNOWLEDGMENTS

We acknowledge stimulating discussions with John H. Nuckolls.

TABLE I

Neutron Data Used in Present Calculation[a]

REACTION			POINTS	Q-VALUE	E-MIN	E-MAX
N,ELASTIC		CROSS SECTION	212	0.0000+ 0	1.0000-10	2.0000+ 1
N,ELASTIC	N	ANGULAR DIST.	18	0.0000+ 0	1.0000-10	2.0000+ 1
N,ELASTIC	N	TOTAL ENERGY DEP.	34	0.0000+ 0	1.0000-10	2.0000+ 1
N,ELASTIC	N	LOCAL ENERGY DEP.	34	0.0000+ 0	1.0000-10	2.0000+ 1
N,N'		CROSS SECTION	15	0.0000+ 0	5.0000- 2	2.0000+ 1
N,N'	N	ENERGY-ANGLE DIST.	14	0.0000+ 0	5.0000- 2	2.0000+ 1
N,N'	N	TOTAL ENERGY DEP.	20	0.0000+ 0	5.0000- 2	2.0000+ 1
N,N'	N	LOCAL ENERGY DEP.	15	0.0000+ 0	5.0000- 2	2.0000+ 1
N,2N		CROSS SECTION	15	-5.9300+ 0	5.9500+ 0	2.0000+ 1
N,2N	N	ENERGY-ANGLE DIST.	9	-5.9300+ 0	5.9500+ 0	2.0000+ 1
N,2N	N	TOTAL ENERGY DEP.	19	-5.9300+ 0	5.9548+ 0	2.0000+ 1
N,2N	N	LOCAL ENERGY DEP.	10	-5.9300+ 0	5.9549+ 0	2.0000+ 1
N,3N		CROSS SECTION	5	-1.2600+ 1	1.2650+ 1	2.0000+ 1
N,3N	N	ENERGY-ANGLE DIST.	6	-1.2600+ 1	1.2650+ 1	2.0000+ 1
N,3N	N	TOTAL ENERGY DEP.	4	-1.2600+ 1	1.2653+ 1	2.0000+ 1
N,3N	N	LOCAL ENERGY DEP.	4	-1.2600+ 1	1.2653+ 1	2.0000+ 1
N,F		CROSS SECTION	1535	2.0000+ 2	1.0000-10	2.0000+ 1
N,F	N	TOTAL ENERGY DEP.	2	2.0000+ 2	1.0000-10	2.0000+ 1
N,F	N	LOCAL ENERGY DEP.	2	2.0000+ 2	1.0000-10	2.0000+ 1
N,F	N	ENERGY-ANGLE DIST.	5	2.0000+ 2	1.0000-10	2.0000+ 1
N,F	N	NEUTRONS/FISSION	6	2.0000+ 2	1.0000-10	2.0000+ 1
N,F	G	ENERGY DIST.	2	2.0000+ 2	1.0000-10	2.0000+ 1
N,F	G	MULTIPLICITY	2	2.0000+ 2	1.0000-10	2.0000+ 1
N,F	N	NEUTRONS/FISSION	2	2.0000+ 2	1.0000-10	2.0000+ 1
N,G		CROSS SECTION	656	5.4800+ 0	1.0000-10	2.0000+ 1
N,G	G	ENERGY-ANGLE DIST.	2	5.4800+ 0	1.0000-10	2.0000+ 1
N,G	G	MULTIPLICITY	2	5.4800+ 0	1.0000-10	2.0000+ 1
N,G		TOTAL ENERGY DEP.	2	5.4800+ 0	1.0000-10	2.0000+ 1
N,G		LOCAL ENERGY DEP.	2	5.4800+ 0	1.0000-10	2.0000+ 1
N,G		CROSS SECTION	652	5.5280+ 0	1.0000-10	2.0000+ 1
N,G	G	ENERGY-ANGLE DIST.	2	5.5280+ 0	1.0000-10	2.0000+ 1
N,G	G	MULTIPLICITY	2	5.5280+ 0	1.0000-10	2.0000+ 1
N,G		TOTAL ENERGY DEP.	2	5.5280+ 0	1.0000-10	2.0000+ 1
N,G		LOCAL ENERGY DEP.	2	5.5280+ 0	1.0000-10	2.0000+ 1
N,XG		CROSS SECTION	20	0.0000+ 0	5.0000- 2	2.0000+ 1
N,XG	G	ENERGY-ANGLE DIST.	20	0.0000+ 0	5.0000- 2	2.0000+ 1

[a]Taken from R.J. Howerton and M. H. MacGregor, UCRL-50400, Vol. 15, Part D, Rev. 1, p. 386.

REFERENCES

1. "The HYLIFE concept; Electricity from Laser Fusion," Energy and Technology Review, Oct. 1979, UCRL-52000-79-10.

   See also: LASL Program Annual Report, 1978, Vol. 3, Sec. 9, "Energy and Military Applications," UCRL 50021-78.

   P. E. Walker, "Remote System Requirements of the High Yield Lithium Injection Fusion Energy (HYLIFE) Converter Concept," UCRL-81309 and references therein; for publication in the Proceedings of the ANS 1978 Winter Meeting, November 12-16, 1978, Washington, D.C.

2. Bernard L. Cohen, "High-Level Radioactive Waste from Light-Water Reactors," in Reviews of Modern Physics, Vol. 49, No. 1, pp. 1-20; January 1977.

   See also B. L. Cohen, Scient. American 236, 21 (1977); and Physics Today, January 1976.

   Alternative Processes for Managing Existing Commercial High Level Radioactive Wastes. Nuclear Regulatory Commission Report NUREG-0043, 1976.

   Alternatives for Managing Wastes from Reactors and Post-Fission Operations in the LWR Fuel Cycle. Division of Nuclear Fuel Cycle and Production. Energy Research and Development Administration Report ERDA-76-43, 1976.

   Environmental Survey of the Reprocessing and Waste Management Portions of the LWR Fuel Cycle. Nuclear Regulatory Commission Report NUREG-0116, 1976.

3. D. H. Berwald and J. J. Duderstadt, "Neutronic Analysis of a Laser-Fusion-Driven Actinide Waste Burner." Transactions of the American Nuclear Soc., Vol. 27, 82 (1977 Winter Meeting at San Francisco).

   J.W.H. Chi et al., "Fusion Driven Actinide Burner Design Study," First, Second, and Third Quarterly Progress Reports, Westinghouse Fusion Power Systems, EPRI Contract RP-473-1 (1976).

   W. C. Wolkenhauer and W. C. Gough, "Transmutation of High Level Radioactive Wastes by Fusion Reactor Neutrons -- A Summary of EPRI Resarch," EPRI Report (1976).

   M. Sshaffer et al., "Imploding Liner Fusion Devices for Fission Waste Transmutation," G. A. Progress Report to be published by EPRI in 1978.

   B. R. Leonard, Jr., "Transmutation of High Level Radioactive Waste," Battelle-Pacific Northwest Labs Presentation, October 24, 1975.

   K. J. Schneider and A. M. Platt, Editors, "High-Level Radioactive Waste Management Alternatives." Battelle Memorial Institute. Pacific Northwest Laboratories, 1974.

4. S. Raman, "Some Activities in the U.S. Concerning Physics Aspects of Actinide Recycling," IAEA Meeting on Transactinium Isotope Nuclear Data. IAEA-186, p. 201 (see also p. 39). Karlsruhe, W. Germany (1975).

5. H. W. Meldner, unpublished calculations, May 1975.

6. J. Henley and H. W. Meldner, Phys. Rev. C12, 407 (1975).

7. John Nuckolls and John Lindl, private communication.

8. John D. Lindl, "Low Aspect Ratio Double Shells for High Density and High Gain," ThC7-1, Proceedings of the Optical Society of America Topical Meeting on Inertial Confinement Fusion, February 1978, San Diego.

9. J. A. Blink, P. E. Walker and H. W. Meldner, "Energy Partition and Neutron Spectra from Laser Fusion Reactor Pellets," Transactions of the American Nuclear Society, Vol. 27, p. 70, 1977 Winter Meeting at San Francisco.

10. G. B. Zimmerman and W. L. Kruer, Comments in Plasma Physics and Controlled Thermonuclear Fusion 2, 85 (1975).

    G. B. Zimmerman, D. Kershaw, D. Bailey and J. Harte, "The LASNEX Code for Inertial Confinement Fusion," ThC6-1, Proceedings of the Optical Society of America Topical Meeting on Inertial Confinement Fusion, February 1978, San Diego.

11. R. J. Howerton, "The LLL Evaluated Nuclear Data Library (ENDL): Translation of ENDL Neutron-Induced Interaction Data into the ENDF/B Format," UCRL-50400, and updates 1978.

12. F. H. Southworth and H. D. Campbell, "Neutron Downscattering in Laser-Induced Fusioning Plasma," Nuclear Technology 30, 434 (1976).

13. A. L. Prindle, D. H. Sisson, D. R. Nethaway, M. V. Kantelo, and R. A. Sigg, Phys. Rev. C 20, 1824 (1979).

SAFEGUARDS

W.A. Higinbotham

Brookhaven National Laboratory, Upton, New York 11973 USA

Abstract

Domestic safeguards have been developed to prevent the theft of nuclear materials or the sabotage of nuclear facilities. International safeguards are intended to detect diversion of materials or mis-use of nuclear facilities by a nation. An important safeguards activity, in both cases, is materials accounting. Conventional accounting employs measurement of weight or volume, the taking of representative samples, and chemical analysis to determine the concentration of U or Pu, and isotopic ratios. Non-destructive assay methods, based on the measurement of the natural or induced radioactive emissions of U and Pu, are of increasing importance for national and IAEA safeguards. These techniques are based on the information developed in the R&D on neutron cross sections and nuclear decay schemes. Calculations of the burnup of uranium fuels in a reactor and of the plutonium in spent fuel depend heavily on the knowledge of nuclear cross sections and on the neutron spectra in operating reactors. Examples of important safeguards non-destructive and other verification techniques are presented.

[Safeguards, calorimetry, gamma-ray spectrometry, neutron interrogation, $^{239,240,241,242}Pu$, $^{235,238}U$]

Institutions have been developed to protect nuclear materials at both the national and international level. These institutions are referred to as nuclear safeguards systems. Both national and international nuclear safeguards systems place emphasis on the measurement of nuclear materials transferred from one nuclear facility to another and of the materials within a processing facility.

It will be useful to indicate the similarities and the differences between domestic and international safeguards systems.

Domestically, a national government takes responsibility for control of the nuclear materials within its jurisdiction in the interest of national security and the general welfare. The threats of concern to a nation are the theft or diversion of nuclear materials to fabricate a nuclear explosive, the theft or diversion of radioactive nuclear materials for dispersal, and the sabotage of nuclear facilities or shipments of nuclear materials.

The three generic safeguards measures employed by a nation are material accounting, physical protection, and measures to prevent diversion or sabotage by individuals who handle nuclear materials or are otherwise authorized access. In the U.S. this latter class of safeguards measures is called "material control". The safeguards measures are designed to counter, insofaras possible, the credible domestic adversaries, which could range from one trusted employee at a nuclear facility to a sophisticated band of terrorists.

The International Atomic Energy Agency applies safeguards to the nuclear facilities within nations. Non-nuclear weapon states which have ratified the Nuclear Non-Proliferation Treaty, must submit all of their nuclear facilities for IAEA safeguards. A number of other nations have agreed to accept IAEA safeguards for all of their nuclear facilities or for only some of them (e.g., India). The U.K. and the U.S. have offered to place all of their non-military nuclear facilities under IAEA safeguards.

The goal of IAEA safeguards is to provide assurance that nuclear materials are not diverted from the declared peaceful applications for use in a nuclear explosive, or for purposes unknown. In this case the state or nation is the potential adversary.

Whereas the objective of national safeguards is to detect and to interrupt adversary activities, the IAEA responsibility is to alert the world should it conclude that a significant diversion has occured or that circumstances prevent it from concluding that no diversion has occured. For the IAEA, materials accounting is the safeguards measure of fundamental importance, with containment and surveillance as important complimentary measures. The exercise of physical protection is reserved to the member states.

Nuclear data is of interest for the measurements upon which both domestic and IAEA safeguards accounting are based. In both cases, the facility operator is required to make accurate measurements of receipts, shipments and internal transfers, to maintain records of the measurements and transfers, and to submit reports to the national regulatory body and to the IAEA. In order to determine whether the book-values in the records reflect the true state of affairs, the equipment in a nuclear processing or research facility is cleaned out, and a physical inventory performed at periods which depend on the capacity and type of facility, after which the book-inventory is compared to the physical inventory.

The book-physical inventory difference will not be exact, since it is based on inexact measurements of the beginning and ending inventory and of the materials transferred during the period between the inventories. It is important for both domestic and international safeguards to know the accuracy of each type of measurement, and to calculate the uncertainty in the final material balance (the difference between book and physical inventory is called the material-unaccounted-for or MUF), by propagating the errors of the many measurements.

IAEA accounting is based on the inde-

pendent verification of some subset of the operator's measurements and on auditing the operator's records and reports. Comparing IAEA measurements to those of the operator checks the veracity and accuracy of data supplied by the operator, enabling the Agency to arrive at a material balance for comparison with that of the facility. The sensitivity of IAEA material accounting is limited by the uncertainties in the operator's measurements and the uncertainties of the measurements made by the IAEA.

There are two general classes of measurements for nuclear materials, analytical chemistry, and physical techniques. The former requires a measurement of weight or volume, the taking of a sample, and chemical analysis of the concentration of uranium or plutonium. The isotopic composition of the uranium or plutonium is also important. The physical techniques, usually referred to as non-destructive assay (NDA), determine the amount of the uranium and/or plutonium contained in a sample, or a container, or a fuel rod by measuring radioactivity emitted spontaneously or that induced by, e.g., irradiating the item with neutrons. The former is called passive NDA, the latter active NDA. Since the spontaneous emission of alpha, beta, gamma-rays and neutrons is specific for each isotope, most NDA measurements require an accurate knowledge of the isotopic composition of the uranium and/or plutonium in the item being assayed (exceptions are X-ray fluorescence and χ or gamma-ray absorption, which depend on the element, rather than the isotopic ratios). For passive NDA, the half-lives and decay schemes are very important. For neutron activation, neutron cross-sections are also important.

At the smaller nuclear processing facilities, it was adequate for both domestic and international safeguards to rely primarily on sampling and chemical analysis for the routine measurements and on assessing periodic material balances for indication of diversion. This is no longer satisfactory for the larger nuclear processing facilities which exist or are to be built. If accounting is to play a role in the detection and apprehension of a diverter in a plant which processes several or many kilograms per day, it would be necessary to perform a material balance for each process area every day or every shift. For this reason, U.S. safeguards R&D has concentrated on the development of on-line and at-line NDA instrumentation, coupled to computers, so that the materials flowing into, out-of, and contained within each unit process can be measured on an essentially real-time basis. The safeguards group at the Los Alamos Scientific Laboratory has led in this development and published many papers on instrument development and on what they call Dynamic Material Control, or DYMAC.

The IAEA has a need, not only for more timely information to verify compliance, but also for instrumentation which is convenient for its inspectors to use. For obtaining material accounting data more rapidly, the Agency is interested in the development of DYMAC instrumentation. In order to perform its safeguards assignment efficiently, the Agency presently employs a number of NDA techniques and has requested assistance in the development of more and better NDA instruments.

Rather than attempt to list the instruments and techniques, useful for domestic and IAEA safeguards, which make use of nuclear data, a few illustrative techniques will be described:

Calorimetry is capable of high sensitivity and precision. It has been used for many years at Mound Laboratory to measure Pu-238 and at Rocky Flats to measure containers with plutonium. It would be a convenient way to measure cans of PuO_2 or mixed U, PuO_2, providing the isotopic composition of the plutonium is well known, and the Am-241 daughter of 14 year Pu-241. The DOE safeguards program is supporting the accurate determination of the half-lives of the isotopes of plutonium and of Am-241, in order to improve the data base for calorimetry.

While the relative abundance of Pu-238 and Am-241 may be small compared to that of Pu-239 and Pu-240, the former isotopes are the major source of heat in commercial grades of plutonium, due to their shorter half-lives. Ultra-high resolution gamma-ray spectrometry is often used to determine the isotopic ratios of the items to be measured by calorimetry.

Gamma-ray spectrometry is the most highly developed of the NDA methods and is an extremely useful tool for the IAEA. Simple instruments, using a sodium-iodide scintillation detector and a two channel pulse-height analyzer, measure the enrichment (U-235/total U) of bulk samples (e.g., UO_2 pellets, containers of UO_2 powder, or large cylinders containing UF_6) to a few percent, relative, in a few minutes. Higher resolution gamma-ray detectors, and multichannel analyzers are required to measure the isotopes of plutonium. Very sophisticated detector-analyzer-computer systems have been developed at Lawrence Livermore Lab, Mound Lab, and Los Alamos, to make accurate isotopic analyses, and to measure the plutonium-americium concentration in well defined sample cells. The latter may be used to replace chemical analysis and mass-spectrometer analysis of laboratory samples and may be employed to analyze liquid plutonium flows at a reprocessing or plutonium-conversion facility.

The gamma-ray decay schemes unravelled by research physicists were an essential base for the development of gamma-ray spectrometry for safeguards. For safeguards it is also important to determine many of the branching ratios accurately. However, the self absorption of gamma-rays in the sample, the energy response of the detector, and the particular geometrical arrangement of each measuring system affect the energy

response of an instrument. Consequently, it is necessary to calibrate such a system using well characterized reference materials.

Active neutron interrogation is finding more uses is safeguards. One example is an instrument to measure the U-235 content of the pellets in low-enriched UO_2 fuel for light water reactors. Developed at Los Alamos, these instruments are now produced commercially and used by U.S. fuel manufacturers to insure that all pellets in each fuel rod have the proper enrichment and to measure the uranium content. Cf-252 is generally used as the neutron source. Either the neutrons produced by the fissions induced, or the fission product gamma-rays are used to measure the U-235 content. Although neutron cross-sections are obviously of interest for this application, the neutron spectrum and the detector response depend on the particular instrumental design. As in the gamma-ray case, each instrument must be calibrated using standards similar in characteristics to the rods being measured. Fabricating and characterizing a set of standard rods for this application costs in the range of a quarter million dollars.

Another example of this class of instrument is a transportable instrument that employs a small isotopic neutron source and moderated He-3 detectors to verify the U-235 content of low enriched uranium fuel assemblies (containing 49 to 220 fuel rods), which was developed at Los Alamos for use by the IAEA.

Passive neutron analysis is useful for the measurement of many items containing plutonium. The neutrons arise from the spontaneous fission of the even isotopes of plutonium and from alpha-n reactions with isotopes of lighter elemens in the samples. 4-Pi detectors are often used to measure the plutonium content in containers of PuO_2 powder, Pu/UO_2 pellets, and containers of fabrication scrap and waste (the measurement of quantities greater than about 1 kg of plutonium are complicated by the self-multiplication or self-induced fissions in the sample). The multiple neutrons resulting from spontaneous fission can be separated from the alpha-n neutrons by supplying autocorrelation analysis. As for other NDA methods, it is necessary to know the isotopic composition of the plutonium and the spontaneous fission parameters for each isotope.

Although none of the safeguards techniques discussed above make significant use of neutron cross section or isotopic decay scheme data, there is one important area which requires calculations of the burnup and transmutation occurring in reactors, and hence involves cross section data. This is the calculation of the production of plutonium as a function of exposure in a given type of reactor. Such calculations are also of interest to an operator of a nuclear power plant. The burnup and net plutonium production varies from one fuel assembly to another and within each fuel assembly. What is of interest for safeguards is the amount of plutonium contained in a batch of fuel assemblies after discharge from a reactor. Although the U.S. presently plans to store spent fuel indefinitely, other nations plan to reprocess spent fuel. The most critical problem for the IAEA, in this case, is to ensure that the plutonium, after dissolution of the spent fuel pellets, is accurately and reliably measured at the head-end of a reprocessing plant.

For reprocessing, the fuel bundles are disassembled, the rods chopped into short sections, and the fuel pellets dissolved in nitric acid. The dissolver solution is transferred into a calibrated vessel where the volume or weight of the solution is determined and samples are drawn for analysis of the uranium and plutonium concentrations. Presumably the IAEA would observe the calibration procedures, obtain the bulk measurement data, and obtain duplicate samples of the solution for independent analysis. In each of these steps, the Agency inspectors would, of necessity, be dependent on the facility staff. A considerable amount of work has been applied, both in the U.S. and abroad, to developing isotope correlation techniques which the IAEA might employ to verify that the reprocessing plant input data are reliable, and also to confirm data on the batch of fuel prior to, during, and following exposure of the fuel in a reactor.

The simplest check is to measure the ratio of plutonium to uranium in the dissolver solution, to estimate the amount of uranium and plutonium that had been consumed, using the reactor operator's data on burnup, and using the fabricator's data for the uranium contained in the batch of fuel assemblies prior to exposure in the reactor, to calculate how much plutonium should have been recovered. This procedure has been used by reactor operators to confirm the input measurement reported by a reprocessor. Given accurate values for the initial uranium content, approximate burnup, and state-of-the-art determination of the Pu/U ratio in the composited dissolver solutions, the results are comparable in accuracy to those obtained by means of bulk measurement and concentration, i.e., about 0.5%. This verification process depends little, if at all, on the calibration of the input accountability vessel.

The IAEA generally will have been given detailed information on the uranium content and enrichment of the fresh fuel assemblies sent to reactors. It may or may not be able to verify information on burnup supplied by the reactor operator. It will have maintained accountancy for the fuel assemblies on the basis of item identification and records. However, there may be some question as to the completeness of this surveillance. By analyzing the data on fission products, uranium and plutonium isotopes, and isotopic abundance of heavier actinides, the IAEA should be able to confirm or to question, the data given it on the prior history of and recovered plutonium of a discharged batch of reactor fuel. Since reprocessor, customer, and the IAEA

are all interested in determining the amount of each, at a reprocessing plant, the investigations have focussed on ratios of combinations of the U and Pu isotopes. In studying the potential use of isotopic ratios, the approach has been both empirical and theoretical. Where the original composition of the low enriched uranium fuel, the reactor history (and type), and the amounts and isotopic compositions of the recovered U and Pu were well known, various U/Pu isotopic ratios were plotted. Since the amount of spent fuel that has been reprocessed is rather limited, empirical data of this sort are also limited and unsatisfactory. It has, however, shown that some ratios are rather different for fuel with zirconium cladding compared to fuel clad in stainless steel.

While it would not be practical to attempt to compute the isotopic distribution to be expected in spent fuel from one-third of a core of a particular reactor, exposed for 30,000 MWd/t, etc. to, let's say, 2%, it should be possible, using cross section data and reactor codes, to determine which isotopic ratios are more or less sensitive to changes in cladding, to operation at high or low power levels, to neutron poisons, etc. What would be of particular interest to the IAEA are ratios which would be strongly affected by misinformation on the original enrichments, or to substitution of spent fuel elements.

The kinds of isotopic ratios under study include the following:

1. recovered ratio of Pu/U vs U-235 consumed.
2. recovered ratio of Pu/U vs (100 - Pu-239)
3. recovered U-236/U-235
4. recovered Pu (total)/U-235
5. Pu-239/Pu-240 vs U-235/Pu-241
6. $(\text{Pu-239})^2/(\text{Pu-240})^2$ vs Pu-240
7. Pu-240/Pu-241 vs U-235/Pu-242

There are many more possibilities. Some appear to be linear or at least monotonically increasing with burnup. Some are more sensitive at lower burnup and others at higher burnup. The data for heavy water moderated reactors will be somewhat different from that for light water moderated reactors. Given so many possible ratios to consider, it seems evident that theoretical studies using cross section data are important.

So far, these studies have considered only natural or low enriched uranium fuels, since these are the fuels in use today. It is premature to worry about verification of fast breeder spent fuels which will not be reprocessed in large amounts for 20 years or more. However, it is probable that a number of developed nations will find it economically and technically advantageous to recycle plutonium and recovered uranium in light water moderated reactors within a few years. Given reliable and accurate data on the U, Pu and isotopic content of fresh U/Pu mixed-oxide fuel and samples of dissolver solution, would it be possible to employ isotopic ratio analysis, like that above, to verify data on burnup and plutonium recovered at a reprocessing plant?

FAST-NEUTRON CAPTURE CROSS SECTIONS OF IMPORTANCE IN TECHNOLOGICAL APPLICATIONS

W. P. Poenitz

Argonne National Laboratory, 9700 South Cass Avenue
Argonne, Illinois 60439, USA

The importance of the capture cross section of the major fertile nuclei, ^{238}U and ^{232}Th, leads to the consideration of these data. The ^{238}U (n,γ) cross section is considered of priority as it is part of the ^{238}U - ^{239}Pu cycle. Experimental techniques used in the measurements of these data are considered. Data measured more recently are compared with provisions made for the possible explanations of differing results. It is concluded that the ^{238}U (n,γ) cross section is known with ~5% above 10 keV and fulfills the uncertainty limit for this cross section set to achieve design accuracy for k_{eff} and the breeding ratio above 500 keV. Below 500 keV, the present uncertainty falls short of the required 1.5 - 3.0% uncertainty. Specific recommendations are made to resolve existing discrepancies and data uncertainties.

[Fast Neutron Capture, ^{238}U, ^{232}Th, ^{240}Pu, Fission Product Nuclei]

INTRODUCTION

Measurement techniques used in the detection of neutron capture events were reviewed by Chrien[1] at the last conference on Nuclear Cross Sections and Technology held in Washington in 1975. There are few new developments, if any, in this area to justify a reconsideration of general measurement techniques. The standard capture cross section, $\sigma_{n,\gamma}$ (Au), was reviewed even more recently by Paulsen[2] and only one new measurement[3] was reported since then and another was revised.[4] However, these additions or changes will cause little, if any, changes of the evaluated standard capture cross section. Some considerations of the standard capture cross sections will be made by Wasson.[5]

Energy is on many peoples mind these days, and therefore it appears appropriate to consider the area more closely related to this topic. It is not generally realized, though well known among experts, that for many countries, specifically the U.S., the largest energy reserves based upon presently achieved levels of technology and at acceptable costs is in uranium and thorium deposits. The utilization of these energy reserves requires however, the breeding of nuclear fuel by some scheme; the LMFBR being the conventional approach, and more recently accelerator breeding and fusion - fission hybrids under serious discussions. It is obvious that nuclear data of uranium and thorium must play a predominant role in the design and evaluation of the economics of specific systems regardless of the breeding scheme being considered. Indeed, sensitivity studies show[6] that the capture cross section of ^{238}U is the most important, surpassed only by the neutron production cross sections (ν, $\sigma_{n,f}$) of the fertile materials. Historically, the most intensively investigated and currently dominating systems involve the ^{238}U - ^{239}Pu cycle. For a variety of reasons the ^{232}Th - ^{233}U cycle is being considered more recently.

A recent study of a large LMFBR benchmark model[7] shows the following distribution of total capture events in the inner core of such reactor:

^{238}U	70%	Fe	4%
^{239}Pu	13%	Ni	2%
^{240}Pu	4%	Cr	2%
^{241}Pu	2%	Rest	3%

The predominant role of the major fertile material is obvious from these numbers, however, a more important role may be expected of the capture in ^{235}U and ^{240}Pu if ^{235}U or reprocessed plutonium are considered as fuel for a first generation of breeder reactors. Capture in ^{240}Pu and fission products becomes more important with increased burn-up or considerations of other parts of the fuel-cyle.[10] Though a case can be made for the specific importance of many nuclei, it is preferable in view of the restricted time and space available to concentrate on the major fertile materials with the emphasis on the fast neutron capture cross section of ^{238}U.

The great importance of the ^{238}U neutron capture cross section would lead up to expect that this reaction process is well documented and uncertainties are low. However, a number of problems persisting for the last 10-15 years suggest substantial uncertainty and limited knowledge. Other problems are of more recent origin. Outstanding problems are:

1. The C/E (calculated vs. experimental) discrepancy for the central reaction rate ratio $^{28}c/^{49}f$ (^{238}U (n,f)/^{239}Pu(n,f)). The calculated ratio is usually found to be 3-9% higher than experimentally determined values[8], resulting in differential data adjustments, or requests for lower evaluated differential data.

2. The small sample central reactivity worth problem which exists for most major fertile and fissile materials.[9] The C/E discrepancy was in the order of ~20% for ^{238}U and adjustments of the capture cross section of ~12% were proposed[9] in order to resolve the discrepancy.

3. A C/E discrepancy of ~13% for $^{28}c/^{28}f$ for GODIVA with ENDF/B-V data resulted in requests for ^{238}U (n,γ) data adjustments.

Calculations with more recent nuclear data files resulted in substantially reduced ^{238}U central worth discrepancies, specifically for advanced fuels.[11] Facilities with harder neutron spectra[12] find agreement between calculated and experimental small sample central reactivity worth.

Commonly accepted goals for the design accuracy in k_{eff} and the breeding ratio are 0.5-1.0% and 2%, respectively.[13] The breeding ratio is directly related to $^{28}c/^{49}f$ and uncertainty levels required to achieve design accuracy were given in the 1.5-3% range by Usachev and Bodkov,[14] and Bohn et al.[6]

These requirements are reflected in nuclear data request lists[15,16] which contain requests for the accuracy of the ^{238}U (n,γ) cross section or its ratio

to ^{235}U (n,f) in the range of 1.5-3% for the lower keV region and 3-7% for the MeV range. Weisbin et al.[17] gave a rather detailed breakdown of the uncertainties which are required to obtain design accuracy over the keV-MeV range. Figure 1 shows the requested accuracy which appears plausible since it reflects sensitivity calculations[5,18]. Weisbin et al., also estimated the present uncertainty of the ^{238}U (n,γ) cross section which is also shown in Fig. 1. The estimated uncertainty exceeds at all energies and by large margins, the requested level of uncertainty which appears an acceptable result. However, specific features and the general magnitude of the uncertainty estimated by Weisbin et al., cannot be as easily agreed upon: Measurement techniques or nuclear properties which would justify the suggestion that the cross section is less uncertain by a factor of 2 in the 41-67 keV range than in the adjacent regions are unknown. The size of the suggested uncertainty might reflect the dispersion of all existing data and ignore the improvements achieved in recent years.

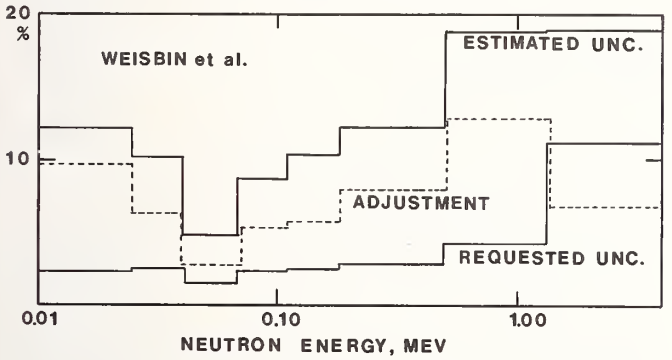

Fig. 1. Uncertainty limit for the ^{238}U (n,γ) cross section required in order to achieve design accuracy and the present uncertainty estimated by Weisbin et al.[23]. Also shown is the adjustment required to obtain agreement between differential and integral data.

In the following we will look in detail at measurements and data for ^{238}U (n,γ) in order to obtain a more realistic estimate of the present uncertainty of this important cross section. In doing so we will consider data which were presented after the conference on Neutron Cross Sections and Technology held at Knoxville in 1971. Older data were discussed by Davey[19] and Poenitz.[20]

Some consideration will also be given to the capture cross sections of ^{232}Th and ^{240}Pu, and, as examples, the fission product nuclei of Rh and Pd.

II. EXPERIMENTAL DATA ANALYSIS

A. Experimental Data Interpretation

Before considering experimental data we should achieve some understanding about their interpretation. Cross section values are at best given with the following information:

E,	the energy of the measurement
ΔE,	the uncertainty of this energy
R,	the resolution
σ,	the average cross section
Δσ,	the estimated total uncertainty of σ
$\Delta\sigma_{stat}$,	the statistical uncertainty of σ
σ_{ST},	the standard cross section or reference cross section used in the measurements.

As pointed out in another paper of these proceedings[21,22], the true uncertainty is most likely larger than the quoted uncertainty because only some errors are accounted for by the experimentor. Insufficient accounting or recognition of uncertainties is only one reason why data are often barely agreeing within their quoted error bars. Another reason is that the energy uncertainties cause uncertainties of the cross section due to the energy dependence of the cross section and of the standard. Data sets measured with different resolutions might differ substantially if the measured cross section is not smoothly varying with energy.

B. Experimental Techniques used in the Measurements of ^{238}U and ^{232}Th Capture Cross Sections

Diffences found between various experimental data sets of fast neutron capture cross sections of ^{238}U and ^{232}Th exceed, by far, the levels of uncertainty found in other important cross section measurements, e.g., ^{235}U (n,f). Thus we may suspect that these differences and discrepancies are caused by the detection of the capture events. Techniques which are used in the detection of capture events are:

Absorption

The capture cross section is only a small fraction of the total cross section and therefore difficult to determine with this technique. Spherical shell transmission measurements were used[24,25] but require extensive Monte Carlo interpretations[26] which depend on many parameters. The structure of the cross sections found in the energy range below 100 keV imply local values of the average level spacings and strength functions which might be different from those determined in the lower-energy range and used in the Monte Carlo calculations.[23]

Activation

There are several reasons why the activation technique should be used in the measurement of ^{238}U and ^{232}Th capture cross sections. One reason is that reactor reaction rate measurements use this technique, thus compatibility can be checked if differential data also use activation. Another reason is that very specific calibration techniques exist which should, in principle, permit accurate determination of capture rates in ^{238}U and ^{232}Th. The alpha-emitters ^{243}Am and ^{237}Np decay to the daughter nuclei of the capture process, ^{239}Np and ^{233}Pa. Samples of ^{243}Am and ^{237}Np which were α-counted in low geometry detectors and which are in equilibruim with their daughters can then be used for the calibration of the γ-counting equipment which detects the decay of ^{239}Np or ^{233}Pa. The uncertainty for this calibration is not expected to exceed 1%.

Prompt γ-Detection Techniques

Several different prompt γ-detection techniques are in use. Large liquid scintillators[27] (LLS) or 4π-NaI-detectors[28] were used to absorb the total γ-energy emitted in the decay of the compound nucleus. The major problem in this technique, if applied to ^{238}U (n,γ) and ^{232}Th (n,γ), is the low neutron binding energy for these reactions. A large background for low energies requires the threshold for the detection of capture events to be set at ~2-3 MeV which results in an efficiency or only ~60-70%. Figure 2 shows the pulse-height spectra obtained with the 1100 litre RPI-LLS[29] (on the left side) and the 1300 litre

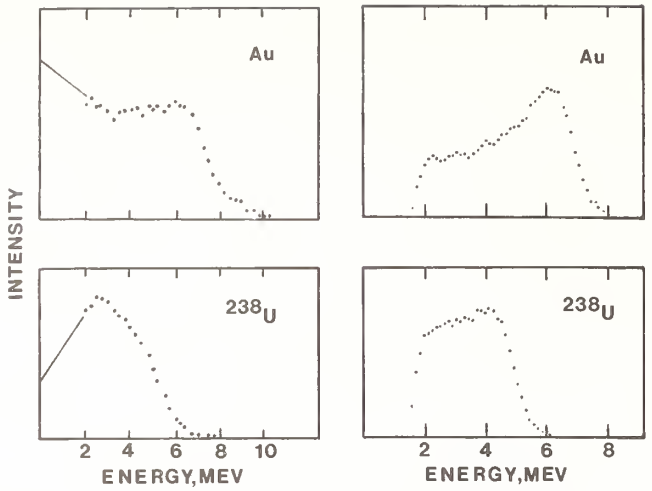

Fig. 2. Pulse-height spectra obtained with a large liquid scintillator. The spectra on the right were measured with a 1100 litre tank at RPI and the spectra on the left were obtained with a 1300 litre tank at ANL.

ANL-LLS[30] (right side) for gold and ^{238}U capture events. It is apprent that a large uncertainty exists due to the extrapolation to zero pulse-height. The figure shows the extrapolation chosen by RPI. The larger LLS from ANL shows improved spectra but the uncertainty for ^{238}U is still large and was estimated to be ~7%. One might suspect that the efficiency of these detectors is sensitive to changes in the primary γ-spectrum. Moxon-Rae detectors[31] were designed to have an efficiency which is proportional to the energy of the detected photon. This results in a proportionability to the total γ-energy released in the decay of the compound state. In other detectors with higher efficiencies, the proportionability to the photon energy is achieved by introducing spectrum weighting techniques.[32] Moxon-Rae detectors and their derivatives are expected to be sensitive to the absorption of γ-rays in the sample and to losses due to electron conversion of transitions which occur on the deexcitation cascades.

Measurements of the ^{238}U (n,γ) cross section were made with all three prompt γ-detection techniques[31,33,34,35] with LINAC accelerators. In all cases the black resonance technique was used for the normalization of the data. It is of interest to compare these data for which the relative differences from the data by Moxon are shown in Fig. 3. The first noticable feature in these differences concerns the several large fluctuations of the values obtained by DeSaussure et al., vs. those reported by Moxon. These fluctuations cannot come from cross section fluctuations because both data sets were integrated over the same bin-widths. The neutron flux spectrum obtained with a LINAC accelerator shows considerable structure which is associated with resonances of light mass nuclei which are present in the structural materials of these facilities. Figure 3 indicates the energies at which resonances in aluminum occur. It appears that the fluctuations in the ratio of the cross section data by DeSaussure et al., and Moxon are coincident with resonances in Aℓ. A check against a theoretically calculated neutron capture cross section suggests that the fluctuations are due to the data by Moxon[31] and not due to the measurements by DeSaussure et al.[33].

The near constant difference between the LLS-tank data and the Moxon-Rae-detector results at low energies suggest a different efficiency for one or

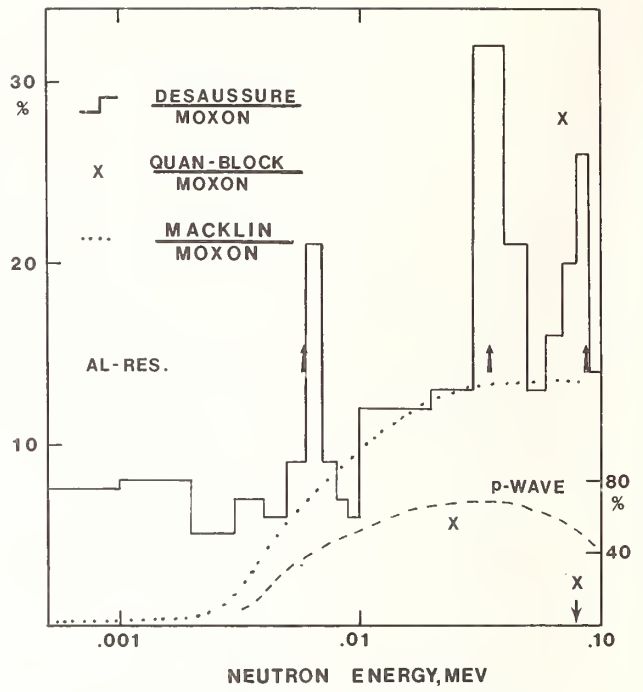

Fig. 3. Differences obtained for the $\gamma^{38}U$ (n,γ) cross section measured with prompt-γ-detection techniques and the black-resonance normalization.

both detectors for the 6.6 eV resonance vs. the average over many S-wave resonances. Chrien[36] points out the anomalously high direct transition of 4.059 MeV between thermal energies and the 6.67 eV resonance. The difference between the LLS data and the Moxon-Rae detector result increases to ~14% at higher energies. This increase might be associated with spectra-changes due to an increasing amount of p-wave capture which is shown in Fig. 3 (right scale). The data by Quan and Block[35] were also obtained with a LLS and normalized with the black-resonance technique, however; an iron-filtered beam was used. Quan and Block measured the ratio of the detection efficiency for 24.3 keV neutron capture and capture in the 6.67 eV resonance. An ~11% difference (±3%) was found and attributed to p-wave contribution to the neutron capture at 24 keV. Without applying this correction the 24 keV value by Quan and Block would have agreed with the result by Moxon. However, if one were to conclude that a similar, though smaller correction should be applied for the LLS measurements by DeSaussure et al., the difference of those data relative to Moxon's values would increase. The ratio of data obtained with the pulse-height spectrum weighting technique relative to the data by Moxon is shown in Fig. 3 in a qualitative manner based upon figures given in Ref. 34. It appears that the pulse-height spectrum weighting technique results in the same normalization difference relative to LLS data as Moxon, however, it yields an even larger change in the range where p-wave neutron capture contributes substantially.

The values by Quan and Block[35] vs. the Moxon data differ at 69.8 keV and 80.3 keV from the 24.3 keV value by ~23% (higher) and ~12% (lower), respectively. The resolution is different for both measurements, thus this difference might indicate fluctuations of the cross section which will be considered next.

C. Cross Section Fluctuations

Fluctuations were found for many cross sections which once were considered to vary smoothly with

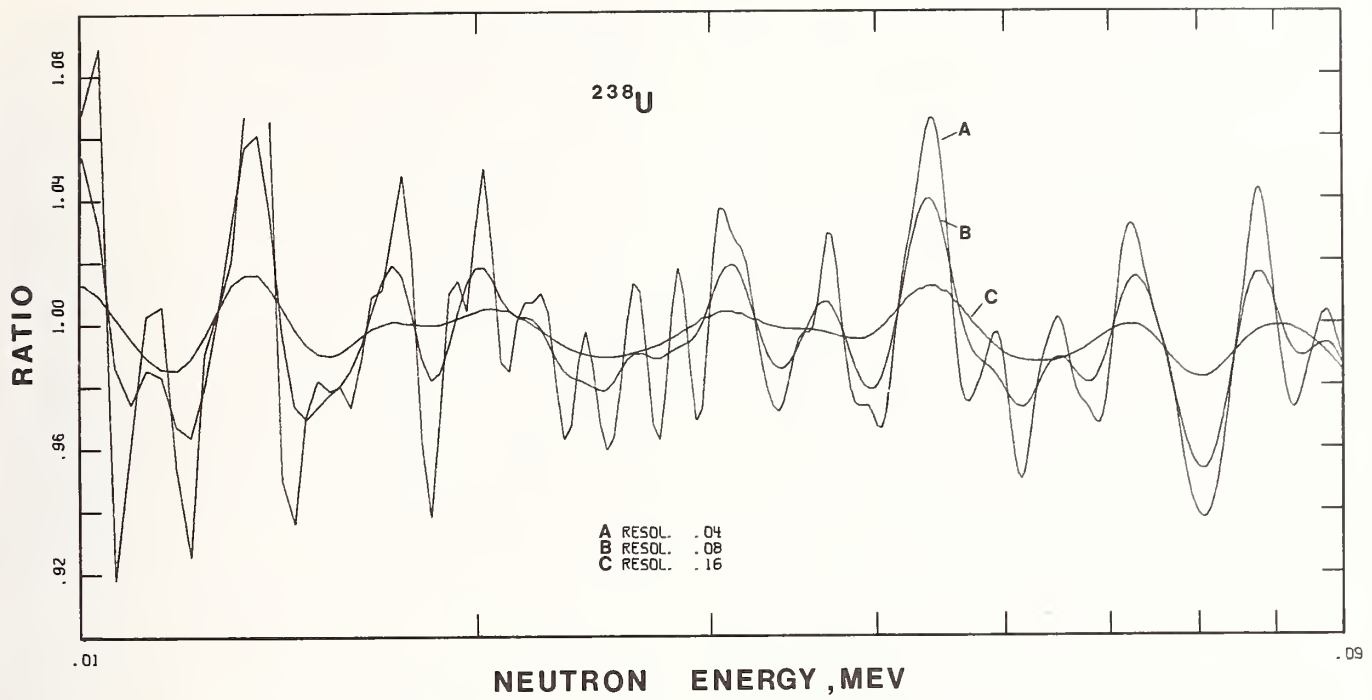

Fig. 4. Fluctuations of the ^{238}U (n,γ) cross section for different resolutions.

energy as long as the resolution was large compared with the compound resonance level spacing. These fluctuations are of importance in the interpresentation of differential cross section data though they should have little impact on the technological applications. Fluctuations of the ^{238}U (n,γ) cross sections were found by DeSaussure et al.,[33] and Spencer and Kaeppeler.[37] A physical interpretation and analysis of these fluctuations was given by Perez et al.[34] The present question is how much must a cross section value measured with the resolution $\alpha = \Delta E/E$ (FWHM) be corrected in order to correspond to the average cross section which varies smoothly with energy (large α). The present analysis of ^{238}U (n,γ) cross section fluctuations is based upon the data by DeSaussure[33] and is similar to the analysis of ^{235}U (n,f) cross section fluctuations by Bowman et al.,[38] but differs with respect to the quoted quantity. In the present analysis $\sigma(\alpha)/\sigma$ (α = .30) was derived which is independent of the cross section normalization and can be directly used in order to apply a correction to measured data. The averaging was carried out with a Gaussian:

$$\frac{\sigma(\alpha,E)}{\sigma(E,\alpha=.3)} = \frac{1}{a\sqrt{2\pi}}\int \frac{\sigma(E')}{\sigma(E,\alpha=.3)} e^{-\frac{(E-E')^2}{2a^2}} dE'$$

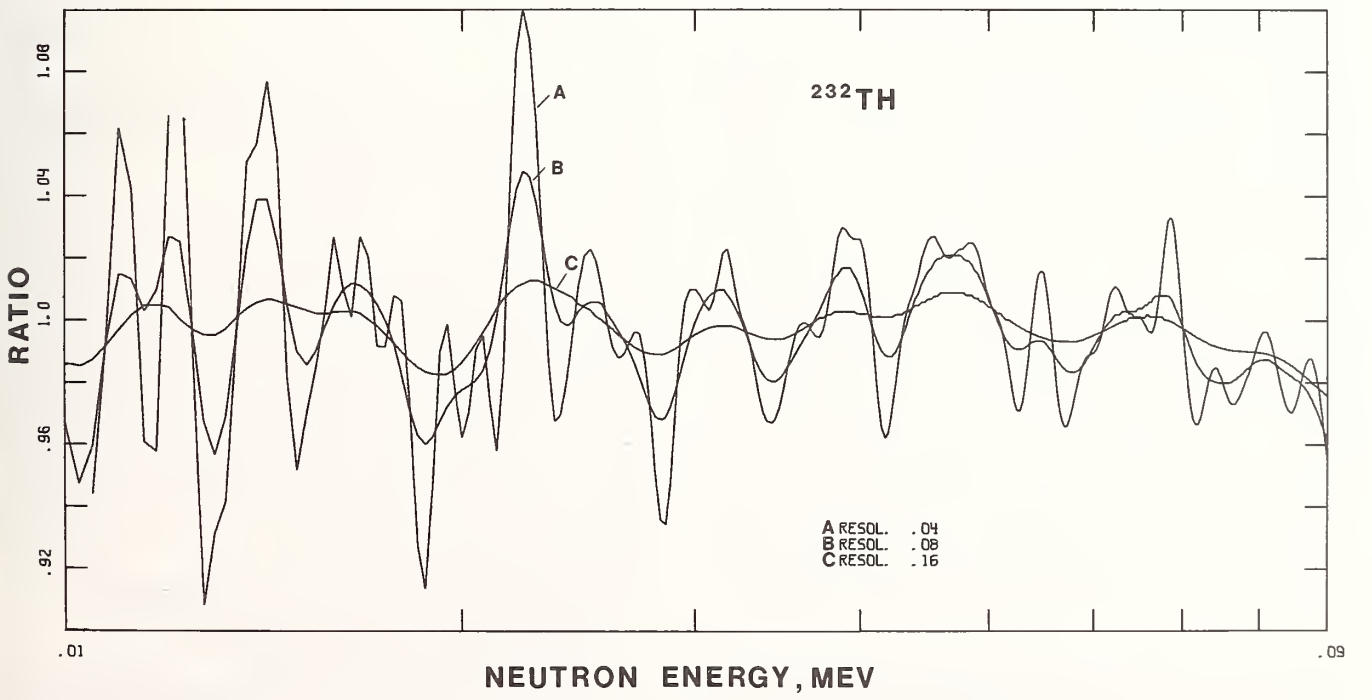

Fig. 5. Fluctuations of the ^{232}Th (n,γ) cross section for different resolutions.

with a = $\alpha E/2\sqrt{2\ell n2}$. Figure 4 shows that substantial corrections may need to be applied in the 10 - 100 keV range if average cross sections are to be derived from individual data points. However, corrections for measurements with a Sb-Be Photo-neutron source or an iron-filtered beam should not exceed 1-2%. A measurement at 30 keV at the ^{7}Li (p,n) ^{7}Be threshold should require only a minor correction. We can conclude from Fig. 4 that fluctuations of the ^{238}U (n,γ) cross section cannot explain the Fe-filter beam data at 69.8 keV and 80.3 keV by Quan and Block.[35] The discrepancy after applying the correction is actually larger at 69.8 keV than previously concluded.

Equivalent information on the fluctuations of the ^{232}Th (n,γ) cross section was derived from the data by Macklin and Halperin[39] and is given in Fig. 5. The fluctuations in ^{238}U (n,γ) and ^{232}Th (n,γ) are compared in Fig. 6 for α = 0.04. It is surprising to find nearly a one-to-one correspondence of maxima and minima between the two cross sections. This appears to hold up even for finer resolutions (α = 0.02 and 0.01) though worse statistics complicates the comparison. It also appears that the areas between major minima labeled "a" through "k" in Fig. 6 are very similar for the two nuclei. It can be concluded that the structure in these data was not caused by the experimental equipment because both data sets were measured with different detector systems[33,39] and the structure in the ^{238}U cross section was confirmed by a measurement at another facility.[37]

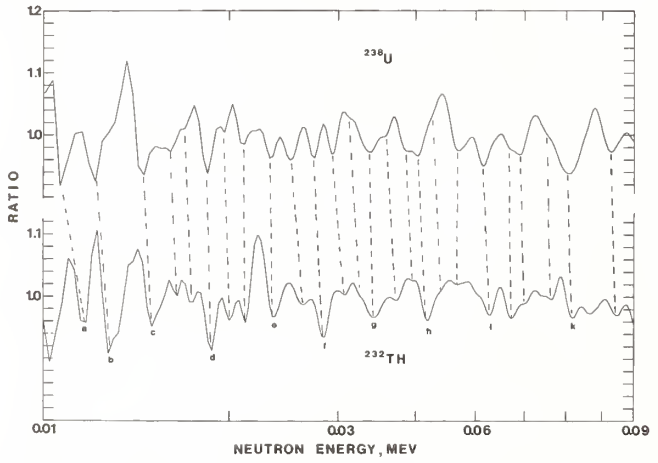

Fig. 6. Comparison of the fluctuations of the neutron capture cross sections of ^{238}U and ^{232}Th.

D. Resonance Self-Shielding and Multiple Scattering Corrections

At higher neutron energies, the cross sections vary rather smoothly with energy. The major effect which may cause erroneous measurement results besides the uncertainty of the detection efficiency are capture events which were caused by neutrons scattered within the sample. Inelastically scattered neutrons have a much higher capture probability due to the higher capture cross section at lower energies. The average flight path length within the sample increases for all scattered neutrons and thus increases the capture probability. Such events cannot be separated by the TOF technique and the effect is most obvious at 14 MeV where measured cross section values were too large by a factor of 4-5 due to these scattered neutrons.

At lower neutron energies the cross section has well separated compound nuclear resonances and resonance self-shielding reduces the measured effective cross section. The effects caused by neutron scattering and resonance self-shielding were treated by Schmitt,[40] Dresner,[41] and Macklin[42] with analytical approximative methods. Bogard,[43] Miller and Poenitz,[26] and Froehner[44] calculated these effects with Monte Carlo techniques. The most frequently used solutions for correcting resonance self-shielding and multiple scattering are those given by Schmitt, Dresner and Macklin. Figure 7 shows the correction calculated by DeSaussure et al.,[33] for a sample with a density of 0.0028 at /b. between 15 and 100 keV. Calculations were carried out for the same sample with the Monte Carlo code SESH by Froehner at several energies. These reults are also shown in Fig. 7. Additional calculations were carried out with a Monte Carlo code which was developed for the higer energy region and thus does not treat resonance self-shielding. However, first order resonance self-shielding effects could be estimated with another code and the combined effect is also shown in Fig. 7. The comparisons of the results from the Monte Carlo techniques and the analytical treatment of the resonance self-shielding and multiple neutron scattering effects shows a difference which exceeds the required uncertainty limit for the ^{238}U (n,γ) cross section in this energy range. The computer code SESH developed by Froehner will be shortly available from the National Computer Code Center at Argonne National Laboratory.

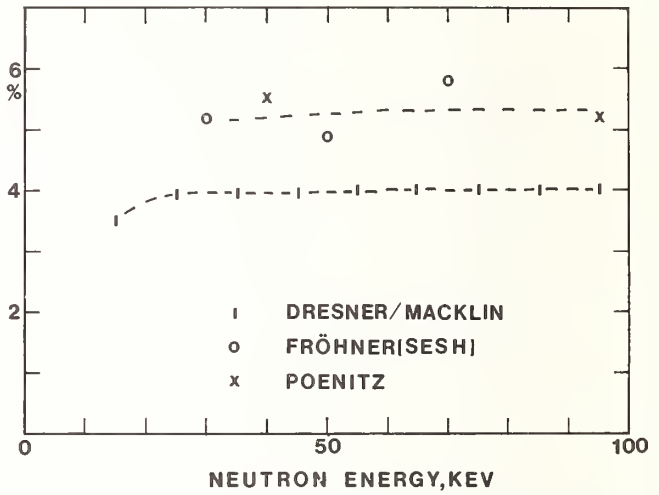

Fig. 7. Comparison of resonance self-shielding and multiple scattering corrections calculated with Monte Carlo techniques and analytical methods.

III. DISCUSSION OF THE EXPERIMENTAL DATA BASE

It is common to use double logarithmic scales for the graphical display of capture cross section data. This choise best accommodates the range of the data which change by ~2 orders of magnitude between 10 keV and 4 MeV. However, data differences which exceed by far the required uncertainty limit for the ^{238}U (n,γ) cross section are suppressed in such displays and are near indistinguishable, therefore in this presentation we are using instead, displays of $\sqrt{E} \cdot \sigma(E)$ which removes about one order of magnitude from the range of the data and permits the display with a linear scale.

A. The Utilization of Independent Experimental Data to Derive Capture Cross Sections with Theoretical Model Calculations

There are substantial discrepancies between some of the experimental data as was discussed before.

Therefore, it should be worthwhile to consider whether other experimental data can be utilized in order to derive additional information which might be helpful in deciding which capture cross section data are realistic and which are not. The capture cross section can be calculated in terms of the statistical model with neutron transmission coefficients derived from the optical model. The gamma strength function, (Γ_γ/D), can be calculated with a giant-dipole resonance for the γ-transition probability and a Fermi-gas model for the level density. In order to follow this outline a substantial number of parameters must be determined with other experimental data. For this presentation we used measurements of the total neutron cross section[44] and of elastic and inelastic scattering cross sections[45] in a fitting procedure in order to determine the optical model parameters for the calculation of the neutron transmission coefficients.[54] The parameters of the giant resonance γ-transition probability can be determined from (γ,n) -cross sections, however, it is common to utilize $\overline{\Gamma_\gamma}$ and <D> values determined with resonances observed in measurements at low energies (1-2 keV above the neutron binding energy) for normalization of the S-wave gamma strength function. Table I shows some of the more recent values and indicates the substantial uncertainty which appears to be mainly due to uncertainties of the average level spacing, <D>. Figure 8 shows the resulting uncertainty for $\sqrt{E}\cdot\sigma$ of ^{238}U (n,γ). Additional parameters which must be considered are the spin-cut-off parameter, σ, and the level density formula parameters, a, which is related to the nuclear temperature.[53] Using the observed average level spacing, <D>, as a constraint, we can use different choices of (a,σ) in order to obtain agreement with experimental capture cross sections in the higher keV range. This is shown in the middle section of Fig. 8. The degrees of freedom of the neutron channel which determine the width fluctuation correction is another parameter which determines the capture cross section below ~200 keV. Figure 8 shows calculations with and without the width fluctuation correction. For all the present calculations $1.0 + T^{0.6}$ was used for the neutron width fluctuation degrees of freedom,[54] where T is the transmission coefficient.

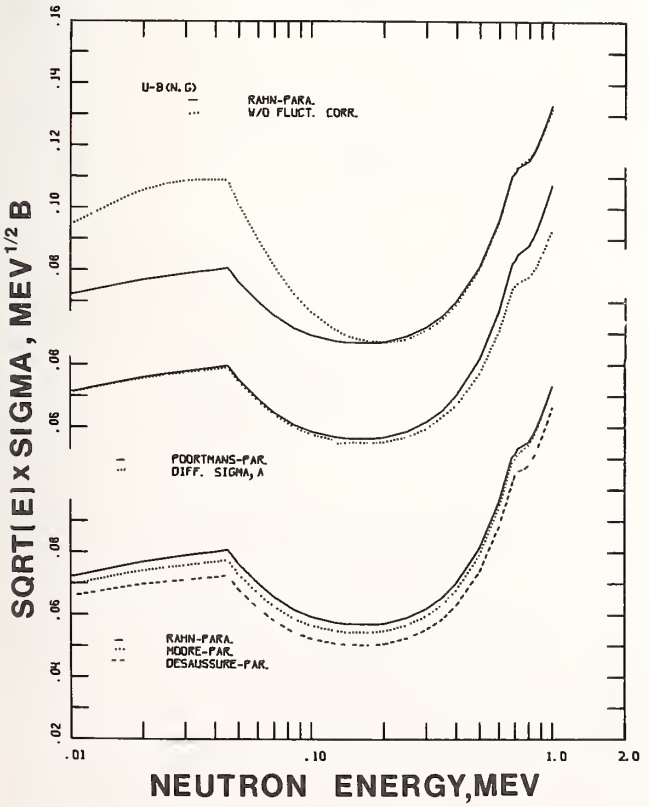

Fig. 8. Changes obtained for capture cross section calculated with the statistical and optical model for the variations of some parameters.

A spherical optical model was used in the present calculations. Some improvements might be expected with a deformed optical model, however, changes will be minor.[55] Γ_γ values for p-wave neutrons were estimated by Moore[49] to be ~5% larger than for S-wave capture, thus expected changes for the capture cross section would be <5%.

TABLE I. Γ_γ and <D> Values Used for Theoretical Model Calculations of the Capture Cross Sections of ^{238}U, ^{232}Th and ^{240}Pu

Nuclei	Author	Reference	$\overline{\Gamma_\gamma}$,meV	<D>,eV
^{238}U	Rahn et al.	46	22.9 ± 1.1	20.8
	DeSaussure et al.	47,48	23.1 ± 0.8	24.8
	Moore, Keyworth	49,50	21.5 ± 1.4	20.9
	Poortmans et al.	51	23.6	22.0
	ENDF/B-V	52	23.5	20.0
^{232}Th	Rahn et al.	46	21.2 ± 0.9	16.7
^{240}Pu	Lynn	53	33	14.0

B. Recent Fast Neutron Capture Cross Section Data of ^{238}U

Figure 9 shows experimental data which were measured absolutely (Ryves et al.,[56] and Panitkin et al.[57]), relative to the H(n,n) cross section (Davletchin et al.[58]), or relative to the ^{235}U (n,γ) cross section (Lindner et al.,[59] and "Present Results," which will be reported at this session. The activation technique was used for the detection of the capture events for all data shown in Fig. 9. A statistical model calculation was carried out as discussed above and the result is shown together with a ±5% range in Fig. 9. The $\overline{\Gamma_\gamma}$ and <D> values used for the normalization are those reported by Rahn et al.[46]. The level density parameters, a and σ, were adjusted

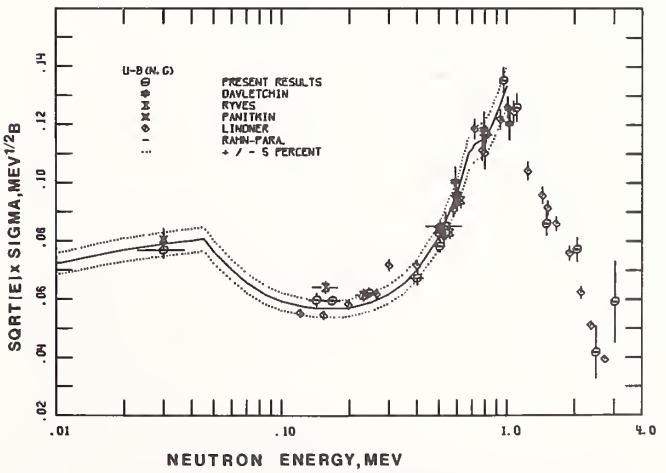

Fig. 9. Comparison of experimental data for ^{238}U (n,γ). Data in this figure were obtained with the activation technique.

in order to obtain a reasonable agreement between the calculated cross section and the experimental data in the higher keV-range. Inspection of Fig. 9 shows that the data fall into a ±5% band with the exception of two points which we can ignore. The larger spread around 150 keV should be noted. The experimental data shown in Fig. 9 suggest somewhat lower values above 500 keV and somewhat higher values around 200 keV. The latter is also supported by measurements relative to the standard capture cross section of gold (Poenitz,[60] and Spencer and Kaeppeler[37]) which are shown in Fig. 10. These data were measured with a large liquid scintillator and have subsequently larger uncertainties. The data by Poenitz are within the ±5% band except around 200 keV as discussed above. The data by Spencer and Kaeppler are generally higher and exclude with their uncertainty limit the ±5% band, though these data overlap with their uncertainties, the uncertainties of the measurements by Poenitz. Also shown in Fig. 10 are measurements by Panitkin et al.[61] relative to the ^{235}U (n,f) cross section. These data were the result of shape measurements and were renormalized to the data by Lindner et al.[59].

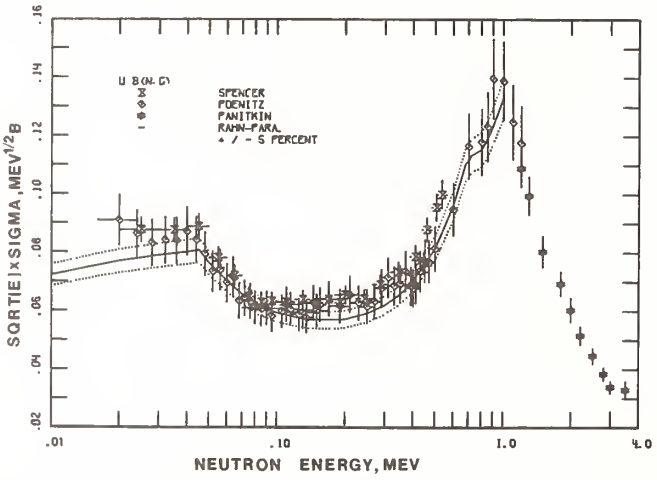

Fig. 10. Comparison of experimental data for the ^{238}U (n,γ) cross section.

Figure 11 repeats some of the data shown in Fig. 9 and shows the recent spherical shell transmission data by Dietze [25] and the results from measurements by LeRigoleur et al.[62]. The pulse-height spectrum weighting technique was used in the latter measurement. The measured values at 45 keV and at 62.5 keV are on or close to a maximum of the fluctuating cross section; thus, values for the average cross section below 100 keV are again well within the ±5% band. However, the values between 100 and 200 kev appear to suggest a decrease of the cross section which could be explained with inelastic scattering to the 4$^+$ level at 148 keV. The calculated cross section does not confirm such a sudden decrease of the capture cross section and other experimental data differ in this energy-range. It is helpful in this context to consider other cross sections measured by LeRigoleur et al.,[62] specifically the capture cross section of ^{103}Rh shown in Fig.17 below, where it is discussed as a fission product. The first three excited levels of ^{103}Rh are at 40, 93 and 297 keV with spins and parities of 7/2$^+$, 9/2$^+$ and 3/2$^-$, respectively. The spin and parity of the ground state are 1/2$^-$, thus only the 3/2$^-$ state represents appreciable competition to neutron radiative capture and elastic scattering and a capture cross section varying smoothly with energy over the 100 - 200 keV range must be expected. The data by LeRigoleur et al., however, show a structure in this range for ^{103}Rh similar to their data for ^{238}U. This suggests that this structure is caused by experimental effects which were not corrected.

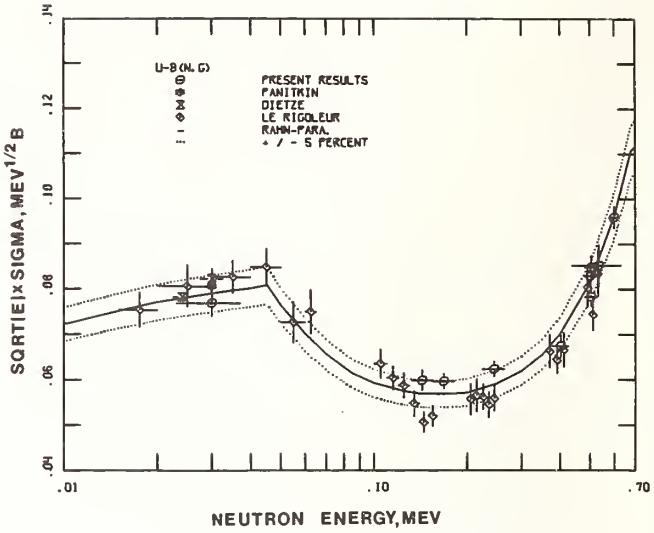

Fig. 11. Comparison of experimental data for the ^{238}U (n,γ) cross section. Data normalized in the keV-MeV range are shown.

A correction of ~1% for cross section fluctuations will decrease the value at 30 keV, and a correction of ~2% will increase the value at 24 keV measured by Dietze.[25]

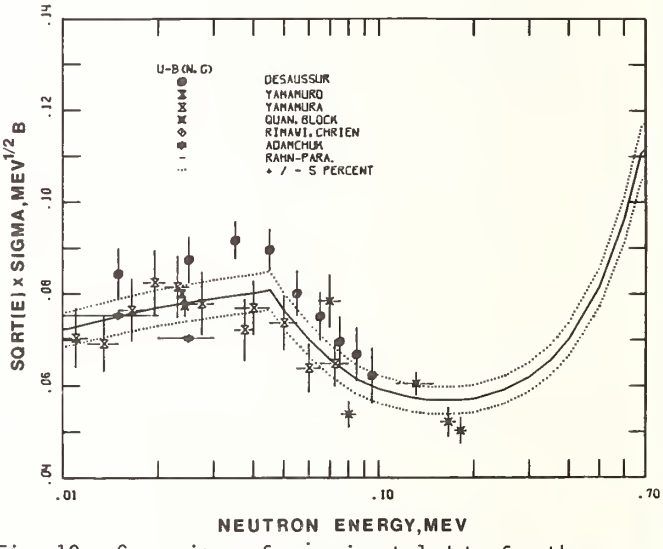

Fig. 12. Comparison of experimental data for the ^{238}U (n,γ) cross section. Data normalized at low energies (eV) are shown.

Figure 12 shows data obtained with white-spectra time-of-flight techniques at LINACs or with Fe-filter beams. These data appear to contradict the result of the model calculation and the ±5% range shown in all previous figures. The exceptions are the data by Rimawi and Chrien,[64] and by Yamamuro et al.[65]. Rimawi and Chrien used an Fe-filtered neutron beam and the activation technique. Yamamuro et al., used the pulse-height spectrum weighting technique and normalized the data to a value obtained previously[66] with an Fe-filtered neutron beam. The agreement between the data by Yamamuro et al., and the ±5% range will improve for several values if corrections for the cross section fluctuations are applied, however, not for the value at 13.5 keV. The data by DeSaussure et al.,[33] are systematically higher than the calculated cross section over the total energy range by

5-15%. The values shown in Fig. 12 are 10 keV-bin averages; therefore, fluctuation corrections do not apply. The data by DeSaussure et al., are the result of an extensive measurement program with detailed reports on the measurements and available data, thus, these data cannot be easily dismissed. Some corrections were proposed[67] but would result in changes well within the uncertainty limits of the reported data. It appears a curious coincident that the measurement,by DeSaussure et al., result in high cross section values compared with other recent data (within the last 8 years) whereas the parameters for $\langle\Gamma_\gamma\rangle$ and $\langle D\rangle$ measured or evaluated by DeSaussure result in the lowest calculated cross section (see Fig. 38).

The two values at 69.8 and 80.3 keV by Quan and Block[35] cannot be improved with corrections for cross section fluctuations, as pointed out above. The values above 100 keV are inconclusive and the implied cross section shape is not supported by the model calculation. It appears that a substantially better foreground to background ratio was obtained in this experiment at 24.3 keV than at all other energies.

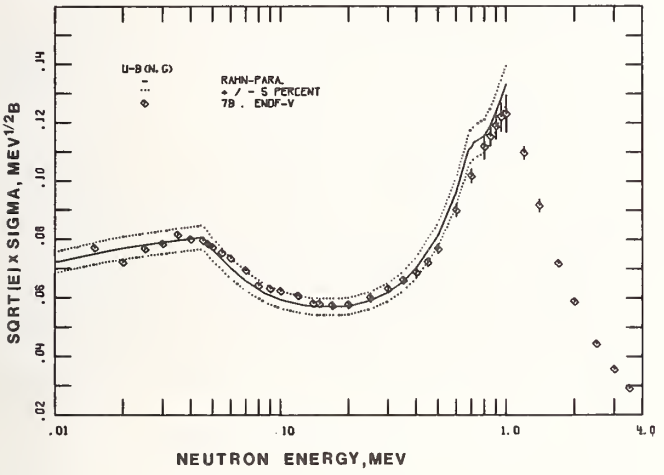

Fig. 13. Comparison of a cross section calculated in terms of the statistical and optical model and the evaluated cross section of ENDF/B-V.

The result of the statistical model calculation which was shown in the previous figures is compared in Fig. 13 with ENDF/B-V.[45,52] The evaluation of ENDF/B-V included all available data up to 1977. Several data sets considered here were not available for this evaluation and one data set used in the ENDF/B-V evaluation (Pearlstein and Moxon[68]) was not considered here because this set has remained preliminary for now more than 6 years. ENDF/B-V cross section values are also found well within the ±5% band considered above. The scattering of values at lower energies appears to come from matching different evaluations. Some differences relative to the calculated cross section are supported by the more recently measured data which were discussed above: Figures 9 and 11 indicate support for somewhat lower values above 400 keV. The optical model fit to the total and inelastic cross section data resulted in an understimation of the inelastic cross section of the 45 keV level between 400 and 800 keV. Somewhat higher cross section values below 200 keV are supported with the data by LeRigoleur et al.,[62] Ryves et al.[56] and recent measurements at ANL. The resulting cross section shape would imply a slower rising inelastic scattering cross section for the 45 keV level than presently obtained with the optical model fit.

C. Recent Fast Neutron Capture Cross Section Data of ^{238}Th

Uncertainty requirements for the capture cross section of ^{232}Th can be expected to be rather similar to those for ^{238}U if a ^{232}Th-^{233}U cycle is considered. The interest in the ^{232}Th - ^{233}U cycle is more recent and only a few newer measurements are available. Some of this more recent data are shown in Fig. 14. Older data are without exception higher than the more recent values, usually by 10-20%. As can be seen in Fig. 14, the values from the more recent fast neutron capture cross section measurements of ^{232}Th are found at best in a ±10% range, suggesting a factor of 2 larger uncertainty for ^{232}Th (n,γ) than for ^{238}U (n,γ). A discrepancy appears to exist between the data by Macklin and Halperin[69] on the one hand and those by Lindner et al.[59] and Poenitz and Smith[70] on the other hand. This discrepancy is in the order of 10-15%. The data by Macklin and Halperin were obtained with the pulse-height spectra weighting technique and recently revised values are shown in Fig. 14. The data by Lindner et al., and Poenitz and Smith were measured relative to the ^{235}U (n,f) cross section and the activation technique was used for the determination of the capture events. Some of the values by Poenitz and Smith were measured with a large liquid scintillator, but normalized to the activation data. Measurements by Chrien et al.[71] and Yamamuro et al.,[66] both taken with an Fe-filtered beam, appear to differ similarly from the data by Macklin and Halperin. DeSaussure and Macklin[72] pointed out that cross section values of the data by Macklin and Halperin between resonances indicate that too much background may have been subtracted from the measured events spectra. It appears that the pulse-height spectrum weighting technique measurements by Macklin lend support for lower ^{232}Th values than those measured by others, whereas they lend support for the higher ^{238}U values measured by DeSaussure et al., at least above 20 keV. The cross section calculated with the statistical model and shown in Fig. 14 was normalized with $\langle\Gamma_\gamma\rangle$ and $\langle D\rangle$ by Rahn et al.[46]. The Columbia University parameters resulted in good agreement for ^{238}U (n,γ) cross sections in the keV-range which suggested the use of ^{232}Th parameters from the same source. Figure 15 shows a comparison with the ENDF/B-V evaluated data file. Agreement is within the +/- 10% range of the experimental data. The difference in shape below the first inelastic scattering level appears to be caused by matching different evaluations in this range.

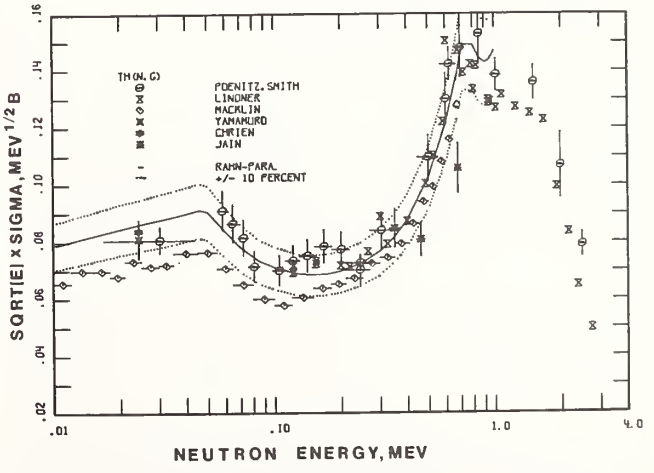

Fig. 14. Comparison of recent data for the capture cross section of ^{232}Th.

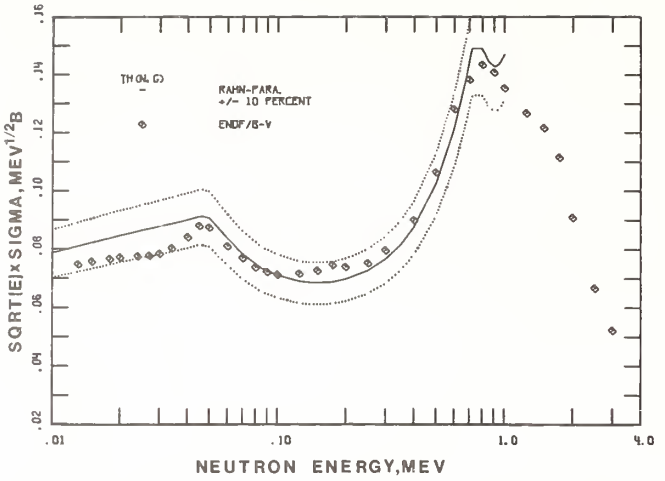

Fig. 15. Comparison of the ^{232}Th (n,γ) cross section and the calculated curve shown in Fig. 14.

D. ^{240}Pu Fast Neutron Capture Cross Section Data

The ^{240}Pu (n,γ) cross section is the major "doorway" for the buildup of higher actinides. It is of importance for burn-up calculations and uncertainty requests [73] are in the order of ~4%. Figure 16 shows the available data. It is obvious that the requested uncertainty has not yet been reached: The spread of all data appears to be over a 30% range. There is a normalization difference of ~25% between the data by Hockenbury et al.[74] and the values obtained by Weston et al.[75]. The recent data by Wisshak and Kaeppeler[76] were measured with very short flight paths of 6.8 and 13.3 cm. These data have a different shape than the data by Weston et al.[75]. The present optical model calculation supports the shape of the data by Weston et al. Wisshak and Kaeppeler point out

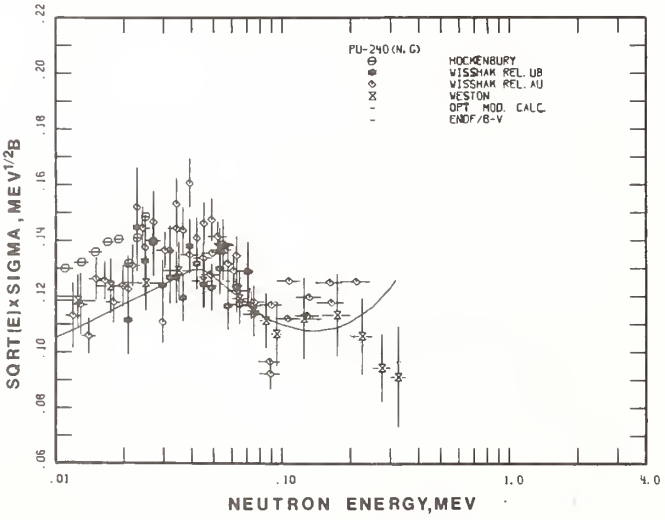

Fig. 16. Comparison of experimental data for the ^{240}Pu (n,γ) cross section and ENDF/B-V.

that their data differs from the results by Weston et al., around 30-40 keV. They measured the ^{240}Pu (n,γ) and the ^{242}Pu (n,γ) cross sections relative to the Au (n,γ) and the ^{238}U (n,γ) cross sections and reported the measured ratios. Therefore, ratios of $\sigma_{n,\gamma}$ (^{238}U)/$\sigma_{n,\gamma}$ (Au) can be derived from both, their ^{240}Pu (n,γ) and the ^{242}Pu (n,γ) measurements. These ratios differ by 20-25% around 30 keV which exceeds the estimated systematic uncertainty by about a factor of 4. A curious point appears to be that Wisshak and Kaeppeler considered the $\sigma_{n,\gamma}$ (^{238}U)/$\sigma_{n,\gamma}$ (Au) ratios which can be derived from their data. However, they apparently obtained different results than can be derived from the tables in which they present their ^{240}Pu (n,γ) and ^{242}Pu (n,γ) data.

E. Fission Product Capture Cross Sections

Capture cross sections of fission product nuclei are the "picture book example" for the proposition that cross sections which are difficult to measure can be calculated with nuclear models for which the parameters were determined with other, reliable experimental data. A survey of fast neutron capture cross sections of fission product nuclei which were calculated with nuclear model codes [77] shows that difference between various calculations may be as large as a factor of 4 if no experimental data exist at all. Values of

$$\delta = \frac{1}{n}\sqrt{\sum\frac{(\sigma_i - \bar{\sigma})^2}{\bar{\sigma}^2}}$$

were considered at 100 keV and 1 MeV, with σ_i the calculated cross section (i = 1...n) and $\bar{\sigma}$ the average of all evaluated cross sections. As an average over all fission product nuclei, δ was 0.31 and 0.32 if no experimental data were available and 0.15 and 0.20 at 100 keV and 1 MeV, respectively, if at least one or two experimental values were reported.

Substantial improvement can be expected if in the absence of differential data, integral values measured in facilities like CFRMF or STEK can be used in the evaluation of fission product nuclei. This approach was used extensively in the evaluation of fission product capture cross sections for ENDF/B-V by Schenter et al.[78]. Requests for fission product capture cross sections usually state requested uncertainties of ~10%.

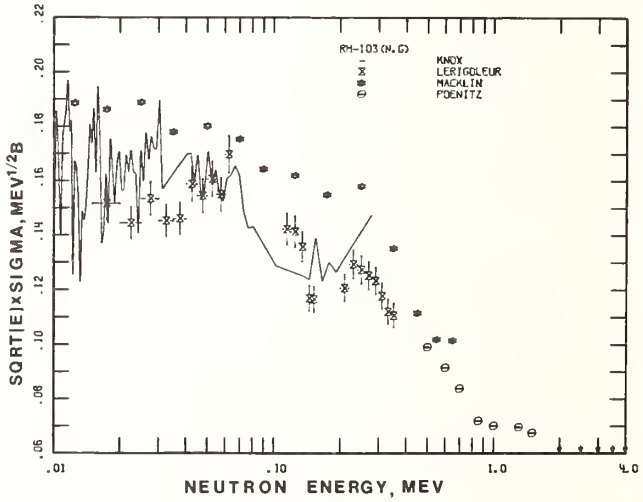

Fig. 17. Comparison of recent experimental data for the capture cross section of the fission product nuclei ^{103}Rh.

Figure 17 shows recent data for the capture cross section of ^{103}Rh. This cross section can be measured by the activation technique and prompt γ-detection techiques. All more recent values shown in Fig. 17 were obtained with the prompt γ-detection technique. Knox et al.[79] and Poenitz[80] used a large liquid scintillator and LeRigoleur et al.[62] and Macklin [81] used the pulse-height spectrum weighting technique. Large fluctuations of the cross section can be seen at low energies as should be expected. The cross section in the 100-300 keV range measured by LeRigoleur et al. shows an unexpected shape which was discussed in con-

text of the ^{238}U (n,γ) cross section above. There appears to be a difference in normalization of ~10-20% between the recent data by Macklin and all other values shown in Fig. 17.

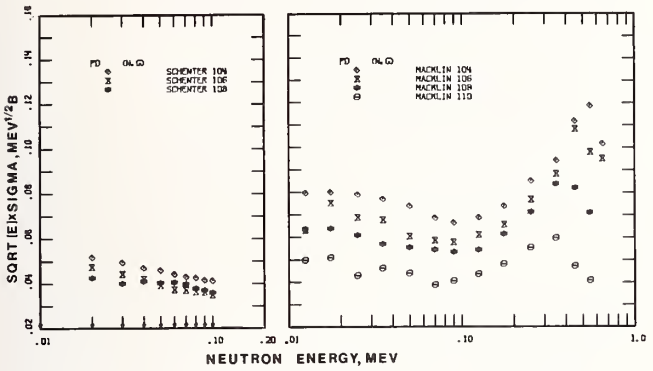

Fig. 18. Comparison of evaluated and experimental data for the even isotopes of Pd.

Figure 18 compares evaluated data by Schenter[78] and experimental values by Macklin[81] for the even isotopes of Pd. The evaluated cross sections are lower for all isotopes and the cross section for ^{110}Pd (n,γ) adjusted with integral values is lower by a factor of 5 than the experimental values for this and the other even isotopes. This cannot be understood from nuclear systematics. The evaluated cross section for the odd isotope ^{105}Pd is larger than experimental differential data (~10-15%). Because the ^{105}Pd (n,q) cross section is much larger than the capture cross sections of the even isotopes,a large part of the substantial difference for the even isotopes is compensated in the elemental cross section shown in Fig. 19. As for ^{103}Rh, recent ANL measurements support lower cross sections than measured by Macklin.

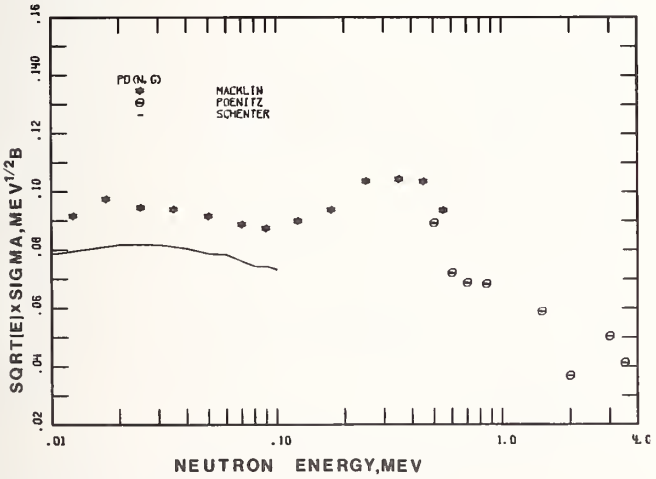

Fig. 19. Capture cross section of Pd.

IV. DISCUSSION, CONCLUSIONS AND RECOMMENDATIONS

^{238}U (n,γ)

Recent fast neutron capture cross section data measured for ^{238}U fall in a ±5% uncertainty band. This suggests that the present data uncertainty above 500 keV is less than one third of the uncertainty estimated by Weisbin et al.,[17] and falls below the required uncertainty limit above this energy (see Fig. 1). The ±5% range is in question below 500 keV where two data sets exceed this range with their estimated uncertainties. The data by DeSaussure et al.,[33] suggest 10 - 12% higher values between 10 and 45 keV than the evaluated data file ENDF/B-V. The data by Spencer and Kaeppeler[37] suggest 8 - 10% higher values between 25 and 45 keV and ~10% higher values between 100 keV and 500 keV. However, the majority of the data apparently does not follow such increases.

The present uncertainty of the ^{238}U (n,γ) cross section is believed to be ±5% above 10 keV and ±10% above 1 MeV. This satisfies the uncertainty limit required to achieve design accuracy for k_{eff} and the breeding ratio above 500 keV but does not fulfill the 1.5 - 3.0% uncertainty requirement below 500 keV.

The present ±5% uncertainty limit of the ^{238}U (n,γ) cross section can not accommodate data adjustments which Weisbin et al.[17] showed are needed in order to obtain agreement between differential cross section data and integral measurement results. Considerations of C/E - ratios require the investigation of all possible sources for existing discrepancies. The C/E discrepancy for c^{28}/f^{49} could be logically caused by:

1. Errors of the differential ^{238}U (n,γ) data.
2. Errors of the experimental integral value.
3. Errors of other differential data which result in a miscalculation of c^{28}/f^{49}.
4. Errors in the computational process.
5. Errors of the differential ^{239}Pu (n,f) and/or ^{235}U (n,f) data.

The C/E - discrepancy of the central reaction rate ratios for GODIVA which was mentioned in the introduction can most likely be explained with errors of other evaluated data which cause a miscalculation of the neutron spectrum[21,82] (above point 3.). Weisbin et al.[17] showed that lowering the experimental integral value for c^{28}/f^{49} by 3% leads to substantially reduced requirements for lowering the differential data. The adjustments required in order to obtain agreement between experimental integral and evaluated differential data would be less than 5% for all but one energy interval; therefore such adjustment would fall below the present uncertainty estimate. This suggests a coordination of measurement techniques between integral and differential measurement groups in order to assure consistency. An extensive effort in this direction is presently underway at Argonne National Laboratory and substantial improvements appear to emerge. Intercomparisons of ^{238}U (n,γ) reaction rate measurements were also made by dosimetry groups for the Big Ten and CFRMF,[83] however, results were reported with uncertainties of 2.2 - 4.9% and differences were 2.0 - 4.5%. This is obviously insufficient considering the requirements shown in Fig. 1.

- *^{238}U capture rate measurements should be compared between groups involved in measuring c^{28}/f^{25} reaction rate ratios for benchmark facilities. Participation by differential data measurement groups is desirable.*

Investigations at Argonne show that different techniques yield a consistency within ± 1 - 1.5%. There is some indication that the thermal capture cross section might be too high. It appears that an uncertainty of less than 1% should be achievable.

The question to be considered next is how to improve on the present ^{238}U (n,γ) differential cross section uncertainty. Present uncertainty levels and differences between data sets measured with prompt

γ-detection techniques are such that a resolution cannot be expected without expensive efforts and long, time-consuming programs. Consideration of the (in)sensitivty of the present model calculations to parameter variations leads to the following recommendation.

- *Absolute values should be measured in the energy range where the lowest uncertainties are required and nuclear model calculations with the constraints given by low energy Γ_γ and D and high-energy $\sigma_{n,\gamma}$ data should be used to provide the shape of the cross section.*

Opportunities for measuring such absolute values exist with iron-filtered beams at 24.3 keV, Sb-Be-sources at 22.8 keV and the forward neutron cone at the threshold of the ^{7}Li (p,n) ^{7}Be-reaction with ~30 keV. Presently available absolute measurements in this range are given in Table II. These values were corrected for cross section fluctuations and referenced to 30 keV. The weighted average is in very good agreement with iron-filtered beam measurements by Rimawi and Chrien[64] and Quan and Block[35] relative to the ^{10}B (n,α) cross section.

TABLE II. Absolute Values of ^{238}U (n,γ) at 30 KeV

Technique	Reference	Value, mb
^{7}Be Associated Activity	Menlove and Poenitz[84]	473 ± 14
	Panitkin et al.[57]	465 ± 23
Spherical Shell Transmission	Belanova et al.[24] and Miller and Poenitz[26]	442 ± 35
	Dietze [25]	470 ± 30
Weighted Average		468 ± 5

^{232}Th (n,γ)

- *Presently available data are inconsistent and uncertain by ±10%. Additional experimental values are required over the total energy range. ^{238}U (n.γ) should serve as an example for finding a solution to the problem.*

^{240}Pu (n,γ)

- *Present data differ in a ± 15% uncertainty range.*

^{240}Pu differs substantially from ^{238}U and ^{232}Th in regard to the available choices for the detection of the capture events. The activation technique might not be applicable and spherical shell transmission experiments might not be possible due to the lack of sufficient material or the complications caused by its high radioactivity. However, the level structure of ^{240}Pu is rather similar to ^{238}U.

- *Measurements relative to the ^{238}U (n,γ) cross section with prompt γ-detection techniques are recommended.*

ACKNOWLEDGEMENTS

The author appreciated discussions with Dr. P. A. Moldauer. This work is supported by the U. S. Department of Energy.

REFERENCES

1. R. E. Chrien, Proc. Conf. Nucl. Cross Sect. + Techn. NBS SP 425, Vol. I, 139 (1975).
2. A. Paulsen, Pros. Symp. Neutr. Stand. + Applic., NBS SP 493, 165 (1977).
3. S. Joly et al., Proc. Conf. Neutron Physics, Harwell, 859 (1978).
4. R. L. Macklin, Oak Ridge Nat'l. Lab., private communication (1978).
5. A. O. Wasson, These Proceedings (1979).
6. E. M. Bohn et al., Argonne National Laboratory, ZPR-TM-240 (1976).
7. L. G. LeSage et al., Proc. NEACRP/IAEA Specialists Meeting, Argonne National Laboratory, 1978.
8. L. G. LeSage, These Proceedings (1979).
9. E. M. Bohn, Argonne National Laboratory Report, ANL-75-14 (1975).
10. S. L. Beaman and C. L. Cowan, Proc. Specialists Meet. Nucl. Data of Pu and Am Isotopes, BNL50991, 287 (1978).
11. S. K. Bhattacharyya
12. W. G. Davey et al., Proc. Conf. Neutron Physics, Harwell, 98 (1978).
13. J. L. Rowlands, Proc. Conf. Neutron Physics, Harwell, 7 (1978).
14. L. N. Usachev and Yu. G. Bobkov, Intern. Nucl. Data Com., INDC (CCP)-19U (1972).
15. Compilation of Requests for Nuclear Data, BNL-NCS-51005 (1979).
16. WRENDA 75, World Request List for Nuclear Data Measurements, INDC (SEC)-46/U+R+I+S (1975).
17. C. R. Weisbin et al., Nucl. Sci. Eng. 66, 307 (1978)
18. C. R. Weisbin et al., ENDF-265 (1978).
19. W. G. Davey, Nucl. Sci. Eng. 39, 337 (1970).
20. W. P. Poenitz, AEC Symp. Series 23, 320 (1971).
21. W. P. Poenitz et al., The Evaluation of ^{235}U (n,f) Above 100 keV, these proceedings (1979).
22. W. P. Poenitz, Argonne National Laboratory, ANL/NDM-45 (1979).
23. W. P. Poenitz, Proc. Conf. Nucl. Data, Helsinki, Vol. I, 209 (1970).
24. T. Belanova et al., J. Nucl. Energy 20, 411 (1966).
25. K. Dietze, Proc. Conf. Neutr. Physics, Kiev, Vol. 3, 200 (1975) and ZFK - 341 (1977).
26. L. B. Miller and W. P. Poenitz, Nucl. Sci.Eng. 35, 295 (1969).
27. B. Diven et al., Phys. Rev. 120, 556 (1960).
28. Yu. B. Adamchuk et al., Proc. Conf. Neutr. Physics, Kiev, Vol. 2, 194 (1977).
29. Z. M. Bartolome et al., Nucl. Sci. Eng. 37, 137 (1969).
30. W. P. Poenitz, Nucl. Sci. Eng. 57, 300 (1975).
31. M. C. Moxon, AERE-R-6074 (1969).
32. R. L. Macklin and J. H. Gibbons, Phys. Rev. 159, 1007 (1967).
33. G. DeSaussure et al., Nucl. Sci. Eng. 51, 385 (1973).
34. R. B. Perez et al., Phys. Rev. 20, 528 (1979).
35. B. L. Quan and R. C. Block, COO-2479-14 (1978).
36. R. E. Chrien, Sem. ^{238}U Res. Capt., INDC(US)-691L, 147 (1975).
37. R. Spencer and F. Kaeppeler, NBS Spec. Publ. 425, 620 (1975).
38. C. D. Bowman et al., Proc. NEANDC/NEACRP Spec. Meeting on Fast Neutron Fission Cross Sections, ANL-76-90, 270 (1976).
39. R. L. Macklin and J. Halperin, Nucl. Sci. Eng. 64, 849 (1977).
40. H. W. Schmitt, Oak Ridge Nat'l. Lab, ORNL-2883 (1960).
41. L. Dresner, Ncul. Instr. and Methods 16, 176 (1962).
42. R. L. Macklin, Nucl. Instr. and Methods 25, 213 (1964).

43. D. Bogard and T. Semler, Conf. Neutr. Cross Sect. Technol. CONF-660303, Vol. I, 502 (1966).
44. F. H. Froehner, Gulf-General Atomics, GA8380 (1968).
45. W. P. Poenitz et al., ANL/NDM-32 (1977), J. W. Meadows et al., ANL/NDM-35 (1978), and A. B. Smith et al., Nucl. Sci. Eng. 47, 19 (1972).
46. F. Rahn et al., Phys. Rev. C6, 1854 (1972).
47. G. DeSaussure et al., ORNL/TM-6152 (1978).
48. D. K. Olsen et al., Nucl. Sci. Eng. 62, 479 (1977).
49. M. S. Moore, Proc. Conf. Neutron Phys., Harwell, 313 (1978).
50. G. A. Keyworth and M. S. Moore, Proc. Conf. Neutr. Phys., Harwell, 241 (1978).
51. F. Poortmans et al., Proc. Conf. Neutr. Phys., Kiev (1977).
52. E. Pennington et al., Am. Nucl. Soc. 16, 591 (1977), see also ENDFB-V, Evalucated Nuclear Data File, National Neutron Cross Section Center, Brookhaven National Laboratory (1979).
53. J. E. Lynn, AERE-R7468 (1974).
54. P. A. Moldauer, Argonne National Lab., ABAREX, Optic.-Stat. Model Cross Section Code, Unpublished (1979).
55. M. P. Fricke et al., GA-10194 (1970).
56. T. B. Ryves et al., J. Nucl. Energy 27, 519 (1973).
57. Yu. G. Panitkin and L. E. Sherman, Atomnaya Energiya 39, 17 (1975).
58. A. N. Davletchin et al., Conf. Neutron Physics, Kiev, Vol. 4, 109 (1975).
59. M. Lindner et al., Nucl. Sci. Eng. 59, 381 (1976)
60. W. P. Poenitz, Nucl. Sci. Eng. 57, 300 (1975).
61. Yu. G. Panitkin and V. A. Tolsikov, Atomnaya Energiya 33, 782 (1972).
62. C. LeRigoleur et al., Conf. Nucl. Cross Sect. and Technol., NBS Spec. Publ. 425, Vol. II, 953 (1975).
63. W. P. Poenitz et al., These Proceedings, "Total Neutron Cross Sections of Heavy Nuclei," (1979).
64. K. Rimawi amd R. E. Chrien, Conf. Nuclear Cross Sections and Technol., NBS Spec. Publ. 425, Vol. II, 920 (1975).
65. N. Yamamuro et al., Conf. Neutron Physics, Harwell, 432 (1978).
66. N. Yamamuro et al., Nucl. Sci. Technol. 15, 637 (1978).
67. Private communication between W. P. Poenitz and G. DeSaussure (1976).
68. S. Pearlstein, private communication, and S. Pearlstein and M. C. Moxon, EANDC (UK), 151 (1973), INDC (UK)-281U (1976).
69. R. L. Macklin and J. Halperin, Nucl. Sci. Eng. 64, 849 (1977).
70. W. P. Poenitz and D. L. Smith, Argonne Nat. Lab., ANL/NDM-42 (1978).
71. R. E. Chrien et al., Nucl. Sci. Eng., to be publ. (1978).
72. G. DeSaussure and R. L. Macklin, Oak Ridge Nat. Lab., ORNL/TM-6161 (1977).
73. L. N. Usachev et al., Conf. Neutron Physics, Harwell, 181 (1978).
74. R. W.Hockenburry et al., Nucl. Sci. Eng. 49, 153 (197π).
75. L. W. Weston and J. H. Todd, Nucl. Sci. Eng. 63, 143 (1977).
76. K. Wisshak and F. Kaeppeler, Nucl. Sci. Eng. 66, 363 (1978), and Nucl. Sci. Eng. 69, 39 (1978).
77. P. Ribon et al., CEA-N-1832, F. Schmittroth and R. E. Schenter, ENDF-194, and others cited in these two reports.
78. R. E. Schenter et al., Evaluation of Fission. Product Nuclei for ENDF/B-V, private communication (1979).
79. H. D. Knox et al., Conf. Nucl. Cross Sections and Technology, Vol. 2, 905 (1975).
80. W. P. Poenitz, unpublished (1979).
81. R. L. Macklin, Private communication (1979).
82. W. P. Poenitz, ANL/NDM-45 (1979).
83. W. N. McElroy, HEDL-TME-77-34.
84. H. O. Menlove and W. P. Poenitz, Nucl. Sci. Eng. 33, 24 (1968).

MEASUREMENT OF THE FAST NEUTRON CAPTURE CROSS SECTION OF ^{238}U RELATIVE TO $^{235}U(n,f)$

L. R. Fawcett, Jr.*, W. P. Poenitz, and D. L. Smith
Argonne National Laboratory, 9700 South Cass Avenue, Argonne, Illinois 60439, USA

The capture cross section of ^{238}U was measured using the activation technique and $^{235}U(n,f)$ as a reference cross section. Capture events were measured by detection of two prominent γ-transitions in the decay of the ^{239}U daughter nuclide, ^{239}Np, employing a high resolution Ge(Li) detector. The system was calibrated with samples activated in a thermal neutron flux relative to the capture cross section of gold, and with an absolutely calibrated α-emitter, ^{243}Am, which decays to ^{239}Np. Cross section measurements were carried out in the neutron energy range from 30 keV to 3 MeV. Emphasis was on absolute values between 150 keV and 1 MeV where the $^{238}U(n,\gamma)$ cross section and its ratio to $^{235}U(n,f)$ are not very sensitive to energy scale uncertainties and the $^{238}U(n,f)$ cross section is small. Background from fission products was found to restrict the accuracy of the measured data at energies > 1.5 MeV.

[($\sigma_c(^{238}U)$, $\sigma_f(^{235}U)$, E_n = 30 keV-3 MeV, activation, ^{243}Am, ^{239}Np, gamma counting)]

Introduction

The radiative capture cross section of ^{238}U is of interest in applied areas due to its important role as a fertile material in various breeding cycles. Calculations of breeding gains and criticality are sensitive to this cross section which is, unfortunately, still rather poorly known. Calculations of capture-to-fission central core reaction ratios for benchmark test facilities using current evaluated data files result in higher values than experimentally determined. This situation has prevailed for more than 10 years and has resulted in continuous requests to lower evaluated differential data. However, most experimental differential cross section data are higher than the evaluated cross section data; thus little support can be seen for further lowering of the ^{238}U capture cross section which is presently on the ENDF/B-file. Many of the problems observed in the data base seem to be associated with unfavorable factors related to measuring ^{238}U capture events. The neutron binding energy is only 4.8 MeV, thus the efficiency for counting capture events with a large liquid scintillator is low and must be expected to be rather uncertain and sensitive to changes in details of the γ-cascades. Low thresholds for inelastic scattering, and the open fission channel at higher energies, hamper all prompt detection techniques. The natural radioactivity of ^{238}U and ^{235}U and their decay products produces additional background which further impedes prompt detection and also complicates the use of the activation technique. Activation nevertheless appears to be the most promising technique because a well-defined calibration method exists for this specific approach.

The present measurements were carried out between 30 keV and 3 MeV. This energy range contributes significantly to the total capture rate in fast reactors. Emphasis was on absolute values in the range from 150 keV to 1 MeV where the cross section varies less with energy than at lower or higher energies. The activation technique was applied and the $^{235}U(n,f)$ cross section was used as a reference.

Irradiations

The $^{7}Li(p,n)^{7}Be$ reaction was used as a neutron source and protons were accelerated by an 8 MV Tandem-Dynamitron accelerator. Proton beam currents were ~15 μ amperes. Several targets consisting of metallic lithium evaporated on a 0.025 cm thick tantalum backing were used. The target thicknesses used provided neutron energy resolutions in the range of 10 to 100 keV. Irradiations were made at zero degrees to the incident proton beam. The diameter of the metallic ^{238}U capture samples was 1.27 cm and their thickness was ~0.025 cm. The ^{238}U material was specifically selected to contain a low amount of ^{235}U (< 400 ppm). The ^{238}U capture samples were mounted on the outside of a low mass ionization fission chamber as shown in Fig. 1. The diameter of the ^{235}U sample was 2.54 cm and its thickness was 210 μg/cm^2. The isotopic composition of this sample was 98.405% ^{235}U, 1.028% ^{234}U, 0.447% ^{236}U, and 0.122% ^{238}U and its mass was recently established relative to several independent mass scales[1] with an uncertainty of ~0.6%. The spacing between the capture samples and the ^{235}U sample was 0.05 cm, half of this was due to the wall of the fission counter and the other half due to the backing of the fissile deposit.

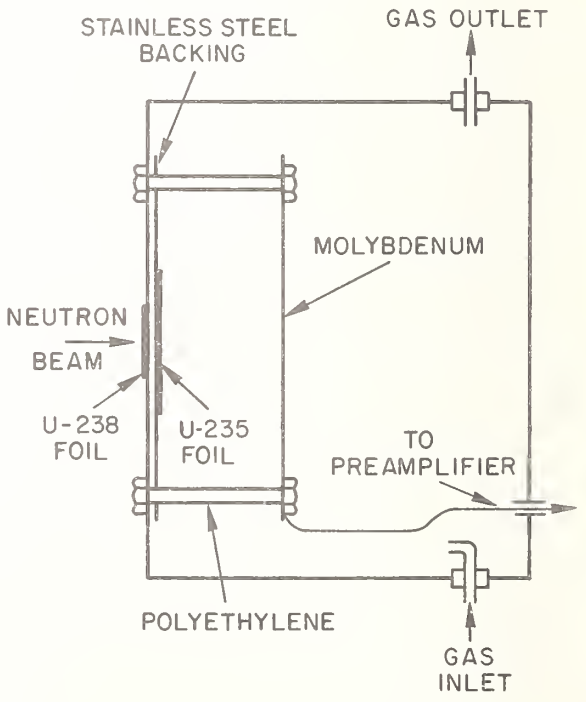

Fig. 1. Schematic of Fission Chamber and Uranium Samples

*Physics Department, Longwood College, Farmville, VA 23901, USA

Irradiations were carried out at 13 energies between 0.03 and 3.0 MeV with irradiation times varying from 45 minutes to 9 hours. The ^{238}U samples and the ionization chamber were usually situated ~2.54 cm from the target; however, at 0.5 MeV samples were irradiated at various distances up to 25 cm. These measurements were used to determine the background produced by neutrons which were scattered from the floor and other structures in the building. The background was found to be on the order of 1% for both the ^{238}U capture and ^{235}U fission processes at the standard position. The spatial variation of the background was known to be small over the region of the experiment from prior time-of-flight measurements with a fission counter. The absolute number of fission events was determined by extrapolating the measured fission fragment energy spectrum to zero pulse-height. A correction for the total fission fragment absorption was calculated using a fission fragment range of 4.1 mg U/cm^2. The average cross section at the average neutron energy was determined from the total number of capture and fission events. The angular distribution of the source neutrons, the path through the samples, isotopic compositions and attenuation in the various materials were taken into account.[2]

Corrections were applied for scattering of neutrons in the samples, the fission chamber and the target structural material using Monte Carlo techniques and data from current ENDF/B - files. A correction was applied to obtain the average cross section at the average energy from the measured average cross section.[3]

Determination of the Capture Events

The capture samples were irradiated in the fast neutron flux, ϕ, for a period of time, T. After the end of the irradiation, a waiting period of $t \geq 4h$ permitted at least 99.9% of the ^{239}U nuclei produced with the capture events to decay to ^{239}Np. The samples were then counted with a Ge(Li) detector for a period of time, θ. The total number of counts observed in this time is given by $C_\gamma = \varepsilon_\gamma \cdot \sigma \cdot n \cdot \phi \cdot F$, where ε_γ is the effective counting efficiency, σ is the cross section to be determined, n is the number of nuclei in the sample, and ϕ is the neutron flux per cm^2 and sec. The time factor, F, is

$$F = \frac{1}{\lambda}(1 - e^{-\lambda T})\, e^{-\lambda t}\,(1 - e^{-\lambda\theta}) \quad .$$

The half-life of ^{239}Np was taken to be 2.355 ± 0.004d.[4] A correction was required for the variation of the flux, θ, during the irradiation. The correction was determined by monitoring the neutron flux with a Long Counter for a series (n) of time intervals (τ). τ was set at 15 minutes. The correction is given by

$$k = n \cdot \frac{1 - e^{-\lambda\tau}}{1 - e^{-n\lambda\tau}} \cdot \frac{\sum a_i\, e^{-\lambda(n-i)\tau}}{\sum a_i} \quad ,$$

with a_i being the relative monitor counts. This correction was found not to exceed 0.2%.

Major transitions in the decay of ^{239}Np result in γ-rays of 106 keV, 228 keV, and 278 keV which occur with 27.2%, 11.5% and 14.5%[5] frequency per decay, respectively. The 106-keV γ-transition cannot be distinguished from several x-rays of ^{239}Pu, therefore, the 228 keV and the 278 keV γ-rays were used in the present measurements. The stability of the counting system was checked for the period of the present experiment and found to be better than 0.4%. This represents a reproducibility limit for the present measurements and is probably caused by the limitations of the reproducibility of mounting the uranium samples in proximity to the Ge(Li) detector. The resolution of the counting system was determined using the 1.33 MeV γ-transition in the decay of ^{60}Co and was found to be 2.6 keV FWHM at 1.33 MeV.

The uranium samples were counted at a distance of ~1.4 cm from the Ge diode. At this close distance the γ-ray absorption in the sample must be determined by integrating over the space angles involved, while considering the effect of the Ge(Li) detector efficiency which is itself dependent on the direction and the position of the entering γ-ray. The 228 keV and the 278 keV γ-rays are frequently in coincidence with the 106 keV transition as well as with some other γ-rays and x-rays.[6] Thus, sum-coincidences must be expected for close-geometry counting. The sum-coincidence probabilities are expected to depend on the sample thickness because the absorption is different for the observed γ-rays and those with which they are in coincidence. Due to these complications the effective sample absorption was not calculated but experimentally determined and made part of the calibration procedure.

Calibration with ^{243}Am-Samples

The ^{239}Np - decay observed in the present experiment also occurs in the decay chain of the α-emitter ^{243}Am. Therefore, very thin ^{243}Am samples (calibrated absolutely by low-geometry α-counting) which are in equilibrium with ^{239}Np can be used for the calibration of the γ-detection efficiency.[7-9]. Two ^{243}Am samples were used in the present experiment to determine the absorption-free effective efficiency for counting ^{239}Np decays by detecting the 228 keV and the 278 keV γ-rays. These samples contained some ^{241}Am, ^{242}Cm and ^{244}Cm which could be separated in an alpha-energy spectrum analysis. The ^{243}Am-decay fraction was 90.05%. The total α-decay rates of the samples were determined by low-geometry α-counting. The values obtained for the number of gammas detected with the Ge(Li) detector to the number of α-decays for the two samples agreed within 0.4% for the 228 keV transition and within 0.3% for the 278 keV transition. The two samples differed in intensity by about a factor of three. Therefore, the result indicated that count rate effects were negligible. The diameter of the ^{243}Am samples was somewhat smaller than the capture samples. The radial dependence of the efficiency was measured with a "point" source and a correction of 0.5% was calculated by fitting the measured values with a 2nd-order polynomial and subsequently integrating over the samples of different size.

The effects of the γ-absorption in the sample and the effective detection efficiency were analyzed by a combination of measurements and Monte Carlo simulation calculations. First, the transmission, T, through the sample was measured in the same geometry as used in the actual sample counts. The measurements were performed as shown in B and C of Fig. 2 using a virgin uranium sample and an ^{243}Am sample. From this measurement, an "effective" absorption coefficient, μ, was deduced, in the parallel-beam approximation, from the formula $T = \exp(-\mu\sigma)$. This value of μ was used to calculate the effective absorption, η, for a uniformly activated uranium sample using the formula

$$\eta = \frac{1}{\mu\delta} \cdot (1 - e^{-\mu\delta}) \quad .$$

The validity of this experimental method was tested by means of the Monte Carlo "experiments". Calculations for geometries B and C of Fig. 2 yielded an effective calculated T and hence a μ value. Simulation of configuration A yielded the absorption, η. Substitution of the calculated μ into the formula calculating η

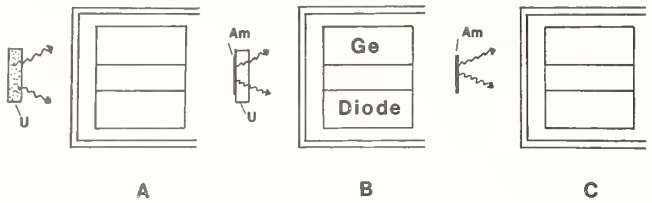

Fig. 2. Schematic Representation of the Three Cases Used in the Present Experiment and Monte Carlo Calculations

yielded a value which agreed with the Monte Carlo result to within 0.05%. This good agreement justifies the use of an experimentally-determined effective absorption coefficient in a parallel-beam approximation to calculate the absorption and efficiency correction for the geometry of the present experiment.

The above considerations do not yet include the effect of the sum-coincidences with all details. Sum-coincidences between the measured 228 keV and 278 keV γ-rays and other transitions reduce the effective absorption of the samples and are thus included in the effective thickness obtained from the transmission experiment. However, the difference between the sum-coincidences obtained for the transmission experiment and for the homogeneously-activated sample must be taken into account. A lower effective absorption is measured in the transmission experiment because the transitions which are in coincidence with the 228 keV and the 278 keV lines have lower energies and are more strongly absorbed in the transmission experiment than in the homogeneously activated sample. The effect was calculated with a simplified decay scheme and the total detection efficiencies for the emitted γ-rays which were calculated by Monte Carlo techniques. It was found that the effect due to coincidences slightly over compensates the increase in absorption caused by the effective opening angle for the detection of γ-rays.

Calibration with Samples Activated in a Thermal Neutron Flux

The thermal neutron capture cross section of ^{238}U is well known. This suggests an alternate method to calibrate the detection efficiency of the Ge(Li) detector and to obtain the effective absorption of the sample. Four capsules were placed on a wheel and rotated in the thermal column of a 10 KW reactor in order to assure equal exposure for each of the capsules. Three of the capsules were made from aluminum and one was made from cadmium. The cadmium capsule and one of the aluminum capusles contained a uranium sample sandwiched by two 0.0025 cm thick gold foils. One of the remaining aluminum capsules contained a single uranium sample and the other a single gold foil. The absolute activation of the gold samples was determined with the $4\pi\beta - \gamma$ - coincidence method employing corrections which have been discussed in detail previously.[10] The uranium samples were counted with the Ge(Li) detector using the procedures described above. The efficiency follows from

$$\varepsilon = \frac{R_{U8}}{R_{Au}} \cdot \frac{\sigma_{Au}}{\sigma_{U8}} \cdot \frac{S_{Au}}{S_{U8}} \quad , R = \frac{C \cdot A}{F \cdot G}$$

where C is the number of counts, A is the atomic weight, F is the time factor defined above, and G is the mass of the sample in gms. The factor S accounts for self shielding of the samples and the activation due to neutrons scattered in the sample.[10,11] S is an average over a Maxwellian spectrum and becomes identical to the Westcott g-factor[12] for very thin samples. The neutron field was well moderated and a minor correction (0.5%) was calculated for the activation by epithermal neutrons using the Westcott formalism and the measured Cd-ratio. A value of 98.65 ± 0.09b was used for the thermal capture cross section of gold.[13] A weighted average of 2.712 ± .006b was obtained from an updated listing of all experimental values[14] of the thermal capture cross section of ^{238}U.

One of the fission products, ^{132}Te, has a half-life of 78.2h and decays with a high frequency (96.9%) by emitting a 228 keV γ-ray.[15] This gamma cannot be separated from the 228 keV γ-ray in the decay of ^{239}Np which is used in the present measurements. Fission events of ^{235}U occur in the thermal neutron activation of the ^{238}U samples and are not negligible. Corrections were calculated and found to be in the range 3.2 - 4.5% for the 228 keV photopeak. The 228 keV γ-ray of ^{132}Te is in coincidence with a 49.7 keV transition (100%),[15] thus sumcoincidences are possible which fall into the 278 keV photopeak of the ^{239}Np - decay. A correction was calculated and found to be 0.3%.

Results

The agreement between the values obtained with the two different techniques is within their respective uncertainties. The efficiency appears to be a linear function of the sample weight and a fit was used to determine the efficiency in the range of the weights of the samples used in the cross section experiment.

Table I contains the different contributions to the uncertainties of the present values. With the exception of the values above 1 MeV, the limiting factor appears to be the uncertainty of the reference cross section which was assumed to be 2%.[16]

Table I. Uncertainties of the Present Cross Sections.

Source	Range, %	Comment
Gamma Detection Efficiency	1.0	Common to all values
^{235}U Sample Mass	0.6	
Total Fission Fragment Absorption	0.5	
Half-life of ^{239}Np	0.2	
^{238}U Sample Mass	0.2	
$^{235}U(n,f)$ Cross Section	2.0	
Statistics and Reproducibility	0.9-23.1	Values are 0.9-3.0% below 1 MeV
Neutron Background	0.3-4.0	0.3% for most values except at higher energies and larger distances from the target
Second Neutron Group	0.1-1.2	Does not apply below 800 keV
Scattering of Neutrons in the Counter, Samples and Neutron Source Structural Material	0.8-1.7	
Fission Product Decay	0.2-4.0	Does not apply below 1 MeV

The cross sections obtained in the present experiment are compared in Fig. 3 with an evaluated cross section.[17] The new experimental data do not support the recent trend to lower values obtained in other measurements[19,20] which influenced the evaluated cross section.

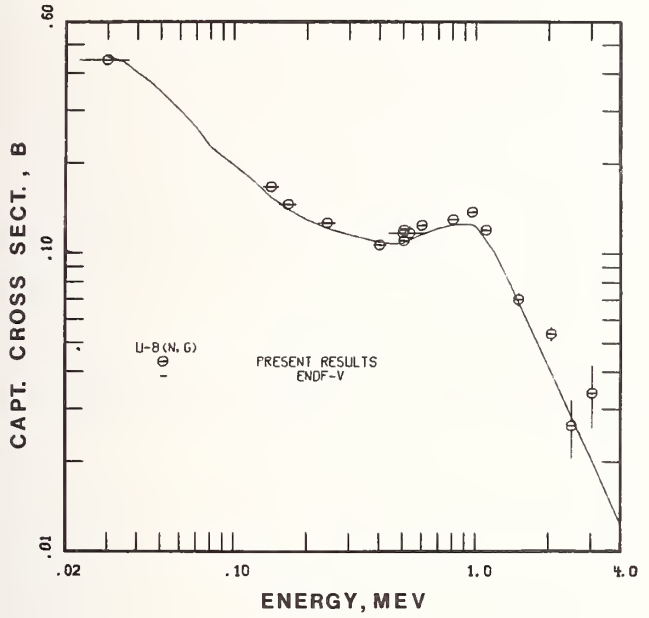

Fig. 3. Comparison of the Present Results with ENDF/B-V

The present data are compared in Figs. 4, 5, and 6 with other experimental data. Only the more recent data were selected for comparison. A detailed discussion of all available data through 1977 is given elsewhere.[17] The present result is in good agreement with that obtained with the prompt detection technique by Poenitz[21] relative to the gold standard capture cross section. Agreement with data by Lindner et al.[18] is reasonable, though the present data are somewhat higher between

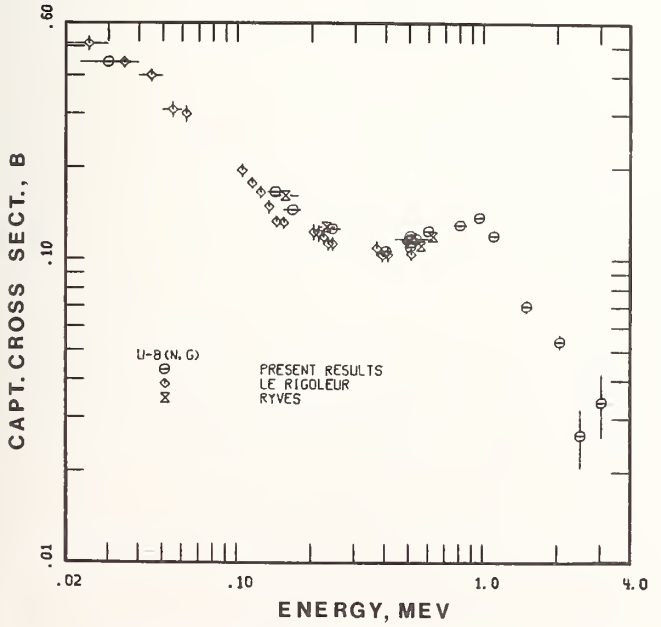

Fig. 4. Comparison of the Present Results with Other Recent Experimental Data

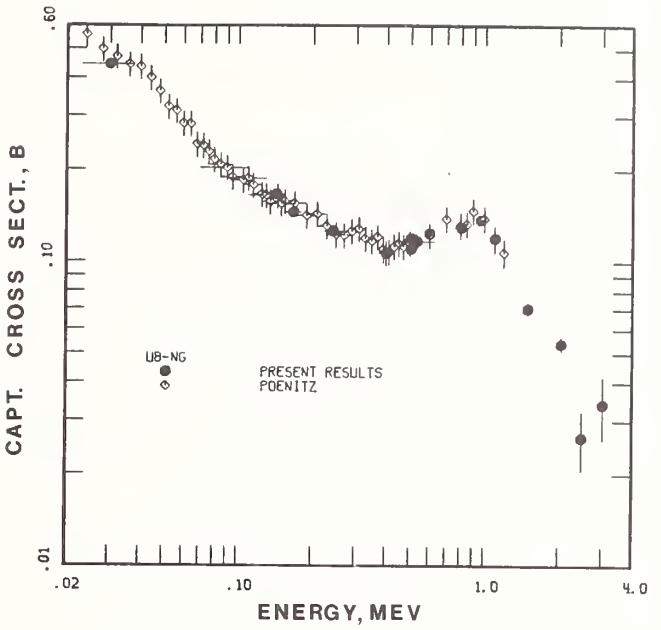

Fig. 5. Comparison of the Present Results with Other Recent Experimental Data

100 and 250 keV and around 1 MeV. The present data agree well with those by Ryves et al.[22] in the former and with the data by Davletshin et al.[23] in the latter energy region. The data by Quan et al.[20] and LeRigoleur et al.[19] agree better with those by Lindner et al. between 100 and 250 keV.

Acknowledgments

Useful discussions with J. Meadows and G. DiIorio were appreciated. This work has been supported by the U. S. Department of Energy.

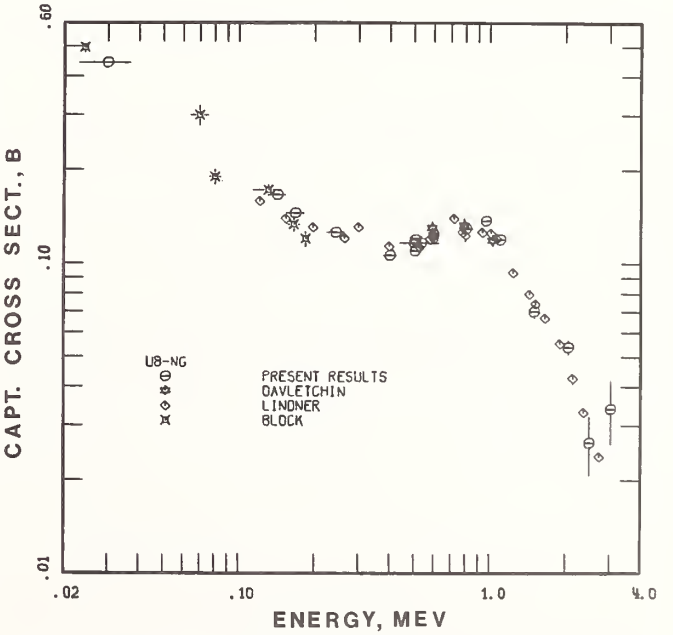

Fig. 6. Comparison of the Present Results with Other Recent Experimental Data

References

1. W. P. Poenitz, J. W. Meadows and R. J. Armani, Argonne National Laboratory Report, ANL/NMD-48, (1979).

2. D. L. Smith and J. W. Meadows, Argonne National Laboratory Reports, ANL-7938, (1972), ANL-7989 (1973) and ANL/NDM-37 (1977).

3. W. P. Poenitz, D. Kompe and H. O. Menlove, Journal of Nuclear Energy, 22, 505 (1968).

4. Evaluated Nuclear Structure Data File, ORNL.

5. D. I. Starozhokov, Yu. S. Popov and P. A. Privalova, Atomnaya Energiya, 42, 4, 319, (1977).

6. D. J. Horen et al., Nuclear Level Schemes A=45 Through A=257, A=239 Drawing 4, Academic Press, Inc., New York and London, (1973).

7. J. F. Barry, J. Bunce and P. H. White, Journal of Nuclear Energy, Parts A/B, 18, 489, (1964).

8. H. Seufert and D. Stegemann, Nucl. Sci. Eng., 28, 277, (1967).

9. W. P. Poenitz, Nucl. Sci. Eng., 40, 383, (1970).

10. W. P. Poenitz, KFK 180, Kernforschungszentrum Karlsruhe, (1963).

11. K. H. Beckurts and K. Wirtz, Neutron Physics, Springer-Verlag, Berlin and New York, (1964).

12. C. H. Westcott, AECL 670, Atomic Energy of Canada Limited, (1958).

13. N. E. Holden, Brookhaven National Laboratory, Personal Communication, (1979).

14. E. T. Tomlinson, G. deSaussure and C. R. Weisbin, EPRI NP-346, Electric Power Research Institute, Oak Ridge National Laboratory, (1977).

15. Nuclear Data Sheets, ORNL, 17, 229, (1976).

16. W. P. Poenitz, Argonne National Laboratory Report, ANL/NDM-45, (to be published), (1979).

17. W. P. Poenitz, E. Pennington and A. B. Smith, Argonne National Laboratory Report, ANL/NDM-32, (1977). The evaluation was updated at a later time to include changes in the evaluated $^{235}U(n,f)$ cross section.

18. M. Lindner, R. J. Nagle and J. H. Landrum, Nucl. Sci. Eng., 59, 381, (1976).

19. C. LeRigoleur, A. Arnaud, and J. Taste, National Bureau of Standards Conference Report, NBS 425, 2, 953, (1975).

20. B. L. Quan, R. H. Pendt and R. C. Block, TANSAO, 23, 498 (1976).

21. W. P. Poenitz, Nucl. Sci. Eng., 57, 300, (1975).

22. T. B. Ryves, J. B. Hunt and J. C. Robertson, Journal of Nuclear Energy, 27, 519, (1973).

23. A. N. Davletshin et al., Proceedings of Conference on Neutron Physics, Kiev, 4, 109, (1975).

SELECTED TOPICS IN RESEARCH PROGRAM ON IBR-2

V.I.Luschikov, L.B.Pikelner, Yu.P.Popov, I.M.Frank, E.I.Sharapov, Yu.S.Yazvitskii
Laboratory of Neutron Physics, Joint Institute for Nuclear Research
Dubna, USSR

The physical start-up of the IBR-2 fast pulsed reactor took place in the Laboratory of Neutron Physics, JINR. Design values for instantaneous thermal neutron fluxes are : 10^{17} $cm^{-2}s^{-1}$ inside the moderator and 10^{16} cm^{-2} s^{-1} from its surface. In combination with the heavy current, short pulse injector (electron induction accelerator LIU-30 being under construction now) it will become a high intensity neutron source for the time-of-flight investigations in the energy range from 10^{-7} to 10^{6} eV. The characteristics of the complex IBR-2 + LIU-30 are described. The neutron beams and their use in the condensed matter and applied research are mentioned. The program for $n\alpha$-, $n\gamma$- and nf- cross section measurements as well as neutron cross section study for few nucleon systems are reported. The prospects for nuclear physics research on the LIU-30 nonmultiplying target facility are outlined using as examples the experiments with polarized neutrons and nuclei and some others. The description is illustrated with the results obtained recently on the operating IBR-30 pulsed reactor.

[pulsed neutron source, IBR-2 reactor, $n\alpha$, $n\gamma$, nn, nf cross sections, polarized neutrons and nuclei, isomeric shift, neutron resonances.]

I. IBR-2 and LIU-30 complex - the high intensity pulsed neutron source

Design characteristics

The periodically pulsed fast reactor IBR-2 with liquid metal cooling is constructed in the Laboratory of Neutron Physics, JINR. The physical start-up of IBR-2 was performed in the end of 1977- beginning 1978. Its operation at design power level is being prepared. The design mean and pulse thermal power is 4 MW and 7700 MW, respectively, pulse duration being 100 μsec and pulse repetition rate - 5 p.p.s. Total neutron yield from the active zone of a volume of 22 l is to be $1.7.10^{17}$ s^{-1}. The instantaneous thermal neutron flux within the moderators will reach 10^{17} cm^{-2} s^{-1} and that from their surface - 10^{16} cm^{-2} s^{-1}. The latter exceeds the thermal neutron flux from moderator surface of best stationary reactors by a factor of 10. Several references, see for example, ref.[1] give details on the IBR-2 characteristics, its construction and operation. The IBR-2 reactor design is new if compared with the previous IBR reactors. Here we employ liquid sodium as a coolant. The reactivity modulation is performed with the help of the moving reflector instead of the rotating part of the active core. The nuclear fuel is 90 kg of plutonium dioxide. The fuel rods are to be replaced once per 4 years period.

The IBR-2 reactor is also designed to operate as a dynamical multiplier of neutrons from the target of the electron induction accelerator LIU-30. Thus provided neutron pulses will be 50 times shorter. The accelerator is being constructed (electron energy 30 MeV, current 250 A in the pulse, pulse duration 0.5 μsec, beam power on a target 200 kW). The accelerator building 160 m long is built. The assembly works started of the electron gun and first module of LIU-30.

Source performances in different regimes

The IBR-2 reactor in combination with LIU-30 is to be a very powerful neutron source to serve the needs of scientists performing physical investigations with the time-of-flight technique. The arrangement of buildings and flight tubes of the whole complex is shown in fig. 1. The measuring pavilions and flight tubes from the IBR-30 reactor (in operation now) are planned to enter the arrangement. The nonmultiplying target of LIU-30 is to be placed instead of the IBR-30 core. This will allow to operate with short neutron and γ ray pulses. The arrangement as a whole will include 20 beams, 14 of them being in the new experimental building with two halls 30 m x 60 m each.

The IBR-2 and LIU-30 complex is to perform in three modes :

- reactor mode (IBR-2), pulse duration 100 μsec
- dynamical booster mode (IBR-2+LIU-30), pulse duration 2 - 10 μsec;

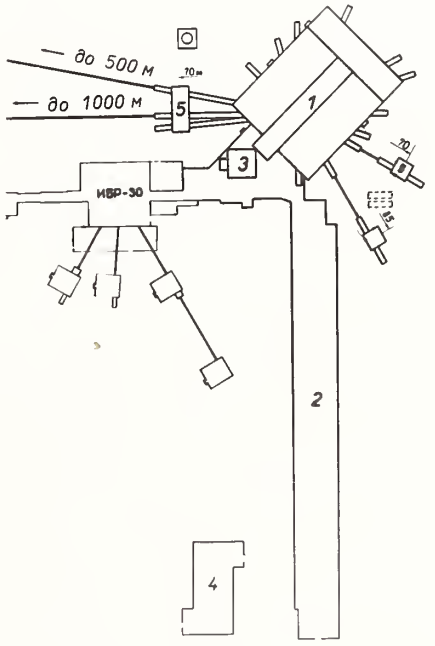

Fig. 1. Arrangement of the buildings and flight tubes of the IBR-2+LIU-30 complex.

- accelerator mode with nonmultiplying target (LIU-30), pulse duration 500 nsec at the beginning and 50 nsec in the future.

The neutron source characteristics for the above mentioned modes are given in Table 1. Line 5 in the Table presents the figures of merit at 1 keV, i.e the intensity of the 1 keV neutron beam on the sample 1 cm^2 with a fixed resolution of 0.1%. In the brackets the flight path to achieve this resolution is indicated. The first mode (IBR-2) is mainly planned for the experiments with thermal and epithermal neutrons. The second mode (IBR-2 + LIU-30) is expected to gain benefits in the experiments under moderate resolution in the energy region up to several hundreds eV. The third mode (LIU-30, pulse duration 50 nsec or less) is to have a higher figure of merit. It will provide means for neutron cross section measurements and other experiments under good resolution in the energy range 10^3 - 10^5 eV.

Table 1. The characteristics of the complex IBR-2 + LIU-30 in three modes

Parameters	IBR-2	IBR-2 + LIU-30		LIU-30	
1 Total neutron yield s^{-1}	1.7×10^{17}	6.6×10^{16}	1.2×10^{16}	6×10^{14}	6×10^{13}
2 Pulse duration μsec	100	10	2	0.500	0.050
3 Pulse repetition rate p.p.s.	5	50	50	50	50
4 Fast neutron flux (E > 10 keV) in the active core					
a) instantaneous $cm^{-2}s^{-1}$	6×10^{17}	2.2×10^{17}	2.0×10^{17}	-	-
b) average $cm^{-2}s^{-1}$	3×10^{14}	1.1×10^{14}	2.0×10^{13}	-	-
5 Resonance neutron flux ($E = 10^3$ eV) on the sample at resolution 0.1% $cm^{-2}\ s^{-1}$	-	-	0.4 (2000 m)	0.32 (500)m)	3.2 (50 m)
6 Thermal neutron flux from the moderator surface					
a) instant. $cm^{-2}s^{-1}$	1.0×10^{16}	3.9×10^{14}	7.2×10^{13}	-	-
b) average $cm^{-2}s^{-1}$	5.8×10^{12}	2.2×10^{12}	4.0×10^{11}	-	-

Neutron characteristics measured during the physical start-up of IBR-2

On January 13, 1978 the IBR-2 reactor was started to operate in the pulse mode at a pulse repetition rate of 50 p.p.s. In February and March 1978 the reactor worked for 100 hrs at an average power of 500 W. The reactor parameters were investigated and are reported in refs.[2,3]. The pulse duration was measured to be equal to 200 μsec instead of expected 100 μsec. Additional measurements showed the possibility to make the pulse shorter by improving the construction of the auxiliary moving reflector.

During the physical start-up the shape of neutron spectrum and neutron fluxes were measured[3]. Data on thermal neutron fluxes obtained by the activation method (gold and copper foils) proved the design value of the flux (Table 1) real. The results of measurements of the spectrum shape at $E > 1$ eV are shown in Fig.2. They were got by the technique of neutron spectra unfolding from readings of the activation thermal, resonance and threshold detectors. The spectrum in the energy range $1 < E < 10^4$ eV should be E^{-x}, where $x \leq 1$. The smooth curve in Fig.2 does not obey this law (there x=1.25). However these results should be regarded as qualitative due to considerable uncertainties of the method conventionally used for the dosimetry purposes. In planning the experiments on IBR-2 it seems reasonable to use some modifications of the empirical formula derived in ref.[4] for resonance neutron fluxes of the IBR-30 reactor:

$$N(E) = \frac{2.7 \times 10^9 \ W}{L^2 \ E^{0.9}} \quad cm^{-2}s^{-1}eV^{-1}$$

where W is the reactor power in MW and L is the flight path (reactor - detector) in m, E is the neutron energy in eV.

II. IBR-2 neutron beams in the future use

The arrangement within the experimental hall of 14 neutron beams of IBR-2 with spectrometers for the time-of-flight investigations are shown in Fig.3. Roman numerals indicate neutron beams. The spectrometers

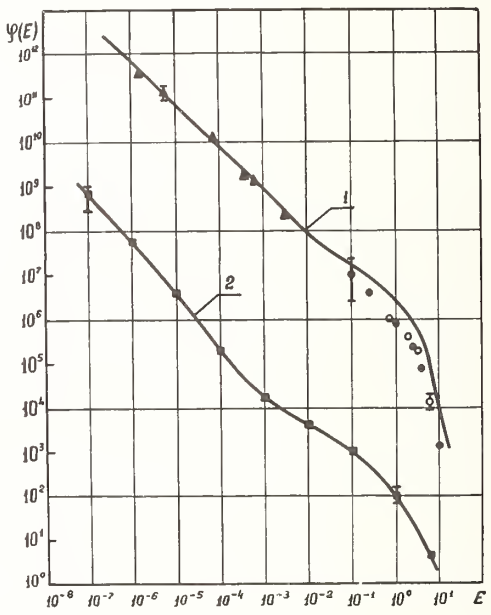

Fig. 2. Spectra of neutrons from the surface of moderator (1) and in the external beam (2) at a distance of 8 m from the reactor core (taken from ref. [3]).
E - neutron energy in MeV
$\varphi(E)$ - neutron flux in $cm^{-2}sec^{-1}$ eV^{-1} per a power of 1 MW, channel diameter being 20 cm.

are given Russian denotions.

Neutron channel for the measurements of double differential cross sections

The flight tube II terminates in the pavilion at a distance of 95 m from the reactor core. Here the spectrometer ДИН (DIN-2) with mechanical chopper is mounted by the Physics-Energy Institute (Obninsk, USSR[5]). Two modifications of the spectrometer allow to study inelastic neutron scattering under moderate resolution with a monochromatic neutron beam up to $10^7 cm^{-2}$ s^{-1} on the sample and under highest possible resolution

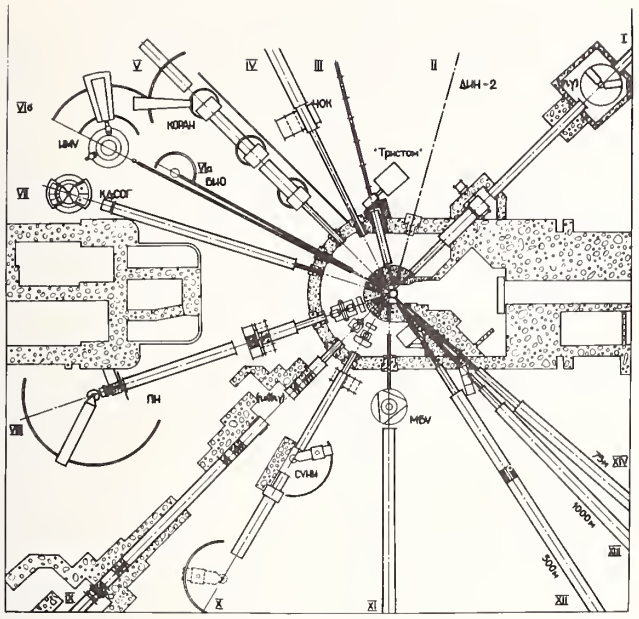

Fig. 3. Arrangement of neutron beams and spectrometers of IBR-2.

up to 10^{-7} eV at a neutron flux of 10^{4} $cm^{-2}s^{-1}$. The figure of merit of the spectrometer is better than that of other time-of-flight spectrometers by an order of magnitude and is comparable with the figure of merit of three-crystal spectrometers at high flux reactors. A broad program for investigations of quantum liquids and ideal crystals, as well as a program for applied research is developed. The latter includes the double differential cross section measurements for the moderator materials of thermal reactors in the temperature range 4 - 200 K.

Neutron channel for the experiments with ultracold neutrons

Experiments with ultracold neutrons (UCN) are performed in the lowest energy part of the maxwellian spectrum, i.e. up to $E_{bound} \sim 10^{-7}$ eV. Below E_{bound} neutrons are totally reflected at any angle of incidence and may be kept in closed vessels. Since the UCN portion in the thermal spectrum is small, i.e. about

$$\frac{1}{8}\,(V_{bound}/V_{th})^{4} \approx 10^{-11},$$

one needs high flux stationary or pulsed reactors to perform experiments with them. Several reviews, for example refs.[6-8], are devoted to these investigations started in Dubna and Munich, and then at some European research centres. Recent issues of BNL-325 already contain data on the cross sections of neutrons at energies ranging from 10^{-4} to 10^{-7} eV. The experiments revealed some uncommon UCN properties and more are still under investigation. But at present the use of UCN for the neutron properties study (such as the lifetime or electric dypole moment EDM) seem to be most interesting from the physical point of view. The search for EDM is directly connected with the T-violation problem in particle interactions. The so-called UCN confinement method for the EDM measurement proposed in ref.[9] was firstly employed in the Institute of Nuclear Physics of USSR Academy of Sciences (Gatchina). An upper EDM limit of 1.6×10^{-24} ecm[10] was obtained.

In Dubna a facility "TRISTOM" is constructed to be used on the neutron channel III of the IBR-2 reactor. Its expected EDM sensitivity will be at a level of 10^{-25} ecm[11]. The neutron channel III is designed for the extraction and guiding of UCN. A hydrogen-containing convertor cooled down to 20 K is to be used as an UCN source together with the neutron shutter to increase the UCN density inside the chamber of the Ramsey type magnetic resonance spectrometer.

Beams for the condensed matter and applied investigations

Seven horizontal channels will be employed (i.e. IV - VIII, X, XI) in the time-of-flight experiments and three inclined ones (not shown in Fig. 3) for neutron irradiation. Neutron beams IV,V,VI are equiped with a liquid hydrogen moderator at a maxwellian spectrum temperature of 50 K. Water moderators (their thickness can be varied from 35 to 55 mm) are mounted on other beams. The temperature of their maxwellian spectrum is 400 K. The program for condensed matter and biological research with the IBR-2 reactor is comprehensive, but, since it has no close connection with the topic of the present conference, it suffices to mention review papers[1,12].

The following installations (Fig.3) are being constructed and partly already built for the implementation of this program:

- spectrometer НОК (COK). To investigate by small angle diffusion neutron scattering the structure of biological crystals and macromolecules in solutions;
- spectrometer КОРА (CORA). To study inelastic thermal neutron scattering by the correlation time-of-flight spectroscopy method;
- diffractometers БИО (BIO). To perform neutron diffraction investigations on complex crystals. Apparatus ИМУ (IMU). To study the behaviour of the matter in pulsed magnetic fields by the time-of-flight diffraction method;
- spectrometers of inverted geometry КДСОГ (KDSOG), СУНИ (SUNI) with neutron monochromatization after scattering. To study the dynamics of organic crystals and energy levels of paramagnetic ions in crystals. The spectrometers will be installed at a distance of 100 m from the reactor and equipped with mirror neutron guides.

ПН - spectrometer of polarized thermal neutrons (PN) based on polarizing mirror neutron guides. Neutron beam will be polarized to 97% in the wavelength range 1 - 6 A at a flux of 10^{7} $cm^{-2}s^{-1}$ on the sample.

- apparatus МБУ (MBU) on the flight tube XI. To perform medical biological investigations with neutrons. This subject is a part of the topic of the present conference. As a preparative step the measurements of the characteristics of the specially designed neutron beam and some radiobiological research were carried out at the IBR-30 reactor. In Fig.4 from ref.[13] there are shown the conventional spectrum (1) and the spectrum (3) obtained after transmission of neutrons through the zirconium hydride and tungsten filters 4 cm and 2.5 cm thick, respectively. The average energy of neutrons transmitted through the filter increased up to 3 MeV and become about that of neutrons (5) from the beryllium target irradiated by deuterons at an energy of E_d=11 MeV. The radiation doses measured on IBR-30 at various filter thicknesses were 0.4 - 1 rad/min (neutrons) and 0.07 - 0.1 rad/min (γ-rays).

According to the results, for IBR-2 one expects to have up to 500 rad/min at a distance of 8 m. This will allow to achieve (using thicker filters) a neutron spectrum with everage energy of 6 MeV at reasonable doses of 50 rad/min. It is equivalent to neutron source at 15 MeV cyclotron with a deuteron current of 100 μA (curve 4). Such beam may serve for neutron diagnostics and maybe neutron therapy.

Neutron flight tube XI will be also equipped with a mirror neutron guide to perform elemental analysis by using capture γ-rays. It has advantages, if applied for the analysis of biological and other objects in comparison with activation method, since the intensity of sample irradiation decreases by a factor of 3 - 4

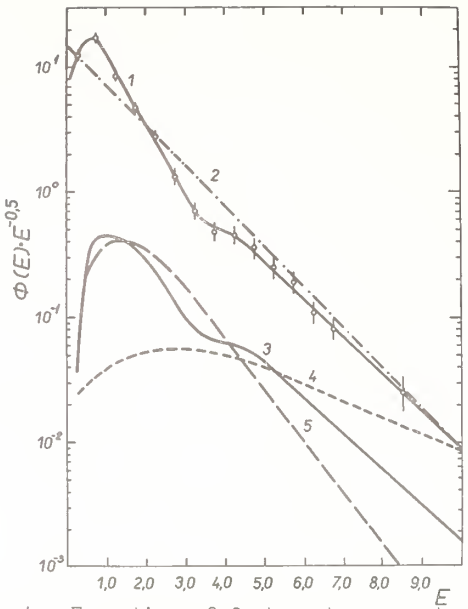

Fig.4. Formation of fast neutron spectra for the medical and biological research.

orders of magnitude. Maximal absolute sensitivity at a level of 10^{-9} g/l is expected for B,Gd, Sm.

In order to implement the materials research program the IBR-2 reactor will have three pneumatictransport systems, so that samples 14 mm in diameter and up to 40 mm long could be irradiated. Pneumatictransport channels are directed to the active core, reflector and moderator. The former provides a mean flux of 3.5×10^{14} $cm^{-2}s^{-1}$ of fast neutrons with energies E=1.5 MeV, instantaneous neutron flux being 7×10^{17} $cm^{-2}s^{-1}$. The irradiated samples will be sent to hot chambers or directly to physical installations. High neutron fluxes from IBR-2 may serve the needs of scientists studying the kinetics of radiation damages characterized by the relaxation time within the 10^{-1} - 10^{-4} sec interval and of those making material research for fusion reactors.

The pneumatictransport system will be also used in the activation analysis by fast and thermal neutrons. The experience acquired at IBR-30 in the express method of activation analysis with Ge(Li) detector[14] proves this field of applied research to be advantageous with the IBR-2 reactor also.

The same is true for the use of thermal neutron fluxes to study the distribution profiles of boron atoms in silicon and other materials. The detailed description of this method having high depth resolution is given in review[15].

III. Nuclear Physics Experiments

The IBR-2 reactor as a very powerful pulsed neutron source could be useful in the study of processes with very small neutron cross sections such as $n\alpha$- , $n\gamma\alpha$ -, n f-, etc. Long neutron pulses are sometimes advantageous, since the instantaneous loading of detectors is lower and slow detectors and secondary-ray spectrometers with moderate response times could be used.

Cross sections and spectra from $n\alpha$-, $n\gamma\alpha$- and $n\gamma$ -reactions

Nearly all experimental data on the structure of compound states (neutron resonances) available at present in the field of neutron spectroscopy contain mainly partial γ-widths of transitions to the ground or to a comparatively simple (few-quasiparticle) nuclear state. They give information only about the few-quasiparticle components of the wave function of compound states. The study of the probability of α-decay of neutron resonances and γ-transitions between nuclear compound states through $(n, \gamma\alpha)$ reaction may provide information about many particle components of the wave function of high excited nuclear states. The investigation of γ-transitions to collective states also serves this aim.

Up to now the resonance α-widths for about a dozen and half nuclei with $65 < A < 178$[16,17] were measured on the IBR-30 reactor. Experimental data obtained on average α-widths (Fig.5), on total α-widths and partial α-widths distributions (Fig.6) are well described in the frame of the statistical theory, the exceptions are the average α-widths of deformed nuclei and total α-widths distributions of J=4 resonances in ^{149}Sm. The amount of helium produced in some materials due to the (n, α) reaction was also estimated[18].

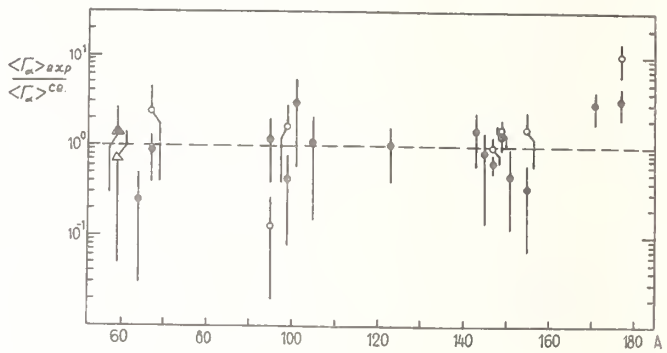

Fig.5. Comparison of experimental average α-widths with theoretical ones in dependence on nuclear mass number.

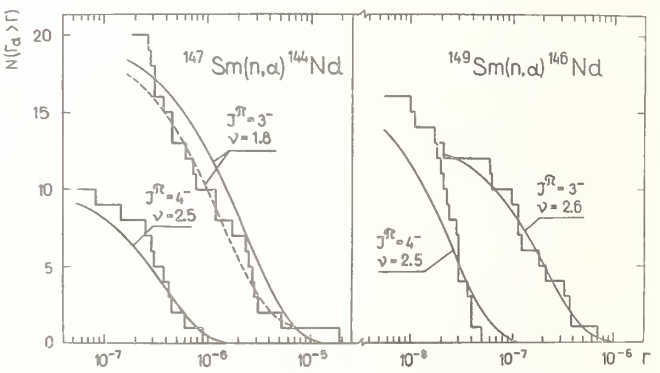

Fig.6. Distribution of partial widths of α-decay of the compound states of ^{144}Nd and ^{146}Nd with different spin J.
Hystograms - experiment;
Solid lines - theory.

With the employment of IBR-2 reactor in combination with LIU-30 the broader range of nuclei could be covered in the study of neutron resonance α-decay in order to explain why the cluster and optical model[17] did not describe satisfactorily the average α-widths of deformed nuclei. Further experiments to measure the (n, α) reaction yield will be made for some materials used in the construction of the reactors.

Experimental data on $\Gamma_{\gamma\alpha}$ in resonances with different spins obtained in the study of the two-step $(n, \gamma\alpha)$ process gave indication of the interesting phenomenon: the prevalence of M1 transitions between compound states[19]. They are the transitions from the 55 eV resonance to the states shown in Fig.7 by dotted lines. However, to be sure about the above mentioned prevalence one should perform the statistically more precise measurements of $\Gamma_{\gamma\alpha}$ in resonances with different J. The values which are now known: 0.16 ± 0.08 and 0.11 ± 0.08 meV for J=3 and 4, respectively. Since $\Gamma_{\gamma\alpha}$ in the $(n, \gamma\alpha)$ process scar-

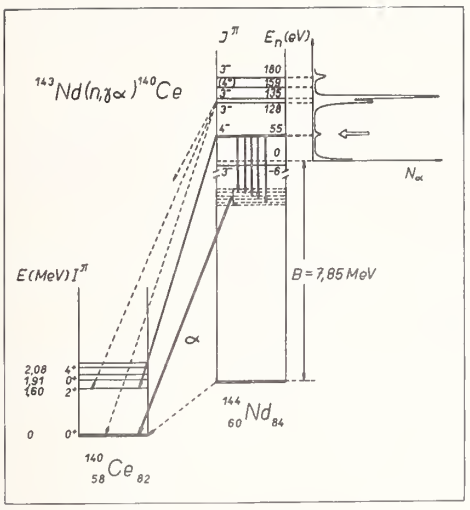

Fig. 7. Scheme for the (n, $\gamma\alpha$) process in ^{143}Nd.

cely changes from resonance to resonance with same spin(due to averaging over many intermediate states), the experiment may be made on 2-3 resonances, if high neutron fluxes were available.

The program for experiments on IBR-2 includes also the measurement of the ^{7}Be(n,2α) reaction cross section in the thermal and epithermal neutron energy range to investigate the parity conservation of nuclear forces[20]. The cross section of the reaction must be small due to parity selection rules. Besides, the target may contain a small (10^3-10^4 less than usual) number of nuclei, since beryllium-7 is radioactive ($T_{1/2}$=53.6 days). So, a very powerful neutron source is absolutely necessary. The IBR-2 reactor will allow to perform more complicate experiments than those with IBR-30. For example, the investigation of $\alpha\alpha$-angular correlations in the decay of ^{150}Sm compound states is planned. It will provide information about the contribution of partial α-transitions with different orbital momenta.

The γ-ray studies in (n,γ) reaction carried out in recent years revealed some deviations from the statistical theory in the description of the decay of highly excited[21] states. That is important for understanding the fragmentation of simple excitations over compound states. The different behaviour of fluctuations in the population of low-lying states in a region of A~100 (spherical nuclei, s-neutrons strength function S_o being minimal) and of A~150 (deformed and transition nuclei, maximum S_o) was established recently[22]. The IBR-2+LIU-30 complex will be used in the further study of the regularities in the population of nuclear states having definite structure, for example, octupole states with spin 3⁻ and others, and in the $\gamma\gamma$- cascade study by coincidence technique.

This part of the program on IBR-2 foresees the use of flight tubes I and IX (tangential flight tube). In order to investigate the average parameters of interaction of neutrons with nuclei, there will be installed Fe- (E=24 keV) and Sc- (E=2 keV) filters on the beams. The background conditions with filtered beams on a pulsed reactor may be improved by a factor of 2-3 orders of magnitude using the time-of-flight technique as compared with the stationary reactor facilities. The calculated intensity of the filtered beams on the fast neutron pulse reactor IBR-2 is equivalent to that from the thermal neutron stationary reactor with a power of ~ 50 MW.

Fission cross sections

Fission process study is being carried out in the Laboratory of Neutron Physics for several years. It will be continued with the IBR-2 + LIU-30 complex. The study goes in two directions. The first is the multiparameter measurement of slow-neutron-induced fission cross sections, i.e. the joint measurements of the kinetical energies of fission fragments, of the instantaneous γ-rays and neutron multiplicities and of the mass distribution of fragments. This will also serve for further improvement of nuclear data necessary for reactor calculations. The comparison of the above mentioned data for many resonances is interesting from the point of view of finding the spin dependence of different characteristics of fission and their correlations. Presently available data are not unambigous, because the variations of the above characteristics from resonance to resonance, if present, are about 1% or even less. So, the success of the experiments strongly depends on the intensity of neutron beams especially in the case of coincident events in different channels of the fission reaction. As is seen from the spectrum in Fig. 8 (the results obtained using fission

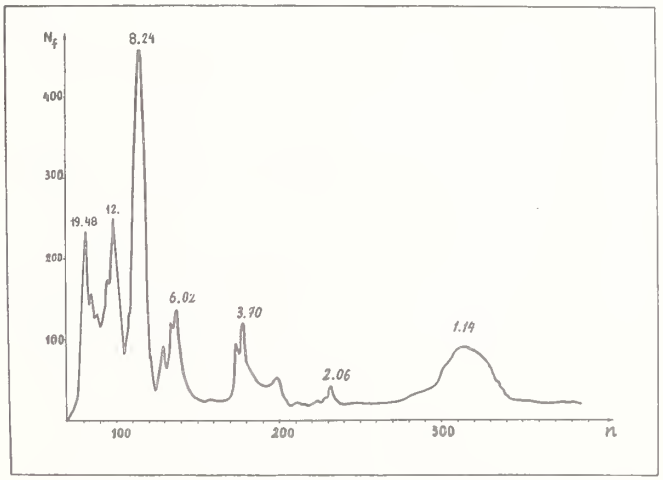

Fig. 8. Time-of-flight resonance spectrum obtained during 10 hrs of measurement with the ^{235}U target and fission fragments Si-detector, the flight path being 75 m, in IBR-30 mode of operation.

fragments Si-detector in ref.[23]) the IBR-2 reactor even at the first step of operation may provide sufficient intensities for such experiments, though not optimal resolution.

The study of the (n,γf) process, i.e. the process of fission after the emission of γ-quanta, is closely connected with the above. The possibility of its existence and calculation of its cross section are reported in ref.[24,25]. The process was searched for (see review papers[2 6]) by measuring the correlation of the multiplicity of fission γ-quanta, average number of neutrons per fission and resonance fission widths Γ_f. However, all data obtained represent only indirect experimental evidence. The direct method for the search of the(n,γf) process was developed in Dubna[27]. It is based on the registration of the X-ray quanta emitted as a result of the internal conversion of γ-quanta preceeding fission and detected in coincidence with a fission event. In Fig. 9 one may see the results obtained in ref [27]. The dependence of the X-ray yield per fission event R on resonance fission widths Γ_f is shown. Since R is proportional to $\Gamma_{\gamma f}$ and the latter (similarly to $\Gamma_{\gamma\alpha}$ under consideration above) is constant from resonance to resonance, the relative contribution of the (n,γf) process must decrease with increasing Γ_f. It seems this may take place (the obtained result $\Gamma_{\gamma f}$ = 2.1 $\pm^{1.2}_{1.7}$ meV), though to be sure one must acquire more data.

The second direction in the measurement of fission cross sections in JINR is connected with nuclear data

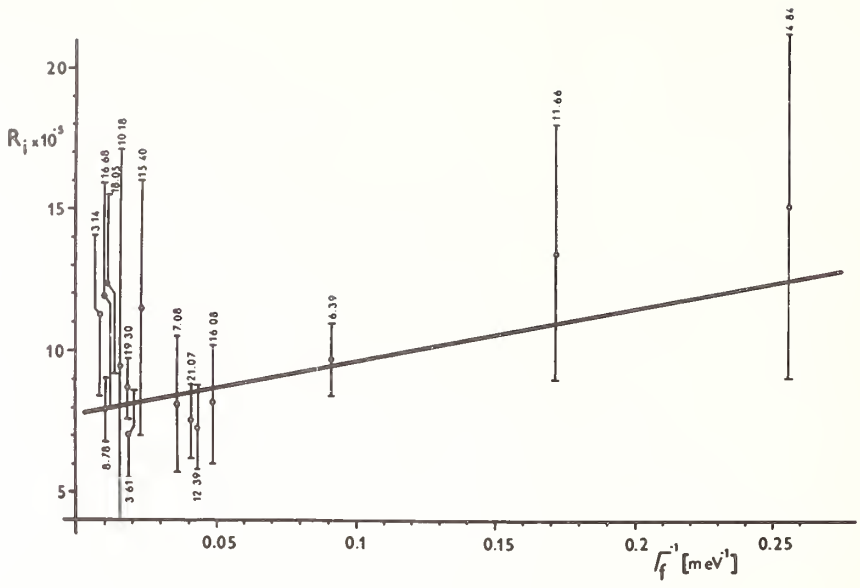

Fig. 9. Results of the (n, γ f) process study on ^{235}U during 260 hrs of measuring time with the IBR-30 in booster mode of operation.

needs for fast neutron reactor calculations. For several years already the Laboratory of Neutron Physics (Dubna) jointly with the Physics-Energy Institute (Obninsk) perform experiments in this field. They include the measurement of transmission functions and self-indication ratios for ^{235}U, ^{238}U, ^{239}Pu and the calculation on their basis of average group cross sections and resonance self-shielding factors [28]. The former performed for a wide range of sample thicknesses at energies from several eV to dozens keV give information about the self-shielding effects in cross sections that could not be obtained by even very precise high resolution cross section measurements made in limitted range of sample thicknesses. Recent ^{235}U and ^{239}Pu results are given in paper [29] contributed to the present conference. The work is to be continued with the IBR-2 + LIU-30 complex.

Precise (n n)- and (nγ)- cross section measurements in the few nucleon systems

The experimental study of the few body problem was initiated on the IBR reactor in 1966 with polarization experiments on an unambigous choice of (n d) scattering lengths[30]. Recent measurements performed with the IBR-30 reactor contributed much to this research. Since the theory of few nicleon systems now attends to nuclei consisting of four nucleons, it is interesting to measure (n^{3}He) scattering lengths. Experimentally they may in principle be obtained from a combination of data on total and coherent scattering cross sections. But the experiment is different due to the competing (n,p) absorption process having a large cross section of 5400 b.

The results first obtained in[31] for the cross section $\sigma_n(^3\mathrm{He})$ are shown in Fig. 10. Different points are taken at different pressures of the ^{3}He-gas in the target (minimal 30 mm Hg) and under different conditions. Fig. 11 presents the whole data on the basis of which one may (by the graphical method) obtain the scattering lengths discussed in ref.[32]. Crosses indicate theoretical results obtained by V.F.Kharchenko (Kiev Institute of Theoretical Physics) with different nucleon-nucleon potentials. As is seen one needs to lessen the uncertainty of data on scattering cross section σ_n and incoherent scattering cross section σ_{inc} available up to now only by the indirect method. The accuracy of σ_n and σ_{inc} is worse than that of the recently

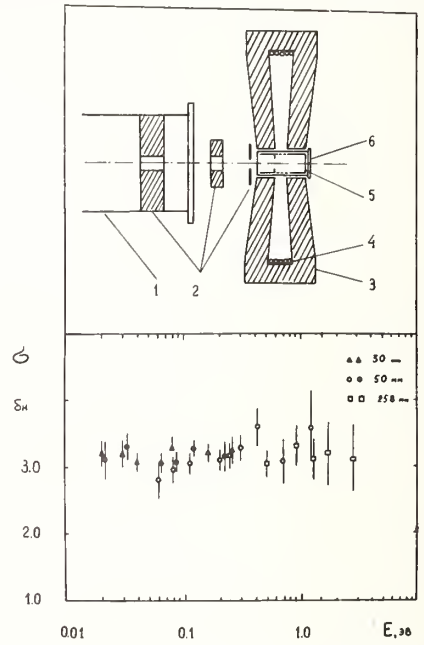

Fig. 10. Experimental lay-out and results obtained for the scattering cross section σ_n (^{3}He) (b) in dependence on neutron energy (eV).

obtained coherent scattering length result a_c[33]. The IBR-2 reactor will bring a possibility for more precise measurements of σ_n and of the direct measurement of σ_{inc} using polarized gaseous ^{3}He target.

The study of radiative neutron capture in ^{3}He is closely connected with the four nucleon problem, though up to now remained practivally unattended both experimentally and theoretically. The results obtained this year in Dubna are shown in Fig.12[34]. The accuracy is not high, but from the qualitative behaviour of the energy dependence one may conclude that at low energies the capture process is of the s-wave nature, while at higher energies - p-wave. The calculation of thermal cross section (M1 transition) were performed taking into account only S-states of ^{3}He and ^{4}He described with the simplest (gaussian) wave functions. The comparison of experimental and theoretical results allowed to estimate an admixture of the "mixed symmetry" state of 0.14%

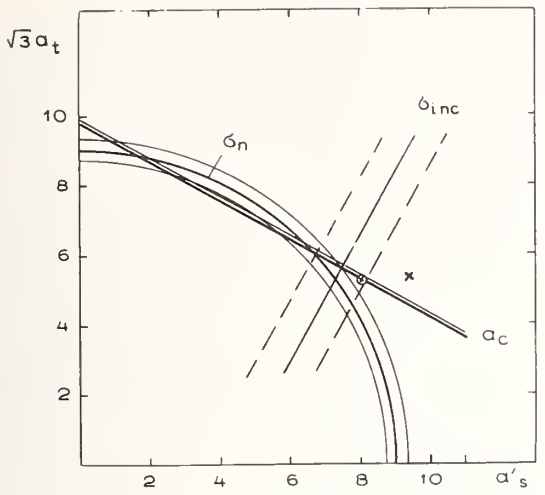

Fig. 11. Data for obtaining the triplet a_t and real part of the singlet a_s' components of scattering lengths in n^3He scattering.

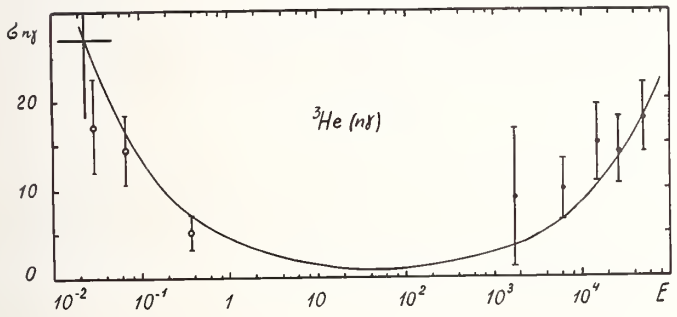

Fig. 12. Neutron radiative capture cross section by ^3He (μb) in dependence on neutron energy (eV).

in ^4He. Theoretical results become multi-meaning, if the D-component of the ^3He, ^4He ground states and various meson exchange currents[35] are taken into account. Thus to have a reliable theory one should perform more precise measurements of thermal cross section $\sigma_{n\gamma}(^3He)$. They are included in the program of experiments on IBR-2.

Precise measurements of the $D(n\gamma)$ radiation capture cross sections are also interesting from the point of view of meson exchange currents as well as of their importance for the reactor calculations. The first stage of measurements is reported in ref,[36] contributed to the present conference. Further measurements are included in the IBR-2 reactor research program. Then it will be possible to carry out a polarization experiment to determine separately the doublet and quartet component of the $D(n\gamma)$ reaction cross section.

Prospects for some other experiments after the start of LIU-30

The problem of the spin dependence of neutron cross section is under discussion for a long time already, but its experimental investigation encounters many methodical difficulties. The apparatus for the measurement of the total cross section of polarized neutrons with polarized nuclei installed at IBR-30 is shown in Fig.13. Its principle components are : the polarized proton target (4) as a neutron polarizer and the $^3He/^4He$ refrigerator (5) at a temperature down to 0.03 K for nuclear polarization. The method for the polarization of neutrons via transmission through the polarized proton tar-

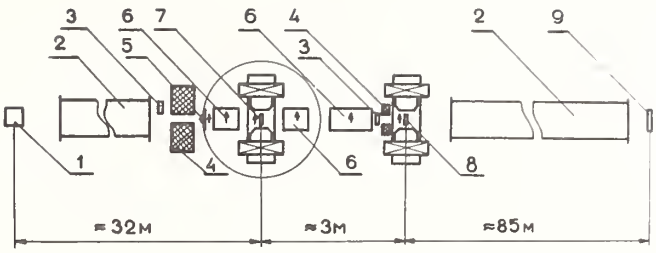

Fig. 13. Apparatus for measuring total cross sections of polarized neutrons with polarized nuclei.

get was developed in Dubna and then used in the Los Alamos and Oak Ridge Laboratories to measure the spins of resonances of fissionable nuclei[37]. In Dubna the rare earth nuclei were mainly investigated in the neutron transmission experiments[38]. As is seen from Fig.14 the

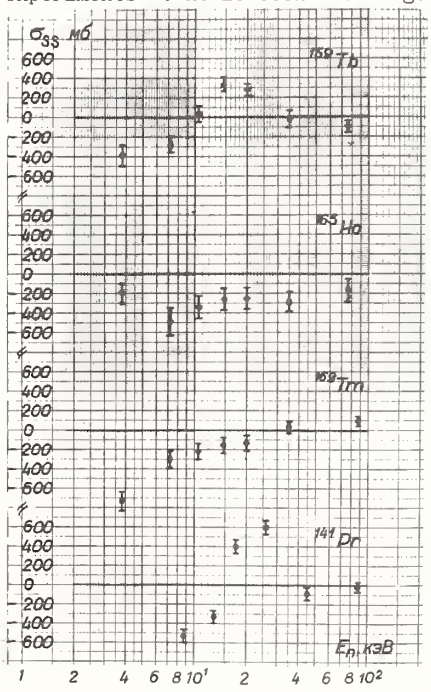

Fig. 14. Data on the spin-spin cross section σ_{ss} via neutron energy E for a number of rare earth nuclei.

nuclei investigated behave quite differently. This is difficult to explain with the introduction of the spin-dependent optical potential. Most probably the cross sections intermediate structure connected with spin value is responsible for that. For the further investigation of the problem one needs to perform the polarization measurements of partial neutron cross sections (scattering and capture cross sections). This will be possible in principle with the LIU-30 facility working in the regime of nonmultiplying target. As for the spin dependence of the neutron strength functions the Dubna-results show its not exceeding 10-15 % (if at all present) for the nuclei investigated.

The same $^3He/^4He$ refrigerator was used for the measurement of magnetic moments of neutron resonances. They were the first systematical investigations of that kind. The results are reported in ref.[39] and shown in Fig. 15. They reveal the collective properties of nuclear high excited states in agreement with theoretical predictions within the thermodynamical approach. The experiments planned for the IBR-2 + LIU-30 are aimed at further enlargement of the number of resonances under investigation in a nucleus and of the number of

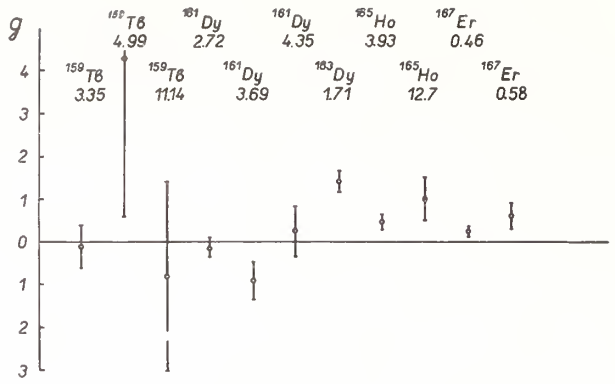

Fig. 15. Gyromagnetic ratios (g-factors) of neutron resonances in a number of nuclei obtained in the experiments with polarized nuclei.

nuclei.

In the near future it seems possible to obtain the new information about the deformation of nuclei excited to about neutron binding energy. Some experiments were done recently in Dubna[40] with an attempt to measure the variation of the mean square nuclear radius after excitation. The method of the isomeric shift of the neutron resonance was proposed and used. The shift ΔE between the resonance energies appearing in different chemical compounds may occur due to hyperfine interaction of the atom electrons with nuclear charge Z. It is described by the formula:

$$\Delta E = \frac{2\pi}{3} e^2 \cdot Z \cdot \Delta |\Psi(0)|^2 \cdot \Delta \langle R^2 \rangle$$

where $\Delta|\Psi(0)|^2$ is the difference in the electron densities of the nucleus between a pair of chemical compounds investigated. Theoretical prediction made by G.Bunatian (Dubna) $\Delta \langle R^2 \rangle \approx -0.1$ fm which leads to a small, but detectable resonance shift of $10^{-3}\,\Gamma$. The preliminary experimental result is $\Delta \langle R^2 \rangle = (-0.6 \pm 0.3)$ fm[40]. The measurements are performed with IBR-30. Their extension is planned for the complex, IBR-2+LIU-30.

IV Conclusions

In the present paper some trends of future investigation with IBR-2, mostly in the field of nuclear physics are reviewed. They include the neutron cross section measurements important both in the study of nuclear structure and in the determination of nuclear constants needed for reactor calculations. Applied fields of research with IBR-2 are outlined also. At the same time the review does not practically cover the investigation of condensed matters, though more than 50% of the experimental program for IBR-2 is devoted to them. The research program developed for the IBR-2 and LIU-30 facilities has the following principle directions:

- investigations in the field of condensed matters and molecular biology;
- studies of fundamental properties of the neutron;
- neutron cross section measurement for the study of highly excited states and nuclear reactions and for applied purposes;
- applied research by using nuclear methods.

In the first step of the IBR-2 operation (regime IBR-2) the investigations of condensed matters will prevail due to rather long times of pulse duration. However, the measurements of (n,α), (n,γ), $(n,\gamma\alpha)$, (n n), (n f) cross sections not requiring good resolution will be also done. The operation of IBR-2 in combination with LIU-30 (IBR-2+LIU-30 regime) will allow to employ shorter pulses more suitable for nuclear experiments. Further shortening of the pulse duration to 500 nsec - 50 nsec (LIU-30 nonmultiplying target regime) will give a possibility of neutron cross section measurements at neutron energies up to 10^5-10^6 eV and other experiments under good energy resolution.

The IBR-2 start-up at full power will give birth to a new generation of high intensity pulsed neutron sources. The need in such sources is now commonly agreed. The neutron fluxes of stationary reactors approached their technical and financial limits. The new generation of neutron sources will include together with the IBR-2 reactor the facilities on proton accelerators being designed or constructed. The IPNS (Argon Lab.) and SNS (Rutherford Lab.) facilities are planned for the condensed matter experiments with thermal and epithermal neutrons and the WNR source (with a coming storage ring) at the meson factory LAMPF to be used for nuclear investigations in a wide energy range.

The outlined possibilities for physical investigations with IBR-2 and LIU-30 are extensive, however, the experience of the pulse reactor IBR-30 operation proves them possible. The present paper is devoted to selected topics in the experimental program proposed for the IBR-2 reactor. Needs and pressures in the future, as well as further experience, may influence of course the actual research program on IBR-2.

References

1. V.D.Anan'ev, D.I.Blokhintsev, Yu.M.Bulkin et al., Pribory i Tehhnika Eksperimenta, No.5,p.17 (1977).
2. I.M.Frank, E.P.Shabalin, Harwell Conference on Neutron Physics and Nuclear Data, Proceed. p.113, Harwell, 1978.
3. V.D.Anan'ev, V.A.Arkhipov, A.I.Babaev et al., Atomnaja Energija, 46, issue 6, p.393, 1979.
4. V.V.Golikov, Zh.A.Kozlov, L.K.Kul'kin et al., JINR 3-5736, Dubna, 1971.
5. V.A.Parfenov, P.S.Klemyshev, I.G.Morozov, A.F.Pavlov, Neutron Inelastic Scattering, Proceed. of a Symp., Vienna, IAEA,p.87, 1978.
6. F.L.Shapiro, Nuclear Structure Study with Neutrons, Plenum Press, London, p.259, 1974.
7. V.I.Luschikov, Physics Today, 42, June 1977.
8. I.M.Frank, International School on Neutron Physics in Alushta, JINR D3-7991, p.19, Dubna 1977.
9. F.L.Shapiro, Uspekhi Fizicheskikh Nauk, 95, p.146, 1968.
10. I.S.Altarev, Yu.V.Borisov et al., Pis'ma JETF, 29, 794, 1979.
11. Yu.V.Taran, JINR P13-10067, P13-10068, Dubna, 1977.
12. Yu.M.Ostanevich, I.M.Frank, E.P.Shabalin, III International School on Neutron Physics, Alushta, JINR D3-11787, p.7, Dubna, 1978.
13. O.V.Komova, V.M.Nazarov, M.Stoica et. al., III Soveschanie po ispol'zovaniju novykh jaderno-fizicheskikh metodov dlja reshenija nauchno tekhnicheskikh i narodno-khoziajstvennykh zadach, Dubna, 1978.
14. M.V.Golovanov, N.A.Gundorin, S.F.Gundorina, et al., JINR 18-12262, Dubna 1979.
15. J.Bogancs et al., JINR-P3-11816, Dubna, 1978.
16. Yu.P.Popov, Sov.J. Nuclei and Particle, 2,issue 4, p. p.925, Moskva, Atomizdat, 1972.
17. Yu.P.Popov, W.I.Furman, III International School on Neutron Physics, p.390, JINR D3-11787, Dubna, 1978.

18. N.P.Balabanov, Yu.M.Gledenov, Yu.P.Popov, et al., "Nejtronnaja Fizika, p.3,p.126, FEI, Obninsk,1974.

19. W.I.Furman, K.Niedzwiedziuk, Yu.P.Popov, et al., Phys.Lett.,b44, p.465, 1973.

20. V.N.Andreev, II International School on Neutron Physics, p.96, JINR, D3-7991, Dubna, 1974.

21. S,F.Mughabghab, R.E.Chrien, Neutron Capture Gamma Ray Spectroscopy, ed.by R.E.Chrien, W.R.Kane, p.265 Plenum Press, N.Y., 1979.

22. V.A.Khitrov, Yu.P.Popov, A.M.Sukhovoj, Yu.S.Yazvitskij ibid, p.655.

23. T.B.Bakalov, A.A.Bogdzel, G.L.Ilchev et al., JINR P3-12796, Dubna, 1979.

24. V.Stavinskij, M.O.Shaker, Nucl.Phys.,62, p.667, 1965.

25. J.E.Lynn, Phys.Lett., 1B, p.31, 1965.

26. A.Michadon, Proceed. Int.Conf.on Interactions of Neutrons with Nuclei, Lowell, ERDA, Conf.-760715, p.641, 1976.

27. Z.Dlouhy, A.Duka-Zolyomi, J.Kristiak, Ts.Panteleev, JINR P3-12562, 1979.

28. A.A.Van'kov, Yu.V.Grigoriev V.F.Ukraintsev et al., FEI-905, Obninsk, 1979.

29. T.Bakalov, G.Ilchev, S.Toshkov et al., Paper contributed to the present Conference and JINR Preprint P3-12404, Dubna, 1979.

30. V.P.Alfimenkov, V.I.Luschikov, V.G.Nikolenko et al., Phys.Lett., 24B, p.151, 1967.

31. V.P.Alfimenkov, G.G.Akopian, J.Wierzbicki et al., Jad.Fiz, 25, 1145, 1977.

32. E.I.Sharapov, III International School on Neutron Physics, Alushta, JINR D3-11787, p.437, 1978.

33. H.Kaiser, H.Rauch, Badurek, et al., Z.Physik, A291, p.231, 1979.

34. V.P.Alfimenkov, S.B.Borzakov, G.G.Bunatian et al., JINR E15-12380, Dubna, 1979.

35. I.S.Towner, F.C.Khanna, Intern.Conf.on Nucl.Phys. with Electromagnetic Interactions, Mainz, Contributions, p.712, 1979.

36. V.P.Alfimenkov, S.B.Borzakov, J.Wierzbicki et al., Paper contributed to the present conference and JINR Preprint P3-12667, Dubna, 1979.

37. M.S.Moore, J.D.Moses, J.A.Keyworth et al.,C18, p.1328, 1978.

38. V.P.Alfimenkov, L.B.Pikelner, E.I.Sharapov, Jaderno-Fizicheskie issledovanija s orientirovannymi jadrami i poljarozovannymi nejtronami, Sov.J. Nuclei and Particles, v.11, issue 2, Moskva, Atomizdat, 1980.

39. V.P.Alfimenkov, L.Lason, Yu.D.Mareev, et al., Nucl.Phys., A267, p.172, 1976.

40. G.G.Akopian, V.A.Vagov, K.Zeidel, JINR P3-11740, Dubna, 1978.

THERMAL NEUTRON CAPTURE CROSS SECTION IN DEUTERIUM

V.P.Alfimenkov, S.B.Borzakov, J.Wierzbicki, B.P.Osipenko, L.B.Pikelner, V.G.Tishin, E.I.Sharapov
Laboratory of Neutron Physics, Joint Institute for Nuclear Research, Dubna, USSR

The radiative thermal nD capture cross section σ_D was measured by the time-of-flight method at the IBR-30 pulsed reactor using Ge(Li) detector, D_2O water sample ant the σ_{Cl} thermal cross section as the standard. The result 487(24) μb is in favour of the theoretical value found in the frame of the three body problem.

[D(n, γ), radiative cross section, thermal neutron capture]

Thermal neutron capture cross section in deuterium σ_D is both of applied and theoretical interest. Heavy water is the common moderator used in nuclear reactors. The accuracy of neutron absorbtion calculations for such moderators depends on the uncertainty of the experimental value of σ_D. The nD capture cross section can be obtained within the few nucleon system theory by sophisticated methods. The comparison with experiment is then necessary to estimate the contribution of meson exchange currents and of admixture states in the triton total wave function.

Meanwhile the modern data on σ_D are contraversary. Most precise values were obtained with activation method by measuring the yield of tritium. But even there the difference between the results (0.57±0.01 mb[1] and 0.520±0.009[2]) much exceeds the experimental accuracy. Data obtained with other methods : 0.60±0.05 [3] and 0.353±0.035 mb[4] (γ-yield from the D(n, γ) reactionwas measured using the NaI(Tl) crystal), and 0.37±0.12 mb (reported in Neutron Cross Section Data, BNL-325 (1964) from the measurement of the diffusion length in heavy water[5]) are less precise.

In the reported here experiment we tried to determine σ_D by measuring the γ-yield from the D(n,γ) reaction using the Ge(Li) detector. The high energy resolution of the spectrometer with Ge(Li) detector helped to avoid the background difficulties usual in the measurement of small cross sections. The measurements were performed by the time-of-flight method at the IBR-30 pulsed reactor, mean power being 20 kW, pulse repetition rate 4 sec^{-1} . The flight path was 33 m. The experimental lay-out is shown in fig. 1. The beam of neutrons 70 x 50 mm was formed by the collimators 1 and 2. The sample 3 was heavy water of a volume of 247.5 ml in the thin glass air-tight container. It was shielded by Li^6F layer 1 cm thick to prevent thermal neutrons from leaving the sample. The coaxial Ge(Li) detector 4 of a volume of 55 cm^3 was mounted at a distance of 16 cm from the beam axis. It was shielded from fast neutrons and γ-rays as is shown in fig.1. Spectra were measured with amplitude analyser in the time window corresponding to incident neutron energy

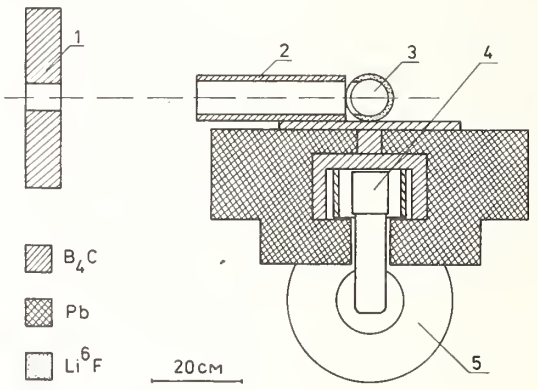

Fig.1. Experimental lay-out for the measurement of the effective nD capture cross section.

from 100 to 15 meV. The energy resolution of the Ge(Li) detector in the neutron beam was 9 keV at an energy of 5-6 MeV. The standard samples were H_2O and NaCl introduced in small quantities in D_2O (99.75 mol %). Then the following relationship between effective cross sections σ_D and σ_S (S -standard sample) holds:

$$\frac{\sigma_D}{\sigma_S} = \frac{\sum N_D}{\sum N_S} \frac{n_S}{n_D} \frac{\varepsilon_S}{\varepsilon_D} \qquad (1)$$

where N_D and N_S are the sums of detector counts under γ-lines, n_S/n_D and $\varepsilon_S/\varepsilon_D$ are the ratios of corresponding concentrations and registration efficiency. In eq.(1) there are no terms responcible for experimental geometry and normalization, since the measurements with the standard and investigated sample are performed simultaneously and under the same conditions. Systematical errors of $\varepsilon_S/\varepsilon_D$ may, however, occur, if the standard γ-line energy is considerably different from investigated, i.e. from E_D = 6.26 MeV. It has just may happened due to the use of the proton line E_H = 2.23 MeV. Therefore, the line E_{Cl} = 6.110 MeV is preferable, though σ_{Cl} accuracy as a standard is less

than that of σ_H. As recently was reported in [6] the partial yield for the 6110 keV line is $I_\gamma = 0.198 \pm 0.005$ at a total capture cross section of 33.2 ± 0.5 b, which gives us the partial cross section $\sigma_{Cl} = 6.57 \pm 0.19$ b.

The introduction of NaCl increased the background under the line E_D=6.26 MeV. Therefore, we undertook two runs of measurements. First, the yield from the E_D line was measured with respect to the E_H line using the solution 238.9 ml D_2O + 8.6 ml H_2O. Then, 1.000 g of NaCl was introduced and the measurement repeated. In this procedure the proton line E_H was the monitor one. The obtained spectra are shown in fig.2 for the region of double escape peaks of 6.26 and 6.11 lines and in fig.3 for the total energy peak 2.23 MeV.

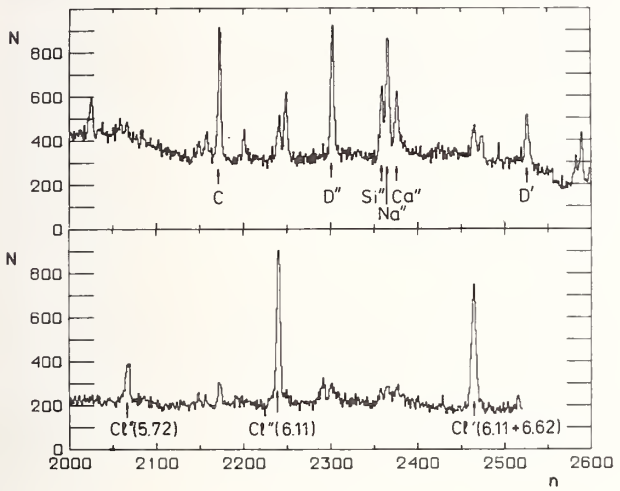

Fig.2. Gamma-ray spectra obtained with the sample

$D_2O+NaCl+H_2O$ (below)

D_2O+H_2O (above)

n is the number of the amplitude analyser channel (energy width being 2.28 keV), N is the number of detector counts after 75 hours of measurement (above), after 11 hours of measurement (below).

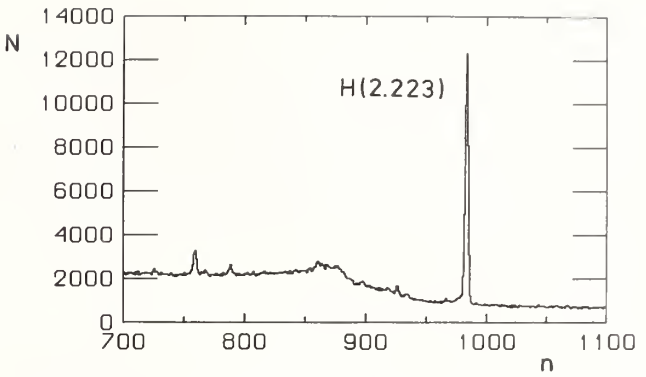

Fig.3. Energy spectrum obtained with the sample D_2O+H_2O near 2.2 MeV

The experimental value for it was found to be equal to

$$(7.41 \pm 0.37) \cdot 10^{-5}$$

The cross section of the radiative thermal capture by deuterons we searched for was obtained to be $\sigma_D = 487 \pm 24$ μb using the partial cross section $\sigma_{Cl} = 6.57 \pm 0.19$ b. It is the preliminary result. The statistical error indicated will be reduced by further collecting the data. The systematical error of the method is limited by the uncertainty of σ_{Cl} as a standard being equal to 2.6 %.

Table 1 enlists present data on σ_D. As is seen we managed to achieve better accuracy of $n\gamma$ measurements even at the first stage of the experiment.

The value we obtained is a little smaller than that from a later paper[2]. But as it was mentioned the result is preliminary and final conclusion will be made when the measurements are completed.

It is interesting to compare the experimental and theoretical estimates. The latter are found in the frame of the dispersion theory[7] and by solving the Fadeev equation[8] using the separable approach. The system

Table 1. Results of σ_D measurements

year	1947	1952	1963	1963	1968	1979
σ_D mb	0.37(12)	0.570(10)	0353(35)	0.600(50)	0.520(9)	0.487(24)
method	diff. length	activation	$n\gamma$	$n\gamma$	activation	$n\gamma$
paper	5	1	4	3	2	present paper

From the two equations similar to eq.(1) one obtains the ratio:

$$\frac{\sigma_D}{\sigma_{Cl}} = \frac{(\sum N_D / \sum N_H)\, D_2O}{(\sum N_{Cl} / \sum N_H)\, D_2O+NaCl} \cdot \frac{n_{Cl}}{n_D} \qquad (2)$$

^{2}H+n formed in neutron capture evidently may have at L=0 the total spin and parity $J=3/2^+$ (quartet channel) or $J=1/2^+$ (double channel). In principle, magnetic dipole transition to the gorund state of triton $I=1/2^+$ may take place in both cases. However, the effective cross section of this process is hindered by some sym-

metry selection rules. The magnetic transition in the D(n, γ) reaction (similar to ^{3}He(n, γ) reaction in[9]) is allowed only between the states with symmetrical spin wave functions. The latter is present in triton, if it has an admixture of S'-states, i.e. the state with mixed symmetry. The weight of S'-states in the total wave function of triton is taken within 1-2% in the the theoretical papers mentioned. Calculation was performed either with or without account for the meson exchange currents.

Table 2. Calculated σ_D values.

Authors	σ_D mb free moments	σ_D mb meson exchange
Phillips [7]	0.15	0.55
Hadjimichael [8]	0.29	0.52±0.05

As is seen from Table 2 the latter case gives larger values. It is interesting to note that the calculated value in the case of meson exchange increases due to the doublet component. Therefore, the polarization technique, which allows separate determination of the doublet and quartet components may serve for the consistent verification of calculated values.

References

1. L.Kaplan, C.R.Ringo, K.E.Wilzbach, Phys.Rev., 87, 785 (1952).
2. J.S.Merritt, J.G.V.Taylor, A.W.Boyd, Nucl.Sci.Eng., 34, 195 (1968).
3. E.T.Jurney, H.T.Motz, Preprint ANL-6797, 1963,p.236.
4. C.C.Trail, S.Raboy, Preprint ANL-6797,1963,p.247.
5. B.W.Sargent, D.V.Booner, P.E.Cavanagh, H.G.Hereward, N.J.Niemi, Can.J.Research, A25, 134 (1947).
6. M.L.Stelts, R.E.Chrien, Nucl.Instr.Meth., 155, 233 (1978).
7. A.C.Phillips, Nucl.Phys.,A184, 337 (1972).
8. E.Hadjimichael, Phys.Rev.Lett., 31, 183 (1973).
9. V.P.Alfimenkov, S.B.Borzakov, G.G.Bunatian, J.Wierzbicki, L.B.Pikelner, E.I.Sharapov, JINR E15-12380, Dubna 1979.

STATUS OF GAMMA RAY PRODUCTION CROSS SECTION DATA

K. Sugiyama
Department of Nuclear Engineering, Tohoku University
Aramaki-Aoba, Sendai, 980, JAPAN

The gamma rays produced by the interaction of neutrons with matter are important aspect of problem concerning the utilization of nuclear energy. This paper presents a review of the gamma ray production cross sections in neutron energy of MeV; experimental measurements and theoretical calculations. Emphasis is given to the applied purpose rather than the nuclear structure studies described by van Heerden at Harwell Conference on Neutron Physics and Nuclear Data last year. Current measurements are discussed not only the discrete lines but continuum fractions of the gamma rays. Some efforts on the theoretical calculations are presented for the explanations of the data.

[(n,xγ) cross sections, fast neutron, gamma rays of discrete and continuum]

Introduction

Study of the gamma rays produced by neutron interaction with matter has been made since the discovery of neutron. A number of papers have been presented in the past and have played an important part for the development of nuclear physics. The analysis of cross sections and angular distributions of the gamma rays of discrete energies following the inelastic scattering of fast neutrons and a comparison with the theoretical calculations provide a good tool for the study of spins and parities of nuclear excited states. Recent survey on this point of view has been given by van Heerden[1] at Harwell Conference on Neutron Physics and Nuclear Data last year.

Some problems of the gamma rays will be important so far as the neutron is concerned; fission and fusion reactor shielding, radiation heating and radiation dose. Accurate gamma ray production cross sections are required to permit calculation of the total radiation fields where neutron are transported through various assemblies.[2] A survey on the gamma ray production and the evaluation of the cross sections has been presented by Young[3] at the 1975 conference on this series.

There exist some unresolved weak gamma rays (continuum components) as well as the resolved gamma rays (discrete lines) in the photon spectrum emitted from the interactions of neutrons with matter. The total (the sum of the above two parts) gamma rays should be studied for the engineering purpose. The present paper describes the status of the production cross sections of the gamma rays caused by fast neutron interaction.

Status of the Cross Section Measurement

There are two kinds of fast neutron sources usefull for the cross section measurements; the monoenergetic and the white. The monoenergetic neutrons produced with Van de Graaff accelerators have been used for the study of nuclear structures by means of the (n,n'γ) reactions. The white spectrum neutrons produced by bremsstrahlung from an electron linear accelerator were proposed for measuring the cross sections of the (n,xγ) reactions by Orphan et al.[4] at GRT in 1969. There have been some discussions about the merit and demerit of the neutron sources in order to obtain the gamma ray production cross sections.[5] Pulsed neutrons from cyclotron machine were also used for the cross section measurements.[6] There is little to choose among these neutron sources. It should be understood that these techniques complement each other.

The measurements using the monoenergetic neutrons have also been performing at several experimental groups aimed at engineering, and the production cross sections of the resolved gamma rays were reported .[7~12] Almost of these papers did not present the production cross section of the continuum components. Efforts were put on higher resolutions for the individual lines and on more accurate measurements for absolute values of the cross section.

Developments of the Ge(Li) detectors have brought higher resolution data for cross sections. It should be noted that some experimental data were reported relative to standard cross section values such as the 846 keV gamma ray from the Fe(n,n'γ) reaction. Some authors,[13~16] however, have pointed out that the differential cross sections of the individual gamma rays exhibited severe fluctuations of values varying with incident neutron energies which has been predicted from the inelastic scattering cross sections of neutrons. The discrepancies of the production cross sections of the 846 keV gamma ray obtained by several experimental groups have been discussed by Young.[3] It should be also checked what different methods were employed for neutron monitoring, gamma ray detection and unfolding techniques as well as neutron sources. From different calibration of neutron energy, the accuracy of the energy has the uncertainty of several tenth- to hundred-keV. The cross section measurement for engineering use should be performed on an absolute value for that reaction.

Experimental data of the gamma ray production cross sections for the engineering purpose have been presented at the 1971 Knoxville conference of this series by Voss et al.[13] of KFK, Hoot et al.[17] of GRT, and Dickens et al.[18] of ORNL. It is interesting that all these measurements started at the same time. Voss et al. illustrated the detailed cross sections from near threshold to MeV region for several individual gamma rays. Hoot et al. stressed the technique based on an electron linear accelerator pulsed neutron source with a system consisted of time-of-flight and Ge(Li) detector, for the measurements of the secondary gamma rays from iron and aluminum at neutron energies from 0.85 to 16 MeV from a Ta-Be target. It was found from an examination of the secondary gamma ray spectra that the gamma ray production cross sections measured for discrete lines represented only a fraction of the total gamma ray production cross section. For the incident neutron energy interval 6.0 to 7.5 MeV, the total gamma ray production cross section for 27 lines from the Fe(n,n'γ) reactions was 2.2 b in comparison with the averaged value 4.3 b which as obtained by Drake et al.[10] who have unfolded their gamma ray spectra measured with a NaI(Tl) detector. Hoot et al. pointed out it is important that the cross section of the many weak lines be accounted for. It was shown that the continuum contribution to the cross section was about a factor of three greater than that from resolved gamma lines for the neutron energy interval from 12 to 17 MeV.

A precise measurement of the discrete lines is

important for the nuclear study of the low-lying excited states. The continuum conponent must not be disregarded for the engineering purposes such as radiation shielding, radiation heating and radiation dose estimations. More details will be described latter.

GRT-IRT group has continued the measurements of the cross sections for C, N, O, Al, Si, Fe and Cu due to interaction of the white neutrons from low energy to 20 MeV.[19] Gamma rays from the ring shaped sample at an angle of about 125° with respect to the incident neutron beam were measured with Ge(Li) detector placed on center line of the neutron flight path.

Comprehensive study for a variety of elements at the ORNL electron linear accelerator facility has started in 1972. A number of experimental data for neutron energies from 0.7 to 20 MeV and gamma ray energies from 0.3 to 10 MeV have been presented for twenty-two elements (Li, C, N, F, Mg, Al, Si, Ca, V, Cr, Fe, Ni, Cu, Zn, Nb, Mo, Ag, Sn, Ta, Au, and Pb).[20] The measurements from the plate shaped sample were made using a heavily shielded NaI(Tl) detector at 125° with respect to the neutron beam line.

The ORNL group has moreover developed a technique in which the production of secondary neutrons and gamma rays from the ring sample were determined by unfolding the pulse height distribution observed in a NE-213 liquid organic scintillation spectrometer.[21] Each event in the scintillation detector are identified as either a neutron or gamma ray by means of a pulse shape discrimination system. The poor energy resolution of the detector[∿30% compared to 7% of NaI(Tl) and 0.003% of Ge(Li) at 1 MeV] does not provide the cross sections of the discrete gamma rays, the total (summed) cross section of the gamma ray production at angle (127°) is only obtained by means of this method. This result allows some comprehensive checking the sum of the differential cross sections for resolved and unresolved (continuum) gamma rays. The technique would be valuable in the data required for neutron transport application since only moderate energy resolution is needed in the field.

Most experimental workers are interesting in the raw data such as pulse height distribution measured by gamma ray detectors. Typical examples which were taken by a NaI(Tl) and Ge(Li) detectors are shown in Figs. 1 to 4. These figures are taken from ref. 10,

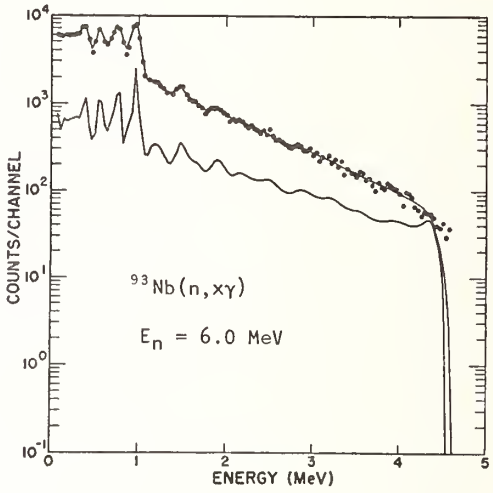

Fig. 10. Gamma-ray pulse-height spectrum and the unfolded solution for 6.0-MeV neutron bombardment of niobium. (Drake et al. 1970)[10]

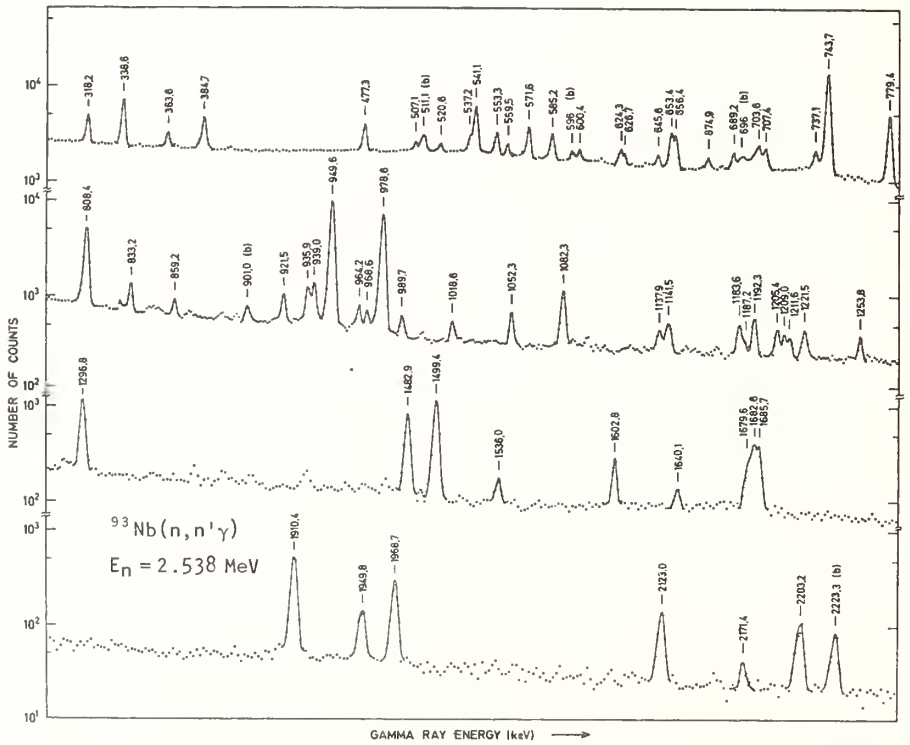

Fig. 2. The gamma ray spectrum produced by inelastic scattering of 2.5 MeV neutrons in ^{93}Nb, measured with Ge(Li) detector. Gamma ray energies are given in keV. (van Heerden and McMurray 1973)[22]

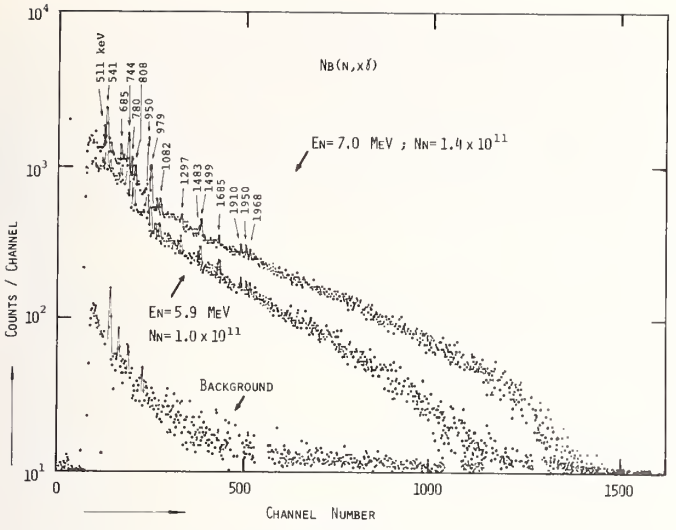

Fig. 3. Gamma ray pulse height spectra from niobium produced by neutron energies 5.9 MeV (lower) and 7.0 MeV (upper) obtained with Ge(Li) detector. Neutron monitoring counts are also shown. (Hino et al. 1979)[12]

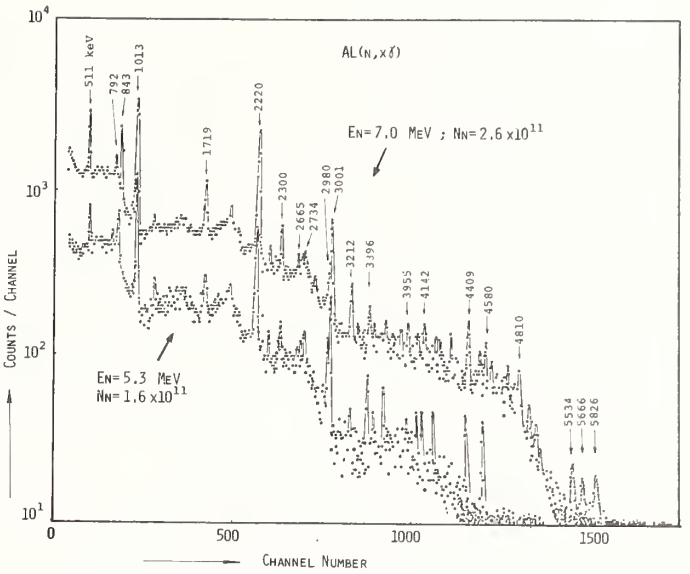

Fig. 4. Gamma ray pulse height spectra from aluminum taken similar to Fig. 3. (Hino et al. 1970)[12]

22 and 23. In the papers aimed at nuclear structure study, emphases are given for individual peaks in the pulse height distribution as shown in Fig. 2. The weak peaks are not prominent even if there exist considerable numbers of gamma rays. It is, however, found that the weak gamma rays should not be ignored as seen in Fig. 1, 3 and 4. The unresolved components become more prominent as the neutron energy or atomic number of material is increased.

The techniques of the neutron monitoring have been improved by means of employments of organic scinillator with neutron-gamma ray discrimination and TOF systems. It is obvious that undesired neutrons from scattering by surrounding materials were ignored to some extent. Efforts have been put on the correction of multiple scattering of neutrons in the sample. The uncertainty in the neutron fluence incident on the sample was improved to below 5 ∿ 6%. For the white neutron source, the uncertainty varies from ∿5 % below 10 MeV to ∿10 % above 10 MeV because of low intensity at high neutron energy region. The large uncertainty above 10 MeV would be due to poor knowledge of neutron cross sections for carbon in the organic scintillator.

Development of the gamma ray detecting system such as one with high resolution, heavily shielded, time gating of one employing a NaI(Tl) anti-Compton annulus counter have brought about considerable suppression of background gamma rays in the energy spectra. The uncertainty in the efficiency of the gamma ray detector comes to below 4 ∿ 6% except for high energy gamma rays. This results in the uncertainty in the extraction of the intensities of the gamma rays to about 5% for the strong isolated peaks and 30% for the weak transitions.

The resultant uncertainty in the differential gamma ray production cross sections have been reported to be below 10% for the strong isolated gamma rays and to be larger for the weak gamma rays which depend on intensities. For the unfolded data, it is impossible to clearly determine the uncertainty. The overall uncertainty in the measurements, apart from background determination and counting statistics, is estimated to be 10 ∿ 15%. Rather poor neutron intensity above 10 MeV in the white neutron sources results in poor statistics, and large uncertinty in the cross sections follow. The cross section measurement at 14 MeV using D-T neutron source from a small accelerator are valuable as a complementary method to the white neutron source. Imrovement in the uncertainty of detecting efficiency is expected to yield more accurate cross sections.

Status of Experimental Data

After the analysis of the pulse height distribution, the gamma ray production cross section is derived. The individual peaks are analyzed and the counts under the peaks are computed in order to obtain the production cross sections of the resolved gamma rays. The cross sections of the discrete gamma rays are reported by a number of authors. No detailed description for the individual gamma rays is given in the present review.

In measurements with the NaI(Tl) detector, the resulting pulse height disributions are unfolded and are converted to the gamma ray energy spectrum using the detector response functions. The unfolded results were reported for the measurements of several elements by Drake et al.[10] The result for niobium at incident neutron energy 6.0 MeV are shown in Fig. 1. The production cross sections of the composite peaks of the individual gamma rays and continuum conponents were derived by means of this technique.

The unfolding technique has been followed by several suthors and the differential cross sections for the weak and the continuum gamma rays were directly derived from the pulse height distributions meaured with NaI(Tl), Ge(Li) or NE-213 detectors. There are, however, some difficulties in application of the unfolding technique; they are "oscillation" and error estimations in the obtained spectrum. This is the same feature as unfolding results in neutron energy spectrum with the NE-213 liquid scintillator.

The GRT-IRT and Tohoku university groups unfolded the residual distribution from which was subtracted the resolved peaks from the total pulse height distribution in order to obtain the continuum component.

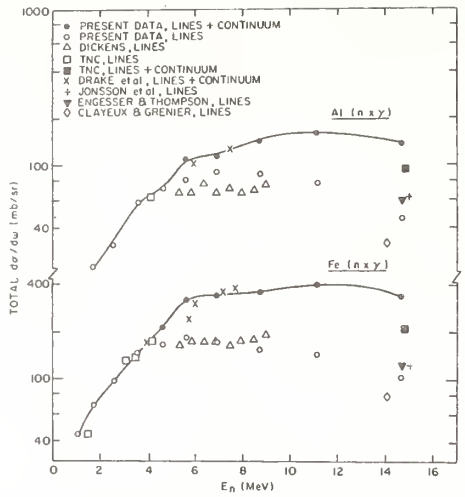

Fig. 5. Total γ-ray production cross sections for $Al(n,x\gamma)$ reactions (upper) and for $Fe(n,x\gamma)$ reactions (lower). The cross sections for discrete lines and for the sum of discrete and continuum γ rays are compared to previous results. A smooth curve connects the present data points for the sum of discrete and continuum γ rays.
(Orphan et al. 1971)[17]

The results of the production cross sections for the $Al(n,x\gamma)$ and for the $Fe(n,x\gamma)$ reactions in neutron energy region from 1 to 15 MeV are shown in Fig. 5 which was taken from the Trans. Am. Nucl. Soc. 14, 897 (1971). It is obvious that the continuum components become significant for incident neutron energy greater than about 5 MeV. Results by Tohoku group are also shown in Fig. 6. The continuum contiribution to the total gamma ray production cross sections were found to be 67 % for Al, and 70 % for Fe near 15 MeV in GRT data, and this contributions becomes large in heavier elements (over 60%) and the higher the neutron energy becomes the more the contribution becomes significant for light elements.

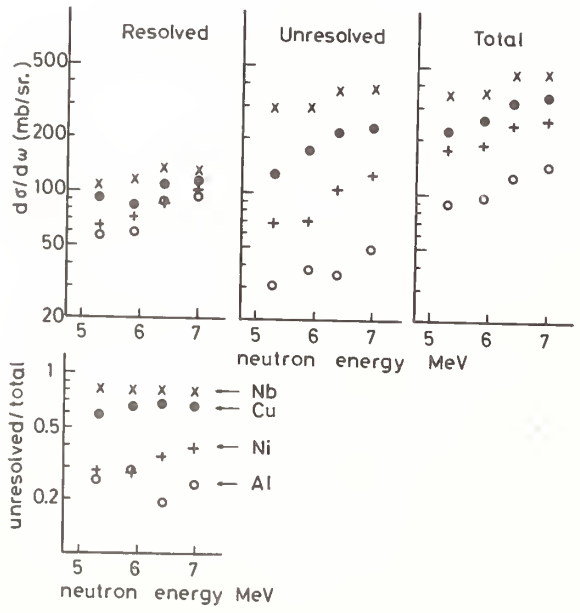

Fig. 6. Differential production cross sections of the resolved, the continuum and the total (summed) gamma rays as a function of incident neutron energy for Al, Ni, Cu and Nb. The ratios of the continuum to the total are also shown. (Hino et al. 1978)[23]

The double differntial cross sections, $d^2\sigma/d\omega dE$, which give the gamma ray spectra were derived by the ORNL group, over a wide energy range of incident neutrons and wide region of atomic number. The examples of the ORNL data are shown in Figs. 7 and 8. Because of poor energy resolution of the NaI(Tl) detector and the bunched bins varying with the energies of gamma rays, the discrete gamma rays are not separated. The summed cross

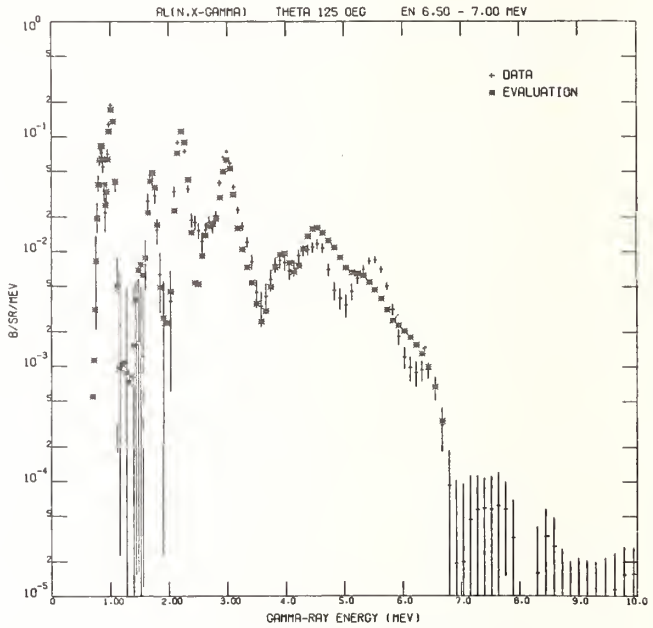

Fig. 7. Doubly differential cross section for aluminum resulting from unfolding the pulse height spectrum obtained with a NaI(Tl) detector in neutron energy from 6.5 to 7.0 MeV. Evaluated data by Young and Foster (LA-4726) is also shown. This figure is taken from Dickens et al. ORNL/TM-5219 (1973)

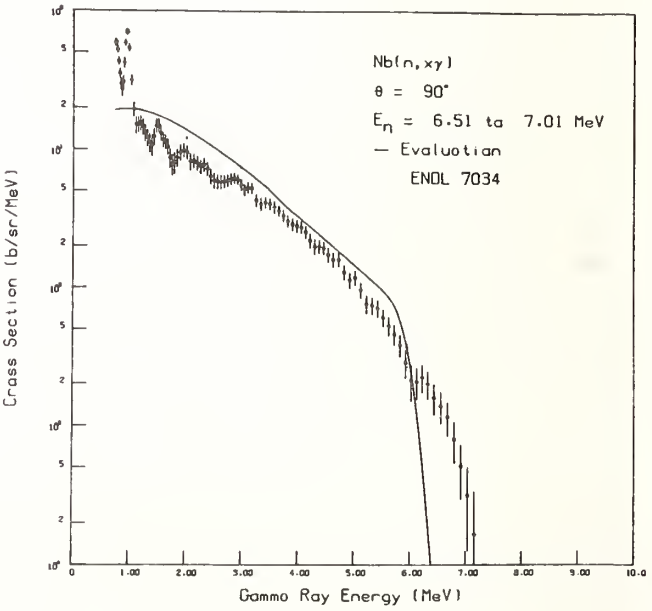

Fig. 8. Doubly differential cross section for niobium resulting of the same as Fig. 7. This figure is taken from Dickens et al. ORNL/TM-4972 (1975)

sections of the discrete lines placed into 100 keV bins, and the unfolded continuum component which are derived from the Ge(Li) detector by the Tohoku group[12] are presented in Figs. 9 and 10. For higher neutron energies, the cross sections are illustrated in Figs. 11 and 12. These are measured with the NaI(Tl)[23] and NE-213 organic scintillator with neutron-gamma discrimination technique.[24] The gamma ray energy bin is not clear for the latter data.

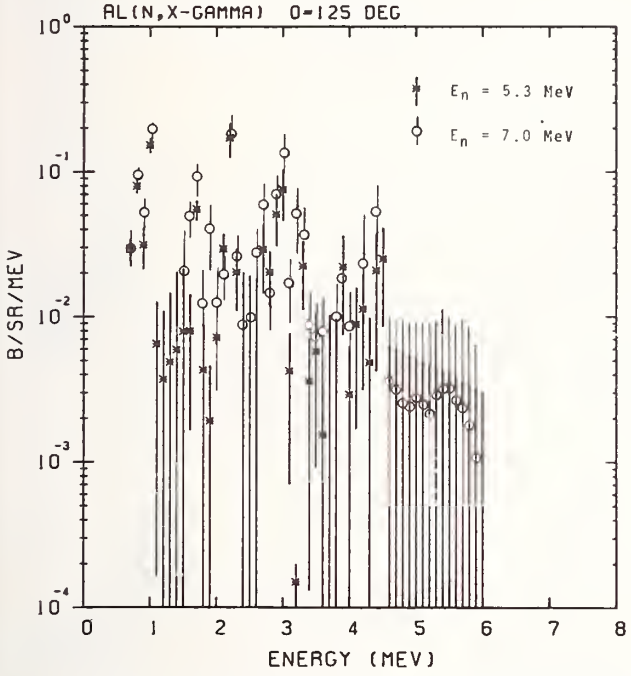

Fig. 9. Doubly differential cross section for aluminum resulting from unfolding the pulse height spectra obtained with Ge(Li) detector as shown in Fig. 4.. (Hino et al. 1979)[12]

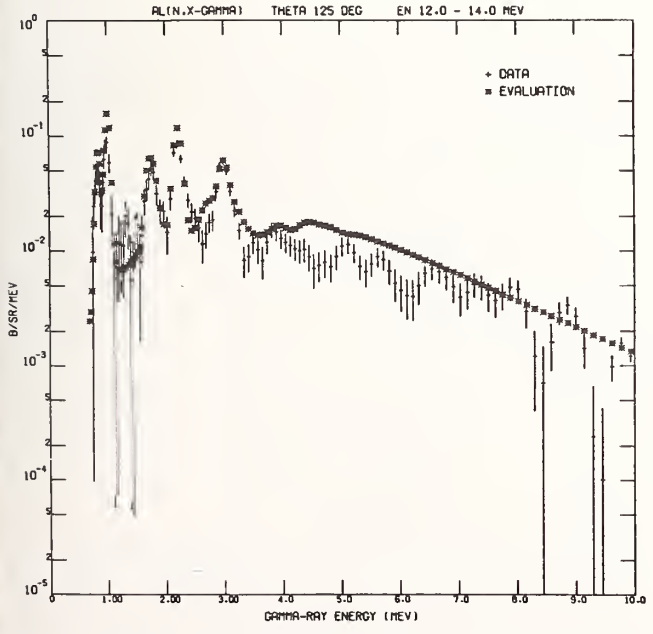

Fig. 11. Doubly differential cross sections for aluminum resulting of the same as Fig. 7, in neutron energies from 12 to 14 MeV. (Dickens et al. ORNL/TM5219)

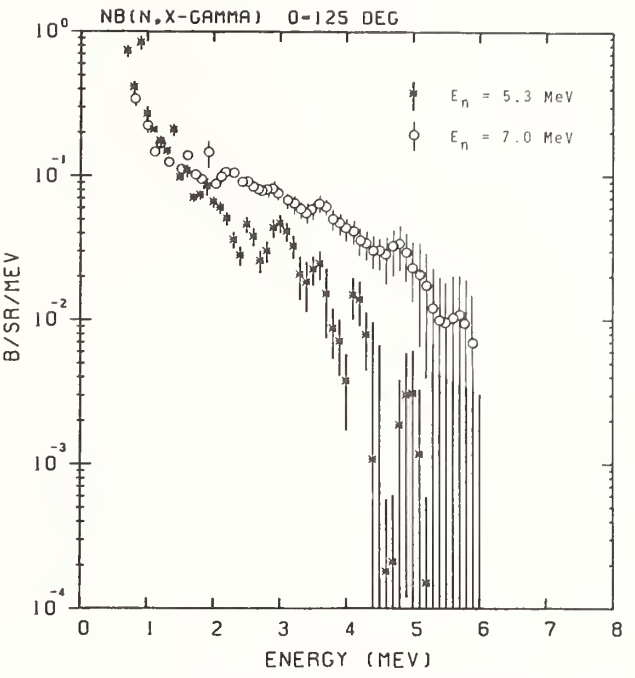

Fig. 10. Doubly differential cross sections for niobium resulting from unfolding the pulse height spectra obtained with Ge(Li) detector as shown in Fig. 3. (Hino et al. 1979)[12]

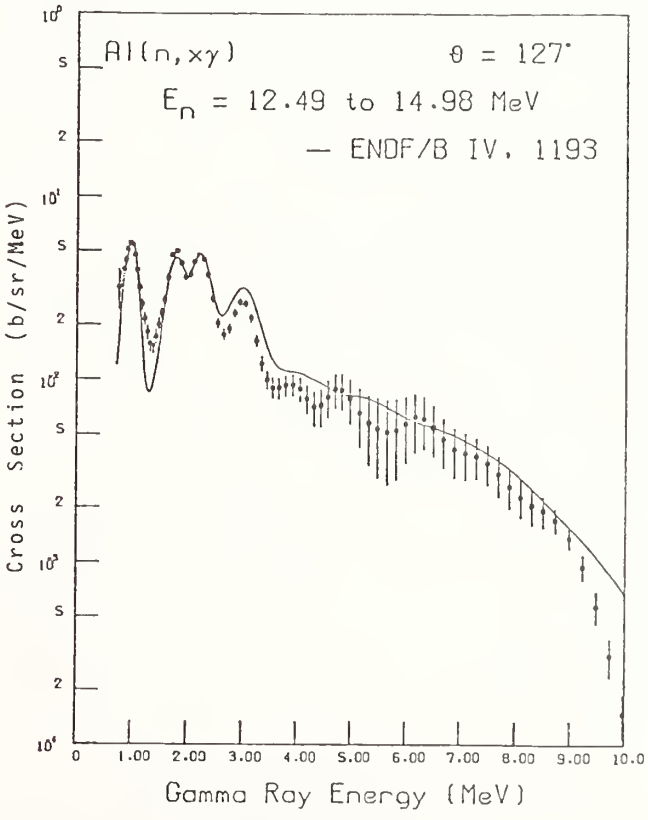

Fig. 12. Doubly differntial cross sections for aluminum resulting from unfolding the pulse height spectrum obtained with NE-213 detector in neutron energies from 12.49 to 14.98 MeV. (Perey, 1978)[24]

The ORNL group has illustrated a graphic representation[20] which is in form as two-dimensional projections of the gamma ray spectra with a fuction of atomic number. These are shown in Fig. 13. The following conclusions are deduced.

In the neutron range from 1.0 and 1.5 MeV, gamma rays arise from deexcitation of low lying levels excited by inelastic scattering. For the higher atomic number, capture is still an important process. Thus, for $Z > 40$, gamma ray spectra generally exhibit two distinct components, one consisting of the relatively hard spectrum due to capture, the other being low-energy gamma rays from inelastic scattering.

In the range from 5 to 6 MeV, neutron capture is no longer contributing appreciably to gamma ray production. All the elements produce gamma ray spectra with maximum energies near that of the incident neutron energy. The most significant variation with atomic number is that from discrete line spectra at low Z to nearly continuous spectra for high A. Clearly, at these neutron energies, measurement techniques for heavier elements must permit determination of this continuum component for the total gamma ray production cross section.

For $10 < E_n < 12$ MeV and $12 < E_n < 14$ MeV, all but the lightest elements produce spectra with appreciable continuum components whose energy is greater than the neutron separation energies (~ 8 MeV). Spectra for Z = 25 to 30 tend to reach higher gamma ray energies than elements of higher or lower Z.

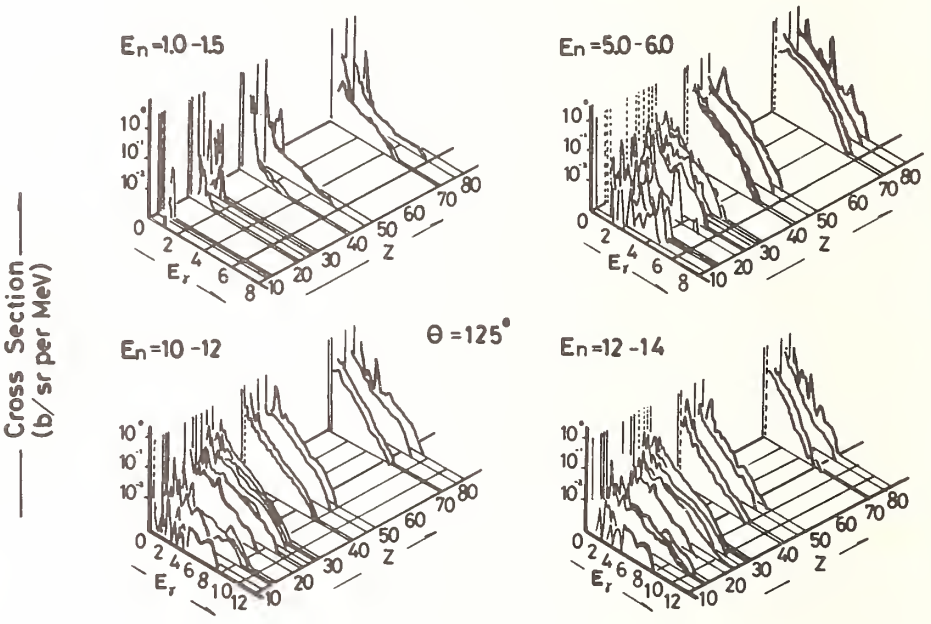

Fig. 13. The graphic representations of gamma ray spectra as a function of atomic number for various energy regions of incident neutrons. The gamma ray energies above 4 MeV, the data have been smoothed to reduced statistical variations. (Dickens et al. 1977)[20]

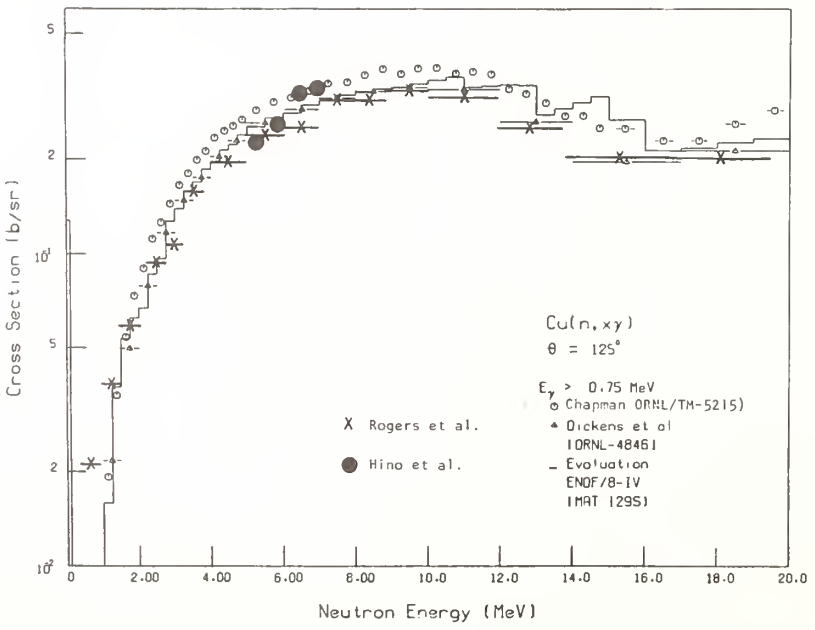

Fig. 14. Total yield of gamma rays having energies greater than 0.75 MeV for the Cu(n,xγ) reaction as a function of incident neutron energy. For comparison, several data and the evaluation are shown. (Chapman 1976)[25]

The integrated cross sections (the excitation functions of total gamma rays with neutron energies) for copper are given in Fig. 14, for comparison between the results reported by several authors, who were Dickens et al,[20] Chapman,[25] Rogers et al.,[19] and Hino et al.[12] The cross sections are integrated for gamma rays having energies greater than 0.75 MeV. It is found out that there is general agreement between these data.

The effect for the different discrimination levels of the gamma ray energies, 0.75 and 0.3 MeV, are also compared. Some discrepansies are found out between the data as shown in Fig. 15. Although measurements are required covering gamma ray energy as low as possible, strong annihilation gamma rays come to prevent a accurate measurement of the lower energy gamma rays. Attempts to detect the low energy gamma rays have been made by Grenier[26] and Dickens et al.[27] No additional data is followed.

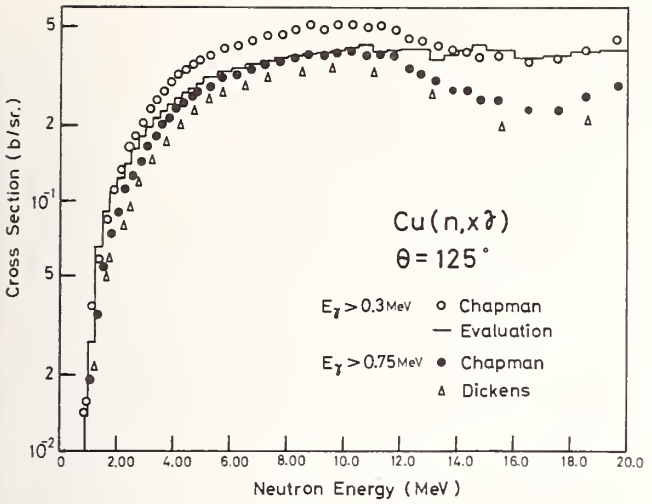

Fig. 15. Total yields are compared between gamma rays having energies greater than 0.75 MeV and neutrons above 0.30 MeV for the Cu(n,xγ) reaction as a function of incident neutron energy. (Chapman 1976)[25]

Status of Compilations, Evaluations and Theoretical Works

The accumulation of the experimental data for the (n,xγ) reactions for many elements or isotopes required a compilation and an evaluation of the data.

Compilations by Chazan[28] and Buchanan et al.[7] were presented before 1970, and POPOP 4[29] and the ENDL[30] were published. These compilations covered only the gamma rays of the discrete energies, except for the ENDL file. Addition to the ENDL system started in 1971 when there were approximately 10 materials with the gamma ray production cross sections.[31] The growth of the ENDF/B evaluated library which were described by Bhat[32] extend to 53 elements and isotopes in the version V compared with 42 elements and isotopes in the version IV (1974).

The United States Department of Energy has determined that ENDF/B-V will, for the present, be limited to users within the United States and AECL-Chalk River, the NNDC News letter No. 79-2 has reported. The present author is, unfortunately, unable to discuss any contents of this new evaluation.

Before 1970, there was little experimental data for the complete gamma ray spectrum, and one has to have recourse to various calculational procedures. Howerton and Plechaty[33] have developed so called "R-parameter formalism" for the calculation of (n,xγ) cross sections and gamma ray spectra above 4 MeV incident neutron energy which has been extended to include more explicit details of the excitation energy .[34] They noticed that for continuum gamma rays with E > 1 MeV the experimental spectra follow the evaporation form:

$$N(E_\gamma) = A\, E_\gamma \exp(-R\, E_\gamma)$$

where the parameters can be determined from experimental data as a function of incident neutron energy. This formalism has been used to calculate the gamma ray production cross sections, in part, for some 60 elements and isotopes in the ENDL data file.[34] The results for Ti (MAT 1286), Cr (MAT 1191), ^{59}Co (MAT 1199), ^{93}Nb (MAT 1189), Mo (MAT 1287), Ta (MAT 1285) and ^{238}U (MAT 1262) have also been included in the

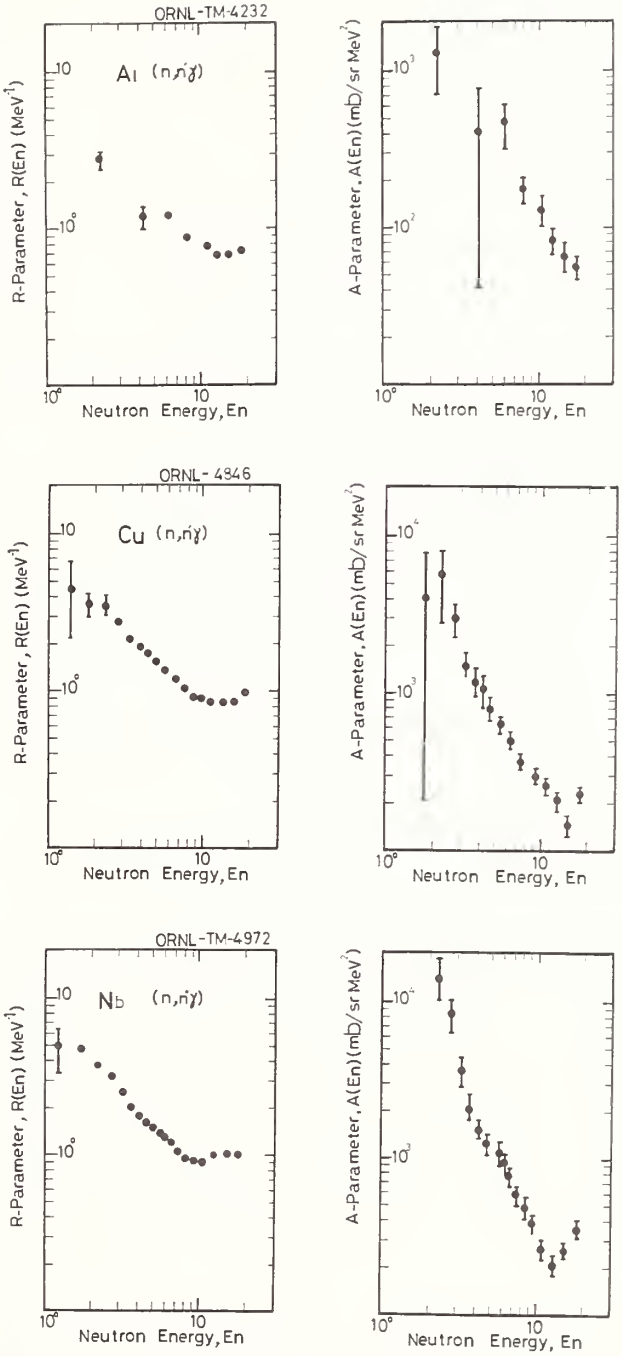

Fig. 16. The values of the parameters in the "R-parameter formalism" for aluminum, nickel and copper in a function of incident neutron energy obtained from the experimental data by the ORNL group.[20] (Hino et al. 1978)[23]

ENDF evaluation library. The agreement with the experimental data are fairly good, but some discrepancies remain.

The Tohoku group[23] has analysed the ORNL data[20] and the Tohoku data[12] using the R-parameter formalism to check its validity. The experimental data were peeled off, and separated into the peak and the continuum component. The continuum components are analysed using the least squares fitting techniques. The parameters A and R are deduced as a function of the neu-

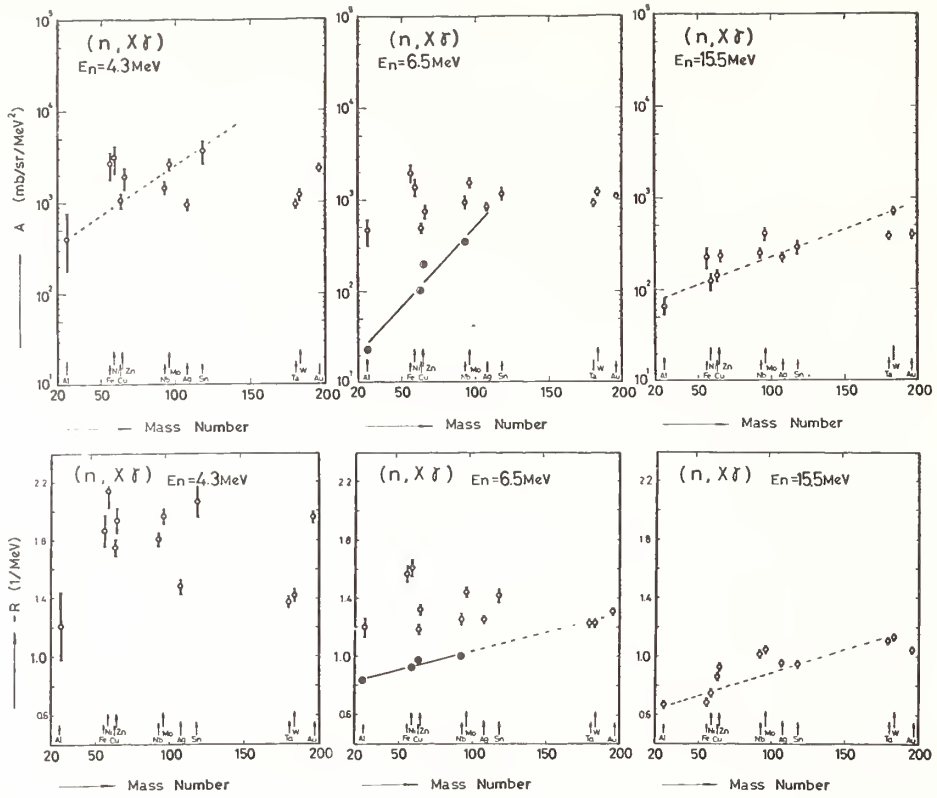

Fig. 17. Mass number dependence of the values of parameters in the "R-parameter formalism" for incident neutron energies 4.3, 6.5 and 15.5 MeV. Experimental data are taken from the ORNL group[20] (open circle), and the Tohoku group[12] (closed circle). (Hino et al. 1978)[23]

tron energy. For the examples, the results of Al, Cu and Nb are shown in Fig. 16. The R-parameters are also shown in Fig. 17 for the incident neutron energies 4.3, 6.5 and 15.5 MeV. The results of the mass dependences for the ORNL data have not brought any clear conclusions except for higher neutron energy. The Tohoku data show a linear behavior for the mass dependency. It is to be noticed that the Tohoku data were performed using the Ge(Li) high resolution detector, and the resolved peaks in the pulse height distributions were correctly rejected in order to obtain the continuum component. It is interesting that the parameters for the gamma ray spectra from the (n,γ) reactions as shown in Fig. 18 behave in a clear fashion.

The parameters for the gamma ray spectra in the (n,γ) reactions are also derived from the (n,xγ) reactions, where the continuum spectrum was decomposed to two parts, (n, x γ) and (n,γ) derived from an assumed linear relation in $N(E_\gamma)/E_\gamma \sim E_\gamma$.

From these results, it is suggested that clear trends of mass dependence for the parameters A and R would be derived from the high resolution measurements. There is a possibility for predicting unknown cross sections and spectra of the (n,xγ) reactions for the elements and isotopes at region of no data by means of a method which sums up known discrete data to compute continuum conponent. The R-parameter formalism which is simple and model independent is useful to predict unknown (n,x γ) cross sections and gamma ray spectra for heavier elements for the engineering purposes.

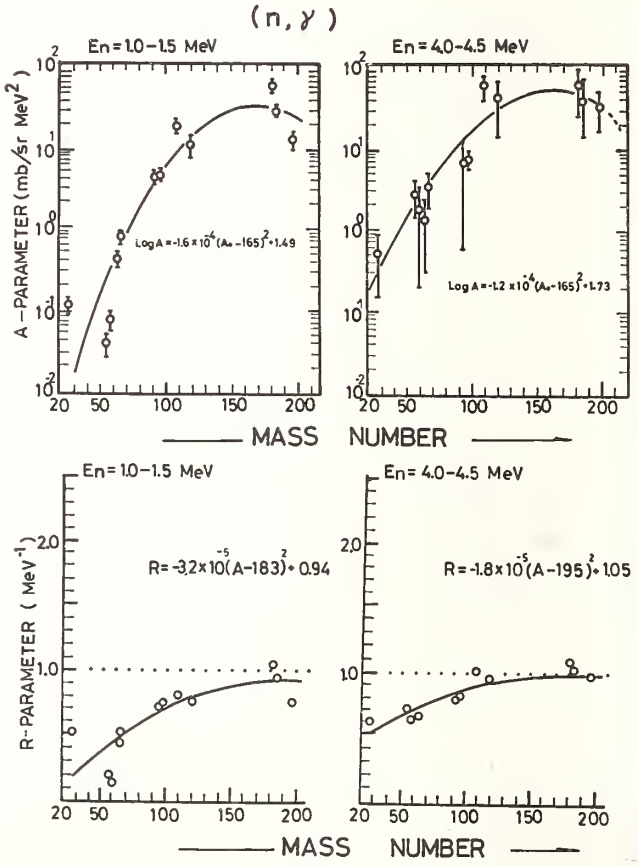

Fig. 18. Mass number dependence of the values of parameters A and R for the radiative capture reactions at incident neutron energies from 1.0 to 1.5, and from 4.0 to 4.5 MeV. The experimental data by the ORNL group[20] are used. (Hino et al. 1978)[23]

Some efforts have been made for the interpretation, extrapolation and evaluation of the gamma ray production cross sections and spectra, based on several nuclear models. Troubetzkoy,[35] Grover and Gilat,[36] Yost,[37] Booth, White and Penny,[38] Takahashi,[39] Fu and Perey,[40] Fu,[41] Arthur and Young,[42] Strohmaier, Uhl and Matthes,[43] and Kitazawa, Harima, Yamakoshi, Sano, Kobayashi and Kawai[44] have contributed to the developments. Young[3] has also described his calculation which used the spin independent statistical theory proposed by Troubetzkoy for the evaluations. The present paper gives only two theoretical works as follows.

After some improvements in the calculations, Fu has performed a calculation of cross sections for neutron interaction with ^{40}Ca, where Hauser-Feshbach theory for binary reactions was extended to include tertiary reactions and also continuum-level spins and parities were included to conserve angular momentum. Results of gamma ray production cross section were compared with observed spectra. An excellent agreement between both values was found as shown in Fig. 19.

In the last year, Kitazawa and his collaborators have presented a new impressive calculations. They used a spin-dependent evaporation model without the parity conservation and including the dipole and quadrupole gamma ray transitions. It started from modified GROGI code made by Takahashi, and the gamma ray spectrum are computed using the radiation width of Brink-Axel type and the level density formula of Gilbert-Cameron type. It was stressed that the inclusion of yrast levels is necessary in dealing with the competition of the neutron and gamma ray emissions from highly excited states. The examples of these results are shown in Figs. 20 and 21 for aluminum and niobium at neutron energy of 14 MeV.

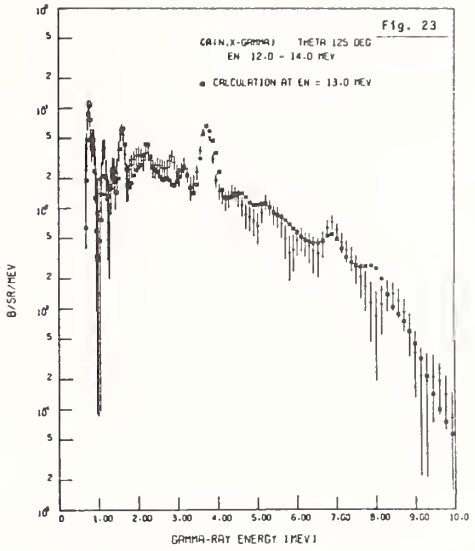

Fig. 19. Calculated and observed gamma ray spectra from calcium. Experimental data is taken from Dickens et al.[45] (Fu 1976)[41]

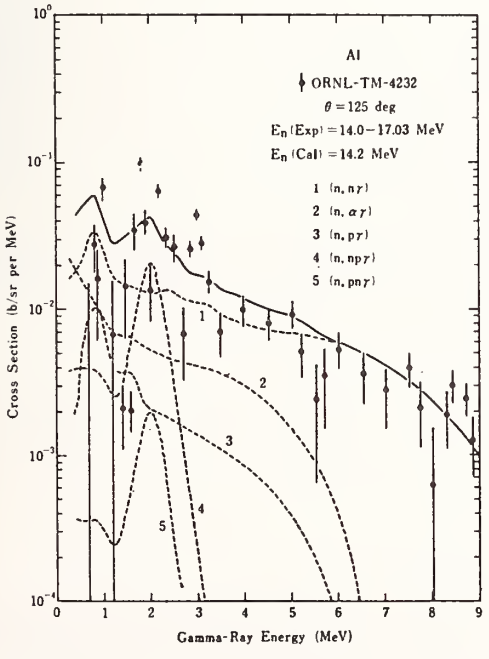

Fig. 20. Calculated and observed gamma ray spectra from aluminum. Dotted lines show the contributions of (n,nγ), (n,αγ), (n,pγ), (n,npγ) and (n,pnγ) processes. (Kitazawa et al. 1978)[44]

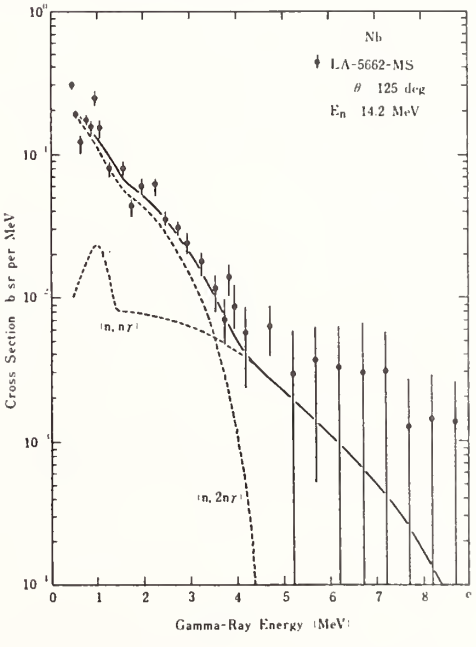

Fig. 21. Calculated and observed gamma ray spectra from niobium. Dotted lines show the contributions of (n,nγ) and (n,2nγ) processes. (Kitazawa et al. 1978)[44]

Concluding Remarks

The situation that there was little experimental data for the (n,xγ) reactions before 1970 has been improved by accumulations of the ORNL measurements using white neutron sources in addition to the GRT-IRT data and nomoenergetic neutron data in other institutes. On details of these data, there still remain some discrepancies between diffent experimental results. Agreements are getting better. Following measurements will be expected in future; for low energy gamma rays, use of high resolution detector for wide neutron energies and for the elments in region of little data. The evaluation of the data would be made below 10 % without difficulties in the near future.

The present paper has not described gamma ray production at lower neutron energy radiatlve capture and from fissionable nuclei for which exist little information after 1975. Further experimental measurement and development of theoretical works are expected.

Acknowledgements

The author would like to thank his collaborators S. Itagaki, Y. Hino and T. Yoshikawa for their assistances and cooperations in preparation of the article.

References

1. I.J. van Heerden, Proc. Conference on Neutron Physics and Nuclear Data, Harwell, UK, 1978 (OECD, 1978) p. 160.

2. Y. Seki, presented paper at Advisory Group Meeting on Nuclear Data for Fusion Reactor Technology, (Vienna, December 1978), and M.A. Abdou, ibid.

3. P.G. Young, Proc. Conference on Nuclear Cross Sections and Technology, Washington, D.C., USA, 1975, ed. by R.A. Schrack and C.D. Bowman (NBS Special Publication 425, 1975) p. 149.

4. V.J. Orphan, C.G. Hoot, A.D. Carlson, J. John, and J.R. Beyster, Nucl. Instr. Meth. 73, 1 (1969).

5. J.K. Dickens and F.G. Perey, Nucl. Instr. Meth. 82, 301 (1970).

6. S. Cierjacks, B. Duelli, P. Forti, D. Kopsch, L. Kropp, M. Lösel, J. Nebe, H. Schwerckert, and H. Unseld, Rev. Sci. Instr. 39, 1279 (1968).

7. P.S. Buchanan, D.O. Neillis, and W.E. Tucker, ORO-2791-32 (1971). Measurements at Texas Nuclear are refered in this report.

8. J.K. Dickens and F.G. Perey, Nucl. Sci. Eng. 36, 280 (1969), ibid. 40, 283 (1970), and J.K.Dickens, ibid. 48, 78 (1972), and G.L. Morgan and F.G. Perey, ibid. 61, 337 (1976).

9. J. Lachkar, J. Singard, Y. Partin and G. Houat, ibid. 55, 168 (1974)

10. D.M. Drake, J.C. Hopkins, C.G. Young, and H. Conde, ibid. 40, 294 (1970), E.D. Arthur, D.M. Drake, M.G. Silbert, and F.G Young, Proc. Conference on Nuclear Cross Sections and Technology, Washington, D.C. USA, 1975, ed. by R.A. Schrack and C.D. Bowman (NBS Special Publication 425, 1975) p. 770, and D.M. Drake, E.D. Arthur, and M.G. Silbert, Nucl. Sci. Eng. 65, 49 (1978).

11. C. Nordborg, L. Nilsson, H. Conde, and L.G. Stromberg, Nucl. Sci. Eng. 66, 75 (1978).

12. Y. Hino, T. Yamamoto, T. Saito, Y. Arai, S. Itagaki, and K. Sugiyama, J. Nucl. Sci. Technol. 15, 85 (1978), T. Yamamoto, Y. Hino, S. Itagaki, and K. Sugiyama, ibid. 15, 797 (1978), Y. Hino, T. Yamamoto, S. Itagaki, and K. Sugiyama, NETU-34 (Department of Nuclear Engineering, Tohoku University 1979), and presented paper at NEANDC Topical Discussion of Progress in Neutron Cross Section Measurements and Evaluation Concerning Structural Materials for Fast Reactors, (Geel, September 1979), and contributed paper in this conference.

13. E. Voss, S. Cierjacks, and L. Kropp, Proc. Third Conference on Neutron Cross Sections and Technology, Knoxville, Tenn. USA, 1971, ed. by R.L. Macklin, p. 218.

14. J.K. Dickens, G.L. Morgan, and F.G Perey, Nucl. Sci. Eng. 50, 311 (1973).

15. D.L. Smith, ANL/NDM-20 (1975), and Nucl. Sci. Eng. 64, 897 (1976).

16. W.E. Kinney and F.G. Perey, Nucl. Sci. Eng. 63, 418 (1976).

17. G.C. Hoot, V.J. Orphan, and J. John, Proc. Third Conference on Neutron Cross Sections and Technology, Knoxville, Tenn. USA, 1971, ed. by R.L. Macklin, p. 227.

18. J.K. Dickens and F.G Perey, ibid. p. 235.

19. V.J. Orphan and C.G. Hoot, Gulf-RT-A10743 (1971), V.J. Orphan, C.G. Hoot, and J. John, Nucl. Sci. Eng. 42, 352 (1970), and Trans. Am. Nucl. Soc. 14, 897 (1971), V.C. Rogers, V.J. Orphan, C.G. Hoot, D.R. Dixon, D. Costello, and G.M. Sandquist, Trans. Am. Nucl. Soc. 22, 817 (1975), and V.C. Rogers, V.J. Orphan, C.G. Hoot, V.V. Verbinski, D. Costello, and S.J. Friesenhahn, Proc. Conference on Nuclear Cross Sections and Technology, Washington D.C., USA, 1975, ed. by R.A. Schrack and C.D. Bowman, (NBS Special Publication 425, 1975) p. 766, V.C. Rogers, D.R. Dixon, C.G. Hoot, D. Costello, and V.J. Orphan, Nucl. Sci. Eng. 62, 716 (1977).

20. J.K.Dickens, G.L. Morgan, G.T. Chapman, T.A. Love, E. Newman, and F.G. Perey, Proc. Conference on Nuclear Cross Sections and Technology, Washington D.C., USA, 1975, ed. by R.A. Schrack and C.D. Bowman (NBS Special Publication 425, 1975) p. 758, and Nucl. Sci. Eng. 62, 515 (1976).

21. G.L. Morgan, T.A. Love, and F.G. Perey, Nucl. Instr. Meth. 128, 125 (1975), and G.L. Morgan and F.G. Perey, Nucl. Sci. Eng. 61, 337 (1976)

22. I.J. van Heerden and W.R. McMurray, Z. Physik 260, 9 (1973).

23. Y. Hino, S. Itagaki, F. Saito, and K. Sugiyama, unpublished.

24. F.G. Perey, presented paper at Advisory Group Meeting on Nuclear Data for Fusion Reactor Technology, (Vienna, December 1978).

25. G.T. Chapman, ORNL/TM-5215 (1976).

26. G. Grenier, Proc. Third Conference on Neutron Cross Sections and Technology, Knoxville, Tenn. USA, 1971 ed. by R.L. Macklin, p. 248.

27. J.K. Dickens, G.L. Morgan and F.G. Perey, Proc. Conference on Nuclear Cross Sections and Technology, Washington, D.C. USA, 1975 (NBS Special Publication 425, 1975) p. 762.

28. N.J. Chazan, UCRL-14007 (1965).

29. W.E. Ford III, CTC-42 (1970).

30. R.J. Howerton etal., UCRL-51370, Vol. 4 (1971).

31. D.J. Dudziak, Proc. Third Conference on Neutron Cross Sections and Technology, Knoxville, Tenn. USA, 1971, ed. by R.L. Macklin, p.367.

32. M.R. Bhat, presented paper at Advisory Group Meeting on Nuclear Data for Fusion Reactor Technology, (Vienna, December 1978).

33. R.J. Howerton and E.F. Plechaty, Nucl. Sci. Eng. 32, 178 (1968).

34. S.T. Perkins, R.C. Haight and R.J. Howerton, Nucl. Sci. Eng. 57, 1 (1975).

35. E.S. Troubetzkoy, Phys. Rev. 122, 212 (1961).

36. J.R. Grover and J. Gilat, Phys. Rev. 157, 802 (1961)

37. K.J. Yost, Nucl. Sci. Eng. 32, 62 (1968).

38. R.S. Booth, J.E. White and S.K. Penny, Nucl. Sci. Eng. 47, 8 (1972).

39. H. Takahashi, Nucl. Sci. Eng. 51, 296 (1973), and Proc. EANDC Topical Discussion on Critique of Nuclear Models and Their Validity in the Evaluation of Nuclear Data, (Tokyo, 1974) JAERI-M 5984, p. 257.

40. C.Y. Fu and F.G. Perey, Trans. Am. Nucl. Soc. 15, 961 (1972), and Atomic Data and Nuclear Tables 16, 409.

41. C.Y. Fu, Proc. Conference on Nuclear Cross Sections and Technology, Washington, D.C. USA, 1975 (NBS Special Publication 425, 1975) p. , and Atomic data and Nuclear Tables 17, 127 (1976).

42. E. Arthur and P.G. Young, Proc. Symposium on Neutron Cross Sections from 10 to 40 MeV, B.N.L., May 1977, ed. by M.R. Bhat and S. Pearlstein, (BNL-NCS-50681, 1977) p. 467.

43. B. Strohmaier, M Uhl, and W.K. Matthes, Nucl. Sci. Eng. 65, 368 (1978).

44. H. Kitazawa, Y. Harima, H. Yamakoshi, Y. Sano, H. Kobayashi, and M. Kawai, Proc. 1978 Seminor on Nuclear Data, (Japanese Nuclear Data Committee), JAERI-M 8163 (1979).

45. J.K. Dickens, T.A. Love, and G.L Morgan, Nucl. Sci. Eng. 53, 277 (1974).

GAMMA-RAY PRODUCTION CROSS SECTIONS FOR FAST NEUTRON INTERACTIONS WITH Al, Ni, Cu AND Nb

Y. Hino, T. Yamamoto†, S. Itagaki and K. Sugiyama

Department of Nuclear Engineering, Tohoku University
Aramaki-Aoba, Sendai, 980 Japan

Gamma-ray production cross sections have been measured for the (n,xγ) reactions in Al, Ni, Cu and Nb at the neutron energies of 5.3, 5.9, 6.4 and 7.0 MeV. The Dynamitron accelerator and a deuterium gas target were used to produce pulsed monoenergetic neutrons. Gamma-rays were detected with a heavily shielded 70-cm^3 coaxial Ge(Li) detector placed at an angle of 125°. A time-of-flight technique was adopted to discriminate against pulses due to scattered neutrons and background radiations. Absolute cross sections of discrete gamma-ray lines are obtained. Total and unresolved gamma-ray production cross sections are also obtained by unfolding the pulse height spectra with a modified "FERDOR" code. The present results are discussed in comparison with previous data, and are in general agreement with those of ORNL.

[Al, Ni, Cu and Nb(n,xγ) reactions, differential cross sections, θ_γ=125°, En= 5.3, 5.9, 6.4 and 7.0 MeV, discrete lines, unresolved gamma-rays, unfolding analysis]

Introduction

Gamma-ray production cross sections of neutron interactions are basic nuclear data for the shielding calculations and for the estimation of gamma-ray heating in fusion reactors. In recent years, some efforts have been made to obtain the gamma-ray production cross sections, but some disagreements exist in previous results, particularly between those from white neutrons and monoenergetic neutrons. The additional data have been required for constructing the accurate evaluations. The present measurement was motivated by these reasons. The gamma-ray production cross sections for Al, Ni, Cu and Nb were obtained using a pulsed monoenergetic neutron source and a Ge(Li) detector. The samples of Al and Ni are important as the structural materials, and Cu is used in many instruments, and Nb is especially of interest in the fusion reactors. The low background and high resolution detection system allowed measurement for many discrete gamma-ray lines as well as total production cross sections. The origins of discrete lines were also studied, and the cross sections of ground-state transitions were summed up to give the total inelastic cross sections.

Experimental Procedures

Neutron Production and Flux Monitoring

The experiment was performed using the 4.5-MV Dynamitron accelerator in Tohoku University. A deuterium gas target was bombarded by pulsed deuteron beams of 2-nsec duration and 2-MHz repetition rate, and monoenergetic neutrons of 5.3, 5.9, 6.4 and 7.0 MeV were produced. The flux of emerging neutrons was monitored by a 2"ϕx2" NE-213 liquid scintillator. The time-of-flight technique was used to discriminate against the pulses from scattered neutrons and other time dependent backgrounds. The detection efficiencies of the NE-213 detector were obtained by the computation using the 05S Monte-Carlo code.[1]

Samples

The samples were natural mixture of high purity metal (>99%), and the hollow cylindrical shape of 2-cm i.d. and 3-cm o.d. and 4-cm long was used for Al, Ni and Cu, and right cylindrical shape of 2-cm dia. by 3-cm long was used for Nb. Each sample was placed at the crossing point of two axes of deuteron beam and the gamma-ray detector as shown in Fig. 1.

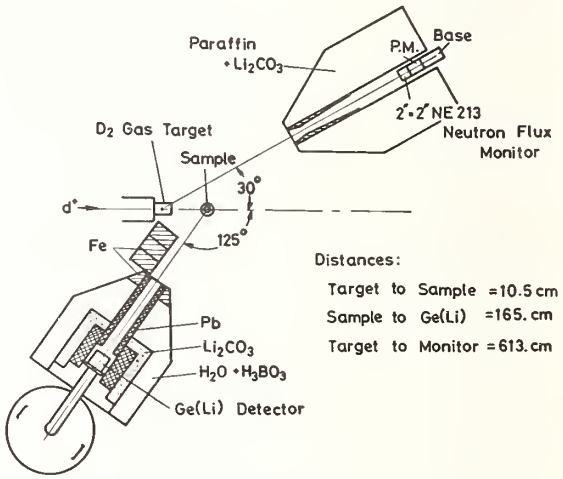

Fig. 1. Experimental arrangement

Gamma-Ray Detector

Gamma-rays from the sample were measured with a 70-cm^3 Ge(Li) detector. The resolution was about 5 keV for 1.33-MeV gamma-rays from a ^{60}Co source. The detector was heavily shielded as shown in Fig. 1. The time-of-flight technique was also adopted to reduce the background radiations. A typical time spectra is shown in Fig. 2.

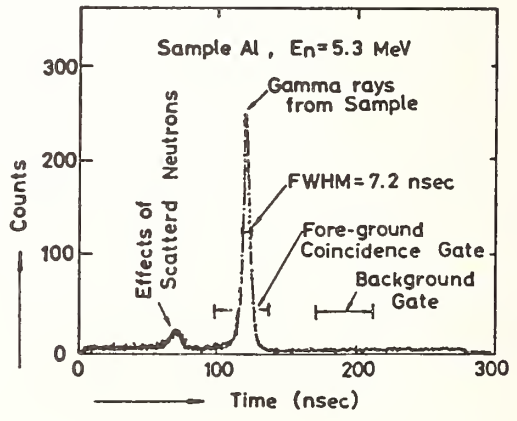

Fig. 2. Time spectrum of pulses from the Ge(Li) detector for aluminum at the neutron energy of 5.3 MeV. The stop pulses were generated by a beam pickup ring.

†Present address: Toshiba Electric Co. Ltd., Tokyo, Shibaura, Japan.

In the data acquisition system, the prompt gamma-rays from the sample and time independent backgrounds were collected at a time by setting the windows of timing discriminator and were stored in a dual 2048-channel pulse height analyser.

Data Analysis

Data Analysis for Discrete Lines

The production cross section of each gamma-ray line is expressed by the formula:

$$\left.\frac{d\sigma}{d\omega}\right|_{\text{at } 125^\circ} = \frac{N\gamma}{N_S \cdot N_n \cdot \varepsilon\gamma \cdot \Omega\gamma} C \qquad (1)$$

in which
$N\gamma$=peak area of the gamma-rays under consideration,
N_S=average number of the sample atoms (atoms/cm^2)
N_n=the number of neutrons incident upon the sample,
$\varepsilon\gamma$=full-energy-peak detection efficiency,
$\Omega\gamma$=the solid angle subtended by the Ge(Li) detector with respect to the sample,
C=the correction factor.
Corrections have been made for attenuation and multiple scattering effects of neutrons, and for the attenuation of produced gamma-rays in the sample.

Probable errors in gamma-ray production cross sections have been estimated as follows:
i) the determination of neutron flux: 5%,
ii) the corrections for attenuation and multiplication of neutron flux: 5%,
iii) the correction for the attenuation of gamma-rays in the sample: 1%,
iv) the determination of detection efficiencies for full energy peaks: 5% for $E\gamma < 3.5$ MeV and 10% for $E\gamma > 3.5$ MeV,
v) the counting statistics of the peak area and the continuum component under the peak: 1% ~ 40%.

Data Analysis for Unresolved Gamma-Rays

There are many peaks in the measured gamma-ray spectra, and almost all prominent peaks have been analysed. However, weak peaks and continuum gamma-ray components still remain, so that an unfolding procedure is necessary to obtain total gamma-ray production cross sections. The "FERDOR"[2] code was modified to resolve the gamma-ray spectra from the Ge(Li) detector, and was renamed "GFERDOR". The attenuation factors of gamma-rays in the sample and some constants were included in the code.

The response functions of the Ge(Li) detector were determined by the measurements of monoenergetic gamma-rays. In the low energy region ($E\gamma < 2.5$ MeV), gamma-rays from radioactive sources of ^{22}Na, ^{24}Na, ^{60}Co and ^{137}Cs were measured. In the high energy region, gamma-rays from ^{7}Li(p,γ), ^{11}B(p,γ) and ^{19}F(p,$\alpha\gamma$) reactions were used. To estimate the effects of scattered gamma-rays in the sample, the ^{60}Co and ^{137}Cs sources were set at the center of hollow-cylindrical samples.

In the unfolding procedure, clean peak components were subtracted from the raw spectra to avoid the undesired fluctuations. Then, the spectra were smoothed and bunched into 100-keV energy bins, and the unresolved gamma-ray production cross sections were obtained by unfolding the data. Total gamma-ray production cross sections were calculated by adding these unresolved and resolved gamma-ray production cross sections.

The error due to unfolding procedure has been estimated to be 10% ~ 30% including the uncertainties of the response functions.

Results and Discussion

Aluminum

Absolute differential cross sections for 21 discrete gamma-ray lines are obtained and listed in Table 1. The gamma-rays of 952-, 984-, 1692- and 1936-keV are caused by (n,pγ) reactions and the rest are due to (n,n'γ) reactions.

The cross sections for intense gamma-ray lines of 843-, 1013-, 2210- and 3001-keV are shown in Fig. 3 together with previous data. The measuerment of Dickens[3] was performed with a Ge(Li) detector and monoenergetic neutrons. Hoot and Orphan[4] used a Ge(Li) detector and white neutrons from an electron linac. The present results are in good agreement with those of the previous measurements.

Table 1. Differential gamma-ray production cross sections for aluminum. (mb/sr)

$E\gamma$ (keV)	E_n= 5.3 MeV	5.9 MeV	6.4 MeV	7.0 MeV
792	2.0 ± 0.2	1.9 ± 0.3	2.6 ± 0.2	2.2 ± 0.2
843	7.1 ± 0.5	8.5 ± 0.7	7.4 ± 0.6	8.3 ± 0.7
952	0.4 ± 0.2	1.1 ± 0.2	1.1 ± 0.2	1.5 ± 0.3
984	2.0 ± 0.4	2.4 ± 0.2	3.3 ± 0.3	3.0 ± 0.4
1013	14.5 ± 1.2	16.5 ± 1.3	18.1 ± 1.3	18.2 ± 1.4
1507			0.6 ± 0.1	1.0 ± 0.2
1692			2.4 ± 0.2	3.3 ± 0.3
1719	5.4 ± 0.4	5.2 ± 0.6	5.9 ± 0.5	7.4 ± 0.7
1936			1.8 ± 0.2	2.8 ± 0.5
2210	14.7 ± 1.7	16.7 ± 2.0	16.0 ± 1.8	17.2 ± 2.2
2300	1.1 ± 0.2	2.4 ± 0.4	2.5 ± 0.3	2.0 ± 0.3
2665			1.1 ± 0.2	2.0 ± 0.3
2732	1.5 ± 0.3	1.8 ± 0.4	2.3 ± 0.4	4.6 ± 0.7
2980	3.1 ± 0.4	2.9 ± 0.4	4.8 ± 0.6	4.4 ± 0.6
3001	6.6 ± 0.8	7.8 ± 0.9	10.8 ± 1.3	11.2 ± 1.3
3212		1.8 ± 0.3	3.5 ± 0.5	3.5 ± 0.5
3396	2.1 ± 0.3	1.9 ± 0.4	2.1 ± 0.3	2.2 ± 0.4
3956	2.2 ± 0.4	2.3 ± 0.4	2.2 ± 0.4	1.0 ± 0.3
4237			1.6 ± 0.3	1.9 ± 0.6
4409	1.7 ± 0.3	2.6 ± 0.5	3.3 ± 0.5	4.8 ± 0.6
4580	2.5 ± 0.4	3.0 ± 0.5	3.5 ± 0.5	1.6 ± 0.4

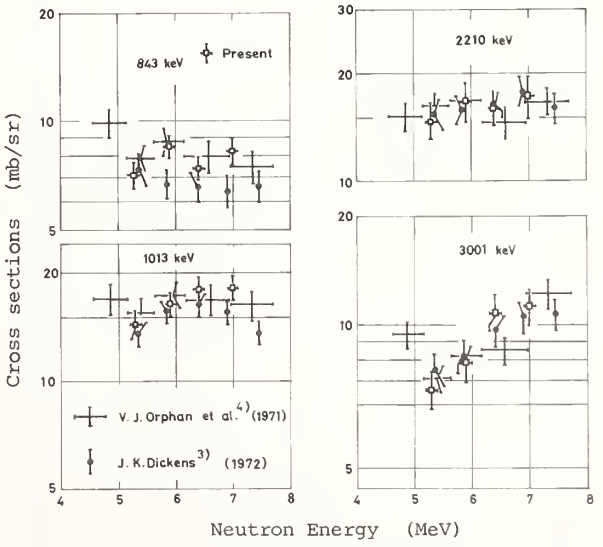

Fig. 3. Cross sections of prominent gamma-rays for Al.

Among 21 resolved gamma-ray lines listed in the Table 1, 9 gamma-ray lines correspond to the ground-state transitions in the $(n,n'\gamma)$ reactions. The summed cross sections for these ground-state transitions are compared with evaluated values of total inelastic cross sections. The present values of 0.68 to 0.88 b are in remarkably good agreement with those of 0.75 to 0.86 b derived from BNL-325[5] in the energy region of 5.3 to 7.0 MeV.

The binned cross sections for resolved and unresolved gamma-rays were summed up to give the spectral gamma-ray production cross sections. This result is compared with those of Dickens et al[6] and are shown in Fig. 4.

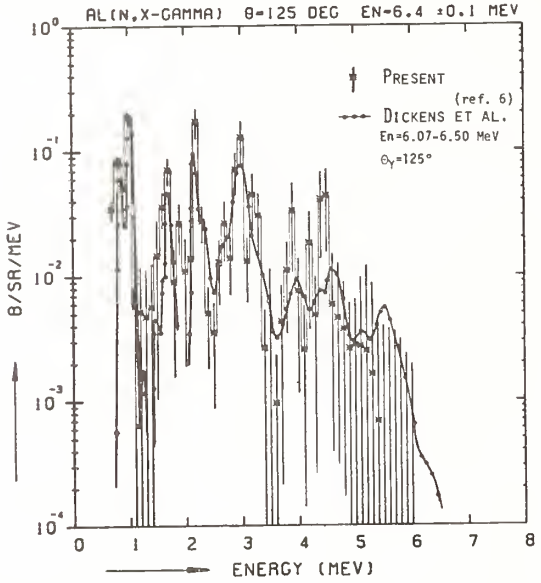

Fig. 4. Spectral gamma-ray production cross sections for aluminum.

Nickel

Table 2. Differential resolved gamma-ray production cross sections for nickel. (mb/sr)

E_γ (keV)	En= 5.3 MeV	5.9 MeV	6.4 MeV	7.0 MeV
433	1.1 ± 0.1	1.3 ± 0.2	1.0 ± 0.4	1.8 ± 0.3
467	1.4 ± 0.2	1.6 ± 0.2	1.5 ± 0.4	3.0 ± 0.4
826	5.6 ± 0.5	5.6 ± 0.5	6.4 ± 0.6	6.4 ± 0.6
935	2.2 ± 0.4	2.6 ± 0.4	3.2 ± 0.4	3.5 ± 0.4
953	3.1 ± 0.4	3.0 ± 0.4	3.0 ± 0.4	3.4 ± 0.4
1005	10.2 ± 0.8	11.5 ± 0.9	13.2 ± 1.0	13.9 ± 1.1
1050		1.0 ± 0.2	1.6 ± 0.3	2.4 ± 0.3
1170	9.7 ± 0.9	11.0 ± 1.0	13.9 ± 1.2	13.9 ± 1.1
1238			1.0 ± 0.2	2.0 ± 0.5
1292	2.1 ± 0.7	4.1 ± 1.1	5.0 ± 1.1	4.7 ± 1.2
1333(D)	33.0 ± 2.7	30.4 ± 2.5	32.2 ± 2.6	31.4 ± 2.5
1436(D)	4.0 ± 1.1	3.2 ± 0.6	3.1 ± 0.6	3.9 ± 1.0
1454(D)	47.0 ± 3.3	43.3 ± 3.2	44.2 ± 3.3	43.6 ± 3.4
1584	1.9 ± 0.2	2.0 ± 0.2	2.0 ± 0.3	1.5 ± 0.2
1792	2.1 ± 0.2	2.3 ± 0.3	2.5 ± 0.3	2.5 ± 0.3
1810	0.9 ± 0.1	0.9 ± 0.2	1.3 ± 0.2	1.1 ± 0.2
2060	1.1 ± 0.2	1.1 ± 0.2	1.1 ± 0.2	1.0 ± 0.2
2158	1.1 ± 0.2	0.9 ± 0.2	1.5 ± 0.2	1.2 ± 0.2
2653	1.2 ± 0.2	1.1 ± 0.2	1.0 ± 0.2	1.0 ± 0.2
2950	1.0 ± 0.2	1.3 ± 0.2	1.1 ± 0.2	1.2 ± 0.2
3020	1.5 ± 0.2	1.6 ± 0.2	1.7 ± 0.3	1.7 ± 0.3
3038	1.0 ± 0.1	1.1 ± 0.2	0.6 ± 0.2	1.0 ± 0.2
3264	2.0 ± 0.3	1.4 ± 0.2	1.8 ± 0.3	1.2 ± 0.2
3593	1.4 ± 0.2	1.6 ± 0.2	1.2 ± 0.2	0.6 ± 0.1
4108	0.9 ± 0.2	1.0 ± 0.2	0.9 ± 0.2	0.8 ± 0.2

* Doudlet peaks are denoted as "(D)"

Production cross sections for 25 resolved gamma-ray lines from natural nickel are listed in Table 2. The gamma-ray lines of 433-, 935-, 1050- and 1238-keV are caused by $(n,p\gamma)$ reactions and the rest are due to $(n,n'\gamma)$ reactions.

Production cross sections for prominent gamma-ray lines of 1005-, 1170-, 1333- and 1454-keV are shown in Fig. 5 together with previous data. The results show good agreement for the 1333(+1321) keV line, smaller values for the 1005 and 1454(+1488) lines, and larger values for the 1170 keV line compared with previous data.[7]

Spectral gamma-ray production cross sections for nickel at the neutron energy of 6.4 MeV are shown in Fig. 6 together with previous data. Dickens et al.[7] used a NaI(Tl) detector and white neutrons from a linac. The agreement between the present results and those of Dickens et al. is very good.

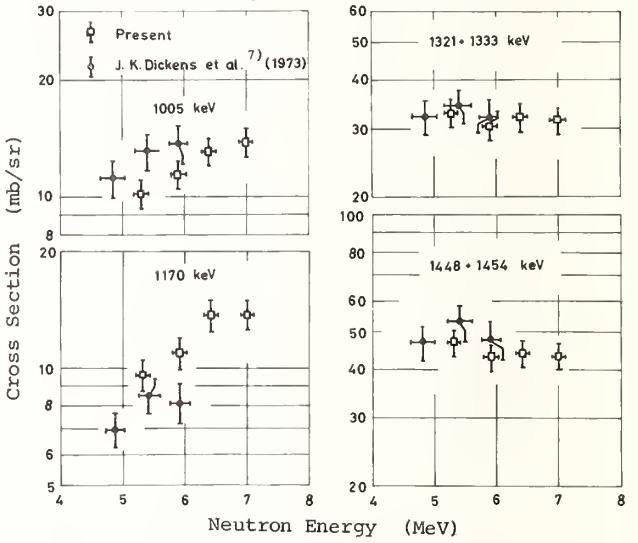

Fig. 5. Cross sections of prominent gamma-rays for Ni.

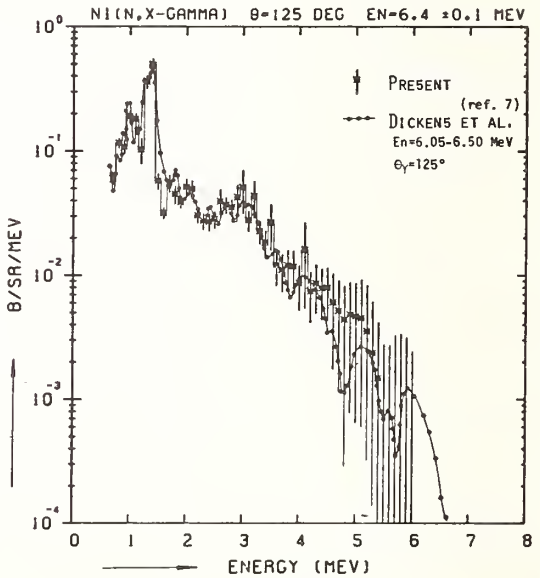

Fig. 6. Spectral gamma-ray production cross sections for natural nickel.

The summed cross sections of ground-state transitions have been obtained and compared with the total inelastic cross sections. For nickel, most of the gamma-rays are due to cascade transitions, and the first excited states of nickel isotopes are 1170, 1333 and 1454

keV for ^{58}Ni, ^{60}Ni and ^{62}Ni, respectively. The sum of the cross sections corresponding to the first excited states, including the unresolved lines of 1321 and 1488 keV, is about 1.0 b in the present energy region. It is an approximation, then, that the small contribution of 1321- and 1488-keV lines can be ignored and to cancel the other weak ground-state transitions. The present value of 1.0 b is in reasonable agreement with total inelastic cross section of 1.1 b derived from BNL-325.

Copper

Differential production cross sections for 21 resolved gamma-rays from natural copper are listed in Table 3. All resolved gamma-rays are due to $(n,n'\gamma)$ reactions in ^{63}Cu and ^{65}Cu. In contrast with nickel, most of gamma-ray lines correspond to the ground-state transitions.

Table 3. Differential gamma-ray production cross sections for natural copper. (mb/sr)

Eγ (keV)	En= 5.3 MeV	5.9 MeV	6.4 MeV	7.0 MeV
643	0.7 ± 0.2	1.0 ± 0.2	1.3 ± 0.2	1.3 ± 0.3
669	7.2 ± 0.6	6.9 ± 0.5	7.4 ± 1.3	7.9 ± 0.6
684	2.0 ± 0.3	2.3 ± 0.3	1.6 ± 0.3	1.1 ± 0.3
770	4.9 ± 0.4	5.6 ± 0.5	6.6 ± 0.8	7.6 ± 0.8
877	1.7 ± 0.4	1.8 ± 0.3	2.7 ± 0.6	3.0 ± 0.7
901(D)	4.4 ± 0.5	4.3 ± 0.4	6.0 ± 0.7	8.2 ± 1.2
962	27.9 ± 2.1	27.8 ± 2.1	31.5 ± 2.4	33.2 ± 2.6
1115	14.6 ± 1.2	15.4 ± 1.3	19.3 ± 1.5	20.0 ± 1.5
1161	1.9 ± 0.4	2.0 ± 0.6	2.3 ± 0.5	3.1 ± 0.6
1245	1.9 ± 0.2	1.8 ± 0.3	1.5 ± 0.2	1.8 ± 0.2
1327	14.9 ± 1.1	15.1 ± 1.2	17.2 ± 1.4	19.2 ± 1.5
1350	2.2 ± 0.4	2.0 ± 0.4	2.3 ± 0.5	3.0 ± 0.6
1412	4.0 ± 0.4	4.0 ± 0.4	4.2 ± 0.5	4.7 ± 0.5
1481	6.5 ± 0.6	5.8 ± 0.5	7.6 ± 0.6	8.5 ± 0.7
1547	3.4 ± 0.4	2.9 ± 0.3	3.8 ± 0.4	3.7 ± 0.4
1625	2.1 ± 0.3	2.2 ± 0.3	2.6 ± 0.3	2.2 ± 0.3
1725	1.1 ± 0.1	1.4 ± 0.2	1.8 ± 0.3	2.1 ± 0.3
1861	5.3 ± 0.5	5.2 ± 0.5	6.0 ± 0.5	5.7 ± 0.5
2011	1.2 ± 0.2	1.5 ± 0.3	1.4 ± 0.3	1.4 ± 0.3
2093	3.3 ± 0.5	3.2 ± 0.5	3.1 ± 0.4	2.8 ± 0.4
2336	1.9 ± 0.3	2.0 ± 0.3	1.9 ± 0.3	2.3 ± 0.4

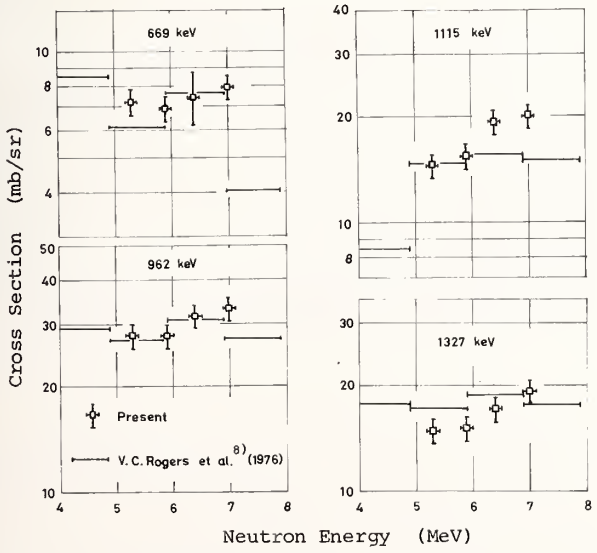

Fig. 7. Cross sections of prominent gamma-rays for Cu.

The summed cross sections of all observed gamma-rays corresponding to the ground-state transitions are 1.2 to 1.5 b in this energy region. This present results are slightly low compared with the total inelastic cross sections of 1.7 to 1.6 b, derived from BNL-325.

The cross sections for prominent gamma-ray lines are shown in Fig. 7 together with previous data. The present results are in good agreement with those of Rogers et al.[8] performed with a Ge(Li) detector and white neutrons from a linac.

Spectral gamma-ray production cross sections for natural copper are shown in Fig. 8. The present results are in good agreement with those of Chapman et al.[9] and the evaluation of ENDF/B-IV[10].

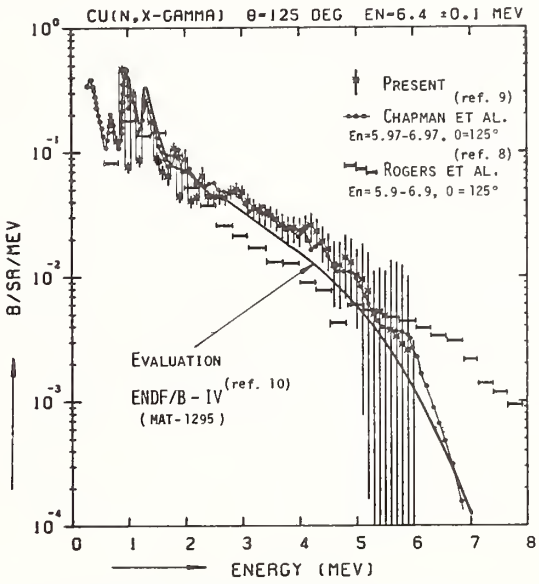

Fig. 8. Spectral gamma-ray production cross sections for natural copper at 6.4 MeV neutron energy.

Niobium

Table 4. Differential gamma-ray production cross sections for niobium. (mb/sr)

Eγ (keV)	En= 5.3 MeV	5.9 MeV	6.4 MeV	7.0 MeV
477	3.7 ± 0.7	4.9 ± 0.7	5.6 ± 1.0	7.7 ± 1.3
541	10.9 ± 1.0	12.3 ± 1.0	13.2 ± 1.2	14 9 ± 1.4
571	2.8 ± 0.6	3.2 ± 0.8	4.0 ± 0.8	3.7 ± 1.0
585	4.7 ± 0.9	4.0 ± 0.9	6.2 ± 1.1	5.6 ± 1.4
655(D)	6.5 ± 0.7	6.5 ± 0.8	7.9 ± 1.2	9.4 ± 1.2
689	6.0 ± 1.2	6.1 ± 1.0	5.5 ± 0.8	5.8 ± 0.8
705(D)	6.5 ± 1.3	6.2 ± 1.1	6.5 ± 1.0	6.7 ± 1.3
744	23.9 ± 1.9	26.5 ± 2.3	29.4 ± 2.3	36.1 ± 2.9
780	12.9 ± 1.2	12.5 ± 1.4	12.5 ± 1.2	13.4 ± 1.7
808	10.1 ± 0.9	11.5 ± 1.1	12.3 ± 1.4	11.3 ± 1.3
833	5.0 ± 0.9	5.7 ± 0.9	5.9 ± 1.0	5.2 ± 0.9
921	5.4 ± 1.3	4.9 ± 1.0	4.8 ± 1.0	5.1 ± 1.6
950	36.9 ± 2.9	41.5 ± 3.0	50.7 ± 3.9	56.1 ± 4.3
979	18.2 ± 1.7	17.6 ± 1.5	21.7 ± 2.1	23.4 ± 2.1
1052	2.2 ± 0.5	2.0 ± 0.4	2.8 ± 0.5	3.5 ± 0.6
1082	3.8 ± 0.7	4.2 ± 0.6	3.9 ± 0.6	4.1 ± 0.8
1297	1.9 ± 0.4	2.1 ± 0.5	2.8 ± 0.5	3.9 ± 0.8
1483	2.7 ± 0.4	2.1 ± 0.4	3.2 ± 0.5	3.2 ± 0.8
1499	5.8 ± 0.5	5.2 ± 0.5	7.8 ± 1.0	8.4 ± 0.9
1685(T)	1.9 ± 0.3	1.9 ± 0.3	2.6 ± 0.5	2.3 ± 0.3
1910	1.4 ± 0.3	1.2 ± 0.3	1.7 ± 0.4	2.1 ± 0.4
1950		0.9 ± 0.3	1.1 ± 0.4	1.4 ± 0.5
1968		0.8 ± 0.3	2.2 ± 0.6	2.3 ± 0.4

* Triplet peak is denoted as "(T)"

For niobium, 23 discrete lines were resolved, and the cross sections are listed in Table 4. The gamma-rays listed in the table are produced from (n,n'γ) reactions, and almost all the intense lines correspond to the ground-state transitions.

In the previous measurement by Drake et al.[11]), discrete lines were not resolved well because of the use of a NaI(Tl) detector. To compare with poor resolution data, the present cross sections near 744-keV and 950-keV lines are summed up. The present results of 740- and 950-keV groups are in reasonable agreement with those of Drake et al..

The summed cross sections of gamma-rays corresponding to the ground state transitions are compared with total inelastic cross sections. The present results are in good agreement with Thomas[12]), and slightly larger than the data of BNL-325. These results are illustrated in Fig. 9.

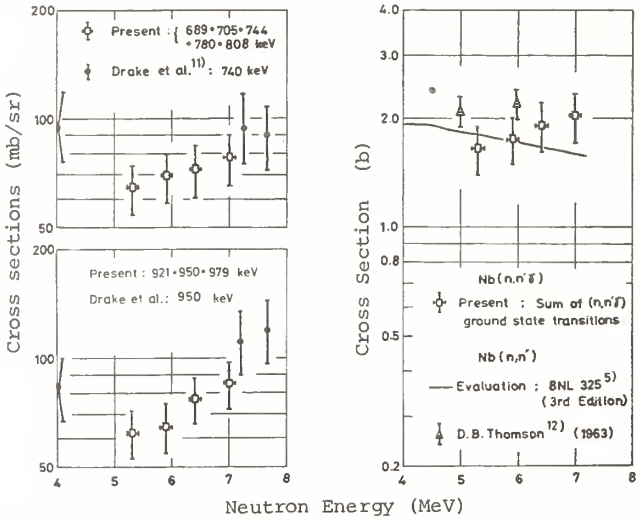

Fig. 9. Cross sections of intense gamma-rays and the summed cross sections of ground-state transitions.

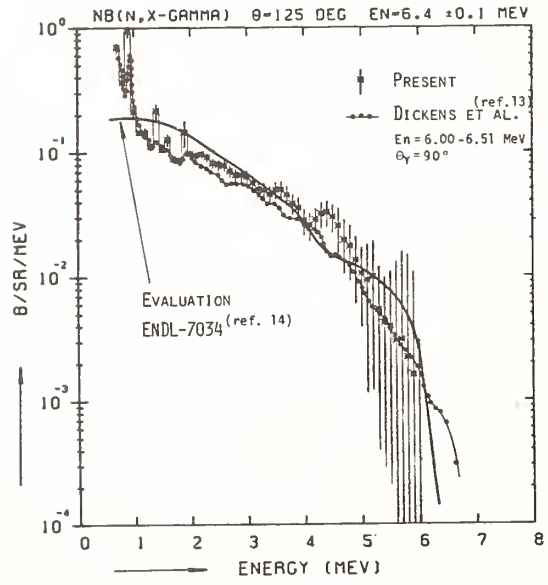

Fig. 10. Spectral gamma-ray production cross sections for niobium at 6.4 MeV neutron energy.

Spectral gamma-ray production cross sections are shown in Fig. 10 together with previous data. Dickens et al.[13]) used a NaI(Tl) detector and white neutrons from a linac. The evaluation of ENDL-7034[14]) was quoted from the data of Dickens et al.. The agreement is very good between the present result and those of Dickens et al., and some disagreements are found between the experimental results and the evaluation.

Conclusion

The results of present measurement are in good agreement with those of recent experiments, especially with ORNL groups. Some disagreements are found in the earlier studies or evaluations.

The summed cross sections of gamma-rays corresponding to the ground-state transitions are in fairly good agreement with total inelastic cross sections, and it may be improved with higher resolution and lower background measurements. This application is very useful to estimate inelastic cross sections because the data can be collected over a wide energy range in a given time with white neutrons.

The higher resolution and higher quality measurements will be expected to allow accurate evaluations and for other applications.

Acknowledgement

The authors are deeply grateful to the supporting staff of the Dynamitron accelerator at Tohoku University for technical assistance.

References

1) R.E. Textor and V.V. Verbinski: ORNL-4160, (1968)

2) D.C. Irving: ORNL-3662, (1965)

3) J.K. Dickens: Phys. Rev. C, Vol 5, pp 100, (1972)

4) C.G. Hoot, V.J. Orphan and J. Joseph: Gulf-RT-A10743, (1972)

5) D.I. Garber and R.R. Kinsey: BNL 325, Third edition, Vol II, (1976)

6) J.K. Dickens, T.A. Love and G.L. Morgan: ORNL-TM-4232, (1973)

7) J.K. Dickens, T.A. Love and G.L. Morgan: ORNL-TM-4379, (1973)

8) V.C. Rogers, D.R. Dixon, C.G. Hoot, D. Costello and V.J. Orphan: NSE 62, pp 716, (1977)

9) G.T. Chapman: ORNL-TM-5215, (1976)

10) M.K. Drake and M.P. Fricke: DNA 3356F, (1974)

11) D.M. Drake, J.C. Hopkins and C.S. Young: NSE 40, pp 294, (1970)

12) D.B. Thomson: Phys. Rev. 129, pp 1649, (1963)

13) J.K. Dickens, G.L. Morgan and E. Newman: ORNL-TM-4972, (1975)

14) E.F. Plechaty, D.E. Cullen, R.J. Howerton and J.R. Kimilinger: UCRL-50400, Vol 16, (1975)

NEUTRON SPECTRUM AT 90° FROM 800 MeV (p,n) REACTIONS ON A Ta TARGET

S. D. Howe, P. W. Lisowski, N. S. P. King and G. J. Russell
Los Alamos Scientific Laboratory*
Los Alamos, New Mexico 87545 USA

H. J. Donnert
Kansas State University
Manhattan, Kansas 66506 USA

The neutron time-of-flight spectrum produced by a thick tantalum target bombarded by 800-MeV protons has been measured at an angle of 90°. The data were taken at the Weapons Neutron Research facility using a cylindrical Ta target with a radius of 1.27 cm and a length of 15 cm. An NE-213 liquid scintillator was used to detect the neutrons over an energy range of 0.5-330 MeV. The neutron yield is presented and compared to a intranuclear-cascade/evaporation model prediction.

[Ta(p,xn), Neutron Yield, 800-MeV Protons, 0.5-350 MeV Neutrons, Intranuclear Cascade Predictions]

Introduction

The Weapons Neutron Research facility (WNR)[1] is a pulsed spallation neutron source operating at the Los Alamos Scientific Laboratory (LASL). The neutron energy spectrum produced by the WNR target has not been well characterized experimentally. Until now, theoretical predictions by a Monte Carlo intranuclear-cascade/evaporation code, NMTC,[2] have been used to represent the expected distribution. In this paper the results of a measurement of the neutron yield from the WNR Ta target are given for energies between 0.5 MeV and 350 MeV. A comparison of the data to a theoretical prediction is also made.

Experiment

A brief description of the WNR is presented here since previous papers[1,3] have given complete details. Up to 1% of the 800-MeV proton beam from the Clinton P. Anderson Meson Physics Facility (LAMPF) is transported to the water-cooled Ta target at the WNR. The target is 2.54-cm diam by 15-cm long. For this measurement, the proton beam consisted of micropulses less than 200 ps wide separated by 11 μs and occurring over intervals of 640 μs. The beam intervals were repeated at 12 Hz.

Collimated and evacuated flight paths perpendicular to the incident proton beam provide neutron beams to outlying detector stations. The experimental arrangement used in this measurement is shown in Fig. 1. The collimators in the shield surrounding the target consisted of two sets of movable copper jaws. These collimators limited the neutron flux to a 2.5 cm spot at the edge of the shield. In conjunction with a third collimator located outside the shield, a 0.95 cm diameter neutron beam was formed and passed through a sweep magnet to remove charged particles. This collimator combination limited the acceptance of the detector to a 2.5 cm square area of the target centered approximately 3.2 cm below the top.

The neutron detector used was a 5.1-cm diam. by 2.5-cm thick NE-213 liquid scintillator located 29.37 meters from the Ta target. The detector bias was set using the 60 keV gamma ray from an ^{241}Am source. This established the neutron energy bias at approximately 425 keV. The efficiency of the detector at this bias was measured up to 31 MeV at the LASL Tandem Van de Graaff accelerator. From 31 MeV to 800 MeV the efficiency was calculated using a Monte Carlo neutron efficiency code.[4,5] The measured detector efficiency and the Monte Carlo calculation are shown in Fig. 2. The calculated efficiency is about 15% higher than the measured value. This discrepancy indicates that the detector efficiency must be experimentally determined above 31 MeV. Work is presently underway on this problem.

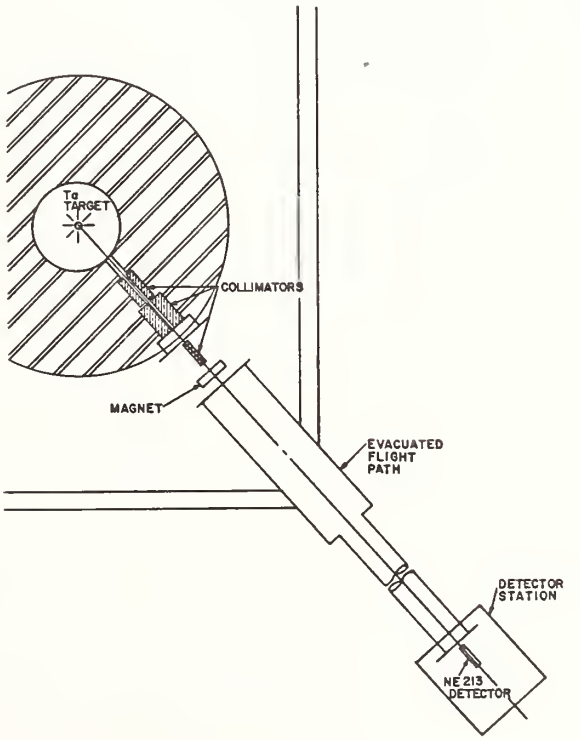

Fig. 1. Experimental setup to measure the neutron yield from the 2.5 cm diam. Ta target.

*Work performed under the auspices of the U.S. Department of Energy.

Electronics

A constant fraction timing discriminator was used to establish the neutron detection threshold and to provide stop signals for an EG&G TDC-100 clock. The clock was operated in a single stop per start mode at 0.5 ns per channel and with a 4 μs dead time. The start signal for the clock was provided by a capacitive pickoff positioned in the proton beam line. The signal generated by this pickoff was amplified and fanned out into two equal signals. One of the signals went to a ORTEC TDC-200 fast trigger whose output started the clock. The output of the clock was then stored in a MODCOMP IV computer. The count rate for this measurement was sufficiently low that the computer dead time was negligible.

The other pickoff signal was used to determine the number of protons incident on the target as follows. The signal was integrated and passed to an ORTEC QD808 charge digitizer. The digitizer, which has a conversion time of ≤ 6 μs, provided a pulse height distribution related to the number of protons in each pulse. The relationship between this spectrum and the number of protons, p, is given in Eq. (1).

$$p = K \beta \left[\frac{\sum_i C_i X_i}{\sum_i C_i} - A \right] \text{(protons)} \quad (1)$$

where C_i is the number of counts in channel X_i, β is the number of clock busy signals, A is the pedestal channel number of the QD808, and K is the constant of proportionality. The value of K was determined by bombarding a set of Aℓ foils with proton micropulses and simultaneously digitizing the pickoff signal using the QD808. By counting the gamma rays of the ^{24}Na, ^{22}Na and ^{7}Be spallation products, the number of incident protons was determined. Two such foil activations were made for this experiment explicity determining both K and A.

Data Reduction

The calculation of neutron yield first involved converting from time-of-flight to energy. This was done relativisitcally. The data were binned so that the energy resolution, ΔE/E, was constant and equaled

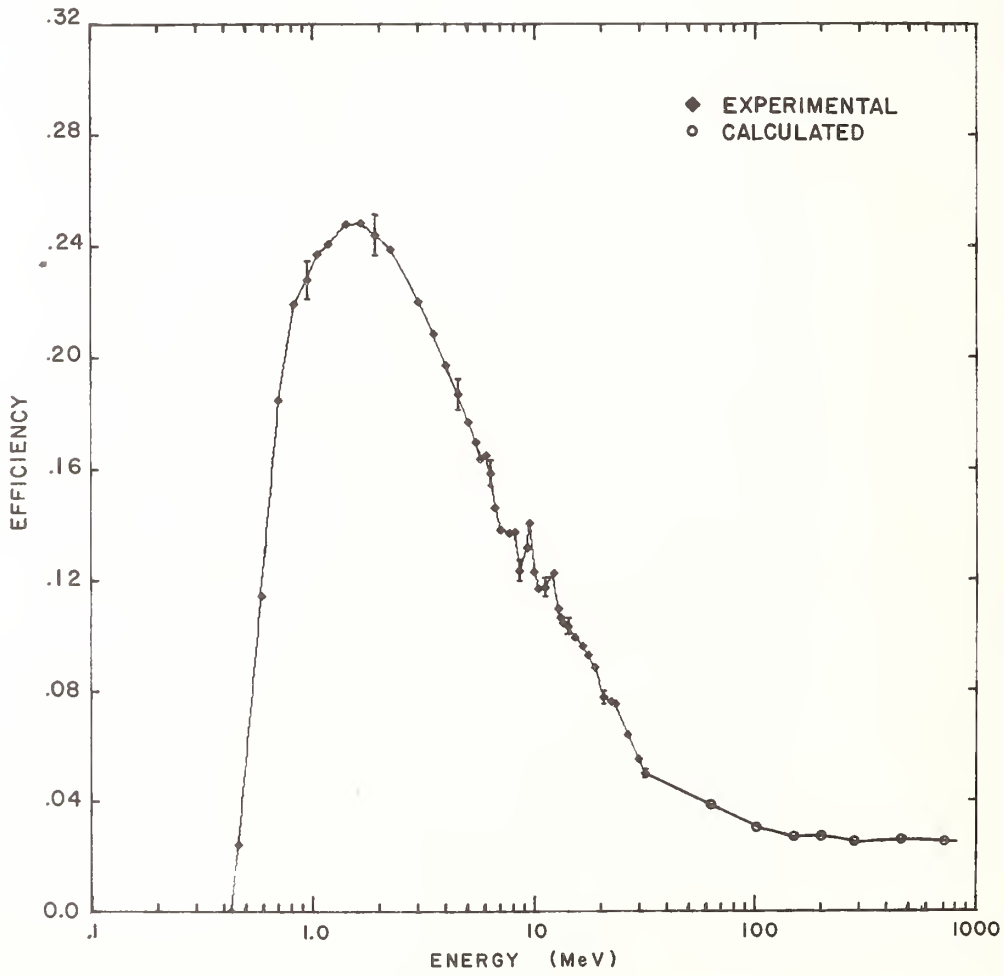

Fig. 2. Efficiency of the NE-123 neutron detector for a 0.43 MeV neutron energy bias. The values above 31 MeV were calculated using a Monte Carlo code. The solid line is a guide to the eye.

0.05. The actual time resolution of the experiment was 42 ps/m as determined from the gamma flash time width.

The neutron yield, Y(E), in energy interval ΔE about energy E is found from:

$$Y(E) = \frac{R(E)}{p \Delta\Omega \ \varepsilon(E)} \quad (n/p \cdot sr \cdot MeV) \qquad (3)$$

where R(E) represents the number of events in ΔE corrected for clock dead time losses[6], p is the incident number of protons, $\Delta\Omega$ is the solid angle subtended by the detector, and $\varepsilon(E)$ is the efficiency of the detector at energy E averaged over ΔE. The solid angle was calculated by a Monte Carlo code.

Statistical errors in this measurement varied from less than 3% around 1 MeV to 5% above 100 MeV. The sources of systematic error include determination of the incident number of protons, calculation of the solid angle, transparency of the collimators to neutrons with energy greater than 100 MeV, and estimation of the neutron detector efficiency above 31 MeV. The magnitude of the systematic errors is estimated to vary from 11% for En $\leq$ 30 MeV to 13% at higher energies. More effort is being made to understand these errors and include their effects.

Results

The experimental results are shown in Fig. 3 and compared with a calculated prediction using the computer code NMTC. The error bars on the experimental data are statistical only. The main features shown by this initial comparison are the low calculated neutron yields at both high and low energies. The two spectra do agree in the energy region around 10 MeV.

The underprediction of the calculations above $\sim$ 50 MeV is consistant with other results[7] obtained using 740-MeV protons but disagrees with 450-MeV proton data.[8] The disagreement at energies below $\sim$ 5 MeV could be due to: a) parameters used in the evaporation model, b) instability in detector bias, c) the inability to calculate proton transport below 20 MeV, and d) use of an outdated neutron cross section library below 20 MeV. The computations are being repeated with more

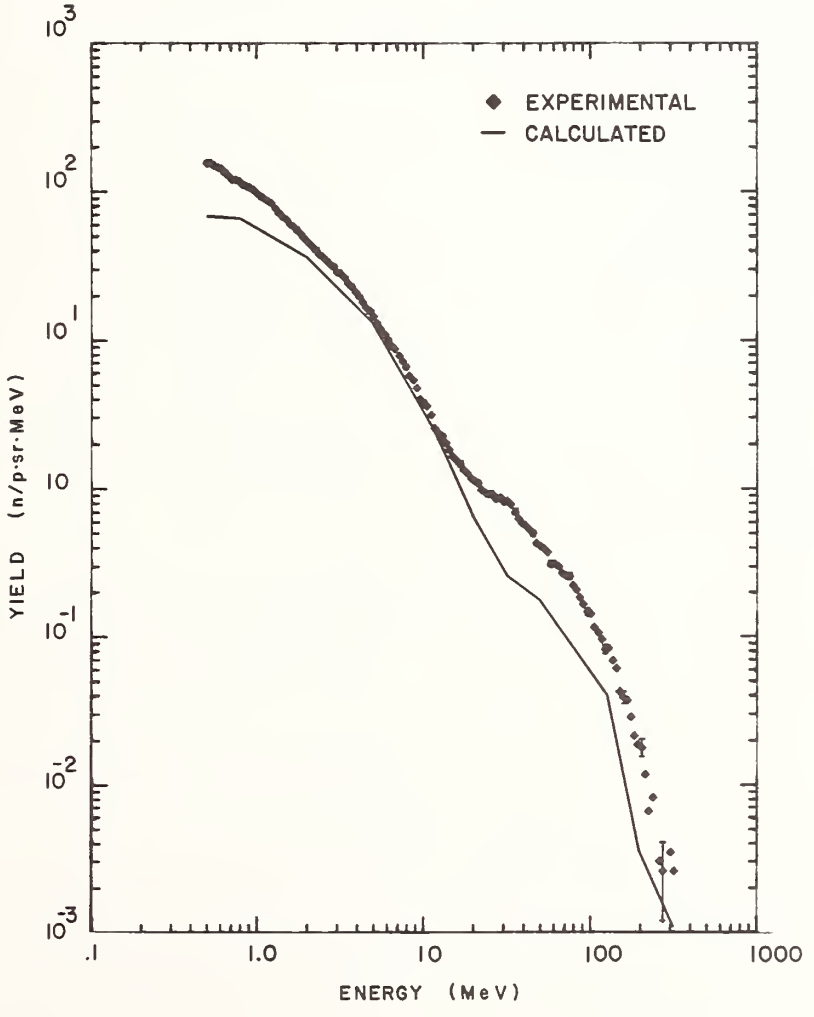

Fig. 3. Neutron yield for the 2.5-cm-diam by 15-cm-long Ta target at the WNR. The solid line was calculated using the Monte Carlo code NMTC. Statistical errors of the data below 100 MeV are represented by the dot size. Typical error bars for data above 100 MeV are shown.

stringent requirements on solid angle and energy resolution binning and using the latest ENDF-B cross sections.

References

1. G. J. Russell, P. W. Lisowski, and N. S. P. King, in Proc. of Intl. Conf. on Neutron Phys. and Nucl. Data for Reac. and Other Appl. Purposes, Harwell, England, 1978.

2. W. A. Coleman and T. W. Armstrong, Oak Ridge Natl. Lab. Report ORNL-4606 (Oct. 1970).

3. G. F. Auchampaugh, in Proc. of Intl. Conf. on Nucl. Cross Sec. for Tech., Knoxville, Tenn., 1979 (to be published).

4. B. Anderson to N. S. P. King, private communication.

5. R. A. Cecil et al., Nuclear Instruments and Methods, 161, 439 (1979).

6. M. S. Moore and references therein, to be published in Nucl. Instr. Meth. (1979).

7. R. Madey and F. M. Waterman, Phys. Rev. C, Vol. 8, No. 6, 2412-2418 (1973).

8. R. G. Alsmiller, Jr., J. W. Wachter, and H. S. Moran, Nucl. Sci. Engr., #36, 291-294 (1966).

ANALYSIS OF NEUTRON YIELD PRODUCED BY HIGH ENERGY PROTON

H. Takahashi and Y. Nakahara
Brookhaven National Laboratory
Upton, New York 11973, USA

Vasil'kov et al.'s experiments for neutron yield and neutron capture distribution produced by 400 and 660 MeV protons were analyzed by using ENDF/B-IV data and the BNL codes NMTC and TWOTRAN. The calculated total neutron radiative capture by ^{238}U is 77 and 60% of the measured values for protons of 660 and 400 MeV, respectively. The calculated distribution has the higher peak in the central part of the target system, and steeper gradient both in the r and z directions, compared to experimental. The leakage rate of neutrons from the target assembly is calculated as more than 20%, which is much higher than the 10% estimated from the experiment. The total neutron captures determined using ENDF/B-IV are 3.8 and 3.0% higher than those determined using ENDF/B-III for protons of 660 and 400 MeV, respectively.

[Neutron yield analysis, High energy proton, 400-660 MeV, Spallation, Evaporation, Fission]

Introduction

Since reprocessing facilities indispensable for the conventional Light Water Reactor to Fast Breeder Reactor fuel cycle are now considered to increase the risk of nuclear weapons proliferation, evaluations have been initiated to find alternative nuclear energy systems not only more proliferation resistant but helpful to stretch uranium resources. A Linear Accelerator Reactor (LAR)[1] is one of these systems of great promise in producing fissile material in conjunction with proliferation resistant fuel cycles.

This reactor uses a high energy proton or deuteron beam from a linear accelerator incident on a Pb-Bi target as an intense neutron source. The target is surrounded by a lattice of Zr-clad rods of fertile-fissile material which is called the blanket. At the initial loading, uranium with 2% enrichment is used.[2] The burning scheme depends on the options described below. Three options for design optimization are present: (1) optimization of the time-integrated production of thermal energy for conversion to power, (2) optimization of the production rate of fissile material, without reprocessing, (3) optimization of the production rate of fissile material, in conjunction with reprocessing. These options correspond to Linear Accelerator Driven Reactor, Linear Accelerator Fuel Regenerator and Linear Accelerator Fuel Producer, respectively.

From the nuclear design point of view for these reactors, the neutron yield per primary proton (or deuteron) and the neutron flux distribution are the most important physical parameters. There have been published, however, few experimental data on these quantities for realistic reactor systems.[3,4]

Recently, a Russian group (Vasil'kov et al.)[5] performed experiments on 56x56x66 cm^3 natural and depleted uranium blocks surrounded by a lead wall for primary proton energies of 300, 400, 500, and 660 MeV.

In this paper, the BNL computer code system for the linear accelerator reactors has been applied to the Russian experimental facilities in order to estimate the accuracy and tendency of the code system. Comparison is made of the neutron radiative capture $^{238}U(n,\gamma)$ reaction density distribution between the measured value obtained by Vasil'kov et al. and our computational results using the cross section data of ENDF/B-III[6] and -IV[7].

The total neutron radiative capture by ^{238}U calculated with the ENDF/B-IV cross section data are 77 and 60% of the measured values for proton energies of 660 and 400 MeV, respectively. These values are 3.9 and 3.0% higher than those calculated by using ENDF/B-III.

Vasil'kov Experiment

In the experiments by Vasil'kov et al.[5], use was made of a target assembled from rectangular blocks of natural (2x4x8 cm^3) and depleted (8x8x16 cm^3) uranium. Total linear dimension of the target was 56x56x64 cm^3 covered with a lead layer of thickness 10 or 20 cm, as shown in Fig. 1.

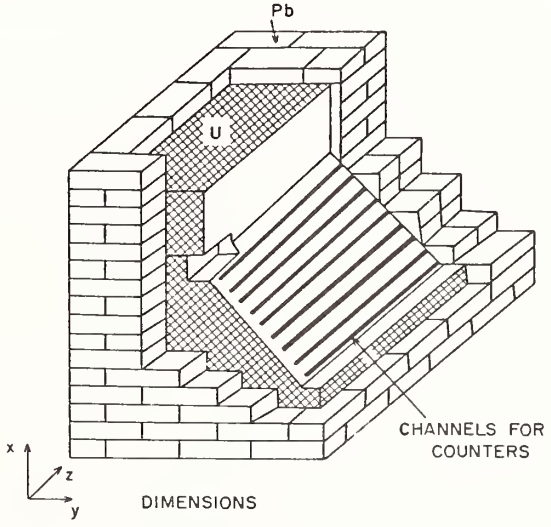

Fig. 1 TARGET IN RUSSIAN EXPERIMENTS

The proton beam was injected into the central part of the target through a beam hole of cross section 8x8 cm^2 and a depth of 16 cm from the front surface of the uranium block. The diameter of the proton beam at the entrance into the target was 4~5 cm.

Experiments were carried out with an extracted beam of 660 MeV protons. For the experiments at proton energies 300, 400 and 500 MeV, the initial 660 MeV protons were slowed down in a polyethylene attenuator.

In the diagonal plane of the target, passing through the axis of the proton beam, a system of channels was made for the arrangement of detectors. Channels were arranged in parallel with the proton beam

and located from 6 to 45 cm from the axis approximately each 3 cm. The dimensions of a channel were 60 cm in length and 2x0.3 cm^2 in cross section.

When the proton beam is absorbed in a uranium target, fast neutrons are generated with an energy of 1~100 MeV (superposition of cascade-evaporation and fission). On being scattered by uranium nuclei, these neutrons slow down to the energy range where radiative capture occurs.

$$^{238}U\ (n,\gamma) \longrightarrow {}^{239}U \xrightarrow{\beta-} {}^{239}Np \xrightarrow{\beta-} {}^{239}Pu$$

During the slowing down, neutrons are multiplied further in consequence of the fission of uranium nuclei.

The density distribution of (n,γ) capture was measured by ^{239}Np, distinguished radio-chemically from uranium samples irradiated at various points in the target. Measuring the density distribution $A(z,r,\phi)$ of the (n,γ) capture in the volume of target and integrating this distribution, Vasil'kov et al., obtained the total number of captures (^{239}Pu yields) per one energetic proton[5]:

$$Y = \rho \int_V A(z,r,\phi)dV \qquad (1)$$

where z is the direction of proton beam, r,ϕ are cylindrical coordinates and ρ is the density of metallic uranium.

Computational Method

The BNL computer code system used in this analysis consists of six main programs: NMTC[8], HIST3D, EPR[7], (DLC-2[6],) TAPEMAKER, ANISN[9], TWOTRAN-II[10]; and auxiliary programs: FIND, SURF, MULTSUM. Overall interrelations of these programs is indicated in Fig. 2.

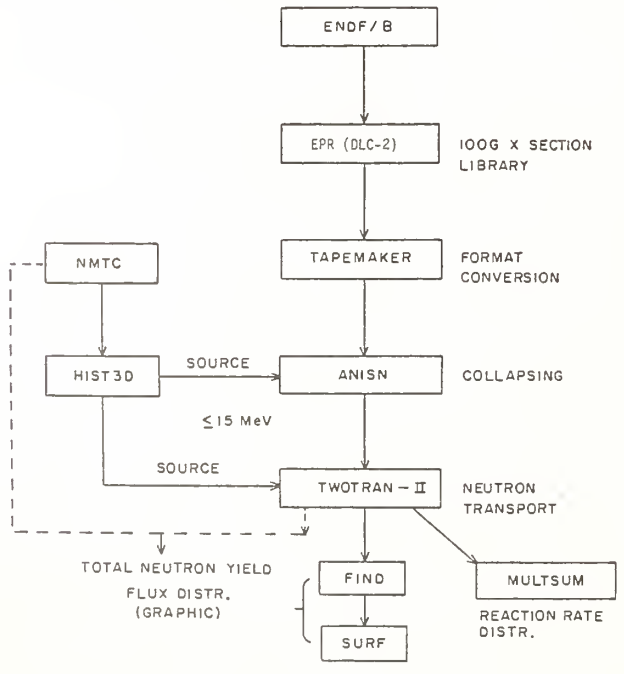

Fig.2 NEUTRONICS PART OF BNL CODE SYSTEM FOR LAR'S

The NMTC is used to calculate the spallation and evaporation processes above 15 MeV by the Monte Carlo method. Collision events of neutrons slowed down below 15 MeV are filed by NMTC. The collision events file is analyzed with HIST3D to obtain neutron distributions which are used as neutron sources in the transport calculations for neutrons in the energy range below 15 MeV. The EPR[7] neutron reaction cross sections are based on ENDF/B-IV. The program EPR is used to make a file containing cross section data only for nuclides selected specifically. TAPEMAKER is used to convert the format of EPR data to that of ANISN, i.e., FIDO format as it is usually called. The EPR 100 group sets are collapsed to fewer energy group sets by the one-dimensional neutron transport code ANISN based on the discrete ordinate S_n method. The final neutron transport calculations are performed with TWOTRAN-II, which is a two-dimensional S_n method program and can take into consideration anisotropies in neutron source and scattering cross sections. MULTSUM has been programmed to calculate reaction rate distributions. The ENDF/B-III cross section data are taken from the DLC-2 100 group set.

In our calculations, the rectangular target of Vasil'kov et al. was replaced by a volume equivalent cylinder of metallic natural uranium with a radius of 31.595 cm and axial length of 64 cm, as shown in Fig. 3. The radius of the beam guide hole is 4.5135 cm. The proton beam radius was taken to be 2.5 cm. Atomic number densities of ^{235}U, ^{238}U and Pb are in units of $10^{24}/cm^3$, 0.00035148, 0.0478546 and 0.033000, respectively.

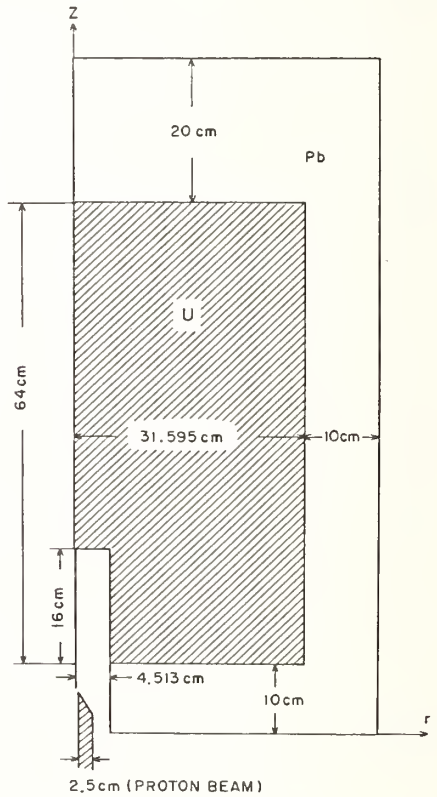

Fig.3 VOLUME EQUIVALENT CYLINDRICAL TARGET IN BNL CALCULATION

The procedure of our calculations is as follows. In the NMTC calculation, the average was taken over 10 batches of 75 protons each. Since the sampling number is large enough, the statistical error is somewhat large.

The P_3 neutron source distribution was prepared for the TWOTRAN-II calculation using HIST3D. As for the anisotropy of neutron scattering, the P_3 approximation was employed and 30 group cross section sets

were prepared using ANISN. In the TWOTRAN-II calculations the S_8 approximation was used. Since the $S_8 - P_3 - P_3 - 30$ group calculations by TWOTRAN are very expensive, sufficiency of the degree of S_n approximation has not been examined.

Since the entire calculation is very expensive, the calculations have been performed only for proton energies of 660 and 400 MeV. Values of neutron capture by ^{238}U are summarized in Table I and are compared in Fig. 4 with experimental values of Vasil'kov et al.[5], and the calculational results of Baraschenkov et al.[4] As is clear from Fig. 4, our model gives conservative results in comparison with experiments, i.e., underestimates of about 23 ∿ 39% in average values depending on proton energies.

Table I. Analysis of Russian experiments by the BNL Code System for LAR.

Target	E_p	^8N_c (IV)	^8N_c (III)	N	^8N_c (Vasil'kov Exp)
Nat. U	660	35.23 ± 3.79	33.92 ± 3.64	24.38 ± 2.62	46. ± 4
U-238	660	32.52 ± 3.49	31.47 ± 3.38	"	-
Oept. U	660	33.78 ± 3.63	32.61 ± 3.50	"	38. ± 4
Nat. U	400	13.44 ± 0.81	12.97 ± 0.79	9.95 ± 0.60	22.1 ± 2.4
Pb-Nat. U	660	26.68 ± 2.40	25.92 ± 2.33	21.10 ± 1.9	27.60
Pb-U-238	660	24.56 ± 2.21	24.13 ± 2.17	"	-

E_p = proton beam energy (MeV)

N = average number of neutrons per one primary proton produced by spallation evaporation reactions in energy range above 15 MeV.

N_c = number of neutrons captured by ^{238}U per one primary proton.

(IV) = ENDF/B-IV

(III) = ENDF/B-III

Vasil'kov Exp = Reference (5)

Pb-Nat. U = Pb target surrounded by natural uranium.

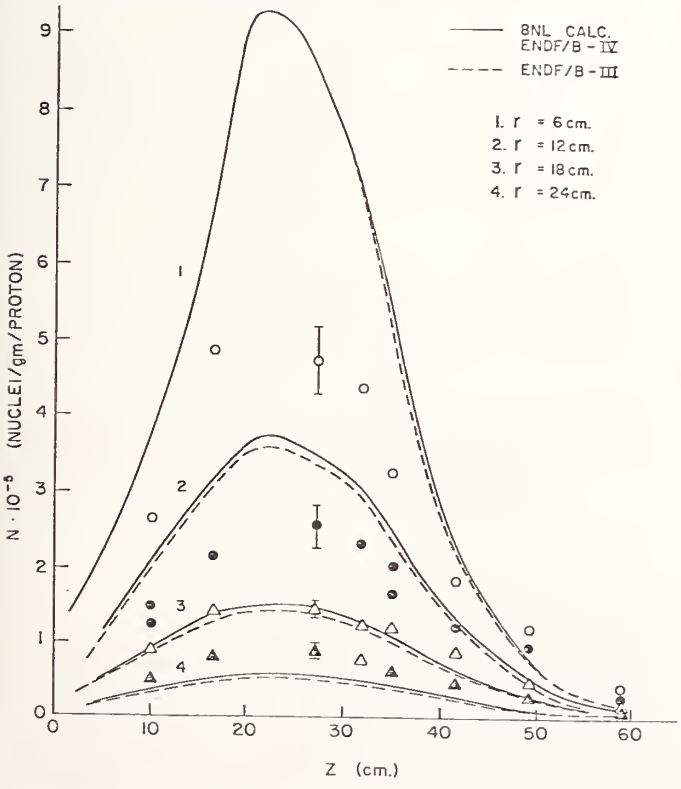

Figure 4 $^{238}U(n,\gamma)$ REACTION DISTRIBUTION
N = NUMBER OF ^{239}Np NUCLEI

Vasil'kov et al. performed experiments also on depleted uranium targets. For the sake of comparison, calculations were performed for the pure ^{238}U target, results for which are also shown in Table I. Although the degree of depletedness is not written in the paper of Vasil'kov et al., if we estimate it as 0.33% (number density percentage of ^{235}U) from the data of ^{235}U fission events summarized in Table II, the value of the total neutron capture by ^{238}U for this depleted uranium can be estimated to be 33.78 ± 3.63, which should be compared with the experimental value 38±4. In this calculation, the spallation and evaporation calculation using NMTC is taken from the results for the natural uranium case, because the difference between them should be small in the case of neglecting high energy fission.

Table II. Number of fission events in Nat. U target (fissions/proton).

	BNL Calculation ENDF/B-IV	ENOF/8-III	Russian Exp[5]
ν_{Total}	10.37 ± 1.11	8.98 ± 0.96	18.5 ± 1.7 (13.7 ± 1.2)
ν_{235}	2.11 ± 0.23	1.99 ± 0.21	3.9 ± 0.4 (1.5 ± 0.1)
ν_{238}	8.26 ± 0.88	6.99 ± 0.75	14.6 ± 1.3 (12.2 ± 1.1)

Proton energy = 660 MeV

Values in ( ) are for depleted uranium

For a proton energy of 660 MeV, Vasil'kov et al. also measured the decrease in the value of neutron captured by ^{238}U when replacing the uranium in the central part of the target with a lead block of dimensions ($8 \times 8 \times 48$ cm^3)[5]. The measured ratio of neutron yields for lead-uranium and uranium target was 0.48 ± 0.2, that is, the value of neutron captured by ^{238}U is calculated as 27.6 ± 11.5 for Pb-U. Which is close to our calculated value of 26.68 ± 2.40.

In Fig. 5, distributions of radiative capture density for ^{238}U are compared between our calculations and the experiments of Vasil'kov et al[5]. The unit of distribution is the number of ^{239}Np nuclei per gram of uranium and per incident proton. In the central region of the target system the calculated distribution has the higher peak and steeper gradient both in the r and z directions. The agreement between calculated and measured values is good for the curve 3. Fig. 5 is, however, somewhat embarrassing. The calculated distribution is larger than the measured one, while the neutron capture yield obtained by integrating the distribution is smaller in the calculation.

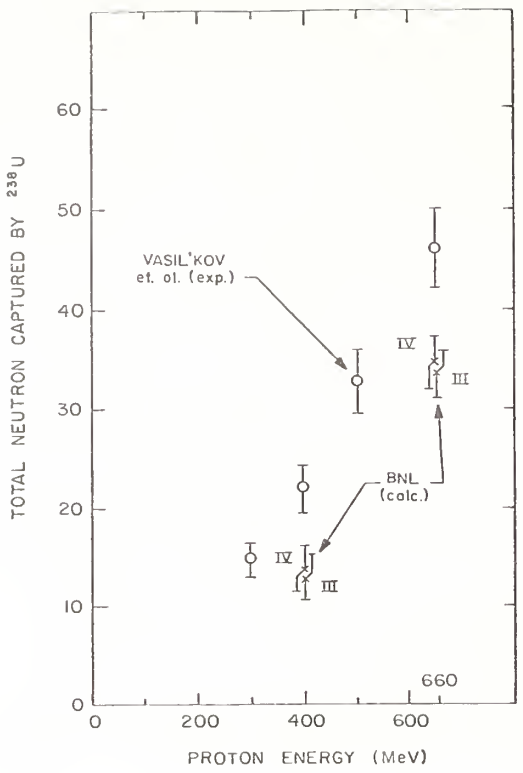

Figure 5 COMPARISON OF TOTAL NEUTRONS CAPTURED BY ^{238}U PER ONE PROTON BY VASIL'KOV et al. EXPERIMENT AND BNL CALCULATION (III & IV FOR ENDF/B - III & IV)

In Table III, the numbers of absorbed, fissioned and leaked neutrons from the assembly normalized to one neutron, which is produced by spallation and evaporation reactions in the energy range above 15 MeV, are shown for several targets and proton energies. The neutron leakage ratio, which is defined by L/(L+A), is from 16.7 to 20.4%. This is higher than the estimation of Vasil'kov et al.

Table III. The fractions of neutron absorption, fission and leakage from assemblies in the energy range less than 15 MeV.

Target	E_p	Absorption A	Fission F	Leakage L	A+L	Leakage Rate $\frac{L}{1+L}$
Nat. U	660	1.741 (1.639)	1.063 (0.921)	0.373 (0.329)	2.114 (1.968)	0.176 (0.167)
U-238	660	1.503 (1.423)	0.770 (0.659)	0.319 (0.283)	1.821 (1.706)	0.175 (0.166)
Nat. U	400	1.605 (1.512)	0.978 (0.843)	0.413 (0.369)	2.018 (1.881)	0.205 (0.196)
Pb-Nat. U	660	1.545 (1.470)	0.852 (0.739)	0.360 (0.322)	1.905 (1.792)	0.189 (0.179)

The values in parenthesis ( ) are calculated by ENOF/B-III and those without parenthesis are calculated by ENOF/B-IV.

A = Absorption fraction normalized to one source neutron which is produced by spallation and evaporation reaction in energy range above 15 MeV.

F = Fission fraction normalized to one source neutron which is produced by spallation and evaporation reaction in energy range above 15 MeV.

L = Net leakage fraction from the system normalized to one source neutron which is produced by spallation and evaporation reaction in energy range above 15 MeV.

The neutron yield in the calculation of Baraschenkov et al. which is cited in the paper of Vasil'kov et al. is defined as

$$Y = N_c^5 + N_c^8 + N_{esc}, \qquad (2)$$

where N_c^5 and N_c^8 give the internal escape defined as the number of radiative neutron captures by ^{235}U and ^{238}U and N_{esc} is the number of neutrons which escape from the block through the side and faces. This yield corresponds to the value of (A+L)·N in our calculation. Although the comparison between two calculations of Baraschenkov and ours is not meaningful, because of the different geometries, the values of Baraschenkov and our results of (A+L)·N are shown in Fig. 6. Our values are substantially smaller than those of Baraschenkov.

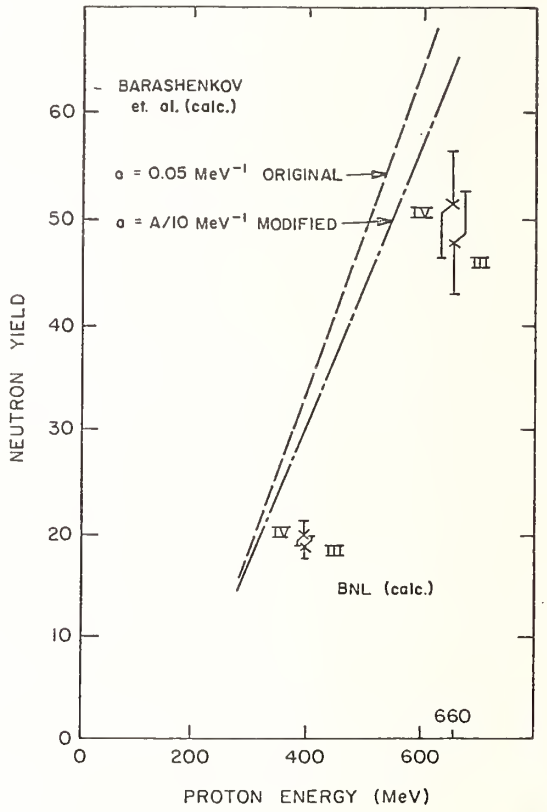

Figure 6 COMPARISON OF NEUTRON YIELDS OBTAINED BY BNL AND BARASHENKOV'S CALCULATIONS FOR EFFECTIVELY INFINITE NATURAL URANIUM TARGET. (III & IV FOR ENDF/B - III & IV)

What causes disagreement between theory and experiment depends on many assumptions and approximations used both in the theory and experiment. The theory is based on assumptions of nuclear structure, nuclear reactions and their measured data. Computation brings in further approximations. When we use the code system available currently, what can be done to improve the calculations is to use higher order approximations in S_n and P_n treatments.

One specific reason for this discrepancy seems to be neglect of the fission process in the energy range higher than 15 MeV in the NMTC code. The fission by high energy protons was calculated as about 80% of the reaction in ^{238}U by Dostrovski et al.[11], but it has been considered that inclusion of fission in the high energy reaction does not change the total number of neutrons produced appreciably. The study by Hahn and Bertini[12] on the competition of spallation-fission in the reaction of protons with heavy elements showed that the total number of neutrons calculated by spallation and evaporation without fission is larger than the number calculated by including the fission reaction because of neglecting the neutrons from fission product nuclei. He used the empirical energy dependent relation for $\Gamma n/\Gamma f$, where Γn, Γf = neutron and fission widths, respectively.

Our preliminary calculation of the fission reaction by the statistical model indicates that the total neutron yield in the reaction at energy higher than 15 MeV is increased about 48% over that without fission. Thus, in order to explain the discrepancy between the experimental results and calculations, it is important to take the fission reaction into consideration.

As shown in Table II, the difference in fission events between experiment and calculation is large, the number of fission events is almost the same as that for energy lower than 15 MeV.

All data calculated by ENDF/B-III are smaller than those calculated by ENDF/B-IV data. The slightly larger value of fission cross section of ^{238}U and ^{235}U from ENDF/B-IV might cause the increase of the fission, leakage and absorption in that case.

Acknowledgement

Work performed under the auspices of the U.S. Department of Energy.

The authors wish to express their acknowledgments to Dr. B. Gol'danskii, Dr. R. Alsmiller and Dr. P. Garvey for their valuable discussions.

References

1. H. Kouts et al., ed., "Informal Meeting on Linear Accelerator Breeders, held at BNL on Jan. 18 & 19, 1977", ERDA Conf. 770107.

2. Dept. of Nucl. Energy, Brookhaven National Laboratory, "Conceptual Design and Economic Analysis of a Light Water Reactor Fuel Enricher/Regenerator", BNL-50838 (UC-80 TID-4500) 1978.

3. V.S. Baraschenkov, A.S. Ii'nov, N.M. Sobelevskii, and V.D. Toneev, Sov. Phys. Usp., 16, 31 (1973).

4. V.S. Baraschenkov and V.D. Toneev, Atomnaya Energiya, 35, 163 (1973).

5. R.G. Vasil'kov, V.I. Gol'danskii, B.A. Pimenov, Yu. N. Potokilovskii, and L.V. Chistyakov, Atomnaya Energiya, 44, 329 (1978).

6. Radiation Shielding Information Center, ORNL, "EPR, Coupled 100-Group Neutron 21-Group Gamma-Ray Cross Section for EPR Neutronics", DLC-37.

7. Radiation Shielding Information Center, ORNL, "100G, 100 Group Neutron Cross Section Data Based on ENDF/B", DLC-2.

8. Radiation Shielding Information Center, ORNL, "NMTC, Monte Carlo Nucleon-Meson Transport Code System", CCC-161.

9. W.W. Engle, Jr., "A Users Manual for ANISN, A One-Dimensional Discrete Ordinate Transport Code with Anisotropic Scattering", K-1693 (1967), contained in CCC-82, RSIC ORNL.

10. K.D. Lathrop and F.W. Brinkely, "TWOTRAN-II: An Interfaced, Exportable Version of the TWOTRAN Code for Two-Dimensional Transport", LA-4848-MS (1973).

11. I. Dostrovsky, Z. Fraenkel, and P. Rabinowitz, P/1615, "Proc. Second United Nations International Conference on the Peaceful Uses of Atomic Energy", Vol, 15, 1958.

12. R. Hahn and H. Bertini, Phys. Rev. 6C, 660 (1972).

CALCULATED PARTICLE PRODUCTION SPECTRA AND MULTIPLICITIES FROM NUCLEON-FISSILE ELEMENT COLLISIONS AT MEDIUM ENERGIES

F. S. Alsmiller, R. G. Alsmiller, Jr., T. A. Gabriel, R. A. Lillie, J. Barish
Oak Ridge National Laboratory
Oak Ridge, Tennessee 37830, USA

A fission channel has been added to the intranuclear-cascade-evaporation model of nuclear reactions so that this model may be used to obtain the differential particle production data that are needed to study the transport of medium-energy nucleons and pions through matter. The earlier work of Hahn and Bertini on the incorporation of fission-evaporation competition into the intranuclear-cascade-evaporation model has been retained and the statistical model of fission has been utilized to predict particle production from the fission process. Approximate empirically derived kinetic energies and deformation energies are used in the statistical model. The calculated residual nuclei distributions are in reasonable agreement with experimental data, but the neutron multiplicities at the higher incident nucleon energies $\gtrsim$ 500 MeV are sensitive to the level density parameter used.

[High Energy Cross Sections, Actinide Fission, Statistical Model, Intranuclear Cascade]

Introduction

For several applications, e.g., studies of the feasibility of converting fertile to fissile material using medium-energy proton beams[1], and in designing facilities to produce an intense source of low-energy neutrons by using medium-energy protons[2], it is necessary to carry out calculations of the transport of medium- and low-energy nucleons and pions through fissionable material. To carry out such transport calculations it is necessary to have available differential particle production data from the collision of nucleons and pions with fissionable nuclei. In this paper a fission channel, that has been added to the intranuclear-cascade-evaporation model of H. W. Bertini[3,4] so that this model can be used to provide this needed differential particle production data, is described and comparisons between calculational results and experimental data are presented.

In a previous paper, H. L. Hahn and H. W. Bertini[5] have shown how the probability of fission may be incorporated into the intranuclear-cascade-evaporation model, but they did not extend their calculations to include particle production following fission. In the present paper, this particle production following fission is included by using a version of the statistical model of fission developed by P. Fong.[6] To a large extent the physical data that occur in the statistical model have been derived from the experimental measurements of D. H. Epperson.[7] Calculations similar to those presented here have previously been given by V. S. Barashenkov and V. D. Toneyev.[8] In the model used here, however, much more reliance is placed on empirically derived constants than in Ref. 8.

Intranuclear-Cascade-Evaporation Model

The intranuclear-cascade-evaporation model of medium-energy nuclear reactions as implemented by Bertini has been described in detail previously[3,4], so only a very simple discussion of those parts of the model that have not been modified will be given here. Basically, the model assumes that nucleon- and pion-nucleus nonelastic collisions may be considered to be a two-step process. In the first step the cascade nucleons and pions are emitted leaving an exicted residual nucleus. In the second step this excited nucleus loses its excitation energy by "evaporating" particles. If the excited residual nucleus has a sufficiently large atomic weight and number, fission will compete with the evaporation process. Hahn and Bertini[5] have considered this competition and have found that reasonably reliable results can be obtained by using an excitation-energy-independent empirically derived formula for the ratio of the neutron width to the fission width in conjunction with the assumption that no fission occurs for elements with atomic number less than 91. After a fission has occurred, two excited residual nuclei remain and further particle emission by evaporation occurs. The work reported here is primarily concerned with estimating the mass, atomic number, and kinetic energy distributions of the nuclei produced from fission and with estimating the kind, number and energy of the particles that are evaporated following fission.

Statistical Model

Let the set (A_f, z_f, m_{of}, E_f) be the nucleon number, proton number, rest mass energy, and excitation energy of the fissioning nucleus. Similarly, let the set $(A_i, z_i, m_{oi}, E_{ir})$ be the corresponding values for the fission fragments where i takes values 1 and 2 corresponding to the light and heavy fragment and r takes values S meaning evaluation at scission time, t_S, and E meaning evaluation at evaporation time, t_E. If

$$m_d = m_{of} - m_{o1} - m_{o2} \; ; \; Q = E_f + m_d \; , \tag{1}$$

conservation of energy gives[6,9]

$$E_{1E} + E_{2E} = Q - K_E = E_{1S} + E_{2S} + D \; , \tag{2}$$

where D is the total "deformation" energy at t_S and K_E is the relative kinetic energy at t_E. Also

$$K_E = K_S + C_S \; ; \; C_S = k \, V_S \; , \tag{3}$$

where K_S is the relative kinetic energy at t_S, C_S is the Coulomb potential energy of the deformed fragments at t_S, and V_S is the Coulomb potential energy of two spherical nuclei in contact.

Conservation of momentum can be carried out relativistically at t_E in the c.m. system. Then

$$\sqrt{p^2+m_{e1}^2} + \sqrt{p^2+m_{e2}^2} = \varepsilon_1 + \varepsilon_2 = m_{ef} \tag{4}$$

$$m_{ei} = m_{oi} + E_{iE} \qquad i = 1,2 \tag{5}$$

$$m_{ef} = m_{of} + E_f = K_E + m_{e1} + m_{e2} \; , \tag{6}$$

and P, the magnitude of the momentum of each fragment, is approximately given by

$$p^2 \simeq 2K_E \, \frac{m_{e1} m_{e2}}{m_{ef}} \tag{7}$$

The kinetic energies of each fragment are obtained using the value of P from Eq. (7) and isotropy in the c.m. system. The density of kinetic energy states will be needed in the statistical model. The relativistic value for this is proportional to $\omega(K_E)$ where

$$\omega(K_E) = P^2 \frac{dP}{dK_E} = \frac{\varepsilon_1\varepsilon_2 P}{m_{ef}} \simeq \frac{A_1A_2}{A_1+A_2}\sqrt{K_E} \qquad (8)$$

The primary postulate of the statistical theory of Fong[6] is that the yield of fission fragments, $N(A_2,E_f)$, is taken to be proportional to the total density of quantum states at scission time, integrated over all variables. The density of excitation states at t_S is written

$$\tilde{\rho}_{iS} = p_{ri} \exp\left[2\sqrt{a_i E_{ic}}\right] \qquad i = 1,2 \qquad (9)$$

$$E_{ic} = E_{iS} - \Delta_i = E_{iE} - \Delta_i - D_i \qquad (10)$$

= excitation energy above the "characteristic" ground-state level[6],

Δ_i = pairing energy,

p_{ri} = preexponential factor, including an integral over all angular momentum states,

a_i = "level density parameter."

For given deformation energies, D_i, the product $\tilde{\rho}_{1S}\tilde{\rho}_{2S}\,\omega(K_E)$, where $\omega(K_E)$ has been given previously, is proportional to the total density of states. Defining

$$R_m = Q - \Delta_1 - \Delta_2 \ , \qquad (11)$$

$P(D,k)$ = probability of a given D and k,

one can write quite generally, using limits determined by the conservation of energy conditions,

$$N(A_2,E_f) \triangleq \int_{z_L}^{z_H} dz_2 \int_{D_{min}}^{R_m - k_{min}V_s} dD \int_{k_L(D)\geq k_{min}}^{(R_m-D)/V_s} dk \int_{kV_s}^{R_m-D} dK_E \int_{0}^{R_m-D-K_E} dE_{2c}$$

$$\times \tilde{\rho}_{2S}(E_{2c})\tilde{\rho}_{1S}(R_m - D - K_E - E_{2c})\omega(K_E)P(D,k) \cdot \qquad (12)$$

The limits z_L, z_H, $k_{min} > 0$, and $D_{min}(z_2) > 0$, are assumed tentatively to be given.

The probability function, $P(D,k)$, and the lower limit, $k_L(D)$, must be found from a theory of deformation energies. For simplicity, we use the two-parameter theory of Fong[10],

$$D_i = \frac{C_i}{2}\beta_i^2 \qquad i = 1,2 \qquad (13)$$

$$D = D_1 + D_2 = D_2(1+D_r) \ ; \ D_r = \frac{C_1}{C_2}\beta_{1r} \ ; \beta_{1r} = \frac{\beta_1}{\beta_2} \qquad (14)$$

$$k = C_S/V_S = \frac{(r_1+r_2)_S}{r_{1S}+r_{2S}+\alpha_1\beta_1 r_{1S}+\alpha_2\beta_2 r_{2S}} \ , \qquad (15)$$

where r_{1S} = radius of spherical nucleus, α_1, and α_2 are parameters (or functions of A_2,z_2) to be determined, and the C's are Mottelson's "stiffness coefficients", furnished by Fong[10,11].

One can solve for $\beta_{1r}(D,k)$. The minimum possible value of k, if β_{1r} is to be real, is given by

$$k_L(D) = \left[1+\sqrt{D/D_o}\ \right]^{-1} \ ; \ D_o = \frac{C_2\left[\left(1+\frac{r_{1S}}{r_{2S}}\right)/\alpha_2\right]^2}{2(1+D_{rp})} \qquad (16)$$

$$D_{rp} = \frac{C_2}{C_1}\left(\frac{\alpha_1 r_{1S}}{\alpha_2 r_{2S}}\right) \ ; \ \frac{r_{1S}}{r_{2S}} = \left(\frac{A_1}{A_2}\right)^{1/3} . \qquad (17)$$

Conversely, the minimum possible value of D(k) is

$$D_L(k) = D_o(1/k-1)^2 .$$

Integrations in Eq. (12) are interchanged systematically so as to bring them into the order: K_E, z_2, E_{2c}; D and k. The upper limit of the E_{2c} integration is E_m where

$$E_m = R_m - K_E - D_{low}(K_E,z_2) \geq 0 \ . \qquad (18)$$

$$D_{low}(K_E,z_2) = D_L(K_E/V_S) \ , \ \text{if } \frac{K_E}{V_S} < k_L(D_{min}) = k_c \qquad (19)$$

$$= D_{min}(z_2), \ \text{if } \frac{K_E}{V_S} \geq k_L(D_{min}) = k_c .$$

The K_E and z_2 integration limits can be worked out to satisfy Eq. (18). Gaussian-type integrations, carried out in Fong's[6] manner give

$$N(A_2,E_f) \ \exp\left[2\sqrt{(a_1+a_2)\bar{E}_m}\right]\sigma_{K_E}\bar{\sigma}_z\bar{\sigma}_{E_{2c}}\bar{p}_{r1}\bar{p}_{r2}\bar{I}_{nn} \qquad (20)$$

$$\bar{E}(A_2,E_f) \equiv \bar{E}_m = \bar{R}_m - \bar{K}_E - \bar{D} \ ; \ \bar{D} = D_{low}(\bar{K}_E,\bar{z}_2) \qquad (21)$$

$$\equiv E_f + \overline{\Delta E_c}\,(A_2,E_f) \ . \qquad (22)$$

The overbars indicate evaluation at a "most probable" value of $z_2 = \bar{z}_2$ and at $\bar{K}_E$, the average value of K_E. Both $\bar{K}_E$ and σ_{K_E}, the variance of the K_E distribution, are taken from experiment, for p on U^{235} (see next section); $\bar{\sigma}_z$ is the variance of the z_2 distribution for fixed $\bar{K}_E$, evaluated at $\bar{K}_E$; $\bar{\sigma}_{E_{2c}}$ is the average of the variance given by the integral, (approximately integrated by Fong[6]),

$$\sigma_{E_{2c}} = \frac{\exp\left[-2\sqrt{(a_1+a_2)\bar{E}_m}\ \right]}{\bar{p}_{r2}\bar{p}_{r1}} \int_0^{E_m} dE_{2c} \ \frac{\exp\left[2\sqrt{a_2 E_{2c}}\ \right]}{\exp\left[-2\sqrt{a_1(E_m-E_{2c})}\ \right]} \times p_{r1}p_{r2} \qquad (23)$$

$$\triangleq \frac{(a_1a_2)^{1/2}}{(a_1+a_2)^{5/4}} E_m^{3/4} \ .$$

The value of $\bar{z}_2$ is found approximately from the condition

$$\frac{d}{dz_2} E_m = 0 \ , \qquad (24)$$

using the Fong-Wing[12] empirical mass formula. Rest mass and pairing energies, taken from Wapstra[13] and Cameron[14] are interpolated to obtain $\bar{R}_m = R_m(A_2,\bar{z}_2)$. For the level density parameters, a_i, we used the formula[15]

$$a_i = \frac{A_i}{B_o}\left[1 + Y_o(A_i - z_i)^2/A_i^2\right] \ , \qquad (25)$$

that the calculated results agree with the experimental data, but it is clear that above about 100 MeV the calculated and experimental fission cross sections are in approximate agreement. The decrease in the fission cross section above approximately 500 MeV where the nonelastic cross section is increasing slightly may be due to the fact that pion production is becoming significant. As the incident proton energy decreases below 100 MeV the calculated fission cross section increases slightly while the very few experimental points do not show the slight increase. This may indicate, as one might expect, that the model becomes inaccurate at the lower energies but more information is needed before this can be said with any certainty.

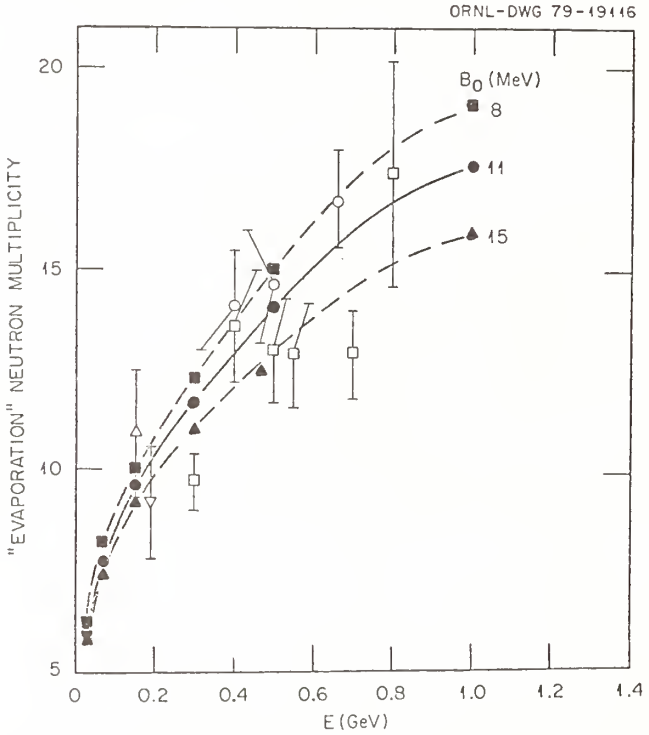

Fig. 2. "Evaporation" neutron multiplicity vs incident proton energy for protons on U^{238}. The experimental data are taken from ▲ Ref. 23, ▽ Ref. 24, □ Ref. 25, and o Ref. 26.

In Fig. 2 the calculated "evaporation" neutron multiplicity is shown as a function of incident energy for protons incident on U^{238}. The designation "evaporation" neutron multiplicity means all neutrons that are obtained from excited "compound" nuclei, and explicitly excludes all neutrons that are emitted during the "cascade" that takes place before a "compound" nucleus is formed. The evaporation neutron multiplicity includes those evaporation neutrons that are emitted before fission takes place, and those evaporation neutrons from the excited nuclei produced by the fission process. The evaporation neutrons have a spectrum that extends into the 25 MeV range, but the large majority are below energies of the order of 10 to 15 MeV.

Also shown in Fig. 2 are a variety of experimental "evaporation" neutron multiplicities for protons on U^{238} taken from Refs. 23-26. These experimentally measured "evaporation" neutron multiplicities are defined only very approximately in the various references and the measured points in Fig. 2 correspond only approximately to the calculated quantities.

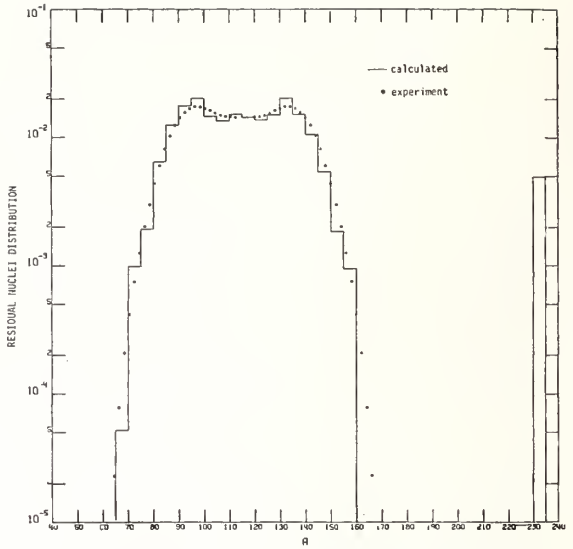

Fig. 3. Residual nuclei distribution from 30 MeV protons on U^{235}. The experimental data for A > 118 is from Ref. 7 and for A < 118 was obtained assuming symmetry as described in the text.

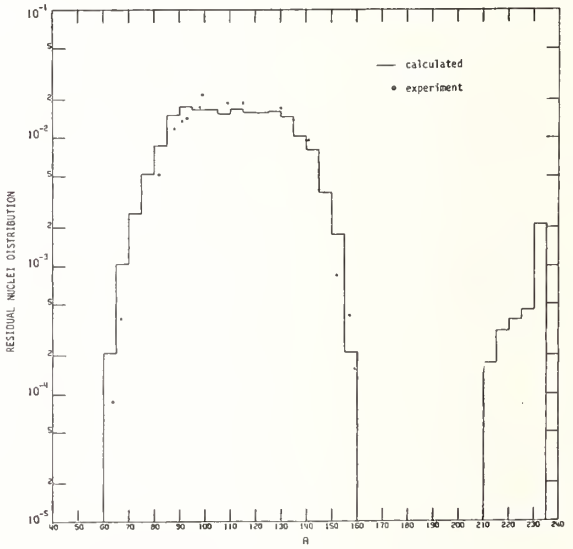

Fig. 4. Residual nuclei distribution from 300 MeV protons on U^{238}. The experimental data are from Ref. 16.

Calculated results are shown in Fig. 2 for three values of the parameter B_0 that occur in the level density formula (see Eq. (25)). As the figure indicates, at the lower energies the calculated evaporatio neutron multiplicity is not sensitive to the value of B_0 used, but at an incident energy of 1 GeV the difference in the multiplicity values for the various B_0 values is appreciable. Considering the large spread in data, it is difficult to decide on "best" value of B_0, but from Fig. 2 it seems that B_0 = 11 MeV is a reasonable value. It should be noted, however, that B_0 enters into the present calculations in a variety o complex ways, and therefore it should not be concluded that this value is necessarily appropriate in any othe context.

In Fig. 3 the calculated distribution of residual nuclei is shown for the case of 30 MeV protons inciden on U^{235} and in Fig. 4 the calculated distribution is shown for the case of 300 MeV protons incident on U^{238}

where B_o and Y_o are constants.

In this paper, the factors $\bar{\sigma}_z\ \bar{p}_{r1}\bar{p}_{r2}\bar{I}_{nn}$ were taken to be approximately those used by Fong[6].

The function D_o in Eq. (16) was evaluated using

$$D_o = \bar{D}_o = \bar{D}(\bar{V}_s/\bar{K}_E - 1)^2 \qquad (26)$$

The Monte Carlo procedures to select the needed parameters for a random mass splitting are to sample A_2 from Eq. (20) by rejection techniques; sample K_E and z_2 from truncated Gaussians; sample E_2 from the integrand of Eq. (23) by rejection. Then

$$E_{2E} = E_{2c} + \Delta_2 + D_2\ ;\ D_2 = D_{low}(K_E,z_2)/(1+D_{rp}) \qquad (27)$$
$$E_{1E} = (E_m - E_{2c}) + \Delta_1 + D_2\ D_{rp}\ .$$

Empirical Determination of Deformation Energy, Mean Kinetic Energy, and Variance of the Kinetic Energy

Correlated experimental postevaporation distributions versus A_2 for the residual nuclei yields, $Y(A_2,E_I)$, average total kinetic energy of the fragment pair, and the variance of the kinetic energy for protons of kinetic energy, E_I, ($\leq$ 30 MeV) incident on U^{235} are available from Epperson. In principle, each of these distributions is an integral over E_f of a preevaporation distribution weighted by the probability of fission at E_f, neglecting any dependence on the prefission values of A_f and z_f. The prefission distributions may be obtained approximately from the postevaporation distribution by using an average emitted evaporation neutron multiplicity $\bar{\nu}$. Thus, taking six values of the incident proton energy, i.e., E_{Ij} for j = 1 to 6, and corresponding intervals in E_f, each with average value E_{fj}, one has

$$Y_j(A_2,E_{Ij}) = \sum_{k=1}^{j} P_f(E_{fk})\Delta E_{fk} N_k(A'_{2k},E_{fk}) \qquad j=1,6$$
$$A'_{2k} = A_2 + \bar{\nu}(E_{fk}) \qquad (28)$$

which may easily be solved for $N_k(A'_{2k},E_{fk})$. The E_{Ij} values used were 7, 10, 15, 20, 25, and 30 MeV and the fission probabilities and neutron multiplicities were computed by using the intranuclear-cascade-evaporation model including the fission channel described in this paper. The N_j's were obtained from Eq. (28) for $E_f \leq E_{f6}$. The same procedure was followed to obtain the functions $\bar{K}_E(A_2,E_{fj})$ and $\sigma_{K_E}(A_2,E_{fj})$.

The next step in the procedure was to fit the yields $N_j(A_2,E_{fj})$ by use of Eq. (20) from the statistical model. In this fitting procedure the quantity $\bar{E}(A_2,E_{fj})$ was determined, and then the quantities $\bar{\Delta E}_c(A_2,E_{fj})$, $\bar{K}_E(A_2,E_{fj})$ and $\sigma_{K_E}(A_2,E_{fj})$ for N_p^{236} form a permanent data set for use in the statistical model code. Interpolation between the values of E_{fj} was used to obtain data at all values less than E_{f6}. When the excitation energy exceeds that corresponding to an incident proton energy of 30 MeV the values of these functions (and the derived average deformation energy) are simply assumed to have the value calculated at E_{f6}.

When the fissioning nucleus is not N_p^{236} a simple scaling procedure is assumed. Thus, if primes are used to indicate values corresponding to N_p^{236},

$$A_2 = \frac{A_f}{236} A'_2 \qquad (29)$$

$$\bar{E}(A_2,E_f) = \left[\frac{(a_1+a_2)_{236}}{(a_1+a_2)_{A_f}}\right] E'(A'_2,E_f) \qquad (30)$$

The functions $K_E(A_2,E_f)$ and $\sigma_{K_E}(A_2,E_f)$ are arbitrarily scaled in the same manner as $\bar{E}(A_2,E_f)$. These assumptions modify the distributions just enough to give the correct reflection in A_2 (since the statistical model predicts symmetrically reflected distributions) and to maintain general shapes.

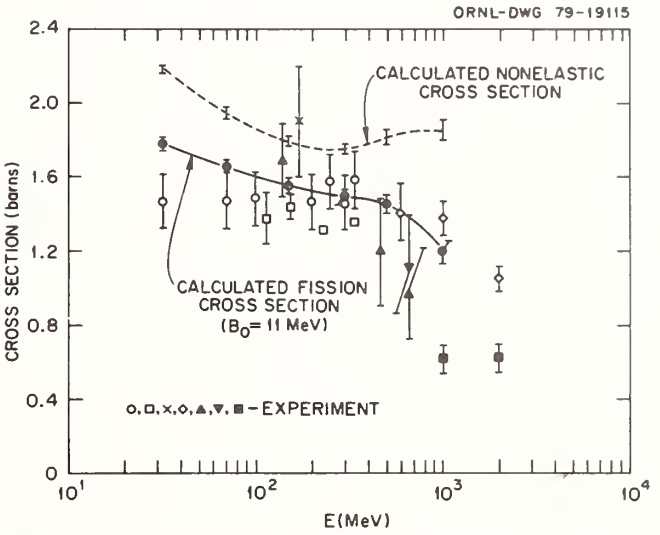

Fig. 1. Nonelastic and fission cross section vs incident proton kinetic energy for protons on U^{238}. The experimental data are taken from o Ref. 16, □ Ref. 17, x Ref. 18, ◇ Ref. 19, ▲Ref. 20, ▼ Ref. 21, and ■ Ref. 22.

Results and Discussion

In Fig. 1. The calculated nonelastic cross section and the calculated fission cross section for protons on U^{238} are shown as a function of incident proton kinetic energy. The points on the calculated curves indicate the energies at which calculations have actually been carried out. The dashed and solid curves are drawn through the calculated points to aid in interpreting the figure. The error bars on the calculated points are statistical only and represent one standard deviation. The fission cross section values shown in the figure were calculated with B_o = 11 MeV (see Eq. 25), but these results are quite insensitive to the yalue used. The calculated results shown in Fig. 1 are not appreciably different from the results obtained earlier by Hahn and Bertini.

Also shown in Fig. 1 are a large variety of experimentally measured values of the fission cross section for protons of various energies on U^{238}. In the figure only representative results are shown from some of the references because of the large number of points available.

Because of the spread in the experimental fission cross section data it is difficult to say precisely

In both figures the calculated results are normalized to unity for A < 160.

The experimental data in Fig. 3 for A > 118 is taken from Ref. 7. Error bars on the measurements were not given in Ref. 7 and therefore are not shown. In Ref. 7 measured values were not given for A values less than 118 so the data points in Fig. 3 were obtained by assuming symmetry about a midpoint defined by 1/2 [236 - average neutron multiplicity]. The experimental data in Fig. 4 was taken from Ref. 13 and again experimental error bars are not shown because they were not given in Ref. 9. The normalization on the experimental data is the same as that used (see above) for the calculated data.

The calculated results in Fig. 3 are in very good agreement with the experimental data over the complete range of A values considered. To some extent, this is to be expected because the experimental data was used in obtaining the functions used in the statistical model, but nevertheless, the good agreement shown in Fig. 3 is very satisfying. The calculated results in Fig. 4 are in good agreement with the experimental data at the larger A values ($A \gtrsim 118$) but overestimate the experimental data somewhat for the lower A values. In both Fig. 3 and 4 the residual nuclei for the larger A values ($A \gtrsim 200$) correspond to incident particle collisions in which no fission occurred. No experimental comparisons between calculated results and experimental data for these higher A residual nuclei are considered here but such comparisons are given in Ref. 5.

Acknowledgement

Research sponsored by the U.S. Department of Energy, Office of Basic Energy Sciences, under contract no. W-7405-eng-26 with Union Carbide Corporation.

References

1. Proceedings of an Information Meeting on Accelerator Breeding, Brookhaven National Laboratory, June 18-19, 1977, NTIS CONF-770107.
2. J. M. Carpenter, Nucl. Instr. Methods 145 133 (1977).
3. H. W. Bertini, Phys. Rev. C 6, 631 (1972).
4. H. W. Bertini, "Spallations Reactions: Calculations" in Spallation Nuclear Reactions and Their Applicatons (D. Reidel Publishing Co., Boston, MA, 1976).
5. R. L. Hahn and H. W. Bertini, Phys. Rev. C 6 660 (1972).
6. P. Fong, Statistical Theory of Nuclear Fission (Gordon and Breach Science Publishers, New York, NY, 1969).
7. D. H. Epperson, "Systematics of Mass Yield Distributions for Nuclear Fission of Neptunium" Dissertation, Dept. of Physics, Duke University, 1978.
8. V. S. Barashenkov and V. D. Toneyev, "Interactions of High-Energy Particles and Atomic Nuclei with Nuclei," Chapter 10, FTD-ID(RS)T-1069-77 (1977).
9. A Michaudon, Proceedings of the International Conference on the Interactions of Neutrons with Nuclei, Lowell, MA, July 6-9, 1976, NTIS CONF-760715-P1.
10. P. Fong, Phys. Rev. Letters 11, (1963).
11. P. Fong, private communication (1978).
12. J. Wing and P. Fong, Phys. Rev. 13C (1964).
13. A. M. Wapstra, Physica 21, 367 (1955).
14. A. G. W. Cameron, Can. J. of Phys. 36, 1040 (1958).
15. K. J. LeCouteur and D. W. Lang, Nucl. Phys. 13, 36 (1959).
16. P. C. Stevenson et al., Phys. Rev. 111, 886 (1958).
17. H. Steiner and H. Jungerman, Phys. Rev. 101, 807 (1956).
18. A. Kjelberg and A. Pappas, Nucl. Phys. 1, 322 (1956).
19. J. Hudis and S. Katcoff, Phys. Rev. 180 1122 (1969).
20. See Ref. 56, p. 352 of Ref. 8.
21. See Ref. 101, p. 352 of Ref. 8.
22. E. S. Matusevich and V. I. Regushevskii, Yadern. Fiz. 7, 1187 (1968) [Transl: Soviet Journal Nucl. Phys. 7, 708 (1968)].
23. E. Cheifetz et al., Phys. Rev. C 2, 256 (1970).
24. E. E. Gross, University of California Report Nos. UCRL-3330 and UCRL-3336 (1956), unpublished.
25. M. Bercovitch et al., Phys. Rev. 119, 412 (1960).
26. R. V. Vasil'kov et al., Yadern. Fiz. 7, 88 (1968) [Transl: Soviet Journal Nucl. Phys. 7, 64 (1968)].

PHOTONEUTRON LEAKAGE FROM THE W(γ,n) REACTION AT RADIATION THERAPY CENTERS

R. J. Holt, H. E. Jackson and J. R. Specht
Argonne National Laboratory
Argonne, Illinois 60439, USA

The energy spectrum of photoneutrons from W(γ,n) was observed for an electron energy of 10 MeV by using the ANL high-current electron linac and a neutron time-of-flight spectrometer.

[W(γ,n), photoneutron energy spectrum for E_e = 10 MeV, E_n = 0.3 - 3.6 MeV]

Introduction

There are a number of radiation therapy facilities which rely upon 10-MeV electron linacs or betatrons. The heads of these accelerators typically contain tungsten bremsstrahlung converters, beam hardeners and photon collimators. Of course, heavy elements such as W or Pb have large photoneutron production cross sections and at energies of $\gtrsim$ 10 MeV a sizeable neutron background can be generated from these elements. Unfortunately, it is extremely difficult to determine the dose equivalent of the leakage neutrons. The primary difficulty is that most neutron detection schemes at these facilities measure only the neutron fluence and not the energy spectrum of the neutrons. Then, it is common practice to assume that the neutron spectrum has the same shape as a fission spectrum, typically that of ^{252}Cf. McCall et al.[1] have demonstrated that this is a poor assumption. This is especially true since the primary neutron spectrum is distorted in its energy dependence by the accelerator head shielding which is usually in the form of W, Fe or Pb. In principle, this spectrum can be calculated using a Monte Carlo technique,[2] provided that the primary neutron spectrum is known. However, the problem is compounded by the fact that there is not a complete set of photoneutron spectra even for the case of W. For example, there were no W(γ,n) data for an electron energy of 10 MeV. For these reasons we have observed the photoneutron energy spectrum for W(γ,n) at angles of 90° and 135° throughout the neutron energy range 0.3 to 3.8 MeV for an electron energy of 10.0 MeV.

Experiment

Since we are only concerned with the spectral shape of the W(γ,n) cross section, the experimental method is relatively simple. An energy-analyzed, 10.0 MeV beam of electrons with a pulse width of 4 ns and a rate of 800 Hz was focused onto an Al electron beam stop and bremsstrahlung converter as shown in Fig. 1. The bremsstrahlung photons irradiated a sample of W powder (10.93 g/cm^3) which was encased in a thin-walled Al can. Photoneutrons from the W then traveled through two 15-m flight paths which were at angles of 90° and 135° with respect to the photon beam axis. The neutrons were detected in plastic scintillators (2.5-cm thick x 20 cm x 5.1 cm) located at the end of each flight path. The neutron energies were measured with a time-of-flight method. The shapes of the forward-produced thick target bremsstrahlung for Al and W are nearly identical, so that no significant shape error was introduced by using an Al converter. The target thickness in the photon beam direction was 0.18 g/cm^2 and 0.036 g/cm^2 in the neutron direction at 90°. The neutron detector efficiency and effects of Bi γ-flash filter were unfolded from the measured spectra. The final results are shown in Fig. 2 for a reaction angle of 90°.

Results

The spectrum shown in Fig. 2 was averaged and plotted in 30-keV increments. The spectrum can be

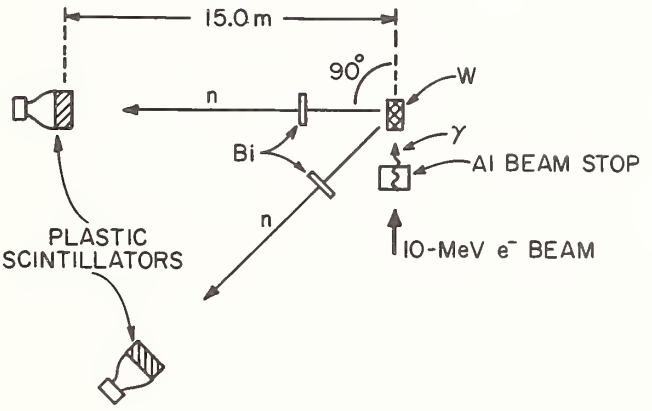

Fig. 1. Schematic diagram of experimental arrangement.

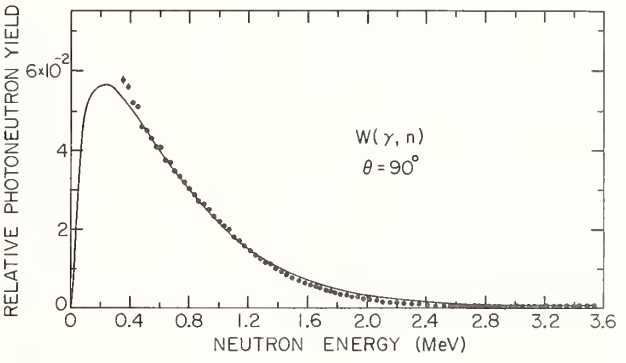

Fig. 2. Relative yield of photoneutrons from the W(γ,n) reaction at 90° for a 10-MeV electron beam.

relatively well-represented by a Maxwellian with a temperature of 0.45 MeV as shown in Fig. 2. The curve in the figure was calculated with the expression

$$N = N_o \, E^{1/2} \, e^{-E/0.45}$$

where N_o = 0.0196. The constant term N_o, of course, has no significance since we have determined only the spectral shape for the W(γ,n) reaction.

There are currently two methods for determining the dose equivalent from this primary spectra. In both methods one must determine the neutron fluence and the contribution from thermal neutrons. The first method, "brute-force," would be to determine with a Monte Carlo technique the spectral shape after transmission through the head shielding. The second method,

"cookbook," was developed by McCall et al.[1] He observed that to a very good approximation one only needs to know the behavior of neutrons with the average energy of the neutron spectrum in order to determine the dose equivalent. We have found the average energy from the Maxwellian shape of the present spectrum to be $\bar{E}$ = 0.67 MeV. Once this is known a simple procedure is described in Ref. 1 to obtain the dose equivalent.

It is expected that the present work will lead to more accurate determinations of neutron dose equivalent of leakage neutrons from 10-MeV electron accelerators.

Acknowledgments

We thank R. C. McCall for bringing this problem to our attention and for useful discussions. This work was performed under the auspices of the United States Department of Energy.

References

1. R. C. McCall, T. M. Jenkins and R. A. Shore, in Proc. of the Fifth International Conference on Small Accelerators, 1979, preprint.

2. R. C. McCall and W. P. Swanson, in Proc. of the Conf. on Neutrons from Electron Accelerators, 1979, preprint.

NELMA PROJECT

I. Objectives of the Methodical Aspects

G. C. Madueme
Department of Physics, University of Ife, Ile-Ife, Nigeria

The significance of the NELMA Project is presented. The main aim is to inject new and useful frontiers into the medical care facilities in Nigeria and to provide broader scopes for applying excited nuclear probes to research in bio-agricultural economics as well as in nuclear and solid state physics.

[Nuclear Methods in Medicine, Nuclear Methods in Agriculture, Oil well Logging]

Introduction

Applications of nuclear science to the material needs of human existence today are readily found within a multifold subject areas such as medicine, chemistry, biology, geology, archeology, food and agriculture, material science as well as a wide range of industrial and technological fields. Some of these areas need proper investigation in Nigeria today as they touch on issues which have decisive importance for the life of the individual; in particular disease, hunger and malnutrition. This project therefore focuses on the areas of life sciences, mainly medicine, biology, food and agriculture. The need for more adequate and improved facilities for health care as well as more adequate and improved agricultural products in the country is such that program-related applied research with such a focus can, for example, make a major contribution to food availability, thereby control the rising cost of food. In response to such needs, a study of the possibility of utilizing in Nigeria an accelerating machine for medical use as well as for bio-agricultural and physical programmes was initiated by the author while at the cyclotron laboratory of the Institute for Nuclear Study, University of Tokyo (1975-1977). The ideas, however, grew earlier out of studies at the Tandem Accelerator laboratory, Uppsala (1970-1975).

The NELMA (Nuclear Energy Laboratory of Medical and Agricultural Sciences) project was conceived to meet the demand made by many observers in the country today that research ought to be beneficial. Hence, in further recognition of the need to maintain a strong relationship between applied science and basic research, the NELMA project is expected to at least

(i) contribute solutions to specific problems in the life sciences and bio-medical physics

(ii) exploit experimental techniques and fundamental concepts to gain a better understanding of ideas related to human biology, food and agricultural science

(iii) maintain a strong basic research which may provide the nourishment that could be valuable in meeting future identified needs.

To achieve these objectives the accelerator laboratory is designed to be provided with 3 beam courses for medical irradiation, isotope production and bio-agricultural science respectively; and another 3 lines for nuclear, solid-state and material physics. Light and heavy ions will be available and beam time will be shared between the pair of 3 beam lines in the ratio 2:1. It is hoped that the scientific community in Nigeria will be better equipped with the aid of this new facility, to meet the challenges of certain health and food-related problems in the society, as well as contribute actively to the acquisition of new knowledge which will further yield benefits to enhance the quality of life of human beings as well as a better understanding of our universe.

In the subsequent sections some of the main objectives of the NELMA project will be outlined. They drive from the use of

a) emitted signals from radionuclides

b) the interaction between radiation and matter

c) the mutual interaction between nuclei, and

d) the interaction between nuclei and their surroundings.

The principal tools in the practical application are the tracer technique and radioactivation analysis.

Medicine and Health Care

Radioisotope production for Medical Use

Production of nuclides of desired purity and radiation properties demands the knowledge of properties such as isotopic abundance of target material and its economy, reaction energy and reaction probabilities. In addition, for the produced radionuclides to be usable, knowledge of the nuclear spectroscopic nature is required e.g. the types of decay, lifetimes and the form of decay schemes. The isotope production unit will be of particular advantage in the case of short-lived isotopes important for biochemistry and physiology e.g. ^{15}O, ^{11}C and ^{13}N. Other examples of medical-use radioisotopes for production and their application potential are shown in the following table:

Table I. Medical-use radionuclides and application potential

Radioisotope	Use	Technique/ Properties
^{55}Fe, ^{59}Fe	Treatment and prevention of blood (haemo-globin) deficiency in the body. Iron transport studies.	Addition in food; tracer method
Au, P	Isotopic diagnostics and therapy for kidney, brain, heart, lungs and thyroid glands	
^{123}I	Liver, lung scans; blood vol. measurements, thyroid studies	
^{99}Tc	Brain scans	Short $T_{\frac{1}{2}}$. Has only a low energy γ
^{252}Cf	Neutron radiography for treatment of tumors	Selective irradiation

Nuclear methods in medicine

The methodical aspects will include studies aimed at establishing the connection between certain diseases and the essential salts of the body; for instance, the implication of change in limestone content of urine for kidney stone and that of sodium accumulation in the body for heart ailments as well as for high blood pressure. Thus, measurement of absorption coefficient for low energy γ-ray or the attenuation when monoenergetic beam is passed through a given part of the body could be used to evaluate the calcium concentration in bone tissue. Evidence of lung infection may be established through trace elements such as Ta, Co and W; while leade poisoning (common among industrial workers) may be detected through X-ray fluorescence method in cases where conventional tracer technique is unsuitable. Emitted signals from radionuclides after activation will be useful in the analysis of materials left at the scene of a crime as well as for detection of forgeries. Also, nuclear reactions of the types $^{19}F(p, \alpha\gamma)\ ^{16}O$ and $^{15}N(p, \alpha\gamma)\ ^{12}C$ will be important for understanding the role of fluorine in the process of tooth care. It is also well known that body measurements of ^{40}K, ^{137}Cs and ^{131}I in thyroid glands yield valuable information on ecological implications of nuclear radiations. In addition, measurement of potassium content in the body will give useful information on the distribution of muscles and fat production in the body as well as on heart diseases and conditions of first year infancy.

Radiation therapy and tumor treatment

Conventional X-ray machines for radiation treatment are increasingly being replaced by accelerating machines. One beam course will be devoted to medical irradiation e.g. for cancer and brain tumor patients.

Livestock, Food and Bio-agricultural Science

The NELMA project aims at contributing in advancing food production in the country. Radiation sources and radioisotope tracers in agriculture and animal science will therefore received the attention they deserve. Research efforts with nuclear techniques will be directed on specific areas such as plant and animal breeding, management of tropical soils, pest control and ruminant livestock. Nuclear methods have the advantages of high sensitivity and more direct approach. In some cases the desired information are obtained via nuclear methods only. It is common knowledge, for example, that the radionuclides ^{60}Co, ^{32}P, ^{14}C and ^{65}Zn are important in pest control, gamma radiation being very useful in eradication certain species of soil parasites.

Soil management, plant and animal science

The investigations will include efficiency studies of solar energy fixation by plants through isotope techniques, research on fertilizer dressings, development of root systems, ion and water intake mechanisms in plants, the influence of ionizing radiation on vegetative processes in plants, protein content and oil content determination as well as the use of ionising irradiation on food and livestock. Some examples of the type of problems to be examined within this group are surmmarised in table II.

Table II. Nuclear methods in agriculture

Nuclides Nuclear reactions	Aim	Technique
Nitrogen, phosphorus and Potassium	Fertilizer efficiency studies; nutrient status of soils	Isotopic dilution analysis, activation analysis

^{14}N, ^{15}N, ^{32}P, ^{33}P and ^{86}Rb	Root activity tests for fertilization technique	Injection into soil and analysis of leaf sample
Na, S, Zn, Cs and Se	Root Propagation Studies	Selective injection into soil or fertilizer
^{11}C, ^{40}K and ^{24}Na	Fast processes taking place in plant organisms	
^{57}Co	Structure of haemoglobin	Mossbauer technique
$^{14}N(p,d)$, $^{14}N(p,n)$ $^{14}N(d,\alpha)$, $^{14}N(d,p)$	Nitrogen content and its depth distribution in single seeds, e.g. maize and beans. Protein loss in various treatment of seeds e.g. rice polishing	Evaluation of energy loss per unit length penetration
	Oil content in seeds	Measurement of dielectricity constant at different frequencies
^{125}I radiation on eggs	Studies on how to produce eggs with more uniform thickness; conservation	Deduction of shell thickness from intensity measurements
Irradiation of perishable food products e.g. meat, fish, fruits, vegetables, yams, onions, grains.	Preservation and increased shelf life. Prevention of food toxins and parasites c.f. heating and freezing	Proper choice of radiation dose
Irradiation of pigs, duck eggs and fish sperm	Metabolism of minerals in domestic animals; breeding and reproduction effects (e.g. fertilization rate)	
$(\rho,\alpha\gamma)$ reactions on liquid food, e.g. orange juice	Analysis of fluids for elemental composition of contamitants	*Proton-induced X-ray fluorescence technique on sample spread on suitable foil
Isotopic diagnostics in animal husbandry and vertinary medicine	Thyroid glands, liver, kidney and brain disorders	Gamma Cameras

* Suitable for the analysis of environmental pollution in air.

Nuclear Physics, Solid State and Materials

Based on the knowledge of nuclear and material properties, nuclear radiations and nuclear spectra the NELMA project will make some impact directly or indirectly on a wide range of industrial and technological activities in Nigeria such as oil and minerals, steel, glass, paper and textiles. (E.g. Logging of oil wells by means of nuclear techniques; use of deuteron induced reactions to obtain a depth profile in material composition analysis and for the control of machine wear).

The extensive applications of basic knowledge point to the need of generating continuously, fundamental results and data for new areas of application. A large number of atomic nuclei can be used at present for various purposes and as probes because we possess a fairly good knowledge of their elementary properties. Estimates show that about 6000 nuclei exist with lifetimes long enough to permit studies on their nature and properties. Only about a quarter of these have been studied of which the knowledge of many nuclei is very rudimentary. One of the greatest challenges to basic research is to extend our knowledge to the unexplored nuclear regions. Many new phenomena would certainly unfold in our quest for the clue to understanding nuclear structure. In addition, significant innovations on instrumentation and experimental techniques are expected as a result of the different needs of the selected areas of accelerator utilization in life sciences and physics.

Conclusions

The applications which have been outlined should constitute some of the most valuable contributions offered to the life sciences by nuclear technology so that the NELMA project would indeed be well justified. On the other hand, the basic physics research will provide not only the nourishment for the applied work but also the knowledge which is essential

for understanding the evolution of the universe; through nuclear reactions by which elements are formed and which also control the processes in the stars. Nuclear research, in particular, which is revealing the many properties of matter and its evolutionary trends through various concepts and laws, perhaps, holds the ultimate answer to the age old question on the structure of matter and its various forms of existence. Hence future discoveries will further affect the life of the individual in many respects.

Acknowledgement

Work supported in part by the Japan Society for the Promotion of Science.

References

1. E. Selin and U. Baverstam, Kosmos 1976 vol. 53 (ed. by N. R. Nilsson and U. Litzen, Swedish Natural Science Research Council publication, 1977) p.185.

2. T. Karasawa, H. Seki, M. Imamura, A. Matsuyama and M. Mitsui, in "The Uses of Cyclotrons in Chemistry, Metallurgy and Biology" (ed. C. B. Amphlett, Butterworths, London, 1970) p.76.

3. B. Sundqvist, L. Gonczi, R. Bergman and U. Lindh, Int. J. Appl. Rad. Isot. 25, (1974) 277.

4. J. Simon, Proceedings of 8th ESNA Annual Meeting, Uppsala, 1977, p.60.
J. G. van Kooij, Ibid p.98.
M. J. Frissel, Ibid p102.

5. G. C. Madueme, in "Nuclear Research and Technology: A viable project in Nigeria?" Unpublished lectures to Physics and Engineering Physics Society, University of Ife, April 1978.

THE $^{127}I(n,2n)^{126}I$ REACTION AS A FAST NEUTRON FLUX MONITOR

D. C. Santry
Solid State Science Branch, Atomic Energy of Canada Limited,
Chalk River Nuclear Laboratories, Chalk River, Ontario, Canada K0J 1J0

The activation method was used to measure the production of 12.88 day ^{126}I as a function of neutron energy. Monoenergetic neutrons were produced with a tandem Van de Graaff using the reaction $D(d,n)^3He$ and $T(d,n)^4He$. Cross sections were measured from a threshold energy of 9.2 MeV up to 20 MeV relative to the known cross sections for the $^{32}S(n,p)^{32}P$ reaction. The study has shown that the $^{127}I(n,2n)$ reaction has a flat response around 14 MeV and this factor combined with the suitable decay characteristics of ^{126}I provides a reaction suitable as a standard for determining integrated fast-neutron fluxes of neutron generators and thermonuclear fusion machines.

[$^{127}I(n,2n)^{126}I$, measured cross section, E_n = 9.2 to 20 MeV, deduced effective σ for $^{127}I(n,2n)$ and $^{32}S(n,p)$ for ^{235}U fission neutron spectrum]

Introduction

The use of threshold detectors to provide information on flux densities, fluences and spectra of fast neutrons has several advantages over instrumental methods. For example, they are inexpensive, simple to use and because of their small size can be placed in any chosen irradiation position and will have a negligible perturbation on the measured flux. They are not sensitive to temperature or to gamma rays, in contrast to other methods such as proton recoil or nuclear emulsions. They work well with pulsed sources, such as cyclotrons, and effects due to coincidences or pile-up do not apply.

Although threshold detectors are used for measuring integral neutron spectra and fast fluxes, there is no widely accepted standard reaction. Perhaps the closest to a standard is the $^{32}S(n,p)^{32}P$ reaction which is also used in personal radiation dosimetry. Many of the factors involved in using the $^{32}S(n,p)$ reaction have been described previously[1]. The validity of its cross section values has been confirmed, since other fast-neutron cross sections measured by Santry and Butler relative to the $^{32}S(n,p)$ values are in excellent agreement with measurements by Paulsen and Liskien using a proton-recoil telescope[2].

The present paper discusses the possible uses of the reaction $^{127}I(n,2n)^{126}I$ as a supplemental standard for measuring neutrons with energies above 9.2 MeV (see Table 1). The cross section for the production of ^{126}I as a function of neutron energy was measured from a threshold energy of 9.2 MeV up to 20 MeV.

Table 1

Nuclear Parameters for Fast-Neutron Flux Monitoring[6]

Reaction	Threshold (MeV)	Half-life of product (days)	Detection
$^{127}I(n,2n)^{126}I$	9.14	13.0	β-counting
			γ-counting (666 keV photon)
$^{32}S(n,p)^{32}P$	∿1.5	14.28	β-counting

Calibration standards

^{137}Cs 30.1 year (662 keV photons)

^{32}P 14.28 day

Experimental

Neutron Irradiation

Monoenergetic neutrons were obtained from the $D(d,n)^3He$ and $T(d,n)^4He$ reactions using a Tandem Van de Graaff Accelerator or a Texas Nuclear Neutron Generator. The irradiation conditions are shown schematically in Figure 1. A collimated deuteron beam strikes a target of either tritium or deuterium and samples to be activated are placed at known angles relative to the incident deuteron beam, i.e., 0 to 150° for tritium and at 0° for deuterium. Samples irradiated subtended half angles of 9° for the tritium target and 6.5° for the deuterium gas cell.

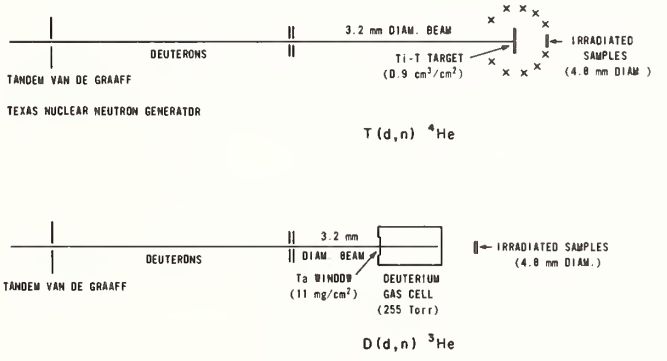

Fig. 1. Fast Neutron Irradiation Cells

Iodine samples were prepared from hexaiodobenzene (C_6I_6), a brown powder, which was pressed into pellets 5 mm in diameter and 1 mm in thickness. This material has the advantage of high iodine content (91.4%) and unlike many other compounds is nonhygroscopic[3]. Powdered sulfur was pressed into pellets of the same dimensions as the C_6I_6.

Neutron Flux Monitoring

In measuring the neutron cross section for iodine, samples of C_6I_6 were sandwiched between pellets of sulfur of the same diameter. Neutron fluxes were therefore calibrated through the known cross sections[1,4] of $^{32}S(n,p)$ reaction. The flux gradient which occurs over the geometrical arrangement of samples was determined by irradiating stacked pellets of known thicknesses and measuring the specific activity of each pellet. Neutron attenuation in the samples was small, calculated to be < 0.2% for 1 mm thick pellets. In practice, the front and rear sulfur samples were counted separately and when corrected for geometry gave the same activity value.

Additional irradiations were performed with tritium and deuterium replaced by hydrogen and thus provided a measure of activation by background neutron production. It was found that there was no contribution to the ^{126}I activity by background neutrons, but there were corrections for the $^{32}S(n,p)$ reaction[5].

For neutrons produced with the (D + D) reaction, there were associated with the monoenergetic group a continuum of neutrons produced by the D(d,np)D or breakup reaction. The energies of the breakup neutrons are low enough that they do not activate the iodine samples to form ^{126}I, but do activate sulfur to form ^{32}P. Corrections for the breakup neutrons were computed from cross section values and the known energy distribution of neutrons from the breakup process[5].

Activity Measurements

The irradiated sulfur samples were ignited to produce weightless sources of 14.22 day ^{32}P which were beta counted with an overall efficiency of 42.2 ± 0.8%[1].

The irradiated C_6I_6 pellets were measured with gamma ray spectrometers, either NaI or Ge(Li) detectors. The radioactivity of all samples was followed to confirm the identity of activities. Immediately after an irradiation some ^{128}I ($t_{½}$ 20 min), formed by the (n,γ) reaction, was observed but decayed away within 3 hours. Figure 2 shows a gamma ray spectrum of C_6I_6 measured one day after an irradiation. There are no interfering activities. Although there are two abundant gamma rays at 388 and 666 keV, measurement of the latter is recommended since detectors are easily calibrated at 662 keV with commercially available ^{137}Cs standardized sources.

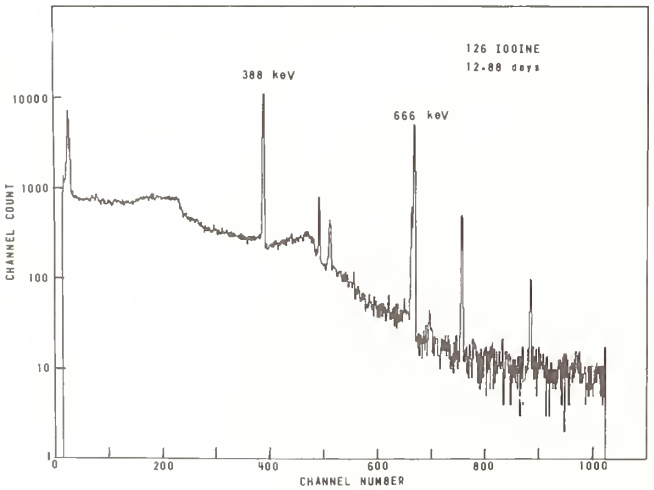

Fig. 2. Gamma-ray spectrum of C_6I_6 irradiated with 14.5 MeV neutrons (decay time 20 hours). All the observed gamma rays are from the decay of ^{126}I.

The radioactive decay of ^{126}I was followed for 58 days and a least squares fit to the decay data gave a half life value of 12.88 ± 0.03 days which is to be compared with 13.0 days as listed by Lederer and Shirley[6]. The absolute values of gammas per disintegration used in this work were 0.32 ± 0.06 for 388.5 keV and 0.30 ± 0.06 for the 666.2 keV transitions[7,8].

Results

From a measure of the ^{32}P and ^{126}I activities and a knowledge of the irradiation histories, cross sections were calculated for the $^{127}I(n,2n)$ reaction. The excitation curve is shown in Figure 3 and the results are listed in Table 2.

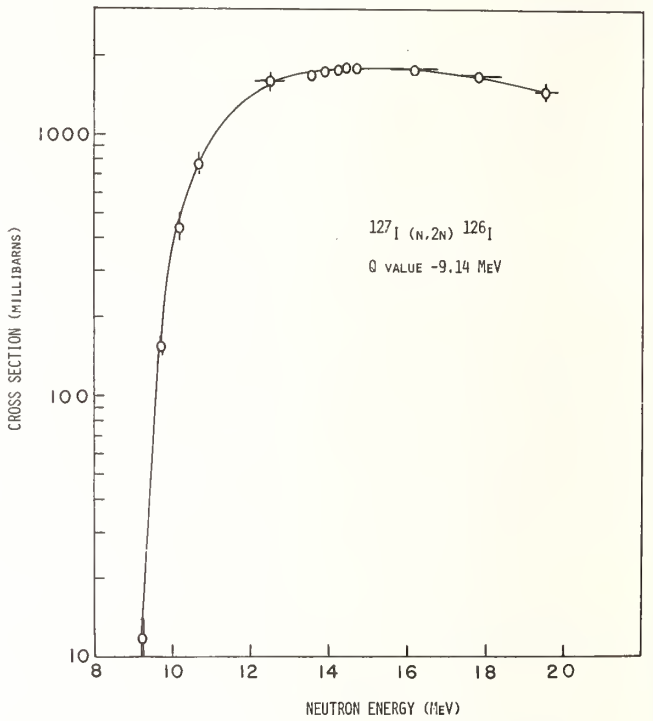

Fig. 3. Excitation curve for the $^{127}I(n,2n)^{126}I$ reaction.

Table 2

$^{127}I(n,2n)^{126}I$ Cross Section Measured Relative to the $^{32}S(n,p)^{32}P$ Reaction

Neutron Energy (MeV)	Cross Section (mb) $^{32}S(n,p)$	$^{127}I(n,2n)$
9.25 ± 0.11	366	11.6 ± 2.3
9.80 ± 0.11	383	155 ± 1.6
10.25 ± 0.11	397	422 ± 35.
10.75 ± 0.11	398	754 ± 60.
12.5 ± 0.4	333	1569 ± 94.
13.58 ± 0.10*	277	1690 ± 101.
13.89 ± 0.06*	263	1720 ± 103.
14.24 ± 0.08*	235	1780 ± 107.
14.50 ± 0.15*	226	1782 ± 107.
14.76 ± 0.20*	216	1766 ± 106.
16.2 ± 0.6	154	1731 ± 104.
17.8 ± 0.5	106	1681 ± 100.
19.6 ± 0.3	80	1424 ± 85.

* Texas Nuclear Neutron Generator

At each energy the cross section value is the average of at least three separate measurements. Errors in the measured cross sections are 6% except near the reaction threshold energy. The values were determined relative to the $^{32}S(n,p)$ cross sections and possible errors of 6% in the latter have not been included, nor has the 20% uncertainty in the gamma ray abundance of the 666 keV transition in the decay of ^{126}I. A more accurate gamma branching ratio for the decay of ^{126}I is desirable, but at present using the value quoted here together with the derived cross section value will give the correct neutron flux. The observed threshold occurs at 9.2 MeV, in agreement with the calculated Q for the reaction, consequently the reaction is sensitive only to the higher energy component of fast neutrons.

Discussion

Previously published values for the $^{127}I(n,2n)$ cross section were made at energies around 14 MeV, but were in poor agreement with each other. The most recent measurements at 14.5 MeV when corrected for the gamma branching ratio now accepted[7] are 1764 ± 140 mb by Barrall, et al.[9] and 1752 ± 80 mb by Lu, et al.[10] These values are in good agreement with 1782 ± 107 mb as measured in this work.

The $^{127}I(n,2n)$ reaction has a flat response around 14 MeV which is the energy region produced by neutron generators or thermonuclear fusion machines. For monitoring (D + T) neutrons, the reaction is not influenced by the presence of extraneous 2.9 MeV (D + D) neutrons produced by deuterium buildup in tritium targets.

Changes in neutron energy as well as flux can be monitored using the $^{127}I(n,2n)$ reaction in conjunction with a low threshold detector, i.e., $^{32}S(n,p)$. For this pair of reactions the resulting products have similar half lives and would be monitoring the same irradiation time period. In the example given in the previous paragraph, a measure of ^{32}P and ^{126}I activities would determine the (D + D) neutrons as well as the (D + T) contribution. Another example would be in monitoring the neutron spectrum of a nuclear reactor. Calculations[5] of an effective cross section for a fission neutron spectrum based on the differential cross section values are given in Table 3. By measuring the ratio of ^{32}P to ^{126}I activities, it is possible to measure deviations from a pure fission spectrum.

Table 3

Effective Cross Section for a Fission-Neutron Spectrum

$$\bar{\sigma} = \int_0^\infty N(E)\sigma \, dE$$

For a ^{235}U spectrum -

$$N(E) = k \exp(-1.036) \sinh(2.29E)^{1/2}$$

$\bar{\sigma}$ $^{127}I(n,2n)^{126}I$ = 1.03 mb

$\bar{\sigma}$ $^{32}S(n,p)^{32}P$ = 63.2 mb

The present study shows that the high cross section for $^{127}I(n,2n)$ reaction combined with the suitable decay characteristics of ^{126}I make the reaction suitable for measuring the high energy neutron component in experiments at accelerators or in nuclear reactors.

References

1. D.C. Santry and J.P. Butler, Can. J. Chem. 41, 123 (1963).
2. A.M. Bresesti, M. Bresesti, A. Rota and R.A. Rydin, Nucl. Sci. Eng. 40, 331 (1970).
3. P.S. Spangler, N.C. Rasmussen and D.J. Rose, Nucl. Sci. Eng. 26, 278 (1966).
4. L. Allen, Jr., W.A. Biggers, R.J. Prestwood and R.K. Smith, Phys. Rev. 107, 1363 (1957).
5. D.C. Santry and J.P. Butler, Can. J. Phys. 50, 2536 (1972).
6. C.M. Lederer, V.S. Shirley, Tables of Isotopes (John Wiley and Sons, Inc., New York, 1978).
7. M.J. Martin, Oak Ridge National Lab. Report, ORNL-5114 (1976).
8. R.S. Grantham, L.C. Whitlock, R.S. Lee, J.H. Hamilton, A.V. Ramayya and K.S.R. Sastry, J. Phys. G: Nucl. Phys. 2, 519 (1976).
9. R.C. Barrall, M. Silbergeld and D.G. Gardner, Nucl. Phys. A138, 387 (1969).
10. W. Lu, N. RanaKumar and R.W. Fink, Phys. Rev. C1, 350 (1970).

RESONANCE NEUTRON RADIOGRAPHY FOR NONDESTRUCTIVE EVALUATION AND ASSAY APPLICATIONS

J. W. Behrens, R. A. Schrack, A. D. Carlson, and C. D. Bowman
National Bureau of Standards
Washington, D. C. 20234, USA

Resonance neutron radiography is being developed at the NBS for both nondestructive evaluation (NDE) and nondestructive assay (NDA) applications. To illustrate the method we determined the distribution of solder between two silver-brazed metal rings and measured the thickness of the braze. Our technique was also used to nondestructively assay ^{234}U, ^{235}U, and ^{238}U in a fresh UO_2 nuclear fuel pellet. The National Bureau of Standards linear accelerator provided a pulsed source of neutrons over the energy range from 0.3 eV to 20 eV. A linear position-sensitive proportional counter (PSPC) was designed and built having a spatial resolution of 1.2 mm. The PSPC had a sensitive length of 50 mm and contained 3 atm ^3He, 7.5 atm Xe, and 0.5 atm CO_2. Transmission values over the resonances were used to identify and assay the materials.

[Epithermal neutron energy, neutron radiography, nondestructive assay, nondestructive evaluation, position-sensitive proportional counter.]

Introduction

Rapid growth in the development of neutron radiography began in the early 1960s. By the mid 1960s thermal neutron radiography was being used by industry. A summary of the early development of neutron radiography has been published by Berger.[1] In 1970 Forman et al.[2] used epithermal neutrons to produce neutron radiographs. A pulsed reactor and a ^6Li-based neutron detector were used. Neutron energy was determined by time-of-flight. In 1972 Kaplan et al.[3] reported work on thermal neutron radiography using a multiwire proportional counter instead of photographic film and in 1975 Priesmeyer and Harz[4] determined the isotopic assay of irradiated nuclear fuel using neutron transmission measurements in the energy range below 20 eV.

To date neutron radiography has primarily been considered as a nondestructive evaluation (NDE) technique. At the National Bureau of Standards (NBS) we are developing a method called resonance neutron radiography.[5] By comparison, this method utilizes epithermal neutrons and a position-sensitive proportional counter (PSPC) and has applicability as both an NDE and NDA (nondestructive assay) technique. To demonstrate and test the method a broad energy spectrum of epithermal neutrons and a linear (i.e., a one-dimensional) PSPC were used with the time-of-flight technique to determine (1) the distribution of solder between two silver-brazed metal rings and to measure the thickness of the braze, and (2) the amount of ^{234}U, ^{235}U, and ^{238}U in a fresh UO_2 nuclear fuel pellet.

Experimental Setup

A test facility for resonance neutron radiography has been established and experiments completed confirm the scientific validity of the method. The apparatus is illustrated in Fig. 1. The NBS 100 MeV electron linear accelerator was used to produce a pulsed-neutron source. The electron beam struck a water-cooled tungsten target. The resulting bremsstrahlung radiation produced neutrons by the (γ,n) reaction in the tungsten. High energy neutrons were moderated using a water moderator. The linac parameters which were used to take the two radiographs are given in Table I.

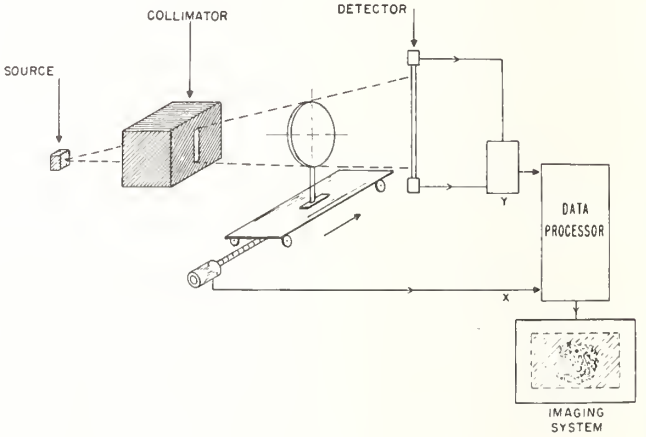

Fig. 1. Illustration of experimental setup for resonance neutron radiography experiments.

The neutron beam was collimated by a narrow slit and passed through the object to be radiographed. The transmitted intensity was detected in the linear PSPC. For the silver solder radiograph a commercially available PSPC[6] containing 4 atm ^3He and 6 atm argon was used. Position sensing was accomplished by charge division from the resistive electrode.[7] The sensitive length was 300 mm and the spatial resolution, measured at the NBS reactor,[8] was 5 mm. This spatial resolution was satisfactory for the 76 mm diameter silver solder braze; however, it was not good enough for radiography of 10 mm diameter fresh nuclear fuel pellets. For the cylindrically shaped nuclear fuel a spatial resolution of 1 mm was desired; however, linear PSPCs with 1 mm spatial resolution were not available commercially. To solve this problem the NBS and ORNL[9] started a collaboration to develop a linear PSPC with 50 mm sensitive length and a 1 mm spatial resolution. Our PSPC contained 3 atm ^3He, 7.5 atm Xe, and 0.5 atm CO_2. Position sensing was accomplished by RC-encoding.[10] The spatial resolution, measured at the ORNL HFIR reactor,[11] was 1.2 mm. This PSPC was used at the NBS for the fresh nuclear fuel radiograph.

Table I. Linac parameters during radiography measurements.

Radiograph	Linac Parameters			
	Repetition rate (Hz)	Maximum electron energy (MeV)	Electron pulse width (μ sec)	Average power on target (kW)
Silver solder braze	600	92	1/2	3.2
Fresh nuclear fuel	720	110	1	4.0

The object under study was moved by a precision-driven tray. The information on position of the tray (x-direction) and position of neutron detection (y-direction) were fed into our data acquisition system along with time-of-flight information. Each position of the tray had assigned to it 262K words of memory from our data storage disk. For a given tray position 2048 time-of-flight channels with 128 pulse height channels per TOF channel were used. The time per channel on the TOF data was 1/4 μ sec. We processed the multi-parameter data to form pictures for particular neutron energies of interest.

Results

Silver Solder Radiograph

For the silver solder radiograph a 5-inch outer diameter, 1-inch inner diameter, 1/2-inch thick brass ring was machined to contain a 3-inch outer diameter, 1-inch inner diameter, 1/4-inch thick steel ring. The steel ring was silver soldered into the center of the brass ring. Solder was purposely omitted from about a 20 degree portion of the full circle. The objective of the experiment was to determine the distribution of the silver solder and to measure its thickness.

For this experiment the PSPC was located at a flight path distance of 8.5 meters from the neutron producing target. The neutron beam was collimated to a slit 6 inches long and 3 mm wide. A total of 26 tray positions were required (25 sample in runs and 1 sample out run) to take the radiograph and each position represented approximately 45 minutes of data collection.

The results of the measurement are shown in Fig. 2. Silver was identified using the time-of-flight information for the neutron energy range centered on the 5-eV resonance of the isotope ^{109}Ag. Position information for "on resonance" (3 to 7 eV) and "off resonance" (10 to 20 eV) conditions gave us transmission values from which the image in Fig. 2 could be constructed. In looking at Fig. 2 it is clear that the distribution of the silver was not uniform and the 20-degree slot is clearly visible. From the transmission values the thickness of the silver was determined. This was done using area analysis on the isolated 5 eV ^{109}Ag resonance. In the more uniform regions the silver thickness averaged about 0.001 inch. This is to be compared to the 0.5 inch total thickness of the sample.

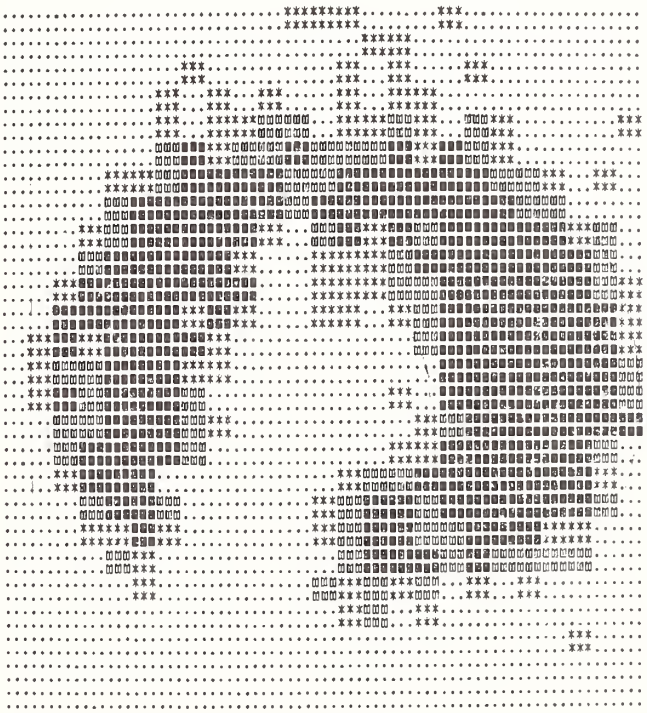

Fig. 2. Image of silver distribution in brazed metal rings.

Fresh Nuclear Fuel Radiograph

For the fresh nuclear fuel radiograph fresh UO_2 nuclear fuel pellets[12] 10 mm in diameter and 10 mm in thickness with ^{235}U enrichments ranging from 1.88 to 3.95 at.% were used. The UO_2 pellets had a mass of 9.1 grams. The objective of the experiment was to assay the ^{234}U, ^{235}U, and ^{238}U in the pellets.

For this experiment the specially built NBS/ORNL PSPC was located at a flight path distance of 4.6 meters from the neutron producing target. The neutron beam was collimated to a slit 2 inches long and 3.2 mm wide. Figure 3 shows typical position information

from an 8-hour linac run where two fuel pellets were being radiographed simultaneously. The ratio of pulse height distributions for sample in and sample out over all time-of-flight channels is plotted as a function of pulse height channel.

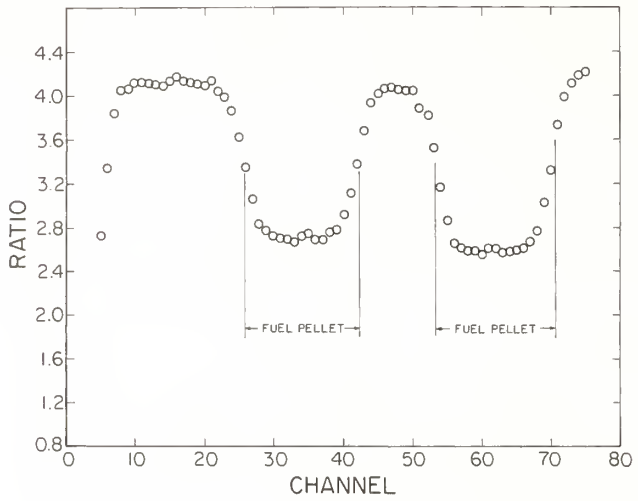

Fig. 3. Typical position information showing two nuclear fuel pellets.

The UO_2 pellet has three major components; ^{235}U, ^{238}U, and ^{16}O. Over the neutron energy range from 1 to 20 eV the ^{16}O total cross section is almost constant; however, the ^{235}U and ^{238}U total cross sections have considerable structure, as shown in Fig. 4(a). Figure 4(b) shows transmission values plotted as a function of TOF channel number. These measured transmission values were determined for a range of positions which were well inside the nuclear fuel pellet. Determination of the isotopic abundance of ^{235}U was accomplished by fitting the nuclear data for ^{235}U and ^{238}U to match these measured transmission values (smooth curve in Fig. 4(b). Starting values for n_1, n_2, and n_3 (^{235}U, ^{238}U, and ^{16}O atoms/barn, respectively) were determined in the following way. Values for n_1 and n_2 were determined by a linear least squares fit of the log of the transmission values using the ^{235}U and ^{238}U total cross section values as basis functions. The value for n_3 was determined by assuming the pellet to be pure UO_2. These n_1 and n_2 values were then used in a more complex nonlinear fitting code where the system response function was included. This system response function was due to the electron and neutron source distributions and the detector electronics response. Values of n_1 and n_2 determined in this manner were within 1.5% of the values determined by gamma spectrometry. The amount of ^{234}U in the pellet was determined using area analysis on the 5.19 eV resonance (see Fig. 4(b)). The n value was within 6% of the value determined by mass spectrometry; however, the statistical uncertainty in our measurement is about 6%.

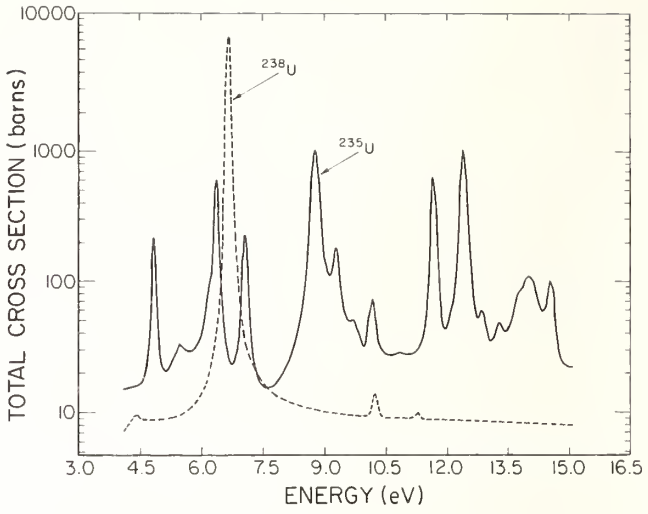

Fig. 4(a). Total cross sections of ^{235}U and ^{238}U from 4.5 to 15.0 eV neutron energy.

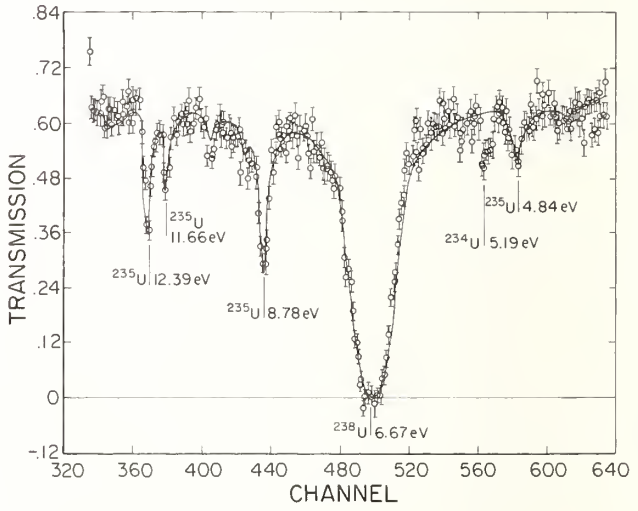

Fig. 4(b). Transmission values for a range of positions well inside a 3.95 at.% ^{235}U nuclear fuel pellet.

Discussion

Our work has demonstrated the use of resonance neutron radiography as an NDE and NDA technique. A number of refinements to our experimental setup and procedures are currently being pursued. The NBS and ORNL are continuing their collaboration to develop high spatial resolution PSPCs. We are currently building an "area" PSPC which has a sensitive area 50 x 50 mm^2 and a spatial resolution of 1 x 1 mm^2. Using this area PSPC would greatly reduce the linac running time necessary to do a radiograph. Improvements in our data acquisition system are being made to accommodate the increased counting rates which will accompany the area PSPC. Further refinements in our data analysis methods are also being made.

Our first radiograph centered on determining the presence of silver within an object. Clearly, other elements and isotopes can be similarly identified through their characteristic neutron resonances. Table II gives an indication of elemental sensitivity using resonance neutron radiography where, for example, the element is mixed in an iron specimen 1-inch thick.

Table II. Sensitivity of resonance neutron radiography.

Sensitivity (atom ppm)*	Element
< 5	Gd
5-10	Sm
10-30	In, Dy, Tm, Ta, W, Au
30-50	Pd, Ag, I, Cs, Pr, Eu, Hf, Re
50-100	Co, As, Rh, Cd, La, Ho, Ir
100-300	Mn, Br, Kr, Mo, Tc, Sn, Sb, Xe, Nd, Er, Lu, Pf, Ti, Bi, Th, U
300-500	Yb, Os, Hg
500-1000	Li, B, Te
1000-1500	Na, Se, Ru, Ba

*Mixed in iron 1" thick.

The use of resonance neutron radiography as an NDA technique for determining the ^{235}U content in fresh nuclear fuel might be valuable in the areas of nuclear material accountability and safeguards. Sections of fresh nuclear fuel rods could be nondestructively assayed at the NBS. These sections would then become reference standards which would be circulated worldwide to calibrate ^{235}U assaying instruments at nuclear fuel fabrication facilities. Resonance neutron radiography might also be a valuable technique at nuclear reprocessing plants as a nondestructive method for nuclear accountability and safeguards. Spent nuclear fuel contains a number of uranium and plutonium isotopes. We will be using resonance neutron radiography to assay a central and an end section from a spent fuel rod. The object of this experiment will be to demonstrate feasibility of the technique with highly radioactive spent fuel, to assay the ^{235}U and ^{239}Pu, and to measure radial and longitudinal gradients in the ^{235}U and ^{239}Pu concentrations.

The feasibility of resonance neutron radiography as an industrial NDE and/or NDA technique rests greatly on the expense and complexity of the pulsed neutron source. To conduct our measurements we utilized the nine section NBS 100 MeV electron linear accelerator. The expense and complexity of the NBS linac are not necessary to produce a sufficient neutron flux over the neutron energy range of interest, i.e., from 0.3 eV to 20 eV. Sufficient neutron intensity might be possible using a one section 10 MeV linac in the manner described by Bowman.[13] Some advantages of neutron production at lower electron energy are (1) reduced capital for the accelerator, (2) reduced physical space requirements, (3) more reliable accelerator operation, (4) lower maintenance, (5) simplicity of operation, and (6) greatly reduced activation of accelerator and neutron target.

Acknowledgments

The authors would like to thank H. Hill, Director of Instrumentation and Controls Division, Oak Ridge National Laboratory for his encouragement and support throughout our collaboration with members of his division on the development of high spatial resolution PSPCs. We give special acknowledgment and thanks to M. K. Kopp and J. A. Williams (ORNL) for sharing with us their years of experience in the field of PSPC development.

We would also like to thank the NBS linac operators and staff for their efforts in providing the electron beam for these measurements.

This work was sponsored in part by the U.S. Nuclear Regulatory Commission.

References

1. H. Berger, Neutron Radiography Methods, Capabilities, and Applications, (Elsevier Publishing Co., New York, 1965).
2. L. Forman, C.U. Benton, D.A. Garrett, and A.D. Schelberg, Rev. Sci. Instrum., 41, 1900 (1970).
3. S. Kaplan, K. Valentine, L. Kaufman, V. Perez-Mendez, "Neutron Radiography with a Multiwire Proportional Chamber-Performance and Projections," Trans. Am. Nucl. Soc., 15, 140 (1972).
4. H.G. Priesmeyer and U. Harz, Atomkernenergie 25, 109 (1975).
5. J.W. Behrens, R.A. Schrack, and C.D. Bowman, "Resonance Neutron Radiography Using a Position-Sensitive Proportional Counter," Trans. Am. Nucl. Soc., 32, 207 (1979).
6. Reuter-Stokes, Inc., Cleveland, Ohio.
7. J.L. Alberi and V. Radeka, IEEE Trans. Nucl. Sci., 23, 251 (Feb. 1976).
8. J.W. Behrens (private communication, Feb. 1978).
9. M.K. Kopp and J.A. Williams, Instrumentation and Controls Division, Oak Ridge National Laboratory, Oak Ridge, Tennessee.
10. C.J. Borkowski and M.K. Kopp, Rev. Sci. Instrum., 46, 951 (1975).
11. J.W. Behrens (NBS) and M.K. Kopp (ORNL) (private communication, Feb. 1979).
12. General Electric Company, Wilmington, North Carolina.
13. C.D. Bowman, "Efficient Neutron Production Using Low-Energy Electron Beams," Proceedings of the International Conference on Nuclear Cross Sections for Technology, Univ. of Tennessee, USA, Oct. 22-26, 1979.

FAST NEUTRON RADIOTHERAPY: FUNDAMENTAL ASPECTS AND CLINICAL RESULTS

J.J. Broerse
Radiobiological Institute TNO
Rijswijk, the Netherlands

Renewed applications of fast neutrons for clinical radiotherapy, were initiated by fundamental radiobiological findings. Studies of the responses of normal tissues and tumour systems after irradiation with fast neutrons had shown two essential differences with the effect after X-irradiation, notably a reduced oxygen effect and a reduced repair of sublethal damage. Furthermore wide variations in relative biological effectiveness had been observed for different tumours and normal tissues. The results of the clinical applications of fast neutrons are promising for specific tumours. However, the studies have indicated the need for coordinated clinical trials on a national and international scale. To allow a direct evaluation of clinical results obtained at the different neutron radiotherapy centers it will be essential to optimize the delivery of the dose to the target volume and to determine the energy dissipation with a sufficient degree of precision and accuracy. The need for better dose distributions and further knowledge of nuclear data, including cross sections, will be exemplified.

[neutron radiotherapy, radiobiology, neutron depth dose, uncertainties, cross sections]

Introduction

Only a few years after the discovery of the neutron, the first patients were treated with these indirectly ionizing particles produced through the d(8)+Be reaction by a 37 inch cyclotron at Berkeley[1]. Historical surveys of the radiobiological and radiotherapeutic experience with fast neutrons can be found elsewhere[2,3]. The radiobiological knowledge available in 1938 was very limited, contradictory in some instances, and did not provide a clear rationale as to why neutrons should give a better result in the cure of cancer than conventional X-rays. The clinical results of these first applications of fast neutrons showed large variations; this was to be expected, since, in general, the patients treated were in an advanced stage of the disease. Another conclusion of the first clinical applications was that late effects in different normal tissues were more serious than anticipated. In later analyses of the data, a number of complications could be attributed to differences in effects of fractionation of neutrons as compared to photons. However, the mechanism of repair of sublethal damage for different types of radiation was not yet investigated. The clinical results were considered to be so unsatisfactory that the neutron irradiations of patients were terminated in 1942.

Only at the end of the fifties did new radiobiological data become available, initially connected with the so-called oxygen effect. Studies on cell systems in vitro showed that a cell population is much more radiosensitive in the presence of oxygen than in its absence. This effect can be described by the oxygen enhancement ratio (OER), which is defined as the ratio of the doses needed for a certain survival level for cells under anoxic and oxygenated conditions. For X- and gamma radiation, this OER has a value between 2.5 and 3.0. Employing the new tissue culture techniques, it was also possible to study the effects of different types of radiations with varying linear energy transfer (LET). From cell survival studies after irradiation with deuterons and alpha-particles, it appeared that the shape of the survival curve for high LET radiation differed from that obtained after irradiation with low LET radiation, such as X- or gamma rays. Furthermore, the OER was lower for radiations with high LET than for low LET[4].

In this paper the actual radiobiological data will be summarized, recent results of the clinical applications of fast neutron beams will be discussed and the characteristics of fast neutron beams will be described. In order to understand interactions of neutrons with biological material and to interpret dosimeter readings, our knowledge on basic physical data (including neutron cross sections) has to be extended especially in the neutron energy range from 15 to 80 MeV.

Present-day radiobiological knowledge

When a biological system is irradiated with neutrons, the energy is dissipated by fast protons, alpha particles and heavy recoils which are produced in the tissue through interactions of the neutrons with the tissue constituents. The secondary particles produced by the neutrons have a higher ionization density than electrons produced by X- or gamma radiation; consequently, neutrons can be described as high LET radiation. As pointed out in the introduction, the OER is considerably reduced for high LET radiation and, on the basis of the research performed with alpha-particles and deuterons, it was expected that the oxygen effect for neutrons would also be lower than for photons. By using an established line of cultured cells derived from human kidney, the oxygen effect was initially studied after irradiation with 15 MeV neutrons produced by the d+T reaction. The survival curves observed have a much steeper slope than those obtained after X-irradiation, indicating that neutrons are more effective per unit dose than X-rays which are used in radiobiology as a standard radiation. Furthermore, it was concluded that the OER for the 15 MeV neutrons was considerably lower than that for X-rays, namely, 1.6 in comparison with the OER of 2.6 for X-rays[5]. Subsequent studies[6] have shown that the OER is independent of neutron energy and remains constant up to high neutron energies produced by the p(100)+Be reaction (see figure 1).

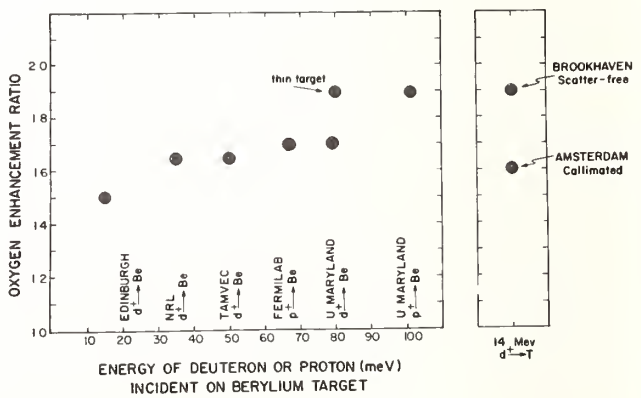

Fig. 1. Values of the oxygen enhancement ratio (OER) for various neutron beams produced by the p+Be, d+Be and d+T reactions (Hall and Kellerer[6])

Since it has been shown that a number of animal tumours contain a certain fraction of anoxic cells, it appeared that the use of neutrons could offer advantages in the treatment of these types of tumours. To evaluate the clinical usefulness of neutrons, however, it is necessary that information be also obtained on the biological effects on tumours and normal tissues in experimental animals and man.

In radiotherapy applications, the required dose is often limited by the risks of late damage to normal tissues such as fibrosis and necrosis. Since it is difficult to study these late effects in a quantitative way, the assessment of normal tissue damage is often based on the scoring of effects occurring relatively early after irradiation. Acute effects on normal tissues can be expressed in a number of radiation syndromes such as the bone marrow and intestinal syndromes which reflect the overall response of the total organism. By the introduction of new techniques, it has also been possible to study the effects on these normal tissues at the cellular level. The survival of bone marrow stem cells can be studied in a quantitative way by the use of the spleen colony technique[7] and the survival of cells in the intestinal crypts by the counting of the regenerating colonies in the intestinal epithelium[8]. The survival curves for effects on normal cell populations[9] show that there is a great variation in the intrinsic cellular radiosensitivity (see figure 2).

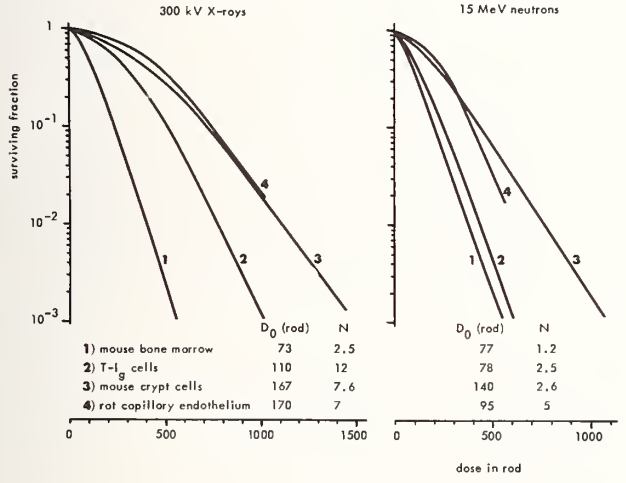

Fig. 2. Survival curves of clonogenic cells in different types of normal tissue (Broerse et al.[9]).

The exponential part of the survival curves can be described mathematically as

$$S = N \cdot e^{-D/D_0},$$

where S is the fraction surviving cells, N is the extrapolation number, D is the dose and D_0 is the reciprocal of the slope of the survival curve at higher doses. The intrinsic radiosensitivity can be described by the initial slope, the shoulder of the survival curve and the final slope at high doses. On the basis of the survival curves, it is possible to calculate the relative biological effectiveness (RBE) of neutrons. A surviving fraction of 10^{-3} for the intestinal crypt stem cells can be obtained after irradiation with 15 MeV neutrons with a dose of approximately 1080 rad (10.8 Gy) and after X-irradiation with a dose of 1500 rad (15 Gy). The ratio of these two doses, 1500/1080 = 1.4, is the RBE for this effect at this level of survival. The RBE is a quantity which is commonly used in radiobiology but it should be realized that it depends on a great number of circumstances, including the physiological conditions of the irradiated cell population, the nature of the biological effect and the dose applied. Furthermore, different RBE values can be obtained for the same dose depending on whether the radiation had been administered as a single dose, fractionated or protracted irradiation.

Parallel with the investigations on the radiation sensitivity of normal tissues, the sensitivity of a number of experimental animal tumour systems has been investigated. Information is presently available on the in vitro survival characteristics of a number of animal tumours. Studies on cell cultures derived from an osteosarcoma, a lymphosarcoma and a ureter carcinoma have shown that these tumours have distinctly different radiosensitivities[9]. The RBE for the various tumour systems is also considerably different; e.g., at a dose of about 100 rad, it varies between 1.8 and 3.0.

The final assessment of the possible advantages of the use of fast neutrons for radiotherapy has to be based on a comparison of the RBE values for effects on tumours with those for effects on normal tissues. For neutron beams of different energies, extensive information is currently available on the RBE as a function of the neutron dose for both normal tissues and experimental tumours. From studies performed with both in vitro and in vivo irradiations of a rhabdomyosarcoma in the rat and an osteosarcoma in the mouse, it could be concluded that, for these types of tumour, the RBE values are generally higher than those for effects on normal tissues (see figure 3). The fundamental radiobiological findings have initiated the renewed application of fast neutrons for clinical radiotherapy.

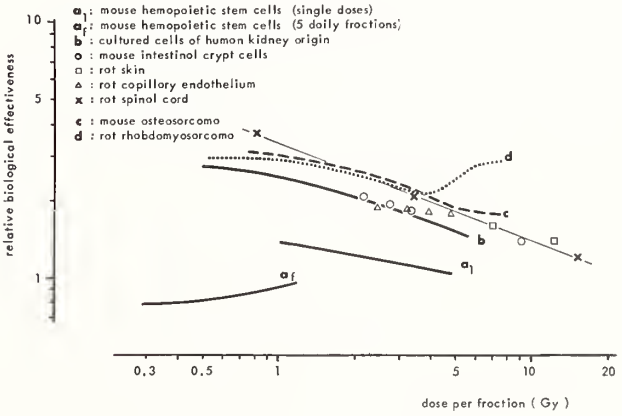

Fig. 3. Relation between the RBE of 15 MeV neutrons and the neutron dose or daily dose per fraction (Broerse et al.[9]).

Clinical results of fast neutron radiotherapy

In the pre-clinical studies special attention was devoted to occurrence of late tissue reactions. It was largely because this was shown not to be true in pig skin for observation periods up to five years[10], that sufficient confidence was gained to try fast neutrons again in the treatment of cancer. In 1969 new radiotherapeutical irradiations with fast neutrons were started at the Hammersmith Hospital in London. In the years following, neutron machines were installed in a number of countries, including the USA, the UK and the Netherlands. Additional centres in Germany and Belgium have recently started clinical irradiations or have plans for neutron radiotherapy at a later stage. The neutron therapy centres are listed in Table I. The final

evaluation of the usefulness of neutrons should come from a careful comparison of the clinical trials performed in the different institutes. The comparability of the clinical results is severely hampered by the fact that the centres have used different fractionation schedules imposed upon them because of the limited availability of the neutron producing cyclotrons. In addition, the various clinics have applied different dose levels due to the fact that the neutron beams employed have different energies. From the experimental radiobiological investigations, it is known that the RBE for neutrons generally decreases with increasing neutron energy.

reaction employed	location	type of machine	maximum deuteron energy (MeV)	deuteron beam (mA)	start of clinical operation	patients treated until end 1978
d+T	Amsterdam	s. tube*	0.25	18	1975	300
	Glasgow	s. tube*	0.25	30	1978	7
	Homburg	r. torget**	0.5	8	1976	260
	Heidelberg	s. tube***	0.25	500	1978	50
	Manchester	s. tube*	0.25	30	1978	50
d+Be	Chiba-shi	cyclotron	30	0.03	1975	400
	Chibo-shi	v.d. Graaff	2.8	--	1967	--
	Dresden	cyclotron	13.5	0.04	1972	450
	Edinburgh	"	15	0.1	1977	210
	Essen	"	14	0.1	1978	70
	Houston	"	50	0.007	1972	440
	London	"	16	0.1	1969	800
	Louvain	"	50	0.02	1978	--
	Seattle	"	21.5	0.04	1973	240
	Tokyo	"	15	0.1	1976	120
	Washington	"	35	0.01	1973	250
p+Be	Batovio	cyclotron	66	0.008	1976	105

* output : $10^{12} s^{-1}$; ** output : $1\text{-}2.10^{12} s^{-1}$; *** output : $5.10^{12} s^{-1}$

Table I. Fast neutron installations in use for clinical applications.

It must be realized that the renewed application of fast neutrons for the treatment of cancer has been in effect for only a relatively short period of time and that the follow-up of patients has not been long enough to allow us to make definite conclusions. The number of treated patients having the different types of cancers is also too limited for a reliable statistical analysis. Thus at the present time the evaluation of the tumour response can only be provisional. Nevertheless there have been a number of remarkable clinical results. During a recent meeting on Fundamental and Practical Aspects of the Application of Fast Neutrons and other high LET Particles in Radiotherapy, clinical data obtained at 10 centers were reviewed[11].

Among the tumours with a poor response to conventional radiotherapy, the brain tumours received particular interest at several institutes. It has to be concluded, however, that the results obtained so far at almost all centers are disappointing with pure neutrons as well as mixed schedules.

The therapeutic benefit with respect to conventional low LET radiation is doubtful for the adenocarcinoma of the breast and for carcinoma of the gastro-intestinal tract.

Encouraging clinical results appear to be obtained for carcinomas of the upper respiratory and digestive tract. The results obtained at London and Houston are summarized in tables II and III, respectively. The data obtained by Catterall et al.[12] show a considerably higher percentage of control for neutrons (76%) than for photons (19%), although for the neutron irradiations more complications have been observed (10/70). The data by Peters et al.[13] indicate a higher percentage of control without complications for the mixed neutron-photon beam than for the photons used for the control group. Among the head and neck tumours the results on salivary gland tumours should be mentioned separately with persisting controls up to 80% obtained by a number of neutron centers.

	neutron series	photon series
Patients in trial		
Total admitted to trial	82	79
Excluded for various reasons	12	16
Included in analysis	70	63
Local control of tumour		
Complete regression clinically:		
Which persisted	53(76%)	12(19%)
Later recurrence	1(1%)	15(24%)
No or incomplete regression	16(23%)	36(57%)
Survival (actuarial percentages)		
Alive at 1 year	53	42
Alive at 2 years	28	15
Severe complications in patients with cured tumours		
Eyes	2	1
Spinal cord	2	
Larynx and pharynx	6	1
Total	10	2

Table II. Clinical results obtained at London for neutron- and photon-treated patients. (Catterall et al.[12]).

	Local Control		Complications		Control without Complications	
	No.	%	No.	%	No.	%
Neutron group:						
Neutrons only, twice/week (N = 49)	23	46.9	10	20.4	14	28.6
Neutrons only, four times/week (N = 19)	7	36.8	1	5.3	7	36.8
Neutron boost (N = 29)	14	48.3	5	17.2	9	31.0
Mixed beam (N = 19)..	11	57.9	0	0	11	57.9
Total (N = 116)	55	47.4	16	13.8	41	35.3
Control group (N = 49)..	28	57.1	12	24.5	23	46.9

Table III. Clinical results obtained at Houston for head and neck cancer (Peters et al.[13]).

The clinical results obtained in the treatment of soft tissue sarcoma, bladder carcinoma and gynecological cancers seem also promising. For the treatment of advanced carcinoma of the cervix (see table IV) higher percentages of local control were observed for either a mixed neutron-photon beam or for photons alone.

HOUSTON 96 patients analyzed

	Local control	Complications
Mixed beam	61 %	7 %
Boost	60 %	20 %
[Photons]	48 %	7 %

NIRS 69 patients

Results for 20 grade III-IVa patients

	Local control	Complications
Neutrons	80 %	25 %
[Photons]	66 %	25 %

Table IV. Clinical results obtained in treatment of the cervix (Dutreix and Tubiana,[11]).

On the basis of clinical experience, it is also possible to make some conclusions concerning the effects on normal tissues[14]. In this analysis, it is important to realize that, for neutron beams, the penumbra is generally larger than for photon irradiations and the damage to normal tissues could probably be attributed to the poorer dose distribution for neutrons in comparison to that for conventional photon irradiations. The results indicate that, except for the effects on brain and spinal cord, the different types of damage (including necrosis) are not essentially more serious than those observed after photon irradiations (including effects on intestinal tract, bone, cartilage, connective tissue and skin).

The clinical experience collected up to now indicates that neutrons could be useful in the treatment of a certain number of tumour types and sites. It should be realized that most neutron radiotherapy studies have been handicapped by a number of factors[11] such as:

1. suboptimal dose distribution due to the low neutron energy or the large penumbra;
2. suboptimal fractionation resulting from lack of cyclotron availability;
3. suboptimal setting-up of patients caused by fixed horizontal beams and too low dose rates.

In spite of these difficulties a number of interesting clinical data have become available and it has to be stressed that due to these handicaps the possible advantages of fast neutron therapy are probably underestimated for many tumour sites. It has to be concluded that improvement of the dose distributions will be indispensable to make the best use of high LET radiation therapy.

Physical characteristics of fast neutron beams

It should be mentioned that the majority of neutron radiotherapy treatments have been performed with cyclotrons constructed for other purposes, essentially unsuitable for clinical work or with neutron generators which technically fall far short of modern megavoltage X-ray machines. In consequence dissatisfying clinical results could reflect more the inadequacy of the delivery of the neutrons to the tumour than the effects of neutrons themselves. Recently Catterall[15] suggested a number of factors to be considered in the production of a neutron machine suitable for treating patients in a comparable way with photons from megavoltage machines now in routine use throughout the world (see table V).

1. The beam must always be available to meet clinicol requirements.
2. The output must give treatment times not exceeding four minutes.
3. Depth dose ond isodose shape must be at least os good os those of ^{60}Co gammo-roys.
4. The neutron generator must be within o hospital.
5. The set-up of neutron treatments must not be compromised.
6. The beom should not be fixed in one position.

Table V. Minimum operational requirements of clinical neutron generators (Catterall[15]).

In order to meet the dose rate requirements, d+T neutron generators should have outputs in excess of 10^{13} s^{-1}. Such a d+T system is not yet operational for neutron radiotherapy. A high intensity d+T neutron source is under construction at Lawrence Livermore Laboratory[16], but little interest has been shown in developing this system into a clinical neutron therapy source. Present day experience has shown that dose rates in excess of 20 $rad.min^{-1}$ can readily be achieved with cyclotrons through the d+Be and p+Be reactions.

Extensive information[17,18] is presently available about the penetration characteristics of different neutron beams (e.g. see figure 4). For d+Be neutrons the depth dose increases with increasing deuteron energy with the d(30)+Be depth dose distribution similar to that of ^{60}Co gamma-rays.

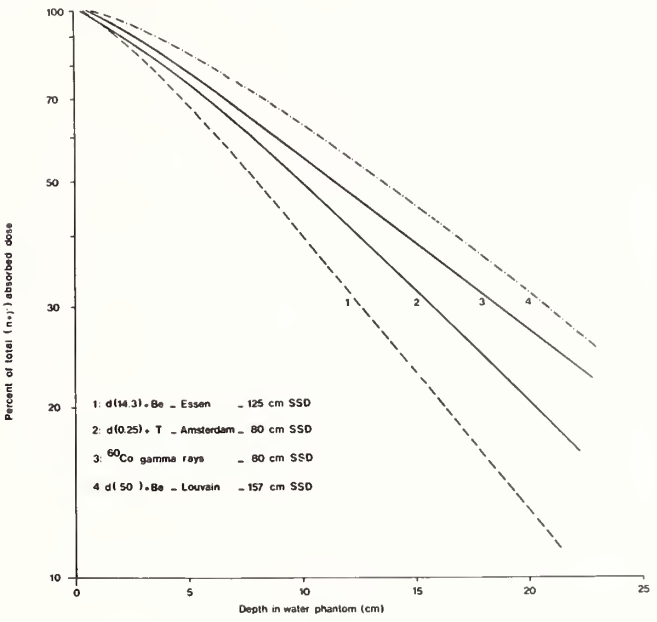

Fig. 4. Central axis depth dose curves (field sizes approximately 10x10 cm^2) for ^{60}Co gamma-rays and three different neutron beams. (Mijnheer and Broerse[18]).

The limited penetration characteristics of d+T neutron beams made it necessary to use multiple fields for the treatment of bladder cancer[19]. The treatment plans for bilateral irradiation and irradiation with six fields (see fig. 5a and 5b) show the considerably improvement obtained with regard to the dose delivery to the target volume.

It was only after the introduction of the six field technique that a local cure rate of 80% was achieved at Amsterdam (without severe skin and intestine complications (versus 30% with ^{60}Co gamma-rays).

The transverse dose distribution is predominantly determined by the scatter from the primary beam. With the exception of small fields the scatter dose generally exceeds several percent of the central axis dose when the shield transmission for such a shield is about 1% of the central axis dose (see fig. 6).

The transverse absorbed dose distributions for cyclotrons show that the penumbral width decreases with increasing deuteron energy. This may be explained by the more forward peaking of the neutrons by the higher energetic deuteron reactions and the decreasing scattering cross section of hydrogen at higher neutron energies[18]. The data for the d+T neutron generators show a much larger penumbra than for the cyclotrons. This is due to the larger target sizes needed to obtain adequate dose rates, the thinner shield and more isotropic emission of the neutrons produced in the d+T reaction. However, the difference in penumbral width becomes smaller if only the neutron dose is considered.

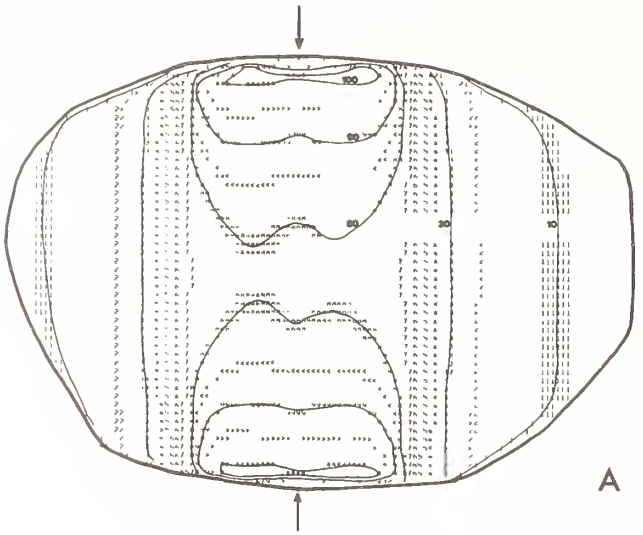

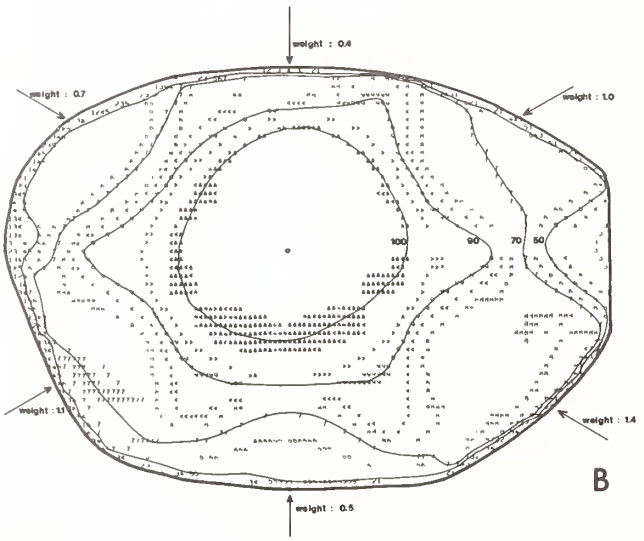

Fig. 5. Treatment plans for effective dose (D_n + 1/3 D_g) for bilateral irradiation (part A) and irradiation with six fields (part B) of bladder carcinoma at Amsterdam for d(0.25)+T neutrons, field size 11 x 9 cm^2 (Mijnheer and Battermann, [19]).

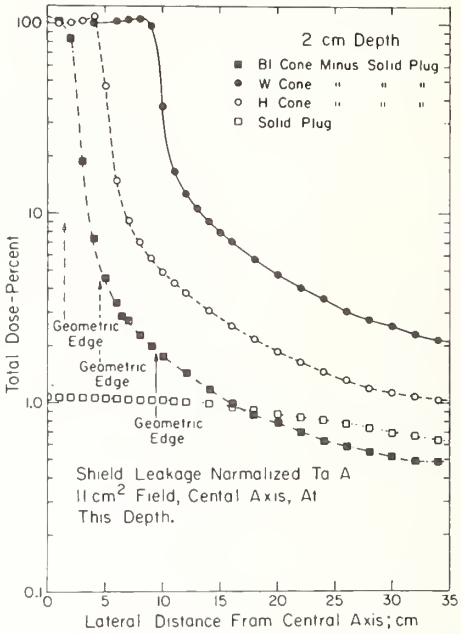

Fig. 6. Off-axis dose distribution for d(50)+Be neutrons for three different field sizes (Bl: 5.1 x 6.6 cm^2; H: 11 x 11.1 cm^2 and W: 20.5 x 20.5 cm^2) in comparison to shield leakage by insertion of a solid plug (Smathers et al. [17]).

It should also be realized, that RBE changes outside the beam may occur. The RBE will decrease due to the increase in the relative gamma ray contribution with increasing distance from the central axis. On the other hand, the RBE may increase due to the smaller absorbed dose per fraction and the lower neutron energy outside the beam as compared to the centre of the beam. Recently, it has been shown [20] that, when allowance is made for changes in the RBE of the neutron component, even with perfect shielding the biologically effective dose outside the useful beam is much higher for d(16)+Be neutrons than for a ^{60}Co machine. The same statement is probably valid for other fast neutron therapy beams, indicating that, in neutron therapy, one has to accept a greater hazard to the patient from stray radiation than with megavoltage X-rays.

Accuracies required for dosimetry in mixed n-γ fields

To obtain an equivocal answer as to which types of cancer will benefit most from neutron treatments, more clinical results have to be collected. Larger numbers of patient data will result from coordination of clinical trials in progress at the different clinics [21]. To allow an evaluation of the responses of tumours and normal tissues it is important to perform the neutron dosimetry with a sufficient degree of precision and accuracy.

Experimental studies on late radiation damage in the spinal cord of rats have shown that a dose increase of 5 to 10 percent in excess of the tolerance level can produce a considerable percentage of paralyzed animals (see figure 7).
There is also evidence from radiotherapy applications that the probability of tumour control is a steep function of dose: deviations of 7 to 10 percent in absorbed dose can be detected clinically [23,24]. In consequence, an overall uncertainty of ± 5 percent in dose to the tumour is generally considered to be necessary which requires accuracy of physical dosimetry to be about 3 percent. With regard to the reproducibility of the delivery of the neutron beam at the biological object, present day technology makes it possible to perform the monitoring with a precision of better than ± 2 percent.

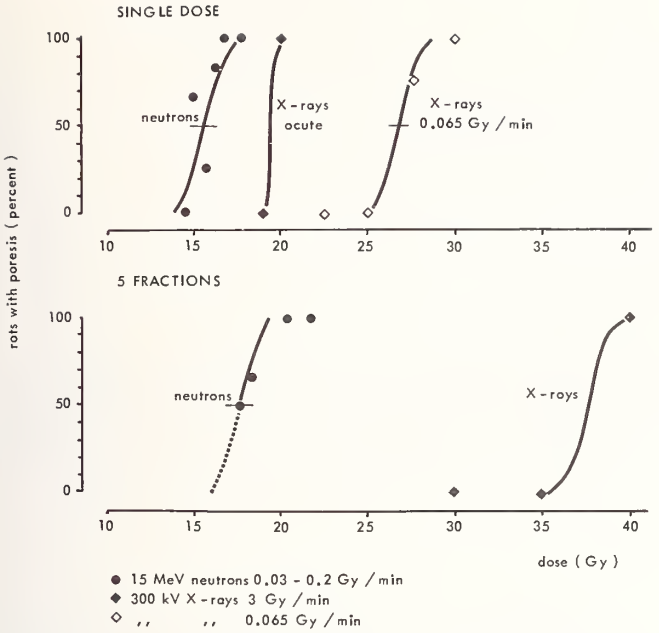

Fig. 7. Dose response curves for induction of paralysis in the rat after single and fractionated irradiations of the spinal cord with X-rays and 15 MeV neutrons (van der Kogel[22]).

The instrument most commonly used for the determination of the total absorbed dose is the tissue-equivalent (TE) ionization chamber[23]. The dose can be derived from ionization charge produced in the cavity by applying a number of conversion factors and corrections (see table VI). As can be seen from the table there are considerable uncertainties in the muscle/TE plastic kerma ratio, especially for the higher neutron energies because of the lack of cross section data in this energy range.

Ionizotion chamber response	R_T	0.2
Chorge saturotion correction	k_{sot}	0.2
T ond P correction	k_{TP}	0.1
Stem correction	k_{st}	0.1
Neutron kermo foctor rotio	$(K_T/K_M)_N$	3 to 10
Photon moss energy obsorption coefficient ratio	$(\mu_{en}/\rho)_t/(\mu_{en}/\rho)_m$	0.2
Displocement correction in phantom	d	1
Moss stopping power ratio for A-150 TE gos chomber	$(s_{m,g})_c/(s_{m,g})_N$	2 to 3
Averoge energy per ion poir ratio for A-150 TE gas chomber	$\overline{W}_C/\overline{W}_N$	3
	overoll uncertointy (quodroture sum)	5 to 11

Table VI. Uncertainties (in percent) in determination of total absorbed dose in a mixed n-γ field.

Recent neutron dosimetry intercomparisons[26,27] have shown that for in-phantom conditions the standard deviation of the results from the average value for total absorbed dose is in the order of 6 to 7 percent. Only for a few specific situations were maximum differences up to 20 percent observed. The participants in the dosimetry intercomparisons employed different physical parameters characterizing the detector response. To exclude the influence of the introduction of differing values for the basic parameters, the relative responses of the TE ionization chambers have also been compared. This analysis showed that the standard deviations for instrument response are of the same magnitude as those calculated for dose and kerma values. This implies that, in addition to the inconsistencies in basic physical parameters, there are also large systematic differences in measurement procedures connected with for example the calibration with photons, gas flow rate, collecting potential, polarity, correction for wall thickness and choice of effective point of measurement in a phantom. The results of the intercomparisons emphasize the need for uniform procedures and techniques for measuring chamber response and for applying the appropriate corrections.

It can further be concluded that more neutron data are necessary to guide and interpret the results of clinical applications and supporting biological studies. A number of neutron radiotherapy installations are under construction and nuclear data will be needed for two purposes[28]. First data are required on the neutron source reactions in order to select the bombarding particle and energy for new accelerators to be designed specifically for radiotherapy. Data will be required to resolve existing spectral differences and to evaluate the usefulness of the p+Be and p+D_2O reactions. Second, new neutron cross section data are essential for neutron energies between 14 and 80 MeV to understand the interactions of high energy neutrons in the body and to interpret dosimeter measurements. The most important nuclear data needed are the energy spectra of charged particles from oxygen and carbon. Also required are reaction cross sections and total cross sections for these elements for the neutron energy range between 14 and 80 MeV.

References

1. R.S. Stone, J.H. Lawrence, and P.C. Aebersold, Radiology 35, 322 (1940).

2. S.B. Field, Curr. Top. in Rad. Res. Quart. 11, 1 (1976)

3. J.T. Brennan, Int. J. Radiat. Oncol. Biol. Phys. 3, 143 (1977).

4. G.W. Barendsen, C.J. Koot, G.R. van Kersen, D.K. Bewley, S.B. Field, and C.J. Parnell, Int. J. Rad. Biol. 10, 317 (1966).

5. J.J. Broerse, G.W. Barendsen, and G.R. van Kersen, Int. J. Radiat. Biol. 13, 559 (1968).

6. E.J. Hall, and A. Kellerer, Europ. J. Cancer Suppl., p. 171 (1979).

7. J.E. Till, and E.A. McCulloch, Radiat. Res. 14, 213, (1961).

8. H.D. Withers, and M.M. Elkind, Int. J. Radiat. Biol., 17, 261 (1970).

9. J.J. Broerse, G.W. Barendsen, J.F. Gaiser and J. Zoetelief, in Radiobiological Research and Radiotherapy, Vol. II, IAEA, Vienna, 1977, p. 19.

10. D.K. Bewley, S.B. Field, R.L. Morgan, B.C. Page and C.J. Parnell, Br. J. Radiol., 40, 765 (1967).

11. J. Dutreix, and M. Tubiana, Europ. J. Cancer Suppl., p. 243 (1979).

12. M. Catterall, D.K. Bewley, and I. Sutherland, Br. Med. Journ. 1, 1642 (1977).

13. L.J. Peters, D.H. Hussey, G.H. Fletcher, P.A. Baumann, and M.H. Olson, Am. J. Roentg., 132, 637 (1979).

14. K.E. Halnan, Europ. J. Cancer Suppl., p. 251 (1979).

15. M. Catterall, Br. J. Radiol., 49, 203 (1976).

16. J.C. Davis, Europ. J. Cancer Suppl., p. 132 (1979).

17. J.B. Smathers, P.R. Almond, V.A. Otte, and W.H. Grant, Int. J. Rad. Oncol. Biol. Phys., 3, 149 (1977).

18. B.J. Mijnheer, and J.J. Broerse, Europ. J. Cancer Suppl., p. 109 (1979).

19. B.J. Mijnheer, and J.J. Battermann, private communication.

20. D.K. Bewley, and B.C. Page, Br. J. Radiol., 51, 375 (1978).

21. K. Breur, and J.J. Battermann, Europ. J. Cancer Suppl., p. 273 (1979).

22. A.J. van der Kogel, Late Effects of Radiation on the Spinal Cord: dose-effect relationships and pathogenesis (Thesis, Radiobiological Institute TNO, Rijswijk, 1979).

23. D.F. Herring, and D.M.J. Compton, in Computers and Radiotherapy, The British Institute of Radiology, London, 1971, p. 51.

24. ICRU report 24, Determination of absorbed dose in a patient irradiated by beams of X or Gamma rays in radiotherapy procedures (ICRU, Washington, 1976).

25. ICRU report 26, Neutron Dosimetry for Biology and Medicine (ICRU, Washington, 1977).

26. ICRU report 27, An International Neutron Dosimetry Intercomparison (ICRU, Washington, 1978).

27. J.J. Broerse, G. Burger, and M. Coppola, A European Neutron Dosimetry Intercomparison Project (ENDIP) Results and Evaluation (Commission of the European Communities, EUR 6004, Luxembourg, 1978).

28. W.G. Cross, in Proc. Int. Conf. on Neutron Physics and Nuclear Data for Reactors and other Applied Purposes, HMSO, 1979, p. 648.

NEUTRON DOSIMETRY

Peter R. Almond
The University of Texas System Cancer Center
M. D. Anderson Hospital and Tumor Institute
Texas Medical Center
Houston, Texas 77030, USA

James B. Smathers
Texas A&M University
Division of Bio-Engineering
College Station, Texas 77843, USA

The basis for measuring absorbed dose with ionization chambers is presented and the major parameters involved are discussed. These included the energy required to produce an ion pair ($\bar{W}/e$) and stopping power ratio's, kerma and tissue equivalence. The necessity for determining the photon absorbed dose along with the neutron dose is discussed, along with measurements of neutron spectrum.

(Neutron dosimetry, ionization chambers, stopping power ratios, kerma, tissue equivalence.)

Introduction

This paper will deal with neutron dosimetry as it applies to the biomedical sciences. In particular the dosimetric requirements for neutron therapy will be considered in some detail, but what is presented will also apply and be of importance for radiobiological experiments carried out with fast neutrons. Since neutrons are always accompanied by photons, it is necessary to select dosimetric systems which make it possible to quantitatively separate the two radiation components. The paper will not deal specifically with the measurement of radiation quality but it should be pointed out that determination of absorbed dose only is of limited value without information on beam quality.

Types of Dosimeters

The type of dosimeter selected will depend upon the type of measurement required. If the absorbed dose output of a neutron source is required then a calorimeter could be used since this gives a fundamental determination of absorbed dose. Several calorimeters have been built and used but they tend to be too insensitive and cumbersome for routine use and are generally used only as a standard for the calibration of secondary instruments, or the determination of the physical parameters used with other dosimeters. Activation detectors can be used, but the determination of kerma from the fluence measurements obtained from the activation detectors requires the knowledge of the neutron spectrum, cross sections and kerma factors. Activation detectors can also be used for relative dose measurements. Other detectors that may be used include silicon diode detectors, thermolumeniscent dosimeters, Geiger-Muller counters. By for the widest use, however, is made of gas detectors. Ionization chambers are used extensively for absorbed dose determination and proportional counter for quality (LET) determination.

Ionization Chambers

Tissue equivalent (TE) ionization chambers are used as the practical method for measuring neutron beam tissue kerma in air and the absorbed dose in a TE phantom. This is based on the fact that TE chambers have been used as the principal dose measuring instrument by the neutron therapy projects in the U.S., Europe, and Japan which are regularly treating patients. The dosimetry system of all the U.S. groups is based on the use of two sizes of commercial ion chambers manufactured with A-150 TE plastic as the chamber wall and collector material. Typically, a 1.0-cm^3 spherical chamber is used as the principal dose-rate calibration instrument, for measurements of neutron beam tissue kerma in air and total absorbed dose in a TE-liquid phantom, and 0.1-cm^3 thimble chamber is used for spatial dose distribution measurements in a TE phantom.

In order to make the total system as homogeneous as possible the chambers are often used with TE gas as well as being used in a TE phantom. The composition of the plastic, phantom material and gas are discussed later on.

The selection of "tissue equivalent" ionization chambers implies an acceptance of the applicability of the Bragg-Gray relationship and in the following sections the concerns associated with the utilization of this theory will be reviewed.

The general dosimetric methods followed have been reviewed in several papers ([1, 2, 3, 4, 5]) and will only be summarized here for completeness. The Bragg-Gray relation can be stated as

$$D = \frac{Q(\bar{w}/e)S_{rd}}{M} \qquad 1$$

where

D = dose; gray
Q = collected charge; Coulombs
$\bar{w}/e$ = average energy required to form an ion pair; Joules/Coulomb
S_r = gas to wall dose conversion factor and is the ratio of the mass stopping powers of the wall and gas.
M = mass of gas in sensitive volume of chamber; kg
d = chamber gas volume correction factor

As can be seen a knowledge of M, the mass of the gas, is one of the required parameters. As the sensitive volume of a chamber is generally difficult to physically calculate (with the desired accuracy) from shop drawings, an alternate method of determining M by exposing the chamber in a calibrated gamma field is generally used. The mass, as computed by this method, is given by

$$M = \frac{Q_\gamma(\bar{w}/e)_\gamma \; S_{r,\gamma} \; TPC_\gamma}{R(f)\;(\mu_{en}/\rho)(wall)\,\mu_{en}/\rho(muscle)(Aw)} \qquad 2$$

TPC = temperature - pressure correction to standard condition

R = exposure, Ckg^{-1}

f = tissue dose to exposure conversion factor for ^{60}Co gamma rays

f = $.3709 \times 10^2$ GyC^{-1} kg

μ_{en}/ρ(wall)/μ_{en}/ρ(muscle = conversion chamber wall dose to muscle dose; = 1.0036 for ^{60}Co

Aw = attenuation of primary beam by material required to establish charged particle equilibrium
= 0.985 for ^{60}Co

other parameters as previously defined, when the calibrated gamma field is from cobalt-60.

The parameters involved in equation 2 can be calculated or measured with accuracies such that the computed value of M has less uncertainty than one based on chamber shop drawings and electric field strength calculations.

Substituting this value of the mass into the Bragg-Gray relation for muscle dose in a neutron field yields equation 3 for the total dose

$$D_n(Gy) = \underset{a}{\left[\frac{(\bar{w}/e)_n}{(\bar{w}/e)_\gamma}\right]} \; X \; \underset{b}{\left[\frac{S_{r,n}}{S_{r,\gamma}}\right]} \; X \; \underset{c}{\left[\frac{Kerma\ (muscle)}{Kerma\ (wall)}\right]} \; X$$

$$\underset{d}{\left[Q_n \; TPC_n \; (C_\gamma)NBS \; f \frac{\mu en}{\rho}(wall) Aw.d \Big/ \frac{\mu en}{\rho}(muscle)\right]} \qquad 3$$

where $(C_\gamma)NBS = \frac{R}{Q_\gamma \; TPC_\gamma}$ = ionization chamber ^{60}Co calibration factor traceable to NBS in kg^{-1}

Bracket d is composed of terms whose magnitures are considered to be measureable or calculable to the accuracy required. The uncertainty is larger, however, for the quantities in brackets a, b, and c.

W

A wide variety of particles contribute to the ionization producted by neutron irradiation: these range from electrons with energies of several MeV to heavy recoil ions with very low energies.

The variation of w with energy has been considered by many authors and variation with energy has been reported for both electrons and heavy ions. [6-18] The most extensive study of a particular gas has been that for methane by McDonald and Sidenius. [19] Using this data to bench mark theoretical and empirical relations, Dennis has evolved a series of relations for w vs energy and ion mass for hydrocarbon gases including tissue equivalent gas mixtures, equations 4 and 5. [20,21]

For E $\leq$ 1 MeV/amu

$$w(E) = w_e \left[1.035 + A(Z)\,(E/M)^{-n(Z)}\right] \qquad 4$$

For E $\geq$ 1 MeV/amu

$$w(E) - w_e \left[E/(E - constant)\right] \qquad 5$$

w(E) = w value for ion of energy E; Joules/Coulomb
w_e = w value for fast electrons; Joules/Coulomb
A(Z) = constant which is ion dependent, see Table 1
E = ion energy; KeV
M = ion mass, amu
n(Z) = constant which is ion dependent, see Table 1

The constant in eqn 5 is determined by equating eqn 4 and eqn 5 at 1 MeV.

The formulation was extended to include nitrogen and carbon-dioxide by modification of the constant A(Z). If the A(Z) as tabulated in Table 1 is multiplied by 0.626, equations 4 and 5 are valid for CO_2 and N.

Table 1

Coefficients Used to Obtain Mean w Values for Heavy Ions in Organic Gases

Ion	A(Z)	N(Z)
Proton	0.1301	0.04902
Helium	1.810	0.5360
Lithium	3.219	0.7630
Beryllium	2.240	0.8208
Boron	1.903	0.7226
Carbon	1.909	0.6337
Nitrogen	1.907	0.5828
Oxygen	2.020	0.5999

For the charged particle fields created by the high energy neutron beams, the relative abundance of the low energy heavy ions and consequently their overall effect on w_n is still clouded by a lack of good experimental data and/or cross section values for theoretical analysis. As a consequence, the values of w_n in use at present are based on measured dose distributions between alphas, protons, and electrons only. Assuming the additivity of ionization produced within the chamber, w_n is calculated using equation 6,

$$\frac{100}{\frac{\%\,D_p}{w_p} + \frac{\%\,D_e}{w_e} + \frac{\%\,D_\alpha}{w_\alpha}} \qquad 6$$

where D = absorbed dose deposited by the various charged particles.

Bichsel and Rubach (1978)[22] fitted single functions to the data for p, α, C+, N+, and O+ ions

and used them to calculate effective values of w_n for spherical ionization chambers with walls of Shonka plastic (A-150) filled with methane-based TE gas (ICRU, 1977 Appendix B)[23] and irradiated with monoenergetic neutrons of energy E_n.

Similar calculations were made by Goodman (1978)[24] and updated by Coyne and Goodman (1978)[25] with slightly different assumptions. Results for both calculations using point energies, E_n, are given in Table 2. For comparison, the values calculated by Dennis (1973)[20] are also included.

Table 2

Effective W-values, W_n for tissue-Equivalent Ion Chambers Irradiated by neutrons of energy E_n

	W_n/eV		
E_n/MeV	Bichsel and Rubach(1978)[22]	Coyne and Goodman(1978)[24]	Dennis (1973)[20]
0.1	----	32.38	34.4
0.5	----	31.87	34.1
1	----	32.31	34.0
2	31.14	31.26	32.4
5	30.92	31.02	30.5
9	31.02	31.12	30.5
14	31.25	31.10	30.3

Bichsel and Rubach (1978)[22] estimated the uncertainty of their calculation to about ± 2 percent (one standard deviation). They also calculated a change of W_n with the volume of the chamber of no more than 0.2 percent. For the values given by Bichsel and Rubach and by Coyne and Goodman, an overall uncertainty of ± 1.5 e V is suggested.

The value which has been widely used in neutron dosimetry is W_n = 30.5 e V for equation 6 (Smith et al., 1975)[26]. A better value based on the above information would be 31 ± 1.5 e V for neutron energies between 0 and 14 MeV. The most satisfying method would consist in evaluating a W value for each neutron spectrum and account could be taken of the fact that, as the depth in phantom at which the measurement is made increases, the dose distribution between protons, alphas, and electrons changes and thus w_n may also change.

Stopping Power Ratio. Sr

The second bracketed term, stopping power ratio, is compromised in its accuracy for the non-homogenous chamber systems due to two basic problems; a lack of knowledge of the equilibrium charged particle spectrum created by the incident neutron fields and the limited range of the low energy, heavy recoils. The latter results in particles existing in the ion chamber cavity with designations, starters, stoppers, and crossers, Figure 1. (27,29) Table 3 illustrates the ion energy equivalent to a range of multiples of the mean distance required to cross the chamber gas volume. If the particle is to lose but a small fraction of its total energy in crossing the gas volume, i.e. relatively constant dE/dx, then energies equivalent to a range of 10 $\bar{x}$ or larger are required.

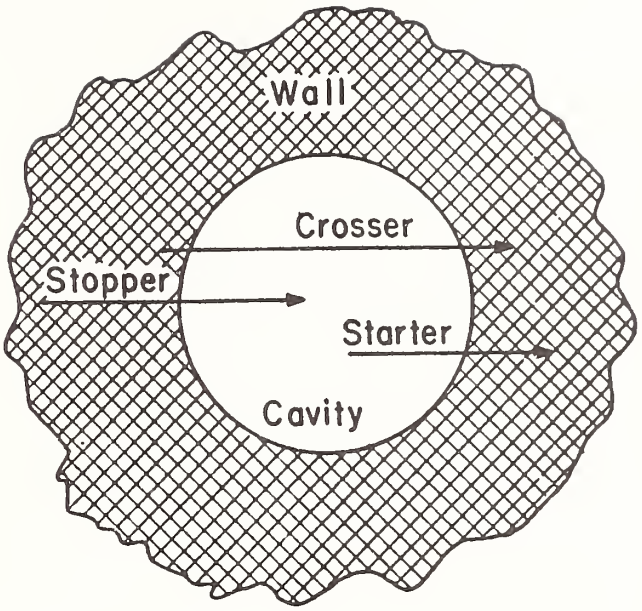

Figure 1. - Gas Volume Ion Interaction Categories

Table 3

Comparison of Heavy Ion Range with Energy

	0.1cc TE Chamber $\bar{x}$ = .155cm	1.0cc TE Chamber $\bar{x}$ = .435 cm
Alpha		
$\bar{x}$ = range	0.057 MeV	0.26 MeV
(2)($\bar{x}$) = range	0.160 MeV	0.8 MeV
(10)($\bar{x}$) = range	1.9 MeV	4.7 MeV
C+ ion		
$\bar{x}$ = range	0.22 MeV	0.86
(2)($\bar{x}$) = range	0.54 MeV	2.7 MeV
(10)($\bar{x}$) = range	7.4 MeV	21 MeV

Reference 30. $\bar{x}$ is the average distance required to cross the gas volume.

For the TE plastic ion chambers the heavy ion recoil dose contribution has been shown to increase with neutron energy, consequently the accuracy with which the ratio is known tends to diminish with increasing neutron energy. (31) The problem is particularly acute at all energies for the non-hydrogenous chambers as only heavy ions exist in this situation, alpha or heavier.

The U.S. neutron therapy groups are using stopping power ratios for TE chambers presently which are calculated on the basis of the equilibrium

proton spectrum only with the heavy ion contribution not included. The rational for this is that at present the error in including the heavy particle effect is probably greater than that incurred in neglecting it. Table 4.

Bichsel and Rubach (1978)[22] have calculated the dose conversion factor for a TE plastic-TE gas ionization chamber which approximates a Bragg-Gray (BG) cavity and for chambers of finite volume, taking into account the ionization due to primary charged particles (protons, helium nuclei, and C, N, and O nuclei) originating in the gas (i.e., starters and insiders), relative to the total ionization; they also accounted for the possible differences in the stopping powers for solids and gases (Williamson and Watt, 1972; [32] Whillock and Edwards, 1978)[33]. The results for the 1 cm^3-volume TE plastic-TE gas chamber used currently as the principal dose calibration instruments by the U.S. neutron therapy groups indicate a value of $S_{r,n}$ = 0.98 - 0.99 for the neutron beams being presently used. The factor is about 1% smaller for the smaller (0.1-cm^3) chambers. The uncertainty is about 4 - 5%. The value is about 1 - 2% lower than the values used previously (Table 4).

Table 4

Dose Conversion Factor, S_r*
used by different groups

Constant	Chamber/Gas	Group 1[a]	Group 2[b]	Group 3[c]
$S_{r,\gamma}$[(d)]	TE plastic/air	1.142	1.140	1.133
	TE plastic/TE gas	1.001	0.995	0.994
	Carbon/CO_2	1.009	---	---
	Mg/Ar	1.14		
$S_{r,n}$	TE plastic/air	1.157	1.177	1.188
	TE plastic/TE gas	1.020	0.995	1.013

a) $S_{r,n} = 0.77\ S_{r,p} + 0.18\ S_{r,\alpha} + 0.05\ S_{r,e}$ (for 50 MeV deuterons on Be)

b) $S_{r,n} = S_{r,p}$

c) $S_{r,n} = S_{r,p}$

d) $S_{r,\gamma} = S_{r,e}$

*Smith, et al. (1975)[26]

Intercomparisons of the ionization chamber technique with calorimetry indicate good agreement between the two dosimetric methods (McDonald, 1979)[34], when either the previous values or the newly indicated values of the physical constants $\bar{W}_n$ and $\bar{S}_{r,n}$ are used, since it is the product of W_n and $S_{r,n}$ which appears in the expression for neutron dose (eqn. 3). It is therefore recommended that the more recent value of $S_{r,n}$ = 0.98 for TE gas be used in conjunction with the more recently indicated value of $\bar{W}_n$. The magnitude of the dose is thus maintained invariant from that indicated previously.

The newly indicated value for 1 cm^3-volume TE plastic-air chambers is $S_{r,n}$ = 1.18 (± 5%), which is also not much different from that used previously (Bichsel and Rubach, 1978)[22].

TE Materials and Kerma

Before considering the kerma ratio correction to tissue dose, it is necessary to consider what is tissue equivalence for neutrons. ([35-40]) The formulation of several proposed TE liquid phantom solutions and ICRU muscle are given in Table 5. A quick comparison indicates that several of the solutions are indeed quite close in matching the elemental weight percentages of muscle. Neglecting any secondary effects such as chemical binding, one can indeed assume the liquids to be muscle equivalent.

Table 5

Tissue-Equivalent Liquids for Muscle Tissue

Compositions	Percent by Weight		
Elements	Frigerio(1)	Goodman(2)	Muscle(3)
C	12.3	12.0	12.3
H	10.2	10.2	10.2
O	72.9	74.2	72.9
N	3.5	3.6	3.5
Ca	0.01	----	0.007
P	0.20	----	0.2
S	0.32	----	0.5
K	0.39	----	0.3
Na	0.07	----	0.08
Cl	0.08	----	----
Mg	0.02	----	0.02

Formulations of Standard 1.07 g/cm^3 Density TE-Liquid

Compound	Formula	Percent by Weight of Compounds listed above	
		Frigerio[(1)]	Goodman[(2)]
Water	H_2O	62.16	65.6
Calcium Phosphate,Monobasic	$Ca(H_2PO_4)_2{:}6H_2O$	0.06	---
Magnesium Nitrate	$Mg(NO_3)_2{:}6H_2O$	0.21	---
Phosphoric Acid (85%)	$H_3PO_4{:}H_2O$	0.60	---
Potassium Bisulfate	$KHSO_4$	1.36	---
Sodium Chloride	NaCl	0.13	---
Sodium Phosphate,Monobasic	$NaH_2PO_4{:}H_2O$	0.11	---
Urea	NH_2CONH_2	7.46	7.60
Glycerol	$CH_2OHCHOHCH_2OH$	2.60	26.8
Ethylene Glycol	$HOCH_2CH_2OH$	25.30	---

(1) Frigerio et al., 1972.[36]

(2) Goodman, 1969.[35]

(3) NBS HB85,(33).[37]

Regrettably, the same assumption cannot be made for the electrically conductive TE plastic, Table 6. The composition of A-150 TE plastic is not the formulation originally reported by Shonka.[38] The composition was changed shortly after the original paper was published and the new formulation labeled A-150. The data given in Table 6 is based on experimental and computational analysis of the element composition of the A-150 plastic. [40,41]

A desirable feature of any TE plastic used in ion chamber construction is that it be electrically conductive. Shonka found that substitution of carbon for oxygen in the theoretical muscle formulation achieved the desired electrical conductivity and maintained the same photon energy absorption coefficient as muscle above 0.1 MeV. [38,40]

The same cannot be said about the equivalence for neutrons, Figure 2. The differences in the oxygen and carbon neutron cross sections clearly will result in a TE plastic (A-150)/ muscle kerma ratio which deviates from one. The ratio will obviously be spectrical dependent and is in the range 1.05 ± .006 for the neutron therapy beams presently used for treating patients. Again, the uncertainty associated with the ratio increases with neutron energy because of a lack of cross sectional information in the energy range 20 to 50 MeV. Even within the energy range for which cross sectional information exists, 0 to 20 MeV, differences of from 5 to 20 percent in the calculated Kerma for muscle exist due to differences in the cross section sets utilized and in the assumptions made in the computational approach. [42-46]

It is recommended that the kerma ratio factors be calculated on the basis of kerma per unit neutron fluence values published in ICRU Report 26 (ICRU, 1977).[23] These calculations will obviously be dependent on the neutron energy spectrum and attempts should be made to obtain information concerning the energy spectrum for different irradiation configurations and depths in a phantom.

Table 6

Percent Elemental Composition by Weight of A-150 Muscle-Equivalent Plastic Compared to ICRU Muscle Tissue

Element	ICRU Muscle[a]	A-150 Plastic[b]
H	10.2	10.2 ± 0.1
C	12.3	76.8 ± .5
O	72.9	5.9 ± .2
N	3.5	3.6 ± .2
Ca	0.007	1.8 ± .1
F	not listed	1.7 ± .1
total	98.9	100.0 ± .5

a) ICRU (1964)[37]

b) Smathers et al. (1977)[41]

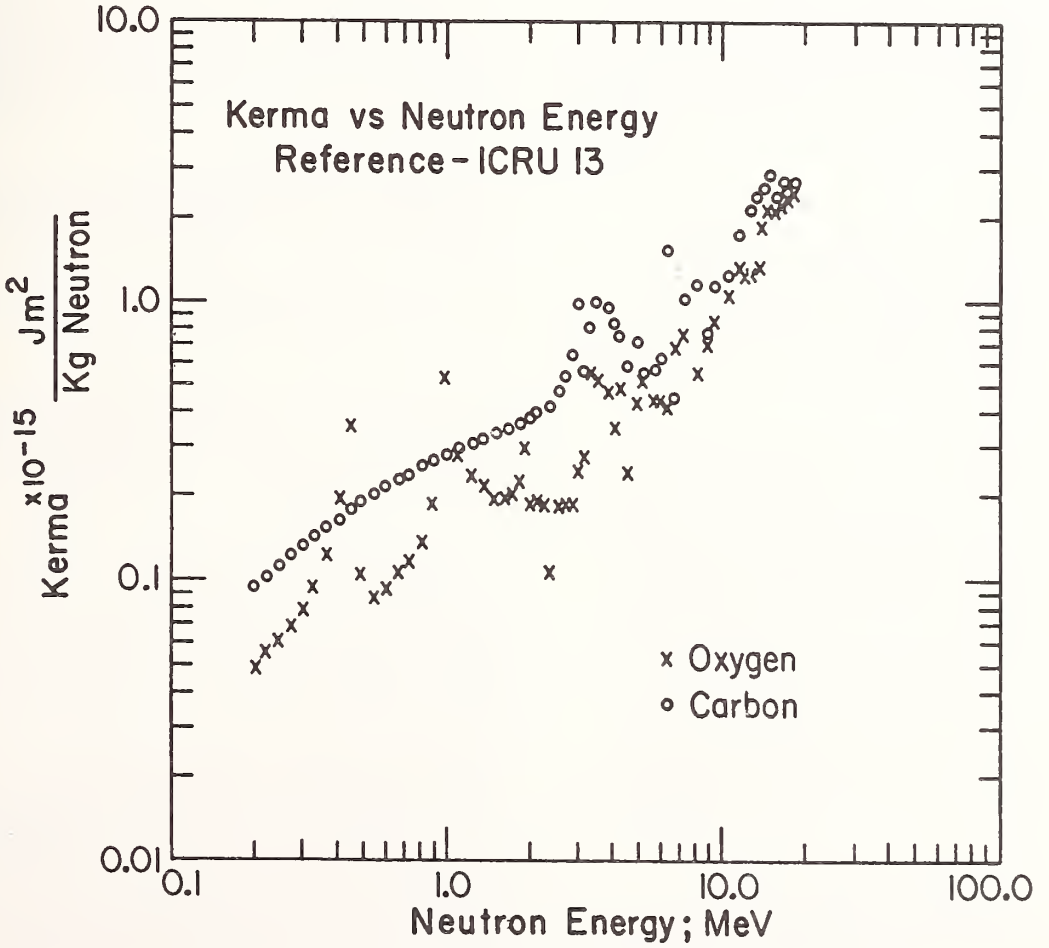

Fig. 2 Neutron Kerma vs Energy Comparison for Oxygen and Carbon

Tissue-equivalent gas is recommended for use in homogeneous TE ionization chambers for measuring the total absorbed dose. The recommended formulation and composition of the TE Gas is given in Table 7. The composition of the gas should be verified by analysis since impurities in the gas may have a significant effect on the chamber response.

Table 7

Tissue-Equivalent Gas[a]

Percent Partial Pressure	Percent Elemental Weight
64.4 CH_4	10.2 H
32.4 CO_2	45.6 C
3.2 N_2	3.5 N
	40.7 O

(a) Rossi, H.H. and Failla, G. (1956)[39]

Displacement correction.d

For absorbed dose specification as a function of depth and/or position in a large tissue-equivalent phantom, the analyses of dosimetric measurements using ionization chambers must account for the displacement of the phantom material brought about by the introduction of the dosimeter. A displacement correction factor should be applied to the measured ionization charge (dose) to compensate for the decreased attenuation and alteration of scattering caused by the displacement of the phantom material by the ion chamber. This results in a dose which would have been measured by a hypothetical ion chamber of zero volume centered at the same location, for which the displacement correction factor would be unity.

It is recommended that the multiplicative displacement correction factors of 0.970 (1-cm^3-volume) and 0.989 (0.1-cm^3 volume) suggested by measurements of Shapiro et al, (1976)[47] with air-filled spherical ion chambers be used. This multiplicative displacement correction factor has been found to have no significant dependence on depth in phantom or on neutron beam size.

N_1- γ Dose Determination

Because of the biological effect differences between equal absorbed doses of neutrons and gammas, the first breakdown of total dose generally made is into photon and neutron dose components. Several of the more frequently used methods (detectors) are given in Table 8. Each of the detectors has some degree of neutron sensitivity and this neutron dose response must be taken into account before an accurate gamma dose fraction may be determined.

As the neutron energy increases, the neutron sensitivity of all the photon detectors increases, thus the detectors have a strong neutron spectral dependence. Also the greater the neutron sensitivity, the larger the uncertainty in the gamma dose thus determined.[48]

The general method separating the two contributions is to measure total dose with a TE chamber and the gamma dose with the photon detector. Knowing the neutron sensitivity factor, the two, neutron and gamma, dose components may be solved for by use of simultaneous equations.

The first four methods listed in Table 8 are in order of increasing magnitude of the neutron/gamma dose response ratio i.e. GM lowest and TLD highest. The GM tube is a miniature version of the standard type and through calibration the dose is related to the counts. The neutron sensitivity is determined in separate experiments in which the detector is exposed to monoenergetic "pure" neutron beams.

The film dosimetry methods are very similar to those used with pure photon or electron sources; only when used in neutron fields, the film must be removed from any protective packaging and shielded with sufficient lead to eliminate the maximum energy external protons generated. It is impossible, however, to eliminate the protons created within the emulsion and this is one source of the neutron sensitivity for the system. Conventional film density vs calibration dose is used for gamma dose determination. Neutron sensitivity is determined by methods similar to those used for GM counters.

One of the standard methods is the use of paired chambers, i.e. graphite-TE plastic or Magnesium-TE plastic. The neutron sensitivity of the chambers can be determined by a series of lead attenuation measurements ([49,50]) and it has been found to vary significantly with neutron spectrum and with the system used. Of the two mentioned above, the magnesium-TE plastic pair has the lower neutron sensitivity.

Thermoluminescent dosimeters are troubled by fading, contaminants having high neutron cross sections (^6Li), and a neutron sensitivity which seems to vary with the annealing procedure. However, their small size and ease of use, many times outweighs the above disadvantages.

The use of proportional counters or scintillation detectors allows the simulataneous separation and quantification of the neutron and photon dose components. With the proportional counters the Linear Energy Transfer, LET, region in which both photon and neutron induced pulses occur increases with neutron energy and the uncertainty of the dose distribution between the sources likewise increases.

The scintillation system suffers similarly as the low energy neutron induced events tend to merge with the photon induced events in the pulse shape discrimination analysis. For a system upper energy range of 35 to 55 MeV, this merging tends to give the system a lower energy cutoff of 2 to 6 MeV.

Because of their significantly different biological effectiveness, the separate neutron and gamma-ray dose components of fast neutron beams should be determined as accurately as possible at all positions of relevance to their clinical application, and this should be done for different field sizes and irradiation conditions.

However, because of the uncertainties in the determination of the relatively small photon dose component leading to resultant overall uncertainties in the separate neutron absorbed dose which can be greater than those of the total absorbed dose, it is recommended that the specification of absorbed dose be in terms of the total dose. That is, the total dose (neutron plus gamma) should be specified at all points, along with the relative contribution of the photon dose component, expressed as a percentage of the total

dose, D_T(percent D_G).

Dose measurements should be stated in 1.07g/cm^3 density TE liquid, without conversion to unit density medium.

Table 8

Detector-Methods Used in Dose Component Measurements

1) Minature GM Counters
2) Lead shielded film
3) Paired chambers
4) Thermoluminescent Dosimeters (CaF_2,^7LiF,^6LiF)
5) Proportional counters
6) Scintillation detectors

Neutron Spectral Measurements

Neutron spectral measurements have been accomplished by many methods, several of which are listed in Table 9. The techniques have been developed over a period of years for use in reactor and neutron physics research. Of thos listed, both proton recoil counters and time-or-flight methods have been used to characterize the neutron beams presently used in treatment. Foil activation is a simpler system but tends to give results having less energy definition than the others mentioned. Again, for neutrons above 20 MeV, deficiencies in the cross section information tend to increase the uncertainty in the data with increasing energy.

The information is of paramount importance since knowing the neutron spectra, one then has the necessary source input for theoretical computation of average w_n, stopping power ratio, and Kerma ratios.

Table 9

Neutron Spectrum Measurement Methods

1) Proton recoil counters
2) Time-of-flight
3) Foil activation
4) Proton telescopes

Discussion

Neutron dosimetry has benefited by groups participating in dosimetry intercomparisons. This has taken place in the USA and Europe (Broerse and Mijnheer 1976[51], Broerse et al, 1977[52], Broerse et al, 1978)[53] and internationally (ICRU 1978)[54] and between the USA and Japan (Almond 1977)[55]. These extensive intercomparison projects have yielded the same conclusions, namely, that to reduce systematic dosimetry differences, it will be necessary to standardize the basic physical parameters and the experimental instruments and techniques employed. The uncertainties in neutron-beam calibration are listed in Table 10.

Table 10

	Uncertainty (%)
Ionization charge	0.2
Charge saturation correction	0.2
T and P correction	0.1
Neutron kerma factor ratio	2
Displacement correction in phantom	1
Dose-conversion factor	
TE-TE gas chamber	4
TE-Air chamber	4
Average energy per ion pair	
TE-gas chamber	5
TE-Air chamber	6
C-CO_2 chamber	6
Determination of M(Gamma-ray Calibration)	2.5
RMS (TE-TE gas)	7
(TE-Air)	8

The publication, "Neutron Dosimetry for Biology and Medicine," Report No. 26, by the International Commission of Radiation Units and Measurements (ICRU, 1977)[23] has provided extensive information on methodology and physical data. It should be emphasized that efforts are being continued to improve the data base of neutron dosimetry. Some of the tables in this paper will therefore contain values which differ from the ones quoted in ICRU Report 26 and may be subject to changes in the future.

At the present a U.S. protocol (AAPM, 1979)[56] is being developed in parallel and in a cooperative effort with the European neutron dosimetry protocol (Broerse and Mijnheer, 1976[57], and Broerse and Mijnheer, 1979)[58] and the main items of the two drafts were recently summarized by Broerse et al., (1979)[59].

Acknowledgement

This work was supported by U.S. Public Health Service Research Grant CA 12542 from the National Cancer Institute.

References

1. D.K. Bewley, Current Topics in Radiation Research, 251-292, North-Holland Publishing Co., Amsterday, 1970.

2. D.K. Bewley, Second Symposium on Neutron Dosimetry in Biology & Medicine, Vol. 1, Neuherberg/Munich, Sept. 30-Oct. 4 (1974) EUR 5273 d-e-f.

3. H. Bichsel, Second Symposium on Neutron Dosimetry in Biology & Medicine, Vol. 1, Neuherberg/Munich, Sept. 30-Oct. 4 (1974) EUR 5273 d-e-f.

4. P. Almond, A. Smith, J. Smathers, V. Otte, Second Symposium on Neutron Dosimetry in Biology and Medicine, Vol. II, Neuherberg/ Munich, Sept. 30-Oct. 4 (1974) EUR 5273 d-e-f.

5. A. Smith, P. Almond, J. Smathers, V. Otte, Medical Physics, Radiology 113 (1), 181-193, 1974.

6. B. Loenard, J. Boring, Rad. Resh, 55 1 (1973).

7. J. Dennis, Proceedings Third Symposium on Microdosimetry, Stresa (Italy), Oct. 18-22, 1971, p. 403-415.

8. H. Delafield, L. Chuang, P. Holt, Second Symposium on Neutron Dosimetry in Biology and Medicine, I, Neuherberg/Munich, Sept. 30-Oct. 4 (1974) EUR 5273 d-e-f.

9. H. Bichsel, Second Symposium on Neutron Dosimetry in Biology and Medicine, Vol. 1 Neuherberg/ Munich, Sept. 30-Oct. 4 (1974) EUR 5273 d-e-f.

10. M. Miller, J. Boring, Phys. Rev. A9 2421 (1974).

11. J. Boring, G. Strohl, F. Woods, Phys. Rev., A140 1065 (1965).

12. Srdoc, Nuclear Inst. Methods 108 327 (1973).

13. J. Phipps, J. Boring, R. Lowry, Phys. Rev., A135, 36 (1964).

14. D. Glenn, Medical Physics 1, 103, (1974).

15. J. Boring, F. Woods, Rad. Resh. 35 472 (1968).

16. I. Myers, Radiation Dosimetry, Chpt. 7, Attix & Roesch Editors, Academic Press, 1968.

17. W. Jesse, Phys. Rev., 122 1195 (1961).

18. J. Booz, Proceedings of the Symposium on Microdosimetry, Ispra: Brussels, EUR 3747 (1968).

19. J. MacDonald, G. Sidenius, Phys. Letters A28 543 (1969).

20. J. Dennis, Phys. Med. Biology 18 379 (1973).

21. H. Bichsel, H. and A. Rubach, Uncertainty of the Determination of Absolute Neutron Dose with Ionization Chambers. Third Symposium on Neutron Dosimetry. Munich. EUR 5848 DE/EN/FR, pp. 549-563 (Commission of the European Communities, Luxembourg), (May, 1977).

23. ICRU, Neutron Dosimetry in Biology and Medicine, Report 26. International Commission on Radiation Units and Measurements. (1977)

24. Goodman, L. J. W_N Computed from Recent Measurements of W for Charged Particles. Basic Data for Neutron Dosimetry. EUR 5848 DE/EN/FR pp. 61-74 (Commission of the European Communities Luxembourg) (1978).

25. Coyne, J.J. and Goodman, L.J. Private communication (National Bureau of Standards, Washington and Columbia University-Brookhaven National Laboratory, Upton, Long Island, New York) (1978).

26. Smith, A.R., P.R. Almond, J.B. Smathers, V.A. Otte, F.H. Attix, R.B. Theus, P. Wootton, H. Bichsel, J. Eenmaa, D. Williams, D.K. Bewley and C.J. Parnell. Dosimetry intercomparisons between fast-neutron radiotherapy facilities. Med. Phys. 2, 191-200, (1975).

27. H. Bichsel, Radiation Dosimetry, Vol. 1, Chpt. 4 Academic Press, 1972, Attix, Roesch, Tochilin Editors.

28. L. Northcliffe, R. Schilling, Nuclear Data Tables, A7, #3, 4 (1970).

29. Linear Energy Transfer, ICRU Report 16, 1970.

30. P. Shapiro, Naval Research Laboratory, Washington, D.C. 20375, Personal Communication.

31. G. Oliver, W. Grant, J. Smathers, Rad. Resh. 61 366 (1975).

32. Williamson, J. and Watt, D. Phys. Med. Biol. 17, 486-492 (1972).

33. Whillock, M.J. and Edwards, A.A., Phys. Med. Biol. 23, 416-425 and Phys. Med. Biol. 23, 1205-1206, (1978).

34. McDonald, J.C., Private Communication, (1979).

35. L. Goodman, Health Physics 16 #6, 763 (1969).

36. N. Frigerio, R. Coley, M. Sampson, Phys. Med. Biol. 17, #6, 792 (1972).

37. ICRU, Physical Aspects of Irradiation, International Commission on Radiation Units and Measurements. Report 10b, 1962, National Bureau of Standards Handbook (Washington: U.S. Government Printing Office) (1964).

38. F. Shonka, J. Rose, G. Failla, Progress in Nuclear Energy, Series XII, 1, Health Physics, Pergamon Press, 160 (1959).

39. H. Rossi, G. Failla, Nucleonics 14 32 (1956).

40. J. Spokas, Rad. Resh. Soc., May 11-15, Miami Beach (1975).

41. Smathers, J.B., V. A. Otte, A.R. Smith, P.R. Almond, F.H. Attix, J.J. Spokas, W.M. Quam and L. J. Goodman, Composition of A-150 tissue-equivalent plastic. Med. Phys. 4, 74 (1977).

42. R. Bach, R. Caswell, Rad. Resh. 35 1 (1968).

43. F. Williamson, P. Mitacek, Proceedings Symposium on Neutron Monitoring for Radiological Protection Vienna, 29 Aug. 2 - Sept. (1966), SM/76-15.

44. J. Dennis, Phys. Med. Biol. 18 379 (1973).

45. ICRU Report 13, Neutron Fluence, Neutron Spectra, and Kerma (1969).

46. R. Caswell, J. Coyne, M. Randolph, 2nd Symposium on Neutron Dosimetry in Biology and Medicine, Neuherberg/Munich, Sept. 30-Oct. 4 EUR 5273 d-e-f, (1974).

47. Shapiro, P., F.H. Attix, L.S. August, R.B. Theus and C.C. Rogers, Displacement correction factor for fast-neutron dosimetry in a tissue-equivalent phantom, Med. Phys. 3, 87, (1976).

48. L. Goodman, Second Symposium on Neutron Dosimetry in Biology & Medicine, Vol. 1, Neuherberg/Munich, Sept. 30-Oct. 4, EUR d-e-f (1974).

49. F. Attix, R. Theus, C. Rogers, 2nd Symposium on Neutron Dosimetry in Biology and Medicine Neuherberg/Munich, Sept. 30-Oct. 4 EUR 5273 d-e-f (1974).

50. M. Clelean, N. Wells, 2nd Symposium on Neutron Dosimetry in Biology and Medicine, Neuherberg/ Munich, Sept. 30-Oct. 4 EUR 5273 d-e-f (1974).

51. Broerse, J.J., and Mijnheer, B.J. (1976), Basic Physical Data for Neutron Dosimetry: Conclusions and Recommendations. Basic Physical Data for Neutron Dosimetry. Rijswijk, The Netherlands, EUR 5629e, pp. 275-321, Broerse, J.J., Ed. (Commission of the European Communities, Luxembourg).

52. Broerse, J.J., G. Burger and M. Coppola (1977). Implications of Dosimetry Intercomparisons for Standarization in Neutron Dosimetry for Biological and Medical Applications. International Symposium on National and International Standardization of Radiation Dosimetry, Atlanta, Georgia, U.S.A.

53. Broerse, J. J., G. Burger, and M. Cappola (1978). A European neutron dosimetry intercomparison project (ENDIP). Results and evaluation. EUR 6004. (Commission of the European Communities, Luxembourg).

54. ICRU (1978). International Commission on Radiation Units and Measurements. An International Neutron Dsoimetry Intercomparison, ICRU Report 27 (International Commission on Radiation Units and Measurements, Washington, D.C.).

55. Almond, P.R., and J.B. Smathers (1977). Physics intercomparisons for neutron radiation therapy. Int. J. Radiation Oncology Biol. Phys. 3, 169.

56. AAPM, Protocol for Neutron Beam Dosimetry, Task Group No. 18, Fast Neutron Beam Dosimetry Physics Radiation Therapy Committee, (1979).

57. Broerse, J.J. and B. J. Mijnheer (1976). Second draft protocol for neutron dosiemtry. In: Basic Physical Data for Neutron Dosimetry. EUR 5629. Broerse, J.J., Ed. (Commission of the European Communities, Luxembourg).

58. Broerse, J.J. and B. J. Mijnheer (1979). Third Draft of a European Protocol for Neutron Dosimetry for External Beam Therapy. (1979). In preparation by European Clinical Neutron Dosimetry Group (ECNEU).

59. Broerse, J.J., B.J. Mijnheer, J. Eenmaa, and P. Wootton (1979). Dosimetry intercomparison protocols for therapeutic applications of fast neutron beams. Proc. Third Meeting on Fundamental and Practical Aspects of Fast Neutrons and Other High LET particles in Clinical Radiotherapy. Eur. J. Cancer. (To be published).

THE CLINICAL APPLICATION OF IN VIVO NEUTRON ACTIVATION ANALYSIS

S. H. Cohn, K. J. Ellis, I. Zanzi and D. Vartsky
Medical Research Center
BROOKHAVEN NATIONAL LABORATORY
Upton, Long Island, New York 11973, USA

J. F. Aloia
NASSAU HOSPITAL
Mineola, New York 11501, USA

(neutron activation, body composition, clinical application, elemental analysis , in vivo measurement)

The development of the in vivo neutron activation technique has opened an era of research into the elemental composition of human beings. Until recently, few data had been recorded on the exact amounts of the elements of which the human body is composed.

Neutron activation is an analytical tool based on nuclear rather than chemical reactions. The essential physical parameters involved include isotopic abundance, cross-section, half-lives of the product isotopes, and energy emission of the product.

Total body neutron activation (TBNAA) designed for in vivo studies requires a beam of fast neutrons to be delivered to the subject. Capture of a neutron by an atom of a target element creates an excited nucleus. This isotope reverts to a stable condition by the emission of one or more gamma rays either immediately (within $\sim 10^{-12}$ s), (prompt gamma activation), or after a decay period characteristic of the activation product (delayed gamma activation). The energy of the gamma ray is characteristic of the target element and its intensity (count rate in a suitable detector) is a measure of the amount of that element. The induced radioactivity in the subject is measured by a suitable detector that has to be shielded against background radiation. The data thereby obtained are treated by standard gamma spectrometric methods of analysis.

There are two essential requirements for the measurement of the body elements by total body neutron activation: a uniform thermal neutron distribution through the body, and uniform counting sensitivity of the whole body counter. Of the two, the first is the more difficult to attain. Clearly, the achievement of the highest degree of uniformity of thermal neutrons is an art, and there is considerable space for the improvement of technique. The uniformity of the neutron flux in the body is a function of the incident neutron energy and the thickness and position of the moderator.

Besides the reduced dose to the patient, there are numerous advantages derived from the use of α,n neutrons over neutrons produced by cyclotrons or neutron generators. The irradiation geometry is substantially improved, and significantly greater stability in neutron output is achieved; thus, the precision of the technique is enhanced. The operation of α,n neutron sources is relatively simple and hence the service of a trained operator is not required, as it is for the operation of neutron generators and cyclotrons. Finally, the design of such a facility for medical applications, permitting it to be located in a hospital environment, is a significant advantage to the patient, as well as to the investigator.

It is clear that if total body neutron activation analysis is eventually to become a part of the armamentarium of the medical profession, the most likely direction of development will be in the application of "portable" α,n neutron sources.

The clinical usefulness of total body neutron activation analysis (TBNAA) is best demonstrated by the studies involving the measurement of total body calcium. TBNAA studies provide data useful for the diagnosis and management of metabolic bone disorders. It should be emphasized, however, that while most of the applications to date have used the calcium measurements, the measurement of sodium, chlorine and nitrogen also appear to be useful clinically.

Total body calcium measurements by means of TBNAA have been used in studies of osteoporosis to establish absolute and relative deficits of calcium in patients with this disease in comparison to a normal contrast population. Changes in total body calcium (skeletal mass) have also been useful for quantifying the efficacy of various therapies in osteoporosis. Serial measurements over periods of years provide long term balance data by direct measurement with a higher precision (±3%) than is possible with the use of any other technique.

In renal osteodystrophy observed in patients with renal failure, disorders of both calcium and phosphorus, as well as electrolyte disturbances, have been studied to provide the necessary data to design dialysis therapy.

Bone changes in endocrine dysfunction have been studied with TBNAA, particularly in patients with thyroid and parathyroid disorders. In parathyroidectomized patients, the measurement of total body calcium, post-operatively, can indicate the degree of bone resorption. Skeletal metabolism and body composition in acromegaly, Cushing's disease, and several other disorders have also been investigated with the use of TBNAA.

Levels of cadmium in liver and kidney have been measured in vivo by prompt gamma neutron activation. Marked differences in cadmium body burdens have been found in cigarette smokers as compared with non-smokers. No correlation has been established between cadmium body burden and hypertension or emphysema as has been hypothesized.

Total body nitrogen and potassium measurements serve as indices of muscle mass and protein content, and hence are useful in studies of the effects of diet and nutrition on cancer patients. An essential requirement for these studies is the in vivo measurement of changes in body composition, primarily revealed by nitrogen content. Currently, the optimal method for measurement of total body nitrogen is prompt gamma neutron activation.

These are but some of the clinical applications which have utilized *in vivo* neutron activation. Clearly, these applications indicate the enormous potential of this technique. There can be little question that *in vivo* neutron activation is a highly sophisticated and useful addition to the techniques for medical research. It has provided new and previously unavailable information, and can be expected to produce even greater amounts of data as the current techniques are refined.

ACCELERATORS FOR RADIONUCLIDE PRODUCTION

John C. Clark
Medical Research Council
Cyclotron Unit
Hammersmith Hospital
London, W12 0HS
United Kingdom

Of 60 questionaires sent out to institutes known to be operating accelerators, replys were received relating to 55 individual accelerators all of which had a program for radionuclide production. The majority of the non-commercially operated accelerators were seen to be concentrating their efforts on producing radionuclides which were not generally available from the 9 commercially operated accelerators. Notable exceptions however were ^{123}I and ^{201}Tl. Some of the problems encountered in the use of these accelerators for large scale radionuclide production will be discussed.

[Accelerator, radionuclide production]

Introduction

There are at least 55 accelerators engaged in radionuclide production at the present time.[1] Their energies range from the 6 MeV deuterons of the Allis-Chalmers classical cyclotrons in St. Louis and Boston to the 800 MeV protons of the linear accelerator at Los Alamos. However, the majority (19) of these accelerators are isochronous cyclotrons with a proton energy between 20 and 30 MeV. Table 2 gives a more detailed breakdown of the distribution. In order to get an up to date picture of the extent of radionuclide production programmes of these accelerators, two of my colleagues recently sent out a questionaire to more than 60 institutes known to be operating accelerators. 48 replies were received relating to the 55 accelerators mentioned above. Unfortunately, no information was received from E. Europe, S. Africa, or S. America. The results are summarized in Table 1. Part A comprises the "non-commercial" accelerators (40 cyclotrons and 2 Linacs and lists for each of those radionuclides (a) which are currently being produced at least once a week, (b) those which are produced less frequently, and (c) those which are expected to be in production by 1980. Part B of the table lists the world's 9 commercially operated cyclotrons and their products.

In order to discuss some aspects of these accelerator operations that may be of interest the present gathering, it is useful to divide them into roughly four energy ranges namely 100-800 MeV, 50-100 MeV, 20-50 Mev, (including the large group at 20-30 MeV), and those up to 20 MeV proton energies. I will avoid any reference to cost effectiveness and dwell only on some of the practicalities of radionuclide production with each group, where possible mentioning some unique aspects.

Accelerators With Proton Energies of 100-800 MeV

Five accelerators with a large scale radionuclide production potential exist in the Western World. Two are linear accelerators, the 200 MeV injector for the alternating gradient synchrotron at Brookhaven[2] and the 800 MeV giant at the Los Alamos meson physics facility.[3,4] The remaining 3 are cyclotrons and include the very large isochronous cyclotron at Vancouver[5] at 500 MeV, and two separated sector cyclotrons at Bloomington, Indiana[6] (200MeV) and Villigen, Switzerland[7], (590 MeV). All these accelerators rely heavily on spallation reactions for radionuclide production. This is a field which is probably much more familiar to some of our participants than myself so I hope my interpretation of the problems stand up to their criticism. The term spallation seems to cover a complex series of nuclear events when incident nucleons with energies in excess of 100 MeV interact with a target, including knock-on cascade, evaporation, fragmentation and for sufficiently high Z materials, fission processes. In addition, secondary nuclear reactions can occur between emitted particles and other target nuclei. Thus one can expect the formation, to a greater or lesser extent, of every element from Z + 2 or 3 above the target to Z =1. At 800 MeV three distinct regions can be seen if the formation cross sections are plotted against mass number. In the case of a bismuth target a peak A = 180 to 200 can be identified due to spallation products near the target mass, a fission product peak between A = 60 and 140, and a fragmentation continuum below A = 40.

To the radionuclide production chemist this can only mean formidable radiochemical recovery and decontamination problems. However, it must be fairly self-evident that several radionuclides of that Z will be present in the product. For example, ^{82}Sr ($t_{\frac{1}{2}}$=25 day) is of interest in the medical field as a source of radiogenic ^{82}Rb ($t_{\frac{1}{2}}$ 1.25 min), a β^+ emitter of potential value in emission tomographic studies of heart and kidney function. The most effective means of production is via spallation of a molybdenum target using 800 MeV protons at LAMPF.[8] All samples of ^{82}Sr however, contain significant amounts of ^{85}Sr ($t_{\frac{1}{2}}$ = 65d) so that great care must be exercised when designing and operating a radionuclide generator[9,10,11] for the in vivo use of ^{82}Rb as a strontium leakage could result in unacceptable ^{85}Sr burdens in the bone. Fortunately, systems have been perfected for this use so that high levels of ^{82}Rb can be available due to this fortunate radiogenic relationship.

The production of high purity ^{123}I ($t_{\frac{1}{2}}$ = 13h) and ^{201}Tl ($t_{\frac{1}{2}}$ = 73h) are further examples of radiogenic purification and will be refered to below.

Accelerators With Proton Energies of 50-100 MeV

There are around 10 accelerators, all cyclotrons, in this group and almost all originally dedicated to nuclear physics work. However, they have now turned some of their attentions to the production of medically useful radionuclides and are recovering some of their operating costs by doing so.

^{123}I seems to be by far the most popular radionuclide to produce, and several ingenious and highly effective target systems have been devised and perfected to produce it via the $^{127}I(p,5n)^{123}Xe \xrightarrow{t_{\frac{1}{2}}= 2.1h} {}^{123}I$ reaction. The relevant nuclear data have recently been reviewed by STOCKLIN AND QAIM.[12] The various chemical

forms of iodine used include I_2,[6-13] CH_2I_2,[14] mixtures thereof,[15] and NaI.[16] In addition the use of liquid Cs and the $^{133}Cs(p,2p9n)^{123}Xe$ reaction has been proposed when protons of variable energy are being dumped.[14] At the Crocker cyclotron, (UC Davis) an elegant target system centred around a stainless steel vessel containing molten NaI is maintained at 650°C by a combination of beam power and a controlled helium flow.[18] The ^{123}Xe is removed from the target by the helium and transported to a remote laboratory where it is recovered and purified cryogenically prior to allowing its decay to ^{123}I. Several important factors such as target thickness and NaI density during irradiation had to be carefully studied before the routine target was perfected. In the use of methylene iodide, CH_2I_2, at at the variable energy cyclotron at Harwell, U.K., different problems arose.[15] Here the aim was to circulate the organic liquid through a titanium target cell and recover the ^{123}Xe using a gas/liquid scrubber. Early experience showed that extensive radiolytic polymerisation of the CH_2I_2 to a thick oil occured at high beam currents making it impossible to pump it around the circuit. However, the application of a classical radiation chemist's radical scavenger, molecular iodine I_2, not only solved the polymerisation problem but also increased the iodine content of the target mixture. The target system has now been in routine use for about 3 years satisfying some of the demand for ^{123}I in the U.K.

Accelerators With Proton Energies of 20-50 MeV

This group includes all the commercially operated cyclotrons and perhaps mention of some of the problems encountered here would be of interest. The major logistic problem is that the accelerator produced product must be available on a routine scheduled basis. Thus a commercial operator would expect his accelerator to be dedicated to radionuclide production and be ready for action at all times. He may even have more than one accelerator! He will also be keen to make the very best use of the beam available from his particular accelerator.

When a charged particle beam interacts with a target the principle method of energy loss is by ionisation; only about one particle in a thousand produce a nuclear reaction and the rest of the energy appears as heat and here lies the major problem for the high current target designer. The internal beam of the cyclotron, where the highest intensities are usually available, has a radial distribution that is approximately triangular with the high intensity towards the centre of the machine. If a target plate is placed at a tangent to the beam the resultant beam pattern will be spread over a larger area. If the plate is then either angled to the tangent or bent to a radius slightly larger than the beam radius a still larger spread can be obtained. The more the beam can be spread out the lower the power density (Wcm^{-2}). The power density in the unspread beam of a typical production cyclotron compares well with those found in the arc welding field, being typically 15-50$KWcm^{-2}$; thermal damage to targets is therefore an ever present hazard. The beam dimensions of the flat field or classical cyclotron, few of which remain in the radionuclide production field, have internal beams of between 15mm X 5mm (Hammersmith 45")[19] and 70mm X 6mm (ORNL 86").[20] A typical isochronous cyclotron might have a beam of 4mm X 1.5mm.[21] Thus beam power dinsities in excess of 50 $KWcm^{-2}$ are easily achieved. The peak power density that can be handled by normal water cooling is about 3$KWcm^{-2}$ so that it can be seen that if the full output potential of the more recently introduced commercial isochronous cyclotron is to be achieved, beam spreading techniques are of prime importance. One manufacturer offers a beam interactive spreader that uses RF driven deflector plates above and below the circulating beam close to the final radius.[22] In other cases the users have found that rotating[23-24] or oscillating the target has helped provide the necessary power density reduction. The use of thin targets in this field is not usually practicable. However, the use of enriched isotopic targets can often give rise to a higher intrinsic yield together with a reduced interfering impurity. The production of ^{201}Tl with protons of up to 28 MeV being a typical example.[25] Of course the use of highly enriched target materials is expensive, so high efficiency recovery procedures have to be devised. Often radionuclides of the target material are also made making target recovery and refabrication more difficult.

Target fabrication includes all the normal metallurgical techniques. A typical target would consist of copper or other high thermal conductivity backing of the shape most suited to the beam spreading criteria outlined above, with a thin layer (typically 0.050 - 0.1mm) of the desired target material deposited and securely fixed in a thermal sense onto its surface. Techinques such as electrodeposition, flame spraying, chemical vapour deposition, vacuum evaporation, soldering, brazing, casting and spot welding finding application, depending on the properties of the specific target material.

Many of the non commercial accelerators in this group do not have provision for internal targets and rely on the extracted or external beam for radionuclide production. Although somewhat less efficient the external arrangement does allow much more scope for target thichness selection and thus the opportunity to optimise a particular nuclear reaction to minimize impurity. The direct production of ^{123}I via the $^{124}Te(p,2n)^{123}I$ reaction is a good example. Several groups have applied themselves to this problem and have found that by using a thin highly enriched (92%) ^{124}Te target and carefully selected proton energy the ^{124}I impurity due to $^{124}Te(p,n)^{124}I$ can be suppressed to below 1% at end of bombardment (EOB).[26-27-28] However, as the half lives of ^{123}I and ^{124}I are 13.3h and 4.3d respectively the ^{124}I level increases quite rapidly with time.

One further advantage of the external beam is that gaseous and liquid targets can be irradiated. These are usually considered impracticable for internal beam irradiation due to the severe space restrictions imposed in the typical modern cyclotron's accelerating region.

The production of ^{81}Rb ($t_{\frac{1}{2}}$= 4.5h) has achieved commercial status using an external beam and is used in the increasingly popular $^{81}Kr^m$ ($t_{\frac{1}{2}}$=13s) radionuclide generator. Krypton-81m has found widespread use in nuclear medicine organ flow studies.[29-30] Once again due to the radiogenic nature of the desired product, $^{81}Kr^m$, the presence of other Rb radionuclides in the generator is in practice of no importance. Thus the most favourable route to large scale production of ^{81}Rb is via the $Kr(p,xn)^{81}Rb$ reactions.[31-32-33] Protons of 20 MeV upwards have been found to be useful here, however the use of enriched ^{82}Kr is essential for the lower energies.[32] Several approaches have been described for the recovery of the Rb from the target walls after irradiation but the most popular seems to be the use of a rotating target liner which can conveniently be washed with water.[31] The Rb is then simply bound to a small column of cation exchanger. $^{81}Kr^m$ may be recovered continously during clinical use in the gas phase, for lung ventilation assessment, by passing humidified air through the column or alternatively, in a solution suitable for infusion for blood flow investigations, by passing isotonic dextrose through the column.[29-30]

Accelerators With Proton Energies Up To 20 MeV

Here external beams and gas targets seem to be the order of day and the most commonly produced radionuclides are ^{13}N ($t_{\frac{1}{2}}$= 10 min), ^{11}C ($t_{\frac{1}{2}}$=20 min), ^{15}O ($t_{\frac{1}{2}}$= 2 min) and ^{18}F ($t_{\frac{1}{2}}$= 110 min). They are almost invariably destined for incorporation into biomolecules or varying complexity for use in emission tomographic studies, description of which is beyond the scope of this presentation. However, there are several features of the production of these radionuclides in a chemical form directly applicable to these syntheses that may be of interest. ^{13}N may readily be produced as $^{13}NO_3^-$ by the ^{16}O $(p,\alpha)^{13}N$ reaction using a water target,[34] a simple reduction reaction yielding high specific activity $^{13}NH_3$.[35] In recent studies ^{11}C produced via the ^{14}N $(p,\alpha)^{11}C$ reactions has been incorporated into brain receptor selective drugs.[36] Here the major aim is to exclude ^{12}C from the target system so that the synthesis should result in very high specific activity biomolecules typically 0.5÷1Ci/μM or better. This is quite a challenging problem and has led workers into designing gas targets to standards usually only found in the ultra high vacuum field. The target gas has also received careful attention to remove traces of CO_2 and hydrocarbons. One group in the field has observed an increasing reluctance of the $^{11}CO_2$ to escape from the target[37] possibly due to selective adsorption sites trapping the desired product rather than being saturated with the undesired $^{12}CO_2$. This is probably a gross over-simplification of events and much work still seems to be necessary before an approach to the theoretical specific activity of ^{11}C is achieved.

In the case of ^{15}O specific activity has not yet received much attention but the chemical form in which ^{15}O may be recovered, after the $^{14}N(d,n)^{15}O$ reaction in target gases of different compositions, has been superficially studied.[38,39] The ^{15}O atom produced here is a highly reactive species and has been seen to react with a variety of substrates including the target gas N_2. Radiation chemical effects can also be seen which alter the initial product composition as evidenced by studies at different beam currents (beam distribution remaining sensibly constant).

Turning to ^{18}F we find that both the reactivity of the nucleogenic atom and specific activity are the problems confronting the target chemist. If recovery of ^{18}F as a molecular F_2 is desired for some synthetic purpose, the addition of carrier F_2 to the Ne target gas (^{20}Ne $(d,\alpha)^{18}F$) is essential as is careful attention to target vessel construction materials and techniques.[40] If recovery as $H^{18}F$ is desired the addition of H_2 to the Ne target gas can under favourable circumstances yield a high recovery of ^{18}F as HF without the addition of carrier[41] which is of value as in the ^{11}C case for the synthesis of receptors specific radiolabelled drugs.

The Place Of Nuclear Data In This Field

It must be obvious that for the generation of any radionuclide adequate nuclear data for the prediction of yields of both the desired product and any impurities are essential. Most of the accelerator groups engaged in this field have when necessary attempted an extension or improvement of the existing cross section data to suit their requirements. Often, however, it is not the nuclear physics that is the limiting factor. Problems of designing a target that will work reliably at the desired beam intensity and produce a recoverable product often seem to make the fine detail sometimes quoted in nuclear data of little practical consequence.

Perhaps to put this into better perspective consider a gas N_2 target for the production of ^{11}C. A calculated yield from the excellent cross section data available is seen in practice only to hold if carrier ^{12}C is present and irradiations are carried out at low beam currents. As the current is increased the ^{11}C production versus beam current becomes grossly non-linear due to a variety of effects which are as yet little understood.[37,40,42]

Factors involved may be simply thermal or induced plasma effects in the beam path both reducing the number of target nuclei in the beam path and also perhaps increasing the mean free path of the product nucleus, enabling it to react with the target walls (e.g. ^{18}F and high specific activity ^{11}C). Further study is going to be essential before problems such as these are to be resolved.

However, the production of radionuclides with an accelerator is a challenging interdisciplinary and multidisciplinary field and the contributions of the workers in the cross section field are gratefully acknowledged.

REFERENCES

1. D.J. Silvster and S.L. Waters in Proceedings of the Second International Symposium on Radiopharmaceuticals. March 19-22, 1979, Seattle, Washington USA. To be published by The Society of Nuclear Medicine, N.Y.
2. L.G. Stang, J. Labelled Cmpds. Radiopharm. 13, 240, (1977).
3. H.A. O'Brien (Jr.) P.M. Grant and A.E. Ogard ,Prog. Nucl. Med. 4 , 93-99, (1978)
4. Ibid 16-22
5. B.D. Pate ibid 61-62.
6. D.L. Friesel and W. Smith ibid 63-71.
7. E. Loepfe, I. Huzar and F. Hegedeus. J.Labelled Cmpds. Radiopharm. 13, 241, (1977).
8. P.M. Grant, M. Kahn and H.A. O'Brien J. Inorg. Nucl. Chem. 37, 413-417, (1975)
9. P.M. Grant, B.R. Erdal and H.A. O'Brien, J.Nucl. Med. 16, 300-304, (1975)
10. Y.Yano, P. Chu and T.F. Budinger J. Nucl. Med. 18, 46-50, (1977).
11. Y.Yano, T.F. Budinger, G. Chiang et.al. J. Nucl. Med., 20, 961-966, (1979).
12. G. Stocklin and S.M. Qaim Proceedings of Internaonal Conference on Neutron Physics and Nuclear Data for Reactors and other applied purposes. Harwell U.K. 25-29 Sept. 1978. Publ. by Her Majesties Stationary Office ISBN 92-64-01870-0
13. J. Godart, J.L. Barat, A. Menthe et. al. Int. J. Appl. Rad. Isotopes 28, 967-969 (1977).
14. A. Schimmel, F.M. Kaspersen and L. Lindner, Int. J. Appl. Rad. Isotopes 30, 63-64, (1979)
15a) J.G. Cuninghame, B. Morris, A.L.Nichols et. al. Int. J. Appl. Rad. Isotopes 27, 597-603, (1976).
b) J.G. Cuninghame, J.I.S. Hill, A.L. Nichols et. al. The Production of Iodine-123 on the Harwell variable Energy Cyclotron: AERE Report 9087, (1978)
16. M.C. Lagunas-Solar, J.A. Jungerman, N.F Peek and C. Bennet. J. Labelled. Cpds. Radiopharm. 16, 224-225, (1979)
17a). J.W. Blue, R. Leonard, S.Jha, and V.J. Sodd Prog. Nucl. Med. 4, 53-60, (1978)
b). J.W. Blue, D.L.Friesel, D.C. Liu and J. Labelled Cmpds. Radiopharm. 16, 101-102 (1979).
18. M.C. Lagunas-Solar Prog.Nucl. Med. 4, 118-128, (1978)
19. D.D. Vonberg, L.C. Baker, P.D. Buckingham et.al. Proceedings of a Conference on The Uses of Cyclotrons in Chemistry Metallurgy and Biology pp. 258-269, Publ. Butterworths (1970) ISBN 0408 70029 7
20. J. A. Martin, R.S. Livingston, R. Murray and M.Rankin Nucleonics 13, 28, (1955).
21. J.L. Need, IEEE Trans. Nucl. Sci. NS-26, 2236, (1979)

22. The Cyclotron Corporation. Berkeley, Ca.
23. M.F. Finlan Proceedings of 5th European Meeting of Radioisotope Producers, Athens pp. 119. Ministry of Culture and Science Greek Atomic Energy Commission (1974)
24. N.N. Krashov, P.P. Dmitryev, et. al. Proceedings of a conference on The Uses of Cyclotrons in Chemistry Metallurgy and Biology pp 159-167. Ed. C.B. Amphlett. Butterworths (1970) ISBN 0 408 70029 7.
25. J.A. Campbell, R.D. Finn, and P.M. Smith J. Labelled Cmpds. Radiopharm. 13, 437, (1977).
26. E. Acerbi, C. Birattari et. al. Int. J. Appl. Rad. Isotopes 26, 741-747 (1975)
27. R. Van Den Bosch, J.J. M. De Goeij et.al. ibid, 28, 255-261, (1977)
28. K. Knodo, R. M. Lambrecht and A.P. Wolf ibid, 28, 395-401 (1977)
29. J.C. Clark, P.L. Horlock and I.A. Watson, Radiochem. Radioanal. Letts. 25, 245-253, (1976).
30. Clinical and Experimental Applications of Krypton-81m. J.P. Lavender Ed. Brit. J. Radiol. Special Report No.15 London, (1978)
31. J.C. Clark, R.D. Finn, et.al. 9th Int. Hot Atom Symposium Blacksburg Va. Sept. 18-23, 1977 (abstract)
32. J. Lamb et. Clinical and Experimental Applications of Krypton-81 m. J.P. Lavender Ed., Brit.J.Radiol. Special Report No. 15, London (1978)
33. T.J. Ruth, R.M. Lambrecht, A.P. Wolf and M.L. Thakur, J. Labelled Cmpds. Radiopharm. 16, 210-211, (1979)
34. R.S. Tilbury, J.R. Dahl and S.J. Marano. J. Labelled Cmpds. Radiopharm. 13, 208, (1977).
35. K.A. Lathrop, P.V. Harper, B.H. Rich et. al. Radiopharmaceuticals and Labelled Compounds Vol.1. pp. 471-481, IAEA Vienna (1973) STI/PUB/344
36. G. Berger, M. Maziere, D.Comar et. al. Int. J. Appl. Rad. Isotopes 30, 393-399, (1979)
37. G. Berger, M. Maziere, J. Sastre and D. Comar. Carrier-free "C formaldehyde": An approach Submitted to J. Labelled Cmpds. Radiopharm.
38. J.C. Clark and P.D. Buckingham pp 122-170 Short Lived Radioactive Gases for Clinical Use Butterworths, London 1975. ISBN 0 407 39770 1
39. H.V. Ruiz and A.P. Wolf J. Labelled Cmpds. Radiopharm. 15, 185-189, (1978).
40. T.J. Ruth and A.P. Wolf. IEEE Trans. Nucl. Sci. NS-26, 1710-1712, (1979)
41. T.J. Tewson, M.J. Welch and M.E. Raichle, J. Nucl. Med. 19, 1339-1345, (1978).
42. M. Cselka, J.E. Gindler and A.M. Friedman, Int. J. Appl. Rad. Isotopes. 28, 804-805, (1977)

TABLE 2

Proton Energy MeV	N° of Accelerators
up to 10	4
10 - 20	6
20 - 30	19
30 - 40	3
40 - 50	6
50 - 60	4
60 - 70	3
70 - 80	3
80 - 100	0
100 - 200	2
200 - 800	3

TABLE 1B

ACCELERATORS FOR RADIONUCLIDE PRODUCTION

B. COMMERCIALLY OPERATED CYCLOTRONS

Firm
Location — Machine Type
Person Supplying Information

Radionuclides Produced

JAPAN

Nihan Medi-Physics
Takarazuka, Hyogo — TCC CS-30
Dr. Masaaki Hazue

F-18, Ga-67, Rb-81, In-111, I-123, Tl-201

NETHERLANDS

Mallinckrodt (formerly Duphar) — Philips (28 MeV protons)
Petten, N. Holland

No Information Given

UNITED KINGDOM

The Radiochemical Centre — Philips
Amersham — (27 MeV protons)
Dr. M. Finlan

Ga-67, In-111, Co-57, As-73, 74, Au-195, Be-7, Bi-206, 207, Co-56, Fe-55, Mn-52,54, Ti-44, V-48

UNITED STATES

Medi-Physics
Dr. A. Fleischer — Scanditronix MC-40
(i) Arlington Heights, Ill

Rb-81, I-123, Tl-201

(ii) Emeryville, Calif. — TCC CS-22

Ga-67, Rb-81, In-111, I-123, Tl-201

(iii) South Plainfield, N.J. — TCC CS-22

Ga-67, Rb-81, I-123

New England Nuclear — (i) TCC CS-22
North Billerica, Mass. — (ii) TCC CS-30
Dr. J. Need — (iii) TCC CS-30

(i) Co-57, Ga-67, Cd-109, In-111
(ii) Ge-68, Au-195, Tl-201
(iii) Ge-68, Au-195, Tl-201

TABLE 1A ACCELERATORS FOR RADIONUCLIDE PRODUCTION: DECEMBER 1978

A. NON-COMMERCIAL ACCELERATORS

Location / Institute / Person Supplying Information — Machine Type / Time Spent on Radionuclide Production

*Radionuclides Produced

BELGIUM

Ghent University
Institute for Nuclear Studies
Dr. C. Vandecasteele
CGR-Mev 520
8 hr/wk

Rb/Kr-81, N-13, (C-11)

Liege University
Cyclotron Research Centre
Dr. M.A. Guillaume
CGR-MeV 520
25 hr/wk

C-11, N-13, O-15, F-18, K-43, Rb/Kr-81, Se-73 Ga-67, In-111

Louvain-la-Neuve University
Nuclear Chemistry Laboratory
Dr. M. Cogneau
CGR-MeV 930
15 hr/wk

Fe-52, I-123, Mg-28, At-211, (Tl-201)

CANADA

Vancouver, B. C.
TRIUMF
Dr. B.D. Pate
TCC CP-42 and TRIUMF 500-MeV

I-123, (C-11, N-13, O-15, F-18, Fe-52, Se-77m, Ga-67, Ge-68, Cd-109, In-111, Xe-127, Tl-201)

Winnipeg
University of Manitoba
Dr. M.I. Gusdal
(50 MeV protons)

I-123, Rb/Kr-81, Rb-84

FINLAND

Turku
Abo Academy
Dr. M. Brenner
Techsnabexport, USSR
(20 MeV protons)
16 hr/wk

C-11, F-18, Rb/Kr-81, O-15, K-43, Fe-52, Br-77, Tl-197-202, Re-181, Bi-206, (I-123)

FRANCE

Orsay
Service Hospitalier Fred. Joliot
Dr. D. Comar
CGR-MeV 520
30 hr/wk

C-11, N-13, O-15, F-18, K-43, Ru-97, Ge-68, Bi-206, (Rb/Kr-81)

GERMAN FEDERAL REPUBLIC

Essen
University Clinic
Dr H.J. Machulla
TCC CV-28
(50%)

C-11, F-18, I-123, (N-13, O-15)

Heidelberg
Inst. F. Nuklearmedizin, DKFZ
Dr. F. Helus
AEG-Compact

N-13, F-18, Rb/Kr-81, I-121, I-123, Hg-197m, O-15, Fe-52, Cu-61, Zn-62, Ru-97, Tl-201, (C-11)

Julich
Inst. f. Chemie 1, KFA
Dr. G. Stocklin
(1) TCC CV-28
24 hr/wk

C-11, F-18, P-30, Cr-48, Br-77, I-123, Cl-34m, Tl-201, Pb-203, (more F-18, and Cr-48)

(2) "Julic"
(45 MeV protons)
12 hr/wk

Mg-28*, I-123, -every two weeks, Br-76,77

Karlsruhe
Kernforschungszentrum
Dr. H. Schweickert
Isochronous
(26 MeV protons)
5 hr/wk

I-123 (500mCi/wk), (double I-123, Rb/Kr-81)

INDIA

Calcutta
Dr. R.S. Mani (Bhabha Atomic Res. Centre, Trombay)
V.E.C.
(60 MeV protons)

(K-43, Fe-52, Ga-67, In-111, I-123, Tl-201)

ITALY

Milan University
Cyclotron Laboratory
Dr. C. Birattari
A.V.F.
(45 MeV protons)
10-15 hr/wk

Rb/Kr-81, I-123, Tl-201, V-48, As-71-74, Cd-107-109, Hg-197, Pb-203, Bi-205-206

JAPAN

Chiba
Natl. Inst, of Radiological Sciences
Dr. T. Hiramoto
CGR-MeV 930
12 hr/wk

C-11, N-13, O-15, F-18, Ti-45, Fe-52, Br-77, I-123

Saitama
Inst. Phys. Chem. Research Sciences
Dr. T. Nozaki
(18 MeV protons)
5 hr/wk

F-18, Mg-28, K-43, Fe-52, Br-77

Sendai
Tohoku University
Dr. S. Morita
CGR-MeV 680
30-40 hr/wk(planned)

(F-18, Br-77)

Tokyo University
Inst. of Medical Science
Dr. Akira Ito
TCC CS-30
2 hr/wk

F-18, Ti-44, Co-56, I-123

NETHERLANDS

Eindhoven
University of Technology
Dr. R.L.P. van den Bosch
AVF
(30 MeV protons)
8 hr/wk

Br-77, I-123, Fe-55, Sr-87m, Cd-109, (Fe-52, Rb/Kr-81

NETHERLANDS Cont.

Groningen University Inst. of Nuclear Physics Dr. W. Vaalburg	AVF (65 MeV protons) 7 hr/wk

C-11, N-13, Co-55, O-15, Fe-52, Rb/Kr-81, I-123, Hg-197

SWITZERLAND

Villigen Natl. Inst. for Nuclear Research Dr. I. Huszar	VEC (72 MeV protons) and Ring Accelerator (590 MeV protons) 3-4 hr/wk

In-111, I-123, (Xe-127)

UNITED KINGDOM

Birmingham University Dept. of Physics Prof. J. H. Fremlin	Fixed-frequency (10 MeV protons) 20 hr/wk

Rb/Kr-81, I-123, Na-22, Po-208, (daily Rb/Kr-81)

Edinburgh M.R.C. Western General Hospital Mr. T. Saxton	TCC CS-30

(O-15, N-13, C-11, Rb/Kr-81)

Harwell Chem. Division AERE Mr. J. G. Cuninghame	VEC (58 MeV protons) 12 hr/wk

I-123, S-38, Nb-92m, Rh-99m, Pu-236, Pu-237, (Tl-201)

London M.R.C. Hammersmith Hospital Mr. I.A. Watson	Classical 45" (8 MeV protons) 37 hr/wk

C-11, N-13, O-15, F-18, K-43, Rb/Kr-81, Fe-52, I-123, Cu-61, Zn-62, Br-77, Ru-97, Cs-129, Pb-203, (K-38)

UNITED STATES OF AMERICA

Bloomington Indiana Univ. Cyclotron Facility Dr. D. L. Friesel	Separated sector VEC (200 MeV protons) (under 1%)

I-123

Boston Mass. General Hospital Dr. G. L. Brownell	Allis-Chalmers (6 MeV deuterons) 40 hr/wk

C-11, N-13, F-18, O-15

Brookhaven National Lab. Upton Long Island, N.Y. Dr. A.P. Wolf	Isochronous 60" (36 MeV protons) 40-50 hr/wk

C-11, N-13, O-15, F-18, K-38, Mn-51, Mn-52, Rb/Kr-81, I-123, At-211, Ne-19, Cl-34m, Fe-55, Br-76, Br-77, Se-97m, Tc-92, Os-191, Au-195m, Pb-203

Brookhaven National Lab. Upton Long Island, N.Y. Dr. Louis Stang	BLIP (Lin. Acc.) (200 MeV protons) 145 hr/week

Mg-28, Fe/Mn-52, Ga-67, Rb/Kr-81, Ru-97, I-123, Ge-68, Cd-109, Sn-113, Te-118, Xe/I-122, Xe-127, W-178

Chicago University Franklin McLean Mem. Res. Institute Dr. P.V. Harper	TCC CS-15 10 hr/wk

C-11, N-13, O-15, F-18, Mn-51

Cleveland, Ohio NASA Dr. J.W. Blue	VEC (45 MeV protons) 8 hr/wk

C-11, Tl-201

Davis, California Crocker Nuclear Lab. Dr. M.C. Lagunas-Solar	VEC (66 MeV protons) 20-35 hr/wk

I-123, Tl-201, N-13, Co-55, Rh-101m

Los Alamos, New Mexico C.P. Anderson Meson Phys. Facility Dr. H. A. O'Brien	LAMPF (Lin. Acc.) (800 MeV protons) 168 hr/wk

Fe/Mn-52, Br/Se-77, Sr/Rb-82, Hf/Lu-172, (Cu-67, Ge-68, Se-72, I-123, Xe-127)

Los Angeles, California U.C.L.A. School of Medicine Dr. N.S. MacDonald	TCC CS-22 50 hr/wk

C-11, N-13, F-18, Zn/Cu-62, Cu-64, Rb/Kr-81, O-15, Cd-107, In-111, I-123

Miami Beach, Florida Mount Sinai Medical Center Mr. J.E. Beaver	TCC CS-30 (27 MeV protons) 100 hr/wk

Rb/Kr-81, Ga-67, In-111, Tl-201, C-11, O-15, (N-13)

Michigan State University Cyclotron Laboratory Dr. P.S. Miller	VEC (50 MeV protons) av. 6 hr/wk

C-11, N-13

New York, N.Y. Sloan Kettering Institute Dr. R.S. Tilbury	TCC CS-15 20 hr/wk

C-11, N-13, O-15, F-18, K-38, Fe-52, Se-73

Oak Ridge, Tennessee O.R.N.L. Dr. S. W. Mosko	Isochronous Cyclotron (55 MeV protons) 2%

No Data Given

St. Louis, Missouri Washington University Dr. M.J. Welch	(1) Allis-Chalmers (6 MeV deuterons)
C-11, N-13, O-15, F-18	
do	(2) 52" Cyclotron (30 MeV ^{4}He) 12 hr/wk
Br-77, Kr-77, Rb/Kr-81	
do	(3) TCC CS-15

(C-11, N-13, F-18)

Washington, D.C. Naval Research Laboratory Dr. R. Q. Bondelid	Sector-Focusing Cycl. (65 MeV protons)

C-11, F-18, I-123

* Radionuclides produced Routinely at least once a week; underlined.
Irregularly or in future; in parenthesis.

EVALUATION OF THE FISSION AND CAPTURE CROSS SECTIONS OF ^{240}Pu AND ^{241}Pu FOR ENDF/B-V

L. W. Weston and R. Q. Wright
Oak Ridge National Laboratory
Oak Ridge, Tennessee 37830, USA

Since there were appreciable new data which were not available for ENDF/B-IV, new evaluations for ^{240}Pu and ^{241}Pu were carried out for ENDF/B-V. The evaluation of the fission and capture cross sections will be reviewed and problem areas discussed. The neutron energy range of concern was from 10^{-5} eV to 20 MeV. Significant changes were made over the entire neutron energy region because of the new experimental data available. The problems in the evaluations due to discrepancies in the nuclear data will be emphasized, particularly the 1-eV resonance in ^{240}Pu and the 0.3-eV resonance in ^{241}Pu. The evaluation of the fission and capture cross sections for ENDF/B-V represents an improvement over the previous evaluation; however, there continues to be a need for accurate experimental data.

(neutron nuclear data evaluations, fission, capture, ^{240,241}Pu)

Introduction

An evaluation of the neutron capture and fission cross sections for ^{240}Pu and ^{241}Pu for ENDF/B-V was necessary because significant new data on these isotopes have become available. Some of these new data were discrepant with previous evaluations,[1,2,3] for example, resonance region of ^{241}Pu and the capture cross section of ^{240}Pu in the keV neutron energy region. In the case of the high energy fission cross sections the new data were superior to those previously available. Also, parts of the ENDF/B-IV evaluation were carried over from earlier versions of ENDF and therefore required updating.

Thermal Energy Range

Plutonium-240

A severe uncertainty in the evaluation of ^{240}Pu was the thermal neutron energy region which is dominated by the 1-eV resonance. About 99% of the thermal capture cross section is due to the influence of the 1-eV resonance. Because of the small quoted uncertainty, a single measurement[4] of the thermal cross section dominates the accepted 2200 m/s cross section as well as the determination of the product of the neutron width and radiation width, $\Gamma_n\Gamma_\gamma$, for the 1-eV resonance. This measurement is that of Lounsbury et al.[4] who report a 2200 m/s capture cross section of 289.5 ± 1.4 barns.

Plutonium-241

There have been two measurements[5,6] of the fission cross section and one measurement[6] of the capture cross section since the previous ENDF evaluation. The fission cross section was raised 2% at the 0.25-eV resonance based predominately on the experiments of Wagemans and Deruytter,[5] and Weston and Todd.[6]

The measurements of Weston and Todd[6] indicated a significantly higher capture cross section (14%) over the 0.25-eV resonance than the previous ENDF evaluation. The ENDF/B-IV evaluation was based on the total and fission cross section measurements of Simpson and Schuman[7] and Watanabe and Simpson.[8] The ENDF/B-V capture in the thermal neutron energy region is based on the measurements of Weston and Todd[6] for the following reasons; 1) the smaller uncertainty of the more direct measurement of the capture cross section, 2) the ENDF/B-IV capture in the resonance region was also determined to be low and 3) integral experiments suggest a higher capture cross section in the thermal neutron energy range. Figure 1 illustrates ENDF/B-V fission compared to Wagemans and Deruytter,[5] and the capture cross section of Weston and Todd[6] compared to ENDF/B-IV and V.

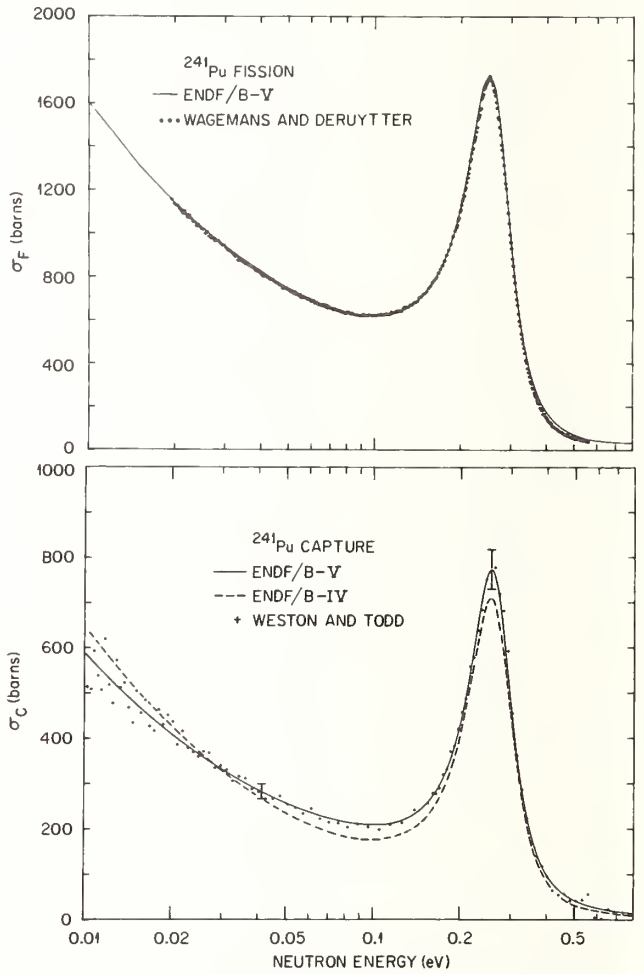

Fig. 1. The fission and capture cross sections of ^{241}Pu from 0.01 to 0.8 eV.

Resonance Region

Plutonium-240

The most severe uncertainty in the evaluation as far as thermal reactors are concerned is in the resonance parameters of the 1-eV resonance. The product of the neutron and radiation widths, $\Gamma_n\Gamma_\gamma$, is determined with an uncertainty of about 1% by the thermal cross section measurement of Lounsbury et al.[4] The individual resonance parameters, Γ_n and Γ_γ, have been measured in

a number of experiments with discrepant results; these are described by Caner and Yiftah[10] and in a review paper by Weigmann et al.[11] In essence, there are two groups of experiments which predict radiation widths which are about 10% apart. This evaluation favors a high value of Γ_γ. The ENDF/B-V values of Γ_n and Γ_γ were taken to be 2.28 and 33.3 meV, respectively, as evaluated by Caner and Yiftah.[10]

Integral experiments yield little information on these resonance widths because they are usually carried out with low ^{240}Pu content as compared to ^{239}Pu and they are most sensitive to the product, $\Gamma_n\Gamma_\gamma$. Thompson and Leonard[12] are using least squares fitting techniques to more accurately determine the widths, Γ_n and Γ_γ, from the available data.

There is a need for careful, accurate experimental measurements to determine the resonance parameters of the 1-eV resonance of ^{240}Pu. Without such additional experimental measurements, the large uncertainty in the cross section of ^{240}Pu below a neutron energy of a few eV will continue to be a problem.

The resonance parameters from 20 to 665 eV for ENDF/B-V are the weighted average of the parameters of Weigman et al.,[11] Asghar et al.[13] and Hockenbury et al.[14] Above 665 eV, the neutron widths of Kolar and Bockhoff[15] were used as was the case for ENDF/B-IV. The fission widths for the subthreshold fission resonances were evaluated from the data of Auchampaugh and Weston,[16] Migneco and Theobald,[17] and Weigman et al.[11]

Plutonium-241

Because of appreciable level-level interference in the fission cross section, this evaluation is in the form of the Adler-Adler[18] multilevel formalism. The data of Weston and Todd[19] had been fit in the Adler-Adler formalism. Fits to the data of Blons,[20] Simpson and Shuman,[7] James,[21] and Moore et al.[22] which were in the Reich-Moore formalism were converted to the Adler-Adler formalism using the computer code, POLLA, and techniques developed by de Saussure and Perez.[23] This evaluation was carried out using these sets of parameters. The resulting capture cross section, and thus the average radiation width, is higher (~40%) than the ENDF/B-IV evaluation. Indications that the capture cross section was low in the previous evaluation had been noted previously.[10,20] Figure 2 illustrates the ENDF/B-V fission cross section compared to the measurements of Blons,[20] and Migneco et al.[24] Figure 3 compares the ENDF/B-V fission and capture cross sections with the measurements of Weston and Todd.[6]

Unresolved Resonance Region

Plutonium-240

The capture cross section of ^{240}Pu in the unresolved resonance region is illustrated in Fig. 4. The average resonance parameters[11] as derived from the resonance region were in good agreement with the average capture cross section measurements of Weston and Todd[25] so these parameters were used for the evaluation. This

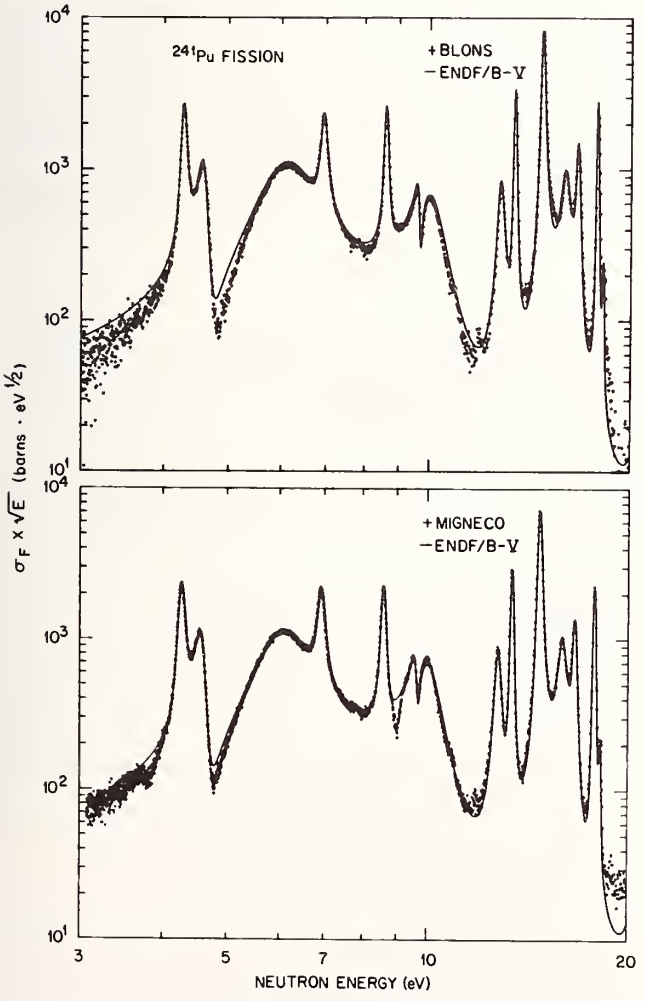

Fig. 2. The fission cross section of ^{241}Pu from 3 to 20 eV.

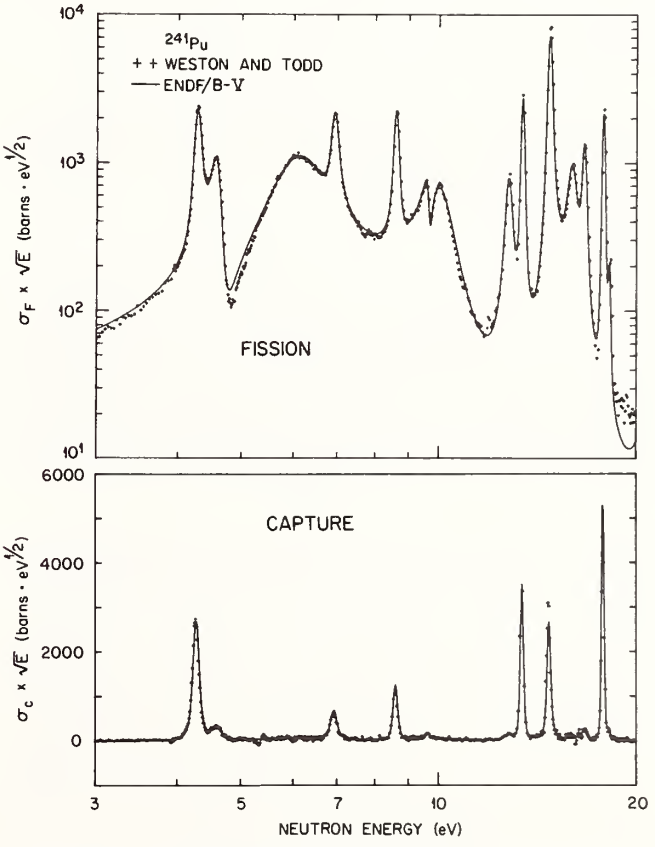

Fig. 3. The fission and capture cross section of ^{241}Pu for ENDF/B-V compared to Weston and Todd from 3 to 20 eV.

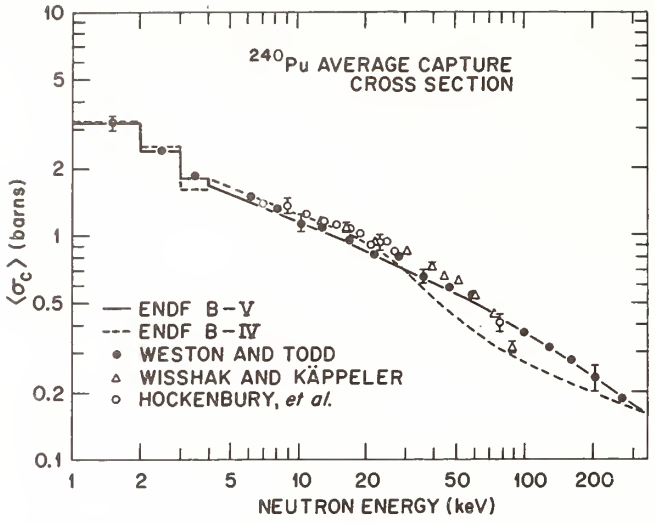

Fig. 4. The average capture cross section of ^{240}Pu from 1 to 300 keV.

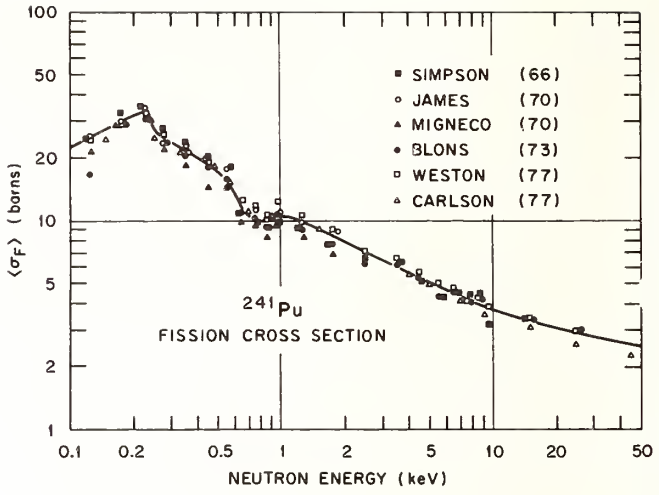

Fig. 5. The fission cross section of ^{241}Pu in the neutron energy range from 0.1 to 50 keV.

evaluation is lower than the measurements of Hockenbury et al.:[14] however, these experimenters[26] indicated their results may have been high because the canning of the sample was not properly taken into account. The measurements of Wisshak and Käppeler were available only in very preliminary form at the time of the evaluation and were not considered. The points of Wisshak and Käppeler[27] in Fig. 4 were converted by the author from ratio measurements with respect to Au using the ENDF/B-V Au cross section. These points are only part of the data and are only intended to be representative of the data. The Wisshak and Käppeler [27] and the Weston and Todd[25] measurements are not very discrepant on a point-by-point basis, but the difference in shape is disturbing.

The fission cross section of ^{240}Pu is small and relatively insignificant from thermal through the unresolved resonance region. The evaluation of this cross section in the unresolved resonance region was based on the data of Behrens et al.[28]

Plutonium-241

The fission cross section of ^{241}Pu in the unresolved resonance region is illustrated in Fig. 5. Most of the experimental measurements[6,17,20,21,29,30] shown in Fig. 5 indicate an unexpected rise between 100 and 200 eV and a dip in the cross section at about 800 eV. These measurements show disturbing discrepancies (~10%) when their quoted uncertainties are considered (~3%). The ENDF/B-V evaluation reproduces the major structure which is common to the experimental results.

The data on the capture cross section of ^{241}Pu by Weston and Todd[6] in the energy region shown in Fig. 5 indicate the same structure (rise between 100 and 200 eV and dip at about 800 eV) which appears in the fission cross section. This is somewhat surprising because if the structure were due to the usual effect of the well-known double fission barrier the fission widths would be modulated. Since the structure appears in the capture cross section as well as in the fission cross section it must be due to one or both components of the strength function, $\langle \Gamma_n/D \rangle$. The evaluation of the capture cross section was based on the data of Weston and Todd[6] since no other differential data are available.

High Energy Region

Plutonium-240

The evaluation of the fission cross section of ^{240}Pu was based upon the ratio to ^{235}U measurements of Behrens et al.[28] These data appeared superior to other available data at the time of the evaluation. Since the evaluation, additional data by Kari and Cierjacks,[31] and Budtz-Jorgensen and Knitter[32] have become available which are in reasonable agreement with the measurements of Behrens. The data of Behrens[28] converted to the fission cross section with the use of the ENDF/B-V fission cross section for ^{235}U are compared in Fig. 6 with the ENDF/B-V evaluation for ^{240}Pu and the ENDF/B-IV evaluation for ^{240}Pu.

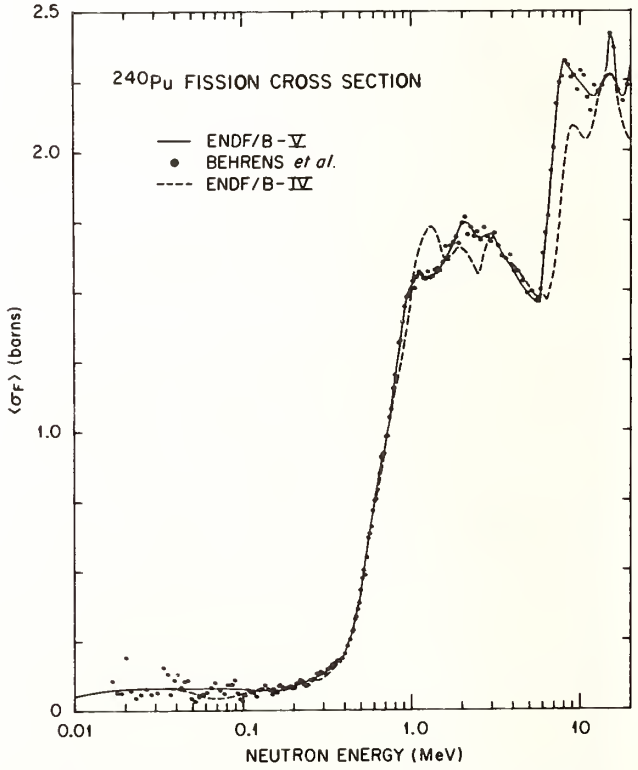

Fig. 6. The fission cross section of ^{240}Pu at high-neutron energies.

The capture cross section of ^{240}Pu above 300 keV is unchanged from Version IV. The changes below this neutron energy were illustrated in Fig. 4.

Plutonium-241

Figure 7 illustrates the experimental data,[30,33-36] the ENDF/B-V, and the ENDF/B-IV evaluations for the high-energy fission cross section of ^{241}Pu. Again the ratio data of Carlson and Behrens[33] were given the principle weight in the evaluation because of accuracy, consistency with ^{240}Pu, and complete coverage of the high-energy neutron range.

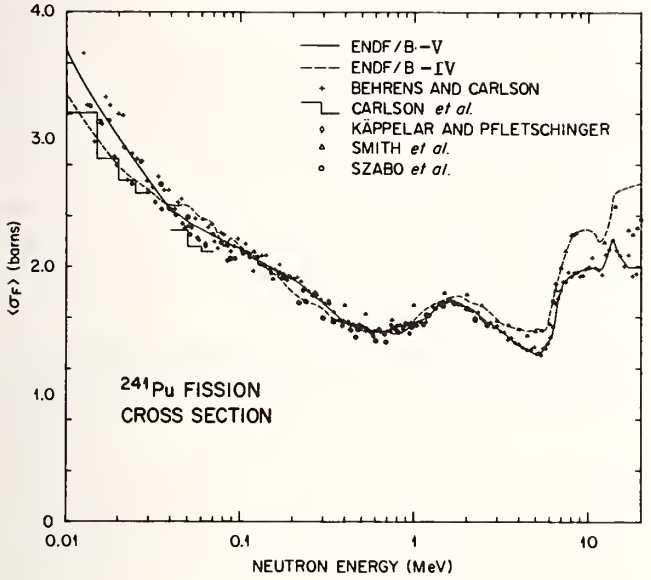

Fig. 7. The fission cross section of ^{241}Pu at high-neutron energies.

Conclusions

The capture and fission cross sections for ^{240}Pu and ^{241}Pu were evaluated from 10^{-5} eV to 20 MeV for ENDF/B-V. Due to new experimental data which have become available the new evaluation is placed on a firmer basis than the earlier evaluation.

In the authors' opinion, three problem areas remain which would require new, careful experimental measurements to resolve. These are listed in decreasing order of importance:

1. The resonance parameters of the 1-eV resonance of ^{240}Pu are not known with a sufficient accuracy. The 1-eV resonance also controls the 2200 m/s capture cross section and so a confirmation of the experiment of Lounsbury et al.[4] would be worthwhile.

2. The capture cross-section measurements on ^{241}Pu of Weston and Todd[6] carried an inordinate weight because they were the only extensive differential capture cross-section measurements from 0.01 eV to 200 keV neutron energy. Another independent measurement would be of value.

3. The ^{241}Pu fission cross section in the unresolved resonance region is uncertain by about 5%. There are a number of experimental measurements but they are discrepant. A careful high-precision measurement of this cross section would be most useful.

Acknowledgment

Research sponsored by the Reactor Research and Technology Division, U. S. Department of Energy under contract W-7405-eng-26 with the Union Carbide Corporation.

References

1. E. Pennington and H. Hummel, ENDF/B-IV, MAT 1265, File 1, Brookhaven National Laboratory (1974).

2. H. Hummel and E. Pennington, ENDF/B-IV, MAT 1266, File 1, Brookhaven National Laboratory (1974).

3. R. E. Hunter, L. Stewart, and T. S. Hirons, "Evaluated Neutron-Induced Cross Sections for ^{239}Pu and ^{240}Pu," LA-5172, Los Alamos Scientific Laboratory (1973).

4. M. Lounsbury, R. W. Durkam, and G. C. Hanna, Proc. Conf. on Nuclear Data for Reactors, Helsinki, IAEA, Vienna (1970) p. 287.

5. C. Wagemans and A. J. Deruytter, Proc. Conf. Nuclear Cross Sections and Technology, Washington, National Bureau of Standard Special Publication, 425, II, p. 603 (1975).

6. L. W. Weston and J. H. Todd, Nucl. Sci. Eng. 65, 454 (1978); for resonance parameters see Nucl. Sci. Eng. 68, 125 (1978).

7. O. D. Simpson and R. P. Schuman, Nucl. Sci. Eng. 11, 111 (1961).

8. T. Watanabe and O. D. Simpson, IDO-16995, Phillips Petroleum, Idaho (1964).

9. H. D. Lemmel, Proc. Symp. Neutron Standards and Applications, National Bureau of Standards, Washington D. C., NBS-493 (1977) p. 170.

10. M. Caner and S. Yiftah, "Nuclear Data Evaluation for Plutonium-240," IA-1243; "Nuclear Data Evaluation for Plutonium-241," IA-1276, Israel Atomic Energy Commission (1972).

11. H. Weigmann, G. Rohr, and F. Pourtmans, Proc. Conf. Resonance Parameters of Fertile Nuclei and ^{239}Pu, Saclay, Commissariat a L'Energia Atomique, NEANDC(E) 163U (1974) p. 219.

12. J. K. Thompson and B.,R. Leonard, Jr., private communication (1978).

13. M. Asghar, M. C. Moxon, and N. J. Pattenden, Proc. Conf. Nuclear Data for Reactors, Paris, IAEA, Vienna (1966); see ref. 7 for revised parameters.

14. R. W. Hockenbury, W. R. Moyer, and R. C. Block, Nucl. Sci. Eng. 49, 153 (1972).

15. W. Kolar and K. H. Bockhoff, J. Nucl. Energy 22, 299 (1968).

16. G. F. Auchampaugh and L. W. Weston, Phys. Rev. C12, 1850 (1975).

17. E. Migneco and J. P. Theobald, Nucl. Phys. A112, 603 (1968).

18. D. B. Adler and F. T. Adler, Proc. Conf. Breeding Economics and Safety in Large Fast Power Reactors, Argonne, Illinois, ANL-6792, Argonne National Laboratory (1963) p. 695.

19. L. W. Weston and J. H. Todd, Nucl. Sci. Eng. 68, 125 (1978).

20. J. Blons, Nucl. Sci. Eng. 51, 130 (1973).

21. G. D. James, Proc. Conf. Nuclear Data for Reactors, Helsinki, 1, p. 267, International Atomic Energy Agency, (1970).

22. M. S. Moore et al., Phys. Rev. 135, B945 (1964).

23. G. de Saussure and R. B. Perez, "POLLA, A Fortran Program to Convert R-Matrix-Type Multilevel Resonance Parameters for Fissile Nuclei into Equivalent Kapur-Peierls-Type Parameters," ORNL-TM-2599, Oak Ridge National Laboratory (1969).

24. E. Migneco et al., Proc. Conf. Nuclear Data for Reactors, Helsinki, 1, p. 437, International Atomic Energy Agency (1970).

25. L. W. Weston and J. H. Todd, Nucl. Sci. Eng. 63, 143 (1977).

26. R. W. Hockenbury, private communication (1978).

27. K. Wisshak and F. Käppeler, Nucl. Sci. Eng. 66, 363 (1978).

28. J. W. Behrens, J. C. Browne, and G. W. Carlson, Nucl. Sci. Eng. 66, 433 (1978).

29. O. D. Simpson et al., Proc. Conf. Neutron Cross Sections and Technology, Washington, CONF-660303, II, p. 910, USAEC (1966).

30. G. W. Carlson, J. W. Behrens, and J. B. Crizz, Nucl. Sci. Eng. 63, 149 (1977).

31. K. Kari and S. Cierjacks, Proc. Conf. Neutron Physics and Nuclear Data, Harwell, p. 905, OECD Nuclear Energy Agency (Paris) (1978).

32. C. Budtz-Jorgensen and H. H. Knitter, Proc. Nuclear Data of Plutonium and Americium Isotopes for Reactor Applications, p. 239, Brookhaven, BNL-50991, Brookhaven National Laboratory (1978).

33. G. W. Carlson and J. W. Behrens, Nucl. Sci. Eng. 68, 128 (1978).

34. F. Käppeler and E. Pfletschinger, Nucl. Sci. Eng. 51, 124 (1973).

35. H. L. Smith, R. K. Smith, and R. L. Henkel, Phys. Rev. 125, 1329 (1962).

36. I. Szabo et al., Proc. Symp. Neutron Standards, Argonne National Laboratory, CONF-701002, p. 257 USAEC (1970).

WHAT CAN BE LEARNED FROM THE CHANNEL ANALYSIS OF THE ^{232}Th NEUTRON FISSION CROSS SECTION

H. Abou Yehia, J. Jary, J. Trochon

Service de Physique Neutronique et Nucléaire
Centre d'Etudes de Bruyères-le-Châtel
B.P. n° 561
92542 Montrouge Cedex, France

and

J.W. Boldeman, A.R. de L. Musgrove

AAEC Research Establishment
Private Mail Bag, Sutherland 2232
N.S.W. Australia

Channel analyses of the neutron fission cross section of ^{232}Th have been made in two laboratories. The calculated fission cross sections and fission fragment anisotropies are compared with the experimental data. Despite some differences in the methods used, the conclusions on the physical aspects of the fission process are very similar.

[^{232}Th, fission channel analysis, statistical model, $\sigma_{n,f}$, $\sigma_{n,\gamma}$, $\sigma_{n,n'}$, $W(E_n,\theta)$, fission barriers derived, triple humped shapes.]

Introduction

The prediction[1] of a triple humped shape for the ground state fission barriers of the thorium isotopes has led to renewed interest in the neutron data for these nuclei and their interpretation. From the proceedings of the recent conference in Julich[2] it is clear that consensus has not yet been achieved on the reliability of the theoretical prediction. This is not surprising in view of the complexity of the problem. One method which may help to clarify the situation is to attempt a comprehensive analysis of all experimental data. The present paper summarises the status of such an analysis of the ^{232}Th neutron data, which has been proceding independently at two laboratories.

Method of analysis

Both analyses are based on the statistical model[3]. The capture of an incident neutron with energy E_n by the target ^{232}Th leads to the formation of a compound nucleus which subsequently decays by neutron emission, gamma ray emission or fission. The various cross sections may be written in the form

$$\sigma_{cc'}(E_n) = \sum_{J\pi} \sigma_c(E,J,\pi) P_{c'}(E,J,\pi), \qquad (1)$$

where c and c' label the entrance and exit channels respectively, $\sigma_c(E,J,\pi)$ is the cross section for formation of the compound nucleus state with total angular momentum J and parity π at the excitation energy E, and $P_{c'}$ is the branching ratio to the channel c' with corrections due to width fluctuations. Thus the cross section for neutron emission to a final state λ of the target nucleus is given by

$$\sigma_{n,n'(\lambda)} = \sum_{J\pi} \sigma_c(E,J,\pi) \frac{T_n(E - E_\lambda,J,\pi) F_{n,n'}}{T_f^t + T_n^t + T_\gamma^t}, \qquad (2)$$

where T_n, T_f and T_γ denote the transmission coefficients for neutron emission, fission and radiative capture respectively and the superscript t signifies summation over all channels for each mode. $F_{n,n'}$ is a level width fluctuation factor. Similar expressions can be written for the fission and capture cross sections.

Despite the similarity of the approach in each analysis, there are significant differences in the method of deriving some of the transmission coefficients. The BRC analysis[4] used transmission coefficients for the compound nucleus formation and neutron emission cross sections, derived by Lagrange from a coupled channel calculation[5]. The fluctuation correction followed the method of Moldauer[6]. For the Lucas Heights analysis, the method adopted followed the procedure of Hofmann et al.[7], with the use of the potential of Moldauer[8], and with fluctuation corrections based on a combination of the methods of ref.[7] and Bertram[9].

The radiative capture transmission coefficient T_γ is related to the average capture width $\bar{\Gamma}_\gamma$ by

$$T_\gamma(E,J,\pi) = 2\pi\rho(E,J,\pi)\ \bar{\Gamma}_\gamma(E), \qquad (3)$$

where $\rho(E,J,\pi)$ denotes the Fermi-gas level density[10] of the compound nucleus, ^{233}Th, in its state (E,J,π). In both analyses, γ ray widths have been calculated according to the Weisskopf formalism[11] and normalised to the measured average radiative width in the resolved resonance region.

For the evaluation of the fission penetrabilities, the fission barriers were parameterised by smoothly joined parabolas following the procedure of Cramer and Nix[12]. The fission penetrabilities were obtained from an exact solution of the Schrödinger equation. For the Lucas Heights calculations, triple humped fission barriers could be parameterised in the analysis. In the BRC method, double humped barriers only could be specified but there is no real loss of accuracy here as the inner barrier is expected to be much lower in height than the outer two barriers and therefore exercises almost no impact on the magnitude of the penetrability. Of course, this is the real problem in the present method of attempting to confirm a triple humped fission barrier shape. The only real difference in the two methods of evaluating the fission penetrabilities is the use of different constant values for the mass inertial parameter. The BRC calculation used the value suggested by Cramer and Nix[12] for a double humped fission barrier. In the Lucas Heights analysis, a different mass inertial parameter

was derived from Dudek[13], who has discussed the deformation dependence of this parameter.

No damping in the outer well was used in either analysis. For the BRC analysis, all triple humped fission barriers which gave rise to a vibrational resonance had both parities which is expected because of the asymmetric deformation of the nucleus at the third minimum. For the Lucas Heights analysis, this additional complication was not adopted because of the already numerous fission barriers.

Finally, the differential fission fragment angular distributions are obtained from

$$\langle\sigma_f(E_n,\theta)\rangle = \sum_{JK\pi} \sigma_f^{JK\pi}(E_n) W_{JK}(\theta), \qquad (4)$$

where the quantum numbers, JKπ, specify the particular fission channel. K is the projection of the total angular momentum J on the symmetry axis of the nucleus. The fission fragment angular distribution, $W_{JK}(\theta)$, for fission through each channel, JK, is given by

$$W_{JK}(\theta) = \frac{1/(2J+1)}{4}\left[\,|d_{1/2,K}(\theta)|^2 + |d_{-1/2,K}(\theta)|^2\right] \qquad (5)$$

where $|d|^2$ is the square of the rotational part of the symmetric-top wave function[14].

Results

The experimental neutron fission cross section shows a great deal of structure accompanied by rapid changes in the fission fragment angular distributions[18-21]. Consequently, a search for a set of barrier parameters which leads to predicted values consistent with all experimental data presents many problems.

The computational procedure involved adjusting the heights (E_B, E_{III}, E_c) and widths ($\hbar\omega_B$, $\hbar\omega_{III}$, $\hbar\omega_c$) of the potential barriers associated with a set of fission channels (Kπ) until good agreement was obtained between calculated and experimental fission cross sections and fission fragment angular distributions. The two procedures were similar to that of Caruana et al.[18] but with one important difference. Whereas in the analysis of Caruana et al. all fission barriers were assumed to have the same triple humped shape and were merely displaced in energy with respect to each other, this restriction was relaxed and different shapes were allowed in the present analyses.

The parameters of the different fission barriers derived in the BRC analysis are shown in table I. The fission cross section calculated with these values is shown for the neutron energy region, 0.7 - 1.5 MeV, in figure 1 and in figure 2 for the range 1.0 - 2.5 MeV together with the experimental neutron fission cross sections[15-17]. The calculated neutron capture cross section is compared with experimental data[22-26] in figure 3. Similarly, the calculated elastic and inelastic scattering cross sections are in good agreement[4] with experimental data but for brevity are not shown here.

The fission barrier parameters obtained from the Lucas Heights analysis are listed in table 2. The set of parameters is somewhat smaller than in table 1, partly because the analysis was terminated at a lower upper energy. No structures in the cross section beyond 1.85 MeV were fitted. Two options (a,b) were tried for the $7/2^-$ barrier associated with the structure in the fission cross section at 950 keV. The calculated fission and neutron capture cross sections are shown in figures 1-3.

Table I. Fission barrier parameters in MeV. BRC fit.

(k,π)	E_B	E_{III}	E_C	$\hbar\omega_B$	$\hbar\omega_{III}$	$\hbar\omega_C$
1/2 +	5.49	5.47	6.86	1.30	0.60	1.30
7/2 −	5.70	5.46	6.875	0.74	0.60	1.05
1/2 +	6.27	5.72	6.86	1.20	1.0	1.23
3/2 +	6.29	5.723	6.77	1.40	1.0	1.40
1/2 +	6.22	5.86	7.24	1.40	1.0	1.40
3/2 +	6.35	5.81	6.92	1.40	1.0	1.40
3/2 +	6.62	5.90	7.01	1.40	1.0	1.40
3/2 −	6.61	5.89	7.00	1.40	1.0	1.40
5/2 +	6.45	5.90	6.96	1.40	1.0	1.40
5/2 −	6.46	5.91	6.97	1.40	1.0	1.40
1/2 +	6.73	6.026	7.62	1.40	1.0	1.40
1/2 −	6.74	6.036	7.63	1.40	1.0	1.40
3/2 +	6.78	6.016	7.29	1.40	1.0	1.40
3/2 −	6.79	6.026	7.30	1.40	1.0	1.40
1/2 +	6.76	6.19	7.43	1.40	1.0	1.40
1/2 −	6.77	6.20	7.44	1.40	1.0	1.40
5/2 +	6.85	6.175	7.23	1.40	1.0	1.40
5/2 −	6.86	6.185	7.24	1.40	1.0	1.40
1/2 +	7.01	6.305	7.54	1.40	1.0	1.40
1/2 −	7.02	6.315	7.55	1.40	1.0	1.40
1/2 +	7.20	6.38	7.70	1.40	1.0	1.40
1/2 −	7.21	6.39	7.71	1.40	1.0	1.40
1/2 +	7.20	6.48	7.54	1.40	1.0	1.40
1/2 −	7.21	6.49	7.55	1.40	1.0	1.40
1/2 +	7.22	6.55	7.57	1.40	1.0	1.40
1/2 −	7.23	6.56	7.58	1.40	1.0	1.40
1/2 +	7.24	6.625	7.52	1.40	1.0	1.40
1/2 −	7.24	6.735	7.55	1.40	1.0	1.40

As a further exercise, the fission barrier parameters derived from the BRC analysis were tried without modification in the Lucas Heights calculation. It was found that the shape of both the fission cross section and the anisotropy were reproduced ; however there was a difference of approximately 30 per cent in the absolute magnitude of the fission cross section.

Table II. Fission barrier parameters in MeV. Lucas Heights fit.
a)b) Options discussed in the text.

	K Π	E_B	E_{III}	E_C	$\hbar\omega_B$	$\hbar\omega_{III}$	$\hbar\omega_C$
a)	$7/2^-$	6.200	5.260	6.577	1.40	0.90	1.25
b)	$7/2^-$	5.70	5.46	6.875	0.74	0.60	1.05
	$1/2^+$	5.650	5.450	7.140	1.40	1.00	1.15
	$1/2^-$	6.250	5.690	6.880	1.40	1.20	1.35
	$3/2^+$	6.130	5.710	6.940	1.40	1.15	1.30
	$3/2^+$	6.550	5.880	6.950	1.40	1.05	1.30
	$5/2^+$	6.500	5.875	6.960	1.40	1.20	1.16
	$5/2^-$	6.650	6.030	6.800	1.40	1.10	1.35
	$1/2^-$	6.700	6.020	6.950	1.40	1.10	1.20
	$1/2^-$	6.800	6.023	6.980	1.40	1.50	1.20
	$3/2^-$	6.800	6.060	6.900	1.40	1.50	1.10
	$1/2^+$	6.900	6.140	7.300	1.40	1.50	1.15

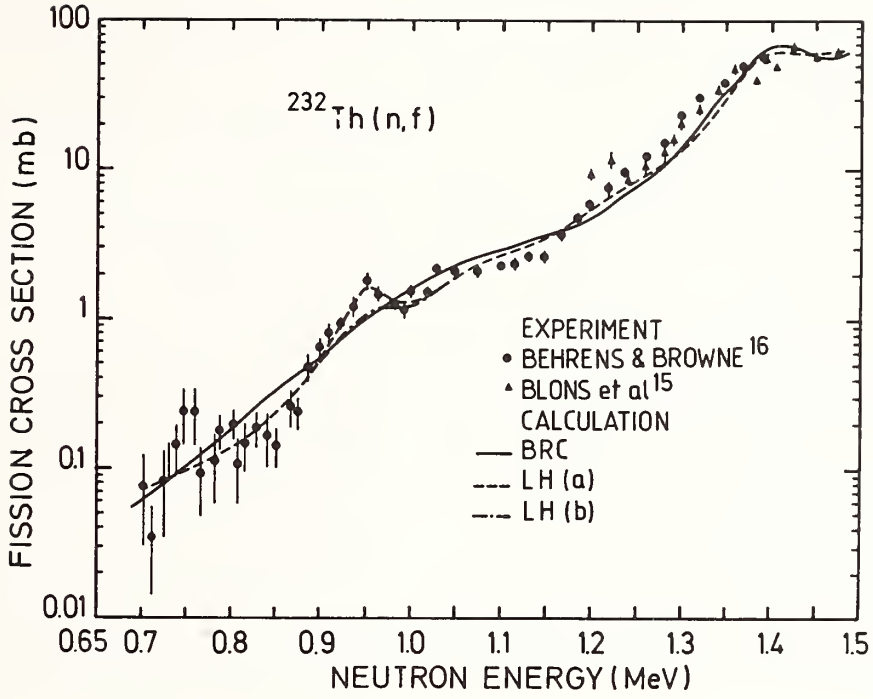

Fig. 1 . The neutron fission cross section for ^{232}Th between 0.7 and 1.5 MeV.

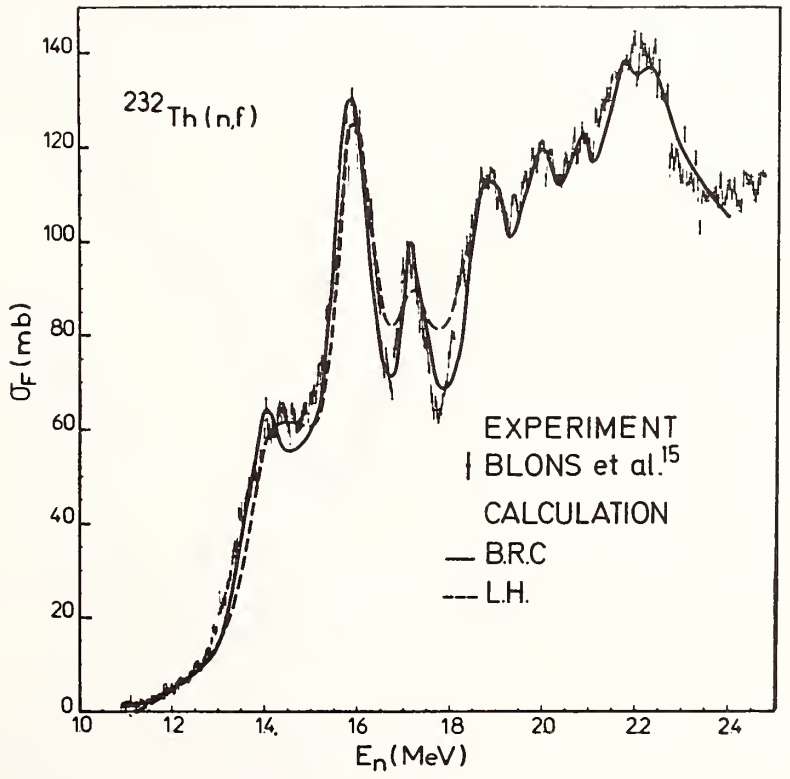

Fig. 2 . The neutron fission cross section for ^{232}Th between 1.2 and 2.5 MeV.

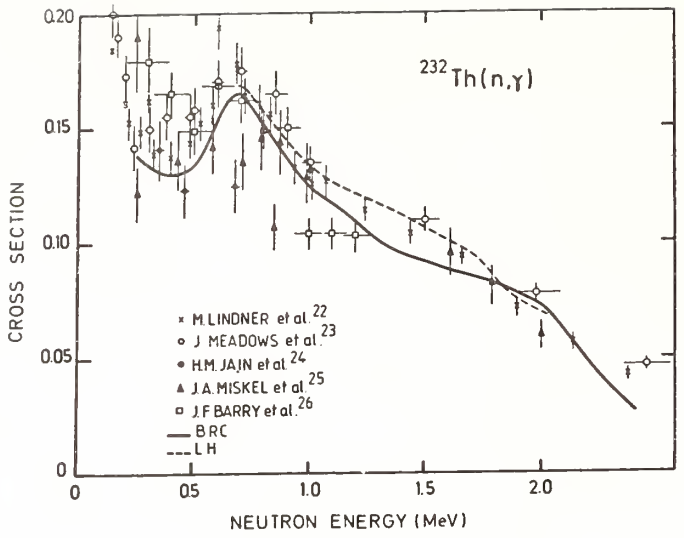

Fig.3. Experimental and calculated neutron capture cross sections.

The fission fragment anisotropies obtained from the fission fragment angular distributions calculated in both analyses are shown in figure 4 together with the experimental data[18-21].

that it is not possible to derive a unique set. Thus the important question to answer is "What can be learnt from these analyses ?".

Despite the difference in the actual values for the different parameters, the physical conclusions derived in each analysis are the same.

1. Throughout the energy range, 0.7 - 1.3 MeV, the fission cross section is dominated by the partial cross section through a K = 1/2 band for which the outer well is too shallow to include a vibrational state. Consequently, there is no vibrational resonance in the partial cross section for this band.

2. For the structure in the fission cross section at 0.95 MeV, which is also associated with a minimum in the anisotropy, the most satisfactory interpretation requires the introduction of a K = 7/2 fission band. However there are difficulties at this energy because of slight differences in the experimental data, which are illustrated by the two Lucas Heights options presented. If, for example, the fission cross section near this energy has a sharply defined peak[16], this can be reproduced in the calculation as a vibrational resonance in the outer minimum of a K = 7/2 fission barrier [fit a in figures 1 and 4]. However the fission fragment anisotropy then shows a very strong minimum (figure 4) which is in disagreement with the experimental data. On the other hand, the

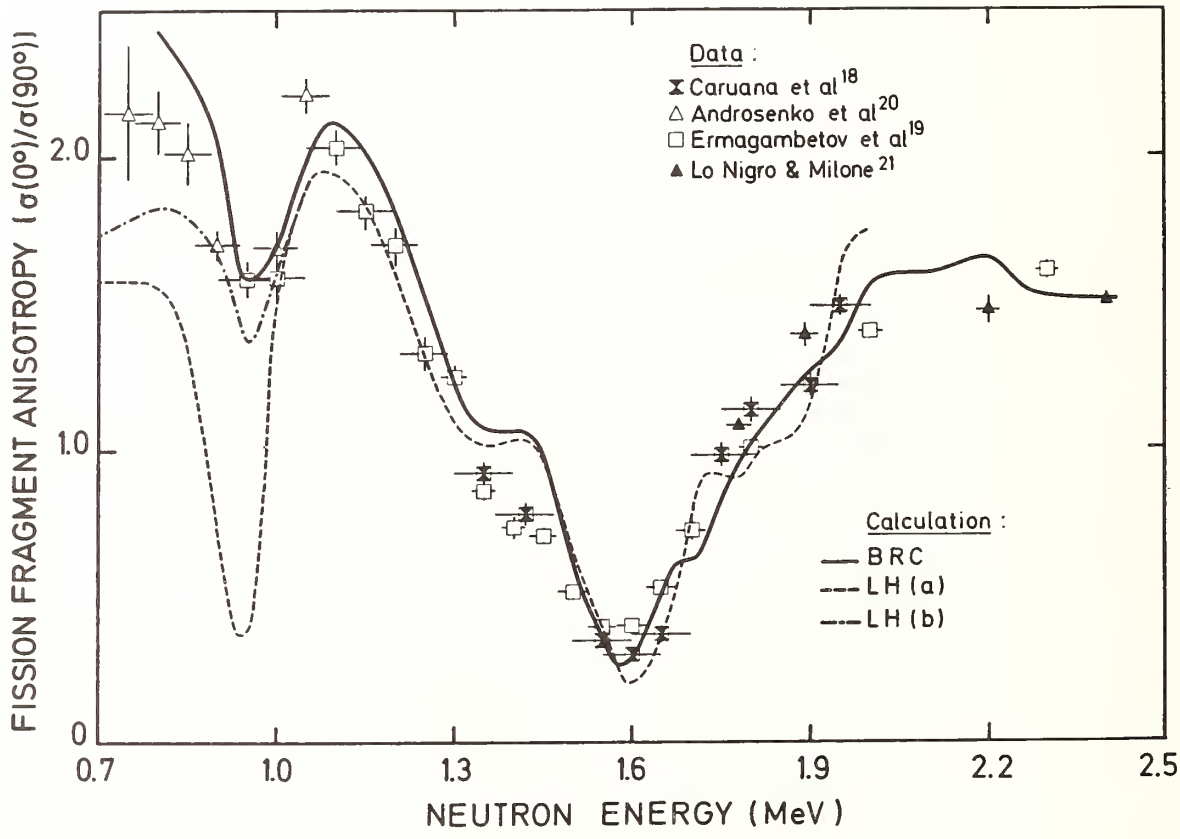

Fig.4. Fission fragment anisotropies.

Discussion

It is clear from both analyses that it is possible to find a set of parameters which leads to predicted cross sections consistent with the experimental data. However it is also clear from tables 1 and 2

fission cross section data from Plattard et al.[17] show a broad peak at this energy which is consistent with the experimental angular distribution data[19,20]. These data can be reproduced with a K = 7/2 barrier in which the outer minimum is too shallow to include a vibrational resonance as in the BRC analysis and Lucas Heights option (b) which, for this case, used the BRC parameters for the 7/2$^-$ band. The broad peak

in the fission cross section corresponds in excitation to the second outer peak of the fission barrier. An alternative explanation to the K = 7/2 barrier can be presented for the structure at 0.95 MeV. The second possibility is that there is a concentration of J = 1/2 strength at this energy because of coupling to compound nuclear states in the first well. If this is the explanation, it cannot be incorporated in the present analyses.

3. The very large resonance at 1.6 MeV which also corresponds to the minimum in the anisotropy results from a vibrational state within the outer well of a K = 3/2 fission barrier, in confirmation of many previous analyses. Presently the interest is in the details and the interpretation of the fine structure superimposed on this peak (figure 5). In fact, the first argument for the triple humped fission barrier for the thorium nuclei was based on the spacing of the fine structure peaks. Blons et al.[15] associated each of these with the partial fission cross section through one of the rotational members of the K = 3/2 barrier. From the spacing of the peaks they derived a moment of inertia constant which was significantly smaller than that for a nucleus within the second well of a double humped fission barrier and was consistent with a more deformed nucleus. Unfortunately, the present analyses disagree with this interpretation and confirm the previous conclusion of Caruana et al.[15]. To fit simultaneously both the fission fragment angular distributions[27] and the absolute magnitude of the fission cross section the shape of the fission barrier was such that the partial cross section through any channel (JKπ) had a FWHM of at least 40 keV for the 1.6 MeV peak. In other words it was not possible to fit the structures with experimental FWHM's of 7 keV and reproduce the magnitude of the fission cross section (Figure 5). Furthermore, although both the present analyses can be criticised because of the large number of adjustable parameters this objection does not alter this basic incompatibility. Consequently, the fine structures must be due to other effects which have not been incorporated in the analyses.

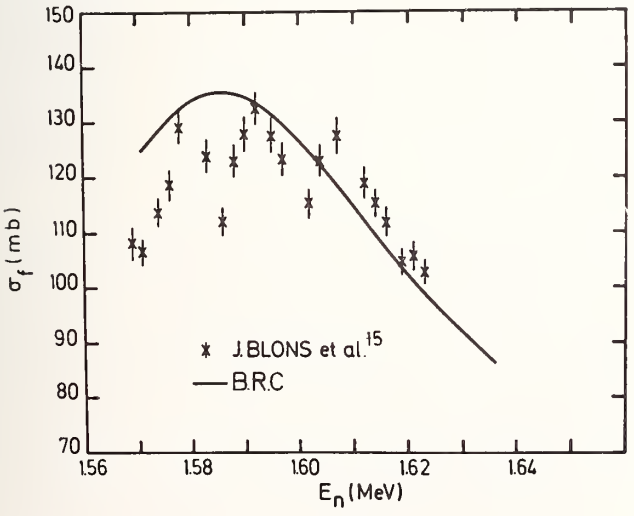

Fig.5. Detail of the experimental and calculated (BRC) fission cross section near E_n = 1.6 MeV.

4. The experimental fission cross section decreases above 2.2 MeV. Neither analysis reproduced this effect. In fact, the calculated cross sections continue to increase because of the rapid increase in the number of open fission channels. One way of reducing this effect tried in the BRC analysis was to increase the inelastic scattering competition above 2.2 MeV. However, it was always apparent that this type of analysis which is based on discrete nuclear levels, becomes unreliable at energies significantly higher than those where these data have been obtained.

5. The striking feature of all fission barriers in tables 1 and 2, is that not one, despite their number, has a shape similar to those that were derived when symmetric deformations only were considered in the calculation of the potential energy surface. Whereas these calculations gave rise to a very low inner peak, the second outer peaks in the barriers from both analyses were similar in height to the outermost peak and all intermediate wells were extremely shallow. In fact, the barriers derived in both analyses are consistent in shape with the triple humped barrier derived when mass asymmetric deformations are considered.

Conclusion

Two separate analyses have been made of the neutron data for ^{232}Th and both have been successful in reproducing most of the experimental data. However, the fission barrier parameters derived are different and both analyses can be criticised because of the large number of fission barriers employed. In fact, the real situation is probably more simple than in either of the two solutions presented. Despite this criticism, the analyses do reveal many of the underlying details of the neutron fission of ^{232}Th and contribute to the growing evidence for a triple humped fission barrier in the thorium region. The details of the data for the neutron fission of ^{230}Th are less complex than those for ^{232}Th and this case presents a better opportunity to arrive at a unique description of the process. When the ^{230}Th case has been resolved, the additional data thereby obtained should allow a fresh re-examination of the data for ^{232}Th.

Acknowledgements

One of the authors, J.W.B., would like to thank the CEA for its hospitality during an attachment at Bruyères-le-Châtel.

References

1. P. Möller and J.R. Nix, IAEA Vienna, "Physics and Chemistry of Fission" Rochester (1973) Vol.1 p. 403.

2. IAEA Vienna "Physics and Chemistry of Fission" Jülich (1979)
D. Paya - Paper B6
B. Leroux, G. Barreau, A. Sicre, T. Benfougal, F. Caĭtucoli, T.P. Doan and G.D. James - Paper B8
J. Blons, C. Mazur, D. Paya and M. Ribrag - Paper B9
J. Blons, C. Mazur, D. Paya and M. Ribrag - Paper B10
S. Plattard, G.F. Auchampaugh, N.W. Hill, R.B. Perez and G. de Saussure - Paper B11
J.W. Boldeman, R.L. Walsh and A.R. de L. Musgrove - Paper B13.

3. W. Hauser and H. Feshbach, Phys. Rev. 87 (1952) 366.

4. H. Abou Yehia, J. Jary and J. Trochon, Report INDC(FR) 34/L - NEANDC(E) 204 "L" (1979).

5. Ch. Lagrange, Bruyères-le-Châtel, Private communication.

6. P.A. Moldauer, ANL/NDM-40 (1978).

7. H.M. Hofmann, J. Richert, J.W. Tepel and H.A. Weidenmüller, Annals of Physics 90 (1975) 403.

8. P.A. Moldauer, Nucl. Phys. 47, (1963) 65.

9. W.K. Bertram, Aust. J. of Phys. 31 (1978) 151.

10. A. Gilbert and A.G.W. Cameron, Can. J. Physics 43 (1965)/466.

11. J.M. Blatt and V.E. Weisskopf, Theoretical Nuclear Physics, Ed. Wiley (1952).

12. J.D. Cramer and J.R. Nix, Phys. Rev. C2 (1970) 1048.

13. J. Dudek, Nucl. Phys. A194 (1972) 552.

14. R.W. Lamphere,Nucl. Phys. 38 (1962) 561.

15. J. Blons, C. Mazur and D. Paya, Phys. Rev. Lett. Vol.35 (1975) 1749 and note CEA-N-1959.

16. J.W. Behrens and J.C. Browne, Phys. Lett. Vol. 69B (1977) 278.

17. S. Plattard et al. Private communication and Ref.2

18. J. Caruana, J.W. Boldeman and R.L. Walsh, Nucl. Phys. A285 (1977) 205.

19. S.B. Ermagambetov and G.N. Smirenkin, Sov. J. of Nucl. Phys. Vol.11 (1970) 646.

20. Kh. D. Androsenko and G.N. Smirenkin JETP Letters 19 (1974) 199.

21. S. Lo Nigro and C. Milone, Nucl. Physics A96 (1967) 617.

22. M. Lindner, R.J. Nagle and J.H. Landrum, Nucl. Sc. Eng. 59 (1976) 381.

23. J. Meadows, W. Poenitz, A. Smith, D. Smith and J. Whalen, ANL/NDM-35 (1978).

24. H.M. Jain, H.P. Anand, M.L. Jhingan, R.N. Jindal, V.C. Deniz and M.K. Mehta, Int. Conf. on Neutron Physics (Harwell 1978).

25. J.A. Miskel, K.V. Marsh, M. Lindner and R.L. Nagle, Phys. Rev. 128 (1962) 2717.

26. J.F. Barry, L.P.O' Connor and J.L. Perkin, Proc. Phys. Soc. (London) (1959) 685.

27. G. Barreau, Thèse de Doctorat d'Etat.Bordeaux - Gradignan University (1977).

MEASUREMENT OF THE INTEGRAL CAPTURE AND FISSION CROSS SECTIONS FOR ^{232}TH IN THE CFRMF

R. A. Anderl and Y. D. Harker
Idaho National Engineering Laboratory
EG&G Idaho
Idaho Falls, Idaho 83415, USA

The recent evaluation of the cross-section data bases for ^{232}Th capture and fission emphasized significant normalization discrepancies between the available differential data. To help resolve the normalization discrepancies, the capture and fission integral cross sections have been measured for ^{232}Th in the fast neutron zone of the Coupled Fast Reactivity Measurements Facility (CFRMF). The cross sections are derived from the radiometric determination of the saturation reaction rates for fission and capture based on the Ge(Li) spectrometric measurement of the absolute gamma emission rates of the 537-keV and 1596-keV lines in the ^{140}Ba - ^{140}La decay and the 311.9-keV line in the ^{233}Pa decay. For capture and fission, respectively, the measured integral cross sections are 291 mb ± 3% and 19.6 mb ± 5%. The ratios of the integral cross sections computed with ENDF/B-IV thorium cross sections and the CFRMF neutron spectrum to the above values are 0.99 for capture and 0.90 for fission.

[^{232}Th(n,f), ^{232}Th(n,γ), Integral Cross Sections, CFRMF, ENDF/B]

Introduction

Recent interest in developing alternate fuel cycles for advanced reactor systems has focused on the use of ^{232}Th as a fertile material for production of ^{233}U fuel. Because a realistic prediction of the production of ^{233}U in various advanced reactor systems (LMFBR, LWBR, and others) depends on an accurate description of the ^{232}Th cross sections, much effort has been expended recently on the measurement and evaluation of the neutron cross sections for ^{232}Th. Meadows et al.[1], have prepared the ^{232}Th cross section file for ENDF/B-V using data obtained up through 1977. As stated by Meadows et al., the cross section data for the ^{232}Th (n,γ) and ^{232}Th (n,f) reactions are very poor and of dubious quality, respectively. Typically, few absolute cross-section measurements are available [none for ^{232}Th (n,γ)]. The data consist primarily of differential cross sections derived from ratio measurements. A comparison of the ^{232}Th (n,γ) cross sections obtained from ratio measurements shows discrepancies in the energy range 20 keV to 1000 keV of up to 50% between the different sets of differential data. For ^{232}Th (n,f), the cross sections based on ratio measurements have normalization problems and energy scale problems in the threshold region. In addition, when the fission ratio-determined cross sections are compared to the little absolute data available, shape discrepancies are noted for energies <1.5 MeV and >1.3 MeV. To resolve the discrepancies, Meadows et al.[1] emphasized the need for better absolute and relative measurements.

Integral measurements in well-characterized neutron fields[2], the ^{235}U fission neutron spectrum, and the fast neutron fields of the CFRMF, $\sum\sum$ facility, and BIG-10, would be helpful in resolving these normalization uncertainties and in testing the differential data. Meadows et al.[1] reference several integral fission measurements made in a reference ^{235}U fission neutron spectrum. The authors note that the measured values range from 71 mb - 83 mb and are consistent with the value of 72.8 mb calculated from their new evaluation and the ENDF/B-V ^{235}U fission neutron spectrum as compared to a value of 69.0 mb calculated using ENDF/B-IV data. No similar integral measurements are identified in the Meadows[1] evaluation for ^{232}Th (n,γ).

Beck et al.[3] have reviewed recently the fast integral data for ^{233}U and ^{232}Th. Included in the review are the results of measurements of ^{232}Th capture and fission reaction rates relative to the ^{235}U fission rate made in the Advanced Epithermal Thorium Reactor (AETR) critical experiments, in the Gas Cooled Fast Reactor Experiments for the ZPR criticals and in recent ZPPR experiments. The results reported as C/E ratios (calculated to experiment with ENDF/B-IV cross-sections used to generate the calculated ^{232}Th (n,f)/^{235}U(n,f) and ^{232}Th(n,γ)/^{235}U(n,f) ratios) indicate a spread of 0.93 to 1.12 for ^{232}Th (n,f) and 0.99 to 1.04 for ^{232}Th(n,γ).

In addition, Green[4] has reported an integral capture measurement for ^{232}Th irradiated with ^{252}Cf spontaneous fission neutrons. His measured value is approximately 13% lower than that calculated using the capture cross section from BNL-325 and his Complex Spectrum for ^{252}Cf fission neutrons.

To help in the resolution of the normalization discrepancies for the capture and fission cross sections for ^{232}Th, we have made integral capture and fission measurements in the fast neutron field of the CFRMF. The purpose of this paper is to present the necessary experimental details and the results of these measurements. More complete information is found in reference 5.

Experimental Details

Irradiation Facility

Irradiation of the thorium foils took place in the fast neutron field of the CFRMF.[6,7,8] Capable of operating at a power level of 100 KW, the reactor produces a neutron flux level of ~10^{12}n/cm^2-sec in the fast neutron experiment region. Spanning the intermediate neutron energy range (1 keV < E_n < 1 MeV) with a mean energy of 0.72 MeV, the CFRMF neutron spectrum is similar to that in a fast reactor. The neutron energy spectrum has been extensively studied by proton-recoil neutron spectrometry, ^{6}Li neutron spectrometry and neutronic calculations.

This facility has been a cornerstone irradiation facility for the Interlaboratory LMFBR Reactor Rate (ILRR) program for precise dosimetry reaction-rate measurements and for an extensive series of integral measurements for "fission-product class" materials.[6] Consequently, it has been selected by the Cross Sections Evaluation Working Group (CSEWG) as a benchmark field for integral testing of data for the Evaluated Nuclear Data File (ENDF/B).

Irradiation Package

A six hour irradiation was made in the CFRMF for each of two Reactor Experiments, 99.96% pure, 1.27 cm diameter thorium metal foils (one - 161.6 mg, 0.01 cm thick; two - 22.2 mg, 0.00127 cm thick). Each foil was wrapped in three thicknesses of 0.00127 cm aluminum foil to minimize the loss of fission gas and

stop all released fragments in the aluminum cladding. Each irradiation package included three 0.4 cm diameter, 0.0127 cm thick gold foils for monitoring the reactor power level. One gold foil was located 2.54 cm above the sample midplane and the other two were located at midplane but displaced 1 cm radially from the sample center.

Post-Irradiation Ge(Li) Spectrometry

Gamma-ray spectra were measured for each of the aluminum-clad thorium foils and the gold monitors, each positioned at a calibrated location in a Ge(Li) spectrometer (65 cm^3 closed-end coaxial detector). The Ge(Li) spectrometer and gamma-ray counting techniques followed are described in references 9 and 10. For the irradiation 1 thorium foil (161.6 mg) six spectra were measured at a source to detector distance of 25 cm for times ranging from 2 days to 21 days after the end of irradiation. For the irradiation 2 thorium foil (22.2 mg), five spectra were measured at source to detector distances of 25 cm and 10 cm for times ranging from 1 day to 110 days after the end of irradiation.

Analysis and Results

Reaction-Rate Determination

Method. The method used for the determination of the thorium capture and fission reaction rates is the radiometric method, described in some detail in references 9 and 11. Briefly, saturation reaction rates are determined by the following expression

$$RR = \frac{A}{b \cdot \varepsilon} \cdot \frac{1}{N} \cdot \frac{1}{Y} \cdot D \cdot \frac{1}{\delta} ,$$

Where A is the measured peak area, b is the gamma-ray branching ratio, ε is the detector efficiency for a point source, N is the number of atoms for isotope of interest in the sample, Y is the fission yield, D is a decay/count factor and δ includes necessary correction factors.

For this specific experiment, the capture reaction rate is based on the absolute measurement of the gamma-emission rate of the 311.9-keV gamma ray from the β^- decay of 27 day ^{233}Pa. The ^{233}Pa activity is produced from the β^- decay of 22 min ^{233}Th which is the neutron capture product for ^{232}Th. The ^{233}Pa activity was measured after a sufficient time to allow for the decay of the ^{233}Th. The fission reaction rate is based on the absolute measurement of the gamma-emission rates of the 537.4-keV gamma ray from ^{140}Ba β^- decay and of the 1596-keV gamma ray from ^{140}La β^- decay. The capture reaction rate for the gold monitor, ^{197}Au, is based on the measurement of the 411.8-keV gamma ray from the β^- decay of ^{198}Au. Decay data for these radionuclides used in the present analysis are summarized in Table I. With the exception of the half-life and branching ratio for ^{233}Pa which are from references 12 and 13 respectively, the decay data were taken from reference 11. A fission yield of 0.0777 $\pm$ 4% was used for ^{140}Ba and ^{140}La.[14]

Peak area determinations were made with the GAUSS-V computer program[15] implemented on a PDP-15 interactive graphics computer system. This analysis was consistent with that used in the measurements used to generate the efficiency curves for the Ge(Li) spectrometer as described by Gehrke et al.[10] Peak efficiencies used in the present analysis were interpolated values based on the previously measured efficiency curves.

Table I. Decay Data for ^{198}Au, ^{233}Pa, ^{140}Ba, ^{140}La

Radionuclide	$T_{1/2}$	E_γ	b_γ
^{193}Au	2.6956(10)[a] d	411.794(7)	95.52(5)
^{233}Pa	26.96(5)d	311.9	38.6(5)
^{140}Ba	12.789(6)d	537.35(5)	24.4(3)
^{140}La	40.26(2)h	1596.18(5)	95.40(8)

[a]Uncertainty in last significant digits as quoted in the references.

Correction Factors. Correction factors were estimated to account for gamma-ray self absorption in the sample foils, for gamma-ray attenuation in the aluminum cladding, for random summing/live timer losses, for coincidence-summing losses, for interferring gamma rays and for neutron resonance self-shielding. Gamma-ray self-absorption corrections of 2.6% and 1.0% were estimated for the 311.9-keV and 537.4-keV lines from the 0.01 cm thick thorium foil. All other gamma-ray self absorption and attenuation corrections for the 0.01 cm and 0.0013 cm thorium foils were less than 0.3%. The values of the mass-absorption coefficients used in the determination of these corrections were obtained using quadration log-log interpolation of the total mass absorption tables of Storm and Israel.[16]

Correction factors for random summing and the live-timer were taken from data available for the spectrometer. For the thorium related gamma-ray measurements these corrections ranged from 1.0% to 1.8% for the 161.6 mg foil and 0% to 0.4% for the 22.2 mg foil.

Two additional factors affect the accurate determination of the fission rate of Th based on a measurement of the gamma-emission rates of the ^{140}La 1596-keV line. As pointed out by Debertin et al.[17], ^{208}Tl which is at the end of the decay chain of natural thorium emits 2615 keV radiation, giving rise to a double escape peak at 1593 keV. This peak, also observed in the background spectrum due to Th present in the environment, interfers with the ^{140}La 1596-keV peak and may contribute to an error in the accurate determination of the peak area of the 1596-keV peak. Secondly, 1596-keV gammas from the ^{140}La decay are emitted in cascade with the lower energy gamma rays. For small source-to-detector distances, this results in coincidence summation losses from the 1596-keV peak. These factors were considered in the analysis as follows. The contribution of the 1593-keV interferring peak to the Gaussian area determination for the 1596-keV peak was minimized by fitting the peak with the low energy Gaussian fit limit within 1 keV of the peak channel. Fission rates computed from the ^{140}La 1596-keV peaks analyzed in this way were found to be consistent with those based on the ^{140}Ba 537-keV peaks. A correction of 1% for coincidence summing losses was required for only one of the spectrum analyses for the 0.00127 cm thick foil. This correction was determined by Greenwood[11] for a source to detector distance of 10 cm for the Ge(Li) spectrometer used in the present measurements.

Even though the CFRMF neutron spectrum in the fast zone is relatively hard, there are a significant number of neutrons in the resonance region such that

neutron resonance self-shielding corrections are required for radiative capture in thorium foils used in the present experiment. Resonance self-shielding corrections were estimated as follows. Using ENDF/B-IV data 69 group (0.25 lethargy) capture cross sections were generated with the PHROG[18] code for samples which were infinitely dilute, infinite diameter disc of thickness 0.01 cm, and infinite diameter disc of thickness 0.00127 cm. Each of these multi-group cross sections was folded with a multigroup representation of the CFRMF fast zone neutron spectrum. The spectral-averaged cross sections for the thick samples relative to that computed from the infinitely dilute sample give a measure of the integral self-shielding correction factor. For the 0.01 cm and 0.00127 cm samples, the radiative-capture self-shielding correction factors were estimated to be 0.951 and 0.987, respectively.

Reaction-Rate Results

Summarized in Table II are infinitely dilute reaction rates for ^{232}Th capture and fission in the CFRMF. The thorium capture and fission reaction rates listed under the Irradiation 1 column are the averages of values determined for each gamma ray from each of six spectra analyzed for the 161.1 mg foil. Listed under the Irradiation 2 column are average reaction rates based on the analyses of five gamma spectra for capture and three gamma spectra for fission. The thorium reaction rates listed include, where applicable, corrections for gamma-ray self-absorption, external gamma absorption, random summing/live-timer losses, coincidence summing and neutron resonance self-shielding.

In parentheses next to the thorium reaction rates are estimates of the total errors and reduced errors for the measured quantities. Details concerning the error propagation can be found in reference 5. It may be noted that the dominant errors contributing to the ^{232}Th(n,γ) reaction rate uncertainty are 1.3% in the branching ratio and 1.5% in the peak efficiency for the 311.9-keV line. Dominant errors contributing to the ^{232}Th(n,f) reaction-rate uncertainty are the 4% fission yield error and 1.5% in the peak efficiencies for the 537.4-keV and 1596.2-keV lines.

Also included in Table II are estimates of the ^{197}Au(n,γ) reaction rates at the sample location for each irradiation. These estimates were made by first correcting by 1% the reaction rates determined for each of the three monitor foils to account for axial and radial flux gradients[8] and then averaging together the three reaction rates. The gold reaction rates do not include corrections for gamma ray self absorption or neutron resonance self-shielding.

Neutron Flux Determination

The neutron flux for each irradiation was determined by correlating the sample-position estimates of the ^{197}Au (n,γ) reaction rates given in Table II to that determined by Harker[6] for a 0.0127 cm gold foil at the sample position. Harker[6] in a separate experiment had correlated the "sample position" 0.0127 cm gold reaction rate to that of a 0.005 cm gold foil at the ILRR monitor position (2.54 cm above midplane). His measurements yielded (4.785 $\pm$ 0.003) X 10^{-14} rps/a for the 0.005 cm foil and (4.859 $\pm$ 0.015) X 10^{-14} rps/a for the 0.0127 cm gold foil. From Rogers et al.[8] a reaction rate of 3.008 X 10^{-14} rps/a for the 0.005 cm ILRR monitor corresponds to a midplane flux of 7.9 X 10^{10} n/cm^2-sec $\pm$ 1.9%. Based on these correlating data and the estimated reaction rates from the present experiments, the neutron fluxes for the present irradiations were determined to be 8.78 X 10^{11}n/cm^2-sec $\pm$ (2.7%, 1.9%) for irradiation 1 and 8.73 X 10^{11}n/cm^2-sec $\pm$ (2.5%, 1.6%) for irradiation 2. In parenthesis are two error values, the first an estimate of the total error in the flux determination and the second an estimate of the error without the 1.9% flux uncertainty from the ILRR fission-chamber measurements.

Table II. Reaction rates for ^{232}Th(n,γ), ^{232}Th(n,f) and ^{197}Au(n,γ) in the CFRMF

Reaction -Eγ	Reaction Rate (reactions/sec-atom)X10^{14} Irradiation 1	Irradiation 2
^{232}Th(n,γ)		
- 311.9	25.64[a] (2.5[a],1.5[b],0.3[c])	25.31 (2.2,1.0,0.4)
^{232}Th(n,f)		
- 537.4	1.716 (4.5,2.0,0.5)	1.727 (4.7,2.5,1.4)
-1596.2	1.715 (4.3,1.6,0.4)	1.706 (4.5,2.1,1.2)
-(537+1596)	1.72[d] (4.2[d],1.2[e])	1.71 (4.3,1.6)
^{197}Au(n,γ)		
- 411.8	33.9 (1.9,1.1)	33.74 (1.6,0.4)

[a] Total percentage error for the above reaction rate. Definition applies for all reaction rates listed.

[b] Reduced error which for Th(n,γ) case does not include a 1.5% peak efficiency error or a 1.3% branching ratio error. For the Th(n,f) case the 4% fission yield error is excluded. For the Au(n,γ) case the 1.5% peak efficiency error is excluded.

[c] Internal error computed from the averaging indicated in the text.

[d] Total percentage error for the above reaction rate which is the weighted average of the above two rates.

[e] Reduced error which does not include the 4% fission yield error.

Integral Cross Sections

Integral cross sections for capture and fission of ^{232}Th irradiated in the CFRMF were obtained by dividing the capture and fission reaction rates given in Table II by the corresponding neutron fluxes given in the previous paragraph. The fission rates used in Table II were those based on the (537+1596) averages. For the first irradiation the integral capture and fission cross sections were determined to be 292 mb $\pm$ (3.7%, 2.4%) and 19.5 mb $\pm$ (5%, 2.3%). The first error in parenthesis for each of these cross sections is the total percentage error at the 1-sigma level. The second error in parenthesis for the capture cross section does not include the 1.5% peak efficiency, 1.3% branching ratio and 1.9% fission-chamber flux uncertainties. For the fission cross section the second error does not include the 4% fission yield error and the 1.9% fission chamber flux uncertainty. Based on averages of the results from both irradiation experiments, the measured integral capture cross section for ^{232}Th in the CFRMF is 291 mb $\pm$ 3.1%. Similarly, the measured integral fission cross section

for ^{232}Th in the CFRMF is 19.6 mb ± 4.7%.

Discussion

As stated earlier, integral measurements are helpful in sorting out normalization difficulties with differential data. Based on the measured integral data from this experiment a simple integral test of the ENDF/B-IV capture and fission cross sections was made as follows. Estimates of the ENDF/B-IV spectral-averaged cross sections were computed using the 620 group capture and fission cross sections from the ENDF/B-IV Dosimetry Library[17] and a 620 group representation of the CFRMF neutron spectrum as given by Harker et al.[6] Calculated integral cross sections are 287 mb for capture and 17.6 mb for fission. The resultant calculated-to-experimental ratios are then 0.99 for capture and 0.90 for fission. These ratios indicate that the integral values for capture deviate by less than the uncertainty in the cross section measurement. However, for fission the deviation is approximately twice the uncertainty in the measured integral value. The capture calculated-to-experimental ratio from the present work is consistent with the corresponding ratios given by Beck et al.[3] However the fission calculated-to-measured ratio is consistent with the lower ratio values given in that review of integral data. The present measurements suggest that the normalization of the ENDF/B-IV capture cross section is consistent with the present integral measurement but the normalization of the ENDF/B-IV fission cross section is too low by 10%.

With the advent of covariance files for many cross sections important to reactor technology the measurements presented here can be used for other than simple integral checks of ENDF/B data, namely, the adjustment of multigroup cross sections based on measured reaction rates. Such analyses require as a-priori information: a multigroup representation of the neutron spectrum, a flux covariance matrix which realistically treats the uncertainties and energy dependent correlations in the flux, multigroup representations of all cross sections and covariance matrices for those cross sections. The results of such analyses would be helpful in evaluating the point-wise differential data base.

Acknowledgements

This work was performed under the auspices of the U.S. D.O.E.

References

1. J. Meadows. W. Poenitz, A. Smith, D. Smith, J. Whalen, R. Howerton, "Evaluated Nuclear Data File of Th-232", U.S. DOE Report ANL/NDM-35 (February 1978).

2. J. Grundl and C. Eisenhauer, "Benchmark Neutron Fields for Reactor Dosimetry", Proceedings of IAEA Consultants Meeting on Integral Cross-Section Measurements in Standard Neutron Fields for Reactor Dosimetry, IAEA, Vienna, Austria, November 15-19, 1976, p.53, IAEA-208 Vol. 1.

3. C. L. Beck, M. J. Lineberry, R. W. Schaefer, S. G. Carpenter, D. C. Wade, and G. A. Ducat, "An Evaluation of Fast Integral Data Related to ^{233}U and Thorium", Proceedings of an American Nuclear Society Topical Meeting on Advances in Reactor Physics, Gatlinburg, Tennessee, April 10-12 1978, p. 27, CONF-780401 (June 1978).

4. L. Green, Nucl. Sci. Eng. 58, 361-370 (1975).

5. R. A. Anderl, "Integral Measurements for ^{232}Th in the CFRMF", EG&G Idaho Internal Technical Report RE-P-79-060 (July, 1979).

6. Y. D. Harker, J W Rogers and D. A. Millsap, "Fission Product and Reactor Dosimetry Studies at Coupled Fast Reactivity Measurements Facility", U.S. DOE Report TREE-1259 (March 1978).

7. J W Rogers, D. A. Millsap and Y. D. Harker, Nucl. Tech. 25, 330 (1975).

8. J W Rogers, D. A. Millsap and Y. D. Harker, "The Coupled Fast Reactivity Measurements Facility (CFRMF)", Proceedings of IAEA Consultants Meeting on Integral Cross-Section Measurements in Standard Neutron Fields for Reactor Dosimetry, IAEA, Vienna, Austria, November 15-19, 1976, p. 117, IAEA-208 Vol. II.

9. R. C. Greenwood, R. G. Helmer, J W Rogers, N. D. Dudey, R. J. Popek, L. S. Kellogg and W. H. Zimmer, Nucl. Tech. 25, 275 (1975).

10. R. J. Gehrke, R. G. Helmer, and R. C. Greenwood, Nucl. Instru. Methods 147, 405 (1977).

11. R. C. Greenwood, R. G. Helmer, J W Rogers, R. J. Popek,, R. R. Heinrich, N. D. Dudey, L. S. Kellogg and W. H. Zimmer, "Radiometric Reaction-Rate Measurements in CFRMF and Big-10", NUREG/CP-0004, Vol. 3, 1207 (1978).

12. Y. A. Ellis, Nucl. Data, Sect. B, 6 257 (1971).

13. R. J. Gehrke, R. G. Helmer and C. W. Reich, Nucl. Sci. Eng. 70, 298 (1979).

14. M. E. Meek and B. F. Rider, "Compilation of fission Product Yields, Vallecitos Nuclear Center", NEDO-12154-2 (January 1977).

15. R. G. Helmer and M. H. Putnam, ANCR-1043, U.S. Atomic Energy Commission (1972).

16. E. Storm and H. I. Israel, Nucl. Data Tables A7, 565 (1970).

17. K. Debertin, U. Schotzig and K. F. Walz, Nucl. Sci. Eng. 64, 784 (1977).

18. R. L. Curtis, F. J. Wheeler, G. L. Singer and R. A. Grimesey, "PHROG - A Fortran IV Program to Generate Fast Neutron Spectra and Average Multigroup Constants", IN-1435, Idaho Nuclear Corporation (April 1971).

19. B. A. Magurno, Editor, "ENDF/B-IV Dosimetry File", BNL-NCS-50446 (April 1975).

THE FISSION CROSS SECTION OF ^{230}Th AND ^{232}Th RELATIVE TO ^{235}U

J. W. Meadows
Argonne National Laboratory
9700 South Cass Avenue
Argonne, Illinois 60439, USA

The fission cross sections of ^{230}Th and ^{232}Th have been measured relative to ^{235}U from near threshold to near 10 MeV. The weights of the thorium samples were determined by isotopic dilution. The weight of the uranium deposit was based on specific activity measurements of a ^{234}U-^{235}U mixture and low geometry alpha counting. Corrections were made for thermal background, loss of fragments in the deposits, neutron scattering in the detector assembly, sample geometry, sample composition and the spectrum of the neutron source. Generally the systematic errors were ~1%. The combined systematic and statistical errors were typically 1.5%.

(NUCLEAR REACTIONS, FISSION ^{230}Th(n,f), ^{232}Th(n,f), cross sections relative to ^{235}U(n,f), threshold to 10 MeV.)

Introduction

Several years ago a measurement program was started at the ANL Fast Neutron Generator with the goal of measuring the fission cross sections of the longer-lived fissionable isotopes relative to ^{235}U with accuracies of the order of 1 percent. This paper reports the results for ^{230}Th and ^{232}Th. These isotopes have received little attention in the past, particularly when compared to the more common uranium isotopes. Inspection of the CSISRS file[1] does show a number of data sets for the ^{232}Th fission cross section including two recent ratio measurements [2,3] but there are only four references[4-7] to ^{230}Th and the agreement between the measurements is poor.

Experimental Method

The experimental method and techniques for making those measurements have been described previously.[8] Briefly, the relative fission rates of pairs of ^{235}U and ^{230}Th or ^{232}Th samples were measured by placing them back-to-back in a double ionization chamber positioned near a monoenergetic neutron source. Neutrons with energies above 5 MeV were produced by the D(d,n)^{3}He reaction. Lower energy neutrons were produced by the ^{7}Li(p,n)^{7}Be reaction. A pulsed and bunched charged-particle beam was used to obtain a pulsed-neutron source and fast timing techniques selected those fissions suitably correlated with the neutron pulse. The data was stored in two time-by-pulse-height arrays for later inspection when time windows and pulse-height discrimination levels were set. Windows were set over the time peak and also to one side to permit simultaneous measurement of any background due to thermal and epi-thermal room-return neutrons. The data from the individual detectors was corrected for the discriminator bias and background. The fission ratios were corrected for neutrons from secondary source reactions such as ^{7}Li(p,pn)^{6}Li, ^{7}Li(p,n)^{7}Be* and D(d,pn)D and for scattering from the ionization chamber and the neutron source assembly. The differences in the geometry and the neutron transmission for the two samples were eliminated by making a second measurement with the sample positions interchanged. Although this greatly reduced the effect of momentum transfer, the fission ratios were explicitly corrected for residual momentum effects as well as deposit thickness and fission fragment angular distribution effects. The background produced by (d,n) reactions with the gas target assembly was measured with an empty gas cell before and after each measurement with a full cell.

Table I. The Isotopic Analyses of the Samples in Weight Percent.

Material	U-235			Th-230	Th-232	
Sample No. / Isotope	5-2	3	SST-5	(51 thru 54)	(31 thru 36)	1
230	____	____	____	99.516	0.383	0.0
232	____	____	____	0.484	99.617	100.0
234	1.028	0.028	0.852	____	____	____
235	98.403	99.856	93.244	____	____	____
236	0.447	0.062	0.334	____	____	____
238	0.122	0.054	5.570	____	____	____
Area Density mg Th/U/cm^2	0.164	0.077	0.081	0.075 - 0.155	0.131 - 0.569	0.127

Samples

Most of the samples were prepared by molecular depositon using a method similar to that described in Ref. 9. Thin layers of uranium or thorium, 2.54 cm in diameter, were deposited onto 0.25 mm thick stainless or 0.13 mm thick platinium plates. One of the uranium deposits, SST5, was made by vacuum evaporation of UF_4 and one of the thorium samples, Th-232-1, was made by evaporation of thorium metal. The isotopic analyses of all materials used is given in Table I.

Absolute fission-cross-section ratios were measured using ^{235}U sample 5-2. The weight used for this deposit, based on specific activity measurements of the original material and on low geometry alpha counting, was 0.8316 mg. This deposit was one of those used in a recent series of measurements where reference ^{235}U deposits from several laboratories were intercompared.[10] The weight based on the intercomparison was 0.833 mg. The other uranium deposits were only used in shape measurements.

The weights of most of the thorium samples were based on specific activity measurements. Enough ^{230}Th was added to the ^{232}Th material to give a convenient alpha count rate and a number of ^{230}Th and ^{232}Th deposits were prepared. The alpha count rate of each deposit was measured in a low geometry alpha counter whose geometry factor was calculable from precisely measured dimensions. The weights of some of the deposits were determined by the isotopic dilution technique. The ^{230}Th half-life obtained from the ^{232}Th samples was 75600 ± 330 y. For the ^{230}Th samples it was 75900 ± 300 y. The best previous measurement gave 75200 ± 1600 y.[11] The weight of Th-232-1 was not determined accurately and it was only used for shape measurements.

The exact composition of these deposits is uncertain. The approximate composition of Th-232-1 is probably fairly well represented by ThO. The other thorium deposits should be ThO_2, however the actual weight of the deposits are ~6 percent larger than the weights of ThO_2 calculated from the isotopic dilution results. These deposits were heated to 700 deg. C but that was not high enough to ensure that they would not be slightly hydroscopic so this excess weight suggests that their approximate composition might be closer to $ThO_2 \cdot H_2O$. The composition of uranium samples 5-2 and 3 is unknown but may be some uranyl oxide hydrate.

Deposit Thickness Correction

In principal the deposit thickness correction can be calculated from the deposit composition and fission fragment range and angular distribution data. In practice, as discussed above, the deposit composition may not be known very well and if the correction is significant it is best to measure it for a particular set of samples.

The effects of deposit thickness, fission fragment angular distribution and momentum transfer cannot be separated. Approximate formulas for estimating losses in thin deposits are developed in Ref. 12. In the measurements reported here the ratio of the fission rates of two deposits was obtained by averaging two measurements, one made with the thorium deposit facing the neutron direction and one made with the uranium deposit in that position. Under these conditions the first order momentum terms cancel and the average specific fission rate of the thorium deposit relative to the reference deposit can be approximated by

$$S_{obs} = S_{true}(1 + C_u - C_{Th})$$

$$C = P(\pi/2)\left(\frac{t}{2R} + \frac{R\gamma^2}{4t}\right) \qquad t > R\gamma$$

where t is the deposit thickness, R is the fragment range, γ is approximately the ratio of the incident neutron momentum to the total momentum of the fission fragments and $P(\pi/2)$ is the normalized fragment angular distribution function evaluated at $\pi/2$. $P(\Theta)$ can be expressed as a power series in $\cos^2\Theta$ and for this purpose one term is usually sufficient although additional terms may be necessary in limited energy regions. Coefficients were obtained from data given in Refs. 13 thru 15. For $t > 1.5R\gamma$ the γ^2 term may be dropped and the effective value of R can be obtained from the slope. Specific fission rates were measured for a series of thorium deposits ranging from 0.13 to 0.57 mg Th/cm^2 with the results shown in Fig. 1. The effective value of R was determined to be 5.1 ± 0.3 mg Th/cm^2.

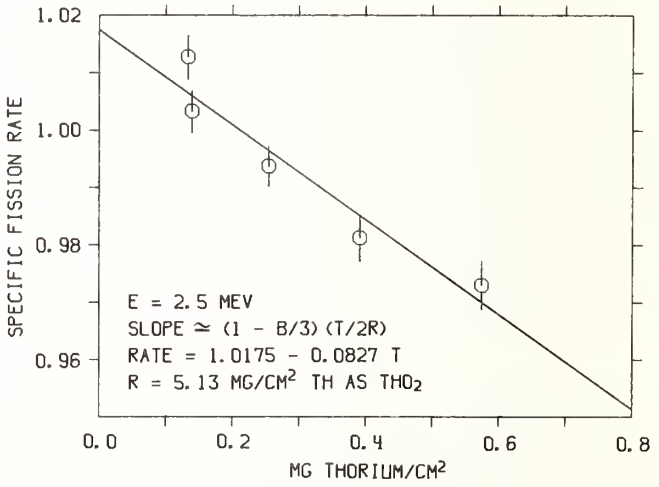

Fig. 1. The dependence of the specific fission rate on deposit thickness for thorium deposits.

Previous measurements for the uranium deposits gave 4.1 mg U/cm^2 for the effective range in sample 3 and 5-2 and 4.7 mg U/cm^2 for SST5.[10]

Calculated ranges based on the data of Alexander and Gazdik[16] and Niday[17] were generally in good agreement. The calculated value for UF_4 was 4.7 mg U/cm^2 in very good agreement with the measurement. In the previous section it was suggested that the composition of the thorium deposits might be approximately represented as $ThO_2 \cdot H_2O$. The calculated range for this material, 5.2 mg Th/cm^2, is in good agreement with the measured value.

Results

The results are shown in Figs. 2 and 3. Points are plotted at average energies and all energy resolutions are full widths at half height of the calculated energy distributions. Error and resolution bars are shown where they exceed the size of the data symbol.

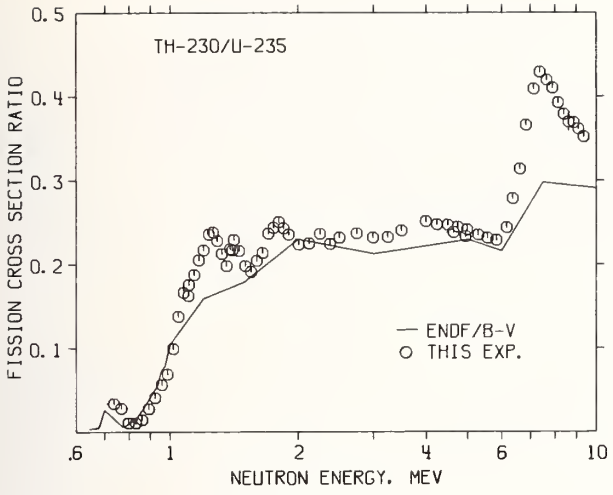

Fig. 2. The ^{230}Th to ^{235}U fission cross section ratios.

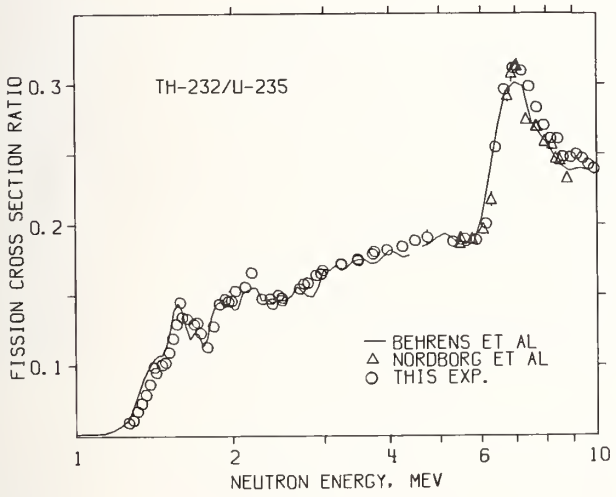

Fig. 3. The ^{232}Th to ^{235}U fission cross section ratios.

Figure 4 shows the combined error, excluding the fission counting errors, as a function of energy for the ^{232}Th measurement. The error for the ^{230}Th measurement is similar. There is a basic error of ~0.8 percent due to the uncertainty in the ratio of the sample masses and an additional 0.2 percent error in the correction for neutron scattering in the detector structure. The large errors near 5 MeV and 10 MeV are caused by the uncertainties in the correction for the lithium and deuteron break-up reactions. The correction for the $^{7}Li(p,n)^{7}Be^{*}$ reaction is significant in the threshold region but its yield relative to the ground state reaction is well known so the error from this source does not exceed 0.5 percent.

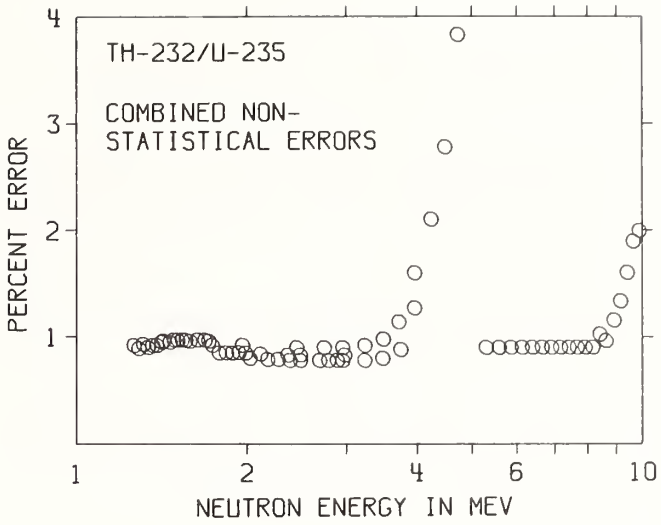

Fig. 4. The energy dependence of the principal systematic errors for the ^{232}Th to ^{235}U fission cross section ratios.

The counting errors are typically 1 percent except in the threshold region where the thorium fission rate was low. Points used for normalization have counting errors of ~0.5 percent. This error includes the counting statistics and also any uncertainty in the extrapolation to account for fission below the bias level. This correction ranged from ~0.5 to ~5 percent depending on the deposit thickness. In making the extrapolation the counts per channel at the bias level were assumed to remain constant down to zero pulse height. It is doubtful if this is true and such a procedure may introduce a systematic error when only one of the fission detectors is considered. However this procedure was used for both detectors and also used in determining the deposit thickness correction so any systematic effect should largely cancel in the ratio. Other corrections and errors are discussed in Ref. 8.

The results for ^{230}Th are shown in Fig. 2. There have been few other measurements for this isotope. Muir et al.[4] made measurements relative to ^{239}Pu using a bomb shot as a pulsed source. When the data from the present experiment is converted to cross sections using ENDF/B-V the agreement is fairly good. The other measurements[5-7] are in very poor agreement.

The results for ^{232}Th are shown in Fig. 3 and compared with two recent ratio measurements. The agreement with the data of Behrens et al.[2] is fair. The two data sets differ by a consistent 3 to 4 percent in magnitude and by ~20 keV in energy in the threshold region. The agreement with the data of Nordborg et al.[3] is fairly good up to ~7 MeV but above the energy the difference is ~5 percent.

Acknowledgment

The author wishes to thank R. J. Armani for his help in preparing the samples and C. L. Callis and A. M. Essling for the isotopic dilution analyses. This work supported by the U. S. Department of Energy.

References

1. Experimental Data File, CSISRS, National Neutron Cross Section Center, Brookhaven National Laboratory.

2. J. W. Behrens, J. W. Magana and J. C. Browne, "Measurement of the Neutron-Induced Fission Cross Section of ^{232}Th Relative to ^{235}U from 0.7 to 30 MeV", UCID-17442, Lawrence Livermore Laboratory (1977).

3. C. Nordborg, H. Conde and L. G. Stroemberg, Proceedings of the International Conference on Neutron Physics, Nuclear Data for Reactors and Other Applied Purposes, p. 910, Harwell, (1978).

4. D. W. Muir and L. R. Vesser, Proceedings of the Third Conference on Neutron Cross Sections and Technology at the University of Tennessee, (March 15-17, 1971), p. 292, CONF-710301(Vol. 1).

5. J. E. Lynn, G. D. James and L. G. Earwaker, Nucl. Phys. A189, 225(1972).

6. M. I. Kazarinova, Yu. S. Zamyatin and V. M. Gorbachev, Soviet Atomic Energy, 8, 125(1960).

7. B. M. Gokhberg, G. A. Otroshchenko and V. A. Shigin, Tr. Tashkentsk. konf. po Mirnomu Ispol'z. At. Energii, Akad. Nauk. Uz. SSR, 1:57(1961). AEC-tr-6398, p. 59.

8. J. W. Meadows, Nucl. Sci. Eng., 68, 360(1978); 65, 171(1978).

9. W. Parker, H. Bildstein and N. Getoff, Nucl. Instr. Methods, 26, 55(1964).

10. W. P. Poenitz, J. W. Meadows and R. J. Armani, "^{235}U Fission Mass and Counting Comparison and Standardization", ANL/NDM-48, Argonne National Laboratory, (1979).

11. R. W. Attree, M. J. Cabell, R. L. Cushing and J. J. Pieroni, Canad. J. Phys. 40, 194(1962).

12. J. W. Meadows, "The Fission Cross Section of ^{239}Pu Relative to ^{235}U from 0.1 to 10 MeV", ANL/NDM-39, Argonne National Laboratory, (1978).

13. R. L. Henkel and J. E. Brolley, Phys. Rev. 103, 1292(1956).

14. J. E. Simmons and R. L. Henkel, Phys. Rev. 120, 198(1960).

15. S. B. Ermagambetov and G. N. Smirenkin, Sov. J. Nucl. Phys. 11, 646(1970).

16. J. M. Alexander and M. F. Gazdik, Phys. Rev. 120, 874(1960).

17. J. B. Niday, Phys. Rev. 121, 1471(1961).

THE EVALUATION OF $^{235}U(n,f)$ ABOVE 100 keV FOR ENDF/B-V AND THE IMPLICATIONS OF A UNIFIED ^{235}U MASS SCALE

W. P. Poenitz, J. W. Meadows, and R. J. Armani
Argonne National Laboratory, 9700 South Cass Avenue, Argonne, Illinois 60439 USA

A previously reported evaluation of $^{235}U(n,f)$ in the fast neutron energy range was updated to include data published up to the 1978 Harwell Conference on Neutron Physics. The shape of the cross section resulting from this evaluation and a normalization factor extracted from data provided within the framework of this evaluation were used by the Subcommittee on Standards and Normalizations of the Cross Section Evaluation Working Group to establish $^{235}U(n,f)$ for ENDF/B-V above 100 keV. ^{235}U sample mass comparisons made between different laboratories were compiled in order to investigate the implications of different sample masses on recent $^{235}U(n,f)$ data. A new intercomparison of several such samples was carried out using absolute and relative alpha-counting and relative fast neutron fission counting. The result of this work is a unified ^{235}U mass scale with an uncertainty of 0.6%.

[$^{235}U(n,f)$ cross sections, shape evaluation, normalization uncertainties, alpha counting]

Introduction

Early evaluations of nuclear data had to cope with experimental values which were sparse in some areas and discrepant in others. Therefore it is not surprising that procedures used in these evaluations were more pragmatic than exact. However, the return to a better defined evaluation methodology was suggested as experimental data became more abundant and consistent.[1] The presently continued effort to evaluate consistent data sets was initiated in 1968[2] with results obtained in a simultaneous evaluation of several cross sections reported in 1970.[1] An independent but similarly motivated evaluation was also reported in 1970.[3] A new simultaneous evaluation of standard cross sections and cross sections important for technical applications seems desirable because the data base has substantially improved since 1970. As a first step the $^{235}U(n,f)$ cross section was evaluated and reported at the Symposium on Neutron Standards and Applications in 1977.[4] This evaluation was updated in order to include more recently reported data.[5] The Subcommittee on Standards and References of the Cross Section Evaluation Working Group (CSEWG) derived the $^{235}U(n,f)$ cross section above 100 keV for ENDF/B-V from a preliminary version of the present evaluation of the shape and a different selection of normalization factors.[6] Consideration of some of the recently reported data sets suggests that differences between these data may in part be caused by differences in the ^{235}U-mass scales. This led to an intercomparison of various mass scales. The implications of a unified mass scale on different data sets and on the evaluation results, including ENDF/B-V will be considered here.

The Evaluation Methodology and the Evaluation of $^{235}U(n,f)$ above 100 keV

An objective evaluation procedure is based upon the available data base and avoids intuition which might be justified with experience but is probably very subjective in nature. Theoretical models and empirical rules with parameter sets determined with other experimental data are useful tools in the evaluation process and provide additional information where primary experimental data are uncertain or discrepant. The current data base contains absolutely measured cross section values for a large number of nuclei and reactions ((n,f), (n,γ), (n,α)). The data base also contains ratios measured between these nuclei and for different reactions. The absolute cross section values and the ratios between them define an overdetermined system with more values determined than unknown quantities. This situation calls for a simultaneous evaluation in order to obtain a consistent data set and to utilize the maximum of the available experimental information. The individual cross sections and the ratios between them are evaluated in a first step and a consistency fit is carried out as a second step. The present report describes the evaluation of the $^{235}U(n,f)$ cross section which is to be used as an input for the consistency fit together with other standard cross sections. The evaluation of these other cross sections and the consistency fit will be described at a later time.

The Evaluation of the Shape and the Normalization

The energy dependence of the cross section is called the shape. The absolute cross section is known in the energy range in which the shape is known if an absolute value is known at any energy. This corresponds well to the experimental determination of fast neutron reaction cross sections: Several factors in the determination of the cross section are common to all energies, e.g. the mass of the sample, often the counting efficiency; or they vary only slightly with energy. Thus, a major part of the uncertainty and of the unknown error is common to all energies. The cross section can be expressed by $\sigma(E) = a \cdot S(E)$, where "a" lumps together the common factors and S(E) is the shape of the cross section. The evaluation of the shape will use a procedure which is independent on the absolute or arbitrary normalization of the cross section. One possibility would be to use the slope, that is

$$\frac{d\sigma}{dE} \Big/ \frac{\sigma}{E} \approx \frac{\sigma_{i+1} - \sigma_i}{E_{i+1} - E_i} \Big/ \frac{\sigma_i}{E_i} \quad ,$$

where σ_i is the cross section at the energy, E_i, in a predefined energy grid. This method appears to have the disadvantage that local data discrepancies can "tilt" the shape over a large energy range. A procedure which stabilizes the shape over large energy ranges is the use of ratios between the cross sections at any two energies,[7] $R_{ik} = \sigma_i/\sigma_k = S(E_i)/S(E_k)$. This procedure is used in the present evaluation. Weighted averages of all R_{ik}'s from different experimental data sets are formed. The R_{ik}'s define a system of equations for the cross sections on a predetermined energy grid. The cross section shape can be reconstructed by an arbitrarily selected starting point, for example $\sigma(E_1) = \sigma_1$.

The weighted average difference between the absolute cross section values of an experimental data set and the arbitrarily normalized shape curve yields a normalization factor. The weighted average of the normalization factors obtained from all the absolute experimental data sets gives the final normalization for the evaluated shape curve. A more detailed description of this evaluation process is given elsewhere[4,5,7]

The Uncertainties and the Weighing of Data

It is the nature of the measuring process to be uncertain. The true uncertainty (which differs from the quoted uncertainty) may be subdivided as follows [1,5,8]:

$\Delta\sigma_R$, the reference uncertainty (mass, standard cross section, etc.), which is usually outside of the responsibility of the experimenter.

$\Delta\sigma_S$, the systematic uncertainty (estimated or calculated from the uncertainties of models and their parameters used to calculate corrections, the subtraction if backgorund, etc.) which is the major responsibility of the experimenter.

$\Delta\sigma_{St}$, the statistical uncertainty (caused by the limited number of events counted), which is the only uncertainty the mathematical faculty bothers to deal with.

$\Delta\sigma_{E}$, the cross section uncertainty caused by the energy uncertainty. Not only the energy dependence of the measured cross section must be considered, but also that of the reference cross section and of other factors (e.g., efficiencies).

$\Delta\sigma_{Res}$, the cross section uncertainty caused by cross section fluctuations and insufficient averaging with the given resolution of the experiment.

$\Delta\sigma_{a}$, the accidental error, which may be revealed if the experiment is repeated. The experimenter would eliminate accidental errors by proving reproducibility, however, the length of some experiments does not permit repetition.

$\Delta\sigma_{u}$, the unknown error which is systematic in nature and caused by not recognizing necessary corrections or underestimating uncertainties.

$\Delta\sigma_{Ps}$, the psychological error which is caused by satisfaction with agreement obtained with values reported by others, thus neglecting the search for additional effects in the measuring process or equipment which would require corrections, or, the opposite, that is the dissatisfaction with a disagreement with prior reported values and the subsequent search for one-directional corrections.

It is assumed that experimental values of the past can be analyzed in terms of the following parameters:

$\bar{E}$, the average energy at which the cross section was measured.

ΔE, the uncertainty of this energy which is needed to derive $\Delta\sigma_{E}$.

R_{es}, the resolution or energy spread which is required to derive $\Delta\sigma_{Res}$.

$\bar{\sigma}$, the average cross section value.

$\Delta\sigma$, the total uncerainty of the measured cross section value.

$\Delta\sigma_{St}$, the statistical uncertainty.

The average energy may have been obtained as an average over the reaction rate, or the neutron flux. In either case, the measured average cross section differs from the average cross section at the average energy and a correction must be applied.

The quoted cross section uncertainty, $\Delta\sigma$, is usually the square root of the sum of the squares of the reference uncertainty, the estimated systematic uncertainty, the statistical uncertainty, and sometimes the reproducibility. The energy uncertainty can be translated into additional cross section uncertainty:

$$\Delta\sigma_E^2 = \left(\frac{d\sigma}{dE}\right)^2 \Delta E^2 + \left(\frac{d\sigma}{d\sigma_R}\right)^2 \left(\frac{d\sigma_R}{dE}\right)^2 \Delta E^2 + \sum_i \left(\frac{dF_i}{dE}\right)^2 \Delta E^2,$$

where the first term is the cross section uncertainty caused by the energy dependence of the measured cross section and the second term is that caused by the reference cross section. The last term is accounting for the uncertainties caused by the energy dependence of corrections and efficiencies.

The square of the inverse of the uncertainty was used for weighing the data in the present evaluation. The cross section equivalent uncertainties caused by the energy uncertainty and by the resolution were added to the quoted uncertainty. For the evaluation of the shape, the total uncertainty was reduced by the uncertainty of the normalization. For the evaluation of the normalization, the total uncertainty was reduced by part of the statistical uncertainty if several cross section values contributed. Finally, it was assumed that the evaluation yields best values which reveal unknown errors in specific experiments.[8] Two standard deviations (2σ) were used in the present evaluation as a criteria for assuming unknown errors in a specific data set and doubling its quoted uncertainty.

Evaluation of the $^{235}U(n,f)$ Cross Section above 100 keV

The data file contains all data reported up to and including the Conference on "Neutron Physics and Nuclear Data for Reactors and Other Applied Purposes", held at Harwell, England, in September 1978. Data reported earlier than the publication by White[9] were only included if reevaluations were available. Data measured relative to the H(n,n) cross section were renormalized to ENDF/B-V[15] values for this reference cross section. Data normalized at low energies were renormalized to a weighted average integral of 243.7 ± 1.0 beV between 7.8 eV and 11.0 eV.[10] Cross section uncertainties caused by energy uncertainties were added as discussed in above. Cross section uncertainties caused by cross section fluctuations were added based upon an analysis by Bowman et al.[11]. The shape was evaluated in an energy grid of 63 grid points. The result was smoothened in order to obtain a more physical shape of the cross section. Table I gives the normalization factors obtained from the absolutely measured data sets. The details of the evaluation and a comparison of the result with the experimental data was given elsewhere.[5]

Table I. Normalization Factors

Set Name	All Norm. Factors	Selected Factors, Present Normalization
Smith	1.006 ± 0.066	1.006 ± 0.066
Barton	1.012 ± 0.029	1.003 ± 0.029
Poenitz BND	1.008 ± 0.030	0.988 ± 0.027
Poenitz VSO_4	1.003 ± 0.038	1.003 ± 0.038
Poenitz AA	1.002 ± 0.038	1.002 ± 0.038
Kari	1.048 ± 0.039	1.048 ± 0.039
Alkharov	1.060 ± 0.035	---
Kuks	1.051 ± 0.041	---
Cance	1.007 ± 0.038	1.007 ± 0.038
White	1.032 ± 0.042	1.032 ± 0.042
Wassen, Meier	0.986 ± 0.039	0.986 ± 0.039
Szabo	1.012 ± 0.032	1.012 ± 0.032
Kaeppeler	1.054 ± 0.037	---
U. Michigan	1.019 ± 0.024	1.019 ± 0.024
Wassen	0.991 ± 0.036	0.991 ± 0.036
Arlt	1.004 ± 0.032	1.004 ± 0.032
Adamov	1.048 ± 0.021	---
U. Michigan, Cf	1.006 ± 0.021	---
Heaton	1.001 ± 0.025	1.001 ± 0.025
unweight. av.	1.018	1.007
weighted av.	1.019 ± 0.005	1.006 ± 0.004

The $^{235}U(n,f)$ cross section of ENDF/B-V above 100 keV was derived from a preliminary version of the present evaluation. Small differences in the shape are due to the later discovery that two data sets [12,13] used the analyses of the H(n,n) cross section by Gammel[14] instead of the ENDF/B-V[15] cross section (Hopkins - Breit[16]). However, the major difference is in normalization (ENDF/B-V is ~ 1.3% higher). The members of the Subcommittee on Normalizations and Standards of the Cross Section Evaluation Working Group (CSEWG) selected normalization factors closely corresponding to the first column of Table I but excluded the value

by Arlt et al.[17] and the averages over the ^{252}Cf spontaneous fission neutron spectrum (the last three values of Table I). A more extensive description of the measurement by Arlt et al.[17] is now available and the value was used in the present evaluation. The average over the ^{252}Cf spontaneous fission neutron spectrum was considered here one of the most important measurements for the normalization of differential experimental values and these values were used in the present evaluation. The present result and ENDF/B-V are compared in Figs. 1 and 2 with more recent experimental data and data reported with low uncertainties.

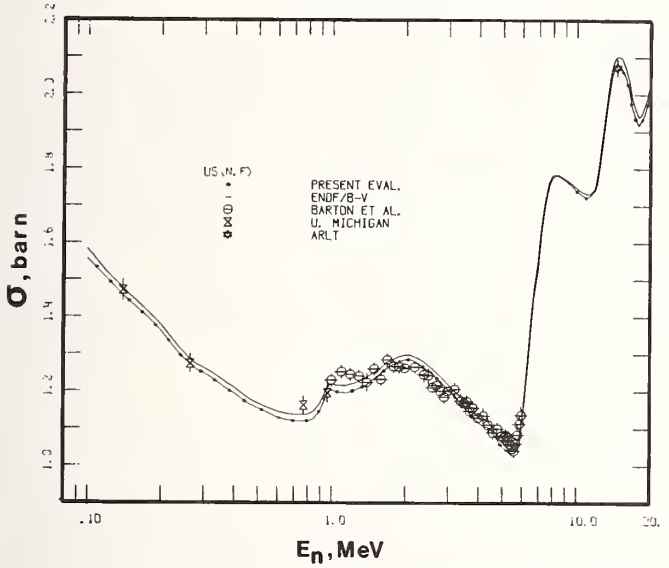

Fig. 1. Comparison of the Result of the Present Evaluation and ENDF/B-V with Experimental Data Reported with Low Uncertainties.

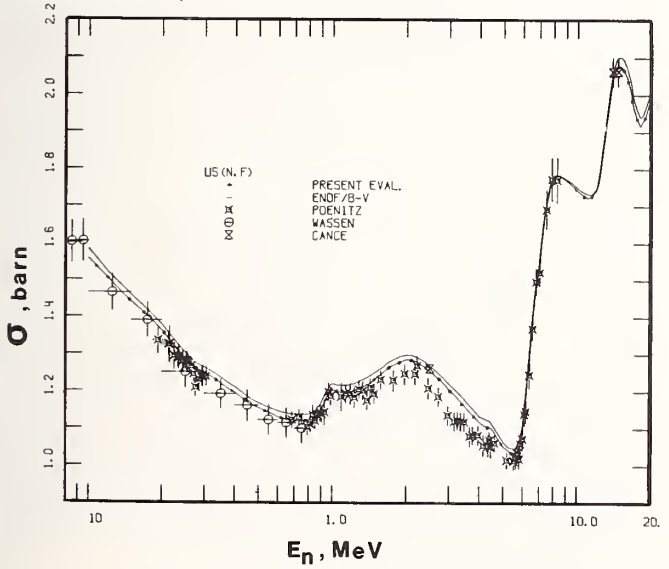

Fig. 2. Comparison of the Result of the Present Evaluation and ENDF/B-V with Recent Experimental Data by Poenitz, Wassen, and Cance and Grenier.

The Intercomparison of ^{235}U Mass Scales

A comparison of the present evaluation result with experimental data reported within the last 15 years shows a reasonable agreement within the general uncertainty level of the data (~3-4%).[5] However, it appears that the agreement in shape is often better than in normalization. An important quantity for the normalization of many absolute data sets is the ^{235}U - mass. Several sample sets are in use at different laboratories and intercomparisons have been carried out among some of these laboratories. Most of these intercomparisons were made with a set of samples established at the National Bureau of Standards (NBS). The mass scale of the NBS sample set is stated with a 1.2% uncertainty. This appears inadequate for future ^{235}U cross section measurements by about a factor of 2-3. However, it may be possible to establish an improved mass scale by utilizing the various intercomparisons carried out in the past.

A Compilation of Previous ^{235}U Sample Intercomparisons

Several intercomparisons of ^{235}U samples were made during the last several years.[18-21] Figure 3 is a schematic diagram which summarizes the relative differences between the stated masses of the samples and those determined relative to other samples by alpha or fission counting. The NBS mass scale, against which most other samples were measured, appears to be higher than any other mass scale. The average difference is 0.7% which is well within the stated uncertainty of 1.2% for the NBS mass scale. The perception of Fig. 3 is that six mass scales agree rather well, possibly within ±0.1 - 0.2%. This would suggest that the ^{235}U mass problem could be considered as solved after adjustment of the NBS mass scale and resolution of the possible inconsistency between the two Meadows' foils. However, closer scrutiny reveals that many of the mass scales of the previous intercomparisons shown in Fig. 3 were not independent. A compilation of past intercomparisons made at various laboratories at different times may be less consistent than an intercomparison of the different mass scales in a single experiment. Therefore, a new attempt was made to compare several samples which were used in cross section experiments and represent four different mass scales.

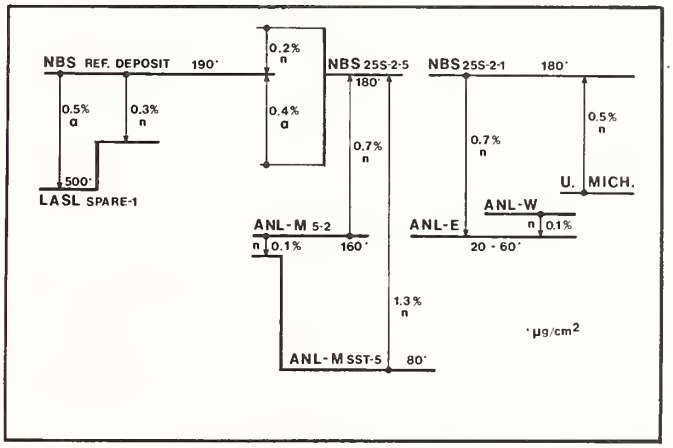

Fig. 3. Comparison of ^{235}U Mass Scales from Various Intercomparisons Reported by Others. n indicates thermal neutron intercomparison and α indicates α-counting intercomparison.

The Intercomparison by Alpha and Fast Neutron Induced Fission Counting

Eight samples were used in the present measurements. These samples were made from three different fissile materials and represented four different mass scales. A detailed description of the samples involved in the intercomparison and of the experimental procedure was given elsewhere.[25] Utilizing the specific activities for the varying materials permits the determination of the fissile mass by alpha-counting. Two low-geometry alpha-counters of similar design were available. Geometry factors were calculated with a Monte Carlo procedure or with an approximate correction to the point source geometry factor. All samples were initially counted at a distance of ~1.6 cm from the

Table II. Sample Masses Obtained from Absolute Alpha Counting and Relative to Four Different Mass Scales, in μg

	ANL R-5	ANL N-U5-3	ANL M-5-1	ANL M-5-2	ANL M-SST-2	LASL S1	LASL S3	NBS 25S-5-2
Present Absolute Alpha Counting, and Specific Activity Compilation	79.55	52.09	1063	831.6	411.7	299.7	1687	229.6
Relative to Fission Mass Scale								
ANL#1	79.25	51.86	1071.5	836.9	417.6	298.7	1686.2	229.3
ANL#2	78.1	51.11	1056	824.6	411.5	294.3	1661.6	226.0
LASL	79.35	51.93	1073	837.8	419.1	299.0	1688.2	229.6
NBS	79.7	52.25	1077	841.4	419.9	300.3	1695.5	230.6
Average Fission Scale	79.10	51.76	1069	835.2	416.8	298.1	1683	228.9
Quoted Mass	79.8	52.1	1066	832	411.5	298.8	1689.4	230.6
Difference Between Quoted Mass and Average Fission Scale; %	+0.9	+0.7	-0.3	-0.4	-1.3	+0.2	+0.4	+0.7

aperture with a typical statistical uncertainty of ±0.3%. Samples with a sufficiently high alpha-activity were also counted at a distance of ~3.6 cm, thus changing the geometry factor by about a factor of four. Comparison of the decay rates obtained at the different distances increased the confidence in the calculated geometry factors. The ratio of values obtained at the second position. to the value obtained at the closest position was 1.0002 ± 0.0009. A comparison was made between the two low-geometry counters using an ^{241}Am sample. A ratio of 1.0008 ± 0.0007 was found. Based on these values, the estimated systematic uncertainty due to the geometry of the counters does not exceed 0.11%. A more serious matter is the interpretation of the measured alpha-spectra. All the spectra show a low-energy tail. The tail was, on the average, ~0.3% of the total count rate. It may be assumed that the tail extends under the alpha-peak. Therefore, we assume that the total amount of these alphas is ~0.4%. One-half, that is 0.2%, were included in the count rate and 0.2% was assumed to be the systematic error.

The present experimental procedure used in the intercomparison of the samples in a fast neutron flux followed that employed for fast neutron fission cross section ratio measurements described in detail elsewhere.[22-24] The measurements were carried out at an average energy of 600 ± 80 keV. The fissile deposits were located back-to-back at a distance of ~5 cm from the neutron source. Measurements were carried out with each sample alternately facing the neutron source or facing away from the source.

Table II summarizes the results from the present measurements. The differences obtained between the various mass scales and an "Unified ^{235}U Mass Scale" is shown in Fig. 4.

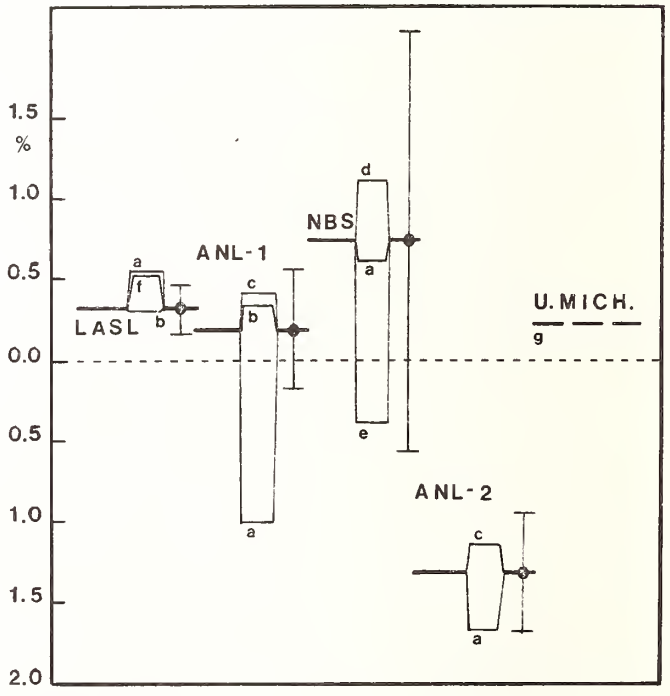

Fig. 4. Comparison of the Four Different Mass Scales Involved in the Present Intercomparison. Vales are shown relative to a "unified mass scale" derived as an unweighted average. a = isotopic composition and half-life, b = isotopic dilution, c= colorimetric comparison with standard, d = thermal neutron comparison with quantitative deposition, e = thermal neutron comparison with ^{239}Pu sample, g = weighting.

The Implications of a Unified ^{235}U Mass Scale

The average of the ^{235}U neutron fission cross section over the ^{252}Cf spontaneous fission neutron spectrum is insensitive to uncertainties of the neutron spectrum and the cross section shape.[12,14] Therefore, this average is not only a good indicator for normalization differences of differential data but also a first check for the proper normalization of evaluated data. The ^{235}U(n,f) cross section was measured at several laboratories within the last 10 years. Data may have been obtained in various experiments using different methods but were usually found to be quite consistent. It is of interest to compare the ^{252}Cf spectrum averaged differential ^{235}U cross sections with experimental values and to consider the changes caused by the unified mass scale developed above.

The differential data sets considered here are:

1. KFK (Kaeppeler[26], Kari[13])
2. NBS (Wassen[12], Wassen and Meier[27], Carlson and Patrick[28])
3. ANL (Poenitz[38,39])
4. LASL (Barton et al.[28], Smith et al.[29], Diven[30], Lemley et al.[31])
5. CEN (Szabo[37])

The experimental data which are to be compared with the average over these differential data sets are:

1. NBS (Heaton et al.[32,33])
2. U. Michigan (Knoll[34])
3. USSR (Adamov et al.[35])

The comparison is made in Fig. 5. The round full circles show the original values and the crosses show the same data after referencing to the unified mass scale.

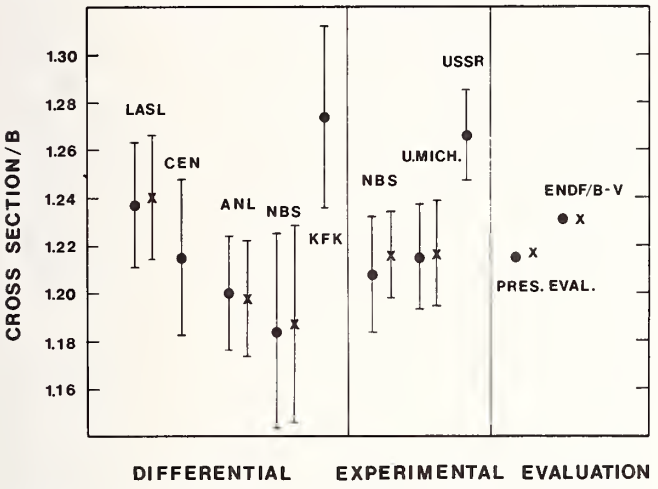

Fig. 5. Comparison of the $^{235}U(n,f)$ Cross Sections Averaged over the ^{252}Cf Spontaneous Fission Neutron Spectrum. Full circles apply for the originally reported data and crosses indicate the changes due to the introduction of the unified mass scale.

The changes are apparently small compared with differences between the various data. This is in part due to the good agreement of the original masses with the unified mass scale (LASL, U. Michigan, ANL (one of the two sets)) or because the change concerns only one set where several data sets contributed to the normalization (differental data by NBS, ANL).

It is of interest to note that the experimental values by Heaton et al.[32] and by Knoll[34] are in near perfect agreement if referenced to the unified mass scale. The neutron source strength determination in both experiments is linked to a longstanding international effort of neutron source intercomparisons. The good agreement between the two values suggests that the remaining possible causes for obtaining different results (scattering corrections, fission event detection, geometry factors) did not introduce any error. The changes of the normalization factors given in Table I due to referencing to the unified mass scale are also small and compensate one another, thus the evaluation results are virtually unchanged (see Fig. 5).

Conclusions

The result of the evaluation of the $^{235}U(n,f)$ cross section by an objective evaluation technique is very well supported by the experiments data which were reported with the lowest uncertainties (Arlt et al.[17], Barton et al.[28], Knoll[34], Cancé and Grenier[36], and Heaton et al.[32]) and in good agreement with many other data sets (Szabo[37], Poenitz[38], Smith et al.[29]). Agreement with data by Wassen[12] is also good after renormalization of these data with an evaluated integral of 243.7 beV between 7.8 eV and 11.0 eV. Some of the most recently reported data are somewhat lower (Poenitz[39], Wassen and Meier[27]) and some are higher (Adamov et al.[35], Kari[13]).

Differences between the mass scales used for some of the experimental data were found not to explain differences between the data. The majority of the data reported in the past has an uncertainty of 2.5 - 4.0%. Any new measurement in this uncertainty range will not substantially improve our knowledge of the $^{235}U(n,f)$ cross section because its weight will be low among many other data sets with similar uncertainty. It is recommended that any new measurements should have an uncertainty of about ~1% in order to be significant.

Acknowledgment

This work was supported by the U. S. Department of Energy.

References

(PC = Private Communication)

1. W. P. Poenitz, AEC Symp. Ser., 23, 331 (1970).
2. J. M. Kallfelz, W. P. Poenitz, B. R. Sengal and B. A. Zolotar, TANSACO, 12, 186 (1969).
3. M. G. Sowerby, B. H. Patrick, Proc. Con. Nucl. Data, Helsinki, 2, 703 (1970).
4. W. P. Poenitz, NBS SP 493, 261 (1977).
5. W. P. Poenitz, ANL/NDM-45, 1979.
6. Subcommittee on Normalization and Standards of CSEWG, see Ref. 5, Appendix II.
7. W. P. Poenitz, P. Guenther, ANL-76-90, 154 (1976).
8. L. N. Usachev, INDC(CCP) - 45/L (1974).
9. P. H. White, J. Nucl. En., A/B, 19, 325 (1965)
10. See Reference 5 and M. R. Bhat, ANL-76-90, 307 (1976).
11. C. D. Bowman et al., ANL-76-90, 270 (1976).
12. O. A. Wassen, ANL-76-90, 183 (1976).
13. K. Kari, KFK 2673, (1978).
14. J. A. Grundl, AEC Symp. Ser., 13, 417 (1970).
15. L. Stewart, et al., LA-7663-MS, 4 (1979).
16. J. C. Hopkins, G. Breit, Nucl. Data A, 9, 137 (1971).
17. R. Arlt et al., ZfK 350, 10 (1977), also INDC/GDR 1-71G.
    I. D. Alkhasov et al., T. U. Dresden, Sec. Phy. 05-37-78 (1978).
18. J. A. Grundl, NBS, PC, (1978), and see Ref. 1.
19. J. W. Meadows, ANL, PC (1978).
20. D. M. Gilliam, R. J. Armani, et al., ANL, PC, (1978).
21. G. F. Knoll, U. of Mich., PC by D. M. Gilliam, NBS.
22. J. W. Meadows, Nucl. Sci. Eng., 49, 310 (1972).
23. W. P. Poenitz, Nucl. Sci. Eng., 40, 383 (1970).
24. J. W. Meadows, Nucl. Sci. Eng., 65, 171 (1978).
    W. P. Poenitz, et al., ANL/NDM-48 (1979).
26. F. Kaeppeler, KFK 1772, (1973).
27. A. O. Wassen, NBS, PC (1978).
28. D. M. Barton, Nucl. Sci. Eng., 60, 369 (1976).
29. R. K. Smith et al., Bull. Am. Phys. Soc. 2, 196 (K4), 5709.
30. B. C. Diven, Phys. Rev., 105, 1350 (1957).
31. J. R. Lemley et al., Nucl. Sci. Eng., 43, 281 (1971).
32. H. T. Heaton II et al., ANL-76-90, 333 (1976).
33. J. A. Grundl, NBS, PC (1978).
34. G. F. Knoll, NBS S. P., 493, 3041, (1977).
35. V. M. Adamov et al., NBS-SP-493, 313, (1977).
36. M. Cance, G. Grenier, Nucl. Sci. Eng., 68, 197 (1978).
37. I. Szabo, J. P. Marquette, ANL-76-90, 208 (1976).
38. W. P. Poenitz, Nucl. Sci. Eng., 53, 370 (1974).
39. W. P. Poenitz, Nucl. Sci. Eng., 64, 894 (1977).

A MEASUREMENT OF U-235 ABSOLUTE ALPHA VALUE IN THE NEUTRON ENERGY RANGE FROM 0.1 to 30 keV

G. V. Muradyan, Yu, G. Schepkin
Yu. V. Adamchuk, M. A. Voskanyan

I. V. Kurchatov Atomic Energy Institute,
Moscow, USSR

[Alpha-value, multiplicity spectrum, multisectional detector, U-235]

In order to measure the neutron-physical constants with high accuracy and to investigate ways of formation and decay of excited nuclei a method has been developed at the I.V. Kurchatov AEI, based on the gamma-quanta and neutrons multiplicity spectrometry.[1,2] During 1974-1978 there have been constructed a number of multisectional 4π-detectors which have demonstrated great possibilities for this method.[3,4,5] A detector permitting the required accuracy of measurements of neutron cross sections and their ratios has been chosen and designed on the basis of these works. The detector with 4π-geometry has 46 sections and was based on NaI(Tl) crystals with the total volume of the scintillator of $\sim$100 1. The detector was used at the 26-m station.

Up to 37 time-of-flight spectra are obtained in each measurement. 16 of them corresponds to 1-fold, 2-fold, ..., 15-fold and 16-fold coincidences between detector sections when the energy released in each section is not less than a given value, E_S and in the whole detector - not less than E_Σ. The selection of coincidencies is performed within the time interval τ_0 beginning from the moment of appearing the pulse with the total energy $E > E_\Sigma$. At the same time analogous time-of-flight spectra are separated under the additional condition of recording fission neutrons within the gate of the width τ_1, delayed for the time τ_2 with respect to the total energy pulse.

In this paper the results of U-235 absolute alpha value measurements are presented. The measurements are carried out by the detector described above over the energy range from 0.1 to 30 keV with the high accuracy - better than 5%. The equipment parameters and measurement conditions are listed in Table I.

At the present time there are a large number of papers on alpha value measurement. However, none of these give the required high accuracy (better than 5%) over a wide range of neutron energy. This is mainly explained by two circumstances. The first one is the high background value in the capture channel, which has many components which depend differently upon the neutron energy and alpha value; the fission gamma-quanta, the background due to neutron capture in construction materials, gamma-background, etc. The second one is connected with finding the equipment constants needed to obtain the alpha value. All this lead to the fact that alpha proves to depend to a great extent on the uncertainties of the background, calibration values, and capture and fission detection efficiencies. These uncertainties confine the accuracy of alpha value to a level of $\sim$15%.

We succeeded in overcoming these difficulties by means of realization of the advantages of the excited nuclei secondary radiation multiplicity spectrometry. The capture and fission detection efficiencies (E_γ and E_f respectively) of the 46 sectional detector are close to 100%. This detector separates well the capture, fission and scattering events (the low B-value and high E_γ/E_n-value). The background caused by scattered neutrons capture in construction materials is reduced greatly in this detector as compared with other ones due to the use of shielding - the converter of a mixture (B^{10} + paraffin) with thickness $\sim$10 cm (0.1 g/cm^3 B^{10} and 0.8 g/cm^3 paraffin). At the same time the shielding-converter enables the recording of the fission neutrons thereby increasing the multiplicity of gamma-quanta recorded in fission as well as it delays a part of these neutrons for a time $\gtrsim \tau_2$ before they will be detected in NaI(Tl) crystals. The latter circumstance is used to make more exact the fraction of the fissions at coincidence ratios K=2,3 where it amounts to only $\sim$3% of the capture. The admixture of fission events at K=1-5, where the portion of capture events is about 90%, is less than 20% (Bo).

The low Bo-value and the possibility of its definition by means of the detection of the part ($\sim$2%) of fission neutrons in NaI(Tl) as well as the low value of background and high efficiencies E_γ and E_f permit obtaining alpha values with the required high (over 5%) accuracy over the whole of measured energy range. Note that in obtaining alpha no data from other measurements were taken and no calculated corrections were made. In Table II the comparison of the present method with one of the best method of alpha measurement (ORNL[6]) is presented. It is seen that the use of the multiplicity spectrometry permits obtaining essentially higher accuracy. This accuracy is better than the needed 5%. To confirm the high accuracy we have performed additional measurements of the U-235 alpha absolute value in the thermal region. In these measurements the time-dependent background did not exceed 3%. The alpha value obtained at thermal energy for U-235 according to our measurements is α_T = 0.168. The good agreement of th obtained α_T-value with the recommended value of α_T = 0.169[7] when the values of this quantity are so low ensures the high (better than 5%) accuracy of alpha in the range 0.1-30 keV. It should be noted that when measuring the α_T -value we did not intend to make more exact the recommended value of α_T although at the optimization of experimental conditions for the thermal energy the present method permitted the accuracy of α_T about 1%.

In the Table III the obtained alpha values for U-235 over the energy range from 0.1 to 30 keV are

presented. In addition estimations of [8] and ENDF/B-III, Mat. 1157 are given for comparison.

Table I.

Experimental conditions \ Energy interval (eV)	100-30000	0.022-0.028
Linac frequency (Hz)	350	40
Linac pulse width (nsec)	60	60
Channel width (nsec)	40	640
Number of channels	32K	32K
E_Σ (keV)	800 250	800
E_ζ (keV)	25	25
τ_1 (nsec)	520 400	520 400
τ_2 (nsec)	600 900	600 900
τ_0 (nsec)	790	790
Filters on the beam	B-10(0.12g/cm^2) or Cd(δ =3mm)	-
	Al(δ =40mm)	-
	Pb(δ =10mm)	Pb(δ =10mm)
Sample-metallic U-235	P=2g ϕ 28mm	P=2g ϕ =28mm

Table II.

Characteristics \ Paper	Present paper	ORNL [6]
1	2	3
Fission background(B) in capture channel in % of capture at α =1	22 at $2 \leq k \leq 5$ 10 at k=3	58
Time-dependent background (F) in capture channel at E = 10keV ($\alpha \approx 0.4$) (%)	9	130
at E_n =0.025 eV ($\alpha \approx$ 0,017) (%)	3	50
$\Delta\alpha/\alpha$ at 10%-uncertainty of F at E_n = 10keV ($\alpha \approx 0.4$) (%)	0.9	13
at E_n =0.025 eV ($\alpha \approx$ 0.17) (%)	0.3	5
$\Delta\alpha/\alpha$ at 3% uncertainty of B at $\alpha \approx$ 0,4 (%)	1.6	4.3
at $\alpha \approx$ 0,17 (%)	3.8	10
Fission detection efficiency ε_f (%)	97	50
Capture detection efficiency ε_γ (%)	97	85
Presence of features in background line	There are not	There are irregulaties
Normalization	Absolute measurement	Over the energy region 0.02-0.4eV

Table III

Energy interval (keV)	value			
	Present paper	[6]	[8]	ENDF/B-III Mat.1157
0,1 - 0,2	0.490	0,60	0.580	0.54
0,2 - 0,3	0.378	0,45	0,434	0.42
0,3 - 0,4	0.429	0,52	0.481	0.40
0.4 - 0.5	0.304	0.35	0.349	0.36
0.5 - 0.6	0.272	0.29	0.294	0.34
0,6 - 0,7	0.331	0.42	0.392	0.39
0,7 - 0,8	0.363	0.45	0.417	0.45
0.8 - 0.9	0.437	0.51	0.485	0.49
0.9 - 1.0	0.549	0.68	0.625	0.50
1 - 2	0.355	0.42	0.386	0.42
2 - 3	0.342	0.41	0.340	0.35
3 - 4	0.323	0.38	0.308	0.34
4 - 5	0.322	0.38	0.327	0.34
5 - 6	0.313	0.38	0.297	0.34
6 - 7	0.386	0.47	0.361	0.34
7 - 8	0.350	0.43	0.368	0.34
8 - 9	0.411	0.51	0.408	0,34
9 - 10	0.335	0.42	0.372	0.35
10 - 20	0.337	0.40	0.391	0.35
20 - 30	0.332	0.39	0.366	0.36
30 - 40	0.368	0.37	0.360	0.36
40 - 50	0.360	0.36	0.350	0.35

References

1. G.V.Muradyan, Yu.G.Shchepkin, Yu.V.Adamchuk, G.V.Ustroev. Preprint IAE-2634, 1976.
2. G.V.Muradyan. Report on the present conference,
3. Yu.V.Adamchuk, M.A.Voskanyan, V.I.Juk, D.A.Markov, G.V.Muradyan, L.Yu.Prokofieva, G.I.Ustroev, A.D.Charitonov, Yu.G. Shchepkin. Proceedings of IV All-Union Conference on neutron physics, Kiev, 1977, Publ.Moscow, v.3, p.113, 1977.
4. Yu.V.Adamchuk, M.A.Voskanyan, G.V.Muradyan, G.I.Ustroev, Yu.G.Shchepkin. Proceedings of IV All-Union Conference on neutron physics. Keiv, 1977, Publ.Moscow, v.2. p.192, 1977.
5. G.V.Muradyan, G.I.Ustroev, Yu.G.Shchepkin, Yu.V.Adamchuk, M.A.Voskanyan, L.Yu. Prokofieva. Proceedings of IV All-Union conference on neutron physics. Kiev, 1977, Publ.Moscow, v.3, p.119, 1977.
6. R.Gwin, E.G.Silver, R.W.Ingle and H.Weaver. Nucl.Sci.Engin., 59, 79 (1976).
7. G.C.Hanna, C.H.Westcott, H.D.Lemmel, R.R. Leonard, Jr., J.S.Storv, P.M.Attree, Atomic Energy Reviue, 7, 3 (1969).
8. V.A.Koshin, G.V.Antzipov. Proceedings of III All-Union conference on neutron physics. Kiev, 1975, v.2, p.3, Moscow,1976.

HIGH-RESOLUTION FISSION CROSS SECTION OF ^{231}Pa*

S. Plattard,+ G. F. Auchampaugh
University of California, Los Alamos Scientific Laboratory
Los Alamos, New Mexico 87545 USA

N. W. Hill, G. de Saussure, R. B. Perez and J. A. Harvey
Oak Ridge National Laboratory
Oak Ridge, Tennessee 37830 USA

The ^{231}Pa fission cross section was measured with high resolution at ORELA from 0.1 to 12 MeV and between 0.4 eV and 10 keV. The data show evidence for 1) fractionated vibrational structures in the threshold region of the fission cross section, and 2) narrow fission resonances above 0.4 eV with an average fission width $\langle\Gamma_f\rangle$ = 8 μeV.

[^{231}Pa(n,f) cross seotion 0.4 eV - 10 keV and 0.1-12 MeV,measured Γ_f below 60 eV.]

Introduction

Previous measurements of the ^{231}Pa(n,f) cross section above 100 keV [1,2] show considerable structure in the threshold region of the fission cross section. These structures have been interpreted[2] as vibrational states of known spin and parity trapped in the second minimum of the double-humped fission barrier of ^{232}Pa. However, since these resonances occur at rather high excitation energy, they may be fragmented into more complex states. To investigate such a possibility, we have undertaken at the Oak Ridge Electron Linear Accelerator (ORELA) a high-resolution fission cross section measurement of ^{231}Pa.

Taking advantage of the high chemical purity of the ^{231}Pa samples (less than 0.1 ppm of fissile elements) a preliminary measurement in the eV region was also carried out. For the first time, narrow fission resonances were observed above 1.3 eV.

Besides the importance of ^{231}Pa for basic fission studies, it is also of interest in the field of reactor design[3] in that it plays a part in the unwanted generation of ^{232}U in the $^{232}Th/^{233}U$ breeder cycle.

Experimental Procedure

The ^{231}Pa(n,f) cross section σ_f relative to the ^{235}U fission cross section was measured with neutrons produced by ORELA used as a pulsed source. Fission fragments were detected by a gas scintillator located on a flight path perpendicular to the electron beam. Table I summarizes the experimental conditions for both the high energy [$0.1 < E_n(MeV) \leq 12$] and the low energy [$0 < E_n(keV) < 10$] measurements.

Table I. Experimental conditions

	$0.1 < E_n(MeV) \leq 12$	$0 < E_n(keV) < 10$
Frequency (Hz)	800	450
Pulse width (ns)	6 - 8	40
Power (kW)	8 - 9	26
Average flight path (m)	41.68	18.30
Filters	none	0.5 mm of Cd.
Duration (h)	632	60

*Work supported in part by the U.S. Department of Energy.

+Permanent address: Centre d'Etudes de Bruyères-le-Châtel, BP561, 92542 Montrouge Cedex, France.

The fission detector consisted of a sealed cylindrical chamber containing a mixture of 98% He and 2% N_2 at STP. The chamber was divided into 3 pairs of optically isolated cells. The distance between two consecutive pairs was 12.5 cm. Each cell was viewed through two circular quartz windows by two XP2020/Q photomultiplier tubes.

Each of the five ^{231}Pa cells contained 53 mg of protactinium in the form of oxide painted on both sides of a semicircular titanium foil (20 cm in diameter and 12.5 μm thick) to a density of approximately 0.3 mg/cm^2. The remaining cell contained 140 mg of uranium enriched to 93% in ^{235}U. The uranium was electroplated on both sides of a semicircular stainless-steel disk (250 μm thick) to a density of 0.5 mg/cm^2.

To define a valid fission event and to reduce alpha pileup background and noise we required a coincidence between the pair of photomultiplier tubes on each cell. The fission events from each cell once digitized and routed by an EG&G TDC 100 clock were stored separately in the computer. Both pulse-height and time-of-flight information were recorded to provide a continuous monitor as a function of neutron energy of the fission bias for each cell.

Data Reduction

$E_n > 0.1$ MeV. After background corrections, which were assumed essentially constant for the ^{231}Pa and ^{235}U time-of-flight (TOF) spectra, the shape of the ^{231}Pa(n,f) cross section was obtained using the ^{235}U(n,f) cross section derived from ENDF/B-V. The ^{231}Pa fission cross section was normalized between 0.9 and 1.1 MeV to the data of Sicre.[2] In this procedure it was assumed implicitly that the efficiency of the detector was independent of neutron energy.

$E_n < 10$ keV. Since the data recorded in this energy region can provide only preliminary results, due to the limited available beam time for this measurement, a simple reduction procedure was adopted. By assuming that the energy dependence of the neutron flux is close to $1/E_n$, $\sigma_f \sqrt{E_n}$ is proportional to the ^{231}Pa TOF spectrum when it is reduced to a constant channel width. The proportionality constant was determined by the ratios of $^{231}Pa/^{235}U$ counts at 230 and 380 keV and from the known fission cross section at 13.16 eV for ^{235}U. As a check of the energy dependence of the neutron flux, the ^{235}U TOF spectrum was compared to $\sigma_f \sqrt{E_n}$. The two sets of data agree to within a few percent between 0.4 and 100 eV.

Results

The ^{231}Pa(n,f) cross section is plotted in Fig. 1 from 0.1 to 12 MeV. The peaks and the strong fluctuations observed below 1 MeV are superimposed on an underlying cross-section characteristic of a neutron-induced threshold fission reaction whose threshold is located around 750 keV. The second chance fission threshold occurs in the vicinity of E_n = 6 MeV leading to a plateau value for σ_f of ∿2 b.

Figure 2 displays a more detailed picture of σ_f between 0.12 and 0.42 MeV. For comparison we have plotted the data of Sicre[2] which were taken with a resolution of 5 keV, except for the 160-keV data point which was taken with a resolution of 2 keV. Below 0.5 MeV, Sicre's data are systematically lower even though the present data were normalized to his cross section in the 0.9- to 1.1-MeV region. However our data are in good agreement with the results reported in Ref. 1 and 4. The striking feature of this figure lies in the considerable amount of fine structure in the cross section which had not been observed in the data of Sicre. This is due to the substantial improvement in the resolution of the present measurement. For instance, at 160 keV our resolution is 0.4 keV. As a result, the shape of the resonance at 156.7 keV which has a FWHM of 2.9 keV is now better defined (peak/valley ratio ≙ 13). However, the wings of this resonance are not fully consistent with a Breit-Wigner shape. This suggests the presence of additional structure centered around the 157-keV peak. In addition, the good energy resolution reveals the presence of other sharp resonances (at least two in the vicinity of E_n = 370 keV) and separates into several components the broad peaks located around E_n = 180 and 330 keV. Table II gives a preliminary list of the peak energies of σ_f together with K^π values extracted from Ref. 2.

Table II. Resonance energies and corresponding K^π values.

E_n(keV)	K^π	E_n(keV)	K^π
156.7	3^+	304.5	
173.3		312.1	
182.3		319.3	
187.4		328.6	0^-
193.8	0^+	336.7	
281.9		371.1	
300.6		375.7	

Below 100 eV (see Fig. 3), a number of fission resonances are observed for the first time except for the 4 rsonances below 1.3 eV already reported by Leonard *et al.*[5] The resonance energies are in very good agreement with those given by Simpson *et al.*[6] in their total cross-section measurement. However, we observe additional resonances above 15 eV. Rather than being clustered around definite energies as observed in several subthreshold cross sections,[7-10] these resonances seem to be uniformly distributed, at least below 100 eV. Because of poor statistics it is not possible at the present time to verify if this behavior is similar in the keV region. From the $g\Gamma_n$ and Γ values reported in Ref. 11, tentative Γ_f values have been calculated and are listed in Table III together with other resonance parameters. A meaningful average fission width $\langle\Gamma_f\rangle$ can be obtained only for those resonances below 15 eV because resonances were missed above this energy in the total cross section measurement. The average fission width for the resonances below 15 eV is 8 μeV, about 3 to 4 orders of magnitude lower than what is generally measured for fissile nuclei. In the energy region analyzed, [1.24 < E_n(eV) < 57.3] no significant enhancement of Γ_f is noted. This is similar to the behavior of the fission widths for the fissile nuclei.

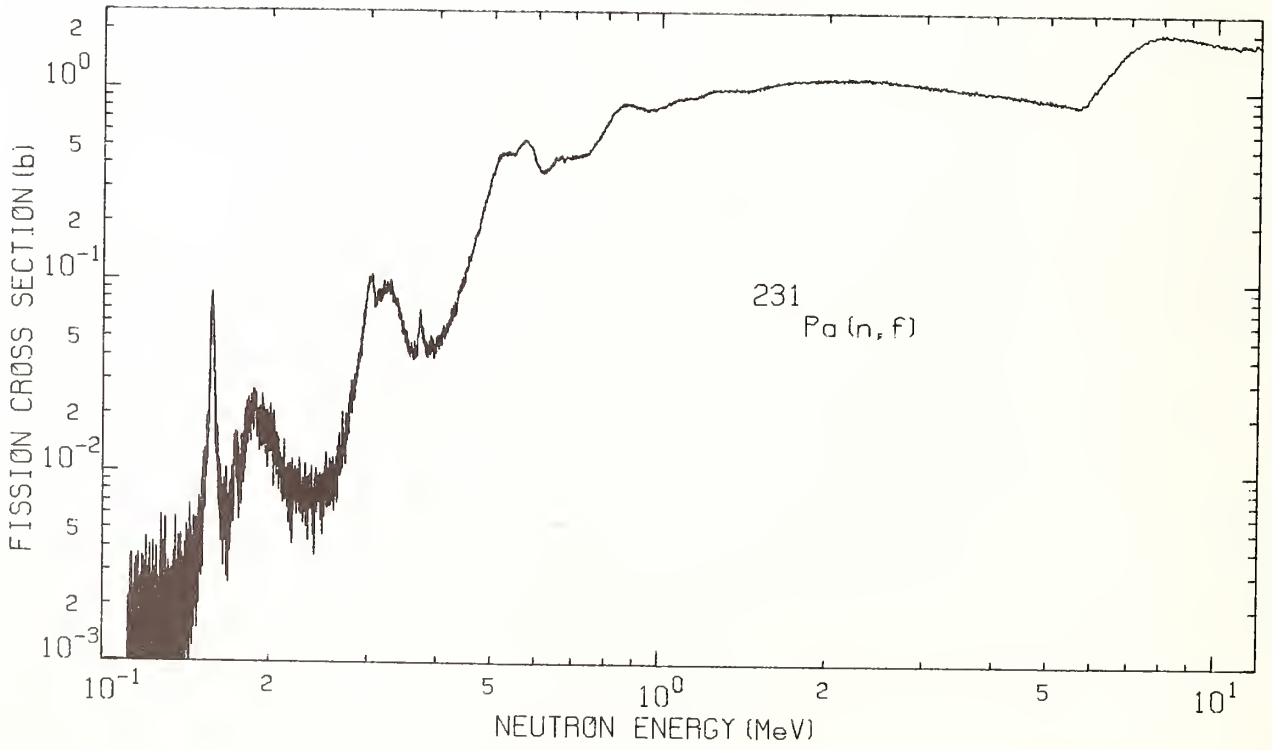

Fig. 1. Fission cross section of ^{231}Pa between 0.12 and 12 MeV. The data are plotted at intervals which correspond to a timing-channel width of 2 ns.

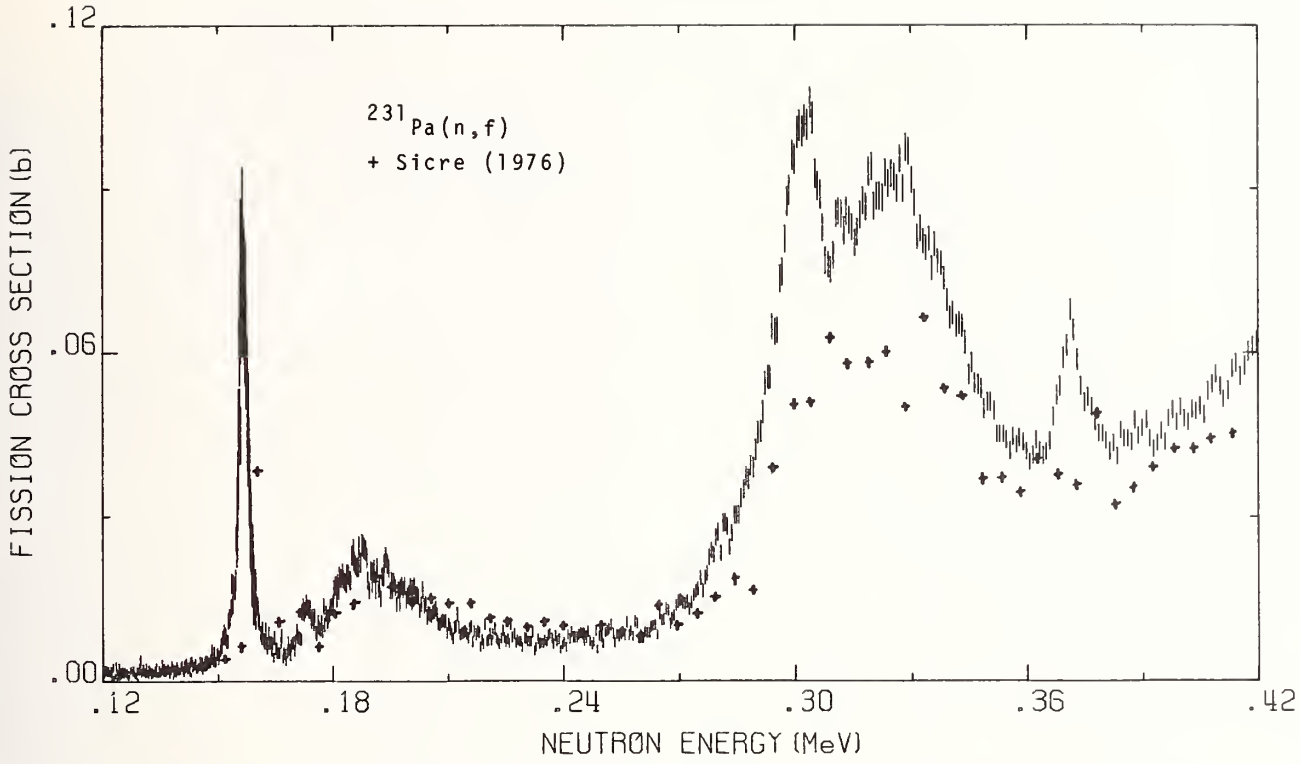

Fig. 2. Fission cross section of ^{231}Pa between 0.12 and 0.42 MeV. The data are plotted at intervals which correspond to a timing-channel width of 6 ns except for the resonance at 157 keV where the channel width was kept at 2 ns. The error bars correspond to one standard deviation. For clarity, the data points of Sicre are plotted with no error bars.

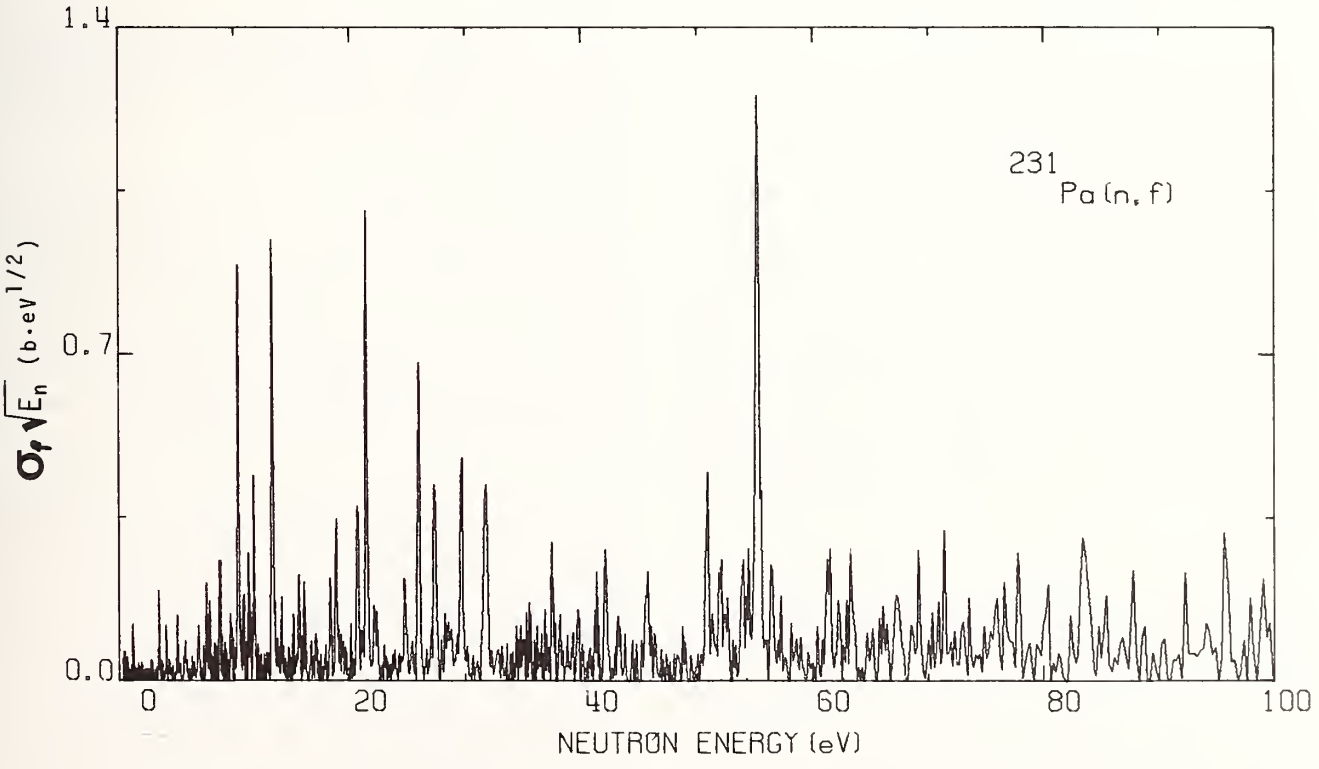

Fig. 3. Fission cross section of ^{231}Pa (multiplied by $\sqrt{E_n}$) between 0.4 eV and 100 eV. The averaged data correspond to a 24-ns channel width.

Table III. Preliminary fission widths and other resonance parameters from 1 eV to 58 eV for ^{231}Pa + n.

E_n(eV)[a]	A_f(b·eV)	$g\Gamma_n$(meV)[a]	Γ(meV)[a]	Γ_f(μeV)
1.24	0.0079	0.0280	46	8
1.40	0.0	0.0012	45	0
1.96	0.0014	0.0071	46	9
2.79	0.0029	0.0099	39	16
3.48	0.0108	0.0470	48	19
4.12	0.0043	0.0850	50	5
4.35	0.0020	0.0600	60	4
4.53	0.0013	0.0170	55	9
5.06	0.0070	0.4900	63	2
5.28	0.0017	0.0850	45	2
5.63	0.0016	0.0470	45	4
5.82	0.0049	0.0580	45	11
6.55	0.0014	0.0490	50	5
6.87	0.0076	0.2500	46	5
7.57	0.0058	0.0930	60	14
7.82	0.0092	0.1820	55	11
8.73	0.0142	0.7400	57	5
9.26	0.0006	0.0460	55	3
9.70	0.0073	0.2300	50	8
10.33	0.0461	0.7000	49	16
10.76	0.0071	0.3410	30	3
11.26	0.0101	0.3620	50	8
11.67	0.0199	0.6830	50	8
12.08	0.0006	0.0216	50	8
13.26	0.0331	0.8010	50	13
13.38	0.0345	1.0970	50	10
14.10	0.0029	0.5780	50	2
15.06	0.0043	0.1090	50	15
15.57	0.0112	0.2010	50	21
16.02	0.0059	0.3280	50	7
16.66	0.0043	0.2290	50	8
16.99	0.0055	0.3060	50	7
18.29	0.0103	1.5140	50	3
18.74	0.0195	0.6930	50	13
19.25	0.0036	0.1760	50	10
19.55	0.0013	0.0800	50	8
20.30	0.0016	0.0410	50	19
20.60	0.0203	0.9990	50	10
21.30	0.0056	0.5540	50	5
21.45	0.0432	0.6480	50	35
22.12	0.0134	0.4700	50	15
24.75	0.0125	0.2790	50	27
25.45	0.0037	0.0910	50	26
25.97	0.0364	1.0700	50	21
26.85	0.0027	0.1550	50	12
27.32	0.0288	0.5540	50	35
28.23	0.0033	0.2020	50	11
28.69	0.0048	0.2680	50	12
29.62	0.0246	1.6870	50	11
30.22	0.0033	0.0550	50	45
31.73	0.0332	3.3800	50	8
32.20	0.0016	0.0570	50	22
32.80	0.0048	0.1800	50	21
33.39	0.0017	0.1400	50	10
35.15	0.0043	0.2000	50	19
36.14	0.0035	0.3900	50	8
36.65	0.0025	1.4500	50	2
36.80	0.0033	0.3600	50	8
37.53	0.0119	0.9800	50	11
38.26	0.0060	0.2000	50	28
39.73	0.0073	1.0500	50	7
41.27	0.0085	0.4500	50	19
42.08	0.0140	0.6500	50	22
43.34	0.0092	1.5100	50	7
44.54	0.0009	0.1900	50	5
44.91	0.0023	0.1100	50	23
45.64	0.0144	1.2200	50	13
46.39	0.0076	0.3300	50	26
47.22	0.0022	1.0300	50	2
48.60	0.0043	0.2920	50	18
50.12	0.0030	0.1300	50	29
50.85	0.0209	0.8560	50	30
51.25	0.0063	0.4900	50	16
51.92	0.0115	0.9800	50	15
52.54	0.0105	2.1800	50	6
53.91	0.0122	0.8080	50	20
54.45	0.0117	1.3600	50	11
55.20	0.0738	9.3600	59	13
56.52	0.0108	0.8300	50	18
57.16	0.0094	1.4200	50	9

[a]Ref. 11

When not reported in Ref. 11, Γ values were assumed to be 50 meV.

Discussion

Sicre[2] concludes from his fission fragment angular distribution measurements on ^{231}Pa ($I^\pi = 3/2^-$ in its ground state) that the resonance at 156.7 keV is a pure vibrational state having $K^\pi = 3^+$. However, our data suggest that this resonance is fragmented. A possible explanation for this fragmentation may be due to a rotational band built on this vibrational state. The resonances of this band would have $J^\pi > 3^+$ and therefore be formed with $\ell \geq 3$ neutrons leading to peak cross sectons on the order of a few mb. This is consistent with the magnitude of the structure observed in the tails of the 156.7-keV peak. However, the spacing of members of such a rotational band is on the order of 20 keV if we assume $\hbar^2/2\mathcal{I} = 2$- to 3-keV as reported for ^{240}Pu[12] and ^{231,233}Th[13,14]. This spacing is much larger than the energy span of the underlying structure. A spacing of a few keV would require a moment of inertia $\mathcal{I}$ incompatible with a stable shape of the nucleus.

To interpret the particular shape of this resonance we propose the following picture in the framework of the calculations of Möller et al.[15,16] This resonance could represent a vibrational state trapped in a shallow asymmetrically deformed third minimum of the triple-humped fission barrier of ^{232}Pa. The additional observed structure would come from coupling between this vibrational state (Class-III state) and more complex states (Class II states) at somewhat less deformation that exhibit an average spacing $\langle D_{II} \rangle$ of a few keV. The gross structures observed by Sicre[2] at approximately 180 and 330 keV were interpreted in terms of $K^\pi = 0^+$ and 0^- rotational band, respectively. We observe more structure than can be accounted for by just two simple rotational bands. As in the case of the 156.7-keV resonance, this additional structure may be due to the fragmentation of the members of the rotational bands.

Since we adopt the model of an asymmetrically deformed third minimum, one should expect to find vibrational states of both parities which can be verified by a WKB calculation.[17] We speculate that the resonance located at 173.3 keV could be a possible candicate for a $K^\pi = 3^-$ vibrational state. Indeed, 1) the peak cross section has a correct magnitude to be formed with $\ell = 2$ neutrons, and 2) its separation from the 3^+ state (16.6 keV below) is comparable to what has been reported by Blons et al.[13] for ^{231}Th and calculated by Möller et al.[16] for this mass region.

We also would like to point out that the average width of the narrow resonances observed in the eV region is in good agreement with that calculated using the the double-humped barrier parameters of Sicre[2] ($\langle \Gamma_f \rangle_{calc} = 7.7$ μeV). A double-humped barrier is not necessarily inconsistent with the triple-humped barrier proposed to explain the fragmentation of the 157 keV resonance. Indeed, if we assume a rather shallow third minimum then the outer two barriers could be approximated by a single barrier with $\hbar\omega_B = .45$ MeV[2]. The agreement between the observed and the calculated average fission width also suggest that the acquired fission strength of the eV resonances is not a result of coupling between the Class I and the Class II states but a result of direct penetration through the total fission barrier.

Conclusion

This measurement has revealed a considerable amount of fine structure in the threshold region of the neutron-induced fission cross section of ^{231}Pa. We speculate that some of the newly observed structure may be due to coupling between vibrational states of the third well to more complex states of the second well of the fission barrier. A more accurate knowledge of the fission mechanism for this nucleus would require a high-resolution measurement of 1) the fission fragment anisotropies between 0.1 and 0.4 MeV, and 2) the fission cross section in the keV region to look for possible intermediate structure. In addition, other experiments such as γ-ray spectra measurements from the ^{231}Pa(d,pγ) reaction for excitation energies below S_n would provide a sensitive probe for determining the depth of the first and second minima of the fission barrier.

Acknowledgments

We are particularly indebted to P. Möller and M. Howard for fruitful discussions and access to their recent results prior to publication. We are grateful to E. Kobisk and P. Kuehn from the Solid State Division of Oak Ridge National Laboratory for the very successful preparation of the ^{231}Pa samples. The staff of ORELA should also be thanked for the smooth operation of the Linac. One of us (S. P.) would like specially to thank the Physics Division of the Los Alamos Scientific Laboratory for its warm hospitality and constant support during this experiment.

References

1. D. W. Muir and L. R. Veeser, in Proceedings of the Conference on Nuclear Cross Sections and Technology, Knoxville, TN, March 15-17, 1971, p. 292.

2. A. Sicre, Ph.D thesis, University of Bordeaux (1976), Report CENBG 7603.

3. F. M. Mann and R. E. Schenter, Nucl. Sci. Eng., 65, 544 (1977).

4. S. M. Dubrovna and V. A. Shigin, Sov. Phys. Doklady, 9, 579 (1964).

5. B. R. Leonard, Jr., and R. H. Odegaarden, Bull. Amer. Phys. Soc., 6, 8 (1961); Hanford Report 67219 (1960).

6. F. B. Simpson, W. H. Burgus, J. E. Evans and H. W. Kirby, Nucl. Sci. Eng., 12, 243 (1960).

7. D. Paya, H. Derrien, A. Fubini, A. Michaudon and P. Ribon, in Nuclear Data for Reactors, IAEA Vienna 1967, II, p. 128; A. Fubini, J. Blons, A. Michaudon and D. Paya, Phys. Rev. Lett., 20, 1373 (1968).

8. E. Migneco and J. P. Theobald, Nucl. Phys., A112, 603 (1968).

9. G. D. James, J. W. T. Dabbs. J. A. Harvey, N. W. Hill and R. H. Schindler, Phys. Rev., C15, 2083 (1977).

10. F. C. Difilippo, R. B. Perez, G. de Saussure, D. K. Olsen, R. W. Ingle, Nucl. Sci. Eng., 68, 43 (1978).

11. BNL 325, 1, Third Edition (1973).

12. H. J. Specht., J. Weber, F. Konecny and D. Heunemann, Phys. Lett., 41B, 43 (1972).

13. J. Blons, C. Mazur, D. Paya, M. Ribrag and H. Weigmann, Phys. Rev. Lett., 41, 1281 (1978).

14. J. Blons, C. Mazur and D. Paya, Phys. Rev. Lett., 35, 1749 (1975).

15. P. Möller and J. R. Nix, in Proceedings of Physics and Chemistry of Fission, IAEA Vienna 1974, I, p. 103.

16. P. Möller and M. Howard, private communication (1979).

17. L. D. Landau and E. M. Lifshitz, in Quantum Mechanics, Pergamon Press (1958), p. 176.

FISSION CROSS SECTION OF ^{245}Cm FROM 10^{-3} EV TO 10^{4} EV

R. M. White, J. C. Browne*, R. E. Howe, J. H. Landrum, and J. A. Becker
University of California Lawrence Livermore Laboratory
Livermore, California 94550, U.S.A.

The neutron-induced fission cross section of ^{245}Cm has been measured from .001 eV to 10 keV using the LLL 100-MeV Linac. The resonance data are analyzed with a multilevel-multichannel R-matrix code. The statistical distribution of R-matrix parameters extracted from the analysis are investigated and comparisons are made with previous work.

[^{245}Cm(n,f), 10^{-3} eV - 10 keV, multilevel R-matrix analysis, deduced levels, $\langle\Gamma_n^o\rangle$, $\langle\Gamma_f\rangle$, $\langle D\rangle$.]

Introduction

The neutron-induced fission cross section of ^{245}Cm described below is part of an ongoing series of measurements aimed at determining neutron cross sections in the transplutonium mass region. Many of these cross sections are important for calculating heavy actinide concentrations in reactor fuel elements. This has application in both production of heavy isotopes and also in actinide-waste recycling schemes. The location of ^{245}Cm in the reactor production chain makes its cross section particularly important. Its predecessor, ^{244}Cm, has a small capture cross section that acts to retard the mass transfer to heavier isotopes. The mass loss to fission or transferred through to ^{246}Cm depends on the fairly large fission and capture cross section of ^{245}Cm and on the energy dependence of the incident neutron spectrum.

Previous measurements and a review of work to date on the fission cross section of ^{245}Cm are given by Browne, et al.[1] The experiment described in this paper was only recently completed (July, 1979) and the conclusions drawn from the R-matrix analysis are preliminary.

Experimental Procedure

The data for this experiment were taken using the LLL 100-MeV linac. Electrons from the linac were focused on a target consisting of water cooled tantalum plates coupled to an H_2O moderator. The data were accumulated in two overlapping measurements from 10^{-3} eV to 100 eV and from 0.5 eV to 10^4 eV respectively with the fission samples viewing only the H_2O moderator at both flight paths. The neutrons were collimated with a series of polyethylene, borated polyethylene and lead collimators and their energies were measured by time-of-flight techniques.

The fission sample consisted of approximately 189 μg of isotopically enriched (>99%) ^{245}Cm electroplated onto a 0.05 mm-thick nickel hemispherical foil to a density of ∿123 μg/cm^2. A fission sample of ^{235}U was also included in this measurement. The ^{235}U sample was prepared by vapor deposition onto 0.006 mm thick titanium foils to a density of approximately 500 μg/cm^2. Fission fragments were detected using a hemispherical ionization chamber for ^{245}Cm and a parallel-plate ionization chamber for ^{235}U. Signals from each chamber were amplified using fast, current sensitive preamplifiers. The ionization chambers used an Ar-CO_2 (96%-4%) mixture at a pressure of approximately one atmosphere.

The neutron flux was measured from 10^{-3} eV to 100 eV using 1-mm thick NE901 (2.4% natural) lithium glass and from 0.5 eV to 10^4 eV using 1-mm thick NE905 (6.6% enriched ^6Li) glass scintillators, which were positioned in the neutron beam between two 5-cm diameter photomultiplier tubes. Fission events from the ionization chambers and signals from the lithium glass scintillators were each collected in time-of-flight arrays of approximately 2000 channels.

Both the ^{245}Cm and ^{235}U low energy (10^{-3} to 100 eV) fission data were reduced to relative cross sections by normalization to the measured flux shape. The ^{235}U relative cross section was normalized to the known 2200 m/sec ^{235}U fission cross section. This normalization constant along with the ratio of the $^{245}Cm/^{235}U$ masses and the relative efficiencies of the two fission chambers, determined from pulse height spectra, provided the proper normalization for the ^{245}Cm relative cross section. The ^{245}Cm resonance data (0.5 to 10^4 eV) were normalized to the low energy cross section between 0.8 and 1.5 eV.

Data Analysis

The fission cross section was analyzed on a CDC 7600 computer with the multichannel R-matrix code, MULTI, of Auchampaugh.[2] The code performs a least-squares fit to total, scatter, fission, and capture cross sections and allows for resolution and Doppler broadening of resonance data. In addition to the MULTI code a sophisticated graphics package utilizing the LLL television monitor display system (TMDS) was written to allow instant graphical comparison of least-squares fits to the fission data with each iteration process. This system allows for convenient and timely analysis of the data. Though there are two compound nuclear states (3^+ and 4^+) formed by the interaction of an ℓ=0 neutron with the $7/2^+$ ground state of ^{245}Cm, all states in the 0-80 eV region were assumed to be of one spin group, namely 4^+. A three channel R-matrix, consisting of one neutron and two fission channels, was used to obtain the fits in Figs. 1 through 4. A constant 40 meV width was used for the capture widths of all resonances in this analysis.

Figure 1 shows the fit to the data from .01 to 10 eV. It is evident that the low energy data are not yet fit perfectly. Two possible reasons are (1) that more than one bound state is necessary to correctly fit the region from .01 to 0.5 eV and (2) that the broad resonance at 1 eV is actually two states. Further work is required to resolve this question. Figure 2 shows the fit from 1 to 10 eV and includes two additional states at 7.5 eV and 9.0 eV not seen in previous measurements. It is clear that an excellent fit to this region has been obtained. Figure 3 is a fit to the region from 10 to 32 eV. A fairly dramatic lack of resonances is apparent from the small cross section in the region from 12 to 20 eV. At least three other measurements have been made[1,3,4] for which analysis is complete and resonance parameters can be compared. Fairly good agreement between this work and that of Browne, et al.[1], and Berreth, et al.[3], is obtained. The major work from 20 to 60 eV is that of Moore and Keyworth[4]. Their data were taken using the Physics 8 nuclear explosion as a

*Now at Los Alamos Scientific Laboratory, P.O. Box 1663, Los Alamos, NM 87545.

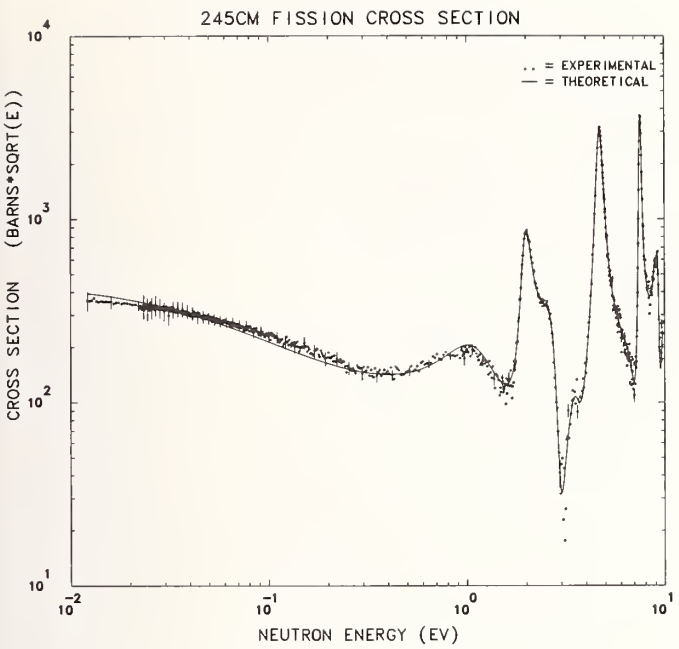

Figure 1. Least-squares multichannel R-matrix fit to ^{245}Cm fission cross section (multiplied by $\sqrt{E_n}$) from .01 to 10 eV.

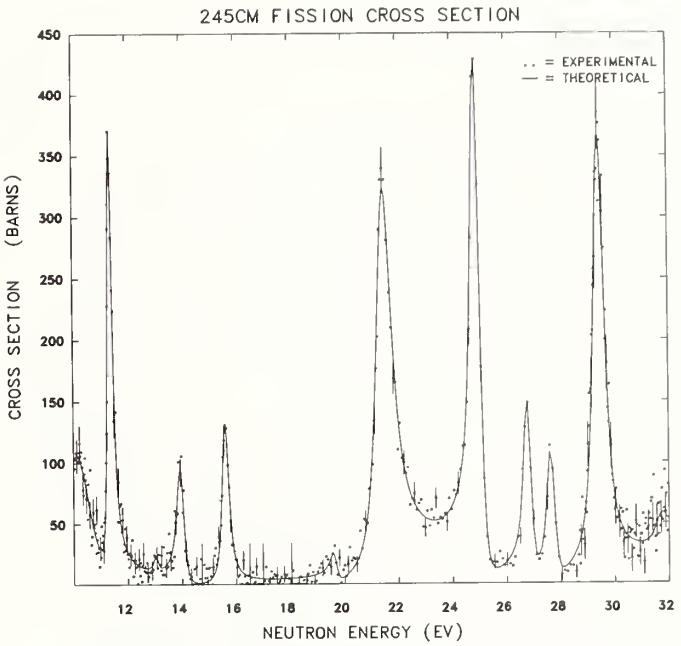

Figure 3. ^{245}Cm fission cross section with R-matrix fit from 10 to 32 eV.

neutron source and to obtain equivalent statistics with a linac would require approximately 2.5 years of continuous running time. In the region of overlap from 20 to 30 eV our data have reasonable statistics however, and there are systematic differences in the neutron and fission widths obtained in this analysis and that of Ref. 4. In the 20 to 30 eV region both the neutron and fission widths are approximately 20% larger for most resonances in the present analysis than those obtained in Ref. 4. This is unfortunate because the present data cannot compare statistically with that of Ref. 4 above 30 eV and the resonance parameters from 30 to 60 eV are needed to make a more meaningful statistical study of the neutron and fission widths. Figure 4 shows a fit to the data from 30 to 80 eV. While the overall fit is reasonable it is nontheless clear that levels are missing and that statistics limit the information that can be obtained from this analysis.

Figure 5 is a plot of the number of levels as a function of energy for the present data to 30 eV and the data of Moore, et al. from 30 to 60 eV. The straight lines are least-squares fits to the region from 0-15 eV and from 25 to 60 eV. The average level spacings are 1.02 eV and 1.48 eV respectively. The problem of two different slopes comes about from the fact that (1) there exists two sets of levels in the 7-9 eV region that are unusually closely spaced and (2) there exists few levels in the 15 to 25 eV region. This problem would be exacerbated were it not

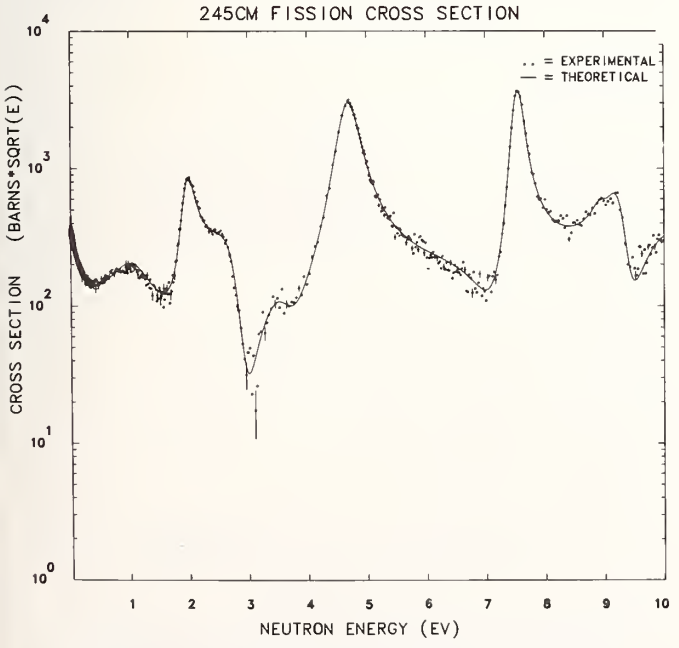

Figure 2. R-matrix fit to ^{245}Cm fission cross section (multiplied by $\sqrt{E_n}$) from 1 to 10 eV.

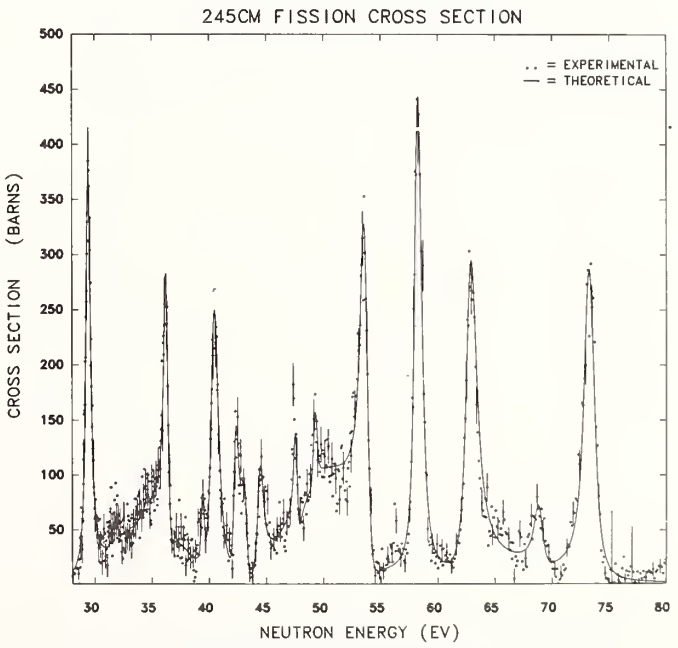

Figure 4. ^{245}Cm fission cross section from 30 eV to 80 eV with R-matrix fit.

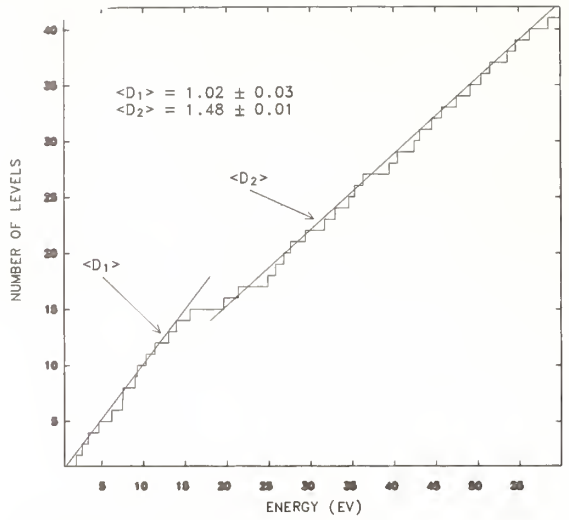

Figure 5. Histogram showing the number of levels observed as a function of energy for the present work to 30 eV and that of Ref. 4 from 30 to 60 eV. The straight lines are least-squares fits to the data. The average level spacings are in units of eV.

for the discovery of two small resonances not seen before at 13.1 and 19.6 eV. Figure 6 is a plot of the number of levels vs. energy for the present analysis which includes 21 levels from 0 to 30 eV. The average level spacing is 1.5 eV. The histogram in Fig. 7 represents the variation of the sum of the reduced neutron widths, $\Sigma g\Gamma_n^\circ$, as a function of energy. The slope of the least-squares fitted straight line yields a strength function of $(1.02\pm0.02)\times10^{-4}$.

Fig. 8 shows the experimental distribution of reduced neutron widths compared to a Porter-Thomas distribution (chi-squared distribution with one degree of freedom) for the 21 levels up to 30 eV. The average reduced neutron width is 0.287 meV. In Fig. 9 we compare the experimental distribution of fission widths with a chi-squared distribution of three degrees of freedom. The maximum likelihood method was applied to the fission widths and yielded the most likely number of degrees of freedom to be

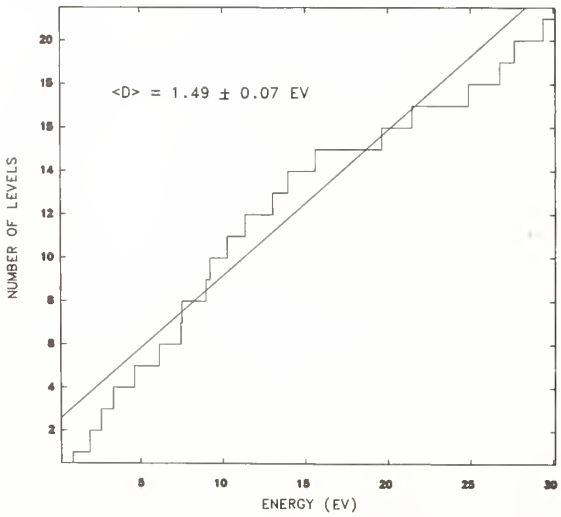

Figure 6. Histogram showing the number of levels observed as a function of energy for the present work to 30 eV.

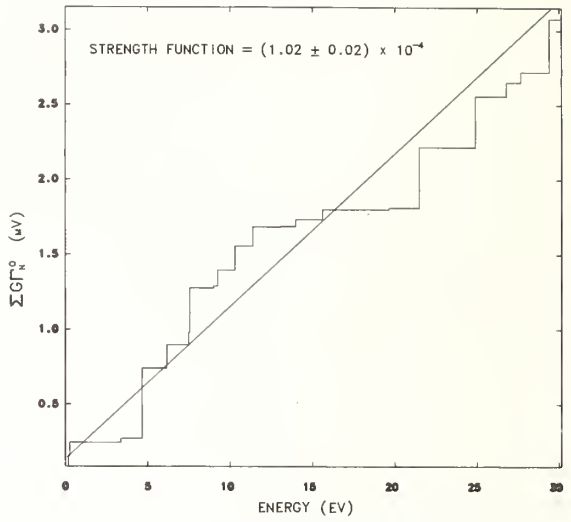

Figure 7. Histogram showing the sum of the reduced neutron widths as a function of energy.

2.8±0.8. In the strong coupling picture of fission, the effective number of open fission channels, N, is equal to $2\pi\langle\Gamma_f\rangle/\langle D\rangle$ which for the present case is 2.3.

Summary

The ^{245}Cm fission cross section has been measured from .001 eV to 10 keV. Preliminary resonance parameters have been obtained for levels below 30 eV. The average fission width is 550 meV. The neutron strength function (1.02×10^{-4}) is in reasonable agreement with neighboring nuclei. The average level spacing with energy appears to be different over the regions from 1 to 15 eV and 25 to 60 eV. For distributions of neutron and fission widths more levels need to be included for more statistically meaningful analysis. In the region of overlap with previous analysis up to 60 eV systematic differences occur which preclude folding in those parameters with the present work.

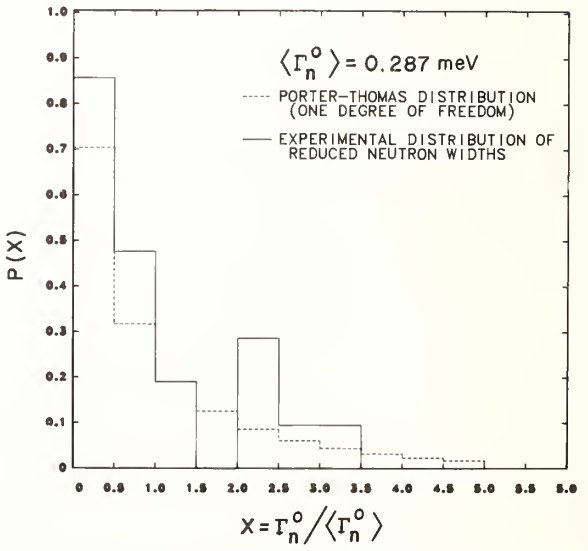

Figure 8. Distribution of reduced neutron widths for 21 levels from the present work to 30 eV.

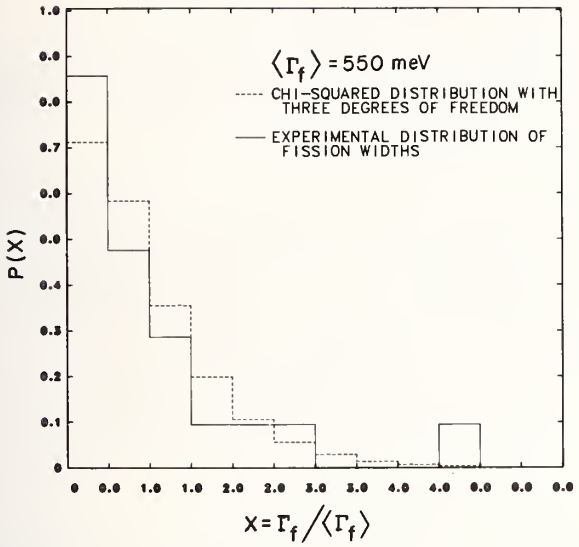

Figure 9. Distribution of the fission widths for 21 levels from the present work to 30 eV.

Acknowledgments

The authors sincerely appreciate the efforts of G. F. Auchampaugh in making his MULTI code and his expertise in analyzing cross sections available to us. Our appreciation also to R. E. Strout, II who developed the graphics display for MULTI and made the total package operational on the Livermore computers. This work was performed under the auspices of the U.S. Department of Energy by the Lawrence Livermore Laboratory under contract number W-7405-ENG-48.

References

1. J.C. Browne, R.W. Benjamin, and D.G. Karraker, Nucl. Sci. Eng., 65, 166 (1978).
2. G. F. Auchampaugh, Private communication.
3. J.R. Berreth, F.B. Simpson, and B.C. Rusche, Nucl. Sci. Eng. 49, 145 (1972).
4. M.S. Moore and G.A. Keyworth, Phys. Rev. C, 3, 1656 (1971).

FIRST AND SECOND CHANCE FISSION CALCULATIONS FOR ACTINIDES AND RELATED TOPICS

G. Maino(°), E. Menapace, M. Motta, A. Ventura
Laboratorio Dati Nucleari - Centro di Calcolo del CNEN, Bologna, Italy

First and second chance contributions to neutron induced fission cross sections in an energy range of interest for reactor applications ($E_n \leq 13$ MeV) were obtained by extensive and consistent calculations for ^{241}Am; moreover, a simplified semiempirical approach was applied to ^{235}U and ^{239}Pu.
[Hauser-Feshbach formalism, optical model, fission probabilities, $E_n \leq 13$ MeV , ^{241}Am, ^{235}U, ^{239}Pu].

Description of the Method

Hauser-Feshbach calculations, corrected for statistical width fluctuations as in ref. [10], were performed to obtain the cross sections via compound nucleus for the "first chance" fission ($=\sigma'_{nf}$) and for the competing channels: radiative capture ($=\sigma_{n\gamma}$), elastic ($=\sigma_{ce}$), total inelastic ($=\sigma_{nn'tot.}$), for which the separate components σ_{n2n} , $\sigma_{nn'\gamma}$, $\sigma_{nn'f}$ ("second chance" fission) were calculated.

The compound nucleus formation cross section σ_c has to be consistent with optical and pre-equilibrium model calculations, according to

$$\sigma_c = \sigma_{tot} - \sigma_{se} - \sigma_{in}(\text{direct}) - \sigma_{nn'}(\text{pre-eq.}) \qquad (1)$$

where σ_{tot} is the total cross section, σ_{se} and σ_{in} (direct) the shape elastic and the direct collective inelastic contributions, respectively, from "coupled channel" OM calculations ("JUPITOR" [1] and "ADAPE" [2] codes); $\sigma_{nn'}$(pre-eq.) is a pre-equilibrium contribution to neutron emission, estimated by a simple extension of the Brown and Muirhead model [3] (PRODE code [4]).

The pre-equilibrium fission is expected to give an important contribution at energies above the upper limit of the interesting interval.

In order to calculate $\sigma_{n,2n}$, $\sigma_{n,n'\gamma}$ and $\sigma_{n,n'f}$ for a target nucleus ${}^{A}_{N}X_{Z}$, the branching ratios P_n, P_γ and P_f for neutron emission, γ-decay and fission, respectively, were determined as functions of excitation energy, spin and parity of the decaying nucleus ${}^{A}_{N}X_{Z}$.

Application to ^{241}Am

The isotope ^{241}Am has been chosen as an example of application. The importance of ^{241}Am in power reactor and fuel cycle problems is discussed, e.g., in ref. [15].

The optical model parameters used in our calculations (Table I) are those of ref. [5], slightly modified at low neutron energies for a better approximation of $\bar{\sigma}_c$ (rel.(2) below) and of the experimental strength function [15] $S_0 = (0.93 \pm 0.10) \times 10^{-4}$: the calculated value is $S_0 = 0.89 \times 10^{-4}$; moreover, we obtain $S_1 = 2.5 \times 10^{-4}$ and a scattering radius $R' = 9.02$ fm, in comparison with the experimental value [17] $R' = (10.1 \pm 0.4)$ fm.

The adiabatic approximation was assumed above 2 MeV.

Table I. Deformed optical model parameters

$V = 47.01 - 0.267\,E - 0.00118\,E^2$ MeV (E in MeV)

$$W = \begin{cases} 3.2 \text{ MeV} & (E \leq 2.26 \text{ MeV}) \\ 2.25 + 0.42\,E \text{ MeV} & (E > 2.26 \text{ MeV}) \end{cases}$$

$V_{S.O.} = 7.2$ MeV

$r_V = 1.259$ fm; $r_W = 1.237$ fm; $r_{S.O.} = 1.259$ fm

$a_V = 0.66$ fm; $a_W = 0.48$ fm; $a_{S.O.} = 0.66$ fm

$\beta_2 = 0.22$; $\beta_4 = 0.03$

As for the quadrupole and hexadecapole ground state deformations, β_2 and β_4 , the experimental values [18] near A=241 are usually higher (by about 10%, on the average) than the theoretical ones [19-20]; in fact, they are strictly related to the adopted radius r_0 . Consistently with r_V in Table I, we adopted $\beta_2 = 0.22$ (ref. [20], where values in agreement with those of ref. [21] for Th, U, Pu nuclei were found) ; our $\beta_4 = 0.03$ is lower than that of ref. [20], but is in agreement with the systematics [18].

By means of these parameters the experimental total cross section [6] was adequately fitted.

As a further check of validity, σ_c obtained in (1) was compared with the ratio:

$$\bar{\sigma}_c(E_n) = \sigma_{nf}(E_n)/P_f(E_n) \qquad (2)$$

where σ_{nf} is the experimental fission cross section [7] (renormalized by a recent evaluation [8] of the standard $\sigma_{nf}(^{235}U)$) and P_f is the fission probability of compound nucleus ^{242}Am measured by Britt and coworkers [9] via the reaction $^{242}Pu(^3He,tf)$. σ_{tot} , σ_c and $\bar{\sigma}_c$ are shown in Fig. 1.

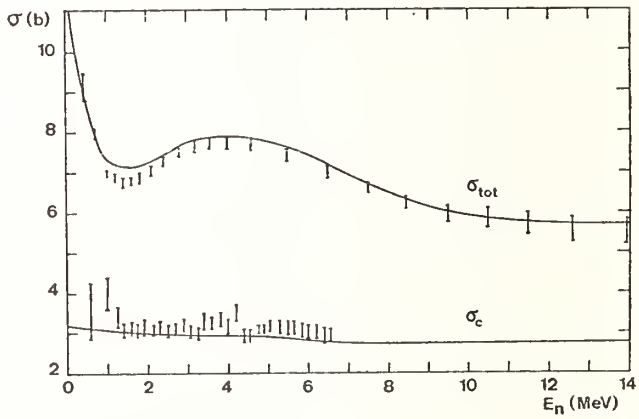

Fig. 1 Total and compound nucleus formation cross sections of ^{241}Am. Solid lines: calculated values. The error bars in σ_{tot} [6] are only statistical; relative systematic errors due to flux monitoring are estimated of the order of .6b. The error bars of $\bar{\sigma}_c$ are estimated from those of σ_{nf} [7] and P_f [9] (see formula (2)).

An "ad hoc" spherical optical potential was found, with the condition of adequately fitting the proper σ_c of (1), and utilized to obtain the neutron penetrabilities for HF calculations of the cross section "via" compound nucleus through a version of HAUSER code [10].

As for the nuclear level densities required in statistical calculations, a composite Gilbert-Cameron formula was used.

The values adopted for the temperature T , the parameter "a" and the spin cutoff σ^2 reproduce the cumulative number of nuclear levels at low energies, $E \leq 1$ MeV (refs. [11] and [12] for ^{241}Am and ^{242}Am, respectively) and, at higher energies, the total level density calculated by a microscopic method, based on shell model potential with pairing interaction treated in the BCS approximation, including collective (rotational)

(°) guest researcher

contributions [13]. In these calculations the assumed "gap parameter" Δ_o was deduced from a general actinide systematics [13]. In this way the calculated average s-wave resonance spacing of ^{241}Am (=0.58 eV) matched the experimental value [15] (=0.57±0.04 eV). In addition, the BCS temperature, at an excitation energy equal to the neutron binding energy in ^{242}Am, made it possible to reproduce by the "black-body" model of ref. [14] the experimental $\overline{\Gamma}_\gamma$=44 meV of ^{241}Am.

This procedure was also used to estimate the level density of the fissioning nucleus ^{242}Am at the first maximum of the fission barrier, where no experimental information is available. In this calculation, we assumed the same average "gap parameter" Δ_o as for the first minimum, and axial symmetry with quadrupole and hexadecapole deformations consistent with the ground state deformations (β_2=0.218 and β_4=0.03) and the adopted barrier parameters of Table II.

We would point out, however, that the hypothesis of axial symmetry at the first maximum has been abandoned in a recent analysis of fission probabilities [9]. (The introduction of axial asymmetry in our formalism has been undertaken).

As pointed out in section 1, for $\sigma_{nn'f}$ theoretical estimate, P_n, P_γ, P_f were calculated for ^{241}Am (compound) by neutron reaction on ^{240}Am through the same code [10].

In fig. 2, the theoretical P_f is compared with the experimental data by Britt and coworkers [9].

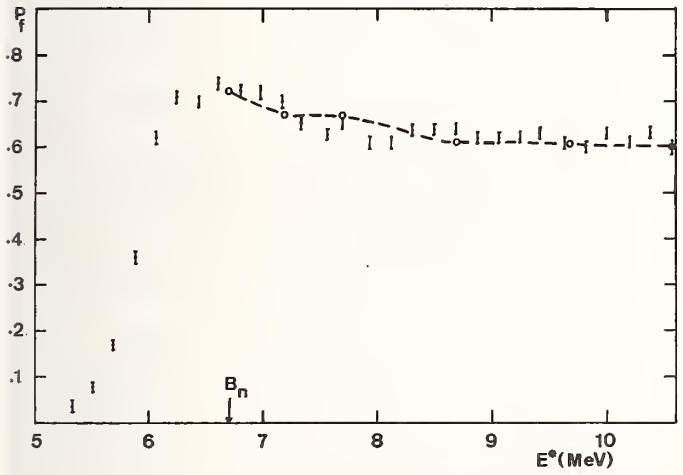

Fig. 2 Fission probabilities of the compound nucleus ^{241}Am. Dashed line: calculated values.

The final results for neutron induced reactions on ^{241}Am are shown in fig. 3, where the absorption and fission cross sections are plotted from 0.1 KeV to 1 MeV, and in fig. 4, where the fission cross section is calculated in the range 1-13 MeV; the relative cross sections of ref. [7] and [27] were renormalized by $\sigma_{nf}(^{235}U)$ of ref. [8]

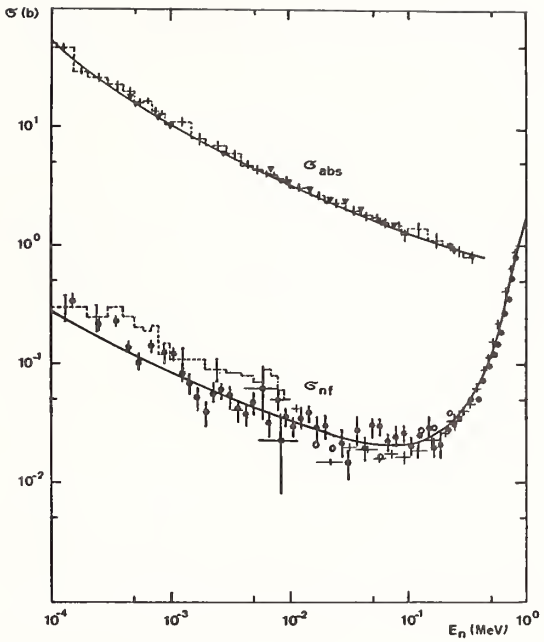

Fig. 3 ^{241}Am absorption and fission cross sections. Solid lines: calculated cross sections; σ_{abs}: ---: ref.[25]; ▼ : ref.[26]; σ_{nf}: ---: ref.[26]; ✱: ref.[27]; ○ : ref.[28]; + : ref.[29].

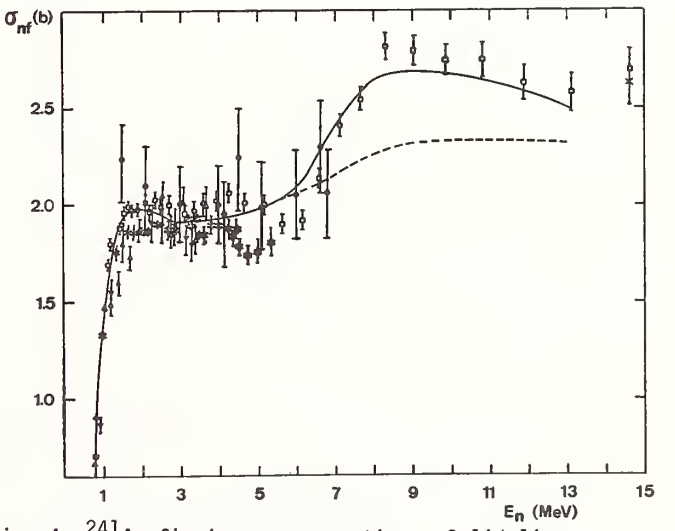

Fig. 4 ^{241}Am fission cross section. Solid line: calculated total fission cross section; dashed line: calculated first-chance fission contribution; Δ : ref.[29]; ✱: ref.[27]; ▼ : ref.[28]; ●: ref.[31]; □: ref.[7]; X : ref.[30]

Table II. Level density and fission barrier parameters

Nucleus	Deformation	T(MeV)	E_o(MeV)	$E_{cut.}$(MeV)	a(MeV^{-1})	Δ(MeV)	σ^2/T(MeV^{-1})
^{241}Am	ground st.	0.320	-0.300	2	22.5	-0.300	104
^{242}Am	ground st.	0.342	-2.000	2	26.0	-0.830	104
^{242}Am	1st saddle	0.350	-1.900	3	29.1	-0.700	100

Parameters of the two-humped fission barrier for ^{242}Am

E_A=6.16 MeV ; $\hbar\omega_A$=0.66 MeV ; E_B=4.80 MeV ; $\hbar\omega_B$=0.42 MeV

Our calculation cannot reproduce the trend of σ_{nf} around 14-15 MeV; in this interval the contribution of the third chance fission (n,2nf), the threshold of which is estimated at about 12.4 MeV, might not be negligible.

First and Second Chance Fission in a Semiempirical Approach

If experimental information about the reactions ${}^{A}_{N}X_{Z}(n,2n){}^{A-1}_{N-1}X_{Z}$, ${}^{A}_{N}X_{Z}(nn'tot.){}^{A}_{N}X_{Z}$ and the fission probability P_f of the compound nucleus ${}^{A}_{N}X_{Z}$,exists, the second-chance fission $\sigma_{nn'f}$ can be estimated by a simplified semiempirical approach, where (ref.[14])

$$\sigma_{nn'f} \simeq (\sigma_{n,2n}+\sigma_{n,n'\gamma})\beta/(1-\beta) \qquad (3)$$

$$\beta(E_n) \simeq \frac{1}{T^2(E_n)} \int_0^{E_{max}} E' \, P_f(E_n-E') e^{-E'/T(E_n)} dE' \qquad (4)$$

T (in energy units) is the thermodynamic temperature of the compound nucleus ${}^{A+1}_{N+1}X_{Z}$, corresponding to the incident neutron energy E_n , and E_{max} is the maximum kinetic energy available to the emitted neutron. The calculations were performed for U-235 and Pu-239; σ_{n2n} "via" compound nucleus in (3) was deduced from the experimental one [22] by subtracting the pre-equilibrium component calculated as in ref.[4] (see fig.5).

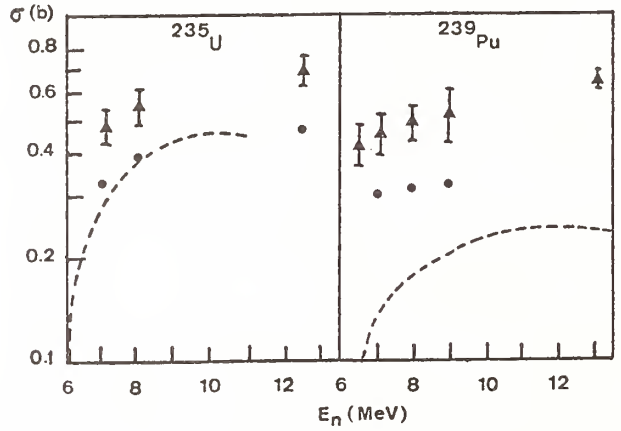

Fig. 5 σ_{n2n}: ▲ = experimental data of ref. 22; ● = compound nucleus component obtained by subtracting the pre-equilibrium contribution; --- = ENDF/B IV calculation.

The "first chance" contribution σ'_{nf}, deduced by difference from total fission, showed an increasing trend by 15% from (nn'f) threshold to 10 MeV for the considered nuclei.

This behaviour is consistent with theoretical predictions of ref. 23-24. In fact, from σ'_{nf} the ratio $\overline{\Gamma}_n/\overline{\Gamma}_f$ as a function of incident neutron energy can be estimated by

$$\overline{\Gamma}_n/\overline{\Gamma}_f \simeq [(1-R)\sigma_{tot}/\sigma'_{nf}] - 1 \qquad (5)$$

where the fraction $R = [\sigma_{se}+\sigma_{in}(direct)+\sigma_{nn'}(pre\text{-}eq.)]/\sigma_{tot}$ was derived by deformed optical model calculation (with the parameters of table I) and the codes of ref. [1,2,4]. The resulting $\overline{\Gamma}_n/\overline{\Gamma}_f$ ratios for ^{235}U and ^{239}Pu (see ref.[14]) are in reasonable agreement with those obtained in ref.[23-24] showing a bumplike structure with a maximum at about 4-5 MeV of neutron energy.

Acknowledgment

We thank Dr. H.C. Britt for providing us with his experimental fission probabilities.

References

1. T. Tamura, Rev. of Mod. Phys., 37, 679 (1965)
2. F. Fabbri and L. Zuffi, CNEN rep. RT/FI(69)7, Bologna (1969).
3. G. Brown and H. Muirhead, Phyl. Mag. 8, 474 (1957).
4. E. Menapace and M. Vaccari, to be published.
5. L. Zuffi, Nucl. Sci. and Eng. 68, 356 (1978).
6. T.W. Phillips and R.E. Howe, Nucl. Sci. and Eng. 69, 375 (1979).
7. J.W. Behrens and J.C. Browne, Livermore rep. UCID-17324 (1976).
8. M.R. Bhat, in Proc. of the Specialists'Meet. on Fast Neutr. Fiss. Cross Sect. of U-233, U-235, U-238 and Pu-239, Argonne Nat. Lab., USA, 1976, ed. by W.P. Poenitz and A.B. Smith, (rep. ANL-76--90, 1976), p. 307.
9. A. Gavron, H.C. Britt, E. Konecny, J. Weber and J.B. Wilhelmy, Phys. Rev. C13, 2374 (1976).
10. F.M. Mann, Hanford rep. HEDL-TME 76-80 (1976).
11. Y.A. Ellis, Nucl. Data Sheets 23, 123 (1978).
12. Y.A. Ellis and R.L. Haese, Nucl. Data Sheets 21, 615 (1977).
13. G. Maino, E. Menapace and A. Ventura, Nuovo Cimento 50A, 1(1979).
14. V. Benzi, in Proc. of the Conf. on Neutr. Phys. and Nucl. Data, Harwell (1978), p. 288.
15. G. Maino, E. Menapace, M. Motta and A. Ventura, CNEN rep. RT/FI(79)6, Bologna (1979).
16. V. Benzi, G. Maino and E. Menapace, Lett. Nuovo Cimento, 21, 231 (1978).
17. T.S. Belanova, A.G. Kolesov, V.M. Nikolaev, V.A. Safonov, V. Ya. Gabeskiriya, V.A. Poruchikov, S.M. Kalebin, R.I. Ivanov and O.M. Gudkov, Sov. Journ. of At. En. 38, 33 (1975).
18. C.E. Bemis jr., F.K. McGowan, J.L.C. Ford jr., W.T. Milner, P.H. Stelson, and R.L. Robinson, Phys. Rev. C8, 1466 (1973).
19. P. Möller, S.G. Nilsson and J.R. Nix, Nucl. Phys. A229, 292 (1974).
20. P.A. Seeger and W.M. Howard, Nucl. Phys. A238, 491 (1975).
21. J. Salvy, review paper presented at the Neutr. Interlab Seminar, Paris (1979).
22. D.S. Mather, P.F. Bampton, R.E. Coles, G. James and P.J. Nind, rep. AWRE-O-72/72, Aldermaston (1972).
23. H.C. Britt, M. Bolsterli ,J.R. Nix and J.L. Norton, Phys. Rev. C7, 801 (1973).
24. V. Metag, S.M. Lee, E. Liukkonen, G. Sleten, S. Bjornholm and A.S. Jensen, Nucl. Phys. A213, 397 (1973).
25. L.W. Weston and J.H. Todd, Nucl. Sci. and Eng. 61, 356 (1976).
26. D.B. Gayther and B.W. Thomas, in Proc. of the Sov. Conf. on Neutr. Phys., Kiev (1977), v. 3, p.3.
27. H.H. Knitter and C. Budtz-Jorgensen, Atomkernenergie, 33, 205 (1979).

28. D.L. Shpak, Yu.B. Ostapenko and G.N. Smirenkin, JETP Lett., 10, 175 (1969).

29. K. Wisshak, F. Käppeler, W. Hage and H. Hettinger, in Proc. of the Conf. on Neutr. Phys. and Nucl. Data, Harwell, (1978), p. 893.

30. M. Cancé, D. Gimat and G. Grenier, contribution to the Neutr. Interlab Seminar, Paris (1979).

31. J.B. Wilhelmy, H.C. Britt, A. Gavron, E. Konecny and J. Weber, in Proc. of the Conf. on Nucl. Cross Sect. and Techn., Washington, 1975, ed. by R.A. Schrack and C.D. Bowman (NBS Special Publication 425, 1975), v. 1, p. 218.

FINITE GEOMETRY AND MULTIPLE SCATTERING CORRECTIONS FOR NEUTRON CROSS SECTION MEASUREMENTS

H. H. Hogue*
Duke University
Durham, North Carolina 27706, USA

A. G. Beyerle
North Carolina State University
Raleigh, North Carolina 27607, USA

Computer programs EFFIGY and EFFIGYC have been developed to calculate finite geometry and multiple scattering corrections for fast neutron cross-section measurements. These programs employ the Monte Carlo method to simulate time-of-flight spectra of neutrons scattered by single- or multiple-element, cylindrical or annular samples illuminated by a pulsed, monoenergetic neutron source. EFFIGY calculates corrections to angular distributions of discrete neutron groups appearing in the scattering spectra for low nuclear excitation. In addition, EFFIGYC corrects the energy distribution of the "continuum" of neutrons produced by (n,n') reactions leading to overlapping levels, and removes a contribution to the scattering spectra due to source neutrons from other than the monoenergetic source reaction.

[neutron, scattering, angular distribution, energy distribution, corrections, computer programs, finite geometry, multiple scattering, Monte Carlo method.]

Introduction

As part of the program of neutron scattering measurements at the Triangle Universities Nuclear Laboratory (TUNL), we have directed considerable effort to the task of making reliable data corrections. A pair of computer programs have been written to correct data for two complementary types of measurements: EFFIGY calculates corrections to angular distribution data, simultaneously for elastic scattering and for inelastic scattering to low-lying excited states resolved in the experiments. Scattering to the continuum and to states at high excitation, which produces a continuous energy distribution of secondary neutrons, is corrected by the companion program EFFIGYC. The TUNL measurement method features a monoenergetic neutron source, using D(d,N) or T(p,n) reactions, and pulsed-beam time-of-flight methods for energy analysis of scattered neutrons. Facility details and data for a series of p-shell elements have been reported.[1-6] Recent system improvements and measurements are reported at this conference.[7-9]

Data correction plays an important role because experimental conditions must be used in the measurements which are less than ideal. Low neutron production and detection probabilities force good experimental geometry to be compromised for an adequate count rate. Large samples, occupying volumes of several cubic centimeters, are placed within a few centimeters of the neutron-production target. Resulting effects of angular averaging and attenuation and multiple scattering in the samples can be large. The monoenergetic neutron production forms neither a point source, nor is it isotropic. This contributes to angular and energy averaging in the scattered neutrons. Also, at most energies, the "monoenergetic" neutron sources contain lower-energy contamination from other reactions. Scattering of this contamination may not be experimentally separable from primary-neutron scattering at higher excitation. Calculation must be used to separate these processes.

The method employed to correct the scattering data in programs EFFIGY and EFFIGYC has evolved from the work of Cox,[10] Kinney,[11] and Velkley et al.[12] Its basic features are Monte Carlo simulation of the scattering experiments and an iterative calculational scheme. The iteration sequence adjusts the cross-section input to the simulation until results in agreement with the experimental data are obtained. Accuracy of the method is limited only by the degree of detail of the experiments included in the simulations, the accuracy of system parameters and cross section input (other than that being adjusted), and the accuracy of the representation of cross section data in the program library. The techniques are quite general and could be adapted readily to other types of measurements having neutrons in the entrance and/or exit channels.

Our purpose in this paper is to acquaint other workers in the field with the existence, features, and method of operation of these programs. The first two sections will detail the iterative process and the simulation techniques, respectively. Following that, operating characteristics and features of the programs will be discussed. Finally, examples of the use of EFFIGY and EFFIGYC in correcting data taken at TUNL will be presented.

Method

Programs EFFIGY and EFFIGYC have the same basic structure. We will discuss them together and note differences where they occur. Figure 1 is a flow diagram for the calculations. Initial steps read data, store it in convenient form, and perform some initial setup operations. The heart of the calculation is contained in a loop which occupies most of the remaining program steps. The calculations performed inside this loop will be discussed below.

Input to a calculation consists of the experimental data, all parameters of the time-of-flight system and neutron source needed for computer modeling of the experiment, and a cross section library. The library contains the total and partial cross sections for the sample material, tabulated versus energy. Also included are angular distributions versus energy for the discrete states which are experimentally resolved. Program EFFIGYC requires, additionally, an angle and energy distribution of secondary neutrons not accounted for by the discrete-state data. We refer to these neutrons as the "continuum-scattered" neutrons.

* Presently of Union Carbide Corporation, Nuclear Division, Oak Ridge, Tennessee.

Inside the iteration loop indicated in Figure 1, a subroutine is called which performs the simulation of the scattering experiment. This simulation includes calculation of time-of-flight spectra for each detector position of the experiment and reduction of the spectra to quantities analogous to the measured, uncorrected cross section data. EFFIGYC's simulation subroutine differs from that of EFFIGY only in that extra coding is needed to accommodate an extra, lower-energy component in the neutron source and to treat the continuum scattering in addition to the scattering via discrete states. Detail of the simulation will be given in the following section.

After the calculation has returned from the simulation step and printed results, a comparison of calculated and experimental angular distribution data is made for each detector position and for each scattering process considered. EFFIGYC makes a channel-by-channel comparison in the experimental and calculated time-of-flight spectra. In either case, discrepancies outside experimental error estimates are used to modify the appropriate entries in the cross section libraries for a new simulation step. Iteration proceeds until convergence between calculated and experimental quantities is reached or to a user-specified maximum number of iterations. Output of data-correction factors and corrected cross sections terminates the calculation.

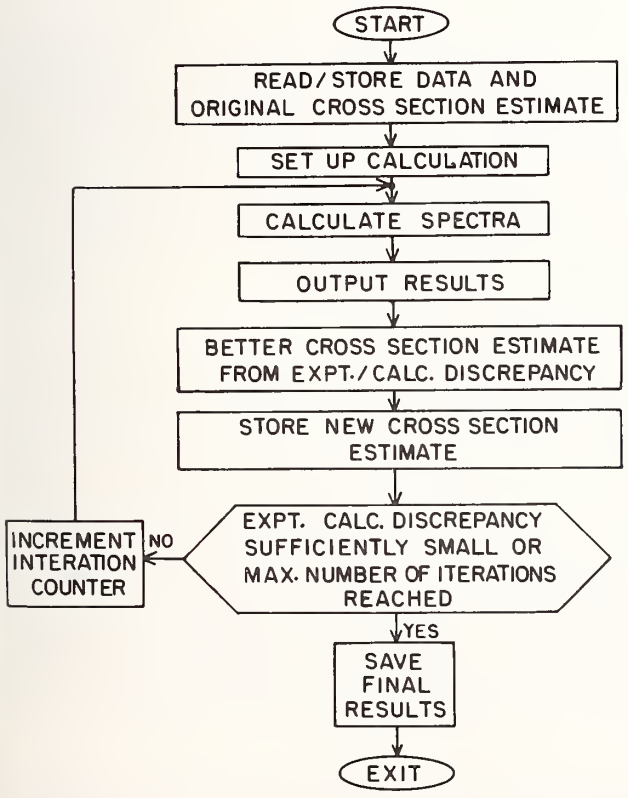

FIGURE 1. Flow Diagram for EFFIGY or EFFIGYC Calculation.

Scattering Simulation

The scattering simulations in EFFIGY and EFFIGYC are based on the experimental arrangement illustrated in Figure 2. All important features of the actual experimental geometry are represented. The neutron source is a volume formed by the intersection of a diverging charged-particle beam and a cylindrical target. Samples are cylindrical, either solid or hollow (case illustrated). The detector volume (not illustrated in the figure) is located in the xy-plane at fixed distance from the sample and at variable scattering angle. Its symmetry axis is along the line joining the sample and detector. The simulation is independent of the relative sizes and separations of the source, sample, and detector components. However, all calculations performed so far have used geometries typical of the TUNL measurements. Sample diameters of 2.5 cm or less and heights between 2.5 and 5.0 cm have been used. Neutron-production targets of length 3 cm and source-sample separations of 8-10 cm have been typical.

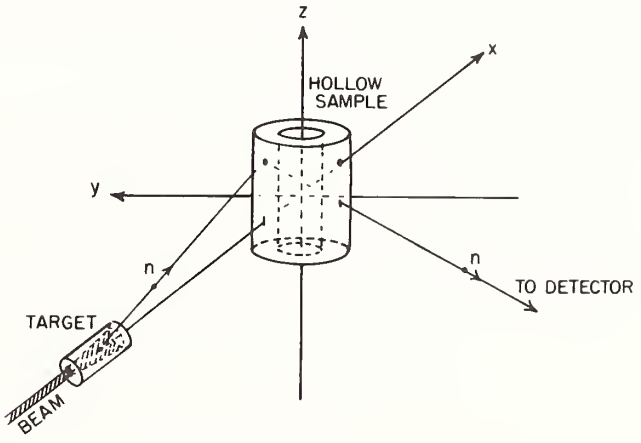

FIGURE 2. Geometry for the Scattering Measurements and Computer Simulations.

The structure of the scattering simulations is indicated in Figure 3. This flow diagram is applicable to the calculations performed by either computer program. A pair of nested loops accumulate the results of a large number of possible neutron histories sampled by the Monte Carlo method. We use the words "neutron history" to signify a collection of neutron scatterings — one for each elastic- and inelastic-scattering process to each detector position. In addition, a neutron history may include multiple scattering in the sample, as explained below. One thousand such histories form a "batch". The variation among batch results furnishes a running estimate of the precision of the calculation. A sufficient number of batches are run to give an estimated precision of one percent, unless otherwise specified.

Calculation of a neutron history begins with a single-scattering calculation. Points in the source and sample volumes are randomly selected, and calculation of the relative source strength at the sample point proceeds. The source-strength calculation in EFFIGYC chooses from either a mono-energetic source component or a lower-energy contaminant group. EFFIGY allows only a monoenergetic component. Angle and energy dependence of the

monoenergetic source flux and flux attenuation in the sample is accounted for. Next, for each detector position, a point in the detector is chosen and for each scattering process, the scattering to that detector point is calculated. Each discrete-scattering process is recorded by adding its scattering strength to the time-of-flight bin corresponding to the neutron energy after that process. Continuum scattering produces a contribution to each accessible time-of-flight bin.

As indicated in Figure 3, EFFIGY and EFFIGYC may choose to calculate a multiple-scattering process after each set of single-scattering processes has been recorded. It is much more efficient to include the calculation of multiple events here rather than in a separate calculation because most of the coding already in place for the single-scattering calculation may be used for the multiple-scattering calculation as well. The only additional requirements for the double-scattering calculation are to select a second point in the sample volume and to calculate the scattered neutron flux at that site. The calculation then proceeds just as for the single-scattering case. After each double-scattering calculation, a triple-scattering calculation may be performed. A program parameter controls the relative number of multiple-scattering processes calculated in each batch.

Following each batch, the accumulated time-of-flight spectra are reduced to quantities analogous to the experimental data. When the calculation, as the experiment, has involved a multi-element sample and the scattering from only one element is to be isolated, a special step is taken. Previously calculated "blank" spectra for a sample containing elements for which the scattering is to be removed are subtracted from the multi-element spectra at each detector angle. This is analogous to what is done in the measurements. In

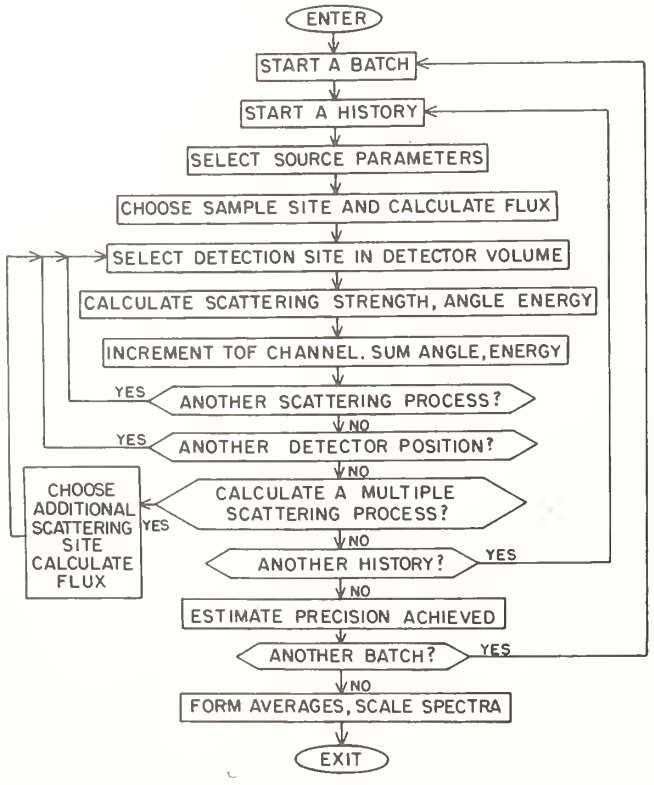

FIGURE 3. Flow Diagram for the Scattering Simulation Steps of Program EFFIGY or EFFIGYC.

EFFIGY, yields from peaks in the time-of-flight spectra identified with the various scattering processes are extracted and normalized to a standard source flux. The attained precision of the calculation is estimated. As precision dictates, an additional batch calculation is called for or the simulation is terminated.

Characteristics and Features

The two computer programs we have discussed perform similar calculations for types of experimental data which are complementary in nature. Much of the input required for the programs is the same. With this in mind, we have designed the programs' input sections to access a set of common input files. This is made possible by a keywording scheme. The input files are broken into sections, each identified by a keyword. Some of the keywords are for program execution control, while others identify the various data types. On input to the programs, data types inapplicable to a particular calculation may be skipped. The scheme allows for efficiency in chaining together calculations also. For example, after data for one beam energy has been corrected, calculation at another energy requires input of beam parameters and the experimental data for that energy. Cross section libraries and system parameters are already resident.

Initial setup of the input files has been made as convenient for the user as possible. Input formats for the various cross sections required for the calculation match those of the Evaluated Nuclear Data Files (ENDF). Therefore, cross section data may be taken directly from ENDF tapes in most cases.

The multi-angle, multi-process capability of the corrections programs has been alluded to in discussing their operation. Present array sizes used limit EFFIGY to 25 detector positions and EFFIGYC to 5. Each program may include up to 10 scattering processes. With such limits, either program will occupy less than 500K bytes (4 bytes per computer word) of core storage on an IBM360 computer. An effort has been made to facilitate changing these array sizes when this is desirable. Variables have been used for array lengths which enter in the calculations.

In general, Monte Carlo calculations require considerable execution time. In the present programs, execution speed has been increased at the expense of program size wherever such trade-offs exist. The typical time requirement for an EFFIGY calculation for each batch of 1000 neutron histories is about five seconds of IBM360 processor time per detector angle and scattering process included. For each batch, EFFIGYC requires about 45 seconds on an IBM360, or about 6 minutes on a DEC10 for the generation of a 256-channel time-of-flight spectrum at one detector position. Calculations performed for the TUNL measurements have required, at each iteration, between 5 and 10 batches to reach the one percent precision level. Agreement between the calculation and the experimental data has typically been reached after no more than three iterations.

A reasonable attempt has been made to provide checks and diagnostic output to aid the users of these programs. A print level parameter has been included, which permits the user to control the quantity of diagnostic print-out he wishes to obtain from the calculation. Besides correction factors, the programs also calculate average energies, scattering angles, attenuation factors, and other quantities which serve as diagnostics.

Examples

Oxygen Angular-Distribution Measurements

The TUNL measurements of the O^{16} angular distribution for energies between 9 and 15 MeV required the largest correction of any of the TUNL discrete-state data. A beryllium oxide sample was used. Scattering by beryllium was removed from the spectra by taking separate runs using a beryllium "blank" having the same number of Be nuclei as the BeO sample. Figure 4 shows (as the crosses) data resulting from the measurement at 12 MeV. Following two iterations in program EFFIGY, the calculated scattering (shown as the curve) was in agreement with the experimental data. The correction factors generated and applied to the experimental data yielded the corrected data shown as the dots in the figure.

Figure 5 breaks down the net correction factor applied to the 12 MeV oxygen data (dashed curve) into its largest components. Neutron flux attenuation by the sample, or out scattering, was the predominate 30% effect. Multiply-scattered neutrons averaged around 10% of those singly-scattered. A correction of <20% was required at forward angles to remove effects of a flux-attenuation difference between the BeO sample and the Be "blanks". Beyond 50°, neutron groups scattered by oxygen and beryllium were separated in the time-of-flight spectra; therefore, no over-subtraction correction was needed.

Iron Neutron-Emission Measurements

In recent work at TUNL reported at this conference, [7] angle and energy distributions of neutrons emitted by several materials have been measured. Correction of the data by program EFFIGYC has begun. Figure 6 shows, as the open circles, a time-of-flight spectrum for 12 MeV neutrons scattered by an iron sample to a lab angle of 125°. This data is from an early set of poor-statistics measurements. The histogram is a near-convergence calculation by program EFFIGYC, in which the scattering to only the ground and first excited states are treated in full angular dependence. All other scattering is calculated via an effective continuum-scattering process with isotropic angular distribution. Higher excited states may be included explicitly in future calculations if this proves necessary.

The calculation shown in Figure 6 is reproduced in Figure 7. That part of the distribution which has been treated as continuum scattering of the mono-energetic part of the neutron source distribution is shown as curve 2. Curve 3 shows the calculated distribution of "breakup" neutrons from the T(p,n) source scattered by the sample. The cross sections of Drosg *et al* [13] were used in the present calculation to determine the source distribution used by the program. The scattered breakup neutrons are seen to contribute significantly to the spectrum. Direct measurements of the source spectra will be used in further calculations to decrease the uncertainty in that part of the data corrections.

Conclusion

We have described a pair of computer programs developed to make corrections to neutron scattering data obtained by the time-of-flight method. Separate programs to handle scattering to discrete states and scattering to the continuum have been written. The methods employed in the simulation of the experimental data collection and reduction are of a general nature. Therefore, modification of the program to treat other types of measurements with neutrons in the entrance and/or exit channels should be possible.

Work continues at TUNL to test the continuum-scattering program, EFFIGYC, and apply it to recent data. In addition, improvements in the program input routine, implemented in EFFIGYC, will be retrofit into the discrete-scattering version, EFFIGY.

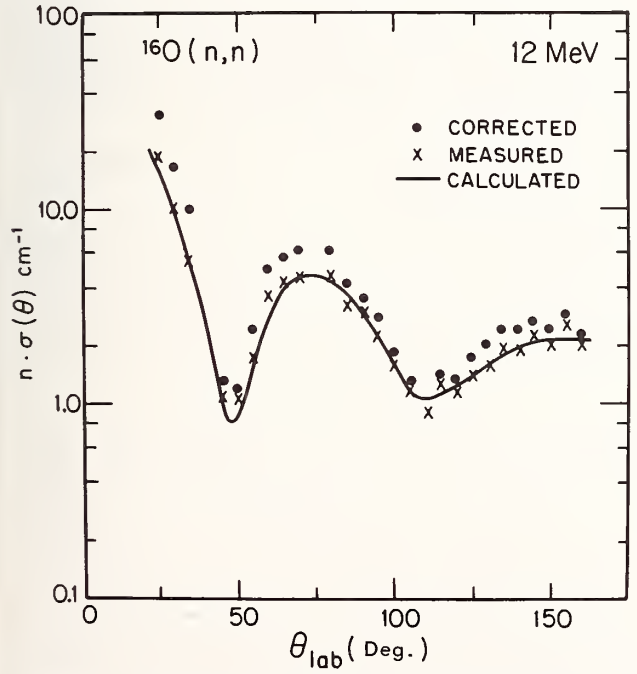

FIGURE 4. Angular Distribution of Neutrons Elastically Scattered by Oxygen. The Ordinate is Differential Cross Section Times the Sample's Oxygen Nuclear Density.

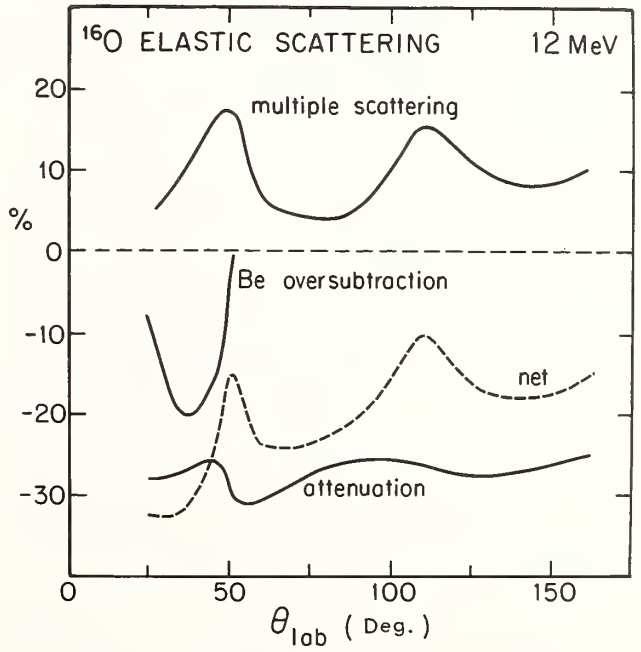

FIGURE 5. The Oxygen 12-MeV Elastic Scattering Correction Factor and its Major Components.

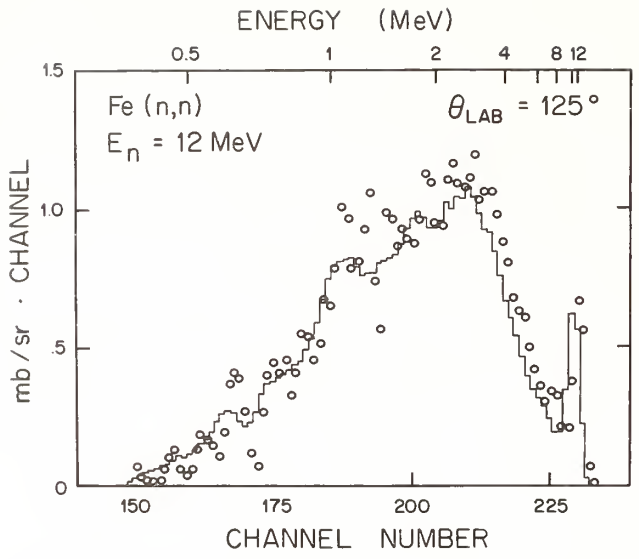

FIGURE 6. Time-of-Flight Spectrum of 12-MeV Neutrons Scattered by an Iron Sample to a Detector Angle of 125°.

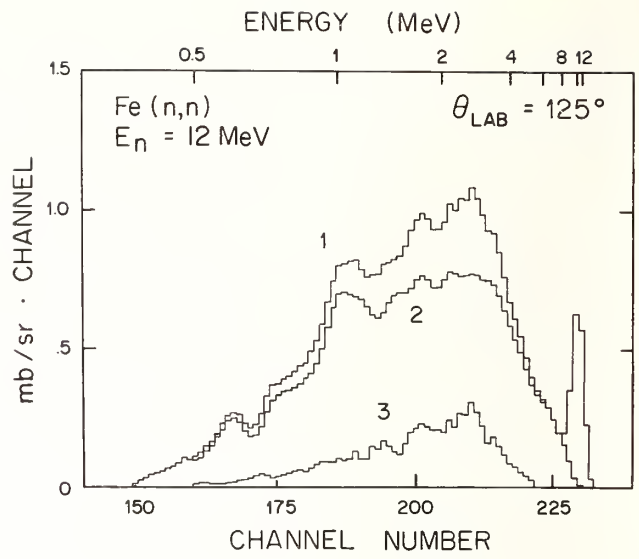

FIGURE 7. Calculated Time-of-Flight Spectrum for 12-MeV Neutrons Scattered by Iron to a Lab Angle of 125°. Two of its Components Isolated by EFFIGYC are shown.

Acknowledgements

The authors wish to thank the personnel of the Oak Ridge Linear Accelerator Facility for use of their computing facilities during latter phases of the program development. Major support for the work was provided by the United States Department of Energy.

References

1. H. W. Newson, E. G. Bilpuch, F. O. Purser, J. R. Boyce, and T. B. Clegg, Nuclear Instruments and Methods 122 (1974), p. 99.

2. D. W. Glasgow, F. O. Purser, J. C. Clement, G. Mack, K. Stelzer, J. R. Boyce, D. H. Epperson, H. H. Hogue, E. G. Bilpuch, H. W. Newson, and C. R. Gould, "TUNL Fast Neutron Facility,", Nuclear Cross Sections and Technology, NBS Special Publication 425, I (Washington, D.C., 1975), p. 99.

3. F. O. Purser, D. W. Glasgow, H. H. Hogue, J. C. Clement, G. Mack, K. Stelzer, J. R. Boyce, D. H. Epperson, S. G. Buccino, P. W. Lisowski, S. G. Glendinning, E. G. Bilpuch, H. W. Newson, and C. R. Gould, "Differential Elastic and Inelastic Scattering of 9-15 MeV Neutrons from Carbon,", ibid, II, p. 866.

4. D. W. Glasgow, F. O. Purser, H. H. Hogue, J. C. Clement, K. Stelzer, G. Mack, J. R. Boyce, D. H. Epperson, S. G. Buccino, P. W. Lisowski, S. G. Glendinning, E. G. Bilpuch, H. W. Newson, and C. R. Gould, Nuclear Science and Engineering 61 (1976), p. 521.

5. H. H. Hogue, P. L. VonBehren, D. H. Epperson, S. G. Glendinning, P. W. Lisowski, C. E. Nelson, H. W. Newson, F. O. Purser, W. Tornow, C. R. Gould, and L. W. Seagondollar, Nuclear Science and Engineering 68 (1978), p. 38.

6. H. H. Hogue, P. L. VonBehren, D. W. Glasgow, S. G. Glendinning, P. W. Lisowski, C. E. Nelson, F. O. Purser, W. Tornow, C. R. Gould, and L. W. Seagondollar, Nuclear Science and Engineering 69 (1979), p. 22.

7. A. Beyerle, S. El-Kadi, G. Glendinning, C. Gould, C. E. Nelson, F. O. Purser, W. Seagondollar, P. Thambiduria, and R. L. Walter, "Double-Differential Neutron Scattering Cross Sections for Fe, Cu, Ni, and Pb Between 8 and 12 MeV," proceedings of this conference.

8. S. El-Kadi, A. Beyerle, C. Gould, A. McDermott, R. Pedroni, P. Thambiduria, C. E. Nelson, F. O. Purser, W. Seagondollar, and R. L. Walter, "Neutron Elastic and Inelastic Scattering from ^{63}Cu, ^{65}Cu, ^{54}Fe, and ^{56}Fe Between 8 and 14 MeV," proceedings of this conference.

9. L. W. Seagondollar, A. G. Beyerle, C. R. Gould, F. O. Purser, S. El-Kadi, S. G. Glendinning, and C. E. Nelson, "Recent Modifications of the TUNL Fast Neutron Cross Section Facility", proceedings of this conference.

10. S. A. Cox, Nuclear Instruments and Methods 56, (1967), p. 245.

11. W. E. Kinney, Nuclear Instruments and Methods 83, (1970), p. 15.

12. D. E. Velkley, J. D. Brandenberger, D. W. Glasgow, and M. T. McEllistrem, Nuclear Instruments and Methods 129 (1975), p. 231.

13. M. Drosg, G. Auchampaugh, and F. Gurule, Nuclear Instruments and Methods 140 (1977), p. 515.

FAST NEUTRON DETECTION CAPABILITIES OF NaI(Tℓ) SCINTILLATOR AND HgI_2 SEMICONDUCTOR GAMMA RAY SPECTROMETERS

F. E. Cecil, K. Killian*, and M. Rymes†
Department of Physics, Colorado School of Mines, Golden, Colorado 80401 USA

The utilization of NaI(Tℓ) scintillators as a high efficiency, fast neutron monitor, through the reaction $^{127}I(n,n')^{127}I^{4}(E_x = 57\ keV)^{127}I(E_x = 0)$, has been established. The total gamma ray production cross sections for the 57 keV gamma ray production cross sections for the 57 keV gamma ray in ^{127}I by inelastic scattering of 3 MeV and 14 MeV neutrons are 0.43 ± 0.04 b and 0.28 ± 0.03 b respectively. Temperature and count rate limitations on this utilization have been determined. The same reaction should allow HgI_2 semiconductor gamma ray detectors with intrinsic energy resolution potentially for superior to NaI(Tℓ) to be utilized to monitor fast neutrons.

[NaI detector, $^{127}I(n,n')^{127}I^*$, $\sigma(n,n')$, excited states in ^{127}I]

INTRODUCTION

Flux measurements of fast neutrons constitute an essential aspect of many areas of applied nuclear physics. In applications such as fast neutron activation analysis, neutron radiology or thermonuclear fusion technology, neutron flux measurements are necessary to meaningful utilization of the associated neutron sources. The lack of neutron interaction with the atomic structure of matter requires that neutron detection involve the indirect measurement of the interaction of the neutron with nuclear matter. Familiar examples of this method are proton recoil scintillometry[1] or activation techniques[2]. We have investigated a novel approach to fast neutron detection utilizing a different form of neutron nucleus interaction than is used as the basis of, say, proton recoil spectrometry. In the method which we have investigated, a conventional NaI(Tℓ) scintillator is exposed directly to the fast neutron flux to be measured. The inelastic scattering of the fast neutrons are detected by absorption, in the scintillator itself, of the subsequent deexcitation gamma ray. For a monoenergetic flux of neutron, the yield of the deexcitation gamma rays, as measured through any standard photomultiplier tube coupling to the scintillator, will be proportional to the associated fast neutron inelastic scattering total cross sections. A measurement of these cross sections will thus allow a given scintillator to be calibrated in the sense that an absolute neutron flux determination will be possible directly given the yield of the associated deexcitation gamma ray.

EXPERIMENTAL PROCEDURE

The particular reactions which we have investigated are to the low lying states of ^{127}I. The nuclear energy level diagram of ^{127}I is shown in Figure 1[3]. Specifically we have measured the total cross sections at neutron energies of 3 and 14 MeV for the production of the 57 keV and 202 keV gamma rays, corresponding to the deexcitation of the first two excited states. The cross sections were measured by exposing a conventional NaI(Tℓ) scintillator to monoenergetic fluxes of neutrons of 3 MeV and 14 MeV, counting the yields of the 57 keV and 202 keV gamma rays (using a standard multichannel analyzer) and comparing these yields to independent measurements of the neutron fluxes. The neutrons were generated by bombarding deuterated or tritiated titanium targets with deuteron beams from Cockcroft-Walton accelerators in the Colorado School of Mines Physics Department. The independent measurements of the neutron fluxes consisted of activation of samples with known cross sections and are described elsewhere[4].

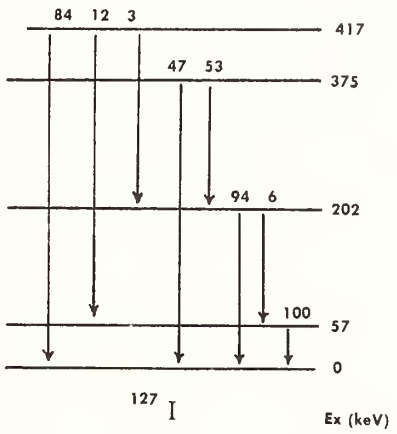

Fig. 1. Level Diagram of ^{127}I.

A typical energy spectrum when a commercial scintillator is exposed to a flux of 3 MeV neutrons is shown in Figure 2(a). The 57 keV and 202 keV transitions are evident. This spectrum is conveniently calibrated using a radioactive ^{133}Ba source, Figure 2(b).

The cross sections which we measured at 3 and 14 MeV for the production of the 57 and 202 keV gamma rays are shown in Figure 3 where they are compared to earlier measurements at energies up to 1.2 MeV[5].

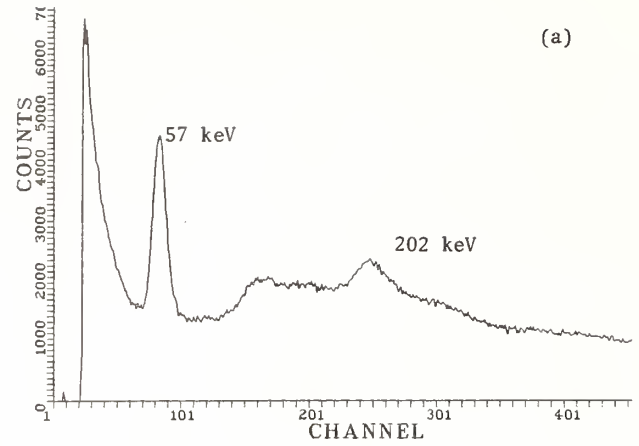

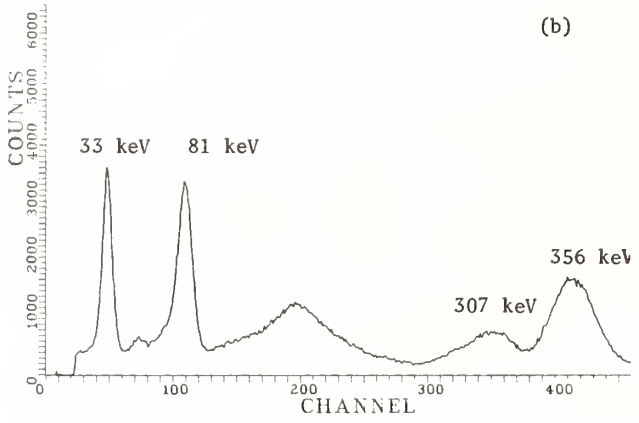

Fig. 2(a). Response of NaI(Tℓ) to flux of 3 MeV Neutrons.
Fig. 2(b). ^{133}Ba Calibration Spectrum.

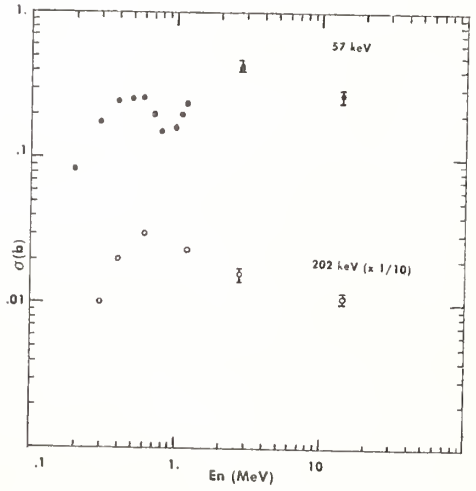

Fig. 3. Measured cross sections. Data below 1.2 MeV from Ref 5.

DISCUSSION

As noted above, the cross sections which we have measured permit an absolute determination of fast neutron fluxes. Consider a specific example. For a 2" (5.08 cm) diameter NaI(Tℓ) scintillator. For the cross section for production of the 57 keV gamma by 3 MeV neutrons of about 0.4 barns and given the density of NaI(Tℓ), the probability for production neutron through the face of the scintillator is about 4.1%. Thus, for example, the 1 3/4" x 2" scintillator facing an isotropic 3 MeV neutron source of 10^8 n/sec at a distance of 1 meter will yield 4.9 x 10^2 57 keV gamma rays per second.

We encountered two notable limitations in the utilization of NaI(Tℓ) scintillator as a fast neutron monitor. We found that thermionic cathode emission obscured the 57 keV level when the system is operated at temperatures above about 250 °F. This is of course a property of phototubes and not the scintillator and will be encountered in any low energy scintillometry using photomultiplier tubes. We also noticed an activation of the crystal following exposure to relatively high fluxes of neutrons. The activation reactions which were observed were $^{127}I(n,\gamma)^{128}I$ (25 min) and $^{23}Na(n,p)^{23}Ne$ (38 sec). A multiscaling of the count rate in the crystal following an exposure to a flux of 14 MeV neutrons of about 10^7 n/(cm^2-sec) is shown in Figure 4 where the half lives noted above are evident. These activation reactions only constituted a practical limitation in cases where we attempted to measure a very low flux of neutrons immediately following exposure to a relatively high flux of neutrons. (The particular study in which this was found was that of DFN Uranium analysis in which we attempted to measure both the source output and the DFN's with the same scintillator.)

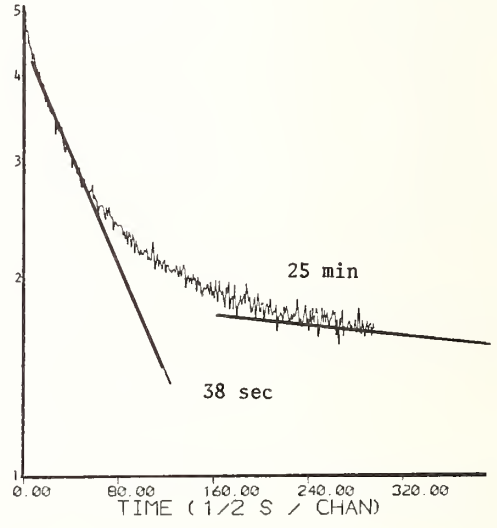

Fig. 4. Multiscaling of total count rate in scintillator following exposure to intense neutron flux.

Within the context of the above limitation due to activation, we should note that the recent development of HgI_2 semiconductor gamma ray detectors[6] affords another application of

the present measurements of the $^{127}I(n,n')$ cross sections to fast neutron monitoring. The 57 keV transition in ^{127}I will, of course, appear if an HgI_2 detector is exposed to a fast neutron flux. The superior resolution of these detectors (1 keV has been observed at a gamma ray energy of about 50 keV)[7] will greatly improve the signal to noise ratio (for comparison the width of the 57 keV line in Fig. 2(a) is about 15 keV). Moreover, the problem of the activation of the Na will obviously be eliminated (although similar activation of the Hg isotopes could pose an analogous problem).

In conclusion the advantages of using NaI(Tℓ) as a fast neutron flux monitor are detailed:

1. high efficiency, comparable to proton recoil and much greater than ^{3}He or ^{6}Li detectors.

2. all the counts are in a single peak; ideal for monitoring.

3. a built-in discriminator against thermal or epithermal neutrons.

4. inexpensive and simple (compared to say a liquid scintillator system requiring n-γ discrimination.

This work was supported by a grant from the U.S. Geological Survey #14-08-0001-G548.

* presently at Martin Marietta Company, Denver, CO.

† presently at Department of Mathematics, University of Colorado at Boulder, CO.

REFERENCES

1. J.B. Marion and J.L. Fowler, ed., "Fast Neutron Physics", Interscience, 1960.

2. S. Nargdwalla and E. Prxybylowics, "Activation Analysis with Neutron Generators", John Wiley, 1968.

3. C.M. Lederca, et al. "Table of Isotopes", John Wiley, 1968.

4. F.E. Cecil, et al. Phys. Rev. C, 19 (1979) 2414.

5. J. Van Loef and D.A. Lind, Phys. Rev 101 (1956) 103.

6. R.C. Whited, et al., Nucl. Inst. and Methods, 162 (1979) 113.

FISSION TRACK RECORDER TECHNIQUES FOR FISSION RATE MEASUREMENTS

H. P. CHOU, R. H. JOHNSON, and F. M. CLIKEMAN
Purdue University
West Lafayette, Indiana 47907, USA

Fused quartz fission track recorders have been used for fission rate measurements. A scanning optical microscope interfaced with a microcomputer has been developed to perform fission track counting. The stability of the system has been extensively checked. An overall reproducibility of ±3% (one standard deviation) has been achieved. Programming for this system provides a partial scanned image, the total number of fission tracks, a track size distribution, and the locations of individual tracks.

[fission rate, fused quartz track recorder, track counting, microcomputer.]

Introduction

The Fast Breeder Blanket Facility (FBBF)[1] was constructed at Purdue University to study the blanket characteristics of fast breeder reactors. This project requires fission rate measurements of ^{235}U, ^{238}U, ^{239}Pu, ^{237}Np, and ^{232}Th for evaluation of computational methods and basic cross section data.

Fission track recorder techniques have been applied for fission rate measurements at several laboratories.[2-4] Figure 1 is a microphotograph of etched fission tracks in fused quartz. A major weakness of this technique is the determination of precise track numbers. Spark counting with plastic fission track recorders is not appropriate for the present work. Visual counting using a microscope is expensive, time consuming, and may involve personal bias. Sophisticated automatic track counting systems using computer-controlled scanning methods have been developed with good results.[5,6] In such systems, however, large computers were devoted to relatively simple pattern recognition.

The goal of the present work was to interface a microcomputer with an available scanning optical microscope to obtain a reliable and inexpensive track counting system.

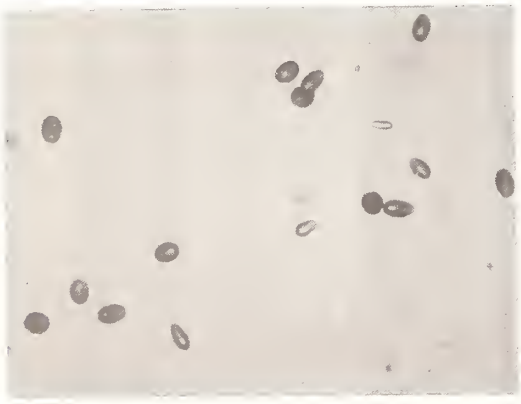

Fig. 1. Microphotograph of fission tracks in a fused quartz track reorder with track density of 200/mm². The recorder was etched in 48% HF for 5 minutes at room temperature.

Track counting system

Apparatus

Figure 2 shows the general diagram of the counting system. The stage of the scanning optical microscope[7] moves the specimen in the x-y plane by two DC motors operating under a built-in control unit. Two light choppers are mounted with the motor assemblies to measure the x and y positions with a resolution of 0.5 μm. When the stage moves, the choppers send out sequential logic pulses of one pulse per 0.5 μm. These pulses are counted by a built-in TTL logic unit to control a scanning pattern. The microscope was designed to scan a rectangular field with the maximum size of 50 mm x 50 mm. The scanning path goes from right to left, moves down in y direction and then travels back. Two signal lines (x and y) were brought out from the logic unit to measure the number of traveling steps. The accuracy of the step size is limited to the accuracy of the choppers, i.e. 0.5 μm.

The light source is a 12 volt, 100 watt, quartz-iodine lamp with a regulated DC power supply. A photo-detector was mounted on the lamp socket to monitor the stability of the light source. The optics of the microscope are arranged for a bright field incident light illumination. The reflected light from the specimen passes through a condenser and a light splitter to a photometer. The photometer consists of a photo-transistor and an amplifier to convert the incoming light intensity to voltage. With a X10 objective lens, the aperture of the photometer projected onto the objective plane has a diameter of 7 μm and defines one picture element. The output of the photometer is fed into a discriminator to determine track events.

A microcomputer system[3] has been interfaced with the microscope for data acquisition and analysis. The interfacing arrangement is also shown in Fig. 2. Whenever the microscope stage travels one step length, a pulse is sent to the interrupt lines of the computer. The computer is programmed to sense this signal and fetches the scanned data from the data line. This arrangement did not require modification of the existing microscope logic unit. The system is programmed to be able to handle an interrupt rate of ≤2000 interrupts per second. For regular scanning operation, the interrupt rate is approximately 330 interrupt per second corresponding to a stage speed of 0.3 mm/s.

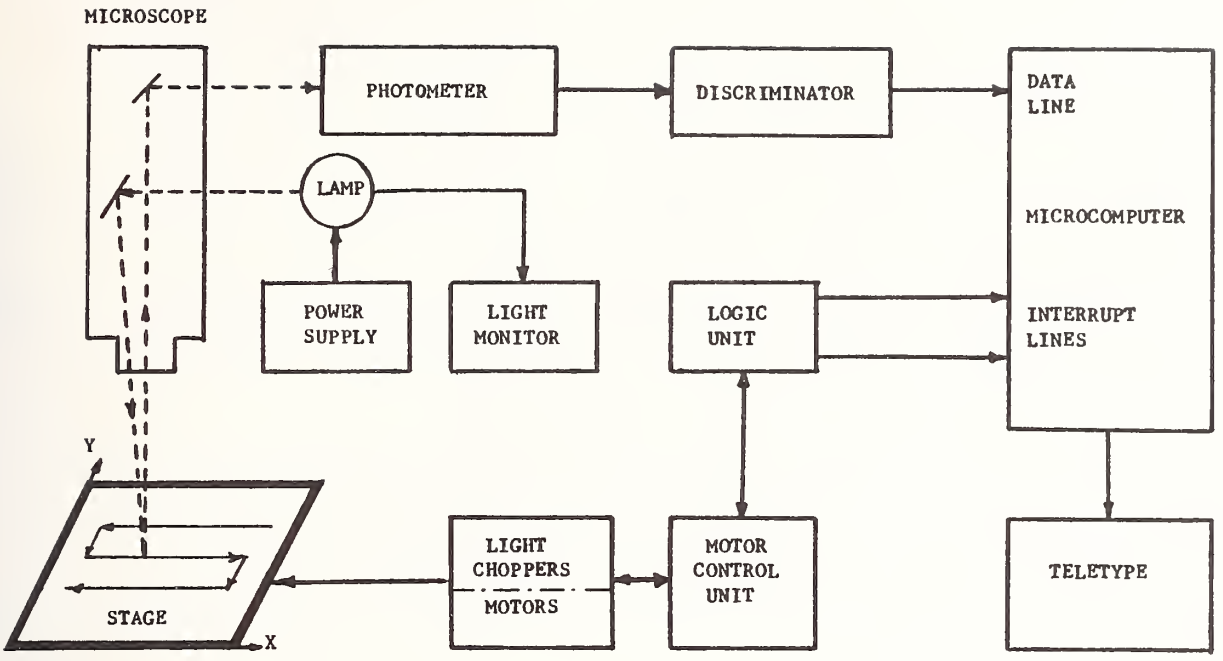

Fig. 2. Block diagram of the automatic track counting system.

Track counting program

The microcomputer is programmed in assembly language and loaded with the object code to save processing time and memory space. The object code is 2000 bytes long and requires 16000 bytes of memory for data storage, although experience has shown that 8000 bytes would be sufficient. An extra 8000 bytes of memory is reserved for the option of storing a partial scanned image and the coordinates of individual tracks.

The track counting program consists of two major parts: an interrupt service routine and a main routine. The interrupt service routine is activated whenever interrupts are received. The main function of this routine is to fetch and store the scanned data for the main routine to analyze. The main routine correlates the scanned data and gives the scanned results. The pattern of the scanned image can be viewed as a matrix with each element corresponding to a picture element. If a picture element falls on a track, its value is one; otherwise the value is zero. Since the size of the scanned field is usually on the order of 10^7 picture elements, it is not feasible to store the entire matrix in the system. In addition, only the picture elements which fall on tracks are important for the track recognition. Therefore, the interrupt service routine tests each picture element to find the positions where a x-path intercepts a track. The interrupt routine then stores intercept points, the intercept length and the current track size. The interrupt service routine provides an option to store a partial scanned image with a size up to 4000 picture elements.

The main routine correlates the scanned data to determine the number, location, and size of tracks. The main routine requires that the last two completely scanned lines be retained in memory. The algorithm for track counting treats any degree of track overlap as simply a large single track. A simple paralyzable counter model is used later for the overlap correction. At the end of each 256 scanned lines, the program types the current number of tracks to assure the operator that the counting is progressing. At the end of each run, the total number of tracks and the track size distribution are printed. The track size distribution gives valuable information on etching and overlap behaviors. An option is provided for the storage of the size and the locations of individual tracks in a 4000-byte data buffer. The contents of the buffer can be dumped onto a floppy disk whenever the buffer is full. The locations of the tracks will be analyzed later in a study of the spatial distribution of fission tracks.

Experimental prodcedure

Kimfol plastic foils, mica, microscope slide glass, and fused quartz were tested to determine the most suitable track recorder material for this counting system. Fused quartz (silica glass) was finally chosen for its advantages of low natural background, low surface imperfections, surface flatness, and high track to background optical contrast. Fused quartz disks with a diameter of 13 mm were cut from flat plates. These disks are pre-etched using 48% HF solution for six minutes, rinsed with water and alcohol, and finally dried in hot air. Disks are examined under an optical microscope to eliminate those with a large number of surface imperfections.

For measurements made in the FBBF, pre-etched track recorders are placed next to fission foils inside stainless steel or lead holders. The holders are placed between fuel pellets inside fuel rods. The fission foils are nickel-plated with a deposit less than 1 mg/cm^2; the active diameter is 6.3 mm. The irradiated track recorders are cleaned and scanned to get the number of background events. To bring out fission tracks, recorders are then etched a second time in 48% HF solution for five minutes with the irradiated side facing up. To ensure etching reproducibility, a fresh solution is used for every track recorder. After cleaning and drying, the track recorders are scanned again to get the total number of track events.

A standardized procedure is used to set up the scanning. The positioning of the lamp, the opening of the field diaphragm, and the aperture of the condenser diaphragm are set up to get the Köhler bright field illumination which gives the best combination of contrast and resolution. A x10 objective lens is used, which has an adequate depth of field to overcome the surface unevenness of the recorders.

Before each run, the light intensity of the lamp is adjusted. The output of the photometer is recorded to check the stability of the photometer. The threshold setting of the discriminator is located on the plateau of a curve of number of tracks versus threshold setting. Since the shape of the curve is dependent on track densities, the curve used was obtained from scanning a track recorder with a track density of approximately 200/mm^2 which is the typical track density in the present work.

A masking plate with a concentric hole is used to cover a track recorder to define a reproducible scanning field. The scanned field is set to cover the hole of the masking plate. The step size in the x direction is 1 μm and the line spacing in the y direction is 5 μm. It takes 12 hours to scan a field of 8 mm x 8 mm, which is determined by the stage speed.

Performance

Figure 3 shows a typical track size distribution of a fused quartz track recorder. A small ^{244}Cm spontaneous fission source[9] is being used for checking the system stability and efficiency calibration. A track recorder with approximately 10000 tracks (density 200/mm^2) was scanned ten times. The reproducibility of the ten readings was ±1% (one standard deviation). The uncertainty was caused by the variation of light intensity, thermal drifting of the photometer, and the differences of scanning paths in each run. To check the uncertainty in the counting procedure, three track recorders, with approximately 5000,10000, and 20000 tracks, were each scanned five times over a period of six weeks. The standard deviation for each recorder was consistent within 3%, but did not follow the Poisson statistics. This larger variation is due to the positioning of the sample, the focusing, and differences among track recorders.

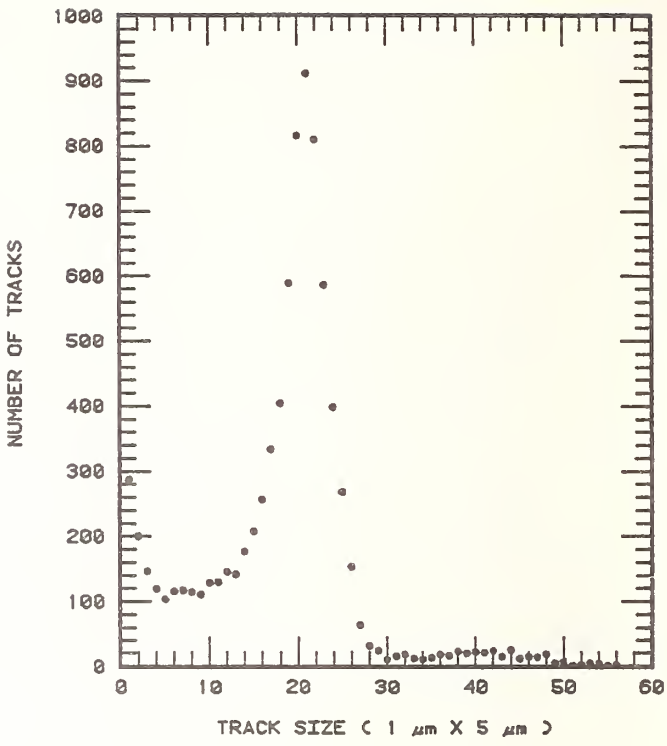

Fig. 3. A typical track size distribution obtained from the track counting system for a fused quartz track recorder.

Several unirradiated track recorders were scanned. The average number of background events was approximately 400. The standard deviation for each recorder ranged from 10% to 30%. The rather poor reproducibility is believed to be caused by the large fraction of small area events and the irregular shape of the surface imperfections.

To investigate the etching effect, several unirradiated and irradiated recorders were etched various periods of time. The results of the unirradiated recorders were within the reproducibility range for etching from 5 to 20 minutes. For recorders with track density less than 300/mm^2, the results were also insensitive to etching from 4 to 6 minutes. However, the results have a ±5% variation for recorders with track densities of 400/mm^2 etched 4 to 6 minutes.

Three recorders were irradiated with the ^{244}Cm source for the same amount of time. They were scanned before and after the final etching to test the overall reproducibility. The results are listed in Table I. The preliminary calibration results have shown that the a efficiency is 68% for a track density of 100/mm^2 and 57% for a track density of 420/mm^2. The decreasing of efficiency is caused by track overlap. A track-density-dependent efficiency curve will be determined from the final calibrations based on the simple paralyzable counter model.[9]

Table I. Scanning results of three track recorders

Sample Number	Number of Fissions	Background Tracks	Total Observed Tracks	Fission Tracks	Efficiency[c] (%)
STR-13	27414 ± 166[a]	324 ± 116[b]	16119 ± 171[b]	15795 ± 207[b]	57.6 ± 0.8[d]
STR-14	27414 ± 166	388 ± 63	16053 ± 204	15665 ± 214	57.1 ± 0.9
STR-15	27475 ± 166	372 ± 76	15712 ± 168	15340 ± 185	55.8 ± 0.8

a. Errors are one standard deviation based on Poisson statistics.
b. Errors are one standard deviation based on four readings.
c. The efficiency is dependent on the fission track density. These three track recorders had a density of 420/mm^2.
d. Errors are propagated from the number of fissions and the number of fission tracks. The systematic error in the ^{244}Cm fission rate (not included in the error propagation) is ±0.3%.

Conclusions

An automatic track counting system has been developed for fission rate measurements. Track counting is performed using a microcomputer. Programming of the system provides the number, size distribution, and locations of fission tracks. Fused quartz is the most suitable track recorder material for the present system. The system has achieved an overall reproducibility of ±3% (one standard deviation) in the counting process.

Acknowledgments

The assistance of Dr. Roland J. Armani (ANL) in the efficiency calibrations is gratefully acknowledged. The authors wish to acknowledge the U. S. Department of Energy and the Electric Power Research Institute for the funds for the construction and operation of the Fast Breeder Blanket Facility.

References

1. K.O. Ott et al., Proc. ANS Topical Meeting on Advances in Reactor Physics, CONF-780401, p.550, Gatlinburg, Tennessee (April 1978).

2. R. Gold and R.J. Armani, Nucl. Sci. Eng., 34, 13(1968).

3. E.L. Draper, Jr., Nucl. Sci. Eng., 46, 31(1971).

4. J.A. Grundl et al., Nucl. Technol., 25, 237(1975).

5. C.E. Cohn and R. Gold, Rev. Sci. Instr., 43, 13(1972).

6. C. Paretti and A. Ricci, Nucl. Instr. Meth., 122, 389(1974).

7. DIGISCAN, manufactured by Kontron Instruments, LTD., Munich, Federal Republic of Germany.

8. SWTPC-6800, manufactured by Southwest Technical Products Corp., San Antonio, Texas, USA.

9. The source was prepared by Argonne National Laboratory. The details are given in Ref. 2.

10. R. Gold and C. E. Cohn, Rev. Sci. Instr., 43, 18(1972).

ANALYSIS OF PARTICULATES FOR VERY LIGHT ELEMENTS BY FORWARD SCATTERING OF ALPHA PARTICLES

G. W. WOLFE
Physics Department, University of Mississippi
University, Mississippi 38677, USA

PIXE analysis is limited to elements heavier than Sodium. A technique has been developed for obtaining quantitative information about the levels of elements Hydrogen through Flourine by forward scattering of 18 MeV alphas, and may be obtained simultaneously with PIXE. Using substrate thicknesses less than 1 mg/cm^2, sensitivities from 2.7 μg/cm^2 for Hydrogen to 124 μg/cm^2 for Carbon, may be obtained after corrections, with determinations accurate to ±15%, in 200 second irradiation times. Substantial corrections must be made.

[^{1}H(α,p),^{7}Li(α,α),^{9}Be(α,α),^{11}B(α,α),^{12}C(α,α),^{12}C(α,α'),^{14}N(α,α),^{14}N(α,α'),^{16}O(α,α),^{16}O(α,α'), ^{19}F(α,α), dσ/dΩ at 18.36 MeV, elastic scattering, elemental analysis, PIXE.]

Introduction

Accurate, sensitive, and quantitative determination of the levels of elements and compounds is one of the most widely used investigative techniques in the sciences today. Many such techniques have been developed. One such method is Particle-Induced X-ray Emission (PIXE), using an ion beam to produce primary X-rays, which are used as "signatures" to identify and determine quantities of elements present is a sample or target.[1,2,3,4]

One shortcoming with PIXE is that it is only practical for elements with Z=11 (Sodium) or greater. Either the X-rays are not detectable, or large self-absorption corrections cast doubts on the validity of analysis for elements with Z<11. But in the earth's crust, and especially in air pollution studies, only 15% of the mass to be studied has Z=>11.

Elastic ion scattering may be used to identify and determine quantities of the remaining 85%, and may be used simultaneously with PIXE. Ion scattering analysis (ISA) has many desirable qualities. It is absolute, multi-element, rapid, non-destructive, and inexpensive on a cost-per-element basis. Used by itself, the method is not new. Backscattering from sources or accelerators off thick targets is an accepted technique.[5,6,7] Nelson and Courtney have developed a PIXE- compatible proton scattering system for light element work on thin targets[8], but they require separate experiments for scattering analysis and PIXE.

Experimental Configuration

The development of an Ion Scattering Analysis system (ISA) for light elements was undertaken subject to the constraints that the method be quantitative, cover elements not seen by PIXE, and be capable of being run simultaneously with PIXE, to reduce beam time charges.

This last requirement was the major source of difficulty inthe development, as will be seen. First and foremost, it required that ISA be done with an 18 MeV beam of alphas, for which the PIXE system had been optimized.

Work was carried out at the Crocker Nuclear Laboratory at the University of California at Davis, on the 193 cm isochronous cyclotron. A beam of 18.36 MeV alphas was produced, and magnetically analyzed twice in the beam line system. Cross-sections were measured in the 76 cm ORTEC scattering chamber, using a 300 μm, 100 mm^2 partially depleted silicon surface barrier detector, and ORTEC 452 spectroscopy amplifier, going into a Nuclear data NP02 512 channel ADC and PDP-15/40 computer for data acquisition and analysis.[9]

The results of these measurements are shown in Figure 1.

Cross-sections were measured in 5° intervals (laboratory) from 30° to 90°, and in intervals of 2.5° from 40° to 60°. A 1/8 mil (3.2 μm) film of Mylar was used for the Carbon, Oxygen and Hydrogen cross-section determination as a standard. A 1/3 mil film of Kapton was used for Nitrogen, a 1/2 mil foil of Beryllium for the Beryllium reaction, and vacuum-deposited commercially prepared foils of NaCl (35 μg/cm2), UF_4 (208 μg/cm^2), and Na_2BO_3 (159 μg/cm^2) were used as standards for the other reactions. The ^{1}H(α,α)H reaction is forbidden above 5° laboratory, but the complimentary reaction ^{1}H(α,p)^{4}He reaction is theoretically possible to 90°.

It was determined that Carbon and Oxygen are not resolveable below a 40° scattering angle, and the H(α,p) reaction is not practical above a 70° angle due to a very low energy signal which begins to be cut off by the discriminator in the ADC. Within this range, the best compromise of maximum cross-section, minimum rate of change of cross-section, best resolution, and absence of line interferences occured at a laboratory scattering angle of 52°, and this angle was used in all subsequent experiments and analyses.

All such further experiments were carried out in the PIXE chamber, after a detector was fitted at the proper angle. The only significant difference is that the beam is magnetically analyzed only once. The alpha detector is kept in air behind a thin plastic window to eleiminate detector discharge in the mechanical pump vacuum of the PIXE target changer. Since the X-ray detector is at 90° to the beam, the target rests at an angle of 45° to the beam.

Table I shows the estimated contributions to the resolution of the ISA system. Note that the major contributions to resolution are the spread in the beam energy and the finite width of the sample, which causes a difference in scattering angles from either side of the sample. Neither of these are correctable at this time. The measured resolution was 235 KeV, in excellent agreement with the estimate.

Table I.
Contributions to Scattering Resolution

Beam energy spread	130 kev
Finite target width	170
Kinematics due to detector width	56
Target at 45° instead of 26°	51
Detector	40
Electronics and MCA	10
Detector window	17
Backing material of sample	10
Air gap between detector and window	10
Quadratic sum	232 kev

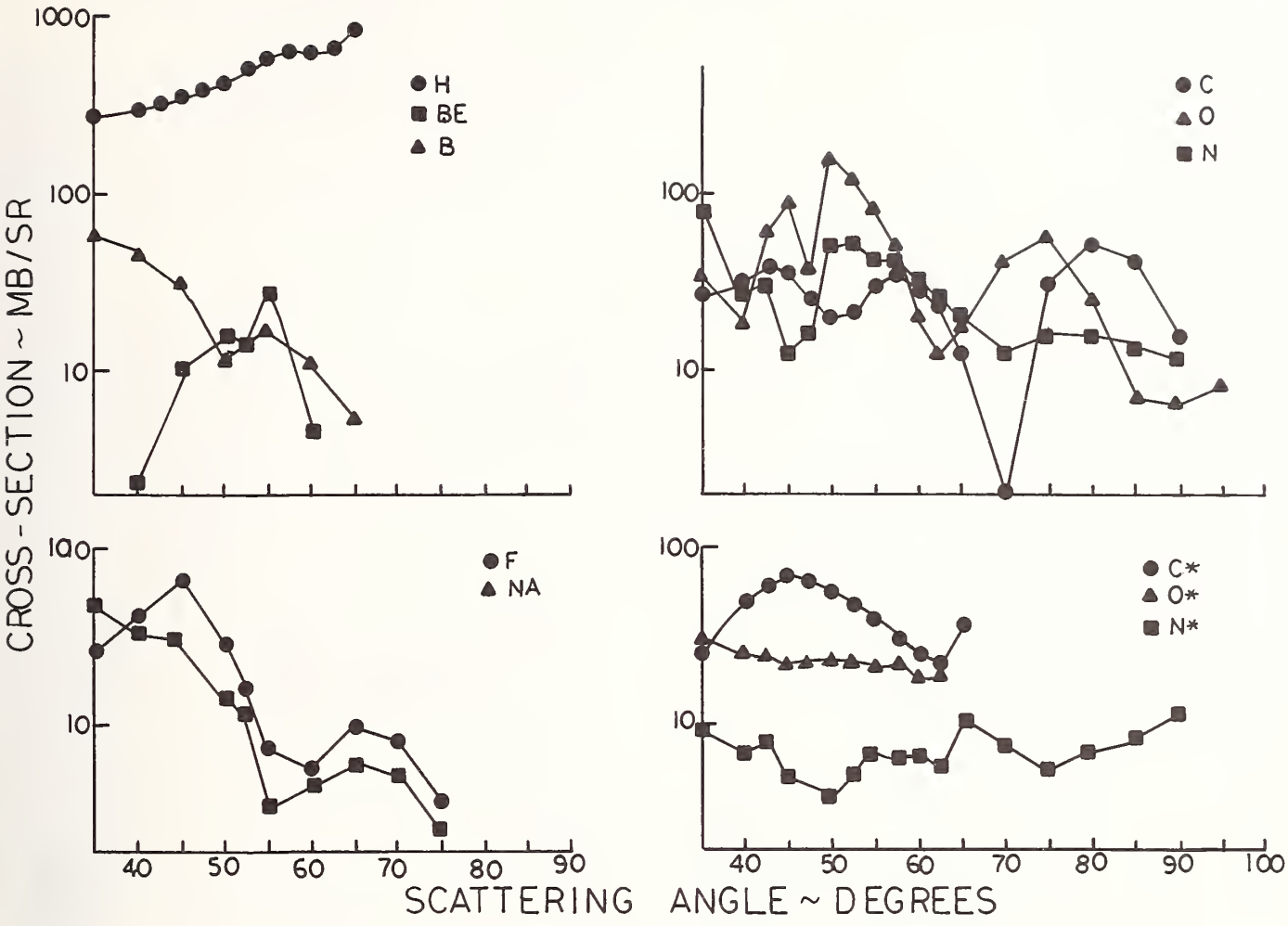

Figure 1. Scattering cross-sections for light elements. $d\sigma/d\Omega$ vs. θ. Elastic except for those marked with "*".

Spectral analysis and data reduction is done with the code RACE[9] after being acquired by DEUCE. The former is a two-pass on-line code which analyzes the PIXE spectrum and then the ISA spectrum. Dead time correction, while used for PIXE, is not used for ISA because of the low (<500 hz) counting rate. In the case of ISA, peaks are located and identified, and then a linear background is subtracted, and elemental levels calculated from a table of cross-sections. If elements are present in the substrate, the substrate values are subtracted. Figure 2 shows an ISA spectrum taken from a sample of particulates from ambient air impacted onto mylar with a Lundgren-type impactor. The vertical scale is logarithmic to show all the peaks more clearly. In addition to the elastic peaks, note the 2+ and 0+ excited states of Carbon, the 0+ and 3- doublet of Oxygen, and the 1+ excited state of Nitrogen. The 2.31 MeV excited state of Nitrogen is parity forbidden in an (α,α) reaction and is not seen. The presence of an excited state may be used for verification of an elastic reaction, and give confirming data on quantity.

Minimum sensitivity of elemental analysis must be computed in a different manner for elements present in the substrate than for elements not present in the substrate. In the latter case, it is necessary to identify the presence of the peak within the background. Using the IUPAP criterion of significance,[1] the number of counts in the peak (N_α) must be more than three times the uncertainty in the background for a peak to be detectable as such. If N_b is the background, then using Poisson statistics, this is

$$N_\alpha \geq 3\sqrt{N_b}\ .$$

However, when a peak is present in the blank substrate, it is not necessary to determine the existence of the peak, only to determine if material is present in addition to the substrate. The minimum sensitivity is, then, only the uncertainty in the substrate elemental concentration. Table II shows minimum sensitivities for elements on 3.2 μm mylar and on Nuclepore brand membrane filters for a 5.00 μcoulomb beam charge of alphas.

Table II

Minimum Sensitivity on Different Substrates $\mu g/cm^2$

	3.2 μm Mylar	Nuclepore Filter
H	2.6	2.7
Li	13.5	14.7
Be	11.0	11.0
B	11.0	35.5
C	38.0	124.5
N	13.0	14.0
O	20.7	17.0
F	12.0	10.0
Na	49.8	53.7

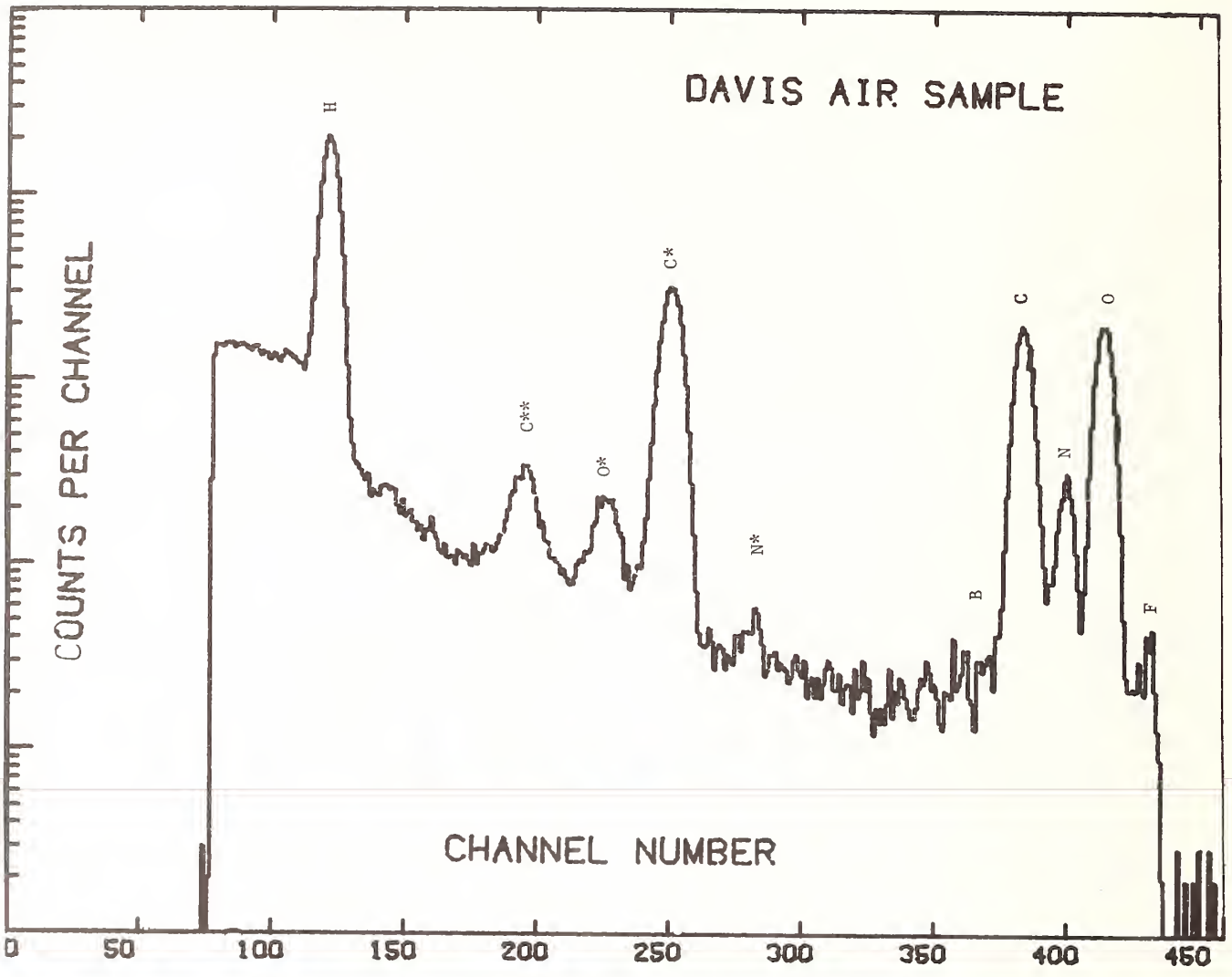

Figure 2. ISA spectrum of atmospheric particulates on mylar

Corrections to Experimental Data

Several difficulties present themselves in ISA work,most arising from the presence of a substrate.

If one is analyzing for all elements, then elements contained in a substrate interfere with elements on a substrate. The blank subtraction problem is a substantial one. Commercially-prepared substrates vary in thickness. Quality control holds these variations to (typically) 5%, but if the sample represents only a 10% mass increase on the substrate, the analyzed sample has a built-in uncertainty of 50%. Very thin substrates, such as the 3.2 μm (1/8 mil) mylar may be used so that thesample is a large percentage of the mass of the sample+substrate. If the substrate has uniform physical dimensions, such as Nuclepore brand membrane filters, the substrates may be pre-sized for thickness by weighing, so that the variations in thickness are reduced to less than 1%, or even 0.5%.

The forward scattering method itself presents difficulties. Straggling causes shift of the beam emergy, so that the system must be re-calibrated for peak location for substrates of different thicknesses. A straight-line recalibration method based on total counts per microcoulomb of beam charge has been used, and gives satisfactory results for samples ranging from 0.4 mg/cm^2 to 1.5 mg/cm^2.

Associated with this difficulty is the fact that deposited samples are not uniform in thickness. Heavier spots have more straggling and the result is not a true gaussian peak, but rather a peak with a low-energy "tail" Integration procedures must be adjusted appropriately.

Also, if the beam energy is reduced by straggling, the scattering cross-section may be altered. Figure 3 shows the measured areal density of Carbon, expressed in counts per microcoulomb of beam vs. the location of the Carbon peak. Since energy loss is approximately proportional to distance traveled, for short distances at least,[10] this should give a straight line. The data are much better fit to a power curve of the form $A(\Delta E+160)^B$, however, where ΔE is the energy shift of the peak in KeV. A correction factor of $(\Delta E/160)^{B-1}$ is applied to analyzed amounts to account for the effect, with satisfactory results. Table III gives the values of A and B, along with the coefficient of determination of the fit r^2, for the most noteworthy elements at 18.36 MeV.

Table III
Cross-Section Energy Shift Parameters

Element	A	B	r^2
H	9.259	1.158	.98
C	.0189	1.793	.99+
C*	.552	1.309	.98
N	.192	1.061	.99
O	3.353	.915	.99
O*	.456	.942	.82

Results of Method

A number of standards of varying areal density were analyzed repeatedly. The method was shown to be reproducible within 4.2% and linear up to 1.2 mg/cm^2 within 5.0%. See figure 4.

A second, more thorough test was based upon comparison of mass loading from ISA/PIXE analysis to gravimetrically determined mass loadings. The results are shown in Table IV. The chi-square factor

$$\chi^2 = \frac{1}{i}\left(\sum_i \frac{1}{\sigma_i^2}(Y_{grav} - Y_{ISA})^2\right)$$

where σ_i is the RMS uncertainty in ISA, Y_{grav} the gravimetric total mass, and Y_{ISA} the total mass by ISA and PIXE methods, over these runs was 3.89. On the whole, the error is acceptable for two-significant-figure determinations, with the average error being 17.1%, with none higher than 38.1%. (Note: samples 1 and 2 are for calibration, and sample 5 was damaged.)

A difference in sample mass was noted between the pre-analysis weighing and post-analysis weighing. An average of 7% weight loss, with a single-case maximum of 40%, was seen. It is suggested that this loss is due to evaporation of volatile matter on the particulate sample in vacuum. This fact must be taken into account when using PIXE-ISA dual analysis.

ISA Analysis may be used to supplement PIXE data. An example of statistical correlations leading to information about chemical structure is seen in Figure 5. Here the concentrations of Silicon (by PIXE) and Oxygen (by ISA) in large (3.5 μm to 20 μm) atmospheric particulates show an excellent correlation, with a correlation coefficient of 0.92. The least-squares slope gives a gives a mass ratio of Silicon to Oxygen of 0.484 . While the elemental ratio of SiO_2 in wind-blown dust is only .877 , the ratio of Silicon to Oxygen in "Average Sedimentary Soil" [11] is .488 , in excellent agreement.

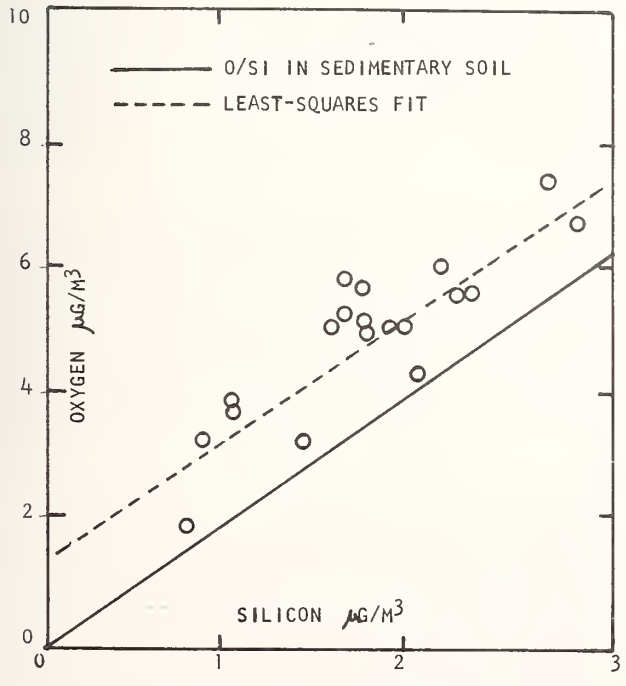

Figure 5. Correlation of Oxygen and Silicon in large atmospheric particulates.

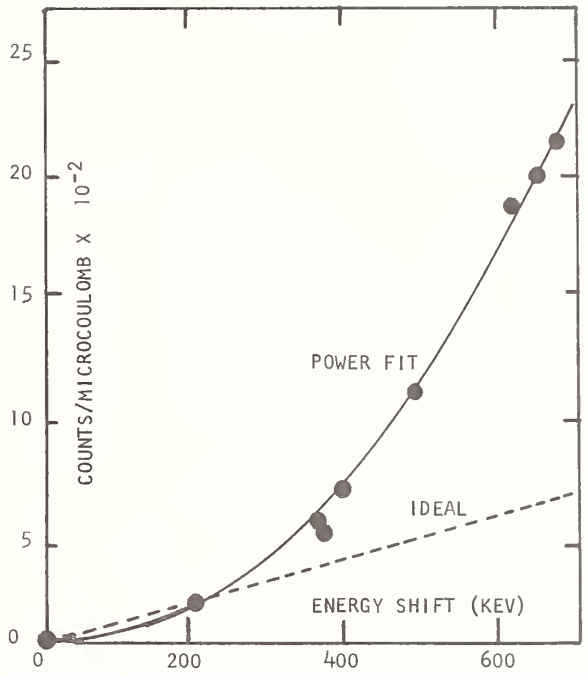

Figure 3. Drift of Cross-section with Straggling

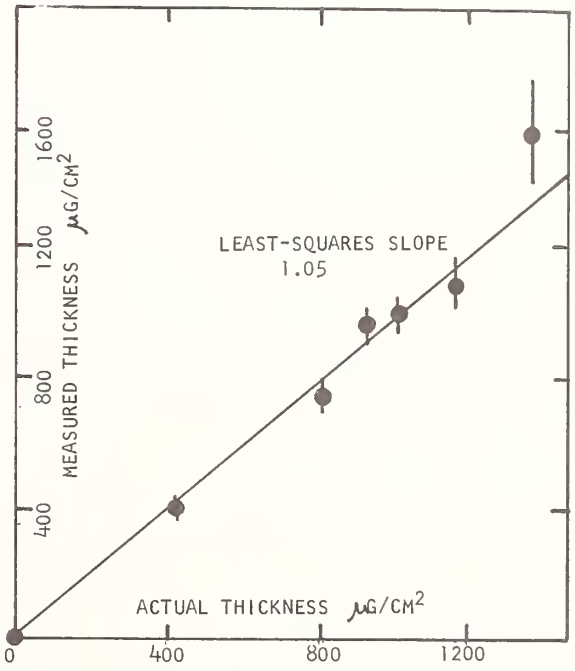

Figure 4. Linearity and Accuracy of ISA method.

Conclusions

ISA is seen to be an effective quantitative tool for identifying the presence of very light elements in thin samples.

As a method for monitoring potentially toxic light elements such as Beryllium, the sensitivity is inadequate for ambient uses. However, as a method for obtaining information about the total atmospheric aerosol mass present on an element-by-element basis, this method can observe all elements simultaneously, with sensitivity adequate to observe 50% or more of the 78 elements present in principle in atmospheric particulate matter using only short irradiations.

Table IV
Comparison of PIXE + ISA to gravimetric values

Sample No.	Net H	Net C	Net O	Other Light Elements	Heavy Elements (PIXE)	Total	Unloaded Sample Weight	Loaded Sample Weight	Net Sample Weight	Error (%)
3	53.1	1898	1668	0	81.8	3700	14300	18333	4033	-9.0
4	70.8	1880	235	0	211.3	2397	14276	16325	2049	14.5
6	51.8	877	245	0	184.0	1357	14120	15706	1586	-16.9
7	25.9	845	0	0	1.4	872	14108	14647	539	38.1
8	70.9	1991	158	0	6.8	2226	14537	16511	1974	11.3
9	73.6	1581	143	0	5.5	1803	14364	15938	1574	12.7

Values in μg for entire sample (13.63 cm^2)
47 mm nuclepore membranes

References

1. T. Cahill, "Ion-excited X-ray analysis of Environmental Samples", J. Zeigler, New Uses of Ion Accelerators, Plenum press, New York (1975)

2. T. Cahill, Cyclotron Analysis of Atmospheric Contaminants, final report to the California Air Resources Board, Project Clean Air. PCA-038 (1972)

3. T. Cahill and P. Feeney, Contribution of Freeway Traffic to Airborne Particulate Matter, final report to the California Air Resources Board, contract ARB-502 (1974)

4. Nucl. Inst. & Methods, V142,1-333 and references therein. (1977)

5. T. Cahill, Application of Alpha Scattering for On-Line Analysis of Atmospheric Aerosols, final report to the National Science Foundation (RANN) on grant NSF-AEN-23469 (1976)

6. J. Zeigler, "Material Analysis by Nuclear Backscattering", New Uses of Ion Accelerators Plenum Press, New York (1975)

7. T. Novakov, A. Harker, and W. Seikhaus, Sulfates in Pollution Particulates, USAEC contract W-7405-ENG-48

8. J. Nelson and W. Courtney, Nucl. Inst. & Meth., 142,127 (1977)

9. J. Harrison and R. Eldred, Advances in X-ray Analysis, V. 17, pergamon press, New York (1974)

10. P. Marmier and E. Sheldon, Physics of Nuclei and Particles, V. 1. Academic press, New York (1969)

11. Handbook of Chemistry and Physics, 51st edition, Chemical Rubber Co. (1971)

The author wishes to thank the Air Quality Group at the University of California, Associated Western Universiites, the National Science Foundation (RANN), and the California Air Resources Board for the opportunity to do this work. Special thanks to Tom Cahill and Robert Eldred.

THE SPECTROMETRY OF MULTIPLICITY OF SECONDARY RADIATION AS A METHOD OF MEASUREMENT OF NEUTRON CROSS-SECTION AND INVESTIGATION OF NUCLEI

G. V. Muradyan
I.V. Kurchatov Atomic Energy Institute,
Moscow, USSR

[Neutron cross section, multiplicity spectrum, α-value, U-235, Cd-113, Cf-252]

The present paper deals with the new method of neutron cross-section measurement and the investigation of ways of formation and decay of excited nuclei. The idea of the procedure from the view-point of measurement of partial neutron cross-sections has been described in [1]. It involves the measurement of total multiplicity sprectum of gamma-quanta and neutrons arising from reactions with neutrons. The object of the present article is the further generalization of the multiplicity spectrometry method and the broadening of the range of problems under investigation. At the same time a brief review of experiments on the multiplicity spectrometry is given.

An ideal installation to study nuclear processes can be a device which enable one to perform the complete analysis of the parameters of all particles resulting in the excited nuclear system, and of particles generated in the process of deexcitation. For instance, under fission of a nucleus by protons it would be possible by means of such a device to measure the proton energy, the energy, the angle of emission and other parameters of all neutrons, gamma-quanta and fragments at the same time. In contrast to the totality of experiments where these values are measured separately the ideal installation gives the complete information on the process, since along with individual values it gives all possible correlations of them.

However, the creation of such a versatile installation at the up-to-date stage of development of experimental technique presents a very severe problem. Besides, in order to obtain physically clear results it is necessary to create the alogrithms selecting from great numbers of data the information which we wish. Therefore, the need arises for searching such a set of simultaneously measured values and of a concrete method of their measurement which reflect the main correlations of values of the process under investigation. In this case the method of measurement should provide the acceptable rate of accumulation of statistics.

As a rule, energy spectra of particles (and fragments), their angular distributions and spins are considered as measurable values. We believe that one more type of spectrum - the multiplicity spectrum should be included in this list. By this definition the distribution of number of particles emitted in the process of deexcitation, for example, the gamma-quanta number emitted in fission, is meant. The A(ν) multiplicity spectrum shows in how many events one particle (ν=1) has been emitted, and in how many events two particles (ν=2) have been emitted, etc.

The multiplicity spectrum can be measured by the multisectional 4π-detector having efficiency ∿100% in the center of which is located the sample (Fig. 1). The ν-fold coincidence events number gives directly the multiplicity spectrum A (ν). For this purpose the detector sections number should be much greater than ν_{max}, and the detecting efficiency ∿100%. Such a device, in principle, can also give angular coordinates of every particle. But here we shall concentrate our attention only on the problem of multiplicity.

The high relative aperture in measuring the multiplicity spectrum follows from the essence itself of this spectrum - from the necessity to detect all (or almost all emitted particles, i.e. the detecting efficiency is ∿100%. Since the particles number is not great, this 100% effect is distributed over a small number of spectrum channels. If the neutrons and gamma-quanta multiplicity spectrum is measured, the relative aperture can be very high since one can use samples with a thickness up to several g/cm^2.

The relation between the multiplicity spectrum and physical parameters of the nuclear process can be found by calculations for every specific case.

Let us consider the case when this connection is so unequivocal that it can be determined without calculations. The question is about the total multiplicity A ($_\Sigma$) of neutrons and gamma-quanta arising at the interaction of slow neutrons with nuclei. In this case the measurement of A (ν_Σ) permits one to pick out scattering, capture and fission events at the same time. This is seen from Fig. 2, where the result of the Imaginary measurement of A (ν_Σ) is shown. Indeed,

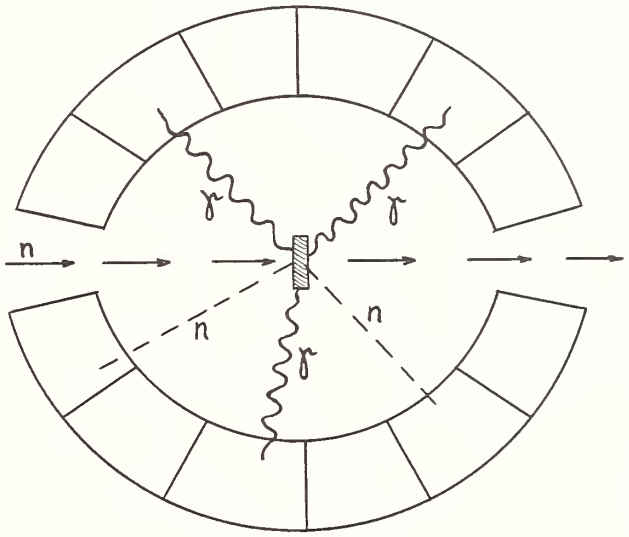

Fig. 1.

for scattering, only one neutron, i.e. $\nu_\Sigma = 1$ is detected; the first peak corresponds to the scattering. In the capture about 4 gamma-quanta are emitted; the second peak corresponds to capture. In fission the total number of gamma-quanta and neutrons is of the order of 10; the third peak corresponds to the fission. Thus, the multiplicity spectrum in the given case reflects the spectrum of the known decay ways of excited nuclei. The experimental detection of additional peaks or peculiarities can be indicative of other, possibly still unknown ways of the deexcitation.

The imaginary experiment given shows that the measurement of A (ν_Σ) allows one to obtain neutron

cross-sections and their rations with a high accuracy. Such measurements are of great significance for a reactor design.

The multiplicity spectrum of gamma-quanta arising from neutron capture permits one in many cases to group neutron resonances in accordance with spin and parity values. It follows from the fact that at the fixed low-lying state of radiation cascade the multiplicity of gamma-quanta in the cascade depends on the spin and parity of the neutron resonance. This dependence to some extent is smeared-out because of Porter-Thomas fluctuations. For $\nu_\gamma = 1$ the smearing is strong but already for $\nu_\gamma = 2$ it drops by one order. At the further increase of ν_γ fluctuations can be intensified. The accuracy of grouping depends on how do the spin difference of A (ν_γ) compete with Porter-Thomas fluctuations.

The problem of fluctuations of the multiplicity spectrum can be of interest in itself, since there exists the connection between fluctuations and the number of channels through which the primary gamma-transition (γI) proceeds in the cascade. As ν_γ increases the energy, $E_{\gamma I}$, of this transition decreases

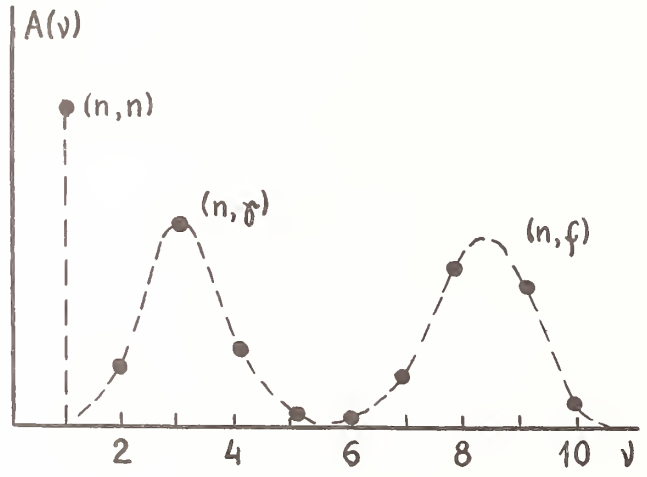

Fig. 2.

on an average. Therefore, studying the dependence of fluctuations upon ν_γ one may obtain information on the dependence of the state densities upon the excitation energy.

The multiplicity spectrum A (ν_γ) or A (ν_γ) permits one to reveal the (n, f) process. It is known that the multiplicity of gamma-quanta in the (n,γf)-process is somewhat higher than in the usual fission. Studying the dependence of A (ν) on E_n one can separate contributions of (n,γf) and (n,f)-processes since cross-sections of these processes depends differently on neutron energies. Note that the relative aperture of the method is far higher than those one uses in the measurements of the mean multiplicity, because A (ν_γ) as compared with J is far more sensitive to the admixture of the (n,γf)-process. Besides, the multiplicity spectrum is measured with the efficiency ~100% whereas the detection efficiency in the measurements of the mean multiplicity must be one order less.

The examples given show that by measuring the multiplicity spectrum one can research a wide range of problems.

Let us turn to concrete installations and results of measurements.

The first installation "Romashka-I" measuring the multiplicity spectrum has been installed in 1974 at I.V. Kurchatov AEI [2]. The detector (Fig. 3) consists of 12 light-isolated NaI(Tl) crystals with the total volume of 16-ℓ. In order to detect neutrons the sample is surrounded with a (n → γ) converter, consisting of the mixture B^{10} with moderator. To measure neutron cross-sections the detector "Romashka-2" similar to "Romashka-I" but with volume of 26-ℓ in addition was used at the 26-m station of I.V. Kurchatov AEI.

Figure 4 shows multiplicity spectra for the spontaneous fission of Cf-252 and the neutron radiative capture in Cd-113. It is seen that "Romashka-2" separates rather well the fission and capture events. Preliminary measurements of the U-238 capture cross-section [3], the α-value and fission and capture cross-sections of U-235 over the energy range from 0.1 to 30 keV [4] were carried out by means of this detector. Cross-sections obtained from U-238 and U-235 agree well with data by other authors. The relative shape of α is in good agreement (the maximum deviation - 3%) with ORNL data [5]. To make the α-value absolute without using data from other work we had to introduce the estimated fission and capture detection efficiencies as well as the multiplicity spectrum

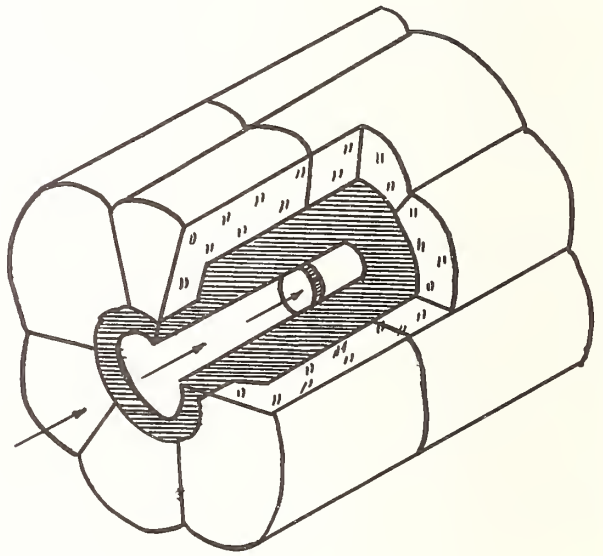

Fig. 3.

shape for the fission in the range $\nu = 2$. This could reduce the accuracy of absolute α-value. Therefore, in addition, the method of measurements has been improved in order to obtain the absolute α-value without reference to calculated corrections. The absolute α-value has been measured by our group by means of 46-sectional detector with the volume of 100-ℓ. These data are pressented in another paper of ours at the present conference.

To investigate possibilities of the method for the spin identification, the multiplicity spectrum of Cd-113 [2] was measured and many new levels have been found. For grouping the resonance through the multiplicity spectrum one can use the known methods of the cluster analysis. But for the given case the method described below is more effective.

The multiplicity spectrum for the i-th neutron resonance was normalized to 1 ($\sum_\nu N(\nu) = 1$) and was presented in the form:

$$N_i(\nu) = a_i N_i(\nu) + (1-a_i)N_2(\nu) \qquad (1)$$

where $N_1(\nu)$ is the corresponding multiplicity spectrum for the first spin state, $N_2(\nu)$ is multiplicity spectrum for the second spin state; a_i is the fraction of the first spin state in the i-th resonance. For isolated levels $a_i = 1$ or 0 depending on whether the level belongs to the first or the second spin state, respectively. The set of equations (1) was solved by a least-squares method with regard to a_i. $N_1(\nu)$ and $N_2(\nu)$ were selected by a interaction method.

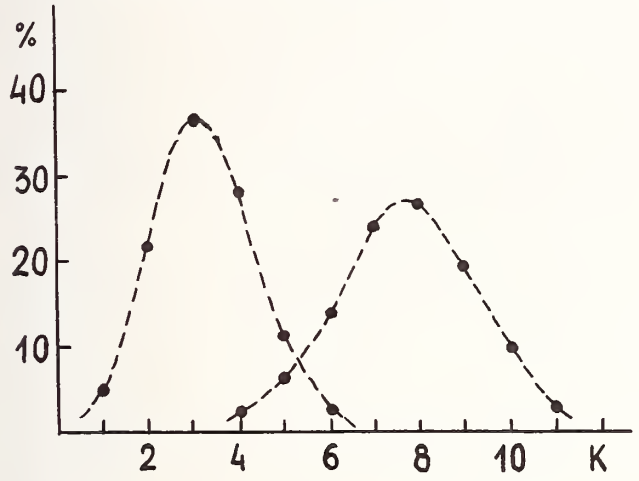

Fig. 4.

Results of such a treatment of 26 levels over the range up to $E_n \sim 1$ keV are presented in Fig. 5. There is seen the clear-cut grouping. The comparison with data obtained by other methods for 13 levels within the same energy range [6] shows the $a_i = 1$ corresponds to J = 1, and $a_i = 0$ corresponds to J = 0 without exception.

Note that the separation of s- and p-neutron cross-sections is possible through the multiplicity spectrum within the range of non-separated resonances. In this case the multiplicity spectrum is averaged over many levels and therefore the Porter-Thomas fluctuations distort the results much less. The treatment of results is similar to that mentioned above.

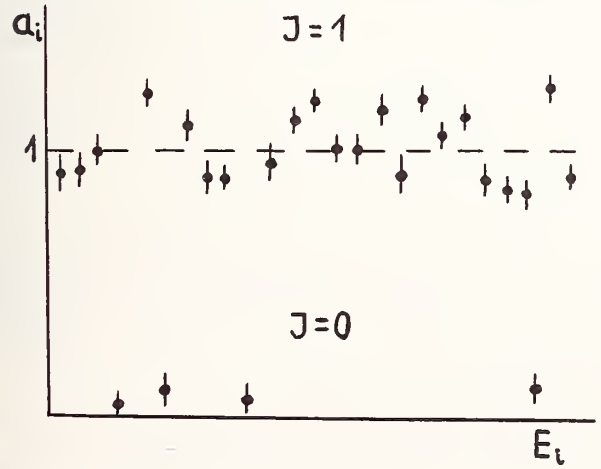

Fig. 5

Now the 46-sectional detector "Romashka" operates at I.V. Kurchatov AEI. The detector geometry permits one to increase the number of sections and to change the converter and sample values. This detector is used to measure the nuclear-physical constants needed for reactor design and for the study of the process of neutron-interaction with nuclei.

Since the relative aperture of the method is rather high it is possible together with the multiplicity spectrometry to perform the spectrometry of individual particles-fission fragments, soft gamma-radiation, etc. The spectrometry of the fragments gives valuable information on all possible correlations in fission and permits one to pick out and study such rare processes as the fission without neutron escape or with escape of a great many neutrons, etc. The spectrometry of soft gamma-radiation permits one to investigate gamma-cascades between levels above the neutron binding energy and definite levels near the ground state. From results of such measurements it is possible to reveal the low-lying isomeric states and identify the spin and parity of nuclear levels. Corresponding detectors can be inserted into the "Romashka" and one can develop high efficiency of detection since its practical to improve the measurement of multiplicity spectrum. Work of such a type have already started at I.V. Kurchatov AEI. Besides, they have already done work with very thin converter that permits one to measure also the total energy of gamma-quanta for low-lying resonances. Work on separation of multiplicity spectra of neutrons and gamma-quanta emitted in fission is also performed.

Thus the measurement of the multiplicity spectrum opens wide possibilities to study nuclei and nuclear processes and to obtain data of great significance.

References

1. G.V. Muradyan, Yu.G. Shchepkin, Yu.V. Adamchuk, G.I. Ustroev. Preprint IAE-2634, 1976.

2. Yu.V. Adamchuk, M.A. Voskanyan, V.U. Juk, D.A. Markov, G.V. Muradyan, L.Yu. Prokofieva, G.I. Ustroev, A.D. Charitonov, Yu.G. Shchepkin. Proceedings of IV All-Union Conference on Neutron Physics, Kiev, 1977, Publ. Moscow, v.3, p. 113, 1977.

3. Yu.V. Adamchuk, M.A. Voskanyan, G.V. Muradyan, G.I. Ustroev, Yu.G. Shchepkin. Proceedings of IV All-Union Conference on Neutron Physics, Kiev, 1977, Publ. Moscow, v. 2, p. 192, 1977.

4. G.V.Muradyan, G.I. Ustroev, Yu.G. Shchepkin, Yu.V. Adamchuk, M.A. Voskanyan, L.Yu. Prokofieva. Proceedings of IV All-Union Conference on Neutron Physics. Kiev, 1977, Publ. Moscow, v. 3, p. 119, 1977.

5. R. Gwin, E.G. Silver, R.W. Ingle and H. Weaver, Nucl. Sci. Eng. 59, 79 (1976).

6. BNL-325, Third Edition, v. 1 (1973).

Neutron Total Cross Section Measurement at WNR

P. W. Lisowski, M. S. Moore, G. L. Morgan, and R. E. Shamu
University of California, Los Alamos Scientific Laboratory*
Los Alamos, New Mexico 87545

The techniques involved in measuring fast-neutron total cross sections at the Weapons Neutron Facility (WNR) of the Los Alamos Scientific Laboratory are described. Results of total cross section measurements on natural carbon covering the range 2.5 to 250 MeV are presented.

[C (n,n), total cross section, 2.5-250 MeV]

Introduction

The Weapons Neutron Research Facility[1,2] is the first operating example of a new class of neutron sources. A part of the 800-MeV proton beam from LAMPF is used to bombard a tantalum target to produce an intense white source of pulsed neutrons. Variable width proton pulses may be supplied to permit a time-of-flight capability covering the neutron energy range from a few meV to several hundred MeV. The first nuclear physics experiments have exploited the fact that the neutron flux from the WNR is particularly suited for measurements in the MeV energy range. One such result, the total cross section of ^{242}Pu measured from 0.7 to 170 MeV, is presented in a separate contribution[3] to this conference. We give here a description of the measurement technique used in that experiment together with results for the total cross section of natural carbon, a measurement which was provided as a reference case for both ^{242}Pu and additional actinide samples.

Experimental Technique

The data were acquired using WNR as the neutron source. Neutrons were produced by spallation processes due to 800-MeV protons incident on a water-cooled aluminum-clad tantalum target (2.5-cm diam. by 15-cm high).

One out of every ten LAMPF H^+ beam pulses[a] was chopped at the injector to provide a 5-μs proton pulse spacing.[b] These pulses were then diverted to the WNR after acceleration by LAMPF using a kicker magnet operating at 12 Hz. The proton pulse width at the WNR target was typically 0.2-ns FWHM. A fiducial signal (t_0) was obtained from a capacitive pick-off located upstream of the target in the proton beam line. In addition to providing a start pulse for the time-of-flight (TOF) electronics, this signal was integrated in an analog-to-digital converter gated by a random signal to provide a measure of the relative proton intensity and the intensity variation.

The cross section measurements were performed using a 31.78-meter flight path. About 30 m of the flight path was evacuated in order to minimize any structure in the neutron flux caused by resonances in air.

The neutron beam at the sample was defined by a main collimator in the flight path located approximately 16-m from the WNR target. For the ^{242}Pu and for one of the reference C results, the collimating geometry and other experimental details slightly different from those of the C measurements described here may be found Ref. 3. For these measurements, larger samples and correspondingly larger collimators were used. Because there are a significant number of high-energy neutrons in the WNR beam, leakage through the collimator and through an aligning sleeve was found to be an important background contribution. The main collimator was composed of brass, iron and lead sections giving an average length of 80 cm. A brass scraper collimator 29-cm long and having a 3-cm diam opening was placed after the samples to remove any neutrons penetrating the aligning sleeve.

A neutron flux monitor was placed in the neutron beam after the main collimator. Because earlier investigations had showed that the number of charged particles[c] in the neutron beam was not a reliable indication of the neutron flux, a two-detector monitor was used. This arrangement consisted of two separate detectors separated by about 8 cm. Each detector was an 0.3-cm thick 2.9-cm square Pilot-B scintillator mounted on an RCA 8850 photomultiplier tube. The first of these detectors acted as a veto counter for the second, thus eliminating a charged particle contribution which was actually greater than the neutron contribution due to the almost 100% efficiency for charged particles.

The transmission samples were placed in a motorized changer, located about 0.5-m downstream of the main collimator. This sample changer was driven by the data collection computer via a Camac interface and stepping motors. An optical encoding system provided positioning accuracy to about 0.03 mm.

Because of the continuous distribution of high-energy charged particles produced along with the neutrons, it was necessary to use a sweep magnet located after the sample changer. This arrangement consisted of a magnet constructed from four ion-pump plate-magnets[d] with an overall length of 20 cm, a separation of 5 cm, and a central field of approximately 1 kG. Tests conducted using a thin fast-plastic detector at the location of the main detector demonstrated that the charged particles were completely removed by the magnet.

The neutron beam was stopped in a beam dump located at the end of an evacuated pipe approximately 30 meters beyond the neutron detector.

Two different neutron detectors were used in the cross section measurements. For the ^{242}Pu and corresponding C reference data, a 10.2-cm diam by 3.1-cm thick cylinder of NE 110 viewed by an RCA 8854 photomultiplier was used. This detector was replaced for

---

a) During these experiments, LAMPF was obtaining with an average current of 460 μA and a 7.44% duty cycle.

b) For the ^{242}Pu experiment, a spacing of 7 μs was used to avoid frame overlap.

* Work performed under auspices of U.S. Dept. of Energy

c) Although no absolute measurements have been made, calculations using the code NMTC indicate that about 0.3 protons/incident proton escape with an average energy of 273 MeV from the cylindrical surface of the target.

d) Available from Permag-Pacific Corporation, 5441 West 104th St., Los Angeles, California 90045.

later measurements by a similar system having a 15.2-cm thick NE 110 cylinder to improve the detection efficiency for high-energy neutrons.

The electronics consisted of a complete TOF system for the main detector and a fast-timing system for the neutron-flux monitor. Anode signals from the two monitor detectors were fed into an Ortec 934 constant fraction discriminator with a bias set below the minimum ionizing peak using a ^{90}Sr electron source. The output of the veto monitor detector was stretched and combined in anti-coincidence with the output of a coincidence between the second monitor detector and a time gating signal. This technique gated out charged particle as well as very short and very long time events. The resulting pulses were counted in a fast (100 MHz) scaler. Deadtime losses for this system were insignificant as the rate in the detector was only about 0.1 counts per micropulse in gated and about 0.6 counts in ungated mode. The time-of-flight spectrum from the main detector system was obtained from an Ortec TDC-100 digital clock operated in single-stop-per-start mode. Time-channel widths were set at 1 ns or 0.5 ns for the two sets of measurements. The proton t_0 signal was used to start the clock. The stop signal was derived from an Ortec 934 constant-fraction discriminator. Data were collected in four pulse-height windows, using bias settings ranging from $\sim$ 2 MeV to $\sim$ 10 MeV. The total open-beam counting rate for the ^{242}Pu experiment with a low bias of $\sim$ 300 keV and a small collimator was about 0.7/micropulse, whereas for the C data with a low bias of $\sim$ 2 MeV and a large collimator, the rate was only about 0.8/micropulse.

The background spectrum was measured by replacing the sample with a 1.9-cm diam by 46-cm long tungsten rod. These background spectra were measured several times and the shape followed roughly that expected for transmission of high-energy neutrons through the collimator. The backgrounds were less than 0.6% below 60 MeV, 0.8% at 100 MeV, and 2% at 200 MeV.

Data were accumulated using a Modcomp/IV computer system via a Camac interface. Time-of-flight spectra of 4096 channels for each bias were recorded along with various scaler signals for diagnostic purposes. The samples were cycled in and out of the beam at about 15-minute intervals, based on a preset number of monitor events. The spectra and scaler readings were recorded on tape at about 2-hour intervals as a backup against computer failure.

The carbon sample for the measurements reported here was one of three machined from a single block of high-purity, high-density, reactor-grade graphite. The measured density of each of the cylinders was found to be 1.836 g/cm^3 and density differences were less than 0.1% among all three. The sample thickness was 1.3682 atoms/barn.

The data reduction was performed using the central computing facility at Los Alamos Scientific Laboratory. The sample-in and sample-out spectra were corrected for dead-time losses and a normalized dead-time corrected background spectrum was subtracted from each. After subtraction of the measured background spectrum, a small time-uncorrelated background, typically less than 1%, was also subtracted.

For data below 60 MeV, the lowest bias data were used. Above 60 MeV, only the highest bias data were used both to lower the time-uncorrelated background and to avoid any contribution from time slewing of the prompt γ-ray peak produced when the beam struck the target.

The data for individual time channels were combined into bins of constant neutron energy resolution, as listed in Table I, and converted to total cross sections as a function of neutron energy.

Results and Comparison with Other Data

The total cross section of carbon has been the subject of many experimental investigations, particularly in the energy range below 15 MeV. Between 15 and 250 MeV, the data are sparse, but several sets of data from different laboratories are available for comparison. The present results are shown in Fig. 1 compared to the ENDF/B-V evaluation.[4] The measurements of the carbon total cross section reported here agree with the ENDF/B-V evaluation below about 8.5 MeV, to about 0.6% for the relatively smooth regions between resonances where energy resolution is unimportant. Above 8.5 MeV, these data agree better with the NBS data,[5] upon which the evaluation was largely based, than the evaluation itself. Comparison with the data of Auchampaugh et al.[6] is of similar quality. Above 15 MeV, the most recent data are those of Auman et al.[7] and Bubb et al.[8] covering the range from 24 to 60 and 20 to 45 MeV, respectively. Agreement with data of Auman et al. is generally better than 1%. The results of Bubb et al.[8] are generally higher than our results, those of Auman et al., or older results of Bowen et al.[9] From 80 to 150 MeV, there exist data from Meadsday and Palmieri[10], Bowen et al.[9], Taylor and Wood[11] and several other less comprehensive cross section measurements.[14-17] Agreement with the present data is within about 2% for Meadsday and Palmieri. The results of Bowen et al. are consistently lower than our data below about 90 MeV; at higher energies their data generally agree within errors with our systematically higher results. Above about 150 MeV, there exist no recent data; however, several sets of early results have been reported. Ragent[15], DeJuren and Moyer[16], and Mott et al.[13] all provide values which compare well with our data between 163 and 220 MeV. Table II provides a summary of selected comparison points covering the energy range of these measurements.

Conclusions

The technique for measuring fast neutron total cross sections at WNR has been described and demonstrated to yield accurate results using C as a test case. Additional data covering the complete energy range 2.5 to 250 MeV have been provided.

TABLE I

NEUTRON ENERGY BINS FOR FIGURE 1

E_n	ΔE_n
2.5 to 8.5 MeV	0.2%
8.5 to 20 MeV	0.5%
20.0 to 60 MeV	1.0%
60 to 250 MeV	2.5%

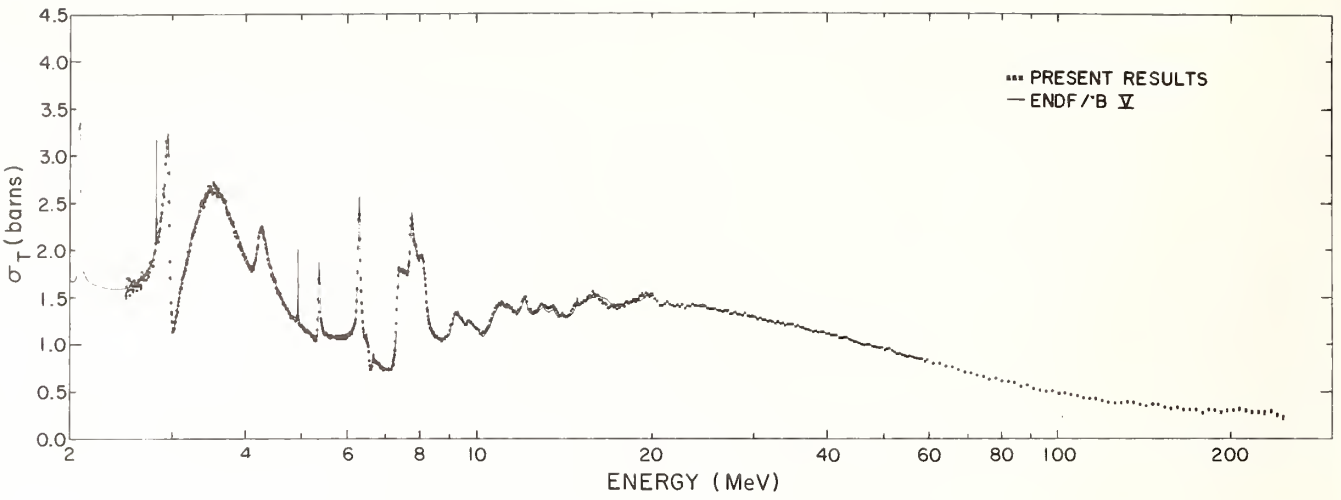

Fig. 1. Present results for the carbon total cross section. The solid curve is from ENDF/B-V evaluation.

Table II. Comparison of the present carbon total cross-section results with other work at selected energies

E_n ΔE_n (MeV)	Present Work Δ_T (b) $\Delta\sigma_T$	Previous Work σ_T (b) $\Delta\delta_T$	Difference δ (%) $\Delta\delta$	Reference
3.60 ± 0.04	2.602 ± 0.012	2.607 -	- 0.2 ± 0.5	ENOF/B-V (4)
5.72 ± 0.15	1.071 ± 0.002	1.078 -	- 0.7 ± 0.2	"
8.64 ± 0.10	1.050 ± 0.004	1.066 -	- 1.5 ± 0.4	"
11.63 ± 0.30	1.346 ± 0.005	1.337 -	+ 0.7 ± 0.4	"
14.20 ± 0.50	1.308 ± 0.004	1.303 -	+ 0.4 ± 0.3	"
16.10 ± 0.26	1.497 ± 0.007	1.502 -	- 0.3 ± 0.5	"
18.13 ± 0.27	1.439 ± 0.007	1.445 -	- 0.4 ± 0.5	"
24.62 ± 2.0	1.393 ± 0.003	1.390 ± 0.002	+ 0.2 ± 0.4	Auman et al(7)
36.33 ± 2.0	1.175 ± 0.004	1.179 ± 0.001	- 0.3 ± 0.4	"
46.17 ± 2.0	0.995 ± 0.004	1.013 ± 0.001	- 1.8 ± 0.5	"
54.36 ± 2.0	0.882 ± 0.005	0.883 ± 0.001	- 0.0 ± 0.6	"
68.90 ± 3.0	0.714 ± 0.004	0.698 ± 0.009	+ 2.2 ± 1.8	Bowen et al(9)
88.2 ± 2.0	0.560 ± 0.006	0.547 ± 0.008	+ 2.3 ± 2.5	Measday (10)
98.10 ± 2.0	0.502 ± 0.006	0.490 ± 0.007	+ 2.4 ± 2.6	"
110.0 ± 2.0	0.445 ± 0.006	0.439 ± 0.006	+ 1.3 ± 2.6	"
119.6 ± 2.0	0.406 ± 0.007	0.403 ± 0.006	+ 0.7 ± 3.2	"
129.4 ± 2.0	0.384 ± 0.007	0.375 ± 0.005	+ 2.3 ± 3.1	"
140.9 ± 2.0	6.362 ± 0.006	0.346 ± 0.005	+ 4.4 ± 3.0	"
156.0 ± 5.0	0.332 ± 0.006	0.325 ± 0.010	+ 2.1 ± 4.8	Mott (13)
180.0 ± 7.0	0.290 ± 0.007	0.311 ± 0.009	- 7.2 ± 5.5	"
216.0 ± 6.0	0.292 ± 0.012	0.296 ± 0.005	- 1.4 ± 5.8	"

References

1. G. J. Russell, P. A. Seeger, and R. G. Fluharty, "Parametric Studies of Target/Moderator Configuration for the Weapons Neutron Research (WNR) Facility," Los Alamos Scientific Laboratory report LA-6020 (March 1977).

2. G. F. Auchampaugh, "Status and Comparison of New, Planned, and Upgraded Pulsed "White" Neutron Source Facilities," International Conference on Nuclear Cross Sections for Technology, Knoxville, TN (1979).

3. M. S. Moore, P. W. Lisowski, G. L. Morgan, G. F. Auchampaugh and R. W. Shamu, "Total Cross Section of ^{242}Pu Between 0.7 and 170 MeV," International Conference on Nuclear Cross Sections for Technology, Knoxville, TN (1979).

4. C. Y. Fu and F. G. Perey, ENDF/B-V evaluation for carbon, MAT 1306, ORNL, Jan. 1977.

5. R. B. Schwartz, R. A. Schrack, and H. T. Heaton, II, "MeV Total Neutron Cross Sections," NBS Monograph 138, Jan. 1974.

6. G. F. Auchampaugh, S. Plattard and W. W. Hill, Nucl. Sci. Eng., 69 (1979) 30.

7. M. Auman, F. P. Brady, J. A. Jungerman W. J. Knox, M. R. McGie, and T. C. Montgomery, Phys. Rev., 5 (1971) 1.

8. I. F. Bubb, S. N. Bunker, M. Jain, J. W. Leonard, A. McIlwain, K. I. Roudston, K. G. Standing, D. O. Wells and B. G. Whitmore, Can. J. Phys. 52 (1974) 648.

9. P. H. Bowen, J. P. Scanlon, G. H. Stafford, J. J. Thresher, and P. E. Hodgsen, Nucl. Phys. 22 (1961) 690.

10. D. F. Measday and J. N. Palmieri, Nucl. Phys. 85 (1966) 129.

11. A. E. Taylor and E. Wood, Phil. Mag. 44 (1953) 95.

12. P. Hillman, R. H. Stahl and N. F. Ramsey, Phys. Rev. 96 (1954) 115.

13. G. R. Mott, G. L. Gurnsey and B. K. Nelson, Phys. Rev. 88 (1952) 9.

14. L. J. Cook, E. M. McMellan, J. M. Petersen and D. C. Sewell, Phys. Rev. 75 (1949) 7.

15. B. Ragent, "The Variation of High-Energy Total Cross Section with Energy," UCRL-2337, 1953 (unpublished).

16. J. Dejuren and B. J. Moyer, Phys. Rev. 81 (1951) 919.

STUDY OF NEUTRON-INDUCED CHARGED PARTICLE REACTIONS ON DEUTERIUM USING A QUADRUPOLE TRIPLET SPECTROMETER

V. Kulkarni, P. Grabmayr, G. Randers-Pehrson, R.W. Finlay and J. Rapaport
Physics Department
Ohio University
Athens, Ohio 45701, USA

S.M. Grimes
Lawrence Livermore Laboratory
Livermore, California 94550, USA

A Quadrupole Triplet Spectrometer similar to the one at Lawrence Livermore Laboratory has been constructed at Ohio University to study neutron-induced charged particle reactions. The D(n,p)2n break-up reaction was studied at incident neutron energies of 11 and 25 MeV, and the angular distribution of the D(n,d)n elastic scattering was measured at E_n = 9 and 11 MeV.

[Quadrupole Triplet Spectrometer; D(n,p)2n; E_n = 11, 25 MeV, $\sigma(E_p)$; D(n,d)n, E_n = 9, 11 MeV, $\sigma(\theta_d)$]

Introduction

The measurement of neutron-induced charged particle reactions is important in both basic and applied nuclear physics. These reactions serve as a tool in the determination of Q-values, energy levels, and angular momentum transfers, and in the studies of few-particle problems, reaction mechanism and nuclear spectroscopy. Among the applied areas are the nuclear data needs of the fusion energy program and dosimetry information in neutron cancer therapy. However, available experimental data on (n,z) reactions are inadequate because of the experimental difficulties involved in these reactions. Low counting rates and high background have been the chronic problems with the traditional techniques. A new technique recently developed at the Lawrence Livermore Laboratory[1] has been implemented at Ohio University.

Quadrupole Triplet Spectrometer (QTS)

This device is a charged particle spectrometer consisting of three magnetic quadrupoles. It is a poor-resolution momentum spectrometer, and the energy resolution is regained by using a suitable detector system. The target for the neutron beam (radiator) is located close to the neutron source. The device permits placement of the detector at a large distance from the neutron source, while retaining a substantial solid angle. The net result is a significant improvement in the signal-to-background ratio. The quadrupole triplet also has the advantage that it may be operated with unit magnification, so that the radiator area can be as large as the detector area.

The Ohio University QTS is shown in figure 1. It is 3.4 m long and has a beam transport tube with

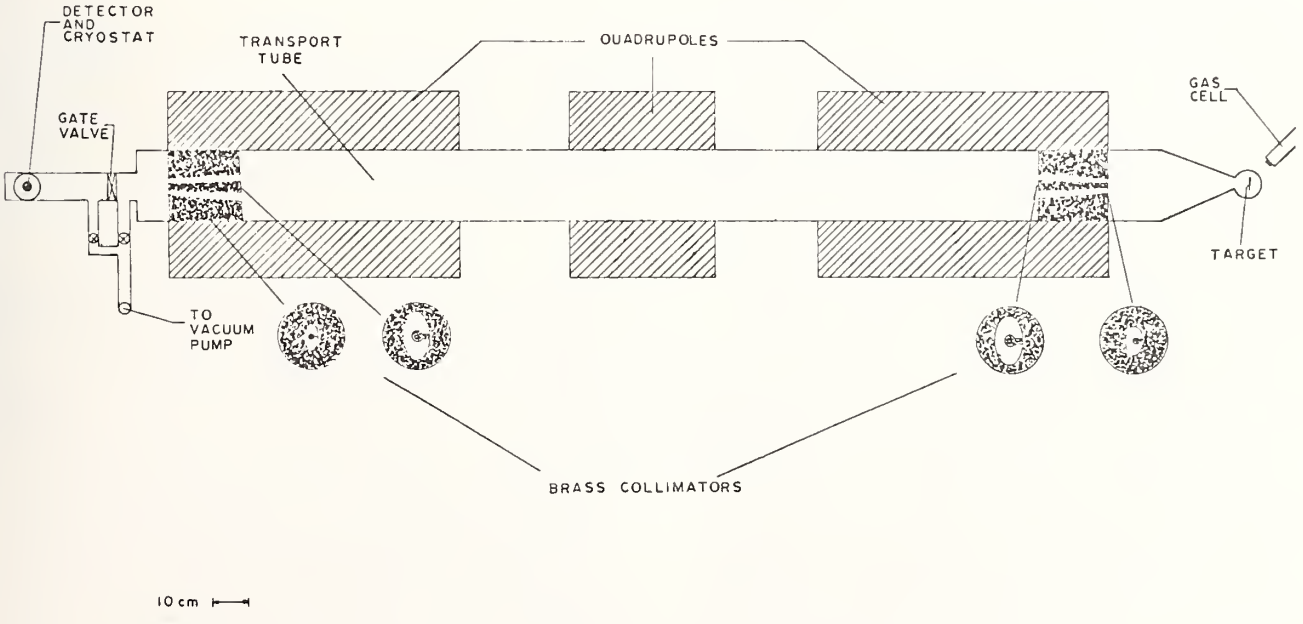

FIGURE 1

The Quadrupole Triplet Spectrometer at Ohio University

20 cm diameter. The magnetic lenses, with lengths 80 cm, 40 cm and 80 cm are placed symmetrically along its length. The distance between two quadrupoles is 30 cm. The radiators are mounted on a ladder which can be moved along a verticle axis, and the entire spectrometer can be rotated about this axis in order to measure angular distributions. The enclosure of the QTS is evacuated to a pressure of $\sim 10^{-6}$ torr. A detector telescope consisting of either two Si surface barrier detectors, or one Si and one intrinsic Ge detector is employed to measure charged particle spectra.

To reduce neutron-induced background, 25 cm long brass collimators enveloping the charged particle trajectory are placed at the entrance and the exit of the spectrometer. Brass shadow bars are also placed at the center of the spectrometer aperture to shield the detector from the direct neutrons from the source (see figure 1). The spectrometer solid angle is 6 - 10 msr depending on the area of the detector.

Charged particles produced in the radiator are focused onto the detector system by the quadrupole triplet. The focusing action of the magnets substantially enhances the solid angle for detecting charged particles over the geometrical solid angle of the detector. The lenses also act as an energy bandpass filter. These two effects define an effective solid angle for charged particles which is a function of the charged particle energy and the magnetic field gradients. The total acceptance of the spectrometer is the product of the solid angle and the efficiency of the detector system. In practice only the acceptance needs to be known and is determined by measuring a spectrum of protons from a thick CH_2 radiator. Energy calibration of the detector is achieved by using charged particle sources.

Experimental Procedure and Results

Neutron-induced charged particle reactions on deuterium have been studied using the QTS. The objective is to obtain cross-sections at various neutron energies and to study the effect of nucleon-nucleon interaction in the few-nucleon system. The D(n,p)2n deuteron break-up reaction was studied at neutron energies of 11 and 25 MeV and the D(n,d)n elastic scattering angular distribution was measured at neutron energies of 9 and 11 MeV. The spectrometer solid angle was restricted to 2 - 3 msr during these measurements by placing a collimator with a circular aperture at the entrance of the spectrometer. This was done to limit the angular spread of the charged particles emitted from the radiator and to improve the energy resolution.

Monoenergetic neutrons were produced using a pulsed deuteron beam obtained from the Ohio University Tandem Van de Graaff Accelerator, and $D(d,n)^3He$ or $T(d,n)^4He$ reactions in a gas cell. The radiator, with 280 mm^2 area, was located 14 to 18 cm away from the neutron source. The neutron flux incident on the radiator was 1.5×10^7 neutrons/sec at 11 MeV and 3×10^6 neutrons/sec at 25 MeV. The radiator was a 0.8 mg/cm^2 deuterated polyethylene (CD_2) film for the break-up experiment and a 3 mg/cm^2 CD_2 film for the elastic scattering experiment. The films were made using 99% pure CD_2 powder* and according to the method outlined by Bartle and Meyer[2]. The uncertainty in the radiator thickness was estimated to be 8%.

* Obtained from Bio-Rad Laboratories, Richmond, California.

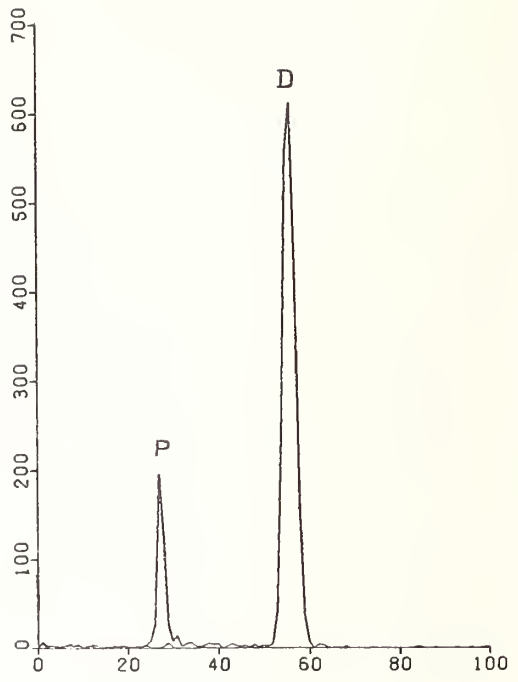

FIGURE 2

Mass spectrum from a thick deuterated polyethylene (CD_2) radiator. The background is also shown.

The ΔE-E detector telescope consisted on a 30 μ thick Si surface barrier detector and a 1000 μ thick Si surface barrier detector for energies up to 11 MeV, and a 200 μ thick Si surface barrier detector and a 3.5 mm thick intrinsic Ge detector for energies about 11 MeV. The Ge detector was constantly cooled with liquid N_2. The effective area of the detector telescope was 280 mm^2.

Time-of-flight and conventional slow coincidence electronics were used to identify charged particle spectra according to their masses in the OU-8000 minicomputer developed at Ohio University[3]. The digital multiplication of the energy and the square of the time-of-flight satisfying the coincidence requirement gave a signal proportional to the mass of the particle. A typical mass spectrum is shown in figure 2.

Proton spectra from a thick CH_2 radiator were measured to obtain energy bandpasses. Proton spectra from a thin (1.1 mg/cm^2) CH_2 radiator was measured to obtain the energy resolution. A thick CD_2 radiator was also prepared to obtain protons and deuterons at the same time. The spectra were stored on-line in an IBM-1800 computer, and charged particle cross sections were calculated using the data analysis code TANKA. The deuteron break-up experiment consisted of a sample-in (radiator) and sample-out (blank) measurements. These measurements took five to six days at each energy. The break-up proton spectrum near 0° shows a peak at the maximum allowed energy corresponding to the final state interaction between the two neutrons. The value of the neutron-neutron scattering length, a_{nn}, is directly related to the width and the shape of this peak. The spectra at E_n = 11 and 25 MeV are shown in figures 3 and 4 respectively. The energy resolution was 170 keV at 11 MeV and 350 keV at 25 MeV.

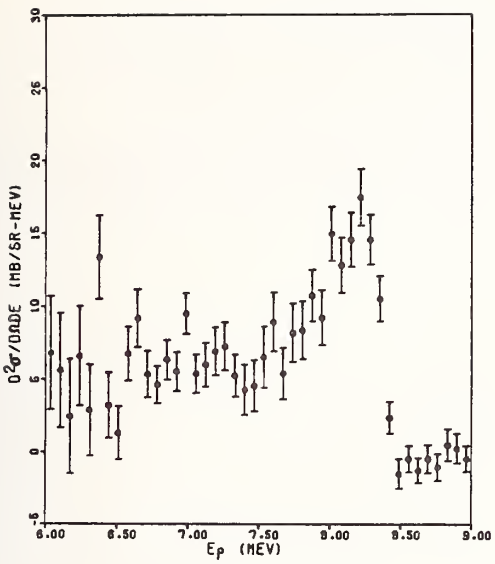

FIGURE 3

The double differential cross section $d^2\sigma/d\Omega Ep$ as a function of proton energy in the D(n,p)2n break-up reaction at E_n = 11 MeV and $\langle\theta p\rangle$ = 2°. The width and the shape of the final state interaction peak are related to the neutron-neutron scattering length a_{nn}.

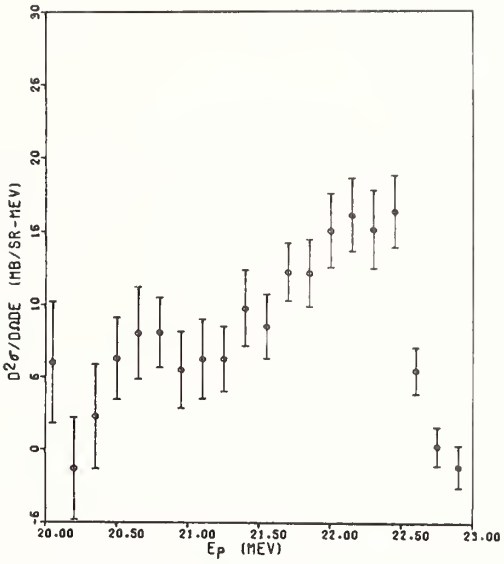

FIGURE 4

The double differential cross section $d^2\sigma/d\Omega dEp$ as a function of proton energy in the D(n,p)2n break-up reaction at E_n = 25 MeV and $\langle\theta p\rangle$ = 2.7°.

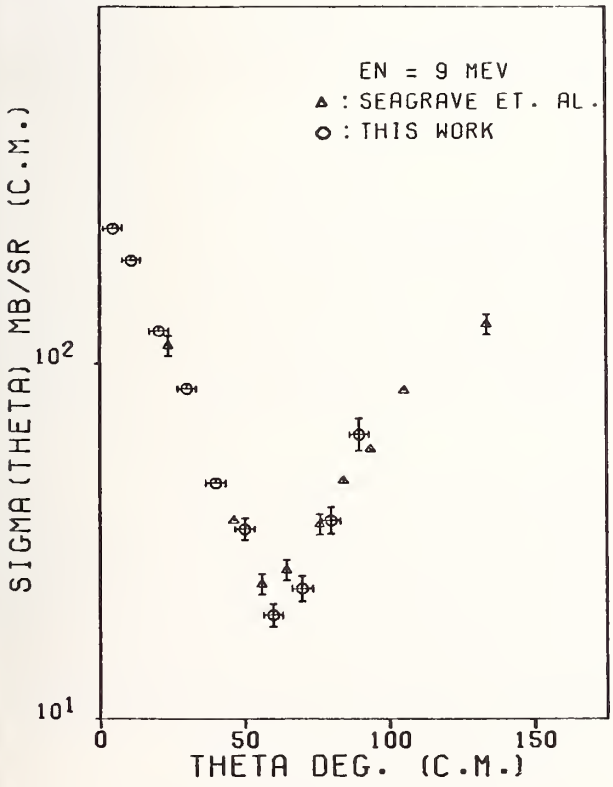

FIGURE 5

The angular distribution of deutrons elastically scattered from 9 MeV neutrons. Statistical errors and estimates of angular spread are shown. The cross sections by Seagrave et al. have been taken from ref. 6.

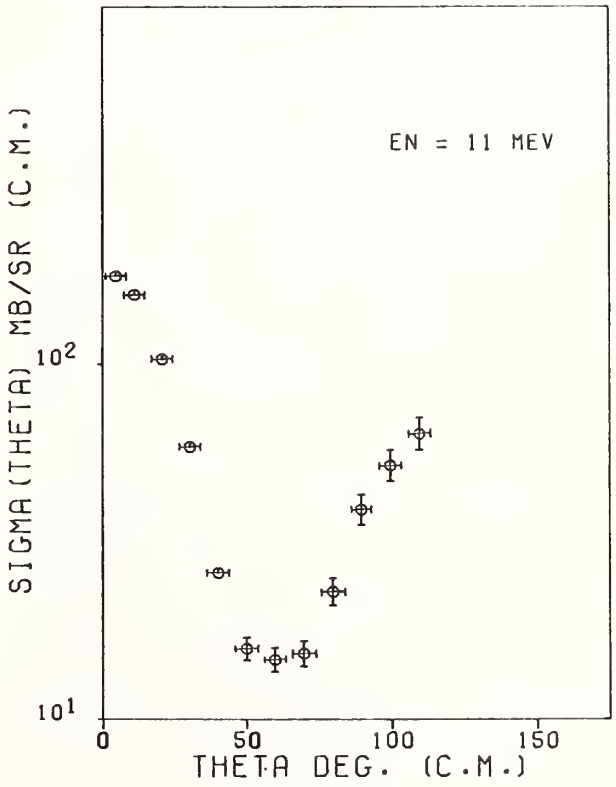

FIGURE 6

The angular distribution of deuterons elastically scattered from 11 MeV neutrons. Statistical errors and estimates of angular spread are shown.

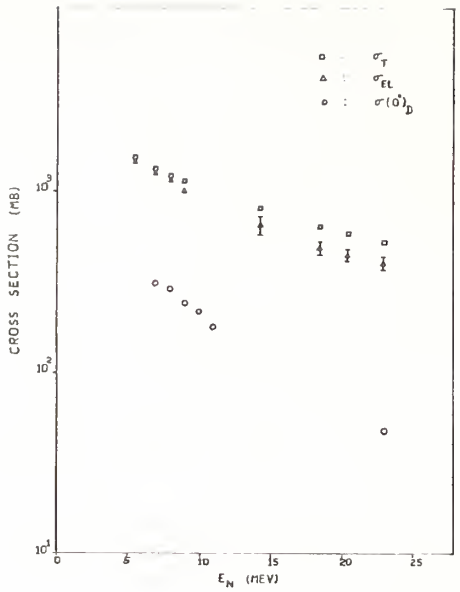

FIGURE 7

Neutron cross sections for deuterium. σ_T and σ_{EL} are the neutron total and total elastic cross sections for deuterium. The values are taken from ref. 6. $\sigma(0°)_D$ are the deuteron elastic differential cross sections measured in this laboratory at $\langle\theta_d\rangle_{lab} = 2.3°$.

The analysis of these data using a computer code based on the Faddeev three-body formalism[4] is in progress with the intention of investigating the discrepancy in the value of a_{nn} reported by Haight et al.[5]. They have obtained a value $a_{nn} = -23 \pm 3$ fm in a similar incomplete experiment performed at 14 MeV, while many other complete experiments, in which two break-up particles are detected, have resulted in a much less negative value of $a_{nn} = -16.6 \pm 0.5$ fm.

The angular distributions of deuteron elastic scattering were measured at incident neutron energies of 9 and 11 MeV, from $\theta_{Lab} = 0°$ to 55° in 5° steps. The results are shown in figures 5 and 6. The 9 MeV results are compared with the data of Seagrave et al.[6].

In addition to the elastic scattering angular distributions, deuteron differential elastic cross sections were measured at 0° at 7, 8, 9, 10, 11 and 23 MeV neutron energies. The results are shown in figure 7, along with the total and elastic cross sections at these energies.

Acknowledgment

Work supported in part by grants from the National Science Foundation and U.S. Dept. of Energy.

References

1. K.R. Alvar, H.H. Barschall, R.R. Borchers, S.M. Grimes, and R.C. Haight, Nucl. Inst. and Meth. 148, 303, (1978)
2. C.M. Bartle and H.O. Meyer, Nucl. Inst. and Meth. 112, 615 (1973)
3. D.E. Carter, Nucl. Inst. and Meth. 160, 165 (1979)
4. P. Doleschall, Nucl. Phys. A201, 264 (1973); Nucl. Phys. A220, 491 (1974)
5. R.C. Haight, S.M. Grimes, and J.A. Anderson, Phys. Rev. C16, 97 (1977)
6. J.D. Seagrave, J.C. Hopkins, D.R. Dixon, P.W. Keaton, E.C. Kerr, A. Niiler, R.H. Sherman, and R.K. Walter, Ann. Phys. 74, 250 (1972)

EFFICIENT NEUTRON PRODUCTION USING LOW ENERGY ELECTRON BEAMS

C. D. Bowman
National Bureau of Standards
Washington, D.C. 20234, USA

A comparison of (γ,n) and atomic cross sections shows that neutron production with an electron beam can be as energy efficient with 10 MeV electrons as with the conventionally used 30 to 100 MeV electrons. Neutron production from W using 100 MeV electrons is compared with a thin W converter followed by a deuterium-containing target using electrons near 10 MeV.

[Bremsstrahlung, electron beams, linear accelerator, neutron physics, neutron radiography, neutrons.]

Introduction

The production of neutrons through the use of electron beams is well established and has played an important role in neutron experimental physics.[1] Conventional accelerators of this type are r-f systems which accelerate electrons in the 30-100 MeV range. The electron beam strikes a tungsten or other heavy metal producing bremsstrahlung which through the (γ,n) reaction produces neutrons in subsequent layers of the target. Above thirty MeV the neutron production is very nearly proportional to the power in the electron beam. The efficiency for this system is about 3000 MeV per electron[2,3] or about 2×10^{12} total neutrons per kilowatt of electron beam power. With conventional accelerators operating in the 5-40 kW range, the method provides a very useful intensity for experimental applications even though the conversion efficiency is not high. These accelerators must be large to achieve the high energy, they usually have a reputation for high maintenance costs, and require a rather large operations staff. If neutrons could be generated with comparable efficiency at a more modest electron energy, the size, operation costs, and operating staff could be significantly reduced. The purpose of this report is to compare the opportunities for neutron production with lower energy electrons with the established methods at higher energy.

Beryllium and Deuterium Targets

For production of neutrons with lower energy electrons, attention is immediately focused on beryllium and deuterium owing to their low reaction thresholds of 1.67 and 2.22 MeV respectively. While these thresholds are quite low compared to heavy elements, the cross sections for the (γ,n) process also are smaller by about two orders of magnitude than the giant resonance cross sections for heavy nuclei. Perhaps for this reason, the possibilities at low energies have been largely overlooked.

It is important to recognize that the yield of neutrons is determined perhaps more by the atomic processes governing attenuation of the γ-rays than by the (γ,n) cross sections which actually produce neutrons. For example, in the case of the heavy material W, the nuclear cross section is about 0.4 barns at the peak of the giant resonance near 14 MeV whereas the atomic cross section at the same energy is 16 barns. The mean free path in W for γ-rays is therefore limited by the atomic cross section. The yield Y of neutrons from a γ-ray beam of intensity I_o is given by

$$Y = \frac{I_o \sigma_n}{(\sigma_a+\sigma_n)} \left[1 - e^{-(\sigma_a+\sigma_n)N} \right] \qquad (1)$$

where N is the target thickness in atoms/cm^2 and σ_a and σ_n are the atomic and nuclear cross sections, respectively. For heavy metals for which $\sigma_a >> \sigma_n$, Eq. (1) reduces to

$$Y \simeq I_o \frac{\sigma_a}{\sigma_a} \left[1 - e^{-\sigma_a N} \right] \qquad (2)$$

For W nearly all of the neutrons are produced within the first mean free path which is about 1 cm. For the lighter targets of Be or deuterium compounds, both the atomic and the nuclear cross sections are much smaller. However, the ratio of atomic to nuclear cross sections is essentially the same. Therefore, neutron yields as high as those from heavy metals are in principle possible if the target thickness is increased to one atomic mean free path. For Be metal at 5 MeV this thickness is 23 cm. While the physical thickness of the target is much greater for the light element compared with the heavy element, the yield might be comparable depending on the details of the energy dependence of the (γ,n) cross section with energy, etc. In those experiments where target size is not an important factor, the lighter targets of deuterium or beryllium might compete.

In order to place these calculations on a more quantitative basis, an estimation of neutron yield per MeV of electron energy has been carried out from first principles. It is necessary of course that conversion of electron energy to bremsstrahlung must be done with the greatest efficiency. This implies the use of a thin heavy metal target which we take to be tungsten followed by a layer of the neutron emitting material. Calculations of Berger and Seltzer[2] are used which take into account bremsstrahlung production and attenuation of the radiation in the heavy target for various incident electron energies. Their calculations show that the maximum conversion efficiency is obtained for a radiator of about half the thickness of the electron range. At 10 MeV the efficiency is about 0.18; for 20 MeV, it is about 0.32.

The bremsstrahlung has been measured by O'Dell et al.[4] at 0° for a tungsten-gold radiator with a thickness 20% of the electron range. The measured spectra estimated from his work are given in Table I. The numbers appearing in the table are the number of γ-rays per MeV per steradian per electron of energy of 8, 10, 15, or 20 MeV. Even though the spectrum is sharply peaked in the forward direction, the effects of angular distribution must be taken into account. This is done in an approximate way by normalizing these spectra to the Berger and Seltzer calculations of total γ-ray energy in the forward hemisphere for a target of optimum conversion efficiency, which are given at the bottom of each column of Table I. It is assumed that all the γ radiation is emitted in the forward direction so as to strike a target containing either deuterium or beryllium. Averaged (γ,n) cross sections for neutron production from deuterium and beryllium were used in these calculations. Neutron yield calculations were carried out for several compounds using the non-nuclear cross sections of Table II.

Table II also gives the thickness of the target giving an attenuation of 1/e for 5 MeV γ-radiation.

Table I. Bremsstrahlung spectra.

Ee(MeV)	8	10	15	20
E_γ(MeV)				
3	.055	.09	.35	1
5	.030	.06	.25	.6
7	.010	.035	.15	.45
9		.01	.10	.35
11			.06	.25
13			.04	.17
15				.10
17				.06
19				.025
Total Energy (MeV)	1.3	1.8	3.75	6.4

The numbers in the table are the number of γ-rays per MeV in the forward steradian of solid angle per incident electron of given energy. The numbers labeled total energy at the bottom of the table are the total energy in the forward hemisphere for a given electron energy.

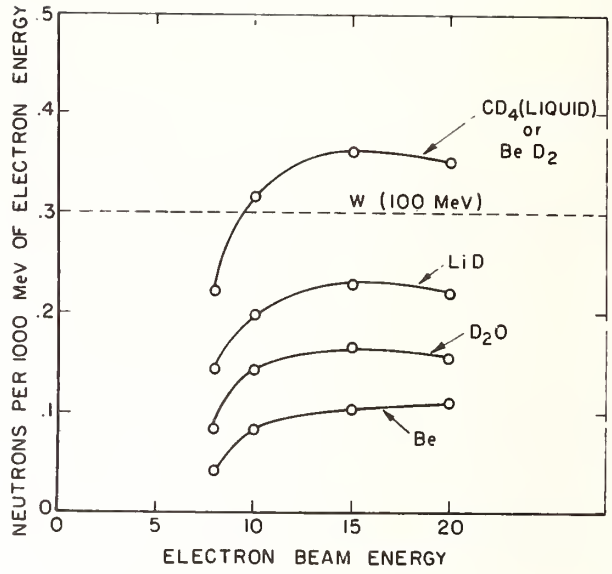

Fig. 1. Neutron production efficiency for various target materials. The number of neutrons produced per 1000 MeV of electron energy is shown vs the electron beam energy for various target materials. A target thick enough to attenuate 5 MeV γ-rays by a factor of 1/e is assumed. The dashed line is the efficiency for 100 MeV electrons on tungsten. Note that no significant gain in efficiency is obtained for an electron energy exceeding 10 MeV.

Table II. Non-nuclear cross sections for various targets.†

Compound	Cross Section (b/molecule)	Cross Section (b/Be and/or D atom)	Thickness (cm) (1/e attenuation)
BeD_2	.52	.18	44
CD_4*	.88	.22	72
^7LiD	.34	.34	48
Be	.35	.35	23
ND_3*	1.12	.37	37
D_2O*	0.91	0.46	33

*Liquid targets.

†For 5-MeV γ-rays.

The bremsstrahlung yield, target thickness, and (γ,n) cross section are folded together to give the neutron yield/per 1000 MeV of electron energy as a function of the energy of the electron beam. The results are shown in Fig. 1 for several different beryllium-and deuterium-containing targets. The efficiency possible using a thick tungsten target with a 100 MeV electron beam also is shown by the dashed line. It is interesting to note that D_2O with 10 MeV electrons is only a factor of two less efficient than W with 100 MeV electrons. A beryllium metal target is a factor of three less efficient than tungsten with 100 MeV electrons. If a CD_4 or BeD_2 target could be used, the neutron production efficiency would exceed that for tungsten at 100 MeV. For deuterium and beryllium containing targets, very little gain in efficiency is obtained by working at electron energies above 10 MeV.

These results have interesting implications for neutron production for some research and industrial purposes. If accelerator technology permits the exchange of current for beam energy, electron accelerators for neutron production need not operate at energies above 10 MeV. The accelerator could be far more modest in space since the length of the accelerator could be greatly reduced. For high power operation, probably D_2O is the only suitable target owing to target heating problems which necessitates a reduction in efficiency by a factor of two. If the neutron source strength requirements are sufficiently low, BeD_2 or even liquid CD_4 might be suitable targets

with greater efficiency than W at 100 MeV. For some experiments, the larger size of the target necessary for use of beryllium or deuterium might be a disadvantage depending on the source strength. Also no neutrons will be produced with energies above 4 MeV. Nevertheless these results indicate that a one-section L-band linac operating at 2000 pps with a 20 amp peak pulse and a pulse width of 30 nsec on a D_2O target could produce 1.2×10^{13} n/sec at an average power of 12 kW. With an induction linac[5] the average current might be higher by a factor of 25 permitting an average source intensity as high as 3×10^{14} n/sec. Developing pulse-switching technology might permit such an accelerator soon. The operating characteristics of these accelerators are compared with that of the Oak Ridge National Laboratory accelerator ORELA in Table III.

Some advantages of neutron production at lower electron energy are (1) reduced capital for the accelerator, (2) reduced physical space requirements, (3) more reliable accelerator operation, (4) lower maintenance, (5) simplicity of operation, and (6) greatly reduced activation of accelerator and neutron target. The disadvantages are less source brightness (larger target) and the unavailability of neutrons above 4 MeV. For industrial applications such as thermal and resonance neutron radiography or various measurements for safeguarding nuclear fuel, the disadvantages do not appear to be serious and the advantages appear to satisfy many of the past reservations about the practicality of industrial accelerators for neutron production.

References

1. E.R. Rae and W.M. Good, "Pulsed Accelerator Time-of Glight Spectrometers" in Experimental Neutron Resonance Spectroscopy, Academic Press, New York, p. 2 (1970).

2. M.J. Berger and S.M. Seltzer, Phys. Rev. C 2 621 (1970).

3. R.G. Alsmiller and H.S. Moran, Nucl. Instrum. Methods 48 109 (1967).

4. A.H. O'Dell, Jr. et al., EG&G Technical Report 1183-2139 "Measurement of Absolute Thick Target Bremsstrahlung Spectra" (1967).

5. N.C. Cristofilos et al., Rev. Sci. Instrum. 35 886 (1964).

Table III. Neutron production with electron accelerators.

	One Section* Linac	Induction Accelerator	ORELA
Energy (MeV)	10	10	140
Current (amps)	20	1000	20
RF frequency	L-band	--	L-band
Pulse width (nsec)	30	30	30
Rep rate (pps)	2000	1000	1000
Length (meters)	2	6(?)	30
Average power (kW)	12	300	84
Average neutron rate	$1.2X10^{13}$	$3X10^{14}$	$1.7X10^{14}$

*Built with existing technology, D_2O target.

PERFORMANCE IMPROVEMENTS OF THE GEEL LINAC NEUTRON SOURCE

J. M. Salomé and K. H. Böckhoff
Commission of the European Communities, Joint Research Centre,
Central Bureau for Nuclear Measurements, 2440 Geel, Belgium

(Linear accelerator, stationary U target, rotating U target, post-acceleration beam compression)

The Geel Electron Linear Accelerator, acronymed GELINA, is a 150 MeV S-band Linac which - together with its targets - serves as a pulsed neutron source in a multiple neutron time-of-flight spectrometer.

It has recently been modernised with the aim of narrowing the electron burst widths down to 3 ns and of increasing the peak currents for the short bursts. The accelerator is shown schematically in Fig.1 and its characteristic parameters in Table I.

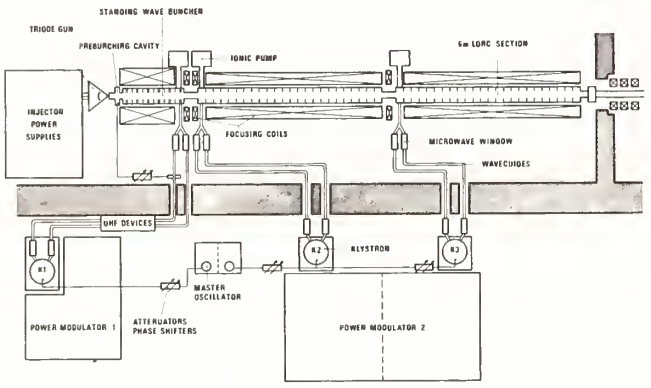

Fig. 1 : Schematics of the Linac.

Table I : Characteristic Parameters of the Linac.

Pulse Width ns	Repetition Rate Hz	Peak Current A	Mean Current µA	Nom Mean Energy MeV	Mean Power kW
4	900	9	32	120	3 8
10	900	9	81	105	8 5
100	880	1 5	132	87	11 5
1000	380	0 22	83	100	8 3
2000	250	0 22	110	100	11

The targets which have been used so far (all were constructed by CERCA-Paris) consist of Uranium alloyed with 10% Molybdenum. They are cooled by Mercury. For more than 13 years stationary cylindrical targets have been used. Their latest design can be seen on Fig. 2.

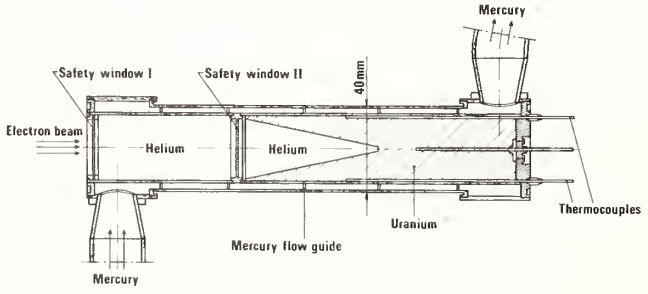

Fig. 2 : Stationary cylindrical Uranium Target.

The natural Uranium/Molybdenum core is cladded with stainless steel and Helium fills the small gap between the cladding and core to improve the heat transfer. Helium is also present in the conical space of the core and between the two windows, both consisting of stainless steel. The temperature can be measured with 3 Chromel-Alumel thermocouples placed near the centre of the heat production and near the clad. The cladded core is cooled by a stream of mercury steered helically around the cylinder.

Another target has been constructed which is geometrically identical with the one just shown. The only difference is that the front part of the uranium core, which produces the major part of the neutrons, has been replaced by 93% enriched Uranium-235. The neutron outputs have been compared for both targets by measuring the flux of moderated neutrons under identical conditions. It turned out that the "U-235 target" produced only 10% more neutrons than the other one. On the other hand the temperatures in the "U-235 target" were 10% higher than in the "Natural Uranium target" under comparable circumstances. This can be seen in Fig. 3. It was concluded therefore, that the use of enriched Uranium is not justified with such a configuration.

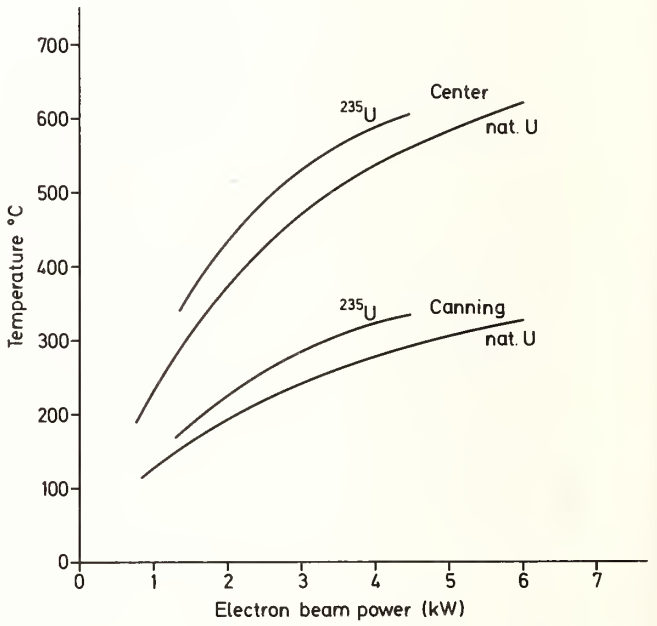

Fig. 3 : Temperatures in the Stationary Targets.

The temperature readings indicate that a beam power of about 6 kW is the limit for this type of stationary cylindrical Uranium-target. The critical point is reached when the Mercury starts to boil (327°C at normal pressure).

Because the modernised accelerator can deliver electron beams with up to 12 kW power there was a need for another type of target to be constructed which could stand such beam power.

Wishing to retain Uranium as target material because of its high neutron/electron "conversion" ratio, we decided to transfer the principle design of the stationary target to a rotary system, (Fig. 4).

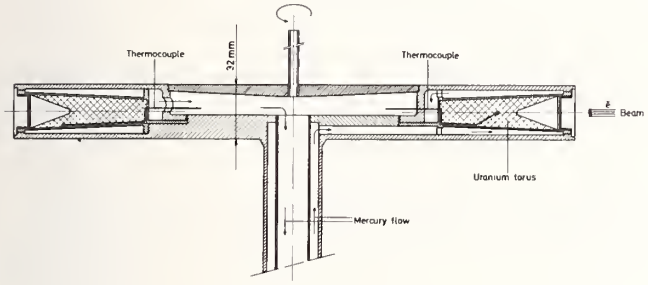

Fig. 4 : Rotary Uranium Target.

The cross sections of both targets look very similar. Fig. 5 gives another schematic view of the rotary target, illustrating the flow of the mercury coolant.

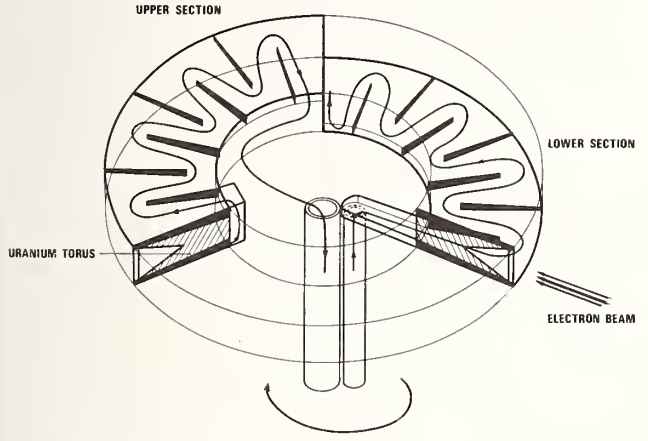

Fig. 5 : Flow of Mercury Coolant within the Rotary Target.

The target is divided into three sectors. The mercury enters each sector individually from a common input pipe in the shaft of the rotor and moves in serpentines along the lower side of the uranium, it then moves further in serpentines on top of the uranium and flows back to a tube in the shaft which is common to the flow from each of the sectors. The height of the passage decreases from the inside to the outside of the cooling cross section. The purpose of this flow guide is to assure equal mercury flow velocities in every part of the circuit.

The contact area between the Uranium clad and the mercury is a factor of 10 larger for the rotary than for the stationary target. The area of the safety windows is enlarged by a factor of 50.

The large reserve in cooling potential allows a decrease in the height of the Uranium annulus to 2 cm and thereby also the height of the target disc to 3.2 cm as compared to the corresponding dimensions of the stationary target (3 cf. 4 cm). Therefore, the moderators can be closer to the source of the neutrons, which results in a 25 % increase in the yield of moderated neutrons for comparable beam power.

The complete assembly of the rotary target with its mercury pump and heat exchanger is shown in Fig. 6. Rotation speed is 20 to 30 rpm.

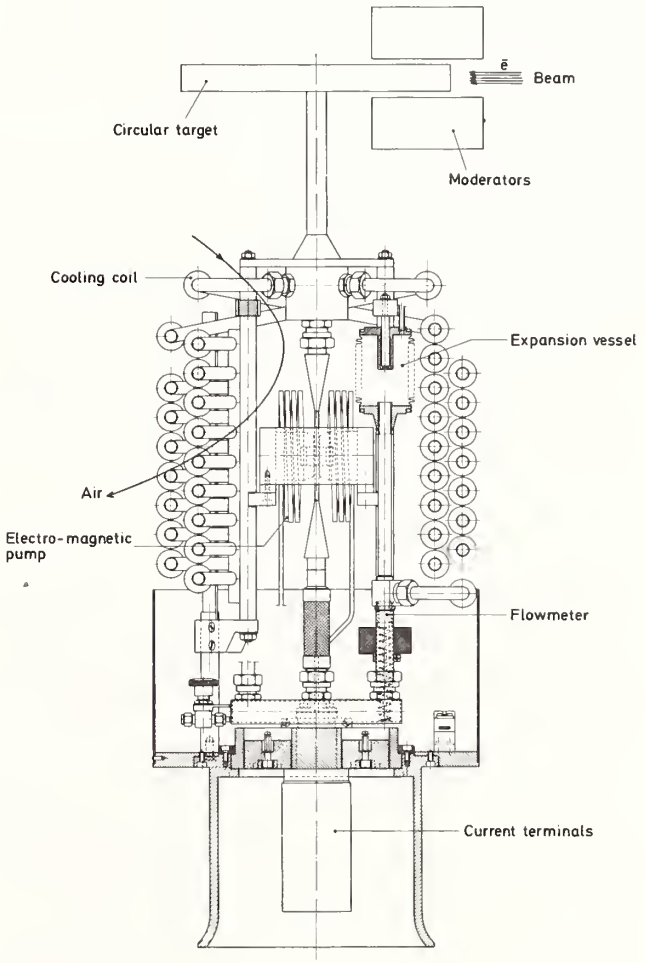

Fig. 6 : Assembly of the Rotary Target System.

The rotary target has been operated now for 500 hours without any problem at a beam power level of 8-9 kW.

The temperatures near the centre of the heat source and near the cladding are lower by a factor of 4.4 and 3.3 respectively than for the stationary

target, all measured at a 6 kW beam power level which is the limit for the stationary target. It may be concluded that the rotary target could be safely operated up to a beam power of 20 kW.

The absolute flux of moderated neutrons from the stationary target as measured with a ^{6}Li glass scintillator at 3.7 kW beam power is shown in Fig. 7. [1]

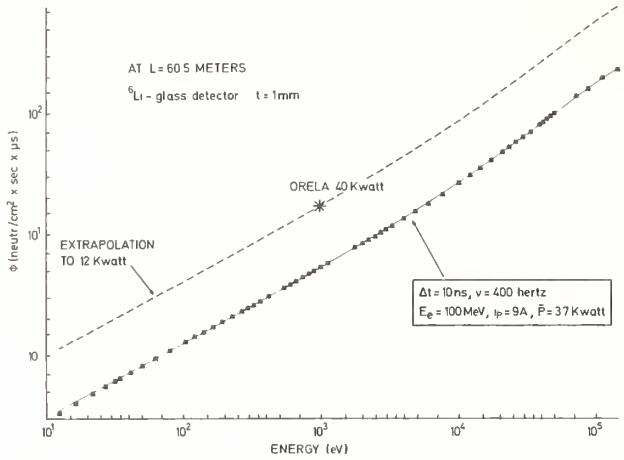

Fig. 7 : Absolute Flux of Moderated Neutrons at GELINA.

Extrapolating this to the maximum possible beam power of 12 kW, one arrives at a neutron yield which is comparable to that of ORELA at 40 kW. At Oak Ridge a Tantalum target is used, together with a water moderator, which gives about a factor of 3 less neutrons than our Uranium target with its polyethylene moderators.

Future development program

Improvements on the injection side

A new gun with an emission of 50A, rather than 25A of the present one, has been developed together with an optimised design of the gun structure and the magnetic field. It has been successfully tested in a laboratory version.

Post-acceleration buncher

A method of post-acceleration bunching is being studied in collaboration with the firm CGR-MEV which aims at an electron pulse compression from 15 ns down to 3 ns, maintaining the charge in the pulse.

The method is based on the following considerations (see Fig. 8) :

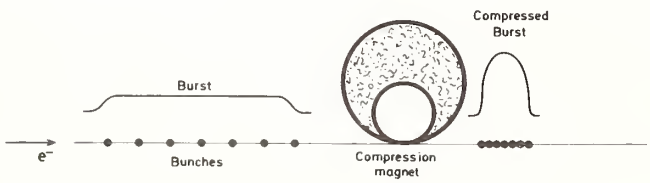

Fig. 8 : Principle of Post-Acceleration Compression.

an electron pulse ("macro-burst") of a travelling or standing S-band linear accelerator consists of a train of micro-bursts, each of about 40 picoseconds duration and 330 picoseconds separation. For short macro-bursts, of the order of 10 ns, the electromagnetic energy stored in the cavities is used for the acceleration of the electrons. Each of the micro-bursts uses up a certain part of that stored energy, with the result that their average energy drops down sequentially from the beginning to the end of the macro-burst.

If we inject after acceleration such a pulse into a 360° magnetic deflection unit, then the electrons of the first micro-bursts of a pulse move on trajectories with larger diameters than those of the later micro-bursts. Because all the electrons have practically equal velocities the macro-burst will be reduced in width when it leaves the magnet, the reduction depending on the difference between the maximum and minimum trajectory lengths. If each micro-burst could have zero energy spread, the initial pulse width would be compressed almost to zero by an appropriate choice of the magnetic field. In reality, however, the micro-bursts have a finite energy spread which limits the compression.

Experiments have been carried out at GELINA aiming at an assessment of these accelerator-immanent limitations. Although the study is not yet complete due to the lack of available beam time, the results obtained so far look very promising and demonstrate the feasibility of the method. It may be expected that a pulse compression from e.g. 15 ns down to ~ 5 ns can be realised, which means that the neutron output at pulse widths of 5 ns can be improved by a factor of about 2.5 with respect to the present situation.

Reference

1. G. Pasquariello, F. Corvi, T. van der Veen, Internal Communication.

RECENT MODIFICATIONS OF THE TUNL FAST NEUTRON CROSS SECTION FACILITY

L.W. Seagondollar, A.G. Beyerle, & C.R. Gould
North Carolina State University & TUNL
Raleigh, North Carolina 27650 USA

F.O. Purser, S. El-Kadi, S.G. Glendinning, & C.E. Nelson
Duke University & TUNL
Durham, North Carolina 27706 USA

The Triangle Universities Nuclear Laboratory fast neutron cross section facility has been modified so that tritium as well as deuterium gas targets may be used and so that two detectors can be used simultaneously to measure angular distributions of neutrons scattered from samples of interest. The targets, the new detector, and associated equipment are described.

[Fast neutron time-of-flight $\sigma(\theta)$ equipment, D and T gas targets, movable detectors.]

Introduction

The overall layout of the TUNL accelerator facility is shown in Fig. 1. In the original TUNL time-of-flight facility[1], deuterons from the tandem accelerator were sent through magnets 1,2,3, and then deflected by a final beam-switching magnet into the time-of-flight area. Neutrons produced in a deuterium gas target were scattered from samples of interest into a movable, heavily-shielded detector. The detector was an 8.9 cm-diameter NE-218 liquid scintillator deep inside a 4400 kg shield made primarily of paraffin and Li_2CO_3 with a double truncated conical collimator for the transmission channel[2] for sample-scattered neutrons to reach the detector. A 111 kg tungsten shadow bar shielded the collimator aperture from neutrons coming directly from the deuterium target. The detector could be moved manually to radial flight paths of 2 m to nearly 4 m and through scattering angles up to 155°. Scattering samples were suspended, one at a time, on a taut 0.4 mm-diameter steel cable.

Recent modifications to be discussed below are: a tritium gas target system, a new beam leg, a second neutron detector and shield, a mechanical aid to shadow bar positioning, a multiple scattering-sample support system, and new electronics arrangements.

Tritium Gas Target System

A cross section of the tritium gas target is shown in Fig. 2. The tritium, usually at about 2 atm absolute pressure, is separated from the vacuum in the beam leg by a 3.5 μm molybdenum foil. In accord with the measurements of Drosg et al.[3], a ^{28}Si collimator and a ^{58}Ni beam stop are used. Foils are cemented in place with epoxy glue[4]. A new foil is used in each week-long run. With no beam on target, the cell is tested at 3 atm absolute using helium. A beam of about 2 μA is then run on the helium-filled cell for at least ten minutes. If the cell integrity appears satisfactory,

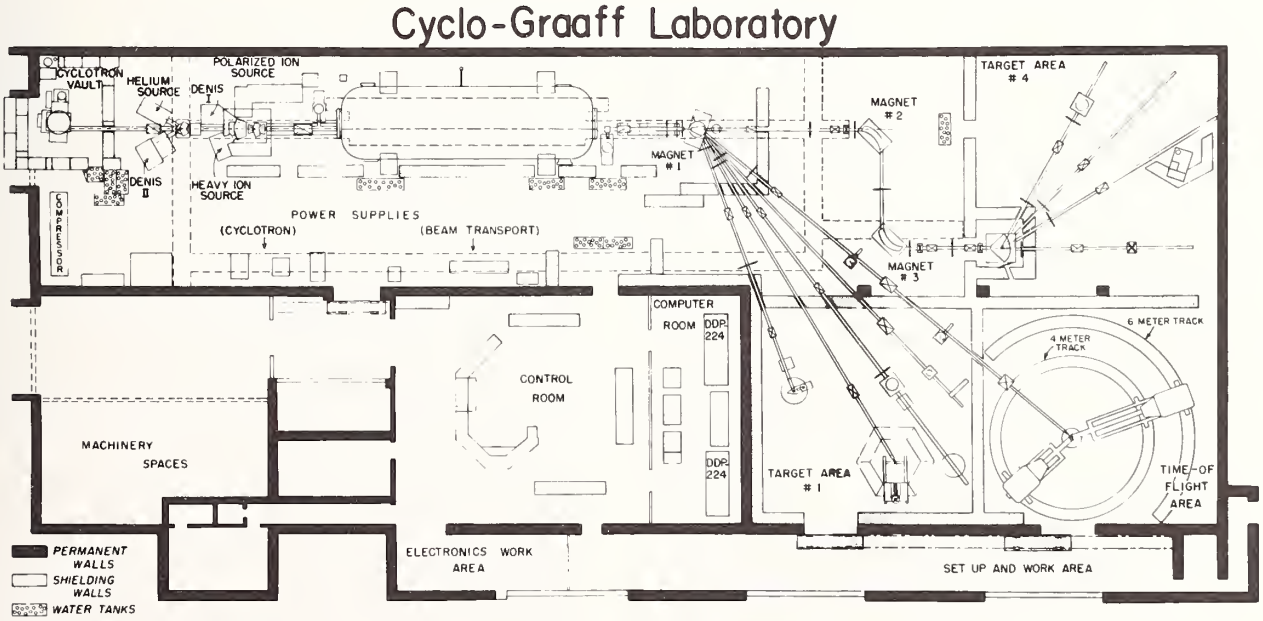

Fig. 1. The Triangle Universities Nuclear Laboratory accelerator facility.

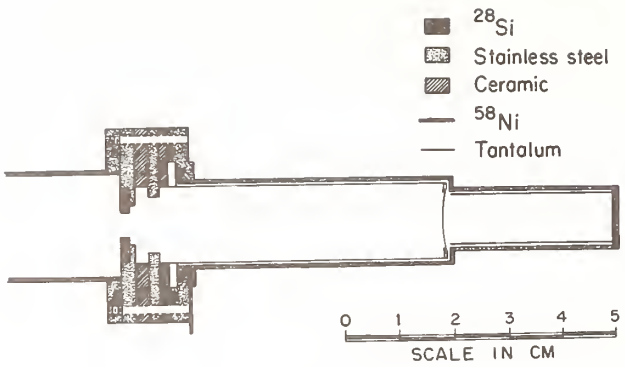

Fig. 2. Cross section of the TUNL gas target. The curved foil is 3.5 μm molybdenum. Gas enters cell through tube at bottom of drawing.

it is evacuated and filled to 2 atm absolute with tritium by means of a heated uranium-tritium furnace. The pressure in the cell is read by a small Bourdon gage which is continuously connected to the cell. During runs, the gage reading is monitored visually by closed circuit television.

A new pressure monitoring system has been developed and calibrated. The Bourdon gage will be replaced with a silicon pressure transducer[5] which puts out a voltage proportional to the pressure on the transducer. The advantages are twofold: the volume of the tritium in the transducer is considerably less than that in the Bourdon gage and the output voltage of the transducer can be used for varied and remote readouts. We have digital readout of the pressure in the target room and in the control room of the accelerator. Also in the control room, the voltage runs a D'Arsonval meter with adjustable upper and lower limit switches on it. If the meter reading is not within these limits, an audio alert sounds. The voltage is also recorded on a strip-chart recorder so we know how the pressure is varying with time.

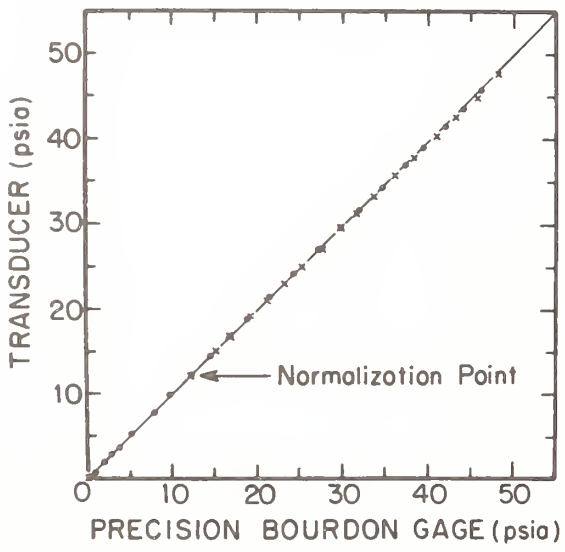

Fig. 3. Calibration of silicon pressure transducer against a precision Bourdon gage. The normalization point was 1 atm -- 14.4 psia on both gages. Readings taken in ascending order are "x"; in descending order "•".

By means of "zeroing" bias, the digital readout was adjusted to 14.4 at atmospheric pressure and the transducer was calibrated against a precision Bourdon gage from "good fore-vacuum" to nearly 50 psia. The calibration curve is shown in Fig. 3.

The target can be used for bombardment of either deuterium or tritium gas. Accelerated particles are either protons or deuterons from a pulsed direct-extraction negative-ion source. Typical average current on target is about 2 μA at a pulse repetition rate of 2 MHz. Widths of charged particle bursts have been measured to be ∿ 1.8 nsec and overall system resolution is ∿3 nsec.

New Beam Leg

The fragility of the thin foil in the gas target demands both health and equipment safety considerations. If the foil should rupture, tritium will get into part of the vacuum equipment and could get into the laboratory. To handle both these problems, a new beam leg 25 m in length was run from magnet #1 (See Fig. 1) to the time-of-flight area. In addition to suitable strong-focussing lenses, beam stop, and alignment-slit electrodes, two special systems exist. The first is an automatically triggered fast-acting valve[6] located just on the target side of magnet #1 (approximately 25 m upstream from the target). The valve consists of a low-mass polyethylene conical cup sitting below a mating conical hole at right angles to the beam line axis. A conducting ring is on the bottom of the cup. Just below the cup, outside the vacuum region, are a few turns of heavy copper. When a rise in pressure near the target triggers a Geissler circuit, a 5 KV capacitor bank discharges through the copper conductor and this slams the cup into the conical hole thus isolating the 25 m beam line from the rest of the TUNL accelerator vacuum system. The valve "closes" in 5-7 msec which is much less than the calculated time for a pressure pulse to traverse the 25 m. As a test, a valve in the vacuum line near the target was opened. The fast-acting valve closed before any observable change occurred in the vacuum on the other side of the valve.

The second special system concerns vacuum pumps on the new beam leg. Very near the target is a large titanium sublimation pump operating with no exhaust to the laboratory. Further upstream towards the magnet are two vacuum stations each having an oil diffusion pump, a LN_2 cooled charcoal trap, a mechanical forepump and an exhaust from the forepump going into PVC lines which are part of our air exhaust system.

Normally the exhaust system keeps the pressure in the time-of-flight area slightly below atmospheric pressure thus causing a continuous flow of air through the region. In addition to air intakes near the ceiling, there is a hood just over the target and tritium filling system, a glove box, a chemical hood and the above mentioned forepump exhausts that feed this exhaust system. The output of the exhaust system is a metal stack that terminates 10 m above the laboratory roof. Tritium monitors sample the air in the stack. If the fast-acting valve closes or if the tritium monitor measures excessive tritium content in the stack, the exhaust rate automatically is stepped up by a factor of ten and alarms sound.

New Neutron Shield and Detector

A second, movable, massively-shielded neutron

detector system has been built. A cross section of the shield (and detector) is shown in Fig. 4. It is similar to our original detector except: 1) it uses a larger scintillator (12.5 cm-diameter, 5 cm-thick), 2) the shield has about 30 cm more material in back of the detector to further reduce background neutrons scattered from the laboratory walls and thus is more massive (approximately 5000 kg), and 3) the radial position of the detector can be adjusted from 2.5 m to almost 6m. The angular swing of the new detector is the same as the older unit. Both detectors are used simultaneously. Both detector carriages pivot about the same axis (the axis of the scattering samples). Detector angles are measured by vernier scales that are part of the precision pivot system. A geared-down, 1/2 hp electric drive is located under each carriage so that a single operator can stand near the vernier scales and "push-button" position either detector at any desired angle within the angular range.

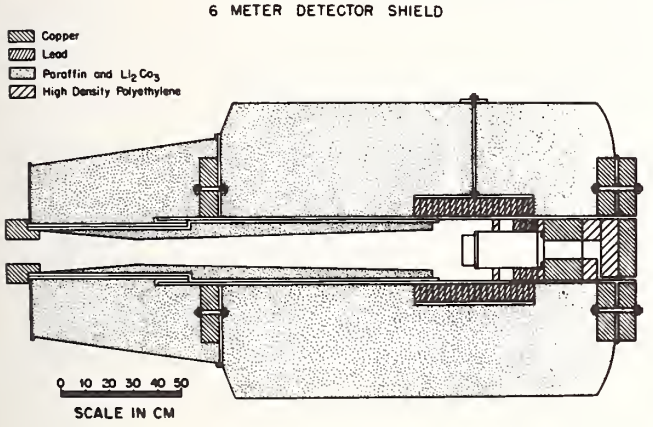

Fig. 4. Cross section of the new detector and and shield.

Both detectors are used with massive tungsten shadow bars. The position of the shadow bar is supposed to be such that: 1) the neutron flux from the target into the collimator aperture will be very greatly attenuated, and 2) there will be minimal "inscattering" of neutrons into the detector that would not have happened if the shadow bar were absent. This inscattering can occur by any of three routes of neutrons: a) from target to shadow bar to aperture, b) from target to scattering sample to shadow bar to aperture, and c) from target to shadow bar to scattering sample to aperture. Unfortunately, the position of the shadow bar that comes closest to satisfying these criteria depends in complex manner upon the scattering angle involved. Precise resetting each shadow bar after each angle change is time consuming, tiring, and subject to different precision by different experimenters. Being unaware that details of an aid to this problem had been published[7], we used a full scale mock-up of the target, scatterer, shadow bar and detector system to determine the optimum position of the shadow bar relative to the axis from the center of the scatterer to the center of the detector. The back corner of the shadow bar closest to the axis travels in a straight line. A point near the front of the shadow bar follows a complex curve not unlike a Maxwellian distribution curve. A base plate was then constructed on which the shadow bar sits. Beneath the back corner is a pin which is constrained to move in straight milled groove beneath this plate. A pin under a point near the tip of the shadow bar is connected to a roller-chain that is moved by rotation of a sprocket and the chain moves over a machined contour of the above ascertained curve. This assembly is mounted on posts connected to the detector shield carriage. With the back pin in the furthest back position, the shadow bar is aligned for the 150° angle. The carriage is then placed at 25° and the sprocket shaft is turned until the pins are in far forward position. If the shadow bar was correctly aligned at 150°, it is good in this 25° position. With this shadow bar mounting, the detector is swung to 60°, 90°, and 120° and the sprocket is rotated to find optimum positions for each of these angles. The angles are marked on a dial connected to the sprocket shaft. During an experimental run, the shadow bars are not moved on the base plate. The position of the shadow bar is determined by the angular position of the sprocket shaft.

Scattering samples are mounted in a chain of "modules" which are connected to 0.4 mm-diameter steel cable that goes over precisely located upper and lower pulleys. The pulleys define the vertical axis of the scatterers. They are far enough away from the height of the target that any of four scattering samples and a section of bare cable can be located at the height of the gas target. The upper portion of the cable goes over the upper pulley and and is attached to a 1 kg weight. The lower portion of the cable makes a 90° turn on the lower pulley, goes to a 2.5 cm-diameter brass drum on which there is a spiral groove, makes about 6 turns around the drum (in the groove), and then goes to another 1 kg weight. The brass drum is mounted on the shaft of a stepping motor[8]. Each module is a 15 cm-length of the 0.4 mm cable with a scattering sample at its center. Couplings are made of 0-80 brass screws and mating 0-80 sleeves. Static breaking strength of the assembly is about 16 kg. The electronic driving circuit for the stepping motor can drive it at speeds of about 1 step/sec to a thousand steps/sec or it can take pulses from computer output and drive the motor. Limit switches prevent driving the assembly too high or too low. Vertical positioning of a sample is determined by use of a precision Zeiss optical level telescope.

The sample can be positioned within about 1/4 mm accuracy using either manual control of the driving circuit or a predetermined number of pulses from the computer. Some assembly breakage has occurred due to resonant transverse vibrations caused by the "stepping" action of the motor. Computer drive is not being used at present and a heavier cable system is being investigated.

New Electronics Arrangement

The electronic equipment for the detectors has been upgraded to take advantage of the superior pulse shape discrimination capabilities of the Canberra Model 2160 NIM modules. The wide dynamic range of these units also permit operation at low bias settings without saturating the circuits for high energy recoil events.

A block diagram of the electronic set-up for one of the scintillators is shown in Fig. 5.

The anode signal from the photomultiplier is used for both pulse shape discriminator information and linear information. The single channel analyzer in the ORTEC 490B is used for setting the bias level for the the experiment. The constant fraction discriminator strobes the pulse shape discriminator unit and also provides the start signal for a Canberra 1443 time-to-amplitude converter. The stop signal

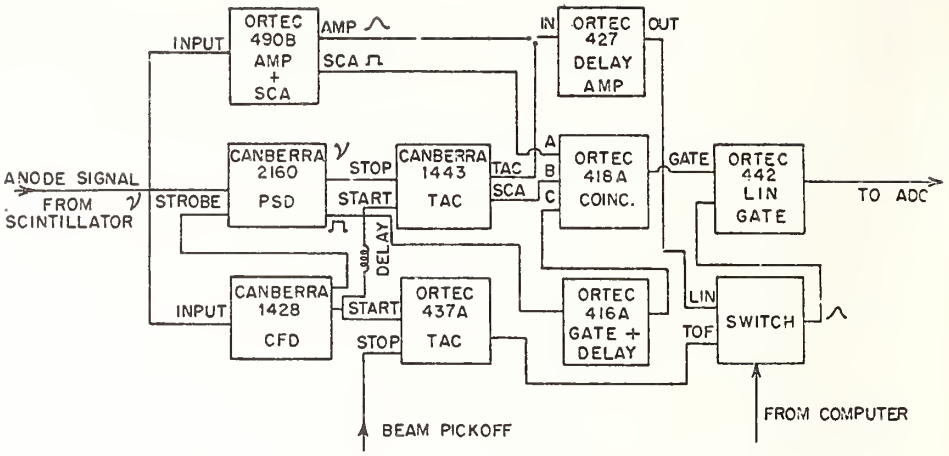

Fig. 5. Block diagram of the electronic circuitry for one neutron detector. Four such systems are used.

comes from the pulse shape discriminator unit which is operated in the n + γ mode, and the single channel analyzer output of the time-to-amplitude converter is used to select neutron and/or gamma ray events. A separate ORTEC 437A time-to-amplitude converter is used for neutron time-of-flight measurement with the stop signal coming from a delayed capacitive beam pick-off pulse. Any of the three signals, neutron time-of-flight, neutron pulse shape discrimination or linear neutron energy can be gated through to an analog-to-digital converter subject to the logic requirements established in the ORTEC universal coincidence unit.

At present, four neutron detectors are operational. The two main detectors are in the heavily shielded systems. These detectors are located at 3.71 m and 5.67 m from the scattering samples for the elastic, discrete inelastic measurements and at 2.76 m and 3.73 m for the low-bias continuum measurements. Two small scintillators are used to monitor neutrons produced in the source reaction. One is at 0° at about 7 m and it is used to monitor timing variations in the pulsed beam. The other is mounted above the reaction plane at about 90° and a flight path of 2 m. It is used for normalizing angular distribution measurements from angle to angle.

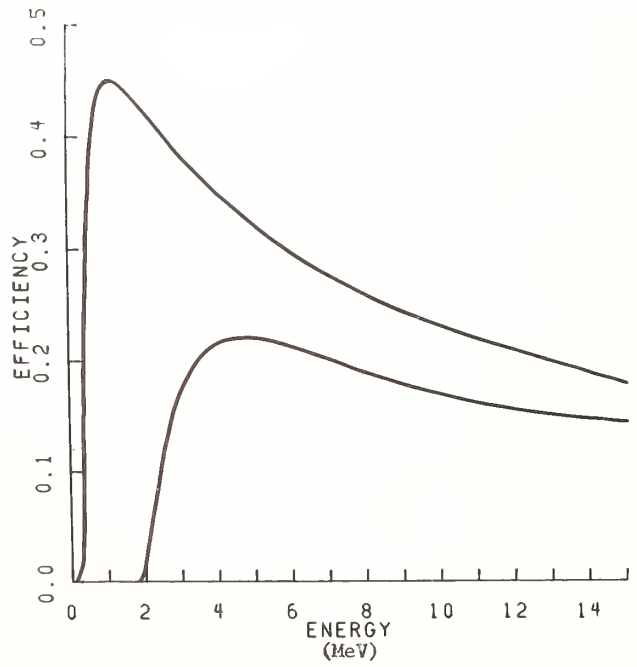

Fig. 6. Efficiency curves for the main neutron detectors. The curves are the same for both detectors. The upper curve is for E_n > 300 keV and the lower curve is for E_n > 1.9 MeV.

New detector efficiency curves have been determined for the two main neutron detectors. Efficiencies for two bias settings (E_n > 1.9 MeV and E_n > 300 keV) were obtained by measuring the response functions of the detectors to monoergic neutrons of 6.0 and 10 MeV from the $^2H(d,n)$ reaction and of 2.5, 5.0 and 10 MeV from the $^3H(p,n)$ reaction. The overlapping data sets spanned the neutron energy range from 300 keV to 13 MeV. The energy range was extended to 16.8 MeV by measuring the 0° excitation functions for the $^3H(d,n)$ reaction. All cross-section data used to convert yields to efficiencies were obtained from the compilation of Drosg[9] except for the 2.5 MeV $^3H(p,n)$ data which were taken from Liskien and Paulsen[10]. Efficiency curves for the two bias conditions are shown in Fig. 6.

Acknowledgment

Research sponsored by the U.S. Department of Energy.

References

1. D.W. Glasgow et al., Nat. Bur. Stand. (U.S.) Spec. Publ. 425, 1, 99 (1975).

2. D.W. Glasgow et al., Nuc. Inst. & Meth., 114, 541 (1974).

3. M. Drosg and G.F. Auchambaugh, Nuc. Inst. & Meth., 140, 515 (1977)

4. A-12 adhesive, Armstrong Products, Inc., Warsaw, Indiana

5. National Semiconductor Device LX1704GB, National Semiconductor Corporation, Sunnyvale California

6. Modeled after a valve developed at Crocker Nuclear Laboratory, University of California-Davis.

7. J.C. Hopkins, J.T. Martin and J.D. Seagrave, Nuc. Inst & Meth., 56, 175 (1967)

8. Type M092-FC08, Superior Electric Company, Bristol, Connecticut.

9. M. Drosg, Nuc. Sci. & Eng., 67, 190 (1978)

10. H. Liskien and A. Paulsen, Nuc. Data Tables, A 11, 569 (No. 7) (1973)

A STUDY OF SOURCE NEUTRON REACTIONS

P. Grabmayr, J. Rapaport, R.W. Finlay and V. Kulkarni
Physics Department
Ohio University
Athens, Ohio 45701 USA

S.M. Grimes
Lawrence Livermore Laboratory
University of California
Livermore, California 94550 USA

The breakup of deuterons incident on deuterium and ^{3}He has been studied at energies between 5 and 8 MeV by the neutron time-of-flight method. Shifting the beam energy by 250 keV results in a better match of the shapes of the continuous spectra of breakup on D and ^{3}He. Thus it is possible to correct contaminations of the source neutron spectra.

[Nuclear Reactions: D(d,n), ^{3}He(d,n), E_d = 4.8, 6.15, 6.40, 6.66, 7.75, 8.00, 8.25 MeV, measured $\sigma(E_n,0°)$, gas target]

Introduction

Accurate cross section measurements are basics for any theoretical interpretations of reaction mechamism or nuclear structure as well as for any application in neutron therapy or reactor design. There exist many data for charged-particle induced reactions because charged particles are easily produced and detected with high precision.

As for neutrons there exists the disadvantage that they have to be produced by reactions. This, in fact, reduces the flux available on target and secondly deteriorates the energy resolution of the projectiles. A further problem is the monochromaticity of the source. Only at very low energies the most common source neutron reactions, the p-T, d-D, d-T and p-Li reactions, are considered truly monoenergetic. At higher energies there are contaminations due to breakup or exitation of other levels. This may distort experimental results, since this contribution is not taken care of in a "sample out" background spectrum. The usual procedure is to set a high bias in the analog branch. This in turn is not possible if a larger range is desired in TOF experiments or if contributions to the low energy part of charged particle spectra by the continuous neutrons are to be expected in (n,α) or (n,p) reactions measured with the Quadrupole-Triplet-Spectrometer (QTS). No bias setting at all is possible in neutron therapy.

Common methods employ measurements of the same reaction at several lower bombarding energies or simulation of the contaminations by means of Monte Carlo Methods. This is a rather laborious and time consuming procedure. A different approach is pursued at Ohio University, which needs only one additional run. Figure 1 shows TOF spectra of the deuteron breakup on different helium and hydrogen gases. The shapes of the different source reaction yields are compared in order to match up the breakup spectrum for the source neutron reactions. Due to the configuration at the Ohio University Tandem Accelerator Laboratory, our interest was focused on the T(d,n)^{4}He and D(d,n)^{3}He reactions at deuteron energies between 5 and 8 MeV.

Experimental

The Ohio University Tandem Accelerator provided a pulsed beam of deuterons with energies between 4.8 MeV and 8.25 MeV. At 6 and 8 MeV respectively, groups of 3 data sets were taken varying the deuteron energy by 250 keV. The gas cell, which contained either deuterium (D), tritium (T) or helium (^{3}He) gas up to 40 psi, was sealed off against the vacuum system by a 5 µm Mo foil. Ta and W foils of similar thickness were also used for comparison of their contribution to the background (figure 2). We have successfully used a 5 µm W foil at 3 µA for a total charge of 1 C. A special double-neck gas cell was developed, which by means of a bellows and motor drive allows the alternative positioning of two gas cells in the deuteron beam. Quick gas cell changes are possible, and successive measurements are easily compared since the interval between them is minimized. Switching the cells from the control room also reduces the radiation dose to the operator.

A standard TOF spectrometer with n-γ discrimination employing a 2" x 8" liquid scintillator

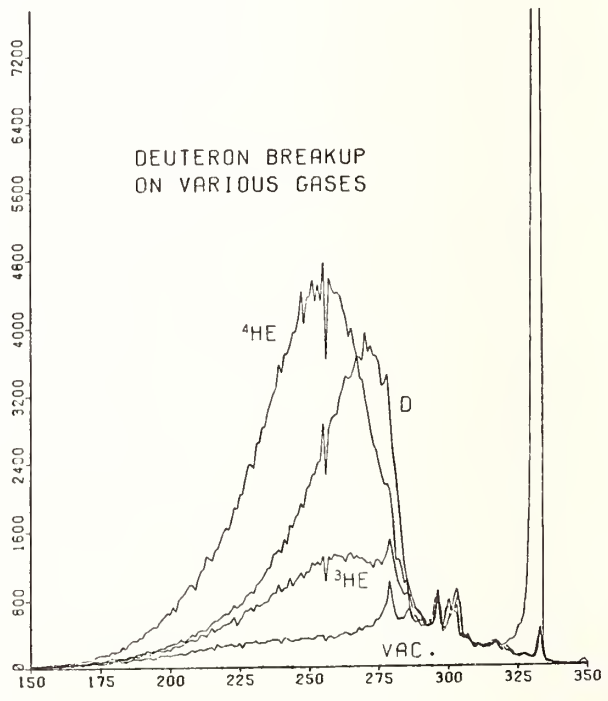

Figure 1. Neutron TOF spectra at 0° obtained by bombarding different helium and hydrogen isotopes with 8 MeV deuterons.

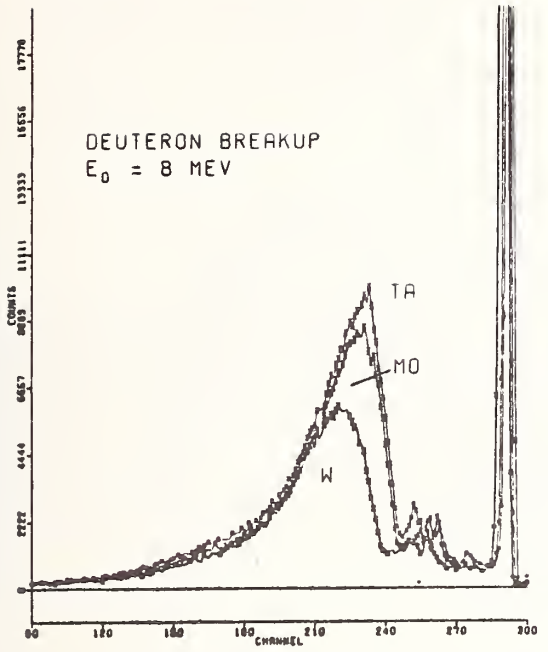

Figure 2. Variation in the continuous neutron TOF spectra due to different entrance foils in the gas cell (5 μm Mo, 5 μm Ta, 8 μm W) at a deuteron energy of 8 MeV.

(NE224) was set up at 0° at a distance of 8.5 m. A repetition rate of 1.25 MHz was chosen in order to reduce deadtime and to allow for setting a bias of 0.7 MeV neutron energy. Electron suppression in front of the gas cell was employed to allow charge normalization for comparison of ^{3}He and hydrogen spectra. "Gas out" runs were taken to determine the contribution of the gas cell to the background. The pressure of ^{3}He was adjusted so that the deuterons experience the same energy loss as in D gas.

Results

The deadtime-corrected and charge-normalized TOF spectra were converted into neutron energy spectra (laboratory system) averaging over 125 keV. Detector efficiencies of the neutron detector as function of neutron energy, if calculated by different codes |1,2| vary in magnitude but show very similar shape. Therefore, the yields were normalized to the well known cross sections of the monoenergetic reaction |3|. Several energy spectra are shown in figures 3 to 5, which were taken at 6 and 8 MeV deuteron. No data are shown for deuteron energy of 4.8 MeV since the breakup is negligible.

In figure 3 the contamination due to oxygen and carbon are very distinctive. By flushing the cell several times with D or ^{4}He, their contribution may be reduced by an order of magnitude. Below neutron energy of 4.5 MeV breakup of the deuterium is observed thus limiting the energy range in TOF or QTS experiments.

In order to compare D and ^{3}He measurements, the total yield and the mean energy of the breakup spectra were calculated within the range of 1 to 4.5 MeV. The average energy of the continuous neutrons produced from ^{3}He or D differs by an amount which is nearly independent of bombarding energy. Except for very low energy, the average energy is 0.25 MeV higher in case of the breakup on D. Therefore, the continuum spectrum of ^{3}He at deuteron energy of 7.75 MeV is plotted against the breakup of D at 8 MeV (figure 4). The D spectrum is arbitrarily normalized to fit the shape between 3.2 and 4.6 MeV. Also shown is the d-D spectrum at the same energy. Figure 5 gives the comparison for deuteron energies at about 6 MeV. Both figures reveal the same features. The shapes of the breakup spectra are similar but not the same due to different kinematics. It is possible to overlap the high energy parts of the breakup spectra. This is sufficient for investigations of certain (n,p) reactions, where the reaction Q-value is in the range of -2 to -4 MeV as for e.g. ^{27}Al, ^{18}O, ^{28}Si, ^{56}Fe, ^{116,118}Sn or ^{92}Zr. In those cases only that part of the deuteron breakup peak has to be matched, which is higher than the threshold energy.

As far as the d-T reaction is concerned, the energy difference between peak and the monoenergetic neutron peak is much larger due to the Q-value of 17.6 MeV. Nonetheless, one has to consider those background neutrons, if a (n,p) cross section measurement at very low proton energies is wanted. Besides a peak due to build up of deuterium in the gas cell, the low energy contamination of the T(d,n)^{4}He reaction arises from the T(d,np)T and from the T(d,2n)^{3}He reactions. The latter one yields a distribution similar to breakup of d on ^{3}He or D, whereas the first one gives a narrow peak. It is thought that a combination of a breakup spectrum and a monoenergetic peak produced by a d-D or p-T reaction might resemble this shape.

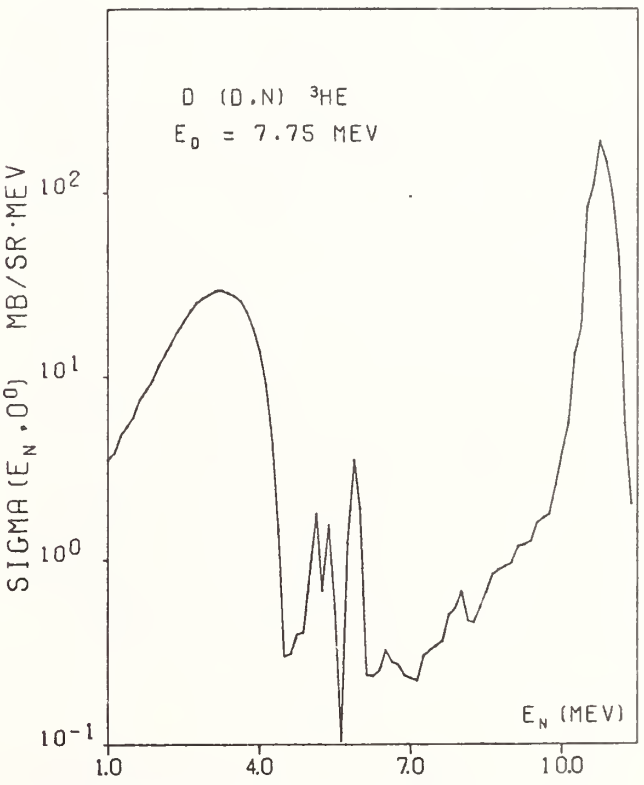

Figure 3. Neutron energy spectrum from the d-D reaction at zero degrees. The spikes at ∿ 5 MeV are due to contaminations by oxygen and carbon.

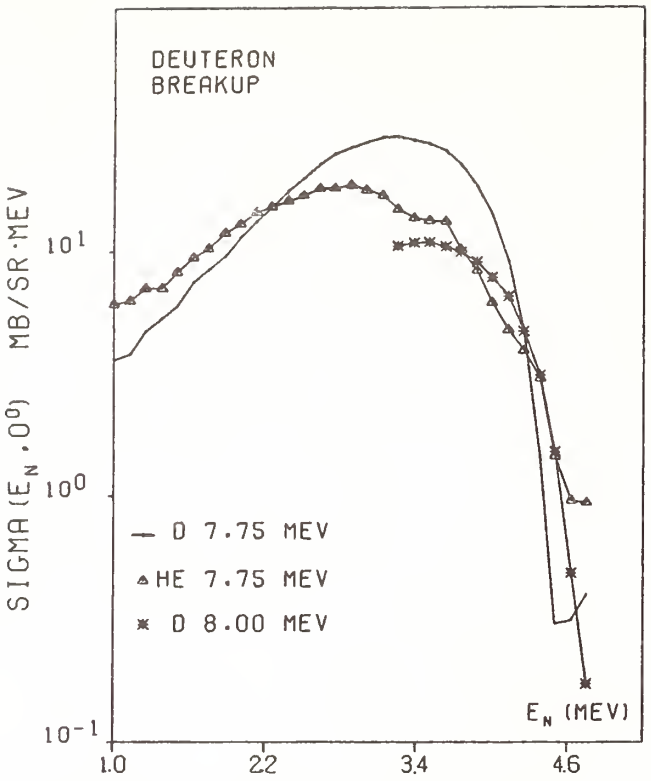

Figure 4. Comparison of the continuous neutron energy spectra after breakup of 8 MeV deuterons on D and ^{3}He. The yield at 8.0 MeV is normalized to fit the shape of the He spectrum in the range of 3.2 to 4.6 MeV.

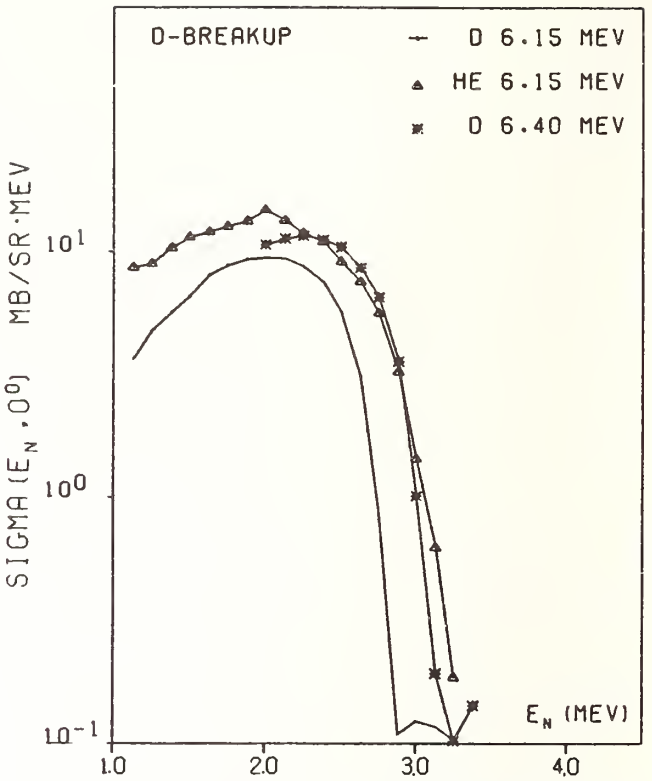

Figure 5. The continuous energy spectra of deuteron breakup on ^{3}He and D at a beam energy of 6 MeV. The d-D spectrum at 6.4 MeV is reduced by a factor 0.55 to match the shape of the ^{3}He spectrum.

Conclusions

Breakup spectra of different neutron producing reactions were investigated in order to correct for low-energy contamination. These corrections are essential if high lying states are looked for in TOF experiments or if low energy (n,p) or (n,α) spectra should be measured with the Quadrupole-Triplet-Spectrometer. The breakup of deuterons on ^{3}He is used to match up the contamination of the neutron spectrum produced by the d-D reaction. There is only one additional "dummy gas" measurement needed to correct for all contributions. Thus, this method is much more efficient and less time consuming than scanning through all neutron energies and/or employing laborious corrections by different Monte Carlo Methods. Much work has been done at higher energies, especially by the group in Wisconsin. The continuous spectra measured by Kerr |4| and Lefevre et al. |5| relate to each other in a similar way as pointed out in this paper. Therefore, it can be anticipated that the described procedure can also be used at higher bombarding energies. Further investigations of the source neutron reactions, which will employ the QTS as a giant proton-recoil-telescope, are underway.

Acknowledgment

Work supported in part by the U.S. Department of Energy, the National Science Foundation and the National Cancer Institute.

References

1. R.J. Kurz, LRL Report UCRL - 11339 (1964)
S.T. Thornton and J.R. Smith, Nucl. Inst. and Meth., 96, 551 (1971)

2. N.R. Stanton, Ohio State University Report, C00-1545-92 (1971)
R.A. Cecil, B.D. Anderson and R. Madey, Nucl. Inst. and Meth., 161, 439 (1979)

3. R.G. Kerr, Phys. Rev., 148, 998 (1966)

4. H.W. Lefevre, R.R. Borchers and C.H. Poppe, Phys. Rev., 128, 1328 (1962)

5. M. Drosg, Nucl. Sci. Eng., 67, 190 (1978)

NEUTRON SPECTRA MEASUREMENTS UPON A SPHERICAL ASSEMBLY OF THORIA *

R. C. Block, M. Becker, D. R. Harris, B. K. Malaviya
S. A. Bokharee, R. W. Emmett, P. S. Feigenbaum
S. H. Levinson, H. T. Maguire, Jr.
Rensselaer Polytechnic Institute
Troy, New York 12181

S. A. Hayashi, S. Yamamoto
Research Reactor Institute
Kyoto University, Japan

A cooperative research program between the Kyoto University Research Reactor Institute (KUR) and the Gaerttner Linac Laboratory at RPI has carried out neutron spectra measurements upon a thoria assembly. The assembly consists of 300 kg of throia contained in a 0.6-m-dia. stainless steel sphere and is the same assembly reported by Nishihara et al.[1] A 1-kw air-cooled spheroidal Ta photoneutron target was developed for use with this assembly. Neutron spectra measurements have been carried out from approximately 1 keV to 15 MeV at radii of 15 and 20 cm with angles of 90° and 130° respectively. The high-energy spectra were obtained with the 50-cm-dia.-by-12.5-cm-thick proton recoil detector at 100 meters, and the low-energy spectra were obtained with the 30-cm-dia.-by-5-cm-thick ^{10}B-Vaseline-plus-NaI detector at 33 meters. In order to compare with experiment, spectra are being calculated with the DTF-IV one-dimensional transport code with ENDF/B-IV data, and results will be presented.

[Thoria, neutron flux spectra, MeV, keV, cross section, ENDF/B, multigroup calculation, time-of-flight, LINAC]

Introduction

A comprehensive program to assess the adequacy of differential nuclear data of thorium via integral experiments has been under way at the Gaerttner LINAC laboratory of Rensselaer Polytechnic Institute (RPI) in cooperation with the Kyoto University Reactor Research Institute (KUR). Our approach involves precision time-of-flight measurements of position-dependent angular flux spectra over a wide energy range in a bulk assembly of simple geometry. Then we compare our experimental spectra with the results of transport theory and Monte Carlo calculations utilizing nuclear data from current ENDF/B and other available data libraries. The interpretation of these results provides meaningful conclusions as to the thorium cross section data. Recently there has been renewed interest in alternative fuel cycles and novel breeder systems involving thorium. The evaluation of these systems and fuel cycles depends critically on accurate thorium nuclear data that go into their analyses. Our measurements provide information both on the quality of current thorium data sets and on changes in thorium data required to conform with these integral experiments.

Experimental Setup and Procedures

The present set of measurements utilize a thoria assembly, currently on loan to RPI from Japan where it was designed, constructed and originally used in conjunction with the integral experiments program at KUR.[1] This assembly+, shown in Fig. 1, consists of about 300 kg of thoria powder (99.9% ThO_2), packed to an average density of approximately 2.70 gm/cm^3 in a spherical airtight stainless steel vessel of 60 cm I.D. (see Ref. 1 for details). Re-entrant holes of 5-cm diameter allow the placement of a target at the center of the sphere and the extraction of a beam reaching to several locations in the assembly

The over-all experimental setup is similar to earlier integral measurements[2,3] at RPI. The electron beam from the Gaerttner Laboratory LINAC is defined by air-cooled aluminum strippers and strikes an especially designed air-cooled spheroidal tantalum target[4] which is imbedded inside the thoria assembly near its center. This target converts the electron beam via brehmsstrahlung into a fission-type spectrum of neutrons, whose angular distribution is very nearly spherically symmetric. The neutron beams extracted through a reentrant hole from different spatial and angular positions in the medium are viewed by detectors located at the end of 100.52 and 33.3 meter flight paths. To cover the energies above about 0.5 MeV, a large 50-cm-diameter, 12.5-cm-thick liquid scintillator is used whose relative neutron detection efficiency has been determined experimentally using the $D(\gamma,p)n$ reaction and also deduced from Verbinski's analysis.[5] For energies below about 1.5 MeV, the principal detector used is a ^{10}B-vaseline-NaI unit which has been calibrated using a combination of measurements and calculation.[2] The signal from the detector is fed into a 31.25-nsec, 18-bit digital clock and the data are stored in an on-line 8-k memory PDP-7 computer. The neutron time-of-flight data are corrected for background, deadtime losses, relative detector efficiency, transmission through materials in the flight path, etc. The spectra from the two detectors are matched in the energy region of overlap.

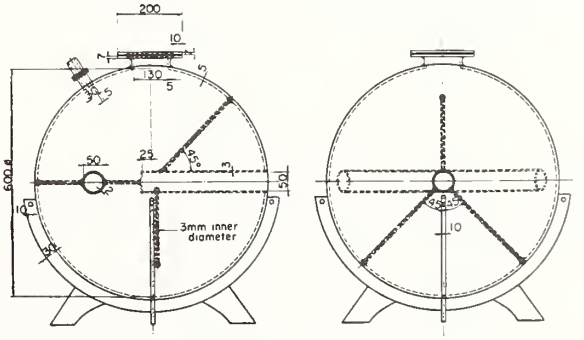

Fig. 1 The Spherical Stainless-Steel Vessel of Thoria Assembly

The experimental parameters and conditions employed in the present set of measurements are summarized in Table I.

* Supported by US DOE Contract No. ET-78-S-02-4933
+ Manufactured by Sintoku-Kinzoku Co., Ltd.

Table I. Experimental Parameters and Conditions

Electron Beam Energy	: 32 and 62 MeV
Pulse Repetition Rate	: 500 pps
Pulse Width	: 19 nanoseconds
Neutron Target	: Air-Cooled Tantalum Spheroid[4]
Electron Beam Power on Target	: 600 - 800 watts
High-Energy Measurements (0.5 - 15 MeV) :	
Flight Path	: 100.52 m
Material in Beam	: 1.5 mm Mylar + 4.262 cm depleted U + .398 cm Al + 10.76 m air.
Low-Energy Measurements (1 keV-1.15 MeV):	
Flight Path	: 33.198 m
Material in Beam	: 1.5 mm Mylar + 4.262 cm depleted U + .158 cm Al + 6.13 m air.

Calculational Approaches

For assessing the neutron cross section data of thorium, the measured spectra are compared with spectra calculated by the one-dimensional transport theory which appropriately models the source-assembly geometry of the experiment. For this purpose we use the one-dimensional discrete S_N code DTF-IV[6] which represents the system in the form of three concentric spherical regions: a target region represented by a black absorber, a void region and a spherical outer shell of thoria. The validity of the spherical representation and of the black-absorber representation of the target are checked through supporting calculations.

This report presents analyses based on nuclear data for thorium and oxygen taken from ENDF/B-IV. Analyses based on ENDF/B-V are underway. The basic data are converted into a 49-group set using SUPERTOG[7] and related codes for input into the transport calculations. For the DTF-IV calculations the source above 720 keV is the measured spectrum from the bare tantalum target. Below this energy the measured bare-target source is joined to a Maxwellian with temperature 0.8 MeV; this Maxwellian was fitted to the measured source shape. The DTF-IV calculations reported here utilized S_{16} quadrature and scattering matrices up to P_8.

Results and Discussion

An earlier set of measurements of neutron spectra on this same thoria assembly were undertaken at the KUR laboratory in Japan. These measurements, reported in Ref. 1, employed a 5-cm long by 5-cm diameter cylindrical low-power lead target which was not specifically designed to yield a completely isotropic distribution of emergent neutrons; this complicates the analysis and interpretation of experimental results using one-dimensional transport theory codes. The smaller flight path lengths used at KUR also limited the experimental resolution. The measured spectra were compared, in this earlier work, to the results of S_N calculations utilizing mainly ENDF/B-III data for thorium and oxygen.

The present integral experiments on the same thoria assembly at the RPI Gaerttner LINAC Laboratory have extended the measurements over a wider range of neutron energies. We also use a more isotropic higher-power neutron source[4] than used at KUR; our analyses utilize ENDF/B-IV data, and ultimately will be extended to ENDF/V. Furthermore Monte Carlo calculations are underway and will provide an additional support to our comparisons.

We include in this paper, our results of neutron angular flux spectra for two positions (r=15 cm, μ=0 and r=20 cm, μ=-.66) in the thoria assembly. As a means of validating the over-all experimental setups at the two facilities, Fig. 2 shows a comparison of the measured spectra at KUR and RPI, for the same position in the assembly when bombarded by a 32-MeV electron beam. The RPI experimental data are presented in the same 49-group structure utilized in the DTF-IV calculation. The over-all agreement is quite good and lends confidence to the reproducibility of the measured spectrum. The higher energy range of the RPI measurement is also evident.

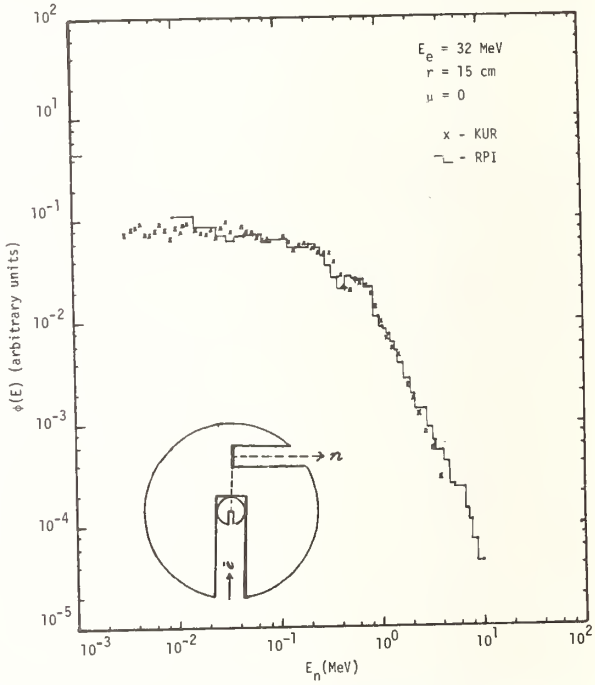

Fig. 2 Comparison of Spectra in The Thorium Assembly Measured at KUR and RPI.

Figure 3 shows a comparison of the measured and calculated (S_{16}, 49-group, ENDF/B-IV) flux spectra for r=20 cm and μ=-0.66. This angular orientation (about 130° with respect to the direction of electron beam) makes this position less susceptible to uncertainties in the source spectrum arising from any contribution of brehmsstrahlung leaking from the target in the forward direction and producing (γ,n) reactions in the thoria. The effect of uncollided flux from the source is also minimized at this position and direction. The overall agreement over most of the energy range is good. Toward lower energies, part of the disagreement is expected to be due to the presence of the 0.133 w/o water present in the thoria powder, which has not been taken into account in these preliminary DTF-IV calculations. Inclusion of the H_2O content can augment the calculated neutron flux by almost a factor of 2 around 10 keV.[1] Improved DTF-IV calculations are under way. However, this sensitivity result points out the ambiguity of interpreting the low-energy data from measurements on a thorium oxide assembly in which the concen-

tration of H_2O is necessarily difficult to ascertain (ThO_2 is highly hygroscopic).

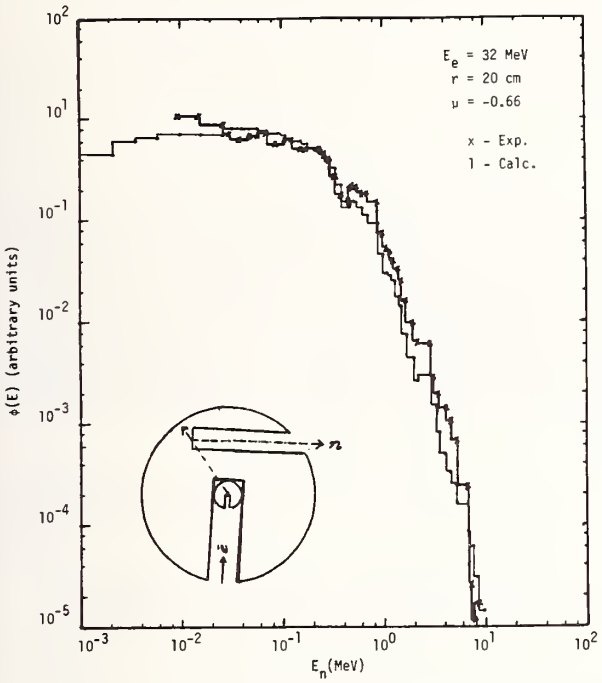

Fig. 3 Comparison of Measured and Calculated (S_{16} OTF-IV, ENOF/B-IV) Spectra in The Toria Assembly.

Our studies with the thoria assembly have shown that transport theory calculations utilizing ENDF/B-IV data can predict the measured spectra well over the high-keV to low-MeV range. To obtain a more comprehensive assessment of thorium data, additional measurements supported by more definitive Monte Carlo calculations are desirable. In order to minimize uncertainties arising from source-related effects, a larger and/or higher-density assembly is needed, so that several locations, well removed from the source and at different angular positions can be studied. The present thoria assembly dimensions correspond to only about 4 mean free paths around 1 MeV. A thorium metal assembly of about 5 times the density and dimensions approximately 10 mean free paths would considerably improve the over-all integral experiment. It will permit experiment-theory comparison of neutron angular flux spectra from locations less sensitive to source-related uncertainties. The effect of moisture content would also be eliminated. Further, in a thorium metal system, complications arising from oxygen resonances will not cloud the interpretation of data.

References

1. Hiroshi Nishihara,Itsuro Kimura,Katsuhei Kobayashi, Shu A. Hayashi,Shuji Yamamoto and Masayuki Nakagawa, "Measurement and Analysis of Neutron Spectrum in Spherical Pile of Thoria," J. Nucl. Sci. and Tech. 14, 426 (1977).

2. B. K. Malaviya, N. N. Kaushal, M. Becker, E. Burns, A. Ginsberg, E. R. Gaerttner, "Experimental and Analytical Studies of Fast Neutron Transport in Iron," Nucl. Sci. Eng., 47, 329 (1972).

3. N. N. Kaushal, B. K. Malaviya, M. Becker, E. Burns, E. R. Gaerttner, "Measurement and Analysis of Fast Neutron Spectra in Uranium Depleted in the Uranium-235 Isotope," Nucl. Sci. Eng. 49, 330 (1972).

4. Saeed A. Bokharee, Richard W. Emmet, Martin Becker, Robert C. Block, Donald R. Harris, Bimal K.Malaviya, Shu A. Hayashi, Shuji Yamamoto, "Photoneutron Target Design for Fast Neutron Spectrum Measurements," Trans. Am. Nucl. Soc., 32, 750 (1979).

5. V. V. Verbinski, J. C. Courtney, W. R. Burrus, T. A. Love, "The Response of Some Organic Scintillators to Fast Neutrons," ORNL-P-993 (1965).

6. K. D. Lathrop, "DTF-IV-A Fortran-IV Program for Solving the Multigroup Transport Equation with Anisotropic Scattering," LA-3373 (1955).

7. B. Q. Wright, J. L. Lucius, N. M. Greene and C. W. Crawen, Jr., "SUPERTOG: A Program to Generate Fine Group Constants and P_n Scattering Matrices from ENDF/B," ORNL-TM-2679 (1969).

INTEGRAL MEASUREMENTS FOR HIGHER ACTINIDES IN CFRMF

Y. D. Harker, R. A. Anderl and E. H. Turk
EG&G Idaho Inc.
Idaho Falls, Idaho 83415, USA

N. C. Schroeder
Exxon Nuclear Idaho Co.
Idaho Falls, Idaho 83401, USA

[integral capture cross section, integral fission cross section, 0.1-2000 keV]

To improve upon the lack of fast integral data for higher actinides, an effort has been underway to measure integral capture and fission cross sections for ^{242}Pu, ^{241}Am and ^{243}Am in the fast neutron zone of the Couple Fast Reactivity Measurements Facility (CFRMF). Fission cross sections are determined based on the Ge(Li) gamma spectrometric measurements of the absolute emission rates of the 537-keV and/or 1596-keV lines in the ^{140}Ba - ^{140}La decay. The capture rate for ^{242}Pu is based on the measurement of the absolute emission rate of the 84.0 keV line in the ^{243}Pu β^- decay. Although the capture cross sections for ^{241}Am and ^{243}Am are not obtained directly, the cross sections for production of ^{242}Cm and ^{244}Cm are based on the quantitative alpha spectrometry and total alpha counting. Measured integral and capture cross sections for ^{242}Pu are 357 mb $\pm$ 10% and 146 mb $\pm$ 15% Corresponding spectral averaged cross sections calculated using ENDF/B-IV data and 489 mb and 238 mb, respectively. For ^{241}Am fission and capture the measured cross sections are 504 mb $\pm$ 12% and 1.01 b $\pm$ 3%, respectively. For ^{243}Am fission and capture, the measure cross sections are 0.352 b and .10 b, respectively.

Introduction

Considerable attention is being focused on the adequacy of neutron cross-section data for higher mass actinides, in particular ^{242}Pu, ^{241}Am, ^{243}Am, ^{242}Cm and ^{244}Cm. The reasons for this interest are varied; however, our involvement stems from fast reactor applications where the impact of these nuclides present in high-burnup plutonium fuel needs to be evaluated. From the reactor physicist's viewpoint, credit for these nuclides must be considered either as fuels or as poisons. In addition, one of the modes of decay for both ^{242}Cm and ^{244}Cm is spontaneous fission. This effect has been estimated to be significant and must be considered in reactor shutdown and startup and also in handling the waste from processing the spent fuel.

As a result of the renewed interest in higher-actinide cross-section data, our program at INEL began a measurement series whereby integral cross-section data would be determined for the fission and capture reactions of ^{241}Am, ^{243}Am and ^{242}Pu. The facility used in this measurement series is the Coupled Fast Reactivity Measurements Facility (CFRMF) which provides a fast neutron environment which is similar in a spectral sense to a typical fast reactor environment. These measurements are similar to and do compliment other integral measurements in fast reactor environments; e.g., the ongoing work in the U.K. The U. K. effort is performing measurements in ZEBRA, PFR and DFR on the higher mass actinides and has reported progress[1-8] in measuring integral fission and capture cross sections for the nuclides reported here. In this paper, the CFRMF measurements on ^{241}Am, ^{243}Am and ^{242}Pu are discussed. Brief descriptions of the CFRMF, sample preparation procedures and analysis procedures are given. The results are presented and compared where applicable with other data derived from either the U.K. measurements or from ENDF/B-IV.

Measurements

Irradiation Facility

These measurements were performed using the CFRMF as the irradiation source. It is a thermal reactor with a fast neutron flux trap in the center of the assembly. The neutron spectrum has been tailored to be similar to the "typical" fast reactor neutron spectrum. An extensive measurement and calculational program has been devoted to characterizing the environment inside the CFRMF. The facility and the results of the characterization effects are described in the references[9-11]. The mean energy of the neutron spectrum has been determined to be 750 keV.

For these measurements, the reactor was operated at a power level which produced a flux integrated over energy of approximately 8.6 x 10^{11} neutrons/cm^2/sec. In each irradiation the actual flux level was determined from .40 cm dia x .0127 cm thick gold foils which were irradiated along with the sample. The measured reaction rates from the gold monitor foils were reduced to absolute flux values using a correlation procedure reported by Harker, et al.[11] and Grundl, et al.[12] The reported accuracy of the absolute flux determined by this method is approximately $\pm$ 3%.

^{242}Pu Measurements

The ^{242}Pu sample, in the oxide form, was irradiated and analyzed inside an aluminum container. The container was designed to have an internal plunger which, when the lid was tightened, forced the sample against the bottom. This was done to insure the location and shape of the sample for counting purposes. The sample was irradiated in the CFRMF and the capture cross section was determined from the 84 keV gamma activity of ^{243}Pu. The fission cross section was determined by measuring the activity of ^{140}La in equilibrium with ^{140}Ba. The ^{140}Ba/^{140}La activity was reduced to a fission cross section using a fission yield of 4.963% reported by Meek and Rider[13]. Table I lists the parameters used in the analysis and the results of the ^{242}Pu measurements.

TABLE I. ^{242}Pu Analysis

	Capture	Fission
m	30.21 mg	30.21 mg
E_γ	84 keV[a]	537 keV/1596 keV[b]
b_γ	0.23 ($\pm$8.7%)	.244($\pm$1.2%/.9540($\pm$.08%)[b]
fission yield		0.04963
$\phi\sigma$	1.26×10^{-13}rps/a	4.81×10^{-13}rps/a
ϕ	8.63×10^{11}n/cm^2/sec	8.63×10^{11}n/cm^2/sec
σ	0.146 b($\pm$15%)	0.557 b($\pm$10%)

[a] From reference 14.
[b] From reference 15.

In a review of the measurements, it was discovered that the sample material did not remain in the bottom of the holder as designed, consequently, the gamma self-absorption factor and sample position during analysis are somewhat uncertain. This problem is considered to be of greater importance in interpreting the capture measurements than in interpreting the fission measurements. As a result, large uncertainties have been assigned to ^{242}Pu values.

^{241}Am to ^{242}Cm Capture Cross-Section Measurements

A sample of ^{241}Am, in the oxide form, was dissolved in nitric acid to make a stock solution. Two aliquots (~1 mg ^{241}Am each) were transferred to 7mm (od)x6.4 cm quartz ampules. Samples were taken to dryness and the ampules sealed. Each ampule was placed inside a thin-walled aluminum capsule for irradiation. Two samples were irradiated; however, the results presented here are from one of the irradiations, the remaining sample is being analyzed at this time.

The post-irradiation analysis was done by isotope dilution alpha spectrometry which proceeded in the following sequence:

1. Ampule was opened. The sample was dissolved in nitric acid and transferred to volumetric flask and diluted to volume.
2. Four mass aliquots (~1g each) were removed, three were spiked with ^{244}Cm. The unspiked fourth sample was processed along with the other three to determine the ^{244}Cm concentration present in the irradiated sample prior to spiking.
3. Each of the aliquots was prepared for and run through an Am-Cm separation[16].
4. Curium fractions from the separation were collected, prepared and electroplated on stainless-steel plates.
5. The prepared sources were analyzed by alpha spectrometry to determine the ^{242}Cm/^{244}Cm atom ratios. From these ratios and the known spike, the concentration of ^{242}Cm was determined in the irradiated sample.

The ^{241}Am concentration was determined in a similar way using ^{243}Am as the spike. A check of the unirradiated ^{241}Am stock solution found it to be free of ^{242}Cm. Similarly the ^{243}Am and ^{244}Cm spikes were checked for purity. From these analyses, the ^{242}Cm/^{244}Cm atom ratio in the curium spike was 1.85×10^{-6} and the ^{241}Am/^{243}Am atom ratio in the americium spike was 1.508×10^{-3}. These ratios were used to correct the ^{242}Cm/^{244}Cm atom ratios in the irradiated stock and the ^{241}Am/^{243}Am atom ratios in the americium determination, respectively.

The results of the isotope dilution alpha spectrometry were quoted as atoms ^{242}Cm/mg ^{241}Am at the time of separation. These ratios were converted to cross sections using the following half-lives:

$T_{1/2}(^{242m}Am)=152$ y $T_{1/2}(^{242}Cm)=162.9$ d

$T_{1/2}(^{242g}Am)=16.01$ h $T_{1/2}(^{241}Am)=432.2$ y

The results of the first irradiation are:

$\phi\sigma(^{241}Am(n,\gamma)^{242g}Am \rightarrow {}^{242}Cm)=9.03\times10^{-13}$ rps/a($\pm$0.8%)

$\phi = 8.97\times10^{11}$ n/cm^2/sec ($\pm$3%)

$\sigma = 1.01$ b ($\pm$3%)

If an isomer ratio of 0.8 as calculated by Mann and Schenter[17] is assumed, then the total $\sigma(n,\gamma)=1.26$ b.

^{241}Am and ^{243}Am Fission Cross-Section Measurements

In the ^{241}Am fission cross-section measurements, the sample (41.9 mg ^{241}Am) in the oxide form was sealed inside a stainless steel capsule for both the irradiation in CFRMF and for the post-irradiation analysis. The fission rate was determined by measuring the intensity 1596 keV gamma activity of the ^{140}La in equilibrium with the ^{140}Ba. The decay parameters for ^{140}La are given in Table I. To reduce the gamma activity from the decay of ^{241}Am, a 1.02 cm lead absorber was placed between the Ge(Li) detector and the source. As a result, a correction factor of 1.704 was applied to the measured count rate to account for the absorption of the 1596 keV gamma in the lead absorber. The fission yield for ^{140}Ba used in this analysis was 0.0577. The results reduced to fission rate and fission cross section are:

$\phi\sigma = 3.90 \times 10^{-13}$ fps/a for ^{241}Am

$\phi = 7.736 \times 10^{11}$ n/cm^2/sec

$\sigma = 0.504$ b for ^{241}Am (n,f) f.p.

In the ^{243}Am fission cross-section measurements, the samples (~1.2 mg ^{243}Am per capsule) were sealed in quartz ampules in the same manner as described in the ^{241}Am capture cross-section measurements. The ^{243}Am stock material was obtained via the Transplutonium Committee from the research materials inventory at ORNL. Prior to shipment to INEL, the material had undergone extensive chemistry to remove any ^{244}Cm. The post-irradiation analysis for fission rate followed the same procedure used for ^{241}Am, except that 487 keV, 815 keV and 1596 keV lines from ^{140}La and 537 keV line from ^{140}Ba were all analyzed and a different procedure was used to obtain the lead absorber corrections. In the ^{243}Am case, the absorption correction for counting the sample at 10 cm from the detector was based on transmission measurements for the absorber configuration using a ^{152}Eu point source and a mixed radionuclide source. The absorption correction for counting the sample at 25 cm from the detector were calculated utilizing mass absorption coefficients from Storm and Israel[18].

In these measurements, the amount of ^{243}Am was determined by counting the activity of ^{239}Np which is in secular equilibrium with parent ^{243}Am. In fact, the actual analysis called for relative measurements of the fission product activities to that of ^{239}Np, consequently there was no need for an absolute mass determination, and other corrections required in absolute measurements.

A fission yield of 0.055[13] was used to determine a fission rate. The results from two separate irradiations are given in Table II.

TABLE II. ^{243}Am Fission Rate and Cross Section

	Irradiation 1	Irradiation 2
$\phi\sigma_f$(fps/a)	3.069×10^{-13}($\pm$2.2%)	3.079×10^{-13}($\pm$2.2%)
ϕ(n/cm^2/sec)	8.74×10^{11}($\pm$2%)	8.70×10^{11}($\pm$2%)
σ_f(barns)	0.351	0.353

Am Capture Cross-Section Measurements

The ^{243}Am capture cross-section measurements were performed at the same time as the fissiosn rate measurements. The capture reaction rate is based on the measurement of the intensities of 744.1 keV and 898.1 keV gamma lines from the decay of the 10.1 h half-life ^{244g}Am relative to the 277.6 keV line from the decay of ^{239}Np (see the ^{243}Am fission cross-section measurements). The decay data for these determinations are listed in Table III. The results of the analyses are given in Table IV.

TABLE III. Decay Data for ^{243}Am Experiment[a]

Radionuclide	$T_{1/2}$	E_γ	b_γ
^{239}Np	2.354d(±.25%)	277.6 keV	.143(±1.4%)
^{244g}Am	10.1 h (±.9%)	744.1 keV	.666(±4.5%)
		898.1 keV	.273(±4.5%)

[a]From INEL Decay Data Master Library.

TABLE IV. ^{243}Am Capture Cross-Section Measurements

	Irradiation 1	Irradiation 2
$\phi\sigma_\gamma$ (rps/a)	8.41×10^{-14}(±15%)	8.70×10^{-14}(±2.3%)
ϕ (r/cm^2/sec)	8.74×10^{11}(±3%)	8.70×10^{11}(±3%)
σ_γ(barns)	0.0962(±3.4%)	0.100(±3.8%)

If the calculated isomer ratio from Mann and Schenter[17] of 0.1 is assumed then the total capture cross section for ^{243}Am is 1.0 barn.

Results

The data from these measurements, from measurements in ZEBRA and PFR and from calculations using ENDF/B-IV are listed in Table V. For the americium reactions, there appears to be a good consistency between the CFRMF results and the ZEBRA/PFR data. The CFRMF neutron spectrum is the "hardest" of the three neutron fields and consequently the capture values should be the lowest and the fission values the highest. Semi-quantitatively, this appears to the the case; however, more quantitative comparison need to be made by using, for example, integrals based on the reported spectra and a common cross section file such as ENDF/B.

For the ^{242}Pu reactions, it is difficult to draw any conclusions; however, in the case of fission, a review of the differential data such as that reported by Davey[19] would suggest that an integral value of 0.557 b is consistent with the differential data over the energy response of the CFRMF.

For ^{242}Pu capture, the sample configuration control problems identified in the measurements places a great deal of uncertainty on the results reported here. It is planned to duplicate the ^{242}Pu measurements using sample containment like that used in the most recent americium measurements.

TABLE V. Comparison of Integral Cross Section Values

Reaction	CFRMF (meas.)	CFRMF (ENDF.)	ZEBRA 12	ZEBRA 14	PFR
$^{241}Am(n,\gamma)^{242g}Am$	1.016		1.50 b	1.275 b	1.29 b
$^{241}Am(n,f)$ f.p.	.504 b			.316 b[a]	
$^{243}Am(n,\gamma)^{244}$ Am	1.0 b			1.51 b	1.39 b
$^{243}Am(n,f)$ f.p.	.352			.23 b[a]	
$^{242}Pu(n,\gamma)^{243}Pu$	.146 b	.238 b			
$^{242}Pu(n,f)$ f.p.	.557 b	.489 b		.26 b	

[a]Fission rate ratio relative to ^{239}Pu fission rate was reported in reference 2. Values shown use a fission cross section for ^{239}Pu of 1.78 b.

Future Work

The measured integral data presented here along with the U. K. integral data and possibly other integral data, form a complimentary set to use in the evaluation of differential data in the intermediate to fast neutron energy range. Further work is planned at INEL to finalize these measurements plus make further comparisons with ENDF/B evaluated data. Capture measurements for ^{243}Am are in progress where the total production of ^{244}Cm will be determined, consequently for ^{243}Am an isomeric capture ratio will be derived. Fission rate measurements using fission chambers are also planned. By doing both chamber measurements and radiometric measurements fission yields for key fission products will be determined also.

Acknowledgements

Mr. I. E. Stepan and the CFRMF operations group performed the irradiations and assisted in sample preparations.

Research is sponsored by the U. S. Department of Energy under contract with EG&G Idaho Inc.

References

1. D. W. Sweet, "Measurements in Progress in ZEBRA AEE Winfrith", UKNDC (75)P71/INDC(UK)-25/U, 39, July 1975.

2. D. W. Sweet, "Actinide Fission Rate Measurements in ZEBRA 14", NEACRP-L-132, 16.838.

3. K. M. Glover, et al., "Cm Production Cross-Section Measurements in ZEBRA", UKNDC(UK)P71/INDC(UK)-25/U, 51, July 1975.

4. R. A. P. Wilshire, et al., "The Cross Section for the Production of ^{242}Cm from ^{241}Am in a Fast Reactor", AERE-R-7363, (1973).

5. K. M. Glover, et al., "Measurement of the Integral Capture Cross Section of ^{243}Am", UKNDC(78)P88/NEANDC(E) 192 U. Vol. 8/INDC(UK) 30/U, 96, June 1978.

6. W. Davies, et al., "Measurement of Neutron Cross Sections in PFR", UKNDC(75)P71/INDC(UK)-25/U, 53, July 1975.

7. W. Davies, et al., " Measurement of Neutron Cross Sections in PFR", UKNDC(78)P88/NEANDC(E) 192 U. Vol. 8/INDC(UK) 30/U, 96, June 1978.

8. K. M. Glover, R. A. P. Wiltshire, D. W. Sweet, "Integral Capture Cross-Section Measurements of Americium Isotopes in the ZEBRA Reactor at Winfrith", Proceedings of the Specialists' Meeting on Nuclear Data of Plutonium and Americium Isotopes for Reactor Applications, Brookhaven National Laboratory, Nov. 20-21, 1978, BNL 50991/NEANDC L-116 P. 367.

9. J W Rogers, D. A. Millsap, Y. D. Harker, "CFRMF Neutron Field Flux Spectral Characterization", Nuclear Technology 25, 330 (1975).

10. J W Rogers, Y. D. Harker, D. A. Millsap, "The Coupled Fast Reactivity Measurements Facility", IAEA Consultants Meeting on Integral Cross-Section Measurements in Standard Neutron Fields for Reactor Dosimetry, Vienna. Austria (Nov. 15-19, 1976).

11. Y. D. Harker, J W Rogers, D. A. Millsap, Fission Product and Reactor Dosimetry Studies at Coupled Fast Reactivity Measurements Facility, TREE 1259/ ENDF 266, March 1978.

12. J. Grundl and C. Eisenhauer, "Benchmark Neutron Fields for Reactor Dosimetry", Proceedings of a Consultants Meeting on Integral Cross-Section Measurements in Standard Neutron Fields for Reactor Dosimetry, IAEA, Vienna, Austria, November 15-19, 1976, P. 53, IAEA-208 Vol 1.

13. M. E. Meek and B. F. Rider, "Complication of Fission Product Yields, Vallecitos Nuclear Center", NEDO-12154-2 (January 1977).

14. P. R. Fields, I. Ahmadl, A. M. Friedman, J. Lerner, D. N. Metta, "Alpha Decay of ^{247}Cm", Nucl. Phys. A160, 460 (1971).

15. R. C. Greenwood, R. G. Helmer, J W Rogers, R. J. Popek, R. R. Heinrich, N. D. Dudey, L. S. Kellogg and W. H. Zimmer, "Radiometric Reaction-Rate Measurements in CFRMF and Big-10", NUREG/CP-0004, Vol. 3, 1207 (1978).

16. H. L. Smith and D. C. Hoffman, Journal of Inorganic Nuclear Chemistry 13, 243 (1956).

17. F. M. Mann and R. E. Schenter, HEDL Evaluation of Actinide Cross Sections for ENDF/B-V, HEDL-TME77-54, August 1977.

18. E. Storm and H. I. Israel, Nucl. Data Tables A7, 565 (1970).

19. W. G. Davey, Nuclear Science and Engineering 26, 149 (1966).

EVALUATION OF ACTINIDE CROSS SECTIONS BY INTEGRAL EXPERIMENTS IN FAST CRITICAL ASSEMBLY FCA

T. Mukaiyama, H. Mitani, K. Koyama, M. Obu and H. Kuroi

Japan Atomic Energy Institute
Tokai-mura, Ibaraki-ken, Japan

The preliminary study has been performed to determine the effects of actinide cross sections uncertainties upon the long term characteristics of the actinide burning reactor. A program for the integral measurement of the actinides is planned at JAERI to improve the actinide cross section data. The small sample (20 gr) perturbation and the reaction rate ratio are to be measured in the neutron spectra of varying hardness. Measurements are planned for ^{237}Np, ^{238}Pu, ^{241}Am and ^{243}Am.

[actinide recycle, fast reactor, cross section evaluation, integral experiment, least square fitting, sample perturbation, neutron spectrum, fast critical facility]

Introduction

One of the major problems which may govern the very future of the nuclear power is the risks from the high-level, long-lived radioactive wastes. Among the radioactive wastes, most of fission products decay to innocuous levels in a relatively short time span of about 500 years, whereas the radiological hazards of actinides continue for a hundred thousands years. In order to alleviate the long-term radiological hazard of actinide nuclides, it has been proposed to recycle actinides in a suitable reactor to transmute them into fission products which are a shorter-term hazard.[1,2] From the neutron economy point of view, the actinide recycle concept may be acceptable especially with the fast reactors because the most of actinide isotopes possess appreciable fission cross sections in the high energy region. The assessment of the actinide recycle concept requires the reliable fission and capture cross sections of the actinides over the whole energy spectrum of potential actinide recycling systems.

Status of Actinide Cross Section

The reliability of the prediction of reactor physics parameters depends upon "the data and the method" used. As far as actinides are concerned, the "data" available at present are much less reliable than the "method". In Table 1, some of one-group actinides cross section sets for fast reactors are shown. The first three sets in Table 1, i.e., ENDL, ENDF/B-IV and FD5, are collapsed using the central spectrum of the NEACRP LMFBR benchmark model[5] calculated using JAERI-Fast[6] set for the first and the second set and FGL5[7] for the FD5 set. The 25-group ENDL set was generated[3] using the Evaluated Nuclear Data Library of Lawrence Livermore Laboratory[4] (U.S.A.) as the source data. In collapsing the multi-group cross section into one-group cross section, the weighting function plays an important role. When the central neutron spectra of the large LMFBR proposed as a benchmark model by Till[5] (a soft spectrum case) and of the Actinide Burning Reactor ABR which utilize only oxide actinides as the

Table 1(a) One-group Capture Cross Section of Actinides in Fast Reactors (unit inbarns)

Isotope	ENDL3[a]	ENDF/B-IV[a]	FD5[7a]	TKSY[9]	ORIGEN[10]
Th232	0.53		0.43		0.44
U233	0.30		0.27		0.40
U234	0.64	0.44	0.61		0.45
U235	0.72	0.72	0.53	0.62	0.57
U236	0.71		0.59	0.61	0.66
U237	0.40				0.41
U238	0.41[b]	0.41	0.29	0.30	0.30
Np237	1.94		1.95	1.72	0.77
Pu238	0.58		0.45	0.50	0.22
Pu239	0.71	0.64	0.55	0.47	0.50
Pu240	0.54	0.56	0.63	0.45	0.42
Pu241	0.62	0.59	0.62	0.47	0.43
Pu242	0.46	0.45	0.39	0.42	0.34
Pu243	0.46				0.57
Am241	1.59		2.01	1.40	0.99
Am242m	0.46		0.11	0.65	0.40
Am243	0.55		1.73	0.91	0.56
Cm242	0.46		0.51	0.68	0.38
Cm243	0.48		0.10	0.44	0.40
Cm244	0.66		0.49	0.53	0.37
Cm245	0.48		0.5[c]		0.40
Cm246	0.47		0.5[c]		0.30
Cm247	0.57		0.5[c]		0.36
Cm248	0.43		0.5[c]		0.31
Bk249	0.53		1.7[c]		0.39
Cf249	0.51		0.5[c]		0.83
Cf250	0.59		0.5[c]		0.42
Cf251	0.58		0.5[c]		0.41
Cf252	0.46		0.5[c]		0.39

a. one group sets with a are collapsed using the central spectrum of the NEACRP LMFBR benchmark model[5] calculated using JAERI-Fast[6] set for ENDL, ENDF/B-IV cases and FGL5[8] data for FD5 case

b. the figures with b are obtained using ENDF/B-IV data

Table 1(b) One-group Fission Cross Section of Actinides in Fast Reactors (unit in barns)

Isotope	ENDL3[a]	ENDF/B-IV[a]	FD5[7a]	TKSY[9]	ORIGEN[10]
Th232	0.010		0.0094		0.014
U233	3.03		2.85		3.15
U234	0.30	0.29	0.29		0.51
U235	2.15	2.12	1.98	2.05	2.03
U236	0.10		0.088	0.10	0.12
U237	0.68				1.82
U238	0.044[b]	0.044	0.043	0.051	0.043
Mp237	0.33		0.31	0.33	0.36
Pu238	1.31		1.13	1.13	1.38
Pu239	1.94	1.94	1.83	1.90	1.85
Pu240	0.36	0.37	0.35	0.41	0.35
Pu241	2.66	2.69	2.69	3.05	2.49
Pu242	0.26	0.28	0.22	0.29	0.28
Pu243	0.81				2.03
Am241	0.44		0.31	0.43	0.46
Am242m	3.97		3.33	3.74	1.83
Am243	0.24		0.19	1.97	0.24
Cm242	0.40		1.23	1.93	0.42
Cm243	2.85		2.89	2.66	0.32
Cm244	0.39		0.38	0.53	0.41
Cm245	3.03		2.3[c]		2.45
Cm246	0.31		0.3[c]		0.30
Cm247	2.31		2.3[c]		2.15
Cm248	0.34		0.3[c]		0.29
Bk249	0.17		0.2[c]		0.13
Cf249	2.87		2.3[c]		2.55
Cf250	0.99		0.3[c]		1.22
Cf251	3.16		2.3[c]		2.03
Cf252	0.68		0.3[c]		1.24

c. the figures with c are derived by the following rule:

capture	fission
even Z, any N 0.5	even Z, even N 0.3
odd Z, even N 1.7	even Z, odd N 2.3
odd Z, odd N 0.1	odd Z, even N 0.3
	odd Z, odd N 3.3

fuel (a hard spectrum case) are used as the weighting spectra , the maximum difference of two sets in one-group capture and fission cross section was 45% and 20%, respectively. This case is rather an extreme one. Even if we assume that the different weighting in collapsing causes 30% and 15% difference in capture and fission cross section, respectively, between the cross section sets, there still exist big differences between the sets especially in the capture cross section. The uncertainty effects of actinide cross sections upon the characteristics of the actinide transmutation system was investigated. In Table 2 the uncertainty level estimated for decay constants and cross sections are given as the reference set for this study. The effect of cross section uncertainties of Table 2 upon the prediction of actinide production in a typical LMFBR is given in Table 3 for the irradiation of 2 years and the cooling of 180 days.

Table 2 Estimated Cross Section and Decay Constant Uncertainties

Nuclide	λ (%)	σ_f (%)	σ_c (%)	$\sigma_{n,2n}$ (%)
U-235	2	5	5	40
U-236	2	15	25	50
U-237	1	25	50	
U-238	3	5	5	40
Np-236	1	30	50	
Np-237	2	20	40	50
Np-238	1	30	50	
Np-239	1	30	50	
Pu-238	1.5	20	50	
Pu-239	1	5	5	40
Pu-240	5	10	20	40
Pu-241	5	10	20	40
Pu-242	5	20	30	50
Am-241	2	30	40	
Am-242m	2	30	50	50
Am-242	1	30	50	50
Am-243	2	30	50	
Cm-242	2	30	50	
Cm-243	3	30	50	50
Cm-244	3	30	50	
Cm-245	3	30	50	

Table 3 Effects of Cross Section Uncertainties[a] upon Actinide Production[b] in LMFBR

Isotope	Uncertainty of Production in %
U-235	3.7
U-236	5.6
U-238	0.5
Np-237	36.4
Pu-238	29.1
Pu-239	3.4
Pu-240	3.1
Pu-241	10.0
Pu-242	7.0
Am-241	9.8
Am-242m	36.4
Am-243	28.9
Cm-242	35.2
Cm-243	61.2
Cm-244	55.0
Cm-245	74.0

a. cross section uncertainties given in Table 2

b. irradiation for 2 years and cooling for 180 days

The Actinide Burning Reactor ABR utilizes the oxide of actinide mixture recovered from the wastes generated by the reproccessing LMFBR fuel of 33000 MWD/MT with the assumptions of reprocessing 30 days after fuel discharge and of 0.5% of uranium and plutonium lost to waste.[11] From this actinide waste, uranium must be partitioned off because the large amount of ^{238}U is unfavorable for the criticality of a reactor and for the hard neutron spectrum necessary for an efficient actinide fission. The volume fraction of ABR is chosen as,

oxide actinide:sodium:structual material=40:40:20.

Recycling calculation has been made for the irradiation of $1x10^{16}n/sec\cdot cm^2$ for 300 days and 300 days cooling per cycle. At the beginning of each cycle, the criticality is adjusted by feeding the fresh actinide mixture from the reprocessing. The actinide concentrations in ABR investigated are tabulated for the initial state of 1st and 20th cycle in Table 4. The effect of the cross section uncertainties upon the atom density of ABR is calculated for the cross section uncertainties given in Table 2 and the atom density uncertainties in the final state of 1st and 20th cycle are given in Table 5. The uncertainties of atom density in Table 5 cause 3% and 17% actinide fuel volume uncertainties at the final state of 1st and 20th cycle, respectively.

Density coefficient of multiplication factor per one percent change of atom density is given in Table 6 for the 1st and 20th cycle of ABR. Assuming no correlation between the uncertainties of different nuclides, the uncertainty of the multiplication factor due to the uncertainties of actinide density of Table 5 is 0.9%Δk and 5.9%Δk for the 1st and 20th cycle.

The multiplication factor uncertainty due to errors of actinide cross section is calculated under the following correlation conditions and for the cross section uncertainties of Table 2;

Case A: full correlation between errors in different energy groups and between errors in different nuclides,

Case B: full correlation between errors in different energy groups only,

Case C: full correlation between errors in different nuclides only,

Case D: no correlation.

The results of the calculation are given in Table 7.

Table 4 Actinide Atom Density in ABR Core unit in $0.6023x10^{24}n/cm^3$

	Initial	20th Cycle
Np-237	1.38(-3)[a]	1.38(-4)
Pu-238	3.65(-5)	1.99(-3)
Pu-239	3.18(-3)	1.99(-4)
Pu-240	1.06(-3)	3.22(-4)
Pu-241	2.91(-4)	5.19(-5)
Pu-242	1.81(-4)	9.63(-4)
Am-241	5.31(-3)	1.34(-2)
Am-242m	0.0	3.08(-4)
Am-243	2.81(-3)	2.78(-3)
Cm-242	2.17(-4)	1.20(-4)
Cm-243	0.0	5.20(-5)
Cm-244	2.06(-4)	6.49(-4)
Cm-245	0.0	4.06(-5)

a. read as $1.38x10^{-3}$

Table 5 Effect of Cross Section Uncertainties[a] on Actinide Atom Density in ABR at 1st and 20th cycle[b]

Isotope	Uncertainty of Atom Density in %	
	1st cycle	20th cycle
U-235	2.2	5.4
U-236	29.1	17.6
U-237	8.6	26.3
U-238	11.9	32.4
Np-237	7.4	30.5
Pu-238	18.9	32.9
Pu-239	2.4	41.7
Pu-240	2.5	26.4
Pu-241	7.2	26.0
Pu-242	10.9	31.5
Am-241	5.6	25.9
Am-242m	39.2	39.2
Am-243	4.9	31.7
Cm-242	29.2	29.8
Cm-243	52.7	61.7
Cm-244	25.7	39.3
Cm-245	52.8	63.9

a. cross section uncertainties given in Table 2
b. each cycle consists of irradiation of 1.0×10^{16}n/sec.cm^2 for 300 days and 300 days cooling

Table 6 Density Coefficient[a] of Reactivity in ABR at 1st and 20th Cycle

	1st cycle	20th cycle
Np-237	-1.03(-2)[b]	-6.61(-4)
Pu-238	2.36(-3)	1.28(-1)
Pu-239	3.10(-1)	1.78(-2)
Pu-240	2.02(-2)	5.22(-3)
Pu-241	3.94(-2)	6.13(-3)
Pu-242	7.46(-3)	3.00(-2)
Am-241	5.27(-2)	1.14(-1)
Am-242m	—	5.97(-2)
Am-243	2.68(-2)	2.03(-2)
Cm-242	4.71(-3)	1.30(-3)
Cm-243	—	8.40(-3)
Cm-244	4.11(-3)	1.22(-2)
Cm-245	—	7.29(-3)

a. (% change of Δk)/(% change of atom density)
b. read as -1.03×10^{-2}

Table 7 Uncertainty in Multiplication Factor of ABR due to Cross Section Uncertainties[a]

CASE[b]	1st cycle		20th cycle	
	cap.	fiss.	cap.	fiss.
A	7.3%	11.%	8.5%	17.%
B	4.6	6.0	7.0	12.0
C	2.4	4.2	3.0	6.5
D	1.6	2.3	2.5	4.4

a. cross section uncertainties given in Table 2
b. see the text at the end of section "Status of Actinide Cross Section"

Improvement of Accracy of Actinide Cross Section by Integral Measurement

Least Square Fitting of Cross Section Utilizing Integral Data

Experiences on cross section evaluation studies suggest that the improvement of accuracy of cross section data is most efficiently achieved by the combination use of differential and integral measurements.

The theory of least square fitting of cross sections utilizing integral data is informative to demonstrate the contribution of the integral data to improvement of the multi-group cross section data. The error of the adjusted group cross section by the least square fitting of integral data is given as follows according to the formula derived by Mitani and Kuroi,[12]

$$\Delta\tilde{\sigma}_i = \Delta\hat{\sigma}_i(1-\delta_{ii})^{\frac{1}{2}}\sqrt{\frac{\hat{M}^T B^{-1}\hat{M}}{(N-n)\sigma^2}} \qquad (1)$$

$$\delta_{ii} = \sum_{jk\ell m}^{nmmn}\rho_{ij}A_{kj}B^{-1}_{k\ell}A_{\ell m}\rho_{mi} \qquad (2)$$

where

n: number of group cross sections to be adjusted
m: number of integral data used for adjusting cross sections
N: n + m
σ^2: a known proportional constant of the weight
ρ_{ij}: (i,j) element of the correlation matrix ρ of cross section
A_{kj}: (k,j) element of the sensitivity coefficient matrix A of integral data
$B^{-1}_{k\ell}$: (k,ℓ) element of the inverse matrix B^{-1} ($B = E+A\rho A^T$)
$\hat{M}$: vector of the difference between the measured and calculated values of the integral data

The quantity $q = \frac{\hat{M}^T B^{-1}\hat{M}}{(N-n)\sigma^2}$ of the third term of Eq.1 has a Chi-square distribution with N-n degree of freedom. The value of q distributes around 1 and the factor of $(1-\delta_{ii})^{\frac{1}{2}}$ is proved to be always smaller than 1.0. Therefore, the behavior of this factor showes how the integral data contribute to improving the accuracy of cross section data.

Program of Integral Experiments in Fast Critical Assembly FCA at JAERI

The small sample perturbation and the reaction rate ratio are the realistic integral data of the actinide elements because of the high radioactivity of actinides and the difficulty of obtaining pure samples. In contrast with the differential measurements, the integral measurements are very accurate, but the information with respect to the energy dependence is not so straightforward. Therefore, the choice of appropriate variety of neutron spectra where integral measurements are taken place is most important to obtain a successful result for improving the cross section data.

The following twelve cores are planned to be built at FCA of JAERI to cover a wide range of neutron spectra. The core composition of twelve cores are given in Table 8. The maximum amount of actinide samples available for perturbation measurements is 20 gr. Therefore, the core configurations are selected so as to satisfy the condition that their critical masses are less than 150 kg of the fissile material. Only 93% enriched uranium metal plates are used and plutonium is not used for this experiments in order to minimize temperature drift during the perturbation measurement. Iron or graphite is used as a diluent material for shifting neutron

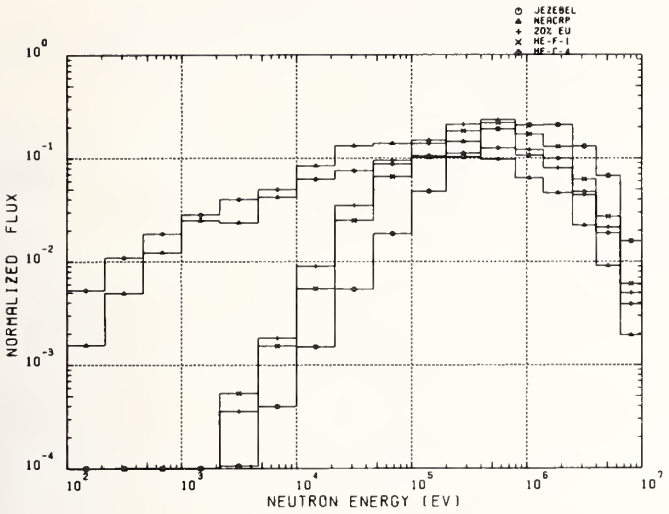

Fig.1(a) Hard and Soft Neutron Spectra among Those of Cores to be built, Spectra of Jezebel[13] and NEACRP LMFBR Benchmark Model for Comparisons

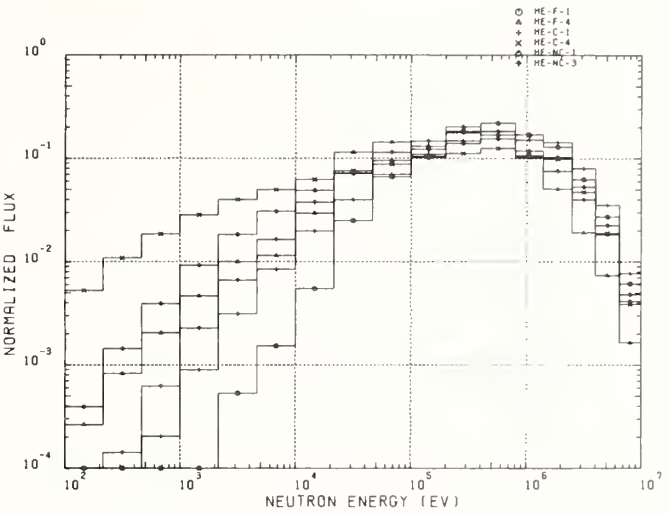

Fig. 1(b) Some of the Spectra of the Cores to be built

Fig. 1 Central Neutron Spectra of Cores
For the Core Name, see Table 8

spectrum appropriately. Natural uranium is also used to adjust the neutron spectrum in the relatively low energy region. Some of the central spectra of these cores are shown in Fig.1. Flg.1(a) showes the hard and soft spectra among those of the twelve cores and the spectrum of the plutonium metal core "Jezebel[13]" and that of NEACRP benchmark model[5] are also shown for the comparison. In Fig.1(b), some of the typical spectra of varying hardness of the planned cores are shown.

The sample perturbations of 20 gr of ^{237}Np, ^{238}Pu, ^{241}Am and ^{243}Am, and the fission rate ratios of these isotopes to ^{235}U are to be measured in these cores.

The values of $(1-\delta_{ii})^{\frac{1}{2}}$ in Eq.1 was calculated with the assumption of 3% errors in the measurements of the perturbation and the fission rate ratio. The result is tabulated in Table 9. From the values of the table and the experiences on the values of the statistical factor in Eq.1, we can conclude that the uncertainty of the group cross section can be reduced by factor 2 to 5 for the important energy region of fast reactors after adjusted by the least square fitting of the integral data measured with 3% error.

Table 8 Volume Fraction of Cores to be built

Core	Fissile		Diluent		NU[a]	Steel[b]	Void
HE-C-1	HEU[c]	29.1%	C[d]	55.6%	0.0%	10.8%	4.5
HE-C-2	HEU	21.2	C	63.5	0.0	10.8	4.5
HE-C-3	HEU	10.6	C	74.1	0.0	10.8	4.5
HE-C-4	HEU	5.3	C	79.4	0.0	10.8	4.5
HE-NC-1	HEU	10.6	C	63.5	10.6	10.8	4.5
HE-NC-2	HEU	10.6	C	52.9	21.2	10.8	4.5
HE-NC-3	HEU	10.6	C	31.8	42.3	10.8	4.5
HE-F-1	HEU	29.1	F[e]	55.6	0.0	10.8	4.5
HE-F-2	HEU	21.2	F	63.5	0.0	10.8	4.5
HE-F-3	HEU	10.6	F	74.1	0.0	10.8	4.5
HE-F-4	HEU	5.3	F	79.4	0.0	10.8	4.5
EU	EU[f]	84.7		0.0	0.0	10.8	4.5

a. natural uranium metal plate
b. structual material
c. 93% enriched uranium metal plate
d. graphite plate
e. steel plate
f. 20% enriched uranium metal plate

Table 9 The values of $(1-\delta_{ii})^{1/2}$ in Eq.1

Energy Group	Upper Energy	Pu-238 (CAP)	Pu-238 (FIS)	Np-237 (CAP)	Np-237 (FIS)	Am-243 (CAP)	Am-243 (FIS)	Am-241 (CAP)	Am-241 (FIS)
1	10.5 Mev.	0.99	0.49	0.86	0.37	0.95	0.33	0.99	0.77
2	4.02 "	0.85	0.07	0.68	0.04	0.88	0.03	0.97	0.63
3	2.48 "	0.81	0.05	0.64	0.03	0.85	0.02	0.97	0.37
4	1.41 "	0.65	0.04	0.50	0.01	0.68	0.01	0.96	0.20
5	0.795 "	0.29	0.04	0.11	0.05	0.19	0.15	0.95	0.85
6	0.399 "	0.23	0.04	0.03	0.13	0.06	0.30	0.89	1.00
7	0.200 "	0.24	0.06	0.03	0.18	0.06	0.35	0.79	1.00
8	100. Kev	0.20	0.06	0.03	0.21	0.04	0.37	0.62	1.00
9	46.4 "	0.15	0.08	0.03	0.29	0.04	0.41	0.44	0.87
10	21.5 "	0.18	0.18	0.03	0.53	0.04	0.55	0.65	0.59
11	9.96 "	0.30	0.31	0.03	0.79	0.08	0.72	0.66	0.92
12	4.61 "	0.44	0.41	0.03	0.93	0.13	0.83	0.34	0.58
13	989. ev	0.57	0.92	0.28	1.00	0.78	0.99	0.52	0.86
14	212. "	0.66	0.98	0.33	1.00	0.16	1.00	0.32	1.00
15	9.74 "	1.00	1.00	1.00	1.00	0.97	1.00	0.92	1.00

Summary

The preliminary study has been made to investigate the cross section requirements for the actinide incineration in the fast reactor system. The effect of the cross section errors causes the large uncertainty in the multiplication factor of Actinide Burning Reactor. The improvement of the cross section errors by factor 2 to 3 will be necessary for the conceptual study and for the engineering study of the concept. Such integral data as the small sample perturbation and the reaction rate ratio can greatly improve the reliability of the actinide cross sections.

References

1. H.C. Claiborne, "Neutron-Induced Transmutation of High-Level Radioactive Waste", ORNL-TM-3964 (1972).

2. K.J. Shneider and A.M. Platt, "Advanced Waste Management Studies, High-Level Radioactive Waste Disposal Alternatives", BNWL-1900, Vols 1 - 4 (1974).

3. T. Mukaiyama, K. Koyama and H. Kuroi, "Generation of Actinide Isotopes Cross Section Set for Fast Reactor Calculations Using Data from ENDL and ENDF/B-IV", JAERI-M8310 (1979).

4. R.J. Howerton, et al., "The LLL Evaluated Nuclear Data Library (ENDL) , UCRL-50400 Vol. 15, Part A (1975) and Part B (1976).

5. C.E. Till, "Specifications for An International Comparison Calculation of A Large Sodium-Cooled Fast Breeder Reactor", NEACRP-A-272 (1976).

6. S. Katsuragi, et al., "JAERI Fast Reactor Group Constants System, Part I and II-1", JAERI-1195 and 1199 (1970), H. Takano, et al., JAERI Fast Reactor Group Constants Set, Version II", JAERI-1255 (1978).

7. J.L. Rowlands, "Actinide cross sections averaged using the central spectrum calculated using FGL5 data for NEACRP LMFBR Benchmark model", NEACRP-A-323 (1978).

8. J.L. Rowlands, et al., "The Production and Perfomance of the Adjusted Cross-Section Set FGL5", *Proceedings of International Symposium on Physics of Fast Reactors, A30 (Tokyo, Oct. 1973)*.

9. K. Tasaka, et al., J. Nucl. Sci. Technol., 14, 519 (1977).

10. M.J. Bell, "ORIGEN-The ORNL Isotope generation and depletion code", ORNL-4628 (1973).

11. ORNL Report, "Siting of Fuel Reprocessing Plants and Waste Management Facilities, Chap. 3, ORNL-4451 (1970).

12. H. Mitani and H. Kuroi, J. Nucl. Sci. Technol. 9, 383 (1972).

13. G.A. Jarvis, et al., Nucl. Sci. Eng. 8, 525 (1960).

NEODYMIUM, SAMARIUM AND EUROPIUM CAPTURE CROSS-SECTION ADJUSTMENTS BASED ON EBR-II INTEGRAL MEASUREMENTS

R. A. Anderl and Y. D. Harker
Idaho National Engineering Laboratory
EG&G Idaho, P.O. Box 1625
Idaho Falls, Idaho 83415

F. Schmittroth
Hanford Engineering Development Laboratory
P.O. Box 1970
Richland, Washington 99352

[Integral Cross Sections, EBR-II, Nd, Sm, Eu Isotopes, Dosimetry]

Integral capture measurements have been made for highly-enriched isotopes of neodymium, samarium and europium irradiated in a row 8 position of EBR-II with samples located both at mid-plane and in the axial reflector. Broad response, resonance, and threshold dosimeters were included to characterize the neutron spectra at the sample locations. The saturation reaction rates for the rare-earth samples were determined by post-irradiation mass-spectrometric analyses and for the dosimeter materials by the gamma-spectrometric method. The HEDL maximum-likelihood analysis code, FERRET, was used to make a "least-squares adjustment" of the ENDF/B-IV rare-earth cross sections based on the measured dosimeter and fission-product reaction rates. Preliminary results to date indicate a need for a significant upward adjustment of the capture cross sections for ^{143}Nd, ^{145}Nd, ^{147}Sm and ^{148}Sm.

Introduction

In recent years, integral data (capture reaction rates and reactivity worth measurements in fast-reactor fields) have played an important role in the evaluation of fission-product capture cross sections of importance to reactor technology, especially the development of fast reactor systems[1]. In the simplest evaluation application for isotopes with sparse or no measured differential data, integral measurements have been used to normalize capture cross sections based exclusively on nuclear model calculations. For isotopes with a more extensive base of measured differential data, integral measurements have been used to make integral tests of cross-section curves based on the differential measurements and nuclear model calculations. Such integral tests have been helpful to the evaluator in sorting out normalization problems between differential measurements. In a more sophisticated application, integral data obtained from measurements in different spectra have been used to adjust both multigroup and/or point-wise cross sections[1]. This latter application requires a realistic treatment of the uncertainties and correlations in the integral data and in the a-priori flux spectra and fission-product cross sections.

A significant fraction of the integral data used in the fission product cross-section evaluation process comprises reactivity worth measurements in the fast reactor spectra of the STEK cores[2] and activation capture rates in the fast neutron field of the Coupled Fast Reactivity Measurements Facility (CFRMF) at the Idaho National Engineering Laboratory[3]. This paper presents the integral capture results for enriched isotopes of neodymium, samarium and europium irradiated in different spectra in the Experimental Breeder Reactor-II (EBR-II). The Nd and Sm cross sections are of importance to fission product poison effects in fast reactors and/or to the establishment of a reliable burnup monitor for fast reactor fuels. Cross sections for the Eu isotopes are needed in the evaluation of europium oxide as a control material. For most of the isotopes in the irradiation, some integral data exist as reactivity worths. Little, if any, integral capture data have been published. The EBR-II experiment differs significantly from experiments in the CFRMF and STEK facilities in terms of neutron spectrum characterization. The neutron fields in the latter two facilities are well characterized by means of neutronic calculations and active neutron dosimetry. Characterization of the neutron spectra in the EBR-II is dependent on the use of passive dosimeters (activation monitors).

Included in this paper are a brief description of the EBR-II irradiation experiment and a detailed presentation of the measured reaction rates for the rare-earth samples and for the neutron spectrum dosimeters. In addition, preliminary results of the application of the FERRET Code[4,5] for spectrum unfolding and for the adjustment of ENDF/B-IV multigroup cross sections based on the measured integral data are presented.

EBR-II Irradiation Experiment

Irradiation Configuration

A detailed description of the irradiation experiment was presented earlier[6]. Only pertinent details will be given here. Shown in Figures 1 and 2 are the subassembly and axial loading patterns for this experiment. The irradiation package consisted of multiple samples (0.1 μg to 50 μg deposits on Ni or V foils) of the isotopically enriched isotopes shown in Figure 2 and dosimeter sets consisting of Co, Cu, Fe, Ni, Ti, Sc, ^{237}Np, ^{235}U, ^{238}U monitors. Two B-7 capsules provided the primary containment of the eight experiment capsules. Each experiment capsule contained up to five subcapsules each of which contained the sample or dosimetry materials.

Reaction-Rate Determination

Dosimeters. Saturation reaction rates for the dosimeters were determined by the radiometric technique[7,8] using calibrated Ge(Li) spectrometers. Decay data for the analysis was taken from reference 8. The fission-rate determinations were based on the consensus fast reactor fission yields given in reference 9. Infinitely-dilute reaction rates for the dosimeters in each set for the irradiation are summarized in Table I. Accurate fission rates for ^{238}U, not given in the table, are difficult to obtain because a large correction is required to account for fission-product activity due to fission of the "grown-in" ^{239}Pu. Uncertainties in the reaction rates for the Co dosimeters reflect significant neutron self-shielding corrections (~factor of 2) required for these monitors.

Rare-Earth Samples. The saturation reaction rates summarized in Table II for the Nd, Sm and Eu samples are based on mass-spectrometric or gamma

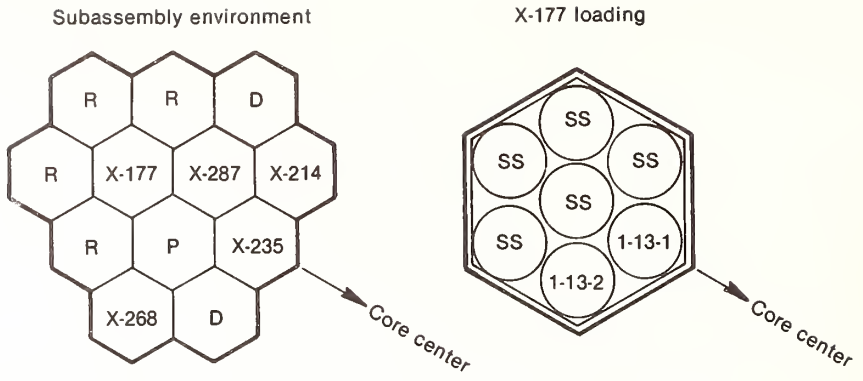

Fig. 1. Subassembly Loading Pattern for EBR-II Irradiation.

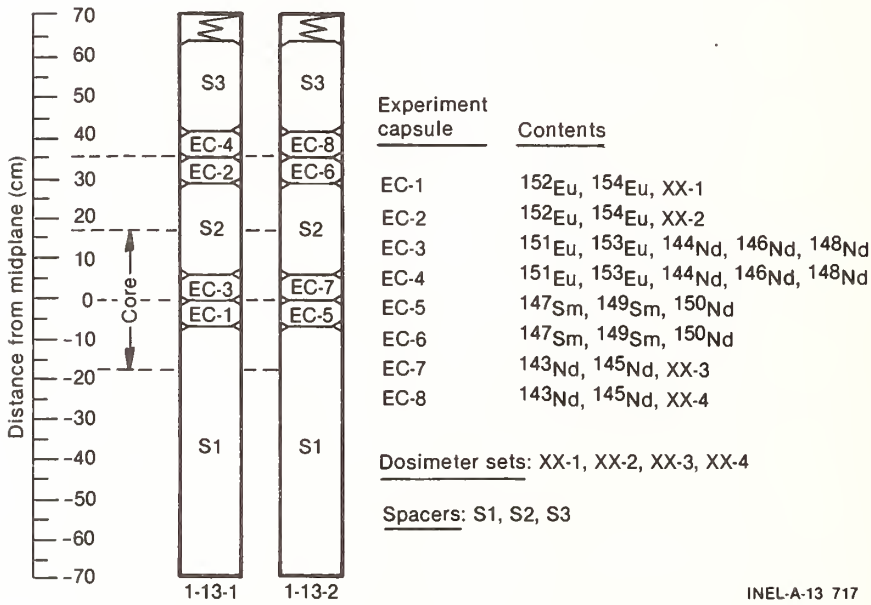

Fig. 2. B-7 Axial Loading Pattern for EBR-II Irradiation.

spectrometric measurements for the post-irradiation samples. For the Nd and Sm isotopes for which integral results are reported here, both the parent and the capture products are stable and the reaction rates are determined easily from mass spectrometer measurements of the (A+1)/A atom ratios for the samples[6]. Prior to mass spectrometric analysis, the rare-earth deposits were chemically isolated from the backing foil. A minimum of three mass-spectrometric analyses were made for the Nd and Sm samples from each axial location. The quoted errors for the Nd and Sm isotopes result from averaging the isotopic data from each mass-spectrometric analysis and accounting for an estimated 0.5% systematic error in the mass-spectrometric determination.

For the Eu isotopes, which involve radioactive parent or capture products, the reaction-rate determination is more complicated. Because a significant fraction of the capture in ^{151}Eu goes to the 9.6 h ^{152}Eu metastable state (estimated to be 41% from the data in reference 3), chemical isolation of the Eu fraction from the Gd and Sm decay products from the 9.6 h activity was required prior to mass-spectrometric analysis for the 152/151 atom ratio. Consequently, the capture rates for ^{151}Eu in the table were derived from decay-corrected measured-atom ratios divided by .59 to account for the isomer production. The errors in the measured capture rates for ^{151}Eu are dominated by a 5% uncertainty estimated for the isomer ratio.

Capture rates for ^{152}Eu are based on decay corrected 153/152 atom ratios obtained from mass spectrometric measurements for Eu samples isolated from the nickel backing and from the Sm and Gd decay products from the decay of the 13.2y ^{152}Eu. The sizable errors estimated for the quoted ^{152}Eu capture rates result from uncertainties in the mass-

TABLE I. Infinitely-dilute Reaction Rates for Dosimeters in EBR-II Experiment X-177

Reaction	Reaction rate (reactions/sec-atom) x 10^{11} XX-1[a]	XX-3	XX-2	XX-4
$^{59}Co(n,\gamma)^{60}Co$	20.2(9)[b]	27.8(12)	64.(5)	70.(6)
$^{235}U(n,f)$	231.(7)	234.(9)	238.(9)	230.(8)
$^{237}Np(n,f)$	63.(4)	50.(2)	19.3(10)	11.0(5)
$^{45}Sc(n,\gamma)^{46}Sc$	3.75(9)	3.72(8)	3.99(9)	4.07(8)
$^{54}Fe(n,p)^{54}Mn$	1.300(22)	0.910(15)	0.2162(37)	0.1024(17)
$^{58}Fe(n,\gamma)^{59}Fe$	0.965(13)	0.998(14)	1.239(16)	1.166(15)
$^{58}Ni(n,p)^{58}Co$	1.74(4)	1.27(3)	0.306(6)	0.152(3)
$^{46}Ti(n,p)^{46}Sc$	0.1570(19)	0.1142(14)	.02364(28)	0.01169(14)
$^{63}Cu(n,\alpha)^{60}Co$	0.00728(12)	0.00527(8)	.00212(3)	0.00104(2)

[a]Label for dosimetry set.

[b]Number in parenthesis is the 1-sigma error in the last significant digits.

TABLE II. Infinitely-dilute (n,γ) Reaction Rates for Rare-Earth Samples in EBR-II Experiment X-177

Isotope	Applicable[a] Dosimeter Set	Reaction Rate (rps/atom)x10^{10}	$\frac{C}{M}$ [c]
^{143}Nd	XX-3	5.03(6)[b]	.822
	XX-4	8.75(5)	.863
^{144}Nd	XX-1	1.06(2)	.997
	XX-4	0.993(11)	.970
^{145}Nd	XX-3	7.64(8)	.653
	XX-4	14.55(9)	.765
^{147}Sm	XX-3	23.11(14)	.658
	XX-2	44.8(5)	.813
^{149}Sm	XX-3	40.9(10)	.721
	XX-2	81.5(27)	1.07
^{151}Eu	XX-1	54.(3)	.705
	XX-4	113.(7)	.794
^{152}Eu	XX-1	52.(5)	.913
	XX-2	75.(8)	1.26
^{153}Eu	XX-1	29.6(15)	.804
	XX-4	61.9(25)	.934
^{154}Eu	XX-1	38.(3)	.757
	XX-2	62.(5)	1.03

[a]Dosimeter set identification which relates rare-earth reaction rates to dosimeter rates in Table I.

[b]Number in parenthesis is the 1-sigma error in the last significant digits.

[c]Calculated-to-measured reaction-rate ratios based on the unadjusted fission-product cross sections and the multigroup fluxes obtained from spectrum unfolding analysis.

spectrometric determination of the 153/152 atom ratios in the unirradiated and irradiated samples. Similarly, the capture rates for ^{153}Eu are based on decay-corrected 154/153 atom ratios obtained from mass-spectrometric measurements. The dominant contribution to the error for the ^{153}Eu capture rate is due to uncertainties in the mass-spectrometric determination of the 154/153 atom ratios.

The capture rates for the ^{154}Eu samples are based on decay-corrected atom ratios determined by the Ge(Li) spectrometric measurement of the relative gamma emission rates of the 123.14-keV and 105.3-keV lines in the β^- decay of ^{154}Eu and ^{155}Eu, respectively. The dominant contributors to the uncertainty in the capture rates are errors in the gamma-ray branching ratios and half-lives used in the computation of the atom ratios from the relative gamma intensities. Decay data from these analyses were taken from the INEL Decay Data Master File[10].

Data Analysis

Neutron Spectrum Characterization

The FERRET data analysis code[4,5] was used to obtain 47 group* representations of the neutron spectra based on the measured reaction rates for the dosimeters in Table I. A priori information for this analysis included the following:

1) 47 group fluxes derived from 29 group fluxes obtained from XY-geometry (for mid-plane) and RZ-geometry (for reflector) neutronics calculations for applicable core configurations of EBR-II[11],

2) parametric representations for the flux covariance matrices,

*Slightly modified version of the HEDL 42 group energy structure with maximum energy extended to 16.91 MeV.

3) 47 group dosimeter cross sections based on ENDF/B-IV, 620 group cross sections collapsed with a weighting function representative of the neutron spectra in EBR-II.

4) parametric representations for the cross section covariance matrices.

The covariance matrices generated for both the fluxes and cross sections are composed of two components: An overall fractional normalization uncertainty, c, and a second term, $r_i r_j \rho_{ij}$, that describes any additional uncertainties and correlations. The correlation matrix is parameterized by

$$\rho_{ij} = (1 - \theta)\, \delta_{ij} + \theta\, e^{-\frac{(i-j)^2}{2\gamma^2}}$$

where θ denotes the strength of the short range correlations and γ denotes their range. For example, completely uncorrelated data or a priori values are described by $\theta=0$ so that $\rho_{ij} = \delta_{ij}$. The values, $\{r_i\}$ are the group-by-group fractional uncertainties.

In the present analysis, a mid-plane a-priori flux was assumed to have a 10% normalization uncertainty of 20% with short-range correlations specified by $\theta= 0.9$ and $\gamma= 3.0$. A reflector a-priori flux was assumed to have a 20% normalization uncertainty and a group-by-group uncertainty of 40%. A more extensive evalution by one of the authors (F. Schmittroth) of the uncertainties and correlations for the dosimeter cross section is beyond the scope of this paper.

Two examples of the spectrum-unfolding analysis which simultaneously treated all four dosimeter sets are illustrated in Figures 3 and 4. In Figure 3, one notes that the adjusted multi-group flux appears to be somewhat softer than the a-priori flux. Group-to-group fractional uncertainties were reduced to as low as 12% in the region of maximum response above the sodium dip (25 keV). Illustrated in Figure 4 is the overall hardening of the a-priori reflector neutron spectrum by the adjustment. The two figures illustrate the significant differences in the energy distribution of the neutron flux between a mid-plane and a reflector location and point to the sensitivity of the reflector reaction rates to resonance capture.

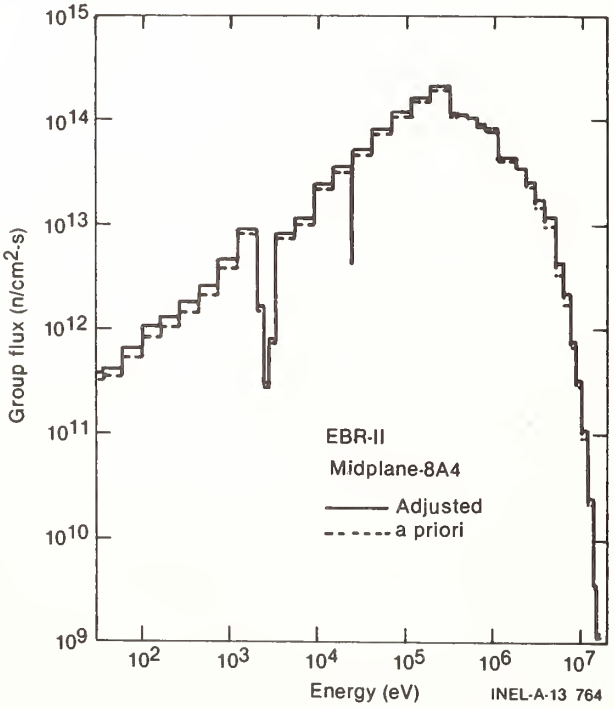

Fig. 3. Comparison of a-priori and adjusted multigroup fluxes for XX-1 dosimeter at midplane.

Cross-Section Adjustment

A least-squares adjustment of the fission-product multigroup cross sections was made with FERRET based on the following a-priori information:

1) Adjusted multigroup fluxes and adjusted flux covariance matrices from the spectrum unfolding analysis,

2) 47 group fission-product cross sections based on ENDF/B-IV,

3) parametric representations for the cross-section covariance matrices.

Summarized in the 4th column of Table II and illustrated by Figures 5-8 are some of the results of the FERRET analysis. The C/M ratios given in Table II present "conventional" integral tests of the fission-product cross sections. For example, both the midplane and reflector C/M ratios for ^{143}Nd indicate the need for an upward adjustment in the cross section throughout the region of sensitivity of the fluxes. The C/M ratios based on the adjusted fission-product cross sections and fluxes were essentially 1 for all cases except those with large errors in the measured reaction rate, e.g., ^{152}Eu. Shown in Figures 5-8 are comparisons of the a-priori and adjusted cross sections for ^{143}Nd, ^{145}Nd, ^{147}Sm and ^{148}Sm, isotopes for which no previous integral capture data have been reported. As expected, the adjustment in the cross section is mainly over the region of maximum response in the neutron fields and the magnitude of the adjustment is approximately given by the inverse of the C/M ratios from Table II.

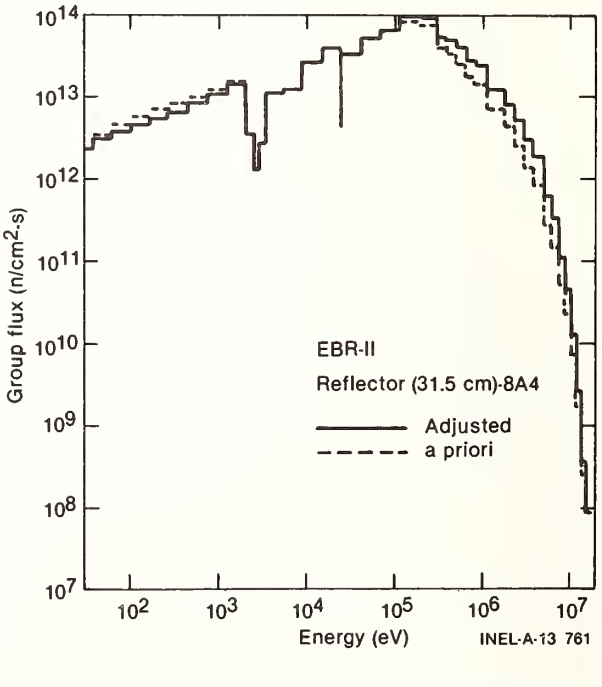

Fig. 4. Comparison of a-priori and adjusted multigroup fluxes for XX-2 dosimeter in the reflector.

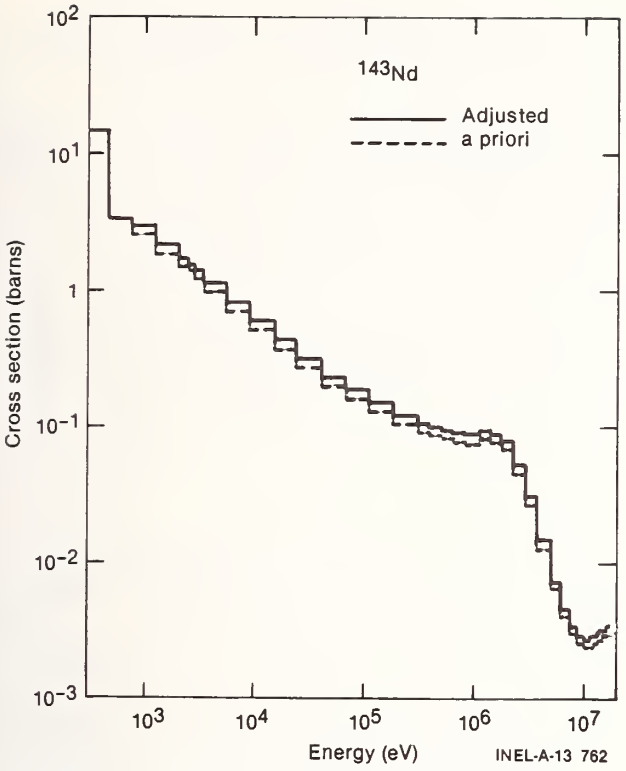

Fig. 5. Comparison of a-priori and adjusted multigroup cross sections for ^{143}Nd

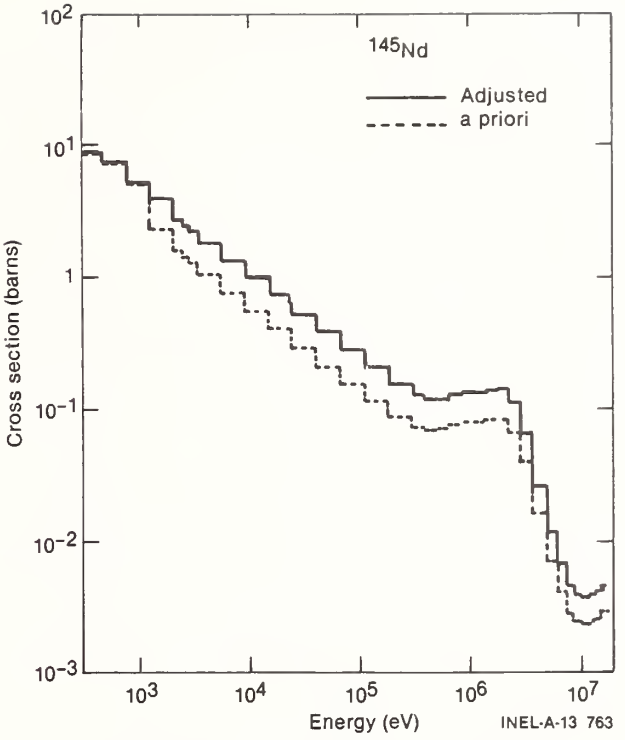

Fig. 6. Comparison of a-priori and adjusted multigroup cross sections for ^{145}Nd.

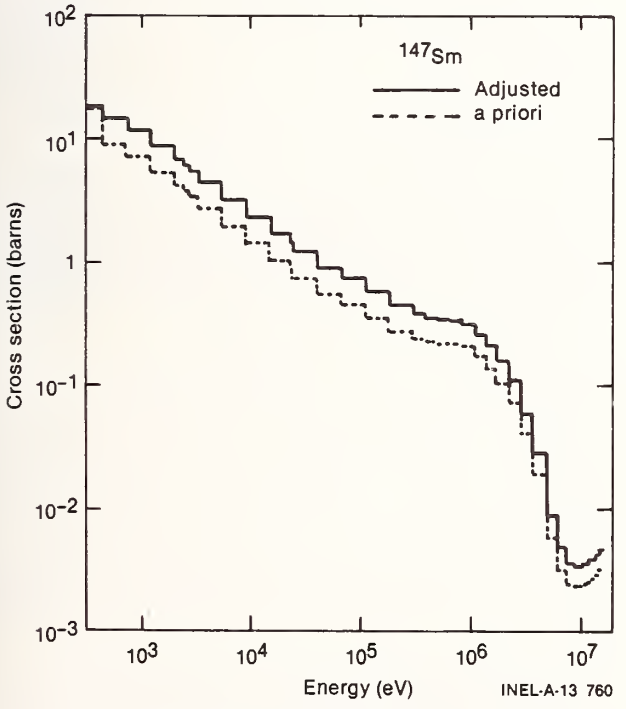

Fig. 7. Comparison of a-priori and adjusted cross sections for ^{147}Sm.

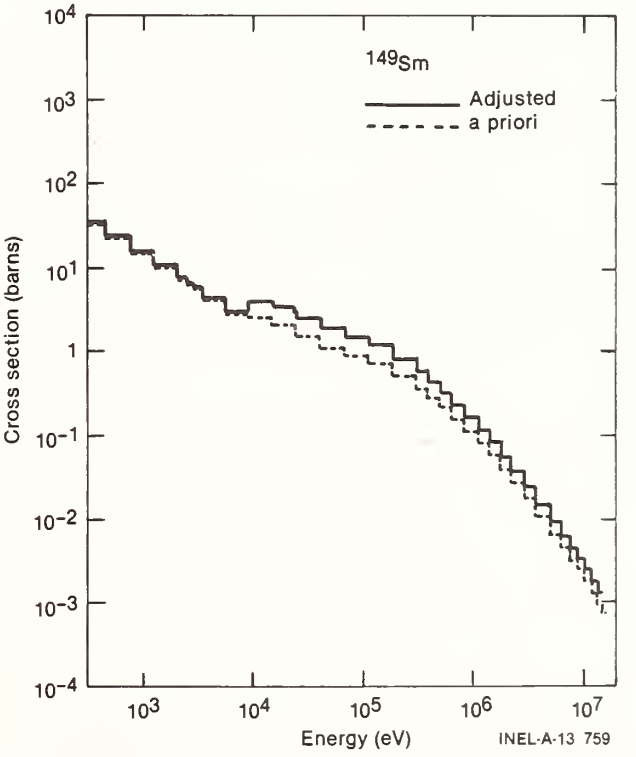

Fig. 8. Comparison of a-priori and adjusted cross sections for ^{149}Sm.

Discussion

Some qualitative comparisons of the present integral results and cross section adjustments with other integral data, measured differential cross sections and/or evaluated cross sections were made. Integral checks of the ENDF/B-IV cross sections for ^{147}Sm and ^{149}Sm based on reactivity-worth measurements in the STEK cores has been reported as C/M ratios[2]. The C/M ratios from the present experiment are in good agree-

ment with the STEK results. For ^{143}Nd, ^{144}Nd and ^{145}Nd, Gruppelaar[13] has reported adjusted cross sections (RCN-2A set) based on reactivity-worth measurements in the STEK cores. A comparison of the adjusted Nd cross sections from the present work with those of Gruppelaar indicates good agreement for ^{145}Nd and reasonable agreement for ^{143}Nd and ^{144}Nd. A comparison of the preliminary EBR-II adjusted cross sections with recent differential data indicates reasonable agreement for ^{149}Sm and ^{145}Nd and good agreement for ^{143}Nd and ^{144}Nd[14].

We consider the present integral results and FERRET analyses to be of more use in data evaluation than just for qualitative comparisons of C/M ratios and adjusted cross sections. Especially of use to the data evaluator are the adjusted cross sections and associated adjusted covariance matrices. The adjusted covariance matrices embody all the uncertainties and correlations associated with these integral experiments. The data could subsequently be used by the evaluator to adjust evaluated point cross sections based on nuclear model calculations and measured differential data[1]. Furthermore, with the advent and utilization of covariance files for ENDF/B cross sections, this approach to data evaluation will utilize in the most consistent way all the measured and calculated information important to determining pointwise cross sections for fission-product isotopes.

In summary, we would like to emphasize the unique features and contributions of the present experiment and analyses. From an experimental standpoint,

1) small sample sizes were required (μg quantities of highly enriched rare-earth samples were prepared with the INEL electromagnetic mass separator),

2) short-time (~30 days) irradiation of samples in different neutron fields of high flux test reactor,

3) spectral characterization of neutron fields by use of passive dosimetry,

4) capture reaction rate measurements based on conventional mass spectrometric and Ge(Li) spectrometric techniques and capabilities at the INEL.

From an analysis standpoint, we have demonstrated the adjustment of cross sections based on the present integral results to be consistent with other evaluations and differential measurements.

Acknowledgement

This work was performed under the auspices of the U. S. Department of Energy.

References

1. H. Gruppelaar and J. W. M. Dekker, "Impact of Integral Measurements on the Capture Cross-Sections Evaluations of Individual Fission-Product Isotopes," ECN-24, (September 1977).

2. M. Bustrann, J. W. M. Dekker, R. J. Heigboer, A. J. Janssen, "Integral Determination of Fission Product Neutron Capture Cross Sections for Applications in Fast Reactors," ECN-27,(September 1977).

3. Y. D. Harker, J W Rogers and D. A. Millsap, "Fission-Product and Reactor Dosimetry Studies at Coupled Fast Reactivity Measurements Facility," U. S. DOE Report TREE-1259 (March 1978).

4. F. S. Schmittroth, "Varied Applications of a New Maximum-Likelihood Code with Complete Covariance Capability," ORNL-RSIC-42, 145 (February 1979).

5. F. Schmittroth, "FERRET Data Analysis Code," HEDL-TME 79-40 (September 1979).

6. R. A. Anderl, Y. D. Harker, R. L. Tromp, J. E. Delmore, "EBR-II Irradiation of Enriched Isotopes of Neodymium, Samarium and Europium," Trans. Am. Nucl. Soc. 28 745 (1978).

7. R. C. Greenwood, R. G. Helmer, J W Rogers, N. D. Dudy, R. J. Popek, L. S. Kellogg and W. H. Zimmer, Nucl. Tech 25, 275 (1975).

8. R. C. Greenwood, R. G. Helmer, J W Rogers, R. J. Popek, R. R. Heinrich, N. D. Dudy, L. S. Kellogg and W. H. Zimmer, "Radiometric Reaction-Rate Measurements in CFRMF and Big-10," NUREG/CP-0004, Vol. 3, 1207 (1978).

9. D. M. Gilliam, R. G. Helmer, R. C. Greenwood, J W Rogers, R. R. Heinrich, R. J. Popek, L. S. Kellog, E. P. Lippincott, G. E. Hansen, W. H. Zimmer, "Reference and Standard Benchmark Fission Yields for U. S. Reactor Dosimetry Programs," NUREG/CP-0004, Vol. 3, 1289 (1978).

10. Private communication from R. L. Bunting and C. W. Reich.

11. Private communication from G. H. Golden, EBR-II Project.

12. B. A. Magurno, Editor, "ENDF/B-IV Dosimetry File," BNL-NCS-50446 (April 1975).

13. H. Gruppelaar, J. W. M. Dekker, A. J. Janssen, H. Ch. Rieffe, "Adjustment of Evaluated Neutron Capture Cross Sections of Neodymium Isotopes to Integral STEK and CFRMF Data," paper presented at the Int. Conf. on Neutron Physics and Nuclear Data for Reactors and Other Applied Purposes, Harwell, 25-29 September, 1978.

14. Private communication from R. E. Schenter.

MEASUREMENTS AND ANALYSES OF NEUTRON TRANSPORT THROUGH IRON

N. E. Hertel, R. H. Johnson, J. J. Dorning, and B. W. Wehring
University of Illinois at Urbana-Champaign
Urbana, Illinois 61801

Integral experiments have been performed using a thick homogeneous spherical shell of iron to test existing neutron cross section data. Neutron leakage spectra were measured for Cf-252-fission and DT-fusion neutron sources using an NE-213 spectrometry system. An associated particle detector monitored the absolute DT neutron source strength and the amount of DD neutron contamination in the DT source spectrum. The leakage spectra were calculated using the continuous-energy Monte Carlo code VIM and the discrete-S_n code ANISN. For neutron energies between 1 and 5 MeV, the calculations underpredicted the leakage spectrum by factors of 2 to 1.4 for the Cf neutron source and of 3 to 2 for the DT neutron source. The large discrepancies are attributed to inadequate representation of cross-section resonance structure (viz., minima); inadequate representation of the angular and secondary energy distributions for continuum inelastic scattering and (n, 2n) reactions may also contribute to these discrepancies.

(Integral tests of ENDF/B-IV; iron)

Introduction

Integral tests of evaluated nuclear data for iron were obtained by comparing measurements and calculations of the absolute energy spectrum of neutrons leaking from a bare homogeneous spherical iron shell containing a neutron source at its center. Iron was selected for testing because of its extensive use as a structural material in traditional nuclear engineering applications, its projected use in fusion reactors,[1] and its use as a shielding material in neutron radiotherapy shielding and collimators.[2]

The measurements were made for neutron energies between 1 and 15 MeV using a NE-213 proton-recoil spectrometer.[3,4] Two different neutron sources were used, a ^{252}Cf fission neutron source and a 14-MeV DT fusion neutron source provided by a neutron generator. The neutron generator drift tube was accommodated by a reentrant hole in the spherical shell.

The leakage calculations of neutron spectra were done using the one-dimensional discrete S_n code ANISN[5] and the continuous-energy Monte Carlo code VIM[6] both with cross section data derived from ENDF/B-IV.[7,8] The Monte Carlo code VIM was also used to investigate the effects of the reentrant hole, the base and supports of the iron sphere, and impurities in the iron.

Experiment

The spherical iron shell used in the integral tests was constructed and used previously by Gulf General Atomic to perform integral tests of iron cross section data in the keV region.[9,10] It is supported on a steel base by two stanchions and pinions. The full-density 38.1-cm radius iron sphere has a shell thickness of 6.5 mean free paths for 14-MeV neutrons and 6.9 mpf for 2-MeV neutrons. Two cylindrical reentrant holes with plugs provide access to the 7.7-cm radius central void.

To perform the ^{252}Cf neutron leakage measurements, a ^{252}Cf sealed needle was suspended in the center of the central void. The neutron source spectrum for ^{252}Cf has been thoroughly investigated at the University of Illinois[3] and was determined to be well-represented above 1 MeV by a Maxwellian distribution ($\phi \propto \sqrt{E}\, e^{-E/T}$) with a temperature T of 1.43 ± 0.02 MeV. The DT neutrons for the DT measurements were produced using a Texas Nuclear neutron generator utilizing a bombarding deuteron energy of 60 keV. One of the reentrant holes was used to accommodate the neutron-generator drift tube.

The absolute normalization of the experimentally determined leakage spectra is essential to extracting information for the comparisons with calculations. Measurements using the ^{252}Cf source were performed on an absolute basis by recording the live time duration of the measurement. Fluctuations in the deuteron beam current and tritium burnup in the target made this difficult when the DT neutron source was used. Therefore, an associated particle system was constructed to monitor the neutron production rate by counting the associated alpha particle from the DT reaction.[11] The associated particle system also served as a monitor of the DD neutron contamination of the DT source spectrum.

The neutron leakage measurements were made using the NE-213 spectrometry system assembled at the University of Illinois.[3,4] The NE-213 proton recoil spectra obtained in the measurements were unfolded using the FORIST unfolding code[12] and the University of Illinois neutron response matrix.[3] Background was measured by placing a paraffin shadow cone midway between the detector and the spherical assembly. For the DT leakage measurement the detector was 265 ± 1 cm from the source (the center of the sphere) and at an angle of 45° to the incident deuteron direction. For the ^{252}Cf measurement, the source-to-detector distance was 227 ± 1 cm. The detector and source were both located approximately 1 m above the concrete floor for all measurements.

Calculations

Calculations of the leakage spectra for the iron sphere were performed with the Monte Carlo code VIM[6] and the one-dimensional discrete-ordinates S_n code ANISN.[5] These calculations were performed using cross-section data derived from ENDF/B-IV.[7,8] The fixed source option of each code was employed. Because of its multidimensional capabilities, the VIM code was also used to analyze the effects of the spherical shell reentrant hole and the base and supports on the DT neutron leakage spectra.

The VIM code is a continuous-energy Monte Carlo code with a combinatorial geometry package which allows for the description of complicated and irregular assemblies for one-, two-, and three-dimensional calculations. Cross section definition in VIM was by composition-independent microscopic data sets derived from ENDF/B-IV for neutron energies between 1 eV and 14.2 MeV. Cross sections are specified pointwise and interpolated linearly in energy to provide a continuous energy cross section description.[6]

The ^{252}Cf source spectrum was randomly generated using a Maxwellian with a 1.43 MeV temperature. The DT source was randomly generated between 13.8 and 14.2 MeV. For all VIM calculations, the source was located in a 0.24-cm radius spherical region at the center of the central void. The results were binned in the 171 group energy structure of the DLC-41/VITAMIN-C multigroup cross section set.[13]

All leakage calculations using ANISN were performed with S_{32} P_3. Previous studies for similar calculations showed that these values were adequate for calculating leakage spectra to the degree of accuracy needed. Eighty spatial intervals were used with 24 of them in the spherical void. All calculations were performed for a distributed source located in the 0.24-cm radius inner mesh of the central void.

The ANISN leakage calculations were performed using two coupled neutron and gamma-ray cross-section sets generated at ORNL, DLC-41/VITAMIN-C[13] and DLC-47/BUGLE.[14] The DLC-41 multigroup cross-section set has 171 neutron groups from 10^{-5} eV to 17.33 MeV and 36 gamma-ray groups from 10 keV to 14 MeV. The multigroup neutron cross sections were generated in MINX from ENDF/B-IV for a weighting function which consisted of a Maxwellian from 10^{-5} eV to 0.125 eV, a 1/E shape from there to 820.8 keV, a fission spectrum from 820.8 keV to 10 MeV, a 1/E shape from 10 to 12.57 MeV, a velocity exponential fusion peak from 12.57 to 15.57 MeV, and a 1/E shape above 15.57 MeV. Calculations were performed using infinitely dilute and self-shielded versions of the DLC-41. The self-shielding was done using the BONAMI code which implements the Bondarenko formalism.

Since the calculations done using the DLC-41 cross section set are large and costly, most leakage calculations for the ^{252}Cf, DT and DD sources were performed using the DLC-47 cross-section set which was collapsed to provide the 45-neutron and 16-gamma-ray multigroup DLC-47 cross section set. The DT distributed source was represented by the 13.50 to 14.19 MeV group and the DD distributed source by the 2.365 to 2.725 MeV group.

Results and Discussion

The DT leakage spectrum at the neutron detector location (45° from the deuteron beam) calculated by VIM with the reentrant hole defined exactly was in good agreement with the VIM results with no reentrant hole (one-dimensional calculation). The agreement for other neutron detector locations was not as good; this was the reason the detector location at 45° was selected for the neutron measurements. The leakage spectrum calculated with VIM which included the base and supports was also in good agreement with the one dimensional VIM results. These comparisons showed that the neutron spectrum at the neutron detector can be adequately predicted by a one-dimensional calculation. The VIM calculation of the leakage spectrum from the sphere incorporating the various impurities demonstrated that the effect of neglecting these impurities in the iron was also small.

^{252}Cf Source

The neutron leakage spectrum calculated using VIM and ANISN (self-shielded DLC-47) for the ^{252}Cf source is shown in Fig. 1. Above 2.5 MeV, the agreement is good; however, the VIM calculation suffers from statistical error at high neutron energies. Below 2.5 MeV, the VIM calculation predicts a higher neutron

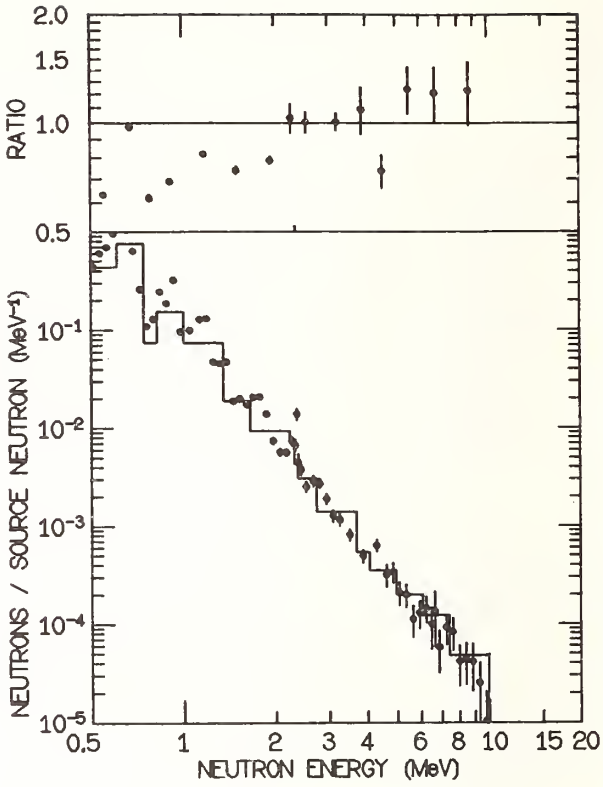

Fig. 1. Neutron leakage spectrum from the iron sphere for the ^{252}Cf source. The circles are the VIM results and the histogram is the ANISN results using DLC-47. The ratios of the ANISN to VIM results are plotted in the top portion of the figure for the DLC-47 group structure.

leakage. The results of the fine-group self-shielded DLC-41 calculation were in good agreement with the DLC-47 results shown here. Figure 2 shows the measured neutron leakage spectrum compared to the DLC-47 calculation. To facilitate this comparison, the calculated spectrum has been smoothed with the resolution used in FORIST to smooth the unfolded spectrum. These measured data agree well with the previous measurements made by Johnson.[15] However, they do not agree with the calculated results. Both the ANISN calculation and the VIM calculation significantly underpredict the measured leakage with the disagreements increasing for lower neutron energies. These results are tabulated in Table I.

The present results are in general agreement with previous results using cylindrical samples ("broomsticks") of iron at ORNL.[16] These "broomstick" experiments revealed disagreement between the measured and calculated transmitted fluxes between 1 and 5 MeV. The conclusion drawn from those discrepancies was that the average iron total cross section in ENDF/B-IV was about 4% high from 1 to 5 MeV. The results of the present work also indicate that a reassessment of the total cross section of iron below 5 MeV is warranted. These deficiencies in the evaluated total cross section are explained in part by errors in the cross sections for inelastic scattering exciting the first three discrete levels in iron. Cramer and Oblow observed that the evaluated inelastic scattering cross section in ENDF/B-IV is 30-100% too large for energies up to 1 MeV above the discrete inelastic level scattering thresholds.[17] Since the first three levels in iron are at 0.861, 1.43, and 2.12 MeV, the lowering of the inelastic cross section in the 1 to 5 MeV region would

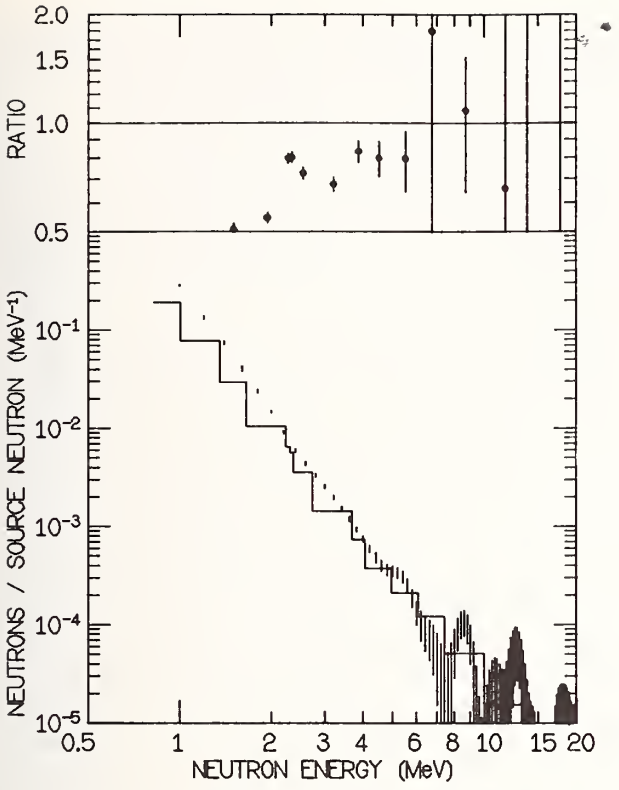

Fig. 2. Neutron leakage spectrum for the iron sphere and the ^{252}Cf neutron source. The ratio of the ANISN calculation (histogram) using the DLC-47 cross-section set to the measured leakage spectrum (± 1 standard deviation error bars) is shown in the upper plot. The calculation was smoothed with the resolution of the unfolded spectrum.

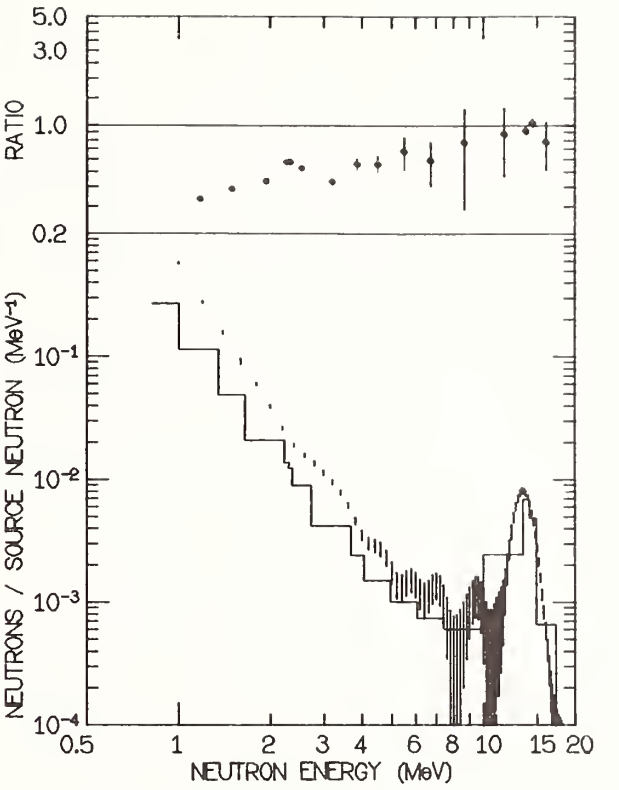

Fig. 3. Neutron leakage spectrum from the iron sphere for the DT neutron source including 5% DD contamination. The ratio of the ANISN calculation (histogram) using the DLC-47 cross-section set to the measured leakage spectrum (± 1 standard deviation error bars) is shown in the upper plot. The calculation was smoothed with the resolution of the unfolded spectrum.

improve the ability to predict the measured leakage spectrum.

The deficiency of the ANISN calculations as compared to the VIM calculations in the 1-2.5 MeV energy region also is the result of inadequate representation of the inelastic scattering cross section. The DLC-47 cross section set used in the ANISN calculation has self shielding applied only to the absorption and elastic scattering cross sections. As a result, the inelastic scattering cross section is too high in the vicinity of the inelastic scattering threshold.[10]

D-T Source

The measured DT neutron leakage spectrum for the iron sphere is compared to the ANISN calculation using DLC-47 in Fig. 3. The source for this ANISN calculation included DD neutron contamination equal to 5% of the DT source strength. This amount of DD contamination was determined to be present during the neutron leakage measurement by use of the associated particle system. However, this calculated leakage spectrum is not significantly different than the one calculated with the fine group DLC-41 assuming no DD contamination. Both ANISN calculations substantially underpredict the measured DT neutron leakage spectrum

Table I. Measured and ENDF/B-IV-calculated neutron leakage for the iron sphere containing the ^{252}Cf neutron source.

Energy Region (MeV)	Measurement (n/source n)	VIM[a] (n/source n)	ANISN,[a] DLC-47 (n/source n)
5 - 10	$(5.0 \pm 1.7) \times 10^{-4}$	$(4.4 \pm 0.5) \times 10^{-4}$	5.2×10^{-4}
2.23 - 5	$(5.6 \pm 0.2) \times 10^{-3}$	$(4.1 \pm 0.3) \times 10^{-3}$	4.1×10^{-3}
1.0 - 2.23	$(8.7 \pm 0.3) \times 10^{-2}$	$(5.2 \pm 0.1) \times 10^{-2}$	4.2×10^{-2}

[a]The calculations were smoothed with the resolution of the measurement (unfolded spectrum).

below 10 MeV, whereas the transmitted 14-MeV neutron peak is accurately predicted by these calculations.

The comparison of the DT neutron leakage spectrum calculated by VIM with that calculated by ANISN revealed an error in VIM. From approximately 10 MeV down in energy, the VIM results were consistently lower (20-30%) than the ANISN results. In the version of VIM ENDF/B-IV cross sections used, the second energy probability tables for continuum inelastic scattering and (n, 2n) events were generated for incident neutron energies up to only 10 and 11.4 MeV, respectively. In order to provide secondary distributions for continuum inelastic scattering, the VIM code extrapolated the data for an incident energy of 10 MeV to 14 MeV resulting in the underprediction of the leakage spectrum from 1 to 10 MeV. Hence, the discrepancy between these VIM and ANISN calculations shows that the results of this integral test are sensitive to inelastic scattering and (n, 2n) data.

Neutrons emitted in continuum inelastic scattering with iron nuclei are forward peaked particularly for neutrons emitted above 3 MeV.[19] However, the ENDF/-B-IV data treats continuum inelastic scattering as isotropic. To approximately incorporate the effect of anisotropy in continuum inelastic scattering for ENDF/-B-IV, an ANISN calculation was performed using a modified version of the DLC-47 cross-section set. The set was modified to include a P_1 component equal to one-half of the P_0 component at zero degrees for neutrons reacting at the source energy. The use of this modified DLC-47 cross section set decreases the discrepancies between the calculated and measured leakage spectra, however this reduction was small compared to that which would be necessary to bring them into even rough agreement. The DT leakage results are summarized in Table II. The number of neutrons calculated to leak from the sphere above 10 MeV using ENDF/B-IV data agrees well with the measured value. Between 5 and 10 MeV this calculation underpredicts the measured value; although the number calculated using the modified DLC-47 cross section set is in slightly better agreement with the measured value in this energy range, both calculations agree with the measurement within experimental error. However, all three calculations grossly underpredict the measured numbers of leakage neutrons in the two lower energy intervals in Table II.

The secondary energy distributions for continuum inelastic scattering and (n, 2n) events are averaged over their angular dependencies in the present ENDF/B-IV data. However, experimentally observed emitted neutron spectra for these reactions in iron[19] indicate that the temperature describing the secondary energy distribution of neutrons emitted in the forward directions is higher than that of neutrons emitted in the backward directions. Since forward scattered neutrons are more likely to escape from the iron sphere, calculations performed with the secondary neutron energy distribution averaged over all emission angles, such as those reported here, should be expected to underpredict the leakage spectrum due to the incorrect effective downward shift in energy of these neutrons. This effect is less important in smaller spheres, such as those used in the LLL pulsed sphere program,[20] since the leakages from them are less significantly affected by forward-scattered neutrons. A calculation which roughly takes into account the recoil energy of the iron nucleus and assumes that the ENDF/B-IV average emission spectrum corresponds to neutron emission at 90°, indicates that the low-energy part of the calculated leakage spectrum would shift upward in energy if these effects were included in the data, and that substantially better agreement between the calculated and measured leakage spectra would result. For example, the computed leakage value at 1 MeV would shift up in energy by about 0.27 MeV and the leakage value at 10 MeV would shift up in energy by about 0.4 MeV. Thus, the inclusion of a correlated angle-energy description for secondary neutrons emitted in continuum inelastic scattering and (n, 2n) events would result in a better prediction of the DT neutron leakage spectrum from the iron sphere. It is recommended that such a change be considered for inclusion in future evaluated nuclear data files.

Conclusions

Comparisons of neutron leakage spectra calculated using ENDF/B-IV data with measured neutron leakage spectra from an iron sphere have been made for a ^{252}Cf fission neutron and a DT fusion neutron source. The neutron leakage results for the ^{252}Cf source in the iron spherical shell showed that the ENDF/B-IV total cross section for iron is too high between 1 and 5 MeV. It was concluded that a poor representation of the inelastic level cross section just above the

Table II. Measured and ENDF/B-IV-calculated neutron leakage for the iron sphere containing the DT neutron source.

Energy Region (MeV)	Measurement (n/source n)	ANISN[a] (n/source n) DLC-41	DLC-47[b]	DLC-47[c]
> 10	$(2.0 \pm 0.1) \times 10^{-2}$	1.9×10^{-2}	1.9×10^{-2}	1.9×10^{-2}
5 - 10	$(5.3 \pm 2.2) \times 10^{-3}$	3.5×10^{-3}	3.7×10^{-3}	4.0×10^{-3}
2.23 - 5	$(2.3 \pm 0.1) \times 10^{-2}$	1.0×10^{-2}	1.1×10^{-2}	1.2×10^{-2}
1.0 - 2.23	$(1.9 \pm 0.1) \times 10^{-1}$	6.2×10^{-2}	6.7×10^{-2}	6.9×10^{-2}

[a] The calculations were smoothed with the resolution of the measurement (unfolded spectrum).

[b] Includes 0.05 DD neutron contamination per DT source neutron.

[c] The continuum inelastic cross sections in the DT source group were changed to have a P_1 component equal to 50% of the P_0 component.

thresholds for the first three levels contributes to this deficiency in the total cross section. The neutron leakage spectrum for the DT source in the iron spherical shell was greatly underpredicted by the calculations done using ENDF/B-IV. The effect of including the anistropy of inelastically scattered neutrons was investigated and found to account for only a small portion of this large discrepancy. It was concluded that a correlated angle-energy description of secondary neutrons emitted in continuum inelastic scattering and (n, 2n) events should be included in future evaluated nuclear data files for iron

Finally, the fact that the computations significantly underpredict the measured spectra in the 1 to 5 MeV region for both the ^{252}Cf and DT sources leads to the historic question of the adequacy of the measured and evaluated total cross section data in the energy regions of the cross section interference minima (windows) immediately below scattering resonances. The low impurity level, combined with the large shell-thickness of the sphere used in the present experiment, increases the significance of the contributions to the leakage spectra of neutrons which stream through portions of the shell at energies in the windows associated with narrow cross section minima. Deeper minima in the total cross section data in the 1 to 5 MeV region would directly increase the leakage calculated in this region in the VIM Monte Carlo calculations and indirectly increase it in the ANISN transport calculations through the self-shielding factors used in developing the multigroup cross section sets. Clearly other experiments, in which the impurity levels were higher than the very low values here and/or the shell thicknesses less than that of the very thick sphere used here, would be far less sensitive to such cross section minima.

References

1. D. J. Dudziak and D. W. Muir, "Review of Magnetic Fusion Energy Neutron Cross-Section Needs: Neutronics Viewpoint," Symposium on Neutron Cross Sections from 10-40 MeV, Brookhaven National Laboratory, May 3-5, 1977, BNL-NCS-50681, p. 59 (1977).

2. W. B. Wilson, "Nuclear Data Development and Shield Designs for Neutrons Below 60 MeV," LA-7159-T, Los Alamos Scientific Laboratory (1978).

3. R. H. Johnson, D. T. Ingersoll, B. W. Wehring, and J. J. Dorning, Nucl. Instr. Meth. 145, 337 (1977).

4. D. T. Ingersoll and B. W. Wehring, Nucl. Instr. Meth. 147, 551 (1977).

5. W. W. Engle, Jr., "A User's Manual for ANISN:A One Dimensional Discrete Ordinates Code With Anisotropic Scattering," K-1693, Oak Ridge National Laboratory (1967).

6. R. E. Prael and L. J. Milton, "A User's Manual for the Monte Carlo Code VIM," FRA-TM-84, Argonne National Laboratory (1976).

7. D. J. Garber and C. Brewster, "ENDF/B Cross Sections," BNL 17100(ENDF-200), 2nd ed., Brookhaven National Laboratory (1975).

8. D. Garber (compiled by), "ENDF-201: ENDF/B Summary Documentation," BNL 17541, 2nd ed., Brookhaven National Laboratory (1975).

9. R. J. Cerbone, J. E. Miller, and A. E. Profio, "Angular Neutron and Gamma-Ray Spectrum Measurements in a Bulk Iron Assembly," GA-9149, Gulf General Atomic, Inc. (1969).

10. R. J. Cerbone, "Reanalysis of the Neutron Spectrum Measurements in an Iron Bulk Assembly," Gulf-RT-A10859, Gulf Radiation Technology (1971).

11. N. E. Hertel, "High-Energy Neutron Transport Through Tungsten and Iron," Ph.D. Thesis, University of Illinois at Urbana-Champaign (1979).

12. R. H. Johnson, "A User's Manual for COOLC and FORIST," PNE-75-107, Department of Nuclear Engineering, Purdue Unviersity, (1975).

13. C. R. Weisbin, R. W. Roussin, E. M. Oblow, D. E. Cullen, J. E. White, and R. W. White, "The Role 'Standard' Fine-Group Cross Section Libraries in Shielding Analysis," Proceedings Fifth International Conference on Reactor Shielding, April 17-23, 1977, Knoxville, Tennessee, 742 (1977).

14. "BUGLE: Coupled 45 Neutron, 16 Gamma-Ray, P_3, Cross Sections for Studies by the ANS 6.1.2 Shielding Standards Working Group on Multigroup Cross Sections," DLC-47, Radiation Shielding Information Center, Oak Ridge National Laboratory (1977).

15. R. H. Johnson, J. J. Dorning, and B. W. Wehring, Trans. Am. Nucl. Soc. 22, 799 (1975).

16. E. M. Bohn, R. E. Maerker, F. J. McCrosson, R. J. LaBauve, B. A. Macqurno, and R. E. Schenter, "Benchmark Experiments for Nuclear Data," Proceedings Conference on Nuclear Cross Sections and Technology, Washington, D.C., March 3-7, 1975, NBS Special Publication No. 425.

17. S. N. Cramer and E. M. Oblow, "Analysis of a Neutron Scattering Experiment on Iron for Neutron Energies from 1 to 15 MeV," ORNL-TM-5548 (1976).

18. N. E. Hertel, B. W. Wehring, and R. H. Johnson, "Comparison of VITAMIN-C Master Library Reaction Cross Sections for Iron with Multi-group Cross Sections Generated by the VIM Monte Carlo Code," Proceedings RSIC Multigroup Nuclear Cross-Section Preparation and Data Manipulation Techniques Seminars-Workshop, ORNL/RSIC-41, March 14-16, 1978, Oak Ridge, Tennessee (1978).

19. O. A. Sal'Nikov, G. N. Lovchikoya, G. V. Kotel' Nikova, V. S. Nesterenko, N. I. Fetisov, and A. M. Trufanov, Soviet J. Nucl. Phys. 12, 620 (1971).

20. Y. F. Hansen, C. Wong, and T. Komoto, and J. D. Anderson, Nucl. Sci. Engr. 60, 27 (1976).

NEUTRON ENERGY SPECTRA IN THE FAST BREEDER BLANKET FACILITY

D. W. Vehar, R. H. Johnson and F. M. Clikeman
School of Nuclear Engineering
Purdue University
West Lafayette, Indiana 47907, USA

Neutron energy spectra have been measured for the initial loading of the FBBF, in the energy range from 1 keV to 3 MeV and for radii of 0.385, 0.563 and 0.711 m. Hydrogen- and methane-filled proton-recoil detectors are used for the measurements. Energy spectra are calculated using the two-dimensional diffusion code 2DB and a self-shielded cross section set based on ENDF/B-IV. Measured and calculated spectra are compared on an absolute basis for a source strength of 10^{10} neutrons per second. The calculations overpredict the measured total flux between 1 keV and 3 MeV at a radius of 0.385 m and underpredict it at a radius of 0.711 m. Thus, the calculated flux decreases with radius more rapidly than the measured flux. The shape of the neutron spectrum is predicted reasonably well at all three radii, although less structure is seen in the calculations due to the large energy group widths.

[Fast reactor, Fast Breeder Blanket Facility, neutron spectrum, proton-recoil, calculated neutron spectrum, 2DB]

Introduction

The Fast Breeder Blanket Facility (FBBF) is a subcritical facility designed to test mock-ups of fast breeder reactor blankets.[1] The experiments are designed to provide information about reaction rates, neutron energy spectra and gamma-ray energy deposition rates as a function of position in the blanket. Comparisons between calculations and experiments should serve as a test of both the calculational methods and the cross sections used for the calculations. Measurements of neutron energy spectra are useful in verifying the calculational methods and aiding in the investigation of any discrepancies between calculations and measurements of integral data. Proton-recoil proportional counting is the method best suited for measurements in the FBBF due to the small size and relatively fine resolution of the detectors. Although the energy range for which proton-recoil gas-filled detectors is limited to approximately 1 keV to 3 MeV, this is the most significant region of the neutron energy spectrum.

Facility Description

A view of the FBBF is shown in Figure 1. At the center of the cylindrical facility are four Cf-252 spontaneous fission sources, each containing approximately 1 mg of Cf-252, and spaced so as to approximate a cosine distribution. The total source strength is approximately 10^{10} neutrons per second. The source rod is lowered into a concrete storage cask below the facility when it is not in operation.

Surrounding the source region are inner and outer transformer regions for shaping the energy spectrum of neutrons from the Cf-252 sources. The neutron energy spectrum at the outer radius of the transformer regions (0.22 m) closely matches that at the core-blanket interface of a commercial LMFBR. The inner transformer contains stainless-steel clad, 4.8 percent enriched fuel rods in a close-packed hexagonal array. The inner transformer has an inner and outer radius of 0.025 and 0.16 m, respectively, and an active height of 0.91 m (3 feet). The outer transformer contains the same type of fuel, but on a wider pitch. Sodium in stainless-steel cans is placed between the rods. The remaining spaces in both transformer regions are filled with boron carbide powder.

The initial loading for the FBBF consists of a two-region blanket, with outer radii of 0.57 and 0.74 m. The fuel is aluminum-clad natural UO_2 fuel rods with an active length of 1.22 m (4 feet). Each fuel rod in the inner blanket is placed in a secondary cladding of stainless steel. The rods are loaded in a close-packed hexagonal array. Number densities of materials in the inner blanket are comparable to those of current LMFBR blankets, with the exception of aluminum, which was substituted for sodium. In the outer blanket, the secondary cladding is aluminum. Since the outer blanket contains only aluminum and natural UO_2, somewhat cleaner experiments are permitted. A carbon-steel and NaCl reflector surrounds the blanket regions.

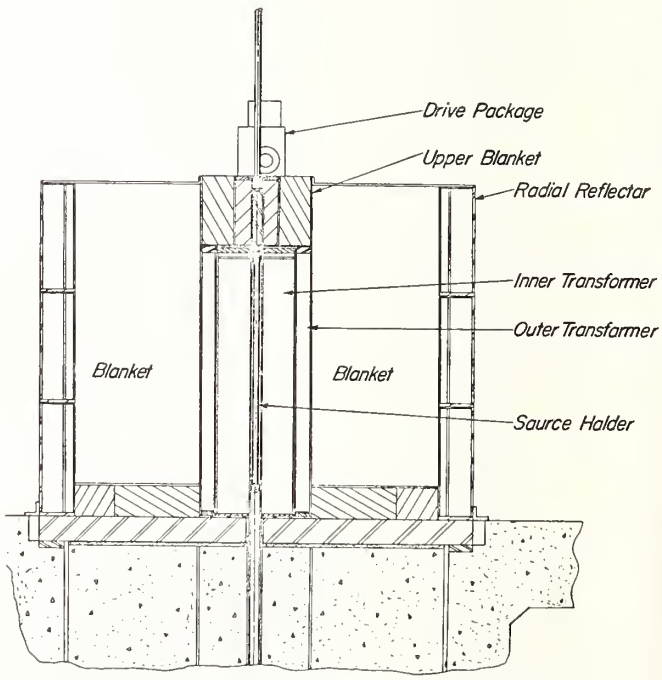

Figure 1. Cross Sectional View of the FBBF

Calculations

Calculated spectra were obtained for the FBBF using the two-dimensional diffusion code 2DB.[2] Region-dependent cross sections for the calculation were generated using the one-dimensional diffusion code 1DX.[3] Resonance self shielding is treated in 1DX by the Bondarenko self-shielding factor method. An external source option was added to the 1DX code to allow the use of a multiregion one-dimensional model of the FBBF.[4] Region-dependent weighting spectra were used to collapse cross sections to 30 energy groups from the 50-group DLC-40/LIB-IV cross section

library.[5] The two-dimensional (R-Z) diffusion calculation was done using a 15-region model in 30 energy groups.

Measurements

Neutron energy spectra were measured using proton-recoil proportional counters. The detector and preamplifiers used were designed to fit inside metal tubing with an inner diameter of 15.3 mm. Thus, only one fuel rod must be removed from the blanket to accommodate the detector and preamplifier. Two hydrogen-filled proportional counters (with different fill gas pressures) and one methane-filled detector are used for the measurements. The three detectors are cylindrical and identical in construction except for the fill gas. The active length of the detector is 25.4 mm (1 inch) with an outside diameter of 12.7 mm (0.5 inch) and a wall thickness of 0.89 mm (0.035 inch). Two-parameter analysis is used for measurements with the hydrogen detectors to distinguish between neutron and gamma-ray events in the detector.[6] The methane detector can be used without gamma-ray discrimination, and single-parameter analysis is used. Neutron spectra are obtained from the proton-recoil data by differential unfolding with the PSNS-N data reduction codes.[7] The PSNS-5 code which actually does the differential unfolding has been rewritten to incorporate a different method of numerical differentiation.[8]

Results

Neutron energy spectra have been measured in the FBBF blanket at radii of 0.385, 0.563 and 0.711 m at a height of 0.460 m above the bottom of the active fuel. This corresponds to the midplane of the transformer region. Figures 2-4 show measured and calculated spectra for each of the three radii. The data are presented on an absolute basis for a neutron source strength of 10^{10} neutrons per second. The experimental data is presented in the figures as vertical bars representing ± one standard deviation statistical error. The systematic errors are not shown, but are estimated to be about 5 percent. Sources of systematic error include the neutron source strength (approximately 3 percent), detector sensitivity (less than 1 percent) and energy calibration errors (less than 0.5 percent). Errors in energy calibration will affect the magnitude of the neutron flux per unit lethargy by the same percentage.

The calculation overpredicts the magnitude of the measured spectrum at 0.385 m by about 30 percent, with the calculation yielding a very slightly softer spectrum. The calculated spectrum shows a dip in group 12 (24.78 - 40.87 keV) corresponding to the 28 keV iron and 35 keV aluminum resonances, and a dip in group 7 (301.97 - 497.87 keV) corresponding to the 440 keV oxygen resonance. The group structure in the calculated spectrum is too coarse, however, to show the other resonances of aluminum and oxygen. At a radius of 0.563 m, the calculation again overpredicts the experimental spectrum, but only by about 12 percent. The calculated spectrum is slightly softer than the experimental spectrum. At a radius of 0.711 m, the calculation underpredicts the experiment by about 9 percent, with the calculated spectrum again softer than the experimental spectrum. It is seen from the figures that the calculation in general predicts a slightly softer spectra than actually measured. In addition, the magnitude of the calculated flux falls off more rapidly than the experimental, although it starts out higher in the inner portion of the blanket. The softening of the spectrum with blanket radius is readily apparent.

Figures 5-7 compare the 2DB calculated spectra with the experimental spectra collapsed to the 30-group structure. The agreement between the calculation and experiment in the shape of the spectra is more easily seen.

The 2DB diffusion code with the present cross section set does a reasonable job of predicting neutron energy spectra in the FBBF blanket. It has problems, however, with the magnitude of the flux. The reasons for this have not been fully resolved.

Acknowledgements

The authors wish to acknowledge the U.S. Department of Energy and the Electric Power Research Institute for the funds for the construction and operation of the Fast Breeder Blanket Facility.

References

1. K.O. Ott, F.M. Clikeman, P.J. Fulford, R.C. Borg, R.H. Johnson and O.H. Gailar, "The Purdue University Fast Breeder Blanket Facility," Proc. ANS Topical Meeting on Advances in Reactor Physics, p. 505, Gatlinburg, Tennessee, April 9-12, 1978, CONF-780401 (1978).

2. W.W. Little, Jr. and R.W. Hardie, "2DB User's Manual -- Revision 1," Battelle Northwest Laboratory, BNWL-821-REV1 (1969).

3. R.W. Hardie and W.W. Little, Jr., "1DX, A One-Dimensional Diffusion Code for Generating Effective Nuclear Cross Sections," Battelle Pacific Northwest Laboratories, BNWL-460 (1968).

4. R.C. Borg, R.H. Johnson and M.P. Sohn, "Cross Section Preparation," FBBF Quarterly Progress Report for the Period April 1, 1978 - June 30, 1978, p.8, Purdue University, COO-2826-9 (1978).

5. R.B. Kidman and R.E. MacFarlane, "LIB-IV, A Library of Group Constants for Nuclear Reactor Calculations," Los Alamos Scientific Laboratory, LA-6287-MS (1976).

6. D.W. Vehar and F.M. Clikeman, "Proton Recoil Proportional Counter Measurements," FBBF Quarterly Progress Report for the Period January 1, 1979 - March 30, 1979, pp.4-11, Purdue University, COO-2826-12 (1979).

7. E.F. Bennett and T.J. Yule, "Techniques and Analysis of Fast Neutron Spectroscopy Proton-Recoil Proportional Counters," Argonne National Laboratory, ANL-7763 (1971).

8. R.H. Johnson and D.W. Vehar, "Neutron Spectrum Unfolding," FBBF Quarterly Progress Report for the Period January 1, 1979 - March 30, 1979, pp.12-13, Purdue University, COO-2826-12 (1979).

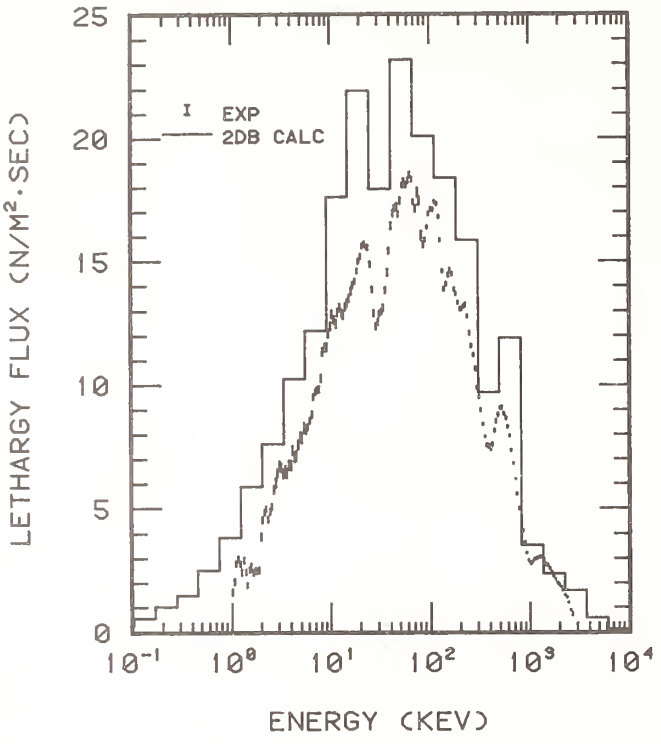

Figure 2. Neutron energy spectrum at a radius of 0.385 m.

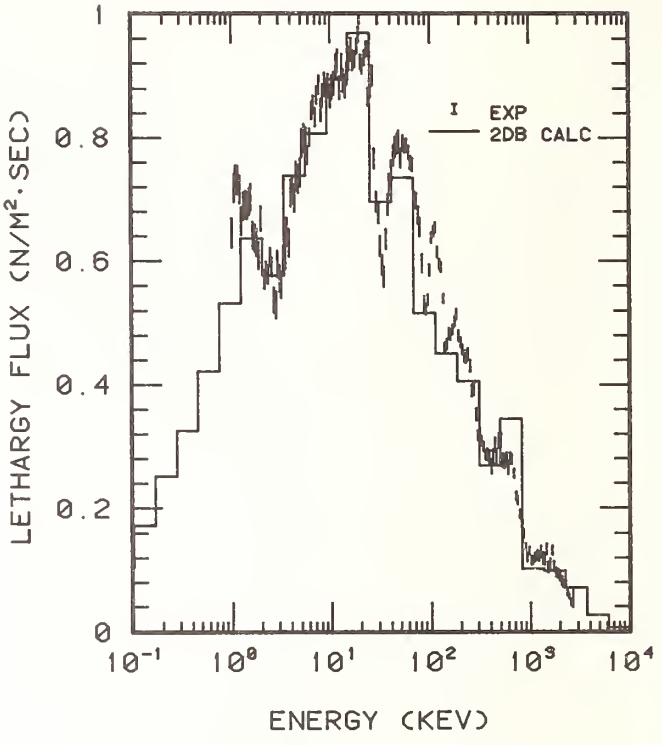

Figure 4. Neutron energy spectrum at a radius of 0.711 m.

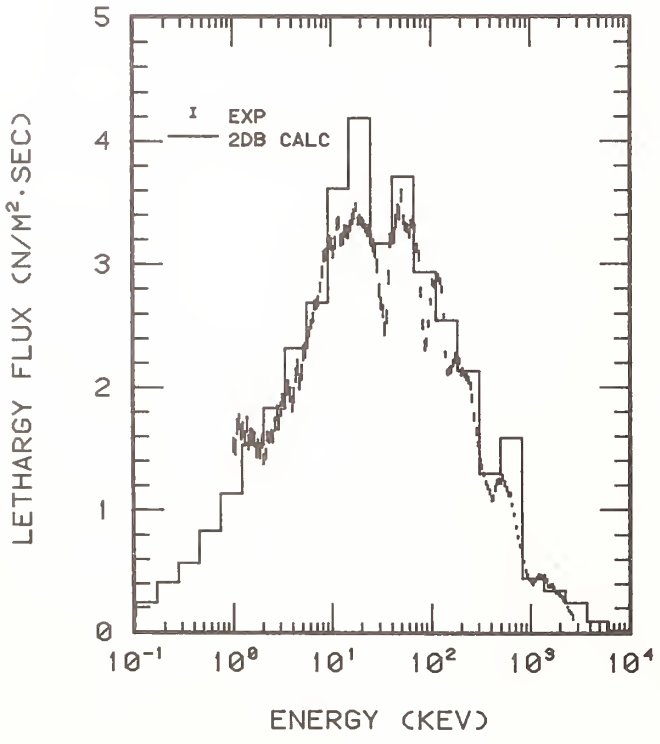

Figure 3. Neutron energy spectrum at a radius of 0.563 m.

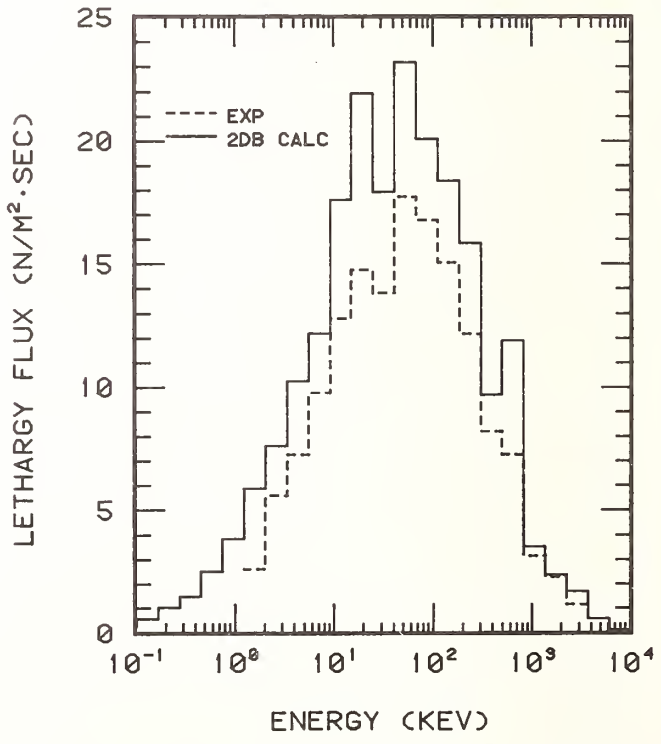

Figure 5. Neutron energy spectrum at a radius of 0.385 m, collapsed experimental spectrum.

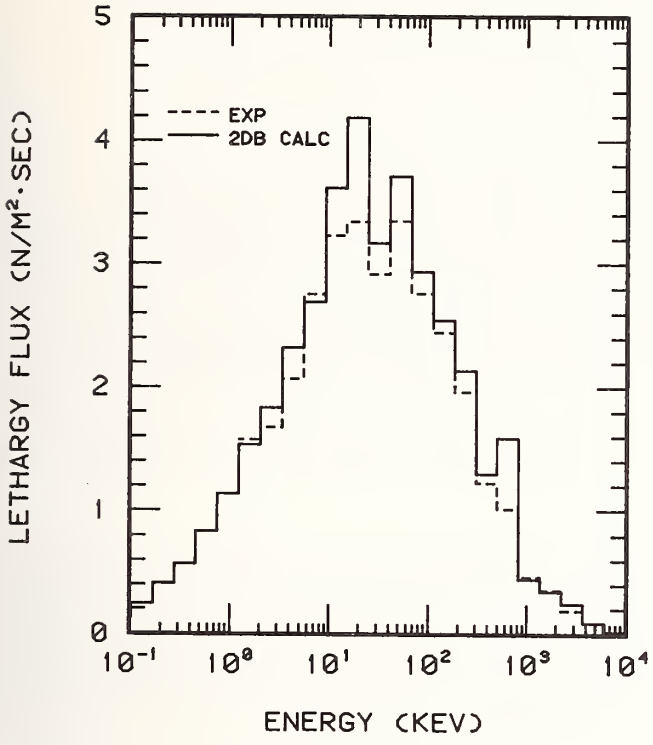

Figure 6. Neutron energy spectrum at a radius of 0.563 m, collapsed experimental spectrum.

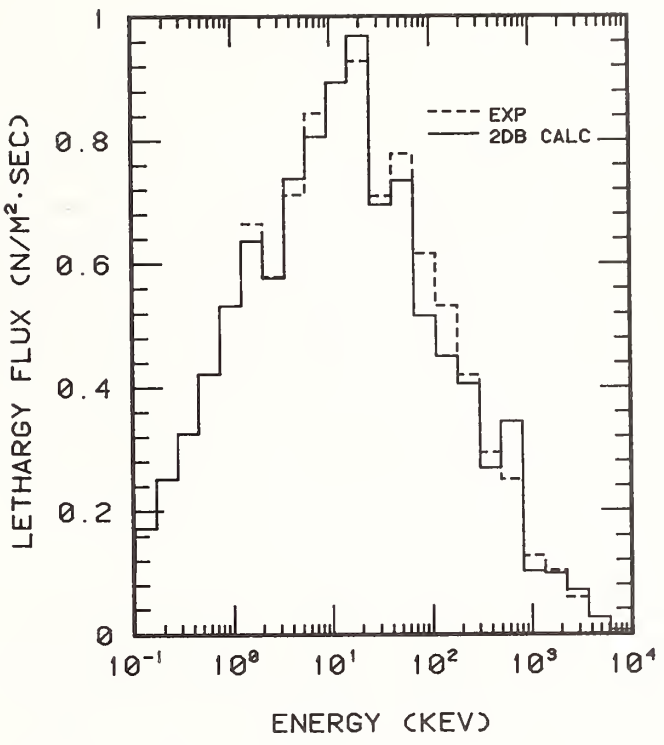

Figure 7. Neutron energy spectrum at a radius of 0.711 m, collapsed experimental spectrum.

^{238}U AND ^{232}TH CAPTURE RATES IN THE FBBF

G. A. Harms, F. M. Clikeman
R. H. Johnson, R. C. Borg
and K. O. Ott
School of Nuclear Engineering
Purdue University
West Lafayette, Indiana 47907, USA

The Fast Breeder Blanket Facility (FBBF) is designed to test mock-ups of fast reactor blankets. The FBBF currently has a two-region blanket consisting of natural UO_2, aluminum, and stainless steel. Neutron capture rates for ^{238}U, ^{232}Th, ^{197}Au, and ^{55}Mn were measured at the midplane of the FBBF. A two-dimensional diffusion calculation of reaction rates in the facility was performed and the results compared with the measurements. The C/E values range from 0.99 to 0.57 for ^{238}U, 0.97 to 0.89 for ^{232}Th, 0.95 to 0.85 for ^{197}Au, and 1.21 to 0.88 for ^{55}Mn. The calculation agreed well for materials not present in the FBBF (^{232}Th and ^{197}Au) but diverged for ^{238}U and ^{55}Mn which are significant constituents of the facility. An independent Monte Carlo calculation gave ^{238}U capture rates that agree well with the experimental results.

[fast reactors, blankets, breeding, capture rates, Fast Breeder Blanket Facility, foil activation]

Introduction

The Purdue University Fast Breeder Blanket Facility[1] (FBBF) is a subcritical, cylindrically-symmetric facility designed to test mock-ups of the blanket regions of commercial fast breeder reactors. The FBBF is driven in its central region by four discrete ^{252}Cf sources spaced on the axis of the facility to simulate a chopped-cosine distribution. The total neutron source rate is approximately 10^{10} neutrons per second. The source is surrounded radially by a two-region transformer that modifies the spontaneous fission neutron spectrum of the ^{252}Cf sources to one that closely approximates the spectrum at the core-blanket interface of a comercial fast breeder reactor. The outer radius of the transformer is 0.22 m. The transformer is surrounded by the blanket region. The current blanket loading has two regions of outer radii 0.57 m and 0.74 m. The inner blanket consists of natural UO_2 fuel rods clad in aluminum with a secondary cladding of stainless steel. The outer blanket also consists of aluminum-clad natural UO_2 fuel rods but with a secondary cladding of aluminum. The outer blanket is surrounded by a carbon steel and sodium chloride reflector of outer radius 0.89 m.

Measurements

A number of fuel rod locations contain removable experimental rods. These locations are identical in every other respect to ordinary rod locations. Special rods were fabricated with removable ends to allow the placement of experimental assemblies between the fuel pellets of these rods. Single foils ranging in thickness from 0.03 mm to 0.13 mm were used to measure activation rates in the FBBF. Gold and thorium foils were placed inside stainless steel covers with a wall thickness of 0.7 mm and overall length of 1.9 mm. Depleted uranium and manganese-copper foils were used without covers. The foil assemblies were then placed at the axial midplane of the FBBF. After irradiation, the foils were removed and counted for neutron capture product activity.

Two counting systems are available: an end-well NaI(Tl) system and a Ge(Li) system. Data acquisition and analysis for the Ge(Li) detector was performed using a Canberra Scorpio 3000 system. The Ge(Li) system was calibrated for energy and absolute efficiency using a mixed radionuclide source and a ^{152}Eu source, both supplied by the National Bureau of Standards. Foils irradiated in the FBBF were counted on the face of the Ge(Li) detector and corrected for geometrical effects by counting a foil at the face of the detector and at a distance of 105 mm from the detector face. Foils with two or more radioactive isotopes present were counted only with the Ge(Li) system. Foils in which a single radioactive nuclide was produced were counted with the NaI(Tl) system and this system cross-calibrated with the Ge(Li) system.

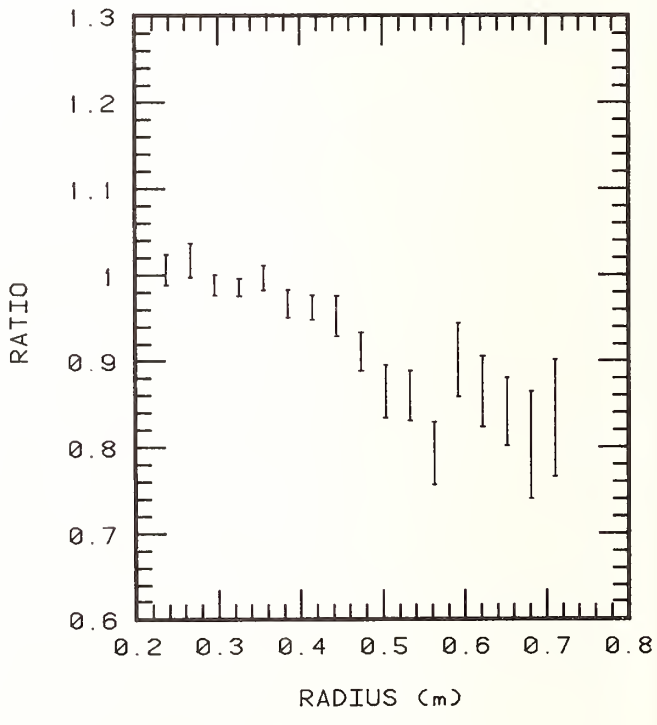

Fig. 1. Ratio of diffusion to Monte Carlo calculations for ^{238}U capture.

The neutron capture rates for the following reactions were measured in the FBBF:

$$^{238}U(n,\gamma)^{239}U \rightarrow ^{239}Np \rightarrow ^{239}Pu$$

$$^{232}Th(n,\gamma)^{233}Th \rightarrow ^{233}Pa \rightarrow ^{233}U$$

$$^{197}Au(n,\gamma)^{198}Au \rightarrow ^{198}Hg$$

$$^{55}Mn(n,\gamma)^{56}Mn \rightarrow ^{56}Fe.$$

The gamma-ray energies, isotopes, and photon yields used are as follows:

1. Uranium- 277.6 keV ^{239}Pu peak, 0.141 ± 0.004 photons per decay[2]
2. Thorium- 311.9 keV ^{233}U peak, 0.36 ± 0.02 photons per decay[3]
3. Gold- 411.8 keV ^{198}Hg peak, 0.955 ± 0.001 photons per decay[4]
4. Manganese- 846.8 keV ^{56}Fe peak, 0.989 ± 0.003 photons per decay.[5]

A more recent measurement of the ^{233}Pa photon yield of 0.386 ± 0.005 photons per decay was reported by Gehrke et. al.[6] The values taken from Refs. 2-5 were used, however, to obtain the results given below. The absolute capture rate for the reaction of interest was calculated from the absolute foil activity and foil irradiation history. The reaction rates were normalized to a neutron source rate of 10^{10} neutrons per second for comparison with the calculations.

Calculations

A two-dimensional 30-group diffusion calculation was performed using the code 2DB.[7] A homogenized 15-region model of the facility was used for the calculation. The active midplane of the facility crosses six regions of the model: the source, inner transformer, outer transformer, inner blanket, outer blanket, and reflector. The remaining 9 regions contain only structural materials at the upper or lower axial extremes of the facility. The 50-group library DLC-40/LIB-IV[8] was collapsed using the code 1DX,[9] a one-dimensional diffusion code for generating nuclear group constants. 1DX employs the Bondarenko method of treating resonance self-shielding.

A continuous-energy Monte Carlo calculation of the FBBF was performed using the code VIM.[10] to reduce the running time of the problem, the active regions of the facility were treated as a series of homogenized concentric cylinders. Reaction rates were available from this calculation only for the materials present in the FBBF. Figure 1 shows the ratio of the diffusion calculation to the Monte Carlo calculation for the reaction $^{238}U(n,\gamma)^{239}U$. The two calculations agree well through the first third of the inner blanket (to a radius of about 0.35 m) beyond which the ratio declines to 0.83 at the outer experimental position of the blanket. The minimum value of 0.79 occurs at the interface between the inner and outer blankets.

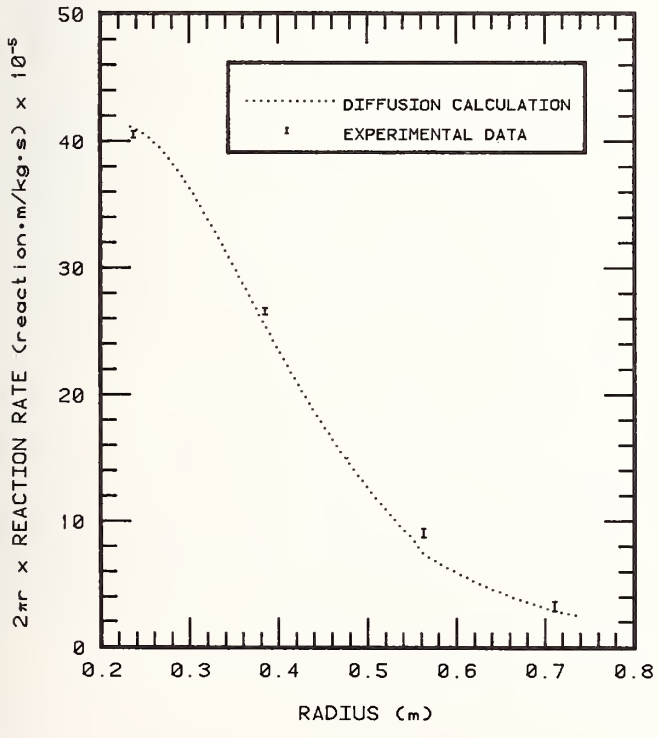

Fig. 2. Diffusion calculation and preliminary experimental results for ^{238}U capture.

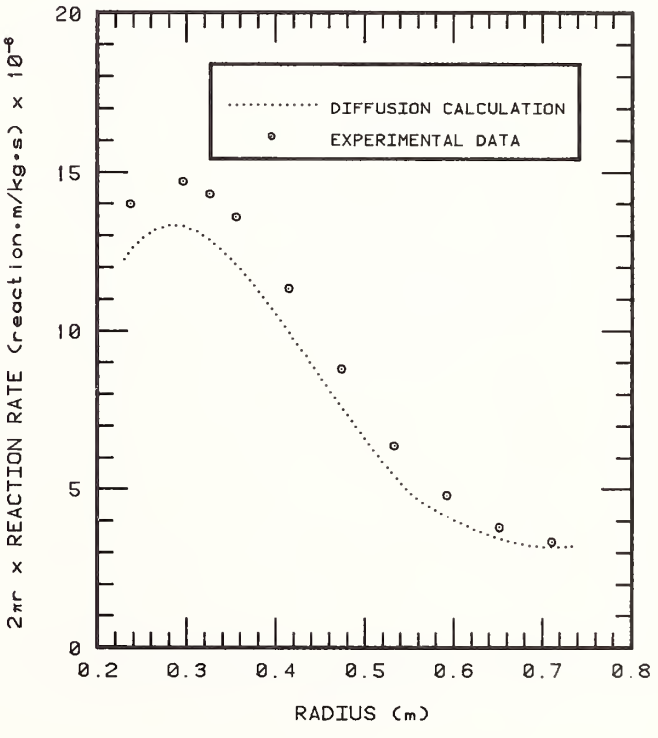

Fig. 3. Diffusion calculation and preliminary experimental results for ^{197}Au capture.

Results

The capture rate for the ^{238}U capture reaction is shown in Fig. 2. The curve indicates the result of the diffusion calculation and the symbols indicate the preliminary experimental data. The error bars shown in this and the following figures include only statistical errors at one standard deviation from the counting process. Systematic error in the calibration of the counting system is about 4% and the errors in the gamma-ray yields used are given above. The uncertainty in the neutron source strength is 3%. A similar plot for the ^{198}Au capture reaction is shown in Fig. 3. In this case, the statistical error is smaller than the symbols used.

The ratio of the reaction rates calculated by the diffusion code to the experimentally determined rates for the capture reactions of ^{197}Au, ^{232}Th, ^{238}U, and ^{55}Mn are shown in Figs. 4 through 7. The error bars shown account only for statistical errors in the counting process. The C/E values for gold and thorium, elements that are not constituents of the FBBF, show less than 10% deviation across both blankets. Neither data set shows a consistent trend across the blanket. The C/E values for manganese, which is present in the stainless steel in the facility, show a downward trend across both blankets from 1.21 at the transformer-blanket interface to 0.88 at the blanket-reflector interface. The C/E values for ^{238}U indicate good agreement between calculations and measurements at the transformer-blanket interface but show a radial dependence similar to the manganese values. Figure 8 shows the ratio of the Monte Carlo results to the experimental results for the ^{238}U capture reaction. Though the combined errors of the calculation and experiment are large, the C/E values fall within the quoted statistical error of unity.

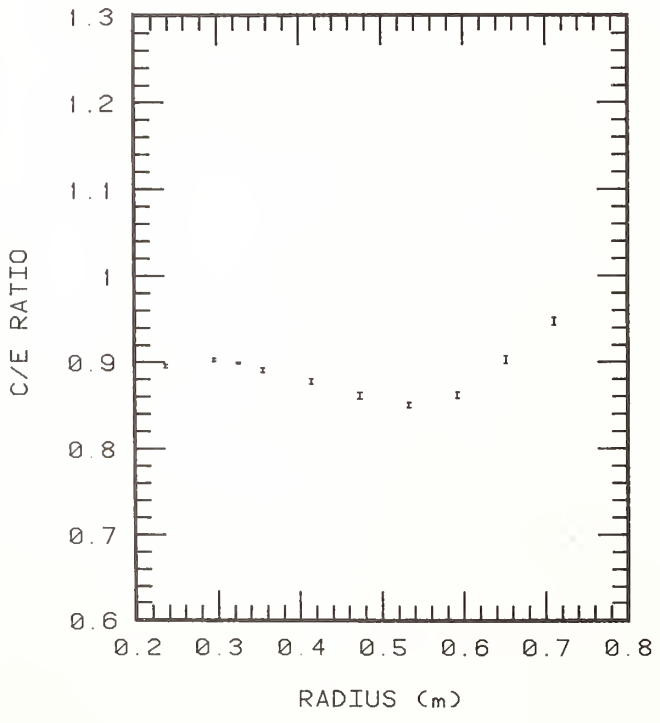

Fig. 4 Ratio of diffusion calculation to preliminary experimental results for ^{197}Au capture.

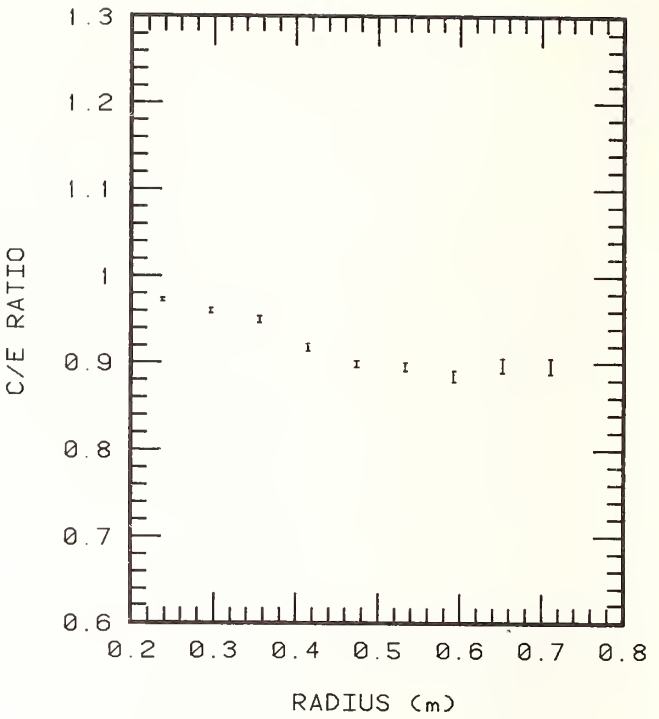

Fig. 5. Ratio of diffusion calculation to preliminary experimental results for ^{232}Th capture.

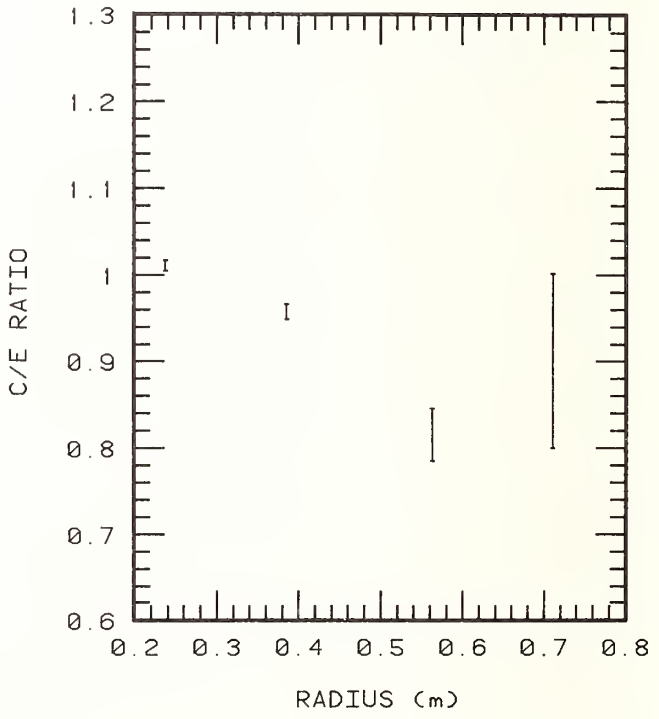

Fig. 6. Ratio of diffusion calculation to preliminary experimental results for ^{238}U capture.

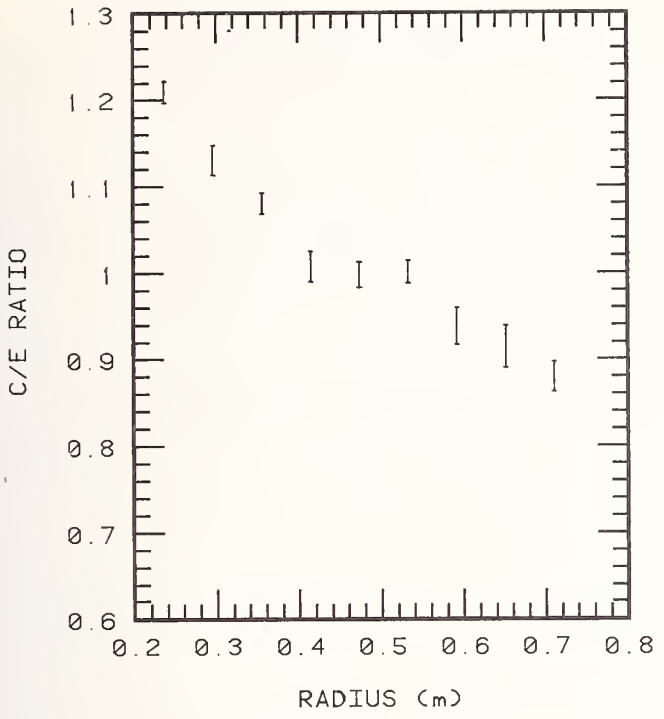

Fig. 7. Ratio of diffusion calculation to preliminary experimental results for ^{55}Mn capture.

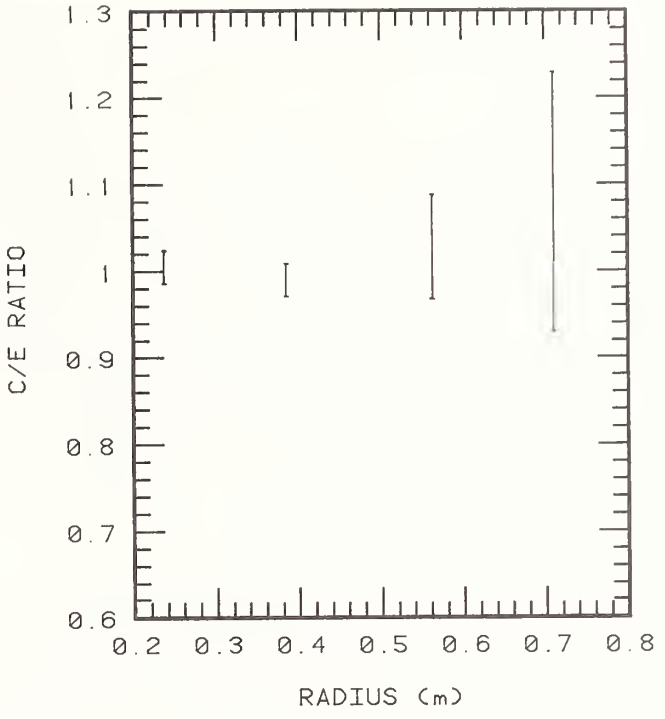

Fig. 8. Ratio of Monte Carlo calculation to preliminary experimental results for ^{238}U capture.

Conclusions

The diffusion calculation predicts the capture rates for ^{197}Au and ^{232}Th, materials present in the FBBF only as foils, with reasonable accuracy. The diffusion calculation of the ^{55}Mn and ^{238}U capture rates, both constituents of the facility, diverge substantially from the measured capture rates. The Monte Carlo calculation predicts the ^{238}U capture rate within statistical error. These preliminary results would indicate that multigroup diffusion theory, even with group constants generated specifically for the blanket, is inadequate to accurately predict neutron capture rates in the blanket regions of fast reactors.

Acknowledgments

The authors wish to acknowledge the U. S. Department of Energy and the Electric Power Research Institute for the funds for the construction and operation of the Fast Breeder Blanket Facility.

References

1. K. O. Ott, F. M. Clikeman, P. J. Fulford, R. C. Borg, R. H. Johnson and O. H. Gailar, "The Purdue University Fast Breeder Blanket Facility," Proc. ANS Topical Meeting on Advances in Reactor Physics, p. 505, Gatlinburg, Tennessee, April 9-12, 1978, CONF-780401 (1978).

2. M. R. Schmorak, Nucl. Data Sheets, 21, 153 (1977).

3. Y. A. Ellis, Nucl. Data Sheets, 24, 289 (1978).

4. B. Harmatz, Nucl. Data Sheets, 21, 377 (1977).

5. R. L. Auble, Nucl. Data Sheets, 20, 253 (1977).

6. R. J. Gehrke, R. G. Helmer and C. W. Reich, Nucl. Sci. Eng., 70, 298 (1979).

7. W. W. Little, Jr. and R. W. Hardie, "2DB User's Manual -- Revision 1," Battelle Northwest Laboratory, BNWL-821-REV1 (1969).

8. R. B. Kidman and R. E. MacFarlane, "LIB-IV, A Library of Group Constants for Nuclear Reactor Calculations," Los Alamos Scientific Laboratory, LA-6260-MS (1978).

9. R. W. Hardie and W. W. Little, Jr., "1DX, A One-Dimensional Diffusion Code for Generating Effective Nuclear Cross Sections," Battelle Pacific Northwest Laboratories, BNWL-954 (1969).

10. R. E. Prael and L. J. Milton, "A User's Manual for the Monte Carlo Code VIM," Argonne National Laboratory, FRA-TM-84 (1976).

GAMMA-RAY HEATING IN THE FAST BREEDER BLANKET FACILITY

K.R. Koch, F.M. Clikeman, and R.H. Johnson
School of Nuclear Engineering
Purdue University
West Lafayette, Indiana 47907, USA

Gamma-ray heating rates in both stainless steel and lead have been measured in the Fast Breeder Blanket Facility using CaF_2:Dy thermoluminescent dosimeters. The TLD responses in stainless steel or lead holders were corrected by applying spectral-weighted f-factors. Corrections for neutron responses were based on CaF_2 TLD neutron sensitivities. Radial experimental heating rates are presented and have been compared to results of a radial calculation performed as three seperate steps: a neutron diffusion calculation, a distributed gamma-production calculation and a gamma-ray transport calculation. The calculation underestimates the gamma-ray heating by 20% and 42% in stainless steel and by 1% and 32% in lead at the smallest and largest blanket radii respectively. The use of the multigroup method in blanket calculations seems to cause underestimations of several nuclear parameters in the outer blanket of the Fast Breeder Blanket Facility.

[fast breeder reactors, blankets, FBBF, gamma-ray heating, thermoluminescent dosimeters, TLD, CaF_2:Dy]

Introduction

Gamma-ray heating rates have been measured in the blanket regions of the Fast Breeder Blanket Facility[1] (FBBF) using CaF_2:Dy thermoluminescent dosimeters (TLD's). The gamma-ray heating rates have been measured in both stainless steel and lead for radial and axial traverses through the first blanket loading of the FBBF. These gamma-ray heating measurements have been made concurrently with measurements of neutron spectra, neutron capture rates, and fission rates, thus allowing intercomparisons of the various measurements and the calculations to provide a well-studied fast breeder blanket. The goal of these experiments is to identify and resolve the shortcomings of blanket calculations.

Facility Description

The FBBF is a cylindrical subcritical assembly which was designed and built at Purdue University to mock-up the blanket neutronics of a fast breeder reactor. A major benefit of the subcritical design is that it allows reproducible measurements which can be compared with calculations on an absolute basis. The assembly is 1.78 m in diameter by 1.45 m in height and consists of two transformer regions containing a neutron source surrounded by an inner blanket, an outer blanket, and a 0.15 m thick steel and sodium reflector. The transformer regions are designed to modify the fission spectrum of the 10^{10} neutrons per second ^{252}Cf source so that the neutron spectrum at the interface with the inner blanket matches the spectrum at the core-blanket interface of an LMFBR. The inner transformer has an outer radius of 0.16 m and the outer transformer has an outer radius of 0.22 m and encircles the inner transformer. Both transformer regions are 1.1 m in height and consist of 4.8% enriched UO_2 fuel rods clad in stainless steel. In addition, the outer transformer has sodium-filled stainless-steel tubes in the interstitial voids.

The two blanket regions are 1.22 m in height and consist of aluminum-clad natural UO_2 fuel rods spaced on a close hexagonal pitch. The inner blanket has a secondary cladding of stainless steel around the fuel rods and the outer blanket has a secondary cladding of aluminum. The inner blanket has an inner radius of 0.22 m and an outer radius of 0.56 m; the outer blanket has inner and outer radii of 0.56 m and 0.74 m. Throughout the blanket, experimental fuel rods are located on radial rays and azimuthal rings. These experimental fuel rods can be disassembled to allow the insertion of experiments directly between the 13.9 mm diameter fuel pellets.

Experiment

TLD Sensitivity

Gamma-ray dose measurements were made with 3.2 mm x 3.2 mm x 0.89 mm CaF_2:Dy TLD chips (TLD-200)[2] and a Harshaw model 2000A - 2000B TLD reader. During preliminary studies of the thermoluminescence characteristics of TLD-200, it was found that reproducible results could be obtained only if a fixed readout schedule was stringently followed. The readout schedule that was used consisted of a fixed fading time of 24 hours between exposure and readout, careful reproduction of TLD reader settings and dark current, and a fixed 3 minute time interval between the starting times of sequential TLD readouts. This readout schedule yielded reproducible responses for the CaF_2 TLD's. Other factors affecting reproducibility are consistency of annealing times and temperatures and the cleanliness and handling of the TLD chips.

A set of 120 TLD chips from a single production batch were used for the gamma-ray dose measurements. The entire 120 chip set was studied for its response characteristics to cobalt-60 gamma rays. Four chips had extremely low responses compared to the rest of the set; they were eliminated and later found to be thinner than the nominal 0.89 mm thickness. The remaining chips had a range of sensitivities with a standard deviation of 4.8%. In addition, each TLD chip had a relative position within the range of responses that was reproducible within statistics. As a result of this information, the set of 116 chips was divided in half at the median of the sensitivities to form two sets of higher precision. The TLD's of each of the two sets were then assigned correction factors normalizing each TLD's response to the set's mean response. These two sets, known as precision sets, had standard deviations of 2.8% for the corrected responses.

The two precision sets were calibrated in the dose range of 0.008 to 0.750 joules per kilogram using a cobalt-60 irradiation facility. The exposure of each calibration run was measured using a gamma-ray exposure-rate meter and an ionization chamber. The measured exposures were accurate to 2% statistical

error and 3% systematic error. Several TLD's from each precision set were exposed simultaneously so that averaged responses of higher precision could be obtained. The TLD's were exposed through a 6.4 mm thick acrylic plastic sheet at several different exposures. The resulting dose versus response curve for each precision set was extremely linear over the calibrated range and was fit to a line forced through the origin using an iterative double-error least-squares method. The resulting fits were extremely good with statistical errors of only 0.9% for the slopes.

Measurements

The gamma-ray heating measurements were made with four TLD's placed in either a stainless steel or lead holder so that averaged responses of higher precision could be obtained. The holders were designed to hold the four TLD's in a 6.4 mm x 6.4 mm x 0.89 mm geometry and thus fit inside of an experimental fuel rod. The holders had overall dimensions of 12.7 mm diameter by 4.37 mm height with 1.59 mm thick walls. Radial measurements were made at the blanket's active midplane along a radial ray of experimental rods. Axial measurements were made over the full active fuel height at four radial positions in the blanket. Background measurements without the ^{252}Cf source in place were made at the same locations so that the fuel's natural activity could be eliminated.

F factors

Each measured TLD dose must be corrected to obtain the dose deposition in the material used as the holder. This correction is based on cavity ionization theory for the TLD-holder geometry. The corrections are made in the form of f-factors (ratio of TLD dose to holder dose).[3] Energy-dependent f-factors are based on the response of the TLD's to electrons of various energies created by a discrete-energy gamma ray interacting in the holder. Energy-dependent f-factors were obtained for the CaF_2-stainless steel and CaF_2-lead combinations of TLD and holder materials.[4] These energy-dependent f-factors were based on a single 3.2 mm x 3.2 mm x 0.89 mm TLD and had to be modified slightly to account for four TLD's per holder. The energy-dependent f-factors then have to be flux weighted using the appropriate gamma-ray spectra. The calculated gamma-ray spectrum at each experimental position was used to flux weight the energy-dependent f-factors to obtain a single f-factor for each holder material at each experimental position. All of the weighted f-factors for both stainless steel and lead are close to unity. The weighted f-factors are approximately constant throughout the blanket because the blanket gamma-ray spectra all have roughly the same shape even though they differ in magnitude; the spectral shapes are almost the same throughout the blanket because the primary production of gamma rays in the blanket is due to the large quantity of ^{238}U. The f-factors are close to unity because the energy-dependent f-factors are close to unity for the dominant energies of the gamma-ray spectra.

Neutron Response

The measured doses must be corrected for the neutron responses of the CaF_2:Dy TLD's since they are in mixed neutron-gamma-ray fields. The CaF_2:Dy TLD's were originally chosen over other TLD's because their neutron response was reported to be smaller. However, it has been found that in the mixed neutron-gamma-ray fields of the FBBF the neutron response is not negligible compared to the gamma-ray response, especially near the transformer-blanket interface. In addition, it was found that very little data concerning the neutron sensitivity of CaF_2 TLD's is available. A set of energy-dependent neutron sensitivities calculated by Rinard and Simons[5] was used along with the calculated neutron fluxes to calculate neutron responses. To help minimize possible errors in the calculated neutron fluxes, neutron correction factors were determined based on the calculated neutron responses and calculated gamma-ray responses. Multiplicative neutron correction factors were calculated as the fractional contribution of the gamma-ray response to the entire response due to both neutrons and gamma rays. The neutron fractional contribution was 13% at a radius of 0.237 m, quickly decreased to 5% at a radius of 0.36 m, and then continued to decrease, reaching a minimum of 3% at a radius of 0.716 m.

Calculations

The gamma-ray heating calculations were performed in three separate steps. First, the facility was modeled in two dimensions and a neutron diffusion calculation was performed using the 2DB[6] computer code. The cross section set used for this calculation was a 30-group set which had been collapsed and self-shielded for each homogenized spatial region using the computer code 1DX[7] and the 50-group, 101-isotope DLC-40/LIB-IV[8] cross section library. From these neutron fluxes, a distributed gamma-ray source was then calculated using partially self-shielded gamma-ray production cross sections based on the coupled DLC-37/EPR[9] cross section library. Finally, a one-dimensional radial gamma-ray transport calculation was performed using the ANISN[10] computer code and the DLC-37/EPR gamma-ray cross sections. The calculation of gamma-ray heating rates in various materials was performed as part of the ANISN calculation and was based on the kerma factors in the DLC-37/EPR cross section library. Several one-dimensional axial gamma-ray transport calculations or a single two-dimensional calculation are planned to provide the axial distributions of gamma-ray heating.

Results

Experimental and calculated results of gamma-ray heating in stainless steel are shown in Fig. 1 for a radial midplane traverse through the blanket. The heating rates are presented as 2 r times the heating rate so that the purely geometrical dependence of flux drop off with radius is not shown. The error bars shown for the experimental results represent statistical errors only and range from 1.7% to 2.4% at one standard deviation. The systematic errors are not shown but are estimated to range from 12% at a radius of 0.237 m to 15% at a radius of 0.716 m. Sources of systematic error include the neutron source strength (approximately 3%), TLD calibration (approximately 3%), f-factors (estimated at 2%) and neutron corrections (estimated at 4%). An additional source of systematic error results from the use of an average blanket background; this error is negligible at a radius of 0.237 m and is estimated to be 3% at a radius of 0.716 m. The ratios of calculation to experiment for the these same results are shown in Fig. 2. The error bars are the experimental statistical errors only. The calculation underestimates the experimental results by 20% at a radius of 0.237 m and by 42% at a radius of 0.711 m.

The experimental and calculated results of the gamma-ray heating in lead are shown in Fig. 3 for a radial midplane traverse through the blanket. The

error bars shown for the experimental results represent statistical errors only and range from 1.6% to 2.2% at one standard deviation; the systematic errors are estimated to be the same as for the stainless steel results. There are four experimental results shown at a radius of 0.237 m, two at 0.355 m, two at 0.474 m, and three at 0.711 m, all of which are the results of four different experimental irradiations. These results indicate that the TLD measurements of gamma-ray heating in the FBBF are reproducible. Figure 4 shows the ratios of calculation to experiment for these lead results. The results for lead show a similar underestimation by the calculation and again the calculation drops off faster than the experimental results. The underestimation of gamma-ray heating in lead by the calculation is 1% at a radius of 0.237 m and 32% at a radius of 0.711 m.

The larger disagreement between calculation and experiment of heating in stainless steel than in lead could be due to neutron activation of the stainless steel holder. Indications are that there is a buildup of activity in the stainless steel holders during the time span of the irradiation and that there is not a buildup in the lead holders. The additional contribution to TLD response caused by holder activity would be larger at the inner radii of the blanket where the neutron fluxes are high and less at larger radii where the neutron fluxes are less. Experiments will be made to estimate the additional TLD response caused by holder activation for each experimental position.

Fission product decay gamma-rays were excluded from the distributed source calculation; this causes the gamma-ray heating in both stainless steel and lead to be underestimated. The decay gamma-ray source was excluded because the DLC-37/EPR cross section library does not include the production cross sections for fission product decay gamma rays. Inclusion of this source could possibly increase the calculated heating rates by 8% or more.[11] However, this can not completely account for the large underestimations by the calculation, especially in the outer blanket.

A likely cause of the large underestimations is the use of multigroup cross sections for a blanket calculation. The cross sections were self-shielded and collapsed over each entire region and thus describe the average cross sections in each region. In a fast reactor blanket the neutron spectrum changes rapidly with radius; this causes region-wise multigroup cross sections to inaccurately represent large regions. This effect was noticed when the 2DB results were compared to the results of a two-dimensional continuous-energy Monte Carlo calculation by the VIM[12] computer code.[13] The continuous-energy cross section formulation allows for spectral changes within a region. The 2DB total neutron flux overestimates the VIM total flux at the inside of the inner blanket and underestimates it at the outside of the inner blanket; the results agree reasonably well in the middle of the inner blanket. The underestimation by the 2DB total flux at the outside of the inner blanket causes the flux at the inside of the outer blanket to be underestimated. This causes the flux at the outside of the outer blanket to be underestimated due to the average description of the outer blanket cross sections. The gamma-ray heating calculations could be improved by using the neutron fluxes calculated by VIM to calculate the distributed gamma-ray source.

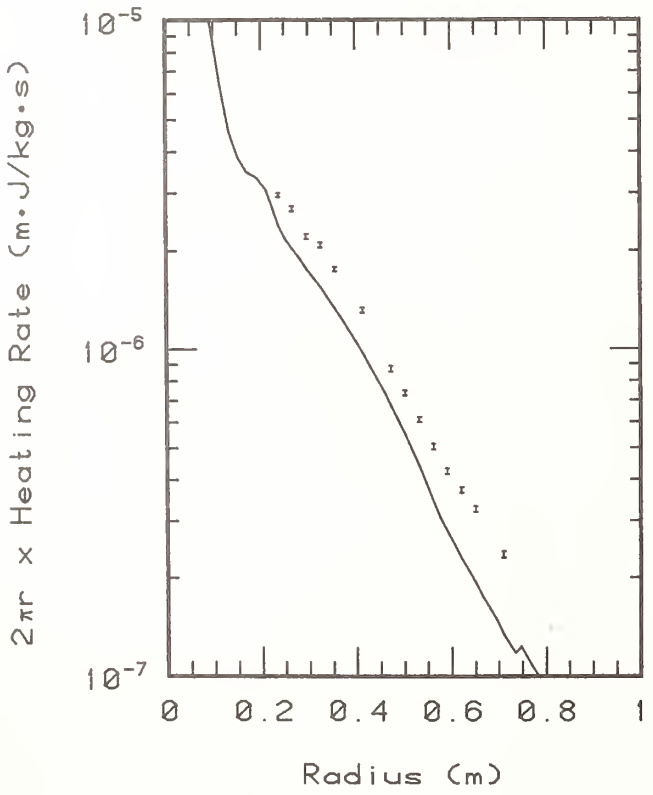

Figure 1. Gamma-ray heating rates in stainless steel as a function of radial position. The error bars shown for the experimental results represent statistical errors. Systematic errors are not shown. The solid line represents the calculated heating rates.

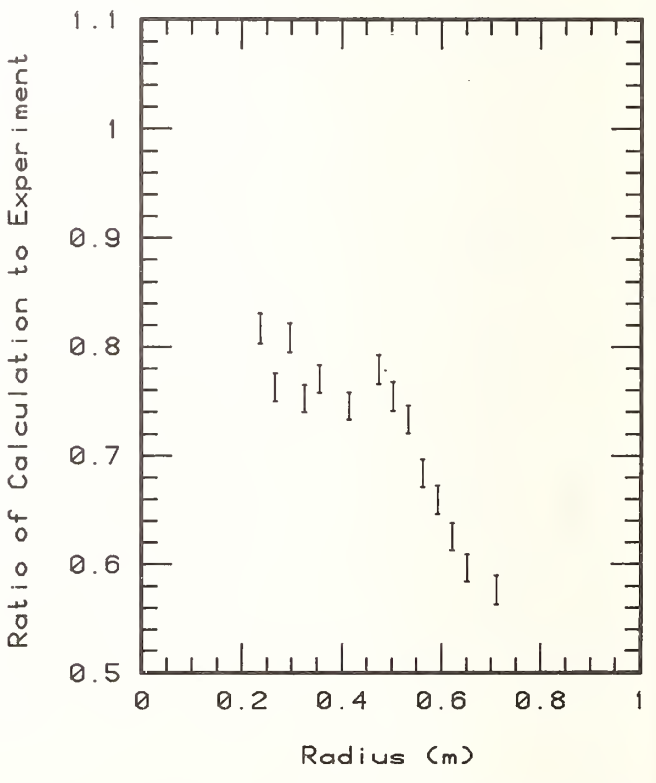

Figure 2. Ratio of calculation to experiment for gamma-ray heating in stainless steel. The error bars represent the the experimental statistical errors only.

Additional underestimations of gamma-ray heating by the calculation may be caused by the gamma-ray production cross sections. Multigroup cross sections which were collapsed over each entire region were used and thus have the same inadequate descriptions that the multigroup neutron cross sections have at points away from the middle of a region. Another error may have been introduced when self-shielding the production cross sections. Only the ^{238}U production cross sections were adjusted because ^{238}U was found to dominate gamma-ray production. The ^{238}U production cross sections were adjusted for self shielding by multiplying by the ratio of the self-shielded ^{238}U neutron capture cross sections obtained from 1DX to the infinitely dilute cross sections of the DLC-37/EPR set.[14] The resulting gamma-ray production cross sections are estimates of the true self-shielded production cross sections but may still have errors associated with them.

Conclusions

Gamma-ray heating measurements were made in the FBBF using CaF_2:Dy thermoluminescent dosimeters. High precision results were obtained by developing and stringently following a readout schedule. The precision of a single batch of TLD's was improved by by eliminating TLD's which had bad response characteristics and by assigning individual normalization factors to each TLD chip. The TLD measurements were corrected for the TLD-holder cavity responses by applying spectral-weighted f-factors. The measurements were also corrected for neutron responses by applying correction factors based on calculated neutron responses. Experiments should be made to estimate the contribution to TLD response caused by neutron activation of the stainless steel holders. Additional calculations are necessary to include the fission product decay gamma rays in the distributed gamma-ray source. The use of the multigroup method in the calculation of neutron fluxes in the FBBF leads to underestimations of the neutron flux in the outer regions of the facility which cause similar underestimations of gamma-ray heating. A calculational method which allows for continuous cross sections in the blanket should be used to calculate the neutron fluxes; this will allow the gamma-ray heating rates to be predicted more accurately.

Acknowledgements

The authors wish to acknowledge the U.S. Department of Energy and the Electric Power Research Institute for the funds for the construction and operation of the Fast Breeder Blanket Facility. The authors wish to thank G.G. Simons for providing the energy-dependent f-factors.

References

1. K.O. Ott, F.M. Clikeman, P.J. Fulford, R.C. Borg, R.H. Johnson and O.H. Gailar, "The Purdue University Fast Breeder Blanket Facility," Proc. ANS Topical Meeting on Advances in Reactor Physics, p. 505, Gatlinburg, Tennessee, April 9-12 1978, CONF-780401 (1978).

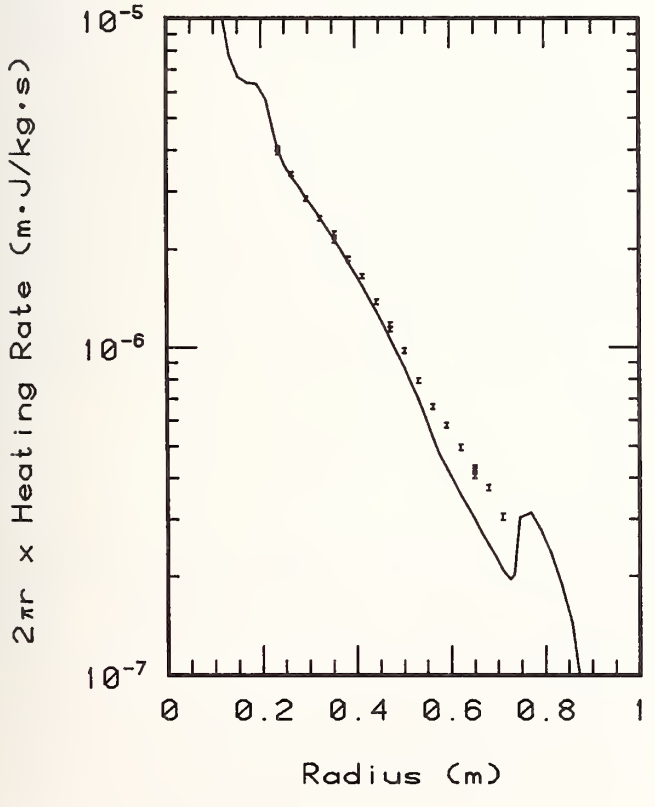

Figure 3. Gamma-ray heating rates in lead as a function of radial position. The error bars shown for the experimental results represent statistical errors. Systematic errors are not shown. The solid line represents the calculated heating rates.

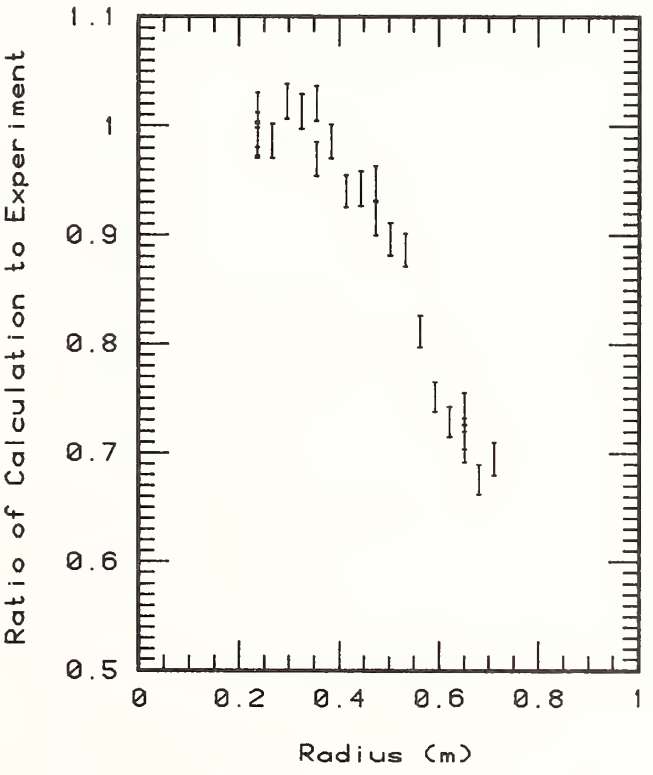

Figure 4. Ratio of calculation to experiment for gamma-ray heating in lead. The error bars represent the the experimental statistical errors only.

2. Harshaw Chemical Co., Solon, Ohio.

3. G.G. Simons and T.J. Yule, Nucl. Sci. Eng., 53, 162 (1974).

4. G.G. Simons, Kansas State University, Private Communication (1978).

5. P.M. Rinard and G.G. Simons, Nucl. Instr. Meth., 158, 554 (1979).

6. W.W. Little, Jr. and R.W. Hardie, "2DB User's Manual -- Revision 1," Battelle Northwest Laboratory, BNWL-821-REV1 (1969).

7. R.W. Hardie and W.W. Little, Jr., "1DX, A One-Dimensional Diffusion Code for Generating Effective Nuclear Cross Sections," Battelle Pacific Northwest Laboratories, BNWL-954 (1969).

8. R.B. Kidman and R.E. MacFarlane, "LIB-IV, A Library of Group Constants for Nuclear Reactor Calculations," Los Alamos Scientific Laboratory, LA-6260-MS (1976).

9. "DLC-37/EPR, Coupled 100-Group Neutron 21-Group Gamma-Ray Cross Sections for EPR Neutronics," Radiation Shielding Information Center, Oak Ridge National Laboratory.

10. W.W. Engle, Jr., "A User's Manual for ANISN, A One-Dimensional Discrete Ordinates Transport Code with Anistropic Scattering," Union Carbide Corporation, K-1693 (1967).

11. G.G. Simons and A.P. Olsen, Nucl. Sci. Eng., 53, 176 (1974).

12. R.E. Prael and L.J. Milton, "A User's Manual for the Monte Carlo Code VIM," Argonne National Laboratory, FRA-TM-84 (1976).

13. "FBBF Quarterly Report for Period April 1, 1979 - June 30, 1979," Purdue University, PNE-79-145, COO-2826-13 (1979).

14. J.H. Paczolt, Jr., "Neutron and Gamma-Ray Calculations for the Purdue University Fast Breeder Blanket Facility," Purdue University, MSNE Project, May 1979.

BENCHMARK TESTS OF JAPANESE EVALUATED NUCLEAR DATA LIBRARY (JENDL)

Y. Kikuchi and A. Hasegawa
Japan Atomic Energy Research Institute
Tokai-mura, Ibaraki 319-11, Japan

T. Hojuyama, M. Sasaki and Y. Seki
Mitsubishi Atomic Power Industries Inc.
1-297 Kitabukuro-cho, Ohmiya-shi, Saitama 330, Japan

T. Kamei
Nippon Atomic Industry Group Co., Ltd.
4-1 Ukishima-cho, Kawasaki-shi, Kanagawa 210, Japan

I. Otake
Power Reactor and Nuclear Fuel Development Corporation
1-9-13 Akasaka, Minato-ku, Tokyo 107, Japan

Various benchmark tests were performed on JENDL-1. JENDL-1 predicted various neutronic characteristics of fast reactors fairly well. It was pointed out, however, that JENDL-1 underestimated the fission rate ratio of ^{239}Pu to ^{235}U and might give some errors in predicting the reaction rate distribution in outer core and blanket region. The effects of cross sections of structural materials were investigated concerning the latter problems.

[JENDL-1, benchmark tests, k_{eff}, reaction rate ratio, reactivity worth, Doppler coefficient, reaction rate distribution, control rod worth, sodium void coefficient, structural materials]

Introduction

The first version of Japanese Evaluated Nuclear Data Library (JENDL-1)[1] has mainly aimed to provide data for fast reactor calculations and its evaluation was made purely on the basis of differential nuclear data. Its compilation work started in 1973 and completed in 1976. Since then various benchmark tests have been made to prove its applicability to fast reactor calculations.

The first stage of tests was done in 1976 on the core center characteristics for selected 27 assemblies. The calculation was based on one dimensional diffusion and first order perturbation approximations by using the reactor constants with 70 groups. As the second stage, applicability was tested to more sophisticated problems on MOZART and ZPPR-3 cores with a two dimensional model. Various problems were pointed out through these integral tests particularly on the cross sections of structural materials and they were further investigated. The comments from the integral tests were taken into account in the evaluation work* for the second version of JENDL (JENDL-2).

Benchmark Tests with 1-D Model

Assemblies

Hardie et al.[2] selected 18 assemblies for tests of ENDF/B-IV. They consist of 12 Pu cores (VERA-11A, ZPR-3-53, ZPR-3-54, SNEAK-7A, ZPR-3-48, ZPR-3-49, ZPR-3-50, ZPR-3-56B, ZPPR-2, ZPR-6-7, SNEAK-7B and ZEBRA-3) and 6 U cores (VERA-1B, ZPR-3-6F, ZPR-3-12, ZPR-6-6A, ZEBRA-2 and ZPR-3-11). We adopted all of them and added MOZART cores[3] (MZA and MZB) and some FCA cores. The characteristics of the added assemblies are shown in Table I. As to Doppler coefficients, we adopted small sample Doppler coefficient measurements at FCA V-1, V-2, VI-1, VI-2, ZPPR-2 and ZPR-3-47, and whole core Doppler measurements at SEFOR.

Table I. Characteristics of 9 Added Assemblies.

Name	Fissile Fuel	Fertile to Fissile Ratio	Core Volume (ℓ)
FCA-V-2	Pu (+U)	2.3	200
FCA-V-1	U (+Pu)	2.6	142
MZA	Pu	3.9	570
FCA-I-1	U	4.0	30
FCA-I-6	U	4.0	24
FCA-III-2S	U	4.0	245
FCA-VI-1	Pu	4.8	423
MZB	Pu	5.8	1800
FCA-VI-2	Pu	6.5	627

Effective Multiplication Factor

Calculated values of the effective multiplication factor are compared with the measured values in Table II and Fig. 1 in the form of the ratio of calculated to experimental data (C/E-value). The results of JAERI-Fast-II[4] and of ENDF/B-IV[2] are also given. The following are observed:

1) JENDL-1 predicts the k_{eff} value very well on an average, but there exists discrepancy of 0.7 % between Pu and U cores.

2) Obvious differences are observed between the results of ZPR-3-53 and -54, which have the same core but different reflectors, i. e., natural uranium for ZPR-3-53 and iron for -54. The k_{eff} value of ZPR-3-54 calculated with JENDL-1 is 2 % higher than that of -53, while the k_{eff} value of ZPR-3-54 with JAERI-Fast-II and ENDF/B-IV is 4 % lower. This may suggest that JENDL-1 has iron cross sections which give less leakage.

3) Without ZPR-3-54, the discrepancy between Pu and U cores becomes small with JAERI-Fast-II and ENDF/B-IV, but it becomes larger with NENDL-1.

* During compilation of JENDL-2, the preliminary data were tested with a one dimensional model and various problems were pointed out from the view point of the integral data. These problems will be taken into account in the final evaluation of JENDL-2.

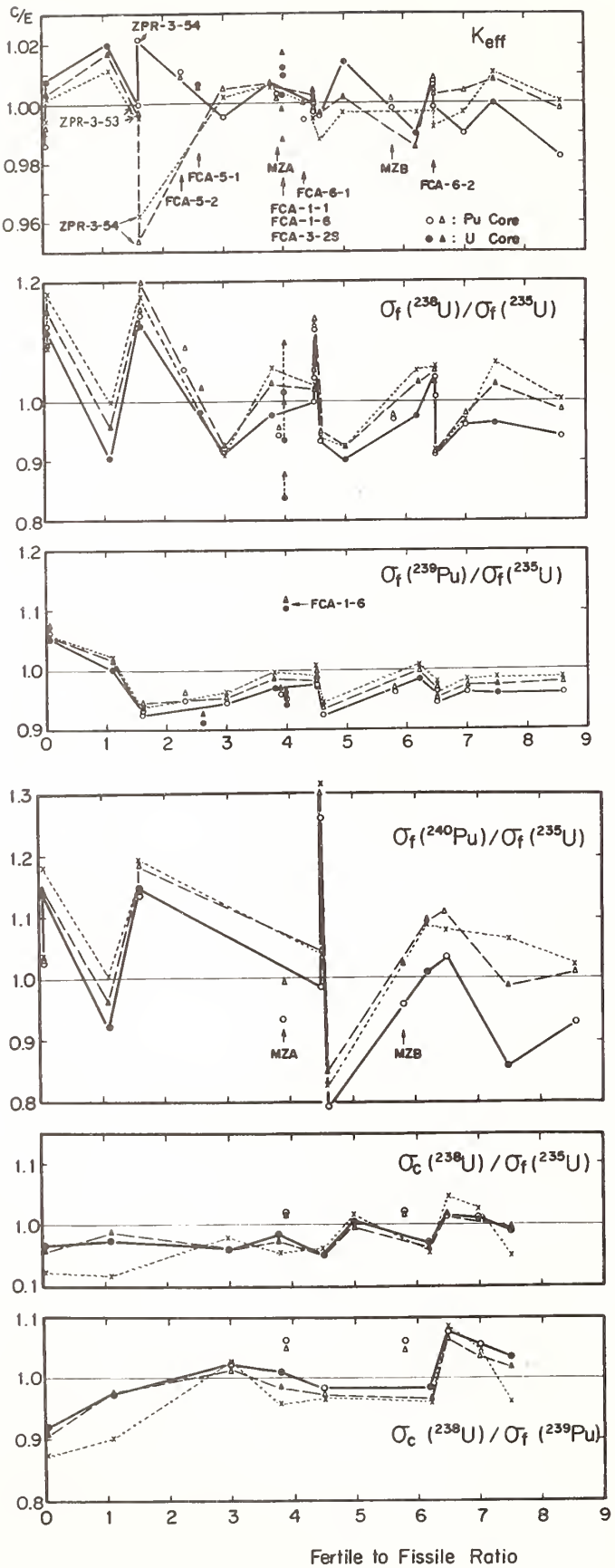

Fig. 1. C/E of k_{eff} and reaction rate ratio vs. fertile to fissile ratio of assemblies.
o—o JENDL-1, Δ---Δ JAERI-Fast-II, x...x ENDF/B-IV

Table II. Effective Multiplication Factors. The value in parenthesis is obtained for 18 assemblies given in Ref. (2).

No. of Cores.	*	JENDL-1	JAERI-Fast II	ENDF/B-IV [2]
Pu-Cores	A	0.9992 (0.9978)	0.9991 (0.9971)	(0.9939)
17 (12)	B	0.0067 (0.0072)	0.0064 (0.0077)	(0.0071)
U -Cores	A	1.0067 (1.0062)	1.0047 (1.0037)	(1.0038)
10 (6)	B	0.0087 (0.0086)	0.0089 (0.0095)	(0.0061)
All	A	1.0020 (1.0006)	1.0012 (0.9993)	(0.9972)
27 (18)	B	0.0074 (0.0076)	0.0073 (0.0083)	(0.0068)

* A: Average of C/E, B: Average of 1-C/E .

Central Reaction Rate Ratio

The C/E values of central reaction rate ratios are shown in Table III and Fig. 1 with those of JAERI-Fast-II and ENDF/B-IV. JENDL-1 shows satisfactory balance in the ratios of ^{235}U fission to ^{238}U fission, ^{238}U capture and ^{240}Pu fission. However JENDL-1 underestimates the ratio of ^{239}Pu fission to ^{235}U fission by 3.5 %. This may attribute to the discrepancy of k_{eff} between U- and Pu-cores as pointed above.

Table III. Central Reaction Rate Ratio.

Quantity	*	JENDL-1	JAERI-Fast-II	ENDF/B-IV**
U -238 Fission / U -235 Fission	A	0.994	1.024	1.037
	B	0.067	0.070	0.075
Pu-239 Fission / U -235 Fission	A	0.965	0.976	0.989
	B	0.046	0.036	0.031
Pu-240 Fission / U -235 Fission	A	1.018	1.068	1.084
	B	0.091	0.096	0.113
U -238 Capture / U -235 Fission	A	0.984	0.982	0.974
	B	0.027	0.026	0.043
U -238 Capture / Pu-239 Fission	A	1.016	0.999	0.976
	B	0.041	0.040	0.059

* A: Average of C/E, B: Average of 1-C/E .
** Values for 18 assemblies taken from Ref. (2).

Central Reactivity Worths

Reactivity worth of ^{239}Pu. The central reactivity worth of ^{239}Pu was calculated for 18 assemblies by using β_{eff} values in Ref. (2). The results are shown in Table IV. The $\overline{C/E}$ value of Pu cores is about 15 % larger than that of U cores for all the three sets. This tendency was also observed in the reactivity worth of the other materials. This suggests that the scaling problem exists in the reactivity worths.

Reactivity worth of the other materials. In order to avoid the scaling problem mentioned above, the calculated and the experimental reactivity worths were normalized to those of ^{239}Pu, and C/E values of the normalized worth were compared in Table V. JENDL-1 a little overestimates the worths of ^{235}U and ^{238}U. This

may be partly due to its underestimation of σ_f (^{239}Pu) mentioned in the reaction rate ratio. The worths of ^{10}B and Cr are predicted with JENDL-1 better than with the other sets. However, the calculated worth of Fe is underestimated with JENDL-1.

Table IV. Central Reactivity Worth of ^{239}Pu.

No. of Cores	*	JENDL-1	JAERI-Fast-II	ENDF/B-IV [2]
Pu Cores 12	A	1.145	1.161	1.174
	C	0.055	0.085	0.089
U Cores 6	A	0.994	0.999	1.007
	C	0.053	0.063	0.055
All Cores 18	A	1.092	1.103	1.115
	C	0.090	0.109	0.112

* A: Average of C/E, C: Stand and deviation of C/E.

Table V. Central Reactivity Worths Normalized to ^{239}Pu Worth.

	*	JENDL-1	JAERI-Fast-II	ENDF/B-IV [2]
^{235}U	A	1.038	1.004	1.014
	C	0.071	0.057	0.060
^{238}U	A	1.080	0.994	0.950
	C	0.204	0.140	0.130
^{10}B	A	0.927	0.911	0.836
	C	0.122	0.112	0.115
Cr	A	0.968	1.309	1.359
	C	0.110	0.309	0.205
Fe	A	0.905	1.018	1.109
	C	0.116	0.129	0.275
Ni	A	1.136	1.153	1.167
	C	0.201	0.154	0.196

* A: Average of C/E, C: Standard deviation of C/E.

Table VI. Doppler Reactivity Coefficients (C/E).

	Assembly	JENDL-1	JAERI-Fast-II
Small Sample Doppler Experiment	FCA V-1	1.09	0.78
	V-2	0.98	0.74
	VI-1	1.13	0.94
	VI-2	1.03	0.90
	ZPPR-2 (Normal)	1.25	1.08
	(Na-voided)	0.96	0.81
	ZPR-3-47	1.04	0.95
Whole Core Doppler Experiment	SEFOR	1.12	1.05
Average of C/E		1.08	0.91
Standard Deviation of C/E		0.09	0.12

Doppler Reactivity Coefficients

The Doppler coefficients are given in Table VI. JENDL-1 overestimates the coefficients by 8 %, while JAERI-Fast-II underestimates them by 9 %. This is mainly caused by the difference in neutron spectra: JENDL-1 gives higher flux in the energy range of 1 keV to 10 keV.

Integral Tests with 2-D Model

Analysis of MOZART Core[5]

Reaction rate distribution in MZB. Figure 2 shows the calculated radial distribution of ^{235}U, ^{238}U, ^{239}Pu and ^{240}Pu fission rates and ^{238}U capture rate with the measured data. The fission rates of ^{235}U and ^{239}Pu are underestimated in the outer core and the blanket. Though this underestimation is observed with the other sets, it is rather significant with JENDL-1. On the other hand the fission rate of ^{240}Pu is overestimated in the outer core and the blanket. The C/E value stays near unity for the fission and capture rates of ^{238}U.

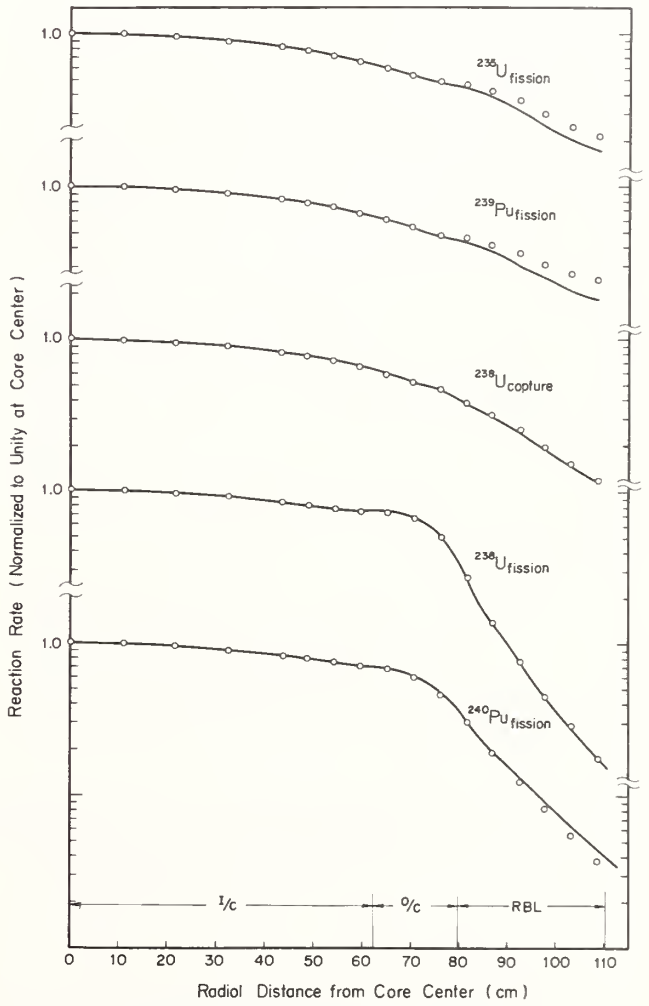

Fig. 2. Reaction rate distribution in MZA.
○: Experiment —: Calculation

Sodium void coefficients in MZB. The sodium void worths were measured in MZB core by traversing the void region in axial and radial directions. The calculated results are compared with the measured ones in Fig. 3. The followings are observed:

1) The C/E value is 1.1 for void in the core center.

2) The calculation very well predicts the sodium void worth in the axial direction.

3) The calculation overestimates the negative sodium void coefficient, when sodium is removed from the outer core. By examing the perturbation component, we considered that this might be caused by overestimation of radial leakage component.

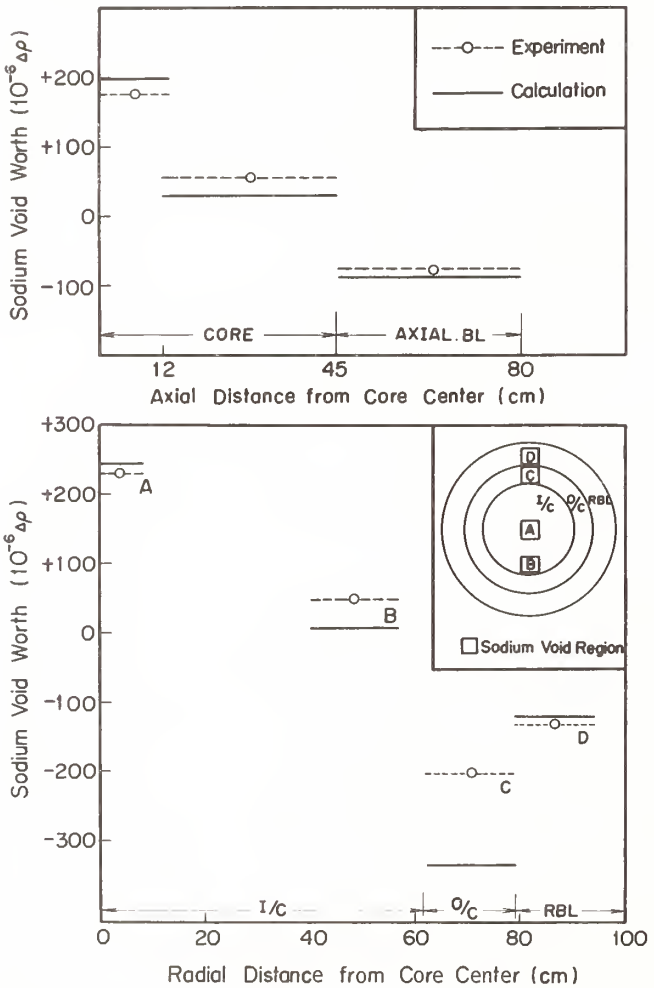

Fig. 3. Axial and radial traverse of sodium void coefficients in MZB.

Control rod worth in MZC. The C/E value is about 0.95 for the central control rod worth. The C/E values depend little on the enrichment of ^{10}B, while the ^{10}B enrichment dependence was often observed with other sets.

Analysis of ZPPR-3[6)]

Worth of multi-control rods in Phase 1B core. The prediction with JENDL-1 is excellent for both single and multi-control rod worths as seen in Table VII. The average of C/E is 0.98 with standard deviation of 2 %.

Table VII. Control rod worths of ZPPR-3 phase 1B core.

No. of Control Rods			Measured Worth ($)	C/E-Value	
Center	Inner Ring	Outer Ring		JENDL-1	JAERI-Fast-II[7)]
		1	1.94	0.97	0.96
	1		2.02	0.98	1.00
	1	1	3.58	0.96	-
1			4.14	0.96	0.96
		2	4.24	1.02	0.97
	2		4.26	0.98	0.99
	3		6.51	0.98	0.99
	3	3	14.33	0.99	0.97
		6	14.88	0.96	0.97
	6	3	20.75	0.97	-
	3	6	22.65	1.00	-
		12	28.96	1.00	0.99
	3	9	28.99	0.97	-
	6	6	30.12	0.96	-
	6	12	44.76	0.97	-
Average of C/E				0.98	0.98
Standard Deviation of C/E				0.02	0.01

Fission rate distribution of ^{235}U in Phase 2 Core. The fission rate distribution was calculated in three cases:

(1) All of six control rods in the inner ring inserted,

(2) six rods in the outer ring inserted, and

(3) three rods inserted in the inner ring and three in the outer ring.

Figure 4 shows the C/E values along X-axis in the cases (1) and (2).
The following can be said:

1) The calculation underestimates the fission rate in the outer core.

2) The underestimation is much enhanced when the control rods are inserted in the outer ring. The C/E value is decreased down to 0.88.

3) The control rods have little effect on the C/E value of reaction rate distribution when inserted in the inner ring.

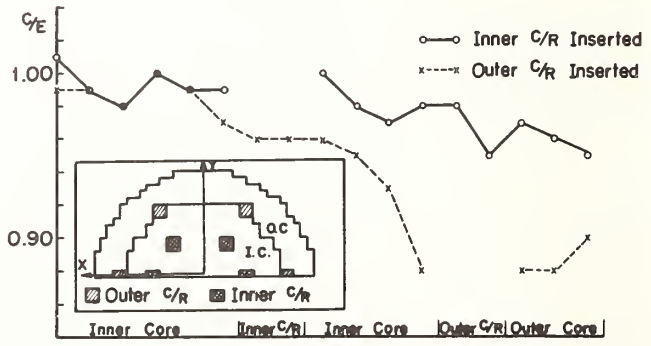

Fig. 4. Fission rate distribution along x-axis in ZPPR-3.

Discussion

Observations through Benchmark Tests

JENDL-1 predicts various quantities of fast reactors very satisfactorily in core center, but the reaction rate distribution shows some anomalous behavior in the outer core and blanket regions, where leakage and spectrum effects have an important role.

Comparison of Macroscopic Cross Sections with Other Sets

Intercomparison of the macroscopic cross section was made with other sets, in order to know the causes affecting neutron leakage and spectrum. (See Appendix as an example.) JENDL-1 has

1) smaller diffusion coefficients above 100 keV,

2) smaller inelastic removal cross section,

3) larger elastic removal cross section above 100 keV and

4) smaller elastic removal cross section below 1 keV.

Cross Sections of Structural Materials

It has been pointed out through reevaluation work for JENDL-2 that JENDL-1 might overestimate the total and elastic scattering cross sections of Fe, Cr and Ni in the energy range of a few hundreds keV to a few MeV and underestimate the inelastic scattering cross section. This is consistent with the observation for diffusion coefficient and slowing down cross section mentioned above, and with underestimation of the central reactivity worth of iron.

Effects of Cross Sections of Structural Materials

In order to know whether the cross sections of structural materials significantly affect the reaction rate distribution mentioned above, the analysis of MZB was made by replacing the cross sections of Fe, Cr, Ni by those of ENDF/B-IV. By this replacement, the radial fission rate distribution was more underestimated in the outer core and blanket regions. Thus its underestimation is not due to the cross sections of structural materials.

The other main effects of the replacement are (1) k_{eff} is decreased by 1.3 % and (2) the neutron flux is enhanced between 200 keV and 1 MeV and is suppressed below 2 keV. The latter may explain partly the difference of Doppler coefficients between JENDL-1 and JAERI-Fast-II, since JAERI-Fast-II took the cross sections of Fe, Cr and Ni from ENDF/B-IV.

Concluding Remarks

It was found through the benchmark tests that JENDL-1 predicted most of characteristics of fast reactors very well. On the other hand, problems in microscopic cross sections of JENDL-1 becomes fairly clear through the tests. The followings can be pointed out from the view point of integral tests.

1) The ratio of σ_f (^{239}Pu)/σ_f (^{235}U) is underestimated by a few percents.

2) σ_f (^{240}Pu) may be overestimated in the energy region below fission threshold.

3) The total and elastic scattering cross sections of Fe, Cr and Ni are overestimated in the energy region of 100 keV to a few MeV.

4) The inelastic scattering may be underestimated for Cr, Fe and Ni.

These points were taken into account in the evaluation for JENDL-2.

Acknowledgment

The authors wish to thank members of working group on JENDL integral test of JNDC for helpful discussion. They also thank T. Narita and H. Takano for production of the group constants.

References

1) S. Igarasi et al.: "Japanese Evaluated Nuclear Data Library, Version-1.", JAERI-1261 (1979).

2) R. W. Hardie et al.: Nucl. Sci. Eng., 57, 222 (1975).

3) C. G. Campbell et al.: Proc. Int. Symp. on Physics of Fast Reactors, Tokyo, Oct. 16-19, 1973, Vol. 1, p. 259 (1973).

4) H. Takano et al.: "JAERI Fast Reactor Group Constants Set, Version II", JAERI-1255 (1978).

5) Y. Seki and T. Hojuyama: Proc. 1978 Seminar on Nuclear Data, p. 319, JAERI-M 8163 (1979)(in Japanese).

6) T. Kamei and M. Iida: Proc. 1978 Seminar on Nuclear Data, p. 329, JAERI-M 8163 (1979)(in Japanese).

7) H. Yoshida et al.: Private Communication.

Appendix: Change of Macroscopic Cross Sections

The change of macroscopic cross sections is given in Table VIII, when the cross sections of Fe, Cr and Ni are replaced by those of ENDF/B-IV in analysis of 1000 MWe FBR.

Significant are increase of D and decrease of Σ_s above 100 keV, increase of Σ_{rem} above 1.4 MeV, and increase of Σ_a and Σ_{rem} below 1 keV.

Table VIII. Change of macroscopic cross sections, when the cross sections are replaced by those of ENDF/B-IV.

Gr.	E_L(eV)*	(Replaced Set - JENDL-1)/JENDL-1 (%)				
		$\Delta\nu\Sigma_f$	$\Delta\Sigma_a$	$\Delta\Sigma_s$	$\Delta\Sigma_{rem}$	ΔD
1	1.4 +6	-0.5	0.9	-2.6	4.8	0.3
2	4.0 +5	0.1	-0.3	-5.9	-3.5	11.3
3	1.0 +5	0.	0.	-3.3	-1.3	3.9
4	1.0 +4	0.2	1.0	-0.8	-3.2	0.4
5	1.0 +3	-0.9	1.6	0.2	0.1	-0.7
6	1.0 +2	0.9	3.4	3.0	3.0	-6.0
7	0.215	0.5	0.9	0.7	0.7	-2.9

* 1.4 +6 denotes 1.4×10^6.

REQUEST FOR EVALUATING NEUTRON CROSS SECTION OF STRUCTURAL MATERIAL FOR SHIELDING APPLICATION

M. Kawai
Nippon Atomic Industry Group Co., Ltd.
4-1 Ukishima-cho, Kawasaki-shi 210, JAPAN

N. Yamano
Sumitomo Atomic Energy Industries, Ltd.
2-6-1 Kaji-cho, Chiyoda-ku, Tokyo 101, JAPAN

K. Koyama
Japan Atomic Energy Research Institute
Tokai-mura, Ibaraki-ken, 319-11, JAPAN

The effect of resonance structure in neutron cross sections of structural mateiral up to a few MeV and the role of the partial inelastic scattering cross sections are investigated from the viewpoint of shielding application by using ENDF/B-IV and JENDL-1. Sensitivity and S_N-transport calculations are performed in the case of iron sphere and slab geometries. The results obtained are as follows: 1) The neglect of resonance self-shielding leads to underestimation of neutron dose rate at the distance of 100 cm from the source by 30 % (for elastic scattering in unresolved resonance region), and 5 % (for inelastic scattering). 2) The neutron flux below 10 keV at 30 cm from the source increases about 60 % by considering low energy discrete levels of ^{57}Fe. 3) Fast neutron spectrum is much affected by the secondary neutron spectrum data of the continuum level.

[Total cross section, elastic scattering cross section, partial inelastic scattering cross section, unresolved resonance, resonance self-shielding effect, structural material, shielding application, sensitivity analysis.]

Introduction

Neutron flux in shielding material shows a strong anisotropy and barely achieves an asymptotic spectrum and decays by the magnitude of about twenty decades from the reactor core to the outside of the biological shields. Additionally, neutron flux in the full range over thermal energy through about 15 MeV is required in order to evaluate the shielding characteristics: such as neutron dose rate, radiation damage, neutron induced radio-activities and gamma-heating. It is not easy to obtain the neutron fluxes to satisfy the required accuracies of shielding design.

Recently, some excellent data processing and radiation transport codes have been developed for shielding calculation. Examples are the RADHEAT-V3[1], AMPX[2], and MINX[3] systems which generate coupled neutron and gamma-ray group constants from the ENDF/B type nuclear data library and the transport codes of DIAC[4], DOT-IV[5] with S_N-approximation and the Monte Carlo code MORSE[6].

The error due to calculations, which overwhelmed the one due to cross section uncertainty, diminishes by adopting these codes. Thus, cross section sensitivity analysis codes, SWANLAKE[7] and ROSETTA[8] were also developed and are used for the investigations of effect of cross section uncertainties upon shielding calculation.

In this work, we have investigated the problems in the neutron cross sections of structural material on shielding application. Iron data was taken as a typical material, since it is the most important and its neutron cross sections have been measured well. The calculations were carried out by using the one-dimensional S_N-transport code ANISN-JR[9] and the sensitivity analysis code ROSETTA-1D. Group cross sections used for the calculations were generated by RADHEAT-V3 system by processing the evaluated data in JENDL-1[10] (Japanese Evaluated Nuclear Data Library Version-1) MAT=1260 and ENDF/B-IV MAT=1192. Large differences between both files are observed in the elastic and inelastic scattering cross sections.

Analysis was performed so as to acertain quantitatively the effects of two items, resonance structure up to a few MeV and the partial inelastic scattering cross sections on neutron penetrating through bulk iron.

Effect of Resonance Structure

Fine Structure in Cross Section

There is observed a fine structure in experimental data of neutron total cross section for structural material up to several MeV, which were measured precisely by 68Cierjacks et al.[11] and 70 Carlson et al.[12] whose results agree well with each other in the detailed structure as shown in Fig. 1. The similar structure is also seen in inelastic scattering cross section of iron measured by 71Perey et al.[13] On the other hand, most evaluated nuclear data are given so as to reproduce the experimental data averaged over the proper energy bins at least. Fig. 1 shows the total and inelastic scattering cross sections for iron in JENDL-1 and ENDF/B-IV comparing with the experimental data in the energy region between 0.92 MeV and 1.0 MeV. For ENDF/B-IV data, fine structures appear in the smooth cross sections for total, elastic and inelastic scattering above 59 keV. Their shapes follow the experimental data, but some peaks are sharper than experimental ones. However, such structures are substituted by the smoothed mean values in the energy range over 400 keV through 15 MeV in JENDL-1.

This difference of cross section treatment gives

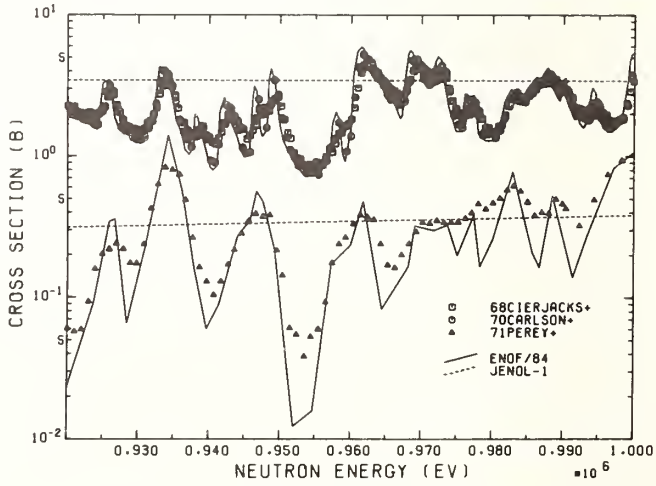

Fig. 1. Total and inelastic scattering cross sections of iron in ENDF/B-IV and JENDL-1.

a significant discrepancy of a self-shielded cross section of iron. Fig. 2 shows Bondarenko type[14] resonance self-shielding factor for capture, elastic and inelastic scattering cross sections of pure iron calculated by using ENDF/B-IV data and the RADHEAT-V3 system. It was found that the resonance self-shielding decreased the value of cross section by 30 % at 400 keV, 22 % at 1 MeV and 7 % at 2 MeV for elastic scattering, and 15 % near 1 MeV for inelastic scattering. Regarding JENDL-1 data, the resonance self-shielding is neglected inevitably above 400 keV. This neglection will bring on the underestimation of neutron flux transmitted through bulk iron as described in the following sections.

Method of Cross Section Sensitivity Analysis

Cross section sensitivity analysis was performed to estimate the effect of resonance structure up to several MeV in elastic and inelastic scattering, and capture cross sections on neutron flux penetrating through iron slabs. In the exact perturbation theory, the change of detector response, ΔR_x, to the change of (n,x) reaction cross section, $\Delta\sigma_x$, is written by the following formulae:

$$R = \iiint S^*(\underline{r},E,\underline{\Omega})\ \phi(\underline{r},E,\underline{\Omega})\ d\underline{r}dEd\underline{\Omega} \qquad (1)$$

$$\Delta R_x = -\iiint N\Delta\sigma_x(E)\ \phi^*(\underline{r},E,\underline{\Omega})\ \phi'(\underline{r},E,\underline{\Omega})\ d\underline{r}dEd\underline{\Omega}$$

for capture, (2)

$$= \iiiint\iint N\Delta\sigma_x(E,\underline{\Omega}\to E',\Omega')[\phi^*(\underline{r},E',\underline{\Omega}')-\phi^*(\underline{r},E,\underline{\Omega})]$$

$$\cdot\phi'(\underline{r},E,\underline{\Omega})\ d\underline{r}dEd\underline{\Omega}\ dE'd\underline{\Omega}'$$

for (n,n) and (n,n'), (3)

where $\phi'(\underline{r},E,\underline{\Omega})$ is forward flux at the position $\underline{r}$, the energy E and the angle $\underline{\Omega}$ in the perturbed system, and $\phi^*(\underline{r},E,\underline{\Omega})$ is adjoint flux obtained by solving the in homogeneous adjoint Boltzman equation with a forcing function $S^*(\underline{r},E,\underline{\Omega})$ i.e. detector response function in the unperturbed system.

In this study, both fluxes in iron slabs were calculated under the following conditions:

1. cross section: ENDF/B-IV MAT=1192,
2. energy group structure: 40 groups with a equi-lethargy width of 0.2 over 1.677 keV through 5 MeV,
3. approximation: S_{16} with P_5 anisotropic scattering,
4. geometry: 10 cm, 50 cm and 100 cm iron slabs,
5. neutron source: fission neutron and monoenergetic 5 MeV neutron located at one edge of iron slab,
6. detector: dosimeter, 1/v-absorber and flat response above 100 keV located at the other edge of slab against source,

The effect of the perturbation, neglection of resonance self-shielding, was calculated by the equations (2) and (3).

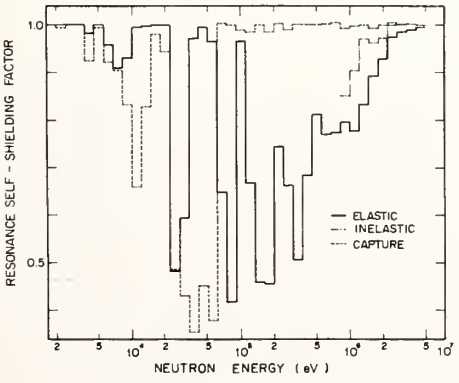

Fig. 2. Resonance self-shielding factors of pure iron by ENDF/B-IV.

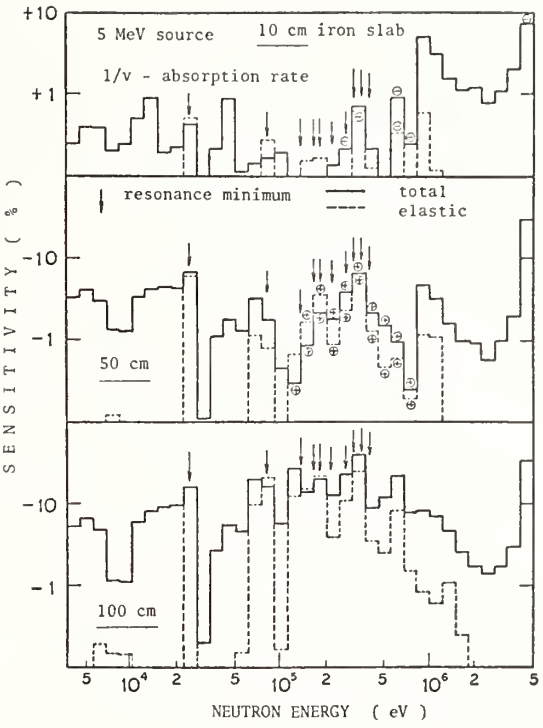

Fig. 3. Sensitivity profiles for 1/v-absorption rate.

Results

The calculated sensitivity coefficient shows that inelastic scattering is effective to neutron response in the thin slab, and that elastic scattering become dominant as the thickness increases. It is high at the resonance minimum and this fact coincides with the window effect of neutron transmission. Fig. 3 is the results for 1/v-absorption rate. The sign of sensitivity to total cross section, which is shown by a solid line, changes from plus to minus as the thickness increase, and its magnitude increases with the global shape maintained. It is also found that the sensitivity coefficients amount to a few ten percents even at the energy above 400 keV. In the figure, a dotted line express the sensitivities to neglecting the resonance self-shielding for elastic scattering. This resembles the sensitivity profile for total cross section, but the difference is observed clearly in the off-resonance energies.

Fig. 4 shows the sensitivities to neglecting the resonance self-shielding for elastic and inelastic scattering, and capture cross section. The effect of elastic scattering is large as a whole. The self-shielding of capture cross section influences only the lower energy region, and is larger on a 1/v absorber than on a neutron dosimeter. The dips are found near 1 MeV for elastic and inelastic scattering because of a cancellation of positive and negative components of the slowing down effects.

The main results are summarized in Table 1. The neglect of resonance self-shielding leads to underestimation of dose rate at the distance of 100 cm from the source by 90 % (for overall elastic scattering), 30 % (for elastic scattering in unresolved resonance region), 5 % (for inelastic scattering), and 0.23 % (for capture). For 1/v-absorption, capture cross section become important at the low energy. For fluence above 100 keV, the results are the same as those of dose rate except for the magnitude being slightly smaller.

Table 1. Influence of resonance self-shielding of neutron penetrating through an iron slab of 100 cm thickness from fission neutron source.

	Flat response above 100 keV (%)				Neutron absorbed dose (%)				1/v absorption (%)			
	(n,n)	(n,n')	(n,γ)	total	(n,n)	(n,n')	(n,γ)	total	(n,n)	(n,n')	(n,γ)	total
5.0MeV ∿1.01MeV	-2.13	-1.06	0.0	-3.19	-2.11	-1.15	0.0	-3.26	-2.73	-0.66	0.0	-3.39
1.01 ∿ 0.453	-25.83	-3.11	-0.01	-28.95	-28.37	-3.33	0.01	-31.69	-11.36	-2.00	0.0	-13.36
453keV ∿204keV	-51.72	0.0	0.0	-51.72	-47.30	0.0	0.0	-47.30	-31.71	0.0	-0.01	-31.72
204 ∿ 111	-8.53	---	-0.01	-8.54	-9.88	0.0	-0.02	-9.90	-20.84	0.0	-0.04	-20.88
5.0MeV ∿1.68keV	-88.20	-4.17	-0.02	-92.39	-90.10	-4.48	-0.22	-94.80	-78.90	-2.66	-2.83	-84.39

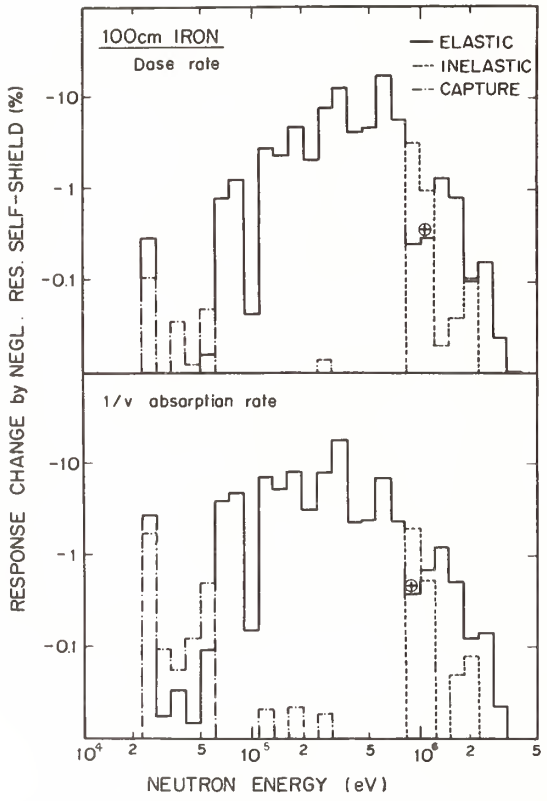

Fig. 4. Sensitivities to neglecting resonance self-shielding effects.

The effects of self-shielding in the energy range above 2.2 MeV are smaller than the value of 0.2 % for all responses. It was also found that the contribution of self-shielding for a needle-like p-wave resonance was almost negligible in the energy range of resolved resonances below 400 keV from the analysis which uses the resonance parameters in JENDL-1 MAT=1260.

Discussion

The resonance self-shielding effects below about 2 MeV were found to play a important role in predicting responses in the results obtained by the exact perturbation theory, although there remained some problems in evaluation of resonance self-shielding factor for capture cross section.

Comparing the sensitivities calculated by perturbation theories with those of direct calculation, good agreements were obtained for the exact perturbation, but not for the linear perturbation as shown in Table 2.

The relative difference of sensitivity was compared with the relative cross section change in Fig. 5.

Table 2. Sensitivities of fluence above 100 keV.

Thickness	Linear Pert.	Exact Pert.	Direct Pert.
50 cm	-90.6%	-58.3%	-59.9%
100 cm	-290.0%	-88.0%	-93.2%

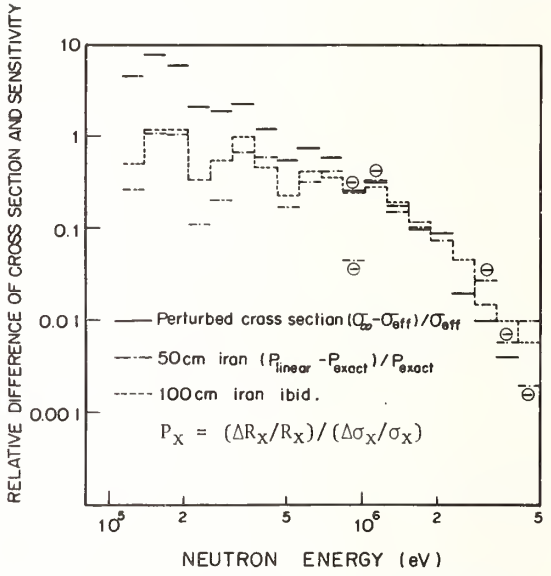

Fig. 5. Error of the linear perturbation results and the perturbed cross section.

It was found that the former was the same as the latter in the higher energy where the cross section change was small. However, the difference became larger than the relative change of cross section with energy decrease and with slab thickness increase because the slowing-down neutron brought in errors in the upper energy regions and the resonance self-shielding effect was large below 400 keV.

Contribution of Partial Inelastic Scattering Cross Section

Difference between JENDL-1 and ENDF/B-IV Data

The inelastic scattering cross sections effectively contribute to softening of neutron spectrum. Fig. 6 shows the total inelastic scattering cross sections of JENDL-1 MAT=1260 and ENDF/B-IV MAT=1192. Agreements are found between both data except for the fine structure in ENDF/B-IV and the data of JENDL-1 below 860 keV. However, there are observed the peculiar differences in both file in the partial inelastic scattering cross section.

There is a limitation in ENDF/B-Format for inelastic scattering cross section that only 40 dicrete levels can be stored. Accordingly, JENDL-1 MAT=1260 has maximum 40 discrete levels from the ^{57}Fe first excited level at 14.6 keV to the 3.90 MeV level of ^{56}Fe and continuum level including the discrete levels

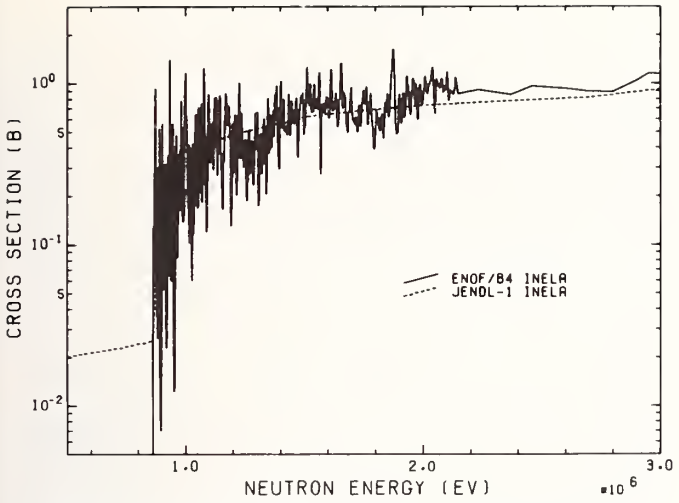

Fig. 6. Comparison of inelastic scattering cross section for iron between JENDL-1 and ENDF/B-IV.

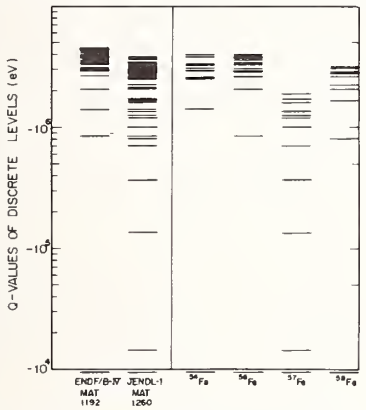

Fig. 7. Level schemes of natural iron in JENDL-1 and ENDF/B-IV.

above 3.91 MeV, while ENDF/B-IV MAT=1192 has 26 levels from 861 keV to almost 5.59 MeV for ^{56}Fe compiled by putting together the levels for which energies are nearly equal to each other. The differences of data compilation are shown in the lowest five levels belonging to ^{57}Fe and ^{58}Fe of JENDL-1 (hereafter called MT=51-55 of MAT=1260), and in the ten levels from 3.93 MeV to 4.59 MeV of ENDF/B-IV (MT=67-76 of MAT=1192) as illustrated in Fig. 7.

Secondary neutron energy spectrum of continuum levels is expressed in the simple Maxwellian in JENDL-1, but in the tabulated form which gives the complicated spectrum based on nuclear model calculation in ENDF/B-IV.

Analysis

The contribution of partial inelastic scattering cross section to neutron flux transmitted through an iron sphere with a 100 cm diameter was examined by using the ad hoc libraries consisting of ENDF/B-IV and JENDL-1 as shown in Table 3. Neutron transport calculations were performed under the following conditions:

1. energy group structure: DLC-II type 100 group over 0.001 eV through 14.9 MeV,
2. approximation: S_{64}-P_{12} approximation,
3. neutron source: 0.65 MeV, 4.5 MeV and 14 MeV monoenergetic sources with 2 cm radius located at the center.

The ad hoc libraries were made so as to investigate 1) the effect of the secondary neutron spectrum data of the continuum level by comparing the neutron

Table 3. Contents of ad hoc libraries.

MAT No.	Contents
1260	JENDL-1 data
1192	ENDF/B-IV data
2600	replacing the data of MT=51-91 in MAT=1192 with those in MAT=1260
2601	replacing the secondary neutron spectrum of continuum level in MAT=1192 with the data in MAT=1260
2602	incorpolating the data of MT=67-76 in MAT=2601 into continuum level (MT=91)
2603	adding the data of MT=51 (first level of Fe-57) in MAT=1260 to the data in MAT=2601
2604	adding the data of MT=51-55 (discrete level of Fe-57 and Fe-58) in MAT=1260 to the data in MAT=2601

fluxes by MAT=1192 with those by MAT=2601, 2) the contribution of MT=67-76 of MAT=1192 by comparing MAT=2601 with MAT=2602, and 3) the contribution of MT=51-55 of MAT=1260 by comparing MAT=2603 and 2604 with MAT=2601. The difference between the results by MAT=2600 and MAT=1192 corresponds to the mixed effects of the three components mentioned above.

Results

Neutron slowing down matrices reflect directly the structure of partial inelastic scattering cross sections. Fig. 8 shows the down-scattering probabilities, $\sigma_{in}(g \to g')$, from the source energy of 4.5 MeV (g=12) of ad hoc libraries. In the figure, three kinds of pattern are shown. The first is consist of MAT=1192, the second is MAT=2601, 2603 and 2604, and the third is MAT=2602. The first curve may be expressed as a linear function of g' (lethargy widths are 0.1 for g=1-49, and 0.25 for g'=50-99) in the range of g'=40-99 (400 keV - 0.4 eV). The third curve is also the same in the range of g'=33-99 (600 keV - 0.4 eV) and its gradient is greater than that of the first. This difference was caused by the secondary neutron spectrum data of the continuum level and the highest discrete levels of MT=67-76 of MAT=1192. The second curve is parallel to the third in the range of g'=40-63 (400 keV - 4.3 keV) and to the first in the range of g'=63-99 (4.3 keV - 0.4 eV). This fact shows

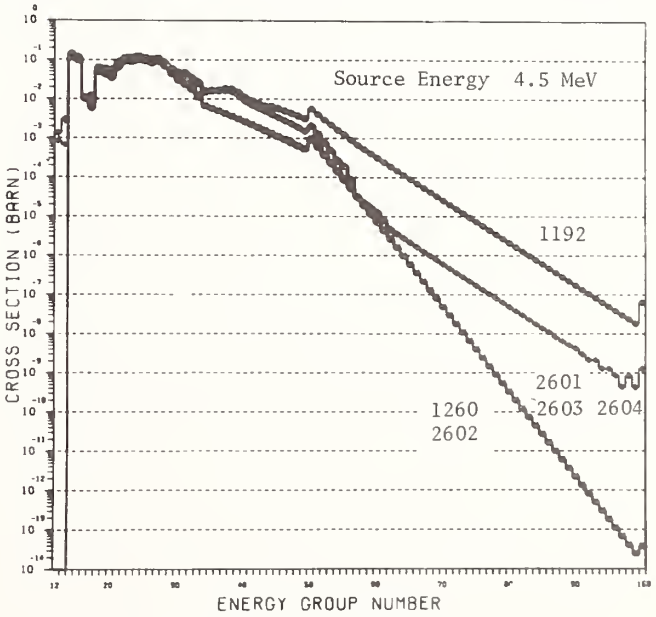

Fig. 8. Down scattering probabilities of ad hoc libraries.

that the slowing down into g'=40-63 was mainly dominated by the continuum level.

The scattering into g'=12, 13 was found only in the cases of MAT=2600, 2603 and 2604, which contain the lowest levels of MT=51-55 of MAT=1260.

The shape of the slowing down cross section of MAT=1192 from 14.9 MeV (g=1) into the groups g'=20-55 (2.2 MeV - 30 keV) is not as simple as that of the other libraries because of the difference of the secondary neutron spectrum data in the continuum level. When the source energy is lower than the energy of the first excited state of ^{56}Fe at 861 keV, the inelastic scattering of MT=51-55 of MAT=1260 contributes to neutron slowing-down significantly.

The differences among the reaction rates in iron calculated with ad hoc libraries are by a factor of two at maximum in the case of 4.50 MeV neutron source.

The figures 9 and 10 show the relative change of neutron spectrum to that calculated with MAT=1192 at the distance of 30 cm from the central source of 0.65 MeV and 14 MeV, respectively. It was found that the epithermal neutron flux below 10 keV was increased by about 60 % by considering low energy discrete levels of ^{57}Fe and ^{58}Fe in the case of 0.65 MeV source, and also by about 20 % for the 14 MeV source. The fast neutron spectrum was also much affected by the secondary neutron spectrum data of the continuum level.

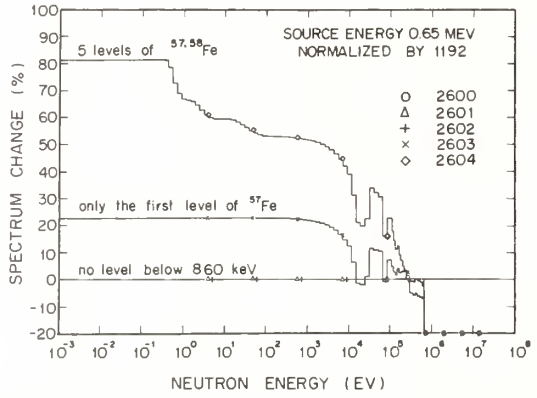

Fig. 9. Neutron spectrum change at the distance of 30 cm from the central 0.65 MeV Source.

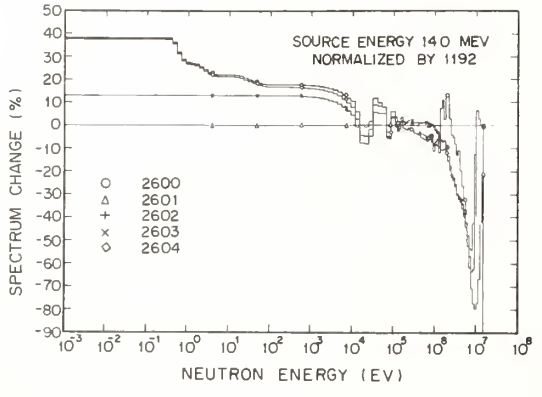

Fig. 10. Neutron spectrum change at the distance of 30 cm from the central 14.0 MeV source.

Conclusion

In the preceding chapters, the effects of resonance self-shielding and the contribution of partial inelastic scattering cross section were evaluated in the typical case of iron as a structural material. The results obtained are as follows: 1) the resonance self-shielding effects of elastic and inelastic scattering cross sections in the unresolved resonance region contribute to the change of dose rate by 30 % and 5 %, respectively. 2) The neutron flux below 10 keV at the distance of 30 cm from the central source increases about 60 % by considering low energy discrete levels of ^{57}Fe and ^{58}Fe. 3) Fast neutron spectrum is much affected by the secondary neutron spectrum data of the continuum level. These results will be true of the other structural materials, although a kind of detector and source condition were limited in this study. The resonance self-shielding effect for capture may be underestimated, since the experimental data of capture cross section are not enough to give the resonance structure of it. For elastic and inelastic scattering cross sections, there were some subjective problems in that the experimental error and the energy resolution may gradate the structures and lead to missing the needle-like peaks. However, the results obtained in this study will be adopted generally because the needle-like p-wave resonance self-shielding effect did not affect neutron flux.

Thus, it has been concluded that the following quantities should be considered for evaluating/compiling cross sections of structural materials; 1) unresolved resonance up to 2 MeV, 2) the discrete inelastic scattering cross sections of an isotope even with a low abundance, and 3) the rigorous secondary neutron spectrum data. This conclusion has been reflected in the evaluation of neutron cross sections for structural material for JENDL-2.

Acknowledgement

This work has been done as one of the activities of the Japanese Nuclear Data Committee.

References

1. K. Koyama, et al., JAERI-M 7155 (1977).
2. N.M. Greene et al., ORNL-TM-3706 (1976).
3. C.R. Weisbin, et al., LA-6486-MS (1976).
4. N. Yamano, et al., Method of Calculation for Anisotropic Transmission Problems by S_N-Transport Code, to be submitted in J. Nucl. Sci. Technol.
5. W.A. Rhoades, The DOT-IV Variable Mesh Discrete Ordinates Transport Code, Proc. 5th Int. Conf. Reactor Shielding, Knoxville, 724 (1977).
6. M.B. Emmett, ORNL-4972 (1975).
7. D.E. Bartine, et al., ORNL-TM-3809 (1973).
8. M. Kawai, et al., to be published.
9. K. Koyama, et al., JAERI-M 6954 (1977).
10. S. Igarasi, et al., JAERI 1261 (1979).
11. S. Cierjacks, et al., KFK-1000 (1968).
12. A.D. Carlson, et al., Nucl. Sci. Eng. 42 28 (1970).
13. F.G. Perey, et al., Proc. of Conf. on Neutron Cross Sections and Technol., Knoxville, 191 (1971).
14. I.I. Bondarenko edited, Group Constants for Nuclear Reactor Calculation (translated from Russian), Constants Bureau, New York (1964).

INTEGRAL EXPERIMENTS FOR FUSION REACTOR DESIGN: EXPERIMENTATION

G. T. Chapman and G. L. Morgan[1]
Oak Ridge National Laboratory
Oak Ridge, Tennessee 37830, USA

Integral experiments that measure the energy spectra of neutrons and gamma rays due to the transport of ∿ 14-MeV T(d,n)^{4}He neutrons through thick steel and borated polyethylene shield configurations have been performed at the Oak Ridge National Laboratory. Descriptions of the facility and experimental techniques are given along with curves showing data representative of the results.

[Integral Experiment, Energy Spectra, Pulse-shape Discrimination, Data Unfolding]

Introduction

Integral experiments have been performed at the Oak Ridge National Laboratory to provide verification of nuclear data and radiation transport methods that are being used in nuclear design calculations for fusion reactors. Using an NE-213 detector and pulse-shape discrimination methods, both neutron and gamma-ray energy spectra were obtained for shields up to a thickness of about 412 g/cm^2. The energy ranges covered were from about 800 keV to 14 MeV for neutrons and from about 800 keV to 10 MeV for gamma rays. The source of neutrons was the T(d,n)^{4}He reaction in targets consisting of 4 mg/cm^2 of TiT deposited on 0.254-cm-thick copper disks. The condition of the target was monitored at all times by the use of a solid-state alpha detector and a small NE-213 neutron detector.

The Facility

The facility, designed[2] and built for conducting the measurements described here, is located in Bldg. 6025 at the Oak Ridge National Laboratory (ORNL). Since this is primarily an office complex, it was necessary to provide shielding to meet all Health Physics requirements in addition to that needed to reduce the backgrounds produced by neutron scattering and/or capture in the room. Figure 1 is a drawing of the facility showing a cut-away section in the environmental control shield to illustrate the arrangement of the components in that shield. The experimental shield, consisting of stainless-steel and borated polyethylene slabs, each 5.08 cm thick by 152 cm in cross section, is contained in a cavity in the environmental shield which provides a minimum of one meter of concrete shielding in all but the forward direction (right in the figure). To reduce the return of thermal neutrons from the wall, iron slabs were placed between the detector and the wall. This, in effect, simulated making the measurements with the detector located within the experimental shield.

The accelerator target, consisting of 4 mg/cm^2 of titanium titride deposited on 0.254 cm thick copper disks, is located in a cylindrical can of iron with a 7.5-cm wall thickness. This can serves to modify the nominal 14-MeV neutron source spectrum to more nearly represent the softer spectrum from the reactor. In addition, the source can with its backup shield of lithiated paraffin in the accelerator drift-tube port, reduces the number of neutrons reflected from the back room wall. As designed and built, the room allows making statistically good measurements with experimental shields as thick as 412 gm/cm^2 in only 3 to 4 hours counting time.

Target Calibration

For the deuteron energies used in this work (E_D < 300 keV) the T(d,n)^{4}He reaction is isotropic in in the center-of-mass system. Therefore, counting the alpha particles emitted into a known solid angle gives an accurate determination of the neutron source strength. The only calibration constant necessary is the solid angle transformation factor (lab to center-of-mass) for the reaction angle at which the alpha particles are observed. This transformation factor is dependent on the deuteron energy and is calculated using the T(d,n) cross section as a function of energy, the stopping power of the target (TiT), and the relative fraction of D^+, D_2^+, and D_3^+ in the incident beam.

The initial test of the technique was carried out using a very low mass target holder in which the alpha particles were detected by a surface-barrier detector at an angle of 165° and a distance of 25 cm. An aperture with a diameter of 0.630 cm defined the active area of the detector. The detector was protected from scattered deuterons by a foil of aluminized mylar with a thickness of 3.8×10^{-4} cm. Pulse height distributions observed in this detector showed a very clean peak, well isolated from noise and free of background. The source strength determined by the alpha particle detector was compared with a simultaneous measurement of the neutrons at 0° (Fig. 2) using a calibrated[3] NE-213 detector (with a suitable calculation of the 0° neutron-solid-angle transformation factor). Agreement was within 3% which is within the uncertainties of 5% on neutron detector efficiency and 3% on alpha particle calibration factor (due mainly to possible variations in the molecular fractions of the incident deuteron beam).

After the environmental-control shield wall and source-modifying can were in place, this same target holder was used to calibrate a neutron monitor consisting of a NE-213 detector at 0°. The production target holder was then installed. This target holder used the same alpha particle detector package (detector, aperture, cover-foil) relocated to 90° and at a distance of about 150 cm. The source strength determined by this alpha-particle detector assembly was then compared to that determined by the calibrated neutron monitor and found to agree within 1%. The solid angle transformation factor at 90° is very nearly equal to unity and is essentially independent of deuteron energy and therefore independent of the relative molecular fractions in the deuteron beam.

Detector and Electronics

The primary neutron/gamma-ray detector used in this work was manufactured at the ORNL ORELA facility and consists of 66.1 gm of NE-213 scintillation liquid contained in a cylindrical cup made of aluminum (4.32×10^{-2} cm wall thickness) and coated on the inside with a titanium dioxide reflector paint. After coating, the inside dimensions of the can were 4.658 cm diam by 4.648 cm deep. The detector was mounted on an 8850 photomultiplier tube. The circuitry used in the pulse-shape discrimination to distinguish between neutrons and gamma rays is essentially standard and state-of-the-art. The data were accumulated with an ND-812 pulse-height analyzer/computer and transferred for permanent storage on a PDP-10 disk via paper tape. Two

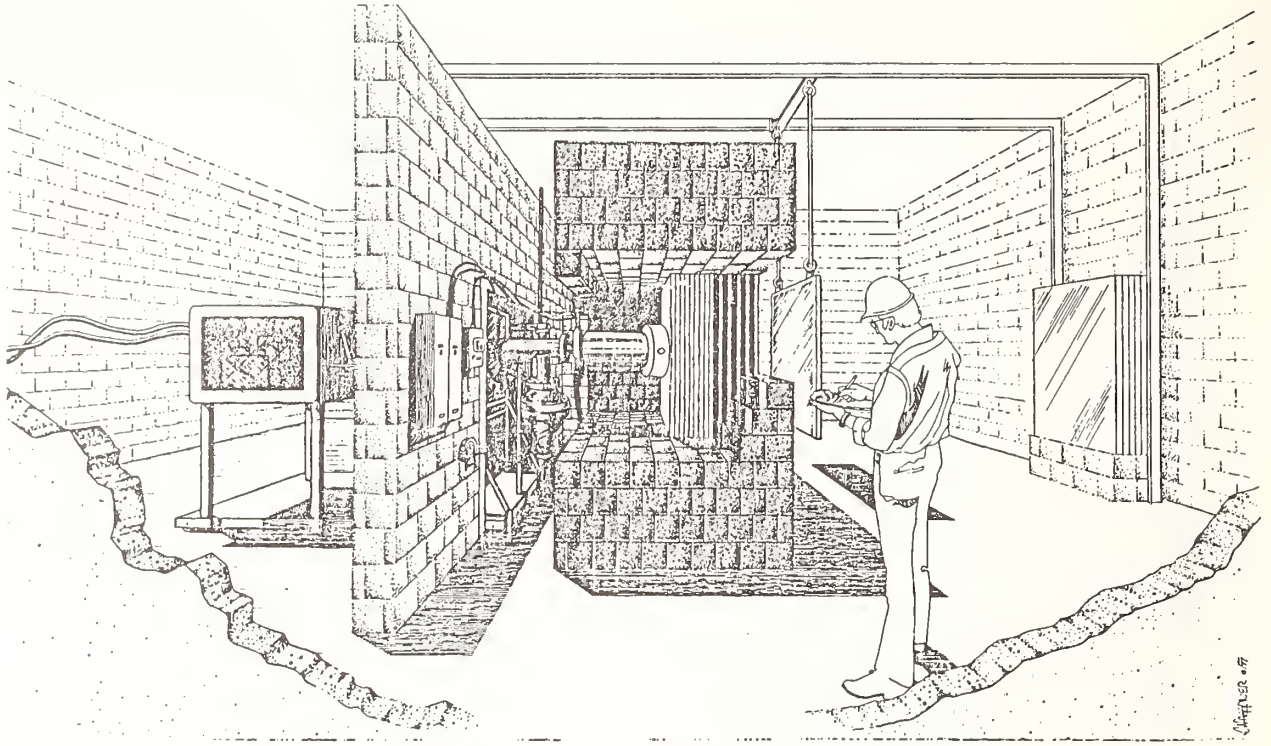

Fig. 1. Artist's sketch of the experimental facility at ORNL.

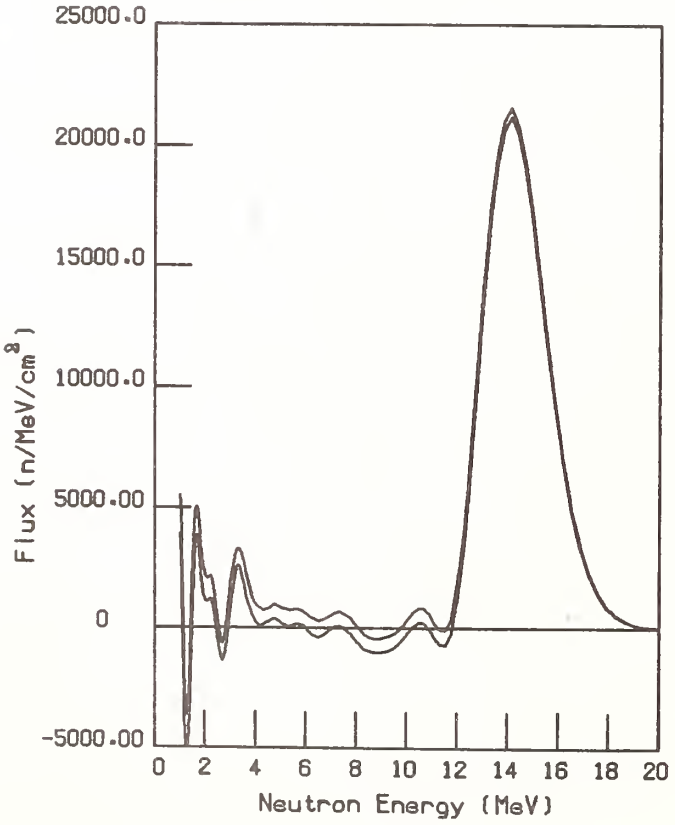

Fig. 2. NE-213 detector response to T(d,n) neutrons.

subsidiary electronic channels are used to monitor alpha and neutron emissions from the target with a surface-barrier alpha-particle detector (see above) and a small NE-213 neutron detector biased at about 10 MeV. Both monitors are located at right angles to the beam and at a distance of about 150 cm from the target. Pulse-height spectra of the detected alpha particles are recorded at all times to monitor for any change in the quality of the target.

Data Analysis

The pulse-height spectra obtained for both neutrons and gamma rays were unfolded to produce the energy spectra using the program FERD.[4] The response matrices required by FERD were obtained by one of us (GLM) using the pulsed neutron beam at ORELA for the neutron data and sources of gamma rays with known energies for the gamma-ray matrix. The detector has an energy resolution that varies as

$$R = \sqrt{300 + 800/E_n}$$

for neutrons, and

$$R = \sqrt{170 + 288/E_\gamma}$$

for gamma rays where R is the FWHM in percent at the given energy in MeV. Indicative of the detector's response are the data shown in Figs. 2 and 3. Figure 2 shows the response to the T(d,n) neutrons at about 14 MeV, and Fig. 3 shows the separation of ^{24}Na gamma rays at 1.37 and 2.76 MeV. All the data are normalized to the source neutron strength as determined by the detection of the associated alpha particles (see above).

Results

A companion paper to this one[4] gives a detailed description of the data and the success in comparing calculations to these measurements. Therefore, only a cursory presentation of representative samples will

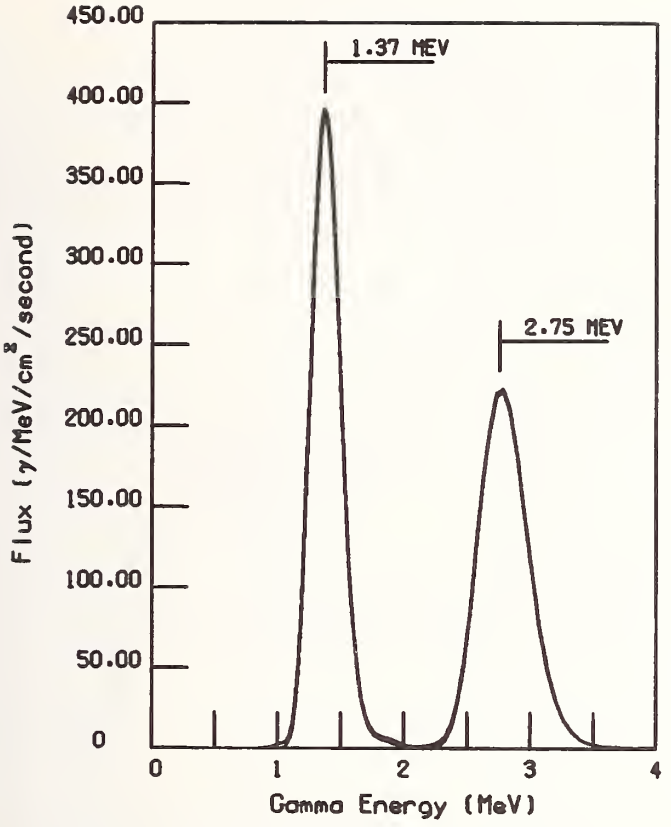

Fig. 3. NE-213 detector response to gamma rays from ^{24}Na.

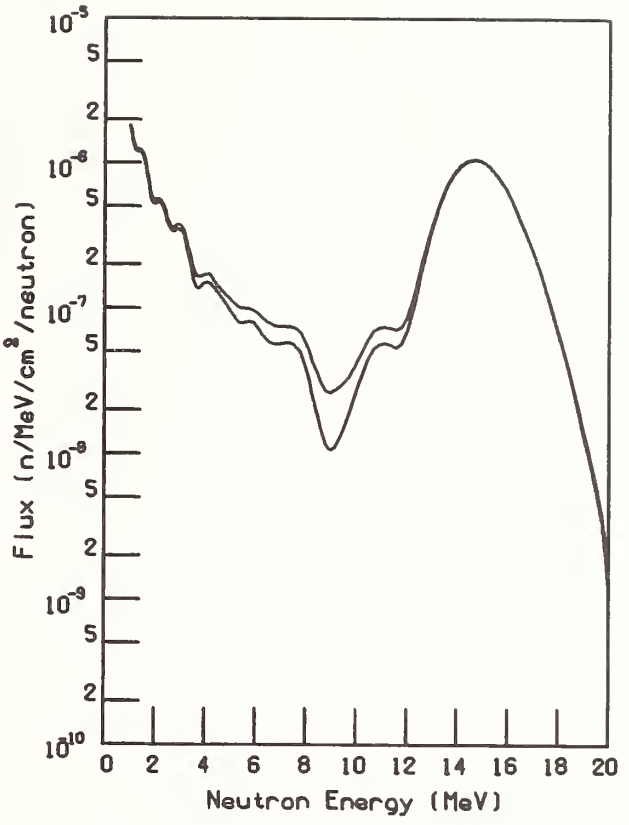

Fig. 4. Neutron energy spectrum measured with no experimental shield in the environment shield.

be given here. First, Figs. 4 through 6 show the neutron energy spectra measured through increasingly thicker shields. The data in Fig. 4 was taken with no experimental shield, whereas, Fig. 5 shows the data taken behind a shield composed of 35.56 cm of stainless steel followed by 5.08 cm of borated polyethylene. An additional 5.08 cm of stainless steel and 5.08 cm of hevimet (tungsten alloy) were added to the 35.56 cm of stainless steel to take the data shown in Fig. 6. The only structure apparent in these data is the peak at above 14 MeV due to source neutrons.

Although NE-213 does not perform as well in detecting gamma rays as it does for neutrons, it is possible to obtain useful gamma-ray spectra as shown in Figs. 7, 8, and 9. As with the neutron data, these figures show the gamma ray spectra taken behind increasingly thick shields. That is, Fig. 7 shows the gamma rays measured behind 15.24 cm of stainless steel, after which the thickness of the shield was increased to 35.56 cm of stainless steel plus 5.08 cm of borated polyethylene for data shown in Fig. 8. An additional 5.08 cm of stainless steel and 5.08 cm of hevimet were added to the shield for taking the data shown in Fig. 9. The apparent structure at 6 to 8 MeV remains outstanding in all of the spectra and may be due primarily to neutron capture in the shield. The apparent peak at about 2 MeV has not been resolved at this time.

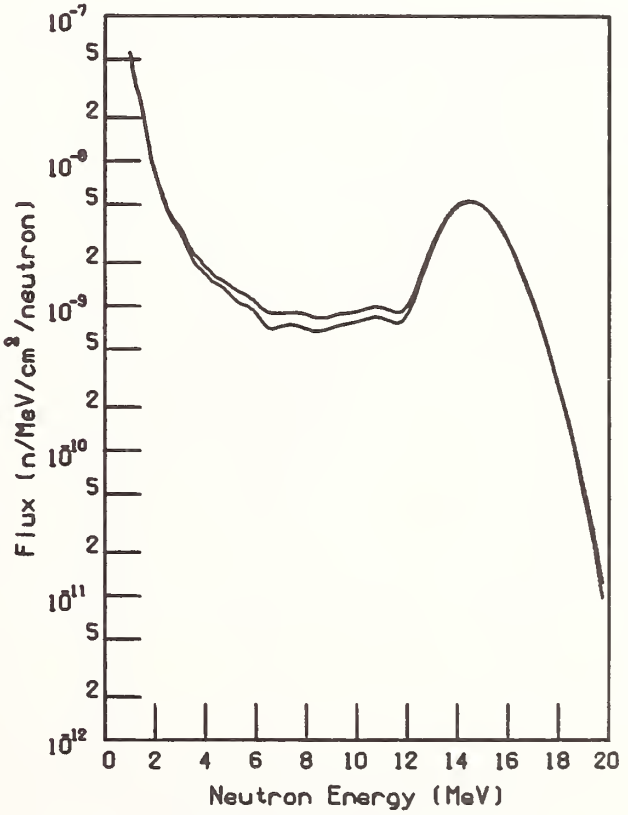

Fig. 5. Neutron energy spectrum measured behind 35.56 cm of stainless steel plus 5.08 cm of borated polyethylene.

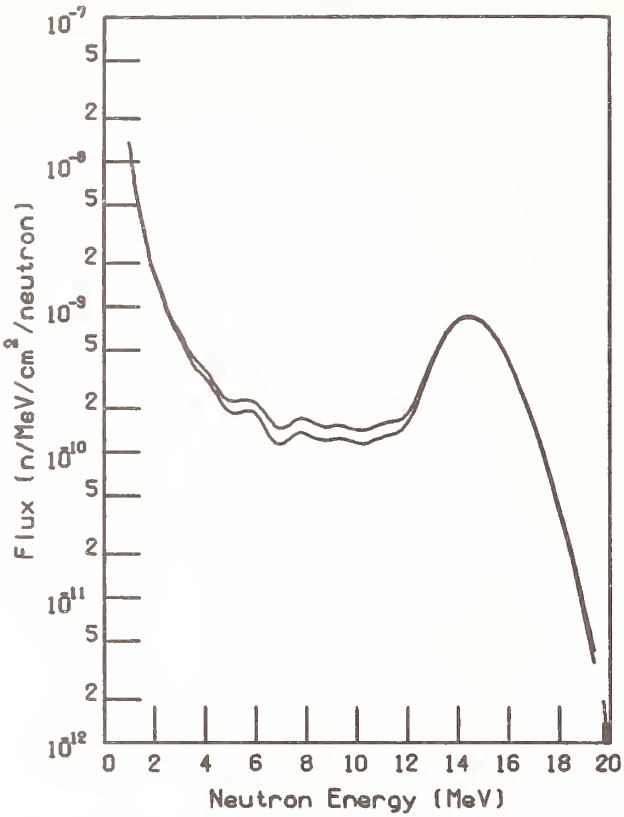

Fig. 6. Neutron energy spectrum measured behind 35.56 cm of stainless steel plus 5.08 cm of borated polyethylene plus 5.08 cm of stainless steel and 5.08 of hevimet.

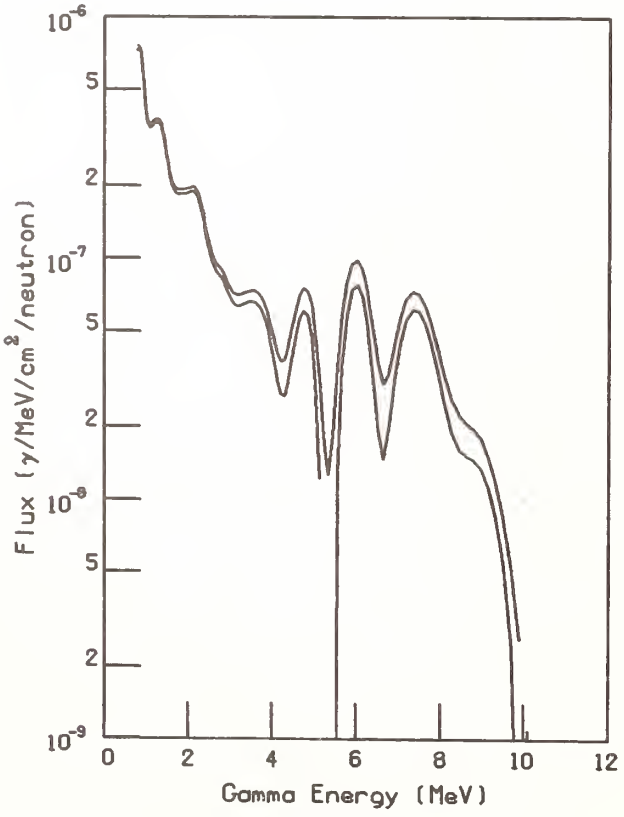

Fig. 7. The gamma-ray energy spectrum measured behind 15.24 cm of stainless steel.

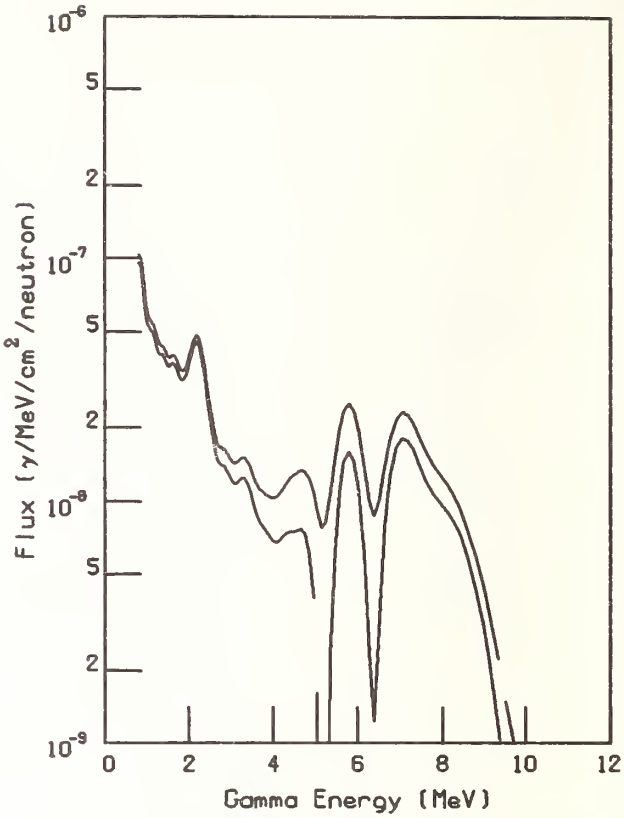

Fig. 8. The gamma-ray energy spectrum measured behind 35.56 cm of stainless steel plus 5.08 cm of borated polyethylene.

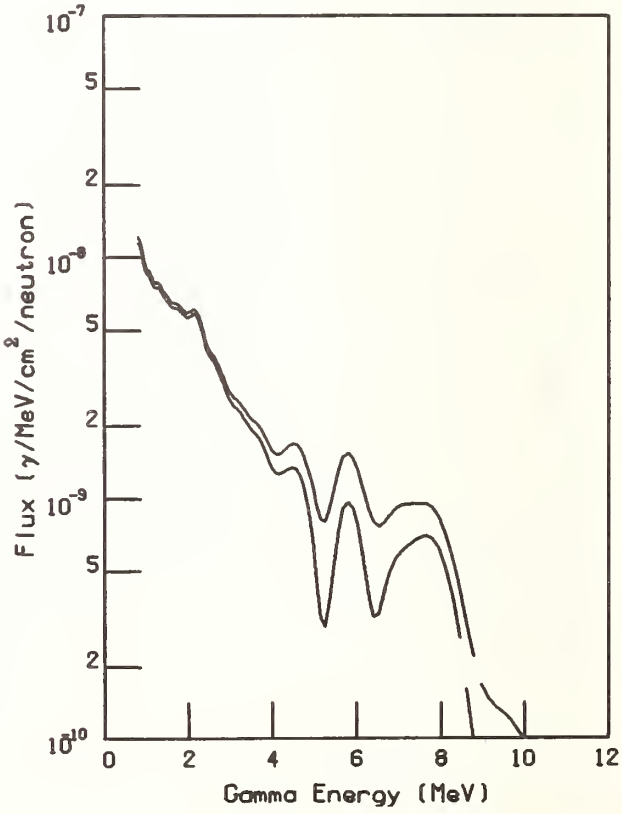

Fig. 9. The gamma-ray energy spectrum measured behind the shield described in Fig. 6.

Acknowledgments

Specific acknowledgment is made of the assistance given by J. W. McConnell of the Engineering Physics Division (ORNL) in computer technology and circuit development. His efforts were a major contribution to the progress made in the program. This work is sponsored by the DOE Office of Fusion Energy under Contract No. W-7405-eng-26 with Union Carbide Corporation.

References

1. Present address: Los Alamos Scientific Laboratory, Los Alamos, New Mexico 87545, USA.

2. E. Oblow in DMFE Integral Experiment Progress Report, 10/76 - 10/77 (ORNL).

3. V. V. Verbinski, W. B. Burrus, T. A. Love, W. Zobel, and N. W. Hill, Nucl. Inst. & Meth., 65, 8 (1968).

4. R. T. Santoro, R. G. Alsmiller, Jr., J. M. Barnes, E. M. Oblow, to be published in the Proceedings of the International Conference on Nuclear Cross Sections for Technology, Knoxville, Tennessee, 1979.

INTEGRAL EXPERIMENTS FOR FUSION REACTOR DESIGN: ANALYSIS

R. T. Santoro, R. G. Alsmiller, Jr., J. M. Barnes, E. M. Oblow
Oak Ridge National Laboratory
Oak Ridge, Tennessee 37830, USA

Integral experiments that measure the energy spectra of neutrons and gamma rays due to the transport of ∿ 14 MeV D-T neutrons through laminated SS-304 and borated polyethylene shield assemblies have been performed. Measured and calculated energy spectra and integrated flux distributions are compared for a typical shield assembly as a function of detector location.

[Integral Experiments, Radiation Transport, Neutron Spectra, Gamma Ray Spectra]

Introduction

A series of integral experiments are being performed at the Oak Ridge National Laboratory to provide verification of the nuclear data and radiation transport methods that are being used in nuclear design calculations for fusion reactors. The experimental program, which is described in detail in a companion paper[1], is currently directed at measuring the transport of ∿ 14 MeV neutrons produced in D-T reactions through laminated slabs of stainless steel type 304 (SS-304) and borated polyethylene (BP). These materials are typical of those expected to be used in the shield of a fusion reactor. The experiments are supported and complemented by an analytic program that attempts to reproduce the measured results by carrying out radiation transport calculations using representative geometries of the experimental configuration and the most current nuclear data and radiation transport codes.

This paper compares neutron and gamma ray energy spectra measured behind a typical shield assembly with those obtained from calculation. The details of the calculations including the model of experimental geometry, the nuclear data, and the radiation transport procedures are described in the next section. The measured and calculated energy spectra are compared and discussed in another section.

Details of the Calculations

The calculated energy spectra were obtained using two-dimensional radiation transport methods using the geometric representation of the experimental configuration shown in Fig. 1. The experimental arrangement was approximated by representing the room, shield assembly, concrete support structure, and detectors in cylindrical geometry with symmetry about the axis of deuteron injection. The components were modeled using 42 radial and 82 axial mesh intervals. The calculational geometry is reduced by eliminating the experimental room walls. The radial boundaries and the axial boundary at r = ∿ 152 cm are treated as albedo surfaces with a reflection factor of 20% for neutrons and gamma rays of all energies. The reduced geometry and reflection factor were carefully chosen to assure that the scalar flux profiles are the same as those obtained with a full experimental room representation. Compressing the geometry results in a smaller core size requirement for the transport codes and a concomittant reduction in code running time.

The neutron source (produced by the reactions of 200 keV deuterons with tritium) is housed in an iron can which was designed to soften the neutron spectrum emitted from the target. The softened spectrum simulates the reflection of neutrons from the vacuum vessel walls in a fusion reactor. The laminated shield assemblies are supported in a bulk concrete superstructure. Neutron and gamma ray spectra are

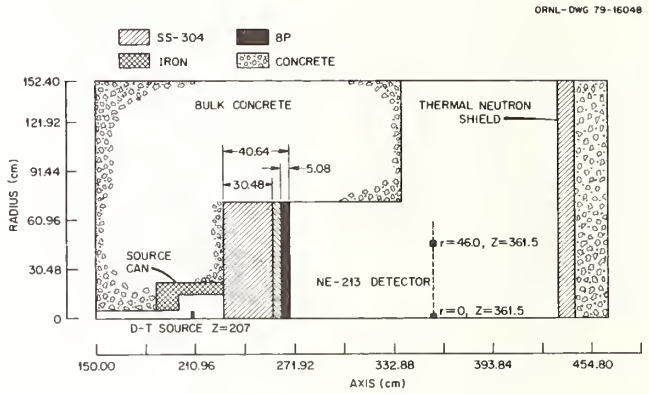

Fig. 1. Calculational geometry of the experimental configuration.

measured as a function of shield thickness and composition with respect to the axis of symmetry. Experiments have been completed for the shield compositions and thicknesses listed in Table I. In this paper, the measured and calculated results are presented only for Experiment 4.

The sequence of calculations to obtain the neutron and gamma ray energy spectra is complex and very detailed and is described fully elsewhere[2], so only a brief discussion of the calculational sequence is given here. The neutrons emitted from the D-T reaction are characterized by an angle-energy relation that depends on the energy of the incident deuteron and the tritium number density in the target. The angular dependence was calculated taking into account the deuteron slowing down in the target. The energies of the emitted neutrons were determined from the kinematic equations for a two-particle reaction. The probability distributions for the emission of neutrons into an angular interval served as the source term for the transport calculations and as the energy weighting functions for collapsing the multigroup transport cross section data.

Separate calculations were performed to determine the first collision and uncollided flux distributions in the geometry mesh used to define the experimental configuration using black absorbers positioned about the neutron source to define the angular interval into which neutrons in a given energy interval are emitted. The angular intervals were selected using the geometry shown in Fig. 1 to account for the neutrons emitted into the solid angle subtended by the source can opening, for those emitted essentially perpendicular to the deuteron axis, and for those emitted into the backward angles. The three separately calculated uncollided flux-first collision source distributions were combined to form a single source term for use in the

Table I. Shield Compositions and Thicknesses

Experiment	Shield Composition: 55-304[a]	5S-304	BP[b]	55-304	BP	55-304	Total Shield Thickness (cm)
	Slab Thicknesses (cm)						
1	0						0
2	15.24[c]						15.24
3	30.48[d]						30.48
4	30.48	5.08	5.08				40.64
5	30.48	5.08	5.08	5.08			45.72
6	30.48	5.08	5.08	5.08	5.08		50.80
7	30.48	5.08	5.08	5.08	5.08	5.08	55.88

[a] Stainless steel type 304
[b] Borated polyethylene
[c] Three 5.08-cm-thick slabs
[d] Six 5.08-cm-thick slabs

two-dimensional discrete ordinates code DOT[3] (S_{12} angular quadrature) to complete the transport calculation. A final scattering source tape generated in DOT was employed to carry out a last-flight transport calculation to obtain the neutron and gamma ray flux distributions at each detector location. Performing the calculations in this sequence assures that ray effects from the D-T neutron source as well as those from intense scattering centers in the experimental apparatus are eliminated.

In all of the calculational procedures, the radiation transport was performed using a 53-neutron, 21-gamma ray energy group transport cross section library. These data were obtained by collapsing the 171-neutron, 36-gamma ray energy group Vitamin C data set (ENDF/B-IV).[4] This library was created as a general purpose cross section data set for the analysis of fusion neutronics problems. The fine group library was collapsed using the ANISN[5] code by representing the experimental components in the emitted neutron angular intervals in spherical geometry and using the energy spectrum in that angular interval as a weighting function. The energy boundaries of the collapsed data library were selected so that the D-T neutron source spectrum could be represented accurately in the transport calculations.

Discussion of Results

The measured and calculated neutron energy spectra at the two detector locations shown in Fig. 1 are compared in Fig. 2. The experimental data were obtained using an NE-213 liquid scintillator.[1] The solid lines indicate the statistical uncertainty in the unfolded measured neutron spectra and the dots are the calculated results. The calculated results were obtained by smoothing the flux per unit energy in each multigroup energy interval with an energy-dependent Gaussian distribution that characterizes the response of the detector and electronic system to neutrons. The data are compared for neutrons with energies above $\sim$ 850 keV which is the lower energy limit at which optimum performance of NE-213 can be achieved. The lower energy limit being governed by such factors as the dynamic range and linearity of the detector system.

The measured and calculated data are in excellent agreement between 850 keV and $\sim$ 11 MeV. The calculated energy spectra are slightly higher than the measured spectra between 11 and $\sim$ 12.5 MeV, in good agreement between 12.5 MeV and $\sim$ 15 MeV, and then

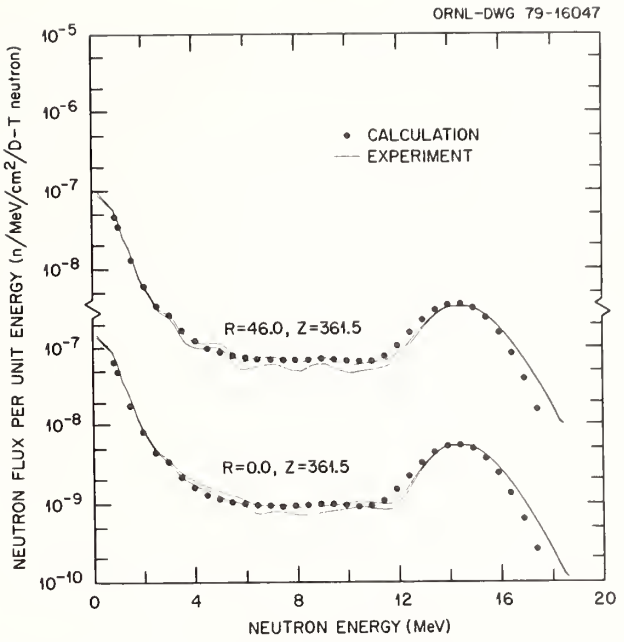

Fig. 2. Comparison of measured and calculated neutron energy spectra versus neutron energy.

exhibit a more rapid roll off at higher neutron energies. The maximum neutron energy emitted from the reaction of 200 keV deuterons with tritium is 15.1 MeV. The differences between the measured and calculated results above this energy is principally a manifestation of Gaussian response of the detector and that the response function is acting on energy intervals that differ between the two data sets.

The differences between the measured and calculated results between $\sim$ 11 and $\sim$ 12.5 MeV are more difficult to identify and may be due to anomalies in the cross sections used in the radiation transport. A detailed investigation of the causes of these differences using sensitivity analyses will be carried out.

The measured and calculated integrated neutron flux distributions are compared in Fig. 3. These data were obtained by integrating the energy spectra shown in Fig. 2. The calculated and measured data are in excellent agreement for energies up to $\sim$ 15 MeV.

The gamma ray energy spectra are compared in Fig. 4 for the two detector locations. The agreement among the measured and calculated data are favorable for gamma ray energies up to $\sim$ 9 MeV. At the higher energies, the differences may not be entirely due to physical causes, but rather the result of uncertainties in unfolding the experimental data or, as in the case for neutrons, a manifestation of the response of the NE-213 detector. The calculated data were obtained using a rather broad energy group structure which may account for the failure to reproduce some of the gamma ray peaks. However, similar trends in the spectra are observed. When the data are compared on an integrated basis as in Fig. 5, then the results are more encouraging.

Analyses of these neutron and gamma ray data are continuing and comparisons for the remaining cases given in Table I are becoming available. Detailed studies of all the results should isolate some of the reasons for differences in the measured and calculated spectra and identify uncertainties and limitations in both the data and calculational methods.

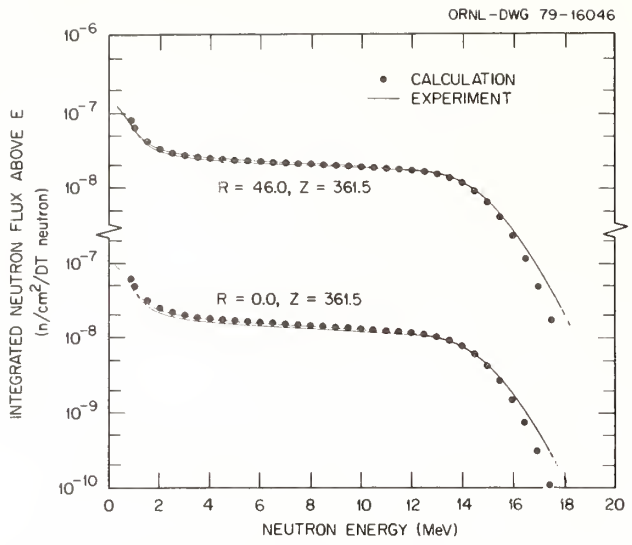

Fig. 3. Comparison of measured and calculated integrated neutron flux above E versus neutron energy.

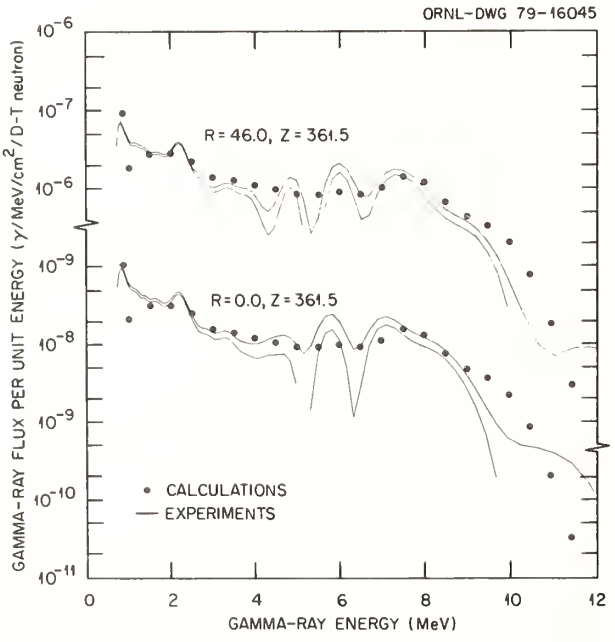

Fig. 4. Comparison of measured and calculated gamma ray spectra versus gamma ray energy.

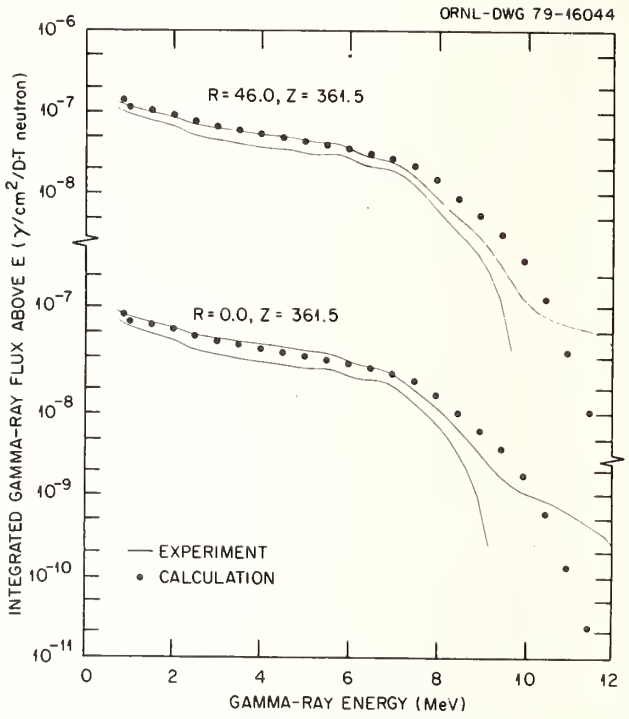

Fig. 5. Comparison of measured and calculated gamma ray flux above E versus gamma ray energy.

Acknowledgement

Research sponsored by the U.S. Department of Energy, Division of Development and Technology, Office of Fusion Energy under Contract No. W-7405-eng-26 with Union Carbide Corporation.

References

1. G. T. Chapman and G. L. Morgan, to be published in the Proceedings of the International Conference on Nuclear Cross Sections for Technology, Knoxville, TN, October, 1979.

2. W. A. Rhoades and F. R. Mynatt, "The DOT III Two-Dimensional Discrete Ordinates Transport Code," ORNL/TM-4280, Oak Ridge National Laboratory (1979).

3. R. T. Santoro, J. M. Barnes, R. G. Alsmiller, Jr. and E. M. Oblow, "Calculational Procedures for the Analysis of Integral Experiments for Fusion Reactor Design," ORNL/TM-7094, Oak Ridge National Laboratory, in preparation.

4. ORNL/RSIC-37, Radiation Shielding Information Center, Oak Ridge National Laboratory (1975) available as DLC/41-Vitamin C.

5. W. W. Engle, Jr., "A User's Manual for ANISN, A One-Dimensional Discrete Ordinates Code with Anisotropic Scattering," K-1693, Oak Ridge National Laboratory (1967).

USE OF NUCLEAR TECHNIQUES IN OIL WELL LOGGING

K. S. Quisenberry
Schlumberger-Doll Research
Ridgefield, Connecticut 06877, USA

Radiation transport codes are being applied to modeling the response of nuclear logging tools. The cross sections, benchmark experiments and neutron source spectral data that are required for this purpose are described. A neutron porosity tool is used to illustrate such calculations.

[Nuclear logging, radiation transport, nuclear data, neutron source shapes.]

Introduction

Oil well logging is the process of making physical measurements in an oil well, after it has been drilled, and then representing the data and resulting parameters of interest as a linear function of depth; the log. Methods today use electrical, acoustical, and mechanical as well as nuclear properties of rock. The parameters measured (e.g. electron density, hydrogen density, type of rock) usually do not directly indicate the quantity and producibility of oil. Rather answers are obtained by inference, after combining the results of several measurements.

To improve the inference process it is useful to have measuring tools that give accurate results, with well known corrections where necessary. For nuclear tools, detailed mathematical calculations can improve the accuracy of the corrections especially where specific conditions are difficult, if not impossible, to simulate experimentally. These calculations require appropriate codes and accurate cross section and spectral data.

The oil well measurement problem shown in Figure 1 is in many ways unique. The region of interest, the rock formation surrounding the borehole, is unaccessible. All measurements are either made in the well or on the surface. Temperature and pressure increase with depth in the earth, with pressures of 20 to 40 MPa and temperatures of up to 150°C common. All measurement apparatus must be contained within a slim pressure housing suspended at the end of a long (up to 10,000 m) cable. The borehole has a diameter of 20 to 40 cm, with walls that are frequently not smooth. The borehole fluid can contain water, dense mud, oil, and corrosive chemicals such as salt (NaCl) or hydrogen sulfide (H_2S). The instruments are lowered to the bottom of the well, and data are recorded as the cable is withdrawn at a constant rate, typically in the range of two-hundred to two-thousand meters per hour. Data signals must be transmitted to the surface where they are decoded, processed, and recorded.

Under field conditions, rapid measurement and high equipment reliability require apparatus designs that maximize accuracy and minimize measurement time. For nuclear tools that use radioactive sources this indicates use of strong sources, but such sources present ever-increasing handling, shielding, and transport problems so source size is limited. Detector size is restricted by the need to fit within the pressure housing, typically $\leq$ 9 cm in outside diameter.

Chemical sources of gamma rays and neutrons are used as are 14 MeV (D,T) neutrons. Integral measurements can be made which are sensitive to the electron density,[1] hydrogen density,[2] and macroscopic capture cross section[3] of the formation. Gamma ray spectroscopy, using NaI(Tl) or germanium detectors, can be applied in several ways. The simplest is to detect

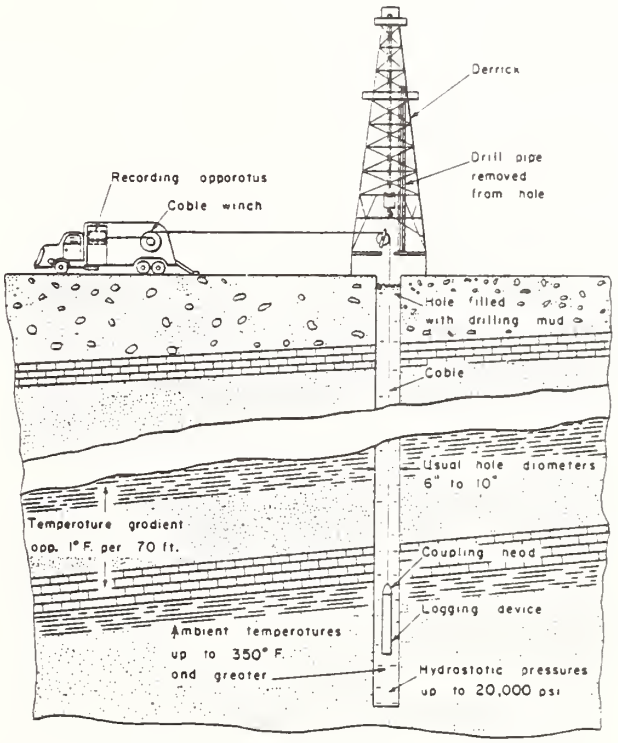

Figure 1 - Schematic Drawing of a Well Logging Operation

natural activity from the potassium, thorium and uranium present in the rocks. Activation analysis can be performed using either chemical or accelerator neutron sources. High energy neutrons (14 MeV) are used to determine fluid saturation by measuring the thermal flux decay time. Recently it has become possible to determine elemental concentrations by detecting inelastic gamma rays from reactions of 14 MeV neutrons.[4]

Neutron Porosity Logging

To illustrate the application to logging of analytical methods and nuclear cross section data, we use as an example a Pu-Be neutron source and ^3He detector based porosity measurement tool. Such a device has been used for some time to provide accurate hydrogen density measurements which are related to the formation porosity. (The assumption that the rock pores are fluid filled with water (H_2O) or hydrocarbons (C_nH_{2n}) yields a direct relationship between hydrogen density and porosity.) This system has been described

in some detail,[2] and only the basic principle will be introduced here to illustrate the use of analytical modeling.

Figure 2 is a plot of the count rate observed in a black thermal neutron detector as a function of source-detector spacing in limestone. The neutron source is Pu-Be and the curves are for porosities of 0, 10 and 30%, respectively. These data are the result of ANISN[5] one-dimensional transport theory calculations with a point source in an infinite medium. This "ideal case" is used to illustrate the concept of the measurement. If a source-detector spacing greater than about 20 cm (in this model) is used, the slope as a function of distance increases monotonically with porosity. By using two or more detectors, this slope can be determined and hence a porosity value derived.

Figure 3 shows a similar calculation for a sandstone matrix. The trends are similar to the previous example but there are significant differences in the calculated slope for a given porosity. This illustrates the dependence of the measurement on the rock matrix. Many other details of the environment significantly influence the response. In general, porosity measurements to an accuracy of about ±1 percent of total volume are desired for porosities between 0 and 40%.

Experimental data from the laboratory and field operating experience confirm that raw porosity data must be corrected for numerous environmental effects, e.g. borehole size, fluid density and salinity, and temperature. Up to now most such corrections have been obtained by laboratory measurements. However, as the degree of accuracy of the answers required from logging data has increased and the wide range of physically occurring environments has become apparent, accurate knowledge of these corrections has become essential over a range impossible to duplicate experimentally. We therefore embarked on an effort to supplement our experimental understanding of nuclear logging tools with detailed, analytical models of each device.

Data Requirements to Calculate Tool Response

The benefits to be realized from the development of reliable theoretical models of logging tools and concepts are now being recognized. In principle, evaluation models will permit the investigation of almost every conceivable neutron source and detector configuration as a function of many borehole and rock matrix parameters. The sophisticated radiation transport computer codes that have been developed will greatly aid in the effort to build good models of nuclear logging tools.

However, the application of radiation transport computer codes is complicated by many of the realities of oil well logging. During the drilling a mud-like fluid lubricates the bit and applies overpressure to prevent blowouts. Mud filtrate can penetrate the formation wall leaving a precipitate, the mudcake, along the rock surface. The borehole diameter and surface texture depend on the type of rock and on drilling conditions. The tool is geometrically complex with the hardware confined inside the pressure housing (often asymmetrically) and with shielding competing for space with electronics and detectors. Logging practices often destroy any remaining geometrical symmetry. The measuring device is almost always eccentered in the well: hence, an accurate model must be three-dimensional, which implies use of Monte Carlo. However, the low counting efficiency of actual tools

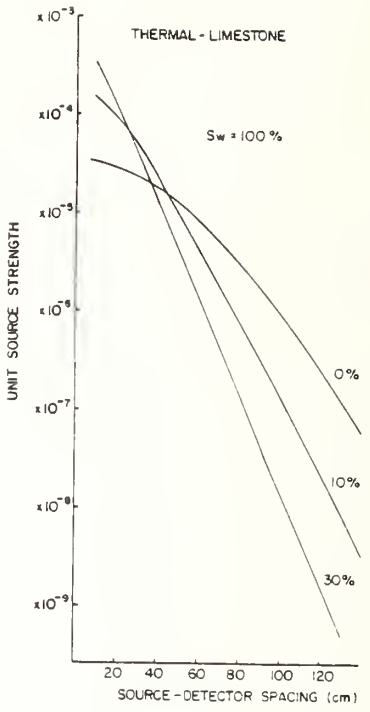

Figure 2 - Count Rate vs Source-Detector Spacing in Limestone

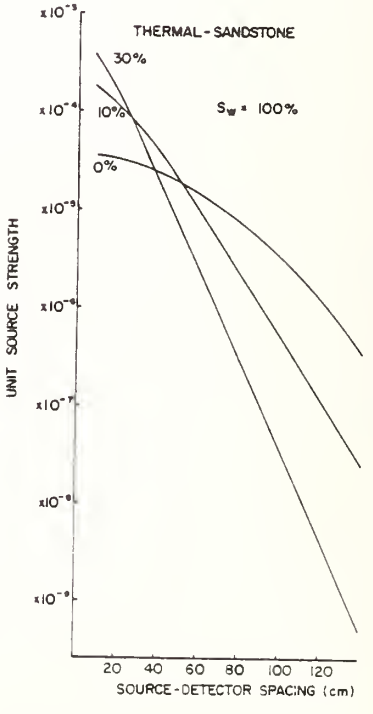

Figure 3 - Count Rate vs Source-Detector Spacing in Sandstone

Table 1 - Nuclear Data Required for Nuclear Logging

Elements	Reaction Cross Section				
	Elastic	Differential Elastic	Inelastic	Capture	γ Production
Silicon	X	X	X	X	X
Calcium	X	X	X	X	X
Carbon	X	X	X	X	X
Oxygen	X	X	X	X	X
Hydrogen	X	X		X	X
Magnesium	X	X	X		X
Iron	X	X	X	X	X
Aluminum	X	X			
Tungsten	X	X	X		
Nickel	X	X	X	X	X
Chromium	X	X	X	X	X
Copper	X	X	X		
Titanium	X	X	X		
Sulfur	X			X	
Chlorine	X			X	X
Manganese	X	X	X	X	
Sodium	X	X		X	
Barium	X	X		X	

($\sim 10^{-5}$) can drastically increase Monte Carlo computing times. Hence, biasing techniques for improving the calculational efficiency are critical. Finally, the formations themselves, though represented as homogeneous media, usually are non-homogeneous on a macroscopic scale.

To illustrate our approach, we are already applying three-dimensional continuous energy Monte Carlo techniques and 2-D transport theory to many of our problems. It is clear that despite the realities of the borehole problem the usefulness of calculated results will be affected by the reliability of basic nuclear data. This is especially true when accuracies of one to a few percent are desired. Some of the elements which are most significant to the analysis of nuclear logging problems are listed in Table 1, along with the major reaction cross sections of interest.

A casual survey of the compiled nuclear data[6] which are available for many of the elements in Table 1 in the energy range of interest to logging (thermal to 14 MeV) does not identify any particular gaps in the measurements of important cross sections. For example, Figure 4 shows the total neutron cross section for silicon, one of the major constituents of sandstone rock. The data do exist to describe the intricate energy dependence of the silicon total cross section for use in the continuous energy Monte Carlo calculations. Figure 5 depicts essentially the same situation for calcium, a major constituent of limestone and dolomite. It appears that the total cross section detail that can be represented for elements like calcium and silicon is comparable to that for hydrogen, oxygen and carbon. However, one important difference is that while we have confidence in the existing nuclear data for elements like hydrogen, oxygen and carbon as a result of benchmark work in reactor programs, we cannot claim the same for the common rock matrix materials (i.e. silicon, calcium, magnesium, etc) for logging applications. Therefore, we see a need to assess the reliability of these nuclear data through analysis of benchmark experiments and cross section sensitivity testing.

In particular, it would be desirable to study the moderation of fast neutrons directly in the media of interest, namely limestone, silica and dolomite. More up-to-date age measurements[7] with well-characterized sources would provide a good test of the space-energy slowing down in these media. An important feature of these measurements is that they are one-dimensional, enabling reliable cross section sensitivity modeling to be performed. Another one-dimensional integral test of these nuclear data would be provided by measurements of neutron leakage spectra[8] from homogeneous spherical assemblies made up of different rock matrix materials.

Finally, in addition to reliable nuclear cross section data there is a need to represent more precisely for modeling the various radioactive source spectra used in nuclear logging. The published shapes of common source spectra (e.g. Pu-Be, Am-Be, Pu-Li) exhibit appreciable scatter. This is particularly clear from examination of three different Pu-Be source spectra shown in Figure 6 (taken from Reference 9). Characteristics of two Be(α,n) sources as compiled by Geiger and Van Der Zwan[10] exhibit significant (>10%) spreads in mean energies (Table 2). The best spectral representations to use in our modeling are unknown. For some logging techniques, details of the source spectra, particularly at high neutron energies (>4 MeV) can greatly affect calculated results. More work is needed to resolve the differences between measured spectra for specific Be(α,n) sources.

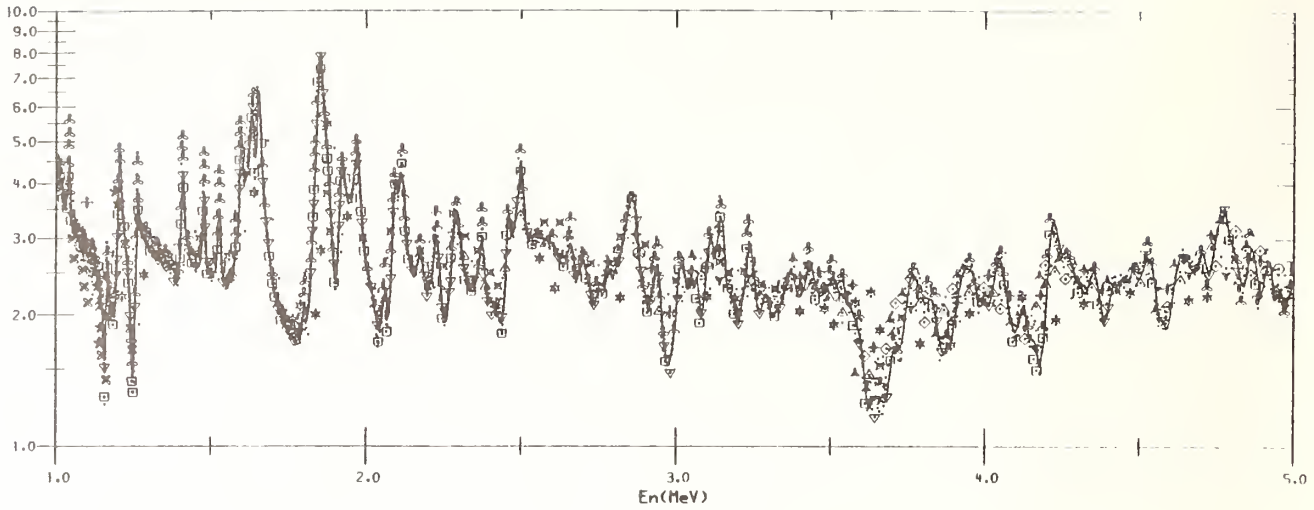

Figure 4 - Total Cross Section of Silicon

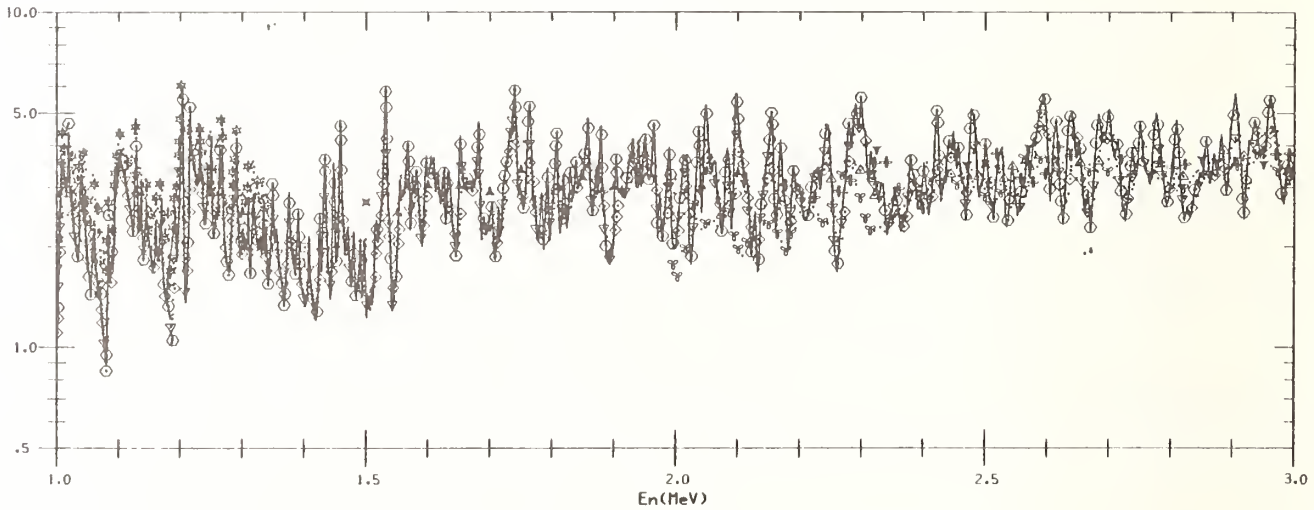

Figure 5 - Total Cross Section of Calcium

Summary

This paper has portrayed nuclear oil well logging and the application of radiation transport models to logging problems. Some of the important nuclear data to be input to these models have been identified. At this time we cannot judge the adequacy of existing nuclear data for logging models and concepts. However, we see the need for better characterizations of radioactive source spectra and for quality integral experiments to provide benchmarks to test these spectra and the nuclear data for common rock materials.

Table 2 - Characteristics of Be(α,n) Source Spectra from the Literature

Source	Fraction of Neutrons with E_n <1.5 MeV (%)	Mean Energy (MeV)
Pu-Be	7 - 33	4.2 - 4.7
Am-Be	15 - 23	3.9 - 4.3

References

1. B. Felder and C. Boyeldieu, "The Lithodensity Log", Sixth European Symposium Transactions, March 26-27, 1979

2. R. P. Alger, S. Locke, W. A. Nagle, and H. Sherman, J. Pet. Tech., 24, 1073 (1972)

3. J. S. Wahl, W. B. Nelligan, A. H. Frentrop, C. W. Johnstone and R. J. Schwartz, J. Soc. Pet. Eng., 10, 365 (1970)

4. R. C. Hertzog, "Laboratory and Field Evaluation of an Inelastic-Neutron Scattering and Capture Gamma Ray Spectroscopy Tool", SPE 7430, 1978

5. W. W. Engle, Jr., "A Users Manual for ANISN: A One-Dimensional Discrete Ordinates Transport Code with Anisotropic Scattering", K-1693 (Rev. 6-6-73)

6. D. I. Garber and R. R. Kinsey, "Neutron Cross Sections Vol II, Curves", BNL-325 Third Edition, 1976

7. J. Tittman, J. Appl. Physics, 26, 394 (1955)

8. R. H. Johnson et al, "Integral Tests of Cross Sections Using Neutron Leakage Spectra from Spheres....", Proceedings of Conference Neutron Cross Sections and Technology, NBS-425, 1975

9. H. W. Patterson and R. H. Thomas, Accelerator Health Physics, Academic Press, 1973

10. K. W. Geiger and L. Van Der Zwan, Nucl. Inst. Meths., 131, 315 (1975)

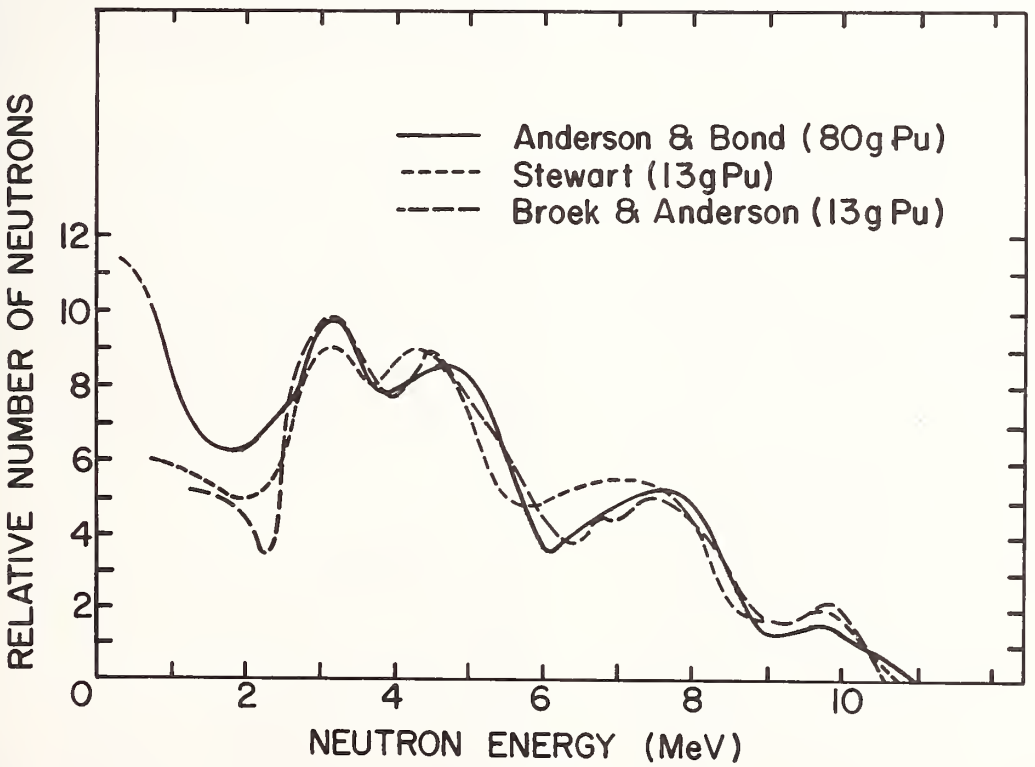

Figure 6 - Comparison of Several Pu-Be Source Spectra

NEUTRON INDUCED RADIOACTIVITY FOR MINERAL EXPLORATION

Frank E. Senftle
U.S. Geological Survey, Reston, Virginia 22092

Borehole neutron activation-gamma-ray spectrometry is a useful method for mineral exploration. Isotopic or accelerator neutron sources are used with either scintillation or semiconductor detectors in the borehole tools depending on the application, rock formation, required measurement time, etc. The basic neutron processes in rock formations are summarized to point out the problem of spectrometer calibration. The source-to-detector distance is an important consideration to achieve optimum sensitivity. There are several possible solutions of the calibration problem. Some of these are demonstrated by applications of neutron activation to mineral exploration in the field. Although many problems still need to be solved to make borehole neutron-gamma-ray spectrometry a more general analytical tool, the method is a powerful qualitative exploration device applicable to many elements in most rock formations. Under certain conditions, e.g., in a coal seam, it can also be a good quantitative tool.

[Borehole Sonde, Accelerator, ^{252}Cf, Source-to-Detector Distance, Capture γ-Ray Analysis]

Introduction

The use of gamma-ray spectroscopy to detect elements for mineral exploration purposes has gained increased acceptance in the mining industry over the past 5 years. The concept of using nuclear techniques for this application is not new. Pontecorvo[1] suggested neutron-gamma-ray logging for oil exploration as early as 1941. The papers published before 1951 were directed toward oil exploration and have been reviewed by Caldwell.[2] The application of nuclear techniques to mineral exploration came later. Some preliminary experiments with a Ra-Be neutron source to detect silver were made in 1951,[3] and in 1955 investigators in the USSR reported using neutron activation techniques to detect aluminum, copper, and manganese in ores.[4] Since then, nuclear technology and instrumentation have progressed so that the practical methods of gamma-ray spectrometry can now be made in situ, e.g., down a relatively deep borehole. Useful field instrumentation has been produced because of the availability of high-resolution gamma-ray detectors, borehole accelerator-type- and ^{252}Cf-isotopic neutron sources, and miniaturized electronics, together with the need for rapid and less costly in situ elemental analyses by the mineral industry. As virtually all the near-surface bonanza-type ore deposits have been found, we now must explore for deep, large-tonnage, low-grade deposits. Thus, the major emphasis is on borehole gamma-ray spectrometry rather than surface-exploration techniques.

Gamma-ray spectrometry in the restricted volume of a water-filled borehole presents some challenging problems. The intensities of the practical neutron sources are low compared with those of nuclear reactors, the detector is not easily shielded from neutrons, the activated samples are ill-defined and are broad gamma-ray sources, and finally, all the borehole electronics must be rugged, low-power, and miniaturized. In spite of the formidable problems, a number of practical exploration systems have been developed and are just becoming commercially available. Although several other nuclear methods have been devised to explore for specific elements in a borehole, we limit this review to the major steps in the development of borehole gamma-ray spectrometry as a mineral-exploration tool.

Early Investigations

Activation logging to determine the presence of elements in reservoir rocks was first exploited for oil exploration by geologists[5-9] using accelerator-type neutron sources. Similar studies[10-12] with isotopic neutron sources were used in the USSR to log boreholes for copper and manganese by means of total-count methods. Rabson[13] and Caldwell et al.[14] were among the first to use neutron-capture spectral logs to detect specific elements. The resolution of their scintillation detectors was not very good, however, and the technique was limited virtually to a qualitative analysis. Most of the other borehole neutron activation techniques before 1970 were based on delayed gamma activation reactions and were also largely qualitative. Although most of the early work was performed by means of continuous-beam borehole accelerators and NaI(Tℓ) detectors, the use of pulsed accelerator neutron sources was later introduced. Chrusciel et al.[15] reviewed the basic physics of pulsed neutron logging, a time-resolution technique that could be used to separate the different types of gamma rays.

Figure 1 shows the fundamental steps in pulsed neutron counting. The gamma-ray analysis is gated to count for set time periods during and after each neutron pulse. The gamma rays produced by inelastic neutron scattering are emitted during the neutron pulse (Gate 1) and the capture plus activation gamma rays are measured after the neutron pulse (Gate 2). The decay or activation gamma-ray activity gradually builds up during each succeeding neutron pulse as the half-lives are generally long compared with the inter-pulse time. The decay gamma rays are measured after the capture gamma-ray activity has decayed to a negligible level, i.e., in the time gate just before the next neutron pulse (Gate 3). The

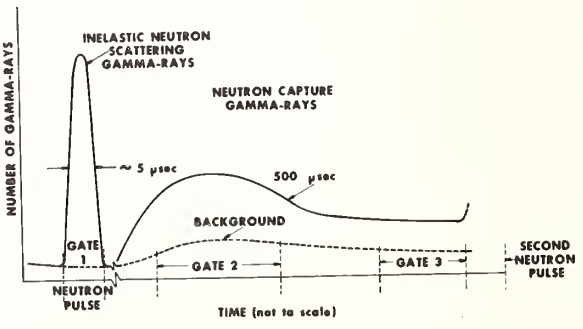

Fig. 1. Relations between time of the neutron pulse and the emission of the several types of gamma rays.

Table I. Comparison of Accelerator-Type and ^{252}Cf-Neutron Sources for Borehole Activation Application.

	Advantages	Disadvantages
Accelerator Type Neutron	1- Can be turned off when not in use - massive shields not required.	1- High energy neutrons cause severe damage to solid-state detector*- difficult to shield.
	2- High neutron energy, greater penetrability - can observe a large sample.	2- Neutron flux is not steady - requires monitoring and integration over measuring period.
	3- Large useful neutron flux of ~10^9 neutrons/sec.	3- Dimensionally large for borehole use - requires sonde 5 to 30 m long.
	4- Useful life of >100 hours.	
^{252}Cf Neutron	1- Neutrons do not cause excessive damage to solid state detectors - can be effectively shielded.	1- Cannot be turned off - needs massive shield.
	2- Neutron flux steady - does not have to be monitored.	2- Relatively low energy neutrons - observed sample therefore only moderately large.
	3- Very small - ideal size for borehole use.	3- Neutron flux 10^6 neutrons/μg ^{252}Cf. Max. practical flux ~6×10^8 neutrons/sec.
		4- ^{252}Cf decays rapidly ($T_{\frac{1}{2}}$ = 2.6 yrs).

*Applies primarily to p-type germanium detectors; n-type germanium is more resistant.

capture gamma rays are determined by subtracting the counts in Gate 3 from those in Gate 2. The number of gamma rays produced by inelastic scattering in Gate 1 is much larger than the sum of the capture and decay gamma rays and does not need to be corrected. Wickmann and Webb[16] and later Wickmann[17] reviewed the use of accelerator - NaI(Tℓ) borehole sondes, and showed that by employing the proper source-to-detector distance and moving the sonde at an optimum speed for a given half-life it was possible to log for oxygen, silicon, and aluminum using the $^{16}O(n,p)^{16}N$, $^{28}Si(n,p)^{28}Al$, and the $^{27}Al(n,p)^{27}Mg$ reactions, respectively. Senftle and Hoyte,[18] using Monte Carlo techniques, examined the neutron fluence rate as depth increased in soil for 3- and 14-MeV accelerator-produced neutrons. Although 14-MeV neutrons provided the greater penetration (larger sample) and higher neutron fluence rate, the spectrum observed with a scintillation detector was complicated by gamma-ray peaks produced by high-energy neutron reactions, e.g., $(n,n'\gamma)$ and (neutron, particle) reactions. They concluded that in order to yield a less complicated spectrum neutrons with a lower energy should be used, e.g., 3 MeV neutrons produced by the (d,d) reaction, in spite of the fact that this reaction yields a hundredfold lower neutron fluence rate.

In 1968, the first ^{252}Cf neutron sources were made available for research purposes. The small size, the relatively high neutron flux, constant over time periods of several hours, and the reliability under field conditions made ^{252}Cf an attractive source of neutrons. The neutrons are emitted with a fission-type spectrum at an average energy of 2.35 MeV, and one can obtain a reasonably uncomplicated delayed-gamma spectrum in a rock matrix even with a NaI(Tℓ) detector. Comparison of results obtained with neutrons produced by ^{252}Cf and an accelerator using a (d,d) reaction indicated that ^{252}Cf could be used in borehole tools for mineral exploration.[19]

In the late 1960's, solid-state Ge(Li) detectors also became available. The vast improvement in resolution of these detectors over scintillation detectors made it possible to resolve many individual gamma-ray lines. Several lists[20-23] of capture gamma-ray lines and their relative intensities were published so that capture gamma-ray analyses could be made in the laboratory. Unfortunately, the requirement that Ge(Li) detectors be cooled to liquid nitrogen temperatures complicated their use in a water-filled borehole configuration. Venting the nitrogen without causing temperature changes was an intractable problem that was eventually solved by using a solid cryogen at the melting point rather than a liquid at the boiling point.

Borehole Gamma-Ray Spectrometers

A borehole neutron activation gamma-ray spectrometer system can be divided into two basic parts, the neutron source and the gamma-ray detector. Two types of neutron sources are used, accelerators and isotopic sources. Because of its high specific neutron emission, ^{252}Cf is the best isotopic source. The advantages and disadvantages of the two types of neutron sources are outlined in Table I. Both types have been used, the choice depending on the application and type of reaction under investigation. Accelerator voltages of 100-150 kV can be obtained in a borehole sonde, and thus a useful neutron flux of about 10^9 neutrons/sec at 14 MeV can be achieved at the target using a (d,t) reaction. A neutron flux with an energy of 3 MeV but two orders of magnitude lower flux can be obtained with a (d,d) reaction. At 1 cm from a ^{252}Cf source of 100 μg, a fluence rate of about 2×10^7 neutrons/cm^2-sec with a fission-type energy distribution and an average energy of 2.35 MeV can be realized.

NaI(Tℓ), Ge(Li), and high-purity Ge crystals have been used for detectors in borehole spectrometers. NaI(Tℓ) is considerably more efficient than Ge(Li) or pure germanium, but the germanium crystals have a much better energy resolution - a highly desirable property for gamma-ray spectrometry. In spite of the poor resolution of scintillation spectrometers, many investigators currently use them in order to obtain significant counts in short counting times, e.g., when the sonde is continuously moved up a borehole. Before 1971, NaI(Tℓ) detectors were used for spectral analysis in all borehole sondes. In 1971, Tanner *et al.*[24] built a borehole sonde using a Ge(Li) detector cooled with melting propane, which

held the crystal close to the temperature of liquid nitrogen for as long as 10 hours (see Figure 2). Nedostup and Prokof'ev[25] constructed a similar sonde in which solid nitrogen frozen by cryogenic evaporation was used. Dumesnil and Andrieux,[26,27] and also Lauber and Landstrom[28] built borehole sondes

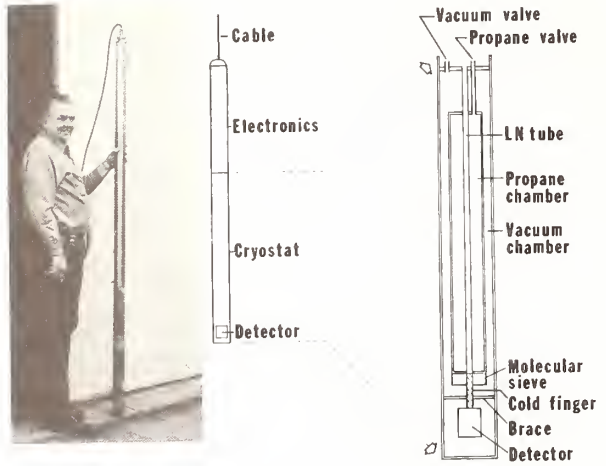

Fig. 2. Picture and sketch of borehole sonde with solid propane-cooled cryostat.

using Ge(Li) detectors which were cooled by liquid nitrogen and vented through flexible tubes to the surface. These liquid-nitrogen-cooled instruments have a depth limitation, and the advantage of using solid propane as a cryogen is obvious. In his doctoral thesis,[29] Andrieux proposed a sonde similar to that shown in Figure 2 except that the Ge(Li) crystal was above the cryostat. An early sonde reported by Fanger et al.[30] closely resembled that proposed by Andrieux. To stabilize the detector temperature and to maximize the operating period, the cryogen ice must remain close to the detector position. Propane ice sinks in liquid propane at the melting point, whereas chlorodifluoromethane, which has also been suggested as a cryogen,[24,31] floats on its melt liquid. Therefore, the configuration of the sonde is dictated by the cryogen used. Chrusciel[32] has reported results using a new sonde built by the Karlsruhe group that has an improved cryostat and electronic system.

In 1975, Boynton[33] devised a sonde cooled by a canister of frozen propane. When the propane melted, the warm canister could be replaced by a second frozen canister. In this way the working time could be extended.

Recent improvements in borehole sondes have been applied to the detector rather than the cryostat. Replacement of the Ge(Li) detector with high-purity germanium makes field operation more practical. High-purity germanium requires cooling only when in use, and if a warm-up inadvertently takes place, one does not lose the crystal. A very recent improvement is the use of n-type, rather than the more common p-type germanium,[34,35] which is about 28 times more sensitive to radiation damage than an n-type detector. This type of detector is especially suitable for use with a 14-MeV accelerator-type neutron source, whose fast neutrons can seriously damage the detector.

Between the neutron source and the detector, a shadow shield of lead or bismuth is generally used to attenuate the direct gamma radiation from the source. The shield also scatters direct neutrons from the source into the wall rock. Although some exceptions are made, the general practice is to mount an isotopic source below the detector to facilitate its attachment and removal. The reverse is true when an accelerator-type neutron source is used. Both source and detector are mounted in a single hermetically sealed casing that can be moved continuously or stepwise in the borehole.

An electronics package consisting of a power supply and a preamplifier-driver is usually mounted above the detector. Although the practice has been to send an analog signal up the borehole, such a signal will obviously show degradation through a long cable, and there will be a subsequent loss of resolution in the spectra. To reduce resolution losses, one can digitize the signal in the sonde and send the digitized rather than the analog signal up the cable. Field systems in which the analog-to-digital converter is built into the borehole sonde have been described and tested by Schulze and Würz[36] and also by Mikesell et al.[37]

Neutron Interaction

Any one of four basic reactions can be used to detect and analyze the elements in the wall rock of the borehole. These are:

1) Delayed gamma-ray analysis following thermal neutron activation.

2) Capture gamma-ray analysis following thermal, epithermal, or resonance activation.

3) Gamma-ray analysis following inelastic neutron scattering.

4) Gamma-ray analysis following particle reactions (n,2n), (n,p) (n,α), etc.

Delayed Gamma Analysis: Ordinary laboratory neutron activation utilizes thermal neutrons from a reactor for analyzing a relatively small sample. As both the neutron fluence rate and the activation cross sections are generally high, the analytical method is sensitive for many elements. In a borehole analysis, the sample is much larger than that used in the laboratory but the available neutron fluence rate is much lower. One cannot fully utilize the much larger sample (1) because of the significant attenuation of the relatively low energy gamma rays emitted, and (2) because the region of maximum activation in the wall rocks is only several centimeters from the edge of the borehole. Consequently, except for a few elements that are easily activated, e.g., aluminum, one must use an intense neutron source. A large ^{252}Cf source would be suitable, but the shield-handling problems in the field are prohibitive. For delayed gamma-ray spectroscopy in a borehole, a neutron generator offers an adequate source intensity for a number of elements, but other problems detract from its usefulness. For instance, a major fraction of the fast neutrons are thermalized at distances so far removed from the borehole that the subsequent gamma rays, which are all less than 3-MeV, are seriously attenuated. This implies a relatively small effective sample (a few kilograms). However, the counting takes place after the source is turned off, and the signal-to-noise ratio is favorable. Although the thermal neutron absorption cross sections are high for many elements, delayed gamma-ray spectroscopy in a borehole is limited in its usefulness by the small sample size, gamma-ray attenuation, and the marginal thermal neutron fluence rate regardless of the neutron source used.

Capture Gamma Ray Analysis: The energy of the radiative capture gamma ray emitted immediately after neutron absorption is characteristic of the excited nucleus. Unlike delayed gamma-ray analysis, capture gamma-ray spectroscopy must be made during, rather than after neutron irradiation; thus the signal-to-noise ratio is lessened by a background of gamma rays. The neutrons from an isotopic neutron source usually are moderated to nearly thermal energies within a few centimeters of the borehole. Because capture gamma rays range in energy up to 11 MeV, attenuation is not as serious as with delayed gamma rays, and the effective sample may be as large as several hundred kilograms. 14-MeV neutrons from an accelerator-type source penetrate to much greater distances and activate a larger sample volume. However, the counting geometry is not as good, and gamma-ray attenuation and scattering are significantly greater in the larger sample than in a sample activated by lower energy neutrons.

Because of the greater probability of pair production from high-energy capture gamma rays, the spectrum is complicated by the formation of single- and double-escape peaks. To adequately resolve the peaks in such a spectrum demands the best energy resolution one can achieve with current semiconductor detectors. Base metals such as copper, nickel, and chromium produce very high energy gamma rays (>7 MeV); because there is little interference from other gamma rays in this energy region, analysis with a low-resolution detector system is possible.

Inelastic Neutron Scattering: The energies of the gamma rays produced when neutrons are inelastically scattered by nuclei are characteristic of the struck nucleus. The cross sections, of course, vary with the initial neutron energy above a given threshold value. The first excited state (threshold) for some elements lies below 5 MeV, but the maximum yield is obtained for higher energy neutrons. Thus, we can adequately measure only a few elements by $(n,n'\gamma)$ reactions using an isotopic source. For this reason and the fact that the inelastic scattering cross sections are considerably lower than those for thermal neutrons, a copious source of high-energy neutrons (i.e., an accelerator) is indicated to make use of these reactions.

Particle Reactions (n,2n), (n,p), and (n,α): For neutrons with an energy greater than about 4 MeV, neutron reactions with some nuclei are possible that result in emission of a particle and the formation of a radioactive element. The gamma rays subsequently emitted by radioactive decay are from the newly formed radionuclide and indirectly indicate the element that initially absorbed the neutron. Therefore, (neutron, particle) reactions can be used for elemental analysis. A common example in borehole activation is the $^{28}Si(n,p)^{28}Al$ reaction, which is detected by the 1.78-MeV decay gamma-ray from ^{28}Al and indicates the presence of silicon. These reactions are limited to a relatively few elements where a 14-MeV neutron source is used, and generally are insignificant where a low-average-energy neutron source, such as ^{252}Cf is used.

Borehole Neutron Dynamics

Although geophysicists have directed the discussion of the dynamics of neutron interactions in rock a formation toward oil exploration,[38-42] it is useful to summarize the salient features with respect to mineral exploration. Whether the neutron source is an accelerator or an isotopic source, virtually all the neutrons are initially emitted from the source with energies much above thermal energy. The capture cross sections for most atomic nuclei for fast neutrons are small compared with the scattering cross sections; therefore scattering is the principal interaction between fast neutrons and atomic nuclei. The two distinct scattering processes are elastic (billiard ball type) and inelastic scattering. The inelastic scattering cross section is a function of the energy of the impinging neutron and the mass of the target nucleus and consequently is relatively high for fast neutrons. Because there is a substantial non-conservative transfer of energy to the struck atom, the neutron rapidly loses energy on successive collisions until it reaches epithermal energies (0.1 - 100 eV). If the energy transferred to the target nucleus is above its first excited state, the excited nucleus returns to the ground state by the emission of a gamma ray. If the energy transferred to the target nucleus is less than the first excited state, there is an elastic collision, i.e., the mechanical energy is conserved. After one or more elastic collisions, the neutron is moderated to the thermal energy of its surroundings. As the neutron energy approaches thermal energy, the capture cross sections of most elements rise rapidly. Once thermalized, the neutron diffuses only a short distance before it is captured by an atomic nucleus. After the neutron has been captured, an excited compound nucleus is formed that emits a capture gamma ray almost immediately ($\sim 10^{-14}$ sec). The resulting radioactive nucleus than decays by emission of a β^- or β^+ particle and an activation (or decay) gamma ray at some later time, according to its half life, and returns to the ground state or stable nucleus (see Figure 3).

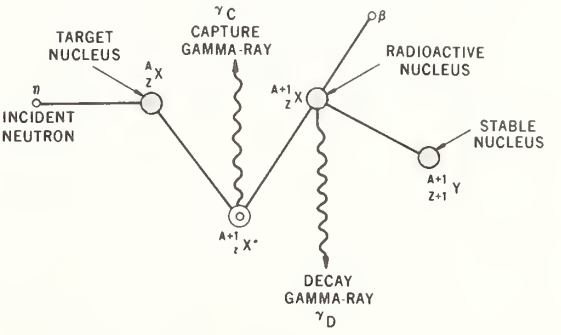

Fig. 3. Sketch showing gamma rays emitted after thermal-neutron capture (from Meyer[77]).

A neutron that leaves the source with an energy E_o starts to lose energy through collision processes with nuclei in the rock formation. At any given time its energy state is defined by its lethargy, $u = \ell n\ (E_o/E)$, where E is the neutron energy at that time. As a result of an elastic collision with an atomic nucleus, the average value of the change in lethargy, i.e., the average logarithmic neutron energy loss, ξ, is

$$\xi = \ell n \frac{E_o}{E_2} - \frac{E_o}{E_1} = \ell n \frac{E_1}{E_2} \qquad (1)$$

which from neutron slowing-down theory can be shown to be

$$\xi = 1 - \frac{(A-1)^2}{2A} \ell n \frac{A-1}{A+1} \qquad (2)$$

where A is the mass of the atomic nucleus in the

center-of-mass system. Thus, equation (2) indicates that the energy a neutron loses during an elastic collision is independent of the initial energy of the neutron, but is a significant function of the mass of the target nucleus, the loss being greater for smaller masses. For this reason hydrogen is by far the most efficient moderator.

The moderating power of a specific nucleus is given by $\Sigma_s\xi$ where Σ_s is the product of the number of the nuclei per cm^3 and the microscopic cross section. Σ_s is energy dependent and is large for hydrogen at low neutron energies only. Oxygen and silicon, which are common elements in most rock formations, have values of Σ_s that are significant (but not large) at high energies. At high energies, Σ_s for hydrogen is less than that for silicon or oxygen and does not rise above Σ_s for those elements until the neutron energy is reduced to less than about 10 keV. However, the change in lethargy, ξ, during elastic collisions is much larger for hydrogen than for silicon or oxygen. Even at high energies the moderating power of hydrogen is higher than that of other rock-forming elements, and the moderating power of a rock formation is generally controlled by the hydrogen concentration (primarily water) in the rock matrix.

In some rock formations, the hydrogen concentration is so low that the moderating power of the other rock-forming elements becomes significant. For instance, dry salt or very nonporous crystalline rocks such as unfractured diabase or granite contain very little water. Lunar rocks contain virtually no water. In these rocks, the moderating power is small and the spatial distribution of neutrons in the rock formation is profoundly affected. Fermi age theory[43] shows that the moderating power is inversely related to the square of the slowing-down length, L_s, of a rock formation. Kreft[44] has compared the calculated and measured neutron slowing-down lengths for several rock types and neutron sources. The mean square distance, $\overline{R^2}$, of a neutron from the source position in a borehole to positions in the rock formation where they attain epithermal energies is related to L_s. Thus, $\overline{R^2} = 6L_s^2$.

The root-mean-square value of R for several materials and sources is shown in Table II. Using a neutron source in a borehole in very dry rock, we find that the neutron on the average can travel considerable distances before reaching epithermal energies. When the neutron energy is reduced to a value at which thermal capture finally occurs, the source of the capture and/or decay gamma ray is so far removed from the detector, that the probability of the gamma ray reaching the detector is very small. Under these circumstances, one would expect a very poor sensitivity to thermal capture or decay gamma rays,[45] and a relatively high observed activity from $(n,n'\gamma)$ reactions (inelastic neutron scattering). Indeed, in anticipation of possibly making analyses on dry lunar rocks, the prominent spectra observed during gamma-ray spectroscopy tests on very dry terrestrial samples were found to be produced by $(n,n'\gamma)$ reactions.[46]

Many elements have strong resonance capture cross sections in the epithermal energy range, so that resonance and epithermal capture processes are also affected by the hydrogen concentration in the rock formation. In thin elemental samples, the capture probability per neutron absorbed is a maximum at resonance neutron energies. As the sample thickness is increased, this probability reaches a saturation

Table II. List of Root-Mean Square Distance Between Source and Point in Matrix at which the Neutron Reaches Epithermal Energy

Neutron Source	Matrix	R_{rms} (cm)	Ref
Ra-Be	Sand, SiO_2	110.8	44
	Limestone, $CaCO_3$	58.5	44
	Dolomite, $(Ca,Mg)CO_3$	49.5	44
	H_2O	17.6	44
	Graphite	47.4	44
	Coal (10% H)	11.3	78
^{252}Cf	Coal (10% H)	8.6	78
Accelerator (d,t) reaction	Sand, SiO_2	112.7	79
	Sand + 5% H_2O	62.2	79
	Sand + 10% H_2O	48.2	79
	Sandstone	67.2	79
	Limestone, $CaCO_3$	61.3	79
	Dolomite, $(Ca,Mg)CO_3$	50.9	79
	Coal (10% H)	18.4	79
	H_2O	16.3	80

value when all the neutrons of resonant energy are filtered out. For relatively dry rock formations, it is conceivable that the capture gamma rays from epithermal and resonance neutron capture in the sample "seen" by the detector may be greater than those produced by thermal capture, particularly for an element of high concentration. Also, the gamma rays from the primary transitions at epithermal energies shift toward higher energies than from the same transitions caused by thermal neutron capture.[81-83] These effects are not generally significant if the hydrogen concentration is more than a half percent, but in dry rock formations it can be a severe problem.[69]

The fact that all the neutron reactions that are useful for elemental analysis are affected by the concentration of hydrogen in the rock formations raises some serious problems. Owing to differences in hydrogen concentrations, the sensitivity and thus the calibration of a borehole sonde for quantitative analysis will vary from formation to formation and, in places even within a given formation because of the change in spatial distribution of thermal neutrons. The maximum density of thermal neutrons in the rock formation will be close to the neutron source if the hydrogen concentration is high, and because of the larger neutron slowing-down length, the neutrons will spread out far from the source in a nonhydrogenous medium. The variable distribution of thermal neutrons is a problem that has not yet been completely solved but that can be minimized by appropriate design of the borehole sonde.

Source-to-Detector Distance

In designing a borehole sonde, we must recognize the importance of the source-to-detector distance. Because thermal and epithermal neutrons are strongly attenuated by water but weakly attenuated by hard rock formations we can best assess the properties of the formation by placing the source as far as possible from the detector.[47] For instance, some years ago Tittman[41] calculated the thermal-neutron density in porous silica for several porosities (water-filled) and at various distances from the neutron source as shown in Figure 4. At that time, the emphasis was placed on porosity measurements for oil exploration, and Tittman pointed out that the source-to-detector spacing should not correspond to the cross-over zone but should be long to obtain the maximum sensitivity to porosity changes. For elemental analysis, however, the thermal neutron

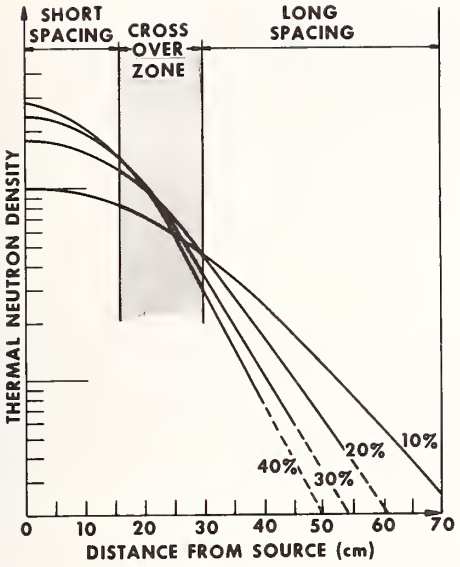

Fig. 4. Calculated thermal-neutron density (from Tittman[41]) as a function of distance from source in porous (water-filled) silica.

fluence rate should be kept as independent as possible of local changes in porosity. Thus, the source-to-detector distance should be adjusted to fall in the cross over zone. As convincing as these arguments seem, they may not be entirely practical. Other limitations must to be considered.

The fact is well known[48-51] that semiconductor detectors are vulnerable to radiation damage when used in close proximity to a strong source of fast neutrons. Ge(Li) and p-type high-purity germanium detectors must be carefully shielded from accelerator-produced neutrons (14-MeV) in order to insure a reasonable working lifetime. The more recently developed n-type germanium detectors[34,35] have considerably better radiation-damage resistance. Although the same limitations apply to isotopic sources, the problem is not as serious because of the lower average energy of the neutrons. Accelerator-type neutron sources and NaI(Tℓ) or gas-type detectors are used in typical borehole sondes. As far as we know, no borehole sondes have yet been constructed in which both a semiconductor detector and 14-MeV neutron source are used. However, the new n-type radiation-resistant germanium offers a possibility of such a combination. In any event, the allowable source-to-detector distance is in part dictated by the source strength and the allowable detector damage.

Another limitation on the source-to-detector distance is the speed of the electronic circuits. The total counting rate across the spectrum (integral count rate) must be low enough so that the spectral resolution is not impaired owing to paralysis of the counting circuits when very short source-to-detector distances are used.

The problems of radiation damage to the crystal and loss of resolution due to circuit paralysis are independent functions of source-to-detector distance, although each is related to the source-to-detector distance. Recent studies[52,53] have been made to solve these problems for ^{252}Cf neutron sources. The fast neutron fluence rate was experimentally measured as a function of the source-to-detector distance for a small standard laboratory ^{252}Cf neutron source (3 μg) for various ore samples in a borehole configuration. The ratio of the neutron fluence rate, ϕ, for any source size to that of the standard source, ϕ_o, can be expressed as

$$\phi/\phi_o = (S/S_o)\ \exp\ (A\ X^2 - X/X_n) \qquad (3)$$

S and S_o are the source and the standard source size in μg, respectively, X is the source-to-detector distance and A and X_n are constants determined with the standard source. Gamma-ray spectral analyses were also made over the same range of source-to-detector distances. The counting rate, ψ, in any given gamma-ray peak for any source size and source-to-detector distance can be similarly expressed as a ratio. Thus,

$$\psi/\psi_o = (S/S_o)\ \exp\ (-\ X/X_g) \qquad (4)$$

where ψ and ψ_o are the counting rates in the specified gamma-ray peak for the source sizes S and S_o, respectively, and X is the source-to-detector distance, and X_g is a constant. Combining equations (3) and (4), one obtains the counting rate for a given gamma-ray photopeak as a function of the source strength and the experimental parameters measured with a standard source. Thus,

$$\psi = \psi_o\ (S/S_o)\ \exp\left[-\left\{1-\sqrt{1+4\ A\ X_n^2\ \ell n\left(\frac{\phi S_o}{\phi_o S}\right)}\right\}\Big/ 2\ A\ X_n X_g\right] \qquad (5)$$

Note that although the required source-to-detector distance can be obtained from either equation (3) or (4), it does not appear in equation (5). If we now specify the fast neutron fluence rate that can be tolerated at the detector commensurate with a practical working lifetime, we can determine the spectral gamma-ray response as a function of source size.

Using a similar analysis, an expression was found to determine the counting rate in a given spectral line as a function of source strength for a given integral counting rate. Thus,

$$\psi = \psi_o\ (S/S_o)\ \exp\left[-\left\{1-\sqrt{1+4\ BX_G^2\ \ell n\left(\frac{CS_o}{C_o S}\right)}\right\}\Big/ 2\ BX_G X_g\right] \qquad (6)$$

where C and C_o are the total counting rate for the given and standard sources, respectively, X_G and B are constants that appear in a counting rate equation similar to the neutron-fluence-rate equation (5), and the other symbols are the same as above. Specifying the maximum counting rate corresponding to the particular counting circuits used, we can determine ψ for any source size.

Figures 5 and 6 show plots of the count rate in the 6610 keV ^{56}Fe double escape photopeak given by equations (5) and (6) for an arbitarily chosen critical neutron fluence rate of 20 n/cm^2-sec at the detector and an integral counting rate of 3000 net counts/sec. Figure 5 is for an iron ore-concrete mix and Figure 6 is for coal. The data show that maximum sensitivity for the iron photopeak can be obtained with a 37-μg ^{252}Cf source in the relatively dry iron ore-concrete mix (~0.2% hydrogen), whereas in the hydrogenous coal matrix (~5% hydrogen) the maximum sensitivity can be obtained with a 2-μg ^{252}Cf source. Solving equation (3) or (5) for X_n, we

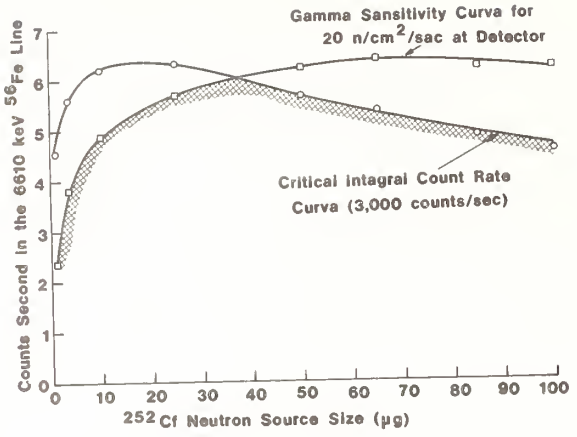

Fig. 5. The gamma-ray count rate in the 6610-keV ^{56}Fe doublet (double-escape peaks) as a function of the size of the ^{252}Cf neutron source for the stated criterion values of the neutron fluence rate and the integral count rate of the detector in an iron ore-concrete mix.

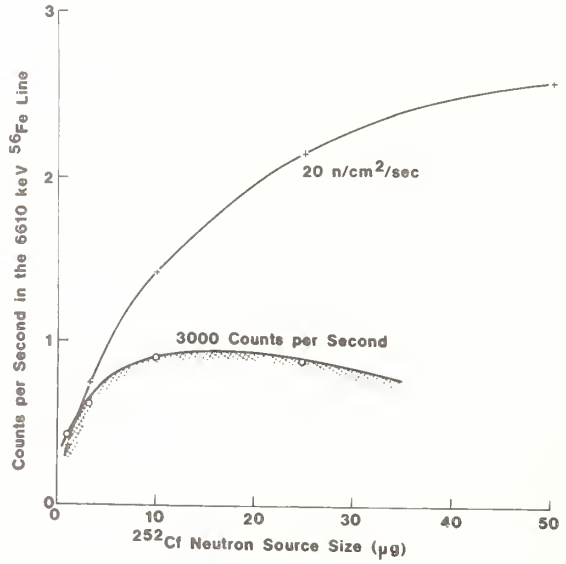

Fig. 6. The gamma-ray count rate in the 6610-keV ^{56}Fe doublet (double-escape peaks) as a function of the size of the ^{252}Cf neutron source for the same conditions as those shown in Figure 5 in a coal matrix.

find that the source sizes required to obtain optimum sensitivity correspond to source-to-detector distances of 61 cm and 32 cm, respectively.

Although the data for a silica matrix in Figure 4 are only approximate, the above calculated source-to-detector distances required to yield a maximum sensitivity are outside the cross-over zone. Thus, the source strengths and source-to-detector distances required to yield maximum sensitivity are not the same as those that yield a minimum effect from porosity changes. Therefore, calibration of a sonde should be made in the formation being measured.

Sonde Calibration

Fanger et al.[54] and Fanger and Pepelnik[55] recognized the above problems and suggested an interesting method they called an "internal concentration determination", which circumvents the need for any direct knowledge of the neutron fluence rate (ϕ), the solid angle (Ω), or the mass (M) of the sample. The counting rate (P_i) of element i is given by

$$P_i = \frac{\phi \cdot \Omega \cdot \varepsilon(E\gamma)_i \cdot I_i \cdot \sigma_i \cdot L \cdot k_i \cdot C_i \cdot M}{A_i} \qquad (7)$$

where $\varepsilon(E\gamma)_i$ is the detector efficiency at the energy $E\gamma$, I_i is the gamma-ray intensity, σ_i is the microscopic thermal absorption cross-section, L is Avogadro's number, C_i is the mass fraction, k_i is the isotopic abundance, and A_i is the atomic mass. If C_o is the mass fraction of a given element, then

$$C_o = \frac{C_o}{\sum C_i} = \frac{C_o}{1} \qquad (8)$$

and substituting equation (7) into equation (8), and cancelling out ϕ, Ω, and M,

$$C_o = \frac{P_o A_o}{\varepsilon(E\gamma) \cdot I_o \cdot k_o \cdot \sigma_o} \cdot \sum_i^n \frac{\varepsilon(E_i) \cdot I_i \cdot k_i \cdot \sigma_i}{P_i A_i} = \qquad (9)$$

$$A_o \left[\sum_i^n A_i\right]^{-1}$$

where the summation is over n elements in the rock formation. All the parameters to calculate A_o are known or can be measured. If the concentration of only one element in the matrix is known or can be estimated reasonably well, the $\sum_i^n A_i$ can be evaluated and the mass fraction of any other element yielding measurable capture gamma radiation can be calculated. Often little is known about the elemental composition, limiting the utility of the technique. However, in a matrix such as coal where the qualitative elemental composition is relatively simple and is known, this is a powerful method to obtain quantitative analysis. Table III shows some field results that were obtained in a borehole in coal[56] by means of this method.

Table III. Comparison of the Elemental Concentration in a Coal Bed Determined by Capture Gamma Ray Analysis In Situ and that Determined by Chemical Analysis of the Drill Core.

Element	Capture Gamma-Ray Analyses*	Chemical Analyses*
Hydrogen	5.0	5.0
Carbon	68.1	68.9
Nitrogen	2.0	1.3
Oxygen	10.6	9.7
Sulfur	3.0	3.0
Aluminum	1.2	1.46
Silicon	2.1	2.41
Iron	0.8	2.18
Titanium	0.032	0.06
Chlorine	0.025	0.024
Ash Content	11.4	12.1
Heat of Combustion	12,258	12,380

*Analyses in percent except for heat of combustion (in BTU).

Schulze[57] and Schulze and Würz[36] have studied the calibration problem from a somewhat different point of view. They have made an excellent study of a model borehole and theoretically investigated the parameters required for elemental analysis. They express the ratio of the concentration of a given element, C, to the peak area, P, as

$$C/P = 1 \Big/ \left[S_{th} K_{th} \phi_{th} + S_{epi} K_{epi} \phi_{epi} + f_R(C) S_R K_{epi} \phi_{epi} \right] t \qquad (10)$$

where the indices th, epi, and R indicate the quantities associated with thermal, epithermal, and resonance capture, ϕ is the neutron fluence rate at the detector position, t is the period of irradiation, and $f_R(C)$ is the resonance self-shielding factor. S is the intensity of a specific gamma ray of an element per neutron captured per unit concentration, and K is a number describing the attenuation within the sample. For example, they define the thermal components of S and K by

$$S_{th} = \varepsilon(E\gamma) \frac{\sqrt{\pi}}{2} \frac{L}{A} \sigma_{th} I_{th} \qquad (11)$$

and

$$K_{th} = \frac{\int \phi_{th}(\vec{r}) \exp(-\mu r/4\pi r^2) \, d\vec{r}}{\phi_{th}(0)} \qquad (12)$$

where $\varepsilon(E\gamma)$ is the detector efficiency at energy $E\gamma$, L is Avogadro's number, A is the atomic mass, σ_{th} is the thermal absorption cross section, and $\phi_{th}(0)$ and $\phi_{th}(\vec{r})$ is the thermal neutron fluence rate at the detector and at a distance r from the detector, respectively. Similar expressions can be written to correspond to the epithermal and resonance capture components. Using these expressions and by experimentally measuring all the parameters in their model borehole, Schulze and Würz investigated the important factors required for borehole analysis. For instance, they showed that the thickness of the water between the sonde and the borehole wall seriously affects delayed gamma ray analyses. They demonstrated that this effect was not as important for capture gamma-ray analyses, but that the water thickness should be minimum. Their results may explain the relatively poor data obtained by Mikesell et al.[37] in a large borehole.

Sohrabpour and Bull[58] recently reported on a Monte Carlo study to predict the peak count rate as a function of element concentration in a tungsten oxide (WO_3) - granite and also in a chalcocite (Cu_2S) - monzonite matrix. Figure 7 shows a typical sensitivity curve obtained by means of the Monte Carlo method in a matrix for which the parameters could be established. Comparison of results obtained by this method with data in the literature shows favorable agreement, although the authors caution that because of experimental uncertainties the differences may be as great as 50 percent.

Calibration is still the major problem in the use of borehole gamma-ray spectrometry for quantitative elemental analysis. Although in some places fairly good quantitative data have been obtained, calibration must be determined for the particular rock formation being studied.

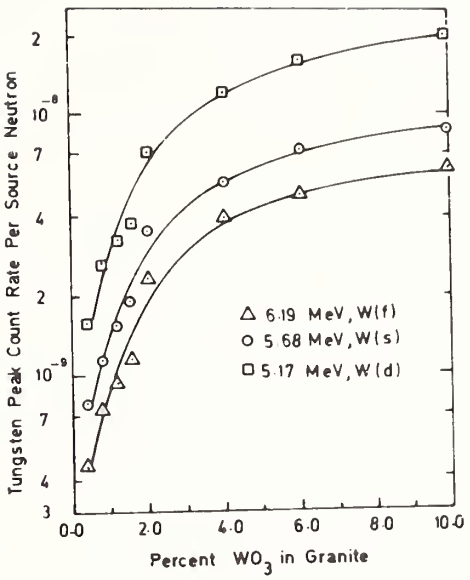

Fig. 7. The 6.19-MeV tungsten full-energy and single- and double-escape count rates per source neutron as a function of tungsten concentration in granite (from Sohrabpour and Bull[58]).

Recent Field Application

During the last decade many papers discussing the application of neutron activation and other nuclear techniques for the exploration and analysis of minerals, but few reports describe actual field experiments in borehole activation and gamma-ray spectrometry. Before 1970, most of the work in the field was done in the USSR. Czubek[59] presented a comprehensive outline of 205 Russian and European papers of the early work; only a few of these papers discuss actual borehole spectroscopy. Nargolwalla et al.[60] have reviewed the more recent field applications of nuclear techniques to mineral exploration.

Neutron absorption by certain nuclides gives rise to high-energy gamma activities that can be discerned easily by low-resolution detectors. For instance, ^{16}N, which is formed by the $^{19}F(n,\alpha)^{16}N$ reaction, emits a high-energy gamma ray (6.13-MeV) that has little interference from other elements. Dumesnil and Andrieux,[61] Selyutin et al.,[62] and Yakubson[63] reported on the borehole spectrometric analysis of fluorine. They found such analyses to deviate about 1 percent of the chemical assays.

Copper is also an element that is easily measured because of its two isotopes and the convenient half life of ^{65}Cu ($T_{1/2}$ = 5.1 min). Landstrom et al.[64] and Bakhterev and Sen'ko-Balantnyi,[65] however, found better sensitivity by using the isotope ^{63}Cu ($T_{1/2}$ = 12.5 hrs), which avoids interferences from ^{28}Al and ^{56}Mn. Moxham et al.[66] circumvented the interference problem by using a high-resolution Ge(Li) detector and a 15-min delay period to eliminate ^{28}Al. They determined a conservative lower limit of detection to be about 0.5 percent copper. Hoyer and Lock[67] made extensive tests using both Am-Be and accelerator-type neutron sources to determine the ^{63}Cu activity. They too found a detection limit of 0.5 percent using 14 MeV neutrons, but felt the technique needed further improvement to be used as a practical field method.

Nargolwalla et al.[68] using a ^{252}Cf neutron source and an improved data reduction system to extract the capture gamma-ray lines from low-resolution data were able to push the sensitivity down to 0.2 percent copper. They concluded that the method was suitable for in-situ logging of porphyry copper deposits. Figure 8 shows a comparison of the capture gamma-ray analyses with the core analyses.

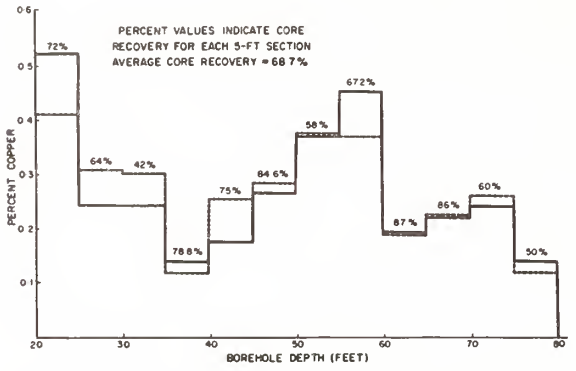

Fig. 8. Comparison of the neutron-capture gamma-ray analysis of a porphyry copper deposit with the chemical analysis of the core (from Nargolwalla et al.[68]). Solid line shows the chemical analysis of the core; the dashed line is the capture gamma-ray analyses.

Nickel has several intense capture gamma rays above 8 MeV that have no serious interferences and do not require high-resolution detectors. To estimate the ore reserves, Volkov et al.[69] used capture gamma-ray analysis to determine the nickel content of several boreholes in a nickel deposit. Later, Nargolwalla et al.[68] successfully logged for nickel in lateritic deposits. They achieved a relative standard error of about 4.2 percent for grades of 1-2 percent nickel. To test the capture technique in dry, low-porosity igneous rocks, Senftle et al.[70] obtained a linear correlation coefficient of 0.65 when analyzing for nickel in the 0.09- to 0.38-percent range. They found that the low correlation with the chemical analyses was probably due to substantial epithermal and resonance neutron absorption in the dry ore, which caused a significant departure of the intensities of the gamma rays from the intensities expected from absorption of thermal neutrons only.

In 1973, Erkhov et al.[71] studied the mercury concentration in a 300-m-deep deposit by the capture gamma-ray technique. Apparently an iron shadow shield between source and detector caused some interference, which was later reduced by use of stainless steel.[72] Borehole neutron-gamma-ray spectroscopy has also been used to determine uranium,[73] sulfur,[56,68,74] silicon,[56,68] aluminum,[56,75] iron,[68] and tungsten[30,76] in various ore deposits.

Coal, because of its high hydrogen concentration, is an ideal matrix in which to study thermal-neutron-capture techniques. Nargolwalla et al.[68] used a capture gamma-ray method to delineate the depth of the coal seam and also were able to measure the sulfur content with an average relative error of less than 8 percent in a range of 1 to 8 percent sulfur. By using high resolution spectrometry, Senftle et al.[56] were able to obtain a complete ultimate analysis of the coal (see Table III).

Conclusions

Neutron-activation gamma-ray spectroscopy in a borehole configuration has been developed to the point that it can be used to yield good semiquantitative data for many elements (~30) in almost any rock formation. In most porous or hydrogenous (e.g., coal) formations, quantitative information, which under some circumstances may be within a few percent of chemical values can be obtained. Calibration is the most serious problem in obtaining good quantitative data in moderately porous to impervious rock types.

Acknowledgements

The author is grateful to his colleagues A. B. Tanner and J. L. Mikesell for their helpful suggestions and review of the manuscript.

References

1. B. Pontecorvo, Oil and Gas Journal 40, 32 (1941).
2. R.L. Caldwell, Nucleonics 16, 58 (1958).
3. F.E. Senftle, unpublished data; Mining Cong. Jour., 56, 21 (1970).
4. Conference of the Academy of Sciences of the USSR on the Peaceful Use of Atomic Energy, July (1955); see also reference 2.
5. A.H. Youmans, E.G. Hopkinson, and R.J. Stewart, Paper 1304-G, in Proceedings of the SPE 34th Annual Fall Meeting, Dallas, Texas Oct (1959).
6. R.L. Caldwell and W.R. Mills, Nucl. Instr. and Methods 5, 312 (1959).
7. J.C. Stick, Petrol. Eng. 32, B-31 (1960).
8. P.A. Wichmann, A.H. Youmans, and E.C. Hopkinson, J. Petrol. Tech. 479 (1967).
9. W.W. Givens, R.L. Caldwell, and W.R. Mills, The Log Analyst IX, 18 (1968).
10. E.M. Lobanov, A.P. Novikov, G.S. Nikanorov, O.M. Romanov, and A.A. Khaidarov, Radiatsionnye Effekty v Kondensirovannykh Sredakh 116, (1964); also Mining Minerals Eng. 2, 261 (1966).
11. E.M. Lobanov, A.P. Novikov, G.S. Nikanorov, and A.A. Khaidarov, Radiatsionnye Effekty v Kondensirovannykh Sredakh 126 (1964); also Mining Minerals Eng. 2, 303 (1966).
12. L.V. Muzyukin and I.P. Sen'ko-Bulantnyi, Geofiz, Sb. Inst. Geofiz. Ural Filial, Akad. Nauk SSSR, No. 6, 77 (1967).
13. W.R. Rabson, Petrol. Eng. 31, B-102 (1959).
14. R.L. Caldwell, W.F. Baldwin, J.D. Bargainer, J.E. Barry, G.N. Salaita, and R.W. Slon, Geophysics 28, 617 (1963).
15. E. Chrusciel, J. Massalski, and A. Starzec, Nukleonika 15, 705 (1970).
16. P.A. Wichmann and R.W. Webb, J. Petrol. Tech. 201 (1970).
17. P.A. Wichmann, 12th Annual Logging Symposium, Trans. SPWLA, G1 (1971).

18. F.E. Senftle and A.F. Hoyte, Nucl. Instr. and Methods 42, 93 (1966).

19. F.E. Senftle, P.W. Philbin, and P. Sarigianis, in Proceedings of the Symposium on the Californium-252, U.S. AEC. Rept. CONF-681032, Jan (1969); Isotopes and Rad. Tech. 1, 411 (1970).

20. L.V. Groshev, A.M. Demidov, V.N. Lutsenko, and V.I. Peliko, Atlas of the Spectra of Gamma Rays from the Radiative Capture of Thermal Neutrons (Pergamon Press, New York, 1959).

21. N.C. Rasmussen, Y. Hukai, T. Inouyi, and V. Orphan, Thermal Neutron Capture Gamma-Ray Spectra of Elements, Rept ARCRL-69-0071 (Mass. Inst. of Tech. Cambridge, Mass; U.S. Air Force Cambridge Res. Lab., Bedford, Mass., 1969).

22. D. Duffey, A. El-Kady, and F. Senftle, Nucl. Instr. and Methods 80, 149 (1970).

23. F.E. Senftle, H.D. Moore, D.B. Leep, A. El-Kady, and D. Duffey, Nucl. Instr. and Methods 93, 425 (1971).

24. A.B. Tanner, R.M. Moxham, F.E. Senftle, and J.A. Baicker, in Proceedings of the American Nuclear Society Topical Meeting, Augusta, GA, USA, U.S. AEC Rept CONF-710402, Vol. III, p. 1-6, (1971); Nucl. Instr. and Methods 100, 1 (1972).

25. G.A. Nedostup and F.N. Prokof'ev, At. Energ. 35, 54 (1973).

26. P. Dumesnil, Bull. Instr. Nucl. 157, no. 43, 31 (1971).

27. P. Dumesnil and C. Andrieux, Ind. At. 14, 29 (1970).

28. A. Lauber and O. Landström, Geophys. Prospect. 20, 800 (1972).

29. C. Andrieux, Spectrometrie Gamma dans les Forages avec un Semicteur Ge(Li) Ph.D., Thesis, l'Universitē de Paris, 75 pp., (1972).

30. U. Fanger, A. Lubecki, R. Pepelnik, and H. Würz, PACT-Bericht 37, Kernforschungszentrum Karlsruhe, West Germany (1973); see also reference 54.

31. J. A. Baicker, Princeton Gamma-Tech, Inc., private communication.

32. E. Chrusciel, in Proceedings of the Krajowym Symposium, Postepy Tech. Izot. Nauce Gospod. Nar., INT 95/I, (1975).

33. G.R. Boynton, Nucl. Instr. and Methods 123, 599 (1975).

34. R.H. Pehl, N.W. Madden, J.H. Elliott, T.W. Raudorf, R.C. Trammell, and L.S. Darken, Jr., IEEE Trans., Nucl. Sci., NS-26, 321 (1979).

35. T.W. Raudorf, R.C. Trammell, and L.S. Darken, Jr., IEEE Trans., Nucl. Sci., NS-26, 297 (1979).

36. G. Schulze and H. Würz, in Proceedings of the Paris Symposium on Californium-252 Utilization, Vol. II, Paris, France, Rept. CONF-760436, V-113 (1976).

37. J.L. Mikesell, D.W. Dotson, F.E. Senftle, R.S. Zych, J. Koger, and L. Goldman, Comptes Rendus, (1979) [in press].

38. C.W. Tittle, Geophysics 26, 27 (1961).

39. C.W. Tittle and L.S. Allen, Geophysics 31, 214 (1966).

40. C.W. Tittle, H. Faul, and C. Goodman, Geophysics 16, 626 (1951).

41. J. Tittman, in Fundamentals of Logging, Lecture Series, Petroleum Engineering Conference, Univ. of Kansas, 115 (1956).

42. J. Tittman, J. Appl. Phys. 26, 394 (1955).

43. S. Glasstone and M.C. Edlund, The Elements of Reactor Theory, (D. Van Nostrand Co., New York, 1952).

44. A. Kreft, Nukleonika 19, 145 (1974).

45. C. Preskitt, J. John, and G. Reynolds, Trans. Am. Nucl. Soc., 12, 471 (1969).

46. F.E. Senftle, P. Philbin, R.M. Moxham, and G. Boynton, Nucl. Instr. and Methods 117, 435 (1974).

47. L.S. Allen, C.W. Tittle, W.R. Mills, and R.L. Caldwell, Geophysics 32, 60 (1967).

48. H. Kraner, C. Chassman, and K. Jones, Nucl. Instr. and Methods 62, 173 (1968).

49. H. Kraner, R. Pehl, and E. Haller, IEEE Trans. Nucl. Sci. NS-22, 149 (1975).

50. F. Goulding and R. Pehl, IEEE Trans. Nucl. Sci. NS-19, 91 (1972).

51. P. Stelson, J. Dickens, S. Raman, and R. Trammell, Nucl. Instr. and Methods 98, 481 (1972).

52. F.E. Senftle, R.J. Macy, and J.L. Mikesell, Nucl. Instr. and Methods 158, 293 (1979).

53. J.L. Mikesell, F.E. Senftle, and R.J. Macy, in Neutron Capture Gamma-Ray Spectroscopy, (ed., R. Chrien and W.R. Kane, Plenum Publishing Co., New York 1979).

54. U. Fanger, D. Hcck, P. Martens, R. Pepelnik, and H. Schmidt, Rept. KFF 1404 (1971), Kernforschungszentrum, Karlsruhe, West Germany (1971).

55. U. Fanger and R. Pepelnik, in the Proceedings of the American Nuclear Society Topical Meeting, Austin, Texas, Rept CONF-720902, p. 245, Sept (1972).

56. F.E. Senftle, A.B. Tanner, P.W. Philbin, G.R. Boynton, and C.W. Schram, Min. Eng. (AIME), 30, 666 (1978).

57. G. Schulze, Rept KFE-2995, Kernforschungszentrum, Karlsruhe, West Germany, Oct (1977).

58. M. Sohrabpour and S.R. Bull, Nuclear Instr. and Methods 161, 281 (1979).

59. J. Czubek, Log Analyst 12, 20 (1971).

60. Nargolwalla, S.S., Nguyen, N.D., and Rehman, A.U. in Nuclear Methods in Mineral Exploration and Production (ed., J.G. Morse, Elsevier Scientific Publishing Co., New York, 1977).

61. P. Dumesnil and C. Andrieux, C.E.N. Commis. Énerg. At., Saclay, Fr., Report CEA-N-1592, 20 pp. (1972).

62. E.G. Selyutin, I.I. Shirokii, and S.N. Alekseev, Yad. Geofiz., Dokl. Vses. Nauch.-Tekh. Konf. XX(Dvadtsat) Let Prorzvod. Primen. Izotop. Istochnikov Yad. Izluch. Nar. Khoz. SSSR, Atomizdat, Moscow, 1968, p. 117 (1972).

63. K.I. Yakubson, Tr. Inst. Geol. Geofiz., Akad. Nauk. SSSR, Sib. Otd. No. 126, 213 (1972).

64. O. Landström, R. Christell, and K. Koski, Geoexploration 10, 23 (1972).

65. V.V. Bakhterev and I.N. Sen'ko-Balantnyi, Razved. Okhr. Nedr 2, 39 (1974).

66. R.M. Moxham, F.E. Senftle, and G.R. Boynton, Econ. Geol. 67, 579 (1972).

67. W.A. Hoyer and G.A. Lock, Trans. Soc. Min. Eng. (AIME) 252, 409 (1972).

68. S.S. Nargolwalla, A. Kung, O.J. Legrady, J. Callag, and H.O. Seigel, in the International Symposium of the Nuclear Techniques Mineral Resource, Paper SM-216/8, IAEA, Vienna, Austria (1977).

69. I.D. Volkov, L.A. Ziv, V.L. Kostin, and A.F. Postel'nikov, Tr. Vses. Nauchno-Issled. Inst. Yad. Geofiz. Geokhim. 13, 86 (1972).

70. F.E. Senftle, R.M. Moxham, A.B. Tanner, P.W. Philbin, G.R. Boynton, and R.E. Wager, Geoexploration 15, 121 (1977).

71. V.A. Erkhov, Y.I. Makarov, V.F. Yaroslavtsev, E.V. Egorov, E.A. Sokolov, and P.A. Ockhur, Razved. Okhr. Nedr 2, 30 (1973).

72. E.A. Sokolov, E.V. Egorov, and I.B. Vysotskii, Metody Razved. Geofiz. 25, 28 (1975).

73. F.E. Senftle, R.M. Moxham, A.B. Tanner, G.R. Boynton, and J.A. Baicker, Nucl. Instr. and Methods 138, 371 (1976).

74. E. Chrusciel, J. Niewodniczanski, and K.W. Palka, in the International Symposium of the Nuclear Techniques on Mineral Resources, Paper SM-216/27, IAEA, Vienna, Austria (1977).

75. H.D. Scott and M.P. Smith, The Log Analyst, 14, 3 (1973).

76. U. Fanger, D. Heck, P. Martens, R. Pepelnik, and H. Schmidt, Rept. KFK 1404, Kernforschungszentrum, Karlsruhe, West Germany (1971).

77. G.L. Meyer, Technical Report Series, No. 126, IAEA, Vienna, Austria, 90 pp. (1971).

78. K. Morstin and J. Wozniah, in the International Symposium of Nuclear Techniques on Mineral Resources, IAEA, Vienna, Austria, 119 (1977).

79. S.A. Kantor, Yadernaya Geofiz. Moscow, Gostoptekhizdat, 126 (1963); also E.M. Filippov, B.S. Vakhtin, and A.V. Novoselov, Neutron-Neutron and Neutron-Gamma Methods in Ore Geophysics, Nauka, Novosibirsk USSR (1972).

80. T.O. Marshall, Health Physics 19, 571 (1970).

81. G.J. Broomhall, Aust. J. Phys. 25, 9 (1972).

82. R.E. Chrien, Report BNL 19191, Brookhaven National Laboratory, Upton, L.I., USA (1974).

83. J.R. Bird, B.J. Allen, I. Bergquist, and J.A. Biggerstaff, Nucl. Data Tables II, 433 (1973).

NUCLEAR TECHNIQUES IN MARINE METAL EXPLORATION

W. Michaelis
Institut für Physik, GKSS Forschungszentrum Geesthacht GmbH
2054 Geesthacht, Germany

The growing concern about the future availability of raw materials has increasingly drawn attention to the extensive marine metalliferous mineral deposits. Nuclear techniques can provide powerful analytical tools for exploring these resources. The measurement of natural gamma radiation, X-ray fluorescence analysis and a variety of neutron techniques based on ^{252}Cf, (α,n) and (d,n) sources are now in use or appear to make progress. Improvement of the relevant cross sections could considerably advance the technical development both in the field and in the laboratory. Particular consideration should be given to a number of energy-dependent cross sections pertaining to neutron and gamma transport in field applications of activation analysis or radiative capture, to neutron cross sections for production of gamma rays from inelastic collisions, to cross sections of threshold reactions which either ensure elemental selectivity or are the source of elemental interferences and, finally, to cross sections for quasi-prompt activation with 14 MeV neutrons.

[Natural gamma radiation, XRF analysis, scattered gamma radiation, neutron inelastic scattering, neutron activation analysis, radiative neutron capture, ^{252}Cf, (α,n) and (d,n) neutron sources, reaction interferences, nuclear reactors, nuclear cross sections, metal exploration.]

1. Introduction

Nuclear techniques for elemental analysis play an increasing role in the exploration, mining and processing of mineral resources. For a number of years they have been successfully applied in many countries with respect to both terrestrial and maritime raw materials, in particular, since the availability of high-resolution semiconductor detectors. The ability to operate devices satisfactorily in environments that preclude the use of most other analytical methods, the possible simplification or even avoidance of sample preparation, the rapid presentation of the results and the high degree of elemental specifity, often accompanied by the potential of multielement analysis, are the main advantages claimed for the methods. Generally, nuclear techniques provide non-contacting quantitative measurements integrated over a significantly large volume of material, and the penetrating radiation often used enables analyses to be made through borehole liners or the walls of conveyor pipes and process vessels. It should be stressed, however, that nuclear methods give little or no information on chemical properties. Therefore, particularly in the exploration phase, nuclear and non-nuclear techniques are often combined.

While at first the application to terrestrial resources was well to the fore, the growing concern about the future availability of raw materials has more and more drawn the attention also to the extensive maritime metalliferous mineral deposits. Among these the heavy mineral sands in stream and shelf areas, the hydrothermal slimes and the manganese nodules in the deep sea are of particular importance[1], the nodules in the Pacific being perhaps the most spectacular metal deposit on the earth at all.

A number of techniques are now in use in marine metal exploration or are being developed. Passive methods are based on the measurement of natural gamma radiation and will be briefly described in section 2. Active interrogation techniques include X-ray fluorescence analyses, measurements of scattered gamma radiation and a variety of neutron techniques which use either inelastic scattering, neutron activation or prompt capture gamma-ray spectroscopy. Applications of these techniques *in situ* or on board ship will shortly be reviewed in sections 3 - 5. Land-based laboratory analyses (section 6) provide an indispensable tool in more fundamental geochemical investigations which require high accuracy, precision and sensitivity. Nuclear cross section data needs will be briefly summarized in section 7.

2. Measurement of Natural Gamma Radiation

The techniques of measuring natural gamma radioactivity in terrestrial uranium exploration campaigns are well established[2-4]. Applications on the sea floor necessitate direct contact of the detector with the sea bed because of the gamma-ray absorption in sea water. In order to enable continuous measurements for useful survey purposes, the spectrometer should be installed in a towed vehicle.

Extensive radiometric contour maps disclosing the variations in the abundances of uranium, thorium and potassium over several areas of the UK continental shelf have been obtained, with only limited other sources of information, by using a towed sea bed spectrometer[5-9] which essentially consists of a 127 mm dia. stainless-steel probe comprising a 76 x 76 mm dia. or 127 x 76 mm dia. NaI(Tl) scintillation detector in an integrated ruggedized assembly. The probe is attached to 850 m of double-armoured coaxial cable, the lowest 30 m of which is enclosed in a flexible reinforced plastic hose to minimize the risk of snagging on sea bed obstacles. Control, analysis and recording facilities are housed within the ship's laboratory. The instrumentation proved to be reliable under strenuous field conditions. The count rates are continuously monitored at speeds up to 7 knots in several energy channels: total activity 100 - 3000 keV, potassium (^{40}K) 1310 - 1610 keV, uranium (^{214}Bi) 1620 - 1940 keV and thorium (^{208}Tl) 2475 - 2970 keV. From extensive marine studies[10] it is known that the abundances of uranium and thorium and their decay daughters, respectively, are abnormally high in rather specific minerals, for instance, in certain of the heavy minerals and in marine phosphorite deposits. Heavy mineral sands which contain monazite, epidote, sphene or zircon are characterized by predominantly high contents of thorium and its decay products, while phosphate deposits, especially those with high apatite content, may be detected via predominantly high abundances of uranium and its decay daughters. The natural radioactivity method has thus considerable potential both for marine mineral exploration and to geological and geochemical mapping (Fig. 1).

Noakes and co-workers[11] have reported preliminary studies with a towed sledge containing four 76 mm x 76 mm dia. NaI(Tl) detectors to map the sea floor off the coast of Florida. They also tested a statically positioned underwater gamma-ray spectrometer with a 65 cm^3 Ge(Li) detector in a stainless-steel housing. High-resolution spectra of phosphate rock and heavy mineral

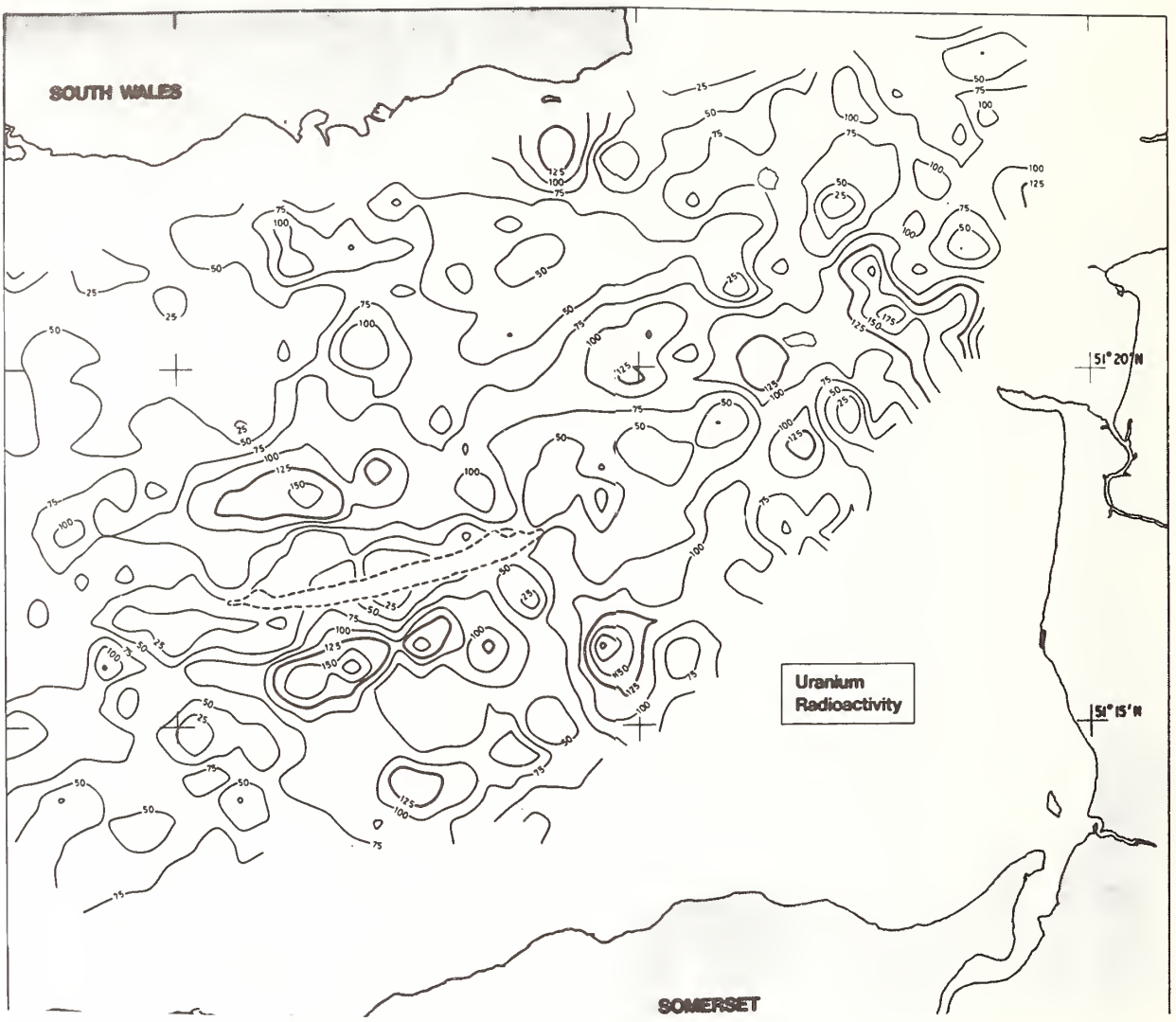

Fig. 1. Contour map of uranium (^{214}Bi) radioactivity as derived from the 1620 - 1940 keV gamma-ray window[8].

sands were found to exhibit distinct differences, thereby allowing differentiation between the two types of deposits. However, since the structure of the spectra is essentially correlated to variations in the uranium and thorium content, the more rugged scintillation counter seems to be sufficient in resolution for these aplications and thus preferable to a semiconductor detector.

For *in situ* analysis of river-bottom sediments Moxham et al.[12] have combined the measurement of natural radioactivity with neutron activation analysis and prompt capture gamma-ray spectroscopy (cf. section 5) using a 45 cm^3 Ge(Li) detector in a sonde configured so as to penetrate the sediments about 60 cm. The natural background spectrum observed contains peaks from several members of the uranium and thorium series, from ^{40}K and from ^{137}Cs and ^{60}Co which originate from bomb tests fallout. Unfortunately, the state of equilibrium in the uranium series cannot be judged, as the diagnostic low-energy lines from ^{235}U, ^{226}Ra and ^{234}Th could not be detected because of absorption in the cryostat housing.

3. Field Applications of X-Ray Fluorescence Techniques

X-ray fluorescence analysis is presumably the most widely adopted techniques for measuring elemental concentrations in the marine environment. The capability of the method is determined by the choice of the source - radioisotope or X-ray tube -, the energy of the primary radiation and the resolution power of the detector which may be a proportional counter, a scintillation or a semiconductor detector. In any case, interelement effects which are mainly due to matrix absorption and the influence of particle size are the chief causes of error, if they are not carefully considered. Another inherent feature is that analysis is performed of only a thin layer of matter. To obtain representative and intermediate- to high-accuracy results, samples must be prepared with attention to detail. The particular advantages compared to other methods are simplicity in instrumentation and rapidity of measurement.

Inexpensive compact and portable analyzers with radioisotope sources and low-resolution detectors are used for limits of detection > 0.1 %. They have been

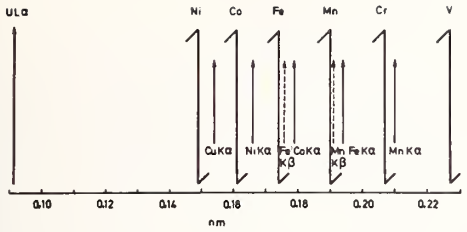

Fig. 2. Wavelength lines and filters used in non-dispersive X-ray fluorescence analysis[18].

reviewed in several articles[13-16]. Non-dispersive spectrometry has been extensively applied[17-20] on board ship in the exploration of Pacific manganese nodules which, on the average, contain 25.8 % Mn, 7.0 % Fe, 1.2 % Ni, 1.1 % Cu, 0.2 % Co and 0.01 % Zn. Balanced differential filters are used for energy selection (Fig. 2). Quantitative analysis of Fe, Mn, Ni and Cu is achieved with adequate reproducibility and accuracy. The method has also been employed for determining a reference element in order to evade weighing on board vessel for atomic absorption spectrometry[21].

In the course of time reliable equipment has evolved for sampling of nodules, sediment and water. Freefall grabs, often combined with bottom photography, sediment tubes and water sampler as well as boomerang corers are now the most important devices. Geological surveying and mapping is achieved with narrow-beam echosounders and air gun seismic.

Cryogenically cooled semiconductor detectors provide energy resolutions sufficient to separate K X-rays from adjacent elements as low as 15 in atomic number. This considerably extends the capabilities of X-ray fluorescence technique towards rapid, simultaneous multielement analysis. Elemental concentrations of a few ppm can be measured, often in the presence of high abundances of few major constituents. The application of ship-borne energy-dispersive equipment has been described by several authors[22-26]. Friedrich and co-workers[22-24] used a 30 mCi ^{238}Pu source and a 30 mm^2 Si(Li) detector with 195 eV resolution for Mn K X-rays during manganese nodule exploration campaigns in the northern equatorial Pacific (Fig. 3). The disclosure of the regional distribution of the elements in nodules within the investigated area and of the zonal elemental distribution within the nodules and, finally, the establishment of geochemical correlations between the absolute Cu and Ni concentrations and the Mn/Fe ratio are the most important results of such studies.

Knoth and co-workers[25,26] have developed energy-dispersive equipment for the on-line determination of metal concentrations in heavy mineral sands. The system consists of a water-flushed vibrocorer sampling device configured so as to penetrate the sea floor up to 10 m and connected to a hydraulic conveying line[27], a hydrocyclone for sample processing and a ship-borne X-ray spectrometer with a ring-shaped ^{109}Cd source, a Si(Li) detector with Be window and appropriate control facilities (Fig. 4). Following successful tests in the North Sea the recovery of sediment depth profiles is at present proved in a tin stone exploration campaign off the coast of Malaysia with promising results obtained so far. The technique is believed to have considerable potential during exploration and geochemical surveys of the continental shelf.

Ultimate performance in X-ray fluorescence analysis may be achieved by combining X-ray tube sources with high-resolution detectors. Knoth and Schwenke[28,29] have developed a spectrometer with totally reflecting sample support for trace analysis at the ppb level and beneath it. Very recently, the equipment was tested for the first time on board ship with great success.

High-sensitivity analyses of marine specimens generally require separation of the salt matrix and preconcentration. Strong chelating reagents such as ammonium pyrrolidine dithio-carbamate (APDC) have been found to satisfy the specific demands[30,31].

Numerous metals have been determined in stream sediments, wholly or in part in the field, by means of either non-dispersive or energy-dispersive analysis or both[32-34].

The performance of *in situ* measurements on the sea bed using energy-dispersive equipment has been reported by Cooper, Wogman and co-workers[35-38]. Though such applications of the technique are seriously impeded by the low energy of the X-rays and the corresponding thin windows required (~10-20 mil. Be), encouraging results have been obtained. The analyzer allows more than 20 elements to be determined quantitatively at the 10 ppm level at water depths to 300 m. A schematic design of the probe is shown in Fig. 5.

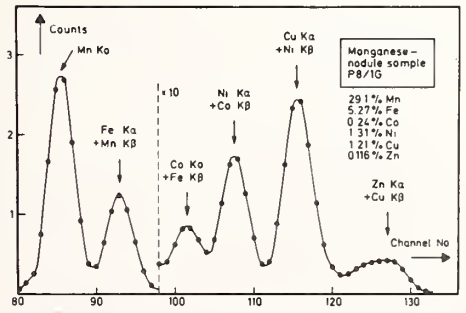

Fig. 3. Characteristic X-ray spectrum of elements Mn to Zn in a manganese-iron nodule sample[22].

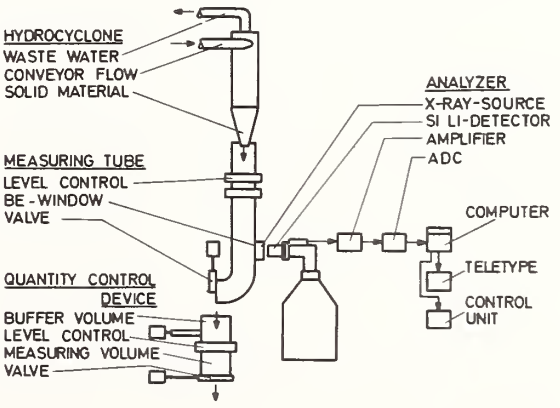

Fig. 4. Sample processing and analysing system for determination of metals in heavy mineral/water mixtures[25,26].

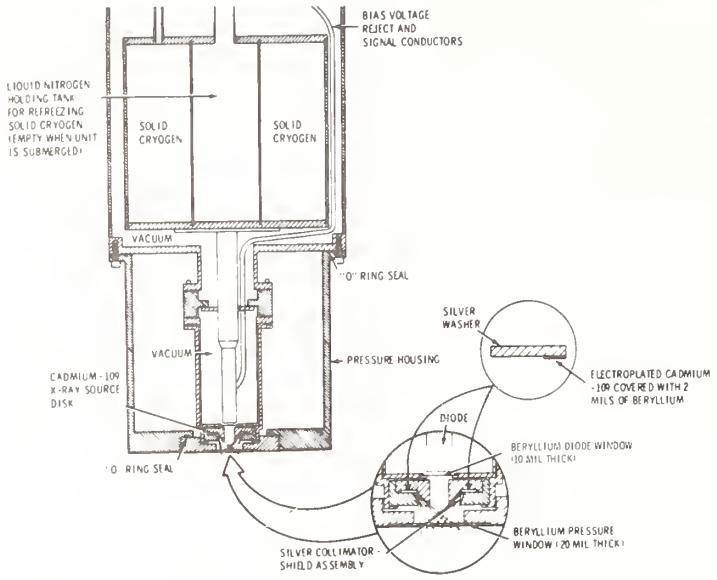

Fig. 5 Schematic design of *in situ* X-ray fluorescence probe[38].

4. Use of Scattered Gamma Radiation

Non-resonant gamma-gamma methods employing radiation from a mono-energetic source are used in two modifications: (i) the bulk density of material may be determined by registering the higher energy interval of the scattered gamma-ray spectrum which is essentially influenced by Compton scattering (density gamma-gamma method), (ii) the intensity measured in the lower part of the spectrum is a function of bulk density as well as effective atomic number as a result of both Compton scattering and photo-electric absorption (selective gamma-gamma method)[39,40]. The latter method is of principal interest in metal exploration, particularly in view of the relatively simple instrumentation, but it suffers from poor specifity and thus inferior accuracy at low elemental concentrations. Therefore, utilization during the past years has been restricted, on the whole, to the favourable case of grade determination of iron ore[41-43] and no applications in the marine environment have come to the knowledge of the writer.

Highly specific, however, though somewhat more elaborate, is the use of the gamma-ray resonance scattering process. This technique has thoroughly been studied and field tested by Sowerby and co-workers[44,45]. It is capable of rapid and accurate analysis of simply prepared bulk mineral samples for copper and nickel. Exact resonance with the nucleus of one of the isotopes of the element to be measured is achieved by using gamma radiation from a heated gaseous source which decays to that isotope. Appropriate sources for copper and nickel determination are $^{65}ZnI_2$ and $^{60}CoBr_2$ (or $^{60}CoI_2$), respectively. Careful shielding of the NaI(Tl) detector against direct radiation from the source is a basic requirement (Fig. 6). Resonance and Compton scattered radiation differ in energy and are pulse-height selected. Drawbacks of the method in field applications are the heavy shielding and high source strengths needed. So far, gamma-ray resonance scattering has been used for bulk analysis of terrestrial ores. It would be intriguing to explore the capability of the technique with respect to the analysis of manganese nodules where just nickel and copper are the elements of main interest; but the high and variable water content of the nodules will probably require appropriate corrections which have to be derived from additional equipment.

5. Field Applications of Neutron Techniques

5.1 General Considerations

In view of the inherently high efficiency of neutron techniques, the desire for versatile multielement analytical equipment using penetrating radiation has led several workers to examine the possibilities of combining a neutron source and a gamma-ray detector for *in situ* analysis during mineral exploration. The availability of sufficiently strong ^{252}Cf spontaneous fission sources has highly stimulated these investigations. In general, the energy resolution of NaI(Tl) detectors is too poor for such applications, since either the reaction utilized results in a spectrum of complex structure or, with a steady-state neutron source, more than one of the possible processes - inelastic scattering, radiative capture and decay of activated nuclides - contribute to the resultant spectrum. Therefore, the development of low-temperature semiconductor detector cryostats[46-51] that are suitable for sea bed measurements provides a very important contribution to this field of activity.

Utilization of inelastic scattering is a domain of pulsed neutron sources which allow significant improvements in signal-to-noise ratios by appropriate gating of the detector. To date, activation analysis and radiative capture assay have mainly been performed using ^{252}Cf sources. Among these two types of measurement, the radiative capture process, from a principal point of view, appears to be the most promising for several reasons. The technique is characterized by a larger effective radial sample thickness and corresponding larger effective sample volume, by a more favourable measurement speed and by the absence of sensitivity to natural radioactivity interference. On the other hand, the measurement of prompt gamma emission from radiative neutron capture sets limits to the choice of the source-detector distance and the detector has to be carefully shielded against neutrons and direct gamma radiation from the source. In activation techniques neutron source and gamma-ray detector can be properly separated.

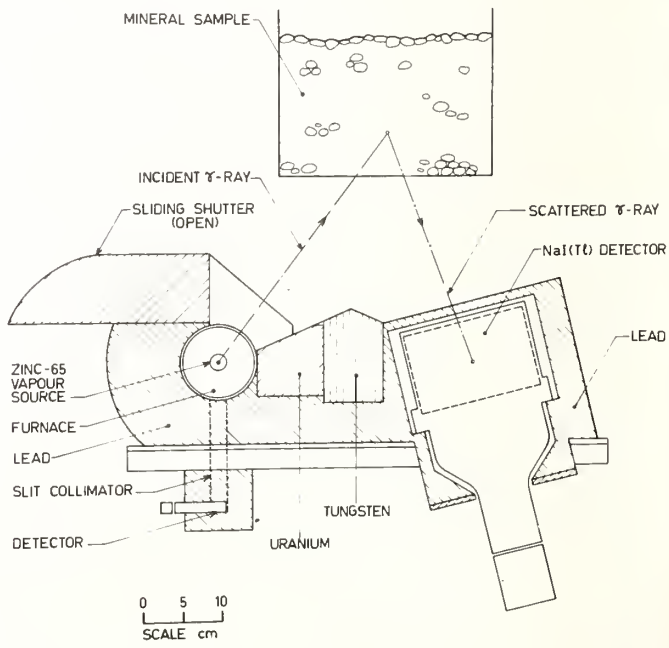

Fig. 6. Cross-sectional view of bulk analyser based on gamma-ray resonance scattering[45].

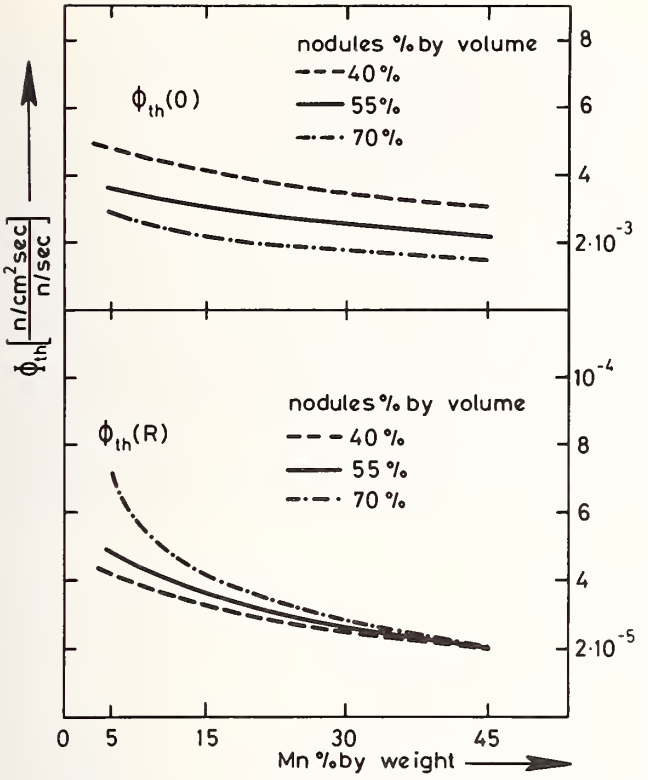

Fig. 7. Dependence of thermal neutron flux upon part by volume and Mn content of nodules at r = 0 and R = 26.5 cm[52].

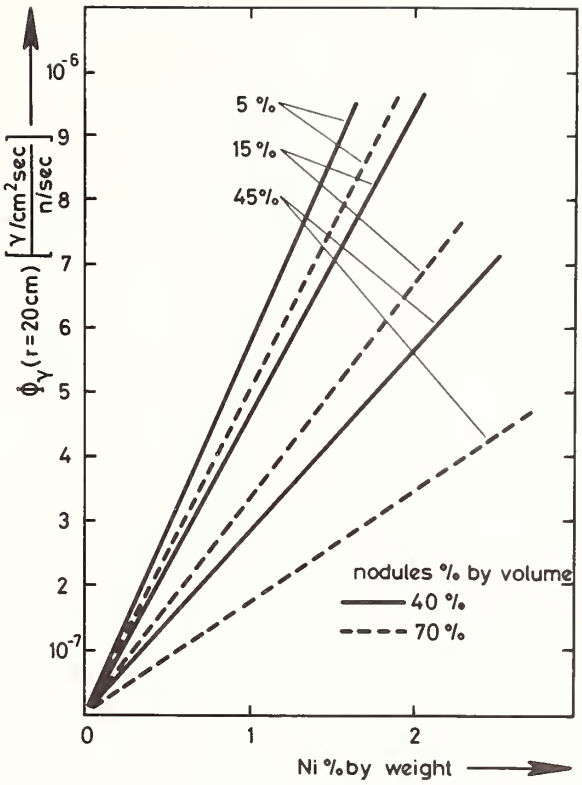

Fig. 8. Dependence of nickel capture gamma-ray intensity at r = 20 cm upon part by volume and Ni and Mn content of nodules[52].

Irrespective of source and interaction process used, the response of the measuring system is a result of manifold interaction processes in neutron and gamma-ray transport. As a consequence, the fundamental reliability of the data often remains in some doubt, in spite of the considerable progress achieved in instrumentation, and the degree of accuracy has to be carefully examined in each case. The most important potential sources of error lie in variations in neutron transport due to inhomogeneity, water content and density effects. These parameters all affect the spatial and spectral distribution of neutrons and thus the gamma-ray intensity at the detector. An example is given in Figs. 7 and 8 for the case of using a ^{252}Cf source in a concentric arrangement of a 53 cm dia. container filled with water and manganese nodules and surrounded by a water reflector[52]. Fig. 7 shows the calculated dependence of the thermal neutron flux at the source position and at the container wall (R = 26.5 cm) on the manganese content of the nodules and their part by volume in the container. As a result of the strong flux variations, the intensity of the 8998 keV nickel capture gamma-rays is quite sensitive to these analytical parameters (Fig. 8). The calculations have been performed using a 26-group transport programme with the ABN group scheme[53].

In the example described the nickel capture gamma-rays originate essentially from capture of thermal neutrons, since the resonance integral of ^{58}Ni is small and the high sea-water content leads to a favourable ratio of thermal to epithermal flux. The problem is further complicated, if the measured spectra are the result of both thermal and epithermal resonance capture[54]. Substantial epithermal capture may pose a serious problem of identification and calibration for quantitative analysis. Similar difficulties arise, when 14 MeV neutron tubes and fast neutron threshold reactions are utilized. In all practical applications a broad spectral distribution is involved in the interaction processes and the strong energy dependence of the cross sections has to be carefully considered.

In order to study and to understand the influence of the various analytical parameters, experimentalists perform simulated laboratory measurements on samples which have been analysed in detail with respect to elemental concentrations, density and water content. This procedure, however, is laborious and time-consuming. Therefore, theoretical calculations are of great benifit for determining the limits of quantitative analysis. They require accurate cross section data and group constants. Unfortunately, the agreement between theoretical and experimental results is often unsatisfactory. One of the reasons for the discrepancies observed may lie in insufficient accuracy of the cross section data used.

Although much profound work has already been carried out, the problems briefly summarized here may be one of the principal causes why neutron techniques, so far, have not yet found wide-spread routine use in marine metal exploration. The discussion also emphasizes the need for monitoring both number and energy of the neutrons which further complicates the instrumentation under anyway unfavourable environmental conditions. Finally, it must be realized that the application of neutrons has to compete with various other well established techniques. Further experimental and theoretical efforts are needed to achieve a common breakthrough and to make available the potential capabilities of the method.

5.2 Pertinent Research

Use of ^{252}Cf sources. Radioisotope neutron sources have several unique advantages. They are simple and reliable and provide a stable source strength and neutron flux. The most important exponent is the ^{252}Cf spontaneous fission source which is characterized by a high neutron yield (4.3×10^9 n $s^{-1}Ci^{-1}$; 2.3×10^{12} n $s^{-1}g^{-1}$), a small volume required (< 0.05 cm^3 per 10^8 n s^{-1}) and a low heat output (0.001 W per 10^8 n s^{-1})[55].

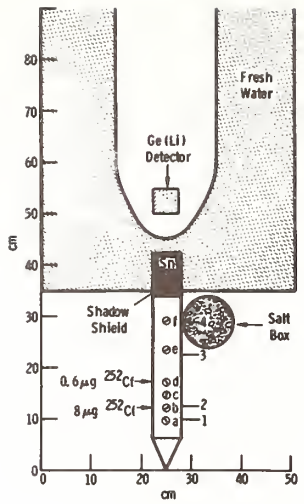

Fig. 9. Sketch of apparatus for *in situ* capture gamma-ray analyses in sea bed exploration[54].

Senftle and co-workers[54,56-60] have thorougly studied the possibilities of using neutron activation and radiative capture for *in situ* analysis. The early work concentrated on establishing and improving techniques [56-59] and on compiling the relevant nuclear data[60]. A more recent feasibility study[54] examined in detail the capabilities and limitations of capture gamma-ray analysis of bottom sediments in sea bed exploration. The experiments were carried out using two ^{252}Cf sources of 0.6 and 8.2 µg and a 45 cm^3 Ge(Li) detector in a canister-cooled cryostat (Fig. 9). To reduce chlorine interference a sheath of fresh water was placed around the detector. The results obtained clearly demonstrate the compositional and density effects on neutron flux and energy distribution and the associated intensity variations of specific capture gamma-ray lines with average neutron energy. Such variations are compatible with pertinent spectroscopic investigations[61,62]. Several measures are suggested by Senftle et al.[54] to reduce these problems. They include (i) changing the configuration of the probe to improve counting statistics, (ii) derivation of an index of spectral hardness from the ratio of two peaks of some common element and (iii) use of a pulsed neutron generator with proper detector gating to increase the selectivity.

Moxham and co-workers[12] have developed a prototype device which allows three modes of data collection: (i) measurement of natural radioactivity (cf. section 2), (ii) neutron activation in the decay mode and (iii) radiative capture gamma-ray analysis (Fig. 10). The sonde has been used *in situ* for the assay of river-bottom sediment. It incorporates a 110 µg ^{252}Cf source and a propane-cooled Ge(Li) detector. The device is capable to penetrate the sediment about 60 cm. Among the elements identified in the activation spectra were ^{64}Cu, ^{66}Cu, ^{52}V, ^{56}Mn, ^{28}Al, ^{24}Na, ^{27}Mg, ^{116m}In and ^{152m}Eu (Figs.11 and 12).Fe, Cu, Mn, Ti, Si, Ca, O, K and Al were present in the capture gamma-ray spectra. Comparison of the spectra from the water-saturated sediments with borehole spectra from a relatively dry deposit, for both modes of operation, revealed significant differences in gamma-ray intensity in spite of equal elemental concentrations. It may be concluded that the high water content of the river bottom greatly increases the thermal flux near the source and tends to favour the decay gamma-ray response more than the capture. Monitoring of both number and energy of neutrons is needed to take flux variations into account.

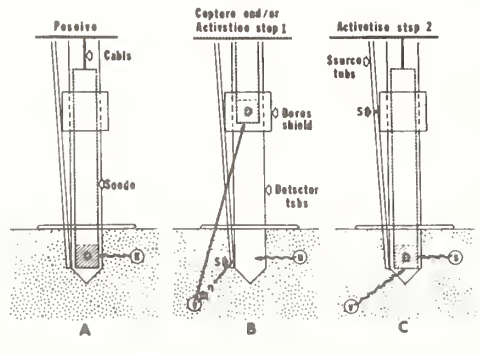

Fig. 10. Diagram showing relative position of sonde and neutron source in three modes of data collection[12].

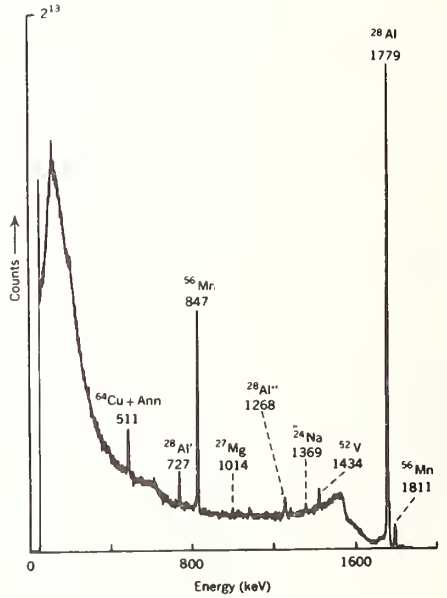

Fig. 11. *In situ* decay gamma spectrum of bottom sediments[12].

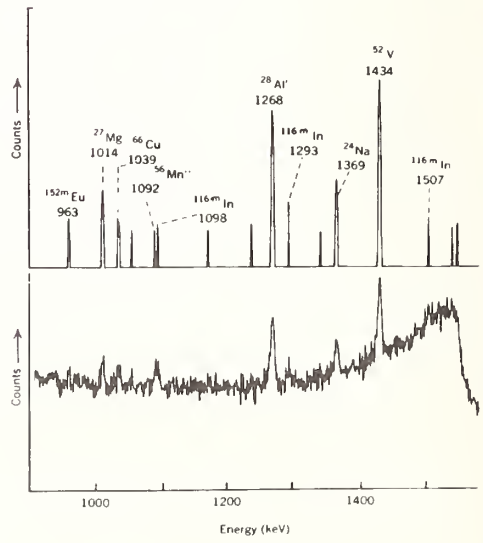

Fig. 12. Details of the gamma-ray spectrum in Fig. 11.

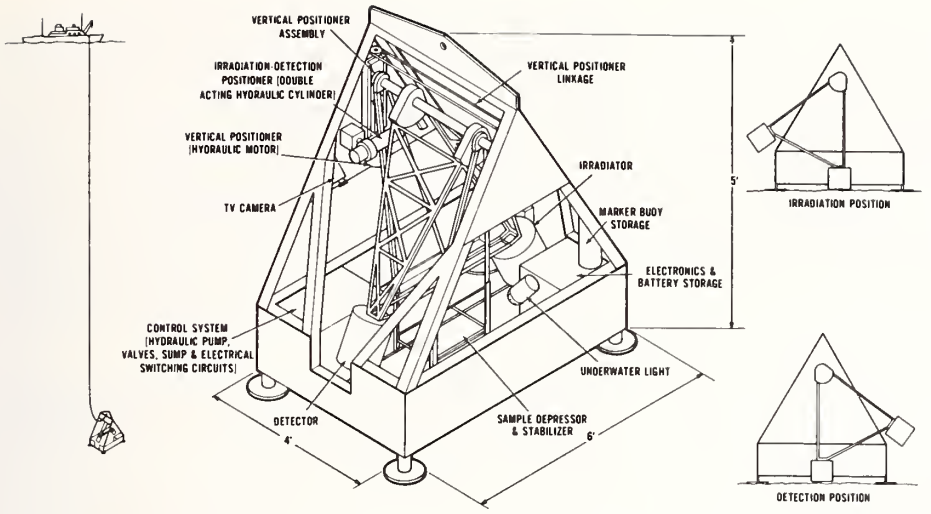

Fig. 13. Design of *in situ* neutron activation probe for water depths to 300 m[38].

By using a probe containing a 1 mg source and a 15 % efficiency Ge(Li) diode Wogman[38] has accomplished activation analysis on the sea floor with the detection of 33 elements (Fig. 13). The design depth of the analyzer is 300 m. The minimum detectable concentrations for metals, based on 2 min irradiation, 40 s decay and 2 min counting time, were found to range from 1 to 100 ppm for Sc, Ti, V, Au, Mg, Mn, Mo and from 0.1 to 1 % for Al, Co, Cu, W, Ni, Nb and Cd.

Fanger and Pepelnik[66] have demonstrated that the (n,γ) method is a powerful tool for *in situ* analyses of manganese nodules, if bulk density and flux distribution are properly monitored by gamma-ray transmission and fission chambers, respectively (Figs.14 and 15). The work was part of a most ambitious project[67-71] aiming at rapid multielement analyses on the ocean floor at water depths up to 6000 m. Unfortunately, the prototype device (Fig. 16) got lost during the first deep-sea field test in the Pacific due to unusual overcharge of the cable, when the sonde was heaved aboard after a short circuit had occurred in the 6 kV power supply. Though promising results had been obtained with respect to the functional capabilities of the analyzer down to 3700 m water depth, the project was discontinued.

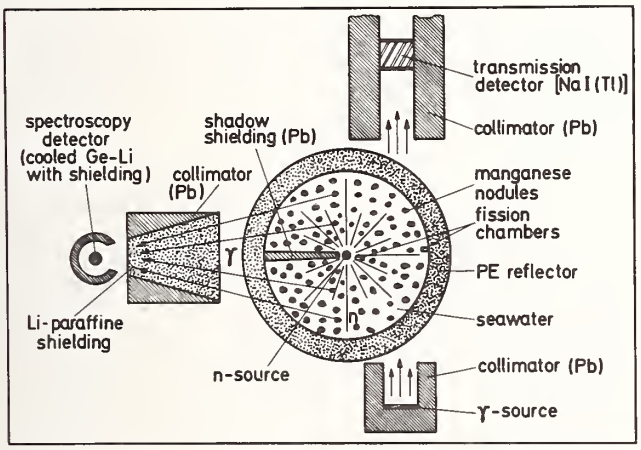

Fig. 14. Scheme of (n,γ) apparatus for *in situ* analysis of manganese nodules[66].

Noakes and co-workers[63-65] have reported activation analysis with a 200 µg Cf source on the sea floor by three different modes of operation: (i) an undersea submersible for deep water capabilities (150 - > 300 feet), (ii) a sled for intermediate depths (50 - 150 feet) and (iii) SCUBA divers for shallow water operations. In addition, a shipboard analytical system incorporating a 1 mg ^{252}Cf neutron irradiator was tested. A health physics study showed that Cf neutron sources can be handled in all phases of the marine work without undue radiation hazards to participating personnel.

In order to increase the neutron flux and, at the same time, to minimize the cost involved in the purchase of Cf (~ $ 10.000/mg), current developments of Wogman and co-workers[38,72-74] are aimed at using a subcritical ^{252}Cf-^{235}U multiplier arrangement with a k_{eff} of up to 0.985 and an associated multiplication factor of 66 (cf. section 6). In field applications such a multiplier assembly could combine the advantage of high flux with that of handling a neutron source of only moderate strength.

Use of 14 MeV neutron tubes and (α,n) sources. Fast neutron activation analysis utilizing threshold reactions of the (n,p), (n,α), (n,n') and (n,2n) type is well suited for the solution of many analytical problems. The most common source is the 14 MeV sealed neutron tube based on the ^{3}H(d,n)^{4}He reaction. Tubes for field applications usually operate with neutron yields between 10^{8} to a few 10^{10} n s^{-1} and corresponding usable fluxes near the target in the range from 10^{6} to 10^{9} n $cm^{-2}s^{-1}$. Devices with higher outputs are generally limited to laboratory experiments (cf. section 6).

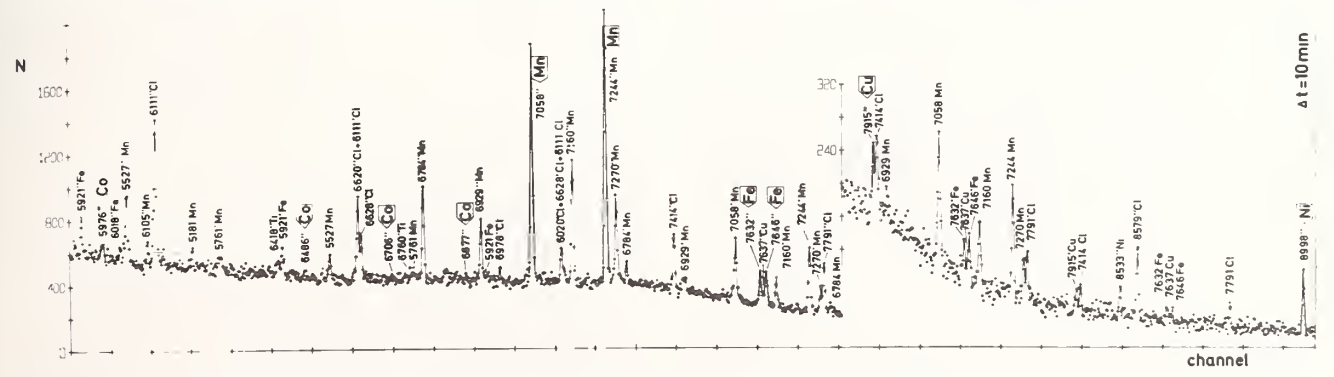

Fig. 15. High-energy section of a typical (n,γ) spectrum from manganese nodules[66].

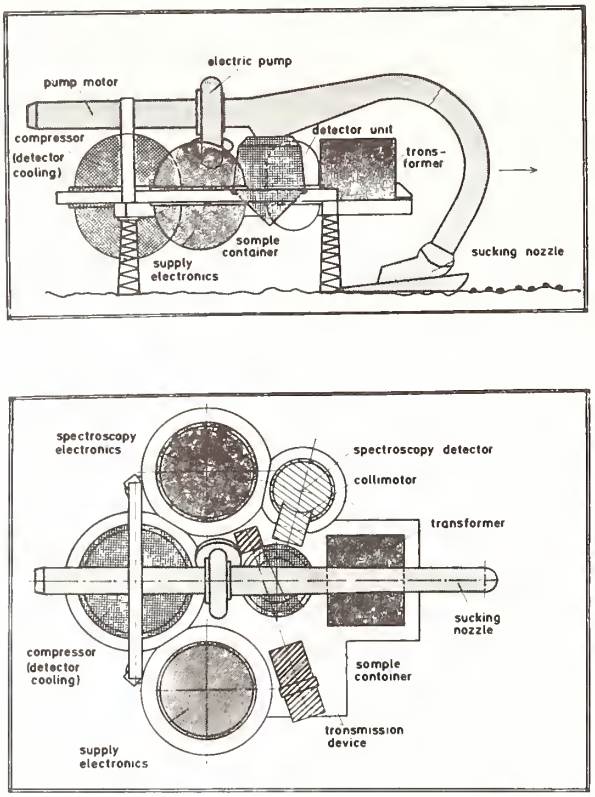

Fig. 16. Scheme of the technical concept for *in situ* (n,γ) analysis of manganese nodules[66].

Pulsed neutron tubes are of particular interest, since they allow time-sequencing between source and detector. In this way gamma-rays from inelastic scattering, radiative capture and radioactive decay can be separated to a large extent (Fig. 17). Common to pulsed and direct current neutron generators is the advantage that they can be turned off simply by de-exciting the high voltage which very much facilitates handling of the source in the field. On the other hand, accelerator stability, primary source strength determination, spatial and spectral flux distribution and standardization require careful consideration. Techniques for the evaluation of systematic errors caused by geometry effects and neutron and gamma-ray attenuation have been described in great detail in the literature[75-78]. The need of multi-group calculations and of corresponding accurate cross section data for exploring the compositional, density and water content effects has already been emphasized before. In some cases, serious problems may arise with the use of 14 MeV neutrons from interfering reactions which lead to the same radioactive nuclides. Typical examples are provided by the reactions $^{27}Al(n,p)^{27}Mg$; $^{30}Si(n,\alpha)^{27}Mg$ and $^{56}Fe(n,p)^{56}Mn$; $^{55}Mn(n,\gamma)^{56}Mn$. Cross section data needs, therefore, refer also to elements not of primary interest in metal exploration. Another drawback of neutron tubes is the limited life of targets.

So far, 56 elements in different matrices have been determined using 14 MeV neutron activation[55]. Detection limits range from 0.1 to 1 mg for Al, Cr, Cu, Zr, Ag and Cd, and from 1 to 10 mg for Mg, Mn, Fe, Ni, Au and Hg, if a flux of 10^9 n cm^{-2} s^{-1} and activation, decay and counting times in the order of a few minutes are assumed. Comprehensive tables may be found elsewhere[79].

Several authors[80-87] have described the application of 14 MeV neutrons including comparisons of this technique with the use of ^{252}Cf sources. Evans and co-workers[83] have developed equipment for underwater *in situ* elemental analysis based on the experience from the orbital gamma-ray spectrometer experiments during Apollo 15 and 16 missions. Additional measurements of the rate of die-away of neutrons may yield supplementary information in field experiments[84], for example, on the hydrogen content of the material. Uranium may be assayed by the detection of delayed fission neutrons. Other authors[85-87] have demonstrated that copper and nickel in manganese nodules can be determined in a rapid and quasi-continuous way by fast-neutron activation techniques (Fig. 18) via the Mn/Fe ratio using well pronounced geochemical correlations (cf. section 3). The method requires no sample preparation and laborious calibration procedures, but interference from low- and intermediate-energy neutron capture in Mn has to be carefully considered.

The measurement of prompt gamma-rays from the inelastic scattering of fast neutrons is another promising technique for elemental analysis[88,89]. The detection limits for the metals Ti, Mn, Fe, Co, Ni, Cu, Zn, Ag and Sn range from 0.5 to 5 % by weight for common neutron sources. Sowerby[89] is currently investigating the capabilities of the method with a ^{238}Pu-Be source. Improvement of the relevant cross section data on the production of gamma-rays in inelastic collisions would be helpful for advancing this technique.

Only little has been reported so far on routine applications of (α,n) sources in spite of their obvious potentiality. The main reasons lie in the limited neutron yields obtainable[55].

6. Laboratory Analyses

In the course of fundamental geochemical investigations nuclear techniques are used extensively for laboratory analyses of samples collected in the field. High accuracy, precision and sensitivity are the most important requirements in these studies. Not only the determination of major and minor constituents, but also quantitative analyses of trace elements are needed, as every element is of potential geochemical interest. In the marine domain, the disclosure of the genesis and growth rate of manganese nodules and the inconsistency of the rates of sediment accumulation and nodule growth are the most intriguing subjects of research[90-101].

Neutron activation analysis, radiochemical or preferably instrumental, using reactor neutrons provides an outstanding analytical tool for multielement geochemical studies[102-104]. Sensitivities range from 10^{-13} to 10^{-9} g for two thirds of the natural elements if a thermal flux of 5×10^{13} n cm^{-2} s^{-1} and a epithermal flux of 10^{12}

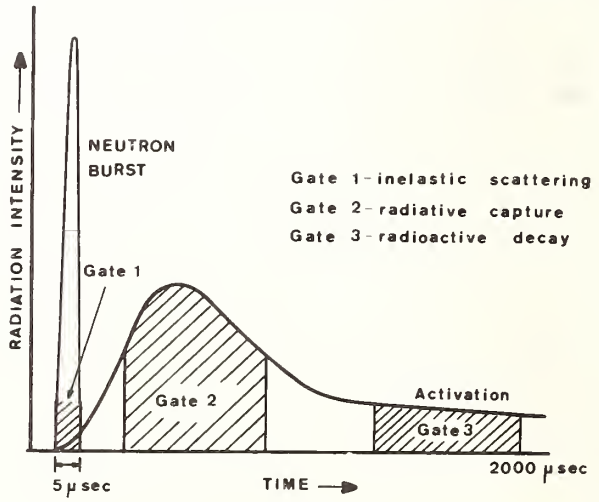

Fig. 17. Time-sequencing for pulsed neutron sources.

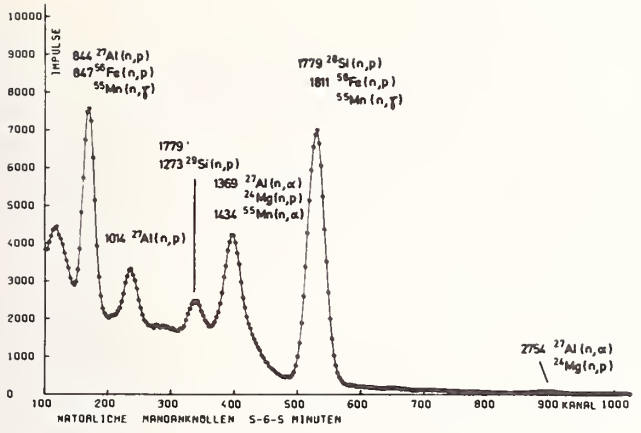

Fig. 18. Gamma-ray spectrum from fast-neutron activation analysis of manganese nodules[87].

n cm^{-2} s^{-1} are available. Wogman and co-workers[72-74] have developed a ^{252}Cf-^{235}U fueled subcritical multiplier which produces a thermal flux on the order of 10^{10} n cm^{-2} s^{-1} with corresponding detection limits between 10^{-9} and 10^{-5} for the majority of the elements. The facility contains six ^{252}Cf sources totaling slightly over 100 mg and placed in a 93 % enriched uranium core with k_{eff} = 0.985. Other important techniques are energy-dispersive X-ray fluorescence analysis and low-level α-, β- and γ-counting[105,106]. With the availability of high-output 14 MeV neutron generators[107,108] the use of fast-neutron threshold reactions will more and more gain in significance[109] and supplement the research at nuclear reactors. Although the primary application of these devices with steady-state yields of 5×10^{12} to 5×10^{13} n s^{-1} is in radiotherapy, the sources are equally well suited for activation analysis. Fig. 19 shows a schematic view of KORONA, a facility now under construction at the GKSS research centre[110]. Characterictic features of the device are the high neutron yield (5×10^{12} n s^{-1}) and, due to the cylindrical target design, the very low flux gradient which minimizes systematic errors caused by geometry effects[111]. For more than 50 elements the detection limits will be in the µg range or even below.

High-accuracy activation analysis requires careful consideration of primary, secondary and second-order reaction interferences. While primary interferences are, in general, well accessible to evaluation in analyses with reactor neutrons, they may rise severe problems with 14 MeV neutron sources. Secondary particles may affect the analytical results in all measurements in which energetic projectiles are applied. This is particularly valid for charged particle- and photon- induced reactions, but may also occur in fast-neutron activation analysis depending on the specific matrix. Second-order effects can be the source of serious systematic errors in activation with reactor neutrons if a high flux and long irradiation times are used. The problem of reaction interferences and their evaluation has extensively been treated in the literature[112-117]. For considering their extent correction by calculation is the preferred procedure, but this requires critically evaluated and accurate data for the relevant cross sections. Unfortunately, the experimental data are often very inconsistent and it is difficult to judge the accuracy of the cross section needed. Reduction of the uncertainties would thus be most helpful.

Besides improvement of sensitivity, high-output 14 MeV neutron facilities extend the analytical potentialities in two respects: (i) the high yield allows utilization of reactions of lower cross section but increased elemental selectivity and (ii) a number of fast-neutron reactions leading to short-lived product nuclides or isomeric states with half-lives between 20 and 1000 ms appear feasible thus permitting rapid assays by means of quasi-prompt activation with detection limits below 0.1 ppm. The latter approach suggests combining the neutron source with an ultra-fast rabbit system (Fig. 19). Numerous cross sections pertaining to high-selectivity and quasi-prompt activation are subject to considerable uncertainties or are even unkown.

7. Summary of Cross Section Data Needs

The discussion of the various techniques in the preceding paragraphs discloses the necessity of further improving a number of cross section data. Particular consideration should be given to some energy-dependent cross sections relevant to neutron and gamma transport in field applications of neutron techniques, to cross sections for production of gamma rays from inelastic collisions, to cross sections of threshold reactions which either ensure elemental selectivity or are the source of elemental interferences and, finally, to cross sections for quasi-prompt activation analysis. These suggestions are summarized in Table I. The accuracy requested is better than 5 % in most cases. It would be very helpful for many applications in nuclear geophysics to have the updated fast-neutron cross sections tabulated in a multigroup scheme beginning with 14 MeV neutrons. In this connection the possible use of (α,n) sources with their broad energy distribution should be kept in mind.

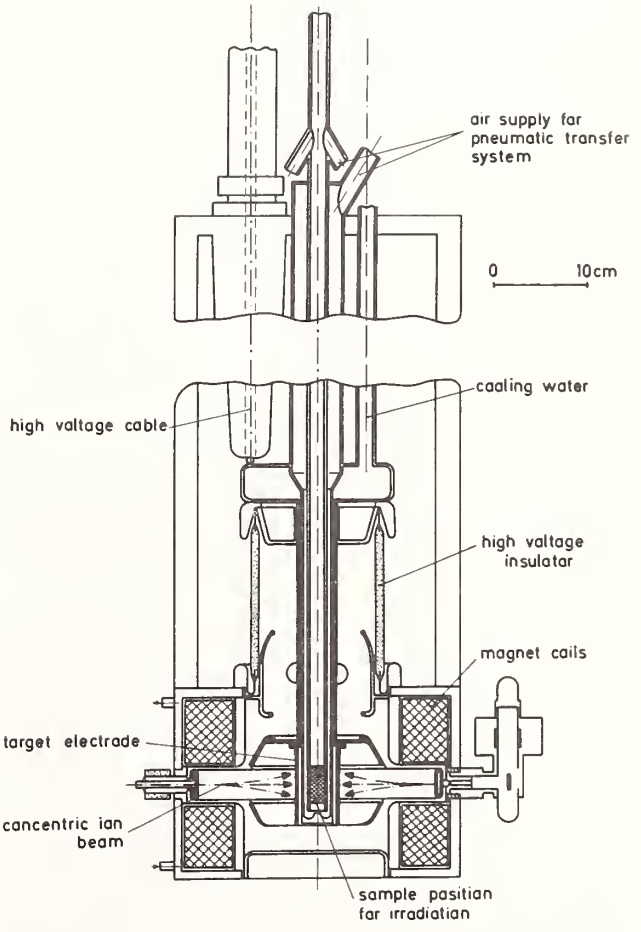

Fig. 19. KORONA - a high-output 14 MeV neutron activation facility combined with an ultra-fast rabbit system.

Table I. Cross section data needs[a]

Reaction	Energy range	Estimated present accuracy[b] %	Half-life of product	Remarks
^{17}O (n,p)^{17}N	thr.-15 MeV	?	4.15 s	c
^{30}Si(n,α)^{27}Mg	thr.-15 MeV	?	9.46 m	d,e
^{35}Cl(n,γ)^{36}Cl	I	15	$3 \cdot 10^5$ a	f
^{46}Ca(n,γ)^{47}Ca	thermal	30	4.54 d	g
	I	30	4.54 d	g
Ti(n,n'γ)	thr.-15 MeV	?	stable	h
^{46}Ti(n,2n)^{45}Ti	14-15 MeV	7	3.08 h	e,i,j
^{48}Ti(n,p)^{48}Sc	thr.-15 MeV	10	44.1 h	
^{50}Ti(n,γ)^{51}Ti	I	10	5.76 m	
^{50}Ti(n,p)^{50}Sc	thr.-15 MeV	?		e,j
^{50}Ti(n,p)^{50m}Sc	14-15 MeV	?	350 ms	e
^{51}V (n,α)^{48}Sc	thr.-15 MeV	20	44.1 h	d
^{50}Cr(n,2n)^{49}Cr	thr.-15 MeV	10	42 m	j
^{52}Cr(n,p)^{52}V	thr.-15 MeV	12	3.75 m	d
^{55}Mn(n,γ)^{56}Mn	epith.-15 MeV	?	2.58 h	d
^{55}Mn(n,α)^{52}V	thr.-15 MeV	15	3.77 m	
Co(n,n'γ)	thr.-15 MeV	?	stable	h
Ni(n,n'γ)	thr.-15 MeV	?	stable	h
^{58}Ni(n,2n)^{57}Ni	14-15 MeV	8	36.0 h	e,i,j
^{61}Ni(n,p)^{61}Co	thr.-15 MeV	10	1.65 h	
Cu(n,n'γ)	thr.-15 MeV	?	stable	h
^{63}Cu(n,γ)^{64}Cu	I	20	12.74 h	
^{63}Cu(n,2n)^{62}Cu	thr.-15 MeV	10	9.78 m	e
^{65}Cu(n,γ)^{66}Cu	I	13	5.10 m	
^{65}Cu(n,p)^{65}Ni	thr.-15 MeV	20	2.52 h	
Zn(n,n'γ)	thr.-15 MeV	?	stable	h
^{64}Zn(n,2n)^{63}Zn	14-15 MeV	8	38.5 m	e,j
^{66}Zn(n,p)^{66}Cu	thr.-15 MeV	10	5.1 m	
^{68}Zn(n,p)^{68}Cu	thr.-15 MeV	20	30 s	
^{68}Zn(n,α)^{65}Ni	14-15 MeV	10	2.52 h	d,i
Zr(n,n'γ)	thr.-15 MeV	?	stable	h
^{90}Zr(n,n')^{90m}Zr	14-15 MeV	?	809 ms	k
^{90}Zr(n,2n)^{89m}Zr	thr.-15 MeV	?	4.2 m	k
^{91}Zr(n,2n)^{90m}Zr	14-15 MeV	?	809 ms	k
^{94}Zr(n,γ)^{95}Zr	thermal	8	65.5 d	g
	I	6	65.5 d	g
^{94}Zr(n,p)^{94}Y	thr.-15 MeV	20	20 m	j
^{96}Zr(n,γ)^{97}Zr	thermal	20	16.8 h	g
	I	8	16.8 h	g
Ag(n,n'γ)	thr.-15 MeV	?	stable	h
^{107}Ag(n,n')^{107m}Ag	thr.-15 MeV	?	44.3 s	
^{107}Ag(n,2n)^{106g}Ag	thr.-15 MeV	20	24 m	
^{109}Ag(n,γ)^{110}Ag	I	25	24.6 s	
^{109}Ag(n,n')^{109m}Ag	thr.-15 MeV	?	39.6 s	
^{109}Ag(n,2n)^{108g}Ag	thr.-15 MeV	15	2.4 m	
Sn(n,n'γ)	thr.-15 MeV	?	stable	h
^{112}Sn(n,2n)^{111}Sn	thr.-15 MeV	30	35 m	j
^{124}Sn(n,2n)^{123m}Sn	thr.-15 MeV	5	40 m	i
^{207}Pb(n,n')^{207m}Pb	14-15 MeV	?	845 ms	
^{208}Pb(n,2n)^{207m}Pb	14-15 MeV	?	845 ms	

[a] Abbreviations used:
[b] thr threshold I resonance integral
In the case of threshold reactions the value given
[c] refers to the 14 - 15 MeV energy range
Of interest to DFN uranium assay; product nucleus
[d] is a delayed neutron emitter
Interfering reaction
[e] σ at 14 MeV strongly energy-dependent
[f] Strong epithermal absorber
[g] Possbile flux detector
[h] σ for production of gamma rays required
[i] Accuracy to be examined
[j] No interfering element
[k] σ very uncertain

There exist several neutron cross section compilation which are widely used[118-121]. More recent experimental data, semiempirical formulae and special systematics may be obtained from some review articles and conference proceedings of late years and the literature cited there[114,115,122].

Not included in Table I, but equally important, are requests for detailed multigroup data for photon attenuation in geological materials. The details required include a breakdown into components for photo-electric, Compton scattering and pair production process up to 11 MeV.

8. Conclusions

Nuclear techniques can provide powerful analytical tools in marine metal exploration. The measurement of natural radioactivity and X-ray fluorescence analysis have been widely applied in the past years with great success. A variety of neutron techniques have been developed with promising results, but their wide-spread routine use in the field has yet to come. Variations in neutron and gamma transport due to compositional, water content and density effects may pose serious problems of identification and calibration for quantitative analysis. Therefore, further experimental and theoretical work is required to ensure the fundamental reliability of the data and to make available the outstanding multielement capabilities of these techniques. In laboratory analyses nuclear methods, in particular activation analysis with reactor neutrons and energy-dispersive X-ray fluorescence spectrometry, are well established. The availability of high-output 14 MeV neutron sources reveals new opportunities for fast-neutron applications with respect to improved sensitivity, selectivity and rapid assay. Improvement and extension of a number of cross section data would be of great benefit for further advancing the development both in the field and in the laboratory.

Acknowledgements

I should like to express my sincere thanks to R.L. Caldwell, J.K. Cochran, P. Eisler, A. El Kady, S. Nargolwalla, J. Noakes, E.A. Schweikert, F.E. Senftle and B.D. Sowerby for their suggestions and for providing me with up-to-date information on the work of their groups.

References

1. J.L. Mero, World Subsea Mineral Resources (V.E. McKelvey, F.F.B. Wang, Eds.), US Geological Survey, Misc. Geological Investigation, MAP I-C 32 (1969)
2. N.M. Saum and J.M. Link, Exploration of uranium ores, Colorado School of Mines, Miner.Ind.Bull. 12 4 (1969) 1
3. B.L. Dickson, A natural gamma technique for direct bulk uranium analysis, Austral.Acad.Sci. 2 (1976) 386
4. M. Bassan, A. Bossin and A. Combaz, Fundamentals of the differential gamma ray log, SPWLA 17th Annual Logging Symp.Trans., Denver, Colorado, 9 June, 1976, B 1
5. C.G. Clayton, Some resent developments and applications of nuclear techniques in the exploitation of mineral resources, CONF - 721091, 1972
6. S.B.U. Bowie and C.G. Clayton, Gamma spectrometer for sea- or lake-bottom surveying, Inst.Min.Metall., Trans., Sect. B 81 (1972) 215
7. J.M. Miller and G.D. Symons, Radiometric traverse of the seabed off the Yorkshire coast, Nature (London) 242 (1973) 184
8. J.M. Miller, P.O. Roberts, G.D. Symons, N.B. Merill and M.R. Wormald, A towed sea-bad gamma-ray spectrometer for continental shelf surveys, Nuclear Techniques and Mineral Resources 1977, (Proc. Symp. Vienna, 1977) IAEA, Vienna (1977) 465
9. C.G. Clayton, Some recent applications of nuclear techniques in the exploration and mining of metalliferous minerals, Nuclear Techniques and Mineral Resources 1977 (Proc.Symp. Vienna, 1977), IAEA, Vienna (1977) 185
10. K.O. Emery and E. Uchupi, Western Atlantic Ocean: Topography, Rocks, Structure, Water, Life and Sediments, Am.Asso. Petroleum Geologists, Mem.17, 379 p. (1972)
11. J.E. Noakes, J.L. Harding and J.D. Spaulding, Locating offshore mineral deposits by natural radioactive measurements, Mar.Technol.Soc. J. 8 5 (1974) 36
12. R.M. Moxham, A.B. Tanner and F.E. Senftle, In situ neutron activation analysis of bottom sediments, Anacostia River, Washington D.C., Mar.Technol.Soc. J. 11 1 (1976) 14
13. J.F. Cameron and C.G. Clayton, Radioisotope Instruments, Part I, Pergamon Press, London (1971)
14. J.R. Rhodes, Applications of portable radioisotope X-ray analyzers in industry and mining, Nucl.Eng. 66 XXII (1970) 48
15. C.G. Clayton, Applications of radioisotope X-ray fluorescence analysis in geological assay, mining and mineral processing, Nuclear Techniques and Mineral Resources (Proc.Symp. Buenos Aires, 1968) IAEA, Vienna (1969) 293
16. J.R. Rhodes, Practical problems in chemical analysis using energy-dispersive X-ray emission spectrometry, Proc.Int.Conf. Inner Shell Ionization Phenom. and Future Applications 4, USAEC, Oak Ridge, Tennessee (1973) 2218
17. J.R. Rhodes and T. Furuta, Multi-element portable radioisotope X-ray analyzer for determination of copper, nickel, iron and manganese, Inst.Min.Metall., Trans. 77 (1968) 162 B
18. H.-M. Lueschow, Non-dispersive X-ray spectrometric analysis of manganese nodules: procedure and results, The Origin and the Distribution of Manganese Nodules in the Pacific and Prospects for Exploration (B. Morgenstein, Ed.), Valdivia Manganese Expl. Group and Hawaii Inst. Geophysics (1973) 103
19. B.-M. Lueschow and G. Kraft, Non-dispersive X-ray spectrometry for manganese nodules from the Pacific, mt 4 6 (1973) 200
20. P. Martinelli, Tête de mesure pour l'analyse semi-automatique des échantillons de minerais et des solutions industrielles, Nuclear Techniques and Mineral Resources 1977 (Proc.Symp. Vienna, 1977), IAEA, Vienna (1977) 431
21. B.-M. Lueschow, D. Lindenberger and G. Kraft, Atomabsorptions-Spektrometrie ohne Wägung an Bord eines Forschungsschiffes, Z.Anal.Chem. 279 (1976) 347
22. G.B. Friedrich, B. Kunzendorf and W.L. Plüger, Geochemical investigation of deep sea manganese nodules from the Pacific on board R/V VALDIVIA - an application of the EDX-technique, The Origin and the Distribution of Manganese Nodules in the Pacific and Prospects for Exploration (B. Morgenstern, Ed.), Valdivia Manganese Expl. Group and Hawaii Inst. Geophysics (1973) 31
23. G.B.W. Friedrich, B. Kunzendorf and W.L. Plüger, Ship-borne geochemical investigations of deep-sea manganese-nodule deposits in the Pacific using a radioisotope energy-dispersive X-ray system, J.Geochem. Explor. 3 (1974) 303
24. B. Kunzendorf, G. Friedrich and W. Plüger, Anwendung eines Radioisotop-EDX-Systems bei der Analyse von Manganknollen, Erzmetall 27 2 (1974) 85
25. J. Knoth, R. Marten, B. Schneider and B. Schwenke, On-line determination of heavy minerals in marine deposits by X-ray spectrometry, Proc. 3rd Int.Conf. Ocean Engineering and Marine Sciences, Düsseldorf (1976) 30; GKSS 76/E/28
26. B. Schwenke and D. Anders, Prospektion mariner Mineralseifen durch Bohrkernentnahme mit in-line Röntgenfluoreszenz-Analyse, mt 8 5 (1977) 157; GKSS 77/E/48
27. J. Ahlf, D. Anders and B. Rosomm, Hydraulic sample conveying system for the exploration of marine sands and placers, Proc.3rd.Int.Conf. Ocean Engineering and Marine Sciences, Düsseldorf (1976) 36; GKSS 76/E/25
28. J. Knoth and B. Schwenke, An X-ray fluorescence spectrometer with totally reflecting sample support for trace analysis at the ppb level, Fresenius Z.Anal.Chem. 291 (1978) 200; GKSS 78/E/50
29. J. Knoth and H. Schwenke, A new totally reflecting X-ray fluorescence spectrometer with detection limits below 10^{-11} g, Fresenius Z.Anal. Chem. (to be published)
30. A.H. Pradzynski, R.E. Henry and E.L. Draper, Determination of trace elements for hydrochemical prospecting by APDC-coprecipitation and X-ray spectrometry, Trans.Am.Nucl.Soc. 24 (1976) 119
31. J. Knoth and H. Schwenke, Trace element enrichment on a quartz glass surface used as a sample support of an X-ray spectrometer for the subnanogram range, Fresenius Z.Anal.Chem. 294 (1979) 273; GKSS 79/E/13
32. C.G. Clayton and T.W. Packer, Analysis of stream sediment and soil samples using a high resolution energy-dispersive X-ray fluorescence spectrometer, Nuclear Techniques and Mineral Resources 1977 (Proc.Symp. Vienna, 1977), IAEA, Vienna (1977) 395
33. J.M. Bansel and C.J. Martell, Automated energy-dispersive X-ray determination of trace elements in stream sediments, LA-6869-MS. GJBX-52 (77)
34. H. Kunzendorf, Radioisotope-excited X-ray fluorescence analysis and its application to geochemical exploration in Greenland, Risø-M-1610
35. J.A. Cooper, H.L. Nielson and N.A. Wogman, Feasibility study of in-situ sediment analysis by X-ray fluorescence, Nucl.Technol. 26 (1975) 224
36. N.A. Wogman, H.G. Rieck and J.R. Kosorok, In situ analysis of sedimentary pollutants by X-ray fluorescence, Nucl.Instrum.Methods 128 (1975) 561
37. N.A. Wogman and K.K. Nielson, In situ parts per million analysis of marine sediments by X-ray fluorescence techniques, Oceans '76, 76 CH 1118 - 9 OEC (1976) 12A1
38. N.A. Wogman, In-situ X-ray fluorescence and californium-252 neutron activation analysis for marine and terrestrial mineral exploration, Nuclear Techniques and Mineral Resources 1977 (Proc. Symp. Vienna, 1977), IAEA, Vienna (1977) 447
39. J.A. Czubek, Recent Russian and European developments in nuclear geophysics applied to mineral exploration and mining, Log Analyst 12 (1971) 20
40. Junji Nakai, On the measurement of rock density and prospecting for heavy metallic ore deposits by using γ-γ logging, Chishitsu Chosajo Geppo 29 1 (1978) 1
41. R.J. Bolmes, Bulk analyzer for grade determination of iron ore fines by backscatter of cobalt-60 gamma radiation, Analytical Chemistry 48 8 (1976) 1155
42. J. Charbucinski, P.L. Eisler, P.J. Mathew and A.W. Wylie, Use of backscattered gamma radiation for determining grade of iron ores in blast holes and development drill holes, Proc.Australas.Inst. Min.Metall., 262 (1977) 29
43. A.W. Wylie and P.L. Eisler, Determining the grade, bulk density and porosity of iron ores by the methods of nuclear geophysics, Atomic Energy in Australia 21 2 (1978) 1
44. B.D. Sowerby and W.K. Ellis, Industrial on-stream analysis using gamma-ray resonance scattering, Nuclear Techniques in the Basic Metal Industries (Proc.Symp. Helsinki, 1972), IAEA, Vienna (1973) 479
45. B.D. Sowerby, W.K. Ellis and R. Greenwood-Smith, Bulk analysis for copper and nickel in ores using gamma-ray resonance scattering, Nuclear Techniques and Mineral Resources 1977 (Proc.Symp. Vienna, 1977), IAEA, Vienna (1977) 499
46. P. Dumesnil and C. Andrieux, Spectrométrie gamma dans les forages par sonde à semiconducteur Ge(Li), Industries Atomiques 11/12 (1970) 3
47. P. Dumesnil, Sonde de radioprospection avec semiconducteur Ge(Li), Bull.Instrum.Nucl. 43 (1971) 31
48. A. Lauber and O. Landström, A Ge(Li) borehole probe for in-situ gamma ray spectrometry, Rep. AE-444, Aktiebolaget Atomenergi, Studsvik, Sweden (1971)
49. A.B. Tanner, R.M. Moxham and F.E. Senftle, A probe for neutron activation analysis in a drill hole using ^{252}Cf and a Ge(Li) detector cooled by a melting cryogen, Nucl.Instrum. Methods 100 (1972) 1
50. G.R. Boynton, Canister cryogenic system for cooling germanium semiconductor detectors in a borehole and marine probes, Nucl.Instrum. Methods 123 (1975) 599
51. F.E. Senftle, R.M. Moxham, A.B. Tanner, G.R. Boynton, G.R. Philbin and J.A. Baicker, Intrinsic germanium detector used in borehole sonde for uranium exploration, Nucl.Instrum. Methods 138 (1976) 371
52. B. Würz and L. Buth, Theoretische und experimentelle Untersuchungen zur Lagerstättenprospektion mit Hilfe von neutroneninduzierter Gammastrahlung, KFK 1771 (1973)
53. L.P. Abagyan, N.O. Bazazyants, I.I. Bondarenko and M.N. Nikolaev, Group Constants for Nuclear Reactor Calculations (ed. I.I. Bondarenko), Consultants Bureau, N.Y., 1964
54. F.E. Senftle, A.B. Tanner, P.W. Philbin, J.E. Noakes, J.D. Spaulding and J.L. Barding, In-situ capture gamma-ray analyses for sea-bed exploration, Nuclear Techniques in Geochemistry and Geophysics (Proc. Panel Vienna, 1974), IAEA, Vienna (1976) 75
55. V. Krivan, Non-reactor activation analysis: recent advances and practical significance, Fresenius Z.Anal.Chem. 290 (1978) 193
56. F.E. Senftle, D. Duffey and P.F. Wiggins, Mineral exploration of the ocean floor by in-situ neutron absorption using a californium-252 source, Mar.Technol.Soc.J. 3 (1969) 9
57. F.E. Senftle, Mineral exploration by nuclear techniques, Mining Congress Journal, January 1970
58. P.F. Wiggins, F.E. Senftle and D. Duffey, Geochemical mapping of the ocean floor using neutron capture gamma rays, Trans.Mar.Technol. Soc. 2 (1970) 1165
59. P.F. Wiggins, F.E. Senftle and D. Duffey, Neutron capture gamma-ray analysis of marine manganese nodules using ^{252}Cf, Trans.Am.Nucl. Soc. 13 (1970) 60
60. F.E. Senftle, B.D. Moore, D.B. Leep, A. El-Kady and D. Duffey, Analytical sensitivities and energies of thermal neutron capture gamma rays, Nucl.Instrum. Methods 93 (1971) 425
61. E.R. Rae, W.R. Moyer, R.R. Fullwood and J.L. Andrews, Gamma-ray spectra from radiative capture of thermal and resonance neutrons in mercury and tungsten, Phys.Rev. 155 (1967) 1301
62. J.R. Bird, J. Bergquist, J.A. Biggerstaff, J.H. Gibbon and W.M. Good, Compilation of keV neutron capture gamma-ray spectra, Nucl. Data Tables 11 6 (1973) 433
63. J.E. Noakes and J.L. Harding, New techniques in seafloor mineral exploration, Mar.Technol.Soc.J. 5 6 (1971) 41
64. J.E. Noakes, G.A. Smithwick, J.L. Barding and A. Kirst, Undersea mineral analysis with californium-252, Proc.Am.Nucl.Soc. Topical Meeting, April 1971

65. J.E. Noakes, J.L. Harding and J.D. Spaulding, Californium-252 as a new oceanographic tool, 8th Ann.Conf.Mar.Techn.Soc., Sept. 11-12, 1972, Washington, D.C., p. 415
66. H.U. Fanger and R. Pepelnik, Exploration of marine ore deposits utilizing spectroscopy of neutron-induced γ radiation, Industries Atomiques & Spatiales 4 (1974)
67. W. Stegmaier, K. Borcherding, L. Bösch, U. Fanger, J. Lange, R. Pepelnik, A. Suppau and U. Tamm, Ein integriertes Manganknollen-Explorationssystem, KFK 1957 (1974)
68. J. Lange, U. Tamm and B. Würz, Entwicklung einer Schleppsonde zur in-situ Analyse von Manganknollen-Lagerstätten, mt 6 2 (1975)50
69. J. Lange and W. Biemann, Development of Components for an In-situ Analysis System for the Exploration of Manganese Nodules, Proc. Offshore Technology Conf., Houston, 5-8 May, 1975
70. B. Würz and H. Eberle, Multielementanalyse von Erzknollen mittels Neutroneneinfang-Gammaspektroskopie, KFK 2160 (1975)
71. J. Lange and U. Tamm, Ein In-situ-Analysensystem zur Exploration von Manganknollen, KFK 2224 (1977)
72. L.E. Bansen, N.A. Wogman, R.W. Perkins and E.D. Clayton, Subcritical multiplication of californium-252 neutrons and its applications, Nucl.Technol. 15 (1972) 422
73. N.A. Wogman, H.G. Rieck, J.C. Laul and K.W. MacMurdo, High-sensitivity isotope analysis with a ^{252}Cf - ^{235}U fueled subcritical multiplier and low background photon detector systems, Nucl. Instrum. Methods 141 (1977) 539
74. R.C. Lloyd, S.R. Bierman, E.D. Clayton and B.M. Durst, Criticality Studies of a Neutron Multiplier Lattice, Rep.BNWL - 2031, UC - 46, Batelle, Pacific Northwest Laboratories, Richland, WA (1976)
75. S.S. Nargolwalla, M.R. Crambes and J.R. DeVoe, A technique for the evaluation of systematic errors in the activation analysis for oxygen with 14 MeV neutrons, Anal.Chem. 40 (1968) 666
76. C. Vandecasteele, R. Van Grieken, R. Gijbels and A. Speecke, Systematic errors in 14 MeV neutron activation analysis for oxygen, I. Neutron and γ-ray attenuation effects, Anal.Chim.Acta 64 (1973)187
77. C. Vandecasteele, R. Van Grieken, R. Gijbels and A. Speecke, Systematic errors in 14 MeV neutron activation analysis for oxygen, II. A general standardization method for the determination of oxygen, Anal. Chim. Acta 65 (1973) 1
78. R. Van Grieken, A. Speecke and J. Hoste, Geometry errors in 14 MeV neutron activation analysis, Radioanal.Chem. 13 (1973) 225
79. S.S. Nargolwalla, Neutron absorption physics in the development and practice of activation analysis, From Idea to Application, Some selected nuclear Techniques in Research and Development, IAEA, Vienna (1978) 81
80. F.E. Senftle and A.F. Boyte, Mineral exploration and soil analysis using in situ neutron activation, Nucl.Instrum.Methods 42 (1966) 93
81. A.F. Boyte, P. Martinez and F.E. Senftle, Neutron activation method for silver exploration, SME Transactions, March 1967, 94
82. F.E. Senftle, P.W. Philbin and P. Sarigianis, Use of ^{252}Cf for mineral exploration: comparison with accelerators for in situ neutron activation of silver, Isotopes and Radiation Technology 7 4 (1970) 411
83. L.G. Evans et al., Apollo remote analysis system applied to surface and underwater in-situ elemental analysis, Proc. ERDA X- and Gamma-Ray Symp., Ann Arbor, MI, May 19-21, 1976, 178
84. R.L. Caldwell, W.R. Mills, L.S. Allen, P.R. Bell and R.L. Beath, Combination Neutron Experiment for Remote Analysis, Science 152 (1966) 457
85. W. Michaelis, B.U. Fanger, A. Müller and R. Pepelnik, Fast-neutron activation analysis of manganese nodules, Proc.3rd.Int.Conf. Ocean Engineering and Marine Sciences, Düsseldorf 1976, 68; GKSS 76/E/26
86. R. Pepelnik, H.U. Fanger, W. Michaelis, Nuclear measuring techniques in mining and processing of manganese nodules, Oceans '76, Washington D.C., 1976, 2C - 1; IEEE J. Oceanic Engineering 2 2 (1977)185; GKSS 77/E/3
87. H.U. Fanger, R. Pepelnik und G. Grondey, Experimentelle Untersuchungen zur Wertmetallanalyse von Manganknollen mittels 14 MeV-Neutronenaktivierungsanalyse, GKSS 77/E/50
88. A.H. Jiggins and F.I. Babbani, Prompt gamma-ray analysis using 3.29 MeV neutron inelastic scattering, Int.J.Appl. Radiation and Isotopes 27 (1976) 689
89. B.D. Sowerby, Elemental analysis by neutron inelastic scatter gamma rays with a radioisotope neutron source, Nucl.Instrum. Methods (to be published)
90. C. Schnier, B. Gundlach and V. Marchig, Trace element investigations of manganese nodules, sediments and pore waters using neutron activation analysis - a contribution to the study of manganese nodules genesis, Proc.3rd.Int.Conf. Ocean Engineering and Marine Sciences, Düsseldorf 1976, 68
91. D. Beye and V. Marchig, Relationship between the growth rate of manganese nodules from the Central Pacific and their chemical constitution, Marine Geology 23 (1977) M 19
92. B. Gundlach, V. Marchig und C. Schnier, Zur Geochemie von Manganknollen aus dem Zentralpazifik und ihrer Sedimentunterlage, Geol.Jb., D 23 (1977) 67 und 91
93. C. Schnier, B. Gundlach and V. Marchig, Trace elements in the pore water and sea water in the radiolarian ooze area of the central Pacific as related to the genesis of manganese nodules, Environmental Biogeochemistry and Geomicrobiology (Ed. W.E. Krumbein) 1978, 859
94. D. Heye, V. Marchig and H. Meyer, The growth of buried manganese nodules, Deep-Sea Res. (in press)
95. V. Marchig, H. Gundlach und C. Schnier, Verhalten von Radiolarienschalen aus dem Zentralpazifik bei der Diagenese, Geol. Rundschau (in press)
96. Colloque International du C.N.R.S. n° 289 SUR LA GENESE DES NODULES DE MANGANESE, Gif-sur-Yvette, 25-30 Septembre 1978
97. T.L. Ku, A. Omura and P.S. Chen, Be^{10} and U-series isotopes in nodules from the central North Pacific, Marine Geology and Oceanography of the Central Pacific Manganese Nodule Province (to be published)
98. D. Heye, Wachstumsverhältnisse von Manganknollen, Geol. Jb. E 5 (1975) 3
99. B. Meyer, Untersuchungen über Beziehungen zwischen Sedimenten und Manganknollen im zentralen Pacific SE von Bawaii, Thesis, Techn. University Braunschweig, 1977
100. S. Krishnaswami and J.K. Cochran, Uranium and thorium series nuclides in oriented ferromanganese nodules: growth rates, turnover times and nuclide behavior, Earth Planet. Sci.Lett. 40 (1978) 45
101. K.K. Turekian, J.K. Cochran, S. Krishnaswami, W.A. Lanford, P.D. Parker and K.A. Bauer, The measurement of ^{10}Be in manganese nodules using a Tandem Van de Graaff accelerator, Geophys.Res.Lett. 6 5(1979) 417
102. G.H. Morrison, Application of activation analysis to the earth sciences, J. Radioanal.Chem. 18 (1973) 9
103. J. Plant, G.C. Goode and J. Herrington, An instrumental neutron activation method for multi-element geochemical mapping, J. Geochem. Explor. 6 (1976) 299
104. V. Krivan, Entwicklungsstand und Bedeutung der Aktivierungsanalyse, Angew.Chem. 91 (1979) 132
105. R.C. Aller and J.K. Cochran, $^{234}Th/^{238}U$ disequilibrium in nearshore sediment: particle reworking and diagenetic time scales, Earth Planet.Sci.Lett. 29 (1976) 37
106. J.K. Cochran and J.K. Osmond, Gamma spectrometry of deep-sea cores and sediment accumulation rates, Deep-Sea Res. 21 (1974) 721
107. R.E. Wainerdi, R. Zeisler and E.A. Schweikert, Activation analysis opportunities using a 5 x 10^{12} to 5 x 10^{13} n/sec 14 MeV generator, Proc.Int.Conf.Mod. Trends Activation Analysis, München 1976, 198; J. Radioanal.Chem. 37 (1977) 307
108. K.A. Schmidt und H. Dohrmann, Die Hochleistungs-Neutronengeneratorröhre KARIN für 14 MeV-Neutronen, Atomkernenergie 27 (1976)159
109. G.G. Santos, L.E. Fite, W.E. Kuykendall, R.E. Wainerdi, A.B. Bouma and W.R. Bryant, Preliminary study on the use of fast-neutron activation analysis on sea-floor compositional mapping, Nuclear Techniques and Mineral Resources (Proc.Symp. Buenos Aires, 1968) IAEA, Vienna (1969) 463
110. H.U. Fanger, R. Pepelnik, P. Rybaczok and W. Michaelis, KORONA - Eine Bestrahlungsanlage hoher Ausbeute für die Aktivierungsanalyse mit 14 MeV-Neutronen, 8. Seminar Aktivierungsanalyse, Neuherberg, November 1979
111. P. Rybaczok and B.U. Fanger, Ein Programm für die Berechnung punktueller und räumlich gemittelter Neutronenflüsse bei einer zylindrischen Flächenquelle, GKSS Report (to be published)
112. J.P. Op de Beeck, A compilation of second order reaction interferences, J. Radioanal.Chem. 3 (1969) 431; 4 (1970) 137
113. W. Maenhaut and J.P. Op de Beeck, Interference by second order reactions in activation analysis, J. Radioanal.Chem. 5 (1970) 115
114. V. Krivan, Estimation of primary reaction interferences in fast particle activation analysis by calculations using cross section data, in NBS Spec.Publ. 422, 2, U.S. Depart. of Commerce 1976
115. V. Krivan and K. Krivan, Tabulation of calculated data on primary reaction interferences in 14-MeV neutron activation analysis, J. Radioanal.Chem. 29 (1976) 145
116. V.K. Yurtchenko, E.N. Gilbert, G.V. Veriovkin and V.A. Mikhailov, Nuclear interferences in activation analysis, J. Radioanal.Chem. 41 (1977) 137
117. A. Bleier, Aktivitätsberechnung bei mehrstufigen Kernreaktionen, Techn. Bericht Nr. R 53 - 24/78 (Juni 1978) Kraftwerk Union AG, Reaktortechnik, Erlangen
118. S.F. Mughabghab and D.I. Garber, Neutron Cross Sections, BNL 325, 3rd Edition, Vol.I(1973)
119. D.I. Garber and R.R. Kinsey, Neutron Cross Sections, BNL 325, 3rd Edition, Vol. II (1976)
120. Handbook on Nuclear Activation Cross-Sections, Technical Reports Series No. 156, IAEA, Vienna, 1974
121. G. Erdtmann, Neutron Activation Tables, Verlag Chemie, 1976
122. Symposium on Neutron Cross-Sections from 10 to 40 MeV (M.R. Bhat and S. Pearlstein, Eds.), BNL-NCS-50681, 1977

NEUTRON CROSS SECTIONS OF IMPORTANCE TO ASTROPHYSICS

John C. Browne
Los Alamos Scientific Laboratory
Los Alamos, NM 87545, USA

Neutron reactions of importance to the various stellar burning cycles are discussed. The role of isomeric states in the branched s-process is considered for particular cases. Neutron cross section needs for the ^{187}Re-^{187}Os, ^{87}Rb-^{87}Sr clocks for nuclear cosmochronology are discussed. Other reactions of interest to astrophysical processes are presented.

[Neutron Cross Sections, Stellar Processes, Nuclear Clocks]

Introduction

Neutron physics has played a major role in the understanding of many phenomena associated with astrophysics. Usually it is common to think of the relevance of neutrons to the formation and abundance of the heavy elements via neutron capture. However, there are other aspects which are important in astrophysical processes. In this paper, we will consider a variety of neutron reactions which affect our understanding in very different ways. We will not summarize the wealth of neutron data that already has been obtained which is relevant to nuclear astrophysics. Rather, we will concentrate on areas where no data or discrepancies exist (or where the data are of insufficient accuracy) so as to affect the ability of the astrophysicist to use the information. In addition, other neutron data that can be used indirectly to calculate important effects will be discussed.

The reader is referred to the article of Burbidge et al.[1] for the classic discussion of nucleosynthesis in stars. Also the review articles of Barnes,[2] Allen, Gibbons, and Macklin,[3] and Clayton and Woosley[4] contain very comprehensive information regarding nuclear cross sections of interest to astrophysics.

Neutron Reactions During Various Stellar Burning Phases

Recently, there has been significant development in the detailed calculations of the evolution of stars through their various hydrostatic and explosive burning cycles.[5,6] Figure 1 shows a schematic diagram of the various stages as they progress toward iron core collapse. The stellar burning cycles are referred to by the main nuclear fuel such a hydrogen-burning, helium-burning, carbon-burning, etc. For carbon burning and future cycles, there can be both hydrostatic and explosive burning differing in temperature as well as time scale. The neutron reactions of importance in each of these cycles is discussed in the following paragraphs.

Hydrogen Burning

This phase involves the formation of ^4He via p-p chains and the C-N-O cycle where the presence of carbon, nitrogen, and oxygen results in ^4He production through a series of proton reactions. There are no neutron reactions of significant importance to this cycle.

Helium Burning and the s-Process

After the hydrogen is exhausted in the stellar core, contraction occurs which increases the temperature to allow hydrogen burning in a shell concentric with the predominantly helium core. Due to the increased outward heat flux, the star expands greatly so that the stellar surface cools and the star

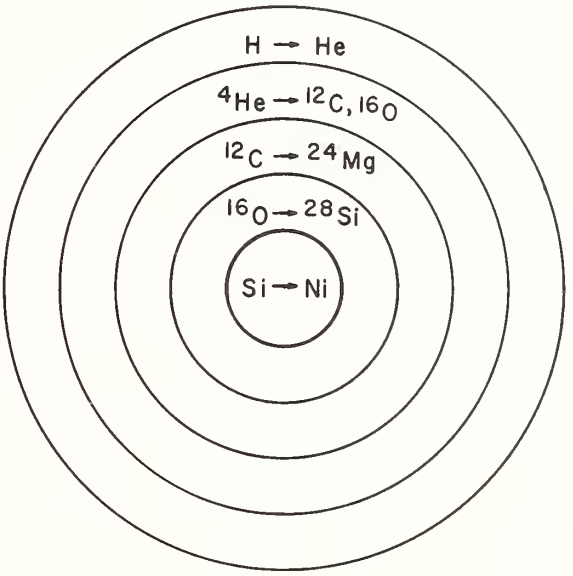

Fig. 1. Schematic diagram of the various stellar burning cycles progressing from hydrogen burning to silicon burning.

becomes a "red giant." The helium in the core will eventually ignite (usually referred to as the helium flash) and the star enters a stage of hydrostatic helium burning. At some point the star will consume its helium in the core and form a helium burning shell. The picture that prevails at this point is one of an inert core, a concentric helium-burning shell surrounded by a concentric hydrogen-burning shell. The calculation of Schwarzchild and Harm[7] indicated that this system exhibited thermal instabilities which lead to helium-shell flashing. Sanders,[8] Ulrich,[9] and Iben[10] have discussed how such a phenomenon may provide an ideal site for the s-process of nucleosynthesis. Sanders and Ulrich argue that mixing of protons from the hydrogen shell into the helium shell during the thermal instability will provide a source of neutrons via the reactions:

$$^{12}C(p,\gamma)^{13}N(\beta^+,\nu)^{13}C;$$

$$^{13}C(\alpha,n)^{16}O;$$

and

$$^{16}O(p,\gamma)^{17}F(\beta^+,\nu)^{17}O\ ;$$

$$^{17}O(\alpha,n)^{20}Ne,$$

where the carbon and oxygen are by-products of the quiescent helium-burning. Iben argues that the $^{22}Ne(\alpha,n)^{25}Mg$ reaction serves as the major source of neutrons where the ^{22}Ne is formed via the following reactions:

$$^{14}N(\alpha,\gamma)^{18}F(\beta^+,\nu)^{18}O(\alpha,\gamma)^{22}Ne.$$

The ^{14}N is a remnant in the helium shell of the hydrogen burning shell. A measurement of the $^{26}Mg(\gamma,n)$ reaction by Berman et al.[11] exhibited a prominent resonance in the ^{26}Mg compound system which was just 54.3-keV above the (γ,n) threshold. In the $^{22}Ne(\alpha,n)$ reaction, the resonance would occur for an α-particle kinetic energy (center-of-mass) of 540 keV. This resonance could affect the neutron production rate dramatically if its alpha width (Γ_α) is significant. The most probable J^π of this resonance was determined to be 1^- by Berman et al. This would require absorption of an $\ell = 1$ alpha particle by $^{22}Ne(0^+)$. This is a difficult experiment because one needs good alpha-energy resolution to observe the resonance and the nature of the noble gas target increases the difficulty. The $^{22}Ne(\alpha,n)$ has been studied between 1.6 and 4.0 MeV by Ashery,[12] but there are no data near this resonance. One solution might be to study the inverse reaction, $^{25}Mg(n,\alpha)^{22}Ne$. Weigmann et al.[13] observed a resonance at $E_n(lab) = 62.88$-keV in the $^{25}Mg(n,\gamma)$ reaction which corresponds very closely in energy (corrected for kinematics) to the resonance observed by Berman et al. If the J^π is 1^-, this corresponds to $\ell = 1$ neutron capture and would require $\ell = 1$ alpha particle emission as mentioned. Although the $^{25}Mg(n,\alpha)$ reaction is a difficult experiment, if one observed resonant α-emission, the implications for s-process neutron production would be very important.

There are also neutron reactions on the light elements that affect the excess number of neutrons available for the s-process capture on iron (and higher A) seed nuclei. These include any neutron reaction on the primary nuclei producing the neutrons, such as ^{14}N, ^{18}O, ^{21}Ne, ^{22}Ne and the by-products of the (α,n) reactions, such as $^{24,25,26}Mg$. Particularly valuable would be the unmeasured neutron capture cross sections for $^{20,21,22}Ne$.

Although the models of Sanders, Ulrich, and Iben provide for different mechanisms and different neutron sources, the common feature is that the s-process takes place during repeated neutron bursts during these helium-shell flashes which last on the order of 10 years followed by a long quiescent period ($\sim$ 2500 years). This is in marked contrast with the original ideas of Burbidge et al.[1] which indicated that the s-process took place slowly on a time scale of thousands of years. Figure 2 shows the abundance (N) times capture cross section (σ) distribution for the s-process. It was recognized as early as 1961 by Clayton et al.[14] that the seed iron nuclei had to be exposed to several neutron fluxes of different strengths to account for Fig. 2. Seeger, Fowler, and Clayton[15] demonstrated that a good fit to the Nσ distribution resulted from an exponential exposure distribution. This is consistent with the helium-shell flashing hypothesis producing an intermittent s-process. The effects on the s-process result from the deviation from the hypothesis of Burbidge et al.[1] that the β-decay lifetimes are much shorter than the mean neutron capture time. In a pulsed s-process, this is no longer true. Ward, Newman, and Clayton[16] and Ward and Newman[17] discussed the effects of a pulsed neutron flux on the s-process. If all β-decays were much faster than the mean neutron capture time, one could not distinguish between the different astrophysical scenarios. But the existence of branch points in the s-process may provide the information necessary to determine whether or not the pulsed s-process is important to the formation of the heavy elements. It is clear from Fig. 2 that the Nσ values on both sides of the magic numbers near A = 90, 140 are needed to determine the steepness of the precipice near these magic nuclei and to the absolute level of the Nσ values on the plateau regions away from the magic numbers. Neutron capture cross sections for nuclei shielded from the r-process are very important in this respect (e.g., $^{134,136}Ba$). This is particularly true if branching to isomeric states is involved.

An example where the branched s-process is important is shown in Fig. 3. It is clear that for the constant exposure model of Burbidge et al., much of the ^{85}Kr would β-decay since the 10.8 yr half-life is shorter than their mean capture lifetime. However, in a pulsed s-process, ^{85}Kr can capture a neutron to form ^{86}Kr and subsequently ^{87}Kr. Since ^{87}Kr will decay to ^{87}Rb, the s-process production of ^{87}Rb clouds the picture of the use of the 5×10^{10} yr β-decay of ^{87}Rb to ^{87}Sr as an r-process chronometer. The r-process chronometer will be discussed in the section on Nuclear Cosmochronology. In addition to this problem, neutron capture on ^{84}Kr can result in the formation of the 4.5-hr first excited state of ^{85}Kr whose main mode of decay is β^- decay to ^{85}Rb. This will affect the neutron current through ^{85}Kr into ^{85}Rb, ^{86}Sr, and ^{87}Sr even if the neutron flux during

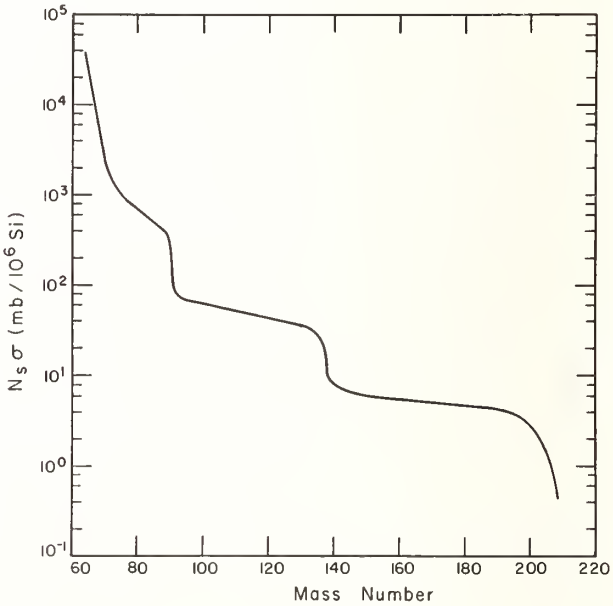

Fig. 2. The s-process abundance (N_S) times neutron capture cross section (σ) plotted as a function of mass number. The precipices near A=90 and 140 are due to the closing of the neutron shell at N=50 and 82.

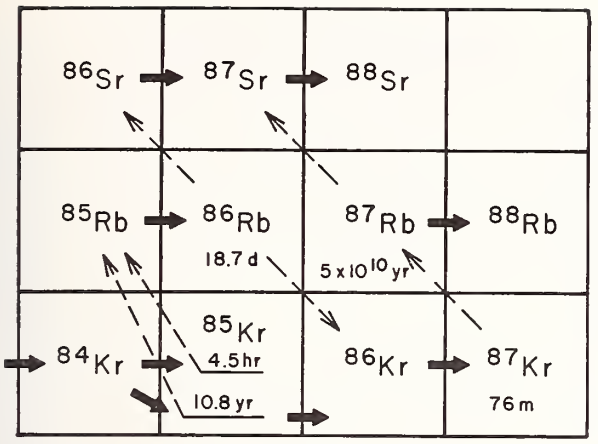

Fig. 3. Diagram of the branched s-process at ^{85}Kr. The 10.8-yr ground state of ^{85}Kr can either β-decay to ^{85}Rb or capture a neutron to form ^{86}Kr. The 4.5-min first excited state can only β-decay to ^{85}Kr.

the s-process path is very high. Therefore, it would be very valuable to have the neutron capture cross sections for ^{84}Kr and ^{86}Kr, but also the branching ratio for 30-keV neutron capture on ^{84}Kr to the g.s. and the first excited state of ^{85}Kr to determine how important the various branches are in the s-process.

Figure 4 shows a different situation for the production of ^{113}In, ^{114}Sn, and ^{115}Sn due to an s-process branch at ^{113}Cd. If the 14-yr 270-keV first excited state of ^{113}Cd is populated significantly by 30-keV neutron capture by ^{112}Cd, then ^{113}In, ^{114}Sn, and ^{115}Sn can be produced in the s-process in amounts which are a large fraction of their solar-system abundance. At this branch point, the neutron-capture cross sections (kT = 30 keV) for ^{113}Cd, ^{114}Sn, ^{115}Sn, and ^{113}In are needed to reduce the sensitivity of the branch calculations. Also, the branching ratio for 30-keV neutron capture to 270-keV state compared to the g.s. for ^{112}Ca + n would provide valuable data to asess its importance.

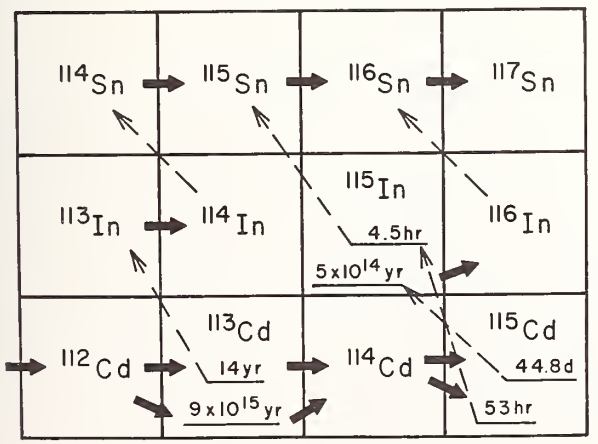

Fig. 4. Diagram of the branched s-process at ^{113}Cd. Population of the 14-yr, 270-keV first excited state of ^{113}Cd can result in the population of ^{113}In, ^{114}Sn and ^{115}Sn.

Figure 5 shows a similar branch point at ^{151}Sm. Since the 90-yr ^{151}Sm can either β-decay or capture a neutron in a pulsed s-process, the amount of ^{152}Gd formed in the s-process will be dependent on this branch. Both ^{152}Gd and ^{154}Gd are shielded from the r-process and therefore provide a constraint on the lower bound of the mean s-process neutron flux so that there is not an overproduction of ^{152}Gd. Neutron capture on ^{151}Eu can result in the population of either the 13-yr g.s. of ^{152}Eu or the 9-hr first excited state both of which can decay to either ^{152}Gd or ^{152}Sm. However, if the pulsed s-process neutron flux is high enough, then the 13-yr ^{152}Eu g.s. can capture a neutron and thus bypass ^{152}Gd. The cross sections which would provide valuable information on the absolute level of the σN curve beyond the s-only ^{148}Sm and ^{150}Sm are the kT = 30 keV neutron capture cross sections for ^{152}Gd and ^{154}Gd as well as the branching ratio for 30-keV capture on ^{151}Eu to the g.s. and first excited state of ^{152}Eu.

The region near ^{176}Lu is another important example of s-process branching. Since ^{176}Lu is shielded from the r-process by ^{176}Yb, the 3.6 x 10^{10} yr half-life for β-decay of ^{176}Lu to ^{176}Hf can be used as a purely s-process chronometer. However, neutron capture on ^{175}Lu can lead either to production of the 127-keV first excited state of ^{176}Lu whose β-decay half-life is 3.7 hrs or the 3.6 x 10^{10} yr g.s. Depending on the branching ratio, fast β-decay to ^{176}Hf will compete with neutron capture on ^{176}Lu. Some of the relevant neutron data has been obtained recently by Beer and Kappeler[18] and will be discussed in the section on Nuclear Cosmochronology.

There are other branch points to be studied which can be important under the hypothesis of a pulsed s-process. A summary of neutron capture cross sections relevant to both the branched and unbranched s-process solutions is listed in Table I. Although many nuclei are listed, there are clearly several important cases in common. Table II lists nuclei for which the kT = 30 keV branching ratios to the ground and isomeric states would be valuable to these studies. There are virtually no data for these cases.

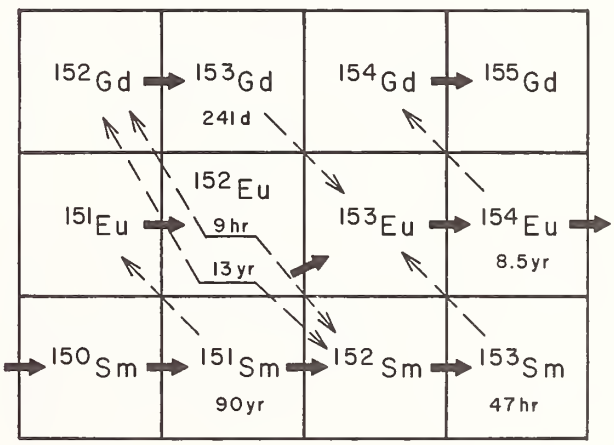

Fig. 5. Diagram of the branched s-process at ^{151}Sm. The branches at ^{151}Sm and ^{152}Eu can affect the amount of ^{152}Gd produced in the s-process. This puts restrictions on the s-process flux so that the low abundance ^{152}Gd is not overproduced.

Table I. Neutron capture cross sections of importance to the s-process (kT = 30 keV) for branched and unbranched solutions.

Ref. 16[a]	Ref. 17[b]	Rev. 19[c]	Ref. 20[a]
		^{58}Fe	^{58}Fe
		^{66,67}Zn	^{64,66,67,70}Zn
		^{70,72,73}Ge	^{70,72,73}Ge
		$^{76-78}$Se	$^{74-78}$Se
^{80,82}Kr	^{80,82,84,86}Kr	$^{82-84}$Kr	$^{78,80,82-84,86}$Kr
		--	^{84}Sr
		--	^{92}Mo
		$^{99-101}$Ru	$^{98-101}$Ru
		$^{104-106}$Pd	$^{102,104-106}$Pd
^{113}Cd		$^{111-113}$Cd	$^{106,108,110-113}$Cd
^{114,115}Sn		--	^{112,114,115}Sn
		--	^{120}Te
		$^{128-132}$Xe	$^{124-136}$Xe
$^{134-136}$Ba		$^{134-137}$Ba	^{130,132,135,137}Ba
			^{136,138}Ce
			^{138}La
		$^{142-145}$Nd	$^{142,143-145}$Nd
			^{152,154}Eu
^{152}Gd	^{152,154}Gd		^{152}Gd
^{160}Dy		^{160}Dy	^{156,158,160}Dy
^{164}Er			^{162,164}Er
^{170}Yb		^{170}Yb	^{168,170}Yb
		$^{177-179}$Hf	$^{174,177-179}$Hf
			^{180}W
			^{184}Os
^{192}Pt		$^{192-195}$Pt	$^{190,192-195}$Pt
^{198}Hg		$^{198-201}$Hg	$^{196,198-201}$Hg

[a] branched s-process.

[b] branched s-process, pulsed-neutron source.

[c] unbranched s-process.

Carbon Burning

The fusion of $^{12}C + ^{12}C$ results when the core remnant from helium burning contracts to produce temperatures near 10^9 K. There are many neutron reactions in this cycle which affect the abundance of nuclei between oxygen and sulfur. Many of the important reactions such as $^{12,13}C(n,\gamma)$ and $^{16}O(n,\gamma)$ have been measured. However, many have not been measured and the accuracy of others could be improved. These are listed in Table III.

Carbon burning can also ignite explosively[21] at temperatures near 2 x 10^9 K. These reactions burn only for a fraction of a second so that an intense bath of free neutrons can become available. This short phase can result in the production of rare isotopes between sulfur and iron. Neutron seed reactions of importance are also listed in Table III. An excellent example of a neutron measurement that directly affected the production of the rare isotope ^{36}S was made by Auchampaugh et al.[22] One chain of reactions involved is

$$^{32}S(n,\gamma)\,^{33}S(n,\gamma)\,^{34}S(n,\gamma)\,^{35}S(n,\gamma)\,^{36}S.$$
$$\searrow\,(n,\alpha)$$

Table II. Unmeasured branching ratios for kT = 30 keV neutron capture important to the branched s-process

Compound Nucleus	Ground State	Isomeric State	
	$t_{1/2}$	E(keV)	$t_{1/2}$
^{85}Kr	10.7 y	305	4.5 hr
^{87}Sr	stable	388	2.8 hr
^{108}Ag	2.4 m	110	127 y
^{110}Ag	24.4 s	118	252 d
^{113}Cd	9 x 10^{15} y	264	14 y
^{115}Cd	2.2 d	173	45 d
^{114}In	72 s	190	50 d
^{115}In	5.1 x 10^{14} y	336	4.5 hr
^{121}Sn	27 hr	6.3	55 y
^{123}Sn	129 d	25	40 m
^{127}Te	9.4 hr	88	109 d
^{129}Te	69 m	106	33.5 d
^{148}Pm	5.4 d	137	41 d
^{152}Eu	13 y	49	9.3 hr
^{166}Ho	27 hr	5	1.2 x 10^3 y
^{176}Lu[a]	3.6 x 10^{10} y	127	3.7 hr
^{177}Lu	6.7 d	970	161 d
^{192}Ir	74 d	160	240 y
^{194}Ir	19 hr	$\leq$ 450	0.47 y
^{210}Bi	5 d	270	3 x 10^6 y

[a] See H. Beer and F. Kaeppler, ref. 18.

Table III. Neutron cross sections important to the carbon burning cycle.

Reaction	Relevance
$^{12,13}C(n,\gamma)$	3
$^{14}N(n,\gamma)$	1
$^{16}O(n,\gamma)$	3
$^{17}O(n,\gamma)$	1
$^{18}O(n,\alpha)$	1
$^{20,21}Ne(n,\gamma)$	3
$^{23}Na(n,\gamma)$	1
$^{24,25,26}Mg(n,\gamma)$	3
$^{27}Al(n,\gamma)$	2
$^{28,29,30}Si(n,\gamma)$	↓
$^{31}P(n,\gamma)$	↓
$^{32,33,34}S(n,\gamma)$	2,4
$^{33}S(n,\alpha)$	2,4
$^{35,37}Cl(n,\gamma)$	4
$^{36,38,40}Ar(n,\gamma)$	↓
$^{36,38}Ar(n,p)$	↓
$^{36,38}Ar(n,\alpha)$	↓
$^{39}K(n,\gamma)$	↓
$^{40,42,43,44,46,48}Ca(n,\gamma)$	↓
$^{40}Ca(n,p)$	↓
$^{48,49,50}Ti(n,\gamma)$	↓
$^{50}V(n,\gamma)$	↓

1 = hydrostatic burning
2 = explosive burning
3 = hydrostatic and explosive burning
4 = seed reaction for abundance of nuclei below iron.

The $^{33}S(n,\alpha)$ reaction can therefore reduce the amount of ^{36}S formed in an explosive process. The cross section had been estimated originally via optical-model calculations by Truran.[23] The result of his calculation was overproduction of ^{36}S by a factor of 10. The measurements of $^{33}S(n,\alpha_0)$ and $^{33}S(n,\gamma)$ by Auchampaugh et al.[22] reduced this factor to 2.5. Further measurements along this chain and other chains will help to clarify the production of rare nuclei in explosive carbon burning.

Oxygen Burning

Fusion of oxygen can occur in a similar manner to the carbon cycle, but at a temperature near 2.5 x 10^9 K. However, this cycle does not last long. There are several neutron reactions in the "hydrostatic" burning phase that are important in determining the evolution of the stellar composition. Those parasitic neutron capture reactions that affect the excess number of neutrons can influence the future composition. Those of importance are listed in Table IV and include poorly known neutron capture cross sections for ^{27}Al, ^{31}P, and ^{32}S.

Oxygen will burn explosively near 4 x 10^9 K with one of the main burning reactions being the $^{16}O(n,\alpha)$ reaction. Similar to the explosive carbon burning phase, there will be an intense bath of neutrons producing nuclei between ^{28}Si and ^{54}Fe. Neutron reactions important to such synthesis are listed in Tables III and IV.

Silicon Burning

After the depletion of oxygen, a very short-lived stage of silicon burning will produce nuclei up to iron. Explosive silicon burning can also occur under certain conditions in ejected debris. Some of the main neutron burning reactions incude $^{16}O(n,\alpha)$, $^{20}Ne(n,\alpha)$, and $^{24}Mg(n,\alpha)$. Other neutron reactions on nuclei between ^{32}S and ^{56}Fe will affect the production of isotopes below iron and any neutron data would be welcome. This is particularly true where little information exists such as for the isotopes of chlorine, potassium, and argon (see Tables III and IV).

Supernovae - r Process

It is during a supernovae explosion, when the density of neutrons is extremely high, that the r-process is believed to occur. Multiple-neutron capture forms nuclei far from the line of β-stability which eventually β-decay back toward this region. Neutron capture cross sections do not directly affect the r-process abundances because the captures occur much faster (∿ 1 s) than β-decays. Thus, there will be considerable smoothing of the final abundances by the nature of the multiple β-decays, many of which involve neutron emission. However, neutron cross sections are indirectly important for determining the r-process abundances in the following way. There are nuclei which can be formed only in the s-process and those which can be formed only in the r-process. The cases that can be formed in both require a knowledge of the s-process abundance, N_s, to extract the r-process portion, N_r, from the solar abundance, N. Improvements in the $N_s\sigma$ curve in Fig. 2 therefore permit better determinations of N_r. These improvements will result from better neutron data near the precipices in Fig. 2 and cross sections on the plateaus for s-only cases, such as ^{134}Ba and ^{136}Ba, ^{160}Dy, ^{170}Yb, and others listed in Table I.

Table IV. Neutron reactions of importance during oxygen and silicon burning cycles.

Reaction	Relevance
$^{16}O(n,\alpha)$	1,2
$^{20}Ne(n,\alpha)$	2
$^{24}Mg(n,\alpha)$	2
$^{27}Al(n,\gamma)$	3
$^{28,29,30}Si(n,\gamma)$	4
$^{31}P(n,\gamma)$	3
$^{32,33}S(n,\gamma)$	3,4
$^{33}S(n,\alpha)$	4
$^{36}Ar(n,\gamma)$	↓
$^{40}Ca(n,\gamma)$	↓
$^{50}Cr(n,\gamma)$	↓
$^{54}Fe(n,\gamma)$	↓

1 = explosive oxygen burning
2 = explosive silicon burning
3 = hydrostatic oxygen burning
4 = seed reactions for abundance of nuclei below iron

Nuclear Cosmochronology

The relative abundance of radioactive nuclei can be used to determine the time scale for nucleosynthesis. Probably the best known of these is the uranium-thorium dating which was extensively developed by Fowler and Hoyle[24] to determine the duration of r-process nucleosynthesis (Δ) in our galaxy. The best current value based on this chronometer assuming an exponential distribution of supernova events in our galaxy is Δ = 7±2 x 10^9 yr.

However, there are other chronometers with which the U-Th clock can be compared. The most promising of these is the ^{187}Re-^{187}Os chronometer proposed by Clayton[25] which involves the 4.5 x 10^{10} yr β-decay of ^{187}Re. Figure 6 shows the s- and r-process paths in the vicinity of Re and Os. ^{186}Os and ^{187}Os are shielded from the r-process and the s-process is unbranched in this region so that we can write

$$N^{186}\sigma_{186} = N^{187}\sigma_{187}$$

where N refers to the isotopic abundance and σ is the Maxwellian-averaged cross section for kT ∿ 30 keV (3 x 10^8 K) appropriate for the site of the s-process. The abundance of ^{187}Os that is found in meteorites is then a composite of s-process material and radiogenic material. One can ultimately obtain a ratio of radiogenic ^{187}Os to its parent ^{187}Re that depends on the ratio of the kT = 30 keV Maxwellian-average neutron capture cross sections for ^{186}Os and ^{187}Os. Using this cross section ratio and the half-life for β-decay, one can obtain a value for Δ. However, nature is never that kind. ^{187}Os has an excited state at 9.8 keV which clearly can be populated in a stellar interior. One therefore needs the ratio of the neutron capture cross sections for a stellar environment or alternatively the neutron capture cross section for the first excited state of ^{187}Os. Woosley and Fowler[2] defined a correction factor, f, as

$$f=[\sigma^*(186)/\sigma^{LAB}(186)]/[\sigma^*(187)/\sigma^{lab}(187)],$$

where the asterisk (*) refers to stellar environment cross sections. Their Hauser-Feshbach calculation yielded a value of f = 0.83. The same calculations predict that $\sigma_{n,n'}$ (E_n = 30 keV) to the 9.8-keV state in ^{187}Os should be about 800 mb. A recent measurement by Winters et al.[27] of the ^{187}Os(n,n') cross section is substantially smaller (< 500 mb). The use of ^{187}Re-^{187}Os depends critically on both the ^{186}Os/^{187}Os cross section ratio and the correction factor, f. Calculating the duration of r-process nucleosynthesis (Δ) using the same model as Fowler and Hoyle for U-Th, Winters, Macklin, and Halperin[28] obtain from their ^{186}Os and ^{187}Os capture data a value of Δ = 10.3±2.5 x 10^9 yr for f = 0.83. The above (n,n') measurement would imply that f is closer to 1.0 in which case one would calculate $\Delta \sim 8 \times 10^9$ yr which agrees incredibly well with the U-Th method. It should be noted that earlier measurements of $\sigma_c(186)/\sigma_c(187)$ reported by Browne and Berman[29] were found to have a systematic error in the $\sigma_c(186)$ cross section. Correction of their results leads to a value of Δ = 11±3 x 10^9 yr for f = 0.83 and Δ = 8.7±3 x 10^9 yr for f = 1.0. It is clear that one may have concordance of the r-process chronometers, ^{187}Re-^{187}Os and U-Th, if further measurements and calculations can improve our knowledge of the correction factor f. In addition, the half-life of ^{187}Re has a large uncertainty at this point and an improved accuracy is critical to use of this chronometer.

Another r-process chronometer that possibly could be used in a similar manner to ^{187}Re-^{187}Os is the ^{87}Rb-^{87}Sr clock, which involves a half-life for β-decay of 4.8 x 10^{10} yr. In this case, the half-life is well measured and one does not have the problem of excited state cross sections. However, in the case of Re-Os, the radiogenic component of ^{187}Os relative to total ^{187}Os is large and the σN equality is a good approximation. In the case of Rb-Sr, the radiogenic enrichment of ^{87}Sr is only on the order of 10%. Also, as can be seen in Fig. 2, σN is decreasing in this mass region as the N = 50 neutron shell is approached. To use this chronometer, therefore, will require very accurate neutron capture cross section measurements (< 5%) over the energy range 1 to 200 keV to determine the temperature sensitivity of the Maxwellian-averaged cross sections. Even if this is possible, we noted in the earlier discussion of s-process branching that it is possible to produce an s-process component of ^{87}Rb in a pulsed s-process environment. If sizable, this would increase the difficulty of using this chronometer. An accurate determination of the capture cross sections of ^{86}Sr and ^{87}Sr as well as any cross sections that affect the s-process path in this region would be valuable.

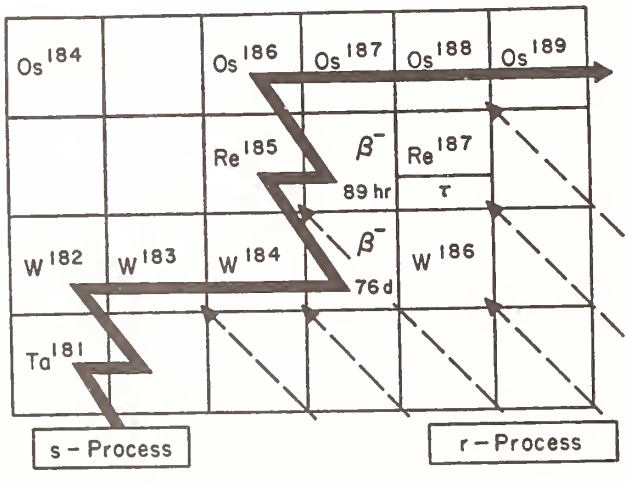

Fig. 6. The s-process path in the vicinity of the Re and Os isotopes. Both ^{186}Os and ^{187}Os are shielded from the r-process and hence are pure s-process nuclei. ^{187}Re is an r-process nucleus hence its β-decay can be used as a chronometer.

The β-decay of ^{176}Lu (3.6 x 10^{10} yr half-life) can be used as an s-process chronometer because it is shielded from the r-process by ^{176}Yb. As mentioned earlier, the use of this chronometer is affected by s-process branching. ^{175}Lu can capture a neutron to form either the long-lived g.s. of ^{176}Lu or the 3.7-hr first excited state. A knowledge of this branching ratio for kT = 30 keV is required to use this chronometer. Such a measurement by Beer and Kappeler[18] is reported at this conference. If they use the same exponential model for s-process nucleosynthesis, Beer and Kappeler obtain a value for the duration of s-process nucleosynthesis which is consistent with the Re-Os and U-Th r-process ages. Improvements could be made for this chronometer if the kT = 30-keV value of the neutron total capture cross section for ^{175}Lu were improved. The current values are 1460±110 mb from Ref. 30 and 1260±190 from Ref. 31. The reader is referred to the article by Beer and Kappeler for more details.

Solar Physics

It was proposed by Kuroda[29] in 1971 that it may be possible to determine the temperature of the sun shortly after formation from the difference in isotopic compositions of terrestrial and extraterrestrial xenon. His analysis of xenon isotope ratio data for carbonaceous chrondrite meteorites, lunar soil samples, and atmospheric samples indicated that xenon found in lunar soil is likely to represent the isotopic composition of almost pure solar xenon. Atmospheric xenon appeared to have the least solar xenon with meteoritic xenon falling in between. He speculated that the solar xenon was transported to the earth, moon, and meteorites via the solar wind early in the history of the solar system. The excess of ^{128}Xe in lunar soil can be explained[33] by cosmic ray neutron capture on ^{127}I. The excess of ^{131}Xe can be explained by cosmic ray neutron capture on ^{130}Ba (or ^{130}Te) as shown by the neutron capture measurements of Browne and Berman.[34,35] However, the excesses at ^{130}Xe and ^{132}Xe can only be explained by neutron capture on ^{129}Xe and ^{131}Xe. Kuroda concludes that neutron capture occurred on these isotopes in the interior of our sun during the deuterium-burning phase. The ratio of the neutron capture cross sections can be related to the ratio of the excess ^{130}Xe and ^{132}Xe and yield the most probable temperature at which the reactions occurred. From this, he concludes that the D(d,n)^{3}He reaction is the probable source of the neutrons. However, it is necessary to measure the ^{129,131}Xe(n,γ) cross sections from 100 eV to 100 keV to provide the information needed to check his hypothesis that the temperature obtained is that of the core of the sun shortly after its birth.

Summary

Nuclear astrophysics poses a wonderful challenge to the neutron physicist, experimentalist and theorist alike. As was seen, there is a need for a large quantity of data across the periodic table. There are neutron measurements needed on abundant nuclei which will be difficult because of the small cross sections involved. There are some where the cross sections are large, but the isotopic abundance is small. There are some measurements which require new and more sensitive techniques, e.g., capture cross sections on the noble gases and isomeric branching ratios for kT = 30 keV.

This paper cannot possibly point out all the areas that neutron physics is of interest to astrophysics. Indeed, the needs will continually change as improvements are made in models of nucleosynthesis. Perhaps the best statement that can be made is that any high-quality neutron measurement will be of interest to the astrophysicist. Some directly because of their bearing on a specific problem. Others will be only indirectly of interest to check calculations or semi-empirical estimates for cross sections that cannot be measured in the laboratory. In the same manner, improvements in nuclear modeling techniques, such as better calculations of level densities and gamma-ray strength functions, will allow the astrophysicist to obtain more accurate data to check various theories.

Acknowledgment

The author would like to thank Stan Woosley and Mike Newman for interesting and helpful discussions.

References

1. E. M. Burbidge, G. R. Burbidge, W. A. Fowler, and F. Hoyle, Rev. Mod. Phys. 29, 547 (1957).

2. C. A. Barnes, in Advances in Nuclear Physics, Vol. 4, ed. by M. Baranger and E. Vogt (Plenum Press, New York, 1971) p. 133.

3. B. J. Allen, J. H. Gibbons, and R. L. Macklin, in Advances in Nuclear Physics, Vol. 4, ed. by M. Baranger and E. Vogt (Plenum Press, New York, 1971) p. 205.

4. D. D. Clayton and S. E. Woosley, Rev. Mod. Phys. 46, 755 (1974).

5. W. D. Arnett, Astrophys. J. 194, 373 (1974).

6. T. A. Weaver, G. D. Zimmerman, and S. E. Woosley, Astrophys. J. 225, 1021 (1978).

7. M. Schwarzchild and R. Harm, Astrophys. J. 150, 961 (1967).

8. R. H. Sanders, Astrophys. J. 150, 971 (1967).

9. R. K. Ulrich, in Explosive Nucleosynthesis, ed. by D. N. Schramm and W. D. Arnett (Univ. of Texas Press, Austin, 1973) p. 139.

10. I. Iben, Ap. J. 196, 525 (1975).

11. B. L. Berman, R. L. Van Hemert, and C. D. Bowman, Phys. Rev. Letters 23, 386 (1969).

12. D. Ashery, Nucl. Phys. A136, 481 (1969).

13. H. Weigmann, R. L. Macklin, and J. A. Harvey, Phys. Rev. C14, 1328 (1976).

14. D. D. Clayton, W. A. Fowler, T. E. Hull, and B. A. Zimmerman, Ann. Phys. 12, 331 (1961).

15. P. A. Seeger, W. A. Fowler, and D. D. Clayton, Astrophys. J. Suppl. 11, 121 (1965).

16. R. A. Ward, M. J. Newman, and D. D. Clayton, Astrophys. J. Suppl. 31, 33 (1976).

17. R. A. Ward and M. J. Newman, Astrophys. J. 219 195 (1978).

18. H. Beer and F. Kappeler, These proceedings, Bull. Am. Phys. Soc. 24, 871 (1979).

19. M. J. Newman, Astrophys. J. 219, 676 (1978).

20. J. Conrad, Ph.D. Thesis, Heidelberg (1976) - unpublished.

21. W. D. Arnett, Astrophys. J. 157, 1369 (1969).

22. G. F. Auchampaugh, J. Halperin, R. L. Macklin and W. M. Howard, Phys. Rev. C 12, 1126 (1975).

23. J. W. Truran, Astrophys. Space Sci. 18, 306 (1972).

24. W. A. Fowler and F. Hoyle, Ann. Phys. 10, 280 (1960).

25. D. D. Clayton, Astrophys. J. 139, 637 (1964).

26. S. A. Woosley and W. A. Fowler, Calif. Inst. of Technology preprint No. OAP-528, October 1978.

27. R. R. Winters, F. Kappeler, K. Wisshak, B. Berman, and J. Browne, Bull. Am. Phys. Soc. 24, 854 (1979).

28. R. R. Winters, R. L. Macklin, and J. Halperin, Phys. Rev. C. (to be publsihed - 1979).

29. J. C. Browne and B. L. Berman, Nature 262, 197 (1976).

30. R. L. Macklin and J. H. Gibbons, Phys. Rev. 159, 1007 (1967).

31. J. R. D. Lepine, R. A. Douglas, H. A. Maia, Nucl. Phys. A196, 83 (1972).

32. P. K. Kuroda, Nature 230, 40 (1971).

33. K. Marti, P. Eberhardt, and J. Geiss, Z. Naturforsch. 21a, 398 (1966).

34. B. L. Berman and J. C. Browne, Phys. Rev. C 7, 2522 (1973).

35. J. C. Browne and B. L. Berman, Phys. Rev. C 8, 2405 (1973).

OPEN PROBLEMS IN NUCLEAR DATA EVALUATIONS

S. Pearlstein
Brookhaven National Laboratory
Upton, New York 11973, USA

Nuclear data measurements are often discrepant or incomplete. Despite these difficulties, after reviewing the information at hand, experts periodically prescribe their best estimates of nuclear data for use by scientists. Some of the obstacles the experts face are poor energy calibrations, inadequate data, overly detailed data, and the necessity for coalescing multi-disciplinary information. These and other aspects of nuclear data evaluation are discussed.

Introduction

The objective of a nuclear data evaluator is to recommend the most probable value of a quantity. Since our knowledge of nuclear forces is incomplete the evaluator must rely on measurements rather than calculations from first principles. However, measurements of the same quantity by different authors are often discrepant. Sometimes the discrepancies are understood when the measurements are corrected for differences in methods, samples, standards, and analysis. But unexplained differences can remain.

In the U.S. most nuclear data evaluations are contributed by the Cross Section Evaluation Working Group (CSEWG), a cooperative effort of over twenty laboratories. CSEWG has identified several nuclear topics that warrant continuous review because of their impact on data evaluation. These topics include Cf-252 nubar, fission energy spectra, thermal fissile parameters, neutron cross-section standards, delayed fission neutrons, neutron energy standards, alpha, fast neutron capture, half-lives, resonance integrals, decay schemes, isotopic abundances, energy per fission, and inelastic scattering for fissile and fertile nuclei. What is hoped for, of course, is that measurement discrepancies will be eliminated and data will converge to universally accepted values. The evaluator and the measurer are helped if accepted measurement standards are used. Those recommended by CSEWG[1] are shown in Figure 1. Although these cover the energy range from thermal to 20 MeV, by no means are they adequate for every situation and secondary standards must be used. This basic list should be reviewed periodically.

No single recipe can be prescribed for an evaluator because each evaluation has its own unique set of conditions. For the purpose of completing a talk on a limitless subject in a finite time I will describe only four additional problems an evaluator might face when recommending data. These problems concern energy calibration, inadequate measurements, highly detailed measurements, and the multidisciplinary approach.

Energy Calibration

In the resonance region for fertile and fissile materials the resonances are closely spaced. In the calculation of isotopic buildup in fuel-cycle studies there can be resonance overlap and screening effects requiring nuclear data with accurate resonance energies. In the study of U-238 resonance energies from 6 eV to 4.6 keV with time-of-flight paths ranging from 20 to 200 meters, the results of sixteen independent measurements were analyzed.[2] Calculating the deviation from the weighted mean values of the resonance energies gave a chi-square of 2 per degree of freedom. After fitting relative to a single set of data chosen as a standard and determining flight path length and zero time corrections a chi-square per degree of freedom approximately equal to 1 was obtained. The uncertainty in measuring the distance of a 200 meter flight path should be as little as 3 or 4 centimeters and the uncertainty in the zero time should be less than a tenth of a microsecond. Some of the corrections as shown in Figure 2 are within the quoted errors but some are not, indicating that some energies were not calibrated well and therefore resonance overlap effects will not be calculated correctly.

Energy calibration in the MeV region also seems difficult. The U-235 fission cross section which is used as a standard has a knee in the cross-section curve at about 6 MeV[3] as shown in Figure 3. A number of experiments have enough data points in this region to permit least squares fitting with a quadratic curve. The smooth curves obtained show apparent energy shifts in the data aside from differences in absolute magnitude as shown in Figure 4. The energy shift in the U-235 fission cross section and other cross sections such as the threshold U-238 fission cross section can dramatically affect calculated reaction rates and contribute to the discrepancy between calculation and experiment for cross-section ratios.

Wider use should be made by measurers of the recommended energy standards. Well known resonances in U-238, Pb-206, Al-27, S-32, Na-23, Si-28, and Fe-56 have been used to provide energy standards[4] in the electron volt to the 100 keV range. The associated correlations between the resonance energies have also been estimated.

Inadequate Measurements

The energy and angular cross sections for neutrons emitted in neutron inelastic scattering, (n,2n), and (n,3n) reactions as a function of incident neutron energy are important in order to calculate neutron energy and angular distributions. Numerous measurements have been made of neutron emission spectra but they fail to be complete or accurate enough to provide a comprehensive data base. Consequently, the evaluator must also rely on nuclear model calculations. The importance of these data was shown in the calculation of the Livermore pulsed-sphere experiments.[5] The time-of-flight spectra emanating from thick shells of material internally pulsed with 14 MeV neutrons was measured as shown in Figure 5. The calculation of the neutrons detected below the elastic peak is very sensitive to the cross section and energy distribution of inelastically scattered neutrons. A calculation using only compound nucleus theory will fail to account for the high energy neutron spectra. It is necessary to include neutrons emitted in the approach to equilibrium. The data in Figure 6 were taken from the thin shell measurements of a large number of materials over a wide mass range. Data were taken at several angles and show that these preequilibrium neutrons are forward peaked.

Several nuclear model codes that include equilibrium and preequilibrium reaction processes have been written that reasonably calculate the cross section and energy distribution of neutrons emitted in

inelastic scattering, (n,2n), and (n,3n) reactions over a wide mass range.[6,7,8] Recently codes have been developed that also calculate the angular distribution of the emitted neutrons.[9] In Figure 6 a comparison is shown between calculation[9] and experiment for the neutrons emitted from niobium. The agreement is quite good but it has not yet been demonstrated that angular distributions can be calculated for a large number of cases using a global set of parameters.

Despite consistent use of nuclear fission data in applications there are many unknowns about the fission process. The total number of neutrons emitted in fission, their mean energy, and the shape of their energy distribution are important quantities. The choice of formalisms to explain fission neutron data is heavily influenced by the proportion of very low and very high energy neutrons emitted. Since the intensity of these neutrons is low the measurements are plagued by poor statistics and the difficulty in separating out room scattered neutrons. The worsening of the data at low and high energies when compared to a Watt spectrum[10] is shown in Figure 7. Recent improvements in analysis tend to show that the true fission neutron shape lies between a Maxwellian and Watt spectrum[11] as shown in Figure 8. Only one set of data is shown here and it will be necessary for a number of experiments to converge at high energies before the shape of the fission spectrum can be resolved.

Highly Detailed Measurements

Two examples of highly detailed nuclear reaction data are neutron capture spectra and neutron elastic scattering cross sections. In the case of neutron capture gamma-ray emission spectra the evaluator finds it difficult to digest and store all the data that are available. For most applications it is only necessary to know the location and intensities of the principal lines and the average intensity of the radiation emitted in coarse energy bins. In other words, some of the detail available is thrown away.

The energy and angular distributions of neutrons elastically scattered from structural materials is becoming available in great detail.[12] Figure 9 shows the elastic scattering cross section for two structural materials; iron and nickel. They are similar and show considerable structure up to an energy of a few MeV. The angular distribution also shows sharp changes as a function of energy as shown in Figure 10. In fact, at some points the angular distribution briefly changes from a forward peaked distribution to one that is backward peaked. This is shown in Figure 11 where at certain energies the average cosine of the scattering angle goes negative in the case of iron. The coarsely measured distributions for nickel do not show this but would probably display the same effect if the measurements were taken in equivalent detail.

Again we approach the limit on how much information can be digested and stored. Changing characteristics of the angular distribution of neutrons scattered in iron resonances could be important in calculating the transport and streaming effects in steel cores and shields. It seems impractical to fully measure and evaluate these data and incorporate their full detail in transport problems. If applications are sensitive to these effects a parametric representation of the energy and angular distribution data may have to be developed.

Multidisciplinary Approach

The results of applying nuclear data can generally be improved if nuclear physics information e.g. measurement and theory of cross sections, can be combined with reactor physics information e.g. criticality, spectrum-averaged ratio, and reactivity measurements. These two types of information are called differential data (with regard to energy or angle) and integral data, respectively. Integral data have the advantage of often being measured to high precision but can be difficult to interpret because of complex geometries and the involvement of many nuclides and reactions.

A least squares fitting process can be used to minimize a chi-square combining differential and integral data with the data appropriately weighted by their uncertainties. The input data covariance matrix can include correlations among the differential and integral data. In addition, correlations among the data are introduced by the least squares fitting process because of the sensitivity of the calculated integral quantities to the differential data.[13] The correlations resulting from fitting a particular set of integral data are important since the reduced independence of the differential data uncertainties can reduce the uncertainty of calculated integral quantities. These correlations explain why differential data used to calculate integral data do not need to be known to as high a precision as the integral data being calculated. However, because the correlations might be characteristic only of a particular set of integral experiments, the adjusted data may be valid for calculating only integral quantities of the same type (similar sensitivities) chosen for fitting.

Consistency between carefully measured differential and integral data is required for a good evaluation. The discrepancy between calculation and experiment for highly self-shielded U-238 cross sections,[14] after an impasse lasting many years, was solved with the blame shared equally by nuclear physics measurements and reactor physics calculations. Still not understood are some discrepancies between calculated and measured fast reactor reactivity coefficients. Any inconsistencies should be pursued until the discrepancies are eliminated.

Conclusion

It has been possible to discuss here only a few of the open problems in data evaluation. The next generation of evaluated data files will place increasing emphasis on the data covariances associated with the recommended values. This will require increased analysis and the reporting of details by measurers and increased effort on the part of evaluators. The results are worthwhile because they will improve the technological basis for nuclear applications.

Acknowledgment

Research sponsored by the U.S. Department of Energy.

References

1. B.A. Magurno, Editor, ENDF/B-IV Cross Section Measurement Standards, August 1975. BNL-NCS-50464 (ENDF-225), NEACRP-148, NEANDC(US)-196, INDC(US)-73.

2. M.C. Moxon, Specialists' Meeting on Resonance Parameters of Fertile Nuclei and Pu-239, pp. 159-190, Saclay, 20-22 May 1974, NEANDC(E) 163, January 1975.

3. M.R. Bhat, Private Communication 1979.

4. F.G. Perey, Proceedings: Neutron Physics and Nuclear Data, pp.104-115, Harwell, September 1978.

5. L.F. Hansen et al., Nucl. Sci. and Eng. 51, 278-295 (1973).

6. L.F. Hansen et al., Nucl. Sci. and Eng. 61, 201-211 (1976).

7. H. Jahn, ibid. 4, pp. 502-507.

8. S. Pearlstein, ibid. 4, pp. 1059-1065.

9. J.M. Akkermans and H. Gruppelaar, Calculation of Preequilibrium Angular Distributions with the Exciton Model Code Preang, ECN-60, May 1979.

10. J.M. Adams, Comparison of U-235 and Pu-239 Fast Neutron Fission Spectra, AERE-R8636.

11. D.G. Madlund and J.R. Nix, Trans. Am. Nucl. Soc., 32, 726 (June 1979).

12. F.G. Perey, Specialists' Meeting on Neutron Data of Structural Materials for Fast Reactors, p. 571 CBNM Geel, 5-8 Dec. 1977.

13. J.B. Dragt, STEK, the Fast-Thermal Coupled Facility of R.C.N. at Petten, pp. 85-105, RCN-122, 1970.

14. J. Hardy and D.R. Finch, Proceedings: Nuclear Data Problems for Thermal Reactor Applications, p. 7-1, EPRI NP-1098, June 1979.

Material	MAT#	Reaction Type	Energy Range	LAB
^{1}H	1269	$\sigma_{n,n}$	1 keV - 20 MeV	LASL
		σ_{Θ}	1 - 20 MeV	
^{3}He	1146	$\sigma_{n,p}$	1 keV - 50 keV	LASL
^{6}Li	1271	$\sigma_{n,\alpha}$	Thr - 100 keV	LASL
^{10}B	1273	$\sigma_{n,\alpha}$	Thr - 100 keV	LASL
^{12}C	1274	σ_{Θ}	1 keV - 2 MeV	ORNL
^{197}Au	1283	$\sigma_{n,\gamma}$	Thr; 10 keV - 1 MeV	BNL
^{235}U	1261	$\sigma_{n,f}$	Thr; 100 keV - 20 MeV	Task Force

Fig. 1. Cross Section Evaluation Working Group cross section standards.

	Experiment		Range (eV)	Length (M)	Corrected Length (M)	Corrected Time (μsec)
1	GARG	64	100-4000	200.0	199.9 ±0.27	-0.120±0.467
2	FIRK	63	6-2000	55.0	55.03±0.53	0.383±1.433
3	ASGHAR	66	6-830	32.54	32.59±0.09	0.253±0.380
4	LEVIN	55	6-40	20.0	19.92±0.31	0.026±4.534
5	HARVEY	55	0-700	20.0	20.06±0.96	0.995±6.759
6	FLUHARTY	56	10-300	30.0	29.39±1.99	-6.148±18.00
7	BOLLINGER	56	4-350	58.70	58.71±5.81	-0.276±68.31
8	JACKSON	62	6.5-6.8	58.90	- -	0.000±7.190
9	BOLLINGER	68	0-200	60.00	59.87±0.38	-0.412±3.724
10	RYABOV	70	6-7	30.00	- -	-1.891±4.932
11	ROSEN	59	90-1300	35.00	34.99±0.05	0.195±0.163
12	MALECKI	71	66-600	30.00	30.01±0.016	0.103±0.048
13	RAHN	72	6-4600	200.0	STANDARD	
14	CARRARO	70	60-5700	100.0	100.00±0.018	0.087±0.029
15	LYNN	55	6-120	20.00	19.98±0.75	0.150±9.695
16	ROHR	70	50-1000	60.00	60.01±0.073	0.069±0.236

Fig. 2. U-238 resonance energy measurements 6-4000 eV.

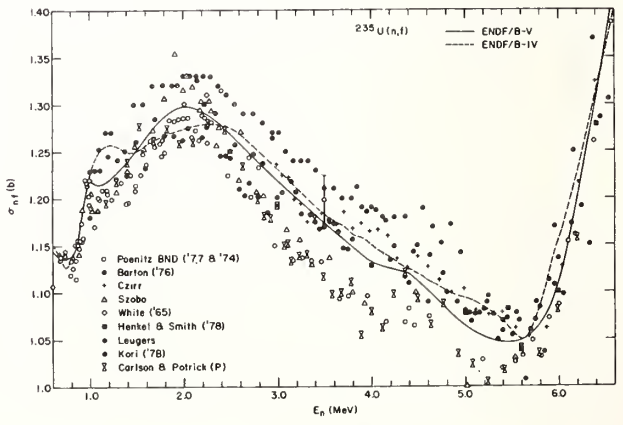

Fig. 3. U-235 (n,fission) experimental data in the MeV region.

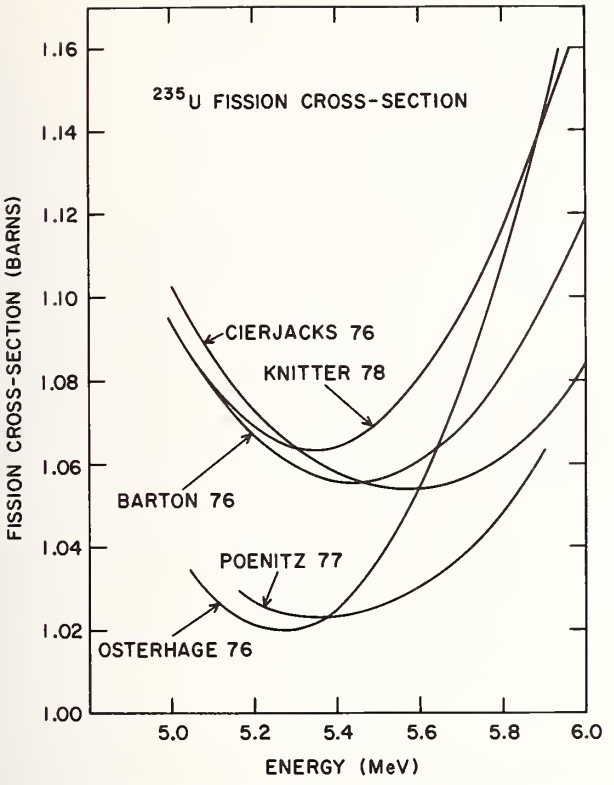

Fig. 4. Least squares fitting of U-235 (n,fission) data 5-6 MeV.

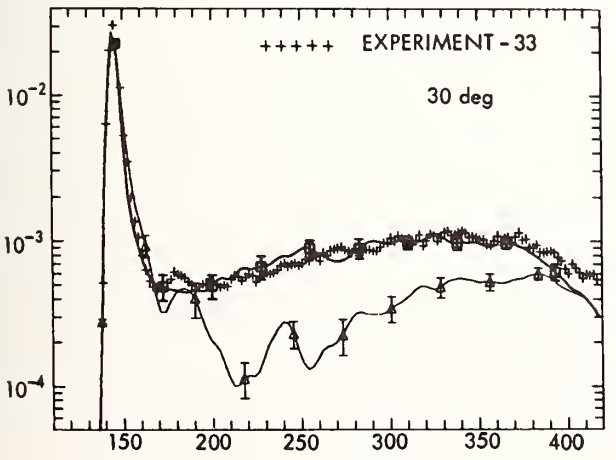

Fig. 5. Pulsed sphere measurements on Iron.

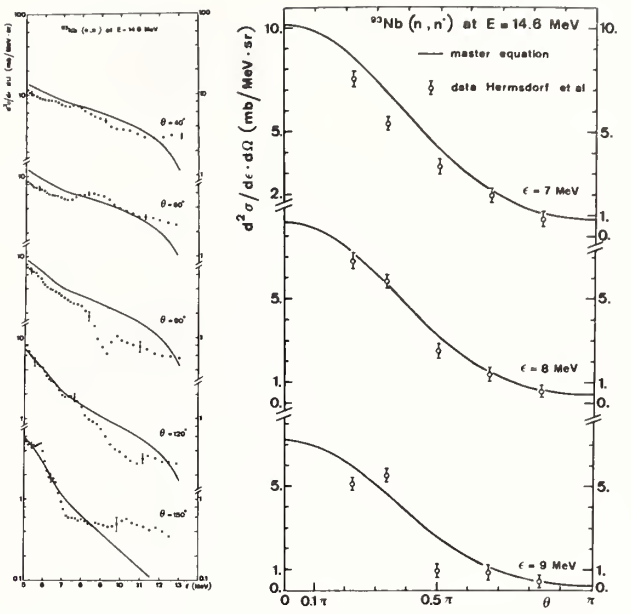

Fig. 6. Neutron emission spectra from Niobium.

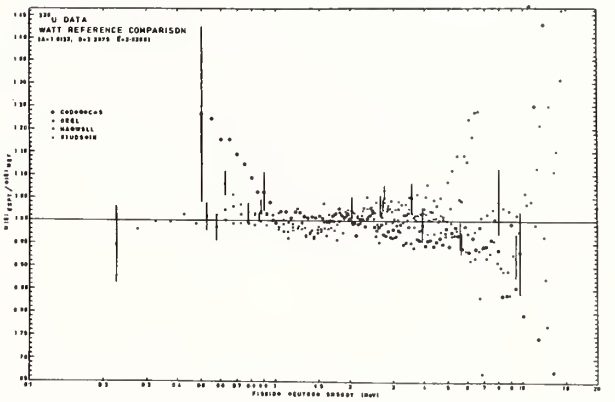

Fig. 7. U-235 Watt spectrum comparison.

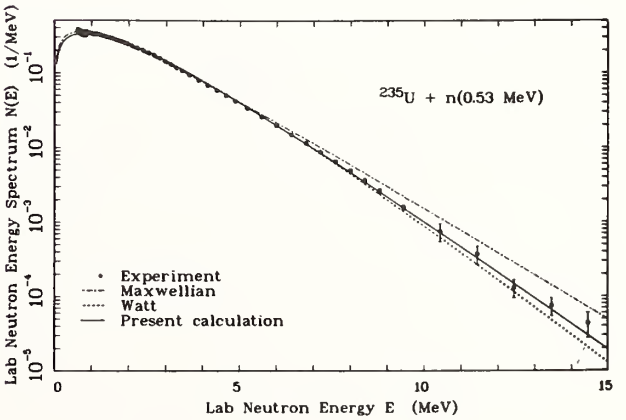

Fig. 8. U-235 Model comparison with spectrum data.

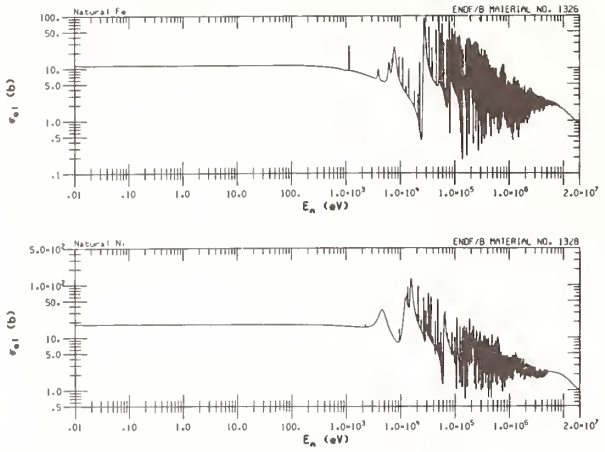

Fig. 9. Elastic scattering cross sections for Fe and Ni.

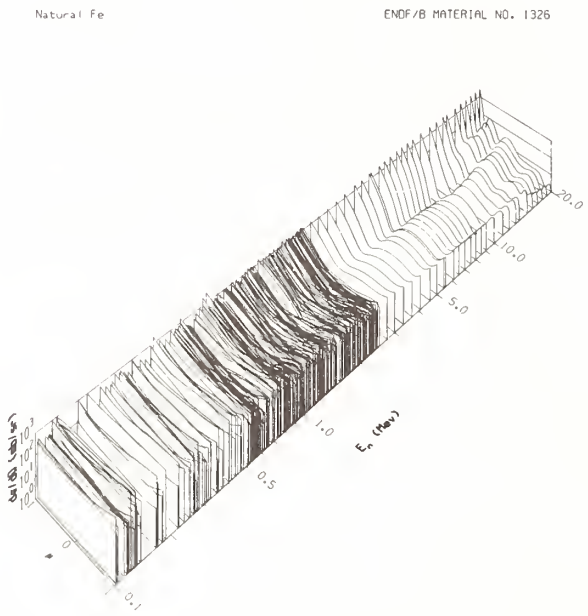

Fig. 10. Elastic scattering angular distributions for Fe.

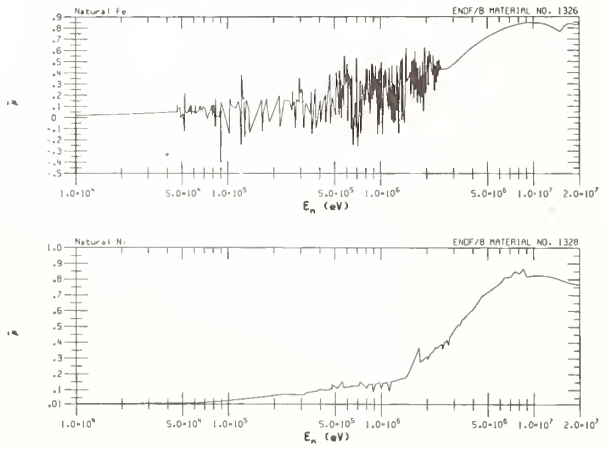

Fig. 11. Mean cosine of the scattering angle for Fe and Ni.

APPLICATION OF NUCLEAR MODELS

P. G. Young, E. D. Arthur, and D. G. Madland
Los Alamos Scientific Laboratory, University of California
Theoretical Division
Los Alamos, New Mexico 87545 U.S.A.

The development of our extensive experimental nuclear data base over the past three decades has been accompanied by parallel advancement of nuclear theory and models used to describe and interpret the measurements. This theoretical capability is important because of many nuclear data requirements that are still difficult, impractical, or even impossible to meet with present experimental techniques. Examples of such data needs are neutron cross sections for unstable fission products, which are required for neutron absorption corrections in reactor calculations; cross sections for transactinide nuclei that control production of long-lived nuclear wastes; and the extensive dosimetry, activation, and neutronic data requirements to 40 MeV that must accompany development of the Fusion Materials Irradiation Test (FMIT) facility. In recent years systematic improvements have been made in the nuclear models and codes used in data evaluation and, most importantly, in the methods used to derive physically based parameters for model calculations. The newly issued ENDF/B-V evaluated data library relies in many cases on nuclear reaction theory based on compound-nucleus Hauser-Feshbach, preequilibrium and direct reaction mechanisms as well as spherical and deformed optical-model theories. The development and application of nuclear models for data evaluation are discussed in this paper, with emphasis on the 1-40 MeV neutron energy range.

(Nuclear reaction theory, nuclear model codes, nuclear data evaluation)

Introduction

The requirements for evaluated nuclear data that result from the various nuclear applications are sufficiently broad that the use of nuclear theory and models is essential to complement the available experimental data base. A number of areas exist where nuclear models play a very important role. A classic example is the problem of determining nuclear data for radioactive or unstable target nuclei which, of course, are very difficult to measure and which are required in a number of applications. Such applications include calculation of neutron absorption and scattering by fission products in thermal and fast reactors; production, depletion, and absorption calculations for actinide nuclides important in waste management and disposal studies; and activation calculations for fusion reactor components and shielding that can involve unstable intermediate nuclei. A second area where nuclear models are very important is the extension of the evaluated data base into the 20-50 MeV incident neutron energy range, where experimental data are much more limited than at lower energies. Although biomedical and shielding data needs have existed in this region for many years, the planned development of d + Li neutron sources, such as the Fusion Materials Irradiation Test facility (FMIT), has given new impetus to developing evaluated data libraries above 20 MeV. It should also be mentioned that in the more common applications models still play an important role in interpolating and extrapolating data such as secondary angular and energy distributions that have not been measured with the same thoroughness as energy-dependent cross sections. For example, the energy range between 9-14 MeV is only sparsely measured for many nuclei. Finally, nuclear models have advanced to a state that they can occasionally be useful to evaluators in deciding among discrepant experimental results.

The use of nuclear theory in data evalations has expanded and become more sophisticated over the years in much the same way that the experimental data base has developed. In this paper we will outline some of the advances that have occurred in the recent past in applying nuclear theory and models to data evaluation. We will describe briefly some of the features of nuclear model codes in common use and will show examples of their application in recent evaluations. Because of time and space limitations, we will restrict the discussion mainly to neutron-induced and fusion reactions in the 1-40 MeV energy region, which excludes the resolved and unresolved resonance regions for the heavier nuclei. We will close with some observations and comments on the recently issued Version V of ENDF/B.

Use of Nuclear Theory in Light Element Evaluations

Nuclear models used in evaluation range from the almost trivially simple to the very complex, depending upon what is appropriate and available for a given situation. An example of the former is the use of simple three-body phase space calculations to represent secondary energy distributions from breakup of light systems. This technique is used in the ^{6}Li ENDF/B-V evaluation[1] to represent the continuum part of the neutron spectrum from the ^{6}Li(n,nd)^{4}He reaction, as illustrated in Fig. 1. Note that elastic scattering is omitted from the calculated curves in Fig. 1. The calculated spectral shape agrees reasonably with the experimental data and provides a useful device for inferring the spectra at unmeasured energies and angles. There are many light nuclei, however, for which such simple representations are unsatisfactory.

At the other end of the complexity scale is the use of sophisticated coupled-channel R-matrix analyses in data evaluations. Such analyses are incorporated in the ENDF/B-V evaluations for ^{4}He, ^{6}Li, ^{10}B, ^{12}C, and ^{16}O, which include the three standard reactions ^{6}Li(n,t)^{4}He, ^{10}B(n,α)^{7}Li and ^{12}C(n,n)^{12}C.

While such applications of R-matrix theory are not new, it is only in relatively recent times that analyses of sufficient detail and thoroughness have been available for light systems so that accurate predictions of results can be made in poorly measured reaction channels of a system. Additionally, by application of the principle of charge independence, predictions can now be extended to different isospin members of a mass system.[2] Such analyses are proving most helpful in providing charged-particle fusion data, and a list of reactions analyzed in this manner at Los Alamos Scientific Laboratory (LASL) is included in Table I. Because this

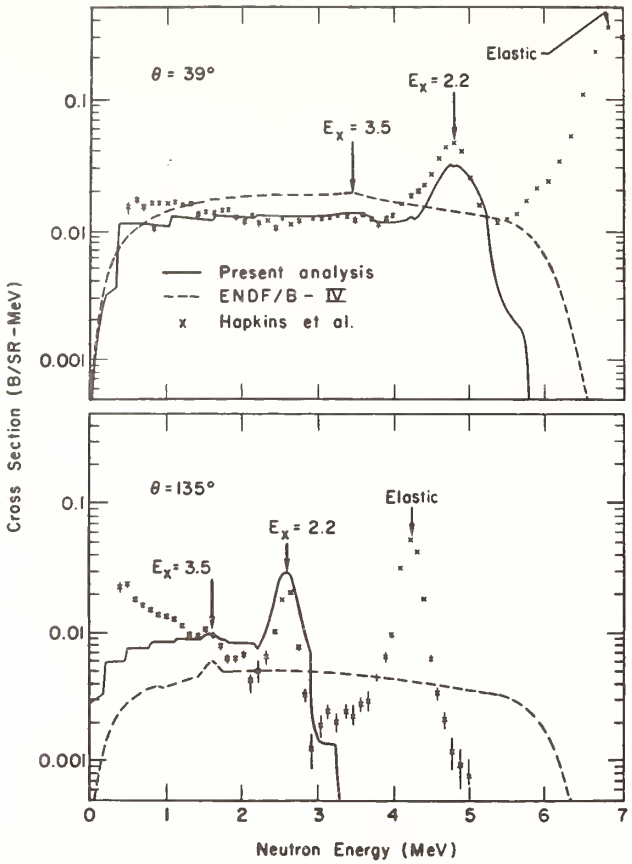

Fig. 1. Neutron emission spectra at laboratory angles of 39 and 135° from 5.74-MeV neutron bombardment of ^{6}Li. As described in Ref. 1, the calculated curves do not include elastic scattering.

topic is the subject of another talk[3] at this conference, no further discussion is included here.

Nuclear Models for Intermediate and Heavy Mass Evaluation

The nuclear models and theories most commonly applied in evaluations of neutron-induced data for heavier nuclei in the MeV region are the spherical and deformed optical models, Hauser-Feshbach statistical theory, direct reaction theory, preequilibrium theory, and fission theory. A number of theoretical improvements have occurred over the past few years, and some of these are cited below. Equally important for data evaluation, however, has been the development and use of improved methods for determining parameters used in model calculations and the coming of age of several multistep Hauser-Feshbach/preequilibrium theory codes that can accommodate the myriad of reaction channels open at incident neutron energies of 20 MeV and higher.

Optical Model Parameterizations

The optical model is still one of the most important tools for a good theoretical evaluation, whether dealing with spherical or deformed target nuclei. In addition to providing a means to calculate energy dependent total, elastic, and reaction cross sections as well as elastic angular distributions, it is also used to compute transmission coefficients that are used in Hauser-Feshbach or direct reaction calculations. There has been increasing recognition over the past several years that the old global or universal parameter sets such as the Wilmore-Hodgson,[4] Perey,[5] or Becchetti-Greenlees[6] parameters, while very useful for scoping

Table I. Charged-Particle Reactions For Which Cross Sections Are Available From Current LASL R-Matrix Analyses

Reaction	Energy Range (MeV)
$T(p,p)T$	E_p = 0-11
$T(p,n)^{3}He$	E_p = 1-11
$^{3}He(p,p)^{3}He$	E_p = 0-20
$^{4}He(p,p)^{4}He$	E_p = 0-30
$^{6}Li(p,p)^{6}Li$	E_p = 0-2.5
$^{6}Li(p,\alpha)^{3}He$	E_p = 0-2.5
$D(d,d)D$	E_d = 0-10
$D(d,n)^{3}He$[a]	E_d = 0-10
$D(d,p)T$[a]	E_d = 0-10
$T(d,d)T$	E_d = 0-8
$T(d,n)^{4}He$	E_d = 0-8
$^{3}He(d,d)^{3}He$	E_d = 0-10
$^{3}He(d,p)^{4}He$	E_d = 0-10
$^{4}He(d,d)^{4}He$	E_d = 0-15
$T(t,t)T$	E_t = 0-2
$T(t,2n)^{4}He$	E_t = 0-2
$^{4}He(t,t)^{4}He$	E_t = 0-14
$^{4}He(t,n)^{6}Li$	E_t = 0-14
$^{4}He(^{3}He,^{3}He)^{4}He$	$E_{^{3}He}$ = 0-11

[a]Results preliminary

studies, are usually not adequate for detailed calculations of specific nuclei. It is far preferable to use optical model parameters that are optimized over a more limited region of A, such as a particular shell, at the same time preserving the accepted trends with energy and mass of the parameters.[7] As a result, there has been a renewal of efforts to determine realistic optical parameters for evaluations over the past few years.

A very useful technique for obtaining neutron optical parameters for spherical and deformed nuclei that does not require extensive automated least-squares fitting and can therefore be performed with modest computing outlay has been developed at Bruyéres-le-Châtel by Lagrange and his coworkers.[8] This technique, referred to as the "SPRT" method, uses s- and p-wave strength functions and the potential scattering radius as data to aid in determination of the real and (surface) imaginary potentials at low energies and then uses the total cross section to establish their energy dependence. Fine tuning of the potential is accomplished by adjusting the spin-orbit strength to match back angle elastic scattering data and the imaginary strengths to match inelastic scattering cross sections. Proton elastic scattering and polarization data can then be analyzed using the derived neutron parameters to provide further information concerning isospin terms, higher energy behavior, etc. The end results are nucleon optical parameters suitable for use over an expanded energy range for a nucleus or nuclei of interest. Such an analysis for ^{93}Nb is reported at this conference[9] with an example of the quality of fit to proton polarization data shown in Fig. 2.

A second technique that also averts extensive fitting for deformed nuclei has been developed by

Madland.[7] With this method, parameters are determined for a spherical optical potential, which is relatively inexpensive to compute, by fitting all available total and differential elastic scattering data. Simple transformations are then sought that will result in realistic deformed model parameters by fitting a much more restricted data set in a fully deformed coupled-channel optical model calculation.

Preliminary results from such an analysis were reported at Harwell[7] and are reproduced in Fig. 3. The solid curves represent neutron total cross sections calculated with a spherical optical model determined by fitting experimental data for all five actinides in Fig. 3. The dashed curve shown for ^{238}U was obtained in a deformed calculation using a simple parameter transformation determined by simultaneously fitting ^{238}U inelastic angular distributions at only two energies (2.5 and 3.4 MeV). The ^{238}U total cross sections calculated with the deformed model agree with experiment to within $\pm$ 3% for neutron energies between 50 keV and 10 MeV. Additionally, the geometrical parameters obtained in this analysis are reasonably similar to ones obtained by Lagrange[10,11] using the SPRT method.

Gamma-Ray Strength Functions

Another important aspect of model calculations is to properly describe gamma-ray emission, both in estimating gamma competition to particle emission and fission in Hauser-Feshbach calculations and in actually computing gamma-ray emission spectra for use in evaluations. In most Hauser-Feshbach calculations, the integral of the product of level density and gamma-ray transmission coefficients is normalized to the experimental value of $2\pi\langle\Gamma_\gamma\rangle/\langle D\rangle$, where $\langle\Gamma_\gamma\rangle$ and $\langle D\rangle$ are the average gamma width and spacing for s-wave resonances. This normalization directly influences the amount of gamma-ray emission occurring, either in the capture reactions or in competition to particle-emission or fission reactions. Experimental data for $\langle\Gamma_\gamma\rangle$ and $\langle D\rangle$ are not always reliable (especially where resonance spacings are large), and for compound systems lacking such data, reliance must be placed upon determination of these quantities from systematics. Since the observed spacing $\langle D\rangle$ can vary drastically between nearby nuclei in closed shell regions, considerable uncertainty can exist in calculations of gamma-ray emission.

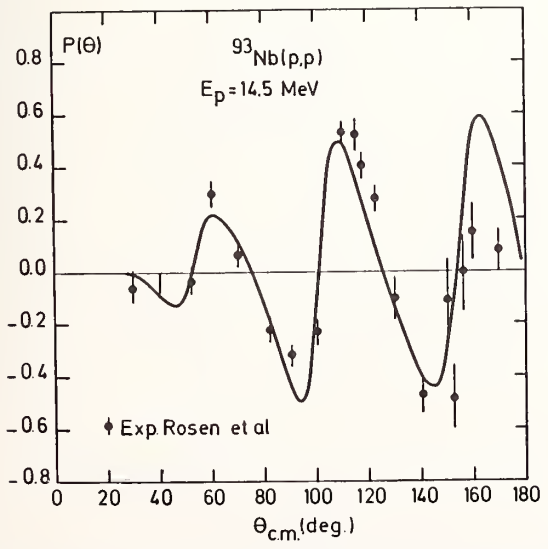

Fig. 2. Calculated and measured proton polarization from ^{93}Nb(p,p) elastic scattering at 14.5 MeV. See Ref. 9 for details.

An alternate approach has been suggested by Gardner[12] that eliminates many of these problems, leading in turn to more accurate capture cross sections where data is unavailable and to a better treatment of gamma-ray competition. This method is based upon determination of the gamma-ray strength function $f(\varepsilon_\gamma)$ defined by

$$\frac{\langle\Gamma_\gamma\rangle}{\langle D\rangle} = \int_0^{S_n} f(\varepsilon_\gamma)\varepsilon_\gamma^{\,3}\rho(S_n-\varepsilon_\gamma)d\varepsilon_\gamma \quad , \tag{1}$$

where S_n is the neutron separation energy, ε_γ is the gamma-ray energy, and ρ is the level density of the compound system. The electric dipole strength function is assumed to have a giant dipole resonance (GDR) form given by

$$f_{E1}(\varepsilon_\gamma) = \frac{k\varepsilon_\gamma\Gamma_{GDR}}{(\varepsilon_\gamma\Gamma_{GDR})^2 + (\varepsilon_\gamma^2-E_{GDR}^2)^2} \quad . \tag{2}$$

The strength function can be extracted from the analysis of neutron capture cross sections measured for stable nuclei or through the analysis of spectral data resulting from capture. Since the strength function is expected to vary smoothly between nearby nuclei, some of the problems mentioned earlier can be eliminated, and one can use it with increased confidence.

An application of this technique by Gardner[12] for the ^{85}Rb(n,γ) and ^{87}Rb(n,γ) reactions is shown in Fig. 4. The same strength function $f_{E1}(\varepsilon_\gamma)$ was used for both reactions shown in Fig. 4; the vastly different capture cross sections result entirely from the different binding energies and level densities used in the two cases.

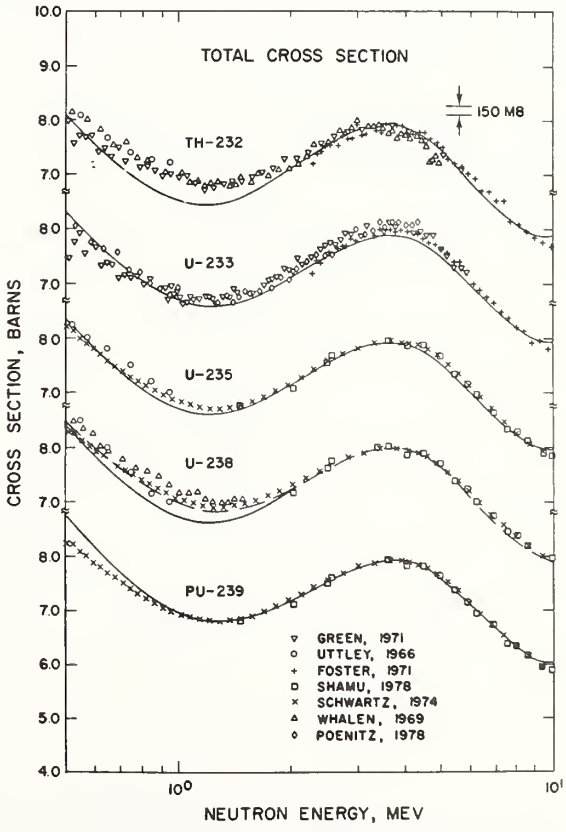

Fig. 3. Calculated and measured neutron total cross sections for five actinide nuclei. See Ref. 7.

Improved Codes for Evaluations

A large number of codes useful for evaluations have been developed in many countries, but space does not permit a thorough discussion here.

One major advance in the past several years that will be discussed, however, is the development of several multistep Hauser-Feshbach statistical-preequilibrium codes that permit calculation of most important reactions in the MeV region. Within the community of ENDF/B evaluators, these codes include the HAUSER[13] code developed at Hanford Engineering Development Laboratory, the TNG[14] code from Oak Ridge National Laboratory, the STAPRE[15] code written in Austria and extensively used at Lawrence Livermore Laboratory and Brookhaven National Laboratory, and the GNASH[16] code developed at LASL. These codes, when used in combination with spherical and deformed optical model codes and the older reaction theory code COMNUC,[17] provide a capability for calculating all important reaction sequences up to 20 MeV or higher.

Typical reaction sequences that can be included in multistep calculations are shown in Fig. 5. The case illustrated is for neutron-induced reactions on ^{89}Y, which were recently calculated with the GNASH code.[18] The first arrow indicates the path from the incident channel to the first compound nucleus $^{90}Y^*$, whose decays correspond to the binary (n,γ), (n,p), (n,α), and (n,n') reactions. The various compound nuclei shown in the diagram are populated in specific energy, spin, and parity states, and each nucleus is permitted to decay by n, p, α, and/or γ emission until the decay sequences terminate. The most complicated sequences shown in Fig. 5 are (n,2nγ), (n,2np), (n,2nα), and (n,3n) reactions, although calculations are not limited to these.

All four multistep Hauser-Feshbach codes mentioned above can carry out these calculations with full allowance for angular momentum effects. The TNG, HAUSER, and STAPRE codes include width fluctuation corrections for the lower energy calculations, whereas GNASH, which is designed for higher energy calculations, does not. All four codes include preequilibrium models that are used to correct the binary reactions for nonequilibrium effects. In the case of TNG, a new model (described in a later paper[19]) has been included to incorporate conservation of angular momentum in the preequilibrium step. This model ensures consistency between the statistical and preequilibrium parts of the calculations. Particle spectra are calculated in all four codes, and all except HAUSER also output gamma-ray spectra. The HAUSER, GNASH, and TNG codes allow input of externally computed direct-reaction cross sections to specific states, which are combined with the Hauser-Feshbach calculations and, in the case of GNASH and TNG, are included explicitly in the gamma-ray cascades. The TNG and HAUSER codes calculate compound nucleus angular distributions, whereas GNASH and STAPRE rely upon external codes for these effects. STAPRE, HAUSER, and GNASH all have fission channels, with a double-humped barrier being available for use in HAUSER and STAPRE.

In the past few years these codes have been extensively developed and used in support of data evaluation, and examples of calculations are given below. The Nuclear Models Subcommittee of the Cross Section Evaluation Working Group has been carrying out code comparison studies with these and other codes, and even more detailed comparisons have been made between codes used at LLL and LASL.[20]

Examples of Recent Calculations

There are a number of examples that can be cited where the above codes have been successfully applied to evaluation problems. The HAUSER code has been used extensively by Mann and Schenter[21] in calculations of actinide cross sections for ENDF/B-V. Similarly, Fu has used TNG for ENDF/B evaluations of ^{40}Ca,[22] ^{56}Fe,[23] and Pb,[24] and for Cu and Nb calculations to 32 MeV.[25] Calculations with STAPRE include comprehensive analyses by M. Gardner of neutron-induced reactions on zirconium isotopes[26] and by D. Gardner of neutron reactions on 33 target states of $^{170-180}Lu$.[27] Additionally, an analysis[28] of neutron reactions on barium isotopes with

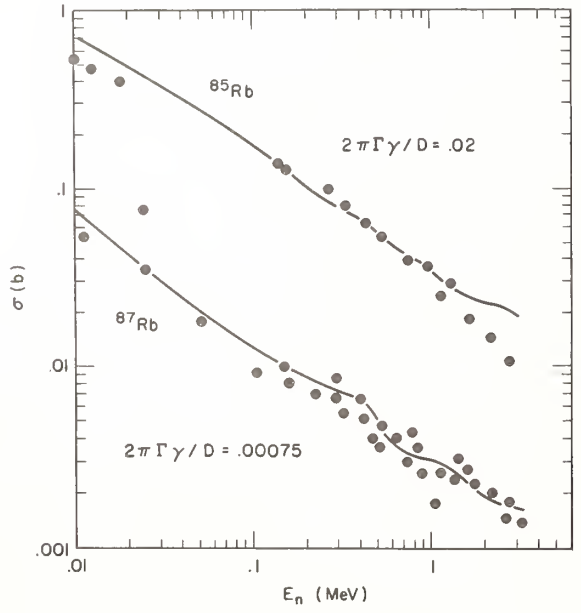

Fig. 4. $^{85}Rb(n,\gamma)$ and $^{87}Rb(n,\gamma)$ cross sections between 10 keV and 3.5 MeV. See Ref. 12 for details.

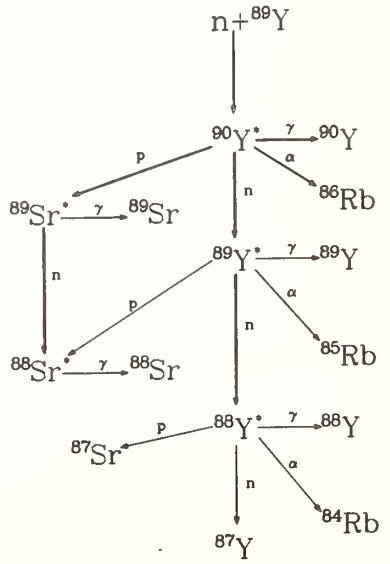

Fig. 5. Sample reaction decay sequences from neutron interactions with ^{89}Y as calculated by Arthur (Ref. 18).

STAPRE has been performed. Recent analyses with the GNASH code include studies of neutron-induced reactions to 20 MeV on a total of 10 isotopes of yttrium and zirconium,[18] to 40 MeV for ^{54}Fe and ^{56}Fe,[29] to 20 MeV for the four principal isotopes of tungsten,[30] and to 22 MeV for ^{235}U and ^{238}U.[31]

To illustrate the potential of such calculations when care is taken with parameterizations, Figs. 6-8 show comparisons between calculated and experimental cross sections from the GNASH analysis of yttrium and zirconium isotopes.[18] In this study, consistency was required of the optical model parameterizations for all the yttrium and zirconium isotopes, and several different types of neutron and charged-particle experiments were fit to determine optical parameters. In addition, a careful study was made using Gardner's method[12] to obtain reliable gamma-ray strength functions.

Gamma-ray energy spectra from GNASH calculations[29] for iron are compared to the experimental data of Chapman et al.[32] at four incident neutron energies in Figs. 9-12. In this case, the model parameters were determined entirely from other measurements, so the comparisons with the gamma-ray spectra provide a test of the calculations. Although the calculations agree relatively poorly with the Chapman data at 14.55 MeV (Fig. 11), they are in reasonably good agreement with the data of Drake et al.[33] at 14.2 MeV, shown in Fig. 13. Thus, there appears to be a discrepancy between the two experiments near 14 MeV, and Arthur's calculations tend to support Drake's measurement.

The neutron emission spectra calculated for 36-MeV neutrons incident on iron are shown at 0, 90, and 180° in Fig. 14. The high energy lines in the spectrum result from Fe(n,n') reactions to discrete states, which were obtained in DWBA calculations and are strongly forward peaked. The angular distributions in the continuum region were calculated from semiempirical relationships determined by Kalbach[34] and based on preequilibrium theory. The breaks in the spectrum in the continuum region indicate the boundaries of 5-MeV wide secondary energy bins, each of which was given a separate angular distribution from the Kalbach formalism. This representation results from an ad hoc modification of the ENDF/B format to accommodate the pronounced forward peaking of spectra at energies above 20 MeV.

The gamma-ray emission spectrum that is calculated for 40-MeV incident neutrons on iron is shown in Fig. 15. Isotropy was assumed for all emitted gamma rays, and the standard ENDF/B formats were adequate to represent the calculations.

Finally, a comparison of calculated fission[31] cross sections for ^{235}U and ^{238}U with experimental data is shown in Fig. 16. In this case, a simple single-hump fission barrier model in the GNASH code was optimized to the data shown, for the purpose of providing adequate fission competition in calculations of (n,xn) reactions.

Comments on ENDF/B-V

The new multistep Hauser-Feshbach codes and the older direct-reaction and compound-nucleus theory codes provide a very useful array of tools for optimizing data evaluations. It is usually preferable in cases where measurements are available to base evaluated total and fission cross sections on direct experimental data. In such cases, the use of nuclear models can ensure consistency of the remaining evaluated cross sections through derivation of parameters which simultaneously describe all channels. Evaluations determined with this match of theory and experiment offer the advantage that the neutron, gamma-ray, and charged-particle data satisfy the basic requirements of conservation of total energy and flux.

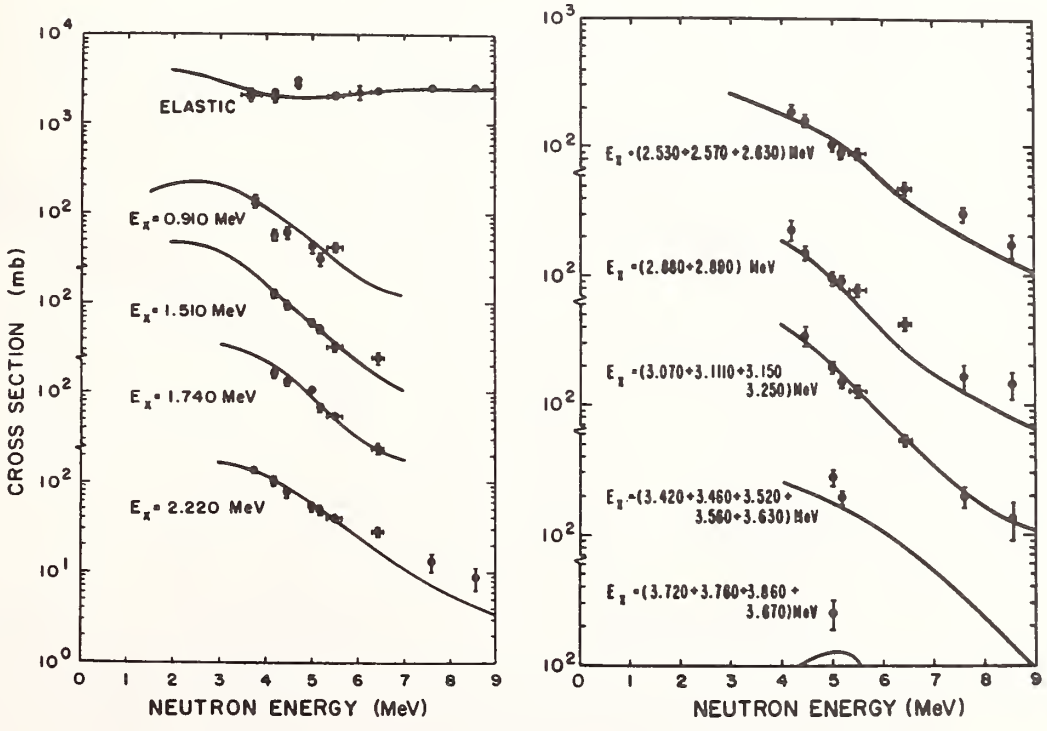

Fig. 6. Measured and calculated elastic and inelastic neutron scattering from ^{89}Y. See Ref. 18 for details.

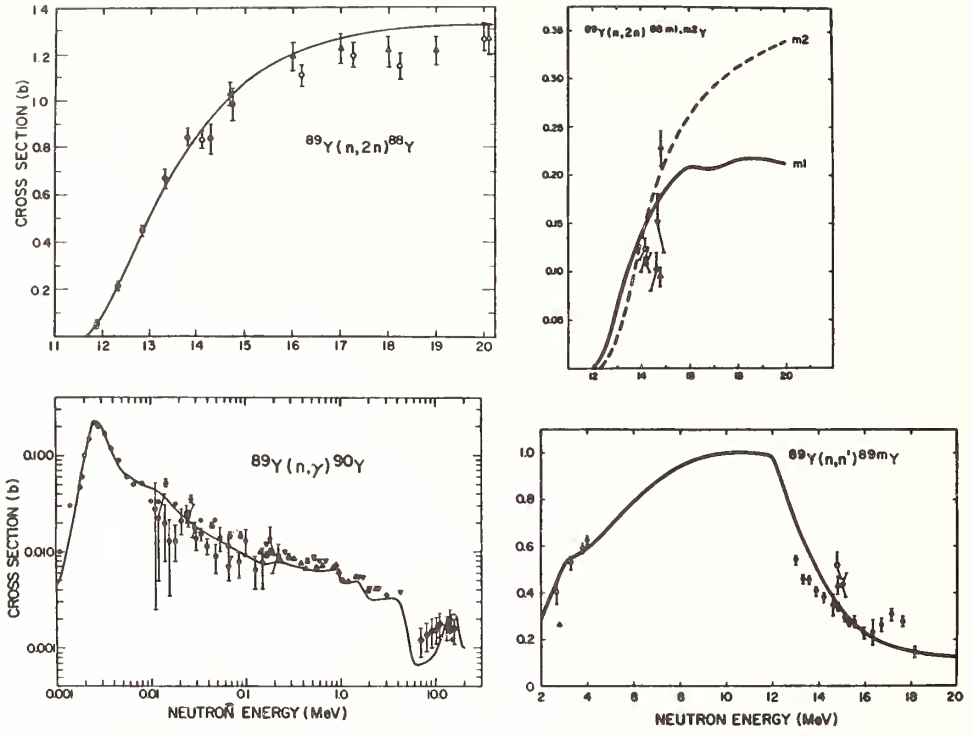

Fig. 7. Measured and calculated cross sections for the $^{89}Y(n,\gamma)^{90}Y$, $^{89}Y(n,n')^{89m}Y$, $^{89}Y(n,2n)^{88}Y$, and $^{89}Y(n,2n)^{88m1,\ m2}Y$ reactions. See Ref. 18 for details.

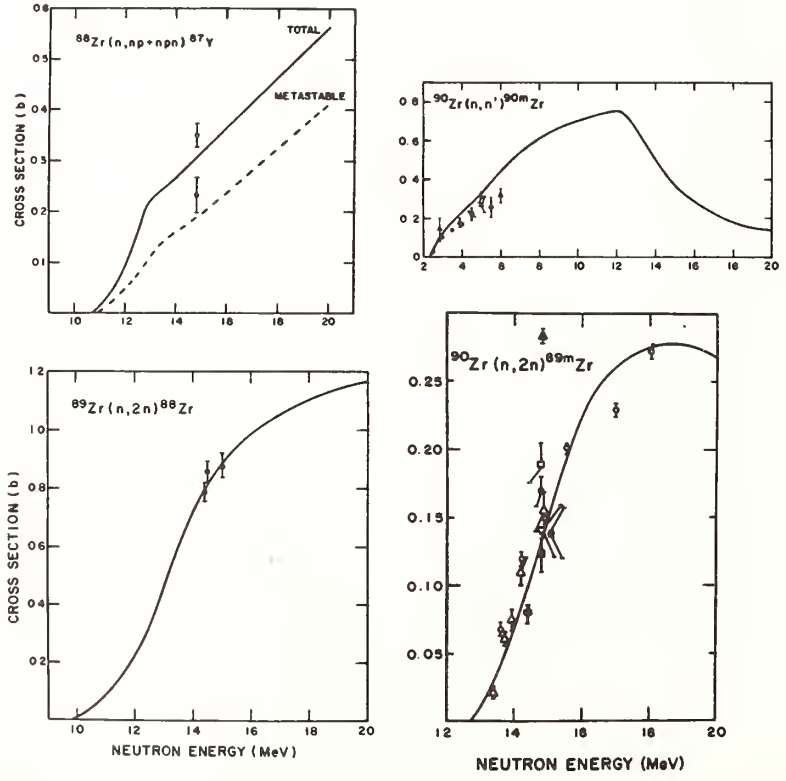

Fig. 8. Measured and calculated cross sections for the $^{88}Zr(n,np)^{87}Y$, $^{89}Zr(n,2n)^{88}Zr$, $^{90}Zr(n,n')^{90m}Zr$, and $^{90}Zr(n,2n)^{89m}Zr$ reactions. See Ref. 18 for details.

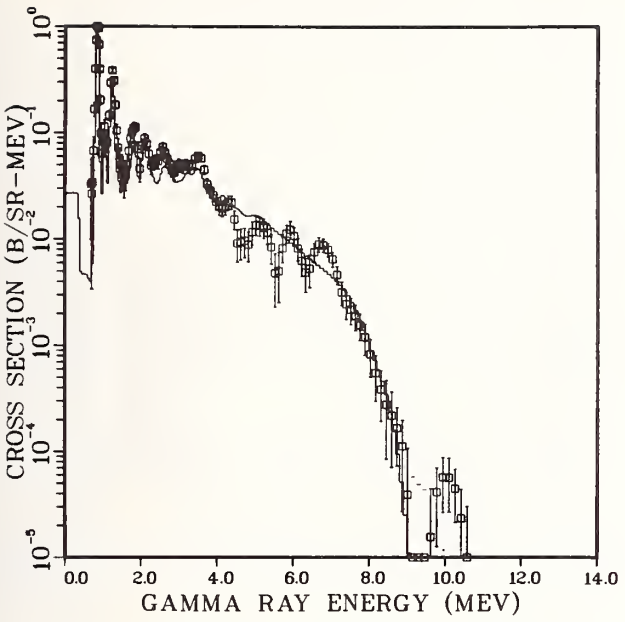

Fig. 9. Calculated gamma-ray emission spectra for 8.76-MeV neutron bombardment of Fe compared to the measurement by Chapman et al. (Ref. 32) at 125°.

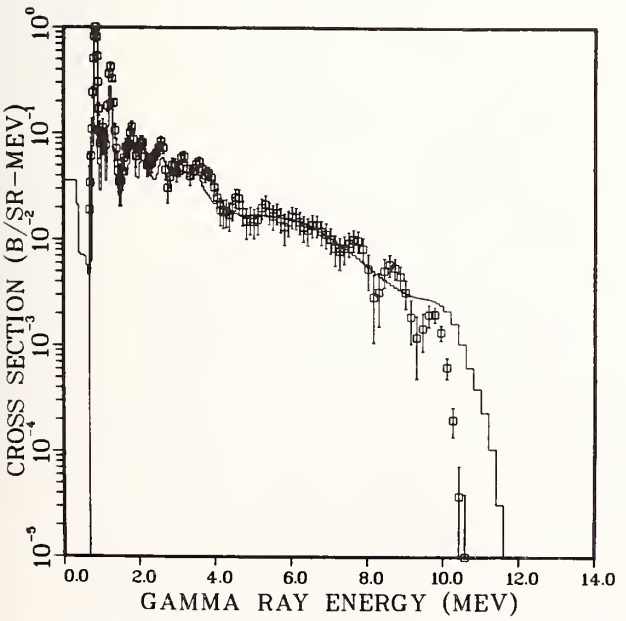

Fig. 10. Calculated gamma-ray emission spectra for 11.5-MeV neutron bombardment of Fe compared to the measurement by Chapman et al. (Ref. 32) at 125°.

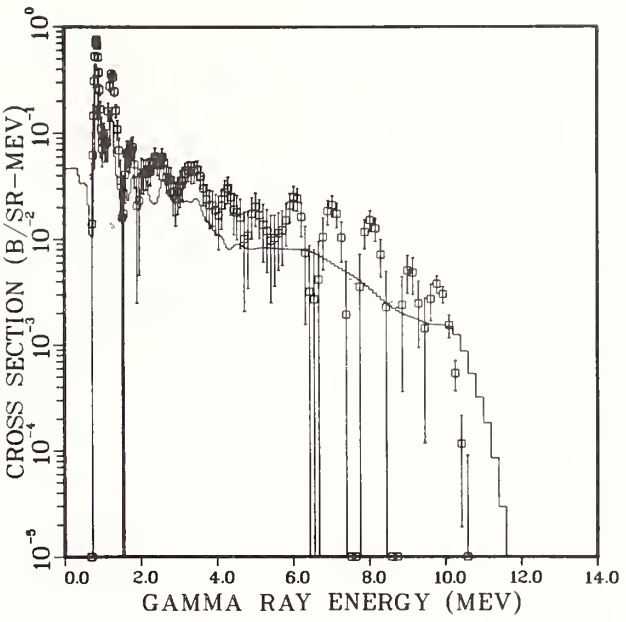

Fig. 11. Calculated gamma-ray emission spectra for 14.55-MeV neutron bombardment of Fe compared to the measurement by Chapman et al. (Ref. 32) at 125°.

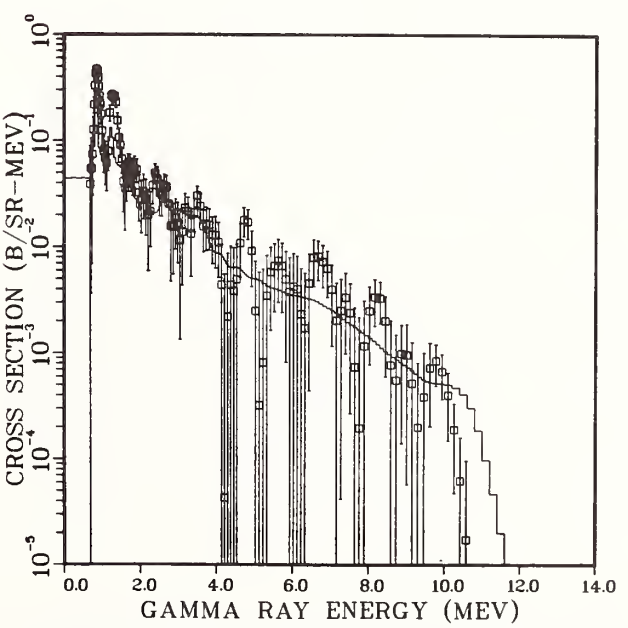

Fig. 12. Calculated gamma-ray emission spectra for 18.85-MeV neutron bombardment of Fe compared to the measurement by Chapman et al. (Ref. 32) at 125°.

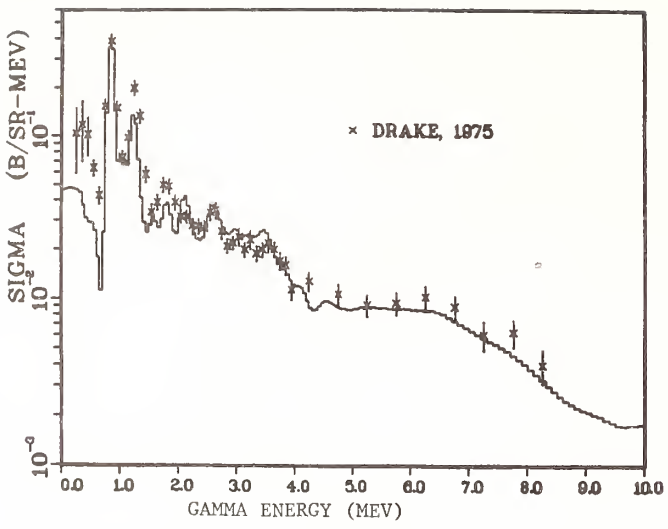

Fig. 13. Calculated gamma-ray emission spectra for 14.2-MeV neutron bombardment of Fe compared to the measurement of Drake et al. (Ref. 33) at 90°.

While nuclear theory has been frequently put to good use in evaluations, its application has tended to be somewhat piecemeal with the result that energy conservation has frequently not been satisfied. Examples of this problem are provided in a recent study of energy balance in ENDF/B-V evaluations by MacFarlane.[35] KERMA factors, which are simply the energy given to charged reactions products, were computed for a variety of nonfissile nuclei at a selection of incident energies by subtracting the energy carried away by neutrons and photons from the total energy (E+Q) available to each reaction. Lower and upper limits based on general considerations were determined for the KERMA factors for most reactions, and tests were made to see if the ENDF/B-V data satisfied the limits.

MacFarlane's results are reproduced in Table II where each evaluation tested is rated as G (good), F (fair), or P (poor) for the energy ranges THER (E_n < 1 keV), FAST (1 keV-2MeV), and FUSN (2-20 MeV). A rating of "P" means that KERMA factors computed in this manner are inadequate for most applications and indicates rather significant (∿1-10%) violations of conservation of total energy.

A disturbing number of "P" ratings occur in Table II. While the KERMA diagnostic is quite sensitive and can indicate rather small violations of energy conservation, a number of cases flagged in Table II do represent significant problems. Additionally, one might take the point of view that conservation of energy should be essentially inviolate in evaluations, in much the same manner that evaluators require that all neutron cross sections sum to the total cross section. Careful, consistent use of nuclear theory in fitting experimental data can help remove problems of this nature in future evaluations.

Summary

Significant advances have occurred over the past several years in applying nuclear theory to data evaluations. Areas highlighted here are the use of R-matrix theory for improving and extending light element evaluations, development of improved methods for determining model parameters, and the availability of several new multistep Hauser-Feshbach/preequilibrium model codes

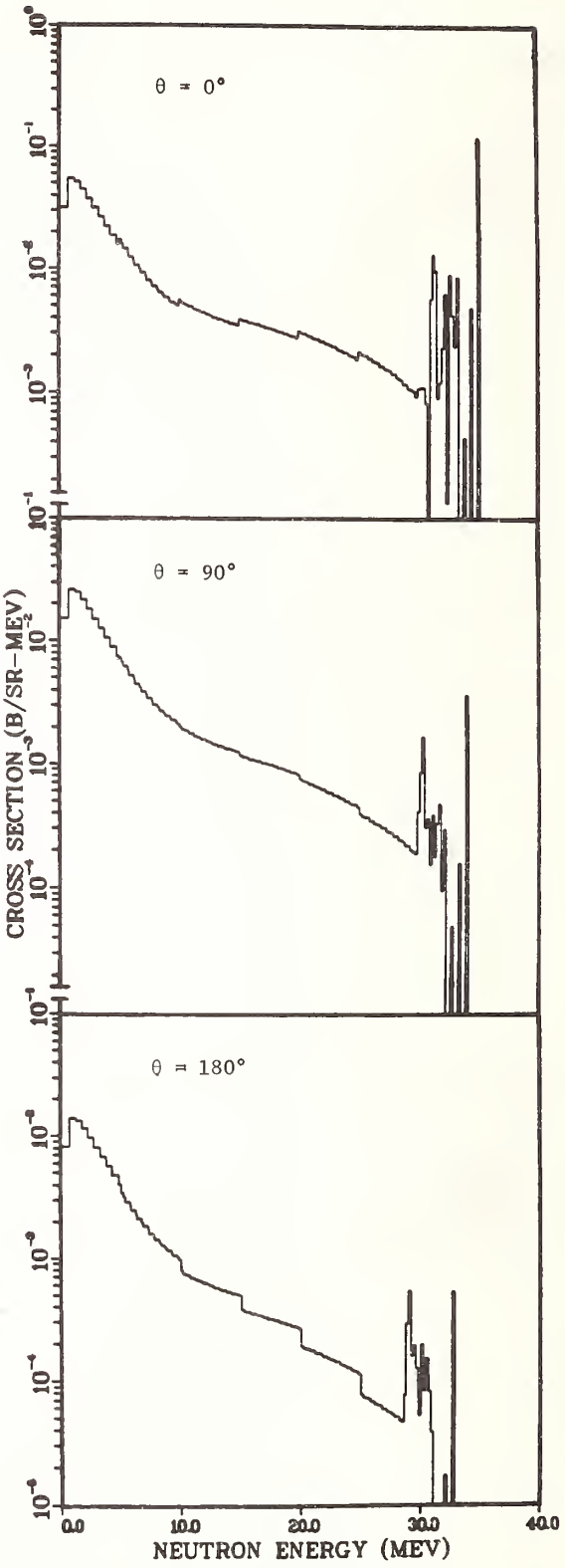

Fig. 14. Calculated neutron emission spectra at 0, 90, and 180° from 36-MeV neutron bombardment of Fe.

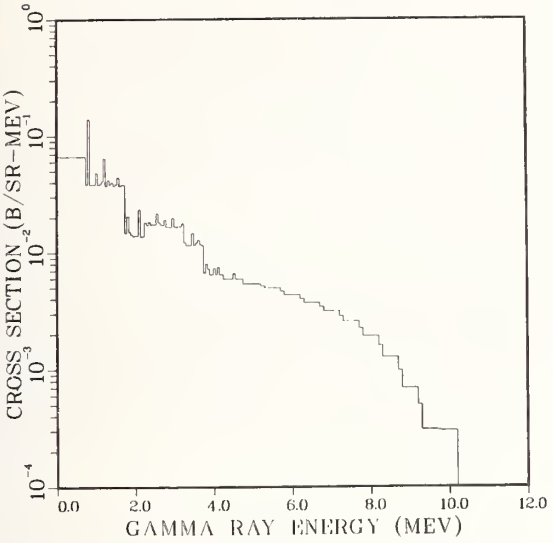

Fig. 15. Calculated gamma-ray emission spectrum from 40-MeV neutron bombardment of Fe.

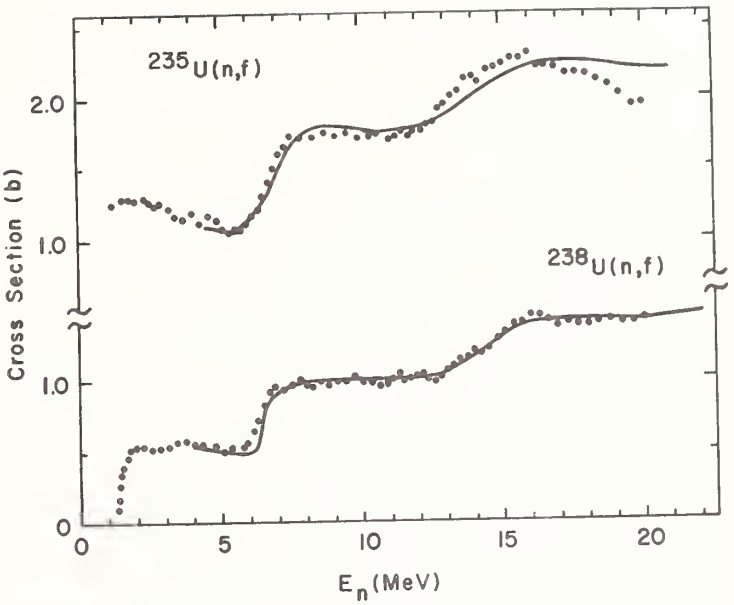

Fig. 16. Measured and calculated $^{235}U(n,f)$ and $^{238}U(n,f)$ cross sections. See Ref. 31 for details.

Table II

QUALITATIVE RATING OF ENERGY BALANCE FOR MATERIALS FROM ENDF/B-V
(G=Good, F=Fair, P=Poor) BY ENERGY RANGE
(THER<1 keV, FAST=1 keV to 2 MeV, FUSN=2 to 20 MeV)

Material	THER	FAST	FUSN	Material	THER	FAST	FUSN
H-1	G	G	G	K	*	*	P
H-2	G	G	G	Ca	G	G	G
Li-6	G	G	G	Ti	G	F	F
Li-7	G	G	G	V	G	G	F
Be-9	G	G	G	Cr	*	*	P
B-10	G	G	G	Mn-55	P	P	P
C	G	G	G	Fe	*	F	P
N-14	G	G	G	Co-59	G	P	P
N-15	G	G	F	Ni	G	P	F
O-16	G	G	G	Cu	*	*	*
F-19	G	G	F	Mo	*	*	*
Na-23	G	G	F	Ba-138	F	F	F
Mg	G	F	F	Ta-181	P+	P	P
Al-27	G	G	F	W-182	P	P	P
Si	G	G	G	W-184	P	P	P
P-31	G	G	F	W-185	P	P	P
S-32	G	G	F	W-186	P	P	P
Cl	*	G	*	Pb	*	G	F

*Tests masked by element effect

+Possibly masked by internal conversion

that permit rather complete calculations in the 1-40 MeV region. Additionally, problems with energy balance in ENDF/B-V evaluations are noted, and we conclude that more consistent use of theory in evaluations is needed so that total energy and flux conservation are maintained.

Time and space limitations have dictated that the scope of this paper be limited. There are many other developments that should lead to further improvement in theoretical calculations. More sophisticated fission models as described by Lynn,[36] Back et al.,[37] and Delagrange et al.[38] are planned or in use in certain model codes, and advances are being made in preequilibrium theory which offer promise of more accurate analyses in the future. Efforts to base model calculations on more fundamental theories, particularly regarding microscopic descriptions of nuclear level densities[39] and the optical model,[40] show promise for applied usage. An improved theoretical description of neutron energy spectra from fission has been developed,[41] and a new "master" code that will combine and refine some of the models presently used is under development at Lawrence Livermore Laboratory.[42] Finally, progress in developing a unifed theory to include both Hauser-Feshbach and direct reaction mechanisms has been made in recent years,[43,44] and multistep direct-reaction calculations as carried out by Tamura et al. [45] might prove useful in extending the evaluated data base to higher energies.

References

1. L. Stewart and P. G. Young, Trans. Am. Nucl. Soc. 23, 22 (1976).
2. D. C. Dodder and G. M. Hale, "Application of Approximate Isospin Conservation in R-Matrix Analysis," Proc. of Intnl. Conf. on Neutron Physics and Nuclear Data for Reactors and Other Applied Purposes," Harwell, England (Sept. 1978), p. 490.
3. G. M. Hale, Bull. Am. Phys. Soc. 24, 881 (1979).
4. D. Wilmore and P. E. Hodgson, Nucl. Phys. 55, 673 (1964).
5. F. G. Perey, Phys. Rev. 131, 745 (1962).
6. F. D. Becchetti, Jr., and G. W. Greenlees, Phys. Rev. 182, 1190 (1969).
7. D. G. Madland and P. G. Young, "Neutron-Nucleus Optical Potential for the Actinide Region," Proc. of Intnl. Conf. on Neutron Physics and Nuclear Data for Reactors and Other Applied Purposes," Harwell, England (Sept. 1978), p. 349.
8. J. P. Delaroche, Ch. Lagrange, and J. Salvy, "The Optical Model with Particular Considerations of the Coupled-Channel Optical Model," IAEA-190 (1976), p. 251.
9. Ch. Lagrange, Bull. Am. Phys. Soc. 24, 870 (1979).
10. G. Haouat et al., "Differential Cross Section Measurements of Fast Neutron Scattering for ^{208}Pb, ^{232}Th, and ^{238}U at 2.5 MeV." NEANDC(E)180 "L" (1977).
11. G. Haouat et al., "Differential Cross Section Measurements for 3.4-MeV Neutron Scattering from ^{208}Pb, ^{232}Th, ^{235}U, ^{238}U, and ^{239}Pu," NEANDC(E)196 "L" (1978).
12. D. G. Gardner and M. A. Gardner, Bull. Am. Phys. Soc. 22, 993 (1977).
13. F. M. Mann, "HAUSER-4: A Computer Code to Calculate Nuclear Cross Sections," HEDL-TME-76-80 (1976).
14. C. Y. Fu, "Development of a Two-Step Hauser-Feshbach Code with Precompound Decays and Gamma-Ray Cascades: A Theoretical Tool for Cross Section Evaluation," Proc. Nucl. Cross Section Tech. Conf., Washington, D.C. (March 1975), NBS Special Publication 425, p. 328.
15. M. Uhl and B. Strohmaier, "STAPRE: A Computer Code for Particle-Induced Activation Cross Sections and Related Quantities," IRK 76/01 (1976).
16. P. G. Young and E. D. Arthur, "GNASH: A Preequilibrium Statistical Nuclear Model Code for Calculation of Cross Sections and Emission Spectra," LA-6947 (1977).
17. C. L. Dunford, "A Unified Model for Analysis of Compound Nucleus Reactions," AI-AEC-12931 (1970).
18. E. D. Arthur, "Calculation of Neutron Cross Sections on Isotopes of Yttrium and Zirconium," LA-7789-MS (1979).
19. C. Y. Fu, Bull. Am. Phys. Soc. 24, 884 (1979).
20. E. D. Arthur, "Comparison of Cross Sections Calculated with Various Statistical Model Codes Using Identical Parameter Sets," in "Applied Nuclear Data Research and Development, July 1-Sept. 30, 1978," compiled by C. I. Baxman and P. G. Young, LA-7596-PR (1978).
21. F. M. Mann and R. E. Schenter, "HEDL Evaluation of Actinide Cross Sections for ENDF/B-V," HEDL-TME-77-54 (1977).
22. C. Y. Fu, Atomic Data and Nucl. Data Tables 17, 127 (1976).
23. C. Y. Fu and F. G. Perey, ENDF/B-V evaluation MAT 1326, personal communication through the National Nuclear Data Center, Brookhaven National Laboratory (1979).
24. C. Y. Fu and F. G. Perey, Atomic Data and Nuclear Data Table 16, 409 (1975).
25. C. Y. Fu and F. G. Perey, J. Nucl. Materials 61, 153 (1976).
26. M. A. Gardner and D. G. Gardner, Bull. Am. Phys. Soc. 22, 993 (1977).
27. D. R. Nethaway and D. G. Gardner, Bull. Am. Phys. Soc. 22, 615 (1977).
28. B. Strohmaier et al, Nucl. Sci. and Eng. 65, 368 (1978).
29. E. D. Arthur and P. G. Young, Bull. Am. Phys. Soc. 24, 863 (1979).
30. E. D. Arthur and C. A. Philis, Bull. Am. Phys. Soc. 24, 871 (1979).
31. L. R. Veeser and E. D. Arthur, "Measurements of (n,3n) Cross Sections for ^{235}U and ^{238}U," Proc. of Intnl. Conf. on Neutron Physics and Nuclear Data for Reactors and Other Applied Purposes, Harwell, England (Sept. 1978), p. 1054.

32. G. T. Chapman et al., "A Re-Measurement of the Neutron Induced Gamma-Ray Production Cross Sections for Iron in the Energy Range 850 keV $\leq E_n \leq$ 20.0 MeV," ORNL/TM-5416 (1976).

33. D. M. Drake et al., Nucl. Sci. and Eng. 65, 49 (1978).

34. C. Kalbach, personal communication (1979).

35. R. E. MacFarlane, "Energy Balance of ENDF/B-V," to be presented at the ANS Winter Meeting, San Francisco, (Nov. 1979).

36. J. E. Lynn, "Cross Section Theory for Actinide Nuclei," Proc. of Intnl. Conf. on Neutron Physics and Nuclear Data for Reactors and Other Applied Purposes, Harwell, England (Sept. 1978), p. 941.

37. B. B. Back et al., Phys. Rev. C10, 1948 (1974); see also Phys. Rev. C9, 1924 (1974).

38. H. Delagrange et al., Phys. Rev. C17, 1706 (1978).

39. L. G. Morretto, Nucl. Phys. A185, 145 (1972).

40. J. P. Jeukenne et al., Phys. Rev. C16, 80 (1977).

41. D. G. Madland and J. R. Nix, Bull. Am. Phys. Soc. 24, 885 (1979); see also, Trans. Am. Nucl. Soc. 32, 726 (1979).

42. D. G. Gardner, personal communication (1979).

43. P. A. Moldauer, Phys. Rev. C12, 744 (1975).

44. H. M. Hofmann et al., Annals of Physics 90, 403 (1975).

45. T. Tamura et al., Phys. Lett. 66B, 109 (1977).

R-MATRIX ANALYSES OF LIGHT-ELEMENT REACTIONS FOR FUSION APPLICATIONS

G. M. Hale and D. C. Dodder
Los Alamos Scientific Laboratory, University of California
Theoretical Division
Los Alamos, New Mexico 87545, USA

Charged-particle reactions, multichannel R-matrix analyses, evaluated fusion cross sections, A = 4-7 nucleon systems.

Comprehensive R-matrix analyses of reactions in light systems done at LASL contain cross-section information of interest in fusion applications. Results for analyses of the 4-, 5-, 6-, and 7- nucleon systems are presented, with particular emphasis on cross sections for the T(d,n), D(d,n) D(d,p), T(t,2n), and ^{6}Li(p,^{3}He) fusion reactions.

Introduction

As fusion designs begin to emerge from the problematic to a more programmatic stage, the need for reliable cross sections for reactions occurring in the plasma becomes increasingly important.[1,2] Many of these reactions involve charged particles in producing the primary energy source of the reactor, in slowing down energetic ions to heat the plasma, in removing and replacing the primary fuels, and in providing diagnostic information about plasma conditions.

Since present plasma confinement concepts are limited to relatively low temperatures, these reactions generally need be considered only at energies below a few MeV. Although most of the important fusion cross sections were measured in this energy range some 25 years ago, it is questionable[3] whether these measurements meet the current or projected nuclear data requirements of fusion technology. Measurements are especially difficult in the critical low-energy region (below ~30 keV), where one has generally assumed the dominance of pure Coulomb repulsion to extrapolate the cross sections. It should be noted, however, that most fusion cross sections large enough to be of interest exhibit resonant behavior at low energies, so that nuclear effects almost certainly modify the pure Coulomb behavior.

The suitability of R-matrix theory for describing reactions in light nuclei has been pointed out at several previous technology conferences.[4-7] In the case of charged-particle reactions of interest in fusion applications, the separation of short-ranged and long-ranged forces explicit in R-matrix theory allows pure Coulomb and angular momentum effects, like barrier penetration, to interact in a simple and natural way with nuclear effects, especially resonances. Also, since the R matrix provides a particularly simple and unitary parameterization of multichannel reaction theory, one has the prospect of using a single set of parameters to describe several reactions simultaneously, and of imposing a large amount of experimental information on the determination of the parameters, resulting in improved statistical reliability of predictions from the fit. In the following sections, we will describe applications of multichannel R-matrix theory to few-nucleon systems in the mass range A = 4-7 having charged-particle reactions of interest in fusion applications. We shall begin, however, with a brief, formal summary of R-matrix theory.

Formal Summary of R-Matrix Theory

Imagine a nuclear scattering process in which A nucleons, initially distributed between two bound particles, come together, interact, and emerge distributed again in two bound particles which can, in general, be different from the initial pair. Different 2-body distributions of the nucleons are called the arrangement channels of the system, and the surface outside of which the nucleons can exist only as 2-body clusters is called the channel surface. Due to the short range of nuclear forces, the channel surface encloses only a relatively small region of configuration space for the nucleons. R-matrix theory relates the wavefunction in the large region outside the channel surface (which is most accessible to experiment) to that inside the channel surface by the device of Green's functions incorporating specialized boundary conditions.

Let us add to Schroedinger's equation describing the A-nucleon system inside the channel surface a boundary-value operator $\mathcal{L}$ so that

$$(H-E+\mathcal{L})\Psi = \mathcal{L}\Psi \quad , \tag{1}$$

and Ψ has the formal solution

$$\Psi = (H+\mathcal{L}-E)^{-1}\mathcal{L}\Psi \quad . \tag{2}$$

If $\mathcal{L}$ is chosen to project onto the channel surface, then Ψ everywhere interior to the channel surface (i.e., the "internal" region) can be related to its projection on the surface through Eq. (2). Furthermore, the Green's function operator,

$$G = (H+\mathcal{L}-E)^{-1} \tag{3}$$

can be made hermitian in the internal region by the appropriate choice of $\mathcal{L}$, even though the hamiltonian H is not hermitian if Ψ evolves to positive-energy channels at the surface.[8] A choice for $\mathcal{L}$ that accomplishes both purposes is

$$\mathcal{L}_B = \sum_c |c)(c|\left(\frac{\partial}{\partial r_c} r_c - B_c\right) \quad , \tag{4}$$

with $|c) = \left(\frac{\hbar^2}{2m_c a_c}\right)^{1/2} \frac{\delta(r_c - a_c)}{a_c} Y_c(\hat{r}_c)$, the "channel surface function", defined in terms of the channel spin-angle eigenfunction of total angular momentum and parity $Y_c(\hat{r}_c)$, and B_c the real, energy-independent boundary numbers specified at the channel surface $r_c = a_c$ which generate the R-matrix theory of Wigner and Eisenbud.[9]

Taking the projection of Eq. (2) on the channel surface, and inserting the forms (3) and (4), one obtains

$$(c'|\Psi) = \sum_c (c'|G|c)(c|\frac{\partial}{\partial r_c} r_c - B_c|\Psi) \quad . \qquad (5)$$

Since Ψ is known outside and on the channel surface (i.e., the "external" region) as a superposition of Coulomb spherical waves,

$$(c|\Psi) \sim I_c(a_c) - \sum_{c'} O_{c'}(a_{c'}) U_{c'c} \quad ,$$

the constants $U_{c'c}$ in the external wavefunction can be expressed in terms of the elements of the R matrix,

$$R_{c'c} = (c'|G|c) \quad . \qquad (6)$$

In matrix form, this relation is[10]

$$U = 2i\, O^{-1} \left[I - R(L-B)\right]^{-1} RO^{-1} + IO^{-1} \quad , \qquad (7)$$

where $L_c = a_c \frac{\partial}{\partial r_c} O_c / O_c |_{r_c = a_c}$

is the logarithmic derivative of the outgoing spherical Coulomb wavefunction evaluated on the surface. The unitarity of the collision matrix U follows from the hermiticity of the R matrix. The point of expressing the collision matrix, from which the results of any scattering measurement - cross section, polarization, etc. - can be calculated, in terms of the R matrix is that R, being surface matrix elements of the internal Green's function, depends only on the properties of the internal hamiltonian H, which is dominated by nuclear forces. External Coulomb and angular momentum effects are separated out and contained in the surface functions O, I, and L. The real and imaginary parts of L = S + iP are usually called the "shift" and "penetrability" functions, respectively, while the phase of O is termed the "hard sphere" phase shift, ϕ.

Finally, if one makes a spectral expansion for G, the familiar form for the R-matrix results. Since we have chosen $\mathcal{L}_B$ to make $H + \mathcal{L}_B$ hermitian, the eigenfunctions $|\lambda)$ satisfying

$$(H+\mathcal{L}_B)|\lambda) = E_\lambda |\lambda) \qquad (8)$$

for eigenvalues E_λ form a complete orthogonal set in the internal region. Assuming the $|\lambda)$'s are normalized, we have the expansion

$$G = \sum_\lambda \frac{|\lambda)(\lambda|}{E_\lambda - E} \quad , \qquad (9)$$

from which it follows immediately that

$$R_{c'c} = (c'|G|c) = \sum_\lambda \frac{\gamma_{\lambda c'}\gamma_{\lambda c}}{E_\lambda - E} \quad , \qquad (10)$$

where $\gamma_{\lambda c} = (c|\lambda)$ is the "reduced width amplitude". The simple pole term of the R-matrix expansion (10), characterized by the parameters $\gamma_{\lambda c}$ and E_λ which depend on the channel radii a_c and boundary condition numbers B_c, can be identified with resonances of the compound A-nucleon system. However, not every pole term need be identified with a resonance in the conventional sense (i.e., one that shows a sufficiently narrow width Γ in the collision matrix to have a relatively long lifetime $\tau = h/\Gamma$). They can also be identified with shorter-lived "direct" processes, like single-particle scattering, stripping, etc., since the R-matrix formalism is not specialized to a particular reaction mechanism. Contributions from these latter processes are especially important in applications to few-nucleon systems, as those discussed in the following section.

Applications

We will describe multichannel R-matrix analyses of the 4-, 5-, 6-, and 7- nucleon systems which contain some of the basic charged-particle fusion reactions, and which illustrate a wide range of R-matrix techniques being used at Los Alamos Scientific Laboratory to analyze reactions among light nuclei. Our general approach in these analyses has been to make use of all available data for all possible 2-body reactions in each system, and to use the full multilevel, multichannel R-matrix expansion (10), approximated only by truncating the sum over levels (λ). For a given choice of channel radii a_c and boundary condition numbers B_c, the R-matrix parameters E_λ and $\gamma_{\lambda c}$ are adjusted by an automated fitting code, EDA,[11] to achieve a best fit in the least-squares sense to all the data included. The code also has the capability to treat the channel radii, as well as normalizations and energy shifts for the experimental data, as adjustable parameters.

Four Nucleons

We shall concentrate on reactions in the ^{4}He system, although the R-matrix parameters are determined in such a way that p-^{3}He (^{4}Li system) and n-T (^{4}H system) scattering are also well represented. This is done by exploiting the fact that the internal hamiltonian H, and thus the R matrix (provided the B_c are chosen correctly), exhibits an approximate symmetry of nuclear forces called charge independence, which is broken weakly by the internal Coulomb interactions.[7] One then says that the R matrix approximately conserves isospin (T), and in the case of the four-nucleon system, that the T = 1 part of the R matrix which describes reactions in the ^{4}He system is essentially the same as that which describes p-^{3}He scattering, which, in turn, is essentially the same as that which describes n-T scattering. Accounting for the differences in the T = 1 R-matrix parameters due to internal Coulomb effects by simply shifting the E_λ's[7] appears to work quite well. The T = 1 parameters for this system were actually determined by fitting most of the available p-^{3}He scattering data below 20 MeV.[12] These parameters, energy-shifted to account for the decreased Coulomb repulsion energy in ^{4}He, were used in a larger analysis of reactions among p-T, n-^{3}He, and d-d where only the energy shift and parameters for the T = 0 part of the R matrix were adjusted to fit the data. In addition, isospin conservation relates the widths in the p-T and n-^{3}He channels for both T = 0 and T = 1 levels to reduce further the number of parameters.

A summary of the data included for each reaction in the ^{4}He system analysis is given in Table I. The types of data to which the table refers generally

include cross sections (both differential and integrated) and polarizations for various spin orientations of the incoming and outgoing particles. The fits are, on the whole, good representations of the experimental measurements for all six reactions.

Table I. ^{4}He System Analysis

CHANNELS INCLUDED: p-T
n-^{3}He
d-D

Reaction	Energy Range (MeV)	No. Observ-able Types	No. Data Points
T(p,p)T	E_p=0-11	2	1317
T(p,n)^{3}He+inv.	E_p=0-11	5	722
^{3}He(n,n)^{3}He	E_n=0-10	2	127
D(d,p)T	E_d=0-10	6	695
D(d,n)^{3}He	E_d=0-10	6	542
D(d,d)D	E_d=0-10	2	705
	TOTALS:	23	4108

Until recently, however, a perplexing exception to the overall quality of the fit has been the low-energy cross sections for the two branches of the d + d reaction - precisely the data most relevant in the four-nucleon system to current fusion interests! The problem is that experimental measurements[13] show large differences in the D(d,n)^{3}He and D(d,p)T cross sections in the few-hundred keV range. The D(d,n) differential cross section has a higher zero-to ninety-degree asymmetry than does the D(d,p) differential cross section, and the integrated cross section for the neutron branch lies 15-20% higher than that for the proton branch. These differences are quite unexpected at first glance, because they occur for mirror reactions which one would expect to be more similar on the basis of charge symmetry. Even taking into account external charge differences in the exit-channel (n-^{3}He and p-T) penetrabilities, etc., would appear to give the opposite effect to that observed - ie, the enhancement of the proton branch. However, we noticed a compensating enhancement of the neutron branch in the p-wave states coming from isospin mixing in the external Coulomb field, although it was not sufficient to explain the experimentally observed differences.

Recently, following the suggestion of Sergeyev[14] that additional isospin mixing from the internal Coulomb interactions may reproduce the observed differences, we have allowed non-zero T = 1 widths in the ^{3}P states of the d-d channel (these widths are zero in the strict isospin-conservation limit). Indeed, the experimental differences are largely reproduced with mixing widths only 2% of the single-particle value which characterizes the d-d widths in the ^{3}P, T = 0 levels. This is entirely consistent with the magnitude of the matrix element one might expect from internal Coulomb mixing, indicating that perhaps anomolous differences even as large as those observed in the d + d reaction cross sections may be explained entirely by Coulomb effects.

The calculations are compared to low-energy measurements of the D(d,n) and D(d,p) cross sections in Figs. 1 and 2. Figure 1 shows the isospin-mixed D(d,n) and D(d,p) integrated cross section calculations compared with various measurements at energies below 500 keV. Figure 2 shows the effect of

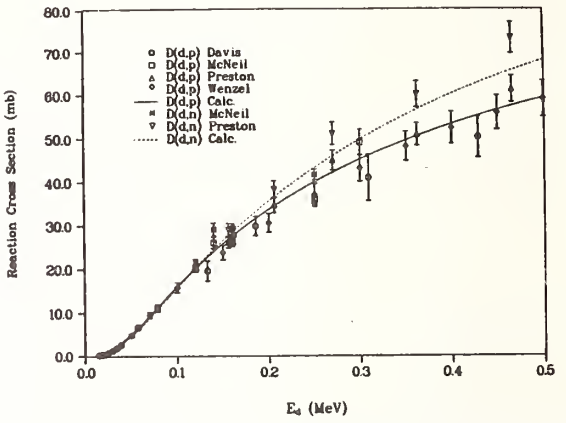

Fig. 1. R-matrix fits (solid curves) to various measurements of the D(d,n)^{3}He (upper points) and D(d,p)T (lower points) cross sections at energies below 500 keV.

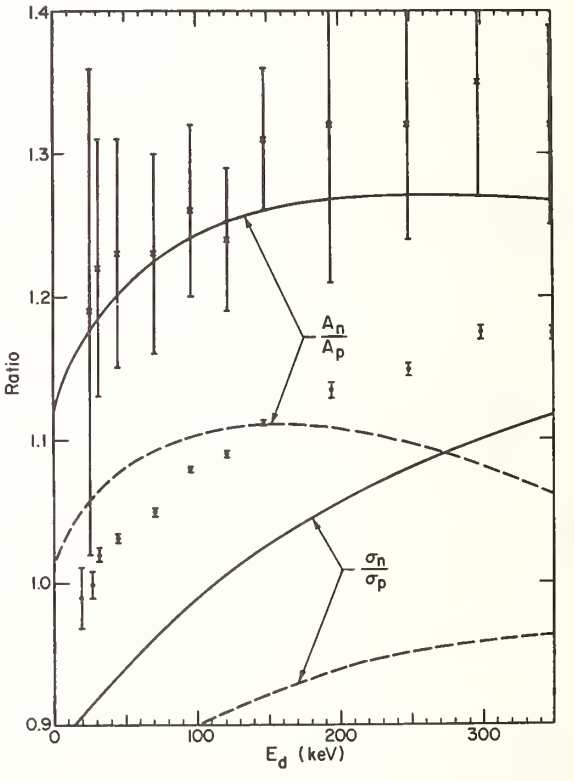

Fig. 2. Ratios of the integrated cross sections, $\frac{\sigma_n}{\sigma_p}$, and of the Asymmetries, $\frac{\sigma_n(0)}{\sigma_n(90)}\Big/\frac{\sigma_p(0)}{\sigma_p(90)}$, for the two branches of the d + d reaction. The points are measurements of Theus et al; the solid and dashed curves are R-matrix calculations with and without internal isospin mixing, respectively.

allowing internal isospin mixing in the calculations on the ratio of the integrated cross sections, and on the ratio of the differential cross section asymmetries for the two reactions. The large values of these ratios observed experimentally in the few-hundred keV region are clearly much better reproduced by including internal isospin mixing in the calculations.

The calculations including internal isospin mixing also show improved agreement with differences in the outgoing neutron and proton polarizations measured at low energies. At higher energies, where differences have been seen to persist in measurements of analyzing powers for the two reactions made with polarized deuterons,[15,16] the situation is not so clear. Some of the analyzing-power differences are improved by the mixing, while others remain unaccounted for. We plan to explore the effect of allowing internal isospin mixing in higher partial waves on these analyzing powers. In addition, we need to investigate a related consequence of internal isospin mixing that has been neglected thus far: the perturbation of the pure isospin relations between p-T and n-^{3}He widths in both the T = 0 and T = 1 levels. However, the results of the analysis at this stage show promise for being able to account sucessfully for data from all the four-nucleon reactions with a single, Coulomb-corrected, charge-independent set of R-matrix parameters.

Five Nucleons

The discussion here will concern mainly reactions in the ^{5}He system, which contains the most prominent of all low-energy fusion processes, T(d,n)^{4}He. A summary of the channels and data included in the ^{5}He analysis is given in Table II. It can be seen that an especially large variety of data types is available for the T(d,n) reaction, including cross sections, measurements for beam and target polarized separately (analyzing powers) and simultaneously (spin correlations), and measurements of outgoing neutron polarizations for both unpolarized and polarized (polarization transfer) configurations of beam and target.

Table II. ^{5}He System Analysis

CHANNELS INCLUDED: d-t
n-^{4}He
n-^{4}He*

Reaction	Energy Range (MeV)	No. Observable Types	No. Data Points
T(d,d)T	E_d=0-8	6	752
T(d,n)^{4}He	E_d=0-8	13	852
T(d,n)^{4}He*	E_d=4.8-8	1	11
^{4}He(n,n)^{4}He	E_n=0-28	2	799
	TOTALS:	22	2414

The fits to a small sample of the 2400 data points are shown for the reactions T(d,d)T, T(d,n)^{4}He, and ^{4}He(n,n)^{4}He in Figs. 3-5. Figure 3 shows cross section and polarization angular distributions for T(d,d)T in the range E_d = 1.2 to 8 MeV. Figure 4 shows fits to a selection of the T(d,n)^{4}He data at energies between 1 and 7 MeV; cross sections and polarizations for ^{4}He(n,n)^{4}He at neutron energies between 0.9 and 24 MeV are shown in Fig. 5. These are representative of the fits to all the data included in the analysis, which are generally quite good.

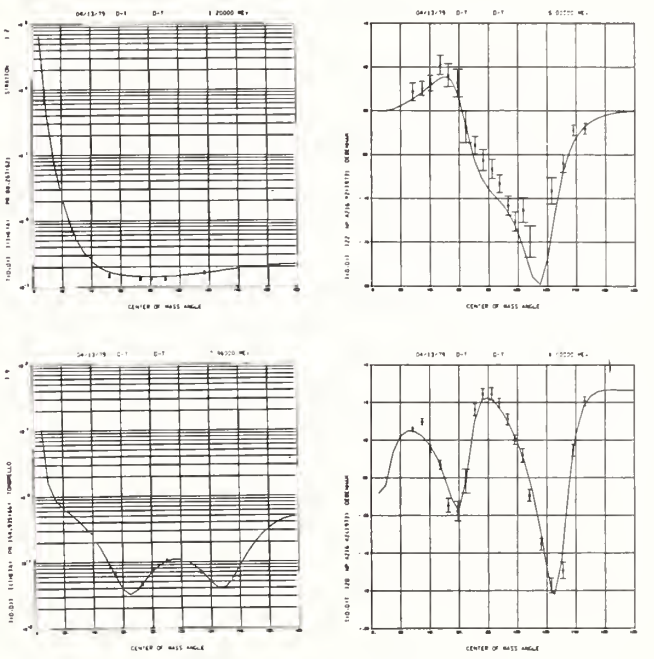

Fig. 3. Fits to T(d,d)T cross sections and analyzing powers at energies between 1.2 and 8 MeV.

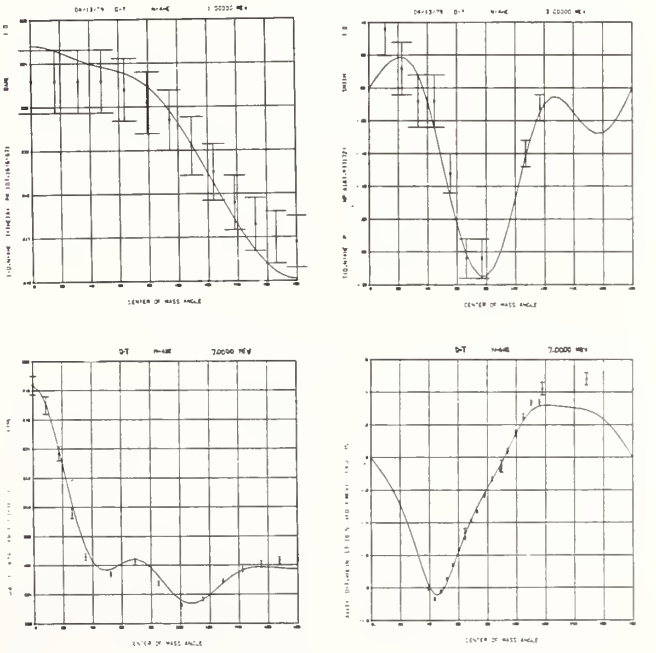

Fig. 4. Fits to T(d,n)^{4}He cross sections and polarization at energies between 1 and 7 MeV.

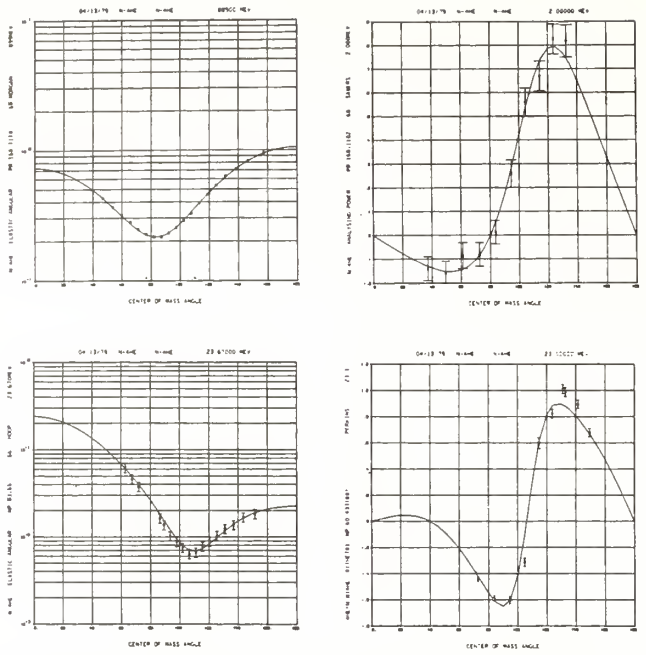

Fig. 5. Fits to $^{4}He(n,n)^{4}He$ cross sections and polarizations at energies between 0.9 and 24 MeV.

The calculated and measured observables for this system, particularly the polarizations, undergo marked changes in angular shape as a function of energy over the range of the analysis (E_x < 22 MeV), due in part to the presence of ten "resonances" at excitation energies E_x < 25 MeV in ^{5}He. Only two of these produce visible structure in the integrated T(d,n) reaction cross section shown in Fig. 6. One is the famous 110-keV resonance responsible for the large low-energy cross section which makes the T(d,n) reaction such an attractive fusion energy process, and the other is a small "bump" at E_d ~ 4.5 MeV.

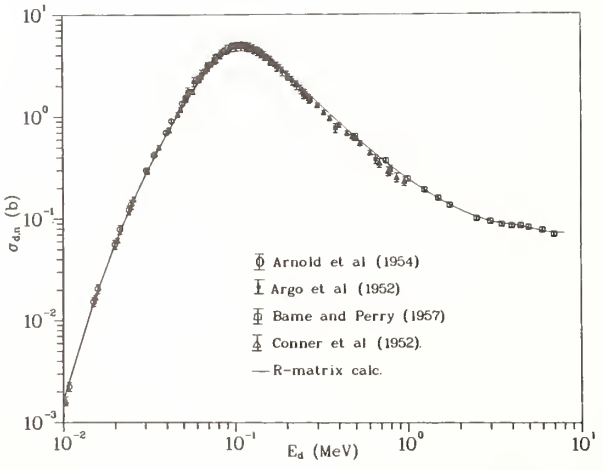

Fig. 6. R-matrix calculation (solid curve) compared to various measurements of the $T(d,n)^{4}He$ integrated cross section at energies below 8 MeV.

The effect of the 110-keV s-wave resonance on the T(d,n) cross section persists down to very low deuteron energies. This can be seen in an expanded plot of the low-energy cross sections shown in Fig. 7, in which the inverse-energy and Gamow-penetrability dependence have been removed. What remains, the so-called "astrophysical S-function", would plot as a horizontal straight line if the assumptions implied by the usual Gamow extrapolation of the low-energy cross sections were valid. In fact, the dashed line labeled "Gamow extrapolation" corresponds to the cross section values reported by Arnold et al.[17] in place of their own experimental measurements[18] ($\bar{\Phi}$) at energies below 20 keV. The R-matrix calculation clearly does not follow the Gamow dependence at low energies due to the resonance, and tends to confirm the behavior of the original measurements.[18]

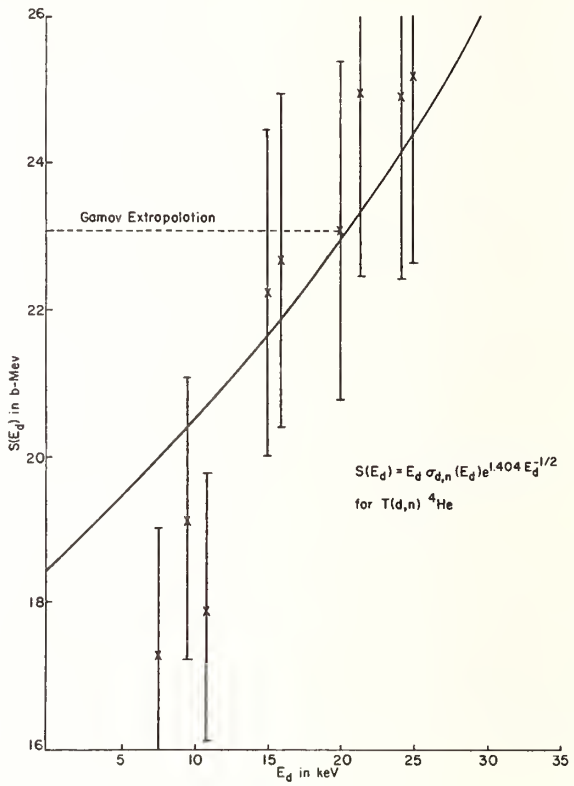

Fig. 7. Astrophysical S-function for $T(d,n)^{4}He$ as a function of laboratory energy. The solid curve is the R-matrix calculation, and the dashed line is the Gamow extrapolation reported by Arnold et al.[17] in place of their measured points[18] ($\bar{\Phi}$) at energies below 20 keV.

We are also doing a similar analysis of reactions in the ^{5}Li ($d-^{3}He$, $p-^{4}He$) system which uses an even more extensive data base. The calculated $^{3}He(d,p)^{4}He$ integrated cross section we obtain peaks at a value nearly in the middle of the broad range of measured values that have been obtained at the peak - from 700 to 900 mb. Neither of the five-nucleon analyses is yet final, since new measurements have been added recently in both cases which appear to conflict with some of the data previously being analyzed, but the essential features of the calculated reaction cross sections discussed here have not changed.

Six Nucleons: ^{6}He System

Our study of reaction in ^{6}He system is motivated by large uncertainties in the $T(t,2n)^{4}He$ cross section

at low energies, corresponding to large discrepancies among the measurements. As can be seen in Table III, very few measurements are available for reactions in this system, making this analysis an example of one of the simplest we have yet done.

Table III. ^{6}He System Analysis

CHANNELS INCLUDED: t-T
n-^{5}He (2n-^{4}He)

Reaction	Energy Range (MeV)	No. Observable Types	No. Data Points
T(t,t)T	E_t=0-2	1	27
T(t,2n)^{4}He	E_t=0-2	1	71
	TOTALS:	2	98

The fits to most of the few available t-t differential elastic scattering cross section measurements are shown in Fig. 8 at triton energies between 1.6 and 2 MeV. Although these fits are quite good, it is doubtful whether they constrain very much the fit to the T(t,2n) reaction cross sections shown in Fig. 9, particularly at low energies. Nevertheless, the R-matrix calculation shows a definite preference for the relatively recent measurements of Serov et al.[19] in the low-energy region. This remains the case even when the Serov data are removed from the fit, indicating that the low-energy behavior of the calculated cross section is actually being determined by consistency with the data at energies above 100 keV, where the measurements are in much better mutual agreement. Of course, the low-energy extrapolation of the cross section is to some extent a function of the extremely simple parameterization of the R-matrix necessitated by lack of data, but the agreement with the Serov data is an indication that this parameterization may be adequate at energies below 2 MeV. In particular, we take into account only contributions from the ^{6}He ground state, and from a level which is responsible for the slight bump in the t+t reaction cross section at energies close to 2 MeV.

Large differences between our calculated curve and some of the earlier measurements at energies below 100 keV (see Fig. 9) result in significant differences between Maxwellian reaction rates calculated from the R-matrix cross sections and those based on the earlier data. Our reaction rates become a factor of two or more lower than those of Greene[21] and of Duane[22] at temperatures below kT = 10 keV.

Seven Nucleons

Although the analysis discussed here is a charge-symmetic R-matrix analysis of all the 7-nucleon reactions, including those in both the ^{7}Li and ^{7}Be systems, we shall mention only the ^{7}Be reactions. This is because similar analyses of reactions in the ^{7}Li system have been discussed elsewhere[5,6,23] in connection with neutron standards applications, and because the ^{7}Be system contains charged-particle reactions of great interest in advanced fusion concepts.[2]

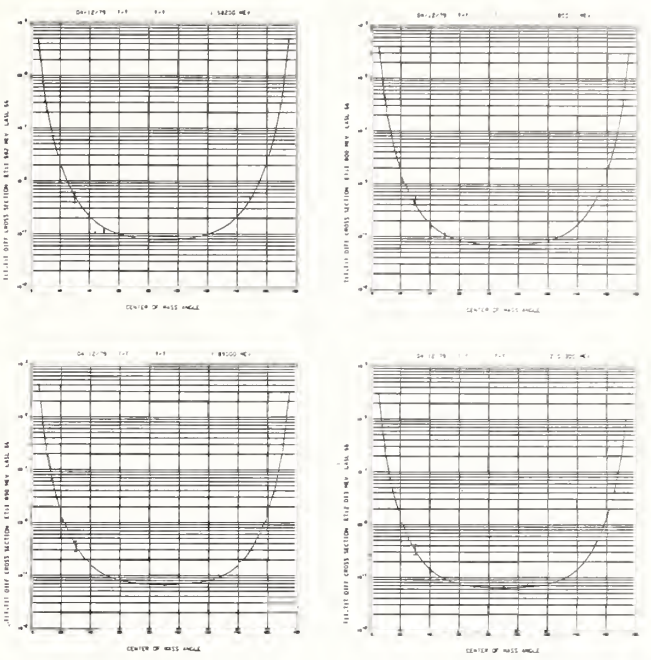

Fig. 8. Fits to T(t,t)T differental cross sections at energies between 1.6 and 2 MeV.

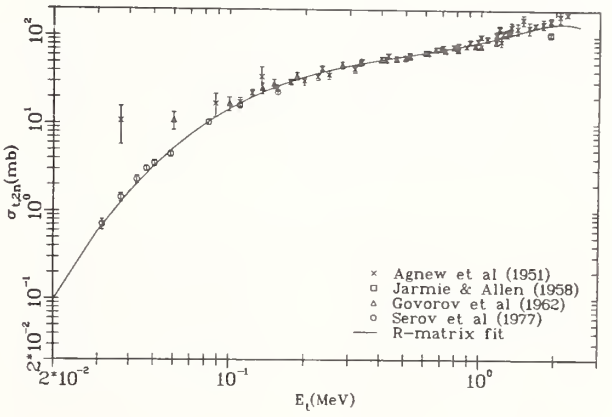

Fig. 9. R-matrix calculation (solid curve) compared with various measurements of the T(t,2n)^{4}He integrated cross section at energies below 2 MeV.

A summary of the data included for the 7-nucleon reactions is given in Table IV. Cross section and polarization measurements are available for the four reactions possible among p-^{6}Li and ^{3}He-^{4}He (^{7}Be system). The fits to some of these are shown for the three independent reactions ^{6}Li(p,p)^{6}Li, ^{6}Li(p,^{3}He)^{4}He, and ^{4}He(^{3}He,^{3}He)^{4}He in Figs. 10-12.

The problem in the ^{6}Li(p,^{3}He)^{4}He reaction, which is of greatest current interest in the ^{7}Be system, has been that the few existing differential cross section measurements have been relative, and the absolute determinations of the integrated cross section have differed by as much as 50%. In the 7-nucleon analysis we described at the Harwell conference[7] as an example of our charge-independent approach, the

Table IV. Seven-Nucleon Analysis

CHANNELS INCLUDED: p-^{6}Li n-^{6}Li ^{3}He-^{4}He t-^{4}He

Reaction	Energy Range (MeV)	No. Observ-able Types	No. Data Points
^{6}Li(p,p)^{6}Li	E_p=0-2.5	1	187
^{6}Li(p,^{3}He)^{4}He+inv.	E_p=0-2.5	3	559
^{4}He(^{3}He,^{3}He)^{4}He	$E_{^3He}$=0-11	2	1487
^{6}Li(n,n)^{6}Li	E_n=0-1.7	3	330
^{6}Li,(n,t)^{4}He	E_n=0-1.7	2	468
^{4}He,(t,t)^{4}He	E_t=0-11	2	1355
	TOTALS:	13	4386

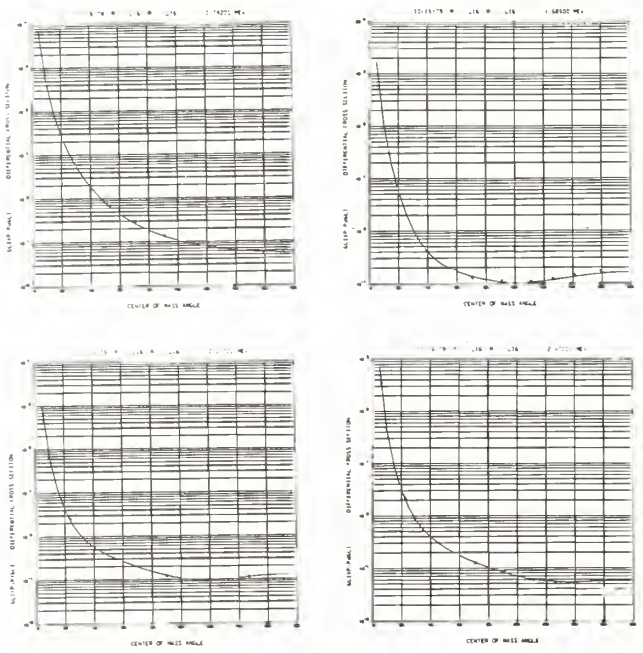

Fig. 10. Fits to ^{6}Li(p,p)^{6}Li cross sections at energies below 2.5 MeV.

experimental cross-section data included for the ^{6}Li(p,^{3}He) reaction required extensive renormalization in almost every case. We have therefore been uncertain about the reliability of the scale of our calculated cross sections, which presumably was determined by data for other reactions in the analysis.

Recently, new absolute measurements of ^{6}Li(p,^{3}He)^{4}He differential cross sections at proton energies between 0.14 and 3 MeV have been made by Elwyn et al.[22] at Argonne National Laboratory. A comparison of their integrated cross sections with our predictions[7] is shown in Fig. 13. It can be seen that the agreement of the calculations with the new measurements is excellent, both in shape and magnitude.

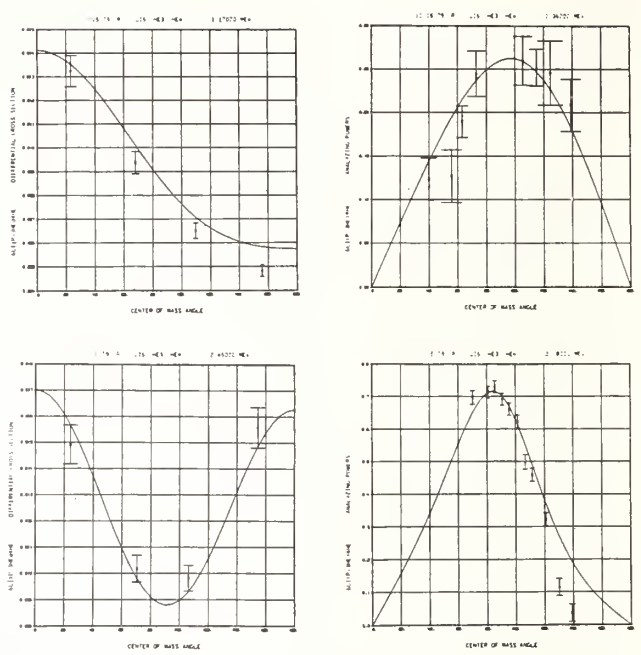

Fig. 11. Fits to ^{6}Li(p,^{3}He)^{4}He cross sections and polarizations at energies below 2.5 MeV.

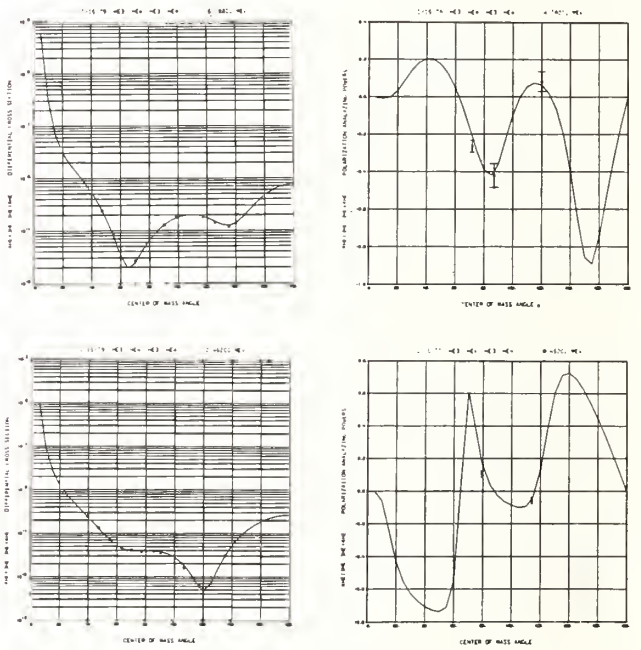

Fig. 12. Fits to ^{4}He(^{3}He,^{3}He)^{4}He Cross sections and polarizations at energies below 10 MeV.

The agreement of the calculated angular distributions with the new data[22] is generally poorer, especially at energies above 2 MeV, indicating that somewhat different interferences among the partial-wave amplitudes are required (possibly even those involving p-^{6}Li d-waves, which have been neglected thus far in the calculations) which do not affect the integrated cross sections.

This comparison indicates that the other 7-nucleon data in the analysis, through unitary and charge-

conjugate relationships, correctly determine the scale of the $^{6}Li(p,^{3}He)$ reaction cross section, much as other ^{7}Li data had constrained values of the $^{6}Li(n,t)$ cross section in the analysis[23] used for the ENDF/B-V ^{6}Li evaluation at low energies.

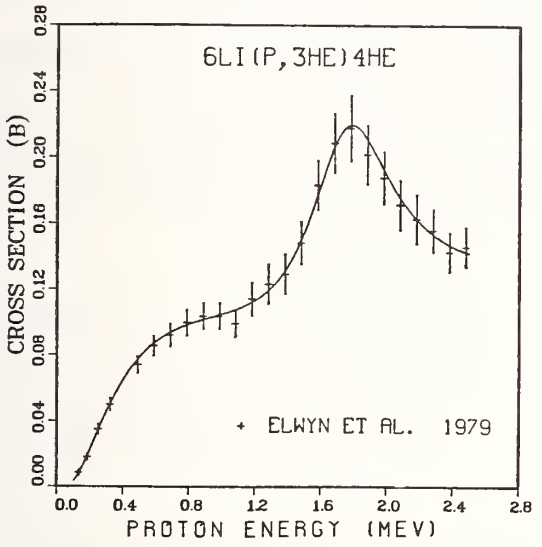

Fig. 13. Predictions from the charge-symmetric 7-nucleon analysis[7] compared with recent measurements of Elwyn et al.[22] for the $^{6}Li(p,^{3}He)^{4}He$ integrated cross section.

Conclusions

As the examples described in the previous section suggest, a great deal of information is available from these multireaction R-matrix analyses, having been determined in most cases by a large and varied collection of experimental input. Clearly, the R-matrix parameters provide detailed information about the spectroscopy of light systems, and even information about the macroscopic properties of nuclear forces. Of more direct concern to the subject of this conference, however, are the smooth (as functions of both energy and angle) charged-particle cross sections which result from them.

The dominance of Coulomb effects in charged-particle cross sections at low energies is modified by nuclear resonances in many cases of interest in fusion applications. This is most apparent for the T(d,n) reaction, but is true to some degree for all the reactions discussed. R-matrix theory provides a framework for fitting and extrapolating these cross sections in which both the long-range effects, like penetration of the Coulomb-angular momentum barrier, and the short-range (nuclear) effects arise in a simple and physically meaningful way. Moreover, the interaction of these effects in the theory leads in general to a different energy dependence for the low-energy cross sections than that obtained from the representations of fusion cross sections commonly used.[24] There are indications from the T(d,n) and T(t,2n) examples that the R-matrix dependence is more nearly correct, but a firm conclusion requires more and better-quality measurements in the low-energy region, such as those forthcoming from the fusion cross-section measurement program at Los Alamos.[3]

At higher energies, the reactions appear to be dominated by broad, overlapping structures, few of which appear as definite bumps in the integrated cross sections. These structures can be associated with definite R-matrix levels, however, with the help of angular distribution measurements, particularly those for polarization observables. Attempting to use all the available experimental data in these analyses also has obvious statistical advantages, especially in cases where direct measurements of the cross sections are conflicting or incomplete. In those cases, the other data included, even for different reactions, can help dictate more correct values for cross sections, as illustrated by the $p+^{6}Li$ example.

We feel that such R-matrix analyses, making maximal use of the available experimental data while imposing some minimal information about nuclear forces, constitute the best technique currently at hand for evaluating light-element cross sections. One obtains from these analyses unified cross-section sets, in which the elastic scattering and reaction cross section for a given system are calculated from the same R-matrix parameters. We therefore suggest that compilers of evaluated charged-particle cross sections make use of these calculations, where available, rather than rely on methods having less physical content and experimental input.

Acknowledgments

K. Witte, who developed and maintains the EDA code, has been our collaborator on several of these analyses. Likewise, S. D. Baker and E. K. Biegert collaborated with us on analyses of the 7-nucleon reactions.

References

1. C. R. Head, "Nuclear Data Requirements of the Magnetic Fusion Power Program of the United States of America," presented at IAEA Advisory Group Meeting on Nuclear Data for Fusion Reactor Technology, Vienna, Austria (1978).

2. R. W. Conn, Bull. Am. Phys. Soc. 24, 869 (1979).

3. N. Jarmie, Bull. Am. Phys. Soc. 24, 883 (1979).

4. D. C. Dodder et al., "Models Based on Multichannel R-Matrix Theory," JAERI-M 5984, p. 1 (1975).

5. G. M. Hale, "R-Matrix Analysis of the Light Element Standards," NBS Special Publication 425, p. 302 (1975).

6. G. M. Hale, "R-Matrix Methods for Light Systems," IAEA-90, Vol. II, p. 1 (1976).

7. D. C. Dodder and G. M. Hale, "Applications of Approximate Isospin Conservation in R-Matrix Analyses," in Neutron Physics and Nuclear Data (Harwell), p. 490 (1978).

8. A. M. Lane and D. Robson, Phys. Rev. 151, 774 (1966).

9. E. P. Wigner and L. Eisenbud, Phys. Rev. 72, 29 (1947).

10. A. M. Lane and R. G. Thomas, Rev. Mod. Phys. 30, 257 (1958).

11. D. C. Dodder, K. Witte, and G. M. Hale, "EDA, an Energy Dependent Analysis Code for Nuclear Reactions," (unpublished).

12. G. M. Hale, J. Devaney, D. C. Dodder, and K. Witte, Bull. Am. Phys. Soc. 19, 506 (1974).

13. See, for instance, R. B. Theus, W. I. McGary, and L. A. Beach, Nucl. Phys. 80, 273 (1966).

14. V. A. Sergeyev, Phys. Lett. 38B, 286 (1972).

15. V. König et al., "Investigation of Charge Symmetry Violation in the Mirror Reactions $^{2}H(d,p)^{3}H$ and $^{2}H(d,n)^{3}He$," submitted to Nucl. Phys. (1979).

16. T. R. Donoghue, Ohio State University, personal communication (1979).

17. W. R. Arnold et al., Phys. Rev. 93, 483 (1954).

18. W. R. Arnold et al., "Absolute Cross Section for the Reaction $T(d,n)He^{4}$ from 10 to 120 keV," LA-1479 (1953).

19. V. I. Serov, S. N. Abramovich, and L. A. Morkin, At. Eng. 42, 59 (1977).

20. S. L. Greene, "Maxwell Averaged Cross Sections for Some Thermonuclear Reactions on Light Isotopes," UCRL-70522 (1967).

21. B. H. Duane, "Fusion Cross Section Theory," BNWL-1685, p. 75 (1972).

22. A. J. Elwyn et al., "Cross Sections for the $^{6}Li(p,^{3}He)^{4}He$ Reaction at Energies Between 0.1 and 3.0 MeV," submitted to Phys. Rev. C (1979).

23. G. M. Hale, "R-Matrix Analysis of the ^{7}Li System," NBS Special Publication 493, p. 30 (1977).

24. In these representations, Coulomb effects are not explicit in the S-function. The simplest example is the Gamow extrapolation (S constant). Other examples are Ref. 20, Ref. 21, and A. Peres, J. Appl. Phys. 50, 5569 (1979).

EVALUATED DATA COLLECTIONS FROM ENSDF*

W. B. Ewbank
Nuclear Data Project
Oak Ridge National Laboratory, Oak Ridge, Tennessee 37830, USA

For several years the Nuclear Data Project has been maintaining an Evaluated Nuclear Structure Data File (ENSDF), which is designed to include critically evaluated values for most nuclear spectroscopic quantities. The information in ENSDF is the same as in the *Nuclear Data Sheets*, which illustrates two particular output formats (drawings and tables). Spectroscopic information for nuclei with $A < 45$ is put into ENSDF from the evaluations of Ajzenberg-Selove and of Endt and van der Leun. An international network has been organized to provide regular revisions of the data file. Computer facilities have been developed to retrieve collections of evaluated data for special calculations or detailed examination.

[Evaluation, nuclear structure data, ENSDF, nuclear levels, radioactivity, nuclear reactions, reaction gamma rays.]

INTRODUCTION

Since 1948, the Nuclear Data Project (NDP) has been a recognized center for the systematic collection and evaluation of data from nuclear structure experiments. The Data Project has helped consolidate the rapid advance of nuclear science by identifying and publicizing conflicting results and by integrating each new measurement with those that preceded it. The organization of nuclear data for publication in *Nuclear Data Sheets*[1] has also led to the development of a natural structure for containing these data.

In 1971 NDP designed a formal structure for entering nuclear structure data into computer files.[2] This structure has been used since then to prepare, maintain, and edit a comprehensive file of Evaluated Nuclear Structure Data (ENSDF), which is used for production of drawings and tables for *Nuclear Data Sheets*.

These computer files of nuclear data are also being used as a means of making the results of basic research quickly and easily available to a broader audience. Radioactivity information, in particular, has wide application in fields such as nuclear medicine, reactor engineering, environmental impact assessment, and nuclear waste management. Often the specialists in these areas have neither the time nor the training to make effective use of the data generated by basic nuclear research. The NDP has made important progress toward providing a channel through which the results of new nuclear measurements can be transferred to any engineer or scientist who needs evaluated data to factor into his or her own work.

The value of a scientific data base is determined largely by four properties, each of which represents a compromise between what would be ideal and what is easily attainable. Ideally, the data base should be:

1. Comprehensive – All related quantities (measurable or derived from "reliable" theory) should be included, together with estimates of their uncertainties.
2. Complete – All available data of each type should be included.
3. Up-to-Date – The consequences of each reliable new measurement should appear quickly throughout the data collection.
4. Accessible – Data should be obtainable from the file according to user-defined needs and should be presentable in a user-defined format.

STATUS AND UPDATING OF ENSDF

ENSDF Current Contents

The Evaluated Nuclear Structure Data File now contains 6800 distinct sets of evaluated nuclear information. This includes:

1930	sets of adopted level properties
1850	decay schemes
3020	nuclear reaction data collections, including
230	(n,γ) reactions
225	(d,p) reactions
500	(charged-particle, $xn\gamma$) reactions

A set of adopted levels and their properties is now included for every nucleus. For nuclei with $A < 45$, ENSDF is based on the evaluations of Ajzenberg-Selove[3] and of Endt and van der Leun.[4]

Several complete collections of level properties have been assembled from ENSDF; e.g., all levels with lifetimes between 1 ps and 1 fs; odd-parity states in even nuclei. A collection of levels with spontaneous fission branching has recently been published.[5]

Most decay scheme information in ENSDF is now as complete as the measurements warrant, usually based on the most recent *Nuclear Data Sheets*. Normalization information is included wherever available, and details of electron capture and internal conversion have been added systematically, so that complete tables of atomic and nuclear radiations can be assembled for approximately 1500 decay schemes.

Regular Revision of the ENSDF Data Base

The ENSDF computer format has been adopted[6] as an international standard for the systematic storage and exchange of nuclear data. At six-month intervals, since 1977, NDP has prepared complete copies of ENSDF on magnetic tape for distribution through the (U.S.) National Nuclear Data Center at Brookhaven National Laboratory. This tape defines the current version of an International File of Evaluated Nuclear Structure and Decay Data.

At the 1977 meeting of the IAEA Advisory Group on Nuclear Structure and Decay Data[6] in Oak Ridge, the responsibility for periodic reevaluation of each mass chain was given to

*Research sponsored by the Division of Basic Energy Sciences, U.S. Department of Energy, under contract W-7405-eng-26 with Union Carbide Corporation.

a specific evaluation center. Evaluation responsibilities were allocated with the intent of reaching and maintaining a four-year cycle. That is, every mass chain would be considered for revision at least every four years.

At present, the mechanism for updating ENSDF is by means of a complete revision of *Nuclear Data Sheets* for an entire mass chain. For older mass chains, where the evaluations were prepared by the Nuclear Data Project, the systematic addition of internal conversion coefficients, average beta energies, and detailed electron-capture ratios was recently completed for several hundred decay schemes. Newer decay data have been incorporated into ENSDF for 380 decay schemes included in the data collections of Kocher[7] and Martin.[8] In general, however, a collection of data extracted from ENSDF will be only as up-to-date as the most recent *Nuclear Data Sheets*.

There may be little justification for more frequent review of all new nuclear measurements. For some groups of radionuclides (e.g., those isotopes used in medicine) or perhaps for specific data items (such as the ^{239}Pu half-life), a more frequent consideration of newer data could be desirable. Evaluations of particular kinds of data are sometimes prepared by special working groups, and there should also be a means of including these in the ENSDF system.

A file of supporting data for ENSDF (called the "working file") has been established to include measurements or evaluations that appear between regular revisions of the data base. Data sets for the working file are prepared in standard ENSDF format and can be processed with the same analysis or publication programs. The working file can provide alternatives or supplements to the International File of evaluated data as documented in *Nuclear Data Sheets*.

Procedures for incorporating important new information into the International File between the regular cycles are being developed by the evaluation network. Documentation of differences between the International File and the published *Nuclear Data Sheets* is especially important. The evaluator or evaluation center which is responsible for the affected mass chain must also accept any changes before ENSDF can be modified. The more frequent evaluation of those data which are especially important or rapidly changing would increase the quality and usefulness of the data base.

USABLE OUTPUT FROM ENSDF

The NDSLIST Program

The standard output format from ENSDF is the same as the input. This format is convenient for making revisions or as input for a succeeding program. A number of data analysis programs have also been developed to operate on standard data sets: to identify and mark inconsistent data, to perform systematic theoretical calculations, or to reformat the data for easier use by a research worker.

Choosing a useful format for presenting the data retrieved from a data file is often as difficult as defining the retrieval. The potential user will often have special requirements (or prejudices?) about how the data should be organized and displayed. Unless the user's preferences are considered, the transfer of information from a data file to the user is seriously inhibited. He will often choose to reorganize the data again by hand, even though the recopying will surely introduce errors.

A general table-formatting program (NDSLIST) has been developed to accept standard ENSDF data sets and to prepare the separate tables of information which are needed to produce the journal *Nuclear Data Sheets*. The program will automatically separate each data set into groups of each kind of record contained in the data set. Each group of records is arranged according to increasing values of one or more data items on each record, and all accompanying information (including comments) is attached to the record in its proper place.

Although NDSLIST normally processes one data set at a time, this is not an essential restriction. A merge capability disables the isotope checking so that information from many data sets can be merged into a single table. The merge feature was used to prepare the table of SF-isomers[5] mentioned previously.

Linking of the merge facility with the ENSDF data-retrieval package makes it possible to select and display carefully tailored blocks of nuclear data. Tables of alpha and gamma radiations were prepared[9] for a recent IAEA Symposium on Transactinide Nuclear Data. The tables were limited to decay of nuclei with $A > 207$ and $T_{1/2} > 1$ s. Only radiations with an absolute intensity greater than one percent were included, and the tables were prepared in order of increasing α- or γ-ray energy, as well as by parent nucleus.

The MEDLIST Program

If a user is interested in the total physical or biological consequences of radioactive decay, it is necessary to include atomic as well as nuclear radiations. A nuclear transition can cause vacancies in the electron shells. The refilling of the electron shells is accompanied by emission of characteristic X-rays and Auger electrons. A second program (MEDLIST) has been developed to combine the basic nuclear data from ENSDF with tables of X-ray and Auger yield to prepare complete lists of radiations emitted by each radionuclide. The γ-ray intensity normalization, the page layout, and the bookkeeping (intensity of omitted weak radiations, etc.) are all performed automatically. Radiations are grouped by type: X-rays included with nuclear γ-rays; Auger lines listed with conversion-electron lines. Several special collections of radioactivity data[7,8,10] have been prepared by MEDLIST.

The MEDLIST program also prepares a computer-readable file of card images, which can be more easily used to make further calculations with the radiation data. This file of atomic and nuclear data radiations has been used[11,12] in reactor and accelerator calculations.

A third summary output from MEDLIST lists the energy emitted as each radiation type and compares the sum with the available energy; i.e., the decay Q-value. Besides giving a gross survey of radiations, the table of energy sums also indicates how completely each decay scheme has been characterized. If the sum of radiated energy is substantially larger or smaller than the branching-adjusted Q-value, then further measurements are probably needed to provide better or more complete information.

A MEDLIST survey of 1500 radioactivity data sets from ENSDF has recently been completed.[13]

SUMMARY

1. An Evaluated Nuclear Structure Data File (ENSDF) has been designed to contain most of the data of nuclear structure physics.

2. ENSDF includes adopted level information for all 1930 known nuclei. Detailed data are available for ~1500 decay schemes.

3. An international network of data evaluation centers has been organized to provide for a four-year cycle of ENSDF revisions.

4. Standard retrieval and display programs can prepare various tables of specific data which can serve as a good first approximation to a complete up-to-date compilation.

REFERENCES

1. *Nuclear Data Sheets*, published by Academic Press. Subscription information available on request to Academic Press, Inc., 111 Fifth Avenue, New York, NY 10003.

2. W. B. Ewbank and M. R. Schmorak, *Evaluated Nuclear Structure Data File — A Manual for Preparation of Data Sets,* ORNL-5054/R1 (February 1978).

3. F. Ajzenberg-Selove, *Nuclear Physics* [e.g., A300, 1 (1978)].

4. P. M. Endt and C. van der Leun, *Nuclear Physics* A310, 1 (1978).

5. W. B. Ewbank, Y. A. Ellis, and M. R. Schmorak, *Nucl. Data Sheets* 26, 1 (1979).

6. *IAEA Advisory Group Meeting on Nuclear Structure and Decay Data, Summary Report,* INDC(NDS)-92/LN (March 1978).

7. D. C. Kocher, *Nuclear Decay Data for Radionuclides Occurring in Routine Releases from Nuclear Fuel Cycle Facilities,* ORNL/NUREG/TM-102 (August 1977).

8. M. J. Martin, Ed., *Nuclear Decay Data for Selected Radionuclides,* Appendix A in NCRP Report No. 58 (November 1978)

9. W. B. Ewbank, in *Proceedings, IAEA Advisory Group Meeting on Transactinium Isotope Nuclear Data* (Cadarache, France, May 1979), to be published.

10. M. J. Martin, *Nuclear Decay Data for Selected Radionuclides,* ORNL-5114 (March 1976).

11. A. G. Croff, R. L. Haese, and N. B. Gove, *Updated Decay and Photon Libraries for the ORIGEN Code,* ORNL/TM-6055 (February 1979).

12. R. G. Alsmiller, T. A. Gabriel, and J. Barish, *Photon Dose Rate from Induced Activity in the Beam Stop of a 400-GeV Proton Accelerator,* ORNL/TM-6238 (February 1978).

13. W. B. Ewbank, Ed., *Atomic and Nuclear Radiations from ENSDF/MEDLIST,* ORNL-5535, to be published.

EVALUATIONS OF FISSION PRODUCT CAPTURE CROSS SECTIONS FOR ENDF/B-V

R. E. Schenter, D. L. Johnson,
F. M. Mann, and F. Schmittroth

Hanford Engineering Development Laboratory

H. Gruppelaar

RCN, Petten, The Netherlands

Capture cross section evaluations have been made for the 36 most important fission product absorbers in a fast reactor system. These evaluations were obtained using a generalized least-squares approach with calculations being performed with the computer code FERRET. These results will provide the major revisions to the ENDF/B-IV Fission Product Cross Section File which will be released as part of ENDF/B-V. Input for the cross section adjustment calculations included both integral and differential experimental data results. The differential cross sections and their uncertainties were obtained from the CSIRS library. Integral measurement results came from CFRMF and STEK Assemblies 500, 1000, 2000, 3000, 4000. Comparisons of these evaluations with recent capture measurements will be presented.

[Capture cross sections; Fast Reactors]

Introduction

There has been extensive activity world-wide, recently, in evaluating fission product capture cross sections, important for fast reactor application. Nuclear data laboratories in Australia, France, Italy, the Netherlands, Japan, the United Kingdom, the U.S.S.R., and the United States have been especially productive in the past few years. Absorption and other effects by fission product nuclei will become increasingly important as fast reactors come on line and begin to operate. Consequently, accurate and complete capture data evaluations will be required. To this end, the ENDF/B-IV fission product cross section file has been updated to produce the ENDF/B-V file, using important new evaluation techniques and recent experimental results from both integral and differential measurements.

In this paper, we present the results of these re-evaluations where use was made of a generalized least squares adjustment procedure[1] to obtain a nominal cross section curve and uncertainty information in the form of a covariance matrix which linked energy points. This procedure involves calculations which use the finite element representation of the FERRET[2] data adjustment code.

Results

Typical results of these evaluations are shown in Figures 1-14, where the "adjusted" curves will be used for ENDF/B-V. Also shown is the data used as input to the FERRET code. This includes both differential and integral data and their uncertainties. Also inputted to the calculation was an "a priori" description which combined multi-group average cross sections obtained from resonance parameters for the resolved resonance region with "smooth" average cross section from ENDF/B-IV for the higher energy region. The resonance parameters used were from ENDF/B-IV or BNL-325[3] as indicated. The histogram or multi-group cross section description in the resonance region is required for the FERRET least squares calculation because following the exact resonance structure takes too many points for the standard computer calculations, especially for the covariance matrix part.

The integral data came from reaction rate measurements in STEK Assemblies 500, 1000, 3000, 4000[4] and CFRMF[5]. ENDF/B-IV evaluations also used earlier CFRMF measurements which helped normalize nuclear models calculations made with the Hauser-Feshbach computer code NCAP[6].

Figure 1 shows results for the important absorber Sm149. As can be seen from the curves, significant changes occur in going from ENDF/B-IV to ENDF/B-V. The ENDF/B-IV result was made with nuclear model calculations where no previous experimental data existed in 1973. Also shown in Figure 1 are "adjusted" cross sections using the FERRET code, comparing various results when only integral data is used or differential data is used. For the Sm149 case, the results are consistent with each other. For some of the other cases shown in Figures 5 - 14, this does not necessarily occur.

Error estimates are outputted from the FERRET code and Figure 2 shows fractional uncertainty versus energy for the Sm149 case, where the final uncertainty changes from about 60% to 10% (1σ) in going from ENDF/B-IV to ENDF/B-V. Figure 4 shows the case of the adjusted curve using STEK measurement compared to recent integral results at EBR-II adjusted by Anderl, et al,[7] for Sm147. The full energy region (1eV-10MeV) evaluation is shown in Figure 5 for Mo97. Comparisons to recent differential measurements by Macklin etal,[8] is shown in Figures 6-10 for Ru101, Ru102, Ru104, Pd104, and Pd108. Finally, results for four of the top ten fission product absorbers (Tc99, Rh103, Ag109, and Cs133) are given in Figures 11-14.

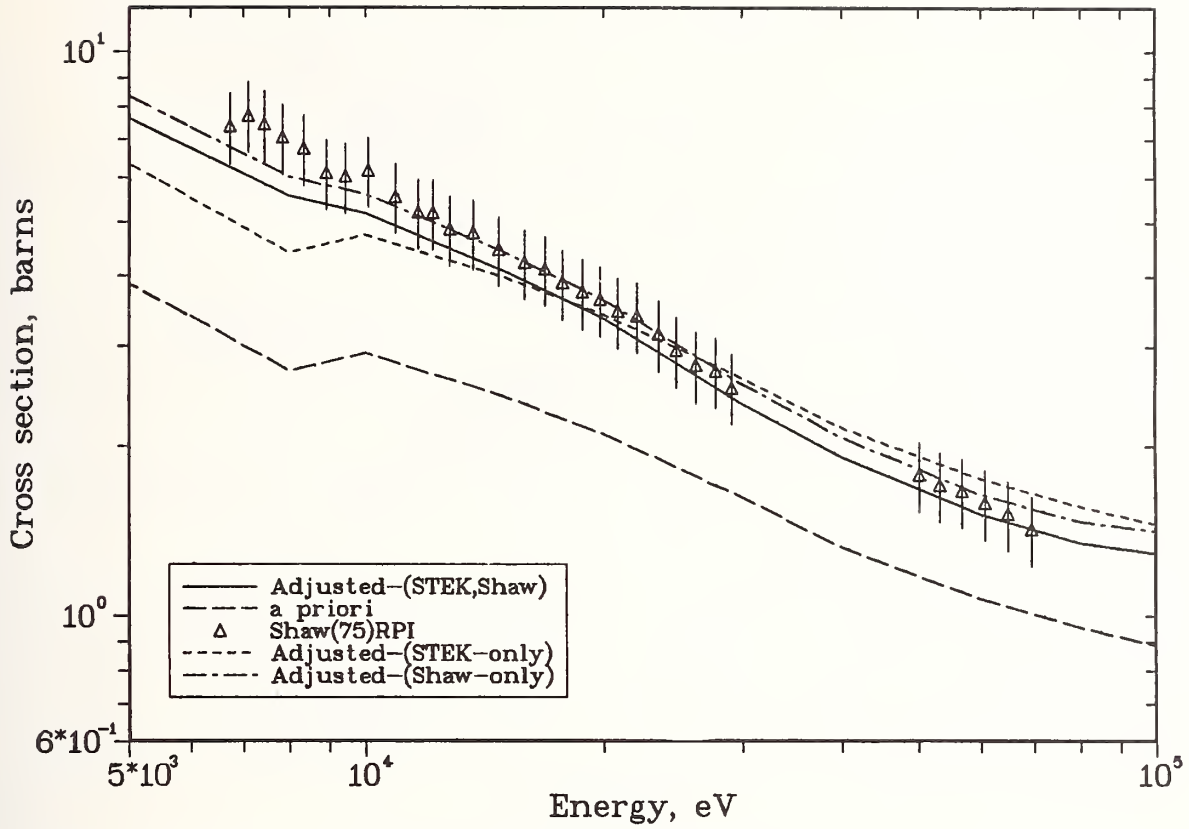

Fig. 1. Sm149 capture cross section evaluations and differential data.

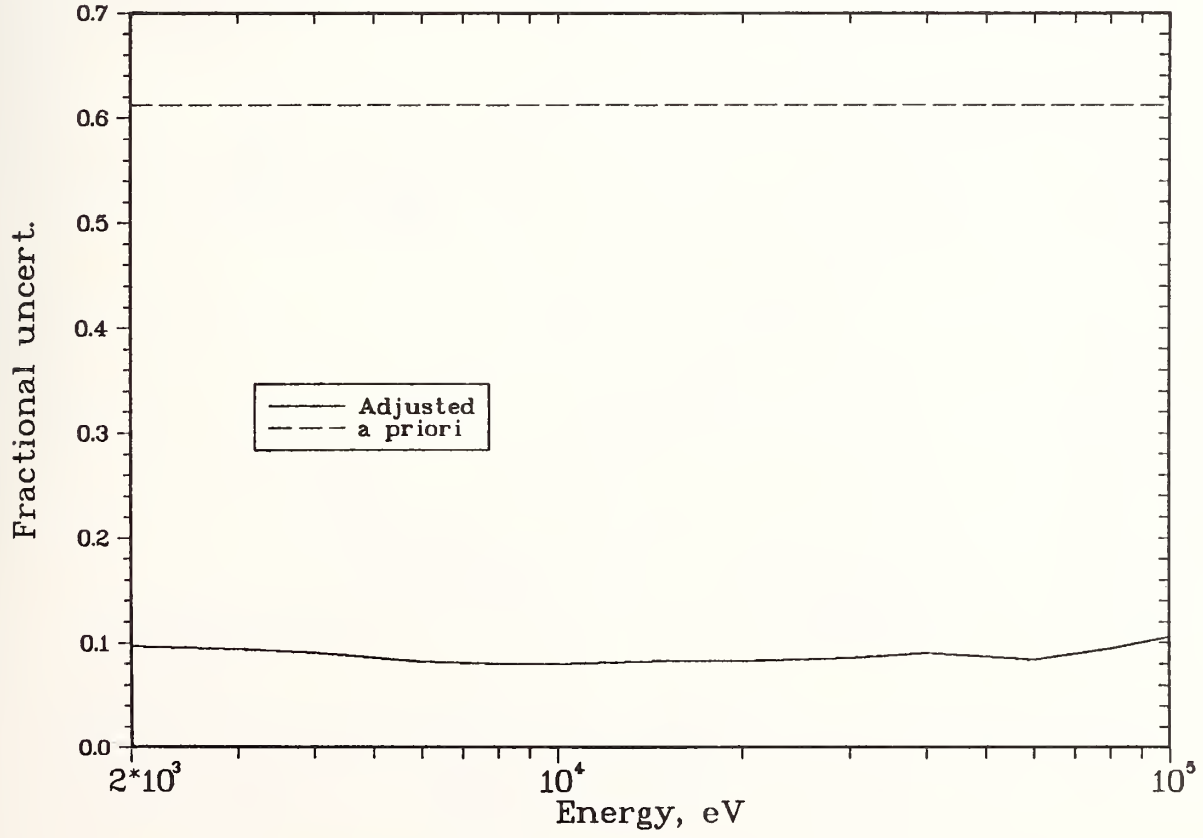

Fig. 2. Sm149 fractional uncertainty evaluations.

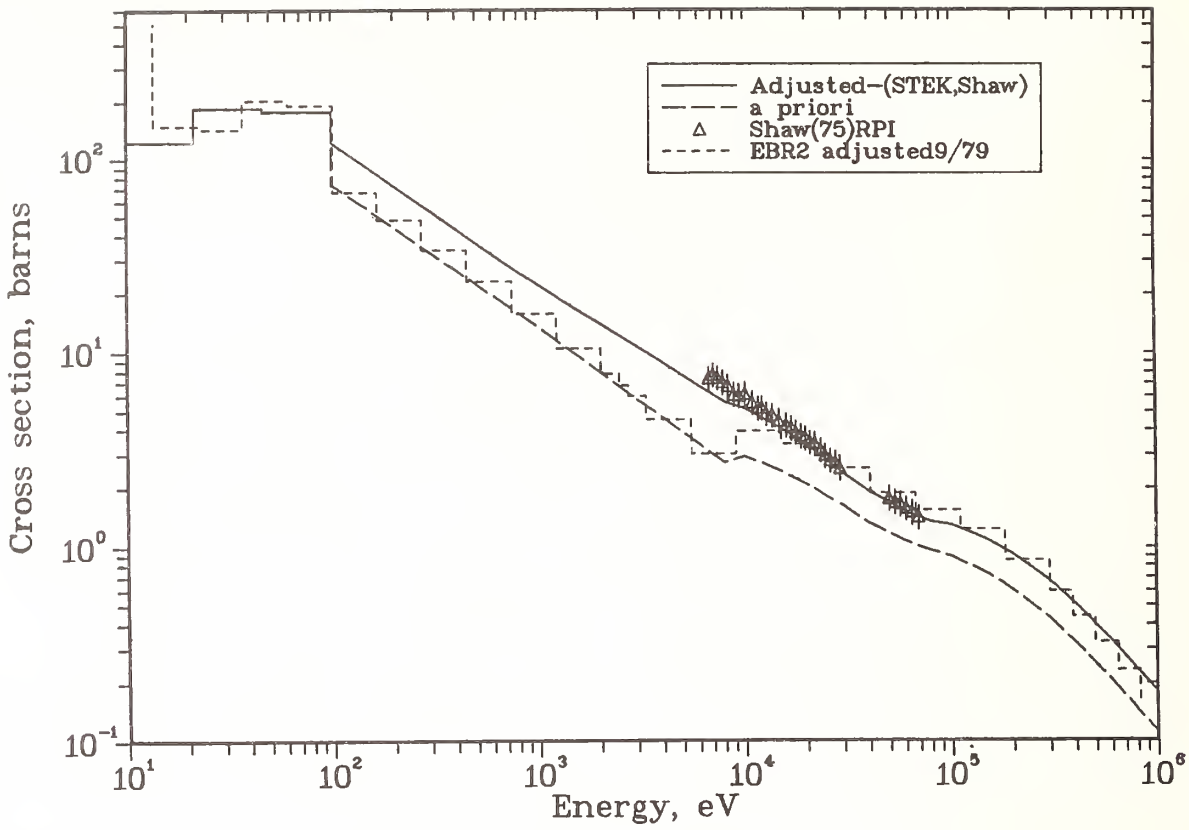

Fig. 3. Sm149 capture cross section evaluation comparison to EBR-II results.

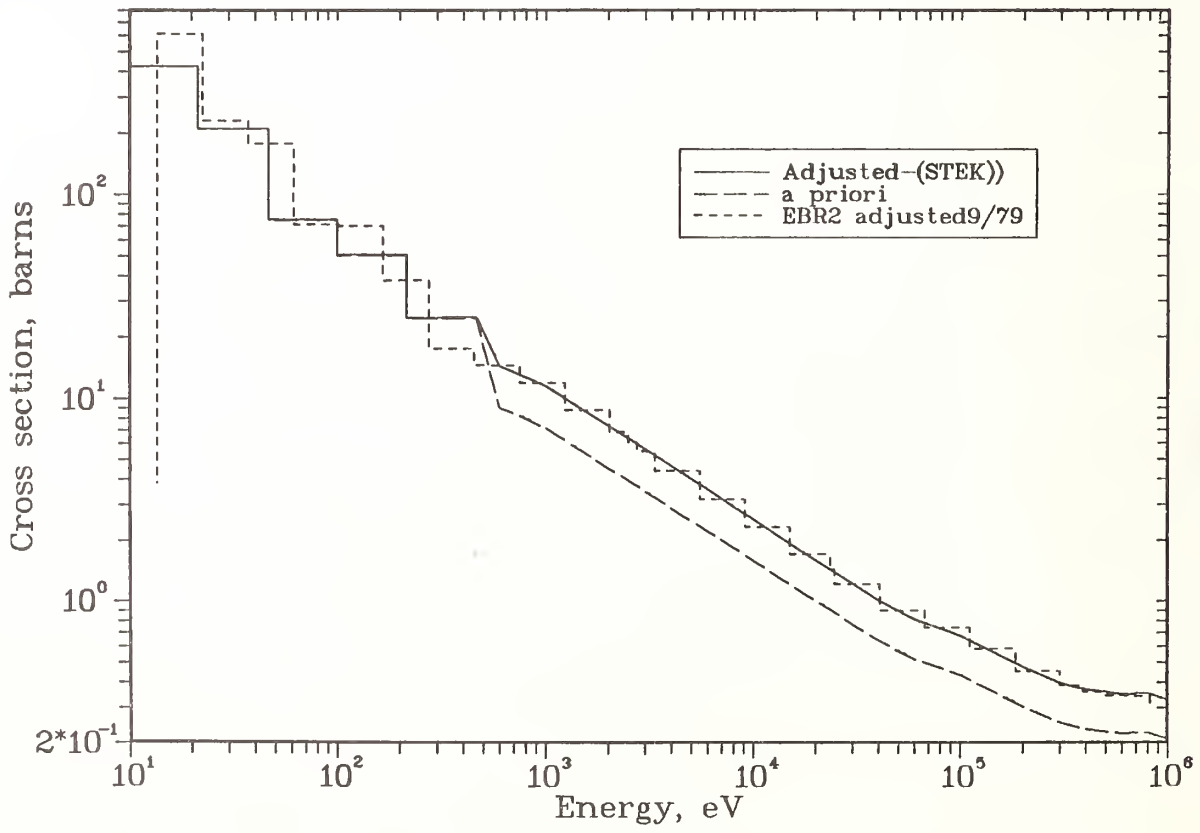

Fig. 4. Sm147 capture cross section evaluation comparison to EBR-II results.

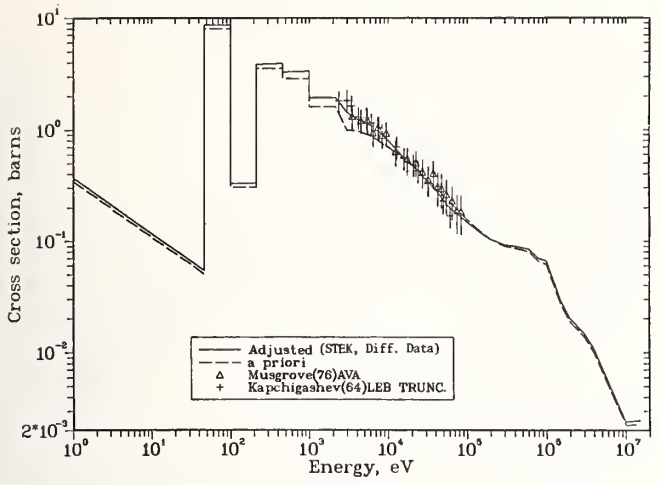

Fig. 5. Mo97 capture cross section evaluations and differential data.

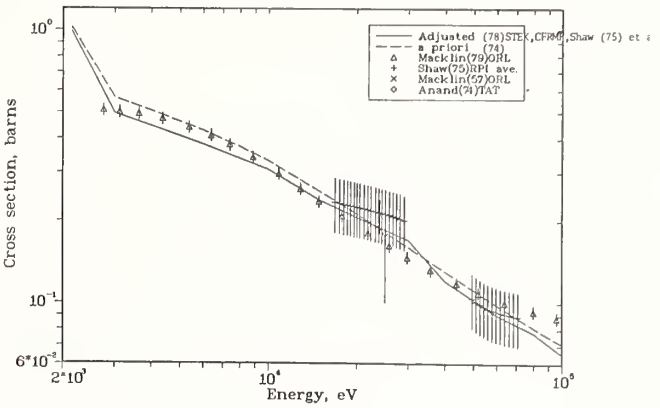

Fig. 8. Ru104 capture cross section evaluations and differential data.

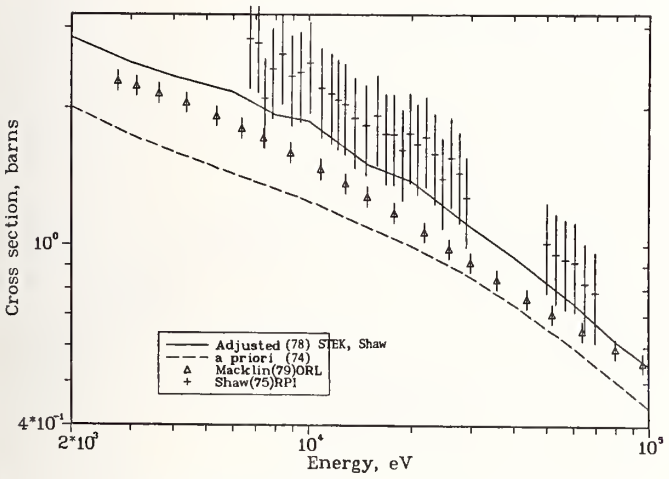

Fig. 6. Ru101 capture cross section evaluations and differential data.

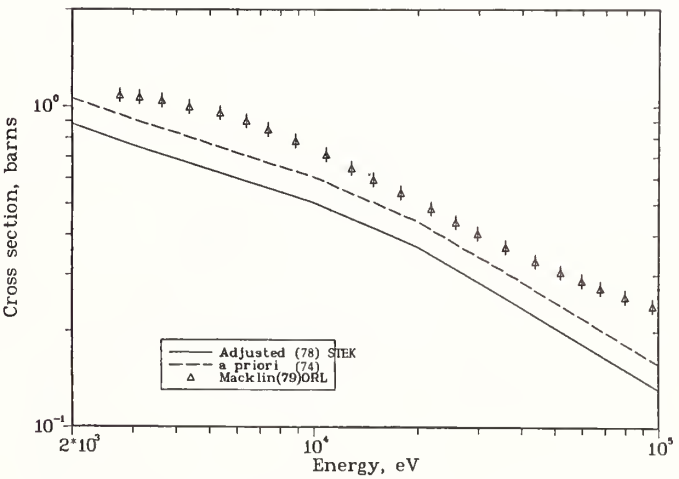

Fig. 9. Pd104 capture cross section evaluations and differential data.

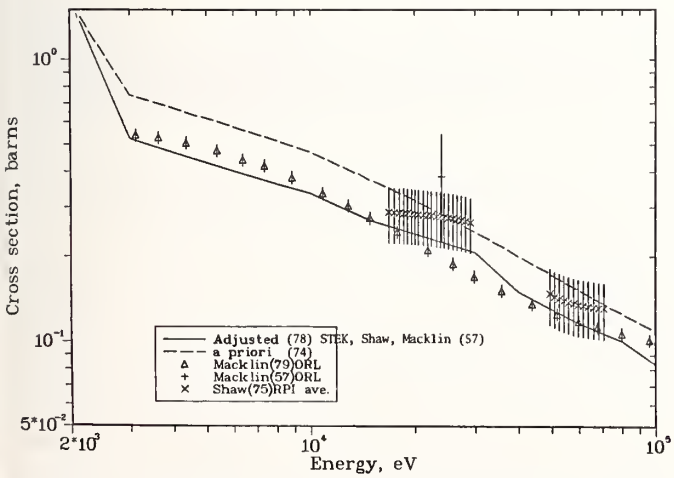

Fig. 7. Ru102 capture cross section evaluations and differential data.

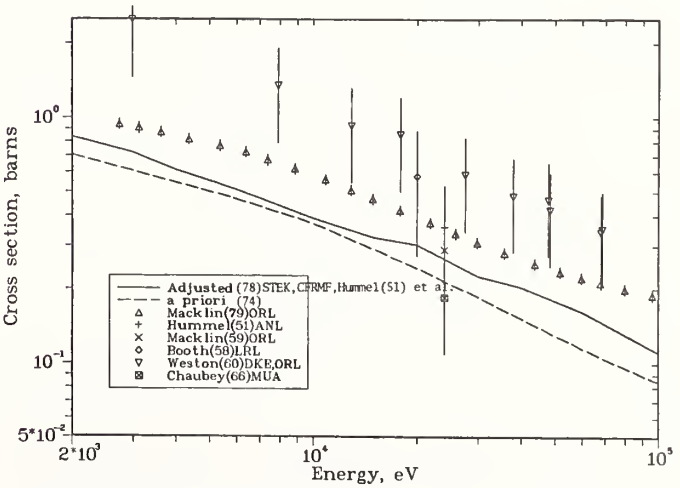

Fig. 10. Pd108 capture cross section evaluations and differential data.

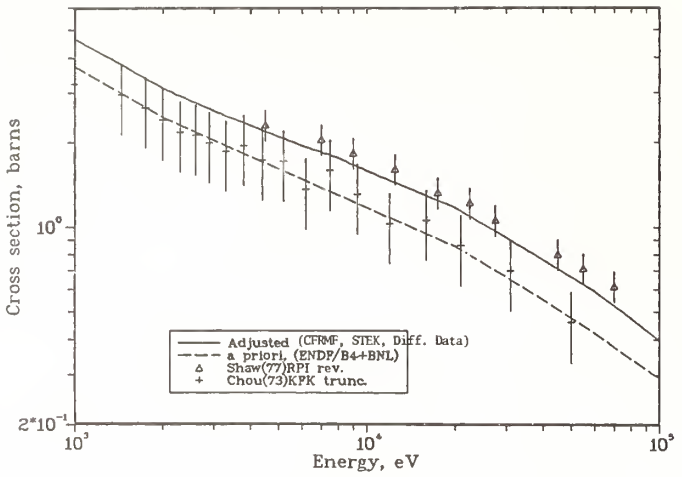

Fig. 11. Tc99 capture cross section evaluations and differential data.

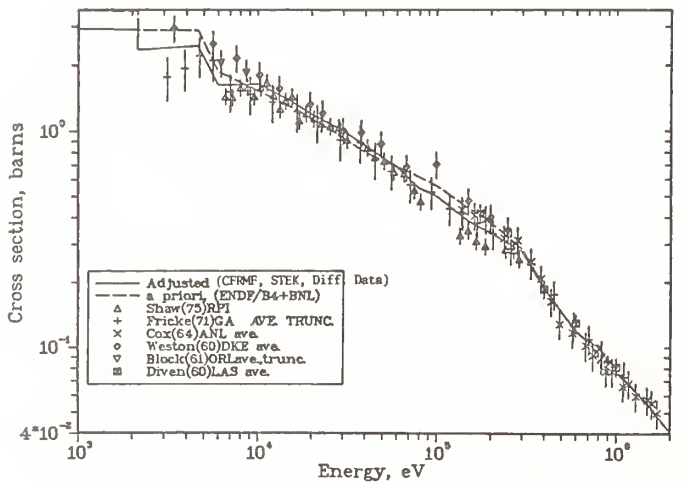

Fig. 12. Rh103 capture cross section evaluations and differential data.

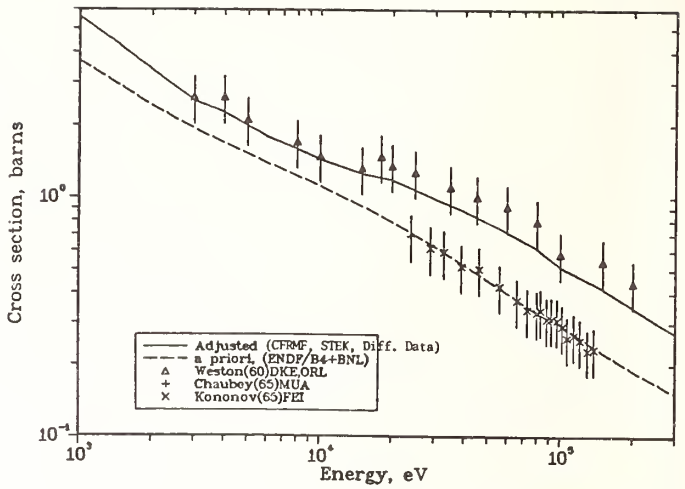

Fig. 13. Ag109 capture cross section evaluations and differential data.

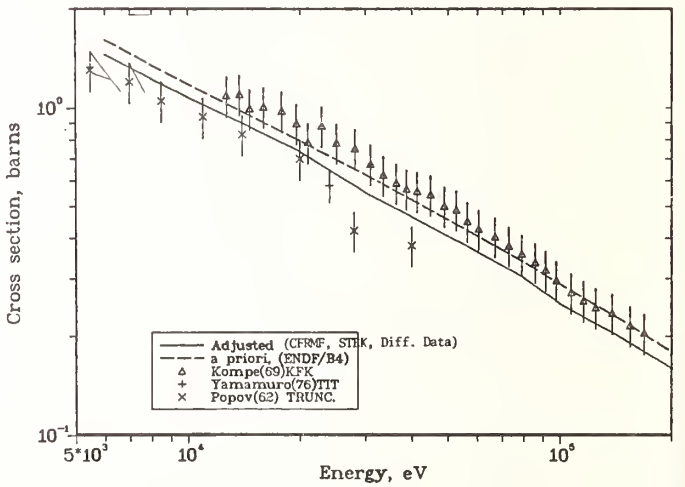

Fig. 14. Cs133 capture cross section evaluations and differential data.

References

1. F. Schmittroth, "Generalized Least-Squares for Data Analysis," HEDL-TME 77-51 (March 1978)

2. F. Schmittroth, "FERRET Data Analysis Code", HEDL-TME 79-40, (Sept. 1979).

3. S.F. Mughabghab and D.I. Garber, "Neutron Cross Sections, Vol. I., Resonance Parameters", BNL 325, June 1973.

4. J.W.M. Dekker, ECN-14, February 1977.

5. Y.D. Harker, et al., EGG Report 1977, Kiamesha Lake Talk, 1972.

6. F. Schmittroth, "Theoretical Calculations of Fast Neutron Capture Cross Sections," HEDL-TME 71-106, (August 1971).

7. R.A. Anderl, et al., "Neodymium, Samarium and Europium Capture Cross Section Adjustments Based on EBR-II Integral Measurements," this conference.

8. R.L. Macklin, et al., "100, 101, 102, ^{104}Ru(n,γ) and ^{103}Rh(n,γ) Cross Sections above 2.6 KeV," to be published.

BETA AND GAMMA DECAY HEAT EVALUATION FOR THE THERMAL FISSION OF ^{235}U

G. K. Schenter and F. Schmittroth
Hanford Engineering Development Laboratory
Richland, Washington 99352, USA

Beta and gamma fission product decay heat curves are evaluated for the thermal fission of ^{235}U. Experimental data that include beta, gamma, and total measurements are combined with summation calculations based on ENDF/B in a consistent evaluation. Least-squares methods are used that take proper account of data uncertainties and correlations.

[^{235}U, fission-products, decay heat, evaluation]

Introduction

There has been an increased interest in fission-product decay heat in recent years, in part because of its importance in loss-of-coolant-accidents (LOCA). Although the need in LOCA is for the total decay heat, there are several reasons for studying the beta and gamma components separately. First, many experimental measurements include only one component or the other. Also, many reactor applications actually depend on the separate components. The individual components also provide a much more severe test of the nuclear data libraries such as ENDF/B that are used in summation calculations to compute decay heat. The present study is devoted to an updated evaluation of the total decay heat and its beta and gamma components for the thermal fission of ^{235}U. A generalized least-squares approach is used that can properly account for important uncertainties and correlations in the data. Although numerous reviews and comparisons of decay heat experiments have been made [see Ref. (1) for a thorough and up-to-date review of decay heat], very few have attempted an objective evaluation that properly weights the various data. And except for a recent evaluation of the total,[2] detailed covariance information has not been included.

Method

Least-squares model equation

In principle, the method is quite simple. One casts the problem into a least-squares format and solves the resulting problem. Techniques[3,4] to keep the problem to a manageable size considerably complicate the situation but are not discussed in depth here. As a first step, we expand the time-multiplied beta decay-heat function $tf_\beta(t)$ in a sum of finite element basis functions $\{\Delta_i(u)\}$:

$$tf_\beta(t) = \sum_i X_{\beta i}\Delta_i(u) \qquad (1)$$

where $u = \ln(t)$, and t denotes cooling time. These basis functions are trivially defined by first establishing a mesh of points $\{t_i\}$ on the cooling-time axis. The i-th basis function is then defined as a triangle of unit height whose vertex is at $u_i = \ln(t_i)$ and whose legs terminate at $u_{i-1} = \ln(t_{i-1})$ and $u_{i+1} = \ln(t_{i+1})$. This representation is discussed in detail elsewhere in this conference and is equivalent to representing $tf_\beta(t)$ as a piecewise linear and continuous function relative to $u = \ln(t)$. The number and spacing of the points $\{t_i\}$ can be chosen to ensure an adequate representation of $f_\beta(t)$. Clearly, Eq. (1) can also be used to represent the gamma decay heat $f_\gamma(t)$ where one replaces the expansion coefficients by $\{X_{\gamma i}\}$.

In Eq. (1), $f(t)$ represents the decay heat from a fission pulse [$f(t)$ could denote beta, gamma, or total decay heat]. If a measurement $f_{m\alpha}$ of $f(t)$ at a time t_α is made, we have

$$f_{m\alpha} = \sum_i A^P_{\alpha i} X_i , \qquad (2)$$

where

$$A^P_{\alpha i} = t_\alpha^{-1}\Delta_i(t_\alpha) . \qquad (3)$$

For a complete set of measurements $\{f_{m\alpha}\}$, Eq. (2) has the standard least-squares form whereby one uses the measurements $\{f_{m\alpha}\}$ to find the least-squares parameters $\{X_i\}$ that define $f(t)$.

Most decay heat measurements are integral measurements such as

$$F(t,T) = \int_t^{t+T} f(t)\,dt \qquad (4)$$

for a finite irradiation time T. Assume that one has a set of integral measurements $\{F_{m\alpha} = F(t_\alpha, T_\alpha)\}$ measured for the respective times $\{(t_\alpha, T_\alpha)\}$. Substitution of Eq. (1) into Eq. (4) yields

$$F_{m\alpha} = \sum_i A^f_{\alpha i} X_i , \qquad (5)$$

where

$$A^f_{\alpha i} = \int_t^{t+T} t'^{-1}\Delta_i[\ln(t')]\,dt' . \qquad (6)$$

Once the set of matrix elements $\{A^f_{\alpha i}\}$ are calculated, Eq. (5) is simply another least-squares model equation, and integral data can be included along with the pulse data in Eq. (2). Other types of integral measurements are treated similarly.

The present evaluation includes total measurements along with beta and gamma measurements. We do

this by defining a single parameter vector $\vec{X}$ that is the union of the beta and gamma parameter vectors:

$$\vec{X} = (\vec{X}_\beta, \vec{X}_\gamma) = (X_{\beta 1}, X_{\beta 2}, \ldots, X_{\gamma 1}, \ldots). \quad (7)$$

In this combined space, all decay heat measurements whether integral or pulse or whether total, beta, or gamma can be included in a single equation of the form

$$\vec{F}_m = A\vec{X}. \quad (8)$$

One simply computes the appropriate A-matrix. The dimensionality of $\vec{X}$ is 2N where N is the number of mesh points used to separately represent $f_\beta(t)$ and $f_\gamma(t)$. In our case N = 54. The measurement vector $\vec{F}_m$ includes all measured data points for all data used plus values obtained from summation calculations. Its dimensionality is several hundred.

Least-squares solution

The least-squares algorithm is defined by the minimization of

$$S_r^2 = (\vec{F}_m - A\vec{X})M_f^{-1}(\vec{F}_m - A\vec{X}) + (\vec{X}-\vec{X}_o)^t M_{xo}^{-1}(\vec{X}-\vec{X}_o). \quad (9)$$

The first term is the usual least-squares form whereby one seeks the least-squares solution $A\vec{X}$ that best represents the data $\vec{F}_m$. The data covariance matrix M_f gives a proper weighting to the data and includes both uncertainties and correlations. The second term allows the specification of prior information for the parameter vector $\vec{X}$. It could represent the results from other experiments or calculations; however, here the only significant prior information that is used is that the decay heat curves must be smooth. This smoothness is assured by assigning prior values $\{X_{oi}\}$ that follow a smooth curve and that are very strongly correlated. Very large uncertainties are specified so that the magnitude of these values does not influence the results.

Covariance parameterization

In order to simplify the construction of the data covariance matrices, the following parameterization was used

$$\frac{(M_f)_{ij}}{F_{mi}\,F_{mj}} = C^2 + r_i r_j \rho_{ij} \quad (10)$$

where

$$\rho_{ij} = \delta_{ij}(1-\theta) + \theta \exp\left[-\frac{\ln^2(E_i/E_j)}{\ln^2(\gamma)}\right] \quad (11)$$

Each parameter has a simple physical interpretation. A fractional normalization uncertainty (complete correlation) is given by C. Any additional uncertainty at the i-th data point is given by r_i. The uncertainties r_i are associated with a short-range correlation where θ gives the strength and γ specifies the range of the correlation.

Data

A brief summary of the data used in the evaluation is given in Table I. The total normalization uncertainty C in column 9 is not quite as indicated. Several experiments included multiple irradiations. In these cases, part of the uncertainty in C was taken as correlated over all values and part was taken as correlated only for data points belonging to a particular irradiation.

The use of calculated values based on ENDF/B and which appear as four separate entries in Table I needs to be clarified. The only case in which realistic uncertainties were assigned to the calculated values is for the total decay heat. In the remaining cases, the sole purpose of the ENDF/B based values was to provide a smoothing constraint as discussed above. The need for three additional calculations is beyond the scope of the present discussion. Constraining calculated values with small uncertainties were not included as separate beta and gamma components because it was felt that only the total calculation was reliable enough to be treated as "measured" data.

Results

The results of the least-squares analysis are given in Table II for cooling times up to 10^6 s. The final uncertainties are calculated in the least-squares analysis and reflect a propagation of the data uncertainties and correlations given in Table I. These uncertainties therefore do not reflect any undetected systematic errors in the input data. However simple statistical checks were made, and in some cases, quoted experimental uncertainties were increased to ensure that the data were not statistically inconsistent. All uncertainties are quoted at one standard deviation (1σ).

The series of graphs in Figs. 1, 2, and 3 show the fractional deviation of the values in the input data from the nominal least-squares values. Note that these comparisons are not for unfolded or otherwise transformed data. For each plot, the comparison is with nominal least-squares values that are calculated for the specific irradiation times peculiar to each data set.

To illustrate the utility of these evaluations, we compare beta and gamma curves calculated from ENDF/B-IV for a pulse irradiation with the evaluated values. Fig. 4 shows that the ENDF/B-IV values show significant deviations that indicate inadequate nuclear data.

In conclusion we wish to note that the present evaluation is in reasonable agreement with the results of a recent evaluation of the total decay heat in support of a new ANS standard. Deviations average about 1% for the pulse curve and are substantially less for longer irradiations.

TABLE 1

Reference	Lab	Date	Type	Form	Irradiation Times (sec)	Cooling Time Range (sec)	# Pts	C Total %	Average R %	Θ	γ
			BETA DECAY HEAT								
Dickens, et al.[5]	ORNL	'77	Scintillator	F	1,10,100	1.7-9950	43	3.	3.6	.5	2.
Friesenhahn, et al.[6]	IRT	'76	Nuclear Calorimeter	F	864000	1.05-15490	80	5.	2.5	.5	2.
Alam and Scobie [7]	SURRC	'74	Scintillator	F	10,100	.3-26.2	62	6.	5.0	.5	2.
Tsoulfarides, et al.[8]	U of Ill.	'70	Scintillator	F	28800	15-11100	6	7.	7.2	.5	2.
McNair, et al.[9]	AWRE	'68	Scintillator	F	10,100000	$1.-5x10^5$	28	10.	4.4	.5	2.
MacMahon, et al.[10]	SURRC	'70	Scintillator	F	10,10000	$5.-10^6$	37	20.	5.5	.5	2.
ENDF/B-IV [11]	-	-	Calculation	tf(t)	BURST	$1-10^6$	53	20.	46.	1.	8*
			GAMMA DECAY HEAT								
Dickens, et al.[5]	ORNL	'77	Scintillator	F	1,10,100	1.7-9950	43	3.	2.4	.5	2.
Friesenhahn, et al.[6]	IRT	'76	Nuclear Calorimeter	F	864000	1.05-15490	80	5.	1.5	.5	2.
Jurney, et al.[12]	LASL	'79	Scintillator	F	20000	4.-148300	12	2.	4.0	.5	2.
Johansson & Nilsson[13]	STUDSVIK	'77	Scintillator	F	4,10,120	10.7-1515	27	6.	3.0	.5	2.
Bunny & Sam[14]	USNRDL	'69	Scintillator	f	∿0	905-259240	9	25.	16.6	.5	2.
Fisher & Engle[15]	LASL	'64	Scintillator	f	∿0	1.5-40.	4	25.	16.6	.5	2.
ENDF/B-IV[11]	-	-	Calculation	tf(t)	BURST	$1-10^6$	53	20.	46.	1.	8*
			TOTAL DECAY HEAT								
Yarnell & Bendt[16]	LASL	'77	Calorimeter	F	20000	10-1005500	76	1.	1.3	.5	2.
Lott, et al.[17]	F-a-R	'73	Calorimeter	F	100,1000,5000	$70-7x10^5$	39	3.5	3.5	.5	2.
ENOF/B-IV[11]	-	-	Calculation	F	20000	$1-10^6$	37	0.	4.2	.8	10.
ENOF/B-IV[11]	-	-	Calculation	tf(t)	BURST	$1-10^6$	53	20.	46.	1.	8*

* a priori

TABLE 2

Cooling Time t (sec.)	$tf_\beta(t)$ (MeV/fission)	Fractional Uncertainty	$tf_\gamma(t)$ (MeV/fission)	Fractional Uncertainty
.100+001	.44722	.073	.35926	.084
.150+001	.54283	.053	.42699	.062
.200+001	.61610	.040	.47516	.046
.300+001	.71229	.032	.53566	.034
.400+001	.77159	.028	.56960	.029
.500+001	.81030	.026	.59191	.026
.650+001	.84161	.025	.61465	.025
.800+001	.85202	.023	.62682	.024
.100+002	.84887	.022	.64371	.020
.150+002	.83813	.021	.67708	.021
.200+002	.79903	.020	.69817	.018
.300+002	.74110	.020	.71880	.017
.450+002	.68662	.019	.73352	.016
.600+002	.64452	.020	.72509	.015
.800+002	.60592	.019	.71633	.015
.100+003	.57366	.019	.69709	.016
.150+003	.52436	.019	.64196	.017
.200+003	.49357	.018	.60044	.018
.300+003	.45981	.018	.53578	.018
.400+003	.44756	.018	.50335	.017
.500+003	.44598	.018	.48813	.017
.650+003	.44902	.018	.48282	.018
.800+003	.45174	.018	.48357	.017
.100+004	.45250	.018	.48433	.016
.150+004	.44101	.018	.50365	.016
.200+004	.42116	.018	.50847	.015
.275+004	.38372	.018	.49850	.016
.350+004	.34983	.018	.47743	.015
.500+004	.30228	.019	.43976	.015
.700+004	.26893	.020	.39476	.015
.850+004	.25498	.020	.36533	.015
.100+005	.24680	.020	.33919	.016
.140+005	.23565	.020	.28365	.017
.170+005	.23219	.019	.25094	.017
.200+005	.23013	.019	.22517	.017
.250+005	.22627	.018	.19688	.018
.325+005	.21963	.018	.17373	.017
.400+005	.21053	.018	.16084	.018
.500+005	.19568	.019	.15052	.018
.600+005	.17997	.019	.14332	.018
.700+005	.16542	.019	.13862	.019
.850+005	.14668	.019	.13212	.018
.100+006	.13200	.020	.12733	.019
.140+006	.10576	.022	.11542	.021
.170+006	.09267	.025	.10942	.022
.200+006	.08298	.028	.10508	.024
.250+006	.07214	.031	.10015	.026
.325+006	.06369	.034	.09721	.027
.400+006	.05999	.038	.09693	.029
.500+006	.05832	.044	.09781	.032
.650+006	.05819	.056	.09941	.038
.800+006	.05887	.073	.10023	.047
.100+007	.05979	.096	.09974	.060

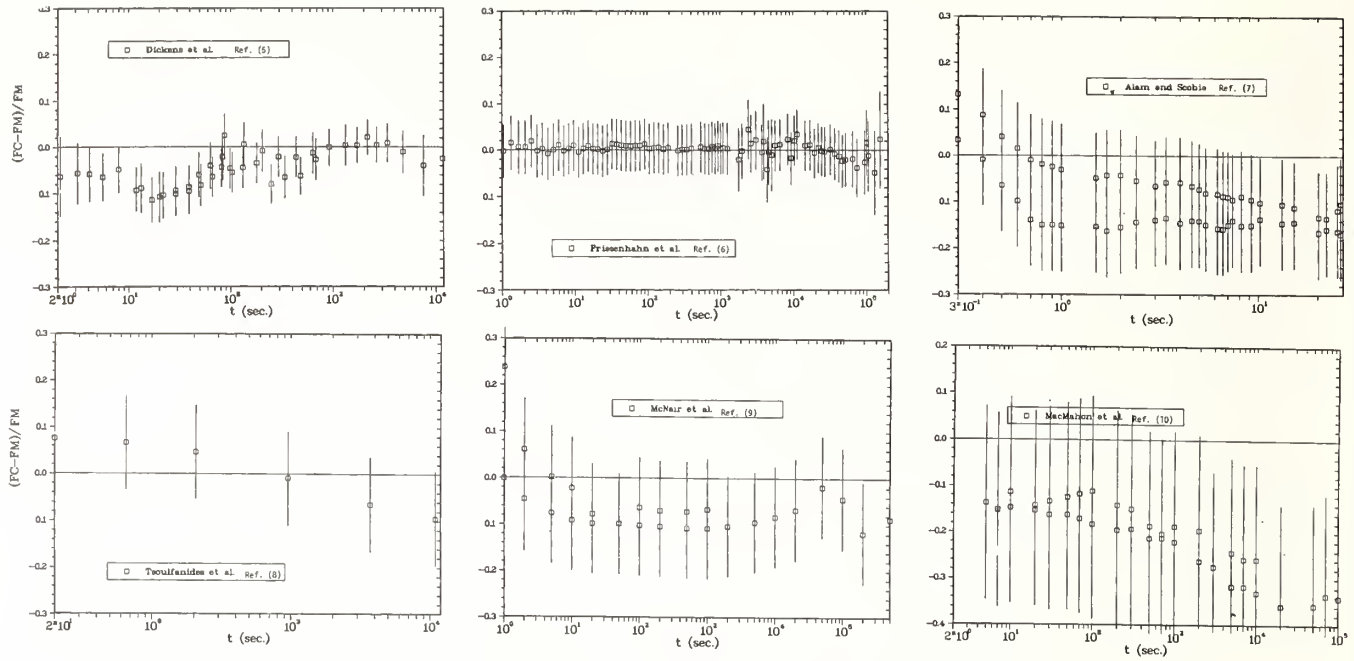

FIGURE 1 COMPARISON OF EVALUATED BETA DECAY HEAT TO MEASUREMENTS

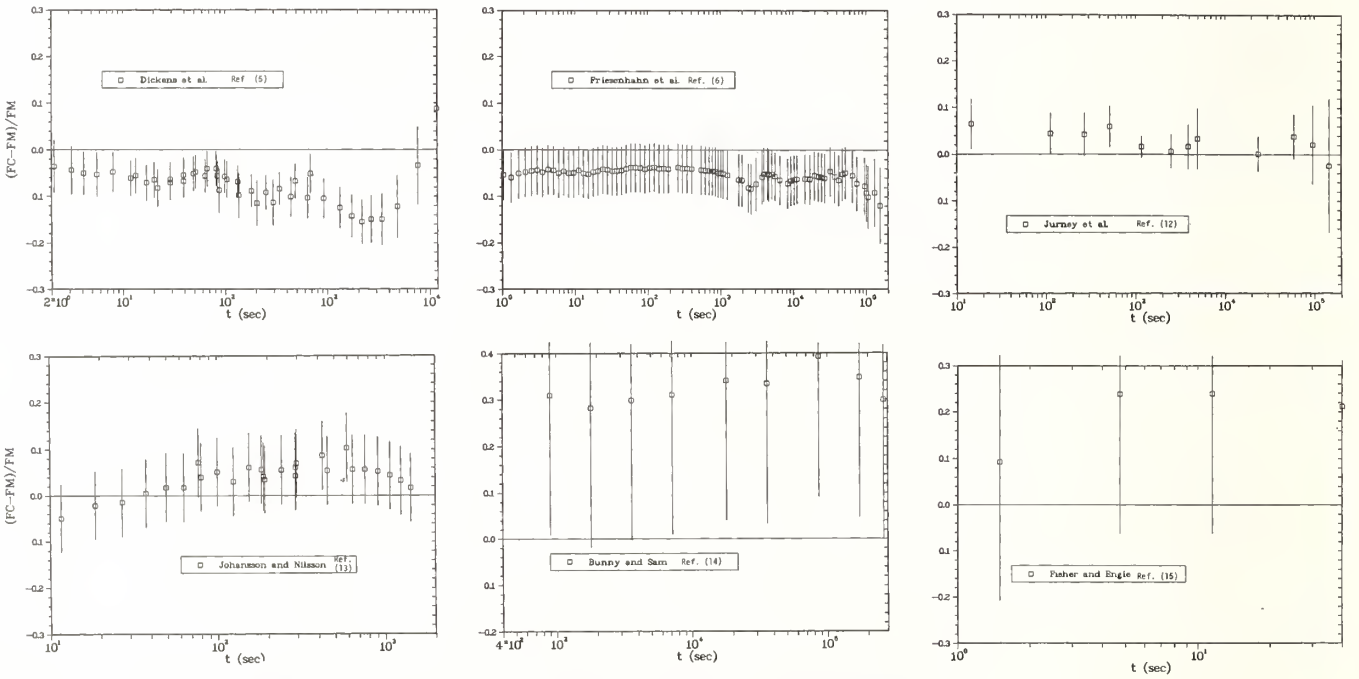

FIGURE 2 COMPARISON OF EVALUATED GAMMA DECAY HEAT TO MEASUREMENTS

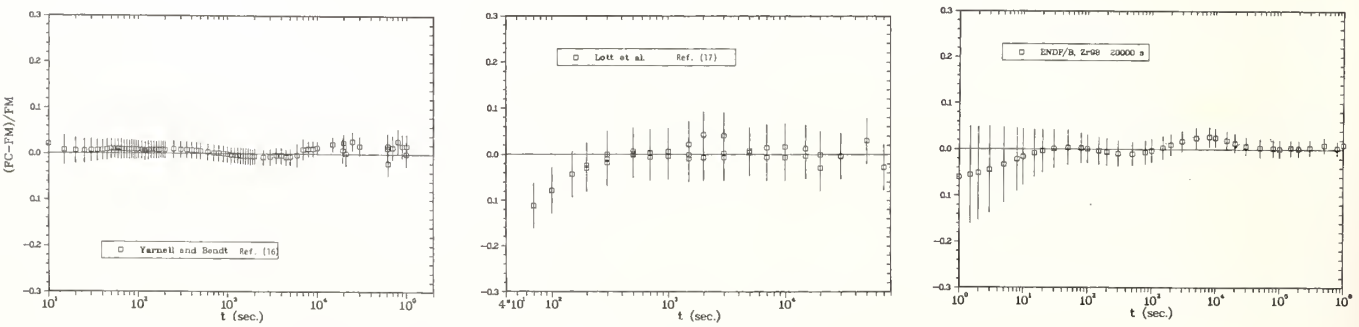

FIGURE 3 COMPARISON OF TOTAL DECAY HEAT TO MEASUREMENTS

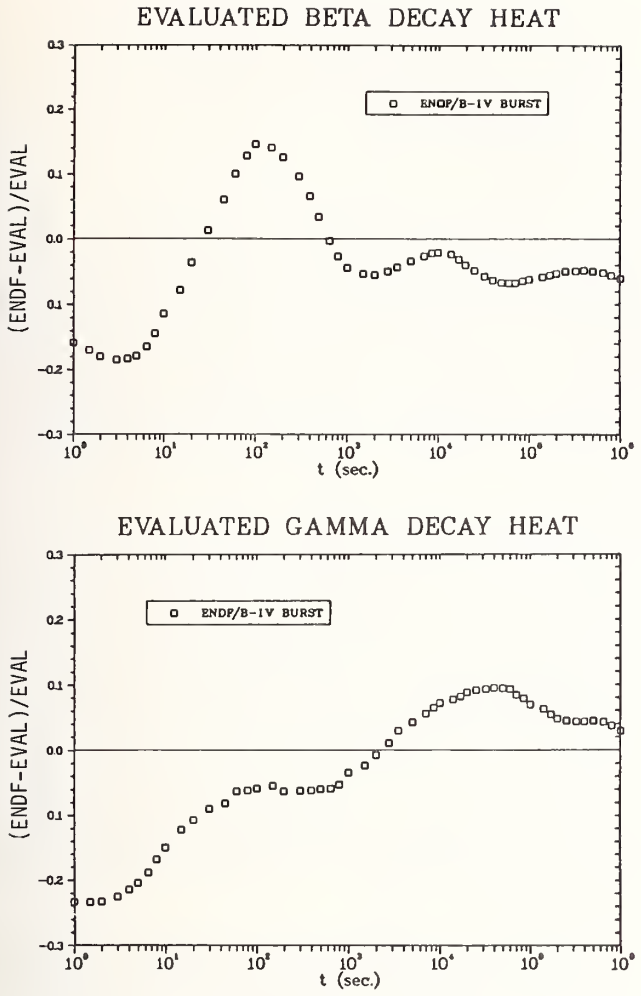

Figure 4 Fractional deviation of ENDF/B-IV values from the evaluated results for a pulse irradiation.

References

1. V. E. Schrock, Progress in Nucl. Energy, 3, 125 (1979).

2. F. Schmittroth and R. E. Schenter, Nucl. Sci. Eng., 69, 389 (1979).

3. F. Schmittroth, "A Method for Data Evaluation with Lognormal Distributions", Nucl. Sci. Eng., 72, 19 (1979).

4. F. Schmittroth, "FERRET Data Analysis Code", HEDL-TME 79-40, Hanford Engineering Development Laboratory (Sept. 1979).

5. J. K. Dickens, J. F. Emery, T. A. Love, J. W. McConnell, K. J. Northcutt, R. W. Peelle, and H. Weaver, "Fission-Product Energy Release for Times Following Thermal-Neutron Fission of ^{235}U Between 2 and 14,000 Seconds", ORNL/NUREG-14, Oak Ridge National Laboratory, (Oct. 1977).

6. S. J. Friesenhahn, N. A. Lurie, N. C. Rogers, and N. Vagelatos, "^{235}U Fission Product Decay Heat from 1 to 10^5 Seconds", EPRI NP-180, Electric Power Research Institute (Feb. 1976).

7. B. Alam and J. Scobie, Ann. of Nucl. Sci. and Eng., 1, 537, (1974).

8. N. Tsoulfanides, B. W. Wehring, and M. E. Wyman, Nucl. Sci. and Eng., 43, 42 (1970).

9. A. McNair, F. J. Bannister, R. L. G. Keith and H. W. Wilson, J. Nucl. Energy, 23, 73, (1968).

10. T. D. MacMahon, R. Wellum and H. W. Wilson, J. Nucl. Energy, 24, 493 (1970).

11. Evaluated Nuclear Data File (ENDF/B-IV) available from, and maintained by, the National Nuclear Data Center at Brookhaven National Laboratory, Upton, New York; see also, T. R. England and R. E. Schenter, "ENDF/B-IV Fission-Product Files: Summary of Major Nuclide Data", LA-6116-MS (ENDF-233), Los Alamos Scientific Laboratory (Oct. 1975).

12. E. T. Jurney, P. J. Bendt, and T. R. England, "Fission Product Gamma Spectra", LA-7620-MS, Los Alamos Scientific Laboratory (Jan. 1979).

13. P. I. Johansson and G. Nilsson, "Measurement of Decay Energy Released in Thermal Fission of ^{235}U", AES-16, Aktiebolaget Atomenergi, Nykoping, Sweden, (March 1977).

14. L. R. Bunney and D. Sam, Nucl. Sci. Eng., 39, 81 (1969).

15. P. C. Fisher and L. B. Engle, Phys. Rev., 134, B796 (1964).

16. J. L. Yarnell and P. J. Bendt, "Decay Heat from Products of ^{235}U Thermal Fission by Fast Response Boil-Off Calorimetry", LA-NUREG-6713, Los Alamos Scientific Laboratory (Jan. 1977).

17. M. Lott, G. Lhianbet, F. Dufreche, and R. deTourreil, J. Nucl. Energy, 27 597 (1973).

FAST NEUTRON SCATTERING CROSS SECTIONS FOR ACTINIDE NUCLEI

G. Haouat, Ch. Lagrange, J. Lachkar, J. Jary, Y. Patin, J. Sigaud
Service de Physique Neutronique et Nucléaire
Centre d'Etudes de Bruyères-le-Châtel
B.P. N° 561
92542 Montrouge Cedex, France

Differential cross sections for neutron elastic and inelastic scattering from ^{232}Th, ^{233}U, ^{235}U, ^{238}U, ^{239}Pu and ^{242}Pu have been obtained at incident energies ranging from 0.6 to 3.4 MeV. The overall energy resolution of the time-of-flight spectrometer was sufficient to easily separate at all energies the elastic and inelastic neutron groups for ^{232}Th, ^{233}U, ^{238}U and ^{242}Pu. Cross sections for groups of states have been obtained for ^{235}U and ^{239}Pu. Comparisons of these results with the latest available evaluations show large discrepancies. The present measured cross sections have been combined with measured total cross sections and low-energy scattering properties in an analysis based on combined coupled-channel and compound-nucleus formalisms. Optical potential parameters and nuclear deformation parameters have been deduced and are discussed.

[Nuclear reactions : ^{232}Th, ^{233}U, ^{235}U, ^{238}U, ^{239}Pu, $^{242}Pu(n,n)$, (n,n'), E_n = 0.6 - 3.4 MeV ; measured $\sigma(E_n,\theta)$, enriched targets ; calculated direct-interaction and compound-nucleus cross sections ; deduced coupled-channel optical potential parameters, quadrupole and hexadecapole deformation parameters].

Introduction

Calculation and design of devices such as fast breeder reactors require cross section data for neutron induced reactions on several actinide nuclei mainly in the energy range from a few hundred keV to ≃ 15 MeV[1]. Among these the elastic and inelastic scattering data are of great importance since the balance between the elastic scattering and the inelastic scattering to the low-lying excited states is important in the slowing down mechanism of fast reactors[2]. The various evaluation files for these cross sections are generally discrepant and based on very few, poor resolution measurements which yield cross sections for many unresolved levels.

Besides the interest in providing accurate data for engineering applications the study of fast neutron scattering from actinides can give insight into the nuclear deformation of these nuclei. The main source of information on nuclear shapes hitherto has been studies of electromagnetic excitation which give the charge distribution of nuclei, or studies of nuclear excitation with charged projectiles which determine the nuclear potential shape. Neutron scattering has contributed little to our knowledge of nuclear deformations in the actinide region, because the techniques have not had, until recently, the requisite energy resolution that permits separation of the neutron groups corresponding to the low-lying collective states at incident neutron energies where the deformation effects are dominant, that is above ≃ 2 MeV.

We have therefore undertaken a series of measurements of fast neutron elastic and inelastic scattering from the actinide nuclei : ^{232}Th, ^{233}U, ^{235}U, ^{238}U, ^{239}Pu and ^{242}Pu. We present here the experimental results, of which some have been already reported[3-5]. The data are then analysed in terms of the direct-interaction and compound-nucleus formalisms. The deduced optical potential parameters and nuclear deformation parameters are discussed.

Experimental details

Differential cross section measurements were carried out using the neutron time-of-flight spectrometer of the Centre d'Etudes de Bruyères-le-Châtel. The experimental set-up has been described in detail elsewhere[3,4], and therefore only a brief description is given here.

The neutron spectrometer was installed near the super EN tandem Van-de-Graaff accelerator for measurements at incident neutron energies ⩾ 2.5 MeV, and at the 4 MV accelerator for measurements below 2.5 MeV. The incident neutrons were produced using the $^{7}Li(p,n)^{7}Be$ reaction. The proton beams were pulsed at a repetition rate of 2.5 MHz and bunched into bursts of width ranging between 0.6 and 0.8 ns (FWHM). The protons were incident on thin targets of 99,8 % pure ^{7}Li evaporated on 1-mm thick tantalum discs. The average current delivered by the tandem accelerator was approximately 2 μA; the beam current from the 4 MV accelerator was typically 8 μA, which required a rotating target.

The neutrons were incident on cylindrical samples located at 0° with respect to the proton beam axis and between 10.2 and 11.9 cm from the target depending on the incident neutron flux strength. The ^{232}Th, ^{233}U, ^{235}U, ^{238}U and ^{239}Pu samples were 1.5 cm diameter solid metal cylinders having the same number of atoms (0.294 mole), to within 0.1 %, and an isotopic enrichment of 99.5 % or greater. The ^{242}Pu sample, with a mass corresponding to 0.186 mole, consisted of powdered $Pu\,O_2$ and had an isotopic enrichment of 93.7 %. Each of the ^{233}U, ^{239}Pu and ^{242}Pu samples was placed in a stainless-steel can which was sealed and put in a polyethylene container. The scattered neutrons were detected by an array of four recoil proton detectors in all measurements except those on ^{242}Pu, for which the data were collected with an array of five detectors. Neutron-gamma pulse shape discrimination was employed to reject most of the γ-ray induced events in the scintillators ; this greatly reduced the time independent background generated in the time-of-flight spectra by spontaneous or delayed fission γ-rays.

The experimental conditions were fixed so as to obtain a global neutron energy resolution of ≃ 8 keV at 0.6 and 0.7 MeV, ≃ 15 keV at 1.0 MeV, ≃ 18 keV at 1.5 MeV, ≃ 22 keV at 2.0 MeV, ≃ 27 keV at 2.5 MeV and ≃ 28 keV at 3.4 MeV. Time-of-flight spectra for the ^{238}U sample are shown in figure 1 to illustrate the experimental resolution at 0.7 and 3.4 MeV incident neutron energies. The absolute values of the differential cross sections were determined by measuring the incident and scattered neutron fluxes with the same detector. The primary neutron flux was monitored during the measurements by using an auxiliary neutron detector. The energy dependence of the detector efficiency was obtained by comparing the direct neutron yield at various angles with the corresponding cross sections for

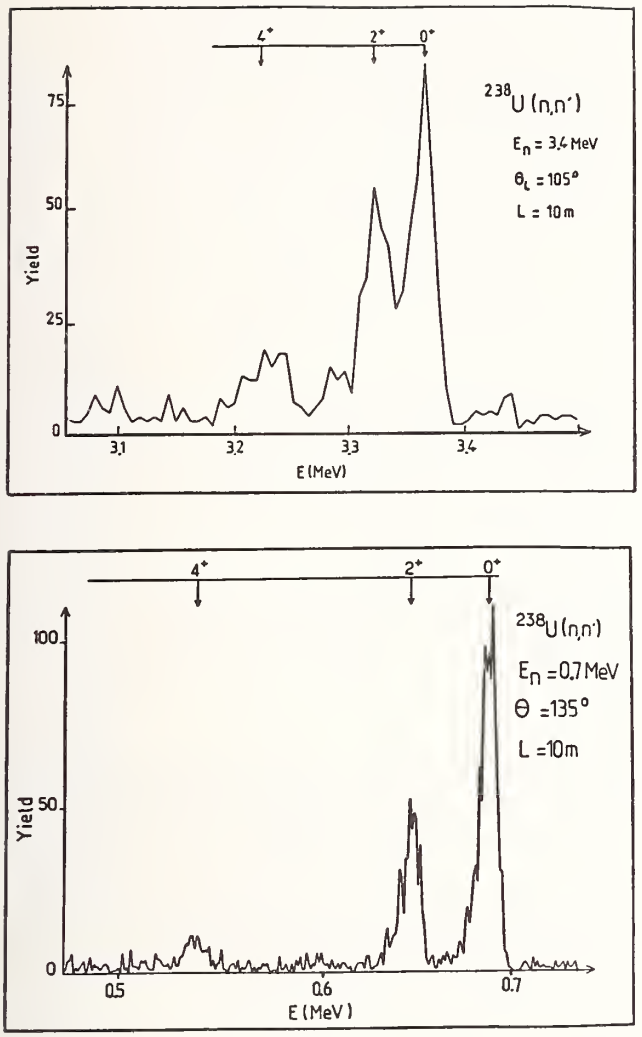

Fig.1. Time-of-flight spectra of 3.4 MeV (above) and 0.7 MeV (below) neutrons scattered from ^{238}U. The elastic scattering peak (0^+) and inelastic scattering peaks corresponding to the first 2^+ (45 keV) and 4^+ (148 keV) states appear clearly in the spectra.

the $^{7}Li(p,n)^{7}Be$ reaction[6]. The neutron scattering differential cross sections were corrected for anisotropy effects in the incident neutron flux and for finite size effects in the sample. These latter corrections included those for neutron flux attenuation by the sample, multiple scattering and geometrical effects. The corrections were made using the analytic method described by Kinney[7] ; they were consistent with the results of Monte-Carlo calculations[8] to within 2 %.

Results

Differential cross sections for neutron scattering from ^{232}Th and ^{238}U were measured at 0.7, 1.5, 2.5 and 3.4 MeV in the angular range from 20° to 160°. The energy resolution of the neutron spectrometer was good enough at all energies to permit an easy separation of the elastic and inelastic scattering neutron groups for these two nuclei (see Fig.1). Cross sections were obtained for the elastic scattering and inelastic scattering to the first 2^+ and 4^+ states of the two isotopes. Figure 2 shows the data for ^{238}U. The recent data of Guenther et al.[9] and Beghian et al.[10] on ^{238}U, which are not plotted on this figure, are in good agreement with the present measurements.

Measurements on ^{233}U were performed at 0.7 and 1.5 MeV between 20° and 160°, the energy spacing of the low-lying collective levels of this nucleus is sufficiently large that data were obtained separately for the elastic scattering ($5/2^+$) and the inelastic scattering to the first $7/2^+$ (40 keV) and $9/2^+$ (92 keV) excited states.

For ^{235}U and ^{239}Pu, data were taken at 0.7 and 3.4 MeV in the angular range 20° - 160°. Because at both energies the experimental resolution is larger than the energy spacing of some levels of ^{235}U, cross sections were determined for the two groups of levels ($7/2^-$, g.s - $1/2^+$, 75 eV - $3/2^+$, 13 keV) and ($9/2^-$, 46 keV - $5/2^+$, 52 keV) ; also, cross sections were obtained at 3.4 MeV energy for the excited state $11/2^-$, 103 keV. However, both the 0.7 - and 3.4 - MeV time-of-flight spectra seem to indicate that the states of the rotational band built on the $1/2^+$ (75 eV) particle level are very weakly excited, since the neutron group corresponding to the $7/2^+$ (84 keV) state of this band is not conspicuous in the spectra. Moreover, scattered neutrons corresponding to the $3/2^+$ (13 keV) and $5/2^+$

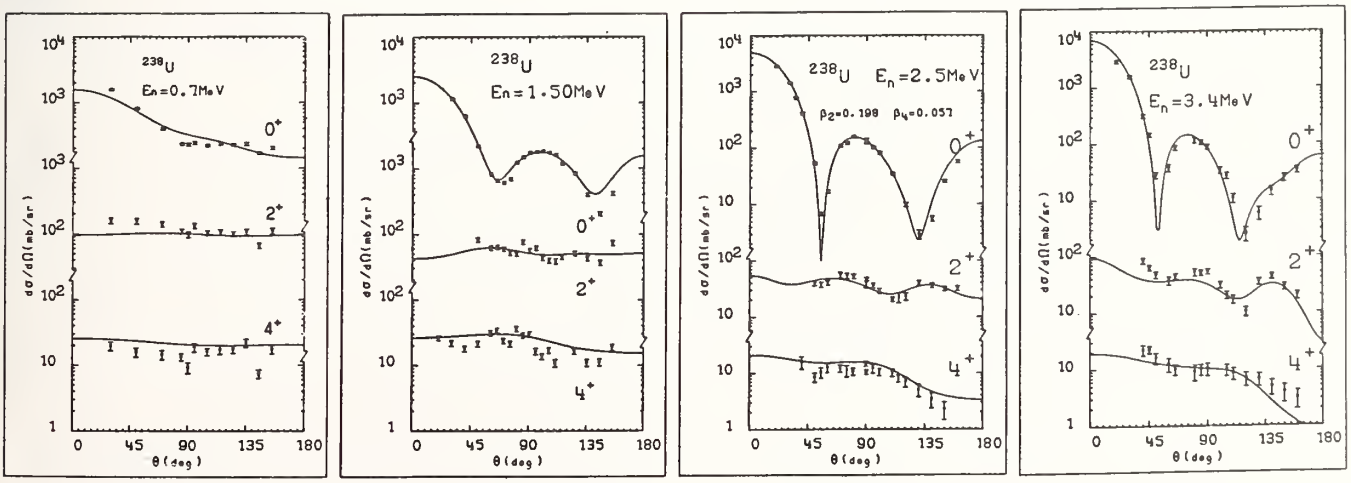

Fig.2. Neutron cross sections at 0.7 - 1.5 - 2.5 and 3.4 MeV for the elastic scattering (0^+) and inelastic scattering to the first 2^+ (45 keV) and 4^+ (148 keV) states of ^{238}U.

(52 keV) do not seem to broaden the elastic $(7/2^-)$ and inelastic $(9/2^-)$ neutron peaks respectively[4].

The 3.4 MeV cross sections of ^{239}Pu were obtained for the three groups of levels : $(1/2^+$, g.s. - $3/2^+$, 8 keV), $(5/2^+$, 57 keV - $7/2^+$, 76 keV) and $(9/2^+$, 163 keV - $11/2^+$, 173 keV). But at 0.7 MeV, the experimental resolution of $\simeq$ 8 keV permitted the separation of the contributions from the various levels and angular distributions were obtained for the ground state $1/2^+$ and the excited states $3/2^+$, $5/2^+$, $7/2^+$. The data appear in fig.3.

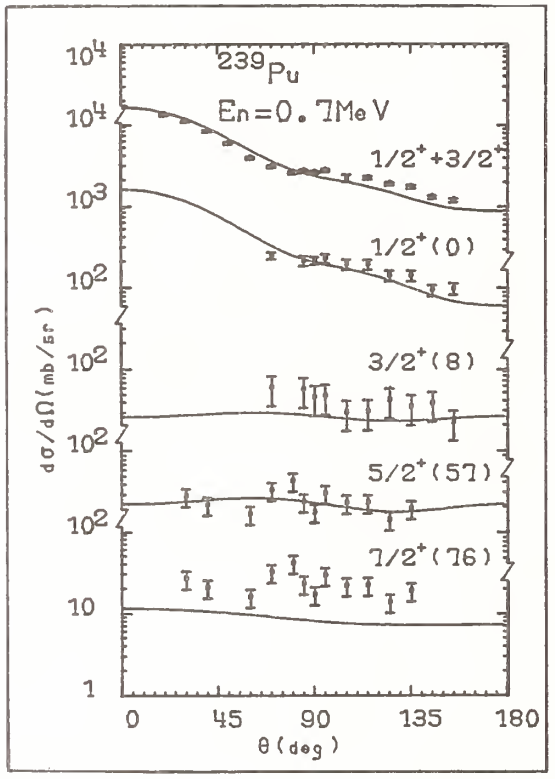

Fig.3. Differential cross sections for ^{239}Pu at 0.7 MeV. The energy of the excited levels is given in keV.

Differential cross sections for ^{242}Pu were measured at 0.6 - 1.0 - 1.5 - 2.0 - 2.5 and 3.4 MeV at angles ranging from 15° to 160°. Extraction of the ^{242}Pu scattering yields was difficult because the time-of-flight spectra contain neutron peaks corresponding to the scattering from stainless steel and carbon of the container and from oxygen of the PuO_2 sample. Figure 4 gives the 2.5 MeV data for the elastic scattering and inelastic scattering to the first 2^+ state (44.5 keV). Cross sections for the first 4^+ state (147 keV) are not presented here because the corresponding neutron group has not been separated from the contaminant peaks produced by scattering from oxygen in the sample and stainless steel of the container.

Discussion

Some of the present data have been compared with the most recent evaluations ENDF/B IV and ENDL 76 : large discrepancies appear mainly at high energies[4]. Figure 5 shows our 3.4 MeV elastic scattering cross sections for ^{232}Th, ^{235}U, ^{238}U and ^{239}Pu along with the angular distributions obtained from the ENDF/B IV (dotted curves) and ENDL 76 (dashed curves) files ; in this figure, the solid lines represent the results of calculations which will be described below. Large disagreements between experimental and evaluated data are observed mainly at angles beyond $\simeq$ 45° : the two minima around 55° and 120° in the measured cross sections are not reproduced by the evaluations. This may be

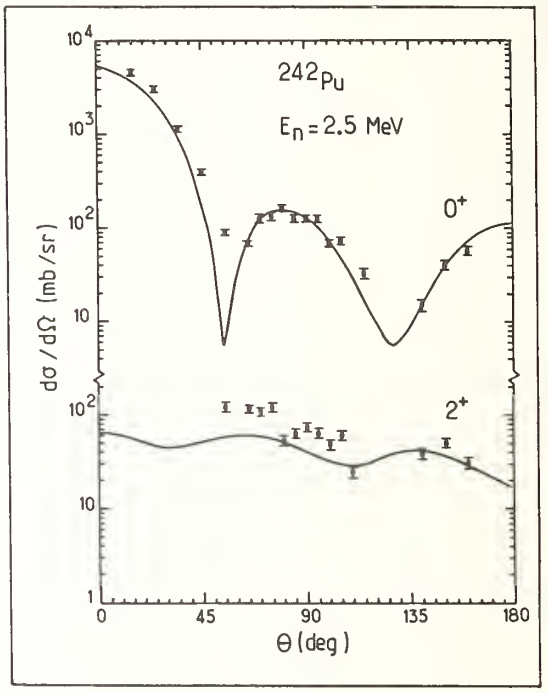

Fig.4. Neutron cross sections at 2.5 MeV for the elastic scattering (0^+) and inelastic scattering to the first 2^+ (44.5 keV) state of ^{242}Pu.

explained by the fact that these evaluations are based on low-resolution measurements which include contributions from many unresolved levels. The disagreement between evaluated and presently measured inelastic scattering cross sections is even worse ; all of the evaluated inelastic angular distributions are considered as isotropic in both files, and the angle-integrated cross sections are much smaller than the experimental data except for the ENDL 76 values for ^{238}U [4]. In fact the ^{242}Pu measurements were undertaken to clarify the situation concerning this nucleus.

A theoretical analysis of the present data has been carried out for the nuclei ^{232}Th, ^{235}U, ^{238}U and ^{239}Pu. Both the direct-interaction (DI) and compound-nucleus (CN) processes were considered in the calculations. The coupled-channel optical model[11] was used to estimate the DI cross sections and the Wolfenstein-Hauser-Feshbach formalism[12], with width-fluctuation corrections, for computing the CN cross sections. Compound-nucleus calculations included as possible exit channels compound elastic scattering and inelastic scattering to discrete and continuum levels, radiative capture and fission. Coupled-channel calculations were performed using a modified version[13] of Tamura's code JUPITOR I [14]. The real and imaginary parts of the optical potential were assumed to have quadrupole and hexadecapole deformations. The geometric parameters, i.e. radii and diffusivenesses, were taken the same for the four nuclei[4] ; they are given in table I. The other optical potential parameters were adjusted separately for each nucleus. They were estimated using

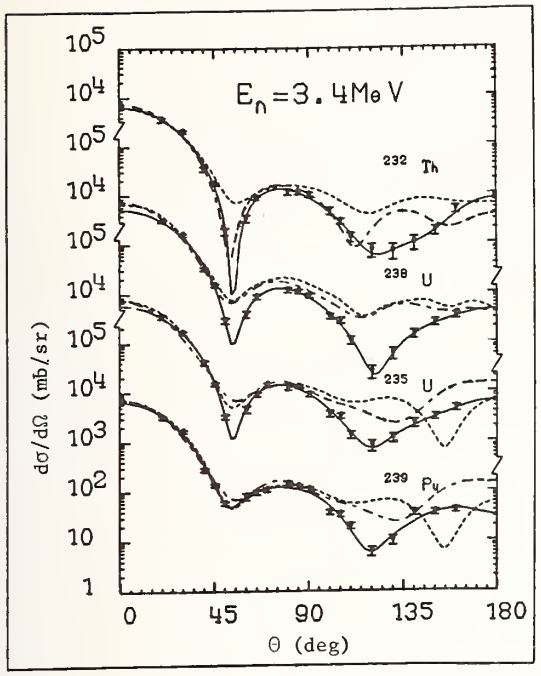

Fig.5. Elastic scattering cross sections at 3.4 MeV for ^{232}Th and ^{238}U, and cross sections for the groups of levels (7/2⁻, 1/2⁺, 3/2⁺) for ^{235}U and (1/2⁺, 3/2⁺) for ^{239}Pu. Solid lines are coupled-channel calculations as described in the text. Dotted and dashed curves are angular distributions from the ENDF/B IV and ENDL 76 files respectively.

the parametrization method proposed by Delaroche, Lagrange and Salvy[15] which consists in analysing an extensive set of neutron scattering properties including s-and p-wave strength functions, potential scattering radius and total cross sections over a wide energy range. The deformation parameters were then adjusted to fit the present elastic and inelastic scattering cross sections.Potential depths and deformation parameters are given in table I.

Calculations for ^{232}Th and ^{238}U assumed a coupling basis 0^+, 2^+, 4^+. Good agreement is found between calculations and measurements, as is illustrated in figure 2 for ^{238}U. The ^{235}U cross sections were computed assuming the strong coupling of the $7/2^-$, $9/2^-$, $11/2^-$ states of the ground state rotational band. The good agreement between experimental and calculated cross sections mentioned in Ref.4 suggests that, as assumed, the states of the rotational band built on the particle level $1/2^+$ (75 eV) are very weakly excited. For ^{239}Pu the six first states of the ground-state rotational band were explicitly coupled. Satisfactory agreement is found for the 3.4 MeV data[4] ; the CN cross sections are found to be negligible at that energy. At 0.7 MeV, on the other hand, the CN contributions to the elastic and inelastic scattering cross sections are important. Data and calculations are compared in figure 3 ; here the CN cross sections are assumed to be isotropic.

Values of the optical potential depths (table I) for the ^{232}Th, ^{235}U, ^{238}U and ^{239}Pu nuclei are very similar; the slight differences between the values of the real potentials might be ascribed to the isospin dependence. Thus except for the potential deformations, these nuclei have the same behaviour with respect to neutron scattering. Concerning the potential deformations, comparison of the quadrupole deformation parameters (table I) implies that the static deformation is rather larger for the even-odd nuclei than for the even-even ones. This difference must be emphasized in further evaluations for transactinides.

For ^{242}Pu, the 2.5 MeV data are compared in figure 4 to calculations performed with the deformed potential parameters given by Lagrange and Jary in their evaluation of the ^{240}Pu and ^{242}Pu cross sections[16] ; these parameters are given in table I. The agreement between measurements and calculations is fairly good (fig.4) although a better fit to the angular distributions would yield more reliable values of the deformation parameters.

Conclusion

In order to study the neutron-nucleus interaction in the actinide mass region, fast neutron elastic and inelastic scattering cross sections have been measured

Table I. Deformed potential parameters used in this study. Radii and diffusivenesses are given in fm. Potential depths and incident neutron energy E are given in MeV. Also given are the quadrupole (β_2) and hexadecapole (β_4) deformations of the optical potential.

Geometric parameters / Nucleus	V_R : REAL POTENTIAL	W_D : SURFACE IMAGINARY POTENTIAL	V_{SO} : SPIN-ORBIT POTENTIAL	QUADRUPOLE DEFORMATION (β_2)	HEXADECAPOLE DEFORMATION (β_4)
	$R_R^\circ = 1.26$ $a_R = 0.63$	$R_D^\circ = 1.26$ $a_D = 0.52$	$R_{SO}^\circ = 1.12$ $a_{SO} = 0.47$		
^{232}Th	46.4(± 0.2) - 0.3 E	3.6(± 0.2) + 0.4 E	6.2 ± 0.3	0.190 ± 0.010	0.071 ± 0.007
^{235}U	46.4(± 0.2) - 0.3 E	3.3(± 0.2) + 0.4 E	6.2 ± 0.3	0.220 ± 0.011	0.080 ± 0.008
^{238}U	46.2(± 0.2) - 0.3 E	3.6(± 0.2) + 0.4 E	6.2 ± 0.3	0.198 ± 0.010	0.057 ± 0.006
^{239}Pu	46.2(± 0.2) - 0.3 E	3.6(± 0.2) + 0.4 E	6.2 ± 0.3	0.220 ± 0.011	0.070 ± 0.007
^{242}Pu	46.0(± 0.2) - 0.3 E	3.5(± 0.2) + 0.4 E	6.2 ± 0.3	0.204 ± 0.010	0.051 ± 0.005

for the ^{232}Th, ^{233}U, ^{235}U, ^{238}U, ^{239}Pu and ^{242}Pu isotopes in the energy range from 0.6 to 3.4 MeV. The cross sections show the characteristic behaviour of these deformed nuclei. Optical potential parameters and nuclear deformations deduced from the analysis of the data indicate that the optical potentials are nearly identical for these nuclei, the differences between the neutron scattering properties being attributable to nuclear deformations.

Acknowledgements

We thank J.P. Delaroche for his assistance in computing the cross sections for ^{242}Pu, D.K. Olsen for his help in collecting the ^{242}Pu data and J.R. Lilley for a careful reading of the manuscript and many useful comments.

References

1. R.M. Lessler (Editor), "World Request List For Nuclear Data" Wrenda 76/77. INDC (SEC) - 55/URSF, August 1976 ;

   J.L. Rowlands, Proc. of an Int. Conf. on Neutron Physics and Nuclear Data (Harwell U.K. 1978) p.7.

2. T. Choong and E. Kujawski, Nucl. Sci. Eng. 60, 326 (1976).

3. G. Haouat, J. Sigaud, J. Lachkar, Ch. Lagrange, B. Duchemin and Y. Patin, Proc. of the Int. Conf. on the Interactions of Neutrons with Nuclei, Lowell, Conf. 760715 P2 (1976) 1330 ; Report NEANDC(E) 180 "L", INDC(FR) 13/L (1977).

4. G. Haouat, J. Lachkar, Ch. Lagrange, Y. Patin, J. Sigaud and R.E. Shamu, Report NEANDC(E) 196 "L", INDC(FR) 29/L (1978).

5. J. Lachkar, G. Haouat, Ch. Lagrange, M. Cates, Y. Patin, J. Sigaud, J. Jary, S. Ferguson and R.E. Shamu, Proc. of an Int. Conf. on Neutron Physics and Nuclear Data, (Harwell U.K. 1978) p. 508.

6. H. Liskien and A. Paulsen, Atomic Data and Nuclear Data Tables 15, 57 (1975).

7. W.E. Kinney, Nucl. Inst. and Meth. 83, 15 (1970).

8. D.E. Velkley, J.D. Brandenberger, D.W. Glasgow and M.T. McEllistrem, Nucl. Inst. and Meth. 129, 231 (1975).

9. P. Guenther, D. Havel and A.B. Smith, Nucl. Sci. and Eng. 65, 78 (1978).

10. L.E. Beghian et al. Nucl. Sci. and Eng. 69, 191 (1979).

11. T. Tamura, Rev. Mod. Phys. 37, 679 (1965).

12. L. Wolfenstein, Phys. Rev. 82, 690 (1951) ; W. Hauser and H. Feshbach, Phys. Rev. 87, 366 (1952)

13. Ch. Lagrange and N. Mondon, Internal Report, Centre d'Etudes de Limeil, France (1973) (unpublished).

14. T. Tamura, Report ORNL 4152 (1967) (unpublished).

15. J.P. Delaroche, Ch. Lagrange, and J. Salvy, Nuclear Theory in Neutron Nuclear Data Evaluation, IAEA-190 Vol.II, 251 (1976).

16. Ch. Lagrange, and J. Jary, Report NEANDC(E) 198"L", INDC(FR) 30/L (1978).

MEASUREMENT OF $^{238}U(n,n'\gamma)^{238}U^*$ CROSS SECTIONS

D. K. Olsen, G. L. Morgan,* and J. W. McConnell
Oak Ridge National Laboratory
Oak Ridge, Tennessee 37830, USA

Production cross sections for gamma-ray transitions produced by 0.5 to 5.0-MeV neutrons on ^{238}U have been measured employing a 95-cm^3 Ge(Li) detector at 125°, the ORELA neutron source, and a recoil proton telescope. From these data and other decay scheme information, inelastic scattering cross sections for levels from 680 to 1224 keV of excitation have been constructed and compared with statistical model calculations and the ENDF/B-V evaluation.

[Measured $^{238}U(n,n'\gamma)$, E_n = 0.5 to 5.0 MeV, deduced $^{238}U(n,n')^{238}U^*(E_x)$ for E_x = 0.680 to 1.224 MeV.]

Introduction

Accurate knowledge of neutron inelastic scattering cross sections, CS, on ^{238}U are important for fast reactor design. Although these CS do not determine neutron balance directly, they influence fast-critical and reactor parameters through the energy transfer mechanism they provide for the neutron flux. Previous measurements of these CS have been reviewed for the ENDF/B-V evaluation.[1] Accurate data is scarce for the threshold shapes of these CS which are sensitive to the model calculations employed and for the CS to the excited rotational bands which provide most of the energy transfer for MeV neutrons. To overcome the resolution and background problems associated with Van de Graaff measurements for the excited bands, we have measured the deexcitation gamma-rays production CS for inelastic levels from 0.680 to 1.224 MeV of excitation employing 0.5 to 5.0-MeV neutrons from the ORELA "white" source. From these CS and other decay scheme information inelastic scattering CS are deduced. In addition to providing needed information for ^{238}U inelastic scattering, these CS provide a stringent test for statistical-model-calculated[2] inelastic scattering from highly deformed actinide nuclei.

Experimental Procedure

Eight hundred 35-nsec FWHM neutron pps were produced from the ORELA Ta target with 35 kW of time-averaged electron power. After being filtered through 0.93 g/cm^2 of ^{10}B to inhibit time overlap and 14.0 cm of Th to attenuate gamma flash, the flux was collimated into a ∿ 7-cm diam beam which traversed a proton-recoil radiator foil and ^{238}U scattering sample. The experimental arrangement is outlined in Fig. 1. The 0.00376-atom/barn ^{238}U sample consisted of a 11.11-cm diam, 0.76-mm thick, 99.92% isotopically enriched disk which was mounted in a vertical plane at a 50° grazing angle to the beam direction with its center 22.181 m from the ORELA target.

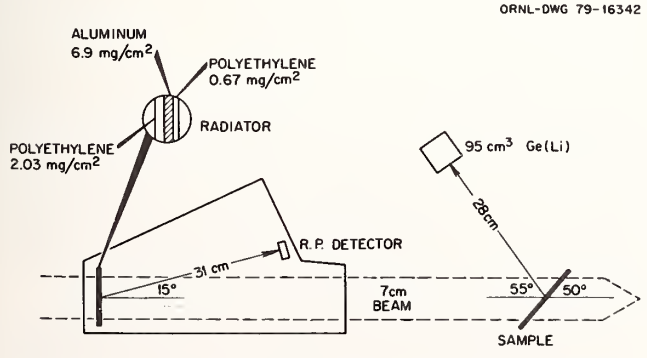

Fig. 1. Experimental arrangement. The radiator and sample centers were positioned 21.430 and 22.181 m from the ORELA target, respectively.

Photons were counted with a 95-cm^3 Ge(Li) detector with its front face 28 cm from the sample center and face-shielded with 1.8 mm of lead. This detector was mounted so that its axis was at 125° and 15° to the beam direction and sample-disk normal, respectively. The flux detector and its operation is described in detail in Ref. 3. It consisted of a radiator at 21.430 m which was composed of 2.0 and 0.67 mg/cm^2 polyethylene foils with a 6.9 mg/cm^2 Al absorber sandwiched between. Recoil protons were counted with 0.30-mm solid-state detector mounted behind an 1.27 cm^2 aperture located 30.6 cm from the radiator center.

Fast timing pulses were obtained from the Ge(Li) detector with an ORTEC 473A constant fraction discriminator operated with slow rise-time reject and from the proton-recoil detector with an ORNL Q3066B crossover timing discriminator. From these fast pulses neutron flight times for both detectors were measured with an EG&G TDC100 time digitizer operated in the single stop mode. Simultaneous slow pulses produced 2048- and 256-channel pulse-height spectra, respectively, for each of 160 timing bins. The efficiency with respect to 4π steradians of the Pb-shielded Ge(Li) detector was measured *in situ* with standard sources to ± 3%. The TOF scale, and hence energy scale since the path length is known to within a few mm, is believed accurate to ± 5 nsec and has been verified by observing the ^{12}C 2.078-MeV transmission dip.[4]

Data Reduction

The counting rate and line shape from the Ge(Li) detector were monitored with 662-keV gamma radiation from a ^{137}Cs source near the sample. After the clock deadtime correction, events from this source showed no counting losses at long flight times; however, at the short flight times of interest peak tailing and a consistent 10% counting loss from pileup and electronic deadtimes were measured.

For spectra from 36-nsec wide incident neutron bins, the number of photon events at 125° for various ^{238}U lines were determined, clock deadtime corrected, normalized to 4π steradians through the efficiency calibration, and corrected for the measured 10% electronic deadtime and pileup loss. Using known[5] n-p CS, analysis of the two-dimensional proton recoil data provided a flux measurement with an estimated systematic uncertainty of less than 5%. Events from an ^{241}Am alpha source mounted in the proton-recoil detector provided a pulse-height energy calibration for the Si diode and assured that after the clock deadtime correction there were no counting losses.

The resultant gamma-ray production CS were corrected for neutron multiple scattering, neutron flux and gamma-ray attenuation, and the small solid

*Present address: Los Alamos Scientific Laboratory, Los Alamos, New Mexico 87545, USA.

angle variations from the finite sample size using Monte Carlo procedures. More experimental details, listings and plots of the CS, and a discussion of errors can be found in Ref. 6. In particular, the overall normalization error is believed to be less than 6% which has been somewhat verified by an accompanying measurement[7] of 478-keV gamma-ray production from neutrons on ^{7}Li. Altogether 28 gamma-ray production CS and 7 branching ratios from weak transitions were measured. In the discussion below it is assumed that the Legendre expansion of the gamma-ray angular distributions contain only zero and second order terms.

Discussion and Conclusions

From these data and other decay scheme information[8] inelastic scattering CS were calculated using the decay scheme shown in Fig. 2 which is mainly from the work of Ref. 8. With this decay scheme population CS were first calculated for each level from 680 to 1224 keV of excitation accounting for all known decays out of each level; low-energy gamma rays, E0 transitions and internal conversion. From these population CS, inelastic scattering CS were calculated by subtracting all known decays into each level from higher-energy excited states. The branching ratios employed are listed in Ref. 6.

Figure 3 compares resulting CS to the $K^{\pi} = 0^{-}$ octupole band with the ENDF/B-V evaluation and the statistical model calculations of Jary et al.[2] The data points with and without error bars are population and inelastic scattering CS, respectively. These levels have appreciable feeding from higher-energy excited states. The smooth curves from threshold to 2.0 MeV which reproduce both the shape and magnitude of the inelastic CS are the statistical-model calculated results of Jary et al.[2] The smooth curves from threshold to 5.0 MeV which overpredict the inelastic CS maxima are from the ENDF/B-V evaluation.

Other examples of the data are given in Fig. 4 which shows inelastic scattering CS to the (1^{-}), (2^{-}), and 3^{-} members of the proposed $K^{\pi} = 1^{-}$ band and to the (0^{+}), 2^{+}, and (4^{+}) members of the proposed first excited $K^{\pi} = 0^{+}$ band. The error bars are statistical only and do not include decay-scheme uncertainties. Reference 1 does not provide an evaluated CS for each level above 827.1 keV of excitation, but clusters them into level groups for which there is an evaluated CS. Figure 5 compares the ENDF/B-V CS for the 965 and 1048-keV level groups with the measured CS summed over the corresponding levels. The CS maxima agree within 10%, but the threshold shapes are discrepant.

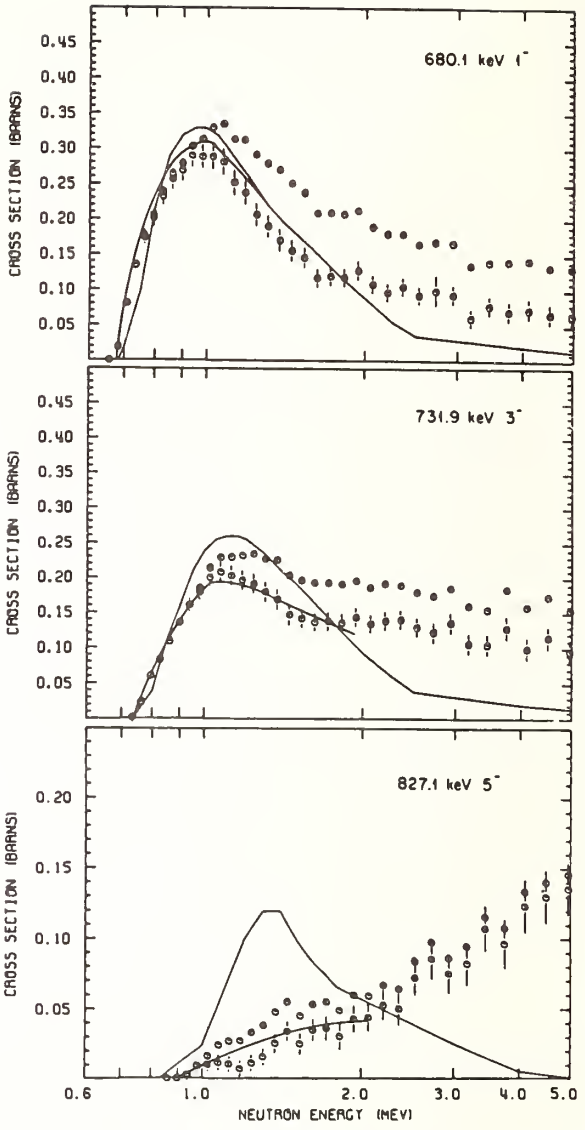

Fig. 3. Inelastic scattering CS to the K = 0 octupole band. Data points with and without error bars are population and inelastic scattering CS, respectively, which differ by the feeding from higher energy excited states. The calculated curves to 2.0 MeV which reproduce both the shape and magnitude of the inelastic scattering CS are from Ref. 2. The curves to 5.0 MeV which overpredict the CS maxima are the ENDF/B-V evaluation.

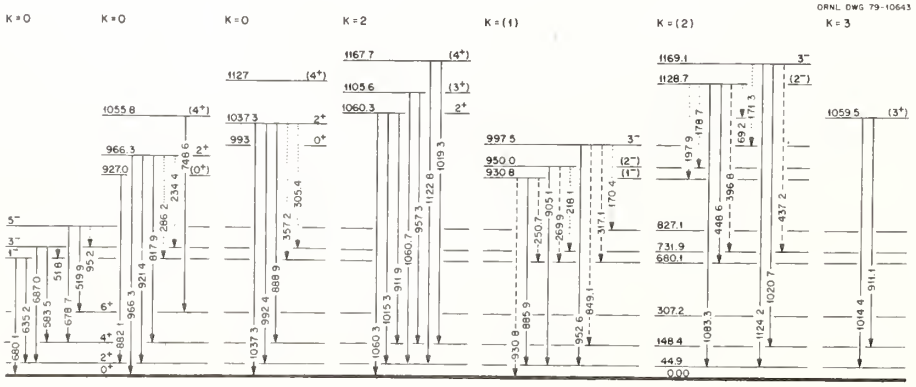

Fig. 2. Proposed ^{238}U rotational band structure of Ref. 8. The solid lines represent transitions whose gamma-ray production CS have been measured in the present work. The dashed and dotted lines represent transitions whose branching ratios have been measured in this work and by other workers, respectively. In addition, CS to levels at 1199.8, 1208.3, and 1223.9 keV of excitation were also measured.

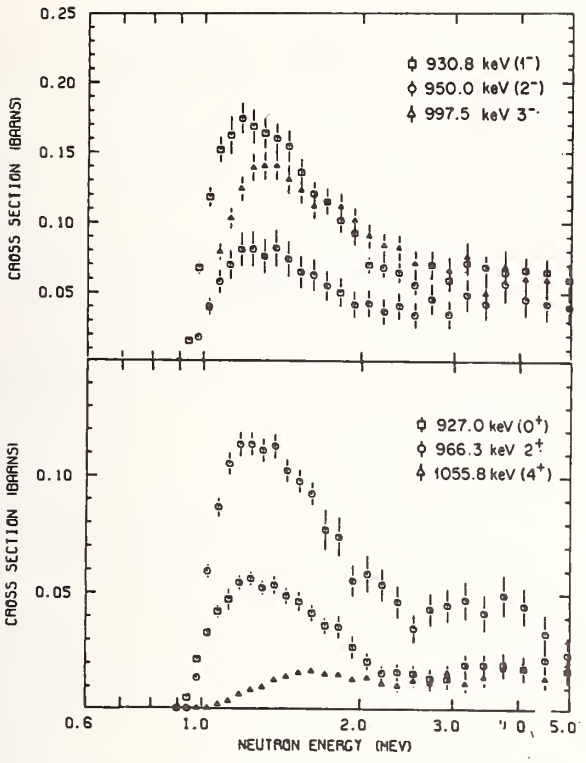

Fig. 4. Inelastic scattering cross sections to the (1^-), (2^-), and 3^- members of the proposed $K^\pi = 1^-$ band and the (0^+), 2^+, and (4^+) members of the proposed first-excited $K^\pi = 0^+$ band.

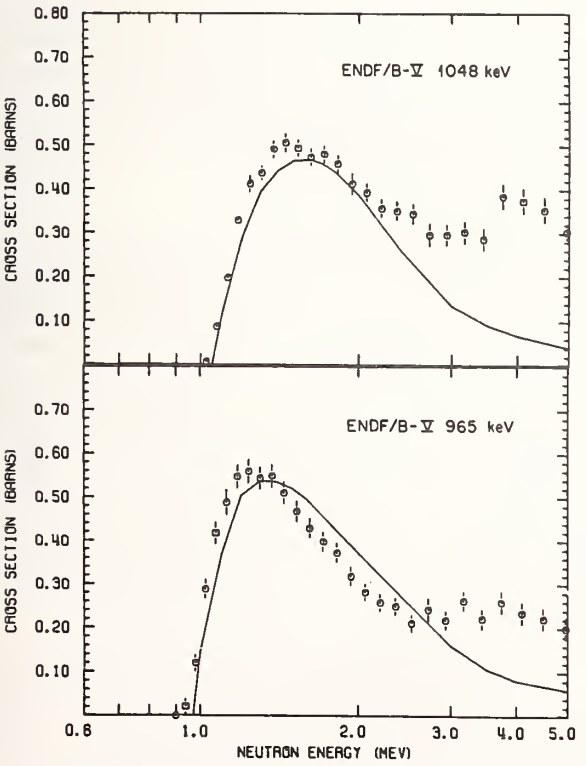

Fig. 5. Comparison between the ENDF/B-V evaluated level-group CS and the corresponding summed measured CS. The 965-keV level group consists of the 927.0, 930.8, 950.0, 966.3, 993, and 997.5 keV levels and the 1048 keV level group consists of the 1037.3, 1055.8, 1059.5, and 1060.3 keV levels.

The deduced inelastic scattering CS are sensitive to imprecisely known decay scheme information whose uncertainties are not contained in the plotted errors. In particular, possible unmeasured E0 transitions, unknown E2-M1 mixing ratios, and discrepant[8] gamma-ray branching ratios all cause confusion. Nevertheless, these results provide the most accurate CS threshold shape determination for these levels and probably the most accurate measurement of the scattering CS to the various individual levels for neutron energies below $\sim$ 1.5 MeV.

Acknowledgement

This work is sponsored by the DOE Office of Energy Technology, Division of Reactor Research and Technology under contract W-7405-eng-26 with Union Carbide Corporation.

References

1. W. Poenitz, E. Pennington, A. B. Smith, and R. Howerton, "Evaluated Fast Neutron Cross Sections of ^{238}U," ANL/NDM-32 (1977).

2. J. Jary, Ch. Lagrange, and P. Thomet, "Coherent Optical and Statistical Model Calculations of Neutron Cross Sections for ^{238}U Between 1 keV and 20 MeV," INDC(FR) 9/L (1977).

3. G. L. Morgan, D. K. Olsen, and J. W. McConnell, NIM 157, 525 (1978).

4. F. Perey, "Covariance Matrices of Experimental Data," Proc. Conf. Neutron Physics and Nuclear Data, Harwell, p. 104, OECD Nuclear Energy Agency (Paris) (1978).

5. J. L. Gammel, in "Fast Neutron Physics," Part II, edited by J. B. Marion and J. L. Fowler (Interscience, New York, 1963).

6. D. K. Olsen, G. L. Morgan, and J. W. McConnell, "Measurement of ^{238}U(n,n'γ) and ^{7}Li(n,n'γ) Gamma-Ray Production Cross Sections," ORNL/TM-6832 (1979).

7. D. K. Olsen, G. L. Morgan, and J. W. McConnell, "Measurement of the ^{7}Li(n,n'γ)^{7}Li*(0.478-MeV) Cross Section from 0.5 to 5.0 MeV," submitted to Nucl. Sci. and Eng.

8. Y. A. Ellis, Nuclear Data Sheets 21, 549 (1977); and references contained therein.

NEUTRON INELASTIC SCATTERING CROSS SECTIONS OF ^{238}U VIA (n,n'γ)

A. Mittler, G. P. Couchell, W. A. Schier, S. Ashar,
J. H. Chang and A. T. Y. Wang
Department of Physics and Applied Physics
University of Lowell
Lowell, Massachusetts 01854

Level cross sections of ^{238}U have been deduced from gamma-ray measurements at 125° following inelastic neutron scattering over an incident energy range of 0.70 to 1.96 MeV. A pulsed source of neutrons was produced via the ^{3}H(p,n)^{3}He reaction. The spectrometer system consisted of a 40-cm^{3} Ge(Li) detector surrounded by a large annular NaI anti-Compton detector, used in conjunction with time-of-flight electronics. Forty-five gamma transitions were observed for twenty-seven levels up to 1516 keV. Finite sample corrections, including neutron attenuation, gamma-ray attenuation and neutron multiple scattering were made for the disc-shaped scatterer. Results are compared to statistical compound-nucleus model calculations and ENDF.

[NUCLEAR REACTIONS ^{238}U(n,n'γ), E_n = 0.70 - 1.96 MeV, measured $\sigma_\gamma(E_n, 125°)$, inferred level cross sections for 20 states. Time-of-flight.]

Introduction

An important process which contributes to the shape of the low energy spectrum in fast reactors is the inelastic scattering for ^{238}U levels at 1 MeV excitation or higher, which results in high energy transfer and large neutron energy losses. The high energy resolution attainable from measured gamma-ray spectra makes the (n,n'γ) technique particularly attractive as the average level spacing near 1 MeV is only about 25 keV. Neutron level cross sections may be inferred from these data if all feeding and branching transitions are observed.

Experimental Methods

The (n,n'γ) measurements on ^{238}U were performed using the University of Lowell 5.5 MV Van de Graaff accelerator. Figure 1 shows the experimental arrangement. A pulsed beam of protons impinged on a solid tritium target producing near monoenergetic neutrons via the ^{3}H(p,n)^{3}He reaction. The target was wobbled and water-cooled to limit deterioration. A disc scattering sample, 3.8 cm in diameter and 1.2 cm in thickness, was located at 8.5 cm from the source of neutrons. De-excited gamma rays from the scatterer were detected by a 40 cm^{3} Ge(Li) detector placed at 125 degrees with respect to the incident neutron flux and 88 cm from the center of the scatterer. An annular NaI(Tl) detector, which surrounded the Ge(Li) detector, was used to detect Compton events. Shielding of these two detectors was accomplished using structures of lead, a lithium carbonate and paraffin mixture and a copper shadow bar. A paraffin block was placed between the scatterer and the Ge(Li) detector to reduce the neutron flux hitting the detector. Neutron monitoring during the data runs was done by a neutron time-of-flight detector (a plastic scintillator mounted on a photomultiplier tube). The 0°-neutron fluence was measured after each run with a long counter and a fission chamber in a TOF system. The absolute efficiencies of these detectors were determined by comparison to a recoil-proton telescope whose absolute efficiency is known.

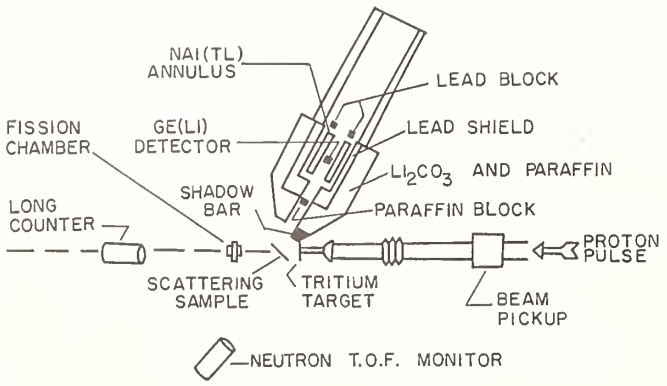

Fig. 1. Experimental arrangement.

The main components of the time-of-flight electronics are shown in Figure 2 and a typical Ge(Li) time spectrum illustrated in Figure 3 indicates the reduction of the neutron events due to the paraffin plug. Two 4096-channel energy spectra were accumulated simultaneously in the multichannel analyzer. One was the time-gated, energy-gated and Compton-suppressed spectrum yielding the accepted data. The other spectrum contained those gamma-ray events which fell in the time window but were rejected by the annulus. This procedure allowed us to determine whether the annulus was removing any "good" (n,n'γ) lines from the spectrum.

Results and Discussion

The ^{238}U level energies shown in Figure 4 were determined from our present study with the exception of the first four excited states. These energies agree in most cases to within 0.5 keV of the (n,n'γ) results of McMurray et al.[1] Spin-parity assignments were taken from Nuclear Data Sheets.[2] There are approximately 15 additional levels for the adopted level scheme in Nuclear Data Sheets[2] for the energy region shown here. Most of these are from Coulomb excitation and ^{238}Pa β-decay studies. Some of the transitions have been multiply-placed in the level scheme. Although one of the primary aims of our experiment was to measure low-energy transitions between energy levels near 1 MeV only four gamma rays were observed for states decaying to those above the one at 307.2 keV.

The 125° data obtained from the energy spectra were converted to gamma-ray production cross sections by performing corrections for the efficiency of the Ge(Li) detector, neutron flux normalization, analyzer dead time, neutron target thickness and finite sample size effects (which included neutron attenuation, gamma-ray attenuation, neutron scattering and the anisotropy of the neutron source). Total uncertainties in the gamma-ray production cross sections were typically 10% for the strong transitions and 20% for the weak ones.

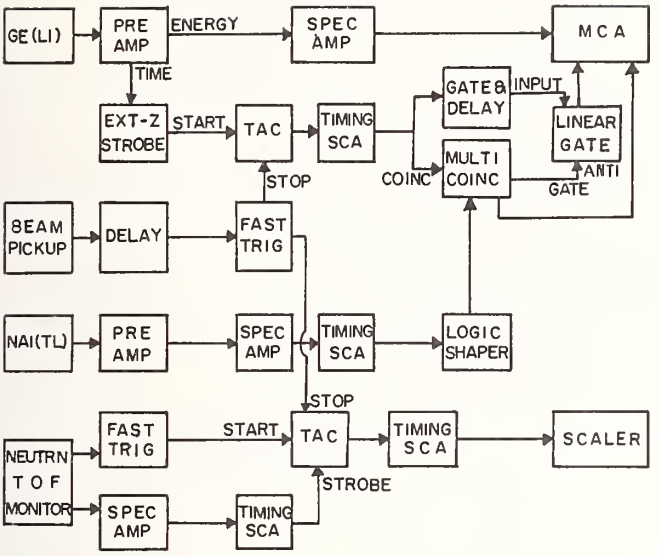

Fig. 2. Time-of-flight electronics.

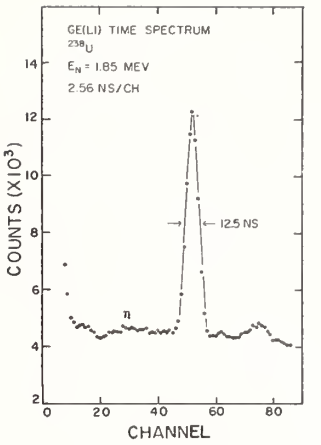

Fig. 3. Ge(Li) time spectrum.

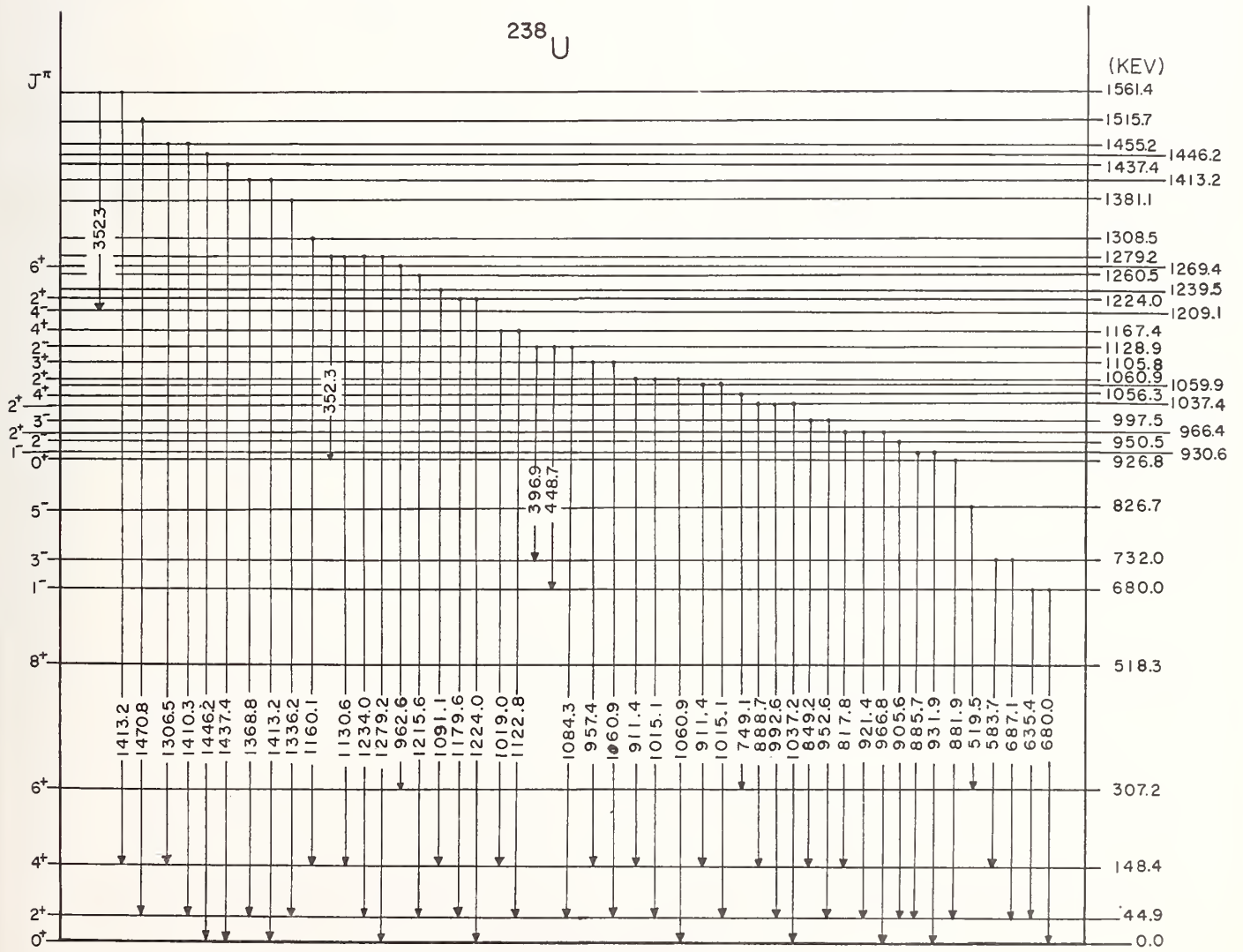

Fig. 4. Energy level scheme for ^{238}U.

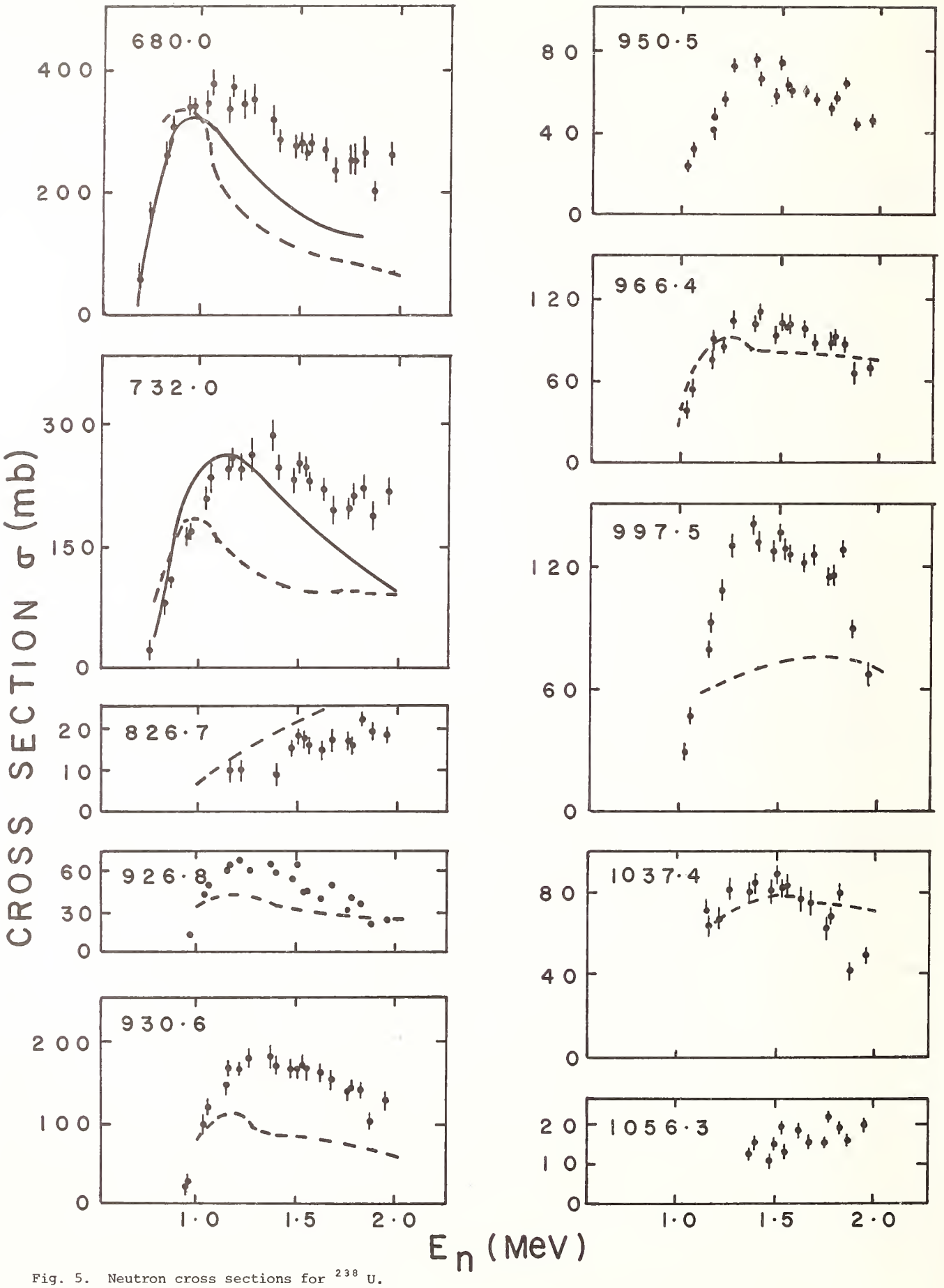

Fig. 5. Neutron cross sections for ^{238}U.

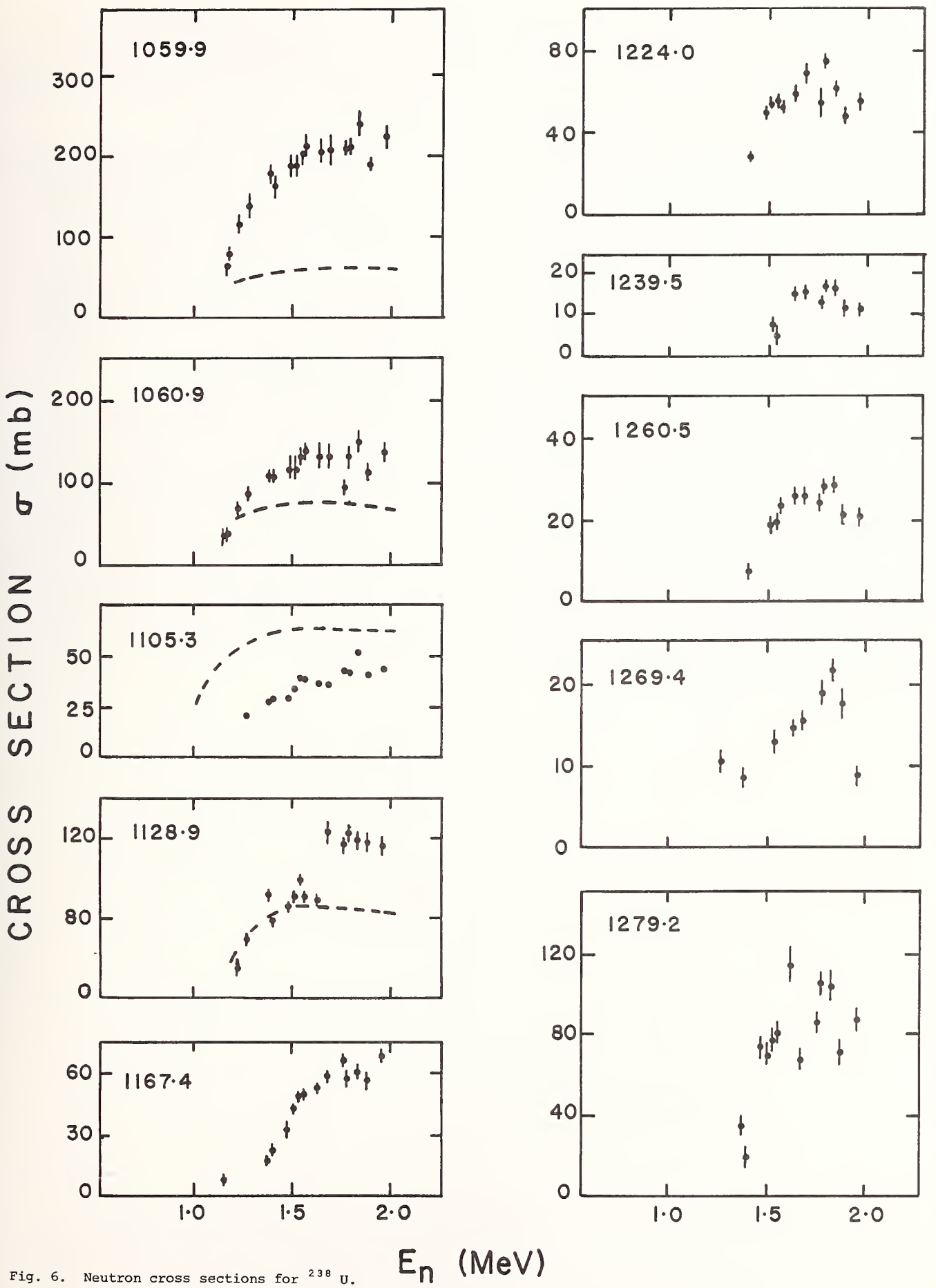

Fig. 6. Neutron cross sections for ^{238}U.

Angle-integrated cross sections for 27 levels were deduced from the gamma-ray production results at 125° by integrating the gamma-ray angular distributions, summing the cross sections for transitions from a particular level and subtracting any feeding to that level. The integration was approximated by multiplying the 125° data by 4π, thereby assuming that contributions due to P_4 and higher-order Legendre polynomials are negligible. Theoretical calculations indicate that at worst this approximation will produce an error of a few percent.

The neutron inelastic cross sections for the first 20 excited states of ^{238}U are shown in Figures 5 and 6. Uncertainties are indicated where they exceed the size of the plotted points. The solid curves are ENDF-V and the dashed curves are statistical compound-nucleus model predictions calculated by the computer code, CINDY[3] using the optical potential parameters of Haouat, Lagrange et al.[4]

Only three ^{238}U inelastic cross sections in ENDF seem to correspond to individual levels. The ENDF values for the 1^- 680.0 keV level and the 3^- 732.0 keV level shown in Figure 5 are significantly smaller than our deduced (n,n') results. The ENDF values for the 5^- 826.7 keV level are approximately 10 times that of our data. Although ENDF lists many more "level" cross sections, the energies must be for groups of levels and therefore cannot be compared directly with our data.

Statistical compound-nucleus model calculations are shown for 12 levels in Figures 5 and 6. Values for the 950.0 keV and 1056.3 keV levels were too large to appear in the plots. In most cases the theoretical values underestimate the measured cross section by a significant amount, suggesting that it may be necessary to include a direct-interaction model calculation.

Future work will involve taking selected high resolution (n,n') measurements in order to see how reliable the (n,n'γ) results are in determining inelastic cross sections for ^{238}U. McMurray et al.[1] has suggested that the disagreement is quite substantial.

Acknowledgements

The authors wish to express their gratitude to Drs. J. J. Egan, G. H. R. Kegel and D. J. Pullen for their assistance in many aspects of this research.

This work was supported in part by the United States Department of Energy.

References

1. W. R. McMurray, E. Barnard, I. J. van Heerden and D. T. L. Jones, Southern University Nuclear Institute Annual Report (196).

2. Y. A. Ellis, Nuclear Data Sheets, 21, #4, Aug. 1977 (Academic Press).

3. E. Sheldon and V. C. Rogers, Computer Physics Communications, 6, 99(1973).

4. G. Haouat, J. Sigaud, J. Lachkar, Ch. Lagrange, B. Ducheim and Y. Patin, Bruyères Report NEANDC(E) 180 "L"; INDC(FR) 13/L (Bruyères-le-Châtel, 1977).

NEUTRON INELASTIC SCATTERING CROSS SECTIONS OF ^{232}TH OBTAINED FROM (n,n'γ) MEASUREMENTS

J.J. Egan, J.D. Menachery, G.H.R. Kegel and D.J. Pullen
Department of Physics and Applied Physics
University of Lowell
Lowell, Massachusetts 01854

The ^{232}Th(n,n'γ) reaction has been studied up to 2.1 MeV bombarding energy for states with excitation energies from 700 to 1700 keV. Seventy-five gamma-ray transitions from forty-three above the first excited state have been observed from a disk scatterer with a 40-cm^3 Ge(Li) detector surrounded by an anti-Compton annulus of NaI(Tℓ). The time-of-flight technique was employed to further reduce background. Cross sections for twenty-two states are reported here. The data have been corrected for the finite sample effects of neutron and gamma-ray attenuation, and neutron multiple scattering. The results are compared to those of McMurray et al. and to the predictions of the compound nucleus statistical model. A compound nucleus plus direct interaction calculation is also shown for the 1^- state at 714 keV.

[NUCLEAR REACTIONS ^{232}Th(n,n'γ) E = 0.7 - 2.1 MeV; measured $\sigma_\gamma(E_n,125°)$; inferred level cross sections for 22 states. Time-of-flight. Comparison with calculated excitation functions]

Introduction

Recent concern about reactor safety, proliferation of plutonium and waste management, along with the limitations of known uranium reserves have led to the consideration of breeder reactors using fuel cycles other than the ^{232}Th/^{233}U fuel cycle. The ultimate choice of fast breeder systems will depend on careful analyses of the often conflicting requirements of economics, reactor safety and proliferation safeguards.

A complete and accurate data base is essential in evaluating the various breeder reactor alternatives. One of the largest uncertainties of these analyses arises from the lack of neutron inelastic scattering cross sections for core and blanket materials. In a fast breeder reactor utilizing the ^{232}Th/^{233}U fuel cycle, neutron inelastic scattering in ^{232}Th provides the strongest slowing-down mechanism and is mainly responsible for the shape of the neutron energy spectrum.

The present work involves the determination of inelastic cross sections for neutrons scattered from states in ^{232}Th at excitation energies near 1 MeV. This is a region where the level density is high and hence presents difficulties for investigation by direct observation of the scattered neutrons. However, the (n,n'γ) technique with its high resolution is ideally suited to such studies.

Experimental Methods

The experimental details for the ^{232}Th(n,n'γ) work are essentially the same as those described in the previous paper on ^{238}U. Neutrons were produced by ^{3}H(p,n)^{3}He. The Ge(Li) detector was used in conjunc-

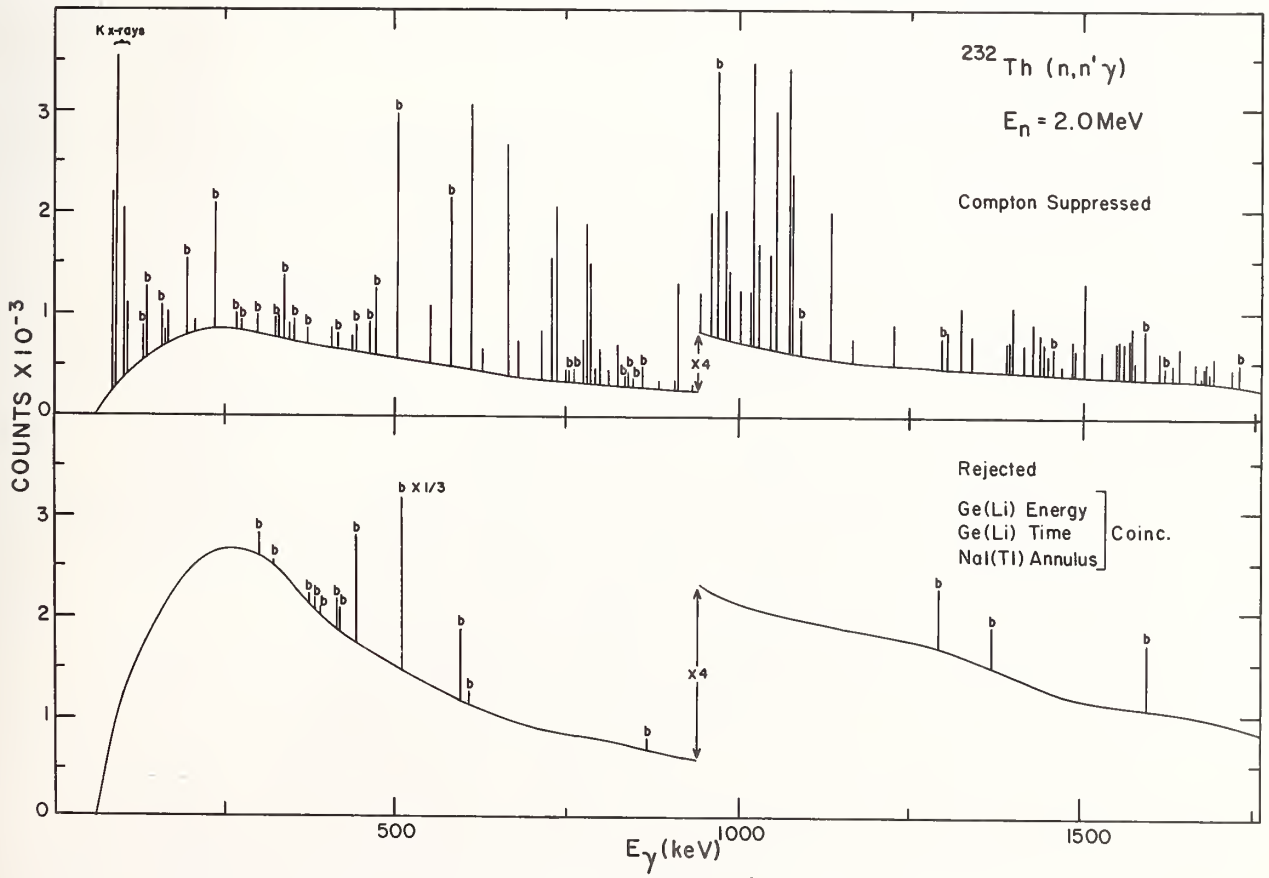

Fig. 1. Simplified representation of a Compton suppressed ^{232}Th(n,n'γ) spectrum (top); and the spectrum of events rejected by the suppression system for the same data acquisition run (bottom).

tion with a time-of-flight system and an NaI(Tl) annulus was employed in order to suppress Compton events. A disk-shaped scattering sample was used resulting in lower gamma-ray attenuation than in cylindrical samples of comparable volume. The incident neutron flux was monitored by a long counter, a fission chamber and an auxiliary time-of-flight system using a plastic scintillator. All measurements were made at 125° to the beam direction, near a zero of the Legendre polynomial of second order, thus facilitating the extraction of neutron cross sections from the data.

Figure 1 is a simplified representation of a ^{232}Th Compton suppressed gamma-ray spectrum and the spectrum of events rejected by the Compton suppression system but accepted in the time window in the Ge(Li) TOF system. Lines marked (b) are due to room background and to natural radioactivity in the thorium sample. Unmarked lines are from the (n,n'γ) reaction. The lower spectrum is plotted on the same scale and was obtained during the same run as the upper one. The advantages of Compton suppression are clearly seen. The sum of these two spectra would result in the spectrum which would have been obtained with time gating but no Compton suppression. None of the Th(n,n'γ) lines were observed in the rejected spectrum.

Results and Analysis

Figure 2 shows the level and decay scheme derived from the present work. The energies of states above 700 keV have been obtained from an analysis of the centroids of the gamma-ray peaks in the twenty-five spectra, the transitions from lower energy levels appearing in all the spectra with those from the highest levels studied appearing in at least five spectra. The spins are taken from the Nuclear Data Sheets.[1]

The decay scheme shows seventy-two transitions from forty-three levels above the 49 keV first excited state. The dashed transitions were definitely observed but there is some doubt as to where they should be placed in the level scheme. The dashed levels at 1716 and 1727 keV are tentatively placed in the level scheme on the basis of the appearance of transitions whose thresholds are in accord with states at those excitation energies.

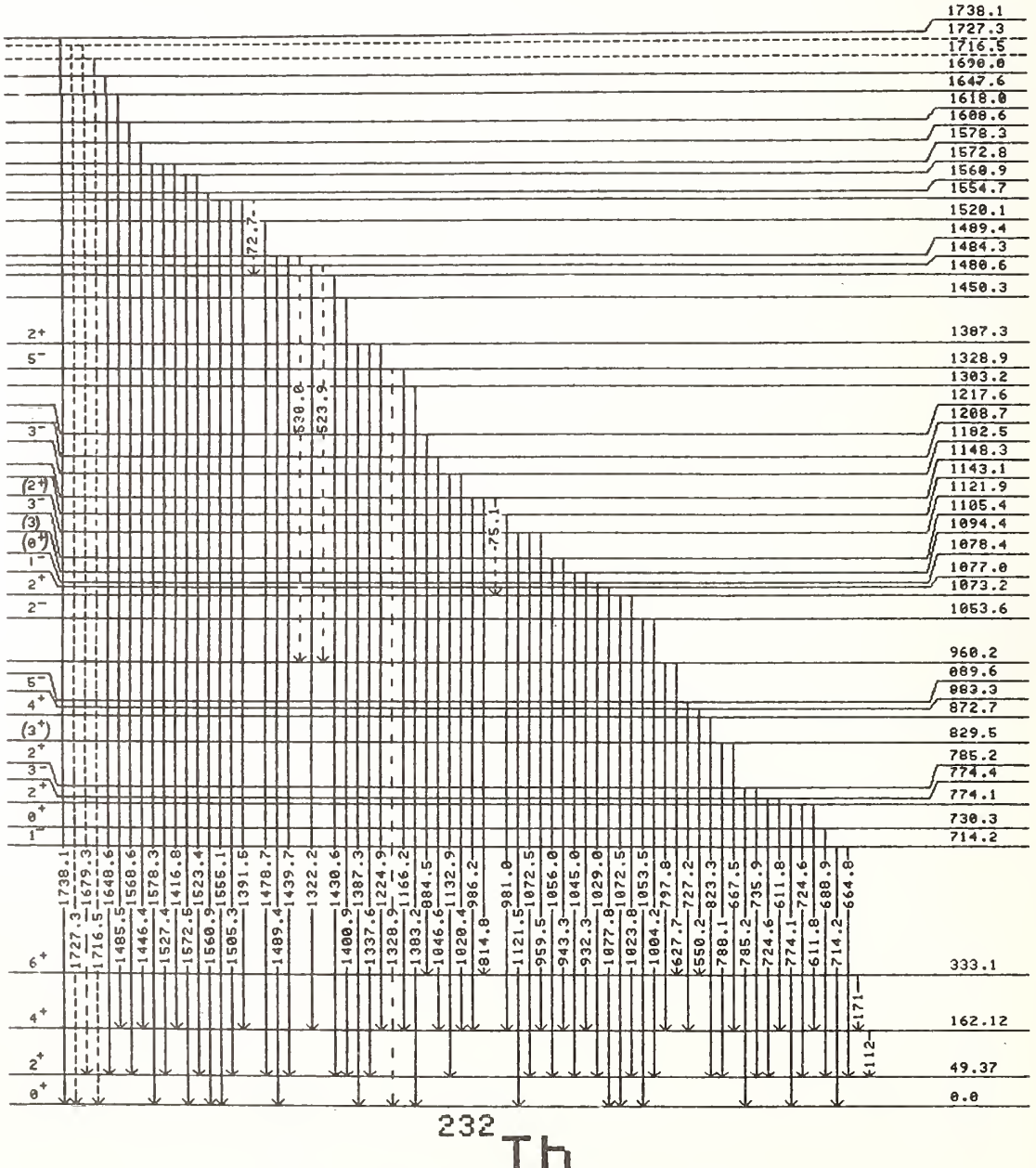

Fig. 2. The level and decay scheme of ^{232}Th

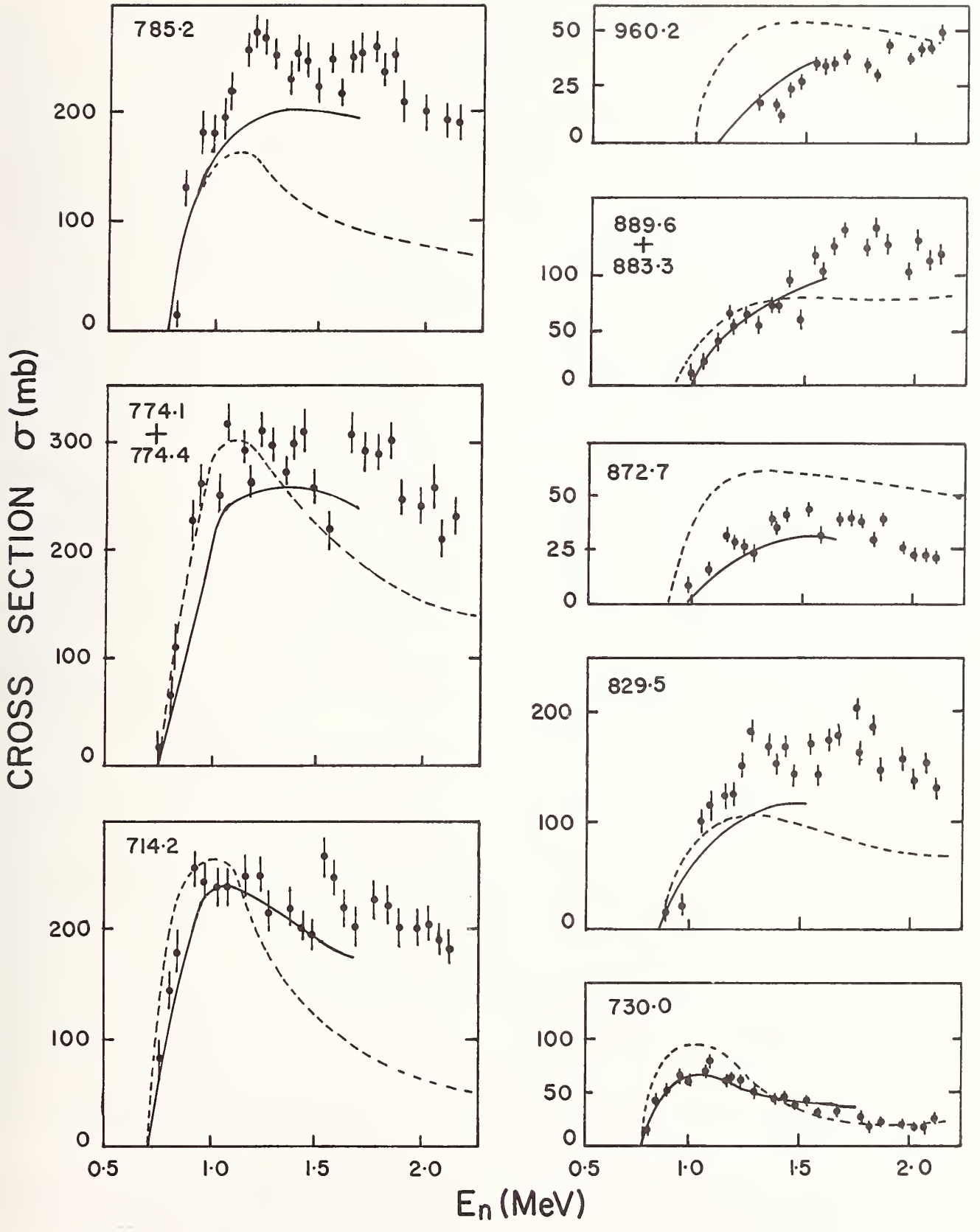

Fig. 3. Cross Sections for levels from 714.2-960.2 keV in ^{232}Th. Solid lines approximate the (n,n'γ) data of Ref. 3. Dashed curves are compound nucleus calculations.

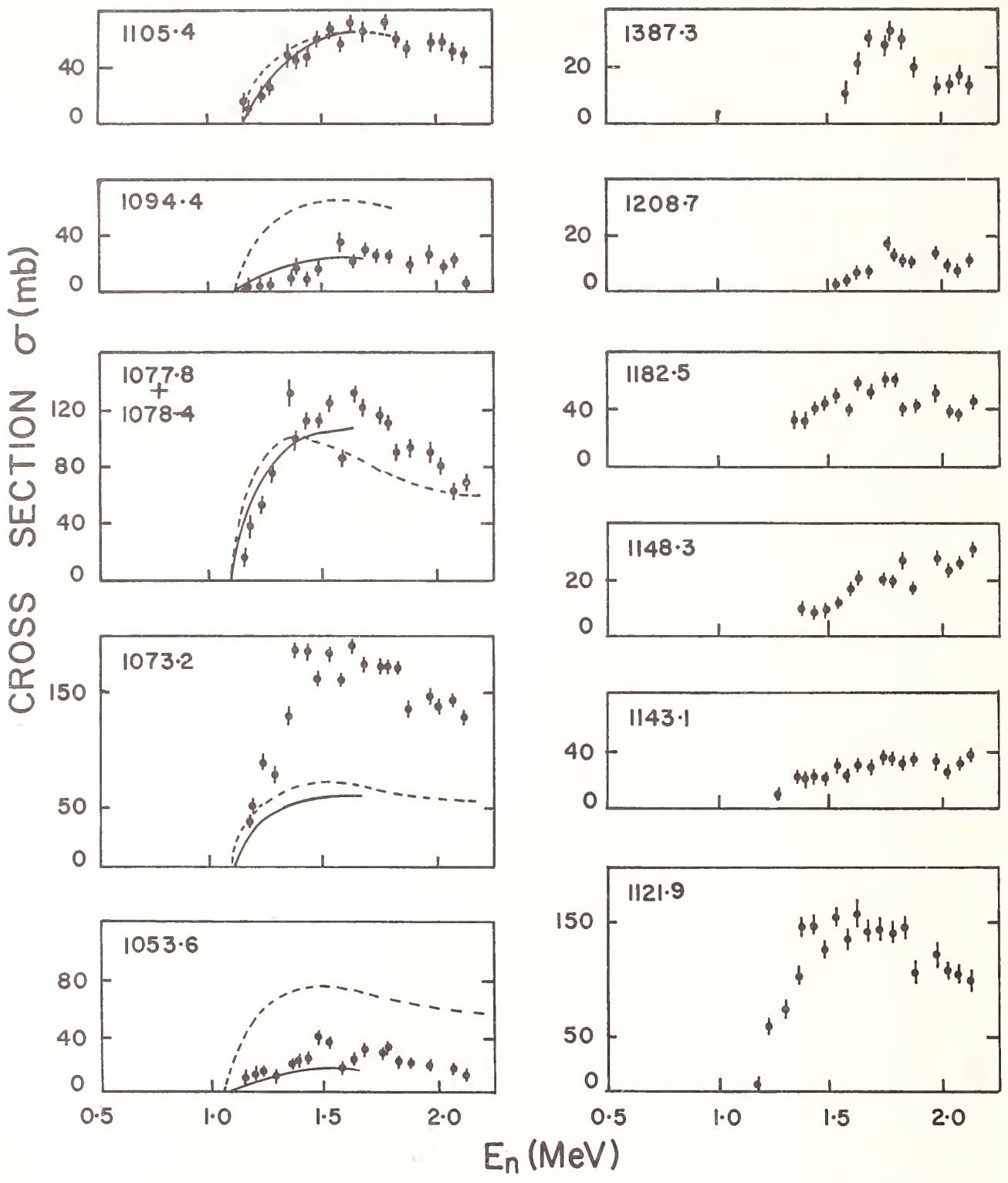

Fig. 4. Cross Sections for levels from 1053.6-1208.7 keV and 1387.3 keV. Solid lines approximate the (n,n'γ) data of Ref. 3. Dashed curves are compound nucleus calculations.

Figures 3 and 4 show the inelastic cross sections for twenty-two states obtained from our (n,n'γ) data by summing the gamma-ray production cross sections for transitions which originate at a level and subtracting off any feeding transitions. The integrated gamma-ray production cross sections were obtained by multiplying the 125° differential cross sections by 4π. The error introduced by assuming that the gamma-ray angular distribution can be represented by a series of even-order Legendre polynomials in which all but the first two terms are neglected is at worst 1%, based upon computations of (n,n'γ) angular distributions for ^{232}Th using the compound nucleus statistical model code CINDY.[2] These calculations showed that the Legendre coefficients a_4, a_6, ... were vanishingly small.

The data have been corrected for the finite sample effects of neutron attenuation and multiple scattering as well as gamma-ray attenuation using the codes NEVES and PENHA which were developed at our laboratory by G. H. R. Kegel to deal with disk scattering geometries. Corrections have also been applied for internal conversion and account has been taken for the variation of the incident fluence over the sample.

The principal causes of uncertainty in the data include statistical errors, ranging from a few percent to as much as forty percent for some very weak transitions, uncertainty in yield extractions (1 - 20%), uncertainty in the incident neutron fluence (5%), and uncertainty in the Ge(Li) detector efficiency (4 - 6%).

The solid curves in Figures 3 and 4 are visual fits to the cross section data reported by McMurray et al.[3] based upon (n,n'γ) measurements. For the most part our results follow the trend of those of McMurray et al. with ours being somewhat higher in magnitude for some of the transitions. The dashed curves represent theoretical calculations based upon the compound nucleus statistical model performed with the code CINDY[2] using the optical potential of Haouat, Lagrange et al.[4] The calculations are in reasonable agreement for some states (e.g. 730 and 1105 keV) while for others there are serious discrepancies in magnitudes, but the general shape is in agreement (e.g. 827 and 1054 keV). However, in certain cases where the cross sections are large, and hence more easily measured, the theory and data are in agreement up to about 1.2 MeV and become seriously discrepant at higher bombarding energies where the theory fails to account for the measured cross section. The effect is readily apparent for the 1^- state at 714.2 keV and for the combination of 2^+ and 3^- states at 774.1 keV and 774.4 keV.

The fact that the measured cross section does not fall as rapidly as the statistical model predicts suggests the possibility of a direct interaction component to the cross section.

Figure 5 shows a preliminary attempt to fit the cross section for the 1^- state at 714 keV using an incoherent sum of compound nucleus (CN) and direct interaction (DI) components. The DI calculations were performed using the code KARJUP, the Karlsruhe version[5] of the coupled channel code JUPITOR[6], with the potential of Haouat et al., coupling this 1^- state to three ground state rotational levels and to the 1^- state at 1077.8 keV in a $0^+/2^+/4^+/1^-/1^-$ scheme. The influence of the DI mechanism becomes perceptible at 1.2 MeV but the summed CN and DI cross section (solid curve) still does not account for the measured values at energies above 1.3 MeV.

The curve labeled CN(con) + DI is an attempt to improve the agreement by adding the DI calculations done at Lowell to the CN calculations of the Bruyères group[7] which use a continuum of levels beyond 1122.8keV rather than the explicit level energies. While this calculation does improve the agreement it is probably a less desirable approach than that represented by the solid curve where only real states are included.

Analysis is in progress on the cross sections for eighteen more states, from (n,n'γ) data and we have recently begun direct neutron measurements from these levels using our high resolution neutron TOF facility. The neutron measurements will supplement the gamma-ray work and should allow us to resolve

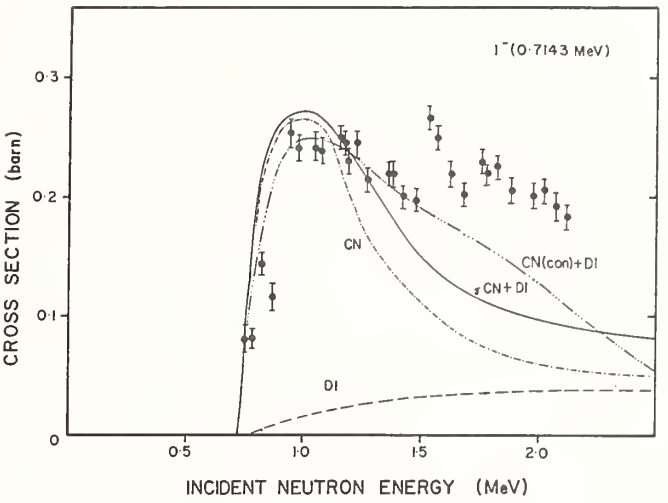

Fig. 5. Comparison of theoretical compound nucleus (CN), direct interaction (DI) and their incoherent sum (CN+DI). The broken curve marked "CN(con) + DI" represents the incoherent sum of the DI magnitude computed with KARJUP at Lowell and the CN magnitude computed at Bruyères, wherein levels above 1122.8 keV in excitation are approximated by a continuum.

difficulties in determining cross sections from gamma-ray data which arise for example when transitions have significant EO strengths.

Acknowledgements

The authors wish to acknowledge Drs. G.P. Couchell A. Mittler and W.A. Schier for their assistance in various phases of this work. We are especially grateful to Dr. Eric Sheldon for his efforts and advice involving the theoretical reaction model computations.

This work was supported in part by a grant from the United States Department of Energy.

References

1. M. R. Smorak, Nuclear Data Sheets 20, 165 (1977).
2. E. Sheldon and V. C. Rogers, Comp. Phys. Comm. 6, 99 (1973).
3. W. R. McMurray, E. Barnard, I. J. van Heerden and D. T. L. Jones, Southern Universities Nuclear Institute Annual Research Report (1976) p. 5.
4. G. Haouat, J. Sigaud, J. Lachkar, Ch. Lagrange, B. Duchemin and Y. Patin, Bruyères Report NEANDC(E) 180 "L"; INDC(FR) 13/L (Bruyères-le-Châtel, 1977).
5. H. Rebel and G. W. Schweimer, Kernforschungszeutrum Karlsruhe Report KFK-1333 (1977).
6. T. Tamura, Oak Ridge National Laboratory Report ORNL-4152 (1967).
7. H. Abou Yehia, J. Jary and T. Trochon, Bruyères Report NEANDC(E) 204 "L"; INDC(FR) 34/L (Bruyères-le-Châtel, March 1979).

NEUTRON TOTAL CROSS SECTION OF ^{233}U FROM 0.01 to 1.0 eV

J. A. Harvey, Cindy L. Moore*, and N. W. Hill
Oak Ridge National Laboratory,
Oak Ridge, Tennessee 37830 USA

At the last Nuclear Cross Sections and Technology Conference, B. R. Leonard stressed the importance of improved total cross section data for ^{233}U in the energy region from 0.1 to 0.2 eV. We have measured the neutron total cross section of ^{233}U from 0.01 to 1.0 eV at ORELA using a repetition rate of 25 sec^{-1} and a 17.872 flight path. Two samples of ^{233}U enriched to 99.76% with inverse thicknesses of 165.2 and 321.1 barns/atom were measured. The data were corrected for neutron and gamma ray backgrounds which were $\lesssim$1%. Results from the two samples are in good agreement. The data are compared to earlier data and to ENDF/B-V evaluation.

[Measured σ_T for ^{233}U, 0.01 to 1.0 eV, resonance at 0.15 eV, ^{233}U-Th breeding cycle]

Introduction

For over 30 years there has been fluctuating interest for reactor technology in the variation with neutron energy of the total, capture and fission cross sections and (the number of fission neutrons per neutron absorbed) of ^{233}U in the thermal energy region. This is because of the thorium-^{233}U breeding cycle which is possible for thermal energy neutrons. Measurements and multilevel analysis of fission and total cross section data of ^{233}U by Moore et al.[1,2] showed the existence of a very small resonance at 0.15 eV which required a two fission channel multilevel analysis to fit the data. The assumption that the number of neutrons per fission, ν, was constant for low energy neutrons predicted a decrease of η of $\sim$4% from 0.04 to 0.15 eV. Measurements by Weston et al.[3] of the fission and capture cross sections showed a 4.5% decrease of η in this energy range, again based on a constant ν. Although Weston et al. normalized their data below 1 eV to the total data of Moore et al., Leonard,[5] at the last NCS&T Conference, concluded that the total cross section computed from Weston's data based on the scattering cross section from the evaluation of Drake et al.[4] differs systematically from the measured total cross section in the energy region from 0.1 to 0.2 eV. In addition, Leonard claimed that the existing total cross section data set of Moore et al.[1] was not in particularly good agreement with that of Pattenden and Harvey[6] in this region. Finally Leonard concluded that "This is a very important energy region for ^{233}U and improved total cross section data would improve the understanding of problems here". In order to satisfy this need we have made measurements of the neutron cross section of ^{233}U from 0.01 to 1.0 eV, which in the energy range from 0.1 to 0.2 eV have an uncertainty of $\lesssim$1%.

Measurements

Neutron transmission measurements have been made upon four samples of ^{233}U at ORELA using a 17.872-meter flight path. The accelerator was operated at a repetition rate of 25 sec^{-1} and an electron burst width of 24 nsec with 1 kW power on a Ta target. Neutrons from the Ta target are moderated in a water moderator (3-cm thick) surrounding the Ta target and a shadow bar prevents the detector from seeing the Ta target. The detector was a ^{6}Li glass scintillator, 1.3 cm thick and 10 cm dia, which is essentially black for the energy region studied in this work. An energy resolution of 0.3% was deduced from the thickness of the ^{6}Li detector and the neutron mean free path in the water moderator. Neutron energies were computed from the flight path and the flight times. The "zero" time reference was established by observing the gamma flash from the target. The uncertainty in flight path was $\leq$0.5 cm resulting in an uncertainty in the energy scale of $\leq$0.1%.

Two ^{233}U sample thicknesses were used with thicknesses of 1.26 and 0.65 mm. In addition to the open beam and sample-in runs, data were also taken with a sample of polyethylene 7.5 cm thick and with a sample of uranium 0.73 cm thick. In order to minimize any drifts in the electronic equipment, complete cycles of the different samples and open beam were taken every 40 minutes for 35 cycles. The ^{233}U samples and open beam were measured for 11 minutes each per cycle and the polyethylene and uranium for 3 minutes each. Corrections for the 1.1-μsec deadtime of the time digitizer were 0.3% at 0.6 eV and 0.2% at 0.08 eV for the open beam and less for the sample-in data. Corrections were made for three types of background (1) a constant room background determined with the accelerator off, (2) a 17.6-μsec background due to 2.23-MeV gamma rays from neutron capture in the water moderator, and (3) a long time background due to scattered neutrons from other experiments in the electron room at ORELA which has a dependence of the form 1/time. At 0.12 eV the correction for all 3 backgrounds was 1.3% for the thick ^{233}U sample, 0.7% for the thin sample and 0.25% for the open beam.

^{233}U Samples

The ^{233}U metal used for the samples was produced over 20 years ago at ORNL from ^{233}Pa decay by separating the ^{233}Pa from highly irradiated thorium shortly after the irradiation to minimize the ^{232}U contamination. Metal foils of various thicknesses, 3.81 x 7.62 cm in area were made by the Metallurgy Division, ORNL, again over 20 years ago. At that time the foils were accurately weighed and measured, and all showed about a one percent non-uniformity in thickness. Some of these foils were used in the measurements of Pattenden and Harvey[6] and Block et al.[7] The isotopic analysis of the ^{233}U is given in

Table I

Isotopic Analysis of the Uranium in the ^{233}U Metal Samples

Mass No.	Atom percent
232	0.6 ppm
233	99.76 ± 0.01
234	0.022 ± 0.001
235	0.007 ± 0.0007
236	1 ppm
238	0.21 ± 0.01

*Summer student, Roberts Wesleyan College, Rochester, New York.

Table I. A spectroscopic analysis and a search[6] for resonances characteristic of specific impurities showed that no impurity was present in sufficient quantity to make any significant error in calculating the ^{233}U thicknesses. However, a chemical analysis showed 0.25% by weight carbon impurity, which was included in calculating the sample thicknesses. The thick sample (Foils No. 4 and 5 of reference 6) has an average inverse sample thickness of ^{233}U of 165.2 b/atom over the beam area used in these measurements and has a transmission of 1/e at ∿0.5 eV. The thin sample (Foil No. 2 of reference 6) has an average inverse thickness of 321.1 b/atom and has a transmission of 1/e at ∿0.08 eV.

Results and Discussion

Figure 1 shows the measured total cross section (in barns) times $\sqrt{E(\text{in eV})}$ for the thick sample as Δ's and for the thin sample as +'s. The solid curve is from the ENDF/B-V evaluation. The data for the thin

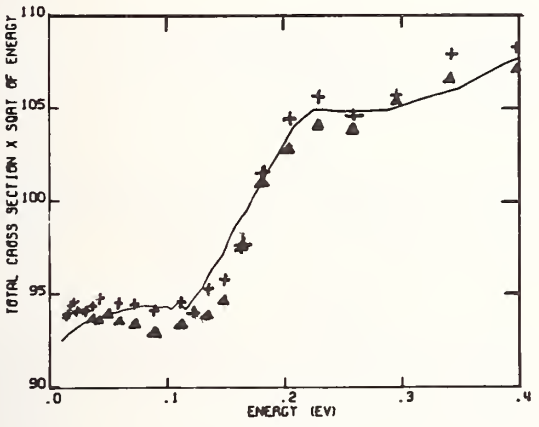

Fig. 1. Comparison of the measured total cross section of ^{233}U times $E^{1/2}$ for the thick ^{233}U sample Δ's, and the thin sample +'s, and the curve of ENDF/B-V.

sample are systematically about 1% higher than the data for the thick sample. Some of this discrepancy probably arises from the uncertainties in the corrections (1.0% for the thick sample and 0.5% due to the thin sample) due to the non-uniformity in the thickness of each foil and because the transmission of only about 20% of the sample area was measured. Even though there is a systematic difference between the measured total cross sections for the two sample thicknesses in this present work the shapes are in excellent agreement. An average of the data for the two thicknesses in the energy range up to 0.3 eV agrees with the data of Pattenden and Harvey[6] and Block et al.[7] to 0.5%. The earlier data of Pattenden and Harvey and Block et al. were obtained from different samples of the same ^{233}U metal. In those measurements the transmission of almost the entire sample area was sampled so the corrections for sample non-uniformity were small.

In the energy region below 0.3 eV the present results are in good agreement (∿1%) with ENDF/B-V except from 0.12 to 0.17 eV. Below 0.2 eV the present data fall more rapidly than ENDF/B-V and are almost 3% lower at 0.15 eV. The present total cross section data in this energy region show the same discrepancy with the data of Weston et al.[3] since the ENDF/B-V was based primarily on the fission and capture data of Weston et al.

Above 0.5 eV the present total cross section data average about 2% higher than ENDF/B-V and about 1% higher than the data of Pattenden and Harvey. There is a large resonance at 0.6 eV in ^{229}Th; however, the abundance of this nuclide produced from alpha decay of the ^{233}U is only 8.9×10^{-5} after 20 years. This would give a contribution of only 0.5 barns at 0.6 eV which would be a 0.4% effect. Resonances in other nuclides produced from ^{229}Th decay should give a negligible contribution.

Conclusions

The total cross section of ^{233}U has been measured with an uncertainty of <1% below 0.3 eV and the data agree with earlier measurements of Pattenden and Harvey to 0.5% in this energy region. The present data disagree with ENDF/B-V and Weston's derived σ_T in the energy region from 0.12 to 0.17 eV where the maximum difference is almost 3% at 0.15 eV. We do not believe that this discrepancy can be attributed to errors in the measured total cross section.

The research was supported by the Division of Nuclear Sciences, U.S. Department of Energy, under contract No. W-7405-eng-26 with the Union Carbide Corporation.

References

1. M.S. Moore, L.G. Miller, and O.D. Simpson, Phys. Rev. 118, 714 (1960).

2. M.S. Moore and C.W. Reich, Phys. Rev. 118, 718 (1960).

3. L.W. Weston, R. Gwin, G. deSaussure, R.W. Ingle, J.H. Todd, C.W. Craven, R.W. Hockenbury, and R.C. Block, Nucl. Sci. Eng. 42, 143 (1970).

4. M.K. Drake, R.C. Dahlberg and B.G. McGehee, "Neutron Cross Sections for Uranium-233", GA-7076, General Atomic (1966).

5. B. R. Leonard, Proceedings of Nuclear Cross Sections and Technology Conference, NBS-425, 281 (1975).

6. N.J. Pattenden and J.A. Harvey, Nucl. Sci. Eng. 17, 404 (1963).

7. R.C. Block, G.G. Slaughter, and J.A. Harvey, Nucl. Sci. Eng. 8, 112 (1960).

TRANSMISSION AND SELF-INDICATION MEASUREMENTS WITH U-235 and Pu-239 in the 2 eV-20 keV ENERGY REGION

T.Bakalov, G.Ilchev, S.Toshkov, Tran Khanh Mai, N.Janeva
Joint Institute for Nuclear Research, Dubna, USSR

A.A.Van'kov, Yu.V.Grigoriev, V.F.Ukraintsev
Physics Energy Institute, Obninsk, USSR

The transmission and self-indication measurements with U-235 and Pu-239 have been carried out using the ^{3}He proportional counter and fission chambers in the 2 eV-20 keV energy region. The TOF technique was used with JINR pulse fast reactor IBR-30 in Dubna as a neutron source, the resolution being 100 nsec/m (^{3}He counter measurements) and 53 nsec/m (fission chamber measurements). The sample thickness was varied from 0.0013 atom/barns to 0.172 atom/barns. Average total cross sections with self shielding factors and self-shielding fission factors were determined for energies within ABBN nuclear constant set.

[self-indication, ^{3}He proportional counter, fission chamber, 2 eV - 20 keV, time-of-flight, self-shielding and fission factors.]

Introduction

The group constants, average cross sections and self shielding factors of U-235, U-238 and Pu-239 in the resonance energy region are of great importance for the fast reactor calculations. The evaluated data are obtained using the results of measurements of neutron cross sections and resonance parameters in the resolved energy region. When extrapolating the latter to the unresolved energy region the errors occur due to the measurement inaccuracy and due to the use of the theoretical model approximation. Therefore,, direct measurements are necessary for the varification of the group constants and, especially, of the resonance self-shielding factors. The present paper is devoted to this problem. Here the fissible isotopes U-235 and Pu-239 were taken ans the object for investigation.

Method

Average cross sections and self-shielding factors can be derived directly from the experimental neutron transmission.

$$\langle T_t(x)\rangle_{\Delta E} = \frac{\int_{\Delta E} G(E)\,\varepsilon(E)\,e^{-\sigma_t(E)x}\,dE}{\int_{\Delta E} G(E)\,\varepsilon(E)\,dE} = \frac{N_{on}}{N_{off}} \qquad (1)$$

Here $\langle T_t(x)\rangle_{\Delta E}$ is the neutron transmission averaged over the spectrum $G(E)$ and detector efficiency $\varepsilon(E)$ in the energy range ΔE; $\sigma_t(E)$ is the total cross section of nuclei under investigation, x is the sample thickness, N_{on} and N_{off} is the detector counting rate with the sample on and off the neutron beam, respectively. The expression (1) transforms into

$$\langle T_f(x)\rangle_{\Delta E} = \frac{\int_{\Delta E} G(E)\,\sigma_f(E)\,e^{-\sigma_t(E)x}\,dE}{\int_{\Delta E} G(E)\,\sigma_f(E)\,dE} = \frac{N_{on}}{N_{off}} \qquad (2)$$

if the detector neutron registration efficiency is proportional to the fission cross section $\sigma_f(E)$. The self-shielding factors of total and fission cross sections[1]

$$f_t = \frac{1}{\langle\sigma_t\rangle}\left[\frac{\left\langle\frac{1}{\sigma_t+\sigma_0}\right\rangle}{\left\langle\frac{1}{(\sigma_t+\sigma_0)^2}\right\rangle} - \sigma_0\right] \qquad (3)$$

$$f_f = \frac{1}{\langle\sigma_f\rangle}\,\frac{\left\langle\frac{\sigma_f}{\sigma_t+\sigma_0}\right\rangle}{\left\langle\frac{1}{\sigma_t+\sigma_0}\right\rangle} \qquad (4)$$

can be determined from the $T(x)$ and $T_f(x)$ values. Here σ_0 is the delution cross section representing the total cross section for the other isotopes in the mixture per an atom of Pu-239 or U-235.

Experiment

The resonance structure of neutron cross sections of U-235 and Pu-239 was investigated in the Laboratory of Neutron Physics (JINR). Transmission and self-indication measurements we carried out at the IBR-30 fast pulse reactor using the time-of-flight spectrometer. The transmission $T_t(x)$ was measured on the 1000 m flight path with the ^{3}He proportional counter. The self indication $T_f(x)$ - on the 59 m and 75 m flight paths with fission chamber. In the former case the so-called "reactor mode" was employed (pulse repetition rate 5 Hz pulse width 70 mcsec), the latter used the linear accelerator mode (100 Hz, 4 mcsec).

The samples were the metal discs from U-235 and Pu-239 48 mm in diameter, tightly packed in stainless steel jackets. A battery of ^{3}He counters [2] was used as the detector with a monotonious cross section function. The multilayer fast fission chambers were used as the fission dedectors[3]. The thickness of U-235 layer was 2mg/cm^2, the total amount being 2 g for Pu-239 - 0.5 mg/cm^2 and o.5 g, respectively. The fragments registration efficiency in the U-235 chamber was 70% and in the Pu-239 chamber - 50%. The transmission measurements resolution was 100 nsec/m and self-indication measurements resolution - 50 nsec/m. The U-235 samples contained 10% of U-238. The correction for U-238 was calculated with parameters derived from the U-238 transmission data. The background consisted of the following components: counter's self-background, the neutron background of the reactor beam and scattered neutrons around the detector. The background was controlled in the process of measurement. For ^{3}He counters the first component was negligible, while for the fission chamber it was rather large, i.e. 10% for uranium chamber and 18% for plutonium at a neutron energy of 10 eV, the sample thickness being maximal.

The time-depending reactor background (the second and third components) was measured in the open beam and for each sample thickness by the resonance filter

technique. Titanium, mongenese, tungsten, indium and cadmium were used as the filters. Besides the background might be determined at the energies of"black" resonances of U and Pu.

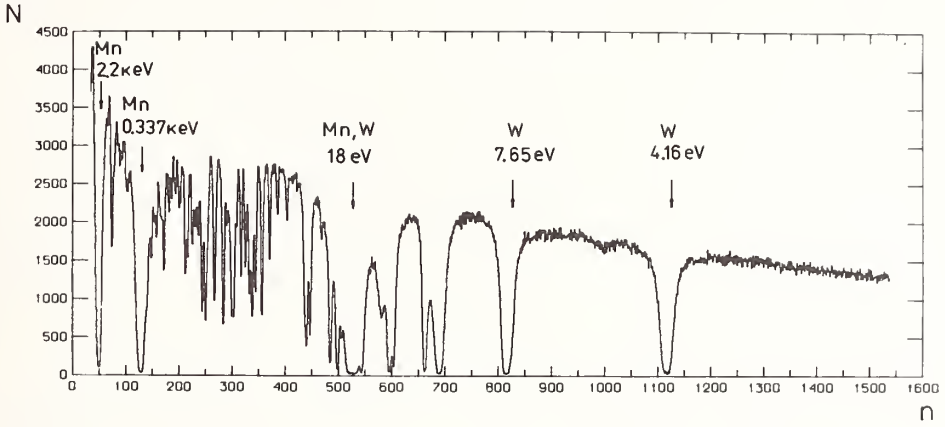

Fig.1. Time-of-flight spectrum for the ^{3}He detector on the 1000 m flight path, channel width 32 mcsec with resonance filters Mn, W on the neutron beam, Pu thickness 0.00823 atom/bn.

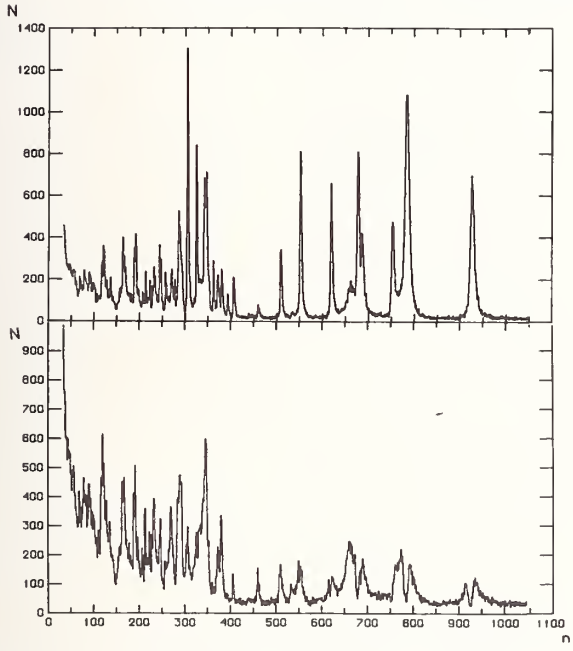

Fig.2. Time-of-flight spectrum for the Pu-239 fission chamber on the 75 m flight path, channel width 2 mcsec.
a) Pu-239 off
b) Pu-239 0.00412 at/bn on

Fig. 2 show the time-of-flight spectra for fission chambers in the open beam and for the plutonium sample 0.00412 atom/barn thick (plutonium self-indication measurements). The deficit of neutrons with energies near 337 eV is observed due to the presence of resonance of manganese present in the material of the neutron guide shelters. Background as a function of channel numbers was approximated on the computer by polynim and subtracted from the experimental spectrum. The background component in the open beam for the ^{3}He detector was found to be about 2 - 5 %, and 20 - 40 % for the maximal sample thickness. For fission chambers they varied from 5 - 15 % in the open beam and up to 30 - 60% for maximal sample thickness.

The final treatment of transmissions and self-indications was carried out by both the least square method and maximum likelihood approach with the use of the apriori information[4,5]. The results are close.

Results

The experimental transmissions $T_t(x)$ and self-indications $T_f(x)$ for 8 U-235 and Pu-239 samples of thickness ranging from 0.0013 to 0.17 atom/barn and from 0.0022 to 0.1234 atom/barn, respectively, after averaging over the energy intervals adopted in the system of constants ABBN[1] are presented in tables 1 and 2.

The self-shielding factors of total and fission cross sections obtained in the treatment of curves $T_t(x)$ and $T_f(x)$ are presented in Tables 3 and 4.

For U-235 and Pu-239 isotopes the errors of the self-shielding factors f_t in the energy range 21.5 - 1 keV are about 8 - 10 % and for energies below 1 keV are about 5 - % for zero delution cross section. For fission self-shielding factors f_f the errors are about 5 % in the energy range 21.5 keV and about 3 - % at energies below 1 keV. The uncertainty of factors f_t and f_f decreases with increasing σ_0 . The uncertainty is mainly due to the uncertainty introduced by the background subtraction procedure.

Statistical errors do not exceed 0.3 % in each run of measurements.

It should be noted that in papers[6,7] there reported the similar data on self-indication of Pu-239 and U-235 in a narrow sample thickness interval (from 0.00015 to 0.00756 atom/barn for Pu-239 and from 0.0036 to 0.049 atom/barn). In comparable ranges of neutron energies and sample thicknesses the results of [6,7] are in agreement with those of the present paper.

Figures 3,4 show self-shielding factors obtained in our experiment, as well as some calculational estimates : ABBN[1] (version 1978, evaluated by Nikolaev e.a., f-factors data published in[10,11]),UKNDL[8],Kidman & Schenter[9]. The figures demonstrate a significant dispersion of data.

Acknowledgement

The authors would like to express their gratitude to L.B.Pikelner, M.N.Nikolaev and A.M.Tsibula for fruitful discussions.

References

1. L.P.Abagian, N.O.Bazazian, et al., Grupovye konstanty dlia rascheta iadernykh reaktorov, M.Atomizdat, 1964.

2. B.Beller, A.A.Van'kov, et al., Kompaktnyi neitronnyi detektor v vide batarei iz proportsionalnykh ^{3}He schetchikov,PTE, 1974,v.6,p.57.

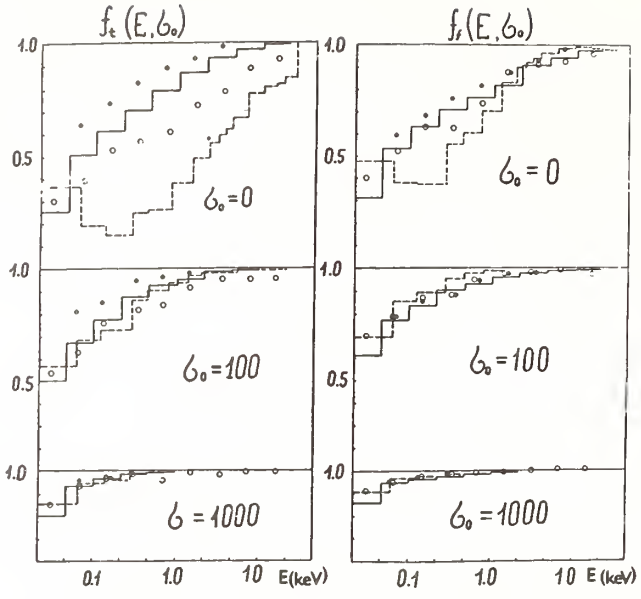

Fig. 3. Resonance self-shielding factors for U-235
Neutron total and fission cross sections.
o experiment
—— ABBN [1]
--- UKNDL [8]
● Kidman and Schenter [9]

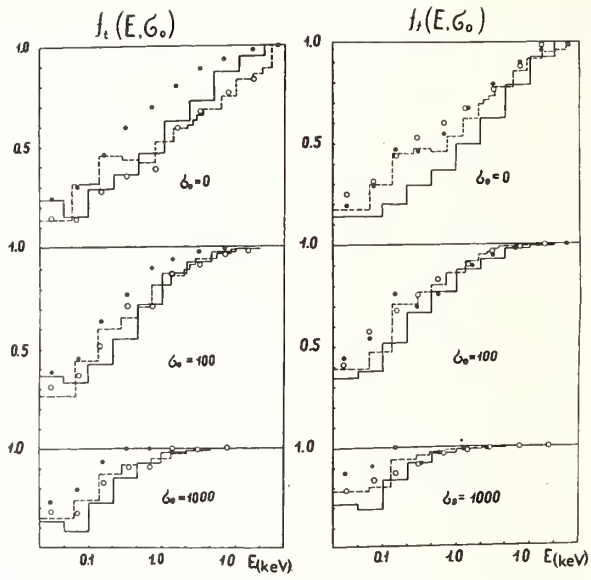

Fig. 4. Self-shielding factors for Pu-239
o experiment
—— ABBN [1]
---UKNDL [8]
● Kidman and Schenter [9]

3. A.A.Bogdzel, Yu.V.Grigoriev, et al., Bystrodeisvuyuschaia ionizatsionnaia kamera s radiatorami iz U-235, PTE,1976, v.1,p.36

4. A.A.Van'kov, Yu.V.Grigoriev et al., Temperaturnaia zavisimost struktury polnogo secheniia U-238 v oblasti nerazreshennykh resonansov, Conf.on Nucl. Data for Reactors, Vienna, 1970, v.1, p.599.

5. T.Bakalov, A.A.Van'kov et al., Baiesovxkii metod obrabotki izmerennykh funktsii propuskanija neitronov dlia opredeleniia faktorov resonansnogo samoekranirovaniia i drugikh srednikh kharakteristik, JINR Communication, P3-12230, 1979

6. J.B.Czirr, R.L.Bramblett, Measurement of Fissions Produced in Bulk Plutonium-239 by 2 eV to 10 keV Neutrons, NSE, v.28, N.1,1967, p.62.

7. R.L.Bramblett, J.B.Czirr, Energy Dependent Shielding Factors for U-235 Foils from Transmission Experiments NSE,v.35, N.3, 1969, p.350.

8. E.Menapace, M.Motta, A 26 group library with self-shielding factors fast reactor calculations from the UK Nuclear Data Files, CNEN-RT/FI(73)-15,1973.

9. R.B.Kidman, R.E.Schenter, Group Constants for Fast Reactor Calculations, HEDL-TME-71-36, March, 1971.

10. A.A.Van'kov, Yu.V.Grigoriev et al., Izuchenie samoekranirovki neitronnykh sechenij tiazhelykh iader, Preprint, FEI-905, 1979.

11. T.Bakalov, A.A.Van'kov et al., Eksperimental'nye issledovaniia effektov rezonansnogo samoekranirovaniia v polnom sechenii i sechenii deleniia plutonia-239, JINR Communication,P3-12404,1979.

Table 1a. Neutron transmission for U-235 measured with the ^{3}He detector.

No.	E_n	Sample thickness in 10^{-2} atom/barn						
		0.257	0.386	1.029	2.145	4.290	8.580	17.160
11	10-21.5 keV	0.956	0.923	0.862	0.736	0.525	0.310	0.097
		±0.011	0.022	0.015	0.013	0.017	0.012	0.006
12	4.65-10	0.954	0.919	0.840	0.704	0.502	0.267	0.077
		±0.009	0.023	0.009	0.011	0.012	0.013	0.009
13	2.15-4.65	0.947	0.904	0.801	0.661	0.449	0.227	0.056
		±0.009	0.025	0.015	0.011	0.012	0.013	0.002
14	1.0-2.15	0.936	0.902	0.780	0.624	0.392	0.187	0.040
		±0.008	0.010	0.011	0.010	0.008	0.008	0.003
15	465-1000 eV	0.918	0.879	0.746	0.564	0.339	0.145	0.028
		±0.011	0.017	0.019	0.016	0.018	0.006	0.002
16	215-465	0.904	0.848	0.704	0.507	0.294	0.127	0.026
		±0.012	0.015	0.019	0.014	0.012	0.005	0.002
17	100-215	0.890	0.826	0.659	0.456	0.240	0.101	0.016
		±0.010	0.015	0.018	0.011	0.010	0.004	0.001
18	4.65-100	0.859	0.788	0.582	0.379	0.192	0.076	0.012
		±0.010	0.014	0.017	0.011	0.009	0.003	0.001
19	21.5-46.5	0.835	0.752	0.566	0.369	0.186	0.080	0.014
		±0.010	0.015	0.016	0.011	0.007	0.003	0.001
20	10-21.5	0.819	0.739	0.550	0.356	0.164	0.062	0.006
		±0.017	0.017	0.016	0.009	0.007	0.003	0.001
21	4.65-10	0.807	0.716	0.526	0.342	0.169	0.072	0.009
		±0.018	0.016	0.016	0.008	0.007	0.003	0.001
22	2.15-4.65	0.907	0.840	0.700	0.516	0.276	0.124	0.019
		±0.010	0.017	0.019	0.013	0.010	0.006	0.001

Table 1b. Transmission through the U-235 samples measured with fission chamber

No.	E_n	Sample thickness in 10^{-2} atom/barn						
		0.129	0.257	0.515	1.029	2.145	4.290	8.580
11	10-21.5 keV	0.980	0.932	0.836	0.858	0.723	0.514	0.297
		±0.011	0.025	0.038	0.012	0.013	0.016	0.019
12	4.65-10	0.980	0.948	0.878	0.831	0.694	0.479	0.233
		±0.009	0.009	0.029	0.012	0.029	0.009	0.005
13	2.15-4.65	0.966	0.944	0.870	0.791	0.658	0.407	0.188
		±0.010	0.006	0.023	0.012	0.027	0.009	0.008
14	1.0-2.15	0.971	0.922	0.857	0.754	0.584	0.345	0.152
		±0.009	0.009	0.021	0.022	0.019	0.012	0.011
15	465-1000 eV	0.953	0.910	0.819	0.682	0.486	0.283	0.690
		±0.009	0.009	0.020	0.021	0.009	0.012	0.005
16	215-465	0.933	0.871	0.751	0.574	0.332	0.163	0.048
		±0.009	0.010	0.018	0.016	0.017	0.012	0.004
17	100-215	0.919	0.858	0.706	0.516	0.267	0.121	0.043
		±0.009	0.011	0.018	0.016	0.013	0.008	0.003
18	4.65-100	0.866	0.772	0.587	0.379	0.171	0.068	0.029
		±0.009	0.012	0.014	0.012	0.008	0.004	0.002
19	21.5-46.5	0.810	0.687	0.487	0.306	0.138	0.048	0.011
		±0.008	0.012	0.012	0.009	0.007	0.003	0.001
20	10-21.5	0.697	0.552	0.385	0.257	0.135	0.047	0.012
		±0.009	0.014	0.009	0.008	0.003	0.003	0.001
21	4.65-10	0 585	0.533	0.337	0.207	0.094	0.029	0.012
		±0.010	0.013	0.008	0.006	0.005	0.002	0.001
22	2.15-465	0.910	0.848	0.726	0.556	0.349	0.143	0.073
		±0.010	0.013	0.020	0.021	0.010	0.010	0.005

Table 2a. Neutron Transmission for Pu-239 measured with the ^{3}He detector

No.	E_n	Sample thickness in 10^{-2} atom/barn						
		0.217	0.412	0.822	1.65	3.29	6.58	12.34
11	10-21.5 keV	0.969	0.923	0.831	0.800	0.594	0.391	0.189
		±0.022	0.023	0.023	0.015	0.018	0.063	0.063
12	4.65-10	0.969	0.907	0.811	0.756	0.520	0.358	0.175
		±0.022	0.027	0.019	0.018	0.013	0.018	0.019
13	2.15-4.65	0.965	0.903	0.786	0.718	0.505	0.334	0.149
		±0.022	0.027	0.017	0.020	0.017	0.034	0.035
14	1.0-2.15	0.958	0.892	0.773	0.699	0.487	0.303	0.139
		±0.033	0.030	0.019	0.014	0.019	0.012	0.017
15	465-1000 eV	0.953	0.871	0.750	0.655	0.452	0.268	0.116
		±0.011	0.026	0.019	0.013	0.015	0.018	0.018
16	215-465	0.917	0.812	0.683	0.561	0.376	0.202	0.086
		±0.011	0.024	0.020	0.013	0.017	0.010	0.008
17	100-215	0.897	0.816	0.698	0.592	0.397	0.219	0.101
		±0.022	0.024	0.018	0.026	0.020	0.015	0.010
18	46.5-100	0.833	0.730	0.578	0.446	0.299	0.150	0.045
		±0.020	0.022	0.015	0.011	0.018	0.010	0.005
19	21.5-46.5	0.901	0.835	0.728	0.659	0.510	0.334	0.184
		±0.020	0.025	0.016	0.017	0.029	0.014	0.014
20	10-21.5	0.774	0.670	0.520	0.397	0.282	0.125	0.044
		±0.025	0.020	0.011	0.010	0.013	0.012	0.008
21	4.65-10	0.906	0.837	0.720	0.627	0.472	0.241	0.092
		±0.018	0.025	0.014	0.013	0.036	0.012	0.008

Table 2b. Neutron transmission for Pu-239 measured with plutonium fission chamber

No.	E_n	Sample thickness in 10^{-2} atom/barn				
		0.217	0.412	0.822	1.65	3.29
11	10-21.5 keV	0.938	0.859	0.818	0.790	0.548
		±0.030	0.028	0.043	0.020	0.050
12	4.65-10	0.951	0.848	0.782	0.703	0.512
		±0.030	0.020	0.026	0.020	0.020
13	2.15-4.65	0.900	0.868	0.738	0.628	0.500
		±0.014	0.012	0.025	0.011	0.015
14	1.0-2.15	0.896	0.825	0.736	0.617	0.471
		±0.050	0.010	0.030	0.040	0.010
15	465-1000 eV	0.855	0.748	0.653	0.491	0.400
		±0.060	0.010	0.015	0.010	0.004
16	215-465	0.766	0.635	0.526	0.358	0.212
		±0.034	0.012	0.010	0.048	0.010
17	100-215	0.738	0.548	0.437	0.308	0.223
		±0.034	0.010	0.017	0.030	0.060
18	46.5-100	0.538	0.385	0.284	0.163	0.076
		±0.024	0.020	0.010	0.015	0.004
19	21.5-46.5	0.485	0.284	0.209	0.166	0.128
		±0.022	0.014	0.025	0.018	0.017
20	10-21.5	0.388	0.212	0.131	0.075	0.041
		±0.016	0.010	0.030	0.008	0.003
21	4.65-10	0.454	0.297	0.356	0.202	0.150
		±0.020	0.010	0.010	0.016	0.008

Table 3. Resonance self-shielding factors of U-235 total and fission cross sections

No.	E_n	$f_t(\sigma_0)$				$f_f(\sigma_0)$			
		o	10	10^2	10^3	0	10	10^2	10^3
11	21.5-10 keV	0.923	0.930	0.965	0.994	0.959	0.966	0.987	0.998
12	10-4.65	0.882	0.905	0.967	0.995	0.931	0.949	0.984	0.998
13	4.65-2.15	0.779	0.830	0.948	0.993	0.912	0.937	0.982	0.997
14	2.15-1.0	0.734	0.772	0.907	0.987	0.883	0.907	0.968	0.995
15	1000-465 eV	0.606	0.700	0.825	0.953	0.740	0.817	0.945	0.992
16	465-215	0.545	0.592	0.812	0.972	0.622	0.696	0.887	0.989
17	215-100	0.507	0.545	0.759	0.961	0.624	0.679	0.861	0.979
18	100-46.5	0.377	0.407	0.633	0.933	0.530	0.584	0.796	0.966
19	46.5-21.5	0.296	0.335	0.542	0.861	0.407	0.476	0.701	0.928
20	21.5-10.0	0.269	0.290	0.406	0.705	0.409	0.450	0.609	0.860
21	10.0-4.65	0.270	0.332	0.489	0.832	0.344	0.379	0.559	0.838
22	4.65-2.15	0.578	0.667	0.826	0.963	0.672	0.725	0.872	0.977

Table 4. Resonance self-shielding factors of Pu-239 total and fission cross sections

No.	E_n	$f_t(\sigma_0)$				$f_f(\sigma_0)$			
		0	10	10^2	10^3	0	10	10^2	10^3
11	21.5-10 keV	0.836	0.918	0.986	0.998	0.974	0.987	0.999	1.000
12	10-4.65	0.785	0.880	0.978	0.998	0.872	0.928	0.986	0.998
13	4.65-2.15	0.728	0.778	0.924	0.990	0.765	0.826	0.948	0.994
14	2.15-1.0	0.598	0.650	0.858	0.981	0.688	0.758	0.920	0.990
15	1000-465 eV	0.386	0.475	0.696	0.909	0.598	0.676	0.831	0.460
16	465-215	0.361	0.450	0.716	0.909	0.541	0.605	0.757	0.927
17	215-100	0.269	0.300	0.521	0.829	0.435	0.485	0.664	0.888
18	100-46.5	0.165	0.190	0.357	0.672	0.300	0.360	0.658	0.835
19	46.5-21.5	0.162	0.184	0.304	0.660	0.235	0.260	0.399	0.778
20	21.5-10	0.124	0.134	0.229	0.609	0.167	0.199	0.366	0.757
21	10-4.65	0.224	0.233	0.303	0.605	0.198	0.225	0.367	0.736

TOTAL-NEUTRON CROSS SECTIONS OF HEAVY NUCLEI

W.P. Poenitz, J. F. Whalen and A. B. Smith
Argonne National Laboratory
9700 South Cass Avenue
Argonne, Illinois 60439, USA

ABSTRACT

Total-neutron cross sections of the heavy and actinide nuclei ^{181}Ta, ^{197}Au, ^{232}Th, ^{233}U, ^{235}U, ^{238}U, ^{239}Pu and ^{240}Pu were measured from 30 keV to 4.8 MeV. The experimental procedures emphasized a high consistency of the measured data. Systematic uncertainties, excluding those associated with sample masses, were $\lesssim$0.5% and statistical uncertainties were typically $\leq$1.0%. At low energies attention was given to resonance self-shielding effects. The experimental results are in good agreement with ^{232}Th, ^{233}U and ^{238}U data previously reported from this laboratory and at higher energies with the comparable values reported by Foster and Glasgow[1], excepting ^{240}Pu which was not studied in the latter work. The measured total-cross-sections were interpreted in terms of a spherical optical model and a deformed coupled-channels model.

[Total neutron cross section, 0.03-4.8 MeV, ^{181}Ta, ^{197}An, ^{232}Th, ^{233}U, ^{235}U, ^{238}U, ^{239}Pu, ^{240}Pu.]

INTRODUCTION

The measurement of total-neutron cross sections is a straight forward task using conventional transmission techniques that are inherently self normalizing and employ relatively simple equipment. This is particularly so when, as in the present work, energy-averaged cross sections are determined. In the latter cases the total cross sections are deduced from the energy-average transmission of neutrons through the sample,

$$\langle T \rangle = \langle \exp(-n\sigma(E)) \rangle. \qquad (1)$$

However, fine energy-dependent structure may be present and then the average transmission yields the average cross section, $\langle\sigma\rangle$, only to the extent that the exponential of Eq. 1 can be approximated by the linear term, $1-n\sigma(E)$, at all energies. This implies samples that are sufficiently thin so that $n\sigma(E) \ll 1$ at all energies.

In view of the simplicity of techniques involved, it is surprising that large discrepancies and/or omissions persist in total-neutron-cross-section data.[2,3] The situation is further complicated by the frequent and erroneous interpretation of reported experimental total-neutron cross sections as "true" average total-neutron cross sections, $\langle\sigma\rangle$, when they are often "effective" average cross sections, σ_{eff}, obtained at room temperature for a specific sample thickness via the inversion of Eq. 1; i.e.,

$$\sigma_{eff} = \frac{-1}{n} \ln \langle T \rangle.$$

An improved knowledge of total-neutron cross sections of heavy nuclei is desirable for a number of technological reasons. Such data are the essential envelope of evaluated data sets to which the individual partial cross sections must conform. The potential accuracy of total-neutron cross sections often can guide the evaluation of partial cross sections. The total-neutron cross section is often one of the most unambiguous model-calculable quantities (e.g., using the optional model) and thus its precise provision can guide the choice of models essential for the extrapolation and interpolation of measured data in the actinide region where radioactivity and/or sample problems make explicit measurements difficult or even impossible. It was the objective of the present work to provide accurate and internally consistent total-neutron cross sections in the heavy and actinide region and to examine their systematics and the model implications.

MEASUREMENT TECHNIQUES AND METHODS

The measurements consisted of the determination of the average transmission of a collimated neutron beam through the heavy-nuclide samples. All the measurements employed fast-neutron time-of-flight techniques at the Argonne National Laboratory Fast Neutron Generator (FNG) in one of two modes. In the "monoenergetic" mode velocity spectra were interpreted to define the primary source and control background with the incident-neutron energy and resolution defined by the neutron source. In the second "pseudo-white" mode the incident neutron energy and resolution was determined from the measured neutron flight times and flight paths using a pseudo-white neutron source. In both modes the ^{7}Li(p,n) ^{7}Be reaction provided the pulsed neutron source with proton bursts of $\approx$ 1n sec at a repetition rate of 2MHz (monoenergetic) or 0.5 MHz (white). The monoenergetic mode was employed from $\approx$ 200 keV-to 4.8 MeV with incident-neutron energy spreads of 40-120 keV. At lower energies the white mode was used with a pseudo-white source-energy spread of $\approx$ 250 keV.

A shield and collimator placed about the neutron source defined a neutron beam at a zero-degree reaction angle having a diameter in the range $\approx$ 0.5 - 1.0 cm.

The Ta, Au, Th, ^{233}U, ^{235}U, ^{238}U, ^{239}Pu and ^{240}Pu measurement samples were all right-circular metallic cylinders with densities ranging from 0.067 at/b (Th) to 0.100 at/b (Ta). The actinide samples were isotopically enriched to between 93.18% (^{235}U) and 99.76% (^{233}U). The Ta, Au, Th and ^{238}U (i.e., U) samples were elemental. Highly active samples were canned in 0.025 cm thick stainless steel shells. Chemical inpurities were negligible. During measurement periods the samples were placed $\approx$ 160 cm from the neutron source, on the collimated beam axis and with neutrons incident on the cylinder bases.

Seven samples and a void (or empty can) were mounted on an eight position wheel which rotated at ~ 3 rpm in a stepping manner alternately placing samples and void in the neutron beam. Eight time-of-flight spectra were obtained correlated with the sample and void positions of the wheel. Thus the cumulative spectra were a sum of a large number of individual short measurements made in rapid sequence. As a consequence any fluctuations of the source intensity were averaged out thus avoiding the conventional source monitor employed in the more usual sample-in, sample-out measurement technique. A number

of samples were referenced to the same void position, thereby increasing the efficiency of the system by nearly 50% relative to the usual "in-out" method. Since the samples see essentially identical source configurations improved measurement consistency can be expected.

A hydrogenous scintillation detector was used at energies above $\approx$ 1 MeV.[2] The detector was placed $\approx$ 780 cm from the source and associated pulse-shape-sensitive circuitry reduced the γ-ray sensitivity. At lower neutron energies, and extending up to $\approx$ 2 MeV, a "Black Neutron Detector" (BND)[4] was used. This device has a high low-energy efficiency with neutron detection down to $\approx$ 10 keV. However, statistical and background considerations set a lower-energy limit of 30-40 keV in the present measurements. A random-event pulser, time correlated with the pulsed-neutron source, was added to the detector signal.[5] This test pulse clearly determined the dead-time perturbations of the entire measurement system. These were usually < 1% and rarely exceeded 2%.

Data acquisition and processing was with an on-line computer system.[6] This system not only properly correlated samples and detector response but also processed the incoming information in "real time" so as to provide continuously updated total-cross-section results. This procedure not only improved the experimental efficiency but also provided for a continual monitoring of experimental progress.

Generally, measurements were made in two sample sets with Th, U and a carbon-reference sample common to both sets. Each set contained a void or empty stainless-steel container position, as appropriate, for the determination of the primary beam intensity. The carbon-reference sample provided a verification of system performance and established the energy scale and energy resolution using well known carbon resonances.[7] The carbon total cross sections resulting from the present measurements generally agreed with those of ENDF/B-V to within $\approx$ 0.5%.[7] Energy calibrations for the lower-energy "white" spectrum measurements were established by observation of well known neutron resonances in iron.[7]

DATA CORRECTIONS

Corrections associated with neutron inscattering, transmission through collimator walls and transmission through the air of the void, and for the isotopic composition of the samples were considered and found negligible. However, resonance self-shielding in the unresolved resonance region was a major concern. The samples were relatively large, therefore, the uncorrected experimental result is the effective, σ_{eff}, total-neutron cross section for the particular sample thickness at a nominal temperature of 293°K. The problem of resonance self-shielding in the unresolved resonance region is well known in the interpretation of neutron capture-cross-section measurements and is usually considered together with neutron-scattering perturbations. Analytical approximations for such corrections have been described by Schmitt,[8] Dresner,[9] and Macklin.[10] Similar corrections using Monte-Carlo techniques have been applied by Bogard and Semler,[11] Miller and Poenitz[12] and Froehner.[13] Detailed self-shielding attention has not been widely given to total-neutron cross sections despite the fact that the self-shielding effects can be large as illustrated, for example, in the context of structural materials, by Smith et al.[14] In the structural region a few very-high resolution results are available from which to determine quantitative self-shielding corrections. In the mass-energy region of the present work such high-resolution data does not exist and approximations used at lower energies[8-13] are not generally applicable. Simple model estimates indicate that self-shielding perturbations in the present context may exceed the experimental uncertainties even above 200 keV. The situation is illustrated by the ^{238}U example of Fig. 1. The potential cross section obtained from the hard-sphere model with $\ell \leq 4$, for example used by Froehner,[13] exceeds the total neutron cross section above $\approx$450 keV. The self-shielding effect should be sensitive to the differences between total and potential cross sections; i.e., to the fluctuating cross section, and is thus underestimated. Calculations using restricted angular momenta, $\ell \leq 2$, e.g. Miller and Poenitz[12]) and reactor codes (e.g., MC^{2}[15])are not much better as they tend to underestimate the potential scattering by only small amounts.

For the present work a Monte-Carlo self-shielding code was developed. It is based upon the single-level Breit-Wigner formulation of the resonances and a potential cross section derived from the optical model.

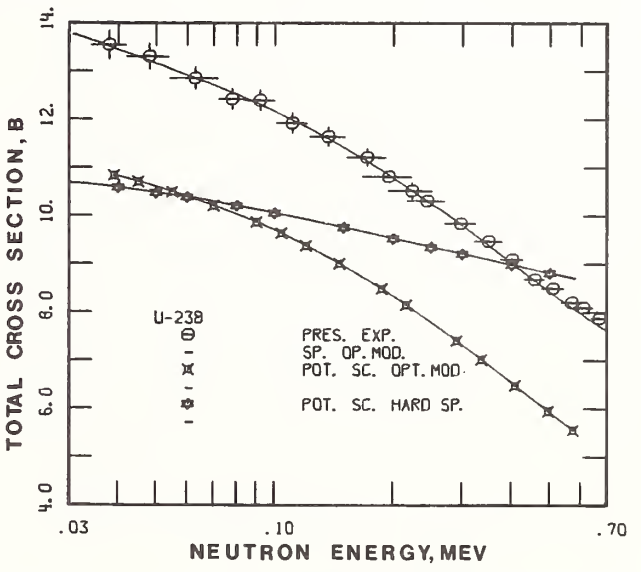

Fig. 1. Comparison of measured and calculated neutron total and potential-scattering cross sections of ^{238}U as discussed in Sec. III of the text.

The cross section is expressed as

$$\sigma_{tot} = \sigma_o \frac{1}{1+X^2} + \sigma_o \left(\frac{\sigma_{pot}}{\sigma_\lambda}\right)^{1/2} \cdot \frac{2X}{1+X^2} + \sigma_{pot} \qquad (2)$$

where

$$\sigma_o = \sigma_\lambda g_J \Gamma_n/\Gamma,\ \sigma_\lambda = 4\pi\lambda^2 \text{ and } X = 2(E-E_o)/\Gamma.$$

Averaging over many resonances yields

$$\sigma_{tot} = \frac{\sigma_\lambda}{4} \cdot \frac{2\pi g_J \overline{\Gamma}_n}{D_J} + \sigma_{pot}. \qquad (3)$$

Using the relationship

$$\frac{2\pi g_J \overline{\Gamma}_n}{\overline{D}_J} = -\ell n\ (|\eta|^2), \qquad (4)$$

with $\eta = e^{-2i\delta}$, between the resonance parameters and the complex optical model phase shift, δ, as derived by Moldauer[16] one obtains

$$\sigma_{pot} = \frac{\sigma_\chi}{2}(1-Re\eta + \frac{1}{2}\ell n(1-T)) = \sigma_{tot} + \frac{\sigma_\chi}{4}\ell n(1-T) \quad (5)$$

where $T = 1- |\eta|^2$ is the optical model transmission coefficient. The potential cross section derived from Eq. 5 is compared with measured and calculational values in Fig. 1.

Eqs. 4 and 5 were used to determine resonance parameters and potential cross sections for use in Eq. 1. Level spacings were calculated from the Fermi-gas model level density formula

$$\rho(E,J) = C \cdot (2J+1) \exp - \frac{(2J+1)^2}{8\sigma^2} \exp (2\sqrt{aE}) \quad (6)$$

where C is the constant for normalization to experimental values in the low eV range. The spin-cut-off factor, σ, and temperature constant, a, are discussed in the literature (e.g., see Refs. 17-19). A Wigner distribution was assumed for the level spacings and a Porter-Thomas distribution for the width fluctuation. An optical potential with a volume-imaginary term was used with parameters adjusted to give good representations of the total cross sections in the 20-300 keV range and of the low-energy potential scattering cross section. The calculation was inclusive of up to four inelastic scattering channels. Doppler broadening was taken into account using the ϕ and χ functions of Ref. 20 in Eq. 1 instead of $1/(1+X^2)$ and $2X/(1+X^2)$ terms.

The resulting calculated self-shielding corrections were small for ^{233}U and ^{235}U (<1% above 40 keV), of intermediate size for ^{239}Pu, ^{240}Pu and Th (<3-5% above 40 keV), and substantial for U, Au and Ta (<7-14% above 40 keV). The present correction for Au agrees very well in the 40-50 keV range with the results of calculations by Schneider and Froehner[21] for samples of similar thickness. The present results are also in good agreement with the sample-thickness dependence of transmissions of neutrons through Ta observed by Byoun and Block.[22]

RESULTS AND ANALYSIS

The results of the present measurements are outlined in Fig. 2. These values are corrected for self-shielding and these corrections, as noted above, can be substantial in some cases. Therefore these correction factors are a matter of continuing experimental and calculational study. The statistical uncertainties in the measured cross sections are typically 1% for Ta, Au, Th, ^{233}U, ^{235}U and U above 100 keV and 2% for ^{239}Pu and ^{240}Pu and for all samples below 100 keV. Uncertainties due to sample densities were estimated to be 0.5-1.0% excepting ^{240}Pu where the measured density was 78% that of the ^{239}Pu sample. The measured density of the ^{240}Pu sample was believed known to 1% but it was not possible to destroy the sample to verify its homogenity.

The present results are in very good agreement with U and ^{233}U values and in resonable agreement with Th results recently measured at this Laboratory.[23,3,2] Extensive comparisons with other previously reported values are not possible here. However, comparisons with the data of Foster and Glasgow[1] are of particular interest as these previously-reported results include all but one of the present samples, appear internally consistent and the energy range extends from well within that of the present measurements to much higher energies of particular interest from the point of view of model derivations. The Foster and Glasgow data are also shown in Fig. 2. In these comparisons averages of the results of Ref. 1 are used consisting of ten values at the lower energies, decreasing to four at the highest energies. The agreement between the two sets of data for Au, ^{233}U, ^{235}U, U and ^{239}Pu is generally good, e.g., better than 1%, in the medium-range of overlap. There is some tendency for the data of Ref. 1 to be slightly lower at low energies and the present values tend to scatter more at their higher-energy extreme. The Ta and Th results of Ref. 1 appear to differ in normalization from those of the present work by $\approx$1-3%.

It is well known that a deformed optical model is more suitable for the description of many features of the neutron interaction with strongly deformed targets than is the simple spherical optical model. This is expected to be true of the representation of the total-neutron cross section although that cross section is not as sensitive to the details of the interaction as some of the partial cross sections. It has been shown, e.g., by Glasgow and Foster,[24] that global-spherical-optical potentials are not particularly suitable for describing the total-neutron cross sections in regions of strong deformation. Much improved descriptions in these regions have been obtained using couupled-channels models, e.g., Zuffi,[25] Madland and Young.[26]

Seven of the eight nuclei studied in the present work are strongly deformed with similar deformations, β, varying from 0.248(Th) to 0.287(^{233}U).[27] A model suitable for the description of the relevant total-neutron cross sections was sought based upon the present measured data, extended to higher energies using the results of Foster and Glasgow[1]; i.e., the data base shown in Fig. 2. Initially, spherical-optical-model parameters were chosen by a simultaneous fit to the experimental total-neutron cross sections of Ta, ^{233}U, ^{235}U, U and ^{239}Pu. The resulting potential parameters are given in Table I. The total-neutron cross sections of the remaining three nuclei were then calculated in a straightforward manner using the derived potential parameters. The spherical-potential parameters of Table I are rather conventional. The absorption is somewhat outside the mean real radius as often suggested[28] and the magnitude of the parameters are similar to those frequently reported in the literature. An exception is the rather narrow and deep surface absorption term but its effective strength, W·a, is again relatively conventional. The results obtained with this spherical potential, shown in Figs. 2 and 3, are in good agreement with the measured values excepting those for Au. The latter exception is expected as the spherical potential is a parameterization of total-neutron cross sections in a deformed nuclear region and should not be suitable for the spherical exception, Au.

Recently, Guenther, et al.,[29] have deduced a coupled-channels model for the description of the neutron interaction with ^{238}U giving particular attention to neutron scattering processes. This model was used to calculate total-neutron cross sections of Th and ^{240}Pu including the consideration of deformation with the results shown in Figs. 2 and 3.[30] Fig. 3 also shows a ^{240}Pu result obtained with the coupled-channels model of LaGrange and Jary.[31] The description of the total-neutron cross sections obtained with the coupled-channels model is marginally better than that obtained with the above simple spherical optical parameterization. The coupled-channels model is far more suitable when dealing with some of the partial-neutron-reaction channels (particularly scattering)[29] and consideration of these same partial reaction channels might well alter the above choice of a

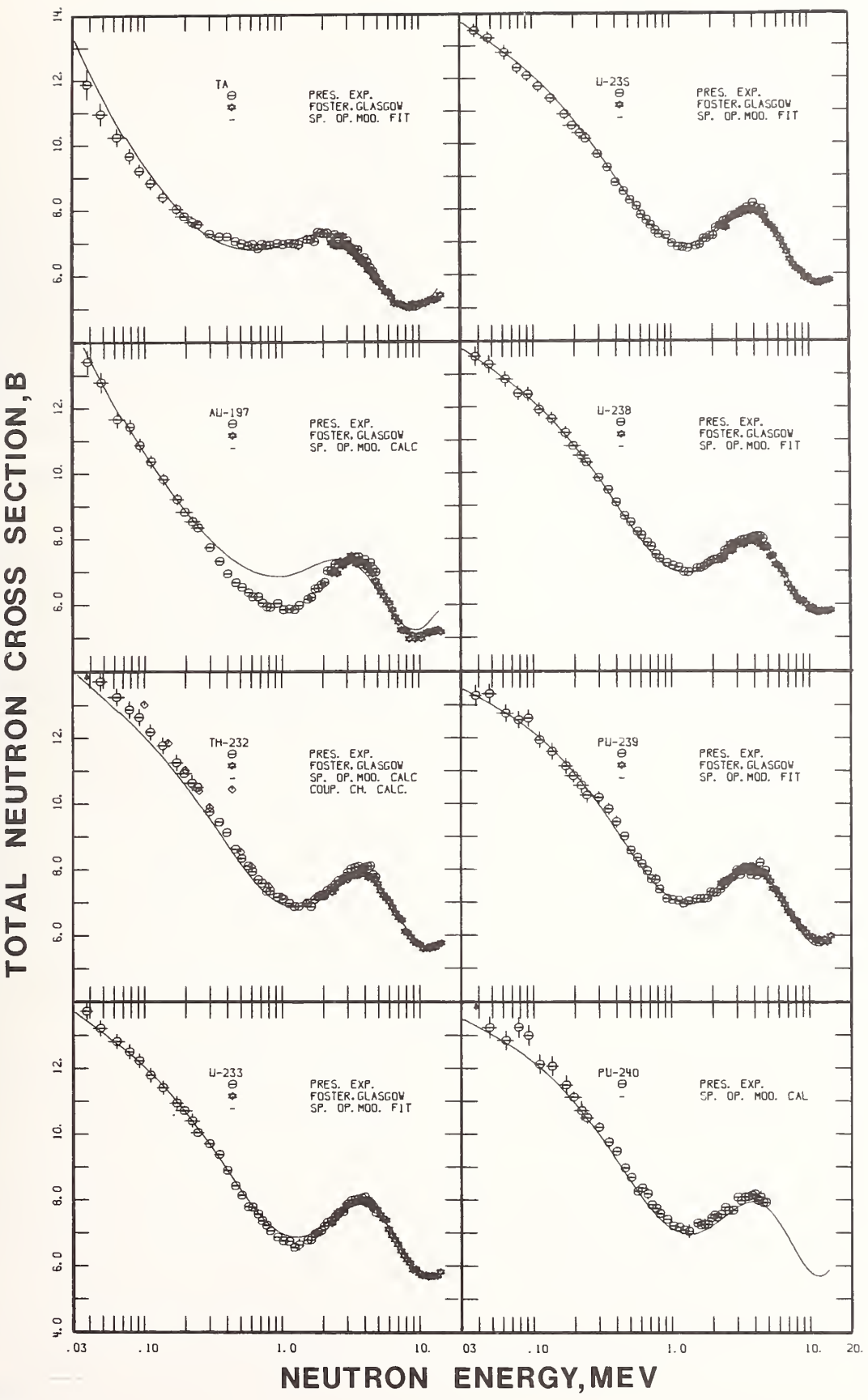

FIGURE 2.

Measured and calculated total-neutron cross sections of Ta, Au, Th, ^{233}U, ^{235}U, U, ^{239}Pu and ^{240}Pu. The present measured values are indicated by circular data points, those of Ref. 1 by star-shaped data points. Curves indicated the results of spherical and deformed optical-model calculations as outlined in Sec. IV of the text.

spherical parameterization. In addition, a properly chosen coupled-channels model has the desirable capability of concurrently treating both spherical nuclei and nuclei of various deformation not a characteristic of the spherical parameterization as illustrated by the above Au total-neutron cross sections.

TABLE I. Spherical-Optical-Potential Parameters[a]

Real Potential[b]

$$V = \underline{45.308} - \underline{0.100}\,E(MeV) - 24.0\,(N-Z)/A, \text{ MeV}$$

$$R = \underline{1.285}\,A^{1/3} + 0.3, F$$

$$a = \underline{0.467}, F$$

Imaginary Potential[c]

$$W = \underline{26.245} + \underline{0.427}\,E(MeV) - 12.0\,(N-Z)/A, \text{ MeV}$$

$$R = \underline{1.403}\,A^{1/3} + 0.3, F$$

$$a = \underline{0.131}, F$$

Spin-orbit Potential[d]

$$V_{so} = 7.0, \text{ MeV}$$

[a] Underlined quantities were determined from fitting procedures.

[b] Saxon form.

[c] Saxon derivative form.

[d] Thomas form.

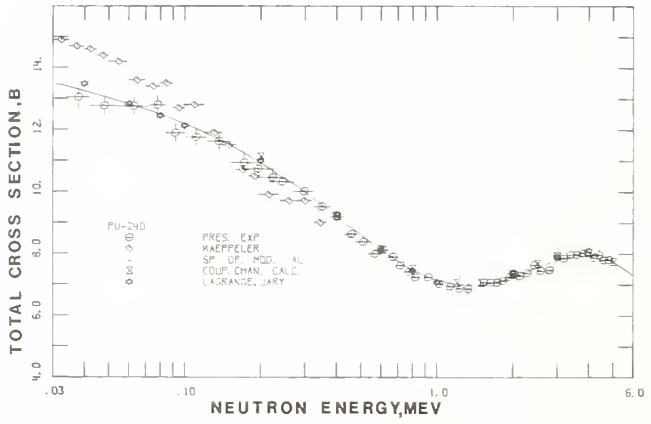

Fig. 3. Measured and calculated total-neutron cross sections of ^{240}Pu. The present measured values are indicated by circular data points. Other symbols and the curve denote the results of calculations as described in Sec. IV of the text.

The present experimental results give new definition to the total-neutron cross sections in a technologically important mass-energy region with particular attention to measurement accuracy, consistency of measured values and the effect of often ignored and frequently substantial self-shielding corrections. The result is a precise total-neutron cross section data base that should bring improved accuracies to important evaluations and better definition to theoretical models.

ACKNOWLEDGEMENTS

The authors greatly acknowledge the consultation and advice of Dr. P. A. Moldauer during the course of this work. The work is supported by the U. S. Department of Energy.

REFERENCES

1. D. Foster and D. Glasgow, Phys. Rev., C3 576 (1971).
2. J. Whalen and A. Smith, Nucl. Sci. and Eng., 67 129 (1978).
3. W. P. Poenitz et al., Nucl. Sci. and Eng., 68 358 (1978).
4. W. P. Poenitz, Argonne National Laboratory Report, ANL-7915 (1978).
5. W. P. Poenitz, Argonne National Laboratory Report, ANL/NDM-36 (1978).
6. W. P. Poenitz and J. F. Whalen, Argonne National Laboratory Report, ANL-8026 (1973).
7. C. Fu and F. Perey, Atomic and Nucl. Data Tables, 22 249 (1978). See also ENDF/B-IV for both carbon and iron reference values.
8. H. W. Schmitt, Oak Ridge National Laboratory Report, ORNL-2883 (1960).
9. L. Dresner, Nucl. Instr. and Methods, 16 176 (1962).
10. R. L. Macklin, Nucl. Instr. and Methods, 26 213 (1964).
11. D. Bogard and T. Semler, Conf. on Neutron Cross Sections and Technology, CONF-660303, 502, Vol. -1 (1966).
12. L. B. Miller and W. P. Poenitz, Nucl. Sci. and Eng., 35 295 (1969).
13. F. H. Froehner, Gulf-General Atomic Report GA-8380 (1968).
14. A. Smith et al., Fast-neutron Total and Scattering Cross Sections of Cr, Fe and ^{60}Ni; NEANDC Topical Conference, Geel (1979).
15. H. Henryson and B. Toppel, Argonne National Laboratory Report, ANL-8144 (1976).
16. P. A. Moldauer, Phys. Rev. Lett. 177 1841 (1976).
17. A. V. Malyshew, Soviet Physics, JETP; 18 221 (1964).
18. N. Abdelmalec and V. Stravinsky, Nucl. Phys, 58 601 (1964).
19. J. E. Lynn, Atomic Energy Research Estabishment Report, AERE-R7468 (1974).
20. L. Dresner, Resonance Absorption in Nuclear Reactors, Pergamon Press, New York (1960).
21. E. Schneider and F. Froehner, Conf. on Nuclear Data for Reactors, Vol. -1,201 (1970) Helsinki; Proc. pub. by IAEA press.
22. T. Byoun and R. Block, Conf. on Neutron Cross Sections and Technology, CONF-710301, Vol. -II, 895 (1971).
23. W. P. Poenitz, et al., Argonne National Laboratory Report, ANL/NDM-32 (1977); also private communication from A. Smith with data available at the National Nuclear Data Center, Brookhaven National Laboratory (1978).
24. D. Glasgow and D. Foster, Phys. Rev., C3 604 (1971).
25. L. Zuffi, Nucl. Sci. and Eng., 68 357 (1978).
26. D. Madland and P. Young, Proc. Conf. on Nuclear Data for Reactors and Other Applications, Harwell (1978).
27. Nuclear Data Tables, A7 495 (1970).
28. P. A. Moldauer, Nucl. Phys., 47 656 (1963).
29. P. Guenther et. al., Argonne National Laboratory Report, ANL/NDM-16 (1975).
30. All coupled-channel calculations were carried out with the computer code JUPREX, P. A. Moldauer, private-communication (1979).
31. C. LaGrange and J. Jary, INDC Report, INDC (FR) -30/L (1978).

Total Cross Section of ^{242}Pu Between 0.7 and 170 MeV

M. S. Moore, P. W. Lisowski, G. L. Morgan, and G. F. Auchampaugh
University of California, Los Alamos Scientific Laboratory*
Los Alamos, New Mexico 87545

R. E. Shamu
Western Michigan University
Kalamazoo, MI, USA

Various evaluations of the neutron cross sections of ^{242}Pu lead to widely different predictions of bulk neutronics properties such as critical mass. These evaluations also show rather different behavior of the energy dependence of the total cross section. We have measured the total cross section of ^{242}Pu from 0.7 to 170 MeV to a statistical accuracy of ≃ 0.5% below 6 MeV, using 8 g of high purity material and the WNR pulsed neutron facility. Recent evaluations by Madland and Young and by Lagrange and Jary are found to be reasonably consistent with the data obtained. Best agreement, however, is found by using the simple prescription

$$\sigma_T(^{242}\text{Pu}) = \sigma_T(^{238}\text{U}) + [\sigma_T(^{239}\text{Pu}) - \sigma_T(^{235}\text{U})]$$

The remarkable accuracy of this description for ^{242}Pu suggests that it could be extended to other deformed actinides for which inadequate amounts of material exist for direct measurements of σ_T in the MeV region, as an evaluation constraint.

[^{242}Pu (n,n), total cross section, 0.7 to 170 MeV]

Introduction

The problem of nuclear data evaluation for transplutonium isotopes is difficult because the experimental data are in most cases limited or nonexistent. The evaluator relies on optical and statistical model calculations, the parameters for which are obtained by extrapolation from those of the more common fissionable materials, or as universal best fits. Frequently, such extrapolations are done subjectively and can lead to markedly different evaluated data sets. The situation that existed for ^{242}Pu prior to 1978 is perhaps typical. There were several evaluations in existence at that time: 1) Dunford and Alter[1] carried out calculations for the ENDF/B system in 1967; this was the basis of ENDF/B IV. 2) The 1973 evaluation by Caner and Yftah[2] was incorporated into the Karlsruhe KEDAK evaluation. 3) Another U.S. evaluation was that of Howerton,[3] done in 1976 for the Lawrence Livermore system ENDL. 4) A third U.S. effort was that of Mann and Schenter[4] of the Hanford Engineering Development Laboratory (HEDL) for the preliminary (1977) version of the special actinide file for ENDF/B. 5) Finally, in 1977, Lagrange[5] carried out an evaluation of ^{242}Pu at Bruyères-le-Châtel. Certain of these evaluations showed large differences in some of the partial cross sections, in particular, in the inelastic scattering and the use of a continuum distribution rather than discrete levels for the final states. Such differences in treatment have little effect when the amount of ^{242}Pu present in the system is dilute, but they can lead to pronounced effects in properties of bulk material. Calculation[6] of the critical mass for three of these evaluations gave 58, 170, and 73 kg for ENDF/B-IV, ENDL, and HEDL-77, respectively. In 1978, two additional evaluations of ^{242}Pu became available, by Madland and Young for ENDF/B-V, also known as LASL-78 and by Lagrange and Jary.[8] These evaluations represented a substantial improvement over the earlier work, but they too did not agree in detail. The range of ^{242}Pu total cross section values produced by various evaluations is shown in Fig. 1. Again, it is the optical model parameterization that appears to be responsible for the difference. Lagrange's general approach[9] to obtaining optical-model parameters may be of interest. He requires parameters to fit three sets of measurements: 1) total cross sections, 2) s- and p-wave strength functions at low energies, and 3) angular distributions of elastic plus inelastic scattering to the lowest states. For ^{242}Pu, the required data did not exist.

*Work performed under auspices of U.S. Dept. of Energy.

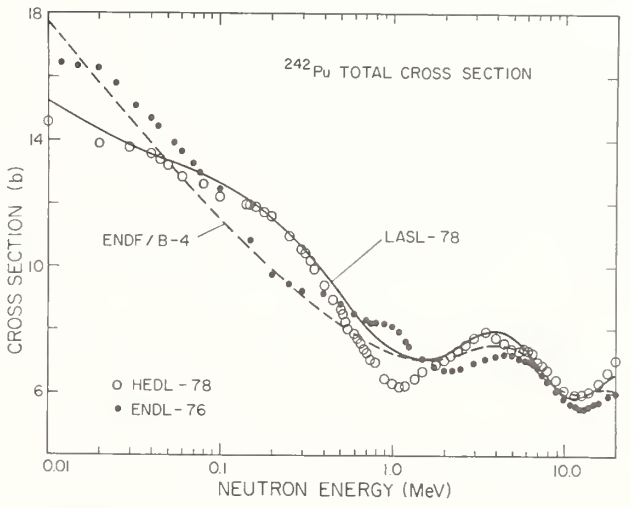

Fig. 1. Comparison of evaluated ^{242}Pu total cross sections from 10 to 20 MeV.

In order to provide an evaluation constraint for the cross sections of ^{242}Pu, we undertook to measure the total cross section at WNR, a pulsed neutron time-of-flight facility that produces spallation neutrons by using pulses of 800-MeV protons from LAMPF.

Experimental Summary

Experimental conditions for the measurement are summarized in Table I. Details of the measurement technique are described in a separate contribution to this conference[10], so that only items particular to the ^{242}Pu measurement will be covered here. The sample was a 15-mm-long, 6-mm-D cylinder of ^{242}Pu metal whose isotopic composition is given in Table II.

The sample thickness was determined by measuring the density and average diameter; the cylinder had been broken from a longer cylinder such that its length was not uniform and did not lend itself to an accurate measurement. The density was determined by weighing the sample in air and in bromobenzene, C_6H_5Br, whose density was calibrated by comparing it to that of

Table I. Experimental conditions for the ^{242}Pu total cross section measurement at WNR.

Repetition rate	1250 to 1500 pulses/sec
Flight path	31.78 m
Target	Water-cooled Ta, no moderator
Proton pulse width	0.16 ns
Neutron pulse width	~ 1.5 ns
Channel width	1 ns
Overall resolution	~ 1.8 ns or 60 ps/m
Sample temperature	~ 300 K (ambient)
Sample thickness	0.0760 x 10^{24} atoms/cm^2
Sample diameter	6.08 mm
Beam diameter at sample	5.08 mm
Detector	10 cm D x 5 cm NE-110
Beam intensity variation	12-15%
Micropulse contamination	0-4%
Data collection time	67 hours

distilled water at a known temperature. The density of the ^{242}Pu metal cylinder was determined to be 19.885 g/cm^3, which can be taken as evidence that there had been no significant nonuniformities introduced in the chill-casting preparation of the cylinder. The average diameter was determined by using micrometer calipers, after carefully filing off the casting ridges. We assign a conservative estimate of 1% as the systematic uncertainty associated with the sample thickness determination.

The sample was contained in a copper can whose end windows had a total thickness of 0.0130 x 10^{24} atoms/cm^2; the ^{242}Pu transmission measurement was carried out by using a matched blank copper can with window thickness of 0.0129 x 10^{24} atoms/cm^2. The sample, and reference samples of ^{235}U metal and natural carbon, were placed in a sample changer between two 102-mm-long collimators of depleted uranium, having a circular aperture of 5.08 mm diameter. The positioning of the sample was checked by ^{60}Co radiography prior to the measurement. Backgrounds were typically less than 1% and were measured by plugging the ^{238}U post collimator with a Ta rod that was 180 mm long. Samples were cycled at 10 to 20 minute intervals; data collection time for the ^{242}Pu sample and its blank, including backgrounds, amounted to 67 hours in three separate runs over a three-week period. Data were collected in four pulse-height windows, using detector bias settings for recoil protons ranging from 300 keV to 4 MeV. For neutron energies above 25 MeV, only the highest bias data were used; at lower energies, data in all four pulse-height windows were summed. The ^{235}U and carbon reference samples gave satisfactory agreement (within 1%) with measurements by Schwartz et al.[11] and Auchampaugh et al.,[12] respectively.

Table II. Plutonium isotopic composition of cast electrorefined ^{242}Pu metal. (Casting 242-1, 141 g Pu)

Pu Mass No.	Atom %
236	$\leq 3 \times 10^{-9}$ (a)
238	0.00043 (a)
239	0.082 (b)
240	0.011 (b)
241	< 0.002 (b)
242	99.91 (b)

(a) Radiochemical analysis

(b) Mass spectrometer analysis

The data obtained were box-averaged in bins ranging from 5 to 99 one ns time channels; the energies listed in Table III correspond to that of the center channel in the box average. The data are plotted in Fig. 2; the solid curve drawn through the data below 20 MeV is not an eyeguide but our simple prescription of calculating the total cross section for ^{242}Pu. This was done before the data had been processed and is discussed in the next section.

Theoretical Estimate of σ_T for ^{242}Pu

It is well known that the 1-20 MeV total cross sections of all the actinide nuclei show very nearly the same features: a size resonance in the region of 4 MeV, and another about 20 MeV. The positions and widths of these resonances depend only weakly on deformation, on nucleon number, on whether the nucleons are paired, etc. The best-known total cross sections are probably those of ^{235}U, ^{238}U, and ^{239}Pu; the ENDF/B-IV evaluations for these three are based primarily on measurements by Schwartz et al. If all four of the actinides under consideration here (i.e., ^{242}Pu plus the "big three") are rigidly deformed, then an adequate description of the total cross section of ^{242}Pu should be given by using that of ^{238}U and correcting for the extra four nucleons by adding the ^{239}Pu-^{235}U total cross section difference. We assume

$$\sigma_T(^{242}\text{Pu}) = \sigma_T(^{238}\text{U}) + [\sigma_T(^{239}\text{Pu}) - \sigma_T(^{235}\text{U})] \qquad (1)$$

This description gives the solid curve plotted in Fig. 2; the data from which it was generated were taken from ENDF/B-IV.

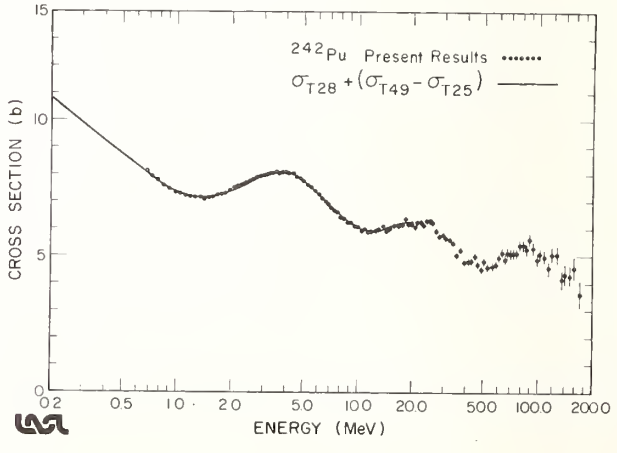

Fig. 2. Present results for the total cross section of ^{242}Pu. The solid line was obtained from equation 1 using ENDF/B-IV data.

It may be noted that if the deformation or any other variable affecting the shape and magnitude of the total cross section vary in such a way that a first-order Taylor's series expansion in A is an adequate description in this region of A and Z, then we also expect Eq. 1 to give an accurate representation. For example, let us use the variable-moment-of-inertia (VMI) model[13,14] to estimate the change in deformation for the ^{242}Pu-^{238}U difference, and for the ^{239}Pu-^{235}U difference. Using the data from the current Nuclear Data Sheets for these four isotopes,[15-18] we can calculate the parameters I_o, the moment of inertia for the nonrotating system, and C, the stiffness parameter of the VMI model, for various common bands. One finds that in going from ^{238}U to ^{242}Pu, I_o increases by 5 ± 1%, whereas in going from ^{235}U to ^{239}Pu, I_o increases by 7.3 ±1.6%. While the uncertainties are overlapping, the analysis based on the VMI model suggests that the deformation correction contained in the ^{239}Pu-^{235}U cross section difference may be slightly too large. This is, however, not substantiated by the data of Fig. 2. In the region of 1.5 MeV, the smooth curve of Eq. 1 is very slightly but systematically above the measured data, and from 2.5 to 3 MeV the smooth curve is slightly below the measurements. The implication is that the observed size resonance near 4 MeV is slightly wider than the predicted shape, and that the actual ^{242}Pu nucleus is perhaps slightly more deformed than Eq. 1 would suggest. The prescription given by Eq. 1 is, however, remarkably accurate for ^{242}Pu. The value of chi-square for this fit is nearly a factor of 10 lower than that for the best of the ^{242}PU evaluations.[7,8] We suggest that the prescription could usefully be extended to other actinide total cross sections, as an evaluation constraint. Using these ^{242}Pu data and the correction obtained from the ^{239}Pu-^{235}U difference gives the total cross sections for ^{246}Cm; using the ^{239}Pu evaluation as the initial values would give data for ^{243}Cm, etc. Careful measurements on a few relatively abundant heavy nuclides could provide total cross section data useful for evaluation work between 1 and 100 MeV for essentially all the transactinide isotopes of interest to various applied programs.

Acknowledgments

The authors especially acknowledge the efforts of Clayton L. Olsen, who performed the measurements of sample thickness and density, and of R. D. Ryder and the WNR opeations staff for the extra effort they put forth during data collection. Thanks are also due to D. G. Madland, Ch. Lagrange, and P. G. Young for illuminating discussions, and for a critical reading of the manuscript.

Table III. Energy dependence of the total cross section of ^{242}Pu. The listed energies are those of the center channels of the bins over which a box average was performed. Cross section uncertainties listed are those due to counting statistics; a conservatively estimated 1% systematic uncertainty should be combined quadratically.

Energy (MeV)	σ_T (b)	$\delta\sigma_T$ (b)	Energy (MeV)	σ_T (b)	$\delta\sigma_T$ (b)	Energy (MeV)	σ_T (b)	$\delta\sigma_T$ (b)
0.676	8.12	0.05	5.51	7.54	0.04	29.4	5.76	0.12
0.726	7.94	0.04	5.80	7.37	0.05	30.8	5.68	0.12
0.783	7.78	0.04	6.08	7.27	0.05	32.2	5.61	0.12
0.844	7.58	0.03	6.31	7.08	0.05	33.7	5.46	0.12
0.908	7.48	0.03	6.54	7.01	0.05	35.3	5.04	0.12
0.975	7.31	0.03	6.79	6.96	0.05	37.1	5.23	0.12
1.041	7.28	0.03	7.06	6.76	0.05	39.0	4.77	0.12
1.111	7.21	0.03	7.35	6.68	0.05	40.8	4.83	0.14
1.182	7.16	0.03	7.66	6.60	0.05	42.5	4.84	0.14
1.256	7.15	0.03	7.98	6.41	0.05	44.3	5.03	0.14
1.332	7.15	0.03	8.33	6.37	0.05	46.2	4.70	0.14
1.410	7.08	0.03	8.70	6.21	0.06	48.3	4.51	0.14
1.492	7.14	0.03	9.10	6.22	0.05	50.5	4.83	0.15
1.576	7.17	0.03	9.52	6.09	0.06	52.8	4.58	0.15
1.665	7.23	0.03	9.95	6.03	0.06	55.4	4.65	0.14
1.758	7.25	0.03	10.37	5.90	0.06	58.1	4.71	0.15
1.855	7.29	0.03	20.83	5.99	0.06	60.6	4.96	0.18
1.956	7.40	0.03	11.31	5.86	0.06	62.8	5.15	0.18
2.06	7.53	0.03	11.83	5.88	0.06	65.1	4.86	0.18
2.17	7.56	0.03	12.39	5.90	0.06	67.6	5.15	0.18
2.28	7.61	0.03	12.98	6.00	0.07	70.2	5.12	0.18
2.39	7.67	0.03	13.62	6.10	0.07	73.0	5.14	0.18
2.50	7.75	0.03	14.31	5.90	0.07	76.0	5.10	0.19
2.62	7.81	0.03	14.95	5.98	0.08	79.2	5.37	0.18
2.74	7.89	0.03	15.53	6.00	0.08	82.5	5.42	0.18
2.86	7.95	0.03	16.14	6.08	0.08	86.1	5.24	0.20
2.98	7.95	0.03	16.79	6.12	0.08	89.1	5.65	0.19
3.10	7.99	0.03	17.47	6.13	0.08	94.1	5.29	0.20
3.22	8.04	0.03	18.21	6.39	0.09	98.5	4.90	0.21
3.35	8.06	0.03	18.98	6.17	0.08	103.3	5.12	0.22
3.49	8.10	0.03	19.82	6.14	0.08	108.4	5.02	0.21
3.64	8.02	0.03	20.6	6.04	0.09	114.0	4.57	0.23
3.79	8.08	0.03	21.4	6.24	0.09	120.0	5.07	0.25
3.96	8.08	0.03	22.2	6.27	0.09	126.6	5.09	0.26
4.14	8.05	0.03	23.1	6.13	0.09	133.7	4.16	0.29
4.33	8.03	0.03	24.0	6.33	0.10	141.5	4.34	0.31
4.53	7.91	0.03	24.9	6.31	0.10	150.1	4.28	0.33
4.75	7.85	0.03	26.0	6.25	0.12	159.5	4.61	0.35
4.98	7.76	0.03	27.0	5.94	0.12	170.0	3.57	0.44
5.24	7.56	0.03	28.2	5.75	0.12			

References

1. C. L. Dunford and H. Alter, "Neutron Cross Sections for Plutonium 238, Plutonium 242, and Curium 244," NAA-SR-1227, 1967.

2. M. Caner and S. Yftah, "Nuclear Data Evaluation for Plutonium-242," Israel Atomic Energy Commission Rerpot IA-1275 (1973).

3. R. J. Howerton, as described in "The LLL Evaluated Nuclear Data Library (ENDL): Descriptions of Individual Evaluations for Z=0-98," by R. J. Howerton and M. H. MacGregor, UCRL-50400 Vol. 15, Part D, Rev. 1 (1978). In this evaluation, Howerton used best-fit optical model parameters of Becchetti and Greenlees, Phys. Rev. 182, 1190 (1969), for data between 0.15 and 20 MeV.

4. F. Mann, R. E. Schenter, "HEDL Evaluation of Actinide Cross Sections for ENDF/B-V," HEDL-TME-77-54 (1977).

5. Ch. Lagrange, "Calculo dans le Cadre du Modele Optique en Voies Couplees de Sections Efficaces Neutroniques pour ^{236}Pu, ^{238}Pu, ^{240}Pu, ^{242}Pu, ^{244}Pu dans le Domaine d'Energie 1 keV-20 Mev." CEA-N-1970, NEANDC(E) 179 "L", INDC(FR)16/L (1977).

6. P. D. Soran, private communciation to P. G. Young (1978).

7. D. G. Madland and P. G. Young, "Evaluation of n + ^{242}Pu Reactions from 10 keV to 20 MeV," LA-7533-MS (1978); see also Trans. Am. Nuc. Soc. 32, 745 (1979).

8. Ch. Lagrange and J. Jary, "Coherent Optical and Statistical Model Calculations of Neutron Cross Sections for ^{240}Pu and ^{242}Pu Between 10 keV and 20 MeV," NEANDC(E) 198 "L", INDC(FR)30/L (1978).

9. Ch. Lagrange, "Critique of Nuclear Models and Their Validity in the Evaluation of Nuclear Data," JAERI-M 5984, NEANDC(J)38L, INDC(JAP)25L, p. 58 (1974).

10. P. W. Lisowski, M. S. Moore, G. L. Morgan, and R. E. Shamu, "Nuetron Total Cross Section Measurement at WNR," Nuclear Cross Sections for Technology, Knoxville, TN (1979).

11. R. B. Schwartz, R. A. Schrack, and H. T. Heaton II, "Total Neutron Cross Sections of Uranium-235, Uranium-238, and Plutonium-239 from 0.5 to 15 MeV," Nuc. Sci. Eng. 54, 322 (1974) and NBS Monograph 138 (1973).

12. G. F. Auchampaugh, S. Plattard, and N. W. Hill, "Neutron Total Cross-Section Measurements of ^{9}Be, ^{10,11}B, and ^{12,13}C from 1.0 to 14 MeV Using the Be(d,n)^{10}B Reaction as a "White" Neutron Source," Nuc. Sci. Eng. 69, 30 (1979); see also G. F. Auchampaugh, C. E. Ragan III, S. Plattard, and N. W. Hill, Los Alamos Scientific Laboratory report LA-6761 (1977).

13. MAJ Mariscotti, G. Scharff-Goldhaber, and B. Buck, "Phenomenological Analysis of Ground-State Bands in Even-Even Nuclei," Phys. Rev. 178, 1864 (1969).

14. G. Scharff-Goldhaber and A. S. Goldhaber, "Extension of the Variable Moment of Inertia Model Toward Magic Nuclei," Phys. Rev. Letts. 24, 1349 (1970).

15. M. R. Schmorak, Nuclear Data Sheets 21, 549 (1977).

16. Y. A. Ellis, Nuclear Data Sheets 21, 549 (1977).

17. M. R. Schmorak, Nuclear Data Sheets 21, 153 (1977).

18. Y. A. Ellis and R. L. Haese, Nuclear Data Sheets 21, 615 (1977).

NEUTRON TOTAL CROSS SECTION MEASUREMENTS ON ^{249}Cf

R. F. Carlton
Middle Tennessee State University, Murfreesboro, Tennessee 37130, USA

J. A. Harvey and N. W. Hill
Oak Ridge National Laboratory, Oak Ridge, Tennessee 37830, USA

M. S. Pandey
Virginia Polytechnic Institute, Blacksburg, Virginia 24061, USA

R. W. Benjamin
Savannah River Laboratory, Aiken, South Carolina 29802, USA

Neutron total cross section measurements have been performed on a sample of ^{249}Cf (5.65 mg total weight) using the ORELA as a source of pulsed neutrons. The sample, whose inverse thickness was 1542 barns/atom, consisted of 85.3% ^{249}Cf and 14.4% ^{249}Bk and was cooled to liquid nitrogen temperature. Analyses were also made of data from a thin sample (1/N = 17430) of 65% ^{249}Cf in the region of the large fission resonance at 0.7 eV. Fifty-five resonances in ^{249}Cf were observed and analyzed over the energy range 0.1 eV to 90 eV using an R-matrix multilevel formalism. The resonance parameters obtained have been used to determine the level spacing and the s-wave neutron and fission strength functions. Thermal total cross section measurements have also been performed.

[^{249}Cf, neutron total cross section, 0.01-90 eV, E_o, level spacing, strength function, fission, multilevel analysis]

Introduction

The calculation of actinide production and depletion in reactors is dependent upon accurate cross section and decay data for nuclides in the reactor production chain. The production chain precursor to the californium isotopes through both neutron capture and β-decay is ^{249}Bk. Although the effects of ^{249}Cf in the production chain are usually quite small because of the large ^{249}Bk capture cross section, they are significant to the extent of the ^{249}Bk decay. Since both ^{249}Bk ($T_{1/2}$ = 320 ± 6d)[1] and its decay daughter ^{249}Cf ($T_{1/2}$ = 351 ± 2y)[1] are highly radioactive and available in only milligram quantities, measurements on these isotopes are difficult. Though studies of ^{249}Cf with low energy neutrons is of practical importance in thermal reactor considerations, they may provide important information concerning systematic trends in fission properties and trends associated with the magic neutron number (152) of the (^{249}Cf + n) system. The only reported study[2] of this system below 13 eV found a strong resonance at 0.071 eV with a fission cross section of 5400 b and a total width of 160 meV which accounted for 85% of the resonance integral. The most comprehensive study of the (^{249}Cf + n) system above 16 eV is that of Silbert,[3] from which 43 resonances were identified and parametrized to obtain neutron and fission resonance parameters. Due to the nature of the nuclear explosion technique, data were not obtained below 16 eV. The present study represents the first attempt to exploit high resolution total cross section measurements in the investigation of neutron and fission properties of ^{250}Cf.

Experimental Procedure

The present measurements were performed at seventeen and twenty-nine month intervals subsequent to initial measurements[4] performed on a 98% ^{249}Bk sample. Sample composition and characteristics are presented in Table I.

Table I. Sample characateristics and experimental conditions for transmission measurements of ^{249}Cf.

Sample Thickness (b/atom)	% Cf	% Bk	Total Weight (mg)	Flight Path (m)	Rep. Rate (pps)	Burst width (nsec)
1542	85.3	14.4	5.65	18	1000	40
17430	68.0	31.9	0.50	18	350	40

Samples were cooled with liquid nitrogen to reduce Doppler broadening of the resonances (which is greater than the instrumental resolution below 100 eV). Sample thicknesses were determined through measurement of the internal diameter of the sample holders and through precise measurement[5] of the ^{249}Cf content. Data collection and processing have been described previously in Reference 6. Background corrected transmission data were used to calculate total neutron cross sections which were then parameterized using the multilevel R-matrix least-squares search program, MULTI,[7] which corrects for resolution and Doppler-broadening.

Results

The neutron total cross section of ^{249}Cf over the energy range 0.1-90 eV is shown in Figure 1 together with theoretical results from MULTI. In running the program, the data were analyzed in segments to obtain approximate estimates for the resonance parameters and these were used as initial estimates for the combined spectrum. The radiative width Γ_γ was held fixed throughout the analysis at 30 meV. All other parameters (E_o, Γ_n, Γ_F) were varied to obtain the best fit.

Table II. Resonance parameters for the n + ^{249}Cf reaction from the present study and two earlier studies.

Energy (eV)	$2g\Gamma_n^o$ [a] (meV)	Γ_F [a] (meV)	$2g\Gamma_n^o$ [b] (meV)	Γ_F [b] (meV)
0.070	0.85 2	127 3	0.741	119
3.88	0.133 5	46 3	0.115	45
5.07	0.319 6	145 6	0.268	154
7.51	0.059 11	62 12	0.063	83
8.65	0.136 10	125 12	0.115	146
9.51	0.471 9	119 5	0.362	97
10.36	0.080 10	173 40	0.078	252
11.88	0.015 5	35 34	0.037	242
13.52	0.231 28	161 30	-	-
			0.403	205
13.71	0.284 30	198 30		
16.03	0.235 30	366 60	0.159	325
16.79	0.495 20	185 10	0.420	163
17.51	0.017 8	30 20	(0.004)	(400)
18.95	0.10 6	<50		
19.8[b]			0.04 1	110 82
21.32	1.76 5	164 7	1.73 17	150 15
21.65	0.35 7	122 30	0.39 4	140 14
22.8			0.2 1	2.4 12
23.41	0.18 4	225 50	0.13 1	106 11
26.0	0.29 4	423 70	0.31 3	320 32
27.64	0.09 2	44 20	0.15 2	75 26
28.15	0.30 2	70 10	0.77 23	15 5
28.7	0.07 7	200 100	(0.01)	(500)
30.37	0.06 3	51 40	0.15 5	28 14
31.0	0.22 4	300 60	.42 8	480 96
31.5	0.22 4	200 60	0.15 3	200 40
33.39	0.21 4	326 90	0.29 3	300 30
34.9			.15 5	40 20
36.35	0.41 4	97 10	1.0 4	50 30
37.11	0.46 10	149 50	0.65 13	130 91
37.56	0.19 7	290 150	(0.1)	(20)
38.1	0.15 15	200 100	(0.08)	(400)
39.88	0.37 5	169 30	0.41 8	220 110
40.30	0.55 4	222 30	0.52 11	110 33
42.7			0.043 9	130 65
43.09	0.041 3	100 100	0.056 11	100 50
45.78	0.38 4	95 15	0.58 35	55 33
46.6			0.072 14	150 90
47.70	0.10 3	500 50	0.32 16	70 53
48.50	0.52 6	324 50	0.44 5	170 17
51.63	0.32 10	357 100	0.24 10	300 225
52.23	1.26 6	132 12	1.15 17	87 17
54.02	0.59 5	465 90	0.65 7	490 50
56.0			0.41 8	230 173
56.28	0.63 10	475 200		
56.4			.49 10	45 34
57.7	0.71 10	638 120	0.60 6	450 45
58.8	0.20 7	190 80	0.51 13	10 3
59.4			0.48 15	260 78
60.8			(0.05)	(1000)
61.1	0.26 13	711 300		
64.2	0.08 8	1035 1000		
65.9	0.74 8	242 50	0.83 9	440 44
69.5	0.12 12	60 68	0.07 1	210 32
74.6	0.12 15	1166 1000		
75.5	0.16 10	130 100		
77.4	0.21 15	605 400		
78.7	0.06 6	44 80		
79.7	0.37 10	149 40		
81.5	0.24 10	40 30		
85.2	0.35 15	490 200		
86.6	0.03 10	150 300		
88.0	0.42 10	188 50		
89.8	0.05 36	10 40		

[a] present work
[b] due to Dabbs below 17 eV; due to Silbert above 17 eV.
[c] In our notation 0.85 2 ≡ 0.85 ± 0.02, etc.

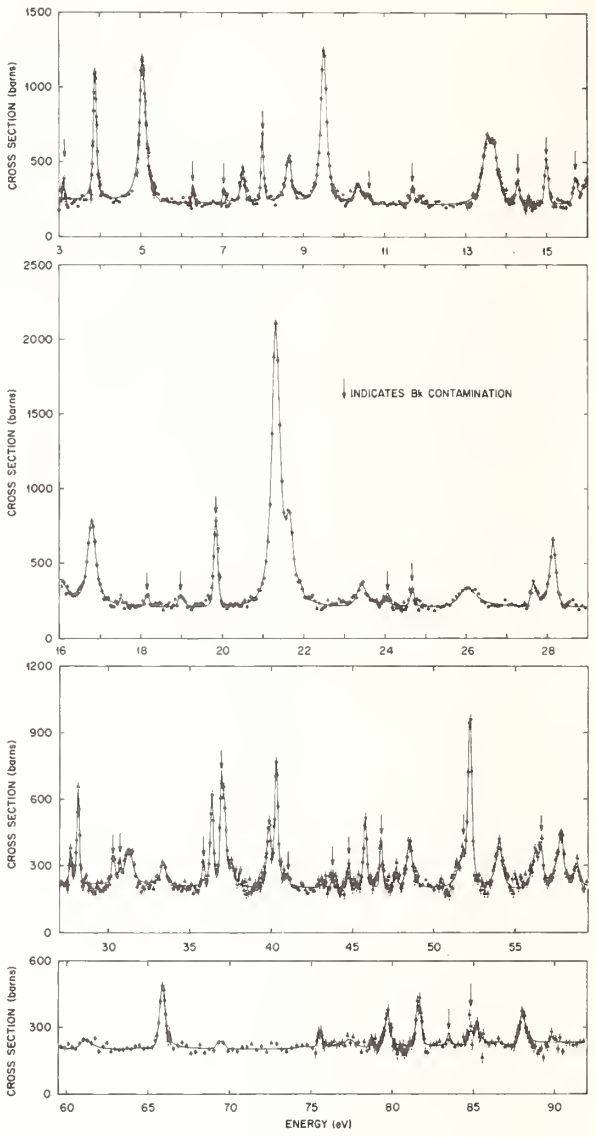

Fig. 1. Total neutron cross section for ^{249}Cf. The solid line is the result of a least squares fit using the program MULTI.

A total of 55 resonances were included in the search in addition to "dummy" resonances at -100 and 200 eV which were necessary to fit the high background. The spin factor g was set to 1/2 and both spin states (4^- and 5^-) were treated identically. In most instances, where overlap occurred, contributions due to ^{249}Bk were calculated with previously determined fixed parameters. The results are presented in Table II along with those of two previous fission cross section measurements. The present results are in substantial agreement with Dabbs, et al.[2] with the exception of the level at 11.88 eV. The level reported by Dabbs at 13.63 was interpreted by the present study to be a doublet. Sixteen of the resonances we report have not been previously reported. We found insufficient statistical evidence for eight of the resonances reported in the Silbert study which is more sensitive to the detection of small fission resonances.

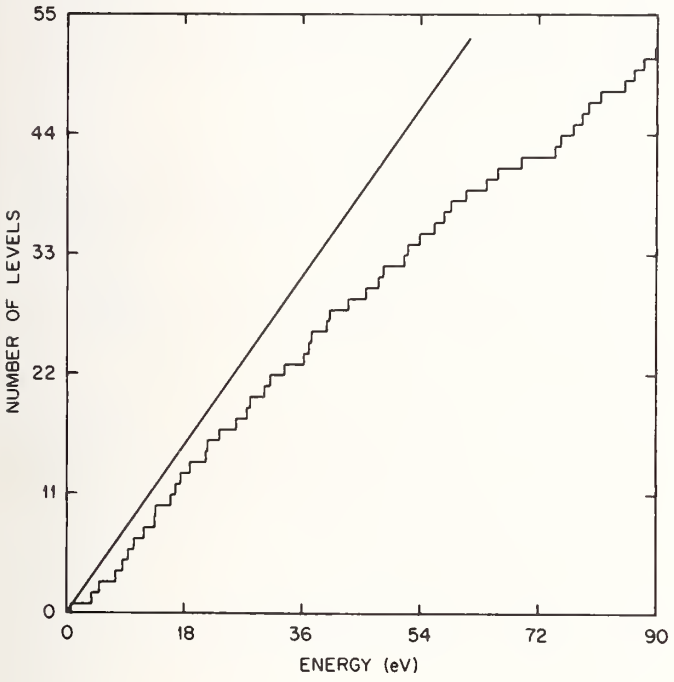

Fig. 2. Cumulative plot of the number of resonances vs. neutron energy for ^{249}Cf. The straight line includes a 25% correction for missed resonances up to 62 eV.

We have plotted in Figure 2 the cumulative number of resonances observed versus the neutron energy. After a correction[8] (amounting to 25%) for missed resonances up to 62 eV, we obtain a value of 1.22 ± 0.12 eV for the observed level spacing $\langle D \rangle$. This result is in good agreement with that reported by Silbert.

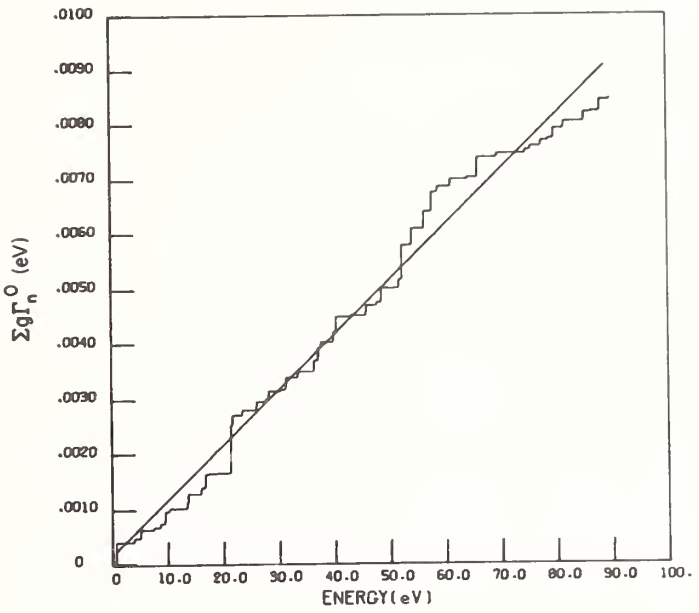

Fig. 3. Cumulative histogram of the reduced neutron width vs. neutron energy for ^{249}Cf. The line is a least squares fit to the histogram.

The s-wave neutron strength function, $S_o = \langle \Gamma_n^o \rangle / \langle D \rangle$, was determined from the slope of a plot of the cumulative sum of reduced neutron widths versus neutron energy as shown in Figure 3, and represents the strength per spin state. This value is presented in Table III in addition to other neutron and fission parameters from the present work and that of Silbert.

Table III. Comparison of various neutron and fission parameters.

	Present Work	Silbert
$\langle D \rangle$	1.22±0.12	1.07±0.12 eV
$\langle \Gamma_n \rangle$	0.260 meV	0.33 meV
$\langle \Gamma_F \rangle$	0.202 eV	0.22 eV
S_o	$(1.06\pm0.22)\times10^{-4}$	$(1.45\pm0.31)\times10^{-4}$
ν_n	1.1±0.2	1.3±0.2
ν_F	3.2±0.5	2.9±0.5

The average reduced neutron width $\langle \Gamma_n^o \rangle$ was determined from the observed strength function (per spin state) and the above expression for S_o. The average fission width was calculated from the sum of observed fission widths up to 62 eV divided by the number of resonances observed to that energy. The effective number of degrees of freedom for the neutron and fission channels has been calculated from the expression

$$\nu = \frac{2\langle \Gamma_x \rangle^2}{\langle \Gamma_x^2 \rangle - \langle \Gamma_x \rangle^2},$$

and by the method of maximum likelihood.[9] The results in Table III represent averages of the two values thus obtained. As can be seen the agreement is good for each of the parameters.

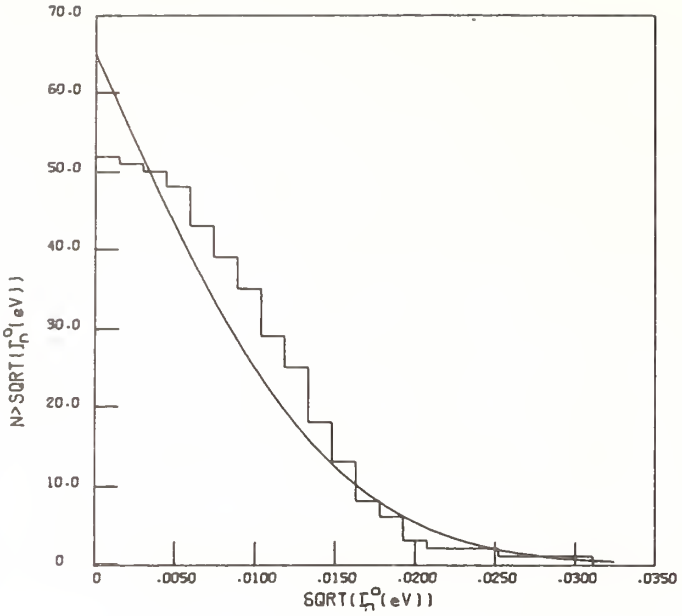

Fig. 4. Distribution of reduced neutron widths for ^{249}Cf. The Porter-Thomas distribution assumes 13 missed resonances.

The distribution of reduced neutron widths is presented in Figure 4. The best agreement of the data with the Porter-Thomas distribution was obtained for the case of thirteen missed resonances. This is corroborated by the fact that Silbert reports five missed resonances, based upon the distribution of observed level spacings when compared to the Wigner distribution, and we miss eight of those reported by Silbert. The same value was also obtained in making the correction for missed levels.

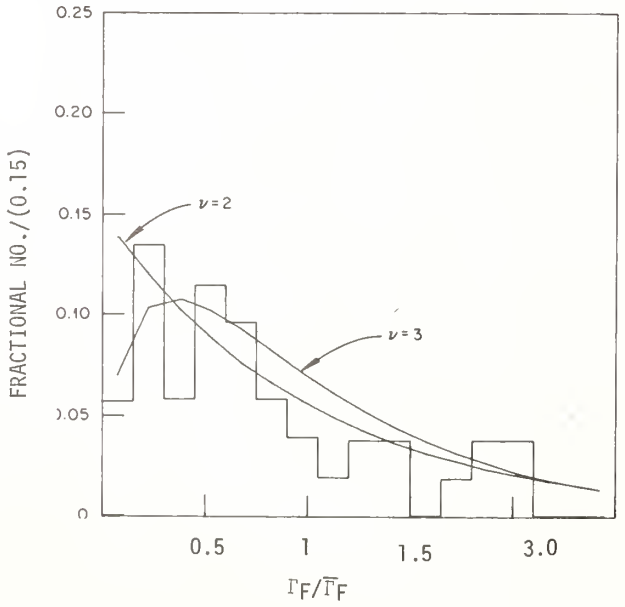

Fig. 5. Distribution of fission widths for ^{249}Cf. χ^2 distributions are also plotted corresponding to 2 and 3 degrees of freedom.

Since the distribution of fission widths is not expected to correspond to the Porter-Thomas distribution, we have treated them differently. In Figure 5 we have plotted the fraction of the fission resonances, observed up to 62 eV, whose ratio, $\Gamma_F/\langle\Gamma_F\rangle$, falls in the ranges indicated. Plotted on this distribution are χ^2 distributions corresponding to two and three degrees of freedom. If emphasis is placed upon the lower ranges, where the uncertainties in fission widths are smaller, we might interpret the result to be in agreement with the value for ν_F given in Table III.

Summary

We have reported sixteen previously unobserved levels up to 90 eV. The uncertainties in reduced neutron widths have been reduced in the energy range below 60 eV. The high background between resonances is still under investigation. When this is understood, resonance integral results will be reported[4] together with results from thermal cross section measurement analyses.

Acknowledgement

Appreciation is expressed to Dr. R. R. Winters for assistance in generating many of the plots included in the paper, and to Dr. C. E. Bemis for determination of the ^{249}Cf content.

The research was sponsored by the Division of Nuclear Sciences, U.S. Department of Energy, under contract No. W-7405-eng-26 with the Union Carbide Corporation.

References

1. H. R. Schmorak, Nuclear Data Sheets 18, 409 (1976).
2. J. W. T. Dabbs, N. W. Hill, C. E. Bemis, Jr., M. S. Moore, G. D. James, and A. N. Ellis, USAEC Report ORNL-4937, p. 181 (1974).
3. M. G. Silbert, Nuc. Sci. Eng. 51, 376 (1973).
4. R. W. Benjamin, J. A. Harvey, N. W. Hill, R. F. Carlton, and M. Pandey, to be submitted to Nucl. Sci. Eng.
5. C. E. Bemis, Private Communication.
6. R. W. Benjamin, C. E. Ahlfeld, J. A. Harvey, and N. W. Hill, Nucl. Sci. Eng. 55, 440 (1974).
7. G. F. Auchampaugh, Report LA-4633 Los Alamos Scientific Laboratory (1974).
8. T. Fuketa and J. A. Harvey, Nucl. Instr. Meth. 33, 107 (1965).
9. J. E. Lynn, The Theory of Neutron Resonance Reactions, p. 224, Clarendon Press, Oxford, England (1968).

INTERCOMPARISON OF COUPLED CHANNEL AND SPHERICAL OPTICAL MODELS IN THE ANALYSIS OF THORIUM NEUTRON CROSS-SECTIONS

S.B. Garg, Amar Sinha and V.K. Shukla
Bhabha Atomic Research Centre
Trombay, Bombay 400 085, India

A comparison has been made of local, nonlocal and deformed optical models in the prediction of neutron cross-sections of ^{232}Th. Coupled channel study makes use of the adiabatic approximation and local and nonlocal optical model parameters have been extracted by making use of the measured total and elastic scattering cross-sections.

[Th (n,n), total and inelastic cross-sections, 1-20 MeV, optical model analysis, local, nonlocal and coupled channel descriptions .]

Introduction

Thorium is an important fertile element which leads to the production of fissile ^{233}U when irradiated with neutrons. It is, therefore, imperative that its nuclear cross-sections should be known with precise accuracy to determine the nuclear characteristics of all those systems which make use of thorium. But the status of its measured cross-sections in the energy range 0.5 MeV to 20 MeV is not yet fully satisfactory. There is insufficient information about elastic and inelastic scattering cross-sections above 2.0 MeV and no measurements exist above 15 MeV. In order to fill this void and to interpolate the data in the measured energy range with an appropriate nuclear reaction model this investigation has been undertaken as a part of the IAEA/NDS sponsored co-ordinated research programme on the Intercomparison of Evaluation of Actinide Neutron Nuclear Data.

^{232}Th is a deformed nucleus with a well defined ground state rotational band consisting of six excited states. Besides these rotational states a few β and γ vibrational states are liable to be excited. All these states can be accounted in the evaluation of total, elastic and inelastic excitation cross-sections by means of a generalized deformed optical model potential as suggested by Tamura[1]. But the computer time involved in these calculations is prohibitively large. Because of this over-riding consideration investigations have been carried out using the other approaches of local and nonlocal spherical optical model and the adiabatic approximation based coupled channel model.

Evaluation of Measured Cross-Sections

Evaluations have been done of measured total[2] and elastic scattering cross-sections[3] by taking into account their experimental uncertainties in order to use them as inputs for the extraction of good local and nonlocal optical model parameters. Evaluation of the measured total cross-sections covers the energy range 100 keV to 15 MeV and that of elastic cross-sections is given in the range 0.3 MeV to 2.0 MeV. The evaluated and recommended total cross-sections are given in Fig.1.

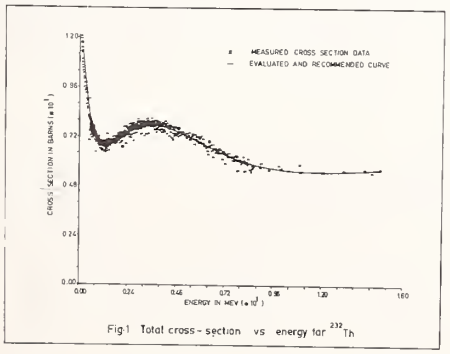

Fig.1 Total cross-section vs energy for ^{232}Th

Spherical Optical Model

Local Potential

Formulation. Local optical model potential with Woods-Saxon form of the real part, derivative Woods-Saxon form of the imaginary part and Thomas-Fermi form of the spin orbit part has been adopted in the calculations. The potential and these various forms are given below:

$$V(r) = V_0 f(r) + i W g(r) + V_{so} h(r) l\cdot\sigma \quad (1)$$

$$f(r) = \left[1 + \exp\{(r-R_V)/a\}\right]^{-1} \quad (2)$$

$$g(r) = \frac{4 \exp\{(r-R_W)/b\}}{\left[1 + \exp\{(r-R_W)/b\}\right]^2} \quad (3)$$

$$h(r) = \left(\frac{\hbar}{m_\pi c}\right)^2 \frac{1}{r a_{so}} \frac{\exp\{(r-R_{so})/a_{so}\}}{\left[1 + \exp\{(r-R_{so})/a_{so}\}\right]^2} \quad (4)$$

where

$$R_V = r_v A^{\frac{1}{3}}$$
$$R_W = r_w A^{\frac{1}{3}} \quad (5)$$
$$R_{SO} = r_{so} A^{\frac{1}{3}}$$

Parameters. The parameters V_o, r_v, a, W, r_W, b, V_{so}, r_{so} and a_{so} have been extracted using the measured evaluated total and elastic scattering cross-section data by searching on them to yield the minimum value of x^2. The following two sets of parameters have been obtained:

(a) Energy range 1.0 MeV $\leq E_n \leq$ 2.0 MeV

V_o = 46.529 MeV, r_v = 1.1595 F
a = 0.757 F, W = 8.15 MeV, r_W = 1.0323F,
b = 0.479 F, V_{so} = 5.524 MeV
r_{so} = 1.1766 F, s_{so} = 0.758 F

(b) Energy range 2.0 MeV $< E_n \leq$ 20.0 MeV

V_o = 43.789 MeV, r_v = 1.2271 F
a = 0.765 F, W = 15.509 MeV
r_W = 1.1236 F, b = 0.490 F
V_{so} = 6.524 MeV, r_{so} = 1.1842 F
s_{so} = 0.758 F

Nonlocal Potential

Formulation. Nonlocal optical model potential[13] with the following Gaussian Kernel has been used in this analysis.

$$h_\ell(r,r') = \frac{1}{\sqrt{\pi}\beta} Q_\ell(\xi) \exp\left[-\left(\frac{r-r'}{\beta}\right)^2\right] + (-1)^{\ell+1} Q_\ell(-\xi) \exp\left[-\left(\frac{r+r'}{\beta}\right)^2\right] \quad (6)$$

where β is a nonlocal parameter and $\xi = 2rr'/\beta^2$. Function $Q_\ell(\xi)$ is a finite polynomial in $(1/\xi)$.

Parameters. We have used the parameters of Engelbrecht and Fiedeldey[4] in the energy range 3.0 MeV to 20.0 MeV except for r_v and r_W which we have scanned to reproduce a close agreement between the measured and calculated total cross-sections. These parameters are:

V_o = 68.64 MeV, r_v = 1.22 F, a = 0.61 F
W = 42.43 MeV, r_W = 1.04 F, b = 0.417 F
V_{so} = 8.0 MeV, r_{so} = 1.217 F,
s_{so} = 0.758 F, β = 0.85

In the energy range 1.0 MeV to 2.0 MeV a search has been performed on V_o, r_v, W and r_W and the following values have been obtained:

V_o = 66.210 MeV, r_v = 1.195 F
W = 31.284 MeV, r_W = 0.944 F

Deformed Optical Model

Formulation. The deformed optical model with adiabatic approximation has been used in the calculations. The potential is given by

$$V(r,\theta,\phi) = V_o f(r) + iW g(r) + V_{so} h(r)\, \ell\cdot\sigma \quad (7)$$

where $f(r)$, $g(r)$ and $h(r)$ have the same forms as given in (2), (3) and (4) respectively. But R_V and R_W are redefined as:

$$R_V = R_{Vo}\left[1 + \sum_\lambda \beta_\lambda Y_{\lambda 0}(\theta)\right]$$
$$R_W = R_{Wo}\left[1 + \sum_\lambda \beta_\lambda Y_{\lambda 0}(\theta)\right] \quad (8)$$
$$R_{Vo} = r_v A^{\frac{1}{3}}$$
$$R_{Wo} = r_W A^{\frac{1}{3}}$$

Parameters. Two sets of parameters given by Fasoli et al[5] and Guenther et al[6] have been examined and based on the analysis of Garg[7] the parameters of Fasoli et al have been selected. These parameters which were originally used upto 8.5 MeV have been adopted in the energy range extending upto 20 MeV. The parameters are:

V_o = 48.412 − 0.963 E + 0.036 E^2 MeV
W = 3.0 + 0.25 E − 6.75/ E^3 MeV
β_2 = 0.25, β_4 = 0.0, V_{so} = 6.5 MeV
r_{so} = r_v = r_W = 1.25 F, a = s_{so} = 0.65 F,
b = 0.47

Analysis

The local and nonlocal optical model parameters have been scanned with CRAPONE[8] code using measured total and elastic scattering cross-sections as the fitting parameters. The reaction cross-section has been split into compound elastic and thirteen discrete level excitation components using the Hauser-Feshbach[9] statistical theory with ABACUS[10] code. These various components have been corrected to account for other exit reaction channels such as capture, fission, (n,2n) and (n,3n). The coupled channel calculations have been performed with ADAPE[11] code based on adiabatic approximation which couples all the six excited states of the ground state rotational band. The excitation energies, spins and parities of the discrete states are given in Table I. The starred states constitute the ground state rotational band.

TABLE I. Energy Level Scheme for ^{232}Th

Energy (MeV)	J^π	Energy (MeV)	J^π
0.0*	0^+*	0.7852	2^+
0.05*	2^+	0.8281*	10^+
0.1624*	4^+	0.873	4^+
0.334*	6^+	1.023	6^+
0.5578*	8^+	1.045	1^-
0.7301	0^+	1.095*	3^-
0.7741	2^+	1.1388*	12^+

The measured and calculated total cross-sections in the energy range 1.0 MeV to 15.0 MeV are given in Table II.

Table II. Comparison of Measured and Evaluated Total Cross-Section (Barns) of ^{232}Th

Energy (MeV)	Measured M	Ad-Deformed D	Local L	Nonlocal N	M-D M %	M-L M %	M-N M %
1.0	6.910	-	6.808	6.687	-	1.47	3.22
1.5	6.822	6.979	6.796	6.759	2.30	0.38	0.92
2.0	7.122	7.733	7.174	7.140	2.96	0.73	0.25
3.0	7.679	7.679	7.800	7.426	0.0	1.58	3.29
4.0	7.741	7.742	7.644	7.468	0.01	1.25	3.53
5.0	7.416	7.452	7.269	7.28	0.48	1.98	1.83
6.0	6.930	6.993	6.821	6.952	0.91	1.57	0.32
7.0	6.453	6.530	6.457	6.618	1.19	0.06	2.56
8.0	6.070	6.137	6.190	6.270	1.10	1.98	3.29
9.0	5.810	5.852	5.961	5.961	0.72	2.60	2.60
10.0	5.661	5.694	5.788	5.73	0.58	2.24	1.22
11.0	5.597	5.644	5.676	5.602	0.84	1.41	0.09
12.0	5.590	5.653	5.626	5.536	1.13	0.64	0.97
13.0	5.623	5.679	5.615	5.528	1.0	0.14	1.69
14.0	5.684	5.697	5.631	5.555	0.23	0.93	2.27
15.0	5.746	5.696	5.665	5.613	0.87	1.41	2.31

It is apparent from this Table that the adiabatic coupled channel theory closely reproduces the measured total cross-sections within 1% from 3 MeV to 15 MeV of neutron incident energies. Upto 2 MeV of neutron energies the measured and calculated cross-sections deviate upto 3%. The local and nonlocal optical models also reproduce the total cross-section reasonably well, the maximum deviation being 3.5%. The predictions of these three models vary amongst themselves upto 2.5% or less. These deviations are within the experimental errors. Beyond 15 MeV measurements do not exist and this evaluation serves to extrapolate these data upto 20 MeV. The evaluated total cross-sections in the energy range 16 MeV to 20 MeV are given in Table III.

TABLE III. Evaluated Total Cross-Sections (Barns) of ^{232}Th

Energy (MeV)	Ad.Deformed D	Local L	Nonlocal N	D-L D %	D-N D %
16.0	5.676	5.706	5.681	0.53	0.09
17.0	5.640	5.753	5.751	2.00	1.97
18.0	5.573	5.802	5.845	4.11	4.88

TABLE III (Continued)

Energy (MeV)	Ad.Deformed D	Local L	Nonlocal N	D-L / D %	D-N / D %
19.0	5.492	5.852	5.870	6.55	6.88
20.0	5.402	5.899	5.915	9.20	9.50

It is seen from this Table that at 18 MeV and beyond these cross-sections deviate from 4% to 9.5%. This difference is of little significance in fission reactors since the fraction of neutrons in this energy range is insignificantly small. Fig.2 depicts the measured and calculated total cross-sections.

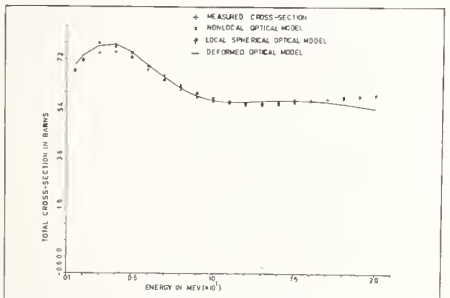

Fig.2 Measured versus predicted total cross-sections based on local, nonlocal and deformed optical models

There are no reliable measurements of elastic scattering cross-sections beyond 2 MeV and thus the model based cross-sections are to be used in all applications. These evaluated cross-sections are shown in Fig.3.

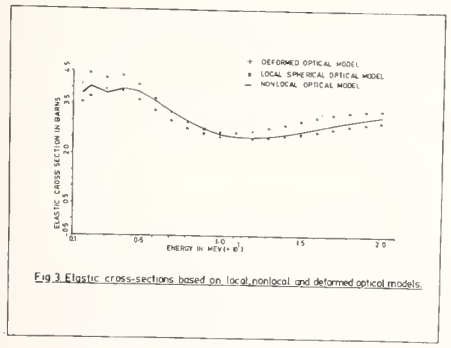

Fig.3 Elastic cross-sections based on local, nonlocal and deformed optical models

It is seen from this Figure that the local and nonlocal potentials produce higher elastic scattering cross-sections than the deformed potential over most of the energy range. The nonlocal calculation varies from 0.8% to 9% and the local calculation varies from 1% to 16% when compared with the deformed one.

The discrete level excitation cross-sections and angular distributions of the elastically and inelastically scattered neutrons have also been calculated but are not given here for want of space. The inelastic cross-sections are shown in Fig.4.

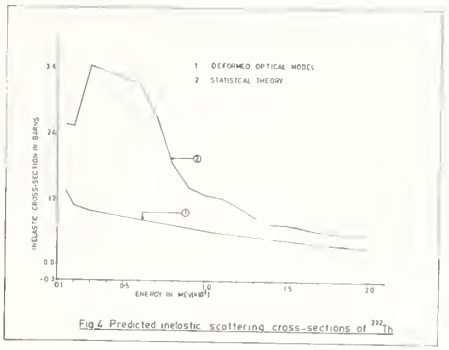

Fig.4 Predicted inelastic scattering cross-sections of ^{232}Th

In this Figure curve 1 is produced by direct excitation of ground state rotational band with coupled channel theory and curve 2 is the result of statistical theory. The bulk of direct excitation cross-section comes from the excitation of first state of the rotational band. At 1 MeV of neutron incident energy statistical calculation gives excitation cross-sections of the first two states well within the experimental errors of the measured values[12]. The measured and calculated cross-sections are given in Table IV.

TABLE IV. Level Excitation Cross-Sections of 1 Mev for ^{232}Th

Level Energy (MeV)	Measured cross-section (barns)	Calculated cross-section (barns)
0.05	1.23 ± 0.10	1.16
0.1624	0.50 ± 0.20	0.33

The calculated total, elastic, inelastic and level excitation cross-sections show similar trends as given by Meadows et al[14] in a recent evaluation.

The sensitivity of calculated cross-sections to deformation parameter has also been examined in the coupled channel theory. It has been noticed that a reduction in this parameter raises the elastic cross-section and lowers the total cross-section. An increase in this parameter produces the oppcsite effect i.e. the elastic cross-section is reduced and the total cross-section is increased but these fluctuations are only marginal and can be ignored. However, the level excitations are found to be very sensitive to deformation parameter.

Conclusions

It has been shown in this paper that the local spherical optical model can provide a good description of the deformed nuclide ^{232}Th. More accurate parameters can still be extracted by putting in measured angular distribution, level excitation and elastic scattering cross-section data. The reliable information about these data is still lacking in the literature.

The nonlocal and deformed optical model parameter search is costly and time consuming. These models may be sparingly used for the extrapolation or interpolation of the data in those energy regions where the measurements are lacking.

Acknowledgement

The authors are thankful to Dr.M.K. Mehta for many helpful discussions and suggestions.

References

1. T. Tamura, Rev.Mod.Phys. 37, 679 (1965).

2. V.K. Shukla and S.B. Garg, Report No:NDE (BARC)-4 (1979).

3. Amar Sinha and S.B. Garg, Report No:NDE(BARC)-1 (1979).

4. C.A. Engelbrecht and H. Fiedeldey, Ann. Phys. 42, 262 (1967).

5. U. Fasoli, D. Toniolo and G. Zago, Nucl. Phys. A 151, 369 (1970).

6. P.T. Guenther, D.G. Havel and A.B. Smith, Nucl. Sci. Eng. 65, 174 (1978).

7. S.B. Garg, Report No:NDE (BARC)-3 (1979).

8. F. Fabbri, G. Fratamico and G. Reffo, RT/FI(77) 3 (1977).

9. W. Hauser and H. Feshbach, Phys. Rev. 87, 366 (1952).

10. E.H. Auerbach, BNL-6562 (Informal Report)(1962).

11. F. Fabbri and L. Zuffi, RT/FI (69) 7 (1969).

12. N.P. Glazkov, Sov.At.Energy 14, 405 (1963).

13. F. Perey and B. Buck, Nucl. Phys. 32 353 (1962).

14. J. Meadows et al, ANL/NDM-35 (1978).

SIMULTANEOUS EVALUATION OF THE NUCLEAR DATA FOR HEAVY NUCLIDES

H. Matsunobu
Sumitomo Atomic Energy Industries, Ltd.
2-6-1 Kaji-cho, Chiyoda-ku, Tokyo 101, JAPAN

Y. Kanda
Graduate School of Engineering Sciences, Kyushu University
Hakozaki-cho, Higashi-ku, Fukuoka 812, JAPAN

M. Kawai and T. Murata
Nippon Atomic Industry Group Co., Ltd.
4-1 Ukishima-cho, Kawasaki-shi, Kanagawa 210, JAPAN

Y. Kikuchi
Japan Atomic Energy Research Institute
Tokai-mura, Naka-gun, Ibaraki 319-11, JAPAN

The nuclear data of ^{235}U, ^{238}U, ^{239}Pu, ^{240}Pu, and ^{241}Pu were simultaneously evaluated in the energy range of 100 eV to 20 MeV by using recent experimental data and theoretical calculations for Japanese Evaluated Nuclear Data Library-Version 2 (JENDL-2). The optical potential parameters were so searched for that the total cross sections of these heavy nuclides were well reproduced with simple systematics.

[JENDL-2, nuclear data, fission cross section, simultaneous evaluation, consistency, absolute measurement, relative measurement, optical potential parameter]

Introduction

Japanese Evaluated Nuclear Data Library-Version 1 (JENDL-1)[1] has been used in Japan since 1977 as the first standard domestic library. Through experiences of its usage, it has been pointed out[2] that the fission rate ratio of ^{239}Pu to ^{235}U was underestimated from the view point of integral experiments. On the other hand, many new experimental data not taken into account in JENDL-1 evaluation were presented in 1976 at NEANDC/NEACRP Specialists Meeting on Fast Neutron Fission Cross Sections of ^{233}U, ^{235}U, ^{238}U, and ^{239}Pu.

In view of these facts, reevaluation was made on the nuclear data of ^{235}U, ^{238}U, ^{239}Pu, ^{240}Pu, and ^{241}Pu for JENDL-2. In this work, a special care was paid for evaluating the fission cross section of ^{235}U so that the consistency could be kept between the relative and absolute measurements for the other heavy nuclides.

The other cross sections of the above five nuclides were also reevaluated by using the experimental data and theoretical calculations in keeping with modification of the fission cross sections. In relation to these reevaluation, the optical potential parameters were so searched for that the experimental data of total cross sections for the above five nuclides were well reproduced by the calculations with simple systematics. In reevaluation of number of prompt neutron per fission, the evaluated data compiled in JENDL-1 were renormalized using the current weighted average value of ^{252}Cf, $^{252}\bar{\nu}_p$ = 3.756.[3]

Simultaneous Evaluation of the Fission Cross Sections

Procedure

Discrepancies are considerably large even among recent measured data, for example, they exceed 10% in keV and MeV regions for the fission cross section of ^{235}U. In selecting the most reliable data among such discrepant ones, we must consider the consistency with the other nuclides. Thus, simultaneous evaluation method was adopted in the present work. The procedure is as follows:

1. Preliminary values on the fission cross section of ^{235}U were obtained on the basis of the recent experimental data.
2. The cross sections of the other nuclides were deduced from the ratio data to fission cross section of ^{235}U by using the preliminary data mentioned above. The deduced data were compared with the absolute measurements for each nuclide. Requirements were derived for modification on the fission cross section of ^{235}U if there exist some discrepancies between the deduced and absolute data.
3. The fission cross section of ^{235}U was reevaluated by taking account of the requirements from the other nuclides.

The data obtained by the procedure mentioned above were examined through the benchmark tests with the integral measurements. The final results were determined by taking account of the results of these tests as well as the present status of the microscopic data.

Evaluation of Each Nuclide

^{235}U : Most of the recent experimental data published after 1975 show systematically low values below 1 MeV compared with the previous data adopted in JENDL-1 evaluation. This tendency of the recent data was taken into account in the present work with the requests from the other nuclides. The fission cross section of ^{235}U was determined on the basis of the data by Perez et al.[4),5)], and Szabo and Marquette[6)] in the energy range of 100 eV to 150 keV, the data by Szabo and Marquette[6)], Poenitz[7),8)], and White[9)] in the energy range of 150 keV to 2.5 MeV, and the data by Barton

et al.[10] and Czirr and Sidhu[11] in the energy range of 2.5 to 20 MeV. The results of evaluation were generally consistent with the requests from the other nuclides in the whole energy range. However, there were large differences between the requests from ^{239}Pu and ^{241}Pu in the energy range of 600 to 800 keV. In this case, the request from ^{239}Pu was adopted taking account of the importance of ^{239}Pu in fast reactor calculation. In this simultaneous evaluation, the fission cross section of ^{235}U in JENDL-1 was increased by maximum 4.5% in the energy ranges of 25 to 150 keV, 1.5 to 4.0 MeV, and 10 to 20 MeV, and decreased by maximum 1.5% in the energy ranges of 150 to 600 keV and 4.5 to 5.5 MeV. The results of evaluation are shown in Fig.s 1 and 2, and compared with JENDL-1, ENDF/B-IV, and the recent experimental data.

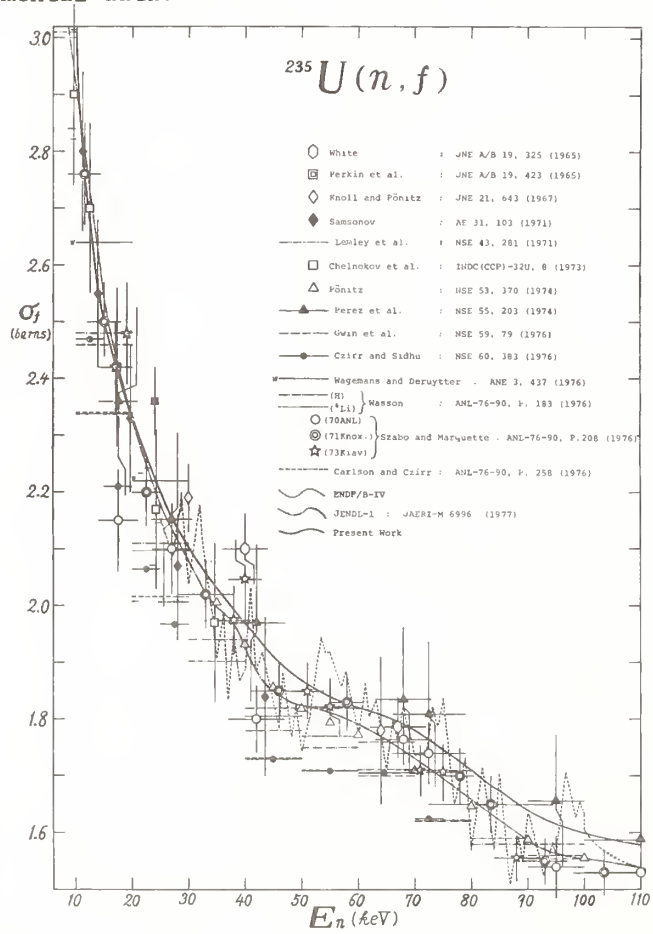

Fig. 1 Fission cross section of ^{235}U in the energy range of 10 to 110 keV.

^{238}U : The fission cross sections were evaluated on the basis of the data of Difilippo et al.[12], Behrens and Carlson[13], Nordborg et al.[14], and Meadows[15),16], which were renormalized with the values of fission cross section for ^{235}U evaluated in the present work. The evaluated results near 14 MeV agree well with the absolute measurements at 13.9 and 14.6 MeV by Cance and Grenier[17] within the errors.

The evaluated values of the capture

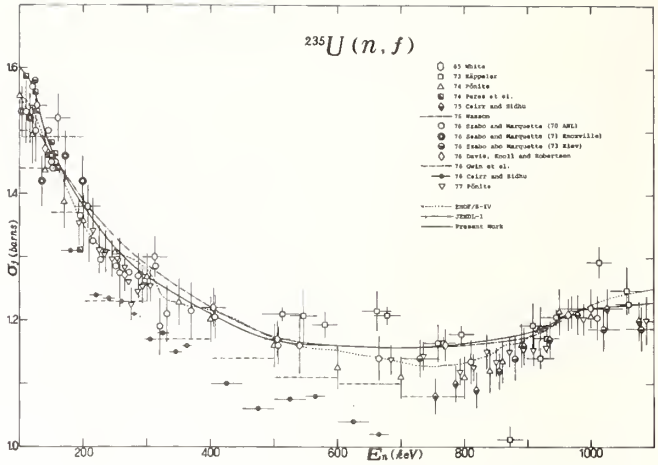

Fig. 2 Fission cross section of ^{235}U in the energy range of 100 keV to 1.1 MeV.

cross sections were determined mainly from the measurements of Poenitz[18], Panitkin and Sherman[19], Moxon[20], Fricke et al.[21], and Menlove and Poenitz[22]. Fig. 3 shows the evaluated curve and the experimental data including the others also. We selected the data measured recently which agreed well with each other. They were measured as being independent of the cross sections for the other heavy nuclides. The data renormalized with the fission cross section of ^{235}U distribute around the evaluated curve not being biassed.

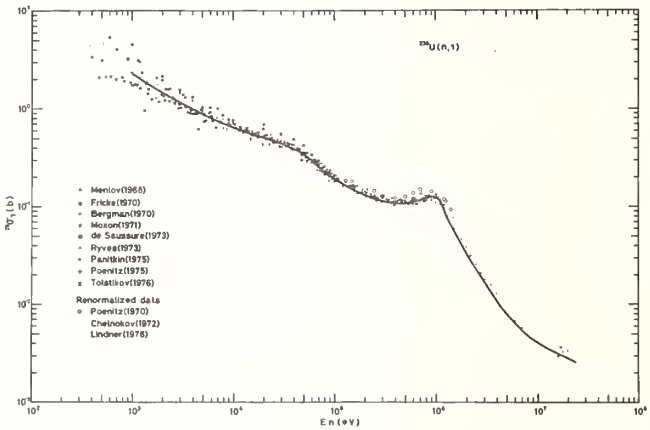

Fig. 3 Neutron capture cross section of ^{238}U. Solid curve shows the present result obtained by simultaneous evaluation with fission cross section of ^{235}U

^{239}Pu : The fission cross section of ^{239}Pu was evaluated on the basis of the following absolute and relative data. As the absolute measurements, the data by Kari and Cierjacks[23], Cance and Grenier[17], Gwin et al.[24], and Gayther[25] were adopted with putting higher weights. As the ratio measurements, the data by Carlson and Bahrens[26], Meadows[27], Kari and Cierjacks[23] Cance and Grenier[17], and Fursov et al.[28] were adopted with putting higher weights. The relative data were derived by

multiplying the ratio measurements by the evaluated fission cross sections of ^{235}U.

The original data by Gayther are normalized using the evaluated value 1.6775 b by Sowerby et al.[29] in the energy range from 10 to 30 keV. In the present work, they were renormalized using the current averaged value 1.760 b. The renormalized data are in good agreement with the data by Gwin et al.. The ratio data by Kari and Cierjacks are considerably low compared with other data. This is due to the low normalization value 1.09 at 14 MeV. Therefore, they were also renormalized using the averaged value 1.130 based on the experimental data around 14 MeV. As the results of evaluation, the relative data distribute between the high and low values of the absolute measurements. The results are shown in Fig.s 4 and 5.

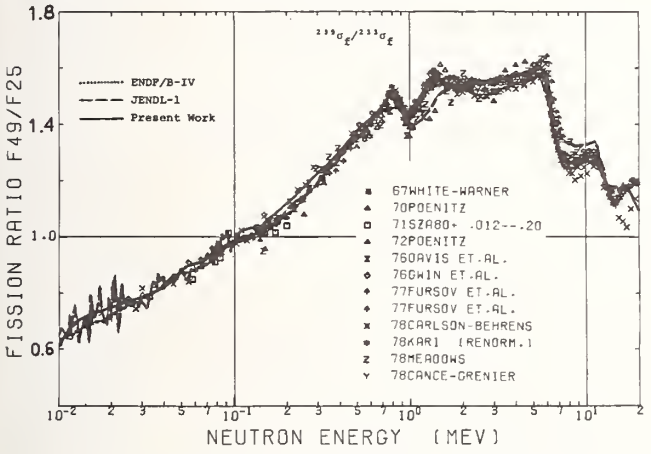

Fig. 4 Fission cross section ratio of ^{239}Pu to ^{235}U.

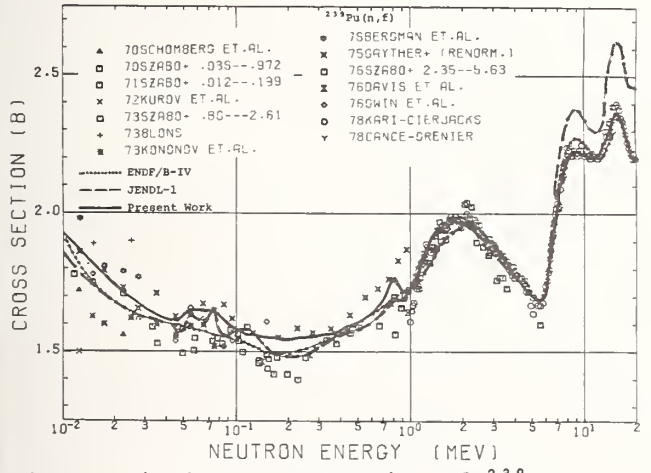

Fig. 5 Fission cross section of ^{239}Pu.

^{240}Pu : Many measurements of the fission cross section ratios have been reported recently. In the energy range of 9 keV to 20 MeV, the evaluated values of the fission ratio relative to ^{235}U were obtained by smoothing the recent experimental ratio data, and the fission cross section for ^{240}Pu was obtained by multiplying the ^{235}U fission cross section evaluated in the present work.

The fission ratio evaluation was made mainly on the data of Wisshak and Käppeler[30] in the energy range of 9 to 55 keV, on the data of Behrens et al.[31] in the energy range of 55 keV to 6 MeV and on the data of Cierjacks[32] in the energy range of 6 to 20 MeV. In the low energy range of 1 to 9 keV, the energy dependence curve of the cross section was determined using the data of Byers et al.[33] and the data of Migneco and Theobald[34]. Then, the fission cross section in the low energy range was obtained by normalizing the curve to the cross section value in the energy range of 9 to 50 keV.

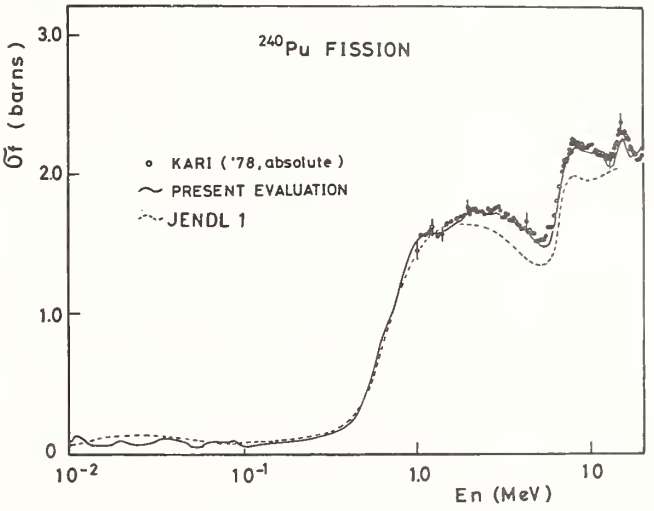

Fig. 6 Fission cross section of ^{240}Pu

^{241}Pu : In the unresolved resonance region below 30 keV the cross sections were evaluated by averaging the absolute measurement with putting higher weights to newer data. In the energy region of 30 keV to 1 MeV, the evaluation was made on the basis of recent relative measurements of Käppeler and Pfletschinger[35], Behrens and Carlson[36], and Fursov et al.[37] which agreed fairly well with each other. The absolute measurements of Szabo et al.[38] are lower than the data deduced from those relative measurements by multiplying the present fission cross section of ^{235}U. The high value of the fission cross section of ^{235}U were determined mainly by the requirements of consistency to the fission cross section of ^{239}Pu. Thus there remains some inconsistency between the absolute and deduced data in ^{241}Pu. The results of evaluation are shown in Fig. 7.

Systematics of Optical Potential Parameter

To estimate some of the cross sections of which experimental data are not available presently, the statistical model calculations were performed with the code CASTHY[39].

Physically, it is difficult to explain all the phenomena of neutron induced reactions with the spherical potential model for the deformed nuclides such as U and Pu. However, it is known as a fact that the simple spherical potential model can predict some trends of the neutron cross sections of these nuclides. For the present estimation, the spherical

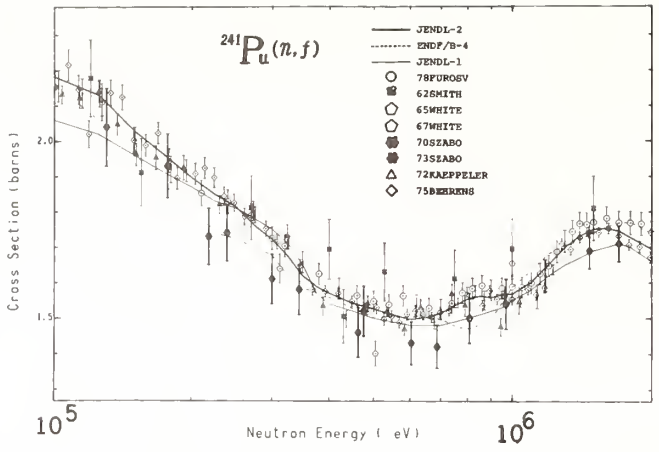

Fig. 7 Fission cross section of ^{241}Pu in the energy range of 100 keV to 2 MeV. The present result is shown by a thick solid curve.

potential model was adopted for simplicity, and effort was made to obtain the optimum potential parameter set. The potential parameters were determined to reproduce the experimental total cross section and s-wave and p-wave strength functions of Th, U and Pu. Also the attention was paid on the relation between the calculated compound nucleus formation cross section and the non-elastic cross section which was evaluated on the basis of the experimental data. After studying the effects of each parameter on the cross sections and the strength functions, the following parameter set was determined.

Real potential well depth (Woods-Saxon):

$V=V_0 - 0.05\ E_n$ MeV, (E_n in MeV)

Imaginary potential well depth (derivative Woods-Saxon):

$W_s=6.5 + 0.15\ E_n$ MeV

Spin-Orbit force (Thomas-Fermi):

$V_{so}=7.0$ MeV

Diffuseness:

a(real) = a(imag.) = a(spin-orbit) =0.47 fm

Nuclear radius parameter:

r_0(real)=r_0(spin-orbit)=1.32 fm

r_0(imag.)=1.38 fm

In this set, only the parameter V_0 varies from nucleus to nucleus, and has tendency to decrease with increasing the mass of target nucleus (see Table 1). To emphasize p-wave absorption, the nuclear radius parameter of the imaginary potential is set larger than that of the real potential. Though the dependence of the parameters on the incident neutron energy En is very simple, the calculated total cross sections using the parameters agree well with the experimental values in the whole energy range of fast neutrons up to 20 MeV, as is shown in Fig. 8.

In Table 1 strength functions calculated with the parameters are compared with the values given in BNL-325 (3rd Ed.) for some nuclides of Th, U and Pu. Values of the parameter V_0 are also listed in Table 1.

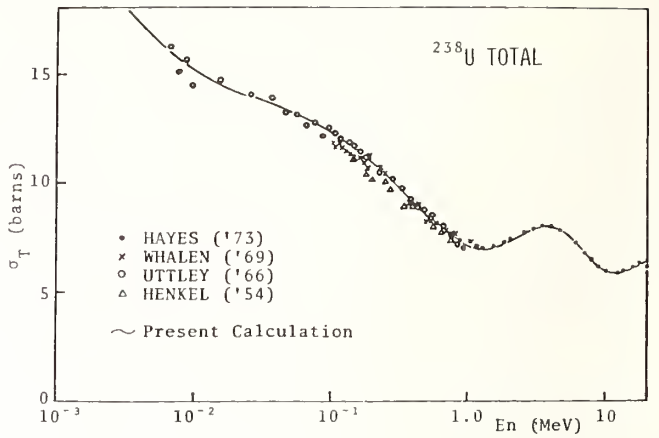

Fig. 8 Total cross section of ^{238}U. The solid curve represents the calculated cross section with the present parameters (V_0=41.0 MeV)

Table 1. Real potential well depth parameter V_0 and strength functions.

Nuclide	V_0 (MeV)	Strength function (in 10^{-4}) Calculated S_0	Calculated S_1	BNL-325 S_0	BNL-325 S_1
^{232}Th	41.5	0.87	1.66	0.84±0.08	1.6±0.2
^{235}U	40.9	0.95	1.57	0.92±0.1	1.8±0.3
^{238}U	41.0	0.83	1.75	1.1±0.1	1.7±0.3
^{239}Pu	40.8	0.85	1.71	1.3±0.1	2.3±0.4
^{240}Pu	40.6	0.88	1.67	0.94±0.09	——
^{241}Pu	40.0	1.03	1.49	0.99±0.14	——

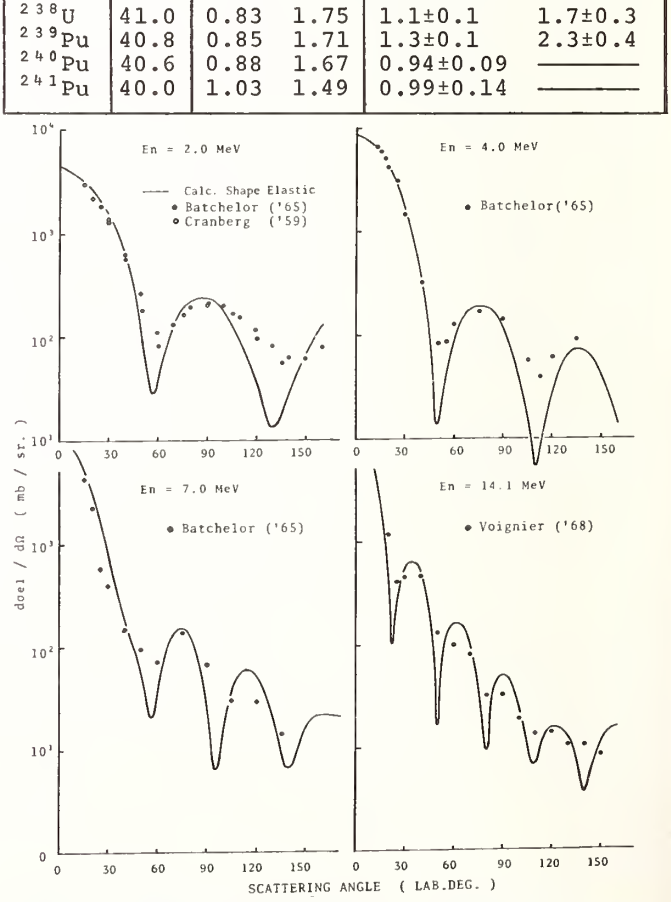

Fig. 9 Differential elastic scattering cross section of ^{238}U.

Fig. 9 shows the comparison of the calculated and experimental values of the differential scattering cross section of ^{238}U. The solid curve represents the calculated cross section with the present parameter set (V_0 = 41.0 MeV). As a whole, good agreements were obtained between the experimental values and the calculated values using the parameters. But there remain some problems in the results of the calculation using the parameters. For ^{239}Pu, the calculated strength functions are somewhat smaller than the experimental values, and the calculated compound nucleus formation cross sections seem to be also somewhat small for fissile nuclides. As an example of the results of the CASTHY calculation, Fig. 10 shows the capture cross section of ^{240}Pu along with experimental data.

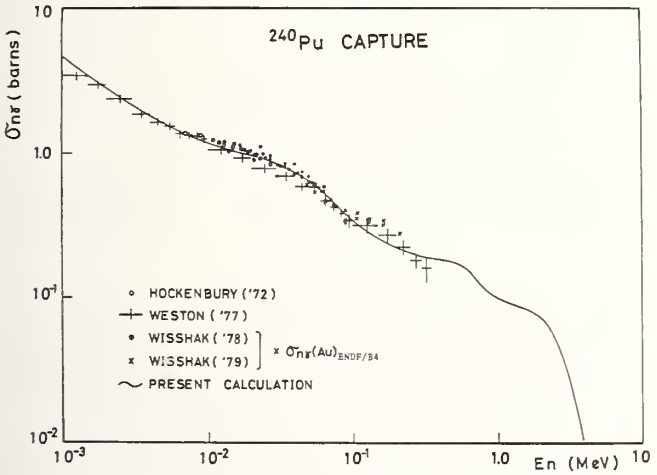

Fig. 10 Capture cross section of ^{240}Pu. The solid curve represents the result of the CASTHY calculation (V_0=40.3 MeV). The normalization with the experimental value was made at En = 40 keV.

Acknowledgment

The authors would like to express their cordial thanks to Dr. S. Igarasi(JAERI) for his advice and encouragement during the present work.

References

1) Igarasi, S. et al. : JAERI 1261 (1979)

2) Kikuchi, Y. et al. : "Benchmark Tests of Japanese Evaluated Nuclear Data Library," Paper presented in this Conference (1979)

3) Smith, J. R. : Symposium Proceedings : Nuclear Data Problems for Thermal Reactor Applications, Section V, Rept No.EPRI 1098 (1979)

4) Perez, R. B. et al. : Nucl. Sci. Eng. 52, 46 (1973)

5) Perez, R. B. et al. : ibid., 55, 203(1974)

6) Szabo, I. and Marquette, G. P. : ANL-76-90 P.208 (1976)

7) Poenitz, W. P. : Nucl. Sci. Eng. 53, 370 (1974)

8) Poenitz, W. P. : ibid., 64, 894 (1977)

9) White, P. H. : J. Nucl. Ener. A/B 19, 325 (1965)

10) Barton, D. M. et al. : Nucl. Sci. Eng. 60, 369 (1976)

11) Czirr, J. B. and Sidhu, G. S. : ibid., 57, 18 (1975)

12) Difilippo, F. C. et al. : ibid., 68, 43 (1978)

13) Behrens, J. W. and Carlson, G. W. : ibid., 63, 250 (1977)

14) Nordborg, C. et al. : ANL-76-90 P.128 (1976)

15) Meadows, J. W. : Nucl. Sci. Eng. 58, 255 (1975)

16) Meadows, J. W. : ibid., 49, 310 (1972)

17) Cancé, M. and Grenier, G. : ibid., 68, 197 (1978)

18) Poenitz, W. P. : ibid., 57, 300 (1975)

19) Panitkin, Yu. G. and Sherman, L. E. : Atomnaya Energiya 39, 17 (1975)

20) Moxon, M. C. : Private Communication to CCDN (1971)

21) Fricke, M. P. et al. : Proc. 2nd Inter. Conf. Nucl. Data for Reactors,P.265(1970)

22) Menlove, H. O. and Poenitz, W. P. : Nucl. Sci. Eng. 33, 24 (1968)

23) Kari, K. and Cierjacks, S. : Proceedings of an International Conference on Neutron Physics and Nuclear Data for Reactors and Other Applied Purposes, P. 905 (1978)

24) Gwin, R. et al. : Nucl. Sci. Eng. 59, 79 (1976)

25) Gayther, D. B. : 4th Conf. on Nuclear Cross-Sections and Technology, P.564(1975)

26) Carlson, G. W. and Behrens, J. W. : Nucl. Sci. Eng. 66, 205 (1978)

27) Meadows, J. W. : ibid., 68, 360 (1978)

28) Fursov, B. I. et al. : Atomnaya Energiya 43, 261 (1977)

29) Sowerby, M. G. et al. : Ann. Nucl. Ener. 1, 409 (1974)

30) Wisshak, K. and Käppeler, F. : Nucl. Sci. Eng. 69, 47 (1979)

31) Behrens, J. W. et al.: ibid., 66,433(1978)

32) Kari, K. and Cierjacks, S. : BNL-50991, P. 57 (1978)

33) Byers, D. H. et al. : LA-3586 (1966)

34) Migneco, E. and Theobald, J. P. : Nucl. Phys. A112, 603 (1968)

35) Käppeler, F. and Pfletschinger, E. : Nucl. Sci. Eng. 51, 124 (1973)

36) Behrens, J. W. and Carlson, G. W. : UCRL-51925 (1975)

37) Fursov, B. I. et al. : Sov. J. Atom. Ener. 44, 262 (1978)

38) Szabo, I. et al. : Conf. on Neutron Physics, Vol. 3, P. 27, Kiev (1973)

39) Igarasi, S. : J. Nucl. Sci. Technol. 12, 67 (1975)

NEUTRON CROSS SECTION STANDARDS

Oren A. Wasson
National Bureau of Standards
Washington, D. C. 20234

A review of the status of the neutron induced reactions which have suitable properties for use as neutron standard cross sections is given. The application of these standards in instruments to measure neutron fluence rate as well as an assessment of the impact of the recent measurements is presented.

Key Words: $^{197}Au(n,\gamma)$; $^{10}B(n,\alpha)$; C(n,n); H(n,n); $^{3}He(n,p)$; $^{6}Li(n,\alpha)$; neutron flux; review; standard cross section; $^{235}U(n,f)$

Introduction

The neutron induced reactions which we now use as standards were first observed over 40 years ago. In spite of the large effort expended since that time, the accuracies achieved do not yet meet the accuracy objectives established years ago. The most accurately known reaction is neutron proton scattering where the uncertainty is at the 1% level. Much work remains to bring the other reactions to this level of accuracy. The status of the cross section standards used for neutron flux measurements in the neutron energy region less than 20 MeV is given. Comparisons with their status at the time of the last conference in this series[1] which was held at the National Bureau of Standards in 1975 is given along with a review of new experiments reported subsequently. The use of these standards in neutron flux detectors as well as the influence of the atomic environment at low energies is reviewed. Reviews of some of the standards have been given at subsequent international conferences.[2-5]

Standard Neutron Induced Reactions

The neutron-induced reactions which are generally considered to be standards are listed in Table 1 along with the standard energy region as well as the number of measurements reported since the review by Carlson[6] at the last conference in the series which was held in 1975. Most of the measurement activity has concentrated on the $^{235}U(n,f)$ reaction in the attempt to attain the goal of 1% uncertainty in this important fission standard. As a matter of fact, ^{235}U has received nearly as much effort as the remaining standards combined. There was even an international conference[2] devoted entirely to the U and Pu fission cross sections which was held at Argonne National Laboratory in 1976. The measurements on $^{6}Li(n,\alpha)$ and $^{10}B(n,\alpha)$ have mostly concentrated on the energy region above 100 keV where earlier experiments differed by 25%. No measurements were reported for the $^{3}He(n,p)^{3}H$ standard. The measurements with hydrogen have been mostly at energies above 20 MeV which is beyond the range of this review. The errors listed are my estimates of the standard deviations which exist at this time.

H(n,n)H Reaction

The hydrogen scattering cross section is the most accurately determined standard. The total cross section is known to better than 1% for neutron energies up to 20 MeV and less accurately at higher energies. However, the angular distribution in the center of mass system deviates from isotropy as the neutron energy increases above several MeV. Since proton recoil telescopes which use only a fraction of the solid angle are the most common flux monitors for energies exceeding 1 MeV, the accuracy with which this standard can be applied is limited by the angular distribution.

There have been two recently published measurements[7,8] of the angular distribution at 25.8 and 27.3 MeV. The results of Cookson et al[7] are plotted in Fig. 1 along with the earlier work of Burrows[9] taken at the same energy. The curves from four different parameterizations from a large range of n,p and p,p measurements[10-13] are also shown. The data which have typical error bars of 3% cannot distinguish between the four curves. Therefore, the Hopkins-Breit[10] parameterization using the Livermore phase shifts, which is the basis of the ENDF/B-V evaluation, should continue to serve as the hydrogen standard.

Table 1 Neutron Standard Reactions and Measurements Reported Since 1975

Reaction	Energy	Error	No. of Measurements
H(n,n)H	< 20 MeV	<1%	4
$^{3}He(n,p)^{3}H$	< 1 MeV	3-5%	0
$^{6}Li(n,t)^{4}H$	<100 keV	2%	6
$^{10}B(n,\alpha)^{7}Li$	<100 keV	2%	3
$^{12}C(n,n)^{12}C$	< 2 MeV	1%	7
$^{197}Au(n,\gamma)^{198}Au$	0.1-3.5 MeV	4%	10
$^{235}U(n,f)$	0.1-20 MeV	3%	21

There has been also two published measurements[14-15] of the analysing power for n-p scattering at 16.9 MeV and 14.5 MeV. The work of Tornow et al[14], which is the highest overall precision ever obtained in any fast neutron polarization experiment, disagrees significantly with predicitions based on global phase shift sets of nucleon-nucleon scattering. It thus appears that the neutron polarization measurements will lead to more accurate determinations of the parameterizations which in turn will improve the angular distribution at the higher neutron energies.

For neutron energies less than 1 MeV, hydrogen gas filled proportional counters[16] have been used for neutron flux monitoring with a relative uncertainty of approximately 1.5% while various forms of proton recoil telescopes are used at higher energies. Both Czirr and Sidhu[17] and Carlson and Patrick[18] cover the 1-20 MeV energy range using only a single shielded recoil proton detector. The Karlsruhe Group[19] has measured neutron flux in the 1-30 MeV range with an uncertainty of 3.5% using solid radiators and gas scintillators. Poenitz[20] has developed a thick plastic scintillator which totally absorbs the neutron beam and is used for absolute flux monitoring in the 0.1-8 MeV energy region.

$^{3}He(n,p)^{3}H$ Reaction

There have been no measurements reported for this reaction since the last conference in 1975. Even the ^{3}He evaluation[21] for ENDF/B-V was carried over intact from both Versions III and IV of ENDF/B. Although the thermal cross section is known to better than 1%, any deviation from the 1/v in the energy region between 11 eV and 5 keV has never been measured. The uncertainty

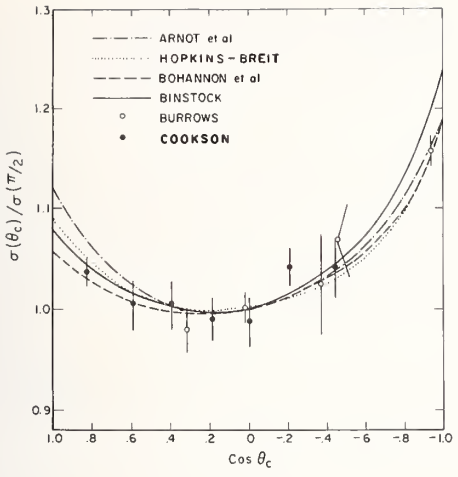

Fig. 1 Angular distribution for (n,p) scattering at 27.3 MeV measured by Cookson et al(7) and Burrows(9). The curves are the parameterizations from refs. 10-13.

in this standard is approximately 3-5% in the energy interval from 0.01-1 MeV.

^{6}Li(n,t)^{4}He Reaction

Although this reaction is usually considered as a standard only for energies less than 100 keV, it is used for neutron flux measurement up to much higher energies where there was a large discrepancy among the various measurements. There have been six (6) measurements of the ^{6}Li(n,t) cross section reported in the 3 keV to 2 MeV region as well as two measurements of the angular distribution at low energies. An excellent listing of all references up to 1977 is given by Derrien and Edwardson[22]. The ^{6}Li- loaded glass scintillator detectors were used in all of the cross section measurements except those of Knitter et al[23,24] who used the difference between the total and scattering cross sections for their results.

The most recent measurement is by Macklin, Ingle, and Halperin[25] who measured the ratio of the ^{6}Li(n,t) reaction to the ^{235}U fission reaction and normalized the results in the 3-70 keV energy range. The results are shown in Fig. 2 as the ratio of the ENDF/B-V ^{235}U cross section to that obtained from their experiment using the ENDF/B-V ^{6}Li(n,α) cross section. This shows that the authors' 240 keV peak cross section is $\sim$ 2% higher and $\sim$ 8% wider than the ENDF/B-V evaluation for ^{6}Li(n,t). The results are also suggestive that the ENDF/B-V evaluation for ^{235}U is also too large in this energy region. Fig. 3 shows the derived ^{6}Li(n,α) cross section as a solid line while the ENDF/B-V standard value is shown by a dashed line.

Also shown by circular points are the absolute measurements of Renner et al[26] which follow the derived curve quite well. This absolute measurement used a ^{6}Li glass scintillator and a thick NE110 plastic scintillator for the neutron flux monitor. The mass of ^{6}Li in the scintillator was determined from transmission measurements at lower neutron energies, while the detector efficiency was calculated from a Monte-Carlo-Program.

The experiment of Lamaze and colleagues[27] was a shape measurement which used a 0.5 mm thick glass scintillator and a hydrogen gas proportional counter for the flux monitor. The published results were normalized to the ENDF/B-V standard in the region from 10 to 100 keV. The quoted uncertainties in the shape measurement were typically 2%.

Table 2 The ^{6}Li(n,t)^{4}He Cross Section Near 240 keV

Reference	σ, barns	Comments
Macklin 1979	3.37	Rel to ^{235}U ENDF/B-V
Renner 1978	3.36 $\pm$ 0.06	Absolute
Lamaze 1978	3.14 $\pm$ 0.08	Rel to H(n,p) Norm <10 keV
Gayther 1977	3.292 $\pm$ 0.122	Rel to ^{235}U Sowerby Eval.
Knitter 1976	3.14 $\pm$ 0.13	From σ_T and σ scatt
Knitter 1977	3.21 $\pm$ 0.13	
ENDF/B-V 1976	3.3087	

The measurement of Gayther[28] was the relative shape of the ^{6}Li(n,α)/^{235}U(n,f) cross section ratio. A thin ^{6}Li-glass scintillator was used to register (n,α) while the fission events in a metallic sample of ^{235}U were registered with fission neutron detectors. The shape of the ^{6}Li(n,α) cross section was obtained by combining the ratio measurement with the ^{235}U(n,f) cross section evaluation of Sowerby et al[29].

Knitter and Colleagues[23,24] deduced the ^{6}Li(n,α) cross section from their measurement of the total cross section and the scattering cross section. The error in the total cross section was less than 2% while the error in the scattering cross section was 5%. A simultaneous fit was made to the total and to the scatter-in cross sections. From the resulting parameters the (n,t) cross section was calculated. This calculation was later expanded to include other data sets and resulted in an approximately 2% increase in the cross section near the resonance peak.

Czirr and colleagues[30,31] have measured ratio of ^{6}Li(n,t) to ^{235}U(n,f) rates from 0.02 eV to 680 keV with an uncertainty of 2% using ^{6}Li glass scintillator and large fission chamber. However the results which were reported in large energy intervals were used to deduce the ^{235}U(n,f) cross section and not the ^{6}Li(n,t) cross section.

Angular distributions for neutron energies less than 25 keV have been reported by Raman et al[32] and Stelts et al[33] and found to be in agreement with the R-Matrix calculation of Hale.[33]

There have been no new measurements in the region below 2 keV where the cross section follows a 1/v dependence to better than 1%.

A comparison of the recent measurements of the peak cross section in the 240 keV resonance is given in Table 2. These values all agree within 7% and indicate the progress made since the last conference. At that time there was a 25% variation in the newer results near the peak of the resonance.

One could argue that ^{6}Li should not be used as a standard in this energy region, but the fact remains that it is used as a flux monitor because it is often more convenient than the other choices.

The ^{10}B(n,α)^{7}Li and ^{10}B(n,$\alpha\gamma$)^{7}Li Reactions

These reactions are generally considered as standards only in the neutron region less than 100 keV where the cross sections show no structure. However, since in practice both reactions are used to measure neutron flux over a wider energy range, it is important that the standard region be extended to higher energies. The form of the flux monitor is either a BF_3-gas proportional counter or a solid target with parallel plate ionization chamber. In both detectors the predominate signal is produced by both alpha particle groups. Another form of monitor is used in which the 478 keV γ ray from the α_1 emission to the first excited state of ^{7}Li is detected.

Since the last conference there has been only one

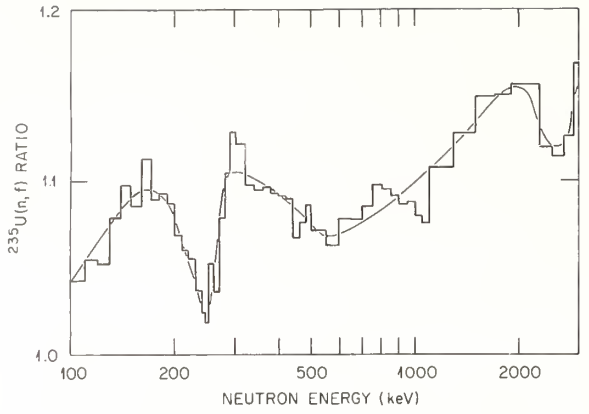

Fig. 2 Ratio of ^{235}U fission cross section of ENDF/B-V to that obtained by Macklin (Ref. 25) using the ENDF/B-V evaluation for ^{6}Li(n,α).

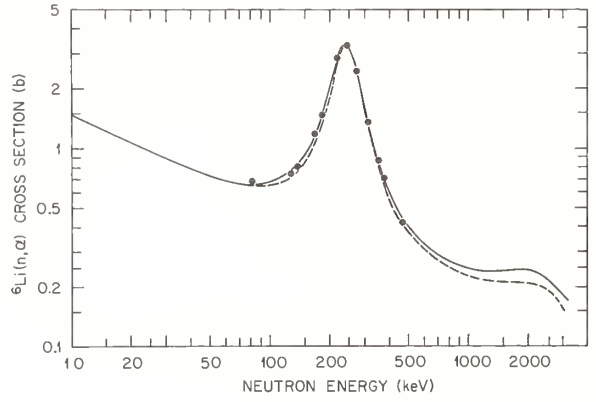

Fig. 3 The ^{6}Li(n,α) cross section of Macklin (Ref. 25) is shown by the solid curve while the dashed curve represents the ENDF/B-V evaluation. The points represent the absolute measurements of Renner et al (Ref. 26).

measurement of the (n,α) cross section. Sealock and Overly[34] measured the angle integrated cross sections for both the ^{10}B(n,α_0)^{7}Li and ^{10}B(n,α_1)^{7}Li* reactions between 0.2 and 1.2 MeV. These results, which had a 12% systematic uncertainty and were unable to resolve discrepancies among earlier measurements, were included in the ENDF/B-V and later evaluations. The angular distribution of the (n,α_1) reaction is forward peaked at the lower neutron energy of 200 keV.

The angular distributions of both the α_0 and α_1 were measured at 2 and 24 keV neutron energies by Stelts et al[33] and found to agree within 2% with the global R Matrix calculation of Hale. The results are shown in Fig. 4. This gives confidence in using the calculation to correct for the neutron energy dependence of the efficiency of solid ^{10}B ionization chambers used for neutron flux monitoring.

There have been two measurements of the shape of the ^{10}B(n,αγ)^{7}Li reaction published since the last conference. Schrack et al[35] measured the shape of this cross section in the energy region from 5 to 700 keV using a hydrogen gas proportional counter for the

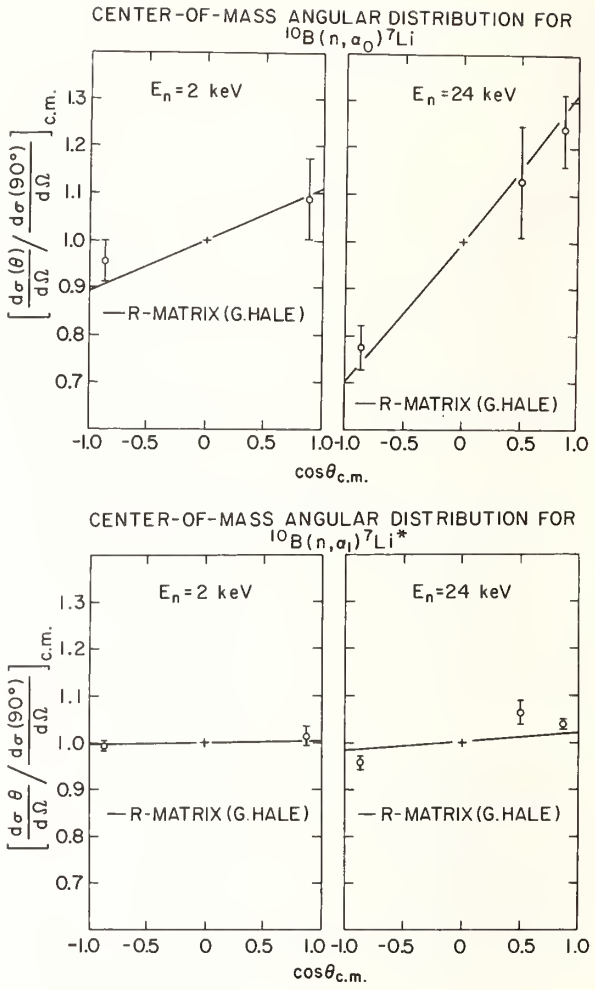

Fig. 4 Angular distributions of ^{10}B(n,α) measured by Stelts et al (Ref. 33).

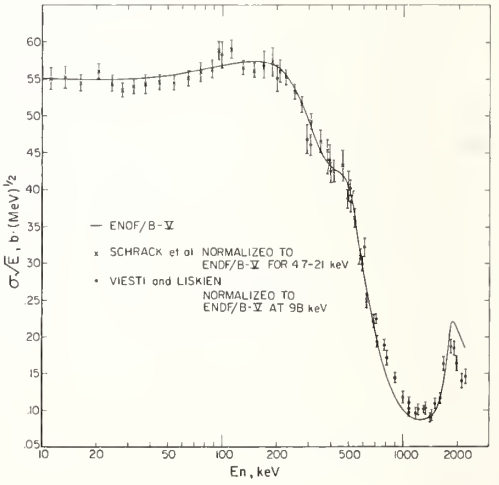

Fig. 5 Measurements of the ^{10}B(n,αγ)^{7}Li reaction from refs. 35 and 36.

neutron flux monitor and a linac-based pulsed neutron source. The 478 keV γ ray was measured with both Ge (Li) and NaI(Tℓ) detectors. Cross sections were obtained by normalization to ENDF/B-V values in the energy region from 4.7 to 21 keV. The overall accuracy is better than 3%.

Viesti and Liskien[36] measured the shape of the cross section in the neutron energy range from 0.1 to 2.2 MeV. The neutron source was the $^{3}H(p,n)^{3}He$ reaction. The neutron flux was deduced from the known angular distribution of the source reaction. The 478 keV γ-rays produced in a boron carbide sample were observed in a Ge(Li) detector. The typical uncertainty was 5%. Cross sections were obtained by normalization to the ENDF/B-V value at 98 keV.

The results of the two experiments are shown in Fig. 5 along with the ENDF/B-V evaluation. In the 0.1 to 0.6 MeV region of overlap the maximum difference of the two experiments is 6%. Also both experiements are within 5% of ENDF/B-V throughout this region. At the higher energies the measurements of Viesti and Liskien[36] deviate by as much as 25% from ENDF/B-V, but are in much better agreement with the evaluation of Liskien and Wattecamps[37] which preceded the data of Viesti and Liskien.

Below 100 keV, it appears likely that the accuracy of evaluated data may reach the 2% uncertainty level. In the energy region from 0.1 to 0.6 MeV it appears that the uncertainty is 5% for the (n,αγ) reaction and greater for the (n,α) reaction. Additional measurements should be done in the energy region above 100 keV in order to extend the standardization limit of these reactions for useful neutron flux monitoring.

$^{12}C(n,n)^{12}C$ Cross Sections

Carbon cross section data are of interest in a number of areas of applied physics in addition to use as a neutron flux monitor. Detailed knowledge of the differential cross sections for scattering is required for calculations of neutron transport in dosimetry and fission and fusion reactors. In neutron scattering experiments where carbon is used as a standard, absolute normalization is generally obtained by replacing the sample with a polyethylene scatterer. Carbon is also the main constituent in many neutron flux monitors such as plastic scintillators and methane filled gas proportional counters.

A review of the status of carbon as a standard which was given by Lackhar[38] in 1977 contains a listing of the previous measurements. The only publications since then have been a measurement of the differential elastic and inelastic cross sections from 8.0 to 14.5 MeV by Haovat et al[39] and a total cross section at 186 eV by Royer and Brugger[40]. Since these data were included in the review by Lackhar, no new conclusions can be inferred.

The total cross section for energies less than 2 MeV is known to better than 1% while the angular distributions are quoted with a precision of better than 5%. The total cross section accuracy is 2% in the 2.8 - 4.8 MeV region while the angle-integrated cross sections deviate from the total cross section by 3 to 5%. The total cross section error is 2% in the 4.8 - 8.5 MeV region and 4% in the 8.5 -15 MeV region. The error in the elastic angular distribution has a global uncertainty of 7%.

The $^{197}Au(n,\gamma)^{198}Au$ Reaction

The gold standard is utilized by either the detection of prompt γ ray emission following neutron capture or by the detection of the ^{198}Au product which decays with a 2.6 day half-life. In the thermal and low resonance energy region, the cross sections are known to better than 1%. However in the unresolved energy region up to 200 keV there is a lot of structure in the cross section which limits its use as a standard, particularly for neutron sources with narrow energy spread. For example near 20 keV Liskien and Weigman[41] show that within a 5 keV energy interval, the fluctuations would limit the accuracy of the average cross section to approximately 4%. At 200 keV, an energy spread of nearly 20 keV is required to limit the effect of the fluctuations on the measure cross section to less than 1%.

A detailed review of the gold standard was presented by Paulsen[42] in 1977 while a summary of the recent measurements [43-52] published since 1975 is given in Table 3. There were no measurements reported in the 3.5 - 14 MeV region or for energies greater than 15 MeV. The quoted standard deviations for the measurements lie in the range from 5 to 8%. It is also important that the results from prompt γ ray detection and activation analysis agree within experimental error[42]. The recent measurements in the 0.2 - 3.5 MeV region are shown in Fig. 6 along with the ENDF/B-V evaluation. The standard deviation in the evaluated data is estimated[53] to be 4%. It thus appears that the gold standard can compete with other neutron flux measuring methods in the 0.2 to 3 MeV energy region.

Table 3 The $^{197}Au(n,\gamma)^{198}Au$ Cross Sections Published Since 1975. The error is that quoted by the authors.

Ref	Author	ΔEn,Mev	Error,%
51	Kononov 77	0.005 - 0.35	7
44	Macklin 75	0.003 - 0.55	3
52	Fort 75	0.1 - 0.5	5
46	Poenitz 75	0.02 - 3.5	∿ 7
47	Lindner 75	0.1 - 3.0	5
45	Paulsen 75	0.2 - 3.0	5
43	Joly 78	0.5 - 3.0	8
49	Gupta 78	1.6 - 2.5	7
50	Csikai 76	^{252}Cf	5
48	Schwerer 76	14.6	60

The $^{235}U(n,f)$ Reaction

The neutron-induced fission cross section of ^{235}U is considered a standard in the energy region from 0.1 to 20 MeV. The region below 100 keV is eliminated because of the structure in the cross section which has been analyzed by Bowman et al[54] and by Liskien and Weigman[55]. The region above 20 MeV is eliminated due to a lack of measurements. A list of the results reported since the 1975 conference are listed[56-76] in Table 4. These references are either to new measurements or to revised values for earlier work. The status of the evaluation of this standard and the effect of the recent improvements in the ^{235}U mass scale in the United States is given by Poenitz[77] in a contribution to this conference while recent reviews have been given by Poenitz,[78] Patrick,[79] and Liskien.[80]

The measurements fall into three groups: 1) absolute, in which the ^{235}U mass and absolute flux are measured; 2) shape measurement; and 3) low energy normalization, in which a shape measurement is extended to low energies where the ^{235}cross section is

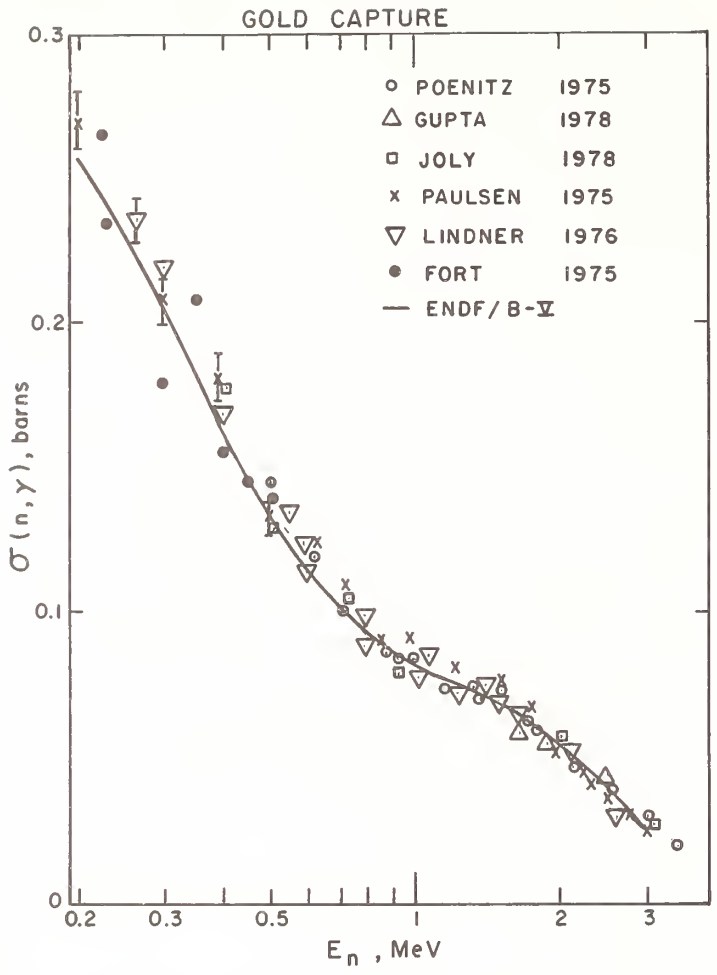

Fig. 6 Measurements of the $^{197}Au(n,\gamma)$ cross section reported in refs. 43, 45, 46, 47, 48, and 52.

well-known. The low energy normalization procedure is discussed in detail by Peelle and de Saussure[81]. The $^{235}U(n,f)$ cross section at thermal energies is thought to be known to a standard deviation of 0.3% while that for the 7.8 - 11.0 eV interval is 0.6% (although recent measurements differ by 5%). The latest measurement of this integral is given in a contribution to this conference by Wagemans et al.[57]

The thermal normalization measurements all used the $^{10}B(n,\alpha)$ or $^{6}Li(n,\alpha)$ reactions for the relative neutron flux determination and electron linacs to produce the neutrons. The absolute measurements at the higher neutron energies used a variety of neutron sources and flux detectors. The sources were produced at electron linacs, Van de Graaffs, cyctotrons, and (α,n) or (γ,n) sources. The absolute flux monitors are black detectors, calibrated scintillators, two types of proton recoil telescopes, and the associated particle technique. The shape measurements which covered the entire 1-20 MeV energy region all used pulsed white neutron sources, long flight paths, and proton recoil detectors. Finally three absolute measurements using the ^{252}Cf fission neutron spectrum were done.

The results obtained at NBS for the 0.2 - 1.2 MeV region[65] are shown in Fig. 7 along with the ENDF/B-V evaluation. The recent absolute measurements using the black detector flux monitor as well as earlier measurements using a hydrogen gas proportional counter flux monitor and low energy normalization[61] are approximately 3% (one standard deviation) lower than the evaluation. The remainder of the recent measurements are shown in Fig. 8. The dip near 280 keV in my earlier measurements[61] has not been observed in more recent measurements by others[62]. It appears that in this region the recent data are lower than the ENDF/B-V evaluation. However, the evaluation still represents the data within a standard deviation of 3%.

The recent results for the 1-6 MeV region are shown in Fig. 9. The shape measurements were normalized to the ENDF/B-V evaluation at 1.2 MeV. The measurements agree well from 1-2.5 MeV, while there is a 10% variation among the various experiments in the 2.5-5.5 MeV region. However recent absolute measurements by Grenier et al[82] at 2.5 and 4.5 MeV should be of value in reducing this discrepency.

The measurements covering the 1-20 MeV region are shown in Fig. 10 along with the ENDF/B-V evaluation. The relative measurements have been normalized to the evaluation at an energy of 1.2 MeV. There are 15% variations in the 15-19 MeV region as well as smaller differences in the 9.5-11 MeV region. The shape in the 5.5-9.5 MeV region appears to be known to within 3%.

The absolute measurements near 14 MeV are shown in Fig. 11. The measurements by Cance and Grenier[72] as well as those of Alkhazov et al[73], both using the associated particle technique, agree within 1.5%. The new measurement by Alkhazov et al replaces the previously reported value of Adamov et al[83] which was nearly 5% larger. We now have two independent measurements near 14 MeV using the same technique which give excellent agreement. The absolute measurements of Kari[67] using a proton recoil detector are 5% (1.5 standard deviations) larger.

The three relative measurements using the proton recoil method and normalized to the ENDF/B-V evaluation at 1.2 MeV are shown in Fig. 12. Only the data of Leugers et al[68] is significantly higher while that of Czirr and Sidhu[70] and Carlson and Patrick[71] agree within the nearly 2% experimental error with the results using the associated particle technique. It thus does not appear that the proton recoil method yields results which are consistently higher than the associated particle method.

The results of the three measurements using the ^{252}Cf fission neutron spectrum are shown in Table 5. The results agree within 3%. The result of Heaton et al[75] will increase by nearly 0.75% as the NBS mass scale is improved. The result of Adamov et al[76] replaces a previous value[83] which was 2% larger. It appears that the $^{235}U(n,f)$ cross section averaged over the ^{252}Cf fission neutron spectrum is now known to better than 3%.

Status of the Standards

A summary of the accuracy of the standard reactions as well as the energy region is shown in Table 1. For hydrogen, the total cross section is known to 1% and the angular distribution to 2 - 3% from the energy region below 20 MeV. In the energy region below 1 MeV the error in the $^{3}He(n,p)^{3}H$ cross section grows from less than 1% to nearly 5%. The $^{10}B(n,\alpha)$ and $^{6}Li(n,a)$ reactions are known within 2% for neutron energies less than 100 keV. For carbon below 2 MeV, the total cross section is known to better than 1% while differential scattering cross section is known to 1 - 2%. The gold capture standard is known within 4% throughout the 0.2 -3.5 MeV region. In general the ^{235}U fission standard is known within 3% from 0.1 - 15 MeV. However there are a few intervals where this uncetainty increases to 6%.

Table 4 $^{235}U(n,f)$ Measurements Since 1975

Year	Author	Energy	Error %	Type
76	Wagemans and Deruytter	0.008 eV - 30 keV		Ther. Norm. Rel to $^{10}B(n\alpha)$
79	Wagemans et al	≤ 30 keV		Ther. Norm. $^{10}B(n,\alpha)$, $^{6}Li(n,\alpha)$
76	Gwin et al	0.02 eV - 0.2 Mev	3.0	Ther. Norm. Rel to $^{10}B(n,\alpha)$
77	Czirr and Carlson	0.02 eV - 1 keV	1.5	Ther. Norm. Rel to $^{6}Li(n,\alpha)$
75	Czirr and Sidhu	0.1 - 680 keV	1.5 - 2.8	Ratio to $^{6}Li(n,\alpha)$
76	Wasson	0.01 - 0.8 MeV	2.8	Low En Norm Rel to H(n,p)
77	Poenitz	0.2 - 8.2 MeV	2.0	Abs. Black Det.
76	Szabo and Marquette	0.01 - 5.5 MeV	2.5	Abs. Scint
78	Davis et al	0.14 - 0.96 MeV	1.7	Abs. γ,n
79	Meier et al	0.2 - 1.2 MeV	2.8	Abs. Black Det.
76	Barton et al	1 - 6 MeV	1.5	Abs. H(n,p)
78	Kari	0.5 - 20 MeV	3.5	Abs. H(n,p)
76	Leugers et al	1 - 20 MeV		Rel to H(n,p)
75	Czirr and Sidhu	0.75 - 4.1 MeV		Rel to H(n,p)
76	Czirr and Sidhu	3 - 20 MeV		Rel to H(n,p)
78	Carlson and Patrick	1 - 20 MeV		Rel to H(n,p)
78	Cance and Grenier	13.9 and 14.6 MeV	1.9	Abs. Assoc. Part.
78	Alkhazov et al	14.7 MeV	1.2	Abs. Assoc Part.
78	Davis and Knoll	Cf Spectrum	1.8	Abs.
76	Heaton et al	Cf Spectrum	2.2	Abs.
79	Adamov et al	Cf Spectrum	1.5	Abs.

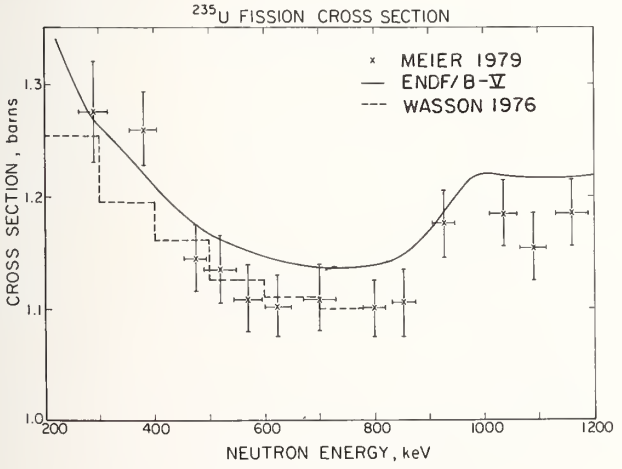

Fig. 7 The ^{235}U fission cross section measurements from refs. 61 and 65.

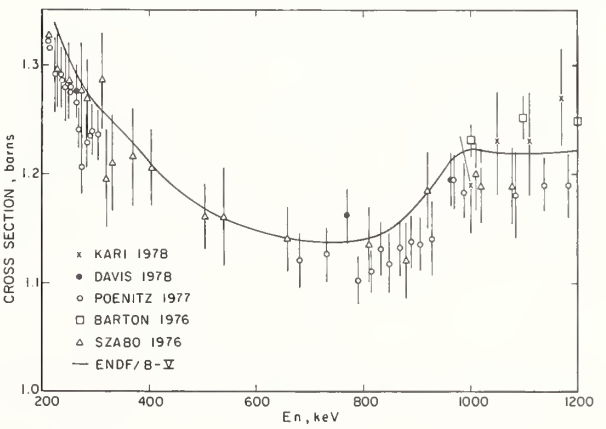

Fig. 8 Recent absolute measurements of the $^{235}U(n,f)$ cross section reported in refs. 62, 63, 64, 66 and 67.

Table 5 The ^{235}U Fission Cross Section Averaged Over the ^{252}Cf Fission Neutron Spectrum

Reference	Experiment	Cross Section, barns
74	Davis and Knoll	1.215 ± 0.022
75	Heaton et al	1.205 ± 0.027
76	Adamov et al	1.241 ± 0.018

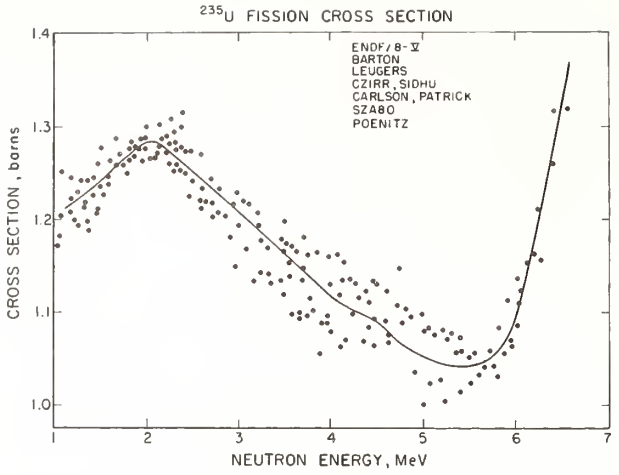

Fig. 9 Recent measurements of the ^{235}U(n,f) cross section reported in refs. 62, 63, 66, 68, 69 70 and 71.

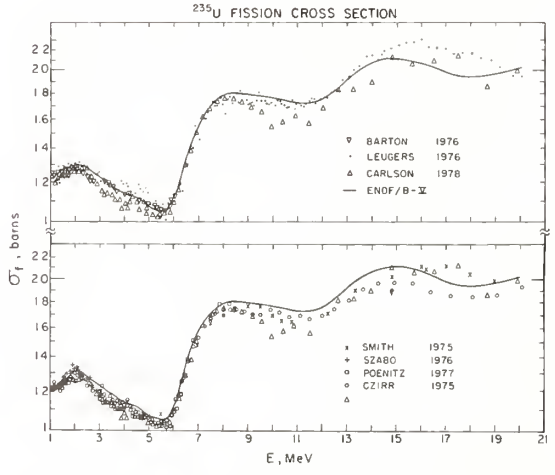

Fig. 10 Recent measurements of the ^{235}U(n,f) cross section reported in refs. 62, 63, 66, 68, 69, 70 and 84.

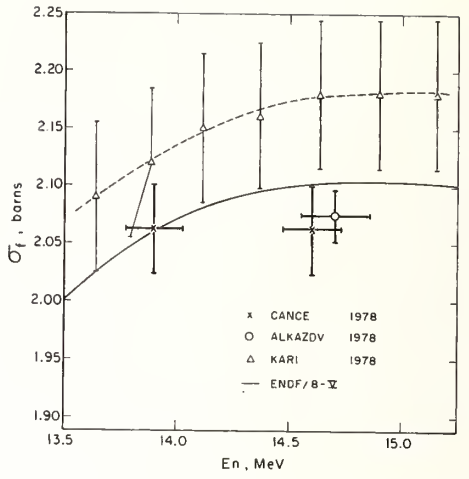

Fig. 11 Absolute ^{235}U(n,f) cross section measurement near 14 MeV reported in refs. 67, 72 and 73.

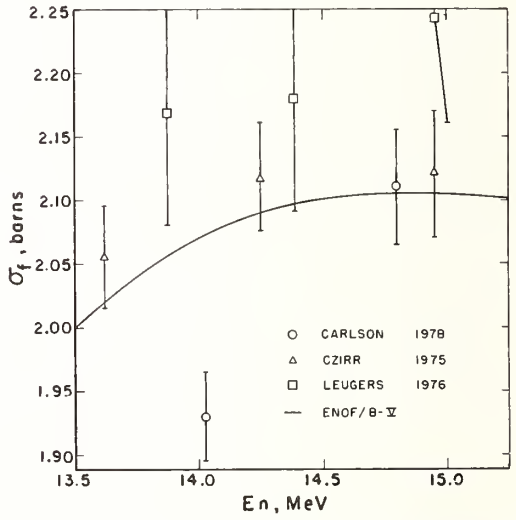

Fig. 12 Relative ^{235}U(n,f) cross sections obtained by normalization to ENDF/B-V at 1.2 MeV from refs. 68, 70, and 71.

References

1. Proceedings of a Conference on Nuclear Cross Sections and Technology, Edited by R. A. S. Schrack and C. D. Bowman, U. S. Government Printing Office, Washington, D. C. 1975, National Bureau of Standards Special Publication 425.
2. Proceedings of the NEANDC/NEACRP Specialists Meeting on Fast Neutron Fission Cross Sections of U-233, U-235, U-238, and Pu-239, Edited by W. P. Poenitz and A. B. Smith, National Technical Information Service, Springfield, Va., 1976.
3. Proceedings of the International Specialists Symposium on Neutron Standards and Applications, Edited by C. D. Bowman, A. D. Carlson, H. O. Liskien, and L. Stewart, National Bureau of Standards Special Publication 493, 1977.
4. Proceedings of the International Conference on the Interactions of Neutrons with Nuclei, Edited by E. Sheldon, Lowell, Massachusetts (1976).
5. Proceedings of an International Conference on Neutron Physics and Nuclear Data, Harwell (1978).
6. A. D. Carlson, Reference 1, p 293.
7. J. A. Cookson, J. L. Fowler, M. Hussain, R. B. Schwartz, and C. A. Uttley, Nucl. Phys. A299, 365 (1978).
8. T. C. Montgomery, B. E. Bonner, F. P. Brady, W. B. Brostc, and M. W. McNaughton, Phys. Rev. C16, 499 (1977).
9. T. W. Burrows, Phys. Rev. C7, 1306 (1973).
10. J. C. Hopkins and G. Breit, Nucl. Data Tables A9, 137 (1971).
11. G. E. Bohannon, T. Burt and P. Signell, Phys. Rev. C13, 1816 (1976).
12. R. A. Arndt, R. H. Hackman, and L. D. Roper, Phys. Rev. C15, 1002 (1977).
13. J. Binstock, Phys. Rev C10, 19 (1974).
14. W. Tornow, P. W. Lisowski, R. C. Byrd, and R. L. Walter, Phys. Rev. Letters 39, 915 (1977).
15. R. Fischer, F. Kierle, H. O. Klages, R. Maschuw, and B. Zeitnitz, Nucl. Phys. A282, 189 (1977).
16. O. A. Wasson, R. A. Schrack, and G. P. Lamaze, Nucl. Sci. Eng. 68, 170 (1978).
17. J. B. Czirr and G. S. Sidhu, Nucl. Sci. Eng. 58, 371 (1975).
18. A. D. Carlson and B. H. Patrick, Proceedings of an International Conference on Neutron Physics and Nuclear Data, Harwell, 1978, p. 880.

19. I. Schouky, S. Cierjacks, P. Brotz, D. Groschel, and B. Leugers, Reference 1, p. 277.
20. W. P. Poenitz, Nucl. Instr. and Meth. 109, 413 (1973).
21. L. Stewart, Los Alamos Report LA-7663-MS, 1979 p. 21 (unpublished).
22. H. Derrien and L. Edvardson, Reference 3, p. 14 (1977).
23. H. Knitter, C. Budtz-Jorgensen, M. Mailly, and R. Vogt, Report EUR-5726E (1977) (Unpublished).
24. H. H. Knitter and C. Budtz-Jorgensen, Proceedings of the International Conference on the Interactions of Neutrons with Nuclei, Lowell, Massachusetts, p. 1387 (1976).
25. R. L. Macklin, R. W. Ingle, and J. Halperin, Nucl. Sci. Eng. 71, 205 (1979).
26. C. Renner, J. A. Harvey, N. W. Hill, G. L. Morgan, and K. Rush, Bull. Amer. Phys. Soc. 23, 526 (1978).
27. G. P. Lamaze, R. A. Schrack, and O. A. Wasson, Nucl. Sci. Eng. 68, 183 (1978).
28. D. B. Gayther, Ann. Nucl. Ener. 4, 515 (1977).
29. M. G. Sowerby, B. H. Patrick, and D. S. Mather, Ann. Nucl. Sci. and Eng. 1, 409 (1974).
30. J. B. Czirr and G. S. Sidhu, Nucl. Sci. and Eng. 60, 383 (1976).
31. J. B. Czirr and G. W. Carlson, Nucl. Sci. and Eng. 64, 892 (1977).
32. S. Paman, N. W. Hill, J. Halperin and J. A. Harvey, Proceedings of the International Conference on the Interactions of Neutrons with Nuclei, Lowell, Massachusetts (1976) p 1341.
33. M. L. Stelts, R. E. Chrien, M. Goldhaber, and M. J. Kenny, Phys. Rev. C19, 1159 (1979).
34. R. M. Sealock and J. C. Overly, Phys. Rev. C13, 2149 (1976).
35. R. A. Schrack, G. P. Lamaze, and O. A. Wasson, Nucl. Sci. and Eng. 68, 189 (1978).
36. G. Viesti and H. Liskien, Ann. of Nucl. Ener. 6, 13 (1979).
37. H. Liskien and E. Wattecamps, Nucl. Sci. and Eng. 68, 132 (1978).
38. J. C. Lachkar, Reference 3, p. 93 (1977).
39. G. Haouat, J. Lachkar, J. Sigaud, Y. Patin, and F. Cocu, Nucl. Sci. Eng. 65, 3331 (1978).
40. R. B. Royer and R. M. Brugger, Nucl. Instr. and Meth. 145, 245 (1977).
41. H. Liskien and H. Weigmann, Ann. Nucl. Ener. 4, 38 (1977).
42. A. Paulsen, Reference 3, p. 165, (1977).
43. S. Joly, J. Voignier, G. Grenier, D. M. Drake, and L. Nilsson, Proceedings of an International Conference on Neutron Physics and Nuclear Data, Harwell (1978) p. 859.
44. R. L. Macklin, J. Halperin, and R. R. Winters, Phys. Rev. C11, 1270 (1975).
45. A. Paulsen, R. Widera, and H. Liskien, Atomkernenergie 26, 80 (1975).
46. W. P. Poenitz, Nucl. Sci. Eng. 57, 300 (1975).
47. M. Lindner, R. J. Nagle, and J. H. Landrum, Nucl. Sci. Eng. 59, 381 (1976).
48. O. Schwerer, M. Winkler-Rohatsch, H. Warhanck, and G. Winkler, Nucl. Phys. A264, 105 (1976).
49. S. K. Gupta, J. Frehaut, and R. Bois, Nucl. Instr. and Meth. 148, 77 (1978).
50. J. Csikai and Z. Dezso, Ann. Nucl. Ener. 3, 527 (1976).
51. V. N. Kononov, B. D. Yurlov, E. D. Poletaev, V. M. Timokhov, Sov. J. Nucl. Phys. 26, 500 (1977).
52. E. Fort and C. LeRigoleur, Reference 1, p. 960 (1975).
53. S. F. Mughabghab, Informal Report BNL-NCS-21774 (1976).
54. C. D. Bowman, G. P. Lamaze, K. C. Duvall, and R. A. Schrack, Reference 2, p. 313.
55. H. Liskien and H. Weigman, Ann. Nucl. Ener. 4, 38 (1977).
56. G. Wagemans and A. J. Deruytter, Ann. Nucl. Ener. 3, 437 (1976).
57. G. Wagemans, G. Coddens, and A. J. Deruytter, Contribution to this conference.
58. R. Gwin, E. G. Silver, R. W. Ingle, and H. Weaver, Nucl. Sci. Eng. 59, 79 (1976).
59. J. B. Czirr and G. W. Carlson, Nucl. Sci. Eng. 64, 891 (1977).
60. J. B. Czirr and G. S. Sidhu, Nucl Sci. Eng. 58, 371 (1975).
61. O. A. Wasson, Reference 2, p. 183 (1976).
62. W. P. Poenitz, Nucl. Sci. Eng. 64, 894 (1977). Values decreased by 1.5%, Private communication (1979).
63. I. Szabo and J. P. Marquette, Reference 2, p. 208 (1976). Also see previous references therein.
64. M. C. Davis, G. F. Knoll, J. C. Robertson, and D. M. Gillian, Ann. Nucl. Ener. 5, 569 (1978).
65. M. M. Meier, O. A. Wasson, and K. C. Duvall, Contribution to this conference.
66. D. M. Barton, B. C. Diven, G. E. Hansen, G. A. Jarvis, P. G. Koontz, and R. K. Smith, Nucl. Sci. Eng. 60, 369 (1976).
67. K. Kari, Karlsruhe Report KfK 2673 (1978) (unpublished).
68. B. Leugers, S. Cierjacks, P. Brotz, D. Erbe, D. Groschel, G. Schmalz, and F. Voss, Reference 2, p. 246 (1976).
69. J. B. Czirr and G. S. Sidhu, Nucl. Sci. Eng. 57, 18 (1975).
70. J. B. Czirr and G. S. Sidhu, Nucl. Sci. Eng. 60, 383 (1976).
71. A. D. Carlson and B. H. Patrick, Ref. 5, 880 (1978).
72. M. Cancé and G. Grenier, Nucl. Sci. Eng. 68, 197 (1978).
73. I. D. Alkhazov, R. Arlt, V. Wagner, F. Vaydkhaze, V. Grimm, V. N. Dushin, S. S. Kovalenko, O. I. Kostochkin, R. Krause, G. Musial, H. G. Ortlepp, K. A. Petrazhak, R. Teichner, and V. I. Shpakov, Technical University of Dresden Report 05-37-78 (1978) (Unpublished).
74. M. C. Davis and G. F. Knoll, Ann. Nucl. Ener. 5, 583 (1978).
75. H. T. Heaton, D. M. Gilliam, V. Spiegal, C. Eisenhauer, and J. A. Grundl, Reference 2, p. 333 (1976).
76. V. M. Adamov, I. D. Alkhazov, L. V. Drapchinsky, V. N. Dushin, A. V. Formichev, S. S. Kovalenko, O. I. Kostochkin, L. Z. Malkin, K. A. Petrzhak, L. A. Pleskachevsky, V. I. Shpakov, R. Arlt, and G. Musial, Contribution to this conference (1979).
77. W. P. Poenitz, Contribution to this conference (1979).
78. W. P. Poenitz, Reference 3, p. 261 (1977).
79. B. H. Patrick, Proceedings of an International Conference on Neutron Physics and Nuclear Data, Harwell (1978) p. 76.
80. H. Liskien, Reference 4, p. 1110 (1976).
81. R. W. Peelle and G. de Saussure, Reference 3, p. 174 (1977).
82. G. Grenier, M. Cancé, D. Gimat, and D. Parisot, Neutron Interlab Seminar, Bruyeres le Chatel, 1979 (Unpublished).
83. V. M. Adamov, B. M. Alexandrov, I. D. Alkhazov, L.V. Drapchinsky, S. S. Kovalenko, O. I. Kostochkin, G. Yu. Kudriavzev, L. Z. Malkin, K. A. Petrzhak, L. Pleskachevsky, A. V. Formichev, and V. I. Shpakov, Reference 3, p. 313 (1977).
84. R. K. Smith et al, Private communication from L. Stewart (1978).
85. C. D. Bowman and J. W. Behrens, Contribution to this conference (1979).

ABSOLUTE MEASUREMENT OF $\bar{\nu}_p$ FOR ^{252}Cf BY THE LARGE LIQUID SCINTILLATOR TANK TECHNIQUE

R. R. Spencer*
Oak Ridge National Laboratory
Oak Ridge, Tennessee 37830, USA

A vigorous effort to dispel the scandal† of the ∿ 2% dispersion in reported experimental values of ^{252}Cf $\bar{\nu}$, the average number of neutrons emitted in spontaneous fission, has been underway over the past 5 years. The goal is to reduce the uncertainty in this fundamental parameter to the ± 0.25% level needed for reactor physics applications. Both new measurements and reevaluation of older measurements are involved. At ORNL a new measurement is being carried out using the large liquid scintillator neutron detector. Findings of the most recent experiment, incorporating improvements suggested in a preliminary study, will be discussed.

($\bar{\nu}$, neutron multiplicity, ^{252}Cf, fission, large liquid scintillator, proton-recoil detector.)

Historical Development

The first measurements of $\bar{\nu}$, the average number of neutrons emitted in fission, were reported by Halban, Joliot, and Kowarski[1] in 1939, incredibly, only four months after the discovery of fission by Hahn and Strassman. These earliest measurements were carried out on systems of uranyl nitrate dissolved in water and, although their derived $\bar{\nu}$ of 3.5 for uranium was somewhat in error, their experiments permitted the important conclusion that no concentration of ordinary uranium in H_2O can result in a self-sustaining chain reaction.[2] At almost the same time Szilard and Zinn[3] had estimated an average of two neutrons per fission in uranium by counting recoils in a helium filled ionization chamber. Shortly thereafter these same experimenters reported[4] a $\bar{\nu}$ value of 2.3 and studied the energy distribution of the emitted neutrons using helium and hydrogen filled chambers. By the end of 1939 $\bar{\nu}$ of uranium, the spectrum of prompt fission neutrons, the number of delayed neutrons and their half-lives had all been studied.[5] In 1940 spontaneous fission was discovered.[6] At this point WW II essentially ended the open publication of fission research.

The late 1940's and early 1950's undoubtedly saw a great deal of activity in the study of neutrons from fission although for the most part the work was unpublished. For example, the apparatuses used by Fowler and by Hanna to study $\bar{\nu}$ of fissile isotopes as a function of energy of the bombarding neutron are described by Henkel.[7] The neutron detectors used in these studies were, in general, of low efficiency (i.e. proton recoil ionization chambers). It was in the mid 1950's that large volume, high efficiency neutron detectors came into prominence. Both the large liquid scintillator[8] device and the manganese bath[9] neutron detectors were introduced. With the former detector delayed coincidence techniques became possible, leading to studies of more complicated aspects of fission such as the variation of ν with fission fragment kinetic energy and mass ratio[10] in addition to more precise values of $\bar{\nu}$ and the second moment of the neutron multiplicity distribution. The first production and isolation of ^{252}Cf from a ^{239}Pu sample irradiated in the MTR reactor in Idaho had been accomplished.[11] It was immediately recognized that the relatively low alpha emission to spontaneous fission ratio of this isotope (∿ 31/1) meant negligible interference from (α,n) reactions in surrounding materials, and therefore it would make an ideal standard source of fission neutrons. But first, precise measurements of the fission neutron energy spectrum and the average number of neutrons emitted, $\bar{\nu}$, were necessary.

Probably the earliest measurement of $\bar{\nu}$ of ^{252}Cf was that of Crane et al.,[9] at Livermore. Using the manganese bath activation technique they obtained a value of 3.10 ± 0.15. Then Hicks et al.,[12] at Berkeley, reported 4.06 ± 0.14 for $\bar{\nu}$ of ^{252}Cf using a large liquid scintillator (and $\bar{\nu}$ of ^{240}Pu as reference). This early large discrepancy undoubtedly provided impetus for new measurements. However, although the magnitude of the difference decreased, the absolute measurements of ^{252}Cf $\bar{\nu}$ which followed have persistently shown a systematic discrepancy between the liquid scintillator method on the one hand and the manganese bath (including boron pile[24]) method on the other. A summary of these measurements from 1963 onward and the latest results prior to this meeting, including recent reevaluations of some of the measurements, is presented in Table I. At this point the discrepancy in the previous measurements has apparently not been reduced sufficiently to derive an absolute $\bar{\nu}_p$ of ^{252}Cf to the ≤ 0.25% accuracy needed for reactor physics applications.

TABLE I. $\bar{\nu}_{total}$ Values for ^{252}Cf

Author	Original Value	Current Status
	Liquid Scintillator	
Asplund-Nilsson et al.[15]	3.808 ± 0.034	3.792 ± 0.040*
Hopkins and Diven[16]	3.780 ± 0.031	3.777 ± 0.031*
Boldeman[17]	3.747 ± 0.015	3.755 ± 0.016*
Spencer et al.[18]	3.792 ± 0.011	3.792 ± 0.011
		Wt'd. Avg. 3.780 ± 0.009
	Manganese Bath	
White and Axton[19]	3.796 ± 0.025	3.815 ± 0.040†
Axton et al.[20]	3.700 ± 0.020	3.743 ± 0.019†
De Volpi and Porges[21]	3.725 ± 0.015	3.747 ± 0.019†
Aleksandrov et al.[22]		3.747 ± 0.036†
Bozorgmanesh[23]	3.744 ± 0.023	3.744 ± 0.023†
	Boron Pile	
Colvin and Sowerby[24]	3.713 ± 0.015	3.739 ± 0.021†
		Wt'd. Avg. 3.748 ± 0.009

Diff. 0.85%

Wt'd. Avg All: $\bar{\nu}_T$ = 3.766 ± 0.006

*Ref. 13

†Ref. 14

*Coworkers: R. Gwin, R. Ingle, R. Shannon, and H. Weaver.

†Herbert J. C. Kouts, Conf. on Nuclear Cross Sections and Technology, NBS-425, 1, 3 (1975).

The Importance of $^{252}Cf\ \bar{\nu}$

The importance of such an accurate value to both fast breeder and thermal reactor systems stems from the use of californium spontaneous fission sources as a standard in measurements of $\bar{\nu}_p(E_n)$, the neutron energy dependence of nubar, for the fissile isotopes of uranium and plutonium. Experimentally it is convenient to measure the energy dependent nubar ratio

$$R(E_n) = \frac{\bar{\nu}_p(E_n)}{\bar{\nu}_p(^{252}Cf)}$$

for each isotope, thereby avoiding a separate measurement of neutron detector efficiency with each experiment. For a reactor the quantities of interest are the neutron-spectrum-averaged values of $\bar{\nu}$ for the combination of heavy metals in the core. Uncertainties in the ratio measurements and in the value of Cf $\bar{\nu}$ contribute directly to uncertainties in the flux-averaged quantities and therefore affect reactor design and cost. For example, sensitivity calculations of a full-scale model LMFBR core[25] indicate that the effect of ν uncertainty is comparable to the more universally recognized sensitivities to σ_f of ^{239}Pu and σ_γ of ^{238}U. It can be seen from Table I of Ref. 25 that a 0.5% uncertainty in $^{252}Cf\ \bar{\nu}$, since it acts in concert on the $\bar{\nu}$ values of all fissionable isotopes through their measured $R(E_n)$'s, in principle results (to first order) in an uncertainty of 0.5% in multiplication factor, k, and a 1% uncertainty in the so-called k-reset breeding ratio. To meet design goals of 0.5% uncertainty in k and 2% in breeding ratio (only $\sim$ 1/2 of which can be taken up by the nuclear parameters) requires that the $^{252}Cf\ \bar{\nu}$ uncertainty be 0.25% or less. Similar conclusions have been reached in the case of light water reactors (LWR). Recent calculations by Becker *et al.*[26] predict that the largest effects on LWR fuel-cycle costs were due to $^{252}Cf\ \bar{\nu}$ with a sensitivity of approximately 4, compared to typical spectrum averaged cross-section sensitivities of about 0.5. However, the importance of $\bar{\nu}$ for thermal systems is diluted through use of direct measurements with thermal neutrons of the related quantity, η, the number of neutrons emitted per neutron absorbed.

The ORNL $^{252}Cf\ \bar{\nu}_p$ Measurement

New measurements of $^{252}Cf\ \bar{\nu}$ by both manganese bath and liquid scintillator techniques have been initiated in the U.S. to try to resolve the discrepancy in this important parameter. At ORNL nubar ratio measurements on the fissile isotopes referenced to ^{252}Cf were already underway using a large liquid scintillator. Thus, the adaptation of the ORNL equipment to an absolute $\bar{\nu}_p$ of ^{252}Cf experiment was a natural and virtually compulsory development.

The 1977 Measurement

In the ORNL measurement an $\sim$ 900 liter gadolinium loaded liquid scintillator tank was placed in the pulsed neutron beam from ORELA approximately 85 m from the neutron-producing target. The tank was carefully aligned so that a 1.27 cm diam collimated beam traversed the scintillator on the axis of a horizontal through-tube built into the tank. In the first experiment[18] done in 1977, an NE-213 proton-recoil detector (0.6 cm thick by 4.8 cm diam liquid volume in direct contact with the photomultiplier face) and a fission chamber containing ^{252}Cf were both positioned on the vertical center axis of the scintillator, the recoil detector being in the beam and normal to it whereas the fission chamber was out of the beam and just above the through-tube bottom. Two graphite plugs were used to reduce neutron escape out the through-tube ends. A schematic of the experimental configuration is given in Fig. 1. Fission events were signalled by coincidence between fragment pulses in the fission detector and the prompt tank pulses from fission gamma rays to allow use of a low fission chamber bias without interference from alpha pulses. When biased well above the alphas, the loss due to the coincidence requirement was only $\sim$ 0.7%. Neutrons scattered from the beam in the NE-213 were signalled by their associated proton recoil pulses and their incident energies defined by recording their time of flight. Pulse shape discrimination was used to reject gamma ray interactions in the NE-213. Some 500 ns after either a fission chamber or proton-recoil detector event a fast scaler was gated on for 50 μs to record subsequent tank pulses from neutrons slowed down and captured in the scintillator. The nubar scaler data were stored according to the number of pulses occurring during this 50 μs and according to the type of initiating event. Thus the observed neutron number distributions, which are required to correct the fission data for neutron pileup, were obtained. Similarly the nubar scaler was triggered by appropriate background gate generators and subsequent tank background pulses were recorded. Since only one neutron enters the tank per proton-recoil event, the fraction of recoil events which resulted in a scintillator tank pulse during the 50 μs counting interval is (after correction for background) a measure of the tank efficiency. These recoil data were used to normalize a Monte Carlo calculation of the total tank efficiency for an isotropic spectrum of neutrons representative of ^{252}Cf fission. This efficiency together with the background corrected fission event nubar data permitted the derivation of $\bar{\nu}_p$ for ^{252}Cf.

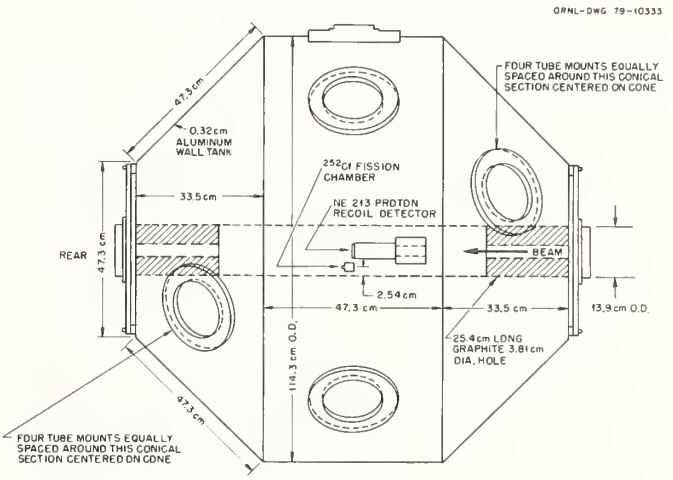

Fig. 1. Schematic cross-section view of the ORNL, gadolinium-loaded scintillator tank with the ^{252}Cf fission chamber and the NE-213 proton-recoil counter in place.

Ideally the tank neutron efficiency calibration should be measured for all regions of the tank at all energies necessary to describe the ^{252}Cf fission neutron spectrum. Using the white spectrum of neutrons available from ORELA, it is possible to kinematically describe scattered neutrons over a sufficiently broad region of energies, but for a somewhat restricted range of scattering angles at each scattered neutron energy. For n,p scattering:

$$E_1 \cong E_0 \cos^2\theta$$

where E_0 is the incident neutron energy as determined by time of flight, E_1 is the scattered neutron energy

as determined from E_0 and the pulse height response to the scattered proton, and θ is the neutron scattering angle with respect to the incident beam. The proton pulse height is calibrated in energy by observing the end point of the pulse height spectrum at each incident neutron time of flight. Thus, the proton-recoil data were reduced to efficiency vs scattering angle for some 16 scattered neutron energy groups from essentially 0 to about 10 MeV. Following a suggestion of Hopkins and Diven[16] the efficiencies were computed from the zeros of the scattered neutron probability distribution thereby avoiding any pile-up correction for these data, i.e.:

$$\text{fraction of neutrons undetected} = 1 - \varepsilon = N(o)/B(o)$$

where ε is the efficiency, N(o) is the observed probability of zeros following a proton-recoil event and B(o) is the probability of zeros in a background nubar gate. Examples of the efficiency data from the 1977 experiment are shown in Fig. 2 along with normalized Monte Carlo calculations of tank efficiency. The latter were carried out using the code DENIS.[27]

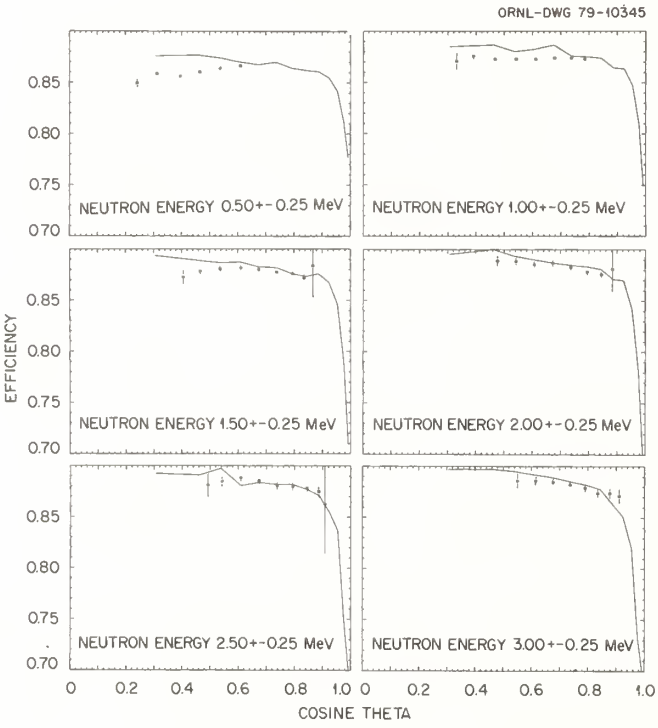

Fig. 2. Experimental (points) and Monte Carlo calculated (lines) tank efficiencies for neutrons from 0.5 to 3.0 MeV energy vs cosine of the neutron scattering angle. The Monte Carlo calculations were carried out for 5° intervals in scattering angle with 10,000 histories at each angle. Straight lines are used as eye guides between the calculated data. Where error bars are not visible in the experimental data, they are of the size of the data points.

The analysis of the 1977 experiment which led to the value $\overline{\nu}_p = 3.783 \pm 0.010$ given in Table I is described in detail in Ref. 18. Briefly, it can be seen in Fig. 2 that the measured efficiencies show a significant decrease at very low scattered neutron energies and that, at the lowest energy shown, there is also a decrease at the higher scattering angles. These disturbances were attributed primarily to two effects. First, there is a preferential loss of detected neutrons at low scattering energies at absorption times beyond the end of the 50 μs counting gate. This is caused by the tens of μs traversal time for thermalized neutrons in the through-tube and was predicted by the Monte Carlo calculations (Fig. 3). In order to accurately predict the low energy drop-off in efficiency, the Monte Carlo calculation was adjusted (by varying the thermal absorption cross section of gadolinium slightly) to fit the measured time of absorption of neutrons at long times as shown in Fig. 4. Second, there is a preferential loss of efficiency at high scattering angles (and low scattered energy) due to the effect of the photomultiplier, primarily absorption of thermalized and eV neutrons by ^{10}B in the glass envelop. This effect was measured for ^{252}Cf neutrons to be 0.35% by simply removing the proton-recoil detector. It was assumed that it could be accounted for in the efficiency calibration by not using data for scattered energies below 1.5 MeV (and the three highest angle points in Fig. 2 for 1.5 MeV). This procedure was not altogether pleasing since these low energy neutron groups carry a high weight in the Maxwellian used to simulate ^{252}Cf neutrons. In addition to these two effects, a possible effect due to multiple scattering[15] in the NE-213 was recognized but presumed to be small due to the relatively flat response with scattered neutron angle of the tank.

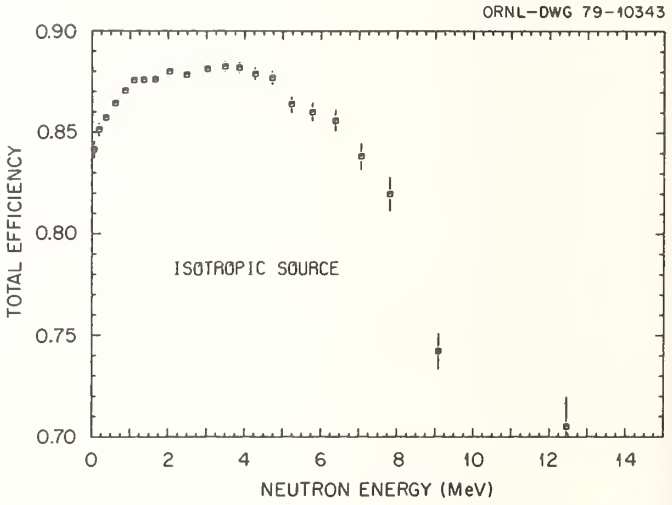

Fig. 3. Monte Carlo calculated total efficiency of the scintillator tank (in 1977) for isotropic neutrons vs neutron energy. The calculation was for 400,000 total histories, weighted by a Maxwellian with average energy of 2.09 MeV.

The 1979 Measurements

As a result of these difficulties in analysis in the 1977 measurement, a new set of measurements with somewhat more optimal conditions are presently underway. The following changes in the experimental arrangement were made: the through-tube diameter was reduced to 8.9 cm OD to reduce the angular dependence of neutron efficiency; a 0.076 cm thick cadmium sleeve was inserted in the through-tube to reduce the number of thermalized neutrons traversing the tube; an 80 μs counting gate (starting 750 ns after an event) was used to reduce any residual "time gate" loss; the diameter of the NE-213 was reduced to 1.9 cm to decrease multiple scattering and a quartz window was used between the NE-213 and P-M; graphite plugs with a 2.54 cm diam hole for the neutron beam were used. With these changes and using a 1 MeV tank bias on the detection of neutrons an ∿ 95% efficiency for ^{252}Cf neutrons was attained and the time gate effect was eliminated

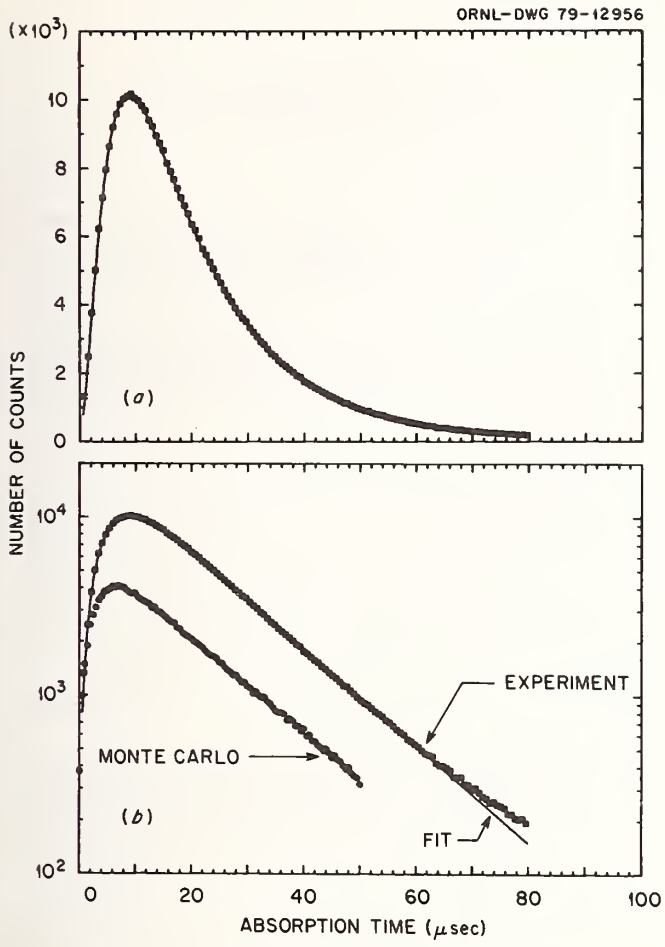

Fig. 4. Linear (a) and semilog (b) plots of the measured (square data points) fission neutron time-to-absorption distribution and a fitted function (solid line) of the form $F(t) = A(e^{-\beta t} - e^{-\lambda t}) - Bte^{-\lambda t}$ with $A = 22319 \pm 63$, $B = 6398 \pm 74$, $\beta = 0.0621 \pm 0.0001$ and $\lambda = 0.382 \pm 0.002$. The Monte Carlo predicted shape shown in the lower figure was fitted (not shown) with the same function and parameters $B/A = 0.110$, $\beta = 0.0613 \pm 0.0005$, and $\lambda = 0.42 \pm 0.03$. The units of B, λ, and β are μsec^{-1} with t in μsec.

(see Fig. 5). Runs were made with the neutron beam entering the P-M base first and entering the NE-213 first so that an average of the two runs could be used to approximately account for the disturbance to ^{252}Cf neutrons caused by the P-M. This effect was unexpectedly about the same as in the 1977 experiment (0.35%). Similar runs were carried out with a 3 MeV bias on tank neutron detection to eliminate delayed gamma rays from fission and thereby verify a 0.3% correction to the low bias result which was calculated from yield data for the delayed isomers. Some results of the efficiency calibration with 1 MeV tank bias are shown in Fig. 6 along with a normalized Monte Carlo calculation using the latest ENDF/B cross sections.

The results of preliminary analyses show that the low and high bias derived ^{252}Cf $\bar{\nu}_p$ values agree within the statistics of the efficiency calibrations (the high bias result is $\sim$ 0.07% lower than the low bias result). The results of various methods of normalizing the Monte Carlo calculation to experiment are also consistent. For example, a single normalization constant using all the experimental data from 0 - 7.5 MeV scattered neutron energy results in a ^{252}Cf $\bar{\nu}_p$ that is within $\sim$ 0.05% of the value obtained by

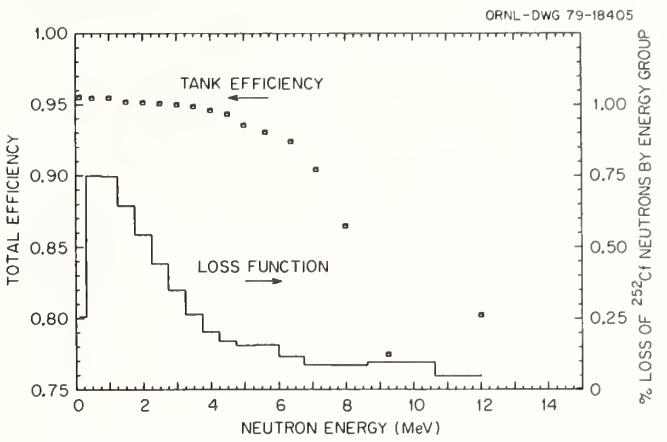

Fig. 5. The 1979 tank total efficiency for isotropic neutrons as a function of energy group are shown as square data points. The histogram shows the % loss of ^{252}Cf neutrons (i.e. a Maxwellian weighting with $\bar{E} = 2.09$) by energy group. Both data sets were obtained from Monte Carlo calculations of the tank efficiency normalized to experiment with a single normalization constant.

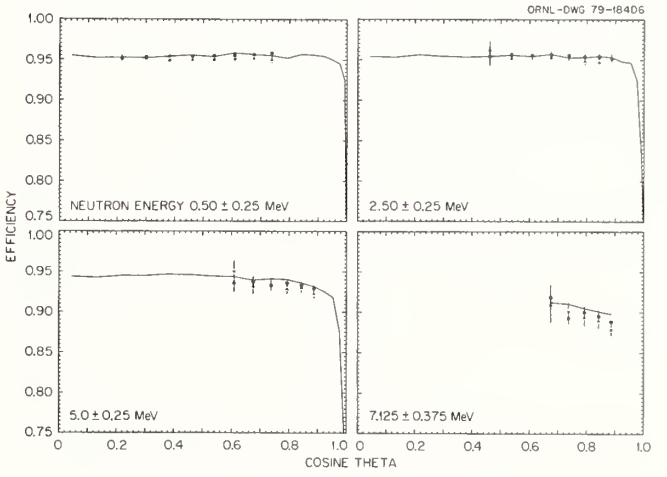

Fig. 6. Measured neutron efficiencies as a function of the cosine of the neutron scattering angle (squares and triangles) for four of sixteen scattered neutron energy groups. The solid line joins Monte Carlo efficiency predictions at 5° angular intervals normalized by a single constant for all energies and angles. Squares were measured with the ORELA neutron beam entering the P-M base first, whereas triangles are for the ORELA beam entering the P-M face first.

normalizing each energy group separately for both the low and high bias runs. Since the Q-values for (n,p) reactions in the materials surrounding the NE-213 are negative and of magnitude $\sim$ 2-4 MeV for the major constituents, the use of proton-recoil data below about 3 MeV should greatly diminish any effect of these "false zeros."[18] This method of normalization led to a reduction of $\sim$ 0.08% in the low bias result. In summary, the two biases and several ways of normalization of the Monte Carlo calculation resulted in values for $\bar{\nu}_p$ of ^{252}Cf from 3.771 to 3.775. Since necessary ancillary measurements for determining uncertainties and/or other small corrections have not yet been carried out with the new system, a tentative value $\bar{\nu}_p = 3.773$ without error is reported here. If calculated in the same manner as in Refs. 17 and 18,

the standard error will be significantly smaller than for the 1977 experiment. This value is 0.43% higher than the value recommended in ENDF/B-V ($\overline{\nu}_p$ = 3.757 ± 0.006).

Conclusion

In conclusion it may be of interest to see what effect this latest value of $\overline{\nu}_p$ for ^{252}Cf has with regard to the thermal parameters of interest to reactor design. Table II, for example, shows a comparison between the 2200 m/s fission cross sections calculated from the relations

$$(\overline{\nu}_p + \overline{\nu}_{delayed})\ \sigma_f = \eta \cdot \sigma_a$$

$$\overline{\nu}_p = R_p \cdot \overline{\nu}_p(^{252}Cf)$$

where η is the number of neutrons emitted per neutron absorbed, and an evaluated set of fission cross sections.[28] For the purpose of this comparison $\overline{\nu}_p$ of ^{252}Cf was taken to be 3.773 without error. It can be seen that relatively little adjustment of the 2200 m/s parameters would be required to obtain complete consistency.

TABLE II

Isotope	R_p	η Ref. 29	σ_a Ref. 28	σ_f Calc.	σ_f Ref. 28
^{233}U	0.659 ± .002[30]	2.295 ± .009	575.2 ± 1.3	529.5 ± 2.6	529.9 ± 1.4
^{235}U	0.644 ± .002[31]	2.081 ± .009	680.9 ± 1.7	579.4 ± 3.1	583.5 ± 1.3
^{239}Pu	0.765 ± .003[31]	2.110 ± .008	1011.2 ± 4.1	737.6 ± 4.0	744.0 ± 2.5
^{241}Pu	0.779 ± .002[30]	2.165 ± .010	1378 ± 9	1009.6 ± 5.3	1015 ± 7

Acknowledgment

This work is sponsored by the DOE Office of Energy Technology, Division of Reactor Research and Technology under contract W-7405-eng-26 with Union Carbide Corporation.

References

1. H. von Halban, F. Joliot, and L. Kowarski, Nature 143, 680 (1939).
2. Louis A. Turner, Phys. Ref. 57, 334 (1940).
3. L. Szilard and W. H. Zinn, Phys. Rev. 55, 799 (1939).
4. W. H. Zinn and L. Szilard, Phys. Rev. 56, 619 (1939).
5. For a description of the many experiments performed in this period one should see: Louis A. Turner, Rev. Mod. Phys. 12, 1 (1940).
6. K. A. Petrzhak and G. N. Flerov, Acad. Sci. (U.S.S.R.) 28, 500 (1940).
7. R. L. Henkel in Fast Neutron Physics II, edited by J. B. Marion and J. L. Fowler, 2031 (1963).
8. C. L. Cowan, F. Reines, F. B. Harrison, E. C. Anderson, and F. N. Hayes, Phys. Rev. 90, 493 (1953).
9. W. W. T. Crane, G. H. Higgins, and S. G. Thompson, Phys. Ref. 97, 242 (1955).
10. W. E. Stein and S. L. Whetstone, Phys. Ref. 110, 476 (1958).
11. S. G. Thompson, A. Ghiorso, B. G. Harvey, and G. R. Choppin, Phys. Rev. 93, 908 (1954).
12. D. A. Hicks, J. Ise, Jr., R. V. Pyle, Phys. Rev. 98, 1521 (1955).
13. J. W. Boldeman, International Specialists Symposium on Neutron Standards and Applications, National Bureau of Standards, NBS Special Publication 493, 182 (1977).
14. J. R. Smith, Seminar on Nuclear Data Problems for Thermal Reactor Applications, Brookhaven National Laboratory, EPRI NP-1098 (1979).
15. I. Asplund-Nilsson, H. Conde, and N. Starfelt, Nucl. Sci. Eng., 16, 124 (1963).
16. J. C. Hopkins and B. C. Diven, Nucl. Phys., 48, 433 (1963).
17. J. W. Boldeman, Nucl. Sci. Eng., 55, 188 (1974).
18. R. R. Spencer, R. Gwin, R. Ingle, and H. Weaver, ORNL/TM-6805 (1979).
19. P. H. White and E. J. Axton, J. Nucl. Energy 22, 73 (1968).
20. E. J. Axton, A. G. Bardell, and B. N. Andric, EANDC(UK)-110, p. 70, National Physical Laboratory (1969).
21. A. De Volpi and K. G. Porges, Phys. Rev., C1, 683 (1970).
22. B. M. Aleksandrov et al., 1975 Kiev Conf., Vol. 5, p. 166.
23. H. Bozorgmanesh, Thesis, U. of Michigan, 1977.
24. D. W. Colvin, M. G. Sowerby, and R. I. MacDonald, Proc. IAEA Conf. Nuclear Data for Reactors, Vienna, I. 307 (1967).
25. J. H. Marable and C. R. Weisbin, Advances in Reactor Physics, Proceedings of an ANS Topical Meeting, Gatlinburg, Tennessee, edited by E. G. Silver, CONF-780401 231 (1978).
26. M. Becker, D. R. Harris, B. Quan, and J. M. Ryskamp, A Review of the Theory and Application of Sensitivity and Uncertainty Analysis, Proceedings of a Seminar-Workshop, Oak Ridge, Tennessee, ORNL/RSIC-42, 75 (1979).
27. J. Poitou and C. Signarbieux, Nucl. Inst. and Meth., 114, 113 (1974).
28. H. D. Lemmel, Conf. on Nuclear Cross Sections and Technology, Washington, D. C., NBS Special Publication 425, 1, 286 (1975).
29. J. R. Smith, Conf. on Nuclear Cross Sections and Technology, Washington, D. C., NBS Special Publication 425, 1, 286 (1975).
30. J. W. Boldeman and A. W. Dalton, AAEC/E172 (1967).
31. R. Gwin, R. R. Spencer, R. W. Ingle, J. H. Todd, and H. Weaver, ORNL/TM-6246 (1978).

DATA DISCREPANCIES IN AND NEW EXPERIMENTS FOR D+D, D+T, AND T+T FUSION REACTIONS

Nelson Jarmie, R. A. Hardekopf, Ronald E. Brown, F. D. Correll, and G. G. Ohlsen
Los Alamos Scientific Laboratory
Los Alamos, New Mexico 87545, USA

We investigate the accuracy of the basic fusion data for the reactions $T(d,n)^4He$, $T(t,2n)^4He$, $D(d,n)^3He$, and $D(d,p)T$ in the 10-100 keV bombarding energy region of interest in the design of fusion reactors, magnetic or inertial. The history of the data base for these reactions, particularly the most critical one: $T(d,n)^4He$, is based on 25-year-old experiments whose accuracy (often assumed to be 5%) has rarely been questioned. In all except the d + d reactions significant differences among data sets exist. The errors of the basic data sets may be considerably larger than previously expected and the effect on design calculations should be significant. Much of the trouble apparently lies in the accuracy of the energy measurements which are difficult at low energies. We feel that systematic errors of up to 50% are possible in the reactivity values of the present $T(d,n)^4He$ data base. The errors in the reactivity would propogate proportionately into the errors in fusion probabilities in reactor calculations. The $D(d,n)^3He$ and $D(d,p)T$ cross sections appear to be well known and consistent. The $T(t,2n)^4He$ cross section is poorly known and may be subject to large systematic errors. Improved absolute measurements in the 10-100 keV bombarding energy region for the above reactions are underway at Los Alamos. The experiment features a windowless cryogenic target, calibration of the target density with a high energy Van-de-Graaff beam, measurement of the beam intensity with a calorimeter, use of a negative ion source for the 10 to 100 keV measurements, and a time-of-flight laser spectrometer to determine the absolute energy. Both the source and target will be capable of handling tritium. Accuracies of better than 5% are anticipated.

[Data discrepancies, 10-100 keV, T(d,n), T(t,2n), d + d reactions, absolute cross section measurement.]

Introduction

The purpose of this work is to investigate the accuracy of the basic fusion reaction data for the reactions $T(d,n)^4He$, $T(t,2n)^4He$, $D(d,n)^3He$, and $D(d,p)T$, and to describe an elaborate experiment in progress at the Los Alamos Scientific Laboratory to remeasure the cross sections with improved accuracy.

The history of the data base for these reactions, particularly the most critical one: $T(d,n)^4He$, is based on 25-year-old experiments whose accuracy (often assumed to be 5%) has rarely been questioned. As reactor experiments and reactor design become more sophisticated and various discrepancies stand out; it will be important to understand the influence of the uncertainty in the basic fusion data. The errors of the basic data sets may be considerably larger than previously expected and the effect on design calculations should be significant. This conclusion provides a motivation for an improved experiment.

The energy region of interest is from 10 to 120 keV bombarding energy. This corresponds, (assuming a triton beam), to a temperature of an interacting D + T plasma of from 0.5 to 20 keV. This difference of energy scale arises from the folding of the Maxwell distribution of velocities in the plasma with the cross section and from a lab to center-of-mass conversion.

The Lawson criterion[1] indicates conditions necessary for "break even" in a burning D + T plasma. It indicates that the optimum plasma temperature for the lowest $n\tau$ is around 20 to 30 keV temperature. Early reactors would likely operate on the lower side of this minimum, say from 1 to 30 keV temperature. This corresponds to a laboratory bombarding energy in the range we are concerned with.

A detailed report of discrepancies in fusion data is being published as a Los Alamos report (LA-8087). A study of the relation of the accuracy of the basic fusion data on the design of nuclear weapons has been done.[2]

Data Survey

$T(d,n)^4He$

The T(d,n) low energy data base rests on three main references. Arnold[3] et al., at Los Alamos, measured $\sigma(90°)$ down to about 10 keV (lab bombarding energy) claiming 2% accuracy. Since the reaction is isotropic in the c.m. system below several hundred keV, the $\sigma(90°)$ is easily converted to an integrated cross section σ_T. Conner, Bonner, and Smith[4] at Rice University measured $\sigma(90°)$ down to 10 keV, with 3% accuracy, and Katsaurov[5] at the Lebedev Institute measured σ_T down to 45 keV claiming 2-3% accuracy. Earlier experiments like those of Jarvis and Roaf[6] in England (20-40 keV, about 10% accuracy) were adjudged to be in some disagreement with the later U.S. experiments and were not commonly used. Most data bases in fusion reactor calculations come eventually from the work of Arnold[3] and Conner[4], sometimes circuitously. Many of the data bases depend on a compilation by Greene[7], whose calculations use mainly the work of Arnold and Conner. The fractional error in the reaction rate in a burning plasma is expected to be equal to the fractional error in the cross section[8].

Figure 1 shows the $T(d,n)^4He$ data. The line is an R-Matrix fit by Stewart and Hale[9] which agrees with standard references 3 and 4, and excludes the Katsaurov data because of an apparent energy shift in the Russian data. Study of the details of Katsaurov's work indicate that it was a carefully done experiment with due regard to the difficult problem of measuring such a low energy. It is not clear in whose work the energy discrepancy lies. The circles, Katsaurov data, are seen to be shifted to lower energies by about 6 keV leading to a cross section discrepancy (standard values low) of 10-30% in the low energy region. Figure 2 shows the low energy detail. Included in this graph is a point by Jarvis and Roaf which, if correct, would agree with the energy scale of Katsaurov. The Jarvis data were also not included in the Stewart and Hale report.

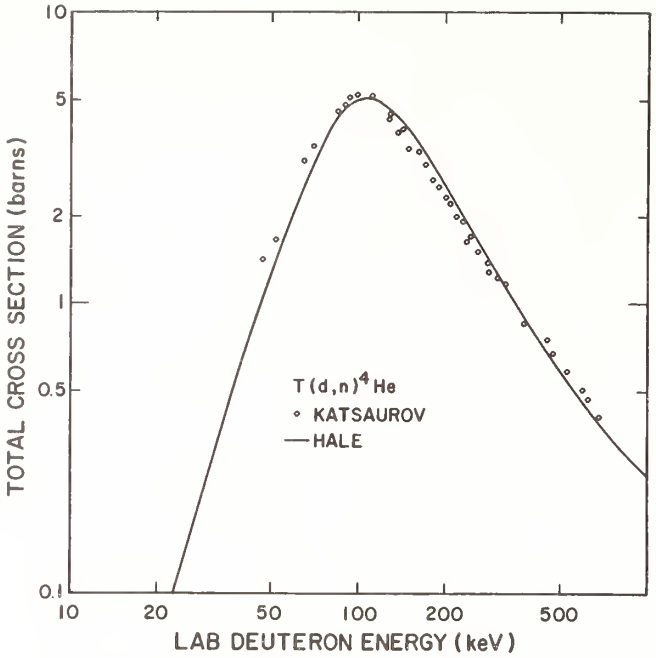

Fig. 1 The $T(d,n)^4He$ total cross-section. The line is an R-Matrix fit (Ref. 9) to known data other than those of Katsaurov. Of note is the apparent energy shift between the Katsaurov values (Ref. 5) and the other data.

The accurate measurement of the bombarding energy is difficult at low energies and is suspected by us to be the main cause of the cross section discrepancies. Because the cross section is falling in a steep exponential, slight energy shifts can produce a large error in the cross section magnitude. One can calculate, for example, that at 20 keV, a shift of only 0.5 keV in the bombarding energy will produce a 10% change in the cross section. At the lower energies the fractional cross section error varies as $dE/E^{3/2}$, so that the effect gets larger as the energy decreases.

The experimental equipment for the $T(d,n)^4He$ reaction was often used in the measurement of similar reactions which also show discrepancies. For example, the main U.S. groups: Bonner, Conner, and Lillie[4], and Arnold[3] et al., also measured the $^3He(d,p)^4He$ reaction total cross section with essentially the same apparatus. Kunz[10], in a subsequent experiment in the low-energy region, disagrees with the above data, having an apparent energy shift of from 5-15 keV higher so that his cross section values are 30-50% lower than the previous work.

It should be noted that Kunz normalizes his absolute scale by also measuring the D(t,n) reaction with his equipment and normalizing to peak of the T(d,n) measurement of Conner, Bonner, and Smith[4]. His agreement with Bonner, Conner, and Lillie at the peak of the resonance is then no surprise, but the disagreement at lower energies again indicates an energy measurement problem.

Detail of the low energy $^3He(d,p)$ reaction is given in Fig. 3. Again the work of Jarvis and Roaf[6] disagree with the Rice and LASL experiments and agree with Kunz[10]. Note that the apparent energy shift of the "standard" work is in the direction opposite to the T(d,n) case in Fig. 2.

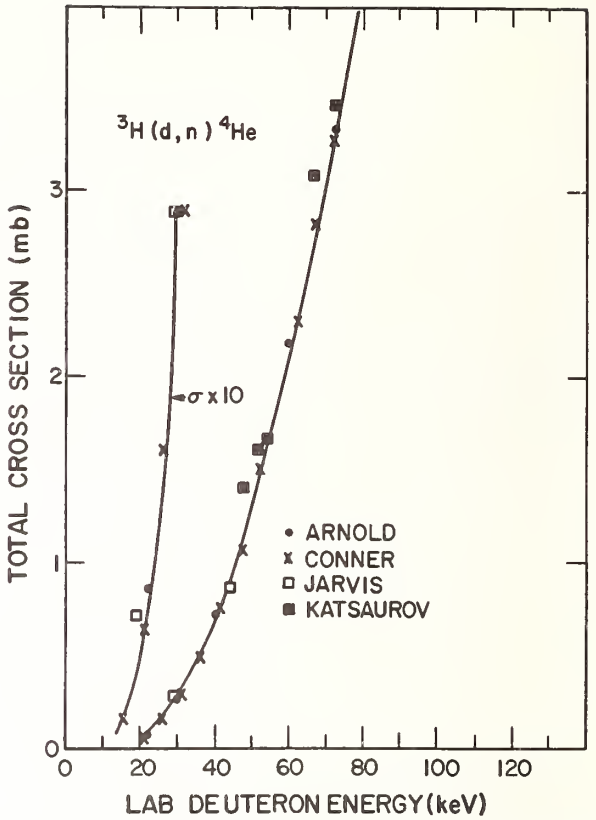

Fig. 2 Low energy detail of the $T(d,n)^4He$ total cross-section data again showing the energy shift of the Katsaurov data (Ref. 5).

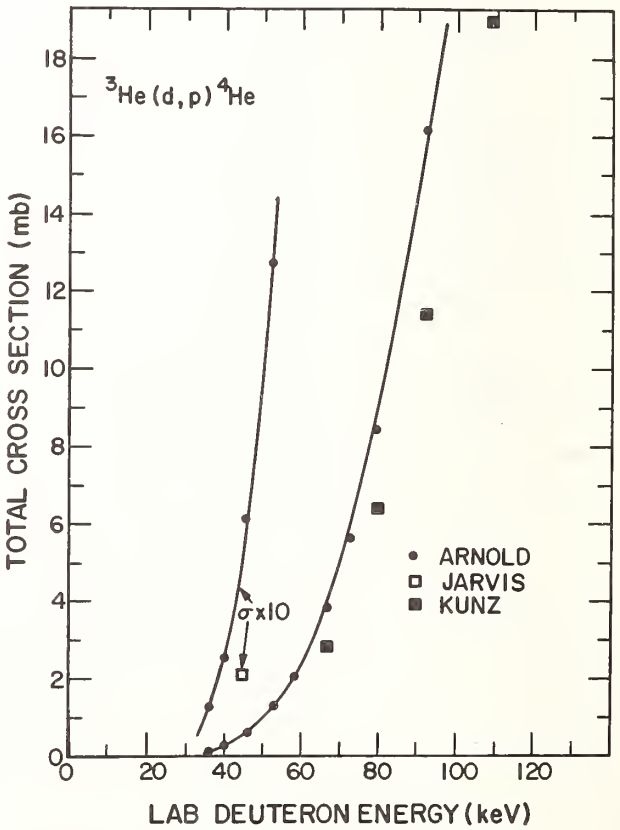

Fig. 3 Low-energy detail of the $^3He(d,p)^4He$ total cross section. It is of interest to compare this figure with Fig. 2.

An unpublished report of a measurement on the $^3He(^3He,2p)^4He$ reaction was made in 1969 by Dwarakanath[11] in which he included a measurement of the $^3He(d,p)^4He$ total cross section. His data are not available in tabluar form. Inspection of his graphical results indicates, paradoxically, that his data agree with Arnold et al. and Bonner, Conner and Lillie at low energies.

The same accelerator and absolute energy measurement used in the Arnold et al.[3] T(d,n) measurement was used by Sawyer and Phillips[12] in the $^6Li(p,^3He)^4He$ reaction. Figure 8 of Elwyn et al.[13] shows the data of Sawyer and Phillips to be high by a factor of 2 or 3 in the low energy region compared to the data of Fiedler and Kunze[14] and Gemeinhardt[15]. It is not clear how much of this discrepancy is due to a possible energy shift.

$T(t,2n)^4He$

Greene's compilation is again the source of data as used in the design codes. His work depends largely on Govorov et al.[16] who measures σ_T from 60 to 1140 keV (5% accuracy). He excludes the data of Agnew[17] et al. (down to 40 keV, $\sigma(90°)$ 4% accuracy). Experiments done since Greene's publication are those of Strel'nikov et al.[18] who measure $\sigma(90°)$ from 40 to 200 keV (15% uncertainty claimed) and Serov, Abramovich, and Morkin[19] who measure $\sigma(0°)$ and σ_T from 30 to 160 keV. Serov's numerical data are available[20]. For completeness we should mention the work of Govorov et al.[21] who measure $\sigma(90°)$ from 230 to 1000 keV; and the measurement of the neutron and alpha spectra by Bame and Leland[22], Wong, Anderson, and McClure[23], and Larose-Poutissou, and Jeremie[24], and Jarmie and Allen[25].

Low energy $T(t,2n)^4He$ data are discrepant and poorly understood. In some cases the total cross section is measured and sometimes the zero degree differential cross section. Comparison of the two kinds of data is not simple because the conversion between the two is not simple, even assuming isotropy in the c.m. system. The reason for this results from the 3-body breakup; and either an angular distribution must be measured or a model dependent calculation made. The conversion is also energy dependent.

In Fig. 4 the zero-degree differential cross section is presented to show the trend of the data. Shown is the prediction of the compilation of Duane[26] which was derived from the Agnew[17] data. The σ_T data of Govorov[16], divided by 10 (which is thought to be a reasonable conversion, see the discussion in ref. 9) follows the Greene curve. The Serov[19,20] data clusters around the Strel'nikov[18] curve. The prediction of Greene[7] (divided by 10) is shown for comparison. It is seen that large differences occur between various data, leading to a considerable lack of reliability in the source of fusion-calculation data sets (Greene's compilation).

Stewart and Hale[9] show that there are severe internal inconsistencies between the various sets of data concerning the conversion from $\sigma(0°)$ to σ_T. This may help explain that when the data are plotted as σ_T vs energy they look somewhat less discrepant. An R-matrix solution by Hale, Young, and Jarmie[27] to the total cross section data of ref's. 16, 20, and 25 up to 2 MeV leads to a prediction of the reactivity of the $T(t,2n)^4He$ reaction about 50% smaller than that predicted by Greene, below 50 keV bombarding energy. The data in this low-energy region are dominated by the work of Serov et al. who made a concerted effort to measure the bombarding energy accurately. Even if they were successful at this difficult task, their energy error is still 2 to 3 keV, and the stated error in their cross sections are from 20 to 30%. Considering the other inconsistencies mentioned, our knowledge of $T(t,2n)^4He$ cross sections is not secure.

$D(d,n)^3He$ and $D(d,p)T$

Many experiments measuring absolute cross section have been done partially because of a report of a narrow resonance near E_d = 100 keV and the comparison of the two branches. Unlike the T(d,n) and T(t,2n) reactions the angular distribution is highly anisotropic at low energies. A good summary of the experiments is given by Theus[28].

McNeill[29] has revised the total cross section data of Arnold et al.[3] upwards by 3-12% to account for improved anisotropy measurements. When this is done, the several absolute experiments agree within experimental errors which are generally 10-15% except for Arnold[3] who quotes 2-5%. It seems then that the data for the d + d reactions are in satisfactory agreement.

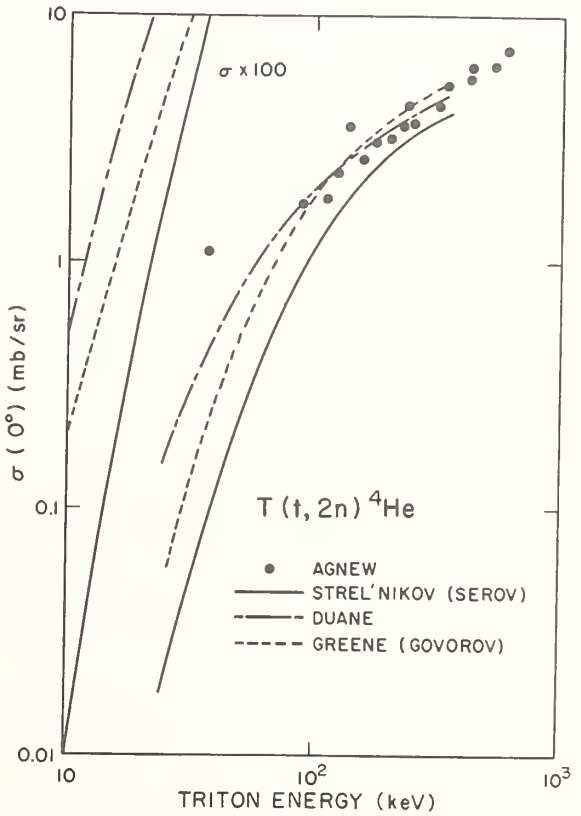

Fig. 4 The $T(t,2n)^4He$ zero-degree differential cross section vs triton bombarding energy. Greene's (Ref. 7) total cross section prediction, based on Govorov (Ref. 16), is divided by 10 to give the curve shown. Duane's prediction (Ref. 26) is based on the Agnew data (Ref. 17). The Serov data (Ref. 20) closely follows the Strel'nikov data (Ref. 18) represented by the solid line.

The d + d data of Arnold et al.[3] were taken with the same apparatus as in their T(d,n) experiment. The apparent agreement of Arnold's d + d data with the other experiments in that system adds another curious heuristic element in the question of the reliability of their T(d,n) data.

Cross Section Experiment

An experiment is now in progress at Los Alamos to measure the absolute cross sections of the reactions under discussion from 10-100 keV bombarding energy to an reliable accuracy of better than 5%. Since knowledge and control of the absolute energy is of some concern, great effort has been made in the design to achieve a good energy measurement.

The schematic of the experiment is shown in Fig. 5. There are several key elements in the experimental design. 1. The target is a windowless, continuous flow, cryogenic device, with the outflowing gas trapped on 4°K surfaces. The avoidance of windows is a critical factor in obtaining a reliable determination of the energy. The target will be capable of handling tritium. A typical target density is about $10^{16}/cm^3$. Precise measurement of gas flow and target temperature is necessary. 2. Because of charge exchange in the target, the beam intensity will be measured by a precision calorimeter following a design by Thomann and Benn[30]. 3. The 5-120 keV ion source will produce a negative beam to eliminate unwanted ion species and supress effects of slitedge scattering. It will be capable of accelerating tritons. Beam currents will be from 1-50 microamps. 4. Energy loss in the target will be explored with a laser spectrometer[31]. This device uses a precise time-of-flight measurement of a beam pulse created by photodetachment of the beam negative ions with a pulsed Nd: YAG laser. Both the laser spectrometer and a precision resistor stack will be used to measure the absolute energy. An attempt will be made to keep all sources of error in the beam energy less than 50 V. 5. Calibration of the target density will be made using a high energy Tandem Van-de-Graaff beam. A reaction with well known cross section, such as D(p,p)D or T(p,p)T will be used. If necessary, the calibrating cross section will be measured separately at Los Alamos to better than 1%.

At this writing, the cryogenic target is complete, the ion source installed and running, the calorimeter complete and tested and all of the beam optic elements installed. Both 100 keV and 10 MeV beams have successfully bombarded a deuterium target and reaction particles have been detected. The laser spectrometer and tritium handling equipment are under construction. A photograph of the system is shown in Fig. 6.

We plan to first measure the D + D system to work out problems in the system; then accelerate tritons to study D + T and finally flow tritium in the target to study the T + T reaction.

Acknowledgments

We would like to acknowledge helpful communications with A. M. Govorov, A. J. Elwyn, R. Santoro, G. M. Hale, L. Stewart, and G. A. Keyworth. The work of Rudy Martinez and Walt Sondheim has been essential in the construction of the experiment.

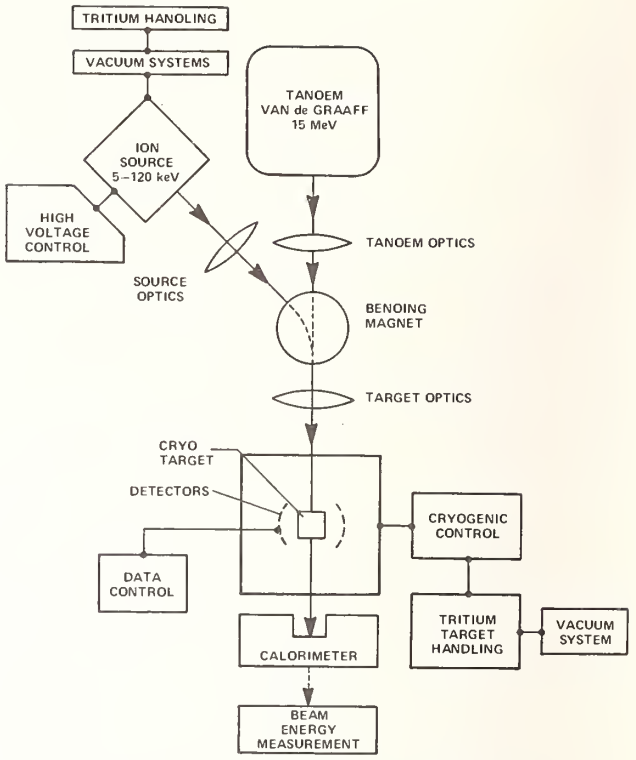

Fig. 5 **LOW ENERGY CROSS SECTION EXPERIMENT**

References

1. F. L. Ribe, T. A. Oliphant, Jr., and W. E. Quinn, Los Alamos Scientific Laboratory report LA-3294-MS (1965), and J. D. Lawson, Proc. Phys. Soc. B70, 6 (1957).
2. N. Jarmie and J. Wallace, private communication.
3. W. R. Arnold, J. A. Phillips, G. A. Sawyer, E. J. Stovall, Jr., and J. L. Tuck, Phys. Rev. 93, 483 (1954). See also, Los Alamos Scientific Laboratory report LA-1479 (1953).
4. J. P. Conner, T. W. Bonner, and J. R. Smith, Phys. Rev. 88, 468 (1952) and T. W. Bonner, J. P. Conner, and A. B. Lillie, Phys. Rev. 88, 473 (1951).
5. L. N. Katsaurov, Akad, Nauk, USSR, Fizicheskii Inst., Trudy, 14, 224 (1962); and, E. M. Balabanov, I. Ia. Barit, L. N. Katsaurov, I. M. Frank, and I. V. Shtranikh, Supplement No. 5 of Soviet Journal of Atomic Energy, Atomnaya Energiya, p. 43 (1957).
6. R. G. Jarvis and D. Roaf, Proc. Roy. Soc. A218, 432 (1953).
7. S. L. Greene, Jr., Lawrence Radiation Laboratory report UCRL-70522 (May 1967).
8. R. Santoro and J. Barish, Nuc. Sci. and Engineering 59, 189 (1976) and ORNL-TM-4933 (1976)
9. L. Stewart and G. M. Hale, Los Alamos Scientific Laboratory report LA-5828-MS (January 1975); See also G. M. Hale, this conference.
10. W. E. Kunz, Phys. Rev. 97, 456 (1955).
11. M. R. Dwarakanath, Thesis, California Institute of Technology (1969).

Fig. 6 The Los Alamos Low Energy Fusion Cross Section Experiment. The 120 keV ion source is on the right; the partially disassembled target at the left. The tandem beam line is hidden.

12. Sawyer and Phillips, Los Alamos, LA-1578 (1953).

13. A. J. Elwyn, R. E. Holland, C. N. Davids, L. Meyer-Schutzmeister, and F. P. Mooring, Phys. Rev. to be published. See also Bull. Amer. Phys. Soc. 23, 97 (1978).

14. O. Fiedler and P. Kunze, Nucl. Phys. A96, 513 (1967).

15. W. Gemeinhardt, D. Kamke and Chr. von Rhoneck, Zeit. fur Physik 197, 58 (1966).

16. A. M. Govorov, Li Ka-Yeng, G. M. Osetinskii, V. I. Salatskii, and I. V. Sizor, Sov. Phys. JETP 15, 266 (1962).

17. H. M. Agnew, W. T. Leland, H. V. Argo, R. W. Crews, A. H. Hemmendinger, W. E. Scott, and R. F. Taschek, Phys. Rev. 84, 862 (1951).

18. Yu. V. Strel'nikov, S. N. Abramovich, L. A. Morkin, N. D. Yur'eva, Bull. Acad. Sci. USSR Ser. Phys. (Isvestia) 35, 149 (1971).

19. V. I. Serov, S. N. Abramovich, and L. A. Morkin, Sov. J. of Atomic Energy 42, 66 (1977).

20. Nat. Nuclear Data Center, Brookhaven Nat. Lab. Data Base CSISRS (EXFØR) #A0007, 770825.

21. A. M. Govorov et al., Sov. Phys.-JETP 14, 508 (1962).

22. S. J. Bame, Jr., and W. T. Leland, Phys. Rev. 106, 1257 (1957).

23. C. Wong, J. D. Anderson, and J. W. McClure, Nucl. Phys. 71, 106 (1965).

24. R. Larose-Poutissou, and H. Jeremie, Nucl. Physics A218, 559 (1974).

25. N. Jarmie and R. C. Allen, Phys. Rev. 111, 1121 (1958).

26. B. H. Duane, in Pacific Northwest Laboratory Report on Controlled Thermonuclear Reactor Technology-1972. W. C. Wolkenhauer, Ed., Battelle Northwest Laboratory report BNWL-1685 (November 1972) p. 75.

27. G. M. Hale, P. G. Young, and N. Jarmie, Los Alamos Scientific Laboratory, Private Communication; see also G. M. Hale, this conference.

28. R. B. Theus, W. I. McGarry, and L. A. Beach, Nucl. Phys. 80, 273 (1966).

29. K. G. McNeill, Phil. Mag. 46, 800 (1955).

30. C. Thomann and J. E. Benn, Nuc. Instr. & Methods 138, 293 (1976).

31. G. G. Ohlsen et al., Bull. Amer. Phys. Soc. 24, 822 (1979).

THE ^{252}Cf $\bar{\nu}$ DISCREPANCY AND THE SULFUR DISCREPANCY

J. R. Smith
Idaho National Engineering Laboratory
EG & G Idaho, Inc.
P.O. Box 1625, Idaho Falls, Idaho 83415 USA

The cantankerous discrepancy among measured values of $\bar{\nu}$ for ^{252}Cf appears at last to be nearing a final resolution. A recent review has summarized the progress that has been achieved through revaluation upward by 0.5% of two manganese bath values of $\bar{\nu}$ and the performance of a new liquid scintillator measurement. A new manganese bath measurement at INEL is in reasonably good agreement with previous manganese bath values of ^{252}Cf $\bar{\nu}$. It now appears that the manganese bath values could still be systematically low by as much as 0.4% because the BNL-325 thermal absorption cross section for sulfur may be as much as 10% low. There is a bona fide discrepancy between measurements of the sulfur cross section by pile oscillators and the values derived from transmission measurements. The resolution of this discrepancy is a prerequisite to the final resolution of the ^{252}Cf $\bar{\nu}$ discrepancy.

[^{252}Cf $\bar{\nu}$, manganese bath, pile oscillator, sulfur, absorption cross section, small-angle scattering]

Introduction

The discrepancy among measured values of $\bar{\nu}$, the total number of neutrons produced per fission event, for ^{252}Cf, has long perplexed both the measurers and the users of this important nuclear datum. In recent years considerable progress has been achieved in understanding this important quantity, which is the standard against which $\bar{\nu}$ values for the fissile nuclei are compared.

The status of measurements of $\bar{\nu}$ for ^{252}Cf was reviewed by the present author at the Symposium on Nuclear Data Problems for Thermal Reactor Applications in May, 1978.[1] A summary table representing the current values for the various experimental results is reproduced in Table I. Two significant developments are represented in the current values shown in Table I: The renormalization upward by approximately 0.5% of the manganese bath values of Axton[2] and Devolpi[3] and the addition of a preliminary result from a new liquid scintillator measurement of $\bar{\nu}_p$ by Spencer. The Spencer value may be revised in Spencer's paper prepared for this meeting.

A striking feature of Table I is the remarkable agreement among the manganese bath values, with the exception of the White-Axton value.[10] The latter measurement has been assigned a relatively large error by its authors, so it carries only a modest weight into a weighted average. An impressive feature of the general manganese bath agreement is the variety of fission assay techniques represented. Axton[2] used a unique fission-fission coincidence technique, DeVolpi[3] used neutron-fission coincidence counting, and Bozorgmanesh[9] and Aleksandrov[11] both used defined solid angle counting. The agreement between the latter two measurements would appear to accentuate the isolation of the White-Axton value.

The close general agreement of the manganese bath results, clustered as they are about 0.5% lower than the weighted average of all measurements, suggests that if this average is near the true ^{252}Cf value, there may be a systematic bias of 0.5% somewhere in the manganese bath method itself. It is therefore appropriate to review the manganese bath method to ascertain where such a systematic problem might lie. Some characteristics might be postulated. The effect should be capable of producing the bulk of the 0.5% correction that is sought. It should preferably raise the value of $\bar{\nu}$ without simultaneously raising the values of η, since these are already in agreement with the higher $\bar{\nu}$ values. Finally, one should not overlook the possibility that the effect lies in something that has been done the same way for so long that we have come to confuse familiarity with accuracy.

TABLE I
^{252}Cf $\bar{\nu}$ Summary

MEASUREMENT	$\bar{\nu}$ (Total)
Liquid Scintillator	
Spencer[4]	3.792±0.011
Boldeman[6]	3.755±0.016
Asplund-Nilsson[7]	3.792±0.040
Hopkins-Diven[8]	3.777±0.031
Manganese Bath	
Axton[2]	3.743±0.019
DeVolpi[3]	3.747±0.019
Bozorgmanesh[9]	3.744±0.023
White, Axton[10]	3.815±0.040
Aleksandrov[11]	3.747±0.036
Boron Pile	
Colvin[12]	3.739±0.021
Wtd. Ave:	3.766±0.007
Ave:	3.765±0.008

The Absorption Cross Section of Sulfur

The sulfur thermal absorption cross section has rather abruptly emerged as perhaps the prime candidate for the dubious distinction of contributing the principal part of a half percent systematic error. This possibility came to light in a review of the sulfur file submitted by Howerton for inclusion in ENDF/B-V. The evaluation is a very old one, with little documentation.[13] The most unsettling part of this review was to find that the thermal capture had been normalized to 0.49 barn at 0.025 eV. For some 20 years the accepted value has been the BNL-325 value[14] of 0.52 barn, with the error variously assigned as 0.02 or 0.03 barn. The difference between 0.49 and 0.52 barn may seem inconsequential to some, but it represents about a quarter percent difference in a manganese bath measurement. An inquiry to Howerton revealed that he has no record of how he arrived at this thermal value. It is presumed that he followed his often-declared preference for selecting

cross sections from the single experiment he judged to be best, rather than resorting to a weighted average. The implied disdain for weighted averages is a fairly common and well-founded attitude. Indeed, it is the use of weighted averages, and an attendant underestimate of the error, that has served to create an unwarranted attitude of contentment towards the 0.52-barn value. Similar problems have plagued the ^{252}Cf ν system, also. The weighted average could well be called the opiate of the evaluator. It is useful as a guide, but should not be used as a crutch.

The cross section chosen by Howerton as best was evidently the Pomerance value,[15] normalized to the current value of the cross section of gold, which was the standard for the measurement. A reexamination of possible reasons for favoring the Pomerance measurement led to the compilation of the comparison shown in Table II. This is a collection of sulfur absorption values, from three sets of pile oscillator measurements,[15-17] that would be derived if the sulfur result were renormalized to current values of cross sections for other materials measured in the same experiment. This table is intended as a test to see which series of measurements has the best internal consistency, and has stood the test of time best, as viewed from the point of view of the sulfur cross section. Included in the comparison are the cross section standards boron, lithium, and gold, plus some low cross-section materials. Manganese has been included because it is the ratio to the manganese cross section that is important in evaluating manganese bath corrections.

TABLE II
Sulfur σ_a

Normalization	Pomerance	Harris	Colmer
Original Value	470 mb	510 mb	490 mb
B = 759 b*	489	545	532
Li = 70.7 b	496	---	529
Au = 98.8 b	489	---	---
Mn = 13.35 b	490	554	511
Co = 37.2 b	511	531	477
K = 2.10 b	481	508	544
Ca = .43 b	493	510	527
Average	493 mb	530 mb	520 mb
Std Dev	9	21	24

*Harwell B = 771 b

The Pomerance set of measurements does appear to have a decided advantage in terms of internal consistency, and this might be considered support for the choice of the Pomerance values. A second glance, however, reveals that the internal consistency of each set is adequate to suggest that the difference in sulfur values may not be a matter of random measurement error alone. One is led to suspect the presence of extraneous effects in the sulfur samples themselves. It is well known that scattering from the sample complicates pile oscillator measurements. All three pile oscillator groups were aware of the scattering problem, and all three dealt with it in their experiments in one way or another. Since there does appear to be some sample-dependent differences, however, one is led to wonder whether the particulate nature of the powdered sulfur samples may have introduced types of scattering that were not typified by the method of correction.

The sort of thing that might be suspected is illustrated by some studies of the ^{242}Pu total cross section by Young.[18] Fig. 1 shows the original, uncorrected data, the same data corrected for moisture content of the oxide sample, and further correction for small-angle scattering from the particles of which the oxide was composed. Measurements on the metallic sample, which were made later, were found to be in good agreement with the corrected data from the oxide sample. Also evident is the structure that is often observed in the vicinity of the cutoff of Bragg scattering from sets of crystalline planes of the sample. The Bragg scattering is a matter of sample composition, and can be seen to be different for the two samples. Both the small-angle scattering and the Bragg cutoff phenomenon can be expected to produce scattering that is both energy-dependent and non-isotropic. Whether these effects would disturb a pile oscillator measurement is not clear, but the comparison in Table II suggests that some sample-dependent complication is present.

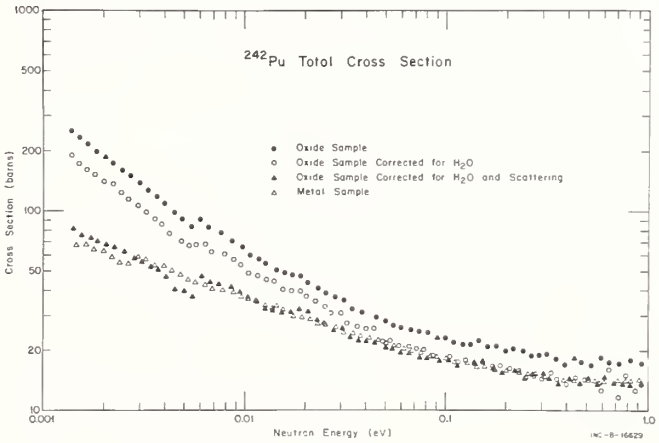

Fig. 1 Neutron total cross section of ^{242}Pu from 0.0015 to 1.0 eV.[18]

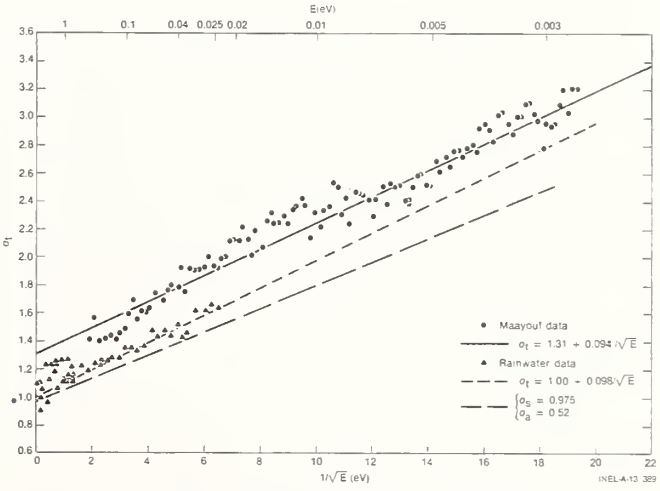

Fig. 2 The total cross section of natural sulfur. Measurements of Rainwater and Maayouf[20] are compared with the behavior indicated by the constants evaluated in BNL 325.[14]

The indication of possible sample-dependent effects in the pile oscillator measurements leads naturally to the question of whether the transmission measurements have been fairly treated. When there are no nearby resonances, the total cross section can be fitted to a simple curve representing the sum of a constant cross section and a 1/V term. The constant term is identified as the scattering cross section, while the 1/V term represents the absorption. There are two published values for the sulfur absorption cross section determined by this method. Both are shown in Fig. 2. Rainwater[19] derived a value of 0.62 barn from his measurements on a powdered sample of sulfur. There is some apparent structure near 0.04 eV, which could be due to a Bragg cutoff that would complicate the interpretation of the data. Maayouf[22] deduced an absorption cross section of 0.59 b. from his measurements on a cast sulfur sample. His data also show structure, but the double-humped nature of the structure suggests that it is an artifact of the rotor transmission, rather than Bragg structure. Maayouf used two different settings of his velocity selector rotor to cover the energy region of the measurement, and the dividing line between the two settings was between the two humps. Although there is considerable separation between the Rainwater and Maayouf data, the slopes are in reasonable agreement, considering the scatter in the data points. Neither measurement appears compatible with the 0.52-barn cross section, which is represented by the lower curve.

A third transmission measurement was made by the present author on the MTR crystal spectrometer, with a velocity selector to eliminate neutrons from higher order reflections in the Bragg beam. The data from the measurement appeared to be very linear on the $1/\sqrt{E}$ plot, with none of the structure evident in the Rainwater and Maayouf data. A fit to the data represented a thermal absorption cross section of 0.57 barn, which is somewhat below the values from the other transmission measurements, but disturbingly above the values from the pile oscillator experiments. The lowest value with which the data could be deemed reasonably compatible was 0.55 b. The high value was tentatively ascribed to uncertainties in the characterization of the cast sulfur block, which was then ten years old. The data were not published, and were subsequently destroyed.

All three total cross section measurements have shown evidence of experimental difficulties that justify their being down-weighted in an evaluation. However, they agree in two significant points: they all yield sulfur capture cross section values well above the results of the pile oscillator measurements, and a curve representing a cross section of 0.52 b. does not appear to be compatible with any of the energy-dependent data. The transmission measurements do indeed have severe experimental problems that are clearly visible. The data comparison of Table II, however, suggests that the pile oscillator measurements may have problems that are no less severe; they may be simply less visible.

An inquiry to Dr. Pomerance, as to whether the intervening 30 years had brought any reason to modify the treatment of his sulfur data, brought a negative reply.[21] However, the reply included some details of his experiment that are very interesting, in the light of the preceding discussion. He supplied the results of the measurements on the individual samples, which included two powdered sulfur samples and two samples of sulfur salts. These values are shown in Table III, both as originally normalized to a gold cross section of 95 barns and as renormalized to the current gold value of 98.8 barns.[14] The salt samples yielded sulfur cross sections near or above the results from the transmission measurements. Pomerance felt that the most likely error would come from the presence of impuritiies in the low cross-section samples. Therefore it was the high values that were considered suspect and discarded. An alternative explanation might be that the differences among Pomerance's samples supports the above-postulated existence of sample-dependent scattering differences.

TABLE III

POMERANCE SULFUR MEASUREMENTS

SAMPLE (wt)	ORIGINAL* σ_a (barns) Molecule	Sulfur	RENORMALIZED* σ_a (barns) Molecule	Sulfur
Sulfur #1 (3.139 g)	0.48 0.475	0.48 0.475	0.50 0.494	0.50 0.494
Sulfur #2 (1.936 g)	0.51 0.40	0.51 0.40	0.53 0.42	0.53 0.42
$PbSO_4$ (5.327 g)	0.76	0.57	0.79	0.62
$Na_2S_2O_5$ (2.218 g)	2.24	0.74	2.52	0.73
AVERAGE VALUES				
All Sulfur		.47		.49
First 3 Sulfur		.49		.51
All Measurements		.53		.55

CROSS SECTIONS ASSUMED

	Au	Pb	Na
Original	95	0.19	0.47
Renormalized	98.8	0.17	0.53

Another curious factor in the Pomerance data set is the fact that the second measurement on the second sulfur sample was about 20% below the first measurement. This puts it nearly as far out of line on the low side as the salt samples are on the high side. Whether the presumption is that something happened to the sample between measurements or that the difference reflects the true reproducibility of the measurements, one wonders whether the high and the low values ought to be accepted or rejected on an equal basis. Rejection of the low measurement would leave three values whose average is 0.51 barn. This would have the rather unsettling consequence that fully 50% of the Pomerance sulfur data would thereby have been rejected. Inclusion of all data would bring the Pomerance average to 0.55 barn.

The puzzle posed by the Pomerance data is the same as that posed by the attempt to reconcile the pile oscillator and transmission measurements. Is it valid to reject the higher values because they "look" too high? Not enough information is available concerning the various samples to allow solution of the problem by evaluative measures alone. New and better measurements are required.

Effects of Sulfur Absorption in the Manganese Bath

To show why a wretched half-barn cross section should be so important to manganese bath measurements and to the ^{252}Cf $\bar{\nu}$ situation, it is necessary to examine briefly the equation describing the response of a manganese bath. When a source of strength Q is irradiated, the observed saturated activity A_s is given by

$$A_s = Q\, f\, \varepsilon\, (1-S)(1-L)(1-P), \qquad (1)$$

where ε represents the efficiency of the counter for detection of a ^{56}Mn disintegration anywhere in the system, S is the loss to neutron absorption in structural material, L is the fraction leaking from the bath, and P is the loss due to (n,p) and (n,α) reactions in oxygen and sulfur. The effect of the sulfur thermal absorption cross section is contained in f, the fraction of neutrons absorbed in manganese in the bath, where f is given by

$$\frac{1}{f} = 1 + \frac{\sigma_s}{\sigma_{Mn}\,(\overline{1+Grs})} + \frac{N_H}{N_{Mn}}\,\frac{\sigma_H}{\sigma_{Mn}(\overline{1+Grs})} \quad . \qquad (2)$$

An uncertainty in the sulfur cross section has an impact not only upon the ratio σ_s/σ_{Mn}, but also upon the ratio σ_H/σ_{Mn}. This follows from the way the latter ratio is determined. To obtain better manganese bath accuracy than can be obtained through the use of individual hydrogen and manganese cross sections, their ratio is determined by making bath activation measurements as a function of $MnSO_4$ concentration. By rearranging equations (1) and (2), we obtain an equation of a straight line in which the independent variable is the modified concentration parameter $N_H/N_{Mn}(\overline{1+Grs})$:

$$\frac{(1-S)(1-L)(1-P)}{A_s} = \frac{1}{Q}\,\frac{\sigma_H}{\sigma_{Mn}}\,\frac{N_H}{N_{Mn}\,(\overline{1+Grs})} + \frac{1}{Q}\left[1 + \frac{\sigma_s}{\sigma_{Mn}\,(\overline{1+Grs})}\right]. \qquad (3)$$

The slope, m, is divided by the intercept, b, of the fitted line, yielding

$$\frac{m}{b} = \frac{\sigma_H/\sigma_{Mn}}{1 + \sigma_s/\sigma_{Mn}\,(\overline{1+Grs})} = R_H \quad , \qquad (4)$$

where R_H is introduced to represent the observed ratio, before correction for the sulfur absorption. The hydrogen-to-manganese cross-section ratio is then simply

$$\sigma_H/\sigma_{Mn} = R_H\,[1 + \sigma_s/\sigma_{Mn}\,(\overline{1+Grs})]. \qquad (5)$$

The cross-section ratio thus derived has improved precision as compared to that derived from individual measurements on manganese and hydrogen, but both its value and its error estimate are correlated with those of the sulfur cross section. To avoid overlooking this important point, it may be instructive to insert the factor R_H directly into Eq. (3), which may then be written

$$Q = \frac{A_s}{(1-S)(1-L)(1-P)} \times \left[1 + \frac{\sigma_s}{\sigma_{Mn}\,(\overline{1+Grs})}\right]\left[1 + \frac{N_H R_H}{N_{Mn}\,(\overline{1+Grs})}\right] \quad . \qquad (6)$$

This form of the equation separates the sulfur effect from the other corrections, and makes it clear that the sulfur correction is independent of concentration. The current BNL-325 value of 0.52 $\pm$ 0.03 barn represents a correction of nearly 4%, and implies an uncertainty of about 0.22% in the derived source strength. That is close to the overall error that is hoped for in the whole manganese bath measurement, but it represents the error from only one correction in one leg of the $\bar{\nu}$ measurement. If the sulfur cross section should really turn out to be 0.57 b or above, as suggested by the transmission measurements and the data from the Pomerance sulfur salt samples, the corresponding shift of $\bar{\nu}$ values from the manganese bath could approach half a per cent.

The sulfur cross section thus has the potential for representing an error of as much as half a per cent in measurements of neutron source strenth by the manganese bath method. A rise in the sulfur absorption cross section would raise manganese bath $\bar{\nu}$ values without imposing a corresponding rise in the η values, since these are determined from ratio measurements only. Finally, the cross-section measurements date back 30 years. The acceptability of the 0.52-b value may be more a matter of familiarity than of accuracy. Thus the sulfur absorption cross section satisfies all of the criteria earlier posulated as characteristics of a possible source of a half per cent systematic effect in manganese bath measurements.

Possible Impact on ^{252}Cf $\bar{\nu}$

Further complicating the picture is the fact that the ^{252}Cf $\bar{\nu}$ measurement by the present author, in its current state of analysis, appears to be headed for the vicinity of 3.77, roughly half a per cent above the other manganese bath values. This is with the traditional value of 0.52 b for sulfur used in the analysis. Since the analysis is still incomplete, it is perhaps premature to conclude that a half per cent systematic effect other than the sulfur absorption cross section has been overcome. In any event, it is essential to the final resolution of the ^{252}Cf $\bar{\nu}$ discrepancy that the current ambiguity in the sulfur absorption cross section be resolved.

As an illustration of the effect of the sulfur cross section, let us suppose that the true value should be found to be 0.57 b. Then the array of $\bar{\nu}$ measurements would take on the aspect shown in Table IV, in which it is assumed that the present author's measurement should continue at its present preliminary value. In the weighted average, it is presumed that the sulfur cross section would be established with sufficient accuracy that the errors assigned in Table I would be maintained, and that the INEL measurement will prove to be at least as accurate as any other manganese bath measurement. The weighted average of Table IV is not a recommended value, because the adoption of a value of 0.57 b for sulfur is certainly not warranted at this point. However, it is useful for putting into perspective the effect of the current unsettled nature of the sulfur cross section.

Conclusion

It is essential that the sulfur absorption cross section be measured with an accuracy approaching 1%. This will improve the accuracy with which neutron source strengths can be measured in the manganese bath and contribute mightily to the final resolution of the ancient ^{252}Cf $\bar{\nu}$ discrepancy.

Acknowledgments

The author is indebted to Dr. H. S. Pomerance for permission to use unpublished details of his sulfur measurements.

This work was supported by the Electric Power Research Institute under contract No. RP 707-4.

TABLE IV
Cf $\bar{\nu}$ Status if Sulfur σ_a = 0.57 b

MEASUREMENT	PROJECTED $\bar{\nu}$ (Total)
Liquid Scintillator	
Spencer	3.792±0.011
Boldeman	3.755±0.016
Asplund-Nilsson	3.792±0.040
Hopkins-Diven	3.777±0.031
Manganese Bath	
Axton	3.757±0.019
DeVolpi	3.761±0.019
Bozorgmanesh	3.758±0.023
White, Axton	3.829±0.040
Aleksandrov	3.761±0.036
Smith	3.78 ±0.02
Boron Pile	
Colvin	3.739±0.021
Wtd. Ave:	3.771±0.006
Ave:	3.773±0.007

REFERENCES

1. J. R. Smith, in "Symposium Proceedings: Nuclear data Problems for Thermal Reactor Applications," EPRI NP-1098, p. 14-1 (1979).

2. E. J. Axton, in "Neutron Standard Reference Data," p. 261 (1974).

3. A. DeVolpi and K. G. Porges, Phys Rev C1, 683 (1970).

4. R. R. Spencer et al., ORNL/TM-6805 (1979).

5. R. R. Spencer, Paper GA2, this conference.

6. J. W. Boldeman, Nucl Sci and Engr 55, 188 (1974).

7. I. Asplund-Nilsson, H. Conde, and N. Starfelt, Nucl Sci and Engr 16, 124 (1963).

8. J. C. Hopkins and B. C. Diven, Nucl Phys 48, 433 (1963).

9. H. Bozorgmanesh, Ph.D. Dissertation, U. Michigan, (1977).

10. P. H. White and E. J. Axton, J. Nucl. Energy 22, 73 (1968).

11. B. Aleksandrov et al., Proc 1975 Kiev Conf. 5, 166 (1975).

12. D. W. Colvin and M. G. Sowerby, in "Physics and Chemistry of Fission (Proc. Symp. Salzberg, 1965)" Vol. 2, p. 25 (1965).

13. R. J. Howerton and M. H. MacGregor, UCRL-50400, Vol. 15, Part D, Rev. 1, p. 115 (1978).

14. S. F. Mughabghab and D. I. Garber, BNL 325, Third Edition, Vol. 1 (1973).

15. H. Pomerance, Phys Rev 83, 64 (1951).

16. S. P. Harris et al., Phys Rev 80, 342 (1950).

17. F. W. C. Colmer and D. J. Littler, Proc Phys Soc (London) 63, 1175 (1950).

18. T. E. Young, F. B. Simpson, and R. E. Tate, Nucl Sci and Engr 43, 341 (1971).

19. L. J. Rainwater et al., Phys Rev 73, 733 (1948).

20. R. Maayouf and I. Hamouda, Atomkernenergie V13, 152 (1968).

21. H. Pomerance, private communication.

22. J. R. smith et al., unpublished.

NEUTRON CAPTURE CROSS SECTION STANDARDS FOR BNL-325

N. E. Holden
Brookhaven National Laboratory
Upton, New York 11973, USA

The most common cross section standards for capture reactions in the thermal neutron energy region are gold, cobalt, and manganese. In preparation for the fourth edition of BNL-325, data on the thermal cross section and resonance integral were evaluated for these three standards. For gold, only measurements below the Bragg scattering cutoff were used and extrapolated to a neutron velocity of 2200 meters/second. A non 1/v correction due to the 4.9 eV resonance was made. The resonance integral is based on Jirlow's integral measurement and Tellier's parameters. The resonance integrals for cobalt and manganese are based solely on integral measurements because the capture widths of the first major resonance either vary by 20% in various measurements (cobalt), or have never been measured (manganese). Recommended thermal cross sections and resonance integrals are respectively gold: 98.65±0.09 barns, 1550±28 barns, cobalt: 37.18±0.06 barns, 74.2±2.0 barns, and manganese: 13.3±0.2 barns, and 14.0±0.3 barns.
[^{197}Au(n,γ), ^{59}Co(n,γ), ^{55}Mn(n,γ), thermal cross section, resonance integral]

Introduction

Neutron capture reaction cross sections are usually measured on a relative basis. The most common absolute standards used in the thermal energy region are gold, cobalt, and manganese. In the epithermal energy range, resonance capture integrals are usually measured relative to gold, with cobalt and manganese as secondary standards.

The Gold Capture Standard

Thermal Neutron Capture Cross Section

Measurements were only considered for which high resolution and accuracy in the wavelength determination were obtained. This would eliminate problems with determination of the incident neutron flux shape and a possible epithermal component, which could contribute significantly due to the 4.9 eV resonance in gold. Table I lists the experiments, which satisfied the above criteria, the reported value and the value recommended. Antonini's result was discarded because it was merely a check on the effectiveness of a slow chopper and the large uncertainty might distort the average result. Steyerl's result is approximately 4½ standard deviations outside the weighted average of other measurements and his foil thickness is uncertain to 5%. Dilg performed measurements on Steyerl's time of flight spectrometer with gold foils of thickness known to 0.02% and obtained results consistent with the other reported experiments. This indicates a problem not with Steyerl's instrumentation, but with his foils.

The cross section was measured below the Bragg scattering cutoff, where scattering contributions to the total cross section become small. The 1/v curve was fitted in this long wavelength region, and extrapolated to a neutron velocity of 2200 meters/second. A correction for the non 1/v portion of the cross section due to the 4.9 eV resonance was made using the Tellier parameters for this resonance, corresponding to 0.90±0.03 barns at 2200 meters/second. The weighted average and recommended value is 98.65±0.09 barns.

Resonance Capture Integral

An absolute resonance integral measurement was made by Jirlow, and a correction for the detailed shape of the epithermal spectrum at the R1 reactor (unknown at the time of Jirlow's measurement) gave a result of 1553±40 barns. A measurement relative to boron by Popovic is estimated to be 1507±100 barns which gives support to Jirlow's measurement but is not included because of lack of details.

From differential data, the total resonance integral, using Wood parameters for the 4.9 eV resonance, is 1597±67 barns, and the total resonance integral, using Tellier parameters for the 4.9 eV resonance, is 1548±40 barns. The Tellier parameters give better agreement with Jirlow's integral measurement, and for the thinnest samples used, Tellier measured approximately six times the number of points about the peak of the resonance as did Wood. Tellier's parameters were used for the non 1/v component calculation for the thermal capture cross section and for the resonance integral giving a gold resonance integral of 1550±28 barns.

The Cobalt Capture Standard

Thermal Neutron Capture Cross Section

Neutron capture in cobalt leads to the compound nucleus ^{60}Co which has a ground state with a 5.27 year half life, and an isomer at 58.6 keV excitation energy with a half life of 10.5 minutes. In addition to the isomeric transition to the ground state, the isomer decays via two weak beta branches of 0.24% and 0.0086%. Since 54.9% of the captures lead to the isomer, the activation cross section of the 5.27 year state will be 0.136% less than the absorption cross section or 0.05 barns less. This factor is used to adjust the various measurements to the same basis.

The results of all experiments are given in Table III, although many are not considered very reliable because of insufficient data on standards, self-shielding, resonance absorption, absolute intensities of gamma rays, conversion coefficients, etc. Table IV lists the most reliable measurements. The resulting cross section is 37.18±0.06 barns. The activation experiments for the 10.5 minute isomer are given in Table V, where the recommended value is 20.4±0.8 barns.

Resonance Capture Integral

Most of the cobalt resonance integral is produced by capture in the 132 eV resonance. The neutron capture width of this resonance is reported in various measurements with a spread of 20%. The resonance integral calculated from differential data is highly uncertain as a result and only integral measurements were considered for the recommended resonance integral. The values considered are given in Table VI, and the recommended result is 74±2 barns. For the 10.5

minute isomer, Table VII lists the experiments with a recommendation of 39±2 barns for this resonance integral.

The Manganese Capture Standard

Thermal Neutron Capture Cross Section

Table VIII lists the various measurements as reported and as revised. In general, there have been no recent measurements of very high accuracy with a detailed error analysis published. The small errors listed with most values correspond to statistical counting uncertainties only. These values have been adjusted to include estimated uncertainties for potential systematic effects. The recommended value is 13.3±0.2 barns.

Resonance Capture Integral

Over seventy percent of the manganese resonance integral is produced by capture in the 336 eV resonance. The neutron capture width of this resonance has never been measured. In fact, the capture width for BNL-325 is being determined by using a recommended resonance integral from integral measurements. The values considered are given in Table IX as quoted, and as revised. The recommended resonance integral is 14.0±0.3 barns.

Table I $^{197}Au(n,\gamma)$ Measurements

Reference	Reported Value (barns)	Recommended Value (barns)
Carter[1] (1953)	98.7 ±0.6	98.72±0.45
Egelstaff[2] (1954)	98.6 ±0.9	98.6 ±0.9
Gould[3] (1960)	98.8 ±0.3	98.7 ±0.3
Teutsch[4] (1962)	98.9 ±0.3	98.8 ±0.3
Als Nielsen[5] (1964)	98.6 ±0.2	98.58±0.22
Antonini[6] (1965)	97.64±4.25	too imprecise
Steyerl[7] (1972)	99.3 ±0.5	apparent error see discussion
Dilg[8] (1973)	98.68±0.12	98.63±0.11

Weighted Average = 98.645 barns ± 0.087 (Internal Error), ± 0.068 (External Error)

Recommended Value = 98.65 ± 0.09 barns

Table II Parameters For The First Resonance In Gold

Reference	E_o(eV)	Γ(meV)	Γ_n(meV)	Γ_γ(meV)	σ_o(barns)
Wood[11]	4.906±0.010	140±3	15.6±0.5	124.4±3	36964
Tellier[12]	4.900±0.005	137.5±2	15.0±0.2	122.5±2.5	36233

Table III $^{59}Co(n,\gamma)$ Measurements

Reference	Reported Value (barns)	Recommended Value (barns)
Wu[13]	40.2 ±0.9	36.0 ±3.0
Colmer[14]	38.2 ±3.0	41.5 ±3.9
Harris[15]	35.7 ±1.8	36.1 ±4
Yaffe[16]	34.2 ±1.4	36.6 ±1.5
Pomerance[17]	34.2 ±1.7	35.7 ±1.8
Grimeland[18]	33.9 ±0.4	36.9 ±1.0
Bernstein[19]	38.4 ±0.6	38.4 ±1.2
Ailloud[20]	35.4 ±1.0	38.5 ±1.6
Eastwood[21]	36.4 ±1.5	36.4 ±1.5
Tattersall[22]	38.2 ±0.7	38.5 ±0.7
Wolf[23]	38.0 ±0.5	38.4 ±0.5
Meadows[24]	36.3 ±0.6	36.3 ±0.6
Cance[25]	35.51 ±0.87	35.51 ±0.87
De Swiniarski[26]	34.9 ±1.0	34.9 ±1.0
Taylor[27]	37.0 ±2.0	37.5 ±1.9
Hüttel[28]	34.8 ±0.2	35.1 ±0.7
Vaninbroukx[29]	37.4 ±0.3	37.3 ±0.3
Carre[30]	38.0 ±0.3	38.0 ±0.3
De Worm[31]	37.7 ±0.4	37.7 ±0.4
Merritt[32]	37.09 ±0.27	37.16 ±0.24
Kim[33]	36.61 ±0.47	37.19 ±0.48
Schuman[34]	38±2	38±2
Silk[35]	37.245±0.11	37.245±0.11
Dilg[8]	37.145±0.07	37.145±0.07

weighted average (barns) = 37.204±0.053 (internal error)
0.075 (external error)

Table IV $^{59}Co(n,\gamma)$ Most Precise and Documented Measurements

Reference	Reported Value (barns)	Recommended Value (barns)
Vaninbroukx[29]	37.4 ±0.3	37.3 ±0.3
Merritt[32]	37.09 ±0.27	37.16 ±0.24
Kim[33]	36.61 ±0.47	37.19 ±0.48
Silk[35]	37.245±0.11	37.245±0.11
Dilg[8]	37.145±0.07	37.145±0.07

weighted average (barns) = 37.178±0.056 (internal error)
0.036 (external error)

Recommended Value = 37.18 ± 0.06 barns

Table V $^{59}Co(n,\gamma)\ ^{60m}Co$ 10.5 Minute Activation Cross Section

Reference	Reported Value (barns)	Recommended Value (barns)
Deutsch[36]	σ^g/σ^m = 1.4 ±0.6	15.2±6.5
Moss[37]	18.3 ±1.7	21.8±2.0
Keisch[38]	σ^m/σ^g = 1.19±0.16	21.8±1.4
Schmidt-Ott[39]	16.5	17.8±(2.0)
Gryntakis[40]	18.80±1.50	19.7±1.6

weighted average (barns) = 20.4±0.84 (internal error)
0.84 (external error)
Recommended Value = 20.4 ± 0.8 barns

Table VI ^{59}Co Resonance Integral Measurements

Reference	Reported Value (barns)	Recommended Value (barns)
Tattersall[22]	↷70	
Johnston[41]	74.8	75.2±5.
Feiner[42]	81±4	74.8±7.2
Eastwood[43]	69.9±3.5	72.3±4.2
Taylor[27]		73.3±7.9
Le Sage[44]	71.0±5	74.0±8.3
Carre[30]	68.7±5.	70.4±7.0
Wall[45]	↷69	
Kim[33]	75.3±0.8	75.8±3.7
Schuman[34]	74.6±3	73.6±7
Hüttel[28]	↷70.3	
Steinnes[46]	77±4	76.2±8.1

weighted average (barns) 74.2±2.0 (internal error)
±0.2 (external error)
Recommended Value = 74 ± 2 barns

Table VII Resonance Integral $^{59}Co(n,\gamma)\ ^{60m}Co$ 10.5 minute state

Reference	Reported Value (barns)	Recommended Value (barns)
Dahlberg[47]		39.2±3.5
Eastwood[43]		38.4±2.3
Gryntakis[48]	39.7±4.3	42.7±4.6

weighted average (barns) 39.2±1.8 (internal error)
±0.3 (external error)
Recommended Value = 39±2 barns

Table VIII ^{55}Mn Thermal Neutron Cross Section

Reference	Reported Value (barns)	Recommended Value (barns)
Coltman[49]	10.7 ±0.2	13.6 ±1.4
Colmer[14]	12.8 ±0.8	13.9 ±1.4
Harris[15]	12.3	13.2 ±1.2
Pomerance[17]	12.8 ±0.6	13.3 ±0.7
Grimeland[18]	12.4 ±0.2	13.3 ±1.0
Bartholomew[50]	12.7 ±0.3	13.5 ±1.4
DeJuren[51]	13.19±0.30	13.38±0.6
Cummins[52]	13.2 ±0.2	13.0 ±0.6
Meister[53]	13.19±0.38	13.18±0.6
Tattersall[22]	13.25±0.15	13.35±0.6
Meadows[24]	13.2 ±0.1	13.26±0.6
Hüttel[54]	13.3 ±0.08	13.4 ±1.0
Bouzyk[55]	13.4 ±0.4	13.5 ±1.0
Sokolowski[56]	13.20±0.15	
Hogg[57]	13.5 ±0.5	13.6 ±1.0
Adib[58]	13.64±0.19	13.64±1.0

Weighted average = 13.32±0.2 barns
Recommended Value = 13.3±0.2 barns

Table IX ^{55}Mn Resonance Capture Integral

Reference	Reported Value (barns)	Recommended Value (barns)
Harris[59]	9.77	12.4 ±1.6
Tattersall[22]	15.5 ±5.0	14.9 ±5.0
Walker[60]	13.8 ±0.8	13.1 ±0.9
Dahlberg[47]	14.12±0.6	14.3 ±0.8
Feiner[61]	15.8	14.2 ±1.2
Jacks[62]	14.1 ±0.3	13.9 ±1.4
Axton[63]	14.6	14.31±0.83
Louwier[64]	15.0 ±1.4	14.2 ±1.5
Kohler[65]	13.52±0.60	13.5 ±1.0
Carre[30]	16.5 ±1	15.15±1.8
Orvini[66]	13.7 ±0.7	14.01±0.97
Ryves[67]	11.7 ±1.7	11.7 ±2.0
Sher[68]	14.4 ±0.5	14.3 ±0.7
Schuman[34]	14.0 ±0.7	14.0 ±1.3
Nanjyo[69]	14.1 ±0.6	14.0 ±1.1
Breitenhuber[70]	15.4	14.5 ±1.2
Van der Linden[71]	13.8 ±0.8	13.8 ±1.2
Gleason[72]	17.0	16.8 ±1.9

weighted average = 14.0±0.27 barns (internal error),
±0.17 barns (external error).
Recommended value = 14.0±0.3 barns.

Acknowledgment

Research sponsored by the U.S. Department of Energy.

References

(1) R.S. Carter et al., Phys. Rev. 92 716 (1953).
(2) P.A. Egelstaff, J. Nucl. Energy 1 57 (1954), see also P.A. Egelstaff., J. Nucl., Energy 5 41 (1957).
(3) F.T. Gould et al., Nucl. Sci. Eng. 8 453 (1960).
(4) H. Teutsch et al., Nukleonik 4 165 (1962).
(5) J. Als-Nielsen, O. Dietrich, Phys. Rev. 133 B925 (1964).
(6) B. Antonini et al., Nucl. Inst. Meth. 33 229 (1965).
(7) A. Steyerl, H. Vonach, Z. Physik 250 166 (1972).
(8) W. Dilg et al., Z. Physik 264 427 (1973).
(9) D. Popovic, Z. Naturforschg. 9a 600 (1954).
(10) K. Jirlow, E. Johansson, J. Nucl. Energy 11 101 (1960), see also E. Johansson, Thesis, Gothenberg (1966).
(11) R.E. Wood, Phys. Rev. 104 1425 (1956), see also R.E. Wood, H.H. Landon, V.L. Sailor, Phys. Rev. 98 639 (1955).
(12) H. Tellier, M. Alix, Saclay CEA Report 1230N (1969).
(13) C.S. Wu et al., Phys. Rev. 71 174 (1947).
(14) F.C.W. Colmer, D.J. Littler, Proc. Phys. Soc. (London) A63 1175 (1950).
(15) S.P. Harris et al., Phys. Rev. 80 342 (1950).
(16) L. Yaffe et al., Phys. Rev. 82 553 (1951).
(17) H. Pomerance, Phys. Rev. 83 641 (1951).
(18) B. Grimeland et al., Compt. Rend. 232 2089 (1951).
(19) S. Bernstein et al., Phys. Rev. 87 487 (1952).
(20) J. Ailloud et al., J. Phys. Rad. 13 171 (1952).
(21) T.A. Eastwood, R.D. Werner, Chalk River Report CI-207 (1959).
(22) R.B. Tattersall et al., J. Nucl. Energy 12 32 (1960).
(23) G. Wolf, Nukleonik 2 255 (1960).
(24) J.W. Meadows, J.F. Whalen, Nucl. Sci. Eng. 9 132 (1961).
(25) M. Cance et al., CEN Saclay Report DPE-SPE 63/503/831 (1963).
(26) R. deSwiniarski et al., CEN Grenoble Report INT/PI-171/135 (1963).
(27) N.K. Taylor, J.K. Linacre, Harwell Report AERE R-4111 (July 1964).
(28) G. Hüttel, P. Liewers, unpublished work cited by K.F. Alexander in Rossendorf Report ZFK-RN23 (1964).
(29) R. Vaninbroukx, Nucl. Sci. Eng. 24 87 (1968).
(30) J.C. Carre, R. Vidal, 1966, Proc. IAEA Conf. on Nuclear Data for Reactor, Paris I, 479 (1966).
(31) J.P. Deworm, European American Nuclear Data Committee Report EANDC (E) 76 106 (1967).
(32) J.S. Merritt, R.E. Green, Can. J. Phys. 46 2325 (1968).
(33) J.J. Kim, F. Adams, Radio Chem. Acta 9 61 (1968).
(34) R.P. Schuman, J.R. Berreth, Idaho Report IN-1296 (May 1969).
(35) M.G. Silk, B.O. Wade, J. Nucl. Energy 24 43 (1970).
(36) M. Deutsch, G. Scharff Goldhaber, Phys. Rev. 83 1059 (1951).
(37) N. Moss, L. Yaffe, Can. J. Chem. 31 391 (1953).
(38) B. Keisch, Phys. Rev. 129 769 (1963).
(39) W.D. Schmidt-Ott, Z. Phys. 174 206 (1963).
(40) E.M. Gryntakis, J.I. Kim, J. Radioanaly. Chem. 46 159 (1978).
(41) F.J. Johnston et al., J. Nucl. Energy 11 95 (1960).
(42) F. Feiner, L.J. Esch, Knolls Atomic Power Lab Report KAPL-2000-12 I.37 (1960).
(43) T.A. Eastwood, R.D. Werner, Can. J. Phys. 41 1263 (1963).
(44) L. Le Sage, R. Sher, Proc. ANS Top. Meet. San Diego, Calif. Vol. II. 175 (1966).
(45) T. Wall, Australian Report AAEC/TM 466 (1968).
(46) E. Steinnes, J. Inorg. Nucl. Chem 34 2699 (1972).
(47) R. Dahlberg et al., J. Nucl. Energy 14 53 (1961).
(48) E.M. Gryntakis, Thesis Munich (1976) (see also ref. 47).
(49) J.W. Coltman, M. Goldhaber, Phys. Rev. 69 411 (1946).
(50) R.M. Bartholomew et al., Can. J. Chem. 31 204 (1953).
(51) J. deJuren, J. Chin, Phys. Rev. 99 191 (1955).
(52) J.D. Cummins, A. H. Spurway, Harwell Report AERE R/M 100 (1957).
(53) H. Meister, Z. Naturforschg 13a 820 (1958).
(54) G. Hüttel, P. Liewers, Kernenergie 6 336 (1963).
(55) J. Bouzyk et al., Nukleonika 8 443 (1963).
(56) E. Sokolowski, R. Bladh, Swedish Report AE-351 (1969).
(57) C.H. Hogg, W.L. Wilson, Idaho Report IN-1317 53 (1970).
(58) M. Adib et al., Atomkernenergie 27 117 (1976).
(59) S.P. Harris et al., Phys. Rev. 79 11 (1950).
(60) W.H. Walker et al., Can. J. Phys. 38 57 (1960).
(61) F. Feiner, Knolls Atomic Power Lab Report KAPL-2000-16 I.3 (1962).
(62) G.M. Jacks, Savannah River Report DP-608 (1961).
(63) E.J. Axton, J. Nucl. Energy AB17 125 (1963).
(64) P.W.F. Louwier, A.H.W. Aten, J. Nucl. Energy AB19 267 (1965).
(65) W. Köhler, H. Schmelz, Nukleonik 9 270 (1967).
(66) E. Orvini et al., J. Inorg. Nucl. Chem. 30 1353 (1968).
(67) T.B. Ryves et al., J. Nucl. Energy 22 465 (1968).
(68) R. Sher, National Bureau of Standards Special Publication 299 253 (1968).
(69) T. Navjyo, J. Nucl. Sci. Techn. 7 126 (1970).
(70) L. Breitenhuber et al., Atomkernenergie 15 83 (1970).
(71) R. Van der Linden et al., J. Radioanal. Chem. 11 133 (1972).
(72) G. Gleason, Radiochem. Radioanal. Letters 23 317 (1975).

NBS NEUTRON MONITOR AND DOSIMETER CALIBRATION FACILITY

K. C. Duvall, O. A. Wasson and M. M. Meier
National Bureau of Standards
Washington, D.C. 20234, USA

A standard neutron flux in the energy range of .2 to 1.2 MeV has been established at the NBS 3 MV positive ion Van de Graff laboratory. The neutron flux is produced from the $^{7}Li(p,n)^{7}Be$ reaction and monitored by a precision calibrated black neutron detector. The flux is emitted within a cone of 4.5° half angle and is spacially uniform to within ±1%. The facility has been recently used for the calibration of neutron monitors and dosimeters submitted by government and industry. The detector responses are measured relative to our standard neutron flux in terms of response per unit fluence. These calibration factors have been determined with an accuracy better than ±5%.

[calibration; dosimetry; detection; facilities; fluence; flux; monitor; neutron; sources; standardization]

Introduction

A standard neutron flux facility has been established at the NBS 3 MV positive ion Van de Graaff laboratory and was briefly described in a paper by O.A. Wasson[1]. The neutron flux in the energy range of .2 to 1.2 MeV is determined accurately to within ±2%. Recently the facility has been used for the calibration of neutron monitors and dosimeters for government and industry. Calibration factors in terms of the monitor response relative to the neutron fluence received have been determined for active neutron monitors. Personnel dosimeters were given specific fluences only. The results of the measurements are presented and discussed.

NBS .2 to 1.2 MeV Neutron Flux Facility

A monoenergetic, pulsed proton beam emitted from the NBS 3 MV Van de Graaff accelerator is incident on an evaporated ^{7}Li metal target. The proton beam is pulsed with 1 μsec intervals and 10 n sec pulse width. Proton currents up to 2.0 μA are available with a 4 mm diameter beam spot at the target position.

Monoenergetic neutrons in the energy range of .2 to 1.2 MeV are produced with the aid of the $^{7}Li(p,n)^{7}Be$ reaction. The experimental geometry is shown in Fig. 1. The neutron source is surrounded by a Li_2Co_3 + wax shield mounted on a movable air table for easy access to the beam line and target. The source shield, along with a grided aluminum floor, serves to reduce the neutron room background. A lithium loaded polyethylene collimator is inserted into the shield allowing the emitted neutron flux to be confined to a cone of 4.5° half angle. The neutron flux within the cone is spacially uniform to better than ± 1%. The beam profile for 1180 keV neutrons at 1.3 m from the source is shown in Fig. 2. The low energy neutron background is less than 0.8% of the direct beam. The γ ray background is nominally less than 1.5 mrem/hr. With this experimental arrangement, a neutron flux of 200 n/cm^2 sec at 1.5 m from the source is typical.

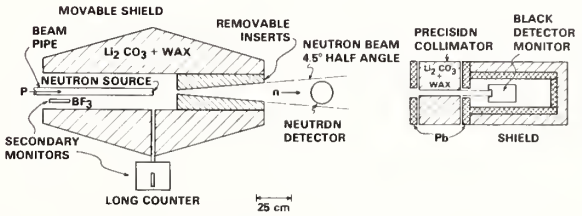

Fig. 1. Experimental geometry.

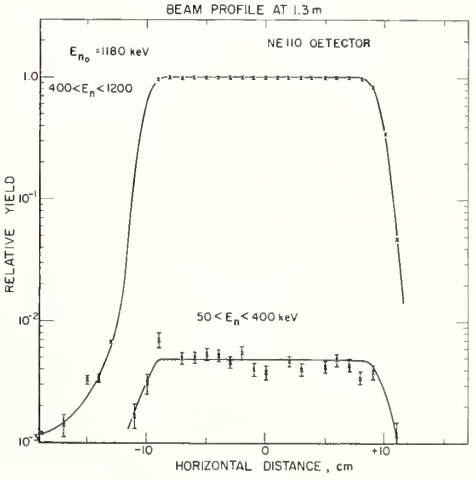

Fig. 2. Neutron beam profile for 1180 keV neutrons at 1.3 m from source. Profile obtained from TOF spectrum of a 1 inch diameter Ne 110 scintillator.

The neutron production rate is monitored at 0° by a precision calibrated black neutron detector[2] positioned 6 m from the neutron source. The black detector consists of a 12.5 cm diameter, 15 cm thick plastic scintillator mounted on a RCA 8854 photomultiplier tube. The black detector efficiency as

a function of energy has been calculated with the use of a Monte Carlo calculation for multiple neutron scattering in a scintillator. The calculated efficiency curve has been compared to several experimentally determined points obtained from absolute measurements using the associated particle method[3]. The independent calibration methods agree to within ± 1.5% in the energy range of .2 to 1.2 MeV. Black detector efficiencies in this energy range are greater than 90%. A black detector pulse height spectrum for a 1200 keV incident neutron flux is shown in Fig. 3. The solid line is the calculated pulse height spectrum.

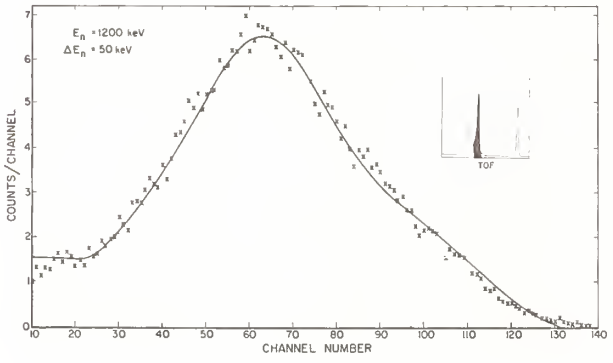

Fig. 3. Black detector pulse height spectrum plotted against the calculated spectrum at 1200 keV neutron energy.

The black neutron detector is enclosed in a borated polyethylene and lead shield. A 4.445 ±0.010 cm diameter, 30 cm deep precisely machined hole allows neutrons in a specific solid angle to strike the black detector. Taking into account the various uncertainties, the neutron flux emitted within the cone can be determined accurately to within ± 2%.

Neutron time-of-flight analysis is used in the determination of neutron energy, energy spread and background levels. The energy spread in the monoenergetic neutron beam which is dependent on the target thickness is 50 keV. Background subtraction is enhanced by the separation in time of γ-ray contributions to the detector rate. A time of flight spectrum is shown in Fig. 4 for a 1 MeV neutron beam. γ-ray and 2 nd repetition, 1-MeV neutrons are isolated along with a second neutron group which will be discussed further.

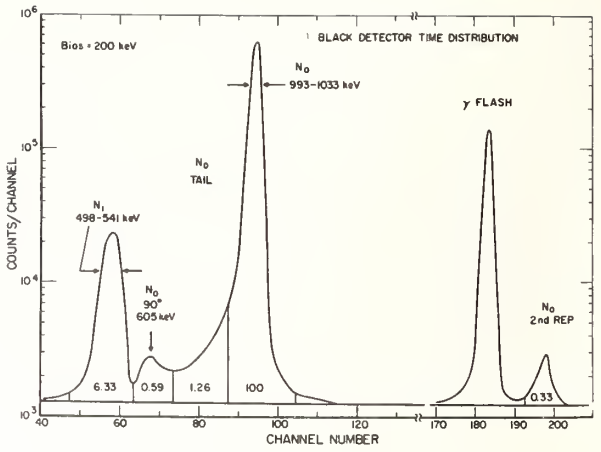

Fig. 4. Black detector time-of-flight spectrum for 1 MeV incident neutron flux. The neutron peaks are identified along with the energy spread and percentage of contribution.

A secondary neutron flux monitor located at a back angle to the source, approximately 180°, is utilized during the irradiation of a thick detector positioned in the center of the neutron cone. The secondary monitor is calibrated with respect to the precision calibrated black detector before and after an irradiation. During the irradiation, the response of monitors and dosimeters placed in the neutron beam for calibration are recorded with respect to the secondary monitor. A 1-inch diameter, 6-inch long BF_3 gas chamber is used for this purpose and rests on the beam pipe within the source shield. However, this secondary monitor is sensitive to proton beam and target conditions and may vary during an irradiation by as much as much 2.5%.

Experimental Procedures

Neutron Monitor and Dosimeter Calibration Measurements

Neutron monitors and dosimeters requiring calibration with respect to our standard neutron flux are positioned in the beam, entirely within the neutron cone. The fluence F(r) received during irradiation is determined from the expression:

$$F(r) = \left(\frac{R}{r}\right)^2 \frac{n_{BF}}{k'} \frac{1}{A_{eff}\, T(R-r)}$$

$$k' = \frac{n_{BF}}{n_{BD}/\varepsilon}$$

where

R — the distance from the source to the rear of the black detector collimator is 565.8 cm.

r — the distance from the source to the neutron monitor or dosimeter requiring calibration.

A_{eff} — the effective area of the black detector collimator.

T(R-r) — the correction for air transmission.

n_{BF} — counts in the secondary monitor.

n_{BD} counts in the black detector.

ε the black detector efficiency.

The neutron monitor response to the specific fluence received is obtained from a scaler associated with the monitor electronics pack. Calibration factors are determined in terms of the ratio of counts to neutron fluence.

An additional complication in determining the fluence received for neutron energies above 600 keV is the presence of a second neutron energy group generated by the $^7Li(p,n)$ source. The contributions to the black detector rate from the two neutron groups are separated in time-of-flight analysis, allowing the fluence received from each neutron component to be determined. The monitor response must be corrected for the response to the lower energy second group. This response is measured separately and applied as a correction in the following expression:

$$K_o = \frac{M}{F_o(r)} - K_1 P$$

$$P = \frac{F_1(r)}{F_o(r)}$$

where

M the monitor response read from a scaler associated with the monitor electronics

$F_o(r)$, $F_1(r)$ the contributions to the total fluence at a distance r from the source for the main neutron group and the second group.

K_o, K_1 the calibration factors determined for the main neutron group and second group.

Some details and results of recent calibrations follow.

Irradiations of Commercial Neutron Monitors

The response of a 3-inch and 9-inch diameter spherical neutron monitor was measured at neutron energies of 235, 515, 754, and 1054 keV. The monitor consisted of a 1/2-inch diameter, 6-inch long BF_3 probe which is inserted into either the 3-inch or 9-inch diameter spherical polyethylene moderator. The monitors were positioned in the neutron cone, 1.5 m from the source. Calibration factors determined for the 754 and 1054 keV energies were corrected for contributions from the second neutron groups by using calibration factors determined from the 235 and 515 keV measurements. The 235 and 515 keV contributions to the 754 and 1054 keV neutron fluences were 7% and 2%, respectively.

Also, several types of thermoluminscent dosimeters were irradiated at the same energies. TLDs were mounted on a water jug and positioned in the beam 1.0 m from the source. The water jug mounting is assumed to allow the backscattering contributions which are present in real life dosimeter applications, to be included in the TLD response. The TLDs received specifically determined fluences for the primary neutron groups and second groups.

Irradiations for Naval Surface Weapons Laboratory

The response of several types of active neutron monitors was required at 552 keV neutron energy. The batch of detectors consisted of 3 cylindrical neutron monitors, a set of Bonner Multisphere neutron monitors, and the 3-inch and 9-inch spherical neutron monitors. The response for each neutron monitor was recorded by some form of attached scaler.

The cylindrical monitor consists of a 1-inch diameter, 3 inch long BF_3 probe enclosed in a 8-inch diameter, 9-1/2-inch long cylindrical polyethylene moderator. Two of the three moderators had been modified by the rounding of one end. The neutron monitors were irradiated at 2.02 m from the source in several orientations with the beam.

The Bonner multi-sphere neutron monitor system consists of a ^6Li-Zinc sulfide scintillator mounted on a photomultiplier tube and inserted into one of the 2, 3, 5, 8, 10-inch diameter spherical moderators. The response was recorded for each moderator and detector combination.

The 3-inch and 9-inch spherical neutron monitors were irradiated at neutron energies of 204 and 1143 keV as well as 515 keV. The correction to the monitor response for the second neutron group at 1143 keV was obtained from previous measurements with a similar monitor.

Discussion

The response measured for the 9-inch sphere submitted by a commercial manufacturer is compared with data obtained by D. E. Hankins[4], LLL for a similar 9-inch sphere. The results are shown in Fig. 5. The two data sets were normalized at 144 keV. The agreement is satisfactory.

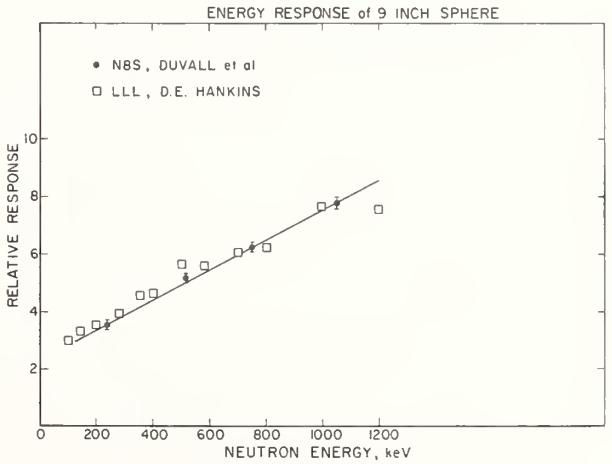

Fig. 5. Energy response of 9-inch sphere. NBS response measurements are compared with data obtained by D. E. Hankins for a similar 9-inch sphere. The two spheres are normalized at 144 keV.

We received 9-inch and 3-inch spherical neutron monitors also from Naval Surface Weapons Lab. The absolute responses measured for these detectors are compared with the measured responses for those submitted by a commercial manufacturer. The results are shown in Figs. 6 and 7. A difference in absolute response of as much as 20% is observed between the two detector sets indicating differences in absolute calibration. However, when the ratio of the 9-inch and 3-inch spheres is considered, the calibration factors cancel and the inherent responses of the two detector sets are compared. Fig. 8 shows that the inherent measured responses are in satisfactory agreement.

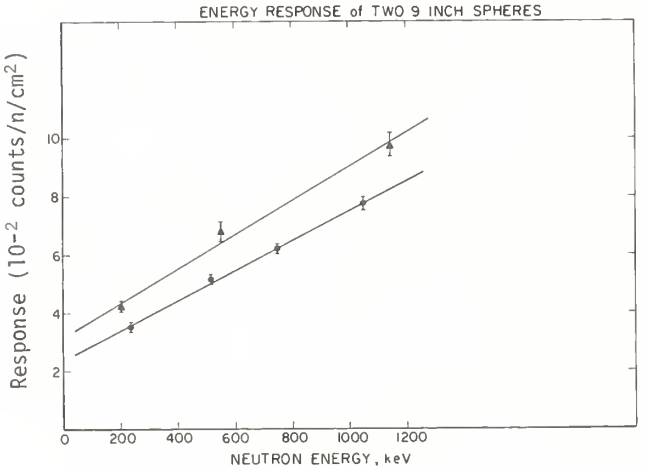

Fig. 6. Absolute response of two similar 9-inch spheres. The measurements indicate a difference in absolute calibration.

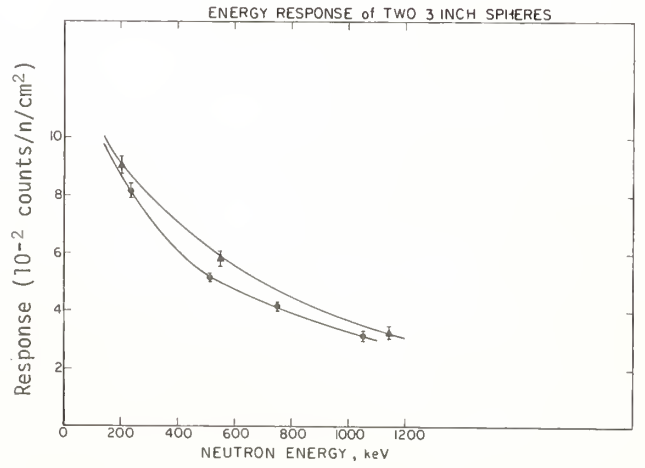

Fig. 7. Absolute response of two similar 3-inch spheres. A difference in absolute calibration is evident also in this data.

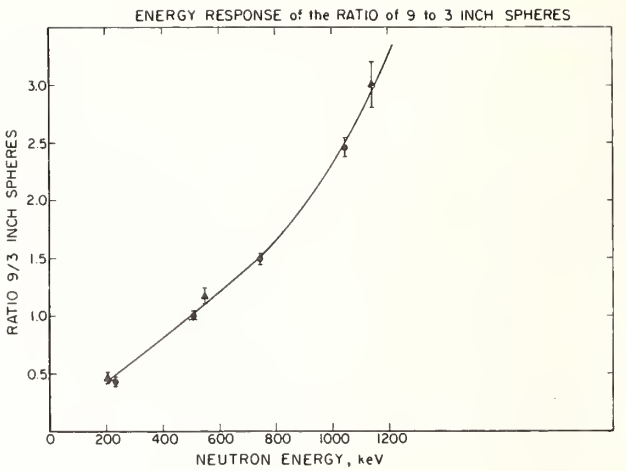

Fig. 8. Absolute response of the ratio of 9 to 3-inch spheres for two similar monitor systems. Predetermined calibration settings are cancelled.

The results of response measurements for the cylindrical neutron monitors in units of counts/n/cm^2 as a function of monitor orientation are listed in Table I. As expected, the response was dependent on the detector orientation in the beam. Table I also illustrates the variation in response for 2, 3, 5, 8 and 10-inch spheres in the 553 keV neutron field.

Table I. Irradiations for Naval Surface Weapons Laboratory at 552 keV

Neutron	Orientation	Calibration factor (counts/n/cm^2)
Cylindrical	1	0.0936 ± 0.0041
	2	0.1328 ± 0.0058
	3	0.1832 ± 0.0081
	4	0.1233 ± 0.0054
	5	0.1080 ± 0.0048
	6	0.1768 ± 0.0078
	7	0.1820 ± 0.0080
	Bkgd	0.0093 ± 0.0004
Rounded Cylindrical	1	0.1083 ± 0.0048
	2	0.1290 ± 0.0057
	3	0.2850 ± 0.0125
	4	0.2654 ± 0.0117
	5	0.2665 ± 0.0117
	6	0.1778 ± 0.0078
	7	0.2839 ± 0.0125
Bonner Multisphere		
2"		0.0055 ± 0.0002
3"		0.0310 ± 0.0014
5"		0.0970 ± 0.0043
8"		0.0799 ± 0.0035
10"		0.0426 ± 0.0019
Bare		0.00021 ± 0.00001
Cd.		0.00015 ± 0.00001

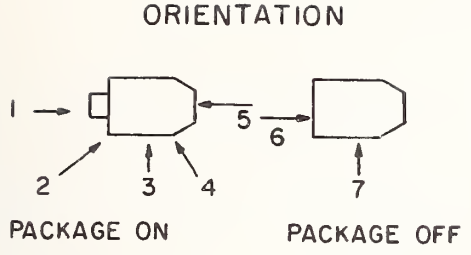

Conclusion

The NBS .2 to 1.2 MeV standard neutron flux facility is now in operation and may be used for the calibration of personnel neutron monitors and dosimeters. Calibration factors may be obtained with better than ±5% accuracy. A detailed list of the nominal experimental uncertainties is given in Table II. Neutron monitors may be exposed to fluxes of the order of 10^2 n/cm^2 sec.

Future efforts will be directed at reducing the measurement errors associated with secondary monitor instability. We believe that calibration measurements to better than ±3% are obtainable.

Table II. Nominal Experimental Uncertainties

r		0.7%
R		0.2%
n_{BF}(STAT)		0.2%
n_{BD}(STAT)		0.2%
ε		1.5%
k' stability		2.5%
A(1 + k)		0.5%
T		0.6%
dead time		0.2%
systematic (In scatt, back scatt, flux uniformity, etc.)		1.0%
M (STAT)		1.0%
M background		0.5%
	Linear	9.1%
	Quad	3.5%

Acknowledgement

We are grateful for the advice and guidance of R. B. Schwartz, who has conducted similar measurements at the NBS filtered neutron beam facility.

References

1. O. A. Wasson, Proceedings of International Specialists Symposium on Neutron Standards and Applications, p. 115 (1977).

2. G. P. Lamaze, Proceedings of a Conference on Nuclear Cross Sections and Technology, p. 73 (1975).

3. M. M. Meier, Proceedings of a Conference on Nuclear Cross Sections and Technology, p. 75 (1975).

4. D. E. Hankins, International Radiation Protection Assoc. IV Congress, Paris, France. April 24-30, 1977.

CAPTURE CROSS SECTION AND GAMMA-RAY SPECTRUM CALCULATIONS FOR MEDIUM-WEIGHT NUCLEI*

M. A. Gardner and D. G. Gardner
Lawrence Livermore Laboratory
Livermore, CA 94550, USA

We have applied a double-peak, energy-dependent Breit-Wigner model of the El gamma-ray strength function to nuclei from As to Rh, to predict their neutron capture cross sections and capture gamma-ray spectra. We found that a consistent set of model parameters could be obtained in this mass region to describe the step in the low-energy tail of the El strength function. This step allows: (a) agreement with photonuclear data at high energies, (b) the correct Γ_γ to be obtained for agreement with neutron capture cross-section data, and (c) the calculation of the observed hardness in the capture gamma-ray spectra. For nuclei at or near the closed, N=50 shell, however, the model's double-peak assumption breaks down. In these cases, good results are still obtained if the same set of model parameters is applied except that the El strength function is formulated in terms of the first, narrower peak.

[Calculated El γ-ray strength functions, calculated σ(n,γ) and γ-ray spectra for ^{75}As, ^{93}Nb, and ^{103}Rh, calculated σ(n,γ) for ^{89}Y and ^{90}Zr.]

Introduction

We are continuing to develop our capability to calculate neutron-induced capture cross sections and capture gamma-ray spectra for both stable and unstable medium-weight nuclei. Our earlier modeling work in this mass region[1-3] related the El gamma-ray strength function to the tail of the giant dipole resonance, assuming it to be represented by a single Lorentzian function. In terms of the classical dipole sum rule, it was expressed as:

$$f_{E1}(E_\gamma) = 3.3 \times 10^{-6} \frac{NZ}{A} F_{SR} \frac{E_\gamma \Gamma_R}{(E_\gamma \Gamma_R)^2 + (E_\gamma^2 - E_R^2)^2} \quad (1)$$

where E_R and Γ_R are the energy and width of the giant dipole resonance and F_{SR} is the fraction of the sum rule that is exhausted. We developed systematics for E_R and Γ_R in cases where experimental data were lacking. From a study of elements ranging from As to Cd, we adopted the expression: $E_R = 35.4/A^{1/6}$ and we parameterized the width in terms of the nuclear deformation parameter, β_2 : $\Gamma_R = (A^{1/3}/1.227)(1. + 1.2.78\ \beta_2^2)$. The expression for the giant dipole width reproduced the literature values to ± 10% or better in this mass region. To obtain values for F_{SR}, we carried out statistical model calculational fits to available experimental neutron capture cross-section data for 12 target nuclei from ^{75}As to ^{103}Rh. In these calculations, we assumed only dipole transitions, an M1 contribution to the capture width of ~ 15%-20%, and the Brink-Axel energy dependence for the El transitions. The El strength functions extracted from these fits, when compared with those predicted by Eq. 1, yielded values for F_{SR}. In general, these values agreed quite well with those inferred from total integrated photoneutron data,[4] as shown in Fig. 1. The value of F_{SR} was somewhat mass dependent: about 0.75 for A = 90 and about 1.1 for A = 94. Two marked exceptions to the general trend were the compound nuclei ^{76}As and ^{104}Rh.

Further, for both of these cases, the experimental thermal neutron capture gamma-ray spectrum was much harder than that calculated. And while this earlier modeling successfully predicted the magnitude of (n,γ) and (p,γ) cross sections in this region, it failed, in general, to reproduce the observed hardness in associated gamma-ray spectra.[5] This was further illustrated by the study of the gamma-ray spectra for the ^{93}Nb(n,γ) reaction.[3] It was found that the El strength function had to be modified by adding a small resonance around 5.5 MeV or by adding a step decrease below 4.5 MeV or by using different combinations of these two, to obtain the harder spectra indicated by experiment. With each modification the capture cross section was reproduced equally well.

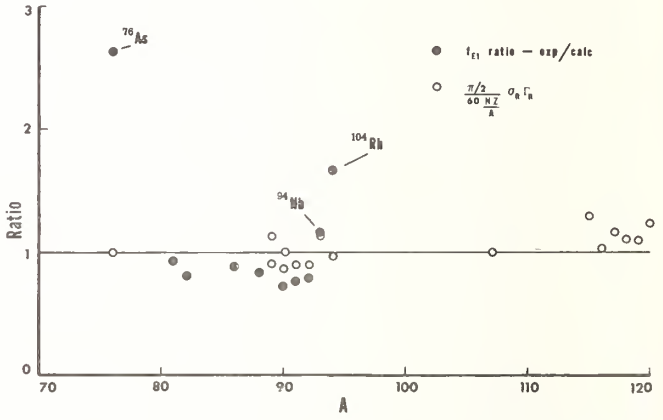

Fig. 1. Ratio of f_{E1} value (at E_γ = 3 MeV) extracted from (n,γ) cross-section measurements to that calculated with Eq. 1 vs. A (closed circles); and total, integrated photoneutron cross section[4] expressed in sum rule units vs. A (open circles).

The present re-investigation in the mass 90 region described in the following sections, makes use of the double-peak, energy-dependent Breit-Wigner (EDBW) model of the El strength function as outlined in the companion paper[6] in this conference. This model is tested to see if a consistent set of parameters can be obtained for this mass range which will yield a step in the low-energy tail of the El strength function that allows: (a) agreement with the photonuclear data at high energies; (b) the correct magnitude of Γ_γ to be obtained for agreement with neutron capture cross section data; and (c) the calculation of the observed hardness in the capture gamma-ray spectra.

*Work performed under the auspices of the U.S. Department of Energy by the Lawrence Livermore Laboratory under contract number W-7405-ENG-48.

Calculational Details

The double-peak, giant dipole parameters were computed making all of the assumptions listed in Ref. 6. This included the assumption that the integrated photonuclear absorption cross section is always 1.25 times the sum rule value. In Fig. 2 are shown the total integrated photoneutron cross sections obtained from the data available in Ref. 4 for V through Bi, expressed in sum rule units. Data from both single and double peak interpretations are included; connecting vertical lines indicate a range of data for the same nucleus. One sees that over most of the full mass range, the relation 1.25 times the sum rule is reasonable, although at around A = 90 and below this value appears to fall off.

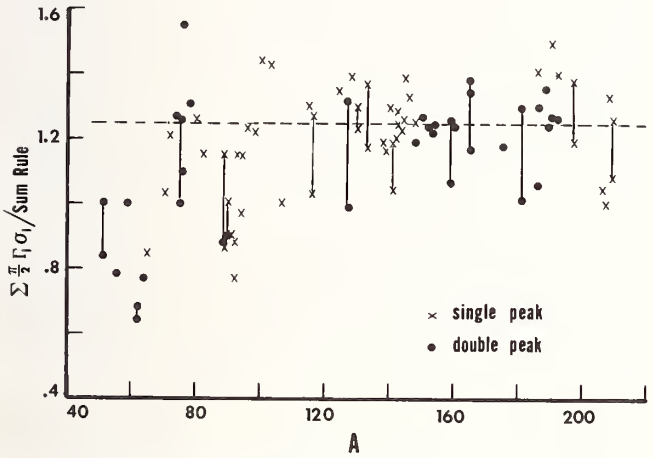

Fig. 2. Total, integrated photoneutron cross sections[4] expressed in sum rule units vs. A.

Remembering that the energy-dependent width is expressed as:

$$\Gamma(E_\gamma) = \Gamma_R \left(\frac{C + E_x}{C + E_\gamma}\right)\left(\frac{E_\gamma^2}{E_x}\right)\left(\frac{2}{E_x + E_R}\right) \qquad (2)$$

we will see that consistent results in this mass 90 range are obtained when E_x is 5 MeV and C ranges from 1 to 5 MeV. This is in agreement with the studies at higher A values.[6]

The latest versions of the statistical model nuclear reaction codes: STAPRE[7] and COMNUC[8] were used. The neutron optical model parameters used in the Y and Zr calculations were the ^{89}Y parameters of Lagrange.[9] Those used for the Nb and Rh calculations were Lagrange's ^{93}Nb parameters.[10] The As calculations were carried out using the neutron parameters of Moldauer.[11] Level densities were computed using the Gilbert-Cameron formalism,[12] as updated by Cook.[13] The constant temperature portion was adjusted to match discrete level input while the Fermi gas portion was adjusted to yield correct D_{obs} values where known.

Results for Nb, As, and Rh

In Fig. 3 is shown the computed capture gamma-ray spectrum (solid circles) for ^{93}Nb compared with the unnormalized, experimental spectrum of Orphan for thermal neutrons (histogram).[14] The calculated spectrum was obtained using the double-peak, EDBW model of the E1 strength function, with the energy-dependent width described by Eq. 2 where E_x = 5 MeV and C = 5 MeV. The insert shows various E1 strength functions for ^{94}Nb as a function of the gamma-ray energy: the short-dashed curve is the f_{E1} obtained using a single-peak Lorentz form with the ^{93}Nb parameters of Ref. 4; the solid and long-dashed curves are f_{E1}'s obtained using the present modeling. The solid curve was computed with an energy-dependent width parameterized with E_x = 5 MeV and C = 1 MeV; the long-dashed curve with a width where E_x = 5 MeV and C = 10 MeV. It should be noted that while all three of the EDBW f_{E1}'s described (where C = 1, 5, or 10 MeV) reproduced the experimental capture cross-section data of Poenitz[15] quite well for neutron energies of 0.3 MeV to 1.7 MeV, the f_{E1} with C = 5 MeV gave the best agreement with the measured gamma-ray spectrum.

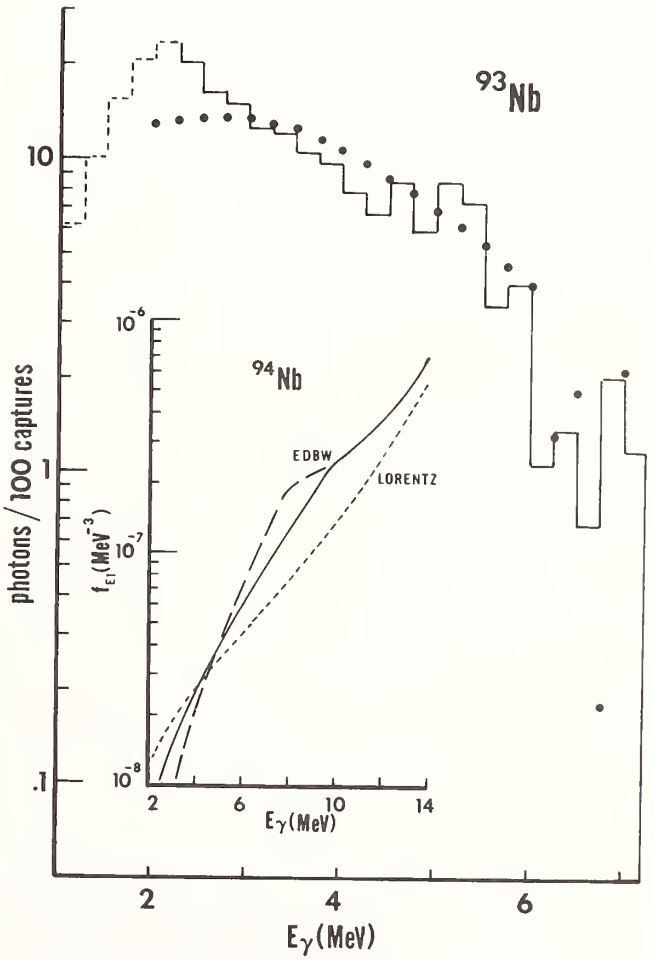

Fig. 3. Comparison of Orphan's[14] measured thermal neutron capture gamma-ray spectrum for ^{93}Nb (histogram) with that calculated via the double-peak, EDBW model (closed circles). Insert compares f_{E1}'s for ^{94}Nb: Lorentz form with parameters from Ref. 4 (short-dashed curve) and EDBW model with E_x = 5 MeV, C = 1 MeV (solid curve), with E_x = 5 MeV, C = 10 MeV (long-dashed curve).

Various calculated gamma-ray spectra for ^{75}As are shown in Fig. 4, again compared with the measured thermal neutron capture gamma-ray spectrum of Orphan (histogram).[14] The double-peak, EDBW model (solid circles) best reproduces the hardness observed in the spectrum, compared with the results obtained using a Lorentz form (open circles) or a Weisskopf formulation (open, inverted triangles) of the E1 strength function. The Lorentz form was computed with one of the sets of the double-peak, giant dipole parameters given in Ref. 4. The EDBW f_{E1} was calculated with an energy-dependent width where E_x = 5 MeV and C = 1 MeV. This same E1 strength function yielded the calculated capture cross section (solid curve) shown in Fig. 5, in good agreement with the more recently measured data sets (shown by the solid symbols).[16-20]

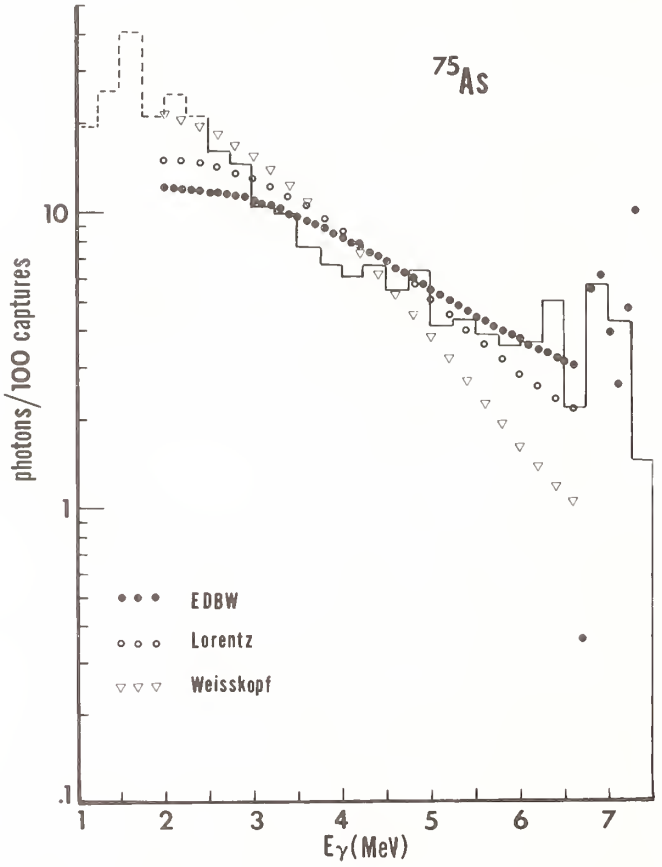

Fig. 4. Comparison of Orphan's[14] measured thermal neutron capture gamma-ray spectrum for ^{75}As (histogram) with calculations: double-peak, EDBW model (closed circles), Lorentz form (open circles) and Weisskopf form (inverted triangles).

In Fig. 6a is shown the computed neutron capture cross section for ^{103}Rh (solid curve) obtained with the present modeling of the E1 strength function. Again the energy-dependent width was described with E_x = 5 MeV and C = 1 MeV. The calculated cross section is in good agreement with the data of Macklin et al. (solid triangles, both upright and inverted)[17,21] and the data of Joly et al. (solid squares).[22] In Fig. 6b the calculated gamma-ray spectrum (solid hexagons) is compared with the measured thermal neutron capture gamma-ray spectrum of Orphan (histogram).[14] The double-peak, EDBW f_{E1}, as described, was used in the spectrum calculation and reproduces the observed hardness reasonably well.

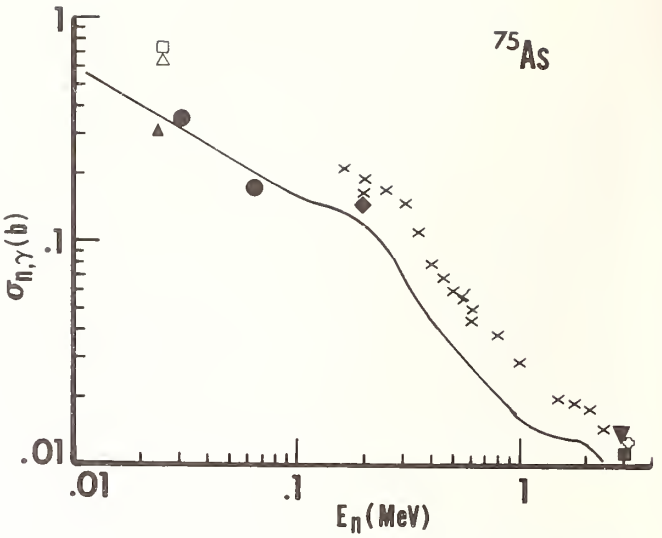

Fig. 5. The calculated (n,γ) cross section for ^{75}As (solid curve) compared with recent measurements[16-20] (solid symbols).

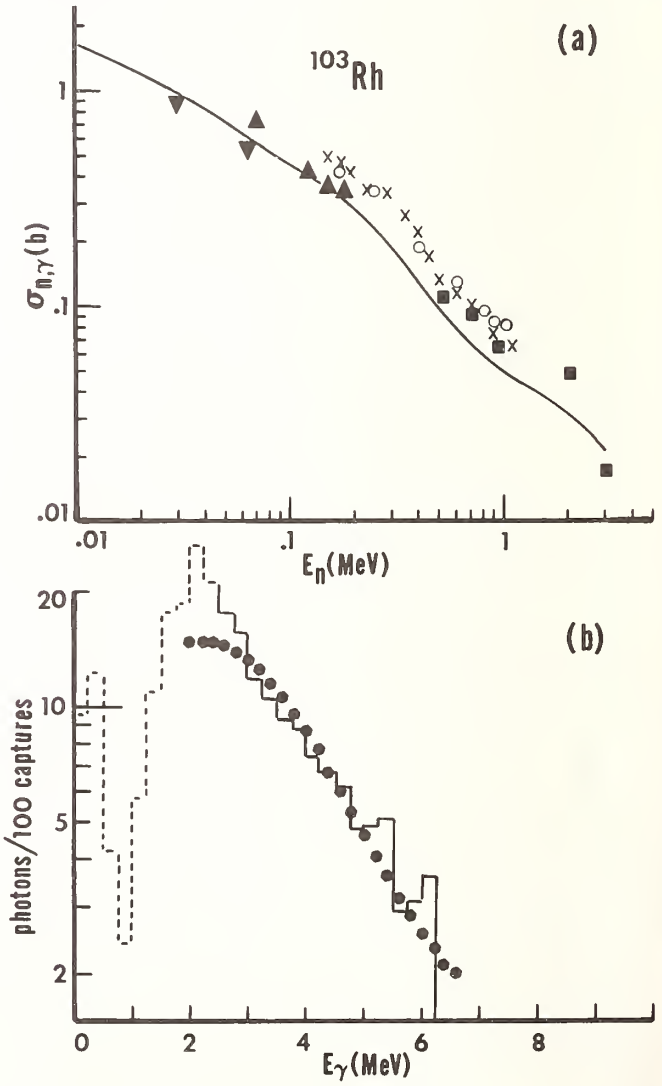

Fig. 6. a) Comparison of the calculated (n,γ) cross section for ^{103}Rh (solid curve) with measurements of Macklin et al.[17,21] (triangles) and of Joly et al.[22] (squares). b) Calculated thermal neutron capture gamma-ray spectrum for ^{103}Rh (solid hexagons) compared with Orphan's measurement[14] (histogram).

Results for Y and Zr

It appears that in the case of nuclei at or near the closed neutron shell, N = 50, the assumption breaks down that these nuclei can still be treated to some extent as prolate spheroids and that their E1 strength functions can be described by two, super-imposed giant dipole resonances. Our studies so far, for nuclei with N = 50 and 51, indicate that the double-peak, EDBW model overestimates the E1 strength function by a factor of two or more at some energies. This leads to neutron capture cross-section calculations that are too high.

In these cases, we do find that if all assumptions and systematics as described[6] are still used but that only the first, narrower resonance is employed to compute the energy-dependent Breit-Wigner E1 strength function, reasonable results are obtained. This may be seen in Fig. 7. Here is shown the single-peak, EDBW E1 strength function (solid curve) as it varies with the gamma-ray energy compared with experimental measurements and with data inferred from photoneutron experiments. The measured f_{E1} values are those of Axel et al. (solid circles)[23] and of Szeflinska et al. (open circles),[24] while the dashed curves were obtained from Lorentz formulations using the resonance parameter sets in Ref. 4. Again, using the single-peak, EDBW model to calculate the capture cross section for ^{89}Y and ^{90}Zr, the results shown in Fig. 8a and 8b are obtained. Both of the computed cross sections (solid curves) resulted from f_{E1}'s with energy-dependent widths where E_x = 5 MeV and C = 1 MeV. The calculated cross sections are in good agreement with the various sets of experimental data.[21,25-30]

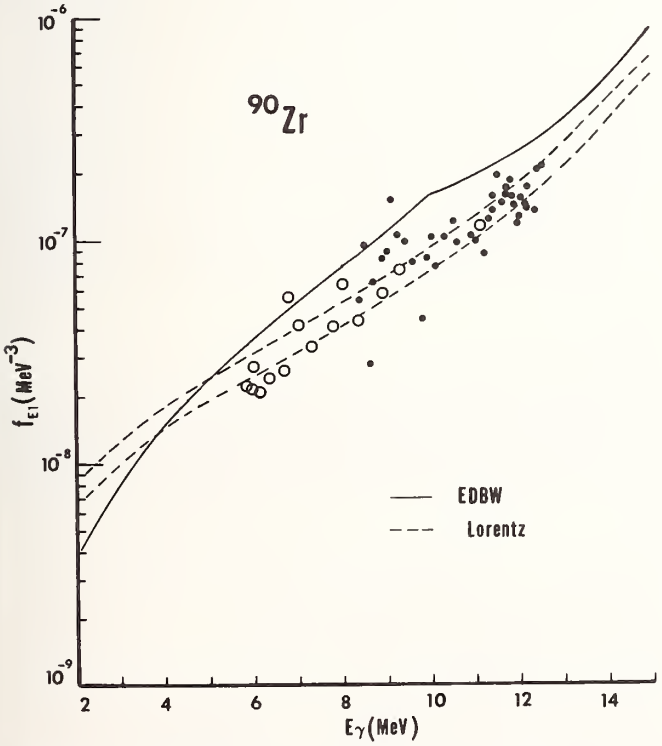

Fig. 7. Comparison of the single-peak, EDBW E1 strength function for ^{90}Zr vs. E_γ (solid curve) with: measurements of Axel et al.[23] (solid circles) and of Szeflinska et al.[24] (open circles); Lorentz form with parameters from Ref. 4 (dashed curves).

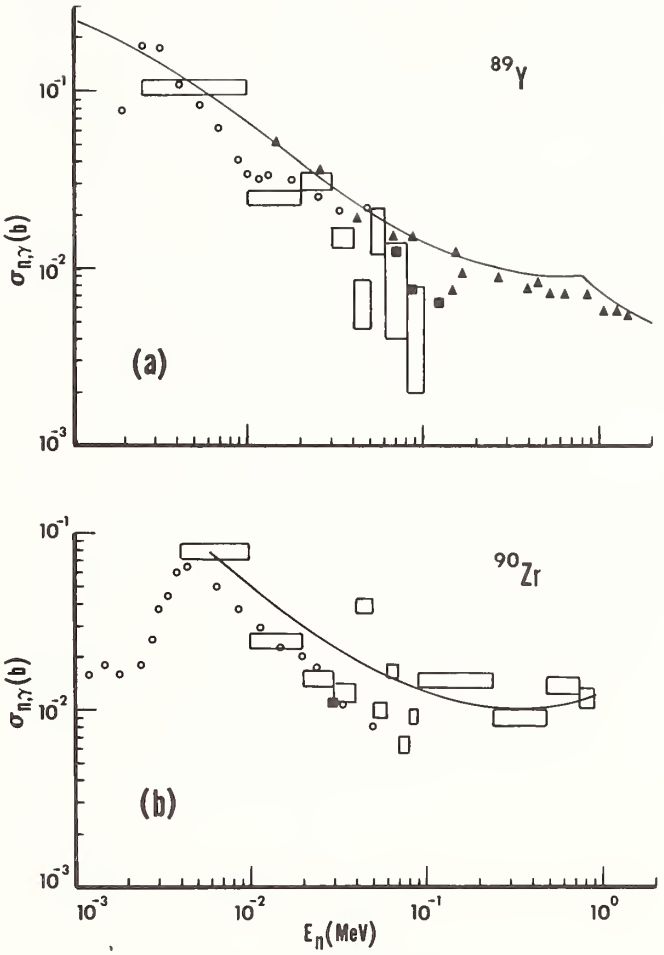

Fig. 8. The calculated (n,γ) cross sections for ^{89}Y and ^{90}Zr (solid curves) compared with measurements.[21,25-30]

References

1. D. G. Gardner and M. A. Gardner, UCID-17566 (July, 1977).
2. D. G. Gardner and M. A. Gardner, Proceedings of the Third International Symposium on Neutron Capture Gamma-Ray Spectroscopy and Related Topics, Brookhaven National Laboratory (1979) 612.
3. M. A. Gardner and D. G. Gardner, Proceedings of an International Conference on Neutron Physics and Nuclear Data for Reactors and Other Applied Purposes, Harwell (1978) 1121.
4. B. Berman, UCRL-78482 (December, 1976).
5. D. G. Gardner, F. S. Dietrich and D. W. Heikkinen, Proceedings of an International Conference on Neutron Physics and Nuclear Data for Reactors and Other Applied Purposes, Harwell (1978) 1126.

6. D. G. Gardner and F. S. Dietrich, "A New Parameterization of the El Gamma-Ray Strength Function," paper GB5, this conference.
7. M. Uhl, Acta Physica Austriaca 31 (1970) 245.
8. C. Dunford, AI-AEC-12931 (July, 1970).
9. Ch. Lagrange, National Soviet Conference on Neutron Physics, Kiev (1975).
10. Ch. Lagrange, private communication.
11. P. Moldauer, Nucl. Phys. 47 (1963) 65.
12. A. Gilbert and A. Cameron, Can. J. Phys. 43 (1965) 1446.
13. J. Cook et al., AAEC/TM-392 (June, 1967).
14. V. J. Orphan et al., AD-717 639 (July, 1970).
15. W. P. Poenitz, ANL/NDM-8 (May, 1974).
16. W. S. Lyon and R. L. Macklin, Phys. Rev. 114 (1959) 1619.
17. R. L. Macklin et al., Phys. Rev. 129 (1963) 2695.
18. G. Peto et al., J. Nuclear Energy 21 (1967) 797.
19. S. S. Hasan et al., Nuovo Cimento 58 (1968) 402.
20. J. Colditz and P. Hille, Anz. Oesterr. Akad. Wiss. Math-Naturwiss. Kl. 105 (1968) 236.
21. R. L. Macklin and J. H. Gibbons, Phys. Rev. 159 (1967) 1007.
22. S. Joly et al., Nucl. Sci. Eng. 70 (1979) 53.
23. P. Axel et al., Phys. Rev. C2 (1970) 689.
24. G. Szeflinska et al., Nucl. Phys. A323 (1979) 253.
25. A. A. Bergman et al., Jad-Fiz. Isseldovanya 3 (1966) 9.
26. D. C. Stupegia et al., J. Nuclear Energy 22 (1968) 267.
27. J. W. Boldeman et al., Nucl. Sci. Eng. 64 (1977) 744.
28. S. P. Kapchigashev, Atomnaya Energiya 19 (1965) 294.
29. R. L. Macklin et al., BAPS 8 (1963) 81.
30. J. W. Boldeman et al., Nucl. Phys. A246 (1975) 1.

A CONSISTENT NUCLEAR MODEL FOR COMPOUND AND PRECOMPOUND REACTIONS WITH CONSERVATION OF ANGULAR MOMENTUM

C. Y. Fu
Oak Ridge National Laboratory
Oak Ridge, Tennessee 37830, USA

The exciton model is modified such that it automatically reduces to the usual evaporation formula after equilibrium has been reached. The result is further modified to conserve angular momentum in a form compatible with the Hauser-Feshbach formula. This allows a consistent description of intermediate excitations from which tertiary reaction cross sections can be calculated for transitions to discrete residual levels with known spins and parities. Level densities used for the compound component of reaction cross sections are derived from direct summation of the particle-hole state densities used for the precompound component.

[Nuclear reactions ^{27}Al, ^{46,48}Ti, ^{51}V, ^{50,52}Cr, ^{54,56}Fe, ^{58,60}Ni, ^{63,65}Cu, ^{93}Nb, E = 14.6 MeV. Calculated $\sigma(n,xn)$, (n,xp), $(n,x\alpha)$, $\sigma(E_n)$, (E_p), (E_α). Hauser-Feshbach and precompound analysis.]

Introduction

Development of fusion energy calls for substantial improvement in the knowledge of neutron cross sections in the energy range from a few MeV to about 40 MeV.[1] In this energy range, the multi-step Hauser-Feshbach model with precompound effects is the most versatile and is considered an indispensible theoretical tool for cross-section evaluations.[2] In analyzing cross sections such as hydrogen and helium productions from 14-MeV neutron-induced reactions, we showed[3] that spin and parity effects are more important in the second step of the calculation than in the first step. However, it is not straightforward to conserve angular momentum even in the first step because the presently available models for precompound reactions do not conserve or even recognize angular momentum. In addition the compound and precompound components are generally calculated in the first step from two physically different models, thus lacking a common basis for carrying out the calculation to the second step.

In this paper we develop a model capable of calculating the compound and precompound cross sections consistently and conserving angular momentum in both compound and precompound reactions. The model becomes that of Hauser-Feshbach[4] at low energies where the precompound effects are negligible. Level densities used for calculating the compound component are made consistent with those used for the precompound component.

Theory

A full derivation of the formula given below has been written up for publication elsewhere.[5] Here we only have enough space for a summary. We shall first write down the final formula and then explain the physical implications of the various components leading to its derivation.

The final formula is

$$\sigma_b(E,\varepsilon)d\varepsilon = \pi\lambda^2 \sum_{J\pi} g_J \sum_{s\ell} T^J_{s\ell} \frac{d\varepsilon}{D_{J\pi}} \sum_{s'\ell'} T^J_{s'\ell'} \Omega_b(I,E,U), \tag{1a}$$

where

$$D_{J\pi} = \sum_b \sum_{I\pi} \int_\varepsilon \sum_p \sum_{s'\ell'} T^J_{s'\ell'} \Omega_b(I,E,U) \tag{1b}$$

$$\Omega_b(I,E,U) = \sum_p D_b(p,E)\, \omega_b(p\text{-}1,h,I,U') + C(E)\, \rho_b(I,U') \tag{1c}$$

$$D_b(p,E) = \int_0^T P_b(p,h,t)dt/\omega(p,h,E) \tag{1d}$$

$$C(E) = \int_T^\infty P(p,h,t)dt/\omega(p,h,E) \tag{1e}$$

$$\rho_b(I,U') = \sum_p \omega_b(p\text{-}1,h,I,U') \quad , \tag{1f}$$

and the various components and notations are explained below.

The compound and precompound components are consistent if the precompound model automatically reduces to the compound model after equilibrium has been reached. This is achieved by introducing a set of master equations containing time-dependent particle-type distributions. Defining $P_b(p,h,t)$, the occupation probability, as the probability that the system will be found in a state with p particles and h holes of type b at time t, the master equations which describe the approach of the nucleus to statistical equilibrium are given by

$$\frac{d\,P_b(p,h,t)}{dt} =$$

$$\left[\frac{P_b(p\text{-}1,h\text{-}1,t)}{P(p\text{-}1,h\text{-}1,t)}\frac{p\text{-}1}{p} + \frac{f_b(p)}{p}\right] P(p\text{-}1,h\text{-}1,t)\, \lambda_+(p\text{-}1,h\text{-}1,E)$$

$$+ \left[\frac{P_b(p+1,h+1,t)}{P(p+1,h+1,t)}\right] P(p+1,h+1,t)\, \lambda_-(p+1,h+1,E)$$

$$- P_b(p,h,t)\left[\lambda_+(p,h,E) + \lambda_-(p,h,E) + \int_0^{\varepsilon_{max}} X_b(p,h,\varepsilon)d\varepsilon\right] \tag{2a}$$

with

$$P(p,h,t) = \sum_b P_b(p,h,t) \tag{2b}$$

and

$$\sum_b f_b(p) = 1 \quad . \tag{2c}$$

The transition rates λ_+ and λ_- are given by Ribansky *et al.*[5] which contain an empirical residual two-body matrix element determined by Kalbach.[6] E is the total energy of the reacting system.

In the first term in Eq. (1), $P(p\text{-}1,h\text{-}1,t)\,\lambda_+(p\text{-}1,h\text{-}1,E)$ represents the total transition rates from (p-1,h-1) states to (p,h) states. Among the p particles in the (p,h) states, (p-1) of them retain the old particle-type distribution $P_b(p\text{-}1,h\text{-}1,t)/P(p\text{-}1,h\text{-}1,t)$, and the newly created particle may have a different particle-type distribution given by $f_b(p)$, which will be determined analytically. Thus the compositions of particle types in the new (p,h) states are given by the quantity in the brackets.

In the second term, $P(p+1,h+1,t)\ \lambda_-(p+1,h+1,E)$ represents the total transition rates from $(p+1,h+1)$ states to (p,h) states. The quantity in the brackets is the fraction of particle type b in the (p,h) states. If we assume that various types of particles annihilate with their respective holes at the same rate, then the compositions of various particles in the newly formed (p,h) states are the same as in the initial $(p+1,h+1)$ states.

The emission rates X_b are given by

$$X_b(p,h,\varepsilon)d\varepsilon = \frac{2S_b+1}{\pi^2\hbar^3}\mu_b\,\varepsilon\,\sigma_b(\varepsilon)d\varepsilon\,\frac{\omega_b(p-1,h,U)}{\omega(p,h,E)} \quad . \qquad (3)$$

where S_b, μ_b, and ε are the spin, reduced mass, and kinetic energy of the emitted particle of type b; U is the residual nucleus excitation energy. Equation (3) differs from that of Kalbach[7] in the absence of the particle-type weighting factor $R_b(p)$. This weighting factor is now time dependent and is built into Eq. (2). The state densities $\omega(p,h,E)$ are given by Williams.[8]

The numerical values of $f_b(p)$ are determined by requiring that after equilibrium has been reached the system will stay in equilibrium. Our definition of equilibrium is

$$P_b(p,h,t \geq T)/\omega(p,h,E) = C(t,E) \qquad (4)$$

where the equilibration time T is the time when all allowed states in the composite system are equally populated. This definition of equilibrium leads to

$$f_b(p) = \frac{1}{N} \qquad (5)$$

where N is the number of particle types included in the calculation.

The initial conditions for numerical integration of Eq. (2) are given by

$$P_b(p,h,0) = \delta_{pp_o}\delta_{hh_o}\,q_b \quad , \qquad (6)$$

where q_b is the fraction of particle type b in the states (p_o,h_o) at time 0. This fraction is previously contained in $R_b(p_o)$.

To conserve angular momentum it is necessary to write the occupation probability as $P_b(p,h,J,t)$ where J is the total spin of the reacting system. Eq. (1) was derived with this definition for the occupation probability. We shall not attempt to solve for this occupation probability. Instead we make the simplifying assumption that

$$\frac{P_b(p,h,J,t)}{\omega(p,h,J,E)} = \frac{P_b(p,h,t)}{\omega(p,h,E)} \qquad (7)$$

so that Eq. (2) can be used directly. This has little to do with our goal of conserving angular momentum. What we have neglected are the angular momentum couplings among the p particles and h holes and their possible influence on the spreading widths and escaping widths. Solution of this problem is beyond our present purpose.

The spin dependent p-h state densities for the residual nuclei are given by

$$\omega(p,h,J,E) = \omega(p,h,E)\,\omega_n(J) \quad , \qquad (8a)$$

where

$$\omega_n(J) = \frac{1}{2\sqrt{2\pi}\,\sigma_n^3}(2J+1)\,e^{-(J+\frac{1}{2})^2/2\sigma_n^2} \quad , \qquad (8b)$$

with

$$\sigma_n^2 = 1.17\,nc/a \quad , \qquad (8c)$$

where $a = \pi^2 g/6$, and c is a constant related to the moment of inertia.[9] Equation (8c) is derived by equating σ_n^2 to $c\tau$ where $\bar{n}$ is the most probable exciton number and τ is the nuclear temperature.[9]

The effective excitation energy U' is given by

$$U' = U - U_{p,h}$$

with

$$U_{p,h} = (h-1.5)\Delta + U_o$$

and[10]

$$\Delta = 12/\sqrt{A}$$

where U_o is the odd-even shift of Gilbert and Cameron[9] and A is the mass number. The pairing correction, $U_{p,h}$, reduces the p-h state densities given ty Williams[8] by a factor of 10 and makes their summation (over p or h) comparable to empirical descriptions such as those given by Gilbert and Cameron.[9]

Finally, converting all inverse reaction cross sections in the cross section formula given by Kalbach[6] into transmission coefficients, $T^J_{s\ell}$ and $T^J_{s'\ell'}$, where s, ℓ, s', ℓ' are the channel spins and orbital angular momenta of the incident and outgoing particles, we obtain Eq. (1). If instantaneous equilibration is assumed, Eq. (1) reduces to the usual Hauser-Feshbach formula. We emphasize that as long as comparable level densities are used, the compound part of our model, as obtained directly from the precompound model developed here, would yield identical results as the conventional compound model.

Parameter Determinations and Calculations

Calculations of neutron, proton, and alpha-particle production spectra for 14.6-MeV neutrons incident on thirteen isotopes are compared with experimental data.[11,12] Parameters of general validity are fixed beforehand. Two parameters are determined from calculations for ^{56}Fe and then used for predicting the other twelve isotopes.

Optical model parameters are taken from Wilmore and Hodgson[13] for neutrons, Becchetti and Greenlees[14] for protons, and Huizenga and Igo[15] for alpha-particles. Calculation of gamma-ray transmission coefficients was described previously in detail.[16] Level density parameters, a, c, and U_o, are calculated from the empirical formalism of Gilbert and Cameron[9] and used in Eq. (1f) as well as Eqs. (8a) to (8c). The single particle density g for each nucleus is calculated from the corresponding parameter a and thus has the effect of shell corrections, as given by Gilbert and Cameron.[9]

A few discrete levels are used for each residual nucleus in the binary step. These levels are given a weight $\Omega_b(I,E,U_c)/\rho(I,U')$, defined in Eqs. (1c) and (1f) with U_c being the continuum cutoff, such that continuity in the calculated spectra across U_c is maintained. A larger number of discrete levels in each residual nucleus is used in the second step such that more than 80% of decays by proton emission excite the discrete levels. Often only a few discrete levels are excited by the second outgoing particles in (n,np) and (n,nα) reactions. In such cases, the calculated tertiary-reaction cross sections are sensitive to the spacings and spins of the residual discrete levels.

The remaining parameters are k, the scale factor

for the residual two-body matrix elements,[7] and q_b, the fraction of particle type b in the states (p_o, h_o) at time 0. A neutron incident on a nucleus sees N neutrons, Z protons, and a maximum of Z/2 alpha clusters. Introducing a parameter f as the clustering probability[7] for alpha particles and using $p_o = 2$ and $h_o = 1$, we have

$$b_n = 0.5\ N/A' + 0.5$$
$$b_p = 0.5\ Z/A'$$
$$b_\alpha = 0.5\ (0.5\ f\ Z/A')$$

where A' = N + Z + 0.5 fZ and the fraction 0.5 accounts for the incident neutron.

The value of k has been determined by Kalbach[6] to be 400 MeV[3]. This value depends strongly on the level density parameters. Since the level densities we used here have strong pairing corrections, the value of k is expected to increase. The value k = 700 MeV[3] was determined by fitting the high-energy half of the 14.6-MeV ^{56}Fe(n,xp) spectrum measured by Grimes *et al.*[11] as shown in Fig. 1. The (n,xn) spectrum, measured by Hermsdorf *et al.*[12] and integrated over angle by Hetrick *et al.*[17] was not used for determining the value of k because of possible presence of collective excitations. We have reported[18] DWBA calculations for 15 of the 26 discrete levels up to 4.5 MeV in 14.5-MeV ^{56}Fe(n,n') reactions. The dashed histograms in the calculated (n,xn) spectrum in Fig. 1 represent such DWBA calculations. Collective strengths in higher-energy levels may not be negligible, making the determination of the parameter k on (n,xn) spectrum somewhat uncertain.

The (n,xn) spectra measured by Hermsdorf *et al.* are the only set covering all thirteen isotopes studied here. Five other sets of measurements for ^{56}Fe, considered previously,[18] are omitted for clarity. The (n,xp) and (n,xα) spectra measured by Grimes *et al.* are probably the only high quality data available.

After the value of k was determined, the value f = 0.2 was found from the high-energy tail of the ^{56}Fe(n,xα) spectrum shown in Fig. 1. This value of f increases the tail of the (n,xα) spectrum near 13 MeV by only 25% from a case calculated with f = 0, thus is weakly determined. A survey[19] of previous calculations for heavier isotopes (A > 100), for which the precompound effect is more pronounced, shows large fluctuations of f with A and shell structures.

With the above parameters, we proceed to predict similar spectra for the other twelve isotopes: ^{27}Al, ^{46,48}Ti, ^{51}V, ^{50,52}Cr, ^{54}Fe, ^{58,60}Ni, ^{63,65}Cu, and ^{93}Nb. Some of the results (^{27}Al, ^{54}Fe, ^{63}Cu, ^{93}Nb) are compared in Fig. 2 with experimental data. The (n,xn) data are for natural elements, so are shown separately in Fig. 3.

The calculated (n,xn) spectra represent sums of partial spectra from (n,n'), 2x(n,2n), (n,pn), and (n,αn) reactions. The (n,xp) spectra are sums of (n,p), (n,pn), and (n,np). The (n,xα) spectra are sums of (n,α), (n,αn), and (n,nα). The dashed curves in Fig. 2 include calculated results from the first step only. The high-energy edge in each (n,xn) spectrum represents the position of the first excited state

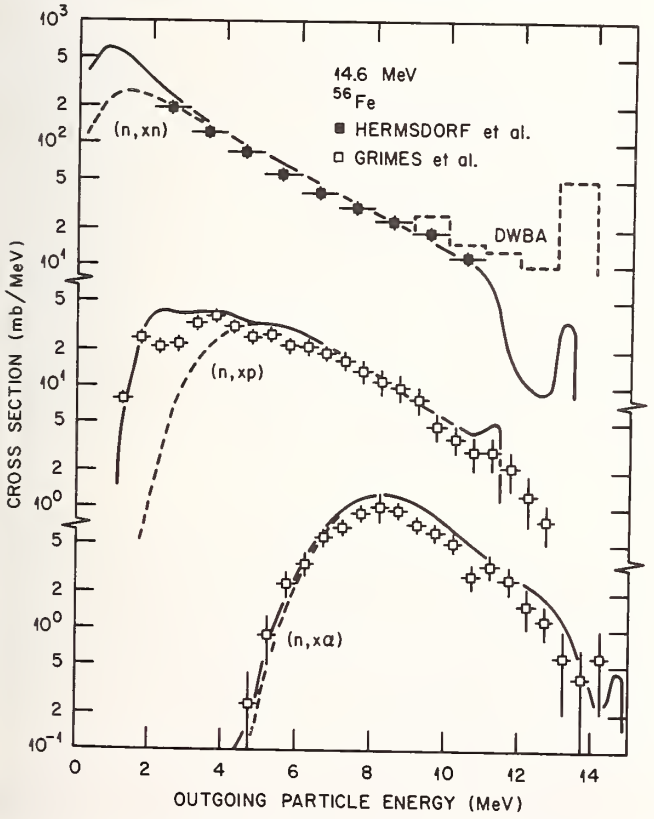

Fig. 1. Calculated and experimental n, p, α production spectra from 14.6-MeV neutrons on ^{56}Fe. The solid curves are calculations. The dashed curves include calculated contributions from the binary step only. The histograms represent DWBA calculations of (n,n') cross sections for 15 discrete levels.

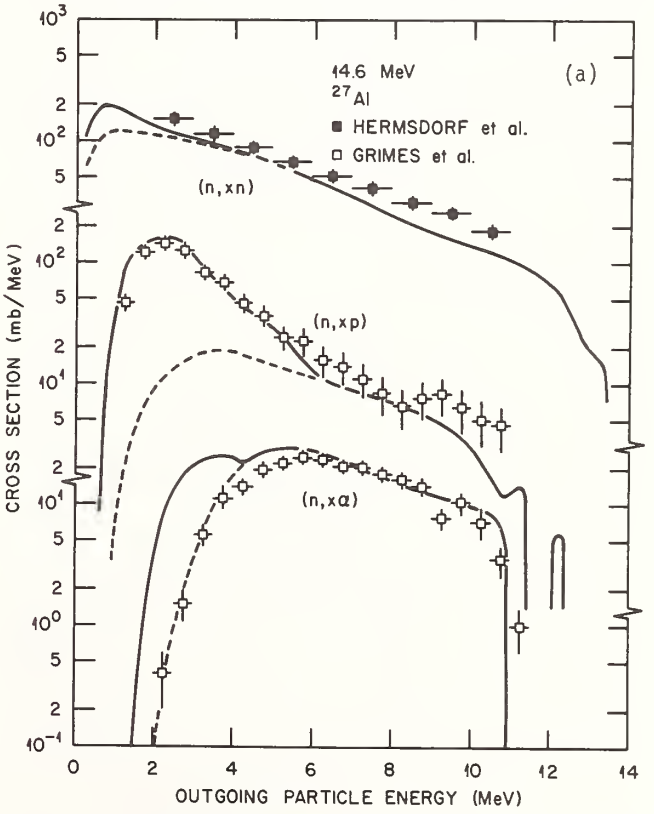

Fig. 2. Calculated and experimental n, p, α production spectra from 14.6-MeV Neutrons on (a) ^{27}Al, (b) ^{54}Fe, (c) ^{63}Cu, and (d) ^{93}Nb. The dashed curved include contributions from the binary step only.

in the residual nucleus in (n,n') reaction, while those in the (n,xp) and (n,xα) spectra correspond to the ground states. The dip in the high-energy tail, when

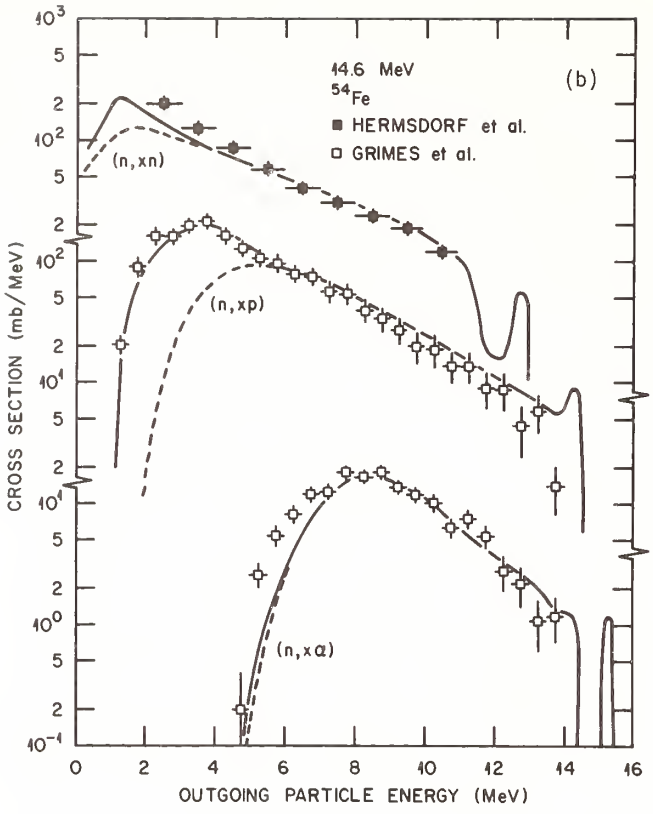

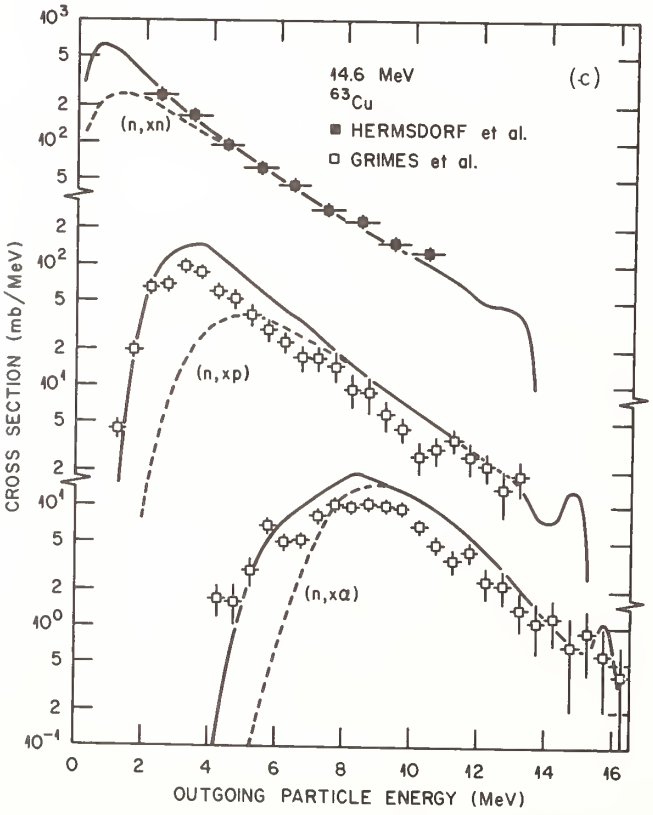

present, is from the odd-even shift, which is the most pronounced in even-even residual nucleus.

Best agreement between calculations and experiments is seen for the (n,xp) spectra. This is probably not surprising since the reactions comprising the (n,xp) spectra are rather pure compound and precompound combinations. The measured (n,xn) spectra contain

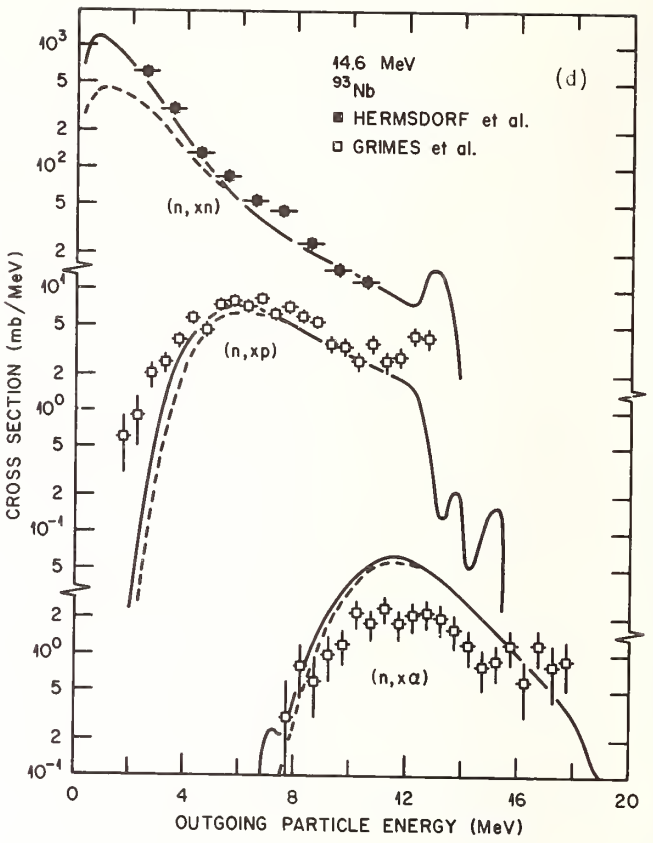

collective excitations. Although DWBA calculations are routinely performed for the low-lying discrete levels for cross-section evaluation works,[16,18,20] it is not straightforward to deal with collective excitations for the continuum states. However, in view of the reasonable agreement between calculated and measured (n,xn) spectra, the collective excitation in continuum states cannot be large in most cases. In several cases, the agreement between calculated and measured (n,xα) spectra is not quite satisfactory. Since the precompound effect is rather small in (n,α)reactions induced by 14.6-MeV neutrons, we speculate that the optical-model parameters used for alpha-particles are not valid for all the isotopes and energies, particularly for low-energy transitions. The conclusion by McFadden and Satchler[21] that a global set of optical-model parameters for alpha-particles could not be found has not yet been challenged.

Conclusion

Our consistent treatment of the compound and precompound reactions leads to a single model that reduces to the usual Hauser-Feshbach model at low energies where the precompound effects are negligible. A single set of parameters, including those for level densities, is used for both modes of reactions. For 14.6-MeV neutron-induced reactions, the second outgoing particle often sees only a few discrete levels in the residual nuclei. Therefore, the multi-step Hauser-Feshbach method is used for describing the tertiary reactions. For the same reason, spin populations in the intermediate nuclei are important, and are calculated with conservation of angular momentum in both modes of reaction.

Acknowledgements

The author wishes to thank D. M. Hetrick of Computer Science Division for making most of the calculations and plots, and Prof. C. Kalbach of Duke Univ. for providing the computer code PRECOA, and Dr.

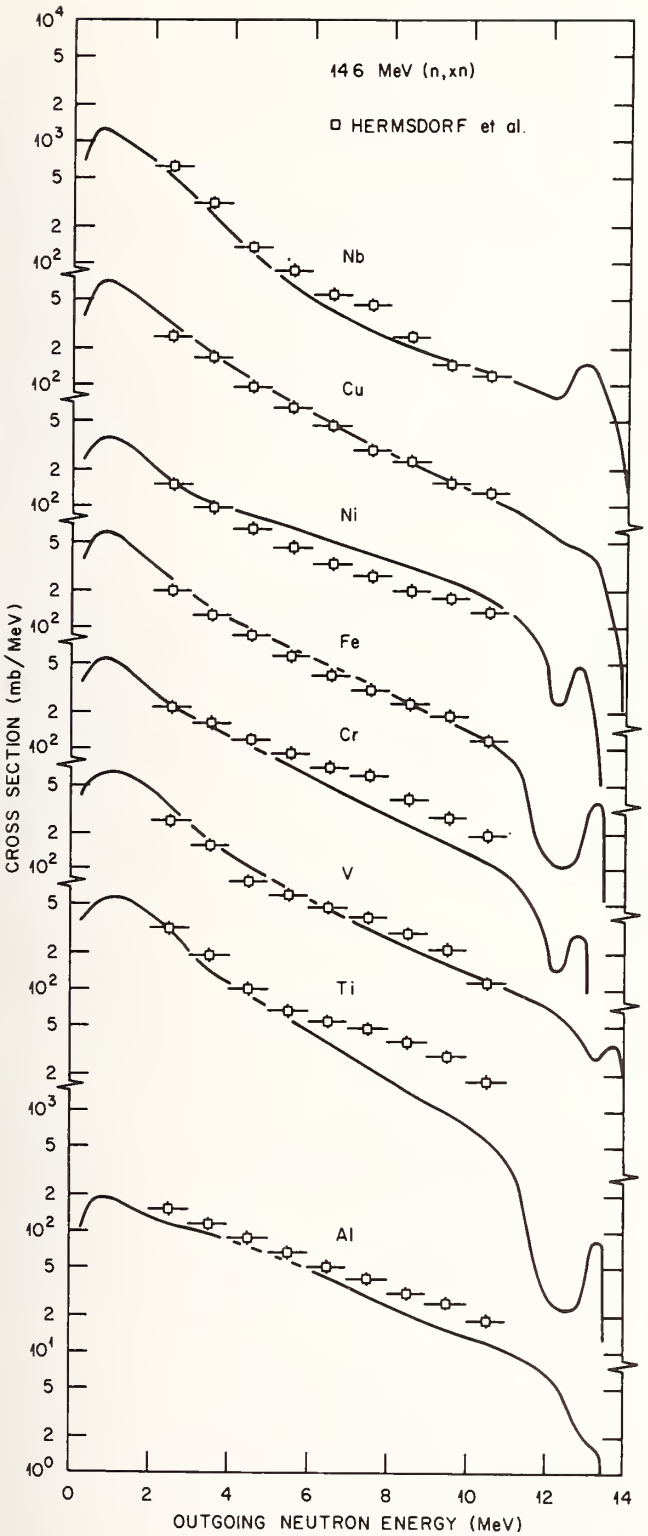

Fig. 3. Calculated and experimental neutron production spectra from 14.6-MeV neutrons on eight natural elements. See Figs. 1 and 2 for some of the results calculated for individual isotopes.

R. C. Haight of Lawrence Livermore Laboratory for sending experimental data prior to publication.

Research sponsored by the U. S. Department of Energy, Office of Basic Energy Sciences, under contract No. W-7405-eng-26 with Union Carbide Corporation.

References

1. M. R. Bhat and S. Pearlstein, Editors, "Symposium on Neutron Cross Sections from 10 to 40 MeV," held at Brookhaven National Laboratory, Upton, New York 11973, May 3-5, 1977, BNL-NCS-50681 (1977).
2. L. Stewart and E. D. Arthur, "Neutron Cross-Section Evaluation at High Energies - Problems and Prospects," p. 435, *ibid.*
3. C. Y. Fu, "Multi-Step Hauser-Feshbach Codes with Precompound Effects: A Brief Review of Current and Required Developments and Applications up to 40 MeV," p. 453, *ibid.*
4. W. Hauser and H. Feshbach, Phys. Rev. 87, 366 (1952).
5. C. Y. Fu, submitted to Phys. Rev.
6. I. Ribansky, P. Oblozinsky, and E. Betak, Nucl. Phys. A205, 545 (1973).
7. C. Kalbach, Z. Physik A283, 401 (1977).
8. F. C. Williams, Jr., Nucl. Phys. A166, 231 (1971).
9. A. Gilbert and A. G. W. Cameron, Can. J. Phys. 43, 1446 (1965).
10. A. Bohr and B. R. Mottelson, Nuclear Structure (W. A. Benjamin, Inc., New York, 1969), p. 169.
11. S. M. Grimes, R. C. Haight, K. R. Alvar, H. H. Barschall, and R. R. Borchers, Phys. Rev. C19, 2127 (1979). R. C. Haight and S. M. Grimes, Lawrence Livermore Laboratory Report UCRL-80235 (1977) and private communication.
12. D. Hermdsdorf, A. Meister, S. Sassonoff, D. Seeliger, K. Seidel, and F. Shahin, Zentralinstitut für Kernforschung, Rossendorf Bei Dresden, ZfK-277 (Ü), (1975).
13. D. Wilmore and P. Hodgson, Nucl. Phys. 55, 673 (1964).
14. F. D. Becchetti and G. W. Greenlees, Phys. Rev. 182, 1190 (1969).
15. J. R. Huizenga and C. J. Igo, Nucl. Phys. 29, 462, (1962).
16. C. Y. Fu, Atomic Data and Nucl. Data Tables 17, 127 (1976).
17. D. M. Hetrick, D. C. Larson, and C. Y. Fu, Oak Ridge National Laboratory Report ORNL/TM-6637, ENDF-280 (1979).
18. C. Y. Fu, in *Nuclear Cross Sections and Technology*, Proceedings of a Conference, Vol. I, p. 325, National Bureau of Standards Special Publication SP-425, Washington, D. C., 1975.
19. H. J. Mang, in *Proceedings of the Second International Conference on Clustering Phenomena in Nuclei*, Vol. II, p. 601, College Park, Maryland, 1975.
20. C. Y. Fu and F. G. Perey, Atomic Data and Nucl. Data Tables 16, 409 (1975).
21. L. McFadden and G. R. Satchler, Nucl. Phys. 84, 177 (1966).

IMPROVED FORMULAS FOR COMPOUND NUCLEUS CROSS SECTIONS

J.W.Tepel
Fachinformationszentrum Energie,Physik,Mathematik
Kernforschungszentrum Karlsruhe
Federal Republic of Germany

H.M.Hofmann
Institut für Theoretische Physik
Universität Erlangen-Nürnberg
Federal Republic of Germany

M.Herman
Institute of Nuclear Research
SWIERK
Warsaw
Poland

In an extension of previous work on the theory of statistical cross sections[1,2] model calculations have been performed in the region of weak absorption, which is of particular interest in applied work involving neutron capture or neutron scattering at low energies. Improved formulas for calculating compound nucleus cross sections and width fluctuation correction factors are presented. Although we agree with Moldauer[3] that the factorization condition for cross sections is not always satisfied in few channel cases where strongly and weakly absorbing channels are mixed, the formulas provide a good description of the computer-generated cross sections. In addition, the structure of the improved formula has been chosen as to describe cases where many weakly absorbing channels contribute.

[Compound-Nucleus Reactions, Cross Sections, Factorization, Statistical Models, Hauser-Feshbach Theory, Width Fluctuation Correction Factor, Elastic Enhancement Factors]

Introduction

Starting from the K-matrix representation of the S-matrix,

$$S = (1+iK)(1-iK)^{-1} \qquad (1)$$

where

$$K_{ab} = \sum_{\mu} \frac{\gamma_{\mu a}\gamma_{\mu b}}{E_\mu - E} \quad , \qquad (2)$$

Hofmann, Richert, Tepel, and Weidenmüller (HRTW)[1,2] derived analytical and numerical results for the calculation of compound nucleus cross sections. In contrast to the often used pole expansion of the S-matrix, where the residues are correlated due to the unitarity condition $SS^{+}=1$, this approach makes use of uncorrelated $\mathcal{N}(0,\sigma_a)$ distributed partial width amplitudes $\gamma_{\mu a}$ (we assume that $\langle \gamma_{\mu a}\gamma_{\mu b}\rangle = 0$, $a\neq b$, i.e. direct reactions are absent) and E_μ drawn from a Wigner spacing distribution. Any real and symmetric K will automatically lead to an unitary S. Separating the S-matrix (1) into an energy averaged part $\langle S\rangle$ and a fluctuating part S^{fl} such that

$$\langle S^{fl}\rangle = 0 \ ,$$

we have

$$S_{ab} = \langle S_{ab}\rangle + S^{fl}_{ab} \quad , \qquad (3)$$

and the elastic and inelastic compound cross sections are given by

$$\sigma^{fl}_{aa} = \langle |S^{fl}_{aa}|^2\rangle \quad \text{and}$$

$$\sigma^{fl}_{ab} = \langle |S^{fl}_{ab}|^2\rangle \ . \qquad (4)$$

Furthermore, we define the elastic enhancement factor W_a by

$$W_a = \langle |S^{fl}_{aa}|^2\rangle / \langle |S^{fl}_{ab}|^2\rangle, \ a=b. \qquad (5)$$

HRTW Approach

In the HRTW approach compound nucleus cross sections are assumed to factorize,

$$\sigma^{fl}_{ab} = \mathcal{T}_a \cdot \mathcal{T}_b, \ a\neq b, \text{ and } \sigma^{fl}_{aa} = \mathcal{T}_a^2 \cdot W_a, \qquad (6)$$

which on introducing "effective transmission coefficients" V_a through

$$\mathcal{T}_a = V_a / \sqrt{\textstyle\sum_c V_c}$$

and applying the unitarity condition $S.S^{+}=1$, or equivalently

$$T_a = 1 - |\langle S_{aa}\rangle|^2 = \sum_b \sigma^{fl}_{ab} \ ,$$

leads to a set of equations

$$T_a = V_a + V_a^2 \, (W_a - 1) \, / \sum_c V_c . \qquad (7)$$

Solution of these equations by iteration is very simple[1] once the enhancement factors W_a are known. For $\sum_c T_c \to \infty$ or $W_c = 1$ one regains the normal Hauser-Feshbach situation where $V_c = T_c$. It is important to note that since the statistical cross sections (6) depend solely on the average S-matrix elements[2], the enhancement factors W_a can be expressed in terms of the set of transmission coefficients T_c. HRTW suggested the following parametrization for W_a:

$$W_a = 1 + 2\left(1+T_a^{\,0.3+1.5\cdot T_a / \sum_c T_c}\right)^{-1} + 2\left((T_a - T_{avg}) / \sum_c T_c\right)^2 \qquad (8)$$

Since this formula has certain undesirable properties as was pointed out by various authors (i.e. the use of $T_{avg} = \sum_c T_c / n$, where n is the number of channels), and some doubt was thrown on the factorizability of CN cross sections by Moldauer[3], we have decided to look into these questions in more detail.

Fit Formulas

Factorization of Compound Cross Sections

Consider the ratio

$$R = \sigma_{ab}^{fl} \cdot \sigma_{cd}^{fl} \; / \; \sigma_{ac}^{fl} \cdot \sigma_{bd}^{fl} \qquad (9)$$

with (a,b,c,d) pairwise different. Factorization as was assumed by HRTW leads to R=1. Moldauer has calculated R for a number of n-channel cases[3] with n=4,8,...,30 using an equal number of weak channels ($T \approx 0.1$) coupled to strong channels ($T \approx 0.9$). We have repeated and extended these calculations for the worst (n=4) of these already rather extreme cases. The results are shown in Fig.1 as a function of the transmission coefficients $T_3 = T_4$, while channels 1 and 2 with $T_1 = T_2 = 0.1$ were kept fixed. It is evident that the deviation of R from 1 is statistically significant for large T- (or cross section) ratios implying non-factorization of cross sections. The curve seems to follow the predictions of Moldauer's integration[4] method with $\nu = 1$. Comparison of the computer generated cross sections with the HRTW model shows that the cross section involving the weakly absorbing channels (usually 1 and 2) is larger than $V_1 \cdot V_2 / \Sigma V_c$, while all other σ_{ab}^{fl}, $a \neq b$ agree well with the formula.

Similarly, elastic enhancement factors W_a^{fact} determined from the data assuming factorization via relations of the type

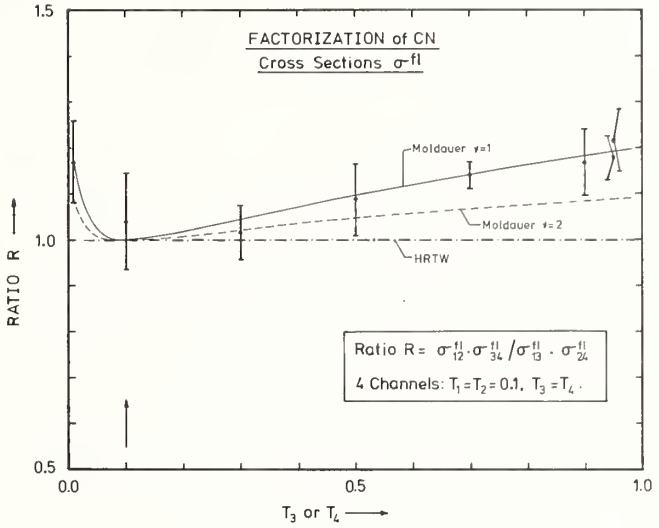

Fig.1 Factorization of CN Cross Sections

$W_a = \sigma_{aa}^{fl} \cdot \sigma_{cd}^{fl} / \sigma_{ac}^{fl} \cdot \sigma_{ad}^{fl}$ agree well with "true" enhancement factors determined via

$$W_a^{true} = \sigma_{aa}^{fl} / \sigma_{ab}^{fl} \;, \; a=b$$

(see Table I).

Table I. Enhancement factors for the 4-channel cases shown in Fig. 1 .

T	W_a^{true}	W_a^{fact}
0.95	2.08 3	2.11 6
0.90	2.23 6	2.24 6
0.70	2.11 5	2.18 7
0.50	2.48 6	2.49 7
0.30	2.54 8	2.47 13
0.10	2.98 13	2.86 14
0.01	2.98 27	3.12 30

It is therefore not surprizing to find good agreement between HRTW calculations and computer-generated cross sections also for the non-factorizing cases of Fig.1 (Table II).

Table II. Model comparisons (mean absolute deviations) for the 4-channel cases of Fig.1

T	Avg. Error	R[a]	HF[b]	Mold I[c]	Mold II[d]	HRTW[e]
0.95	1.7%	1.18	23.5%	10.8%	3.6%	4.0%
0.90	3.4%	1.16	25.3	9.5	5.0	4.9
0.70	2.3	1.14	24.6	10.4	4.6	2.8
0.50	3.3	1.11	31.5	5.8	9.0	4.7
0.30	6.2	1.02	32.4	6.6	9.9	2.4
0.10	5.9	1.04	48.8	2.5	18.0	11.4
0.01	8.2	1.22	37.8	2.8	15.7	6.2

[a] eq.(9) [b] Hauser-Feshbach [c] $\nu = 1$ [d] $\nu = 2$ [e] eq. (10)

Comparing the columns labelled Mold I (W_a=3), Mold II (W_a=2) and HRTW in Table II it seems that the mean fit error depends more on the precice choice of W_a than on the question of factorizability.

Elastic Enhancement Factor

The HRTW expression for the elastic enhancement factor W_a as given by eq. (8) contains a correction term which becomes operative mainly in cases where a single strong channel is mixed with several weak ones, as is the case at isobaric analogue resonances. The use of T_{avg} produces a sizeable correction to the average W for the strong channel. Although this is a desirable feature at IAR, low energy neutron reactions involve a small number of weak channels, often mixed with a large number of very weak gamma channels. Here the formula leads to $W_a > 3$ and values of 5 may even be reached. We have used the proposal of Yoshida[5] and replaced T_{avg} by

$$\overline{T} = \sum_c T_c^2 \; / \sum_b T_b \; .$$

A new fit formula

$$W_a = 1+2\left[1+T_a{}^{a_1+a_2 \cdot T_a/\sum_c T_c}\right]^{-1} + a_3 \cdot \left[(T_a-\overline{T})/\sum_c T_c\right]^2 \cdot (T_a/\sum_c T_c), \quad (10)$$

with preliminary values of the coefficients a_1=0.36, a_2=1.15, and a_3=20 leads to

$$\chi^2_{new} \approx \chi^2_{HRTW} \; .$$

This formula has the advantage that the introduction of very weak channels do not change any results. As is shown in Fig.2, W changes rather more rapidly towards 3 at the weak absorption limit. Still missing from the formula is the requirement of Agassi, Weidenmüller, and Mantzouranis[6] that $W_a \to 2$ when $\sum_c T_c \to \infty$ for all $T > 0$ (strong absorption, although individual T's may be $\ll 1$).

Conclusions

1) Although factorization of compound cross sections does not hold in all cases, in practice it is a good assumption.
2) We have presented a formula for the elastic enhancement factor W_a which can also deal with a large number of weak channels.
3) It is necessary to improve the structure of eq. (10) so that the limit of Agassi et al.[6] is satisfied. In addition, the limit of very weak absorption, $T \approx 0.001$-0.1 has not been sufficiently investigated, since Monte-Carlo calculations are unable to produce data of good statistical accuracy in reasonable computing time.

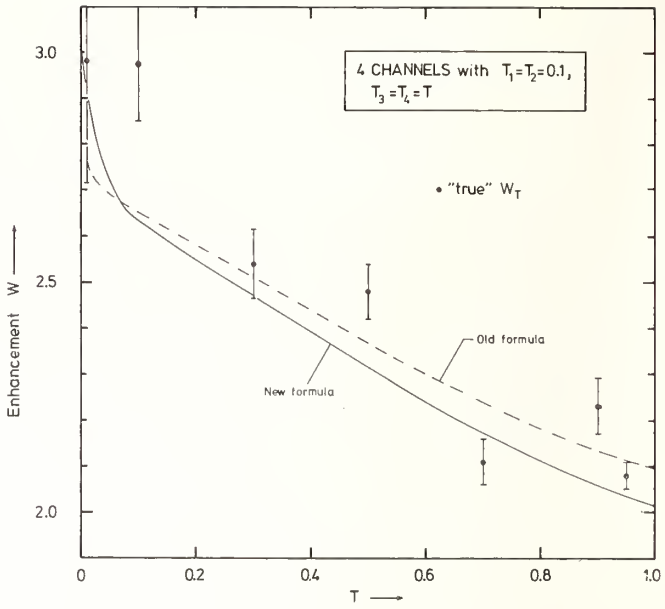

Fig.2 Elastic enhancement factor W_a as a function of T for the 4 channel cases introduced in Fig.1 and Tables I and II.

References

1. J.W.Tepel, H.M. Hofmann, and H.A. Weidenmüller, Phys. Lett. 49B,1 (1974).
2. H.M.Hofmann, J.Richert, J.W.Tepel, and H.A.Weidenmüller, Ann.Phys.(NY) 90, 391 and 403.
3. P.A.Moldauer, Phys. Rev. C11, 426(1975)
4. P.A.Moldauer, Phys. Rev. 135,B642 (1964), P.A.Moldauer, Phys. Rev. 123,968 (1961).
5. S.Yoshida and K.Yazaki, Nucl.Phys. A255, 173 (1975).
6. D.Agassi, H.A.Weidenmüller, and G. Mantzouranis, Physics Reports 22C,145 (1975).

NEUTRON EMISSION SPECTRA INDUCED BY 14-MeV NEUTRONS FROM THE EVALUATED NUCLEAR DATA FILE (ENDF/B-V) - A CRITICAL REVIEW

D. M. Hetrick, D. C. Larson, and C. Y. Fu
Oak Ridge National Laboratory
Oak Ridge, Tennessee 37830, USA

Neutron emission spectra induced by 14.6-MeV incident neutrons, retrieved from ENDF/B-V, are graphically compared with experimental data by Hermsdorf *et al.*[1] and Clayeux and Voignier.[2] The elements selected for the comparisons include Na, Mg, Al, Si, Ca, Ti, V, Cr, Fe, Ni, Cu, Nb, W, and Pb. In addition to comparing the evaluated total neutron emission spectra with experimental data, individually evaluated spectra from contributing reactions are presented. Only a few of the evaluated spectra were found to agree well with the measured spectra; namely, those evaluations which utilized advanced nuclear model codes with precompound effects and competing binary and tertiary reactions. Recommendations for removing several defects in most evaluations are made.

[ENDF/B-V, neutron emission spectra, 14.6 MeV, nuclear model codes.]

Introduction

Graphical comparisons of ENDF/B-V neutron emission spectra with experimental data induced by 14-MeV incident neutrons are presented. The elements chosen for the comparisons are those considered important for fusion reactor applications and include Na, Mg, Al, Si, Ca, Ti, V, Cr, Fe, Ni, Cu, Nb, W, and Pb. On each graph, individually evaluated emission spectra from contributing reactions and total emission spectra from the ENDF/B-V files are shown. Thus, disagreement with the experimental data, if any, may be attributed to specific evaluated spectra. Experimental data are available only for the total emission spectra.

Deficiencies in the ENDF/B-V neutron emission spectra for several materials are uncovered and discussed.

Experimental Data

Experimental data given by Hermsdorf *et al.*[1] and Clayeux and Voignier[2] were utilized for this work. There are numerous other data sets available, but since they are generally in agreement with data of Hermsdorf *et al.*, they have been left off the plots for the purpose of clarity. However, the data of Clayeux and Voignier have been included since they have been used frequently for evaluation work, and since they sometimes differ significantly from the data of Hermsdorf *et al.* and others, we felt it useful to include them for comparison. In addition, the energy-integrated cross sections obtained from the data of Clayeux and Voignier are much larger than the calculated results, due to the large intensity of low energy neutrons indicated in their work.

In their report, Hermsdorf *et al.* presented the laboratory angular distributions of secondary neutrons integrated over 1.0-MeV energy intervals. We have fitted a series of Legendre coefficients by least squares to the angular data for elements Na, Mg, Al, Si, Ca, Ti, V, Cr, Fe, Ni, Cu, Nb, W, and Pb for each energy interval given. For each energy interval, the integrated cross section was computed for different polynomial orders to obtain the total differential cross section. The integral obtained from the order that gave the best visual fit to their data (generally $\ell = 3$) was compared with the evaluated data. Graphical results are presented in Fig. 1-3. The error bars shown in these figures correspond to the errors given in the report by Hermsdorf *et al.* plus their estimated 10% systematic error.

The data of Clayeux and Voignier were taken directly from tables in their report. Whereas Hermsdorf *et al.* obtained cross sections from the bombardment of the materials by 14.6-MeV neutrons, Clayeux and Voignier's data were given for 14.0-MeV neutrons. The data of Clayeux and Voignier for the elements Mg, Al, Si, Ca, Fe, Ni, Cu, and Pb were used in this paper.

ENDF/B-V Files

In Figs. 1-3 the differential cross sections versus outgoing neutron energy are plotted for all reaction types that produce secondary neutrons. In all figures, the incident neutron energy was 14.6 MeV. The differential cross section for each reaction type was obtained from

$$\frac{d\sigma(E\rightarrow E')}{dE'} = m\,\sigma(E)\,p(E\rightarrow E') \qquad (1)$$

as given in Ref. 3. Here $\sigma(E)$ is the cross section for incident energy E as given in File 3 of the ENDF/B-V library, m is the neutron multiplicity, and $p(E\rightarrow E')$ represents the energy distribution for the secondary particle. The energy distribution is broken down into partial energy distributions,[3]

$$p(E\rightarrow E') = \sum_{k=1}^{NK} p_k(E)\, f_k(E\rightarrow E') \quad , \qquad (2)$$

where $f_k(E\rightarrow E')$ represents the distributions of the secondary neutron energies E' calculated from data given in File 5 of the library. At a particular incident neutron energy E,

$$\sum_{k=1}^{NK} p_k(E) = 1 \quad , \qquad (3)$$

where $p_k(E)$ is the fractional probability that the distribution $f_k(E\rightarrow E')$ applies at E. NK is the number of partial distributions, and, with the exception of reaction types for the elements Ni, W-182, W-183, W-184, and W-186, is equal to 1.

The energy distributions $f_k(E\rightarrow E')$ are described by different analytic formulations. Each formulation, or energy distribution law, has an identification number (LF number) associated with it.[3] Note in Figures 1-3 that the curves are shown for evaluated emission spectra from all of the contributing reactions. Data from the (n,n') discrete curves were taken from the inelastic level excitation cross sections in File 3 of the ENDF/B-V files. For each excited state of an element, the cross section was calculated for the incident energy by interpolation and the outgoing neutron energy was calculated by subtracting the reaction Q-value from the incident energy. These results were combined into 1.0-MeV bins. Figures 1-3 display the total differential cross section obtained by summing the curves via

linear-linear interpolation from all neutron-producing reactions present in the evaluation. This total neutron emission cross section is compared with the data of Hermsdorf *et al.*[1] and Clayeux and Voignier.[2]

Discussions and Conclusion

Sodium (Fig. 1)

The evaluation is in reasonable agreement with the data of Hermsdorf. However, outgoing neutrons with energies greater than 6.5 MeV are under-estimated by about 30%, indicating the lack of a precompound component. Only the cross section of the discrete level at 0.44 MeV was given in ENDF/B-V at E_n = 14.6 MeV.

Magnesium (Fig. 1)

The data of Clayeux and those of Hermsdorf are in disagreement, with the evaluation lying approximately between them. The evaluation somewhat underestimates (see Ref. 4) a 14-MeV pulsed sphere measurement performed at Livermore, indicating that the Hermsdorf data are probably correct. The evaluation also underestimated this data set at most neutron energies by 30% to 40%, and would benefit by the inclusion of a precompound component.

Aluminum (Fig. 1)

For this material, the two data sets shown are in good agreement. However, there are too few neutrons below 2 MeV in the evaluation. This may be caused by omission of neutrons from the (n,pn) and (n,αn) reactions. The evaluation also overestimates the number of neutrons with energies greater than 6 MeV.

Silicon (Fig. 1)

The evaluated spectrum for silicon appears too low in intensity from 6 to 8 MeV, but otherwise is in good agreement with both data sets.

Calcium (Fig. 1)

The two data sets shown are in sharp disagreement for Ca. From the fact that a precompound component has not been included in the evaluation (see Ref. 5), it may be concluded that the evaluated spectrum is too low from 4 to 10 MeV and the Clayeux data for Ca are in serious error.

Iron (Fig.2)

The evaluated spectrum is in good agreement with the experimental data. The evaluation of various partial neutron production spectra was based on an advanced nuclear model analysis[6] of several measured total neutron production spectra.

Copper (Fig. 2)

The evaluated spectrum needs more high energy neutron intensity between 8 and 13 MeV.

Lead (Fig. 3)

There is good agreement between the evaluation and the data. The evaluation had adequate data support, and was coupled with a nuclear model analysis.[7] The bump in the (n,n') spectrum near 1 MeV reflects the use of a giant dipole for the gamma-ray channels in the calculation.

Titanium, Vanadium, Chromium, Nickel, Niobium, Tungsten

These materials appear to have similar deficiencies in their neutron spectra. First,neutron intensity in the (n,n') spectrum above the (n,2n) threshold is too high. This indicates that competition between the neutron channels in the (n,2n) reaction and the gamma-ray channels in the (n,n'γ) reaction does not seem to have been properly considered. Second, there are too few (or too many in the case of Nb) high energy neutrons, indicating that precompound and/or direct interaction effects have not been treated correctly in model calculations or were based on inadequate estimates. It appears that both deficiencies can be removed by using one of the recently developed nuclear model codes, GNASH[8] or TNG[9,10] An early version of TNG* was used for the analysis of neutron spectra for Fe and Pb, showing reasonable success as evidenced in this report.

From the discussions above we conclude that the ENDF/B-V evaluations for the neutron spectra resulting from 14.6-MeV neutron interactions are reasonably good for Fe and Pb and fair for Na, Al, and Si. Further evaluation is required for Mg, Ca, Ti, V, Cr, Ni, Cu, Nb, W-182, W-183, W-184, and W-186. From the nature of the deficiencies shown we recommend that advanced nuclear model codes[8-10] employing precompound emission be used in future evaluations to assure consistency among various partial cross sections and spectra and for extrapolating to energy ranges in which measurements have not been made.

*A multistep Hauser-Feshbach code with precompound effects.

Acknowledgment

Research sponsored by the U.S. Department of Energy, Office of Basic Energy Sciences, under contract No. W-7405-eng-26 with Union Carbide Corporation.

References

1. D. Hermsdorf, A. Meister, S. Sassonoff, D. Seeliger, K. Seidel, and F. Shahin, Zentralinstitut für Kernforschung Rossendorf Bei Dresden, ZfK-277 (U), (1975).

2. G. Clayeux and J. Voignier, Centre d'Etudes de Limeil CEA-R-4279 (1972).

3. D. Garber, C. Dunford, and S. Pearlstein, "Data Formats and Procedures for the Evaluated Nuclear Data File, ENDF," ENDF-102, BNL-NCS-50496 (1975).

4. M.K. Drake and M.P. Fricke, Defense Nuclear Agency Report DNA 3479F (1975).

5. C.Y. Fu, Atomic Data and Nuclear Data Tables 17, 127 (1976).

6. C.Y. Fu, "Development of a Two-Step Hauser-Feshbach Code with Precompound Decays and Gamma-Ray Cascades: A Theoretical Tool for Cross Section Evaluations," Conf. Proc. Nuclear Cross Sections and Technology, Washington, D. C. 1975, NBS-SP-425, p. 328 (1975).

7. C. Y. Fu, private communication (1978).

8. E. D. Arthur and P. G. Young, "Cross Sections in the Energy Range from 10 to 40 MeV calculated with the GNASH Code," Symp. on Neutron Cross Sections from 10 to 40 MeV, Brookhaven National Laboratory, Upton, New York, 1977, Eds. M. K. Bhat and S. Pearlstein, BNL-NCS-50681, p. 467 (1977).

9. C. Y. Fu, "Multi-Step Hauser-Feshbach Codes with Precompound Effects: A Brief Review of Current and Required Developments and Applications up to 40 MeV," *ibid*, p. 453 (1977).

10. C. Y. Fu, A Consistent Nuclear Model for Compound and Precompound Reactions with Conservation of Angular Momentum," to be published in the proceedings of this conference.

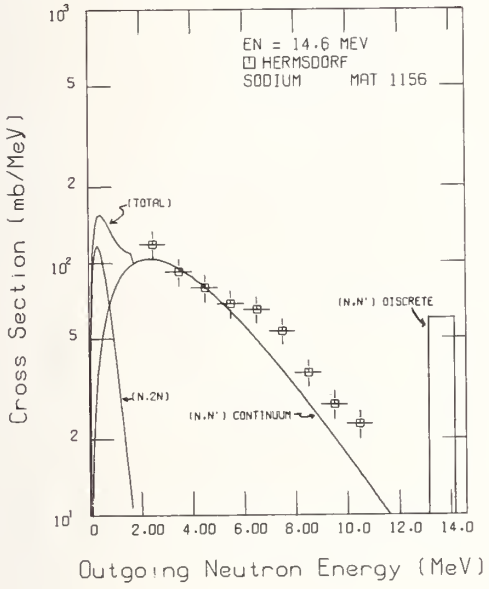

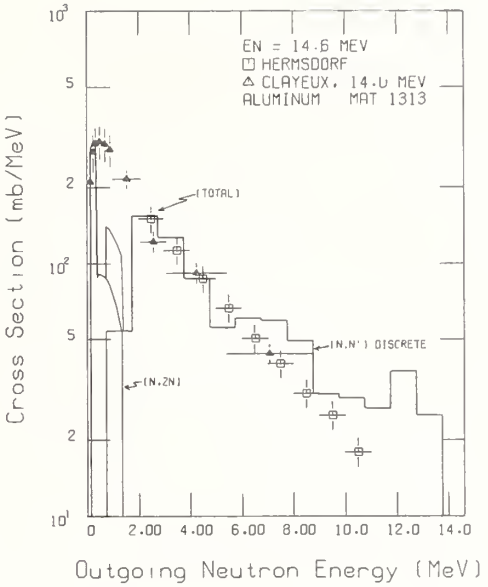

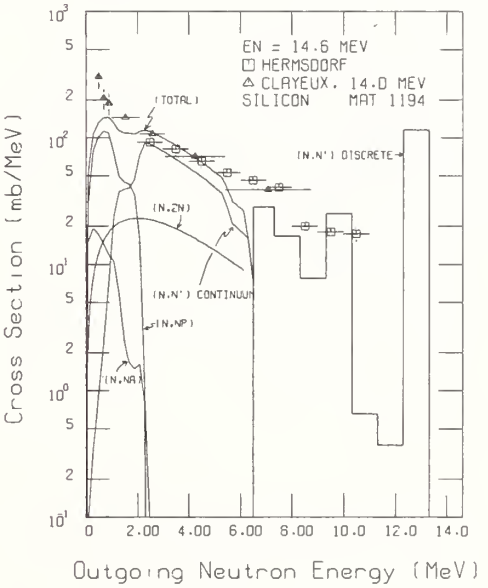

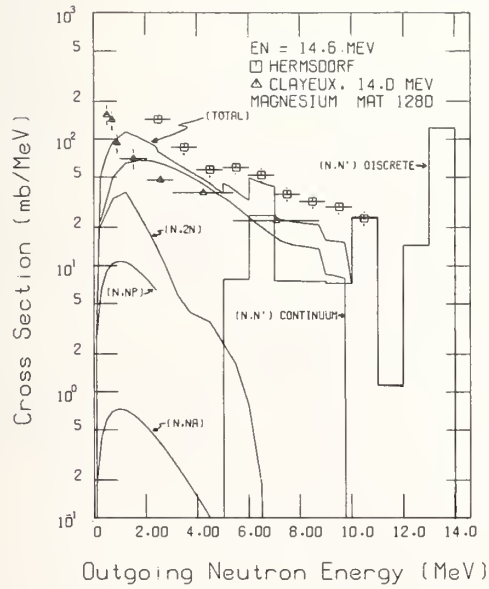

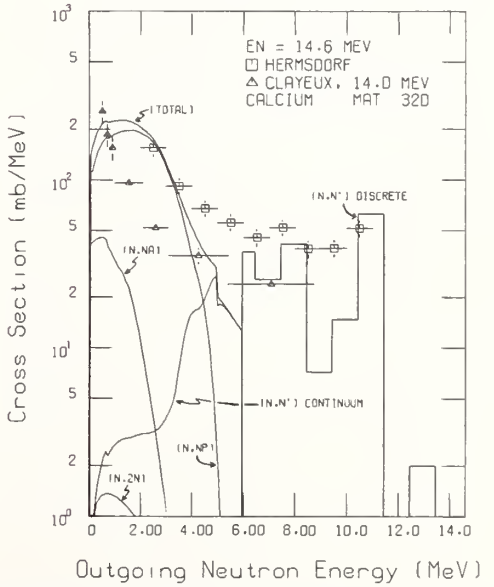

Fig. 1. Partial and Total Neutron Emission Spectra from the ENDF/B-V Files Compared with the Experimental Data of Hermsdorf *et al.* and Clayeux and Voignier for the Elements Sodium, Magnesium, Aluminum, Silicon, and Calcium.

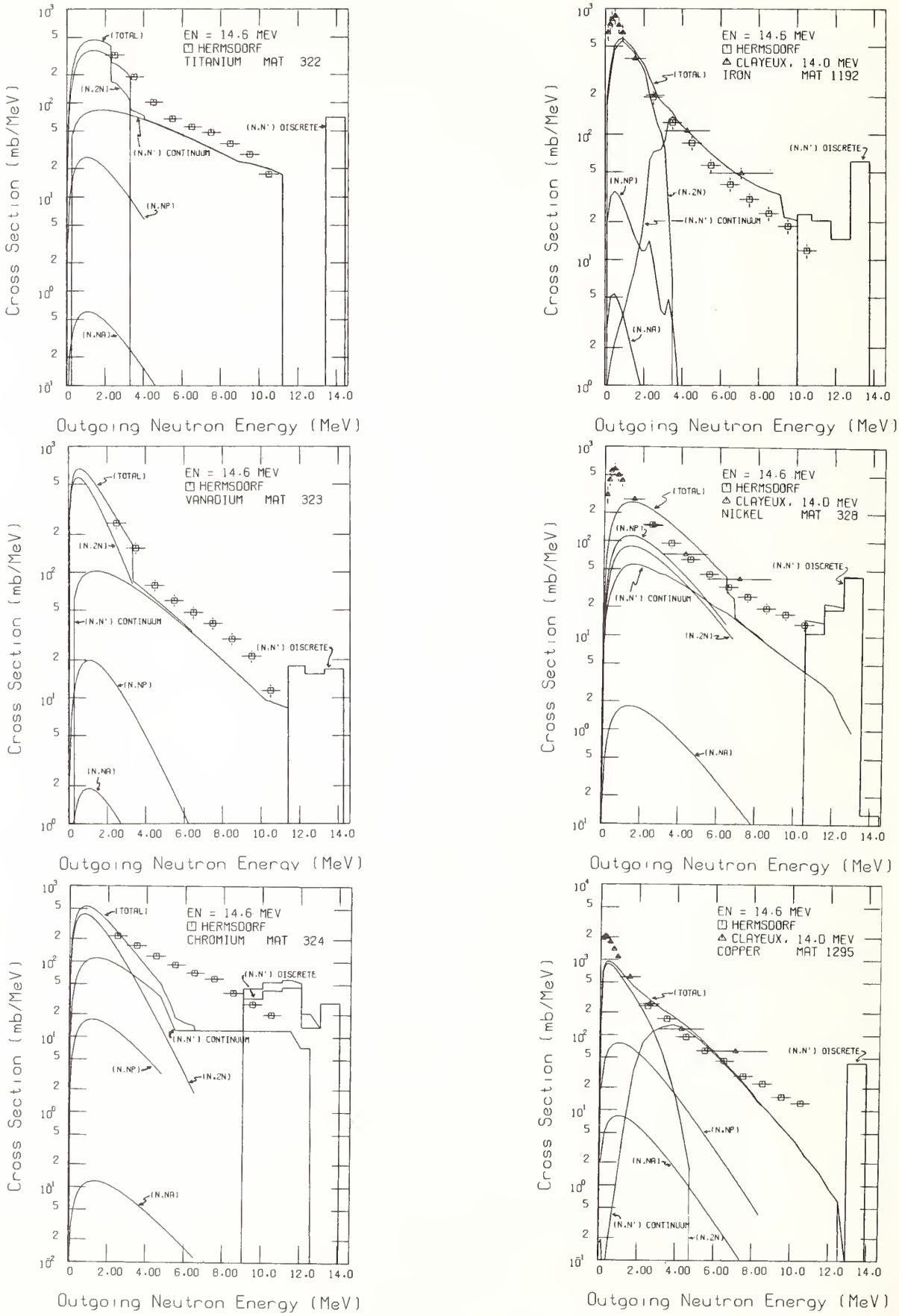

Fig. 2. Partial and Total Neutron Emission Spectra from the ENDF/B-V Files Compared with the Experimental Data of Hermsdorf *et al.* and Clayeux and Voignier for the Elements Titanium, Vanadium, Chromium, Iron, Nickel, and Copper.

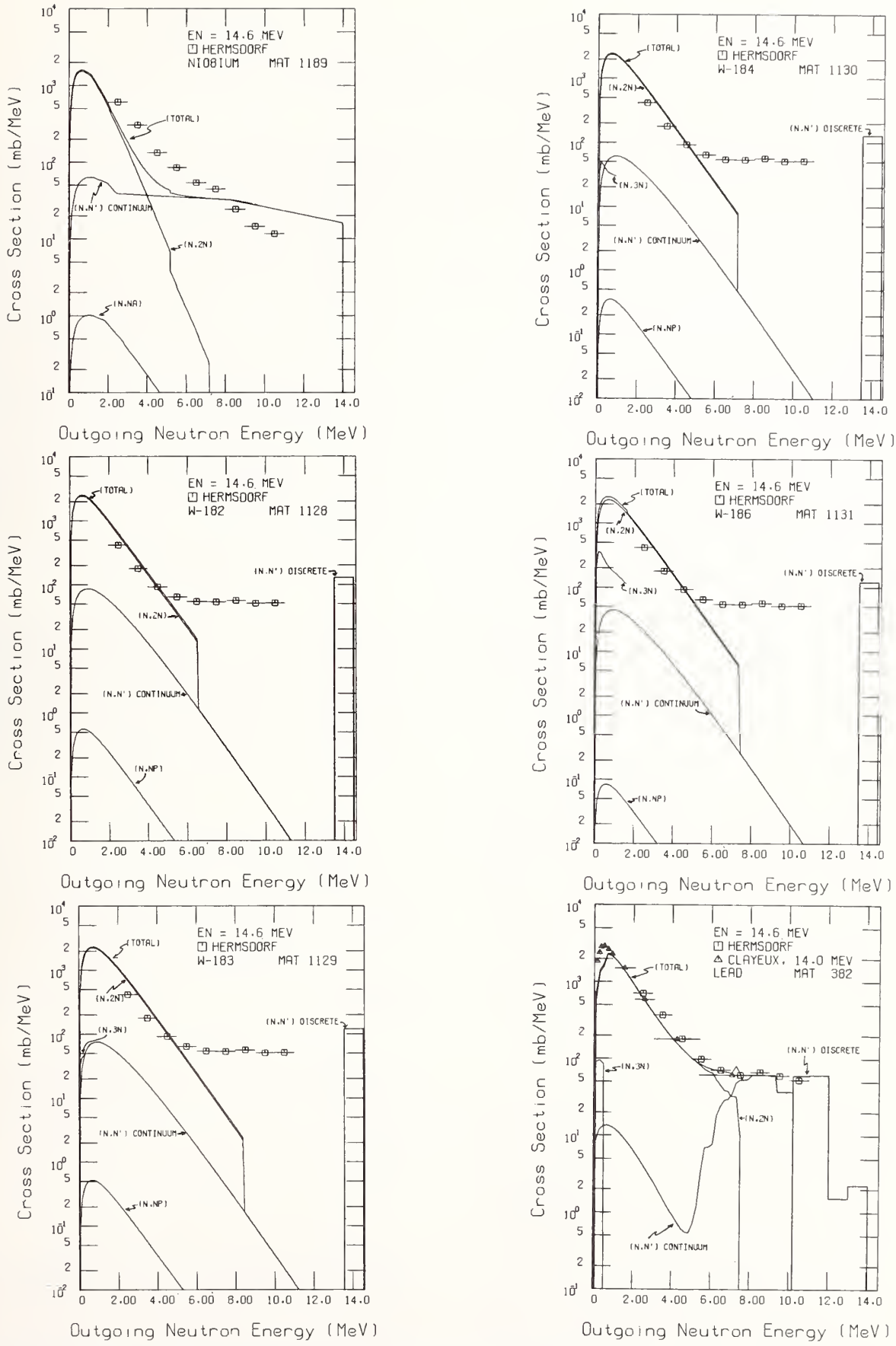

Fig. 3. Partial and Total Neutron Emission Spectra from the ENDF/B-V Files Compared with the Experimental Data of Hermsdorf *et al.* and Clayeux and Voignier for the Elements Niobium, Tungsten, and Lead.

A NEW PARAMETERIZATION OF THE E1 GAMMA-RAY STRENGTH FUNCTION*

D. G. Gardner and F. S. Dietrich
Lawrence Livermore Laboratory
Livermore, CA 94550, USA

We have satisfactorily correlated the giant dipole (GD) parameters of peak energy, width, and cross section for elements from V to Bi, assuming two overlapping peaks with a separation dependent on deformation. The energy dependence of the GD resonance is assumed to have a Breit-Wigner form, but with an energy-dependent width. The resulting gamma-ray strength function model is used to predict neutron capture cross sections and gamma-ray spectra for isotopes of Ta, Os, and Au.

[GD parameter systematics, E1 γ-ray strength functions, calculated σ(n,γ) and γ-ray spectra for ^{181}Ta and ^{197}Au, calculated σ(n,γ) for ^{186,187,188}Os.]

Introduction

In this paper we present a preliminary attempt to parameterize two aspects of the E1 giant dipole resonance (GDR): its energy dependence and its width. The motivation for this work is the desire to be able to calculate both the cross section for low-energy neutron or proton capture reactions and the resulting capture gamma-ray spectrum. To do this requires knowledge of of the E1 (and to a much lesser extent the M1) gamma-ray strength function. The E1 strength function, for medium weight to heavy nuclei, at least, is usually related to the low-energy tail of the GDR, obtained by extrapolation from the peak under the assumption of a Lorentz functional form.

It has been observed for many years that there are at least two practical problems associated with this type of extrapolation. Firstly, strength functions inferred from various types of experimental measurements often lie below the low-energy Lorentz extrapolation, and secondly, for several nuclei the shape of the Lorentz tail is clearly wrong.[1-3] For these nuclei there is a distinct and sometimes severe loss of strength below 5 or 6 MeV, together with an occasional resonance-like bump somewhat above 6 MeV. A third problem sometimes arises for nuclei away from closed shells, and where photonuclear measurements are used to derive the GDR peak parameters. Depending on whether a single-hump or a double-hump Lorentz function is used to fit the data, as much as a factor of 2 difference in magnitude of the extrapolated tail may be observed. A recent example of this involves isotopes of Os,[4] which will be discussed in a later section of this paper. Since the strength function cannot depend on the preference of the person fitting the photonuclear data, with respect to a single or double peak, there appears to be some basic error involved in the assumption of a single-peak resonance.

Functional Form of the GDR

While it has been traditional to fit photoabsorption cross sections with the sum of one or two Lorentz curves, other forms have been used in the past, including the Breit-Wigner form.[5-10] Dover, et al., discuss the assumptions under which either the Breit-Wigner or the Lorentz form may be derived.[11] The Breit-Wigner form with a constant width produces a low-energy tail that is even larger in magnitude than a Lorentz extrapolation using the same peak parameters. In addition, the Breit-Wigner tail is flatter than the Lorentz, and hence has an even poorer energy dependence. In the past there have also been attempts to utilize an energy-dependent width,[6,8,11] but, to our knowledge, not fully in conjunction with the Breit-Wigner shape. In the following discussion we assume that the sum of one or two energy-dependent Breit-Wigner (EDBW) functions will best represent photoabsorption cross section, and hence the E1 gamma-ray strength function. We next attempt to estimate a reasonable energy dependence for the width. In the following discussion we argue that two EDBW functions should always be employed.

The photoabsorption cross section $\sigma_{\gamma a}(E_\gamma)$, expressed in terms of a Breit-Wigner function with a constant width Γ_R is

$$\sigma_{\gamma a}(E_\gamma) = \frac{\sigma_0(\Gamma_R/2)^2}{(\Gamma_R/2)^2 + (E_\gamma - E_R)^2} \qquad (1)$$

Here E_R is the energy at the center of the peak, and σ_0 is the peak cross section. We wish to replace Γ_R by $\Gamma(E_\gamma)$, and make the assumption that $\Gamma(E_\gamma)$ is primarily a damping width of one-particle - one-hole states into states of increasing exciton number. As a guide we can look at the rate expressions from precompound model treatments. For example, Williams[12] gives for the rate for increasing the exciton number n by one unit:

$$\lambda_+(n) = \frac{2\pi}{\hbar}|M|^2 \frac{g(gE - C_{p+1,h+1})^2}{p + h + 1} \qquad (2)$$

Here n = p + h, g is the single particle level density at the Fermi level, |M| is the effective matrix element for residual interactions, and $C_{p,h}$ is a correction due to the Pauli principle. The energy of the system is E, which we will take to be E_γ.

Systematics[13] for $|M|^2$ from medium-energy precompound reaction studies have shown that, to a fair approximation

$$|M|^2 \alpha (g^3E)^{-1}$$

This has an unrealistic energy dependence at low energies (a region of no concern to the precompound studies), but it leads to a linear dependence of $\Gamma(E_\gamma)$ on Eγ. Instead, we choose to use the form

$$|M|^2 = \frac{k_1}{k_2 + g^3E} \qquad (3)$$

where k_1 and k_2 are adjustable parameters to be obtained from fitting data. Because we are accustomed to viewing strength functions in relation to the Lorentz extrapolation, we express k_1 in terms of E_X, the energy at which point the EDBW function will intersect the Lorentz function at or below the peak energy E_R. If we then express k_2 as C in units of g^3, we arrive at an expression for the damping width as a function of excitation (or gamma-ray) energy:

*Work performed under the auspices of the U.S. Department of Energy by the Lawrence Livermore Laboratory under contract number W-7405-ENG-48.

$$\Gamma(E_\gamma) = \Gamma_R\left(\frac{C + E_x}{C + E_\gamma}\right)\left(\frac{E_\gamma^2}{E_x}\right)\left(\frac{2}{E_x + E_R}\right) \qquad (4)$$

We see from Eq. 4 that $\Gamma(E_\gamma)$ approaches a linear dependence on E_γ, when E_γ becomes large compared to C. Our preliminary studies so far indicate a reasonable range for the parameter C is 1 to 5 MeV, and E_x is usually 5 of 6 MeV. Furthermore, if $\Gamma(E_\gamma)$ is related to the imaginary part of the optical model potential, one would expect $\Gamma(E_\gamma)$ to increase linearly for awhile, and then at some energy to remain constant or even begin to decrease. In this work we allow $\Gamma(E_\gamma)$ to increase to Γ_R and then to remain constant. Thus $\Gamma(E_\gamma) \leqslant \Gamma_R$ for all values of E_γ.

A Double-Peak Model of the GDR

To avoid the problem referred to earlier, of photonuclear data that may be described almost equally well in terms of either a single or a double GDR peak, we have studied the usefulness of a model for the GDR that consists always of two overlapping peaks, even in the regions of low β_2 values around closed shells. To do this we have taken all of the resonance parameters listed in Berman's compilation,[14] for 80 nuclei from V to Bi. These encompass some 99 sets of parameters; no attempt was made to eliminate questionable or poor data sets.

In our model we have made a number of sometimes extreme, simplifying assumptions:

1) All nuclei are prolate spheroids to some degree, and we take it that $\Gamma_{R1}\,\sigma_{01} = \Gamma_{R2}\,\sigma_{02}/2$.

2) From an examination of the photonuclear data for well-deformed nuclei, we assume $\sigma_{01} = \sigma_{02}$, i.e., both peak cross sections are equal. Hence $\Gamma_{R1} = \Gamma_{R2}/2$.

3) The integrated photonuclear absorption cross section is always 1.25 times the sum rule value.

4) The two widths, Γ_{R1} and Γ_{R2}, are independent of the deformation parameter β_2, but do vary with mass, roughly as $A^{-1/3}$.

5) The average energy of the two peaks is that of a prolate spheroid, i.e.,

$$E_R = (E_{R1} + 2\,E_{R2})/3 \qquad (5)$$

The mass dependence of E_R may be taken as

$$E_R = 31.2\,A^{-1/3} + 20.6\,A^{-1/6} \qquad (6)$$

The ratio of the two peak energies is related to the ratio of the major to minor axes of the prolate spheroid, and thus to β_2. We find

$$\frac{E_{R2}}{E_{R1}} = F(\beta_2) = 0.95\left[\frac{2.126 + 0.822\beta_2}{2.126 - \beta_2}\right] \qquad (7)$$

When the term in brackets in Eq. 7 was derived and compared with the values in Ref. 14, it appeared that a reduction by 5% was in order. This gave rise to the factor of 0.95.

6) The apparent width of two overlapping peaks of equal height, and with widths differing by a factor of two, can satisfactorily be represented by a function involving the square of the difference of the peak energies, plus the average of the two widths. Thus

$$\Gamma_R = a\,(E_{R2} - E_{R1})^2 + 3/4\;\;\Gamma_{R2}, \qquad (8)$$

where a is a constant.

The above assumptions yield the following expression for Γ_R,

$$\Gamma_R = a\left[\frac{3E_R(F(\beta_2) - 1)}{1 + 2F(\beta_2)}\right]^2 + 3/4\,\frac{b}{A^{1/3}} \qquad (9)$$

where again a and b are constants. The model was tested by the least squares fitting of Eq. 9 to the 63 parameter sets in Ref.[14] for the 52 nuclides from Cu to Bi that are treated as single-peak resonances. The results of the fit gave the parameter values

$$a = 0.3974$$

$$b = 29.699$$

Figure 1a shows the ratio of experimental to calculated single-peak widths versus A. The connected points represent two or more different data sets for the same nucleus, and thus give some feeling for the spread within the data. For most nuclei, the calculated width is within 10% of the measured value. The notable exceptions appear in the mass 90 region. A companion paper[15] in this Conference will concentrate on this mass region, and investigate the breakdown of one or two of the assumptions of the present model that seem to occur near the N = 50 closed shell.

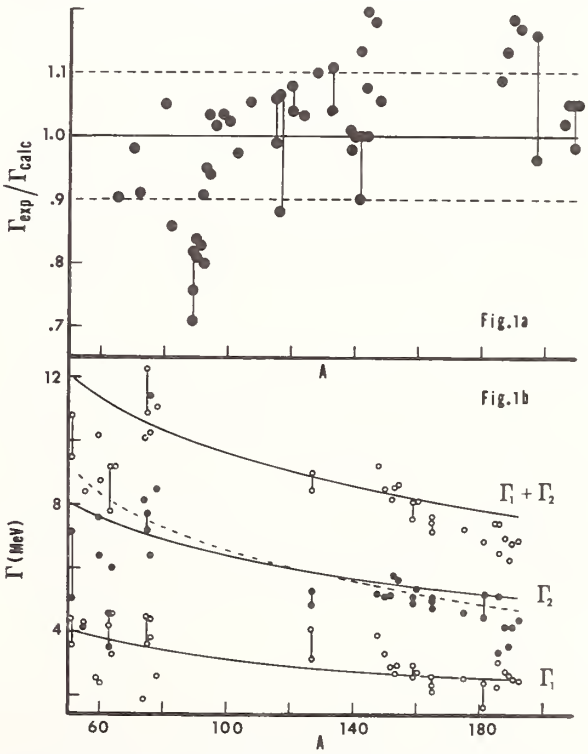

Fig. 1. a) Ratio of experimental widths for single-peak E1 resonances to widths calculated from Eq. 9. b) Predicted widths (solid lines) for double-peak resonances from Eqs. 10, compared with values from Ref. 14; dashed line results from assumption of $A^{-1/2}$ dependence of the widths.

If the two-peak model has any validity, it should be able to predict the widths of the two peaks in cases where they have been resolved. Covariance terms connect all of the six parameters in the two-peak data sets, because they come from a single fitting analysis; errors in one parameter may be compensated by errors in other parameters. Also some of the data sets are more representative of oblate rather than prolate spheroids. Nevertheless, the general trends should be predictable.

The analysis of the single-peak data yielded the result that the $A^{1/3}$ dependent term was $3/4\ (29.699/A^{1/3})$. This we identify with the width of the second peak, Γ_{R2}. Thus

$$\Gamma_{R2} = 29.699/A^{1/3}$$
$$\Gamma_{R1} = \Gamma_{R2}/2 \qquad (10)$$
$$\Gamma_{R1} + \Gamma_{R2} = 3/2\ \Gamma_{R2}$$

These predictions are compared in Fig. 1b with 36 data sets for 28 nuclides which were specified in terms of two peaks in Ref. 14. The solid lines are the predicted values, and empty and filled circles are the measurements. Keeping in mind that none of these 36 data sets were used to fix the parameters in the double-peak model, it appears that there is substantial agreement with the predictions.

In the heavy mass region, however, the data suggest that the supposed $A^{-1/3}$ dependence of the width is not strong enough. The single-peak data were refit using an $A^{-1/2}$ dependence for Γ_{R2}, which resulted in the dashed line in Fig. 1b. This improves the fit in the heavy mass region, but elsewhere the agreement is lessened. The dashed curve was used in the following analysis of Ta, Os and Au, merely because it provided better results than the solid curve.

Application of the Model to Ta, Os, and Au

We have applied the EDBW model with the double-peak GDR to calculate neutron capture cross sections and capture gamma-ray spectra for the targets ^{181}Ta, ^{186,187,188}Os, ^{187}Re, and ^{197}Au. The statistical model codes COMNUC and STAPRE were employed. Good results were obtained for all except ^{197}Au, where the calculated spectra lacked sufficient high-energy gamma rays.

^{181}Ta

The capture cross section was calculated for neutrons up to 3 MeV, and the results are compared with the measurements of Lindner[16] and of Poenitz[17] in Fig. 2, along with a typical capture gamma-ray spectrum. The Oak Ridge data[18] in this case were for neutrons in the energy range of 1-2 MeV. The calculations did not include the inelastic scattering gamma rays, and so are not shown below 2 MeV. An equally good fit was achieved when the spectrum from s-wave neutrons was compared with the measurements of Orphan.[19]

^{186,187,188}Os

Here we show our calculated neutron capture cross sections for ^{186,188}Os in Fig. 3, and for ^{187}Os in Fig. 4. The solid lines are the calculations, and the points represent the recent data of Macklin and Winters.[20] In Fig. 4 we also show the double-peak EDBW strength function computed for our model, together with the Lorentz extrapolations of the single-peak and double-peak fits to the ^{188}Os photoneutron data of Berman.[4,14] These produce the larger cross section shown in Fig. 4.

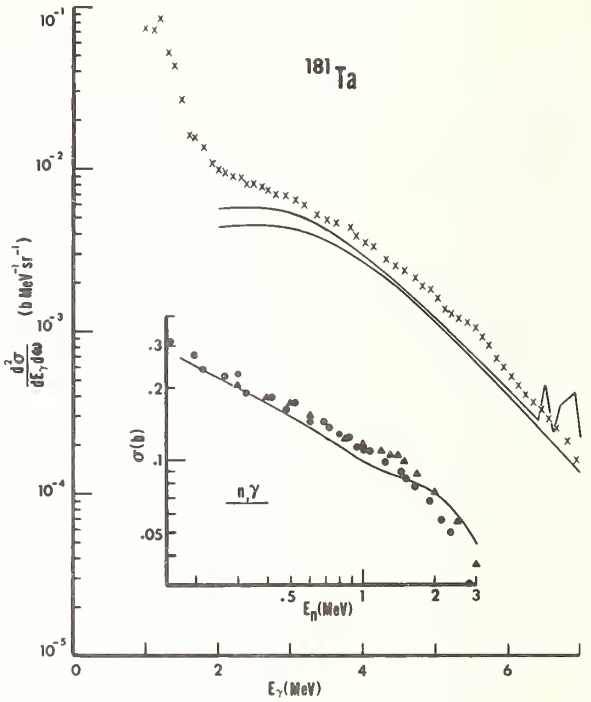

Fig. 2. Comparison of the measured capture gamma-ray spectrum for ^{181}Ta with neutrons between 1 and 2 MeV (x) from Ref. 18 with calculations (solid lines) at these two energies. Insert compares the calculated (n,γ) cross section with measurements by Lindner[16] (circles) and Poenitz[17] (triangles).

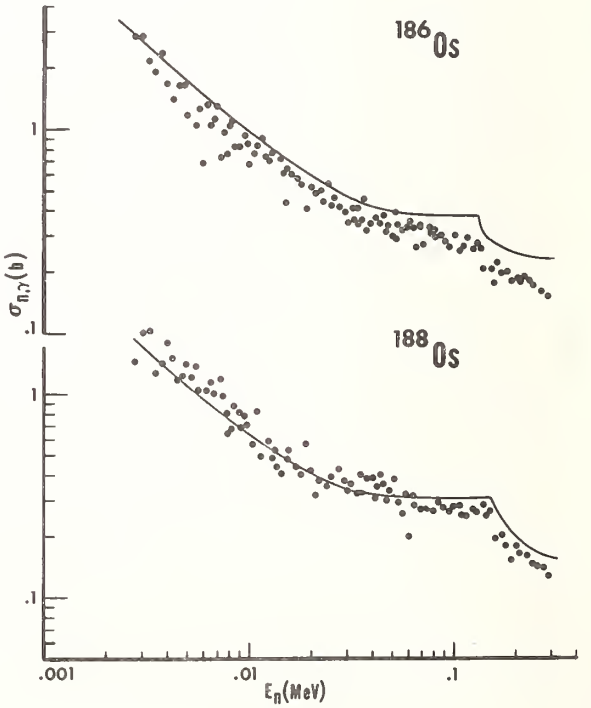

Fig. 3. Comparison of the calculated (n,γ) cross sections for ^{186,188}Os with the data of Macklin and Winters.[20]

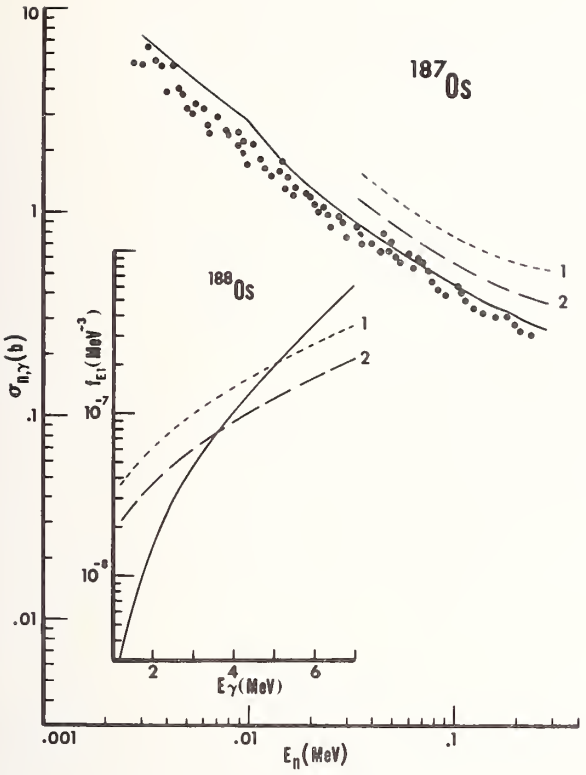

Fig. 4. Comparison of the calculated (solid line) (n,γ) cross section for ^{187}Os with the data of Macklin and Winters.[20] Insert shows the E1 strength functions used. The short dash (1) and long dash (2) strength functions represent, respectively, extrapolations of the single- and double-peak fits of Berman,[4,14] which yield the indicated cross sections.

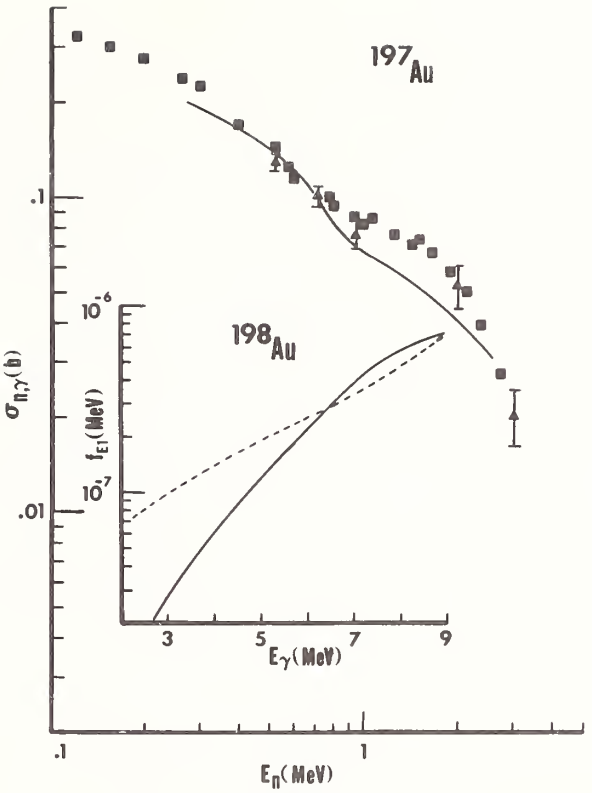

Fig. 5. Comparison of the calculated (solid line) (n,γ) cross section for ^{197}Au with the data of Lindner[16] (squares) and Joly[21] (triangles). Insert shows the E1 strength function used, compared with the extrapolation of the Saclay[14] results (dashed line).

^{197}Au

The calculated neutron capture cross section and two sets of measurements[16,21] are presented in Fig. 5. The EDBW strength function is shown in the insert, compared with the Lorentz extrapolation of the peak parameters measured at Saclay.[14] While the calculated cross section is adequate, the capture gamma-ray spectrum is not. We have computed this spectrum at a variety of neutron energies, and with several sets of values for the parameters E_x and C in Eq. 4. A typical result appears in Fig. 6, where some Oak Ridge data[22] are given. We have not been successful in producing the degree of hardness in the spectra that the Oak Ridge data as well as the thermal capture data of Orphan all seem to exhibit. The reason is clear when our calculated strength function is compared with those extracted from various types of experimental measurements, as presented in a report by Earle, et al.[23] While our results compare well at gamma-ray energies of 4 and 10 MeV, inbetween the data require an abrupt loss of strength near 8 MeV which our calculations do not reproduce.

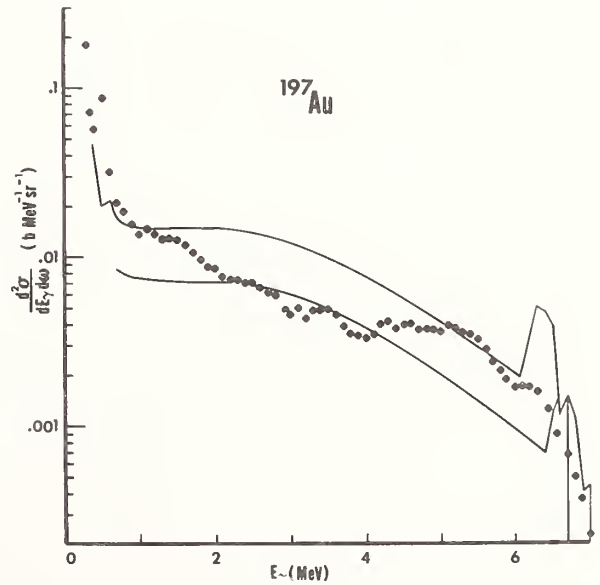

Fig. 6. Comparison of the measured capture gamma-ray spectrum[22] of ^{197}Au with neutrons from 0.2 to 0.6 MeV (circles) with the calculations (solid lines) at these two energies.

References

1. G. Bartholomew et al., Advances in Nuclear Physics, Vol. 7, Chapter 4 (Plenum Press, New York, 1973).
2. E. D. Earle et al., Can. J. Phys. 52, 989 (1974).
3. V. Soloviev et al., Nucl. Phys. A304, 503 (1978).
4. B. Berman et al., Phys. Rev. 19, 1205 (1979).
5. M. Danos and W. Greiner, Phys. Rev. 134, 284 (1964).
6. M. Danos and W. Greiner, Phys. Lett. 8, 113 (1964).
7. M. Danos and W. Greiner, Phys. Rev. 138, 876 (1965).
8. P. Carlos et al., Nucl. Phys. A219, 61 (1974).
9. P. Carlos et al., Nucl. Phys. A225, 171 (1974).
10. E. Gordon and R. Pitthan, Nucl. Instru. Methods 145, 569 (1977).
11. C. Dover et al., Annals of Phys. 70, 458 (1972).
12. F. Williams, Phys. Lett. 31B, 184 (1970).
13. C. Kalbach-Cline, Nucl. Phys. A210, 590 (1973).
14. B. Berman, UCRL-78482 (Dec. 1976).
15. M. A. Gardner and D. G. Gardner, "Capture Cross Sections and Gamma-Ray Spectrum Calculations for Medium-Weight Nuclei," paper GB1, this conference.
16. M. Lindner et al., Nucl. Sci. Eng. 59, 381 (1976).
17. W. Poenitz, ANL/NDM-15 (June, 1975).
18. G. Morgan et al., ORNL-TM-3702 (Feb., 1972).
19. V. Orphan et al., GA-10248 (July, 1970).
20. R. Macklin and R. Winters, private communication prior to publication.
21. S. Joly, Nucl. Sci. Eng. 70, 53 (1979).
22. G. Morgan and E. Newman, ORNL-TM-4973 (Aug., 1975).
23. E. Earle et al., AE-515 (Aug., 1977).

GAMMA-RAY PRODUCTION CROSS SECTIONS FOR MeV NEUTRONS

H. Kitazawa and Y. Harima
Tokyo Institute of Technology
O-okayama, Megro-ku, Tokyo, Japan

H. Yamakoshi
Ship Research Institute
Shinkawa, Mitaka-shi, Tokyo, Japan

Y. Sano and T. Kobayashi
Toshiba Research and Development Center
Toshiba-cho, Saiwai-ku, Kawasaki-shi, Kanagawa, Japan

M. Kawai
NAIG Nuclear Research Laboratory
Ukishima-cho, Kawasaki-ku, Kawasaki-shi, Kanagawa, Japan

Gamma-ray production cross sections for MeV neutrons are calculated for several nuclei over the wide nuclear mass number from 27 to 208. The results are compared with experimental data. It is found that the model and assumptions adopted in the present calculation are adequate for description of the gross dependence of gamma-ray production cross section on neutron energy and nuclear mass number, unless the radiative neutron capture process is dominant in comparison with other possible ones.

[Gamma-ray production cross section, spin-dependent evaporation model, yrast level, gamma-ray strength function.]

Introduction

Gamma-ray production cross sections and spectra are requested for heating calculations, for shielding design calculations, and for material damage estimates. Recently, many experiments in ORNL[1] have been carried out for measurements of the gamma-ray production cross section for 1- to 20-MeV neutrons. However, these data are not evaluated enough to fit for extensive technological applications. In the present paper we will understand appearances of the gamma-ray production cross section and spectrum for a variety of nuclei from light to heavy, within the framework of a evaporation model.

Model and Assumptions

(1) Calculations are based on the spin-dependent evaporation model which does not follow the parity conservation and takes account of the dipole and quadrupole transitions.
(2) Concept of the yrast level[2] is applied.
(3) The Brink-Axel type[3] is adopted for gamma-ray strength function.
(4) The gamma-ray width Γ_γ^D for electric dipole radiation is normalized to El sum-rule.[4]
(5) The ratio $\Gamma_\gamma^Q/\Gamma_\gamma^D$ is set equal to 0.05.
(6) The Gilbert-Cameron formula[5] is used for calculation of nuclear level densities.
(7) The Becchetti-Greenlees optical potentials[6] are used for neutrons and protons. For alpha particles, the Huizenga-Igo potential[7] is used.

Calculations and Discussions

Optical Potential

Fig. 1 shows that the shape of gamma-ray spectra is not susceptible to the optical potential adopted in calculation, while the absolute value of gamma-ray production cross section is much more influenced by the potential. Namely, the use of the potential which gives the observed total cross section is essential to gamma-ray production calculations.

Yrast Level

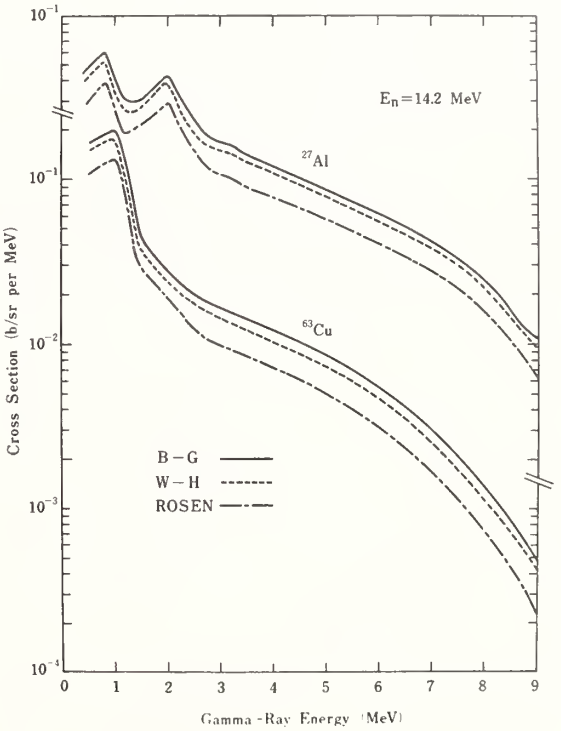

Fig. 1. Gamma-ray spectra from ^{27}Al and ^{63}Cu for 14.2-MeV neutrons, calculated with the optical potentials of Becchetti-Greenlees(B-G), Rosen et al.(ROSEN),[8] and Wilmore-Hodgson(W-H).[9]

As seen from Fig. 2, the inclusion of yrast levels is inevitable for expecting the appearance of a peak around 1 MeV. This peak is formed by quadrupole gamma-rays resulting from the decay of excited states along a yrast line. The yrast level is probably needed in dealing with the competition between the particle and gamma-ray emissions from highly excited states.

Influence of the Channel-opening

Fig. 3 shows that gamma-rays due to two-particles emission reactions contribute to the low energy part

of the calculated spectrum. This is because these reactions populate low energy levels in residual nuclei.

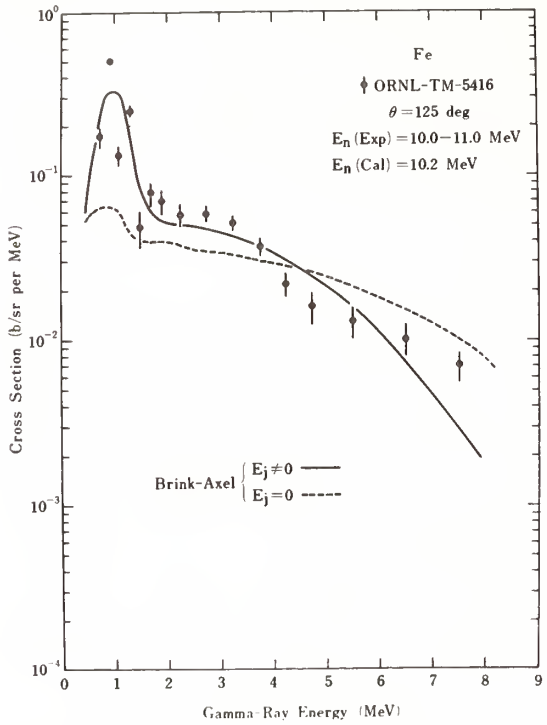

Fig. 2. Calculated and observed gamma-ray spectra from Fe. The calculated spectra are obtained with the Brink-Axel type's gamma-ray strength function, including ($E_j \neq 0$) and not including ($E_j = 0$) yrast levels.

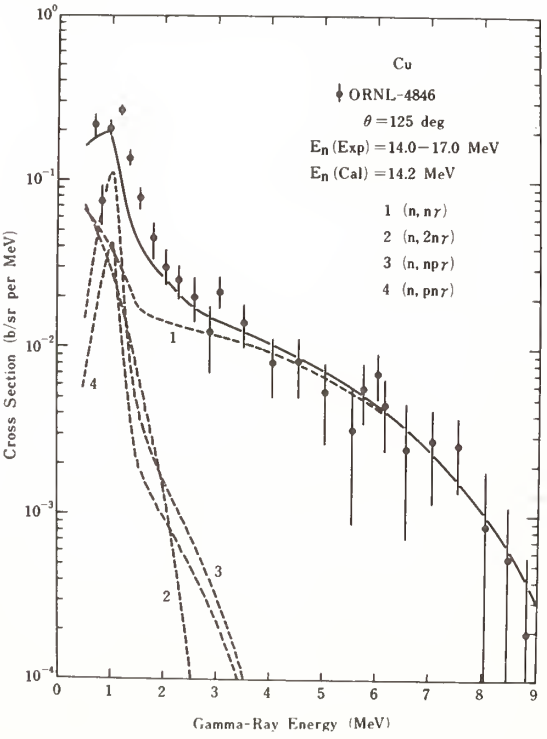

Fig. 3. Calculated and observed gamma-ray spectra from Cu. Dotted lines show the contributions of (n,nγ), (n,2nγ), (n,npγ) and (n,pnγ) processes.

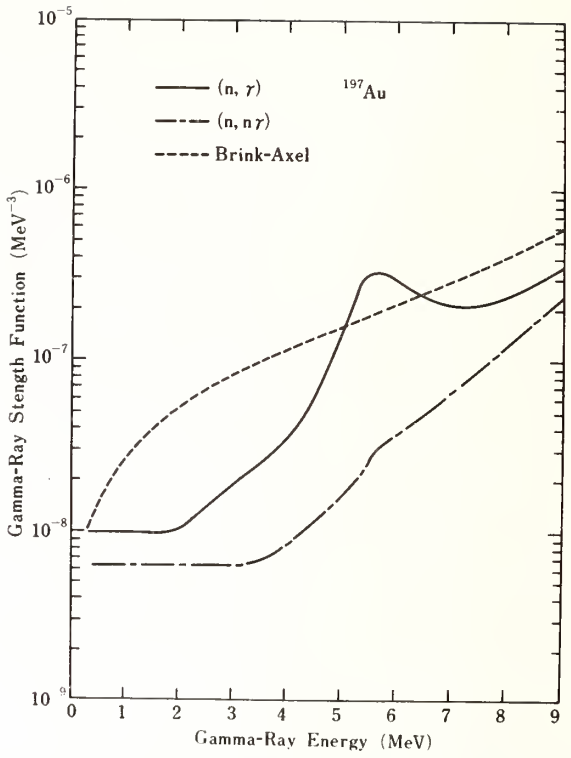

Fig. 4. Gamma-ray strength functions for ^{197}Au(n,γ) and ^{197}Au(n,nγ) processes and of Brink-Axel. The (n,γ) strength function is derived from ORNL experimental data for incident neutron energies between 0.2 and 0.6 MeV, using the spectrum fitting method, and the (n,γ) strength function from ORNL experimental data for incident neutron energies between 7.01 and 7.97 MeV in the same way.

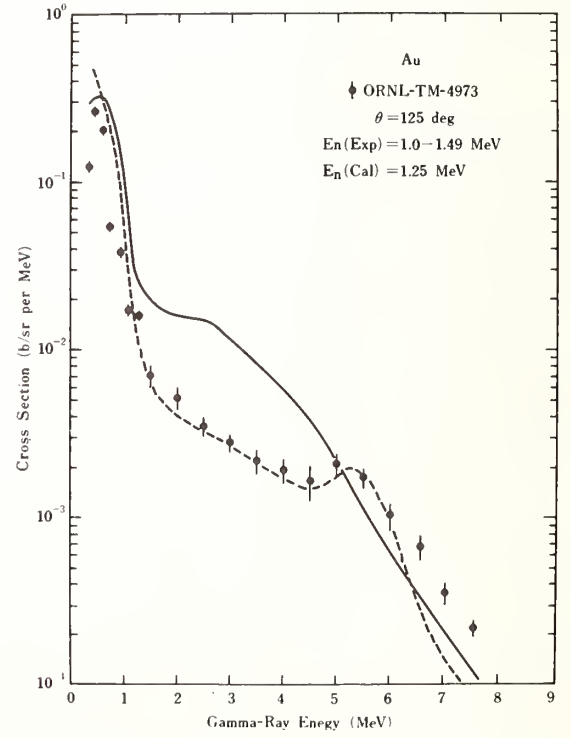

Fig. 5. Calculated and observed gamma-ray spectra from ^{197}Au. The continuous line is obtained with the Brink-Axel type's gamma-ray strength function, and the dotted line with the one derived from experimental data.

Gamma-ray Strength Function

Bollinger et al.[10] have shown that the E_γ^5-law for radiation width, predicted by the Brink-Axel theory, is more plausible than the E_γ^3-law in the Weisskopf theory.[11] But, our results suggest that the Brink-Axel type's gamma-ray strength function has a tendency to overestimate the lower energy part in the calculated spectrum and to underestimate the higher energy part. This is visualized in Fig. 4, where the Brink-Axel type's strength function for gold is compared with ones for capture and inelastic scattering gamma-rays. The latter strength functions are obtained by a spectrum fitting method.[12] In conclusion, the Brink-Axel type's strength function is not always powerful in all range of neutron energy, as seen from Fig. 5, especially at the energy where capture process is dominant.

Acknowledgement

The authors wish to thank Dr. Hiroshi Takahashi of Brookhaven National Laboratory for showing us the importance of present works in fission and fusion reactor designs and for support of the GROGI-3 code. Our thanks also go to Prof. Nobuhiro Yamamuro of Tokyo Institute of Technology and to Dr. Shungo Iijima of NAIG Nuclear Research Laboratory for helpful suggestions.

References

1. J. K. Dickens et al., Nucl. Sci. Eng. 62, 515 (1977).

2. J. R. Grover and J. Gilat, Phys. Rev. 157, 814 (1967).

3. P. Axel, Phys. Rev. 126, 671 (1962).

4. J. S. Levinger and H. A. Bethe, Phys. Rev. 78, 115 (1950).

5. A. Gilbert and A. G. W. Cameron, Can. J. Phys. 43, 1446 (1965).

6. F. D. Becchetti and G. W. Greenlees, Phys. Rev. 182, 1190 (1969).

7. J. R. Huizenga and G. Igo, Nucl. Phys. 29, 462 (1962).

8. L. Rosen et al., Ann. Phys. 34, 96 (1965).

9. P. E. Hodgson, Nuclear Reactions and Nuclear Structure (Clarendon, Oxford, 1971).

10. M. L. Bollinger and G. E. Thomas, Phys. Rev. C2, 1951 (1970).

11. J. M. Blatt and V. S. Weisskopf, Theoretical Nuclear Physics (Wily, New York, 1952).

12. G. A. Bartholomew et al., Advance in Nucl. Phys. 7, 229 (1973).

SEMIEMPIRICAL CALCULATION OF EXCITATION FUNCTIONS

E. L. Petersen
Naval Research Laboratory
Washington, D. C. 20375

A simple model for the calculation of excitation functions is described. The geometrical cross section, allowing for transparency, is divided into statistical, direct and preequilibrium portions. These cross sections are allocated to individual reactions by examining the relative contributions of all possible reactions emitting the same number of particles. The cross section for each reaction product is then calculated as a function of energy. A computer code has been written that calculates excitation functions in the range between 5 and 80 MeV for reactions emitting from one to six particles. The results are compared with experimental values for proton reactions with ^{27}Al, ^{58}Ni, ^{59}Co, and ^{209}Bi.

[Nuclear Reactions, Semiempirical Model, Excitation functions E = 5 - 80 MeV, $^{27}Al(p,xy)$, $^{59}Co(p,xy)$, $^{58}Ni(p,xy)$, $^{209}Bi(p,xy)$]

Introduction

There are a number of theoretical approaches to calculations of nuclear reaction cross sections, such as Hauser-Feshbach, preequilibrium, Monte Carlo, etc. However, as successful as these are, they are awkward to use for a global view of nuclear reactions and nuclear excitation functions in the region of 10 MeV to 100 MeV. This paper presents a simple model that appears to be useful for describing the gross structure of nuclear excitation functions. Rather than starting at the detailed level of angular momentum states or excitons, the model starts with a calculation of the total reaction cross section. The cross section is then separated into direct and statistical fractions, for which in turn pre- and post equilibrium contributions are estimated. At any given energy there are only a few reactions that compete for their share of the cross section. The model assumes that the winners of this competition are decided on the basis of elementary concepts such as reaction Q value. It then assumes simple forms for the individual excitation functions and combines these for an overall view of the various reactions that take place.

Calculations

Total Cross Section

The model starts with a very simple paramaterization of the total reaction cross section (nonelastic cross section). The cross section is basically the geometrical cross section, modified at low energies by the Coulomb barrier if the incident particles are charged, and at high energies by the nuclear transparency.

$$\sigma_t = \pi(R + \lambda\!\!\!^{-})^2\left(1 - \frac{B}{E}\right) \cdot F$$

The transparency (F) is expressed in terms of an absorption coefficient which in turn can be expressed in terms of real and imaginary optical potentials[1]. The real potential $V=52.5 - 0.5E + 0.0025E^2$ is essentially standard, but the imaginary potential $W = 2.5 + 22.0(\exp(-E/40) - \exp(-3E/40))$ has been slightly modified from the usual parameterizations in order to lead to the experimental total cross sections.

A portion of the total cross section that corresponds to a surface area defined by one unit of angular momentum, modified by the Coulomb barrier and transparency, is assigned as leading to direct reactions. The rest of the cross section is assumed to be described by standard statistical considerations. However, as the energy increases, the reaction mechanisms change so that several particles are emitted, some of which may be preequilibrium and some post equilibrium. Therefore both the direct and statistical cross sections have to be modifed to allow for this type of two-step process. The model assumes the following energy dependence above 15 MeV to obtain the preequilibrium components of the cross section.

$$\sigma_s = \sigma_s \exp\left\{-(E - 15)/2.5\ A^{2/3}\right\}$$

$$\sigma_d = \sigma_d \exp\left\{-(E - 15)/30.0\right\}$$

$$\sigma_p = \sigma_t - (\sigma_s + \sigma_d)$$

The direct cross sections will determine the high-energy tail of the excitation function for single particle emission, while the preequilibrium cross section will determine the high-energy tail for reactions emitting two or more particles. Figures 1 and 2 show the total cross section and its components for two nuclei.

Statistical Contributions

The excitation function for a given reaction that is part of the statistical decay of the compound nucleus is calculated in four steps. The model calculates the relative probability of this reaction relative to competing reactions, the location of the peak in its cross section, the value of the cross section at the peak, and the energy dependence of the excitation function.

The reactions that take place are determined by competition with each other for fractions of the total statistical cross section. It is well known that neutron and proton emission compete with the emission of $^{6}LI^{*}$, the dineutron(2n), ^{8}Be, and many

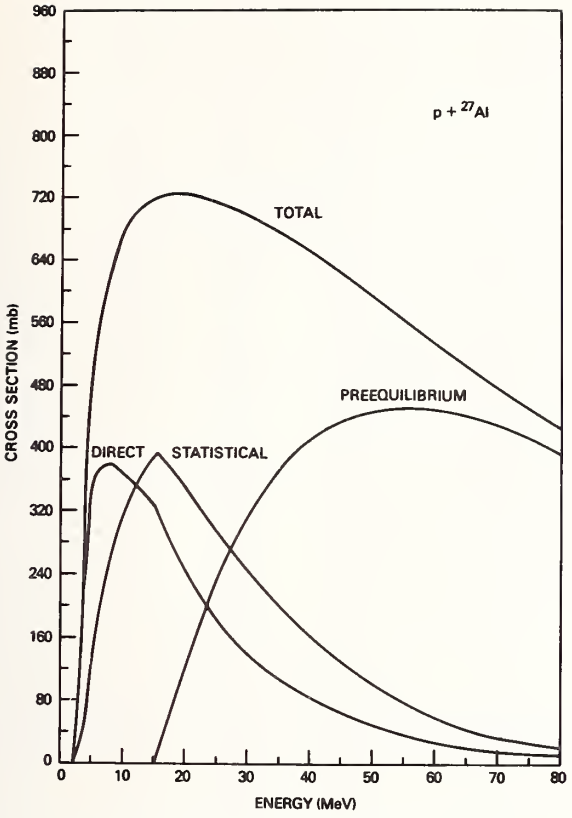

Fig. 1 Reaction cross sections calculated for protons on Aluminum.

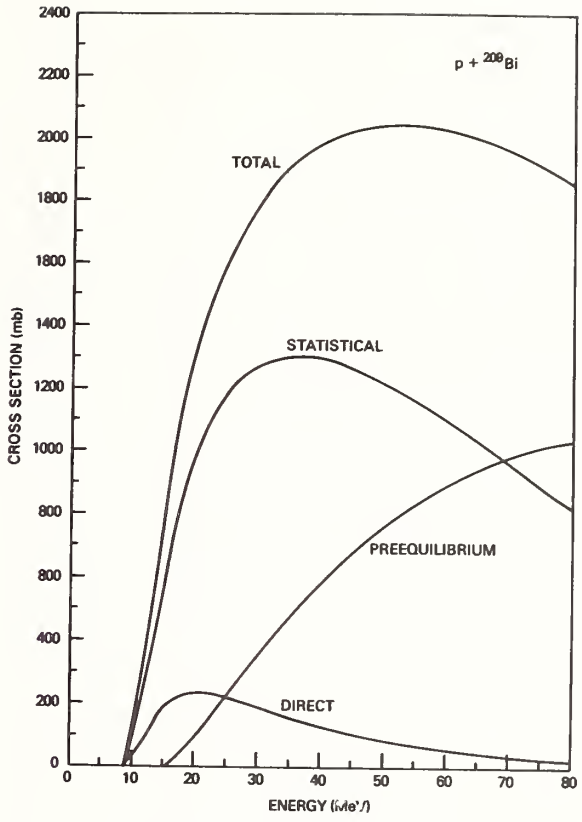

Fig. 2 Reaction cross sections calculated for protons on Bismuth.

other composite particles[2]. This model carries this concept slightly further and says that all reactions emitting two particles are competing with each other as if they are emitting composite particles, and that this is occurring in an energy region in which competition from one particle emission is only a secondary effect. In the same way, there are separate competitions for three particles, four particles, etc.

The principal items that enter into the competition are the Q value, the Coulomb barrier, the odd-even effect, shell effects, and the nuclear temperature (T). The Coulomb barrier is calculated with a simple barrier penetration approach given in Evans[3], in which the term E/B is treated as a constant and used as one of the variable parameters in the model. The odd-even effect is calculated as $12.0/\sqrt{A}$[4] and the shell effect is introduced following the approach of Blann[5] and Rosenzweig[6]. The nuclear temperature is approximated as $13.0/\sqrt{A}$.

The location of the peak cross section for a given reaction depends on several energies characteristic of that reaction.

$$Ep = Th + B + ER + 2T(N-0.5)$$

where Th is the threshold, B is the Coulomb barrier, and ER is the average residual energy in the final nucleus. The factor 2T(N-0.5) assumes that the average particle carries off 2T except for the last particle emitted which carries off T.

The peak cross section is then assigned by subtracting the contributions of the reactions emitting fewer particles from the total and dividing the remainder according to the weighting factors calculated above. The shape of the statistical excitation function is assumed to be: $\sigma(E) = \sigma \exp(a \cdot \ln^2 x)$ where $x = (E-Th)/(EP-Th)$ and a is 3.0 if E>EP and 1.3/T if E<EP. A second approximation is obtained by normalizing the excitation functions point by point so that their total equals the assumed total. This allows for regions in which the assumed shape does not fill in between one particle and two particle emission, or where there is a lot of competition between adjacent particle groups.

Direct and Preequilibrium Contributions

The direct and preequilibrium components are assigned in a similiar way. The preequilibrium competition is weighted as suggested by Cline[7], with evaporation following the preequilibrium emission described with the statistical approach used above. The assumed shape here consists of a straight line up to the peak value followed by a decay governed primarily by the transparency factor. These two components are also normalized pointwise.

Results

The model assumes that all adjustable parameters are independent of target and of energy so that it should predict excitation functions for all nuclei. Table 1 shows a sample of the basic numbers that are calculated. Figures 3 - 6 show the excitation functions calculated from these numbers, and corresponding experimental values taken from the literature. We want to predict the total reaction cross section, and the peak location, the magnitude of the

REACTIONS OF 1H WITH 59CO

	PARTICLES EMITTED	REACTION PRODUCT	Q VALUE	THRESHOLD TRUE	THRESHOLD EFFECTIVE	ENERGY AT PEAK	CROSS SECTION PEAK	CROSS SECTION TAIL
1	N	59NI	-1.86	1.89	1.89	11.48	153.71	11.93
2	P	59CO	-0.00	0.00	1.38	9.74	213.21	235.92
3	D	58CO	-8.24	8.38	10.24	18.28	4.48	0.07
4	A	56FE	3.24	0.00	6.42	17.14	107.86	64.46
5	N N	58NI	-10.86	11.04	14.58	23.69	88.61	26.30
6	P N	58CO	-10.47	10.64	15.85	23.90	327.97	196.04
7	P P	58FE	-7.38	7.50	15.73	26.44	79.08	51.27
8	D N	57CO	-16.81	17.10	22.66	29.74	1.69	10.89
9	D P	57FE	-15.19	15.45	24.50	33.10	0.74	11.34
10	T N	56CO	-21.93	22.31	28.17	35.19	0.45	5.51
11	T P	56FE	-16.58	16.86	26.56	37.28	0.31	10.45
12	H N	56FE	-17.34	17.63	27.33	38.05	0.20	6.93
13	H P	56MN	-20.26	20.60	34.97	43.27	0.01	1.53
14	A N	55FE	-7.97	8.10	18.34	28.45	57.47	35.30
15	A P	55MN	-6.95	7.07	22.27	31.26	4.96	18.04
16	A D	54MN	-14.95	15.21	31.11	39.70	0.04	1.21
17	N N N	57NI	-23.05	23.44	30.60	39.02	39.20	17.91
18	P N N	57CO	-19.04	19.36	28.29	35.38	150.20	95.97
19	P P N	57FE	-17.42	17.71	30.03	38.62	84.26	59.33
20	P P P	57MN	-19.33	19.66	36.22	45.76	2.43	1.25
21	D N N	56CO	-28.19	28.67	37.94	44.96	1.27	6.56
22	D P N	56FE	-22.83	23.22	36.20	46.92	0.98	9.21
23	T N N	55CO	-32.02	32.57	42.46	48.71	0.06	1.03
24	T P N	55FE	-27.78	28.25	41.81	51.92	0.24	8.78
25	H N N	55FE	-28.54	29.03	42.58	52.69	0.15	5.58
26	A N N	54FE	-17.27	17.56	31.91	41.66	11.96	10.99
27	A P N	54MN	-17.18	17.47	36.64	45.23	6.60	23.99
28	A P P	54CR	-15.02	15.27	40.15	50.67	0.14	0.92
29	N N N N	56NI	-33.31	33.88	45.33	53.58	4.45	2.63
30	P N N N	56CO	-30.42	30.93	43.61	50.64	97.99	58.50
31	P P N N	56FE	-25.06	25.48	41.74	52.46	88.39	44.18
32	P P P N	56MN	-27.98	28.45	49.25	57.56	5.11	1.98
33	D N N N	55CO	-38.28	38.93	52.44	58.69	0.13	1.15
34	D P N N	55FE	-34.04	34.61	51.48	61.59	0.56	8.10
35	T P N N	54FE	-37.08	37.71	55.56	65.31	0.04	5.87
36	H N N N	54FE	-37.84	38.49	56.34	66.08	0.03	3.13
37	A N N N	53FE	-30.88	31.41	49.15	57.43	4.03	9.30
38	A P N N	53MN	-26.12	26.56	50.10	57.72	1.25	8.67
39	P N N N N	55CO	-40.50	41.19	58.32	64.57	13.27	12.76
40	P P N N N	55FE	-36.26	36.88	57.06	67.17	71.77	48.45
41	P P P N N	55MN	-35.25	35.85	60.74	69.73	7.61	3.12
42	D P N N N	54FE	-43.34	44.07	65.42	75.17	0.16	5.09
43	T P N N N	53FE	-50.70	51.56	72.64	80.92	0.02	3.47
44	H N N N N	53FE	-51.46	52.33	73.42	81.69	0.02	1.85
45	A N N N N	52FE	-41.33	42.03	63.05	71.30	2.07	3.32
46	A P N N N	52MN	-38.17	38.82	65.69	73.33	1.93	8.10
47	P N N N N N	54CO	-54.60	55.52	75.58	81.45	8.49	11.08
48	P P N N N N	54FE	-45.56	46.33	71.18	80.93	21.36	21.24
49	P P P N N N	54MN	-45.47	46.24	75.22	83.81	14.30	8.00
50	D P N N N N	53FE	-56.96	57.92	82.35	90.62	0.11	3.20
51	T P N N N N	52FE	-61.14	62.18	86.45	94.70	0.02	2.07
52	H N N N N N	52FE	-61.90	62.95	87.23	95.48	0.01	1.09
53	A P N N N N	51MN	-48.68	49.51	79.65	86.00	0.98	6.55

Table 1 Calculated cross sections and energies for protons on Cobalt. The calculated numbers shown here are the basis for the excitation functions shown in figure 4b. The calculation of these numbers and of the excitation functions takes 8 seconds on a Systems 32/55 minicomputer.

cross section at the peak and in the tail, and the shape of the excitation function for the individual reactions. The quality of agreement between the calculated values and the experimental results appears to be good enough so that the model deserves further development.

References

1. K. Kikuchi and M. Kawai, Nuclear Matter and Nuclear Reactions (North-Holland Publishing Co., Amsterdam, 1968).

2. T. Ericson, Phil. Mag. Sup., 9, 425(1960).

3. R. D. Evans, The Atomic Nucleus (McGraw-Hill Book Company, Inc., New York, 1955).

4. A. Bohr and B. R. Mottelson, Nuclear Structure W. A. Benjamin, Inc., New York, 1969).

5. M. Blann, Nuclear Physics, 80, 223(1966)

6. N. Rosenzweig, Phys. Rev. 105, 950(1957); Phys. Rev. 108, 817(1957).

7. C. K. Cline, Nuclear Physics, A193, 417(1972).

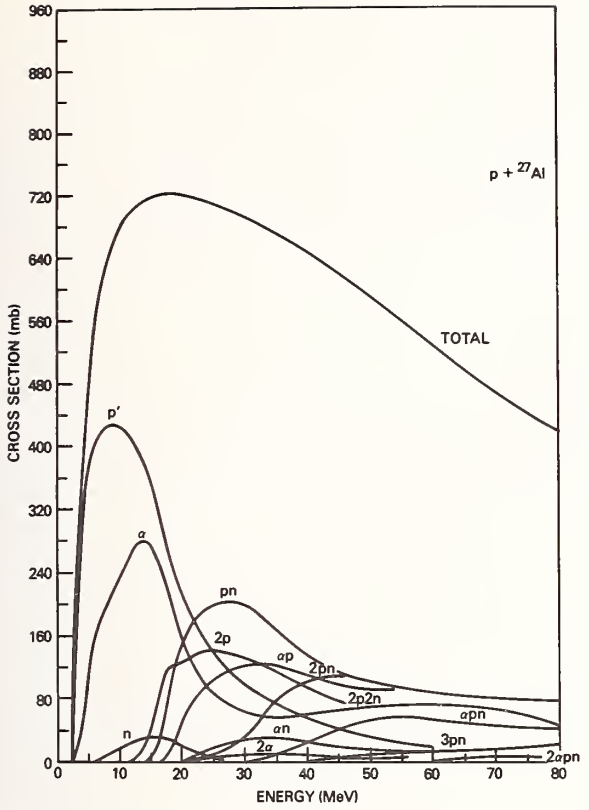

Fig. 3b Calculated cross sections for protons on Aluminum.

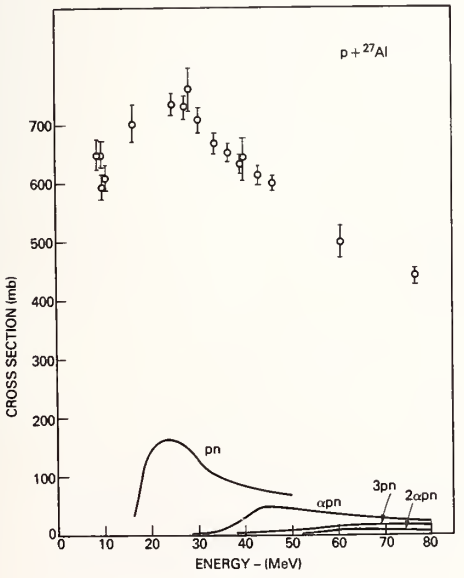

Fig. 3a Experimental cross sections for protons on Aluminum, taken from the literature. The points indicate measurements of the total reaction cross section. The smooth curves have been drawn by eye through the experimental data.

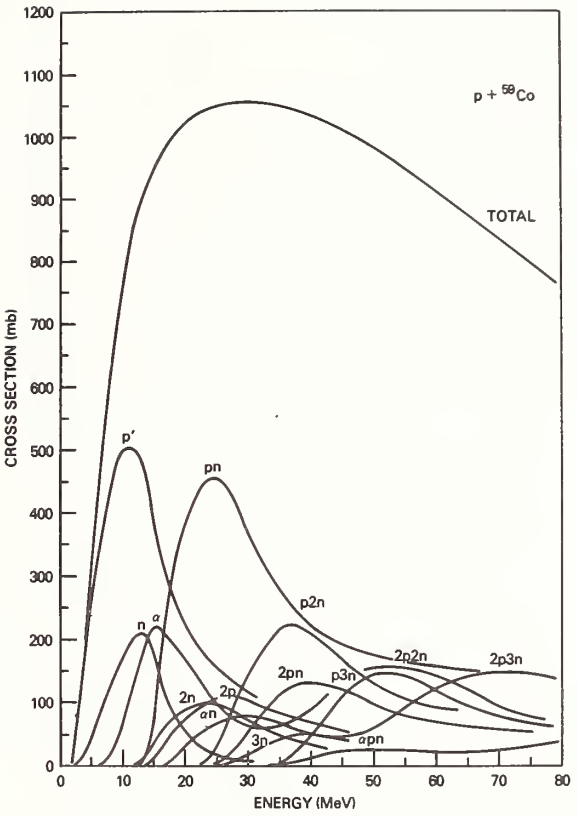

Fig. 4b Calculated cross sections for proton on Cobalt.

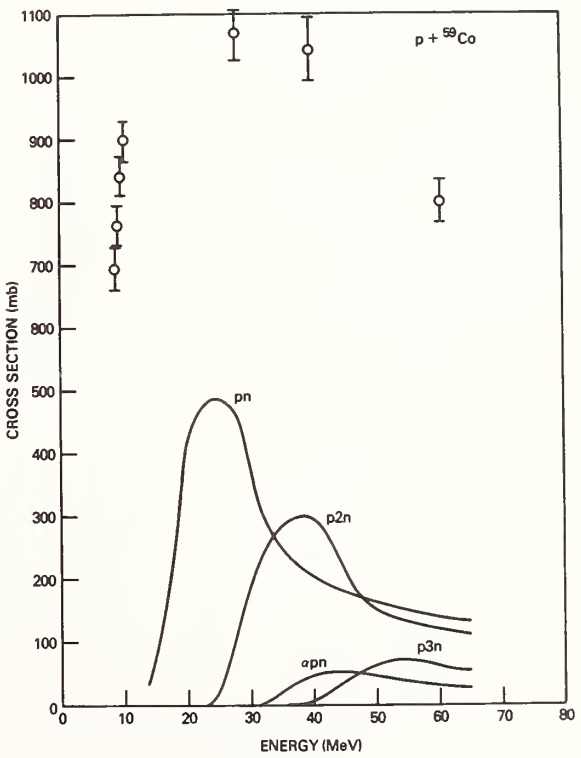

Fig 4a Experimental cross section for proton on Cobalt

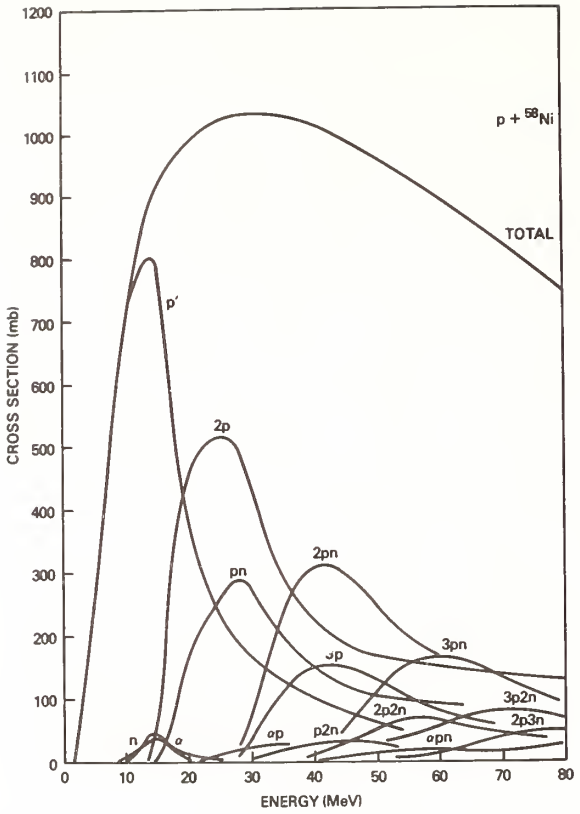

Fig. 5b Calculated cross sections for proton on Nickel.

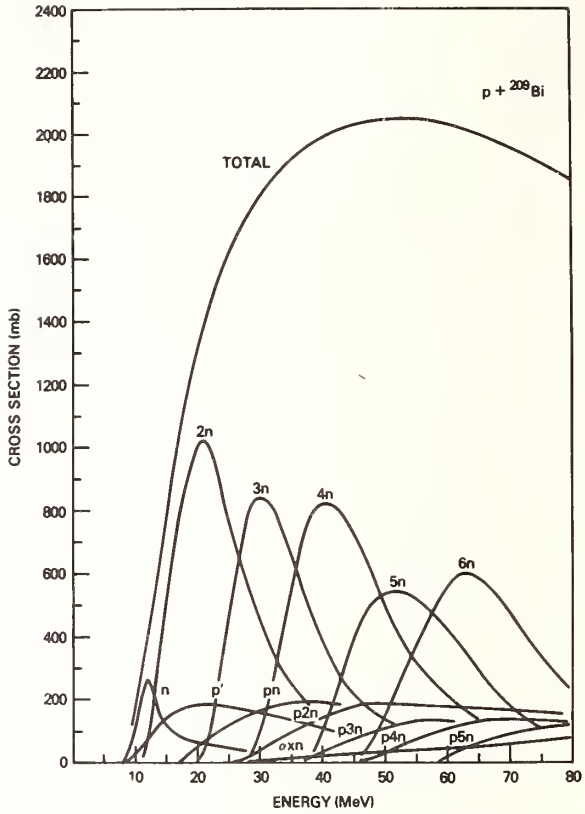

Fig. 6b Calculated cross sections for protons on Bismuth

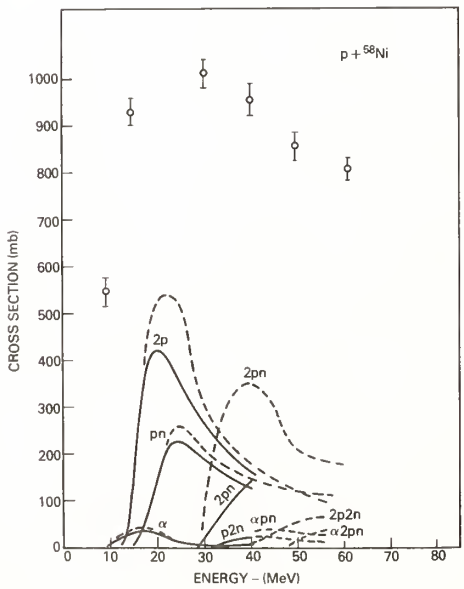

Fig. 5a Experimental cross sections for protons on Nickel. The two sets of curves were obtained by different experimenters and are presented to indicate the difficulty of the experiments.

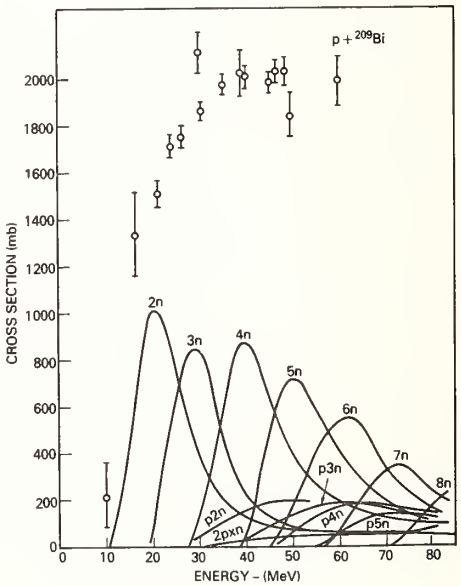

Fig. 6a Experimental cross sections for protons on Bismuth. The total cross section points were obtained for Lead.

R-MATRIX ANALYSIS OF NEUTRON ELASTIC AND INELASTIC SCATTERING DATA

H.D. Knox, R.O. Lane, D.A. Resler and P.E. Koehler
John E. Edwards Accelerator Laboratory
Ohio University
Athens, Ohio 45701 USA

A multichannel multilevel R-matrix analysis program capable of analyzing neutron elastic and inelastic scattering data has been developed. The program has been used to analyze ^{7}Li + n data with good fits obtained for elastic and inelastic (0.478 MeV level) cross sections up to 8 MeV. A description of the program and the results of the ^{7}Li + n study are given.

[Multilevel, multichannel, R-matrix, neutron, elastic cross section, inelastic cross section, ^{7}Li + n]

Introduction

Accurate evaluations of many of the neutron induced reaction cross sections are necessary for the light nuclei having applications in the fusion energy program. For example, in addition to the ^{7}Li tritium breeding reactions which are of fundamental importance to the D-T fusion reactor concept, ^{7}Li + n elastic and inelastic processes are also important because of nuclear heating, shielding and radiation damage effects. To provide evaluations of these cross sections, a multilevel multichannel R-matrix analysis program has been developed. The program can be used to analyze neutron differential elastic and inelastic scattering data to the first two excited states of the target nucleus. Though the program was developed with the goal of analyzing ^{7}Li + n scattering data, it can be used for other nuclei with only slight modification. A description of the program and the results of the ^{7}Li + n study will be given here.

Description of the Program

The program accepts the experimental differential elastic and inelastic cross sections to be analyzed in the form of Legendre polynomial expansion coefficients, B_L. With data in this form the fitting process is sometimes easier since partial waves contributing to particular resonances are frequently evident from a plot of the B_L coefficients versus energy. Also with this form of input, large amounts of diverse experimental data can be condensed to more manageable arrays. Starting with the usual R-matrix parameters, the level energies, E_λ, the reduced width amplitudes, $\gamma_{\lambda c}$, and the channel radii, the code computes the elements of the R-matrix

$$R_{c'c}^{J^\pi} = \sum_\lambda \frac{\gamma_{\lambda c'}\gamma_{\lambda c}}{E_\lambda - E} + R_{o_{c'c}}^{J^\pi}$$

where the term $R_{o_{c'c}}^{J^\pi}$ is a constant background term representing contributions to the cross section of levels far removed from the region of interest. The sum is over levels of the same J^π and λ can have a maximum value of five. Orbital angular momentum values, ℓ, up to and including three are allowed. A total of fifteen J^π values are allowed and for each of the three particle channels four angular momentum channels are permitted. For each J^π the elements of the scattering matrix (S-matrix) are then computed from the R-matrix

$$S^{J^\pi} = \Omega\,(1-2i\,P^{1/2}\,(1-R^{J^\pi}L_o)^{-1}\,R^{J^\pi}P^{1/2})\,\Omega$$

following Lane and Thomas[1]. Finally, using the formalism of Blatt and Biedenharn[2], the Legendre expansion coefficients are calculated for comparison with the experimental data. Phases used in the

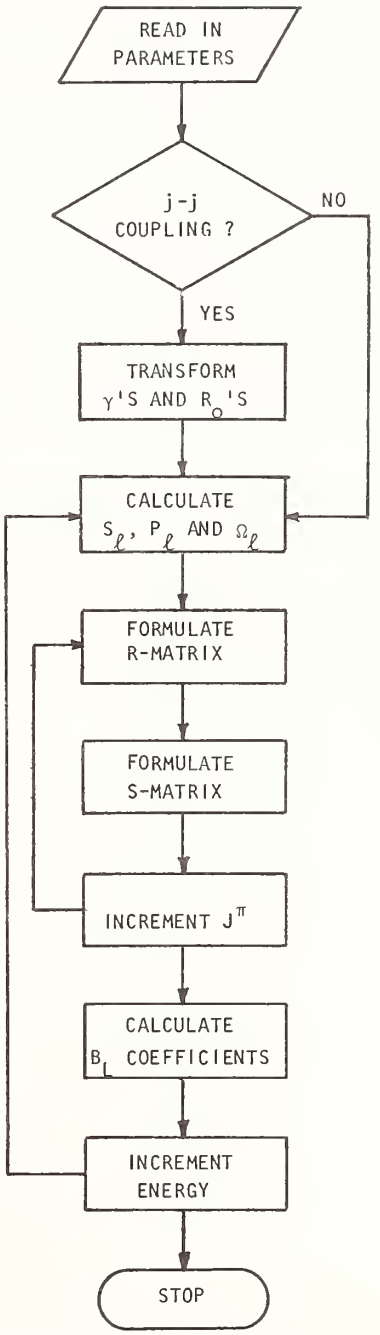

FIGURE 1
A simplified flow diagram of the R-matrix analysis code.

latter calculation were changed to agree with the notation of Lane and Thomas[1].

Frequently, it is desirable to compare parameters for an R-matrix analysis with those from model calculations for the same nucleus either to aid in the fitting process or to provide a check of the theoretical calculations. To conform with available model calculations, one must have the option of undertaking the R-matrix analysis in either the channel or j-j angular momentum coupling schemes. If j-j coupling is to be used, a transformation to the channel coupling scheme must be made prior to the calculation of the B_L coefficients since the formalism of Blatt and Biedenharn[2] assumes the use of the latter scheme. This transformation is most efficiently carried out if performed on the reduced widths and R_o's in the j-j scheme immediately after they are read in as shown in Figure 1. If postponed until later in the calculation, e.g. after the S-matrices have been calculated, transformations must be performed at each neutron energy of the analysis.

The program presently operates on an IBM 370 computer with a Tektronix 4025/4631 graphics terminal used to provide a visual comparison of the experimental data and the calculated fits. The program requires approximately twenty seconds of CPU time for the calculation of five B_L coefficients for each of the three particle channels at a given energy.

^{7}Li + n Analysis

The analysis of the ^{7}Li + n system included fitting of elastic and inelastic neutron scattering data up to 8 MeV incident neutron energy. Elastic data used in this analysis included the work of Lane et al.[3] below 2 MeV and data from 2 MeV to 8 MeV recently obtained at Ohio University[4,5].

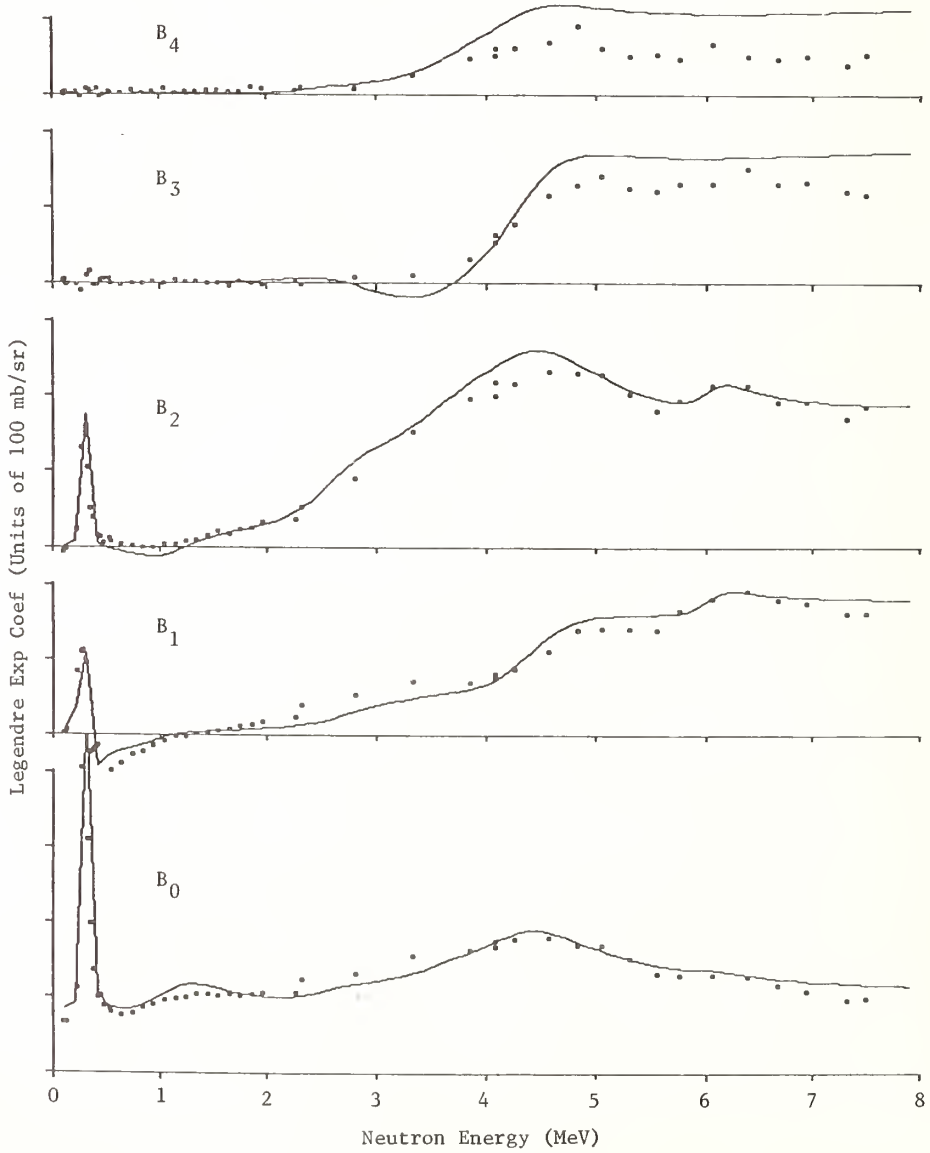

FIGURE 2

A plot of the Legendre expansion coefficients for neutron elastic scattering for ^{7}Li. Increasing order of B_L goes from bottom to top. Neutron energies are given in the laboratory system while the B_L are in the center-of-mass system. The experimental data below 2 MeV are from Reference 3 and above 2 MeV are from References 4 and 5. The curves are the final fits to the data obtained in the present work.

Integrated cross sections for inelastic scattering to the first excited state of ^{7}Li

$$^7\text{Li(n,n')}^7\text{Li}^* \rightarrow \gamma + {}^7\text{Li} \quad Q = -0.478 \text{ MeV}$$

have been measured by Morgan[6] and by Dickens et al.[7] and data of the latter are shown in Figure 3. In both of these experiments the differential cross section for gamma emission was measured at a single angle. Because of the spins of the levels in ^{7}Li involved, the reaction is isotropic. Due to the relatively smooth energy dependence, this reaction has been suggested as a possible standard in other gamma-ray producing reactions if the cross section were known to sufficient accuracy. In addition to these gamma-ray measurements, the differential neutron scattering data of Knitter et al.[8] and Hopkins et al.[9] along with recent work at Ohio University[5] for this inelastic reaction were included in this analysis. Inelastic scattering to the second excited state of ^{7}Li

$$^7\text{Li(n,n')}^7\text{Li}^* \rightarrow \alpha + t \quad Q = -4.633 \text{ MeV}$$

is important as a tritium breeding reaction. Though attempts were made in the present work to predict the cross section for this reaction, no serious analysis could be undertaken due to the lack of experimental data below about 9 MeV.

The number of possible parameters in this analysis is quite large. With the three particle channels for some J^π as many as nine angular momentum channels are possible, implying both the R- and S-matrices are 9 x 9. To eliminate some of the parameters, the off-diagonal R_o's were set equal to zero and not varied during the analysis. Other parameters that remained fixed during the analysis were the channel radii which were chosen to be 4.3 F and the boundary conditions which were assumed to be independent of J and for each ℓ were set equal to the shift factors evaluated at 4 MeV i.e. the midpoint of the energy region studied. The analysis was carried out in the channel coupling scheme for angular momentum.

One difficulty in undertaking the analysis of the ^{7}Li + n system is the present lack of knowledge of the structure of the compound ^{8}Li nucleus. The ^{7}Li + n total cross section shows only slow variations with energy with few clear indications of the domination of individual states. Below about 10 MeV excitation energy seven unbound states are known in ^{8}Li at excitation energies of 2.26, 3.21, 5.4, 6.1, 6.53, 7.1 and 9 MeV. A level diagram for ^{8}Li is shown in Figure 4. The level at E_x = 6.53 MeV is very narrow ($\sim$ 40 keV) and was not included in the present analysis. Of the remaining levels only two have known spins and these are the 3^+ level at E_x = 2.26 MeV and the J = 1 level at E_x = 3.21.

Numerous combinations of possible J^π values for the known levels in ^{8}Li were tested and although reasonable fits were obtained for the data in some energy regions, satisfactory fits for the entire 0 to 8 MeV neutron energy region could not be obtained for either the elastic or inelastic cross section. Good fits were obtained only after the assumption of the presence of four additional levels in ^{8}Li was made. The final fits to the elastic data are shown in Figure 2. The agreement between the experimental data and calculated fits is generally very good. Some small discrepencies between the two exist in the 1 to 3 MeV energy region particularly in B_o and B_1. It was this energy region that proved to be the most difficult to fit and in which three of the four new levels are assumed to occur. At the upper energies, the differences between the calculated fits and experimental data are probably due to background effects i.e. possible broad levels occurring at higher excitation energies.

The final fit to the first inelastic cross section is shown in Figure 3. The data shown here are the ^{7}Li(n,n'γ)^{7}Li data of Dickens et al.[7]. There are some discrepencies between these data and those of Morgan[6] particularly regarding the shape of the cross section near threshold and the overall normalization. The data of Morgan[6] are generally lower than those of Dickens et al.[7] and show a faster rise in the cross section near threshold.

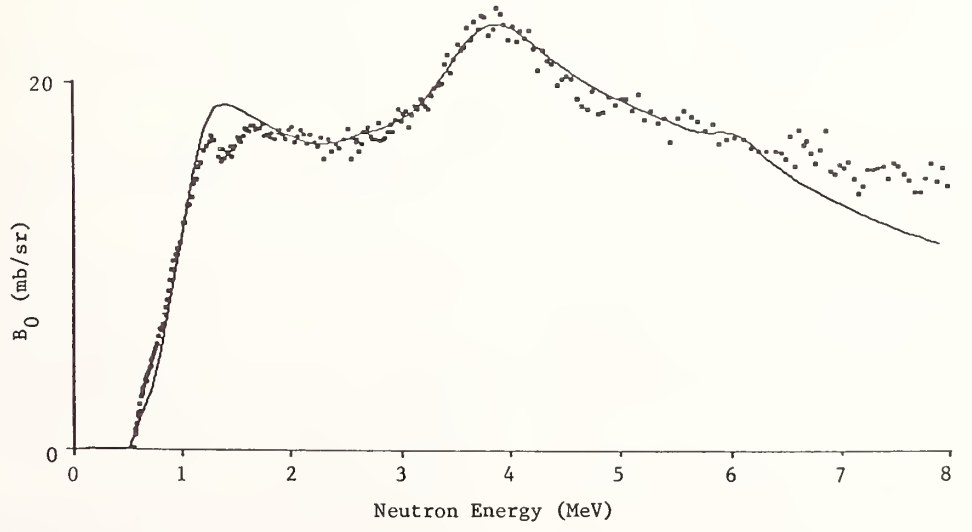

FIGURE 3

A plot of B_o versus neutron energy for the ^{7}Li(n,n')^{7}Li* $\rightarrow \gamma +$ ^{7}Li (0.478 MeV) reaction. The data are the σ (125°) measurements of Dickens et al.[7]. The reaction is isotropic in the center-of-mass system. The curve is the final fit to the data from the present analysis.

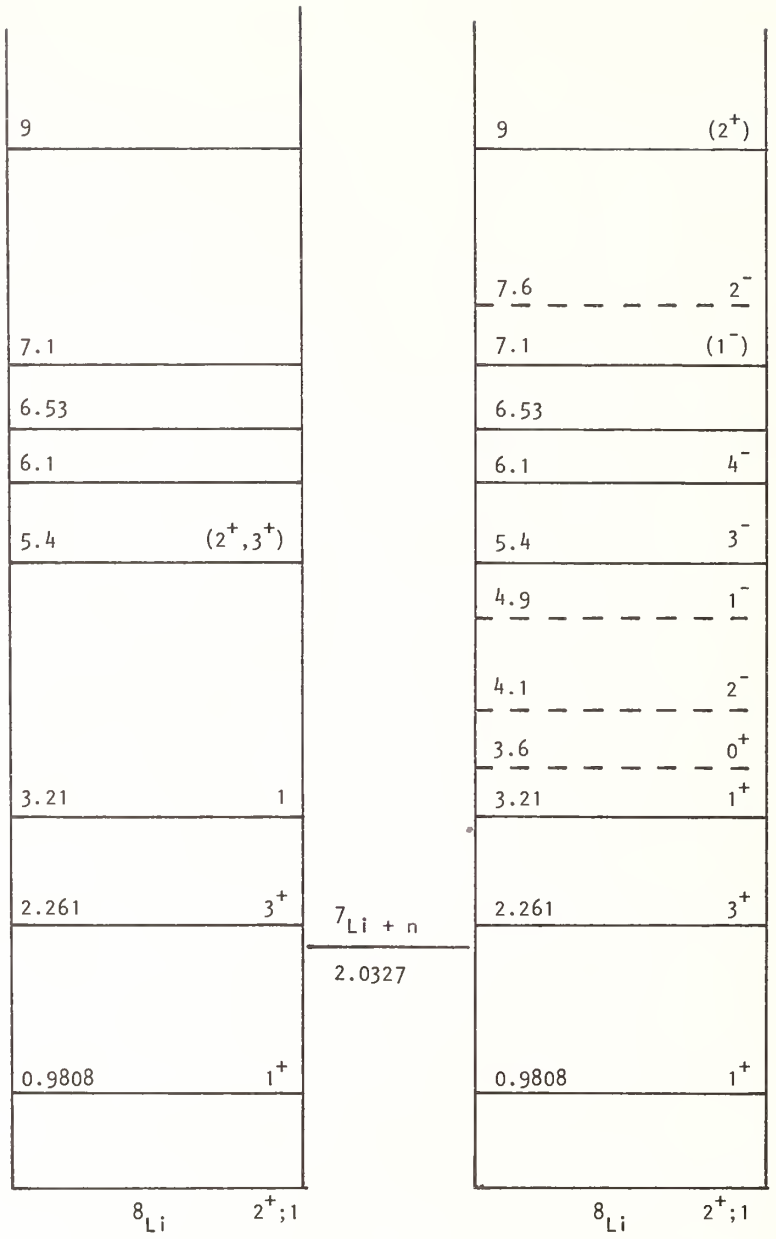

FIGURE 4

Energy level diagram on the left is for ^{8}Li prior to the present analysis. On the right is a proposed energy level diagram based on the results of the present study. New levels predicted here are indicated by dashed lines.

With the exception of the region near ∿ 1.2 MeV neutron energy, the present analysis is in better agreement with the data of Dickens et al.[7]. At higher energies the difference between the calculated fit and the experimental data is again probably due to broad levels at higher energies excluded in the present study.

Based on this analysis, a proposed level diagram for ^{8}Li is shown in Figure 4. Previously known levels in the ^{8}Li system are indicated by solid lines while the new levels predicted from the present work are indicated by dashed lines. The existence of several of the levels shown in the diagram has been predicted by others. In an earlier analysis of ^{7}Li(n,n'γ)^{7}Li (0.478 MeV level), Freeman et al.[10] proposed that the level at E_x = 3.21 MeV was 1^+. Other possible assignments of 1^- and 2^- could not be ruled out at that time. The present work confirms the original 1^+ assignment.

In an analysis of differential scattering and polarization below 2 MeV, Lane et al.[5] found it necessary to assume the presence of broad 2^- and 3^- levels above E_n = 2.5 MeV. These levels correspond to the 2^- and 3^- levels at E_x = 4.1 and 5.4 MeV in the present analysis.

Presser and Bass[11] have made predictions for the J assignments of the levels at E_x = 5.4 and 7.1 MeV based on an analysis of ^{7}Li(n,n'γ)^{7}Li (0.478 MeV level) data. For these two levels J = 2, 3 or 4 and J = 3 or 4 were predicted respectively. For the lower level the present assignment of 3^- is

consistent with that work. For the level at E_x = 7.1 MeV the present assignment is 1^-. This should not be considered definite since an unambiguous J^π assignment was not possible with the data used in the analysis.

A recent cluster model calculation also confirms many of the J^π assignments made in the present study. Stöwe and Zahn[12] have predicted 1^+, 0^+, 1^-, 2^-, 3^- and 4^- levels in ^{8}Li at energies in good agreement with the present work.

The proposed level structure shown in Figure 4 is then quite reasonable both from the standpoint of the excellent fits obtained in the present analysis and from earlier work on the ^{8}Li system.

Conclusion

The simultaneous R-matrix analysis of neutron elastic and inelastic data for ^{7}Li has been quite successful in providing new consistent evaluations of these important cross sections up to approximately 8 MeV incident neutron energy. Moreover, this analysis has revealed much new structure information for the ^{8}Li system where very little progress has been made for over two decades. With the exception of the very narrow level of E_x = 6.53 MeV excluded in the present analysis, spin and parity assignments to all known levels in ^{8}Li have been made along with the predictions of several previously unknown levels. Many of the J^π assignments are in agreement with model calculation or predictions of earlier analyses. The quality of the fits to the experimental data obtained in the present work combined with these corroborating predictions indicate that the proposed structure shown in Figure 4 in an accurate representation of the ^{8}Li system.

The analysis program is currently being updated to include two-body charged-particle channels. As new experimental data become available other reactions will be included in the analysis, thus providing evaluations for as many cross sections as possible for the fusion energy program. Similar analysis for other nuclei e.g. ^{11}B + n and ^{6}Li + n having applications in the fusion program are planned.

Acknowledgments

This work was supported by the U.S. Department of Energy.

References

1) A.M. Lane and R.G. Thomas, Rev. Mod. Phys. 30 257 (1958).
2) J.M. Blatt and L.C. Biedenharn, Rev. Mod. Phys. 24, 258 (1952).
3) R.O. Lane, A.J. Elwyn, and A. Langsdorf, Jr., Phys. Rev. 136, B1710 (1964).
4) H.D. Knox, R.M. White and R.O. Lane, Nucl. Sci. Eng. 69, 223 (1979).
5) R.O. Lane, "Study of Structure of Light Nuclei with Neutrons," Progress Report, Sept. 1, 1977 - August 30, 1978, C00-2490-9, Ohio University (1978)
6) G.L. Morgan, Oak Ridge National Laboratory Report ORNL/TM-6247 (1978).
7) L.K. Dickens, T.A. Love, and G.L. Morgan, Oak Ridge National Laboratory Report ORNL/TM-4538 (1974).
8) H.H. Knitter and M. Coppola, Proc. Conf. Neutron Cross Sections and Technology, Washington D.C., 1968, ed. D.T. Goldman (National Bureau of Standards, Washington D.C., 1968) p. 827.
9) J.C. Hopkins, D.M. Drake, and H. Conde, Nucl. Phys. A107, 139 (1968).
10) J.M. Freeman, A.M. Lane, and B. Rose, Phil. Mag. 46, 17 (1955).
11) G. Presser and R. Bass, Nucl. Phys. A182, 321 (1972).
12) H. Stöwe and W. Zahn, Nucl. Phys. A289, 317 (1977).

CALCULATION OF PROMPT FISSION NEUTRON SPECTRA

David G. Madland and J. Rayford Nix
Theoretical Division
Los Alamos Scientific Laboratory
University of California
Los Alamos, New Mexico 87545, USA

We present a new calculation of the prompt fission neutron spectrum N(E) as a function of both the fissioning nucleus and its excitation energy. The calculation, based upon standard nuclear-evaporation theory, accounts for the physical effects of (1) the distribution of fission-fragment residual nuclear temperature, and (2) the energy dependence of the cross section for the inverse process of compound-nucleus formation. Using a residual nuclear temperature distribution based upon the Fermi-gas model, we have performed calculations for two different assumptions concerning the cross section for compound-nucleus formation. Use of a constant cross section leads to a closed expression for the neutron energy spectrum while use of an energy-dependent cross section, calculated with the optical model, yields a numerical integration. Results obtained for the two assumptions agree well with experimental data although there is a preference for the energy-dependent cross section calculation.

[RADIOACTIVITY, FISSION Calculation of prompt fission neutron spectrum as function of fissioning nucleus and excitation energy. Nuclear-evaporation model, Fermi-gas model. Comparisons to ^{235}U(n,f) and ^{252}Cf(sf) experimental prompt neutron spectra.]

Introduction

Nuclear reactor design and other applications require knowledge of the prompt fission neutron spectrum N(E) as a function of both the fissioning nucleus and its excitation energy. The dependence upon fissioning nucleus and incident neutron energy is particularly important in cases where fission neutron spectrum measurements do not exist or are not possible. We study these dependencies by use of standard nuclear-evaporation theory to calculate the neutron energy spectrum in the fission-fragment center-of-mass system, and then transform these results to the laboratory system.

The center-of-mass neutron energy spectrum is obtained by integrating the nuclear-evaporation spectrum[1] for fixed residual nuclear temperature over the distribution function of this temperature. The nuclear temperature is that of the residual nucleus following neutron emission from the evaporating fission fragment. The physical origins of the residual nuclear temperature distribution are the initial distribution of fission-fragment excitation energy and the subsequent fragment cooling as neutrons are emitted. Following the integration, the resulting center-of-mass neutron energy spectrum is transformed to the laboratory system under the assumption that the neutrons are emitted isotropically from the moving fragments.

Our calculations have been performed using a triangular approximation to the residual nuclear temperature distribution determined by Terrell on the basis of experiment and the Fermi-gas model.[2] Two different assumptions have been tested for the inverse process of compound-nucleus formation. Use of a constant compound-nucleus formation cross section yields a closed expression for N(E) involving the exponential integral and the incomplete gamma function. Use of an energy-dependent formation cross section, calculated with the optical model, yields a numerical double-integral expression. Comparisons to experimental data demonstrate the importance of including both the distribution of residual nuclear temperature and the energy-dependent compound-nucleus formation cross section. The calculations and results obtained using the constant compound-nucleus cross section are discussed in the next section and those obtained with the energy-dependent cross section in the section following that. We then compare the results of both calculations with experimental data. Our conclusions are presented in the final section.

Constant Compound-Nucleus Cross Section

The nuclear-evaporation spectrum corresponding to a fixed residual nuclear temperature T is given approximately by[1]

$$\phi(\varepsilon) = c(T)\, \sigma_c(\varepsilon)\, \varepsilon \exp(-\varepsilon/t) , \quad (1)$$

where ε is the center-of-mass energy, $\sigma_c(\varepsilon)$ is the cross section for the inverse process of compound-nucleus formation, and c(T) is the normalization integral defined such that $\phi(\varepsilon)$ is normalized to unity when integrated from zero to infinity. All distributions in this paper are normalized in this way. In the case of a constant compound-nucleus cross section σ_c, the normalization integral c(T) has the value $1/\sigma_c T^2$.

The initial distribution of total fission-fragment excitation energy is approximately Gaussian in shape, with a total average value given by

$$\langle E^* \rangle = \langle E_r \rangle + B_n + E_n - \langle E_f^{tot} \rangle . \quad (2)$$

Here $\langle E_r \rangle$ is the average energy release, B_n and E_n are the separation energy and kinetic energy of the neutron inducing fission, and $\langle E_f^{tot} \rangle$ is the total average fission-fragment kinetic energy. For spontaneous fission both B_n and E_n in Eq. (2) are zero. In calculating $\langle E_r \rangle$ and B_n we use the experimental and systematic masses compiled by Wapstra and Bos[3] where available and otherwise the droplet-model mass formula of Myers.[4] Measured values of $\langle E_f^{tot} \rangle$ are also used where available and otherwise the formula

$$\langle E_f^{tot} \rangle = c_1(Z^2/A^{1/3}) + c_2 ,$$

where Z and A are the atomic number and mass number of the fissioning nucleus and c_1 and c_2 are determined by least-squares adjustment to experimental data. For low-excitation fission we use (c_1, c_2) values of (0.13323 Mev, -11.64 MeV) determined by Unik et al.,[5] and for high-excitation fission the values (0.1071 MeV, 22.2 MeV) obtained by Viola.[6]

In a study of experimental distributions of fission-fragment kinetic energy and neutron number Terrell obtained the distribution of kinetic energy that governs neutron emission.[2] This distribution was transformed into the distribution P(T) of fission-fragment residual nuclear temperature by use of the Fermi-gas model where the excitation energy E^*, the nuclear temperature T, and the nuclear level-density parameter a are related by $E^* = aT$.[2] Terrell observed that if the resulting temperature distribution is approximated by the sharp cutoff triangular distribution

$$P(T) = \begin{cases} 2T/T_m^2 , & T \leq T_m \\ 0 , & T > T_m \end{cases} \qquad (3)$$

then the maximum temperature T_m is related to the initial total average fission-fragment excitation energy $\langle E^* \rangle$ by

$$T_m = (\langle E^* \rangle / a)^{\frac{1}{2}} . \qquad (4)$$

For the present studies we use the approximation summarized by Eqs. (3) and (4) to calculate the residual nuclear temperature distribution. We use the simple relationship

$$a = A/(11\ \text{MeV}) \qquad (5)$$

for the nuclear level-density parameter, where A is the mass number of the fissioning nucleus. It must be noted that a slight adjustment in T_m from the value predicted by Eqs. (4) and (5) could in principle be required.

The neutron energy spectrum in the fission-fragment center-of-mass system, $\Phi(\varepsilon)$, is obtained by integrating Eq. (1) over the temperature distribution given by Eq. (3). This yields

$$\Phi(\varepsilon) = \int_0^\infty \phi(\varepsilon)\, P(T)\, dT \qquad (6a)$$

$$= (2\varepsilon/T_m^2)\, E_1(\varepsilon/T_m) , \qquad (6b)$$

where $E_1(x) = \int_x^\infty [\exp(-u)/u]du$ is the exponential integral. This result has been obtained previously by Kapoor et al.[7] The average center-of-mass neutron energy $\langle \varepsilon \rangle$ is the first moment of Eq. (6b) and has the value $(4/3)T_m$.

The transformation of the fission-fragment center-of-mass neutron energy spectrum $\Phi(\varepsilon)$ to the laboratory system, under the assumption that the neutrons are emitted isotropically from a fission fragment moving with average kinetic energy per nucleon E_f, is accomplished by use of the general result

$$N(E) = \frac{1}{4\sqrt{E_f}} \int_{(\sqrt{E}-\sqrt{E_f})^2}^{(\sqrt{E}+\sqrt{E_f})^2} [\Phi(\varepsilon)/\sqrt{\varepsilon}]d\varepsilon , \qquad (7)$$

where E is the laboratory neutron energy.[2] Inserting Eq. (6b) and interchanging the order of integration, we obtain for the laboratory prompt fission neutron spectrum

$$N(E) = (1/3\sqrt{E_f T_m})\, [u_2^{3/2}\, E_1(u_2) - u_1^{3/2}\, E_1(u_1) + \gamma(\tfrac{3}{2}, u_2) - \gamma(\tfrac{3}{2}, u_1)] , \qquad (8)$$

where $u_1 = (\sqrt{E} - \sqrt{E_f})^2/T_m$,

$u_2 = (\sqrt{E} + \sqrt{E_f})^2/T_m$,

and $\gamma(a,x) = \int_0^x u^{a-1} \exp(-u)du$

is the incomplete gamma function. The mean laboratory neutron energy $\langle E \rangle$ is the first moment of Eq. (8) and has the value $E_f + (4/3)T_m$.

Since there are two fission fragments, each emitting approximately the same average number of neutrons,[8] but each moving with generally quite different average velocities, the transformation given by Eq. (7) must be separately applied to each fragment. This leads to

$$N(E) = \frac{1}{2} [N_L(E) + N_H(E)] , \qquad (9)$$

where the subscripts refer to light and heavy fragments. Equation (8) is used to evaluate each term of Eq. (9). The values of the average kinetic energy per nucleon for each fragment transformation are given by

$$E_f^L = \frac{\langle A_H \rangle}{\langle A_L \rangle} \frac{\langle E_f^{tot} \rangle}{A} \quad \text{and} \quad E_f^H = \frac{\langle A_L \rangle}{\langle A_H \rangle} \frac{\langle E_f^{tot} \rangle}{A} \qquad (10)$$

where $\langle A_L \rangle$ and $\langle A_H \rangle$ are the average integer fragment atomic mass numbers as obtained from Unik et al.[5] The mean laboratory neutron energy for the spectrum given by Eq. (9) is

$$\langle E \rangle = \frac{1}{2} (E_f^L + E_f^H) + \frac{4}{3} T_m . \qquad (11)$$

The prompt fission neutron spectrum calculated from Eq. (9) for the fission of ^{235}U induced by 0.53-MeV neutrons is shown in Fig. 1. Also shown are the Watt and Maxwellian spectra[2] calculated for the same fissioning system by using temperatures T_W and T_M, respectively, constructed to yield mean energies identical to that given by Eq. (11) for the present claculation. These temperatures have the values $T_W = (8/9)T_m$ and $T_M = (1/3)(E_f^L+E_f^H) + (8/9)T_m$. In Fig. 2 the same calculated spectra are compared by forming ratios to the present calculation. The Watt spectrum is accurate to within a few percent for laboratory neutron energies between 0 and about 7 MeV and smaller than the present calculation for higher energies because the Watt temperature T_W is less than T_m. The Maxwellian spectrum is a much less accurate physical approximation, particularly at energies greater than about 5 MeV where it is most sensitive to the large value of T_M, which must account for the motion of the fission fragments as well as the center-of-mass motion of the emitted neutrons. Finally, the dependence of the present calculation upon the fissioning nucleus and the incident neutron energy is illustrated in Figs. 3 and 4. Figure 3 illustrates how the high-energy portion of the spectrum increases as the charge of the fissioning nucleus increases, for thermal-neutron-induced fission. Figure 4 illustrates a similar behavior of the spectrum as the kinetic energy of the incident neutron increases, for the fission of ^{235}U.

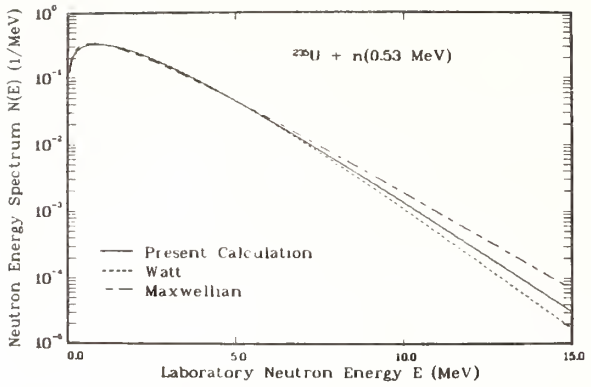

Fig. 1. Prompt fission neutron spectrum in the laboratory system for the fission of ^{235}U induced by 0.53-MeV neutrons. The solid curve gives the present spectrum calculated from Eqs. (8) and (9). The values of E_f^L, E_f^H, and T_m are, respectively, 1.062, 0.499, and 1.018 MeV. The mean laboratory energy, calculated from Eq. (11), is 2.138 MeV and is equal to the mean energy of both the calculated Watt and Maxwellian spectra which are shown for comparison.

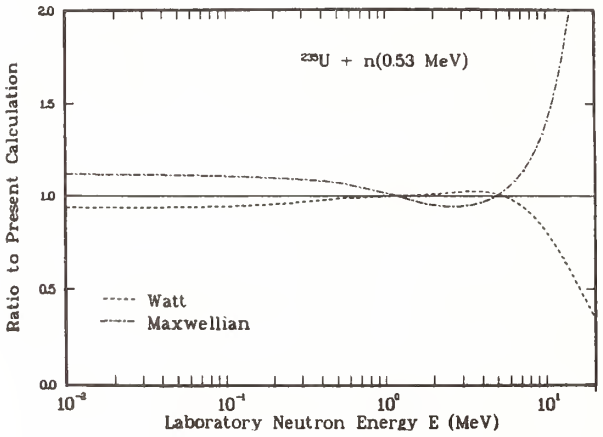

Fig. 2. Ratio of Watt spectrum and the Maxwellian spectrum to the present spectrum, corresponding to the curves shown in Fig. 1.

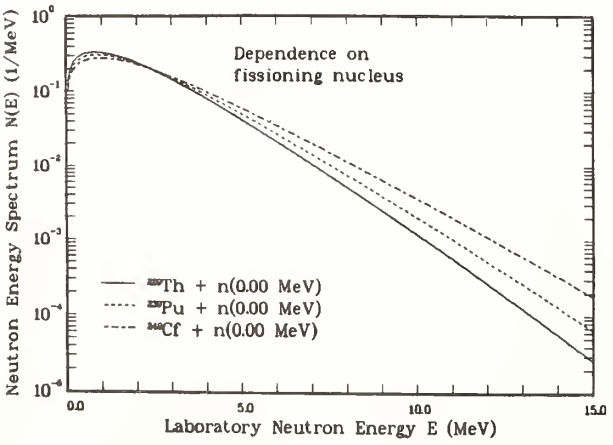

Fig. 3. Dependence of the prompt fission neutron spectrum upon the fissioning nucleus, for thermal-neutron-induced fission, as calculated from Eqs. (8) and (9).

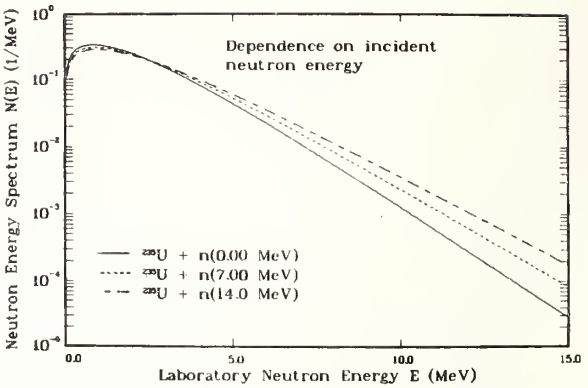

Fig. 4. Dependence of the prompt fission neutron spectrum upon the kinetic energy of the incident neutron, for the fission of ^{235}U, as calculated from Eqs. (8) and (9). The values of E_f^L and E_f^H, obtained from Eq. (10), are held fixed for all incident neutron energies. The 14-MeV spectrum is calculated for first-chance fission only.

Energy-Dependent Compound-Nucleus Cross Section

In this section we calculate the prompt fission neutron spectrum in the case of an energy-dependent cross section for the inverse process of compound-nucleus formation. We obtain this cross section using the optical model. The calculation proceeds exactly as in the previous section except that the integrations must now be performed by numerical methods. The complete expression for the numerical integration is obtained by combining Eqs. (1), (3), and (6a) into Eq. (7) which yields the double integral

$$N(E) = \frac{1}{4\sqrt{E_f}} \int_{(\sqrt{E}-\sqrt{E_f})^2}^{(\sqrt{E}+\sqrt{E_f})^2} \sqrt{\varepsilon}\, \sigma_c(\varepsilon) \left[\int_0^{T_m} (2T/T_m^2) \right.$$

$$\left. \times\, c(T)\, \exp(-\varepsilon/T)\, dT \right] d\varepsilon \qquad (12)$$

where the normalization integral c(T) is given by

$$c(T) = \{\int_o^\infty \nu\, \sigma_c(\nu)\, \exp(-\nu/T) d\nu\}^{-1}$$

Gauss-Laguere and Gauss-Legendre quadrature of order 32 are used to evaluate the three integrals appearing in Eq. (12). We represent the optical-model compound-nucleus formation cross section by a cubic-spline fit to a calculated array of 75 points extending from 1 keV to 30 MeV.

Following the numerical integration of Eq. (12) for E_f values and energy-dependent cross sections appropriate to each fragment, we obtain the laboratory prompt fission neutron spectrum using Eq. (9). Calculations were performed for the fission of ^{235}U induced by 0.53-MeV neutrons using three, well-known, neutron-nucleus global optical-model potentials. These are the potentials of Moldauer,[9] Wilmore and Hodgson,[10] and Becchetti and Greenlees.[11] The results are shown in Fig. 5 where the ratios of the three calculations to the constant compound-nucleus cross section calculation of Fig. 1 are plotted. The results are similar for the three potentials,

namely, there is approximately a 10% enhancement at a laboratory energy of about 700 keV and a gradual decrease above 2 MeV, relative to the constant cross section calculation. These structure changes are due to the gradual decrease of $\sigma_c(\varepsilon)$ with energy and the relative maxima and minima of $\sigma_c(\varepsilon)$ below the 1-MeV region.

Comparisons with Experimental Data

We compare our results to experimentally determined prompt fission neutron spectra in Figs. 6 and 7 for, respectively, the fission of ^{235}U induced by 0.53-MeV neutrons[12] and the spontaneous fission of ^{252}Cf.[13] Calculations using the constant compound-nucleus cross section agree reasonably well with this data although they are slightly high in various portions of the tail region. In both figures a clear preference exists for the energy-dependent compound-nucleus cross section calculation shown for the case of the Wilmore-Hodgson optical potential. This is evident in the high-energy region as well as in the 1-MeV region where the data appear to support the existence of enhanced structure. However, our energy-dependent calculation is unable to reproduce the magnitude of this structure in the case of ^{252}Cf(sf).

Conclusions

A new calculation of the prompt fission neutron spectrum has been presented. The calculation demonstrates the importance of accounting for the physical effects of the residual nuclear temperature distribution and the energy-dependence of the cross section for the inverse process of compound-nucleus formation. The calculation predicts clear dependencies upon fissioning nuclear species and incident neutron energy. Fission neutron spectra can now be calculated in regions devoid of experimental spectrum measurements.

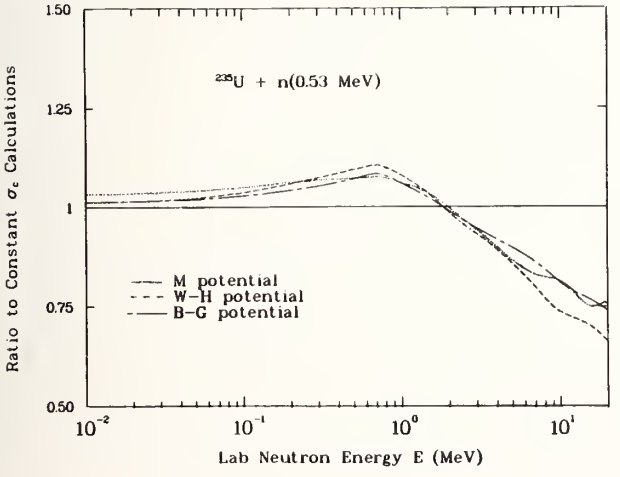

Fig. 5. Ratio of the prompt fission neutron spectra calculated with energy-dependent compound-nucleus cross sections to that calculated using the constant compound-nucleus cross section shown in Fig. 1, for the fission of ^{235}U induced by 0.53-MeV neutrons. The dotted curve is for the potential of Moldauer, the dashed curve is for the potential of Wilmore and Hodgson, and the dot-dashed curve is for the potential of Becchetti and Greenless. The E_f^L and E_f^H values are the same for all four of the calculations.

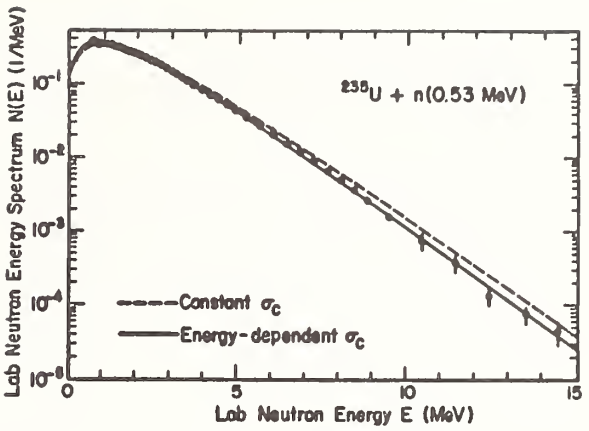

Fig. 6. Prompt fission neutron spectrum for the fission of ^{235}U induced by 0.53-MeV neutrons. The dashed curve gives the constant cross section calculation identical to that of Fig. 1 and the solid curve depicts the energy-dependent cross section calculation using the optical potential of Wilmore and Hodgson. In both cases the same values of E_f^L and E_f^H have been employed. The experimental data are those of Johansson and Holmquist.

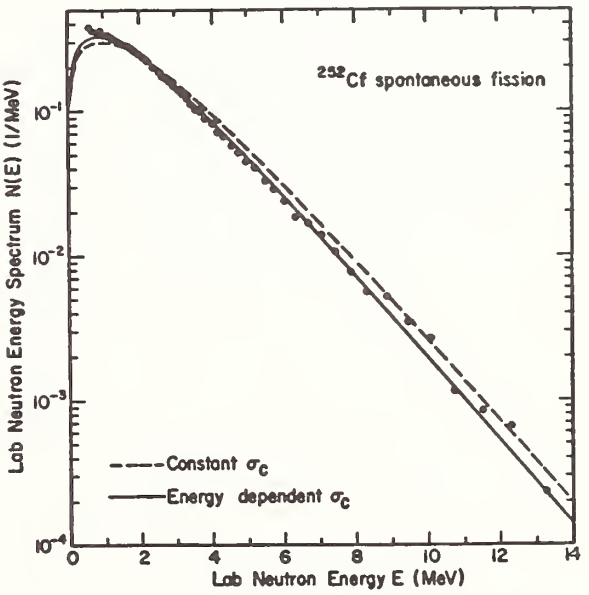

Fig. 7. Prompt fission neutron spectrum for the spontaneous fission of ^{252}Cf. The dashed curve gives the constant cross section calculation where the values of E_f^L, E_f^H, and T_m are, respectively, 0.984, 0.553, and 1.209 MeV. The solid curve depicts the energy-dependent cross section calculation using the optical potential of Wilmore and Hodgson. In both cases the same values of E_f^L and E_f^H have been employed. The experimental data are those of Boldeman, et al.

References

1. V. Weisskopf, Phys. Rev. 52, 295 (1937).

2. J. Terrell, Phys. Rev. 113, 527 (1959).

3. A. H. Wapstra and K. Bos, Atomic Data Nucl. Data Tables 19, 177 (1977).

4. W. D. Myers, Droplet Model of Atomic Nuclei (IFI/Plenum Data Co., New York, 1977).

5. J. P. Unik, J. E. Gindler, L. E. Glendenin, K. F. Flynn, A. Gorski, and R. K. Sjoblom, in Proceedings of the Third IAEA Symposium on the Physics and Chemistry of Fission, Rochester, New York, USA, 1973 (IAEA, Vienna, 1974), Vol. II, p. 19.

6. V. E. Viola, Jr., Nucl. Data A 1, 391 (1966).

7. S. S. Kapoor, R. Ramanna, and P. N. Rama Rao, Phys. Rev. 131, 283 (1963).

8. J. Terrell, Phys. Rev. 127, 880 (1962).

9. P. A. Moldauer, Nucl. Phys. 47, 65 (1963).

10. D. Wilmore and P. E. Hodgson, Nucl. Phys. 55, 673 (1964).

11. F. D. Becchetti and G. W. Greenlees, Phys. Rev. 182, 1190 (1969).

12. P. I. Johansson and B. Holmquist, Nucl. Sci. Eng. 62, 695 (1977).

13. J. W. Boldeman, D. Dulley, and R. J. Cawley, Trans. Am. Nucl. Soc. 32, 733 (1979).

SIMPLE PARAMETERIZATION FOR OPTICAL REACTION CROSS SECTIONS

K.H. Narasimha Murthy*, A. Chatterjee and S.K. Gupta
Nuclear Physics Division, Bhabha Atomic Research Centre, Trombay
Bombay 400 085, India

* C S I R Junior Research Fellow, Mysore University

Optical model reaction cross sections for neutrons, protons and alpha particles, are directly parametrized using simple expressions reflecting the mass number and energy dependence. The cross sections can be calculated within an accuracy of 5-10% over the whole periodic table and the energy range upto 50 Mev. These cross sections are useful inputs for calculating various partial reaction cross sections using statistical models of nuclear reactions.

[Optical reaction cross sections for neutrons, protons, alphas, over the periodic table, energies upto 50 MeV, inputs for further calculations]

Introduction

The scattering between the projectile and the target nucleus can be adequately described by an optical potential over the energy range encompassing tens of MeV. Apart from describing the elastic process, optical model yields also the total reaction cross section, henceforth referred to as the optical reaction cross section. Using statistical models one can further describe the break-up of the optical reaction cross section into various partial modes such as emission of a neutron, a proton or an alpha particle. The sequential processes such as emission of several particles can also be described using the same emission rate equation. This equation involves the inverse cross section of the emitted particle as a function of energy. The inverse cross section is the optical reaction cross section of the excited residual nucleus with the emitted particle as the projectile. This is approximated as the optical reaction cross section between the residual nucleus in its ground state and the (emitted) particle. Thus optical reaction cross sections are required as the properties of the incident projectile and the emitted particle. Usually the optical reaction cross sections at all the required energies for a given particle-target combination are obtained by solving numerically the Schrodinger equation for several partial waves. In a global calculation, therefore, a large amount of computation time is spent in calculating the optical reaction cross sections. The parametrization of the optical reaction cross sections in simple analytic forms is of immense utility in computing the reaction cross sections using the statistical theories. In the present work we describe a parameterization for neutrons, protons and alpha particles both in the target mass-number and energy spaces. The present work can be considered as a considerable improvement over the parameterization of Dostrovsky et al[1] who used the continum model cross sections as the input.

Methodology

Choice of optical model parameters: For neutrons and protons the optical model subroutine[2] SCAT was used to calculate the reaction cross sections at energies 1-50 MeV for 23 nuclei in the mass-range 20-214. The most useful global optical model parameter set is that of Becchetti and Greenlees[3] both for neutrons and protons. The parameter set of Perey[4] can also be considered quite a good description for neutrons. The optical parameter set of Mani et al[5] was also considered since the tabulation using this set is widely used. It can be considered as a reasonable choice but not necessarily the best. For alpha particles there does not exist a clear-cut global phenomenological parameter set, however Huizenga and Igo's[6] table can be considered to be a reasonable one. Therefore it was decided to use these cross sections in the energy range 2-46 MeV and the mass range 20-206 directly in the fitting procedure.

Fitting Procedure for neutrons: For a given projectile the optical reaction cross section is a function of (laboratory) energy, mass number and atomic number. For energy dependence in the case of neutrons the optical reaction cross section σ_R (in millibarns) is written as

$$\sigma_R(E) = \lambda E + \mu + \frac{\nu}{E} \qquad \ldots (1)$$

where λ, μ and ν are mass-dependent parameters. E is the neutron laboratory energy in MeV. Expression(1) is a slight modification of the expression of Dostrovsky et al[1]. An extra term λE has been added to account for size resonance effects in the optical reaction cross section.

In a linear least squares fit code values of σ_R for each nucleus were fed to determine λ, μ and ν individually. Systematic dependences as a function of target mass number A were looked for in these three parameters. It was possible to describe λ, μ and ν using 7 constants in the following manner.

$$\lambda = \lambda_0 A^{-1/3} + \lambda_1$$
$$\mu = \mu_0 A^{1/3} + \mu_1 A^{2/3} \quad \ldots (2)$$
$$\nu = \nu_0 A^{4/3} + \nu_1 A^{2/3} + \nu_2$$

Inserting expression(2) in expression(1) the optical reaction cross section for any target nucleus plus neutron at any energy can be calculated. It was found that the low energy behaviour cannot be described very well by expression(1), however the emission rate expressions are proportional to $\varepsilon \sigma_n(\varepsilon)$ rather than $\sigma_n(\varepsilon)$. Hence the parameterization of expression (2) along with $\sigma_n(\varepsilon)$ given by expression(1) were used to determine the 7 parameters, fitting simultaneously $\varepsilon \sigma_n(\varepsilon)$ values in the linear least squares fit code. The resultant values of the parameters are listed in table I. The values of $\varepsilon \sigma_n(\varepsilon)$ are described well by these parameters.

Fitting procedure for charged projectiles:

It was found that for the charged projectiles it is not possible to describe the cross section behaviour as a function of energy using a simple polynomial expression in energy. Hence it was decided to segment the charged particle cross sections into two domains, one below the Coulamb barrier E_c and the other above E_c. The expression for E_c is

$$E_c = \frac{1.44\, Z_p Z_T}{1.5 A^{1/3} + \delta_p} \text{ MeV} \quad \ldots (3)$$

Here Z_p and Z_T are atomic numbers of projectile and target respectively. δ_p is chosen as zero for protons and 1.2 for alphas. For laboratory energy ε (in Mev) below E_c, the reaction cross section is described as

$$\sigma_n(\varepsilon) = p\varepsilon^2 + q\varepsilon + r \quad (\varepsilon < E_c) \quad \ldots (4)$$

while for values above E_c an expression similar to (1) is used. Matching the two expressions for the value and the derivative at E_c, q and r can be eliminated and the following expression is obtained.

$$\sigma_n(\varepsilon) = P(\varepsilon - \xi)^2 + \lambda\varepsilon + \mu + \frac{\nu}{\xi}\left(2 - \frac{\varepsilon}{\xi}\right) \quad \ldots (5)$$
where $\xi = E_c$ when $\varepsilon < E_c$
$= \varepsilon$ when $\varepsilon > E_c$

Using optical model values of σ_n (in millibarn), the parameter of expression(5) were determined. It was realized that p and ν play a dominant role below the coulamb barrier E_c. So the behaviour of these parameters was considered in terms of E_c while the behaviour of λ and μ was examined as function of target mass number A. The following parameterization was found successful

$$P = P_0 + \frac{P_1}{E_c} + \frac{P_2}{E_c^2}$$
$$\lambda = \lambda_0 A + \lambda_1 \;, \quad \mu = \mu_0 A^{\mu_1} \quad \ldots (6)$$
$$\nu = A^{\mu_1}\left[\nu_0 + \nu_1 E_c + \nu_2 E_c^2\right]$$

In this set only μ_1 appears in a nonlinear form. Hence its value was fixed from individual fits and an overall linear least square fit was carried out to determine the remaining 9 parameters of expression(6) using expressions(5) and the optical reaction cross sections for all the nuclei.

The parameters obtained for protons and alphas are shown in table I. The cross sections σ_n of eqn (5) should be set to zero for ε less than the greater of the two roots of the quadratic equation $P\varepsilon^2 + q\varepsilon + r = 0$. This is reasonably correct as the cross sections are negligible in these cases.

Summary

The optical reaction cross sections for various available global optical model parameter sets have been successfully parameterized using simple analytic expressions. It is found that these expressions describe the cross section to an accuracy better than 5 - 10% over the mass range 16-214 and energy range 1-50 MeV. Extrapolation beyond this mass range should also be reasonably accurate using the present parameterization. It should be emphasized that (1) the present parameterization serves as a useful interpolation formula in the mass and energy ranges.(2) the present paramaterization implies $\varepsilon \sigma_n(\varepsilon)$ is a polynomial in ε, analytic integration of emission rate expressions for the energy spectra in statistical models to obtain total emission rates is quite straightforward. Using the present parameterization which is being extended to include other projectiles such as deuterons, tritons and helium-3, calculation of a large number of cross sections for several reactions are being contemplated employing the exact solution of exciton model[7] discussed elsewhere in this conference.

References:

1. I.Dostrovsky, Z. Fraenkel and G.Friedlander Phys. Rev 116, 683 (1959).

2. W.R.Smith, Computor Phys. Commun.1, 106 (1959)

3. F.D.Becchetti, Jr., and G.W.Greenlees, Phys.Rev. 182, n04, 1190 (1969)

4. F.G.Perey, Phys.Rev. 131 , 745 (1963)

5. G.S.Mani, M.A.Melkanoff and I.Iori. Reports C.E.A. 2379 and 2380 (1963)

6. J.R.Huizenga and G.T.Igo. Report ANL-6373 (1961)

7. S.K.Gupta and A.Chatterjee, this conference.

Table I. Parameters for neutrons, protons and alpha particles.

All parameters will lead to cross sections in millibarns

if energy and coulomb barrier are in MeV

Optical model set	P_0	P_1	P_2	λ_0	λ_1	μ_0	μ_1	ϑ_0	ϑ_1	ϑ_2
NEUTRONS:										
Mani et al	-	-	-	10.140	-9.92	232.1	37.16	0.455	-46.7	758.5
Becchetti and Greenlees	-	-	-	31.550	-23.92	294.9	38.11	1.563	-116.1	2749.1
PROTONS:										
Mani et al	12.97	15.65	-348.5	0.0247	-7.01	300.4	0.4	330.2	-223.6	-3.250
Perey	10.53	52.53	-414.0	0.0309	-10.16	327.9	0.4	323.7	-243.4	-3.037
Becchetti and Greenlees	15.72	9.65	-449.0	0.00437	-16.58	244.7	0.503	273.1	-182.4	-1.872
ALPHA PARTICLES:										
Huizenga and Igo	10.95	-85.21	1146.0	0.0643	-13.96	781.2	0.29	-304.7	-470.0	-8.582

EXACT SOLUTION OF THE EXCITON MODEL MASTER EQUATIONS FOR NUCLEAR REACTIONS

S.K. Gupta and Ambar Chatterjee
Bhabha Atomic Research Centre
Bombay 400 085, India

An exact solution is obtained for the time integrated Pauli master equations of the exciton model. The solution expresses the mean lifetimes of exciton states in terms of the various transition rates of the model in a simple closed form. Using these solutions both the preequilibrium and equilibrium components of nuclear reactions can be obtained in an integrated manner. The solutions are applicable also for the case of the generalized master equations which can be used to calculate angular distributions. An application of the solutions for the calculation of neutron spectra in the neutron induced reactions on ^{93}Nb is discussed.

[Exciton model, master equations, preequilibrium and equilibrium components, neutron angular distributions.]

Introduction

In the region of large nuclear level densities it is appropriate to use statistical concepts in discussing nuclear reactions. The theory of the compound nucleus envisages the formation of a statistically equilibrated system which then decays. The preequilibrium emission of particles prior to equilibrium is also amenable to a statistical interpretation. The quantum statistical description of a system approaching equilibrium is a set of Pauli master equations. In a unified statistical theory of nuclear reactions[1] a probability matrix is constructed which obeys a probability balance equation. The probability balance equation is essentially a time integrated form of the Pauli master equations.

The existing closed formulations of the preequilibrium model employ approximate solutions of the master equations. Alternatively numerical time integration of the master equations upto the equilibration time has also been employed. When approximate closed forms are used the extent of error involved is unknown, while numerical integration of the master equations is time consuming. In both these cases, the equilibrium component has to be added seperately. An integrated description of both the preequilibrium and equilibrium components is possible when the master equations are solved completely, as is the case with matrix methods[2,3].

In this work an exact closed form solution of the master equations is obtained. This has the advantage of the integrated description mentioned above with the simplicity of a closed form.

Transition and Emission Rates

The intermediate states of the system are enumerated in terms of the number of excitons, n with p excited particles and h holes (n = p+h). For a system with excitation energy E, the state density is given by

$$\omega(p,h,E) = \frac{g^n (E - A_{p,h})^{n-1}}{p!\,h!\,(n-1)!} \qquad (1)$$

with

$$A_{p,h} = (3p^2 - h^2 - n)/(4g) \qquad (2)$$

where g is the single particle level density. The transition rates for the allowed two body transitions, $\Delta p = \Delta h = 0, \pm 1$ are given by

$$\lambda^0 = \frac{2\pi}{\hbar} M^2 \frac{g^2}{2} \frac{p^2 + h^2 + 4ph - p - h}{n} (E - C_{p,h}) \qquad (3)$$

$$\lambda^+ = \frac{2\pi}{\hbar} M^2 \frac{g^3 (E - C_{p+1,h+1})^2}{2(n+1)} \qquad (4)$$

$$\lambda^- = \frac{2\pi}{\hbar} M^2 \frac{g}{2} ph(n-2)\left[1 - \frac{(p-1)(p-2) + (h-1)(h-2)}{8g(E - A_{p,h})} \left(\frac{n-1}{n-2}\right)\right] \qquad (5)$$

with

$$C_{p,h} = p^2/g \qquad (6)$$

where M^2 is the square of the average two body matrix element, and has been parameterized in terms of the mass number of the target as

$$M^2 = 400/(A^3 E) \quad \text{MeV}^2 \qquad (7)$$

The rate of emission of a particle β with energy ε from an exciton state is given by

$$W_\beta(p,h,\varepsilon)\,d\varepsilon = \frac{(2s_\beta + 1)}{\pi^2 \hbar^3} \mu_\beta \sigma_\beta \varepsilon\, Q_\beta(p) \frac{\omega(p - p_\beta, h, U)}{\omega(p,h,E)} d\varepsilon \qquad (8)$$

where s_β, μ_β and p_β are the spin, reduced mass and nucleon number of the emitted particle; U is the residual nucleus excitation energy; σ_β is the optical reaction cross section of the inverse reaction; and $Q_\beta(p)$ is a combinatorial factor given by,

$$Q_\beta(p) = \frac{(p - p_\beta)!}{p!} \sum_{i=0}^{p - p_\alpha} \frac{(p - p_\alpha)!}{i!\,(p - p_\alpha - i)!} \left(\frac{Z}{A}\right)^{i - \pi_\beta} \left(\frac{N}{A}\right)^{p - p_\alpha - i - \nu_\beta} \times \frac{(\pi_\alpha + i)!}{(\pi_\alpha + i - \pi_\beta)!} \frac{(p - \pi_\alpha - i)!}{(p - \pi_\alpha - i - \nu_\beta)!} \qquad (9)$$

where π_β, ν_β and π_α, ν_α are the proton and neutron numbers of the emitted particle and the projectile respectively with $p_\beta = \pi_\beta + \nu_\beta$ and $p_\alpha = \pi_\alpha + \nu_\alpha$

Equations (1) to (9) are from ref[4].

Master Equations

A generalized form of the master equations, which can describe angular distributions, has been given by Mantzouranis et al[5]. At any time t the system is characterized by the exciton number n and a direction Ω. The generalized master equation is

$$\frac{d}{dt} q(n,\Omega,t) = \sum_m \int d\Omega' q(m,\Omega',t)\, W_{mn}(\Omega',\Omega) - q(n,\Omega,t) \sum_m \int d\Omega' W_{nm}(\Omega,\Omega') \qquad (10)$$

where $q(n,\Omega,t)$ is the probability of finding the system in class (n,Ω) at time t and $W_{nm}(\Omega,\Omega')$ is the transition rate from class (n,Ω) to (m,Ω'). The latter is a product of the transition rates λ^+, λ^- or λ° and an angular-dependent factor

$$G(\Omega,\Omega') = G(\Omega',\Omega) = \left[\int d\Omega \frac{d\sigma}{d\Omega}\right]^{-1} \frac{d\sigma}{d\Omega}(\Omega,\Omega') \qquad (11)$$

where $d\sigma/d\Omega$ is the differential free nucleon-nucleon scattering cross section. By using the result[6]

$$\int d\Omega' G(\Omega',\Omega) P_\ell(\cos\theta') = \mu_\ell P_\ell(\cos\theta) \qquad (12)$$

and expanding $q(n,\Omega,t)$ in a series of Legendre Polynomials,

$$q(n,\Omega,t) = \sum_\ell \eta_\ell(n,t) P_\ell(\cos\theta) \qquad (13)$$

the master equations reduce to

$$\frac{d}{dt}\eta_\ell(n,t) = \mu_\ell\left[\lambda^+_{n-2}\eta_\ell(n-2,t) + \lambda^-_{n+2}\eta_\ell(n+2,t)\right] - \eta_\ell(n,t)\left[W_n + \lambda^-_n + (1-\mu_\ell)\lambda^\circ_n + \lambda^+_n\right] \qquad (14)$$

where

$$W_n = \sum_\beta \int W_\beta(p,h,\varepsilon)\, d\varepsilon \qquad (15)$$

are the total emissionrates. Eqn.(14) can be written in a time integrated form

$$-D_\ell(n) = \Lambda^+_\ell(n-2)\zeta_\ell(n-2) + \Lambda^-_\ell(n+2)\zeta_\ell(n+2) - \frac{\zeta_\ell(n)}{\tau_\ell(n)} \qquad (16)$$

where $\Lambda^+_\ell(n) = \mu_\ell \lambda^+_n$; $\Lambda^-_\ell(n) = \mu_\ell \lambda^-_n$;

$\tau_\ell(n) = \left[W_n + \lambda^-_n + (1-\mu_\ell)\lambda^\circ_n + \lambda^+_n\right]^{-1}$;

$\zeta_\ell(n) = \int_0^\infty \eta_\ell(n,t)\, dt$ and $D_\ell(n) = \eta_\ell(n,0)$

are the coefficients of expansion of the initial condition.

The time integrated master equations(16) form a system of linear algebraic equations for each value of l with $n = n_\circ, n_\circ+2, \ldots$ where $n_\circ$ is the initial exciton number. The angle independent situation is a special case of the above and can be obtained by setting $\ell = 0$ with $\mu_\circ = 1$.

Exact Solution

The system (16) can be solved by a straightforward elimination process. The solution can be expressed in the following recurrence form

$$\frac{\zeta_\ell(n_\circ)}{\tau_\ell(n_\circ)} = \sum_{k \atop (\Delta k=2)} \alpha_{kn_\circ} D_\ell(k) \qquad (17a)$$

$$\frac{\zeta_\ell(n)}{\tau_\ell(n)} = \Lambda^+_\ell(n-2)\zeta_\ell(n-2)\mathcal{F}_n + \sum_{k\geq n \atop (\Delta k=2)} \alpha_{kn} D_\ell(k) \qquad (n>n_\circ) \qquad (17b)$$

Here the quantities $\mathcal{F}_n$ are continued fractions,

$$\mathcal{F}_n = \frac{1}{1-}\,\frac{F_n}{1-}\,\frac{F_{n+2}}{1-}\cdots \qquad (18)$$

with

$$F_n = \Lambda^+_\ell(n)\tau_\ell(n)\Lambda^-_\ell(n+2)\tau_\ell(n+2) \qquad (19)$$

These continued fractions satisfy the identity,

$$\mathcal{F}_n = 1/(1 - F_n \mathcal{F}_{n+2}) \qquad (20)$$

The coefficients α in eqns.(17) are given by,

$$\alpha_{nn} = \mathcal{F}_n$$
$$\alpha_{kn} = \Lambda^-_\ell(k)\tau_\ell(k)\mathcal{F}_k \alpha_{k-2,n} = \mathcal{F}_n \prod_{m=n+2 \atop (\Delta m=2)}^{k} \Lambda^-_\ell(m)\tau_\ell(m)\mathcal{F}_m \qquad (k>n) \qquad (21)$$

These coefficients satisfy the identity,

$$\alpha_{kn} = \Lambda^-_\ell(n+2)\tau_\ell(n+2)\mathcal{F}_n \alpha_{k,n+2} \qquad (22)$$

The solutions (17) are easily verified by direct substitution in the time integrated master equation (16).

The solutions discussed above are for an arbitrary initial condition. The case where only the initial exciton state is populated at t = 0 is the one most often used. In this case the initial condition is[5]

$$q(n,\Omega,0) = \Theta\left(\tfrac{\pi}{2}-\theta\right)\frac{\cos\theta}{\pi}\,\delta_{nn_\circ} \qquad (23),$$

and the solutions (17) take on a particularly simple form

$$\frac{\zeta_\ell(n_\circ)}{\tau_\ell(n_\circ)} = \eta_\ell \mathcal{F}_{n_\circ} \qquad (24a)$$

$$\frac{\zeta_\ell(n)}{\tau_\ell(n)} = \Lambda^+_\ell(n-2)\zeta_\ell(n-2)\mathcal{F}_n = \eta_\ell \mathcal{F}_{n_\circ} \prod_{k=n_\circ \atop (\Delta k=2)}^{n-2} \Lambda^+_\ell(k)\tau_\ell(k)\mathcal{F}_{k+2} \qquad (n>n_\circ) \qquad (24b)$$

where $\eta_\ell \delta_{nn_\circ}$ are coefficients of the Legendre Polynomial expansion of the initial condition(23). Our expressions for μ_ℓ and η_ℓ are identical to the ones described in ECN-60 (ref.6).

Calculation of Energy Spectra

In terms of the solutions $\zeta_\ell(n)$, the partial lifetimes of the exciton states for particle emission at an angle θ are given by

$$t(n,\theta) = \sum_\ell \zeta_\ell(n) P_\ell(\cos\theta) \qquad (25)$$

and the total lifetimes are

$$\tau_n = \int t(n,\theta)\, d\Omega = 4\pi\, \delta_0(n) \qquad (26)$$

The double differential cross section for a channel (α,β) is

$$\frac{d^2\sigma}{d\varepsilon\, d\Omega} = \sigma_\alpha \sum_n W_\beta(p,h,\varepsilon)\, t_n(\theta) \qquad (27)$$

where the emission rates W_β are given by eqn(8). As an illustration we describe our calculations for neutron emission arising from the 15 MeV neutron bombardment of ^{93}Nb. The optical reaction cross sections $\sigma_\beta(\varepsilon)$ have been obtained from an empirical parameterization described elsewhere in this conference[7]. The use of this empirical formula makes the integral in (15) analytic and the calculations become quite simple to carry out. A value of σ_α = 1690 mb is assumed for this case. For simplicity the Pauli correction terms $C_{p,h}$ and $A_{p,h}$ have been neglected in the emission and transition rates. The effect of the Pauli correction is discussed below. For the expansion in terms of $P_\ell(\cos\theta)$ values of ℓ upto ℓ = 8 were retained. The initial exciton state has been assumed to be n_0 = 3, with the initial condition (23).

The first curve in Fig.1 illustrates the exciton number dependence of F_n with $\ell = 0$ [see eqn(19)] . F_n decreases rapidly beyond the peak at n = 17 and this corresponds to a convergence of the continued fractions $\mathcal{F}_n$ [eqn(18)] . Thus it was found convenient to evaluate the $\mathcal{F}_n$ by means of successive convergents[8]. The lifetime τ_n of the n th exciton state shows a similiar peak and thus corresponds to the equilibrium state. The quantity $W_n\tau_n$ represents the total emission. It consists of an early decreasing part corresponding to the preequilibrium emission and a broad peak corresponding to emission near the equilibrium state. The relative contributions of preequilibrium and equilibrium emissions can be gauged from this curve. The dotted curve shows a curve for $W_n\tau_n$ using the approximate closed form solution of Wu and Chang[9]. It is seen that the approximate closed form becomes inaccurate with increase in exciton number and it is also apparent that an equilibrium part has to be added separately.

When the Pauli correction terms are included the peak in the F_n curve occurs at n = 13 and is considerably more narrow, thereby producing a more rapid convergence of the continued fractions. However the final results for the emission spectra are nearly identical.

The calculated emission spectra for neutron emission at the three centre of mass angles 40°, 90° and 150° are shown as solid lines in Fig.2. The contribution from the (n,2n) reaction is important for $\epsilon < 6$ MeV in spectra shown. Although it is possible to calculate this within the framework of the exciton model we have, for simplicity, estimated the contribution from a simple evaporation model:

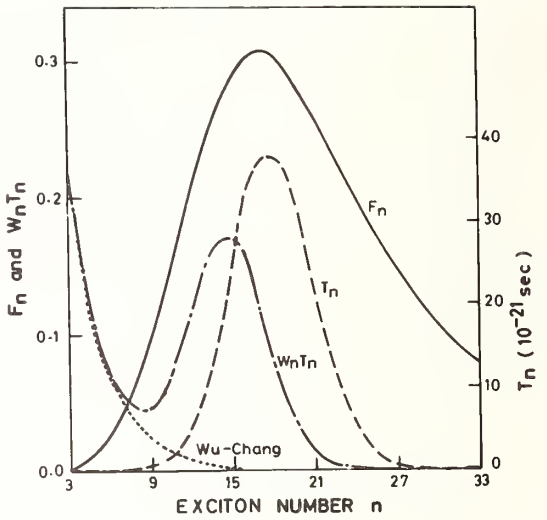

Fig.1.

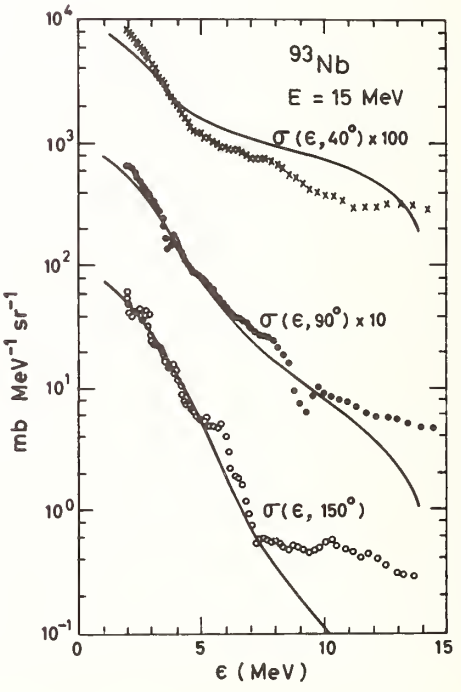

Fig.2.

$$\frac{d^2\sigma(n,2n)}{d\varepsilon\, d\Omega} = \frac{\sigma(E)\,\varepsilon\, e^{-\varepsilon/T}}{4\pi\, T^2\left[1-(1+E/T)e^{-E/T}\right]} \qquad (28)$$

Here the total (n,2n) cross section $\sigma(E)$ is assumed to be 1260 mb and a temperature T = 0.845 MeV is taken. E is taken to be the maximum excitation energy (E = 6.17 MeV).

The calculated spectra are seen to be in general agreement with the experimental data of Hermsdorf et al[10] also shown in Fig.2. There is some disagreement at the high energy end of the spectra particularly at 150°.

Summary

Exact closed form expressions are obtained for the lifetimes of the exciton states. Use of these expressions leads to an integrated description of the preequilibrium and equilibrium components of nuclear reactions in a simple way. The use of the empirical optical reaction cross sections makes calculations using this model quite simple to carry out.

References

1. D. Agassi, H.A. Weidenmüller and G. Mantzouranis, Phys. Rep. 22C, 147 (1975).

2. F.J. Luider, Z. Physik, A284, 187 (1978). F.J. Luider, Preequilibrium theory and slaves of the master equation, ECN-17, Netherlands Energy Research Foundation Report Series (1977).

3. L. Faugere and O. Bersillon, A new approach for interpreting nuclear spectra within a preequilibrium model, INDC(FR) 18/L, International Nuclear Data Committee, IAEA, Vienna (1977).

4. C. Kalbach, Z. Physik A283, 401 (1977). C. Kalbach, PRECO-B Programme for calculating preequilibrium particle energy spectra, Triangle Universities Informal Report (1977).

5. G. Mantzouranis, D. Agassi and H.A. Weidenmüller, Phys. Lett. 57B, 220 (1975). G. Mantzouranis, H.A. Weidenmüller and D. Agassi, Z. Physik A276 (1976).

6. J.M. Akkermans, Phys. Lett. 82B, 20 (1979). J.M. Akkermans and H. Gruppelaar, ECN-60, Netherlands Energy Research Foundation Report Series (1979).

7. K.H. Narsimha Murthy, A. Chatterjee and S.K. Gupta, this conference.

8. M. Abramouitz and I.A. Stegun, Handbook of Mathematical Functions (US Nat. Bu. of Standards: Washington) pg. 19 (1968).

9. J.R. Wu and C.C. Chang, Phys. Lett. 60B, 423, (1976).

10. D. Hermsdorf et al. report ZFK-277 (1974) Zentralinstitut fur Kernforschung Rossendorf bei Dresden.

DELAYED NEUTRON CALCULATIONS USING ENDF/B-V DATA

T. R. England
Los Alamos Scientific Laboratory, University of California
Theoretical Division
Los Alamos, New Mexico 87455 USA

R. E. Schenter and F. Schmittroth
Hanford Engineering Development Laboratory
Richland, Washington 99352 USA

Data from 20 fission yield sets in ENDF/B-V are used with the emission probabilites (Pn) of 105 delayed neutron precursors to calculate 6-group and total equilibrium delayed neutron yields ($\bar{\nu}_d$). Results are compared with recent evaluations and selected measurements of $\bar{\nu}_d$. Least squares data adjustment methods are in progress to improve agreement; preliminary results indicate significant improvement when fission yields are adjusted.

The extensive fission-product yields and delayed neutron emission probabilities to be incorporated in ENDF/B-V permit calculations of $\bar{\nu}_d$ and its individual nuclide and decay group components. In addition, there are now sufficient measurements of the neutron spectra from individual precursors to permit aggregate spectral calculations. At the IAEA Fission-Product Nuclear Data Meeting in Petten in 1977,[1] it was noted that the future effort in improving delayed neutron data should emphasize improvement in Pn values and fission-product yields for use in calculations of aggregate delayed neutron properties, including the delayed neutron spectra. This report shows the current status of such calculations, except for spectra, using very recent precursor data.[2] We expect to calculate spectra during the next few months as these data become available for ENDF/B evaluation.

Calculations of $\bar{\nu}_d$ have been in periodic progress as part of the ENDF/B fission yield testing since Version-IV. Evaluated $\bar{\nu}_d$ values are not included in the fission yield evaluation process; therefore, assuming accurate and extensive Pn values, the calculated $\bar{\nu}_d$ values serve as a very sensitive indication of the quality of fission-product yields. *The reader should recognize that fission-product yield testing is the primary purpose of $\bar{\nu}_d$ calculations; however, the results are sufficiently accurate to justify the emphasis suggested at the 1977 Petten Meeting.*

Table I lists Pn values for 105 precursors, the percent contribution to the $\bar{\nu}_d$ of ^{235}U thermal fission and other information. Based simply on energetics, all are probable delayed-neutron precursors; 67 have measured Pn values and 38 have Pn values we have estimated based on a simple phenomenological model. Since 1977, there have been 18 new measurements, identified in Table I, all being previously incorporated in preliminary ENDF/B-V files based on energetics. Use of the newly measured Pn values in place of the previous model estimates alters the calculated $\bar{\nu}_d$ for ^{235}U by only 0.017%. Model estimates of the remaining 38 unmeasured values are unlikely to significantly alter the calculated $\bar{\nu}_d$, particularly because these collectively contribute only ∿7% in these calculations. However, very large errors in some individual Pn estimates are likely. The estimated values can be identified in Table I by the lack of a tabulated uncertainty. Measured values in Table I incorporate values from the preliminary data at the March 1979 Consultants' Meeting in Vienna.[2] Data differing from that of Ref. 1 are also identified.

Table II lists the results of calculations and comparative results from evaluations and selected measurements. The T, F, and H following the fissionable nuclide refer, respectively, to Thermal, Fast, and High energy (∿14 MeV) fission. Because of the large number of $\bar{\nu}_d$ measurements, particularly for some (but not all) of the fissionable nuclides, only a selection of these can be listed in this paper. R. Tuttle prepared an extensive review of measurements of $\bar{\nu}_d$ and an evaluation for the Vienna Conference;[2] his preliminary evaluations are listed in Table II. The uncertainties listed for the calculations are based on fission-product yield uncertainties in ENDF/B-V and the Pn uncertainties in Table I. A 100% uncertainty was assigned to the estimated Pn values, but this is not a significant component of the listed $\bar{\nu}_d$ uncertainty. Except for ^{235}U thermal fission, the calculated uncertainties are probably too small. The $\bar{\nu}_d$ calculations are sensitive to the yield distribution along each mass chain. This distribution is based on models using parameters derived largely from ^{235}U independent yields. Errors in the most probable charge or nuclear pairing effects could readily alter the $\bar{\nu}_d$ values, even if mass chain yields are exact. Thus, the yield uncertainties for some nuclides far from stability are likely too small. We suspect that the calculated $\bar{\nu}_d$ from ^{238}U fast fission for example, is small because of the large Z-pairing used in the yield evaluation.[3,4] Most (∿90%) of the delayed neutrons are emitted from odd-Z precursors, and a relatively small error in the pairing could create a large error in $\bar{\nu}_d$. In any case, the yield uncertainties for very unstable nuclides probably do not adequately reflect the paucity of data available to predict model distribution parameters for most of the 20 yield sets used in this report.

Calculations of $\bar{\nu}_d$ require a mass imbalance of the yielded fission products of only ∿0.01 units out of ∿236, a stringent demand on the fission yields, and one that is not incorporated into the fission-product yield evalaution procedure. In view of this requirement, it is remarkable that only ∿5 of the 20 calculated values appear in significant error when compared with evaluations or measurements and their respective uncertainties.

TABLE I

DELAYED NEUTRON PRECURSORS

PRECURSOR CS ZZAAAS	HALF-LIFE (s)	Pn (%)	NO. OF SPEC MEAS	% of $\bar{\nu}_d$ U235(T)
Zn 300790	2.74	1.1	0	< 0.01
Ga 310790	3.00	0.102±0.015[a]	1	< 0.01
Ga 310800	1.66	0.87 ±0.05[a]	1	< 0.01
Ga 310810	1.23	12.2 ±0.9[a]	1	0.05
Ga 310820	0.60	21.0 ±1.4[a]	0	0.08
Ga 310830	0.31	56.0	0	0.01
Ge 320830	1.9	0.17	0	< 0.01
Ge 320840	1.2	10.0	0	0.18
Ge 320850	0.234	20.0	0	0.05
Ge 320860	0.259	22.0	0	0.01
As 330840	5.6	0.13 ±0.06	0	0.02
As 330850	2.03	22.0 ±8.0[b]	4	1.94
As 330860	0.9	10.5 ±2.2	0	0.53
As 330870	0.73	44.0 ±14.0	0	1.72
Se 340870	5.60	0.19 ±0.03[b]	0	0.08
Se 340880	1.52	0.5 ±0.3[b]	0	0.10
Se 340890	0.41	5.0 ±1.5	0	0.34
Se 340900	0.555	11.0	0	0.15
Se 340910	0.27	21.0 ±8.0	0	0.02
Br 350870	55.7	2.54 ±0.10[b]	6	2.88
Br 350880	16.0	6.9 ±0.3[b]	1	7.96
Br 350890	4.38	13.9 ±1.0[b]	2	10.38
Br 350900	1.92	21.2 ±2.4[b]	2	8.18
Br 350910	0.542	10.9 ±1.8[b]	1	1.51
Br 350920	0.362	22.0 ±6.0	0	0.45
Br 350930	0.201	41.0	0	0.07
Kr 360920	1.85	0.033±0.003	0	0.03
Kr 360930	1.29	1.95 ±0.11[b]	0	0.58
Kr 360940	0.208	5.7 ±2.2[b]	0	0.71
Kr 360950	0.50	9.5	0	0.04
Rb 370920	4.53	0.0119±0.0006[b]	1	0.03
Rb 370930	5.86	1.37 ±0.08[b]	3	2.79
Rb 370940	2.76	10.3 ±0.5[b]	4	10.41
Rb 370950	0.384	8.8 ±0.4[b]	3	4.07
Rb 370960	0.201	13.9 ±0.7[b]	1	1.62
Rb 370970	0.170	27.8 ±2.5[b]	2	1.23
Rb 370980	0.119	16.0 ±1.0[b]	1	0.02
Rb 370990	0.076	15.0 ±3.0[a]	0	< 0.01
Sr 380970	0.40	0.27 ±0.09[a]	0	0.31
Sr 380980	0.65	0.36 ±0.11[a]	0	0.14
Sr 380990	0.6	3.4 ±2.4	0	0.68
Sr 381000	1.046	5.0	0	0.04
Y 390971	1.11	0.06 ±0.02[b]	0	0.05
Y 390970	3.7	0.33	0	0.97
Y 390981	0.65	3.44 ±0.95[b]	0	2.16
Y 390980	2.0	0.54	0	1.10
Y 390990	1.4	1.2 ±0.8	0	1.60
Y 391000	0.756	5.5	0	1.67
Zr 401040	3.783	0.11	0	< 0.01
Zr 401050	0.559	1.4	0	0.07
Nb 411030	15.669	0.13	0	0.16
Nb 411040	1.00	0.71	0	0.30
Nb 411050	1.80	2.9	0	0.42
Nb 411060	0.535	5.5	0	0.05
Mo 421090	1.033	0.53	0	< 0.01
Mo 421100	1.892	1.3	0	< 0.01
Tc 431090	50.00	1.7	0	< 0.01
Tc 431100	0.83	3.1	0	< 0.01
Ag 471220	1.5	1.4	0	< 0.01
Ag 471230	0.39	4.6	0	< 0.01
Cd 481280	0.83	0.11	0	< 0.01
In 491271	2.0	0.72 ±0.04[a]	0	0.01
In 491270	3.76	0.72 ±0.04[a]	0	0.01
In 491280	0.84	0.063±0.008[a]	0	< 0.01
In 491291	0.99	3.5 ±0.5[a]	0	0.09
In 491290	2.5	3.5 ±0.5[a]	1	0.18
In 491300	0.58	1.39 ±0.08[a]	1	0.07
In 491310	0.28	1.66 ±0.19[a]	0	0.03
In 491320	0.13	4.1 ±0.8[a]	0	0.02
Sn 501330	1.47	0.02	0	< 0.01
Sn 501340	1.04	17.0 ±7.0	1	0.11
Sn 501350	0.291	8.6	0	< 0.01
Sb 511341	10.4	0.086±0.012	0	0.01
Sb 511350	1.71	14.0 ±2.0	3	1.16
Sb 511360	0.82	23.0 ±8.0	0	0.20
Sb 511370	0.284	20.0	0	0.59
Te 521360	17.5	0.9 ±0.4	2	0.78
Te 521370	2.8	2.2 ±0.5	0	0.53
Te 521380	1.4	5.6 ±1.6	0	0.21
Te 521390	0.424	6.3	0	0.02
I 531370	24.5	7.2 ±0.7	3	13.11
I 531380	6.53	2.6 ±0.3	2	2.34
I 531390	2.38	10.2 ±0.9	1	5.65
I 531400	0.60	22.0 ±6.0	1	2.71
I 531410	0.47	39.0 ±13.0	0	0.32
I 531420	0.196	16.0	0	0.06
I 531430	0.328	18.0	0	< 0.01
Xe 541410	1.72	0.043±0.003	0	0.03
Xe 541420	1.24	0.41 ±0.03	0	0.10
Xe 541430	0.30	1.2	0	0.03
Xe 541440	1.00	0.73	0	< 0.01
Cs 551410	24.9	0.053±0.004	1	0.13
Cs 551420	1.69	0.19 ±0.10	2	0.29
Cs 551430	1.78	1.6 ±0.2	3	1.34
Cs 551440	1.001	2.8 ±0.7	2	0.56
Cs 551450	0.58	14.0 ±2.0	1	0.46
Cs 551460	0.335	13.4 ±0.7	1	0.13
Cs 551470	0.21	25.0 ±3.0	1	< 0.01
Ba 561470	2.2	5.2 ±0.5[a]	0	0.27
Ba 561480	-	23.9 ±2.1[a]	0	0.14
Ba 561490	0.917	0.03	0	< 0.01
Ba 561500	1.798	0.24	0	< 0.01
La 571470	10.0	0.5 ±0.17[a]	0	0.26
La 571490	2.864	0.81	0	0.03
La 571500	0.648	0.94	0	< 0.01

[a] Measured subsequent to Ref. 1

[b] Change in Pn or uncertainty subsequent to Ref. 1

TABLE II

COMPARISON OF DELAYED NEUTRONS PER 100 FISSIONS

Fission Nuclide	$\bar{\nu}_d$ Calculated ENDF/B-V	$\bar{\nu}_d$ Evaluated ENDF/B-V	$\bar{\nu}_d$ TUTTLE 1979[b]	$\bar{\nu}_d$ Selected Measurements	Group Components of $\bar{\nu}_d$ (Calculated %; ENDF/B-V) 1	2	3	4	5	6
Th232F	4.76 ±0.34 (4.51)[a]	5.27	5.31 ±0.23	4.96±0.30[e]	3.6	17.5	16.6	35.6	21.7	4.9
Th232H	3.03 ±0.29 (2.77)	3.00	2.85 ±0.13	3.1 ±0.3[d]	3.8	14.5	16.3	41.3	16.6	7.4
U233T	0.846±0.066 (0.803)	0.74	0.667±0.029	0.66±0.04[e]	6.5	27.3	20.3	34.9	9.5	1.6
U233F	0.916±0.089 (0.870)	0.74	0.731±0.036	0.78±0.08[c]	7.4	27.9	21.1	30.7	11.5	1.3
U233H	0.708±0.095 (0.657)	0.47	0.422±0.025	0.43±0.04[d]	6.9	23.4	21.8	33.5	12.9	1.5
U235T	1.77 ±0.081 (1.66)	1.67	1.621±0.050	1.58±0.07[e]	2.9	22.1	15.9	35.4	19.0	4.6
U235F	1.98 ±0.18 (1.84)	1.67	1.673±0.036	1.71±0.17[c]	2.8	21.3	17.8	35.7	18.8	3.7
U235H	0.978±0.097 (0.902)	0.93	0.927±0.029	0.95±0.08[d]	4.5	22.2	20.2	35.6	15.2	2.3
U236F	2.26 ±0.19 (2.09)	-	2.21 ±0.24	-	2.3	20.3	15.4	36.1	21.7	4.1
U238F	3.51 ±0.27 (3.13)	4.40	4.39 ±0.10	4.12±0.25[e]	1.1	15.7	11.0	36.0	28.9	7.2
U238H	2.69 ±0.21 (2.38)	2.60	2.73 ±0.08	2.83±0.13[d]	1.8	13.6	11.6	37.7	27.9	7.4
Np237F	1.28 ±0.13 (1.15)	-	-	-	3.0	23.8	14.3	35.9	20.2	2.7
Pu239T	0.769±0.058 (0.675)	0.645	0.628±0.038	0.61±0.05[e]	2.9	29.1	14.0	33.3	18.9	1.7
Pu239F	0.724±0.090 (0.612)	0.645	0.630±0.016	0.65±0.06[c]	3.4	26.3	14.4	32.9	20.9	2.2
Pu239H	0.387±0.062 (0.325)	0.430	0.417±0.016	0.43±0.04[d]	6.5	22.2	16.0	33.6	20.2	1.6
Pu240F	0.923±0.11 (0.798)	0.900	0.95 ±0.08	0.88±0.09[e]	2.8	26.7	12.4	34.3	20.7	3.1
Pu241T	1.58 ±0.13 (1.34)	1.62	1.52 ±0.11	1.57±0.15[e]	1.9	23.2	9.6	33.7	26.9	4.7
Pu241F	1.49 ±0.16 (1.24)	1.62	1.52 ±0.11	-	2.1	23.4	10.6	34.4	25.3	4.1
Pu242F	1.41 ±0.14 (1.20)	-	2.21 ±0.26	1.6 ±0.5[c]	2.6	24.7	10.3	34.0	23.5	4.9
Cf252S	0.690±0.092 (0.538)	0.89	-	-	4.6	30.1	9.3	30.3	24.2	1.6

[a] Values in parantheses used only measured Pn values.

[b] May 1979 revision of NSE 56 p.37, 1975 article to be published.

[c] Krick and Evans, NSE 47 p.311 (Here, average values between 0.1 and 1.8 MeV are listed).

[d] C. F. Masters et al. NSE 36 p.202 (High energy values at 14.9 MeV).

[e] G. R. Keepin et al. NSE 6 p.1 (Probable error converted to standard deviation).

There is now an effort to improve the calculated $\bar{\nu}_d$ using least squares data adjustment methods, incorporating integral data. To date, fission yield adjustments, limited to the most descrepant values in Table II, have resulted in significant improvements; the adjustment of Pn values is still in progress but appears less promising.

In Table I, a total of 32 precursors are identified as having neutron spectral measurements.[2] For ^{235}U thermal fission, these account for ∿82% of the total $\bar{\nu}_d$ and should, therefore, be adequate for calculations of the aggregate spectral shape.

References

1. "Fission Product Nuclear Data (FPND)-1977," Proc. of the Second Advisory Group Meeting on Fission Product Nuclear Data, Petten, Netherlands (Sept. 5-9, 1977), IAEA-213.

2. "IAEA Consultants' Meeting on Delayed Neutron Properties," Vienna, Austria (March 26-30, 1979). (Preliminary data supplied by R. J. Tuttle.)

3. T. R. England, R. E. Schenter, B. F. Rider, and J. L. Liaw, "Status of ENDF/B-V Fission Yields," 3rd ASTM-Euratom Symposium on Reactor Dosimetery, Ispra, Italy (Oct. 1-5, 1979).

4. David G. Madland and Talmadge R. England, "The Influence of Pairing on the Distributions of Independent Yield Strengths in Neutron-Induced Fission," LA-6430-MS [ENDF-240], (July 1976).

UTILIZATION OF THE REACTION $^{10}B(d,n)^{11}C$ AS A HIGH TEMPERATURE DEUTERIUM PLASMA DIAGNOSTIC

L. K. Len and F. E. Cecil
Department of Physics
Colorado School of Mines
Golden, Colorado 80401

We have measured the thick target yield of the reaction $^{10}B(d,n)^{11}C$ for monoenergetic deuteron beams of energies between 75 and 170 keV. These yields, together with recently published range energy relations for hydrogen ions in matter, permitted our deduction of the reaction cross section as a function of energy. By integrating the cross section over a Maxwell Boltzman population distribution, we obtained the reaction yields for Boron samples exposed to a deuterium plasma of temperatures between 20 x 10^6 and 200 x 10^6 °K.

Measurements of the thick target yield for the reaction $^{10}B(d,n)^{11}C$ have been reported down to energies of 300 keV[1]. These results, however, cannot be applied directly to the measurement of the deuterium plasma temperature in current controlled thermonuclear reaction research which has a temperature range of 10^7 to 10^8 K. This is because the reaction depends on the value of $\langle\sigma V\rangle$ (integrated over the entire ion distribution in the plasma) which for the temperatures between 10^7 and 10^8 K has a maximum value corresponding approximately to an energy of 100 keV with a FWHM of about 60 keV. Clearly, the existing results are out of the useful range.

In order to obtain the measurements needed for such application in temperature diagnostics, we have measured the thick target (i.e., thickness > particle range) yield for $^{10}B(d,n)^{11}C$ reaction, down to 75 keV.

Data between 960 and 220 keV were taken with the Cyclotron at the University of Colorado (CU), while those between 75 and 170 keV were measured using a Cockcroft Walton accelerator in the Physics Department, Colorado School of Mines (CSM).

The experimental procedure consists of the bombardment of a sample of natural metallic Boron target with a beam of deuterons. The beam current was maintained at 200 μA for a period of between 3 and 30 minutes, depending on the operating voltage (i.e., beam energy).

The target was cooled to dissipate the heat generated during the bombardment to prevent target blow-off.

At the end of the process, the activation level in the Boron sample is measured by counting the 511 keV annihilation quanta following the β^+ decay of ^{11}C. The efficiency of the NaI(Tℓ) detector used in the counting of the 511 keV gamma photons was calibrated using a standard ^{22}Na source.

Since the reaction yield of ^{11}C under consideration is a sensitive function of deuteron energy, it is important to know the beam energy. By mapping the thick target yield of the reaction $^{11}B(p,\gamma)^{12}C$ against the known resonance at 163 keV, our beam energy was calibrated to within about 1 keV accuracy. A consistency check on the CSM data was provided by a measurement of the yield of the reaction $^{12}C(p,\gamma)^{13}N$. In doing this measurement, we found (by using the same techniques as employed in the $^{10}B(d,n)^{11}C$ measurements) a yield of (9.0 ± 1.0) x 10^{-15} ^{13}N/proton at a proton bombarding energy of 168 keV, which is in agreement with the value (7.5 ± 0.5) x 10^{-15} ^{13}N/proton quoted by Bailey and Stratton[2].

The thick target yields of the $^{10}B(d,n)^{11}C$ reaction obtained from the measured ^{11}C activity are shown in Figure 1 (referred to as CSM and CU data) where they are compared to the measured yields at energies up to 1 MeV reported by Young et al.[1] (referred to as RSI data). The results are in good agreement with each other.

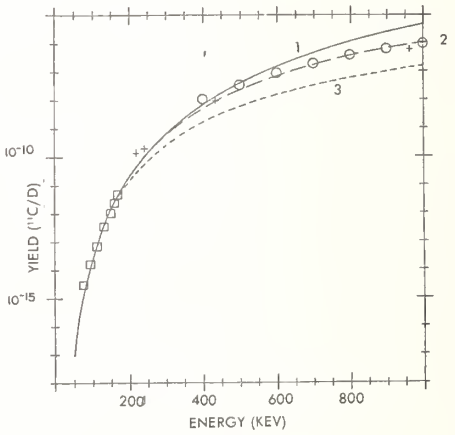

Fig. 1. Thick target yields for reaction $^{10}B(d,n)^{11}C$ for monoenergetic deuteron beam on natural Boron. The squares are the CSM data, the crosses are CU data and the circles are the data from Reference 1. The curves are the yields calculated with Equation 4 and with the three parameter sets of Table 1.

A parameterization of the thick target can be obtained by considering n particles with incident energy E bombarding on a target of thickness Δx which has a density of N nuclei/cm³. The number of reactions is then given by

$$N_o(E) = Nn\sigma(E)\Delta x \qquad (1)$$

where σ(E) = reaction cross section at energy E and Δx is assumed to be sufficiently small so that E does not change appreciably. Thus the thin target yield is

$$dY = N\sigma(E)\Delta x \qquad (2)$$

For a target with thickness ℓ, the thick target yield is

$$Y(E) = \int_0^{\ell} N\sigma(E')dx$$

$$Y(E) = \int_0^{E} \frac{\sigma(E')}{\frac{1}{N}\left|\frac{dE}{dx}\right|} dE'$$

$$= \int_0^{E} \frac{\sigma(E')}{\varepsilon(E')} dE' \qquad (3)$$

where $\varepsilon(E)$ is the stopping power. (A slowly varying function of energy.)

For the present case, we have a 19.8% isotopic abundance of ^{10}B in natural Boron, thus

$$Y(E) = \int_0^{E_\ell} (0.198) \frac{\sigma(E')}{\varepsilon(E')} dE' \qquad (4)$$

The stopping power $\varepsilon(E')$ in (keV atom^{-1} cm^{-2}) is taken from Ziegler and Anderson[3]. As the $^{10}B(d,n)^{11}C$ reaction is a non-resonant charged particle reaction, at energies below the Coulomb barrier ($\tilde{\sim}$ 3 MeV), $\sigma(E)$ is dominated by the Coulomb penetration factor[4], $\sigma(E)$ can thus be written as

$$\sigma(E) = \frac{S(E)}{E} e^{\frac{-2\pi Z_1 Z_2 e^2}{hV}} \qquad (5)$$

where V is the relative velocity between d and ^{10}B, and where S(E) is a slowly varying function of the energy in the absence of any narrow resonances[4]. We assume a Taylor series for S(E)

$$S(E) = A + BE + CE^2 \qquad (6)$$

and obtained optimum values of the constants A, B, and C by performing a chi-square fitting between the calculated, parameterized Y(E) values (as given by Equation 4) and the measured values of Y(E) for energies between 75 and 240 keV. In addition, two sets of one-parameter fits were obtained for which (i) B and C were constrained to be zero, and (ii) A and C were constrained to be zero.

The three parameters sets thus obtained are given in Table 1, and with these values, the predicted yields are calculated using Equations (4), (5), and (6). The three curves in Figure 1 show the prediction for each of the parameters set. It should be noted that all three sets give comparable fits to the measured (experimental) yields for energies below 240 keV, while parameter set 2 (A = C = 0, B $\neq$ 0) provides an excellent fit to the data up to 1 MeV.

Table 1. Parameters for Equation 3

Parameter Set	A (keV-cm^2)	B (cm^2)	C (keV^{-1}cm^2)
1	1.4×10^{-20}	-1.0×10^{-22}	6.0×10^{-25}
2	1.2×10^{-20}	0	0
3	0	1.0×10^{-22}	0

In order to utilize these measurements for ion-temperature diagnostic purposes, it should be understood that the deuteron population in a plasma is not monoenergetic, but exhibit an energy distribution. By integrating over the entire distribution, the thick target yield per incident deuteron of ^{11}C for natural Boron exposed to a deuterium plasma at a given temperature T is given by

$$Y(T) = \int_0^{\infty} N(E)Y(E)V\, dE \quad (^{11}C\ d^{-1}\ cm\ s^{-1}) \qquad (7)$$

where Y(E) is as defined by Equation (4)

N(E) is the normalized population distribution of the plasma incident upon the Boron.

V is the velocity of deuteron (the Boron is assumed at rest)

If one assumes that the deuteron population in the plasma is well-described by the Maxwell-Boltzman distribution, then

$$N(E) = \frac{2\pi}{(kT)^{3/2}} E^{1/2} e^{-E/kT} \qquad (8)$$

The integrand of Equation (7) (analogous to the 'Gamow Peak' of Astrophysics[5], which determines the extent of overlap between $\sigma(E)$ and N(E) curves) is plotted in Figure 2 for T = 6×10^7 K and 1×10^8 K. The curves exhibit maxima at about 70 and 100 keV for the two temperatures respectively. Parameters set 2 and 3 give nearly identical results. The two peaks of Figure 2 imply that the most relevant data required for this diagnostic technique at temperatures between 6×10^7 K and 1×10^8 K correspond to those in the energy range of 50 and 200 keV, this is just what has been measured in the present work. The thick target yields as a function of ion-temperature have been evaluated for temperatures between 2×10^7 and 2×10^8 K for all the three sets of parameters. The results are plotted in Figure 3. The average values for the three yields at each of the temperatures are listed in Table 2.

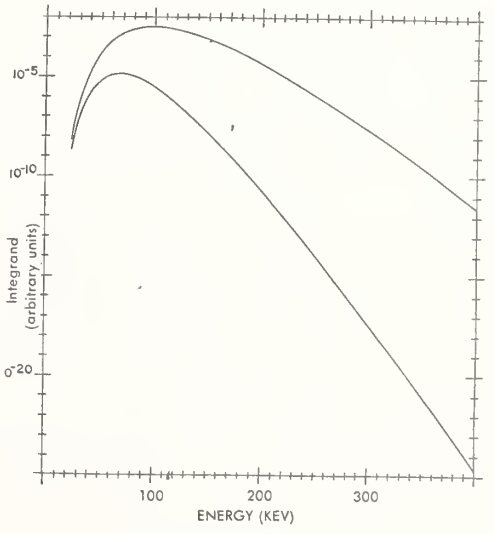

Fig. 2. The integrand of Equation 7. Essentially the overlap of the thick target yield and Maxwell-Boltzman distributions for deuterium plasmas of temperatures 6×10^7 °K and 1×10^8 °K.

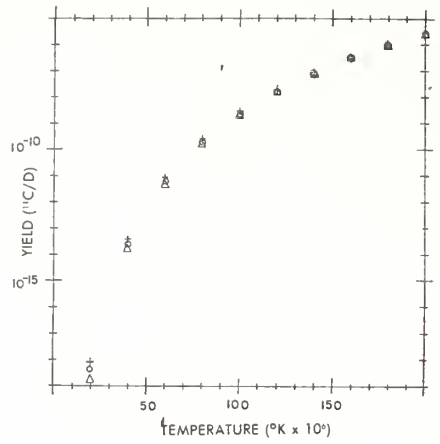

Fig. 3. The thick target yield per incident deuteron as a function of temperature. The three values at each temperature correspond to the three parameter sets of Table 1; circle is set 1, cross is set 2 and triangle is set 3.

Table 2. Thick Target Yields Per Incident Deuteron as a Function of Temperature.

T(x 10^6 K)	Y(T)	Y(T,ρ) with $\rho=5\times10^{13}$ cm^{-3}
20	4.923×10^{-19}	4.102×10^{-6}
40	2.886×10^{-14}	2.405×10^{-1}
60	6.393×10^{-12}	5.327×10^{1}
80	2.045×10^{-10}	1.704×10^{3}
100	2.505×10^{-9}	2.087×10^{4}
120	1.746×10^{-8}	1.455×10^{5}
140	8.435×10^{-8}	7.029×10^{5}
160	3.155×10^{-7}	2.629×10^{6}
180	9.785×10^{-7}	8.154×10^{6}
200	2.626×10^{-6}	2.188×10^{7}

As an example of the utilization of Figure 3, consider a sample of Boron exposed to a plasma having a density of ρ cm^{-3}, contained in a cube of side L. The number of particles having energy between E and E + dE is $(\rho L^3)N(E)dE$, where N(E) is the population distribution. The frequency at which these particles collide with any one particular wall is $(\rho L^3)N(E)dE\ (V/L)\ (1/6L^2)$, where V is the velocity of the particles. Consider one of the walls to be the Boron sample, then the yield will be $(\rho/6)N(E)$ $(\rho/6)N(E)VdEY(E)$, and the total yield will be given by

$$Y(T,\rho) = \frac{\rho}{6}\int_0^\infty Y(E)N(E)VdE$$

$$= \left(\frac{\rho}{6}\right) Y(T) \qquad (9)$$

$Y(T,\rho)$ has been calculated with $\rho = 5 \times 10^{13}$ cm^{-3} and listed in Table 2. The profile of Figure 3 shows that for temperatures significantly less than 10^7 K, the yield becomes prohibitively small; and for temperatures significantly greater than 10^8 K, this technique loses its sensitivity (compare the two order of magnitude increase in yield between 40 and 60 million K to the factor of two increase between 180 and 200 million K). It should also be emphasized that Figure 3 assumes a Maxwellian Distribution. If another distribution is assumed, the integration required by Equation (7) must be repeated.

REFERENCES

1. F.C. Young, et al., Rev. Sci. Instrum., 48, 432 (1977).
2. C.L. Bailey and W.R. Stratton, Phys. Rev. 77, 194 (1950).
3. J.F. Ziegler and H.H. Anderson, The Stopping and Ranges of Ions in Matter; Vol. 3, Hydrogen, (1977), Pergamon Press, NY.
4. C.A. Barnes in Advances in Nuclear Physics, Eds. M. Baranger and E. Vogt, Vol. 4 (1971), Plenum Press, NY, pp. 142.
5. Donald Clayton, Principles of Stellar Evolution and Nucleosynthesis, (1968), McGraw Hill, NY, pp. 302.

MEASUREMENT OF THE 2.35-MeV WINDOW IN O + n

C. H. Johnson, J. L. Fowler†, N. W. Hill and J. M. Ortolf*
Oak Ridge National Laboratory, Oak Ridge, Tennessee 37830 USA

Calculations are made showing that the ion temperature of a deuterium plasma with a Maxwellian distribution can be found by measuring the transmission of the d-d neutrons through liquid oxygen. The method is useful for temperatures up to 6 keV. It does not depend on the absolute neutron yield but does require accurate total neutron cross sections for oxygen. In this experiment the cross section of natural oxygen was measured from 2.0 to 3.0 MeV by neutron time-of-flight at the Oak Ridge Electron Linear Accelerator (ORELA). The fitted cross sections have a 110.9 ± 1.7 mb minimum at 2351.5 keV.

[Fusion, calculate deuterium plasma neutron spectrum, measured σ_T for O(n,n), 2 to 3 MeV, 2.35-MeV resonance minimum.]

Introduction

Stelson and Barnett[1] suggested that the ion temperature for a deuterium plasma can be deduced from the transmission of the neutrons from the plasma through a thick scatterer of liquid oxygen. The method is independent of the absolute ion density and absolute d-d cross section and not very sensitive to uncertainties in the shape of the d-d excitation function. The principle is illustrated in Fig. 1. The three neutron spectra were calculated for deuterium plasmas with Maxwellian distributions at ion temperatures of 1, 6 and 10 keV and normalized to the same peak heights. At a low temperature the spectrum is narrow and centered near 2.45 MeV but, as the temperature increases, it shifts upward in energy and is broadened by the kinematic effects. The figure also shows a curve for the neutron total cross section of oxygen. This curve was relatively well known[2,3] before the present work. Since the minimum cross section at the 2.35-MeV s-wave resonance is only about one-tenth of the non-resonance cross section, a thick oxygen scatterer has a relatively narrow high transmission "window" at 2.35 MeV. We see that the overall transmission of a plasma neutron spectrum increases with temperature. Thus, given accurate neutron cross sections for oxygen near the minimum, one can deduce the ion temperature by performing a relatively simple transmission measurement.

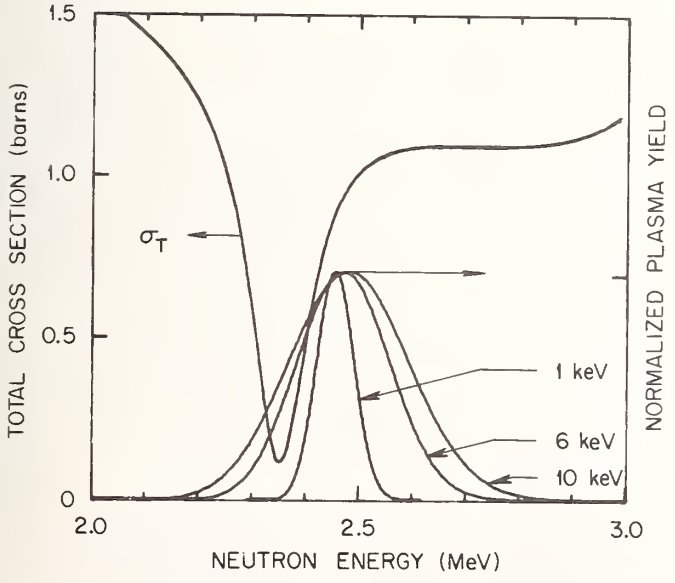

Fig. 1. Neutron total cross section of oxygen (left ordinate) and predicted neutron spectra for a deuterium plasma (right ordinate).

Theory

The spectra in Fig. 1 were calculated as discussed by Faust and Harris,[4] by integration over the Maxwellian distribution and over all laboratory angles between the product nuclei produced in the $D(d,n)^3He$ reaction. We wrote a computer code to calculate the spectrum from Eq. (11) of Faust and Harris and to calculate the transmission of this spectrum through oxygen. The masses and Q-values for the (d,n) reaction are known.[5] For the (d,n) cross section we use the expression[6]

$$\sigma_{d,n} = S(E_d)\, E_d^{-1} e^{-2\pi\eta} \qquad (1)$$

where $2\pi\eta = 2\pi Z_1 Z_2 e^2/\hbar v = 44.40/E_d^{1/2}$,

$$S(E_d) = 1.05 + 0.003\, E_d,$$

and E_d is the deuteron energy in keV in the laboratory system. The units of $\sigma_{d,n}$ are millibarns but, as stated above, absolute values are not required. Hale and Dodder[6] deduced the $S(E_d)$ for low energy deuterons (1 to 50 keV) from an R-matrix evaluation. (Actually, the energy dependent term in $S(E_d)$ has a negligible effect on the transmissions.)

To calculate the overall transmission through oxygen for the plasma neutrons we need accurate neutron cross sections and a corresponding analytical expression near the 2.35-MeV minimum. We could use a multilevel R-matrix for which the level parameters of the s-wave resonance would be based on the present work and the parameters for more distant levels would be obtained from the literature.[2,7] For simplicity we use the R-matrix formalism only for the s-wave resonance and describe the off-resonance cross sections by empirical non-theoretical parameters. For s-waves the single-level approximation for the 0.9976 fraction of ^{16}O is

$$\sigma_o(E) = 0.9976\ (4\pi/k^2)\ \sin^2\left[-kr+\tan^{-1}\left(\frac{k r \gamma^2}{E_o - E}\right)\right], \qquad (2)$$

where k is the neutron wave number for neutron energy E and where the parameters r, γ^2 and E_o are the boundary radius, neutron reduced width and resonance energy, respectively. (The units in Eq. (1) and the following are barns and MeV.) We parameterize the total cross section by the expression

*Summer student from State University College of New York at Buffalo now in graduate school at the University of Illinois.
†Now in Dept. of Physics, Univ. of Tennessee, Knoxville.

$$\sigma_T(E) = \sigma_0(E) + A + B\Delta E + C(\Delta E)^2 + \sigma_1(E), \quad (3)$$

$$\text{where } \sigma_1(E) = \frac{2.0}{1+[(3.2-E)/D]^2} \quad (4)$$

and $\Delta E = E_0 - E$. The last term, $\sigma_1(E)$, describes the broad resonance tails above 2.8 MeV. There are seven adjustable parameters, namely, r, γ^2, E_0, A, B, C and D.

Measurements

The time-of-flight method

Neutron transmission measurements were made by the time-of-flight method at the 200-m flight path at ORELA. Electrons were accelerated in 5-ns bursts and allowed to strike a Be-clad water-moderated target to produce a broad neutron spectrum. Collimators in the evacuated flight path defined a 7.6-cm diameter neutron beam. Filters of 0.3 gr/cm^2 of ^{10}B and 3.8 cm of uranium attenuated low energy neutrons and γ rays. The flux was monitored by a fission counter near the source. To minimize effects of possible variations in flux the samples were oscillated in and out of the beam several times for each measurement.

The neutron detector was a 2.0-cm thick NE-110 plastic scintillator. Neutron flight times were measured relative to the initial γ-ray burst, and neutron energies was calculated relativistically. Data were collected in a time channels corresponding to 1.0 keV at the 2.35-MeV resonance or to about a third of the overall 2.8-keV energy resolution. Uncertainties related to resolution broadening and time-of-flight measurements are negligible for present purposes.

For the energy region of interest there are three small backgrounds: 1) room background, 2) γ rays which are generated by capture in the hydrogen in the source and decay with a 17 μsec half-life, and 3) γ rays from the ^{10}B(n,αγ) reaction in the pyrex face of the detector photo-tube. To facilitate the measurement of the γ-ray backgrounds the data were recorded in three contiguous ranges of pulse height. From the γ rays observed in the higher ranges at late times when there were no proton recoils we deduced the corrections to the proton recoil spectra in all ranges. The final cross sections show that the uncertainties in background subtraction are negligible. All counts were corrected for the 1108 nsec deadtime in the digital time analyzer. We expect the deadtime corrections to be accurate and the following results, which involve corrections from 1% to 43% for the various measurements, show no evidence of errors. Larson, et al.[8] give further details of measurements at ORELA.

Thin sample measurements

Our main effort was devoted to cross sections near the 2.35-MeV minimum, but in this section we describe auxiliary experiments to find the off-resonance cross sections. We measured the transmission for oxygen by repeatedly alternating a 7.62-cm thick BeO sample with a "matching" Be sample. Altogether the BeO and Be were cycled 400 times in five experiments which took 200 hours. After correcting for deadtime losses and backgrounds we added counts from the five experiments and converted to cross sections. Figure 2 shows the cross sections from 2.0 to 3.0 MeV. The data have been averaged over time channels to give point spacings of about 5 keV at the minimum and 20 keV off resonance. The curve is a least squares fit obtained using Eqs. (2-4); Table I lists the best fit parameters. The uncertainties are statistical except for the parameter A, for which the statistical part was only ±2 mb and the main uncertainty is related to the composition of the sample, as discussed below. The deviations of points from the curve near 2.9 MeV are attributed to the narrow 2.889 MeV resonance,[2] which is omitted from the fitting equation.

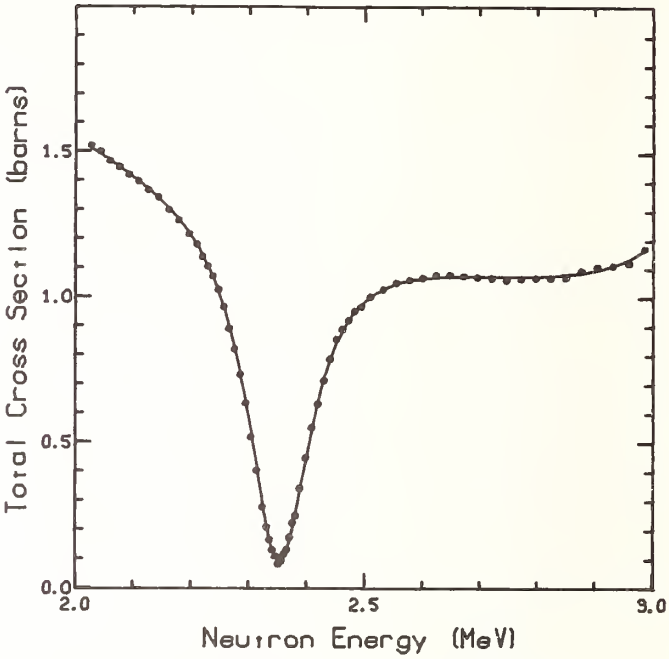

Fig. 2. Neutron total cross section of oxygen determined from the relative transmission of "matched" BeO and Be scatterers. The curve is a seven-parameter fit from Eqs. (2-4).

Perhaps we could have terminated the experiment at this point if we had had complete confidence in the scatterers. We do have confidence in the matching Be sample; it was machined and weighed carefully and has an areal density of 0.5494 atoms/barn. The dimensions and weight of the BeO scatterers are also known but there are small uncertainties in composition.

The BeO scatterers were fabricated by pressing 99.94% BeO powder with 0.4 mole percent Li_2O at 1000°C in a graphite die. The density of the pressed sample was nearly that of BeO. To determine the residual Li_2O in the BeO we made a preliminary evaluation of σ_T for oxygen from the observed transmission. These results showed a very small peak resulting from the 257-keV Li resonance.[9] By comparison of the fitted peak to the resonance cross section[10] of Li we find the sample has 0.6 ± 0.2 atomic percent Li, a little less than in the original mixture.

If we were to make the reasonable assumption that the sample is a uniform mixture of Li_2O and BeO, we would conclude that its areal density for Be is 0.25% less than for the matching Be sample. Because of this slight mismatch we would expect a very small dip at the 622-keV Be resonance.[9] Actually, the preliminary analysis revealed a peak rather than a dip. By fitting this peak and comparing to the known resonance[10] we find the areal density of the Be in the BeO to be 1.2 ± 0.3% more, rather than 0.25% less, than in the matching Be.

We considered two possible explanations for this discrepancy. The first was that the BeO sample was more dense in the center. We rejected that because the overall density was nearly that of BeO and because the resulting oxygen cross section at low energies would be too low relative to the thermal value.[9] The second explanation, which we accept, is that the sample has uniform density but is not stoichiometric. Thus the BeO sample has 0.5486 atoms/barn of oxygen.

The total cross section for oxygen was found from the observed transmission T by the expression,

$$\sigma_T = \frac{-\ln T}{0.5486} - 0.012\ \sigma_{Be} - 0.006\ \sigma_{Li} \qquad (5)$$

where σ_{Be} and σ_{Li} are known[10] cross sections for Be and Li. At the 2.35 MeV resonance the subtraction for Li and Be is 36 mb with a ±7 mb uncertainty from fitting the Li and Be resonances at 257 and 660 keV. This uncertainty is propagated to the parameter A in Table I. The possible systematic uncertainty in our assumption of a non-stoichiometric mixture is not included.

Table I. Best-fit parameters for Eqs. (2-4) for pure oxygen as deduced from measurements with BeO-Be and with liquid oxygen. Numbers in parenthesis are uncertainties in the last significant figures. Parameters indicated by asterisks are recommended. The parameter A should be increased for impure oxygen.

Parameter	Units	BeO-Be	Liquid Oxygen
r	fm	4.98(1)*	
γ^2	MeV	0.0429(2)	0.0438(1)*
E_o	MeV	2.3508(2)	2.3507(1)*
A	barn	0.0820(80)	0.1001(17)*
B	barn-MeV^{-1}	0.19(1)*	
C	barn-MeV^{-2}	0.40(3)*	
D	MeV	0.063(4)*	

Measurements with liquid oxygen

A thick liquid oxygen scatterer was used to obtain good statistics and small systematic uncertainties near the 2.35-MeV resonance. Figure 3 shows the scatterer, a cryostat designed and used previously by Kalyna[3] for similar measurements at Columbia University.

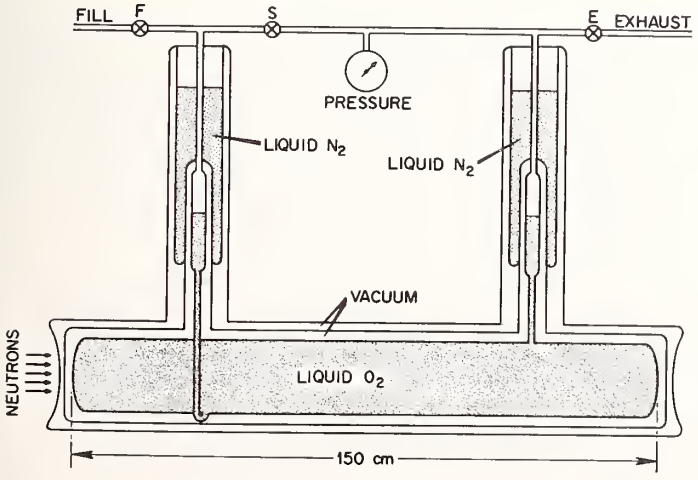

Fig. 3. Liquid oxygen cryostat.

In thirteen experiments we measured the transmission relative to a matching "dummy" cylinder. Each experiment required about fourteen hours during which time the cryostat and dummy were cycled about five times. The same uranium and boron filters were used as above. Also a 36-cm liquid oxygen filter was added for seven of the thirteen experiments. This filter, by removing most neutrons outside of the 2.35-MeV resonance, eliminates backgrounds that might be created by a broad spectrum of fast neutrons reaching the detector room before the neutrons of interest. The measurements with and without the filter proved that such backgrounds were negligible.

The "dummy" scatterer was an evacuated cylinder whose length and end plates matched the cryostat. To confirm the matching we measured the relative transmission for a broad neutron spectrum with both scatterers evacuated. The relative transmission was 0.9990 ± 0.0005; hence, the uncertainty in matching was negligible.

To determine the length of the oxygen container we placed the cryostat unfilled at right angles to the beam at 80 m from the source and made shadow graphs using the highly collimated electromagnetic radiation. We averaged for the slight curvature of the end plates. The resulting length, 149.9 ± 0.3 cm, was later corrected for the shrinkage of stainless steel to the temperature of liquid oxygen.[11]

To fill the cryostat we evacuated it and then filled from a reservoir of high purity liquid oxygen through valve F in Fig. 3 with valve S closed and the exhaust valve E open. When the filling was complete, as indicated by the exhaust being liquid rather than gas, the cooling nitrogen reservoirs were filled, valves E and F were closed and valve S was opened. The liquid oxygen then cooled itself by boiling in the closed system while it consumed considerable liquid nitrogen. After about ten hours it became quiescent at about one-third atmosphere pressure. The quiescent condition continued for the many days of the measurements; the temperature of the liquid oxygen increased gradually and the pressure increased at about one-tenth atmosphere per day. Upon completion of the first six experiments we evacuated the cryostat and refilled it from a fresh supply for the last seven experiments.

To find the areal density of the sample we used a precision absolute gauge to measure the oxygen vapor pressure of the closed system, found the corresponding density of the liquid oxygen from Scott's tabulation,[11] and calculated the areal density for the sample length. The pressures for the thirteen measurements ranged from 0.308 to 0.836 atm. and the corresponding areal densities ranged from 6.69 to 6.47 atom/barn.

The liquid oxygen was produced by Linde Air Products and distributed in 168-L containers by Tennessee Welding Company of Knoxville, TN. The distributor determined the oxygen percentage in a gas sample from each container using either a Taylor oxygen analyzer or the Linde-Shaker method. They reported 99.68% oxygen by volume of gas for the first supply and 99.71% for the second, which was transferred two weeks later. After our final experiment we extracted a liquid sample from the lower connector of the cryostat and had the resulting gas analyzed at this laboratory by gas chromatographic comparison to 99.99% oxygen. The gas was found to contain 0.06% Ar and less than 0.01% N_2; i.e., 99.93% oxygen. From these two independent analyses we conclude the purity was 99.8 ± 0.1%.

The impurities are of consequence only at the 2.35-MeV minimum where the cross sections of argon and nitrogen are much larger than for oxygen. We need not know the exact relative amounts of Ar and N_2 because the neutron cross section for monatomic Ar at 2.35 MeV is about the same as for diatomic N_2. On the basis of average cross sections[10] we corrected the observed minimum by -3.3 ± 1.6 mb to account for the 0.2 ± 0.1% impurity.

Figure 4 is a typical result (experiment 2). The points show averages over channels, with finer averaging at the minimum. The curve was obtained by least-squares adjustment of A, γ^2 and E_0 in Eqs. (2-4) with the other four parameters fixed from Table I. Essentially the position, width and minimum have been fitted. In this figure, and in similar figures for the other twelve experiments, points on the wings of the resonance are fitted remarkably well considering that the transmissions were 0.1% or less. This shows that backgrounds have been subtracted properly.

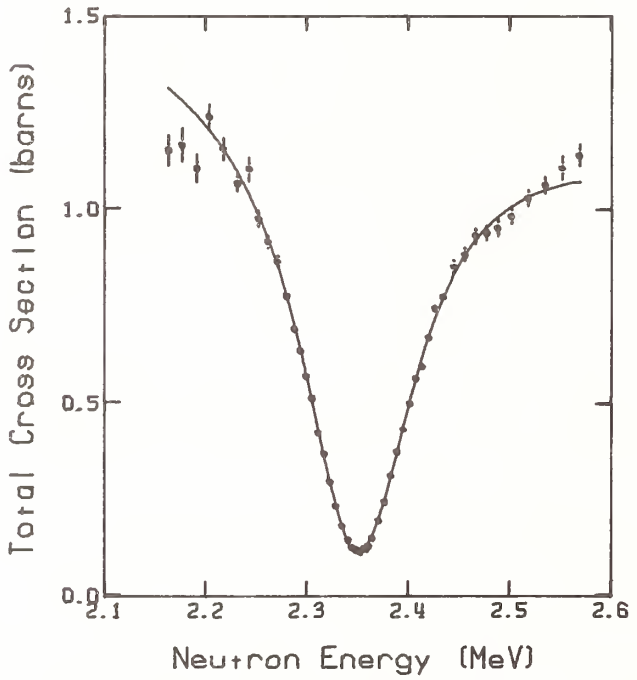

Fig. 4. Neutron total cross section of oxygen from experiment 2 for liquid oxygen. The curve is a three-parameter fit.

Table II summarizes the thirteen experiments and the best-fit parameters. Since the experiments were performed with variations in technique in an effort to reveal any systematic errors, it is significant that the variations in the best-fit parameters are consistent with the counting statistics. As discussed above the experimental variations included the use of two different shipments of liquid oxygen, a range of temperatures for the liquid, and an oxygen filter for the seven experiments indicated in the table. Also a neutron collimator near the detector was enlarged to increase the counting rate a factor of two for the last four experiments. Other minor variations were made but no systematic errors were discovered.

The mean values and uncertainties of A, γ^2 and E_0 from Table II are included in Table I. For γ^2 or E_0 the uncertainty is the standard error of the mean. For the background parameter, A, the ±1.7 mb uncertainty comes mostly from the 3.3 ± 1.6 mb subtraction for impurities of Ar and N_2 in the oxygen. The other small uncertainties in A are ±0.34 mb standard error, ±0.2%(±0.2 mb) in sample length and ±0.2%(±0.2 mb) in the conversion from pressure to density[11] of liquid oxygen.

Table II. Least-squares parameters for the liquid oxygen experiments.

Experiment Number	A (barns)	γ^2 MeV	E_0 MeV
1	0.0997	0.0439	2.3508
2	0.0996	0.0438	2.3508
3	0.0981	0.0436	2.3509
4[a]	0.0995	0.0435	2.3510
5[a]	0.1013	0.0437	2.3510
6[a]	0.0989	0.0441	2.3508
7	0.0999	0.0435	2.3510
8[a]	0.0990	0.0440	2.3507
9[a]	0.1008	0.0436	2.3506
10	0.1012	0.0438	2.3506
11[a]	0.1026	0.0442	2.3505
12	0.1012	0.0435	2.3505
13[a]	0.0997	0.0437	2.3504

a. Experiments with additional 36-cm liquid oxygen filter.

Discussion

For the averaged parameters in Table I for the liquid oxygen experiment the resonance minimum is 110.9 ± 1.7 mb at 0.8 keV above the resonance energy E_0. (The minimum of 93 ± 8 mb from the BeO-Be experiment does not agree within the quoted uncertainty, but we discard this value because of possible further systematic uncertainties related to the BeO sample, as discussed above.)

Using the same cryostat Kalyna[3] found a 95 ± 5 mb minimum at 2362 keV. We believe we made several significant improvements over Kalyna's early work. Fowler, Johnson, Haas and Feezel[12] found a 0.13 b minimum. However, that result had a large uncertainty because it involved a 30% correction for resolution when a T(p,n) source was used and a factor-of-two correction when a Li(p,n) source was used.

For measuring the temperature of a deuterium plasma we recommend the resonance parameters from the liquid oxygen experiment and the non-resonance parameters from BeO-Be measurements. These values, which are indicated by asterisks in Table I, are for pure oxygen. In practice the liquid oxygen will have a small impurity of Ar and N_2 just as in the present measurement. In that case the parameter A should be increased 1.6 mb for each 0.1% impurity by volume of the gas.

Figure 5 shows the predicted transmission versus ion temperature of the d-d plasma neutrons for three thicknesses of liquid oxygen. The transmission for a given thickness rises rapidly with temperature and falls slowly; the ordinate in the figure shows the ratio to the maximum. A thick sample gives a desirable strong energy dependence but a small transmission. Thus, a compromise thickness must be chosen.

The main uncertainty in the present work is the ±1.7 mb in the minimum which was propagated from the uncertainty in impurity of the oxygen. This error will propagate to a small uncertainty in ion temperature. For example, for a scatterer of 5 atoms/barn the uncertainty for 4 keV ions is ±0.025 keV. It increases at higher temperatures where the curve in Fig. 5 has less slope. But it is probable that uncertainties about the Maxwellian distribution in the plasma and in the measurement of transmission will outweigh the errors of the present work.

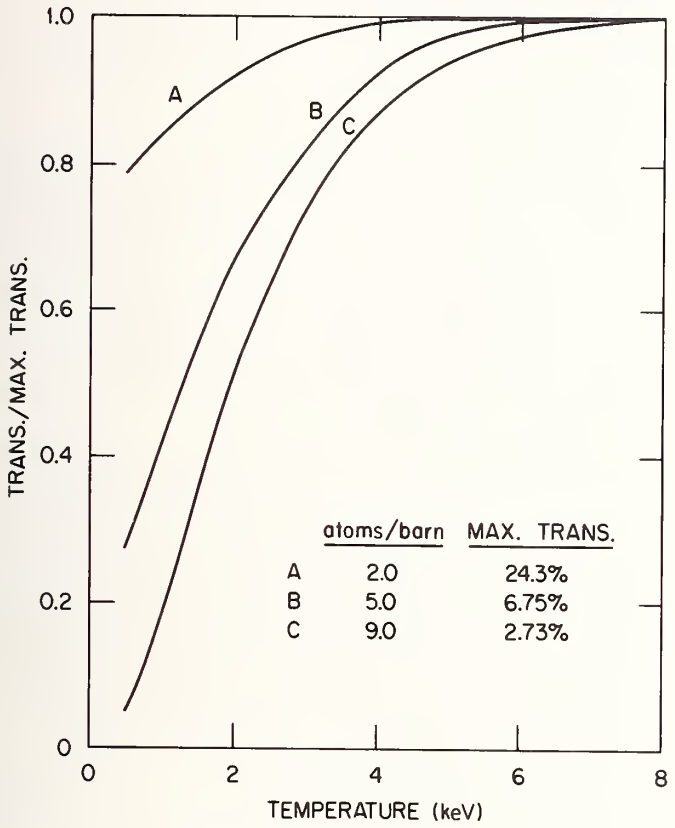

Fig. 5. Predicted neutron transmission versus ion temperature of a deuterium plasma for three thicknesses of oxygen. The ordinate shows the ratio to the listed maximum transmission.

Acknowledgements

We are indebted to Drs. P.H. Stelson and C.F. Barnett for suggesting this problem and for discussions of fusion spectra. We are also grateful to Dr. J.P. Felvinci for the loan of the cryostat from Columbia University, to Dr. J.A. Harvey for helpful discussions of the experiment and to J.L. Heatherly for the oxygen analysis. This research was sponsored by the Division of Nuclear Sciences, U.S. Department of Energy, under contract No. W-7405-eng-26 with the Union Carbide Corporation.

References

1. P.H. Stelson and C.F. Barnett, Bull. Am. Phys. Soc. 23, 882 (1978).
2. J.L. Fowler, C.H. Johnson and R.M. Feezel, Phys. Rev. 8, 545 (1973).
3. J. Kalyna, Neutron Total Cross Section of Oxygen at 2.37 MeV, Doctoral Thesis, Columbia University (1971).
4. W.R. Faust and E.G. Harris, Nucl. Fusion 1, 62 (1960).
5. A.H. Wapstra and K. Bos, Atomic and Nucl. Data Tables 19, 177 (1977).
6. G.M. Hale and D.C. Dodder, paper FB3 of these proceedings and private communication.
7. C.H. Johnson, Phys. Rev. C 7, 561 (1973).
8. D.C. Larson, C.H. Johnson, J.A. Harvey and N.W. Hill, Oak Ridge National Laboratory Report No. ORNL/TM-5612 (1976).
9. Resonance Parameters, compiled by S.F. Mughabghab and D.I. Garber, Brookhaven National Laboratory Report No. 325 (National Technical Information Service, Springfield, Virginia, 1973) 3rd ed., Vol. I.
10. Neutron Cross Section Curves, compiled by D.I. Garber and R. R. Kinsey, Brookhaven National Laboratory Report No. 325, 3rd ed., Vol. II.
11. R.B. Scott, Cryogenic Engineering, (D. Van Nostrand Co. Inc., Princeton, N.J., 1959).
12. J.L. Fowler, C.H. Johnson, F.X. Haas and R.M. Feezel, Proceedings of the 3rd Conf. on Neutron Cross Sections and Technology, CONF-710301, Vol. 1, 179 (1971).

THE STATUS OF NEUTRON DOSIMETRY AND DAMAGE ANALYSIS FOR THE FUSION MATERIALS PROGRAM

L. R. Greenwood
Argonne National Laboratory
9700 South Cass Avenue
Argonne, Illinois 60439, USA

The status of neutron flux and spectral measurements is described for fusion material irradiations at reactor, T(d,n), Be(d,n), and spallation neutron sources. Such measurements are required for the characterization of an irradiation in terms of displacement damage, gas and transmutant production. Emphasis is placed on nuclear data deficiencies with specific recommendations for cross section measurements and calculations.

[Neutron dosimetry; nuclear activation cross sections; displacement damage]

Neutron irradiations for the U.S. Fusion Materials Program require accurate measurements of the neutron flux and spectrum to characterize the irradiation in terms of neutron fluence, displacement damage, and gas and transmutant generation. Such knowledge is vitally important if materials effects are to be correlated between facilities and extrapolated to fusion reactor environments. All too often in the past, adequate neutron dosimetry has been lacking for materials irradiations, making it very difficult to compare effects measured in different facilities. The multiple-foil activation technique, including stable product He monitors, is being used routinely at all current irradiation facilities, including reactors, T(d,n), Be(d,n) and spallation neutron sources. Neutron fluxes can generally be measured to within 10-30% in the energy ranges where most of the displacement damage is generated. Spectral-averaged damage cross sections can be calculated with 10-15% errors due to dosimetric uncertainties, owing to large covariance effects. However, the damage cross sections themselves rely on nuclear data of generally poorer accuracy (10-50%), as discussed later.

The multiple foil activation technique is described in previous papers,[1,2] including nuclear half-lives, gamma branching-ratios, and activation cross sections. For Be(d,n) dosimetry, the activation cross sections, taken primarily from ENDF/B-IV[3] below 20 MeV, were extrapolated to 44 MeV[4] using available data to 28 MeV[5] and the THRESH code.[6] The cross sections have been tested in Be(d,n) fields at E_d = 14-40 MeV. Table I summarizes the results of these tests, comparing estimated cross-section errors (described below) to errors measured in the indicated energy ranges. Similar integral tests pertinent to reactor dosimetry, using ^{235}U and ^{252}Cf fission sources, have also been reported recently.[7]

Two computer codes are presently being used to determine the flux spectrum and associated errors from the integral activation measurements. SANDANL[8] uses a Monte Carlo technique to vary the input to SAND II.[9] More recently, we have developed the code STAYSL,[10] which uses a least-squares technique to solve the variance-covariance matrix for a minimum value of χ^2. The STAYSL code has been modified to accept the same input data as SANDANL, thereby taking advantage of our previously developed nuclear cross section and associated error libraries as well as cadmium cover and neutron self-shielding routines.

Experience with both the SANDANL and STAYSL codes shows that the largest source of uncertainty in the input data is the starting spectrum. Activation errors are typically less than 2% and their covariances are negligible. Cross section errors are currently derived from McElroy *et al*;[11] however, these files will be replaced by ENDF/B-V data, including covariance effects, in the near future. Cross section errors, summarized in Table I, are typically 5-30% in energy regions which most directly contribute to the activation integrals. However, the errors rapidly increase to 30-100% at high neutron energies, especially above 28 MeV where there are virtually no experimental measurements.

Unfortunately, input flux errors are very poorly known and must be estimated, in a somewhat subjective manner, from either neutronics calculations (reactors), remote active spectrometry (accelerators), or previous experience. We have estimated that input flux uncertainties are generally 30-80%, depending on energy. However, the errors may be much larger in some energy regions. For example, no flux measurements have been made at Be(d,n) sources below 1 MeV. In the worst case, maximum flux errors can be increased until they no longer have any influence on the output. However, this procedure will not work if the reaction sensitivities are too low in a particular energy region. In this case, basic physics or past experience must be used to set reasonable error limits.

Covariance effects may be very significant in flux unfolding; however, such data are very poorly known at present. A cross-section covariance file will eventually be made available in ENDF/B-V. Input flux correlations are probably quite large, but they are totally unknown. We have estimated input flux and cross-section covariances for the STAYSL code. A Gaussian function has been used assuming that nearby flux and cross section energy groups must be very highly correlated, although distant groups may be uncorrelated. If the input fluxes are completely uncorrelated, then discontinuities may appear in the output spectrum, especially at resonance energies. However, a correlation full-width at half-maximum of several flux groups removes this undesired effect and appears to be analagous to smoothing the iterations in the SAND II code. Longer term correlations are assumed to be arbitrarily small and have little noticeable effect. Correlations between different cross sections could be quite large since a poorly-known cross section is often experimentally normalized to a well-known one. However, such effects must be very carefully correlated with cross-section variances, delaying the availability of such files in ENDF/B-V.

Figure 1 shows a flux spectrum determined by STAYSL for the Oak Ridge Research Reactor (ORR) at core position E7 at a reduced power of 1 MW.

Table I. Comparison of Estimated Cross Section Errors with Integral Test Results for Be(d,n), E_d = 14 - 40 MeV. The 90% energy sensitivity limits are given.

Reaction	Energy Range (MeV)	Estimated Range of Errors (±%)	Measured Integral Errors (±%)
$^{115}In(n,n')^{115m}In$	2 - 23	8 - 20	3
$^{238}U(n,f)$	2 - 30	6 - 15	4
$Ti(n,p)^{46}Sc$	5 - 33	5 - 50	14
$Ti(n,p)^{47}Sc$	3 - 33	15 - 50	15
$^{48}Ti(n,p)^{48}Sc$	7 - 27	15 - 50	7
$Fe(n,p)^{54}Mn$	4 - 33	10 - 40	6
$^{56}Fe(n,p)^{56}Mn$	6 - 23	10 - 30	4
$^{59}Co(n,p)^{59}Fe$	5 - 24	10 - 40	8
$^{58}Ni(n,p)^{58}Co$	4 - 23	6 - 30	9
$^{60}Ni(n,p)^{60}Co$	6 - 23	10 - 40	14
$^{27}Al(n,\alpha)^{24}Na$	7 - 21	6 - 15	3
$^{54}Fe(n,\alpha)^{51}Cr$	6 - 28	15 - 40	36
$^{59}Co(n,\alpha)^{56}Mn$	7 - 24	10 - 40	4
$^{45}Sc(n,2n)^{44m}Sc$	13 - 27	10 - 20	14
$^{58}Ni(n,2n)^{57}Ni$	13 - 28	20 - 30	14
$^{59}Co(n,2n)^{58}Co$	12 - 27	10 - 20	9
$^{59}Co(n,3n)^{57}Co$	22 - 36	20 - 40	28
$Zr(n,2n)^{89}Zr$	13 - 28	15 - 30	13
$^{93}Nb(n,2n)^{92m}Nb$	10 - 22	10 - 20	7
$^{169}Tm(n,2n)^{168}Tm$	10 - 23	10 - 20	7
$^{169}Tm(n,3n)^{167}Tm$	18 - 30	10 - 30	9
$^{197}Au(n,2n)^{196}Au$	9 - 24	10 - 20	9
$^{197}Au(n,3n)^{195}Au$	18 - 29	10 - 30	6
$^{197}Au(n,4n)^{194}Au$	27 - 40	15 - 30	11
$^{238}U(n,2n)^{237}U$	7 - 16	20 - 40	11

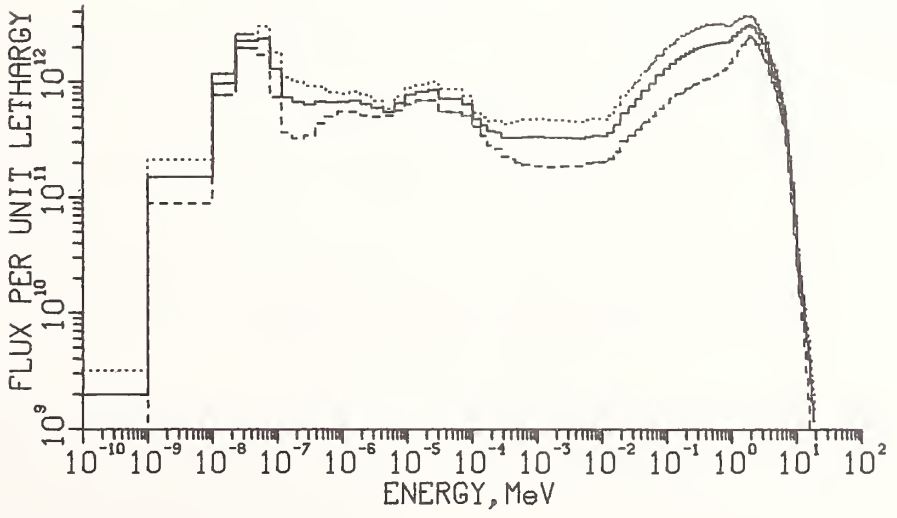

Figure 1. STAYSL results for core position E7 in the Oak Ridge Research Reactor using 21 reactions. The dashed lines represent one standard deviation. Differential flux times neutron energy is plotted.

Twenty-one reactions were used including cadmium covers and fissle monitors. Whereas the thermal and fast (>1 MeV) group fluxes are determined to ± 10-30%, much larger errors are seen for the energy region between 1 and 500 keV. This effect is symptomatic of mixed-spectrum reactors (part thermal and part fast) since, unfortunately, there are no nuclear reactions which have their principal sensitivity (cross section x flux) in the 1-500 keV energy region. Cadmium covered foils do not extend beyond the resonance region and most effective thresholds are above 1 MeV. The ^{93}Nb(n,n') ^{93m}Nb(13.6Y) reaction would help, especially for long irradiations. Otherwise, we must rely on neutronics calculations.

A typical unfolded spectrum for a Be(d,n) irradiation at E_d = 40 MeV at the U.C. Davis Cyclotron is shown in Figure 2. As can be seen, the flux errors are about 10-30% in the 2-30 MeV energy range. Lower energies are difficult to unfold since thermal reactions have a significant contribution (20-40%) to their activation from neutrons above 1 MeV, and there have been no measurements below 1 MeV. Fluxes above 30 MeV are hampered by a lack of cross section data. The most desirable reactions for dosimetry at accelerator based sources (*e.g.*, the FMIT Li(d,n) facility under construction at Hanford Engineering Development Laboratory) are those having multiple, long-lived activation products from a single element. Table II lists activation cross sections which are particularly in need of further measurement or calculation.

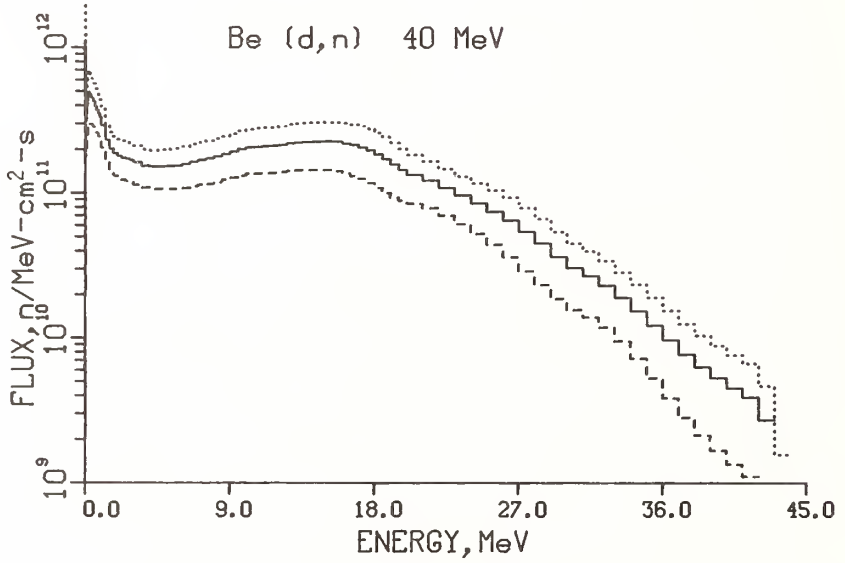

Figure 2. STAYSL results for Be(d,n) irradiation at U.C. Davis Cyclotron at 6 mm using 12 reactions. The dashed lines represent one standard deviation.

Neutron dosimetry at spallation neutron sources is complicated by two factors. First of all, neutrons extend up to very high energy (300-800 MeV) and it does not appear to be possible to extend the activation technique to such high energies (>50 MeV). Secondly, the presence of high energy protons complicate the dosimetry since, for example, (p,d) or (p,np) reactions cannot be distinguished from (n,2n) reactions. Fortunately, neither problem has been found to be very serious in recent tests at the Zero Gradient Synchrotron at Argonne.[12] The neutron flux above 20 MeV is less than 1% of the total and can probably be determined reasonably well by computer calculations. The proton fluxes were also measured by proton activation reactions and appear to be about 1% of the neutron flux with an average energy between 100 and 200 MeV. Fortunately, such high energy protons contribute little to radiation damage and do not produce more than 10% of any of the neutron activation reaction products. Proton activation reaction cross sections are needed to refine such measurements and the spallation reaction on ^{27}Al leading to ^{7}Be and ^{22}Na is extremely useful since it can also be used to measure the absolute proton beam intensity.

Dosimetry at T(d,n) sources, such as the Rotating Target Neutron Source, RTNS II, at Lawrence Livermore Lab can routinely provide neutron fluences to within ± 7%, using only the ^{93}Nb(n,2n) ^{92m}Nb reaction to monitor the 14.8 MeV neutrons. However, longer irradiations will require a longer-lived monitor, such as ^{54}Fe(n,p) ^{54}Mn. Experiments farther back from the source, involving larger masses of material, will also have to contend with backscattered neutrons at much lower energy. This can present some mathematical problems in the unfolding technique, especially if the 14 MeV neutrons dominate the activations. Small errors in the 14 MeV cross sections can then translate into much larger errors in the lower energy neutron flux. Tests are now being planned to study this problem.

The importance of accurately measuring the neutron flux spectrum in various fusion materials irradiations is illustrated in Table III, which shows the contribution of various neutron flux groups to displacement damage production in nickel. At Be or Li(d,n) sources, 90% of the materials damage is generated by neutrons in the 2-30 MeV energy range where fluxes can now be routinely determined to 10-30%. Hence, the fluxes below 2 MeV and above 30 MeV are not very important. At mixed-spectrum reactors, the problem is somewhat more difficult since about 20% of the damage is generated in the 0.1 - 1 MeV energy

region where flux measurements are very difficult, especially for long irradiations. We would particularly like to emphasize that 20-30% of displacement damage in reactors may come from neutrons below 1 MeV since, in the past, experimenters have often neglected this region, only measuring the flux above 1 - 2 MeV (*e.g.*, by the $^{54}Fe(n,p)$ reaction). This can lead to very large errors (50-100%) in the computed damage rates, especially if a fission spectrum is incorrectly assumed below 1 MeV.

In conclusion, neutron dosimetry can presently provide the fusion materials program with flux and spectral accuracies of 10-30% except in the 1-500 keV region in mixed-spectrum reactors and below 2 MeV or above 30 MeV at accelerators. Fortunately, such errors are not particularly important since the output fluxes from SANDANL or STAYSL are very highly correlated. Hence, spectral-averaged damage rates can be routinely measured to ± 10-15%. For example, using the output covariance matrix from STAYSL for the ORR spectrum in Fig. 1, we compute the displacement damage in nickel to be 28.8 ± 3.0 barns. It should also be pointed out that the displacement cross sections themselves have much larger errors (10-50%) since they depend on all nuclear reactions, including elastic scattering as well as angular distributions, many of which are very poorly known. A comprehensive program is thus needed to measure and calculate cross sections for both activation and damage calculations to improve the data base for fusion materials studies.

Table II. Threshold activation reactions needed for fusion related dosimetry. Elements with multiple reactions and long-lived products are particularly desirable.

Reaction	Energy Range (MeV)	Reaction	Energy Range (MeV)
$^{93}Nb(n,2n)^{92m}Nb$	9 - 28	$^{59}Co(n,p)^{59}Fe$	4 - 28
$(n,n')^{93m}Nb$	0.1 - 10	$(n,2n)^{58}Co$	10 - 30
$Fe(n,X)^{54}Mn$*	1 - 40	$(n,3n)^{57}Co$	20 - 40
$^{54}Fe(n,\alpha)^{51}Cr$	7 - 25	$(n,4n)^{56}Co$	30 - 50
$^{58}Ni(n,p)^{58}Co$	2 - 25	$^{197}Au(n,2n)^{196}Au$	8 - 25
$(n,2n)^{57}Ni$	12 - 36	$(n,3n)^{195}Au$	15 - 35
$(n,3n)^{56}Ni$	22 - 40	$(n,4n)^{194}Au$	23 - 45
$^{60}Ni(n,p)^{60}Co$	3 - 30		

* Total production from element is required.

Table III. Fraction of displacement damage in nickel as a function of neutron energy in mixed-spectrum reactors and Be(d,n) sources.

Reactor (ORR)(Fig. 1)		Be(d,n), E_d = 40 MeV (Fig. 2)	
Energy Range (MeV)	Damage (%)	Energy Range (MeV)	Damage (%)
< 0.01	0.6	< 2	5
< 0.1	3.7	2 - 5	5
0.1 - 0.4	9.2	5 - 10	15
0.4 - 1	13.8	10 - 15	25
1 - 2	24.8	15 - 20	25
2 - 4	32.2	20 - 25	15
4 - 6	11.2	25 - 30	5
> 6	5.2	> 30	5

References

1. L. R. Greenwood, R. R. Heinrich, R. J. Kennerley, and R. Medrzychowski, Nucl. Technol. 41, 109 (1978).

2. L. R. Greenwood, R. R. Heinrich, M. J. Saltmarsh, and C. B. Fulmer, Integral Tests of Neutron Activation Cross-Sections in a $^{9}Be(d,n)$ Field at E_d = 40 MeV, to be published in Nucl. Sci. and Eng. (1979).

3. ENDF/B-IV, National Neutron Cross Section Center, Brookhaven National Lab; ENDF/B-IV Dosimetry File, B. A. Magurno, BNL-50446 (1975).

4. L. R. Greenwood, Extrapolated Neutron Activation Cross Sections for Dosimetry to 44 MeV, ANL-FPP TM-115 (1978).

5. B. P. Bayhurst, J. S. Gilmore, R. J. Prestwood, J. B. Wilhelmy, N. Jaime, B. H. Erkkila and R. A. Hardekopf, Phys. Rev. C12, 451 (1975).

6. S. Pearlstein, Neutron-Induced Reactions in Medium Mass Nuclei, BNL-16271 (1971); THRESH 2, BNL (1975).

7. M. F. Vlasov, A. Fabry, and W. N. McElroy, Status of Neutron Cross Sections for Reactor Dosimetry, INDC (NDS) - 84/LM (1977).

8. G. R. Odette, Trans. Am. Nucl. Soc. 22, 803 (1975).

9. Neutron Flux Spectra Determination by Multiple Foil Activation, AFWL-TR-67-41 (1967).

10. F. G. Perey, Least-Squares Dosimetry Unfolding: The Program STAYSL, ORNL-TM-6062 (1977).

11. W. N. McElroy and L. S. Kellogg, Nucl. Technol. 25, 180 (1975).

12. M. A. Kirk and L. R. Greenwood, "Neutron Flux and Spectral Measurements for an E_p = 500 MeV Spallation Source with Tantalum and Uranium Targets," to be published, 1979.

NUCLEAR DATA NEEDS FOR FMIT

R. E. Schenter, F. M. Mann and D. L. Johnson
Hanford Engineering Development Laboratory
Richland, WA 99352

The Fusion Material Irradiation Testing Facility (FMIT) is designed to test samples in a high energy neutron environment so that data obtained in fission reactors can be extrapolated to that needed in fusion devices. Although most of the flux is centered around ∿14 MeV, the neutron distribution will extend from thermal energies to 50 MeV.

Data needed in design include total, elastic, and removal cross sections for shielding, neutron yields for source calculations, and selected transmutation cross sections for dose determinations. Data needed for operation include transport and dosimetry cross sections for flux determinations, damage energy, transmutation, and gas production cross sections for damage analyses, and selected data for machine operation and maintenance. Detailed reaction lists are given.

[Nuclear Data Needs for FMIT]

Introduction

The Fusion Materials Irradiation Test (FMIT) facility[1] is a d + Li neutron source which will more rapidly expand the materials data base to fusion energies. This national facility is being designed by the Hanford Engineering Development Laboratory for the U.S. Department of Energy and should start operation in 1984. The d + Li reaction (E_d = 35 MeV, I_d = 0.1 A) will provide an intense source of neutrons (∿4 * 10^{16} n/sec) peaking at about 14 MeV and ranging up to E_n=50 MeV.

Design Needs

The end of Title II design (i.e., the period of final design) is early 1981. Therefore the data needed for design must be obtained consistent with the design schedule.

Because of the intense deuteron beam, beam spill is of great concern. During operation the major shielding requirements will be from neutrons produced by deuteron interactions. The magnitude of this source can be appreciated by noting that a 0.01% beam spill will result in a 10μA current, a current which many experimentalists would desire to have in their research machines.

The major materials that the deuterons may strike are the accelerator (Cu or some coating such as Au), the high energy beam transport system (e.g. aluminum or stainless steel), and the lithium target. The neutron yield must be known as a function of neutron energy and emission angle. It must also be known as a function of deuteron energy for those materials in the accelerator structure.

After the machine is turned off, gamma radiation from delayed activity becomes predominate. These radioactive nuclides come not only from the deuterons striking the accelerator, the beam transport system, and the Li target (which will have Na, K and Ca impurities), but also from the neutrons produced by the deuteron interactions. Note that impurities, rather than the main material, may be the most important gamma source. The amount of delayed activity will have a major impact on choice of materials and placement of bending magnets, quadrupole focusing magnets, and shielding materials.

In order to determine shielding requirements, transport calculations will be needed. The most likely shielding materials are ordinary concrete, high density concrete, iron, and soil. For each, the neutron differential scattering cross sections as a function of incoming and outgoing energy and of outgoing angle are needed.

Other areas of concern are the production of prompt gamma radiation so that proper wall cooling and instrumentation can be designed. Besides moderating the neutrons, the shields will heat up, thus requiring accurate kerma factors. Finally estimates of damage parameters for the target must be made so that it has an adequate life expectancy.

Operational Needs

Whereas the needs for nuclear data for the design phase will be quickly over, the needs for data during operation will grow more stringent as experimenters learn more from their samples. The experimenters will want to know the flux and damage parameters seen by the samples.

Presently, the damage parameters which are thought to be most important are displacements, helium and hydrogen production, and transmutations. These quantities will have to be available for the materials the experimenters will use and for energies from 0-50 MeV, with the most precise results being needed around 15 MeV.

In order to calculate the displacements per atom, the recoil spectra of the atoms must be found. Using standard kinematic formulas this reduces to knowing the energy-angle differential cross sections for the various nuclear reactions possible, with elastic and inelastic scattering being the most important. Doran et al., have shown that the effect of secondary emission is unimportant. Gas production involves not only (n,pγ) and (n,αγ) cross sections but also all other reactions which can produce hydrogen or helium with (n,np), (n,pn), and (n,αn) usually being the most important. Transmutation may be important for those materials where small amounts of impurities can cause significant property changes. Although not a damage parameter, the experimentalists will want to know the induced radioactivity of their sample so that post-irradiation experiments can be properly planned.

The experimenters will also want to know the

Table I. Possible Dosimetry Reactions.

$^{23}Na(n,2n)^{22}Na$	$^{59}Co(n,p)^{59}Fe$
$^{27}Al(n,\alpha)^{24}Na$	$^{59}Co(n,2n)^{58}Co$
$^{54}Fe(n,\alpha)^{51}Cr$	$^{59}Co(n,3n)^{57}Co$
$^{54}Fe(n,p)^{54}Mn$	$^{59}Co(n,4n)^{56}Co$
$^{58}Ni(n,p)^{58}Co$	$^{93}Nb(n,2n)^{92}Nb$
$^{60}Ni(n,p)^{60}Co$	$^{90}Zr(n,2n)^{89}Zr$
$^{58}Ni(n,2n)^{57}Ni$	$^{90}Zr(n,3n)^{88}Zr$
$^{58}Ni(n,3n)^{56}Ni$	$^{90}Zr(n,p)^{90m}y$
$^{89}Y(n,2n)^{88}Y$	$^{197}Au(n,2n)^{168}Tm$
$^{89}Y(n,3n)^{87}Y$	$^{197}Au(n,3n)^{195}Au$
$^{107}Ag(n,2n)^{106m}Ag$	$^{197}Au(n,4n)^{194}Au$
$^{107}Ag(n,3n)^{105}Ag$	$^{197}Au(n,5n)^{193}Au$
$^{169}Tm(n,2n)^{168}Tm$	$^{238}U(n,2n)^{237}U$
$^{169}Tm(n,3n)^{167}Tm$	
$^{169}Tm(n,4n)^{166}Tm$	

energy dependent flux at their sample positions. Among the ways available are passive and calculational dosimetry. The materials that will be used as dosimetry foils, helium accumulation monitors, and solid state track recorders are not yet precisely known. A likely set of foil material is shown in Table I. It will be important to know their responses not only in the peak response region, but also in the wings. Unfortunately, data above 15 MeV is lacking for many of these reactions. For calculational dosimetry to be accurate, both the d + Li source spectrum and the neutron transport cross sections must be known. Presently[2] the source spectrum is known to ~15% for E_n>2 MeV. The transport cross sections are fairly poorly known for E>15 MeV, and these cross sections must be known for each of the materials in the samples. Fortunately, the same data needed for displacement calculations are needed here.

It is likely that even after construction has started, fine-tuning of the design will occur, especially in those areas where initially there were large uncertainties. More concern will also be evidenced in the selection and design of diagnostic instrumentation.

General Notes

Not only are the cross sections needed, but also their uncertainties. In fact it is highly desirable to have a full covariance matrix for the data. This is extremely important for design purposes, since the facility must be conservedly designed, so often nominal values + 2σ are used. During operation, unfolding and uncertainty analyses will require covariance information.

Much of the needed data will come from nuclear model calculations. Such calculations require computer codes capable of multi-particle emission and pre-equilibrium treatment. However, such calculations must be anchored and verified by experimental data. For some uses, only experiment will provide data of sufficient accuracy.

Some of the needed base is already in place. ENDF/B-V,[3] the standard nuclear data library in the U.S., extends to E_n = 20 MeV. However the data above 8 MeV is usually of lower quality than the data below 8 MeV, while the data above E_n = 15 MeV is poorly known. Shielding libraries for accelerators by Alsmiller[4] and Wilson[5] are based mainly on nuclear model calculations and extend past 50 MeV. There is also scattered experimental data[6] but the major efforts have been initiated by the FMIT project. The d + Li neutron spectra for E_d = 35 MeV have been measured[7] with measurements for deuteron and neutron activation and for wall heating in progress.

Summary

Much nuclear data will be needed for successful operation of the FMIT facility. Some of the needs (mainly those in design) must quickly be satisfied, while others will be long term. Some of the long term needs await on the sample choices of the experimenters.

Fortunately, there is much overlap in the data needs, not only within the FMIT project but also between FMIT and proposed fusion devices. Table II provides a listing of the FMIT most important needs and their time tables.

References

1. E. W. Pottmeyer, Jr. "The Fusion Materials Irradiation Test Facility at Hanford", First Topical Meeting on Fusion Reactor Materials, Bal Harbour, Florida, Jan. 1979. Conference proceedings will be published in the Journal of Nuclear Materials.

2. F. M. Mann, F. Schmittroth, L. L. Carter and J. O. Schiffgens, "The Spatial Dependence of Flux and Damage in the FMIT Test Cell," proceedings of this conference.

3. The Evaluated Nuclear Data Library (ENDF/B) is maintained at the National Nuclear Data Center, Brookhaven National Laboratory.

4. R. G. Alsmiller, Jr. and J. Barish, "NCDATA - Nuclear Collision Data for Nucleon - Nucleus Collisions in the Energy Range 25 to 400 MeV" ORNL-4220, Oak Ridge National Laboratory (1968).

5. W. B. Wilson, "Nuclear Data Development and Shield Design for Neutrons Below 60 MeV", LA-7159-T, Los Alamos Scientific Laboratory (1978).

6. R. C. Haight, "Review of Nuclear Data: 10 to 40 MeV" in BNL-NCS-50681, Brookhaven National Laboratory (1977).

7. D. L. Johnson, F. M. Mann, J. W. Watson, J. Ullman, and W. G. Wyckoff, "Measurements of Neutron Spectra from 35 MeV Deuterons on Thick Lithium for the FMIT Facility," Proceedings of this conference.

TABLE II

Nuclear Data		Design Needs (by 6/80)			Operational Needs	
		Neutron Sources	Gamma Sources	Shielding	Damage Parameters	Dosimetry
$\frac{d\sigma}{d\Omega dE_n}$	(d + accelerator, Li target)	X	X	X		X
$\frac{d\sigma}{d\Omega dE_n}$	(n + shielding)	X	X	X		
$\frac{d\sigma}{d\Omega dE_n}$	(n + samples)				X	X
σ_{act}	(d + accelerator, Li target)		X			
σ_{act}	(n + samples, accelerator)		X		X	X
σ_{gas}	(n + samples)				X	X
$\sigma_{transmutation}$	(n + samples)				X	X

Accelerator materials include Cu, coatings on Cu (e.g. Au), beam pipe (e.g. Al, Fe C or Ta scrappers), and focusing devices (e.g. Cu, Fe).

Sample materials will be limited only by the experimenters' imagination, but certainly will include steels, refractory materials, Cu, Al insulators.

Shielding materials include concrete (Si, O, Ca, C), soil, and iron.

THE SPATIAL DEPENDENCE OF FLUX AND DAMAGE IN THE FMIT TEST CELL

F. M. Mann, F. Schmittroth,
L. L. Carter, and J. O. Schiffgens
Hanford Engineering Development Laboratory
Richland, Washington 99352

Experimental Li(d,n) thick target yields have been combined with nuclear models to determine the microscopic Li(d,n) cross section as a function of incoming deuteron energy ($E_d \leq 40$ MeV), of outgoing neutron energy ($0 \leq E_n \leq 50$ MeV), and of outgoing neutron angle ($0 \leq \theta \leq 180°$). A generalized least squares adjustment procedure using all the experimental data for $14 \leq E_d \leq 50$ provided the overall normalization and the angular distribution, while the Serber stripping model and the evaporation model provided the neutron energy dependence.

The cross sections are applied to the conditions appropriate to the FMIT (Fusion Materials Irradiation Testing) facility to determine flux and damage parameter levels inside the test cell.

[Li(d,n), fitted thick target yield, $E_d \leq 40$ MeV; deduced σdpa, σHe for Cu at FMIT]

Introduction

With the continuing progress toward breakeven fusion facilities, more thought is being directed toward the materials that will be used in power-producing fusion reactors. Unfortunately, there presently does not exist any facility capable of producing very large peak fluxes ($\sim 10^{15}$ n/cm^2-s) of high energy neutrons ($\sim$14 MeV) or of large fluxes ($\sim 10^{14}$ n/cm^2-s) of high energy neutrons over large volumes (500 cm^3). Because of the severe limitation of producing dense targets of deuteron or tritium, the RTNS (Rotating Target Neutron Source) or any other d+t source is restricted to much lower fluxes ($\sim 10^{13}$ n/cm^2-s) in small volumes ($\sim$1 cm^3).

High fluxes of high energy neutrons can be produced from d+Li reactions. The Fusion Material Irradiation Test Facility (FMIT)[1] now being designed at the Hanford Engineering Development Laboratory for the U.S. Department of Energy will produce high energy neutrons with sufficient fluxes in large volumes. This paper describes, using relatively simple, yet accurate models, the neutron environment (including expected displacement and helium production rates) of such d+Li facilities[2,3] with particular attention to the nominal operating parameters of FMIT.

FMIT will have 35 MeV deuterons striking a flowing liquid lithium target 1.9 cm thick. In order to reduce heating problems in the lithium jet, the beam will be disbursed with present designs being Gaussian in shape with full widths at half maximum values (FWHM) of 3 cm in width and 1 cm in height. Over 99.9% of the beam will hit the Li jet. A stainless steel backing plate of .22 cm will constrain the Li and will separate the target space from the experimental volume in the test cell.

Since the peak fluxes of greater than 10^{15}n/cm^2-s will occur within 3 cm of the rear of the backing plate, the source of neutrons cannot be modeled as a point. Persiani[4] has analyzed the neutron environment using the experimental data of Daruga et al.,[5] and of Saltmarsh et al.,[6] but treating the source as a point. For a more accurate description, the cross sections for producing neutrons are needed as a function of distance into the lithium and of the angle between the incident beam direction and the neutron's path. Since the position within the lithium is related to the deuterons' instantaneous energy (ignoring small straggling effects), the dependence of cross section on position can be converted into a dependence on deuteron energy. In addition, since most material property changes will depend on the energy distribution of the neutrons striking the material, the dependence of the cross section on neutron energy must also be known. Thus, the unperturbed energy dependent neutron flux as a function of neutron energy at a point in the test cell can be found from

$$\frac{d\phi}{dE_n} = \int_0^{E_{d\text{-inc}}} dE_d \; \frac{d^3\sigma}{dE_d \, d\Omega \, dE_n} \; \frac{I(y,z)}{(dE_d/dx)\, r^2} \; dydz \qquad (1)$$

where $d^3\sigma/dE_d \, d\Omega \, dE_n$ is the differential cross section for producing neutrons, $E_{d\text{-inc}}$ is the incident deuteron energy, dE_d/dx is the relationship between energy loss and the position parallel to the beam (x), $I(y,z)$ is the deuteron current distribution, and r is the distance between the neutron source point and the point of interest in the test volume. Note that Equation 1 ignores scattering (both neutron and deuteron) within the target as well as neutron scattering outside the target. The equation also ignores the slight loss of deuteron intensity (less than 5%) as they pass through the lithium due to nuclear reactions and the extremely slight divergence of the deuteron beam.

Neutron Source Term

Introduction

All the quantities in Equation 1, except the differential cross sections, are known from geometry, target design, or well established physics. Unfortunately, there is not enough experimental data to determine these cross sections. Instead, models tested against experiment must be used.

Angular Yields

Using the least squares adjustment computer code FERRET[7], the energy dependence of six angular functions forming the angular yields were determined using all the experimental data [5,6,8-14] for deuterons on lithium with $14 < E_d < 45$ MeV. A major problem in using experimental data is that the data do not span all neutron energies; rather only neutrons above some threshold energy are observed. Therefore using the preliminary version of the model, and the energy dependence from the very low energy measurement of the HEDL-UCD (threshold = .4 MeV at E_d = 35 MeV) all the data were corrected to zero neutron energy.

To explain the neutron yield and spectra from 160 MeV deuteron bombardment of thin targets, Serber[15] in 1947 treated the deuteron as very weakly bound with the energy and angle of the spectator neutron being determined by the average internal motion of the target nucleus. Although slight differences exist depending whether the target nucleus is opaque or transparent, these differences are relatively minor. The resulting formula is

$$\frac{d\sigma}{d\Omega}_{\text{Serber}} = \frac{1.}{[1 + (\theta/\theta_s)^2]^{3/2}} \qquad (2)$$

where $\theta_s = (5720/E_d).^{1/2}$ However, the theory presupposes that $E_d >> E_B$, the deuteron binding energy ($\sim$2.2 MeV). Thus it is not surprising that a slightly different formula was more successful in the preliminary model.

$$\frac{d\sigma}{d\Omega}_{\text{Pre}} = \frac{1.}{1 + (\theta/\theta_p)^2} \qquad (3)$$

where $\theta_p = (1800/E_d).^{1/2}$ For an isotropic angular distribution in the center of mass system, the laboratory angular distribution would be a linear combination of unity and cosine (θ). However, an analysis of the HEDL-UCD data for E_n=1 to 2 MeV shows a $1 + \alpha \cos^5\theta$ dependence. Therefore $\cos^5\theta$ was added along with sin θ to complete the six angular functions. Functions peaking at $\theta \sim 20°$ were also tried but their parameters were too uncertain to be meaningful.

So as not to presuppose the deuteron energy dependence of each of the six angular functions, the energy range was broken into 9 groups, 0 - 5 MeV, 5 - 10 MeV, 10 - 15, 15 - 19, 19 - 22, 22 - 25, 25 - 30, 30 - 35, and 35 - 40 MeV. Thus 54 parameters were adjusted by FERRET, which at the same time kept track of the various correlations of the 32 data points. By requiring a smooth variation as a function of deuteron energy, the parameters and their covariance matrix were found.

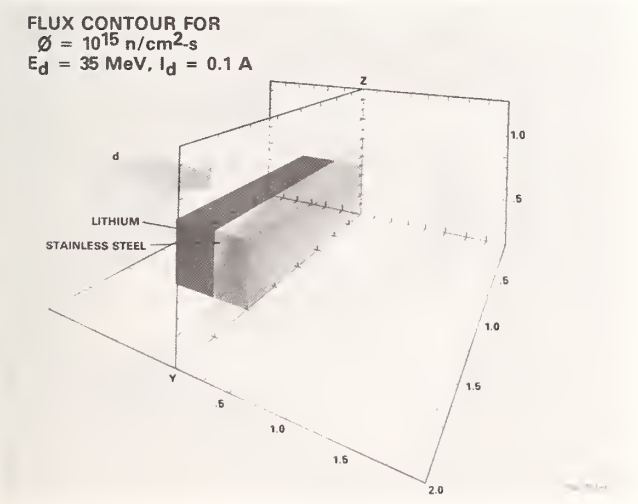

Fig. 1. Flux contour for $\phi = 10^{15}$n/cm^2-s.

Figure 1 shows the 10^{15} n/cm^2-s flux contour for the reference FMIT design. As can be seen, the contour is shaped like a football. Figure 2 displays the volume which has a flux greater than a minimum value ϕ. The figure also displays that volume which contains a region having an average flux ϕ. Since flux is linearly related to deuteron current, Figure 2 can be used to determine the volume for different deuteron currents.

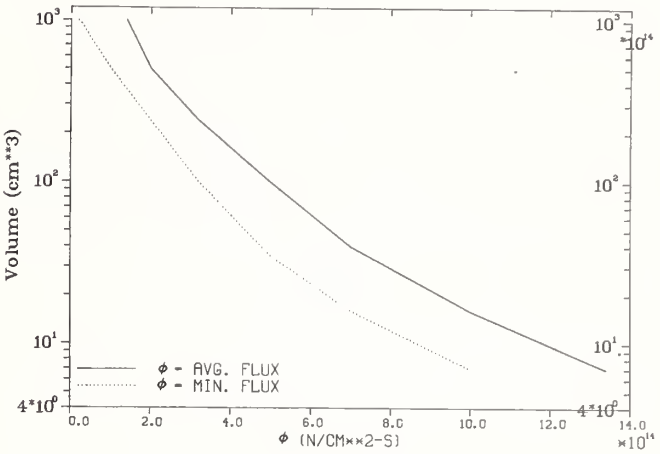

Fig. 2. Volume in test cell having flux greater than minimum value and having average flux of given value.

Neutron Spectra

The determination of the neutron spectra is much more difficult because so much more data are required. Even if experimental neutron spectra were available, the magnitude of the quantity of the data and the need to use non-linear parameters make the use of a code like FERRET inadvisable. Instead, simple models for stripping and for evaporation are used with their parameters being adjusted to fit the HEDL-UCD experiment at E_d = 35 MeV.

The model for stripping relies mainly on the Serber model. August, et al.,[16] have shown that this model which was developed to explain results using 160 MeV deuterons gives the proper shape of the high energy distribution ($E_n > E_d/2$) at 0° for a thick target for incident deuteron energies of interest at FMIT.

For the highest neutron energies ($E_n > E_d$) the Serber model breaks down for d + Li. Here the dominant reaction is the stripping of ^{7}Li to the ground and first excited states of ^{8}Be. Because only two states are involved (and both are unbound), the classical picture fails and one must resort to a quantum mechanical treatment or to experiment. The latter choice is taken with a deuteron energy independent microscopic cross section $\sigma(\theta)$ used for each state for $E_d < E_n < E_d + Q(\theta)$.

The evaporation part of the model is also in two parts. The first part is the classical evaporation model [17] which predicts the energy spectrum of the neutrons which are boiled off as the first particle out after a compound nucleus is formed. The second part, a linear term in neutron energy, represents all succeeding evaporations.

Comparison with Experiment

Figure 3 presents a comparison between the model results (corrected for the experimental neutron detec-

tion threshold) and the measurements between 15 and 40 MeV. The results of the model pass through the data of Nelson, et al.,[9] Daruga, et al., [5] Amols et al., [11] Johnson, et al.,[12] and Saltmarsh, et al.[6]. The calculations are lower than the measurements of Lone, et al., [8] and Weaver, et al., [10] but higher than those of Goland, et al.[13] It should be noted that the data of Lone, et al., show a very large yield for low energy neutrons (E_n>2), which is very uncertain due to uncertainties in detection efficiency. If the 2.3 MeV detection threshold of Lone, et al., is used instead of their 0.3 MeV threshold, the C/E's change to .89, .92, .85 respectively. The data of Goland, et al., on the other hand, show a drastic fall off for neutrons below 5 MeV, maybe explaining why the model predicts more neutrons than they observed. Overall, there seems to be little deuteron energy dependence or angular dependence in the differences between the model and the measurements.

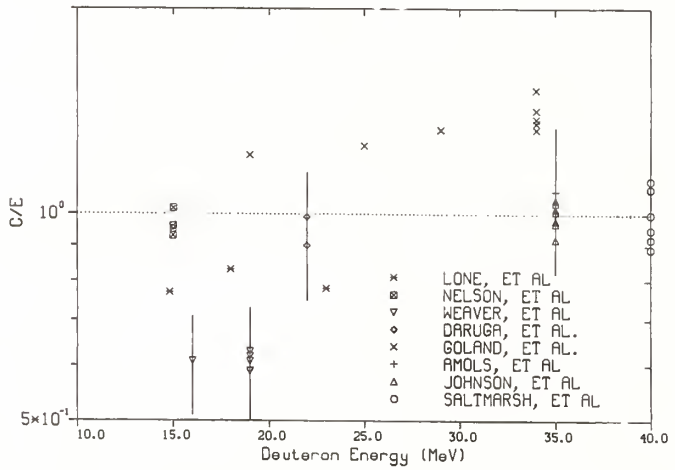

Fig. 3. Comparison between experimental data and results of fit.

Damage Parameters

Although much attention is paid to flux, the experimentalists who will use FMIT will be more interested in predicting damage rates, such as displacement and helium production.

Unfortunately, the nuclear data needed for such calculations are in very poor shape. Data is needed past 40 MeV, but ENDF/B,[18] the main U.S. nuclear data library extends only to 20 MeV. Therefore, data for isolated materials, but not for iron or stainless steel, have been obtained over the desired energy range. To provide an idea of the usefulness of FMIT, damage parameters for Cu, the evaluated material closest to iron, have been used. The displacement cross sections are from ORNL[19] with E_{damage} - 30 eV. Because the ORNL calculations for helium production do not agree with measured values [20,21] and do not include processes such as (n,2nα) new calculations using the computer code HAUSER*5[22] were performed.

Figures 4 and 5 show equal displacement and equal helium production contours, similar to those for flux shown in Figure 1. The helium contours are slightly more peaked along the deuteron beam axis, resulting in He/dpa contours which are hyberloid in shape, opening away from the target. As seen from Figure 6 which displays the predicted volumes having damage rates greater than a given value, there will exist in

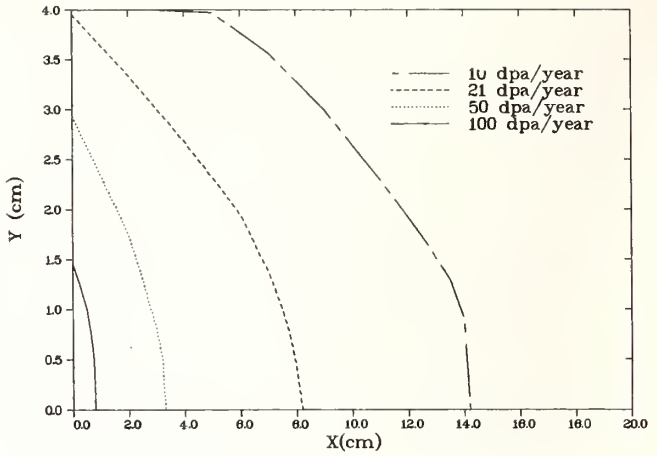

Fig. 4. Displacement rate contours in test cell.

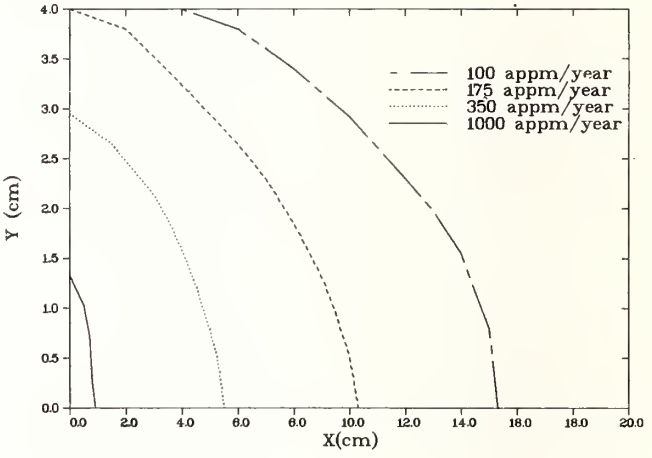

Fig. 5. Helium production rates in test cell.

FMIT over a 100 cm^3 of unperturbed space having damage rates greater than that of a first wall of a 1 MW/m^2 fusion device.

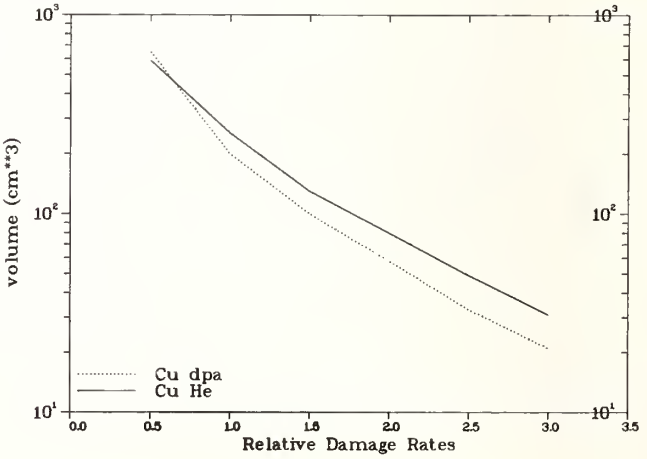

Fig. 6. Volumes in test cell for given displacement and helium product rates.

Conclusion

The unperturbed neutron spectra, displacement rate, and helium production in the FMIT test cell have been calculated using a source term which agrees well with experimental results. The predicted values show that there exists significant volumes having damage rates greater than that of the first wall of a fusion reactor.

References

1. E.W. Pottmeyer, Jr., "The Fusion Materials Irradiation Test Facility at Hanford" presented at the 1st Topical Meeting on Fusion Reactor Materials, Miami Beach, FL., Jan. 1979; to be published in the Journal of Nuclear Materials.

2. M.J. Saltmarsh and R.E. Worsham "INGRID - an Intense Neutron Generator for Radiation-induced Damage Studies in the CTR Material Program", ORNL-TM-5233, Oak Ridge National Laboratory, Oak Ridge, TN. (Jan. 1976).

3. F. Grand and A.N. Goland, "An Intense Neutron Source Based Upon the Deuterium - Stripping Reaction", Nucl. Inst. Meth. 145 (1977) 49 P. Grand (ed.), "Accelerator - Based Neutron Generator", BNL-20159 and addendum BNL-2048, Brookhaven National Laboratory, Upton, NY (Jan. 1975 and Jan. 1976).

4. P.J. Persiani, W. Becker, and J. Donahue, "Neutron Spectra for the 40-MeV Deuteron Lithium Source System", Trans Am Nucl. Soc.(1977) 795. P.J. Persiani, W. Becker, and J. Donahue, "Neutron Spectra and Basic Data Requirements for (d,Li) and (d,Be) Target Systems", in BNL-NCS-50681, Brookhaven National Laboratory, Upton, NY. (1977).

5. V.K. Daruga and N.N. Krasnov, "Production of Strong, High-Energy Neutron Fluxes by a Cyclotron by Irradiating Thick Lithium and Beryllium Targets with 22-MeV Deuterons", Atomic Energy 30 (1971) 493, translated from the Russian Atomnaya Energiya 30 (1971) 399.

6. M.J. Saltmarsh, C.A. Ludemann, C.B. Fulmer, and R.C. Styles, "Characteristics of an Intense Neutron Source Based on the d + Be Reaction "Nucl. Inst. Meth. 145 (1977) 81. M.J. Saltmarsh, C.A. Ludemann, C.B. Fulmer, and R.C. Styles, "Neutron Yields and Dosimetry for Be (d,n) and Li (d,n) Neutron Sources at E_d = 40 MeV" in NBSIR 77-1279, National Bureau of Standards Washington, DC, (July 1977).

7. F. Schmittroth, "Generalized Least-Squares for Data Analysis," HEDL-TME 77-51 Hanford Engineering Development Laboratory, Richland WA., (March 1978).

8. N.A. Lone, "Neutron Spectral Distributions from Proton and Deuteron Bombardment of Thick Li and Be Targets at 14.8, 18, & 23 MeV" in NBSIR 77-1279, National Bureau of Standards, Washington, DC, (July 1977).

9. C.E.Nelson, F.O. Purser, P.Von Behren, and H. W. Newson, "Neutron Spectra from Deuteron and Proton Bombardment of Thick Lithium Targets", in BNL-NCS-50681, Brookhaven Nat'l Lab., Upton, NY (1977).

10. K.W. Weaver, J.D. Anderson, H.H. Barschall, and J.C. Daves, "Neutron Spectra from Deuteron Bombardment of D, Li, Be, and C", Nucl. Sci. Eng., 52 (1973) 35.

11. H.I. Amols, J.F. Dicello, M. Awschalon, L. Coulson, S.W. Johnson, and R.B. Theus, "Physical Characterization of Neutron Beams Produced by Protons and Deuterons of Various Energies Bombarding Beryllium and Lithium Targets of Several Thicknesses", Med. Phys. 4 (1977) 486.

12. D.L. Johnson, F.M. Mann, J.W. Watson, J. Ullmann, and W.G. Wyckoff, "Measurements and Calculations of Neutron Spectra from 35 MeV Deuterons on Thick Lithium for the FMIT Facility", presented at the 1st Topical Meeting on Fusion Reactor Materials, Miami Beach, FL., (Jan. 1979); to be published in Journal of Nuclear Materials.

13. A.N. Goland, C.L. Snead, Jr., D.M. Parker, and R.B. Theus, "Use of Li (d,n) Neutrons for Simulation of Radiation Effects in Fusion Reactors" IEEE Transactions on Nuclear Science, NS-22 (1975) 1776. Also see first article under Reference 2.

14. L.R. Greenwood, R.R. Heinrick, M.J. Saltmarsh, and C.B. Fulmer, "Integral Tests of Neutron Activation Cross Sections in a ^{9}Be (d,n) Field at E_d = 40 MeV", submitted to Nucl. Tech.

15. R. Serber, "The Production of High Energy Neutrons by Stripping", Phys. Rev 72 (1947) 1008.

16. L.S. August, F.H. Attip, G.H. Herling, P. Shaprio and R.B. Theus, Phys. Med. Bio. 6 (1976) 931.

17. See, for example, P. Marmier and E. Sheldon, Physics of Nuclei and Particles, Vol. 2, p. 1233, Academic Press, Inc., NY (1970).

18. The Evaluated Nuclear Data File, maintained at the National Nuclear Data Center, Brookhaven National Laboratory, Upton, NY. The current version is ENDF/B-V.

19. C.Y. Fu and F.G. Perey, J. Nucl. Mat., 61 (1976) 153.

20. S.M. Grimes, R.C. Haight, J.D. Anderson, K.R. Alvar, and R.R. Borchers "Development of a Spectrometer for the Measurement of (n,xp), (n,xd) and (n,xα) Cross Sections, Angular Distributions, and spectra at E_n = 15 MeV" in BNL-NCS-50681, Brookhaven National Laboratory, Upton, NY. (May 1977).

21. H. Farrar IV, D.W. Kneff, R.A. Britten, and R.R. Heinrick, "Fluence Mapping of RTNS-I by Helium Accumulation and Foil Activation Methods" in BNL-NCS-50681, Brookhaven National Laboratory Upton, NY, (May 1977).

22. F.M. Mann, "HAUSER*5, A Computer Code to Calculate Nuclear Reaction Cross Sections," HEDL-TME 78-83, Hanford Engineering Development Laboratory, Richland, WA, (1979).

MEASUREMENTS OF NEUTRON SPECTRA FROM 35 MeV DEUTERONS ON THICK LITHIUM FOR THE FMIT FACILITY

D. L. Johnson and F. M. Mann
Hanford Engineering Development Laboratory*
Richland, Washington 99352. U.S.A.

J. W. Watson,† J. Ullmann and W. G. Wyckoff
University of California at Davis
Davis, California 95616. U.S.A.

Neutron yield spectra were measured for 35 MeV deuterons on thick natural lithium. The time of flight technique was used and data were obtained for laboratory emission angles of 0° to 150°. The yield of neutrons greater than 1 MeV was determined at each angle and was integrated to find the total yield.

[Nuclear reactions, Li(d,xn), thick target yields and spectra; E_d= 35 MeV; angular distribution, 0°- 150°; total yield, time-of-flight technique; Fusion Materials Irradiation Test (FMIT) facility]

Introduction

The Fusion Materials Irradiation Test (FMIT) facility (1) is currently being designed by the Hanford Engineering Development Laboratory (HEDL) at Richland, Washington, U.S.A. This facility will make use of the intense source of high energy neutrons produced by 35 MeV deuterons incident upon a thick lithium target in order to study radiation effects in fusion reactor materials. Samples are to be exposed to the forward neutron flux (which peaks at ∿ 14 MeV) that results when a 0.1 amp deuteron beam is stopped in a 2 cm. thick jet of liquid lithium which also carries away the deposited heat.

Accurate knowledge of the characteristics of such a source is required for design and operation. There have been several measurements of the neutron yield spectra made with deuterons of similar energies on thick lithium. Some of the most recent measurements are described in the articles in references (2) & (3). These data were insufficient to meet FMIT needs primarily for one or more of the following reasons: 1) The deuteron energy was different; 2) Measurements were taken only at or near 0° relative to the beam direction. (Neutrons emitted over a wide range in angles are important for damage in test specimens, for penetration in shield walls, and for activation and heating of materials surrounding the target); 3) The highest energy portion of the spectra (up to the maximum kinematically allowed energy) was not observed. (These neutrons are the most penetrating through thick shielding walls); 4) The lowest energy portion of the spectra was not observed (neutron damage is significant down to ∿0.1 MeV and activation by low energy neutrons is very important).

Most of the data required for FMIT can be obtained from time-of-flight measurements similar to those in references (2) & (3) with a thick target in which one obtains the yield spectrum integrated over deuteron energy as observed at long distances from the target. However, for calculations of the neutron flux spectra at positions very close to the target in the FMIT test cell, additional information is needed because it is necessary to take explicit account of the spatial dependence of the source. For such calculations, the differential neutron production cross section is required as a function of deuteron energy (from 0 to 35 MeV) and also of neutron emission angle and energy. There are few measurements of the differential cross section for appropriate deuteron energies. An approach to obtain the differential data from thick target data is described in references (4,12) The FMIT target geometry is also discussed there and preliminary calculations of the neutron environment for irradiation experiments in FMIT using such differential data are described in references (4, 5, & 12).

Here we describe only experimental aspects and results of neutron yield spectra measurements with 35 MeV deuterons on thick lithium. Our measurements are quite similar to the 40 MeV measurements of Saltmarsh et al., (3, 6) however, there are some different techniques used and here we have emphasized obtaining complete spectra over a rather complete angular distribution, including back angles.

Experiment

The neutron yields and spectra were obtained using the time-of-flight (TOF) technique with a pulsed beam. The data obtained directly were the time distributions of neutrons observed by a detector placed far from the target. Neutrons were produced by very short bursts of incident deuterons. The time distribution measured with very short equal time channels, was then converted to an energy distribution after correction for background and electronic dead time losses. In addition, energy dependent corrections for detector efficiency and the probability for neutron loss between target and detector were made. To obtain the neutron yield spectrum in units of (neutrons/μC-Sr-MeV), the energy distribution was divided by the solid angle (Sr) of the detector for neutrons from the target and the integrated charge (μC) deposited in the target by the deuteron beam.

The measurements were performed using deuterons accelerated by the isochronous cyclotron of the University of California at Davis. The target and detector geometry are illustrated in figure 1. The beam entered the experimental room through a thick concrete and iron wall. It passed through a large scattering chamber before proceeding to the lithium target about 4 meters downstream.

Details of the lithium target system are shown in the inset of figure 1. A very thin walled (0.025cm) stainless steel scattering chamber tube was used which was only 2.54 cm diameter X 30 cm long. The target was a solid cylinder of 99.6% natural lithium which was 2 cm thick and filled the tube diameter. This design was used because it was desired that neutrons down to ∿ 0.5 MeV could be observed with as little perturbation as practical, caused by secondary scat-

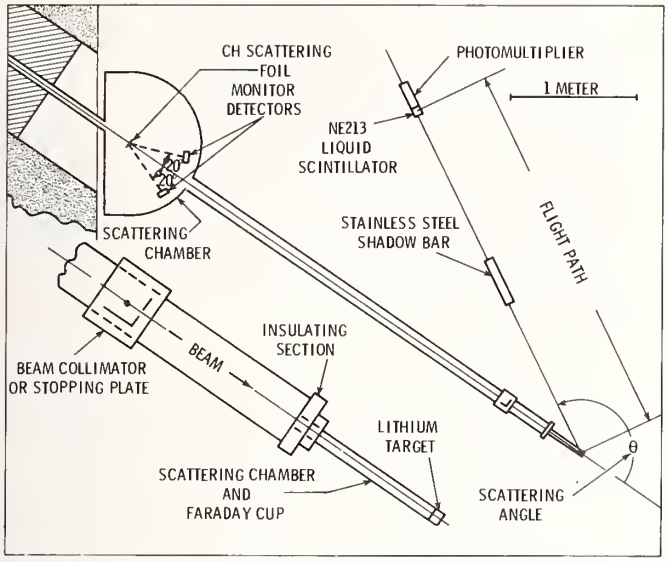

Fig. 1. Diagram of experimental geometry. Inset shows details of target and beam collimator.

tering or absorption in the scattering chamber walls or the lithium target itself. Furthermore, measurements were desired for angles as far back as 150° with respect to the incident beam direction (as in fig. 1) with little structural material along or near the flight path from target to detector.

The beam could be focused to a spot about 1 cm in diameter on target. A beam defining aperture (0.32 cm thick copper with 1.27 cm diameter hole) was placed about 0.7 meters upstream of the lithium to prevent a drift or halo in the beam from striking the beam tube or scattering chamber walls. A small fraction of the beam did hit the aperture itself, however, the source of background which was produced was localized in space and could be measured and corrected for. Some of the background measurements were made when the beam was stopped in a plate made of the same material as the aperture which was rotated to the same position.

Neutrons were detected by a cylindrical NE 213 liquid scintillator that was 5.08 X 5.08 cm diameter and coupled to an RCA 8575 photomultiplier. The detector axis was aimed at the target center. The neutron flight path was considered to be the distance from target center to detector center. Measurements were made with the detector placed at angles of 0°, 4°, 8°, 12°, 20°, 30°, 45°, 70°, 105°, & 150° relative to the beam direction.

For most angles and flight paths, all background due to neutrons not coming directly from the target was measured using a cylindrical stainless steel shadow bar (38.1 X 6.35 cm diameter) placed midway between the target and detector. The shadow bar was completely removed for foreground measurements. The target, shadow bar and detector were carefully aligned at each angle using a laser.

The electronic circuitry provided three pulses to an on-line computer data acquisition system for every event detected. A time-of-flight (TOF) pulse, a pulse height pulse (PH) and a pulse shape discrimination pulse (PSD) were provided. The TOF pulse was obtained from the output of a time to amplitude converter (TAC) which was started by a fast pulse from the photo tube anode and stopped by a pulse derived from every other cycle of the cyclotron R.F. The PH pulse was derived from a photo tube dynode and was proportional to the energy deposited in the detector by either a neutron or gamma ray event. The PSD pulse was proportional to the rise time of the dynode signal and was used to separate neutrons from gamma rays. It was obtained from another TAC which was started by the anode pulse and stopped by a pulse corresponding to the cross-over time of the double-delay line shaped dynode pulse. The computer analysis program used these pulses to provide, among other things, separate 512 channel (∿200 ns) time of flight spectra for neutrons and gamma rays respectively.

The integrated charge of the beam incident on the target and run-to-run normalization were monitored using a stationary neutron detector, similar to the main detector, that was placed about 3 meters from the target at an angle of about 30°. Beam currents required to keep electronic dead time losses within acceptable limits were quite small, going as low as ∿ .002 na. A secondary monitor such as used here was necessary because normal electronic charge integration, using the Faraday cup, was not accurate for such low currents. The monitor was calibrated to charge units by comparison to the Faraday cup charge which was obtained accurately with a high beam current.

The time structure and phase shifts of the deuteron beam pulses were monitored using one of the detectors in the large scattering chamber. This was done by observation of the time of flight of deuterons scattered elastically from the thin (∿ 1 mg/cm^2) CH target using the technique described in reference (7). This method was used to monitor beam tuning and for aligning background and foreground TOF spectra obtained with the main detector.

Data and Analysis

A long flight path was desired in order to obtain the best energy resolution for the highest neutron energies. The fractional resolution ($\Delta E/E$) is proportional to the uncertainty in the time of detection, increases with the square root of the neutron energy, but is inversely proportional to the flight path. Flight paths as long as 6 meters were possible in the forward direction, with 5 meters for 70° and 105°, but only 3 meters for 150°. Fortunately, the maximum kinematically allowed neutron energy drops significantly with increasing angle from 49.84 MeV at 0° to 27.87 MeV at 150°.

The uncertainty in the time of detection includes both the width of beam bursts and jitter and walk in electronics. It is believed to correspond to the width of prompt gamma flash peaks which were observed to have a full width at half maximum (FWHM) of about 1.5 ns. Using this value, the resolution for the maximum neutron energy with a 6 meter flight path was estimated to be $\Delta E/E \sim 4.9\%$. (FWHM)

With a flight path of 6 meters, the electronic discriminator on the neutron detector was adjusted to prevent overlap of the highest and lowest energy neutrons detected from successive bursts and to give an additional time gap of about 4 ns. The same threshold was used for all long flight path measurements and the corresponding neutron energy threshold was accurately determined from each neutron TOF spectrum after background subtraction. The average value was found to be 9.27 ± 0.06 MeV.

To obtain neutron spectra at lower energies, the measurements were repeated for all angles using a flight path of about 0.814 meters. The electronic threshold for these measurements was set crudely at

about 0.17 MeV (± 50%) equivalent electron energy using a gamma source. The corresponding neutron energy threshold was obtained more accurately from the TOF spectra as for the long flight path measurements. The average was found to be 0.90 ± 0.04 MeV. This threshold allowed a rather large time gap between the highest and lowest energy neutrons in the TOF spectra.

Background due to room scattered neutrons was measured for the larger emission angles using only the shadow bar technique. Normalization for subtraction of shadow bar background was obtained from the neutron monitor. Figure 2 shows examples of foreground, background (negative) and net spectra - note time increases from right to left. For forward angles, however, the shadow bar shielded not only the target, but all or part of the aperture as well, hence background from the aperture was not properly measured using only the shadow bar. For the long flight path measurements, only angles up to 8° had this problem, whereas for the short flight path measurements, angles up to 30° were affected.

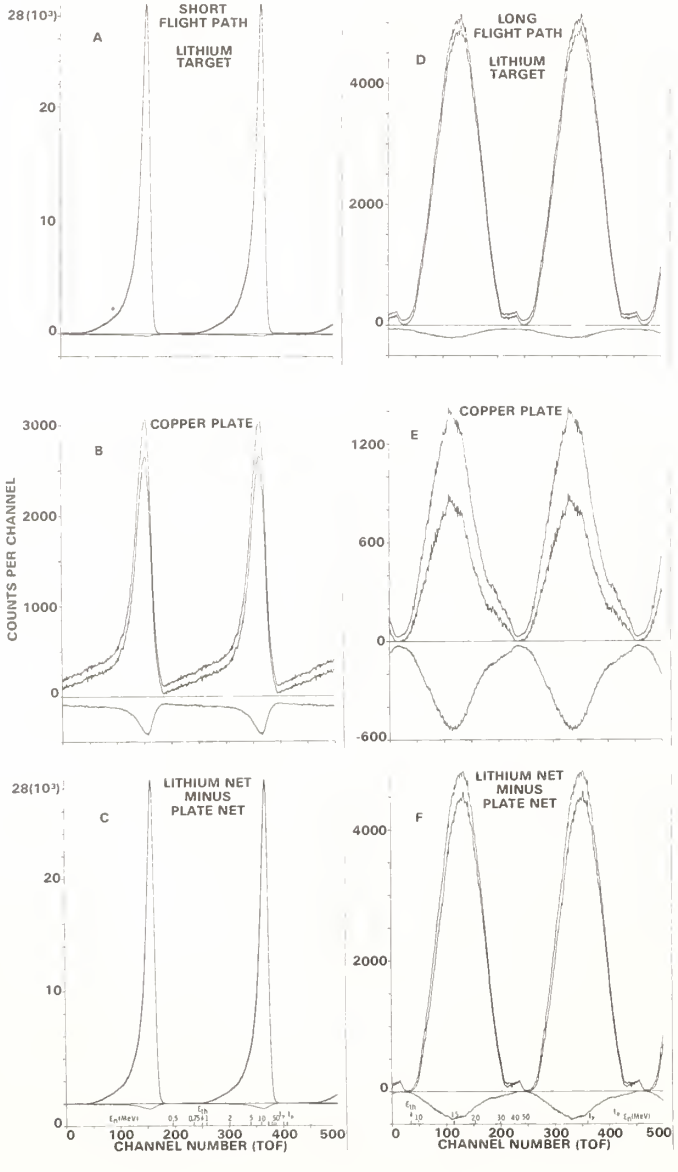

Fig. 2. Examples of neutron background subtraction for data taken at 4°. A, B and C = short flight path data. D, E and F = long flight path data.

To determine the background emitted from the aperture at each forward angle affected, separate measurements of the foreground and shadow bar background were made with the beam stopping in the plate which replaced the aperture. After subtraction of the shadow bar background (normalized with the neutron monitor), we obtained a net plate TOF spectrum believed to have the same time dependence as prompt neutrons emitted from the aperture in the direction of the detector. (See figures 2B and E). This net plate spectrum was subtracted from the net target spectrum (as in figure 2C and F) with normalization obtained by requiring zero net counts in the gap region after subtraction.

In the TOF spectra, the time that the beam pulse hit the target (t_o) is needed in order to determine the time of flight as a function of channel number. This is normally obtained by correcting back from the target gamma flash peak by the time (t_γ) it takes light to traverse the flight path. For the long flight path measurements, however, this gamma flash was not observed because the energies of prompt gamma rays from the target were well below the detector threshold. Gamma flash peaks were observed from beam bursts hitting either the aperture or plate, however. The time that the beam hit the target (t_o) was then calculated from such a peak using the known geometry, the beam energy, and the velocity of light. Examples of t_o and t_γ as well as the neutron energy scale are shown in figure 2 C and F.

The detector efficiency was calculated as a function of neutron energy for each of the threshold values using a version of the Stanton code (8) that was updated by McNaughton (9). This code uses electron equivalent energies for threshold values. These were obtained by conversion of the neutron threshold energies to equivalent electron energies using the expression relating the equivalent light output given in reference 8. An additional 15% was added to the equivalent electron thresholds as suggested in reference 8 for small detectors.

The values obtained by this method were 0.20 and 5.00 MeV for the 0.90 and 9.27 MeV neutron thresholds respectively. The efficiencies calculated for these thresholds provided spectral shapes of long and short flight path measurements at a given angle that agreed fairly well in the overlap region. Furthermore, there was no systematic dramatic rise or fall in spectra near threshold which would indicate a serious threshold error.

The neutron energy spectra obtained from both the short and long flight path measurements at a particular angle were normalized relative to one another over the energy range of 12.5 to 17.5 MeV. Generally less than 10% differences were seen. The absolute normalization was obtained from the short flight path data primarily because background subtractions were less and, for neutron energies about 1-2 MeV above threshold, the uncertainty in detector efficiency was less. The dividing energy for short and long flight path spectra was 15 MeV.

Uncertainties in the spectra are from the following sources. Uncertainties due to statistics and background subtraction were less than 10% except near the lowest and highest energies in each spectra. For each angle there is a separate normalization uncertainty that is typically about 6.5% and is due largely to uncertainty in the integrated charge. Finally, an overall normalization uncertainty of 15% is estimated, due to normalization and relative uncertainties in the detector efficiency.

Results

Results of the spectral measurements have been binned in 1 MeV steps for energies greater than 1 MeV and are shown in figure 3A & B. Data for 8° is not complete. For neutron energies less than the incident deuteron energy, the data are quite similar to the 35 MeV data at 0° by Amols et al (10) and to the 40 MeV data for 0° to 90° by Saltmarsh et al (6). On the other hand, the 34 MeV data of Goland et al (11) for 0° to 20° is only about one half the magnitude of this data and their spectra drop sharply below 5 MeV.

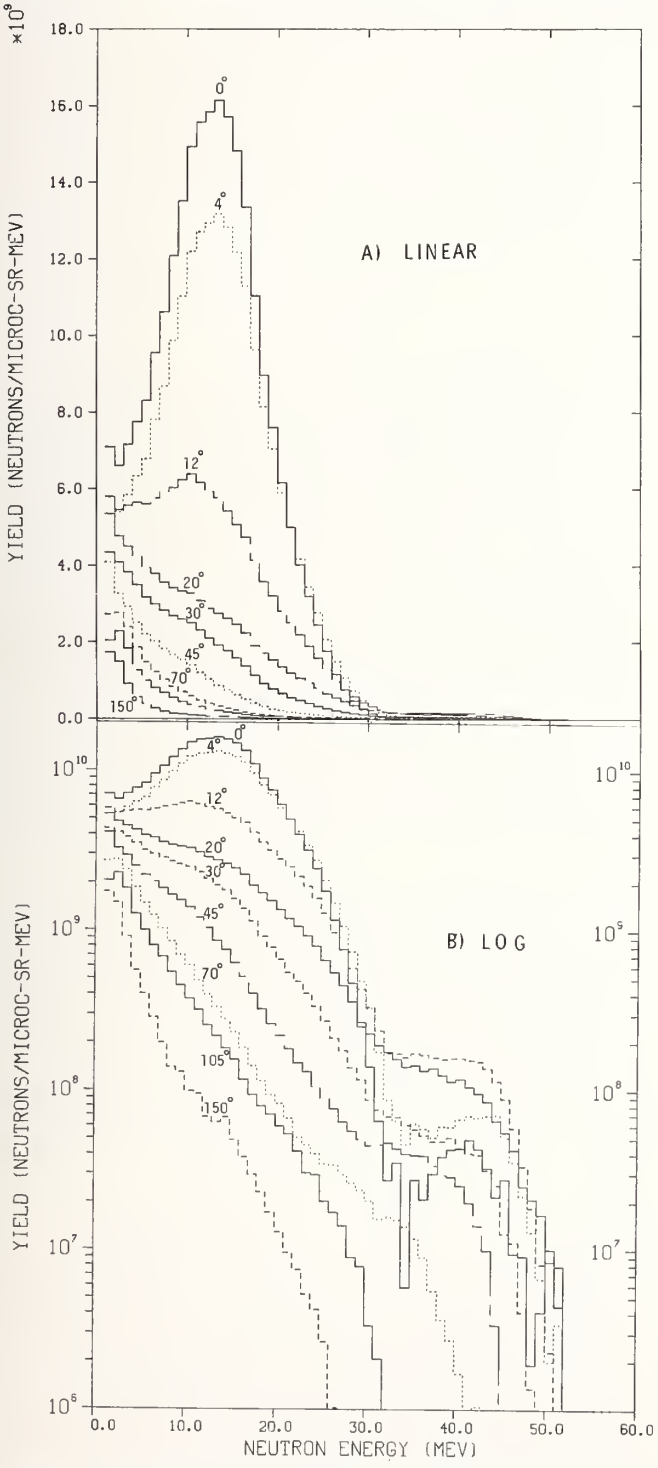

Fig. 3. Neutron yield spectra as a function of emission angle for 35 MeV deuterons on thick lithium.

The bulk of our neutron yield spectra are well described (4) by the combination of a (d,n) stripping reaction contribution (which is very forward peaked and leads to the broad maximum near 14 MeV) plus an evaporation contribution (which is more isotropic and decreases roughly exponentially with energy in the experimental energy range).

For neutron energies greater than the incident deuteron energy we find a shoulder in the spectra which was not shown by previous experimenters having similar deuteron energies. This shoulder is caused by ^{7}Li(d,n) reactions which populate primarily the ground and first excited states of ^{8}Be. The yield of this stripping reaction peaks somewhere in the range of 12° to 20° as seen in our data. These highest energy neutrons are very important for shielding considerations because of their deep penetration in thick walls. For radiation damage they are currently estimated to play only a small role, however, because of their low yield relative to the bulk of neutrons below 30 MeV.

The data shown in figure 3 were integrated over neutron energy to obtain the yield of neutrons above 1 MeV. The yield of neutrons above 0 MeV was estimated for each angle, by assuming the yield from 0 to 1 MeV equaled the yield from 1 to 2 MeV (a small correction). The results are shown in figure 4. Also shown is a plot of the product of the yield and $2\pi \sin\theta$ (θ= lab. angle). This curve shows the relative contribution as a function of emission angle to the total neutron yield. By integrating this curve over angle, the total yield was found to be 3.0 (10^{11}) neutrons/μC (4.8 neutrons/100 deuterons). In the FMIT target design, only the yield forward of 90° is useful. Fortunately about three-fourths of the neutrons or 2.2 (10^{11}) neutrons/μC (3.5 neutrons/100 deuterons) are produced in the forward hemisphere.

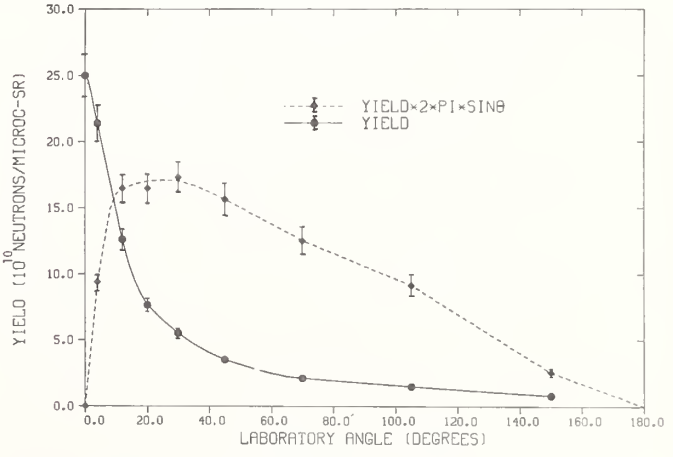

Fig. 4. Total yield of neutrons greater than 0 MeV as a function of emission angle (θ).

Summary and Conclusions

We have measured the thick target neutron yield spectra over a very large range of angles from 0° to 150° in order to provide data for a nuclear model which will be used for predictions of the neutron flux in FMIT, in particular for very small distances from the target. The measurements covered as wide an energy range as possible (1-50 MeV) and we see a significant shoulder in the spectra of neutrons having energies greater than the incident deuteron energy. The energy integrated yield of neutrons has been obtained as a function of angle and also the total yield, integrated

over angle. With simple interpolations, the data can be used directly without the aid of a model to obtain neutron flux spectra at long distances from the source target.

References

1. E.W. Pottmeyer, Jr., "The Fusion Materials Irradiation Test Facility at Hanford," Proceedings of First Topical Meeting on Fusion Reactor Materials, Miami Beach, Florida, Jan. 1979 - to be published in the Journal of Nuclear Materials.

2. "Symposium on Neutron Cross-sections from 10 to 40 MeV." BNL-NCS-50681 (1977).

3. "Cross-sections and Yields for High Energy Neutron Source Reactions." NBSIR 77-1279 (1977).

4. D.L. Johnson, F.M.Mann, J.W.Watson, J.Ullman and W. .Wyckoff, "Measurements and Calculations of Neutron Spectra from 35 MeV Deuterons on Thick Lithium for the FMIT facility," Proceedings of the First Topical Meeting on Fusion Reactor Materials, Miami Beach, Florida, Jan. 1979 - to be published in the Journal of Nuclear Materials.

5. J.O. Schiffgens, R.L.Simons, F.M.Mann, and L.L. Carter, "Spatial Variations of Damage Parameters in FMIT and Their Implications," Ibid.

6. M.J.Saltmarsh, C.A.Ludeman, C.B.Fulmer, and R.C.Styles, "Characteristics of an Intense Neutron Source Based on the d+Be Reaction." Nucl. Instr. and Meth. 145 (1977) 81 and ORNL/TM-5696.

7. J.W.Watson, C.A.Miller and F.J.Wilson, "A Beam Burst Width Monitoring and Phase Stabilization System for Cyclotrons." Nucl. Instr. & Meth. 133 (1976) 399.

8. N.R.Stanton. "A Monte Carlo Program for Calculating Neutron Detection Efficiencies in Plastic Scintillators." COO-1545-92. (Feb. 1971)

9. M.W.McNaughton, N.S.P.King, F.P.Brady, & J.L. Ullmann. "Improved Predictions of Neutron Detection Efficiency Resulting from New Measurements of $^{12}C(n,p)$ and $^{12}C(n,d)$ Reactions at 56MeV." Nucl. Instr. & Meth. 129 (1975) 241.

10. H.I.Amols, J.F.Dicello, M.Awschalom, L.Coulson, S.W.Johnsen, & R.B.Theus. "Physical Characterization of Neutron Beams Produced by Protons and Deuterons of Various Energies Bombarding Beryllium and Lithium Targets of Several Thicknesses." Medical Physics 4 (1977) 486.

11. A.N.Goland, C.L.Snead, Jr., D.M.Parkin, and R.B. Theus. "Use of Li(d,n) Neutrons for Simulation of Radiation Effects in Fusion Reactors." IEEE Trans. Nucl. Sci. NS-22 (1975) 1776.

12. F.M.Mann, F. Schmittroth, L.L.Carter and J.O. Schiffgens, "The Spatial Dependence of Flux and Damage in the FMIT Test Cell". Proceedings of this conference.

* Operated by Westinghouse Hanford. This work supported by the U.S. Dept. of Energy, under contract No.DE-AC14-76FF02170.

† Present address: Physics Dept., Kent State Univ., Kent, Ohio 44242, USA.

MEASURED AND EVALUATED BISMUTH DATA FOR FUSION-FISSION-HYBRID AND ELECTRO-NUCLEAR BREEDING APPLICATIONS*

P. T. Guenther, A. B. Smith, D. L. Smith and J. F. Whalen
Argonne National Laboratory
9700 South Cass Avenue
Argonne, Illinois 60439, USA

R. Howerton
University of California
Lawrence Livermore Laboratory
Livermore, California 94550, USA

Neutron total and scattering cross sections of elemental bismuth are measured to energies of approximately 4.5 MeV. The experimental results are used to deduce an optical-statistical model that is quantitatively descriptive of the measured values and of higher-energy results reported in the literature. The measured and calculated values, together with the body of information available in the literature, are utilized to derive a comprehensive evaluated nuclear-data file in the ENDF format. This evaluation extends from 10^{-5} eV to 20 MeV, addresses neutron induced and photon-emission processes and is oriented toward the needs of fusion-fission-hybrid and electro-nuclear breeding applications.

[Bi(n_t), (n,n) and (n,n') measured to 4.5 MeV; optical-model interpretations and comprehensive evaluation in ENDF format.]

INTRODUCTION

It has been suggested that the fusion-fission hybrid concept represents a nuclear-energy system of considerable potential.[2] One aspect of the strategy of such systems is the production of fissile fuel for subsequent burning in LWR or other conventional fission reactors. In this concept the hybrid itself is largely free of fission products with their attendent problems while, at the same time, providing a rich source of fissile material. With this concept neutron economy is essential and means to multiply the intensity of the primary fusion-neutron source are sought. It has been suggested that one alternative is a bismuth blanket about the primary fusion source as the very large bismuth (n,2n) cross section provides an effective "eta" approaching that of a fissionable multiplier.[3] In addition, bismuth and its alloys have attractive low-melting points and heat-transfer properties. These same nuclear and molecular properties make bismuth a promising primary target in electro-nuclear-breeding concepts.

The above concepts have not been widely examined due to the unavailability of a generally accepted bismuth evaluated data file for use in neutronic calculations. The provision of such a file is impeded by the sparsity of microscopic nuclear data upon which to base it. The present work was undertaken with the objective of providing a comprehensive evaluated data file in the widely-used ENDF format. As a part of this effort basic microscopic nuclear-data measurements and associated interpretations were pursued in order to strengthen the essential physical foundation.

EXPERIMENTAL METHODS

The measurement samples were machined into right-circular cylinders from ingots of chemically-pure elemental bismuth. Two transmission sample sizes were used each having a diameter of 2.5 cm with transmission thickness of 2 cm and 4 cm, respectively. The scattering samples were 2 cm in diameter and 2 cm long with neutrons incident upon the lateral surface. It was assumed that the samples were of uniform density and this assumption was supported by the consistency of the results obtained with different samples.

The neutron total cross sections were deduced from the measured transmissions of approximately monoenergetic neutrons through the measurement samples in a conventional manner.[4] The neutron source was the $Li^7(p,n)Be^7$ reaction. The neutron energy was determined to within 10 keV by control of the incident proton beam. Neutrons were detected using conventional pulsed-beam time-of-flight techniques in such a manner as to provide suitable control of background and source perturbations. Concurrent measurements of the neutron total cross sections of elemental carbon assured the fidelity of the measurement system. The details of the method and the particular apparatus have been extensively described elsewhere.[5]

The neutron scattering measurements were made using the pulsed-beam time-of-flight technique and the 10-angle scattering apparatus at the Argonne Fast Neutron Generator. Again, the neutron source was the $Li^7(p,n)Be^7$ reaction. Scattered-neutron flight paths were 5.0 to 5.5 m. Relative sensitivities of the hydrogenous neutron detectors were determined by observation of neutrons emitted at the spontaneous fission of ^{252}Cf.[6] The normalization of the relative detector sensitivities was determined by the observation of neutrons scattered from hydrogen (i.e., polyethylene). Thus all of the measured neutron-scattering cross sections were determined relative to the well known H(n,n) cross sections.[7] Concurrent with the bismuth measurements, carbon-scattering cross sections were determined in order to verify the performance of the measurement system. The experimental results were corrected for perturbations due to beam attenuation, multiple events and the angular resolution of the apparatus using a combination of Monte-Carlo and analytical computational techniques. The details of the measurement apparatus and procedures, the data reduction, and the correction procedures have been extensively described elsewhere.[8]

EXPERIMENTAL RESULTS

One objective of the experimental measurements was the determination of energy-average total cross sections comparable with, the differential scattering measurements (below), the predictions of energy-averaged models, and with the evaluated data sets.

*This work supported by the U. S. Department of Energy. A comprehensive report of this work is given in Ref. 1.

The measurements extended from ≈1.2 to 4.5 Mev in steps of ≲50 keV. Incident-neutron energy resolutions were 35-50 keV. the statistical accuracies of the individual measured values were in the range of 1-3%. Systematic uncertainties were believed to be much smaller. The results obtained with the two sample thicknesses (i.e., 2 cm and 4 cm) were separately averaged over 100 keV intervals. The associated cross-section uncertainties were ≈1%. The results obtained with the two sample thicknesses were in good agreement. Thus, it was concluded that sample-size-perturbation effects must have been small (i.e., ≲1%).

The present measured values are in good agreement with the previously reported results of Refs. 9, 10, 11 and 12 as illustrated by the comparisons of Fig. 1. The differences between equivalent averages constructed from the various data sets is ≲2% throughout the range of the present experiments.

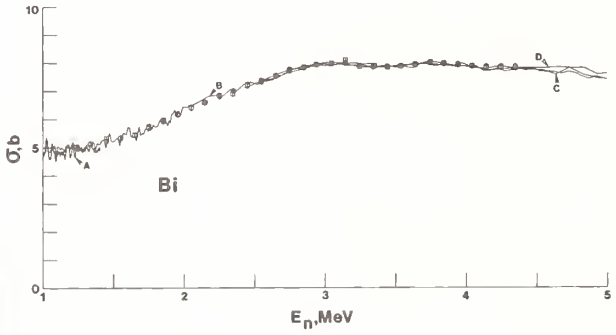

Fig. 1. Measured Neutron Total Cross Sections of Elemental Bismuth. The present results are indicated by data points. Curves indicate previously reported values as follows; A = Ref. 9, B = Ref. 10, C = Ref. 11 and D = Ref. 12.

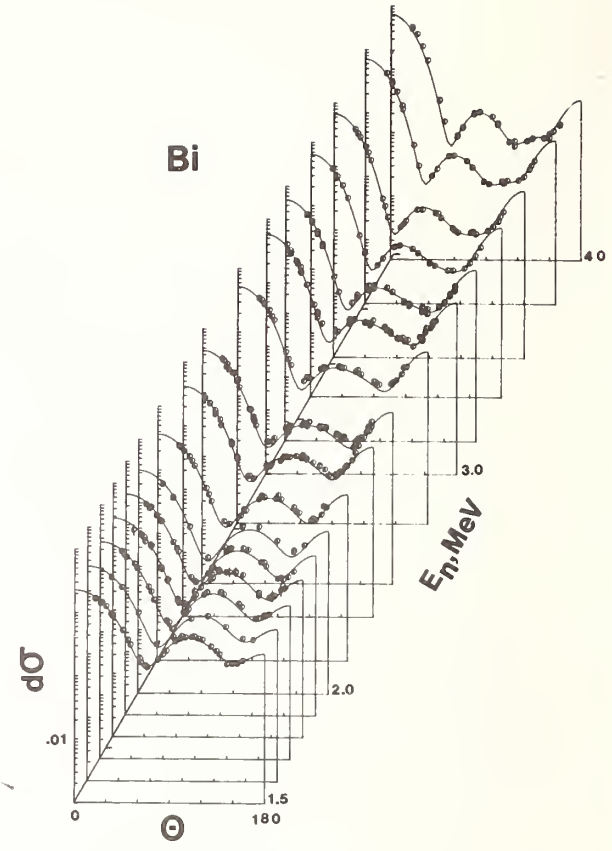

Fig. 2. Differential-Elastic-Scattering Cross Sections of Elemental Bismuth. The present measured values are indicated by data points. Curves denote the results of model calculations as discussed in the text. Dimensionality is b/sr and scattering angle is lab. deg.

The elastic-scattering measurements were made over a number of years with various incident energies, energy resolutions, scattering angles and accuracies. Data, measured over the incident-energy range ≈1.5 to 4.0 MeV, were sorted into incident-energy intervals of ≲100 keV and combined to obtain composite angular distributions at the mean energy of the sorting interval. This procedure was very good at the higher measured energies but somewhat less suitable at the lowest measured energies where fluctuations were clearly evident in the total-neutron cross section. The incident-neutron resolutions varied from ≈20 to 50 keV and the scattered-neutron resolutions were sufficient to clearly distinguish the elastic-neutron group from all known inelastic-neutron components. The individual measurements involved concurrent determination of ten or twenty differential values distributed over the angular range ≈20 to 160 deg. The relative scattering angles were known to ±0.5 deg. and the absolute angular scale was determined to ≈1.0 deg. The accuracies of the individual differential values varied. In the best cases the differential-cross-section uncertainties were ≈5% and in the poor cases ≈10%. A measure of the validity of the above uncertainties was the consistency of the results obtained over a several-year period with various experimental configurations.

The elastic-scattering results are outlined in Fig. 2.

In some of the lower-energy cases there appeared to be systematic differences between distributions obtained at widely separated times and subsequently combined to form the composite distributions. These differences could easily be expected from the fluctuations evident in the neutron total cross sections (as noted above). The angle-integrated neutron elastic-scattering cross sections were obtained by least-square fitting an eight-order Legendre-polynomial series to the measured differential values. The resulting angle-integrated values were believed known to ≈5%. They were consistent with measured neutron elastic and inelastic-scattering cross sections to well within respective experimental uncertainties. The present elastic scattering results generally agree with those reported by Tanaka et al,[13] and Smith et al,[9] and with some isolated results from other sources (see Ref. 1).

The inelastic-neutron-scattering measurements were made concurrently with the above neutron-elastic-scattering determinations. Six inelastically-scattered-neutron groups were observed corresponding to excitation energies of 895 ± 12, 1606 ± 14, 2590 ± 15, 2762 ± 29, 3022 ± 21 and 3144 ± 15 keV. These excitation energies were determined from the individual measured values and the corresponding uncertainties defined as the RMS deviation of the individual values from the average. A comparison of the measured values with the levels reported in the literature[14] indicated that the first two observed excitations corresponded to discrete levels (897(7/2-)

and 1609 (13/2), keV) while the remainder were the result of contributions from a number of previously reported levels. All of the observed differential-inelastic-neutron distributions were essentially isotropic. The angle integrated inelastic-neutron cross sections corresponding to the various excitations were determined by least-square fitting the observed differential distributions with low-order legendre polynomial expansions. The resulting angle-integrated cross sections are shown in Fig. 3. The respective

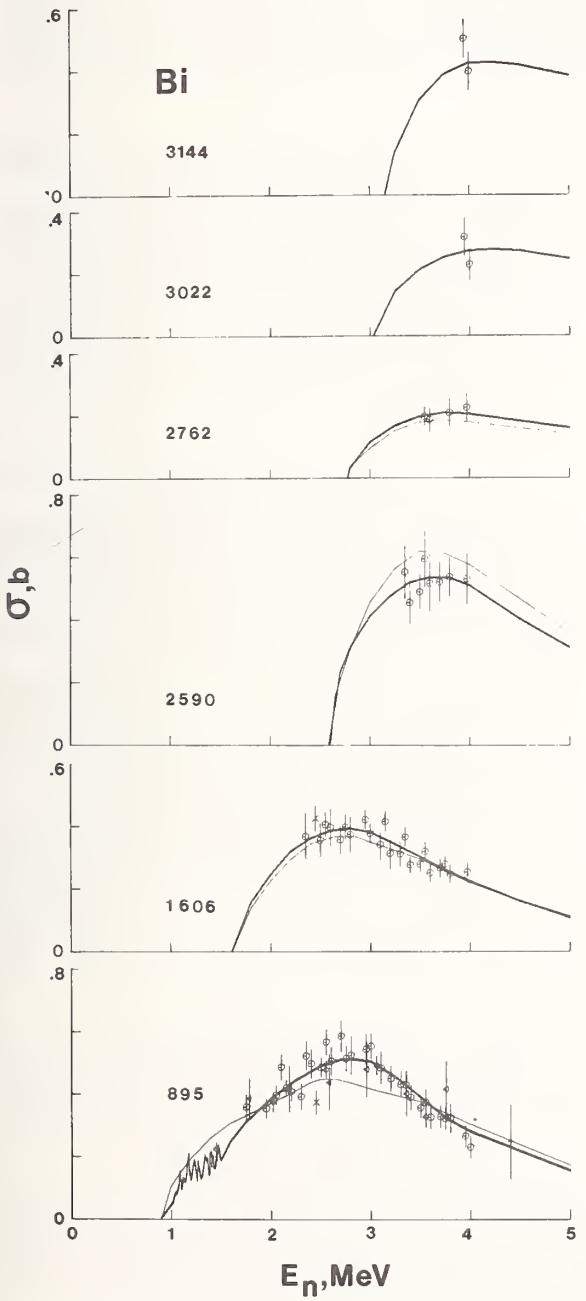

Fig. 3. Inelastic-Neutron Excitation Cross Sections of Bismuth. The present experimental results are indicated by circular data points. The corresponding observed excitation energies are given in each section of the figure in keV. The heavy curves are "eye-guides" constructed through the available experimental information. The light curves indicate the result of model calculations as described in the text. Previously reported experimental values are denoted by symbols and discussed in Ref. 1.

uncertainties were governed by the same factors applicable to the above elastic-scattering measurements. In addition, the experimental resolution was not complete in those cases where the observed neutron group consisted of a number of unresolved components. In the best cases the uncertainties associated with the angle-integrated inelastic-scattering cross sections were in the 5-10% range. Beyond the experimental uncertainties associated with the measurements there may be some residual effects from the physical fluctuations evident, for example, in high-resolution neutron total-cross section measurements.[10] There are a few previously-reported experimental values. The present work reasonably extrapolates to the lower-energy results of Smith et al,[9] and of Tanaka et al.[13] Other inelastic-data comparisons are given in Ref. 1 and Fig. 3.

INTERPRETATIVE MODEL

The objective was the deduction of an optical-statistical model suitable for extrapolating and interpolating the present measurements for the formulation of a comprehensive evaluated file. A simple spherical model was assumed. This assumption is reasonably justified as ^{209}Bi consists of only one proton added to the doubly-closed shell at A = 208. Compound-nucleus processes were calculated using the procedures of Hofmann et al.[15] In doing so the excitation of states to energies of ≈3.0 was explicitly treated using the spin and parity assignments of Ref. 14. The excitation of higher-energy levels was treated as a statistical continuum following the concepts of Gilbert and Cameron.[16] The choice of model parameters was entirely based upon the measured differential-elastic-scattering cross sections. The parameter selection was made by chi-square fitting the observed elastic scattering at incident neutron energies of ≤3.0 MeV. The parameter values for the final potential are summarized in Table 1. The above po-

TABLE 1. Spherical Optical-Model Parameters

Real Potential[a]	
Strength (V)	43.296 Mev
Radius (R_o^v)[b]	1.300 F
Diffuseness (a^v)	0.58 F
VR_o^2	73.17 MeV · F²
Imaginary Potential[c]	
Strength (W)	11.91 MeV
Radius (R_o^w)	1.320 F
Diffuseness (a^w)	0.20 F
Wa^w	2.382 MeV · F
Spin Orbit Potential[d]	
Strength (V_{so})	4.35 MeV

[a] Saxon Form.
[b] All Radii in Form $R = R_o A^{1/3}$.
[c] Saxon Derivative Form.
[d] Thomas Form

tential provides a quantitative description of the measured differential elastic-scattering cross sections as illustrated in Fig. 2. There are some deviations between measured and calculated values at a few and, primarily, lower energies. This is not surprising as the total cross section shows fluctuating structure into the several MeV region that was clearly not averaged in the elastic scattering measurements. The calculated neutron total cross sections agree with the measured values throughout the present experimental range to within ≲3%. The calculation of neutron-inelastic-scattering cross sections using the above model was very much inhibited by a lack of knowledge of the spins and parities of the levels involved. Given this marginal situation only the excitation of the first four observed groups was explicitly calculated and the higher energy excitations were lumped into the continuum contribution. The results of the calculations are compared with the measured values in Fig. 3. Generally the calculated results agree with the measured values to within at least 10-20% and in some cases the agreement is much better. In view of the above, the present potential was accepted as a reasonable basis for subsequent extrapolations and interpolations requisite to the comprehensive evaluation.

EVALUATION

Throughout this evaluation the emphasis was on a data file for high-energy (e.g., fusion-fission hybrid) applications. Therefore, while attention was given to low-energy resonance properties, they were not dealt with in great detail and, in particular, the resonance region is described by point-wise data rather than resonance parameters. The file is in rigorous ENDF formats and has been transmitted to the National Nuclear Data Center, Brookhaven National Laboratory. Interested parties can obtain the file therefrom or contact the present authors directly.

The data base for the evaluated neutron-total cross sections consisted primarily of the measured results of the present work and those reported from Refs. 17, 9, 10, 11 and 12. The evaluation follows detailed resonance behavior up to 0.1 MeV, fluctuating structure from 0.1 - 1.5 MeV and energy-averaged behavior from 1.5 - 20 MeV as illustrated in Fig. 4. Some qualitative guidelines as to the accuracies of the above evaluated-neutron-total cross sections are; 10-20% below 100 keV, 5-10% from 0.2-0.5 MeV, 2-5% from 0.5-1.5 MeV, 1-2% from 1.5-5.0 MeV, and 2-5% from 5-20 MeV.

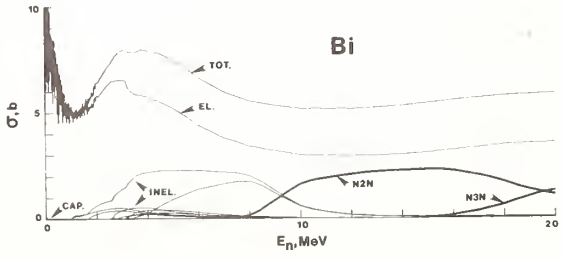

Fig. 4. Summary of Evaluated Files.

Below neutron energies of ≲3.0 MeV the evaluated elastic-scattering cross sections were dictated by the differences between neutron total cross sections and the non-elastic cross sections. At higher energies all of the partial cross sections are not well known and thus the evaluated elastic-scattering cross sections were based upon the predictions of the above model, slightly adjusted to bring exact agreement with the evaluated neutron-total cross sections and to improve the agreement with the measured differential elastic-scattering distributions of Refs. 18 and 19. The resulting evaluated neutron elastic-scattering cross sections were believed to be generally known to ≲5% throughout the energy range of the evaluation.

The discrete evaluated inelastic scattering cross sections were based upon the six excitation functions shown in Fig. 3, extrapolated to 10 MeV using the above model. The continuum inelastic scattering cross section was determined from the difference between total and partial cross sections commencing at an incident energy of approximately 3 MeV. The continuum emission spectrum included a pre-compound component as verified by the sphere transmission measurements reported in Ref. 20. The relative magnitudes of the various inelastic components are illustrated in Fig. 4.

A notable feature of the neutron interaction with bismuth is the very small radiative capture cross section and resonance integral. The evaluation makes use of the fragmentary information available but the results must be considered only qualitative. This is of little concern in most applications as radiative capture processes in other nuclides will far dominate in the overall capture in a realistic system.

An outstanding feature of the interaction of fast neutrons with bismuth is the very large (n;2n) and (n;3n) cross sections. This feature makes bismuth particularly attractive in a number of high-energy applications. The present evaluation is based primarily upon the recent large-scintillator results of Refs. 21 and 22. These two sets of measurements are relatively consistent and, with some minor adjustments near 17 MeV, essentially form the present evaluation of the (n;2n) and (n;3n) cross sections. The estimated uncertainties are generally in the 10-15% range. The very large relative size of these two cross sections is illustrated in Fig. 4.

There are a number of energetically possible Bi(n;X) reactions. All of them are strongly inhibited by the coulomb barrier and generally have very small cross sections. Of these, the evaluation considers only three; (n;p), (n,α) and (n;n',α). All of these cross sections are relatively very small.

Evaluated photon-production cross sections are provided based primarily upon the formalism of Perkins et al.[23] Using this method energy balance is assured and the procedure is substantiated by experimental comparisons.

SUMMARY

The present measurements give new definition to neutron total and scattering cross section of elemental bismuth to energies of 4-5 MeV. The experimental results were used to derive an optical-statistical model. The measured and calculated results together with those previously reported in the literature were used to deduce a comprehensive evaluated nuclear data file in the ENDF format. This file is particularly oriented toward fusion-fission hybrid and other high-energy applications and makes possible the quantitative assessment of the neutronic performance of such systems.

REFERENCES

1. P. T. Guenther, A. B. Smith, D. L. Smith, J. F. Whalen and R. Howerton, Argonne National Laboratory Report, ANL/NDM-51, in press.
2. Final Report of Ad-Hoc Experts Group in Fusion, DOE Report, DOE/ER-0008 (1978), J. Foster, Chairman.
3. Fusion-Fission Hybrid Study Summary Report, July 1978, Argonne National Laboratory, unpublished.
4. D. Miller, "Fast Neutron Physics," Vol.-II, Eds. S. Marion and J. Fowler, Interscience Pub., New York (1963).
5. A. B. Smith and J. F. Whalen, Argonne National Laboratory Report, ANL/NDM-33 (1977).
6. A. B. Smith, P. T. Guenther and R. Sjoblom, Nucl. Instr. and Methods, 140 397 (1977).
7. J. Hopkins and G. Breit, Nucl. Data, A9 137 (1971).
8. P. T. Guenther, "Elastic and Inelastic Scattering of Fast Neutrons from the Even Isotopes of Tungsten," Thesis, University of Illinois (1977).
9. A. B. Smith et al., Nucl. Sci. and Eng., 41 63 (1970).
10. S. Cierjacks, P. Forti, D. Kopsch, L. Kropp, J. Nibe and H. Unseld, Kernforschungzentrum Karlsruhe Report, KFK-1000 (1968), as revised.
11. D. Foster and D. Glasgow, Phys. Rev., C3 576 (1971).
12. A. Carlson and H. Barschall, Phys. Rev., 158 1142 (1967).
13. S. Tanaka et al., Nucl. Phys., 179 513 (1972).
14. Nuclear Data Sheets for A=209, M. J. Martin compiler (1970).
15. H. Hofmann et al., Ann. Phys. (NY) 90 403 (1975).
16. A. Gilbert and A. G. W. Cameron, Can. Jour. Phys., 43 1446 (1965).
17. U. Singh, Phys. Rev., C13 124 (1976).
18. B. Holmqvist and T. Wiedling, Aktiebolaget Atomenergi Report, AE-430 (1971).
19. C. Zafiratos et al., Phys. Rev. Lett., 14 913 (1965).
20. J. Kammerdiener, Lawrence Livermore Laboratory Report, UCRL=51232 (1972).
21. J. Frehaut and G. Mosinski, Proc. Conf. on Nucl. Cross Sections and Tech., National Bureau of Standards Pub., NBS-425 (1975).
22. L. Veeser, E. Arthur and P. Young, Phys. Rev., C16 1792 (1977).
23. S. Perkins, R. Haight and R. Howerton, Nucl. Sci. and Eng., 57 1 (1975).

THE INFLUENCE OF NUCLEAR DATA UNCERTAINTIES ON THORIUM FUSION-FISSION* HYBRID BLANKET NUCLEONIC PERFORMANCE

E. T. Cheng and D. R. Mathews
General Atomic Company
San Diego, California 92138, U.S.A.

The fusion-fission hybrid blanket proposed for the Tandem Mirror Hybrid Reactor employs thorium metal as the fertile material. Based on the ENDF/B-IV nuclear data, the ^{233}U and tritium production rate and blanket energy multiplication averaged over the blanket lifetime of about 9 MW-yr/m^2 are 0.76 and 1.12 per D-T neutron and 4.8, respectively. At the time of the blanket discharge, the ^{233}U enrichment in the thorium metal is about 3%. The thorium cross sections given by the ENDF/B-IV and V were reviewed, and the important partial cross sections such as (n,2n), (n,3n) and (n,γ) were found to be known to ±10—20% in the respective energy range of interest. A sensitivity study showed that the ^{233}U and tritium production rate and blanket energy multiplication are relatively sensitive to the thorium capture and fission cross section uncertainties. In order to predict the above parameters within ±1%, the Th(n,γ) and Th(n,νf) cross sections must be measured within about ±2% in the energy range 3—3000 keV and 13.5—15 MeV, respectively. The present level of uncertainty in these data is ±10 and 5%. This indicates that although presently adequate for preliminary design, additional cross section measurements to improve the accuracy of the Th(n,γ) and Th(n,νf) cross sections in these energy ranges may be needed in order to accurately calculate the blanket performance thorium-base fusion-fission hybrid reactor blankets.

(Fusion-fission hybrid blanket, Th(n,2n), Th(n,3n), Th(n,νf), Th(n,γ), tritium breeding, uranium production, blanket energy multiplication, cross section uncertainty, cross section sensitivity)

Introduction

A wide variety of fusion-fission hybrid system concepts have been recently suggested and evaluated by many investigators.[1] The concept of placing a blanket of fertile material around a fusion plasma to form a hybrid system is most attractive because of the flexibility such a system can have to produce either thermal power or fissile fuel, or both. In these concepts, the blankets consist of either a ^{238}U or ^{232}Th fertile zone which serves to multiply the fusion neutrons via (n,2n), (n,3n) and (n,νf) reactions, to enhance the thermal power output through fission reactions, and/or to produce fissile fuels (^{239}Pu or ^{233}U) from ^{238}U(n,γ) or ^{232}Th(n,γ) reactions. In general, the uranium-base blankets produce a large amount of thermal power, multiplying the incident fusion neutron energy by about a factor of 10 by fast fission of the ^{238}U. They also produce up to two fissile atoms per D-T neutron in addition to the breeding of adequate tritium to sustain the system (T/n $\geq$ 1). The thorium-base blankets produce more modest amounts of thermal power which is generally only two or three times that of the incident fusion neutrons. The fissile atom production rate in these blankets is not more than one per D-T neutron if the self-sustaining tritium production is to be maintained.[2,3] When either uranium or thorium blanket is exposed to the fusion neutron environment the bred fissile fuel concentration accumulates so as to increase the fissioning rate and thus the thermal power output. The net fissile fuel production rate changes relatively little, however, until very high fissile concentrations (~10%) are reached, whereupon production and fission tend to equilibrate.

Because of tne higher blanket thermal output in the uranium or fissile enriched blankets which is mainly due to fission reactions, the fission product and actinide inventories in these blankets can be large. The local nuclear heating and after-shutdown decay heat are thus high compared to those of the thorium-base blankets which possess more modest blanket thermal output. The fission product decay heat can cause meltdown of the fuel if a loss of coolant flow accident occurs, which is a severe concern from the safety point of view and necessitates use of diverse and redundant blanket auxiliary cooling systems. Assuming only adiabatic heating, the afterheat meltdown time for a high power density uranium-base blanket can be as short as one minute. For the lower power thorium-base blanket designs, the afterheat adiabatic meltdown time can be as long as one hour under similar loss of cooling circumstances.[4]

Thorium-base hybrid blankets are also attractive because of the bred fuel. ^{233}U is superior to ^{239}Pu for use in a thermal spectrum burner reactor.[5] In addition to superior fuel cycle performance ^{233}U offers the possibility for isotopic denaturing with ^{238}U which may improve proliferation and diversion resistance.

In the Tandem Mirror Hybrid Reactor (TMHR) study,[4] a helium-cooled thorium metal blanket was chosen as the gas-cooled blanket candidate based on the consideration of better bred fuel (^{233}U versus ^{239}Pu), good fuel production and economics, positive net electricity production and reasonable tolerance of the loss of coolant flow accident.[6,7]

The performance of thorium blanket concepts for fusion-fission hybrid systems depend on the neutron and energy multiplication in the blanket through (n,2n), (n,3n) and fission reactions. The thorium cross section uncertainties and their effect on the blanket nucleonic performance are naturally of concern from the blanket design point of view. The thorium partial cross sections such as (n,2n), (n,3n) around the D-T neutron energy range and (n,γ) in the intermediate energy range are expected to be subject to uncertainties of about ±10—20%. The thorium fast fission cross section is also known to ±5% only. A sensitivity study of these cross section uncertainties is the main purpose of this paper. From the results of this study, the desired accuracies of the related partial cross sections can thus be recommended for the accurate computation of the performance of thorium fusion-fission hybrid blankets.

The blanket configuration and nucleonic performance are described briefly in the next section. A

* Work supported by Department of Energy, Contract DE-AT03-76ET51011.

review of the status of the thorium nuclear data is then given, followed by a discussion of the sensitivity study of the thorium cross section uncertainties to the nucleonic performance of this blanket. The concluding remarks and recommendations of this study are summarized in the last section.

Thorium Fusion-Fission Hybrid Blanket Model

The helium cooled thorium metal TMHR blanket consists of a 10 mm first wall, a 0.11 m thick thorium metal zone, a 0.4 m Li_2O zone and a 0.1 m 316 stainless steel reflector/hot shield. The blanket configuration and material compositions are tabulated in Table I.

Table I. Thorium Fusion-Fission Hybrid Blanket Configuration and Material Compositions

Zone	Thickness (m)	Composition	Remarks
1	1.90	Vacuum	Plasma
2	0.10	Vacuum	Vacuum
3	0.01	Inconel 718	First wall
4	0.11	6.5% Inconel + 10% helium + 83.5% thorium[a]	^{233}U production
5	0.40	6.5% Inconel + 10% helium + 83.5% Li_2O[a]	Tritium breeding
6	0.10	10% helium + 90% 316 SS	Reflector/ hot shield

[a] 90% of the theoretical density of this material is considered to account for the packing effect.

The neutronic calculations were performed using the one-dimensional discrete ordinates transport code, ANISN[8] with P_3S_6 approximation in cylindrical geometry. All the nuclear data except thorium are from the DLC-37[9] library which is based on ENDF/B-IV and were collapsed into 25 neutron and 21 gamma-ray group structure using an 1/E weighting spectrum. The group energy boundaries are the same as given in Ref. 10. The thorium nuclear data and all partial cross sections studied in this paper are from the DLC-41[11] library which used ENDF/B-IV data and were also collapsed into the same group structure using the same weighting spectrum.

The resonance self-shielding correction of thorium cross section is not treated in this study. The effects of the group collapsing weighting function and resonance self-shielding correction are not known. However, from the published results of the ^{238}U blankets,[12,13] it is known that the effect of the weighting function is very small[12] and the resonance self-shielding correction may reduce the $^{238}U(n,\gamma)$ reaction rate by about 4%.[13] It is believed that the results of this sensitivity study will still apply to the case when the weighting function and resonance self-shielding correction are treated.

When the blanket is fresh without neutron irradiation, the thorium metal zone contains no ^{233}U, and only fast fission of the thorium metal contributes to the blanket energy multiplication, which is defined as the ratio of total blanket nuclear heating to the incident D-T neutron energy. As the neutron irradiation proceeds, the ^{233}U concentration increases and its fissioning also adds to the blanket energy multiplication. The $Th(n,\gamma)$ reaction rate also increases due to the increase of neutron population in the blanket. However, ^{233}U fission burns the ^{233}U atoms and results in a slight decrease of the net ^{233}U production rate. The tritium production rate, which relies on the $^{6}Li(n,\alpha)$ and $^{7}Li(n,n'\alpha)$ reactions with the neutrons leaking into the lithium zone from the thorium zone, increases as the ^{233}U concentration in the blanket becomes larger. The irradiation lifetime of the blanket module is limited by the burnup limit of the thorium metal. This burnup design limit is about 1% at the peak location, which occurs immediately behind the first wall and corresponds to an accumulated first wall neutron exposure of about 9 MW-yr/m^2. After the 9 MW-yr/m^2 blanket lifetime is reached, the ^{233}U concentration in the thorium metal is about 3%. The blanket is then discharged and replaced with fresh blanket modules. The nucleonic performance of the thorium fusion-fission hybrid blanket at the beginning and end of life are presented in Table II. Note that in this table the time averaged tritium breeding ratio is about 1.12, adequate for tritium self-sufficiency, although it is 1.00 at the beginning of life and increases to 1.24 tritons per D-T neutron at the end of life. The net ^{233}U production rate which is 0.80 and 0.73 at the beginning and end of life, respectively, is time-averaged to be 0.76 atoms per D-T neutron. The blanket energy multiplication, which is about 2.7 at the beginning of life, increases to 7.1 at the end of life, with a time-averaged value, $\bar{M}$, of about 4.8.

Table II. Nucleonic Performance of the Thorium Fusion-Fission Hybrid Blankets at the Beginning and End of Life (Reactions per D-T Neutron)

Nucleonic Performance Parameter	Beginning of Life (No ^{233}U)	End of Life (3% ^{233}U)
$^{6}Li(n,\alpha)$	0.8995	1.1407
$^{7}Li(n,n'\alpha)$	0.1018	0.1021
Tritium breeding ratio	1.0013	1.2428
$Th(n,\gamma)$	0.7983	0.9429
$Th(n,2n)$	0.3208	0.3114
$Th(n,3n)$	0.1083	0.1044
$Th(n,f)$	0.1005	0.1105
$Th(n,\nu f)$	0.3611	0.3798
$^{233}U(n,\gamma)$	—	0.0208
$^{233}U(n,2n)$	—	0.0031
$^{233}U(n,3n)$	—	0.0003
$^{233}U(n,f)$	—	0.2641
$^{233}U(n,\nu f)$	—	0.6942
Net ^{233}U production	0.7983	0.6546
Blanket energy multiplication[a]	2.7	7.1

[a] Defined as the ratio of blanket thermal output to incident D-T neutron energy.

As stated in the previous section, this blanket concept utilizes the neutron and energy multiplications from $Th(n,2n)$, $Th(n,3n)$ and thorium fast fission as well as ^{233}U fission reactions when ^{233}U atoms accumulate. From Table II we see that the additional number of neutrons coming out of the $Th(n,2n)$ and $Th(n,3n)$ reactions is about 0.54 per D-T neutron. It is almost

Table III. Fractional Contributions to Nuclear Reaction Rates in the Thorium Fusion-Fission Hybrid Blanket in Specified Energy Ranges

Energy Range (MeV)	Th(n,2n)	Th(n,3n)	Th(n,νf)	Th(n,γ)	^{6}Li(n,α)	^{7}Li(n,n'α)	^{233}U(n,νf)[a]
13.5 - 14.9	90.1	98.4	78.6	11.7	0.0	40.7	4.6
2.5 - 13.5	9.9	1.6	12.6	2.5	0.2	59.3	4.6
0.41 - 2.5	—	—	8.8	18.9	2.4	—	29.5
3.4×10^{-3} - 0.41	—	—	0.0	57.5	53.4	—	57.0
0.35 - 3.4×10^{-3}	—	—	—	8.0	26.5	—	3.8
Thermal - 0.35×10^{-3}	—	—	—	1.4	17.5	—	0.5

[a]At the end of life, ~3% ^{233}U in the thorium.

unchanged throughout the blanket lifetime. The amount of multiplied neutrons due to fissioning is a function of accumulated ^{233}U concentration in the blanket due to the fissioning of ^{233}U. At the beginning of life it is only 0.26 per D-T neutron, increasing to about 0.70 at the end of life. The overall number of available neutrons are thus about 1.80 and 2.24 per D-T neutron at the beginning and end of life, respectively.

The contributions of the various partial nuclear cross sections in each specified energy range are presented in Table III. From this table we see that the most important Th(n,2n), Th(n,3n) and Th(n,νf) reactions are in the high energy range, particularly around the D-T neutron energy, i.e., 13.5 - 15 MeV. The energy below 13.5 MeV also contributes about 10 and 21% to the Th(n,2n) and Th(n,νf) reactions, respectively. The tritium production from ^{7}Li(n,n'α) reactions also favors the high energy ranges as can be seen from Table III. However, more than 50% of the ^{233}U production from ^{232}Th(n,γ) reactions and tritium production from ^{6}Li(n,α) reactions occur in the energy range 3.4 - 410 keV. In the range 0.4 - 2.5 MeV, the ^{233}U production rate is about 19% of the total. About 27% of the tritium production from ^{6}Li(n,α) reactions is from the energy range of 0.35 - 3.4 keV. When the ^{233}U concentration reaches 3%, ^{233}U fissioning occurs mostly in the intermediate energy range, namely about 57% in the range 3.4 - 410 keV and about 30% in the range 0.4 - 2.5 MeV. Table III also reveals that the source neutron energy group, 13.5—15 MeV produces about 12% of the total ^{233}U.

Cross Section Uncertainties

As explained in the previous sections, this thorium fusion-fission hybrid blanket employs thorium in metal form. The blanket nucleonic performance is highly dependent on the status of the thorium nuclear cross section uncertainties. In order to provide information for evaluating the importance of sensitivity to partial cross section uncertainty, the status of the thorium nuclear cross sections, which include (n,2n), (n,3n), (n,γ), (n,νf), (n,elastic) and (n,inelastic), are reviewed in this section.[14] Based on this review, the results of this sensitivity study can be evaluated to offer recommendations for further improvement in cross section data. Also included in this section are the status of the ^{233}U(n,νf) cross section, and those of the constituents of iron- and nickel-based structural alloys, namely Cr, Ni and Fe. The impact of the tritium producing cross sections, ^{6}Li(n,α) and ^{7}Li(n,n'α), are also discussed.

Neutron Multiplication Reactions

The principal neutron multiplication reactions in a hybrid fusion-fission blanket using thorium appear to be the Th(n,νf), Th(n,2n) and Th(n,3n) reactions, and after some blanket exposure, the ^{233}U(n,νf) reaction.

Th(n,νf). The number of prompt neutrons per fission event ($\bar{\nu}_p$) in ^{232}Th appears to be known to about ±1% and is not likely to be a significant source of uncertainty. The Th(n,νf) cross section appears to be known to about ±5% above 1 MeV. Below 1 MeV, the Th(n,νf) cross section is highly uncertain but very small. The ENDF/B-IV Th(n,νf) cross sections are 10 to 15% smaller than recent differential cross section measurements. A larger ^{232}Th(n,νf) cross section will be used in the ENDF/B-V data set for ^{232}Th. The ^{232}Th prompt fission neutron energy spectrum appears to be representable with a Maxwellian fission neutron temperature of 1.21 ± 0.05 MeV.

Th(n,2n) and Th(n,3n). The Th(n,2n) cross sections appear to be known to about ±15%. The ENDF/B-V ^{232}Th(n,2n) cross section will be significantly lower than the ENDF/B-IV data above 8 MeV (about 10% lower in the important 13 to 15 MeV energy range). The ^{232}Th(n,3n) cross section uncertainty is estimated to be about ±30%. Essentially no direct experimental data exists because ^{230}Th has too long a half life to use the activation method.

^{233}U(n,νf). The ^{233}U(n,νf) cross section is relatively well known and should be uncertain to ±5% or less over the entire energy range of interest with considerably smaller uncertainty in the low thermal range near 0.025 eV. The prompt fission neutron energy spectrum of ^{233}U is also well known and very similar to ^{235}U.

Fissile Production Reaction

The ^{232}Th(n,γ) cross section in the 10 to 1000 keV energy range has been the subject of considerable discussion in recent years. Much of the discussion has been caused by the publication of very low (20 to 25%) Th(n,γ) data by Macklin and Halperin,[15] with very small claimed uncertainties. The uncertainty in the older activation data of Lindner, *et al.*, has recently been drastically reduced by new measurements of the ^{233}Pa decay gamma ray emission probability. It now appears likely that the Macklin and Halperin Th(n,γ) measurement was afflicted with similar (but more severe) problems as occurred in the Moxon and Chaffey ^{238}U(n,γ) measurements using the same technique which were later revised upward. It is significant to note that the Th(n,γ) cross section measured by Moxon and Chaffey[16] using a technique with known problems agreed very well with the Macklin and Halperin data in the 10 to 100 keV energy range where the two experiments overlap.

The uncertainty in the ENDF/B-IV Th(n,γ) cross section in the 3 to 3000 keV energy range is estimated to be ±10% in spite of the much larger differences in the published experimental cross section data. This is because of the excellent agreement between calculated and integral experiment values of $^{232}\sigma_c/^{239}\sigma_f$ obtained

in the fast breeder fission reactor programs in both the U.S.[17] and Switzerland.[18] The uncertainty in the evaluated (n,γ) reaction data for ^{232}Th appears to be similar to or maybe even slightly less than for ^{238}U in this energy range.

The uncertainty in the Th(n,γ) cross sections at energies above about 3 MeV increase rapidly to ±20% or more. The Th(n,γ) reaction is small above 3 MeV so that hybrid fusion blanket design uncertainties are not much affected by the increased uncertainty.

Other Reactions

The neutron energy spectrum in the thorium portion of the blanket and the number and energy spectrum of the neutrons reaching the lithium region will be influenced by other cross sections such as the Th-elastic and inelastic cross sections as well as (to a lesser extent) by the cross sections of the Inconel used in the first wall and as the thorium region cladding and structural support.

Thorium Total Cross Section. The ENDF/B-IV Th total cross section data appears to be 10 to 20% too low particularly below 1 MeV and will be revised upward for the ENDF/B-V library. The ENDF/B-V Th total cross sections are claimed to be known to ±3% over the 0.01 to 14 MeV energy range with about ±5% uncertainty above about 15 MeV. The transmission through the thorium region to the lithium region is directly affected by this uncertainty.

Thorium Elastic and Inelastic Cross Sections. Measured elastic scattering cross sections usually include some contributions from low Q value inelastic scattering which are almost impossible to experimentally separate. From a computational point of view, no significant error is introduced by this fact although published uncertainties for the elastic cross sections are increased by this experimental problem. The Th(n,n) cross section is probably known to about ±10% over the 0.1 to 15 MeV energy range. It should be noted that the ENDF/B-IV and ENDF/B-V evaluations differ significantly with the ENDF/B-V data higher by about 10% below about 80 keV and about 10% lower in the 1 to 4 MeV range. This is because of the onset of significant inelastic competition above about 50 keV. Elastic scattering angular distributions computed from model calculations agree reasonably well with experimental data where available.

Considerable experimental data on the Th(n,n') reaction has been obtained since the ENDF/B-III/IV Th(n,n') evaluations were performed. The claimed uncertainty in the ENDF/B-V evaluated Th(n,n') data is ±10 to 15%. The ENDF/B-V Th(n,n') data will be about 15 to 20% higher than the ENDF/B-IV data in the 1 to 7 MeV energy range with considerable differences in the details of the inelastic scattering angular distributions. The details of the angular distributions are not very significant to blanket design studies except for their impact on the mean energy loss per collision which is important in determining the neutron energy spectrum in the throium region which strongly affects the tritium production in the lithium region by the ^{7}Li(n,n'α)T threshold reaction.

Structural Material Cross Sections. The Cr, Fe and Ni cross sections are known to the same, or in most cases, better accuracy than the thorium cross sections. Since Inconel is only about 7% of the thorium and lithium regions, the uncertainties in these cross sections will not be very significant in the overall system uncertainties and a conservative simplification would be to assume the same uncertainties for Cr, Fe and Ni as for thorium.

^{6}Li(n,α)T and ^{7}Li(n,n'α)T Reactions. The ^{6}Li(n,α)T reaction is a well known reaction that is often used as a secondary standard against which other cross sections are measured. The uncertainty in the ^{6}Li(n,α)T reaction cross sections should be ±5% or less over the energies of interest in hybrid fusion-fission blanket designs. A study performed by Steiner and Tobias[19] showed that the ^{6}Li(n,α) cross section is adequate for tritium breeding calculations within 1%. The ^{7}Li(n,n'α)T reaction is somewhat less important in this type of hybrid blanket design, since more than 90% of the tritium breeding is contributed from the ^{6}Li(n,α)T reaction. In this case, the current evaluation may be adequate in predicting the nucleonic performance within 1 to 2%.[19]

Sensitivity Study

Method of Study

The method of the cross section sensitivity study employed here is based on the linear perturbation theory as described by Bartine, *et al.*[20] The calculations of the sensitivities were performed using the ORNL developed sensitivity analysis code, SWANLAKE.[21] The direct and adjoint flux distributions required to perform the sensitivity calculations were computed using ANISN. The agreement of the Th(n,γ) and ^{6}Li(n,α) reaction rates in the direct and adjoint calculations is excellent within about 1%. The calculations for fission reaction rates are also in good agreement within about 2%. The ^{7}Li(n,n'α) reaction rates differ by about 4%. However due to its relatively small contribution to the overall tritium breeding, ~ 10%, the overall tritium breeding ratios still agree within 1%.

Results and Discussions

The overall sensitivities of the thorium partial cross sections to the nucleonic performance of the thorium fusion-fission hybrid blanket are presented in Tables IV and V for the blanket at the beginning and end of life, respectively. All quantities are given in units of percent per 1% of cross section increase.

At the beginning of life, the ^{233}U production rate is mostly affected by the (n,γ) and (n,νf) cross section uncertainties. It increases by about 0.44 and 0.14% if the (n,γ) and (n,νf) cross sections are raised by 1%, respectively. At the end of life, it becomes less sensitive and drops to 0.28% for Th(n,γ) cross section. The effect due to Th(n,νf) cross section uncertainty is also very small. These results are revealed in Tables IV and V.

Table IV. Sensitivities of Thorium Partial Cross Section Uncertainties to ^{233}U Production, Thorium Fission and Tritium Production Rates in a Thorium Fusion-Fission Hybrid Blanket at the Beginning of Life (Percent per 1% Cross Section Increase)

Cross Section Type	Th(n,γ)	Th(n,f)	^{6}Li(n,α)	^{7}Li(n,n'α)	Tritium Breeding Ratio
(n,n)	0.051	0.002	-0.036	0.127	-0.020
(n,n')	0.055	-0.030	-0.120	0.138	-0.094
(n,2n)	0.077	-0.021	0.028	0.194	0.045
(n,3n)	0.085	-0.010	0.052	0.212	0.068
(n,νf)	0.142	1.008	0.132	-0.127	0.106
(n,γ)	0.443	-0.009	-0.370	-0.015	-0.334

The tritium breeding ratio is sensitive to the Th(n,γ) cross section uncertainty at the beginning of life. It decreases by about 0.33% as the Th(n,γ) cross section is raised by 1%. However at the end of life,

Table V. Sensitivities of Thorium Partial Cross Section Uncertainties to ^{233}U Production, Thorium and ^{233}U Fission and Tritium Production Rates in a Thorium Fusion-Fission Hybrid Blanket at the End of Life [a] (Percent per 1% Cross Section Increase)

Cross Section Type	Th(n,γ)	Th(n,f)	^{233}U(n,f)	^{6}Li(n,α)	^{7}Li(n,n'α)	Tritium Breeding Ratio
(n,n)	0.064	0.003	0.017	0.013	-0.139	-0.011
(n,n')	0.067	-0.003	-0.028	-0.010	-0.727	-0.072
(n,2n)	0.084	-0.019	0.019	-0.022	0.215	-0.001
(n,3n)	0.092	-0.008	0.021	-0.007	0.335	0.022
(n,νf)	0.140	1.005	0.132	0.134	-0.129	0.112
(n,γ)	0.282	-0.015	-0.149	-0.008	-0.028	-0.010

[a] 3% ^{233}U in thorium.

the tritium breeding ratio becomes relatively insensitive to all cross section uncertainties. This can also be observed from Tables IV and V. The thorium fission reaction rate and thus the blanket energy multiplication are very sensitive to the Th(n,νf) cross section uncertainty. The fission reaction rate increases by about 1% as the corresponding cross section is raised by 1%, no matter whether the blanket is fresh or irradiated. The ^{233}U(n,f) reaction rate, which becomes very important toward the end of life when the ^{233}U concentration increases, is also sensitive to the Th(n,γ) and Th(n,νf) cross section uncertainties. It changes by about -0.15 and 0.3%, respectively, as the Th(n,γ) and Th(n,νf) cross sections increase by 1%.

If the cross section uncertainties shown in the evaluated files as discussed in the previous section are coupled with the above calculated sensitivities, the adequacy of the currently available thorium nuclear data for hybrid design calculations can be assessed. From the previous section, the Th(n,νf) and ^{233}U(n,νf) cross sections appear to be known to about ±5%. This means that the blanket energy multiplication will be known only to about ±2.5 and 4% at the beginning and end of life, respectively. However, all the ^{233}U and tritium production rates seems to be within ±1% due to these cross section uncertainties. The Th(n,2n) and Th(n,3n) cross section uncertainties are about ±15 and 30%, respectively. The uncertainties in predicting the ^{233}U and tritium production rates are thus about ±1.2 and 7% and ±2.8 and 2%, respectively, due to the Th(n,2n) and Th(n,3n) cross section uncertainties. The blanket energy multiplication, however, can be predicted within ±0.5%. The Th(n,γ) cross section is known to about ±10% in the 3—3000 keV range. The uncertainties due to this cross section uncertainty in predicting the ^{233}U and tritium production rates and blanket energy multiplication are up to ±4.5, 3.3 and 2%, respectively. The Th(n,n) and Th(n,n') cross sections are known to about ±10 and 10—15%, respectively. However, the hybrid blanket does not appear to be sensitive to these cross section uncertainties.

Concluding Remarks and Recommendations

The sensitivities of the nucleonic performance characteristics of a typical thorium fusion-fission hybrid blanket to the important thorium partial cross section uncertainties were calculated. The conclusions and recommendations of this study are summarized as follows:

1. The ^{233}U production rate is sensitive to the Th(n,γ) cross section uncertainty. In order to obtain a confident ^{233}U production rate within ±1%, the Th(n,γ) cross section must be measured accurately within about ±2% versus the presently available ±10%, particularly in the energy range 3—3000 keV.
2. The thorium fission reaction rate and thus the blanket energy multiplication depend significantly on the accuracy of the Th(n,νf) cross section itself. For the blanket energy multiplication to be within ±1%, the Th(n,νf) cross section must be measured within about ±2% versus the present ±5%, in the high energy range 13.5—15 MeV.
3. The tritium breeding ratio is sensitive to both Th(n,γ) and (n,νf) cross section uncertainties. In order to predict the tritium breeding within ±1%, the Th(n,γ) and (n,νf) cross sections could be accurate within about ±3 and ±10%, respectively.

In general, it appears that the hybrid blanket performance is not highly sensitive to the nuclear data uncertainties. The accuracy with which the important reaction cross sections is presently known appears to be adequate for preliminary design but it is expected that further measurements of Th(n,γ) cross section, particularly in the 3 to 3000 keV range, and of the Th(n,νf) cross section in the 13.5 to 15 MeV range will be needed for accurate detailed design.

Acknowledgment

The author E. T. Cheng would like to thank K. R. Schultz for his encouragement and helpful discussion.

References

1. W.C. Wolkenhauer, ANS CONF-780508, p. 132 (1978).
2. J.A. Maniscalco, L.F. Hansen and W.O. Allen, ibid, p. 159.
3. A.G. Cook and J.A. Maniscalco, Nucl. Technol., 30, 5 (1976) and references cited therein.
4. R.W. Moir, "Interim Report on the Tandem Mirror Hybrid Reactor Design Study," Lawrence Livermore Laboratory Report UCID-18078 (1979).
5. K.R. Schultz, General Atomic Report GA-A14475, (1977); Trans. Am. Nucl. Soc., 27, 344 (1977).
6. K.R. Schultz, *et al.*, "A Gas-Cooled Blanket for the Tandem Mirror Hybrid Reactor," to be presented at the ANS Winter Meeting, San Francisco, CA, November 11—15, 1979.
7. E.T. Cheng, "Nucleonic Performance Aspects of the Thorium Fusion-Fission Hybrid Blanket Designs," ibid.
8. W.W. Engle, Jr., "A User's Manual for ANISN," K-1693, Oak Ridge Gaseous Diffusion Plant (1967).
9. D.M. Plaster, *et al.*, ORNL-TM-4873 (1975).
10. E.T. Cheng, *et al.*, Nucl. Technol., 45, 77 (1979).
11. DLC-41, Radiation Shielding Information Center, Oak Ridge National Laboratory (1978).
12. B.R. Leonard, *et al.*, *NUCLEAR CROSS SECTIONS AND TECHNOLOGY*, NBS Spec. Pub. 425, p. 608 (1975).
13. R.C. Haight, *et al.*, Nucl. Sci. Eng., 61, 53 (1976).
14. J. Meadows, *et al.*, Argonne National Laboratory, ANL/NDM-35 (1977).
15. R.L. Macklin and J. Halperin, Nucl. Sci. Eng., 64, 849 (1977).
16. M.C. Moxon and C.A. Chaffey, TRDWP, P. 8 (1963).
17. N.M. Steen, Trans. Am. Nucl. Soc., 28, 712 (1978).
18. K. Gmuer, *et al.*, Trans. Am. Nucl. Soc., 28, 719 (1978).
19. D. Steiner and M. Tobias, Nucl. Fusion, 14, 153 (1974).
20. D.E. Bartine, *et al.*, Nucl. Sci. Eng., 53, 504 (1974).
21. D.E. Bartine, *et al.*, ORNL-TM-3809 (1973).

SENSITIVITY OF THE PERFORMANCE OF SYMBIOTIC ENERGY SYSTEMS TO TRITIUM PRODUCTION DATA

J. P. Renier
Nuclear Engineering Applications
Computer Sciences Division at
Oak Ridge National Laboratory
Union Carbide Corporation, Nuclear Division
Oak Ridge, Tennessee 37830, USA

J. G. Martin
University of Lowell
Lowell, MA 01886, USA

For D-T fusion-powered U-233 factories, economics and robustness are strongly affected by the need to breed tritium. The sensitivity analysis of the symbiotic energy system to tritium production data is performed for systems with neutronically uncoupled lithium and thorium blankets. Neutronics calculations utilizing XSDRNPM with 100 neutron group libraries and AMPX cross-section processing, revealed only a minor tritium breeding change between ENDF/B-IV and -V data for ^{6}Li, ^{7}Li, and Pb. For blankets with no multipliers, breeding is most sensitive to the ^{7}Li cross-sections, which are not known with precision, and on which ENDF/B-V has introduced no modifications. Differences of 7% in tritium breeding result into uncertainties in U-233 production costs of typically 15%, while the number of supported fission converters (CR=0.9) varies by 25%. Clearly more certainty in the ^{7}Li data is needed to properly assess the potential of symbiotic systems.

[Symbiotic energy system, CTR, tritium breeding, U-233 production, fuel cycle, cross-section uncertainty, economics, denatured fuel, ENDF/B-V]

Introduction

The recent non-proliferation policy statements[1] have led to an emphasis on alternative energy sources, which minimize the acessibility to materials directly useful for weapons production. The need to minimize the proliferation of sensitive facilities, while extending the use of the available fuel resources, have spurred renewed interest in symbiotic energy systems and denatured (less than 12 w% U-233 in U) fuel cycles.

In symbiotic energy systems, fissile material is bred in drivers (e.g. nuclear fission- or fusion-driven breeders) and is used in burners (e.g. advanced converter fissile reactors). In the drivers, two fissile materials can be bred : U-233 from thorium, and fissile plutonium from U-238. The breeding of fissile plutonium is avoided because this fuel cannot be easily denatured. In addition, we emphasize U-233 factories to take advantage of ample thorium resources and the high conversion ratios achievable with U-233 fuel in thermal reactors. Also, for metallic fuel in the CTR (Controlled Thermonuclear Reactor) blankets, thorium metal alloys exhibit more desirable metallurgical properties than uranium.

The fissile fuel produced in the fusion-powered factories feeds separate advanced fission reactors with high conversion ratios, which generate thermal power for conversion to electricity or process heat. Note that a certain net amount of power may be needed to drive the fuel factory.

Since large amounts of weapons-grade fissile material are generated in the nuclear drivers, we wish to maximize the number of proliferation-proof denatured (DU-233) fissile burners per driver. The concept evaluations were performed for CTR blanket configurations that attempt to maximize fuel (U-233) production, and minimize power production within the blanket. It can be shown[2] that cost and support ratio optimization of symbiotic systems depend on minimizing the energy generation in the fusion reactor blankets. Heat removal from fusion reactors is expensive, and burning U-233 fuel in the fusion factory lowers the support ratio. Reprocessing and fabrication of the fusion blanket are also important components of the U-233 production cost.

In addition, for CTR's surrounding D-T fusioning plasmas, enough tritium must be bred to make the system self-sufficient. Fusion-powered U-233 factories, based on D-T cycles, are the most interesting because of the higher attainable "plasma performance" Q values. They constitute a possible near-term fusion application, and the evaluation of their performance is sensitive to nuclear data, especially the tritium production cross-section of the ^{6}Li and ^{7}Li isotopes. The nuclear reactions involved are : $^{6}Li(n,\alpha)T$ + 4.8 MeV and $^{7}Li(n,n'\alpha)T$ - 2.47 MeV.

Different conceptual types of tritium and U-233 breeding blankets were evaluated, and on the basis of the results obtained, the neutronic results were utilized as a basis for evaluations of the performance of the overall system (fuel cycle and power cost, support ratio, energy doubling time, etc.).

The sensitivity analysis of the performance of conceptual symbiotic energy systems to lithium cross-section uncertainties is done for systems, whose principal components are displayed in Figure 1.

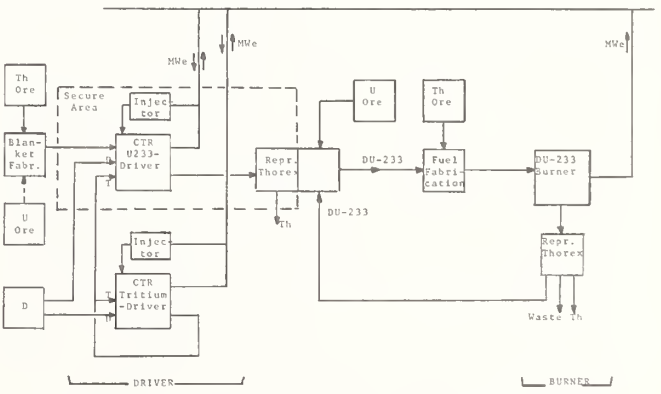

Fig. 1. Conceptual Symbiotic Energy System based on D-T Fusion Driven CTR's.

Cross-Sections

The neutronic calculations of conceptual fusion-driven blankets were performed with 100 neutron group cross-section sets, based on ENDF/B-IV and -V data. The multigroup cross-sections were obtained as follows :

ENDF/B-IV based multigroup sets for ^{6}Li, ^{7}Li, Pb, Fe, Ni, Cr, ^{233}U, ^{232}Th, etc., were taken from the DLC-37 multigroup (100 neutron, 21 gamma ray groups) coupled cross-section library.[3] The kerma factors were taken from the DLC-37 library.

ENDF/B-V multigroup cross-section (100 neutron groups) library for ^{6}Li, ^{7}Li, Pb, Fe, Cr, Ni were generated with the AMPX-II modular code system.[4] The same neutron group structure was taken as for the DLC-37 library. The XLACS-II module of AMPX-II was used to produce weighted multigroup neutron cross-sections from ENDF/B-V point data.

The 100 neutron group ENDF/B-IV and -V based tritium production cross-sections ($^{6}Li(n,\alpha)T$ and $^{7}Li(n,n'\alpha)T$) of natural lithium are shown in Figure 2. No significant differences are apparent between the two versions.

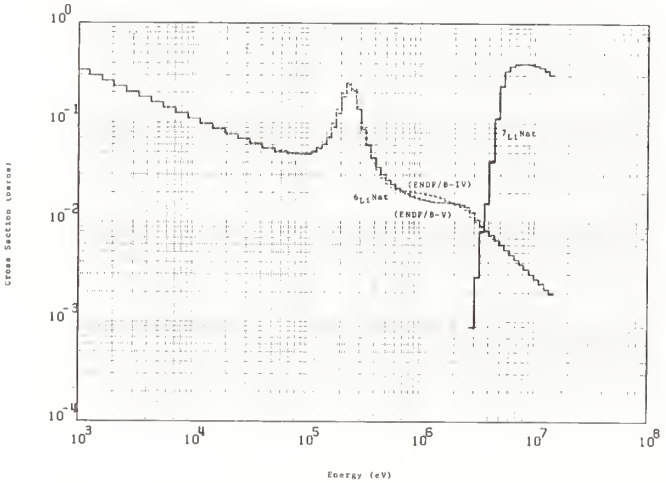

Fig. 2. Tritium Production Cross-Section of Natural Lithium.

It has been reported[5] that the $^{6}Li(n,\alpha)T$ cross-section is known to 1% at 10 keV, 2% at 30 keV, 3% at 230 keV, 5% at 750 keV and above. ENDF/B-V has introduced no modifications on the $^{7}Li(n,n'\alpha)T$ cross-section, although its uncertainty estimates[6] are 15% from threshold to 14 MeV. In addition, the tritium breeding depends on the secondary neutron energy distribution of the $^{7}Li(n,n'\alpha)T$ reaction, which has a 20% uncertainty. Note that for blankets with no neutron multipliers, breeding is most sensitive to the ^{7}Li cross-section. Recent measurements[7,8] of tritium breeding of lithium blankets have shown discrepancies between experiments and calculations. The reported[7] discrepancies in tritium yield from ^{6}LiH were small, while the experimental tritium yield from ^{7}LiH samples was 11±5% smaller than calculations based on ENDF/B-III. In another measurement[8] the tritium yield in a 1-m-diam lithium metal sphere was 35% lower than the measured value, with about half of the discrepancy perhaps caused by the too high value of the $^{7}Li(n,n'\alpha)T$ cross-section. It was recommended that the ^{7}Li cross-section be reduced by ∿15 to 20% with respect to the ENDF/B-III values, which are similar to those of ENDF/B-V. In addition, differences of about 7% in tritium breeding[9] were found by using data obtained from the ENDF/B and UKNDL libraries.

Neutronic Analysis

The neutronic calculations of CTR conceptual blankets, surrounding D-T fusioning plasmas, are performed with a revised version of the discrete ordinates code XSDRN-PM[10], which incorporates a fuel depletion option. A S_4P_3 approximation was used in all the calculations, and was verified with several $S_{16}P_8$ calculations.

The tritium and U-233 breeding blankets may be neutronically coupled. However, this introduces conflicts between the neutronic spectrum requirements for optimum tritium production and optimum ratio of U-233 production to blanket heating. If on the other hand, neither economics, material and engineering design, nor the centralization of sensitive facilities seems to be enhanced by coupling, the two blanket regions may be separate; in fact, they may belong to different reactors altogether. In the analysis, the neutronically uncoupled blankets are matched subject to the requirement that the system be self-sufficient in tritium.

Since the conceptual designs of CTR blankets are still very speculative, we will restrict ourselves to simple geometries for the neutronic calculations.

Tritium Producing Blankets. We considered a simplified spherical breeder, 5-m. inner wall radius, with 1.2 cm. steel first wall, 100 cm. thick region of lithium metal or Pb-Li metal alloy, and a 10 cm. steel outer region. Different compositions of tritium breeding blankets were evaluated, and the neutronic results were utilized for U-233 production cost and support ratio calculations of the overall symbiote.

A synopsis of some of the results obtained is shown in Table 1. The use of the endothermic (n,2n) reaction of Pb in a lithium blanket increases the tritium yield by 7%. The fraction of tritium produced by the $^{7}Li(n,n'\alpha)T$ reaction decreases from 51% to 15%, by switching to a Pb-Li metal alloy. Since the uncertainty in the $^{7}Li(n,n'\alpha)T$ cross-section is higher than in $^{6}Li(n,\alpha)T$, a smaller tritium yield from ^{7}Li produces a smaller uncertainty in the tritium production of Pb-Li alloys. However, an additional uncertainty in the tritium breeding is introduced by the Pb(n,2n) cross-section uncertainty[11] of ±7% at 14 MeV. Neutronic calculations were performed to ascertain the effect of the Pb(n,2n) uncertainty on the tritium yield. A ±7% change introduces a variation of +0.42%, -0.47% in the tritium breeding. A simultaneous decrease of 7% for Pb(n,2n) and 15% for $^{7}Li(n,n'\alpha)T$ gives a 1.9% decrease of the tritium yield. Pb-Li alloys seem to have a smaller sensitivity to present cross-section uncertainties than lithium metal blankets, and in addition they have higher breeding gains.

	ENDF/B-IV					ENDF/B-V				
	Total tritium yield from				Total Energy (MeV)	Total tritium yield from				Pb(n,2n) Activity
	^{6}Li	^{7}Li	Total			^{6}Li	^{7}Li	Total		
Li^{Nat}	0.782	0.808	1.59	1.32*	14.5	0.780	0.802	1.58	1.32*	0.0
Pb - Li^{Nat} (33%-67%)	1.447	0.253	1.69	1.41*	16.1	1.425	0.246	1.67	1.39*	0.533
Pb - Li(30%^{6}Li) (33%-67%)	1.520	0.182	1.70	1.42*	16.3	1.532	0.184	1.72	1.43*	0.535

Sensitivity of the tritium yield to ±7% uncertainty of Pb(n,2n) cross-section

	Change Pb(n,2n)	Total tritium yield from ^{6}Li	^{7}Li	Total	Pb(n,2n) Activity
	+7%	1.442	0.236	1.678(+0.42%)	0.551(+3.1%)
Pb - Li^{Nat} (33%-67%)	0%	1.425	0.246	1.671	0.533
	-7%	1.407	0.255	1.663(-0.47%)	0.517(-3.4%)

* At 85% blanket closure, 2% tritium recuperation losses, otherwise at 100% and 0%, recpectfully

Table 1. Tritium Yield of Lithium Blankets per Fusion Neutron.

Several sensitivity studies have been performed to determine the effect of cross-section uncertainties on the tritium breeding of lithium metal blankets.

Santoro et al[12] concluded that ENDF/B-III data give tritium breedings which are most sensitive to changes in $^{7}Li(n,n'\alpha)T$ cross-section. A 15% change in cross-section introduces a 6.8% change in tritium yield of a natural lithium ORNL blanket design. Tobias and Steiner[13] concluded that, using ENDF/B-III data, the $^{6}Li(n,\alpha)T$ uncertainty caused a 1% breeding ratio change and the $^{7}Li(n,n'\alpha)T$ and secondary neutrons uncertainties introduce a change in excess of 5% in the tritium breeding. The $^{7}Li(n,n'\alpha)T$ uncertainty of 15% introduced a change of 4.9% in the tritium yield of the lithium metal blanket, which we analyzed.

For a symbiotic system, only 0.32 (see Table 1) tritium atom per 14 MeV fusion neutron is available for the U-233 producing CTR. An error on the tritium breeding ratio will therefore be amplified in the U-233 production yield per CTR driver (U233-Driver + Tritium-Driver).

U-233 Producing Blankets. The heat generated in the blanket increases with time during a cycle because of the continuous build-up of U-233 in the thorium fuel. This tends to decrease the ratio of net fissile production to blanket heat generation. The fact that the U-233 inventory and heat production builds up during a cycle necessarily implies an under-utilization of the thermal installation of the U233-driver at BOC (beginning-of-cycle), and an extra penalty. Analyses of clean blankets give an incomplete indication of the heat removal requirements of the factory. [In blanket concepts involving continous fueling such as LiF-BeF_2-ThF_4 molten salt blanket, the U-233 buildup could be minimized. However, the tritium yield is too low to make the system self-sufficient. In addition, difficult engineering challenges are introduced with molten salts.] Also, shaping the plasma burn, so as to keep the blanket maximum power density below a preset value, improves the economics of fusion-driven symbiotic systems.[14]

We considered spherical breeder blankets, 5-m. inner radius, 1.2 cm. steel first wall, with a 40 cm. thick thorium metal blanket. A 5 cm. of lead, used as an endothermic neutron multiplier, and 1.2 cm. of steel separate the thorium region from the first wall; 10 cm. of steel backs it. Heat is removed with helium gas.

For illustrative purposes, Table 2 shows the results of neutronic calculations of a thorium metal blanket. The CTR was simulated at an effective plasma performance, $Q' = \eta_I \times Q = 4.0$ (where η_I, injector efficiency and Q, plasma performance). Other parameters were : 500 Mwatt power injected into the plasma, 400 watt/cc maximum power density in thorium metal fuel, operation with coastdown at EOC (end-of-cycle), 85% blanket closure, 4% structural, 2% reprocessing losses of U-233, energy of the charged particles and radiation fully absorbed by first wall. Observe that, while the net U-233 production rate stays almost constant, the blanket power increases rapidly during a cycle of the U233-driver.

Month	Power Injected (Mwatt)	Net U-233 Produced (kg/month)	Blanket Power (MWth)	Maximum Power Density (watt/cc)
1	500	1715	5390	140
4	500	1725	7160	190
7	500	1735	9140	245
10	500	1750	11360	305
13	500	1760	13840	370
14	500	1765	14740	390
15	475	1670	15080	400

Table 2. Results of a typical Fuel-Cycle Calculation of a U233-Driver Blanket.

Fuel Cycle and Power Cost

The sensitivity studies of fuel cycle, power cost and support ratio, are based on detailed mass and energy flow balances, assuming 85% blanket closure for the fusion breeders, and 2% fissile fuel losses in reprocessing and refabrication.

The computer code that is used to analyze the scenarios, is a complex cost analysis and optimization code[15], that incorporates US INFCE and NASAP preliminary economic guidelines. An effective interest rate (without inflation) of 4.525%, and an appropriate sinking fund depreciation, are used. The method of indifference pricing is applied. Operations-and-Maintenance, and taxes are not included in this analysis. The fusion drivers and the fission burners are operated at 75% capacity factor, with a 40% heat-electrical conversion thermal efficiency. A refueling down-time of two weeks is used for the U233-drivers. A 30 year lifetime is assumed for the CTR drivers and the fissile burners.

DU-233 Fissile Burner. The burners are CANDU advanced converter reactors (ACR), one GWe, burning denatured U-233 fuel, with a conversion ratio, CR = 0.9 and a ratio of capture-to-fission cross-section, $\alpha = 0.1$. The following unit cost values are used :

Balance of plant : $690 / kwe-installed
Nuclear island : $170 / kwe-installed
Fuel fabrication : $590 / kg-HM
Fuel reprocessing : $240 / kg-HM

U233-Driver. The method used for the capital unit cost calculations of the CTR's is similar to the one reported by Kostoff[16] of the Office of Energy Research of DOE. Beam injector cost is assumed proportional to the electric power that goes into the neutral beams. Injection efficiency is assumed to be 50%. In particular the cost components are estimated as follows :

Beam injector : $\beta(1.5)$ x ACR balance of plant=$1030/kw
Nuclear island : 0.7 x ACR balance of plant= $480/kwe
Balance of plant:1.0 x ACR balance of plant= $690/kwe
Fabrication thorium metal fuel : $130 / kg-Th
Reprocessing thorium metal fuel :$275 / kg-Th

Fabrication and reprocessing costs of the U233-driver amount to approximately M$700 per blanket loading.

Tritium-Driver. For the driver for the tritium factory, the costs are estimated as follows :

Beam injector : $\beta(1.5)$ x ACR balance of plant=$1030/kw
Nuclear island : 0.7 x ACR balance of plant= $480/kwe
Balance of plant:1.0 x ACR balance of plant= $690/kwe
Tritium recuperation : 0.8 x ACR balance of plant = $550/kwe

Sensitivity of the Performance

The nuclear data that are used for tritium breeding calculations, and especially the (n,α) and $(n,n'\alpha)$ rections in lithium, are not particularly good. For example, it has been reported[9] that the results for the tritium breeding in typical reactor blankets may differ by 7% by using cross-section data from the ENDF/B and the UKNDL libraries.

Performance sensitivity calculations to nuclear data uncertainties are performed for symbiotic energy systems, whose principal characteristics have been

described. Figure 3 displays the U-233 indifference cost of a symbiote, whose CTR drivers are simulated at an effective plasma performance, $Q' = 2.5$ (plasma performance, $Q = 5$, injection efficiency, $\eta_I = 50\%$).

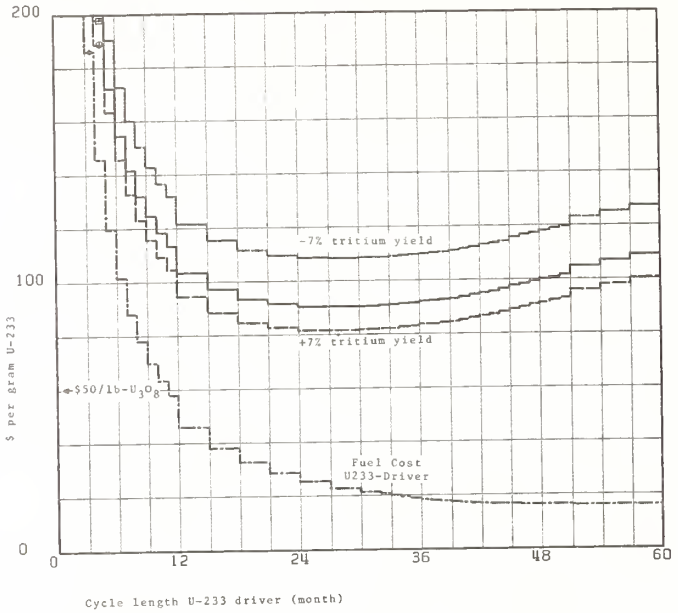

Fig. 3. Indifference U-233 Production Cost of a Symbiotic Energy System (Q=5).

The U-233 production cost is very sensitive to the cycle length of the U233-driver; for small irradiation periods, the effect of the high fabrication and reprocessing costs of the thorium blanket is very strong. For longer cycle lengths, shaping the pulse so as to keep the blanket maximum power density below a given value, permits the achievement of a higher discharged U-233 inventory, and it improves the economics of the symbiote.[14] However, a too long coast-down decreases the net U-233 production rate, and increases the effect of the fixed capital charge rate of the CTR drivers.

Table 3 displays the principal results of the performance sensitivity calculations. Values shown are at the minimum U-233 production cost level.

Figure 3 and Table 3 display the high potential of CTR-driven symbiotic systems. Observe that the number of advanced converter fissile reactors that can be driven is very high, but is very sensitive to the tritium production cross-sections. The support ratio is also much larger than LMFBR drivers.[15] Note that a production cost of $100 per gram U-233 corresponds to an equivalent yellowcake cost of approximately $100 per pound of U_3O_8 (at $75/SWU, 0.2% SW tails, 20 w% u-235 in U, 1.4 equivalence U-233/U-235). CTR-driven scenarios could therefore become competitive with U-235 driven cycles in the near future.

The uncertainties of the $^6Li(n,\alpha)T$, $^7Li(n,n'\alpha)T$ cross-sections and its secondary energy distribution escallate into greater uncertainties in the U-233 production cost and the number of advanced fissile burners that can be supported by the fusion drivers. For example, a -7% change in tritium yield of a tritium-driver causes a +20% increase of the U-233 production cost and a -26% decrease of the support ratio per driver, when operated at Q = 5. A -7% change in tritium yield in a Pb-Li metal blanket tritium-driver causes smaller changes : +11% and -18%, respectfully. The cross-section uncertainties cause smaller changes in the tritium yield of Pb-Li blankets, and the

A. Tritium-Driver : Lithium metal blanket

Q	$1030/kw Injection Cost: U-233 Cost ($/gr-U233)	$1030/kw Injection Cost: Number of ACR per Driver	$2060/kw Injection Cost: U-233 Cost ($/gr-U233)	$2060/kw Injection Cost: Number of ACR per Driver
5	90 +20.0% -9.6%	31 -26.2% +20.5%	110 +22.6% -11%	31 -26.2% +20.5%
8	67 +17% -8.2%	49 -25.8% +20.0%	79 +19.6% -9.5%	49 -25.8% +20.0%
10	63 +14.5% -7.0%	59 -25.2% +19.3%	73 +17.1% -8.3%	59 -25.2% +19.3%

B. Tritium-Driver : Pb-Li^{Nat} metal blanket
Injection cost CTR Drivers : $1030/kw

Q	400 watt/cc*: U-233 Cost ($/gr-U233)	400 watt/cc*: Number of ACR per Driver	200 watt/cc*: U-233 Cost ($/gr-U233)	200 watt/cc*: Number of ACR per Driver
5	81 +11.4% -7.2%	38 -17.6% +16.3%	89 +10.4% -6.5%	37 -18% +15.7%
8	61 +9.5% -6%	59 -17.7% +15.4%	83 +7% -4.4%	51 -16% +14%
10	58 +8% -5%	71 -17% +14.7%		

* Maximum allowed power density in blanket of U233-Driver
** Values shown are at minimum U-233 production costs.

Table 3. Sensitivity of a $\mp 7\%$ Change in Tritium Breeding on the U-233 Production Cost and ACR Support Ratio.

sensitivity of production cost and support ratio is even smaller.

A 100% increase in the CTR injection cost causes typically a 22% increase in U-233 production cost. Decreasing the maximum allowed power density in the thorium blanket from 400 watt/cc to 200 watt/cc causes typically a 9% increase in U-233 cost. The sensitivity to cross-section uncertainties remains about the same.

Conclusions

Factories powered by D-T fusioning plasmas are currently the most interesting ones, because of the higher fusion interaction rates attainable. However, the need to make the symbiotic system self-supporting in tritium implies that the evaluation of the performance will be very dependent on the tritium breeding. This fact emphasizes the need for better lithium cross-section data, especially ^7Li data.

It has been shown above that the present uncertainties in the lithium cross-section data may introduce an uncertainty as high as 20% in the cost of the produced U-233 fuel, even if no other uncertainties are present.

The attractiveness of a symbiotic energy system depends on high support ratios to keep overall cost down. A decrease in the tritium available for U-233 production results in a lower number of fissile reactors that can be supported, and therefore a large uncertainty in the benefits associated with D-T fusion-driven U-233 factories.

The use of Pb-Li metal blankets in a symbiotic system gives lower U-233 production cost, higher support ratios of the drivers, and smaller changes to present lithium cross-section uncertainties.

Clearly, careful optimization of the factory design and evaluation of symbiotic scenarios are tainted by this built-in uncertainty.

References

1. Statement by the President on Nuclear Policy, Summary Fact Sheet, Office of the White House Press Secretary, Washington DC (October 1976).
2. J. P. Renier and J. G. Martin, *D-T and D-D Cycles for Fusion-Powered U-233 Factories*, ANS Conference, San Francisco (November 1979).
3. Revision, *DLC-37/EPR : Coupled 100-Group Neutron, 21 Gamma-Ray Cross-Sections for EPR Neutronics*, ORNL-TM-5249 (1976).
4. N. M. Greene, et al., *AMPX-II : A Modular Code System for Generating Multigroup Neutron-Gamma Libraries from ENDF/B*, ORNL-TM-3706 (March 1976, Revised December 1978).
5. M. R. Bhat, *Evaluated Files of Nuclear Cross-Section for Fusion Reactor Calculations*, Brookhaven National Laboratory, BNL-NCS-25295 (1978).
6. D. Steiner, (Ed), *The Status of Neutron-Induced Nuclear Data for Controlled Thermonuclear Research Applications*, Critical Reviews of Current Evaluations, USNDC-CTR-1 (1974).
7. A. Hemmendinger, C. E. Ragan, and J. M. Wallace, *Tritium Production in a Sphere of ^{6}LiD Irradiated by 14-MeV Neutrons*, NSE, 70, 274-280 (1979).
8. H. Bachmann, U. Fritscher, F. W. Kappler, D. Rusch, H. Werle, H. W. Wiese, *Neutron Spectra and Tritium Production Measurements in a Lithium Sphere to check Fusion Reactor Blanket Calculations*, NSE, 67, 74-84 (1978).
9. O. N. Jarvis, *Nuclear Data for Fusion Reactors*, Proceedings of an International Conference on Neutron Physics and Nuclear Data for Reactors and other Applied Purposes, Harwell, UK (September 1978).
10. L. M. Petrie and N. M. Greene, *XSDRN-PM : AMPX Module with One-Dimensional S_n Capability for Spatial Weighting*, ORNL-TM-3706 (March 1976, Revised December 1978).
11. J. Frehaut and G. Mosinski, *Measurement of (n,2n) and (n,3n) Cross-Sections at Incident Energies between 8 and 15 MeV*, International Symposium on the Interaction of Fast Neutrons with Nuclei, Gaussig, DDR, CEA-CONF-3424 (November 1975).
12. R. G. Alsmiller, R. T. Santoro, J. Barish, T. A. Gabriel, *Comparison of the Cross-Section Sensitivity of the Tritium Breeding Ratio in Various Fusion-Reactor Blankets*, ORNL-TM-4696 (October 1974).
13. M. Tobias and D. Steiner, *Cross-Section Sensitivity of Tritium Breeding in a Fusion Reactor Blanket : Effects of Uncertainties in Cross-Sections of ^{6}Li, ^{7}Li and ^{93}Nb*, ORNL-TM-4200 (June 1973).
14. J. P. Renier and J. G. Martin, *Managing the Fusion Burn to Improve Symbiotic System Performance*, 8th Symposium on Engineering Problems of Fusion Research, San Francisco (November 1979).
15. J. P. Renier, *JPRFUEL : A Scenario Cost Analysis, Fuel Resource Utilization, and Optimization Code*, (to be published).
16. R. H. Kostoff, *Status and Prospects of Advanced Fissile Fuel Breeders*, Third US/USSR Symposium on Fusion-Fission Hybrids, CONF/90103 (January 1979).
17. J. P. Renier, T. J. Hoffman and J. G. Martin, *The Economics of Fusion-Driven Symbiotic Energy Systems*, ANS Conference, Atlanta (June 1979).

MEASUREMENT OF (n,α) CROSS SECTIONS ON Cr, Fe AND Ni IN THE 5 TO 10 MeV NEUTRON ENERGY RANGE

A. Paulsen, H. Liskien, F. Arnotte and R. Widera
Commission of the European Communities
Joint Research Centre, Central Bureau for Nuclear Measurements
2440 Geel, Belgium

A measuring programme has been set up at the CBNM Van de Graaff accelerator facility for the determination of (n,α) cross sections on the main constituents of fast reactor structural materials, namely the elements Cr, Fe and Ni. The α-particles are detected in a reaction chamber by telescope counter arrangements at five observation angles between 14 and 140°. The experimental apparatus and procedure are explained. The results for nickel and iron in the energy range from 5 to 10 MeV are presented. Corresponding measurements on chromium are running.

[Cr,Fe,Ni(n,α) cross sections, 5-10 MeV, angular distributions]

Introduction

Helium formed in stainless steel through (n,α) reactions influences the mechanical and dimensional properties of nuclear reactor structures. For thermal reactors this helium formation is mainly governed by the two-step process $^{58}Ni(n,\gamma)^{59}Ni(n,\alpha)^{56}Fe$, but for fast reactors the (n,α) reactions on the constituents of stainless steel are dominant [1]. Cross section measurements for these (n,α) reactions have been carried out in very few cases at 14 MeV neutron energy. Therefore the measurement of elemental (n,α) cross sections of Cr, Fe and Ni is requested by the designers of fast reactors in the neutron energy range from threshold (~ 5 MeV) to 15MeV [2]

Experimental

As the (n,α) reactions on most of the involved main isotopes lead to stable nuclei activation techniques are not applicable. To study the elemental (n,α) cross sections of Ni, Fe and Cr we designed a reaction chamber for direct α-particle detection during neutron irradiation at the 7 MV electrostatic accelerator of the CBNM. A cross section view of this chamber is shown in Fig. 1.

Five charged particle detector telescopes, each consisting of two energy loss detectors (proportional counters) and one total energy detector (surface barrier counters) in a triple-coincidence arrangement, are registering the charged particles emitted from a thin metallic foil (about 3 mg/cm^2) in the center of the chamber. The mean observation angles relative to the incoming neutron beam are 14,51,79,109 and 141°. All the energy loss detectors are combined in two pairs of proportional counters, one pair on each side of the sample. A neutron collimator is used between neutron source and reaction chamber to keep random coincidences at an acceptable level and to suppress neutron-induced charged particle production in the surface barrier counters. In the middle of the chamber a movable slide permits to insert different samples (the sample to be studied, a reference sample, a background position and a radioactive α-source).

The electronics of this chamber are sketched in Fig. 2. After extraction of the timing information by the indicated threshold discriminators the analogue signals from each pair of proportional counters are summed and led together with the five E-signals to the multiparameter data acquisition system (ND 6600) which serves in this case as a fivefold biparametric analyzer.

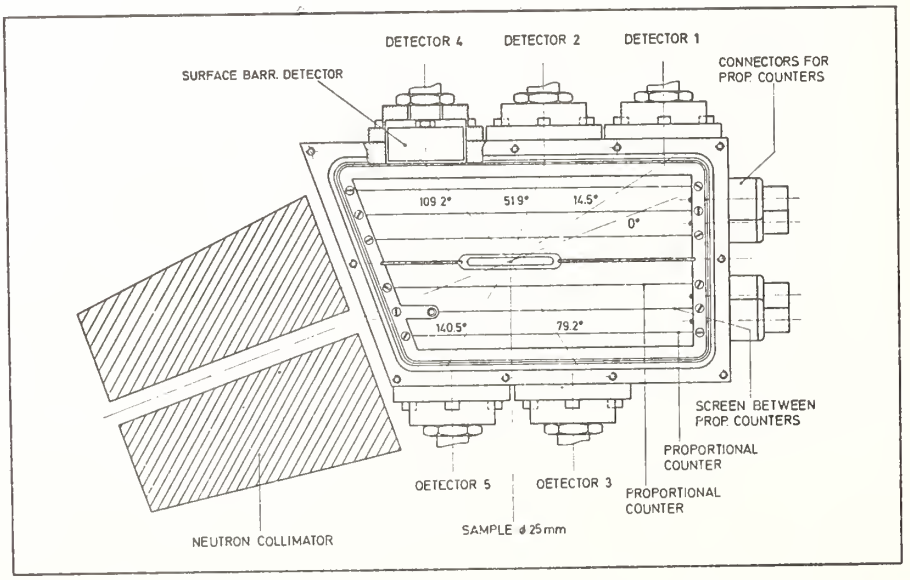

Fig. 1 : Cross-section view of reaction chamber and neutron collimator

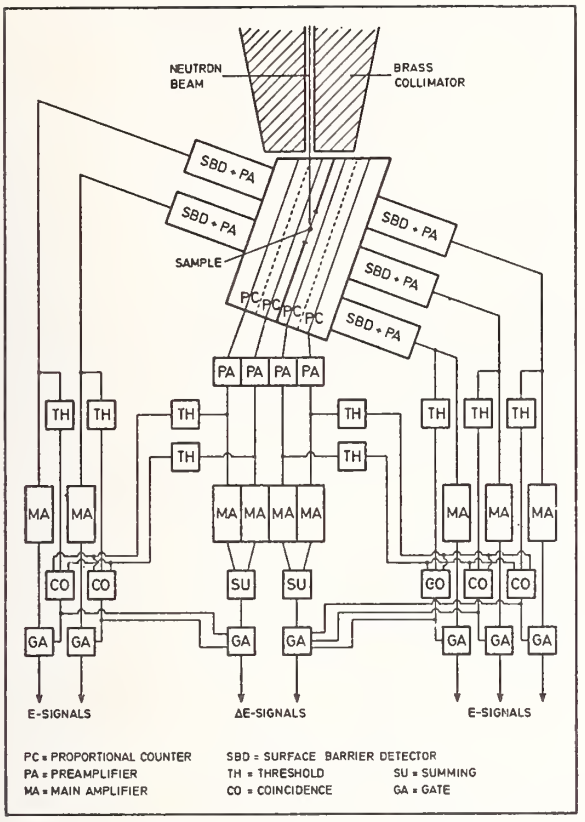

Experimental set-up for reaction chamber.

Fig. 2 : The detector electronics used with the reaction chamber

Fig. 3 indicates the measuring procedure. The differential (n,α) cross sections for the five observation angles are calculated from the observed reaction rates. Since the information about the neutron flux is deduced from a measurement of the recoil proton scattering rate from a polyethylen foil into detector 1 (about 14° observation angle) the final differential cross sections are directly proportional to the assumed differential n-p scattering cross section[3]. Besides the reaction rates and foil characteristics the result depends furtheron in good approximation only on the ratio of the detector solid angles which are measured with an ^{241}Am α-source. The dynamic range of the electronics used is insufficient to record simultaneously the spectra of emitted protons and α-particles. Consequently the recoil protons are observed in a separate run. Since the deuterium gas pressure in the target for the D(d,n) neutron source is very stable in time the beam charge integrator serves as a neutron monitor linking the runs.

Evaluation of differential cross sections from measured

reaction rates $R_i^{n,\alpha} = \Phi_n \cdot N \cdot \left(\frac{d\sigma}{d\Omega}\right)_i^{n,\alpha} \cdot \Omega_n \cdot \Omega_i$, i = 1 to 5

$$\left(\frac{d\sigma}{d\Omega}\right)_i^{n,\alpha} = \frac{R_i^{n,\alpha}}{\Phi_n \cdot N \cdot \Omega_n \cdot \Omega_i}$$

Φ_n : neutrons/sr·s

N : nuclei/cm²

as a similar equation is valid for $\left(\frac{d\sigma}{d\Omega}\right)_1^{n,p}$ of the elastic n-p scattering

$$\Phi_n = \frac{R_1^{n,p}}{\left(\frac{d\sigma}{d\Omega}\right)_1^{n,p} \cdot P \cdot \Omega_n \cdot \Omega_1}$$

P : H nuclei/cm²

$$\Longrightarrow \left(\frac{d\sigma}{d\Omega}\right)_i^{n,\alpha} = \left(\frac{d\sigma}{d\Omega}\right)_1^{n,p} \frac{R_i^{n,\alpha} \cdot P \cdot \Omega_1}{R_1^{n,p} \cdot N \cdot \Omega_i}$$

Fig. 3 : Explanation of measuring procedure

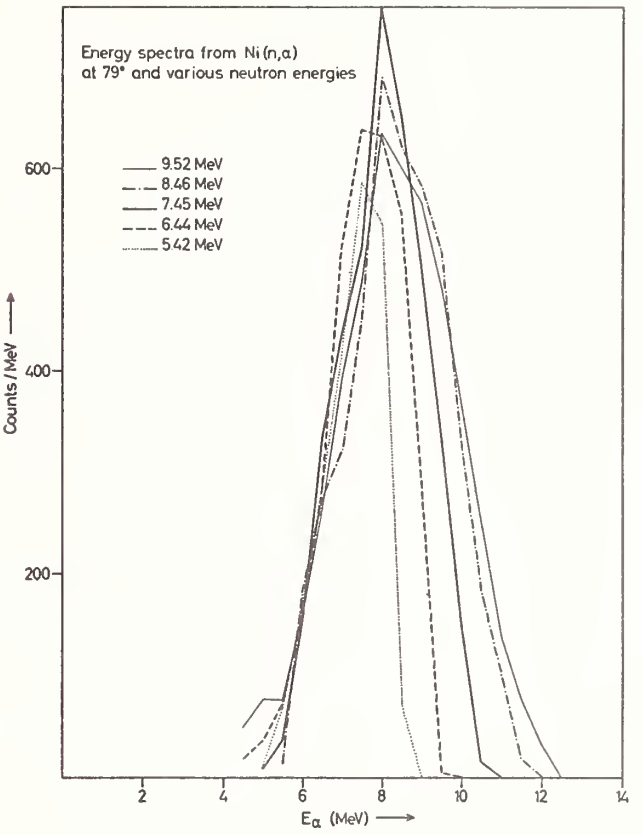

Fig. 4 : α-particle spectra from nickel at 79° observation angle, corrected for energy losses in the sample foil and counter gas

Results

For nickel and iron results are available whereas the measurements on chromium are running. The hyperbola-like curved α-mountain is clearly identified in the bi-parametric (E,ΔE) pulse height spectra of the five detectors. An integration over the ΔE-axis and correction for energy losses in the sample foil and counter gas yields rather clean α-spectra which are shown in Fig. 4 for nickel and 79° observation angle and which are similar for iron.

These spectra can be well fitted with a so-called compound nucleus evaporation shape. The constant low-energy boundary is due to the Coulomb barrier of the separating nuclei and the high-energy boundary increases with increasing neutron energy, according to the increase of energy available to the reaction.

The determination of average Q-values through average α-energies permitted the transformation of the angular distributions into the center-of-mass system. Fig. 5 shows some of the Ni c.m. angular distributions. Fig. 6 and 7 show the relative fitting coefficients for Legendre polynomials up to the second order for the Ni and Fe c.m. angular distributions respectively. Values of A_1/A_0 are roughly zero and values of A_2/A_0 are decreasing with increasing neutron energy. Both statements are in qualitative agreement with the expectations from a reaction model of the compound nucleus theory. The data points shown around 14 MeV refer to ^{58}Ni(n,α) measurements of Seebeck and Bormann [4] and Khan et al. [5] with the isotropic ^{58}Ni(n,nα) contribution subtracted and to the ^{56}Fe(n,α) measurement of Dolya et al. [6] assuming a negligible ^{56}Fe(n,nα) contribution.

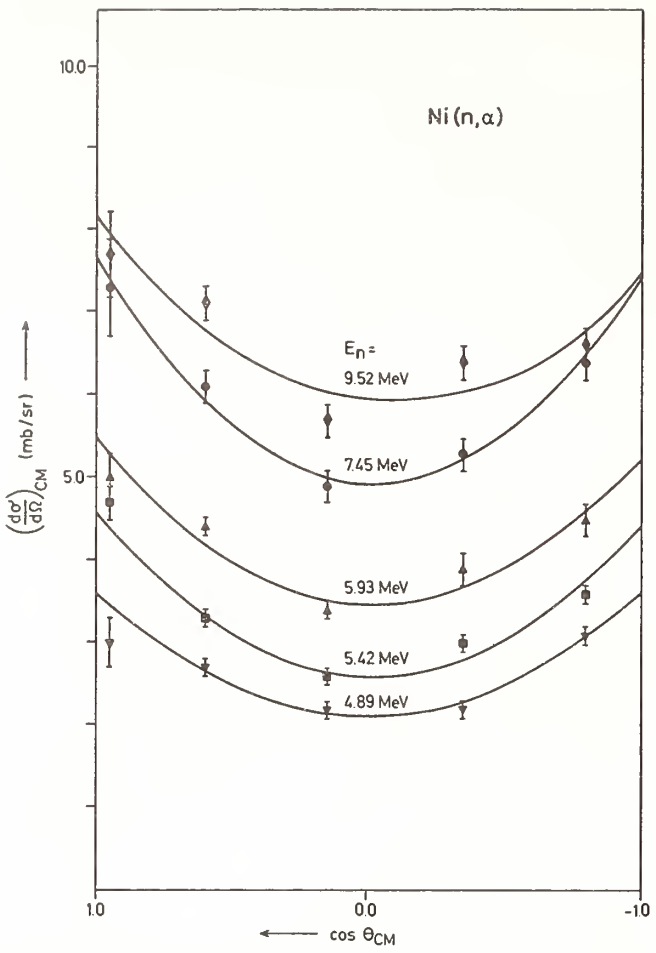

Fig. 5 : c.m. angular distributions of α-particles from Ni

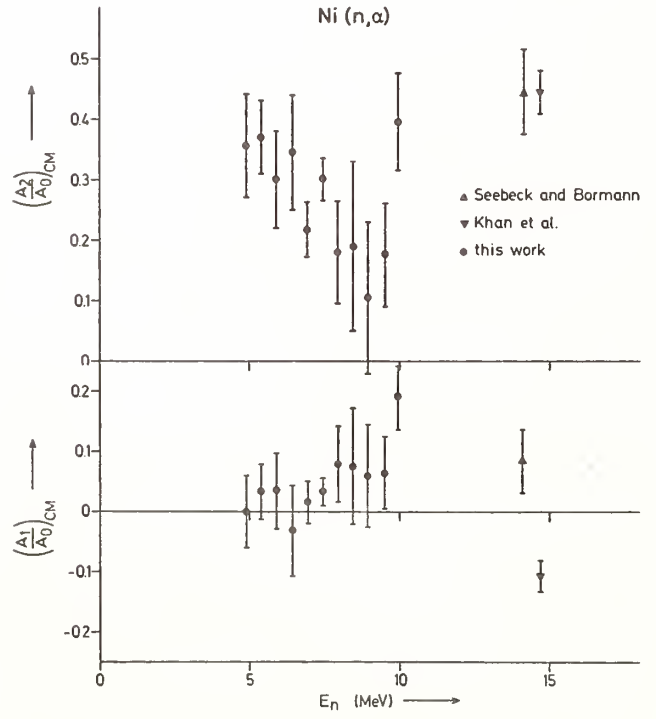

Fig. 6 : Relative c.m. fitting coefficients for Legendre polynomials up to the second order for the angular distributions of α-particles from Ni

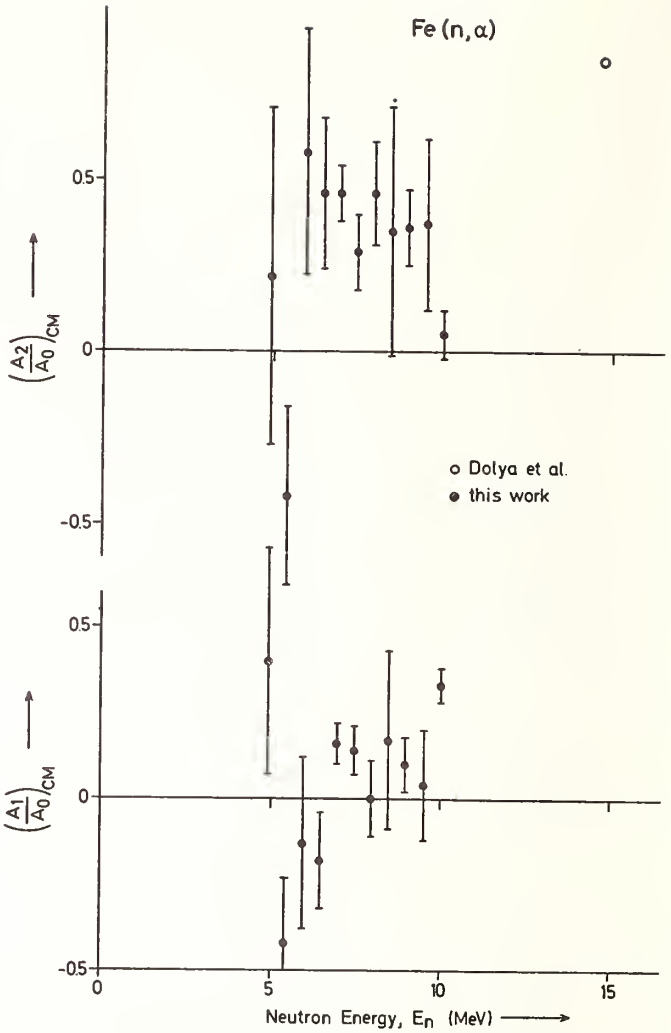

Fig. 7 : Relative c.m. fitting coefficients for Legendre polynomials up to the second order for the angular distributions of α-particles from Fe

The resulting angle-integrated Ni(n,α) cross sections are shown in Fig. 8. The two existing data points for elemental nickel are a quadrupole spectrometer measurement at 15 MeV from Livermore [7] and a high sensitivity gas mass spectrometer measurement at 14.8 MeV of Farrar IV and Kneff [8]. All results are in reasonable agreement with a cross section curve constructed from the KEDAK data file [9] and which is based on theoretical model calculations having the ^{58}Ni(n,α) contribution normalized to a 14 MeV measurement. A measurement on ^{58}Ni, ^{60}Ni and ^{62}Ni at 14.7 MeV by Dolya et al. [6] results in 131 $\pm$ 13 mb for natural nickel and is considerably higher than the elemental nickel results.

The corresponding Fe(n,α) results are shown in Fig. 9. Again the two existing data points around 15 MeV for elemental iron of Grimes et al. [7] and Farrar IV and Kneff [8] are in good agreement. But these results are also in reasonable agreement with the result of Dolya et al. [6] which adds up to 54 $\pm$ 5 mb at 14.7 MeV from measurements on the isotopes ^{54}Fe, ^{56}Fe, ^{57}Fe and ^{58}Fe. The cross section curve constructed from the KEDAK data file [9] is again based on theoretical model calculations having only the very small contributions from ^{54}Fe and ^{58}Fe normalized to experimental 14 MeV values. This curve is in a rather rough agreement with the results

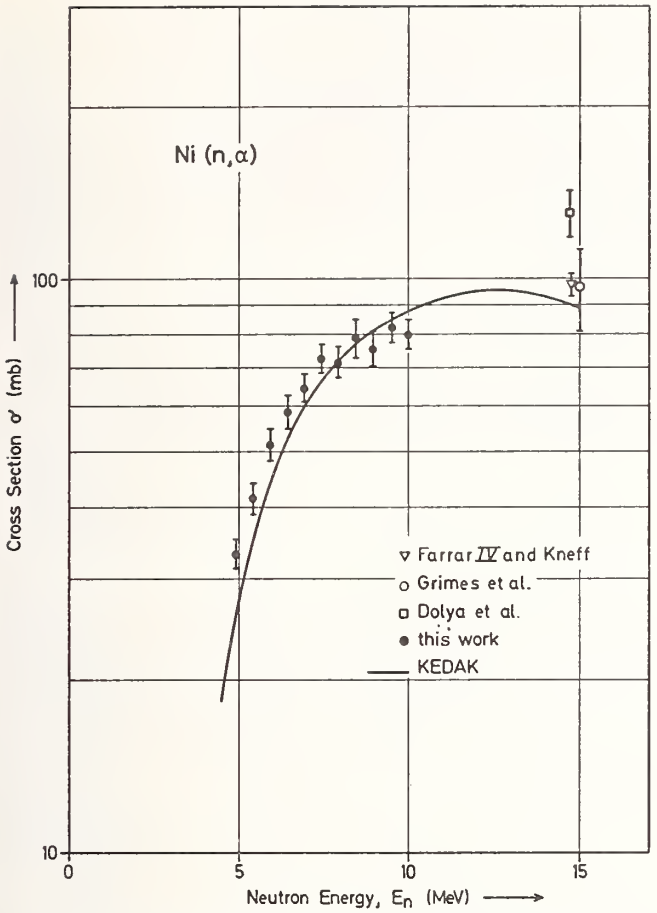

Fig. 8 : The resulting angle-integrated Ni(n,α) cross sections in comparison with existing data

of this work, but is is about a factor of two higher than the experimental results around 15 MeV.

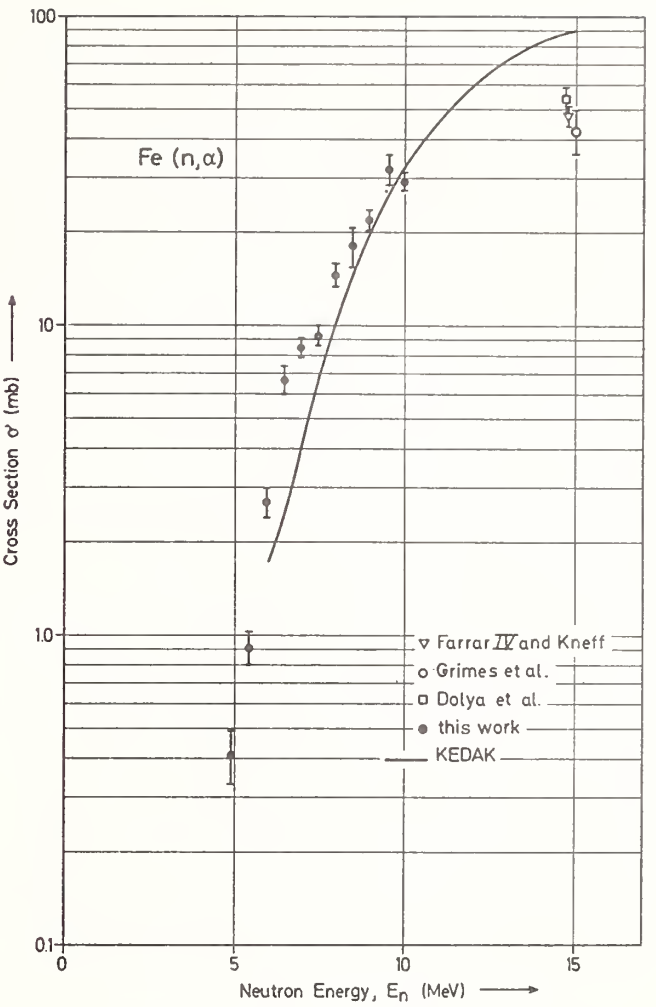

Fig. 9 : The resulting angle-integrated Fe(n,α) cross sections in comparison with existing data

References

1. B. Goel, Nucl.Sci.Eng. 69, 99 (1979).

2. WRENDA 76/77, World Request List for Nuclear Data, Report INDC(SEC)-55/URSF, IAEA Nuclear Data Section, Vienna (1976).

3. J.C. Hopkins and G. Breit, Nucl.Data Tables, A9, 137 (1971).

4. U. Seebeck and M. Bormann, Nucl.Phys., 68, 387 (1965).

5. N.A. Khan, S. Mubarakmand and Mahmud Ahmad, Nucl.Phys., A202, 123 (1973)

6. G.P. Dolya, A.P. Klyucharev, V.P. Bozhko, V.Ya. Golovnya, A.S. Kachan and A.I. Tutubalin, Proc. 3rd All-Union Conference on Neutron Physics, Kiev June 9-13, 1975, Part 4 p. 173.

7. S.M. Grimes, R.C. Haight, K.R. Alvar, H.H. Barshall and R.R. Borchers, Phys.Rev., C19, 2127 (1979).

8. H. Farrar IV and D.W. Kneff, Trans.Am.Nucl.Soc., 28, 197 (1978).

9. KEDAK-3, Evaluations for the German Nuclear Data Library KEDAK-3, Part I: Non-Fissile Materials, compiled by B. Goel, Report KFK 2386/II. Gesellschaft für Kernforschung mbH, Karlsruhe (1977).

NEUTRON NUCLEAR CROSS SECTION DATA FOR FUSION TECHNOLOGY

C.V. SRINIVASA RAO and J. RAMA RAO
Laboratories for Nuclear Research, Andhra University, Visakhapatnam-530003, INDIA.

The investigations on the interaction of fast neutrons with the potential structural materials are of primary importance for the design of fusion reactor. Cross sections for nine fast neutron induced reactions in the isotopes of Molybdenum, which is a candidate for the first wall of the fusion reactor, have been measured using the versatile mixed powder technique and the high resolution Ge(Li) detector.

The high light of the present work is a new element of procedure, self-absorption effects and self-scattering effects which are taken into account experimentally.

A study of the trends of the fast neutron cross sections was undertaken which is generally very useful from the view point of fusion reactor technology. This is because one requires the cross section data for various nuclides in the isotopes and isotonic chains (transmuted species) of the natural elements composing the potential structural materials.

[^{94,92}Mo(n,2n); $^{100, 98,97,96}$Mo(n,p); ^{92}Mo(n,α), 14 MeV, statistical model, experimental trends].

Introduction

Interest in 14 MeV neutrons has been greatly stimulated in recent years by two important applications - material damage studies for controlled fusion reactors and neutron radiotherapy. Even though the plasma physical feasibility of controlled fusion power has as yet not been demonstrated, joint effort is already needed since the anticipated technological problems are considerably greater than those which have been encountered in fission reactor technology. In this present paper, the author considers just one aspect of the diverse problems and discuss the needs and status of neutron nuclear data.

In the present state of the art the Deuterium-Tritium-Lithium (D-T-Li) fuel cycle seems to be the most promising candidate for the release of thermonuclear energy. In the D+T fusion, 80 % of the total energy is carried off by 14 MeV neutrons, and therefore, studies on the interactions of fast neutrons with potential structural materials are of prime importance for the design of fusion reactor.

As sufficiently intense 14 MeV neutron sources are not available at present for the engineering testing of the working conditions of the fusion reactors, accurate cross section data for all the elements are needed for the calculation of the Tritium breeding, radiation shielding, radiation damage, neutron multiplication and so on.[1,2,3,4]

There have been several reviews of the available fast neutron cross section data from the view point of fusion reactor technology[1,4,5,6]. It has been shown that all types of cross sections in the energy range 13-15 MeV are essential.

As far as nuclear reactions induced by 14 MeV neutrons are concerned, most extensive investigations have been carried out in the case of (n,2n), (n,p) and (n,α) reactions.[7-12] The data on (n,2n) reaction are important for calculating the neutron multiplication and that on (n,p) and (n,α) reactions for evaluating the radiation damage.[13] Although the existing data appear to be rather extensive, some of them have larger uncertainties than the errors indicated with the result, they are inconsistent with one another. Hence, it is clearly necessary to resolve the discrepancies with improved accuracy.

It is by now established that Molybdenum is one of the most important structural materials, because of its special physical properties, it is the potential candidate for the first wall material in a fusion reactor[14] which is subject to intense flux of energetic neutrons as well as tremendous amount of charged particle radiation. The neutron multiplication and hence the fuel cycle in a fusion reactor are greatly influenced by the cross section for (n,2n) reactions in the isotopes of Mo and also their radioactive descendants. Likewise (n,p) and (n,α) reaction cross section throw some light on the extent of radiation damage to the structural components of fusion reactor. In view of the unprecedentally large flux of neutrons the product nuclei formed in these reactions may themselves become secondary targets and give rise to a chain of neutron induced reactions. In this way, the cross section data in the lighter nuclei too become interesting. It is in this context that trends of fast neutron cross sections in lighter nuclei come in handy to make an approximate prediction of an unmeasured cross section in an isotope.

Experimental Details

a) Irradiation and monitor reactions:

Neutron irradiations were carried out at the 600 keV cockroft-Walton accelerator of Andhra University, Waltair, India. Neutrons were produced through the T(d,n)α reaction. The samples were placed at 90° to the incident deuteron beam, such that neutrons irradiating the samples had their energy, (14.2 ± 0.2) MeV. This energy was chosen from the view point of the utility of

the data for fusion reactor technology. The neutron flux was of the order of $10^8 n/cm^2/sec$. The flux constancy was monitored by a BF_3 counter embedded in a paraffin block. Specpure metallic form of the sample with purity 99.9 (supplied by J.M.C. high purity materials division, England) was thoroughly mixed with specpure aluminium[15] which served as the monitor through one of the following reactions:

(i) $^{27}Al(n,\alpha)^{24}Na$; $T_{1/2}$ = 15 h. σ = 115±3 mb. Ref.(16)

(ii) $^{27}Al(n,p)^{27}Mg$; $T_{1/2}$ = 9.5m, σ = =72±5 mb. Ref.(17)

The mixed powders were pressed in thin perspex discs so that the thickness of the sample wafer was 1 or 2 mm.

b) Counting and calculation of the Cross Section:

After irradiating the mixed powder, gamma counting was made on a 35 cc. high resolution Co-axial Ge(Li) detector (FWHM: 4.6 at 1332 keV) in conjunction with a ND512 channel analyser system. Figs. 1 and 2 show typical gamma-ray spectrum of the irradiated sample. The relative photopeak efficiency of the detector was calibrated by employing the simulation technique which also takes into account the self absorption and scattering of gamma rays within the sample.[18]

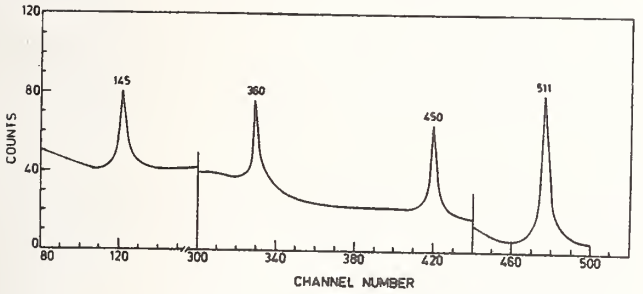

Fig. 1: Gamma-ray Spectrum of Irradiated (Mo+Al) Powder Sample.

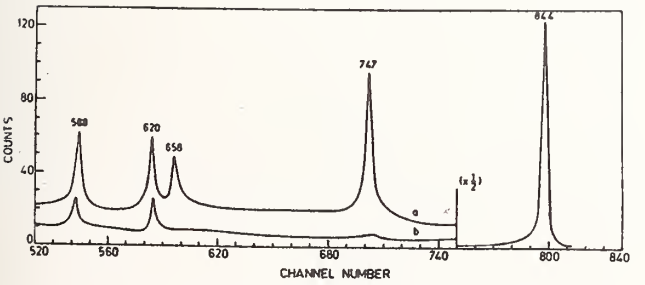

Fig. 2: Gamma-ray Spectrum of Irradiated (Mo+Al) Powder Sample.

The cross section was calculated by using the expression

$$\sigma = \sigma_m \frac{A\lambda}{A_m\lambda_m} \cdot \frac{P_m}{P} \cdot \frac{\theta_m}{\theta} \cdot \frac{N_m}{N} \cdot \frac{[1-\exp(-\lambda_m t_i)][\exp(-\lambda_m t_a) - \exp(-\lambda_m t_b)]}{[1-\exp(-\lambda t_i)][\exp(-\lambda t_a) - \exp(-\lambda t_b)]}$$

where A is the area under the photopeak of the selected gamma-ray counted in the time interval t_a to t_b, λ is the disintegration constant of the residual nucleus formed in the reaction, P is the relative photopeak efficiency for the selected gamma-ray, corrected for self-absorption and scattering within the sample, θ is the absolute gamma-ray abundance in photons per disintegration in the decay of the residual nucleus formed in the reaction, N is the number of nuclei of the particular stable isotope present in the sample exposed for irradiation, t_i is the time of irradiation, t_a is the time that has elapsed since the end of irradiation to the beginning of counting t_b is the interval between the end of irradiation to the end of counting. The parameters subscripted with 'm' denote the corresponding terms for the monitor reactions. The half lives (hence λ) and θ were taken from the recent tabulation of Bowman and MacMurdo.[19]

Measurements

The cross sections measured in the present investigations are given in Table I together with the half-lives ($T_{1/2}$), the energy of the gamma-ray (E_γ), and absolute gamma-ray abundance (θ) in photons per disintegration of the product nuclides, along with the literature values.

In order to make a theoretical comparison, the total cross section for each reaction were compared with predictions based on statistical theory on one hand and semiempirical estimates on the other.

Table II shows such a comparison in the case of (n,2n) reactions studied for Molybdenum. It can be seen from columns (5) and (6) that in these cases the predictions of the statistical theory turn out to be gross overestimates, this behaviour can be understood in terms of the fact that the statistical assumption becomes increasingly poor for lighter nuclei which contain smaller number of nucleons. Some decrease in the cross section from what is expected on the basis of statistical theory could also arise from the circumstance that the first outgoing neutron is emitted in the pre-equilibrium phase i.e. before the statistical equilibrium is reached. Such a pre-equilibrium neutron usually carried away large amount of energy with the result the residual nucleus is left with so low excitation energy that the second neutron emission is energetically forbidden. Thus, the cross sections would be deminished.

In Table III is shown a similar comparison of experimental and theoretical values of (n,p) and (n,α) reaction cross section at 14 MeV. It can be seen from columns (5) and (6) that statistical theory generally underestimates (n,p) and (n,α) cross sections. The enhancement of the observed cross section over the predictions of the statistical theory is often attributed to direct interaction effects in (n,p) reactions. A part of the increase can also be traced to preequilibrium proton emission.

Table - I

Experimental cross sections for (n, 2n), (n,p) and (n,α) reactions at 14.2 ± 0.2 MeV.

Sl. No.	Reactions	$T_{1/2}$	E(keV)	θ	$\sigma_{expt.}$	Literature Values	Ref.
1.	$^{94}Mo(n,2n)^{93m}Mo$	6.9h	1479	1.0	3.5±0.5	0.12±0.03	20
2.	$^{92}Mo(n,2n)^{91m}Mo$	65s	652.9 511	0.497 1.0	19±3	22.1±1.6 16.2±1.2 17.4±3.2	21 22 23
3.	$^{92}Mo(n,2n)^{91m+g}Mo$	15.49m	511	0.94	226±11	211±16 201±17 209±22	21 22 23
4.	$^{100}Mo(n,p)^{100m}Nb$	11m	620	0.6	9±1	-	
5.	$^{92}Mo(n,p)^{92}Nb$	51m	787	0.95	10±1.2	4.1±0.5 7.3±0.8 2.6±0.7	24 25 13
6.	$^{97}Mo(n,p)^{97m}Nb$	54s	743.4	0.993	5±1.1	7.4±0.8	22
7.	$^{96}Mo(n,p)^{96}Nb$	23.5h	1092	0.49	12±2	21.3±1.5 19.2±2.1	22 14
8.	$^{92}Mo(n,\alpha)^{89m}Zr$	4.18m	587.8	1.0	2.1±0.5	9.4±0.9 7.4±0.6 3.6±0.6	22 21 13
9.	$^{92}Mo(n,\alpha)^{89m+g}Zr$	78.5h	910	1.0	24±6	18.7±1.5 28.1±2 25±3 22±3	24 26 14 13

Table - II

Comparison of experimental and theoretical cross sections for (n,2n) reactions at 14.2 MeV in Molybdenum.

Sl. No.	Reaction	Expt. Values			Theoretical Values			
		σ_m	σ_g	Total	Stat.[18]	Pearlstein[27]	Fink[26]	Body[28]
1.	$^{94}Mo(n,2n)^{93}Mo$	3.5±0.5	2.5±0.3	6±0.8	1584	1148	1418	865
2.	$^{92}Mo(n,2n)^{91}Mo$	19±3	-	226±11	307	321	575	200

Table - III

Comparison of experimental and theoretical cross sections for (n,p) and (n,α) reactions at 14.2 MeV in Molybdenum.

Sl. No.	Reactions	Expt. Values			Theoretical Values			
		σ_m	σ_g	Total	Stat.[18]	Levkovskii[29]	Fink[26]	Gardner[30]
1.	$^{98}Mo(n,p)^{98}Nb$	-	-	10±1	16.4	12.76	9.49	9.4
2.	$^{97}Mo(n,p)^{97}Nb$	5±2	9.5±1	15±3	6.9	16.98	18.6	20.3
3.	$^{96}Mo(n,p)^{96}Nb$	-	-	12±2	7.1	22.74	37.8	28.6
4.	$^{92}Mo(n,\alpha)^{89}Zr$	2.12±0.5	-	24±6	27.3	30.97	24.2	-

In columns (5),(7),(8) and (9) experimental values are compared with various semiempirical estimates, it can be seen that no single formula fits all the experimental data, although each of them has a measure of success in reproducing part of the experimental results. Extrapolations to other regions involves uncertainties.

The general conclusion that can be drawn from the above comparisons is that the neutron data needs of the fusion reactor designers cannot be met by theoretical extrapolations.

Experimental Trends

Experimentally observed trends of neutron induced reaction cross sections are of great help to the fusion reactor physicist if the trends are well defined they allow the predictions of an unmeasured cross section falling in their line. In 1966 Csikai and Petö[31] showed that (n,2n) cross sections of isotones increase linearly with neutron excess of the residual nucleus $(N-Z)_R$ for a given residual excitation; U_R. About a decade later, Cindro and Holub[32] revised these trends in the light of accurate experimental data acquired with Ge(Li) detectors. They found a structureless trend for high values of $(N-Z)_R$ and for large residual excitations U_R. Subsequently Pai and Andrews[33] re-examined the trends from a theoretical point of view. They tried to explain both the trends in terms of the competition between gamma emission and neutron emission. However, the theoretical fits to the experimental data are far from satisfactory. Most of these studies on the trends were confined to medium and heavy mass nuclides, for which the neutron excess progressively increases to a significant value.

However, lighter nuclei are characterised by low values of neutron excess and there have been fewer studies on the trends, inspite of their usefulness in controlled fusion reactor. For this reason the trends of the (n,2n) cross sections in light elements are re-evaluated. In the light of the present experimental results as well as those of other investigators. The reactions have been grouped according to the residual excitation energy into three classes, $U_R=2\pm1$ MeV, 4 ± 1 MeV and 6 ± 1 MeV, for each group the experimental (n,2n) cross sections is plotted as a function of neutron excess $(N-Z)_R$ of residual nucleus. Figs. (3) and (4) show these plots.

It can be seen from Fig. (3) in the region of light elements the (n,2n) reaction cross sections increase linearly with neutron excess for residual excitation energy $U_R = 2\pm1$ MeV. This trend is surprisingly simple and at the same time general in the sense that it encompasses not only isotones (as found by Csikai and Petö) but also for almost all the nuclides in the lighter half of the periodic table. This may be viewed as a generalised Csikai-Petö trend. However it differs from the gross structure trend proposed by Cindro and Holub for heavy nuclei.

Fig. (4) shows the plots for $U_R=4\pm1$ MeV and 6 ± 1 MeV. It is interesting to note from Fig. (4) that while the trend at $U_R=4\pm1$ MeV trend to resemble the gross structure trend of Cindro and Holub, the one at $U_R=6\pm1$ MeV is already flat and structureless.

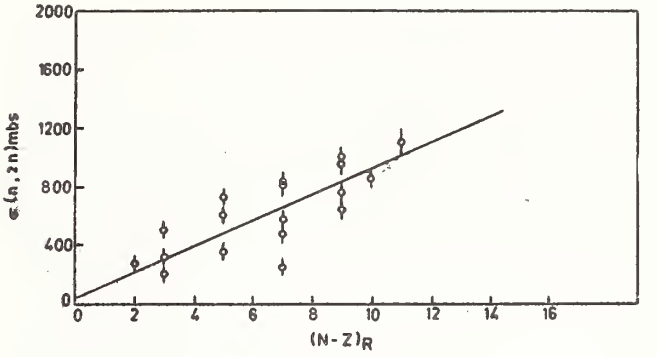

Fig. 3: The Experimental Cross Sections $\sigma(n,2n)$ as a Function of $(N-Z)_R$ at $U_R = 2\pm1$ MeV.

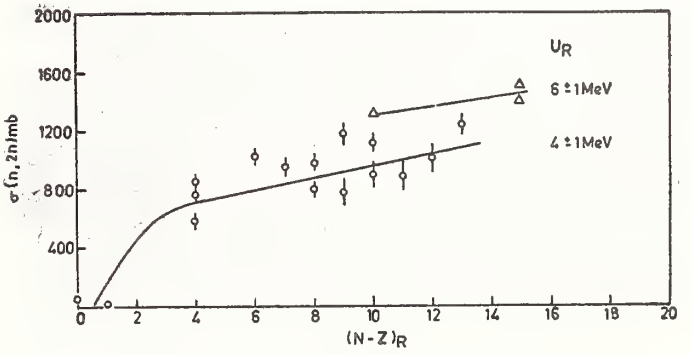

Fig. 4: The Experimental Cross Sections $\sigma(n,2n)$ as a Function on $(N-Z)_R$ at $U_R = 4\pm1$ and $U_R = 6\pm1$

In conclusion, it may be said that the present series of measurements of the fast neutron cross sections in some elements of fusion reactor interest have contributed to carefully measured experimental cross section values to remove discrepancies and help update the experimental data.

The trends of (n,2n) cross sections of lighter nuclei studied in the present work, have revealed new features different from those observed previously for heavier nuclei. The present trends are rather well defined in the region of elements of fusion reactor interest so that unmeasured cross sections can be readily assessed in realising the dream of the present century - an operating fusion reactor.

Acknowledgement

One of us (CVS) is grateful to the Department of Atomic Energy, Government of India and National Bureau of Standards, Washington, D.C. for providing financial assistance during the present investigations.

References

1. L. Stewart,
'Status of neutron induced nuclear data for controlled thermonuclear research applications, USNDC-CTR-I (1974) pp.11.

2. D.Steiner,
Nucl.Sci.Engg. 58, 107 (75).

3. D. Steiner and M.Tobias.
Nucl. Fusion, 14, 153 (1974).

4. S.M. Qaim, R. Wolfle and G. Stocklin,
Atomiki Kozlemenyev 18, 335 (1976).

5. D. Steiner,
Proc. Conf. Nucl. Cross Section and Technology, Washington, D.C., March 1975 (NBS-Special Publication 425 (1975) p. 646.

6. R.C. Haight,
Review of Neutron Data, 10-40 MeV,
Proc. Symp. Neutron Cross Section From 10-40 MeV, Brookhaven, May 1977.
BNL-NCS-50681 (1977), p. 201.

7. S.M. Qaim,
Proc. Int. Conf. on Neutron Physics and Nuclear Data for Reactors and Other Applied Purposes, Harwell, U.K. (1978).

8. EXFOR MASTOR - FILE INDEX, IAEA.

9. K. Tsukade,
JAERI 1252 (1977).

10. S.M. Qaim,
Handbook of Spectroscopy, Vol. III CRC. West Palm beach, Fla 33400, USA.

11. S.M. Qaim,
Proc. Specialist Meeting on Neutron Data of Structural Materials for Fast Reactors, GEEL, Belgium 5-8 Dec.,1977.

12. S.M. Qaim and N.I. Molla,
Nucl. Phys. A283, 269 (1977).

13. S.M. Qaim, R. Wolfle and G. Stocklin,
Chemical and Nucl. Data, Univ. of Kent, Cantebury (1971) p. 121.

14. S.M. Qaim and G. Stocklin,
Proc. of the 8th International Conf. on Fusion Technology (1974).

15. P. Venugopala Rao and R.W. Fink,
Phys. Rev. 154, 1023 (1967).

16. J.C. Robertson, B.Audric and P.Kolkowski
Jour. Nucl. Energy 27, 53 (1973).

17. N. Lakshmana Das,
Andhra University, Waltair, India,
Private Communication (1978).

18. C.V. Srinivasa Rao,
Thesis Submitted to the Andhra University (1979), India.

also

Communicated to Nucl. Instr. Meth. (the Netherlands).

19. W.W. Bowman and K.W. MacMurdo,
Atomic and Nuclear Data Tables, 13, 89 (1974).

20. Yu. P. Gangraskii and I.F. Kharisov,
Sov. J. Nucl. Phys. 12, 611 (1971).

21. R.A. Sigg and P.K. Kuroda,
Jour. of Inor. and Nucl. Chem. 37, 631 (1975).

22. Weh-deh-Lu, N. Rana Kumar and R.W.Fink,
Phys. Rev. C1, 358 (1970).

23. S.M. Qaim,
Nucl. Phys. A185, 614 (1972).

24. W. Lu, N. Rana Kumar and R.W. Fink,
Phys. Rev. C1, 350 (1970).

25. V.K. Tikku, H. Singh and B.Sethi,
B.A.R.C. Conf. Chandigarh (India), 2, 115 (1972).

26. W.Lu and R.W. Fink,
Phys. Rev. C4, 1173 (1971).

27. S. Pearlstein,
Jour. Nucl. Energy 27, 81 (1973).

28. Z.T. Bödy and J. Csikai,
Atomic Energy Review, 11, (1973).

29. V.N. Levkovskii,
Sov. Nucl. Phys. 18, 361 (1974).

30. D.G. Gardner and S. Rosenblum,
Nucl. Phys. A96, 121 (1967).

31. J. Csikai and G. Petö,
Phys. Lett. 20, 52 (1966).

32. E. Holub and N. Cindro.
Jour. of Phys. G (Nucl. Phys.) 2, 405 (1976).

33. M.L. Pai and D.G. Andrews.
Can. Jour. Phys. 55, 2145 (1977).

PRODUCTION CROSS SECTIONS FOR (n,t) REACTIONS IN ^{40}Ca, ^{54}Fe, ^{86}Sr, ^{89}Y, ^{102}Pd, ^{112}Sn, $^{106,114}Cd$, ^{130}Te, ^{139}La, ^{204}Pb, and ^{205}Tl with 14.6 MeV Neutrons

T. W. Woo and G. N. Salaita
Southern Methodist University
Dallas, TX 75275 U.S.A.

The cross sections for (n,t) reaction of 14.6 MeV neutrons with isotopes of the natural elements calcium, iron, yittrium, palladium, tin, lanthanum, and lead, and with enriched isotopes stronium-86, cadmium-114, tellurium-130, and thallium-205 were measured by the activation technique using high-energy resolution gamma-ray spectrometry. The experimental results are generally in good agreement with cross section values obtained from an empirical equation and with recently reported measurements. The cross section ratio of (n,t) and (n,p) were calculated on the basis of the statistical model.

Introduction

A literature survey of (n,t) reaction cross sections at 14-15 MeV shows that for the light mass nuclei the cross section values are well established. However, for medium and heavy mass nuclei the reported information is relatively small and often in disagreement. In many cases only one, as an upper limit, cross section value has been reported.

The (n,t) measurement is of importance in regard to the validity of the cluster model of the nucleus.[1] If the nuclear surface exhibits a tendency for clustering into ^{2}H, ^{3}H, ^{3}He, ^{4}He, etc. groupings, the emission of such groups should be detectable, especially since many of the reactions are energetically possible with 14.6 MeV neutrons. Reactions involving the emission of ^{2}H, ^{3}H, and ^{3}He have generally low cross section values and are more difficult to investigate.

The dependence of the (n,t) cross section on the relative neutron excess (N-Z)/A, though weaker than for the (n,p) and (n,α) can be correlated to the neutron absorption cross section $\sigma_c(n)$ as follows[2,3,4]

$$\sigma(n,t) = \sigma_c(n)\,\alpha_t \quad , \qquad (1)$$

where α_t is the probability of triton emission. Equation (1) may be written in terms of the nucleon radius and the deBroglie wavelength $\lambda\!\!\!^{-}$ as

$$\sigma(n,t) = \pi r_0^2 (A^{\frac{1}{3}} + \lambda\!\!\!^{-}/r_0)^2 \alpha_t \quad . \qquad (2)$$

For 14 MeV neutrons, $\lambda\!\!\!^{-}/r_0 \simeq 1$ with $r_0 = 1.2$ F. Then

$$\sigma(n,t) = 4.52(A^{\frac{1}{3}}+1)^2 \alpha_t \times 10^{-26}\ \text{cm}^2 \quad . \qquad (3)$$

α_t is established empirically in terms of N,Z and A of the target nucleus in the form

$$\alpha_t = a \exp[b(N-Z)/A] \ ,$$

where a and b are constants. From a least-squares fit of the experimental data[5] the values of a and b are found to be 1.7×10^{-4} and -13, respectively. Equation (2) may be used for establishing the gross trend of the (n,t) cross section and for estimating unknown values in medium and heavy mass nuclei.

Experimental Method

In contrast to the common reactions such as (n,p), (n,α) and (n,2n), the (n,t) and (n, ^{3}He) reactions for medium and heavy mass nuclei are considered "rare" due to their rather small reaction cross section values. These values vary from a few to a few tens microbarns. As a consequence of the small cross section values, the measurements are difficult due to the low induced activities.

High purity powder samples placed in 20 ml vials were irradiated by positioning them near the accelerator where the neutron flux density was about 10^{10} neutrons $cm^{-2}sec^{-1}$. In order to avoid ambiguous identification of the product nucleus, the lightest isotope of each natural element has been chosen when possible. For measurements on ^{86}Sr, ^{114}Cd, ^{130}Te, and ^{205}Tl, enriched isotopes were employed as target materials. In all other cases elements of natural isotopic composition were used. The chemical composition and purity of each target material is given in Table 1.

In studies of (n,t) reactions on ^{40}Ca, ^{54}Fe, ^{89}Y, ^{102}Pd, ^{106}Cd, ^{112}Sn, ^{139}La, and ^{204}Pb target samples were irradiated without any external flux monitor since an (n,p), (n,α), or (n,2n) reaction on one of the isotopes of the element was employed as an interan standard. In the case of the enriched isotopes, external monitors such as As, Al, and Tl were used. The reaction cross sections were calculated from the areas of the respective photopeaks of the (n,t) and monitor reaction products. Correction for gamma-ray branching, internal conversion, detector efficiency, and isotopic abundance were applied. Information on the reactions employed as neutron flux monitors is given in Table 2 together with the cross-section data.

The (n,t) product activities were identified by their characteristic gamma-ray peaks using high-energy resolution Ge(Li) detector spectrometer. For further confirmation a check of the half-lives of several activities were also carried out.

In general the cross section obtained by the activation method would giva a sum of the (n,t), (n,dn), and (n,p2n) reactions. However, for the majority of the isotopes utilized the Q-values for the (n,dn) and (n,p2n) reactions are greater than 15-MeV, whereas for (n,t) reactions the values range from 5.24- to 13.2-MeV as shown in Table 2. In the case of ^{139}La and ^{205}Tl the Q-values for (n,p2n) reaction are 15.39-MeV and 13.91-MeV, and the respective values for (n,dn) reaction are 13.17- and 11.69-MeV. However, since the residual energy available for the reactions is much greater for (n,t) than either of former competing reactions, we assume the latter to be favored; any contribution from (n,dn) and (n,p2n) is assumed to be within the limits of the experimental error of the measured (n,t) reaction cross section values.

Table 1

INFORMATION ON THE IDENTIFICATION OF (n,t) REACTIONS

REACTION	TARGET MATERIAL (Grams)	PURITY	IRRADIATION TIME (Hours)	HALF LIFE OF (n,t) PRODUCT	E_γ (KeV)
$^{40}Ca(n,t)^{38}K$	CaF_2(34)	99.99%	0.5	7.7 min	2167
$^{54}Fe(n,t)^{52m,g}Mn$	Fe(63)	99.99%	1	21 min	1433.6
				5.7d(g)	744.1
$^{86}Sr(n,t)^{84}Rb$	*$Sr(NO_3)_2$(2.415)	99.9999%	3.75	33 d	881.5
$^{89}Y(n,t)^{87m}Sr$	Y_2O_3(23)	99.9999%	5.5	2.83 h	388
$^{102}Pd(n,t)^{100}Rh$	Pd(137)	99.5%	6	20 h	540
$^{106}Cd(n,t)^{104m,g}Ag$	Cd(174)	99.99%	1.16	33 min	555.8
				69 min	767.4
$^{112}Sn(n,t)^{110m,g}In$	Sn(181)	99.99%	4	4.9 h	884.7
				69 min	657.5
$^{114}Cd(n,t)^{112}Ag$	*Cdo (1.142)	99.9999%	6	3.13 h	617.4
$^{130}Te(n,t)^{128g}Sb$	*Te(1)	99.9999%	6	8.9 h	314
$^{139}La(n,t)^{137m}Ba$	La_2O_3(30.63)	99.999%	0.153	2.55 min	661.6
$^{204}Pb(n,t)^{202}Tl$	Pb(249)	99.9%	6	12.0 d	440.2
$^{205}Tl(n,t)^{203}Hg$	*Tl_2O_3(1.117)	99.9999%	8	46.76 d	279.2

*Enriched isotope.

Theoretical Consideration

Brown and Muirhead[6] pointed out that for measurement of the (n,p) reaction cross section by the activation technique one can assume two processes by which the proton is emitted; one is by direct interaction between the incident particle and the target nucleons, the other is from the decay of a compound nucleus, which is formed by the incident particle and the target nucleus. We have made an attempt to test the applicability of these assumptions to (n,t) reactions.

Due to the low cross section values, an investigation of the (n,t) reaction mechanism in medium and heavy nuclei is possibly only by comparison between the measured and calculated cross sections. We have used the statistical model for calculating the cross section ratios of (n,t) and (n,p) reactions at 14.6-MeV neutron energy. By comparing the measured cross section ratio of (n,t) and (n,p) reactions with ratio obtained from calculations, one can obtain the relative strength of the direct interaction process.

Calculation of the cross section ratio for the compound nucleus can be reduced to the determination of the relative emission probability Γ_t/Γ_p. The emission probability Γ_b for b particle is given by the expression[7]

$$\Gamma_b = M_b(2S_b+1)\int_{E_{bmin}}^{E_{bmax}} E_b\sigma_b(E_b)\omega(U)dE_b \ , \qquad (4)$$

M_b, S_b and E_b are respectively the mass, spin and kinetic energy of the emitted particle; $\sigma_b(E_b)$ is the cross section for compound nucleus formation by the inverse reaction, and $\omega(U)$ is the level density of the residual nucleus at U excitation energy. The even-odd effect was taken into consideration in the excitation energy $U = E + Q_b - E_b + n\delta$ by adding $n\delta$, where n is 0, 1, and 2 in the case of even, odd-mass and odd end-nuclei, respectively; here E is the kinetic energy of the incident particle, Q_b is the Q-value for particle b, and

$$\delta = 10\cdot A^{-\frac{1}{2}} \text{ MeV} \ , \qquad (5)$$

where A is the mass number.[8]

The cross section ratio $\sigma(n,t)/\sigma(n,p)$ is given by

$$\frac{\sigma(n,t)}{\sigma(n,p)} = \frac{\Gamma_t}{\Gamma_p} = \frac{M_t(2S_t+1)}{M_p(2S_p+1)} \times \frac{\int_0^{E+Q_t} E_t\sigma_t(E_t)\omega(U_t)dE_t}{\int_0^{E+Q_p} E_p\sigma_p(E_p)\omega(U_p)dE_p} \ . \qquad (6)$$

The values of $\sigma_t(E_t)$ and $\sigma_p(E_p)$ were obtained by extrapolating and interpolating the data of Shapiro.[9] These data are given for rectangular potential. Data from the same table were applied to a round-off potential taking into account the Kikuchi relation[10] between the B maximum of rectangular potential and B_{eff} maximum of the effective coulomb barrier.

$$B_{eff} = B\left[1 - \frac{1.7}{R}\right], \quad (7)$$

where $R = 1.5A^{\frac{1}{3}} \times 10^{-13}$cm, and $R_t = (1.5 \times A^{\frac{1}{3}} + 1.21) \times 10^{-13}$cm are the nuclear radii for the proton and triton, respectively. The level density $\omega(U)$ is given by the Fermi gas model

$$\omega(U) = C \exp\left[2(aU)^{\frac{1}{2}}\right] \quad (8)$$

The value of the level density parameter was obtained from the relation[11] $a = A/8.7\ MeV^{-1}$. The multiplication constant C was disregarded for the cross section ratio because ot its weak mass number dependence.[12]

Table 2

ACTIVATION CROSS SECTIONS FOR (n,t) REACTIONS BY 14.6 MeV NEUTRONS

REACTION	Q VALUE* (MeV)	Monitor Reactions	Monitor Cross Section (Mb)	(n,t) REACTION CROSS SECTION (μb) Present Work Theo.	Present Work Exp.	Literature Values	Reference
$^{40}Ca(n,t)^{38}K$	13.15	$^{44}Ca(n,p)^{44}K$	40±5		16±4	27±8	(13)
						< 20	(14)
						100	(15)
						31±5	(16)
						180±20	(17)
$^{54}Fe(n,t)^{52m}Mn$	13.01	$^{56}Fe(n,p)^{56}Mn$	103±6	108	105±42	95±30	(13)
						600±100	(18)
$^{54}Fe(n,t)^{52g}Mn$	12.63	$^{56}Fe(n,p)^{56}Mn$	103±6		17±6	10±5	(13)
$^{86}Sr(n,t)^{84g}Rb$	10.74	$^{75}As(n,2n)^{74}As$	970±80	50	30±8		
$^{89}Y(n,t)^{87m}Sr$	10.20	$^{89}Y(n,\alpha)^{86g}Rb$	5±1	45	2±0.6	3.8±1.0	(13)
$^{102}Pd(n,t)^{100}Rh$	9.22	$^{106}Pd(n,p)^{106m}Rh$	6.0±2	69	64±22		
$^{106}Cd(n,t)^{104m}Ag$	8.89	$^{112}Cd(n,p)^{112}Ag$	15±1.3	74	57±12		
$^{106}Cd(n,t)^{104g}Ag$	8.87	$^{112}Cd(n,p)^{112}Ag$	15±1.3		24±5		
$^{112}Sn(n,t)^{110m}In$	9.11	$^{118}Sn(n,\alpha)^{115}Cd$	1.1±0.08	64	33±6		
$^{112}Sn(n,t)^{110g}In$	9.11	$^{118}Sn(n,\alpha)^{115}Cd$	1.1±0.08		28±7		
$^{114}Cd(n,t)^{112}Ag$	6.32	$^{27}Al(n,\alpha)^{24}Na$	116±3	34	36±8		
$^{130}Te(n,t)^{128g}Sb$	5.24	$^{27}Al(n,\alpha)^{24}Na$	116±3	21	24±8		
$^{139}La(n,t)^{137m}Ba$	7.12	$^{139}La(n,p)^{139}Ba$	8.7±0.6	28	18±5	21±5	(13)
$^{204}Pb(n,t)^{202}Tl$	5.86	$^{204}Pb(n,2n)^{303}Pb$	1740±140	28	29±7	32±10	(2)
$^{205}Tl(n,t)^{203}Hg$	4.94	$^{203}Tl(n,2n)^{202}Tl$	1950±200	24	33±8		

*All Q values are negative.

The (n,t) reactions investigated by the activation technique, their Q-values, and the measured cross sections are given in Table 2 together with data available from the literature. It can be seen from Table 2 that in the case of ^{40}Ca, ^{54}Fe, ^{89}Y, ^{139}La, and ^{204}Pb there is a good agreement between the results of this work and the recently reported values by Qaim.[2,13] Also listed in Table 2 are values of (n,t) reaction cross sections calculated by using Equation (3). It can be seen that the latter values are in fair agreement with the measured values, except for ^{89}Y and ^{139}La where the measured values are for the isomeric states production and are therefore partial cross sections.

A study of the systematic trends in the (n,t) reaction cross sections based on a plot of $\sigma(n,t)$ vs the atomic member of the target nucleus, reveals that the value of σ increases with increasing Z up to $Z \simeq 30$ and decreases thereafter reaching a plateau in the heavy mass region. Qaim[19] made a comparison of the (n,t) cross sections obtained via tritium counting with those obtained via gamma-ray spectroscopy of the activation products by 14.6 MeV neutrons. He found that in the light mass region the two cross sections are very close, indicating that the activation product is formed via triton emission. However, for target nuclic with A > 40, the cross sections obtained via the activation

technique are higher than those measured via the tritium counting. The latter were obtained from fast neutrons produced via break-up of 53-MeV deuteron on beryllium. Solely from the point of view of energetics the emission of a triton should be favored over the emission of three particles. It is possible that, for the higher energy break-up neutron, collision dynamics and statistical processes play important roles in the energy transfer and distribution in the compound nucleus and consequently enhance the emission probability of three particles over that of a bound triton. It appears that the 14.6 MeV data contain contributions only from the (n,t) reactions whereas the break-up data given the sum of (n,t) and (n,xt) cross sections.

The decrease in the cross section for Z > 30 may be attributed to the increasing Coulomb barrier and therefore a decrease in the residual energy available for the reaction. Table 3 lists both the theoretical and experimental cross-section ratios for (n,t) and (n,p) reactions. Listed also are the E_p+Q_t and $E+Q_p$ values. From the table it can be seen that the experimental cross-section ratios for ^{40}Ca, ^{54}Fe, ^{86}Sr, ^{106}Cd, ^{112}Sn and ^{205}Tl are larger than the calculated ratios, whereas for ^{114}Cd this trend is reversed. A tentative conclusion is that the contribution from direct interaction processes in the (n,t) reaction is stronger than in the (n,p) reaction for the former six target nuclei and the reverse for ^{114}Cd. In order to substantiate these and other conclusions, it is necessary to investigate the excitation function of the reactions and to determine the angular distribution and energy spectra of tritons. Such measurements are difficult to carry out with present techniques due to the low cross section values for (n,t) reaction at 14.6 MeV.

Table 3

TRITON AND PROTON PRODUCTION CROSS SECTION RATIO

REACTION	E+Q(MeV)	REACTION	E+Qp(MeV)	$\sigma(n,t)/\sigma(n,p)$ MEASURED	$\sigma(n,t)/\sigma(n,p)$ CALCULATED†
$^{40}Ca(n,t)^{38}K$	1.45	$^{40}Ca(n,p)^{40}K$	14.07	3.40×10^{-5}	1.03×10^{-6}
$^{54}Fe(n,t)^{52}Mn$	1.59	$^{54}Fe(n,p)^{54}Mn$	14.68	3.94×10^{-7}	2.93×10^{-8}
$^{86}Sr(n,t)^{84}Rb$	3.86	$^{86}Sr(n,p)^{86}Rb$	15.5	1.5×10^{-3}	3.05×10^{-6}
$^{106}Cd(n,t)^{104}Ag$	5.72	$^{106}Cd(n,p)^{106}Ag$	15.19	1.66×10^{-4}	4.78×10^{-6}
$^{112}Sn(n,t)^{110}In$	5.49	$^{112}Sn(n,p)^{112}In$	14.72	2.35×10^{-3}	2.68×10^{-6}
$^{114}Cd(n,t)^{112}Ag$	8.28	$^{114}Cd(n,p)^{114}Ag$	10.77	1.2×10^{-2}	0.179
$^{205}Tl(n,t)^{203}Hg$	9.66	$^{205}Tl(n,p)^{205}Hg$	13.6	1.1×10^{-2}	5.92×10^{-4}

†All values are obtained from Equation (6).

Acknowledgements

We would like to express our appreciation to the Robert A. Welch Foundation for financial support of this work.

References

1. D. H. Wilkinson, Phil. Mag. 4, 215 (1959).
2. S. M. Qaim and G. L. Stocklin, Nucl. Phys. A257, 233 (1976).
3. V. N. Leokovski, JEPT (Sov. Phys.) 18, 213 (1964).
4. V. N. Levkovski, Sov. J. Nucl. Phys. 18, 361 (1974).
5. T. W. Woo and G. N. Salaita, ANS Trans. 28, 91 (1978).
6. G. Brown and H. Muirhead, Phil. Mag. 2, 473 (1957).
7. J. Csikai, K. Jost and A. Szalay, Acta Phys. Acad. Sci. Hung. 24, 199 (1968).
8. A. E. Green, Nucl. Phys. (McGraw-Hill Book Co., New York, 1955, p. 250).
9. M. M. Shapiro, Phys. Rev. 90, 171 (1953).
10. K. Kikuchi, Progr. Theor. Phys. 17, 643 (1957).
11. D. Bodansky, Ann. Rev. Nucl. Sci. 12, 79 (1962).
12. M. El-Nadi and M. Wofik, Nucl. Phys. 9, 22 (1958).
13. S. M. Qaim and G. L. Stocklin, J. Inorg. Nucl. Chem. 35, 19 (1973).
14. A. P. Baerg and G. C. Bowes, Can. J. Chem. 39, 684 (1961).
15. E. Weigold and R. N. Glover, Nucl. Phys. 32, 106 (1962).
16. M. Bormann, F. Dreyer, H. Neuert, I. Rishle and U. Zielinsky, Nuclear Data for Reactors, Vol. I, p. 225, IAEA, Vienna (1967).
17. P. N. Tiwari and E. Kondaiah, Phys. Rev. 167, 1091 (1968).
18. D. M. Chittenden, II, D. G. Gardener and R. W. Fink, Phys. Rev. 122, 860 (1961).
19. S. M. Qaim and R. Wolfle, Nucl. Phys. A295, 150 (1978).

KEV NEUTRON CAPTURE CROSS SECTIONS FOR THE S-PROCESS ISOTOPES OF SE, BR AND KR AND THE ABUNDANCE OF KRYPTON IN THE SOLAR SYSTEM

B. Leugers and F. Käppeler
Kernforschungszentrum Karlsruhe GmbH
Institut für Angewandte Kernphysik
P.O.B. 3640, D-7500 Karlsruhe
Federal Republic of Germany

F. Fabbri and G. Reffo
CNEN, Centro di Calcolo
Bologna, Italy

The neutron capture cross sections of natural Kr, ^{84}Kr and three samples enriched in ^{83}Kr ^{82}Kr and ^{80}Kr were measured with the time-of-flight technique in the energy range between 3 and 250 keV. The energy resolution was 1.5 ns/m. Capture gamma rays were detected by two C_6D_6 detectors using the pulse height weighting technique off-line. From these data, Maxwellian averaged cross sections $\langle\sigma v\rangle/v_T$ have been determined for all stable Kr isotopes with an accuracy of typically 10 %, except for ^{78}Kr and ^{86}Kr, where the uncertainties are 30 % and 100 %, respectively. In addition, the cross sections for all s-process isotopes of Se, Br and Kr were calculated with a Hauser Feshbach formalism with width fluctuation corrections, using carefully evaluated level densities and radiative decay widths. In the calculations all available experimental information about these cross sections was considered to include the local behavior of parameters. With this improved set of cross sections, the solar system abundance of Kr was determined from s-process systematics.

Se(n,γ), Br(n,γ), Kr(n,γ), neutron capture cross sections, 3-250 keV, s-process systematics, solar Kr abundance.

Introduction

For many isotopes there is a parallel interest in keV neutron capture cross sections from reactor physics and nuclear astrophysics as well. While the impact of neutron capture on the neutron economy of reactors is evident, its importance to astrophysics has been emphasized e.g. by Clayton[1] or by Allen et al.[2] Most of the elements heavier than Fe were predominantly synthesized by neutron capture reactions and from the observed abundances one can distinguish two synthesizing processes, one of which is characterized by neutron capture events on a slow time scale (s-process). As stars are assumed to be the site of the s-process the corresponding neutron energy distribution follows a Maxwellian distribution for thermal energies around 30 keV. Hence, it is necessary to know the differential cross sections between ∿1 and 200 keV for the determination of effective, average cross sections $\langle\sigma v\rangle/v_T$.

The mass region around krypton is especially interesting for an analysis of the s-process. For the radioactive isotopes ^{79}Se and ^{85}Kr the competition between β^--decay and neutron capture leads to a branching of the synthesis path which is determined by the neutron flux, the temperature and the respective cross sections. If the cross sections are known the other parameters can be evaluated using common s-process synthesis models. Moreover, and this point

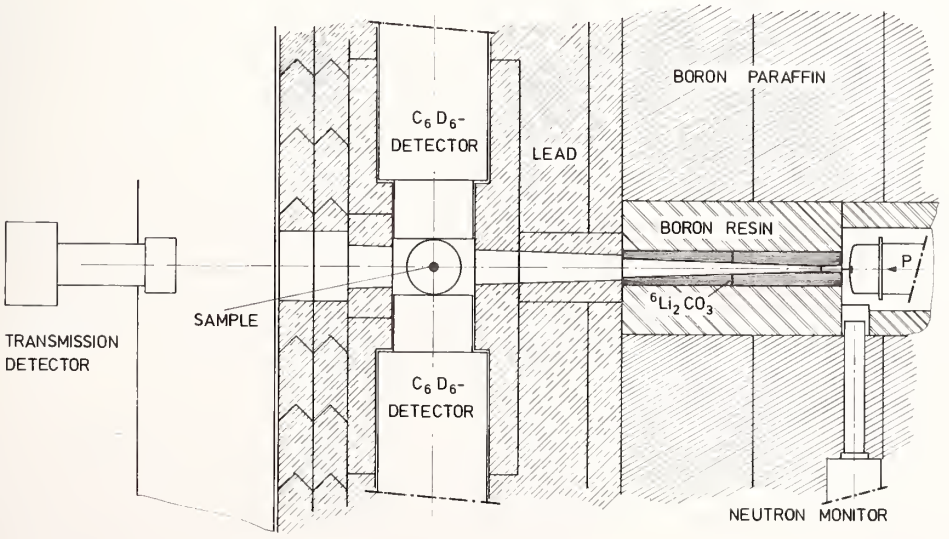

Fig. 1. Schematic view of the experimental set-up for neutron capture cross section measurements in the keV-region.

will be outlined here, the solar krypton abundance can be determined from s-process systematics via the pure s-process isotope ^{82}Kr. For reactor physics krypton may be of interest as a tag gas to identify failed fuel elements. For that reason Maguire et al.[3] have investigated the neutron capture and the total cross sections of natural krypton and of a sample enriched in ^{78,80}Kr up to neutron energies of 4 keV. Beside the work of Maguire et al. no experimental information on fast neutron cross sections was available for krypton so far. We have measured the capture cross sections for natural krypton, ^{84}Kr and three mixtures enriched in ^{83} Kr, ^{82}Kr and ^{80}Kr. In addition, the capture cross sections of all Se, Br and Kr isotopes relevant to the s-process were calculated.

Experiment

The measurements were carried out at the Karlsruhe 3 MV Van de Graaff accelerator with the experimental setup shown in Fig. 1. Neutrons were produced via the ^{7}Li(p,n) reaction using a pulsed proton beam of 500 ps pulse width, 1 MHz repetition rate and 5 µA average current. A continuous neutron energy spectrum from ∿2 to 250 keV was obtained by bombarding sufficiently thick metallic Li-targets with protons of 2.03 MeV energy. Neutron energies were determined by the time-of-flight (TOF)technique with a resolution of 1.5 ns/m. This corresponds to a resolution of 200 eV at 30 keV neutron energy.

As the distance between neutron target and sample was only 61 cm, effective collimation and shielding of the neutron target was essential to keep backgrounds at a manageable level. The double tapered collimator consists of $^{6}LiCO_3$ pressed to 85 % of its crystal density. The main neutron shield is made of boron loaded resin whereas in the outer parts boron paraffin is used. For suppression of gamma radiation from the collimator or from the room, the detectors are surrounded by a 20 cm thick shield of antimony free lead.

The prompt capture gamma rays were registered by two C_6D_6 liquid scintillation counters of 1 l volume. All events were recorded in a two dimensional array of 1024 TOF and 16 pulse height channels for off-line application of the weighting technique. Coincident events in both detectors were stored in a separate TOF-spectrum. This was of twofold interest: - It provides a measure for the probability that two gamma rays of a single cascade are recorded in the same detector. Therefore too large a weight would be attributed to such events. - Furtheron, the coincidence rate provides information on the average multiplicity of the cascade, an additional valuable information about the capture process.

A difficult problem was the design of a suited sample canning. The best solution we found was a sphere of stainless steel with 0.5 mm wall thickness and 2 cm diameter which could withstand gas pressures up to 500 atm. The highest gas pressure during the experiment was 280 atm. All cross sections were measured relative to ^{197}Au as a standard. Three gas filled spheres, an empty sphere for background correction, an additional canning with a graphite sphere inside to correct for the neutron sensitivity of the system and a sphere with a 1 mm thick gold disk were mounted on a sample changer perpendicular to the plane of Fig. 1. The samples were changed cyclically in intervals defined by the neutron flux monitor.

Typical TOF spectra are shown in Fig. 2. As can be seen the spectrum b) for the empty sphere exhibits

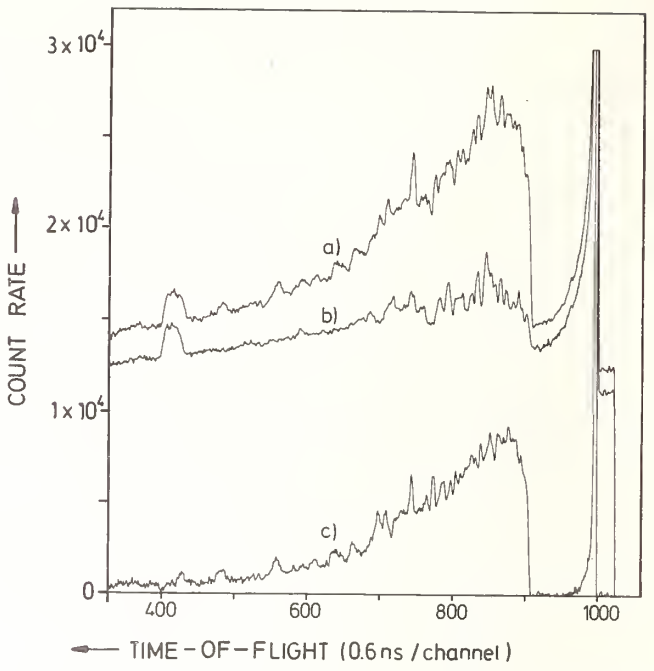

Fig.2. Typical TOF-spectra for illustration of backgrounds,
a) sphere with natural krypton, b) empty sphere,
c) natural krypton after subtraction of spectrum b) and a remaining, time-independent background.

a variety of resonances. In order to avoid systematic uncertainties, this type of background is best be subtracted before the pulse height weighting function is applied. The peaks in spectra a) and b) near channel 400 are correlated with the accelerator pulses and therefore subtract out completely.

The resulting cross section for natural krypton is shown in Fig. 3. The error bars on the data points represent the statistical uncertainties which vary smoothly from 20 % at 10 keV to 3 % at 200 keV neutron energy. The overall systematic uncertainty amounts to ∿5 %. From a comparison with the cross sections of the other samples it is found that most of the resonances observed in natural krypton can be attributed to ^{84}Kr.

The experimental cross sections were averaged over the expected stellar neutron spectrum which corresponds to a Maxwell distribution for kT = 30 keV, 99.5 % of which lies within the neutron energy range of this experiment. The Mawellian averaged cross sections for the various samples together with the isotopic compositions define a system of linear equations which can be solved to derive the Maxwellian averages of all stable krypton isotopes. Unfortunately, the cross section of ^{78}Kr turned out to be rather high which complicates the procedure as this isotope contributes only to one mixture at a significant level. Nevertheless, with meaningful limits on the ^{78}Kr cross section it will be possible to deduce a best set of Maxwellian average cross sections for all stable Kr isotopes. As an example, the preliminary value for ^{82}Kr is included in Table I.

Theoretical Calculations

Parallel to the experimental effort, theoretical calculations of capture cross sections of all s-process isotopes of Se, Br and Kr have been carried out to provide a data basis for systematic s-process studies. The relevant range spans from 1 keV to 400 keV. As no valence capture can be expected in this mass region[4]

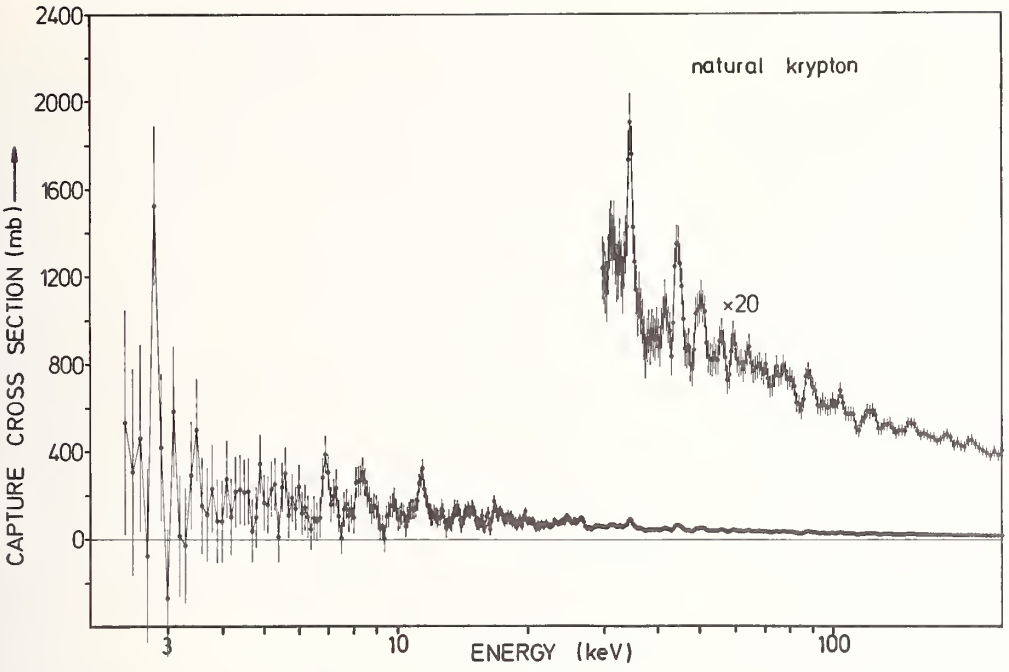

Fig. 3. The neutron capture cross section of natural krypton between 3 and 250 keV

a reaction mechanism was used which considers only capture via compound nucleus formation. The usual Hauser-Feshbach statistical model formalism with width fluctuation correction was used as applied in Refs.[5,6]. We will not discuss here the model adopted, but wish instead to point out the particular care which was devoted to the determination of the parameters required by the model itself. This is important because it has been shown earlier[7] that the accuracy of the calculated cross sections depend most on the reliability of the relevant model parameters.

In view of this extensive use was made of the systematics of the involved parameters as illustrated in Ref. [7] This systematics were specialized as far as possible to the local behavior of parameters, as it results from the neighboring isotopes. Accordingly, an extensive analysis of all experimental information on the Se, Kr, and Br isotopes was carried out.

As shown in Ref. [7] in the energy region relevant to the present discussion one can retain that in first approximation capture cross sections are proportional to the ratio of the radiative decay widths $\Gamma_\gamma(E,J,\Pi)$ to the mean level spacing $D(E,J,\Pi)$. Therefore our attention was concentrated on the best determination of those parameters.

Level density. As indicated in Ref. [8] a phenomenological approach was adopted in order to describe low excitation level densities and a Fermi gas model was used at high energies. The level density parameter "a" appearing in the law valid at high energies was determined from the statistical analysis of resonance schemes whereever possible. The local systematic behavior of "a" vs. neutron number was then determined in order to interpolate "a" in those cases (all Kr isotopes) where no resonance schemes were available. Spin and parity distribution laws used at high energies are those predicted by the Fermi gas theory.[7] At low energies, the high energy spin distribution law was fitted to the low-lying level scheme spin distribution by means of the maximum likelihood method. Low-lying level parity distributions could not be studied according to Ref. [7] because in most cases the level schemes available were not sufficiently shared between the two parities.

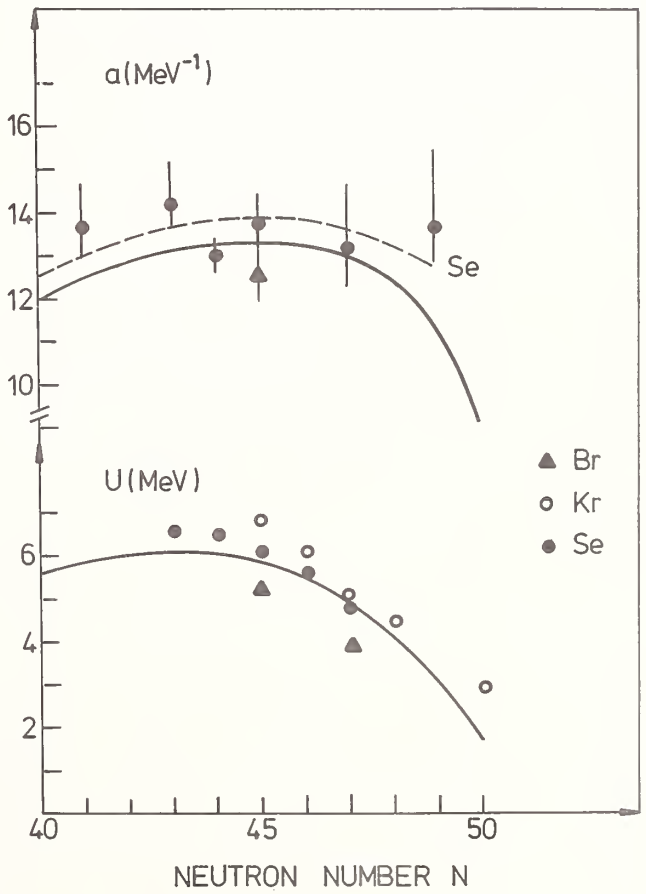

Fig. 4.(Above)The local behavior of the level density parameter a.
(Below)The systematic trend of the energy U where the two laws of the adopted composite level density are tangent. U completely determined the total density of levels and excitation energies below U.

Fig.4 shows the level density parameter "a" and the energy U, where the calculated level densities for low and high excitation energies were linked together.

Radiative decay widths. The radiative decay widths were calculated according to the suggestions by Brink-Axel as applied in Refs.[7,8]. Accordingly one guesses that at the excitation energies involved Γ_γ only depends on the already discussed low-lying level density and on giant resonance parameters (GRP). In particular it is proportional to the photoabsorption cross section at the peak of the dipole giant resonance. The GRP depend on the oblate or prolate character of nuclei and on the deformation parameter ß. They were determined in all cases from the GRP systematics mentioned in Refs.[7,9]. These criteria for the choice of best parameters allowed for an absolute determination of $\Gamma_\gamma(E,J,\pi)$ without any renormalization to experimental values which were only used to check the model predictions. In cases where no Γ_γ^{EXP} was available, the calculated values were checked with those interpolated from the Γ_γ-systematics of Refs .[9,10].

Optical model parameters. No special care was devoted to the choice of the optical model parameter set (OMP) because it affects the calculated neutron cross sections to a rather small extent (10-15 %) compared to the other parameters involved. Taking into account the energy range of interest we considered that our OMP set had to reproduce the experimental values of s- and p-wave strength functions S_0, S_1, the scattering radius R as well as the total and elastic cross sections. Of all the OMP sets available from literature, the one by Ref. [11] proved to be the most satisfactory.

In Table I the most important parameters adopted are given together with the calculated and experimental cross sections for the Kr-, Br-, and Se-isotopes.

The Krypton Abundance in the Solar System

With the Se, Br and Kr cross sections determined in this work it is now possible to calculate isotopic abundances created in the s-process with improved accuracy. Using the formalism given by Ward and Newman[13] the abundance N times the cross section $\langle\sigma\rangle$ which is a smoothly varying function of mass number and characteristic to the s-process can be written as

$$N\langle\sigma\rangle_A = G_1 \prod_{i=S}^{A} \left(1 + \frac{1}{\tau_{01}\langle\sigma\rangle_i}\right)^{-1} + G_2 \prod_{i=S}^{A} \left(1 + \frac{1}{\tau_{02}\langle\sigma\rangle_i}\right)^{-1} \qquad (1)$$

where $N\langle\sigma\rangle_A$ denotes the product for mass number A. $G_{1,2}$ is determined by the seed abundance and S means the atomic number of the seed. The product $N\langle\sigma\rangle$ is strongly determined by the cross section $\langle\sigma\rangle_i$ and by the constants $\tau_{01,2}$ which characterize the strength of the s-process neutron flux. The seed for the s-process are the isotopes of the iron abundance peak. It is found that the dominating abundance of ^{56}Fe allows to neglect contributions from other isotopes to a good approximation.

With that formalism the $N\langle\sigma\rangle$-curve as a function of mass number can be calculated if the involved cross sections $\langle\sigma\rangle_i$ are known. Taking the data set of Leugers[14] one obtains the $N\langle\sigma\rangle$ curve which is shown in Fig. 5. The criterion for a reasonable choice of the parameters for the neutron flux distribution is that the curve fits the empirical $N\langle\sigma\rangle$-values of those nuclei which are produced by the s-process exclusively, such as ^{58}Fe, ^{70}Ge, ^{76}Se and ^{96}Mo. Of course, also an overproduction of any nuclei must be avoided.

Table I. Adopted values for the level density parameter a, the matching energy U, and the spin cut off factor σ^2. In addition the values of radiative widths $\Gamma_\gamma^{CALC}(B_n,J,\pi)$ and for the lowest possible spin are compared to the corresponding experimental quantities taken from Ref.[12]. In the last two columns the experimental and calculated values of neutron capture cross sections averaged over a Maxwellian distribution for kT = 30 keV are given.

Compound Nucleus	a $(MeV)^{-1}$	U (MeV)	σ^2	Γ_γ^{CALC} (meV)	Γ_γ^{EXP} (meV)	cross sections for kT=30 keV: $\langle\sigma_{n,\gamma}^{CALC}\rangle$ (mb)	$\langle\sigma_{n,\gamma}^{EXP}\rangle$ (mb) this work (preliminary)	$\langle\sigma_{n,\gamma}^{EXP}\rangle$ (mb) literature
^{79}Kr	13.1	6.5	4.1	279	230	290		
^{81}Kr	13.25	6.8	4.25	300	290±30	233		
^{82}Kr	13.15	6.o	8.2	197	-	813		
^{83}Kr	13.00	5.1	5.0	196	230±50	99	105±15	
^{84}Kr	12.5	4.6	6.5	160	-	350		
^{85}Kr	11.4	3.6	4.7	236	215±60	30		
^{86}Kr	9.0	2.8	3.7	297	-	68		
^{77}Se	14.15	6.2	3.8	222	230±50	135		
^{79}Se	13.7	6.1	3.1	242	230±55	80		
^{80}Se	12.98	6.5	4.0	200	-	274		
^{81}Se	13.08	4.7	3.4	200	230±100	41		40
^{80}Br	13.25	6.8	3.9	310	315±50	672		815
^{82}Br	13.0	6.0	4.0	200	275±40	366		370

Beside the s-only nuclei mentioned above, also ^{82}Kr is synthesized completely by the s-process. In this case, where abundance determinations by chemical methods are very difficult and uncertain, the systematics of the $N\langle\sigma\rangle$-curve can be used to define the krypton abundance in the solar system. With $N\langle\sigma\rangle = 490$ (mb) from the calculated curve and $\langle\sigma\rangle = 105$ (mb) from Table I the abundance of ^{82}Kr results as $N_{^{82}Kr} = 4.67$, normalized to the silicon abundance $N_{Si} \equiv 10^6$. This result is accurate to about 20 %, mainly determined by the ^{81}Kr cross section. As the isotopic composition is practically constant in the solar system, the ^{82}Kr abundance yields immediately a total solar krypton abundance of $N_{Kr} = 40.3$. This value is 16 % lower than the value given by Cameron[15] which was determined simply by interpolation between isotopic abundances of neighboring elements..

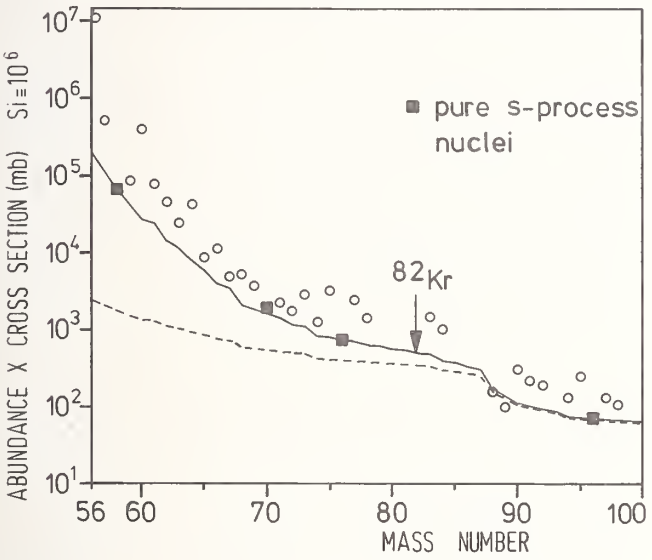

Fig. 5. The calculated $N\langle\sigma\rangle$curve vs. mass number compared to the empirical values. The arrow indicates the position of the s-only nucleus ^{82}Kr.

References

1. D.D. Clayton, in Proceedings of the 2nd Int. Conf. on Nuclear Data for Reactors, Helsinki, 1970, IAEA, Vienna, (1970) Vol. I, p. 35.

2. B.J. Allen, J.H. Gibbons, and R.L. Macklin, Advances in Nuclear Physics, Eds. M. Baranger, E. Vogt, Vol. 4 (1971) 205.

3. H.T. Maguire, Jr., H.M. Fisher and R.C. Block, in Proceedings of the Int. Conf. on Neutron Physics and Nuclear Data for Reactors and Other Applied Purposes, Harwell 1978, OECD Nuclear Energy Agency, p. 472.

4. B.J. Allen and A.R. de L. Musgrove: Advances in Nuclear Physcis, Plenum Press (1977).

5. H. Grupplaar, G. Reffo, Nucl. Sci. Eng. 62, 756 (1977).

6. G. Reffo, F. Fabbri, Nucl. Sci. Eng. 66, 251 (1978).

7. G. Reffo, CNEN Report RT/FI (78) 11 (1978) and IAEA Winter Courses on Nuclear Physics and Reactors, Trieste (February 1978).

8. V. Benzi, G. Reffo, M. Vaccari, IAEA-169 (1974) p. 123.

9. G. Reffo, INDC(NDS) 87 (1978).

10. V. Benzi, R. D'Orazi, G. Reffo, M. Vaccari, CNEN Report RT/FI (72) 6 (1972).

11. F. Perey, Phys. Rev. 131, 745 (1963).

12. S.F. Mughabghab and D.I. Garber; BNL 325, 3rd ed., Vol. 1 (1973).

13. R.A. Ward, M.J. Newman, D.D. Clayton, Astrophys. J. Supp. 31, 33 (1976).

14. B. Leugers, Thesis, University of Karlsruhe (1979).

15. A.G.W. Cameron, Proceedings of the Conf. on Explosive Nucleosynthesis, Austin, Texas (1973), Univ. of Texas Press, p. 3.

COMPLETE EVALUATION OF ^{241}Am BETWEEN THERMAL ENERGY AND 15 MeV-NUCLEAR MODELS USED-CONSISTENCY WITH INTEGRAL DATA

E. FORT, M. DARROUZET, H. DERRIEN, P. HAMMER, L. MARTIN-DEIDIER
C.E.N. CADARACHE - B.P. N°1
13115 - SAINT PAUL-LEZ-DURANCE - FRANCE

In this evaluation both integral and microscopic data are considered as reference data. Calculations are performed with SLBW formalism in the resolved resonance region and statistical formalism elsewhere. Neutron penetrabilities are obtained from coupled channel calculations, considering ^{241}Am as a symmetric rotationnal nucleus. For fission the agreement is excellent between evaluated and integral data and is confirmed by the most recent microscopic measurements. High values for capture cross-sections are supported by integral measurements.

[Microscopic data analysis, coupled channels, complete damping, integral data, consistency]

Justification of data needs

^{241}Am has a non negligible contribution to the breeding ratio and reactivity balance of fast breeders.[1] Neutron capture by this nucleus leads to ^{238}Pu formation with all the problems[2] correlated to α residual heat or neutron emission by spontaneous fission (^{242}Cm) or $^{16}O(\alpha,n)$ reaction.

Evaluation method

The first step consists of a critical analysis of microscopic experimental data in order to select the values on which the evaluation will be based. The calculations are performed by adjusting only the parameters considered as unknown or known with poor accuracy, within the limits allowed by the systematics. In other words, the parameters are chosen so as to preserve the consistency between all the energy ranges. An other consistency is searched by comparing averaged evaluated data with averaged cross sections measured in critical facilities or power reactors having various neutron spectra. These integral experiments are critically analyzed.

An ideal situation occurs when microscopic and integral data agree. In some extent it is the case for ^{241}Am.

Formalism-Evaluation results

Thermal and resolved resonance region

In this energy range the work was already presented.[3] We will report here only the main conclusions. After examination of all available data [WESTON'S[4] (Oak-Ridge absorption), KALEBIN'S et al[5] (Melekess transmission), and DERRIEN and LUCAS[6] (Saclay transmission + fission)], the parameters given by DERRIEN and LUCAS were chosen because they result from better experimental conditions and are extended to higher energy. On the other hand, they permit a good representation of the Saclay's total and Oak-Ridge's absorption cross sections. In the resolved resonance region, cross sections have to be calculated using SLBW formalism. In the thermal region a good representation is obtained by the use of a negative energy resonance and for capture by the addition of a 1/v background as recommended by WESTON[4] with the following results at 0.0253 ev :

$$\sigma_{n,n} = 9.10b,\ \sigma_{n,\gamma} = 579b,\ \sigma_{n,f} = 3.16b$$

Unresolved resonance region (E < 40 KeV) - Averaged parameters

The averaged parameters are of importance for the calculations (statistical formalism) in this energy range and for parametrization of the optical model to be used at higher energy.

Great care was taken for average spacing ($D^{l=0}$) determination which was obtained by MONTE-CARLO sampling[6] and maximum of likelihood method applied to reduced neutron width distribution. These two methods gave very close results. For "s" wave, averaged parameters were extracted from resolved resonance parameters. For "p" waves they have been obtained by fitting capture cross section below ($S^{l=1}$) and above 40 KeV ($\Gamma_\gamma^{l=1}$). For the radiative width we obtain $\Gamma_\gamma^{l=1} \simeq 2\ \Gamma_\gamma^{l=0}$ in qualitative agreement with calculations where the difference according to the parity of low lying level densities in ^{242}Am is taken into account.

The averaged parameters are as follows :

$D^{l=0} = (0.55\pm0.05)ev$, $S_0 = (0.94\pm0.09)10^{-4}$,

$S_1 = (2.43\pm0.4)10^{-4}$, $\langle\Gamma_\gamma^{l=0}\rangle = (43.8\pm0.7)meV$,

$\Gamma_\gamma^{l=1} = (85\pm7)meV$, $\langle\Gamma_f\rangle = (0.24\pm0.05)meV$

Statistical and continum region E > 40 KeV

Experimental data. There are data for total, capture or absorption and fission cross sections.

Total cross section : The only existing data are those recently published by PHILIPPS and HOWE[7] and obtained in good experimental condition. They are a necessary basis for evaluation purpose (see figure 1).

Capture or absorption cross section : Obtained by different technics the values given by WISSHAK et al (capture)[8,9] and by GAYTHER and THOMAS[10] (absorption) are in fairly good agreement and were selected as reference data for the evaluation. WESTON'S and TODD'S data are lower by 10-20% (see figure 2).

Fission cross section : There are numerous data, especially between 1 KeV and 5 MeV. They show large spread below 300 KeV. Above the same energy we have the same conclusions as B.H. PATRICK[11].

Our fitting procedure was based on mean values which are represented by those of KNITTER and BUDTZ-JORGENSEN[12] (see figure 3). Above 5 MeV there are essentially the data of BEHRENS and BROWNE[13] and some data at 14 MeV including the must recent data of CANCE et al[14] at 14.6 MeV.

Evaluated data. A recent version of the statistical code FISINGA was used[23]. For a reaction (n,x) induced by neutrons, the cross section is written as follows :

$$\sigma_{nx} = \pi\lambda^2 \sum_{J,L,L'} g_J \frac{T_n^{J,L}\, T_x^{J,L'}}{\sum_{J'',L''} T^{J'',L''}}\, S_{n,x}^{J,\pi} \qquad (1)$$

In this expression the quantities T and S stand respectively for penetrabilities and width fluctuation correction factors. J,L (and similar superscripts) are compound nucleus spin and orbital momentum.

For neutron channels, the penetrabilities are extracted from generalyzed penetrabilities $T^{L,J,j}$ calculated with the coupled channels code ECIS[15] by the mean of the simple relationship :

$$T^{L,J} = \frac{(L+1)\ T^{L,J,j^+=L+s} + L\ T^{L,J,j^-=L-s}}{2L+1} \qquad (2)$$

^{241}Am was treated as a symmetric rotationnal nucleus and only the three first states of the fundamental rotationnal band were coupled.

The parametrization was chosen so as to reproduce PHILIPPS and HOWE data for total cross section and the values determined for S^0, S^1 and scattering radius.

The potential depths are very close to what LAGRANGE[16] proposes for odd Plutonium isotopes. Deformation parameters determination was inspired from MOLLER'S et al[17] recommendations.

The penetrabilities for gamma channels are written as follows :

$$T_\gamma^{J,\pi}(E) = 2\pi \frac{\Gamma_\gamma^{J,\pi}(E=0)}{D^{J,\pi}(E=0)} \times \frac{\int_E^{B_n+E} \rho^{J,\pi}(\varepsilon)\, \phi^I(B_n+E-\varepsilon)\, d\varepsilon}{\int_0^{B_n} \rho^{J,\pi}(\varepsilon)\, \phi^I(B_n+E-\varepsilon)\, d\varepsilon} \qquad (3)$$

where ϕ is the Brink-Axel type profile function.

^{241}Am is generally believed to have a double humped fission barrier, the outer barrier being well below the inner one.

Since, no experimental data (except those questionnably obtained by bombshot) do show intermediate structure it is reasonnably allowed to assume a complete damping for the coupling between class I and class II states. If the two barriers are labelled A and B, total fission penetrabilities are, according to LYNN[18] :

$$T^{J,\pi} = \frac{T_A^{J,\pi} \times T_B^{J\pi}}{T_A^{J,\pi} + T_B^{J,\pi}} \qquad (4)$$

with :

$$T_{AorB}^{J,\pi} = \sum_i T_{i\ AorB} + \int_{E_{cf}}^{\infty} \rho_{F\ AorB}^{J,\pi}(\varepsilon)\, T_f^0(E+B_n-\varepsilon)\, d\varepsilon \qquad (5)$$

The sum represente the contribution from discrete fission channels and the integral the one from continuum.

In these expressions, T_f^0 is the tunnelling probability through the fundamental barrier, while $\rho^{J,\pi}$ is the fission channel density for given spin J and parity π at deformations corresponding to barrier A or B. $\rho^{J,\pi}$ has the following expression :

$$\rho^{J,\pi}(E^*) = C_1 C(J)\, e^{E^*/\Theta} \quad \text{for } E^* \leq B_n, \qquad (6)$$

$$\rho^{J,\pi}(E^*) = C_2 C(J)\, \frac{e^{2\sqrt{af(E^*-\Delta)}}}{(E^*-\Delta)^{3/2}} \quad \text{for } E^* > B_n, \qquad (7)$$

where $C(J) = (2J+1)\, e^{-(J+1/2)^2/2\sigma^2}$

and $af = a_c\left(1 + \frac{K}{E^*+\Delta}\right)$

The constants in expression (6) come from LYNN'S work[18]

The calculated values reproduce well KNITTER'S and BUTZ-JORGENSEN'S data from 300 KeV to 5.5 MeV. They agree well with averaged values in the resolved resonance region. In the intermediate energy range, they are lower than all experimental data except the recent one from HAGE et al[19] (see figure 4).

Above 6 MeV the formalism of the code SI2N[24] used to calculate (n,2n), (n,3n) and (n,2nf), (n,3nf) cross sections is similar to the one described in reference[22]. Unfortunately there are only data for total fission cross section.

The calculated values for fission probabilities of ^{240}Am and ^{239}Am should be compared to experimental values if available. The parameters used in calculations are listed in Table I.

Table I. Parameters values used in calculations

Optical model - Code ECIS

V_r	= 47.0	- 0.3 E_{MeV}	
W_D	= 2.7	+ 0.4 E_{MeV}	E < 10 MeV
	= 6.7	MeV	E > 10 MeV
$V_{S.O.}$	= 7.5	MeV	
β_2	= 0.22		
β_4	= 0.036		

Statistical model - Code FISINGA

Compound nucleus A+1

$D^{l=0}$ = 0.55 ev a = 27.8 MeV^{-1} σ^2 = 42.9

$\Gamma_\gamma^{l=0}$ = 43.8 meV $\Gamma_\gamma^{l=1}$ = 85 meV

S_0 = $0.91.10^{-4}$ S_1 = $2.43.10^{-4}$

V_A = 6.22 MeV $\hbar\omega_A$ = 0.65 MeV

V_B = 5.61 MeV $\hbar\omega_B$ = 0.45 MeV

Target nucleus A Code SI2N

$D^{l=0}$ = 0.372 ev a = 26.8 MeV^{-1} σ^2 = 42.9

$\Gamma_\gamma^{l=0} = \Gamma_\gamma^{l=1}$ = 65 meV

S_0 = $0.92.10^{-4}$

V_A = 6.2 MeV $\hbar\omega_A$ = 0.8 MeV

V_B = 5.7 MeV $\hbar\omega_B$ = 0.52 MeV

Nucleus A-1 Code SI2N

$D^{l=0}$ = 0.366 ev a = 27.2 MeV σ^2 = 43.56

$\Gamma_\gamma^{l=0} = \Gamma_\gamma^{l=1}$ = 53 meV

S_0 = $0.92.10^{-4}$

V_A = 6.5 MeV $\hbar\omega_A$ = 0.65 MeV

V_B = 5.4 MeV $\hbar\omega_B$ = 0.45 MeV

Integral data

Both fission and capture cross sections were determined by integral experiments.

^{241}Am fission was measured relatively to ^{235}U fission by using small fission chambers (ϕ = 12.7 mm) calibrated by α spectrometry. The experiments were carried out in critical facilities (MASURCA, ERMINE) fueled either with Uranium (R3, RONA 3) or Plutonium [ZONA 1, OP40 (k_∞=1) OP50 (k_∞=1)][20]. The enrichments of these media cover the whole range of the french

type fast breeders.

The accuracies on $\frac{^{241}Am\ \sigma_f}{^{235}U\ \sigma_f}$ values are ± 2.5% (1σ)

The experiments performed in OSIRIS, RAPSODIE and PHENIX to measure capture cross section were of irradiation type[21]. Neutron capture by ^{241}Am leads to ^{242m}Am, ^{242}Pu, ^{242}Cm and ^{238}Pu formation.

The ratio Cm/Pu, Am/Pu were measured respectively by α spectrometry and double isotopic dilution.

Isotopic contents of Pu, Am and Cm were determined by mass spectrometry after chemical separation.

The capture rate of ^{241}Am samples were normalized to those of ^{238}U samples irradiated in same conditions.

The accuracies on $\frac{^{241}Am\ \sigma_c}{^{238}U\ \sigma_c}$ values are ± 5% (1σ)

Consistency between evaluated and integral data

It is interesting to note that the integral experiments give internally consistent results (see table II). The energy interval of main sensitivity, as obtained from cell calculations in fundamental mode, is located between 9 KeV and 1.35 MeV.

TABLE II. Integral data compared to calculated values

For $\langle\sigma_f\rangle(^{241}Am)/\langle\sigma_f\rangle(^{235}U)$		For $\langle\sigma_c\rangle(^{241}Am)/\langle\sigma_c\rangle(^{238}U)$	
Integral experiments	$\frac{E - C}{C}$ (%)	Integral experiments	$\frac{E - C}{C}$ (%)
OP40	- 2 ± 3	RAPSODIE	+ 12% ± 8
OP50	- 1 ± 3	OSIRIS	+ 8 ± 8
RONA 3	- 1 ± 3	PHENIX	+ 9 ± 5
R3	- 5 ± 3		
ZONA 3	- 10 ± 3		
ZONA 1	- 1 ± 3		

For fission the experiments are numerous enough so that their informations can be considered as significant. In particular, in the energy range between 9 KeV and 40 KeV for which the contribution to total fission rate is about 20% they support evaluated data, i.e. low values.

For this energy region they give helpfull informations to solve the discrepancy between microscopic data, a discrepancy which is very difficult to solve on the basis of microscopic experimental technic arguments only.

For capture, since there are too few experiments, the presently available integral results can provide only a global tendency. In any case they confirm the data of WISSHAK and GAYTHER with an high degree of validity since there are about 65% of the total neutron number in the energy region of interest.

Conclusion

In an evaluation work, we consider that integral data (averaged cross section) should be treated on the same footing as microscopic data. With respect with this opinion the evaluation we present is satisfactory. For the future the improvements would concern mainly the energy region above 6 MeV for which there is a lack of microscopic data.

References

1. P. Hammer, Proceedings of an International Conference, p. 551, Harwell, September 1978.
2. L. Costa, private communication.
3. H. Derrien, E. Fort and D. Lafond, Proceedings of a specialist's meeting on nuclear data of Plutonium and Americium isotopes for reactor applications, Brookhaven National Laboratory, Nov. 20-21 1978.
4. L.W. Weston and J.H. Todd, Nuclear Science and Engineering 61, 356 (1976).
5. S.M. Kalebin et al, UDC 621-039-556, Translated from AF Vol. 40, N°4, p. 303 (1976).
6. H. Derrien and Lucas, Proceedings Conference Nuclear cross section and Technology, Vol. 2, p. 637, NBS special publication 425, Washington D.C. (1975).
7. T.W. Phillips, R.E. Howe, UCRL - 81176 (1978).
8. K. Wisshak, F. Kappeler and W. Hage, Proceedings of a specialist's meeting on the nuclear data of higher Plutonium and Americium isotopes for reactor applications, Brookhaven, Nov. 20-21 1978.
9. K. Wisshak, F. Kappeler and W. Hage, Proceedings Int. Conf. on neutron physics and nuclear data for reactors and other applied purposes, Harwell (September 1978), p. 893.
10. D.B. Gayther and B.W. Thomas, Proceedings of IV National Sov. Conf. on neutron physics (Kiev, 1977) Vol. 3.
11. B.H. Patrick, Proceedings of a specialist's meeting on nuclear data of Plutonium and Americium isotopes for reactor applications, Brookhaven National Laboratory, Nov. 20-21 1978.
12. H.M. Knitter and C. Budtz-Jorgensen, Proceedings Int. Conf. on neutron physics and nuclear data for reactors and applied purposes, Harwell (September 1978), p. 889.
13. J.W. Behrens and J.C. Browne, Lawrence Livermore report UCID-17324 (1976).
14. M. Cance, D. Gimat and G. Grenier, Neutron interlab Seminar, BRC 25-27 June 1979.
15. J. Raynal, Equations couplées et DWBA, Aussois (1968), Report Lycen-6804.
16. C. Lagrange, CEA-N-1970, NEANDC(E) 179 "L", INDC (FR) 16/L.
17. P. Möller, S.G. Nilson and J.R. Nix, Nuclear Physics A 229 (1974), 292.
18. J.E. Lynn, AERE - R 7468.

19. W. Hage, F. Käppeler and K. Wisshak, NEANDC(E) 202 U, Vol. V, p. 17.

20. M. Darrouzet and L. Martin-Deidier, CEA-N-2063

21. A. Giacometti, M. Darrouzet, P. Hammer, M. Lucas, F. Prost-Marechal and M. Robin, COlloque international sur la physique des réacteurs à neutrons rapides, Aix-en-Provence, Septembre 1979.

22. J. Jary, CEA-R-4647.

23. E. Fort, D. Lafond and F. Ribaud, The statistical code FISINGA, to be published.

24. E. Fort and J.P. Doat, The statistical code SI2N, unpublished.

FIG. 1

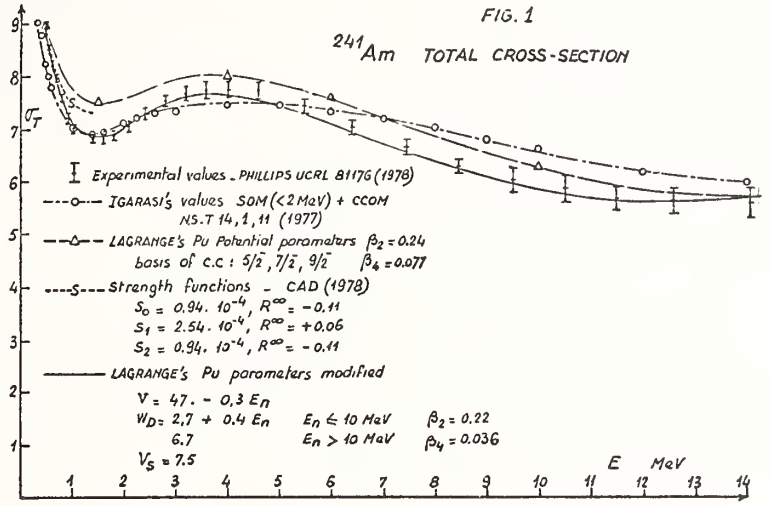

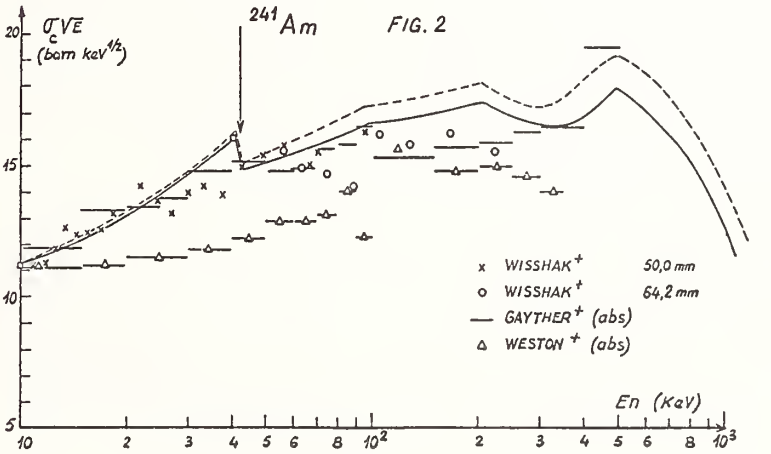

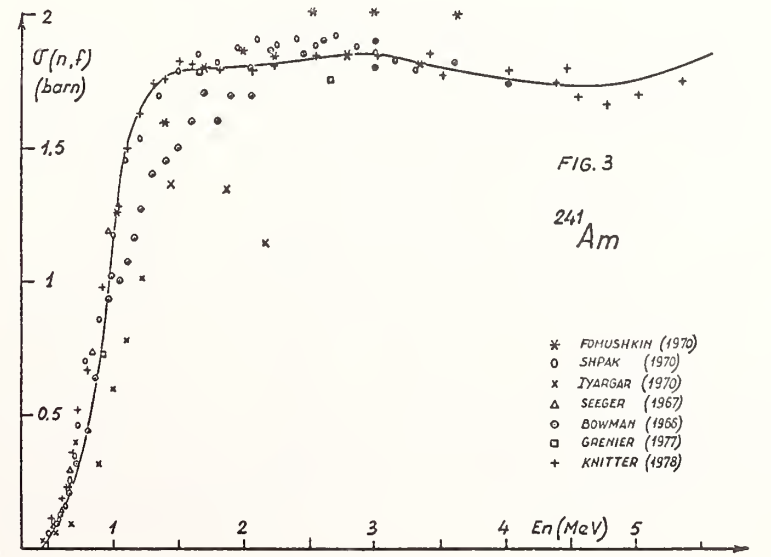

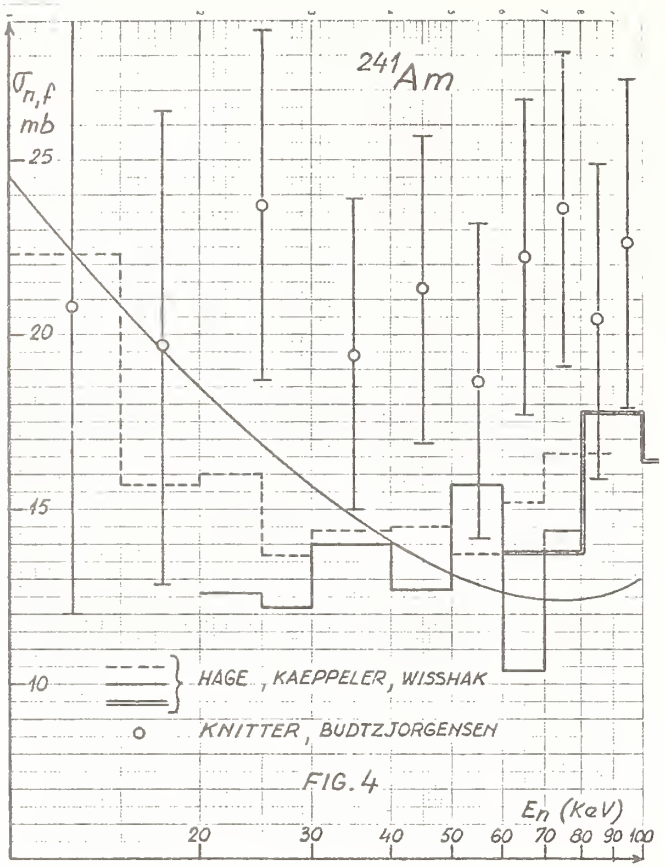
$\sigma_{n,f}$
mb
25
20
15
10
^{241}Am
HAGE , KAEPPELER, WISSHAK
KNITTER, BUDTZJORGENSEN
FIG. 4
E_n (KeV)
20 30 40 50 60 70 80 90 100

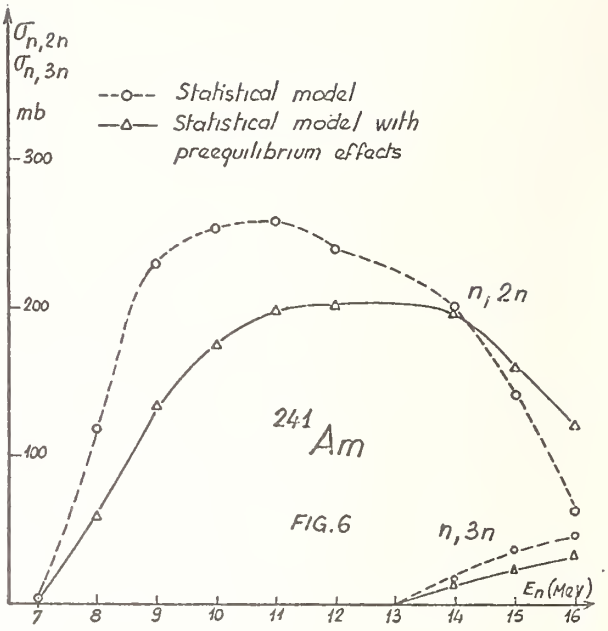
$\sigma_{n,2n}$
$\sigma_{n,3n}$
mb
300
200
100
--o-- Statistical model
—Δ— Statistical model with preequilibrium effects
n, 2n
^{241}Am
FIG.6
n, 3n
E_n(MeV)
7 8 9 10 11 12 13 14 15 16

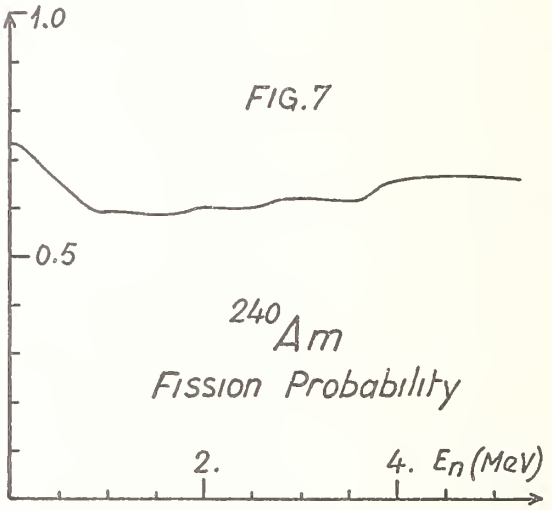
1.0
0.5
FIG.7
^{240}Am
Fission Probability
2.
4. E_n(MeV)

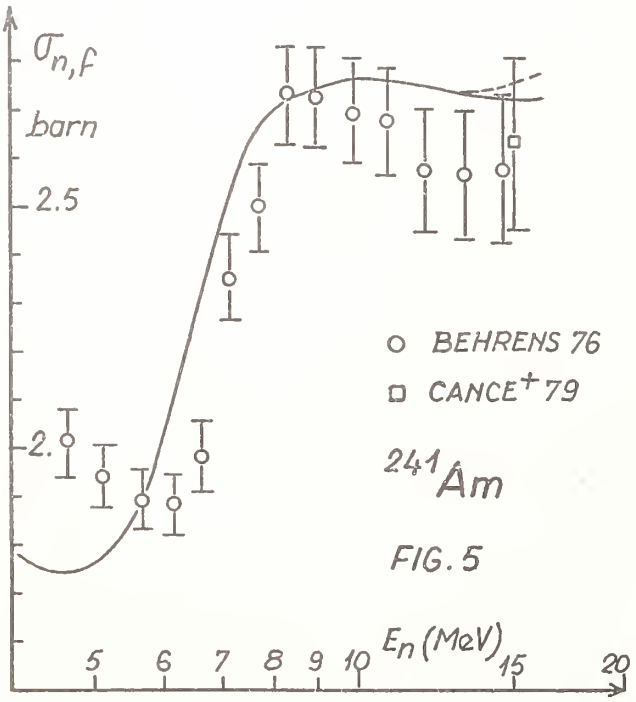
$\sigma_{n,f}$
barn
2.5
2.
BEHRENS 76
CANCE+79
^{241}Am
FIG. 5
E_n(MeV)
5 6 7 8 9 10 15 20

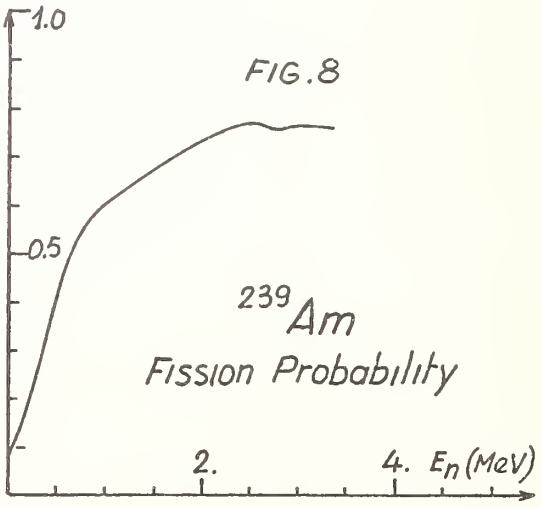
1.0
0.5
FIG.8
^{239}Am
Fission Probability
2.
4. E_n(MeV)

THE BRANCHING RATIO IN ^{242}Am FOLLOWING NEUTRON CAPTURE IN ^{241}Am

K. Wisshak, J. Wickenhauser, and F. Käppeler
Kernforschungszentrum Karlsruhe GmbH
Institut für Angewandte Kernphysik
Federal Republic of Germany

The branching ratio in ^{242}Am has been determined in a differential experiment at neutron energies of 14.75 meV and 30 keV. For that purpose, the total capture cross section has been determined with an accuracy of ∿5 % in the energy range 10-250 keV using kinematically collimated neutrons from the ^{7}Li(p,n) and T(p,n) reaction. The partial capture cross section to the ground state of ^{241}Am was measured by activation. At 14.75 meV monochromatic neutrons were obtained from a triple axis spectrometer at the FR2 reactor and at 30 keV quasi monoenergetic neutrons were produced by the ^{7}Li(p,n) reaction at proton energies 25 keV above threshold. The ^{2429}Am nuclei were detected via the electron spectrum emitted in the beta decay to ^{242}Cm. The electrons were separated in a mini orange spectrometer from the intense alpha-, gamma- and X-ray background of the ^{241}Am sample. Preliminary results show good agreement with existing integral measurements and theoretical calculations.

[^{241}Am(n,γ), capture cross section, 10 - 250 keV, isomeric ratio in ^{242}Am at 14.75 meV and 30 keV]

Introduction

Neutron capture in ^{241}Am populates two different levels in ^{242}Am, the ground state with a half-life of 16 h and an isomeric state with a half-life of 152 y. In the neutron flux of a reactor nuclei in the ground state will decay predominantly into ^{242}Cm whereas nuclei in the long lived isomeric state are mostly transmuted by fission or by a second capture event. The isomeric ratio (IR), defined as the relative population of the ground state to the total capture cross section is therefore of interest for build-up calculations. In particular it influences the amount of ^{242}Cm produced during burnup. This nucleus is of special importance for fuel handling and waste management because of the strong neutron radiation associated with its high spontaneous fission rate.

Until now only integral measurements have been performed to determine the isomeric ratio IR. At thermal energies several experiments have been carried out yielding a mean value of IR = 0.9 [1]. For fast neutrons IR = 0.84 has been obtained by Dovbenko et al.[2] at a mean neutron energy of ∿300 keV. Preliminary data of Koch et al.[3] indicate a similar result. In addition

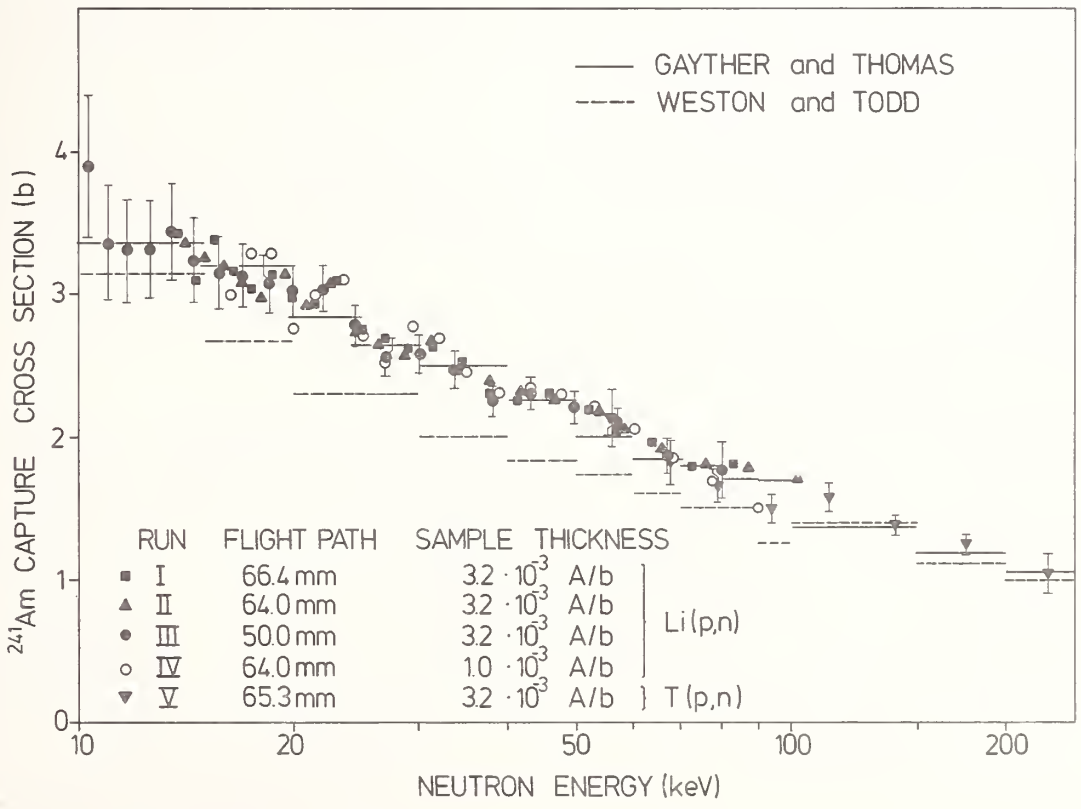

Fig. 1. The neutron capture cross section of ^{241}Am. The values given are obtained by multiplying the experimental ratios with the evaluated cross section of gold taken from ENDF/B-IV. A comparison is made to the data of the absorption cross section given in Refs.[10,11]. The error bars shown only for part of the data indicate the uncertainty of the measured ratio only.

there exist theoretical calculations by Mann and Schenter[4] who quote IR = 0.805 at 30 keV.

The aim of the present experiment is to determine IR in a differential measurement at thermal and fast energies. This has been achieved by the following experiments: The total capture cross section of ^{241}Am was measured by the same technique as applied recently for some plutonium isotopes[5,6]. Kinematically collimated neutrons were produced in the energy range from 10 to 250 keV using a pulsed Van de Graaff accelerator and the ^{7}Li(p,n) and T(p,n) reaction. The samples were positioned at a flight path of ∿6 cm and capture events were registered by a Moxon-Rae detector.

The partial capture cross section to the ground state of ^{242}Am has been determined by activating thin ^{241}Am samples in a flux of 14.75 meV and 30 keV neutrons. The ^{242g}Am nuclei produced are detected by observing the electrons from the beta decay to ^{242}Cm with a mini orange spectrometer[7,8]. The measurements are performed relative to gold which yields a beta spectrum with compatible endpoint energy.

Total Capture Cross Section

The experimental method to determine capture cross sections of highly radioactive actinide isotopes has been described already in Refs.[5,6]. Details of the measurement on ^{241}Am will be published[9]. The result for the total capture cross section of ^{241}Am is shown in Fig. 1. Four runs have been performed in the energy range from 10 to 100 keV using the ^{7}Li(p,n) reaction for neutron production. Data were recorded with two different samples at three flight paths. In the energy range from 50 to 250 keV one measurement has been carried out using the T(p,n) reaction for neutron production. The overall experimental uncertainties are 4-6 % for energies between 20 and 160 keV and increase to ∿10-14 % at lower and higher energies. In Fig. 1 a comparison is made to the data of the total absorption cross sections of Refs.[10,11].

Capture Cross Section to the Ground State

Measurements

To determine the capture cross section to the ground state a thin ^{241}Am sample (10 mm in diameter and ∿1 mg/cm^2 thick) and a gold sample were activated for about 16 h in a neutron flux at thermal and fast energies.

The thermal flux was provided by the FR2 Reactor at Karlsruhe. As the experimental method is very sensitive it was possible to perform the activation with monochromatic neutrons. A neutron intensity of ∿10^6 s^{-1} was obtained from a triple axis spectrometer at an energy of 14.75 meV. At that energy the total capture cross section has a well defined value and any contribution of epithermal neutrons captured in the strong resonances at 0.3 and 0.6 eV are avoided.

The fast flux was obtained from a 3 MV Van de Graaff accelerator using the ^{7}Li(p,n) reaction. The proton energy was adjusted 25 keV above the reaction threshold in order to get a kinematically collimated neutron beam. The opening angle of the neutron cone is 120° and the energy distribution has a mean value of 30 keV and a full width at half maximum of ∿20 keV. The samples were located at a distance of only 1 mm from the neutron target. A dc proton current of 60 µA produced a neutron intensity of ∿2 x 10^8 s^{-1} at the sample position. Activation in a kinematically collimated neutron beam offers the advantage that except the activated samples the neutrons hit no other materials within a distance of at least 1 meter. Consequently, any disturbance of the activation due to scattered neutrons with lower energies is avoided. The neutron beam intensity was monitored continuously during the activation in order to correct for possible fluctuations.

After the activation the decay of the ^{242g}Am nuclei was observed via the electrons emitted in beta-decay to ^{242}Cm. An experimental setup of relatively low expense for a selective detection of electrons in a high background of alpha-, gamma- and X-ray

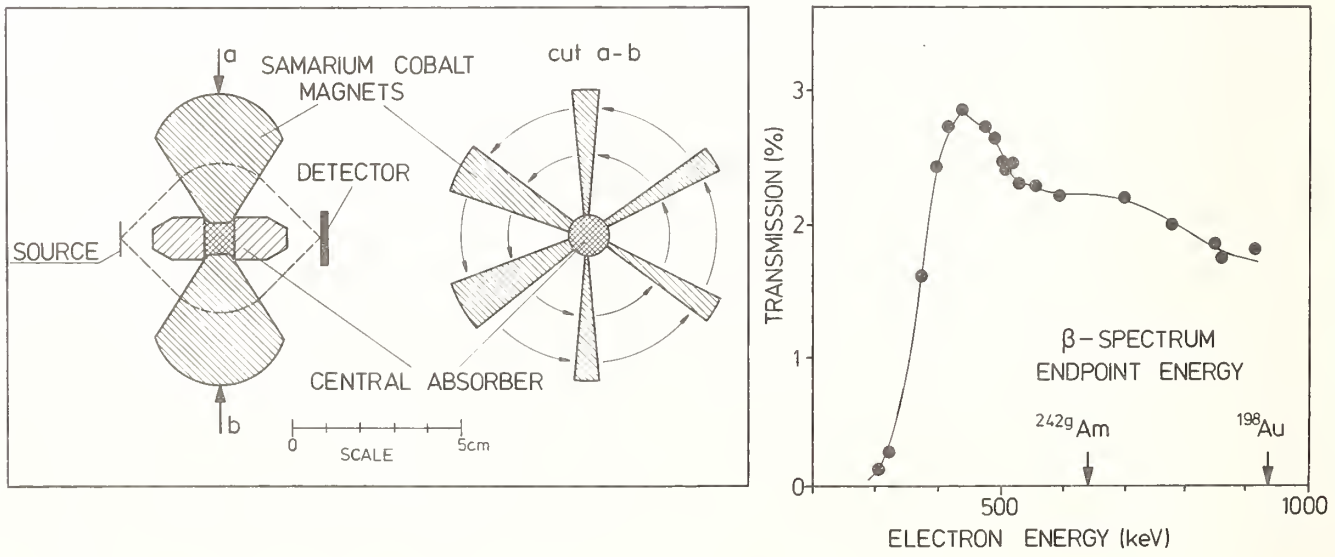

Fig. 2. Schematic setup of the mini orange spectrometer. The electron transmission of the system is given in the right part of the figure.

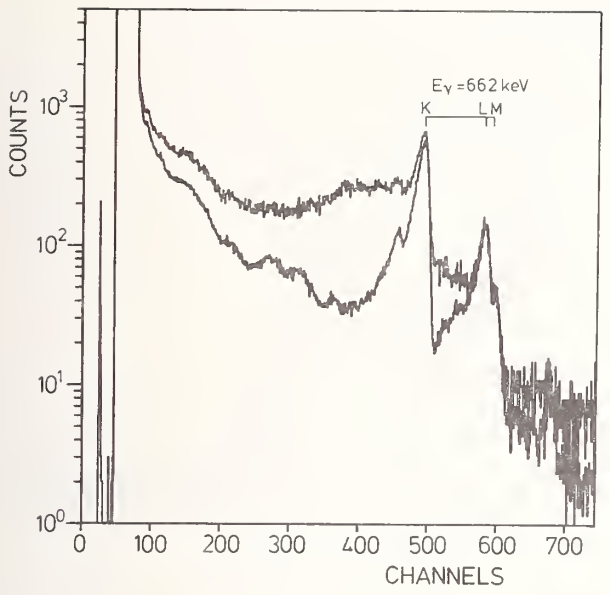

Fig. 3. Electron spectrum of the ^{241}Am sample before and after the activation with neutrons of 14.75 meV.

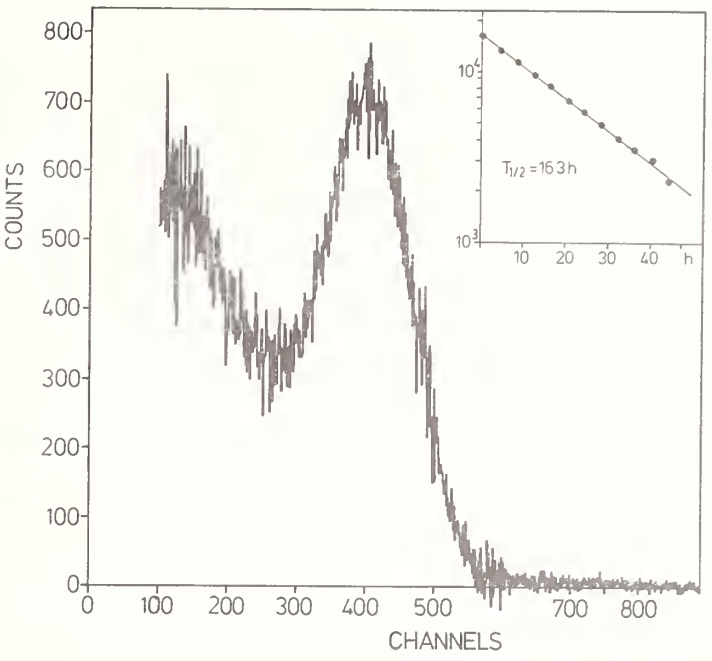

Fig. 4. Beta-spectrum of the decay $^{242g}Am \rightarrow {}^{242}Cm$ as measured with the mini orange spectrometer (activation with neutrons of 14.75 meV). The decrease of the measured intensity is given in the insert.

radiation is the mini orange spectrometer[7,8]. It is kind of an orange type beta-spectrometer the dimensions of which have been minimized by using small permanent magnets instead of coils for the production of a toroidal magnetic field. A schematic view of the spectrometer is shown in Fig. 2. A set of 6 wedge shaped samarium cobalt permanent magnets produces a toroidal field in the gaps.

In this field electrons emerging from the sample are bent around a central absorber towards a Si(Li) detector. The central absorber suppresses gamma radiation and absorbs X-rays and alpha-particles. The total diameter of the system is of the order of 10 cm. The special shape of the permanent magnets allow to taylor the transmission curve for electrons within a wide range so that a large part of the beta spectrum can be observed in a single measurement. The energy of the electrons is determined by the Si(Li) detector.

The total efficiency of the spectrometer which is shown in the right part of Fig. 2 is measured using conversion lines from a ^{206}Bi source. The efficiency amounts to 2-3 % for energies between 400 and 800 keV and decreases very sharply at low energies. In this way the upper part of the beta-spectrum which was used as an evidence for the capture events, is detected with high probability. On the other hand the low energetic conversion electrons from the decay of ^{241}Am are strongly suppressed and cannot lead to an overload of the detector. The endpoint energies in the decay of ^{242g}Am and ^{198}Au are also indicated in Fig. 2.

Fig. 3 shows electron spectra from an ^{241}Am sample measured with the mini orange spectrometer before and during the first four hours after the sample was activated with thermal neutrons. The background is dominated by the K, L and M conversion lines of the gamma transition of 622 keV in the

Table I. Preliminary results for the capture cross section to the ground state and for the isomeric ratio

Neutron Energy	Experimental results for the capture cross section to the ground state of ^{242}Am relative to gold	Adopted cross sections for the determination of IR	Capture cross section to the ground state of ^{242}Am	Isomeric ratio
30 keV	$R_{fast} = \frac{\sigma_{\gamma,\,^{242}Am}}{\sigma_{\gamma,Au}} = 3.42 \pm 0.24$	$\sigma_{\gamma,Am} = 2.48 \pm 0.12$ b $\sigma_{\gamma,Au} = 0.586 \pm 0.015$ b	$\sigma_{\gamma,\,^{242g}Am} = 2.00 \pm 0.15$ b	IR=0.81±0.07
14.75 meV	$R_{th} = \frac{\sigma_{\gamma,\,^{242g}Am}}{\sigma_{\gamma,Au}} = 5.88 \pm 0.41$	$\sigma_{\gamma,Am} = 818 \pm 26$ b $\sigma_{\gamma,Au} = 129 \pm 0.4$ b	$\sigma_{\gamma,\,^{242g}Am} = 758 \pm 53$ b	IR=0.93±0.07
	$C = \frac{R_{fast}}{R_{th}} = 0.515 \pm 0.015$			$\frac{IR_{fast}}{IR_{th}} = 0.77 \pm 0.05$

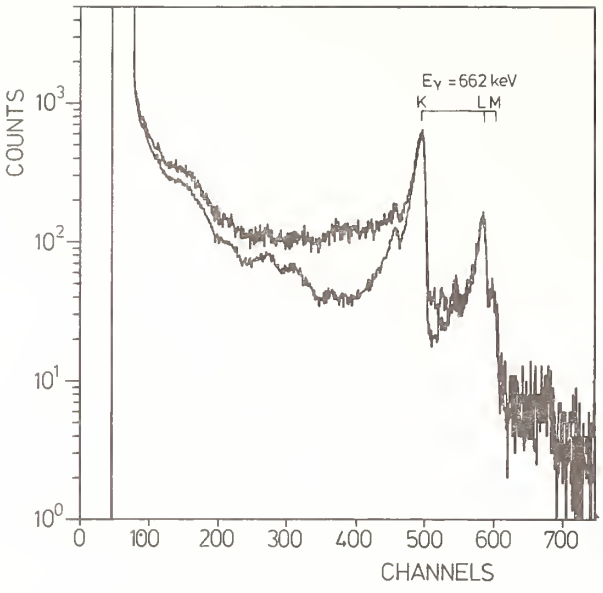

Fig. 5. Electron spectrum of the ^{241}Am sample before and after the activation with neutrons of 30 keV energy.

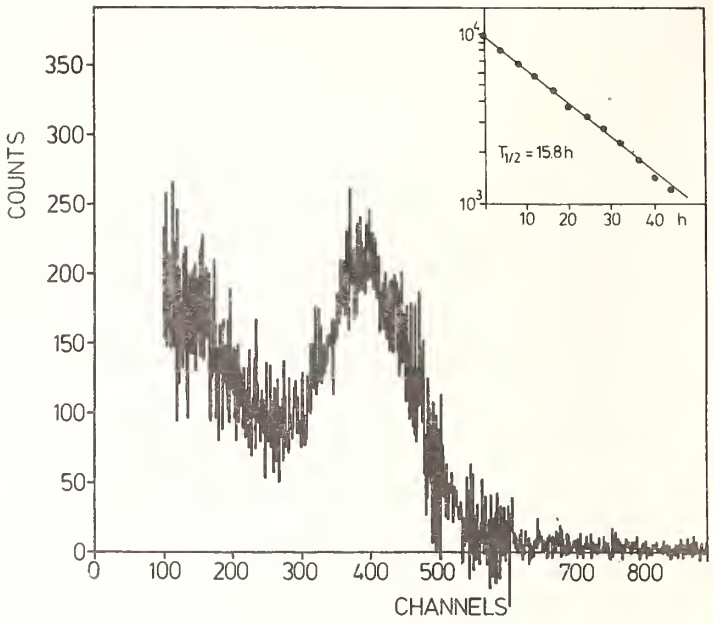

Fig. 6. Beta spectrum of the decay ^{242g}Am → ^{242}Cm as measured with the mini orange spectrometer (activation with neutrons of 30 keV). The decrease of the measured intensity is given in the insert.

decay of ^{241}Am. The difference of both spectra is given in Fig. 4, showing the upper part of the beta spectrum of the ^{242g}Am decay. The shape of the spectrum is determined to a large extent by the transmission of the spectrometer. The decrease in intensity as observed in 4 h intervals over a period of two days is plotted in the insert. The observed half life agrees with the decay constant of ^{242g}Am with an accuracy better than 2 % thus confirming the reliability of the background subtraction. The respective spectra measured after activation with fast neutrons are shown in Figs. 5 and 6.

The spectra of Figs. 3 and 5 have been obtained in a first preliminary experiment.Further measurements will be made with two significant improvements. In the first run a 20 µm thick aluminium foil had to be placed in front of the sample to suppress a residual alpha background from the outer parts of the sample baking which were not shielded by the central absorber. This reduced the resolution of the spectrometer to about 25 keV. In the meantime a better collimation allowed to omit the aluminium foil so that further experiments can be made with an energy resolution of ∿4 keV which is determined by the sample thickness. This improves the measurement in a twofold way: Most of the background is then concentrated in a few channels around the full energy peak of the conversion lines of the gamma transition at 662 keV. Also, the transmission of the spectrometer which is measured via the numerous conversion lines of a ^{206}Bi source can be determined with improved accuracy. Another change in the experimental setup concerns the lithium target used for the production of fast neutrons. With an improved cooling a proton beam intensity up to 150 µAmp can be applied in further activations which certainly increases the signal-to-background ratio by a factor of two.

Data Evaluation

To calculate the capture cross section to the ground state of ^{242}Am the total number of ^{242g}Am and ^{198}Au nuclei produced in the activation must be determined from the measured spectra. This was performed under the assumption that the respective beta spectra exhibit the shape of an allowed transition. Then one can calculate the fraction of the total spectrum above a distinct threshold energy. In our case 8 % of the spectra were used for analysis which leads to a threshold energy of 450 keV in case of ^{242g}Am and of 680 keV in case of ^{198}Au.

The preliminary results obtained until now are compiled in Table I. The ratio of the capture cross section to the ground state in ^{242} Am and gold could be determined with a total accuracy of ∿7 % at both energy points. The statistical accuracy of the measurement is ∿1 %. However, the ratio of the fast and thermal value (the quantity C in Table I) could be determined with a better accuracy of 3 % since in this case the transmission of the spectrometer and the sample mass cancel out.

For the determination of the isomeric ratio IR from the experimental data the total capture cross sections of ^{241}Am and gold are required. The respective values are given in the second part of Table I. The data at 14.75 meV were calculated from the 2200 m/sec values of 625 b for ^{241}Am[12] and 98.8 b for gold[13] assuming a 1/v -dependence of the cross sections. For the 30 keV point a weighted cross section for the experimentally determined energy distribution was calculated from the data given in Fig. 1 for ^{241}Am and from the ENDF/B-IV file for gold.

Preliminary results for the capture cross section to the ground state in ^{241}Am and the isomeric ratio are given in the third part of Table I. As mentioned already the accuracy of the data will be improved in further experiments.

Conclusions

A new experimental method has been applied to determine the capture cross section to the ground state in ^{242}Am and the isomeric ratio in neutron

capture of ^{241}Am at thermal and fast energies. The measurements yield differential data which are therefore completely independent from the existing integral experiments. Due to the high sensitivity a sufficient signal-to-background ratio can be achieved even with a relatively low neutron flux. At present only preliminary results can be given. Final data will be obtained in new experiments performed with an improved setup and after a detailed analysis of systematic uncertainties. In principle, measurements at higher neutron energies than 30 keV are possible, since the decreasing absolute value of the cross section is compensated by an increasing neutron yield of the $^{7}Li(p,n)$ reaction.

Acknowledgements

The authors appreciate the assistance of Dr. Reichardt and Mr. Härdle during the activation at the FR2 reactor. We thank Drs. van Audenhove and Pauwels from the CBNM Geel for the preparation of the ^{241}Am samples and Dr. Hanser and Mr. Feurer for the preparation of a mass separated ^{206}Bi source. The continuous and strong support of the Van de Graaff crew in providing the neutron beam is gratefully acknowledged.

References

1. J.E. Lynn, B.H. Patrick, M.G. Sowerby, and E.M. Bowery, "Evaluation of Differential Nuclear Data for Americium Isotopes. Part I.^{241}Am", AERE-R8528, United Kingdom Atomic Energy Authority, Harwell (1979).

2. A.G. Dovbenko, V.I. Ivanov, V.E. Kolesov, and V.A. Tolstikov. "Radiative Capture of Neutrons by ^{241}Am" LASL Translation Report LA-TR-71-74, Los Alamos Scientific Laboratory (1971).

3. L. Koch, R. Ernstberger, Kl. Kammerichs, "Proceedings of the First Technical Meeting on the Nuclear Transmutation of Actinides" Ispra (1977), EUR 5897 e.f,p. 247, OECD Nuclear Energy Agency (1977).

4. F.M. Mann and R.E. Schenter, Nucl. Sci. Eng. 63, 242 (1977).

5. K. Wisshak and F. Käppeler, Nucl. Sci. Eng. 66 363 (1978).

6. K. Wisshak and F. Käppeler, Nucl. Sci. Eng. 69, 39 (1979).

7. J. van Klinken and K. Wisshak, Nucl. Instr. Meth. 98, 1 (1972).

8. J. van Klinken, S.J. Feenstra, and G. Dumont, Nucl. Instr. Meth. 151, 433 (1978).

9. K. Wisshak and F. Käppeler, submitted for publication to Nucl. Sci. Eng.

10. L.W. Weston and J.H. Todd, Nucl. Sci. Eng. 61, 356 (1976).

11. D.B. Gayther and B.W. Thomas, Proc. of IV National Sov. Conf. on Neutron Physics, Kiev (1977) Vol. 3, p. 3.

12. B. Goel, Proceedings of a Specialists' Meeting on Nuclear Data of Plutonium and Americium Isotopes for Reactor Application, Brookhaven, BNL 50991, NEANDC L-116 p. 177, Brookhaven National Laboratory (1978).

13. S.F. Mughabghab and D.J. Garber, "Neutron Cross Sections", Vol. 1, "Resonance Parameters", BNL-325, 3rd ed., Brookhaven National Laboratory (1973).

EVALUATION OF THE ^{237}Np NEUTRON CROSS SECTIONS IN THE ENERGY RANGE FROM 10^{-5} ev TO 5 MeV

H. Derrien and E. Fort
C.E.N. Cadarache - B.P. N°1
13115 - Saint Paul Lez Durance - FRANCE

The ^{237}Np neutron cross-sections have been evaluated in the energy range from thermal to 5 MeV. A set of resonance parameters including a negative level, is recommended after examination of the available experimental data. This set is used 1) to calculate the cross-sections from the thermal region to 150 ev, and 2) to provide the statistical parameters suitable to the calculations in the unresolved region. At higher energies the transmission coefficients T_e are calculated by the coupled channel optical model code ECIS.[1] They are then used as input in the statistical model code FISINGA.[2] The optical model parameters, including the deformation parameters, are those used by Lagrange[3] for the Pu isotopes, slightly modified to reproduce at 40 KeV the total cross-sections obtained from the pure statistical parameters. The recommendations of Lynn[4] concerning the level density parameters have been used. In this paper we describe the various steps of the evaluation.

[Evaluation, neutron cross-sections, resonances, optical model, statistical model]

The thermal region

Total[5,6], capture[7,8] and fission[9] experimental data are available in the thermal region. Some of these data are quite old and the large discrepancies in the results (30% on the total or the capture cross-sections) do not permit an accurate evaluation of the thermal cross-sections. Fortunately, the capture cross-section has been recently measured by Weston et al[10] in the energy range from thermal to 30 KeV. Preliminary results normalized to 173 barns at 0.0253 ev are available. We have renormalized the Weston data by comparison to the absorption cross-sections obtained from the Saclay total cross-section[14] in the energy range 1 ev to 40 ev ; this renormalization leads to a value of 181 barns for the capture cross-section at 0.0253 ev. This new value and the shape of the Weston data are well reproduced by the resonance parameters given in table I. They are of course associated to other resonances parameters up to 150 ev. The Γ_f values have been choosen to reproduce the fission data of Leonard[9] below 1 ev.

TABLE I. Resonance parameters for the thermal region

Energy (ev)	$2g\,\Gamma_n$ (mev)	Γ_γ (mev)	Γ_f (mev)
- 1.000	1.8960	40.0	4.40×10^{-3}
0.490	0.0384	40.0	0.89×10^{-3}

Table II shows the experimental data compared to ENDF/B- V and the present evaluation (see also figure 1 for the calculated data between 0.01 ev and 1 ev).

TABLE II. Cross-sections at 0.0253 ev

	Experimental data (Barns)	ENDF/B-V	Present evaluation
Total	180 ± 22 (ref 5) 240 ± 20 (ref 6)	186.6	195.14
Capture	184 ± 6 (ref 7) 169 ± 3 (ref 8) 173 (ref 10)	169.1	181.0
Fission		0.017	0.018
Scattering		17.5	14.12

Figure 1 - Fission and capture cross-section of ^{237}Np in the thermal region. The curve represents our evaluation.

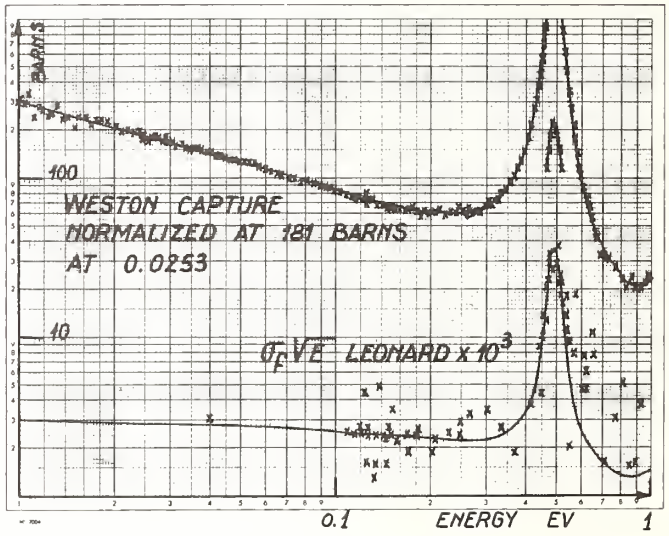

The resonance parameters

Experimental data

The resonance parameters obtained from the old measurements[5,6,12,13] have not been considered. We have only examined 6 important sets of data obtained by Gravilov et al[11] (fission), Paya et al[14] (total and fission), Plattard et al[15] (fission), Mewissen et al[16] (total, capture and scattering), Kolar et al[17] (fission), Keyworth et al[18] (polarization). In the following, we compare the parameters obtained by these experimentators.

The neutron widths

In the 0 to 50 ev neutron energy interval, there is a remarkable agreement between the results obtained by Paya et al at Saclay and by Mewissen et al at Geel. The agreement is within 1% on the average and does not exceed ± 2% on the important individual values. At higher energy the agreement is not so good : the Geel values are smaller than those from Saclay (5% on average in some energy ranges). A greater part of these discrepancies can be explained by the deterioration of the resolution in the Geel experiments compared to Saclay - missed resonances and apparition of more non resolved doublets in the Geel measurements.

The capture widths

In the energy range 0-50 ev two sets of Γ_γ values are available : those from Saclay (Paya et al[14]) and those from Geel (Mewissen et al[15]). The data are in good agreement ; the Saclay average value is (40.00 ± 1.20) mev compared to (41.2 ± 1.9) mev at Geel. Above 50 ev, there are only values from Saclay. The value of 40 mev should be attributed to the resonances for which there is no experimental value.

The fission widths

A complete set of Γ_f values is found in the Saclay data in the energy range 0-155 ev with the fluctuations typical of the classe I states in the fission intermediate structure. Between the structures, only the orders of magnitude of Γ_f are given. This is sufficient to give a good representation of the very weak fission cross-section in the corresponding energy range. We do not consider the fission area of the class II states. In the energy range where they are given, the fission cross-section should be obtained directly from the Plattard et al[15] experimental data.

As a matter of fact, two series of fission measurements have been performed at Saclay : the first by Paya et al[14] and the second by Plattard et al[15]. According to the authors, we should adopt those of Plattard et al made with improved experimental conditions. In any case, the Γ_f widths obtained from both measurements are in agreement, after a renormalization of Paya et al data by a factor of 0.625 (reevaluation of the U235 amount in the sample). The fission widths were also measured at Geel (Kolar et al[17]) in the energy range 20-50 ev with the purpose of studying the properties of the 40 ev class II state. There is a complete inconsistency in these results when compared to the Saclay data. The discrepancies are of 1 or 2 orders of magnitude. Due to the lack of information concerning the normalization, we have therefore disregarded the data of Kolar et al.

At low energy, it is possible to compare a few value obtained by Gravilov et al[11], Leonard et al[9] and Paya et al[14] as it is shown in table III. The results are consistent and,

TABLE III

Resonance energy ev	$\Gamma_f \times 10^6$ ev		
	PAYA x $\frac{5}{8}$	GRAVILOV	LEONARD
0.490	0.78	1.3	1.0
1.320	3.37	4.1	4.3
1.480	0.98	1.1	1.0

in particular, show that the fission cross-sections of Saclay match reasonably well the Leonard data just above the thermal region.

The spin of resonances

The spin assignments have been made by Keyworth et al[18] for 94 resonances in the energy range 1.4-101.1 ev from transmission and fission measurements using polarized neutron beam and polarized target. Data for 10 resonances are also reported by Mewissen et al[15] from transmission and scattering measurements, in complete agreement with Keyworth et al.

The recommended resonance parameters

The best experimental conditions of resolution were achieved on a large energy range by Paya et al[14] and by Plattard et al[15] in their transmission and fission measurements. Then the most complete set of resonance parameters is therefore the one obtained by the Saclay group. We have choosen this set as the basis of our evaluation, preferring a consistent set obtained by one group of experimentators to the one which could be obtained by averaging all the available data.

Finally, the recommended set of resonance parameters can be summarized in the following way :

1) The parameters of the negative level and of the resonance at 0.49 ev have been choosen to reproduce the thermal data of Weston et al[10] and Leonard et al[9].

2) For the other resonances, the energies, $2g\Gamma n$ and Γ_γ values are from Paya et al[14], and the Γ_f values from Plattard et al[15].

3) The spin assignments are those from Keyworth et al[18].

The average resonance parameters

The following values have been deduced from the above set of recommended resonance parameters.

s-wave strength function	So	= (0.994 ± 0.120) 10^{-4}
s-wave level spacing	D	= (0.56 ± 0.05) ev
s-wave capture width	$\langle\Gamma_\gamma\rangle$	= (40.00 ± 1.20) mev
Effective potential scattering radius	R'	= (9.54 ± 0.50) fm

The values of So and $\langle\Gamma_\gamma\rangle$ are those evaluated by Paya et al[14]. As for the level sapcing and the effective potential scattering radius, the evaluation has been done as follows.

Level spacing

An accurate determination of the level spacing from the resonance data cannot be done without a good estimation of the number of the missed levels in the experimental cross-sections. The methods used for this estimation are based on the deviation existing between the statistical properties of the observed parameters and those corresponding to the Porter-Thomas (P-T) and Wigner distributions. As a matter of fact, the results obtained by several authors working on the same sample of data are often contradictory. The 237 Np evaluation of the level spacing has been done by Mewissen et al[16] and by Paya et al[14]. The first author obtained D = (0.742 ± 0.032) ev from the P-T distribution of the neutron widths in the energy range 0-200 ev ; the second obtained D = 0.50 ev from a Monte-Carlo simulation of the total cross-section between 0 ev and 50 ev and from the P-T distribution up to 100 ev. It should be however noted that the value proposed by Mewissen et al[16] is larger than the experimental value of 0.68 ev which is observed in the energy range 0-50 ev.

We think that the determination of the 237 Np level spacing must be done on the sample of 73 resonances observed in the 0-50 ev energy interval where the variation of the number of resonances detected between 0 and E remains a linear function of the energy E. Nevertheless, even in this sample one can hardly describe the $2g\Gamma n^0$ experimental distribution by a P-T law only by taking into account the missed weak values of $2g\Gamma n^0$ (figure 2) ; one observes on the experimental distribution a lack of values around $2g\Gamma n^0 = 0.14$ followed by an excess of values around $2g\Gamma n^0 = 0.23$. This effect can be attributed to the presence of several doublets of unresolved resonances. Figure 2 shows an example of a distribution which can be obtained after correction of the effect of 5 doublets ; the resulting

distribution is well described by a P-T law with D = 0.56 ev (73 observed resonances + 10 non observed weak resonances + effect of 5 doublets). This value is identical to that obtained for 241 Am[19] which presents the same experimental features in the resonance region.

Effective potential scattering radius

The effective potential scattering radius R' can be obtained from a least square shape analysis of the experimental transmission in the resonance region including a large number of resonances. The accuracy achieved on the potential scattering cross-section $4\pi R'^2$ is limited by the thickness of the sample used in the transmission measurement ($dT/T = -n d\sigma$). For 237 Np the best conditions were obtained at Saclay with a sample of n = 0.0064 at/barn. But, with such a thin sample, 1% error on the transmission leads to 1.6 barns error on the potential scattering cross-section, i.e. 6.7% error on R'. The value R' = (9.54 ± 0.50)fms that we recommend has been obtained from the analysis of the Saclay transmission in the energy range 22-30 ev where the accuracy on the transmission is expected to be better than 1%.

Figure 2 - Integral distribution of ^{237}Np neutron widths, 1) corrected of the effect of 5 doublets, 2) non corrected. The P-T laws (the curves) take into account the missed weak levels.

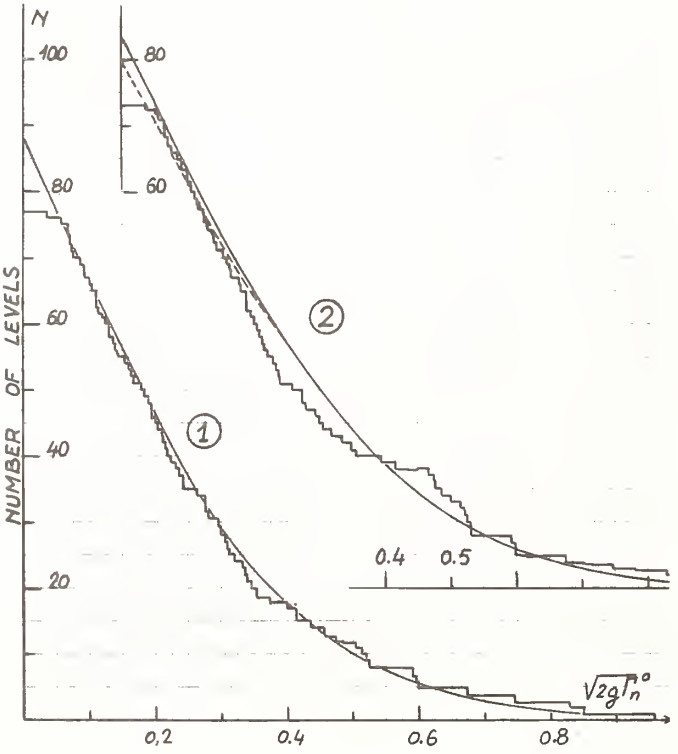

The cross-section in the unresolved region (0.15 Kev to 40 Kev)

Experimental data

The experimental data are shown on figure 3. Some important sets of data have been obtained at Los Alamos from bomb-shot experiments : elastic scattering, capture and fission from Hoffmann et al[20], fission from Brown et al[21] and from Giacoletti et al[22]. These data, at least in the low energy a part, are not consistent with the data obtained from classical experiments or with what we should expect from rough systematics. They have not been considered in our evaluation. The other data are the total cross-sections from Paya et al[14] (up to 4 Kev) and from Adamchuk et al[6] (up to 12 Kev), the preliminary capture cross-section from Weston et al[10] and the fission from Plattard et al[15].

Calculated data

We have performed a Hauser-Feshbach statistical model calculation of the total, elastic and capture cross-section between 0.15 Kev and 40 Kev, by using the neutron strength function So and S1 as input in the FISINGA code. The contribution of higher angular momentum (less than 0.6% of the total cross-section at 40 Kev) has been neglected. The s-wave neutron parameters (So, D, $\langle\Gamma_\gamma\rangle$) are those obtained above. The S1 value is choosen to reproduce the Weston capture data[10] renormalized at low energy as it has been explained above. The accuracy on S1 is obviously affected by the preliminary nature of the Weston data. We obtained :

$$S_1 = (1.82 \pm 0.20) \times 10^{-4}$$

The p-wave average capture width was taken equal to that for s-wave. The calculated total cross-sections is between Paya et al[14] and Adamchuk et al[6] values.

Due to the intermediate structure in the fission channels, a statistical model calculation of the fission cross-section in this energy range is not possible. We therefore chose the experimental data of Plattard[15] averaged in 100 ev energy interval up to 4 Kev. At higher energy, Plattard's values seem to be too low (according to the author, there was a problem of background evaluation). Between 4 Kev and 40 Kev, the cross-sections are very low and should be obtained by interpolation between the Plattard[15] data (0.0085 barn around 4 Kev) and the value of 0.010 barns obtained from the calculation at 40 Kev (see the next section).

The cross-sections at higher energy (40 Kev to 5 Mev)

Experimental data

The capture data to be considered here are those from Stupegia et al[23], from Nagle et al[24] and from Weston et al[10]. Between 0.15 Mev and 0.4 Mev the data of Weston et al and Nagle et al are in good agreement. But there is a systematic deviation between Stupegia et al and Nagle et al up to 1 Mev where the cross-sections differ by a factor of 2. As for the fission cross-sections the available data are very numerous. More than 15 measurements have been made in the high energy range ; we cannot, in this paper, examine all these results. Most of them are shown in the figure 3 (see the references on the figure). In the plateau of the first chance fission the dispersion in the different results is about 20%. The most recent data are from Plattard et al[15] and from Berhens et al[25] ; they show a discrepancy of about 10%.

Calculated data

To obtain a complete set of cross-sections in this energy range a coupled channel optical model calculation (ECIS code) has been performed with the parameters presented in table IV. These parameters are those used by Lagrange[3] for the Pu isotopes and sligthly modified to match between 1 Kev and 40 Kev the total cross-sections calculated from a pure statistical model (So, S1 and R').

Figure 3 - Neutron cross-sections of ^{237}Np. Only a few experimental points are presented for each authors. The curves are the calculated cross-sections

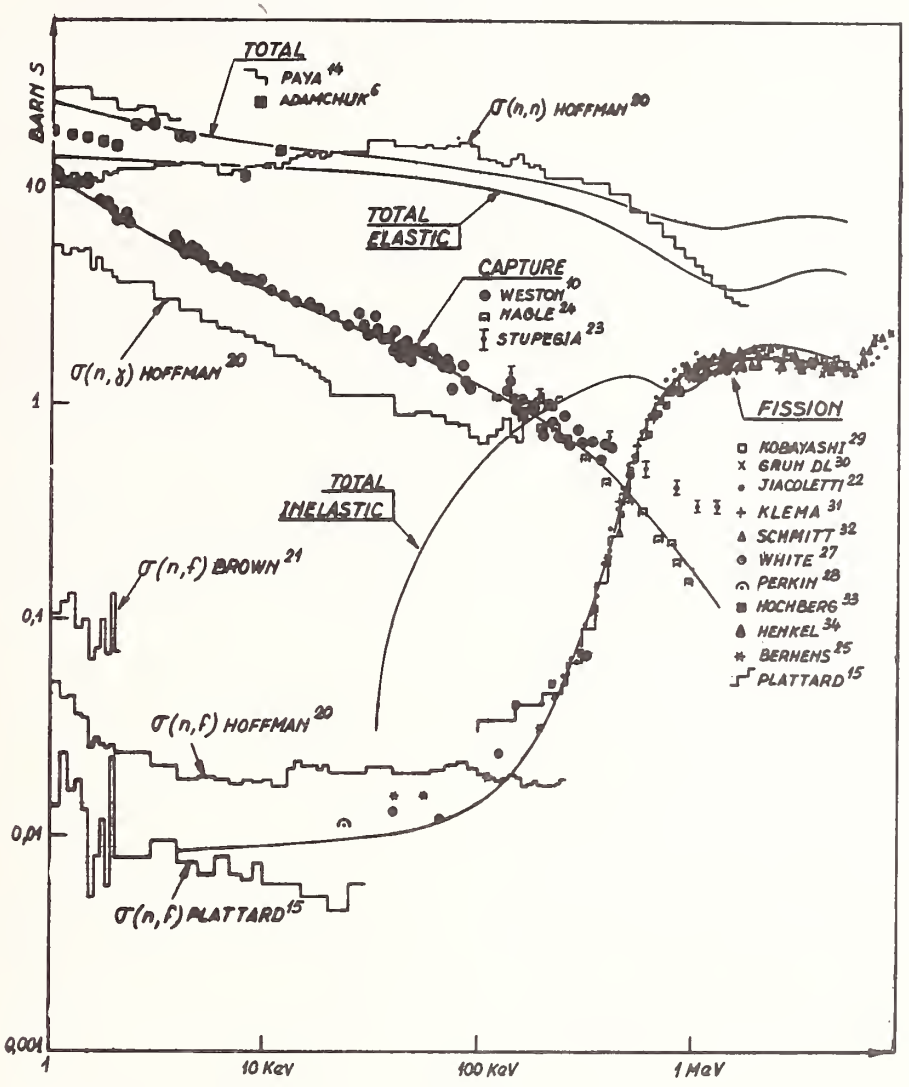

TABLE IV

Potential	Depth (Mev)	Radius (fm)	Diffuseness (fm)
Real	47.569-0.3E	7.643	0.620
Surface imaginary	2.7 +0.4E	7.643	0.620
Real spin orbit	7.5	7.674	0.620
Deformation parameters β_2 = 0.218 ; β_4 = 0.055			

The transmission coefficients Te obtained from ECIS were then used as input in FISINGA in order to calculate the capture, elastic, inelastic and fission cross-sections. Other important parameters are needed which are mainly the following :

1) Fission barrier parameters of 238 Np (compound nucleus). We have assumed a double humped fission barrier and used the method proposed by Lynn[4] for two separated peaks to calculate the total fission transmission ceofficients. The parameters for the barrier of the fondamental were :

V_A = 0.59 Mev and V_B = 0.50 Mev above the neutron binding energy ;
$\hbar\omega_A$ = 0.50 Mev and $\hbar\omega_B$ = 0.40 Mev ;
The density of the fission channels were those recommended by Lynn[4].

2) Level density parameters of 237 Np target. The discrete low lying levels were taken from Nuclear Data Sheets[26] ; a Fermi gaz type of level density relation was assumed for excitation energies larger than 1 Mev with a = 27.90.

3) Level density parameters of 238 Np coumpound nucleus. They were choosen according to $\langle D \rangle_{J=0}$ = 0.56ev at neutron binding energy, which corresponds to a = 28.10.

The calculated capture cross-sections are in agreement with Weston et al[10] data in the 40 Kev-400 Kev energy range, and slightly larger than Nagle et al[24] data at 1 Mev. The calculated fission cross-sections agree fairly well with Behrens et al[25] data in the first chance fission plateau. At 40 Kev we obtain 0.010 barn in agreement with the few available experimental data (White et al[27], Perkin et al[28]).

TABLE V

En (MeV)	TOTAL ELASTIC			CAPTURE			FISSION			TOTAL INELASTIC			TOTAL		
	This work	KEDAK	ENDF/ B-V	This work	KEDAK	ENDF/ B-V	This work	KEDAK	ENDF/ B-V	This work	KEDAK	ENDF/ B-V	This work	KEDAK	ENDF/ B-V
0.001	13.73	14.39		10.65	11.36								24.42	25.77	
0.010	12.52	12.64		3.15	3.19								15.68	15.84	
0.020	12.04	12.06		2.41	2.40								14.47	14.47	
0.030	11.75	11.72		2.12	2.08								13.88	13.81	
0.040	11.28	11.43	10.67	1.87	1.82	1.59	0.011	0.010	0.011	0.098	0.121	0.390	13.26	13.38	12.66
0.100	10.13	10.32	9.60	1.21	1.10	1.10	0.015	0.019	0.026	0.497	0.620	0.715	11.86	12.06	11.44
0.200	8.74	8.96	8.20	0.816	0.79	0.79	0.034	0.039	0.039	0.939	1.144	1.031	10.53	10.94	10.06
0.500	6.02	6.47	6.10	0.414	0.350	0.350	0.498	0.424	0.465	1.359	1.569	1.371	8.29	8.82	8.29
0.800	4.60	4.90	4.90	0.216	0.186	0.186	1.329	1.152	1.240	1.110	1.565	1.433	7.25	7.80	7.76
1.500	3.49	4.16	3.80	0.091	0.079	0.079	1.550	1.533	1.610	1.668	1.467	1.571	6.80	7.24	7.06
2.500	3.86	4.33	3.86	0.043	0.038	0.038	1.624	1.617	1.697	1.864	1.446	1.975	7.39	7.44	7.57
3.500	4.21	4.56	4.06	0.027	0.024	0.024	1.531	1.540	1.614	1.735	1.469	2.252	7.50	7.60	7.95
5.000	4.06	4.44	3.89	0.018	0.015	0.015	1.486	1.464	1.505	1.594	1.519	2.220	7.16	7.44	7.63

Conclusions

Table V shows some calculated values of the total, elastic, inelastic, capture and fission cross-sections compared to ENDF/B-V and KEDAK. Below 200 keV, these three sets of values are in good agreement. In this energy region the accuracy is better than 10% on total, total elastic and capture cross-sections. Furthermore, all evaluations agree on very weak values of the fission cross-section below 100 keV. Above 100 keV the evaluation depends on the values adopted 1) for the total cross-sections which has not been measured at high energy and 2) for the fission cross-section for which there is a large number of measurements but a spread of more than 20% in the experimental results. It is obvious that the calculated total inelastic cross-section depends strongly on the choice of the total and the fission cross-sections, whatever the hypotheses made on the density of the inelastic channels. For instance, our calculated total inelastic cross-section shows a well marked minimum around 1 MeV which does not exist in the ENDF/B-V data. At this energy the difference between our evaluation and ENDF/B-V is more than 20%. This is mainly due to a difference of more than 5% on the calculated total cross-sections.

REFERENCES

1. J. Raynal, Report LYCEN-6804.
2. E. Fort, D. Lafond and F. Ribaud, to be published.
3. Ch. Lagrange, CEA-N-1970 (1977).
4. J.E. Lynn, AERE-R-7468 (1974).
5. Smith et al, Phys. Rev. 107 (1957), 525.
6. Adamchuk et al, Sov. J. Nucl. En. 6, 420 (1960).
7. Eberle et al, KFK-1456, 51 (1971).
8. Tattersall et al, J. Nucl. En., 12, 32 (1960).
9. Jr. Leonard et al, Bull. Am. Phys. Soc., 4, 31 (1959).
10. L. Weston and J.H. Todd, private communication (1979).
11. K.A. Gravilov et al, Atomnaya Energiya, 28, 362 (1969).
12. Slaughter et al, Bull. Am. Phys. Soc., 6, 70 (1961).
13. Cline et al, Bull. Am. Phys. Soc., 4, 270 (1959).
14. D. Paya et al, FRNC-TH-431 (Thesis) (1972).
15. S. Plattard et al, Nucl. Sci. Eng., 61, 477 (1976).
16. L. Mewissen et al, Nucl. Sci. Eng., 70(2), 155, (1979).
17. W. Kolar et al, Zeitschrift fur Physik, 248, 355 (1971).
18. G.A. Keyworth et al, Phys. Rev. C, 8, 2352 (1973).
19. H. Derrien et al, Specialist's meeting Pu, Am isotopes, Nov. 20-21 (1978), BNL-50991.
20. M.M. Hoffman et al, Bull. Am. Phys. Soc., 16, 1181 (1971).
21. W.K. Brown et al, Nuclear Physics, A156 (1970) 609.
22. R.J. Giacoletti et al, Nucl. Sci. Eng., 48, 412 (1972).
23. Stupegia et al, Nucl. Sci. Eng., 29, 218 (1967).
24. R.J. Nagle, 71 Knoxville vol. 1, 259 (1971).
25. J.W. Behrens et al, UCID-17370 (1977).
26. Y.A. Ellis, Nuclear data sheets, vol. 23, N°1 (1978).
27. P.H. White et al, Physics and chemistry of fission, Salzburg, March 1965, vol. 1, page 219.
28. J.L. Perkin et al, Jour. Nucl. En. AB, 19(6), 423 (1965).
29. W. Kobayashi et al, EANDC(J)-26, 39 (1972).
30. J.A. Grundl, Nucl. Sci. Eng., 30, 39 (1967).
31. E.D. Klema, Phys. Rev., 72, 88 (1947).
32. H.W. Shmitt et al, Phys. Rev. 116, 1575 (1959).
33. B.M. Hochberg et al, AEC-TR-6398 (1961).
34. R.L. Henkel et al, LA-1495 (1952).

MEASUREMENT OF THE TOTAL Nd-145 NEUTRON CROSS SECTION

V.A.Anufriev, A.G.Kolesov, S.I.Babich, V.A.Safonov
Research Institute of Atomic Reactors,
Dimitrovgrad, USSR

total cross section, Nd-145, fast chopper, resonance parameters, 0.02-350 eV

The total cross section of Nd-145 in the energy range from 0.02 to 350 eV has been measured by the time-of-flight method at the SM-2 reactor neutron spectrometer. The measurements were carried out using a sample of Nd_2O_3 enriched in Nd-145 (84.8 %). In the studied energy range 21 levels of Nd-145 have been found and for 19 of them the resonance parameters have been calculated by the area and shape methods. To describe the total experimental cross section in the energy range from 0.02 to 1 eV a "negative" level with E_0 = 2.5 eV and $2g\,\overset{\circ}{\Gamma}_n$ = 0.95 meV has been introduced. This neutron level contributes 85 % to the total cross section for this neutron energy range. The total cross section with E_0 = 0.025 eV has been determined to be 64±4 b. Based on the parameters obtained the resonance capture integral I has been calculated (I = 245±30 b).

AUTOMATED SYSTEM FOR NUCLEAR DATA MEASUREMENTS AND OPTIMIZATION

N.G.Volkov, A.N.Gudkov, V.V.Kovalenko,
V.M.Kolobashkin, V.A.Kubjak,
N.I.Morozova, E.V.Poljushkina,
K.G.Finogenov
Moscow Engineering Physical Institute
Moscow, USSR

A computized system for simulation and optimization the experiments for fission products yields measurements is described. In the course of simulating the shape of the apparatus gamma-ray spectrum is calculated, thus providing the experimenter with means for experiment planning and optimization.

[fission products, gamma-ray spectrum, apparatus spectrum, simulation, optimization, data library, full energy peak, peak/Compton ratio, multiplets]

Introduction

While designing an automated control system for nuclear data measurements one has to take into consideration features peculiar to the experiment as an object of control:

- a multiple of various factors which have an influence upon planning and performing the experiment;
- an intricate time dependence of the processes in the sample of fissionable material;
- the impossibility of measurement control without access to the computized nuclear data library;

the ambiguity of optimization of the measurement process and necessity of using various criteria depending on the data obtained in the test runs.

Because of these particular features it is next to impossible to formulate the strict algorithm of measuring system functioning which causes the necessity of development of optimal control test for each series of measurements. This can be done with great efficiency by means of simulation of the processes in the experimental device using a computer in the interective mode.

Simulated experiment

The essence of the simulated experiment is as follows. The sample of fissionable material is exposed to neutron irradiation for the time T_i. During the exposure fission products are accumulated in the sample. Accumulation of each nuclid is determined by its yield Y (which depends on the energy spectrum of neutrons), its half-life period, characteristics of the isobaric chain to which this nuclid belongs, irradiation time T_i, the intensity of the neutron flux and some other conditions.

On the next stage of the experiment gamma-rays of fission products are recording with a Ge(Li) detector. As the elemental composition of the sample and its gamma-ray spectrum is continuously changing due to transitions in the isobaric chains the result of measurements (apparatus spectrum) tepends on the irradiation time T_i and delay time T_d elapsed after the end of T_i.

In the process of simulating the apparatus spectrum it is necessapy to take into account not only the form of the calculated gamma-spectrum, but also such characteristics of spectrometer as energy resolution, efficiency of registration and others, as well as energy dependence of these characteristics. The tipical apparatus srectrum of the fission products compound comprises hundreds of peaks superposed upon the approximately exponential distribution.

The task of simulating the experiment is calculation of the apparatus spectrum shape in some restricted energy range, while the task of optimization is finding such experimental conditions which lead to the most suitable shape of the apparatus spectrum when interesting peaks are singlets and have suffisient hights.

Data base

The calculation of the apparatus spectrum requires to take into account the multitude of the experimental conditions such as energy resolution, efficiency, characteristic times T_i and T_d and so on as well as nuclear characteristics of fission products (yields, half-lives, energies of gamma-rays and their emission probabilities etc.).

The experimental conditions are set from the display keyboard in the course of a dialogue with a computer, while characteristics of fission products are stored on permanent storage units (magnetic disks).

It is characteristic of the data base for nuclear fission experiments that it must comprise a great amount of miscellaneous data, such as:

list of fission products;

information about each nuclid, including half-life, independent yield and a list of energies with gamma-ray emission probabilities;

a description of all isobaric chains, consisting of names of nuclids belonging to each chain, ways of transitions, branching coefficients;

ordered list of energies which enables to find neighbours of the line in question.

Some of these data (e.g. half-lives or energies of gamma-quanta) are constants; others depend on experimental conditions

such as fissile material and energy distribution of neutrons and consequently must be stored as multidimensional matrixes.

The values of data mentioned above are to be corrected from time to time if new more reliable infomation has been made available. This makes it necessary to revise the stored data regularly, which procedure can be done either by deleting old data sets and creating new ones, or by selected comparing and substitution obsolete values. The last, much more effective operation may also be performed in the interactive mode.

Data library

Nuclear characteristics of fission products constitute a specialized data library where information about approximately 500 products of fission is stored in three indexed data sets. Records in these data sets represent the following structures:

structure ENERGY, comprising the value of gamma-ray energy concatenated with the chemical symbol of the element (a key of the record), absolute quantum yield of the line asa well as the referances to the keys of records where appropriate data about neighbouring lines from both sides is written. Thus the information about multiplets is easily obtained;

structure CHAIN, which comprises atomic mass (a key of the record), list of elements belonging to this chain, decay constants of these elements as well as matrixes of auxiliary coefficients, permitting fast calculation of fission products activities. Each of the fission products has its own structure CHAIN;

structure SIZE with chemical symbol of the nuclid (a key of the record), length of the relevant isobaric chain and number of gamma-lines of the specific element.

The designed data structure presents much advantage in modification and complementing the library contents, occupies small area in the main memory of the computer and leads to the time economy calculations. Together with characteristics of specific spectrometer and programms for activiti calculation it presents means for investigating the supposed course of the planning experiment and the influense and significance of all the environmental factors, such as features of sample and conditions of its irradiation, characteristics of gamma spectrometer, the timing of the experiment etc. The optimization of the experiment can be performed in the automatic mode if the criteria of optimization are developed, or by means of successive survey of variants of the planning experiment in order to find optimal conditions. This work also should be done interactively.

Results

Table I shows an example of simulated apparatus spectra in the vicinity of I50.99 keV line of ^{85m}Kr.

Table I. Results of calculation of the spectra

Nuclid	Energy, keV	Full energy peak, p/s	Peak/Compt. ratio
KR 92	I42.40	0.00E+00	0.00E+00
CEI4I	I45.45	I.44E+0I	2.66E-02
TEI3IM	I49.70	I.23E+0I	2.28E-02
TEI3I	I49.80	8.07E+02	I.49E+00
***KR85M ***	I50.99	4.04E+02	7.45E-0I
SBI32M	I5I.I0	3.30E+0I	6.I0E-02
XEI38	I53.96	I.34E+02	2.48E-0I
NDI49	I55.88	6.94E+00	I.28E-02
BAI43	I56.55	3.I8E-I0	5.88E-I3
a) T_i=I000 min, T_d= I0 min			
KR 92	I42.40	0.00E+00	0.00E+00
CEI4I	I45.45	I.43E+00	2.74E-02
TEI3IM	I49.70	2.08E+00	3.98E-02
TEI3I	I49.80	5.52E+0I	I.07E+00
KR 85M	I50.99	9.78E+0I	I.87E+00
SBI32M	I5I.I0	2.55E-09	4.89E-II
XEI38	I53.96	I.44E-0I	2.77E-03
NDI49	I55.88	I.72E+00	3.30E-02
BAI43	I56.55	0.00E+00	0.00E+00
b) T_i= I50 min, T_d= I50 min			
SBI34	297.00	0.00E+00	0.00E+00
BAI45	297.82	0.00E+00	0.00E+00
TCI08	302.77	0.00E+00	0.00E+00
SBI30M	303.30	7.38E-0I	5.67E-02
KR 85M	304.47	7.4IE+00	5.69E-0I
BAI40	304.84	3.I0E-0I	2.38E-02
RHI05	306.3I	I.46E-0I	I.I2E-02
TCI0I	306.86	5.27E+00	4.05E-0I
SBI33	308.90	3.57E-I6	2.74E-I7
c) T_i= I50 min, T_d= I50 min			

In the simulation run, whose results are shown in part a of the Table I times are chosen so that full energy peak of this line has maximum value. As it can be seen from the Table Ia apparatus peak in these conditions will present a multiplet

consisting of lines of $^{131}I_{Te}$, ^{85m}Kr, ^{132m}Sb and ^{138}Xe. Peak/Compton ratio is about 0.7 which is rather small.

Part b of the Table I presents the results of simulating with more optimal characteristic times T_i and T_d. Though the absolute value of reak hight is somewhat diminished, the peak/Compton ratio is much larger now. What is more important still, the apparatus peak is not a quadruple now but a doublet in which the side peak of $^{131}I_{Te}$ is not very high.

Examination of another line of ^{85m}Kr with energy 304.47 keV (part c of the Table I) shows that its full energy peak is small enough (because of small value of quantum yield of this line), but it can be considered as a singlet and will be safely identified.

On Fig.I the simulated spectrum is shown in the wider energy range. The multiplets which are supposed to be in a real spectrum are easily seen and values of absolute peak hights and peak/Compton ratios can be predicted.

The designed system of simulation and optimization can be used while preparing and planning the investigations of fuel elements of reactors of different types, in fission products characteristics measurenments and in other nuclear data experiments. Besides that it can be used for the investigation of the optimization criteria, for evaluation of the influence of the experimental technique on its results and in some other fields.

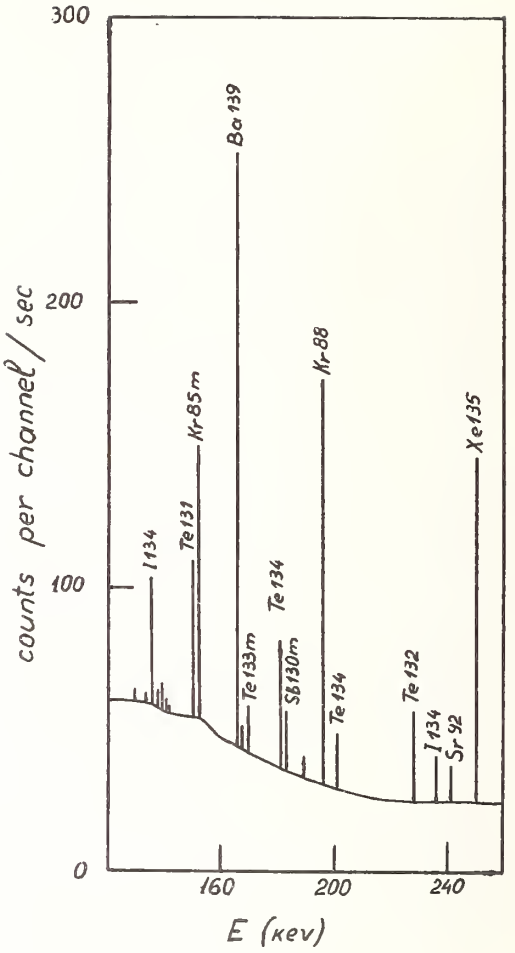

Fig.I Simulated apparatus spectrum

NEUTRON RESONANCES OF ODD-ODD RADIOACTIVE ISOTOPES

Vertebnyi V.P., Vorona P.N., Kaltchenko A.I., Krivenko V.G.
Institute for Nuclear Research, Ukr.SSR Academy of Sciences, Kiev, USSR

Kiev nuclear reactor WWR-M was used to study low energy neutron resonances for the set of radioactive isotopes: odd-odd isotopes ^{192}Ir, ^{154}Eu, ^{152}Eu and odd-even one ^{155}Eu. It was found an argument that odd-odd isotope radiative widths are much larger than those for neighbouring odd-even isotopes. Neutron resonance energies for ^{192}Ir are those (in eV): 0.252; 0.55; 2.07; 3.14; 4.38; 9.47; 12.87, for ^{154}Eu - 0.196; 0.898; 1.42; 5.2; 5.7; 6.9; 9.4. for ^{155}Eu - 0.603; 4.2; 10.8. The observed average level spacings D_{obs} after including corrections for missing of the weak levels are those: ^{192}Ir - (0.63±0.14) eV, ^{154}Eu - (0.92±0.17), ^{152}Eu - (0.25±0.04) eV. The resonance parameters and their properties are discussed just as the neutron cross sections of nuclei - fission products - ^{153}Eu, ^{154}Eu and ^{155}Eu.

(Neutron resonance; ^{154}Eu; ^{155}Eu; ^{192}Ir; D; Γ_γ)

The low-energy neutron resonances of several radioactive isotopes have been studied with time-of-flight method at Kiev atomic WWR-M reactor. Radioactive fission products europium 154 and 155 just as the radioactive odd-odd isotopes europium 152 and iridium 192 were investigated. The results for Eu152 were reported in[1]. Eu152 resonances if were fitted with one-level Breight-Wigner formula: the average radiative width $\bar{\Gamma}_\gamma$ was found to be much larger than those for the stable europium isotopes. We suggested that $\bar{\Gamma}_\gamma$ increased with the growth of nucler excitation energy U more rapidly than it followed from semiempirical $\bar{\Gamma}_\gamma$ systematics[2]. Theoretical background for this suggestion has recently appeared[3]. Generally speaking, the Γ_γ depends upon U in a complex way. However, in a rough approximation $\Gamma_\gamma \sim U^n$. Theoretical and empirical evaluations of index n are contradictory: n varies from 0.8 to 3.5. The study of neutron interactions with odd-odd isotopes may get additional data to establish the validity of that or those theoretical evaluation, as the odd-odd isotopes often have the excitation energy much larger than the neighbouring isotopes of the other class.

Neutron resonances of the Eu154 and Eu155 isotopes

Some preliminary data were presented by authors in[4]. Since that two subsequent irradiations in the reactor of a new Eu153 sample have been fulfilled. Transmission measurements for this sample were carried out in the energy range 0 - 20000 eV, however the notable changes in transmission were observed for neutron energy less than 20 eV. The transmission measurements of the first irradiated sample were repeated after 576 days. These data were used for evaluation of half-life for Eu155 isotope. It was shown from our new measurements that rather large energy-independent component in the total neutron cross section observed in our earlier work[4] was a water traces effect. The radioactive isotopes were obtained by the neutron irradiation of the high enriched Eu153 isotope samples in the atomic reactor: $Eu153 + n \rightarrow Eu154 (\sim 8.5\ y) + n \rightarrow Eu155 (\sim 5y)$. There were also such β-decays: $Eu155 \rightarrow Gd155$; $Eu156 \rightarrow Gd156$. We have not found any influence of Eu156 decay on the measured transmissions, however we have found several strong resonances due to Gd156 traces. Experimental details are given in our previous works[4]. The thermal neutron fluences were determined using Boron 10 burnup. They were as follows: $3.5 \cdot 10^{20}$ n/cm^2 - first sample; $0.9\ 10^{20}$ n/cm^2 - second sample, first irradiation; $2.2 \cdot 10^{20}$ n/cm^2 - second sample, second irradiation. Fig.1 shows the total cross section of Eu153 - II (second sample) for example in energy range (0.02-4.0) eV; curve 1

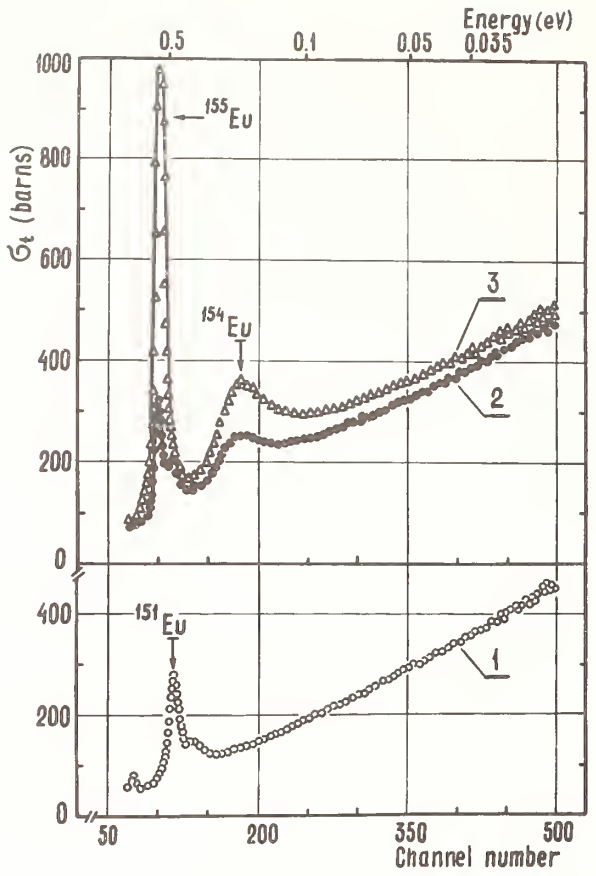

Fig 1. Low energy Eu154 and Eu155 resonances

refers to the sample before irradiation, curves 2 and 3 refer to the same sample after the first and the second irradiations correspondingly. These values were calculated using the initial Eu153 concentration. Eu153 burnup after the first irradiation was about 4%, after the second - about 7%. On curve 1 it is well seen the resonances of Eu151 at energies 0.46 and 0.32 eV. On curve 2 these resonances reduced due to the Eu151 burning, but the new ones appeared at energies 0.603 and 0.195 eV. After the second irradiation the total cross section at the energy 0.603 eV increased in 3.4 times, while the increase at the energy 0.195 eV was only in 1.8 times. At small fluences Φ the amount of the Eu154 isotope follows Φ, but the amount of the Eu155 isotope follows Φ^2. Thus it is clear that the resonance at 0.195 eV energy is due to the Eu154, and at 0.603 eV energy - to the Eu155. This way was used to identify the other resonances. This identification was confirmed by the results obtained after comparison the cross sections of the same sample just after the irradiation and after 576 days, when some amount of Eu154 and Eu155 isotopes had decayed. Fig.2 shows the difference $\Delta\sigma \equiv (n\sigma)_{t=0} - (n\sigma)_{t=576} / n^0_{153}$ for irradiated sample Eu153-1 (first sample) We can see the noticeable decrease of the observed total cross section at 0.603 eV due to the decay of Eu155 and also we can see the noticeable increase in the vicinity of thermal energy point due to the appearence of the Gd155 isotope with very large cross section near the thermal energy point.

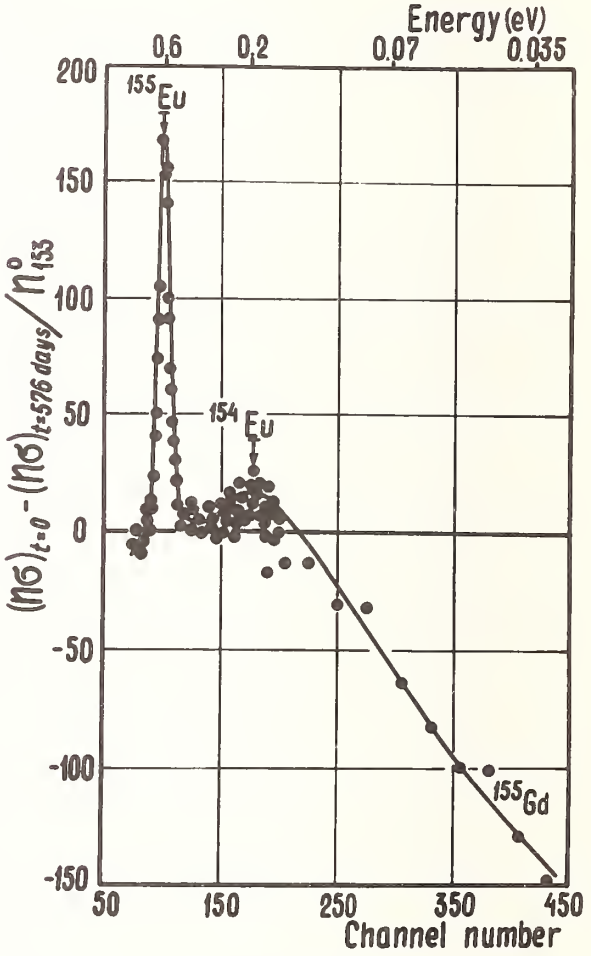

Fig.2. Eu155 decay effect

The decay of Eu154 is less prominent. The isotopes' concentrations were determined using the kinetic equations for isotope concentration and observed resonance cross sections. Resonance parameters were calculated with the shape method.

For Eu155 resonance at 0.603 eV we obtained $\sigma_0 = (117000 \pm 12000)$ barn, Eu154 resonance at 0.195 eV σ_0 is equal (2690 ± 160) barn

The resonance parameters of Eu154 and Eu155 isotopes are given in Table I.

Table I. Europium resonance parameters

Energy, eV	: Γ_γ , meV	: $g\Gamma^0_n$, meV
	Eu 154	
0.1955 ± 0.0005	140^{+10}_{-5}	0.077 ± 0.001
0.860 ± 0.004	-	0.026 ± 0.002
1.366 ± 0.001	135 ± 3	0.169 ± 0.007
List of other Eu154 resonances (energy in eV 3.51 (Eu155?);4.15(Eu155?);5.19;5.61;6.81; 9.42;10.1;10.9;13.7		
	Eu 155	
0.603 ± 0.001	96 ± 1	3.44 ± 0.01
List of other Eu155 resonances (energy in eV) 3.51 (Eu154?);4.15(Eu154?);10.7;16.6		

Neutron resonances of odd-odd isotope Ir192

This experiment in general is similar to those dealing with the radioactive europium isotopes. The transmission of the Ir191 (88.8%) sample was measured before and after the irradiation in atomic reactor; energy range - 0.02 - 100 eV, fast chopper has resolution about 55^{nsec}/m. In addition, the transmission of natural iridium just as the samples enriched by iridium 191 and 193 were measured with resolution 1.8 μsec/m. The parametersof the samples will be presented in other place. Ir total cross sections in the energy range (0.02-4) eV have been also measured. Inhomogeneity of enriched samples was the reason for some scattering of the cross section values. However, average weighted values agreed with the value for natural sample. Total cross sections at V_n= 2200 m/sec are equal:950±25 barn for Ir191, 125±5 barn for Ir193, 475±20 barn for natural iridium. Resonance identification and resonance parameters agreed with the results of evaluation /5/. For example, the cross sections change after irradiation in one of the low energy range is shown in Fig.3. Fluence was calculated using burnup of Boron-10. This value was $1.0 \cdot 10^{20} n/cm^2 \pm 10\%$.

The Westcott parameter is r=0.15±0.03 for vertical irradiation channel. $\hat{\sigma}$ = $\sigma_0(g+rs)$=1200±200 barn is for Ir191 sample with rough account of neutron selfshielding. Using these data we have calculated the burnup for Ir191 - 12% and Ir192 input -11%. The burnup was also calculated using the wing of 0.655 eV resonance; the value 9% was found. Hence, the value of total neutron cross section for Ir192 was obtained for V_n=2200 m/sec - (1100±200) barn. This result is in a striking agreement with Boehm value - (1100±400)barn[6]. We consider this coincidence as an accidental event. We hope to obtain more precise value after accounting of the isotope burnup kinetics. These data have been used for normalizing of Ir192 resonance parameters. These parameters calculated with shape method[7] are collected on Table II. Neutron widths may have the systematic error about 20%;

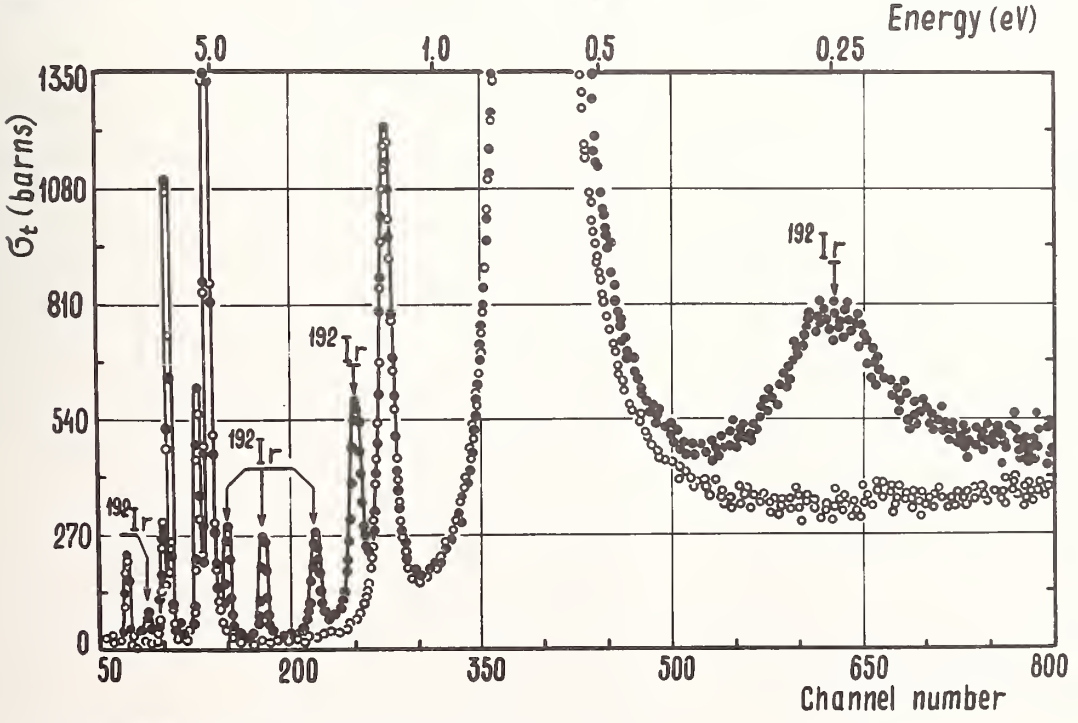

Fig.3.Low energy Ir192 resonances

they are not provided.

Table II. Iridium resonance parameters

Energy, eV	Γ_γ, meV	$g\Gamma_n^o$, meV
	Ir 191	
0.656 ± 0.001	74.1 ± 0.3	0.314±0.001
5.37 ± 0.01	82 ± 2	1.4 ± 0.1
6.13 ± 0.01	76 ± 7	0.11 ± 0.01
	Ir 192	
0.252	-	-
0.557	-	-
1.574 ± 0.001	97 ± 2	0.292 ± 0.003
2.071 ± 0.001	103 ± 4	0.175 ± 0.003
3.129 ± 0.002	96 ± 5	0.25 ± 0.01
4.391 ± 0.002	107 ± 7	0.38 ± 0.01
9.47	-	-
12.87	-	-
	Ir 193	
1.305 ± 0.002	87 ± 4	0.38 ± 0.01

Table III. Average resonance parameters of odd-odd and neighbouring isotopes

Isotope	J	U MeV	D_{obs} eV	$\bar{\Gamma}_\gamma$ meV	a MeV^{-1}	$\bar{\Gamma}_\gamma A d^{1/2} / U(1-0.01I^2)$	$\bar{\Gamma}_\gamma / (U/a A^{2/3})^{7/2}$
Eu151	$5/2^+$	6.31	0.70	92	21.25	55	53
Eu152	3^-	7.44	0.25	160	21.82	84	56
Eu153	$5/2^+$	6.44	1.10	95	21.43	56	52
Eu154	3^-	7.29	0.92	145	20.85	77	45
Eu155	$5/2^+$	6.32	4.80	96	20.84	57	46
Tm169	$1/2^+$	6.59	7.30	87	20.49	51	29
Tm170	1^-	6.94	3.70	122	20.16	68	32
Lu175	$7/2^+$	6.92	1.10	70	20.98	46/41	20
Lu176	7^-	6.4	2.10	60	20.67	74/37	21
Ta180	8^+	6.06	1.10	51	21.25	97/35	23
Ta181	$7/2^+$	6.06	4.40	58	21.14	45/40	25
Ta182	3^-	6.28	4.20	67	21.02	49/45	25
Ir191	$3/2^+$	6.20	3.00	75	20.75	56/51	25
Ir192	4^-	6.62	0.63	100	19.57	76/64	21
Ir193	$3/2^+$	6.10	7.00	87	18.42	60/59	19

Discussion

The mean resonance parameters are represented in Table III. They were calculated using our data for radioactive isotopes europium 152, 154, 155 and iridium 192. After completion of our experiments the paper of Anufriev et al.[8] was published in which neutron resonances for Eu154 and 155 were investigated. Our results are in agreement within the limits of errors with the results[8]. The only exception is resonance at 1.372 eV: we obtained Γ_γ for this resonance equal to (135 ± 3) meV, Anufriev has Γ_γ = (108±5)meV. The low lying resonance Γ_γ -widths for Ir191 agree well with the results[9] but disagree with the results[10]. The mean radiation widths $\bar{\Gamma}_\gamma$, and the mean observed level spacings D_{obs} are represented on Table III for odd-odd heavy isotopes and the neighbouring odd-even ones. Our results just as the results of references 8-13 have been used there. Take note of the mean level spacings to be much less for all odd-odd target nuclei than for the neighbouring ones (as a rule).

Quantitatively within factor 2 the mean level spacings are in agreement with the calculated ones, obtained with the semiempirical systematics by Gilbert-Cameron[14]; the excitation energy is $U = B_N - P_N$; B_N - bound energy, P_N - neutron pairing energy. The mean radiative widths of odd-odd nuclei are much larger than those for neighbouring nuclei. It takes place for Eu152 and 154, Tm170, Ir192, and Pm148[13]. The mean radiative widths of Tantalum isotopes are comparable one with other. One of the best empirical systematics of Malecky et al.[2] predicts the following dependence:

$$\bar{\Gamma}_\gamma = 10.5\ UA^{-1}\ a^{-1/2}\ (1-0.01\ I^2)$$

Here Γ_γ is proportional to the excitation energy U. Recently Zaretsky and Sirotkin[8] in the frame of finite Fermy-system theory have given the approximate expression for $\bar{\Gamma}_\gamma$: $\bar{\Gamma}_\gamma = 3.10^{-3}\alpha\ (U/a\ A^{1/3})^{7/2}$. It is very important that this theory doesn't contain any free parameters contrary to many other works. It is necessary to note that thermodynamic method developed by Kuklin[16] led to the similar expression for $\bar{\Gamma}_\gamma$ if suppose that temperature is T = U/a. In order to compare the theory and experiment the last two columns of Table III contain the values

$$\bar{\Gamma}_\gamma\ A\ a^{1/2}/U(1-0.001\ I^2) \text{ and } \bar{\Gamma}_\gamma / [U/a\ A^{2/3}]^{7/2}$$

For the cases where it is important to take into account the spin factor we give two figures for each value - with account the spin factor (upper) and without it (lower). Systematics[2] satisfactory describes the general

trend in Γ_γ dependence upon A but it does not give the correct values of Γ_γ for odd-odd nuclei. The account of spin factor in Malecky systematics fails to predict the values with large spin.

Zaretsky-Sirotkin approximate formulae gives the consistent results for the neighbouring isotopes of different classes. However, general trends are predicted with accuracy of factor 2.

Thus, the investigation of neutron resonances of new odd-odd nuclei gives as an additional evidence of validity of Zaretsky-Sirotkin formulae. Surely, for more convincing conclusions it is necessary to determine Γ_γ values both for larger amount of resonances and for the larger number of nuclei. The total neutron cross section for Europium 154 and 155 for thermal point don't contradict with the earlier works[17,13] and with the recent work[8]. It follows due to our data that the capture cross sections at V_n= 2200 m/sec for Eu154 is equal to (1250±160) barn, Eu155 to (3950±400) barn, Ir192 to (1100±200) barn. The large value of radiative strength function $\overline{\Gamma_\gamma}/D$ attracts attention to this fact for odd-odd nuclei. This is the reason to expect the larger capture cross sections for odd-odd isotopes than for isotopes of other classes.

References

1. V.P.Vertebnyi,P.N.Vorona,A.I.Kalchenko, V.G.Krivenko,S.L.Lvov,V.A.Pshenichnyi. Report KINI-76-16,Kiev,1976.Jadernaja Fizika,26,issue 6,1137,1977.
2. H.Malecki,L.B.Pikelner,I.M.Salamatin, A.I.Sharapov.Jadernaja Fizika,13,240,1971.
3. D.F.Zaretsky ,V.K.Sirotkin. Jadernaja Fizika,27,1534,1978.
4. V.P.Vertebnyi,P.N.Vorona,A.I.Kalchenko, V.G.Krivenko,S.V.Lvov,V.A.Pshenichnyi. Neitronnaja Fizika (Proc.IV National Soviet conf.on neutron physics,Kiev) v.2, p.207,1977.
5. Neutron Cross Sections,BNL-325,Third Edition,1973.
6. Boehm.Phys.Rev.,105,974,1957.
7. V.A.Pshenichnyi,V.K.Rudyshin.Report KINI-73-5,Kiev,1974.
   V.A.Pshenichnyi.Report KINI-74-16,Kiev, 1974.
8. V.A.Anufriev et al. Atomnaja energija,46, 158,1979.
9. H.H.London. Phys.Rev.,100,1414,1955.
10. J.Brunner,F.Widder. Conf. on Nucl.Data for Reactors, Paris,1966, paper 20.
11. G.E.Stokes. CINDA 76/77,v.2,p.1269.
12. J.P.Roberge,V.L.Sailor.Nucl.Sci.Eng.,7, 502,1960.
13. J.A.Harvey et al. CINDA 76/77, v.2, p.1370; G.E.Stokes, R.P.Shuman,O.D.Simpson. Nucl.Sci. Eng.,33,16,1968. T.S.Belanova et al. Neitronnaja Fizika (Proc. III National conf. on neutron physics, Kiev) v.3, p.205, 1976.
14. A.Gilbert, A.G.W.Cameron. Canad.J.Phys., 43, 1446, 1965.
15. G.J.Kirouak, H.M.Eilang, C.A.Conroad, R.E.Slovacek, K.W.Seemann. Nucl.Sci.Eng., 52,310,1973.
16. R.N.Kuklin. Jadernaja Fizika, 2,409,1965; Jadernaja Fizika, 7,541, 1968.
17. R.S.Mowatt. Canad.J. Phys., 48, 1933, 1970.
18. V.F.Razbudey, V.P.Vertebnyi, A.V.Muravitsky. Neitronnaja Fizika (Proc. III National Soviet conf. on neutron physics, Kiev) v.3,p.161, 1976.

PERTURBATION THEORY AND SENSITIVITY ANALYSIS IN FISSION PRODUCTS KINETICS

L.N.Usachev, Yu.G.Bobkov, A.S.Krivtsov
Institute of Physics and Power Engineering, Obninsk, Kaluga Region, USSR

Earlier the authors have published the procedure of determining the nuclear data accuracies which provide target accuracies of the fast reactor core characteristics and different important actinide nuclides build-up. This procedure is based on the sensetivity analysis and the optimal planning of the experiments. The development of this procedure for the fission products kinetics problem is reported in the given paper. The perturbation theory for the evolution equation was realized for the system of basic and adjoint equations describing the fission products kinetics in the fast reactor. Neutron capture and radioactive decay were taken into account for 190 nuclides with the lifetime over 24 hours.For 700 short-lived nuclides there were taken into account only for radioactive decays. The target accuracies of the fission products average capture cross section, the residual heat generation, the build-up of fuel burn-up indicators, were chosen for sensitivity analysis and experiment planning approach realization.

[Fission products kinetics, sensitivity analysis, residual decay heat, capture cross section of pseudo fission product, ratio $^{134}Cs/^{137}Cs$.]

Introduction

The authors have decided to take up the problem of fission products kinetics in order to draw on their methodic experience gained in working other problems of reactor physics. Formerly the generalized perturbation theory was developed aimed at calculating sensitivities of different important reactor values - ratios of linear functionals by neutron flux[1], bilinear by the neutron flux and neutron importance[2]. For an US reader let us point out that these are the same sensitivities, which have been derived by Stacey from the variational principle[3] (see discussion 4,5,6). Later the sensitivities have been used in the procedure of the experiments set optimal planning under the condition of minimizing their total cost for determining fast reactor nuclear data requirements.[7,8] The summary of the mentioned works has been made by Rowlands.[9] The work on the requirements for actinide characteristics accuracies done by the authors together with V.E.Kolesov a year ago[10] methodically is already quite close. The sensitivities calculation is performed with the use of the perturbation theory for evolution type equations, first developed by Gandini.[11] A modification of this will be presented below as applied to fission products kinetics.

As applied to the fission products residual heat generation the sensitivity analysis is described in the summarizing report by Devillers.[12] Devillers pointed out the necessity of supplementing his investigation with calculating the sensitivities to the fission products capture cross-sections. It has been done in the given work along with recalculating the sensitivities to the variations of yields and decay data. The generality of approach to calculating the sensitivities enables one to perform calculation for different values in a standart way. As an illustration of the procedure the calculations have been also performed for the pseudo fission product capture cross-section sensitivities. The required accuracies have been determined by experiment planning approach for the 10% target accuracy of the FP capture cross-section. The accuracy of calculating the ratio ^{134}Cs to ^{137}Cs has been also analyzed.

Mathematical Description of FP Kinetics

A set of equations describing fission products (FP) kinetics in a reactor takes the vector form:

$$\frac{d\bar{n}(t)}{dt} = \hat{A}\bar{n}(t) + \bar{f}(t), \quad \bar{n} = \bar{n}_o \Big|_{t_o} \qquad (1)$$

Here $\bar{n}^t(t) = \{n_1(t),\dots,n_i(t),\dots,n_m(t)\}$ is a FP concentrations vector at a time moment t. The matrix describes nuclide transformation and its diagonal elements take the form $-(\lambda + \sigma_c\Phi)$, where λ is the probability of radioactive decay, σ_c - a neutron capture cross-section, Φ - a neutron flux. The vector components - $n_i(t)$ are numbered in such a way that as a result of β^-- and β^+ - decay and neutron capture the component number always increases. Respectively all the elements above the diagonal in the $\hat{A}$ matrix are equal to zero. The components of vector $\bar{f}^t(t)=\{f_1(t),\dots,f_i(t),\dots,f_m(t)\}$ are the rates of the i-nuclide formation at the fission of all fissionable nuclei of every kind - "k" in the neutron field Φ with the corresponding cross-sections of σ_{fk}, the concentrations - n_k and the Y_{ik} - i-nuclide yields; $f_i(t) = \sum_k Y_{ik}\Phi n_k(t)\,\sigma_{fk}$. The Y_{ik} values should be considered as cumulative yields until all short-lived FP are taken into account in equation (1). The $\bar{f}(t)$ vector in equation (1) is a given source. According to the $\hat{A}$ matrix structure the solving of the equations set (I) is reduced to the successive solving of the equations for one function $n_i(t)$ in order of increasing the component number of the vector n(t).

The solution of n(t) obtained, one can calculate a number of values of interest. For example, the scalar product of the solutions vector by a certain vector $\bar{P}$ at $t=t_F$, that is:

$$Q = (\bar{n}(t)\,\bar{P}) \Big|_{t_F} = \sum_{i=1}^{m} n_i(t_F)P_i \qquad (2)$$

Among the values of this class are, for example, FP radioactive decay heat generation that is of interest:

$$Q \equiv \langle E \rangle = \sum_{i=1}^{m} n_i \lambda_i \left(\langle E_\gamma \rangle_i + \langle E_\beta \rangle_i \right) \Big|_{t_F}, \qquad P_i \equiv \lambda_i \left(\langle E_\gamma \rangle_i + \langle E_\beta \rangle_i \right), \tag{3}$$

and also the single FP buildup:

$$Q \equiv n_i \Big|_{t_F}, \quad P_k = \delta_{ik} \tag{4}$$

We may also be interested in the ratio of two scalar products:

$$Q = \frac{(\bar{p}_1 \bar{n})}{(\bar{p}_2 \bar{n})} \Big|_{t_F} \tag{5}$$

Into this category of values falls, for example, the pseudo FP neutron capture cross section:

$$Q \equiv \langle \sigma \rangle = \frac{\sum_{i=1}^{m} n_i \sigma_i}{\sum_{i=1}^{m} n_i} \Big|_{t_F} \tag{6}$$

or the ratio of concentration of two FP

$$Q = \frac{n_j}{n_k} \Big|_{t_F} \tag{7}$$

The entire theory becomes more substantial if the adjoint equation is considered as well:

$$-\frac{d\bar{n}^+}{dt} = \hat{A}^t \bar{n}^+, \quad \bar{n}^+ = \bar{P} \Big|_{t_F}, \text{for } Q = (\bar{n}\bar{p}) \tag{8}$$

$$\bar{n}^+ = \frac{(\bar{p}_1 \bar{n})}{(\bar{p}_2 \bar{n})} \left(\frac{\bar{p}_1}{(\bar{p}_1 \bar{n})} - \frac{\bar{p}_2}{(\bar{p}_2 \bar{n})} \right) \Big|_{t_F}, \text{ for}$$

$$Q = \frac{(\bar{p}_1 \bar{n})}{(\bar{p}_2 \bar{n})} \tag{9}$$

Here the sign at the time derivative is changed for the inverse one, the matrix A - for the transposed $\hat{A}^t$, the boundary conditions are set at the end of the time interval, the solution is performed in the opposite direction of time and begins from the last component of the vector $\bar{n}^+(t)$.

In order to obtain the perturbation theory formula for the sensitivities, along with equations (I) the perturbed equation should be written

$$\frac{d\bar{n}'}{dt} = \hat{A}'\bar{n}' + f' \qquad \bar{n} = n'_o \Big|_{t_o} \tag{10}$$

multiply equation (10) by $\bar{n}^+$, and equation (8) by $\bar{n}^+$, subtract the second expression from the first one, integrate with respect to the time from t_o to t_F. Then we derive the expression

$$(\bar{n}'\bar{n}^+)\Big|_{t_F} - (\bar{n}'\bar{n}^+)\Big|_{t_o} = \int_{t_o}^{t_F} \bar{n}' \delta \hat{A} \bar{n}^+ dt + \int_{t_o}^{t_F} (\bar{n}^+ \bar{f}')\, dt. \tag{11}$$

Carrying on the same operations with unperturbed equation (1) we similary have

$$(\bar{n}\bar{n}^+)\Big|_{t_F} - (\bar{n}\bar{n}^+)\Big|_{t_o} = \int_{t_o}^{t_F} (\bar{n}^+ \bar{f}) dt \tag{12}$$

For boundary condition (8) we have

$$(\bar{n}\bar{p})\Big|_{t_F} \equiv Q = \int_{t_o}^{t_F} (\bar{n}^+ \bar{f}) dt + (\bar{n}\bar{n}^+)\Big|_{t_o}$$

The latter formula for the $(\bar{n}\bar{p})$ scalar product provides a possibility of independent functional calculation through solving the adjoint equation. It enables one to check numerical solution algorithms. Subtracting expression (12) from expression (11) we derive:

$$\delta Q = \int_{t_o}^{t_F} \bar{n}^+ \delta \hat{A} \bar{n}' dt + \int_{t_o}^{t_F} (\bar{n}^+ \delta \bar{f}) dt + (\bar{n}' - n)\bar{n}^+ \Big|_{t_o} \tag{13}$$

Here: $\delta \bar{f} = \bar{f}' - \bar{f}$; for boundary condition(8): $\delta Q = Q' - Q$; for boundary condition (9):

$$\delta Q = \frac{(\bar{p}_1 \bar{n})}{(\bar{p}_2 \bar{n})} \left(\frac{(\bar{p}_1 \delta \bar{n})}{(\bar{p}_1 \bar{n})} - \frac{(\bar{p}_2 \delta \bar{n})}{(\bar{p}_2 \bar{n})} \right) = \delta \frac{(\bar{p}_1 \bar{n})}{(\bar{p}_2 \bar{n})}$$

In the first integral of the rigt part of (13) we may change $\bar{n}'$, for $\bar{n}$ at small perturbation. Here we do not consider the boundary conditions perturbations on $\bar{n}$, i.e. $\bar{n}' = \bar{n}\big|_{t_o}$.

Suppose $\delta \hat{A} = \sum_i \frac{\partial A}{\partial a_i} \delta a_i$ and $\delta f = \sum_i \frac{\partial f}{\partial b_i} \delta b_i$

and finally the sensitivity coefficients are put in square brackets in the following expression:

$$\frac{\delta Q}{Q} = \sum_i \frac{\delta a_i}{a_i} \left[\frac{a_i}{Q} \int_{t_o}^{t_F} \bar{n}^+ \frac{\partial \hat{A}}{\partial a_i} \bar{n}\, dt \right] + \sum_j \frac{\delta b_j}{b_j} \left[\frac{b_j}{Q} \int_{t_o}^{t_F} \bar{n}^+ \frac{\partial \bar{f}}{\partial b_j} dt \right] \tag{14}$$

In the case when the values being perturbed enter into not only A and F, but directly into the expressions of the values of interest $Q = (\bar{p}\bar{n})$ and $Q = \left(\frac{p_1 n}{p_2 n}\right)$, that is in P, P_1, P_2, or only into these values, one should also calculate the"direct" sensitivity coefficients components from the formula:

$$\frac{\delta Q}{Q} = \frac{\delta a_i}{a_i} \left[\frac{a_i}{Q} \frac{\partial Q}{\partial a_i} \right], \tag{15}$$

where only P, P_1, P_2 values are differentiated.

In concluding to present the algorithm we should point out that the adjoint vector components have a sense of the importance of the proper nuclides respectively to contribution to the chosen functional. This sense is obvious when considering the perturbation theory formula. But one can derive the a adjoint itself on the basis of the principle

of importance conservation.

Practical Realization of Algorithm

The algorithm described was realized by the authors in the YIELD code. At present the kinetics of 190 fission products with the half-life $\geqslant$24 hours is being calculated taking into account FP burn-up and build-up at neutron capture, β^+ and β^- transitions and isomeric transfers. The remaining 700 short-lived nuclides are taken into account as the precursors of 190 nuclides mentioned above. For the time being the calculations were performed on the basis of evaluated data files from Cook's Australian library[14], from which 26-group constants of the ABBN type were obtained and then were reduced to one-group ones for the typical fast reactor spectrum. At one-group cross-sections set certain additions and corrections were introduced. For the code the library of FP yields, decay and FP resinal decay heat based on Rose and B rrows work[15] was organized.

Illustrations of Calculations. Decay Heat Generation

Coefficients of sensitivities of decay heat generation to 190 FP neutron capture cross-section, yields and decay variations were calculated from formulae (14) and (15) taking into account (3). The results were compared to those by Devillers[12] for the times $\geqslant$5 days. As Devillers' work[12] lists contributions to the dispersion from individual components on the plots, and the tables give an idea of the errors of FP yields and decay data accepted, we were able to see that the sesitivity fits these values within the factor 1.5 without performing a detailed analysis of the errors. As to contribution to heat generation dispersion from the capture cross-section errors, Devillers's work was devoid of it and we supplemented his plot with another curve assuming that the errors in FP capture cross-sections are 30% and that there is an independence of these errors.

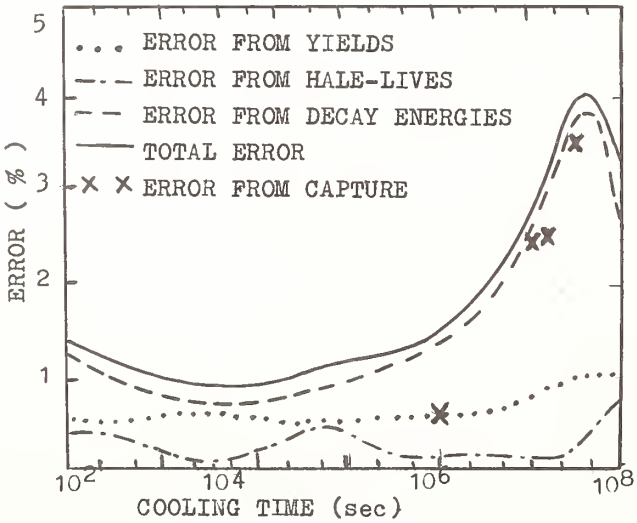

Estimation of the error of the residual heat generation after ^{235}U irradiation by fast neutrons. During 900 days, $\Phi = 4.3 \cdot 10^{15}$ n/cm^{2}sec. A figure from Devillers' work[12] supplemented with the error due to capture cross-section uncertainty.

From the fact that heat generation accuracies appeared to be better that target accuracies: 10% or even 5%, then the application of the experiment planning approach to the given problem turned out aimless.

Average FP Capture Cross-section

The capture cross-sections used in our code are characterized by the following values of average cross-sections per couple of pseudo FP for a typical reactor with uranium oxide fuel and a flux 10^{16} n/cm^{2}sec depending on the time interval from the start of operation.

days	30	60	90	120	150	180	240
cross-section 10^{-24} cm^2	.322	.334	.338	.342	.344	.345	.347

The analogous increase of cross-sections with the time of reactor operation had been pointed out in the summerizing report by Rowlands[13].

For an average capture cross-section per pseudo FP couple were calculated the sensitivities to the variations of yields and certain nuclides capture cross-sections. Planning with the target accuracy of 10% demonstrated the sufficiency of the achieved accuracy of decay data and FP yields. On the assumption of the independence of different nuclides capture cross-section errors the accuracy of 30% is also sufficient. However an assumption of the error correlated over all nuclei is more realistic. The required value of this component is equal to 7%. This requirement is yet to be satisfied. To met this request carrying out measurements by different methods both in microscopic and integral experiments is needed.

Sensitivities of $^{134}Cs/^{137}Cs$ ratio

As an example of sensitivity analysis for a ratio of two FP nucliedes we performed the sensitivities calculation for the ratio mentioned. The concentrations of ^{133}Cs and ^{137}Cs, caused by the nuclei fission either directly or after the decay are proportional to the flux Φ. The concentration of ^{134}Cs, building up through the ^{133}Cs neutron capture is proportional to Φ^2 therefore this ratio increases with the fluence growth and is used for measuring it. That is why sensitivity coefficients for this value may be of interest.

The calculation was performed for irradiating uranium of a 20% enrichment with the typical fast reactor spectrum and flux 10^{16}n/cm^{2}sec for 240 days.

Table of Sensitivities of $^{134}Cs/^{137}Cs$ Ratio to Nuclear Data Variations Multiplied by 100

A	Z	σ_c	λ_β	Y_5	Y_8	Y_9
133	54(m)	-0.02	1.5	51.5	6.1	3.7
133	54(g)	-0.06	5.9	32.5	3.9	2.4
133	55	97.3	stab.	$6 \cdot 10^{-7}$		
134	55	- 2.8	-6.95	0.005		
136	55	-0.005	0.005	-0.0006		
136	54	-0.04	stab.	-0.04		
137	55	0.18	0.79	-80,6	-10.2	-9.2

Using the sensitivities from the table one can by means of the experiment planning algorithm described in work[7] determine the required accuracies of all the values related to the point in order to attain a certain target accuracy in calculating the ratio of two cesium isotopes.

Conclusion

The mathematical approach formulated in this paper is expected to be used for the analysis of errors and the determination of the nuclear data accuracies required in different aspects of the fission products kinetics problem.

References

1. Usachev L.N. Perturbation theory for the breeding and for other number ratios pertaining to various reactor processes. J.Nucl.Eng., A/B, 1964, v.18, p.371.
2. Usachev L.N., Zaritskij S.M. Use of Perturbation Theory for Calculations of Neutron Life-time, Inserted Sample Worth and Delayed Neutron Effective Fraction Variations. BITsYaD, v.2, p.242, Moscow, 1965, Atomisdat.
3. Stacey W.M., Jr. "Variational Methods in Nuclear Reactor Physics". Academic Press, New-York, 1974.
4. Gandini A. "Comments on Variational Theory and Generalized Perturbation Method". Nucl.Sci.Eng., 57, 3, p.248, 1975.
5. Stacey W.M., Jr. "Response to Comments on Variational Theory and Generalized Perturbation Method". Ibid. p.249.
6. Greenspan E. "Variational Versus Generalized Perturbation Theories-Are They Different?" Ibid. p.250.
7. Usachev L.N., Bobkov Yu.G. Planning of an optimum set of microscopic experiments and evaluations for reactors." INDC(CCP)-19/U, IAEA, Vienna, 1972.
8. Bobkov Yu.G., Pyatnitskaya L.T. and Usachev L.N. "Planning of Neutron Data Experiments and Evaluations for Reactors." Obninsk, 1974, INDC(CCP)-46L. IAEA, Vienna, 1974.
9. Rowlands J.L. "Nuclear data for reactor design, operation and safety. Proc. of an International Conference, Harwell, September 1978, p.7.
10. Usachev L.N., Bobkov Yu.G., Kolesov V.E., Krivtsov A.S. "Determination of transactinide nuclear data required accuracy for burn-up calculation in fast reactors." Ibid. p.181.
11. Gandini A. "A Method of Correlation of Burnup Measurements for Physics Prediction of Fast Power Reactor Life". Nucl. Sci. Eng.38, 1 (1969).
12. Devillers C. "The importance of fission product nuclear data in reactor desing and operation". In Proceedings of the second advisory group meeting (Petten, 5-9 sept. 1977) on "Fission product nuclear data" (FPNP)-1977, vol-1,p.61, IAEA, Vienna, 1978.
13. Rowlands J.L. "Needs and accuracy requirements for fission product nuclear data in the physics design of power reactor cores". Ibid. p.41.
14. Cook J.L. Australian AEC report AAEC/TM-549 (1970).
15. Rose P.E. and Burrows T.W. "ENDF/B Fission Product Decay Data. BNL-NCS-50545 (ENDF-243), (1976).

TOTAL NEUTRON CROSS SECTION OF ^{45}Sc AT THE 2 KEV INTERFERENCE MINIMUM

V.F.Razbudey, A.V.Muravitsky, V.P.Vertebnyi, A.L.Kiriluk
Institute for Nuclear Research, Kiev, Ukrainian SSR, USSR

The scandium neutron cross section at 2 keV interference minimum σ_{min} is equal to 0.27 ± 0.07 barn from measurements at the WWR-M reactor. This figure is much lower than the value of 0.71 ± 0.03 barn recently reported by other authors.[3]

Transmissions T of a high purity metalic scandium 22.5-cm-thickness sample were measured with scandium filters of variable thickness (from 63 to 173 cm).

The simple formula suited for experiments like the present one was deduced for σ_{min}:

$$\sigma_{min} = \sigma_{tot}^{obs} - \frac{1}{2n} \ln\left(1 + \frac{n}{N}\right)$$

where $\sigma_{tot}^{obs} \equiv -\frac{1}{n} \ln T$ is an observed total cross section of the sample, n and N are thicknesses (atom/barn) of the sample and the filter respectively.

[Total cross sections; resonance neutrons; ^{45}Sc]

Introduction

Existence of a deep interference minimum at 2 keV in the Sc total cross section energy dependence has resulted in broad use of Sc filters to produce intensive quasimonochromatic neutron beams at atomic reactors[1,2]. However, the total cross section at this minimum, σ_{min}, is not considered wellknown. In accordance with the recent work[3] this value is equal to 710 ± 30 mb while the previous works[4,5] adduce 50^{+120}_{-50} and 85 mb respectively (the latter result is obtained by evaluation of the available experimental data). Besides that the Sc filter used in[2] has much higher transmission than it follows from[3]. The present work is aimed to resolve these discrepancies.

Idea of the experiment

It is well-known that a Sc filter, installed in reactor channel, transforms white neutron beam into a monochromatic one with the energy approximately equal to the interference minimum energy $E_{min} \approx 2$ keV. Transmission T of a scandium sample placed after the Sc filter is equal to

$$T = \int_0^\infty J(E) e^{-(N+n)\sigma(E)} dE \Big/ \int_0^\infty J(E) e^{-N\sigma(E)} dE. \quad (1)$$

Here I(E) is a reactor neutron beam spectrum, modified by energy dependence of detector efficiency, n and N are thicknesses (atom/barn) of the sample and the filter respectively.

When the filter thickness is large enough the integration region is practically limited by small energy interval near the interference minimum energy; $-\infty$ may be substituted for the low limits of the integrals in (1). In this case the following approximations may be used:

$$\sigma(E) \approx \sigma_{min} + B(E - E_{min})^2 \quad (2)$$

$$J(E) \approx J(E_{min}) + C(E - E_{min}) \quad (3)$$

where B and C are some constants. Substituting (2) and (3) into (1), we obtain

$$T = e^{-n\sigma_{min}} \sqrt{\frac{N}{N+n}} \quad (4)$$

and

$$\sigma_{tot}^{obs} = \sigma_{min} + \frac{1}{2n} \ln\left(1 + \frac{n}{N}\right) \quad (5)$$

where σ_{tot}^{obs} is an observed total cross section: $\sigma_{tot}^{obs} \equiv -\frac{1}{n} \ln T$.

The formula (5) describes the observed total cross section dependence on filter and sample thicknesses when N is large. On the other hand it allows to determine σ_{min}

using experimental data of σ_{tot}^{obs} obtained at large N.

If $n \ll N$ the expression (5) may be transformed into more simple one:

$$\sigma_{tot}^{obs} = \sigma_{min} + \frac{1}{2N} \qquad (5a)$$

The minimum thickness of the filter at which the expression (5) is correct must be determined in experiment. The constancy of the quantity $\sigma_{tot}^{obs} - \frac{1}{2n} \ln(1 + \frac{n}{N})$ may be used as a criterion.

Experiment

The neutron beam from the horizontal channel of the WWR-M reactor crossed the boron and scandium filters, scandium sample and reached the detector, disposed 4 m from the sample (Fig.1). The Sc filter with the thickness

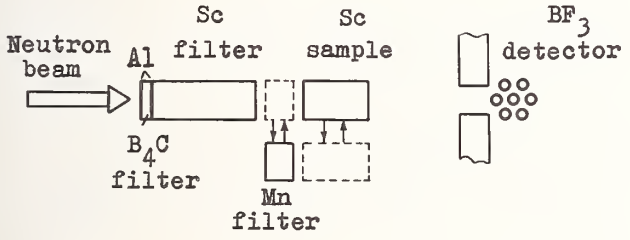

Fig. 1. Arrangement of experiment

varied from 2.5 to 7 atom/barn and the 0.9025-atom/barn-thickness sample were made of the same 99.8% pure metallic scandium (trade mark Sk MP-2). The boron filter consisted of B_4C powder (0.222 g/cm^2) in aluminium container with total thickness of the walls in beam 1.84 g/cm^2. A proportional BF_3 counter battery was used as a neutron detector. The detector efficiency was 0.125% at E = 2 keV. The sensible window of the detector was 4.8x5.8 cm.

Transmission T is determined as

$$T = (I - \Phi)/(I_o - \Phi_o)$$

where I, I_o are detector counting rates when the sample is in and out of the beam. Φ_o (and Φ respectively) is background which may be written as $\Phi_o = \Phi^R + K_o(\Phi_o^{Mn} - \Phi^R)$ where Φ^R is room background ($< 0.03\%$ of I_o) and K_o ($\Phi_o^{Mn} - \Phi^R$) is higher energy neutron contribution.

Φ_o^{Mn} is a detector counting rate with the extra filter of manganese (12, 15 g/cm^2) in the beam and K_o is a background distortion factor for this filter. The value of K_o has been evaluated by means of fitting the water sample transmission calculated from the known hydrogen[6] and oxygen[7] total cross sections to the measured one. More details about this one can find in[8].

Results

The observed total cross section σ_{tot}^{obs} versus filter thickness is plotted in Fig.2.

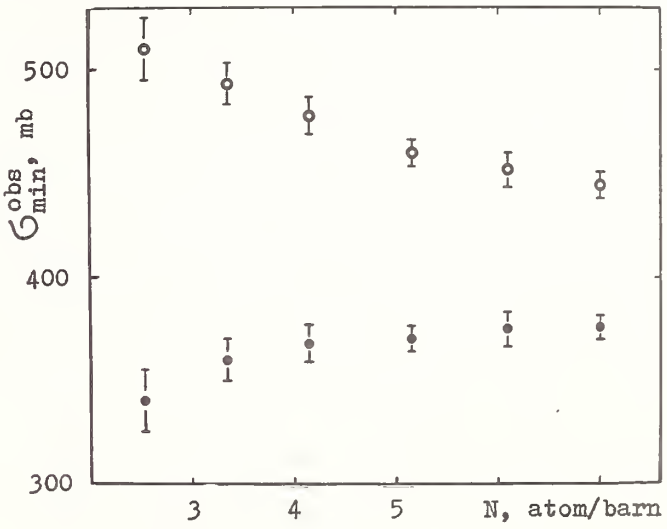

Fig. 2. Observed ^{45}Sc total cross section vs. filter thickness (open dots). Value $\sigma_{tot}^{obs} - \frac{1}{2n} \ln(1 + \frac{n}{N})$ (black dots).

Corrections for air and incomplete removal of 2 keV neutrons by Mn filter are 10 mb and ≤ 3 mb respectively. σ_{tot}^{obs} is equal to 444 mb at the maximum thickness (6.955 atom/barn) of the Sc filter and may be considered as the upper limit of σ_{min} because more detailed analysis (see below) results in its decrease only.

The black dots in Fig.2 show the quantity $\sigma_{tot}^{obs} - \frac{1}{2n} \ln(1 + \frac{n}{N})$. As one can see it becomes constant at N 6 atom/barn. Therefore the expression (5) is true at $N \geq 6$ atom/barn. Since the value $\frac{1}{2n} \ln(1 + \frac{n}{N})$ is 68 mb at N = 6.955 atom/barn σ_{min} is equal to 376 mb. After substruction of impurity contribution 113 $\pm$ 60 mb (71 mb is due to hyd-

rogen and 42 mb is due to the rest of elements in the sample) the value of σ_{min} is 263 ± 70 mb. The components contributing to the error are the following: statistical error is 2.3 mb, systematic error of the measu rement is 3.3 mb, uncertainty of the impurity correction is 60 mb.

Our value of the ^{45}Sc total cross section at 2 keV minimum is 2.7 times lower than the value[3] and 5 times higher than the value[4](see the table).Disagreement with[3] is far beyond the error bars.Disagreement with the value obtained in[4] we consider not very sharp taking into account the relatively large errors.Besides our value can be diminished if some unknown impurities would be found in our scandium material.

Table I. Total neutron cross section of ^{45}Sc at 2 keV minimum

References	4	3	Present work
σ_{min},mb	50^{+120}_{-50}	710 ± 30	263 ± 70

It should be noted that the ration Φ/I when changing N reaches its minimum at N = 6 atom/barn (Fig.3). Existence of such minimum on dependence curve Φ/I testifies that the Sc total cross section at 2 keV essentially exceeds the cross section at some higher energy interference minima.

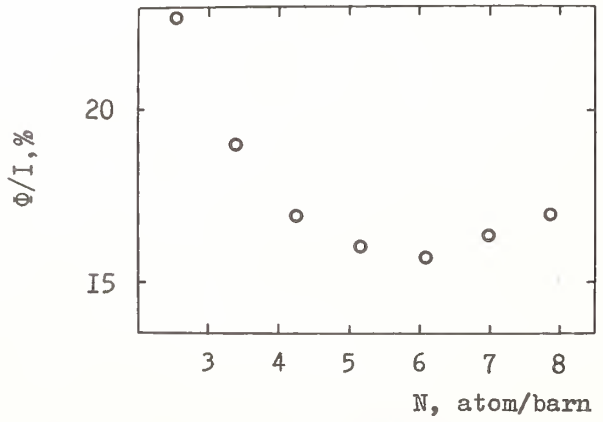

Fig. 3. Share of high energy neutrons in the beam recorded with 1/v - detector.

The authors are grateful to Drs. M.F.Vlasov, N.L.Gnidak, A.V.Murzin, E.A.Pavlenko, N.A.Trofimova for useful discussions.

References

1. O.D.Simpson, L.G.Miller, Nucl.Instr.Meth. 61, 245 (1968).
2. V.P.Vertebnyi, A.L.Kiriluk, N.L.Gnidak, N.A.Trofimova, Neitronnaja Fizika (Proc. III National Soviet Conf. on neutron physics, Kiev) v.3,p.151 (1976).
3. R.E.Chrien, H.I.Lion, R.C.Block, U.N. Singh, K.Kobayashi, Proc. Symposium on Neutron Standards and Appl., NBS Spec. Pub. 493,p.255 (1977).
4. W.E.Wilson, Dissertation (University of Idaho, 1966). The data have been taken from the work by O.D.Simpson and L.G.Miller, Nucl.Instr.Meth., 61,245 (1968).
5. B.A.Magurno, S.F.Mugharghab, Proc. Conf. on Nuclear Cross Sect. and Tech., NBS Spec.Pub. 425,v.1,p.357 (1975).
6. R.C.Block, F.Voshiaki, K.Kobayashi, T.Osaki, Journ.Nucl.Sci.Technol.,12,1 (1975).
7. BNL-325, Third Ed. (1973).
8. V.P.Vertebnyi, N.L.Gnidak, A.V.Grebnev, A.L.Kiriluk, G.M.Novoselov, E.A.Pavlenko, Jadernyje konstanty (1979).

SCATTERING CROSS SECTIONS OF NEUTRONS UP TO 3.0 MEV BY CHROMIUM, IRON AND NICKEL ISOTOPES

M.V.Pasechnik, I.A.Korzh and E.N.Mozhzhukhin
Institute for Nuclear Research of the Ukrainian
Academy of Sciences, Kiev, USSR

Experimental differential cross sections for the elastic and inelastic neutron scattering on $^{50,52,54}Cr$, ^{54}Fe and $^{58,60,62,64}Ni$ and excitation functions for three lowest levels of the above isotopes in 1.5-3.0 MeV energy range are presented. The experimental data are compared with the calculations using the optical model and statistical theory without and with account of level width fluctuations.

[$^{50,52,54}Cr$, ^{54}Fe, $^{58,60,62,64}Ni$(n,n), (n,n'), 1.5-3.0 MeV, TOF, $\sigma(E,\theta)$, $\sigma(E,E_{n'},\theta)$, optical, statistical and coupled-channel analysis.]

Introduction

One of the basic trends of atomic science in our country is the development of fast neutron reactors [1]. The present research was carried out according to the development program of fast neutron reactor, in which heat removal is realized by means of dissociable gas N_2O_4 [2]. In such reactors the irradiation and corrosion stability of the structural materials of core must satisfy high requirements [3]. Special chromium-nickel steels and alloys on the base of chromium satisfy this requirements. The choice of such investigation objects as chromium, iron and nickel was caused primarily by these requirements.

On the other hand, investigation of the fast neutron interaction with nuclei of separated isotopes is connected with the problem of applicability of different models to neutron cross section calculations. The measurements on separated isotopes already allowed to find the shell and isotopic effects in fast neutron scattering [4], nuclei deformability influence on the scattering processes [5]. They allowed also to distinguish the basic components of the real and imaginary parts of the optical potential [6].

At last, there are no experimental data in the available literature on neutron scattering processes by the separated isotopes of the above nuclei in this energy range. All this justifies the systematic research of elastic and inelastic neutron scattering on these isotopes.

Experimental Method

Measurements of differential cross sections of elastic and inelastic scattering were carried out on time-of-flight neutron spectrometer based on the electrostatic generator EG-5 [7]. Monoenergetic neutrons were obtained from $T(p,n)^3He$ reaction. The proton pulse duration was ~ 1 ns and the repetition frequency was 4 MHz. The energy spread of neutron flux was ± 50 keV. The neutrons outgoing at 0° with respect to the proton beam were scattered by cylindrical scatterers, placed at 10cm distance from the target perpendicular to the plane, in which the detector was placed. The isotope scatterers with enrichment 90-99% and masses 43-177 g were metal oxide powders (only ^{52}Cr was the metal powder) filled into thin-walled containers. The container material influences were accounted for at the background measurements.

The scattered neutrons were detected by scintillation detector (stilbene crystal 5.0 x 5.0 cm coupled with PM FEU-30), placed at 2.1 m distance from the scatterer at 9 angles in the 20-150° range. Neutron flux was monitored by the oriented long counter.

Typical spectrum of neutrons with 3.0 MeV initial energy scattered by ^{60}NiO at 150° is shown in Fig.1.

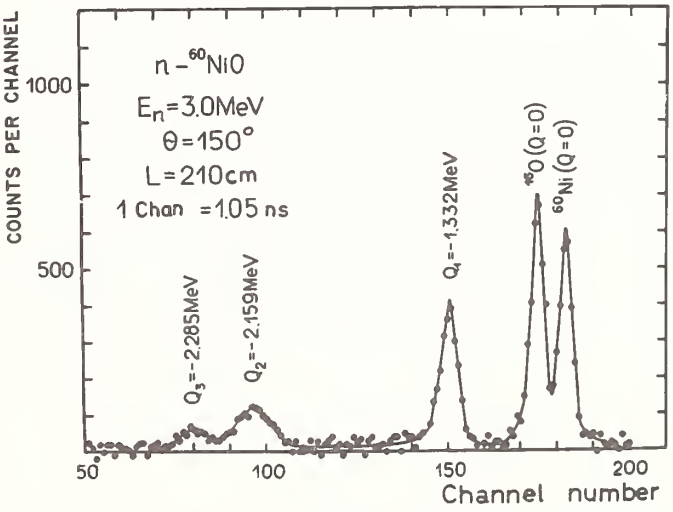

Fig.1. Time spectrum of 3.0 MeV neutrons scattered at 150° by ^{60}NiO.

The dependence of detector effectivity on neutron energy and absolute values of inelastic scattering cross sections was determined by means of (n,p) scattering measurements. The hollow polyethylene scatterer 5.01 cm high, 0.88 cm ext. dia, 0.57 cm int. dia and 1.6 g mass was used in these measurements. Elastic scattering cross sections on the oxide molecules were obtained from measuring direct and scattered neutron fluxes. Those for nickel isotopes were obtained by subtracting the oxygen elastic cross sections from the molecular cross sections. The experimental data are corrected by analytical method for attenuation of neutron flux in the sample, multiple scattering and finite geometry and also for anisotropy of neutron output from the target.

Results and Discussion

Figs. 2 and 3 show the angular distributions of elastically and inelastically scattered neutrons [8,9]. Errors shown in the Figs. include statistical errors of measurements,

errors in scattering cross sections on oxygen or hydrogen and also errors connected with cross section calculation procedure. Total errors are equal to 5-20% for elastic scattering by the oxide samples, 3-6% for elastic scattering by the metal ^{52}Cr sample and 5-10% for inelastic scattering.

Data of the other authors available for

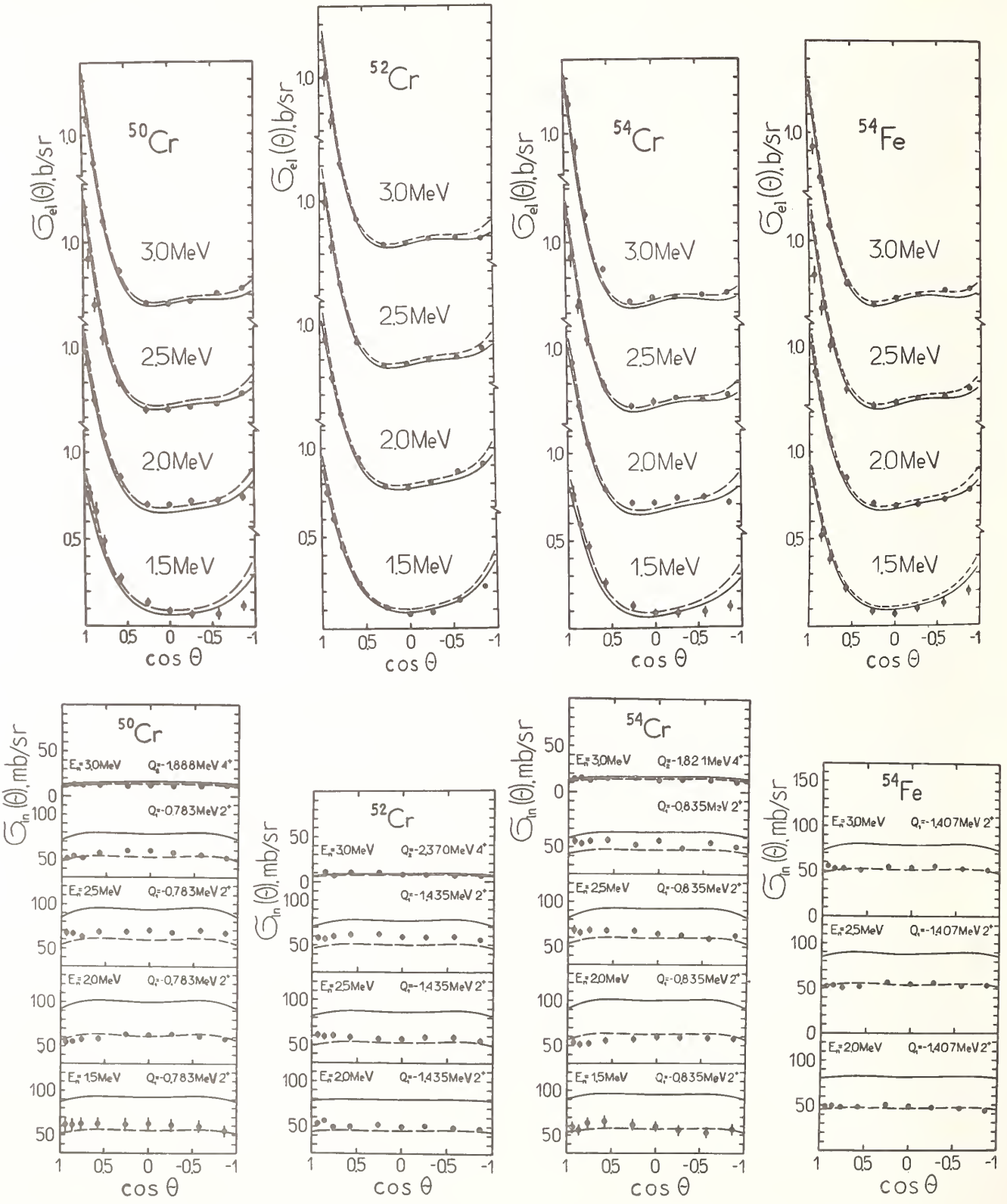

Fig.2. Experimental differential cross sections of the elastic and inelastic scattering by $^{50,52,54}Cr$ and ^{54}Fe isotopes (points) and calculated ones using optical and statistical models (curves). The compound cross sections are calculated without (solid curves) and with (dashed curves) account of level width fluctuations.

some angles and energies within the experimental errors coincide with our data except[10] and are not cited here.

Figs. 4 and 5 show our results and those of other authors on energy dependence of partial cross sections of inelastic neutron scattering with the excitation of first three levels of the investigated chromium and nickel isotopes. The partial experimental cross sections of inelastic scattering with excitation of separate levels of the isotopes are obtained by means of integration of differential cross sections of inelastic scattering measured at investigated neutron energies. Da-

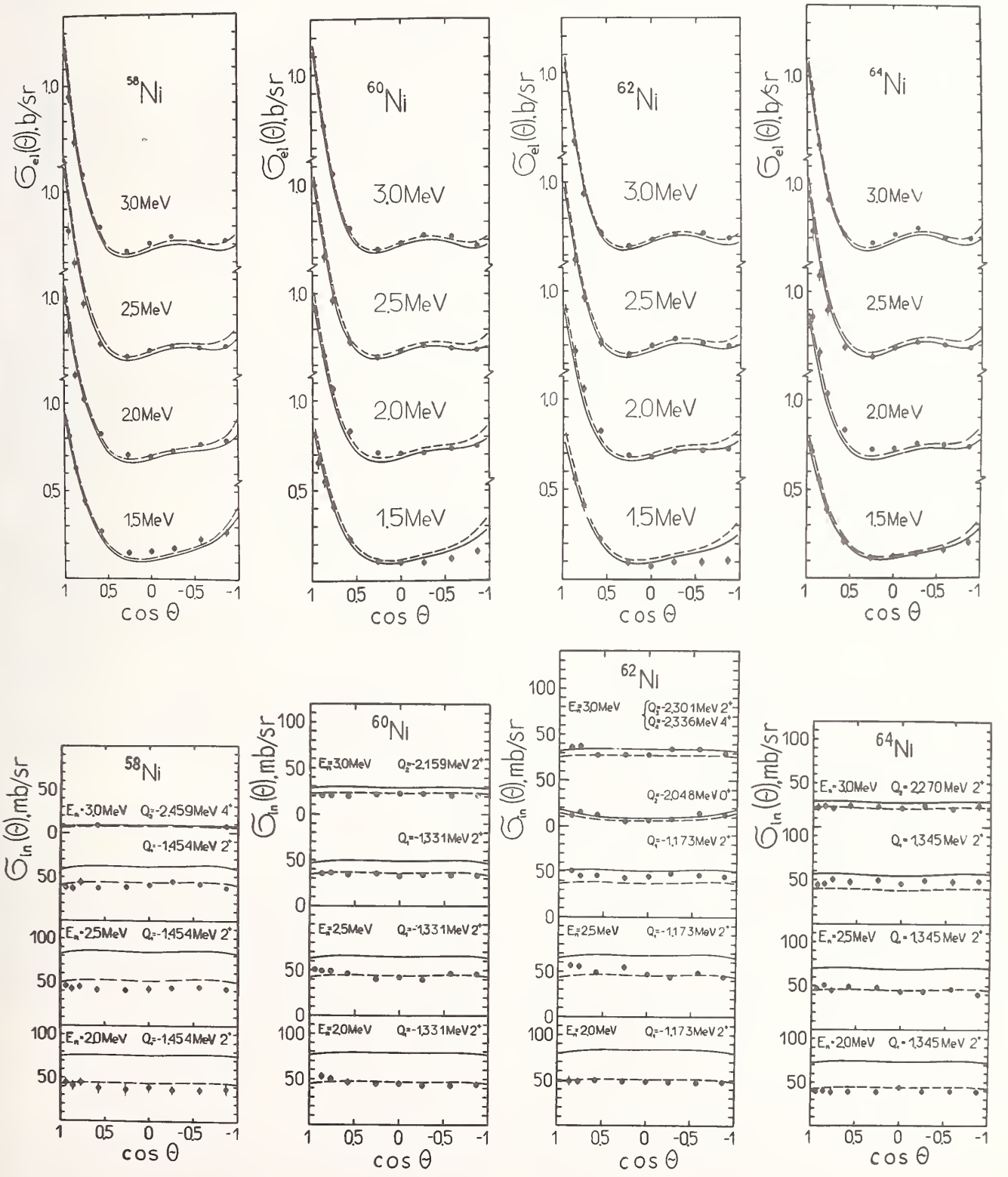

Fig.3. The same, as in Fig.2, for ^{58,60,62,64}Ni isotopes.

ta[11] presented for nucleus of natural nickel are recalculated for all nickel isotopes considering their abundances. All the data are in satisfactory agreement except[10,11], which were obtained from measurement of inelastic neutron scattering cross section on natural nickel, and [12,13] for ^{52}Cr and ^{54}Cr, obtained by γ-ray measurements from (n,n'γ) reaction.

Isotropy or symmetry of the experimental angular distributions of inelastically scattered neutrons permits to carry out an optical and statistical analysis of the data on neutron scattering in the investigated energy range on chromium, iron and nickel isotopes.

Theoretical Analysis

Experimental data on angular distributions of elastically and inelastically scattered neutrons as well as energy dependence of inelastic scattering cross sections are analysed with the optical and statistical nuclear models.

Calculations of total cross sections and angular distributions of elastically scattered neutrons are carried out using the six-parametric potential in such form:

$$V(r)=-V_c f(r)-iW_c g(r)+V_{so}\left(\frac{\hbar}{m_\pi c}\right)^2 \frac{1}{r}\frac{df(r)}{dr}\,\vec{\sigma}\cdot\vec{l}, \qquad (1)$$

where

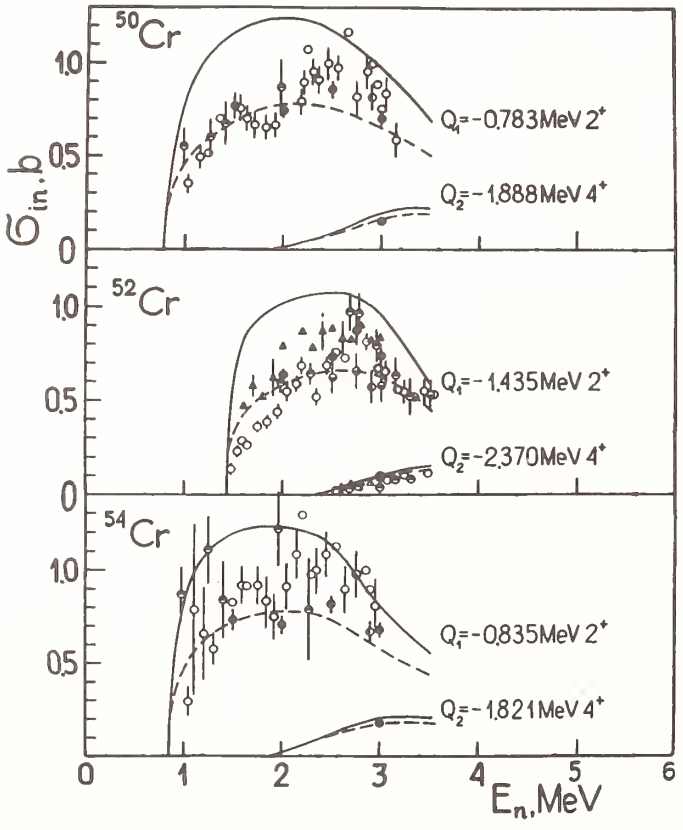

Fig.4. Excitation functions of ^{50,52,54}Cr levels at neutron inelastic scattering: ● - this work, ⊖ - 12, ▲ - 13, ◐ - 19, ○ - 20, ⊖ - 26. The solid and dashed curves are results of the calculations by means of statistical theory without and with account of level width fluctuations respectively.

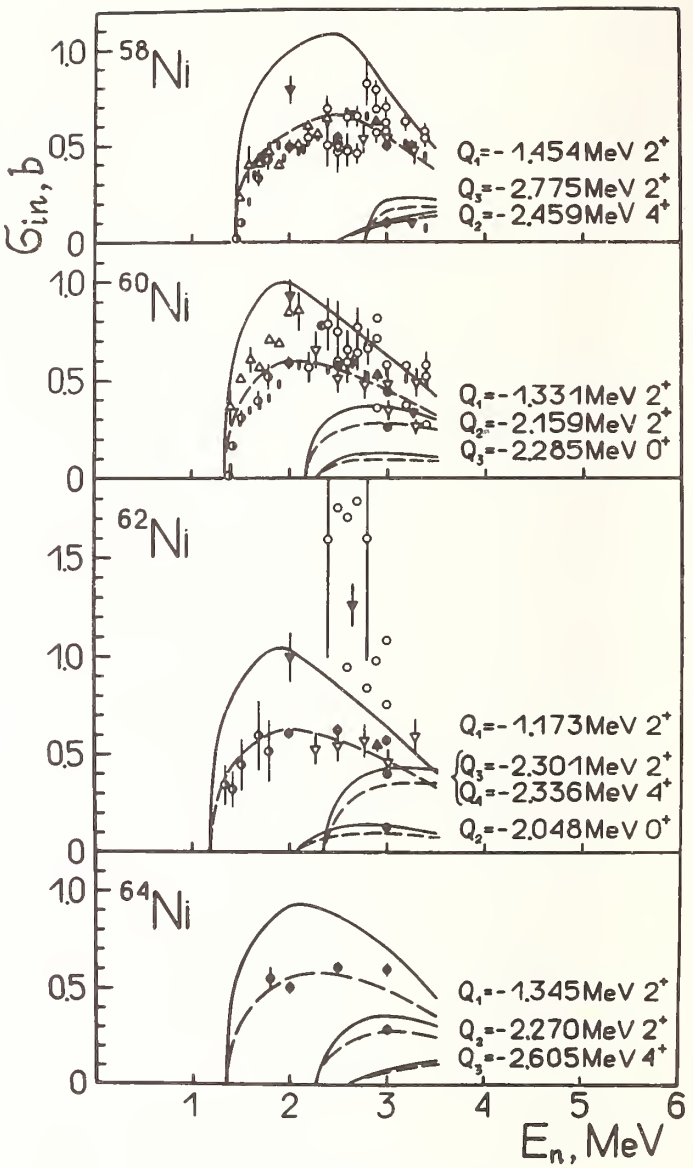

Fig.5. The same, as in Fig.4, for ^{58,60,62,64}Ni isotopes: ● - this work, ▼ - 10, ○ - 11, △ - 13, ▲ - 21, ▽ - 22, ◑ - 23, ❙ - 24, ◐ - 25.

$$f(r)=\left[1+\exp\frac{r-R}{a}\right]^{-1}, \quad g(r)=\exp\left[-\left(\frac{r-R}{b}\right)^2\right].$$

V_c, W_c, V_{so}, a, b and r_o are parameters of the potential. Nuclear radius is taken in $R=r_o A^{1/3}$ form. Cross section calculation method using optical model with potential in form (1) is described in [14]. Optical model cross section calculations are carried out with averaged parameters, which were obtained from analysis of data on neutron scattering in 1.5-6.1 MeV energy range[15]:

V_c=(48.7-0.33E) MeV, W_c=(7.2+0.66E) MeV,
V_{so}=7.5 MeV, a=0.65 Fm, b=0.98 Fm, (2)
r_o=1.25 Fm.

Nuclear optical model allows to calculate only shape elastic scattering. But in the investigated neutron energy range significant part of scattering proceeds through formation of compound nuclei. That is why before making

comparison of the calculated angular distributions with the calculated ones it is necessary to add to the cross sections calculated with optical model the compound elastic cross sections. The latter are calculated by means of Hauser-Feshbach formalism without[16] and with[17] consideration of the Moldauer corrections for level width fluctuations. The calculation program for elastic and inelastic scattering cross sections by means of statistical model both without and with consideration of the corrections for level width fluctuations is described in[18].The neutron transmission coefficients necessary for calculations of compound scattering cross sections are determined by means of optical nuclear model with potential in form (1) and the averaged parameters (2). The experimental data and the differential scattering cross sections calculated by means of optical and statistical models without and with consideration of the Moldauer corrections for level width fluctuations (solid and dashed curves respectively) are plotted in Figs. 2 and 3 for comparison. The similar comparison for integrated cross sections of inelastic scattering is given in Figs. 4 and 5.

Figs. 2 and 3 show a satisfactory agreement between the experimental data on elastic scattering cross sections and theoretical calculations. The comparison of experimental and theoretical data on differential and integrated cross sections of the inelastic scattering given in Figs. 2-5 enables one to conclude that the cross sections, calculated by means of statistical theory accounting the level width fluctuations agree well with experimental ones. This circumstance as well as the isotropy of inelastic scattering angular distributions leads to the conclusion, that the main mechanism of neutron inelastic scattering by even chromium, iron and nickel isotopes in energy range 1.5-3.0 MeV is the compound nuclei formation.

A good agreement of the calculated cross sections for investigated isotopes with experimental ones allows to hope for succesfull use of the optical potential parameters verified in this paper for prediction of scattering cross sections in wider neutron energy range for nuclei of middle atomic weight.

References

1. А.П.Александров, Атомная энергия и научно-технический прогресс, М.,Наука,1979,с.204.
2. Атомная наука и техника в СССР, М., Атомиздат, 1977, с.69.
3. М.В.Пасечник, И.Е.Кашуба, М.Б.Федоров, Т.И.Яковенко, Ядра и радиационная стойкость конструкционных материалов, К., Наукова думка, 1978.
4. М.В.Пасечник, Атомная энергия, 44, 70 (1978); Укр. физ. ж., 14, 1958(1969).
5. Е.А.Андреев, В.К.Басенко, С.П.Ситько, Ядерная физика, 23, 12(1976); R.Shamu et al., Нейтронная физика. Матер. III всесоюзной конф. по нейтронной физ.,Киев,1975г. М., ЦНИИатоминформ, 1976, ч.1У, с.237.
6. H.Feshbach, Proc. Int. Conf. on the Interactions of Neutrons with Nuclei, Lowell, July, 1976, v.1, p.13.
7. В.В.Жук, А.А.Козарь, И.А.Корж, В.А.Мищенко, Э.Н.Можжухин, Н.С.Назаров, М.В.Пасечник, В.С.Подобайло, Н.М.Правдивый, И.Е. Санжур, И.А.Тоцкий, Нейтронная физика. Матер. II Всесоюзной конф. по нейтронной физ., Киев, 1973 г., Обнинск, изд. ФЭИ, 1974, ч.1У, с.203.
8. И.А.Корж, В.А.Мищенко, Э.Н.Можжухин, М.В. Пасечник, Н.М.Правдивый, И.Е.Санжур, Нейтронная физика. Матер. III Всесоюзной конф. по нейтронной физ., Киев, 1975 г., М., ЦНИИатоминформ, 1976, ч.1У, с.220.
9. Н.М.Правдивый, И.А.Корж, В.А.Мищенко, Э.Н. Можжухин, И.Е.Санжур, Нейтронная физика. Матер. 1У Всесоюзной конф. по нейтронной физ., Киев, 1977 г., М., ЦНИИатоминформ, 1977, ч.I, с.273.
10. K.Tsukada et al., Nucl. Phys., A125, 645 (1969).
11. P.Guenther, A,Smith and J.Whalen, Nucl. Sci. Eng., 59, 106(1976).
12. D.M.Van Patter et al., Phys. Rev., 8, 1246(1962).
13. Д.Л.Бродер и др., Атомная энергия, 16, 103(1964).
14. И.А.Корж, И.Е.Кашуба, Укр. физ. ж., 10, 536(1965); М.В.Пасечник, Нейтронная физика средних энергий, К.,Наук.думка, 1969.
15. М.В.Пасечник, И.А.Корж, И.Е.Кашуба, Нейтронная физика. Матер. Всесоюзной конф. по нейтронной физ., Киев, 1971 г., К., Наукова думка, 1972, ч.I, с.253.
16. W.Hauser and H.Feshbach, Phys. Rev., 87, 366(1952).
17. P.A.Moldauer, Phys. Rev., B135, 642(1964); Rev. Mod. Phys., 36, 1079(1964).
18. И.А.Корж, И.Е.Кашуба, А.А.Голубова, Нейтронная физика. Матер. III Всесоюзной кон конф. по нейтронной физ., Киев, 1975 г., М., ЦНИИатоминформ, 1976, ч.1У, с.203.
19. М.Б.Федоров, Т.И.Яковенко, Нейтронная физика. Матер. II Всесоюзной конф. по нейтронной физ., Киев, 1973 г., Обнинск, изд.ФЭИ, ч.III, с.56.
20. P.T.Karatzas et al., Nucl. Sci. Eng., 67, 34(1973).
21. М.В.Пасечник, М.Б.Федоров, Т.И.Яковенко, Нейтронная физика. Матер.Всесоюзной конф. по нейтронной физ., Киев, 1971 г., К., Наукова думка, 1972, ч.I, с.277.
22. M.A.Etemad, AE-481, Studsvik, 1973.
23. V.C.Rogers, L.E.Beghian,and F.M.Glikeman, Nucl. Sci. Eng., 45, 297(1971).
24. J.H.Towle, R.Batchelor and W.B.Gilboy, Nucl. Data for Reactors. Proc. Int. Conf., Vienna, 1967, v.1, p.367.
25. D.I.Garber et al., BNL-400, III Ed., v.2, Brookhaven, 1970.
26. E.Almen-Ramström, AE-503, Studsvik, 1975.

NEUTRON SCATTERING BY NICKEL ISOTOPES IN ENERGY RANGE 5-7 MEV

I.A.Korzh, V.A.Mishchenko, E.N.Mozhzhukhin, M.V.Pasechnik, and N.M.Pravdivy
Institute for Nuclear Research of the Ukrainian Academy of Sciences, Kiev, USSR

Differential cross sections for elastic and inelastic scattering of 5.0, 6.0, and 7.0 MeV neutrons by nickel and its even isotopes are measured. The experimental data are compared with the theoretical values calculated using the optical model, statistical theory of nuclear reactions, and coupled-channel method.

[^{58,60,62,64}Ni(n,n),(n,n'), Ni(n,n), O(n,n), 5.0 MeV, TOF, $\sigma(E,\theta)$, $\sigma(E,E_{n'},\theta)$, optical, statistical, and coupled-channel analysis.]

Introduction

The experimental data on fast neutron interactions with even nickel isotopes are important for some reasons. Firstly, nickel is a component of structural materials of nuclear reactors. Therefore, the cross section data on fast neutron interactions with nickel nuclei, obtained with a sufficient accuracy, are important for reactor physics and technology. Secondly, theoretical analysis of the reliable experimental data by means of the disposable neutron interaction models enables one to determine the applicability limits of the models for predictions of neutron reaction cross sections as well as to investigate the role of various reaction mechanisms.

The even nickel isotopes neutron scattering cross sections have been investigated up to 3 MeV in our laboratory previously [1]. There are enough accurate data in this energy range, while the experimental information at higher energies is very scarce, although its importance for the practice and theory is obvious. To reduce this data lack we have measured the differential cross sections of elastic and inelastic neutron scattering by even nickel isotopes at the energies 5.0, 6.0, and 7.0 MeV.

The results of the measurements and theoretical calculations of the differential cross sections for 5.0 MeV neutrons elastically and inelastically scattered by the isotopes ^{58,60,62,64}Ni and elastically scattered by natural nickel are given in this paper. The differential cross sections of 5.0 MeV neutron elastic scattering by oxygen are also obtained.

Experimental Procedure

The spectra of neutrons scattered by the investigated samples were measured with the fast neutron time-of-flight spectrometer at the electrostatic generator EG-5 [2] in its modified version[3]. The arrangement of the experiment and the spectrometer parameters are given in Table 1.

In the measurements of the neutron scattering spectra NiO oxide powder samples high-enriched by the corresponding isotope were used. As hydrogenous scatterer for normalizing the inelastic neutron cross sections a polythene sample was used. The powder samples were placed in thin-walled brass containers, which contributions into the scattering were taken into account under background measurements.

Experimental Results

The measured spectra of scattered neutrons were used for obtaining the differential cross sections for neutrons elastically scattered by the nickel isotope oxides and by natural nickel as well as for obtaining the differential cross sections for neutrons inelastically scattered by the nickel isotopes with excitation of the first 2^+-levels.

Table 1

1. Beam parameters:	E_d=1.94 MeV, f=4 MHz, I_{mean}= 5 μA, τ_{pulse}=1.0-1.5 ns.
2. Neutron source:	D(d,n)^{3}He reaction, Ti-D target (thickness 340 keV) on thin Mo-backing.
3. Distances:	target-scatterer - 10 cm, scatterer-detector - 2.6 m.
4. Neutron detector:	stylbene crystal 5x5 cm and P.M. FEU-30, n-γ-discrimin.
5. Monitor:	stylbene crystal 3x4 cm and P.M. FEU-30, current integr.
6. Spectrometer parameters:	integral nonlinearity - 0.3%, differential nonlinearity - 4.0%, intrinsic time resolution - 2 ns.
7. Measurement angles:	20, 30, 40, 55, 65, 75, 90, 105, 125, 135, 150°.

The differential cross sections for neutrons elastically scattered by the nickel isotopes were determined by subtracting the cross sections of neutron elastic scattering by oxygen from the measured cross sections of neutron elastic scattering by the nickel isotope oxides. Since the available data on cross sections of 5 MeV neutron elastic scattering by oxygen considerably differ[4,5], these cross sections were determined from our measurements. This was performed by subtracting the measured natural nickel cross sections from the NiO oxide molecular cross sections composed from the measured nickel isotope oxide molecular cross sections considering the nickel isotope abundances.

The absolute differential inelastic cross sections were obtained by normalizing the measured relative angular distributions of inelastic scattered neutrons to the well-known cross sections of neutron scattering by hydrogen.

The measured scattering cross sections were corrected for anisotropy of the neutron yield from the source, for neutron flux attenuation in the scatterer, and the elastic scattering cross sections also for multiple scattering of neutrons in the scatterer and angular resolution of the experiment (for the inelastic scattering the two latter corrections are negligibly small because the anisotropy of the angular distributions is relatively

small). The corrections for the flux attenuation, applied according to the recipes of papers [6], are equal to 10-11% for the powder samples and 7-8% for the polythene sample. The corrections for the multiple scattering and angular resolution, which depend on the scattering angle, reach up to 6% and 15% respectively, for the powder samples.

The experimental cross sections of 5.0 MeV neutron elastic and inelastic scattering by the nickel isotopes are given in Figs. 1 and 2. Most of the data are obtained for the

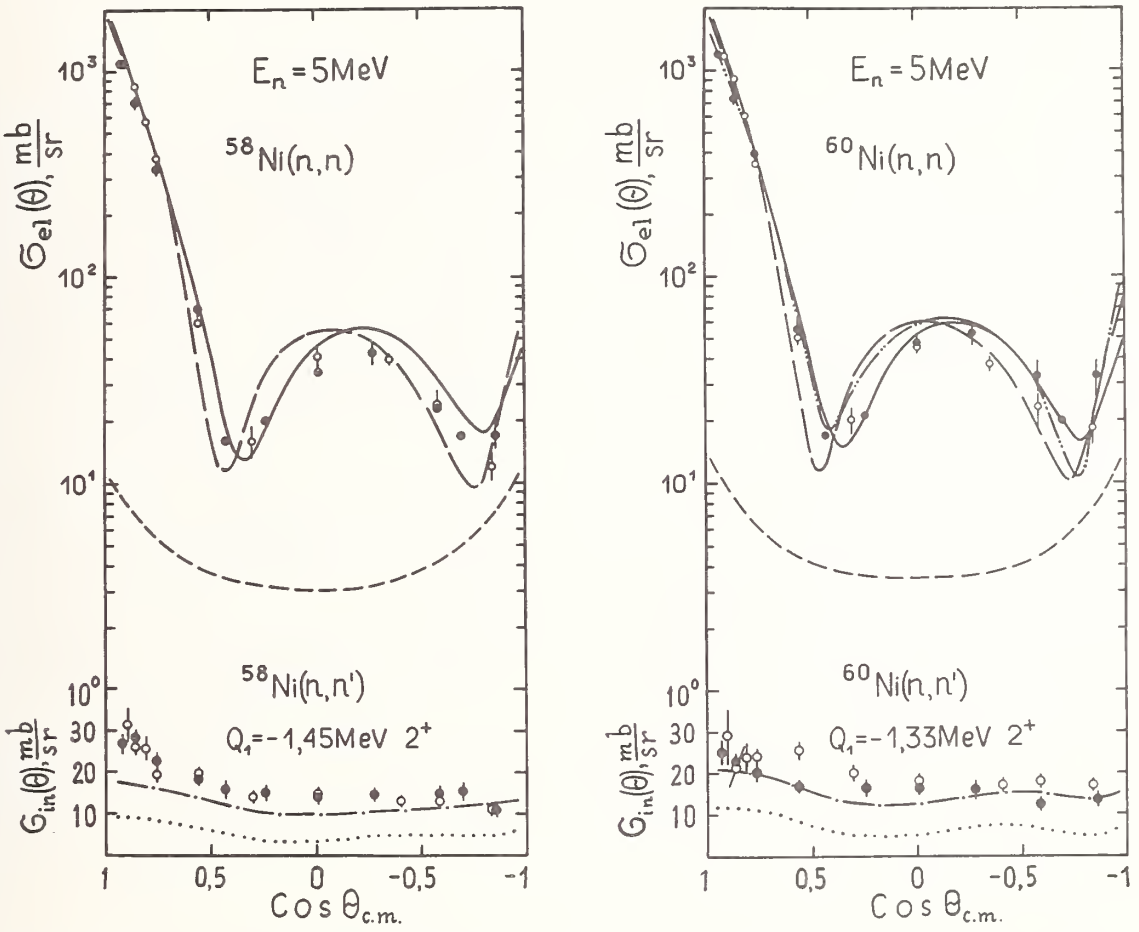

Fig.1. Experimental (● - this work, O - 7) and calculated (curves) differential cross sections for 5 MeV neutrons elastically and inelastically scattered by ^{58}Ni and ^{60}Ni. In the elastic scattering cross sections the shape components are calculated using the optical model with our (————), Rosen (—— ——), and Wilmore-Hodgson (——··——) parameters and the compound ones using statistical theory (– – – – –). The calculated inelastic scattering cross sections are the sums (—·—·—) of the compound and direct (·····) components.

first time. At the comparable neutron energy only the data of paper [7] for ^{58}Ni and ^{60}Ni are available, and they are plotted in Fig.1 for comparison. Both results are in agreement. The errors of our data plotted in Figs. 1 and 2 are the total ones and include the experimental, normalizing, and correction errors as well as the errors of cross sections of neutron scattering by oxygen, for the elastic scattering.

The differential cross sections of the 5.0 MeV neutron elastic scattering by natural nickel with their total errors as well as the data of paper[5] obtained at the comparable energy are given in Fig.3. There are general agreement in form of the angular distributions, but the cross section values are in considerable disagreement. The differential cross sections of 5.0 MeV neutron elastic scattering by oxygen with their total errors as well as those available in literature at the comparable energies[4,5] are also given in Fig.3. The noticeable disagreements between the three data sets are caused, perhaps, by different experimental conditions, in particular, by different neutron energy spreads.

Theoretical Analysis

The complexity of process of neutron scattering by nuclei, when the energy is several MeV, necessitates using for analysis of the experimental data a set of nuclear models, as the different stages and types of scattering require different theoretical model approaches.

The shape elastic cross sections as well as the transmission coefficients, which are necessary for the calculations with statistical theory, were calculated using the optical model with spherical potential[8]:

$$V(r) = -V_c f(r) - iW_c g(r) + V_{so}\left(\frac{\hbar}{m_\pi c}\right)^2 \frac{1}{r}\frac{df(r)}{dr}\vec{\sigma}\cdot\vec{l}, \quad (1)$$

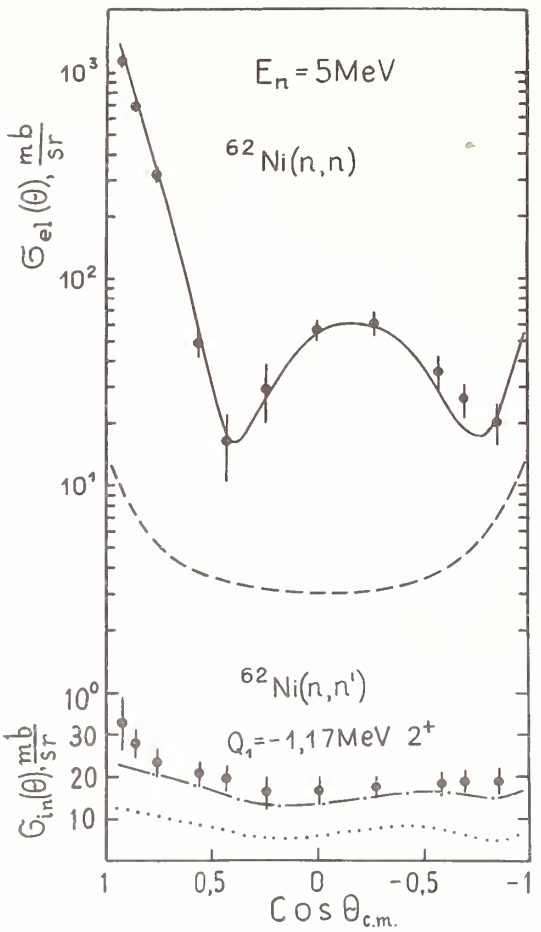

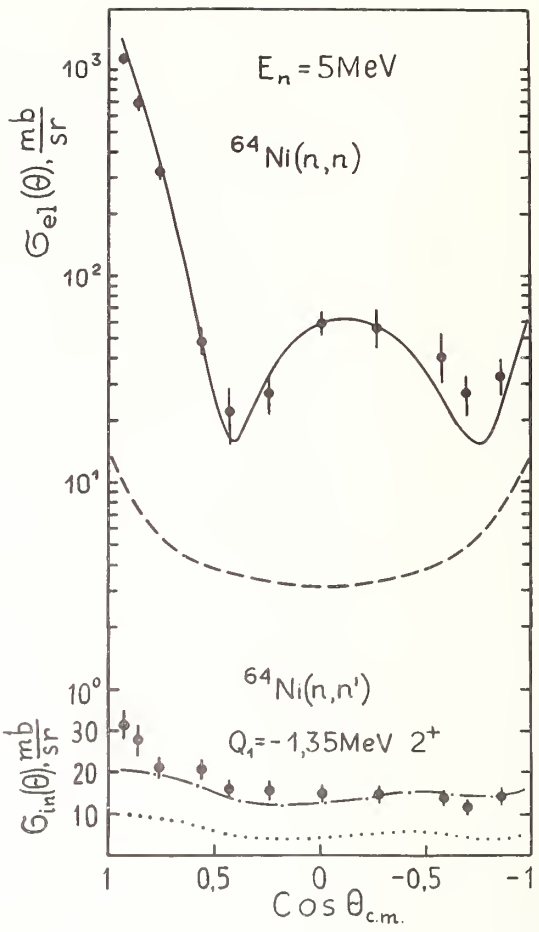

Fig.2. The same, as in Fig.1, for ^{62}Ni and ^{64}Ni isotopes.

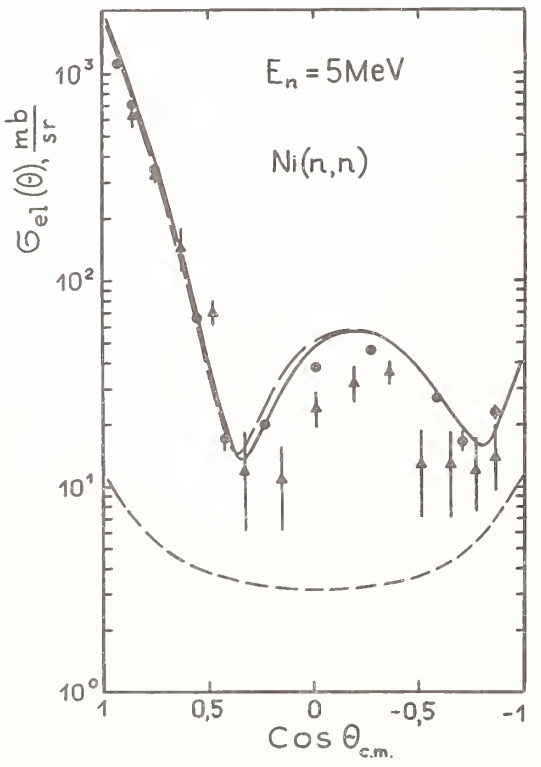

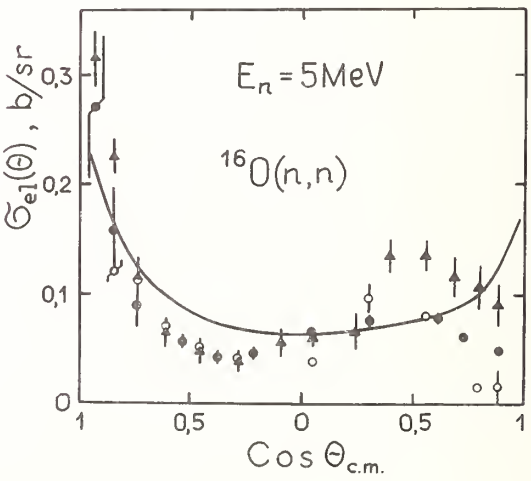

Fig.3. Experimental (● - this work, ○ - 4, ▲ - 5) and calculated (curves) differential cross sections for 5 MeV neutrons elastically scattered by natural nickel and oxygen. The optical model calculations are carried out with our (————) and Holmqvist (—— ——) parameters. The compound elastic cross sections are calculated with statistical theory (— — — —).

where

$$f(r)=\left[1-\exp\frac{r-R}{a}\right]^{-1},\quad g(r)=\exp\left[-\left(\frac{r-R}{b}\right)^2\right],$$

and the unified potential parameter set[9]:

$$V_c=(48.7-0.33E)\ \text{MeV},\quad W_c=(7.2+0.66E)\ \text{MeV},$$
$$V_{so}=7.5\ \text{MeV},\quad a=0.65\ \text{Fm},\quad b=0.98\ \text{Fm},\qquad (2)$$
$$r_o=1.25\ \text{Fm}.$$

For the analysis of the neutron elastic cross sections some other sets of the potential parameters were also used: those of Rosen[10] - for ^{58}Ni and ^{60}Ni, of Wilmore-Hodgson[11] - for ^{60}Ni, and of Holmqvist[12] - for natural nickel.

The compound neutron scattering cross sections were calculated with the statistical theory taking into consideration the level width fluctuations[13] by means of the calculation method presented in papers[14]. As the level schemes of the nuclei are known only for low excitation energies, the concurrence of continuum spectra level excitations at high excitation energies were taken into account by means of statistical description of highly excited nuclear states.

For the calculations of residual nuclei level density with a definite spin and both parities at the effective excitation energy U the relation of Fermi-gas model with phenomenological accounting the residual nucleon interaction was used[15]:

$$\rho(U,i)=\frac{2i+1}{24\sqrt{2}\,a^{1/4}U^{5/4}\sigma^3}\exp\left[2\sqrt{aU}-\frac{(i+1/2)^2}{2\sigma^2}\right],\qquad (3)$$

where a is the main level density parameter, related to the density of one-particle states near the Fermi-surface g: $a=\pi^2 g/6$. The spin cutoff parameter σ is determined by the expression:

$$\sigma^2=\frac{6}{\pi^2}\sqrt{aU}\,\langle m^2\rangle,\qquad (4)$$

where $\langle m^2\rangle$ is the mean square of total momentum projections for individual particles, which approximately relates to the mass number A[16]: $\langle m^2\rangle=0.24A^{2/3}$. For the parameter σ the following approximate dependence on a, U, and A was used[16]: $\sigma^2=0.146\sqrt{aU}A^{2/3}$. The parameter a =6.2 MeV^{-1} and the excitation energy U accounting the pairing energy equal to 1 MeV[17] were used in the calculations.

In the statistical calculations only neutron output channels were considered. Therefore, for ^{58}Ni the competiting proton and α-particle output channels were taken into account by the factor $(\sigma_a-\sigma_{np}-\sigma_{n\alpha})/\sigma_a$.

It is natural to expect significant contributions of direct inelastic scattering in this energy range. Therefore, the calculations based on statistical theory only do not result in adequate interpretation of experimental inelastic cross sections both in shape and in value. The calculations of the direct inelastic cross sections were carried out using the formalism of coupled-channel method developed by Tamura[18]. The method[19], based on the assumption of vibrational nature of first excited levels and approximation of strong coupling of only this level with the ground state, was used in the calculations. The averaged parameters of optical potential (2) (except W_c diminished for 20% in order to obtain the same values of σ_t as in the spherical optical model) with potential (1) were used.

The values of the quadrupole dynamic nuclear deformation parameters β_2 for the nickel isotopes were taken 0.20 for ^{58}Ni, 0.22 for ^{60}Ni, 0.22 for ^{62}Ni, and 0.20 for ^{64}Ni.

The inelastic scattering cross section components calculated with statistical theory and coupled-channel method were summed according to the formula:

$$\sigma^T_{nn'}=\sigma^{CN}_{nn'}\left(\frac{\sigma_a-\sigma^D_{nn'}}{\sigma_a}\right)+\sigma^D_{nn'},\qquad (5)$$

where $\sigma^{CN}_{nn'}$ is compound inelastic scattering cross section, $\sigma^D_{nn'}$ is direct inelastic scattering cross section calculated by means of coupled-channel method, σ_a is absorption cross section.

The comparison of the calculated differential elastic cross sections with the experimental ones justifies the conclusion, that the applied optical-statistical approach is adequate for interpretation of the data for nickel and its isotopes. Even the differential cross sections for neutron elastic scattering by oxygen on the whole are interpretable by means of the applied approach. The calculation results obtained with the other sets of optical potential parameters are also in agreement with the experimental data.

The differential cross sections of inelastic neutron scattering with excitation of the first 2^+-levels of the isotopes ^{58,60,62,64}Ni calculated by means of statistical theory and coupled-channel method are in satisfactory agreement with the obtained experimental data at 5.0 MeV neutron energy. The relative contributions of the compound and direct inelastic scattering into the summary cross sections for the nickel isotopes essentially depend on the incident neutron energy. So, at the energy 3.0 MeV the direct inelastic scattering cross sections don't exceed 20% of the summary ones, while at the neutron energy 5.0 MeV their contributions achieve 40-50%.

References

1. M.V.Pasechnik, I,A.Korzh, and E.N.Mozhzhukhin, Proc. of this Conference; Н.М.Правдивый, И.А.Корж, В.А.Мищенко, Э.Н.Можжухин, Нейтронная физика. Матер. IУ Всесоюзной конф. по нейтронной физ., Киев, I977 г., М., ЦНИИатоминформ, I977, ч.I, с.273.
2. В.В.Жук, А.А.Козарь, И.А.Корж, В.А.Мищенко, Э.Н.Можжухин, Н.С.Назаров, М.В.Пасечник, В.С.Подобайло, Н.М.Правдивый, И.Е.Санжур, И.А.Тоцкий, Нейтронная физика. Матер. II Всесоюзной конф. по нейтронной физ., Киев, I973 г., Обнинск, изд.ФЭИ, I974, ч.IУ, с.203.
3. И.А.Корж, В.А.Мищенко, И.Е.Санжур, Укр. физ. ж., I979 (in press).
4. L.F.Chase, R.G.Johnson, R.V.Smith, F.J.Voughn, and M.Walt, AFSWC-TR-61-15, 1961.
5. R.W.Hill, Phys. Rev., 109, 2105(1958).
6. C.A.Engelbrecht, Nucl. Instr. and Meth., 80, 187(1970); 93, 103(1971).
7. P.Boshung, J.T.Lindow, and E.F.Shrader,

Nucl. Phys., A161, 593(1971).

8. F.Bjorklund, S.Fernbach, Phys. Rev., 109, 1295(1958).

9. М.В.Пасечник, И.А.Корж, И.Е.Кашуба, Нейтронная физика. Матер. Всесоюзной конф. по нейтронной физ., Киев, 1971 г., К., Наукова думка, 1972, ч.I, с.253.

10. L.Rosen, J.G.Beery, A.S.Goldhaber, and E.H.Auerbach, Ann.of Phys., 34, 96(1965).

11. D.Wilmore, P.E.Hodgson, Nucl. Phys., 55, 673(1964).

12. B.Holmqvist, Arkiv för Fysik,38,403(1968)

13. P.A.Moldauer, Phys. Rev., B135,642(1964); B136, 947(1964); Rev. Mod. Phys., 36, 1079(1964).

14. И.А.Корж, И.Е.Кашуба, А.А.Голубова, Нейтронная физика. Матер. III Всесоюзной конф. по нейтронной физ., Киев, 1975 г., М., ЦНИИатоминформ, 1976, ч.IУ, с.203; В.М.Бычков и др., Вопросы атомной науки и техники. Сер. "Ядерные константы", вып.19, М., Атомиздат, 1975, с.110; Г.В.Анцыпов и др., Вопросы атомной науки и техники. Сер. "Ядерные константы", вып.20, М., Атомиздат, 1975, с.164.

15. A.Gilbert, A.G.W.Cameron, Can. J. Phys., 43, 1446(1965).

16. U.Faccini, E.Saetta, En. Nucleare, 15, 54 (1968); D.W.Lang, Nucl. Phys., 77, 545 (1966); E.Erba, U.Faccini, and E.Saetta-Monichella, Nuovo Cimento,22, 1237(1961).

17. C.C.Lu, L.G.Vaz, and J.R.Huizenga, Nucl. Phys., A190, 229(1972).

18. T.Tamura, Rev. Mod. Phys.,37, 679(1965).

19. А.В.Игнатюк, В.П.Лунев, В.С.Шорин, Вопросы атомной науки и техники. Сер. "Ядерные константы", вып.13, М., ЦНИИатоминформ, 1974, с.59.

NEUTRON-SPECTROMETRIC ANALYSIS OF THE SAMPLES

V.M. Ivanov, L.V. Karin, V.I. Nazarenko,
N.I. Kroshkin, V.A. Safonov

V.I.Lenin Research Institute of Atomic Reactors
Dimitrovgrad, USSR

Potentialities of sample non-destructive analysis based on resonance neutron transmission through samples have been studied in energy range from 0.1 to 50 eV. Measurements of unirradiated and irradiated samples were performed with a mechanical chopper. Quantitative contents of both initial U-238 nuclei and built up Pu-240 and Pu-242 as well as some built up fission products have been determined. High activity of the samples doesn't affect the measurement results.

[spectrometric analysis,0.1-50eV,transmission,samples,number of nuclei,measurements]

Introduction

Neutron spectrometry is one of the feasible non-destructive methods for sample analysis based on the transmission of the collimated neutron beam through the sample of interest.[1,2] Since each isotope has its own typical absorption line the analysis of the transmitted neutron beam makes it possible to estimate in the sample the presence of the nuclei of one or another isotope and to judge of the amount of the nuclei in the sample according to the decrease in the number of resonance neutrons. The value for dips in the neutron transmission spectra is determined by the dependence of the total cross-section of the material on the neutron energy and by the sample thickness. The neutron energy range from 0.1 to 50 eV is the most convenient one for the analysis. It is within this energy range that the sufficient for the analysis number of strong resonance nuclei of actinides is located.[3]

This paper presents the results from the measurements of five samples to ascertain the potentialities of the method. The real fuel elements from BOR-60 reactor in Dimitrovgrad and from PWR-365 reactor in Novovoronezh were used in the experiments. These investigations aimed to study the effect of fission fragments on the potentialities of the above sample analysis and to ascertain the possibilities for measuring the absolute contents of U-235, U-238, Pu-240, Pu-242 and fission fragments observed.

Experimental Setup

To perform the neutron spectrometric analysis of samples the neutron time-of-flight spectrometer was used. The spectrometer consisted of a neutron selector with four magnetically suspended rotors positioned within the neutron beam of the SM-2 reactor horisontal channel.[4] The measurements were carried out at the rates of 830 and 1660 r/m that corresponds relatively to the resolutions of 450 and 230 ns/m with the rotor slit width of 1.6 mm. The collimator slit width was 1 mm.

Targets

The measurements were carried out at one point (defined by the collimator dimension of 1 x 6 mm^2) for each of five samples. Samples 1 and 2 were prepared from BOR-60 fuel element end-blankets and samples 3, 4, 5 - from PWR-365 fuel elements. Samples 1 and 3 were tested before reactor irradiation. Cylindrical samples 2, 4, 5 of 18 mm length were investigated after irradiation. The initial isotopic content of the samples was taken from the data on standard fuel elements. The samples characteristics are presented in Table I.

Table I. Sample characteristics

Sample	Initial isotopic content		Burn - up, kg/TU
	U - 235	U - 238	
1 - BOR-60	0.45	99.55	-
2 - BOR-60	0.45	99.55	4
3 - PWR-365	3	97	-
4 - PWR-365	3	97	15
5 - PWR-365	3	97	30

The samples were placed vertically. The collimator axis was normal to the axis of the samples. The geometry of measurements is given in Fig.1. The measurements with samples 1, 2 were carried out at the rotor rotation

speed of 830 r/m and with samples 3, 4, 5 at that of 1660 r/m.

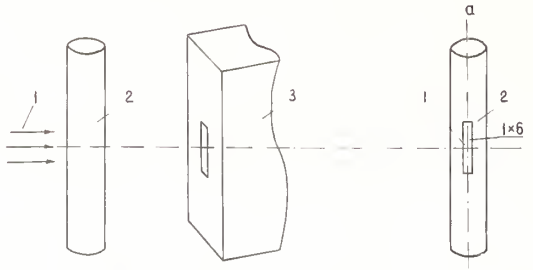

Fig. 1 The measurement geometry: 1 - neutron beam, 2 - sample, 3-collimator, a - front view.

Measurement Results and Discussion

The transmission curves for the samples studied are shown in Figs. 2 and 3.

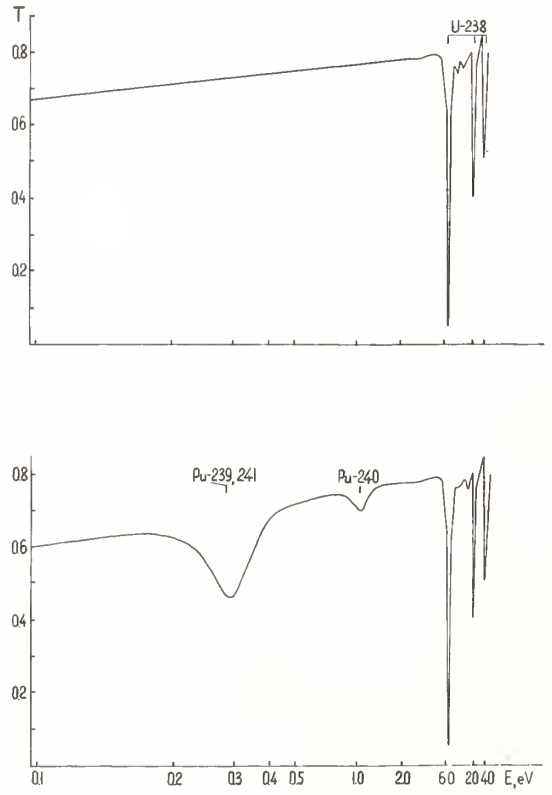

Fig. 2 Transmission through BOR-60 samples: a)before irradiation in the reactor, b) 4 kg/TU burn-up.

For end-blankets 1 and 2 (Fig.2) U-238 was reliably identified according to its neutron resonances (E_0=6.67; 20.90; 36.80eV) and for the irradiated sample 2 Pu-239 was determined according to the neutron resonance of 0.296 eV and Pu-240 - according to that of 1.056 eV.

The comparison of transmission curves for PWR-365 fuel elements with different burnups are of considerable interest. U-238 and U-235 (E_0=6.79 eV), built-up Pu-240, Pu-242 (E_0 = 2.67eV) as well as four nuclei of the fission fragments with a relatively large neutron width, Nd-145 (E_0=4.35eV), Cs-133 (E_0=5.90eV), Sm-152 (E_0=8.05eV), Xe-131 (E_0=14.4 eV) were reliably identified for samples 3,4 and 5 (Fig.3).

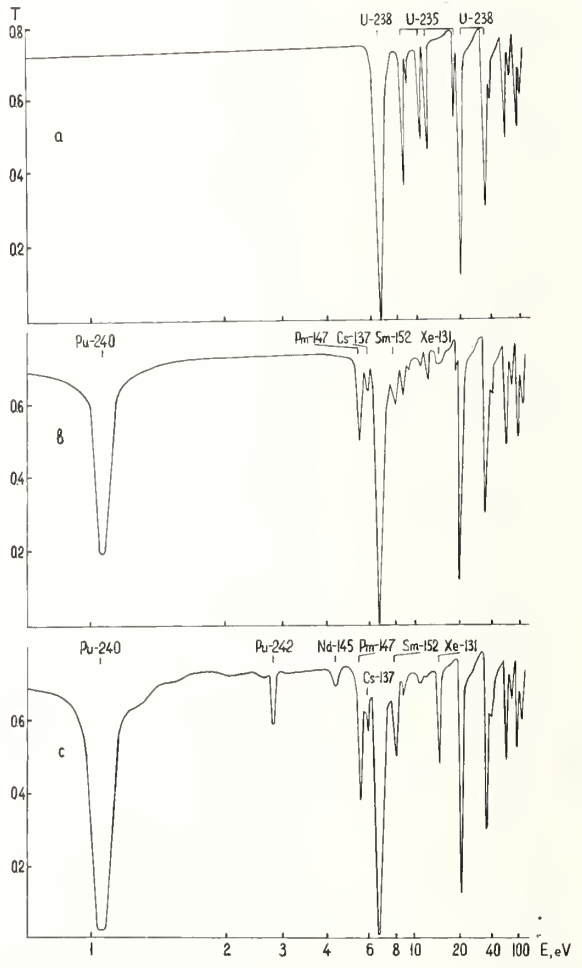

Fig. 3 Transmission through PWR-365 samples: a)before irradiation, b)15 kg/TU burn-up, c) 30 kg/TU burnup

Using the resonance parameters quoted in paper [3] some identified singled out resonances were quantitatively analyzed by the area method (Table II). U-235 nuclei are not quantitatively estimated as far as the uranium resonance levels fall within those of another nuclei and the area method doesn't allow to separate reliably those resonances. The amounts of U-235 and U-238 initial products calculated from the data on isotopic and chemical contents, density and sample dimentions are given in the first columns of Table II. The following columns deal with the results of the measurements.

Table II. Thickness of irradiated samples, nucl./cm^2

Sample	Isotopes						
	Design values for initial product		Measurement results				
	U - 235	U - 238	U - 238 E_0=6.67eV	Pu-240 E_0=1.056eV	Pu-242 E_0=2.67eV	Xe-131 E_0=14.4eV	Nd-145 E_0=4.35eV
1. BOR-60	$4.5 \cdot 10^{19}$	10^{22}	10^{22}	-	-	-	-
2. BOR-60	$4.5 \cdot 10^{19}$	10^{22}	$7.45 \cdot 10^{21}$	$6.47 \cdot 10^{17}$	-	-	-
3. PWR-365	$4.01 \cdot 10^{20}$	$1.29 \cdot 10^{22}$	$1.29 \cdot 10^{22}$	-	-	-	-
4. PWR-365	$4.01 \cdot 10^{20}$	$1.29 \cdot 10^{22}$	$1.23 \cdot 10^{22}$	$1.09 \cdot 10^{19}$	-	-	-
5. PWR-365	$4.01 \cdot 10^{20}$	$1.29 \cdot 10^{22}$	$1.22 \cdot 10^{22}$	$3.49 \cdot 10^{19}$	$5.78 \cdot 10^{18}$	$2.88 \cdot 10^{18}$	$2.3 \cdot 10^{19}$

It should be noted that a high value for gamma-background from irradiated samples is a matter of some difficulties for the personnel but at the same time it doesn't essentially affect the background characteristics of the device and thereby doesn't complicate the identification of the resonance levels and, therefore, has no effect on the measurement results.

In conclusion one should dwell on such important characteristics for the neutron spectrometric analysis as the accuracy and sensitivity. In estimating the number of nuclei in the samples the major errors result from the inaccuracy in the data on the resonance parameters and in the estimation of the area for neutron resonance on the transmission curve, in particular for "black" samples. The accuracy of the resonance parameters so far known is essentially different for various nuclei and resonances and according to the data [3] amounts about 3 % for U-235, about 5 % for U-238, about 4 % for Pu-239 and about 6.5 % for Pu-240. The error introduced to the value of the area for resonance ranges from 8 to 10 %. These values make a major contribution to the total error which was taken into consideration in estimating the number of nuclei in the above investigations and ranges from 10 to 15 %. It is possible to increase the accuracy in estimating the number of nuclei in the presence of the sample-witnesses for which the number of nuclei was determined accurate to about 1 %. The error can be minimised to about 2 % by using the shape method during the treatment of the measurement results that would therefore lead to the reduction of the total error in the sample content assessment to about 3-5 %.

The method is essentially sensitive to Pu-240 and Pu-242 which have an intensive resonance neutron absorption. Table III presents the sensitivity values obtained for Pu-240 and Pu-242 (nucl/cm^2, mg/cm^2). These values were achieved according to the statistical accuracy of about 1 % (the measurement time was about 6 hs) and correspond to resonance "dip" value of about 5 %.

Table III. Sensitivity of the method for plutonium isotopes

Isotope	Resonance energies, eV	Thickness	
		nucl./cm	mg/cm^2
Pu-240	1.056	$4 \cdot 10^{17}$	0.16
Pu-242	2.67	$2.5 \cdot 10^{18}$	1.0

Conclusion

The neutron spectrometric analysis within the neutron resonance energy range from 0.01 to 50 eV can be considered as one of the preferable non-destructive methods. With improving the measurement and calculation techniques this method allows to determine the number of U-235 nuclei and to observe the U-235 depletion particularly in the highly enriched initial fuel. The method is adequate for both irradiated and unirradiated samples. The high activity of the samples doesn't affect the measurement results.

References

1. H.G. Priesmeyer, U. Harz, ATKE 25(1975) 109.
2. S.I. Babich, Yu.S. Zamyatnin, V.M. Ivanov, L.V. Karin, N.I. Kroshkin, V.I. Nazarenko. Preprint RIAR - 15 (349), Dimitrovgrad, 1978.
3. Neutron Cross Section, BNL-325, Third Ed., v.1.
4. S.M. Kalebin, G.V. Rukolaine, V.S. Artamonov, S.N. Nikolsky, N.G. Kocherygin, G.A. Pelevin, Preprint RIAR - 131, Dimitrovgrad, 1972.

RESONANCE PARAMETERS OF Nd-147 ($T_{1/2}$= 11ds) ISOTOPE NEUTRON LEVELS

V.A. Anufriev, S.I. Babich, V.N. Nefedov,
V.A. Poruchikov, V.S. Artomonov
Research Institute of Atomic Reactors,
Dimitrovgrad, USSR

R.N. Ivanov, S.M. Kalebin,
Institute of Theoretical and Experimental Physics,
Obninsk, USSR

time-of-flight method, Nd-147, resonance parameters, 0.01 to 170 eV

The results have been presented on the measurements of Nd-147 ($T_{1/2}$ = 11 ds) radioactive nucleus neutron resonances. The measurements have been performed by the time-of-flight method at the SM-2 reactor neutron spectrometer. Nd-147 was accumulated during neutron irradiation ($1.5 \cdot 10^{21}$ n/cm^2) of Nd oxide (97.5 % of Nd) in SM-2 reactor. The content of Nf-147 ($2.3 \cdot 10^{19}$ at./b) in the irradiated sample was determined from decay produced Pm-147 which was analyzed on three resonance levels with the energies of 5.36, 6.57 and 6.92 eV. In the range from 0.01 to 170 eV eleven levels of Nd-147 have been found and for seven of them the resonanceparameters have been calculated by the area method (see Table below). From the obtained parameters the resonance capture integral I has been calculated (I = 210 ± 90 b).

E, eV	$2g\Gamma_n$, meV	E, eV	$2g\Gamma_n$, meV
4.79	0.36 ± 0.20	22.5	26.4 ± 10.4
6.26	0.76 ± 0.27	33.3	44 ± 28
10.32	2.6 ± 1.3	68.4	-
12.77	4.3 ± 2.1	109.8	-
17.26	5.6 ± 3.3	116.7	-
		167.9	-

NEUTRON PARAMETERS OF CURIUM 242, 244-248 ISOTOPES IN THE RESINANCE REGION

S.I.Babich,N.G.Kocherygin,A.G.Kolesov.V.A.Poruchikov,
V.A.Safonov,V.N.Nefedov,V.S.Artomonov
Research Institute of Atomic Reactors
Dimitrovgrad, USSR

T.S.Belanova, R.N.Ivanov, S.M.Kalebin
Institute of Theoretical and Experimental Physics
Obninsk, USSR

transmission measurements, fast chopper,neutron parameters, Cm isotopes

The transmission measurements have been made on curium oxide samples using the fast chopper at the SM-2 reactor. The resonance parameters were obtained for curium 242,244-248 isotopes levels.

The values of the mean level spacings - D , the average radiation widths - , the neutron strength function - S_o, the resonance absorbtion integrals - $I_{0.4}$ and the energy regions of measurements are given in Table below.

Curium isotopes	Nuclear data				
	D , eV	,meV	$S_o \cdot 10^4$	$I_{0.4}$,barn	Energy region, eV
242	17.6±3.3	55±15	0.64±0.32	115±53	270
244	13 ±2	37±5	0.8 ±0.3	640±50	280
245	1.5±0.1	-	0.9 ±0.2	-	50
246	31 ±6	27±3	1.3 ±0.7	105±9	160
247	-	123±35	-	-	20
248	16 ±4	25±3	1.4±0.8	266±25	100

THE OKLO PHENOMENON AND THE ROLE OF NUCLEAR DATA IN IT'S STUDY

E. ROTH(+) - R. HAGEMANN(++) - RUFFENACH(++)

The study of the OKLO phenomenon requires, but also provides, in some cases better nuclear data than were available at the time of it's discovery. Examples of this situation are given particularly for rare earth's fission yields and neutron capture cross sections.

(Natural fission reactor, Gabon, age of deposit, fluence, fission products, duration, temparature)

Introduction

The story of the discovery of the OKLO phenomenon has been told at other occasions (1). In this paper I wish to emphasize how important, for the understanding of the processes that led to the occurence of natural fission chain reactions, are precise nuclear data, such as fission yields and neutron cross sections.

Small uncertainties on nuclear quantities make it impossible to choose qualitatively between various geophysical hypothesis.

But, more important perhaps to this audience, is the fact that the study of those fossil reactors contributes to improve the knowledge of such quantities.

General pictures of the OKLO quarry and of the "nuclear reactors"

It is situated in the south-eastern part of Gabon. The Gabonese Republic lies at the equator in Western Africa. (fig I)

The geologic formation where the uranium deposit is found is known as Francevillien. It has been thoroughly studied.[2]

It is a sedimentary, precambrian series, that rests upon a cristalline (granitic) base.

In one of the sandstone layers, close to an upsurge of the cristalline bed, and covered by pelitic layers, uraniferous material is found.

Within an area several hundred meters long and at depths varying by 50 meters, nine reaction zones have been discovered. A tenth has been reported about 1.5 km south from the quarry.[3] (fig.2)

The characteristics that enabled chain reactions to take place were :

a) the age of the deposit. It is roughly two billions years old, and at that time natural uranium was about 3 % rich in 235_U .

b) The chemical concentration of uranium. It is high, often more than 20% now.

c) The thickness of the layers. It exceeds often several decimeters.

d) Enough water, and little nuclear poison present at the time of deposition.
Those necessary conditions for divergence were met at OKLO.

(+) DCh - CEN. Saclay - BP n° 2 - 91190 Gif-sur-Yvette (France)
To whom correspondence should be addressed.
(++) DCAEA - CEN. Saclay - BP n° 2 - 91190 Gif-sur-Yvette.

In the regions explored up to now about 800 tons of uranium were involved in nuclear reactions, and a total quantity of about 6 tons of uranium 235 underwent fission.

However, due to a conversion factor of .4 to .5 and to decay, the present deficit in 235_U at OKLO is only about 600 kilograms.

A total energy of 500 billions megajoules was evolved, corresponding to the continuous operation of a 1000 MW_{th} reactor for about 15 years, or rather of a 15 kilowatt source for one million years, as we will see.

As soon as the proof of chain reactions was offered, by both the chemical and the isotopic compositions of rare earths present in the uranium ore, the following questions were raised.

How did the "reactors" start, how were the reactions sustained and finally brought to an end ?

To establish these, in turn we wanted to know , quantitavely, the "burn up" of the ore, i.e the integrated fluence it underwent. Together with the fluence the instantaneous flux, or power level, provides the duration of the reaction.

Finally an evaluation of temperatures reached is important to understand moderation and cooling mechanisms. A knowledge of the proportions of fissions that occured in 238_U (α) and 239_{Pu} (β) also contributes to the total picture. Isotopic analysis of fission products and uranium provide many of the answers, when the necessary nuclear data are at hand,[4] as can be seen from the following section, and 9.

Use of nuclear data to evaluate physical parameters characterising the chain reactions

Measurement of total fluence τ

From observed variations in isotopic composition of uranium one can calculate the fluence τ .

As first approximation (without considering the formation of Pu and it's decay to 235_U).

$$\tau_m = \frac{1}{\sigma_5 - \sigma_{c8}} \ln W \qquad (1)$$

where $$W = \frac{(N_5/N_8)_n}{(N_5/N_8)} \qquad (2)$$

N_5, N_8 are the number of atoms of 235_U and 238_U present now in the sample.

$\left(\frac{N_5}{N_8}\right)_n$ is the "normal" ratio usually observed.

σ_5 is the total neutron cross section of 235_U (fission plus capture)

σ_{c8} is the capture cross section of 238_U.

When the "restitution factor" C is taken into account the formula becomes :

$$\tau = \frac{1}{(1 - C)\sigma_5 - \sigma_{c8}} \qquad (3)$$

WHERE $C = N_8 \cdot \sigma_{c8} / N_5 \sigma_5$

From an isotope of a fission product

if ρ is the fission yield of this isotope

σ_c it's capture cross section

No the total number of atoms of this isotope that were formed

N the remaining number of atoms, after neutron capture.

then :

$$\frac{No - N}{No} = 1 - \frac{\ln W + \sigma_{c8}\tau}{\ln W + \sigma_{c8}\tau - \sigma\tau} \cdot \frac{\exp(-\sigma_{c8}\tau) - W\exp(-\sigma_c\tau)}{\exp(-\sigma_{c8}\tau) - W}$$

from this formula $\sigma_c \tau$ is derived.[5]

Spectral index and resonance integral

From the well known formula

$$\sigma_c = \sigma_0 + r\,I \qquad (4)$$

one also derives r "spectral index" from σ_c measured, σ_0 (2200 m/s cross section), and I (resonance integral), tabulated.

Proportion of ^{238}U (α) and ^{239}Pu (β) fissions.

One uses two isotopes showing fission yields different for the three nuclides ^{235}U, ^{238}U, ^{239}Pu (table I).

From every measured isotope yield one derives a linear relation between α and β that can be represented by a straight line. The use of two isotopes supplies two linear relations, or graphically two straight lines, whose intersection in the α, β plane has the desired values of α and β as coordinates. (fig. 3 from 5).

Duration of the reaction (Δt)

It is calculated from nuclides decaying both by neutron capture and natural decay. This method is analogous to that used in geophysics to evaluate exposure times of meteorites.

Δt from Plutonium 239

(^{239}Pu formation obeys the following equation :

$$\frac{dN_9}{dt} = N_8\sigma_8\phi - N_9\sigma_9\phi - N_9\lambda_9$$

Equilibrium is reached when $\frac{dN_9}{dt} = 0$

then $N_9 = \frac{N_8\sigma_{c8}\tau}{\sigma_9\tau + \lambda_9\Delta t}$

As ^{235}U is formed from ^{239}Pu.

$$\frac{dN_5}{dt} = -N_5(1-C)\sigma_5\phi = -N_5\sigma_5\phi + N_9\lambda_9$$

finally $N_9 = \frac{N_5 C(\sigma_5\tau)}{\lambda_9 \Delta t}$

and as $\beta = \frac{N_9\sigma_{f9}}{N_5\sigma_{f5}/1-\alpha-\beta}$

$$\Delta t = \frac{\sigma_{f9}\cdot\sigma_5}{\sigma_{f5}} \cdot \frac{1-\alpha-\beta}{\beta} \cdot \frac{C\cdot t}{\lambda_9} \qquad (5)$$

It is seen that one must calculate C, α and β in order to obtain Δt.

Δt from ^{99}Tc

Fig (6) shows the desintegration scheme of ^{99}Tc to ^{99}Ru (T 1/2 = 2.10^5 y).

99 T_c is produced with a high fission yield, and produces also ^{100}Ru by neutron capture.

When such competition arises between two different modes of decay of a nucleus, leading to two discernable end-product, and when one of them has a constant relaxation time the duration of the other can be calculated.[5]

Age of the reaction

The age of the uranium deposit can be calculated from conventionnal isotope geochemistry, applied to elements unperturbated by the fissions. Thus, from isotopic lead analysis and/or uranium-lead ratios, in normal zones of the quarry, or from Rubidium-Strontium studies on the pelite cover, ages can be calculated.

However, in addition, an important method of cross-checking ages has been developped.[6]

From the above mentionned nuclear data, namely total fluence and conversion factor, the number of fissions that took place in a given volume of ore can be calculated, and expressed as a proportion, of the number of atoms of Uranium undergoing fission. Under the assumption that the system has behaved as a closed box the present ratio of a given stable fission nuclide to the remaining Uranium isotope provides a "chronometer".

The comparison of ages calculated by such timekeepers (they are as many, in principle, as stable fission nuclides) with those resulting from well established methods leads to two different kinds of results.

- a check of the validity of the closed box model. This is of primary geochemical importance, and in the present case leads also, element by element to an evaluation of the stability of fission products and transuranium elements buried in the same environment as Uranium.[1] and [11]

- a check of the values of fission yields and capture cross sections for some nuclides.

When the abundance of an isotope of an element can be interpreted, according to the closed box model, one should be able to calculate the abundances of the other isotopes of the same element in the same way, in cases where they are also formed directly in fission. Discrepancies must lead to check nuclear data. Several examples of this situation have been quoted in the litterature (see[7]) and are illustrated by the attached tables (tables 2 to 4) of sentivity of τ and Δt to σ_{f5}, and of isotopic composition to ρ

Temperature measurements

A situation similar to that arising from the comparison of different methods of measuring ages develops in the case of evaluation of temperatures at which the chain reactions took place.

Non-nuclear methods are founded on thermal conduction estimates, observation of fluid inclusions, mineralogical observations (nature of cristalline species, reflecting power of graphitized deposits, etc...).

Nuclear determinations are based on the measurement of isotopic ratios in Lutetium. Lutetium is not a fission product and is present during the reaction and has two isotopes : ^{175}Lu and ^{176}Lu. The neutron cross section of the latter is particularly sensitive to temperature. In our laboratories a model has been developed to calculate this temperature from Lutetium isotopic ratios (see [8]). Gadolinium 155 can be used also for neutron temperature measurement in a similar way, though(fig. 4) shows that it's variation with temperature is in the opposite direction of that of ^{176}Lu.(fig. 5) shows the parametric variations of $\hat{\sigma}\,^{176}Lu$. with λ.

The validity of the results is again sharply dependent on the relative stability in the deposit of Uranium and rare earths and the coherence of evaluations from differents methods provide both geochemical evidence of this stability, and again needs to rest on well established nuclear data.[11] They may therefore lead to reconsider the existing litterature, specially when data arising from two different sets of isotopes are compared.

Conclusions

The study of the OKLO phenomenon has already led to the reinvestigation of many fission yields and neutron cross sections. [3]

The necessity that geochemical deductions be coherent when obtained by using different independant nuclear groups of data is a particularly sensitive test on some of these.

Preservation of part of a "reactor" in zone two of the OKLO quarry has been undertaken in order, to keep the road open to further sampling for further investigations.

Aknolwledgments

Dr DEVILLERS and Dr HOLLIGER worked out the temperature measurements methods. Many ideas developed have benefited by discussions with Mr NAUDET.

References

1. E. ROTH in Proceedings of the Conference in high-level radioactive solid waste forms at Denver (Colorado), USA, 1978. ed. bg Leslie A. CASEY (Office of Nuclear Material Safety and Safeguards U.S. - Nuclear Regulatory Commission) Washington D.C. USA NUREG/CP-0005.

2. In the OKLO phenomenon Proceedings of a symposium held in Libreville (1975) ed. by International Atomic Agency (IAEA) Vienna (1975) see P. MOLINA and J.C. BESOMBES, and references quoted.

3. R. NAUDET - private communications, and in 2 and 4.

4. Natural fission reactors. Proceedings of a technical Committee Meeting held in Paris 1977 edited by IAEA Vienna 1978.

5. J.C. RUFFENACH - Thesis Paris 1979.

6. C. DEVILLERS - J.C. RUFFENACH - J. MENES - Monique LUCAS - R. HAGEMANN - G. NIEF in 2.

7. W.J. MAECK, F.W. SPRAKTES, R.L. TROMP, J.H. KELLER in 2. W.J. MAECK, J.E. DELMORE, R.L. EGGLESTON, F.W. SPRAKTES in 4.

8. Philippe HOLLIGER - Thesis Paris 1978 and C. DEVILLERS and Ph. HOLLIGER to be published in Eart and Planetary Science Letters.

9. J.C. RUFFENACH, R. HAGEMANN and E. ROTH to be published in zeitschrift fur Naturforschung.

10. F.B. RIDER and M.E. MEEK - Nedo 12154-2 (D) 1977.

11. G. COWAN in 2 and 4

12. M. LUCAS - R. HAGEMANN - R. NAUDET et al.in 4.

13. M.E. MEEK and B.F. RIDER - Nedo 12154 (1972)

14. M.E. MEEK and B.F. RIDER - Nedo 12154-1 (1974)

15. B.F. RIDER and M.E. MEEK - Nedo 12154-2 (D) (1977)

FIG (1) Location of the OKLO quarry.

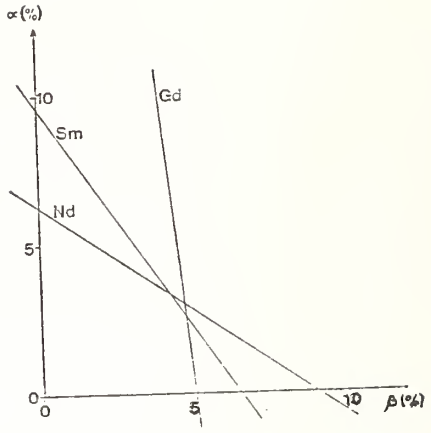

FIG (3) From [5]
Determination of α and β .

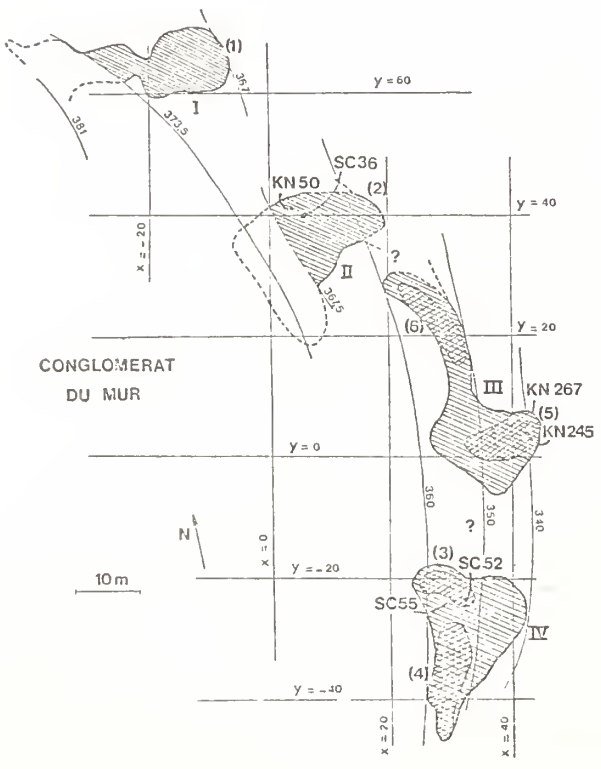

FIG (2) from [8]
Map of the "reactor's zone.

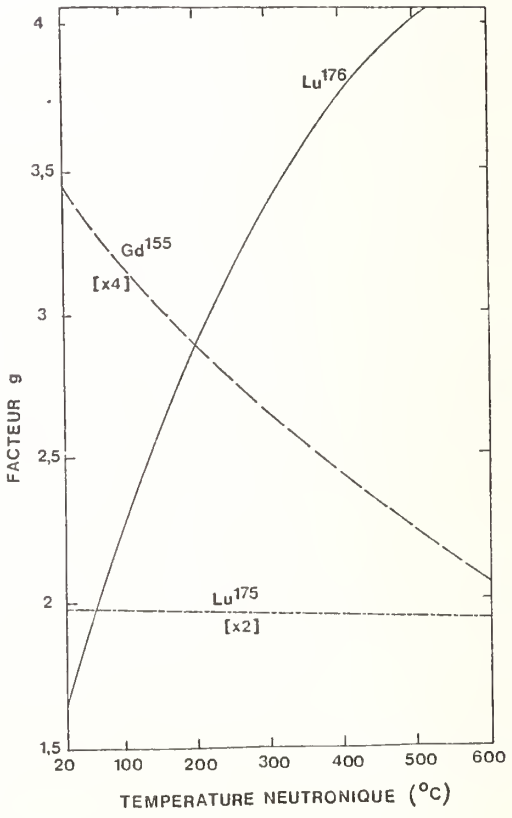

FIG (4) from [8]
g factors for ^{155}Gd , ^{176}Lu , ^{175}Lu

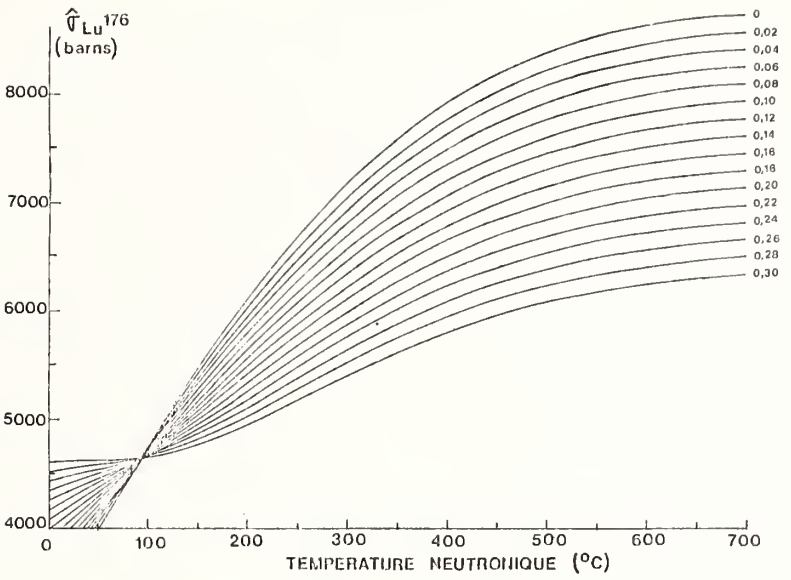

FIG (5) from [8]

Effective cross section-temperature relations for different spectral indexer.

FIG (6) from[5]
Desintegration schema of ^{99}Tc

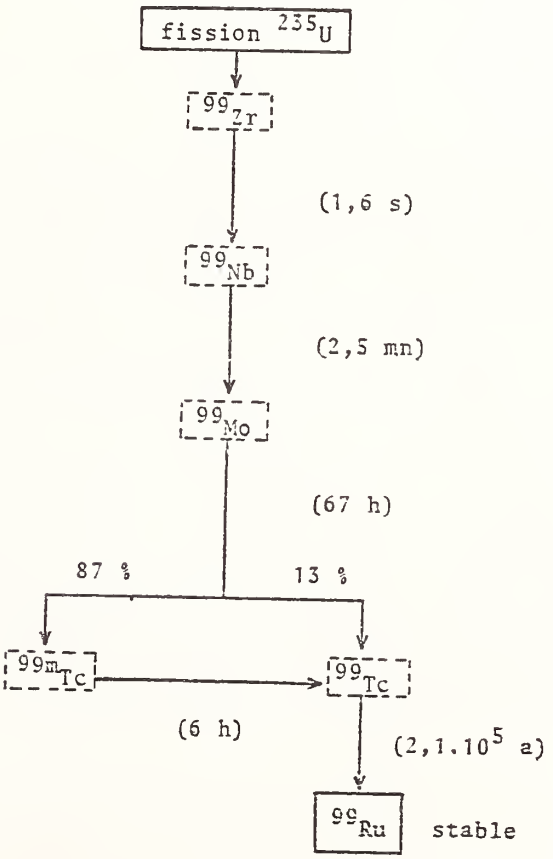

(ρ_{99} = 6,13 %)

TABLE I

FROM REF. 10

SAMARIUM FISSION YIELDS (F.Y.) AND ISOTOPIC PERCENTAGES (I.P.) FROM ^{235}U, ^{238}U AND ^{239}PU FISSIONS

	^{235}U		^{238}U		^{239}PU	
MASS NUMBER :	F.Y.	I.P.	F.Y.	I.P.	F.Y.	I.P.
144	-	-	-	-	-	-
147	2.229	61.14	2.514	51.87	2.050	49.29
148	-	-	-	-	-	-
149	1.075	29.49	1.601	33.03	1.244	29.91
150	-	-	-	-	0.00012	0.03
152	.268	7.35	.519	10.71	0.591	14.21
154	.0736	2.02	.213	4.39	0.273	6.56
TOTAL	3.646		4.847		4.159	

TABLE 2

SENSITIVITY OF τ, λ, AND AND C TO σ_s IN BARNS OF NEODYMIUM

σ IN BARNS	$\sigma_{143} = 325$ $\sigma_{147} = 64$ $I = 714$	$\sigma_{143} = 266$	$\sigma_{143} = 335 - 100\,\lambda$ $= 338 - 100\,\lambda$ ($t = 400°C$) $\sigma_{147} = 52 + 600\,\lambda$
τ	1.33 10^{21}	1.63 10^{21}	1.36 10^{21}
λ	0.13	0.13	0.17
C	0.47	0.57	0.49
t IN 10^9 YEARS	1.98	1.78	1.96
REFERENCES :	FROM BNL 325	FROM MAEK IN 2	FROM NAUDET 12

TABLE 3

SENSITIVITY OF CALCULATED DURATION TO $\sigma_{99}\tau_c$ AND α

SAMPLE KN 50-323 $\tau = 1.12\ 10^{21}\ n/cm^2$

	$\sigma_{99}\ \tau_c = 19 + 340\ \alpha$	$\sigma_{99}\tau_c = 20 + 186\ \alpha$
$\alpha = .16$		$1.\ 10^6$
$\alpha = .17$	$\Delta t = 5.10^6$	$1.7\ 10^6$
$\alpha = .18$		$3.6\ 10^6$
REFERENCES :	FROM BNL 325	FROM NAUDET [12]

TABLE IV

COMPARISON OF OBSERVED AND CALCULATED ISOTOPIC COMPOSITIONS FOR NEODYMIUM

ISOTOPES	MEASURED SAMPLE KN 50-3548	CALCULATED ASSUMING $\alpha = 2\ \%$ FISSION YIELDS FROM [13]	FROM [14]	$\beta = 5\ \%$ FROM [12]
143 + 144	55.08	55.82	54.81	55.01
145 + 146	33.45	33.59	33.59	33.45
148	8.17	8.28	8.29	8.22
150	3.30	3.31	3.31	3.32

THE SET OF FISSION YIELDS USED FOR THE LAST COLUMN PROVIDES THE BEST AGREEMENT

THREE MILE ISLAND

A. R. Buhl
Technology for Energy Corporation
10770 Dutchtown Road, Knoxville, Tennessee 37922

(T.M.I. sequence of events, hydrogen bubble myth, China syndrome myth, reactor safety system, reactor cooling)

The Three Mile Island accident was the worst accident ever experienced by the nuclear power industry. Although the radiation exposures were extremely low, the potential for greater public exposure did exist. Fortunately, the health and safety of the public were not affected by radiation, nor was anyone killed or injured; however, thousands of lives were disrupted by fear and anxiety and by a limited evacuation.

I had the opportunity and responsibility to work on the recovery from this accident from both sides. For the first week and a half, I worked for the Nuclear Regulatory Commission as director of the organization responsible for risk assessment and was directly involved in the recovery effort. Upon leaving the government (incidently, I had resigned long before the Three Mile Island accident), I immediately began working for the industry in its recovery efforts.

Events like that at Three Mile Island are unacceptable to our society - not so much in terms of the economic costs as in the fear that they arouse in the public. I think that much of the fear caused by the Three Mile Island accident was the result of three or four myths concerning the incident, which are still very much alive. What I'd like to do is to expose these myths and then describe the accident sequence.

I will describe what I saw and what I think really happened at Three Mile Island. If I had to choose one word to describe the Three Mile Island (TMI) accident, I would select the word "confusion." Clearly, the TMI operators were confused very early on by what the alarms and instruments were telling them. I define the "accident" as starting at 4:00 AM and lasting until about 8:00 that evening (about 16 hours). In the first 10 seconds of this accident there were some 48 alarms on the control panel. During the entire 16-hour period, there were some 1800 alarms. Confusion existed among those who were trying to make decisions, both inside and outside the control room. Misinformation ran rampant in both directions — that is, from the site and to the site. There was very poor telephone communication with the plant personnel. The public was equally confused by what the NRC and the utility spokesmen were telling them. Perhaps the most serious factor, as far as public confidence and the effect of TMI over the long term, was the very poor public information system.

The least productive thing I've ever done is to attack the press, and when I talk about poor public communication at TMI, I'm not blaming the press. I think the public confusion was caused primarily by the NRC and by the utility spokesmen. This area needs substantial improvement.

Now, to the major myths surrounding the TMI accident. I think the biggest error in the assessment of the incident at the time was what I call the explosive hydrogen bubble myth. The explosive hydrogen bubble that put fear into so many people never existed — such an explosion was impossible! This single item aroused the greatest fear in the public. In fact, on the Sunday morning following the creation of the explosive hydrogen bubble myth, a priest gave general absolution to the congregation at a nearby church. I am told that this occurred in many other churches in the Harrisburg area.

The second myth is that the TMI operators are to blame for the accident. In my view, the operators did what they were trained to do. These were experienced operators. Unfortunately, the training and operating environment proved to be inadequate in some areas. These deficiencies are now being corrected.

The third myth is that the "China syndrome" was imminent. When I was with the NRC, we were constantly concerned with the probability of core melt and were evaluating what the consequences of such an eventuality might be. I can assure you (and I've never understood why this was not affirmed publicly) that, using all the evaluations that were available to them, the senior staff at the NRC concluded that, under core melt conditions, the safety systems and containment would prevent a major radioactive release.

The fourth myth is that the emergency feed-water valves, which were closed before the accident occurred, caused the accident. Not true! This human error did contribute to the confusion during the accident, however. In retrospect the accident could have been terminated instantly if either of two courses of action had been followed. One was for the operators to walk away for the first couple of hours and let the safety systems operate by themselves. The second was for someone to push the one button on the control panel that would have closed the block valve.

Now, I will describe the accident at TMI. Actually, what happened was not so much a nuclear accident as it was a series of errors and failures caused by a lack of understanding of some very fundamental engineering. The accident occurred in the reactor containment building. I shall describe what happened during the course of the accident (Table 1). I put a star at the release valve (Fig. 1) to indicate that it was the star culprit in the accident. There are two significant fundamental priciples that dictate safety, whether a plant is under an accident condition or whether it is operating in normal circumstances. First, the water (as liquid) in the primary system must always cover the core. So, the first safety principle is "please keep water cooling the core of any reactor at all times." Second, in the secondary system water flows into the steam generator and through the turbine and is subsequently cooled by water from the cooling tower and pumped back into the steam generator. This is the so-called heat sink in engineering lingo. The second fundamental safety principle is "maintain a system to remove heat from the water in the primary loop." Again, the

two principles — keep the water flowing in the primary loop and to keep it from becoming steam continue to cool the primary water using the secondary loop.

What happened before the accident? There were two conditions of concern. First, the relief valve (A in Fig. 2), which functions very much like a pressure relief valve on a pressure cooker, had been leaking for about three days before the accident. Second, the emergency feed-water valves (B in Fig. 2), which provide emergency water to the secondary loop, had been closed for some reason. This was a clear violation of technical specifications. Nevertheless, these two negative conditions existed before the accident began. The accident began at 4:00 AM. The feed pumps and the condensate pumps, located within the secondary loop, tripped; the turbine tripped; and the emergency feed-water pumps began operating. All these are normal occurrences; they happen often. The plant is designed precisely for these occurrences. The safety systems came on, as they were designed to do. When high pressure was indicated, the relief valve opened, as it was designed to do. The reactor shut down some 8 seconds into the accident. The first indication of difficulty came at 4:01 AM when the relief valve failed to close. The plant has a backup valve that, had it been closed, would have terminated the accident. Unfortunately, the operators did not realize that the relief valve was stuck in the open position.

At 4:01 the safety valve temperature alarm came on, which was an indication that something was amiss in the safety valve or in the relief valve region. At 4:02 the drain tank, which collects the steam flowing out of the pressurizer through the relief valve, showed malfunction — another indication of difficulty. At 4:02 the steam generator boiled dry. Very quickly the plant was getting to the stage at which the two safety principles I mentioned were in jeopardy. At 4:03 the operators turned off the safety system that was providing emergency cooling water to the core. When this system came on, as designed, the operators saw it, but because they were primarily concerned with something called pressurized level (the level of the water in the pressurizer), they turned off the safety system to eliminate what they believed would be too much water! The drain tank again showed malfunction and opened a valve; again indicating some problem with the flow into the drain tank. At 4:04 the drain tank alarmed and opened.

At 4:06 the primary water was boiling. At 4:08 the operator discovered that the emergency feed-water valves were closed, and he opened them. At this point, water, as liquid, was not cooling the core, and water in the secondary system was not of sufficient volume to remove heat from the primary loop. Eight minutes into the accident the operator discovered this and turned on the water from the condensate storage tank to provide a "heat sink." The accident continued.

At 4:08 the sump pump came on automatically. The drain tank (shown on the top of containment to the left) had opened a rupture disk and water had spilled into the bottom of the reactor building. The sump pump came on to pump this water to the adjacent building, into a tank designed for this purpose. Unfortunately, the pump continued to operate, unnoticed for several hours, much as a sump pump in one's basement, and proceeded to fill and, in fact, overflow the storage tank.

The operator had asked the computer repeatedly about the relief valve condition, but it was not until some time later, after asking again, that the reactor operator recognized that this valve was open. All this time, from 4:00 to 6:22, the relief valve had been open, dumping primary water into the reactor building, and the operators had not known it was happening.

At 5:41 the last reactor coolant pumps were turned off by the operator. At 6:22 the operator discovered the open relief valve and closed it. For the operators, from 6:22 AM on until later that evening, the whole situation became a wrestling match to keep water in the primary and secondary systems because these systems had been substantially overheated. At 7:24 AM a general emergency was declared, based on the activation of radiation alarms inside the containment. The accident progressed on through the day, spilling more water into containment. At 7:50 PM the main coolant pumps were turned back on. This terminated the accident phase and led to some of the more exciting parts of the accident, such as the hydrogen bubble myth, and many others, in the following days. Fortunately, radiation releases from the accident were very small, as shown in Table II.

This has been a very quick summary of the accident. My conclusion, based on my own involvement in supporting the recovery phase of this accident, is that reactors and nuclear power will be much safer in the future because of TMI. I think it's extremely unfortunate that the people of Harrisburg, and the people around the world, were so misinformed — we were responsible for frightening a lot of people!

The TMI accident was the worst in our commercial nuclear power experience. Although the effects on public health were small — no one was killed or injured — the potential for greater exposure existed. The threat was great, but potential consequences were limited. If I learned anything from my experiences at TMI, it is that commercial nuclear plants are safer than I had ever believed them to be, and, that by applying the lessons learned at TMI, they will become even safer in the future.

Our generation faces major energy decisions primarily because of inadequate domestic supplies of oil and natural gas, and because of predicted future world shortages of energy products. Decisions will be based on environmental and economical factors as well as safety considerations. Weighing these factors, nuclear power remains a very attractive energy option. Our experiences with TMI have redoubled my conviction that the United States must maintain a solid commitment to nuclear power.

The nuclear industry may suffer further slowdowns and delays, but the technology to provide nuclear energy safely is within reach. There are no alternatives to nuclear power if America is to regain its economic viability. Imported oil is the heart of inflation. What is at stake is the national economy — jobs and a way of life based on freedom of choice.

TABLE I

SEQUENCE OF EVENTS IN THE
THREE MILE ISLAND UNIT TWO ACCIDENT

Approximate Time	Event
Before Accident	A Relief valve leaking (Fig. 2) B Emergency feed-water valves closed (Fig. 2)
4:00 AM	C Condensate pump & feed pump tripped (Fig. 2) D Turbine tripped (Fig. 2) E Emergency feed-water pumps tripped (Fig. 2)
4:01 AM	A Relief valve opened (Fig. 2) F Reactor shutdown (Fig. 2) A Relief valve failed to close (Fig. 2) G Safety valve temperature alarm came on (Fig. 2)
4:02 AM	H Drain (relief) tank alarmed (Fig. 1) I Steam generator boiled dry (Fig. 2)
4:03 AM	J Cooling water safety system turned off (Fig. 2)
4:04 AM	H Drain tank alarms again and opens (Fig. 1)
4:06 AM	K Primary water boiling (Fig. 2)
4:08 AM	B Emergency feed-water valve opened (Fig. 2) L Sump pump started (Fig. 1)
4:15 AM	H Drain tank bursts (Fig. 1)
4:25 AM	B Operator asked computer about condition of relief valve (Fig. 2) L Sump pump radiation alarm (Fig. 1)
5:25 AM	B Operator again asked computer about condition of relief valve (Fig. 2)
5:41 AM	M Last two reactor coolant pumps stopped by operator (Fig. 2)
6:22 AM	B Operator discovers open relief valve and closes it (Fig. 2)
7:24 AM	General emergency declared
7:56 AM	Containment automatically isolated
1:50 PM	N Hydrogen detonation in containment (28 psig) (Fig. 1) P Containment sprays turned on (Fig. 1)
7:50 PM	Q Reactor coolant pump started by operator (Fig. 1)

TABLE II

HEW, EPA, & NRC JOINT REPORT CONCLUDES OFFSITE DOSE FROM TMI ACCIDENT WAS VERY SMALL

— Collective person dose out to 50 mile radius (Person-rem)	
High estimate	5,300
Best estimate	3,300
Low estimate	1,600
Natural background	270,000
— Average individual dose (annual)	1.5 mrem
— Maximum possible individual	86 mrem
— Natural background individual	116 mrem

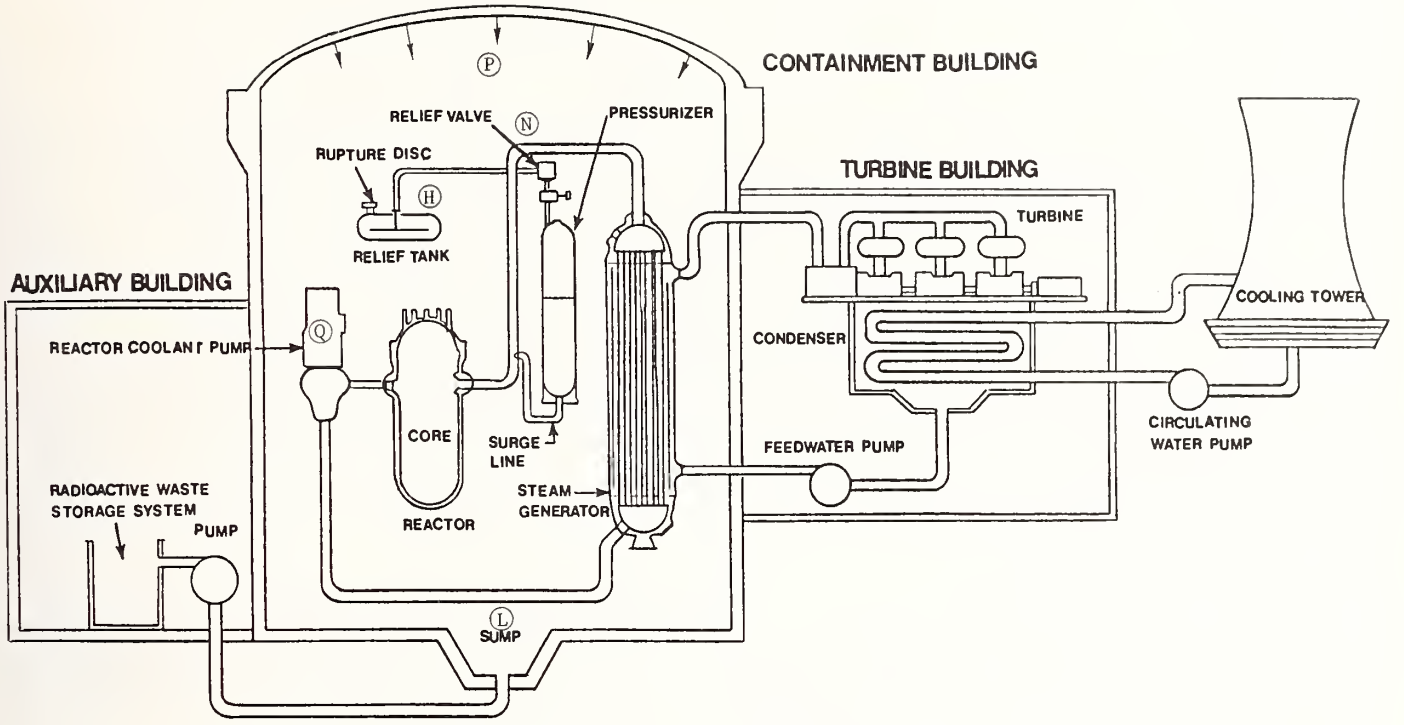

Fig. 1 Three Mile Island Unit Two Plant Layout

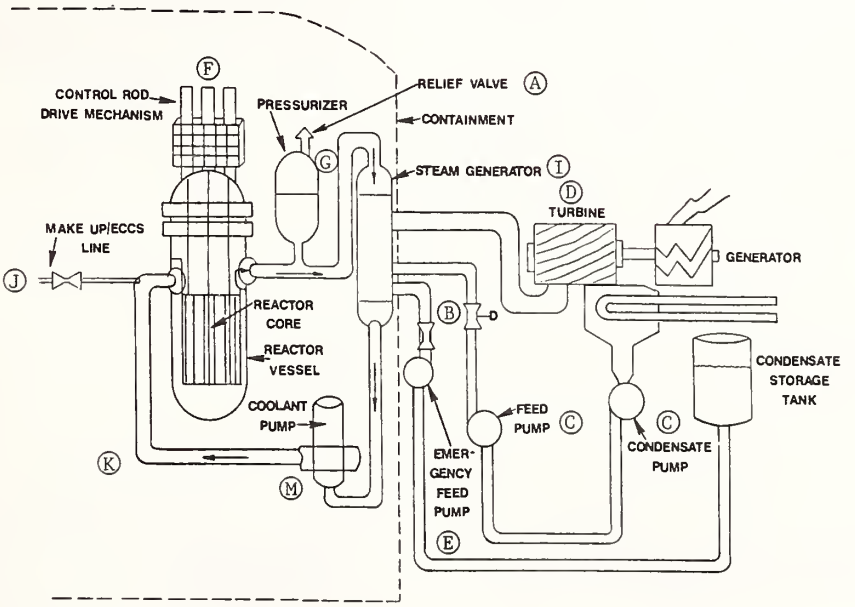

Fig. 2 Schematic of the Accident in Three Mile Island Unit Two

STATUS AND COMPARISON OF NEW, PLANNED, AND UPGRADED PULSED 'WHITE' NEUTRON SOURCE FACILITIES SINCE 1970

G. F. Auchampaugh

University of California, Los Alamos Scientific Laboratory, Los Alamos, New Mexico 87545

The status of pulsed 'white' neutron sources has changed in the last several years. The Weapon Neutron Research (WNR) facility at the Los Alamos Meson Physics Facility has become operational. Work has continued on the conceptual design for the proton storage ring at WNR, which will increase the proton intensity on target by 50 to 1000 times and modify the frequency of the proton beam from 1 to 720 Hz. A prebuncher has been installed at the Oak Ridge Electron Linear Accelerator to compress 15-ns-wide pulses into about 3-ns-wide pulses without loss in neutron intensity. Also, the electron linear accelerator at Geel has been upgraded with new waveguides, increasing the electron energy to 150 MeV, and with modifications to the buncher and gun, which improve the performance of the machine at narrow pulses. The Atomic Energy Research Establishment at Harwell has just finished construction of a new 136-MeV electron linear accelerator which will be commissioned this fall. The characteristics of these new facilities are discussed and compared in this paper.

("White" neutron sources, HELIOS, GELINA, WNR, PSR, ORELA, KFK, comparison neutron yields)

Introduction

It has been at least nine years since the status of pulsed 'white' neutron source facilities was last reviewed.[1,2] During this time several new facilities have either become operational or will become operational shortly, and others have been upgraded or modified to increase neutron intensity and improve neutron-energy resolution. The justification for these new facilities and the modifications to existing facilities has been to address the increasing requests from the fast breeder and magnetic fusion energy programs for nuclear data in the kiloelectron-volt and million-electron-volt regions. This talk is a review of the status of the new electron linear accelerator (linac) at Harwell, the upgrading of the linac at Geel, the installation of the buncher at the Oak Ridge linac, the proton linac at the Los Alamos Meson Physics Facility, the addition of the proton storage ring to this facility, and the improvements in pulse width at the sector-focussed cyclotron at Karlsruhe.

HELIOS

A new zero-load 136-MeV, 8-section, L-band electron linac has been built at Harwell (HELIOS) to replace the 55-MeV linac. This machine can accommodate a wide range of experiments with different beam conditions, both simultaneously and individually, from photonuclear studies to nuclear and condensed matter studies with neutrons. The pulse width can be varied from 5 to 5000 ns and the peak beam current from 1 to 6 A. The frequency of the electron beam pulse can be varied up to 2 kHz. A maximum of 90 kW of beam power can be delivered, but it will be limited to 50 kW on target in normal operation.

One of the unique features of this facility is that it can multiplex the beam into several target cells on a pulse-to-pulse basis with different beam conditions for each target cell. A layout of the facility, showing the four target cells, is given in Fig. 1. The fast neutron cell (FNC), booster cell (BC), and condensed matter cell (CMC) will be used to study the interaction of neutrons with matter. The low energy cell (LEC) will be used for photonuclear studies. The pulse width and peak current will be varied from pulse to pulse, thereby optimizing the beam conditions for each target cell and effectively increasing the available machine time by about a factor of 2. Anticipated neutron yields for the different target cells under optimum conditions are given in Table I.

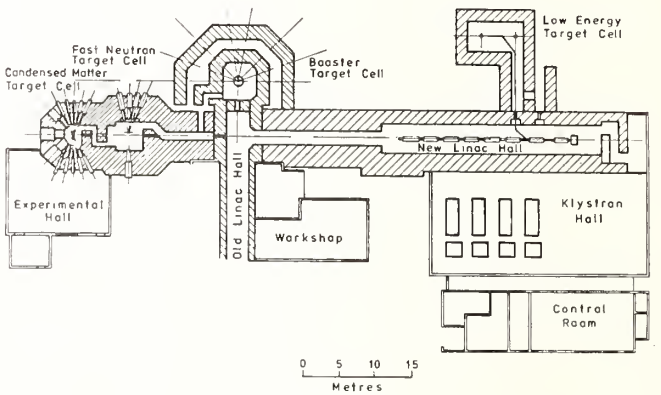

Fig. 1. The 136-MeV linac at Harwell (HELIOS).

Concurrent with the high degree of flexibility built into this facility are a large number of flight tubes and experimental stations. The BC, which contains the Harwell neutron multiplying uranium assembly, has 11 flight tubes between 10 and 300 m long. The BC will be used primarily in the energy region below approximately 100 keV. The target cell, flight tubes, and experimental station are part of the original Harwell linac. The FNC, which contains a normally unmoderated, water-cooled natural uranium target, will be used to study neutron interactions in the energy region from a few tens of kiloelectron volts to a few tens of million electron volts. Eventually, the FNC will have five flight tubes between 20 and 400 m long. Currently, a 150- and a 70-m-long flight tube are being built.

The CMC, which contains a uranium target with moderator, will be used to study the properties of matter with neutrons of less than a few electron volts. Provisions are made for 18 flight tubes several meters in length.

Table I. Design Characteristics for HELIOS

Cell	Max. Electron Power in Target (kW)	Typical Neutron Pulse Width (ns)	Pulse Frequency (Hz)	Max. Neutron Output (n/s) x 10^{13}
FNC	8	5	2000	2.2
	30	40	1000	11
BC	5	100	390	30
CMC	50	2000	300	17
		5000	150	18

The uranium target (Fig. 2) that will be used in the FNC and the CMC consists of uranium plates cladded in varying thicknesses in either Zircalloy for the CMC target or tantalum for the FNC target to compensate for electron energy loss heating. The uranium target will have a total thickness of about 7 cm. The cooling system for the target is designed to handle 50 kW of beam, although the machine will deliver only 30 kW in the short-pulse mode. Tantalum was chosen as the cladding material for the FNC target because it has a higher level density than zirconium (the main component of zircalloy) and will, therefore, perturb the beam less in the kiloelectron-volt region.

Initially, the accelerator will be funded to run 24 hours per day, 5 days per week, with about 5500 hours of machine time available to the user each year. At least one-quarter of the funding is expected from the condensed matter program and, by multiplexing the beam, about 50% of an equivalent single target time will be devoted to nuclear studies with neutrons above a few electron volts, about 25% of the time to the condensed matter studies with neutrons below a few electron volts, and the remaining time to photonuclear studies and miscellaneous electron and gamma irradiations.

The data acquisition system that supports the neutron physics program at HELIOS includes two PDP 11/34 computers which act as a front end to a PDP 11/45 computer. The 11/45 has 128K (K = 1024) words of core. One of its several functions is to control up to seven experimental stations, each equipped with a CAMAC crate and a time scaler. The scaler is connected to the 11/45 through a direct memory access channel. The scaler, which can accept up to four inputs, has a word length of 16 bits, a minimum dead time of 200 ns, and a minimum channel width of 128 ns. The experimenter uses the manual switches in the scaler to select up to four blocks of channels and widths (common to all four inputs). The CAMAC crate is connected to the 11/45 through a branch highway interface unit. The crate is equipped with scalers and control units for a sample changer. The 11/45 also acts as a peripheral driver for two DEC magnetic tape units, two DEC RK05 disk units, two Tektronix 4012 graphic terminals, line printer, and a CDC 80, 40-megabyte disk unit. The maximum shared data rate with the time scalers connected to the 11/45 is 10 000 events per second. The data are stored on the RK05 disks and transferred to tape for processing at the Harwell IBM 370 computer.

One of the 11/34 computers, configured for single-parameter, high data rate experiments, takes advantage of the memory increment feature to handle rates higher than 10 000 events per second. The other 11/34, configured for dual-parameter experiments, has a 512K mass storage memory unit. Multiparameter data also are stored on the CDC 80 disk. Currently, six users, including those on the satellite computers can be accommodated with this system.

GELINA

In early 1977 the Central Bureau for Nuclear Measurements at Geel, Belgium upgraded the 66-MeV linac to a 150-MeV linac (GELINA). The objective was to deliver high peak current electron pulses of short duration for high-resolution measurements in the kiloelectron-volt and million-electron-volt regions. The machine is of the S-band type and consists of one standing wave buncher section and two traveling wave sections, as shown in Fig. 3. The design characteristics of the machine, with estimates of the maximum neutron output per second calculated from the Harwell numbers for a uranium target, are given in Table II.

Figure 4 shows the two mercury-cooled natural uranium targets designed for the facility. One is stationary and can handle about 6 kW, whereas the other rotates and is designed to handle higher powers. The rotating target has been tested to 10 kW, but calculations indicate that it may be able to handle as much as 30 kW.

For those measurements that require a moderated neutron spectrum, two semicircular disks of either polyethylene or water in beryllium containers 7 cm in radius and 4 cm in thickness can be placed on the top and bottom of the uranium target, as shown in Fig. 5. Under these conditions, the target is shielded by a

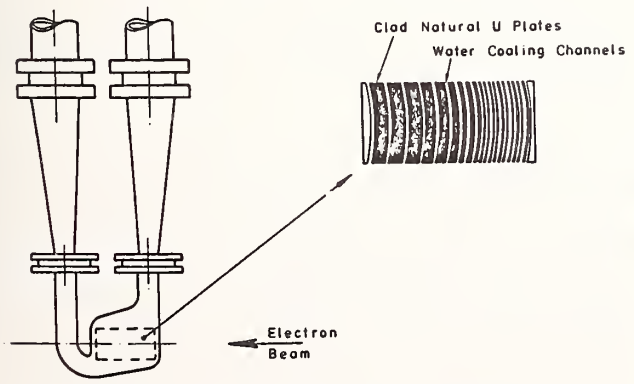

Fig. 2. High-power natural uranium target for HELIOS.

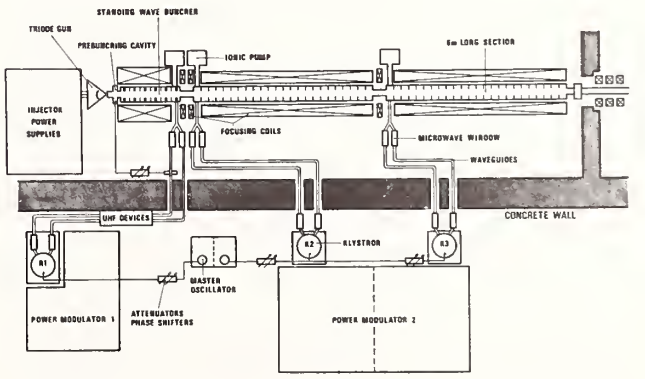

Fig. 3. The 150-MeV linac at Geel (GELINA).

Table II. Design Characteristics for GELINA

Max. Electron Power in Target (kW)	Typical Neutron Pulse Width (ns)	Pulse Frequency (Hz)	Max. Neutron Output (n/s) x 10^{13}
3.9	4	900	1.1
8.5	10	900	2.3
11	2000	250	3.0

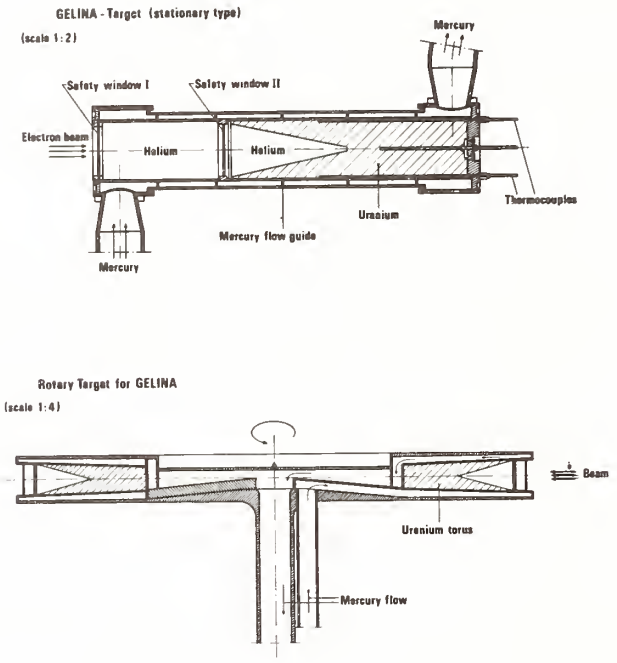

Fig. 4. Stationary target (upper figure) and high-power rotary target (lower figure) for GELINA.

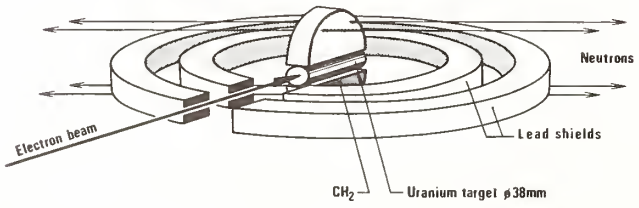

Fig. 5. Natural uranium target/moderator configuration showing lead shadow shields (GELINA).

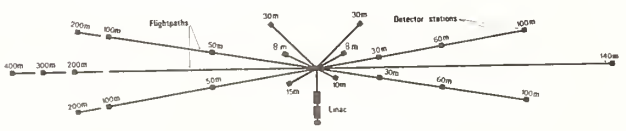

Fig. 6. GELINA flight path and detector stations.

series of concentric lead rings to restrict the field of view of the detectors to only the moderator surfaces.

Figure 6 shows the 12 flight tubes, between 8 and 400 m long, and 22 detector stations provided for the user. The large number of detector stations means that on an annual average, five to six flight tubes are being used simultaneously.

The machine is scheduled to operate 24 hours per day, 5 days per week. During 1978 about 3200 hours of machine time were available to the users. Following is a breakdown (in percent) by pulse width: 55% (4-5 ns), 38% (10-20 ns), 1.3% (2000 ns), and the remaining time under miscellaneous beam conditions.

At present, data can be collected at eight data acquisition stations. Six are equipped with multichannel analyzers (five with 4K and one with 16K of core) and two with minicomputers (32K). The accumulated data are transferred via special interface units and a transmission control computer to the disk storage of an IBM 370/138 central computer that is used for data analysis. Four new multiparameter, distributed processing data acquisition and reduction systems will be installed as stand-alone units before the end of 1979.

WNR

The Weapons Neutron Research (WNR) facility is part of the Clinton P. Anderson Meson Physics Facility (LAMPF) at the Los Alamos Scientific Laboratory (LASL). The approximately 1-km-long, 800-MeV proton linac consists of a 750-keV Cockroft Walton injector, a 100-MeV Alvarez linac operating at 201 MHz, and an 805-MHz side-coupled linac. The linac accelerates simultaneously pulsed beams of H^+ and H^- that have a frequency of 120 Hz, a width of 500 μs, and a time average current of 1 mA for the H^+ beam and about 100 μA for the H^- beam. The H^+ beam characteristics are given in Table III. The important parameter for neutron production at the WNR facility is the peak current of the micropulse, not the time average current. To achieve higher average currents, LAMPF has increased the pulse width, rather than significantly increasing the peak current. The quantities in parentheses in Table III are the present values for a pulse width of 500 μs.

The proton pulse for the WNR facility is obtained by suitably structuring either all or part of the macropulse with a fast helical chopper preceding the Alvarez linac, and then deflecting this structured pulse into the WNR beam line using a pulsed magnet located at the end of the accelerator. The characteristics of the two basic WNR pulse structures, using the values in parentheses in Table III, are given in Table IV. The neutron intensities[3] have been calculated[4] for a tungsten target using the Monte Carlo code MCN.

In the micropulse mode, individual micropulses are selected out of the macropulse in one of two ways: one micropulse per macropulse at a frequency of 120 Hz, or a minimum of one micropulse per microsecond for a total of 500 micropulses for a 500-μs-wide macropulse. In the latter mode, the entire macropulse is deflected into the WNR beam by a 'slow'-pulsed magnet that operates at a maximum frequency of 12 Hz. This mode is useful if beam overlap is not important because it can increase the number of micropulses per second to 6000.

In either micropulse mode the combined intensity of the two satellite peaks, which are separated from

the center peak by 5 ns, can be adjusted to be less than 0.5% of the center peak intensity. Because of limitations in state-of-the-art fast-pulse technology, the center peak intensity is currently about one-third to one-half that of the maximum micropulse peak intensity. Therefore, in the micropulse mode, the true number of protons per second and, consequently, the number of neutrons per second per steradian in Table IV should be reduced accordingly.

In the macropulse mode, the WNR pulse occurs at the end of the LAMPF pulse. It is deflected into the WNR beam line by a 'fast'-pulsed magnet that operates at a maximum frequency of 120 Hz. At present, the magnet will deflect only an approximately 3-μs-wide pulse.

The WNR facility (Fig. 7) consists of three target areas. The high-power target (Target 1) is located below the main proton beam line after the protons are bent 90° into the ground. In this geometry the high-energy component (≥ 300 MeV) is drastically suppressed and all flight tubes look at the same orientation of the target without moderator. The target shielding can handle about 2×10^{15} n/s or about 2% of LAMPF at maximum design average current. The low-power target (Target 2) is located on the same level as the main proton beam line opposite from Target 1. The room surrounding the target is shielded to handle about 0.1% of LAMPF. A third potential target area exists in the beam line after the bending magnet for Target 1. It also is shielded only for about 0.1% of LAMPF.

Table III. LAMPF pulse structure. Quantities in parentheses are the present values for a 500 μs macropulse.

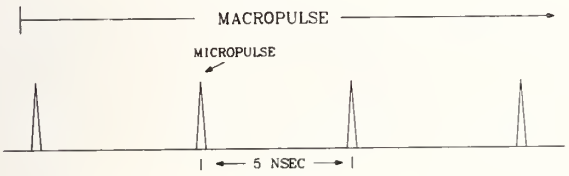

Macropulse Width	= ~ 500 μsec
Macropulses/sec	= 120
Macropulse Average Current	= 1 mamp (360 μamp)
Peak Current during Macropulse	= 17 mamp (6 mamp)
Micropulse Width	= ~ 40 psec
Protons/Micropulse	= 5×10^8 (1.8×10^8)

Table IV. Typical WNR operating conditions. The actual neutron and proton rates in the micropulse mode are somewhat less than those given. See text for further explanation.

MICROPULSE MODE (PULSE WIDTH ~ 200 psec)

A. One Micropulse per Macropulse

Macropulses/sec	= 120
Protons/sec	= 2.16×10^{10}
Neutrons/sr/sec	= 2.09×10^{10} (W, E ≥ 0.1 MeV)

B. Separation Between Micropulses ≥ 1 μsec

Micropulses/Macropulse	= Macropulse Width/Micropulse Sep.
Macropulses/sec	= 12
Protons/sec	= 1.08×10^{12}
Neutrons/sr/sec	= 1.1×10^{12} (W, E ≥ 0.1 MeV)

MACROPULSE MODE (25 nsec ≤ PULSE WIDTH ≤ 3 μsec)

Macropulses/sec	= 120
Protons/sec	= $0.11 - 12.9 \times 10^{12}$
Neutrons/sr/sec	= $0.12 - 13.9 \times 10^{12}$ (W, E ≥ 0.1 MeV

A schematic drawing of Target 1 is shown in Fig. 8. The target is located in the center of an evacuated 1.8-m-diam double-walled iron vessel. The 10-cm spacing between the two walls of the vessel can be filled with borated water to reduce the scattered neutron background from the inner walls of the vessel. The shielding around the target consists of iron and magnetite and borated concrete with a total thickness of 3.8 m. The flight tubes are arranged so that each flight tube serves as a 'get-lost' hole for the diametrically opposite flight tube. The 21-m-square building surrounding the target serves as a short flight path (5 to 15 m) experimental area (Experimental Area 1).

Flight tubes 1, 2, 9, 10, 11, and 12 can be extended beyond the experimental building to distances up to 300 m. Flight tubes 3, 5, 6, 7, and 8 terminate in get-lost holes in the outer walls of the experimental building and flight tube 4 connects Target 1 to Target 2. Most flight tube center lines point at the center of the target; flight tubes 3, 5, 6, and 8 are horizontally displaced 7.5 cm from the target center. Currently, flight tube 11 has an experimental station at 30 m, with plans for one at 70 m. Flight tube 1 has experimental stations at 30 and 80 m and will be extended to 200 m in FY 1980. Flight tubes 2 and 12 can be extended to several hundred meters, whereas 9 and 10 can be extended conveniently only to ~ 30 and 50 m, respectively.

A schematic drawing of Target 2 is given in Fig. 9. The room is designed to reduce wall and floor neutron scattering by having the walls 6 m from the center of the room and by supporting any experimental equipment with a low-mass floor. Four penetrations through the wall that join the beam channel with the room are provided at angles of 30°, 45°, 60°, and 90°. Hardware is being installed to bring the proton beam through the 30° penetration. The 90° penetration can be used for a flight tube that can be extended to 100 m for either a target placed in the beam channel or for a target or sample placed at the center of the room. In addition, there are nine penetrations in the outer wall that allow flight tubes of 30 m to several hundred meters in length. The apex of the penetrations through the wall that joins Target 2 with the beam channel permits the placement of a detector at this point to measure the neutron spectrum at various

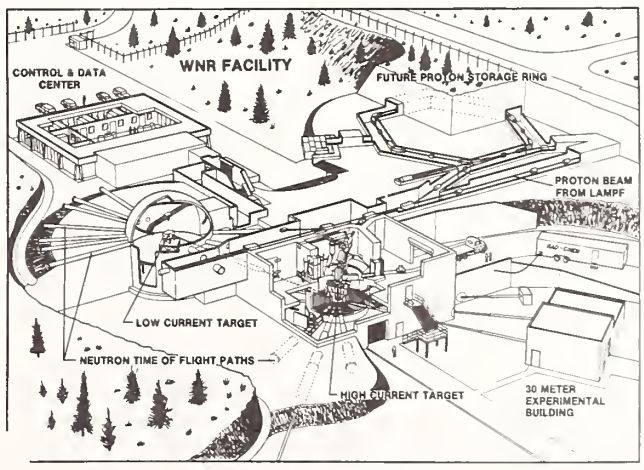

Fig. 7. WNR facility.

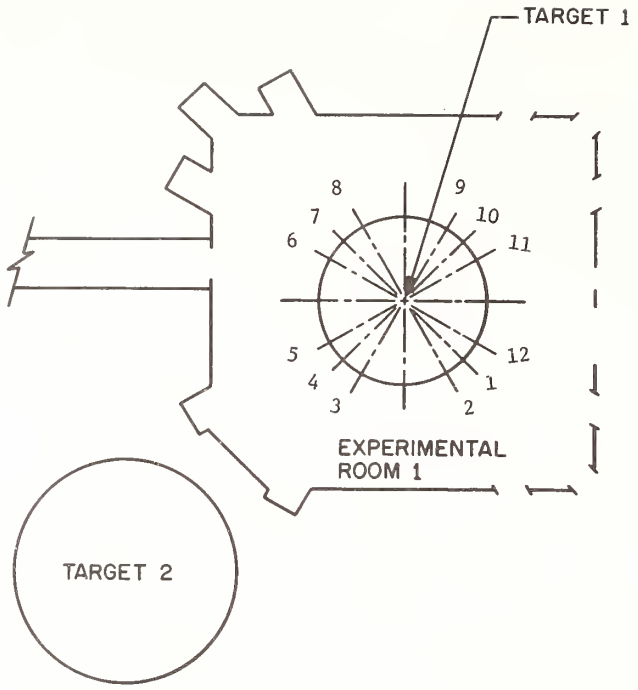

Fig. 8. High-current target (Target 1) and Experimental Room 1 showing orientation of flight tubes. Flight tubes 1, 2, 9, 10, 11, and 12 can be extended from 30 to 270 m. Flight tubes 3, 5, 6, 7, and 8 terminate in outer wall of room 1. Flight tube 4 connects Target 1 with Target 2.

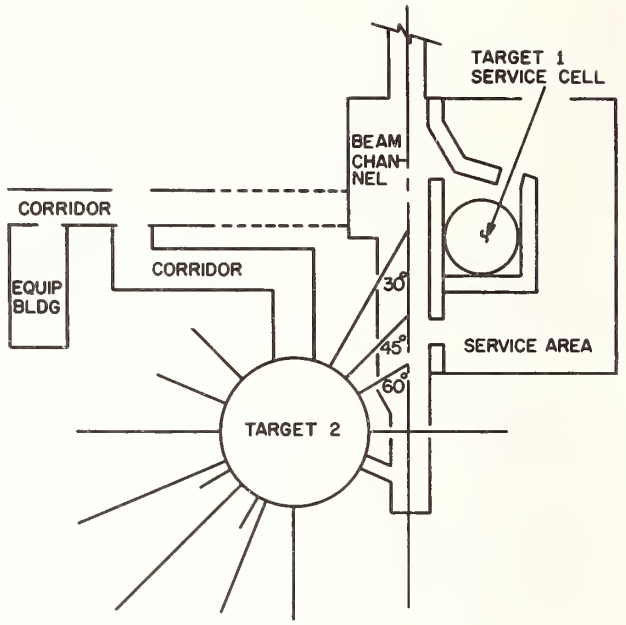

Fig. 9. Low-power area (Target 2), beam channel, and Target 1 service cell area. Proton beam will be brought into Target 2 through 30° penetration.

angles to the proton beam direction for thin targets placed in the beam channel. This high degree of flexibility allows the room to be used either as a low-power target area, a large scattering chamber, or an experimental area.

The service area (Fig. 9) is a shielded room directly above Target 1 that is used to work on the target/moderator assembly without exposing personnel to high radiation levels. This room has leaded-glass viewing ports, a crane for hoisting the assembly unit from the crypt, and remotely controlled mechanical manipulators. The target and/or moderators can be replaced in less than one day with this equipment.

An isomeric view of the high-current target/moderator assembly is shown in Fig. 10. Only two of the four moderator, and one of the two target mechanism, support arms are shown. All arms work independently of each other and can be controlled remotely from outside the target crypt. Not only can the target be cooled with water, but provisions were made to circulate water in the water moderators and to cool the polyethylene moderators, as well. The moderators and target can be moved vertically 25 cm and 12 cm, respectively. This permits investigating the scattered neutron background from the walls of the target crypt by positioning the target/moderator out of the line of sight of the flight tubes.

The present targets are made from either a tantalum or tungsten rod 2.5 cm diam by 15 cm long. About 50% of the energy of the 800-MeV proton beam is deposited in the target and removed by the two 0.7-mm-thick cylindrical water channels shown in the insert of Fig. 10. The cooling system for the target is designed to handle about 20 kW of beam.

The moderator material is either polyethylene or water or a combination of both. The polyethylene moderator is 6.5 cm thick and the water moderator is 7.0 cm thick. Both moderators are 200 by 300 mm in area, with the 200-mm edge parallel to the axis of the target.

Monte Carlo calculations[5] were made to study the neutron yields from the bare targets and target/moderator configurations and the neutron pulse width emerging from the surfaces of the moderator and target for a delta function input pulse of 800-MeV protons. The results from the pulse width calculations for the polyethyene and water moderators and for the bare tantalum target are shown in Fig. 11. Figure 11 shows the standard deviation (σ) of the neutron pulse from the large surface area of the moderator and from the cylindrical surface of the bare target. The shape of the neutron pulse is asymmetrical with an exponential tail and a full width at half maximum of about 2σ. The timing characteristics of our water moderator agree well with the results of a similar study by Camarda[6] for the National Bureau of Standards target/moderator. The pulse width for the polyethylene moderator is about 30% narrower than that for the water moderator. This difference is mainly due to the higher hydrogen atom density in the polyethylene, rather than to the 8% thicker water moderator. The polyethylene moderator also has the advantage that it does not have to be canned like water and, therefore, the neutron spectrum does not have 'windows' because of resonances in the canning material. However, this advantage must be weighed against the fact that polyethylene quickly becomes radiation-damaged and may have to be replaced often for structural reasons.

The results from the calculation of neutron yields for the target/moderator and bare tantalum target configurations are shown in Fig. 12. The polyethylene and water moderators give about the same neutron yield, so only the polyethylene yield is plotted. The bare tantalum target yield is calculated

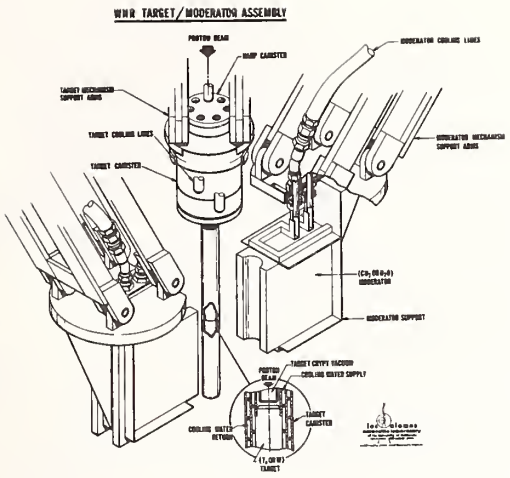

Fig. 10. WNR target/moderator assembly.

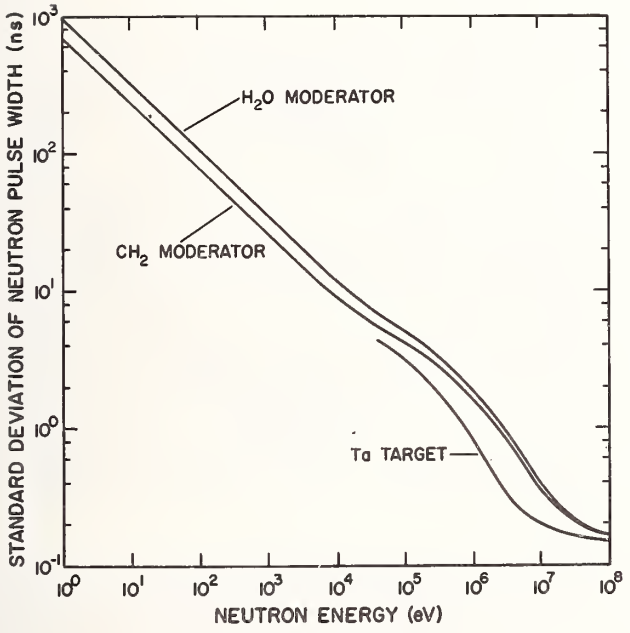

Fig. 11. Pulse width characteristics of the WNR CH_2 and H_2O target/moderator configurations and bare Ta target. The CH_2 moderator is 6.5 cm thick and the H_2O moderator is 7.0 cm thick. Both are 200 by 300 mm in area. The full width at half maximum of the neutron pulse is approximately twice the standard deviation of the pulse width.

without any moderator surrounding the target, but with water in the cooling channels. The effect of the cooling water on the shape of the spectrum for the bare target is negligible; there is no 1/E component to the spectrum below approximately 100 keV.

Measurements have been made of the neutron yield and spectrum shape for the bare target configuration. In general, these data reproduce the calculated results up to 10 MeV. However, above this energy the measured yield exceeds the calculated yield by as much as a factor of three at 100 MeV. No detail comparison has been made for the target/moderator configuration.

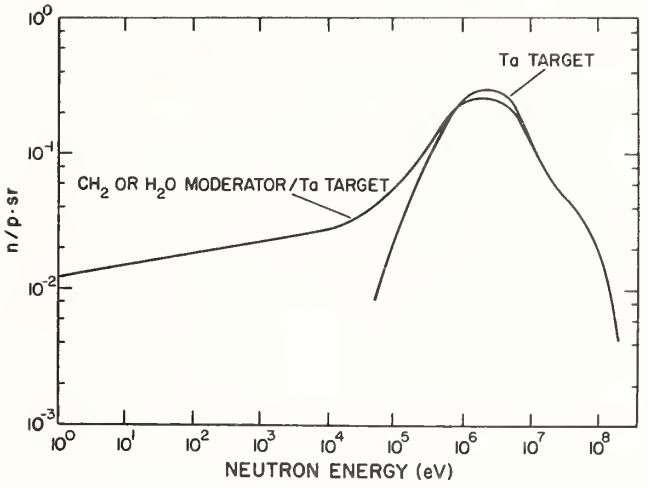

Fig. 12. Neutron yields per proton per steradian for the CH_2 and bare targets. Both the CH_2 and H_2O moderators give the same yield. The yields are for a 12.7-cm-diam circular area centered on the surface of the rectangular moderator.

The WNR operation is closely linked to the LAMPF schedule, although WNR can be down for additional reasons, such as for kicker, and chopper failures. The LAMPF schedule is broken down into four or five cycles per year with each cycle lasting from five to seven weeks. From August 1978 through August 1979, LAMPF was scheduled for 604, 8-hour shifts. About 76% of this time was used for the WNR programs. The time was divided between the material science and neutron physics programs. We do not foresee more time becoming available from LAMPF, nor do we expect the 50% division of time between the two main WNR programs to change significantly in future cycles.

The computer facility associated with the WNR facility consists of two MODCOMP-IV/25 computers, each with 128K, 16-bit memory. The system acquisition computer (SAC) controls up to four experimental stations, each consisting of an input terminal, refresh scope, and a display panel. Also connected to the SAC are two 9-track, tape units, a 12-in. Calcomp plotter, four 1.2-megaword diskpack units, and a CAMAC serial highway system. In addition, the SAC controls and monitors the magnets and quadrupole lenses that transport the proton beam from the kicker magnet to the WNR target as well as the target temperature and radiation monitoring equipment. The data acquisition computer (DAC) essentially acts as a disk driver for a 1-megaword fast disk. The disk can sustain a total input rate of about 9000 words/second. Both single and multiparameter data can be taken with the system. In the multiparameter mode, data can be transferred event by event to tape or single parameter slices of the data can be stored on the DAC disk at about 1000, 16-bit words/sec. Most data taken at the WNR facility are transferred to tape and read in at the central computer facility (CCF) at LASL. The physics division at LASL plans to lease a 1-megaword (32-bit) VAX computer that will be used for data reduction and preliminary data analysis. This computer will be connected to the CCF.

Future plans for reconfiguring each computer to perform both the SAC and DAC functions will improve reliability by providing a back-up system. The beam line functions now controlled by the SAC will be transferred to a new dedicated computer. Also, LASL

is developing a 1-megaword (24-bit) semiconductor memory unit that will be connected either to the MODCOMP computers directly or to satellite computers attached to the MODCOMP computers.

PSR

The proton storage ring (PSR) is an extension to the WNR facility that we plan to have operational by 1985. It will initially store 100 μA of H^- beam and could eventually store 400 μA without any redesign of the ring and associated hardware. The frequency of the pulses ejected from the ring can be varied from 1 to 720 Hz, depending on how the ring is filled and how many pulses are circulating in the ring at any one time. Initially, the pulse widths available will be either 1 or 270 ns. The addition of the PSR to the WNR will increase the neutron intensity by two to three orders of magnitude and will provide more simultaneity for neutron physics and material science measurements.

The PSR is located upstream of Target 1 at the same elevation as the proton beam line (Fig. 7). It will be decahedral in shape with a beam circulating time of approximately 360 ns. There will be two RF buncher cavities in the ring; the one operating at 2.8 MHz will be used for the long-pulse operation, and the other operating at 603.75 MHz will be used for the short-pulse operation. A fast kicker, requiring at least 60 ns between each group of pulses circulating in the ring ejects the pulses back into the main beam line. Therefore, at most, six 1-ns-wide pulses can be circulating in the ring.

In the short-pulse mode (Fig. 13), the ring is filled 120 times per second. About the last 72 μs of each macropulse is structured so that 1 out of every 12 micropulses is injected into the ring, thus forming 6 super micropulses that are extracted from the ring at regular intervals between macropulses. The characteristics of this mode are given in Table V under the heading Super-Micropulse Mode.

PSR has two basic modes of operation. In the long-pulse mode (Fig. 14), the entire macropulse is structured so that there is a 60-ns gap every 270 ns. The ring is filled and dumped 12 times per second. The characteristics of this mode are given in Table V under the heading Super-Pulse Mode.

Although the proton numbers in Table V assume that LAMPF can deliver 100 μA of H^- beam to the PSR, that is not possible at this time. There is, however, a developmental program at LASL to design an H^- source that will be capable of currents far in excess of those required by the PSR. Preliminary results indicate that when the PSR is fully operational, such a source will be available.

ORELA

The major modification to the Oak Ridge electron linac (ORELA) has been the installation of a 2.7-m-long buncher between the electron gun and the pre-buncher. The buncher can achieve high instantaneous peak currents by compressing a 15-ns (50-J) pulse to about 3 ns with essentially no loss in beam power.[7] A schematic diagram of the buncher used in a study[7] of the buncher parameters is shown in Fig. 15. Calculations were made for a 15-ns pulse with a total charge of 1 μC. Because of the large space charge effects, the calculations include an applied longitudinal magnetic field of several kilogauss to prevent the beam from spreading out radially. The buncher has six decelerating gaps and three accelerating gaps. The voltage applied to the gaps varies such that a decelerating gap reduces the kinetic energy of the electrons in the front of the pulse relative to the kinetic energy of the electrons in the back of the

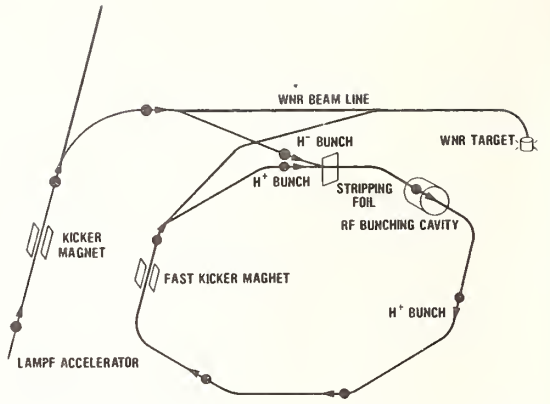

Fig. 13 The short-pulse (1-nsec) mode of operation for PSR.

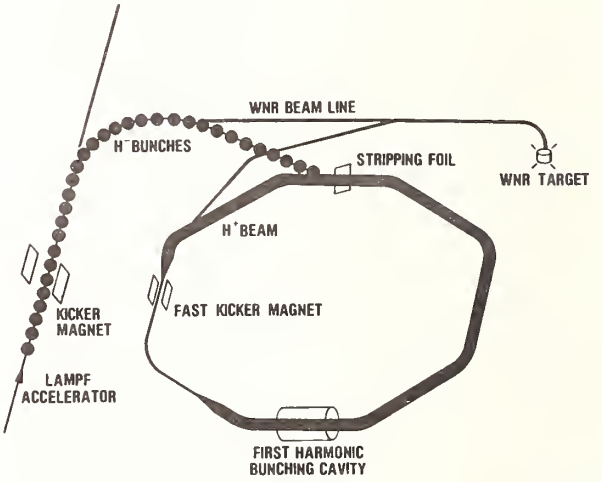

Fig. 14 Long-pulse (270-ns) mode of operation for PSR.

Table V. Typical PSR operating conditions. Proton rates assume that LAMPF will deliver 100 μA of H^- beam to PSR. If PSR is upgraded to handle 400 μA of beam, the number of macropulses/second in the super-pulse mode will increase from 12 to 48.

SUPER - MICROPULSE MODE (STORED PULSE WIDTH ~ 1 nsec)	
1 Micropulse injected into ring every 60 nsec	
Super-Micropulse	= 200 micropulses
Super-Micropulses/Macropulse	= 6
Macropulses/sec	= 120
Protons/sec	= 7.2×10^{13}
Neutrons/sr/sec	= 7×10^{13} (W, E $\geq$ 0.1 MeV)
SUPER - PULSE MODE (STORED PULSE WIDTH = 270 nsec)	
54 Micropulses injected into ring every 360 nsec	
Super-Pulse	= 75000 micropulses
Macropulses/sec	= 12 (possible expansion to 48)
Super-Pulses/sec	= 12
Protons/sec	= 4.5×10^{14}
Neutrons/sr/sec	= 4.9×10^{14} (W, E $\geq$ 0.5 eV)

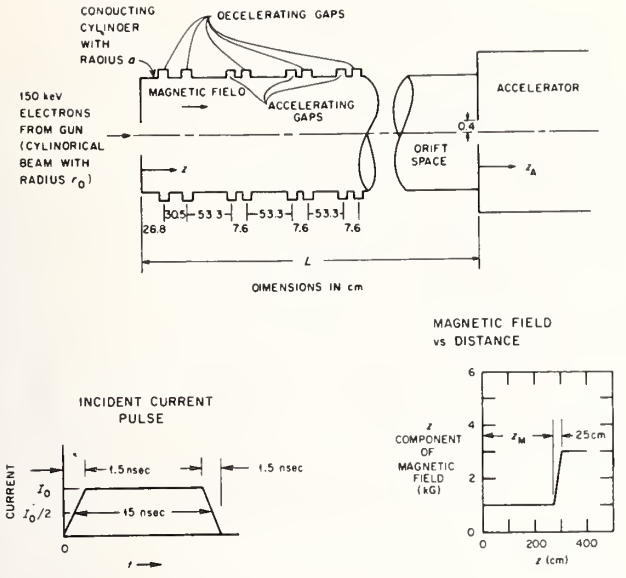

Fig. 15. ORELA prebuncher geometry. Shown is the shape of the incident current pulse and the z-component of the magnetic field as a function of distance.

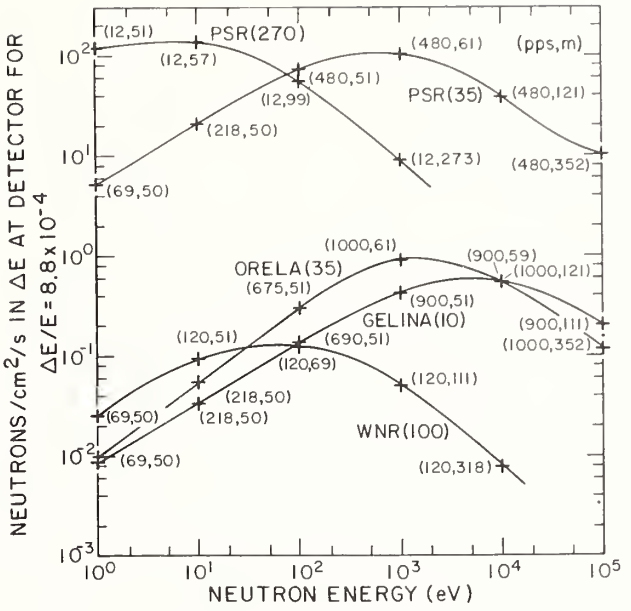

Fig. 16. Comparison of neutron facilities for the low-energy region (< 100 keV). The two quantities in parentheses represent frequency and flight path to achieve maximum neutron flux in the energy interval ΔE for the given resolution. The quantity in parentheses by the facility name represents pulse width in nanoseconds. Machine and neutron characteristics used in calculations are given in Table VI.

pulse. An accelerating gap increases the kinetic energy of the electrons in the back of the pulse relative to the kinetic energy of the electrons in the front of the pulse. The gaps have been designed for a maximum voltage of about 50 kV. In the first test of the buncher, with one-third of the design voltage applied to the gaps, a 17-ns pulse (FWHM) was compressed to about 8 ns with only a 7% loss in power. The energy in the pulse was 15 J. At present, ORELA cannot deliver 50 J per 15-ns pulse, but it has done so in the past and is expected to do so in the future with improvements in gun fabrication. Therefore, to be conservative, I will use 30 instead of 50 J per pulse when I compare facilities.

KFK

In 1972, Cierjacks[1] reviewed the characteristics and performance of the sector-focussed cyclotron at Karlsruhe (KFK). Since then a substantial improvement in the spectrometer resolution has been achieved by optimizing the phase condition of the accelerated deuteron beam, using a computer-controlled beam diagnostic system, and by applying modified neutron detectors with improved time characteristics. Total cross-section data have been taken with a spectrometer resolution of < 0.8 ns and an average beam current of 10 μA at a beam pulse frequency of 50 kHz.[8]

Comparison of the Neutron Source Facilities

I have chosen the procedure outlined by Rae and Good[2] for my comparison of the various neutron source facilities because it uses all the parameters of the facility. With this procedure, the fractional energy resolution is held constant at all energies by varying only the flight path. The value of ΔE/E is chosen to correspond to the minimum value for a moderated neutron source at some minimum flight path. The timing uncertainty introduced by the moderation process is included in the overall resolution by folding it in quadrature with the machine pulse width. In addition, a 1/v filter is assumed to prevent overlap of high energy neutrons with the low-energy neutrons of the previous burst. Neutron output is maximized when the pulse rate is reduced until the time-of-flight of the neutron is greater than about four times the overlap time. In this way the different repetition rates of the facilities that influence the neutron output at low energy are included in the calculations. Rather than introduce new conditions, I have kept the minimum flight path at 50 m and used 2.2 cm for the equivalent flight path uncertainty for the moderation process. These give 8.8×10^{-4} for the fractional energy resolution. Also, I have allowed the flight path to increase to 400 m to maintain this resolution and used 1% for the transmission of the filter at the overlap energy.

The WNR, GELINA, ORELA, and PSR facilities are compared in Fig. 16 for the energy region from 1 to 100 000 eV. The pertinent parameters used to calculate the neutron flux within the given energy resolution for each facility are given in Table VI. The two quantities in parentheses in Fig. 16 represent the pulse frequency and flight path necessary to achieve maximum neutron flux at the desired resolution. The HELIOS facility is not included because no experimental or calculational data of the neutron flux are available in this energy region. The plot[2] of the flux from the Harwell booster, run at its heat transfer limit of 5 kW, should be valid for the BC target. Generally, if we use the WNR facility for comparison, the BC flux should be slightly higher below 10 eV, about the same at 100 eV, and about three to four times higher at 10 000 eV. The calculational data presented in Fig. 12 are used for the WNR. For the PSR, these data are adjusted by the difference in average currents between the two facilities. The experimental data of Weston[9] are used for ORELA and the experimental data for a uranium target[10] taken at Geel at 4 kW are used for

Facility	Pulse Frequency (Hz)	Pulse Width (ns)	Average Beam Current or Power	N(E) (n/sr/sec/eV)
GELINA	900	10	8.5 kW	$1.0 \times 10^{10}\ E^{-0.90}$
ORELA	1000	35	50 kW	$1.3 \times 10^{10}\ E^{-0.75}$
WNR	120	100	69 namps	$4.1 \times 10^{9}\ E^{-0.90}$
PSR	480	35	54 μamps	$3.2 \times 10^{12}\ E^{-0.90}$
	12	270	72 μamps	$4.3 \times 10^{12}\ E^{-0.90}$

Table VI. Neutron facility parameters for low-energy calculations of neutron flux for facility comparisons.

GELINA. The GELINA data have been adjusted to the new power level of 8.5 kW, assuming that the moderator coupling efficiency for the new rotating target is 0.7.[10] The importance of pulse frequency to maintain maximum neutron flux is quite evident in Fig. 16. For example, the PSR (270) can run at its maximum frequency of 12 Hz for energies down to 1 eV, whereas ORELA has to reduce its frequency to 69 Hz at 1 eV, with a corresponding reduction in neutron output.

The WNR, PSR, HELIOS, ORELA, and KFK facilities are compared in Fig. 17 for the energy region from 0.01 to 1000 MeV. The pertinent parameters used in these calculations are given in Table VII. The GELINA data are not included because the performance of this facility is similar to HELIOS except that the flux is about a factor of 2 lower. For the high-energy calculations, the overlap filter is ignored. Because most target dimensions are on the order of several centimeters, I have retained the flight path uncertainty of 2.2 cm, except for KFK where I used 1 cm in determining the resolution of the system. For HELIOS, I used the experimental data from ORELA,[11] assuming that the shape of the neutron spectrum is independent of whether the target material is uranium or tantalum, and I normalized the shape using the expected neutron intensity for the FNC target.

Acknowledgement

I gratefully acknowledge the contributions made by M. S. Coates, J. E. Lynn, and D. A. Boyce of Harwell; F. Käppeler and H. O. Klages of Karlsruhe; K. H. Böckhoff and H. Weigmann, of Geel; and J. A. Harvey of Oak Ridge. I thank G. J. Russell of LASL for his help with the target/moderator calculations.

References

1. S. Cierjacks, "The Karlsruhe Fast Neutron Time-of-Flight Facility," Proc. Int. Conf. Nuclear Structure Study with Neutrons, Budapest, 1972, (Plenum Press, London and New York, 1974), pp. 299-311.

2. E. R. Rae and W. M. Good, "Pulsed Accelerator Time-of-Flight Spectrometers," in Experimental Neutron Resonance Spectroscopy, J. A. Harvey, Ed. (Adademic Press, New York, 1970), Chap. 1, pp. 1-99.

3. G. J. Russell, "Initial Target/Moderator Configuration for the Weapons Neutron Research Facility," Trans. Amer. Nucl. Soc. 27, 861 (1977).

4. E. D. Cashwell, J. R. Neergaard, W. M. Taylor, and G. D. Turner, "MCN: A Neutron Monte Carlo Code," Los Alamos Scientific Laboratory report LA-4751 (January 1972).

5. G. J. Russell, P. A. Seeger, and R. G. Fluharty, "Parametric Studies of Target/Moderator Configurations for the Weapons Neutron Research (WNR) Facility," Los Alamos Scientific Laboratory report LA-6020 (March 1977).

6. H. S. Camarda, "Monte Carlo Studies of D_2O and H_2O Neutron Moderators for Time of Flight Experiments," Nucl. Instrum. Methods 106, 205 (1973).

7. R. G. Alsmiller, Jr., F. S. Alsmiller, J. Barish, and T. A. Lewis, "Calculations Pertaining to the Design of a Prebuncher for an Electron Linear Accelerator," Part. Accel., 9, pp. 187-200 (1979).

8. S. Cierjacks, G. Schmatz, D. Erbe, and B. Leugers, "Progress Report on Nuclear Data Research in the Federal Republic of Germany," NEANDC (E)-192 U, Vol. V, p. 1 (1978).

9. L. Weston, Oak Ridge National Laboratory, unpublished data (1979).

10. H. Weigmann, Central Bureau for Nuclear Measurements, private communication (1979).

11. G. L. Morgan, Oak Ridge National Laboratory, unpublished data (1979).

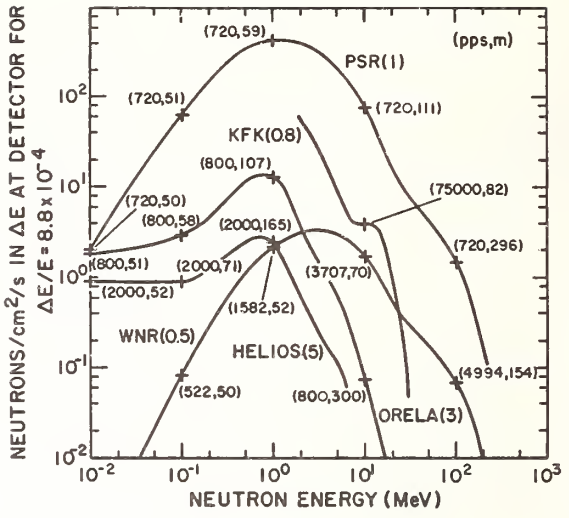

Fig. 17. Comparison of neutron facilities for the high-energy region (> 100 keV). Machine and neutron characteristics used in the calculations are given in Table VII.

Table VII. Neutron facility parameters for high-energy calculations of neutron flux for

Facility	Pulse Frequency (Hz)	Pulse Width (ns)	Average Beam Current or Power	$\int E \cdot N(E)dE$ (n/sr/sec)
HARWELL	2000	5	8 kW	1.75×10^{12}
ORELA	800	3	25 kW	4.0×10^{12}
KFK	75000	0.8	10 μamps	7.6×10^{12}
WNR	< 6000	0.5	< 166 namps	1.08×10^{12}
PSR	720	1.0	11.5 μamps	6.9×10^{13}

NEUTRON CROSS SECTION MEASUREMENTS AT ORELA

J. W. T. Dabbs
Oak Ridge National Laboratory,
Oak Ridge, Tennessee 37830 USA

ORELA (Oak Ridge Electron Linear Accelerator) has been for the last decade the most powerful and useful pulsed neutron time-of-flight facility in the world, particularly in the broad midrange of neutron energies (10 eV - 1 MeV). This position will be enhanced with the addition of a pulse narrowing "prebuncher", recently installed and now under test. Neutron capture, fission, scattering, and total cross sections are measured by members of the Physics and Engineering Physics Divisions of ORNL, and by numerous guests and visitors. Several fundamental and applied measurements will be described, with some emphasis on instrumentation used. The facility comprises the accelerator and its target(s), 10 evacuated neutron flight paths having 18 measurement stations at flight path distances 8.9 to 200 meters, and a complex 4-computer data acquisition system capable of handling some 17000 32-bit "events"/sec from a total of 12 data input ports. The system provides a total of 2.08×10^6 words of data storage on 3 fast disk units. In addition a dedicated PDP-10 timesharing system with a 250 megabyte disk system and 4 PDP-15 graphic display satellites permits on-site data reduction and analysis. More than 10 man-years of application software development supports the system, which is used directly by individual experimenters.

[Electron linac, pulsed neutron source, time-of-flight, neutron cross sections, data acquisition, computers, $^{238}U\sigma_{tot}$, majority logic, inelastic neutron scattering, gas scintillator, prebuncher]

Introduction

The Oak Ridge Electron Linear Accelerator (ORELA) is a powerful pulsed electron accelerator dedicated to the function of producing short intense bursts of neutrons over a wide range of energy. It was commissioned in 1969 and in the intervening decade has been used for an extremely large number of experiments utilizing the neutron time-of-flight technique. Principally, measurements have been made on neutron capture, fission, scattering and total cross sections for nuclides over the entire periodic table. Many other types of measurements have also been made, e.g., determinations of $\bar{\nu}$ and α for heavy elements, inelastic scattering experiments, etc. Until the present time, ORELA continues to be the most useful and most powerful pulsed neutron time-of-flight facility in the world, particularly in the broad midrange of neutron energies (10 eV - 1 MeV).

The staff consists of 19 persons associated with the Engineering Physics Division and 10 persons associated with the Physics Division of Oak Ridge National Laboratory. The Co-directors of the accelerator are J. A. Harvey (Physics) and R. W. Peelle (Engineering Physics). The Engineering Physics Division primarily supports applied measurements and the Physics Division primarily supports fundamental measurements at the accelerator. Both divisions continue to have numerous visitors and collaborators from other institutions and universities throughout the world. The staff is supported by 7 persons in accelerator operations and development, 16 craft and maintenance personnel, 1 computer software expert and 1 computer hardware expert.

Description of ORELA Facility

Figure 1 is a list of the characteristics of the electron accelerator and its neutron production rates. In general all of the specifications shown in Figure 1 have been met in actual practice for the largest part of the life of the facility. In recent months some difficulty has been encountered with electron gun fabrication problems. This has led to power restrictions associated with excessive grid emission ("dark current"). The grid pulse shaping network has also recently presented rise time problems for narrow pulse widths and we have suffered reductions in power because of this. Wide pulse power outputs as high as 60 J/pulse have been obtained over long periods of time for several important experiments in the past[1] and there is reason to expect that this power

ORELA SPECIFICATIONS

L-band, 1300 megacycles
10-140 MeV electrons
15 amp peak current (τ <24 nsec)
2-1000 nsec burst width
5-1000 pulses per second
50 kw electron beam (τ >24 nsec)
10^{11} neutrons/pulse (τ >24 nsec, Ta target)
10^{14} neutrons/sec (average, 50 kw)
4×10^{18} neutrons/sec (peak, 15 amps)

Fig. 1

level will be again obtainable, once the gun problem has been resolved. Improvements in the grid pulse shaping network are also being pursued.

Figure 2 shows a layout of the facility. The facility comprises the accelerator and its targets, 10 evacuated neutron flight paths having 18 measurement stations at flight path distances of 8.9-200 meters and a complex 4-computer data acquisition system. Two types of targets are used. The most commonly used target is a tantalum metal, water cooled target which is shown in Figure 3. An alternate target for high energy neutron work is essentially a large block of beryllium metal which replaces the tantalum target described above. A hydraulic mechanism permits remote target changes and storage. With the aid of a mains-frequency beam sweeping system the tantalum target is capable of absorbing up to 75 kW, although 60 kW is the maximum power which has been actually used for extended periods.[1] As seen in Figure 2, the flight paths are for the most part symmetrically disposed on either side of the accelerator at ∿15° intervals.

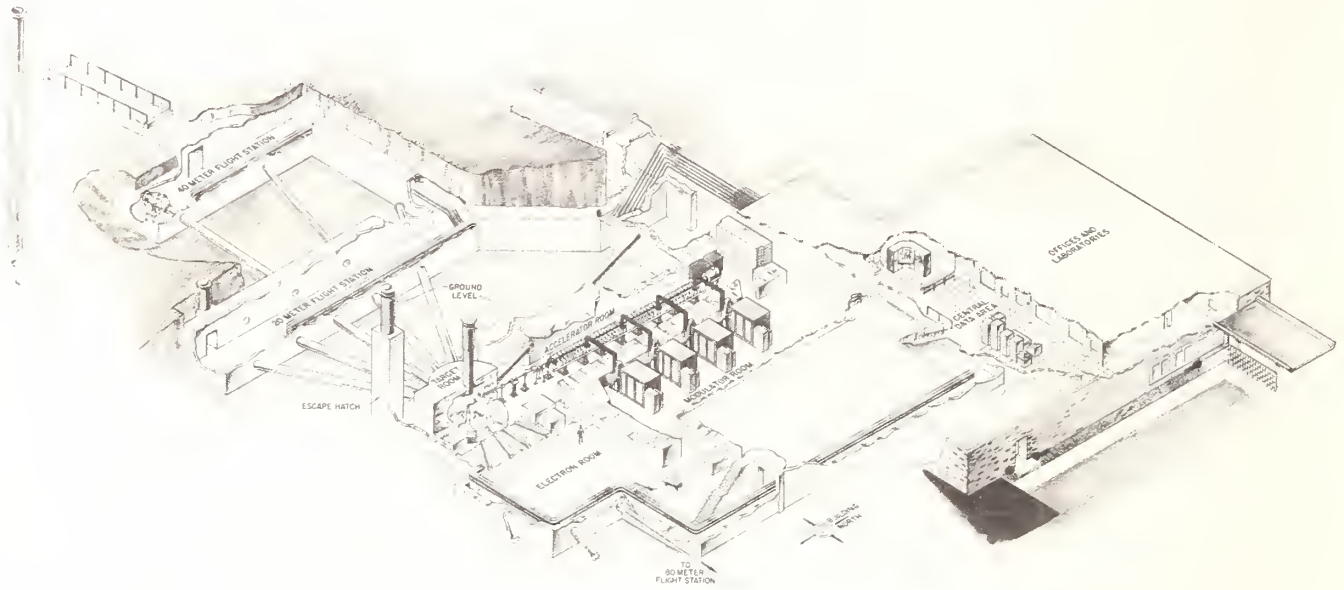

Fig. 2. ORELA

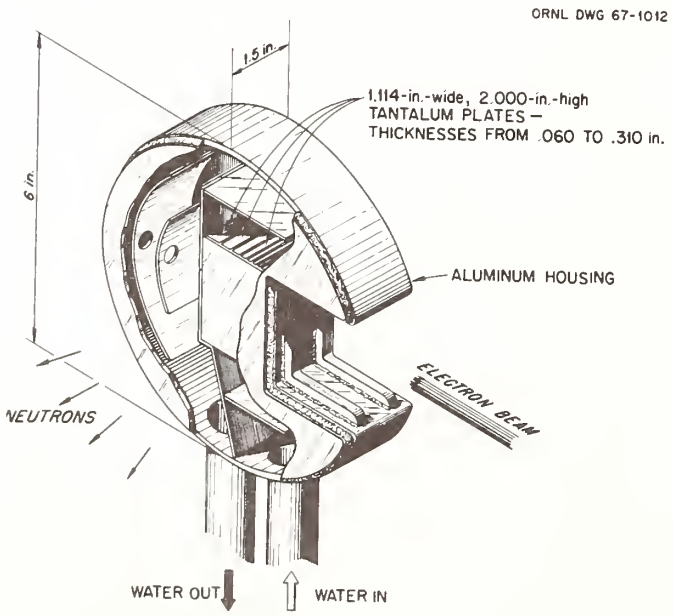

Fig. 3. ORELA target. The housing material has been changed to Beryllium.

Table I gives a listing of these flight paths, their angular positions, location of the various stations together with their primary present use and the names of some users. Among these flight paths, flight paths number 1 and 6 are used for the highest resolution work because of their angular positions perpendicular to the water moderator disk of the standard tantalum target. Flight path 9 is particularly suitable for experiments in which gamma rays are detected because at its angular position very few gamma rays accompany the neutrons down the flight path. Usually, each flight path is equipped with a "shadow bar" which prevents direct viewing of the Ta portion of the target. This reduces the effect of the γ-flash by a large factor.[2]

Table I

Flight Path No.	Angle (degrees)	Station (Meters)	Type of experiment	Contact Person
1	90°	18,80,200	Transmission	J.A. Harvey
2	75°	9,33	Fission	J.W.T. Dabbs
3	60°	10,33	Inelastic	R. Winters
			Solid State	H. Mook
4	60°	20	Fission	R. Gwin
5	75°	20,85	Capture	L.W. Weston
			Fission, $\bar{\nu}$	R.R. Spencer
6	90°	20,40,150	Transmission	D.K. Olsen
			Subthreshold fission	G. de Saussure
7	105°	20,40	Capture	R.L. Macklin
8	120°	20	n,n'γ	D.K. Olsen
9	165°	50	(n,xn'γ),(n,xγ)	G.T. Chapman
11	105°	12	(n,γ spectra)	G. Slaughter

Figure 4 illustrates contributions to the energy resolution available at ORELA in the worst case, i.e., Doppler broadening associated with a heavy element target, flight path length error associated with two of the shortest flight paths, and the pulse width error associated with a 40 ns pulse and 8 ns data bins, in the three regimes from left to right in the figure. The smooth curve for underground explosions is drawn through points given by Diven.[3]

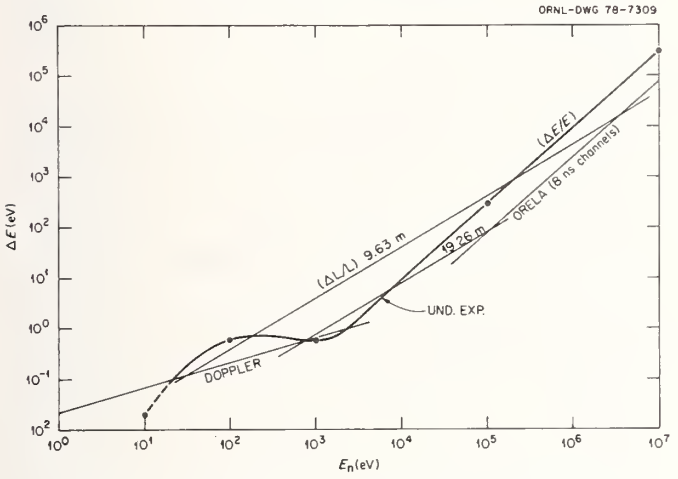

Contributions to Energy Resolution, Underground Explosion and Orela (40 ns Burst)

Fig. 4

Perhaps the most important factor which makes ORELA so useful is the very multiplicity of flight paths and working stations. As will be seen in Table I there are 10 flight paths and 18 working stations. Over the last 5 months an average of 5.4 of these stations were producing data at any given operating time. This situation mandates a powerful system for the cumulation and storage of data.

On-line Data Acquisitions Systems

Generally speaking the time-of-flight portion of each experiment requires that events at a particular time after the accelerator burst must generate a digital word which describes the time at which the event occurred. In a number of cases information such as pulse height must also be folded into this digital word. In the ORELA system the standard word comprises 32 bits. Four bits are reserved for identifying the particular detector involved. Two other bits are reserved for system control and the remainder are used for time-of-flight information and in many cases other information such as pulse height. Each "event" is presented to the data acquisition computer as two 16 bit words which, taken together, comprise the 32 bit word. Almost all of the experiments at ORELA utilize the TDC-100 time digitizer[4] to produce the time of flight portion of the data. Approximately 12 of these units are in use at ORELA.

The data acquisition computer complex comprises 3 model SEL-810B computers which are 16 bit 32K word units with a cycle time <1 μs. Each of these computers has 4 input ports which permit the reception of data from 4 experiments simultaneously under a buffering and priority scheme which avoids distortion of the data in one experiment by another. Input rates totalling 5000 events/second are permissible provided no average individual rate exceeds 1800/second. Each of the 3 computers is equipped with an extremely fast head-per-track disk. Total storage capability of these 3 units is 2.08 x 10^6 channels. Each of these channels can store a count of 65 536. These disks are used only for data storage during data acquisition and for a short time thereafter. Rather elaborate facilities are provided for observing the data with the aid of a cathode ray tube and a light pen on each of the 3 data acquisition computers as the data are being acquired. A fourth SEL-810B computer is used as a peripheral equipment controller or PEC. This computer drives a line printer, card reader, 2 plotters, 2 magnetic tape drives, a paper tape reader, and a paper tape punch, as well as a high speed link via a PDP-15 to the remainder of the facility.

The largest of the ORELA computer facilities is located in the same hall with the data acquisition computers. A PDP-10 time sharing computer with 240 K 36 bit words of main memory and with 250 Mbytes of magnetic disk storage serves as the main data storage and analysis computer. A schematic diagram of the entire computer system is shown in Figure 5.

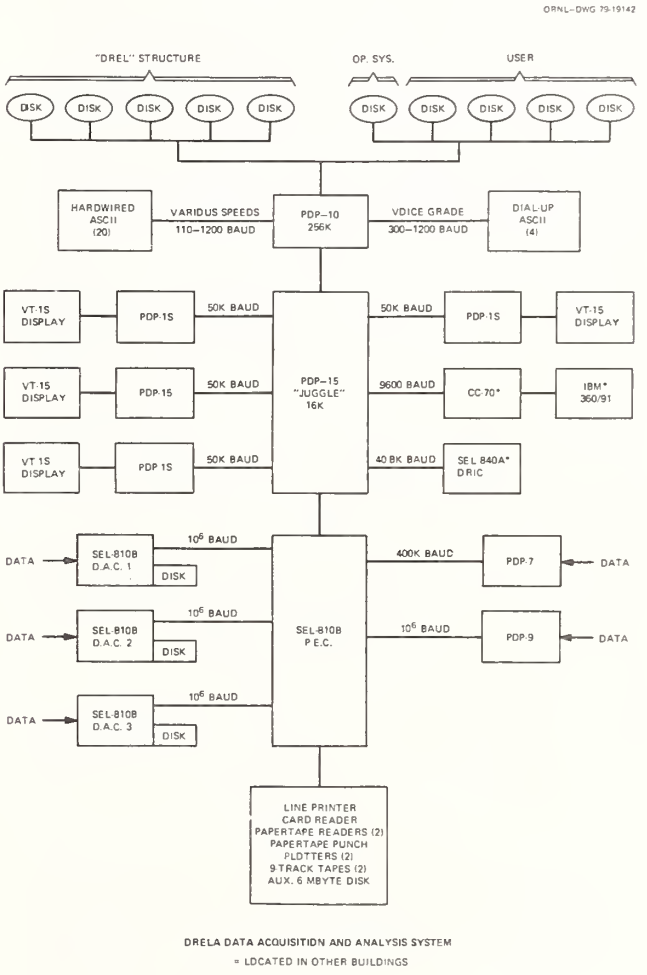

ORELA DATA ACQUISITION AND ANALYSIS SYSTEM
* LOCATED IN OTHER BUILDINGS

Fig. 5

The PDP-10 computer may be accessed by 24 users simultaneously. Four user stations are equipped with graphic display terminals which permit visual analysis of data. Four telephone dial-up lines are also provided. Major output functions are handled by a 300 line/minute line printer, two drum plotters, and two 9-track magnetic tape drives attached to the PEC. No operator is required, except during one 4-hour downtime/week for maintenance; users mount their own 25 Mbyte disk packs.

Recent Improvements

During the last year, the following improvements have been made to the data acquisition and handling system at ORELA:

1. A new 1000 card per minute card reader which replaced a 400 card per minute card reader has been installed on the PEC and is operating without problems.
2. Bids are out for two new 75 inch per second tape units which will replace the 45 inch per second tape units.
3. An additional 16K for each SEL 810B has been installed and software is currently being changed to make use of it. Each SEL now has 32K of core.
4. The amount of core for the PDP-15 displays has been increased from 12K to 16K for 3 of them and to 32K for the fourth. Software has been changed to make use of the new memory.
5. The high speed link between the PEC and the PDP-15 (PDP-10) has been installed increasing the speed from 80 KBaud to 800 KBaud.
6. A Motorola M6800 microprocessor to control two Calcomp plotters has been installed on the PEC and is operating without problems.
7. Bids for the RP04 disk for the PDP-10 are going out. The first RP04 will add 80 000 disk blocks; each additional RP04 will add 160 000 disk blocks.
8. The PEC disk has been replaced. The new disk is twice as fast, and has twice the storage.

Almost all data are handled in a standardized format called "ORELA Data Files" or ODF. Very substantial facilities exist for performing operations upon these data files so as to facilitate background subtractions, resolution corrections, curve fitting, averaging, summation, and alignment. The latter capability uses a program called "ESHIFT" which automatically aligns sets of data taken with different zero times and flight path distances to a common flight path distance and zero time. In this way one can, for example, reduce the data from a number of detectors to a common time (hence energy) scale. Extensive plotting capabilities are usable with well chosen default options to minimize the effort required.

Some Experiments at ORELA

Experiments Reported at this Conference[5]

The following is a list of 7 papers presented at this conference which involved ORELA:

Neutron Total Cross Sections of H, C, O, and Fe from 500 keV to 60 MeV

High Resolution Neutron Fission Cross Section of ^{231}Pa

Measurement of $^{238}U(n,n'\gamma)$ and $^{7}Li(n,n'\gamma)$ gamma ray production cross sections

Neutron Total Cross Section of ^{233}U from 0.01-1.0 eV

Neutron Total Cross Section Measurements on ^{249}Cf

Absolute Measurement of $_{p}$ for ^{252}Cf by the Large Liquid Scintillator Tank Technique

Measurement of the 2.35 MeV Window in ^{16}O + n

Papers at Meeting of Division of Nuclear Physics[6]

Six papers based on ORELA work were presented at last week's American Physical Society meeting:

M1 Ground-state Radiative Strength in ^{207}Pb for E_x = 6.74-7.34 MeV

Statistical Distributions of Spacings of Resonances in ^{64}Zn, ^{66}Zn, ^{68}Zn and ^{70}Zn Nuclei

Neutron Capture Cross Sections in ^{67}Zn

High Resolution Neutron Total Cross Sections in ^{67}Zn

^{187}Os 30 keV Inelastic to Elastic Cross Section Ratio

Measurement of Fission Cross Section of ^{241}Am

Discussion of Selected Experiments

Because of restricted space only a few carefully selected experiments will be discussed herein. These experiments represent recent improvements in techniques of data acquisition and reduction or new instruments.

Precision Total Cross Section Measurements

The most prevalent material in modern nuclear reactors is ^{238}U. Accordingly the nuclear properties of this nuclide are among the most important. Until recently it could not be said that the total cross section of ^{238}U as a function of neutron energy had been well measured in spite of some 24 previous determinations. At ORELA, two very carefully fashioned experiments have now been completed[7] in which a precision determination of the total cross section for energies up to 4 keV and 100 keV were made. These measurements were characterized by the following features: (1) 7 sample thicknesses, (2) black resonace background determinations for each sample thickness, (3) precise determination of time dependent gamma ray backgrounds, (4) especially careful attention to the response of the neutron detectors used, (5) careful determination of the accelerator-on background.

After appropriate background subtractions had been performed the data were subjected to simultaneous multi-level fits for all 7 samples Figure 6 shows the results of such a fit. For clarity the results

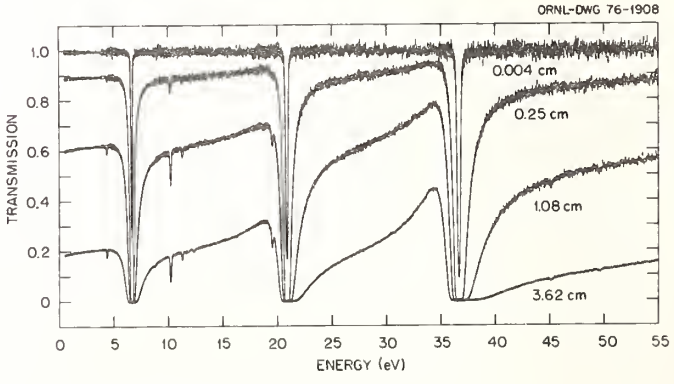

Fig. 6. Transmission of ^{238}U.

for only 4 of the 7 samples are shown. Each curve consists of data and a line which corresponds to the simultaneous least squares fitting curve appropriate for that sample. It is essentially impossible to see the calculated curve because the fit is so perfect. It is important to note that the response of the detector played a very important role in a readjustment of the best values for the neutron width of many of the resonances which were studied. This was important in resolving a long standing discrepancy. A similar experiment to this is being planned for ^{232}Th for the near future.

It is interesting to consider the data storage requirements for such an experiment. In the proposed thorium experiment[8] 8 transmission samples will be used. A typical measurement cycle will consist of the following steps: open beam measurement, 8 samples in succession, 8 samples in succession with black resonance filters in place, 2 successive measurements with different thicknesses of C_2H_2 for gamma ray background determinations and one period with a thick beam stop in place. This cycle of 20 individual determinations will be repeated once per hour for a period of roughly 5 weeks. All measurement spectra but three will occupy 23 535 channels. The total data requirement is 431 874 channels. There are at present at ORELA at least 4 distinct experiments or types of experiments which require this order of data acquisition capability. One proposed experiment is expected to require 900 000 channels of data storage.

Medium Energy Neutron Detector

For neutrons in the energy range 10 keV to 1 MeV it has long been difficult to have a detector which did not show a strong dependence on some threshold bias. Recently a detector has been developed by N. W. Hill of ORNL which removes this dependence in a new way and very well. The detector (Figure 7) consists of a block of NE-110 plastic scintillator and 3 or more photomultiplier tubes attached to its various faces with epoxy. In the particular unit shown in

Fig. 7. Majority logic neutron detector.

Figure 7 the NE-110 is 2 cm thick and 6 cm square. Photomultipliers (in this case 2" diameter 8850 units) may be attached to each of the edges and to the face opposite the entrance face. Thus, up to 5 photomultipliers may be coupled to the scintillator. The bias for each discriminator-photomultiplier is set

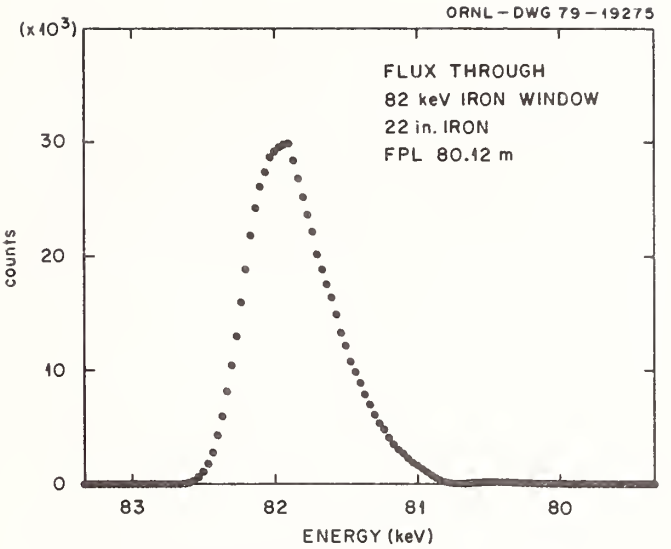

Fig. 8. Incident flux.

well below the single photoelectron level; indeed, it is set at the edge of the amplifier noise. A two-out-of-N majority logic circuit then serves to require a single photoelectron coincidence between at least two of the photomultipliers. This arrangement turns out to be extremely advantageous. The counting rates which are found, of course, depend upon the efficiency of the NE-110 in stopping a neutron of that particular energy; however, the response is almost totally independent of the actual bias settings within reasonable variations, say 20-30%. The net result is that this detector provides an extremely reliable detector which is very reproducible under almost all circumstances.

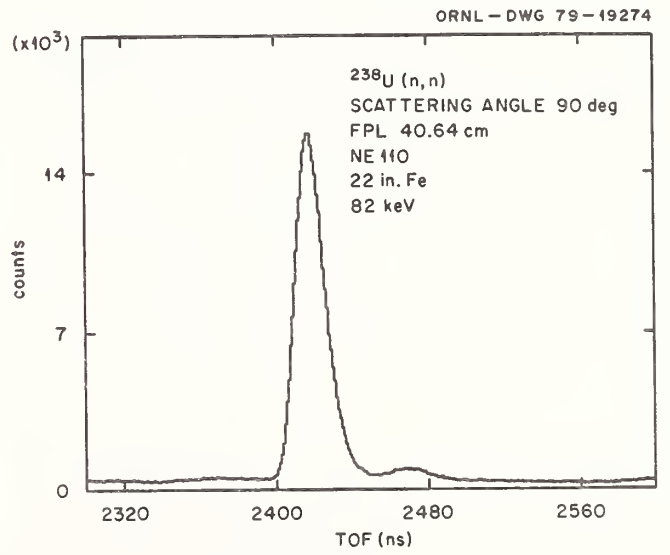

Fig. 9. Scattered flux.

Figure 8 shows the transmitted neutron beam through a 50 cm iron filter at 82 keV. In a recent experiment at ORELA[9] such a beam was allowed to scatter from a sample of ^{238}U and the scattered neutrons were detected with a time-of-flight base of 60 cm into this new detector. The result of this measurement is shown in Figure 9 where the data are plotted as a function of time-of-flight. The small secondary peak to the right

of the main peak represents inelastically scattered neutrons of energy 35 keV. These neutrons have been scattered from the 44 keV level in ^{238}U. The main peak, of course, represents elastically scattered neutrons. This inelastic scattering and similar inelastic scattering from a few other levels provide an important contribution to neutron moderation in reactors which has been previously difficult to measure. This type of measurement obviously requires further development but the new detector appears to provide a means to obtain such important information in the future.

$^{6}Li(n,\alpha)$-Xenon Gas Scintillator Beam Monitor

In connection with fission cross section measurements over a wide range of energy (thermal-20 MeV) it is desirable to use the $^{6}Li(n,\alpha)$ reaction because the cross section is both well known and smooth at the lower energies. The fission reaction in ^{235}U has traditionally been used at higher energies as the cross section standard. It is, of course, useful to allow these two standards to overlap in energy for normalization and and/or consistency checks. The ^{235}U ENDF/B-V fission cross section does not, however, truly become smooth until energies above 300 keV are reached.

It is well known that the usual ^{6}Li glass neutron detector has a large response to the gamma flash associated with the electron pulse at a linear accelerator; in fact recovery from the gamma flash in times less than $\sim$8 μs is very unusual. At short flight paths such as 9 meters this means that data cannot be obtained for energies higher than roughly 280 keV. Note that this does not permit the above mentioned overlap to occur. For this reason, among others, it was decided to develop a new type of neutron beam monitor. The first approach consisted of a sandwich comprising 2 sheets of 0.15 mm thick NE-110 with a thin layer of ^{6}LiF between the two sheets (in fact evaporated onto one of the surfaces). While this detector appeared to give excellent response, it was found that a very substantial amount of moderation of the neutrons occurs in the front layer of plastic scintillator (NE-110). This moderation is sufficiently severe that neutrons initially of 10 keV lead to an artifically enhanced response which may differ from that expected from the cross section of ^{6}Li by as much as 25%. In addition above 400 keV the presence of knock-on proton response also leads to a strong increase in response above that expected from the lithium cross section alone. A curve showing the magnitude of these errors is illustrated in Figure 10.

As a result of the realization that substantial errors existed in the response of the sandwich plastic scintillator, a new detector was developed which replaces the hydrogenous plastic scintillator with xenon gas.[11] The basic principle remains the same. A view of this detector is shown in Figure 11. The xenon gas scintillator system has proved itself to be quite reliable and reproducible and has the advantage that its response shows no anomalies up to above 800 keV when used at 9 meters, except strong dips where two Xe resonances at 9.4 and 14.4 eV occur. The response from the gamma flash is back to base line in about 0.7 μsec and could be improved by electronic modifications. The usual problems of gas purity have

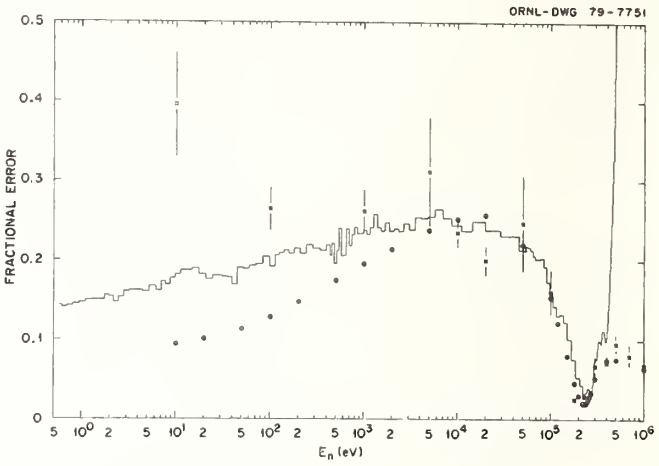

Fig. 10. Correction curves (measured) circles are calculations of R. L. Macklin. Crosses are Monte Carlo calculations of L. M. Petrie.

been addressed by utilizing a thermally driven gas circulation system and 2 gas purification elements.[10]

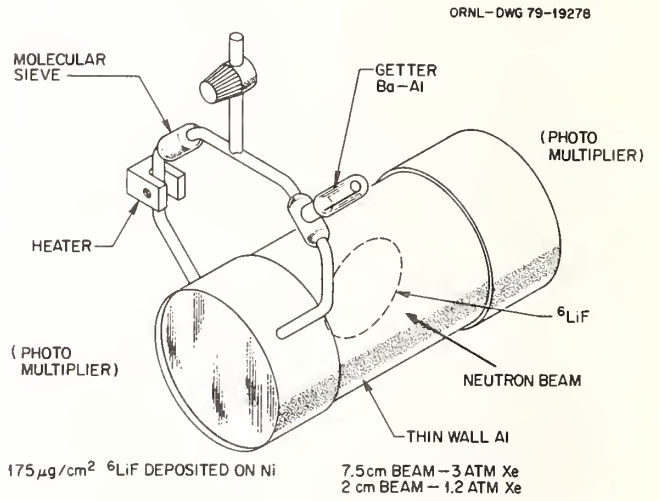

$^{6}Li(n,\alpha)$ – Xe GAS SCINTILLATOR

Fig. 11.

Future Directions at ORELA

In the previous paper[12] Dr. G. F. Auchampaugh has already mentioned the use of an electron prebuncher at ORELA. Recently this system was tried in a preliminary experiment. Figure 12 shows the result of applying 1/3 of the design buncher voltages to the buncher gaps. The prebuncher reduced the pulse width

at the target from 17 nanoseconds to 8 nanoseconds and

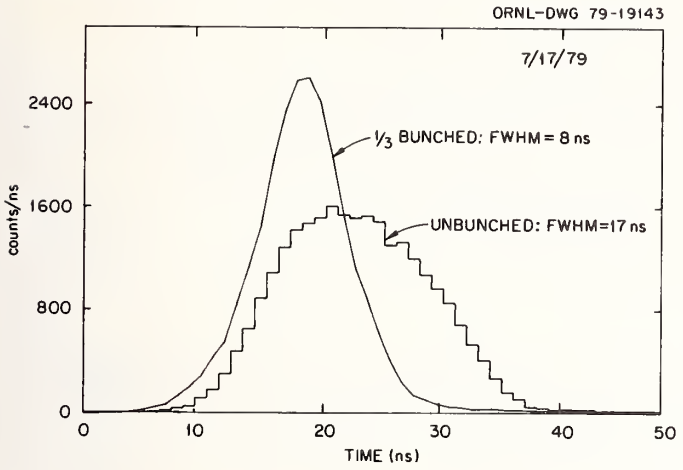

Fig. 12. Partially bunched and unbunched ORELA pulses.

represents only a first approach. At the moment some difficulty with vacuum leaks in several sections of the buncher have appeared. These are being repaired and further tests of the buncher system will be performed as soon as practicable.

A "hidden" advantage of such a buncher is that experiments that require high resolution (short pulses) and experiments that require high power (and, at present, wide pulses) can both be done simultaneously. This may increase the "utilization factor" of 5.4 mentioned above to perhaps 7 or 8.

Recently, it was realized that ORELA could produce neutron fluxes large enough to be usable in transmission measurements up to 80 MeV. In view of a very urgent need for total cross sections to be used in the shielding design of FMIT (Fusion Materials Irradiation Test Facility), such measurements on some 11 materials over the energy range up to 60 or 80 MeV have recently been made.[13] These experiments used the Be block alternate target at ORELA and were performed with an 80 meter flight path. It was found necessary to operate at somewhat reduced power and to put a filter of 20 cm polyethylene in the beam to bring the deadtime corrections to reasonable values, even with a 1 μs deadtime time digitizer. An energy resolution of .01E-.03E was obtained. Clearly this new direction is viable and useful. In the case of the FMIT design, it has been estimated that more accurate data will save roughly one million dollars in construction costs.

The research was sponsored by the Division of Nuclear Sciences, U.S. Department of Energy, under contract No. W-7405-eng-26 with the Union Carbide Corporation.

References

1. M. S. Moore et al., Phys. Rev. C 18, 1328-1348 (1978). Note that Dr. G. F. Auchampaugh has used 30 J/pulse for ORELA in his comparisons (ref. 11).
2. R. L. Macklin, Nucl. Inst. Meth. 91, 79 (1971).
3. B. Diven, Ann. Rev. Nucl. Sci. 20, 79 (1970).
4. Manufactured by EG&G-ORTEC, Oak Ridge, Tennessee.
5. Papers AB1, EB7, FC2, FC5, FC9, GA2, GC2, respectively [BAPS II, 24, 860 ff (1979)].
6. Papers EC10, GC5, GC6, GC7, GC10, GC13, respectively, [BAPS II, 24, 812 ff (1979)].
7. D. K. Olsen et al., Nucl. Sci. Eng. 69, 202 (1979).
8. D. K. Olsen, private communication.
9. R. R. Winters, private communication.
10. J. W. T. Dabbs, Report NEAND L-116, (BNL-50991), p. 313; Brookhaven National Laboratory, May, 1979.
11. J. W. T. Dabbs, BAPS II, 24, 651 (1979).
12. G. F. Auchampaugh, BAPS II, 24, 887 (1978) (previous paper, this conference).
13. A portion of these results are to be found in D. C. Larson et. al. in paper AB1, this conference (see ref. 5).

USE OF HIGH RESOLUTION γ-RAY SPECTROSCOPY FOR NEUTRON CROSS SECTIONS*

M. L. Stelts
Brookhaven National Laboratory, Upton, New York 11973

The use of high resolution spectroscopy to resolve some problems in neutron cross section measurements will be discussed. Topics included are: Measurements of capture cross sections with the time-of-flight technique in the presence of high backgrounds, measurements of activation cross sections, and determination of neutron fluxes. The use of high resolution spectral data to determine resonance spins will be discussed. Data will be presented on measurement of p-wave neutron strength functions from high resolution γ-spectra from average neutron capture at 2- and 24-keV energy.

(Neutron capture, neutron strength functions, photon strength functions, γ-ray spectra, average resonance capture)

Introduction

High resolution γ-ray spectroscopy has seen much use as a tool for the measurement of neutron induced cross sections and those quantities (i.e. neutron and γ-ray strength functions, spin and parities of nuclear levels and nuclear level densities) important in the calculations of neutron cross sections. This usage increased markedly with the development of germanium semiconductor detectors in the early 1960's. I shall give a brief review of the neutron reaction process and describe a few experiments which use high γ-ray spectroscopy to measure these neutron induced cross sections. I shall then concentrate on the (n,γ) reaction and the extraction of nuclear information for high resolution measurements. Finally I shall describe in detail the Average Resonance Capture (ARC) technique and its value in extraction of the ratios of electric dipole to magnetic dipole strength and p-wave to s-wave neutron strength. The strengths and limitations of the method together with its interaction with nuclear spectroscopy will be discussed.

Activation Technique

When a neutron of energy, E_n, is incident on a target, a state of energy E_n+S_n is formed, where S_n is the separation energy of the neutron. This state can decay in a variety of ways. At high energies one or more particles can be emitted; at low energy only neutron and γ-ray emission is possible (excepting the fissile nuclei). Any excited states in the final nucleus will generally decay rapidly to the ground state. If the final nucleus is radioactive, and emits γ rays, high resolution γ-ray detectors can be used to measure the resulting activity. I shall not attempt to survey the current research efforts but refer the reader to references 1-5.

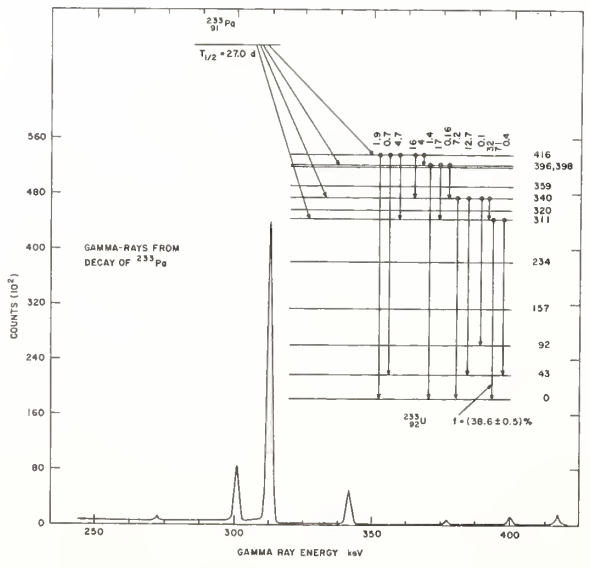

Fig. 1: A portion of the γ-ray spectrum from the decay of ^{233}Pa. The levels in ^{233}U populated by the β decay of ^{233}Pa are shown. The prominent line at 311 keV was used to measure the activation relative to the 400 keV line from Au.

I would like to mention two examples of the activation technique. The first is a measurement of the ^{232}Th[4] capture cross section at thermal, 2- and 24-keV neutron energy at the Brookhaven High Flux Beam Reactor tailored beam facility.[6] Here neutron capture forms ^{233}Th which rapidly decays to 27-day ^{233}Pa. The cross section was measured relative to Au with simultaneous irradiation and counting of the activity. Figure 1 shows the γ-ray spectrum and the pertinent decay scheme. The peaks are clearly distinguished from background and the relative peak areas can be determined to high precision. What is crucial to the accuracy of the experiment is the branching ratio of the 311 keV line. This ratio has been determined by two separate laboratories to be (38.6±0.5)%[7] and (38.6±1.5)%.[8] This information from nuclear spectroscopy is crucial to a precise measurement with this technique.

The second example is from some recent 24-keV neutron capture cross section measurements.[5] Shown in Fig. 2 is the spectrum of γ rays from the activation of a sample of natural Nd + Au. The lines due to the respective targets are shown. It is clear that without high resolution it would have been impossible to do this experiment with a natural target.

Inelastic Neutron Scattering

Several recent studies[9-12] of the excitation function for inelastic neutron scattering demonstrate the rich interaction between cross section measurement and high resolution nuclear spectroscopy. In these experiments the γ-ray spectra are measured as a function of neutron bombarding energy. The branching ratios from each state excited are determined. The results from the relatively simple spectrum at low bombarding energy can be used to determine the more complex decay schemes resulting at high energies where more levels are populated. Thus these experiments yield both precise inelastic scattering cross section and nuclear spectroscopic information.

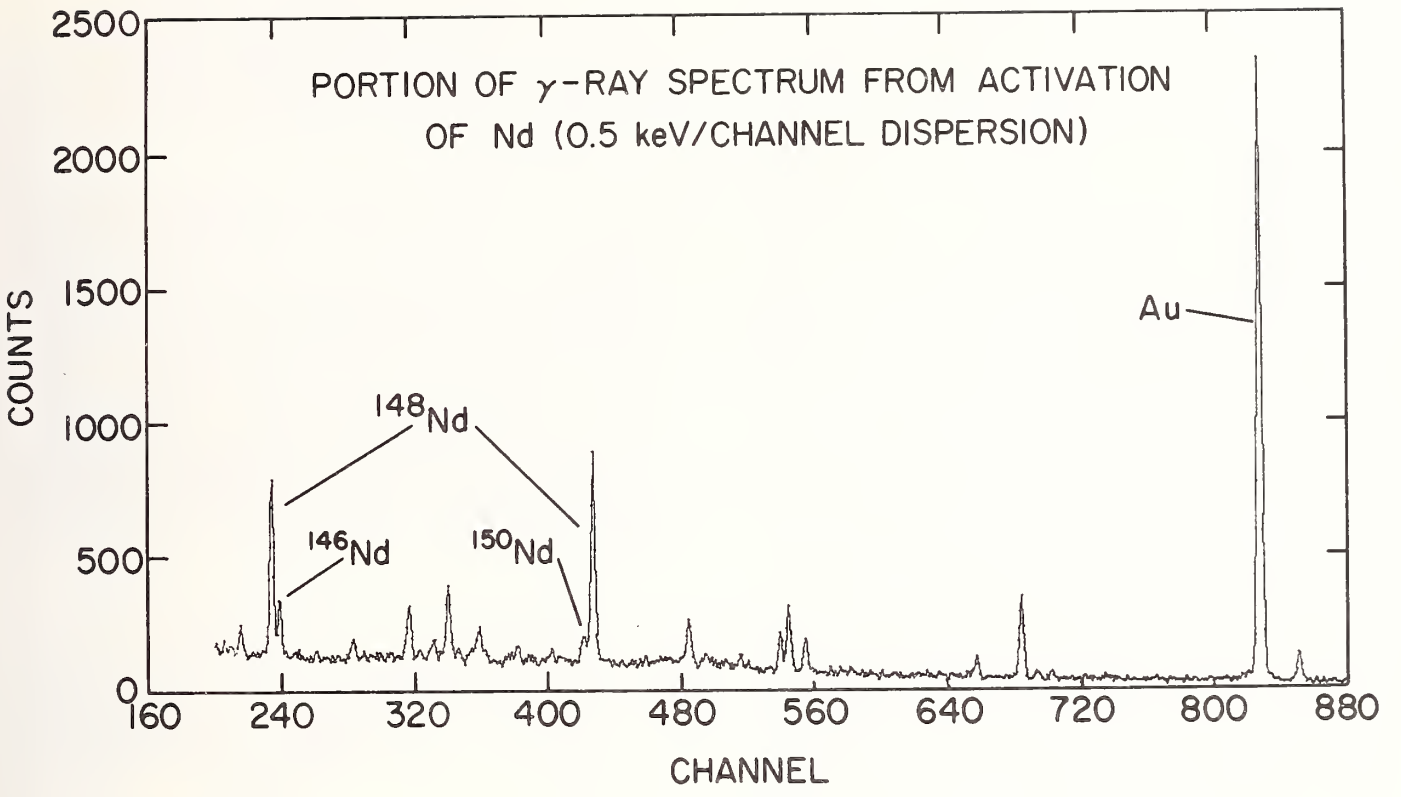

Fig. 2: A portion of the γ-ray spectrum from activation of natural neodynium with 24-keV neutrons. The γ rays are assigned by the isotopic number of the targets.

The (n,γ) Reaction

Consider the neutron capture reaction shown schematically in Fig. 3. A neutron is captured at energy E_n+S_n in the compound nucleus. Deexcitations can occur directly as primary γ rays to final states which have spins and parities which satisfy the (normally dipole) Electromagnetic Selection Rules. These γ rays appear as discrete lines when the final states are at low excitation energies but gradually approach a continuum as the final state level spacing approaches the detector resolution. Decays from these states at high excitation will populate low-lying levels. Deexcitation of these low-lying levels give rise to discrete secondary γ rays. Thus the typical capture spectrum for a typical medium to heavy nucleus will consist of discrete high energy γ-ray lines merging into a continuum as the γ-ray energy decreases. Discrete lines appear again at low energies due to secondary γ rays from low-lying states.

The measurement of these spectra is important for both applied reasons and for testing nuclear models. Unfolding the detector response from measured spectra when the detector has low resolution is subject to large uncertainties. However a germanium detector, operated as a pair spectrometer[13,14] has a very simple response as shown in Fig. 4. The largest single component of the response is in the peak which can be approximated as a δ function on the scale of energy variation of the other components. The other components are either independent of--or vary slowly with the incident γ-ray energy. This simple response enables unfolding of the detector response in a simple straightforward manner[14] to extract γ-ray spectra for energies $\gtrsim$ 1.5 MeV. This has been done[15] for capture spectra from ^{181}Ta (n,γ) as a function of incident neutron energy and the results are shown in Fig.5.

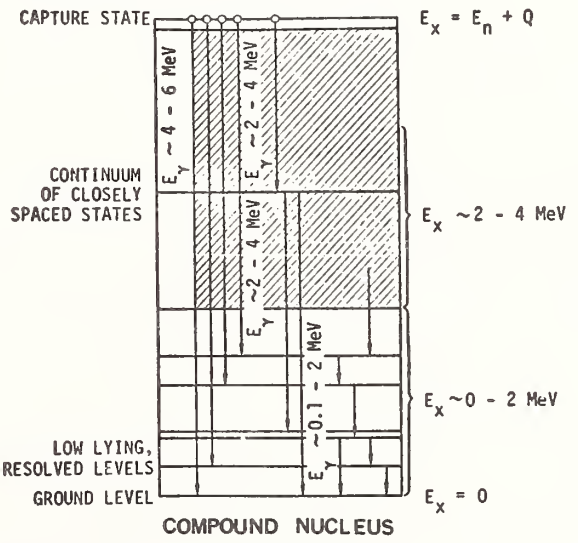

Fig. 3: Schematic representation of the (n,γ) reaction showing representative decays of the excited compound system.

Let us now consider γ-ray spectra from isolated neutron resonances or from thermal capture where only a few resonances influence the capture state. The cross section to a final state, f, from initial state, i, allowed by the EM selection rules is:

$$\sigma_{if} \propto 2\pi\lambda^2 \frac{g\Gamma_n\Gamma_{\gamma f}}{\Gamma} \qquad (1)$$

where $g = \frac{2J+1}{2(2I+1)}$ is the statistical factor for neutrons on a target with spin I and a resonance of spin

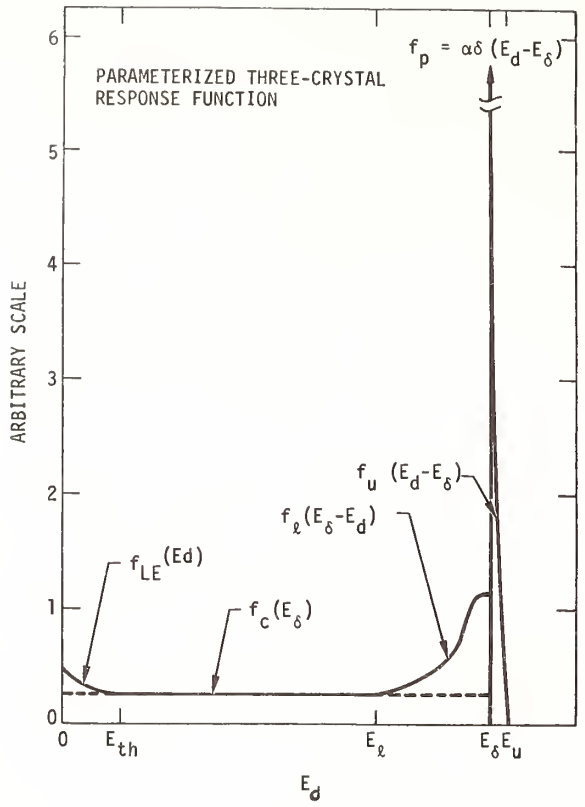

Fig. 4: The parameterized response function of a three-crystal pair spectrometer.

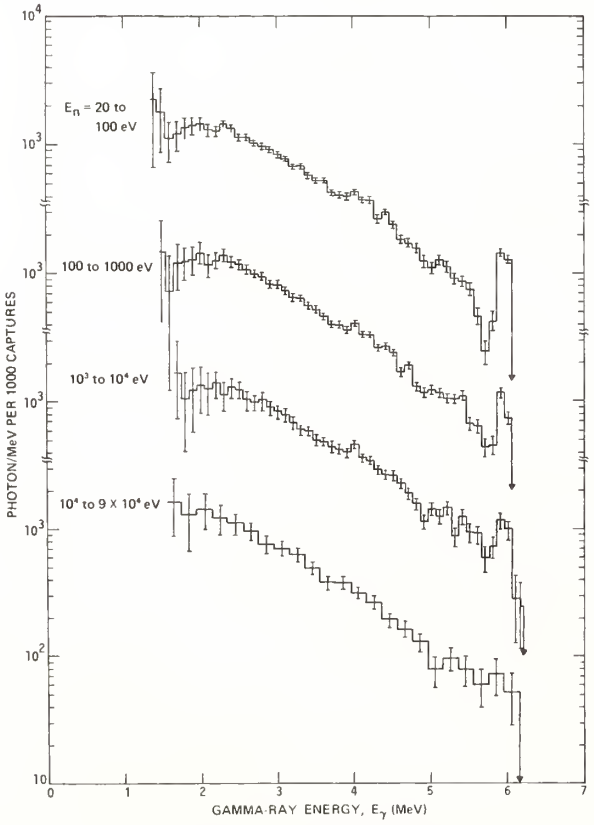

Fig. 5: The unfolded γ-ray spectra from the ^{181}Ta (n,γ) reaction as function of incident neutron energy.

J, λ^2 is the neutron wave length, Γ_n and Γ are the neutron and total width, respectively, of the resonance and $\Gamma_{\gamma f}$ is the partial radiative width. The reduced (by a kinematic factor) radiative widths, $\Gamma^\circ_{\gamma f}$, are expected to follow a Porter-Thomas[16] distribution

$$P(s) = [(s/2)^{1/2}\Gamma(1/2)]^{-1}\, e^{-s/2}$$

where $s = \Gamma^\circ_{\gamma f}/\langle\Gamma^\circ_{\gamma f}\rangle$. Thus we expect large variation in γ-ray intensities as we change initial or final states. The population of low-lying states (with corrections for primary feeding) is from a very large number of states at high excitation. Thus the fluctuations should average out and there should be little variation in the intensity of γ rays from these states for differing initial states with the same spin.

This property has been used with a Ge(Li) detector to measure between resonance capture cross sections for ^{238}U[17] and ^{232}Th[4] where the signal to noise ratio would be poor with low resolution detectors. Figure 6 shows the capture cross section for ^{232}Th measured with this technique.

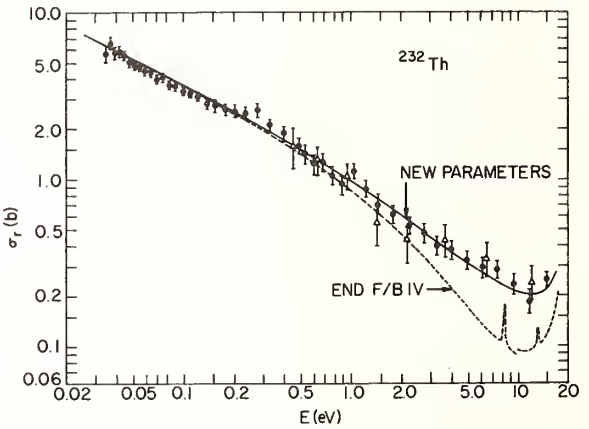

Fig. 6: Capture cross section of ^{232}Th measured with high resolution detection of secondary γ rays.

The non-primary population of a low-lying state is expected to be a function of the spins J_i, J_f, of the initial and final states. A simple argument is as the cascade proceeds via dipole radiation the probability of populating states with $|\bar{J}_i-\bar{J}_f| \gtrsim 2$ is quite reduced. Thus the ratios of intensities of γ rays from states of quite different J_f should be a function of capture state spin. Coceva and Giacobbe[18] have used this technique to measure the spins of resonances in ^{166}Ho. Figure 7 shows the ratio of selected secondary ray intensities as a function of neutron resonances below 400 eV neutron energy. The separation of 3^+ and 4^+ states is excellent. They used this separation to extend the measurement of the s-wave neutron strength function ($S_0=(\Sigma g\Gamma_n)/\Delta E$) where ΔE is the averaging interval into the unresolved resonance region for spin 3^+ and 4^+ resonances. They found no evidence for spin dependence of the neutron strength functions.

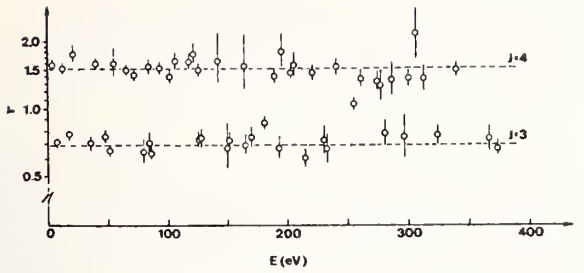

Fig. 7: The ratio between the intensity of the 149.4 keV γ-ray line and the sum of the intensities of the 239.1- and 371.8 keV lines in ^{166}Ho for resonances below 400 eV from the data of Coceva and Giacobbe.[18] Note the clear distinction between the resonance spin states.

Let us now consider the reduced radiative widths $\Gamma^{\circ}_{\gamma f}$. In the Single Particle (SP) model and Giant Dipole Resonance (GDR) models the reduction factors assume different forms[19,20] For E1 radiation for SP

$$\Gamma^{\circ}_{\gamma f}(E1) \propto \frac{\Gamma_{\gamma f}}{E_{\gamma}^{3} D_J A^{2/3}} \qquad (3)$$

where E_γ is the γ-ray energy, D_J is the average level spacing for intial state spin J and A is the mass number of the compound nucleus. For the GDR model[21] an approximation to the GDR for an "average" nucleus is:

$$\Gamma^{\circ}_{\gamma f}(E1) \propto \frac{\Gamma_{\gamma f}}{E_{\gamma}^{5} D_J A^{8/3}} \qquad (4)$$

The SP M1 estimate is:

$$\Gamma^{\circ}_{\gamma f}(M1) \propto \frac{\Gamma_{\gamma f}}{E_{\gamma}^{3} D_J} \qquad (5)$$

It appears from available data[19,20,32,35] that the GDR model for E1 strengths is in better agreement than the SP model. The E_γ^5 dependence shown in Eq. (4) is an approximation good at 7- to 8-MeV γ-ray energy. The data on M1 strengths is not as complete. There is some evidence that E_γ^5 dependence is not unreasonable[36] and this could be explained by an M1 giant resonance at 8-10 MeV. In any case a reduction factor of E_γ^{-5} is generally accepted for γ rays in the 6-8 MeV range.

The prediction of the statistical model, based on the assumption of complex initial states and random matrix elements is that the distribution of these reduced widths should follow the Porter-Thomas distribution, Eq. (2). To test this hypothesis it is necessary to examine transitions from isolated resonances of known J_I^{π} to states of known J_f^{π}. Large numbers of transitions are necessary to achieve reasonable accuracy. The analysis must be done carefully since the most probable width is 0. The function used to test the hypothesis is the χ^2 distribution.

$$\chi^2(s,\rho) = \frac{(\rho s)^{\rho-1}}{\Gamma(\rho)} e^{-\rho s} \qquad (6)$$

where $s = \Gamma^{\circ}_{\gamma f}/\langle\Gamma^{\circ}_{\gamma}\rangle$, $\rho=\nu/2$, where ν is the number of degrees of freedom and Γ is the gamma function. For ν=1 this reduces to the Porter-Thomas distribution, Eq.(2). Four careful experiments[22-25] have been done which give consistent values for ν. These are listed in Table I.

Table I

Nucleus	ν	Reference
^{116}In	$1.42^{+.14}_{-.08}$	22
^{150}Sm	∿1.4	23
^{178}Hf	$1.38^{+.18}_{-.13}$	24
^{182}Ta	1.38±0.11	25

A data set of 1240 E1 transitions was used for determining ν for ^{182}Ta. The distribution of widths is shown in Fig. 8 with the fit for the maximum likelihood value of ν=1.38 and Eq. (6) for ν=1,2. I am aware of no theoretical explanation for these results.

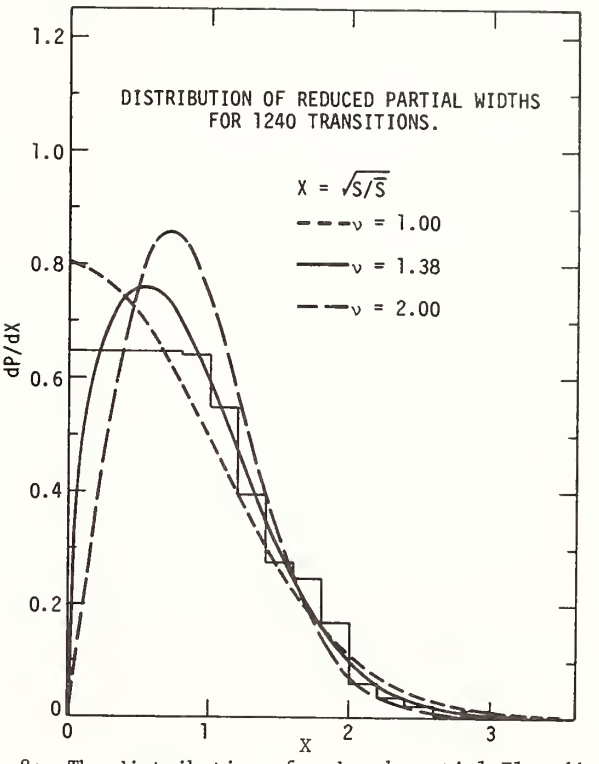

Fig. 8: The distribution of reduced partial E1 radiative widths for ^{182}Ta. The fit for ν=1.38 is the maximum likelihood fit of a chi-squared function to the data. The Porter-Thomas (ν=1) and exponential (ν=2) curves are shown for comparison.

The resolved resonance method is the most straightforward way of extracting the partial radiative widths and thus testing the models. It is easy to get absolute values for the widths, and there is little problem with admixture of partial-waves in the neutron channel. The accuracy of the average widths are generally limited by the Porter-Thomas fluctuations. If we make the conservative assumption that the distribution of partial radiative widths follows the Porter-Thomas distribution (Eq. (2)), then an average over ν transitions will follow the χ^2 distribution with ν degrees of freedom (Eq. (6)). This function is plotted in Fig. 9 for several values of ν. From these curves we can conclude that we must have a sufficient number of neutron resonances and an adequate sensitivity to guarantee seeing transitions of a given multipolarity to each possible final state that can be populated. The accuracy of the final average will have fractional standard deviation given by:

$$\sigma = \sqrt{2/\nu}. \qquad (7)$$

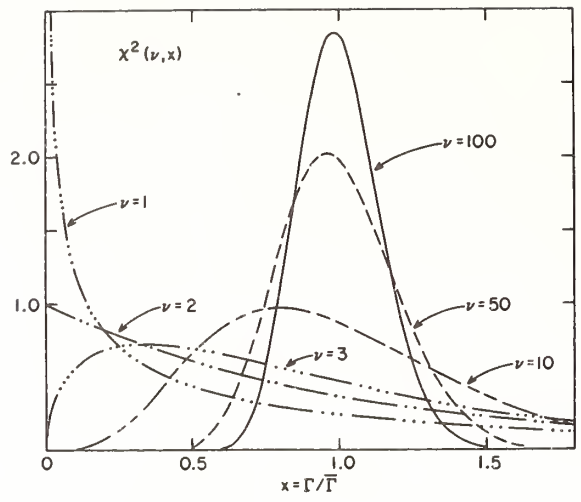

Fig. 9: The χ^2 distribution function for values of ν from 1 to 100.

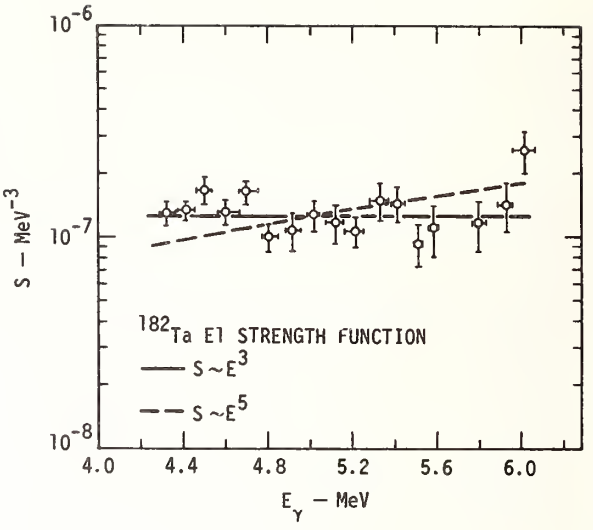

Fig. 10: The E1 strength functions for ^{182}Ta from the resolved resonance method.

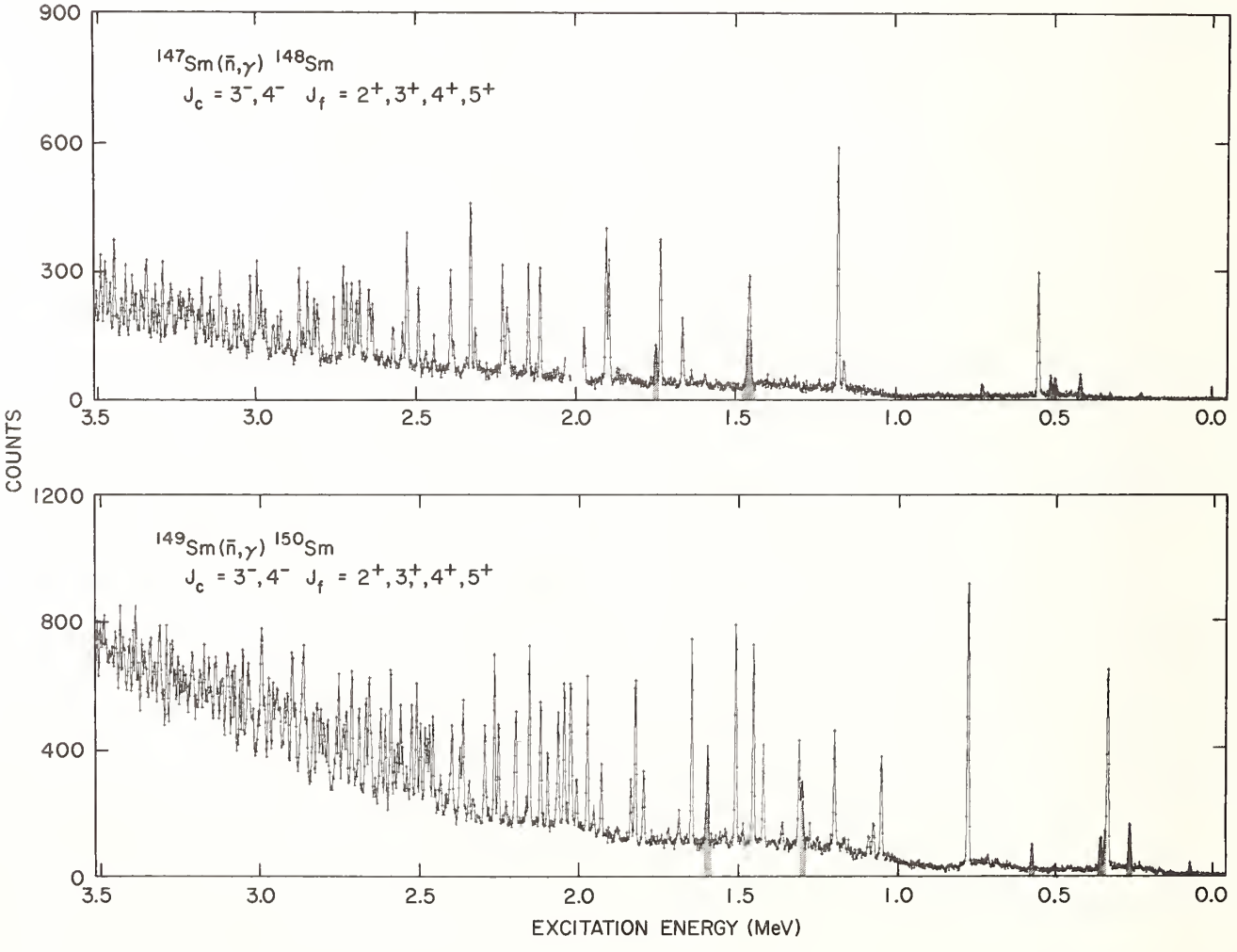

Fig. 11: Typical 2-keV ARC spectra. Note the uniformity of γ-ray intensities. The most prominent lines are due to E1 radiation following s-wave capture.

The average reduced radiation width from $^{181}Ta(n,\gamma)^{182}Ta$[25] is shown in Fig. 10 as a function of E_γ. A reduction factor of somewhat less than E_γ^{-5} is expected for this energy region.

The resolved resonance primary γ-ray spectra technique has been used in many experiments[18,22-30] because of the rich amount of nuclear physics information that can be extracted. The disadvantages of the technique is that a considerable investment of time is required in the collection, and in the careful analysis of the data. The first problem could be alleviated as more intense neutron sources become available.

Average Resonance Capture

Neutron capture γ-ray spectra from isolated neutron resonances show marked variations in the intensities of transitions to individual final states. If the spectra were averaged over many initial states the fluctuations will be reduced as discussed in the previous section. The reduced intensities to final states of the same J^π averaged over ν resonances will be expected to be distributed as a χ^2 function with ν degrees of freedom and show a variance $\sigma = \sqrt{2/\nu}$. Therefore if we can design a neutron source which can average over a sufficient number of resonances, and have adequate experimental sensitivity we can be guaranteed to see every allowed dipole transition. The γ rays will be grouped in bands whose intensities are a function of J^π of the final state and the multipolarity of the transitions.

This technique was first developed by Bollinger and Thomas[31,32] at Argonne National Laboratory in the late 1960's. They used an internal target arrangement

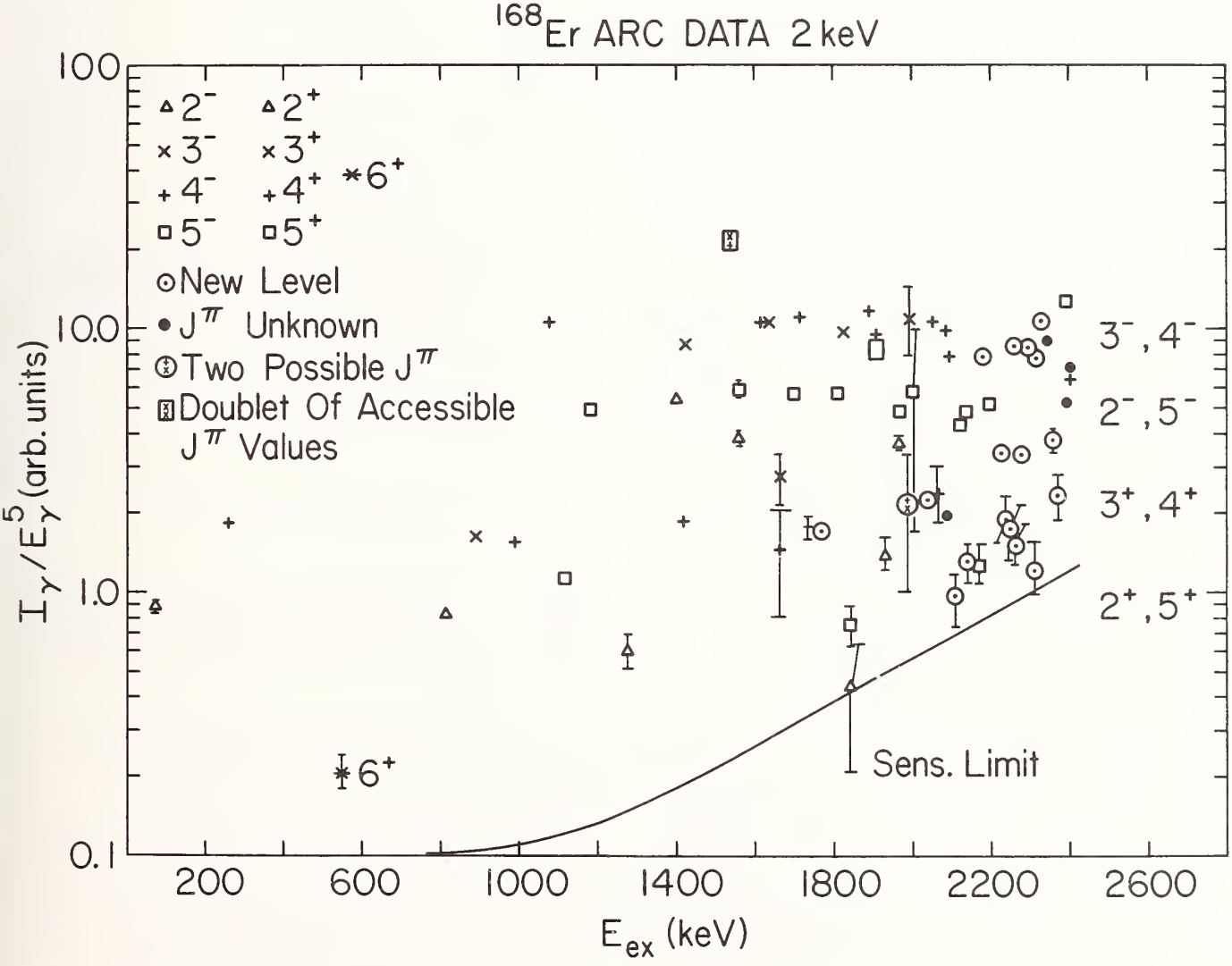

Fig. 12: Reduced intensities, I/E_γ^5, for 2-keV ARC on ^{167}Er. The transitions are labeled by the J^π of the final state.

with the incident neutron spectrum chosen by surrounding the sample with boron absorbers to remove low energy neutrons from the reactor spectrum. The tailored beam facility[6] at the HFBR at Brookhaven uses external beams formed by transmission of reactor spectrum neutrons through total cross section dips caused by interference between s-wave resonances and potential scattering. A Sc-Ti filter and a Fe-Al filter give from beams at 2- and 24-keV energy with widths of 900 and 1900 eV, respectively. These beams are broad enough to encompass many neutron resonances in most medium to heavy nuclei but narrow enough that they do not affect the detector resolution.

Since ARC populates all final states (subject to the electromagnetic selection rules) the spectra will exhibit many more lines than will be seen at thermal capture. It is necessary to use the simple response of a pair spectrometer[13] to adequately resolve the lines even at moderate excitations. Spectra from 2-keV neutron capture by ^{147}Sm and ^{149}Sm are shown in Fig. 11. These are typical of the kinds of spectra generated with ARC. Note that the intensities do fall into bands and there is a general decrease in intensity as the energy decreases due to the E_γ^5 factor. The grouping into bands is demonstrated nicely in Fig. 12 which shows the reduced intensities (I/E_γ^5) for 2-keV capture on ^{167}Er as a function of excitation energy. As can be seen the intensities are a function of the J^π of the final states. Data such as these have seen extensive use as an empirical tool for assignment of spins and parities. I would now like to examine these intensity ratios quantitatively to find what information can be extracted about neutron- and γ-ray strength functions.

The resonance averaged capture cross section[32] for a transition to a final state, f is given by

$$\overline{\sigma_{n,f}} = 2\pi\lambda^2\left\{\sum_{J,\ell}\frac{g_J}{D_J}\left(\overline{\frac{\Gamma_n\Gamma_{\gamma f}}{\Gamma}}\right)\right\}, \tag{8}$$

where ℓ is the orbital angular momentum of the neutron populating the resonance with spin J, D_J is the average level spacing for resonances with spin J and the rest of the variables are as defined in Eq. (1). Lynn[33] has shown that Eq. (8) can be rewritten in terms of averages of the individual widths by introducing fluctuation factors $F_{1,2}$ that account for correlation between Γ_n and Γ subject to assumption of Porter-Thomas fluctuations and $\Gamma = \Gamma_n + \Gamma_\gamma$. Then

$$\bar{\sigma}_{n,f} = 2\pi\lambda^2\left\{\sum_{J,\ell}\frac{g_J}{D_J}\frac{\bar{\Gamma}_n\bar{\Gamma}_{\gamma f}}{\bar{\Gamma}}\ F_{1,2}\left(\frac{\Gamma_\gamma}{\Gamma_n}\right)\right\} \tag{9}$$

where F_1 is used if J is an outer spin (only one way of forming J from $(\vec{s}, \vec{\ell}, \vec{I})$ where $\vec{s} = 1/2$ is the neutron spin) and F_2 is used for inner spins. The formalae for $F_{1,2}$ are given in Lynn[23] and will not be repeated here. F_1 varies between 1 and 0.68 with a minimum at $\Gamma_\gamma/\Gamma_n \sim 1$. F_2 behaves similarly with a range between 1 and 0.8.

We can now use the definitions of the s- and p-wave neutron strength function[34] to calculate $\bar{\Gamma}_n$ in Eq. (9).

$$S_0 = \frac{\langle g\Gamma_n^0\rangle}{D^0} = \sum_{s,J} g\ S\ (J,0) \tag{10}$$

$$S_1 = 1/3\ \frac{\langle g\Gamma_n^1\rangle}{D^1} = 1/3\ \sum g\ S\ (J,\ 1) \tag{11}$$

where D^0, D^1 are the average level spacings for s- and p-wave levels, s is the channel spin and Γ_n^0 Γ_n^1 are the reduced neutron widths[34] for s- and p-wave neutrons. Note that

$$\sum_s S(J,\ell) = \frac{\Gamma_n^\ell(J)}{D_J^\ell} \tag{12}$$

where ℓ is the orbital angular momentum.

Proposed expressions for reducing average partial γ-ray widths for E1 and M1 radiation have been given in Eqs. (3-5). It appears that the GDR formalism describes the reduced E1 widths[20,35,36] but the situation is not as clear for M1 radiation. There is some evidence that the photon energy dependence of M1 radiation follows that of E1 radiation with about 1/7 the strength.[20,32,36] For reasons of simplicity and since the range of excitation energies over which final states can be resolved is much less than the γ-ray energies I make the assumption that both M1 and E1 radiation have the same energy dependence

$$\Gamma^\circ_{\gamma f}(E1,M1) = \frac{\Gamma_{\gamma f}(E1,M1)}{D_J E_\gamma^5} \tag{13-1}$$

and thus

$$\frac{\Gamma^\circ_{\gamma f}(M1)}{\Gamma^\circ_{\gamma f}(E1)} = R, \tag{13-2}$$

a constant for a given nucleus.

If we further assume the neutron strength functions to be spin independent we can use the preceding definitions to rewrite Eq. (9), assuming only s- and p-wave capture as

$$\bar{\sigma}_{J_f^{\pi f}} = 2\pi\lambda^2\sqrt{E_n}\ E_\gamma^5\ S_0\left\{\sum_{J,s} g_J D_J F_1\ \frac{\bar{\Gamma}^\circ_{\gamma f}(E1,M1)}{\bar{\Gamma}_{sJ}} + \frac{S_1}{S_0}\frac{(ka)^2}{1+(ka)^2}\cdot\sum_{J,s} g_J F_{1,2} D_J\ \frac{\bar{\Gamma}^\circ_{\gamma f}(E1,M1)}{\bar{\Gamma}_{sJ}}\right\} \tag{14}$$

where the appropriate selection and vector addition rules are implicit in the $\bar{\Gamma}^\circ_{\gamma f}$ and the limits of the summations. The factor $(ka)^2/1+(ka)^2$ is the penetrability of p-wave neutrons relative to s-wave neutrons, k is the neutron wave number and, a is the nuclear radius.

If we made the following assumptions, $\Gamma_n \ll \Gamma_\gamma$, Γ_γ is independent of ℓ, and $D_J = D_0/2J+1$ then we can write Eq. (14) as:

$$\bar{\sigma}_{Jf^{\pi f}} \sim \left\{\sum_{s,J}^{s\text{-wave}} \bar{\Gamma}^\circ_{\gamma f}\ (E1,M1) + \frac{S_1}{S_0}\frac{(ka)^2}{1+(ka)^2}\sum_{s,J}^{p\text{-wave}} \bar{\Gamma}^\circ_\gamma\ (E1,M1)\right\}$$

If this equation is valid then the intensity of the population of the final state J_f can be determined by counting the number of paths allowed from all incident neutron channel and applying the appropriate

weighting for E1 vs. M1 strength and for relative p-wave to s-wave capture. This gives a simple, gross picture of the process but for real nuclei the assumption that $\Gamma_n \ll \Gamma_\gamma$ is not generally valid at 2 and 24 keV.

If we consider Eq. (14) the only factor which has not been discussed is D_J. Here we shall use the following form[40] for the dependence of D on J:

$$\frac{1}{D_J} = \frac{1}{D_0}\,(2J+1)\; e^{-\frac{1}{2}\left(\frac{J+1/2}{\sigma_c}\right)^2} \qquad (15)$$

where σ_c is the spin cutoff factor which experimentally appears to range from 3-5. D_0 is determined from experimental measurements. We can now write:

$$g_J D_J = \frac{D_0}{2(2I+1)}\; W_c(J,\sigma_c)$$

where

$$W_c(J,\sigma_c) = e^{+\frac{1}{2}\left(\frac{J+1/2}{\sigma_c}\right)^2} \qquad (16)$$

The level density is assumed independent of the capture state parity. If we further assume that the p-wave strength functions are independent of s, then we can write Eq. (14) as:

$$\sigma_{J_f^{\pi f}} = \frac{2\pi\lambda^2\,\overline{\Gamma_\gamma^\circ}(E1)\sqrt{E_n}\; D_0 S_0 E_\gamma^5}{2(2I+1)} \left\{ \sum_{sJ^\pi}^{s\text{-wave}} C(J^\pi,E_n) R\Delta(J_f,J) \right.$$

$$\times\left(\frac{\delta_1(\pi,\pi_f)}{R} + \delta_0(\pi,\pi_f)\right) + \frac{S_1}{S_0}\,\frac{(ka)^2}{1+(ka)^2} \sum_{sJ^\pi}^{p\text{-wave}}$$

$$\left. C(J^\pi,E_n) R\Delta(J_f,J) \left(\frac{\delta_1(\pi,\pi_f)}{R} + \delta_0(\pi,\pi_f)\right) \right\}. \qquad (17)$$

The coefficient

$$C(J^\pi,E_n) = \frac{W_c(J,\sigma_c)}{\bar{\Gamma}_{J\pi}}\; F_{1,2}\left(\frac{\Gamma_\gamma}{\Gamma_n}\right).$$

The functions Δ, δ_0, δ_1 are functions that return 1 or 0 as the appropriate dipole selection rules are obeyed, i.e.

$|\bar{J}-\bar{J}_f| \le 1$, $J \neq 0$ for dipole

$\pi = -\pi_f$ for E1-

$\pi = \pi_f$ for M1-radiation.

Since the calculation of Eq. (17) is rather tedious a computer code, SPARC, was written to compute the ratios of intensities to all final states populated by dipole radiation from initial states formed by s- and p-wave capture. Equation (17) was extended in the code to allow different neutron strengths for $p_{1/2}$ and $p_{3/2}$ capture.

Let us now consider neutron capture on ^{167}Er. Good spectroscopic information is available[37] on ^{168}Er and the averaging is quite reasonable. Figure 12 shows the 2-keV ARC data where I/E_γ^5 is plotted vs. excitation energy. The states are labeled with their spin and parity. The intensities of the bands are described qualitatively by the 'number of paths' argument. The $7/2^+$ target provides $3^+,4^+$ capture states with s-wave neutrons. The strongest final states are the $3^-,4^-$ formed by E1 transitions from these states. The $2^-,5^-$ state intensities are reduced a factor of 2 because only 1/2 the paths are available. The positive parity state pattern follows similar arguments for p-wave capture.

Figure 13 shows average reduced intensities (I/E_γ^5), normalized to $I(4^-)=1.0$, for each final state J^π. Only states of known J^π were included. Note that the intensity ratios between positive and negative parity states are considerably less at 24 than at 2 keV due to the stronger p-wave component.

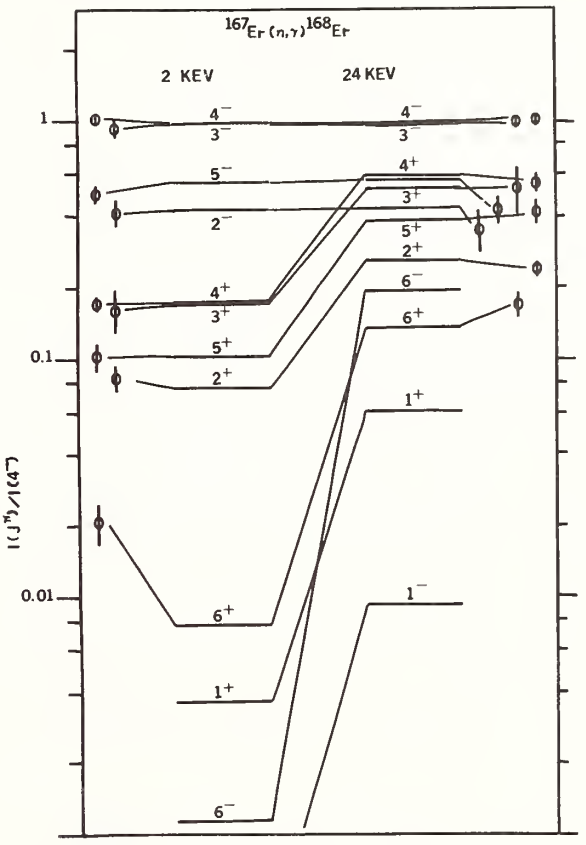

Fig. 13: Average reduced intensities for ARC primary γ-ray transitions for allowed final states for known spins and parities compared to the calculation of ARC intensities for s- and p-wave capture on ^{167}Er followed by dipole radiation.

Most ARC experiments do not measure absolute intensities. Our experimental data is thus limited to the ratios of the final state intensities as a function of J^π. Therefore, we can hope to extract only the ratios, $R = \Gamma_{\gamma f}^\circ(M1)/\Gamma_{\gamma f}^\circ(E1)$ and S_1/S_0. On examination of Eq. (17) we can see that the positive parity states (populated by s-wave-M1 and p-wave-E1 processes) should be most sensitive to R at 2 keV where p-wave capture is small; and to S_1/S_0 at 24 keV where p-wave capture is almost as strong as s-wave. By using an iterative procedure to keep consistency we can find R, S_1/S_0.

For the calculation of ARC on ^{167}Er, the parameters of BNL-325[34] were used: $S_0=(1.8 \pm 0.2) \times 10^{-4}$, $\Gamma_\gamma=87$ meV. The average spacing of 4.0 eV was used with $\sigma_c=4.0$ to compute $D_0=40.0$ eV for Eq. (15). Figure 14

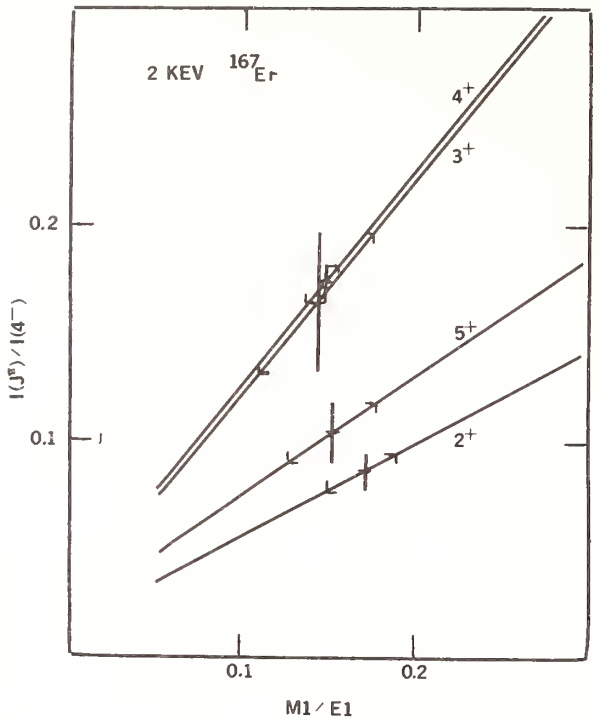

Fig. 14: The intensity ratios for the positive parity final states in ^{168}Er from 2-keV ARC plotted vs. $\Gamma^\circ_{\gamma f}(M1)/\Gamma^\circ_{\gamma f}(E1)$. $S_1 = 1.38 \times 10^{-4}$ for this calculation.

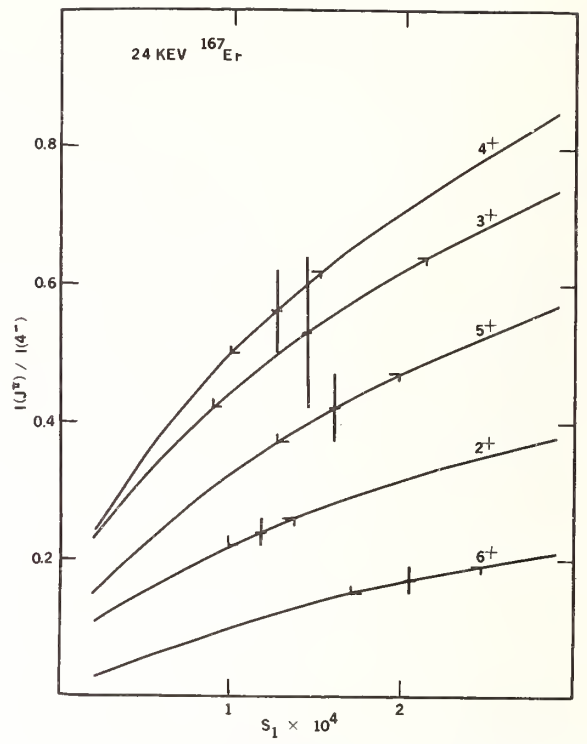

Fig. 15: The intensity ratios for the positive parity final states in ^{168}Er from 24-keV ARC plotted vs. S_1. $\bar{\Gamma}^\circ_{\gamma f}(M1)/\bar{\Gamma}^\circ_{\gamma f}(E1) = 0.15$ for this calculation.

shows the intensity ratios of the positive parity states to the 4^- state as a function of R for S_1=1.38 x 10^{-4}. A weighted average for R, determined from this figure gives a reasonable R=0.150(12). Using this value and computing the 24-keV ratios for the same states gives S_1=1.38(10) x 10^{-4} relative to S_0=1.8 x 10^{-4} where the error includes the uncertainty in S_0. The p-wave strength has not been measured but this value is consistent with systematic trends in this mass region and the value is considerably more precise than most p-wave strength function measurements in the vicinity.

Let us look again at Fig. 13. The calculation agrees with experiment for all states except the 6^+ for which we have data. The discrepancy is most marked at 2 keV. The calculations are insensitive to reasonable changes in σ_c and $S_{1,1/2}/S_{1,3/2}$. A small amount of E2 admixture could explain the difference. I will return to this point later.

The next case examined was ARC on ^{154}Sm. Here the 0^+ target allows population of final states 1/2, 3/2, 5/2. Again there is sufficient spectroscopic data[38] to assign final state spins and parities in ^{155}Sm. As with ^{167}Er, the pertinent parameters, S_0=1.8(5) x 10^{-4}, Γ_γ=78 meV and D_0=224 eV were taken from BNL-325.[34] The averaging was not as good and hence the experimental ratios are less certain than ^{167}Er. The experimental and calculated averages with R=0.24(7), S_1/S_0=1.17(39) are given in Table II.

Only the ratio of $(1/2,3/2)^+/1/2^-$ at 24 keV does not agree within experimental uncertainties. Although the experimental uncertainties are large there is a systematic trend for the high spin states to be populated more strongly than the calculation indicates. This might be explained by a d-wave admixture. Again the calculation was insensitive to variations in σ_c and $S_{1,1/2}/S_{1,3/2}$.

Finally let us consider ^{238}U.[40] The possible final state spins are the same as for ^{154}Sm. For ^{238}U the S_0 (1.1(1) x 10^{-4}) and S_1 (1.7(3) x 10^{-4}) strength functions[34] are well measured as well as the level spacing (D_0=35.5) and Γ_γ(24 meV). A value of R=0.24 was assumed. Table III shows the comparison between calculation and experiment.

Table II

Experimental and calculated intensity ratios $(I(J^\pi)/I(1/2^-)$ for ^{154}Sm. S_0=1.8 x 10^{-4}, S_1=2.1 x 10^{-4}, R=0.24

	2 keV		24 keV	
J^π	Exp.	Calc.	Exp.	Calc.
$1/2,3/2^-$	1.00	1.00	1.00	1.00 Norm.
$1/2,3/2^+$	0.37(5)	0.40	0.94(11)	1.31
$5/2^-$	0.023(8)	0.022	0.21(4)	0.17
$5/2^+$	0.096(13)	0.091	0.58(12)	0.70

Table III

Experimental and calculated intensity ratios $I(J^\pi)/I(1/2^-)$ for ^{238}U. S_0=1.1 x 10^{-4}, S_1=1.7 x 10^{-4}, R=0.24

	2 keV		24 keV	
J^π	Exp.	Calc.	Exp.	Calc.
$1/2,3/2^-$	1.00	1.00	1.00	1.00 Norm.
$1/2,3/2^+$	0.34(4)	0.34	1.07(10)	1.25
$5/2^-$	--	0.015	0.27(3)	0.14
$5/2^+$	0.18(6)	0.069	0.61(7)	0.66

The agreement is not good for the $5/2^+$ states at E_n=2 keV and the $5/2^-$ states at E_n=24 keV. The difference could be lessened by adding E2 and d-wave admixtures. Adding E2 would contribute the largest fraction to the $5/2^+$ intensities via the $1/2^+ \rightarrow 5/2^+$ transitions and a d-wave admixture would contribute the largest fraction to the $5/2^-$ final states via the $3/2^+, 5/2^+ \rightarrow 5/2^-$ (via E1) transitions.

Let us now consider whether such contributions are reasonable. For the SP model, estimates[35] of Γ/D for different multipolarities give, for A=239, E_γ=4.3 MeV.

$$\frac{\Gamma_{SP}(E1)}{D} \approx 4.5 \times 10^{-9} E_\gamma^3 A^{2/3} = 1.38 \times 10^{-5}$$

$$\frac{\Gamma_{SP}(M1)}{D} \approx 1.4 \times 10^{-9} E_\gamma^3 = 1.11 \times 10^{-7}$$

$$\frac{\Gamma_{SP}(E2)}{D} \approx 3.3 \times 10^{-15} E_\gamma^5 A^{4/3} = 7.2 \times 10^{-9}$$

We know that $\Gamma_\gamma^\circ(E1)/\Gamma_\gamma^\circ(M1) \sim 5$ in this mass region and that the SP M1 strength approximately agrees[20] with experiment. This would imply an E1 enhancement of .04 which is reasonable, and $\Gamma_{SP}(E1)/D = 5.55 \times 10^{-7}$. The enhancement factor for E2 radiation necessary to bring the $5/2^+$ intensity into agreement with experiment would be ~ 5, which might not be unreasonable.

A 24-keV d-wave admixture was estimated using $P_2/P_0 = (ka)^4/9 = 7.6 \times 10^{-4}$ for relative d- to s-wave pentrabilities and the assumption that the d-wave and s-wave neutron strength functions are comparable. This assumption can account for only $\sim$ 16% of the difference. This is not too discouraging. The d-wave strength functions are difficult to measure and there is basically no data available. In the near future I will expand the computer code to include E2 and d-wave admixtures and examine many more nuclei to study these effects systematically.

Conclusions

High resolution γ-ray spectroscopy has seen and will continue to see wide use in the measurement of neutron cross sections and associated properties. The ability to get a distinctive 'signal' allows the experimenter to clearly distinguish the process he wants to measure in the presence of high backgrounds and competing processes. To properly determine the relationship of this signal to to the process being measured requires detailed spectroscopic information about the energy levels, spins and branching ratios of the final nucleus. This process is often an iterative one. For example, in ARC the intensity pattern of the γ-ray spectra, (which are a valuable aid in finding the excitation energies, spins and parities of final states) are predicted through knowledge of the neutron- and photon-strength functions. Once the final state levels, and their spins and parities are well established, the procedure can be reversed and more precise information extracted on these strength functions.

There are many problems in neutron physics and nuclear spectroscopy which remain to be solved. High resolution γ-ray spectroscopy is a tool that joins the two fields in a rich and profitable relationship.

References

*Work supported by US DOE contract EY-76-C-02-0016.

[1] S. M. Qaim, "Recent Advances in the Study of Some Neutron Threshold Reactions", Proc. of an Int'l. Conf. on Neutron Physics and Nuclear Data, Harwell, 1978, p. 1088.

[2] N. I. Molla and S. M. Qaim, Nucl. Phys. A283, 269 (1977).

[3] M. Lindner, R. J. Nagle, and J. H. Landrum, Nucl. Sci. and Eng. 59, 381 (1976).

[4] R. E. Chrien, H. I. Liou, M. J. Kenny and M. L. Stelts, "Neutron Cross Sections of ^{232}Th", BNL-25407 (to be published in Nucl. Sci. and Eng.)

[5] Thomas Bradley, M. L. Stelts, R. E. Chrien and Z. Parsa, "Stellar nucleosynthesis and the 24-keV cross sections of some heavy nuclei",(contributed paper to this conference).

[6] R. C. Greenwood and R. E. Chrien, Nucl. Inst. & Meth. 138, 125 (1976).

[7] R. J. Gehrke, R. G. Helmer and C. W. Reich, Nucl. Sci. and Eng. 70, 298 (1979).

[8] W. P. Poenitz and D. L. Smith, "Fast Neutron Radiative Capture Cross Sections of ^{232}Th," ANL-NDM-42 (1979).

[9] T. L. Weil, T. W. Godfrey and R. W. Harper, Bull. Am. Phys. Soc. 24, 658 (1979).

[10] Ugo Abbondanno, Ferruccio Demanins, Maria Rosa Malisan and Giancarlo Nardelli, Nucl. Phys. A305 117 (1978).

[11] E. Barnard and D. Reitmann, Nucl. Phys. A303, 27 (1978).

[12] Yasuharu Sugiyama and Shiroh Kikuchi, Nucl. Phys. A264, 179 (1976).

[13] M. L. Stelts and R. E. Chrien, Nucl. Inst. & Meth. 155, 253 (1978).

[14] Marion L. Stelts and John C. Browne, Nucl. Inst. & Meth. 133, 35 (1976).

[15] M. L. Stelts and J. C. Browne, Nucl. Sci. and Eng. 67, 344 (1978).

[16] C. E. Porter and R. G. Thomas, Phys. Rev. 104, 483 (1956).

[17] H. I. Liou and R. E. Chrien, Nucl. Sci. and Eng. 62 463 (1977).

[18] C. Coceva and P. Giacobbe, Nucl. Phys. A293, 167 (1977).

[19] G. A. Bartholomew, E. D. Earle, A. J. Ferguson, J. W. Knowles, and M. A. Lone, "Gamma Ray Strength Functions", p. 229 of "Advances in Nuclear Physics", Vol. 7, Michel Baranger and Eric Vogt (Ed.), Plenum Press (N.Y.) (1968).

[20] Carol M. McCullagh, "A Survey of Radiative Dipole Strength Functions", Ph.D. thesis, State University of New York at Stony Brook (1979).

[21] Peter Axel, Phys. Rev. 126, 671 (1962).

[22] F. Corvi and M. Stefanon, Nucl. Phys. A233, 185 (1974).

[23] F. Becvar, R. E. Chrien and O. A. Wasson, Nucl. Phys. A236, 198 (1974).

[24] M. Stefanon and F. Corvi, Nucl. Phys. A281, 240 (1977).

[25] M. L. Stelts and J. C. Browne, Phys. Rev. C16, 574 (1977).

[26] S. Raman, R. F. Carlton, G. G. Slaughter and M. R. Medor, Phys. Rev. C18, 1158 (1978).

[27]J. C. Wells, Jr., S. Raman and G. G. Slaughter, Phys. Rev. C18; 707 (1978).

[28]D. A. McClure, S. Raman and G. G. Slaughter, Phys. Rev. C16, 1278 (1977).

[29]R. F. Carlton, S. Raman and G. G. Slaughter, Phys. Rev. C15, 883 (1977).

[30]R. F. Carlton, S. Raman, J. A. Harvey and G. G. Slaughter, Phys. Rev. C14, 1439 (1976).

[31]G. E. Thomas, D. E. Batchley, and L. M. Bollinger, Nucl. Inst. and Meth. 56, 325 (1976).

[32]L. M. Bollinger and G. E. Thomas, Phys. Rev. C5, 1951 (1970).

[33]J. E. Lynn, "The Theory of Neutron Resonance Reactions", Clarendon Press, Oxford, 1968, p. 224.

[34]S. F. Mughabghab and D. I. Garber, BNL-325, Vol. I, "Resonance Parameters", 1963.

[35]M. Aslam Lone, "Photon Strength Functions", p. 161 of "Neutron Capture Gamma Ray Spectroscopy", Robert E. Chrien and Walter R. Kane (Ed.), Plenum Press, New York (1979).

[36]Lowell M. Bollinger, "Neutron Capture Gamma Rays p. 783 of "Photonuclear Reactions and Applications", Barry L. Berman (Ed.) CONF-730301 (1973).

[37]W. F. Davidson et al., Institut Laue-Langevin, Grenoble (to be published).

[38]K. Schreckenbach et al. Institut Laue Langevin and Brookhaven National Laboratory (to be published).

[39]T. von Egidy, J. A. Cizewski, C. M. McCullagh, S. S. Malik, M. L. Stelts, R. E. Chrien, D. Breitig, R. F. Casten, W. R. Kane and G. J. Smith, "Levels in ^{237}U Studied by Resonant Neutron Capture", BNL 26034 (1979) (submitted to Phys. Rev. C).

[40]T. Koeling, Nucl. Phys. A307, 139 (1978).

[41]H. G. Börner, H. R. Koch, H. Seyfarth, T. von Egidy, W. Mampe, J. A. Pinston, K. Schreckenbach and D. Heck, Z. Phys. A286, 31 (1978).

NEW FISSION FRAGMENT DETECTORS FOR CROSS SECTION AND ANGULAR DISTRIBUTION MEASUREMENTS AT CBNM

H.-H. Knitter and C. Budtz-Jørgensen
Commission of the European Communities
Joint Research Centre, Central Bureau for Nuclear Measurements
B.2440-Geel, Belgium

The accurate knowledge of the fission cross section of the highly active minor actinides belonging to the uranium based fuel cycle are of growing importance as the nuclear industry matures. For the measurement of such cross sections two fission fragment detectors are described which can be used in the presence of very high alpha backgrounds rates. For the understanding of the physics of the fission process, angular and energy distribution measurements can be helpful, for example for the determination of the quantum numbers J and K of the transition states. For this purpose a detector was developed which has an angular efficiency of 2 π, an angular resolution of 5 % on cos ϑ, an energy resolution of 1.5 % and a timing resolution sufficient for the application in time-of-flight experiments.

[fission fragments, ionization chambers, actinides, $\sigma_{nf}(E)$, $\sigma_{nf}(E,\vartheta)$, mass distribution.]

Introduction

The knowledge of the neutron induced fission cross section is not only requested for the major actinide isotopes ^{235}U, ^{238}U and ^{239}Pu to an accuracy of 1/2 to 1 %; but also for many of the so called minor isotopes rather stringent requests exist. Fig. 1 shows the production ways for the minor isotopes which are generated in the uranium based fuel cycle.

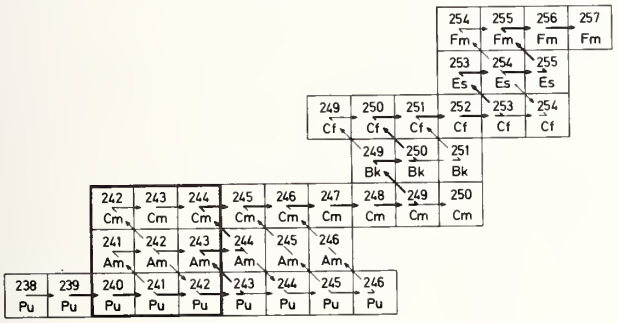

Fig. 1 : Part of nuclide chart with heavy element production line for slow neutrons.

The thick arrows indicate the main line for heavy element production by thermal neutron irradiations of uranium. For problems related to uranium based reactors the nine isotopes of the first three lines and columns starting at ^{240}Pu are the most important minor isotopes from the application point of view. They are present in considerable amounts in the fuel inventory produced by light water reactors. The typical composition of light water reactor plutonium is 60 %, 25 %, 12 % and 3 % for ^{239}Pu, ^{240}Pu, ^{241}Pu and ^{242}Pu respectively. Therefore the higher plutonium isotopes become real constituents of reactor fuel material and their characteristics have to be considered. Surely the requests have not been met for capture and fission cross sections for the higher plutonium isotopes ^{240}Pu and ^{241}Pu[1-2]. Also ^{238}Pu is of importance, since it is proposed as spike material for proliferation-resistant fuel cycles[3-4]. The cross sections for the americium and curium isotopes are needed for calculations of heat and neutron source strength of burned fuel elements, fuel cycle strategy etc... Although the knowledge of these cross sections has improved during the last years, they are not yet good enough known to satisfy the needs[1]. ^{241}Am could be an exception[5].

All these isotopes including the one of ^{238}Pu have half-lives ranging between 163 days for ^{242}Cm and 7380 years for ^{243}Am and yield therefore specific activities between about 10^{11} and 10^{6} s^{-1} mg^{-1}. With neutron intensities available from the Geel electron linac with a nominal energy resolution of 0.5 ns.m^{-1}, typical neutron induced specific fission rates of 0.1 to 10 s^{-1} mg^{-1} are obtainable in measurements on actinide nuclei with fission threshold covering the subthreshold region from 1 eV on. Using a Van de Graaff accelerator above some hundred keV neutron energy and monoenergetic beam technique one gets about the same fission rates and can perform measurements with better energy resolution at higher energies. The neutron induced fission cross section measurements can be disturbed of course also by the spontaneous fission rate. For a partial spontaneous fission half-life of 4.10^{10} years one has a spontaneous fission rate of 1 s^{-1} mg^{-1}. Table I summarizes the total and spontaneous fission half-lives of the above mentioned isotopes.

Table I. Total half-lives and spontaneous fission half-lives of some Pu, Am and Cm isotopes.

Isotopes	τ_{total} (years)[6]	τ_{SF} (years)[7]
^{238}Pu	$(8.775 \pm 0.004)\cdot 10^{1}$	$(4.77 \pm 0.13)\cdot 10^{10}$
^{240}Pu	$(6.537 \pm 0.010)\cdot 10^{3}$	$(1.31 \pm 0.05)\cdot 10^{11}$
^{241}Pu	$(1.44 + 0.02)\cdot 10^{1}$	$2.5\cdot 10^{15}$ *
^{242}Pu	$(3.763 \pm 0.020)\cdot 10^{5}$	$(6.842 \pm 0.075)\cdot 10^{10}$
^{241}Am	$(4.322 \pm 0.005)\cdot 10^{2}$	$(1.05 \pm 0.03)\cdot 10^{14}$
^{242m}Am	$(1.52 \pm 0.07)\cdot 10^{2}$	$(9.5 \pm 3.6)\cdot 10^{11}$
^{243}Am	$(7.38 \pm 0.04)\cdot 10^{3}$	$(3.35 \pm 0.31)\cdot 10^{13}$
^{242}Cm	$(4.460 \pm 0.10)\cdot 10^{-1}$	$(6.56 \pm 0.58)\cdot 10^{6}$
^{243}Cm	$(2.85 \pm 0.02)\cdot 10^{1}$	$1.2\cdot 10^{11}$ *
^{244}Cm	$(1.811 \pm 0.002)\cdot 10^{1}$	$(1.344 \pm 0.002)\cdot 10^{7}$

* Theoretical estimates S. Raman[8]

One can deduce from the half-lives, that it is the alpha activity which represents the major difficulty in the measurement of the neutron induced fission cross section. Only in the cases of ^{242}Cm and ^{244}Cm it is in addition the spontaneous fission rate which presents problems. ^{241}Pu decays mainly by β-emission. The alpha decay, the partial half-life for it is $(6.0 \pm 0.1)\cdot 10^{5}$ years, does not seriously disturb the measurements.

In view of the foregoing, fission fragment detectors used in measurements of neutron induced fission cross sections of these highly active isotopes must have the following characteristics :

1. Good discrimination possibilities between alpha particles and fission fragments.
2. Timing resolution in the nanosecond range such that it can be used for T-O-F technique and spontaneous fission event suppression.
3. Low sensitivity for neutrons and γ-rays.
4. Resistant against radiation damage.
5. High fission event detection efficiency.

In the search for such a detector some of the generally available charged particle detector types can be excluded. For example solid state detectors are excluded due to point 3 and 4, plastic scintillators due to point 4 and gaseous proportional counters are to the points 1 and 2.

Very often ionization chambers were successfully used for fission cross section measurements. The normal design, a closely spaced parallel plate detector filled with a gas with high electron drift velocity, shows excellent performance with respect to the mentioned points. But the discrimination properties are washed out for alpha background rates higher than 10^6. The reason is, that the detector has a low pulse height ratio between the smallest fission signals and the highest alpha signals, since the electrode distance is much smaller than the particle range.

We have developed two types of fission ionization chambers[9-10] with special properties to suppress alpha pile-up. Both were used in the measurements of neutron induced and angle integrated fission cross sections of highly active isotopes like ^{240}Pu and ^{241}Am covering the energy range from 1 eV to 10 MeV and to 5.3 MeV respectively.

A third chamber type was constructed to measure the angular distribution of fission fragments with respect to the incident neutron beam.

All chambers will be described in detail and their utility will be demonstrated by the measurements which were done with them.

Parallel plate ionization chamber with special characteristics

The first chamber[9] is of the parallel plate type. But contrary to other designs the distance between the electrodes has been chosen longer than the ranges R of the fission fragments. Part a of fig. 2 shows the electrodes of the chamber and an ionization track which has an angle ϑ with respect to the normal of the electrode. The time dependence of the induced charge q(t) from the ionization electrons is shown in fig. 2b. As long as all electrons move under the action of the electric field towards the collector plate with the same speed, a signal with constant rise is induced. At the time t_1, when the first electrons reach the collector, the rise becomes smaller until all electrons have been collected at time t_2. The time t_1 is given by :

$$t_1 = (d - R \cdot \cos \vartheta)/v \qquad (1)$$

and depends for monoenergetic particles of the same type and a given electrode distance from the angle between the track and the normal and the electron drift velocity v in the working gas. For methane and

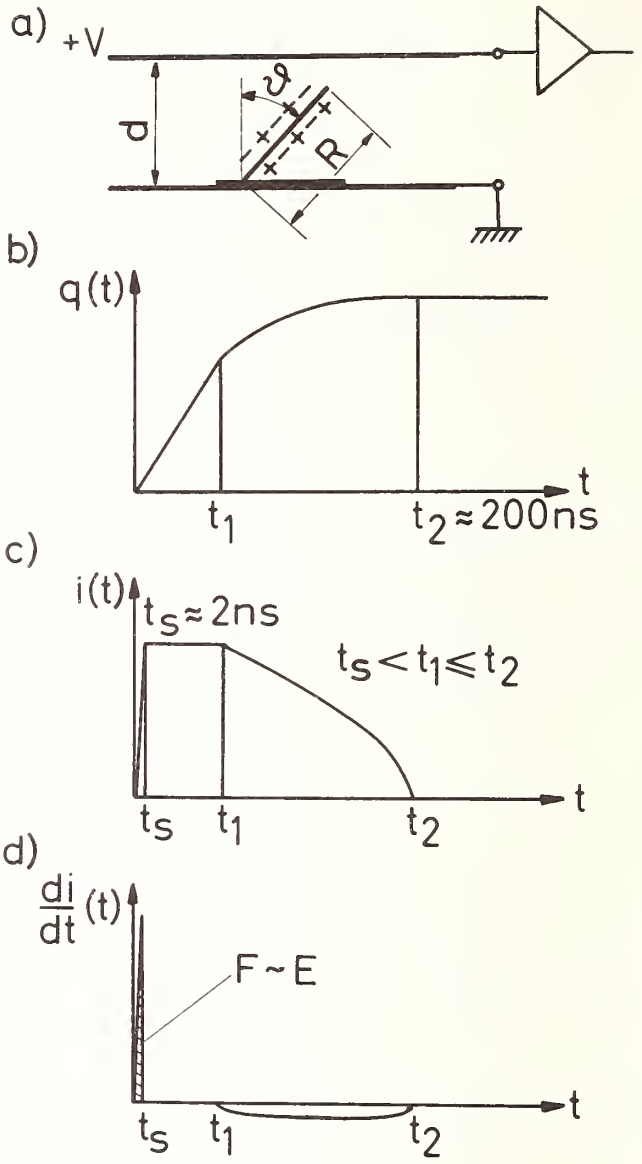

Fig. 2 : Part 2a shows schematically the parallel plate chamber with an ion track. R is the range of the ionizing particle, ϑ the emission angle formed by the track and the normal of the electrodes, and d the distance between the electrodes. The parts 2b, 2c and 2d show the charge, the current and the time differentiated current as function of the time respectively.

500 Vcm^{-1} bar^{-1} v is about 10 cm μs^{-1}. The time $t_2 = d/v$ in the present chamber is about 200 ns. The pulse height of the charge signal at t_2 for monoenergetic particles depends only on the direction of the track in the chamber and is given by

$$q(t_2) = e \cdot N_e \cdot (1 - \frac{\bar{x}}{d} \cdot \cos \vartheta) \approx E \cdot (1 - \frac{\bar{x}}{d}) \cdot \cos \vartheta \qquad (2)$$

with

$$\bar{x} = \frac{\int_0^R x \cdot \rho(x)\, dx}{\int_0^R \rho(x)\, dx} \qquad (3)$$

where $\rho(x)$, e, N_e, and E are the ionization density of the track, the electron charge, the number of ion-pairs and the particle energy respectively. The direction dependence of the charge pulse is a fact, which can be used to investigate e.g. fission fragment angular distributions.

The current pulse shown in fig. 2c has a pulse height which is proportional to the number of ionization electrons and hence to the kinetic energy of the fission fragments. The sharp rise of the current pulse depends in principle only on the time it takes the fission fragments to stop in the gas. This time is about 2 ns. That means, that a differentiation of the current pulse results in the extremely sharp pulse as shown in fig. 2d. The area of the pulse is proportional to the fission fragment energy. To our knowledge, this is the first time that a fast pulse if formed from an ionization chamber applicable to fast timing in the ns-range and carrying the energy information with it.

The experimentally obtained time resolution with this chamber is $\Delta t \leqslant 1.5$ ns. Moreover the short width and the energy proportionality ensures that the chamber can operate with a high alpha background being able to discriminate between signals from alpha pile-up and fission fragments. The ratio between pulse heights from fission fragments to those from alpha particles is larger than 12. In a parallel plate chamber with a distance between the electrodes smaller than the range of the fission fragments this ratio is considerably smaller depending on the electrode distance. In reality the power of this type of design cannot be wholly exploited, since the rise time of commercially available preamplifiers is about 10 ns and their electronic noise sets a limit to how sharp an electronic differentiation can be performed. Using delay line clipping we obtained pulses of 30 ns width. Although this is one order of magnitude more than is ideally obtainable, the chamber has proven to operate satisfactorily with a sample of 1.6 mg of ^{240}Pu which produces an alpha background of $1.5 \cdot 10^7$ s^{-1}. With the experience we have got with this chamber it is expected that the chamber can handle up to 5.10^7 alphas s^{-1} having clear separation between the two sorts of particles and keeping a fission fragment detection efficiency of better than 96 %.

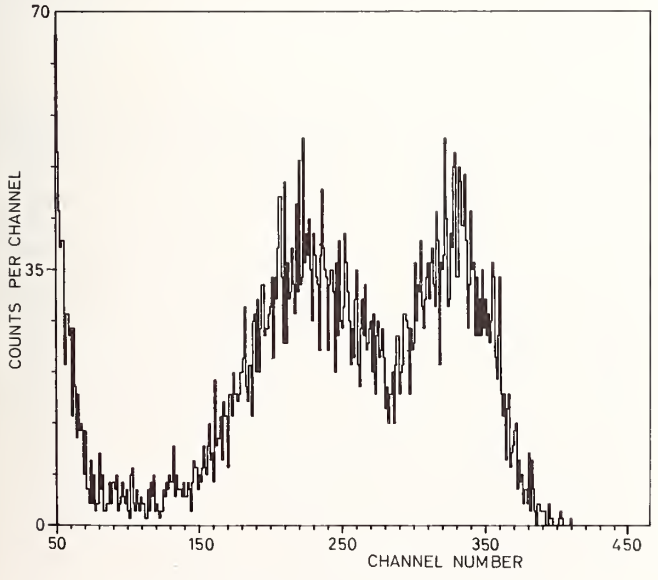

Fig. 3 : Neutron induced fission fragment energy spectrum of ^{240}Pu, obtained with the parallel plate chamber.

A neutron induced fission fragment spectrum of ^{240}Pu obtained with the present detector is shown in fig. 3. It was obtained by integrating the fast pulse with a fast linear gate opened with 40 ns wide pulses from a constant fraction discriminator. Observe the clear separation between the alpha pile-up and the fission fragments. In this case the fission fragment detection efficiency is 98 % and was determined by the thickness of the ^{240}Pu deposit of 200 $\mu g/cm^{-2}$.

With this chamber the fission cross section of ^{240}Pu was measured in the energy range from 150 keV to 10 MeV using the CBNM 7 MV Van de Graaff accelerator. The energy range from 1 eV to 2.5 MeV was covered using the same detector at an eight meter flight path and 10 ns resolution at the CBNM electron linac. Fig. 4 shows as an example a part of the fission cross section results of ^{240}Pu obtained in the region between 10 keV and 300 keV. The picture shows the very complex structure and strong variations of the subthreshold fission cross section near to the threshold. One can see how the class-II states are going to overlap with increasing neutron energy.

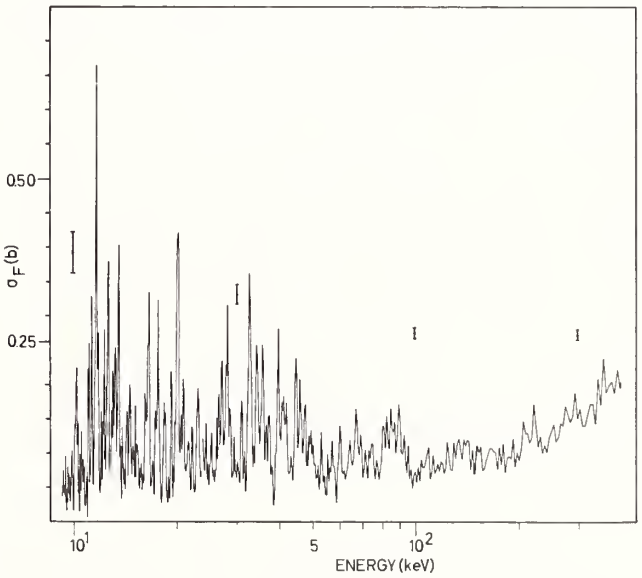

Fig. 4 : Fission cross section of ^{240}Pu in the neutron energy range from 10 to 300 keV.

The compensation chamber

This second fission fragment detector[10] is intended for even higher alpha activities in the active volume of the chamber. The underlying idea of this detector is based on the fact that the ranges of 5 to 6 MeV alpha particles are much longer than the ranges of fission fragments.

Fig. 5 shows the working principle of this detector.

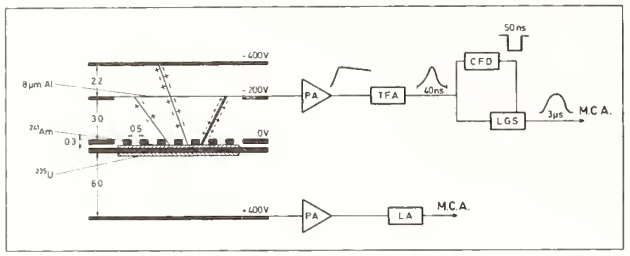

Fig. 5 : Schematic drawing of the fission chamber with intrinsic suppression of alpha background. The distances between the electrodes are given in mm. The track of a fission fragment stopping in the thin Al foil is shown as a thick line. The tracks of the alpha particles, thin lines, pass the Al foil, except in the rare cases where the alpha particle loses too much energy in the edges of the collimator.

The lower half of the chamber is a normal parallel plate ionization chamber and it is used for the detection of ^{235}U fission fragments. The ^{235}U fission cross section is used as a standard. Methane at NTP was used as counter gas because of its large electron drift velocity. The upper chamber, which is used to detect fission fragments from ^{241}Am, contains a middle electrode consisting of a 8 μm thick Al foil. The thickness is chosen such that fission fragments moving normal to the sample will just be stopped in the foil, whereas 5.4 MeV alpha particles will pass the foil, stopping in the outer electrode. The distances between the three electrodes have been chosen such that the alpha particles create nearly the same amount of ionization charge in the two parts of the chamber. Hence, under the influence of the electric field, no net charge will flow to the middle electrode. That means, in principle, that no signal pulse will arise from the alpha particles. For the fission fragments of course the detector behaves as a normal parallel plate chamber, with an electrode distance smaller than the range of fission fragments.

In order to ensure that all alpha particles from the ^{241}Am sample will pass the middle electrode a collimator, a 0.3 mm stainless steel plate with about 1500 holes of 0.5 mm diameter, is placed above the sample. The typical efficiency of such a collimator is about 13 %.

First tests of the chamber were made with a weak ^{241}Am source. When the electric field in the upper part of the chamber was increased to the same field strength as in the lower part, nearly all alpha-particle pulses were reduced disappearing in the electronic noise from the preamplifier. This noise corresponded to about 100 keV particle energy loss in the gas volume of the detector. However, about four percent of the pulses were unaffected. These signals originate from alpha particles which have passed through the edges of the collimator holes losing so much energy that they cannot pass the Al foil, as indicated in fig. 5. A computer simulation showed that it is the "badly" collimated alpha particles which determine the frequency of large pile-up pulse heights.

Fig. 6 gives the simulated pulse pile-up distributions with 10^7 and 10^8 alpha s^{-1} passing the sensitive volume of the chamber.

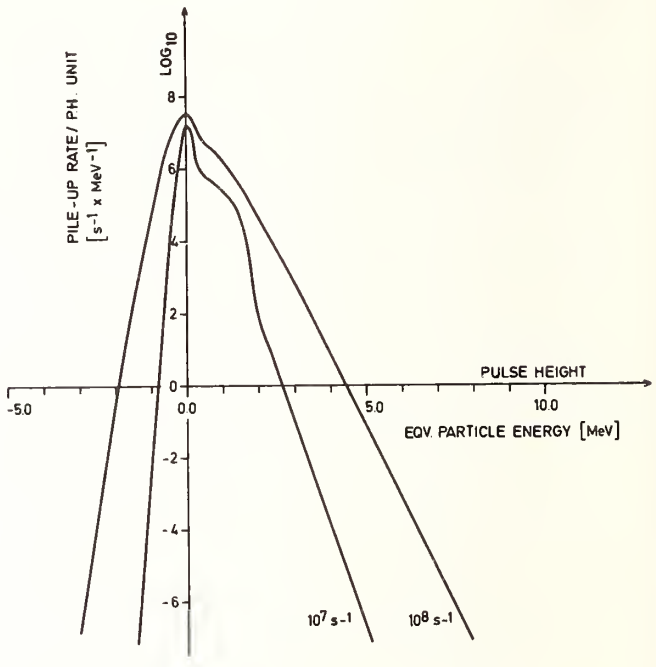

Fig. 6 : Calculated pulse pile-up frequency distributions for the compensation chamber. For each single alpha event a rectangular pulse of 40 ns width was used in the calculations. The amplitudes of the single events were obtained from the experimental pulse-height distribution, recorded from a week ^{241}Am source where pile-up could be neglected.

As the fission fragments give a spectrum above 8 MeV it is evident that the alpha pulses at these rates can be clearly separated from the fission fragment pulses.

Actual measurements were done with samples of 4 mg ^{241}Am, so that up to 5.10^7 alphas enter the chamber. Looking at the preamplifier output on an oscilloscope, one observes such a rate has the effect of a drastic increase in the electronic noise.

The reduction of pulse pile-up obtained by this chamber is illustrated in fig. 7 which shows the result of a measurement of the "noise" from the chamber. A test pulse was fed through the preamplifier, and then to a spectroscopic amplifier with 0.1 μs shaping time. With zero electric field between the outer and the middle electrode a pulse height spectrum was recorded, shown as the broken curve in fig. 7. Then the compensation field was increased to the same value as in the lower part of the chamber. The recorded spectrum is shown as the full curve in fig. 7. The noise is reduced by a factor seven as one can see from the ratio of the FWHM of the two spectra.

The chamber was tested under accelerator

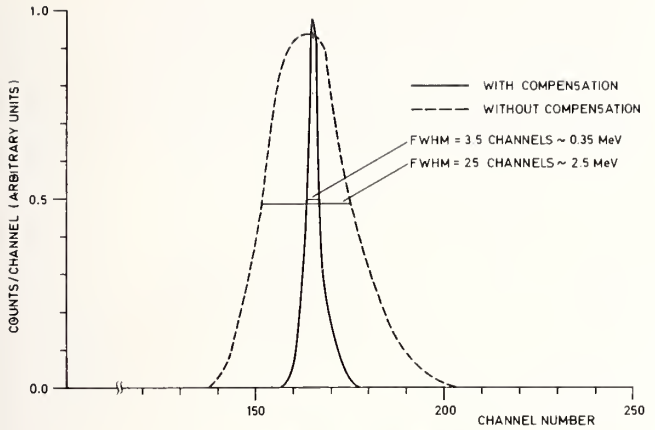

Fig. 7 : "Noise" from the chamber measured with a test pulser. Broken line without and full line with compensation field.

conditions. Fig. 8 shows a fission fragment pulse-height spectrum obtained with a monoenergetic 1.5 ns pulsed neutron beam of 3 MeV from the 7 MV Van de Graaff accelerator of the CBNM. For the lower spectrum the measured time-uncorrelated background has been subtracted, and it demonstrates that only a very little fraction of less than 2 % of the fission spectrum is influenced by the alpha signals. The discrimination capabilities of this chamber can be best seen by the fact, that we could determine the spontaneous fission half-life of the sample material to about 2.10^{14} years. That means, that one fission fragment could be detected out of 5.10^{11} alphas.

This detector has been successfully used in the measurement of the neutron induced fission cross section of ^{241}Am in the energy range from 1 eV to 5.3 MeV. The measurements were performed using both, the Van de Graaf and the electron linear accelerator of the CBNM and the results have been published[11-12].

Ionization chambers for fission fragment angular distribution measurements

Contrary to the two previous fission fragment detectors, this is not a chamber which is intended to operate with a high alpha particle background rate, but should serve to measure fission fragment angular distributions. The fragment angular distributions are interesting from the physics point of view, because they allow one to get information on the spin J and the projection of K of the spin on the nuclear symmetry axis of the transition state to fission[13].

Fig. 9 shows the principle of the fission detector for angular distribution measurements. A version with two grids was already proposed by Ogawa et al.[14] and a similar chamber was used in measurements of angular correlations between fission fragments and γ-rays by Kapoor et al.[15] and very recently for angular correlation measurements in ternary fission by Choudhury et al.[16] The present design is a conventional single grid chamber. The charge signal q_{ca} extracted from the cathode depends on the orientation of the particle track given by the relation

$$q_{ca} \approx E \cdot \left(1 - \frac{\overline{x}}{d} \cdot \cos \vartheta\right) \qquad (4)$$

as discussed earlier.

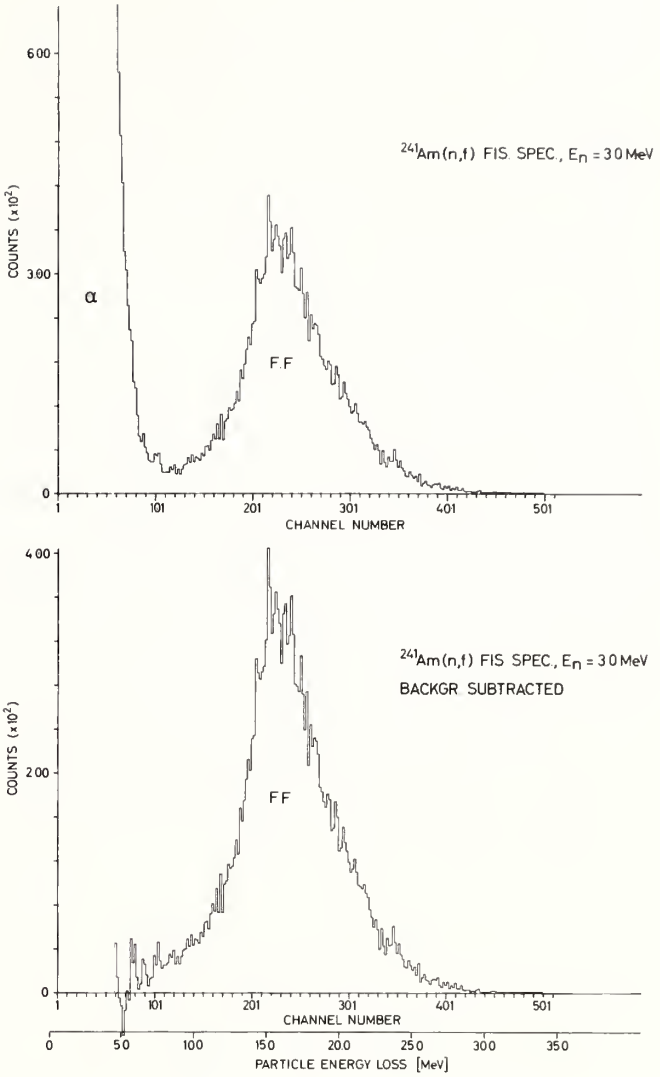

Fig. 8 : The upper part shows the total pulse-height spectrum obtained from the compensation chamber when it is irradiated with a 1.5 ns pulsed neutron beam of 3 MeV from the Van de Graaff accelerator. In the lower spectrum the measured time-uncorrelated background was subtracted. The fission fragment count rate was 1 s^{-1}.

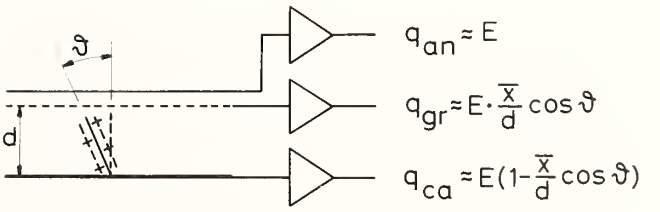

Fig. 9 : Schematic drawing of a detector capable for angle determination, energy determination and ns-timing.

Hence, the pulse height distribution of this signal leads directly to the cos ϑ-distribution of the ion tracks in the case of monoenergetic particles. The situation is more difficult when fission fragments are detected since $\bar{x}$ (E,A,Z), the distance from the origin of the track to the centre of the ion distribution, is a function of the particle type and energy. The anode signal $q_{an} \approx E$ is only dependent on the particle energy due to the inserted Frisch grid. The two signals q_{ca} and q_{an} were fed to a multiparameter data acquisition system, ND 6660, where they were digitized and stored event by event. At the same time the quantity

$$v = 1 - \frac{q_{ca}}{q_{an}} \approx \frac{\bar{x}}{d} \cos \vartheta \qquad (5)$$

was formed and the two-parameter spectrum of q_{an} and v was generated. The one-parameter spectrum of v belonging to a certain value of q_{an}, then gave the cos ϑ-distribution $W_E(\cos \vartheta)$ for fission fragments with a particular energy. These distributions are smeared out somewhat, since a fission fragment is not unambiguously defined by its energy, which means that $\bar{x}(E,A,Z)$ will vary at a particular energy depending on the distribution of A and Z. But the effect is small since the distributions $W_E(\cos \vartheta)$ fall off sharply at their upper end, where $v \approx \bar{x}/d$. From the fall off of the experimental distributions it was estimated that $\delta\bar{x}/\bar{x}$ is smaller than 5 %. The average value $\langle \bar{x}(E)/d \rangle_{A,Z}$ was determined as the width $\Delta(q_{an})$ of each individual distribution. Then, instead of v a new quantity $v' = v/\Delta(q_{an}) \simeq \cos \vartheta$ was used to generate the fission fragment integrated cos ϑ distribution W(cos ϑ). An example of such a distribution is shown in fig. 10, which was obtained from a measurement with thermal neutron induced fission of ^{235}U.

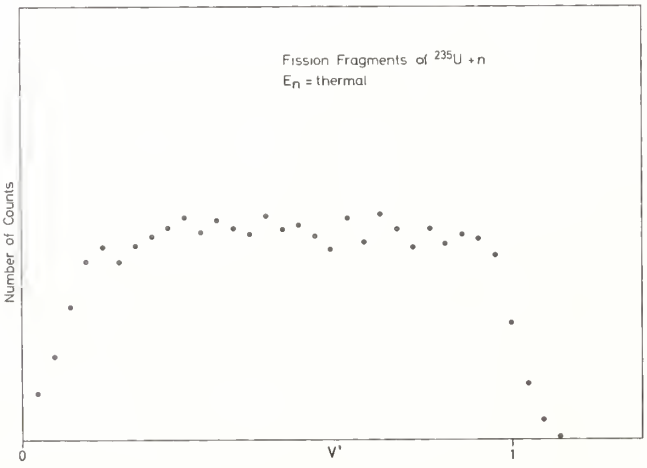

Fig. 10 : Measured distribution of v' = cos ϑ for the fission fragments from a natural uranium target irradiated with thermal neutrons.

The shape of the distribution is nearly rectangular, which is to be expected from an isotropic distribution, although a loss of events at cos $\vartheta \simeq 0$ in the 300 $\mu g \cdot cm^{-2}$ thick sample of natural uranium can be observed. From the fall off of the distribution we estimate that the resolution on cos θ is < 5%.

Fig. 11 shows the experimental distribution from the same target at 1.60 MeV, which stems essentially from ^{238}U. In order to correct the experimental ^{238}U distribution for effects due to the uranium layer thickness we used the ^{235}U distribution as an isotropy standard and divided the two distributions with each other to obtain the corrected angular distribution of the fission fragments for ^{238}U; see fig. 12.

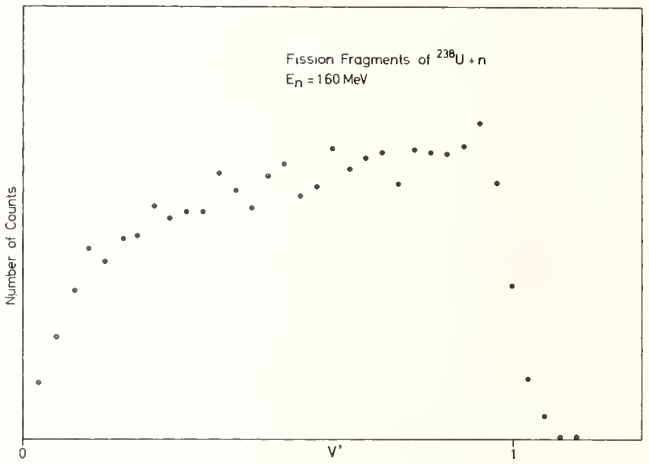

Fig. 11 : Measured distribution of v' = cos ϑ for the fission fragments from a natural uranium target irradiated with 1.60 MeV neutrons.

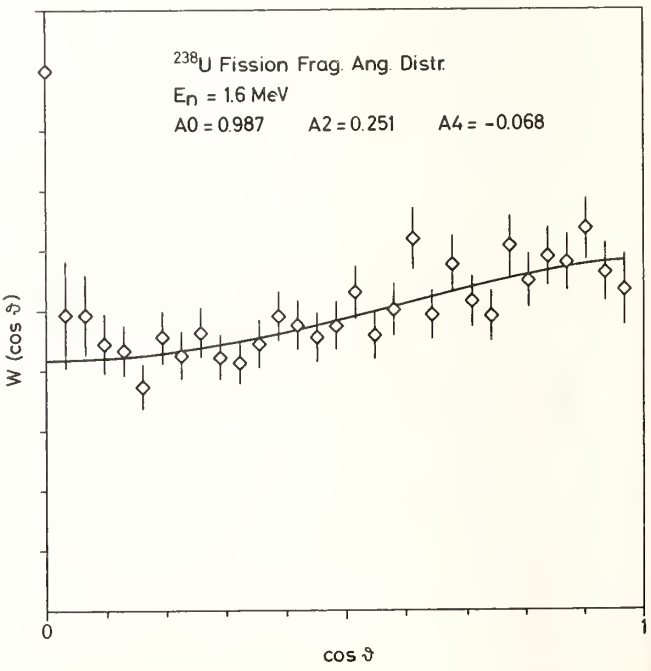

Fig. 12 : Angular distribution of ^{238}U fission fragments at 1.60 MeV incident neutron energy. Full line represents least squares fit with even Legendre polynomials up to A4.

At present tests have been made to investigate the possibility of getting the angular information from the grid signal q_{gr} instead of using the cathode signal q_{ca}. The grid signal has a more complicated wave form than the other signals, see fig. 13.

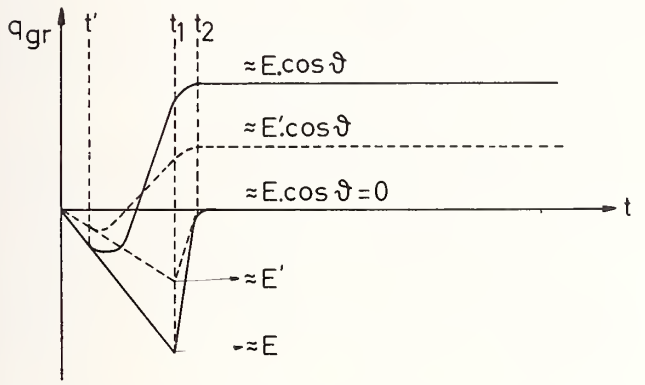

Fig. 13 : The time dependence of charge pulses from the Frisch grid is plotted for charged particles of energy E and E' and angles ϑ and ϑ=90° respectively. t' is the time between the formation of the ion track and the time that the first electron passes the grid. t_1 and t_2 are the electron drift times from the cathode to the Frisch grid and from the cathode to anode respectively.

It starts with a constant negative slope until the time t', where the first ionization electrons reach the grid. Then the slope changes to a positive value as more and more electrons leave the grid and are collected at the anode. The grid signal saturates at a positive value

$$q_{gr}(t_2) \approx E \cdot \frac{\bar{x}}{d} \cdot \cos\vartheta \qquad (6)$$

at the time t_2 when all electrons have been collected. The treatment in the main amplifier of these particulary shaped signals must be performed with a long differentiation time if linearity has to be preserved. A differentiation time of 10 μs was chosen since this is long compared to the electron drift time t_2 of about 0.5 μs for the present chamber. The advantage of using the grid pulses instead of the cathode pulses is, that angular information can be obtained from a double chamber, where both fission fragments are detected in coincidence. Using the two grid signals q_{gr1}, q_{gr2} and the two energy signals q_{an1}, q_{an2} from such a chamber the quantity

$v = q_{gr1}/q_{an1} + q_{gr2}/q_{an2} \approx ((\bar{x}_1 + \bar{x}_2)/d) \cdot \cos\vartheta$

was formed.

Fig. 14 shows the distribution of v from a double chamber loaded with a ^{252}Cf source on a 50 $\mu g \cdot cm^{-2}$ vyns foil. This distribution is close to the cos ϑ distribution since no correction for the energy dependence of $\bar{x}$ is needed. This can be avoided because the sum $\bar{x}_1 + \bar{x}_2$ is approximately constant for the two fission fragments. This is also seen from the rather sharp fall off of the distribution of v. An interesting feature of this detector is the possibility of measuring the combined distribution of angle and mass in fission processes. This is illustrated in fig. 15 where the mass distribution for spontaneous fission of ^{252}Cf is given as function of cos ϑ.

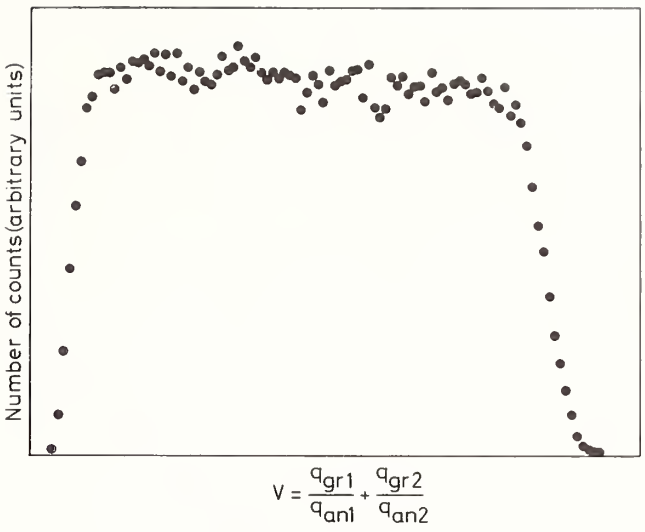

Fig. 14 : Measured distribution of v obtained from the twin chamber.

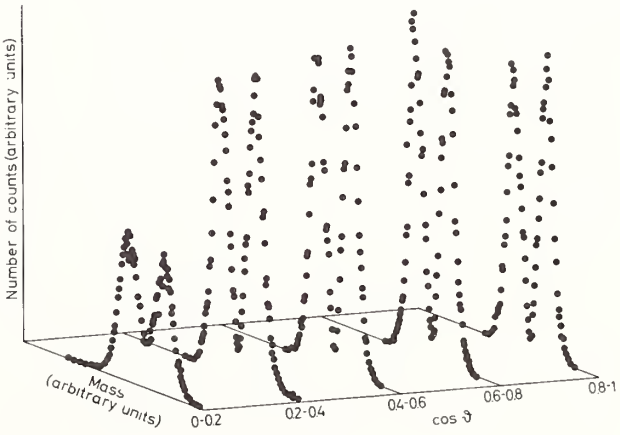

Fig. 15 : A two parameter plot of the number of spontaneous fission events of a ^{252}Cf source versus the fission fragment mass and the angle of the fragment track with respect to the normal of the electrodes obtained with the twin Frisch grid chamber is shown.

Five mass distributions corresponding to the cos ϑ intervals 0.0-0.2, 0.2-0.4, 0.4-0.6, 0.6-0.8 and 0.8-1.0 respectively are shown. The fragment mass μ was determined using the two energy signals with the simple relation

$$\mu_{1(2)} = A \frac{E_{2(1)}}{E_1 + E_2} \qquad (7)$$

where A is the mass of the fissioning nucleus.

No correction for neutron evaporation has yet been made. In this example there should of course be no angular dependence of the mass distribution, but it is observed that the peak to valley ratio of the distributions and the intensities decrease for

ϑ near to 90°. This effect is due to the high energy losses in the backing foil for fission fragments emitted under grazing angles.

The angular information can also be taken from each half of this chamber separately. By forming the two quantities $v_1' \approx \cos \vartheta_1$ and $v_2' \approx \cos \vartheta_2$ the two parameter distributions of $\cos \vartheta_1$ and $\cos \vartheta_2$ could be generated. Fig. 16 shows an isometric plot of this distribution.

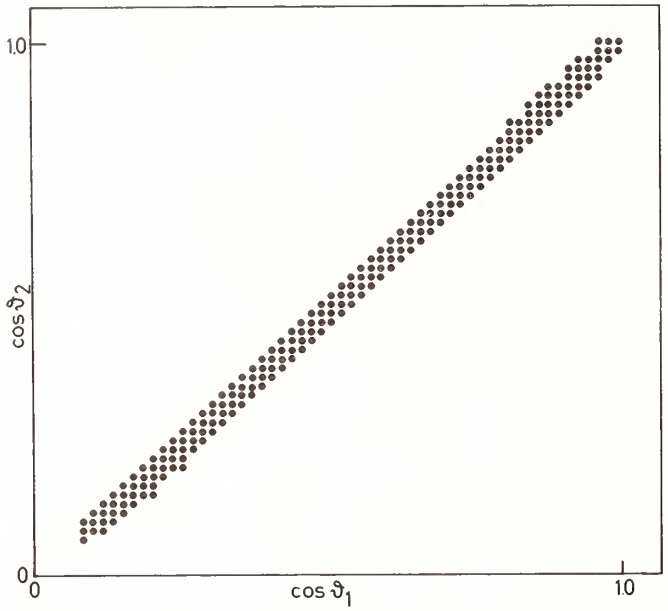

Fig. 16 : Isometric plot of the two parameter distributions of $v_1' \approx \cos \vartheta_1$ and $v_2' \approx \cos \vartheta_2$.

Channels with counts higher than half the maximum value of the distribution are indicated as points. The distribution is centered on the line $\cos \vartheta_1 = \cos \vartheta_2$, which is to be expected for two complementary fragments, and it has a spread of 0.05. From this it can be concluded that the chamber allows a determination of $\cos \vartheta$ with a resolution of 0.05. It should be pointed out that the high efficiency of about 100 % is the great advantage of these detectors compared to conventional detection systems used in particle angular distribution measurements. Moreover, it is often more interesting to measure $W(\cos \vartheta)$ instead of $W(\vartheta)$ since the analysis in many cases is performed with an expansion of the Legendre polynomials $P_k(\cos \vartheta)$. In order to use this chamber also in neutron time-of-flight experiments a timing signal can be extracted from the cathode.

Concluding Remarks

Since all our fission fragment detectors were used in actual measurements, a kind of overview about their performance and their applicability can be given. It is clear, that whenever possible the simple parallel plate chamber should be used, because it has the higher efficiency and it is insensitive to angular distribution effects which could influence the angle integrated cross section measurement. The compensation chamber however, allows one to operate with higher alpha activities. In Table II, the lower limits for the half-lives of fictive materials are given, whose fission cross sections still could be measured using the CBNM facilities. In the case of a material with fission threshold 0.5 mg and 4 mg are needed for the parallel plate and compensation chamber respectively.

Table II : Column 2 and 4 give the amounts of materials needed to get about the same neutron induced fission rate as in our experiment[12] on ^{241}Am for actinides with and without fission threshold respectively. Column 3 and 5 give the half-lives which such materials may have.

Detector	Min. amount of material with threshold	Half-life	Min. amount of material without threshold	Half-life
Parallel Plate chamber	0.5 mg	> 500 years	10 μg	> 10 years
Compensation chamber	4 mg	> 20 years	80 μg	> 0.4 years

When the material has no fission threshold 10 μg and 80 μg are the "minimum" amount of material for the first and second detector respectively. The grided chambers in the single and twin version complete our fission fragment detection instruments. Since more physical parameters can be determined in addition to the simple event detection, their applications are related more towards basic physics problems. At present a single chamber is being used also for the measurement of angular distributions of the neutron fluence standard reaction ^{6}Li(n,α)T.

References

1. R. Chrien, Editor, Proc. NEANDC Specialists Meeting on Nuclear Data of the higher Plutonium and Americium Isotopes for Reactor Applications, Report BNL-50991 (1979).

2. H.-H. Knitter, Proc. IAEA Second Advisory Group Meeting on Transactinium Isotope Nuclear Data, Cadarache, France, 2nd-5th May 1979, to be published.

3. G. Locke, Proc. der Reaktortagung, Düsseldorf, 30.3-2.4.1976, p. 439.

4. AGNS, Nuclear Industry, Sept. 1978, p. 24.

5. H. Derrien, E. Fort and D. Lafond, Proc. Second Advisory Group Meeting on Transactinium Isotope Nuclear Data, Cadarache, France, 2nd-5th May 1979, to be published.

6. W.B. Ewbank, Proc. IAEA Second Advisory Group Meeting on Transactinium Isotope Nuclear Data, Cadarache, France, 2nd-5th May 1979, to be published.

7. A. Lorenz, Report INDC(NDS)-96/N (1978), p. 10.

8. S. Raman, Proc. First IAEA Advisory Group Meeting on Transactinium Isotope Nuclear Data, Karlsruhe, Germany, 1975 "General Survey of Applications".

9. C. Budtz-Jørgensen and H.-H. Knitter, Report BNL-50991, p. 239 (1979).

10. C. Budtz-Jørgensen and H.-H. Knitter, Nucl. Instr. Meth., 154, 122 (1978).

11. H.-H. Knitter and C. Budtz-Jørgensen, AKTE 33, 205 (1979).

12. H.-H. Knitter and C. Budtz-Jørgensen, Proc. of Int. Conf. on Neutron Physics and Nuclear Data, Harwell (1978), p. 899.

13. R. Vandenbosch and J.R. Huizenga, Nuclear Fission, Academic Press, New York and London, p. 109 (1973).

14. I. Ogawa, T. Doke and M. Tsukada, Nucl. Instr. Meth. 13, 169 (1961).

15. S.S. Kapoor and R. Ramanna, Phys. Rev. 133, B 598 (1964).

16. R.K. Choudhury, S.S. Kapoor, D.M. Nadkarni and P.N. Rama Rao, Extended Synopses of Int. Symposium on Physics and Chemistry of Fission, Jülich, May 1979, p. 177, IAEA-SM-241.

Addendum

When the present paper was ready we got knowledge of the paper of R.K. Choudhury, S.S. Kapoor, D.M. Nadkarni and P.N. Rama Rao in Nucl. Instr. Meth. 164, 323 of 15. August 1979, which describes about the same twin fission fragment chamber. This group uses, however, for the extraction of the angular information the amplitude of the first negative going part of the grid pulse, see fig. 13. The shape of this part of the grid pulse varies strongly with the energy and the angle of the fragment. Therefore, the electronic treatment of this part of the pulse is more delicate than for the positive and part which remains constant.

LEAST SQUARES METHODOLOGY APPLIED TO LWR-PV DAMAGE DOSIMETRY, EXPERIENCE AND EXPECTATIONS

J. J. Wagschal†, B. L. Broadhead, and R. E. Maerker
Oak Ridge National Laboratory
Oak Ridge, Tennessee 37830, USA

†On leave from The Hebrew University, Jerusalem, Israel.

The development of an advanced methodology for Light Water Reactors (LWR) Pressure Vessel (PV) damage dosimetry applications is the subject of an ongoing EPRI-sponsored research project at ORNL. This methodology includes a generalized least squares approach to a combination of data. The data include measured foil activations, evaluated cross sections and calculated fluxes. The uncertainties associated with the data as well as with the calculational methods are an essential component of this methodology. Activation measurements in two NBS benchmark neutron fields (^{252}Cf ISNF) and in a prototypic reactor field (*Oak Ridge Pool Critical Assembly* - PCA) are being analyzed using a generalized least squares method. The sensitivity of the results to the representation of the uncertainties (covariances) was carefully checked. Cross element covariances were found to be of utmost importance.

[least squares unfolding, adjustment, ISNF, ^{252}Cf, standard fields, dosimetry, LWR-PV damage]

Introduction

A program has been initiated between ORNL and EPRI[1] which has as its ultimate goal the accurate estimation and reduction of the uncertainty in pressure vessel lifetime of the older LWRs in this country due to neutron-induced embrittlement. The starting point of this program is the development of a methodology which accurately predicts the fluence and spectrum at the pressure vessel from surveillance dosimetric data obtained at another location. The procedure involves unfolding the spectrum at the pressure vessel from the reaction rate data together with a calculation of the neutron fluence spectrum at the two locations and corresponding reaction rates, the latter using the differential cross section data. The unfolding employs the least squares technique,[2] in which the set of data (i.e., differential cross sections, differential fluxes, measured reaction rates) is adjusted to give the most consistent results. This unfolding is accomplished within the framework set by the uncertainty information describing the data, i.e., the covariances.

In order to develop differential cross section data which are more consistent with integral data obtained in relatively well-known fields, the least squares procedure was first applied to integral fission measurements performed in two standard NBS fields — the ^{252}Cf and ISNF facilities[3,4] — and the present paper is essentially devoted to describing this application. Later on, the procedure will be used to bring in a third field — the ORNL Pool Critical Assembly — which has somewhat larger flux uncertainties. Finally, it is intended that this methodology will be used to predict the fluence level and the spectrum in the pressure vessel of an operating LWR, together with an estimate of the uncertainties, from surveillance data.

In this paper we describe in some detail the procedure used to calculate the covariances of all the original data that completely describe the measurements made with double fission chambers in the two aforementioned NBS fields, i.e., the integral measurements themselves, the differential fission cross sections, and the differential fluxes. Following this, we present some results of an adjustment procedure on the data and indicate how these results would change if various parts of the original covariances were neglected.

Measurements

We wanted to start with "clean" measurements with little or no modeling approximations in the calculations. Since we wanted to be able to interact closely with the experimentalists in order to derive credible covariances, the NBS standard fields were analyzed. The ^{252}Cf field is essentially a free field and does not involve any transport calculations (except for applying corrections due to scattering in the source capsule and in the detectors). The ISNF is a spherical cavity in the thermal column of the NBS reactor. Small ^{235}U foils are located in spherical symmetry around the cavity. The neutron spectrum in the field arises from ^{235}U thermal fission modified by carbon reflection. The lower end of the spectrum is shaped by a concentric spherical boron shell. Fission integral ratios have been measured in both fields using NBS back-to-back double fission chambers. The detailed description of the fields, the experimental techniques and the measured values can all be found in References 3, 4, and 5. A recent uncertainty analysis including the derivation of a covariance matrix can be found in References 5 and 6. The measured values are given in Table I, and the corresponding standard deviations and correlation matrix are given in Table II. Additional measurements in NBS fields and in other standard fields will be included at a later stage of our project. The measured values of reaction rates in the ORNL-PCA, which have not yet been released, will also be included in a later stage of our work. The analysis of this prototypic neutron field necessitates the use of more complicated 2-D transport calculations.

Table I. Measured and calculated* values of fission integrals in NBS standard neutron fields.

Exp.	Field	Reaction	Measured	Calculated
1	^{252}Cf	25	1.205 barns	1.239
2		49/25	1.500	1.447
3		28/25	0.2644	0.2531
4	ISNF	49/25	1.555	1.138
5		28/25	0.0920	0.0894

*Fission cross sections and ^{235}U fission spectrum were taken from ENDF/B-V.

Calculations

ISNF flux calculations

The one-dimensional model of the ISNF is given in Fig. 1. Transport calculations were performed using the XSDRNPM module of AMPX[7] with 171-group VITAMIN-C[8] (based on ENDF/B-IV) data. Since previous work[9] on the representation of the thermal fission spectrum of ^{235}U indicated that the ENDF/B-IV Maxwellian shape was poor for energies above $\sim$ 4 MeV, the new ENDF/B-V thermal Watt representation was used. The S_8 angular quadrature

Table II. Relative standard deviations and correlation matrix associated with measured values of fission integrals.

Exp.	Field	Reaction	Relative Standard Deviation (%)	Correlation Matrix 1	2	3	4	5
				^{252}Cf			ISNF	
1		25	2.1	1.0	-0.1916	0.3995	-0.2140	0.1354
2	^{252}Cf	49/25	1.3	-0.1916	1.0	0.1349	0.9516	0.0
3		28/25	1.1	0.3995	0.1349	1.0	0.1106	0.6524
4	ISNF	49/25	1.3	-0.2140	0.9516	0.1106	1.0	0.0160
5		28/25	0.62	0.1354	0.0	0.6524	0.0160	1.0

and P_3 scattering expansions were found to give adequate accuracy.

Fission integrals

All the measured fission integrals were calculated using ENDF/B-V fission cross sections. These fission cross sections were processed from the ENDF/B-V files into 174 groups according to the VITAMIN-E[10] specifications. The ^{252}Cf field values were obtained by folding these cross sections with a 174-group Maxwellian fission spectrum characterized by a temperature of 1.42 MeV.[3] The ISNF field values were obtained in a similar way by folding the fission cross sections with the calculated flux at the ISNF central region. All calculated values are given in Table I alongside the corresponding experimental values and, as was expected, some disagreement exists. The calculated value of the ^{235}U fission integral in the ^{252}Cf field is higher than the experimental value, and all calculated fission integrals relative to the ^{235}U fission integrals are smaller than the experimental values. In Table III these deviations are expressed in percent as well as in units of standard deviations. Taking into account only the experimental uncertainties, all deviations are higher than their corresponding standard deviations, and the ratios of the ^{238}U to ^{235}U fission integrals in both fields deviate by more than four experimental standard deviations. Taking into account the contribution of the covariances in each fission cross section to the uncertainty in the calculated values (considering only autocorrelations), four deviations are already about equal to or less than one joint standard deviation. Including the uncertainty in the flux (^{252}Cf fission spectrum and ISNF central flux) further reduces the deviations in units of joint standard deviations. Finally, however, introducing the cross element correlations of the fission cross sections reduces the joint standard deviation and emphasizes the deviations of the two fission ratios in the ^{252}Cf field.

Least squares unfolding (adjustment)

In order to reduce computation time and storage requirements and thus enable us to perform many calculations, a 17-group subset of VITAMIN-C (and E) was used to calculate all covariances and sensitivities. In each of the 17 groups we have only about 10% or less of the ^{252}Cf fission spectrum, the ISNF central flux and of the fission integrals.

Fission cross-section covariances

The 17-group ^{235}U and ^{239}Pu fission covariance matrices were processed from ENDF/B-V file 33 uncertainty information using the current version of PUFF.[11] The ^{238}U fission covariance data used in this work were taken from ORNL internal files. Preliminary tests with ENDF/B-V ^{238}U data indicated no dramatic change in the results. All cross element covariances are zero for the lowest five energy groups (below 87 keV) and are set equal to the ^{235}U auto-covariance matrix for higher energies since most fission cross sections are measured as ratios to ^{235}U fission.

^{252}Cf fission spectrum covariance

Since the fission spectrum used in our calculations was Maxwellian with a temperature of 1.42 MeV, a covariance was calculated using a 2% uncertainty in the temperature.[3] A more realistic covariance matrix for the ^{252}Cf fission spectrum is being developed now.

ISNF flux covariance

The uncertainty in the flux of the ISNF is the combined propagated uncertainty in the ^{235}U thermal fission spectrum, driving the ISNF, and in the cross sections and densities of the structural materials (B,C,Al) of the ISNF. The procedure for the calculation of the ISNF flux covariance matrix is detailed in Reference 12 and will only be outlined here. The propagated uncertainty in a calculation due to the uncertainties in the contributing parameters is obtained from the covariance of these parameters and

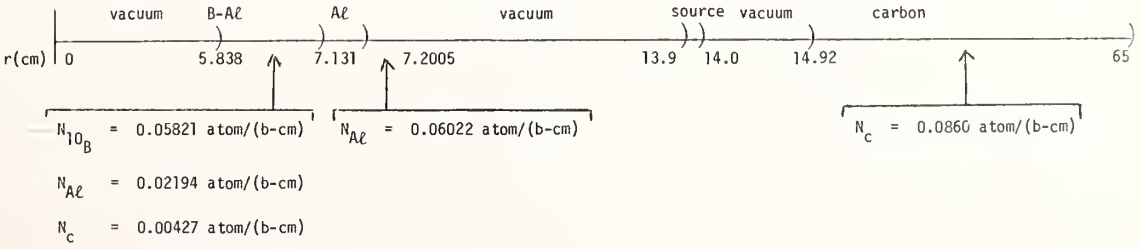

Fig. 1. NBS-ISNF 1-D model parameters.

Table III. Deviations, D, of calculated, C, from experiment, E, values.

Exp.	Field	Reaction	$\frac{C-E}{C}$ (%)	D in units of joint standard deviations due to * Measurement	Fission Cross Sections	Fission Spectrum and Flux	Cross Element Covariance of Fission Cross Section
1		25	2.74	1.30	0.96	0.96	0.96
2	^{252}Cf	49/25	-3.66	-2.75	-1.01	-1.01	-1.54
3		28/25	-4.46	-4.21	-1.39	-1.24	-1.94
4	ISNF	49/25	-1.49	-1.16	-0.48	-0.45	-0.56
5		28/25	-2.97	-4.76	-1.02	-0.63	-0.69

*Going from left to right, the joint standard deviation includes all previous contributions.

from the corresponding sensitivities of the calculated result to the contributing parameters. The sensitivities were obtained from FORSS[13] using forward and adjoint ANISN[14] fluxes. The covariance matrices of the contributing parameters were calculated by PUFF using ENDF/B-V uncertainty file data.

Numerical results

All the carefully prepared data described earlier in this paper were used as input to the least squares module UNCOVER[2] of the FORSS system. The data are: a) measured fission integrals and their covariances, b) calculated fission integrals, c) flux covariances (^{252}Cf and ISNF fields), d) differential fission cross section covariances (including cross element covariances), e) sensitivities of the calculated fission integrals (and ratios) to the fission cross sections and to the flux. The output consists of the "most likely" values of the fluxes, the fission integrals and the differential fission cross sections, given the uncertainties and correlations in the input data. In addition to the "most likely" values we also obtain new reduced uncertainties and correlations reflecting all the information used in our data combination (also known as adjustment or unfolding).

ISNF central flux. The changes in the originally calculated ISNF flux are given by the solid line in Fig. 2. The uncertainty in the flux was reduced by a few percent above ∿ 1 MeV and by about thirty percent at lower energies.

Although this result *is* the "most likely" flux based on all our carefully gathered data, it is tempting to check what the result would have been if we did not have the correlations in the fission integral measurements (dotted curve) or the cross element covariances in the fission cross sections (dashed line). It is easier to try to answer these questions by looking at the fission integrals and at the differential fission cross sections.

Fission integrals. A comparison of the differences between adjusted integral values, A, and the original experimental values, E, (both normalized to the original calculated values, C) is given in Table IV. The most likely values, A, are closer to the E values than the original C values were, and the signs of C-E and A-E are the same. Neglecting the correlations in the integral measurements results in a *different behavior* of the adjusted values in the two fields. We might point out, for example, that the correlation coefficient of the 49/25 measurements in the two fields is ∿ 0.95, their relative standard deviations are about the same (see Table II), and their adjustments are similar.

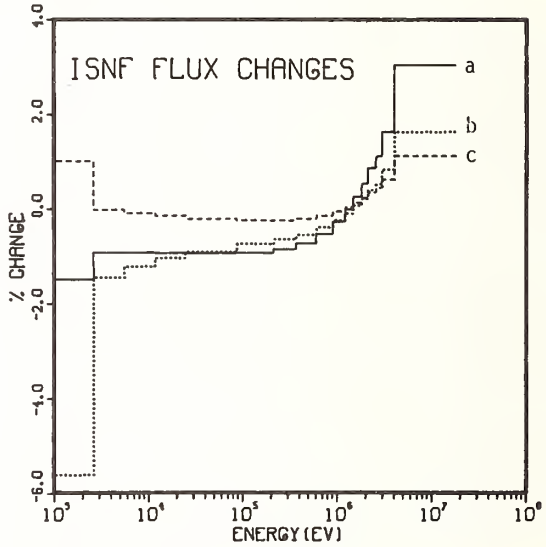

Fig. 2. ISNF flux adjustments.
a - "most likely"
b - correlation in integral measurements neglected
c - cross element covariance neglected

However, when the measurement correlations are neglected, the adjustments are quite different [Table IV(a)]. Although neglecting the cross-element covariances results in closer agreement between measured and adjusted integral values [Table IV(b) and (c)], it is obviously incorrect when the resulting adjusted differential cross sections are considered as will be seen in the following section.

Differential fission cross sections. The most likely fission cross sections, given our full detailed uncertainty data, are obtained by changing the measured differential cross sections according to Fig. 3. Neglecting all correlations in the measured fission integrals, cross element covariances, and assuming no flux uncertainties results in the adjustment given in Fig. 4. This adjustment is what simple-minded "intuition" might have suggested, namely: a) reduction of the ^{235}U fission cross section to decrease C-E of the 25 fission integral in the ^{252}Cf field and b) increase of the ^{238}U and ^{239}Pu fission cross sections in order to further increase the calculated ratios. However, since all the fission cross sections are strongly correlated they cannot be changed independently. Neglecting the correlations in the measured integrals (Fig. 5) results in adjustments that are only quantitatively different from Fig. 3. On the other hand, neglecting the cross element covariances (Fig. 6) produces a profound difference in the adjustment of the fission cross sections.

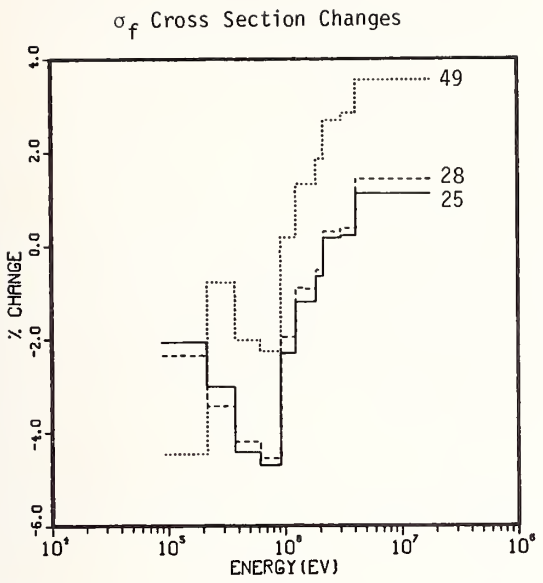

Fig. 3. Fission cross section adjustments.

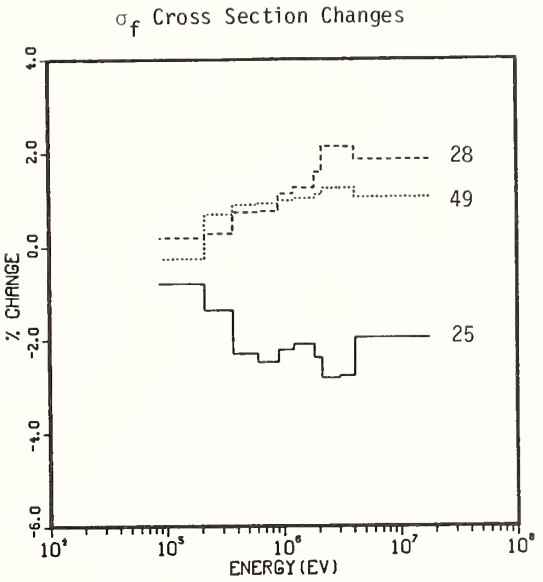

Fig. 4. Fission cross section adjustments neglecting cross element covariances and correlations in fission integral measurements and assuming no flux uncertainties.

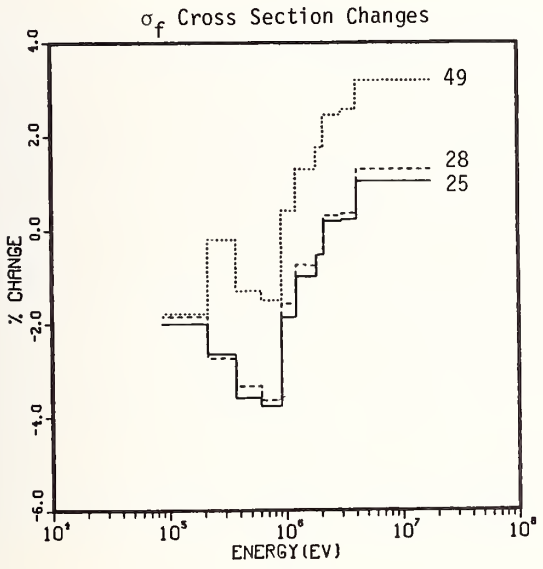

Fig. 5. Fission cross section adjustments neglecting correlations in fission integral measurements.

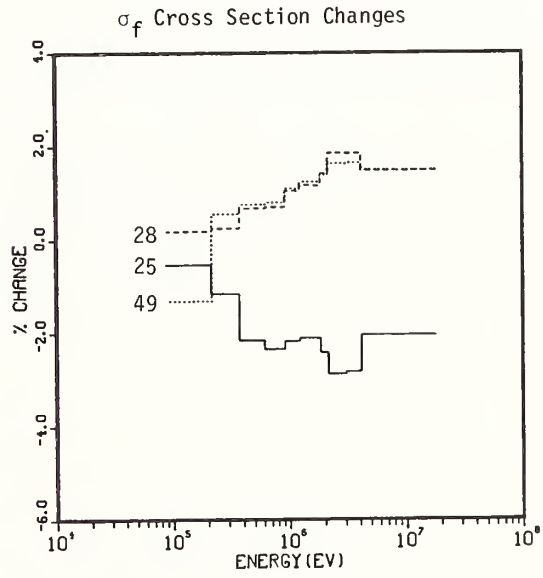

Fig. 6. Fission cross section adjustment neglecting cross element covariances.

Table IV. Comparison of adjusted, A, fission integrals.

Exp.	Field	Reaction	$\frac{C-E}{C}$ (%)	$\frac{A-E}{C}$ (%)	$\frac{A-E}{C}$ (%) neglecting: a) Fission integral measurement correlations only	b) Cross element fission cross section covariances only	c) (a) + (b) + flux uncertainties
1		25	2.74	1.43	1.65	0.52	0.51
2	^{252}Cf	49/25	-3.66	-1.18	-1.27	-0.25	-0.42
3		28/25	-4.46	-0.67	-0.86	-0.13	-0.38
4	ISNF	49/25	-1.49	-0.97	0.32	-0.18	0.24
5		28/25	-2.97	-0.35	-0.06	-0.09	0.00

Summary and Conclusions

In the present work we have demonstrated the feasibility of the application of the generalized least squares unfolding procedure as part of the advanced methodology developed for estimating light-water reactor pressure-vessel radiation damage. Covariance matrices for integral measurements and fluxes were derived and covariance matrices for fission cross sections were processed and compiled. Although the scope of this work is rather limited, it was demonstrated that credible covariances can be obtained, and that the quality of these covariances is indeed reflected in the results. Future work will concentrate on broadening the data base to include threshold reactions and their differential and integral covariances, and on application of the methodology to actual operating U.S. light water reactors.

Acknowledgment

We are indebted to J. A. Grundl and his group at the NBS and in particular to D. M. Gilliam and C. M. Eisenhauer for their continuing help.

References

1. Electric Power Research Institute Project RP-1399, under Union Carbide Corporation contract W-7405-eng-26 with the U. S. Department of Energy.

2. F. G. Perey, ORNL/TM-6062 (ENDF-254) (October 1977); see also handout H of RSIC Workshop-Seminar (August 1978) by J. H. Marable describing the UNCOVER code.

3. J. A. Grundl, C. M. Eisenhauer, and E. D. McGarry, in NUREG/CR-0551 (1978). The fission spectrum we used is the reference Maxwellian in this report. The 2% uncertainty in the temperature was estimated from the experimental point data of Green.[15]

4. C. M. Eisenhauer, J. A. Grundl, A. Fabry, in NBS Special Publication 493, 329 (March 1977).

5. J. J. Wagschal, R. E. Maerker, D. M. Gilliam, Trans. Am. Nucl. Soc. 33 (1979).

6. J. J. Wagschal and R. E. Maerker, Third ASTM-EURATOM Symposium on Reactor Dosimetry, Ispra (Varese), Italy, October 1979.

7. N. M. Greene *et al.*, ORNL/TM-3706 (March 1976).

8. R. W. Roussin *et al.*, in ORNL/RSIC-41, 107 (October 1978).

9. B. L. Broadhead and J. H. Marable, in ORNL/RSIC-42, 161 (February 1979).

10. C. R. Weisbin *et al.*, ORNL-5505 (ENDF-274) (February 1979).

11. C. R. Weisbin *et al.*, ORNL/TM-4847 (ENDF-218) (August 1975); see also, RSIC Code Collection PSR-93.

12. B. L. Broadhead *et al.*, Trans. Am. Nucl. Soc. 30, 590 (1978).

13. J. L. Lucius *et al.*, ORNL-5316; see also handouts describing FORSS, RSIC Workshop-Seminar (August 1978).

14. W. W. Engle, Jr., "Users Manual for ANISN," K-1693 (1967).

15. L. Green, J. A. Mitchell and N. M. Steen, Nucl. Sci. Eng. 50, 257 (1973).

^{235}U (n,f) CROSS SECTION MEASUREMENTS AND NORMALIZATION PROBLEMS *

C. WAGEMANS +, G. CODDENS ++, A.J. DERUYTTER
Nuclear Physics Laboratory, B-9000 Gent, Belgium
and
Nuclear Energy Center, S.C.K./C.E.N., B-2400 Mol, Belgium

At Gelina measurements of the ^{235}U fission cross section were performed relative to $^{10}B(n,\alpha)^{7}Li$ and $^{6}Li(n,\alpha)^{3}H$ independently. The neutron energy range from thermal up to 30 keV was covered, allowing a normalization to the 2200 m/s reference cross section. Surface barrier detectors and back-to-back foils were used. Thus the fission fragments and the neutron flux are measured at the same time and from the same position in the neutron beam. Special attention is given to problems such as background determination, overlap filters, normalization and secondary standards (resonance integrals). Especially the present status of the resonance integrals $\int_{7.8\ eV}^{11\ eV} \sigma_f(E)dE$ and $\int_{0,1\ keV}^{1\ keV} \sigma_f(E)dE$, often used for normalization purposes, is reviewed. Finally, an intercomparison of the present $\bar{\sigma}_f$-values as well as a comparison with other recent results is made.

(^{235}U, $\sigma_{n,f}$, measured 0.02 eV to 30 keV, normalized to 2200 m/sec reference, fission integrals)

Introduction

A good knowledge of the $^{235}U(n,f)$ cross section in function of the neutron energy is very important for reactor calculations and for fission theory. It is also required if one wants to use this cross section as a secondary standard. However, despite worldwide efforts employed during the last decennia, our present knowledge of the ^{235}U neutron induced fission cross section remains unsatisfactory. Several authors claim precisions of the order of 1%, but the reported values are up to 15 % different. (See Table III). Possible explanations for these differences were discussed by Deruytter [1], Leonard et al [2], Peelle and De Saussure [3], Carlson and Czirr [4] and Bath [5]. To reduce these discrepancies or at least to investigate part of their origins a new series of σ_f measurements was performed at Gelina. The $^{10}B(n,\alpha)$- and $^{6}Li(n,\alpha)$-reactions were used as neutron flux monitors and the neutron region from 0.02 eV up to 30 keV was covered. Another goal of the present measurements was to improve the accuracy on the value of the fission integral $\int_{7.8\ eV}^{11\ eV} \sigma_f(E)dE$, which, according to Leonard [6], was only 2.8 %. This is not sufficient if one wants to use this integral for normalization purposes [7].

Experimental Method

Pulsed neutrons with a broad energy spectrum were produced by bombarding an uranium target (with a polyethylene moderator) with the 100 MeV electron beam of Gelina. A ^{10}B or ^{6}Li layer was mounted back-to-back with a ^{235}U layer in the center of a large evacuated detection chamber (ϕ= 50 cm). The $^{10}B(n,\alpha)$ or $^{6}Li(n,\alpha)$ particles and the $^{235}U(n,f)$ fragments were detected by two collinear 20 cm^2 gold-silicon surface barrier detectors placed outside the neutron beam with which they made an angle θ_{lab} = 90°. According to the data of Stelts et al [8] this is the best geometry to eliminate anisotropy effects. After amplification, a fast timing signal was derived from each detector signal and sent into two halves of a 8192 channels time-of-flight analyser with a variable channel width (accordeon). So the fission fragments and the (n,α) particles were detected simultaneously and from the same position in the neutron beam; this has definite advantages compared to several other measuring procedures.

With this apparatus a series of three experiments was performed at short flight paths; a fourth one was done at a 30 m station. The detailed experimental conditions for all these measurements are summarized in Table I. The first and the second measurements covered the thermal neutron energy region and were done under identical conditions, except that the flux determination was relative to ^{10}B in the first experiment and ^{6}Li in the second. A third experiment covering about the same neutron energy region was performed with a different set of background filters in order to investigate the influence of the choice of the background filters on the experimental results.

In a last experiment we moved to a 30.445 m flight path in order to extend the neutron energy range up to 30 keV. In all these experiments, the background was determined using the black resonance technique. The background was very low. In the thermal region e.g. it was less than 0.5 %, increasing to 1-2 % in the eV-region.

The ^{235}U layer was prepared by electrospraying of uranylacetate on an Al disk. The thickness of the layer is 2 mg/cm^2 with an isotopic enrichment of 99.5 % ^{235}U. The ^{10}B layer was prepared by evaporating elemental boron in vacuum. In this way a very

---

* Work performed at CBNM Geel in the frame of a research association contract between CBNM Geel and SCK/CEN

+ NFWO
++ IIKW

TABLE I - EXPERIMENTAL CONDITIONS

Experiment number	Neutron Energies	Neutron flux determination	Linac parameters	Flight path length (m)	Neutron filters	
					Common filters	Background
I	thermal - 200 eV	^{10}B (n,α)	30 ns, 100 Hz	7.757	Mn	Cd, Rh, W, Pd, Co
II	thermal - 200 eV	^{6}Li (n,α)	30 ns, 100 Hz	7.757	Mn	Cd, Rh, W, Pd, Co
III	thermal - 200 eV	^{6}Li (n,α)	24 ns, 100 Hz	9.450	-	Co, Cd Co, W, Au, Rh, Mn
IV	1 eV - 30 keV	^{10}B (n,α)	20 ns, 400 Hz	30.445	^{10}B, Al	Mn, Co, Pd, W, Ta

homogeneous layer with a thickness of 184 μg/cm^2 and an isotopic enrichment of 93% was obtained. The ^{6}Li layer was prepared by evaporating ^{6}LiF in vacuum. Its thickness is 176 μg/cm^2 with 99.32 % enrichment. All these layers were deposited on a 0.1 mm thick aluminium disk.

Treatment of data

The data reduction was done using the computer code ANGELA [9]. For each experiment we first determined an analytical expression for the background by fitting expressions

$$y = \sum_{i=0}^{n} a_i \, (\ln T)^i \qquad (1a)$$

or

$$y = \sum_{i=0}^{n} a_i \, T^i \qquad (1b)$$

to the background values obtained from the black resonances. Here T is the time-of-flight, y is the counting rate and a_i are constants. Since it is difficult to establish a well understood background shape which is fully supported by physical arguments, the major criterium for the adoption of a certain analytical expression for the description of the background shape is the goodness of the χ^2-value. The ratios of the fission t.o.f. spectra and the corresponding neutron t.o.f. spectra yield the (unnormalized) $\sigma_f(E)\sqrt{E}$-values by application of the formula :

$$\sigma_f(E)\sqrt{E} = k \, \frac{N_f(E) - B_f(E)}{N_n(E) - B_n(E)} \qquad (2)$$

where

- k is a normalization constant
- $N_f(E)$ the number of fission counts at energy E
- $B_f(E)$ the fission background at energy E
- $N_n(E)$ the number of ^{10}B (n,α) or ^{6}Li (n,α) counts at energy E
- $B_n(E)$ the corresponding background at energy E

In (2) a $\frac{1}{v}$-shape was assumed for the ^{6}Li (n,α) and ^{10}B (n,α) cross sections. In the thermal neutron energy runs, the fission cross section was normalized to the fission integral

$$\int_{0.0206\ eV}^{0.06239\ eV} \sigma_f(E)\, dE = 19.26 \pm 0.08 \text{ barn eV}$$

as determined by Deruytter et al [7] and corresponding to a thermal σ_f value of 587.6 ± 2.6 b. The high energy run IV (see table I) was normalized using the fission integral

$$\int_{100\ eV}^{200\ eV} \sigma_f(E)\, dE = 2157 \pm 30 \text{ barn. eV}$$

as obtained from the first and the second experiment.

Results and discussion

The fission cross section data obtained from these measurements are represented graphically as a function of the neutron energy in Fig. 1-3. Fig. 1 shows the mean $\sigma_f\sqrt{E}$-values calculated from the measurements I and II in the neutron energy region from 0.02 eV to 1 eV. In Fig. 2 the σ_f versus E curve obtained from the same data set is given in the neutron energy region from 0.5 eV to 30 eV. Fig. 3a and b finally show the σ_f-data from 30 eV up to 30 keV as obtained from the measurement IV.

TABLE II - FISSION INTEGRALS (barn eV) DEDUCED FROM THE MEASUREMENTS I, II AND III

Neutron energy region	I	II	III
0.03 - 0.10	23.9	23.9	24.2
0.10 - 0.50	65.2	64.5	65.5
0.50 - 1.0	30.4	30.2	30.0
1 - 10	373	372	377
10 - 20	546	537	515
20 - 30	380	378	381
30 - 40	588	587	554
40 - 50	344	345	342
50 - 60	643	643	627
60 - 100	997	991	1015
100 - 200	2149	2166	2105
7.8 - 11.0	248.9	246.8	246.8

Table II gives a comparison of the numerical values of the fission integrals calculated from the three low energy experiments (I,II,III). The statistical accuracies of the measurements I and II were comparable and both of them are much better than in experiment III, only performed for control purposes. Taking into account this statistical accuracy and the uncertainty of the normalization and of the background determination, we obtained an overall accuracy of about 1.5 % on the values quoted in Table II for the experiments I and II. Within their respective errors

TABLE III - THE AVERAGE CROSS SECTIONS (barn) OBTAINED IN OUR MEASUREMENTS COMPARED WITH OTHER RECENT MEASUREMENTS, MAINTAINING THEIR ORIGINAL NORMALIZATION

Energy interval	de Saussure (14,15)	Ryabov (16)	Silver (17)	Lemley (18)	Blons (19)	Gayther (20)	Perez (21)	Perez (22)	Czirr (23)	Gwin (11)	Czirr (12)	Wagemans (7, 10)	This work
0.02 - 0.1 eV										379.1	381.7	384.1	383.8
0.1 - 0.5										157.2	159	159.1	162.1
0.5 - 1.0										61.54	61.03	60.64	60.60
1 - 10	40.14											40.64	41.39
10 - 20	52.95	46.09					50.57					52.62	54.15
20 - 30	36.27	35.05			34.28		36.14					38.08	37.90
30 - 40	57.06	52.12			57.31		55.65					59.02	58.81
40 - 50	33.33	32.21			34.00		33.38					34.57	33.83
50 - 60	61.99	51.10			64.47		61.81					64.59	64.33
60 - 100	24.34	24.23	25.75	24.05	25.15		24.55			23.58	24.02	25.40	25.37
100 - 200	21.03	21.39	21.03	20.90	21.03		21.03		19.9	20.47	20.23	21.25	21.57
200 - 300	20.86	20.83	20.61	20.15	20.77		~20.92		19.8	19.74	19.93	20.91	21.47
300 - 1000	11.58	11.69	11.59	11.09	11.71		11.69		10.71	11.08	10.76	11.53	11.99
1 - 10 keV		4.41	3.99	3.99	4.38		4.35			4.08		4.41	4.26
10 - 20		2.98	2.77	2.34	2.54	2.53		2.53	2.35	2.46		2.64	2.57
20 - 30		2.51	2.37	2.10	2.20	2.17		2.18	2.17	2.11		2.22	2.23

TABLE IV - COMPARISON OF FLUX DETERMINATION AND NORMALIZATION METHODS APPLIED IN THE QUOTED σ_f-MEASUREMENTS ON ^{235}U

Authors	Neutron flux determination	Normalization	Corresponding σ_f° (barn)
De Saussure et al. (1967)	^{10}B (n,α)	$\int_{0.45\ eV}^{10\ eV} \sigma_f$ (E) dE/E = 127.9 barn (Bowman et al. 1966)	577.1
De Saussure (1971)	^{10}B (n,α)	$\int_{7.8\ eV}^{11\ eV} \sigma_f$ (E) dE = 240 barn eV (Deruytter et al. 1971, 1973)	587.6
Ryabov et al. (1970)	^{10}B (n,α)	σ_f° = 582 barn	582
Silver et al. (1971)	^{10}B (n,α)	σ_f of de Saussure et al. (1967) between 100 and 200 eV	577.1
Lemley et al. (1971)	^{6}Li (n,α)	σ [^{6}Li (n,α)]	
Blons (1972)	^{10}B (n,α)	$\int_{100\ eV}^{200\ eV} \sigma_f$ (E) dE = 2103 barn eV (De Ssnssure, 1971)	587.6
Gayther et al. (1972)	calibrated boron-vaseline plug	$\bar{\sigma}_f$ = 2.349 barn in the interval 10 - 30 keV (Sowerby et al. 1974)	580.2
Perez et al. (1973)	^{10}B (n,α)	$\int_{100\ eV}^{200\ eV} \sigma_f$ (E) dE = 2103 barn eV (De Saussure, 1971)	587.6
Perez et al. (1974)	^{10}B (n,α)	$\int_{2\ keV}^{10\ keV} \sigma_f$ (E) dE = 31.643 barn keV (Perez et al. 1973)	577.1
Czirr et al. (1975)	^{6}Li (n,α)	σ_f° = 585.4 barn	585.4
Gwin et al. (1976)	^{10}B (n,α)	σ_f of ENDF-B III between 0.02-0.4 eV	580.2
Wagemans and Deruytter (1976)	^{10}B (n,α) | ^{6}Li (n,α) |	$\int_{7.8\ eV}^{11\ eV} \sigma_f$ (E) dE = 240 barn eV	587.6
Czirr and Carlson (1977)	^{6}Li (n,α)	$\int_{0.02\ eV}^{0.1\ eV} \sigma_f$ (E) dE of Leonard et al. (1975)	585.4
This work	^{10}B (n,α) ^{6}Li (n,α)	$\int_{0.0206\ eV}^{0.06239\ eV} \sigma_f$ (E) dE = 19.26 ± 0.08 barn eV (Wagemans and Deruytter, 1971)	587.6

there is a good overall agreement between the results of these three measurements. This is an important fact considering the rather different experimental conditions (cfr. Table I). Our results allow the following two conclusions :

(i) the choice of either ^{10}B (n,α) or ^{6}Li (n,α) as a flux monitor has no impact on the σ_f data in the neutron energy region from 0.02 eV to 200 eV if thin foils and surface barrier detectors are used. Furthermore, the good agreement between the σ_f data relative to ^{10}B and to ^{6}Li (n,α) is an indication that our experimental method is not sensitive to anisotropy effects [8] in the neutron flux determination.

(ii) in the quoted energy region, the contribution of the background determination to the error on σ_f is less than 0.4 % and depends on the neutron energy.

In Table III the average fission cross sections obtained from these experiments are summarized and compared with the results of other recent measurements. Below 30 eV we adopted the mean value of our first and our second experiment with an overall uncertainty of about 1.5 %. Above this energy, the data from experiment IV were used, with an overall uncertainty of about 3 %. To compare the results of all these measurements, we have to take into account their different normalization procedures, summarized in Table IV. Within their respective errors, our present results agree with the previous data of Deruytter and Wagemans [7,10]. Above 1 keV however, the present σ_f values are slightly lower than these previous data, resulting in a better agreement with most other results in this energy region. Considering the different normalization, also the low energy parts ($\lesssim$ 1 eV) of the most recent measurements [10,11,12] normalized at thermal energy are in rather good agreement with the present results. Table V summarizes the present status of the important fission integral $\int_{7.8\ eV}^{11\ eV} \sigma_f(E)\,dE$. While the older data as given by Leonard [6] are up to 6 % different, it is encouraging to see that the most recent data of Czirr and Carlson [12], Gwin [13] and ourselves are in perfect agreement. We are confident that the required accuracy of 1 % for this integral is well approached now. In Table VI we compare the most recent values for the fission integral $\int_{0.1\ keV}^{1\ keV} \sigma_f(E)\,dE$ after a renormalization to σ_f^o = 587.6 barn. This integral has been suggested by Peelle and De Saussure [3] for

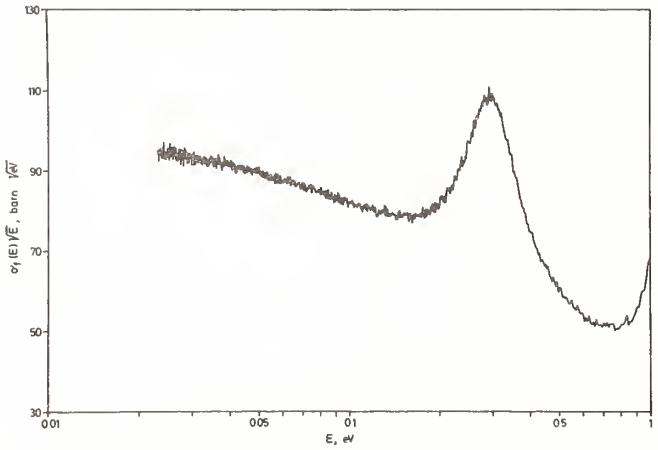

Fig. 1. $\sigma_f\sqrt{E}$-values between 0.02 and 1 eV

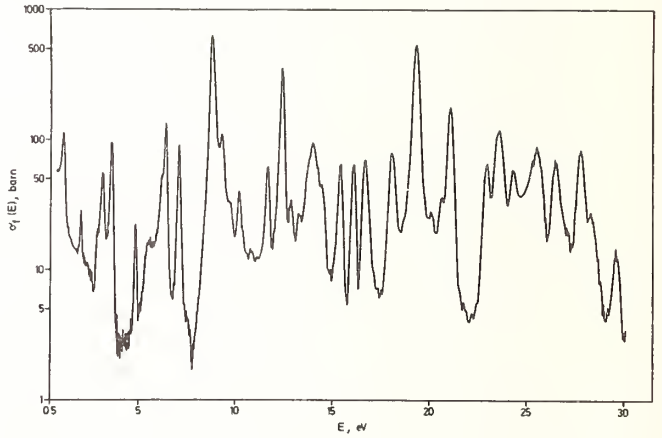

Fig. 2. $\sigma_f(E)$ values between 0.5 eV and 30 eV

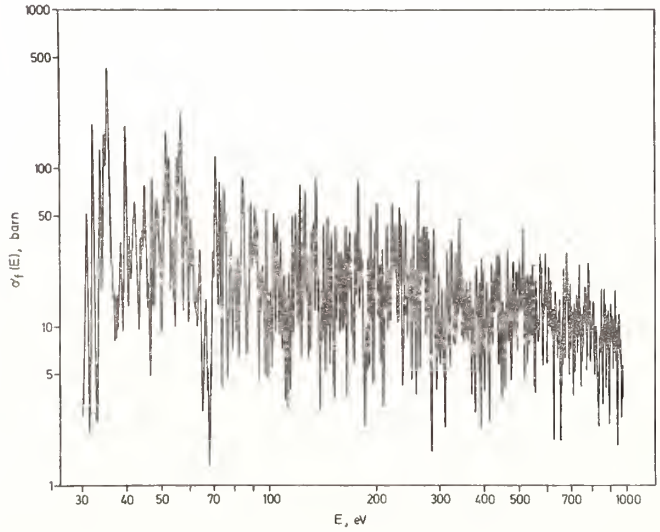

Fig. 3a. $\sigma_f(E)$-values between 30 eV and 1 keV

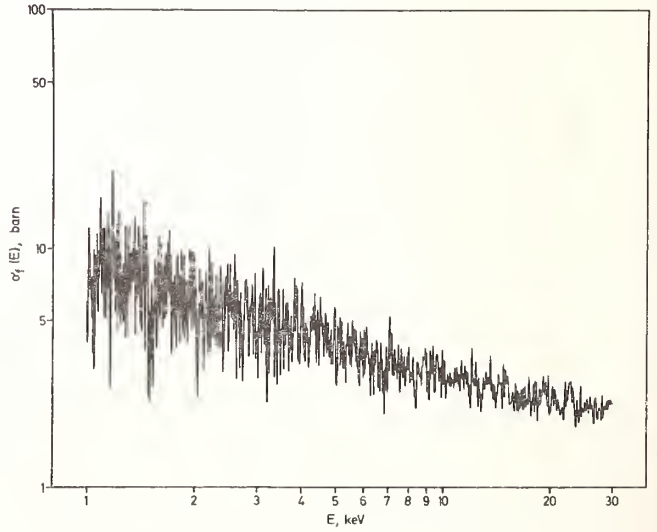

Fig. 3b. $\sigma_f(E)$-values between 1 keV and 30 keV

TABLE V - VALUES OF THE FISSION INTEGRAL $I = \int_{7.8\ eV}^{11\ eV} \sigma_f(E)\, dE$

AFTER A COMMON NORMALIZATION TO σ_f^o = 587.6 barn

Reference	I (barn eV)
Bowman et al. (1966) [26]	254 ± 7 [a]
De Saussure et al. (1966) [14]	243 ± 5 [a]
Deruytter and Wagemans (1971) [10]	245 ± 2 [a]
Gwin et al. (1976) [11]	238 ± 3 [a]
Czirr and Carlson (1977) [12]	246 ± 4
Gwin et al. (1979) [13]	247
This work (1979)	247 ± 3

[a]) values as evaluated by Leonard [6]

TABLE VI - VALUES OF THE FISSION INTEGRAL $I = \int_{0.1\ keV}^{1\ keV} \sigma_f(E)\, dE$

FROM THE MOST RECENT MEASUREMENTS AFTER A COMMON NORMALIZATION TO σ_f^o = 587.6 barn

Reference	I (barn keV)
Sowerby et al. (1974) [24], evaluation	12.4 ± 0.25
De Saussure et al. (1967) [14]	12.3
Gwin et al. (1976) [11]	11.8
Wagemans and Deruytter (1976) [10]	12.3 ± 0.4
Wasson (1976) [25]	11.9
Czirr et al. (1977) [11]	11.6
This work (1979)	12.7 ± 0.4

normalization purposes. The situation here is less satisfactory: the inclusion of the recent values of Czirr and Carlson [12] and of the present authors does not improve the situation. The data spread remains about 7 %.

Conclusion

The ^{235}U (n,f) cross section has been measured in the neutron energy region from thermal up to 30 keV. The average fission cross sections obtained are in good agreement with other recent measurements. Furthermore, in the neutron energy region below 200 eV consistent σ_f data are obtained when using a 1/v shape for the ^{6}Li (n,α) and ^{10}B (n,α) reactions. For the important $\int_{7.8\ eV}^{11\ eV} \sigma_f(E)\, dE$ fission integral a value of 247 ± 3 barn is obtained, in good agreement with the most recent published data.

Acknowledgements

The authors wich to thank Dr. M. Nève de Mévergnies (C.E.N./S.C.K.) for a critical reading of the manuscript. Mr. K.H. Böckhoff (CBNM) is acknowledged for his continuous support to these measurements. Last but not least our thanks go to Mr. R. Barthélémy for skilful technical assistance and to Mr. J. Van Gils for help with the data reduction.

References

1. A.J. Deruytter, Proc. Symp. on Neutron Standards and flux normalization, Argonne, Illinois, October 1970, CONF-701002, p. 221
2. B.R. Leonard, D.A. Kottwitz, J.K. Thompson in Evaluation of the Neutron Cross Sections of ^{235}U in the Thermal Energy Region, EPRI-NP-167 (1976)
3. R.W. Peelle and G. De Saussure, Proc. Symp. on Neutron Standards and Applications, Gaithersburg, MD, March 1977, NBS Spec. publ. 493, p. 174
4. G.W. Carlson and J.B. Czirr, Report ANL-76-90, 1976, p. 258
5. M.R. Bath, Report ANL-76-90, 1976, p. 307
6. B.R. Leonard, Jr., Report ANL-76-90, 1976, p. 281
7. A.J. Deruytter and C. Wagemans, Journ. of Nucl. En., Vol. 25, (1971), p. 263
8. M.L. Stelts, R.E. Chrien, M. Goldhaber, M.J. Kenny and C.M. McCullagh, Phys. Rev.C, 19,4 (1979) p. 1159, and the references therein
9. C. Bastian, The Angela-System, EUR-report in preparation
10. C. Wagemans and A.J. Deruytter, Annals of Nucl. En. Vol. 3 (1976) p. 437
11. R. Gwin, E. Silver and R. Ingle, Nucl. Sc. Engng, 59 (1976), 79
12. J.B. Czirr and G.W. Carlson, Nucl. Sc. Engng 64(4), 1977, 892
13. R. Gwin, 1979, private communication by W. Poenitz
14. G. De Saussure, R. Gwin, L. Weston, R. Ingle, R. Fullwood and R. Hockenbury (1976) Report ORNL-TM-1804
15. G. De Saussure (1971) private communication
16. Y. Ryabov, So Don Sik, N. Chikov and M. Kurov (1970) Report JINR P3-5113
17. E. Silver, G. De Saussure, R. Perez, R. Ingle (1971). Proc. Third Conf. Neutron Cr. Sect. Techn. (Knoxville) CONF-710301, 728
18. J. Lemley, G. Keyworth and B. Diven (1971) Nucl. Sci. Engng 43, 281
19. J. Blons (1972) Nucl. Sc. Engng 51, 130
20. D. Gayther, D. Boyce and J. Brisland (1972) Proc. Panel on Neutr. Stand.Ref.Data (Vienna), 201
21. R. Perez, G. De Saussure, E. Silver, R. Ingle and H. Weaver (1973) Nucl. Sc. Engng 52, 46
22. R. Perez, G. De Saussure, E. Silver, R. Ingle and H. Weaver (1974) Nucl. Sc. Engng 55, 203
23. J. Czirr and G. Sidhu (1975) Report UCRL-77377
24. M.G. Sowerby, B.H. Patrick and D.S. Mather, Ann. Nucl. Sc. Engng, 1 (1974), 409
25. O. Wasson, Report ANL-76-90, 1976, p. 183
26. C. Bowman, G. Auchampaugh, S. Fultz, M. Moore and F. Simpson (1966) Proc. Conf. Neutron Cr. Sect. Techn., (Washington D.C.) p. 1004

ABSOLUTE MEASUREMENT OF THE U-235 FISSION CROSS SECTION FROM 0.2 - 1.2 MEV

M. M. Meier, O. A. Wasson, K. C. Duvall
National Bureau of Standards
Washington, D. C. 20234

The absolute U-235 neutron induced fission cross section has been measured at the NBS 3MV Van de Graaff laboratory from 0.2 to 1.2 MeV. The neutron flux monitor was a large plastic scintillator whose efficiency was both calculated and measured with the associated particle technique. The neutron source was the $^{7}Li(p,n)^{7}Be$ reaction. Pulsed-beam time-of-flight techniques were used. The fission detector consisted of a large volume multiplated chamber with a measured mass of ^{235}U. The cross sections, which were measured with a typical one standard deviation of 2.8%, are approximately 3% lower than the ENDF/B-V evaluation.

(Absolute fission cross section; neutron detector; neutron flux monitor; neutron standards; U-235 fission cross section).

Introduction

The neutron induced fission cross section of ^{235}U is the standard by which most fission cross sections are determined. The present absolute measurement is part of a series of measurements at NBS to improve the knowledge of this important standard. Previous experiments at NBS were an absolute measurement[1] using a Cf source by Heaton et al; a white source measurement[2] relative to H(n,p) from 10-700 keV which was normalized to the 7.8-11 eV resonance integral; and a measurement[3] relative to H(n,p) from 1-20 MeV by Carlson and Patrick.

Experimental

The physical layout of the experimental area associated with the NBS 3 MV positive ion Van de Graaff is shown in Fig. 1. For these measurements, the source was neutrons produced by bombarding metallic lithium targets, nominally 40 keV thick, with pulses of protons 5-10 ns wide at a 1 MHz repetition rate. The target spot was defined by two collimators in the proton beam line which were also used in the neutron collimators alignment. Neutrons which were produced at angles other than 0^{o} were absorbed in a massive shield of paraffin loaded with Li_2CO_3. Machined inserts of lithium loaded polyethylene collimated the neutron beam to a cone with a half-angle of 4.3^{o}.

The black detector[4,5] which monitors neutron flux was located in a massively shielded enclosure 5.9 m from the target. A collimator with 5.067 cm^2 circular cross section defined the solid

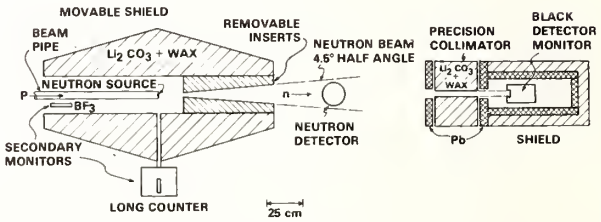

Fig. 1. NBS Monicored Neutron Flux Facility

angle subtended by the detector and insured that all the neutron flux is incident on the reentrant hole of the detector. This collimator and the source shield collimator were optically aligned to be coaxial with the proton collimators.

The energy and spatial characteristics of the beam have been extensively studied.[6] The spatial profile is flat to within 1%, consistent with the $^{7}Li(p,n)$ angular distribution in this energy range. Off-energy components of the beam have been investigated by using plastic and ^{6}Li loaded glass scintillators in conjunction with time of flight. These studies, conducted at the fission chamber distance (1.3 m), showed negligible contamination of the beam with energy degraded neutrons which might be generated in the shield and collimator. For example, for 600 keV neutrons, the components of background with energies between 100 and 220 keV and between 50 and 80 keV are less than 0.4% and 0.2% respectively. It is worth noting that neutrons below 100 keV are lost in the flat continuum of the time spectrum.

The efficiency of the flux monitor has been calculated using Monte Carlo techniques and the calculations were experimentally verified by the associated particle technique.[7] In addition, the flux measuring capability of this facility has been intercompared in the energy range of interest and found to be in agreement with those of other national standards laboratories.[8,9]

A multiplate fission chamber containing ^{235}U deposits totaling 170mg was used to detect fission events. The chamber was located in the neutron beam 1.3m away from the source such that the collimated beam did not illuminate the massive flanges of the chamber, but completely illuminated the fissionable deposits. The fission rate was monitored as the position of the chamber was radially varied by ± 5 cm in order to verify that the deposits were entirely within the neutron beam.

The data were simutaneously accumulated from black detector and fission chamber. Events were stored in two dual parameter arrays according to their respective pulse height and times of flight. Pulses were continuously injected into both sets of electronics to measure losses due to dead time and pile up.

Properties of the Large Multi-plated Fission Chamber

The geometry of the large multiplated fission chamber is shown in Fig. 2. This is the same chamber which was used at the NBS linac to measure the ^{235}U cross section in the 10-800 keV energy region using a hydrogen gas proportional counter as a flux monitor. The 10 deposits, which have a nominal thickness of 100$\mu g/cm^2$, were painted on both sides of 0.0025cm thick Al backings within a 10cm by 18cm area. Since there are 25% variations in the thickness at the ^{235}U deposits, it is essential to have the uniform neutron beam previously mentioned for the cross section measurements. The neutron scattering corrections for this chamber were calculated by Czirr[10] to be 0.2% per barn of Al and are of the order of 1% in the 0.2-1.2 MeV energy intervals.

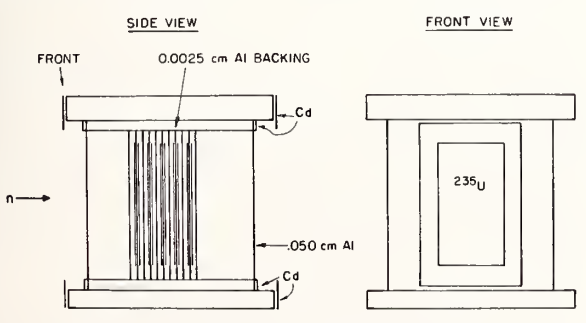

Fig. 2. Multiplate Fission Chamber

The ^{235}U content of the chamber was measured relative to the NBS reference deposits by means of thermal neutron fission counting at the NBS reactor. The 1.5% uncertainty in the mass measurement is due mainly to the uncertainties in scattering from the Pt backings of the reference deposits, the fragment absorption in the deposits, and the zero extrapolations of the fission spectra. The approximate 0.75% decrease in the NBS mass scale has been included in the mass determination.

The spectrum produced by 500 keV neutrons is shown in Fig. 3. The errors in the zero extrapolation and fragment absorption in the large chamber do not contribute to errors in the ^{235}U cross section since the same values are used in both the mass determination at the reactor and the cross section measurement at the Van de Graaff.

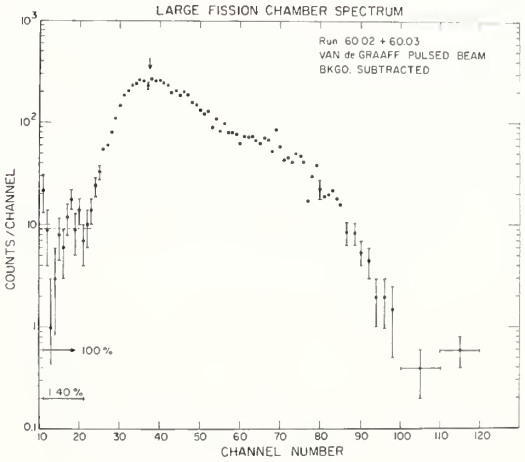

Fig. 3. Pulse Height Spectrum for Fission Chamber Events. En = 500 keV.

The contributions of α particle pile up and low energy neutron background were eliminated by using pulsed-beam and time-of-flight techniques. The timing spread produced by the 10cm extent of the fission chamber deposits did not permit resolution of the lower energy neutron group from the $^{7}Li(p,n)^{7}Be$ reaction for neutron energies greater than 700 keV. The contribution of these neutrons was deduced from the flux monitor measurements.

Response of the Black Detector

The quantity of interest from the black detector is the total number of neutrons incident upon it. We obtain this number from the background corrected pulse height spectrum by fitting the data with the Monte Carlo based calculation. Fitting parameters are neutron energy, a Poisson parameter which is related to photoelectron production at the photomultiplier cathode, and horizontal and vertical scale factors.

The neutron energy is fixed at the value determined by time-of-flight and the other parameters are permitted to vary until a best fit as determined by a χ^2 minimum is obtained. Over this energy range the Poisson parameter varied by less than 10% and the horizontal scale factor changes were consistent with changes in the electronics gains. A typical fit is shown in Figure 4.

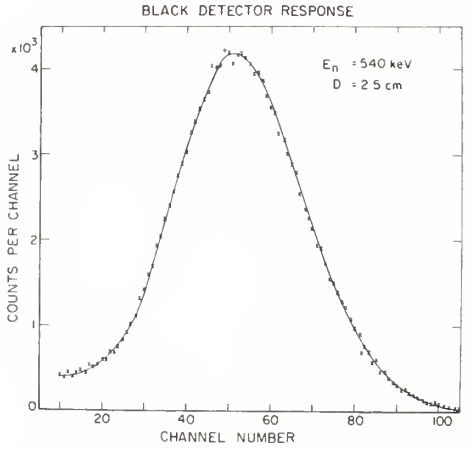

Fig. 4. Experimental (x) and calculated (solid curve) response for the black detector.

After obtaining such a fit, the analysis is done by forming the ratio $Y(i)/\varepsilon(i)$, the total number of black detector events above the ith channel divided by the Monte Carlo efficiency for that channel. This ratio, the total number of neutrons incident on the detector, varies by less than 0.1% (or the statistical error, if greater) over the low pulse height region. Due to this good agreement of calculation and experiment and the fact that the above ratio appears in the cross section calculation, the latter is insensitive to the particular values of $[Y(i), \varepsilon(i)]$ that are chosen.

The error associated with the total number of neutrons is a combination of the last error and the uncertainty in the determination of black detector efficiency. The calculation and associated particle determination of detector efficiency agreed to within the 1.5% accuracy of the experimental technique. Although the calculation may be more accurate than this, we choose to assign the conservative value derived from experiment to it.

The actual analysis of the data is complicated by the real spectrum of source neutrons. Fig. 5 shows a time-of-flight spectrum for 1013 keV neutrons generated by the black detector at 5.9 meters. The complex of lower energy neutrons due to $Li(p,n_1)$ events, to scattering in the target backing and to proton straggling in the surface contamination of the target are

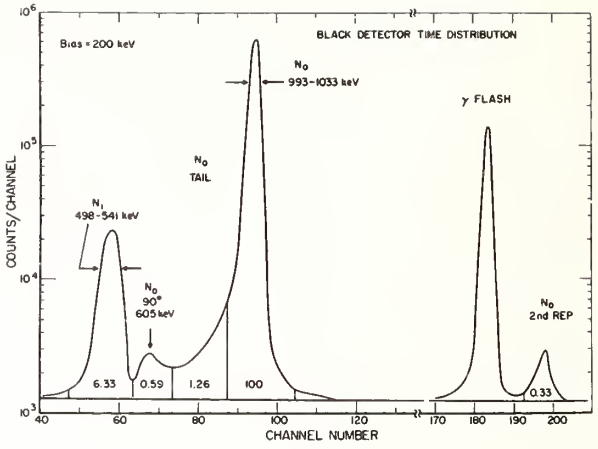

Fig. 5. Time-of-flight spectrum for the black detector. Relative contributions of several time domains are indicated.

completely unresolved in the relatively slower fission chamber at 1.2 m.

To correct for these off energy events, the black detector (time resolved) data are analysed as described above for a number of adjacent time domains in the vicinity of the n_0 peak. The average energy of each of these domains is determined by time of flight, and average fission cross sections at these energies are calculated using ENDF/B-V evaluated data. The number of fission chamber events are then reduced by a correction factor which is a function of the number of neutrons in each time domain and its associated cross section.

Corrections to Neutron Flux Measurement

Several corrections to the neutron flux measurement are made due to perturbations introduced by the collimator and the shield surrounding the flux monitor and by the air between monitor and fission chamber.

The collimator in front of the monitor is a brass walled cylinder with a diameter of 2.54 cm and length of 30 cm. Neutron transmission through the downstream walls of the collimator cause the effective area of the collimator to exceed the geometrical area by a factor of (1+k). This energy dependent correction, k, varies between 0.8 and 1.4% using the ENDF/B-IV total cross section values for the materials in brass. To check this correction, four different collimators, with diameters ranging from 2.54 to 4 cm were used to make flux measurements. The measurements agreed and were independent of collimator area.

The background which occurs at the same neutron flight time as the primary neutron energy group was measured by plugging the collimator hole. The results of these measurements, as shown in Fig. 6, vary between 0.2 and 1.0%.

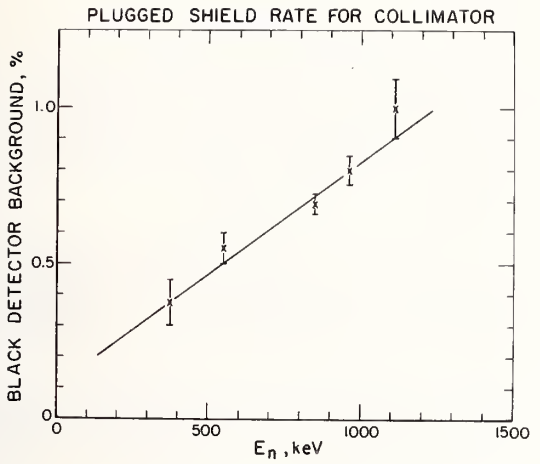

Fig. 6. Energy dependence of background that is unresolved in time from the primary neutron group.

The collimator in-scatter was measured by varying the distance between the collimator and the detector and found to be less than 0.2% at the 27 cm position used in the experiment. The increase in detector efficiency due to return scattering into the detector by neutrons which leak out of the detector was calculated to be less than 0.1%. This value was experimentally confirmed by removing the detector shield. Thus no correction for this effect was applied.

The air absorption between the fission chamber and the flux detector was calculated by using ENDF/B-IV values for the oxygen and nitrogen total cross section. The absorption varied between 4 and 8%. The assigned error is 10% of the absorption.

Calculation of the ^{235}U Fission Cross Section

The fission cross section is obtained from the following expression:

$$\sigma_{nf} = \frac{235.04}{0.6022} \frac{Y_{fc}}{Y_{bd}} \left(\frac{r}{R}\right)^2 \frac{A}{M} (1+k) \frac{\epsilon}{d} \frac{T_{air} T_{fc}}{S_{fc}}$$

where Y_{fc} is the net fission chamber yield
Y_{bd} is the net neutron monitor yield
A is the geometric area of collimator
(1+k) is the energy dependent variation of effective collimater area
r is the distance to the center of the fission chamber
R is the distance to the end of the collimator
M is the ^{235}U mass of the fission chamber
ϵ is the flux monitor efficiency
d is the dead time correction
T_{air} is the air transmission
T_{fc} is the transmission of half of fission chamber
S_{fc} is the scattering correction for fission chamber

The typical values of the parameters are shown in Table 1 along with their uncertainties. Each measurement required over 20 hours of beam time in order to acquire 10^4 events in the fission chamber. The dominant systematic errors in the measurement are the flux monitor efficency uncertainty and the fission chamber mass uncertainty. The errors in the table represent one standard deviation. We assume all errors to be statistically independent so that the total systematic error is 2.3%.

Cross Section Results

The final values of the ^{235}U cross section are shown in Fig. 7. The typical 2.8% error bars represent the total one standard deviation uncertainty which includes the statistical as well as the systematic errors. The solid line represents the ENDF/B-V evaluation, while the dashed curve indicates the earlier measurement done on the NBS linac using the same fission chamber. The latter result is a shape measurement which was normalized to a value of 242.7 $\pm$ 1.3 ev-b for the 7.8-11 eV integral. The approximately 3% uncertainties are not shown in order to simplify the figure.

The present absolute measurements agree with the earlier NBS measurements and are approximately 3% (one standard deviation) lower than the ENDF/B-V evaluation.

TABLE I

VARIABLES AND UNCERTAINTIES FOR CROSS SECTION CALCULATION

Quantity	Nominal Value	Uncertainty, %
r	133.13 cm	0.2
R	565.9 cm	0.07
A	5.067 cm^2	0.5
k	0.015	0.2
M	0.1713 gm	1.5
ϵ	0.92	1.5
d	1.0015	0.2
T_{air}	0.92	0.6
T_{fc}	0.92	0.2
S_{fc}	1.01	0.2
IN SCATT.	0.001	0.05
BACK SCATT.	0.001	0.2
N_1	0.03	0.05
N_o TAIL	0.02	0.2
FLUX UNIFORMITY		0.2
FLUX ( )	0.001	0.1
Y_{fc}	500/hr.	1.1
Y_{bd}	100/sec.	0.1
	TOTAL LINEAR	7.6
	QUAD	2.6

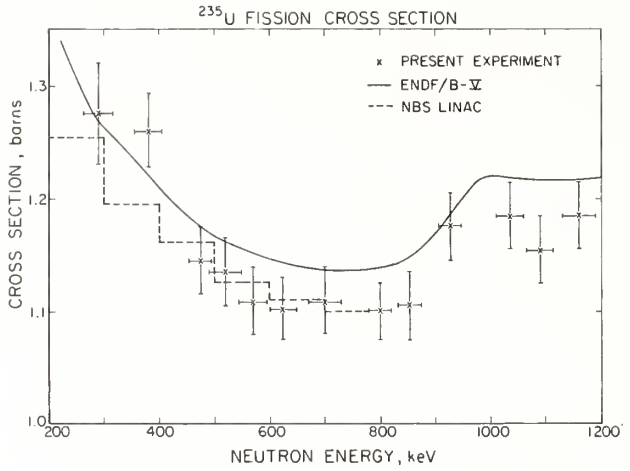

Fig. 7. Fission cross section for ^{235}U. This report (x), Ref. 2 (dashed curve) and ENDF/B-V evaluation (solid curve).

ACKNOWLEDGEMENTS

It is a pleasure to acknowledge the hospitality of the Los Alamos Scientific Laboratory to one of the authors (M. M. M.) and to thank the secretarial staff of LASL Group Q-1 for assistance in the preparation of this manuscript.

REFERENCES

1) H. T. Heaton II, J. A. Grundl, V. Spiegel, Jr., D. M. Gilliam and C. Eisenhauer, NBS Special Publication 425, Proceedings of a Conference on Nuclear Cross Sections and Technology, p. 266 (1975).

2) O. A. Wasson, Proceedings of NEANDC/NEACRP Specialists Meeting on Fast Neutron Fission Cross Sections, Argonne National Laboratory, ANL-76-90 and Supplement (1976).

3) A. D. Carlson and B. H. Patrick, Proceedings of an International Conference on Neutron Physics and Nuclear Data, Harwell, p. 880 (1978).

4) W. P. Poenitz, ANL-7915, Argonne National Laboratory (1972).

5) G. P. Lamaze, M. M. Meier and O. A. Wasson, NBS Special Publication 425, op. cit., p. 73, (1975).

6) O. A. Wasson, NBS Special Publication 493, op. cit., p. 115 (1977).

7) M. M. Meier, NBS Special Publication 493, Proceedings of a Symposium on Neutron Standards and Applications p. 221 (1977).

8) V. D. Huynh, NBS Special Publication 493, op. cit., p. 244 (1977).

9) K. C. Duvall, M. M. Meier, O. A. Wasson, and V. D. Huynh, J. Res. Nat. Bur. Stand. (U.S.) 83, No. 6, 555-562 (1978).

10) J. B. Czirr, Private Communication (1978).

^{237}Np FISSION CROSS SECTION MEASUREMENTS IN THE MeV ENERGY REGION

A. D. Carlson and B. H. Patrick*
National Bureau of Standards
Washington, DC 20234, U.S.A.

Measurements of the energy dependence of the ^{237}Np neutron fission cross section have been made from 1 to 20 MeV at the NBS neutron time-of-flight facility. These data were measured relative to the hydrogen scattering cross section with an annular proton telescope. The error for these shape measurements is 2-3% throughout the entire energy region.

[Cross section, fission, Neptunium-237, MeV neutrons, standard, Uranium-235]

Introduction

The ^{237}Np cross section has important applications in neutron dosimetry and has been considered as a cross section standard in the MeV energy region. This cross section has a relatively smooth energy dependence with a low effective threshold energy and can be utilized where a large flux of low energy background neutrons could cause a problem for some of the standards. Relatively few measurements have been made of this cross section. Most of the data which have been obtained are relative to the ^{235}U (n,f) cross section and thus are limited in accuracy by that standard. The present shape measurements are relative to the well determined hydrogen scattering cross section and extend from ~1 to 20 MeV.

Experimental Details

The data obtained during this investigation utilized two different experimental geometries and will be referred to in this paper as the low energy measurements (1-3 MeV) and the high energy measurements (3-20 MeV).

The data were obtained at the 60-m station of the NBS linac neutron time-of-flight facility. The low-energy measurements employed an unmoderated tungsten neutron target. For the high-energy measurements a tungsten converter (which was not seen by the detectors) and a beryllium target were used in order to increase the yield of high-energy neutrons and reduce the bremsstrahlung gamma flash. For all the measurements a 0.358 g/cm^2 boron overlap filter and a 0.318 cm thick piece of uranium for gamma-flash reduction were used. The linac was operated at a 720 pps rep rate with a pulse width of 20 ns.

An annular proton telescope similar to that described by Sidhu[1] was used at a flight path of 61.7 m to measure the energy dependence of the neutron flux. The NBS detector employs a slightly different geometry with a larger containing vessel and a tapered shadow shield in order to reduce the background. This detector is shown in Figure 1. For the low-energy measurements a polyethylene film of 0.31 mg/cm^2 was utilized. The high-energy measurements were made with three film thicknesses (2.08, 10.7, and 44.2 mg/cm^2) in order to cover the range from 3 to 20 MeV with satisfactory counting rate. The measurements made with these films utilized the same geometry. The data were then self-normalized with the weights of the polyethylene films. The background was determined from a series of measurements with and without the polyethylene film in place and with and without a tantalum cap over the Si(Li) detector. The tantalum cap was thick enough to stop 20 MeV proton recoils. The ambient background for all measurements was determined from a time window located just before the linac pulse. The net background for this detector was small, typically 2-3%. In Figure 2 the pulse-height distribution obtained with the detector for 3.2 MeV neutrons is shown. As is shown in this figure, the energy-dependent bias was set in the region where the net count rate per pulse height channel scatters around zero. The bias was large enough so that events from ^{12}C(n,p) and ^{12}C(n,α) reactions in the polyethylene foil were not counted. The intrinsic resolution of the 2 mm thick Si(Li) detector is better than 2% for ^{241}Am alpha particles, when the outer portion of its surface area is masked off. The pulse-height resolution observed in this experiment was dominated by the angular spread of the proton recoils and the energy loss of the protons in the polyethylene film.

A multiplate fission ionization chamber similar to that of Ref. 2 was used to measure the ^{237}Np fission rate. The chamber was located 63.65 m from the neutron producing target. The detector contained five fission foils with 100 μg/cm^2 deposits of ^{237}Np evaporated onto both sides of 0.0025 cm aluminum backings. The chamber was filled with a one atmosphere mixture of 96% Ar + 4% CO_2 counting gas. The wall of the chamber is .05 cm aluminum. The change in the fission-fragment losses in the films as a result of fission fragment angular distribution effects was calculated to be less than 0.1% over the energy range of this experiment. The fission-fragment angular distribution measurements of Simmons[3] were employed in these calculations.

For the ^{237}Np fission chamber only an ambient background was subtracted from the foreground data. The assumption of no time dependent background is based on a measurement[4] of a 0.2% background at 250 keV with a ^{235}U fission chamber located near the ^{237}Np chamber. The two fission chambers were of the same construction. It is expected that the percentage background will decrease with increasing neutron energy and should be smaller for ^{237}Np than for ^{235}U.

A typical pulse-height distribution obtained with this counter is shown in Figure 3. A single pulse-height bias was used for the neutron energy range of this experiment.

Electronics

The electronic setup for each detector was basically the same and is shown in Figure 4. Current preamplifiers were used so that the preamplifier could recover within one μs of the gamma flash and permit data to be obtained to above 20 MeV neutron energy. The only preamplifier pulses which were analyzed were those in the proper time window with amplitudes above a preset level. The preset level was set just above the noise. The time window was set to include the energy interval of interest and exclude the gamma flash. Both pulse height and time-of-flight data were accumulated with a computer and stored in a two-parameter format on a million word disk. The two-parameter data permitted the setting of the bias

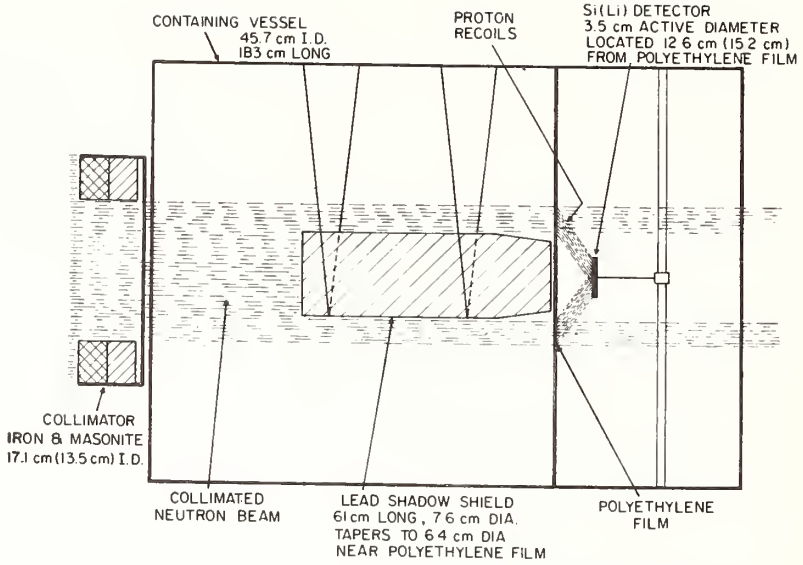

Fig. 1. Experimental setup for the annular proton telescope. Dimensions which are different for the low-energy measurements are shown in parentheses.

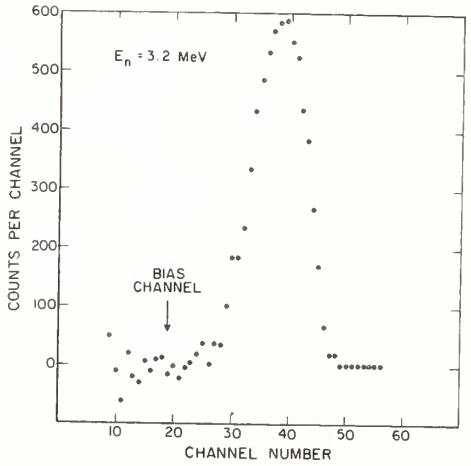

Fig. 2. Pulse-height distribution observed with the proton telescope for a neutron energy of 3.2 MeV.

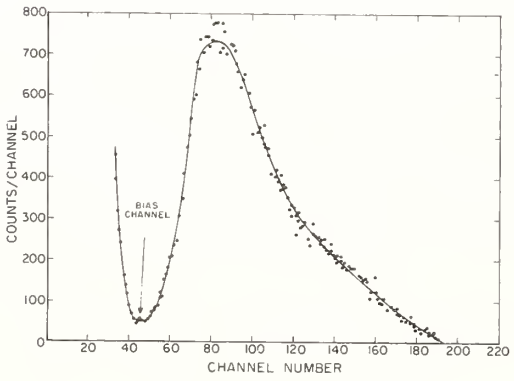

Fig. 3. Pulse-height distribution observed with the parallel plate fission chamber.

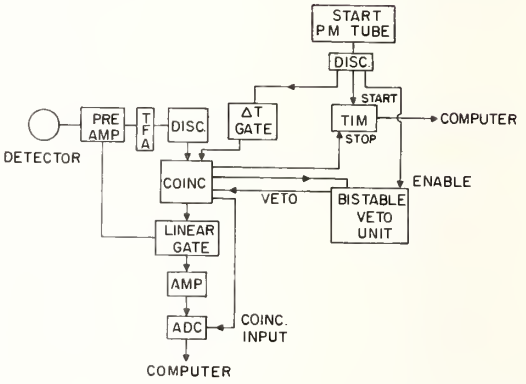

Fig. 4. Block diagram of the electronics employed for each of the detectors.

channels after the experiment had been completed. Tags were employed so that both detector systems could use the same ADC and time digitizer. The time-of-flight data were stored in 8 ns channels which were subsequently grouped into 32 ns bins for the data analysis. The data acquisition system was operated in a one-count-per-beam-pulse mode through the use of a veto unit. Due to the low count rate and the nearly equal flight paths for the two detectors, the dead-time corrections for the two detectors were nearly equal so no dead-time corrections were made to the data. This introduces an error of $<<0.1\%$.

The timing information from the proton telescope system required a walk correction resulting from the discriminator triggering at different times for small signals than for large signals. This correction was determined with a pulser adjusted to produce pulses of the same shape as those produced by an ^{241}Am α source. The signals from the pulser were varied in amplitude with a precision attenuator. The pulse-height energy scale was deduced from the linac measurements. The results of these measurements are shown in Figure 5. These corrections were used to shift the time-of-flight of the proton-recoil events.

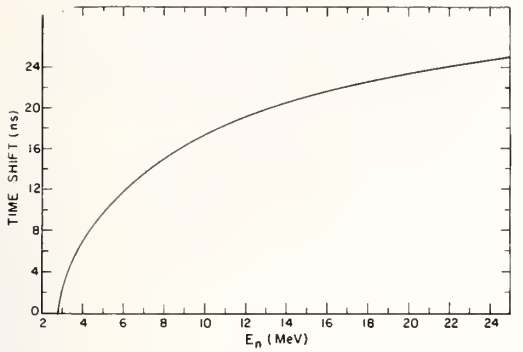

Fig. 5. Walk corrections for the proton telescope versus energy.

Measurements were made with both detectors to determine if gain shifts or baseline shifts were affecting the data acquisition system. These effects can occur if RF pickup or gamma flash adversely affect the electronics. The time dependence of such shifts was investigated from measurements made with and without a radioactive source near the detector with the linac on. The difference between the counting rates from these two runs is the constant rate due to the radioactive source modified by the gain or baseline shifts. For the ^{237}Np fission chamber, the measurement employed a ^{252}Cf neutron source placed near the detector but out of the linac beam. The results of that measurement are shown in Figure 6. The proton telescope measurement was made with an ^{241}Am α source placed between the lead shadow shield and the Si(Li) detector. It was located such that no proton recoils from the polyethylene film were intercepted by the source. The results of that measurement are shown in Figure 7. For both detector systems there is no indication of structure within the statistics of the measurements. A check of the peak positions in the pulse height distributions for the ^{237}Np measurements confirms the ^{237}Np result.

The neutron energy scale for both the proton telescope and the fission chamber was checked by measuring the position[5] of the 2.079 MeV resonance in carbon. A 5.08 cm thick carbon sample was used. The agreement in both cases was within one time-of-flight channel.

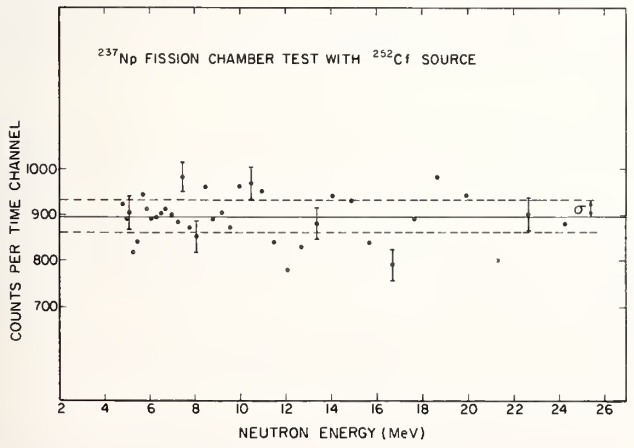

Fig. 6. Baseline and gain shift test for the fission chamber. The solid line near the center of the figure is the constant count rate from the ^{252}Cf neutron source assuming no shifts.

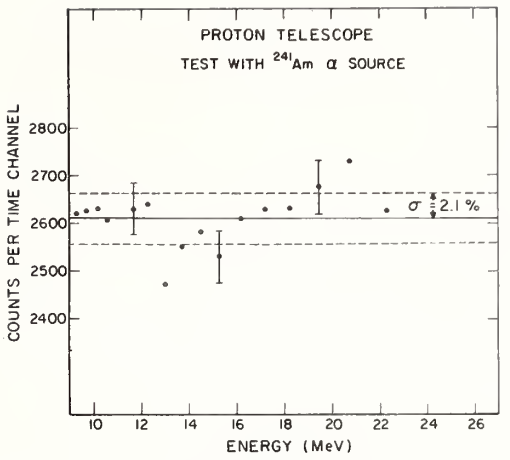

Fig. 7. Baseline and gain shift test for the proton telescope. The solid line near the center of the figure is the constant count rate from the ^{241}Am α source assuming no shifts.

Data Analysis and Comparisons with Previous Measurements

The shape of the neutron flux was obtained by dividing the count rate vs time-of-flight data from the proton telescope by the hydrogen scattering cross section, taking into account the angular range of the proton recoils. The hydrogen cross section and angular distribution data were taken from the analysis by Hopkins and Breit.[6] The fission chamber data were then divided by the flux which had been interpolated to the same energy mesh. Many separate runs were combined for each polyethylene film thickness. For the high-energy measurements the data for the different film thicknesses were combined using only those regions where a bias channel could be set where the net count rate per channel scatters around zero. The high-energy data were normalized to the low-energy data at 3 MeV.

The statistical uncertainty of the measurements is 2-3%. The systematic errors considered are transmission corrections (<0.1%), hydrogen scattering angular distribution (0.2%), walk correction (0.5%), fission fragment angular distribution (<0.1%), deadtime correction (<<0.1%), and fission chamber background (<0.1%). Thus it is believed that the total error is ~2-3%.

Simultaneous with these measurements of the ^{237}Np fission cross section, measurements were also made of the ^{235}U fission cross section.[4] The ^{237}Np/^{235}U fission ratio was formed from these data sets and for purposes of comparison normalized from 1-2 MeV to the measurements of Behrens.[7] The present low energy ratio measurements are shown in Fig. 8 compared with those of Behrens[7] and Stein.[8] The shape agreement among these data sets is reasonably good. The Stein data disagree somewhat in normalization with those of Behrens. The present high energy ratio measurements compared with those of Behrens are shown in Fig. 9. Significant differences are evident in certain energy regions, particularly near ~6, 10 and 16 MeV.

In order to make comparisons with other ^{237}Np cross section measurements, a normalization must be established for the present shape measurements. The normalization was deduced from the Behren's ^{237}Np/^{235}U fission cross section ratio averaged from 1 to 2 MeV combined with the ^{235}U fission cross section[4] averaged

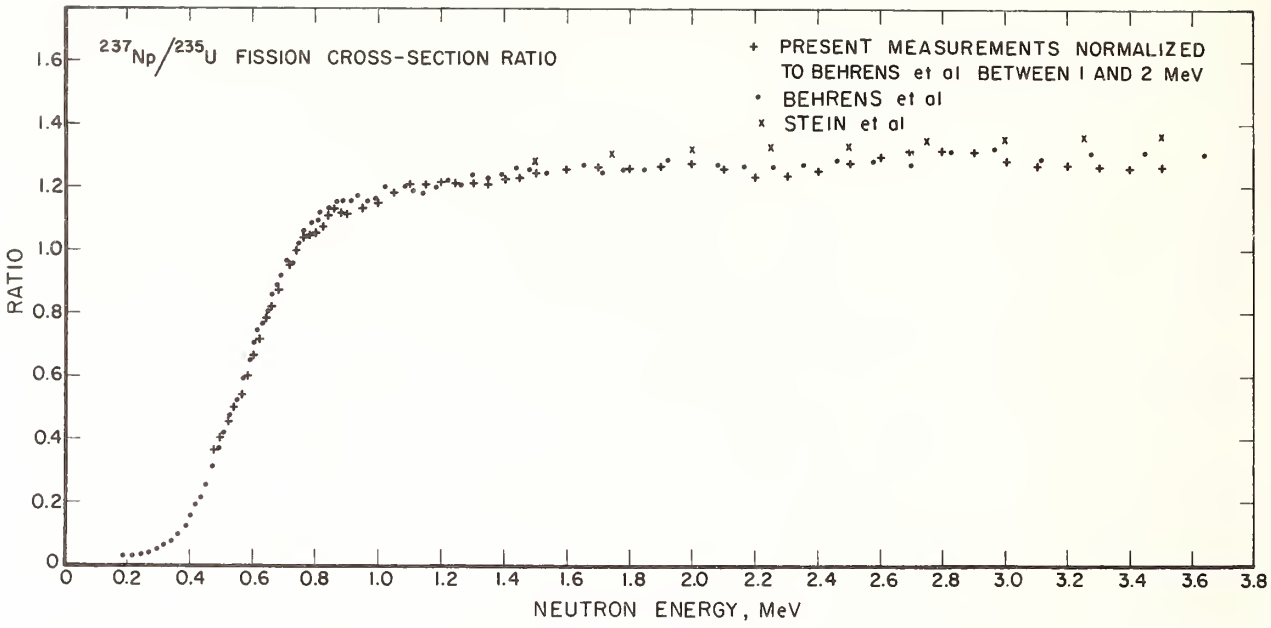

Fig. 8. Comparison of the present low energy measurements of the $^{237}Np/^{235}U$ fission ratio with those of Behrens et al.[7] and Stein et al.[8]

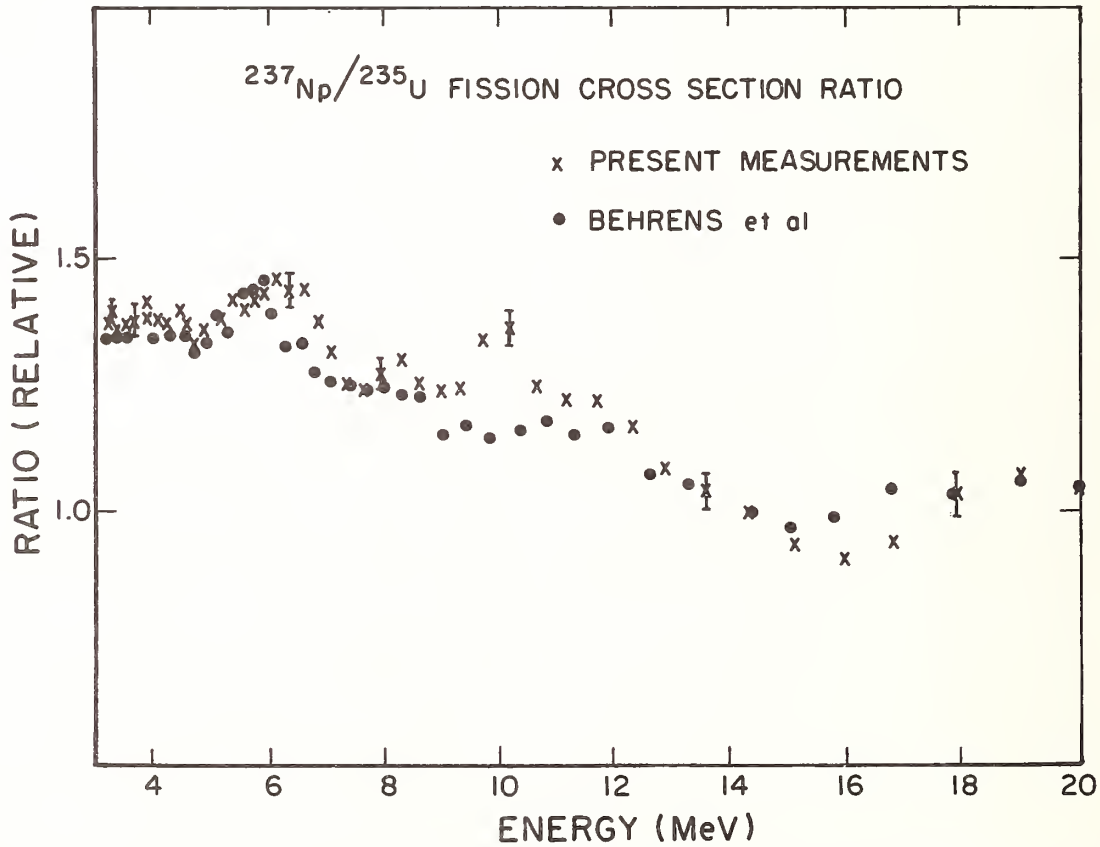

Fig. 9. Comparison of the present high energy measurements of the $^{237}Np/^{235}U$ fission ratio with those of Behrens et al.[7]

from 1 to 2 MeV. The present measurements with this normalization are shown in Fig. 10. Also shown are some of the ^{237}Np measurements which cover a relatively large energy interval and can provide shape comparisons with the present measurements. The measurements of Henkel[9], which employed a long counter for neutron flux measurement, agree reasonably well with the present measurements from ~3 to 8 MeV; however, the measurement at ~14 MeV disagrees significantly with the result from the present investigation. The linac measurements of Plattard[10] lie systematically higher than the present measurements but have a similar shape. The measurements of Jiacolettil[11] have a different shape than the present measurements above ~5 MeV. The normalization procedure adopted for the present measurements does not agree with ENDF/B-V.[12]

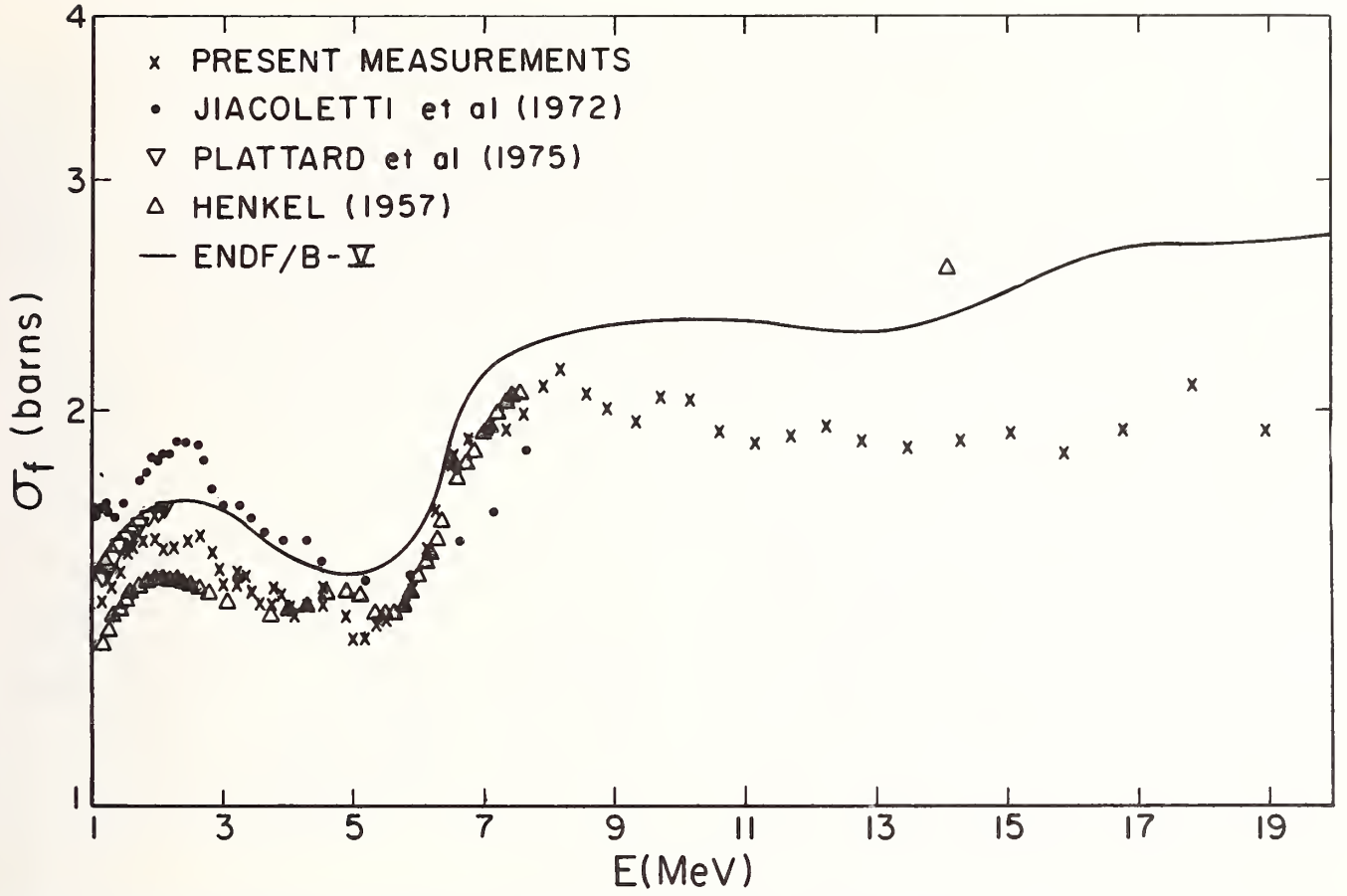

Fig. 10. Comparison of the present measurements of the ^{237}Np fission cross section with those of Jiacoletti et al.,[11] Plattard et al.,[10] and Henkel.[9] Also shown is the ENDF/B-V evaluation.

The shape agreement is reasonably good up to ~8 MeV, but ENDF/B-V is consistently high above that energy.

Summary

The present measurements provide a determination of the shape of the ^{237}Np fission cross section relative to the hydrogen scattering cross section from 1-20 MeV with small systematic errors and statistical uncertainties of 2-3%. The agreement with previous measurements is fair at low neutron energies and worse at higher energies. Unfortunately the poor data base for ^{237}Np(n,f) implies a considerable effort if it is to be used as a cross section standard.

References

*Guest Worker from UKAEA, Atomic Energy Research Establishment, Harwell, United Kingdom.

1. G. S. Sidhu and J. B. Czirr, Nucl. Instrum. Methods, 120, 251 (1974).
2. J. B. Czirr and G. S. Sidhu, Nucl. Sci. Eng., 58, 371 (1975) and Nucl. Sci. Eng., 57, 18 (1975).
3. J. E. Simmons and R. L. Henkel, Phys. Rev., 120, 198 (1960).
4. A. D. Carlson and B. H. Patrick, Proceedings of An International Conference on Neutron Physics and Nuclear Data for Reactors and Other Applied Purposes, Harwell, U.K., 1978, Pub. by OECD Nuclear Energy Agency, p. 880.
5. H. T. Heaton, II, et al., Nucl. Sci. Eng., 56, 27 (1975).
6. J. C. Hopkins and G. Breit, Nucl. Data Tables, A9, 137 (1971).
7. J. W. Behrens et al., Measurement of the Neutron-Induced Fission Cross Section of ^{237}Np Relative to ^{235}U Fission from 0.02 to 30 MeV, UCID-17370, Lawrence Livermore Laboratory, Livermore, CA, Jan. 19, 1977.
8. W. E. Stein et al., Proceedings of A Conference on Neutron Cross Sections and Technology, Washington, DC, 1968, ed. by D. T. Goldman (NBS Special Publication 299, 1968), p. 627.
9. R. L. Henkel, USAEC Report LA-2122, Los Alamos Scientific Laboratory, June 1957.
10. S. Plattard et al., Nucl. Sci. Eng., 61, 477 (1976).
11. R. J. Jiacoletti et al., Nucl. Sci. Eng., 48, 412 (1972).
12. ENDF/B-V, Report ENDF-201, edited by R. Kinsey, available from the National Nuclear Data Center, Brookhaven National Laboratory, Upton, NY (to be published).

ABSOLUTE FAST FISSION CROSS SECTION MEASUREMENTS ON ^{237}Np

D. J. Grady, G. T. Baldwin, and G. F. Knoll
The University of Michigan
Ann Arbor, Michigan 48109, USA

We have extended our series of absolute fission cross section measurements to ^{237}Np at 770 and 964 keV. Nearly monoenergetic fluxes of neutrons were obtained using La-Be and Na-Be photoneutron sources. These small, spherical sources were calibrated in the U of M manganese bath facility, using NBS-II as a standard. Dual target foils were used in symmetric orientation to allow accurate calculation of the average neutron flux magnitude. Deposit masses were determined by microbalance weighings. Fission fragments passing through limited solid angle apertures were recorded on polyester track etch films. Preliminary results give values of 1.191 and 1.365 barns at 770 and 964 keV, respectively. Final error estimates are expected to be between 2 and 3%.

(Absolute fission cross sections, ^{237}Np, photoneutron sources, manganese bath)

Introduction

The establishment of a reliable ^{237}Np fission cross section standard requires the accurate determination of benchmark absolute fast fission neutron cross sections. These measurements help serve to anchor cross section shape results produced by other methods. In particular the smooth threshold-like behavior of this fission cross section makes absolute measurements in the 500 to 1000 keV range quite important. We have used existing facilities at the University of Michigan for performing two such absolute measurements using La-Be and Na-Be photoneutron sources with respective energies of 770 and 964 keV. Together with the established data analysis procedures and confidence acquired through past experience with similar measurements, we expect these results to provide a valuable contribution to the ^{237}Np fission cross section data base.

The experimental techniques used to measure absolute fission cross sections at the University of Michigan have been previously documented in earlier reports.[1,2,3] For completeness, however, a brief summary of our procedure is reviewed in the next section. Following sections will discuss in more detail those aspects of the measurements peculiar to the ^{237}Np isotope.

Overview of Experimental Procedure

The photoneutron source is activated in the thermal neutron flux of the University of Michigan Ford Nuclear Reactor. The source is then immediately transferred by remote handling to the source well of a cadmium-lined brass cylinder containing the fission targets and detectors under vacuum. The experimental containment package is then suspended in the center of a shielded, low albedo room for the duration of the target irradiation.

Two 1 mg/cm^2 $^{237}NpO_2$ target foils positioned in dual "compensated beam" geometry, each with an associated polyester track etch detector defined by a limited solid angle aperture, comprise the fission rate determination apparatus illustrated in Figure 1.

After an exposure period sufficient to acquire 1% counting statistics (17 to 65 hours), the photoneutron source is removed from the experimental package and placed in the manganese bath. Comparison of the induced manganese activity from the photoneutron source with that from our reference ^{252}Cf spontaneous fission neutron source yields the absolute photoneutron source strength.

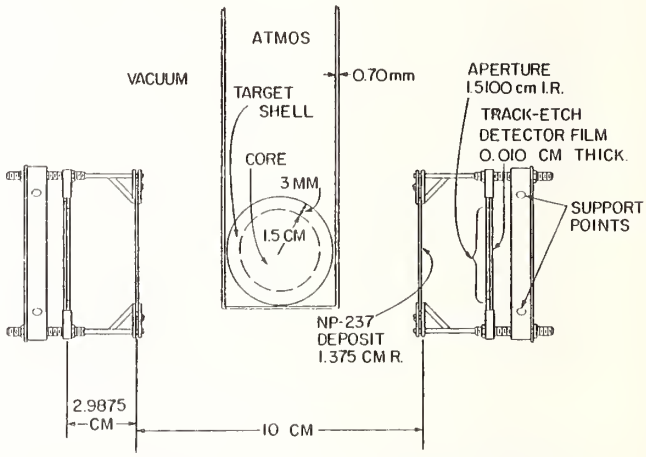

Fig. 1. Fission rate determination apparatus

The latent fission tracks are developed to diameters of about 14 μm by etching the films in potassium hydroxide. The films are then gridded to 1 mm x 1 mm squares on an index bench and then counted manually with the aid of a binocular microscope.

Photoneutron Sources

Activation

The monoenergetic photoneutron sources used in this work are the La-Be (neutron energy of 770 keV) and the Na-Be (neutron energy of 964 keV) spheres described by Davis, et. al.[4] The sources are activated in a flux of 10^{13} $n/cm^2/sec$ to produce the ^{24}Na and ^{140}La core activities. Gammas emitted from the core region interact by the (γ,n) reaction in the surrounding beryllium shell to liberate neutrons. Typical neutron strengths of 5x10(7) and 1.5x10(6) n/sec were thus obtained for the Na-Be and La-Be sources, respectively.

Spectrum Modeling

The VES Monte Carlo computer code was used to determine the energy and angular distributions of photoneutron emission, by modeling the neutron and gamma transport within the multi-region photoneutron source. This program was adapted from an original version described by Vesely[5], and subsequently developed by several workers at the University of Michigan.

The neutron energy spectra obtained by the program for the La-Be and Na-Be sources are shown in Figure 2 and Figure 3. They are used in the neutron spectrum correction factor which is discussed in the section "Significant Correction Factors". The neutron emission distribution as a function of the angle with respect to the source surface normal is used in the calculation of the average scalar flux at the fission targets.

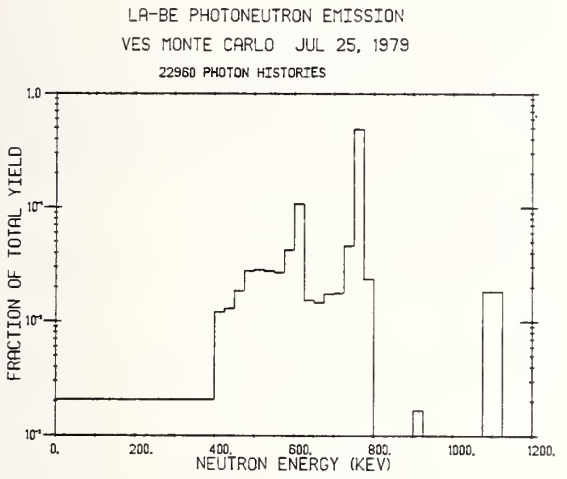

Fig. 2. La-Be photoneutron energy spectrum

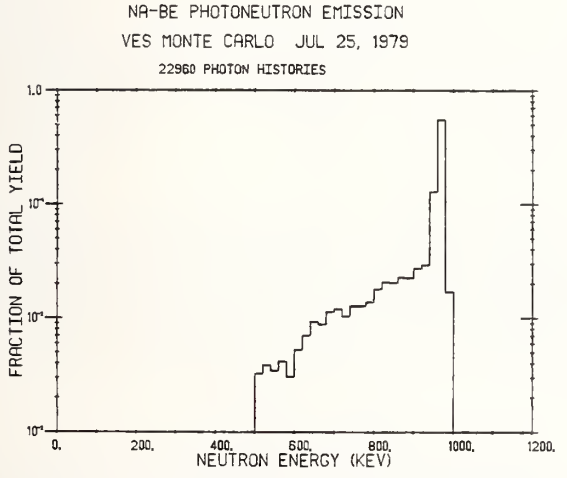

Fig. 3. Na-Be photoneutron energy spectrum

Neutron Source Strength

Following the ^{237}Np foil irradiation, the photoneutron source is transferred to a continuously sampled manganese bath. A time history of the source neutron strength is obtained by detecting a fixed fraction of the induced manganese activity. A computer program unfolds the time dependence of this activation history to obtain a relative indication of neutron strength at the time of source insertion in the bath.

This same procedure is duplicated before and after each photoneutron run using the reference ^{252}Cf spontaneous fission neutron source. These results, together with the previously calibrated ^{252}Cf source strength on 12/27/75 (1.0417×10^7 ±0.58% n/sec) and half life (2.643 ± 0.005 years) yield the absolute photoneutron source strength.

Past measurements at this laboratory[1,2,4] have made reference to the secondary national neutron standard NBS-II. This source was not available for ^{237}Np measurements. A two year history of ^{252}Cf vs. NBS-II cross-calibrations was used to obtain the above-stated neutron strength and associated error. Our experimentally-determined Cf half life (2.663 ± 0.051 years) agreed well with the value quoted above to add further credence to our source strength determination.

Target Foils

Description

The target foils were prepared by the Oak Ridge National Laboratory. They are approximately 1 mg/cm^2 vapor deposits of $^{237}NpO_2$ of radius 1.375 cm on 2.0 cm radius, .0254 cm thick platinum backings. Isotopic purity of the neptunium was quoted as 99.99% ^{237}Np with trace neptunium and plutonium impurities.

Mass Determination

Consistent target mass determination has yet to be made to within acceptable uncertainty. Gravimetric results from ORNL quoted with approximately ±10 μg error were not confirmed by independent mass assays done by alpha counting at the National Bureau of Standards. The NBS results state ±300 μg uncertainty primarily due to alpha energy spectrum degradation by the relatively thick foil deposits, such that short lived impurity alphas cannot be accurately discriminated from the longer lived primary alphas of ^{237}Np. Further work is being done with thinner deposits to better determine the activity ratios for the ^{237}Np and its impurities.

The masses used in the analysis here are those of the ORNL weighings.

Irradiation Geometry

The benefits derived from using the compensated beam geometry in conjunction with limited solid angle detection have been discussed in previous papers.[3,4] The total fission rate determined from the two track detectors is far less sensitive to the exact photoneutron position. This technique is considerably less susceptible to spacing measurement errors and their propagation through flux and detector efficiency calculations.

Two fission runs were performed for each neutron source at deposit-deposit spacings of approximately 10 cm and 14 cm. The two independent measurements permit the evaluation of a systematic room return component to the neutron flux (its relative contribution would be expected to be higher at larger source-target spacings). No such component was observed (within experimental error), as was expected, due to the threshold-like behavior of the fission cross section. Hence, no explicit correction was made and the results of the two runs were simply averaged.

Flux and Detector Efficiency

A computer code calculates the scalar neutron flux and aperture detection efficiency at each of eleven points on the target foil, evenly spaced along a radius in increments of equal area rings. The point flux is evaluated by an integral of the photoneutron emission angular distribution over the source surface.

The efficiency for detection of fission events at these same points is an anisotropy-compensated numerical integration over the aperture acceptance solid angle. The product of the point-wise flux and efficiency values is then numerically averaged over the target foil and weighted by the deposit density distribution.

Fission fragment angular anisotropy literature data for ^{237}Np are scarce. For a fission fragment emission anisotropy described by the function $1 + A(\cos^2\theta)$, where θ = polar angle of fragment emission with respect to the incident neutron, we find values of A = 0.10, 0.17 for La-Be and Na-Be, respectively.[6] We are currently planning to do our own determination of these two anisotropies at the Argonne National Laboratory Tandem Dynamitron.

Fission Rate Determination

The fission fragment detectors used were polyester track etch films. Track etch detectors were chosen for their high intrinsic efficiencies for fission fragments (~100%) and inherent insensitivity to high gamma backgrounds. After exposure these films are etched in 6.0 N potassium hydroxide at 68° C for about four hours resulting in track sizes of approximately 14 μm. The films are next gridded and finally hand counted using a binocular microscope. The films are counted by different individuals until the results agree to within 0.5%.

Significant Correction Factors

Several correction factors are applied to various aspects of the data analysis. The major factors are compiled in Table I and are briefly discussed here.

Manganese Bath

The correction factor is source dependent and is the sum of several competing loss and gain mechanisms. These include source and dry well self-absorption, leakage of neutrons from the bath, neutron streaming losses from the dry well opening, photoactivation of the natural deuterium content of the bath and parasitic fast neutron capture by ^{16}O(n,α) and ^{32}S(n,p) reactions. The values in the table are for the La-Be and Na-Be sources, respectively.

Neutron Inscatter

Inscatter from the components of the experimental package acts to increase the flux at the target. Scattering from the containment package, cadmium shield and detector assemblies are handled using a point source-point scatterer-point target approximation and scattering is treated isotropically. A Monte Carlo program was written to calculate the scattering from the target backings and target holders.

Neutron Spectrum

The measured cross section must be modified to account for the finite neutron energy distribution of the photoneutron sources. The correction factor is obtained by weighting the ENDF/B-IV fission cross section shape with the Monte Carlo-determined neutron energy spectrum. This factor is quite large because of the strong variation of cross section with energy in this region of the ^{237}Np fission cross section.

Table I. Correction Factors (in %)

	770 keV	964 keV
Manganese Bath	-0.333	-0.555
Neutron Inscatter		
- 10 cm spacing	+4.100	+3.250
- 14 cm spacing	+5.390	+4.380
Neutron Spectrum	+17.350	+6.860

Results and Comparisons

The results of our determination of the absolute fission cross section measurements along with comparable ENDF/B-IV values are listed in Table II.

Table II. Absolute ^{237}Np Fission Cross Sections (barns)

E_n (keV)	This Work	ENDF/B-IV
770	1.191	1.182
964	1.365	1.465

We emphasize that these are preliminary results. Final results with error bars will be published pending completion of more accurate mass determination, measurement of the fission fragment anisotropies and recalibration of our reference spontaneous fission source (^{252}Cf) with the NBS-II neutron standard.

Acknowledgements

We wish to thank the Department of Energy for their support of this work. We wish also to thank William Moshier and Donald McKeon for their assistance in both the experimental and analytic aspects of these measurements.

References

1. D. M. Gilliam and G. F. Knoll, "An Absolute Determination of the ^{235}U Fission Cross Section at 964 keV", Trans. Am. Nuc. Soc. 15, 946(1972).

2. J. C. Robertson, M. C. Davis, J. C. Engdahl and G. F. Knoll, "The Fission Cross Section of ^{235}U at 265 keV", Trans. Am. Nuc. Soc. 21, 503(1975).

3. G. F. Knoll, "Absolute Fission Cross Section Measurements Using Fixed Energy Neutron Sources", NBS Special Publication 493.

4. M. C. Davis, G. F. Knoll and J. C. Robertson, "Absolute Measurement of ^{235}U and ^{239}Pu Fission Cross Sections With Photoneutron Sources", Proc. of the NEANDC/NEACRP Specialists Meeting, June 28-30, 1976, ANL (NEANDC(US)-199/L) p.225.

5. Vesely,F. Bensch and H. Hejtmanek, "A Monte Carlo Program for the Determination of the Energy Spectrum of Photoneutron Sources", Nukleonik, 11, 300(1968).

6. B. M. Gokhberg, G. A. Otroshchenko, and V. A. Shigin, "Effective Fission Cross Sections of ^{229}Th, ^{230}Th, and ^{237}Np, and Anisotropic Fission Cross Sections of ^{230}Th and ^{237}Np", Proc. of the Tashkent Conference on the Peaceful Uses of Atomic Energy, V.1, 59, (AEC-tr-6398).

THE CROSS SECTION FOR THE $^{56}Fe(n,p)$ REACTION FOR 14.73 MeV NEUTRONS

by T. B. Ryves and E. J. Axton

National Physical Laboratory

Teddington, Middlesex

TW11 OLW, UK

A value for the cross section for the $^{56}Fe(n,p)^{56}Mn$ reaction for 14.73 Mev neutrons has been derived from a critical evaluation of measurements performed as part of an international comparison of fast neutron flux density organized by the Bureau International des Poids et Mesures between 1974 and 1978.

[$^{56}Fe(n,p)$ cross section, 14.73 MeV, evaluation]

Introduction

The international comparison of fast neutron flux density organized by the Bureau International des Poids et Mesures (BIPM) between 1974 and 1978 is now concluded [1]. One part of the comparison in which five laboratories participated was the 14 MeV comparison using natural iron foils as the transfer method. These laboratories were Bureau Central de Mesures Nucleaires, Geel (BCMN), Electrotechnical Laboratory, Tokyo (ETL), Institut de Metrologie D. I. Mendeleev, Leningrad (IMM) and the National Physical Laboratory, Teddington (NPL). Sets of three foils of pure natural iron 2.54 cm in diameter and 80 mg cm $^{-2}$ in thickness were circulated to each participating laboratory who then irradiated the foils in their standard 14 MeV neutron flux. The basis of the comparison was the induced $4\pi\beta$ count rate produced in the foils, corrected to saturation and normalized to unit neutron fluence. At the suggestion of Dr F G Perey the data have been subjected to a critical evaluation with a view to deriving a value for the cross section for the $^{56}Fe(n,p)^{56}Mn$ reaction at the neutron energy used in the intercomparison. Although the energy originally specified for the intercomparison was 14.80 MeV, subsequent investigations on the part of some of the participating laboratories indicated that the actual measurements were performed at slightly different energies. It was therefore necessary to make small corrections to the assumed neutron energies in order to obtain a consistent set of data. This further necessitated making corrections to the estimations of neutron flux density. Finally the normalized foil activities were corrected to a common 'median' energy using an assumed slope for the variation with neutron energy of the iron cross section.

Evaluation of the date

The results of the participating laboratories were presented in separate reports to BIPM, together with more detailed reports [2-9], wherein the methods of determining the neutron flux density were discussed. The main problems of the evaluation have been to unify the results by ensuring consistency in (a) the neutron energies at which measurements were made (b) the corrections applied to determine the neutron flux density and foil activity, and (c) the uncertainties at 1σ confidence level, and also to specify the covariances which exist between measurements.

Neutron Energy

The neutron energies claimed by the participating laboratories, and the consistent energies used in the evaluation, are given in Table I. It was noted that ETL and NPL used almost identical conditions for obtaining neutrons (a 130 keV deuteron beam striking a new $\sim$270 μg cm^{-2} Ti-T target, with measurements at 0° to the direction of the beam), although these laboratories quoted quite different neutron energies. However a recent measurement under these conditions at NPL [10], using a Si surface barrier detector, yielded a neutron energy of 14.70 MeV, and the ETL calculated estimate was 14.75 MeV, so a compromise value of 14.72 MeV was taken for these two laboratories as a basis for this evaluation. On this basis the BIPM neutron energy at an angle of 27° for a thicker, 550 μg cm^{-2} Ti-T target using 140 keV deuterons was 14.63 MeV. The IMM neutron energy at an angle of 8° for a 250 μg cm^{-2} Ti-T target using 140 keV deuterons became 14.72 MeV, much below their quoted energy of 14.80 MeV. (However it was noted that in a subsequent and apparently similar set of runs in the intercomparison using a fission counter as transfer instrument their quoted energy was reduced to 14.76 MeV). The BCMN value of 14.80 MeV was unaltered, since they used much higher energy deuterons of 650 keV and neutrons at 70° to the direction of the beam.

We have assumed that each laboratory actually made measurements at the evaluation neutron energies E_n shown in Table I. In the case of the associated particle measurements (BIPM, ETL, IMM) this involved altering the solid angle conversion factors J as originally used to the appropriate corrected factors J', where the neutron flux density is $\emptyset \alpha J$. We have assumed that J' can be evaluated without appreciable error at the mean neutron energy, rather than by averaging J over the target neutron spectrum, which is not very well known. The foil activity A ($\alpha\sigma'_{Fe}$, the total ^{56}Mn production cross section) was then further corrected to the median energy of 14.73 MeV using the relation derived from ref.16 that $d\sigma'_{Fe}/dE_n = (-0.0123 \pm 0.0006)\%$ keV^{-1}. These corrections are listed in Table II.

In the case of the proton recoil telescope measurement at NPL, where $\emptyset \alpha 1/\sigma_H$ and σ_H is the

180° neutron-proton differential scattering cross section, $A/\emptyset$ was adjusted by a factor σ'_H/σ_H to correspond to 14.72 MeV, and then by correction of σ'_{Fe} to 14.73 MeV as before. Some of the IMM measurements employing a stilbene crystal also depended on the hydrogen scattering cross section, and these results were adjusted in a similar fashion.

The BCMN foil activity was adjusted from 14.80 to 14.73 MeV using $d\sigma'_{Fe}/dE_n$ as above.

Other corrections

In the course of the evaluation the NPL intercomparison measurements were reviewed and a correction was introduced relating to standard iron foils which were used to monitor the fluence. No other significant corrections to the data were made, since so far as could be ascertained, all the participating laboratories made equivalent corrections in obtaining the neutron flux density. There was a lack of detailed information in some cases, especially on the values of J and σ_H used in obtaining the neutron flux density. Table I shows the input data taken from Table 2e of reference 1, and also the revised data after the evaluation.

Uncertainties and correlations

Systematic uncertainties were generally estimated by the participating laboratories (except for IMM) at approximately the 99% confidence level, and then halved to give 1σ levels. This recipe is a compromise between the assumptions (a) that the uncertainty has infinite degrees of freedom and a Gaussian probability distribution, when the factor would be about 0.4, and (b) that the uncertainty has a rectangular probability distribution, when the factor would be about 0.6. The 1σ uncertainties for the participating laboratories are listed in Table III. These uncertainties are mostly based on their reports to BIPM, apart from those due to our evaluation of the uncertainty in neutron energy (see below). All the 1σ systematic uncertainties were finally combined by adding in quadrature.

It is clear that the proton recoil telescope measurements (BCMN, NPL) and the stilbene crystal results (IMM) are correlated through σ_H. The adopted energy of the experiments (see the previous section) had an estimated 3σ uncertainty of $\pm$ 60 keV, corresponding to a 1σ uncertainty of $\pm$ 30 keV, which mostly affected the associated particle methods (BIPM, ETL, IMM). It was assumed that this energy uncertainty was 70% correlated between BIPM, ETL, IMM and NPL, the correlation of NPL being of the opposite sign to the other laboratories. In the case of IMM, who used both associated particle and stilbene crystal methods for measuring neutron flux, we have assumed that their final result was an average value of the three methods.

Analysis of data and derivation of cross section

One method to derive a reaction cross section from the intercomparison results would be to convert each of the 18 intercomparison measurements into a cross section value and to derive a weighted mean value after giving due attention to the complex correlations between the measurements of laboratories using the same or similar methods, and between measurements using the same foils at different laboratories. However, this method does not at the same time demonstrate clearly how each laboratory's measurements stand in relation to the others. The least squares technique described below is therefore preferred since it yields more information, and the covariance problems are easier to handle.

The first stage of the analysis is to derive optimum values for the foil activities per unit neutron fluence using the least-squares technique described by Hayes and Axton[11], which reduces the problem to the choice of only one arbitrary zero. In this example a set of six iron foils were provided as transfer instruments. Each of five laboratories irradiated some or all of the samples in its own absolutely calibrated field of 14 MeV neutrons, and the basis for the intercomparison is the saturation β-particle counting rate induced in the foils by unit neutron fluence.

The output data consists of the systematic error, or bias, (x), made by each laboratory and the optimum value for each foil activity, together with a covariance matrix of random errors. These estimates are necessarily relative to the bias of one particular laboratory which is taken to be zero. There is no way to determine the true origin, $(\bar{x})$, and the best choice will depend on the particular circumstances. The most likely position of the true zero is that which gives a weighted mean of zero for the x's. It is the difficulty associated with the determination of the weights for the measuring laboratories which presents the greatest problem in this type of analysis.

It was decided that the weight for each laboratory should be derived from the variance-covariance matrix, (Table IV) derived in the previous section for the systematic uncertainties in the value of $A/\emptyset$. It will be recalled that only the random uncertainties in the value of $A/\emptyset$ were used to determine the weights for the Hayes-Axton analysis.

The calculated biases of the laboratories, (x), and best values of $A/\emptyset$ for the foils are given in Table V.

The second stage of the analysis is to derive a cross section value from each optimum foil activity according to the equation

$$\sigma'_{Fe} = \frac{A}{\emptyset} \frac{M}{LaM} \frac{1}{E\beta(1+k)}$$

where σ'_{Fe} is the cross section, A is the saturated β activity, $\emptyset$ is the neutron flux density, M is the atomic weight, L is Avogadro's number, a is the isotopic abundance of ^{56}Fe and m is the mass of the foil. $E\beta$ is the β efficiency N_c/N_γ as determined by $4\pi\beta\gamma$ coincidence counting at NPL, where N_c and N_γ are the coincidence and γ count rates. k is a small correction which combines the effects due to the efficiency of the β counter to γ rays and the complex decay scheme of ^{56}Mn. A small correction was then made to allow for the production of ^{56}Mn by the $^{57}Fe(n,np+pn+d)^{56}Mn$ reactions by reducing the cross section by (0.13 ± 0.04) %.

The conversion of the activities into cross section values introduces a further uncertainty due to that in the β particle counting efficiency,

which is partly correlated and partly uncorrelated between different foils (see Table VI). The random (uncorrelated) part is added to the foil covariance matrix which is then used to provide the final weighted mean cross section value with its associated random and systematic uncertainties. Several other common systematic uncertainties, e.g. in the ^{56}Mn half-life, isotopic abundance of ^{56}Fe, the correction for ^{56}Mn production by the competing reactions, are negligible.

Cross section results

The average value of σ_{Fe}, the $^{56}Fe(n,p)^{56}Mn$ cross section, was calculated, as discussed in the previous section, to be (109.2 ± 1.0) mb. The uncertainty was the sum in quadrature of four components: random uncertainty of $\bar{x}$ (0.15%), systematic uncertainty of $\bar{x}$ (0.76%), random uncertainty in the mean σ_{Fe} (0.33%) and systematic uncertainty in $E\beta$ (1+k) (0.2%).

It is interesting to compare this value of σ_{Fe} with values derived independently by several of the participating laboratories, which were based on the same or similar measurements. The result from ETL[12] was (107.1 ± 3.1) mb at 14.80 MeV, based on $4\pi\beta\gamma$ coincidence counting of their own foils. However they have subsequently reduced the estimate of their neutron energy to 14.75 MeV, which would alter this result. Their values of $E\beta$ and k used in the β counting were close to the values used here but apply to foils of slightly different thickness. The BCMN value[3] was 109.8 mb at 14.80 MeV, based on an absolute measurement of the foil activity with a calibrated NaI crystal. The derived value for their β counting efficiency agreed very closely with the value used here, as did their cross section when converted to our median energy of 14.73 MeV. The IMM result[13] was (110.9 ± 1.7) mb at 14.80 MeV, based on $4\pi\beta\gamma$ coincidence counting with a β counting efficiency of only 0.38 and a k-correction of nearly 10%. Their iron foils were irradiated at distances between 3 and 7 cm from the target, which seem rather close in view of possible geometrical uncertainties.

Discussion

The intercomparison has yielded a value for σ_{Fe} of (109.2 ± 1.0) mb at 14.74 MeV, in fair agreement with the measurements of Robertson et al [14] and Ryves et al [9] and the evaluation of Simons and McElroy [15]. It is 5% above the ENDF/B-IV Dosimetry File evaluation of Dudey and Kennerley [16], due to the weight given there to the measurements of Liskien and Paulsen [17] which are now obsolete [18]. The present evaluation depends entirely on a consistent assignment of neutron energies for the measurements, and an assessment of correlated and uncorrelated 1σ uncertainties. It is apparent that the cross section results of the participating laboratories differ over quite a large range of approximately 3%, but the reasons for these differences are unresolved. It is possible that there is some fine structure in the $^{56}Fe(n,p)$ excitation function. If such an intercomparison were repeated it would be advantageous to: (a) measure the absolute activities of the iron foils, e.g. by $4\pi\beta\gamma$ coincidence counting, or with a calibrated NaI crystal (b) measure (not calculate) the neutron energy to at least ± 20 keV, perhaps with a Si detector, or work at about 95° to the direction of low energy deuteron beam, when the neutron energy from the D-T reaction is close to 14.00 MeV and almost independent of the deuteron energy (c) use several methods for determining neutron flux density to reduce correlations (d) have more laboratories participating.

Acknowledgements

We are grateful to all the participating laboratories for supplying detailed information about their measurements.

References

1. V. D. Huynh, Results of the international comparison and flux density measurements for monoenergetic fast neutrons, CCEMRI(111)/79-1 (1979).
2. H Liskien and A Paulsen, Internal Report CBNM-VG-1 (1974).
3. H Liskien and A Paulsen, Internal Report CBNM-VG-6 (1975).
4. E Teranishi, T Michikawa, T Kinoshita, K Kudo, A Fukuda, H Sekiguchi, M Kageyama, H Watanabe, I Nashiyama, I Sakamoto, T Nishijima and N Takata, Bul. Electrotech. Lab. 41, 693 (1977).
5. V D Huynh, Proces-Verbaux du Comite International des Poids et Mesures, 2e Serie, 44, 92 (1976).
6. V D Huynh, Internal Report BIPM-72/2 (1976).
7. V T Shchebolev, I A Kharitonov, C V Jablokov and Z A Ramendik, Metrologia 11, 65 (1973).
8. V T Shchebolev, I A Kharitonov, C V Jablokov and Z A Ramendik, Metrologia 8, 61 (1974).
9. T B Ryves, P Kolkowski and K J Zieba, Metrologia 14, 127 (1978).
10. T B Ryves and K J Zieba, to be published in Nucl. Instr. and Meth.
11. J G Hayes and E J Axton, Metrologia 6, 21 (1969).
12. K Kudo, Nucl. Instr. and Meth. 141, 325 (1977).
13. Z A Ramendik, G M Stukov and V T Shchebolev, Atomnaya Energiya 42, 136 (1977).
14. J C Robertson, B N Audric and P Kolkowski, J. Nucl. Energy 27, 531 (1973).
15. R L S Simons and W N McElroy, Evaluated Reference Cross Section Library, BNWL-1312 (1970).
16. N D Dudey and R Kennerley, in ENDF/B-IV Dosimetry File, BNL-NES-50446 ed. B A Magurno (1975).
17. H Liskien and A Paulsen, J. Nucl. Energy 19, 73 (1965).
18. H Liskien, private communication (1979).

Table I Intercomparison results

			BIPM REPORT		EVALUATION (14.73 MeV)		
Lab	Method*	Foil no	E_n MeV	A/ϕ $\times 10^{-4}$	E_n** MeV	A/ϕ $\times 10^{-4}$	random uncertainty
BIPM	AP	44	14.68	3.20	14.63	3.205	0.13
		45		3.14		3.145	0.16
		48		3.16		3.165	0.17
ETL	AP	44	14.75	3.21	14.72	3.267	0.3
		45		3.14		3.196	0.3
		48		3.17		3.226	0.3
BCMN	T	44	14.80	3.22	14.80	3.247	0.8
		45		3.22		3.247	0.9
		48		3.18		3.207	0.9
NPL	T	44	14.67	3.216	14.72	3.156	0.29
		45		3.193		3.143	0.20
		48		3.205		3.141	0.36
		47		3.231		3.187	0.11
		49		3.195		3.133	0.47
		57		3.174		3.115	0.15
IMM	AP,CM	47	14.80	3.24	14.72	3.282	0.3
	NP	49		3.17		3.211	3.0
		57		3.19		3.231	0.6

*AP - associated particle

T - proton recoil telescope

CM - n-αcoincidence

NP - Stilbene spectrometer

** Evaluated measurement energy

Table II Correction factors used for (A/ϕ) ratios

Lab	J/J'	σ'_{Fe} to 14.73MeV	correction	σ'_H/σ_H	k	overall factor
BIPM	1.0140	0.9878				1.0017
ETL	1.0190	0.9988				1.0177
BCMN		1.0085				1.0085
NPL		0.9988	0.984[b]	0.9967	1.0020	0.981[b]
IMM	1.022	0.9988		1.004		1.013[a]

a Average value for associated particle and stilbene crystal methods

b Average value for iron foils

Table III 1-σ uncertainties %

	NPL	BCMN	BIPM	ETL	IMM
Neutron flux					
σ_H	0.8	0.8			
geometry	0.3	0.4			
n scatter, atten	0.15	0.25			
background	0.1				
Si(p,X)	0.1				
aperture edge effect	0.25				
radiator composition	0.1	0.75			
p scatter	0.1				
energy, ±30 keV	0.18	0.18	0.58	0.68	0.6
α-count			0.25		
α-solid angle			0.25	0.5	
D(d,p)T reaction			0.1	0.1	
Si(n,X)			0.1	0.1	
α-scatter				0.3	
neutron flux density					0.75
correlated random					0.3
weighting of methods					0.5
Foil					
$d\sigma'_{Fe}/dE_n$ correction			0.1		
distance		0.15	0.2	0.5	0.3
correlated random	0.4				
counter-plateau	0.5	0.15	0.3	0.2	0.3
Total uncertainty	1.14	1.23	0.79	1.05	1.20

Note: correlated uncertainties are underlined.

Table IV Covariance matrix for lab weights

	BIPM	ETL	BCMN	NPL	IMM
BIPM	0.620				
ETL	0.193	1.110			
BCMN	0.000	0.000	1.500		
NPL	-0.051	-0.060	0.640	1.300	
IMM	0.080	0.100	0.320	0.320	1.440

Table V Evaluated (A/Ø) ratios ($\times 10^4$)

Foil	44	45	48	47	49	57	Bias
Lab							%
NPL	3.156	3.143	3.141	3.187	3.133	3.115	-1.35±0.21
BCMN	3.247	3.247	3.207				+1.22±0.72
ETL	3.267	3.196	3.226				+1.13±0.25
BIPM	3.205	3.145	3.165				-0.69±0.15
IMM				3.282	3.211	3.231	+1.78±0.45
Best value	3.225	3.173	3.187	3.230	3.175	3.159	
Uncertainty (%)	0.20	0.20	0.23	0.26	0.76	0.31	

Table VI Data for iron foils

Foil no	mass mg	$E_\beta(1+k)$	% uncertainty in $E_\beta(1+k)$ random	systematic (correlated)
44	412.79	0.7174	0.354	0.2
45	405.67	0.7269	0.304	
47	413.67	0.7229	0.507	
48	408.52	0.7220	0.346	
49	408.08	0.7201	0.446	
57	402.45	0.7263	0.415	

^{12}C + n POLARIZATION MEASUREMENTS AND THE CARBON STANDARD

J. L. Weil, T. W. Burrows† and F. D. McDaniel††
University of Kentucky
Lexington, Kentucky 40506, USA

The asymmetry of polarized neutrons scattered from carbon has been measured at several angles for neutron energies of 4.60, 4.82 and 5.17 MeV. From an analysis of the measured asymmetries together with previously measured total and differential cross sections, the scattering phase shifts of carbon have been determined with more precision and accuracy than previously available, making carbon more useful as a neutron scattering standard.

[C(n,n), measured asymmetry, E_n = 4.6 - 5.2 MeV, calculated scattering phase shifts.]

Introduction

These measurements were undertaken for two reasons; to improve the precision of the $^{12}C(n,n)^{12}C$ scattering phase shifts, and to test a prediction that carbon would be a good polarization analyzer in the energy range $4.5 \leq E_n \leq 5.3$ MeV. More precise phase shifts will improve the usefulness of carbon as a neutron scattering standard, since scattering cross sections can be easily calculated at any place in the range of energy where the phase shifts are known. The analyzing power can also be calculated from the phase shifts. A prediction of large analyzing power was made by Galati et al.[1] based on a phase shift analysis of differential cross section measurements on $^{12}C(n,n)^{12}C$ in the energy range $3 \leq E_n \leq 7$ MeV. Those derived phase shifts are shown in Fig. 1.

Experimental Method

Neutrons with a polarization of 12-16% were produced using the $D(d,n)^3He$ reaction. Deuterons from the University of Kentucky Van de Graaff accelerator were incident on a 3 cm long gas cell filled with 2 atm of deuterium and sealed from the vacuum with a 3.45 micron Mo foil. Neutrons coming off at 45° to the incident beam direction were used for the scattering. The energy spread of the neutrons is given in Table I.

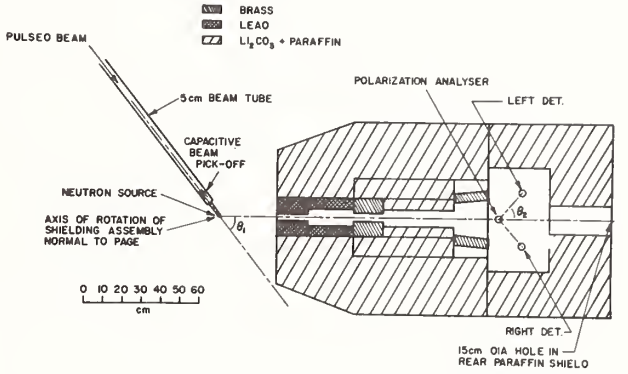

Fig. 2. Experimental apparatus used for measuring the asymmetry.

The experimental setup is shown in Fig. 2. Most of the data were taken with a 4 cm diameter by 6 cm high cylinder of reactor grade graphite as the scattering sample. Some points were also measured with a 2 cm diameter x 6 cm high sample to check the accuracy of the corrections for sample size effects.

The scattered neutrons were detected in two NE218

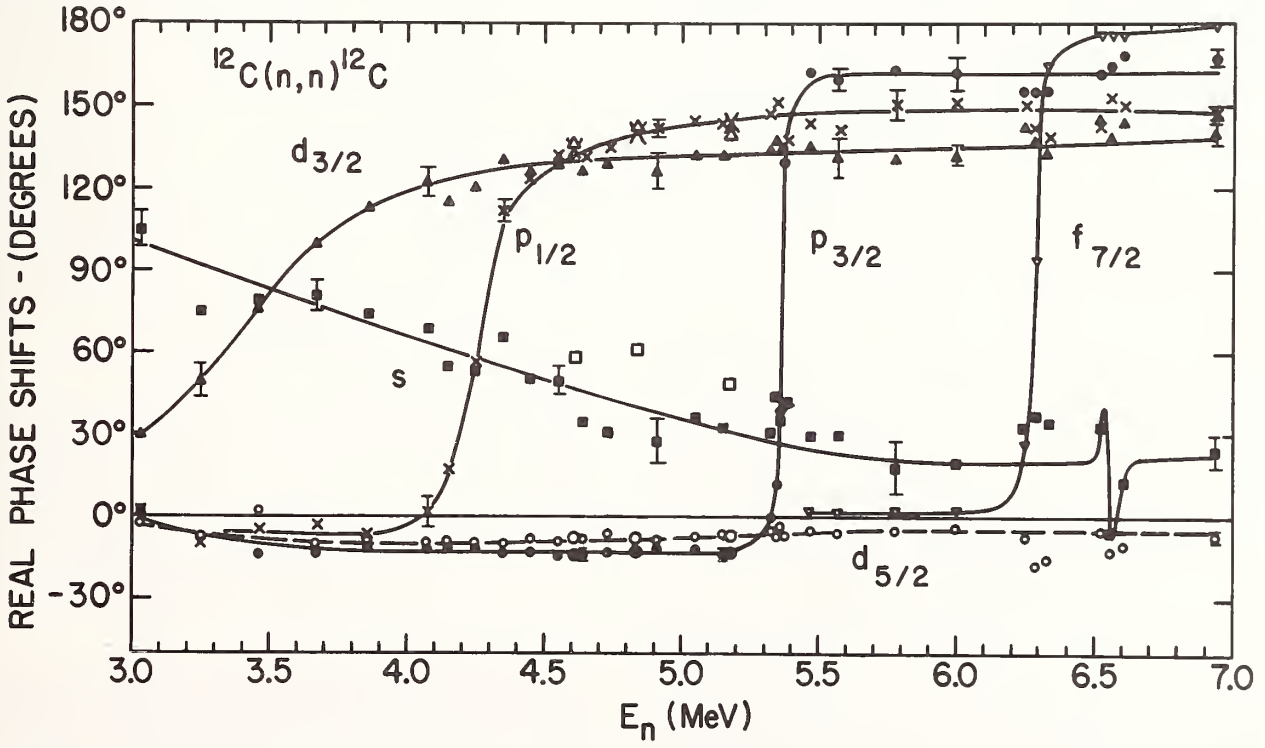

Fig. 1. Phase shifts from Galati $\sigma(\theta)$ measurements. Oversize and open symbols at 4.60, 4.82 and 5.17 MeV are the phase shifts from the present work.

Table I. Neutron Energies, Energy Spreads and Scattering Angles

E_n (MeV)	ΔE_n (MeV)	θ_{lab}
4.60	0.32	50°, 70°, 85°, 135°
4.82	0.29	50°, 70°, 85°, 120°, 135°, 150°
5.17	0.25	70°

liquid scintillators 3.8 cm high x 3.5 cm diameter coupled to 56 AVP phototubes. The incident neutron beam was very tightly collimated with copper apertures and the whole polarimeter was housed in a massive Li_2CO_3 loaded paraffin shield to reduce room background. Brass shadow bars of 20 and 28 cm length near the detectors served to further attenuate the neutrons coming directly from the neutron source by factors of 3 to 20.

The incident deuteron beam was pulsed in the accelerator terminal and bunched with a Mobley compression system into bursts of about 1 ns duration. The time-of-flight method and gamma-ray suppression by pulse shape discrimination were used to further reduce the background. The detection system was electronically biased to accept only those neutrons above 1.68 MeV. The system and methods are modified slightly from those of Sherwood et al.[2] For each data point, scattering measurements were made with the polarimeter at ± 45° relative to the incident deuteron beam in order to cancel out geometrical asymmetries. At each angle, sample-out measurements were made to determine the background which was then subtracted. If N_R and N_L represent the numbers of neutrons detected by the right and left detectors respectively, then the measured asymmetry is given by

$$P_1(45°)\ A_2(\theta_2) = \frac{N_L - N_R}{N_L + N_R}$$

Experimental Results

The asymmetry in the scattering of polarized neutrons from carbon was measured at three incident neutron energies. The energies and laboratory scattering angles are given in Table I. The asymmetries have been corrected for finite geometry and for multiple scattering using the Monte Carlo program PMS1[3] and also corrected for the variation of intensity of the incident neutrons across the face of the sample. The latter correction was small ($\lesssim$ 2.5%) but the finite geometry and multiple scattering corrections ranged from 30% to 70% for the large diameter sample. After correction, the asymmetries measured with the large and small scattering samples agreed to within 0.3%. The overall uncertainty in the measured asymmetries is estimated to range from 6% to 18%.

The asymmetries measured in this work are shown in Figs. 3, 4 and 5, along with asymmetry measurements made by Drigo et al.[4] at nearby energies. The polarization predicted by the Galati phase shifts was averaged over the neutron energy range of the present work, then multiplied by a value of incident neutron polarization $P_1(45°)$ determined as described below, and the resulting asymmetry vs. angle is plotted in the same figures.

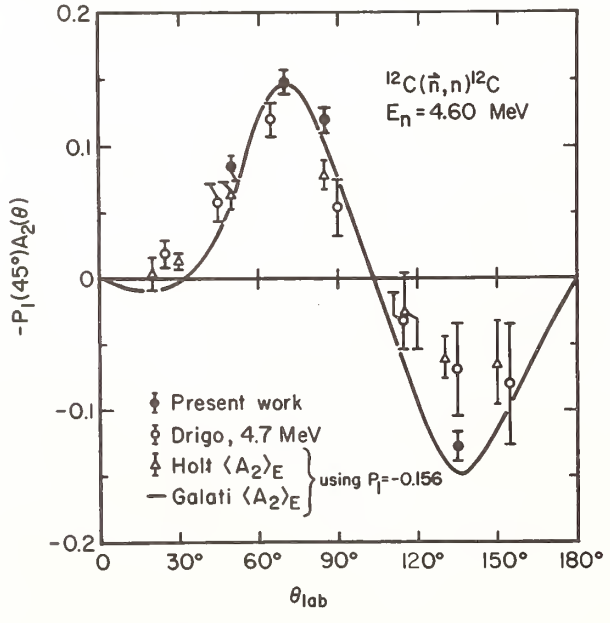

Fig. 3. Asymmetry measurements from this work and by Drigo. Calculated asymmetries from results of Holt and Galati.

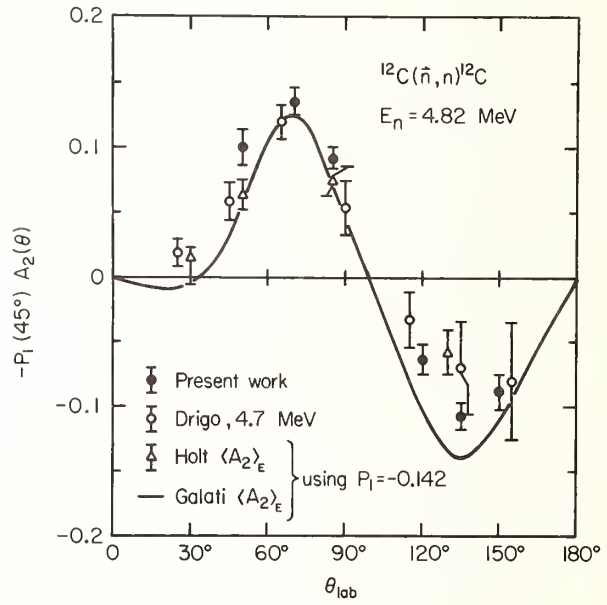

Fig. 4. See caption of Fig. 3.

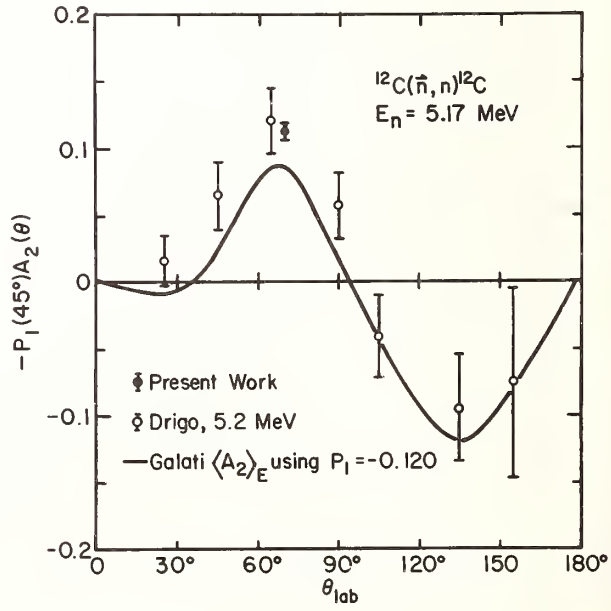

Fig. 5. See caption of Fig. 3.

Analyzing powers measured by Holt et al.[5] were also energy averaged, multiplied by our derived value of $P_1(45°)$, and plotted on the figures for comparison.

The three polarization experiments agree reasonably well in the forward hemisphere at all three energies, but at 4.60 and 4.82 MeV, in the backward hemisphere, the Drigo and Holt asymmetries are somewhat smaller in magnitude than the present work. The asymmetries predicted by the Galati phase shifts have the same general shape as the measurements, but differ in magnitude from the present data in at least one hemisphere at each energy, indicating a need for some modification of those phase shifts.

Analysis

The data were analyzed by doing a least-squares fit simultaneously to the total cross section, the differential scattering cross section and the presently measured asymmetries at each of the three energies, with the carbon scattering phase shifts and the $D(d,n)^3He$ source polarization as adjustable parameters. The total cross section was taken from NBS 138[6] and was energy averaged over the range of energy spread used in the asymmetry measurements so as to be comparable to the asymmetry. The measured differential cross sections given in Galati et al.[1] were also averaged over the same energy interval before fitting.

The phase shift values determined in this analysis are given in Table II and are also shown as oversize symbols in Fig. 1. There it can be seen that the $P_{1/2}$, $P_{3/2}$ and $D_{5/2}$ phase shifts from the present analysis agree very well with the values determined by Galati. Our $D_{3/2}$ phase shift is slightly larger than Galati's, though not outside the combined uncertainties of the two experiments. The S-wave phase shifts determined from the present work do appear to disagree significantly with those of Galati, being somewhat higher.

Not only are the $S_{1/2}$ and $D_{3/2}$ phase shifts determined with the aid of the asymmetry different from those derived from the differential cross sections alone, but the uncertainties are 2-3 times smaller, as

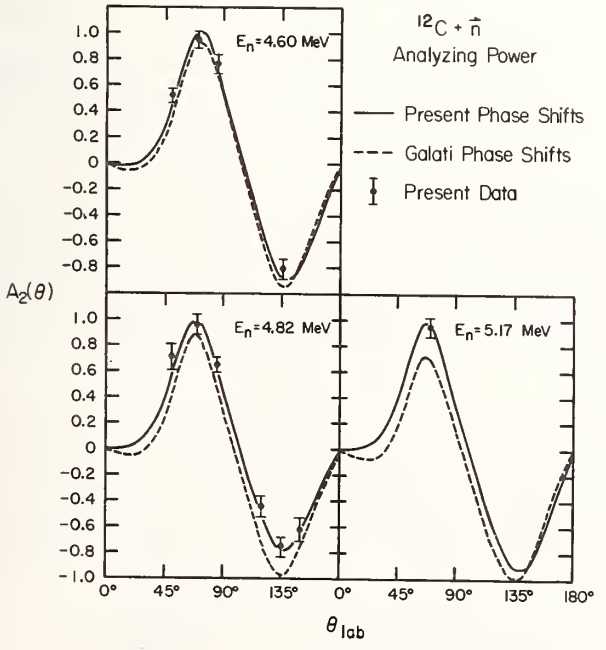

Fig. 6. Carbon analyzing power calculated from phase shifts deduced in the present work, and from Galati phase shifts. The data points are our asymmetries divided by the $D(d,n)^3He$ polarization determined in the least squares fit.

Table II. $^{12}C(n,n)^{12}C$ Scattering Phase Shifts (degrees)

E_n (MeV)	δ_S 1/2	δ_P 3/2	δ_P 1/2	δ_D 5/2	δ_D 3/2
4.60	57	-15	133	-8.0	136
4.82	61	-13	141	-8.6	142
5.17	50	-14	144	-7	140

Table III. Phase Shift Uncertainties (energy averaged)

	$\delta_{S_{1/2}}$	$\delta_{P_{3/2}}$	$\delta_{P_{1/2}}$	$\delta_{D_{5/2}}$	$\delta_{D_{3/2}}$
Galati, et al.	±9°	±2°	±3°	±2°	±8°
This work	±3-6°	≤±3½°	±3-4°	<±3°	±2-3°

can be seen from the preliminary estimates given in Table III. The other three phase shifts are determined with about the same precision in the two analyses. The effect of these relatively small changes in the phase shifts on the predicted carbon analyzing power is shown in Fig. 6. It can be seen that the asymmetry is indeed quite sensitive to the phase shifts, and that even poor resolution measurements with a precision of only 6-18% are of great help in pinning down the values.

The differential scattering cross sections are also significantly affected by the changes in the phase shifts. The cross sections calculated from the new and old phase shifts show differences ranging up to 10%, depending on incident energy and scattering angle. Such differences can be measured experimentally with careful work, and hence are significant for the use of carbon as a standard.

It should also be noted that these measurements and analysis show that carbon is an excellent polarization analyzer, with an analyzing power close to 100% at a scattering angle of 70° over a neutron energy range of at least 4.5 to 5.3 MeV.

Acknowledgment

This research was supported in part by a grant from the National Science Foundation.

References

† Present address, NNCSC, Brookhaven National Laboratory.

†† Present address, North Texas State University.

1. W. Galati, J. D. Brandenberger and J. L. Weil, Phys. Rev C 5, 1508 (1972).

2. J. E. Sherwood, F. D. McDaniel and M. T. McEllistrem, Nucl. Instr. and Meth. 107, 317 (1973).

3. T. G. Miller, F. P. Gibson and G. W. Morrison, Nucl. Instr. and Meth. 80, 325 (1970).

4. L. Drigo, C. Manduchi, G. Moschini, M. T. Russo Manduchi, G. Tornielli and G. Zannoni, Nucl. Phys. A181, 177 (1972).

5. R. J. Holt, F. W. K. Firk, R. Nath and H. L. Schultz, Nucl. Phys. A213, 147 (1973).

6. R. B. Schwartz, R. A. Schrack and H. Thompson Heaton, II, "MeV Total Neutron Cross Sections", NBS Monograph 138, U.S. Government Printing Office, Washington (1974).

PARASITIC ABSORPTION AND LEAKAGE CORRECTIONS FOR $MnSO_4$ BATHS

H. Goldstein and L. Chen
Columbia University
New York, N.Y. 10027, USA

Using ENDF/B-V cross sections plus new evaluations for sulfur, corrections for fast neutron absorption and leakage have been calculated for measurements of $\bar{\nu}$ by the $MnSO_4$ bath techniques. Transport calculations were performed in spherical geometry, chiefly with ANISN, using a specially devised 118 group cross section set.

[$MnSO_4$-bath, $\bar{\nu}$, ^{252}Cf, O(n,α), O(n,p), S(n,α), S(n,p), leakage]

Introduction

At the previous meeting in this series H.J.C. Kouts[1] referred to the 2.5% discrepancy then existing between the scintillator and $MnSO_4$-bath measurements of $\bar{\nu}$ for ^{252}Cf as "unsettling", adding: "this must absolutely be cleared up." Although the magnitude of the discrepancy has decreased somewhat in the intervening years, it still seems to be highly significant. Accordingly, a computational project has been undertaken to re-evaluate some of the corrections inherent to the $MnSO_4$-bath technique. These include absorptions arising from the O(n,α), O(n,p), S(n,p) and S(n,α) reactions. Because the reactions are significant mainly in the MeV range they are referred to as "fast neutron absorption." One other correction is relatively accessible to calculation--the leakage fraction through the external surface of the tank. This paper constitutes a progress report on the present status of the calculations.

Description of Computational Problems

The actual source-tank arrangement was approximated by a one-dimensional spherical geometry consisting of four regions: 1) a source region of 1 cm radius containing no material, 2) a source cavity, essentially empty out to 7.62 cm radius, 3) a layer of pure aluminum, .03" (or .0762 cm) thick, 4) the $MnSO_4$ bath out to a radius of r_4 cm. It was assumed there is no reflector outside the bath. For most of the calculations r_4 = 52.07 cm, corresponding to the smallest dimension of a cylindrical tank employed by J.R. Smith (private communication) although other radii were used on occasion. The spherical geometry substantially overestimated the actual leakage from the cylindrical tank, but it was possible to calculate an accurate correction (see below). For all other purposes the spherical approximation is adequate.

Cross sections employed were derived from ENDF/B-V, except for sulfur, for which a new evaluation was used, produced by the Brookhaven National Nuclear Cross Section Center. Multigroup cross sections were processed by MINX through P_3-order transfer coefficients. A special 118 group structure was constructed from the 171 Vitamin-C groups. Some of the finer groups in Vitamin-C were combined at high energies (> 12 MeV) in the epithermal range, and at several other energy intervals. However additional groups were introduced to delineate the lowest three resonances in Mn, and to give a better picture of the resonance behavior of the O(n,α) reaction in the 4-6 MeV range.

Transport calculations were performed mainly with ANISN. A series of optimization calculations indicated the desirability of setting the computational parameters at S_{48} and Δr = 0.2 cm. As these choices resulted in long computer runs, some problems were performed with reduced quadrature order and broader space intervals. The fission source spectrum was of the Maxwellian evaporation form. A variety of $MnSO_4$ concentrations were assumed, with N_{Mn}/N_H ratios varying from 3.647×10^{-3} to 2.817×10^{-2}, although most of the results reported here are for a ratio of .01818 (the "standard solution").

Parasitic Fast Neutron Absorption

Table 1 lists the absorption per source neutron for the four fast-neutron reactions, assuming standard solution, outer radius = 52.07 cm and a source temperature of 1.39 MeV. It will be noted from the table that the tank is so large that the absorptions are for present purposes identical with those resulting from a point isotropic source in an infinite medium. Various characteristics of these absorption rates can therefore be more easily studied in terms of the infinite medium geometry. For example, Table 2 shows the effect of varying the Maxwellian source temperature, other parameters being kept the same as in Table 1. In the Table, R stands for the reaction absorption rate, and $\bar{E}$ the average source energy, assuming a Maxwellian shape. The large values of the derivative, especially for the (small) O(n,p) absorption rate, is consistent with the high energy thresholds of the reactions.

Table 1. Fast Neutron Absorptions per Source Neutron

r_4 = 52.07 cm	N_{Mn}/N_H = .01818		θ = 1.39 MeV
O(n,α)	0.388%	S(n,p)	0.0806%
O(n,p)	0.00199%	S(n,α)	0.0948%
		Fast	0.0821%
		Thermal	0.0127%

Total = 0.5654% (Total, infinite medium, = 0.5723%)

Table 2. Dependence of Parasitic Absorption On Variation of Source Temperature

N_{Mn}/N_H = .01818 , Reference θ = 1.39 MeV

Reaction	$\frac{\partial \ln R}{\partial \ln E}$
O(n,p)	7.10
O(n,α)	2.93
S(n,p)	2.13
S(n,α) [fast]	1.59

Variation of the fast absorption rates with $MnSO_4$ concentration has been studied primarily in the infinite medium. Table 3 shows that when expressed in absorption rate per nucleus the O(n,α) absorption per source neutron is nearly independent of concentration. Over the entire range a 13.5% change in oxygen concentration produces only a 2.7% change in the absorption per nucleus. Considering the three most concentrated solutions only the effect is even more striking--a 6.2% change in concentration changes R/N_o by only 0.19%. Similar effects are seen for other reactions.

Table 3. Variation of O(n,α) Absorption With $MnSO_4$ Concentration

N_{Mn}/N_H	N_O (per barn cm)	R/N_o
3.647×10^{-3}	.03384	0.10915
4.611×10^{-3}	.03415	0.10865
1.329×10^{-2}	.03619	0.10648
1.797×10^{-2}	.03690	0.10645
2.833×10^{-2}	.03843	0.10628

For purposes of the experimental corrections it therefore suffices to assume that the absorption rate per nucleus is constant. These results further suggest that the variation in the absorption rate for a change in a group cross section is directly given in terms of the group absorption rate. This can be seen by symbolically writing the absorption rate as an inner product over neutron phase space

$$R_x = < \Sigma_x \phi >$$

so that on changing Σ_x we have

$$\delta R_x = < \delta\Sigma_x \phi > + < \Sigma_x \delta\phi >$$

A variation in Σ_x may be due to a change in the microscopic cross section or to a change in concentration. In the latter case

$$\delta R_x = \delta N_x < \sigma_x \phi > + < \Sigma_x \delta\phi >$$

The observed constancy of absorption rate per nucleus is equivalent to saying that δR_x is given only by the first term on the right, and that therefore the second term is negligible. If this is generally assumed then the fractional change in R_x arising from a fractional change in the cross section in some group G is simply

$$\frac{\Sigma_x^G}{R_x} \frac{\delta R_x}{\delta \Sigma_x^G} = \frac{R_x^G}{R_x}$$

where R_x^G is the contribution of group G to R_x. Detailed calculations with a linear perturbation code show that this conclusion holds to within 10% even in the worst case.

Leakage Correction

The full range of leakage calculations has not yet been performed. For a spherical unreflected tank of outside radius 52.07 cm, $N_{Mn}/N_H = .0182$ and $\theta = 1.390$ MeV, the leakage rate per source neutron is 0.452%. The fractional change in the leakage per fractional change in $\bar{E}$ is about 2.6, indicating that most of the leakage is at high energy. However the fraction of the leakage in the lowest ("thermal") group is unexpectedly high, about 23%. Since the lower groups do not yet include thermal upscattering, it is not at all clear that the transport of thermal neutrons has been correctly described. More accurate values will have to await projected calculations including upscattering.

The experimental tank used by J.R. Smith is much closer to a right square cylinder with above radius and half-length. An approximate corrected value for the leakage in this geometry has been obtained by assuming that in each group the ratio of the leakage for the infinite reflected to the unreflected sphere is independent of radius in the range of r from 52 cm to about 75 cm. Using reflected leakages obtained from calculations on a very large sphere ($r \sim 90$ cm), the corrected leakage for the actual tank was found to be 0.197%, less than half that of the unreflected 52 cm sphere.

Acknowledgment

Research sponsored by Electric Power Research Institute under contract RP707-3 with Columbia University.

Reference

1. H.J.C. Kouts, "Neutron Cross Section Needs", p. 6 of NBS Special Publication 425, Proceedings of a Conference on Nuclear Cross Sections and Technology, Washington, 1975.

THE APPLICATION OF A TIME-CORRELATED ASSOCIATED PARTICLE METHOD FOR ABSOLUTE CROSS-SECTION MEASUREMENTS OF HEAVY NUCLIDES

R. Arlt, W. Grimm, M. Josch, G. Musiol, H.-G. Ortlepp, G. Pausch, R. Teichner, and W. Wagner
Technical University of Dresden, Dresden 8027, GDR

and

I. D. Alkhazov, L. V. Drapchinsky, V. N. Dushin, S. S. Kovalenko, O. I. Kostochkin, K. A. Petrzhak, and V. I. Shpakov
V. G. Khlopin Radium Institute, Leningrad 197022, USSR

The joint fission cross-section measurements program of the V. G. Khlopin Radium Institute and the Technical University of Dresden is described. The errors and uncertainties of the time correlated associated particle method of fission cross-section measurements for 2.6, 8.5, and 14.7-MeV neutrons are discussed. Experimental results of absolute fission cross-section measurements of ^{235}U, ^{238}U, ^{237}Np, and ^{239}Pu for 14.7 MeV-neutrons and of ^{235}U for 2.6 and 8.2-MeV neutrons are given.

[fission cross sections, absolute measurements, time correlated associated particle method, 2.6, 8.2, and 14.7 MeV-neutrons.]

Introduction

According to the 1976 NEANDC/NEACRP Specialists' Meeting on Fast Neutron Cross Sections the following recomendations are given to achieve a higher accuracy in fission cross-section measurements: [1,2]
-a variety of techniques and detectors should be used and in addition to measurements with "white spectrum" neutron sources, experiments at few spot point neutron energies should be carried out;
- the corrections to be applied to the raw data of measurements should be minimal;
- the sources of background should be carefully investigated;
- $^{238}U(n,f)$, $^{235}U(n,f)$, $^{239}Pu(n,f)$ cross sections and their ratios should be measured with the same experimental set-ups to recognize systematical errors.

Up to this time, most of fission cross-section measurements have been carried out using the "white spectrum" neutron sources. In a considerable part of these measurements a standard had been used, for example the cross section of (n,p)-scattering.

At the V. G. Khlopin Radium Institute the absolute measurements of fission cross sections for 14,7 MeV-neutrons were started in 1972.[3] These measurements developed futher since 1975 in collaboration with Technical University of Dresden. The joint program provided the increase of the number of neutron energy spot points and parallel independent measurements with the same targets using different set-ups. This program corresponds to most of the recomendations mentioned above.

The time correlated associated particle method (TCAPM) was employed because of the low level of corrections to be applied to the experimental data. The increase of the number of neutron energy spot points caused some experimental problems, which were mainly connected with the associated particle (AP) detection. In the present work the TCAPM was applied in connection with the $T(d,n)^4He$ (E_n = 14.7 MeV) and $D(d,n)^3He$ (E_n = 2.6 and 8.2 MeV) reactions. Experimental data have been obtained for nuclides ^{235}U, ^{238}U, and ^{239}Pu. The ^{237}Np fission cross-section measurements had also been included in our program, following the suggestion to use this value as a secondary standard.[4]

Time correlated associated particle method (TCAPM)

The base idea of TCAPM is illustrated in Fig. 1.

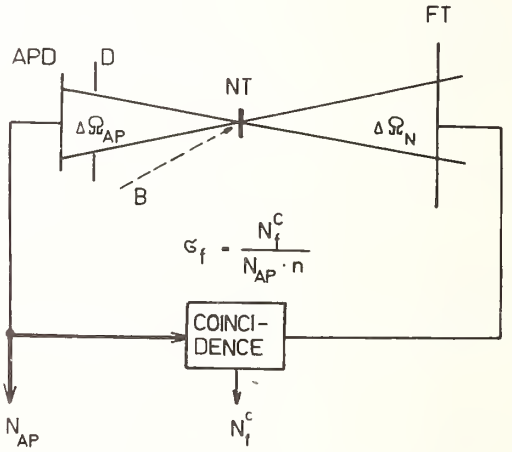

Fig. 1. Scheme of the TCAPM

A charged particle beam (B) is hitting a target (NT), where neutrons and associated particles are produced The associated particles detector (APD) is counting all charged particles within the solid angle $\Delta\Omega_{AP}$ fixed by the diaphragm D. The detector produces the timing signals for all neutrons within the cone $\Delta\Omega_N$. The fission target (FT) should be large enough to make the base of the neutron cone to be situated inside the fission target. The fission events are registered in coincidence with the associated particles. Provided the two main geometrical constraints are met: 1) the solid angle of the cone of neutrons associated with the detected alphas is sufficiently smaller than that subtended by the fissionable target, and 2) the fission target nonuniformity is negligible, the indused fission cross section

σ_f can be determined from the formula

$$\sigma_f = N_c/(N_{ap} \cdot n),$$

where N_c is the number of the coincidences, N_{ap} is the number of the associated particles and n is the number of fissionable nuclei per cm^2.

The TCAPM has the following advantages:
- the exact knowledge of the AP-detection efficiency is not necessary;
- no geometrical factors are to be taken into account;
- fission events induced by background neutrons (scattered neutrons or neutrons from other reactions) are considerably suppressed;
- the systematical errors of the experimental data are relatively small.

Typical corrections and errors of the measurements are summarized in Table 1.

Table 1. Typical values of corrections and measurement errors of the TCAPM.

	Correction (in %)	Error (in %)
Coincid. statistics	-	0.5-1 0
Targets		
Areal density	-	0.7-1.0
Layer nonuniformity	-	0.2-1.0
Chamber efficiency		
Discrim. threshold	+(0.5-1.5)	0.1-0.3
Fragm. absorption	+(0.3-1.0)	0.2
AP detection		
Statistics	-	negligible
Background	+(0.3-4.0)	0.1-0.5
Neutron cone		
Neutr. scattering	+(1 - 3)	0.3
Cone broadening	no correct.	0.2
Random coincidences	-(2 - 5)	0.2-0.5

Fissile targets

The fissionable samples were prepared and calibrated at the V. G. Khlopin Radium Institute. The fissile materials were deposited on 0.1 mm thick polished Ni - Cr - alloy disks, 21 mm in diameter, using a method of high frequency sputtering on rotated and cooled backings. Alpha counting was used in a low and intermediate ($2/3\pi$) geometry to measure the areal density, accuracy of about 1% being achieved.

The following α-decay half-lives were used to calculate the deposit densities:
$T(^{235}U) = (7.0381 \pm 0.0048) \cdot 10^8 y$ (ref.[5])
$T(^{238}U) = (4.4683 \pm 0.0029) \cdot 10^9 y$ (ref.[5])
$T(^{237}Np) = (2.14 \pm 0.01) \cdot 10^6 y$ (ref.[6])
$T(^{239}Pu) = (2.4335 \pm 0.0029) \cdot 10^4 y$ (ref.[7])

The nuclides of high purity were used to prepare the fissionable samples. The admixtures of other nuclides did not exceed 0.1 per cent.

The deposit nonuniformity was determined separately. The high α-activity samples (^{239}Pu and ^{237}Np) were scanned by a detector with a small entrance diaphragm. The ^{235}U samples were investigated using a low geometry counting system with diaphragms of different diameters placed in front of the deposit. To measure the deposit nonuniformity in the case of ^{238}U an optical method (ellipsometry) and electron X-ray microprobe analysis were used.

Fission events detection efficiency

Parallel plate pulse current ionization chambers were used in all the measurements for fission events detection. To estimate the detection efficiency we have to calculate the absorption of the fission fragments in the fissile layer and take into account the counting losses due to timing discriminator threshold. The absorption of fission fragments was calculated as a function of the fissile layer thickness, the neutron energy, the range of fission fragments and the fission product anisotropy.[8,9] The counting losses due to discriminator threshold have been found to be less than 1%. This value was obtained by the pulse-height spectrum analysis.

Corrections and uncertainties due to the neutron cone geometry

The calculations of the neutron fluence attenuation due to the scattering on structural materials were performed by the method based on the solution of the inverse problem of the radiation transfer theory.[10] The transfer equations were solved by the Monte-Carlo method, the real geometry of the experiment and all the structural materials as well as the air and the chamber gaseous mixture being taken into account. The cross-section values from the ENDI-2[11] and angular distributions from Ref. 12 were used in calculations. The statistical errors of the calculations did not exceed 0,1 - 0,2%. The calculations results are practicaly insensitive to the accuracy of both geometrical parameters and nuclear data involved. The correction values calculated did not exceed 3%, and their total errors were estimated to be less than 0,3% in all the cases.

The Coulomb multiple scattering of the associated particles leads to broadening of the neutron cone. However, the systematic error will be negligible if the topography of the neutron cone is known and its long-time stability is ensured.

Broadening of the neutron cone was calculated according to Mollier's charged particle multiple scattering theory.[13] The calculation results showed this broadening to be about 2° even in the most critical case of 2.6-MeV neutrons.

Nevertheless, the cone profile was mapped and its long-time stability controlled carefully for each AP-counting system, the cone profile being measured by a small plastic scintillator in coincidence with the AP. An example of the cone profile for the case of 2.6-MeV neutrons is shown in Fig. 2.

Experimental results

The fission cross-section measurements have been carried out using the neutron generator (150 keV deuteron energy) of Technical University of Dresden (for 2.6 and 14.7-MeV neutrons) and the tandem-generator of Central Institute for Nuclear Research, Rossendorf, GDR (for 8.2-Mev neutrons). The electronic data acquisition system including two CAMAC

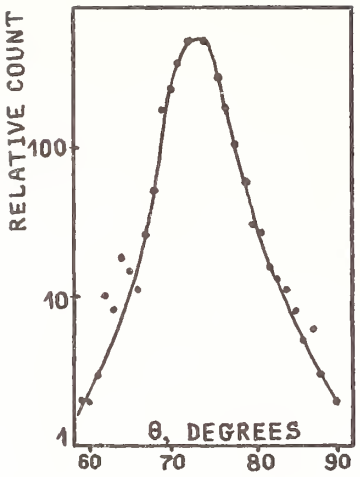

Fig. 2. Neutron cone profile in the case of 2.6- MeV neutrons

crates was connected on-line to KRS-4200 (Robotron Dresden) computer. The set-up block--diagram has been published earlier.[14]

a) Measurements for 14.7-MeV neutrons

The $T(d,n)^4He$ reaction was employed to produce neutrons. A 100 microns thick NE-102A plastic scintillator with time photomultiplier was used in this case to detect the associated α-particles. The main features of the experiment are given in Table 2.

Preliminary data on these measurements have been published earlier.[15,16] Recently, special efforts have been made to investigate the sources of background in the AP detection. Fig. 3 shows all the components of this background.

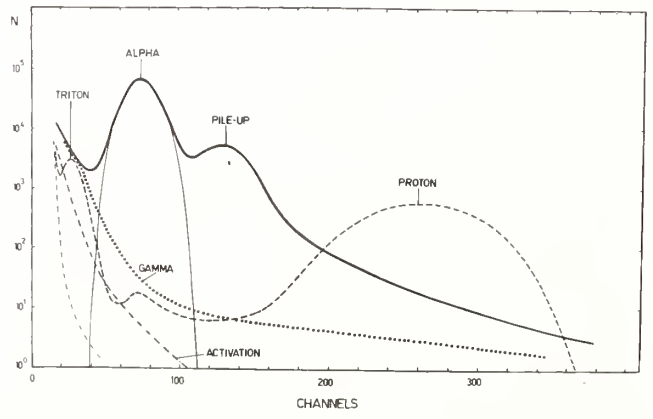

Fig. 3. Pulse-height spectrum of the AP-channel for the case of 14.7-MeV neutrons.

The main component of the background is due to γ-rays and is found to be 0.3%.

The results of measurements are listed in Table 3. The correction values and the measurement error components are similar to that listed in Table 1.

Table 2. Main features of the measurements for 2.6 and 14.7-MeV neutrons

	2.6 MeV	14.7 MeV
Neutron targets	0.3 - 0.6 mg/cm^2 Ti - D	Ti - T
Backings	0.5 mm thick, Cu	
Deuteron energy	120 keV	130 keV
Beam current	300-400 μA	10-30 μA
Beam diaphragm	Ø 3 mm	Ø 2 mm
AP angle with respect to beam	90°	165°
Chamber angle	77°	15°
Neutron energy (MeV)	2.60±0.15	14.70±0.15
Number of AP per sec	10^4	$(1-2)\cdot10^5$
Time resolution of coincidence sirquit	2-3 nsec	2 nsec

b) Measurements for 2.6-MeV neutrons

The main features of these experiments are given in Table 2. The method proposed earlier [17] was applied to register 700-keV helions of $D(d,n)^3He$ reaction. The surface-barrier detector with 100 μm-depth of depleted zone was used to detect helions, being protected from scattered deuterons by 230 μg per cm^2 thick aluminium filter. The ^3He pulse-height spectrum was monitored continuously during the measurements. An example of such spectrum is shown in Fig. 4.

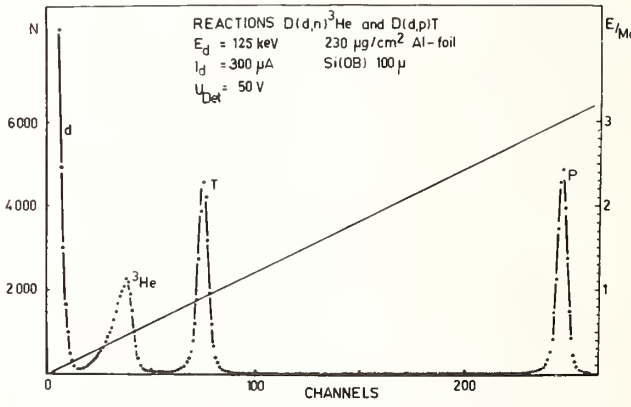

Fig. 4. Pulse-height spectrum of the AP-channel for the case of 2.6-MeV neutrons.

The proton and triton background under the ^3He peak was rather small, the background value being determined by linear extrapolation. The background due to scattered deuterons was found to be negligible on the basis of the good separation of the ^3He peak from noise and scattered deuterons. The separation of ^3He peak depends strongly on the quality and thickness of the aluminum filter.

The measured value of ^{235}U fission cross section for 2.6-MeV neutrons was found to be 1.215 ± 0.028 barns. The measurement error component are the same as listed in Table 1.

Table 3. Measurements results for 14.7-MeV neutrons (in comparison with data obtained in V. G. Khlopin Radium Institute)

Nuclide	Fission cross section (barns)	
	This work	Radium Institute
^{235}U	2.085 ± 0.023	2.096 ± 0.034
^{238}U	1.166 ± 0.021	1.178 ± 0.024
^{237}Np	2.226 ± 0.024	2.292 ± 0.044
^{239}Pu	2.394 ± 0.024	2.505 ± 0.045

c) Measurements for 8.2-MeV neutrons

The D(d,n)^{3}He reaction was used to produce neutrons with energy of 8.2 MeV. This neutron energy corresponds to the second fission plateau. A modified method described earlier by Shuster[18] and Bartle et al[19] was applied to detect associated 3-MeV helions. A target of thin deuterated polyethylene film was used for neutron production. Associated helions were detected by $\Delta E - E_r$ telescope comprising two thin (12 μm and 40 μm) completely depleted silicon detectors. In this way α-particle background in $\Delta E - E_r$ energy window of two channel discriminator[20] was decreased to 2 - 3% of total ^{3}He count. The background was determined by replacement of deuterated polyethylene target with carbon foil as described by Bartle et al.[19]

To increase fission counting rate the measurements were carried out with the ionization chamber containing five successive targets of fissionable nuclide. The Monte-Carlo method permits to perform correct calculations of the neutron fluence attenuation.

Experimental set-up (Fig. 5) was placed inside a 45 cm diameter vacuum chamber coupled to the ion guide of the tandem-generator. In Table 4 the main features of the experiment are summarized.

Fig. 6 shows charged particle spectrum measured at deuteron energy of about 8 MeV.

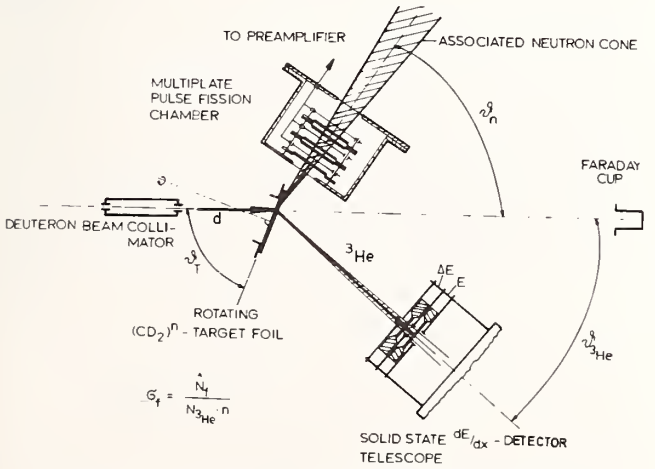

Fig. 5. Scheme of the experimental set-up for the case of 8.2-MeV neutrons.

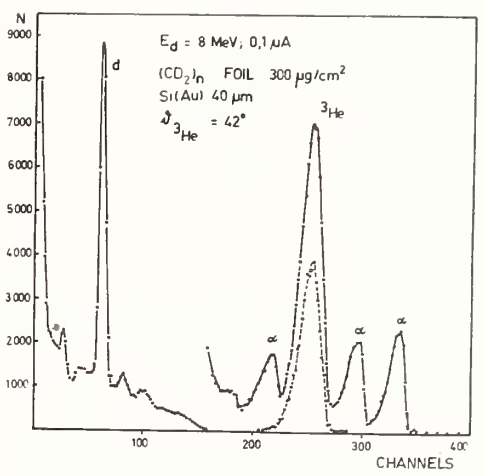

Fig. 6. Charged particle spectrum measured at deuteron energy of about 8 MeV with the target of deuterated polyethylene

The ^{3}He peak was identified by coincidences with neutrons, detected with the use of (n,γ)-discrimination.

In Fig. 7 a contour map of the two-dimensional $(\Delta E, E_r)$-spectrum is shown. A fast two-channel analyser was used as a particle identifier for the associated ^{3}He particles.[20]

The fission cross-section value of ^{235}U obtained in these measurements is 1.74 ± 0.11 barns. This value is in good agreement with estimated one proposed in ENDF-B/IV.

The values of corrections and measurement errors are given in Table 5. The measurement time was not sufficient to get a good statistics. Therefore, the result is preliminary, but it shows that the AP counting system developed enables precise fission cross-section measurements in the region of the second fission plateau. Futher efforts will be made in future to get the results with better accuracy.

Table 4. Main features of the measurements for 8.2-MeV neutrons

Neutron target thickness	0.6-1.0 mg/cm²
Neutron target diameter	20 mm
Deutron energy	9 MeV
Average beam current	400-600 nA
Beam collimator	2 diaphragms Ø 3 mm
Angle of AP $\vartheta_{^3He}$	42°
Angle of fission chamber ϑ_n	55.5°
Angle of neutron target ϑ_T	68°
Average number of AP per sec	300-800
Telescope time resolution	2 nsec
Telescope energy resolution	130 keV/90 keV
^{235}U layer density (mg/cm²)	1.422 ± 0.013

Summary

Absolute fission cross-section measurements at several spot point neutron energies (2.6, 8.2, 14.7 MeV) have been carried out using the time correlated assiciated particle

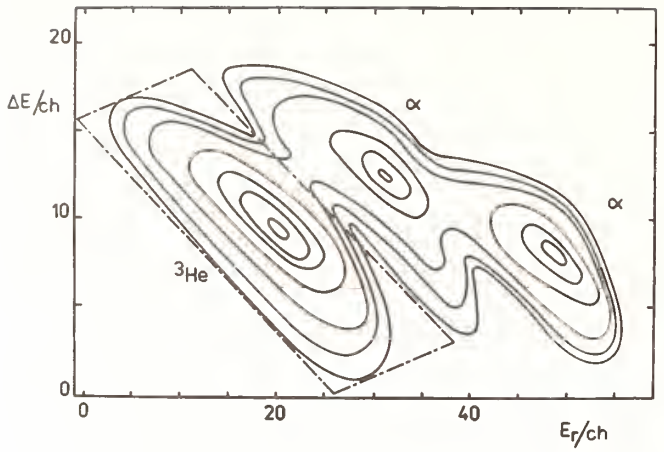

Fig. 7. Contour map of the two-dimensional spectrum of the AP-channel for the case of 8.2-MeV neutrons

Table 5. Values of corrections and errors of measurements for 8.2-MeV neutrons

	Correction (in %)	Error (in %)
Coincidence statistics		5.6
Targets		
Areal density		0.9
Layer nonuniformity		1.14
Chamber efficiency		
Extrapolation to zero pulse height	+ 3.3	1.4
Fragment absorption	+ 2.2	0.2
AP detection		
Statistics		negligible
Alpha background	+ 2.1	0.5
Neutron cone		
Neutron scattering	+ 0.23	0.4
Cone broadening		0.5
Random coincidences	-7	2

method. The method applied provides a high accuracy of measurements not only for 14-MeV neutrons but also for the neutron energies in the region of the first and the second fission plateaus.

Acknowledgements

Authors wish to thank the scientific staff headed by professor W. Meiling for the help and provision of experiment electronics, the operating staff of the tandem-generator and the neutron generator for their help with deuteron beams, the personnel of Design Bureau and Experimental Shop of Technical University and in particulary R. Sprung and W. Zeifert for technical assistance.

Special thanks are due to Dr. Hermsdorf for gracious providing of compilated data.

References

1. Proc. of the NEANDC/NEACRP Spec. Meeting on Fast Neutron Cross Sect. of U-233, U-235, U-238, and Pu-239. Argonne, 1976, ANL-76-90.
2. M. G. Sowerby, ANL/ND-77-1, p. 23.
3. I. D. Alkhazov et al, In Proc. of 2-nd Conf. on Neutron Physics, Kiev, USSR, vol. 4, p. 13.
4. S. Cierjacks, In Proc. of Internat. Spec. Symp., on Neutr. Stand. and Appl., Gaithersburg, 1977, NBS 493, p. 278.
5. A. H. Jaffey et al, Phys. Rev. C4, 1889 (1971).
6. F. P. Brauer et al, J. Inorg. Nucl. Chem. 12, 234 (1960).
7. Second IAEA Panel Meeting on Neutron Standard Ref. Data, 20-24 November, 1972.
8. R. Arlt et al, Preprint 05-5-79 of Techn. University of Dresden. Dresden, GDR, 1972.
9. G. W. Carlson, Nucl. Instrum. Meth. 119, 97 (1974).
10. V. N. Dushin, In proc. of VIII Internat. Symp. on the Interact. of Fast Neutr. with Nucl., Gaussig, GDR, 1978, ZfK-382, p. 153.
11. The Lawrence Livermore Laboratory Evaluated Neutron Data Library (ENDL-2), Report UCRL-50400, vol. 15.
12. M. N. Nikolaev, N. O. Bagazianz, Anizotropiya uglovogo rasseyaniya neitronov (Atomizdat, Moskva, 1972).
13. G. Moliere, Z. für Naturforschung. 3a, 78 (1948).
14. R. Arlt et al, Preprint 05-23-79 of Techn. Univ. of Dresden, Dresden, GDR, 1979. (Submitted to Nucl. Instr. and Meth.).
15. I. D. Alkhazov et al, Preprint 05-37-78 of Techn. Univrsity of Dresden, Dresden, GDR, 1978. (Submitted to Atomnaya Eherg.)
16. R. Arlt et al, See ref. 10, p. 180.
17. R. B. Galloway, A. Waheed, Nucl. Instr. and Meth. 128, 505 (1975).
18. D. G. Shuster, Nucl. Instr. and Meth. 76, 35 (1969).
19. C. M. Bartle et al, Nucl. Instr. and Meth. 144, 437 (1977).
20. R. Arlt et al, Report ZfK-350, Dresden, GDR, 1978, p. 209.

ABSOLUTE MEASUREMENTS OF INDUCED FISSION CROSS SECTIONS OF HEAVY NUCLIDES FOR BOTH ^{252}Cf FISSION SPECTRUM NEUTRONS AND 14.7 - MEV NEUTRONS

V. M. Adamov, I. D. Alkhazov, S. E. Gusev, L. V. Drapchinsky, V. N. Dushin, A. V. Fomichev, S. S. Kovalenko, O. I. Kostochkin, L. Z. Malkin, K. A. Petrzhak, L. A. Pleskachevsky, and V. I. Shpakov
V. G. Khlopin Radium Institute, Leningrad 197022, USSR

and

R. Arlt and G. Musiol
Technical University of Dresden, Dresden 8027, GDR

An application of the time correlated associated particle method to absolute induced fission cross-section measurements for ^{252}Cf fission spectrum neutrons and 14.7-MeV neutrons is described. The errors and uncertainties of the proposed modification of the TCAPM are given. New results of absolute cross-section measurements of ^{234}U and ^{236}U for both ^{252}Cf fission spectrum neutrons and 14.7-MeV neutrons as well as of ^{235}U for 14 - 15-MeV neutrons are presented. The experimental results of cross-section measurements of ^{233}U, ^{238}U, ^{237}Np, ^{239}Pu, and ^{242}Pu obtained earlier have been revised on the basis of more realistic calculations of neutron scattering.

[Fission cross section, absolute measurements, time correlated associated particle method, ^{252}Cf fission spectrum neutrons, 14.7-MeV neutrons]

Introduction

Absolute measurements of fission cross sections of ^{234}U and ^{236}U induced by ^{252}Cf fission spectrum neutrons and 14.7-MeV neutrons as well as repeated measurements of fission cross section of ^{235}U for 14-15-MeV neutrons have been made at V.G. Khlopin Radium Institute as part of a continuing program which began in 1972. The earlier developed time correlated associated particle method was used to perform these measurements. This method is such as to minimize the number and the values of corrections to the experimental data.

Measurements for ^{252}Cf fission spectrum neutrons

Spontaneous fission fragments of the neutron source were the associated particles for the ^{252}Cf fission spectrum neutron measurements, the number of neutrons being determined by the number of these fragments measured and by the average number of prompt neutrons, $\bar{\nu}$, a value known to a high precision (0.4%).

The advantage of the method in this case are as follows:
- there is no need of either neutron flux determination or 100% detection efficiency of ^{252}Cf fragments;
- the effects connected with scattered neutrons are reduced to minimum.

Because of the absence of single-valued correlation between the neutron and associated fragment directions, the angular dimension of the target as seen from the source should be taken into account.

The following corrections are to be introduced into the results measured:

1. For the solid angle subtended by the target of nuclide measured.
2. For neutron scattering which causes neutron flux attenuation.
3. For the nonuniformity of the target layer thickness.
4. For the efficiency of the fissile nuclide fragment detection.

The geometrical conditions of the measurements and experimental set-up were described earlier.[1,2] A flat target of a fissionable nuclide and ^{252}Cf source of the smallest possible dimension, both deposited on thin backings, were fixed in assembly by means of the thin supports (see Fig. 1).

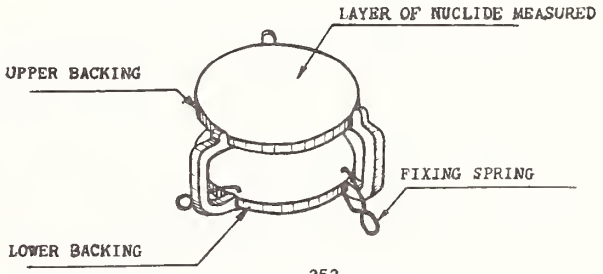

Fig. 1. Assembly for holding the ^{252}Cf source and fissionable nuclide target

The fission events of both the source and the target as well as coincidences between them were registered in the measurements. The cross-section values were calculated using the formula:

$$\sigma_f = \frac{N_c}{N_f \bar{\nu} G n},$$

where N_c is the number of coincidences, N_f is the number of ^{252}Cf fission events; $\bar{\nu}$ is the ^{252}Cf prompt neutron average number; G is geometrical factor, which is defined by the solid angle subtended by the target, by the dependence of effective layer thickness on the neutron angular distribution, and by the neutron scattering; n is the number of fissile nuclei per 1 cm^2.

The assembly design ensured fixing the source relative to the fissionable layer with

an accuracy of ± 10 microns; this gave a correct determination of the geometrical factor. The mass of structural materials in the vicinity of both the target and the source was minimized and did not exceed 1.5 g. The other structural elements were spaced at a distance of 20 - 30 cm from the assembly. The effect of neutron scattering on these elements was minor because of the small solid angle and was suppressed to a large degree due to the high time resolution of coincidence circuit (20 nsec).

In our previous works the geometrical factor was computed analyticaly under certain assumptions.[3] In particular the effects of neutron multiple scattering and neutron spectrum attenuation were neglected and obsolescent data on neutron cross sections were used.[4]

Recently a new method to calculate finite geometry effects was developed based on the inverse problem of the irradiation transfer theory.[5] The set of transfer equations was solved by the Monte-Carlo method for real experimental conditions taking into account all the structural materials and the gaseous mixture filling the chambers. The group approach (number of groups was 20) was realized in calculations. Group cross sections were obtained from the files of the ENDL-2 library[6] by averaging over the fission spectrum. In case of elastic scattering the angular distributions of scattered neutrons were taken from Ref. 7.

Statistical accuracy of calculations was about 0.1%. The total error in the definition of the geometrical factor value includes also the uncertainties of the cross-section values used in the calculation and the errors in distance measuring. The latter error component was estimated by variation of geometrical values in the limits of errors.

The losses in the fission events counting occur because of both the absorption of fragments in the target layer and the discrimination in the counting channel. The correction for the fission fragment absorption was introduced using the expression proposed by White.[8] The correction for channel discrimination was determined using the fragment pulse-height spectrum analysis.

As in previous measurements, the fission fragments of both ^{252}Cf source and nuclide measured were detected by ionization current pulse chambers. The coincidences were registered by circuits with triple duplication. The operation of these circuits were in addition checked by a time-amplitude converter.

Fission targets were prepared of nuclides of mass-separator purification by high frequency sputtering on rotating cooled backings. The admixtures of other nuclides in the targets did not exceed 0.1%. The deposit uniformity had been checked by α-counting scanning. The masses of fissionable deposits were determined by α-counting with a low geometry surface-barrier detector. The following α-decay half-lives were used to calculate the deposit masses:

$T(^{234}U) = (2.488 \pm 0.016) \cdot 10^5 y$ (see ref.[9])

$T(^{236}U) = (2.391 \pm 0.018) \cdot 10^7 y$ (see ref.[10])

To prepare the targets we had rather small amounts of fissionable substances available. Therefore, we did not succed in good uniformity of deposits. The nonuniformity of the targets were 5%. Besides, the masses of fissionable deposits were too small (50 $\mu g/cm^2$) to allow sufficient counting statistics. Therefore the data obtained have rather high errors and are to be regarded as preliminary. Later on these measurements are supposed to be repeated to get more precise results. The components of data errors are presented in Table 1.

Table 1. Error components for ^{252}Cf fission spectrum neutron measurements (in %)

Error sources	Nuclides	
	^{234}U	^{236}U
$\bar{\nu}$ (^{252}Cf)	0.35	0.35
Geometrical factor	0.71	0.71
Measurement of α-activity	0.36	1.04
Half-life	0.64	0.80
Coincidence statistics	4.5	4,5
Extrapolation to fragment zero pulse-height	0.30	0.45
Correction for fragment absorption	0.30	0.30
Total fission cross-section error	4.65	4.78

The results of measurements are given in Table 2. These results were obtained for the first time. The method of calculation of geometrical factor, described above, was employed to recompute the fission cross sections of a number of nuclides using the experimental data obtained earlier. All the results of these computations are given in Table 2 as well.

Table 2. Measurement results for ^{252}Cf fission spectrum neutrons

Nuclides	Fission cross section (mb)	
	This work	Other authors
^{233}U	1910 ± 29	-
^{234}U	1220 ± 60	-
^{235}U	1241 ± 18	1207 ± 52 (ref.[20])
		1204 ± 29 (ref.[21])
^{236}U	610 ± 30	-
^{238}U	344 ± 6	324 ± 14 (ref.[20])
^{239}Pu	1831 ± 27	1800 ± 60 (ref.[22])
^{242}Pu	1092 ± 18	-

Measurements for 14 - 15-MeV neutrons

The method used to perform the measurements of fission cross section of ^{234}U and ^{236}U for 14.7-MeV neutrons has been described earlier.[1,2] Neutrons were produced by the $T(d,n)^4He$ reaction using a 130-keV deuteron beam. The fission target was set up at the angle of 15° with respect to the direction of the beam. Accurate calculation under real experimental conditions gave neutron energy value 14.7 ± 0.2 MeV. We detected associated

alphas in a small solid angle as well as coincidences between alphas and fission events of the target. The main geometrical constraint was met: the base of the neutron cone, determined by the alphas detected, is situated inside the fission target.

The fission cross sections were calculated from the formula:

$$\sigma_f = \frac{N_c}{N_\alpha n},$$

where N_c is the number of coincidences, N_α is the number of associated alphas, n is the number of fissionable nuclei per 1 cm^2.

The experimental set-up allows one to vary the position angles of the alpha detector and the fission target such as to vary the neutron energy from 14.0 - 14.7 MeV. To detect associated alphas a surface-barrier detector was used. The pulse-height spectrum of charged particles is given in Fig. 2. The peaks of alphas and protons from $D(d,p)^3H$ reaction, which have nearly the same energy, were effectively separated by means of 600 $\mu g/cm^2$ thick filter placed in front of the detector.

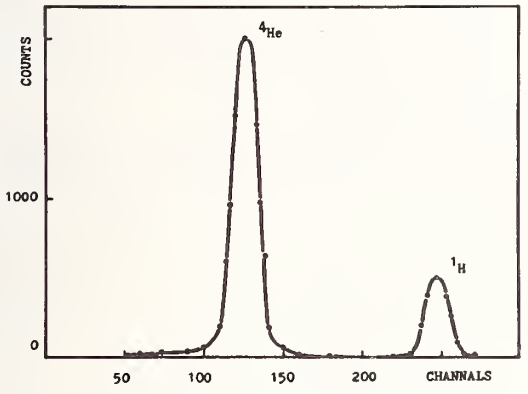

Fig. 2. Charged particle pulse-height spectrum measured by associated particle detector

The background in the amplitude window for α-particle detection was determined by replacement of the tritium target with a deuterium one and was found to be negligible (less than 0.1%). The fission events were detected by pulse current ionization chamber.

The following corrections were introduced into the experimental data: for the neutron flux attenuation, for the efficiency of the fission detection, for the random coincidences.

The correction for the neutron flux attenuation was calculated by the method mentioned above and used to compute the geometrical factors. The calculations in this case were much simpler due to the strong collimation of the neutron cone. The effects of neutron multiple scattering and the decrease of energy of neutrons entering target after scattering were taken into account. In calculating the fission events caused by neutrons with decreased energy the values of fission cross sections were taken from Ref. 11. The set-up design provided a very small amount of structural materials in the vicinity of the targets. The thickness of the backings did not exceed 0.9 mm. Therefore, the total value of correction was less than 2%.

The neutron cone could be larger than that of detected alphas due to Coulomb scattering of alphas in neutron generator target. This circumstance does not affect the result if the diameter of the fission target is rather large and the base of neutron cone is completely within the surface of this target. To determine the value of this broadening the neutron beam profile was measured by means of plastic scintillator of 2 mm diameter in coincidence with alphas. This profile as shown in Fig. 3 is narrower than the fission target.

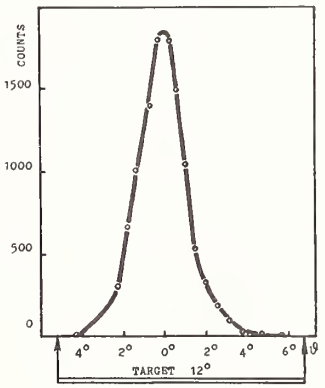

Fig. 3. Neutron cone profile (in comparison with fissionable nuclide target angular dimension)

In addition, the calculation according to the theory of charged particle multiple scattering [12,13] has shown that the broadening of neutron beam is described by the Gaussian distribution with half-width of no more than 10', i.e. a negligible value.

Because of neutron beam collimation the coincidence number is 20 - 30 times less than the total fission number which results in high level of random coincidences. The accurate definition of the correction for random coincidences electronic set-up was used which provided for the simultaneous separate recording of both total coincidences and random ones by the same circuit.

The targets of fissionable nuclides described above were used in the measurements. The corrections for absorption of fragments in the deposits calculated according to Carlsson [15] were equal to zero because of large tranfer velocity brought in by neutron momentum. The corrections for extrapolation to zero pulse-height obtained, as in previous case, by the pulse-height spectrum analysis were found to be below 1%. The nonuniformity of the fissionable deposits leads to appreciable distortion of the results because of neutron beam collimation. The correction for nonuniformity was evaluated only approximately, thus, the errors of results include the maximum value of nonuniformity. The components of errors as well as the values of errors themselves are presented in Table 3. The results obtained are presented in Table 4. As in the previous case, these results are regarded as a preliminary ones due to high values of errors.

We have earlier performed analogous measurements; the results for some heavy nuclides

were published. To carry out these measurements we had the tritium and fissionable targets on backings of significant thickness (2 - 3 mm) which resulted in the increased effect of neutron attenuation and corresponding high values of corrections (of the order of 10%). The corrections were calculated by means of analytical method including a number of assumptions. Now the corrections for the effects of finite geometry have been recalculated by means of the more precise Monte-Carlo method described above. The corrected data obtained are given in Table 4.

Table 3. Error components for 14.7-MeV neutron measurements (in %)

Error sources	Nuclides ^{234}U	^{235}U	^{236}U
Measurement of α-activity	0.36	0.62	1.04
Half-life	0.64	0.20	0.80
Coincidence statistics	1.00	0.70	1.00
Neutron flux attenuation	0.30	0.30	0.30
Extrapolation to fragment zero pulse-height	0.20	0.20	0.20
Correction for fragment absorption	0.20	0.30	0.20
Nonuniformity of fissionable deposit	5.00	1.00	4.50
Background in associated particles	0.05	0.05	0.05
Total fission cross-section error	5.17	1.46	4.81

Table 4. Measurement results for 14.7--MeV neutrons

Nuclides	Fission cross section (barns) This work	Other authors
^{233}U	2.254 ± 0.043	2.360 ± 0.080 (ref.[11])
^{234}U	1.91 ± 0.11	2.09 ± 0.06 (ref.[23])
^{236}U	1.62 ± 0.08	1.63 ± 0.05 (ref.[11])
^{238}U	1.178 ± 0,024	1.29 ± 0.02 (ref.[24])
		1.193 ± 0.020 (ref.[25])
		1.149 ± 0.025 (ref.[17])
^{237}Np	2.292 ± 0.049	2.36 ± 0.09 (ref.[11])
		2.50 ± 0.07 (ref.[11])
^{239}Pu	2.505 ± 0.051	2.61 ± 0.08 (ref.[11])
		2.58 ± 0.09 (ref.[11])
^{242}Pu	2.050 ± 0.040	-

To check the validity of new calculations performed the ^{235}U fission cross section was remeasured. At the same time another measurement of this nuclide was performed using another set-up in Dresden (GDR) in collaboration with the Technical University of Dresden.[16] In both cases the thin target backings (not more than 0.3 mm) and the minimal masses of structural materials were used. The values of corrections for neutron scattering were found to be 1.9% and 2.4% respectively.

The results of these measurements as well as the data of previous measurements recorrected by the new method for the neutron scattering are listed in Table 5. The good agreement between the given values confirms that the method used ensures accurate calculations of the corrections. It should be noted that the results obtained are in good agreement with the data given in ref.[17,18]

In order to measure in detail the dependence of ^{235}U fission cross section on neutron energy in the region of 14 - MeV cross-section measurements were performed for 14.0 - MeV and 14.5 - MeV neutrons, neutron energy being varied by the choice of the angle between the deutron beam and the neutron cone axis (45° and 90°). The results given in Table 5 show that the ^{235}U fission cross section is constant over the neutron energy range of 14.0 - 14.7 MeV. The same conclusion was drawn by Cance and Grenier.[19] Such absence of energy dependence favours the use of this value as a standard one, since the errors of neutron energy determination does not lead to the error in the cross-section measurement.

Table 5. Results of the ^{235}U fission cross--section measurements for 14 - 15-MeV neutrons (barns)

	14.7 MeV	14.5 MeV	14.0 MeV
This work	2.096±0.031	2.101±0.034	2.084±0.034
Previous measurements	2.089±0.040		
Measurements at Technical University	2.085±0.023		
Other authors	2.063±0.039 (ref.[17,19])		2.062±0.039 (ref.[19])
	2.075±0.040 (ref.[18])		
	2.191±0.040 (ref.[25])		
	2.213±0.022 (ref.[24])		

It should be emphasized that the fission cross-section values for 14-MeV neutrons obtained by the absolute measurements (these results and results by Cance and Grenier (ref. 17,19) are systematically lower than the data of "shape" measurements (for example[18,25]).

References

1. V.M.Adamov, et al, Voprosy Atomnoi Nauki i Techniki, Serija "Jadernye Konstanty", USSR, N° 24, p. 8, (1977).
2. V. M. Adamov, et al, in Proc. of International Specialists Symposium on Neutron Standards and Applications, Gaithersburg, USA, 1977 (NBS Special Publication 493, 1977), p. 313.
3. V. M. Adamov, et al, Preprint Radievogo Instituta RI-52, Leningrad, 1976.
4. I. Laigner, J. J. Schmidt, D. Woll, Tables of Evaluated Neutron Cross Sections for Fast Reactor Materials (KFK 750, Karlsruhe, 1968).
5. V. N. Dushin, in Proc. of the VIII Inter-

national Symposium on Interaction of Fast Neutrons with Nuclei, Gaussig, GDR, 1978 (ZfK-382, 1979), p. 153.

6. Evaluated Neutron Data Library ENDL-2 (Report UCRL-50400, v.15, Lawrence Livermore Laboratory).
7. M. N. Nikolaev, N. O. Bagazjanz, Anizotropija uglovogo raspredelenija neitronov (Atomizdat, Moskva, 1972).
8. P. H. White, Nucl. Instr. Meth. 79, 1 (1970).
9. Yu. S. Zamjatnin, Jadernye Konstanty, USSR, N° 14, p. 3 (1974).
10. K. H. Fleming, A. Ghiorso, B. B. Cunningham, Phys. Rev. C4, 1889 (1971).
11. W. Hart, AHSB(S)R 169 (United Kingdom Atomic Energy Authority, 1969).
12. G. Moliere, Z. Naturforsch. 3a, 78 (1948).
13. H. Bethe, Phys. Rev. 89, 1256 (1953).
14. P. Ikelaar, M. J. Wiel, W. Terba, J. Phys. C4, 102 (1971).
15. G. W. Carlsson, Nucl. Instr. Meth. 119, 97 (1974).
16. I. D. Alkhazov, et al, Technische Universität Dresden Informationen 05-37-78, Dresden, 1978.
17. M. Cance, G. Grenier, in Proc. of NEANDC/NEACRP Spec. Meeting on Fast Neutron Cross Sections of U-233, U-235, U-238, and Pu-239, Argonne, USA, 1976 (ANL-76-90, 1976) p. 237.
18. J. B. Czirr, G. S. Sidhu, Nucl. Sci. Eng. 57, 18 (1975).
19. M. Cance, G. Grenier, Nucl. Sci. Eng. 68, 197 (1978).
20. J. A. Grundl et al, Trans. Amer. Nucl. Soc. 15, 945 (1972).
21. H. T. Heaton II, J. A. Grundl et al, in Proc. of Conf. on Nucl. Cross Sections and Technology, Washington, D. C. USA, 1975 (NBS Special Publication 425, 1975), v. 1, p. 266.
22. H. Pauw, A. H. W. Aten, Jr., J. Nucl. Energy, 25, 457, 1971.
23. P. H. White, J. C. Hodgkinson, G. J. Wall et al, in Proc. of Salzburg Symp. on Phys. and Chem. of Fission (IAEA, Salzburg, EANDC (UK) 53 S, 1965).
24. B. Lengers, S. Cierjacks, P. Brots et al, in ref. 17, p. 246.
25. M. G. Sowerby, B. H. Patrick, Annals of Nucl. Sci. and Eng., 1, 409 (1974).

OBSERVATIONS ON THE CONFERENCE

Herbert Goldstein
Columbia University
New York, New York

I am glad that in his introduction Hank Motz has partially "gotten me off the hook" by stressing that it's not my job to give a summary. At the previous conference in this series, in 1975, the summary was presented by a panel of three experts headed by E. P. Wigner. I am clearly a poor substitute on all accounts. The best that I can hope to offer are some overall impressions or observations on the Conference. Indeed, because most of the time there were three simultaneous sessions, it would be better to say impressions of one-third of a Conference. You may have attended an entirely different one-third of a Conference than I did, and your conclusions may therefore be quite different. It's not even a randomly selected one-third, because there is a natural bias to try to select papers of interest to me. I was only partially successful in my attempt. That fellow you saw running back and forth across the corridor from one room to the other was me. I always seemed to come into a session just as they finished the paper I wanted to hear.

The designation of my talk as "impressions" or "observations" is particularly useful, because it gives me leave to mention something of the history of this series. This Conference is the fifth in a series that started back in 1966, although its origins were earlier than that. There were a group of us in the '60s who were attempting to devise some type of meeting or conference that would bring together the separate groups of those who were measuring cross sections and those who were using cross sections. Before that time there was very little in the way of conversation between the two groups. There were only some sort of formal notes passed between them. Our first conference in 1966 was, therefore, an attempt to overcome that barrier. It was not completely successful. We had a hard time, I remember, explaining what this peculiar process of evaluation was. Neither the measurers nor the users quite understood. Still, the idea seemed to catch on. Successive conferences were held in 1968, 1971, and 1975. Today, observing the fifth conference, I think we can apply the words of a famous commercial: "Baby, you've come a long way!" There is now a firm partnership among the measurers, users, and evaluators of cross sections. Very often they wear each other's hats.

Well, what sort of a meeting have we had? Certainly, from the point of view of the hospitality that we received, it's been a very successful meeting, as I'm sure you will agree. I don't know what kind of strings our hosts pulled, but they have even managed to give us five days of perfect weather. And if you don't think that is a major accomplishment, you should be here at other times in Knoxville and see what the weather can be. One might get the impression they also arranged to have a whiskey named appropriately for this conference. Coming up on the road from the Hyatt Regency Hotel to the Center here, you are confronted with a big billboard that advertises Benchmark Bourbon Whiskey. For the actual arrangements and the program, we owe a great thanks to the Deputy Chairmen of the meeting, Fred Maienschein of ORNL and Pete Pasqua of UT, and to our Secretary, Cleland Johnson. And above all, I think, we must tender our grateful thanks to the staff who have taken care of us so well--even though I'm somewhat doubtful as to just what it was that they put in the tea we had in the breaks!

Especially, we are indebted to someone who, to the sorrow of all of us, could not be here--Joe Fowler has been the prime mover of this conference and was really the one who pushed it through. Regrettably, a few months before the meeting, when he had already rounded up most of the invited speakers, he became quite ill and had to undergo heart surgery. Since then, he has had a stormy convalescence; and unfortunately, he has not recovered quite well enough to be here. I miss Joe Fowler terribly in this meeting. It does not seem to be a proper conference without his vigorous enthusiasm and his infectious laughter. We all, I know, wish him well and hope that he will have a speedy and complete recovery.

The previous meeting, held four years ago in Washington, was, I believe, the first in this series to be called an international meeting and to have a title referring to nuclear cross sections rather than neutron cross sections. These designations have been continued in our present meeting, so it's fair to try to compare them and to note any changes. Statistically, the two meetings are almost the same. The number of papers here is down slightly. The number of people attending is just about the same--maybe slightly lower. Comparing the domestic and foreign contribution, the number of papers from outside America went up somewhat compared to 1975, and since the number of papers from the U.S. went down somewhat, there seems to be something of a trend. So, I think we can congratulate ourselves that we have been really running an international meeting. I must say though, parenthetically, that as coming from the host country, I have been somewhat embarrassed at the repeated discussions of data sets generated in the U.S. which are not available in general. It struck me as being what the British call "bad form." One would hope that at an international conference, we could really talk on an equal basis.

Both in 1975 and now the program committee tried very hard to broaden the conference so as to include applications involving charged particles, and to go beyond the range of fission and fusion situations, e.g. to include cross section questions for neutrons above 20 MeV. In that respect, it seems to me there wasn't much difference between the two conferences. In both of them there were about the same number of tutorial papers, trying to introduce us to fields outside of what, perhaps, are our normal interests. In addition, there were some contributed papers referring to such exotic fields; with somewhat fewer in this conference than in the previous one. Some of these tutorial papers outside our standard concerns said rather frankly that they had at best only minor needs for cross sections. Others, such as the papers on medical cancer radiation studies or the papers on applications for geological prospecting, presented some interesting problems but not ones having the same degree of difficulty or sophistication as in fission or fusion. Perhaps what is even more important, these fields seem to lack the kind of funding structure that would support work on cross sections to meet their particular needs. Of course, astrophysics can always be depended upon to post some interesting and challenging problems of cross section measurement and predictions--problems that the physicists particularly like to tackle. And we were promised that if we succeed in solving the shopping list of questions presented here, by the time of the next conference they will have a whole batch of new ones!

It should be noted that there was a significantly increased interest in neutron cross sections in the

range from 20 to 40 MeV. Most of the new interest arises out of the use of "white" sources, particularly deuterons on beryllium or lithium targets, in such widely dispersed fields as cancer radiation therapy and radiation damage in the solid state. We heard repeated mention of a new gadget--the Fusion Materials Irradiation Facility--which is being designed now and which will be operational in a few years, producing intense beams of neutrons up to 40 MeV.

With all due acknowledgment to the significance of these new fields, I felt, nonetheless, that the overwhelming majority of both the papers and those attending were still concerned with fission-fusion applications and, in particular, with neutron cross sections from the thermal range up to 20 MeV. What, perhaps, is the difference from the previous meeting is that there has been a shift from the classical fields of core physics and shielding devices to topics which we have usually considered as more peripheral--safeguards, waste disposal, dosimetry, radiation damage, or fuel cycles of an exotic nature. Again, in some of the cases there didn't seem to be much of interest from the cross section point of view. As I recall, Willie Higginbotham got up and said in the first sentence of his paper that there were no safeguard interests in cross sections. But there certainly were serious needs presented in waste disposal, dosimetry, and radiation damage. Don Smith, for example, gave one of the best papers I've heard at this conference, in a masterful review of the radiation damage and dosimetry problems, and convinced me, for one, of the importance and seriousness of the cross section needs for these areas.

Well, if we look primarily at neutron cross sections and at the fission and fusion applications, what sort of a meeting has it been? A very normal, active, busy scientific meeting, I would say. The corridors, refreshment room, Smokey's Palace and all, have been humming with exchanges and comparisons of data, questions being asked, experiments being planned. Even the regularly scheduled sessions, by and large, have been well attended with intent and responsive audiences. I have been impressed with the general high level of competence and sophistication of the papers. In short, there is every evidence that this sort of artificial field we created some fifteen years ago--this mixture of users of cross sections and of those who measure them--has reached a level of maturity, of steady, competent progress.

But by the same token, at least based on the part that I attended, there have been few surprises, few exciting developments, to set things buzzing, to leave people raring to get back to their laboratories and institutions to try out something new. About the closest to that kind of excitement that I heard was the paper by Dr. Muradyan on a novel detector, the Romashka detector. Using multiple coincidences among a large number of detectors surrounding the sample, the detector measures primarily the multiplicity of particles emitted from the sample. One can, therefore, rather clearly distinguish among neutron scattering events, where there wouldn't normally be more than one particle coming out, capture events where there would be a moderate multiplicity of resultant particles, and fission events, where there would be a larger multiplicity. It seems to me we have here a fresh approach (though it has its forerunners in some experiments that have been done at ORNL), and it appears to provide a clean way of separating between various kinds of events in simultaneous measurements.

Otherwise, I noted relatively little new in experimental techniques. I observed in particular that there are still very few people who are willing or capable of doing differential experiments in that wide empty range between 7 and 13 MeV. If I counted correctly, it appears that the only groups involved in this area are the TUNL Laboratory people here in this country and a combined Russian-Dresden group. Considering the importance of this region for fusion applications and for reactor shields, one would hope that more people would make such measurements.

One other experimental paper that struck me particularly was on the study of fine structure of the fission cross section in what would normally be called sub-threshhold materials, for example, ^{231}Pa, where the interpretation of the cross section fitted in very neatly with a triple hump barrier representation of the fission process. At each of these conferences we add one more hump to the fission barrier. What's for the next time?

Controversies about particular cross sections can be depended to liven up a conference of this nature. In 1975, for example, there was much discussion about discrepancies. A lot was said, for example, about the ^{6}Li(n,α) measurements at the resonance. This time I heard only one reference to that particular problem, and indeed that was a remark about how much better things are now than they were four years ago. Also, the question of fission decay heat, which was a controversy at that time, seems to be satisfactorily resolved now, according to the measurements and comparisons presented by Dickens early Monday. However, we still have our share of discrepancies and controversies. We still have the problems of the ^{238}U (n,γ) reaction. That seems never to leave us--it appears to provide a lifework for some people. And there is always the attempt at changing the ^{238}U inelastic cross sections. There it is mostly, I think, a matter of trying to force agreement with fast criticals, especially so as to resolve the discrepant central reactivity worth that has also been with us, one feels, from time immemorial. Perhaps that will be solved shortly with some very clever measurements which are underway here in Oak Ridge. The very first paper we had on Monday, by Herb Kouts, reminded us of the pronouncement in the 1975 conference that the discrepancy on $\bar{\nu}$ for ^{252}Cf, between the liquid scintillator and the $MnSO_4$ bath techniques, was a national scandal, and we heard the reiteration that four years later it is still a national scandal. But again, while we did not see the resolution of it this time, there seems to be hope. Indeed, new values were whispered around in the corridors for measurements by those two different techniques that are now a good deal closer; and J. R. Smith pointed out how a shift in a sulphur cross section (which depends mostly on rather primeval values) might very well take care of the difference. We can hope for a final resolution in a year or two.

A new discrepancy or controversy has come to the fore, one which might turn out to be quite important for fusion applications. It concerns the ^{7}Li(n,n't) reaction, which we saw in several papers may have a really crucial effect on the design of breeding blankets for fusion reactors. A particularly fine paper was presented by Dr. Swinhoe on this reaction, presenting British measurements, and supporting evidence, indicating the cross section is at least 10% lower than previously thought. Undoubtedly this report will spark some new investigations.

Getting away from the measurements of cross sections, I have been impressed by the number, and especially the quality, of the cross section evaluations presented here--some of those from the United States, and especially those presented by the

French participants. These evaluations struck me as being painstaking, knowledgable, with a good deal of thought and intelligence having gone into them. Noticeable has been the number of experimenters who have switched hats temporarily and performed evaluations directly for ENDF/B. It is a trend to be welcomed, and one would hope it would continue. We were also treated to a discussion of the growing complexity of the nuclear models which are used in the evaluation. While these models are developed on the basis of our knowledge of nuclear physics, they are not constructed primarily to answer questions of nuclear physics, e.g. not to do global fits, but rather to fit and extrapolate data for particular elements. One development which seems to be just starting now--and I think it's been long overdue--has been attempts to make a consistent, complete analysis by some sort of unified model code. Right now, we do a patch job, with an optical model code here, a coupled channel code there, or a direct interaction program here, each with somewhat different parameters and different assumptions, and without recognition of the interrelations between these. We might look forward to some admittedly monster-size code which does it all in one throw of the dice.

The appearance of these new high-quality evaluations underscores a problem that I sense will be of growing importance to us in the U.S.--the long time interval before such "state-of-the-art" cross section data are fed into reactor or shield calculations. There are two aspects to the problem. One is the time-lag built into the cycle of ENDF/B cross section sets. The evaluations described here this week can enter into the stream of official ENDF/B sets only as part of ENDF/B-VI, and that is so many years downstream the powers-that-be don't even want to set a date. Meanwhile, we are practically frozen into sets with old and poor evaluations. Those who manage ENDF/B should provide--and publicize widely--some mechanism for making the new evaluations available promptly and in suitable format, even if they have to be used in parallel with officially approved ENDF/B sets. The other aspect relates to the size and required computing time for our cross section processing codes. Even minor changes in input point cross section data often call for the running of such elaborate and time-consuming processing codes that an elapsed time of two months for such changes is not unusual. No wonder there is a tendency to take the easy way out and keep using an existing multigroup library long after it has been obsoleted by the existence of new and better microscopic data. Some way should be provided to provide more easily for changing input data, preferably by interactive communication with the computer.

There were, however, some aspects which I looked for in this meeting which seem to be absent. The buzz phrases in the 1975 meeting were "sensitivity analysis" and "uncertainty analysis." Just to remind you of the difference between these, sensitivity analysis talks about what is the change in an integral experiment--or in integral calculational result--for a change in a given cross section. It is a variational derivative of the particular integral quantity with respect to a cross section change. Uncertainty analysis convolutes the variational derivative with the covariance matrices (i.e., uncertainty matrices) for the cross section, leading to the uncertainty in the integral quantity that is traceable to uncertainty in the cross sections.

When I first saw the program for this meeting, I looked at the titles of the papers and wondered, "What has happened to sensitivity analysis?" There didn't seem to be any discussion or any papers with that phrase in the title. Well, it hasn't disappeared, in fact. There were a lot of papers that discussed or used both sensitivity analysis and uncertainty analysis. In fact, these techniques have grown to the status that we sort of take them for granted and use them just as regular tools. But, for the most part, sensitivity analysis is being used to produce adjusted cross sections. In effect, one says: "If I know how much effect on an integral experiment a change in cross section will produce, and I find out how much the result of an integral calculation differs from the experiment, then I can go and move that cross section in value a little bit and change the calculation until it agrees with experiment." The technique is not particularly new, and it's not the original motivation behind the creation of the idea of sensitivity analysis. When I first saw sensitivity analysis used in this manner to produce adjusted sets, I called it a number of things, of which "perversion" was the most polite. Listening to some of the papers this week, I have had a slight change of heart about it, mainly as the result of the quality of the discussions and of the efforts that had gone into the way the procedure is being used, specifically in the French work, and in some of the work here at Oak Ridge described in a paper by Dr. Yeivin. In these papers adjustment based on sensitivity analysis has been used in a very intelligent manner, both to modify the cross sections and to select those integral experiments which are most dependable.

I must say, however, that I'm still upset about it. No matter how you clothe the description of the adjustment procedure it bears a very close resemblance to the favorite technique of my undergraduate days when we called it a "fudge factor": the right answer divided by the wrong answer! My difficulty with it, I think, was highlighted by the very fine paper presented by Dr. LeSage--an analysis of a very carefully chosen set of integral experiments of high quality in which he tried to analyze separately the uncertainties due to the experiments themselves and the uncertainties resulting from the calculational methods involved. Very roughly, if you take the difference between a measured integral quantity and calculated value, and subtract from this difference the expected uncertainty arising from the measurement technique and the calculational method, then the result should be the measure of errors in the cross section input. But Dr. LeSage found that the calculational errors are hard to pin down quantitatively and are often the same order of magnitude as the uncertainties which might be attributed to cross sections. So that when you make an attempt to adjust the cross sections, you're also grappling with very uncertain errors in the calculational methods used to obtain the integral experiment figures. One begins to question whether you are correcting the cross sections to agree with experiments or to compensate for the errors of your calculational difficulties. I'd like, for example, to make a comparison of the adjusted cross sections for sodium as developed, say, for fast reactor core analysis with those which were adjusted to meet the shielding experiments. I wonder how well they agree between them.

But, as I said, this is not what sensitivity analysis had been invented for. One of its first purposes was to try to give a quantitative underpinning to the statement of accuracy to which one wants a cross section measured. On the basis of the sensitivity analysis, one could say, "I need a cross section of such and such an accuracy." And some such applications of sensitivity analysis have

indeed been made. But the other reason for sensitivity analysis was to provide a physical understanding of why neutrons and gamma rays in bulk materials behave the way they do. What we seek to find is the connection between the microscopic interaction and the macroscopic behavior. In the period between the 1975 meeting and now, a number of elegant and ingenious tools have been designed, based on sensitivity analysis and its offspring--contributon fluxes--at Oak Ridge and at Los Alamos to help us reach this kind of understanding. There is none of it in the present meeting; it has totally disappeared and I can't quite understand why. One answer I've been getting is that the funding agencies won't support that kind of effort, even though people agree in the long run it must help. Surely, if you understand how neutrons and gamma rays behave in bulk materials, it must certainly help in assessing computational methods and in knowing how to use cross sections. The indifference to this type of analysis is strange. You always require that sort of attempt at "understanding" in making and reporting microscopic cross section measurements--there it's called "nuclear physics." The result, I would say, is that for the past few years we have not had any reactor physics, only reactor computations. There's a big difference between the two. I hope things will change in the future.

Well, my time is running out and there are obviously a number of questions that one might ask about this meeting. One is, have we had too many meetings? In a tutorial paper on fusion needs for cross sections, Dr. Haight presented a slide which listed the meetings within the past five years at which similar talks and analyses of cross section needs for fusion had been presented. As I recall, it listed about six or seven meetings between 1975 and the present one which had similar papers. Nonetheless, I have come to the feeling that a meeting such as the one we've just had was indeed necessary. For one thing, we can't all expect to go to Harwell and to Kiev and the rest, in addition to Knoxville. There are many of us who can attend only one out of every five or six of these meetings; and for those of us it gives us a welcome chance to catch up with what's going on. More important, the researchers in the field--a field which, as I said, is somewhat of a creation of the application needs--have difficulty in finding a proper home in the various professional societies. So a meeting in this series is great, not only as a place to present our results, but also to enable us to get together and compare notes, and not least, to boost our morale a bit.

The obvious next question is "When should the next meeting be?" or, rather, if I may ask: "Should there be a next meeting?" Indeed, I think that's part of a much bigger question. Let me refer back to my statement that this was a normal, busy, regular, professional scientific meeting, about the same size and scope as we had four years ago. That surprised me a good deal. There seemed to be relatively little cognizance of what's going on in the outside world. I acknowledge that thorium got a big play in this conference compared to the last conference. There were any number of papers that discussed thorium cross sections--experiments and calculations. But consider what seems to be in the wind now--what's happening in that outside world from which we've insulated ourselves for five days. The funding agencies have been warning us of coming cuts in support for cross section work. They seem to be coming for two reasons. One is that we are being successful; we're getting closer and closer to the goals that have been set for us. That was evident both in the papers of Odelli Ozer that started off this conference and in that of Dr. Hammer in which he compared the accuracies needed and the accuracies available now and concluded that you're getting pretty close to them today. But the other, perhaps more important reason, is the shifting emphasis away from the neutronic area, per se, to questions involving primarily various safety aspects of nuclear energy. While there may be some interaction between neutronics and safety, nonetheless there is relatively little need for cross sections in the safety area.

But there are other events in the wind.

I come from the battle zone--from New York State. I come from a campus on which we have been trying for 17 years to get a small Triga research reactor activated, from a campus which a few months ago saw our President, Dr. McGill, get up and say that as long as he's President of the University, the reactor will not be activated. When we pressed him for his reasons, he admitted that there was no question about the safety of the reactor, but that very frankly, he's scared. He is frightened of the physical mob damage that would be done to the University if we went ahead. We have had a Master Energy Plan announced for New York State for the next 15 years which is notable for its omission of any role for nuclear energy. In their summary report, the proponents say frankly why. Not that there are overwhelming doubts on the safety of nuclear energy, rather that it will not be acceptable to the public. We heard last night a preview of the Kemeny Commission recommendations, which, if they are taken seriously (and I think they are likely to), will mean, in effect, a long delay in any future progress in nuclear energy in this country.

So, with these developments as a background, it wouldn't have surprised me to have come to this conference to have found very poor attendance and even poorer interest--a lackadaisical interest in the situation. The bustling, active, vigorous meeting that we have had was therefore something of a surprise. At first I thought it was just a case of the corpse walking and talking because it didn't know it was dead. But as I listened to the talks and I saw the professional and competent way that we've been plugging at the problems of implementing nuclear energy, of grappling with how to best use it and develop it to fill our needs well past the beginning of the 21st century, of how to get at the proper mix of various types of cycles to use our resources intelligently, I came to the feeling you here at the conference are wiser and more farsighted than I am. The true lesson of this conference is a reaffirmation that nuclear energy is necessary for all of the countries represented here, and that the outside world, despite the present perturbations, will eventually realize it.

We shall yet overcome.

Registrants:

Mohamed A. Abdou
Associate Director
Argonne National Laboratory
9700 South Cass Avenue
Argonne, IL 60439

William L. Alford
Professor
Auburn University
Nuclear Science Center
Auburn, AL 36830

T. G. J. Al-Janabi
Iraq Atomic Energy Commission
Tuwaitha - Baghdad
P. O. Box 765
Republic of Iraq

Peter R. Almond
The University of Texas
System Cancer Center M. D.
Anderson Hospital & Tumor Inst.
6723 Bertner
Houston, TX 77030

F. S. Alsmiller
Oak Ridge National Laboratory
P. O. Box X
Oak Ridge, TN 37830

R. J. Alsmiller
Oak Ridge National Laboratory
Building 6025
Oak Ridge, TN 37830

Noel Amherd
Project Mgr. Fusion
E.P.R.I.
3412 Hillview Avenue
Polo Alto, CA 94304

Robert A. Anderl
Associate Scientist
EG&G Idaho, Inc.
P. O. Box 1625
Idaho Falls, ID 83401

Edward D. Arthur
Los Alamos Scientific Lab.
T-2 MS 243
Los Alamos, New Mexico 87545

F. Atchison
Science Research Council
Rutherford Laboratory
Chilton, Didcot, Oxon OX11 OQX
England

George F. Auchampaugh
Staff Member
L.A.S.L.
P-3 MS 442
Los Alamos, New Mexico 87545

George T. Baldwin
University of Michigan
3059 PML North Campus
Ann Arbor, MI 48109

J. Barhen
Research Staff
Oak Ridge National Laboratory
P. O. Box X, Bldg. 4500 North
Oak Ridge, TN 37830

J. Barish
Oak Ridge National Laboratory
Building 6025
Oak Ridge, TN 37830

J. M. Barnes
Oak Ridge National Laboratory
Building 6025
Oak Ridge, TN 37830

H. H. Barschall
Professor
University of Wisconsin
Engineering Research Building
Madison, WI 53706

D. E. Bartine
Nuclear Physicist
Oak Ridge National Laboratory
Oak Ridge, TN 37830

H. Beer
Kernforschungszentrum
Karlsruhe Gmb H Institut fur
Angewandte Kernphysik
Postfach 3640 D-7500 Karlsruhe
Federal Republic Germany

James W. Behrens
Physicist
National Bureau of Standards
Washinton, D.C. 20234

Zane W. Bell
Research Staff Member
Oak Ridge National Laboratory
P.O. Box X, Bldg. 4500 North
Oak Ridge, TN 37830

Richard W. Benjamin
Staff Physicist
Savannah River Lab
ElduPont
Aiken, SC 29801

Albert G. Beyerle
Graduate Student in Physics
North Carolina State University &
Triangle Universities Nuclear Lab
Raleigh, NC 27607

R. A. Bhatti
Nuclear Fuels Engineer
Power Department Public Service
Indiana
100 E. Main Street
Plainfield, IN 46016

B. L. Bishop
Oak Ridge National Laboratory
Building 6025
Oak Ridge, TN 37830

Robert C. Block
Professor
R. P. I.
Troy, NY 12181

Karl Heinz Bockhoff
Head of Linac Group
Central Bureau for Nuclear Measurements
CEC, JRC
Geel, Belgium

M. Thiuse Bogaert

T. S. Bohn
Senior Engineer
EG&G Idaho, Inc.
P. O. Box 1625
Idaho Falls, ID 83401

Jean Yves Boutin
CEA France
B P 561
92542 Montrouge
France

Charles D. Bowman
National Bureau of Standards
Center for Radiation Research
Washington, D.C. 20234

Thomas E. Bradley
Visiting Researcher
Brookhaven National Lab
Building 510A
Upton, NY 07933

Faid Brahim
Physicist
CSTN Center of Sciences &
Technology Nuclear
P. O. Box 1017
Alger-Gare, Algeria

J. J. Broerse
Rep-Institutes of the Organ. for
Health Research TNO
151 Lange Kleiweg-Rijswijk (ZH)
The Netherlands

John C. Browne
Group Leader
Los Alamos Scientific Lab
P. O. Box 808
Los Alamos, New Mexico 87545

Arne O. Bull
University of Oslo Vernetjenesten
Postboks 1060, Blindern
Oslo 3 Norway

Thomas W. Burrows
Brookhaven National Laboratory
Associated Universities, Inc.
Upton, NY 11973

Allan D. Carlson
National Bureau of Standards
Center for Radiation Research
Washington, D.C. 20234

Robert F. Carlton
Professor
Middle Tennessee State University
Box 407 M.T.S.U.
Murfreesboro, TN 37132

John M. Carpenter
Technical Director
Argonne National Laboratory
9700 South Cass Avenue
Argonne, IL 60439

F. Edward Cecil
Asst. Professor of Physics
Department of Physics
Colorado School of Mines
Golden, CO 80401

George T. Chapman
Oak Ridge National Laboratory
P. O. Box X, Building 4500 North
Oak Ridge, TN 37830

Yung-An Chao

Hwai-Pwu Chou
Research Assistant
Purdue University
School of Nuclear Engineering
W. Lafayette, IN 47907

R. E. Chrien
Sr. Physicist
Brookhaven National Laboratory
Upton, NY 11973

S. W. Cierjacks
Senior Scientist
U.F.K.
Postfach 3640
Karlsruhe, Federal Republic Germany

John C. Clark
Medical Research Council
Cyclotron Unit
Hammersmith Hospital
London, U.K.

Gerritt Coddens
Gent State University
S.C.K. Ken Mol
Belgium

Stanton H. Cohn
Brookhaven National Laboratory
Medical Research Center
Upton, NY 11973

Henri Conde
National Defence Research Institute
S-104 50 Stockholm 80
Sweden

Robert W. Conn
Professor
University of Wisconsin
Madison, WI 53706

Etieene Cornelis
RUCA University Antwerp
B 2020 Antwerpen
Belgium

F. Corvi
Central Bureau for Nuclear Measurements
CEC, JRC
2440 Geel, Belgium

Charles L. Cowan
General Electric
598 Elvis Drive
San Jose, CA 95123

J. Joseph Coyne
U. S. Department of Commerce
National Bureau of Standards
Washington, D.C. 20234

William G. Cross
Chalk River Nuclear Laboratories
Atomic Energy of Canada Limited
Chalk River, Ontario
Canada KOJ 1JO

J. Bart Czirr
Physicist
1810 E Yoo N
Mapleton, Utah 84663

J. W. T. Dabbs
Physicist
Oak Ridge National Laboratory
Building 6010
P. O. Box X
Oak Ridge, TN 37830

Jean-Paul Delaroche
Engineer
Centre d'Etudes de Bruyeres - le Chatel
B. P. No. 651
92542 Montrouge Cedex
France

Jack DeVeaux
Graduate Student
University of Illinois
214 Nuclear Energy Laboratory
Urbane, IL 61820

J. K. Dickens
Physicist
Oak Ridge National Laboratory
P. O. Box X, Building 4500 North
Oak Ridge, TN 37830

H. L. Dodds, Jr.
Associate Professor
University of Tennessee
Nuclear Engineering Building
Knoxville, TN 37916

Charles L. Dunford
Brookhaven National Laboratory
Upton, New York 11973

Colin Durston
Nuclear Engineer
Brookhaven National Laboratory
Associated Universities, Inc.
Upton, NY 11973

Kenneth C. Duvall
Physicist
National Bureau of Standards
Washington, D.C. 20234

James J. Egan
Associate Professor
University of Lowell
Department of Physics
Lowell, MA 01854

Sadiq El-Kadi
Student
Duke University
Physics Department
Durham, NC 27706

Alexander Elwyn
Senior Scientist
Argonne National Laboratory
9700 South Cass Avenue
Argonne, IL 60439

Bernard A. Engholm
Senior Staff Engineer
General Atomic Co.
P. O. Box 81608
San Deigo, CA 92138

Michael Fanell
Physics Associate
Brookhaven National Laboratory
Upton, NY 11973

L. R. Fawcett, Jr.
Associate Professor
Physics
Longwood College
Farmville, VA 23907

A. T. G. Ferguson
United Kingdom Atomic Energy Authority
Nuclear Physics Division 721
AERE-Harwell, Oxon OX11 ORA
England

Roger W. Finlay
Professor
Ohio University
Physics
Athens, OH 45701

W. E. Ford, III
Oak Ridge National Laboratory
Oak Ridge, TN 37830

Eric Fort
Comm cearíat aI P
Energie Atomique
C.E.A. France

James Freim
Research Specialist
Babcock & Wilcox - LRC
P. O. Box 1260
Lynchburg, VA 24502

C. Y. Fu
Research Staff Member
Oak Ridge National Laboratory
P. O. Box X, Building 4500 North
Oak Ridge, TN 37830

Tony A. Gabriel
Oak Ridge National Laboratory
Building 6025
Oak Ridge, TN 37830

Donald G. Gardner
Chemist
Lawrence Livermore Lab
L-425
Livermore, CA 94550

Maureen A. Gardner
Chemist
Lawrence Livermore Lab
L-234
Livermore, CA 94550

S. B. Garg
International Atomic Energy Agency
Karntner Ring 11
P. O. Box 590
A-1011 Vienna, Austria

Jagadish Garg
Professor Physics Department
University of Albany
1400 Washington Avenue
Albany, NY 12222

Siegfried Gerstl
Los Alamos Scientific Lab
P. O. Box 1663 T-1, MS 269
Los Alamos, NM 87545

Herbert Goldstein
Professor
Nuclear Science & Eng.
Columbia University
Mudd Building
287 Eng. Terrace
New York, NY 10027

Peter Grabmayr
Post-Doctorial
Physics Department
Ohio University
Athens, OH 45701

Daniel J. Grady
University of Michigan
3059 Phoeniv Memorial Laboratory
Ann Arbor, Michigan 48109

Lawrence Green
Fellow Scientist
Westinghouse
P. O. Box 10468
Pittsburgh, PA 15036

N. M. Greene
Oak Ridge National Laboratory
P. O. Box X
Oak Ridge, TN 37830

Lawrence R. Greenwood
Physicist
Argonne National Laboratory
9700 S. Cass Avenue
Argonne, IL 60439

Cudmar Grosshoeg
Chalmers University of Technology
Department of Reactor Physics S-412
96 Gothenburg
Sweden

Khunab Gul
Principal Scientific Officer
Pakistan Institute of Nuclear Science
and Technology
Pinstech P. O. Nilore
Rawalpindi, Pakistan

Dunstan Guo
Research Geophysicist
Chevron Oil Field Research Company
P. O. Box 466
La Habra, CA 90631

Reginald Gwin
Research Staff Member
Oak Ridge National Laboratory
P. O. Box X, Building 4500 North
Oak Ridge, TN 37830

Hans Haggblom
Studsvik Energiteknik AB
S611 82
Nykoping, Sweden

Robert C. Haight
Physicist
Lawrence Livermore Laboratory
P. O. Box 808
University of California
Livermore, CA 94550

Gerald M. Hale
Los Alamos Scientific Laboratory
T-2 MS 243
Los Alamos, NM 87545

Philippe Hammer
C.E.N.
Cadarache, France

Lusia F. Hansen
Senior Physicist
Lawrence Livermore Laboratory
P.O. Box 808
University of California
Livermore, CA 94550

Gerard Haouat
Engineer
Centre d'Etudes de Bruyeres - 1e
B.P. No. 651 92542 Montrouge
Cedex, France

Robert A. Hardekopf
Staff Member
Los Alamos Scientific Laboratory
Group P-9 MS-480
Los Alamos, NM 87544

Yale D. Harka
Scientist
EG&G Idaho
P. O. Box 1625
Idaho Falls, ID 83415

Gary A. Harms
Graduate Student
Purdue University
School of Nuclear Engineering
W. Lafayette, IN 47907

Robert Harper
Graduate Student
Auburn University
Nuclear Science Center
Auburn, AL 36830

J. A. Harvey
Oak Ridge National Laboratory
P. O. Box X
Oak Ridge, TN 37830

W. W. Havens, Jr.
Professor
Columbia University
Department of Applied Physics &
Nuclear Engineering
New York, NY 10027

Philip Hemmig
Physicist
U. S. Department of Energy
Washington, D.C. 20585

David N. Hetrick
Research Staff Member
Oak Ridge National Laboratory
P. O. Box X, Building 4500 North
Oak Ridge, TN 37830

William A. Higinbotham
Senior Scientist
Brookhaven National Lab
Accounts Payable Section
Upton, Long Island, NY 11973

N. W. Hill
Dev. Eng
Oak Ridge National Laboratory
P. O. Box X, Building 6010
Oak Ridge, TN 37830

Yoshio Hino
Tohoku University
Sendai, Japan

Richard W. Hoff
Chemist
Lawrence Livermore Laboratory
P. O. Box 808
University of California
Livermore, CA 94550

Henry H. Hogue
Oak Ridge Y-12
Box Y, Building 9203A
Oak Ridge, TN 37830

Norman E. Holden
Physicist
Brookhaven National Laboratory
Building 197
Upton, NY 11973

Steven D. Howe
Graduate Student
Los Alamos Scientific Lab
P. O. Box 1663
Los Alamos, NM 87545

Henry Hubeny
Engineer
Argonne
1013 Hinswood Drive
Darien, IL

Raymond E. Hunter
Los Alamos Scientific Laboratory
Group TD - 2, MS-220
Los Alamos, NM 87545

Daniel T. Ingersol
Staff - Reactor Phys. & Shlding
Oak Ridge National Laboratory
P. O. Box X
Oak Ridge, TN 37830

S. Iwasaki
Research Assistant
Tohoku University
Sendia, Japan 980

Nelson Jarmie
Staff Scientist
Los Alamos Scientific Lab
Mail Stop 456
Los Alamos, NM 87545

D. Jassby
Research Physicist
Princeton University
P. O. Box 451, Forrestal
Princeton, NJ 08544

T. K. Jindeel
Iraq Atomic Energy Commission
Baghdad, Iraq

Cleland H. Johnson
Oak Ridge National Laboratory
P. O. Box X, X10 Building 6010
Oak Ridge, TN 37830

David L. Johnson
Senior Scientist
Westinghouse Hanford Company
P. O. Box 1970, Mailstop W/F429
Richland, WA 99352

Richard H. Johnson
Asst. Professor
School of Nuclear Engineering
Purdue University
West Lafayette, IN 47907

Ronald G. Johnson
Physi
Na ional Bureau of Standards
Washington, D. C. 20234

Peter Daniel Johnson
O. C. D. E.
Nuclear Energy Agency Data Bank
B. P. 9 Gif-sur-Yvette
F91190 France

F. Kaeppeler
Kernforschungszentrum
Karlsruhe Gmb H Institut fur
Angewandte Kernphysik
Postfach 3640, D-7500 Karlsruhe
Federal Republic Germany

Constance Kalbach-Walker
Consultant
Triangle University Nuclear Lab
Duke University
Durham, NC 27706

John Kallfelz
Professor
Georgia Tech
School of N. E.
Atlanta, GA 30332

P. R. Kasten
Director GCRP
Oak Ridge National Laboratory
P. O. Box X
Rak Ridge, TN 37830

Masayoshi Kawai
Researcher
NAIG Nuclear Research Laboratory
4-1 Ukishima-cho
Kawasaki, Japan 210

G. A. Keyworth
Physics Division Leader
Los Alamos Scientific Lab
P. O. Box 1663, MS-434
Los Alamos, NM 87545

Yasuyuki Kikuchi
Senior Nuclear Engineer
Nuclear Data Center
Japan Atomic Energy Research Inst.
Tokai Research Establishment
Tokai-Mura, Naka-Gun
Ibaraki-Ken, Japan

Itsuro Kimura
Professor
Research Reactor Institute
Kyoto University
Kumatori-Cho Sennan-Gun
Osaka, Japan

Robert R. Kinsey
Physicist
Brookhaven National Laboratory
Upton, NY 11973

Hideo Kitazawa
Research Laboratory for Nuclear Reactors
Tokyo Institute of Technology
2-12-1, O-okayama, Meguro-ku
Tokyo, Japan

Dr. Hans-Otto Klages
Institut fur Kernphysik I
Postfach 3640, D-7500
Karlsruhe 1, Germany

Ron J. Knight
Embassy of Australia
1601 Massachusetts Avenue
Washington, D.C. 20036

Hans-Hermann Knitter
Comm. of the European Communities
Central Bureau for Nuclear Measurements
CEC, CBNM, Steenweg
Naar Retie, Geel, Belgium 2440

Kenneth R. Koch
Research Assistant
Purdue University
School of Nuclear Engineering
W. Lafayette, IN 47907

Herbert J. Kouts
Department Chairman
Brookhaven National Laboratory
Upton, NY 11973

Nikoloy I. Kroshkin
Institute of Reactors
Dimitrovgrad, USSR

Vivek Kulkarni
Graduate Student
Physics Department
Ohio University
Athens, OH 45701

H. Küsters
Nuclear Research Center
P. O. Box 3640
Karlsruhe, Germany

Christian LaGrange
Los Alamos Scientific Laboratory
P. O. Box 1663
Los Alamos, NM 82545

George P. LaMaze
Physicist
National Bureau of Standards
Washington, D.C. 20234

Raymond O. Lane
Professor
Ohio University
Department of Physics
Accelerator Laboratory
Athens, OH 45701

Robert G. Lanier
Nuclear Chemist
Lawrence Livermore Lab
L-234
Livermore, CA 94550

Duane C. Larson
Research Staff Member
Oak Ridge National Lab
P. O. Box X, Bldg. 4500 North
Oak Ridge, TN 37830

T. S. Lefler, Jr.
President
Techlase
P. O. Box 85
Pinellas Park, FL 33565

Leo G. LeSage
Applied Physics Division
Argonne National Laboratory
Bldg. 316
Argonne, IL 60439

Peretz Levin
Research Engineer
GA-Tech
Atlanta, GA 30332

R. A. Lillie
Oak Ridge National Laboratory
Bldg 6025
Oak Ridge, TN 37830

Horn-ing Liou
Physics Associate
Brookhaven National Laboratory
Upton, NY 11973

Paul W. Lisowski
Staff Member
Los Alamos Scientific Laboratory
MS 442
Los Alamos, NM 87545

J. L. Lucuis
Oak Ridge National Laboratory
Oak Ridge, TN 37830

Joseph C. McDonald
Associate
Sloan-Kettering Institute
1275 York Avenue
New York, NY 10021

Richard D. McKnight
Nuclear Engineer
Argonne National Laboratory
9700 South Cass Avenue
Argonne, IL 60439

Victoria McLane
Physics Association
Brookhaven National Laboratory
T-197
Upton, NY 11973

George S. McNeilly
Oak Ridge National Laboratory
P. O. Box X
Oak Ridge, TN 37830

Robert MacFarlane
Los Alamos Scientific Laboratory
MS 243
Los Alamos, NM 87545

R. L. Macklin
Physicist
Oak Ridge National Laboratory
P. O. Box X
Oak Ridge, TN 37830

David G. Madland
Los Alamos Scientific Laboratory
T-2, MS 243, Box 1663
Los Alomos, NM 87545

G. C. Madueme
University of IFE
Department of Physics
Nigeria ILE-IFE, Nigeria

R. E. Maerker
Project Leader
Oak Ridge National Laboratory
P. O. Box X, Bldg. 4500 North
Oak Ridge, TN 37830

F. C. Maienschein
Director
Oak Ridge National Laboratory
P. O. Box X, Bldg. 4500 North
Oak Ridge, TN 37830

Frederick M. Mann
Senior Engineer
HEDL
P. O. Box 1970
Richland, WA 99352

James H. Marable
Oak Ridge National Laboratory
P. O. Box X
Oak Ridge, TN 37830

A. Marcinkowski
Institute of Nuclear Research
Warsaw, Hoza 69
Warsaw, Poland

Margarete Mattes
Institut fur Kernenergetik
D7000 Stuttgart -80
Pfaffenwaldring 31
Germany

James W. Meadows
Chemist
Argonne National Laboratory
9700 South Cass Avenue
Argonne, IL 60439

Mehrzad Mahdavi
Grad, Student Res. Asst.
University of Michigan
2540 Loudonderry
Ann Arbor, MI 48104

Michael M. Meier
Physicist
Los Alamos Scientific Lab
P. O. Box 1663
Los Alamos, NM 87545

Heiner W. Meldner
Physicist
Lawrence Livermore Laboratory
University of California
P. O. Box 808
Livermore, CA 94550

Enzo Menapace
Comitato Nazionale Energia
Nucleare (CNEN)
Centre Di Calcolo
Bologna, Italy

Walfried Michaelis
Institute for Physics
Gesellschaft fur
Kernenergieverwertung in
Schiffbau and Schiffahrt mbH
2054 Geesthacht-Tesperhude
Reaktorstation, Germany

Laurence F. Miller
University of Tennessee
Department of Nuclear Engineering
Knoxville, TN 37916

Arthur Mittler
Associate Professor
University of Lowell
Department of Physics
Lowell, MA 01854

Fellah Mohamed
Doctor in Physics
CSTN Center of Sciences & Technology
Nuclear
P. O. Box 1017
Alger-Gare, Algeria

Peter A. Moldauer
Senior Physicist
Argonne National Laboratory
Department 316
9700 S. Cass Avenue
Argonne, IL 60439

Henry T. Motz
Asst. to Associate Director Research
Los Alamos Scientific Laboratory
P. O. Box 1663
Los Alamos, NM 87545

Takehiko Mukaiyama
Scientist
Japan Atomic Energy Research Inst.
Tokai-Mura
Ibaraki, Japan

Henzik Muzadyan
Senior Scientist
Institute of Atomic Energy
Moscow, U.S.S.R.

S. Nair
Research Officer
Central Electricity Generating
Boacd
United Kingdom

Ralf-Dieter Neef
KFA Julich - IRE
Postfach 1913, D-5170
Julich, Germany

Ronald O. Nelson
Staff
Los Alamos Scientific Laboratory
MS 805
Los Alamos, NM 87545

David Kurt Olsen
Oak Ridge National Laboratory
P. O. Box X, Building 6010
Oak Ridge, TN 37830

Odelli Ozer
Project Manager
E.P.R.I.
P. O. Box 10412
Palo Alto, CA 94303

Apostolos Panayotou
Professor of Physics
University of Athens
Nuclear Physics Laboratory
104 Solonos Street
Athens, Greece 144

Raymond Pannetier
Centre d'Etudes De Limeil
Boite Postale 27
94190 Villeneuve St Georges
Republic of France

Mitrofan V. Paseshnik
Head, Nuclear Physics Department
TNR - Kiev
Kiev-1 Zankoverkaje 5, 35
Kiev, U.S.S.R. 252001

P. F. Pasqua
University of Tennessee
315 Nuclear Engineering Bldg.
Knoxville, TN 37916

Arno Paulsen
Commission of the European Communities
Central Bureau for Nuclear Measurements
CEC, CBNM, Steenweg naar Retie
Geel, Belgium 2440

Sol Pearlstein
Physicist
Brookhaven National Laboratory
Building 197
Upton, Long Island, NY 11973

R. W. Peelle
Group Leader
Oak Ridge National Laboratory
P. O. Box X, Building 4500 North
Oak Ridge, TN 37830

R. B. Perez
Physicist
Oak Ridge National Laboratory
P. O. Box X, Building 4500 North
Oak Ridge, TN 37830

Edward Peterson
Physicist
Naval Research Laboratory
Washington, D.C. 20375

S. Plattard
Visiting Staff Member
Los Alamos Scientific Laboratory
Los Alamos, NM 87545

W. P. Poenitz
Physicist
Argonne National Laboratory
9700 South Cass Avenue
Building 314
Argonne, IL 60439

Fred Poortmans
SCK/CEN
B 2400 MOL
Belgium

Augustus Prince
Nuclear Physicist
Brookhaven National Laboratory
Upton, NY 11973

Karl S. Quisenberry
Director - Nuclear
Schlumberger - Doll Research Center
P. O. Box 307
Ridgefield, CT 06877

Charles Ragen III
Los Alamos Scientific Laboratory
Los Alamos, NM 87544

S. Raman
Physicist
Oak Ridge National Laboratory
Building 6010
Oak Ridge, TN 37830

Gerhard Randers-Pehrson
Post Doc
Ohio University
Physics Department
Athens, OH 45701

James Craig Robertson
Professor
University of New Mexico
Department of Chemical,
Nuclear Engineering
Albuquerque, NM 87106

George Rogosa
Federal Government
3 Hitching Post Place
Rockville, MD 20852

Y. Ronen
Oak Ridge National Laboratory
Oak Ridge, TN 37830

E. Roth
Deputy Division Chemistry Head
CEA France
B.P. N2 DO1-DRA C.E.N. Saclay
Gif/Yvette 91190
France

Carl Rouse
Staff Scientist
General Atomic Center
P. O. Box 8106
San Diego, CA 92138

Robert W. Roussin
RSIC
Oak Ridge National Laboratory
P. O. Box X
Oak Ridge, TN 37830

Ted Rupp
Senior Scientist
EG&G
P. O. Box 809
Los Alamos, NM 87544

Gary J. Russell
Staff Member
Los Alamos Scientific Laboratory
Group P-9, MS 805, P. O. Box 1663
Los Alamos, NM 87545

J. C. Ryman
Oak Ridge National Laboratory
Oak Ridge, TN 37830

T. B. Ryves
National Physical Laboratory
Teddington, Middlesex TW11 OLW
United Kingdom

George N. Salaita
Professor of Physics
Southern Methodist University
Physics Department
Dallas, TX 75275

Max Salvatores
CEN
Cadarache, France

R. T. Santoro
Oak Ridge National Laboratory
Building 6025
Oak Ridge, TN 37830

Dallas C. Santry
Chalk River Nuclear Labs
Atomic Energy of Canada
Ontario, Canada, KOJ 1JO

Gerard deSaussure
Physicist
Oak Ridge National Laboratory
P. O. Box X, Building 4500 North
Oak Ridge, TN 37830

Windried Skherer
Institut fur Reaktorentwicklung
der Kemforschungsanlage Julich
GmbH
517 Julich 1, W. Germany

Josef J. Schmidt
Section Head
IAEA
Vienna International Centre
P. O. Box 100
A-1400 Vienna, Austria

Frank Schmittroth
Scientist
Westinghouse Hanford
Box 1970
Richland, WA 99352

Bruce G. Schnitzler
Nuclear Engineer
EG&G Idaho, Inc.
P. O. Box 1625
Idaho Falls, ID 83401

Horst Scholermann
P.T.B. Bundesallee 100
33 Braunschweig, West Germany

R. A. Schrack
Physicist
National Bureau of Standards
Center for Radiation Research
Washington, D.C. 20234

A. J. Scott
Reactor Physics
EG&G Idaho, Inc.
P. O. Box 1625
Idaho Falls, ID 83401

L. W. Seagondollar
Professor
North Carolina State University
Raleigh, NC 27607

Frank E. Senftle
U. S. Department of the Interior
Geological Survey
Washington, D.C. 20242

Robert E. Shamu
Professor of Physics
Western Michigan University
Department of Physics
Kalamazoo, MI 49008

E. I. Sharapov
The Joint Institute for
Nuclear Research
Head Post Office, P.O.Box 79
10 10 00 Moscow, U.S.S.R.

M. Adib Shihata
Reactor and Neutron Physics Division
Atomic Energy Establishment
Cairo, Egypt

Vladimar I. Shpakov
V. G. Khlopin Radium Institute
Leningrad, U.S.S.R.

Udit N. Singh
Senior Physicist
Combustian Engineering, Inc.
Department 9492-425
Windsor, CT 06095

Alan B. Smith
Physicist
Argonne National Laboratory
9700 South Cass Avenue
Argonne, IL 60439

Donald L. Smith
Physicist
Argonne National Laboratory
Applied Physics Division
Building 314
Argonne, IL 60439

J. Richard Smith
854 Clare View Land
Idaho Falls, ID 83401

Maurice Soleilhac
Centre D'Etudes De Limeil
Boite Postale 27
94190 Villeneuve - St Georges
Republic of France

R. R. Spencer
Physicist
Oak Ridge National Laboratory
P. O. Box X, Building 4500 North
Oak Ridge, TN 37830

M. L. Stelts
Brookhaven National Laboratory
Physics Department
Building 510A
Upton, NY 11973

Howard Stewart
Engineer
Tennessee Valley Authority
1410 Commerce Union Bank Building
Chattanooga, TN 37405

Jim Strachan
Physicist
Princeton University
Plasma Physics Laboratory
Princeton, NJ 08540

Kazusuke Sugiyama
Professor
Tohoku University
Department of Nuclear Engineering
Faculty of Engineering
Sendai, Japan

N. B. Sullivan
Physicist
University of Lowell
University Avenue
Lowell, MA 01854

M. T. Swinhoe
Research Fellow
United Kingdom Atomic Energy Authority
Liaison Office, British Embassy
Washington, D.C. 20008

Hiroshi Takahashi
Physicist
Brookhaven National Laboratory
Upton, LI, NY 11793

Hideki Takano
Japan Atomic Energy Research Inst.
Takai-mura
Ibaraki-ken, Japan

Jurgen W. Tepel
Fach-informations-zentrum
Energie Physik Mathematik
Kernforschungszentrum, 7514
Eggenstein-Leopoldshafen 275 Karlsruhe
Federal Republic of Germany

Charles E. Till
Division Director
Argonne National Laboratory
Applied Physics Division
Argonne, IL 60439

Jean-Pierre Trapp
CEA-France

Jean Trochon
Engineer
Centre d'Etudes de Bruyeres-le-Chatel
B.P. no 651 92542 Montrouge
Cedex, France

Feldman Uri
Research Worker
ADA Israel
P. O. Box A
Ha Israel, Kiriat Motzkin

Lev N. Usachev
Physics Power Engineers Institute
Obninsk, U.S.S.R.

Golikov Vassily
The Joint Institute for Nuclear Research
JINR, Head Post Office, P.O.Box 79
10 10 00 Moscow
U.S.S.R.

David W. Vehar
Grad Instru. Research
Purdue University, Nuclear Eng.
W. Lafayette, IN 47907

V. P. Vertibnyi
Institut Yader NYKH Issledovaniy
AN UKRAI NSKOl SSR Prospekt
Nauki 11g Kiev
U.S.S.R.

Jean Claude Vidal
CPMM
CEA France
BP 561 92562
Montrouge, France

Juan Volkis
Comision Nacional de Energia Atomia
Dept. de Reactores
Av. del Libertador 8250
Buenos Aires, Argentina 1429

Nikolay G. Volkov
The Joint Institute for Nuclear Research
Head Post Office, P. O. Box 79
10 10 00 Moscow, U.S.S.R.

J. J. Wajschal
Research Staff
Oak Ridge National Laboratory
P. O. Box X
Oak Ridge, TN 37830

Gail Waite
Physics Associate
Brookhaven National Laboratory
Upton, NY 11973

Richard L. Walter
Professor
Duke University
Department of Physics
Durham, NC 27706

Oren A. Wasson
National Bureau of Standards
Center for Radiation Research
Washington, D.C. 20234

C. C. Webster
Oak Ridge National Laboratory
Oak Ridge, TN 37830

Bernard W. Wehring
Professor
University of Illinois
Nuclear Engineering Lab
Urbana, IL 61801

Jesse L. Weil
Professor
University of Kentucky
College of Arts & Sciences
Department of Physics and Astronomy
Lexington, KY 40506

C. R. Weisbin
Group Leader
Oak Ridge National Laboratory
P. O. Box X, Building 4500 North
Oak Ridge, TN 37830

Fred G. Welfare
Research Specialist
Babcock & Wilcox
Research & Development Division
P. P. Box 1260
Lynchburg, VA 24505

R. M. Westfall
Oak Ridge National Laboratory
Oak Ridge, TN 37830

Lawrence W. Weston
Research Staff Member
Oak Ridge National Laboratory
P. O. Box X, Building 4500 North
Oak Ridge, TN 37830

Stanley L. Whetstone
U. S. Department of Energy
ER-23, MS J-309
Division Nuclear Physics
Washington, D.C. 20545

J. E. White
Oak Ridge National Laboratory
Oak Ridge, TN 37830

J. R. White
Oak Ridge National Laboratory
Building 6025
Oak Ridge, TN 37830

Roger M. White
Physicist
Lawrence Livermore Laboratory
University of California
P. O. Box 808
Livermore, CA 94550

T. Wiedling
The Studsvik Science Research Lab
Nykoping Sweden

Jerry Wilhelmy
Los Alamos Scientific Laboratory
MS 514
Los Alamos, NM 87545

M. L. Williams
Oak Ridge National Laboratory
Oak Ridge, TN 37830

Robert M. Williamson
Physics Department
Oakland University
Rochester, MI 48063

William B. Wilson
Staff Member
Los Alamos Scientific Laboratory
P. O. Box 1663
Los Alamos, NM 87545

Gerhard Winkler
Physicist
Argonne National Laboratory
9700 South Cass Avenue
Building 314
Argonne, IL 60439

Sidney W. Winslow
Nuc. Coord.
B. M. D. A. T. C. Hsu A1
Box 1500
Huntsville, AL 35807

Ron Winters
Oak Ridge National Laboratory
Building 6010
Oak Ridge, TN 37830

Gordon W. Wolfe
Assistant Professor of Physics
The University of Mississippi
College of Liberal Arts
Department of Physics & Astronomy
University, MS 38677

T. G. Worlton
Physicist
Argonne National Laboratory
9700 South Cass Avenue
Argonne, IL 60439

R. O. Wright
Oak Ridge National Laboratory
Oak Ridge, TN 37830

Yoshimaro Yamanouti
Research Associate
Ohio University
Athens, OH 45701

Y. Yeivin
Research Staff
Oak Ridge National Laboratory
ATTN: Becky Thomas
ORNL Cashier
P. O. Box X, Building 4500 North
Oak Ridge, TN

Miss Fatiha Youcef-Ettoumi
CSTN Center of Science &
Technology Nuclear
P. O. Box 1017
Alger-Gare, Algeria

Phillip G. Young
Los Alamos Scientific Laboratory
T-2, MS 243, P. O. Box 1663
Los Alamos, NM 87545

Boris D. Yurlov
State Department
Washington, D.C. 20545

Bernard Zeitnitz
Institut fur Kernphysik I
Postfach 3640, D-7500
Karlsruhe 1, Germany

Element S	A	Quantity	Energy (eV) Min	Max	Type	Documentation Ref	Vol	Page	Date	Lab	Comments
H	001	TOTAL XSECT	3.0+6	4.2+7	Expt	79KNOX	AB	4	1079	NBS	Kellie+TOF.GRPH.CFD ACCEPTED VALUE
H	001	ELASTIC SCAT		2.0+7	Revw	79KNOX	GA	1	1079	NBS	Wasson+STATUS OF STANDARDS.
H	001	DIFF ELASTIC		2.0+7	Revw	79KNOX	GA	1	1079	NBS	Wasson+STATUS OF STANDARDS.GRPH.
H	001	POLARIZATION		1.7+7	Revw	79KNOX	GA	1	1079	NBS	Wasson+STATUS OF STANDARDS.
H	002	TOTAL XSECT	7.0+6	2.3+7	Expt	79KNOX	EC	7	1079	OHO	Kulkarni+6 ES.GRPH.CFD DEL,SEL.
H	002	ELASTIC SCAT	5.1+6	1.5+7	Expt	79KNOX	AB	2	1079	NIL	Gul+DRVD FROM LEG FIT.CFD EXPT,TH.
H	002	ELASTIC SCAT	7.0+6	2.3+7	Expt	79KNOX	EC	7	1079	OHO	Kulkarni+6 ES.GRPH.CFD TOT,DEL.
H	002	DIFF ELASTIC	1.5+7		Expt	79KNOX	AB	2	1079	NIL	Gul+TOF.ANGDIST.GRPH,TBL.CFD EXPT,TH
H	002	DIFF ELASTIC	9.0+6	1.1+7	Expt	79KNOX	EC	7	1079	OHO	Kulkarni+2 ES.TOF.ANGDISTS.GRPHS.
H	002	N,GAMMA	NDG		Revw	79KNOX	DB	3	1079	DUB	Luschikov+ MEAS TBD.
H	002	N,GAMMA	2.5-2		Expt	79KNOX	DB	4	1079	DUB	Alfimenkov+TOF.REL CL.TBL.CFD TH,EXP
H	002	N2N REACTION	1.1+7	2.5+7	Expt	79KNOX	EC	7	1079	OHO	Kulkarni+2 ES.TOF.DBL DIFF.GRPHS.
HE	003	N,GAMMA	2.5-2		Revw	79KNOX	DB	3	1079	DUB	Luschikov+ MEAS TBD.
HE	003	N,PROTON	2.5-2	1.0+4	Expt	79KNOX	AC	6	1079	NBS	Bowman+2ES.B-10(N,A)/HE-3(N,P) RATIO
HE	003	N,PROTON	2.0+3	2.5+4	Expt	79KNOX	AC	6	1079	ORL	Bowman+ORELA.B10(N,A)/HE3(N,P) RATIO
HE	003	N,PROTON		1.0+6	Revw	79KNOX	GA	1	1079	NBS	Wasson+STATUS OF STANDARDS.GRPH.
LI		NONEL GAMMA		2.0+7	Revw	79KNOX	CA	1	1079	LRL	Haight+CS FOR FUSION.NDG.
LI		NONEL GAMMA	7.0+5	2.0+7	Revw	79KNOX	DB	5	1079	TOH	Sugiyama.REVIEW.DATA STATUS.NDG
LI	006	TOTAL XSECT	3.0+6	4.0+7	Expt	79KNOX	AB	4	1079	NBS	Kellie+TOF.GRPH.CFD ENDF/B-V
LI	006	N,TRITON	2.5-2		Expt	79KNOX	CA	3	1079	HAR	Swinhoe.CS MEAS AS SYSTEM CHECK.
LI	006	N,TRITON	1.0+0	1.0+3	Expt	79KNOX	AC	2	1079	NBS	Czirr+B-10/LI-6 CS RATIO.TBL.GRPH.
LI	006	N,TRITON	NDG		Revw	79KNOX	GC	8	1079	GGA	Cheng+ENDF/B-IV,V REVIEWED.
LI	006	N,TRITON		1.0+5	Revw	79KNOX	GA	1	1079	NBS	Wasson+STATUS OF STANDARDS.GRPH.
LI	006	N,TRITON	2.0-2	3.0+4	Expt	79KNOX	IB	2	1079	GHT	Wagemans+ U235 REL LI6.
LI	007	TOTAL XSECT	3.0+6	4.0+7	Expt	79KNOX	AB	4	1079	NBS	Kellie+TOF.GRPH.CFD ENDF/B-V
LI	007	DIFF ELASTIC	7.0+6	1.4+7	Revw	79KNOX	CA	1	1079	LRL	Haight+CS FOR FUSION.GRPHS.
LI	007	DIFF ELASTIC	5.1+6	1.5+7	Expt	79KNOX	AB	3	1079	TOK	Baba+TOF.3 ES,6 ANGS.GRPHS CFD ENDF
LI	007	DIFF ELASTIC	1.0+5	8.0+6	Exth	79KNOX	GB	7	1079	OHO	Knox+MULTI-CHANL,LVL R-MATRIX.CURVS.
LI	007	DIFF INELAST	7.0+6	1.4+7	Revw	79KNOX	CA	1	1079	LRL	Haight+CS FOR FUSION.GRPHS.
LI	007	DIFF INELAST	5.1+6	1.5+7	Expt	79KNOX	AB	3	1079	TOK	Baba+TOF.3 ES,6 ANGS.GRPHS CFD ENDF
LI	007	DIFF INELAST	5.0+5	8.0+6	Exth	79KNOX	GB	7	1079	OHO	Knox+MULTI-CHANL,LVL R-MATRIX.CURVS.
LI	007	NONEL GAMMA		2.0+7	Revw	79KNOX	CA	1	1079	LRL	Haight+CS FOR FUSION.NDG.
LI	007	NEUT EMISSN	5.1+6	1.5+7	Expt	79KNOX	AB	3	1079	TOK	Baba+TOF.3 ES,6 ANGS.GRPHS CFD ENDF
LI	007	N,TRITON	NDG		Revw	79KNOX	GC	8	1079	GGA	Cheng+ENDF/B-IV,V REVIEWED.
LI	007	N,N TRITON	4.7+6	1.4+7	Expt	79KNOX	CA	3	1079	HAR	Swinhoe.ACT.GRPH.CFD ENDF,OTH EXPTS.

Element S	A	Quantity	Energy (eV) Min	Max	Type	Documentation Ref	Vol	Page	Date	Lab	Comments
LI	007	N,N TRITON	2.8+6	2.0+7	Revw	79KNOX	CA	1	1079	LRL	Haight+CS FOR FUSION.GRPHS
BE	007	N,ALPHA REAC	NDG		Revw	79KNOX	DB	3	1079	DUB	Luschikov+ THR,EPI-THR TBD. (N,2A).
BE	009	TOTAL XSECT	1.0+6	2.0+7	Revw	79KNOX	CA	1	1079	LRL	Haight+CS FOR FUSION.NDG.
BE	009	DIFF ELASTIC	7.0+6	1.5+7	Revw	79KNOX	CA	1	1079	LRL	Haight+CS FOR FUSION.NDG.
BE	009	DIFF INELAST	7.0+6	1.5+7	Revw	79KNOX	CA	1	1079	LRL	Haight+CS FOR FUSION.NDG.
BE	009	NEUT EMISSN	NDG		Revw	79KNOX	CA	1	1079	LRL	Haight+CS FOR FUSION.NDG.
B	010	TOTAL XSECT	1.0+6	2.0+7	Revw	79KNOX	CA	1	1079	LRL	Haight+CS FOR FUSION.NDG.
B	010	N,GAMMA		1.2+6	Revw	79KNOX	GA	1	1079	NBS	Wasson+STATUS OF STANDARDS.GRPH.
B	010	N,TRITON	2.0-2	3.0+4	Expt	79KNOX	IB	2	1079	GHT	Wagemans+U235 REL B10.
B	010	N,ALPHA REAC	1.0+0	1.0+3	Expt	79KNOX	AC	2	1079	NBS	Czirr+B-10/LI-6 CS RATIO.TBL,GRPH.
B	010	N,ALPHA REAC	2.5-2	1.0+4	Expt	79KNOX	AC	6	1079	NBS	Bowman+2ES.B-10(N,A)/HE-3(N,P) RATIO
B	010	N,ALPHA REAC	5.0-1	1.0+4	Exth	79KNOX	AC	4	1079	NBS	Carlson+SOLID B10 VS BF3.TH CFD EXPT
B	010	N,ALPHA REAC	2.0+3	2.5+4	Expt	79KNOX	AC	6	1079	ORL	Bowman+ORELA.B10(N,A)/HE3(N,P) RATIO
B	011	TOTAL XSECT	1.0+6	2.0+7	Revw	79KNOX	CA	1	1079	LRL	Haight+CS FOR FUSION.GRPHS.
B	011	DIFF INELAST	4.8+6	6.0+6	Revw	79KNOX	CA	1	1079	LRL	Haight+CS FOR FUSION.NDG.
B	CMP	N,ALPHA REAC	5.0-1	1.0+4	Exth	79KNOX	AC	4	1079	NBS	Carlson+SOLID B10 VS BF3.TH CFD EXPT
C	012	TOTAL XSECT	1.0+6	2.0+7	Revw	79KNOX	CA	1	1079	LRL	Haight+CS FOR FUSION.NDG.
C	012	TOTAL XSECT	2.5+6	2.5+7	Expt	79KNOX	EC	6	1079	LAS	Lisowski+TRNS,GRPH.CFD ENDF,OTHS.TBL
C	012	TOTAL XSECT		1.5+7	Revw	79KNOX	GA	1	1079	NBS	Wasson+STATUS OF STANDARDS.
C	012	ELASTIC SCAT		1.5+7	Revw	79KNOX	GA	1	1079	NBS	Wasson+STATUS OF STANDARDS.
C	012	DIFF ELASTIC		1.5+7	Revw	79KNOX	GA	1	1079	NBS	Wasson+STATUS OF STANDARDS.
C	012	POLARIZATION	4.6+6	5.2+6	Expt	79KNOX	IB	7	1079	KTY	Weil+3ES.ASYM.CALC SCAT PHASE SHIFTS
C	012	N,GAMMA		6.0+6	Theo	79KNOX	AB	5	1079	WAU	Johnson.(N,G),(G,N),(P,G) CALC.CFD.
C	012	NONEL GAMMA		2.0+7	Revw	79KNOX	CA	1	1079	LRL	Haight+CS FOR FUSION.NDG.
C	012	NONEL GAMMA	7.0+5	2.0+7	Revw	79KNOX	DB	5	1079	TOH	Sugiyama.REVIEW.DATA STATUS.NDG
C	012	NEUT EMISSN	NDG		Revw	79KNOX	CA	1	1079	LRL	Haight+CS FOR FUSION.NDG.
C	012	N,DEUTERON	2.7+7	6.1+7	Revw	79KNOX	CA	1	1079	LRL	Haight+CS FOR FUSION.NDG.
C	012	N,ALPHA REAC	2.7+7	6.1+7	Revw	79KNOX	CA	1	1079	LRL	Haight+CS FOR FUSION.NDG.
C	013	TOTAL XSECT	1.0+6	2.0+7	Revw	79KNOX	CA	1	1079	LRL	Haight+CS FOR FUSION.NDG.
C	013	DIFF INELAST	4.8+6	6.0+6	Revw	79KNOX	CA	1	1079	LRL	Haight+CS FOR FUSION.NDG.
C	013	GAMMA,N		1.0+7	Theo	79KNOX	AB	5	1079	WAU	Johnson.COUPL CHANL CALC CFD EXPT
N	014	NONEL GAMMA		2.0+7	Revw	79KNOX	CA	1	1079	LRL	Haight+CS FOR FUSION.NDG.
N	014	NONEL GAMMA	7.0+5	2.0+7	Revw	79KNOX	DB	5	1079	TOH	Sugiyama.REVIEW.DATA STATUS.NDG
N	014	N,PROTON	2.7+7	6.1+7	Revw	79KNOX	CA	1	1079	LRL	Haight+CS FOR FUSION.NDG.
N	014	N,DEUTERON	2.7+7	6.1+7	Revw	79KNOX	CA	1	1079	LRL	Haight+CS FOR FUSION.NDG.

Element S	A	Quantity	Energy (eV) Min	Max	Type	Documentation Ref	Vol	Page	Date	Lab	Comments
N	014	N,ALPHA REAC	2.7+7	6.1+7	Revw	79KNOX	CA	1	1079	LRL	Haight+CS FOR FUSION.NDG.
O	016	TOTAL XSECT	2.4+6		Expt	79KNOX	GC	2	1079	ORL	Johnson+ORELA,TOF.TRNS. 2.35 MEV CS.
O	016	DIFF ELASTIC	1.2+7		Theo	79KNOX	EC	1	1079	TNL	Hogue+FINITE GEOM,MULT SCT CORR.GRPH
O	016	DIFF ELASTIC	5.0+6		Expt	79KNOX	GD11		1079	IJI	Korzh+TOF.CFD OPTMDL.GRPH.
O	016	N,PROTON	2.7+7	6.1+7	Revw	79KNOX	CA	1	1079	LRL	Haight+CS FOR FUSION.NDG.
O	016	N,DEUTERON	2.7+7	6.1+7	Revw	79KNOX	CA	1	1079	LRL	Haight+CS FOR FUSION.NDG.
O	016	N,ALPHA REAC	2.7+7	6.1+7	Revw	79KNOX	CA	1	1079	LRL	Haight+CS FOR FUSION.NDG.
F	019	NONEL GAMMA		2.0+7	Revw	79KNOX	CA	1	1079	LRL	Haight+CS FOR FUSION.NDG.
F	019	NONEL GAMMA	7.0+5	2.0+7	Revw	79KNOX	DB	5	1079	TOH	Sugiyama.REVIEW.DATA STATUS.NDG
NA	023	NEUT EMISSN	NDG		Revw	79KNOX	CA	1	1079	LRL	Haight+CS FOR FUSION.NDG.
NA	023	NEUT EMISSN	1.5+7		Revw	79KNOX	GB	3	1079	ORL	Hetrick+EVAL DATA CFD MEAS.GRPHS.
MG		NONEL GAMMA		2.0+7	Revw	79KNOX	CA	1	1079	LRL	Haight+CS FOR FUSION.NDG.
MG		NONEL GAMMA	7.0+5	2.0+7	Revw	79KNOX	DB	5	1079	TOH	Sugiyama.REVIEW.DATA STATUS.NDG
MG		NEUT EMISSN	NDG		Revw	79KNOX	CA	1	1079	LRL	Haight+CS FOR FUSION.NDG.
MG		NEUT EMISSN	1.5+7		Revw	79KNOX	GB	3	1079	ORL	Hetrick+EVAL DATA CFD MEAS.GRPHS.
AL	027	NONEL GAMMA		2.0+7	Revw	79KNOX	CA	1	1079	LRL	Haight+CS FOR FUSION.NDG.
AL	027	NONEL GAMMA	1.4+7		Theo	79KNOX	GB	6	1079	TIT	Kitazawa+SPIN DEP EVAP MDL.GRPHS.CFD
AL	027	NONEL GAMMA	5.3+6	7.0+6	Expt	79KNOX	DB	6	1079	TOH	Hino+TOF.4ES.TBL,GRPH.CFD ORL EXPTS
AL	027	NONEL GAMMA	7.0+5	2.0+7	Revw	79KNOX	DB	5	1079	TOH	Sugiyama.REVIEW.GRPHS.DATA STATUS
AL	027	NXN REACTION	1.5+7		Theo	79KNOX	GB	2	1079	ORL	Fu.H-F,PRE-COMPD CALC.CURVS.CFD EXPT
AL	027	NEUT EMISSN	NDG		Revw	79KNOX	CA	1	1079	LRL	Haight+CS FOR FUSION.NDG.
AL	027	NEUT EMISSN	1.5+7		Expt	79KNOX	AB10		1079	TOK	Iwasaki+TOF.ANGDIST,INTEG.GRPHS.CFD
AL	027	NEUT EMISSN	1.5+7		Revw	79KNOX	GB	3	1079	ORL	Hetrick+EVAL DATA CFD MEAS.GRPHS.
AL	027	N,PROTON	NDG		Eval	79KNOX	AB	7	1079	ORL	Fu+LEAST SQUARES CALC.NDG.TBD.
AL	027	N,PROTON	1.5+7		Theo	79KNOX	GB	2	1079	ORL	Fu.H-F,PRE-COMPD CALC.CURVS.CFD EXPT
AL	027	N,ALPHA REAC	4.7+6	1.4+7	Expt	79KNOX	CA	3	1079	HAR	Swinhoe.ACT.GRPH.CFD ENDF.
AL	027	N,ALPHA REAC	1.5+7		Revw	79KNOX	CA	1	1079	LRL	Haight+CS FOR FUSION.TBL.
AL	027	N,ALPHA REAC	1.5+7		Theo	79KNOX	GB	2	1079	ORL	Fu.H-F,PRE-COMPD CALC.CURVS.CFD EXPT
SI		TOTAL XSECT	3.0-3	5.0+1	Expt	79KNOX	AC	3	1079	LAS	Brugger+TOF.3 T.SINGLE CRYSTAL.GRPH
SI		NONEL GAMMA		2.0+7	Revw	79KNOX	CA	1	1079	LRL	Haight+CS FOR FUSION.NDG.
SI		NONEL GAMMA	7.0+5	2.0+7	Revw	79KNOX	DB	5	1079	TOH	Sugiyama.REVIEW.DATA STATUS.NDG
SI		NEUT EMISSN	NDG		Revw	79KNOX	CA	1	1079	LRL	Haight+CS FOR FUSION.NDG.
SI		NEUT EMISSN	1.5+7		Revw	79KNOX	GB	3	1079	ORL	Hetrick+EVAL DATA CFD MEAS.GRPHS.
P	031	NEUT EMISSN	NDG		Revw	79KNOX	CA	1	1079	LRL	Haight+CS FOR FUSION.NDG.
S		NEUT EMISSN	NDG		Revw	79KNOX	CA	1	1079	LRL	Haight+CS FOR FUSION.NDG.

Element S	A	Quantity	Energy (eV) Min	Max	Type	Documentation Ref	Vol	Page	Date	Lab	Comments
S	032	ABSORPTION	2.5-2		Revw	79KNOX	GA	4	1079	INL	Smith+CS ERROR EFFECT UPON CF-252 NU
S	032	N,PROTON	4.0+6	2.0+7	Eval	79KNOX	AB	7	1079	ORL	Fu+LEAST SQUARES CALC.GRPH.TBL.
CA		NONEL GAMMA		2.0+7	Revw	79KNOX	CA	1	1079	LRL	Haight+CS FOR FUSION.NDG.
CA		NONEL GAMMA	7.0+5	2.0+7	Revw	79KNOX	DB	5	1079	TOH	Sugiyama.REVIEW.GRPHS.DATA STATUS
CA		NEUT EMISSN	NDG		Revw	79KNOX	CA	1	1079	LRL	Haight+CS FOR FUSION.NDG.
CA		NEUT EMISSN	1.5+7		Revw	79KNOX	GB	3	1079	ORL	Hetrick+EVAL DATA CFD MEAS.GRPHS.
CA	040	N,PROTON	1.5+7		Exth	79KNOX	GC	12	979	SMU	Woo+(N,T)/(N,P) RATIO CALC CFD MEAS.
CA	040	N,TRITON	1.5+7		Exth	79KNOX	GC	12	979	SMU	Woo+ACT.TBL.CFD OTH EXPT.
SC	045	TOTAL XSECT	2.0+3		Expt	79KNOX	GD	9	1079	IJI	Razbudey+TRNS.CS=0.263+-0.007 B.CFD.
TI		NXN REACTION	1.5+7		Theo	79KNOX	GB	2	1079	ORL	Fu.H-F,PRE-COMPD CALC.CURVS.CFD EXPT
TI		NEUT EMISSN	NDG		Revw	79KNOX	CA	1	1079	LRL	Haight+CS FOR FUSION.NDG.
TI		NEUT EMISSN	1.5+7		Revw	79KNOX	GB	3	1079	ORL	Hetrick+EVAL DATA CFD MEAS.GRPHS.
TI		N,ALPHA REAC	1.5+7		Revw	79KNOX	CA	1	1079	LRL	Haight+CS FOR FUSION.TBL.
TI	046	NXN REACTION	1.5+7		Theo	79KNOX	GB	2	1079	ORL	Fu.H-F,PRE-COMPD CALC.NDG.
TI	046	N,PROTON	1.5+7		Revw	79KNOX	CA	1	1079	LRL	Haight+CS FOR FUSION.GRPH
TI	046	N,PROTON	1.5+7		Theo	79KNOX	GB	2	1079	ORL	Fu.H-F,PRE-COMPD CALC.NDG.
TI	046	N,ALPHA REAC	1.5+7		Theo	79KNOX	GB	2	1079	ORL	Fu.H-F,PRE-COMPD CALC.NDG.
TI	048	NXN REACTION	1.5+7		Theo	79KNOX	GB	2	1079	ORL	Fu.H-F,PRE-COMPD CALC.NDG.
TI	048	N,PROTON	1.5+7		Revw	79KNOX	CA	1	1079	LRL	Haight+CS FOR FUSION.GRPH
TI	048	N,PROTON	1.5+7		Theo	79KNOX	GB	2	1079	ORL	Fu.H-F,PRE-COMPD CALC.NDG.
TI	048	N,ALPHA REAC	1.5+7		Theo	79KNOX	GB	2	1079	ORL	Fu.H-F,PRE-COMPD CALC.NDG.
V	051	NONEL GAMMA		2.0+7	Revw	79KNOX	CA	1	1079	LRL	Haight+CS FOR FUSION.NDG.
V	051	NONEL GAMMA	7.0+5	2.0+7	Revw	79KNOX	DB	5	1079	TOH	Sugiyama.REVIEW.DATA STATUS.NDG
V	051	NXN REACTION	1.5+7		Theo	79KNOX	GB	2	1079	ORL	Fu.H-F,PRE-COMPD CALC.NDG.
V	051	NEUT EMISSN	NDG		Revw	79KNOX	CA	1	1079	LRL	Haight+CS FOR FUSION.NDG.
V	051	NEUT EMISSN	1.5+7		Revw	79KNOX	GB	3	1079	ORL	Hetrick+EVAL DATA CFD MEAS.GRPHS.
V	051	N,PROTON	1.5+7		Theo	79KNOX	GB	2	1079	ORL	Fu.H-F,PRE-COMPD CALC.NDG.
V	051	N,ALPHA REAC	1.5+7		Revw	79KNOX	CA	1	1079	LRL	Haight+CS FOR FUSION.TBL.
V	051	N,ALPHA REAC	1.5+7		Theo	79KNOX	GB	2	1079	ORL	Fu.H-F,PRE-COMPD CALC.NDG.
CR		TOTAL XSECT	1.0+6	4.5+6	Expt	79KNOX	BB	9	1079	ANL	Smith+50-100KEV RESOL.GRPH.CFD.
CR		ELASTIC SCAT	1.5+6	4.0+6	Expt	79KNOX	BB	9	1079	ANL	Smith+DRVD FROM LEG FIT.3-5 PCT ACC.
CR		DIFF ELASTIC	1.5+6	4.0+6	Expt	79KNOX	BB	9	1079	ANL	Smith+ANGDISTS.GRPH.5-8 PCT ACC.
CR		DIFF ELASTIC	1.4+7		Expt	79KNOX	BB	5	1079	IRK	Winkler+TOF.10PCT.ANGDIST CFD OPTMDL
CR		DIFF INELAST	1.5+6	4.0+6	Expt	79KNOX	BB	9	1079	ANL	Smith+ANGDISTS,INTEG.GRPHS.CFD ENDF.
CR		DIFF INELAST	4.0+6	1.2+7	Expt	79KNOX	BB	5	1079	IRK	Winkler+TOF.DBL.DIF.ANGINTEG GRPH.

Element S	A	Quantity	Energy (eV) Min	Max	Type	Documentation Ref	Vol	Page	Date	Lab	Comments
CR		NONELASTIC	1.5+6	4.0+6	Expt	79KNOX	BB	9	1079	ANL	Smith+TOT- INTEG EL = SNE.5 PCT ACC.
CR		NONEL GAMMA		2.0+7	Revw	79KNOX	CA	1	1079	LRL	Haight+CS FOR FUSION.NDG.
CR		NONEL GAMMA	7.0+5	2.0+7	Revw	79KNOX	DB	5	1079	TOH	Sugiyama.REVIEW.DATA STATUS.NDG
CR		NXN REACTION	1.5+7		Theo	79KNOX	GB	2	1079	ORL	Fu.H-F,PRE-COMPD CALC.CURVS.CFD EXPT
CR		NEUT EMISSN	NDG		Revw	79KNOX	CA	1	1079	LRL	Haight+CS FOR FUSION.NDG.
CR		NEUT EMISSN	1.5+7		Revw	79KNOX	GB	3	1079	ORL	Hetrick+EVAL DATA CFD MEAS.GRPHS.
CR		N,ALPHA REAC	5.0+6	1.5+7	Expt	79KNOX	GC	10	1079	GEL	Paulsen+EXPT IN PROGRESS.NDG.
CR	050	DIFF ELASTIC	1.5+6	3.0+6	Expt	79KNOX	GD	10	1079	IJI	Pasechnik+TOF.ANGDISTS.GRPH.CFD CALC
CR	050	DIFF INELAST	1.5+6	3.0+6	Expt	79KNOX	GD	10	1079	IJI	Pasechnik+TOF.ANGDISTS.GRPH.CFD CALC
CR	050	NXN REACTION	1.5+7		Theo	79KNOX	GB	2	1079	ORL	Fu.H-F,PRE-COMPD CALC.NDG.
CR	050	N,PROTON	1.5+7		Theo	79KNOX	GB	2	1079	ORL	Fu.H-F,PRE-COMPD CALC.NDG.
CR	050	N,ALPHA REAC	1.5+7		Theo	79KNOX	GB	2	1079	ORL	Fu.H-F,PRE-COMPD CALC.NDG.
CR	052	DIFF ELASTIC	1.5+6	3.0+6	Expt	79KNOX	GD	10	1079	IJI	Pasechnik+TOF.ANGDISTS.GRPH.CFD CALC
CR	052	DIFF INELAST	4.0+6	1.2+7	Expt	79KNOX	BB	5	1079	IRK	Winkler+1.43,1.46MEV LVL.CFD DWBA.
CR	052	DIFF INELAST	1.5+6	3.0+6	Expt	79KNOX	GD	10	1079	IJI	Pasechnik+TOF.ANGDISTS.GRPH.CFD CALC
CR	052	NXN REACTION	1.5+7		Theo	79KNOX	GB	2	1079	ORL	Fu.H-F,PRE-COMPD CALC.NDG.
CR	052	N,PROTON	1.5+7		Theo	79KNOX	GB	2	1079	ORL	Fu.H-F,PRE-COMPD CALC.NDG.
CR	052	N,ALPHA REAC	1.5+7		Theo	79KNOX	GB	2	1079	ORL	Fu.H-F,PRE-COMPD CALC.NDG.
CR	054	DIFF ELASTIC	1.5+6	3.0+6	Expt	79KNOX	GD	10	1079	IJI	Pasechnik+TOF.ANGDISTS.GRPH.CFD CALC
CR	054	DIFF INELAST	1.5+6	3.0+6	Expt	79KNOX	GD	10	1079	IJI	Pasechnik+TOF.ANGDISTS.GRPH.CFD CALC
MN	055	RES INT ABS	5.0-1		Eval	79KNOX	GA	5	1079	BNL	Holden.BNL 325.RIA=14.0+-0.3 BARNS.
MN	055	N,GAMMA	2.5-2		Eval	79KNOX	GA	5	1079	BNL	Holden.BNL 325.CS=13.3 +-0.2 BARNS.
MN	055	NEUT EMISSN	NDG		Revw	79KNOX	CA	1	1079	LRL	Haight+CS FOR FUSION.NDG.
FE		TOTAL XSECT	1.0+6	4.5+6	Expt	79KNOX	BB	9	1079	ANL	Smith+50-100KEV RESOL.GRPH.CFD.
FE		ELASTIC SCAT	1.5+6	4.0+6	Expt	79KNOX	BB	9	1079	ANL	Smith+DRVD FROM LEG FIT.3-5 PCT ACC.
FE		DIFF ELASTIC	1.5+6	4.0+6	Expt	79KNOX	BB	9	1079	ANL	Smith+ANGDISTS.GRPH.5-8 PCT ACC.
FE		DIFF ELASTIC	1.2+7		Theo	79KNOX	EC	1	1079	TNL	Hogue+FINITE GEOM,MULT SCT CORR.GRPH
FE		DIFF INELAST	1.5+6	4.0+6	Expt	79KNOX	BB	9	1079	ANL	Smith+ANGDISTS,INTEG.GRPHS.CFD ENDF.
FE		NONELASTIC	1.5+6	4.0+6	Expt	79KNOX	BB	9	1079	ANL	Smith+TOT- INTEG EL = SNE.5 PCT ACC.
FE		NONEL GAMMA		2.0+7	Revw	79KNOX	CA	1	1079	LRL	Haight+CS FOR FUSION.NDG.
FE		NONEL GAMMA	1.0+7		Theo	79KNOX	GB	6	1079	TIT	Kitazawa+SPIN DEP EVAP MDL.GRPHS.CFD
FE		NONEL GAMMA	7.0+5	2.0+7	Revw	79KNOX	DB	5	1079	TOH	Sugiyama.REVIEW.DATA STATUS.NDG
FE		NXN REACTION	1.5+7		Theo	79KNOX	GB	2	1079	ORL	Fu.H-F,PRE-COMPD CALC.CURVS.CFD EXPT
FE		NEUT EMISSN	NDG		Revw	79KNOX	CA	1	1079	LRL	Haight+CS FOR FUSION.NDG.
FE		NEUT EMISSN	1.5+7		Revw	79KNOX	GB	3	1079	ORL	Hetrick+EVAL DATA CFD MEAS.GRPHS.

Element S	A	Quantity	Energy (eV) Min	Max	Type	Documentation Ref	Vol	Page	Date	Lab	Comments
FE		N,ALPHA REAC	5.0+6	1.5+7	Expt	79KNOX	GC10	1079		GEL	Paulsen+ANGDISTS,ANGINTEG.GRPHS.CFD.
FE	054	EVALUATION	3.0+6	4.0+7	Eval	79KNOX	AB	9	1079	LAS	Arthur+H-F CALC.DWBA MOLS.GRPHS.CFD.
FE	054	DIFF ELASTIC	8.0+6	1.2+7	Expt	79KNOX	BB	3	1079	TNL	El Kadi+TOF.3ES.GRPHS.CFD OPTMDL,OTH
FE	054	DIFF ELASTIC	1.5+6	3.0+6	Expt	79KNOX	GD10		1079	IJI	Pasechnik+TOF.ANGDISTS.GRPH.CFD CALC
FE	054	DIFF INELAST	8.0+6	1.2+7	Expt	79KNOX	BB	3	1079	TNL	El Kadi+TOF.PRELIM.NDG.ANAL TBC
FE	054	DIFF INELAST	1.5+6	3.0+6	Expt	79KNOX	GD10		1079	IJI	Pasechnik+TOF.ANGDISTS.GRPH.CFD CALC
FE	054	NXN REACTION	1.5+7		Theo	79KNOX	GB	2	1079	ORL	Fu.H-F,PRE-COMPD CALC.CURVS.CFD EXPT
FE	054	N,PROTON	1.0+6	2.0+7	Eval	79KNOX	AB	8	1079	HED	Schenter+ENDF/B-V.LST SQ.GRPHS.CFD.
FE	054	N,PROTON	1.5+7		Theo	79KNOX	GB	2	1079	ORL	Fu.H-F,PRE-COMPD CALC.CURVS.CFD EXPT
FE	054	N,PROTON	1.5+7		Exth	79KNOX	GC12		979	SMU	Woo+(N,T)/(N,P) RATIO CALC CFD MEAS.
FE	054	N,TRITON	1.5+7		Exth	79KNOX	GC12		979	SMU	Woo+ACT.G,M ISOMER CS.CFD TH.TBL.
FE	054	N,ALPHA REAC	1.5+7		Theo	79KNOX	GB	2	1079	ORL	Fu.H-F,PRE-COMPD CALC.CURVS.CFD EXPT
FE	056	EVALUATION	3.0+6	4.0+7	Eval	79KNOX	AB	9	1079	LAS	Arthur+H-F CALC.DWBA MOLS.GRPHS.CFD.
FE	056	DIFF ELASTIC	8.0+6	1.2+7	Expt	79KNOX	BB	3	1079	TNL	El Kadi+TOF.3ES.GRPHS.CFD OPTMDL,OTH
FE	056	DIFF INELAST	8.0+6	1.2+7	Expt	79KNOX	BB	3	1079	TNL	El Kadi+TOF.PRELIM.NDG.ANAL TBC
FE	056	NXN REACTION	1.5+7		Theo	79KNOX	GB	2	1079	ORL	Fu.H-F,PRE-COMPD CALC.CURVS.CFD EXPT
FE	056	N,PROTON	4.0+6	2.0+7	Eval	79KNOX	AB	7	1079	ORL	Fu+LEAST SQUARES CALC.GRPH.TBL.
FE	056	N,PROTON	1.5+7		Theo	79KNOX	GB	2	1079	ORL	Fu.H-F,PRE-COMPD CALC.CURVS.CFD EXPT
FE	056	N,PROTON	1.5+7		Expt	79KNOX	IB	6	1079	NPL	RYVES+CS=109.2+-1.OMB.CFD EVAL,EXP.
FE	056	N,ALPHA REAC	1.5+7		Theo	79KNOX	GB	2	1079	ORL	Fu.H-F,PRE-COMPD CALC.CURVS.CFD EXPT
FE	058	N,GAMMA	2.5-2	2.0+7	Eval	79KNOX	AB	8	1079	HED	Schenter+ENDF/B-V.LST SQ.GRPHS.CFD.
CO	059	RES INT ABS	5.0-1		Eval	79KNOX	GA	5	1079	BNL	Holden.BNL 325.RIA=1550+-28 BARNS.
CO	059	N,GAMMA	2.5-2		Eval	79KNOX	GA	5	1079	BNL	Holden.BNL 325.CS=98.65+-0.09 BARNS.
CO	059	NEUT EMISSN	NDG		Revw	79KNOX	CA	1	1079	LRL	Haight+CS FOR FUSION.NDG.
NI		TOTAL XSECT	2.0-3	2.2+0	Expt	79KNOX	AC	7	1079	CAI	Adib+TOF.TOT CS DEP ON WAVELENGTH,E
NI		ELASTIC SCAT	2.0-3	2.2+0	Expt	79KNOX	AC	7	1079	CAI	Adib+TOF.COH,INCOH SCT CS GVN.CFD
NI		DIFF ELASTIC	5.0+6	7.0+6	Expt	79KNOX	GD11		1079	IJI	Korzh+3ES.TOF.CFD OPT,STAT,CC MDL.
NI		DIFF INELAST	5.0+6	7.0+6	Expt	79KNOX	GD11		1079	IJI	Korzh+3ES.TOF.CFD OPT,STAT,CC MDL.
NI		NONEL GAMMA		2.0+7	Revw	79KNOX	CA	1	1079	LRL	Haight+CS FOR FUSION.NDG.
NI		NONEL GAMMA	5.3+6	7.0+6	Expt	79KNOX	DB	6	1079	TOH	Hino+TOF.4ES.TBL,GRPH.CFD ORL EXPTS
NI		NONEL GAMMA	7.0+5	2.0+7	Revw	79KNOX	DB	5	1079	TOH	Sugiyama.REVIEW.DATA STATUS.NDG
NI		NXN REACTION	1.5+7		Theo	79KNOX	GB	2	1079	ORL	Fu.H-F,PRE-COMPD CALC.CURVS.CFD EXPT
NI		NEUT EMISSN	NDG		Revw	79KNOX	CA	1	1079	LRL	Haight+CS FOR FUSION.NDG.
NI		NEUT EMISSN	1.5+7		Revw	79KNOX	GB	3	1079	ORL	Hetrick+EVAL DATA CFD MEAS.GRPHS.
NI		N,ALPHA REAC	1.5+7		Revw	79KNOX	CA	1	1079	LRL	Haight+CS FOR FUSION.TBL.

Element S	A	Quantity	Energy (eV) Min	Max	Type	Documentation Ref	Vol	Page	Date	Lab	Comments
NI		N,ALPHA REAC	5.0+6	1.5+7	Expt	79KNOX	GC10	1079		GEL	Paulsen+ANGDISTS,ANGINTEG.GRPHS.CFD.
NI	058	DIFF ELASTIC	2.4+7		Expt	79KNOX	BB 4	1079		OHO	Yamanouti+TOF.ANGDISTS.GRPHS OPTMOL
NI	058	DIFF ELASTIC	1.5+6	3.0+6	Expt	79KNOX	GD10	1079		IJI	Pasechnik+TOF.ANGDISTS.GRPH.CFD CALC
NI	058	DIFF ELASTIC	5.0+6	7.0+6	Expt	79KNOX	GD11	1079		IJI	Korzh+3ES.TOF.CFD OPT,STAT,CC MDL.
NI	058	DIFF INELAST	2.4+7		Expt	79KNOX	BB 4	1079		OHO	Yamanouti+TOF.ANGDISTS.GRPHS OPTMOL
NI	058	DIFF INELAST	5.0+6	7.0+6	Expt	79KNOX	GD11	1079		IJI	Korzh+3ES.TOF.CFD OPT,STAT,CC MDL.
NI	058	DIFF INELAST	1.5+6	3.0+6	Expt	79KNOX	GD10	1079		IJI	Pasechnik+TOF.ANGDISTS.GRPH.CFD CALC
NI	058	NXN REACTION	1.5+7		Theo	79KNOX	GB 2	1079		ORL	Fu.H-F,PRE-COMPD CALC.NDG.
NI	058	N,PROTON	1.5+7		Theo	79KNOX	GB 2	1079		ORL	Fu.H-F,PRE-COMPD CALC.NDG.
NI	058	N,ALPHA REAC	1.5+7		Theo	79KNOX	GB 2	1079		ORL	Fu.H-F,PRE-COMPD CALC.NDG.
NI	060	TOTAL XSECT	1.0+6	4.5+6	Expt	79KNOX	BB 9	1079		ANL	Smith+50-100KEV RESOL.GRPH.CFD.
NI	060	ELASTIC SCAT	1.5+6	4.0+6	Expt	79KNOX	BB 9	1079		ANL	Smith+DRVD FROM LEG FIT.3-5 PCT ACC.
NI	060	DIFF ELASTIC	1.5+6	4.0+6	Expt	79KNOX	BB 9	1079		ANL	Smith+ANGDISTS.GRPH.5-8 PCT ACC.
NI	060	DIFF ELASTIC	2.4+7		Expt	79KNOX	BB 4	1079		OHO	Yamanouti+TOF.ANGDISTS.GRPHS OPTMOL
NI	060	DIFF ELASTIC	1.5+6	3.0+6	Expt	79KNOX	GD10	1079		IJI	Pasechnik+TOF.ANGDISTS.GRPH.CFD CALC
NI	060	DIFF ELASTIC	5.0+6	7.0+6	Expt	79KNOX	GD11	1079		IJI	Korzh+3ES.TOF.CFD OPT,STAT,CC MDL.
NI	060	DIFF INELAST	1.5+6	4.0+6	Expt	79KNOX	BB 9	1079		ANL	Smith+ANGDISTS,INTEG.GRPHS.CFD ENDF.
NI	060	DIFF INELAST	2.4+7		Expt	79KNOX	BB 4	1079		OHO	Yamanouti+TOF.ANGDISTS.GRPHS OPTMOL
NI	060	DIFF INELAST	1.5+6	3.0+6	Expt	79KNOX	GD10	1079		IJI	Pasechnik+TOF.ANGDISTS.GRPH.CFD CALC
NI	060	DIFF INELAST	5.0+6	7.0+6	Expt	79KNOX	GD11	1079		IJI	Korzh+3ES.TOF.CFD OPT,STAT,CC MDL.
NI	060	NONELASTIC	1.5+6	4.0+6	Expt	79KNOX	BB 9	1079		ANL	Smith+TOT- INTEG EL = SNE.5 PCT ACC.
NI	062	DIFF ELASTIC	5.0+6	7.0+6	Expt	79KNOX	GD11	1079		IJI	Korzh+3ES.TOF.CFD OPT,STAT,CC MDL.
NI	062	DIFF ELASTIC	1.5+6	3.0+6	Expt	79KNOX	GD10	1079		IJI	Pasechnik+TOF.ANGDISTS.GRPH.CFD CALC
NI	062	DIFF INELAST	1.5+6	3.0+6	Expt	79KNOX	GD10	1079		IJI	Pasechnik+TOF.ANGDISTS.GRPH.CFD CALC
NI	062	DIFF INELAST	5.0+6	7.0+6	Expt	79KNOX	GD11	1079		IJI	Korzh+3ES.TOF.CFD OPT,STAT,CC MDL.
NI	064	DIFF ELASTIC	5.0+6	7.0+6	Expt	79KNOX	GD11	1079		IJI	Korzh+3ES.TOF.CFD OPT,STAT,CC MDL.
NI	064	DIFF ELASTIC	1.5+6	3.0+6	Expt	79KNOX	GD10	1079		IJI	Pasechnik+TOF.ANGDISTS.GRPH.CFD CALC
NI	064	DIFF INELAST	1.5+6	3.0+6	Expt	79KNOX	GD10	1079		IJI	Pasechnik+TOF.ANGDISTS.GRPH.CFD CALC
NI	064	DIFF INELAST	5.0+6	7.0+6	Expt	79KNOX	GD11	1079		IJI	Korzh+3ES.TOF.CFD OPT,STAT,CC MDL.
CU		TOTAL XSECT	2.0-3	2.2+0	Expt	79KNOX	AC 7	1079		CAI	Adib+TOF.TOT CS DEP ON WAVELENGTH,E
CU		ELASTIC SCAT	2.0-3	2.2+0	Expt	79KNOX	AC 7	1079		CAI	Adib+TOF.COH,INCOH SCT CS GVN.CFD
CU		NONEL GAMMA		2.0+7	Revw	79KNOX	CA 1	1079		LRL	Haight+CS FOR FUSION.NDG.
CU		NONEL GAMMA	1.4+7		Theo	79KNOX	GB 6	1079		TIT	Kitazawa+SPIN DEP EVAP MDL.GRPHS.CFD
CU		NONEL GAMMA	5.3+6	7.0+6	Expt	79KNOX	DB 6	1079		TOH	Hino+TOF.4ES.TBL,GRPH.CFD ORL EXPTS
CU		NONEL GAMMA	7.0+5	2.0+7	Revw	79KNOX	DB 5	1079		TOH	Sugiyama.REVIEW.GRPHS.DATA STATUS

Element S	A	Quantity	Energy (eV) Min	Max	Type	Documentation Ref	Vol	Page	Date	Lab	Comments
CU		NXN REACTION	1.5+7		Theo	79KNOX	GB	2	1079	ORL	Fu.H-F,PRE-COMPD CALC.CURVS.CFD EXPT
CU		NEUT EMISSN	NDG		Revw	79KNOX	CA	1	1079	LRL	Haight+CS FOR FUSION.NDG.
CU		NEUT EMISSN	1.5+7		Revw	79KNOX	GB	3	1079	ORL	Hetrick+EVAL DATA CFD MEAS.GRPHS.
CU		N,ALPHA REAC	1.5+7		Revw	79KNOX	CA	1	1079	LRL	Haight+CS FOR FUSION.TBL.
CU	063	DIFF ELASTIC	8.0+6	1.2+7	Expt	79KNOX	BB	3	1079	TNL	El Kadi+TOF.3ES.GRPHS.CFD OPTMDL,OTH
CU	063	DIFF INELAST	8.0+6	1.2+7	Expt	79KNOX	BB	3	1079	TNL	El Kadi+TOF.PRELIM.NDG.ANAL TBC
CU	063	NONEL GAMMA	1.4+7		Theo	79KNOX	GB	6	1079	TIT	Kitazawa+SPIN DEP EVAP MDL.GRPHS.CFD
CU	063	N2N REACTION	NDG		Eval	79KNOX	AB	7	1079	ORL	Fu+LEAST SQUARES CALC.NDG.TBD.
CU	063	NXN REACTION	1.5+7		Theo	79KNOX	GB	2	1079	ORL	Fu.H-F,PRE-COMPD CALC.CURVS.CFD EXPT
CU	063	N,PROTON	1.5+7		Theo	79KNOX	GB	2	1079	ORL	Fu.H-F,PRE-COMPD CALC.CURVS.CFD EXPT
CU	063	N,ALPHA REAC	3.0+6	1.0+7	Expt	79KNOX	BC	6	1079	ANL	Winkler+ACT.TBP.SPEC AVG CS CALC.
CU	063	N,ALPHA REAC	1.5+7		Theo	79KNOX	GB	2	1079	ORL	Fu.H-F,PRE-COMPD CALC.CURVS.CFD EXPT
CU	065	DIFF ELASTIC	8.0+6	1.2+7	Expt	79KNOX	BB	3	1079	TNL	El Kadi+TOF.3ES.GRPHS.CFD OPTMDL,OTH
CU	065	DIFF INELAST	8.0+6	1.2+7	Expt	79KNOX	BB	3	1079	TNL	El Kadi+TOF.PRELIM.NDG.ANAL TBC
CU	065	N2N REACTION	1.0+7		Eval	79KNOX	AB	7	1079	ORL	Fu+LEAST SQUARES CALC.GRPH.TBL.
CU	065	NXN REACTION	1.5+7		Theo	79KNOX	GB	2	1079	ORL	Fu.H-F,PRE-COMPD CALC.NDG.
CU	065	N,PROTON	1.5+7		Theo	79KNOX	GB	2	1079	ORL	Fu.H-F,PRE-COMPD CALC.NDG.
CU	065	N,ALPHA REAC	1.5+7		Theo	79KNOX	GB	2	1079	ORL	Fu.H-F,PRE-COMPD CALC.NDG.
ZN		NONEL GAMMA	7.0+5	2.0+7	Revw	79KNOX	DB	5	1079	TOH	Sugiyama.REVIEW.DATA STATUS.NDG
ZN		NEUT EMISSN	NDG		Revw	79KNOX	CA	1	1079	LRL	Haight+CS FOR FUSION.NDG.
GA		NEUT EMISSN	NDG		Revw	79KNOX	CA	1	1079	LRL	Haight+CS FOR FUSION.NDG.
AS	075	N,GAMMA	1.0+4	3.0+6	Theo	79KNOX	GB	1	1079	LRL	Gardner+DBL PEAK,EDBW MDL.CFD MEAS.
AS	075	SPECT N,GAMM	Maxw		Theo	79KNOX	GB	1	1079	LRL	Gardner+DBL PEAK,EDBW MDL.GRPH.CFD.
AS	075	RESON PARAM	1.0+4	3.0+6	Theo	79KNOX	GB	1	1079	LRL	Gardner+DBL PEAK,EDBW MDL.G STF.
SE		NEUT EMISSN	NDG		Revw	79KNOX	CA	1	1079	LRL	Haight+CS FOR FUSION.NDG.
SE	077	N,GAMMA	1.0+3	4.0+5	Theo	79KNOX	GD	1	1079	KRU	Leugers+30 KEV CS.TBL.H-F CALC.
SE	077	RESON PARAM	1.0+3	4.0+5	Theo	79KNOX	GD	1	1079	KRU	Leugers+WG CALC.CFD EXPT.KT=30 KEV.
SE	078	N,GAMMA	5.3+5	1.3+6	Expt	79KNOX	CC	1	1079	IBJ	Herman+ACT.GRPHS.CFD STAT MDL CALCS.
SE	079	N,GAMMA	1.0+3	4.0+5	Theo	79KNOX	GD	1	1079	KRU	Leugers+30 KEV CS.TBL.H-F CALC.
SE	079	RESON PARAM	1.0+3	4.0+5	Theo	79KNOX	GD	1	1079	KRU	Leugers+WG CALC.CFD EXPT.KT=30 KEV.
SE	080	N,GAMMA	5.3+5	1.3+6	Expt	79KNOX	CC	1	1079	IBJ	Herman+ACT.GRPHS.CFD STAT MDL CALCS.
SE	080	N,GAMMA	1.0+3	4.0+5	Theo	79KNOX	GD	1	1079	KRU	Leugers+30 KEV CS.TBL.H-F CALC.
SE	080	RESON PARAM	1.0+3	4.0+5	Theo	79KNOX	GD	1	1079	KRU	Leugers+WG CALC.CFD EXPT.KT=30 KEV.
SE	081	RESON PARAM	1.0+3	4.0+5	Theo	79KNOX	GD	1	1079	KRU	Leugers+WG CALC.CFD EXPT.KT=30 KEV.
SE	082	N,GAMMA	5.3+5	1.3+6	Expt	79KNOX	CC	1	1079	IBJ	Herman+ACT.GRPHS.CFD STAT MDL CALCS.

Element S	A	Quantity	Energy (eV) Min	Max	Type	Documentation Ref	Vol	Page	Date	Lab	Comments
BR		NEUT EMISSN	NDG		Revw	79KNOX	CA	1	1079	LRL	Haight+CS FOR FUSION.NDG.
BR	080	N,GAMMA	1.0+3	4.0+5	Theo	79KNOX	GD	1	1079	KRU	Leugers+30 KEV CS.TBL.H-F CALC.
BR	080	RESON PARAM	1.0+3	4.0+5	Theo	79KNOX	GD	1	1079	KRU	Leugers+WG CALC.CFD EXPT.KT=30 KEV.
BR	082	N,GAMMA	1.0+3	4.0+5	Theo	79KNOX	GD	1	1079	KRU	Leugers+30 KEV CS.TBL.H-F CALC.
BR	082	RESON PARAM	1.0+3	4.0+5	Theo	79KNOX	GD	1	1079	KRU	Leugers+WG CALC.CFD EXPT.KT=30 KEV.
KR		N,GAMMA	1.0+3	4.0+5	Exth	79KNOX	GD	1	1079	KRU	Leugers+TOF.MAXW AVG CS.TBL.H-F CALC
KR	079	N,GAMMA	1.0+3	4.0+5	Theo	79KNOX	GD	1	1079	KRU	Leugers+30 KEV CS.TBL.H-F CALC.
KR	079	RESON PARAM	1.0+3	4.0+5	Theo	79KNOX	GD	1	1079	KRU	Leugers+WG CALC.CFD EXPT.KT=30 KEV.
KR	080	N,GAMMA	1.0+3	4.0+5	Exth	79KNOX	GD	1	1079	KRU	Leugers+TOF.MAXW AVG CS.TBL.H-F CALC
KR	081	N,GAMMA	1.0+3	4.0+5	Theo	79KNOX	GD	1	1079	KRU	Leugers+30 KEV CS.TBL.H-F CALC.
KR	081	RESON PARAM	1.0+3	4.0+5	Theo	79KNOX	GD	1	1079	KRU	Leugers+WG CALC.CFD EXPT.KT=30 KEV.
KR	082	N,GAMMA	1.0+3	4.0+5	Exth	79KNOX	GD	1	1079	KRU	Leugers+TOF.MAXW AVG CS.TBL.H-F CALC
KR	082	RESON PARAM	1.0+3	4.0+5	Theo	79KNOX	GD	1	1079	KRU	Leugers+WG CALC.CFD EXPT.KT=30 KEV.
KR	083	N,GAMMA	1.0+3	4.0+5	Exth	79KNOX	GD	1	1079	KRU	Leugers+TOF.MAXW AVG CS.TBL.H-F CALC
KR	083	RESON PARAM	1.0+3	4.0+5	Theo	79KNOX	GD	1	1079	KRU	Leugers+WG CALC.CFD EXPT.KT=30 KEV.
KR	084	N,GAMMA	1.0+3	4.0+5	Exth	79KNOX	GD	1	1079	KRU	Leugers+TOF.MAXW AVG CS.TBL.H-F CALC
KR	084	RESON PARAM	1.0+3	4.0+5	Theo	79KNOX	GD	1	1079	KRU	Leugers+WG CALC.CFD EXPT.KT=30 KEV.
KR	085	N,GAMMA	1.0+3	4.0+5	Theo	79KNOX	GD	1	1079	KRU	Leugers+30 KEV CS.TBL.H-F CALC.
KR	086	N,GAMMA	1.0+3	4.0+5	Theo	79KNOX	GD	1	1079	KRU	Leugers+30 KEV CS.TBL.H-F CALC.
KR	086	RESON PARAM	1.0+3	4.0+5	Theo	79KNOX	GD	1	1079	KRU	Leugers+WG CALC.CFD EXPT.KT=30 KEV.
SR	086	N,PROTON	1.5+7		Exth	79KNOX	GC12		979	SMU	Woo+(N,T)/(N,P) RATIO CALC CFD MEAS.
SR	086	N,TRITON	1.5+7		Exth	79KNOX	GC12		979	SMU	Woo+ACT.TBL.CFD TH CALC.G ISOMER.
Y	089	N,GAMMA	5.0+5	3.0+6	Expt	79KNOX	CC	5	1079	BRC	Grenier+TOF.GRPHS.CFD STATMDL,OTH.
Y	089	N,GAMMA	1.0+3	1.0+6	Theo	79KNOX	GB	1	1079	LRL	Gardner+DBL PEAK,EDBW MDL.CFD MEAS.
Y	089	N,TRITON	1.5+7		Exth	79KNOX	GC12		979	SMU	Woo+ACT.TBL.CFD TH CALC.M ISOMER.
Y	089	RESON PARAM	1.0+3	1.0+6	Theo	79KNOX	GB	1	1079	LRL	Gardner+DBL PEAK,EDBW MDL.G STF.
ZR		NEUT EMISSN	NDG		Revw	79KNOX	CA	1	1079	LRL	Haight+CS FOR FUSION.NDG.
ZR	090	N,GAMMA	1.0+3	1.0+6	Theo	79KNOX	GB	1	1079	LRL	Gardner+DBL PEAK,EDBW MDL.CFD MEAS.
ZR	090	RESON PARAM	1.0+3	1.0+6	Theo	79KNOX	GB	1	1079	LRL	Gardner+DBL PEAK,EDBW MDL.G STF.
ZR	096	TOTAL XSECT	3.0+2	4.0+4	Expt	79KNOX	CC	4	1079	BOL	Coceva+TOF.TRNS SPEC.RES ANAL.
ZR	096	RESON PARAM	3.0+2	4.0+4	Expt	79KNOX	CC	4	1079	BOL	Coceva+TRNS.E0,I,PI,WN 14 RES.TBL.
ZR	096	STRNGTH FUNC	3.0+2	4.0+4	Expt	79KNOX	CC	4	1079	BOL	Coceva+S0,S1 DRVD.
NB	093	TOTAL XSECT	1.0+4	1.1+7	Theo	79KNOX	CC	2	1079	LAS	Lagrange+J.L.M. OPTMDL CALC.CFD.
NB	093	DIFF ELASTIC	1.0+4	1.1+7	Theo	79KNOX	CC	2	1079	LAS	Lagrange+J.L.M. OPTMDL CALC.CFD.
NB	093	POTNTAL SCAT	1.0+4	5.0+7	Theo	79KNOX	CC	2	1079	LAS	Lagrange+J.L.M OPTMDL CALC.CFD.

Element S	A	Quantity	Energy (eV) Min	Max	Type	Documentation Ref	Vol	Page	Date	Lab	Comments
NB	093	N,GAMMA	5.0+5	3.0+6	Expt	79KNOX	CC	5	1079	BRC	Grenier+TOF.GRPHS.CFD STATMDL,OTH.
NB	093	N,GAMMA	1.0+4	3.0+6	Theo	79KNOX	GB	1	1079	LRL	Gardner+DBL PEAK,EDBW MDL.CFD MEAS.
NB	093	SPECT N,GAMM	Maxw		Theo	79KNOX	GB	1	1079	LRL	Gardner+DBL PEAK,EDBW MDL.GRPH.CFD.
NB	093	NONEL GAMMA		2.0+7	Revw	79KNOX	CA	1	1079	LRL	Haight+CS FOR FUSION.NDG.
NB	093	NONEL GAMMA	5.3+6	7.0+6	Expt	79KNOX	DB	6	1079	TOH	Hino+TOF.4ES.TBL,GRPH.CFD ORL EXPTS
NB	093	NONEL GAMMA	7.0+5	2.0+7	Revw	79KNOX	DB	5	1079	TOH	Sugiyama.REVIEW.GRPHS.DATA STATUS
NB	093	NXN REACTION	1.5+7		Theo	79KNOX	GB	2	1079	ORL	Fu.H-F,PRE-COMPD CALC.CURVS.CFD EXPT
NB	093	NEUT EMISSN	NDG		Revw	79KNOX	CA	1	1079	LRL	Haight+CS FOR FUSION.NDG.
NB	093	NEUT EMISSN	1.5+7		Expt	79KNOX	AB10		1079	TOK	Iwasaki+TOF.ANGDIST,INTEG.GRPHS.CFD
NB	093	NEUT EMISSN	1.5+7		Revw	79KNOX	GB	3	1079	ORL	Hetrick+EVAL DATA CFD MEAS.GRPHS.
NB	093	NEUT EMISSN	1.5+7		Theo	79KNOX	GB11		1079	TRM	Gupta+EXCITON MDL.SPEC FOR 3 ANGS.
NB	093	N,PROTON	1.5+7		Theo	79KNOX	GB	2	1079	ORL	Fu.H-F,PRE-COMPD CALC.CURVS.CFD EXPT
NB	093	N,ALPHA REAC	1.5+7		Revw	79KNOX	CA	1	1079	LRL	Haight+CS FOR FUSION.TBL.
NB	093	N,ALPHA REAC	1.5+7		Theo	79KNOX	GB	2	1079	ORL	Fu.H-F,PRE-COMPD CALC.CURVS.CFD EXPT
NB	093	RESON PARAM	1.0+4	3.0+6	Theo	79KNOX	GB	1	1079	LRL	Gardner+DBL PEAK,EDBW MDL.G STF.
NB	093	STRNGTH FUNC	1.0+4	5.0+7	Theo	79KNOX	CC	2	1079	LAS	Lagrange+J.L.M OPTMDL CALC.CFD.
MO		NONEL GAMMA		2.0+7	Revw	79KNOX	CA	1	1079	LRL	Haight+CS FOR FUSION.NDG.
MO		NONEL GAMMA	7.0+5	2.0+7	Revw	79KNOX	DB	5	1079	TOH	Sugiyama.REVIEW.DATA STATUS.NDG
MO	092	N2N REACTION	1.4+7		Expt	79KNOX	GC11		1079	AUW	Srinivasa+REL AL.ISOM CS.TBL.CFD.
MO	092	N,ALPHA REAC	1.4+7		Expt	79KNOX	GC11		1079	AUW	Srinivasa+REL AL.ISOM CS.TBL.CFD.
MO	094	N2N REACTION	1.4+7		Expt	79KNOX	GC11		1079	AUW	Srinivasa+REL AL.TBL.CFD EXPT,TH.
MO	096	N,PROTON	1.4+7		Expt	79KNOX	GC11		1079	AUW	Srinivasa+REL AL.TBL.CFD EXPT,TH.
MO	097	N,GAMMA	1.0+1	1.0+7	Eval	79KNOX	FB	5	1079	HED	Schenter+LEAST SQ CALC.GRPH.CFD.
MO	097	N,PROTON	1.4+7		Expt	79KNOX	GC11		1079	AUW	Srinivasa+REL AL.TBL.CFD EXPT,TH.
MO	098	N,PROTON	1.4+7		Expt	79KNOX	GC11		1079	AUW	Srinivasa+REL AL.TBL.CFD EXPT,TH.
MO	100	N,PROTON	1.4+7		Expt	79KNOX	GC11		1079	AUW	Srinivasa+REL AL.TBL.CFD EXPT,TH.
TC	099	N,GAMMA	1.0+3	1.0+5	Eval	79KNOX	FB	5	1079	HED	Schenter+LEAST SQ CALC.GRPH.CFD.
RU	101	N,GAMMA	2.0+3	1.0+5	Eval	79KNOX	FB	5	1079	HED	Schenter+LEAST SQ CALC.GRPH.CFD.
RU	102	N,GAMMA	2.0+3	1.0+5	Eval	79KNOX	FB	5	1079	HED	Schenter+LEAST SQ CALC.GRPH.CFD.
RU	104	N,GAMMA	2.0+3	1.0+5	Eval	79KNOX	FB	5	1079	HED	Schenter+LEAST SQ CALC.GRPH.CFD.
RH	103	N,GAMMA	1.0+4	4.0+6	Revw	79KNOX	DB	1	1079	ANL	Poenitz+GRPHS.FLUCTUATIONS NOTED
RH	103	N,GAMMA	1.0+3	1.0+6	Eval	79KNOX	FB	5	1079	HED	Schenter+LEAST SQ CALC.GRPH.CFD.
RH	103	N,GAMMA	1.0+4	3.0+6	Theo	79KNOX	GB	1	1079	LRL	Gardner+DBL PEAK,EDBW MDL.CFD MEAS.
RH	103	SPECT N,GAMM	Maxw		Theo	79KNOX	GB	1	1079	LRL	Gardner+DBL PEAK,EDBW MDL.GRPH.CFD.
RH	103	RESON PARAM	1.0+4	3.0+6	Theo	79KNOX	GB	1	1079	LRL	Gardner+DBL PEAK,EDBW MDL.G STF.

Element S	A	Quantity	Energy (eV) Min	Max	Type	Documentation Ref	Vol	Page	Date	Lab	Comments
PD	102	N,TRITON	1.5+7		Exth	79KNOX	GC12	979		SMU	Woo+ACT.TBL.CFD TH CALC.
PD	104	TOTAL XSECT	1.0+0	4.0+4	Expt	79KNOX	CC	3	1079	GEL	Staveloz+TRNS.TOF.RES PAR ANAL.NDG.
PD	104	N,GAMMA	1.0+4	4.0+6	Revw	79KNOX	DB	1	1079	ANL	Poenitz+GRPHS.FLUCTATIONS NOTED.
PD	104	N,GAMMA	2.0+3	1.0+5	Eval	79KNOX	FB	5	1079	HED	Schenter+LEAST SQ CALC.GRPH.CFD.
PD	104	RESON PARAM	NDG		Expt	79KNOX	CC	3	1079	GEL	Staveloz+NDG.PRELIM.TBC.
PD	105	TOTAL XSECT	1.0+0	2.0+3	Expt	79KNOX	CC	3	1079	GEL	Staveloz+TRNS.TOF.RES PAR ANAL.NDG.
PD	105	DIFF ELASTIC	1.0+0	4.0+4	Expt	79KNOX	CC	3	1079	GEL	Staveloz+TOF.RES PAR ANAL.NDG.
PD	105	N,GAMMA	1.0+0	4.0+4	Expt	79KNOX	CC	3	1079	GEL	Staveloz+TOF.RES PAR ANAL.NDG.
PD	105	N,GAMMA	1.0+4	4.0+6	Revw	79KNOX	DB	1	1079	ANL	Poenitz+GRPHS.FLUCTATIONS NOTED.
PD	105	RESON PARAM	1.0+0	2.0+3	Expt	79KNOX	CC	3	1079	GEL	Staveloz+WN,WG.NDG.AVG WG GVN.
PD	105	STRNGTH FUNC	1.0+0	2.0+3	Expt	79KNOX	CC	3	1079	GEL	Staveloz+SO GVN.200 RES.D GVN.
PD	106	TOTAL XSECT	1.0+0	4.0+4	Expt	79KNOX	CC	3	1079	GEL	Staveloz+TRNS.TOF.RES PAR ANAL.NDG.
PD	106	N,GAMMA	1.0+4	4.0+6	Revw	79KNOX	DB	1	1079	ANL	Poenitz+GRPHS.FLUCTATIONS NOTED.
PD	106	RESON PARAM	1.0+0	1.5+3	Expt	79KNOX	CC	3	1079	GEL	Staveloz+WN DRVD.PRELIM.TBC.
PD	106	STRNGTH FUNC	1.0+0	2.0+4	Expt	79KNOX	CC	3	1079	GEL	Staveloz+GRPH.PRELIM.TBC.
PD	108	TOTAL XSECT	1.0+0	4.0+4	Expt	79KNOX	CC	3	1079	GEL	Staveloz+TRNS.TOF.RES PAR ANAL.NDG.
PD	108	DIFF ELASTIC	1.0+0	4.0+4	Expt	79KNOX	CC	3	1079	GEL	Staveloz+TOF.RES PAR ANAL.NDG.
PD	108	N,GAMMA	1.0+0	4.0+4	Expt	79KNOX	CC	3	1079	GEL	Staveloz+TOF.RES PAR ANAL.NDG.
PD	108	N,GAMMA	1.0+4	4.0+6	Revw	79KNOX	DB	1	1079	ANL	Poenitz+GRPHS.FLUCTATIONS NOTED.
PD	108	N,GAMMA	2.0+3	1.0+5	Eval	79KNOX	FB	5	1079	HED	Schenter+LEAST SQ CALC.GRPH.CFD.
PD	108	RESON PARAM	1.0+0	1.5+3	Expt	79KNOX	CC	3	1079	GEL	Staveloz+NDG.PRELIM.TBC.
PD	108	STRNGTH FUNC	1.0+0	1.5+3	Expt	79KNOX	CC	3	1079	GEL	Staveloz+SO GVN.TBC.
PD	110	TOTAL XSECT	1.0+0	4.0+4	Expt	79KNOX	CC	3	1079	GEL	Staveloz+TRNS.TOF.RES PAR ANAL.NDG.
PD	110	N,GAMMA	1.0+4	4.0+6	Revw	79KNOX	DB	1	1079	ANL	Poenitz+GRPHS.FLUCTATIONS NOTED.
PD	110	RESON PARAM	1.0+0	4.0+4	Expt	79KNOX	CC	3	1079	GEL	Staveloz+WN DRVD.PRELIM.TBC.
PD	110	STRNGTH FUNC	1.0+0	4.0+4	Expt	79KNOX	CC	3	1079	GEL	Staveloz+GRPH.PRELIM.TBC.
AG		NONEL GAMMA	7.0+5	2.0+7	Revw	79KNOX	DB	5	1079	TOH	Sugiyama.REVIEW.DATA STATUS.NDG
AG	107	N,GAMMA		1.7+1	Expt	79KNOX	AC	1	1079	BNL	Liou+HFBR.LATTICE BINDING EFFECT.
AG	107	RESON PARAM	1.6+1		Expt	79KNOX	AC	1	1079	BNL	Liou+16.3 EV RES.WG GVN.GRPH.
AG	109	N,GAMMA	1.0+3	1.0+5	Eval	79KNOX	FB	5	1079	HED	Schenter+LEAST SQ CALC.GRPH.CFD.
AG	CMP	N,GAMMA	1.6+1		Expt	79KNOX	AC	1	1079	BNL	Liou+AGC1,AG2(O).CAPT YLD MEAS.
AG	CMP	RESON PARAM	1.6+1	1.7+1	Expt	79KNOX	AC	1	1079	BNL	Liou+AGC1,AG2(O).16.3 EV RES.WG GVN.
CD		NEUT EMISSN	NDG		Revw	79KNOX	CA	1	1079	LRL	Haight+CS FOR FUSION.NDG.
CD	106	N,PROTON	1.5+7		Exth	79KNOX	GC12	979		SMU	Woo+(N,T)/(N,P) RATIO CALC CFD MEAS.
CD	106	N,TRITON	1.5+7		Exth	79KNOX	GC12	979		SMU	Woo+ACT.G,M ISOMER CS.CFD TH.TBL.

Element S	A	Quantity	Energy (eV) Min	Max	Type	Documentation Ref	Vol	Page	Date	Lab	Comments
CD	113	SPECT N,GAMM		1.0+3	Revw	79KNOX	EC	5	1079	KUR	Muradyan.MULT SPEC.BRIEF REVIEW.
CD	114	N,GAMMA	5.3+5	1.3+6	Expt	79KNOX	CC	1	1079	IBJ	Herman+ACT.GRPHS.CFD STAT MDL CALCS.
CD	114	N,PROTON	1.5+7		Exth	79KNOX	GC	12	979	SMU	Woo+(N,T)/(N,P) RATIO CALC CFD MEAS.
CD	114	N,TRITON	1.5+7		Exth	79KNOX	GC	12	979	SMU	Woo+ACT.TBL.CFD TH CALC.
CD	116	N,GAMMA	5.3+5	1.3+6	Expt	79KNOX	CC	1	1079	IBJ	Herman+ACT.GRPHS.CFD STAT MDL CALCS.
IN		NEUT EMISSN	NDG		Revw	79KNOX	CA	1	1079	LRL	Haight+CS FOR FUSION.NDG.
IN	115	N,GAMMA	5.0+3	3.5+5	Expt	79KNOX	GD	6	1079	FEI	Kononov+TOF.SO,S1,S2 FROM CS CURVS
IN	115	STRNGTH FUNC	5.0+3	3.5+5	Expt	79KNOX	GD	6	1079	FEI	Kononov+TOF.SO,S1,S2 FROM CS CURVS
SN		NONEL GAMMA		2.0+7	Revw	79KNOX	CA	1	1079	LRL	Haight+CS FOR FUSION.NDG.
SN		NONEL GAMMA	7.0+5	2.0+7	Revw	79KNOX	DB	5	1079	TOH	Sugiyama.REVIEW.DATA STATUS.NDG
SN		NEUT EMISSN	NDG		Revw	79KNOX	CA	1	1079	LRL	Haight+CS FOR FUSION.NDG.
SN	112	N,GAMMA	2.4+4		Expt	79KNOX	CC	10	1079	BNL	Bradley+ACT.REL AU197.TBL.30 KEV CAL
SN	112	N,PROTON	1.5+7		Exth	79KNOX	GC	12	979	SMU	Woo+(N,T)/(N,P) RATIO CALC CFD MEAS.
SN	112	N,TRITON	1.5+7		Exth	79KNOX	GC	12	979	SMU	Woo+ACT.G,M ISOMER CS.CFD TH.TBL.
SB		NEUT EMISSN	NDG		Revw	79KNOX	CA	1	1079	LRL	Haight+CS FOR FUSION.NDG.
TE	130	N,TRITON	1.5+7		Exth	79KNOX	GC	12	979	SMU	Woo+ACT.TBL.CFD TH CALC.G ISOMER.
I	127	INELST GAMMA	3.0+6	1.4+7	Expt	79KNOX	EC	2	1079	CSM	Cecil+2ES.57,202 KEV G PROD CS.GRPH.
I	127	N2N REACTION	9.3+6	2.0+7	Expt	79KNOX	DC	9	1079	CRC	Santry+ACT.REL S-32.TBL,GRPH.CFD
I	127	NEUT EMISSN	NDG		Revw	79KNOX	CA	1	1079	LRL	Haight+CS FOR FUSION.NDG.
CS	133	N,GAMMA	5.0+3	1.0+5	Eval	79KNOX	FB	5	1079	HED	Schenter+LEAST SQ CALC.GRPH.CFD.
BA		DIFF ELASTIC	1.4+7		Expt	79KNOX	BB	5	1079	IRK	Winkler+TOF.10PCT.ANGDIST CFD OPTMDL
BA		DIFF INELAST	4.0+6	1.2+7	Expt	79KNOX	BB	5	1079	IRK	Winkler+TOF.DBL.DIF.ANGINTEG GRPH.
BA	130	N,GAMMA	2.4+4		Expt	79KNOX	CC	10	1079	BNL	Bradley+ACT.REL AU197.TBL.30 KEV CAL
BA	138	DIFF INELAST	4.0+6	1.2+7	Expt	79KNOX	BB	5	1079	IRK	Winkler+1.44 MEV LVL.GRPH CFD CC MDL
BA	138	N,GAMMA	MAXW		Expt	79KNOX	CC	11	1079	KFK	Beer+ACT.REL AU-197.TBL.30 KEV CALC.
LA	139	N,TRITON	1.5+7		Exth	79KNOX	GC	12	979	SMU	Woo+ACT.TBL.CFD TH CALC.M ISOMER.
CE	140	N,GAMMA	MAXW		Expt	79KNOX	CC	11	1079	KFK	Beer+ACT.REL AU-197.TBL.30 KEV CALC.
ND		SPECT N,GAMM	2.4+4		Revw	79KNOX	IA	3	1079	BNL	Stelts.HIGH RESOL SPEC TO DERIVE CS.
ND	142	N,GAMMA	5.0+3	3.5+5	Expt	79KNOX	GD	6	1079	FEI	Kononov+TOF.SO,S1,S2 FROM CS CURVS
ND	142	STRNGTH FUNC	5.0+3	3.5+5	Expt	79KNOX	GD	6	1079	FEI	Kononov+TOF.SO,S1,S2 FROM CS CURVS
ND	143	N,ALPHA REAC	NDG		Revw	79KNOX	DB	3	1079	DUB	Luschikov+ ALF WIDS, J, PI TBD.
ND	144	N,GAMMA	5.0+3	3.5+5	Expt	79KNOX	GD	6	1079	FEI	Kononov+TOF.SO,S1,S2 FROM CS CURVS
ND	144	STRNGTH FUNC	5.0+3	3.5+5	Expt	79KNOX	GD	6	1079	FEI	Kononov+TOF.SO,S1,S2 FROM CS CURVS
ND	145	TOTAL XSECT	2.0-2	3.5+2	Expt	79KNOX	GD	5	1079	NIR	Anufriev+CHOPF,TOF. 0.025 EV CS GVN.
ND	145	RES INT ABS	2.0-2	3.5+2	Expt	79KNOX	GD	5	1079	NIR	Anufriev+RIA CALC=245+-30 BARNS.

Element S	A	Quantity	Energy (eV) Min	Max	Type	Documentation Ref	Vol	Page	Date	Lab	Comments
ND	145	RESON PARAM	2.0-2	3.5+2	Expt	79KNOX	GD	5	1079	NIR	Anufriev+AREA,SHAPE ANAL.19 RES.NDG.
ND	146	N,GAMMA	2.4+4		Expt	79KNOX	CC10		1079	BNL	Bradley+ACT.REL AU197.TBL.30 KEV CAL
ND	146	N,GAMMA	5.0+3	3.5+5	Expt	79KNOX	GD	6	1079	FEI	Kononov+TOF.SO,S1,S2 FROM CS CURVS
ND	146	STRNGTH FUNC	5.0+3	3.5+5	Expt	79KNOX	GD	6	1079	FEI	Kononov+TOF.SO,S1,S2 FROM CS CURVS
ND	147	RES INT ABS	4.8+0	1.7+2	Expt	79KNOX	GD14		1079	NIR	Anufriev+CALC RIA = 210+-90 BARNS.
ND	147	RESON PARAM	1.0-2	1.7+2	Expt	79KNOX	GD14		1079	NIR	Anufriev+11 LVLS.TBL RES,2*G*WN.
ND	148	N,GAMMA	2.4+4		Expt	79KNOX	CC10		1079	BNL	Bradley+ACT.REL AU197.TBL.30 KEV CAL
ND	148	N,GAMMA	5.0+3	3.5+5	Expt	79KNOX	GD	6	1079	FEI	Kononov+TOF.SO,S1,S2 FROM CS CURVS
ND	148	STRNGTH FUNC	5.0+3	3.5+5	Expt	79KNOX	GD	6	1079	FEI	Kononov+TOF.SO,S1,S2 FROM CS CURVS
ND	150	N,GAMMA	5.0+3	3.5+5	Expt	79KNOX	GD	6	1079	FEI	Kononov+TOF.SO,S1,S2 FROM CS CURVS
ND	150	STRNGTH FUNC	5.0+3	3.5+5	Expt	79KNOX	GD	6	1079	FEI	Kononov+TOF.SO,S1,S2 FROM CS CURVS
SM	144	N,GAMMA	5.0+3	3.5+5	Expt	79KNOX	GD	6	1079	FEI	Kononov+TOF.SO,S1,S2 FROM CS CURVS
SM	144	STRNGTH FUNC	5.0+3	3.5+5	Expt	79KNOX	GD	6	1079	FEI	Kononov+TOF.SO,S1,S2 FROM CS CURVS
SM	147	TOTAL XSECT	1.5+0	3.0+5	Expt	79KNOX	CC	6	1079	JAE	Mizumoto+TOF.TRNS.RES PAR ANAL.
SM	147	N,GAMMA	2.5+3	4.0+5	Expt	79KNOX	CC	6	1079	JAE	Mizumoto+TOF.GRPH AVG CAPT CS.CFD.
SM	147	N,GAMMA	1.0+1	1.0+6	Eval	79KNOX	FB	5	1079	HED	Schenter+LEAST SQ CALC.GRPH.CFD.
SM	147	N,GAMMA	5.0+3	3.5+5	Expt	79KNOX	GD	6	1079	FEI	Kononov+TOF.SO,S1,S2 FROM CS CURVS
SM	147	SPECT N,GAMM	1.0+5	3.5+6	Revw	79KNOX	IA	3	1079	BNL	Stelts.HIGH RESOL SPEC TO DERIVE CS.
SM	147	N,ALPHA REAC	NDG		Revw	79KNOX	DB	3	1079	DUB	Luschikov+ TOT ALF WIDTHS. TBD.
SM	147	RESON PARAM	1.5+0	2.0+3	Expt	79KNOX	CC	6	1079	JAE	Mizumoto+CAPT,TRNS.AVG WG GVN.
SM	147	STRNGTH FUNC	0.0+0	2.0+3	Expt	79KNOX	CC	6	1079	JAE	Mizumoto+CAPT,TRNS.SO,S1 GVN.GRPH.
SM	147	STRNGTH FUNC	5.0+3	3.5+5	Expt	79KNOX	GD	6	1079	FEI	Kononov+TOF.SO,S1,S2 FROM CS CURVS
SM	148	N,GAMMA	5.0+3	3.5+5	Expt	79KNOX	GD	6	1079	FEI	Kononov+TOF.SO,S1,S2 FROM CS CURVS
SM	148	STRNGTH FUNC	5.0+3	3.5+5	Expt	79KNOX	GD	6	1079	FEI	Kononov+TOF.SO,S1,S2 FROM CS CURVS
SM	149	TOTAL XSECT	1.5+0	3.0+5	Expt	79KNOX	CC	6	1079	JAE	Mizumoto+TOF.TRNS.GRPH RES PAR ANAL.
SM	149	N,GAMMA	2.5+3	4.0+5	Expt	79KNOX	CC	6	1079	JAE	Mizumoto+TOF.GRPH AVG CAPT CS.CFD.
SM	149	N,GAMMA	1.0+1	1.0+6	Eval	79KNOX	FB	5	1079	HED	Schenter+LEAST SQ CALC.GRPH.CFD.
SM	149	N,GAMMA	5.0+3	3.5+5	Expt	79KNOX	GD	6	1079	FEI	Kononov+TOF.SO,S1,S2 FROM CS CURVS
SM	149	SPECT N,GAMM	1.0+5	3.5+6	Revw	79KNOX	IA	3	1079	BNL	Stelts.HIGH RESOL SPEC TO DERIVE CS.
SM	149	N,ALPHA REAC	NDG		Revw	79KNOX	DB	3	1079	DUB	Luschikov+ TOT ALF WIDTHS. TBD.
SM	149	RESON PARAM	1.5+0	5.0+2	Expt	79KNOX	CC	6	1079	JAE	Mizumoto+CAPT,TRNS.AVG WG GVN.
SM	149	STRNGTH FUNC	0.0+0	4.0+2	Expt	79KNOX	CC	6	1079	JAE	Mizumoto+CAPT,TRNS.SO,S1 GVN.GRPH.
SM	149	STRNGTH FUNC	5.0+3	3.5+5	Expt	79KNOX	GD	6	1079	FEI	Kononov+TOF.SO,S1,S2 FROM CS CURVS
SM	150	N,GAMMA	5.0+3	3.5+5	Expt	79KNOX	GD	6	1079	FEI	Kononov+TOF.SO,S1,S2 FROM CS CURVS
SM	150	STRNGTH FUNC	5.0+3	3.5+5	Expt	79KNOX	GD	6	1079	FEI	Kononov+TOF.SO,S1,S2 FROM CS CURVS

Element S	A	Quantity	Energy (eV) Min	Max	Type	Documentation Ref	Vol	Page	Date	Lab	Comments
SM	152	N,GAMMA	5.0+3	3.5+5	Expt	79KNOX	GD	6	1079	FEI	Kononov+TOF.SO,S1,S2 FROM CS CURVS
SM	152	STRNGTH FUNC	5.0+3	3.5+5	Expt	79KNOX	GD	6	1079	FEI	Kononov+TOF.SO,S1,S2 FROM CS CURVS
SM	154	N,GAMMA	5.0+3	3.5+5	Expt	79KNOX	GD	6	1079	FEI	Kononov+TOF.SO,S1,S2 FROM CS CURVS
SM	154	SPECT N,GAMM	NDG		Revw	79KNOX	IA	3	1079	BNL	Stelts.HIGH RESOL SPEC TO DERIVE CS.
EU	151	N,GAMMA	5.0+3	3.5+5	Expt	79KNOX	GD	6	1079	FEI	Kononov+TOF.SO,S1,S2 FROM CS CURVS
EU	151	STRNGTH FUNC	5.0+3	3.5+5	Expt	79KNOX	GD	6	1079	FEI	Kononov+TOF.SO,S1,S2 FROM CS CURVS
EU	153	TOTAL XSECT		2.0+4	Expt	79KNOX	GD	7	1079	IJI	Vertebnyi+ TRNS.LOW E GRPH.RES ANAL
EU	153	N,GAMMA	5.0+3	3.5+5	Expt	79KNOX	GD	6	1079	FEI	Kononov+TOF.SO,S1,S2 FROM CS CURVS
EU	153	N,GAMMA	2.5-2		Expt	79KNOX	GD	7	1079	IJI	Vertebnyi+CS = 1250+-160 BARNS.
EU	153	RESON PARAM	2.0-1	1.4+1	Expt	79KNOX	GD	7	1079	IJI	Vertebnyi+ TRNS. TBL WG,G*WN RED.
EU	153	STRNGTH FUNC	5.0+3	3.5+5	Expt	79KNOX	GD	6	1079	FEI	Kononov+TOF.SO,S1,S2 FROM CS CURVS
EU	154	TOTAL XSECT		2.0+4	Expt	79KNOX	GD	7	1079	IJI	Vertebnyi+ TRNS.LOW E GRPH.RES ANAL
EU	154	N,GAMMA	2.5-2		Expt	79KNOX	GD	7	1079	IJI	Vertebnyi+CS = 3950+-400 BARNS.
EU	154	RESON PARAM	6.0-1	1.7+1	Expt	79KNOX	GD	7	1079	IJI	Vertebnyi+ TRNS. TBL WG,G*WN RED.
GD		N,GAMMA	5.0+5	3.0+6	Expt	79KNOX	CC	5	1079	BRC	Grenier+TOF.GRPHS.CFD STATMDL,OTH.
GD	155	N,GAMMA	5.0+5	3.0+6	Expt	79KNOX	CC	5	1079	BRC	Grenier+TOF.GRPHS.CFD STATMDL,OTH.
GD	156	N,GAMMA	5.0+5	3.0+6	Expt	79KNOX	CC	5	1079	BRC	Grenier+TOF.GRPHS.CFD STATMDL,OTH.
GD	156	N,GAMMA	5.0+3	3.5+5	Expt	79KNOX	GD	6	1079	FEI	Kononov+TOF.SO,S1,S2 FROM CS CURVS
GD	156	STRNGTH FUNC	5.0+3	3.5+5	Expt	79KNOX	GD	6	1079	FEI	Kononov+TOF.SO,S1,S2 FROM CS CURVS
GD	157	N,GAMMA	5.0+5	3.0+6	Expt	79KNOX	CC	5	1079	BRC	Grenier+TOF.GRPHS.CFD STATMDL,OTH.
GD	158	N,GAMMA	5.0+5	3.0+6	Expt	79KNOX	CC	5	1079	BRC	Grenier+TOF.GRPHS.CFD STATMDL,OTH.
GD	158	N,GAMMA	5.0+3	3.5+5	Expt	79KNOX	GD	6	1079	FEI	Kononov+TOF.SO,S1,S2 FROM CS CURVS
GD	158	STRNGTH FUNC	5.0+3	3.5+5	Expt	79KNOX	GD	6	1079	FEI	Kononov+TOF.SO,S1,S2 FROM CS CURVS
GD	160	N,GAMMA	5.0+5	3.0+6	Expt	79KNOX	CC	5	1079	BRC	Grenier+TOF.GRPHS.CFD STATMDL,OTH.
GD	160	N,GAMMA	5.0+3	3.5+5	Expt	79KNOX	GD	6	1079	FEI	Kononov+TOF.SO,S1,S2 FROM CS CURVS
GD	160	STRNGTH FUNC	5.0+3	3.5+5	Expt	79KNOX	GD	6	1079	FEI	Kononov+TOF.SO,S1,S2 FROM CS CURVS
HO	166	SPECT N,GAMM	4.0+2		Revw	79KNOX	IA	3	1079	BNL	Stelts.HIGH RESOL SPEC TO DERIVE CS.
ER	166	N,GAMMA	5.0+3	3.5+5	Expt	79KNOX	GD	6	1079	FEI	Kononov+TOF.SO,S1,S2 FROM CS CURVS
ER	166	STRNGTH FUNC	5.0+3	3.5+5	Expt	79KNOX	GD	6	1079	FEI	Kononov+TOF.SO,S1,S2 FROM CS CURVS
ER	167	SPECT N,GAMM	2.0+3	2.4+4	Revw	79KNOX	IA	3	1079	BNL	Stelts.HIGH RESOL SPEC TO DERIVE CS.
ER	168	N,GAMMA	5.0+3	3.5+5	Expt	79KNOX	GD	6	1079	FEI	Kononov+TOF.SO,S1,S2 FROM CS CURVS
ER	168	STRNGTH FUNC	5.0+3	3.5+5	Expt	79KNOX	GD	6	1079	FEI	Kononov+TOF.SO,S1,S2 FROM CS CURVS
ER	170	N,GAMMA	5.0+3	3.5+5	Expt	79KNOX	GD	6	1079	FEI	Kononov+TOF.SO,S1,S2 FROM CS CURVS
ER	170	STRNGTH FUNC	5.0+3	3.5+5	Expt	79KNOX	GD	6	1079	FEI	Kononov+TOF.SO,S1,S2 FROM CS CURVS
YB		N,GAMMA	5.0+3	2.0+5	Expt	79KNOX	CC	9	1079	KFK	Beer+TOF.REL AU-197 GRPH.CFD.

Element S	A	Quantity	Energy (eV) Min	Max	Type	Documentation Ref	Vol	Page	Date	Lab	Comments
YB	170	N,GAMMA	5.0+3	2.0+5	Expt	79KNOX	CC	9	1079	KFK	Beer+TOF.REL AU-197 GRPH.CFD.
LU	175	N,GAMMA	5.0+3	2.0+5	Expt	79KNOX	CC	9	1079	KFK	Beer+TOF.REL AU-197 GRPH.CFD.
LU	175	N,GAMMA	MAXW		Expt	79KNOX	CC11		1079	KFK	Beer+ACT.REL AU-197.TBL.30 KEV CALC.
LU	176	N,GAMMA	MAXW		Expt	79KNOX	CC11		1079	KFK	Beer+ACT.REL AU-197.TBL.30 KEV CALC.
TA	181	TOTAL XSECT	3.0+4	4.8+6	Expt	79KNOX	FC	7	1079	ANL	Poenitz+TRNS.GRPHS.CFD OPTMDL CALCS.
TA	181	N,GAMMA	1.0+6	3.0+6	Theo	79KNOX	GB	5	1079	LRL	Gardner+EDBW MDL WITH GDR.CURV.CFD.
TA	181	N,GAMMA	5.0+3	3.5+5	Expt	79KNOX	GD	6	1079	FEI	Kononov+TOF.SO,S1,S2 FROM CS CURVS
TA	181	SPECT N,GAMM	2.0+1	1.0+4	Revw	79KNOX	IA	3	1079	BNL	Stelts.HIGH RESOL SPEC TO DERIVE CS.
TA	181	SPECT N,GAMM	1.0+6	2.0+6	Theo	79KNOX	GB	5	1079	LRL	Gardner+EDBW MDL WITH GDR.CURV.CFD.
TA	181	NONEL GAMMA		2.0+7	Revw	79KNOX	CA	1	1079	LRL	Haight+CS FOR FUSION.NDG.
TA	181	NONEL GAMMA	7.0+5	2.0+7	Revw	79KNOX	DB	5	1079	TOH	Sugiyama.REVIEW.DATA STATUS.NDG
TA	181	NEUT EMISSN	NDG		Revw	79KNOX	CA	1	1079	LRL	Haight+CS FOR FUSION.NDG.
TA	181	STRNGTH FUNC	5.0+3	3.5+5	Expt	79KNOX	GD	6	1079	FEI	Kononov+TOF.SO,S1,S2 FROM CS CURVS
W		DIFF ELASTIC	4.3+6	8.6+6	Theo	79KNOX	CC	8	1079	BRC	Delaroche+OPTMDL,STATMDL.CFD.GRPH.
W		N,GAMMA	5.0+5	3.0+6	Expt	79KNOX	CC	5	1079	BRC	Grenier+TOF.GRPHS.CFD STATMDL,OTH.
W		NONEL GAMMA		2.0+7	Revw	79KNOX	CA	1	1079	LRL	Haight+CS FOR FUSION.NDG.
W		NEUT EMISSN	1.5+7		Theo	79KNOX	CC	7	1079	LAS	Arthur+PRE-EQUIL STATMDL.GRPH.CFD.
W		NEUT EMISSN	NDG		Revw	79KNOX	CA	1	1079	LRL	Haight+CS FOR FUSION.NDG.
W		NEUT EMISSN	1.5+7		Revw	79KNOX	GB	3	1079	ORL	Hetrick+EVAL DATA CFD MEAS.GRPHS.
W	182	TOTAL XSECT	3.0+5	5.0+6	Theo	79KNOX	CC	8	1079	BRC	Delaroche+OPTMDL,STATMDL.CFD EXP.NDG
W	182	DIFF ELASTIC	1.0+4	1.5+7	Theo	79KNOX	CC	8	1079	BRC	Delaroche+OPTMDL,STATMDL.CFD EXP.NDG
W	182	DIFF INELAST	1.0+4	1.5+7	Theo	79KNOX	CC	8	1079	BRC	Delaroche+OPTMDL,STATMDL.CFD EXP.NDG
W	182	N,GAMMA	5.0+5	3.0+6	Expt	79KNOX	CC	5	1079	BRC	Grenier+TOF.GRPHS.CFD STATMDL,OTH.
W	182	N2N REACTION	2.0+5	2.0+7	Theo	79KNOX	CC	7	1079	LAS	Arthur+PRE-EQUIL STATMDL.GRPH.CFD.
W	183	TOTAL XSECT	3.0+5	5.0+6	Theo	79KNOX	CC	8	1079	BRC	Delaroche+OPTMDL,STATMDL.CFD EXP.NDG
W	183	DIFF ELASTIC	3.4+6		Theo	79KNOX	CC	8	1079	BRC	Delaroche+OPTMDL,STATMDL.CFD.GRPH.
W	183	DIFF INELAST	3.4+6		Theo	79KNOX	CC	8	1079	BRC	Delaroche+OPTMDL,STATMDL.CFD.GRPH.
W	183	N,GAMMA	5.0+5	3.0+6	Expt	79KNOX	CC	5	1079	BRC	Grenier+TOF.GRPHS.CFD STATMDL,OTH.
W	183	N2N REACTION	2.0+5	2.0+7	Theo	79KNOX	CC	7	1079	LAS	Arthur+PRE-EQUIL STATMDL.GRPH.CFD.
W	184	TOTAL XSECT	3.0+5	4.0+6	Theo	79KNOX	CC	7	1079	LAS	Arthur+PRE-EQUIL STATMDL.GRPH.CFD.
W	184	TOTAL XSECT	3.0+5	5.0+6	Theo	79KNOX	CC	8	1079	BRC	Delaroche+OPTMDL,STATMDL.CFD EXP.NDG
W	184	ELASTIC SCAT	3.0+5	4.0+6	Theo	79KNOX	CC	7	1079	LAS	Arthur+PRE-EQUIL STATMDL.GRPH.CFD.
W	184	DIFF ELASTIC	4.0+5	4.0+6	Theo	79KNOX	CC	8	1079	BRC	Delaroche+OPTMDL,STATMDL.CFD.GRPH.
W	184	DIFF INELAST	3.0+5	4.0+6	Theo	79KNOX	CC	7	1079	LAS	Arthur+PRE-EQUIL STATMDL.GRPH.CFD.
W	184	DIFF INELAST	4.0+5	4.0+6	Theo	79KNOX	CC	8	1079	BRC	Delaroche+OPTMDL,STATMDL.CFD.GRPH.

Element S	A	Quantity	Energy (eV) Min	Max	Type	Documentation Ref	Vol	Page	Date	Lab	Comments
W	184	N,GAMMA	5.0+5	3.0+6	Expt	79KNOX	CC	5	1079	BRC	Grenier+TOF.GRPHS.CFD STATMDL,OTH.
W	184	N,GAMMA	5.0+3	2.0+5	Expt	79KNOX	CC	9	1079	KFK	Beer+TOF.REL AU-197 GRPH.CFD.
W	184	N2N REACTION	2.0+5	2.0+7	Theo	79KNOX	CC	7	1079	LAS	Arthur+PRE-EQUIL STATMDL.GRPH.CFD.
W	186	TOTAL XSECT	3.0+5	5.0+6	Theo	79KNOX	CC	8	1079	BRC	Delaroche+OPTMDL,STATMDL.CFD EXP.NDG
W	186	DIFF ELASTIC	1.0+4	1.5+7	Theo	79KNOX	CC	8	1079	BRC	Delaroche+OPTMDL,STATMDL.CFD EXP.NDG
W	186	DIFF INELAST	1.0+4	1.5+7	Theo	79KNOX	CC	8	1079	BRC	Delaroche+OPTMDL,STATMDL.CFD EXP.NDG
W	186	N,GAMMA	2.4+4		Expt	79KNOX	CC	10	1079	BNL	Bradley+ACT.REL AU197.TBL.30 KEV CAL
W	186	N,GAMMA	5.0+5	3.0+6	Expt	79KNOX	CC	5	1079	BRC	Grenier+TOF.GRPHS.CFD STATMDL,OTH.
W	186	N2N REACTION	2.0+5	2.0+7	Theo	79KNOX	CC	7	1079	LAS	Arthur+PRE-EQUIL STATMDL.GRPH.CFD.
RE	187	N,GAMMA	NDG		Theo	79KNOX	GB	5	1079	LRL	Gardner+EDBW MDL WITH GDR.NDG.
OS	186	N,GAMMA	1.0+3	3.0+5	Theo	79KNOX	GB	5	1079	LRL	Gardner+EDBW MDL WITH GDR.CURV.CFD.
OS	187	N,GAMMA	1.0+3	3.0+5	Theo	79KNOX	GB	5	1079	LRL	Gardner+EDBW MDL WITH GDR.CURV.CFD.
OS	188	N,GAMMA	1.0+3	3.0+5	Theo	79KNOX	GB	5	1079	LRL	Gardner+EDBW MDL WITH GDR.CURV.CFD.
OS	190	N,GAMMA	2.4+4		Expt	79KNOX	CC	10	1079	BNL	Bradley+ACT.REL AU197.TBL.30 KEV CAL
OS	190	N,GAMMA	5.3+5	1.3+6	Expt	79KNOX	CC	1	1079	IBJ	Herman+ACT.GRPHS.CFD STAT MDL CALCS.
OS	192	N,GAMMA	2.4+4		Expt	79KNOX	CC	10	1079	BNL	Bradley+ACT.REL AU197.TBL.30 KEV CAL
OS	192	N,GAMMA	5.3+5	1.3+6	Expt	79KNOX	CC	1	1079	IBJ	Herman+ACT.GRPHS.CFD STAT MDL CALCS.
IR	191	TOTAL XSECT	2.0-2	1.0+2	Expt	79KNOX	GD	7	1079	IJI	Vertebnyi+ TRNS.LOW E GRPH.RES ANAL
IR	191	N,GAMMA	2.5-2		Expt	79KNOX	GD	7	1079	IJI	Vertebnyi+CS = 1100+-200 BARNS.
IR	191	RESON PARAM	6.5-1	1.3+1	Expt	79KNOX	GD	7	1079	IJI	Vertebnyi+ TRNS. TBL WG,G*WN RED.
AU	197	TOTAL XSECT	3.0+4	4.8+6	Expt	79KNOX	FC	7	1079	ANL	Poenitz+TRNS.GRPHS.CFD OPTMDL CALCS.
AU	197	RES INT ABS	5.0-1		Eval	79KNOX	GA	5	1079	BNL	Holden.BNL 325.RIA=74.2+-2.0 BARNS.
AU	197	N,GAMMA	5.0+5	3.0+6	Expt	79KNOX	CC	5	1079	BRC	Grenier+TOF.GRPHS.CFD STATMDL,OTH.
AU	197	N,GAMMA	2.5-2		Eval	79KNOX	GA	5	1079	BNL	Holden.BNL 325.CS=37.18+-0.06 BARNS.
AU	197	N,GAMMA	1.0+5	3.0+6	Theo	79KNOX	GB	5	1079	LRL	Gardner+EDBW MDL WITH GDR.CURV.CFD.
AU	197	N,GAMMA	1.0+5	3.5+6	Revw	79KNOX	GA	1	1079	NBS	Wasson+STATUS OF STANDARDS.GRPH.
AU	197	N,GAMMA	5.0+3	3.5+5	Expt	79KNOX	GD	6	1079	FEI	Kononov+TOF.SO,S1,S2 FROM CS CURVS
AU	197	SPECT N,GAMM	2.0+5	6.0+5	Theo	79KNOX	GB	5	1079	LRL	Gardner+EDBW MDL WITH GDR.CURV.CFD.
AU	197	NONEL GAMMA		2.0+7	Revw	79KNOX	CA	1	1079	LRL	Haight+CS FOR FUSION.NDG.
AU	197	NONEL GAMMA	1.3+7		Theo	79KNOX	GB	6	1079	TIT	Kitazawa+SPIN DEP EVAP MDL.GRPHS.CFD
AU	197	NONEL GAMMA	7.0+5	2.0+7	Revw	79KNOX	DB	5	1079	TOH	Sugiyama.REVIEW.DATA STATUS.NDG
AU	197	NEUT EMISSN	NDG		Revw	79KNOX	CA	1	1079	LRL	Haight+CS FOR FUSION.NDG.
AU	197	STRNGTH FUNC	5.0+3	3.5+5	Expt	79KNOX	GD	6	1079	FEI	Kononov+TOF.SO,S1,S2 FROM CS CURVS
HG		NEUT EMISSN	NDG		Revw	79KNOX	CA	1	1079	LRL	Haight+CS FOR FUSION.NDG.
TL	205	N,PROTON	1.5+7		Exth	79KNOX	GC	12	979	SMU	Woo+(N,T)/(N,P) RATIO CALC CFD MEAS.

Element S	A	Quantity	Energy (eV) Min	Max	Type	Documentation Ref	Vol	Page	Date	Lab	Comments
TL	205	N,TRITON	1.5+7		Exth	79KNOX	GC	12	979	SMU	Woo+ACT.TBL.CFD TH CALC.
PB		NONEL GAMMA		2.0+7	Revw	79KNOX	CA	1	1079	LRL	Haight+CS FOR FUSION.NDG.
PB		NONEL GAMMA	7.0+5	2.0+7	Revw	79KNOX	DB	5	1079	TOH	Sugiyama.REVIEW.DATA STATUS.NDG
PB		NEUT EMISSN	NDG		Revw	79KNOX	CA	1	1079	LRL	Haight+CS FOR FUSION.NDG.
PB		NEUT EMISSN	1.5+7		Revw	79KNOX	GB	3	1079	ORL	Hetrick+EVAL DATA CFD MEAS.GRPHS.
PB	204	N,TRITON	1.5+7		Exth	79KNOX	GC	12	979	SMU	Woo+ACT.TBL.CFD TH CALC.
BI	209	EVALUATION	1.0-5	2.0+7	Eval	79KNOX	GC	7	1079	ANL	Guenther+CURVS.IN ENDF FORMAT.
BI	209	TOTAL XSECT	1.2+6	4.5+6	Expt	79KNOX	GC	7	1079	ANL	Guenther+TRNS.GRPH.CFD.OPTMDL CALC.
BI	209	DIFF ELASTIC	1.5+6	4.0+6	Expt	79KNOX	GC	7	1079	ANL	Guenther+TOF.GRPH.CFD.OPTMDL CALC.
BI	209	DIFF INELAST	1.5+6	4.0+6	Expt	79KNOX	GC	7	1079	ANL	Guenther+TOF.GRPH.CFD.OPTMDL CALC.
BI	209	NEUT EMISSN	NDG		Revw	79KNOX	CA	1	1079	LRL	Haight+CS FOR FUSION.NDG.
TH	230	FISSION	Tr	1.0+7	Expt	79KNOX	EB	4	1079	ANL	Meadows.REL U235.GRPH.CFD ENDF OK.
TH	232	TOTAL XSECT	3.0+4	4.8+6	Expt	79KNOX	FC	7	1079	ANL	Poenitz+TRNS.GRPHS.CFD OPTMDL CALCS.
TH	232	TOTAL XSECT	1.0+5	1.4+7	Revw	79KNOX	GC	8	1079	GGA	Cheng+ENDF/B-IV,V REVIEWED.
TH	232	TOTAL XSECT	NDG		Revw	79KNOX	IA	2	1079	ORL	Dabbs. ORELA RVW.NDG.MEAS TBD.
TH	232	TOTAL XSECT	3.0+5	2.4+6	Theo	79KNOX	EB	2	1079	BRC	Yehia+H-F,STATMDL CALC.NDG.
TH	232	TOTAL XSECT	1.0+6	2.0+7	Theo	79KNOX	FC	10	1079	TRM	Garg+CC,OPTMDL CALC CFD EXPTS.GRPHS.
TH	232	ELASTIC SCAT	1.0+6	2.0+7	Theo	79KNOX	FC	10	1079	TRM	Garg+CC,OPTMDL CALC CFD EXPTS.GRPHS.
TH	232	DIFF ELASTIC	1.0+5	1.5+7	Revw	79KNOX	GC	8	1079	GGA	Cheng+ENDF/B-IV,V REVIEWED.
TH	232	DIFF ELASTIC	3.0+5	2.4+6	Theo	79KNOX	EB	2	1079	BRC	Yehia+H-F,STATMDL CALC.NDG.
TH	232	DIFF ELASTIC	7.0+5	3.4+6	Expt	79KNOX	FC	1	1079	BRC	Haouat+4ES.GRPHS.CFD EVAL,OPTMDL TH.
TH	232	TOT INELAST	1.0+6	2.0+7	Theo	79KNOX	FC	10	1079	TRM	Garg+CC,OPTMDL CALC CFD EXPTS.GRPHS.
TH	232	DIFF INELAST	1.0+6	7.0+6	Revw	79KNOX	GC	8	1079	GGA	Cheng+ENDF/B-IV,V REVIEWED.
TH	232	DIFF INELAST	7.0+5	2.1+6	Expt	79KNOX	FC	4	1079	LTI	Egan+DIN FROM DNG.GRPHS.CFD STATMDL.
TH	232	DIFF INELAST	3.0+5	2.4+6	Theo	79KNOX	EB	2	1079	BRC	Yehia+H-F,STATMDL CALC.NDG.
TH	232	DIFF INELAST	7.0+5	3.4+6	Expt	79KNOX	FC	1	1079	BRC	Haouat+4ES.GRPHS.CFD EVAL,OPTMDL TH.
TH	232	N,GAMMA	1.0+4	4.0+6	Revw	79KNOX	DB	1	1079	ANL	Poenitz+GRPHS.RECOMMENDATIONS GVN.
TH	232	N,GAMMA	2.0+3	2.4+4	Revw	79KNOX	IA	3	1079	BNL	Stelts.HIGH RESOL SPEC TO DERIVE CS.
TH	232	N,GAMMA	2.5-2	1.5+7	Revw	79KNOX	GC	8	1079	GGA	Cheng+ENDF-B/IV,V REVIEWED.(N,3N).
TH	232	N,GAMMA	3.0+5	2.4+6	Theo	79KNOX	EB	2	1079	BRC	Yehia+H-F,STATMDL CALC.GRPHS.CFD EXP
TH	232	SPECT N,GAMM	2.0+3	2.4+4	Revw	79KNOX	IA	3	1079	BNL	Stelts.HIGH RESOL SPEC TO DERIVE CS.
TH	232	INELST GAMMA	7.0+5	2.1+6	Expt	79KNOX	FC	4	1079	LTI	Egan+125 DEG.TOF.INFERRED LVL CS.
TH	232	N2N REACTION	2.5+6	1.5+7	Revw	79KNOX	GC	8	1079	GGA	Cheng+ENDF-B/IV,V REVIEWED.
TH	232	NXN REACTION	2.5+6	1.5+7	Revw	79KNOX	GC	8	1079	GGA	Cheng+ENDF-B/IV,V REVIEWED.(N,3N).
TH	232	FISSION	Tr	1.0+7	Expt	79KNOX	EB	4	1079	ANL	Meadows.REL U235.GRPH.CFD OTH EXPTS.

Element S	A	Quantity	Energy (eV) Min	Max	Type	Documentation Ref	Vol	Page	Date	Lab	Comments
TH	232	FISSION	2.5-2	1.5+7	Revw	79KNOX	GC	8	1079	GGA	Cheng+ENDF/B-IV,V REVIEWED.
TH	232	FISSION	3.0+5	2.4+6	Theo	79KNOX	EB	2	1079	BRC	Yehia+H-F,STATMDL CALC.GRPHS.CFD EXP
TH	232	NU(BAR)	NDG		Revw	79KNOX	GC	8	1079	GGA	Cheng+ENDF/B-IV,V REVIEWED.
TH	232	F NEUT DELAY	1.0+6	1.4+7	Theo	79KNOX	GB	12	1079	LAS	England+2ES.CALC CFD EVAL,EXPTS.TBL.
TH	232	SPECT FISS N	Fiss		Revw	79KNOX	GC	8	1079	GGA	Cheng+ENDF/B-IV,V REVIEWED.
TH	232	SPECT FISS N	Maxw		Theo	79KNOX	GB	9	1079	LAS	Madland+PROMPT FISS SPEC.CURVS.CFD.
TH	232	FISS YIELD	3.0+5	2.4+6	Theo	79KNOX	EB	2	1079	BRC	Yehia+H-F,STATMDL CALC.GRPHS.CFD EXP
PA	231	FISSION	4.0-1	1.2+7	Expt	79KNOX	EB	7	1079	ORL	Plattard+2 E RANGES.GRPHS.RES TBL.
PA	231	RESON PARAM	1.0+0	6.0+1	Expt	79KNOX	EB	7	1079	ORL	Plattard+RES OBS FOR FIRST TIME.
U	233	TOTAL XSECT	3.0+4	4.8+6	Expt	79KNOX	FC	7	1079	ANL	Poenitz+TRNS.GRPHS.CFD OPTMDL CALCS.
U	233	TOTAL XSECT	1.0-2	1.0+0	Expt	79KNOX	FC	5	1079	ORL	Harvey+TRNS.GRPH.CFD ENDF/B-V,OTH.
U	233	DIFF ELASTIC	7.0+5	1.5+6	Expt	79KNOX	FC	1	1079	BRC	Haouat+2ES.GRPHS.CFD EVAL,OPTMDL TH.
U	233	DIFF INELAST	7.0+5	1.5+6	Expt	79KNOX	FC	1	1079	BRC	Haouat+2ES.GRPHS.CFD EVAL,OPTMDL TH.
U	233	FISSION	1.5+7		Expt	79KNOX	IB	10	1079	TUD	Adamov+ ABSOL MEAS. TBL. CFD.
U	233	FISSION	FISS		Expt	79KNOX	IB	10	1079	TUD	Adamov+ CF252 SPEC.TBL.ABSOL MEAS.
U	233	NU(BAR)	NDG		Revw	79KNOX	GC	8	1079	GGA	Cheng+ENDF/B-IV,V REVIEWED.
U	233	F NEUT DELAY	1.0+6	1.4+7	Theo	79KNOX	GB	12	1079	LAS	England+THR E ALSO.CFD EVAL,EXPT.TBL
U	233	SPECT FISS N	NDG		Revw	79KNOX	GC	8	1079	GGA	Cheng+ENDF/B-IV,V REVIEWED.
U	234	FISSION	1.5+7		Expt	79KNOX	IB	10	1079	TUD	Adamov+ ABSOL MEAS. TBL. CFD.
U	234	FISSION	FISS		Expt	79KNOX	IB	10	1079	TUD	Adamov+ CF252 SPEC.TBL.ABSOL MEAS.
U	235	EVALUATION	1.0+2	2.0+7	Eval	79KNOX	FC	11	1079	SAE	Matsunobu+TOT,NG,NF,EL,INEL.GRPHS.
U	235	TOTAL XSECT	3.0+4	4.8+6	Expt	79KNOX	FC	7	1079	ANL	Poenitz+TRNS.GRPHS.CFD OPTMDL CALCS.
U	235	TOTAL XSECT	NDG		Revw	79KNOX	DB	3	1079	DUB	Luschikov+ TRNS, SELF INDIC TBD.
U	235	TOTAL XSECT	2.0+0	2.0+4	Expt	79KNOX	FC	6	1079	DUB	Bakalov+TOF,TRNS,SELF INDIC.TBLS.
U	235	DIFF ELASTIC	7.0+5	3.4+6	Expt	79KNOX	FC	1	1079	BRC	Haouat+2ES.GRPHS.CFD EVAL,OPTMDL TH.
U	235	DIFF INELAST	7.0+5	3.4+6	Expt	79KNOX	FC	1	1079	BRC	Haouat+2ES.GRPHS.CFD EVAL,OPTMDL TH.
U	235	N,GAMMA	1.0+2	3.0+4	Revw	79KNOX	EC	5	1079	KUR	Muradyan.MULT SPEC.BRIEF REVIEW.
U	235	N2N REACTION	6.0+6	1.3+7	Theo	79KNOX	EB	9	1079	ITY	Maino+H-F,OPTMDL CALC.GRPH.CFD.
U	235	FISSION	3.0+4	3.0+6	Expt	79KNOX	DB	2	1079	ANL	Fawcett+U238 NG REL U235.CFD ENDF,EX
U	235	FISSION	NDG		Eval	79KNOX	AB	7	1079	ORL	Fu+LEAST SQUARES CALC.NDG.TBD.
U	235	FISSION	1.0+5	2.0+7	Eval	79KNOX	EB	5	1079	ANL	Poenitz+CFD ENDF/B-V,EXPTS.GRPHS.
U	235	FISSION	Tr	1.0+7	Expt	79KNOX	EB	4	1079	ANL	Meadows.TH230,232 RATIOS.GRPHS.CFD.
U	235	FISSION	1.0-3	1.0+2	Expt	79KNOX	EB	8	1079	LRL	White+CM245 NF REL U235.
U	235	FISSION	1.0+6	2.0+7	Expt	79KNOX	IB	4	1079	NBS	Carlson+ NP237/U235. GRPH. CFD.
U	235	FISSION	1.0+5	2.0+7	Revw	79KNOX	GA	1	1079	NBS	Wasson+STATUS OF STANDARDS.GRPH.

Element S	A	Quantity	Energy (eV) Min	Max	Type	Documentation Ref	Vol	Page	Date	Lab	Comments
U	235	FISSION	4.0-1	1.2+7	Expt	79KNOX	EB	7	1079	ORL	Plattard+2 E RANGES.PA231 REL U235.
U	235	FISSION	2.0-2	3.0+4	Expt	79KNOX	IB	2	1079	GHT	Wagemans+REL B10,LI6.GRPHS,TBL.CFD.
U	235	FISSION	NDG		Revw	79KNOX	DB	3	1079	DUB	Luschikov+(N,GF)TO BE SEARCHED FOR.
U	235	FISSION	2.0+0	2.0+4	Expt	79KNOX	FC	6	1079	DUB	Bakalov+TOF,TRNS,SELF INDIC.TBLS.
U	235	FISSION	1.4+7	1.5+7	Expt	79KNOX	IB10		1079	TUD	Adamov+ ABSOL MEAS. TBL. CFD. 3ES.
U	235	FISSION	2.6+6	1.5+7	Expt	79KNOX	IB	9	1079	TUD	Arlt+ ABSOL MEAS. 3ES. CS GVN. CFD.
U	235	FISSION	FISS		Expt	79KNOX	IB10		1079	TUD	Adamov+ CF252 SPEC.TBL.ABSOL MEAS.
U	235	RES INT FISS	7.8+0	1.1+1	Expt	79KNOX	IB	2	1079	GHT	Wagemans+ RIF GVN. CFD OTHERS.
U	235	ALPHA	1.0+2	5.0+4	Expt	79KNOX	EB	6	1079	KUR	Muradyan+TOF.5 PCT ACC.TBL.CFD.
U	235	F NEUT DELAY	1.0+6	1.4+7	Theo	79KNOX	GB12		1079	LAS	England+THR E ALSO.CFD EVAL,EXPT.TBL
U	235	SPECT FISS N	5.3+5	1.4+7	Theo	79KNOX	GB	9	1079	LAS	Madland+THERMAL E ALSO.CURVS.CFD.
U	235	FISS PROD G	Maxw		Eval	79KNOX	AA	4	1079	ORL	Dickens.DECAY HEAT STANDARD.GRPHS.
U	235	FISS PROD G	2.5-2		Eval	79KNOX	FB	6	1079	HED	Schenter+DECAY HEAT EVAL.TBLS,GRPHS.
U	235	FISS PROD B	Maxw		Eval	79KNOX	AA	4	1079	ORL	Dickens.DECAY HEAT STANDARD.GRPHS.
U	235	FISS PROD B	2.5-2		Eval	79KNOX	FB	6	1079	HED	Schenter+DECAY HEAT EVAL.TBLS,GRPHS.
U	235	RESON PARAM	TR	1.0+7	Theo	79KNOX	EB	9	1079	ITY	Maino+H-F,OPTMDL CALC.WN/WF.CFD.
U	236	FISSION	FISS		Expt	79KNOX	IB10		1079	TUD	Adamov+ CF252 SPEC.TBL.ABSOL MEAS.
U	236	FISSION	1.5+7		Expt	79KNOX	IB10		1079	TUD	Adamov+ ABSOL MEAS. TBL. CFD.
U	236	F NEUT DELAY	1.0+6		Theo	79KNOX	GB12		1079	LAS	England+CALC CFD EVAL,EXPTS.TBL.
U	238	EVALUATION	1.0+2	2.0+7	Eval	79KNOX	FC11		1079	SAE	Matsunobu+TOT,NG,NF,EL,INEL.GRPHS.
U	238	TOTAL XSECT	6.6+0	6.8+0	Exth	79KNOX	AC	5	1079	NBS	Bowman+SOLID VS GAS GRPH.CFD TH
U	238	TOTAL XSECT	3.0+4	4.8+6	Expt	79KNOX	FC	7	1079	ANL	Poenitz+TRNS.GRPHS.CFD OPTMDL CALCS.
U	238	TOTAL XSECT	8.8+2	1.0+5	Revw	79KNOX	IA	2	1079	ORL	Dabbs. ORELA CS MEAS REVIEWED.GRPH.
U	238	TOTAL XSECT	NDG		Revw	79KNOX	DB	3	1079	DUB	Luschikov+ TRNS, SELF INDIC TBD.
U	238	DIFF ELASTIC	7.0+5	3.4+6	Expt	79KNOX	FC	1	1079	BRC	Haouat+4ES.GRPHS.CFD EVAL,OPTMDL TH.
U	238	DIFF INELAST	7.0+5	2.0+6	Expt	79KNOX	FC	3	1079	LTI	Mittler+CS FOR 20 STATES.GRPHS.CFD.
U	238	DIFF INELAST	1.0+6	5.0+6	Expt	79KNOX	FC	2	1079	ORL	Olsen+DIN CALC FROM DNG.GRPH.CFD.
U	238	DIFF INELAST	7.0+5	3.4+6	Expt	79KNOX	FC	1	1079	BRC	Haouat+4ES.GRPHS.CFD EVAL,OPTMDL TH.
U	238	N,GAMMA	1.0+4	4.0+6	Revw	79KNOX	DB	1	1079	ANL	Poenitz+GRPHS.RECOMMENDATIONS GVN.
U	238	N,GAMMA	3.0+4	3.0+6	Expt	79KNOX	DB	2	1079	ANL	Fawcett+REL U235 NF.GRPH.CFD ENDF,EX
U	238	N,GAMMA	1.0+2	3.0+4	Revw	79KNOX	EC	5	1079	KUR	Muradyan.MULT SPEC.BRIEF REVIEW.
U	238	SPECT N,GAMM	NDG		Revw	79KNOX	IA	3	1079	BNL	Stelts.HIGH RESOL SPEC TO DERIVE CS.
U	238	INELST GAMMA	7.0+5	2.0+6	Expt	79KNOX	FC	3	1079	LTI	Mittler+TOF.DIN FROM DNG.GRPHS.CFD.
U	238	INELST GAMMA	5.0+5	5.0+6	Expt	79KNOX	FC	2	1079	ORL	Olsen+SPEC,G PROD CS.GRPHS.DIN CALC.
U	238	FISSION	NDG		Eval	79KNOX	AB	7	1079	ORL	Fu+LEAST SQUARES CALC.NDG.TBD.

Element S	A	Quantity	Energy (eV) Min	Max	Type	Documentation Ref	Vol	Page	Date	Lab	Comments
U	238	FISSION	1.0+2	3.0+4	Revw	79KNOX	EC	5	1079	KUR	Muradyan.MULT SPEC.BRIEF REVIEW.
U	238	FISSION	1.5+7		Expt	79KNOX	IB10		1079	TUD	Adamov+ ABSOL MEAS. TBL. CFD.
U	238	FISSION	FISS		Expt	79KNOX	IB10		1079	TUD	Adamov+ CF252 SPEC.TBL.ABSOL MEAS.
U	238	FISSION	1.5+7		Expt	79KNOX	IB	9	1079	TUD	Arlt+ ABSOL MEAS. CS GVN. CFD.
U	238	ALPHA	1.0+2	3.0+4	Revw	79KNOX	EC	5	1079	KUR	Muradyan.MULT SPEC.BRIEF REVIEW.
U	238	F NEUT DELAY	1.0+6	1.4+7	Theo	79KNOX	GB12		1079	LAS	England+2ES.CALC CFD EVAL,EXPTS.TBL.
U	238	FISS YIELD	1.6+6		Revw	79KNOX	IA	4	1079	GEL	Knitter+OVERVIEW OF VARIOUS DETC.
U	238	RESON PARAM	6.7+0		Exth	79KNOX	AC	5	1079	NBS	Bowman+6.67 EV RES.MOLEC VIBRATION
U	CMP	TOTAL XSECT	6.6+0	6.8+0	Exth	79KNOX	AC	5	1079	NBS	Bowman+U-238.U3O8 VS UF6.GRPH.CFD TH
U	OXI	TOTAL XSECT	6.6+0	6.8+0	Exth	79KNOX	AC	5	1079	NBS	Bowman+U-238.U3O8 VS UF6.GRPH.CFD TH
NP	237	EVALUATION	1.0-5	5.0+6	Eval	79KNOX	GD	4	1079	CAD	Derrien+RES PARS.CS TBLS,GRPHS.CFD.
NP	237	FISSION	7.7+5	9.6+5	Expt	79KNOX	IB	5	1079	MHG	Grady+ ABSOL.2 ES.PRELIM CS GVN.CFD.
NP	237	FISSION	1.0+6	2.0+7	Expt	79KNOX	IB	4	1079	NBS	Carlson+TOF.CS AND NP237/U235 RATIO.
NP	237	FISSION	1.5+7		Expt	79KNOX	IB10		1079	TUD	Adamov+ ABSOL MEAS. TBL. CFD.
NP	237	FISSION	1.5+7		Expt	79KNOX	IB	9	1079	TUD	Arlt+ ABSOL MEAS. CS GVN. CFD.
NP	237	F NEUT DELAY	1.0+6		Theo	79KNOX	GB12		1079	LAS	England+CALC CFD EVAL,EXPTS.TBL.
PU	239	EVALUATION	1.0+2	2.0+7	Eval	79KNOX	FC11		1079	SAE	Matsunobu+TOT,NG,NF,EL,INEL.GRPHS.
PU	239	TOTAL XSECT	3.0+4	4.8+6	Expt	79KNOX	FC	7	1079	ANL	Poenitz+TRNS.GRPHS.CFD OPTMDL CALCS.
PU	239	TOTAL XSECT	NDG		Revw	79KNOX	DB	3	1079	DUB	Luschikov+ TRNS, SELF INDIC TBD.
PU	239	TOTAL XSECT	2.0+0	2.0+4	Expt	79KNOX	FC	6	1079	DUB	Bakalov+TOF,TRNS,SELF INDIC.TBLS.
PU	239	DIFF ELASTIC	7.0+5	3.4+6	Expt	79KNOX	FC	1	1079	BRC	Haouat+2ES.GRPHS.CFD EVAL,OPTMDL TH.
PU	239	DIFF INELAST	7.0+5	3.4+6	Expt	79KNOX	FC	1	1079	BRC	Haouat+2ES.GRPHS.CFD EVAL,OPTMDL TH.
PU	239	N2N REACTION	6.7+6	1.1+7	Theo	79KNOX	EB	9	1079	ITY	Maino+H-F,OPTMDL CALC.GRPH.CFD.
PU	239	FISSION	2.0+0	2.0+4	Expt	79KNOX	FC	6	1079	DUB	Bakalov+TOF,TRNS,SELF INDIC.TBLS.
PU	239	FISSION	1.5+7		Expt	79KNOX	IB10		1079	TUD	Adamov+ ABSOL MEAS. TBL. CFD.
PU	239	FISSION	FISS		Expt	79KNOX	IB10		1079	TUD	Adamov+ CF252 SPEC.TBL.ABSOL MEAS.
PU	239	FISSION	1.5+7		Expt	79KNOX	IB	9	1079	TUD	Arlt+ ABSOL MEAS. CS GVN. CFD.
PU	239	F NEUT DELAY	1.0+6	1.4+7	Theo	79KNOX	GB12		1079	LAS	England+THR E ALSO.CFD EVAL,EXPT.TBL
PU	239	SPECT FISS N	Maxw		Theo	79KNOX	GB	9	1079	LAS	Madland+PROMPT FISS SPEC.CURVS.CFD.
PU	239	FISS PROD G	Maxw		Eval	79KNOX	AA	4	1079	ORL	Dickens.DECAY HEAT STANDARD.GRPHS.
PU	239	FISS PROD B	Maxw		Eval	79KNOX	AA	4	1079	ORL	Dickens.DECAY HEAT STANDARD.GRPHS.
PU	239	RESON PARAM	TR	1.0+7	Theo	79KNOX	EB	9	1079	ITY	Maino+H-F,OPTMDL CALC.WN/WF.CFD.
PU	240	EVALUATION	1.0+2	2.0+7	Eval	79KNOX	FC11		1079	SAE	Matsunobu+TOT,NG,NF,EL,INEL.GRPHS.
PU	240	TOTAL XSECT	3.0+4	4.8+6	Expt	79KNOX	FC	7	1079	ANL	Poenitz+TRNS.GRPHS.CFD OPTMDL CALCS.
PU	240	N,GAMMA	1.0+4	4.0+6	Revw	79KNOX	DB	1	1079	ANL	Poenitz+GRPHS.RECOMMENDATIONS GVN.

Element S A	Quantity	Energy (eV) Min	Max	Type	Documentation Ref	Vol	Page	Date	Lab	Comments
PU 240	N,GAMMA	1.0-5	2.0+7	Eval	79KNOX	EB	1	1079	ORL	Weston+ENDF/B-V.GRPHS.PROBLEMS GVN.
PU 240	FISSION	1.0-5	2.0+7	Eval	79KNOX	EB	1	1079	ORL	Weston+ENDF/B-V.GRPHS.PROBLEMS GVN.
PU 240	FISSION	1.0+0	3.0+5	Revw	79KNOX	IA	4	1079	GEL	Knitter+OVERVIEW OF VARIOUS DETC.
PU 240	F NEUT DELAY	1.0+6		Theo	79KNOX	GB12		1079	LAS	England+CALC CFD EVAL,EXPTS.TBL.
PU 240	FRAG SPECTRA	NDG		Revw	79KNOX	IA	4	1079	GEL	Knitter+OVERVIEW OF VARIOUS DETC.
PU 240	RESON PARAM	1.0-5	2.0+7	Eval	79KNOX	EB	1	1079	ORL	Weston+ENDF/B-V.PROBLEMS DISCUSSED.
PU 241	EVALUATION	1.0+2	2.0+7	Eval	79KNOX	FC11		1079	SAE	Matsunobu+TOT,NG,NF,EL,INEL.GRPHS.
PU 241	N,GAMMA	1.0-5	2.0+7	Eval	79KNOX	EB	1	1079	ORL	Weston+ENDF/B-V.GRPHS.PROBLEMS GVN.
PU 241	FISSION	1.0-5	2.0+7	Eval	79KNOX	EB	1	1079	ORL	Weston+ENDF/B-V.GRPHS.PROBLEMS GVN.
PU 241	F NEUT DELAY	1.0+6		Theo	79KNOX	GB12		1079	LAS	England+CALC CFD EVAL,EXPTS.TBL.
PU 241	FISS PROD G	Maxw		Eval	79KNOX	AA	4	1079	ORL	Dickens.DECAY HEAT STANDARD.GRPHS.
PU 241	FISS PROD B	Maxw		Eval	79KNOX	AA	4	1079	ORL	Dickens.DECAY HEAT STANDARD.GRPHS.
PU 241	RESON PARAM	1.0-5	2.0+7	Eval	79KNOX	EB	1	1079	ORL	Weston+ENDF/B-V.PROBLEMS DISCUSSED.
PU 242	TOTAL XSECT	6.8+5	1.7+8	Expt	79KNOX	FC	8	1079	LAS	Moore+TOF.GRPH CFD ENDF,CALC.TBL.
PU 242	DIFF ELASTIC	6.0+5	3.4+6	Expt	79KNOX	FC	1	1079	BRC	Haouat+6ES.GRPHS.CFD EVAL,OPTMDL TH.
PU 242	DIFF INELAST	6.0+5	3.4+6	Expt	79KNOX	FC	1	1079	BRC	Haouat+6ES.GRPHS.CFD EVAL,OPTMDL TH.
PU 242	FISSION	1.5+7		Expt	79KNOX	IB10		1079	TUD	Adamov+ ABSOL MEAS. TBL. CFD.
PU 242	FISSION	FISS		Expt	79KNOX	IB10		1079	TUD	Adamov+ CF252 SPEC.TBL.ABSOL MEAS.
PU 242	F NEUT DELAY	1.0+6		Theo	79KNOX	GB12		1079	LAS	England+CALC CFD EVAL,EXPTS.TBL.
AM 241	EVALUATION	1.0-5	1.5+7	Eval	79KNOX	GD	2	1079	CAD	Fort+GRPHS.OK WITH INTEGRAL DATA.
AM 241	TOTAL XSECT	5.0+5	1.4+7	Theo	79KNOX	EB	9	1079	ITY	Maino+H-F,OPTMDL CALC.GRPH.CFD.
AM 241	POTNTAL SCAT	NDG		Theo	79KNOX	EB	9	1079	ITY	Maino+H-F,OPTMDL.VAL GVN.
AM 241	ABSORPTION	1.0+2	1.0+6	Theo	79KNOX	EB	9	1079	ITY	Maino+H-F,OPTMDL CALC.GRPH.CFD.
AM 241	N,GAMMA	5.0+5	1.4+7	Theo	79KNOX	EB	9	1079	ITY	Maino+H-F,OPTMDL CALC.GRPH.CFD.
AM 241	N,GAMMA	1.5-2	3.0+4	Expt	79KNOX	GD	3	1079	KRU	Wisshak+2ES.ACT.TBL.GND.ISOMER RATIO
AM 241	N,GAMMA	1.0+4	2.5+5	Expt	79KNOX	GD	3	1079	KRU	Wisshak+5 PCT ACC.GRPH.CFD.
AM 241	FISSION	1.0+0	5.3+6	Revw	79KNOX	IA	4	1079	GEL	Knitter+OVERVIEW OF VARIOUS DETC.
AM 241	FISSION	1.0+2	1.5+7	Theo	79KNOX	EB	9	1079	ITY	Maino+H-F,OPTMDL CALC.GRPH.CFD.
AM 241	RESON PARAM	NDG		Theo	79KNOX	EB	9	1079	ITY	Maino+H-F,OPTMDL CALC.WG,D CALC.
AM 241	STRNGTH FUNC	NDG		Theo	79KNOX	EB	9	1079	ITY	Maino+H-F,OPTMDL.VAL GVN.
CM 242	TOTAL XSECT	NDG		Expt	79KNOX	GD15		1079	NIR	Babich+TRNS.RES PAR ANAL.
CM 242	RES INT ABS	4.0-1		Expt	79KNOX	GD15		1079	NIR	Babich+TRNS.RIA GVN.
CM 242	RESON PARAM		2.7+2	Expt	79KNOX	GD15		1079	NIR	Babich+TRNS.TBL WG,D FOR G ISOTOPES.
CM 242	STRNGTH FUNC		2.7+2	Expt	79KNOX	GD15		1079	NIR	Babich+TRNS.SO GVN.
CM 244	TOTAL XSECT	NDG		Expt	79KNOX	GD15		1079	NIR	Babich+TRNS.RES PAR ANAL.

Element S	A	Quantity	Energy (eV) Min	Max	Type	Documentation Ref	Vol	Page	Date	Lab	Comments
CM	244	RES INT ABS	4.0-1		Expt	79KNOX	GD15	1079	NIR	Babich+TRNS.RIA GVN.
CM	244	RESON PARAM		2.8+2	Expt	79KNOX	GD15	1079	NIR	Babich+TRNS.TBL WG,D FOR G ISOTOPES.
CM	244	STRNGTH FUNC		2.8+2	Expt	79KNOX	GD15	1079	NIR	Babich+TRNS.SO GVN.
CM	245	TOTAL XSECT	NDG		Expt	79KNOX	GD15	1079	NIR	Babich+TRNS.RES PAR ANAL.
CM	245	FISSION	1.0-3	3.0+1	Expt	79KNOX	EB 8	1079	LRL	White+LINAC.R-MATRIX FIT.GRPHS.CFD.
CM	245	RESON PARAM	1.0-3	3.0+1	Expt	79KNOX	EB 8	1079	LRL	White+R-MATRIX.PRELIM.GRPHS WF,WN.
CM	245	RESON PARAM		5.0+1	Expt	79KNOX	GD15	1079	NIR	Babich+TRNS.TBL WG,D FOR G ISOTOPES.
CM	245	STRNGTH FUNC	0.0+0	3.0+1	Expt	79KNOX	EB 8	1079	LRL	White+21 LVLS.STF,D GVN.PRELIM.
CM	245	STRNGTH FUNC		5.0+1	Expt	79KNOX	GD15	1079	NIR	Babich+TRNS.SO GVN.
CM	246	TOTAL XSECT	NDG		Expt	79KNOX	GD15	1079	NIR	Babich+TRNS.RES PAR ANAL.
CM	246	RES INT ABS	4.0-1		Expt	79KNOX	GD15	1079	NIR	Babich+TRNS.RIA GVN.
CM	246	RESON PARAM		1.6+2	Expt	79KNOX	GD15	1079	NIR	Babich+TRNS.TBL WG,D FOR G ISOTOPES.
CM	246	STRNGTH FUNC		1.6+2	Expt	79KNOX	GD15	1079	NIR	Babich+TRNS.SO GVN.
CM	247	TOTAL XSECT	NDG		Expt	79KNOX	GD15	1079	NIR	Babich+TRNS.RES PAR ANAL.
CM	247	RESON PARAM		2.0+1	Expt	79KNOX	GD15	1079	NIR	Babich+TRNS.TBL WG,D FOR G ISOTOPES.
CM	248	TOTAL XSECT	NDG		Expt	79KNOX	GD15	1079	NIR	Babich+TRNS.RES PAR ANAL.
CM	248	RES INT ABS	4.0-1		Expt	79KNOX	GD15	1079	NIR	Babich+TRNS.RIA GVN.
CM	248	RESON PARAM		1.0+2	Expt	79KNOX	GD15	1079	NIR	Babich+TRNS.TBL WG,D FOR G ISOTOPES.
CM	248	STRNGTH FUNC		1.0+2	Expt	79KNOX	GD15	1079	NIR	Babich+TRNS.SO GVN.
CF	249	TOTAL XSECT	1.0-2	9.0+1	Expt	79KNOX	FC 9	1079	ORL	Carlton+TRNS.GRPH.TBL RES PARS.CFD.
CF	249	SPECT FISS N	Maxw		Theo	79KNOX	GB 9	1079	LAS	Madland+PROMPT FISS SPEC.CURVS.CFD.
CF	249	RESON PARAM	1.0-2	9.0+1	Expt	79KNOX	FC 9	1079	ORL	Carlton+TRNS.TBL.WF,2*G*WN RED.
CF	249	STRNGTH FUNC	1.0-2	9.0+1	Expt	79KNOX	FC 9	1079	ORL	Carlton+SO,D DRVD.TBL.CFD.
CF	252	FISSION	Spon		Revw	79KNOX	EC 5	1079	KUR	Muradyan.MULT SPEC.BRIEF REVIEW.
CF	252	NU(BAR)	Spon		Revw	79KNOX	GA 4	1079	INL	Smith+NU DISCREPANCY.TBLS.S EFFECT.
CF	252	NU(BAR)	Spon		Expt	79KNOX	GA 2	1079	ORL	Spencer+PRELIM RESULT.CFD OTHS.ABSOL
CF	252	NU(BAR)	Spon		Revw	79KNOX	GA 2	1079	ORL	Spencer+ALL DATA REVIEW.CFD PRESENT.
CF	252	F NEUT DELAY	Spon		Theo	79KNOX	GB12	1079	LAS	England+CALC CFD EVAL,EXPTS.TBL.
CF	252	SPECT FISS N	Spon		Theo	79KNOX	GB 9	1079	LAS	Madland+PROMPT FISS SPEC.CURVS.CFD.
Many		F NEUT DELAY	1.0+6	1.4+7	Theo	79KNOX	GB12	1079	LAS	England+11 ELEMENTS.CFD EVAL,EXP.TBL

AUTHOR INDEX

☆ U.S. GOVERNMENT PRINTING OFFICE : 1980 O - 327-189 : QL 3

NBS-114A (REV. 9-78)

U.S. DEPT. OF COMM. BIBLIOGRAPHIC DATA SHEET	1. PUBLICATION OR REPORT NO. NBS SP 594	2. Gov't. Accession No.	3. Recipient's Accession No.

4. TITLE AND SUBTITLE

Proceedings of the International Conference on Nuclear Cross Sections for Technology

5. Publication Date

September 1980

6. Performing Organization Code

7. AUTHOR(S) Editors: J. L. Fowler, C. H. Johnson, and C. D. Bowman

8. Performing Organ. Report No.

9. PERFORMING ORGANIZATION NAME AND ADDRESS

NATIONAL BUREAU OF STANDARDS
DEPARTMENT OF COMMERCE
WASHINGTON, DC 20234

10. Project/Task/Work Unit No.

11. Contract/Grant No.

12. SPONSORING ORGANIZATION NAME AND COMPLETE ADDRESS *(Street, City, State, ZIP)*

U. S. Department of Energy
National Bureau of Standards, U. S. Department of Commerce
International Union of Pure and Applied Physics
The American Physical Society
The American Nuclear Society
Oak Ridge National Laboratory
University of Tennessee
with the cooperation of the International Atomic Energy Agency

13. Type of Report & Period Covered

Final

14. Sponsoring Agency Code

15. SUPPLEMENTARY NOTES

Library of Congress Catalog Card Number: 80-600128

☐ Document describes a computer program; SF-185, FIPS Software Summary, is attached.

16. ABSTRACT *(A 200-word or less factual summary of most significant information. If document includes a significant bibliography or literature survey, mention it here.)*

These proceedings are the compilation of 203 papers presented at the International Conference on Nuclear Cross Sections for Technology held at the University of Tennessee, Knoxville, October 22-26, 1979. Invited papers reviewed nuclear data needs for standard fission reactors, alternate fuel cycles, fusion reactors, biomedical applications, and applications in industry, as well as integral experiments, cross section measurements, cross section standards, and cross section evaluations. There were 165 contributed papers on these subjects with some emphasis on cross section measurement techniques and evaluation of cross section data.

17. KEY WORDS *(six to twelve entries; alphabetical order; capitalize only the first letter of the first key word unless a proper name; separated by semicolons)*

Biomedical; conference; fission; fusion; nuclear cross sections; reactors; standards; technology.

18. AVAILABILITY ☒ Unlimited

☐ For Official Distribution. Do Not Release to NTIS

☒ Order From Sup. of Doc., U.S. Government Printing Office, Washington, DC 20402.

☐ Order From National Technical Information Service (NTIS), Springfield, VA. 22161

19. SECURITY CLASS (THIS REPORT) UNCLASSIFIED

21. NO. OF PRINTED PAGES 1056

20. SECURITY CLASS (THIS PAGE) UNCLASSIFIED

22. Price $21.00

USCOMM-DC